

**PROCEEDINGS OF THE
13TH INTERNATIONAL CONFERENCE
ON STRUCTURES IN FIRE
SIF'24**

Edited by

Luís Simões da Silva, Paulo Vila Real, Aldina Santiago,
Helder Craveiro, Luís Laím

Proceedings of the 13th International Conference on Structures in Fire

Hosted by

University of Coimbra

Proceedings of the 13th International Conference on Structures in Fire (SiF 2024)

1st Edition, 2024

Hosted by University of Coimbra

19 June to 21 June 2024

Editors: Luís Simões da Silva, Paulo Vila Real, Aldina Santiago, Hélder Craveiro, Luís Laím

Published by CMM – Portuguese Steelwork Association © 2024

Editorial Coordination: Joana Filipe Albuquerque

ISBN: 978-989-35292-2-5

https://doi.org/10.30779/cmm_SIF24

All rights reserved. No parts of this publication may be reproduced, stored in a retrieval system, or transmitted in any form or by any means, electronic, mechanical, photocopying, re-cording or otherwise, without the prior permission of the copyright owner.

CMM assumes no liability regarding the use for any application of the material and information contained in this publication.

Publisher's note

This text was prepared based on the reproduction of the originals prepared by the authors. Therefore, the publisher cannot accept any responsibility for the content, nor for possible errors in the text.

Organised by:



Co-organization



PREFACE

This book presents the proceedings of the Thirteenth International Conference Structures in Fire. The conference took place at the Department of Civil Engineering, University of Coimbra, Portugal, from 19 to 21 June 2024, under the auspices of the SIF movement.

Structural fire safety is a crucial aspect of the design of buildings and infrastructures. Significant advances in research have increased the knowledge on this topic. However, until the 1990s, there were few forums for structural fire engineers to exchange ideas and share research findings. SIF (Structures in Fire) specialised workshop series was conceived in the late 1990s and the “First International SIF Workshop” was held in Copenhagen, Denmark in 2000, followed by workshops in Christchurch, New Zealand (2002), Ottawa, Canada (2004) and Aveiro, Portugal (2006). The series of workshops evolved into conferences and the 2008 event in Singapore was the fifth International Conference on Structures in Fire. This was followed by events in East Lansing, USA (2010), Zurich, Switzerland (2012), Shanghai, China (2014), New Jersey, USA (2016), Belfast, UK (2018), Brisbane, Australia (2020) and Hong Kong, China (2022). Information about previous conferences, including complete proceedings, can be found at www.structuresinfire.com.

The main mission of SIF conferences is to provide an opportunity for researchers and engineers from the global structural fire engineering community to participate, share and discuss the recent findings, innovations and developments with their peers in an open and international forum. Following the great success of the previous International Conferences, the University of Coimbra was selected to host the 13th International Conference on Structures in Fire.

As with most of the recent conferences, the number of papers submitted far exceeds the number of papers that can be accommodated in the three-day programme, even with two parallel sessions. SIF 2024 received 249 abstracts before the deadline and accepted 172 abstracts after the review process by at least three reviewers from the scientific committee.

These proceedings represent 132 full papers, collectively representing the state of the art in fundamental knowledge and practical application of structures in fire. Forty-two countries from around the globe have contributed to them. The papers are grouped into the following research topics: Applications of Structural Fire Engineering, Composite Structures in Fire, Concrete Structures in Fire, Timber Structures in Fire, Masonry Structures in Fire, Steel Structures in Fire, Experimental Research of Structures in Fire, Numerical Modelling of Structures in Fire, Other Topics Related to Structures in Fire.

Finally, the Organizing Committee would like to thank the continuous support from the SIF Steering Committee chaired by Prof Jean-Marc Franssen. We also would like to thank to the Scientific Committee chaired by Prof Paulo Vila Real, the authors and all the supporting staff (and volunteer team) from the Institute for Sustainability and Innovation in Structural Engineering (ISISE) in Coimbra, for making SIF 2024 a successful conference.

Aldina Santiago and Luís Simões da Silva
Chairs, Organizing Committee
University of Coimbra, Portugal

Paulo Vila Real
Chair, Scientific Committee
University of Aveiro, Portugal

COMMITTEES

Organizing Committee

Prof. Luís Simões da Silva, University of Coimbra
Prof. Aldina Santiago, University of Coimbra
Dr. Hélder Craveiro, University of Coimbra
Prof. Luís Laím, University of Coimbra
Dr. Ana Francisca Santos, University of Coimbra
Dr. Hugo Caetano, University of Coimbra

Steering Committee

Prof. Jean Marc Franssen (Chair), University of Liège
Prof. Paulo Vila Real, University of Aveiro
Prof. Venkatesh Kodur, Michigan State University
Prof. Kang Hai Tan, Nanyang Technological University
Prof. Thomas Gernay, Johns Hopkins University

Chair of Scientific Committee

Prof. Paulo Vila Real, University of Aveiro

Members of Scientific Committee

AbdelHamid Bouchair	Guo-Qiang Li	Muhammad Masood Rafi
Alar Just	Haiyan Zhang	Negar Elhami-Khorasani
Aldina Santiago	Hélder Craveiro	Nicola Tondini
Alexandre Landesmann	Ignacio Paya Zaforteza	Norman Werther
Ali Morovat	Ian Burgess	Nuno Lopes
Ali Nadjai	Iolanda del Prete	Olivier Vassart
Ana Espinós	Jean-Marc Franssen	Panwei Du
Ananth Ramaswamy	Jian Jiang	Paulo Piloto
Andrea Frangi	Jiayu Hu	Pedro Palma
Andy Buchanan	Joachim Schmid	Peter Schaumann
Anil Agarwal	João Paulo Rodrigues	Piergiacomo Cancelliere
Ann Jeffers	João Ramôa Correia	Pietro Gambarova
Anthony Abu	Jochen Zehfuß	Pradeep Bhargava
Antonio Bilotta	John Gales	Raul Zaharia
Bin Zhao	Kang Hai Tan	Richard Emberley
Bo Wu	Katherine Cashell	Roberto Felicetti
C.S. Manohar	Kazunori Harada	Ruben Van Coile
Carlos Couto	Leroy Gardner	Serdar Selamet
Chao Zhang	Li Ye	Shan-Shan Huang
Charles Clifton	Liming Jiang	Shengxin Fan
Christian Dagenais	Linus Lim	Srishti Banerji
Christophe Renaud	Lou Guobiao	Susan Lamont
David Barber	Luís Laím	Suwen Chen
David Lange	Luís Simões da Silva	Takeo Hirashima
Donatella De Silva	Luke Bisby	Thomas Gernay
Dong Zhang	Mahen Mahendran	Timo Jokinen
Eleni Asimakopoulou	Manuel Romero	Tom Molken
Emidio Nigro	Maria Galorck	Tomaž Hozjan
Eric Tonicello	Marion Charlier	Vasant Matsagar
Erica Fischer	Mark Green	Venkatesh Kodur
Faris Ali	Markus Knobloch	Weiyong Wang
Felix Wiesner	Martin Mensinger	Yong Du
Florian Block	Massimo Fragiaco	Yong Wang
François Hanus	Michael Klippel	Yuzhuo Wang
František Wald	Michal Jandera	Zhi Zhang
Fuminobu Ozaki	Mitsuo Ozawa	Zhong Tao
Gaurav Srivastava	Mohannad Zeyad Naser	

TABLE OF CONTENTS

Preface	v
Committees	vi
Author Index	xvii

Applications of Structural Fire Engineering

A refined cylinder fire model for steel beam temperature calculation under localized fire conditions <i>Wei Junjie and Zhang Chao</i>	3
Analyzing the impact of fire intensity and bridge geometrical characteristics on the thermo-structural response of bridge girders during tanker fire incidents <i>Augusto M. Gil and Venkatesh K. R. Kodur</i>	15
Application of cost-benefit analysis methodology for fire safety measures in structural fire engineering <i>Andrea Lucherini, Shuna Ni, David Unobe, Thomas Gernay, Ranjit Kumar Chaudhary, Mengying Peng and Ruben Van Coile</i>	25
Behaviour of simple steel joints under natural fire curves: A case study <i>Niccolò Passarini and Nicola Tondini</i>	37
Calculation of fire protected steel section temperatures in performance-based fire design – EC3 calculation method generalized for non-uniform fire exposure <i>Timo Jokinen and Risto Ranua</i>	49
Comparing various methods for estimating the fire decay and the cooling phase in structural fire engineering <i>Andrea Lucherini, Ruben Van Coile and Bart Merci</i>	61
Enhancing composite bridges fire safety through performance analysis: Lessons from an actual bridge fire incident on the influence of cross-section, constitutive model, and finite element type <i>Juan José Pagán-Martínez, Ignacio Paya-Zaforteza and Antonio Hospitaler-Pérez</i>	73
Numerical calculation on frame at elevated temperatures <i>Batuhan Der, František Wald, Petr Červinka, Martin Vild and Jiří Vaněk</i>	85
Optimising airport structural fire design with fire spread models: A case study on integrating gozone with SAFIR <i>Jeremy Chang, Antonio Gamba, Linus Lim, Peter Armstrong and Konstantinos Papaioannou</i>	93
Performance-based analysis and structural optimization of existing buildings: Case study and developments <i>Julien Duboc and Eric Tonicello</i>	105
Probabilistic fire assessment of bridges: An Italian case study <i>Patrick Covi and Nicola Tondini</i>	115
Smart performance-based structural fire design <i>Zhuojun Nan, Mhd Anwar Orabi, Xinyan Huang and Asif Usmani</i>	127

The fire engineering challenge associated with a steel beam penetrating a compartment wall <i>Edwin Ayala, Mark Davison and Cristian Maluk</i>	139
 Composite Structures in Fire	
A user interface to compare the lifetime costs of prescriptive and performance-based fire designs of composite buildings <i>Chenzhi Ma, Ruben Van Coile and Thomas Gernay</i>	153
Behaviour of modular building incorporating CFST columns subjected to compartment fire <i>Lalita Lama, Thomas Gernay, Huu Tai Thai, Tuan Ngo and Brian Uy</i>	165
Concrete-filled closed built-up cold-formed steel columns in fire with restrained thermal elongation <i>Hélder D. Craveiro, Rohola Rahnavard, Luís Laím and Aldina Santiago</i>	177
Enhancement of the fire performance of steel-reinforced concrete-filled steel tubular slender columns with high-performance materials <i>David Medall, Carmen Ibáñez, Ana Espinós and Manuel Luis Romero</i>	189
Fire behaviour of concrete-encased concrete-filled steel tube slender columns under concentric and uniaxial eccentric load <i>Nuoxin Wu and Kang Hai Tan</i>	201
Fire behaviour of timber-concrete composite constructions under fire exposure <i>Philipp Peifer and Catherina Thiele</i>	213
Fire performance of protected high strength concrete-filled steel tubular columns <i>Utsab Katwal, Zhong Tao, Qingtao Huang and Maroun Rahme</i>	225
Fire resistance of earthquake-damaged CFST columns filled with plain and fiber-reinforced concrete <i>Smita Singh and Anil Agarwal</i>	235
Heating of fire protected steel beams with unfilled cavities formed between the steel profile and overtop steel deck of composite slabs – Experimental and numerical studies <i>Bin Zhao and Hoang-Tung Vu</i>	243
Influence of laps on the behaviour of a composite slab under membrane action in fire <i>Moe Horie, Takeo Hirashima, Haruka Kanada and Yusuke Shintani</i>	255
Investigations on headed studs in profiled steel sheeting at elevated temperatures <i>Kurt Tutzer, Georg Knallinger, Mohamad Mohamad and Martin Mensinger</i>	267
Load-bearing performance of concrete-filled steel tubular columns with high-strength steel sheets in the core exposed to fire <i>Shaghayegh Ameri, Michael Schäfers, Martin Mensinger and Jochen Zehfuß</i>	277
Mechanical behaviour of vacuum-infused GFRP composites at elevated temperatures – Influence of fibre architecture <i>Eloísa Castilho, João P. Firmo, Mário Garrido, João R. Correia, Afonso Ataíde and Marcos Roque</i>	289
Numerical investigation on different fire protection systems for steel-concrete composite beams with demountable shear connectors <i>Vicente Alberó, Ana Espinós, Andrés Lapuebla-Ferri and Manuel Luis Romero</i>	301

Parametric numerical study of fire experiments on steel-concrete composite floors <i>Chenzhi Ma and Thomas Gernay</i>	313
Simulation of built-up cold-formed steel-lightweight concrete (CFS-LWC) composite beams subjected to elevated temperatures <i>Rohola Rahnavard, Hélder D. Craveiro, Rui A. Simões, Luís Laím, Aldina Santiago and Leroy Gardner</i>	325
 Concrete Structures in Fire	
A model for the effect of thermal spalling in RC columns <i>David L. Peña, Carmen Ibáñez, Vicente Albero, Antonio Hospitaler, Andrés Lapuebla-Ferri and Héctor Saura</i>	337
A new tabulated procedure to fire-design RC ribbed slabs <i>Fabricio Longhi Bolina</i>	347
Application of the method of parallel sections (MPS) for the assessment of the thermo-mechanical performance of precast prestressed concrete roof/floor members in fire <i>Bruno Dal Lago and Matteo Mostachetti</i>	359
Confined Slab Spalling Test (CSST): A screening tool to assist concrete mix design in tunnel projects <i>Roberto Felicetti, Francesco Lo Monte, Umberto Cardu, Federico Martellozzo and Nicola Valiante</i>	371
Efficient and reliable fire risk assessment of RC column <i>Akshay Baheti, David Lange and Vasant Matsagar</i>	383
Enhancing fire resistance of geopolymer concrete utilizing recycled aggregates, copper slag, and glass spheres: A comprehensive study <i>Tawzia Manzoor, Asif H. Shah and Javed Ahmad Bhat</i>	395
Experimental investigation on the concrete behavior in the cooling phase of thermal cycles at high temperature <i>Jan Lyzwa and Jochen Zehfuss</i>	405
Experimental investigation on thermal performance of 3D printed concrete elements subjected to fire <i>Jin Qiu, Liming Jiang, Jinjin Wang, Yiwei Weng and Asif Usmani</i>	417
Experimental study on thermo-hydral response of cracked concrete subjected to elevated temperatures <i>Yu-Qing Ge, Chao Jiang, Hao-Chuan Zhang, Xiang-Lin Gu and Xiao-Bin Song</i>	427
Fire behaviour of reinforced concrete beams strengthened in shear using embedded through-section (ETS) steel or CFRP bars – Fire resistance tests and numerical thermal modelling <i>Adriana S. Azevedo, João P. Firmo and João R. Correia</i>	439
Fire-induced spalling of normal strength concrete with different types of blended portland cement <i>Tim Pittrich, Ludwig Stelzner and Frank Weise</i>	451
From xai into causal inference: A quantification of polypropylene fibers effect in mitigating fire-induced spalling across concrete grades <i>Mohammad Khaled Gazi al-Bashiti and M.Z. Naser</i>	463
High-temperature bond strength of GFRP reinforcing bars for informing design recommendations <i>Bronwyn Chorlton, Naeim Roshan, Hamzeh Hajiloo and Mark Green</i>	473

Influence of design moment redistribution to the fire resistance of fibre-reinforced lightweight aggregate concrete continuous slabs <i>Christopher Kevinly, Panwei Du, Bak Koon Teoh and Kang Hai Tan</i>	483
Investigating the high-temperature behavior of polymer concrete <i>Srishti Banerji, Venkatesh Kodur, Ahmed Almaadawy, Manish Sah and David Unobe</i>	493
Load-induced thermal strain of high-strength concrete at elevated temperatures <i>Dinh Ba Le, José L. Torero and Vinh Dao</i>	503
Numerical analysis of load-bearing fire tests of a composite slab with laps <i>Haruka Kanada, Shimono Kisei, Moe Horie, Takeo Hirasima, Kei Kimura and Yusuke Shintani</i>	515
Post-fire bond strength of steel reinforcing bars to concrete using beam-end specimens <i>Nima Tajik, Negar Elhami-Khorasani, Ravi Ranade and Anthony Tessari</i>	525
Post-fire damage classification of reinforced concrete structures using thermal analysis <i>Nima Tajik, Negar Elhami-Khorasani, Ravi Ranade, Anthony Tessari and Fernando Szasdi-Bardales</i>	535
Post-fire structural performance of corroded concrete beams <i>Ethan Phillion, Kathryn Chin, Austin Martins-Robalino and John Gales</i>	545
Quantifying the link between in-depth temperature gradients and onset of fire-induced concrete spalling <i>Ho Yin Lam, Kai Teng Eunice Lim and Cristian Maluk</i>	557
Response of structural concrete elements to thermo-mechanical loads <i>Biswajit Pal and Ananth Ramaswamy</i>	567
Spalling tests of ultra-high performance concrete: Influence of polipropylene fibers, drying and heating rate <i>V. Albero, D. Hernández-Figueirido, L. Reig, M. Roig-Flores, A. Melchor-Eixea, A. Piquer and A. Pitarch</i>	579
Structural fire assesment of an existing tunnel using performance based approach and design <i>Eric Tonicello and Julien Duboc</i>	589
Structural fire design of blast damaged concrete columns <i>Kevin Mueller, Daksh Patel and Kyle Root</i>	599
Structural modelling coupled with large-scale fire tests for determining spalling of concrete structures: A real application case to the mont-blanc tunnel vault <i>Dorjan Dauti, Julien Viale, Jos Bienefeld, Maikel Lopez, Clifford Chinaya, Xavier Duponchel, Nicolas Roges and Jean Noel Pontarollo</i>	609
Temperature effects on the bond behaviour of reinforcement in fibre-reinforced lightweight aggregate concrete <i>Christopher Kevinly, Panwei Du and Kang Hai Tan</i>	621
Test of a full-scale concrete slab with step exposed to a long-duration ISO fire <i>Mami Saito, Yusuke Shintani, Toshihiko Nishimura and Kei Kimura</i>	631
Unravelling the dynamics of fire-induced concrete spalling: A focus on thermal energy in a two-stage mechanism <i>Ramin Yarmohammadian and Roberto Felicetti</i>	641

Experimental Research of Structures in Fire

- A new approach to the assessment of the fire resistance of structures 655
Tom Lennon, Octavian Lalu and, Diana Duma
- Apparatus for assessing the load-induced thermal strain of concrete at elevated temperature 665
Kajanan Selvaranjan, Maurizio Guadagnini, John L. Provis and Giacomo Torelli
- Assessment of burnout performance of a concrete beam using a novel electric radiant panel 677
Balša Jovanović, Robby Caspeele, Edwin Reynders, Geert Lombaert, Florian Put, Andrea Lucherini and Ruben Van Coile
- Characterization of the change in polymer concrete overlays due to vehicle fire exposure 689
Ikwulono David Unobe and Shuna Ni
- Concrete splitting of post installed rebars at high temperatures: Experimental investigation 701
Fatima Ben Mouhou, Nicolas Pinoteau, Omar Al Mansouri, Roberto Piccinin, Kresimir Nincevic, Sébastien Rémond and Dashnor Hoxha
- Dynamic response assessment of RC structure exposed to natural fire 713
Muhammad Noman, Muhammad Yaqub and Salman Khan
- Experimental study of the loadbearing performance of light gauge steel frame (LSF) walls exposed to fire on two sides 725
Iziengbe Inerhunwa, Danny Hopkin, Grzegorz Kimbar, Michael Spearpoint, Georgios Kanellopoulos and Piotr Turkowski
- Hybrid fire test on a concrete-filled steel tube (CFST) column 737
Majid Hamidi Iravani, Masoud Adelzadeh and Hamzeh Hajiloo
- Introduction to the jet fire and force loading coupled test device 745
Yanhong Zhang, Guobiao Lou, Guoqiang Li, Mengjie Wang and Honghui Qi
- Performance of FREEDAM joints under fire – Experimental assessment 757
Ana Francisca Santos, Aldina Santiago, Hélder Craveiro and Luís Simões da Silva
- Temperature distribution and residual strength of mortar infilled modular rectangular steel columns exposed to standard fire 767
Seulgi Han, Junyoung Gwak, Sunhee Kim, Inrak Choi and Sungmo Choi
- Thermal performance of fire protection materials under non-standard heating regimes: An experimental parametric study 777
Antonio Cibelli, Donatella de Silva, Francesco Dionisio and Emidio Nigro
- Updating french car park fire scenarios for modern vehicles: HRR experimental study 789
Jean-Baptiste Tramoni, Mathieu Suzanne, Gildas Auguin and Christophe Thauvoye

Masonry of Structures in Fire

- Simplified verification method for the classification of thermally insulating vertically perforated bricks in case of fire 803
Heiner Kruse and Catherina Thiele

The comprehensive study of the thermo-mechanical behaviour of masonry walls <i>Armita Obaei, Javad Eslami, Anne-Lise Beaucour, Dashnor Hoxha, Albert Noumowe and Pierre Pimienta</i>	815
 Numerical Modelling of Structures in Fire	
A computational modeling approach for steel gravity frames with composite floor systems subjected to fire <i>Mohammed A. Morovat, Joseph A. Main, Jonathan M. Weigand, Fahim H. Sadek and Long T. Phan</i>	829
A numerical investigation on fire resistance of steel warehouse based on fire protection optimization <i>Pegah Aghabozorgi, Aldina Santiago and Luís Laím</i>	839
Chemo-thermo-hygro-mechanical analysis of blended concretes under fire loading <i>Simon Peters and Günther Meschke</i>	849
Experimental and analysis of precast concrete sandwich panels façade (PCSPF) systems at elevated temperatures <i>Ali Nadjai, Donatella De Silva, Gabriella De Rosa, Naveed Alam and Faris Ali</i>	861
Fire fragility assessment for bridge structures <i>Donatella de Silva, Andrea Miano, Gabriella De Rosa, Francesco Di Meglio, Andrea Prota and Emidio Nigro</i>	873
Integrated analysis of loading eccentricity on response of a column under travelling fire <i>Rabinder Kumar, Naveed Alam and Ali Nadjai</i>	883
Numerical analysis of steel-concrete composite shear wall at elevated temperature <i>Bhatt Nav Raj, Mahbub Khan, Huu Tai Thai, Tuan Ngo and Brian Uy</i>	895
Numerical design calculation of the cardington frame joints <i>Batuhan Der, František Wald, Petr Červinka and Martin Vild</i>	905
Numerical investigation of the structural fire response of tunnel structures with rectangular cross-sections <i>Thomas Thienpont, Florian Put, Balša Jovanović, Ranjit Kumar Chaudhary and Ruben Van Coile</i>	915
On the fire development and modelling for automated rack supported warehouses <i>Margherita Autiero, Donatella de Silva and Emidio Nigro</i>	927
Optimising diagrid design for fire resistance in high-rise buildings <i>Zhiruoyu Wang, Mhd Anwar Orabi, Zhunjun Nan, Matthew Mason, Weiyong Wang and David Lange</i>	939
Response of composite bridge girders exposed to realistic fire scenarios using a deep learning based approach <i>Mustesin Ali Khan, Aatif Ali Khan, Nan Zhuojun, Ghazanfar Ali Anwar, Katherine Cashell and Asif Usmani</i>	949
Structural bolt heating and cooling: Numerical study <i>Gordon Chen, Anthony Abu and Gregory MacRae</i>	959
Thermo-mechanical analysis and validation of SAFIR for historic forms of construction <i>Octavian Lalu, Tom Lennon, Diana Duma and Thomas Gernay</i>	971

Validation of numerical simulations for hot-dip galvanized composite beams and connection details with experimental data 983
Maria-Mirabela Firan, Justus Frenz, Jie Li, Annika Kapfhammer, Jochen Zehfuß and Martin Mensinger

Validation of structural fire simulations: From small-scale experiments to real, large-scale fires 995
Wulan Shofa Aisyah, Augustin Guibaud, Jose Torero and Alejandra Albuerne

Other Topics Related to Structures in Fire

CFD-based analysis of thermocouple measurements in the fire decay and cooling phases in relation to the adiabatic surface temperature 1009
Florian Put, Andrea Lucherini, Ruben Van Coile and Bart Merci

Delivering sustainable buildings: Implications and challenges for structural fire engineering 1021
Marion Charlier and Andrea Lucherini

Prediction of structural failures in a fire accident for firefighters' safety 1033
Aatif Ali Khan, Mustesin Ali Khan, Nan Zhuojun and Asif Usmani

Revisiting structural fire resistance requirements for carparks 1045
Sigurjon Ingolfsson, Adam Glew, Julian Mendez, Eoin O'Loughlin and Alistair Morrison

Simulations and tests of steel plates protected by intumescent paint exposed to fire 1057
Véronique Saulnier, Salah Eddine Ouldboukhitine, Sébastien Durif and Abdelhamid Bouchair

Steel Structures in Fire

Charpy impact test in the post-fire verification of structural steel susceptibility to brittle fracture 1069
Mariusz Maslak, Michal Pazdanowski, Marek Stankiewicz and Paulina Zajdel

Deep learning-driven real-time prediction of fire-induced collapse of steel portal frames 1081
Wei Ji, Guo-Qiang Li, Shaojun Zhu, Yong Du, Liu Zhi, Zongjun Xia and Zhifei Chen

DSM design for cold-formed steel lipped channel beams failing in global modes under fire conditions 1093
Natan Sian das Neves, Alexandre Landesmann and Dinar Camotim

Experimental and numerical investigation on collapse modes and mechanisms of planar steel triangle trusses exposed to fire 1105
Jinyu Li, Guo-Qiang Li, Shaojun Zhu, Wei Ji, Yao Wang, Honghui Qi, Xiuzhi Zheng and Kun Ding

Experimental and numerical response of steel trusses exposed to a localized fire 1117
Kathryn Chin, Chloe Jeanneret, Panagiotis Kotsovinos and John Gales

Failure analysis of an aluminium warehouse columns due to time-dependent strain 1127
Marko Goreta, Neno Torić and Ivica Boko

Failure analysis on the global behaviour of carbon and stainless steel frame structures under fire conditions 1137
Nuno Lopes, João Cabral and Paulo Vila Real

Fire dynamics and structural response of sprinklered warehouse with steel trusses using computational modelling 1149
Dilip Neupane and Zhongcheng Ma

Fire resistance of partially enclosed structural carbon steel hollow columns <i>Luís Laím, Aldina Santiago and Hélder D. Craveiro</i>	1161
Fire resistance testing of steel tension members with hollow section protected by intumescent coating <i>Dustin Häßler, Andreas Becker, Richard Fürst and Sascha Hothan</i>	1173
Fire-induced collapse early-warning method for planar multi-story steel frame structures <i>Yao Wang, Guo-Qiang Li, Shaojun Zhu and Xiuzhi Zheng</i>	1185
Guidance for incorporating high-temperature creep in fire-induced progressive collapse of steel-framed buildings <i>Svetha Venkatachari and Venkatesh Kodur</i>	1195
Heated steel bearing elements continuing through fire compartment boundaries <i>Anita Ogrin, Friderik Knez and Urška Blumauer</i>	1207
In situ test procedure to determine the fire resistance of existing steel structures with aged intumescent coating <i>Richard Fürst, Dustin Häßler, Ludwig Stelzner and Sascha Hothan</i>	1217
Lateral-torsional buckling of steel beams supporting cross-laminated timber slabs in fire <i>Aatish Jeebodh, Buick Davison, Martyn S. McLaggan, Ian Burgess, Danny Hopkin and Shan-Shan Huang</i>	1229
Modelling thermal creep of ultra-high-strength steels under steady state temperature conditions <i>Sara Uszball, Faranak Faghihi and Markus Knobloch</i>	1241
Numerical and experimental study on critical temperature of axially loaded steel members under fire conditions <i>Hao Tang, Shouchao Jiang and Tingna Zhang</i>	1253
OpenSEES simulation of the plasco tower collapse using an integrated simulation approach <i>Ramakanth Domada, Aatif Ali Khan, Anwar Orabi and Asif Usmani</i>	1265
Progressive collapse of steel frames subjected to parametric fire curves <i>Luca Possidente, Boban Cvetanoski, Nicola Tondini and Fabio Freddi</i>	1277
Resistance models for thin-walled steel beams under non-uniform temperature using machine learning <i>Carlos Couto, Qi Tong and Thomas Gernay</i>	1287
Structural behaviour of automated rack supported warehouses in fire situation <i>Margherita Autiero, Donatella de Silva, Naveed Alam and Emidio Nigro</i>	1299
 Timber Structures in Fire	
An empirical model of fallout of char layer of glue laminated timber walls heated by ISO 834 standard fire for various duration <i>Shoma Makino, Anyang Sun, Kazunori Harada and Daisaku Nii</i>	1313
Application of the European charring model to cross laminated timber in parametric fire <i>Alanen Mika, Malaska Mikko and Pajunen Sami</i>	1325
Burning behaviour of a timber ceiling: A bench-scale investigation <i>Joshua Madden, Mabelle Kriel, Felix Wiesner, Wenxuan Wu, Ryan Hilditch, Adam Ervine and David Lange</i>	1337

Determination of char layer density profile during structural timber fire experiments <i>Fernando Pérez Pérez, Joachim Schmid and Andrea Frangi</i>	1349
Embedment strength of dowelled connections of glulam timber at high temperatures <i>Shunsuke Saito, Takayuki Kikuchi, Yukito Nakayama, Marina Totsuka and Takeo Hirashima</i>	1359
Experimental fire studies comparing the charring behaviour of timber protected with thin intumescent coatings and fire rated plasterboard <i>Stavros Spyridakis, Felix Wiesner, Anwar Orabi and Cristian Maluk</i>	1371
Fire development in large compartments with mixed-timber-section ceiling <i>Cheng Chen, Tianwei Chu, Guillermo Rein, Asif Usmani and Liming Jiang</i>	1383
Influence of adhesive type on heat induced delamination in tension loaded shear lap cross laminated timber samples exposed to radiant heat flux <i>Čolić A., Wiesner F., Spearpoint M., Hopkin D. and Bisby L.</i>	1395
Influence of surface slot shape on the temperature rise and burning behavior of wood under intense heating <i>Anyang Sun, Kazunori Harada and Daisaku Nii</i>	1407
Numerical investigations on fire performance of timber frames with dowel-type connections <i>Yukito Nakayama, Marina Totsuka and Takeo Hirashima</i>	1419
Numerical modelling of the charring performance of cross-laminated timber exposed to standard fire <i>Mika Alanen, Topi Julin, Mikko Malaska, Mikko Salminen and Aleksi Ojala</i>	1431
Parametric experimental study on GLT columns stability during natural fire tests including the cooling phase <i>Silvio Renard, Thomas Gernay, Fabienne Robert, Jochen Zehfuß, Robert McNamee, Patrick Bamonte and Jean-Marc Franssen</i>	1443
Probabilistic modelling of wood charring rates: A parametric study and next steps <i>Jakub Šejna, Dominik Štraus, Kamila Cábová and František Wald</i>	1455
Study on the fire design method of timber members treated with surface plastering application <i>Lingzhu Chen, Xi Chen, Qingfeng Xu, Mingqian Wang, Yubing Leng and Fuwen Zhang</i>	1465
Towards alternative fire design solutions for wood-to-wood connections <i>Anne Davidson, Ethan Phillion, Lilyana Mladenova, Rwayda Al Hamd, Beth Weckman and John Gales</i>	1477

AUTHOR INDEX

A			
Abu, A.	959	Chen, G.	959
Adelzadeh, M.	737	Chen, L.	1465
Agarwal, A.	235	Chen, X.	1465
Aghabozorgi, P.	839	Chen, Z.	1081
Aisyah, W. S.	995	Chin, K.	545, 1117
Al Hamd, R.	1477	Chinaya, C.	609
Al Mansouri, O.	701	Choi, I.	767
Al-Bashiti, M. K. G.	463	Choi, S.	767
Alam, N.	861, 883, 1299	Chorlton, B.	473
Alanen, M.	1431	Chu, T.	1383
Albero, V.	301, 337, 579	Cibelli, A.	777
Albuerne, A.	995	Čolić, A.	1395
Ali, F.	861	Correia, J. R.	289, 439
Almaadawy, A.	493	Couto, C.	1287
Ameri, S.	277	Covi, P.	115
Anwar, G. A.	949	Craveiro, H.	177, 325, 757, 1161
Armstrong, P.	93	Cvetanoski, B.	1277
Ataíde, A.	289		
Auguin, G.	789	D	
Autiero, M.	927, 1299	Dal Lago, B.	359
Ayala, E.	139	Dao, V.	503
Azevedo, A. S.	439	Dauti, D.	609
		Davidson, A.	1477
B		Davison, B.	1229
Ba Le, D.	503	Davison, M.	139
Baheti, A.	383	De Rosa, G.	861, 873
Bamonte, P.	1443	Der, B.	85, 905
Banerji, S.	493	Di Meglio, F.	873
Beaucour, A-L	815	Ding, K.	1105
Becker, A.	1173	Dionisio, F.	777
Bhat, J. A.	395	Domada, R.	1265
Bienfelt, J.	609	Du, P.	483, 621
Bisby L.	1395	Du, Y.	1081
Blumauer, U.	1207	Duboc, J.	105, 589
Boko, I.	1127	Duma, D.	655, 971
Bolina, F. L.	347	Duponchel, X.	609
Bouchaïr, A.	1057	Durif, S.	1057
Burgess, I.	1229		
		E	
C		Elhami-Khorasani, N.	525, 535
Cábová, K.	1455	Ervine, A.	1337
Cabral, J.	1137	Eslami, J.	815
Camotim, D.	1093	Espinós, A.	189, 301
Cardu, U.	371		
Cashell, K.	949	F	
Caspeepe, R.	677	Faghihi, F.	1241
Castilho, E.	289	Felicetti, R.	371, 641
Červinka, P.	85, 905	Firan, M-M	983
Chang, J.	93	Firmo, J. P.	289, 439
Charlier, M.	1021	Frangi, A.	1349
Chaudhary, R. K.	25, 915	Franssen, J-M	1443
Chen, C.	1383	Freddi, F.	1277
		Frenz, J.	983

Fürst, R.	1173, 1217		
G			
Gales, J.	545, 1117, 1477		
Gamba, A.	93		
Gardner, L.	325		
Garrido, M.	289		
Ge, Y-Q	427		
Gernay, T.	25, 153, 165, 313, 971, 1287, 1443		
Gil, A. M.	15		
Glew, A.	1045		
Goreta, M.	1127		
Green, M.	473		
Gu, X-L	427		
Guadagnini, M.	665		
Guibaud, A.	995		
Gwak, J.	767		
H			
Hajiloo, H.	473, 737		
Han, S.	767		
Harada, K.	1313, 1407		
Häßler, D.	1173, 1217		
Hernández-Figueirido, D.	579		
Hilditch, R.	1337		
Hirashima, T.	255, 515, 1359, 1419		
Hopkin, D.	725, 1229, 1395		
Horie, M.	255, 515		
Hospitaler, A.	73, 337		
Hothan, S.	1173, 1217		
Hoxha, D.	701, 815		
Huang, Q.	225		
Huang, S-S	1229		
Huang, X.	127		
I			
Ibáñez, C.	189, 337		
Inerhunwa, I.	725		
Ingolfsson, S.	1045		
Iravani, M. H.	737		
J			
Jeanneret, C.	1117		
Jeebodh, A.	1229		
Ji, W.	1081, 1105		
Jiang, C.	427		
Jiang, L.	417, 1383		
Jiang, S.	1253		
Jokinen, T.	49		
Jovanović, B.	677, 915		
Julin, T.	1431		
K			
Kanada, H.	255, 515		
Kanellopoulos, G.	725		
Kapfhammer, A.	983		
Katwal, U.	225		
Kevinly, C.	483, 621		
Khan, A. A.	949, 1033, 1265		
Khan, M.	895		
Khan, M. A.	949, 1033		
Khan, S.	713		
Kikuchi, T.	1359		
Kim, S.	767		
Kimbar, G.	725		
Kimura, K.	515, 631		
Kisei, S.	515		
Knallinger, G.	267		
Knez, F.	1207		
Knobloch, M.	1241		
Kodur, V.	15, 493, 1195		
Kotsovinos, P.	1117		
Kriel, M.	1337		
Kruse, H.	803		
Kumar, R.	883		
L			
Laím, L.	177, 325, 839, 1161		
Lalu, O.	655, 971		
Lam, H. Y.	557		
Lama, L.	165		
Landesmann, A.	1093		
Lange, D.	383, 939, 1337		
Lapuebla-Ferri, A.	301, 337		
Leng, Y.	1465		
Lennon, T.	655, 971		
Li, G.	745, 1081, 1105, 1185		
Li, J.	983, 1105		
Lim, K. T. E.	557		
Lim, L.	93		
Lo Monte, F.	371		
Lombaert, G.	677		
Lopes, N.	1137		
Lopez, M.	609		
Lou, G.	745		
Lucherini, A.	25, 61, 677, 1009, 1021		
Lyzwa, J.	405		
M			
Ma, C.	153, 313		
Ma, Z.	1149		
MacRae, G.	959		
Madden, J.	1337		
Main, J. A.	829		
Makino, S.	1313		
Malaska, M.	1431		
Maluk, C.	139, 557, 1371		

Manzoor, T.	395	Paya-Zaforteza, I.	73
Martellozzo, F.	371	Pazdanowski, M.	1069
Martins-Robalino, A.	545	Peifer, P.	213
Maslak, M.	1069	Peña, D. L.	337
Mason, M.	939	Peng, M.	25
Matsagar, V.	383	Pérez, F. P.	1349
McLaggan, M. S.	1229	Peters, S.	849
McNamee, R.	1443	Phan, L. T.	829
Medall, D.	189	Philion, E.	545, 1477
Melchor-Eixea, A.	579	Piccinin, R.	701
Mendez, J.	1045	Pimienta, P.	815
Mensing, M.	267, 277, 983	Pinoteau, N.	701
Merci, B.	61, 1009	Piquer, A.	579
Meschke, G.	849	Pitarch, A.	579
Miano, A.	873	Pittrich, T.	451
Mika, A.	1325	Pontarollo, J. N.	609
Mikko, M.	1325	Possidente, L.	1277
Mladenova, L.	1477	Prota, A.	873
Mohamad, M.	267	Provis, J. L.	665
Morovat, M. A.	829	Put, F.	677, 915, 1009
Morrison, A.	1045		
Mostachetti, M.	359	Q	
Mouhou, F. B.	701	Qi, H.	745, 1105
Mueller, K.	599	Qiu, J.	417
N		R	
Nadjai, A.	861, 883	Rahme, M.	225
Nakayama, Y.	1359, 1419	Rahnavard, R.	177, 325
Nan, Z.	127, 939, 949, 1033	Raj, B. N.	895
Naser, M.Z.	463	Ramaswamy, A.	567
Neupane, D.	1149	Ranade, R.	525, 535
Neves, N. S.	1093	Ranua, R.	49
Ngo, T.	165, 895	Reig, L.	579
Ni, S.	25, 689	Rein, G.	1383
Nigro, E.	777, 873, 927, 1299	Rémond, S.	701
Nii, D.	1313, 1407	Renard, S.	1443
Nincevic, K.	701	Reynders, E.	677
Nishimura, T.	631	Robert, F.	1443
Noman, M.	713	Roges, N.	609
Noumowe, A.	815	Roig-Flores, M.	579
		Romero, M. L.	189, 301
O		Root, K.	599
O'Loughlin, E.	1045	Roque, M.	289
Obaei, A.	815	Roshan, N.	473
Ogrin, A.	1207		
Ojala, A.	1431	S	
Orabi, A.	127, 939, 1265, 1371	Sadek, F. H.	829
Ouldboukhitine, S. E.	1057	Sah, M.	493
		Saito, M.	631
P		Saito, S.	1359
Pagán-Martínez, J. J.	73	Salminen, M.	1431
Pal, B.	567	Sami, P.	1325
Papaioannou, K.	93	Santiago, A.	177, 325, 757, 839, 1161
Passarini, N.	37	Santos, A. F.	757
Patel, D.	599		

Saulnier, V.	1057	Vaněk, J.	85
Saura, H.	337	Venkatachari, S.	1195
Schäfers, M.	277	Viale, J.	609
Schmid, J.	1349	Vila Real, P.	1137
Šejna, J.	1455	Vild, M.	85, 905
Selvaranjan, K.	665	Vu, H-T	243
Shah, A. H.	395		
Shintani, Y.	255, 515, 631	W	
Silva, D.	777, 861, 873 927, 1299	Wald, F.	85, 905, 1455
Simões da Silva, L.	757	Wang, J.	417
Simões, R. A.	325	Wang, M.	745, 1465
Singh, S.	235	Wang, W.	939
Song, X-B	427	Wang, Y.	1105, 1185
Spearpoint, M.	725, 1395	Wang, Z.	939
Spyridakis, S.	1371	Weckman, B.	1477
Stankiewicz, M.	1069	Wei, J.	3
Stelzner, L.	451, 1217	Weigand, J. M.	829
Štraus, D.	1455	Weise, F.	451
Sun, A.	1313, 1407	Weng, Y.	417
Suzanne, M.	789	Wiesner, F.	1337, 1371, 1395
Szasdi-Bardales, F.	535	Wu, N.	201
		Wu, W	1337
T			
Tajik, N.	525, 535	X	
Tan, K. H.	201, 483, 621	Xia, Z.	1081
Tang, H.	1253	Xu, Q.	1465
Tao, Z.	225		
Teoh, B. K.	483	Y	
Tessari, A.	525, 535	Yaqub, M.	713
Thai, H. T.	165, 895	Yarmohammadian, R.	641
Thauvoye, C.	789		
Thiele, C.	213, 803	Z	
Thienpont, T.	915	Zajdel, P.	1069
Tondini, N.	37, 115, 1277	Zehfuß, J.	277, 405, 983, 1443
Tong, Q.	1287	Zhang, C.	3
Tonicello, E.	105, 589	Zhang, F.	1465
Torelli, G.	665	Zhang, H-C	427
Torero, J.	503, 995	Zhang, T.	1253
Torić, N.	1127	Zhang, Y.	745
Totsuka, M.	1359, 1419	Zhao, B.	243
Tramoni, J-B	789	Zheng, X.	1105, 1185
Turkowski, P.	725	Zhi, L.	1081
Tutzer, K.	267	Zhu, S.	1081, 1105, 1185
U			
Unobe, D.	25, 493, 689		
Usmani, A	127, 417, 949, 1033, 1265, 1383		
Uszball, S.	1241		
Uy, B.	165, 895		
V			
Valiante, N.	371		
Van Coile, R.	25, 61, 153, 677, 915, 1009		

**APPLICATIONS OF STRUCTURAL
FIRE ENGINEERING**

A REFINED CYLINDER FIRE MODEL FOR STEEL BEAM TEMPERATURE CALCULATION UNDER LOCALIZED FIRE CONDITIONS

WEI Junjie¹, ZHANG Chao^{2*}

ABSTRACT

This paper presents the application of a recently developed novel theoretical fire model for calculating the temperatures of steel beams located inside a localized fire. A calculation method is developed based on the novel fire model and is implemented in the finite element software ANSYS. Localized fire tests of I-beams, with and without ceiling, are utilized to validate the efficiency of the novel calculation method. The new method adequately predicts the non-uniform temperature distribution of exposed steel beam in localized fire and the Mean Absolute Percentage Error (MAPE) for all the investigated cases are within $\pm 25\%$. Notably, the deviations between the predicted and measured values of the maximum steel beam temperature are less than 61°C across all test conditions. The method proposed in this paper provides a feasible way for structural fire engineering design in localized fires without the need of FDS.

Keywords: novel methodology, temperature prediction, steel beam, realistic fires, localized fire model

1. INTRODUCTION

Over the past decades, numerous fire tests [1,2] and theoretical studies [3-5] have been carried out for developing calculation methods for structural fire safety design. Most of these studies utilized standard fire or simulated compartment fires that assume uniform heating conditions. However, real fire exposure conditions for steel beams are generally nonuniform because of the randomly distributed combustible materials, the non-symmetry of ventilation, and other factors [6]. The main challenge in structural fire analysis for realistic fires is accurately calculating the nonuniformly distributed thermal boundary conditions at the exposed surfaces. To date, several empirical correlations have been proposed to calculate the heat fluxes to the exposed steel beams located just above a localized fire, as documented in studies such as [7-10]. However, empirical correlations are often derived solely from curve fitting of specific test data. As a result, they may lack physical significance and fail to provide generalizable models. To model complex fire scenarios, the CFD (computational fluid dynamics) code FDS (fire dynamics simulator) [11] is often used. Due to the limitation of the one-dimensional heat conduction assumption for the solid phase in FDS, coupling analyses between FDS and finite element codes (e.g., ANSYS) are often required to accurately predict the three-dimensional heat conduction in fire exposed structures [12]. This needs the utilization of specially developed fire-structure interfaces, often developed based on the concept of adiabatic surface temperature (AST) [13]. Analytical models have also been developed for calculating the radiation from localized fire (flame) to exposed targets. However, existing analytical models typically assume the flame to be a various opaque solid shape and cannot calculate heat flux within the flame [14-16]. To address

¹ Phd Candidate, School of Civil Engineering, Wuhan University

e-mail: junjwe@whu.edu.cn

² Professor, School of Civil Engineering, Wuhan University

e-mail: chao.zhang@whu.edu.cn

this limitation, a novel fire model [17,18] has been recently developed to estimate the thermal radiation from localized fire to exposed surfaces located within and outside the flame. This paper presents the implementation of the novel model in Ansys for calculating the temperatures of steel beams subjected to localized fire. The detailed calculation process of this method will be introduced in the following sections, and its results will be compared with experiment data found in the literature.

2. THE NOVEL LOCALIZED FIRE MODEL

As shown in Figure1, the novel model divides the three-dimensional space within the localized fire radius into a series of concentric hollow cylinders of equal height and equal width. The reasonable element size (the height and width of the hollow cylinder) can be taken as 0.01 m. Every hollow cylinder (elementary graybody) is assumed as a homogenous, isotropic, and absorbing-emitting gray emitter. The radiant incident heat flux of the localized fire to any target surface can be calculated as:

$$\dot{q}_{inc}'' = \sum_{i=1}^N \int_0^H F(i, z) \cdot \varepsilon(i, z) \cdot \tau_m(i, z) \cdot \sigma [T(i, z) + 273]^4 dz \quad (1)$$

where $F(i, z)$ and $\tau_m(i, z)$ are the configuration factor and transmissivity between element (i, z) and the target surface, respectively; $\varepsilon(i, z)$ and $T(i, z)$ are the emissivity and gas temperature of the element (i, z) . Here, i is the number of the element in the radius direction; and N is the number of divisions along the radius. σ is Stefan–Boltzmann constant. Detailed information of the model and methods to determine the model parameters can be found in [17,18].

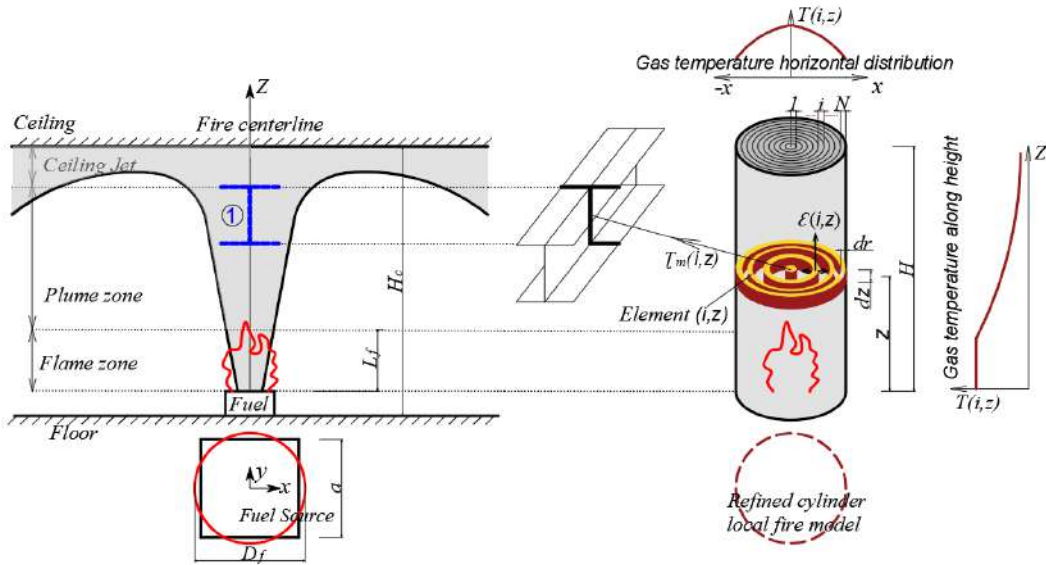


Figure 1. Refined cylinder fire model. H is the localized fire model height. L_f is the intermittent flame height. a is the side length of the fire source. D_f is the equivalent diameter of fire source. z is the vertical distance from element (i, z) to fire source. dz and dr is the height and width of one element (hollow cylinder). r is the distance between the target surface and fire centerline.

3. TEMPERATURE CALCULATION METHOD

Heat can be transferred from flames and hot gases to structures by radiation and convection. The net heat flux \dot{q}_{net}'' received by an exposed surface can be defined by the sum of these two terms:

$$\dot{q}_{net}'' = \varepsilon_s (\dot{q}_{inc}'' - \dot{q}_{emiss}'') + \dot{q}_{conv}'' = \varepsilon_s \dot{q}_{inc}'' - \varepsilon_s \sigma T_s^4 + h_c (T_g - T_s) \quad (2)$$

Where ε_s is emissivity and absorptive of the exposed surface; \dot{q}_{emiss}'' is emissive power of the exposed

surface; \dot{q}_{conv}'' is convective heat flux between the exposed surface and the surrounding gas; T_s is temperature of the exposed surface; h_c is film coefficient; and T_g is temperature of the surrounding gas.

In current structural fire design codes, the absence of a calculation approach to predict the net heat flux of structure members in localized fires presents a significant challenge. A commonly employed method entails utilizing the AST [13] computed by FDS to approximate the actual thermal boundary for heat transfer analysis, commonly referred to as the Ansys-AST Method. Nevertheless, integrating FDS with Ansys poses difficulties due to disparities in spatial and temporal resolutions between the fire and structural domains. In this study, we introduce a new approach named the Ansys-LocFire method, which integrates the novel localized fire model with Ansys software for thermal analysis. The incident heat flux (\dot{q}_{inc}'') is determined by the novel localized fire model outlined in Section 2, while the convective heat flux (\dot{q}_{conv}'') is computed using the Newton formula. The combined value, representing the incident total heat flux, is then inputted into Ansys as the surface load. Additionally, the thermal radiation emitted by high-temperature steel beams to the surrounding air (\dot{q}_{emiss}'') is accounted for concurrently within Ansys. As illustrated in Figure 2, all surfaces of the I-beam receive both radiation and convective heat flux. For more accurate calculation, the number of heat flux measurement points and finite element elements needs to be sufficient. Several assumptions underpin the calculation process:

- Due to complex air flow and radiation shielding between the web and flange plate, it is simply assumed that the heat flux in the grooves of the I-beam is uniform.
- Following the suggestion in Annex G of EC1 part 1-2 [19], a rectangular shape replaces the I-shape, with the assumption that the heat flux of the web and flange remains constant regardless of changes in their dimensions. Specifically, we consider the heat flux value to be equivalent to the heat flux measured at the midpoint of each surface, as illustrated in Figure 2.
- The temperature of the surrounding air is set at 20°C when calculating the emissive power of the steel beam.
- Despite the temporal and spatial variation in the temperature of the steel beam, it is simply assumed to be constant at 20°C for the calculation of maximum convective heat flux. Note that for radiation calculation, the steel temperature is varied,

Through the Ansys-LocFire method, we aim to provide a more cohesive and effective solution compared to existing methodologies, addressing the complexities inherent in coupling FDS and Ansys models. A detailed flowchart which illustrates steps for structure member temperature calculation in the proposed model is shown in Figure. 3. However, the accuracy and applicability of this method hinge upon various factors, including the fidelity of the localized fire model and the validity of the assumptions made.

Nevertheless, the simplification and assumptions made above are considered to be on the conservative side, they may be further refined to obtain more accurate results. In the following section, two experiments found in literatures will be employed to validate the proposed method.

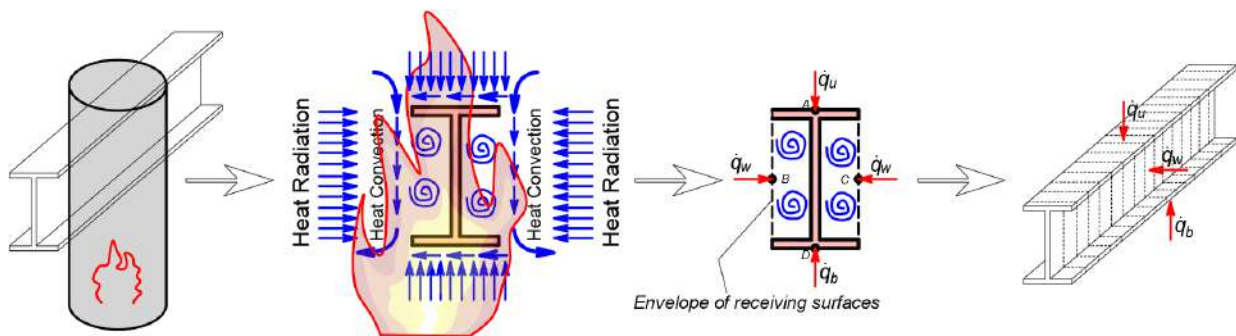


Figure 2. The heat transfer analysis model

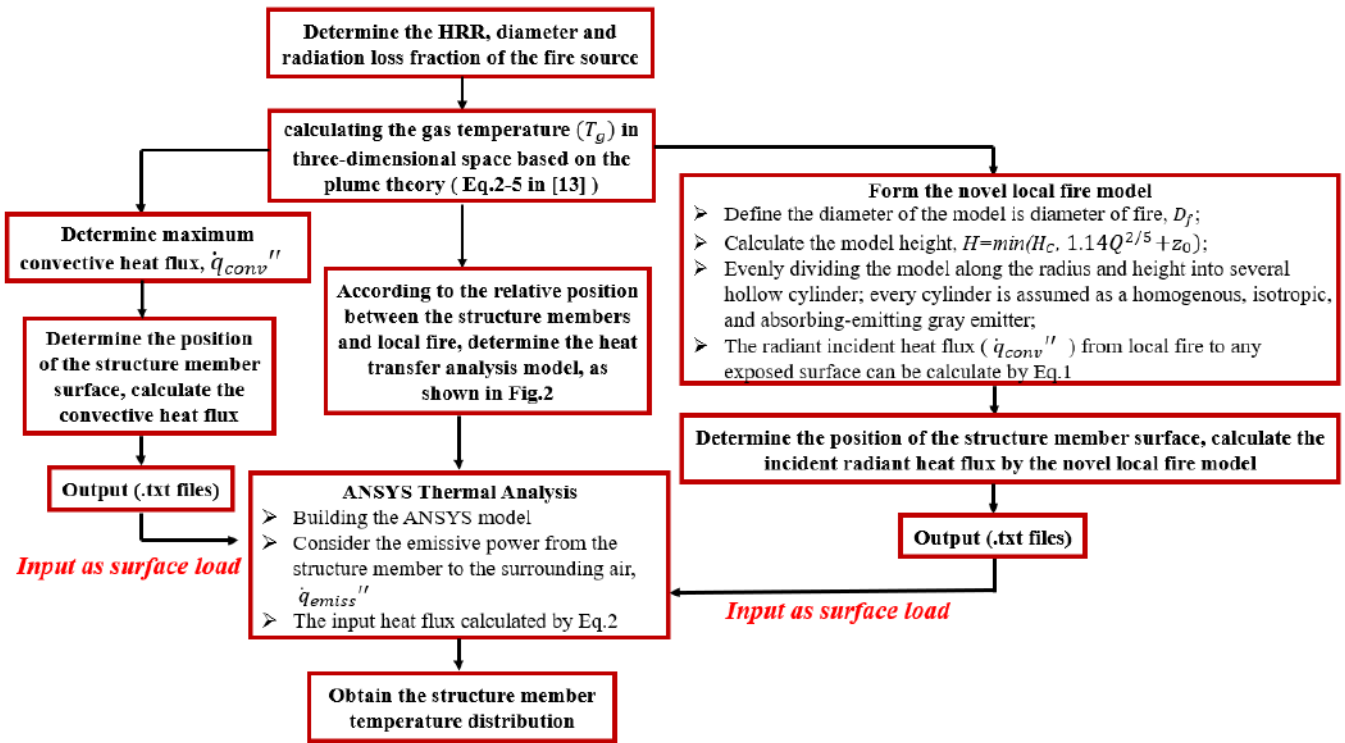


Figure 3. Flowchart of the Ansys-LocFire method for the temperature calculation

4. VALIDATION STUDY: CEILING BEAMS ABOVE LOCALIZED FIRE

4.1 Description of the experiment

Hasemi carried out a series of experiments [20] in which a I-section bare steel beam beneath the ceiling was impinged or engulfed by the localized fire. Figure 4 shows the experimental layout in Hasemi et al.'s experiments. The dimension of the steel beam was $3.6 \times 0.075 \times 0.15$ m (Length \times Width \times Height), with a thickness of 5 mm in the web and 6 mm in the flange. The ceiling was made of mineral fiber perlite board with dimension of $3.6 \times 1.83 \times 0.024$ m (Length \times Width \times Height). The distance from the burner to the lower flange of the beam was H_B . A 0.5 m diameter round porous propane burner were used as the fire source. Further details of the experiments can be found in [21]. All test scenarios are listed in Table 1.

Table 1. Test Conditions of Hasemi experiments

Test no.	Q(kW)	H_B (m)	L_f/H_B	The computation domain	Grilde numbers	Mesh resolution ($\delta x/D^*$)
1	100	1.0	1.1	4m(X) \times 2m(Y) \times 1.4m(Z)	273000	0.043
2	150	1.0	1.5			0.037
3	200	1.0	1.8			0.033
4	95	0.6	1.8	4m(X) \times 2m(Y) \times 1m(Z)	195000	0.044
5	130	0.6	2.2			0.039
6	160	0.6	2.5			0.036

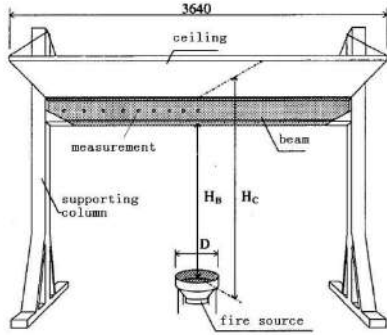


Figure 4. Experimental Setup of Hasemi Tests

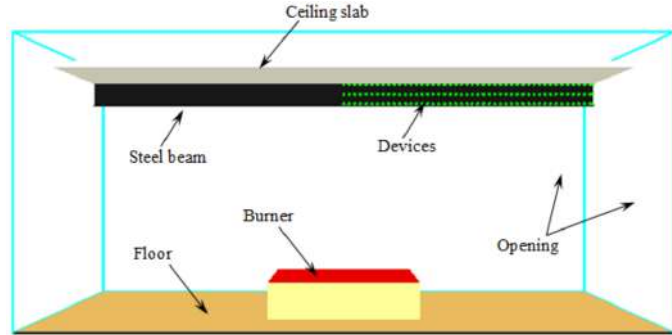


Figure 5. FDS Model of Hasemi Tests

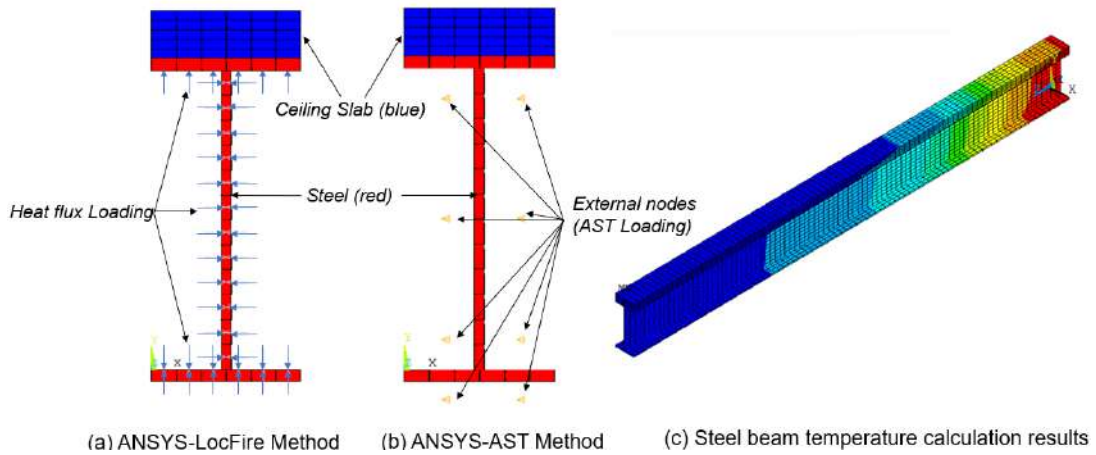


Figure 6. FEM simulation for steel beam temperature calculation

4.2 FDS simulation and FEM simulation

Figure 5 shows the FDS numerical model for the localized fire test. All computational domain boundaries except the ground are open. The flanges and web of the beam are modeled as steel sheets with thickness of 6mm and 5mm, respectively. Ceiling is modeled as 24 mm thick perlite board. The emissivity of all solid surfaces was taken as 0.9 [5]. Other properties of the materials were taken from [21]. Mid-stretched grids were used in X, Y and Z directions (the grid size in fire region is 2cm, and other regions are 4cm). The computational domain, total grid number and the mesh resolution ($\delta x/D^*$) are detailed in Tabel.1.

Figure 6a shows the surface loading in the Ansys-LocFire method. By symmetry, one half of the composite beam was used. The width of the ceiling slab was taken as the steel I beam in the Ansys model. The three dimensional (3D) layered shell element SHELL131 in Ansys 2022R1 [22] was used. The composite section of the steel upper flange and perlite slab was divided into one steel layer and five perlite layers to consider thermal conduction between the upper flange and the slab. Figure 6b shows the Ansys-AST method [12] in the thermal analysis for the ceiling beam composite. An additional external node was defined for each element (SHELL131) to apply the thermal boundary condition using the concept of AST. The temperature of the external node was taken as the AST transferred from FDS.

4.3 Heat flux validation

In Figure 7, the comparison of predicted values from the four methods with the test data in all conditions is presented. For the bottom surface of the lower flange, the novel fire model exhibits the smallest Mean Absolute Percentage Error (MAPE) at 35%. Its Root Mean Square Error (RMSE) and Mean Absolute Error (MAE) are 7.4 kW/m² and 4.3 kW/m², respectively. The FDS predictions show the smallest RMSE and

MAPE, with values of 6.4 kW/m^2 and 4.1 kW/m^2 , respectively, and a MAPE of 43%. The Wakamatsu formula yields RMSE, MAE, and MAPE of 11.9 kW/m^2 , 6.5 kW/m^2 , and 57%, respectively. The Myllymaki and Kokkala formula predicts RMSE, MAE, and MAPE of 8.6 kW/m^2 , 5.3 kW/m^2 , and 50%, respectively. When comparing with test data for the web surface, the novel fire model demonstrates the smallest RMSE, MAE, and MAPE, with values of 7.0 kW/m^2 , 4.4 kW/m^2 , and 43%, respectively. Therefore, the novel fire model exhibits the better performance in heat flux estimation.

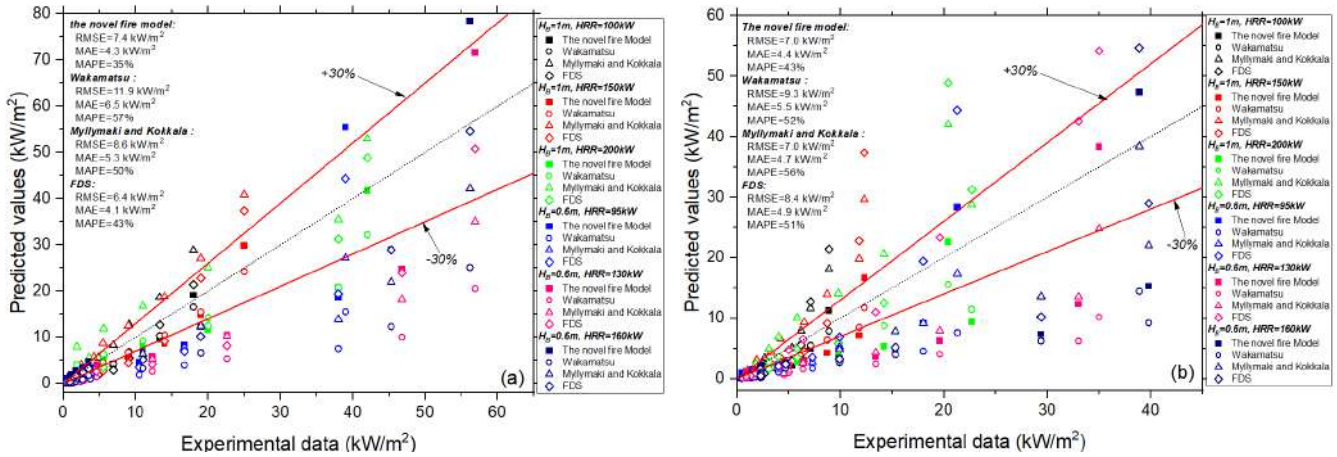


Figure 7. Comparison of heat flux calculated by all methods: (a) Bottom surface of the lower flange; (b) Web Surface

4.4 Steel temperature validation

The heating rate of steel is a crucial parameter. During steady-state localized fires, the temperature of the steel member near the flame stabilizes after reaching a certain value. Due to space limitation, Figure 8 only depicts the steel temperature-time curve at the center section with an HRR of 100 kW. The Ansys-LocFire method's predictions exhibit the most accurate final steady temperatures, with deviations of $13 \text{ }^\circ\text{C}$, $3 \text{ }^\circ\text{C}$, and $-17 \text{ }^\circ\text{C}$ in the bottom flange, web, and upper flange, respectively. Its MAPE values are 9%, 4%, and 28% in the bottom flange, web, and upper flange, respectively. The Ansys-AST method shows deviations of $12 \text{ }^\circ\text{C}$, $11 \text{ }^\circ\text{C}$, and $-35 \text{ }^\circ\text{C}$ in the final steady temperature predictions for the bottom flange, web, and upper flange, respectively, with MAPE values of 17%, 15%, and 22% in the respective regions. The Wakamatsu method predicts deviations of $57 \text{ }^\circ\text{C}$, $53 \text{ }^\circ\text{C}$, and $56 \text{ }^\circ\text{C}$ in the final steady temperature for the bottom flange, web, and upper flange, respectively, with MAPE values of 25%, 25%, and 13%, respectively. The Myllymaki and Kokalla method exhibits deviations of $163 \text{ }^\circ\text{C}$, $187 \text{ }^\circ\text{C}$, and $229 \text{ }^\circ\text{C}$ in the final steady temperature predictions for the bottom flange, web, and upper flange, respectively, with MAPE values of 70%, 91%, and 110%, respectively.

Figure 9 illustrates the steel temperature-time curve at the section 0.75m from the beam midpoint with an HRR of 100 kW. The deviations of the Ansys-LocFire method in the final steady temperature predictions are $12 \text{ }^\circ\text{C}$, $-1 \text{ }^\circ\text{C}$, and $-26 \text{ }^\circ\text{C}$ in the bottom flange, web, and upper flange, respectively, with MAPE values of 5%, 7%, and 28%, respectively. The Ansys-AST method shows deviations of $-47 \text{ }^\circ\text{C}$, $-51 \text{ }^\circ\text{C}$, and $-77 \text{ }^\circ\text{C}$ in the final steady temperature predictions for the bottom flange, web, and upper flange, respectively, with MAPE values of 22%, 21%, and 43%, respectively. The Wakamatsu method predicts deviations of $15 \text{ }^\circ\text{C}$, $7 \text{ }^\circ\text{C}$, and $-13 \text{ }^\circ\text{C}$ in the final steady temperature for the bottom flange, web, and upper flange, respectively, with MAPE values of 6%, 4%, and 23%, respectively. The Myllymaki and Kokalla method exhibit deviations of $58 \text{ }^\circ\text{C}$, $52 \text{ }^\circ\text{C}$, and $42 \text{ }^\circ\text{C}$ in the final steady temperature predictions for the bottom flange, web, and upper flange, respectively, with MAPE values of 28%, 33%, and 12%, respectively. Overall, the Ansys-LocFire method demonstrates stable and accurate estimation performance.

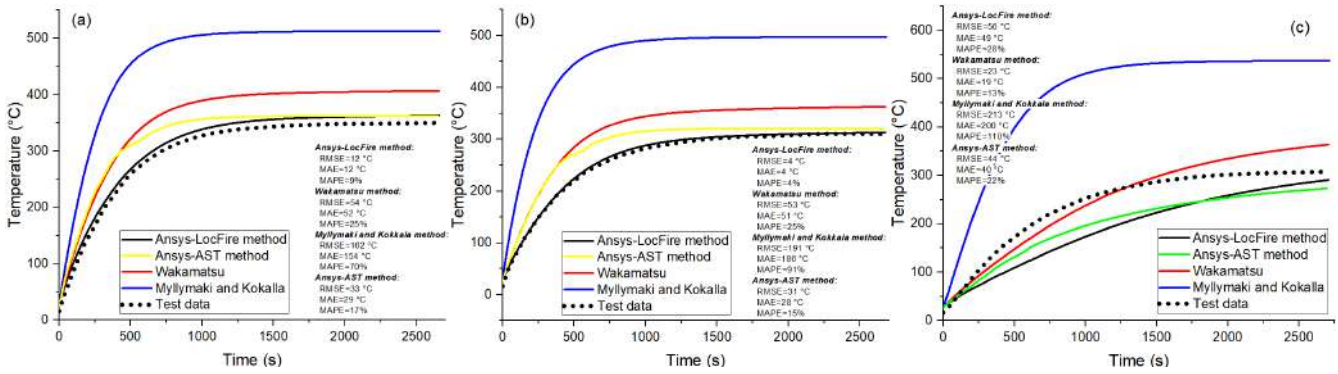


Figure 8. Temperature-time curve of steel at the mid-span section: (a) bottom flange; (b) web; (c) upper flange

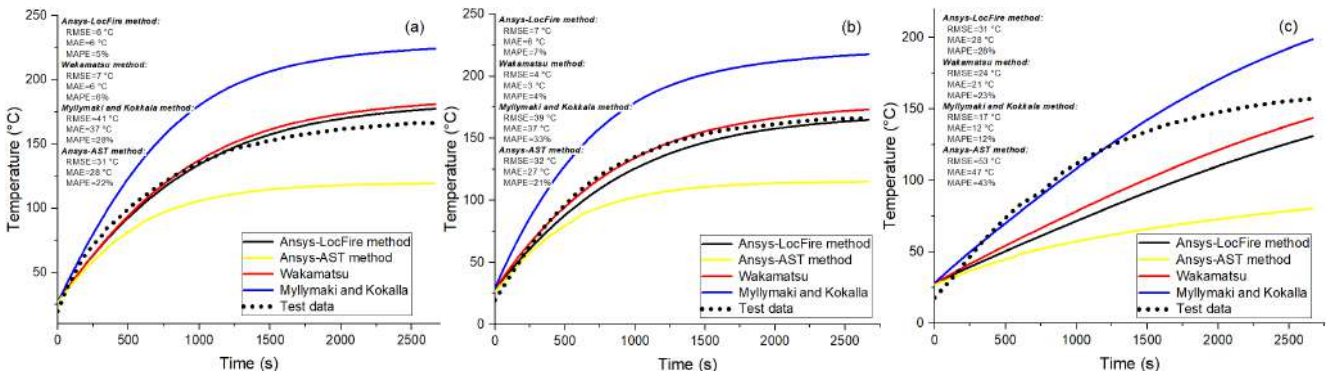


Figure 9. Temperature-time curve of steel at the section 0.75m from beam midpoint: (a) bottom flange; (b) web; (c) upper flange

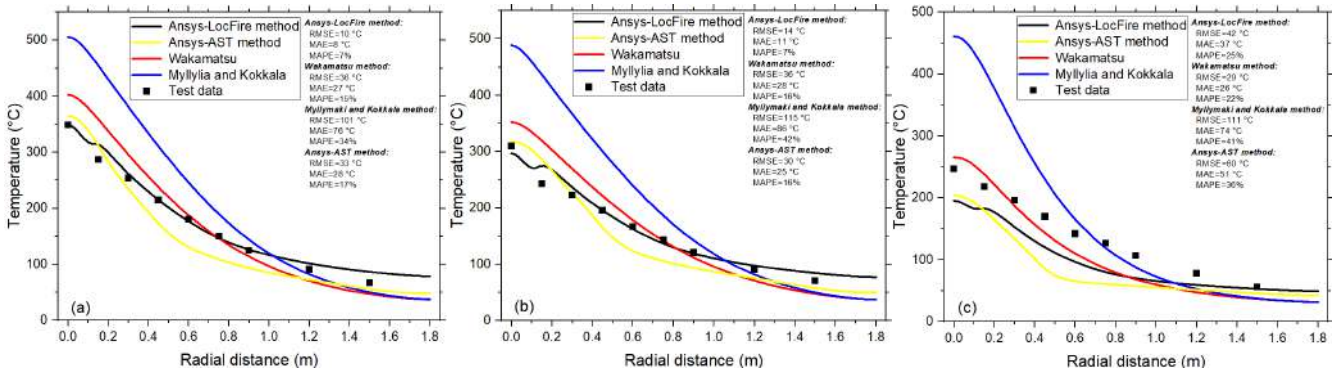


Figure 10. Steel Temperature Distribution along the beam for the case with HRR of 100kW: (a) bottom flange; (b) web; (c) upper flange

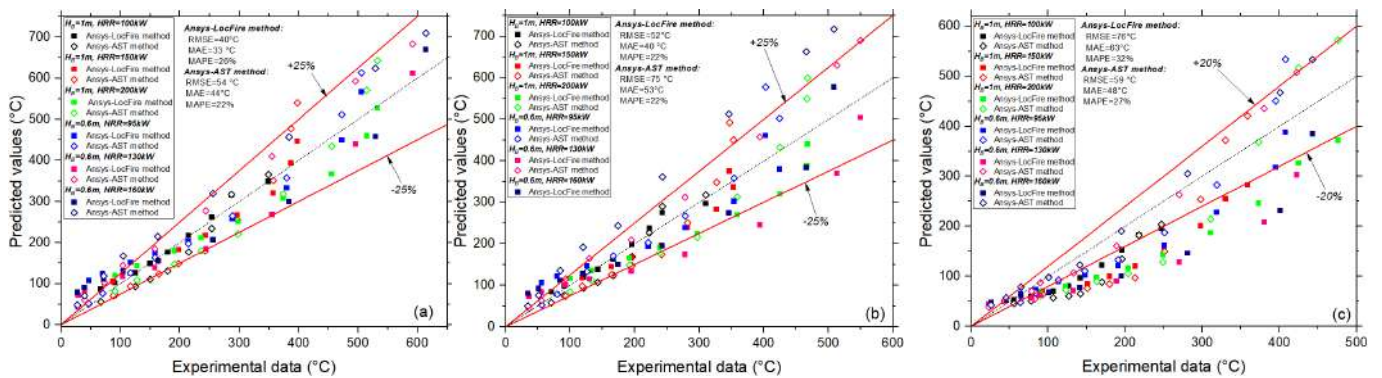


Figure 11. Steel temperature comparison for all cases: (a) bottom flange; (b) web; (c) upper flange

Figure 10 illustrates the comparison of steel temperature distribution along the beam length at an HRR of 100 kW. The temperature of the steel beam decreases as the radial distance from the flame center increases. In the Ansys-LocFire method, convection heat transfer inside fire radius is not considered because the temperature of the steel member in the flame is close to that of the gas. Consequently, this results in a flat section of the steel temperature distribution curve at the flame radius. The Ansys-LocFire method yields the best results, exhibiting the smallest RMSE, MAE, and MAPE in the lower flange and web temperature predictions. Compared with test data, the MAPE of the Ansys-AST method is 17%, 16%, and 36% in the bottom flange, web, and upper flange, respectively. The MAPE of the Wakamatsu method is 15%, 16%, and 22% in the bottom flange, web, and upper flange, respectively. The MAPE of the Myllymaki and Kokkala method is 34%, 42%, and 41% in the bottom flange, web, and upper flange, respectively. In addition, the deviations between the predicted and measured values of the maximum temperature of the steel beam temperature are 61 °C, 20 °C, 56 °C, -1 °C, 48 °C, -6 °C in test no.1 to test no.6, respectively

In Figure 11, a comparative analysis is presented, showcasing the temperatures forecasted by both the Ansys-LocFire and Ansys-AST methods against the actual test values across all test points under all test conditions. The MAPE for the Ansys-LocFire method is determined to be 26%, 22%, and 32% for the bottom flange, web, and upper flange, correspondingly. Conversely, the MAPE for the Ansys-AST method is observed to be 22%, 22%, and 27% for the bottom flange, web, and upper flange, respectively.

5. VALIDATION STUDY: BEAMS WITHOUT CEILING SURROUNDED BY LOCALIZED FIRE

5.1 Description of the experiment

Figure 12 illustrates a schematic of the test setup conducted by NIST [23], comprising the W16×26 beam specimen, reaction frames, and HSS (hollow structural section) loading beams. The length of the beam specimen was 6.17 m, and it was simply supported with a bearing-to-bearing length of 5.86 m. The gas burner was positioned 1.1 m below the lower flange of the steel beam, with a distance of 1.6 m between the lower flange of the beam and the floor. All components of the structural steel frames were designed in accordance with ANSI/AISC-360 (2010). Thermocouples were strategically installed to measure the surface temperatures of the lower flange, upper flange, and mid web. Table 2 provides the matrix of the NFRL tests considered in this paper.

Table 2. The matrix of the NFRL tests

Burner Size	Test no.	Heat Release Rate Q(kW)
1m×1m	Test 1,2	Increased in 100 kW increments up to 500 kW
	Test 3,4,5	Fixed at 400 kW
	Test 7	Fixed at 700 kW
	Test 8,9	$(4.5 \cdot t^2 + 250) \text{ kW} \leq 1600 \text{ kW}$

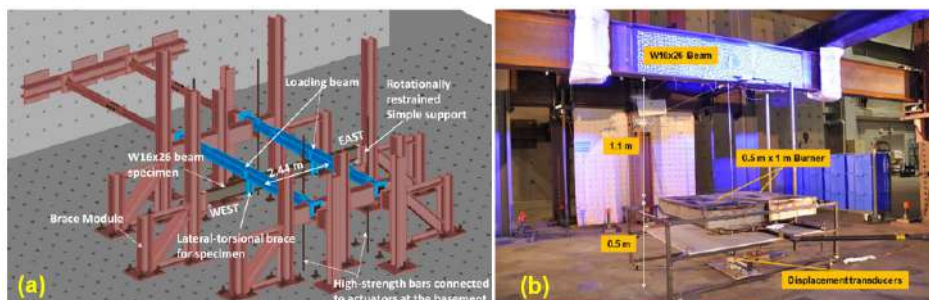


Figure.12 Experimental design: (a) Test setup;(b) Photograph of burner in the test setup

5.2 FDS simulation and FEM simulation

Figure 13 displays the FDS model geometry and computational meshes used for the NFRL structural fire tests. The dimensions of the computational domain were 7.2 m (X)× 1.2 m (Y)× 3.6 m (Z). Mid-stretched grids were employed in X, Y and Z directions, with a grid size of 2cm in the fire region and steel beam region, and 4cm in other regions. This grid configuration has been validated as accurate and effective [24]. The steel sections were modeled as obstructions with zero thickness, and a user-defined solid boundary condition, named “STEEL”, was applied. The default combustion model for propane was utilized. Four side boundaries and the top boundary were modeled as open, while the floor was assumed to be a solid wall. The DEVICE command in FDS was employed to output data, including the AST and steel temperature, at selected points. Figure 14(a) and Figure 14(b) shows the thermal boundary loading in the Ansys-LocFire method and Ansys-AST method, respectively.

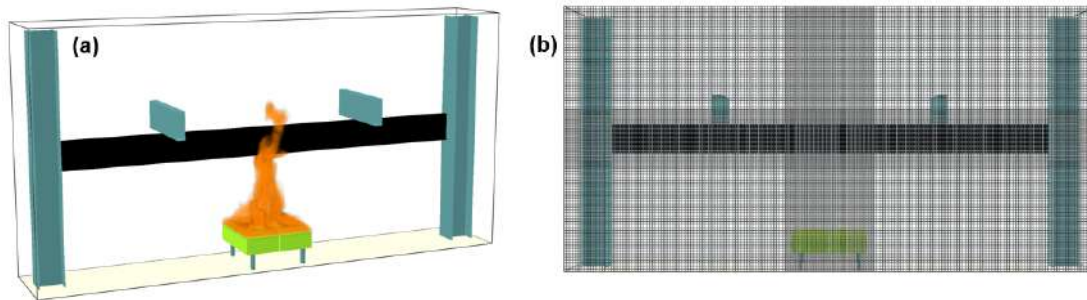


Figure 13. FDS numerical model: (a) Geometry; (b) Mesh

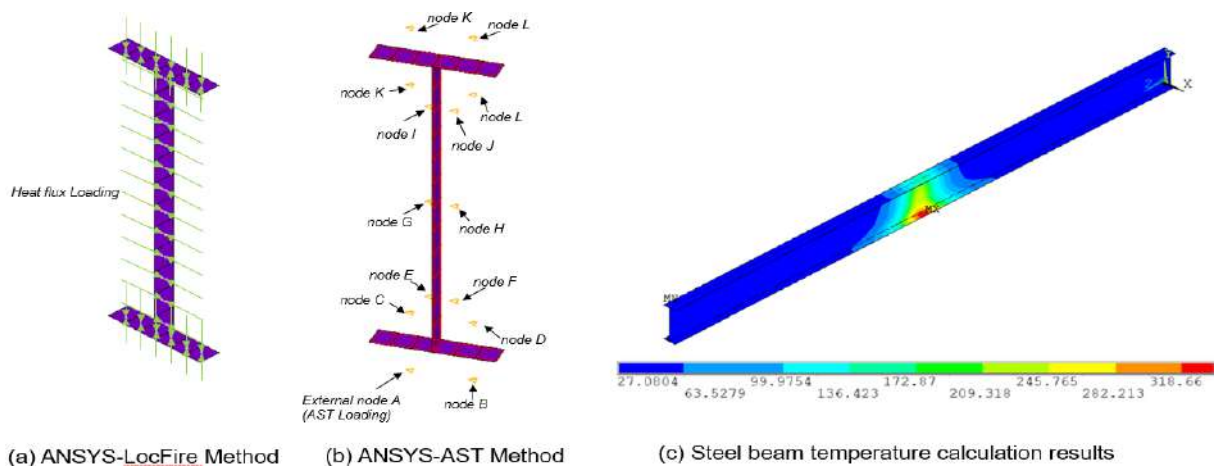


Figure 14. FEM simulation for steel beam temperature calculation

5.3 Steel temperature validation

Figure 15 depicts the time-steel temperature curves of the lower flange, web, and upper flange of the mid-section of the beam under four localized fire conditions. Upon comparison with measured values at all test points and times, it is evident that the Ansys-AST method yields better prediction results. The MAPE for the Ansys-AST method are 11.6%, 14.7%, 41.6%, and 19.5% for the four localized fire tests, respectively. During four localized fire tests, the deviation between the final predicted temperature values and the test data varies across different components. For the lower flange, the deviations are: -26 °C, 0 °C, -47 °C and 28 °C; for the web, they are 6 °C, 45 °C, 17 °C and 81 °C; and for the upper flange, they are: -6 °C, 7 °C, 74 °C and 78 °C. The MAPE of the Ansys-LocFire method's prediction values are 24.3%, 34.8%, 47%, and 44.5% for the four localized fire tests. In the lower flange, its deviations between the predictions and test

data are: 19 °C, 40 °C, 21 °C, and 48 °C; on the web, they are: 88 °C, 126 °C, 116 °C, and 134 °C; and on the upper flange, they are: 37 °C, 78 °C, 146 °C, and 82 °C. Overall, the steel temperature estimation of the Ansys-LocFire method performs well in the bottom flange but poorly in the web and top flange. It can be attributed to the approximate calculation approach employed for the heat flux of the web and upper flange.

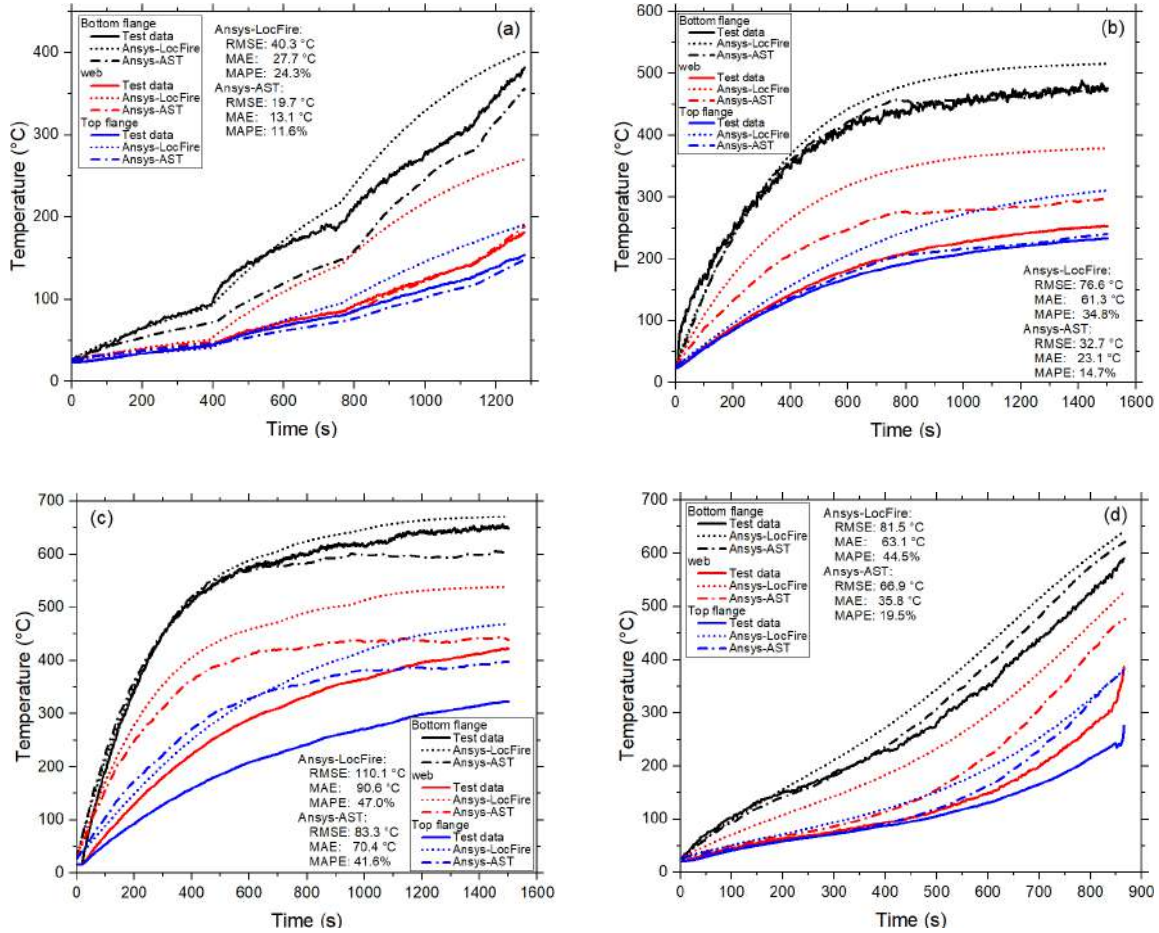


Figure 15. Temperature-time curve of steel at the mid-span section: (a) Test 1,2; (b) Test 3,4,5; (c) Test 7; (d) Test 8,9

Despite variations in working conditions, the distribution of steel beam temperature along the beam length direction exhibits a consistent trend. Due to space limitations, Figure 16 displays only the comparison between the temperature distributions calculated by the Ansys-LocFire method and the Ansys-AST method in test no.7, alongside the corresponding measured values. Compared with the test data, the MAPE of the Ansys-AST method predictions are 17.3%, 17.3% and 18.0% for the bottom flange, web and upper flange, respectively. The MAPE of the Ansys-LocFire method predictions compared to the test data are 31.1%, 31.3%, and 46.7% for the bottom flange, web, and upper flange, respectively. The Ansys-LocFire method tends to generate predictions that are excessively high near the flame and excessively low farther away from it, particularly noticeable in the upper flange.

In Figure 17, a comparative analysis is presented, showcasing the temperatures forecasted by both the Ansys-LocFire and Ansys-AST methods against the actual test values across all test points under diverse conditions. The MAPE for the Ansys-LocFire method is determined to be 23%, 23.7%, and 27.9% for the bottom flange, web, and upper flange, correspondingly. Conversely, the MAPE for the Ansys-AST method is observed to be 16%, 14.7%, and 15% for the bottom flange, web, and upper flange, respectively.

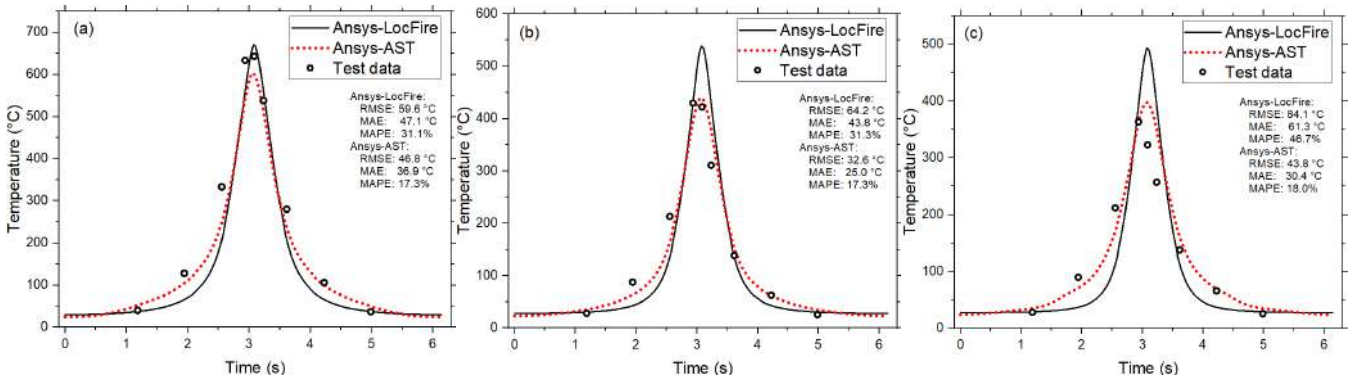


Figure 16. Steel Temperature Distribution along the beam for Test no.7: (a) bottom flange; (b) web; (c) upper flange

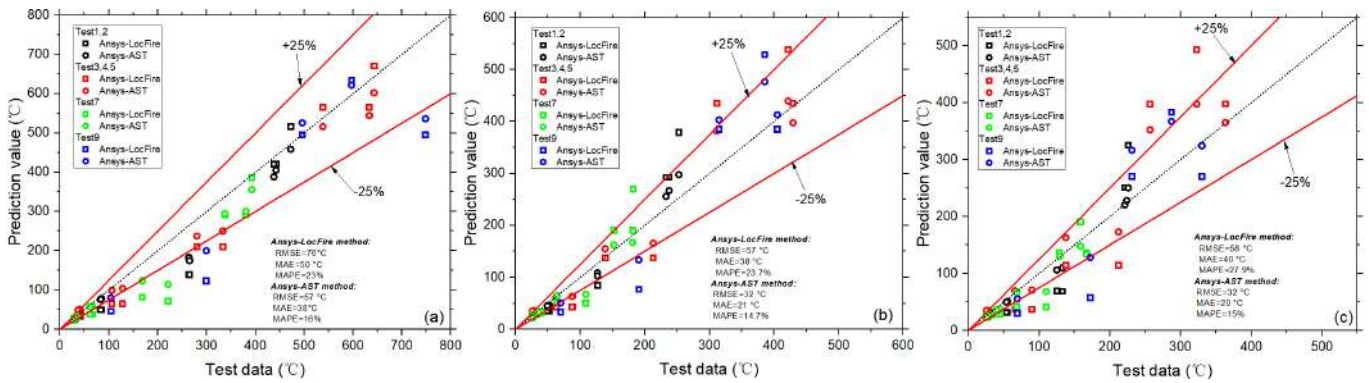


Figure 17. Steel Temperature Comparison for all test conditions: (a) bottom flange; (b) web; (c) upper flange

6. CONCLUSION

Theoretical local fire models play a pivotal role in performance-based structural fire safety design, enabling the handling of diverse design scenarios. This paper presents a pioneering approach that integrates a local fire model with an FEM code to perform comprehensive fire-structure simulations. Specifically, the application of the Ansys-LocFire method demonstrates successful prediction of steel beam temperatures under localized fire exposure. Validation studies encompass temperature development and distribution for the steel beam, both with and without a ceiling. The Mean Absolute Percentage Error (MAPE) of the Ansys-LocFire method's predicted results, compared to experimental values, remains within $\pm 25\%$ across all measured points and test conditions. Moreover, discrepancies between predicted and measured maximum steel beam temperatures are consistently less than 61°C across all test conditions.

REFERENCES

1. Choe L, Varma AH, Agarwal A, Surovek A, Fundamental behavior of steel beam-columns and columns under fire loading: experimental evaluation, *Journal of Structural Engineering*, 2011;137: 954-66.
2. Kodur VKR, Performance-based fire resistance design of concrete-filled steel columns, *Journal of Constructional Steel Research*, 1999;51: 21-36.
3. Yin YZ, Wang YC, Analysis of catenary action in steel beams using a simplified hand calculation method, Part 1: theory and validation for uniform temperature distribution, *Journal of Constructional Steel Research*, 2005;61: 183-211.
4. Usmani AS, Rotter JM, Lamont S, Sanad AM, Gillie M, Fundamental principles of structural behaviour under thermal effects, *Fire Safety Journal*, 2001;36: 721-44.

5. Zhang C, Usmani A, Heat transfer principles in thermal calculation of structures in fire, *Fire Safety Journal*, 2015;78: 85-95.
6. Jiang L, Chen S, Usmani A, Feasibility of dimensionally reduced heat transfer analysis for structural members subjected to localised fire, *Advances in Structural Engineering*, 2018;21: 1708-22.
7. Wakamatsu T, Hasemi Y, Kagiya K, Kamikawa D, Heating mechanism of unprotected steel beam installed beneath ceiling and exposed to a localized fire: verification using the real-scale experiment and effects of the smoke layer, *Fire Safety Science*, 2003: 1099-110.
8. Myllymaki J, Kokkala M, Thermal exposure to a high welded I-beam above a pool fire, *First International Workshop on Structures in Fires*, 2000: 211-26.
9. Kokkala M, Heat transfer to and ignition of ceiling by an impinging diffusion flame, VTT Research Report 586, Technical Research Centre of Finland, Espoo, Finland, 1989.
10. You HZ, Faeth GM, An investigation of fire impingement on a horizontal ceiling," NBS-GCR-79-188, U.S. Department of Commerce, Washington, DC (1979).
11. McGrattan K, Hostikka S, Floyd J, McDermott R, Vanella M, *Fire dynamics simulator user's guide*, NIST Special Publication 1019-Sixth Edition, National Institute of Standards and Technology (NIST), Gaithersburg, Maryland; 2021.
12. Zhang C, Silva JG, Weinschenk C, Kamikawa D, Hasemi Y, Simulation Methodology for coupled fire-structure analysis: modelling localized fire tests on a steel column, *Fire Technology*, 2015;52: 239-62.
13. Zhang C, Li G-Q, Wang R, Using adiabatic surface temperature for thermal calculation of steel members exposed to localized fires, *International Journal of Steel Structures*, 2013;13: 547-56.
14. Beyler CL, *Fire Hazard Calculations for Large, Open Hydrocarbon Fires*. SFPE Handbook of Fire Protection Engineering, Section 3-11, 3rd Society of Fire Protection Engineers, Maryland, USA.
15. Tondini N, Thauvoys C, Hanus F, Vassart O, Development of an analytical model to predict the radiative heat flux to a vertical element due to a localised fire, *Fire Safety Journal*, 2019;105: 227-43.
16. Ji J, Ge F, Qiu T, Experimental and theoretical research on flame emissivity and radiative heat flux from heptane pool fires, *Proceedings of the Combustion Institute*, 2021;38: 4877-85.
17. Wei J, Zhang C, A Refined Cylinder Fire Model for Thermal Radiation Calculation from Localized Fire to Exposed Horizontal Surface. *International Journal of Heat and Mass Transfer*, 2024, (uncorrected proof). <https://doi.org/10.1016/j.ijheatmasstransfer.2024.125539>.
18. Wei J, Zhang C, A Novel Fire Model for Thermal Radiation Calculation from Localized Fire to Exposed Vertical Surface. *International Journal of Thermal Sciences*, 2024 (submitted).
19. Eurocode 1: actions on structures, part 1-2: general actions: actions on structures exposed to fire. BSI, 2002.
20. Hasemi Y, Yokobayashi S, Wakamatsu T, Ptchelintsev A, "Fire Safety of Building Components Exposed to a Localized Fire—Scope and Experiments on Ceiling/Beam System Exposed to a Localized Fire," in *Proceedings from ASIAFLAM*, Kowloon, Hong Kong, pp. 351–361, (1995).
21. Zhang C, Li G-Q, Integrated Fire-Structure Simulation of a Localized Fire Test on a Ceiling Steel Beam, *Advanced Steel Construction*, 2017: 132-43.
22. ANSYS, User Manual, Version 2022 R1 ANSYS Inc., 2022.
23. Choe L, Ramesh S, Hoehler M, Seif M, Gross J, Zhang C, Bundy M, National Fire Research Laboratory Commissioning Project: Testing Steel Beams under Localized Fire Exposure, NIST Technical Note 1983, Fire Research Division Engineering Laboratory, NIST, 2018.
24. Zhang C, Yu H-X, Choe L, Gross J, Li G-H, Simulating the fire-thermal-structural behavior in a localized fire test on a bare steel beam, *Engineering Structures*, 2018;16 3: 61-70.

ANALYZING THE IMPACT OF FIRE INTENSITY AND BRIDGE GEOMETRICAL CHARACTERISTICS ON THE THERMO-STRUCTURAL RESPONSE OF BRIDGE GIRDERS DURING TANKER FIRE INCIDENTS

Augusto M. Gil¹, Venkatesh K. R. Kodur²

ABSTRACT

Bridge fires, like the recent incidents on the I-95 overpass in Philadelphia and the I-10 expressway in Los Angeles, both in 2023, demonstrate the vulnerability of bridge structures to high temperature exposure. These fires, often fueled by hydrocarbons, behave differently from building fires, posing serious challenge to the stability and integrity of structural elements. Unlike building codes, current bridge design codes and standards lack specific fire protection provisions for bridges structures. To address this gap, this study employs computational fluid dynamics (CFD) simulations with the Fire Dynamics Simulator (FDS) to realistically model bridge fires. While previous research focused on steel bridges, this study investigates parameters affecting fire exposure in concrete bridges, such as girder depth and spacing, span and clearance heights, as well as fire intensity in terms of burning area. By integrating FDS simulations with finite element analysis, the thermal response of concrete bridge girders is traced and its influence on the structural response is analyzed. The results clearly demonstrate that bridge structures are exposed to significant thermal gradients during severe fire incidents, and several factors related to the bridge geometry and fire exposure conditions can contribute to this. This behaviour is reflected on the difference between temperatures measured at the midspan cross-section and at a cross-section near the support locations. These differences can determine the failure mode and time of bridge girders and should be taken into consideration to properly assess their fire resistance.

Keywords: Bridge fires; fire dynamics modelling; finite element modelling; parametric studies

1 INTRODUCTION

Recent bridge fire incidents have shown the potential destructive impact of fires on bridge structures. Notable recent cases include the collapse of an I-95 (interstate express way) overpass near Philadelphia in June 2023 [1], and the large damage to an elevated section of I-10 in Los Angeles in November 2023 [2], which are among the most travelled expressways in the United States. The large damage to these bridges is due to lack of fire protection measures, mainly fire resistance, which are not required for bridge structures as per current codes and standards [3]. Besides, current fire resistance provisions developed for structural members in buildings cannot be applied to bridge structures due to fundamental differences in the structural configuration, material characteristics and fire exposure conditions.

Some key differences between building and bridge fire scenarios are the fuel source and resulting fire severity in each scenario. While building fires are based on the combustion of cellulose-based materials, bridge fires typically involve burning of hydrocarbon-based fuels (resulting from collision of oil tankers), which can lead

¹ Ph.D. Candidate, Department of Civil and Environmental Engineering, Michigan State University, East Lansing, MI, United States
e-mail: masierog@msu.edu, ORCID: <https://orcid.org/0000-0001-6167-7638>

² University Distinguished Professor, Department of Civil and Environmental Engineering, Michigan State University, East Lansing, MI, United States
e-mail: kodur@egr.msu.edu, ORCID: <https://orcid.org/0000-0003-2058-2725>

to a faster rise of temperatures as well as higher peak temperatures during a fire incident. Another important difference is the heat progression on the surface of the member. Unlike buildings, bridges are open spaces and structural members experience a non-uniform rise in temperatures on their surface as a result of the fire dynamics. Previous studies have shown that a significant thermal gradient can be developed in all directions of bridge structures during a fire event, especially in long-span bridges [4-5]. Such gradients can vary depending on the geometric characteristics of the bridge, girder depth, spacing between girders, and span length, as hot gases and smoke gets entrapped between the girders and lead to concentration of heat.

Nominal temperature-time relations, such as the ones presented in Figure 1 (a), are commonly used to evaluate the fire resistance of building members in closed furnaces. While standardized curves with higher severity have been developed to evaluate the fire resistance of structural members exposed to hydrocarbon fires, they cannot represent accurately the thermal gradients developed during bridge fires and can lead to non-realistic fire scenario. An alternative to these standardized fire curves is the use of computational fluid dynamics (CFD) simulations to predict temperatures on the surface of structural members in both space and temporal domains based on fire-driven fluid flow [6]. CFD models are developed on the principles of fire dynamics and energy conservation equations to formulate thermal balance of a meshed volume. The Fire Dynamics Simulator (FDS) developed by the National Institute of Standards and Technology (NIST) is an open-source software that is commonly used for modelling fire dynamics and predict the development of fires [7].

Previous studies have used fire simulations to model bridge fires and combined its results with finite element analysis to evaluate the fire resistance of bridge members more realistically. Most of these studies have focused on steel bridge girders or cable-stayed bridges, considering specific scenarios based on assumptions from real fire incidents [8-10]. In these fire models, fire intensity is specified in terms of heat release rate per unit area (HRRPUA), so the total heat released is dependent on the specified burning area [11]. Figure 1 (b) presents the HRRPUA used in some previous studies that modelled bridge fires, through which it is possible to observe that common values ranged around 2,500 kW/m² [12-18]. Alos-Moya et al. [5] investigated the structural response of a steel bridge under various HRRPUA levels to find the level that resulted in a fire resistance time similar to what was observed during a real fire incident in that bridge. They also examined different discretization sizes for transferring temperatures from FDS to finite element models, focusing solely on steel girders. On another study, Peris-Sayol et al. [12] identified factors such as fire location, vertical clearance, and wind effects that influence bridge fire behaviour. Other studies have used similar ranges of HRRPUA for evaluating the behaviour of bridges under specific conditions.

While previous studies have provided useful information for fire modelling of steel bridges, still limited data is available on the effect the bridge geometrical characteristics, specifically for concrete bridges [19-20]. This paper aims to address some of these factors, analysing the impact of several varying factors from tanker fires on the fire exposure of bridge girders. Such information can form the basis to the development of standard fire exposure conditions to be used in the fire evaluation of bridge members. An FDS model will be used to evaluate the effect of the following parameters on the fire response: girder depth and spacing, bridge clearance and span length, as well as the burning area and resulting fire intensity.

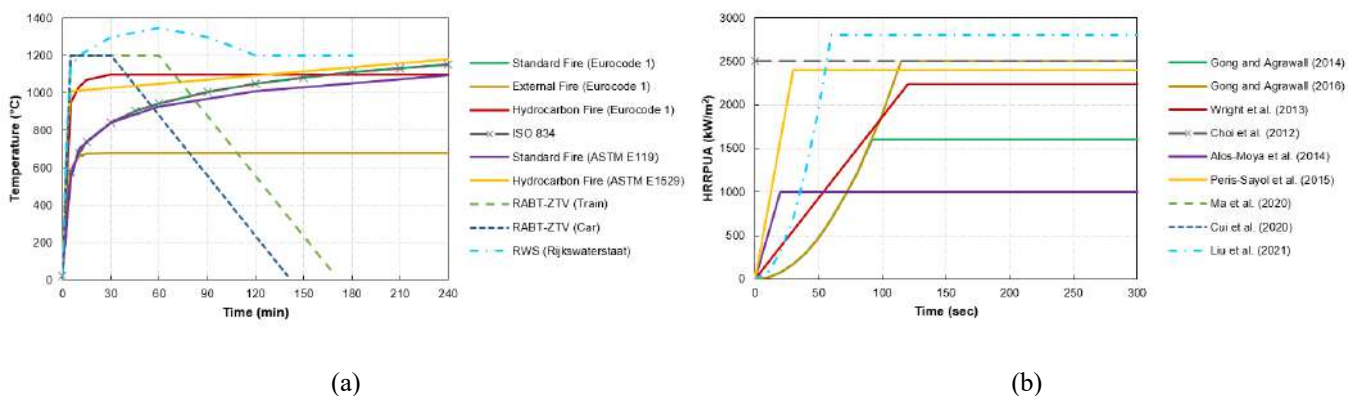


Figure 1. (a) Temperature-time curves used in standard furnace testing; (b) HRRPUA-time curves used in different studies

2 METHODOLOGY

A hypothetical bridge fire scenario was modelled in the FDS to evaluate the progression of fire temperatures along bridge members under varying fire conditions. The results from these simulations are used as input in a finite element-based model developed in ABAQUS to evaluate the fire response of prestressed concrete bridge girders. Details on the development of both numerical models are presented in the following sections.

2.1 Fire Dynamics Model

The FDS model consists in a control volume with defined boundary conditions, which is discretized to delineate the analysis area. The control volume must be chosen to adequately represent the volume influenced by the fire and at the same time be small enough to allow the model to run within a reasonable computing time. In this study, the control volume includes the entire bridge structure, including its girders, deck, parapets, and abutment walls. The volume is discretized in approximately 300,000 parallelepiped cells of 0.20x0.20x0.20 m. The meshed boundaries are modelled as open vents to represent a fire in an open space. The size of the control volume varies depending on the bridge geometry (span length, clear vertical spacing, and width), which will on the studied variable in each model.

Within this volume, bridge components are modelled as obstructions, affecting the flow of flames and gases. This included girders, deck, parapets and abutment walls, as illustrated in Figure 2 (a). FDS limits the geometry of the model components to parallelepipeds, which means that none of the components can be modelled diagonally. Thus, girders are considered to have rectangular sections in the FDS model based on the bottom flange width and height. A layered surface composed by concrete was assigned to all bridge components (obstructions) in the model with thermal properties of concrete from the software library.

A fire source and a combustion model are specified within the model to initiate the fire simulation. In FDS, this is typically specified by defining its characteristics such as size, location, intensity, and duration, often represented by creating an obstruction volume within the control volume. Fire intensity properties are then assigned to the burning surfaces of this volume in terms of HRRPUA and ramp-up time. Currently there is no standardized procedure or guidelines for modelling bridge fires, which results in varying heating procedures adopted by different authors. According to the NFPA 502 [18] report, the HRR of a tanker fire ranges between 200-300 MW. However, in FDS fire intensity is specified in HRRPUA, which means that the resultant HRR can vary depending on the burning area defined in the model. As part of this study, two burning areas were considered as part of the variables of the parametric studies. The two selected burning areas are 30 m² and 80 m², which represent the truck bed area and an additional area of fuel spillage on the road, respectively. The burning area is considered to be 1 m above the ground level to represent the tanker height.

A HRRPUA of 2,500 kW/m² was selected as the fire intensity in order to result in a total HRR of 75 MW and 200 MW for the selected burning areas. A t-squared ramp-up time of 60 seconds along with the selected HRRPUA were chosen based on studies in the literature that used values in the same range. A decay phase was not specified in this study, as the high fuel volume in a tanker is enough for burning for hours and would probably be extinguished before being totally consumed. The FDS model also necessitates the specification of a reaction mechanism to simulate the combustion behaviour of the fuel being studied. In this case, the FDS6 N-Octane reaction was chosen as it closely aligns with the chemical composition and burning characteristics of gasoline, ensuring a realistic representation of the fire dynamics within the simulation.

Finally, measuring devices (sensors) are incorporated at specific locations to record analysis outputs, such as temperatures. The Solid-Phase Device is utilized for recording the Adiabatic Surface Temperature at specific locations on the surface of bridge components. These measuring points included the bottom flange of girders and the bottom of the deck across both transversal and longitudinal directions of the bridge. Notably, these measurement lines are carefully positioned to intersect the burning area, ensuring the worst-case fire scenario is adequately captured. Figure 2 (b) illustrates the distribution of data collection points (yellow dots) across the bridge. Given the high complexity and computational cost of

mapping element or nodal temperatures to be input in the thermal/structural (ABAQUS) model, multiple devices are positioned along the girder's length in the FDS model. These devices, placed at one-meter intervals, facilitate the application of temperatures along the girder surface in the subsequent ABAQUS model.

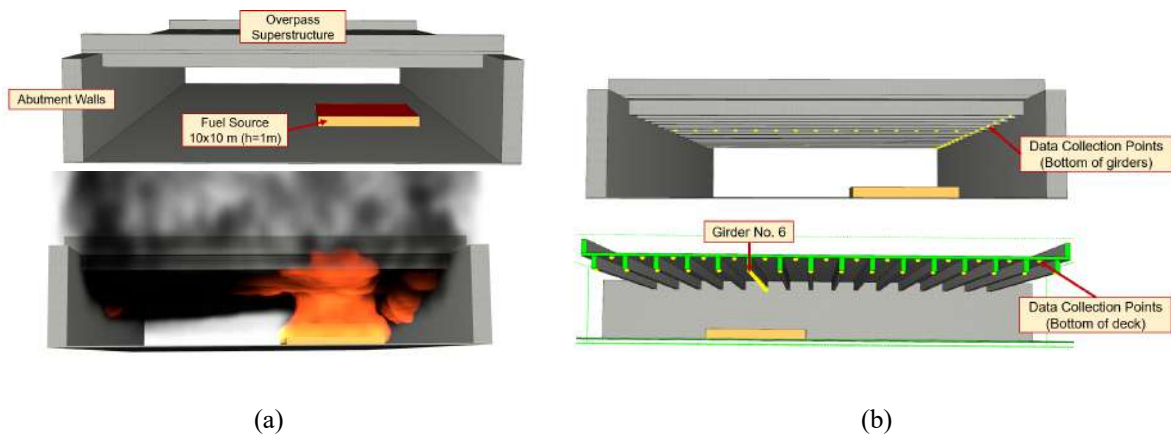


Figure 2. (a) Bridge girder model in FDS; (b) Data collection points

2.2 Structural Fire Model

A finite element model developed in ABAQUS is used to trace the thermal and structural response of prestressed concrete bridge girders. This model is capable of tracing the behavior of members under combined effects of mechanical and thermal loads generated by the FDS model. The analysis is carried out at incrementing time steps. At each time step, the model performs: (1) computation of the transient field temperature from the FDS model; (2) heat transfer analysis to evaluate temperature distribution within the member; (3) calculation of stresses and strains due to combined effects of thermal and mechanical loading; and then, (4) calculation of deflections, flexural and shear strengths. The model considers temperature-dependent thermal and mechanical properties of steel and concrete and is capable of accounting for varying thermal and structural loading conditions. More details on the specimen geometry, including discretization, material models, and failure criteria can be found elsewhere [21].

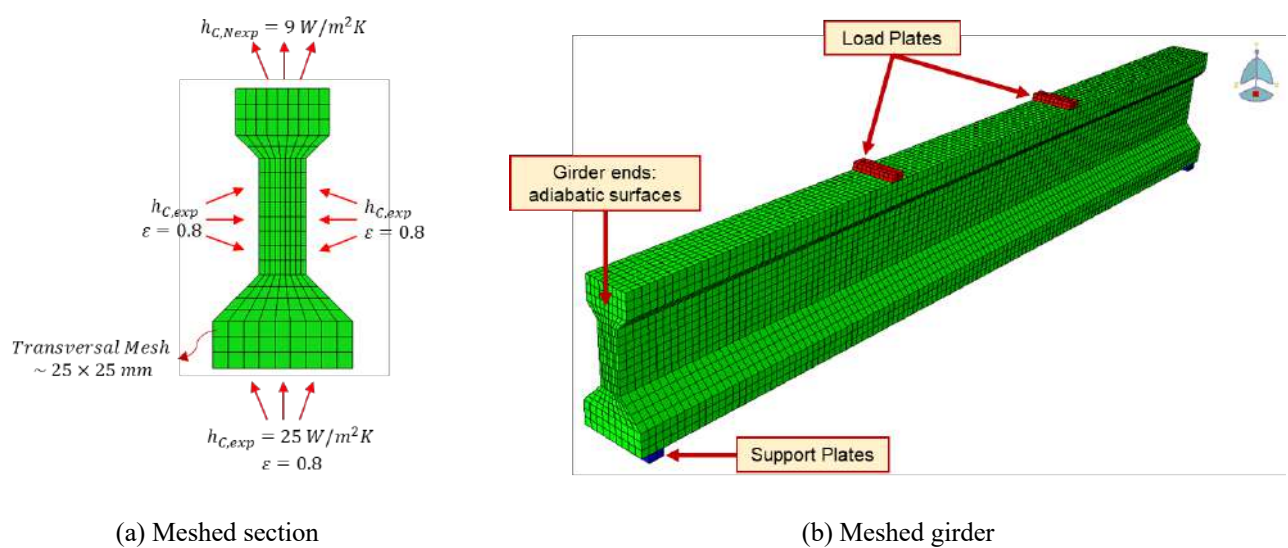


Figure 3. Discretization of a prestressed concrete girder in the ABAQUS model: (a) Cross-section; (b) Girder

2.3 Key Variables

As part of this study, five influencing parameters related to the bridge geometry (girder depth and spacing between girders), bridge geometry (span length and clearance height), and fuel source (in terms of burning area). Table 1 presents the range of variables for each studied parameter. In terms of girder depth, two standard AASHTO sections were selected (Type I and Type IV) in order to investigate the level of influence this parameter has to keep entrapped hot gases and smoke between the girders and increase its exposure to elevated temperatures. In addition, two girder spacings (1.5 m and 3.0 m) were investigated, as they can also contribute to heat propagation underneath the girders. Since these parameters are related to each other, two bridge structures were simulated in FDS: smaller girder (Type I) with smaller spacing (1.5 m); bigger girder (Type IV) with larger spacing (3.0 m). In relation to the bridge geometry, two span lengths (12 and 24 m) and clearance heights (5.0 m and 8.0 m) were evaluated for each combination of girder type/spacing. In relation to the fuel source, the selected fire intensity (2,500 kW/m²) was simulating considering three different fuel spillage areas varying from 30 to 120 m², which generated a heat release rate between 75 and 300 MW, respectively.

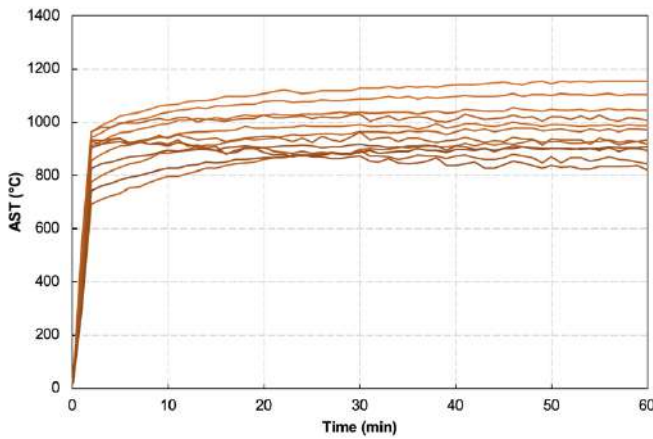
Table 1. Key variables studied as part of parametric studies

Parameter		Variables
Girder geometry	Girder depth (D)	700 mm (AASHTO Type I) 1,400 mm (AASHTO Type IV)
	Girder spacing (S)	1.5 m (shorter girder spacing) 3.0 m (larger girder spacing)
Bridge geometry	Bridge length (L)	12 m (shorter span) 24 m (longer span)
	Bridge height (H)	5.00 m (minimum clearance) 8.00 m (intermediate clearance)
Fuel source	Spillage area (A)	30 m ² (tanker area) – 75 MW 80 m ² (tanker + spill) – 200 MW

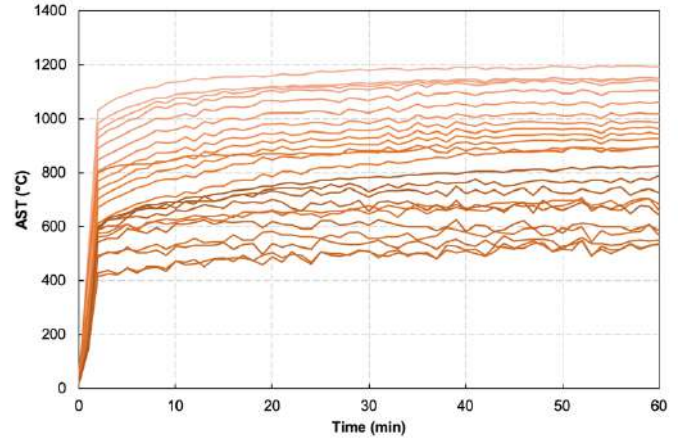
3 RESULTS

3.1 Fire Response

Results from the FDS model include the adiabatic surface temperatures (AST) measured at different points along the length of the bridge below girder and the deck close to the fire source. Figure 4 presents the AST recorded as a function of time from two analysed scenarios, that were exposed to the same fire intensity (total HRR of 75 MW) and minimum clearance (5 m), but two different bridge designs with varying spans: a small bridge spanning 12 meters and a medium bridge spanning 24 meters. The results clearly show that higher thermal gradients are developed in the longer bridge. The difference in thermal gradients in bridges of difference (structural) sizes can be attributed to the fact that the larger bridge presents bigger volumes for heat propagation. Besides, such behaviour can be attributed to the larger girder spacing adopted in these scenarios, which also permit a faster propagation of heat. It is also possible to observe that the longer span bridge experienced slightly higher maximum temperatures compared to the small bridge. However, the average AST for all measured points throughout the bridge is higher for the smaller bridge (965°C) compared to the longer girder (856°C).



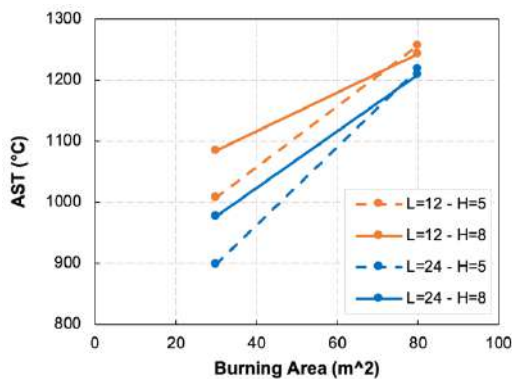
(a) Small bridge (12 m-long span)



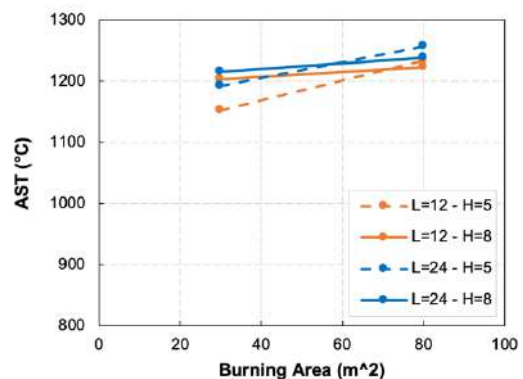
(b) Medium bridge (24 m-long span)

Figure 4. Adiabatic surface temperature measured at different along the length of the girder and the deck

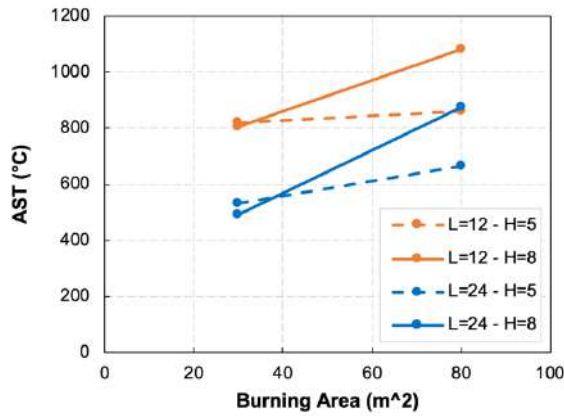
Figure 5 presents the minimum and maximum temperatures registered on the bottom of the girder and the deck for each scenario analysed in terms of burning area. The two burning areas used in the analysis were 30 m^2 and 80 m^2 , which result in a total HRR of 75 MW and 200 MW, respectively. It can be seen that the maximum temperatures recorded on the bottom of the girder (Figure 5a) were higher in the bridges with longer spans ($L=12$), as well as for the bridges with higher clearance ($H=8$). This can be explained by the fact that hot gases quickly concentrate on the space between the girders in the smaller bridge, leading to faster increase of AST when compared to the bridge with longer span. For this reason, it is not possible to observe a significant difference in the maximum temperatures recorded on the deck surface (Figure 5b). This difference is more predominant for the HRR of 75 MW, but it becomes less pronounced when the bridge is exposed to a larger burning area, and the maximum registered AST are very similar. A similar trend can be noted when analysing the minimum temperatures registered along the girder (Figure 5c), where it can be observed that a more significant gradient is developed for the bridges with longer span ($L=24$) and smaller clearance ($H=5$). A similar trend is observed in the minimum temperatures recorded on the deck surface (Figure 5d), but much less significantly. Overall, it is clear that the studied parameters can affect the development of a fire on a bridge and that it can lead to significant thermal gradients along the girder and the deck.



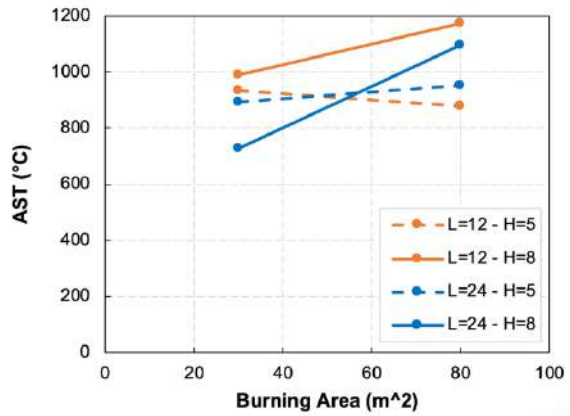
(a) Maximum Temperature - Girder



(b) Maximum Temperature - Deck



(c) Minimum Temperature - Girder

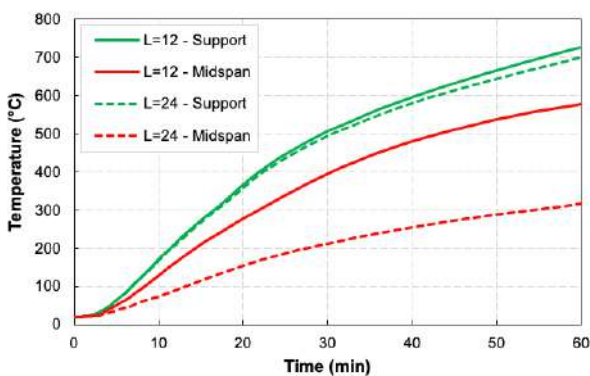


(d) Minimum Temperature - Deck

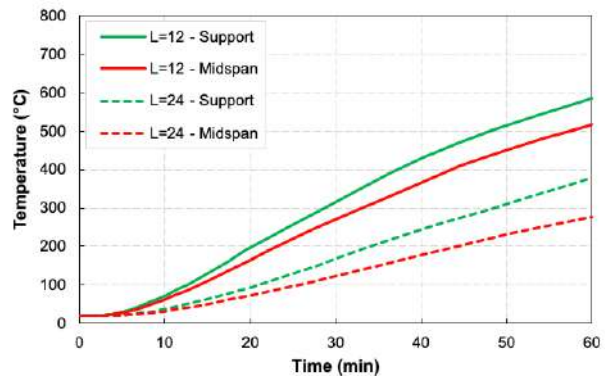
Figure 5. Maximum and minimum adiabatic surface temperature at the bottom of the deck and the girder

3.2 Thermal Response

The temperatures obtained in the fire model (FDS) were used as input in the finite element model (ABAQUS) to analyse the thermal response of bridge girders under realistic fire conditions. Figures 6a and 6b present the temperatures predicted by the model at the corner prestressed strand location and at the centre of the web of two girders from a smaller (12 m) and a larger (24 m) bridge. Both selected scenarios consisted of bridges with a clearance height of 8 m exposed to a lower fire intensity (30 m^2). These conditions were selected to be presented here due to the fact that they have produced the highest thermal gradients along the bridge in each case of bridge over its length. Based on the results presented in these graphs, it can be observed that the thermal gradient from fire exposure is reflected on the temperatures measured at different locations along the length of the girder (support and midspan locations). For instance, while the temperatures at the corner rebar (Figure 6a) were very similar for both girders at the support locations, there is a large difference between these girders at the midspan cross-section, both of them with a significant reduction when compared to the support cross-section. Temperatures at the support location are similar for both girders because they were right above the fire source, but as one of the girders was much longer, heat is dissipated to the environment and reduces the temperatures at the structural member at this location. This behaviour was also observed in the temperatures measured at the centre of the web under same conditions (Figure 6b). Results from all modelled scenarios could not be presented here due to space constraints, but a detailed analysis of all cases will be presented in a future journal publication.



(a) Corner prestressed strand



(b) mid-height of web

Figure 6. Thermal response of girders from bridges with higher clearance (8 m) exposed to a smaller burning area (30 m^2)

3.3 Structural Response

The structural response of the girders analyzed in the previous section are presented in Figures 7a and 7b in terms of flexural and shear strength degradation as a function of fire exposure time. It can be observed that in both scenarios the girders reached failure in the cross-section close to the supports before than the midspan cross-section. This is attributed to the fact that this section experienced higher temperatures in the prestressed strands due to the fact that was located right above the burning area. In addition, it can be noted that the girders experience shear failure around 8 minutes before flexural failure. A factor that may have contributed to this behaviour is related to the concentration of hot gases on the volume between girders, as explained earlier in this paper, which contributes to increase the temperatures on the web of the girders. Overall, it can be noted that the structural response of concrete bridge girders can be significantly affected by thermal gradients and temperature variations related to different bridge structures.

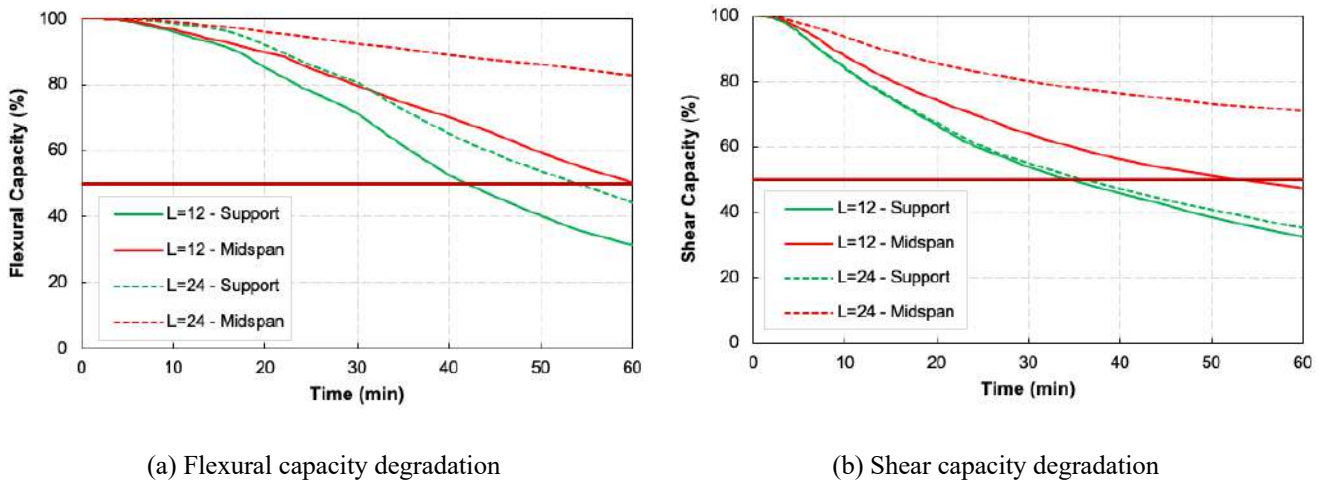


Figure 7. Capacity degradation of girders from bridges with higher clearance (8 m) exposed to a smaller burning area (30 m²)

4 CONCLUSIONS

This paper presented the development of an FDS model using PyroSim to evaluate fire scenarios in bridges. FDS was applied to investigate the influence of different bridge design parameters on the fire behaviour. Results from the fire simulations demonstrate that bridge span length and clearance height present a significant influence on the temperatures recorded on the surface of structural members. While the maximum temperatures recorded in all simulations was very similar for all the cases studied, it was observed that the minimum temperatures at the end of one hour of fire simulation had great variance in different scenarios. These differences between minimum and maximum temperatures demonstrate that a significant thermal gradient is developed on the surface of structural members exposed to open-air fires. Bridges with smaller span lengths (12 m) and higher clearance heights (8 m) experienced higher temperatures, while bridges with longer spans (24 m) and lower clearance heights (5 m) experienced higher thermal gradients. In addition to this, the effect of fire intensity was assessed in terms of burning area for a constant HRRPUA. While it was not observed significant difference in the temperatures recorded on the deck surface, it was observed that the larger burning area (80 m²) resulted in higher temperatures on the bottom of the girders compared to the smaller burning area (30 m²). This can affect the structural response of concrete girders during fire exposure. Overall, the results infer that bridge structures are exposed to significant thermal gradients during fire incidents, and several factors related to the bridge geometry and fire exposure conditions should be taken into consideration for realistic fire resistance assessment.

REFERENCES

1. Kodur, V.K.R., Gil, A.M. & Naser, M.Z., Fire-induced collapse of an I-95 overpass in Philadelphia: Causes, collapse mechanism, and mitigation strategies. *Engineering Structures* 303, 117578 (2024). <https://doi.org/10.1016/j.engstruct.2024.117578>
2. Gorman, S. & Trotta, D., Arson determined as cause of Los Angeles freeway fire, Reuters, Nov. 14, 2023. Available at: <https://www.reuters.com/world/us/los-angeles-freeway-closed-by-fire-creating-commuter-headache-2023-11-13/>
3. AASHTO LRFD Bridge Design Specifications, 9th Edition. Washington, DC: American Association of State Highway and Transportation Officials, 2020.
4. Hu, J., Usmani, A., Sanad, A. & Carvel, R. Fire resistance of composite steel & concrete highway bridges. *J Constr Steel Res* 148, 707–719 (2018). <https://doi.org/10.1016/j.jcsr.2018.06.021>
5. Alos-Moya, J., Paya-Zaforteza, I., Garlock, M.E.M., Loma-Ossorio, E., Schiffner, D. & Hospitaler, A., Analysis of a bridge failure due to fire using computational fluid dynamics and finite element models. *Engineering Structures* 68, 96-110 (2014). <https://doi.org/10.1016/j.engstruct.2014.02.022>
6. Yu, X., Jeffers, A.E., A comparison of subcycling algorithms for bridging disparities in temporal scale between the fire and solid domains. *Fire Safety Journal* 59, 55-61 (2013). <https://doi.org/10.1016/j.firesaf.2013.03.011>
7. Mc Grattan, K., Hostikka, S., McDermott, R., Floyd, J., Weinschenk, C. & Overholt, K.: Fire dynamics simulator User's guide, NIST Special Publication 1019, 6th Ed. Gaithersburg, MD, USA; 2013.
8. Gong, X. & Agrawal, A.K., Safety of Cable-Supported Bridges during Fire Hazards. *Journal of Bridge Engineering* 21 (2016). [https://doi.org/10.1061/\(ASCE\)BE.1943-5592.0000870](https://doi.org/10.1061/(ASCE)BE.1943-5592.0000870)
9. Aziz, E., Kodur, V., Glassman, J. & Garlock, M., Behavior of steel bridge girders under fire conditions. *Journal of Constructional Steel Research* 106, 11-22 (2015). <https://doi.org/10.1016/j.jcsr.2014.12.001>
10. Kodur, V.K.R. & Naser, M., Fire hazard in transportation infrastructure: Review, assessment, and mitigation strategies. *Frontiers of Structural and Civil Engineering* 15, 46-60 (2021). <https://doi.org/10.1007/s11709-020-0676-6>
11. Hu, J., Carvel, R. & Usmani, A., Bridge fires in the 21st century: A literature review. *Fire Safety Journal* 126, 103487 (2021). <https://doi.org/10.1016/j.firesaf.2021.103487>
12. Peris-Sayol, G., Paya-Zaforteza, I., Alos-Moya, J. & Hospitaler, A., Analysis of the influence of geometric, modeling and environmental parameters on the fire response of steel bridges subjected to realistic fire scenarios. *Comput Struct* 158, 333-345 (2015). <https://doi.org/10.1016/j.compstruc.2015.06.003>
13. Liu, Z., Silva, J.C.G., Huang, Q., Hasemi, Y., Huang, Y. & Guo, Z., Coupled CFD–FEM Simulation Methodology for Fire-Exposed Bridges. *Journal of Bridge Engineering* 26 (2021). [https://doi.org/10.1061/\(ASCE\)BE.1943-5592.0001770](https://doi.org/10.1061/(ASCE)BE.1943-5592.0001770)
14. Cui, C., Chen, A. & Ma, R., Stability assessment of a suspension bridge considering the tanker fire nearby steel-pylon. *Journal of Constructional Steel Research* 172, 106186 (2020). <https://doi.org/10.1016/j.jcsr.2020.106186>
15. Ma, R., Cui, C., Ma, M. & Chen A., Numerical simulation and simplified model of vehicle-induced bridge deck fire in the full-open environment considering wind effect. *Structure and Infrastructure Engineering* 17, 1698-1709 (2021). <https://doi.org/10.1080/15732479.2020.1832535>
16. Choi, J., Haj-Ali, R. & Kim, H.S., Integrated fire dynamic and thermomechanical modeling of a bridge under fire. *Structural Engineering and Mechanics* 42, 815-829 (2012). <https://doi.org/10.12989/sem.2012.42.6.815>
17. Gong, X. & Agrawal, A.K., Numerical Simulation of Fire Damage to a Long-Span Truss Bridge. *Journal of Bridge Engineering* 20 (2015). [https://doi.org/10.1061/\(ASCE\)BE.1943-5592.0000707](https://doi.org/10.1061/(ASCE)BE.1943-5592.0000707)
18. National Fire Protection Association (NFPA). NFPA 502 Standard for road tunnels, bridges, and other limited access highways. Quincy, MA, USA; 2008.
19. Kodur, V.K.R. & Gil, A.M., Fire hazard in concrete bridges: review, assessment and mitigation strategies. *Structure and Infrastructure Engineering* (2023). <https://doi.org/10.1080/15732479.2022.2152465>
20. Kodur, V.K.R. & Naser, M.Z., Importance factor for design of bridges against fire hazard. *Engineering Structures* 54, 207-220 (2013). <https://doi.org/10.1016/j.engstruct.2013.03.048>
21. Gil, A. & Kodur, V.K.R., Evaluating Shear Response of UHPC Bridge Girders Exposed to Fire. *Fire Technol* (2023). <https://doi.org/10.1007/s10694-023-01506-4>

APPLICATION OF COST-BENEFIT ANALYSIS METHODOLOGY FOR FIRE SAFETY MEASURES IN STRUCTURAL FIRE ENGINEERING

Andrea Lucherini¹, Shuna Ni², David Unobe³, Thomas Gernay⁴, Ranjit Kumar Chaudhary⁵, Mengying Peng⁶, Ruben Van Coile⁷

ABSTRACT

In fire safety engineering, cost-benefit analysis offers a systematic approach to determining whether the anticipated benefits of a fire safety measure justify its costs. Nonetheless, significant disparities persist in the methodologies employed for cost-benefit analysis, alongside a lack of quantitative data concerning the costs and economic impact of fire protection in buildings. In a recent research project, a reference methodology was suggested, based on the concept of Present Net Value (PNV) assessment and a combination of specialized construction database, fire statistics, and numerical modelling for estimation of the cost components. This study presents the application of this methodology to a specific case study related to structural fire engineering. The case study illustrates the implementation of the methodology to a nine-story office building, as well as data gathering, examination of fire statistics, and loss estimation, while it also demonstrates how the methodology aids decision-making when evaluating multiple design alternatives. The cost-benefit analysis considers various thicknesses of Sprayed Fire Resistive Material (SFRM) applied to the building steel gravity frames corresponding to 1-hour, 2-hour, and 3-hour of fire protection. For all cases, the estimated benefit of the investment in fire protection on the steel members exceeds the cost. For the specific case study, the use of a 3-hour fire rated thickness is found as providing the highest benefit, and the sensitivity analysis confirms the robustness of the investment recommendation.

Keywords: Fire safety; cost-benefit analysis; fire protection; fire statistics; structural fire engineering.

1 INTRODUCTION

Fires in buildings can lead to costly damages as well as loss of lives and injuries. Installed to protect buildings from fires and to limit the damage from such outbreaks, fire safety measures are common features in buildings. However, it is important to understand the benefits they bring to the building safety. An initial consideration is ensuring that the residual risk remains acceptable. While every design carries residual fire

¹ PhD, Senior Researcher, Slovenian National Building and Civil Engineering Institute (ZAG), Slovenia
e-mail: andrea.lucherini@zag.si, ORCID: <https://orcid.org/0000-0001-8738-1018>

² PhD, Assistant Professor, University of Maryland, College Park, USA
e-mail: shunani@umd.edu, ORCID: <https://orcid.org/0000-0002-8795-176X>

³ PhD, Assistant Professor, Schreiner University, Kerrville, USA
e-mail: dunobe@schreiner.edu, ORCID: <https://orcid.org/0000-0001-7145-5027>

⁴ PhD, Assistant Professor, Johns Hopkins University, Baltimore, USA
e-mail: tgernay@jhu.edu, ORCID: <https://orcid.org/0000-0002-3511-9226>

⁵ PhD, Ghent University, Belgium
e-mail: ranjitektumar.chaudhary@ugent.be, ORCID: <https://orcid.org/0000-0002-1104-5859>

⁶ MSc, PhD Student, Ghent University, Belgium
e-mail: mengying.peng@ugent.be, ORCID: <https://orcid.org/0009-0000-8199-0939>

⁷ PhD, Professor, Ghent University, Belgium
e-mail: ruben.vancoile@ugent.be, ORCID: <https://orcid.org/0000-0002-9715-6786>

risk, it must be mitigated to a level deemed acceptable by decision-makers [1]. Determining this acceptability does not solely rely on understanding the costs and benefits of fire protection measures, but also on assessing the perception of exposure. This pertains to whether decision-makers can tolerate the likelihood of the risk materialising, particularly concerning low-probability-high-consequence events [1]. Once this tolerability criterion is satisfied, the discussion shifts to whether further risk reduction is necessary, and if additional safety systems can be incorporated into designs. However, these investments come at a cost, and as safety levels increase (e.g., through improved structural reliability), the marginal benefits decrease [1-2]. Therefore, a method is required to evaluate the cost-effectiveness of fire protection investments.

To understand their value, *Cost-Benefit Analysis (CBA)* detailing the costs and benefits of the systems provides a systematic method to assess whether the projected benefits from a fire safety measure outweigh its costs [2]. CBA measures the usefulness of the investment, typically quantified in monetary terms, though it could be assessed in other terms like environmental impact. On one side, the investment incurs a monetary cost, including maintenance. On the other side, a monetary value is assigned to the net benefit gained from the fire safety investment, usually in terms of avoided losses. After discounting appropriately, these costs are compared, aiding decision-makers in identifying the design that optimizes the building's lifetime utility. It is crucial to consider the perspective of the decision-maker in this process. Code-makers and legislators have different goals compared to private owners. Code-makers assess whether increased fire safety measures for a class of buildings lead to an overall increase in societal welfare, considering an assumed tolerable residual fire risk in society. Private owners, however, focus on their return on investment if they invest beyond societal requirements. These differing viewpoints result in variations in how certain costs, for instance insurance expenses, are viewed [3-4].

Carrying out such an analysis requires methods for estimating both the cost of the fire safety measures and the losses caused by fires. Currently, different approaches are discussed in literature [2] and applied in the fire safety context [5-6]. Despite considerable interest, a clearly established methodology for conducting CBA in fire safety engineering is lacking [7]. It is unclear which approach should be favoured and why, how cost-effectiveness is evaluated, which costs are considered, and how the preferred design solution is defined. In addition, there is a lack of quantitative data on the costs and economic impact of fire safety measures in buildings, uncertainties surrounding fire frequency and severity, and complexities in quantifying the indirect consequences of fire events, which hinder objective decision-making [4].

In this context, the authors conducted a research project supported by the Fire Protection Research Foundation (research affiliate of NFPA). The aim of the research was to examine contemporary methods for estimating costs and losses resulting from fires, and to evaluate cost-benefit analyses. Subsequently, based on a critical literature review, a reference methodology for conducting Cost-Benefit Analyses (CBA) of fire protection measures in buildings was developed [4]. This paper outlines the application of this CBA methodology for a case study relevant for structural fire safety engineering. The case studies encompass the evaluation of the net benefit associated with passive fire protection on steel framing members in a multi-story office building.

2 METHODOLOGY FOR COST-BENEFIT ASSESSMENT

The proposed methodology for cost-benefit analysis of fire protection based on *Present Net Value (PNV)* evaluation combines specialized construction database, fire statistics, and numerical modelling [4, 8, 9, 10]. The methodology clarifies the minimum requirements for assessing cost-effectiveness, and highlights that only a PNV evaluation can be used to compare design alternatives. First, the fire protection cost estimation is performed, including selecting the building category from a list of updated building categories, computing the cost of the entire building and the cost of installation and maintenance of fire protection using construction databases, and computing multipliers, representative of buildings in the selected category. Then, the losses caused by fires are computed based on the definition of the fire hazard and its probability, followed by the estimation of both the direct (material and human) and indirect losses. The proposed methodology is illustrated in the flowchart in Figure 1.

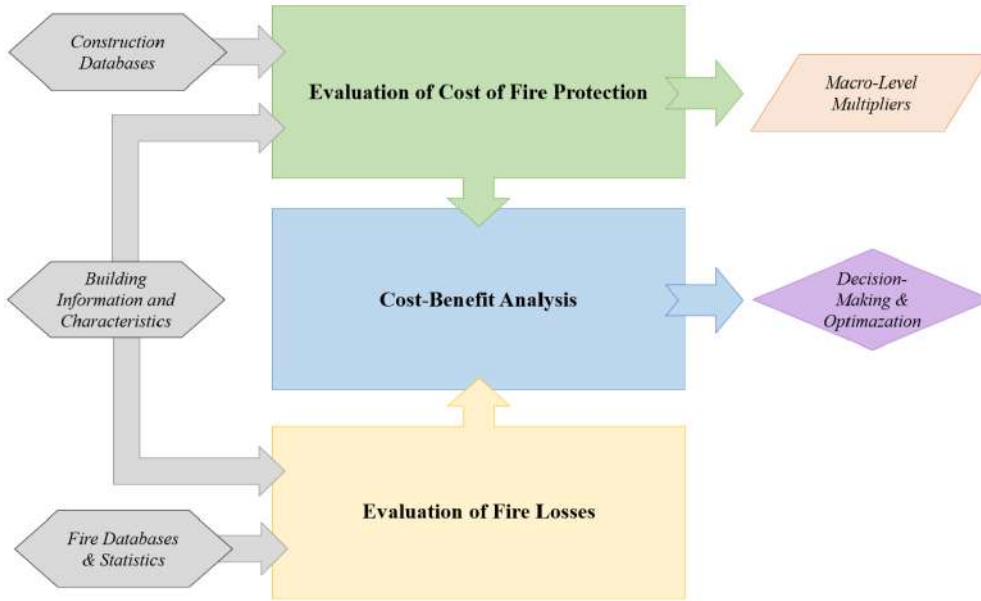


Figure 1. Flowchart of the methodology to assess the cost and benefit of fire protection in buildings

When comparing different options in terms of fire protection measures, the objective is to determine the design with the highest lifetime utility [11]. The lifetime utility of an investment is conceptually represented by equation (1), where Z is the total (net) utility, B is the benefit derived from the safety feature's existence, corresponding with the avoidance of the (expected) fire damage in the reference state absent of the additional safety investment, C is the cost of construction or implementation (including maintenance); A is the obsolescence cost, and D is the direct and indirect costs in case of failure.

$$Z = B - C - A - D \quad (1)$$

Since the scope is focused on the costs and benefits of the safety measure (as opposed to evaluating these for the entire structure), the terms in equation (1) can be simplified in equation (2) and equation (3), where C_{dd} and C_{id} are the PNV for the direct and indirect losses, respectively (with the subscript o and p refer to the original configuration and the proposed configuration), C_I is the PNV of the investment costs, C_M is the PNV of the maintenance costs, and C_A is the PNV cost resulting from building obsolescence.

$$B - D = (C_{id} + C_{dd})_o - (C_{id} + C_{dd})_p \quad (2)$$

$$C + A = C_I + C_M + C_A \quad (3)$$

These terms also allow the evaluation of a *Cost-Benefit Ratio (CBR)*, $(C+A)/(B-D)$, or *Benefit-Cost Ratio (BCR)*, $(B-D)/(C+A)$. While such terms are frequently reported, they only allow for guiding decisions on a single design alternative. Such ratios do not allow comparing multiple alternatives, and thus the lifetime utility or PNV evaluation has been recommended by the authors [4].

Cost evaluation involves aggregating the total expenses for materials, labour, and equipment necessary for installing and maintaining the considered fire protection systems. These costs are appraised using the RSMMeans database [12], which utilises data representative of the USA market. Loss evaluation encompasses both direct and indirect losses. Direct losses pertain to the “damage caused to a building, its contents and occupants during the course of a fire” [7], comprising both material (structural and non-structural elements, along with contents) and human losses (civilian and firefighter fatalities and injuries). Indirect losses are defined as the “costs associated with a fire after it is extinguished” [7]. Examples include expenses related to the unavailability or loss of critical infrastructure or items of unique value, environmental damage and pollution/waste, losses incurred due to business interruption, and cascading effects on suppliers or clients of an affected company [4]. As various scenarios lead to different losses, these losses are weighted based on their likelihood of occurrence.

Assessing fire-related losses is a complex task. In this regard, the methodology relies on a blend of statistical information and predictive modelling. Where reliable data are accessible, the efficacy of a fire protection system can be gauged by contrasting fire loss data from buildings with and without such systems (yet otherwise similar). However, such detailed data may not always be available. In instances where fire loss data lack the requisite granularity to distinguish between similar buildings equipped with different fire protection systems, predictive simulations are employed alongside statistical data.

The methodology is usually applied (also in this study) from a societal viewpoint regarding costs and benefits. Consequently, the aim is to evaluate which fire protection standards bring most benefits to society, which can inform evolution of codes and specifications. Cost elements involving the redistribution of funds within society (e.g., the impact of implementing safety measures on insurance premiums) can thus be disregarded. These studies begin with the current level of fire protection within society, enabling the use of fire statistics collected from real fires. Within the extended research project [4], a series of illustrative case studies have been presented to provide practical examples for the application of the presented cost-benefit methodology. The case studies rely on several assumptions and simplifications, and the input parameters are evaluated using statistics, existing data, numerical simulations, and/or expert judgment. The calculations are completed in JupyterLab [13] (Python) scripts, which are available through the project website.

3 CASE STUDY: PASSIVE FIRE PROTECTION ON STEEL FRAMING MEMBERS IN A MULTI-STORY OFFICE BUILDING

3.1 Case study description

The described illustrative case study applies the presented prototype methodology for the cost-benefit evaluation of the passive fire protection for steel moment-frame commercial professional services buildings (COM4 occupancy class - commercial building, professional/technical/business services [14]). The assessment is done considering a combination of statistical data and numerical simulations using the structural fire engineering software SAFIR [15]. These simulations supplement fire loss statistics to estimate the impact of different fire safety alternatives. This is needed due to the insufficient granularity of fire loss statistics in distinguishing between buildings with varying fire safety measures. These simulations help estimate the expected structural damage levels depending on the implemented fire safety measures, with subsequent loss calculations derived from these damage assessments.

The building prototype is a nine-story steel-concrete composite building with a floor plan area of 2,090 m² for a total floor area of 18,810 m². The building design is based on the FEMA/SAC project for the Boston area post-Northridge [16]. The steel members of the interior gravity frames of the building (beams and columns) are protected with Sprayed Fire Resistive Material (SFRM). The evaluation considers different thicknesses of SFRM corresponding to 1-hour, 2-hour, and 3-hour of protection from qualified UL assemblies.

3.2 Input parameters

Cost estimates, sourced from the RSMeans database [12], are detailed in Table 1, with additional information provided on macro-level cost multipliers for the SFRM application. The reconstruction cost is the combined cost of demolition, disposal and (renewed) construction. Notably, maintenance costs for the SFRM are not considered in this analysis.

As regards to the loss assessment, the fire risk parameters outlined in Table 2 are adopted. The assessment of fatality and injury risk is conducted utilizing the concepts of Value of Statistical Life (VSL) and Value of Statistical Injury (VSI) methodology [4]. Fire frequency is aligned with the reported fires, while non-reported fires are presumed to cause minimal losses. The analysis does not incorporate the potential impact of early fire suppression by occupants or emergency services, leading to an overestimation of the frequency of structurally significant fires. Consequently, from this standpoint, the case study presents an upper limit for evaluating the cost-effectiveness of investments in passive fire protection measures.

Table 1. Cost parameters

Parameter	Value	Cost multiplier
Construction cost	1,674 USD/m ²	
Demolition cost	59.82 USD/m ²	
Disposal cost	0.145 USD/m ²	
Re-construction cost	1,734 USD/m ²	
Cost of SFRM – fire resistance rating 1 hour	13.7 USD/m ²	0.82%
Cost of SFRM – fire resistance rating 2 hour	23.8 USD/m ²	1.42%
Cost of SFRM – fire resistance rating 3 hour	41.0 USD/m ²	2.45%

The fatality and injury rates shown in Table 2 and used in the subsequent cost-benefit analysis are obtained from the published sources listed. These values are from recent data collected on both the civilian and firefighter casualties and injuries from fires across the United States. The property loss areas are obtained from Manes and Rush [17], which is based on 2014 USA fire statistics. In accordance with the Federal Emergency Management Agency (FEMA), the replacement cost for the contents of a commercial office building is valued at 100% of the construction cost of the property [21]. For office buildings, the indirect loss was estimated as 25% of the direct loss [22], and this indirect loss value is added to the total property loss to obtain the total monetary losses from a fire incident. A discount rate of 3% is adopted, based on [23]. Obsolescence is neglected (i.e., an obsolescence rate of 0% is adopted).

Table 2. Parameters for estimating the benefits of fire protection (i.e., fire risk parameters)

Parameter	Value	Reference
Fire frequency (reported fires)	0.00423 per year	[17]
Civilian fatality rate	0.89 per 1,000 reported fires	[18]
Civilian injury rate	1.4 per 100 reported fires	[18]
Firefighter fireground fatality rate	6.9 per 100,000 reported fires	[19]
Firefighter response fatality rate	6.3 per 100,000 reported fires	[19]
Firefighter fireground injury rate	1.62 per 100 reported fires	[20]
Firefighter response injury rate	0.37 per 100 reported fires	[20]
Average damage area – no structural failure	83.5 m ²	assumption (compartment)
Average damage area – structural failure	18,810 m ²	assumption (whole building)
Content loss (% of total construction costs)	100%	[21]
Indirect loss (% of direct costs)	25%	[22]
Effect of structural failure on casualties	1 firefighter fireground fatality 4 firefighter fireground injuries no effect on civilians	assumption

The event tree illustrated in Figure 2 is considered to evaluate the different scenarios associated with the three thickness of SFRM. For each design, the event tree defines two scenarios: (i) “no structural failure”, and (ii) “structural failure”. The probability of each scenario is evaluated from numerical simulations of the thermal-structural response. The outcomes for each scenario are evaluated based on the statistics and assumptions outlined in Table 2. Specifically, the average fire-related losses are highly dependent on the occurrence of significant structural failure in a frame member, as such failure could lead to breaches in

compartmentation and extensive structural damage beyond the compartment of fire origin. It is assumed that if the structural frame withstands the fire without collapsing, losses remain confined to the compartment of fire origin, whereas if the frame collapses during the fire, the entire building is deemed lost. Additionally, it is reasonable to anticipate that structural failure could impact fatalities and injuries. Instances of fire-induced structural failures are fortunately rare, resulting in a lack of available data. In this analysis, it is assumed that building failure leads on average to one fatality and four injuries for firefighters on the fireground, while civilian casualties are presumed unaffected, assuming evacuation is completed prior to collapse. The probabilities associated with each branch of the event tree are derived from numerical simulations, as detailed in the subsequent section. Risk assessment for a design then incorporates both the consequences of each scenario and their associated probabilities within the framework of PNV evaluation.

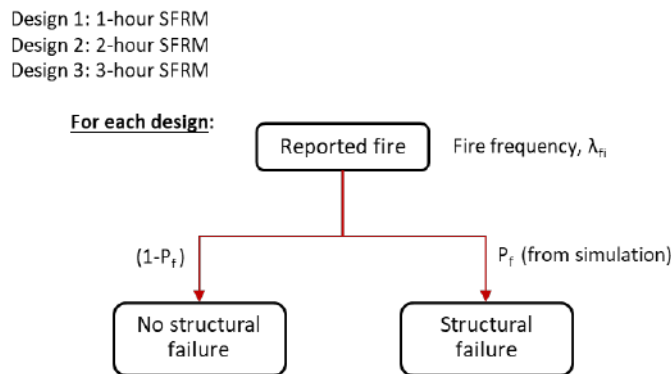


Figure 2. Event tree defining the scenarios for the cost-benefit analysis

3.3 Numerical model for assessing fire losses for the design alternatives

The primary structure of the office building is modelled using the finite element software SAFIR [15]. The design and dimensions of the frame members, derived from the FEMA/SAC prototype developed for post-Northridge designs in the Boston area, are extensively detailed in a prior study [24] and shown in Figure 3. To ensure computational efficiency, a 2D frame model is utilized for probabilistic analyses.

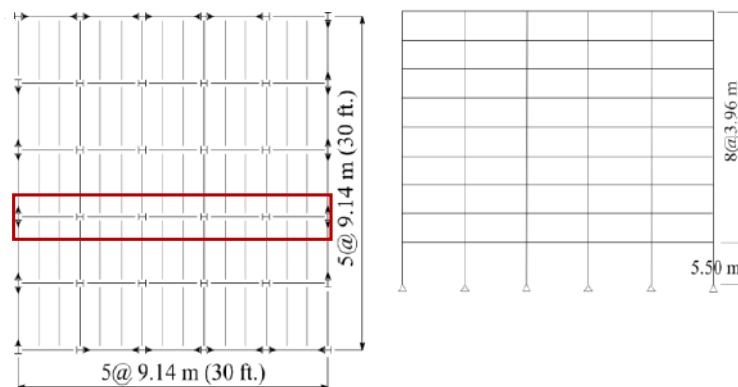


Figure 3. Analysed gravity frame for the multi-story office building

The building is categorized as Type I B, necessitating a 2-hour ICC fire resistance rating for the primary structural frame members. The insulation materials chosen are X829 CAFCO BLAZE-SHIELD II for the columns and N823 UL CAFCO BLAZE-SHIELD II for the beams and girders. Additionally, thickness variations for achieving 1-hour and 3-hour fire resistance ratings are assessed, as the cost-benefit analysis explores different fire protection alternatives. The member sections and fire protection thicknesses are detailed in Table 3, ranging from 10 to 48 mm.

Table 3. SFRM insulation thickness for the various members of the gravity frames

Member type	Storey	Size	1-hour [m]	2-hours [m]	3-hours [m]
COLUMNS	1	W14x145	0.011	0.022	0.033
	2	W14x145	0.011	0.022	0.033
	3	W12x120	0.011	0.022	0.033
	4	W12x120	0.011	0.022	0.033
	5	W14x90	0.015	0.030	0.044
	6	W14x90	0.015	0.030	0.044
	7	W12x65	0.016	0.032	0.048
	8	W12x65	0.016	0.032	0.048
	9	W8x48	0.016	0.032	0.048
BEAMS	1-8	W16x26	0.010	0.021	0.033
	9	W14x22	0.010	0.021	0.033

The distributed dead load on the floors amounts to 4.60 kN/m², with a typical live load for office occupancy at 2.40 kN/m². After reduction, the live load becomes 0.96 kN/m². These values are unfactored. According to the ASCE load combination for ambient temperature design, considering the reduced live load, a distributed load of 7.05 kN/m² is calculated. For fire situations, the ASCE load combination yields a distributed load of 5.99 kN/m². However, for a probabilistic cost-benefit evaluation, it is crucial to consider the expected value of loading rather than the code value. The expected loading value is determined based on a literature review conducted by Jovanović *et al.* [25]. The total load effect is described by $K_E(G + Q)$, where K_E is the model uncertainty with expected value of 1.0, G is the permanent load with expected value equal to the nominal value (i.e., 4.60 kN/m²), and Q is the imposed load with expected value equal to 0.2 times the nominal value (i.e., 0.48 kN/m²). As a result, the beams are subjected to a uniformly distributed load of 5.08 kN/m² multiplied by the tributary width of 9.14 m, for a total of 46.4 kN/m.

To account for uncertainties, several parameters are treated as probabilistic [26], including the fuel load, the compartment opening factor, the thermal properties of the SFRM, and the yield strength of the steel at elevated temperatures. For the fuel load for office occupancy, two probability distributions are considered and compared: the one derived from a recent NFPA study (Generalized Extreme Value distribution, mean of 1,116 MJ/m² with a standard deviation of 604 MJ/m²) [27] and the one prescribed in Eurocode 1 (Gumbel distribution, average 420 MJ/m² and 80% fractile 511 MJ/m²) [28]. For the opening factor, the distribution is calculated according to the JCSS formula [29] (truncated lognormal distribution with mean 0.2 and standard deviation 0.2), where the maximum opening factor is calculated from Eurocode 1 [28] assuming that window glass is immediately broken when fire breaks out. The thermal properties of the boundaries of enclosure are: conductivity 0.48 W/mK, density 1440 kg/m³, and specific heat 840 J/kgK. For the SFRM properties, the temperature-dependent conductivity, specific heat, and density are evaluated from a probabilistic model calibrated on a NIST study of three sprayed fire resistive materials.

The model adopts the probabilistic formulation outlined by Elhami Khorasani *et al.* [30] and is integrated into SAFIR under the name SFRM_PROBA for Sprayed Fire Resistive Material. Regarding the steel, which has a nominal yield strength of 345 MPa, the material model follows the stress-strain relationship in Eurocodes. However, the temperature reduction of yield strength conforms to a logistic EC3-based probabilistic model [30]. This material is incorporated into SAFIR as STEC3PROBA.

The structure undergoes initial loading at ambient temperature to determine the ultimate uniformly distributed load on the beams, which amounts to 82.8 kN/m. Consequently, the anticipated loading during a fire scenario is calculated as $46.4/82.8 = 56\%$ of the ambient temperature capacity. Subsequently, the structural response is assessed under fire conditions. Single-compartment fire scenarios are simulated, given their higher frequency compared to multi-compartment fires. The structural analysis focuses on the gravity frame members of the nine-story building. For each design variation (e.g., differing thicknesses of fire

protection) and each fuel load distribution, 100 simulations are conducted. Fire curves are generated in accordance with the Eurocode parametric fire model [28]. The fire curves, derived from running 100 iterations with varying fuel loads and opening factors, are depicted in Figure 4. It is observed that the NFPA fuel load distribution leads to more severe fires compared to the Eurocode fuel load distribution, as expected due to the significantly higher values of fuel loads.

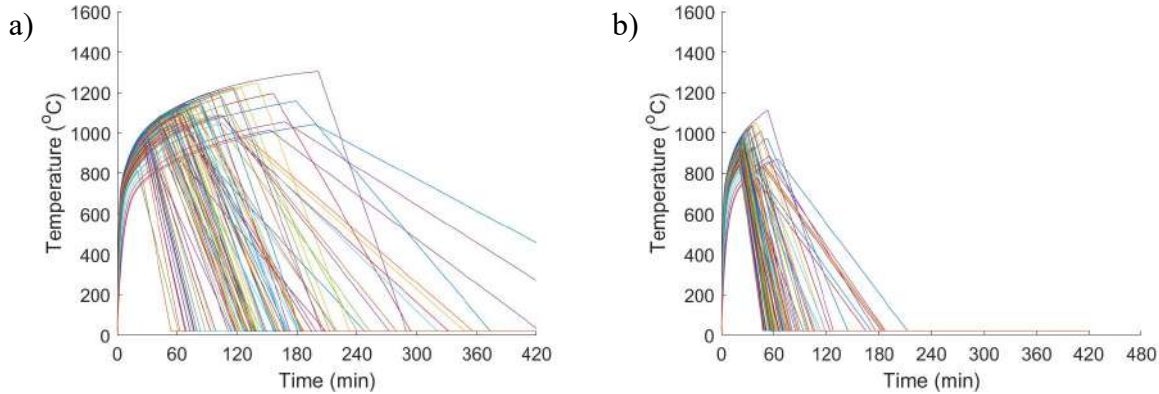


Figure 4. Gas temperature-time curves according to the Eurocode parametric fire curves methodology [28] considered in the simulations, based on two fuel load distributions for office occupancy: NFPA (a) and Eurocode (b) fuel load distributions

4 RESULTS

4.1 Probabilistic structural analysis

Figure 5 illustrates the progression of vertical deflections in the fire-exposed beams for two specific scenarios. A notable divergence in response is evident between the instance resulting in failure (1-hour fire protection) and the one which does not fail (2-hour fire protection). Failure is identified when the simulation is unable to achieve equilibrium under the applied loading and fire exposure, assessing the structural response until full fuel burnout (simulations conducted for 7 hours). It is evident that the absence of numerical convergence correlates with a rapid escalation in deflections within the frame members, indicating a loss of stability, as depicted in Figure 5. Failures typically originate in the beams. It is noteworthy that, while composite floors are not included in the model, the prescriptive design practice in the US requires only a very limited amount of wire mesh reinforcement in the slab (about $60 \text{ mm}^2/\text{m}$) which does not allow development of alternative load paths and redistribution (such as membrane action) through the floors. This has been evidenced by recent full-scale experiments at the NIST.

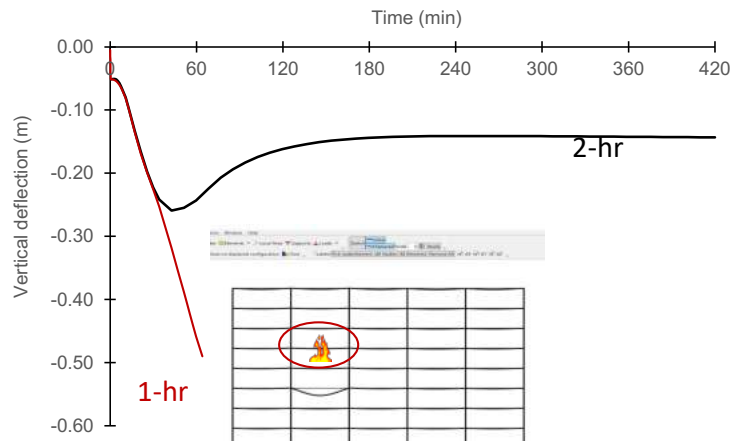


Figure 5. Evolution of the vertical deflections at mid-span of the beam in the fire compartment, for a case that fails (1-hr fire protection) and a case that survives the fire (2-hr fire protection)

The numerical results are presented in Table 4. The probability of failure is determined by dividing the number of failed simulations by the total 100 simulations conducted. As anticipated, the likelihood of failure diminishes with an increase in the thickness of SFRM. Moreover, the probability of failure is higher with the NFPA fuel load distribution compared to the Eurocode fuel load distribution, reflecting the greater fuel load values documented in the former study [27]. With the Eurocode distribution, the probability of failure for the prescribed 2-hour fire protection is calculated to be 15% in the event of an uncontrolled structurally significant fire, while 79% for the NFPA fuel load distribution. In the absence of any fire protection, the building is deemed to fail in all cases of structurally significant fires.

Table 4. Probability of failure for the steel frame structure with different fire protection levels

Design fire rating	Fuel load distribution model	
	NFPA	Eurocode
SFRM prescriptive 1-hour	0.97	0.73
SFRM prescriptive 2-hour	0.79	0.15
SFRM prescriptive 3-hour	0.64	0.08

4.2 PNV evaluation

Table 5 outlines the PNVs across the various considered fire safety alternatives. Utilizing both models for fuel load distribution, each prescribed rating for SFRM yields a positive PNV, indicating that the benefits outweigh the costs. Consequently, under the studied conditions, these safety measures can be recommended as beneficial from an economic perspective. Particularly, both the NFPA and Eurocode fuel load density models advocate for a 3-hour fire resistance rating as the most optimal solution. This alignment is significant as it corresponds with the current prescriptive guidelines, which typically require either a 2-hour or 3-hour fire resistance rating for primary frame members. For generalization, it is advisable to conduct further modelling including other designs and explicit consideration of the potential redistribution of loads following the failure of a primary beam within a three-dimensional structural model, as this could alter failure rates and consequences.

It is important to note that the BCR is highest for the 2-hour fire resistance rating. Nonetheless, particularly when considering in the NFPA fuel load, there is an additional net benefit in opting for the 3-hour fire resistance rating. While the PNV evaluation accurately identifies the optimum solution, the BCR does not (as discussed in [4]). In essence, if the initial choice is to adopt the design with the highest BCR (2-hour rating), subsequent cost-benefit analysis regarding additional protection (upgrading to a 3-hour rating) would reveal a positive BCR for the transition (assuming equal costs and disregarding additional expenses associated with a phased approach). Whereas the PNV directly discerns the optimal outcome, a BCR approach will only converge to the same conclusion through iterations.

Table 5. Cost-benefit indicators

Design fire rating	NFPA fuel load		Eurocode fuel load	
	PNV [USD]	BCR	PNV [USD]	BCR
SFRM prescriptive 1-hour	114,950	1.45	3,090,108	13.03
SFRM prescriptive 2-hour	2,156,338	5.82	10,090,093	23.58
SFRM prescriptive 3-hour	3,691,715	5.79	10,633,751	14.79

4.3 Sensitivity analysis

A parametric study is carried out to investigate the impact of the assumptions regarding the damaged area in instances where failure does not occur. While failure typically assumes total building damage, the scenario shifts when the building maintains stability, allowing for variations in the damaged area affected by significant deformations and fire-induced damages beyond the compartment of fire origin. As illustrated

in Figure 6, the PNV is plotted as a function of the damaged areas, expressed as a percentage of the total floor area. It is evident that this variable significantly influences the PNV. The efficacy of fire protection is most pronounced when the assumed damaged area in the absence of failure is minimal. In such instances, successful fire protection, by preserving structural stability, mitigates repair costs. Conversely, presuming extensive damage across the floor area even without failure diminishes the benefit of fire protection, as repair costs persist despite structural stability. Nonetheless, the PNV remains positive until the damaged area approximates 90% of the total floor area. This underscores the cost-effectiveness of high-rated SFRM in this scenario. Even lacking precise data on fire-induced damaged areas, this sensitivity analysis indicates the robustness of the presented conclusion, irrespective of assumptions regarding the damaged area in the absence of failure.

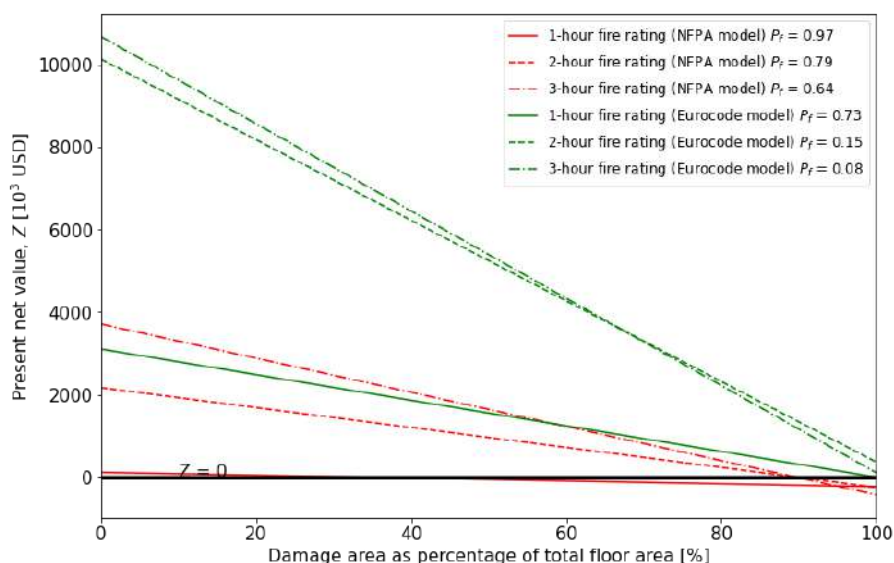


Figure 6. Cost-effectiveness of the passive fire protection for varying fire-induced damaged area

5 CONCLUSIONS

Evaluating the costs and benefits of safety measures is a vital aspect of making well-informed decisions. Once a minimum threshold of tolerability is met (which is imperative), decision-makers can choose to prioritise an alternative design with either a greater or lesser investment in safety. A logical approach to inform this decision-making process involves conducting a Cost-Benefit Analysis (CBA) for each design option. In the field of fire safety engineering, CBA takes into consideration both the investment costs and the benefits derived from enhanced building performance during a fire, including reductions in injuries, casualties, direct losses, and indirect losses.

A methodology for conducting cost-benefit analysis of fire protection in buildings is presented and applied to an illustrative case study. The case study involves a nine-story office building, and the cost-benefit analysis is applied to assess passive fire protection alternatives, in particular different thicknesses of Sprayed Fire Resistive Material (SFRM) applied to the building steel gravity frames and corresponding to 1-hour, 2-hour, and 3-hour of fire protection. As expected, the probability of failure decreases with an increase in SFRM thickness, and the probability of failure is largely affected by the assumed fuel load distribution. Nevertheless, the PNV for the different fire resistance ratings always returns a positive value (i.e., benefit of the investment exceeds the cost), meaning that these fire safety measures can be recommended as beneficial from an economic perspective. In particular, the use of a 3-hour fire rated thickness of SFRM is found as providing the highest PNV. The sensitivity analysis on the assumption of the damaged area in the absence of structural failure shows that this parameter has a significant effect on the PNV. Nevertheless, it confirms the robustness of the investment recommendation because this conclusion holds almost regardless of the assumption for damage area in the absence of failure.

The presented results demonstrate the strength and relevance of the proposed methodology based on the concept of Present Net Value (PNV) and potential applications for structural fire engineering. The insights and suggestions presented in this research study underline how results obtained from the cost-benefit evaluations, adapted from the presented case study with project-specific inputs, can support decision making of various fire safety strategies for both private stakeholders (e.g. business/building owner, insurance companies) and society (e.g. policy makers).

ACKNOWLEDGMENTS

The authors gratefully acknowledge the Fire Protection Research Foundation (FPRF) and the National Fire Protection Association (NFPA) for the funding through the project “Economic Impact of Fire: Cost and Impact of Fire Protection in Buildings”. The authors thank Amanda Kimball, Birgitte Messerschmidt, and the members of the Project Technical Panel for their support. Dr Lucherini would also like to gratefully acknowledge the financial support for the FRISSBE project within the European Union's Horizon 2020 research and innovation programme (GA 952395).

REFERENCES

- [1] Van Coile R., Hopkin D., Lange D., Jomaas G., Bisby L. (2019). The Need for Hierarchies of Acceptance Criteria for Probabilistic Risk Assessments in Fire Engineering. *Fire Technology*, 55:1111–46.
- [2] Sunstein C.R. (2018). *The cost-benefit revolution*. MIT Press.
- [3] Lundin J, Frantzich H. (2002). Cost-benefit and risk analysis-basis for decisions in the fire safety design process. *Proceedings from the 4th International Conference on Performance-based codes and Fire Safety Design Methods*, 370-381.
- [4] Van Coile R., Lucherini A., Chaudhary R.K., Ni S., Unobe D., Gernay T. (2023). Economic impact of fire: cost and impact of fire protection in buildings”. National Fire Protection Association (NFPA).
- [5] Butry D.T., Brown M.H., Fuller S.K. (2007). *Benefit-cost Analysis of Residential Fire Sprinkler Systems*. Gaithersburg, MD
- [6] Hopkin D., Fu I., Van Coile R. (2020). Adequate fire safety for structural steel elements based upon life-time cost optimization. *Fire Safety Journal*, 103095.
- [7] Ramachandran G. (2002). *The economics of fire protection*. Routledge, London, UK.
- [8] Van Coile R., Lucherini A., Chaudhary R.K., Ni S., Unobe D., Gernay T. (2023). Cost-benefit analysis in fire safety engineering: State-of-the-art and reference methodology. *Safety Science*, 168, 106326.
- [9] Unobe I. D., Lucherini A., Ni S., Gernay T., Chaudhary R., Van Coile R. (2024). State of the Art Methodologies for the Estimation of Fire Costs in Buildings to Support Cost–Benefit Analysis. *Fire Technology*.
- [10] Gernay T., Ni S., Unobe D., Lucherini A., Chaudhary R.K., Van Coile R. (2023). Cost-benefit analysis of fire protection in buildings: application of a present net value approach”. *Fire Technology*, 59, 2023–2053.
- [11] Van Coile R., Jomaas G., Bisby L. (2019). Defining ALARP for fire safety engineering design via the Life Quality Index. *Fire Safety Journal*, 107, 1-14.
- [12] RSMMeans. (2020). *Building Construction Costs with RSMMeans Data 2021*. 79th ed. Rockland, MA: RSMMeans Co.
- [13] Kluyver T., Ragan-Kelley B., Pérez F., Granger B.E., Bussonnier M., Frederic J., *et al.* (2016). *Jupyter Notebooks—a publishing format for reproducible computational workflows*. IOS Press, *Positioning and Power in Academic Publishing: Players, Agents and Agendas*, 87-90.
- [14] Federal Emergency Management Agency (2003). *Multi-Hazard Loss Estimation Methodology: Earthquake Model, HAZUS-MH MR4*.
- [15] Franssen J.M., Gernay T. (2017). Modeling structures in fire with SAFIR: theoretical background and capabilities. *Journal of Structural Fire Engineering*, 8, 300–323.

- [16] Federal Emergency Management Agency. SAC. (2000). FEMA 355C: State of the Art Report on System Performance of Steel Moment Frames Subject to Earthquake Ground Shaking. Washington D.C.
- [17] Manes M., Rush D. (2019). A Critical Evaluation of BS PD 7974-7 Structural Fire Response Data Based on USA Fire Statistics. *Fire Technology*, 55, 1243–93.
- [18] National Fire Protection Association (NFPA). (2022). Fires by occupancy or Property Type.
- [19] Fahy RF, Petrillo JT. (2022). Firefighter Fatalities in the US in 2021. National Fire Protection Association (NFPA).
- [20] Campbell R, Evarts B. (2021). United States Firefighter Injuries in 2020 Key Findings. National Fire Protection Association (NFPA).
- [21] Federal Emergency Management Agency (FEMA). (2015) Earthquake loss estimation methodology, Hazus-MH 2.1: Advanced engineering building module (AEBM) - Technical and user's manual. Washington, DC.
- [22] Ramachandran G., Hall J.R. (2002). SFPE Handbook of Fire Protection Engineering, Measuring Fire Consequences in Economic Terms, 79.
- [23] Fischer K. (2014). Societal decision-making for optimal fire safety. *Bericht IBK*, 357.
- [24] Gernay T., Elhami Khorasani N. (2020). Recommendations for performance-based fire design of composite steel buildings using computational analysis. *Journal of Constructional Steel Research*, 166, 105906.
- [25] Jovanović B., Van Coile R., Hopkin D., Elhami Khorasani N., Lange D., Gernay T. (2021). Review of Current Practice in Probabilistic Structural Fire Engineering: Permanent and Live Load Modelling. *Fire Technology*.
- [26] Gernay T., Elhami Khorasani E., Garlock M. (2019). Fire Fragility Functions for Steel Frame Buildings: Sensitivity Analysis and Reliability Framework. *Fire Technology*.
- [27] Elhami Khorasani N., Salado Castillo J.G., Saula E., Josephs T., Nurlybekova G., Gernay T. (2020). Application of a Digitized Fuel Load Surveying Methodology to Office Buildings. *Fire Technology*.
- [28] EN1991-1-2. (2002). Eurocode 1: Actions on structures - Part 1-2: General actions - Actions on structures exposed to fire. European Standard.
- [29] JCSS (2001). JCSS Probabilistic Model Code: Part 2: Load Models.
- [30] Elhami Khorasani N., Gardoni P., Garlock M. (2015). Probabilistic Fire Analysis: Material Models and Evaluation of Steel Structural Members. *Journal of Structural Engineering*, 04015050, 1–15.

BEHAVIOUR OF SIMPLE STEEL JOINTS UNDER NATURAL FIRE CURVES: A CASE STUDY

Niccolò Passarini¹, Nicola Tondini²

ABSTRACT

The paper analyses the behaviour of steel joints subjected to fire in the framework of the Fire Safety Engineering (FSE) approach. In particular, the performance of simple steel joints of an unprotected open steel car park to be built in Italy, whose global fire behaviour was investigated under relevant natural fire scenarios of burning cars, is shown. Three types of joints were investigated, i.e. end plate joint, fin plate joint, and double angle cleat joint, and they were subjected to a thermal action corresponding to the Hasemi model included in Annex C of EN 1991-1-2. First, the structural checks were conducted according to Annex D of EN 1993-1-2. Then, 3D detailed nonlinear finite element (FE) models of the joints were developed in ABAQUS, where the concrete slab and the modelling of accurate boundary conditions were included. None of the joints exhibited satisfactory behaviour according to Annex D of EN 1993-1-2, whereas the numerical results showed that only the end plate joint with a thin plate was able to withstand the entire duration of the fire, which was the required fire performance objective. The paper thoroughly describes all the modelling assumptions and outcomes of the analyses.

Keywords: Steel joints; natural fire curves; numerical modelling; open car park

1 INTRODUCTION

In the framework of Fire Safety Engineering (FSE), global thermomechanical analyses of a significant part of a structure or even of the whole structure are usually performed. In the case of steel-framed structures, finite element models are developed with beam and shell elements that typically suffice to capture the global response of the structural system under fire. In this way, the behaviour of the joints is generally assumed to be ideal, and their ability to ensure the transmission of additional resisting mechanisms throughout the entire duration of the fire scenario is checked *a posteriori*. In the case of using a performance-based approach, the regulations require explicit verification of the joints in different phases of the fire, taking into careful consideration all indirect actions that may affect their response. In fact, the behaviour of the joints may influence the response of steel structures under fire [1,2]. Several works analysed the effect of joints in fire conditions, e.g. [3-6]. During experimental tests, large tensile forces can be observed as well as the reversal of bending moment in the joint during the cooling phase, possibly even causing the collapse of the joint [7-9]. Guidance of joint checks in fire conditions are given in Annex D of EN 1993-1-2 [10], where temperature distribution and reduction factors for both bolts and welds at elevated temperature are provided. The European research project COSSFIRE [11] proposed design recommendations for simple steel and steel-concrete composite joints subject to natural fire curves. Indeed, in the framework of this research project, parametric analyses were conducted on beam-to-column joints to

¹ Mr, Research Engineer, Department of Civil, Environmental and Mechanical Engineering, Italy
e-mail: niccolopassarini98@gmail.com

² PhD, Associate Professor, University of Trento, Department of Civil, Environmental and Mechanical Engineering, Italy
e-mail: nicola.tondini@unitn.it, ORCID: <https://orcid.org/0000-0003-2602-6121>

develop efficient and economically simple fire design rules. On these premises, this paper investigates the fire behaviour of simple steel joints of an open steel car park to be built in Italy, whose global fire behaviour was investigated by Somlavilla and Tondini [12] under relevant fire scenarios of burning cars. In particular, the fire scenario relevant for the column, represented by 4 localised fires of burning vehicles surrounding it, was investigated by applying the Hasemi model included in Annex C of EN 1991-1-2 [13] and the LOCAFI model [14]. The latter model will be included in the next generation of EN 1991-1-2. This paper thoroughly analysed the fire behaviour of three simple beam-to-column joints: end plate joint, fin plate joint, and double angle cleat joint.

2 CASE STUDY

The structure is an unprotected steel open car park to be built in Italy (see Figure 1), whose comprehensive description can be found in Somlavilla and Tondini [12]. For the benefit of the reader, a brief description is given hereinafter. The car park is a 3 to 4-storey split-level of dimensions 48 m x 40 m x 9/12 m (interstorey height = 3 m) with 16-m long IPE 500 steel-concrete composite beams and 220-mm deep steel decking spanning transversally over 5-m long beams. In the transverse direction, HE 120 B 5-m long profiles were employed between each column. The beam-to-column joints are pinned. An S460M steel grade was used. For the column, an HE 260 M with low utilisation ratio in the fire situation was identified as a potential option in the context of overdesign to avoid using partially encased or fireproofed profiles. Class C35/45 concrete inside the ribs and over the upper beam flange (plain slab of 8/10 cm) was employed. A reinforcement welded wire mesh 200 mm x 200 mm ϕ 10 mm B450C was added to the slab. The live load was taken equal to 2.5 kN/m². The open car park was subjected to relevant fire scenarios per the Italian Fire Prevention Code [8] and others in Europe, e.g. France. In particular, the global analysis, performed in SAFIR [16], focused on the fire scenario of 4 burning vehicles around the column, i.e. 3 Class 3 vehicles and 1 commercial vehicle. The outcomes of the global analysis showed that the structure survived the whole duration of the fire, with the maximum vertical displacement of the slab above the commercial vehicle being in the order of 50 cm [12]. Figure 1 shows the vertical displacements of the car park in the cooling phase after 40 min. However, the numerical global modelling did not include the behaviour of the joints. Thus, the joint fire performance was carried out after the analysis based on the evolution of the forces during the entire fire duration.

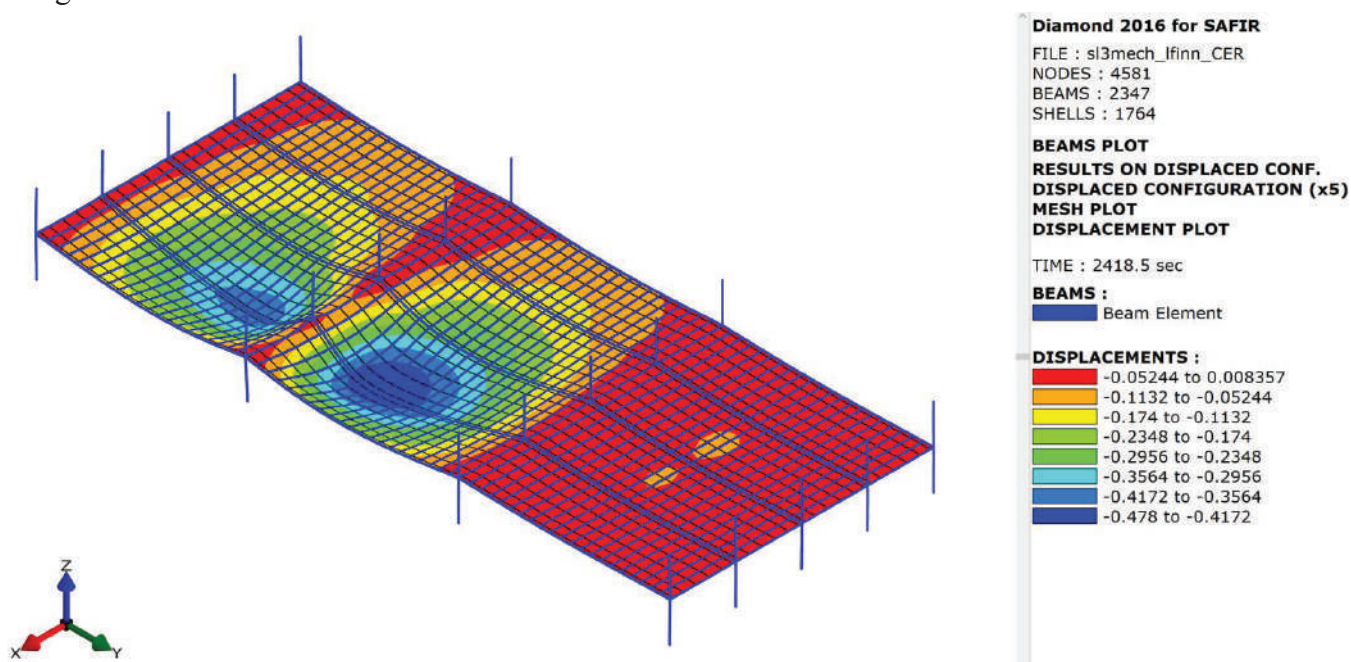


Figure 1. Vertical displacement after 40 min. Deformed shape amplified by 5.

2.1 Joint design

Three types of simple beam-to-column joints were analysed: i) end plate joint; ii) fin plate joint; and iii) double angle cleat joint. Their design was carried out in accordance with EN 1993-1-8 [17,18]. Since they were pinned, they were designed to have sufficient rotational capacity at the ultimate limit state so they cannot develop high internal bending moments. Moreover, ductility criteria were ensured so that the development of combined shear and bending forces into the joint does not cause brittle failure modes, i.e. rupture of bolts or welds. Therefore, plasticisation of the plates composing the joint was guaranteed by imposing Mode 1 failure of the T-stub and the welds were designed as being full strength. As a result, the plates were made of S275 steel grade. Based on the rotational capacity and ductility criteria, the design led to the joints between the major axis of the HE 260 M column and the IPE 500 beam, whose characteristics are shown in Figure 2.

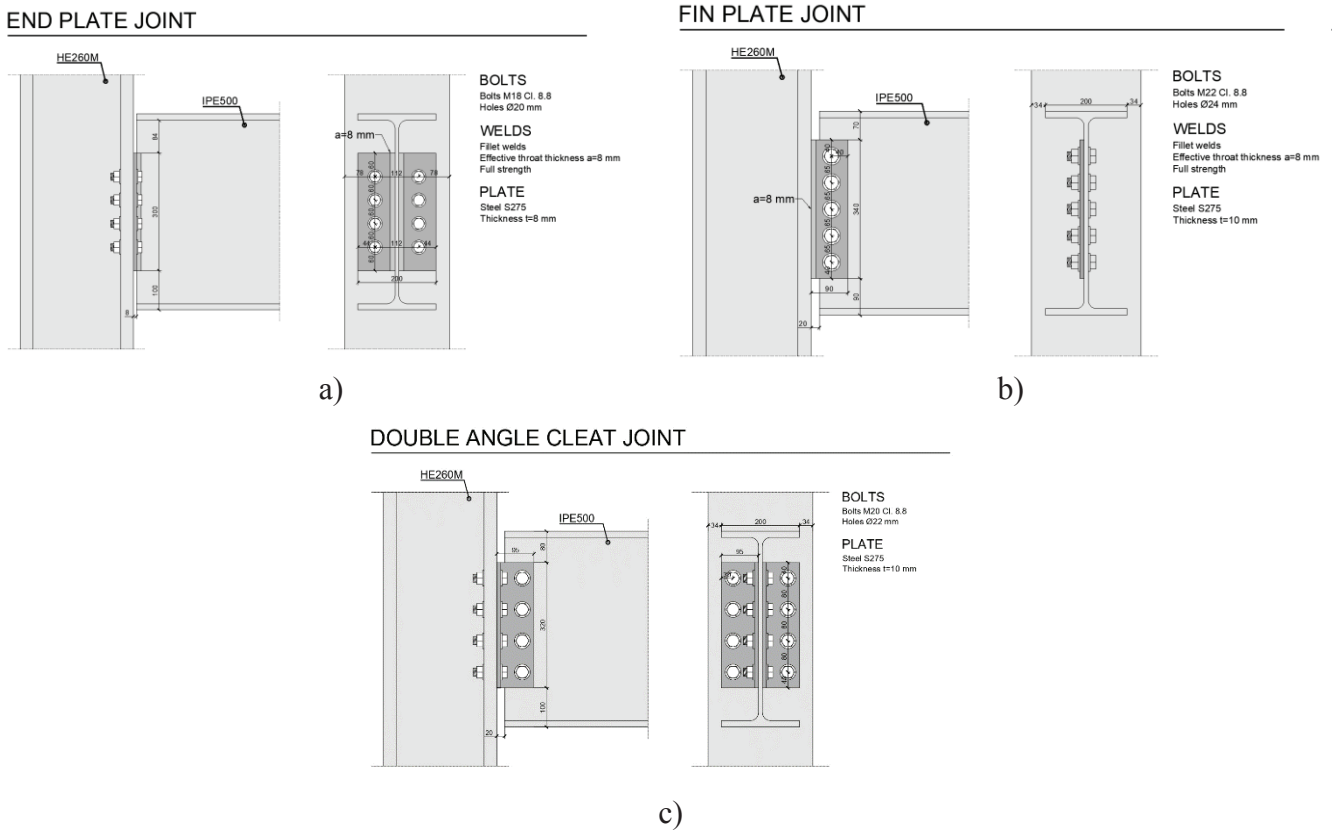


Figure 2. Joint design: a) end plate joint; b) fin plate; c) double angle cleat joint.

3 JOINT CHECK IN FIRE CONDITIONS

This section shows the checks of the joints in fire conditions per Annex D of EN 1993-1-2. In particular, the beam-to-column joint shown in Figure 3 was analysed, which undergoes the highest thermal actions given that it is located just above the burning commercial vehicle and is the most affected by the indirect actions owing to the expansion and contraction of the beam. Being the joint close to the ceiling, the thermal action applied to the joint was obtained from the Hasemi model [13].

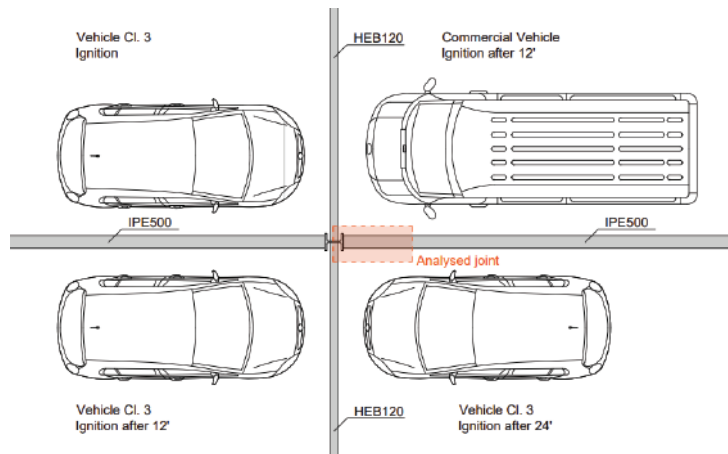


Figure 3. Analysed joint in fire conditions.

3.1 Actions on the joint

In order to verify the joint under fire conditions, the evolution of the shear force, axial force, and temperature over time was extracted from the global analysis. Specifically, these curves were obtained from the closest beam element to the joint. The verification at multiple time instances was performed because it was not clear beforehand which condition was the most critical for the various components of the joint. Indeed, after approximately 15 min, the maximum compressive force was observed, but at that time, the temperature in the joint did not reach its maximum value. When the temperature reached its maximum value at about 30 min, the shear force attained its minimum due to the redistribution of loads among the cooler elements, and the compressive force reduced due to the loss of stiffness of the beam. Another critical phase was the end of the fire scenario since, due to the contraction of the beam during the cooling phase and the deformative state, significant tensile axial forces developed in the joint.

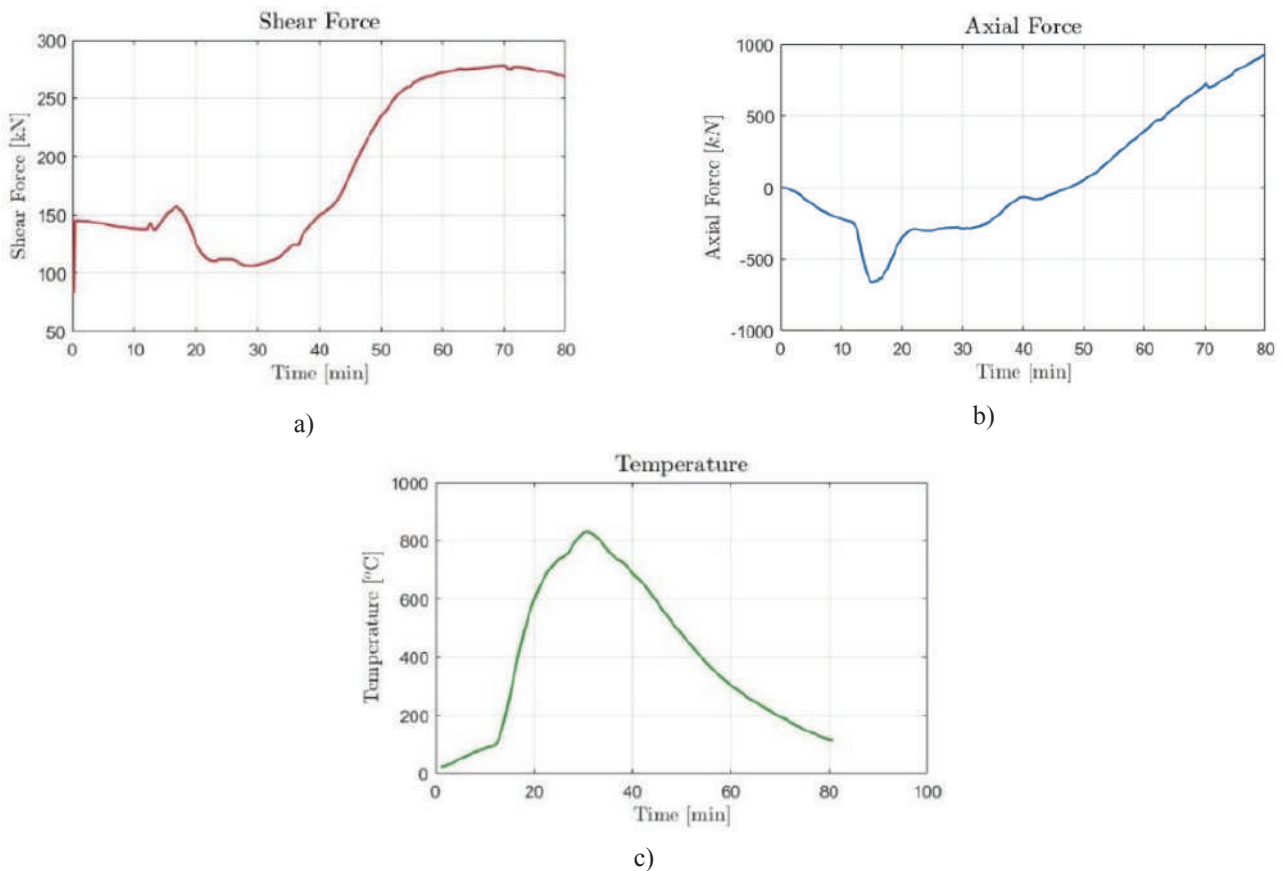


Figure 4. Evolution of the shear force, axial force and temperature in the beam element closest to the joint.

3.2 Structural checks according to EN 1993-1-2

Annex D of EN 1993-1-2 provides the guidelines for performing the structural checks of joints at elevated temperature. A formula is provided to calculate the temperature at the various components of the joint based on the temperature of the beam bottom flange θ_0 . Moreover, Annex D also provides the reduction coefficient factors of strength for bolts and welds. The reduction factors were applied to the relationships to calculate the resistance of individual components at high temperatures. In order to consider the interaction between axial force and shear force on the individual components of the joint, a linear interaction domain was assumed. Only the checks related to the bolts for each joint type are shown for brevity. It is possible to observe that none of them exhibited satisfactory behaviour. The thermal action generated by the Hasemi model determined such high axial forces in the heating and cooling phases that even overdesign was not a viable option. Thus, a more accurate analysis was performed by means of nonlinear finite element modelling. At the same time, the construction detailing recommendations for steel joints developed in the COSSFIRE project [11] were satisfied for all the joints. However, they were developed for uniform heating along the beam, which is not the case in the selected fire scenario. Moreover, the parametric heating curves used in [11] induced much lower temperatures in the joints than in this work.

Table 1. Structural checks in fire condition of each selected joint type

Time t (min)	8	17	31	42	50	67	80
Shear force V_{Ed} (kN)	139	157	109	156	237	277	267
Axial force N_{Ed} (kN)	-200	-618	-285	-81	62	622	927
Beam temperature θ_0 (°C)	79	417	832	658	480	225	116
End plate joint							
Bolt utilisation ratio (-)	0.55	0.62	2.01	1.09	0.87	1.31	1.53
Fin plate joint							
Bolt utilisation ratio (-)	0.48	1.30	6.05	1.13	0.57	1.32	1.70
Double Angle Cleat Joint							
Bolt utilisation ratio (-)	0.37	1.01	4.68	0.87	0.44	1.02	1.31
Bolt utilisation ratio (-)	0.51	0.56	1.65	0.93	0.76	1.10	1.27

4 NUMERICAL MODELLING

To understand the actual nonlinear behaviour of the selected joints under natural fire conditions, it was decided to model them using the finite element software ABAQUS [19]. The three-dimensional model includes the modelling of the beam-to-column joint, taking into account the presence of the composite slab and considering the shear connection between the beam and the slab as full strength. The welded wire mesh was also incorporated into the slab and located at 40 mm from the top edge, as shown in Figure 5a. The geometrical model includes the column with a height of 1950 mm and the beam with a length of 1360 mm, including the plain slab 80 mm thick and 1000 mm wide.

In order to investigate the thermo-mechanical behaviour of the joint, it was chosen to perform a sequentially coupled thermal stress analysis. Hence, an uncoupled heat transfer and then a mechanical analysis was conducted. Given the convergence issues that the nonlinear modelling of concrete may pose, an explicit solver was chosen for the mechanical analysis, whereas an implicit solver was used for the thermal analysis.

The model was meshed with first-order, reduced-integration elements. However, such elements tend to be susceptible to hourglassing; hence, the mesh was sufficiently refined through a careful convergence analysis to minimise the occurrence of it. The convergence analysis led to the use of finite elements with a maximum size ranging from 20 mm in the slab to 3 mm in the bolts. The mesh was refined in areas of higher stress concentration, such as around the bolts or in the connection between the slab and the column. DC3D8 and

DC3D6 finite elements were used for the heat transfer analysis, while C3D8R and C3D6 finite elements were employed for the dynamic explicit analysis. The size and geometry of the mesh are the same for both the mechanical and thermal analysis. The reinforcing bars were instead modelled using T3D2 truss elements. Figure 5b shows the model of the double angle cleat joint. The total number of finite elements is 165000.

For the thermal analysis, all exposed surfaces were subjected to the heat flux derived from the Hasemi model. As a result, the beam was divided into 3 zones to better capture the effect of the fire given the distance from the fire axis (Figure 5c). The coefficient of heat transfer by convection was considered as $\alpha_c = 35 \text{ W/m}^2\text{K}$, the emissivity of the fire was taken as $\varepsilon_f = 1$ and the surface emissivity of the steel member as $\varepsilon_m = 0.7$ [13].

In the mechanical model, interaction between the beam and column in the bolted connection was modelled using surface-to-surface contact. This type of contact does not allow any penetration during the loading process. Friction between the surfaces was modelled using the classical Coulomb model with a friction coefficient of $\mu = 0.35$. Hard contacts were used to simulate the properties of a normal contact. A tie constraint was utilised to connect the weld to the column, plate, and beam web. The same tie constraint was used to connect the shear studs to the upper flange of the beam. The interaction between the reinforcing bars and the slab was modelled using an embedded region, and the same constraint was applied between the shear studs and the slab.

Since the stresses on the joint depend on the global behaviour of the structure, it would be necessary to model the entire beam with its corresponding slab for a total length of 16 m. Due to computational limitations and to maintain accuracy, it was decided to model only the detail of the joint by conducting a displacement control analysis. In fact, to replicate the joint's axial restraint provided by the surrounding structure and the loading conditions, the displacements and rotations obtained from the global analysis were imposed to the beam. In particular, with reference to the coordinate system shown Figure 5, the displacements in the y and z axes, as well as the rotations around the x-axis, were imposed on the section of the beam. The x-y plane passing through the centre of the web column was assumed as a plane of symmetry to reduce computational cost. This assumption was made because the rotations of the column obtained from the global analysis are negligible. Additionally, the translation of the slab along the x-axis was also constrained to recreate the actual confinement conditions generated by the continuity of the slab.

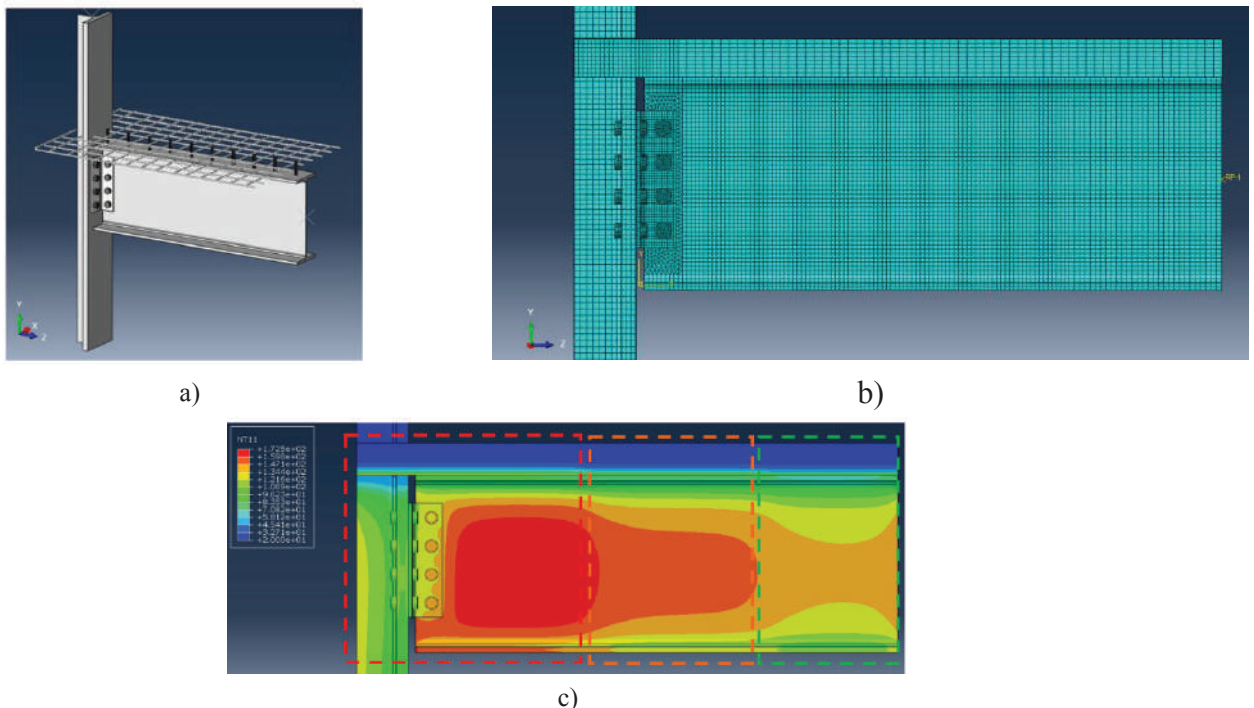


Figure 5. Finite element model in ABAQUS: a) 3D representation of the joint model without concrete to show the welded wire mesh; b) mesh of the joint model; c) selected zones for the application of different heat fluxes derived from the Hasemi model and thermal field after 15 min

4.1 Material properties

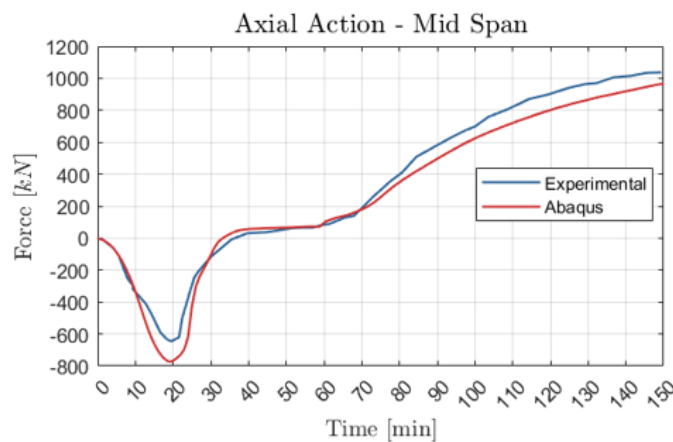
Concrete thermal and mechanical properties were selected according to EN 1992-1-2 [20] and EN 1994-1-2 [21]. The concrete behaviour was modelled by exploiting the concrete damaged plasticity model [19]. It describes the inelastic behaviour of concrete incorporating isotropic damage and isotropic tensile and compressive plasticity. The fracture energy was taken $G_f = 0.024$ N/mm, assuming a compressive strength of 35 MPa and maximum aggregate size of 8 mm.

The thermal and mechanical properties of structural steel used for plates, beam, column, and weld, were taken into account according to EN 1993-1-2 [10]. The Eurocode provides a stress-strain relationship that considers the increased ductility of steel at high temperatures, resulting in an ultimate strain of $\varepsilon_{su} = 20\%$.

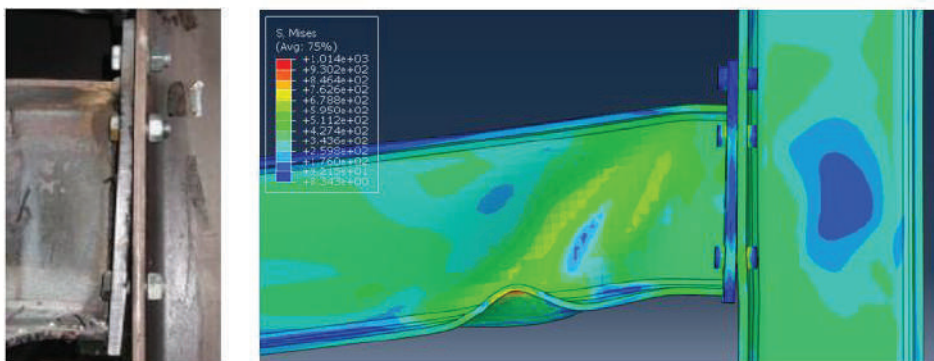
The thermal and mechanical properties of reinforcement steel were taken according to EN 1992-1-2 [20]. The thermal properties of the bolts were taken as those of the structural steel. However, regarding the mechanical properties, such as the stress-strain relationship, the standards do not provide specific guidelines. Therefore, the constitutive relationship for Grade 8.8 bolts under heating and cooling phases proposed by Hanus et al. [22] was employed. It accounts for the non-reversibility of the mechanical properties of Grade 8.8 bolts, and it is based on the maximum temperature (T_u) reached by the bolt during the fire scenario. As an example, assuming $T_u = 700$ °C, the ultimate strain becomes $\varepsilon_{u,\theta} = 20\%$.

4.2 Validation of the FE model

The validation of the FE model with the aforementioned assumptions was conducted against experimental data obtained from six tests on steel sub-frames under natural fire performed by Santiago et al. [8]. The experimental layout consists of two insulated HEA300 columns and an unprotected IPE300 beam with 5.70 m span, supporting a concrete slab. The analysed joint is an extended end plate. The comparison in terms of the evolution of the axial force and of the deformed shape is illustrated in Figure 6 and the agreement is reasonably good.



a)



b)

Figure 6. FE element validation against experimental data: a) axial force evolution in the beam; b) deformed shape.

5 RESULTS OF THE NUMERICAL ANALYSIS

5.1 Thermal analysis

In this section, the results of the thermal analysis will be discussed. In order to evaluate the accuracy of the thermal model implemented in ABAQUS, a comparison between the steel temperatures of the beam obtained from the ABAQUS model and the ones obtained in SAFIR is shown. The comparison was conducted in a beam section located 1 m from the joint. As can be seen from the images below, the temperatures obtained through the 3D simulation with ABAQUS agree well with those computed through 2D thermal analyses in SAFIR.

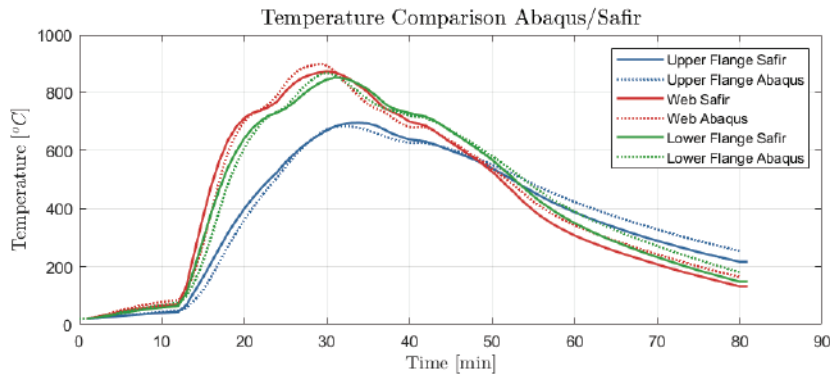
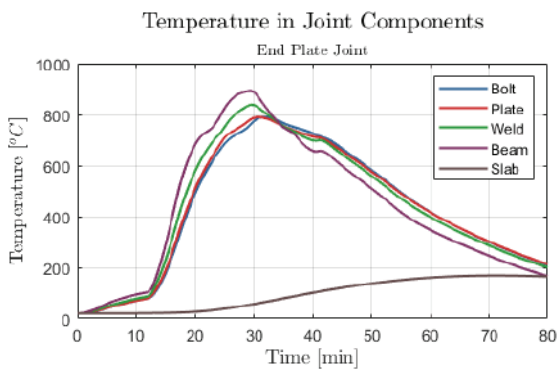
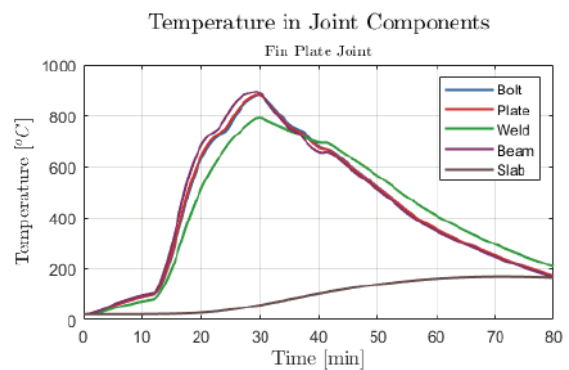


Figure 7. Comparison between the thermal analysis results of SAFIR and ABAQUS at 1 m from the joint.

Figure 8 shows the temperature in the joint components derived from the 3D models. As can be seen from Figure 8a, the end plate joint region exhibits higher thermal inertia due to the greater material density. Consequently, the joint components heat up and cool down at a slower rate than the beam. The temperature of the bolt shank remained relatively low compared to the temperature in the bolts connected to the beam web of the other joints because it received heat only through conduction from the bolt head and the column flange. The choice to use a massive profile for the column is therefore beneficial for the bolts in case of end plate joint. In the fin plate joint (Figure 8c), temperatures reached very high values (over 850°C) in both the bolts and the plate. This phenomenon occurred because both components were in contact with the beam web, which, being very thin, reached elevated temperatures. At a temperature of 850°C, the strength of the bolts is reduced to 5 % of the ambient temperature strength and, considering that the bolts will be subjected to further shear action due to the high rotations of the beam, this type of joint will unlikely be able to transfer shear forces throughout the fire scenario. Even in the case of the double angle cleat joint (Figure 8b), temperatures of over 850°C were reached in the bolt shank on the beam side. However, in this case, the cleats allow for greater rotational capacity.



a)



b)

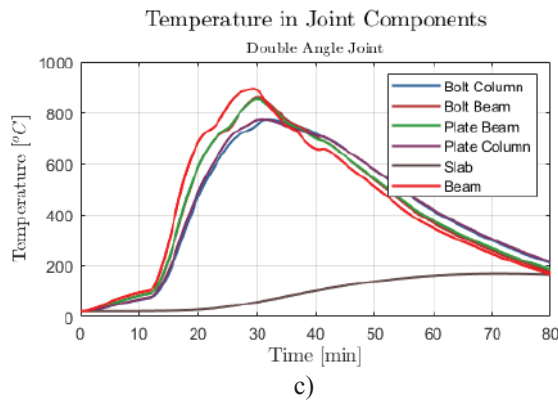


Figure 8. Temperature evolution in joint components: a) end plate joint; b) fin plate joint; c) double angle joint.

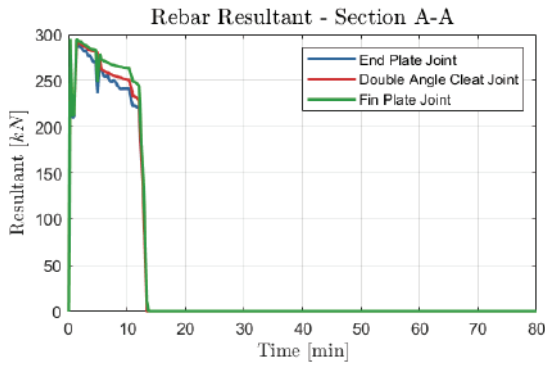
5.2 Mechanical analysis

Based on the thermal analyses of the three joints, the mechanical analyses were performed. Since the behaviour of the slab is similar for all joint types, its description will be reported first. The slab cracked at the initial stages of the analysis, and the reinforcement bars reached their ultimate strain within 14 minutes of the fire scenario. Therefore, after 14 min, both the slab and the reinforcement could no longer transmit stresses (see Figure 9a), and the axial force, moment, and shear force had to necessarily pass through the joint components.

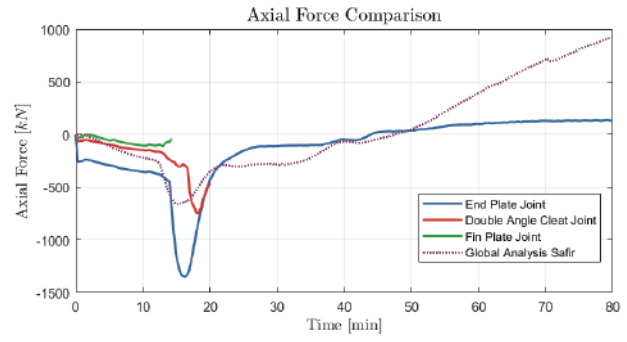
The end plate joint did not collapse throughout the fire scenario. The flexibility of the end plate allowed for rotation while limiting the stresses transmitted to the bolts, which reached lower temperatures with respect to the ones connected to the beam web of the other joints. During the peak of the heating phase, after 30 min, the top bolt row reached an equivalent plastic strain of 15% (a) due to excessive rotations of the joint. During the cooling phase, however, due to the residual deformations of the lower flange of the beam and the stiffness recovery, the bottom bolt row was subjected to tension, as depicted in Figure 11. Indeed, by analysing the equivalent plastic strain in the bolts shown in Figure 10a, it can be observed that the plastic strain in the bottom bolt row increased, even during the cooling phase. Neither the plate nor the beam web exhibited high plastic strain values, while the weld reached critical values of equivalent plastic strain in the upper part, but not sufficient to cause collapse. Figure 9b depicts the axial force in the IPE500 close to the joint. Initially, an axial compressive force developed due to the axial restraint and rotation of the joint. After approximately 14 minutes, when the lower flange of the beam came in contact with the column, the axial compressive force increased until it reached values of more than 1000 kN. Subsequently, due to the loss of stiffness in the beam, the axial compressive force decreased and remained constant until approximately 40 minutes. After 40 minutes, during the cooling phase, a significant axial tensile force developed in the global SAFIR model, while the tensile force in the ABAQUS model reached much lower values. Thanks to the three-dimensional modelling, the end plate deformations were captured, which accommodated the beam contraction, reducing the axial tensile force in the joint. Therefore, using a thin end plate allows for a significant reduction in tensile stresses generated during the cooling phase.

The fin plate joint exhibited a brittle collapse (see Figure 12), because all the bolts reached the ultimate strain after approximately 14 minutes, corresponding to the attainment of the ultimate strain in the reinforcement bars. The 10-mm thick plate did not allow for plate bearing; thus, rotation of the joint is only possible through the deformation of the bolts, as shown in Figure 12. This analysis confirms that using fin plate joints in such cases is discouraged, as also highlighted in [11].

The collapse of the double angle cleat joint occurred after 20 minutes of the analysis due to a fracture in the bolts on the beam side. Although this type of joint has a large rotational capacity due to the deformability of the plates, it was not sufficient to prevent the fracture of the bolts on the beam side, as shown in Figure 13. In this respect, Figure 10 shows the attainment of the ultimate plastic strain of the bolt rows on the beam side. At the moment of collapse, neither the angle cleats nor the bolts on the column side developed significant plastic strain. In addition, as for the fin plate joint, despite the double angle cleat joint complies with the design recommendations provided in the COSSFIRE report [11], it did not withstand the heating phase. In sum, the end plate joint revealed as a suitable option for simple steel joints under natural fires.

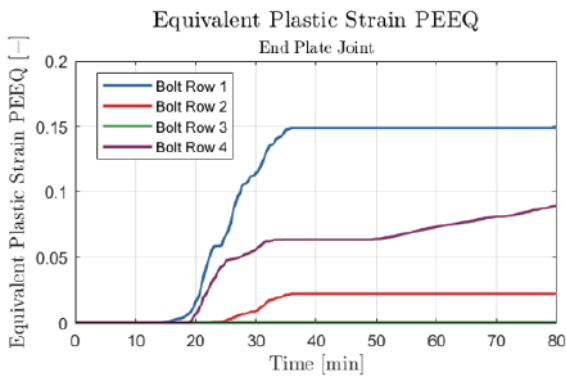


a)

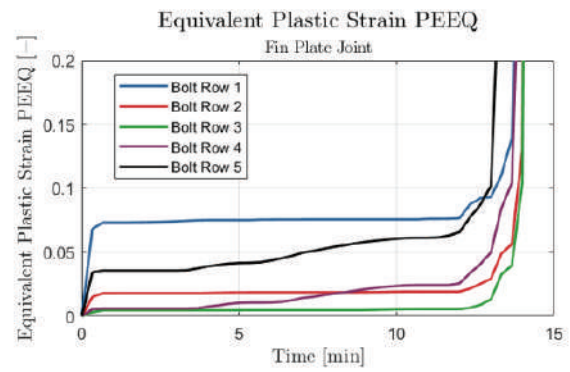


b)

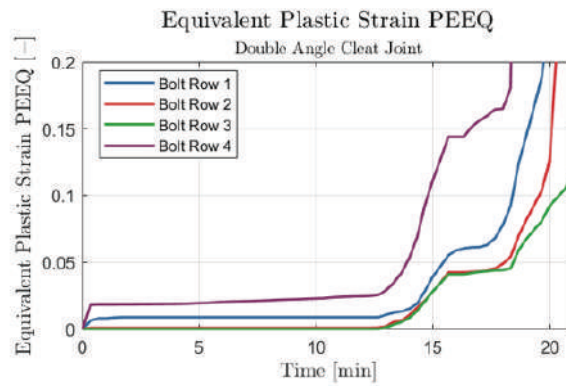
Figure 9. a) Reinforcement bar force resultant; b) Axial force evolution in the different joint solutions.



a)



b)



c)

Figure 10. Equivalent plastic strain in the bolts: a) end plate joint; b) fin plate joint; c) double angle cleat joint.

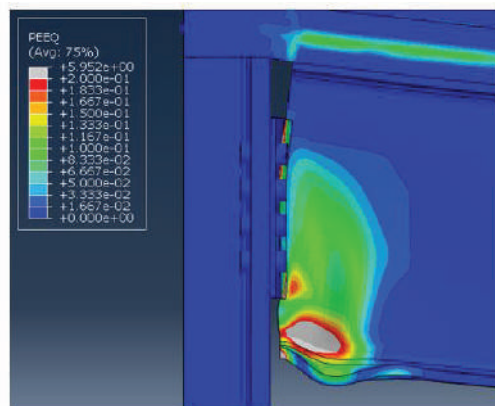
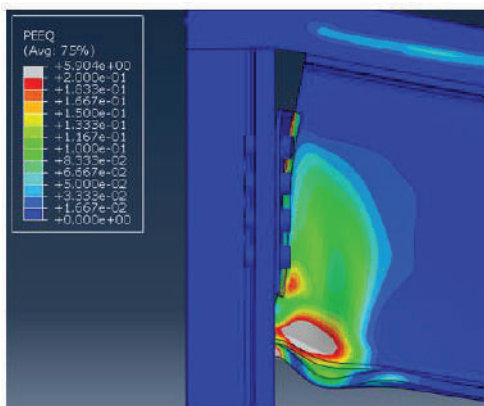


Figure 11. Equivalent plastic strain field in the end plate joint: a) at 30 min of the fire scenario; b) at 80 min of the fire scenario.

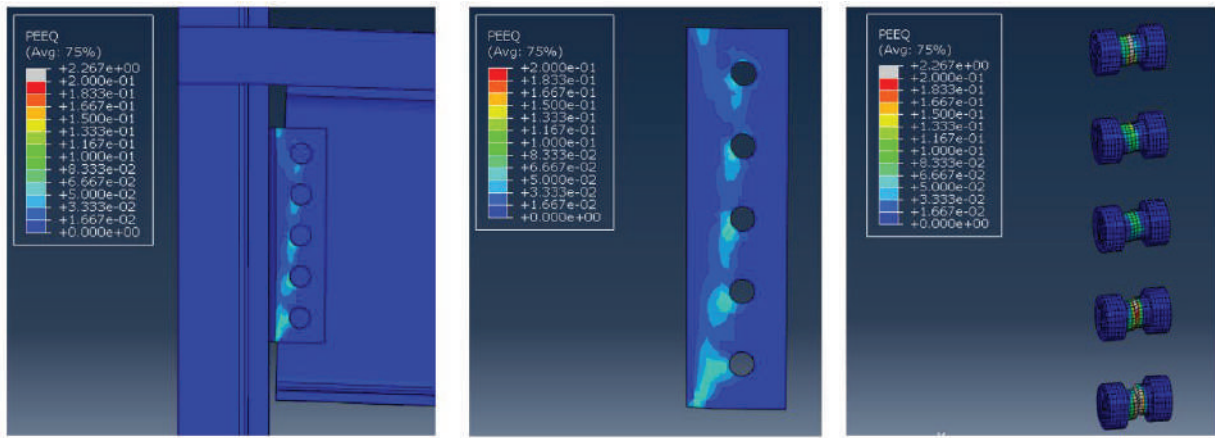


Figure 12. Equivalent plastic strain field in the fin plate joint at failure (14 min).

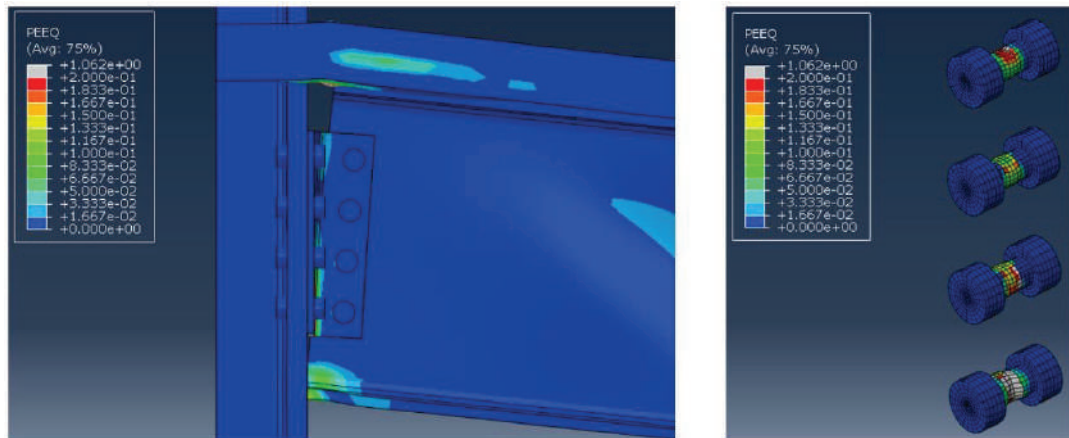


Figure 13. Equivalent plastic strain field in the double angle cleat joint at failure (20 min).

6 CONCLUSIONS

The paper described a comprehensive analysis of the fire behaviour of simple steel joints under a natural fire curve representative of the scenario of burning vehicles. A global analysis of an unprotected open steel car park was performed without explicitly modelling the joints. The structural checks of the joints in fire conditions was performed according to Annex D of EN 1993-1-2. All the 3 different joint types, i.e. end plate, fin plate and double angle cleat, did not exhibited satisfactory behaviour according to EN 1993-1-2, posing the issue of performing more refined analyses. Indeed, the thermal action generated by the Hasemi model determined such high axial forces in both the heating and the cooling phases that even overdesign was not a viable option. Refined nonlinear numerical simulations of the three joint types were performed under the selected fire scenario. Appropriate boundary conditions were applied to capture indirect actions accurately. The analysis results showed that only the end plate joint did not collapse. It was observed that using a very thin end plate ($t=8$ mm) significantly reduces the tensile forces on the bolts that occurred during the cooling phase. Instead, both the double angle cleat joint and the fin plate joint exhibited brittle failure of the bolts during the heating phase, occurring after 20 and 14 minutes of analysis, respectively. Although the fin plate and the double angle cleat joints complied with the design recommendations provided in the COSSFIRE report, they did not withstand the heating phase. However, the recommendations were developed based on parametric analyses in which the temperature along the beam was uniform, and the temperatures in the joint were much lower than the temperatures reached in this paper. For the case study under investigation and the selected fire scenario, the use of end plate joints as simple steel joints is recommended.

ACKNOWLEDGMENT

The authors acknowledge the Italian Ministry of Education, Universities and Research (MUR), in the framework of the project DICAM-EXC (Departments of Excellence 2023-2027, grant L232/2016).

Moreover, the information about the structural design provided by design B&V Eng-Arch Office, Corso Novara 99, Turin, Italy, is also acknowledged.

REFERENCES

1. Burgess IW, Davison JB, Huang SS, Dong G. The role of connections in the response of steel frames to fire. *Struct Eng Int*;22(4):449–61, 2012.
2. Wald F, Simoes da Silva L, Moore DB, Lennon T, Chladná M, Santiago A, Benes M, Borges L, Experimental behaviour of a steel structure under natural fire, *Fire Safety Journal*, 41, 509–522, 2006.
3. Block FM, Davison JB, Burgess IW, Plank RJ, Principles of a component-based connection element for the analysis of steel frames in fire, *Engineering Structures* 49, 1059–1067, 2013.
4. Spyrou S, Davison JB, Burgess IW, Plank RJ. Experimental and analytical investigation of the ‘tension zone’ component within a steel joint at elevated temperatures. *J Constr Steel Res*, 60:867–96, 2004.
5. Spyrou S, Davison JB, Burgess IW, Plank RJ. Experimental and analytical investigation of the ‘compression zone’ component within a steel joint at elevated temperatures. *J Constr Steel Res*, 60:841–65, 2004.
6. Gernay T, Franssen JM, The introduction and the influence of semi-rigid connections in framed structures subjected to fire, *Fire Safety Journal* 114, 103007, 2020.
7. Santiago A, Silva L, Vila Real P, Vaz G, Gameiro Lopes A, Experimental evaluation of the influence of connection typology on the behavior of steel structures under fire. *Engineering Journal*, 46, 2008.
8. Silva Da LS, Santiago A, Vila Real PV, Moore D, Behaviour of steel joints under fire loading, *Steel and Composite Structures*, 5 (6), pp. 485-513, 2005.
9. Choe L et al., Compartment Fire Experiments on Long-Span Composite-Beams with Simple Shear Connections Part 2: Test Results, NIST Technical Note 2055, 2019, <https://doi.org/10.6028/NIST.TN.2055>.
10. European Committee for Standardisation, Eurocode 3 Design of steel structures - Part 1-2: General rules - Structural fire design, 2005.
11. Zhao B, Roosefid M, Breunese A, Franssen JM, Zilli G, Zhao B, Hanus F, and Koutlas G. Connections of steel and composite structures under natural fire conditions (COSSFIRE), RFCS Final report, 2011.
12. Somnavilla M, Tondini N, Fire performance of a steel open car park in the light of the recent development of the localised fire model “LOCAFI”, Proceedings of 11th International Conference on Structures in Fire (SiF 2020), Brisbane, Australia, 30 November – 2 December, 2020.
13. European Committee for Standardisation, Eurocode 1 Actions on structures Part 1-2: General actions - Actions on structures exposed to fire, 2002.
14. Tondini N., Thauvoye C., Hanus F., Vassart O. (2019) Development of an analytical model to predict the radiative heat flux to a vertical element due to a localised fire, *Fire Safety Journal*, 105:227-243.
15. Ministero dell’Interno, D.M. 3 agosto 2015 “Approvazione di norme tecniche di prevenzione incendi”, ai sensi dell’articolo 15 del decreto legislativo 8 marzo 2006, n. 139, Roma, 2015.
16. Franssen J.-M., Gernay T. (2017) Modeling structures in fire with SAFIR©: Theoretical background and capabilities. *Journal of Structural Fire Engineering*, 8 (3), 300-323.
17. European Committee for Standardisation, Eurocode 3 Design of steel structures - Part 1-8: Design of joints, 2005.
18. Jaspart JP and Weynand K, Design of Joints in Steel and Composite Structures. ECCS Eurocode design manuals, ECCS, 2016.
19. ABAQUS/Standard User’s Manual, Version 6.9. Dassault Systèmes Simulia Corp, United States, 2009
20. European Committee for Standardisation, Eurocode 2 Design of concrete structures Part 1-2: General rules - Structural fire design, 2004.
21. European Committee for Standardisation, Eurocode 4 Design of composite steel and concrete structures Part 1-2: General rules - Structural fire design, 2004.
22. Hanus F, Zilli G, Franssen J.-M., Behaviour of Grade 8.8 bolts under natural fire conditions—Tests and model, *Journal of Constructional Steel Research* 67:1292–1298, 2011.

CALCULATION OF FIRE PROTECTED STEEL SECTION TEMPERATURES IN PERFORMANCE-BASED FIRE DESIGN – EC3 CALCULATION METHOD GENERALIZED FOR NON-UNIFORM FIRE EXPOSURE

Timo Jokinen¹, Risto Ranua²

ABSTRACT

This paper presents modifications to the Eurocode 3 (EC3) temperature development calculation method for fire protected steel sections, that try to generalize the method for non-uniform fire exposure to better serve the demands in performance-based fire design (PBD). This paper expands a previous study (Jokinen, Ranua, Salminen, 2022), which only considered unprotected steel sections. A simple procedure for determining the required fire protection ratings in PBD is also presented. The validation studies for the modified method are presented utilizing 2D FEM (Finite Element Method) heat transfer analyses with SAFIR software. 36 different validation cases were studied with rock wool fire protection or with intumescent paint fire protection. The modified method was also benchmarked against a simplified application of the original EC3 method. The proposed calculation method had moderately good agreement with FEM validation. However, in some cases the modified method tended to produce notably hotter temperatures than with FEM, but this is conservative in terms of practical design. The proposed method is presented only as a supplementary tool for determining appropriate fire protections in PBD, and it should be used in tandem (not as a substitute) with more advanced structural analysis to better account for the indirect effects of the design fires in PBD (i.e. using FEM to also account indirect actions and displacements from thermal expansions, thermal gradients within cross-sections, non-linear material models, etc.).

Keywords: steel structures, fire protected section temperature, performance-based fire design, SAFIR, FDS

1 INTRODUCTION

The calculation methods presented in the Eurocodes don't fully explain how to calculate the temperature development of fire protected steel sections for the members exposed to non-uniform fire in performance-based fire design (PBD). Therefore, this paper aims to present modified calculation formulas for these situations and tries to validate them against 2D FEM (Finite Element Method) heat transfer analyses. A simple procedure for determining the required fire protection ratings in PBD is also presented. This paper expands the studies shown in [1], which only considered unprotected steel sections.

2 CALCULATION METHODS

2.1 Calculation method presented in EC3

If the conditions outside a fire protected steel section have uniform temperature distribution, the temperature development of the steel section can be calculated using the formulas given in Eurocode

¹ Senior Fire Safety Specialist, M.Sc, Markku Kauriala Ltd, Fire engineering and fire safety design consultants, Finland
e-mail: timo.jokinen@kauriala.fi ORCID: <https://orcid.org/0000-0002-7391-989X>

² Senior Fire Safety Consultant, M.Sc, Markku Kauriala Ltd, Fire engineering and fire safety design consultants, Finland
e-mail: risto.ranua@kauriala.fi

EN 1993-1-2 (EC3) section 4.2.5.2 [2] (also, there seems to be no changes to these equations in the upcoming Eurocode 2nd generation revisions):

$$\Delta\theta_{a,t} = \frac{\lambda_p \left(A_p/V \right) (\theta_{g,t} - \theta_{a,t})}{d_p c_a \rho_a (1 + \Phi/3)} \Delta t - (e^{\Phi/10} - 1) \Delta\theta_{g,t} \quad (\text{but } \Delta\theta_{a,t} \geq 0 \text{ if } \Delta\theta_{g,t} > 0) \quad (1)$$

$$\Phi = \frac{c_p \rho_p}{c_a \rho_a} d_p \left(A_p/V \right) \quad (2)$$

where

$\Delta\theta_{a,t}$ is the fire protected steel section temperature change during time step Δt [$^{\circ}\text{C}$]

$\theta_{a,t}$ is the fire protected steel section temperature at time t [$^{\circ}\text{C}$]

A_p/V is the section factor for steel members insulated by fire protection material [$1/\text{m}$]

A_p is the appropriate area of fire protection material per unit length of the member (calculated using the inner surface dimensions of the fire protection) [m^2/m]

V is the volume of the steel member per unit length [m^3/m]

c_a is the specific heat of steel [J/kgK]

c_p is the specific heat of the fire protection material [J/kgK]

d_p is the thickness of the fire protection material [m]

λ_p is the thermal conductivity of the fire protection material [W/mK]

ρ_a is the unit mass of steel ($7850 \text{ kg}/\text{m}^3$) [kg/m^3]

ρ_p is the unit mass of the fire protection material [kg/m^3]

Δt is the time step ($\Delta t \leq 30 \text{ s}$) [s]

$\theta_{g,t}$ is the ambient gas temperature at time t [$^{\circ}\text{C}$]

$\Delta\theta_{g,t}$ is the change of the ambient gas temperature during the time step Δt [K]

In the Eurocode by default, the values for c_a are temperature dependent, the values for c_p are temperature independent and the temperature dependency for λ_p , and ρ_p is not directly specified. However, in this study all these variables c_a , c_p , λ_p , and ρ_p can be temperature dependent in all shown methods for increased accuracy (see chapter 2.3). The temperature of the fire protection material layer $\theta_{p,t}$ is assumed to follow the average from the ambient gas temperature and the steel temperature:

$$\theta_{p,t} = \frac{\theta_{g,t} + \theta_{a,t}}{2} \quad (3)$$

2.2 Modified calculation method for performance-based fire design

In performance-based fire design, the temperature distribution around the steel section is often not uniform (e.g. in localized fires, in travelling fires, etc.), and the net heat fluxes can differ significantly from each other around the section (Figure 1a). This poses a problem when trying to utilize the aforementioned EC3 calculation method.

In fire simulations (for example when using Fire Dynamics Simulator, FDS [3]), it's common to utilize Adiabatic Surface Temperatures (AST) [4] when transferring the temperature data from the simulation to the structural analysis. Adiabatic surface temperature method takes into account the convective and radiative heat transfer between the gas and the solid structure and converts them to a single equivalent AST value. Especially in FDS, which utilizes rectilinear meshing of the simulation model, these AST values are often measured from four different main directions (Figure 1a & b). Therefore, the following modification is proposed to the section temperature calculation principle: The original fire protected steel section is separated to four identical "virtual" sections and the heating of each of them is calculated separately in the corresponding four different AST temperatures with only one side of the section exposed to ambient at each case (Figure 1c). The temperature development of the whole steel section can now be calculated after each time step just by adding together the partial temperature changes from each side of the section.

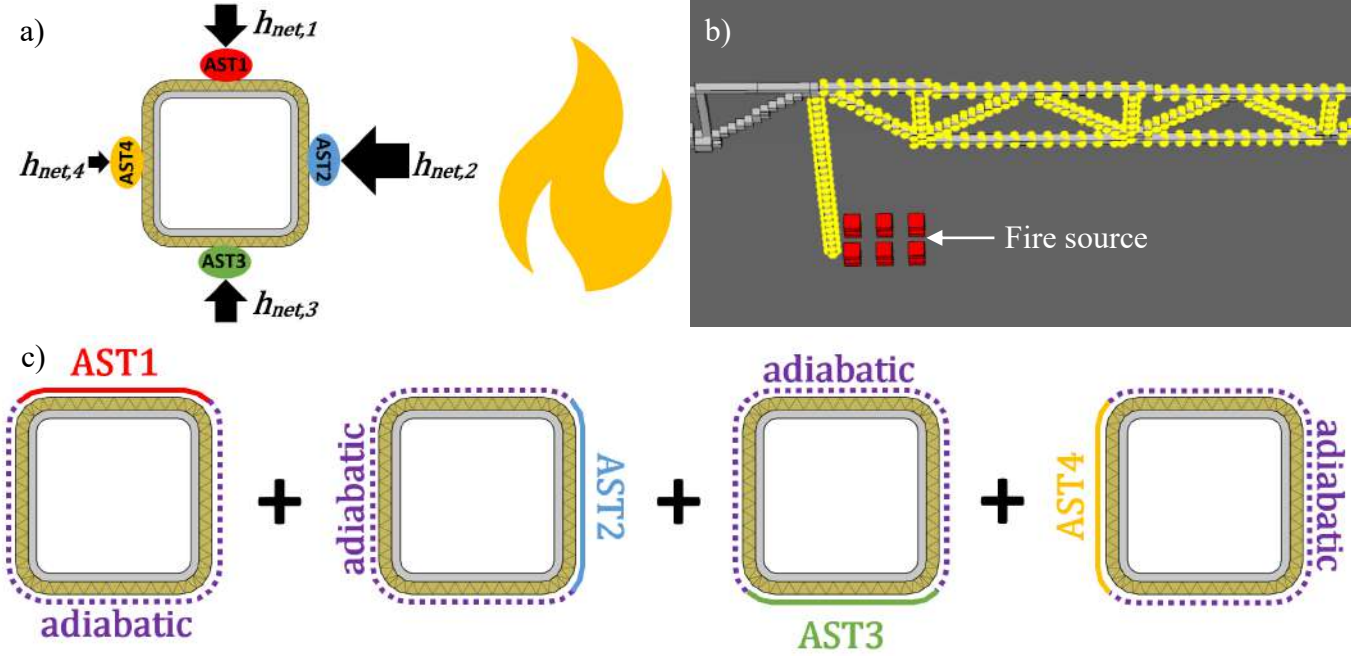


Figure 1. The principle for determining the temperatures that heat the structural steel sections using virtual adiabatic surface temperature (AST) measurement devices in fire simulations. a) The placement of AST measurement devices around the steel section and their corresponding net heat fluxes. b) A detail from an FDS model. c) The section temperature calculation principle in the proposed modified method for fire protected steel sections in non-uniform fires

This calculation can be done by modifying the previous Eurocode formulas the following way:

$$\theta_{a,t+1} = \theta_{a,t} + \Delta\theta_{a,t} \quad (\text{but } \theta_{a,t+1} \leq \max(\theta_{a,unp,0}, \dots, \theta_{a,unp,t-1}, \theta_{a,unp,t})) \quad (4)$$

$$\Delta\theta_{a,t} = \sum_{k=1}^n \Delta\theta_{a,t,k} \quad (5)$$

$$\Delta\theta_{a,t,k} = \frac{\lambda_{p,k} \left(\frac{A_{p,k}}{V} \right) (\theta_{AST,k,t} - \theta_{a,t})}{d_{p,eff} c_a \rho_a (1 + \Phi_k/3)} \Delta t - (e^{\Phi_k/10} - 1) \Delta\theta_{AST,k,t} \quad (\text{but } \Delta\theta_{a,t,k} \geq 0 \text{ if } \Delta\theta_{AST,k,t} > 0) \quad (6)$$

$$\Phi_k = \frac{c_{p,k} \rho_{p,k}}{c_a \rho_a} d_{p,eff} \left(\frac{A_{p,k}}{V} \right), \quad \theta_{p,k,t} = \frac{\theta_{AST,k,t} + \theta_{a,t}}{2} \quad (7), (8)$$

where

- $\Delta\theta_{a,t,k}$ is the partial temperature change in the fire protected steel section resulting from the adiabatic surface temperature acting on the corresponding side of the section at time t [°C]
- $\theta_{a,unp,t}$ is the section temperature in similar unprotected steel section at time t [°C]. This can be calculated, for example, by using the methods presented in [1]
- $A_{p,k}/V$ is the section factor for fire protected steel member on each of the four different sides of the section [1/m] (see Figure 1c, the section factor values are calculated using the inner surface dimensions of the fire protection like in the EC3 method). The sum of each side should result in the original section factor of the entire section, i.e. $\sum_{k=1}^4 (A_{p,k}/V) = A_p/V$
- $\theta_{AST,k,t}$ is the adiabatic surface temperature on each side of the section at time t [°C]
- $\lambda_{p,k}$ is the temperature dependent thermal conductivity of the fire protection material on each side of the section at time t [W/mK]
- $c_{p,k}$ is the temperature dependent specific heat of the fire protection material on each side of the section at time t [J/kgK]
- $\rho_{p,k}$ is the temperature dependent unit mass of the fire protection material on each side of the section at time t [J/kgK]
- $d_{p,eff}$ is the effective thickness of the fire protection material (see chapter 2.3) [m]

$\theta_{p,k,t}$ is the temperature of the fire protection material on each side of the section at time t [°C]
 n is the number of sides exposed to ambient (i.e. by default $n = 4$)

As shown in equation (4), in the heating phase of the fire the temperature development of the fire protected steel section is limited below the temperature development of similar unprotected steel section, because without this limit the fire protected steel section may heat up quicker than the similar unprotected steel section in some rare cases (e.g. when using very small fire protection material thicknesses), which obviously would not make any sense. This is an oversight in the original EC3 method also.

These equations do not incorporate the shadow effect correction factors (i.e. the slight slowdown in the temperature development observed in concave sections due to parts of the section remaining obscured by other parts of the section), because the original EC3 method didn't utilize it either. Nevertheless, adding shadow effect correction should be possible in a similar way than shown in [1], but this has not been studied here.

If one or more steel member side is obstructed by walls, floor slabs, etc., the value of n is lowered and the obstructed side is disregarded, which results in an adiabatic boundary condition to the obstructed sides of the section. This should be a conservative assumption for wide range of different obstruction materials, since usually the heat flux direction is from the steel section towards the obstruction at least during the heating phase [5]. Conversely, assuming a constant 20 °C temperature to the obstructed section side may lead to too large “cooling effect” from the obstruction and the steel temperature development may be underestimated.

2.3 Thermal properties of the fire protection materials

Two different types of fire protection are studied: rock wool fire protection (RW) and intumescent paint fire protection (IP).

The density of rock wool can significantly affect its fire protection abilities, so a relatively heavy fire protection rock wool is chosen with a density of 170 kg/m³ at 20 °C. A thermal material model for the chosen rock wool type is determined based the methods proposed by Schleifer [6] (where the thermal conductivities are calculated as a function of the rock wool density) and the resulting temperature dependant thermal properties are shown in Figure 2.

The intumescent paint is modelled with an effective fire protection material thickness that remains constant during the whole fire, and the swelling of the intumescent layer is taken into account with an effective (or apparent) thermal conductivity model as proposed by Lucherini [7]. In this model, the thermal conductivity is relatively high when the intumescent temperature is below 100 °C (when no swelling has occurred), after that the conductivity lowers as the temperature increases until it reaches 400 °C and then the conductivity remains at a constant value (when full swelling has occurred). The specific heat and density of the intumescent are assumed to remain constant, and their effective values are determined based on [8, 9]. The resulting thermal properties are shown in Figure 3. This exact material model for the intumescent paint was used in [10], where the steel section temperature development had relatively good agreement between experimental and numerical methods (however the test series had only one fire protected experiment).

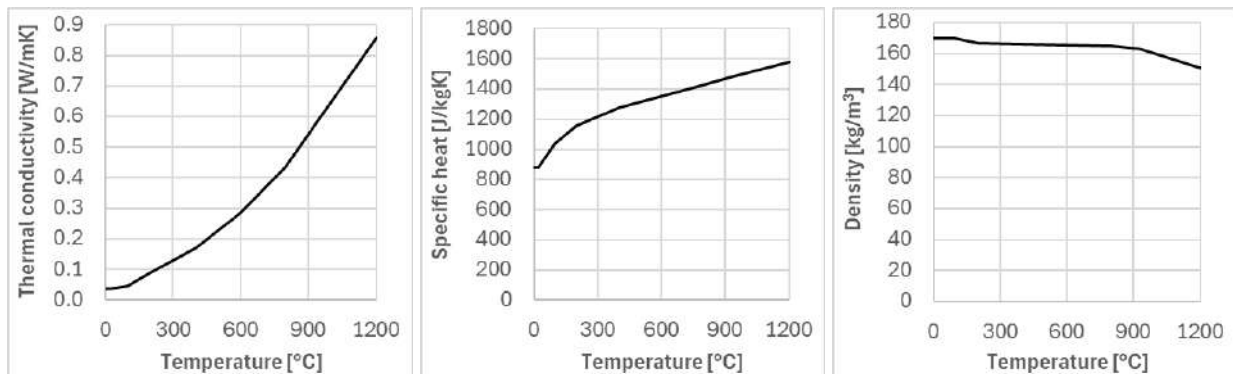


Figure 2. Utilized temperature dependant thermal material properties for rock wool (RW) fire protection [6]

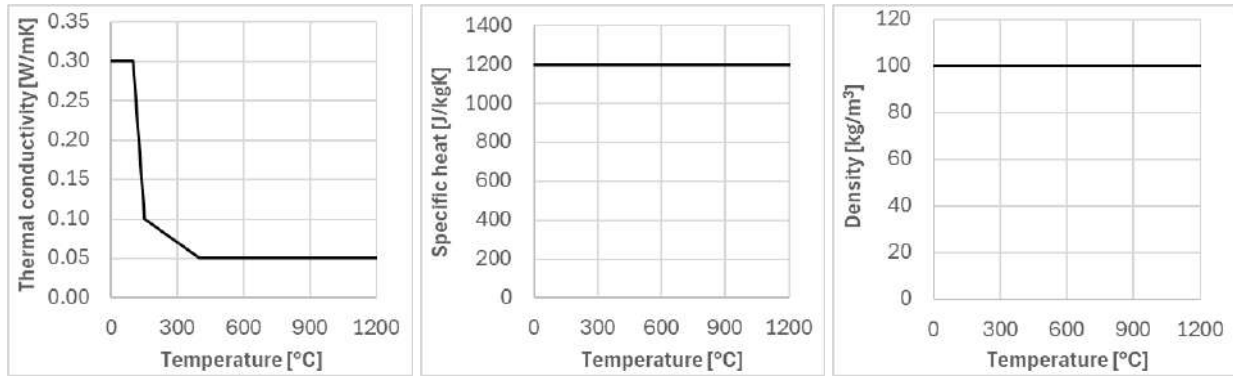


Figure 3. Utilized effective / apparent thermal material properties for intumescent paint (IP) fire protection [7-10]

2.4 Determining the required fire protection rating in performance-based fire design

In performance-based fire design the required fire protection often must be converted to equivalent R-class (R30, R45, R60, etc.), because most fire protection system manufactures do not provide an easy way to utilize their products directly in natural fires. The required fire protection rating can be determined by using the following simple procedure, which has also been utilized in this study (see Figure 4. An application of this procedure in a real case study can also be seen in [11]):

1. The following steps are proceeded, if the unprotected steel section exceeds the member critical temperature, or if there is too small safety margin, or if the structure fails the analysis using more advanced models (e.g. failure in the FEM analysis of the structure). The temperature development of the unprotected steel members can be calculated by using the methods shown in [1].
2. The steel section temperature development is calculated in standard fire [12] (ISO-fire, ISO834 fire) with fire protection by utilizing the regular EC3 method as shown in chapter 2.1.
3. The thickness of the chosen fire protection material is optimized in such a way that the steel section temperature in ISO-fire is exactly the same as the member critical temperature $\theta_{a,crit}$ at the chosen fire protection rating time point (e.g. $\theta_{a,t} = \theta_{a,crit}$ at 45 min in R45, etc.).
4. The steel section temperatures are calculated again in the design fire exposure using exactly the same fire protection material properties and layer thickness than in previous step by utilizing the method shown in chapter 2.2. If the section temperature remains now below the critical temperature of the member, the fire protection rating is sufficient for the studied design fire in PBD.

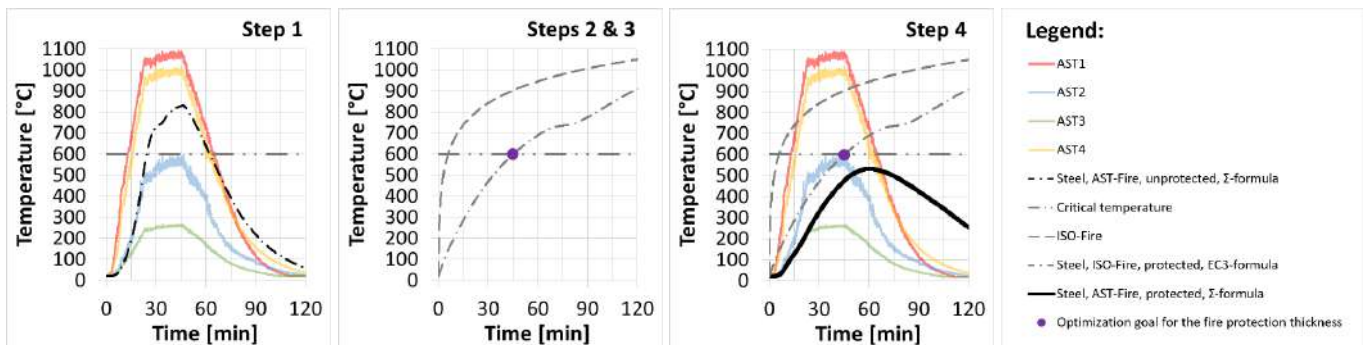


Figure 4. Method for determining the required fire protection rating in performance-based design (R45 in this case)

3 VALIDATION CALCULATIONS USING FEM

3.1 Validation methods and models

This paper also aims to present validation studies for the presented modified calculation method (hence referred here also as the Σ -formulas) by comparing the section temperature development with the Σ -formulas to the development of section temperature average calculated using 2D FEM analysis with SAFIR software [13] (version 2022.d.5). SAFIR is extensively validated [13, 14, 15, 16] and widely used software for analysing structures in elevated temperatures. In addition to the FEM analysis, the modified calculation

method is also benchmarked against the regular EC3 calculation method (section 2.1) by substituting the $\theta_{g,t}$ in the EC3 equations with a simple average temperature curve from the non-uniform AST values:

$$\theta_{g,t} = \theta_{AST,avg,t} = \frac{\sum_{k=1}^n \theta_{AST,k,t}}{n} \quad (9)$$

The validation studies are started by calculating the sections in standard fire exposure and then four different non-uniform fire exposures are studied (Fires 1-4 or F1-F4, Figure 5). The AST data in these four fire exposures originates from FDS simulations of different cases. Three different steel sections are analysed (CFRHS150x100x5, CFRHS200x200x10 and HEB300) and, as mentioned before, two different fire protection materials are studied (rock wool and intumescent paint). The validation studies focus on relatively low fire protection classes (R30 and R45 with critical temperatures of 400, 600 or 650 °C), but some higher protection classes are also studied (R90 with $\theta_{a,crit}$ of 600 or 650 °C). Some additional variables are also briefly studied (the effect of obstructed surfaces, the effect of longer fire durations, the effect of noise in the temperature data and the effect of peaks and valleys in the temperature data).

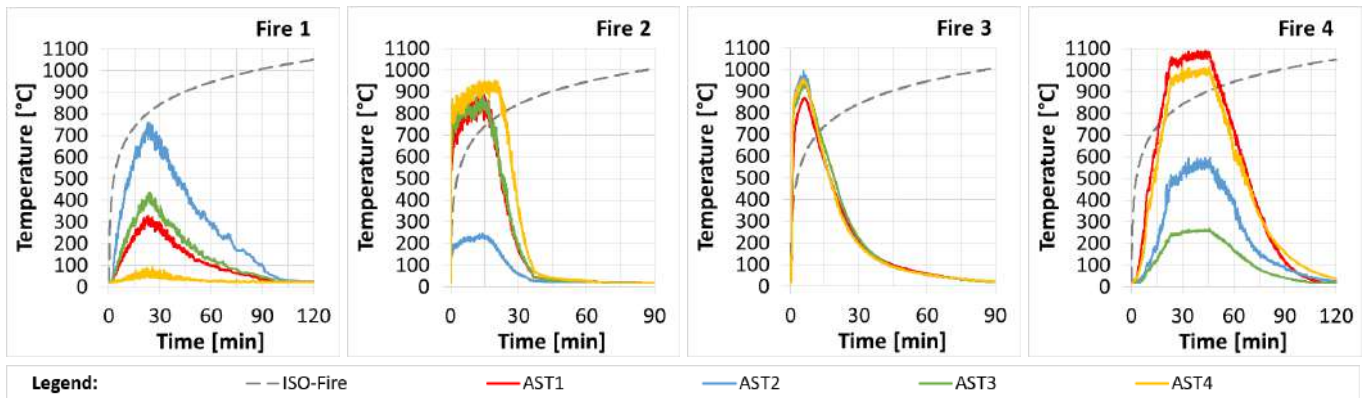


Figure 5. Fires 1-4 (or F1-F4) that are used in the validation calculations. Standard fire shown as a comparison

In the SAFIR validation, 2D section is modelled with four temperature frontier constraints acting on the section boundaries (Figure 6). The heat exchange in the internal cavity is also taken into account in tubular sections by utilizing a void constraint. In the SAFIR models, the parameters for the steel and the surface layers ($c_a, \lambda_a, \rho_a, \varepsilon_a, \alpha_c$) follow the values described in Eurocodes [2, 12] (e.g. $\alpha_c = 35 \text{ W/m}^2\text{K}$ in natural fires, $\varepsilon_a = 0.7$) and the material properties for the fire protection are as shown in chapter 2.3. The emissivities of the fire protection materials are set to $\varepsilon_p = 0.8$. The SAFIR models consist of 400 – 23840 elements depending on the section type and fire protection thickness, and a maximum calculation time step of 1.0 s is used. From the resulting SAFIR temperature data, an average steel section temperature curve is calculated as a weighted arithmetic mean where the element temperature is weighted by the element area (elements of the fire protection material are omitted from the average). Figure 7 shows examples from the resulting temperature gradients and SAFIR section temperature curves compared against the two formulas. All the analysed validation cases, their parameters and summary of their results are presented in Table 1.

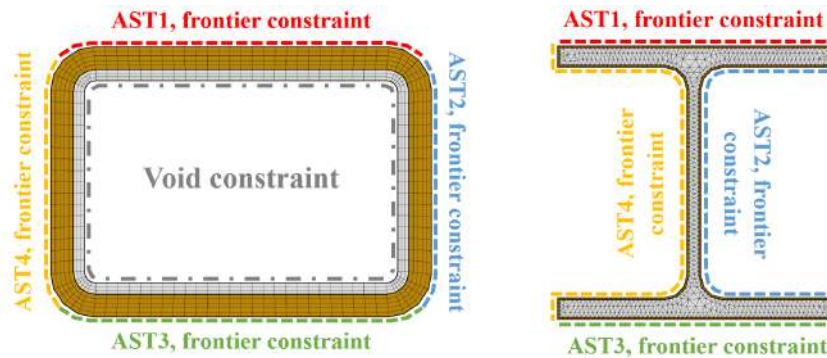


Figure 6. Examples of the SAFIR 2D heat transfer analysis models used in the validation calculations:
a) CFRHS150x100x5 section with rock wool fire protection (R30, $\theta_{a,crit} = 600 \text{ °C}$, $d_{p,eff} = 10.0 \text{ mm}$),
b) HEB300 section with intumescent paint fire protection (R45, $\theta_{a,crit} = 650 \text{ °C}$, $d_{p,eff} = 2.5 \text{ mm}$)

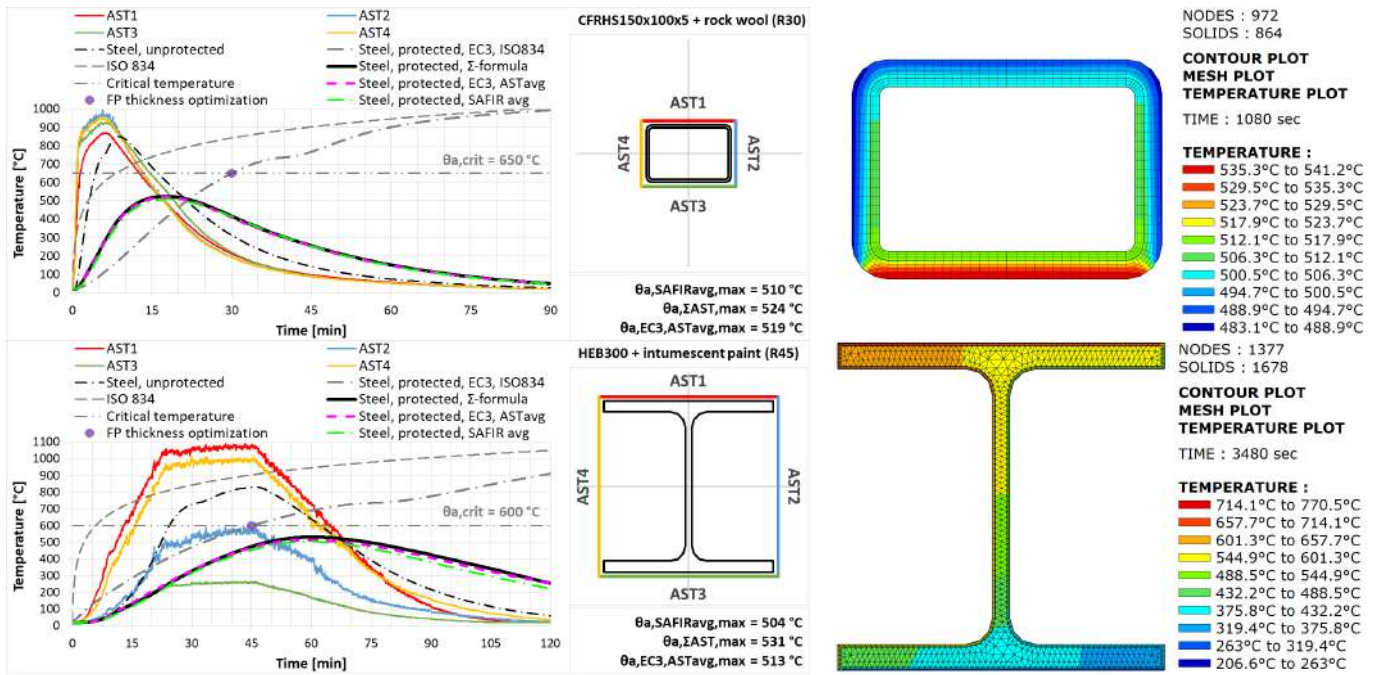


Figure 7. Left: Example figures comparing the section temperature development with fire protection using SAFIR model averages (dash dot green curves) vs. Σ -formulas (solid black curves) vs. simpler EC3-formulas (dashed magenta curves). Right: The corresponding temperature gradients at the hottest timepoint in the SAFIR models. Example calculations shown for a R30 rock wool protected closed section (top) and for a R45 intumescent paint protected open section (bottom)

3.2 Validation results in standard fire

Cases 1 – 8 are analysed in standard fire and the resulting temperature curves are shown in Figure 8. Cases 1 – 4 are with rock wool and 5 – 8 are with intumescent paint fire protection.

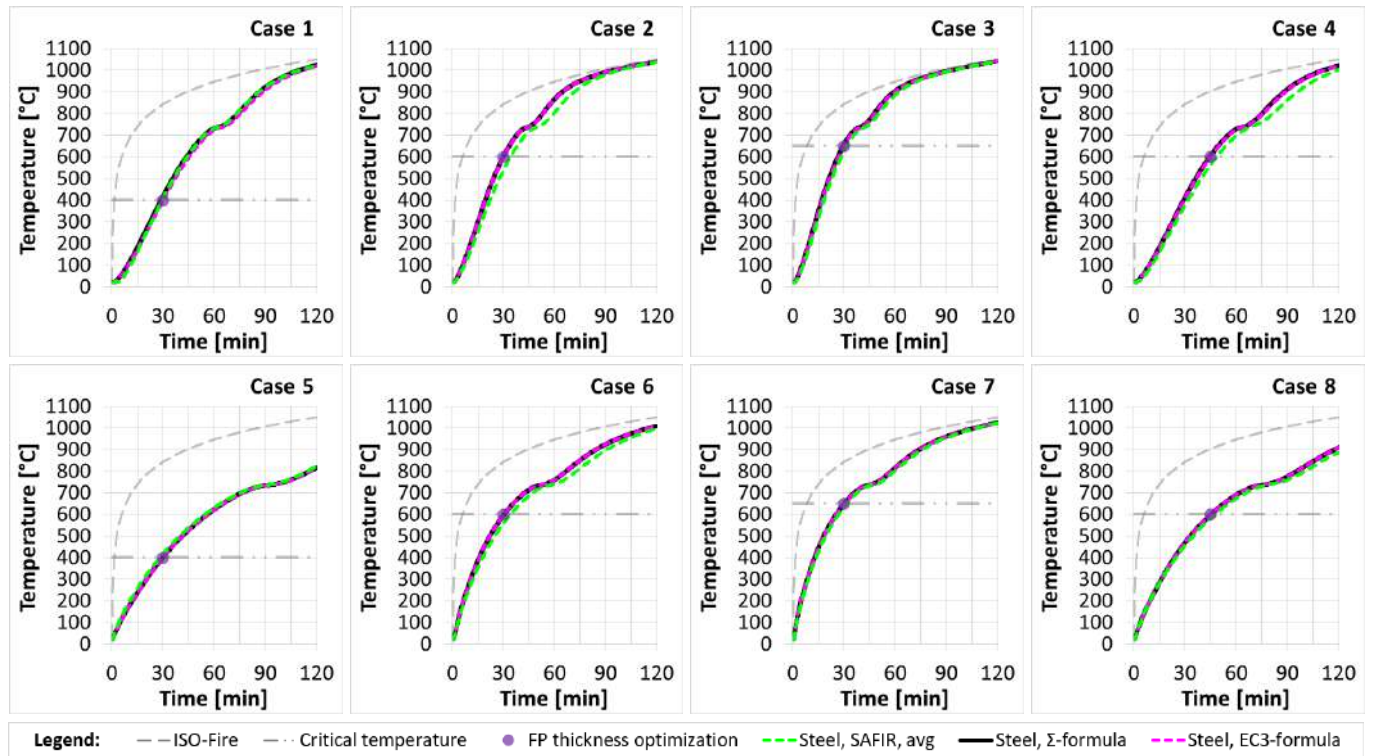


Figure 8. Temperature results in standard fire. Cases 1 – 4 with RW and 5 – 8 with IP fire protection

3.3 Validation results in non-uniform fire

Cases 9 – 16 are analysed in the non-uniform fires F1 – F4 and the resulting temperature curves are shown in Figure 9. Cases 9 – 12 are with rock wool and 13 – 16 are with intumescent paint fire protection.

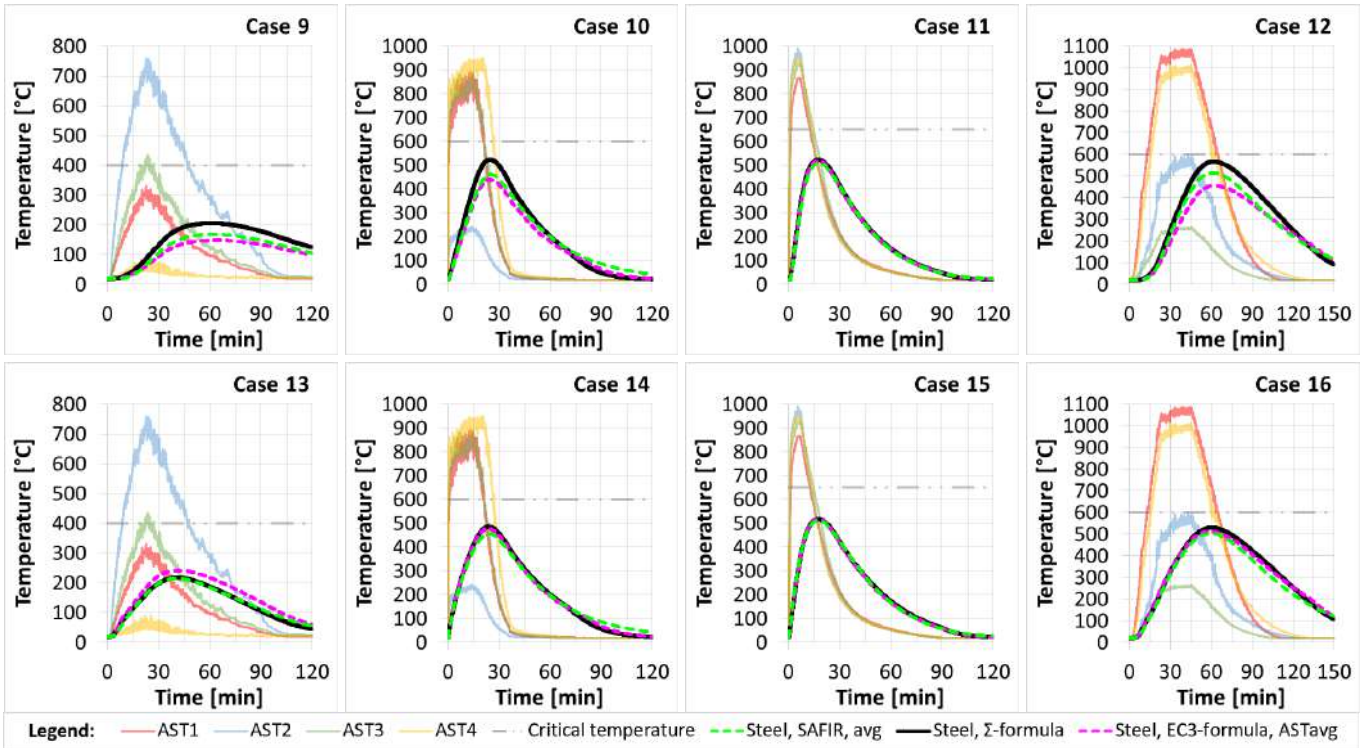


Figure 9. Temperature results in non-uniform fires F1 – F4. Cases 9 – 12 with RW and 13 – 16 with IP fire protection

3.4 Validation results in other cases

Cases 17 – 24 are analysed in non-uniform fires when the cool side of the member is obstructed (i.e. the coolest temperature curve is replaced with an adiabatic surface), and the resulting temperature curves are shown in Figure 10. Cases 17 – 20 are with rock wool and 21 – 24 are with intumescent paint fire protection.

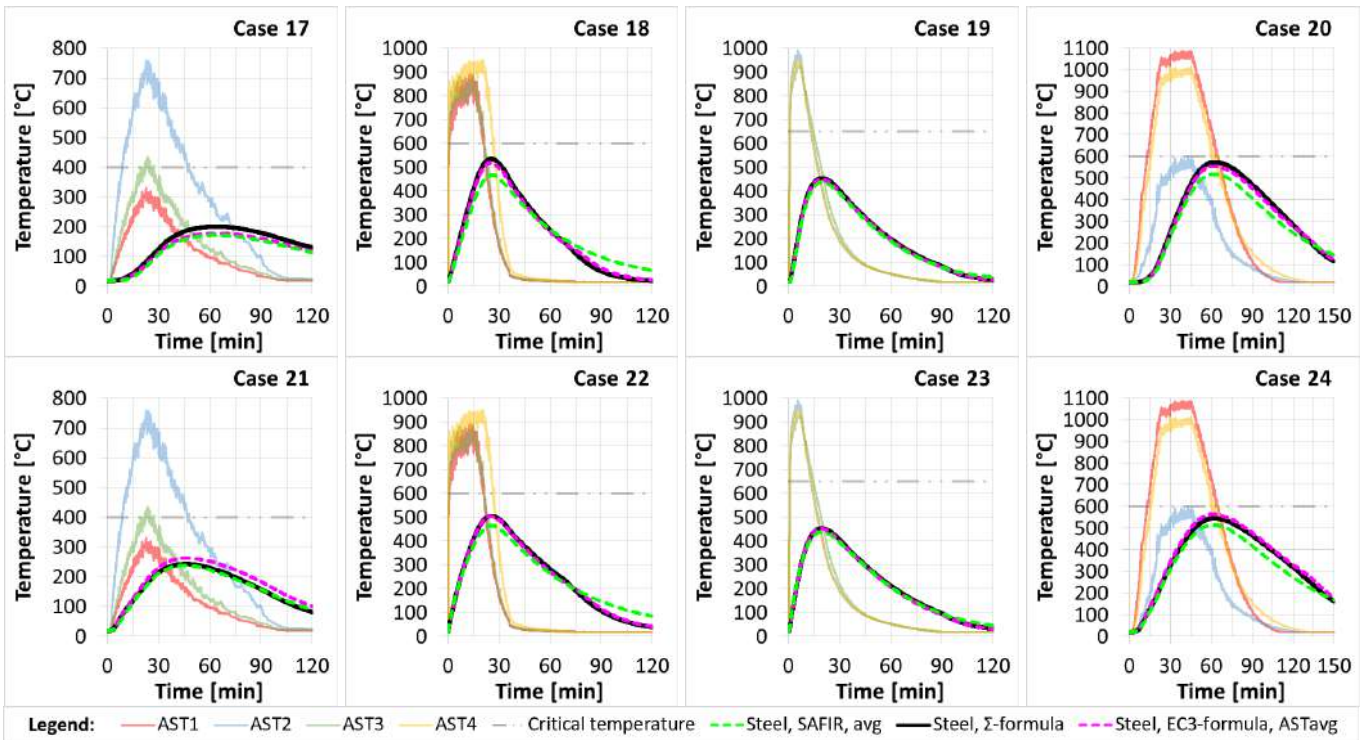


Figure 10. Temperature results in non-uniform fires when the cool side of the section is obscured (adiabatic surface)

Cases 25 – 28 (Figure 11) are analysed in non-uniform fires when fires F3 and F4 are significantly extended by stretching the AST data at the hottest timepoints. The fire protection ratings are also increased from R30 and R45 to R90. Cases 25 – 26 are with rock wool and 27 – 28 are with intumescent paint fire protection.

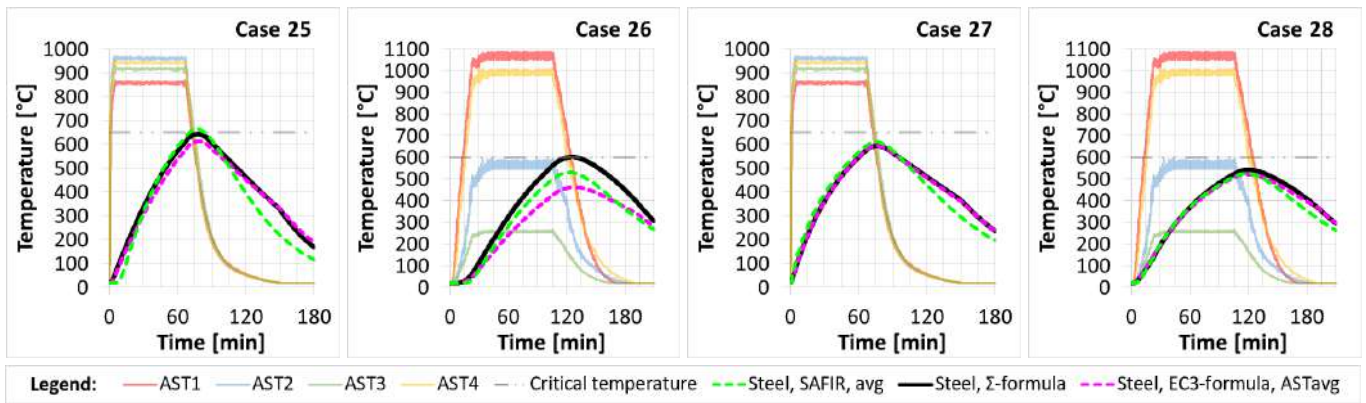


Figure 11. Temperature results when the fire durations of Fires 3 – 4 are significantly lengthened at the middle

Cases 29 – 32 (Figure 12) are analysed in Fire 4 when random noise is added to the AST data ($\pm 15\%$) and when the noise is smoothed out from the data (exponential smoothing with a damping factor of 0.95). Cases 29 & 31 are with rock wool and 30 & 32 are with intumescent paint fire protection. These should also be compared against the corresponding regular cases 12 and 16.

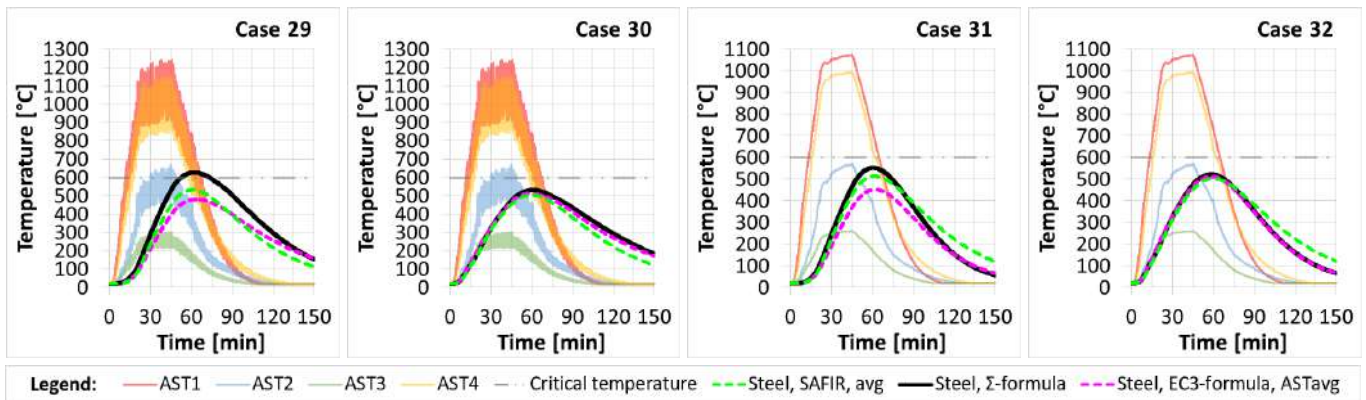


Figure 12. Temperature results when more noise is added to the AST data or the noise is smoothed out from the data of Fire 4

Cases 33 – 36 (Figure 13) are analysed with multiple peaks and valleys in the AST data with a new Fire 5 which is artificially generated (with sinusoidal functions and lines). Cases 33 – 34 are calculated with perfectly smooth AST data and cases 35 – 36 with slightly noisy AST data ($\pm 2\%$ random noise). Cases 33 & 35 are with rock wool and 34 & 36 are with intumescent paint fire protection.

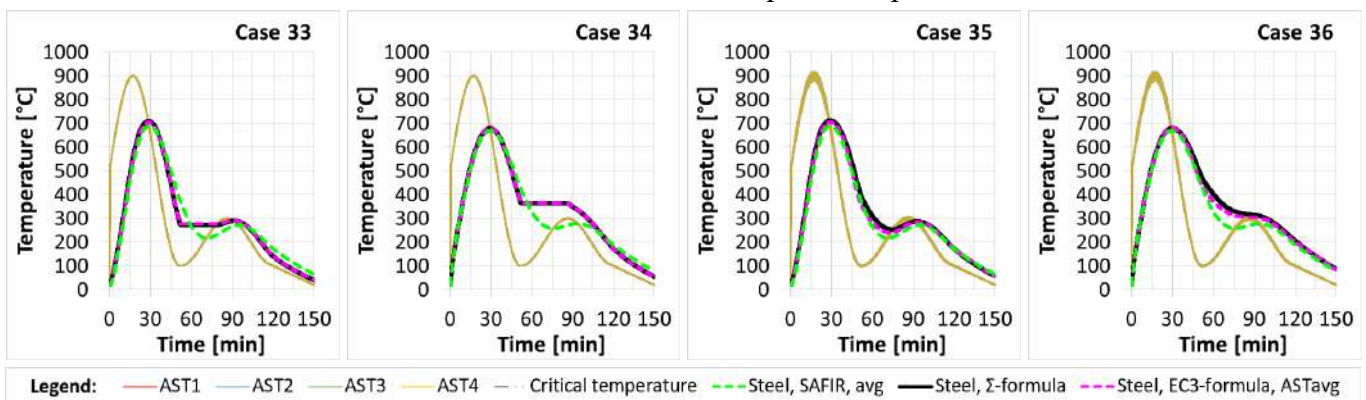


Figure 13. Temperature results with multiple peaks and valleys in the AST data (Fire 5). Perfectly smooth AST data in cases 33 – 34 and slightly noisy AST data in cases 35 – 36

3.5 Validation result tables

All the analysed validation cases, their parameters and summary of their results are shown in Table 1, and the used symbols are shown in the following equations. Most important benchmark values are the differences in the maximum steel section temperature values with different calculation methods compared

against SAFIR results (equations (10) - (13)), but maximum, minimum, mean, and standard deviation values are also recorded from these differences during the entire run at 60 s intervals (equations (14) - (15)). The summary of the deviations from the hottest SAFIR steel temperatures values are shown in Table 2 with the summary values separated to the two different fire protection materials.

$$\Delta\theta_{a,\Sigma AST} = \max(\theta_{a,\Sigma-formula}(t)) - \max(\theta_{a,SAFIR,avg}(t)), \quad t = 0 \dots t_{end} \quad (10)$$

$$\Delta\theta_{a,EC3} = \max(\theta_{a,EC3-formula,ASTavg}(t)) - \max(\theta_{a,SAFIR,avg}(t)), \quad t = 0 \dots t_{end} \quad (11)$$

$$\Delta\theta_{a,\Sigma AST,\%} = \frac{\Delta\theta_{a,\Sigma AST}}{\max(\theta_{a,SAFIR,avg}(t))}, \quad \Delta\theta_{a,EC3,\%} = \frac{\Delta\theta_{a,EC3}}{\max(\theta_{a,SAFIR,avg}(t))} \quad (12), (13)$$

$$\Delta\theta_{a,\Sigma-formula}(t) = \theta_{a,\Sigma-formula}(t) - \theta_{a,SAFIR,avg}(t), \quad t = 0 \text{ s}, 60 \text{ s}, 120 \text{ s} \dots t_{end} \quad (14)$$

$$\Delta\theta_{a,EC3-formula,ASTavg}(t) = \theta_{a,EC3-formula,ASTavg}(t) - \theta_{a,SAFIR,avg}(t), \quad t = 0 \text{ s}, 60 \text{ s}, 120 \text{ s} \dots t_{end} \quad (15)$$

Table 1. All the analysed validation cases, their parameters and summary of their results

#	Fire	Section	FP class	$\theta_{a,crit}$ [°C]	FP mtr.	$d_{p,eff}$ [mm]	$\Delta\theta_{a,\Sigma AST}$		$\Delta\theta_{a,EC3}$		$\Delta\theta_{a,\Sigma-formula,AST}(t)$ [°C]				$\Delta\theta_{a,EC3-formula,ASTavg}(t)$ [°C]			
							max [°C]	max [°C]	max [%]	max [%]	max	min	mean	st.dev	max	min	mean	st.dev
1	ISO	RHS150x100x5	R30	400	RW	21.8	-	-	-	-	25	-3	4	8	21	-17	-7	10
2	ISO	RHS200x200x10	R30	600	RW	6.2	-	-	-	-	64	0	31	22	62	0	30	21
3	ISO	RHS150x100x5	R30	650	RW	10.0	-	-	-	-	35	0	14	12	28	0	12	10
4	ISO	HEB300	R45	600	RW	12.8	-	-	-	-	54	0	33	13	49	0	29	11
5	ISO	RHS150x100x5	R30	400	IP	5.9	-	-	-	-	0	-22	-9	6	0	-23	-11	6
6	ISO	RHS200x200x10	R30	600	IP	1.3	-	-	-	-	38	0	26	10	38	0	26	10
7	ISO	RHS150x100x5	R30	650	IP	1.9	-	-	-	-	18	0	9	5	18	0	9	5
8	ISO	HEB300	R45	600	IP	2.5	-	-	-	-	24	0	13	7	24	0	13	7
9	F1	RHS150x100x5	R30	400	RW	21.8	38	-20	22 %	-12 %	38	0	27	11	3	-21	-12	8
10	F2	RHS200x200x10	R30	600	RW	6.2	62	-23	13 %	-5.0 %	64	-38	5	34	2	-29	-19	7
11	F3	RHS150x100x5	R30	650	RW	10.0	14	9	2.8 %	1.8 %	22	-5	4	7	17	-8	2	6
12	F4	HEB300	R45	600	RW	12.8	51	-60	9.9 %	-12 %	61	-26	30	25	18	-61	-18	27
13	F1	RHS150x100x5	R30	400	IP	5.9	3	27	1.2 %	13 %	12	-11	-2	6	33	0	22	9
14	F2	RHS200x200x10	R30	600	IP	1.3	29	22	6.4 %	4.8 %	30	-30	-2	20	25	-23	-1	15
15	F3	RHS150x100x5	R30	650	IP	1.9	6	6	1.1 %	1.1 %	6	-17	0	5	6	-17	-3	5
16	F4	HEB300	R45	600	IP	2.5	27	9	5.3 %	1.8 %	46	-14	22	16	33	-2	19	9
17	F1, 3 sides	RHS150x100x5	R30	400	RW	21.8	29	6	17 %	3.7 %	30	0	21	8	9	0	6	2
18	F2, 3 sides	RHS200x200x10	R30	600	RW	6.2	67	50	14 %	11 %	68	-60	-3	45	55	-50	-5	35
19	F3, 3 sides	RHS150x100x5	R30	650	RW	10.0	18	12	4.1 %	2.8 %	18	-11	6	9	13	-10	3	7
20	F4, 3 sides	HEB300	R45	600	RW	12.8	54	36	10 %	7.0 %	65	-31	33	27	46	-23	24	18
21	F1, 3 sides	RHS150x100x5	R30	400	IP	5.9	5	25	2.0 %	10 %	13	-9	3	5	31	0	21	7
22	F2, 3 sides	RHS200x200x10	R30	600	IP	1.3	40	38	8.5 %	8.2 %	40	-50	-1	33	39	-46	-2	29
23	F3, 3 sides	RHS150x100x5	R30	650	IP	1.9	16	15	3.8 %	3.4 %	17	-15	1	9	15	-16	-2	9
24	F4, 3 sides	HEB300	R45	600	IP	2.5	31	49	6.0 %	9.4 %	53	-7	29	17	62	0	43	18
25	F3, extended	RHS150x100x5	R90	650	RW	47.5	-22	-52	-3.2 %	-7.8 %	107	-22	29	43	112	-55	8	54
26	F4, extended	HEB300	R90	600	RW	34.1	70	-70	13 %	-13 %	85	0	48	23	13	-74	-40	30
27	F3, extended	RHS150x100x5	R90	650	IP	9.0	-18	-17	-2.9 %	-2.9 %	71	-37	-1	33	67	-38	-3	32
28	F4, extended	HEB300	R90	600	IP	6.2	17	-3	3.2 %	-0.6 %	40	-6	8	12	18	-7	0	7
29	F4, noisy	HEB300	R45	600	RW	12.8	94	-52	18 %	-9.8 %	112	0	71	33	47	-57	-2	35
30	F4, noisy	HEB300	R45	600	IP	2.5	27	8	5.3 %	1.6 %	71	0	39	25	51	0	27	16
31	F4, smooth	HEB300	R45	600	RW	12.8	39	-61	7.5 %	-12 %	41	-72	-12	42	1	-74	-52	25
32	F4, smooth	HEB300	R45	600	IP	2.5	18	9	3.6 %	1.8 %	23	-64	-18	33	27	-66	-20	34
33	F5, smooth	RHS150x100x5	R30	650	RW	10.0	19	15	2.7 %	2.1 %	54	-100	-2	35	59	-95	-1	34
34	F5, smooth	RHS150x100x5	R30	650	IP	1.9	10	9	1.4 %	1.4 %	107	-61	16	44	107	-61	16	44
35	F5, noisy	RHS150x100x5	R30	650	RW	10.0	20	15	3.0 %	2.2 %	46	-7	18	16	25	-21	10	12
36	F5, noisy	RHS150x100x5	R30	650	IP	1.9	10	9	1.4 %	1.4 %	82	-6	29	24	60	-6	20	16
							max				max	min	mean	st.err	max	min	mean	st.err
							94	50	22.2 %	12.8 %								
							-22	-70	-3.2 %	-13 %								
							28	0.4	6.5 %	0.5 %								
							25.9	33	6.3 %	7.3 %								

Table 2. Summary: deviations from the maximum steel temperatures separated to the two fire protection materials

	All cases				Only rock wool cases				Only intumescent paint cases			
	$\Delta\theta_{a,\Sigma AST}$ max [°C]	$\Delta\theta_{a,EC3}$ max [°C]	$\Delta\theta_{a,\Sigma AST}$ max [%]	$\Delta\theta_{a,EC3}$ max [%]	$\Delta\theta_{a,\Sigma AST}$ max [°C]	$\Delta\theta_{a,EC3}$ max [°C]	$\Delta\theta_{a,\Sigma AST}$ max [%]	$\Delta\theta_{a,EC3}$ max [%]	$\Delta\theta_{a,\Sigma AST}$ max [°C]	$\Delta\theta_{a,EC3}$ max [°C]	$\Delta\theta_{a,\Sigma AST}$ max [%]	$\Delta\theta_{a,EC3}$ max [%]
Max.	94	50	22.2 %	12.8 %	94	50	22.2 %	10.7 %	40	49	8.5 %	12.8 %
Min.	-22	-70	-3.2 %	-13.1 %	-22	-70	-3.2 %	-13.1 %	-18	-17	-2.9 %	-2.9 %
Mean	28	0	6.5 %	0.5 %	40	-14	9.6 %	-2.9 %	16	15	3.3 %	3.9 %
St.dev.	26	33	6.3 %	7.3 %	29	40	7.2 %	8.1 %	15	17	2.9 %	4.6 %

4 DISCUSSION

Overall, the validation analyses show that the agreement between SAFIR section temperature curves and the two calculation formulas is moderately good, but not as good as in the corresponding studies for unprotected steel sections [1]. The agreement seems poorer if the fire exposure is very non-uniform and the agreement also seems poorer with rock wool fire protection compared to intumescent paint fire protection. However, since the proposed modified method tends to overestimate the maximum steel section temperatures in the less accurate cases, the method seems to be safe to use in the practical design (i.e. the error results in conservative section temperatures). Conversely, using the regular EC3 method and just averaging the non-uniform fire exposure to single temperature curve tends to sometimes overestimate and sometimes underestimate (sometimes significantly) the maximum steel section temperature, therefore the simpler method might not be safe to use in the practical design. The largest observed underestimation in the proposed modified method was -3 % but with the simpler EC3 method largest underestimation was as high as -13 %. When considering only the cases protected with intumescent paint, the differences between the methods become much less evident while the modified method still fares slightly better (Table 2).

Poorer accuracy with rock wool fire protection may result from larger protection layer thickness (Figure 6) and very temperature dependant material model (Figure 2). In the calculation formulas, the fire protection layer follows a single temperature curve (see equations (3) and (8)) and thus the material properties are constant on the whole layer during each time point. Whereas in the SAFIR models the fire protection layer has multiple elements in multiple different temperatures and has thus multiple different material properties during each time point. In the intumescent paint models the protection layer thicknesses are smaller and the material model is less temperature dependent (Figure 3), so the error might be less pronounced there.

The amount of noise in the temperature data does have an effect to the resulting steel section temperatures when using the calculation formulas. However, more noise tended to produce more conservative results when using the proposed modified calculation formulas (and the opposite might be true with the simpler EC3 formulas). Totally smooth data may also lead to too rapid cooling in the cooling phase (see Cases 31 and 32), so having a moderate amount of noise in the input temperature data might even be beneficial in these methods (and some amount of noise is typical when using FDS simulations).

Cases 33 and 34 demonstrate a minor fundamental flaw in the equations (1) and (6); i.e. the section temperature cannot decrease if the ambient temperature is increasing, which results in an unrealistic steel temperature plateau at the ambient temperature valley when using perfectly smooth input temperature data (see Figure 13). However, this too is mostly fixed just by having small amount of noise in the temperature data, and getting rid of this constraint from these equations would result in overall poorer accuracy.

The proposed method is presented only as an additional tool for determining appropriate fire protections in performance-based fire design, but to be safe the final designs should also be analysed using more advanced methods to better account for the indirect effects of the design fires (i.e. using thermo-mechanical FEM analysis of the steel structure or part of the structure to account indirect actions and displacements from thermal expansions, thermal gradients within cross-sections, non-linear material models, etc.).

5 CONCLUSIONS

The paper presented calculation formulas for calculating fire protected steel section temperature development in non-uniform fire exposure in PBD (a modified method and a simpler application of the

original EC3 method), their validation analyses and a simple procedure for determining the required fire protection ratings in performance-based fire design.

The proposed modified calculation formulas were benchmarked against SAFIR models and the agreement between them was moderately good. However, in some cases the new formulas tend to produce notably hotter temperatures than with FEM, but this is conservative in terms of practical design. Using the presented simpler method, where the non-uniform temperatures curves are averaged to a single input curve and utilizing the original EC3 calculation formulas, can also have good agreement with FEM but it may also sometimes produce quite unconservative (i.e. too cold) steel section temperature values. Nevertheless, the final designs should also be analysed using more advanced methods to better account for the indirect effects of the design fires (i.e. using FEM to account indirect actions and displacements from thermal expansions, thermal gradients within cross-sections, non-linear material models, etc.).

Rock wool fire protections had poorer agreement with FEM than intumescent paints fire protections, but this is most likely explained by the differences in the protection layer thicknesses and temperature dependency of the material models.

The smoothness of the input temperature data does have an effect to the steel section temperature output at least partially due to a minor fundamental flaw present in both calculation formulas. However, having a moderate amount of noise in the input temperature data might even be beneficial with these methods (which is typical when using FDS simulations).

REFERENCES

1. Jokinen, T., Ranua, R., Salminen, M. 2022. Steel section equivalent uniform temperature distribution in performance-based fire design – EC3 calculation method generalized for non-uniform fire exposure. In: Proceedings of 12th International Conference on Structures in Fire (SiF'22)
2. EN 1993-1-2. 2005. Eurocode 3: Design of steel structures. Part 1-2: General rules. Structural fire design.
3. Fire Dynamics Simulator (FDS), <https://pages.nist.gov/fds-smv/>
4. Wickström, U., McGrattan, K. 2007. Adiabatic surface temperature for calculating heat transfer to fire exposed structures. Proceedings of the Eleventh Interflam Conference
5. Heinisuo, M., Jokinen, T. 2014. Tubular composite columns in a non-symmetrical fire. Magazine of Civil Engineering. 49. 107-120. 10.5862/MCE.49.11
6. Schleifer, V. 2009. Zum Verhalten von raumabschliessenden mehrschichtigen Holzbauteilen im Brandfall. PhD Thesis No. 18156. ETH Zurich. Switzerland. <https://doi.org/10.3929/ethz-a-005771863> (in German)
7. Lucherini, A. 2020. Fundamentals of thin intumescent coatings for the design of firesafe structures. PhD Thesis, School of Civil Engineering, The University of Queensland. <https://doi.org/10.14264/uql.2020.1021>
8. Kolsek J., Cesarek P. 2015. Performance-based fire modelling of intumescent painted steel structures and comparison to EC3. J Constr Steel Res 104:91–103. <https://doi.org/10.1016/j.jcsr.2014.10.008>
9. de Silva D., Bilotta A., Nigro E. 2019. Experimental investigation on steel elements protected with intumescent coating. Constr Build Mater 205:232–244. <https://doi.org/10.1016/j.conbuildmat.2019.01.223>
10. Malaska, M., Alanen, M., Salminen, M., Jokinen, T., Ranua, R. 2023. Fire Performance of Steel-Timber Hybrid Beam Section. Fire Technology. <https://doi.org/10.1007/s10694-023-01471-y>
11. Jokinen, T., Ranua, R., Salminen, M. 2024. Holistic Performance-Based Fire Design of Steel Structures—Case Study: Sports Hall. Fire Technology. <https://doi.org/10.1007/s10694-023-01519-z>
12. EN 1991-1-2. 2002. Eurocode 1: Actions on structures. Part 1-2: General actions. Actions on structures exposed to fire
13. Gernay, T., Franssen, J.M. 2017. "Modeling structures in fire with SAFIR®: Theoretical background and capabilities". Journal of Structural Fire Engineering, Vol. 8, issue 3
14. Pintea, D., Franssen, J.M. 1997. Evaluation of the thermal part of the code SAFIR by comparison with the code TASEF. Proc. 8th Int. Conf. on Steel Structures, Vol. 2, M. Ivan ed., MIRTON, Timisoara
15. Franssen, J.M. 2003. Heat transfer by radiation in internal cavities with a complex shape. Proc. of the SEI-SFPE conf. Designing structures for fire, Baltimore, DEStech Publ. Inc.
16. Zaharia, T., Gernay, T. 2012. Validation of the Advanced Calculation Model SAFIR Through DIN EN 1991-1-2 Procedure. 10th Int. Conf. ASCCS, Singapore

COMPARING VARIOUS METHODS FOR ESTIMATING THE FIRE DECAY AND THE COOLING PHASE IN STRUCTURAL FIRE ENGINEERING

Andrea Lucherini¹, Ruben Van Coile², Bart Merci³

ABSTRACT

The current research study discusses the relevance and main characteristics of the fire decay and cooling phase of post-flashover compartment fires, crucial phases for ensuring structural integrity during and after fire. The study evaluates and compares various engineering methods for performance-based structural fire engineering, ranging from analytical formulations to zone-models, focusing on the fire decay and cooling phase. Comparative analysis of methods reveals discrepancies in defining the fire heat release rate and thermal boundary conditions to structural elements during these phases. A case study is presented to investigate the range of defined fire conditions in terms of estimated temperature evolutions and the consequent in-depth temperature profiles and thermal energy gain within load-bearing element according to the various methodologies. This research stresses the necessity for refined methods to properly consider the fire decay and cooling phase in modern performance-based design procedures to ensure the fire safety of structural systems.

as well as the in-depth temperatures and thermal energy experienced by structural elements

Keywords: Fire decay; cooling phase; fire dynamics; natural fires; compartment fires; structural fire engineering; fire safety

1 INTRODUCTION

Traditionally, design methodologies for structural systems exposed to fire adopt the standard fire curve as the only design scenario for post-flashover fires. This fire exposure is represented by a monotonically growing temperature-time curve, often claimed to represent the worst-case scenario for traditional construction materials during the growing and fully-developed phases of a typical natural fire [1]. However, research in the last decades has highlighted the relevance of adopting holistic performance-based methodologies for the design of fire-safe structures that ensure structural integrity until complete fuel burnout [2]. These approaches analyse the behaviour of load-bearing systems during all the typical fire phases in an enclosure: growing, fully-developed, decay, and cooling [3]. The distinction between the fire decay and cooling phase has been extensively explained in [3] and the most important aspects are recalled in Section 2 below. During these phases, the load-bearing capacity of structural elements may continue to decrease due to the continuous penetration of the heat wave and the possibly irreversible reduction of the mechanical properties, resulting in reduced strength and/or stiffness [4-5]. Indeed, delayed failure may occur during or after the fire decay and cooling phase, and a few cases have been reported [6-7].

¹ PhD, Senior Researcher, Slovenian National Building and Civil Engineering Institute (ZAG), Slovenia
e-mail: andrea.lucherini@zag.si, ORCID: <https://orcid.org/0000-0001-8738-1018>

² PhD, Professor, Ghent University, Belgium
e-mail: ruben.vancoile@ugent.be, ORCID: <https://orcid.org/0000-0002-9715-6786>

³ PhD, Professor, Ghent University, Belgium
e-mail: bart.merci@ugent.be, ORCID: <https://orcid.org/0000-0002-2600-0098>

Recent research has proposed different engineering approaches to evaluate the thermal exposure of natural fires on structural elements. These methods rely on different assumptions and simplifications: from analytical formulations to zone-models and computational fluid dynamics (CFD) simulations [8]. However, there is limited understanding on how these approaches can be reliably adopted to reproduce realistic natural fire exposures, including all phases. In particular, even though numerous studies related to this topic are being published, little effort is placed in clarifying the differences between the fire decay and the cooling phase and their treatment remains highly inconsistent [3]. For instance, one of the most adopted methodologies, the Eurocode parametric fire curves (EPFC), adopts a simplified linear approximation for the “cooling” phase, which mixes up fire decay and cooling and is not based on fundamental physical principles or a comprehensive research study [9]. Other examples relate to experimental and modelling studies aimed at assessing the load-bearing capacity of structural elements under fire conditions which include different formulations of the fire decay and cooling phase [2, 4-7, 10-11]. In particular, experimental campaigns, for instance using standard furnaces [6-7], lack comprehensive definition and characterisation of the reproduced thermal conditions and justification for the selected fire scenarios.

This paper discusses the relevance and main characteristics of the fire decay and cooling phase of post-flashover compartment fires and compares several methods for performance-based structural fire engineering, focusing on the definition of the thermal boundary conditions to structural elements during all the fire phases. Special attention is paid on the definition of the fire heat release rate and the estimated temperature evolution for the fire exposure definition, as well as the in-depth temperatures and thermal energy experienced by structural elements according to the various methodologies.

2 FIRE DECAY AND COOLING PHASE

2.1 The various fire phases

Even if the structural fire engineering practice has been traditionally concentrating on the fully-developed phase of post-flashover fires (focus on its duration and temperatures), the fire decay and cooling phase are facing an increasing interest for ensuring the stability and integrity of structures in performance-based design approaches. Even though their treatment has been often mixed up, recent research has carefully defined and discussed their main characteristics and differences (refer to Figure 1) [3].

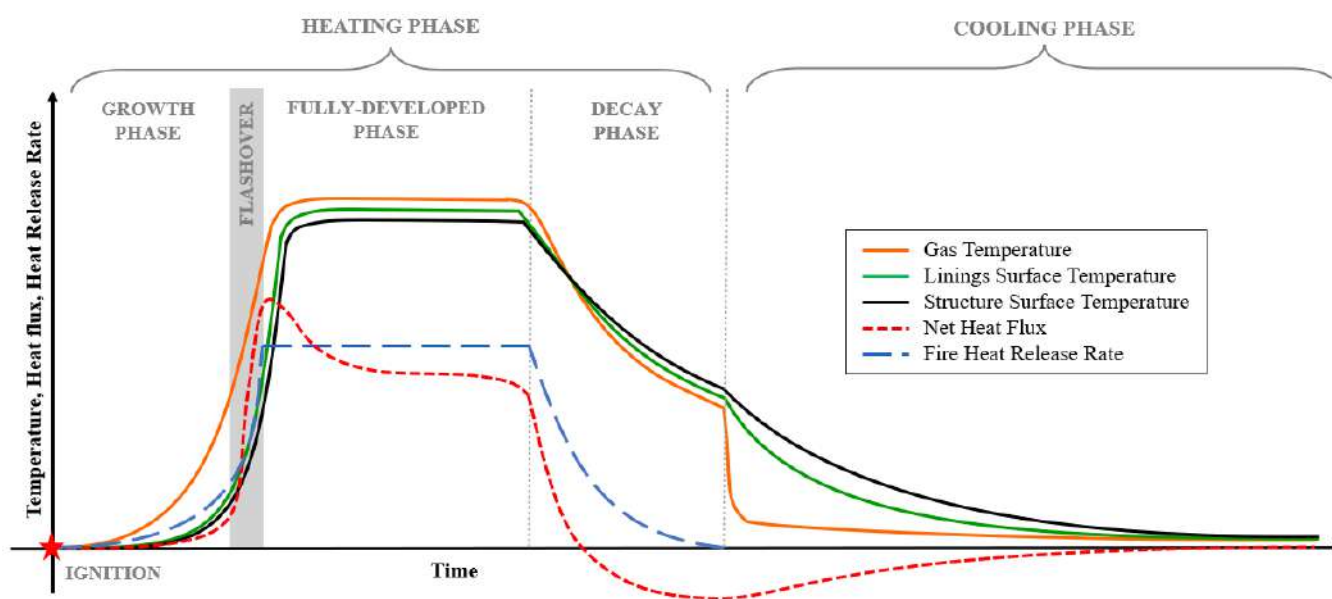


Figure 1. Comparison between gas, compartment linings surface temperatures, structural element surface temperature, net heat flux, and fire heat release rate during the various phases of a post-flashover compartment fire [3]

2.2 Thermal boundary conditions

To perform an accurate assessment of the fire performance of structures, it is important to understand the various phases that occur during a fire event and, more importantly, properly define the thermal conditions at the boundaries of the structural element under analysis [12]. A general definition of the thermal boundary conditions to an exposed structural element j can be written in accordance with equation (1), which considers the convective heat transfer with the surrounding gases and radiative heat transfer with the various compartment elements i and the fire flames [3]:

$$\dot{q}_{net,j}'' = h_c(T_g - T_{s,j}) + \sum_{i=1}^n F_{i-j} \bar{\epsilon} \sigma (T_i^4 - T_{s,j}^4) + \dot{q}_f'' \quad (1)$$

where $\dot{q}_{net,j}''$ [W/m²] is the net heat flux received at the exposed surface of the structural element j under analysis, which has a surface emissivity ϵ_j [-] and a surface temperature $T_{s,j}$ [K]; h_c [W/m²K] is the convective heat transfer coefficient; T_g [K] is the temperature of the surrounding gases; σ is the Stefan–Boltzmann constant (5.67×10^{-8} W/m²K⁴); F_{i-j} [-] is the view factor between the structural element j under analysis and another compartment element i , which has a surface emissivity ϵ_i [-] and a surface temperature T_i [K]; $\bar{\epsilon}$ [-] is the effective emissivity, which can be calculated combining the emissivities of the emitting and receiving body (ϵ_i and ϵ_j); \dot{q}_f'' [W/m²] is the radiative heat flux from the fire flames. Equation (1) can be utilized to accurately characterise the heat transfer occurring at the element surface throughout different fire phases. The objective is to accurately replicate the heat fluxes experienced by the compartment elements being studied.

However, within the structural fire engineering practice, the fire exposure is commonly defined by a single temperature-time curve and the thermal boundary conditions are simplified as equation (2):

$$\dot{q}_{net}'' = h_c(T_g - T_s) + \epsilon \sigma (T_g^4 - T_s^4) \quad (2)$$

This equation is also in line with the thermal boundary conditions defined in Eurocode 1 [13], which are characterised by a single-temperature time curve and given heat transfer coefficients (convective and effective emissivity) and therefore to be considered as a theoretical adiabatic surface temperature [14]. This concept applies well for the fully-developed fire phase, where the compartment is characterised by an optically-thick medium (smoke) and a single gas temperature can provide an appropriate estimation of radiative and convective heat transfer from the compartment gases to the analysed structural element.

However, even if the concept (i.e. mathematical expression) can be also applied to other phases, in the fire decay and cooling phase, the theoretical adiabatic surface temperature cannot be readily interpreted as corresponding to a single physical gas temperature because of the significantly different contributions of convection and radiation [3]. In the fire decay and cooling phase, equation (1) represents a more appropriate and generalised expression for the definition of the thermal boundary conditions to structural elements during and after fire. However, this solution may become complex, for instance the quantification of the radiative heat flux from the fire flames (\dot{q}_f'') and the radiation exchange between compartment elements.

In any case, in order to reproduce realistic fire conditions as boundary condition for structural fire engineering calculations, during the various fire phases, the thermal boundary conditions should be specified in accordance with the fire dynamics within the compartment. This is particularly relevant for the fire decay and cooling phase, which significantly differ from the fully-developed fire phase and have been traditionally overlooked.

3 COMPARING METHODS

Recent research advances have been critically analysing and proposing various engineering approaches to estimate the thermal exposure of post-flashover compartment fires on load-bearing structural elements. The available literature offers a vast range of methods of various complexities, which have been more or less successful and worldwide adopted by the structural fire engineering practice [8]. Table 1 lists and compares

the main methods for performance-based structural fire engineering, focusing on the definition of the thermal boundary conditions to structural elements during all the fire phases.

Table 1. Comparison between available methods to estimate the thermal exposure of post-flashover compartment fires, focusing on the defined thermal boundary conditions to structural elements during the various fire phases

Method	Type	Fully-developed phase	Fire decay phase	Cooling phase
Standard fire curve [13]	Analytical	Single T-t curve	Not included	Not included
Eurocode parametric fire curves (Annex A) [13]	Analytical	Single T-t curve	Unclear distinction decay/cooling Onset of decay/cooling at fuel burnout Single T-t curve with linear decay	
iBMB parametric fire curves [15]	Analytical	Single T-t curve	Distinction between fire decay and cooling Onset of fire decay at 70% fuel load Single T-t curve with parabolic decay	
BFD curves [16]	Analytical	Single T-t curve	Distinction between fire decay and cooling Onset of fire decay at 70% q_f Single T-t curve with parabolic decay	
Lucherini <i>et al.</i> [17]	Analytical	Single T-t curve	Not included	Onset of cooling at fuel burnout Convective cooling with ambient temperature (T_g) Radiation exchange with surrounding elements (T_w)
OZone [18-19]	Zone model	Single T-t curve	Distinction between fire decay and cooling Onset of fire decay at 70% fuel load Single T-t curve	
C-FAST [20], B-RISK [21]	Zone model	Single T-t curve	Distinction based on input fire HRR Single T-t curve	
FDS [22]	CFD	Distinction between various phases based on input fire HRR Various thermal boundary conditions		

The various methods compared in Table 1 rely on different assumptions and simplifications: from analytical formulations to zone-models and computational fluid dynamics (CFD) simulations. Starting with the ISO 834 standard fire curve, this approach only examines the fully-developed fire phase with a monotonically increasing temperature-time curve and structural elements are tested or assessed for a specific duration. This method does not have any consideration of the fire decay and cooling phase and it has been extensively criticised over the last few decades [1].

The following analytical methods introduce the fire decay and cooling phase, even though these are not often distinguished or comprehensively defined. The Eurocode parametric fire curves [13] are a widely adopted methodology which was developed starting from the Swedish fire curves and offers analytical expressions to generate the temperature-time fire curves as a function of the compartment geometry, fuel load, and compartment linings. However, after the fully-developed phase, the fire curve is simplified into a linear decay relationship, which confuses fire decay and cooling and prescribes constant cooling rates with no physical basis [9]. In addition, the fire heat release rate is not made explicit. However, the duration of the fully developed phase is calculated based on the total fuel load, therefore assuming that the end of the fully-developed phase corresponds to fuel burnout (hence onset of cooling) and disregarding the fire decay phase [3].

Similar methods based on analytical parametric fire curves are the iBMB parametric fire curves [15], which have been adopted in the German annex of Eurocode 1, and the BFD curves [16]. Both methods have been obtained from regression analyses of simulations or fire tests data and they calculate key durations and temperatures to define temperature-time fire curves which can be subdivided in four parts: growth, fully-developed, decay and cooling. After the fully-developed fire phase, both methods theoretically foresee a fire decay phase, which commences when 70% of the total fuel load has combusted, and then a cooling

phase. These phases are characterised by a parabolic/exponential decay curve. However, the authors do not provide any distinct specification to define the thermal boundary conditions during the fire decay and cooling phases (i.e. continuous temperature-time curve).

A zone-model, such as OZone [18-19], C-FAST [20] and B-RISK [21], adopts fundamentals of thermo- and fluid-dynamics to typically simplify the fire compartment in two zones, an upper layer constituted by hot smoke and a lower layer constituted by cold air at ambient temperature. They enable the direct input and control of the time-history of the fire heat release rate, therefore the distinction between the various fire phases is up to the user. In OZone, the fire heat release rate is defined according to the advanced fire models from Annex E of Eurocode 1 [13], where the fire decay begins when 70% of the total fuel load has combusted, followed by a cooling phase. Nevertheless, for the quantification of the fire exposure, also zone-models typically provide a single temperature-time curve, which is usually taken as the temperature evolution of the upper (smoke) layer.

In general, the above-mentioned methods define a single temperature-time (T-t) curve to define the thermal boundary conditions to structural elements in fire conditions. This temperature evolution is usually treated as a theoretical adiabatic surface temperature [14] and equation (2) is usually adopted in accordance with Eurocode 1 [13]. However, as discussed in Section 2.2, this simplification may introduce significant errors in the fire decay and cooling phase due to the major differences in the compartment fire dynamics with the fully-developed fire phase, which has been traditionally the main focus of structural fire calculations [3].

Directly defining the fire heat release rate, separating the various heat transfer components, and defining comprehensive thermal boundary conditions (e.g. net heat flux) are usually possible in more complex methodologies, like the Computational Fluid Dynamics (CFD) software Fire Dynamics Simulator (FDS) [22]. However, this approach typically requires a much more accurate level of detail and overall effort.

With a view on developing an analytical model to estimate the thermal exposure to structural elements during a natural fire, focusing on the cooling phase and separately considering the convection and radiation heat transfer contributions, a simplified model based on a first-principles approach has recently been proposed [17]. According to this methodology, first, the compartment thermal conditions during the heating phase are approximated according to the Eurocode parametric fire curves [13]. After fuel burnout, the compartment gases are assumed to return to optically thin conditions and the gas temperatures to return to ambient values, while the compartment solid elements (e.g. linings) slowly cool down by convection and provide radiation exchange to the exposed structural elements. While these simplifications introduce quantitative errors, they enable an analytical solution for transient heat conduction that captures all key heat transfer processes.

4 METHODOLOGY

4.1 Case study definition

In order to compare the discussed methods to estimate post-flashover compartment fires for performance-based structural fire engineering, a case study has been selected from the existing literature with specific ventilation conditions, geometry, compartment linings materials (i.e. thermal inertia), and fuel load density. The chosen case is extracted from the series of full-scale fire tests carried out in 1999-2000 at the BRE Cardington facilities within the scope of the “Natural Fire Safety Concept 2 (NFSC2)” series [23]. The series was conducted on a compartment measuring 12 m x 12 m in plan, 3.4 m in height, a traditional compartment with incombustible linings where flashover and ventilation-controlled fires are expected. The testing campaign involved a total of eight scenarios, which differed for ventilation conditions, fuel load composition, and compartment boundaries. Test 8 is chosen for analysis, an exemplar case which has been largely used for various past analyses and modelling studies [23-25]. This scenario is characterised by an opening factor of $0.10 \text{ m}^{0.5}$ (unique opening, 7.2 m wide and 3.4 m high), a fuel load density of 680 MJ/m^2 (80% wood cribs and 20% plastic, by calorific value), and insulating compartment linings with an approximated thermal inertia of $740 \text{ J/m}^2\text{s}^{0.5}\text{K}$ [23-24].

The case study has been modelled according to some of the available methods presented in Section 63: analytical formulations like the Eurocode parametric fire curves [13], the German iBMB parametric fire curves [15], and the BFD temperature-time curves [16]; the first-principles model for the cooling phase proposed by Lucherini *et al.* [17]; and the zone-model OZone [18-19]. All the relevant model parameters (i.e. geometry, compartment ventilation condition, compartment linings materials, fire growth rate and heat release rate, fuel load density, etc.) have been defined and calculated in accordance with the above-mentioned case study. As regards to the compartment linings, they were defined in line with the thermal inertia reported in the test series and they were modelled with the following constant thermo-physical material properties: thermal conductivity 0.45 W/mK, mass density 1150 kg/m³, and specific heat capacity 1000 J/kgK (properties similar to lightweight concrete, with a thermal inertia equal to 720 J/m²s^{0.5}K).

4.2 Thermal analysis and comparison

The main outcomes of the various models are then analysed and compared. In particular, the various cases are compared in terms of the time-history of the fire heat release rate and several temperature evolutions, which include the compartment gas phase (T_g), the compartment linings surface (T_w), as well as the theoretical adiabatic surface temperature (T_{adb}). The various approaches and the corresponding thermal exposures during all the fire phases are compared, and their implications are discussed.

To investigate the implications of the various estimated fire exposures for structural fire engineering, a pure conduction one-dimensional heat transfer model is formulated to investigate the heat transfer within structural elements exposed in the analysed compartment. The solid is discretised into a number of finite elements, associated to nodes, and it explicitly solves a one-dimensional heat conduction problem by resolving energy-balance equations in the main direction of the heat flow. The heat transfer model focuses on the thermal boundary conditions and the heat penetration within the lightweight concrete compartment linings, assumed as load-bearing elements like a compartment ceiling/slab or wall. The thickness of the load-bearing element is set to 200 mm to ensure its thermal thickness, taking into consideration the defined material properties and thermal conditions. The solid space is discretised in finite elements with a thickness of 1 mm, and the time step is set to 0.01 s, following numerical stability criteria.

The thermal conditions at the fire-exposed surface are defined according to the various methodologies, which include both the heating and the cooling phases of the fire scenario. When the thermal boundary conditions for the fire exposure are expressed as a single temperature-time curve and not stated otherwise, the thermal boundary conditions (radiation and convection) are defined in accordance with Eurocode 1, as reported in equation (2), with a convective heat transfer coefficient equal to 35 W/m²K (advanced fire models) and a surface emissivity equal to 0.8 [13]. As a result, the temperature profiles within the structural element obtained following the different methodologies are analysed and compared to investigate the implications of various thermal boundary conditions at the exposed surface on the in-depth temperatures experienced by the load-bearing structure, both during the heating and cooling phase.

Finally, the effects of the various estimated fire conditions are compared in terms of the thermal energy accumulated within the solid (i.e. load-bearing element) during and after the fire. In particular, the evolution of the total in-depth thermal energy gain (per unit area) within the structural element, E''_{th} [MJ/m²], is calculated in accordance with equation (3) [17]:

$$E''_{th}(t) = \int_0^d \rho c_p \Delta T(x, t) dx \quad (3)$$

where, ρ is the mass density [kg/m³], c_p is the specific heat capacity [J/kgK], and $\Delta T(x, t)$ [K] is the time-varying in-depth temperature rise (above ambient temperature, 20°C) within the thickness of the solid (d [m]). The rise and decrease of the in-depth thermal energy accumulated in the structural material are compared at the end of the fully-developed fire phase, as well as at fuel burnout and onset of cooling.

5 RESULTS AND DISCUSSION

5.1 Fire heat release rate

To investigate the thermal conditions produced by the various models for the presented case study, the analyses first investigate the time history of the fire heat release rate assumed by the various models and compared to the experimental data, as shown in Figure 2. The fire heat release rate represents the most important parameter to characterise the fire conditions and dynamics inside the compartment. Information about the fire heat release rate also enables the distinction between the fire decay and cooling phase [3].

As regards to the experimental data shown in Figure 2, the estimated fire heat release rate follows a typical trend for ventilation-controlled compartment fires, with a rapid growth phase (about 10 min) and a quasi-steady fully-developed fire phase (about 20 min). The fire decay begins after around 30 minutes and has a long duration (approximately 45 min) with a gradual decrease branch, typical of charring fuels like wood cribs [3]. After about 70 minutes, the fire reaches fuel burnout and the onset of the cooling phase.

For the various engineering methods, the fire heat release rate can be an input or output depending on its characteristics. The fire heat release rate is usually an input for zone models, as well as for applications in Computational Fluid Dynamics (CFD). As regards the zone-model OZone [18-19], the fire heat release rate is defined according to the advanced fire models from Eurocode 1 [13]. Fuel load densities, effective heat of combustion, fire growth rates, and maximum values of fuel-controlled fire heat release rates are prescribed, and engineers can estimate the ventilation-controlled (based on opening factor) or fuel-controlled (based on building occupancy) maximum fire heat release rate for each specific case. This value is assumed constant throughout the entire fully-developed fire phase, while the decay phase is assumed to decrease linearly starting when 70% of the total fuel load has been burnt and completed when the fuel load has been completely burnt. Figure 2 reports the resulting time history of heat release rate obtained for the presented case study according to this methodology. In this case, due to the large compartment size, the maximum heat release rate is limited by the fuel conditions, in particular the maximum heat release rate per unit area and therefore the fire size (36 MW). Nevertheless, even if it contains strong assumptions, the methodology is generally robust and provides a clear definition of the fire decay phase and fuel burnout.

In contrast, the Eurocode parametric fire curves [13] do not have this rigorous definition of the energy contribution (i.e. fire heat release rate) and the fire decay phase, as for the natural fire models. It is common belief that Eurocode parametric fire curves methodology is based on the same principle as natural fire models. However, the duration of the fire fully-developed phase is in effect calculated assuming that the total fuel load is consumed during the fully-develop phase at a steady-state heat release rate (ventilation- or fuel-controlled) and therefore the end of this phase should correspond to the beginning of the cooling phase, without any decay phase [3]. In the case presented in Figure 2, according to this methodology, the duration of the fire fully-developed phase is calculated based on the opening factor and the total fuel load and the fire results ventilation-controlled, with a maximum fire heat release rate equal to 62.7 MW. The recently-proposed model for the cooling phase [17] adopted the same assumption to allow for a consistent comparison of the EPFC cooling rates with cooling rates obtained through a first-principles approach.

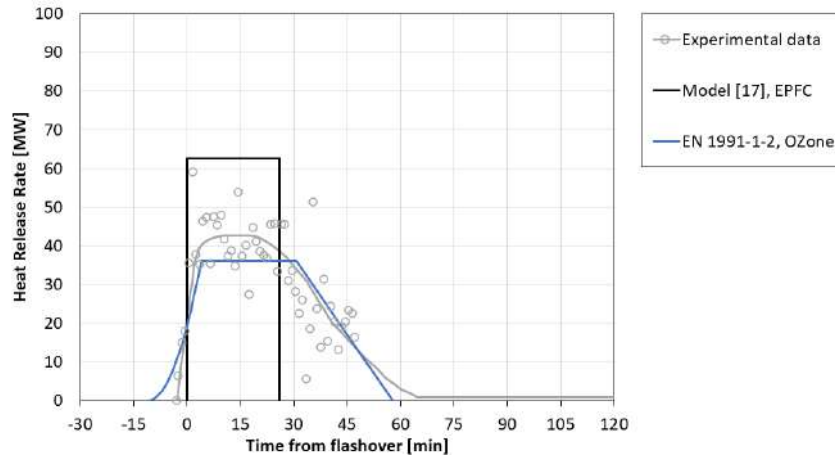


Figure 2. Fire heat release rate according to different methods, including experimental data [25]

5.2 Compartment temperatures and thermal boundary conditions

For the selected case study, the thermal exposures in terms of temperature-time curves estimated according to different methods for post-flashover compartment fires and obtained experimentally from the large-scale fire test are compared and shown in Figure 3. Similarly to Figure 2, since some methods include the growth phase of the fire and other not, for illustration purposes, the temperature-time curves are shifted to achieve flashover at the same instant (assumed to occur when the smoke layer temperature achieves 550°C [26]).

The different methods can be adopted to reproduce a range of natural fire exposures, but each approach evidences specific characteristics and shortcomings. As it has been already underlined by several other researchers [9], the results confirm that the constant cooling rate of the Eurocode parametric fire curves is noticeably inaccurate to reproduce the thermal exposure during the fire decay and cooling phase. Indeed, after the fully-developed phase, temperatures are normally characterised by a parabolic/exponential decreasing branch. Regarding the other methods, the iBMB parametric fire curves appear to define the most critical scenario (highest temperatures and longest fully-developed phase duration), while the zone-model OZone specifies the lowest temperatures, amongst the studied approaches.

While Figure 3 seems to demonstrate an overall agreement between models and experiments, this is purely based on temperature measurements and does not describe the heat transfer environment. Indeed, the thermal exposure to structural elements during fire directly depends on the defined thermal boundary conditions. In most cases, a single temperature-time curve is defined, as it is usually treated as a theoretical adiabatic surface temperature with given heat transfer coefficients [14].

The only method that attempts to separate the convective and radiative heat transfer during the cooling phase is the one proposed by Lucherini *et al* [17]. As shown in Figure 3, at fuel burnout (end of the fully-developed phase), the compartment gas temperature (T_g) quickly drops to ambient temperature and the compartment elements cool down by natural convective cooling, which also defined radiative heat exchange between the exposed compartment surfaces (T_w). In order to provide a direct comparison between the various temperature-time curves, Figure 3 also reports the adiabatic surface temperature (based on Eurocode 1 heat transfer coefficients) for this case, which was calculated starting from the net heat flux to the structural element estimated according to the defined thermal boundary conditions. In general, the simplified method offers reasonable agreement with the temperature evolution, as it is based on a correct phenomenological description of the compartment conditions during the various fire phases, explicitly including consistent treatment of the thermal boundary conditions and the fire heat release rate.

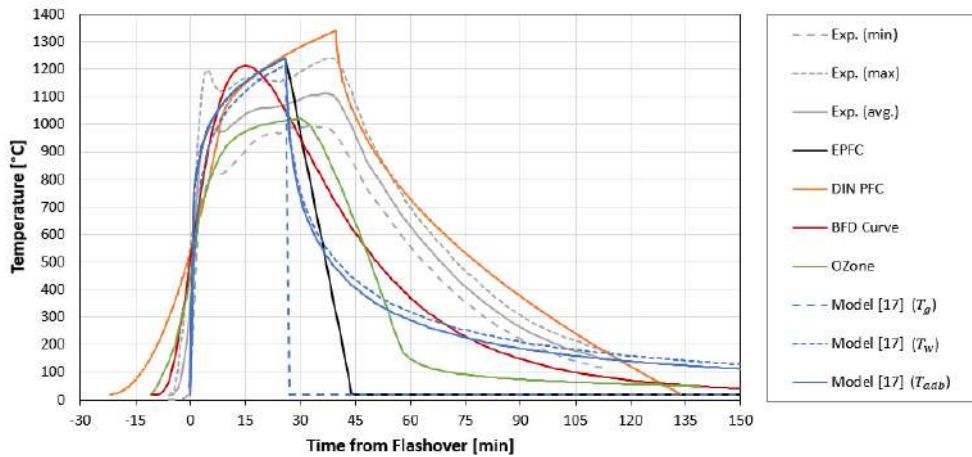


Figure 3. Comparison between experimental results [23] and the temperature-time curves estimated according to different methods (shifted to achieve flashover at the same instant, defined when temperature reaches 550°C) [26]

5.3 In-depth temperature profiles and accumulated thermal energy

To investigate the actual implications of the various estimated fire exposures and defined thermal boundary conditions for structural fire engineering, the heat penetration and in-depth temperature profiles within the studied load-bearing element (lightweight concrete wall/slab) are analysed thanks to the described one-dimensional heat transfer model (refer to Section 4.2).

Figure 4 reports and compares the in-depth temperature profiles within the analysed structural element according to different methods at the end of the heating phase, i.e., the instant of maximum fire (gas) temperature, and 30 minutes later. Without a doubt, the observed in-depth temperature profiles illustrates the direct consequence of defining the temperature-time curves shown in Figure 3. As regards to the end of the heating phase, the temperature profiles within the structural element are distinctive for the defined thermo-physical properties (i.e. thermal diffusivity), with higher surface temperatures and deeper thermal penetrations when the fire exposure achieves higher temperatures and the fully-developed phase lasts for longer durations (i.e. iBMB parametric fire curve). As regards to the temperature profiles during cooling, the surface temperature is again directly dependent on the fire exposure and the surface thermal boundary conditions. However, the thermal penetration in the load-bearing material is affected by the total thermal energy that has been provided (and lost) at the exposed surface, which is the direct effect of the thermal boundary conditions. For instance, the direct comparison between the temperature profile for the iBMB parametric fire curve and BFD curve highlights how, even if the surface temperature is practically identical 30 minutes after the instant of maximum fire (gas) temperature, the thermal penetration for the iBMB curve is significantly deeper due to the longer fully-developed phase with higher temperatures.

The effects of the various estimated fire conditions according to the different methods is then more evident when the rise and decrease of thermal energy accumulated within the solid (i.e. load-bearing element) is calculated according to equation (3) and compared. Figure 5 displays the temporal evolution of the total in-depth thermal energy gain (per unit area) within the structural element (E''_{th}) during the whole fire event. In particular, Figure 5 also highlights the instant of maximum fire temperature, which corresponds to the end of the fully-developed fire.

Figure 5 underlines how, even if the thermal energy gain during the fully-developed phase is almost identical for most cases (except OZone), during the fire decay and cooling phase, the accumulated thermal energy in the analysed structural element differs significantly between the various methods. More importantly, in most models, the energy gain does not stop at the end of the fully-developed phase, but still increases up to additional 30 minutes and more than 35% (BFD curve). On the contrary, according to the cooling phase model [17], in which the fully-developed phase is assumed as fuel burnout and convective cooling occurs after this point leading to significant heat losses, the end of the fully-developed phase corresponds to the beginning of thermal energy decrease and solid cooling. Similar conditions are also produced by the iBMB parametric fire curve.

In conclusion, this result evidences the impact of the definition of the thermal boundary conditions and the significant differences between the various approaches in terms of the amount of the thermal energy which is absorbed by fire-exposed structural elements.

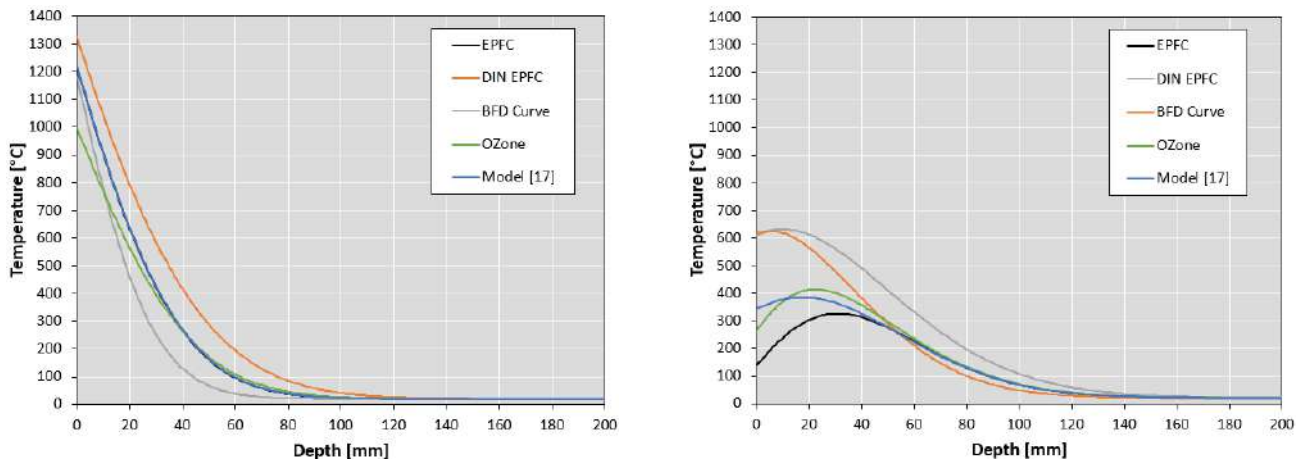


Figure 4. In-depth temperature profiles within the analysed structural element according to different methods at the instant of maximum fire (gas) temperature (left), and 30 minutes later into the fire decay or cooling phase (right)

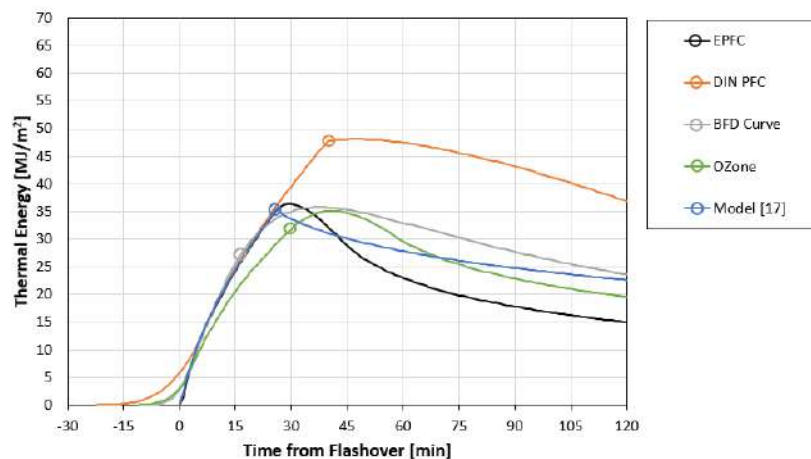


Figure 5. Total in-depth accumulated thermal energy within the analysed structural element according to different methods, highlighting the instant of maximum fire temperature (circles)

6 CONCLUSIONS

The current research study aims at discussing the fire decay and cooling phase of post-flashover compartment fires. Despite their distinct heat transfer characteristics, these phases are often mixed up, yet they play crucial roles in ensuring the structural integrity and stability of fire-safe structures.

The study examines their primary characteristics, and it underlines how the existing methodologies lack explicit and homogenised definitions of the fire decay and cooling phase and the corresponding thermal boundary conditions, often simplified into a single temperature-time curve. In addition, comparing how different methods define and treat the fire decay and cooling phase clarifies how the assumed/defined fire heat release rate and thermal boundary conditions can have a direct effect on the thermal energy and in-depth temperature profiles of structural elements, hence the assessment of their load-bearing capacity.

This research study highlights how specific methods may under- or over-estimate the thermal exposure of the fire decay and cooling phase, although the overall fire exposure is the most relevant aspect because the definition of the single phases provides little relevance to the overall assessment. In any case, this study

confirms that the relevance of properly considering the fire conditions during the fire decay and cooling phase in modern performance-based methodologies for structural fire engineering.

ACKNOWLEDGMENTS

The authors would like to gratefully acknowledge the financial support for the FRISSBE project within the European Union's Horizon 2020 research and innovation programme (GA 952395) and for the FIRESafeTimber project within the European Union's Horizon Europe Marie Skłodowska-Curie Postdoctoral Fellowship (GA 101064840).

REFERENCES

- [1] Law A., Bisby L.A. (2020). The rise and rise of fire resistance. *Fire Safety Journal*, 116, 103188.
- [2] Gernay T., Franssen J.M. (2015). A performance indicator for structures under natural fire. *Engineering Structures*, 100, 94-103.
- [3] Lucherini A., Torero J.L. (2023). Defining the fire decay and the cooling phase of post-flashover compartment fires. *Fire Safety Journal*, 141, 103965.
- [4] Gernay T. (2019). Fire resistance and burnout resistance of reinforced concrete columns. *Fire Safety Journal*, 104, 67-78.
- [5] Gernay T. (2021). Fire resistance and burnout resistance of timber columns. *Fire Safety Journal*, 122, 103350.
- [6] Gernay T., Franssen J.-M., Robert F., McNamee R., Felicetti R., Bamonte P., Brunkhorst S., Mohaine S., Zehfuß J. (2022). Experimental investigation of structural failure during the cooling phase of a fire: Concrete columns. *Fire Safety Journal*, 134, 103691.
- [7] Gernay T., Zehfuß J., Brunkhorst S., Robert F., Bamonte P., McNamee R., Mohaine S., Franssen J.-M. (2022). Experimental investigation of structural failure during the cooling phase of a fire: Timber columns. *Fire and Materials*, 1-16.
- [8] Khan A.A., Usmani A., Torero J.L. (2021). Evolution of fire models for estimating structural fire-resistance. *Fire Safety Journal*, 124, 103367.
- [9] Hopkin D., Van Coile R., Hopkin C., LaMalva K., Spearpoint M., Wade C. (2022). Design Fires and Actions. In: International Handbook of Structural Fire Engineering, *The Society of Fire Protection Engineers Series*.
- [10] Gernay T., Pei J., Tong Q., Bamonte P. (2023). Numerical analysis of the effects of fire with cooling phase on reinforced concrete members. *Engineering Structures*, 293, 116618.
- [11] Thienpont T., Van Coile R., Caspeele R., De Corte W. (2021). Burnout resistance of concrete slabs: Probabilistic assessment and global resistance factor calibration. *Fire Safety Journal*, 119, 103242.
- [12] Torero J.L., Law A., Maluk C. (2017). Defining the thermal boundary condition for protective structures in fire. *Engineering Structures*, 149, 104-112.
- [13] EN 1991-1-2:2002. Eurocode 1: Actions on structures – Part 1.2: General actions – Actions on structures exposed to fire. *European Committee for Standardization (CEN)*. Brussels, Belgium.
- [14] Wickström U. (2016). Temperature calculation in fire safety engineering. *Springer Cham*.
- [15] Zehfuss J., Hosser D. (2007). A parametric natural fire model for the structural fire design of multi-storey buildings. *Fire Safety Journal*, 42(2), 115-126.
- [16] Barnett C.R. (2002). BFD curve: a new empirical model for fire compartment temperatures. *Fire Safety Journal*, 37(5), 437-463.
- [17] Lucherini A., Jovanovic B., Torero J.L., Van Coile R., Merci B. (2024). Thermal characterisation of the cooling phase of post-flashover compartment fires. *International Journal of Thermal Sciences*, 199, 108933.
- [18] Cadorin J.F., Franssen J.M. (2003). A tool to design steel elements submitted to compartment fires—OZone V2. Part 1: pre- and post-flashover compartment fire model. *Fire Safety Journal*, 38(5), 395-427.
- [19] Cadorin J.F., Franssen J.M. (2003). A tool to design steel elements submitted to compartment fires - OZone V2. Part 1: pre- and post-flashover compartment fire model. *Fire Safety Journal*, 38(5).
- [20] Richard D. Peacock R.D., Reneke P.A., Forney G.P. (2021). CFAST – Consolidated Model of Fire Growth and Smoke Transport (Version 7). Volume 2: User's Guide. NIST Technical Note 1889v2, *National Institute of Standards and Technology (NIST)*.

- [21] Wade C., Baker G., Frank K., Harrison R., Spearpoint M. (2016). B-RISK User Guide and Technical Manual. SR364, *Building Research Association of New Zealand*.
- [22] National Institute of Standards and Technology (NIST). (2022). Fire Dynamics Simulator (FDS). <https://pages.nist.gov/fds-smv/>
- [23] Lennon T., Moore D. (2003). The natural fire safety concept - full-scale tests at Cardington. *Fire Safety Journal*, 38, 623-643.
- [24] Welch S., Jowsey A., Deeny S., Morgan R., Torero J.L. (2007). BRE large compartment fire tests - Characterising post-flashover fires for model validation. *Fire Safety Journal*, 42(8), 548–567.
- [25] Kumar S. *et al.* (2005). Natural fire safety concept - The development and validation of a CFD-based engineering methodology for evaluating thermal action on steel and composite structures”. *Report EUR 21444 EN*.
- [26] Drysdale D. (2011). An introduction to fire dynamics. *John Wiley & Sons*, 3rd Edition.

ENHANCING COMPOSITE BRIDGES FIRE SAFETY THROUGH PERFORMANCE ANALYSIS: LESSONS FROM AN ACTUAL BRIDGE FIRE INCIDENT ON THE INFLUENCE OF CROSS-SECTION, CONSTITUTIVE MODEL, AND FINITE ELEMENT TYPE

Juan José Pagán-Martínez¹, Ignacio Paya-Zaforteza², Antonio Hospitaler-Pérez³

ABSTRACT

Bridges are vital components of transportation systems, yet their susceptibility to fire damage remains a significant concern. Despite this, empirical investigations and design guidelines for enhancing bridge fire safety are lacking, particularly those based on real fire events. Analysing the December 2022 fire incident under the "Puente de las Flores" in Valencia, Spain, this study fills this gap by assessing the impact of girder cross-sections, finite element types and constitutive models on bridge response. Through Computational Fluid Dynamics (CFD) and thermomechanical numerical models, the paper evaluates the performance of box-girders versus I-girders and compares different model approaches. Results indicate that box-girders exhibit superior fire resistance due to their enclosed configuration, providing thermal shielding and multiple load paths. Additionally, the study highlights the importance of incorporating instabilities in mechanical models for accurate predictions. By deriving insights from a real fire incident, this research contributes to advancing the fire safety standards of composite bridges, offering valuable guidance for structural fire engineering.

Keywords: Post-fire bridge assessment; composite steel-concrete girder; numerical modelling; forensic engineering

1 INTRODUCTION

Bridges serve as critical links in transportation networks, facilitating the smooth flow of goods and people. However, their vulnerability to fire-induced damage poses a significant threat to public safety and infrastructure resilience. Despite the potential consequences of bridge fires, there is a notable dearth of empirical studies and design guidelines focused on mitigating these risks. Compared to tunnel or building fires, which have been extensively studied in the literature [1–4], bridges possess distinctive structural characteristics and require specialized analysis as the analysis of key distinctive parameters of bridge, tunnel and building fires carried out by Alos-Moya et al. [5] points out. This specialized analysis requirement combined with the importance of bridge fires and the lack of standards has spurred considerable research efforts over the past decade, as evident in the literature reviews conducted by Garlock et al. [6], Hu et al., 2021 [7], Liu et al. [8] and Nicoletta et al. [9]. A thorough analysis of these works reveals important gaps in the current body of knowledge.

¹ Structural Fire Engineer, Universitat Politècnica de València, Spain,
e-mail: juapagma@alumni.upv.es, ORCID: <https://orcid.org/0009-0003-1469-5595>

² Full professor, ICITECH, Universitat Politècnica de València, Spain,
e-mail: igpaza@cst.upv.es, ORCID: <https://orcid.org/0000-0002-3995-8772>

³ Full professor, ICITECH, Universitat Politècnica de València, Spain,
e-mail: ahospitaler@cst.upv.es, ORCID: <https://orcid.org/0000-0001-7108-3104>

In this context, this paper aims to enhance the fire safety of composite girder bridges through a comprehensive performance analysis investigating the influence of structural models and girder cross-sections on their fire response. To reach this goal, this research builds upon the previous analysis of the “Puente de las Flores” (“Bridge of the Flowers”) fire [10], a composite box-girder bridge in Valencia, Spain. On December 4th, 2022, a fire broke under the “Bridge of the Flowers”, provoked significant damage in one span of the bridge and forced the bridge closure. In contrast with other fire incidents affecting bridges with composite I-girders like the MacArthur Maze fire, the bridge did not collapse and was back to service after repairs were carried out. Figure 1 summarizes the post-fire condition of the bridge. Spalling occurred in the walls of Abutment 2 (where fire load was present, refer to Figure 1a) and, in a more limited extension, in the triangular deck module close to the Abutment 2 (Figure 1b). Additionally, visual inspection also revealed an important local buckling in the two sections of the lower flange of the diaphragm girder (Figure 1c) as well as out of plane displacements in sections of both longitudinal and transverse girders. Cracks with different length also appeared in three weldings (Figure 1d). An elevation of the deck in the area close to the abutment was also observed (Figure 1e).



Figure 1. Post-fire visual inspection of the “Bridge of the Flowers”. (a) Overall view of the most damaged area indicating maximum spalling (S_{max}) in Abutment 2 as well as the diaphragm girder main damage. (b) Concrete deck spalling and overall view of out-of-plane displacements. (c) Detail of local buckling on diaphragm girder. (d) Detail of welding crack, (e) Detail of deck uplift movement noticed by the inclination of the expansion joint

The authors of this paper analysed this incident using information from in-situ tests as well as numerical models (see Figure 2a, 2b and 2c). Results of this investigation [10] confirmed the resilient post fire bridge behaviour and prompted inquiries into the potential impact of design choices and structural analysis methodologies on the fire consequences. To explore these aspects, this study examines the bridge response across the five scenarios outlined in Table 1, encompassing various possibilities of deck cross-sections and structural modelling strategies.

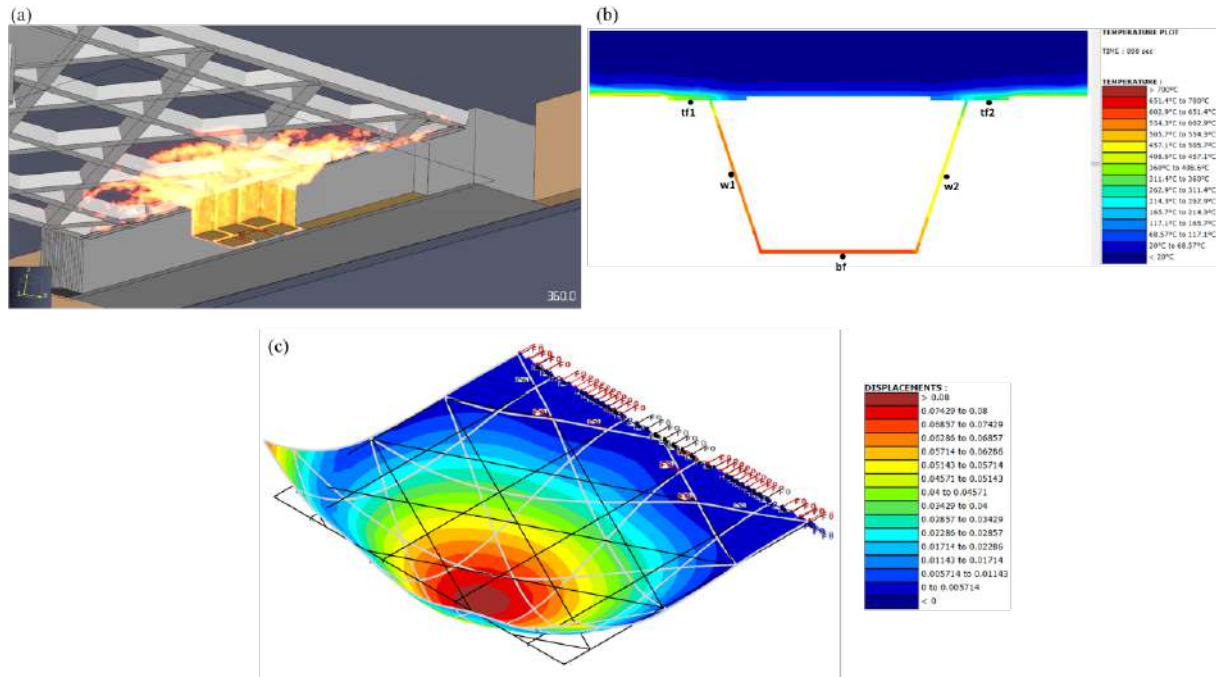


Figure 2. (a) Computational Fluid Dynamics Model. Flame spread after 6 min corresponding to peak heat release rate. (b) Temperature in a typical cross-section of a transversal girder after 15 min. (c) Mechanical model. Vertical displacements after 12min

Table 1. Classification of scenarios for the proposed analysis

Scenario ID	Section Type ⁽¹⁾	Mechanical Model
BG	Box Girder (original analysis)	Fiber-type beam for the steel beams, shell finite elements for the concrete slab [10].
IG	Equivalent I-shaped Girder.	Fiber-type beam for the steel beams, shell finite elements for the concrete slab.
BGb	Box Girder	Fiber-type beam for the steel beams incorporating effects of instabilities using a modified effective stress in compression [11], shell finite elements for the concrete slab.
IGb	Equivalent I-shaped Girder	Fiber-type beam for the steel beams incorporating effects of instabilities using a modified effective stress in compression [11], shell finite elements for the concrete slab.
DG	Diaphragm Girder	Shell finite elements for diaphragm beam, Fiber-type beam elements for stud connectors, shell finite elements for the concrete slab

Note (1). Dimensions of original box-girder elements and diaphragm girder can be obtained from [10]. I-shaped equivalent models (i.e. IG and IGb) are derived from the original box-girder geometry [10] while ensuring an equivalent mechanical capacity, i.e. with identical cross-section area and inertia as the original box-girder configuration. Therefore, the equivalent I-shaped girder maintains consistent dimensions in terms of height (between 450mm and 600mm) and width (between 700mm to 1,000mm), as well as retaining both upper and lower flanges, with a single web resulting from the merging of the two web areas from the box-girder cross-section.

2 THERMAL ANALYSIS

A finite element (FE) heat transfer analysis was conducted to calculate the temperature distribution within the bridge elements over time. In order to incorporate gas phase data from numerical fire simulations (CFD

model) into SAFIR [12] as boundary input, the concept of adiabatic surface temperature (T_{AST}), as proposed by Wickström [13] was used. The materials and its associated thermal properties were implemented within the heat transfer analysis in line with the recommendations of EN 1992-1-2 [14] for reinforced concrete, and EN 1993-1-2 [15] for carbon steel as outlined in the original analysis [10]. Location of the selected girders below is shown in Figure 3 (L1, L2, T1, T2 and D1).

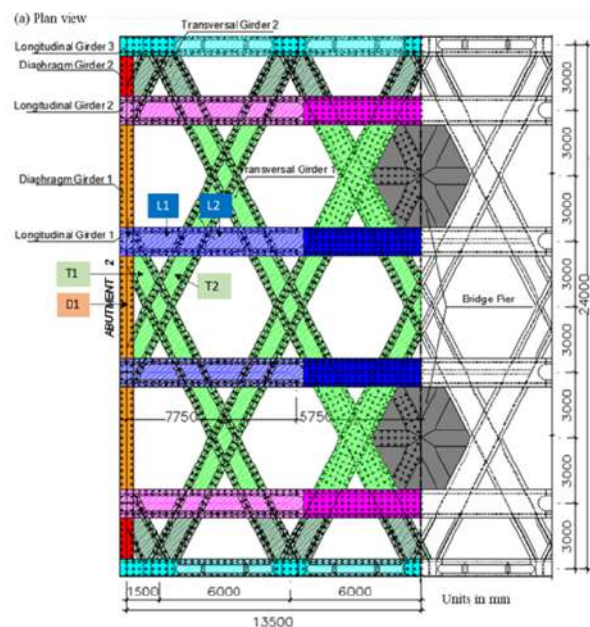


Figure 3. Plan view of the structural elements in the span affected by the fire – Abutment 2

Figure 4a and 4b depict the temperature evolution and distribution, respectively, of the diaphragm girder above the fire zone (D1 in Figure 3). The diaphragm girder, unchanged as part of this analysis and originally designed as I-shaped [10], sustains a maximum temperature of 712°C after about 17 minutes, notably at Node bf3 (Figure 4a).

According to Eurocode EN 1993-1-2 [15], at this temperature, the yield strength, proportional limit, and modulus of elasticity reduce to 22%, 7.2%, and 13% of their ambient values, respectively. This thermal weakening, along with structural restraints, contributed to local buckling of the lower flange at the extreme section of D1 (refer to Figure 1a). However, buckling of the top flange is prevented due to its connection to the concrete slab. Steel temperatures of D1 never exceeded 723°C, critical for steel embrittlement, explaining positive tensile test results on specimens extracted from the girder.

Temperatures in adjacent diaphragm girder sections are not shown as they are unchanged as per the original analysis [10] and affected by lower temperatures (maximum values around 325°C), even below 400°C, the temperature at which the yield strength of steel starts decreasing.

Figure 4c to 4j display the temperature evolution in two sections of the transverse girders (sections T1 and T2, refer to Figure 3 for location) located in the vicinity of the fire load for the box girder (BG) and equivalent I-shaped girder (IG) model.

For the box-girder case, peak temperatures of 650°C (bottom flange of Section T1) and 520°C (most exposed web of Section T2) are observed. At these elevated temperatures, the modulus of elasticity of the steel is significantly reduced (35% at 650°C and 54% at 520°C of their respective values at ambient temperature) as well as the proportional limit (reduced to 12.5% at 650°C and 54% at 520°C of the values at ambient temperature).

Conversely, for the I-shaped girder case, peak temperatures of 800°C (bottom flange of Section T1) and 690°C (node bf3 of Section T2) are observed. At these elevated temperatures, the yield strength is reduced to 11% and 25.4% respectively, similarly, the modulus of elasticity of the steel is significantly reduced (5% at 800°C and 8.5% at 690°C of their respective values at ambient temperature) as well as the proportional limit (reduced to 9% at 800°C and 14.8% at 690°C of the values at ambient temperature).

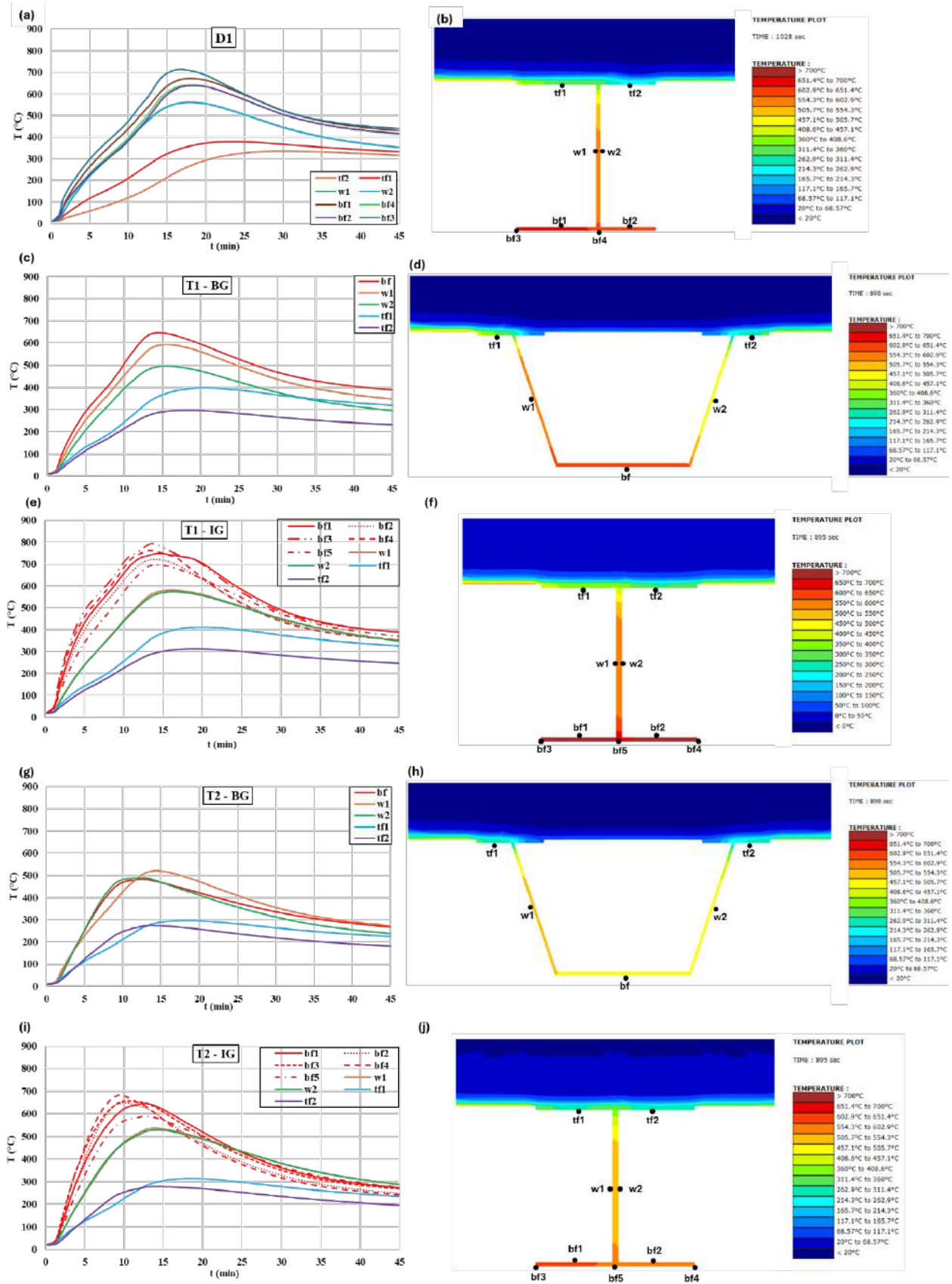


Figure 4. Temperatures in diaphragm girder D1 (a) and (b). (a) Time evolution. (b) Distribution within the girder cross section after 17 min. (c) to (j) Temperatures in representative sections of transversal girders T1 and T2. Images on the left show evolution of temperatures with time whereas images on the right show cross section temperatures after 15 min. Sections location is shown in Figure 3. BG and IG means Box-girder scenario and I-Shaped girder scenario respectively.

The temperature evolution in sections L1 and L2 is shown in Figure 5, (refer to Figure 3 for location). For the box-girder case, the maximum temperature reached is 425°C and occurs in the most exposed web of Section L1. In the other section (L2), the maximum temperatures are around 250°C (Section L2-w1). On this basis, when the maximum temperatures are reached, the yield strength, the proportional limit, and the modulus of elasticity are 94.5%, 40.5%, and 67.5% of their values at ambient temperature (significantly lower reduction). In contrast, for the I-shaped girder case, peak temperatures of 550°C and 330°C are achieved for L1 and L2 respectively. It should be noted that, although web temperatures are still higher than in the box-girder case, the maximum values are now reached along the bottom flange instead of the web, reducing the yield strength, the proportional limit, and the modulus of elasticity to 62.5%, 27%, and 45.5% of its value at ambient temperature in the worst-case scenario (L1).

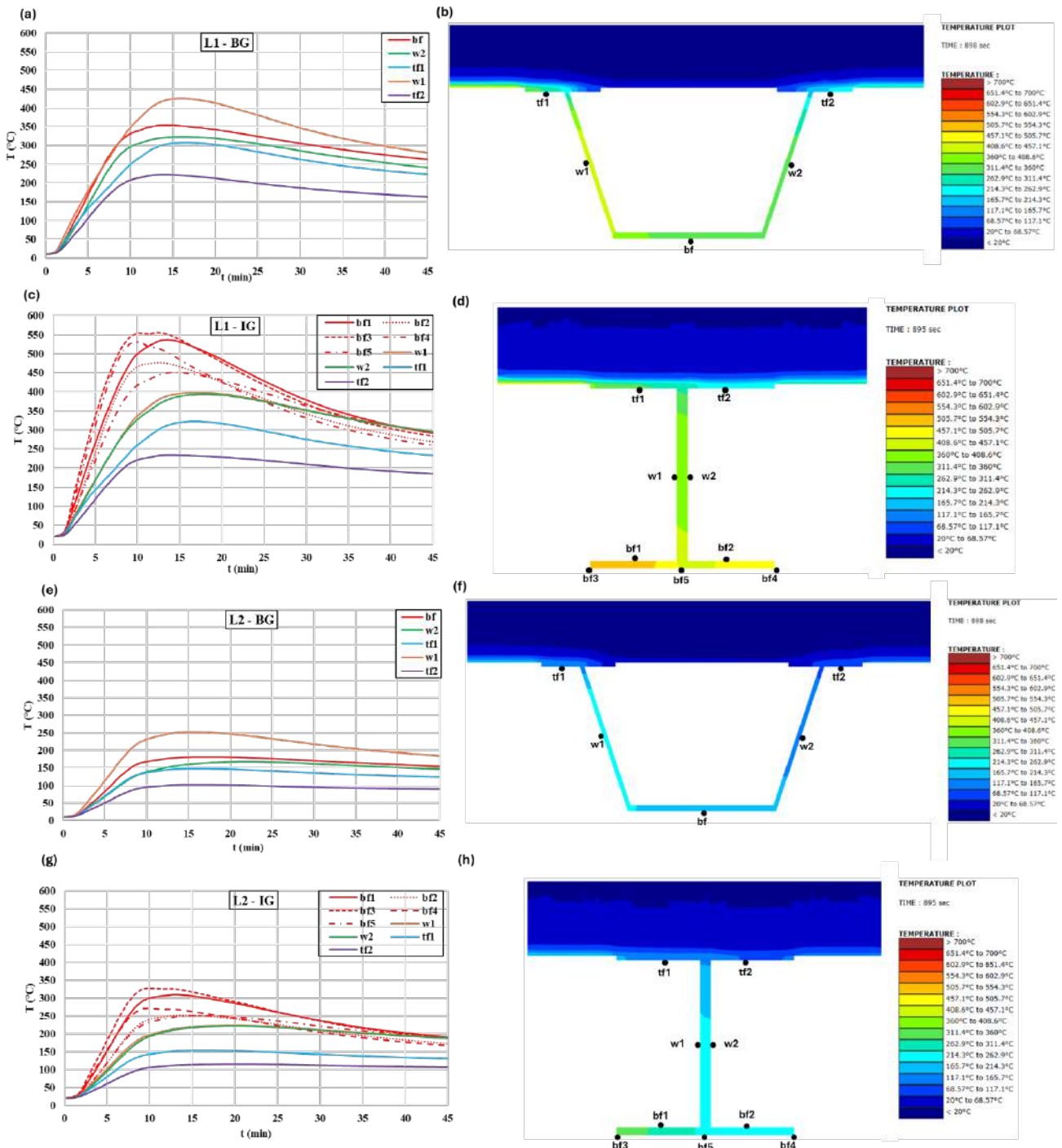


Figure 5. Temperatures in representative sections of transversal girders L1 and L2. Images on the left show evolution of temperatures with time whereas images on the right show cross section temperatures after 15 min. Sections location is shown in Figure 3. BG and IG means Box-girder scenario and I-Shaped girder scenario respectively.

Opting for an I-shaped girder design would have exacerbated the damage to Section T1 even above the damage induced to the diaphragm 1 (D1) girder, likely leading to buckling along the bottom flange, which, in comparison with the longitudinal girders it would have been worsened by the reduced thickness of the flange of the transverse girders. Additionally, Section T1 would have clearly exceeded the 723°C threshold, critical temperature for steel embrittlement.

Furthermore, the box-girder geometry acts as a thermal insulator, shielding the non-directly exposed web from direct fire impingement. Heat transfer within the internal cavity occurs at a comparatively slower rate. In contrast, the I-shaped girder geometry concentrates a higher temperature field along the bottom flange, which is exposed along the upper and lower surfaces simultaneously, facilitating faster temperature propagation across the single girder web.

3 MECHANICAL ANALYSIS

3.1 General characteristics of the structural models

As previously outlined in Table 1 above, 5 different scenarios have been analysed covering 3 different structural models and 2 different section types (box girder -BG- and I-shaped girder -IG-). The structural response to fire was analysed using SAFIR software [12]. Only self-weight loads are implemented within the structural analyses.

For the scenarios BG and IG the same structural approach as per the original analysis [10] was followed, fiber-type beam elements were used to model steel girders, while shell finite elements represented the concrete slab (Refer to Figure 6a). Steel reinforcement within the concrete slab was smeared laterally, and their contribution was modelled with a uniaxial approach. Material properties have been implemented as specified in [10]: Class A reinforcement with a yield strength of 500 MPa, structural steel with a yield strength of 355 MPa, and concrete with compressive strength of 30.0 MPa and tensile strength of 3.0 MPa. Shell elements employed an elevated temperature plastic-damage model with transient creep. Boundary conditions included non-linear vertical springs at the composite deck-abutment connection and restraints at pier connections and substructure edges to account for structural rigidity. Nodes of beam and shell elements are assumed to share a common reference plane, aligning with the mid-surface of the concrete slab. This fixed reference plane maintains rigid behaviour between steel beams and the concrete slab throughout the analysis.

Scenarios BGb and IGb are based on the BG and IG structural model (fiber-type elements for girders and shell elements for concrete slab) but incorporating effects of instabilities using a modified effective stress in compression [11]. In this model, compression stress-strain relationship of steel girders is adjusted, including the proportional limit, effective yield strength, and the strain equivalent to the beginning of the horizontal plateau. Elastic stiffness during unloading after initial plastic deformation is reduced using a damage model, considering the plastic deformation of steel plate within the girder. Reduction levels depend on plate slenderness and boundary conditions of each steel plate.

For the scenario DG, the diaphragm girder (D1) and concrete slab has been modelled fully with shell finite elements and fiber-type beam elements for the stud connectors (Refer to Figure 6b). The steel beam flanges and web are represented with 4 integration points in plan and 8 in depth, ensuring accurate representation. Node layers for all shell elements are positioned at their structural thickness centerlines. To simulate shear studs, a connector beam element was employed, spaced at 300 mm intervals in the longitudinal beam direction and a length matching the distance between the top flange mid-thickness and that of the slab structural thickness. These connectors possess a consistent modulus of elasticity of 500 GPa for robust shear response. Additionally, a fictitious rectangular area of 0.01 m² was assigned to enhance stiffness. These connector beam elements effectively bridge vertically aligned nodes within the slab shell layer and the top flange shell layer. Boundary conditions included vertical restraint along the composite deck-abutment connection and horizontal restraint along the connection between the diaphragm girder and the adjacent girders. Horizontal restraint is also implemented at the edge of the concrete slab section. Figure 6 below shows a conceptual illustration of structural modes.

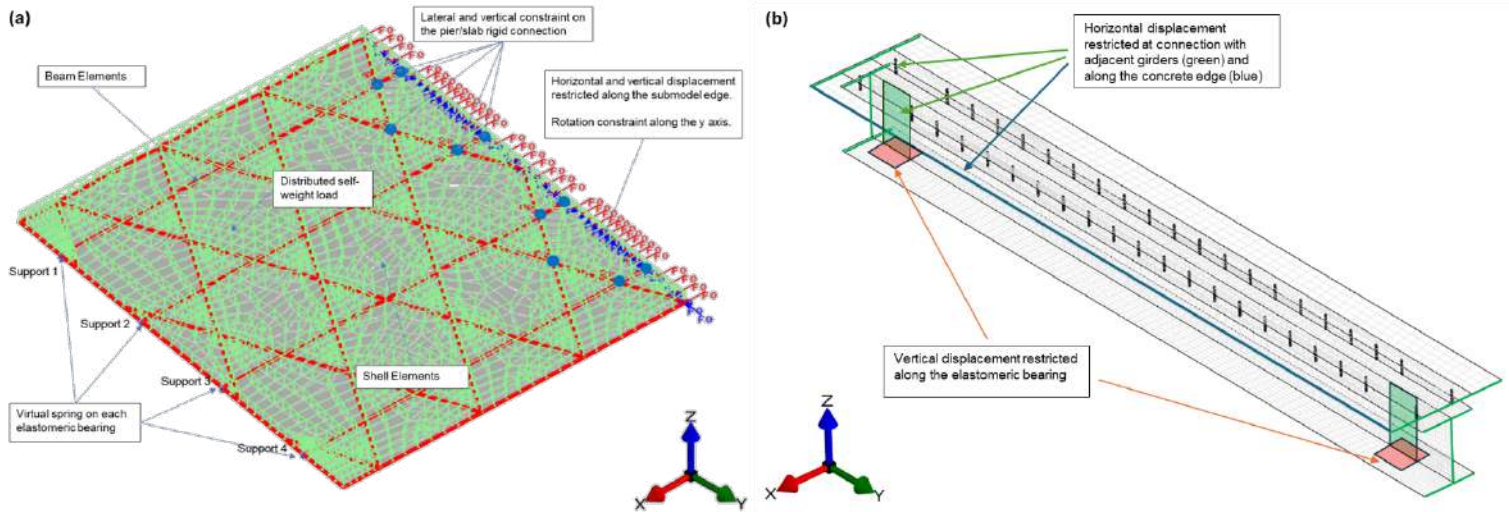


Figure 6. Mechanical models. (a) Scenarios BG, BGb, IG and IGb [10]. (b) Scenario DG

3.2 Comparative Analysis

Figure 7 presents vertical displacement data across various mechanical models up to 25 minutes, aligning with the analysis time for the original scenario (BG). Node 924 (Figure 7a) consistently exhibits the maximum vertical deflection, ranging from 78mm to 113mm (Refer to Table 2 below), peaking after 12 minutes and gradually diminishing as the fire load decreases. Extreme nodes along the diaphragm girder (Nodes 60 in Figure 7a) experience substantial vertical uplift, ranging from 70mm to 180mm after 12 minutes of fire exposure. This uplift is attributed to the lateral expansion of heavily affected girder elements due to rising temperatures, constrained by colder adjacent longitudinal and transversal girders. Data for the node where transversal girders T1 and T2 cross (Refer to Figure 3) is excluded due to its close resemblance to Node 446.

The comparative analysis depicted in Table 2 and Figure 7b to 7e provides the following insights:

- Solely considering section type (Figure 7b), I-shaped girders (IG) exhibit significantly larger vertical displacements compared to box-girders (BG), ranging from 37% higher vertical deflection (i.e. Node 924) to 2.5 times higher uplift (Nodes 55 and 60). This is expected due to higher temperatures within the IG, leading to increased material degradation and expansion rates. This enhancement of material expansion, constrained by colder elements, results in higher vertical uplift at the diaphragm girder extremes (Nodes 55 and 60). Symmetric vertical displacements are observed across the entire model for these scenarios, with a slight tendency for uplift in the central zone towards the end of the analysis. This uplift rate is slightly higher for I-shaped girders across all scenarios.
- Comparing different section types while incorporating a modified effective stress in compression (Figure 7c, BGb vs IGb) reveals a similar trend, with IGb experiencing higher deflection (58%) than BGb. However, asymmetry arises in the uplift at extreme nodes when implicit local instability is incorporated. While Node 60 uplift is comparable between scenarios, Node 55 is significantly higher for the IGb (by 50%). This asymmetry in displacements between bridge sides becomes explicit when the modified effective stress in compression is incorporated. Although this is a common condition for all scenarios, the mechanical constraint causing uplift is slightly reduced on the right-hand side area (facing the abutment, toward Node 60) due to its slightly elevated temperature compared to other areas, however this difference is only noted in the IGb and BGb scenarios.
- Maintaining the same section type (BG) and comparing mechanical behavior (Figure 7d, BGb vs BG) shows maximum deflections occurring in the BG scenario (69% higher) and significantly higher vertical uplift (3.2 times higher). Symmetry in displacements is disrupted when modified effective stress in compression is incorporated. Similar trends are observed in IG scenarios (Figure

7e, IGb vs IG), with IG exhibiting higher deflection (46%) and significantly higher vertical uplift at extreme nodes compared to IGb.

Figure 8 below depicts the axial load for the different scenarios, in the original scenario (BG), the following results were obtained:

- Initially, elements closest to the fire experience tension or minimal compression at ambient temperature but heating during the fire induces significant compression. Transversal girders (T1) above the fire heat at a similar rate to the diaphragm girder, limiting its expansion less than longitudinal girders. Figure 8a (BG) illustrates the rapid transition of the diaphragm girder segment from minimal axial load to substantial compression under elevated temperatures, driven by constraints from less affected elements and adjacent girders.

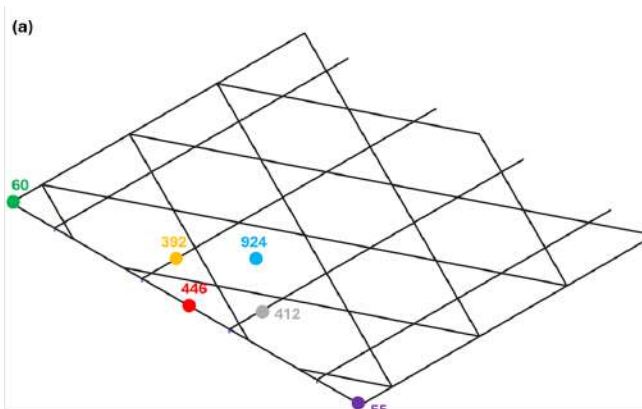


Table 2. Peak vertical displacements. Absolute values and variation with respect to Scenario BG

Scenario	Peak vertical displacements					
	Absolute value (mm)			Variation with respect to Scenario BG (%)		
	Node 392	Node 924	Node 446	Node 392	Node 924	Node 446
BG	47.1	82.7	11.8	-	-	-
IG	63.0	113.2	55.1	33.7	36.8	365.9
BGb	28.3	49.0	3.0	-40.0	-40.8	-75.0
IGb	46.7	77.7	4.0	-0.8	-6.0	-66.6

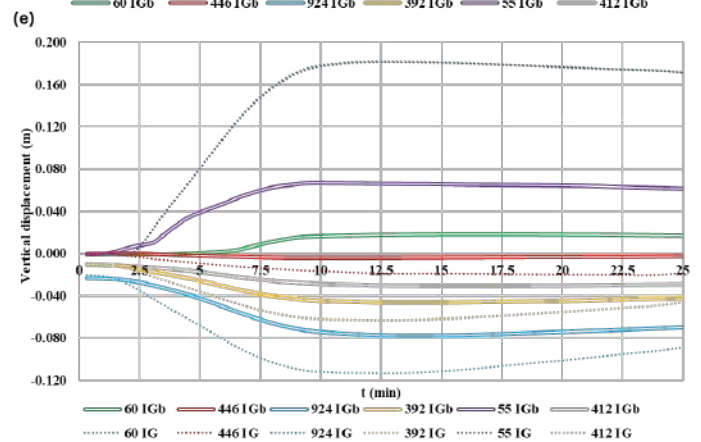
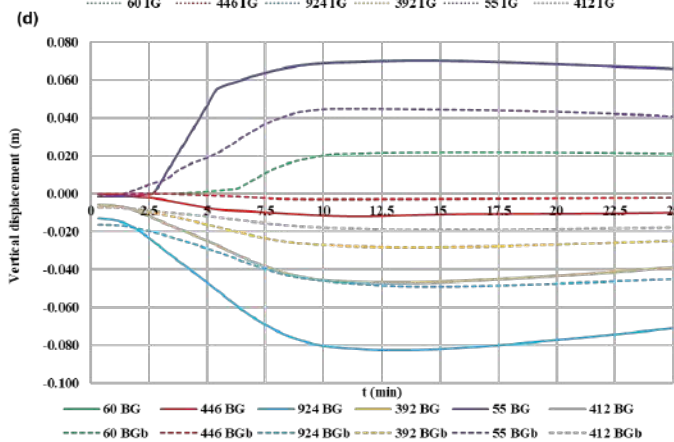
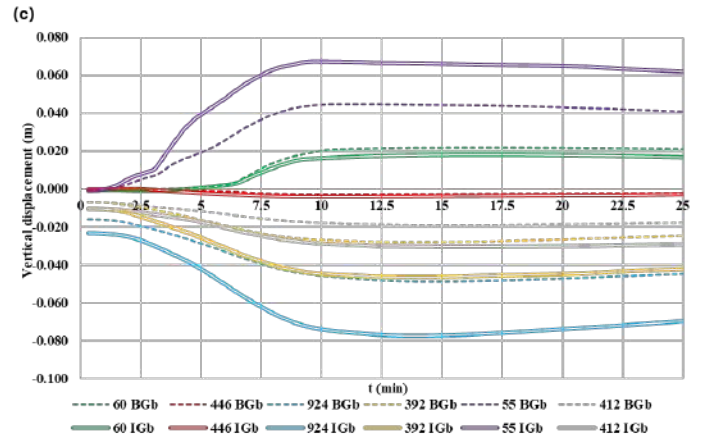
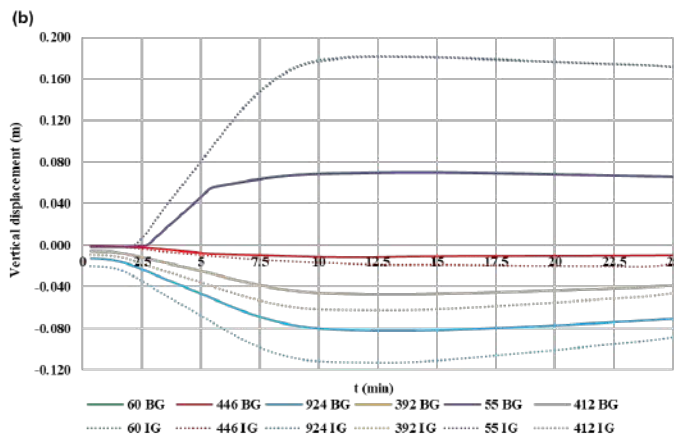


Figure 7. Vertical displacement results. (a) Location of nodes for reference. (b) Comparison between BG and IG scenarios. (c) Comparison between BGb and IGb scenarios. (d) Comparison between BG and BGb scenarios. (e) Comparison between IG and IGb scenarios

- As the diaphragm girder compresses, opposing elements heat up, relax their restraint, and shift from tension to compression. Following a 4-minute period, compression in the diaphragm girder decreases, but it increases again as the fire fully develops, inducing additional compressive forces in adjacent girders. Steel girders near the fire load experience a significant increase in compression, contributing to local buckling observed on site due to proportional limit reduction and decreased stiffness from Young's modulus reduction.

The comparative analysis depicted in Figure 8a to 8d provides the following insights:

- In examining the effects of section type alone (Figure 8a), it becomes evident that the I-shaped girders scenario (IG) demonstrates greater compressions in the transversal girder (T1) compared to the box-girders scenario (BG). Similarly, slightly higher tension (or reduced compression) is observed for the longitudinal and diaphragm girders (L1 and D1) in the IG model. This trend aligns with the observations from the original analysis.
- When incorporating a modified effective stress in compression and comparing different section types (Figure 8b, BGb vs IGb), a similar pattern emerges between I-shaped and box girders (IGb and BGb) for the longitudinal and diaphragm girders (L1 and D1). However, higher compressions are observed along the transversal girder T1 for the BGb scenario compared to IGb. This reversal of behaviour contrasts with the observations from Figure 8a without the modified stress, where greater compression was seen for the IG scenario relative to the BG scenario.

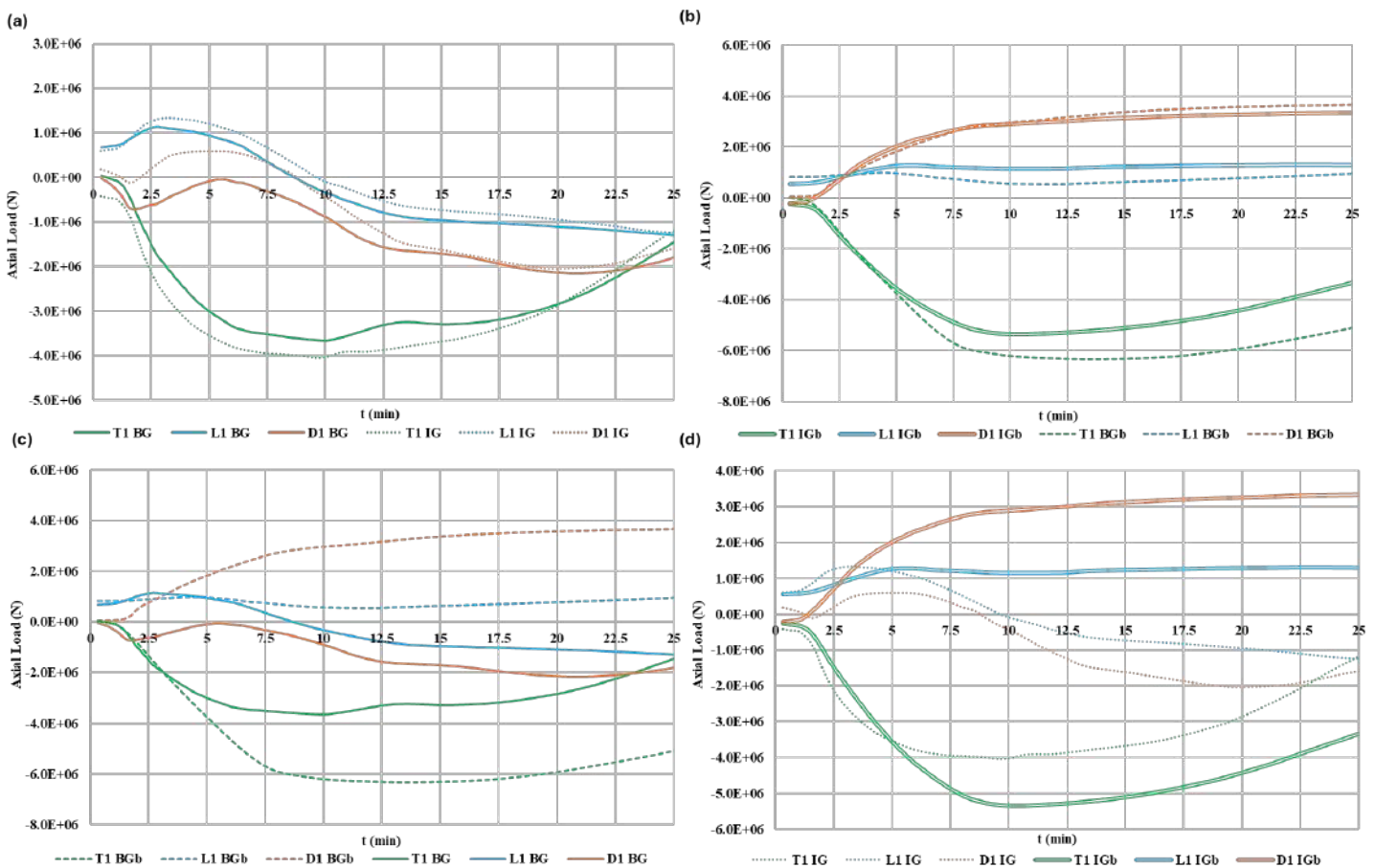


Figure 8. Axial load results. Negative values indicate compression forces and positive values indicate tension forces. Refer to Figure 3 for T1, L1 and D1 location. (a) Comparison between BG and IG scenarios. (b) Comparison between BGb and IGb scenarios. (c) Comparison between BG and BGb scenarios. (d) Comparison between IG and IGb scenarios

- Maintaining the same section type (BG) and comparing mechanical behaviour (Figure 8c, BGb vs BG and Figure 8d, IGb vs IG), it is evident that the transversal girder T1 experiences amplified compression when the modified stress in compression is incorporated for both scenarios (IGb and BGb). However, the trend of variation during the analysis remains consistent with the fire-type beam scenarios (IG and BG). Conversely, girders D1 and L1 exhibit an amplification of tension stresses from the onset of the fire, which stabilizes after a period of growth and does not transition to compression, unlike in the fire-type beam scenarios.

Figure 9 depicts the displaced configuration of the DG scenario after 10 minutes, as shown in Figure 6b (shell finite elements for diaphragm beam D1, fiber-type beam elements for stud connectors, and shell finite elements for the concrete slab).

The results illustrate how local buckling manifests within the shell elements of the diaphragm beam D1 along the central section of the lower flange and web. However, the post-fire analysis and in-situ investigations reveals that steel buckling predominantly occurred near the diaphragm girder supports rather than at the element center. Notably, the mechanical analysis operates under several assumptions that may deviate from the real fire incident. One such assumption involves employing a constant temperature as a boundary condition for the entire D1 element (see Figure 3). Temperature evaluations from the original analysis via CFD [10] indicate that the highest temperatures occur near the abutment recess, closer to the D1 supports. Consequently, considering a quasi-constant axial stress along the D1 girder, these support areas are more susceptible to buckling. Additionally, a simplification has been made regarding mechanical constraints on supports (see Figure 6b), assuming a fixed mechanical constraint throughout the analysis in lieu of a nonlinear, temperature-dependent connection with the rest of the structure. Nevertheless, utilizing full 3D shell model demonstrates the capability to capture local instabilities as part of the mechanical analysis. Modelling the diaphragm beam with non-uniform heating in the longitudinal direction will be part of future works.

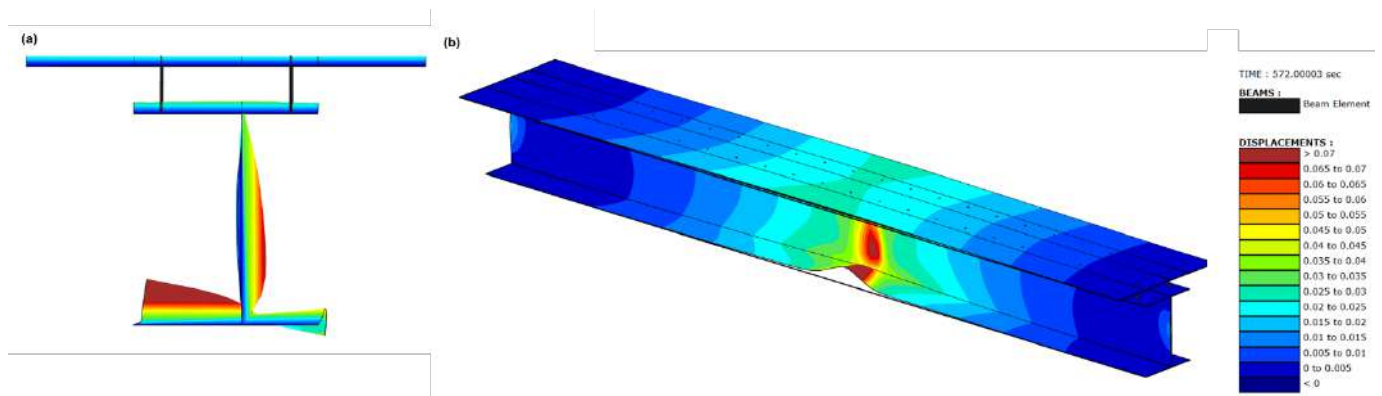


Figure 9. Displacement results for the DG scenario at 10 min. (a) XZ plane. (b) Isometric view

4 CONCLUSIONS

This comparative analysis of thermal and mechanical responses, based on an original study of the Valencia bridge fire incident [10], highlights the profound influence of girder cross-sections and the either implicit or explicit incorporation of local buckling on the structural behaviour of composite bridges under fire conditions.

The temperature evolution highlights the vulnerability of structural elements, with significant implications for material properties such as yield strength, proportional limit, and modulus of elasticity. The findings underscore the importance of selecting appropriate girder designs, with the box-girder geometry proving advantageous due to its ability to act as a thermal insulator and shield non-directly exposed sections from direct fire impingement. Conversely, the I-shaped girder design concentrates higher temperatures along the bottom flange, exacerbating damage and potentially leading to critical structural failures.

I-shaped girders (IG) exhibit significantly larger vertical displacements compared to box-girders (BG) due to higher temperatures within the IG, leading to increased material degradation and expansion rates. When integrating a modified effective stress model in compression, this difference in displacements between I-shaped girder and box girder scenarios is further accentuated (IGb vs BGb). In addition, this modified effective stress model reveals (a) a non-symmetric uplift behaviour at extreme nodes and (b) reduced peak deflections in comparison with the non-modified stress models.

I-shaped girder scenarios demonstrate greater compressions in transversal girders compared to box-girder scenarios, with slightly higher tension observed in longitudinal and diaphragm girders. Incorporating modified effective stress in compression alters the behaviour, with transversal girders experiencing higher compression in BG scenarios compared to IG scenarios.

DG scenario shows that utilizing a full 3D shell model demonstrates the capability to capture local instabilities accurately, enhancing the overall mechanical analysis for specific elements.

Overall, the analysis provides valuable insights into the structural behaviour under fire conditions, emphasizing the importance of section types, material properties, and mechanical constraints in predicting and mitigating potential structural failures.

5 REFERENCES

- [1] Ingason H, Li YZ, Lönnemark A. Tunnel Fire Dynamics. New York, NY: Springer New York; 2015. <https://doi.org/10.1007/978-1-4939-2199-7>.
- [2] Duffy C, Harvey N, MacDonald M. NFPA 502: Standard for Road Tunnels, Bridges, and Other Limited Access Highways. 2023.
- [3] Hua N, Tessari A, Elhami Khorasani N. Characterizing damage to a concrete liner during a tunnel fire. *Tunnelling and Underground Space Technology* 2021;109:103761. <https://doi.org/10.1016/j.tust.2020.103761>.
- [4] Rinaudo P, Paya-Zaforteza I, Calderón PA. Improving tunnel resilience against fires: A new methodology based on temperature monitoring. *Tunnelling and Underground Space Technology* 2016;52:71–84. <https://doi.org/10.1016/j.tust.2015.11.021>.
- [5] Alos-Moya J, Paya-Zaforteza I, Hospitaler A, Rinaudo P. Valencia bridge fire tests: Experimental study of a composite bridge under fire. *Journal of Constructional Steel Research* 2017;138:538–54. <https://doi.org/10.1016/j.jcsr.2017.08.008>.
- [6] Garlock M, Paya-Zaforteza I, Kodur V, Gu L. Fire hazard in bridges: Review, assessment and repair strategies. *Engineering Structures* 2012;35:89–98. <https://doi.org/10.1016/j.engstruct.2011.11.002>.
- [7] Hu J, Carvel R, Usmani A. Bridge fires in the 21st century: A literature review. *Fire Safety Journal* 2021;126:103487. <https://doi.org/10.1016/j.firesaf.2021.103487>.
- [8] Liu Z, Li G-Q, Paya-Zaforteza I, Cai CS, Huang Q. Fire Hazards in Bridges: State of the Art, Recent Progress, and Current Research Gaps. *J Bridge Eng* 2023;28:03123003. <https://doi.org/10.1061/JBENF2.BEENG-5790>.
- [9] Nicoletta B, Kotsovinos P, Gales J. Review of the fire risk, hazard, and thermomechanical response of bridges in fire. *Can J Civ Eng* 2020;47:363–81. <https://doi.org/10.1139/cjce-2018-0767>.
- [10] Pagan-Martinez JJ, Paya-Zaforteza I, Hospitaler-Perez A. Post-fire assessment of composite steel-concrete box-girder bridges: lessons from a recent incident. *Journal of Constructional Steel Research JCSRES-D-23-01583R1* 2024. <https://doi.org/10.1016/j.jcsr.2023.108425>.
- [11] Franssen J, Cowez B, Gernay T. Effective stress method to be used in beam finite elements to take local instabilities into account. *Fire Saf Sci* 2014;11:544–57. <https://doi.org/10.3801/IAFSS.FSS.11-544>.
- [12] Franssen J-M, Gernay T. Modeling structures in fire with SAFIR: theoretical background and capabilities. *JSFE* 2017;8:300–23. <https://doi.org/10.1108/JSFE-07-2016-0010>.
- [13] Wickström U, Duthinh D, McGrattan KB. *Adiabatic Surface Temperature for Calculating Heat Transfer to Fire Exposed Structures.*, NIST; 2007.
- [14] CEN. Eurocode 2: Design of concrete structures - Part 1-2: General rules - Structural fire design 2005.
- [15] CEN. Eurocode 3: Design of steel structures - Part 1-2: General rules - Structural fire design 2005.

NUMERICAL CALCULATION ON FRAME AT ELEVATED TEMPERATURES

Batuhan Der¹, František Wald², Petr Červinka³, Martin Vild⁴, Jiří Vaněk⁵

ABSTRACT

This paper presents an experiment with a steel frame and a validation of its numerical design calculation. The study validates the Component Based Finite Element Method (CBFEM), which is a numerical design calculation model for the analysis and design of steel connections and members at elevated temperatures. The elevated temperature experiment was conducted as part of the FISHWALL RFCS project 101034083, which focuses on the design of a sandwich panel fire wall. The experiment is used to validate and verify the numerical design calculation where the members are analyzed by the shell finite element model by Geometrical and Material Nonlinear Analysis with Imperfections (GMNIA) and the joints are analyzed by Component Based Finite Element Method (CBFEM).

Keywords: Steel member; fire design; numerical calculation; LTB

1 INTRODUCTION

In fire, the stiffness and strength of steel members and connections are reduced at elevated temperatures, resulting in a decrease in resistance. EN 1993-1-2:2005 [1] suggests that the design of insulated steel members exposed to fire, assuming a uniform temperature in the cross-section, taking into account the mechanical properties of steel at elevated temperatures, can be analyzed using simplified analytical methods. When designing a steel beam, ambient temperature actions with reduction factors for the mechanical properties of structural steel at elevated temperature can be used to consider the influence of fire action [2]. Experimental investigation is the most accurate way to calculate the fire resistance of steel members. However, it is not applicable due to the cost and size limitations of currently used furnaces. Many models can be used to calculate the fire moment resistance of steel beams. They are analytical, numerical and CBFEM models. The solid models can provide high accuracy compared to experimental results. On the other hand, the main disadvantage of solid models is the computation time. Therefore, shell elements are a very good alternative to solid elements. The CBFEM simulates the behavior of steel plates using shell element and evaluates the design parameters based on different design specifications.

Liu et al. [3] conducted experimental tests at the University of Manchester to investigate the effects of restraint on the thermal expansion of unprotected beams from protected columns and adjacent cooler beams.

¹ Ph.D. Student, Czech Technical University in Prague,
e-mail: batuhan.der@fsv.cvut.cz, ORCID: <https://orcid.org/0000-0003-1091-9101>

² Prof. Ing., Czech Technical University in Prague
e-mail: wald@fsv.cvut.cz, ORCID: <https://orcid.org/0000-0003-2416-8951>

³ Ing., IDEA RS s.r.o.
e-mail: petr.cervinka@ideastatica.com, ORCID: <https://orcid.org/0009-0000-4435-7106>

⁴ Ph.D, Brno University of Technology
e-mail: vild.m@fce.vutbr.cz, ORCID: <https://orcid.org/0000-0002-2327-3162>

⁵ Ing, PAVUS, a.s.
e-mail: vanek@pavus.cz,

The test setup for the high temperature test is shown in Figure 3.8. The focus of this experimental work was to investigate the influence of different connection types on the failure temperature of the connected members at different load levels. The results of the Cardington full-scale frame fire tests were used to supplement the experimental work. These tests included flush end plate and web cleat connections associated with three loading levels (20%, 50%, and 70% of the moment capacity of the beam) and three degrees of horizontal restraint (8 kN/m; 35 kN/m; and 62 kN/m). Santiago [4] carried out experimental and numerical studies on six steel subframes exposed to natural fire conditions. The objective of this study was to investigate the behavior of the connections under the combined bending moment and axial force developed during a natural fire. The study focused on three types of connections: head plate, flush end plate, and extended end plate. Wang et al [5] conducted ten fire tests on medium-scale restrained steel subframes to investigate the relative behavior and robustness of different types of steel connections in steel frames. The types of joints studied are fin plate, web cleat, flush endplate, flexible endplate, and extended endplate joints. structures in fire. The top flange of the beam was protected to consider the effect of concrete slabs. The column ends were restrained to study the effects of axial restraint on the beam and joints. Very large deflections were observed in the mid-scale steel beams without failure.

The prEN 1993-1-14 [6] describes two design methods for finite element models: numerical simulation (NS) and numerical design calculation (NDC). Simulation generally uses volume models and geometric and material nonlinear analysis with imperfections and provides results similar to experimental results. A validated simulation is used to generate numerical experiments for sensitivity studies of significant parameters. However, the generation of the simulation is very time consuming and costly. Shell elements are recommended for modeling plates in the finite element model design of the steel frame in the numerical calculation. In steel connection design, curve fitting, analytical and finite element models are used to model stiffness, resistance and deformation capacity. CBFEM [7] is a method for analyzing and designing connections and members of steel structures. It is a combination of component method and finite element method. Der et al [8] verified the model to design the steel members at elevated temperatures.

2 EXPERIMENTAL STUDY

2.1 Test Objective and Specimens

The primary objective of the fire test was to investigate the behavior of the non-structural fire wall, composed of sandwich panels and a fusion joint between two frames, when exposed to fire. The test specimen consisted of two steel frames penetrating a non-structural fire wall made of sandwich panels, vertically spanned between a concrete slab at the bottom and steel decks at the top, fixed to a supporting steel structure [9].

2.2 Test Description

The test specimen consisted of a non-load bearing fire wall made of sandwich panels stretched horizontally between two non-exposed HEA 140 steel columns, connected to unprotected steel structures consisting of either steel portal frames on the fire exposed side or single HEA 320 steel columns on the other side, by means of two different fusion systems, Figure 1. Each portal frame consisted of a single HEA 320 steel column connected by a moment resisting bolted connection (8 pcs. M20x60 bolts) to a steel beam IPE 360 supported at its free end by a forked support fixed to a beam HEB 500 as part of a horizontal support frame placed around the furnace. The part of the HEB 500 located inside the furnace was adequately fire protected with mineral wool 50 mm, density 100 kg/m³, wrapped with ceramic blanket insulation Cerablanket 1430, 13 mm, density 128 kg/m³. The two steel portal frames were connected with an IPE 140 steel beam, which was fixed at the upper end of the columns. The IPE 140 beam was fireproofed all around with mineral wool 50 mm and Cerablanket 1430, 13 mm. The columns of the portal frames were approximately 3.2 m high, while the span of the beams was approximately 6.25 m. The HEA 320 steel columns were also attached to the horizontal support frame placed around the furnace. The height of the columns was approximately 4.8 m. 15 mm thick steel base plates were welded to the bottom of the columns and bolted to large 700x30 mm

steel plates placed on the bottom of the furnace. The lower end of the columns on the fire exposed side were fire protected. The steel grade was S275 for steel members and plates and 8.8 for bolts.

The fire resistance test was performed on May 17, 2023 in the test hall PO 1 in the horizontal furnace PAVUS lab Veselí n.L., Czech Republic, with internal dimensions of width 3 000 mm, length 8 460 mm and height 3 250 mm. The test furnace was heated by a set of oil burners according to a nominal standard firing curve. The temperatures inside the furnace were measured by means of plated thermocouples (PTM) and recorded at minute intervals. The rate of horizontal and vertical deflection was measured by deflectometers. Since displacement sensors cannot be installed inside the furnace due to the high temperatures, draw-wire displacement sensors were installed outside the furnace and then attached to the specimen by means of stainless steel rods welded to the top flange of the beams to measure both vertical and horizontal displacements at different locations along the heated steel portal frames: at the beam-column joints and at the beam mid-span. The total length of the stainless-steel rods was 800 mm, of which 250 mm was directly in the heated space of the furnace.

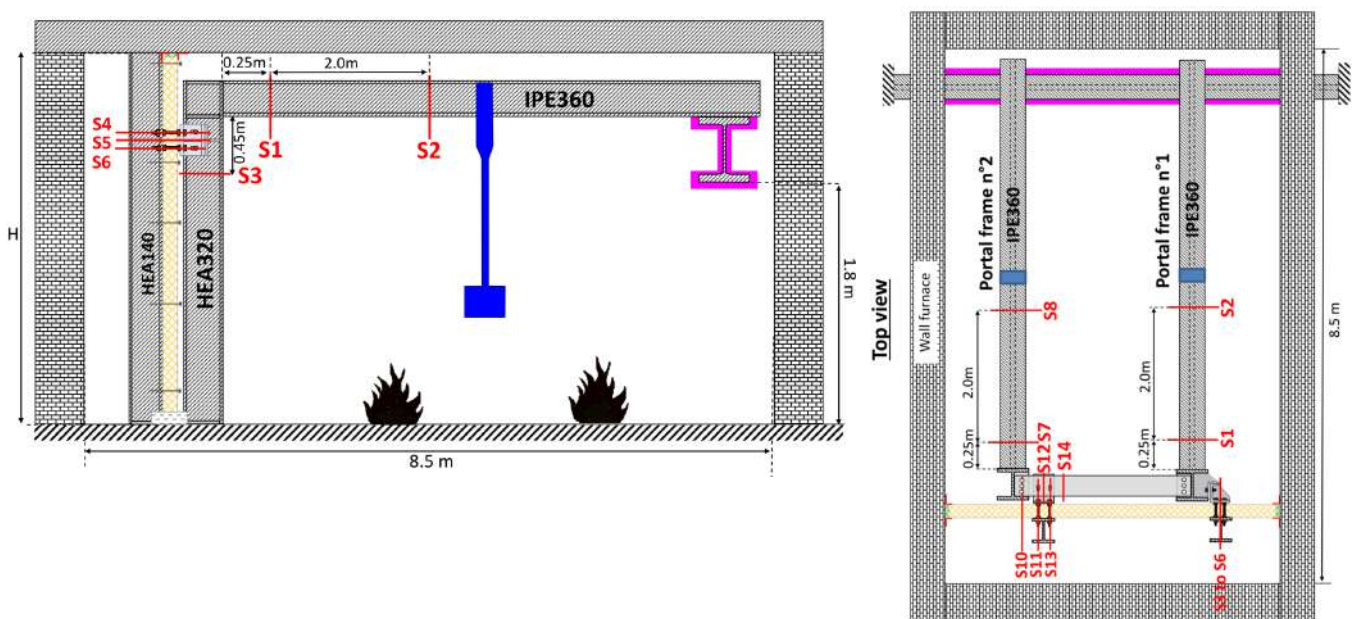


Figure 1. Test Configuration [9]

3 NUMERICAL DESIGN CALCULATION

3.1 CBFEM

Component-based Finite Element Method (CBFEM) is a method to analyze and design joints of steel structures. The CBFEM is the combination of the analytical component method and the numerical finite element method (FEM). The finite element method is used to solve the distribution of internal forces. The plastic limit strain, recommended as 5% in EN 1993-1-5 [10], is used to evaluate the resistance of steel plates. The model is generated using the commercial software IDEA StatiCa [11] to study the behavior of the steel member. IDEA StatiCa Member can perform three types of analysis: material nonlinear analysis, linear buckling analysis, and geometric and material nonlinear analysis with imperfections.

3.2 Model Description

Figure 2 indicates the geometric configuration of the steel frame based on the study [9]. The steel frame consists of IPE beams and HEB columns. The material properties of the steel members are considered as nominal values. Rigid supports were added at the ends of the beams. The bottom part of columns was fixed in the movement and rotation. All members are meshed with 4-node quadrangle shell elements.

MNA	✓	100.0 %
MNA Plates	✓	0.0 < 5.0 %
LBA		6.12
GMNIA	✗	64.8 %
GMNIA Plates	✓	0.1 < 5.0 %

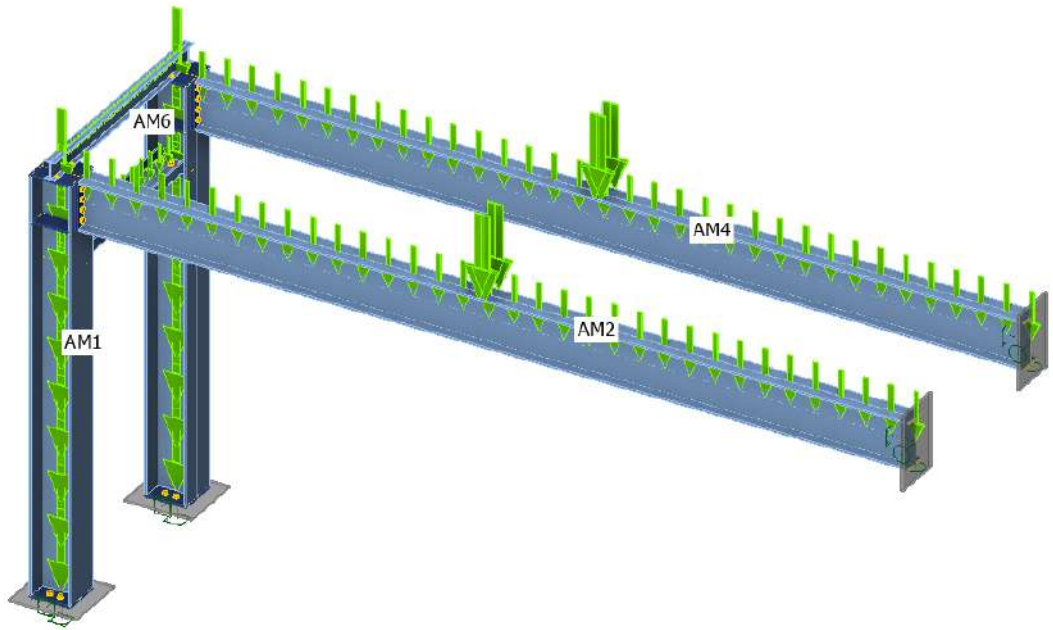


Figure 2. The CBFEM model

To simulate the fire behavior of steel frame, it is necessary to assign the temperature-dependent mechanical properties of the structural material. For steel, the reduction factor of strength and modulus of elasticity of steel at elevated temperatures of individual plate proposed by EN 1993-1-2 [12] are adopted.

3.3 Material Properties

Models use simplified material curves based on the design specifications. The models the plates with an elastic-plastic material with a nominal yield plateau slope $\tan^{-1}(E/1000)$ according to EN 1993-1-5 [10]. The von Mises yield criterion governs the response of the material under load. It is assumed that the material behaves elastically until it reaches the design yield strength, f_{yd} . EN 1993-1-5 recommends the value of 5 % plastic strain limit to simulate the behavior of plates. Figure 3 displays the theoretical true and engineering stress-strain curves as well as the material model used in the CBFEM model.

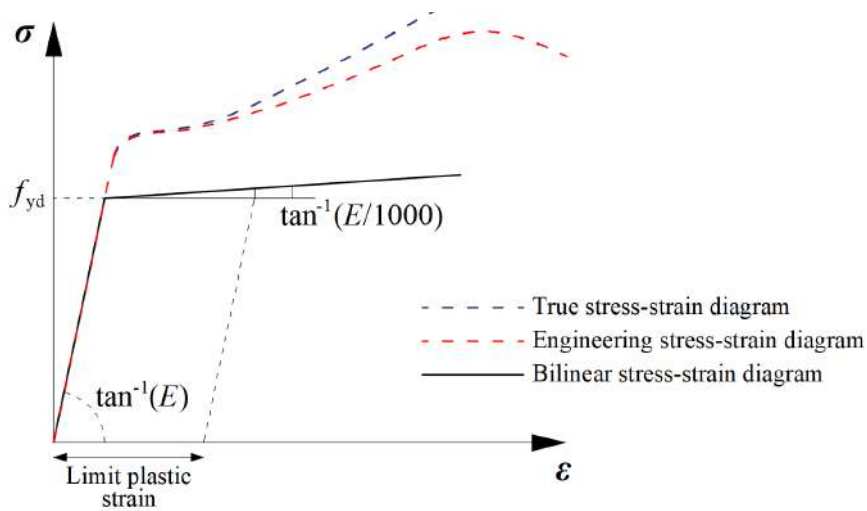


Figure 3. Material model for numerical design calculation

4 RESULTS

4.1 Verification on steel beam

In this chapter, the numerical calculation is verified based on the steel beam at elevated temperatures. The verification study was performed by the linear buckling analysis (LBA) module of the IDEA Member application. The influence of different loading conditions, boundary conditions, and the beam span are investigated. The resulting elastic critical moments from IDEA Member are compared to the elastic critical moments based on analytical and numerical models. The procedure of analytical and numerical calculations is explained by Der et al. [2]. The LBA provides the buckling shapes of steel beams in order to consider the imperfection effect on steel beams. Figure 4 and Figure 5 shows the summary of elastic critical moment and LTB resistance comparison, respectively.

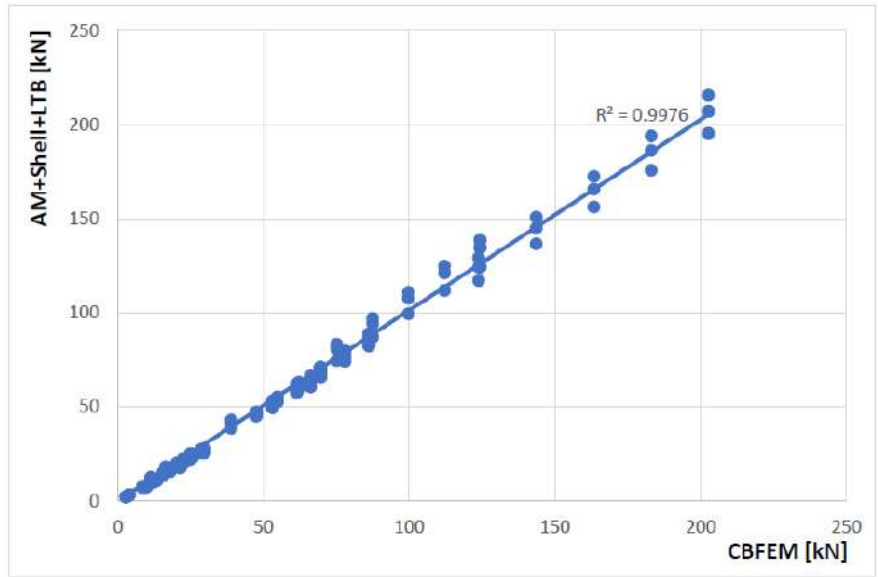


Figure 4. Summary of the elastic critical moment comparison

The GMNIA (geometrically and materially nonlinear analysis with imperfections) module of the IDEA Member provides the lateral torsional buckling moment resistance. Initial geometric imperfections were applied following the beam's eigenmodes obtained by linear buckling analysis (LBA).

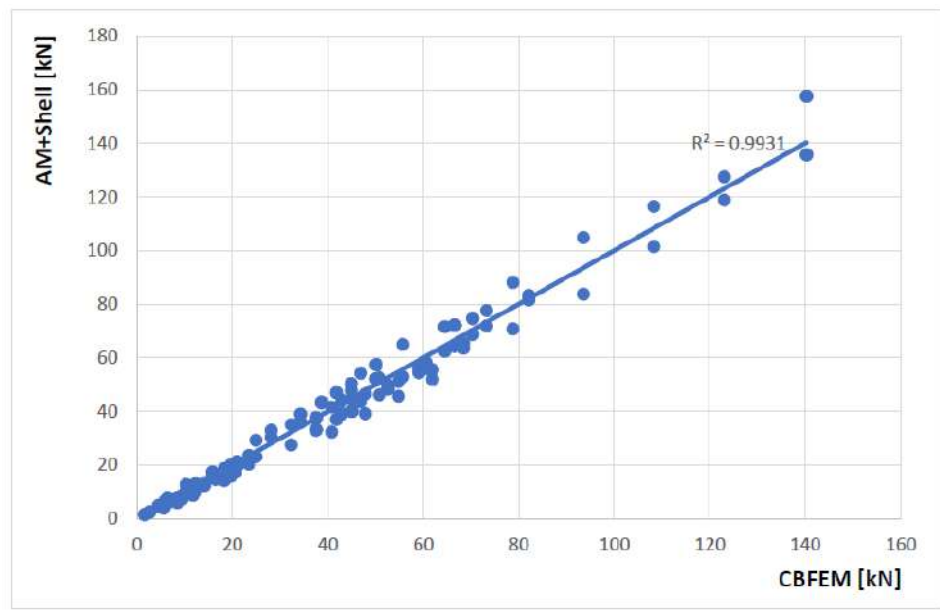


Figure 5. Summary of LTB resistance comparison

The section proposed a CBFEM model to calculate the fire resistance of steel beams in terms of different moment values. The CBFEM model was verified by the shell model in Abaqus code and analytical models. The main drawbacks of the shell model can be defined as the uncertainty in the degree of warping constraint and the differences between real section dimensions and the geometry used in the shell model leading to different torsion and warping constants. The lateral-torsional buckling resistance from the analytical model becomes higher than that from the shell model because the analytical model includes bending resistance depending on the reduction factor in the yield strength of steel. According to Eurocode, the yield strength of steel does not have a reduction until 400°C. However, the results from the shell model were consistent with analytical results and they showed that using a simple shell model is possible to predict the moment resistance of the beam at elevated temperature.

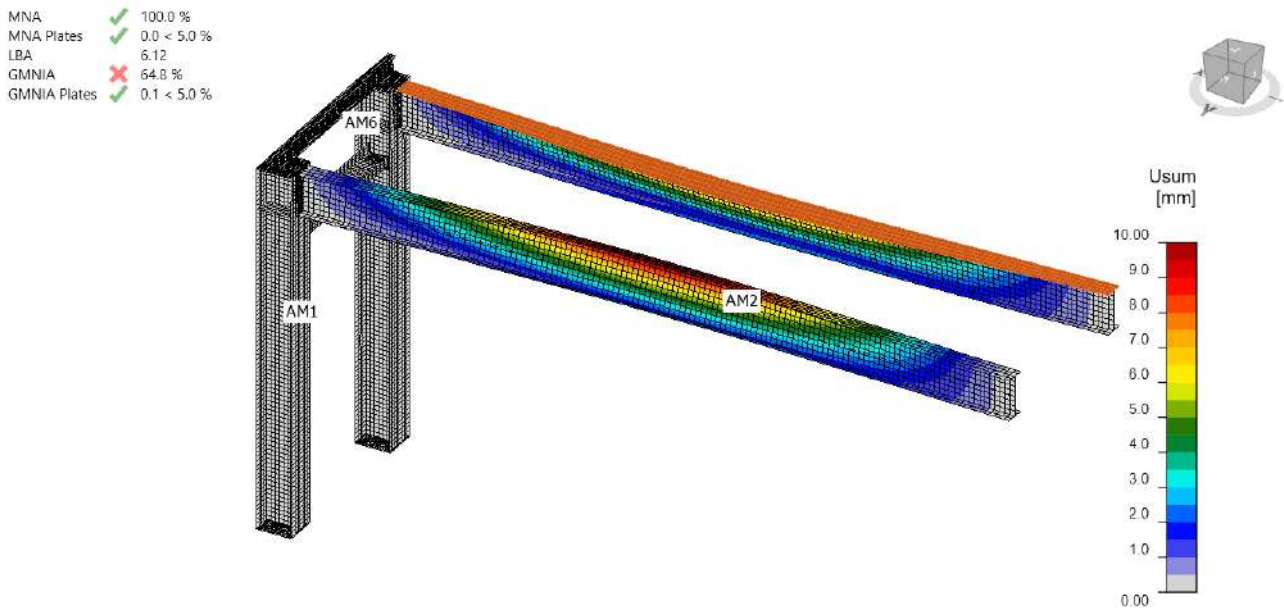


Figure 6. Linear buckling analysis of steel frame in the CBFEM

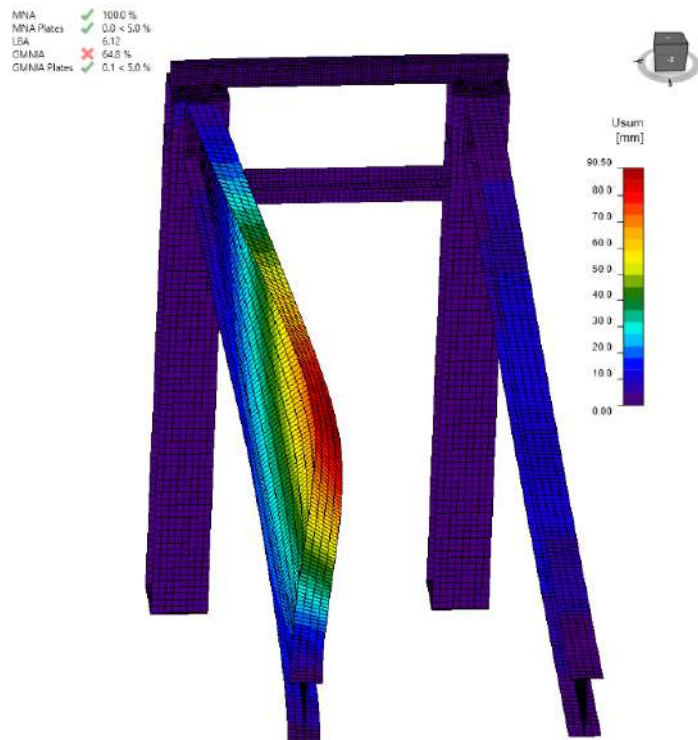


Figure 7. The deformed shape of rafter analyzed by GMNIA

4.2 Validation on steel frame

The tested frame was analyzed in the CBFEM. The geometry, cross sections, and loads are used according to input data [9]. Load effects considered in the model are the self-weight of steel members and two-point loads with 25 kN in the middle of the span of the main beams. Figure 6 and Figure 7 exhibit the results of LBA and GMNIA of the CBFEM to investigate the behavior of tested specimens at elevated temperatures. As seen in Figure 8, the CBFEM may capture a similar failure mode compared to the experimental test. It can be also seen, Figure 9, that the predicted load for the steel frame is calculated as 64.8% of the applied one.



Figure 8. Test specimen during and after the fire test

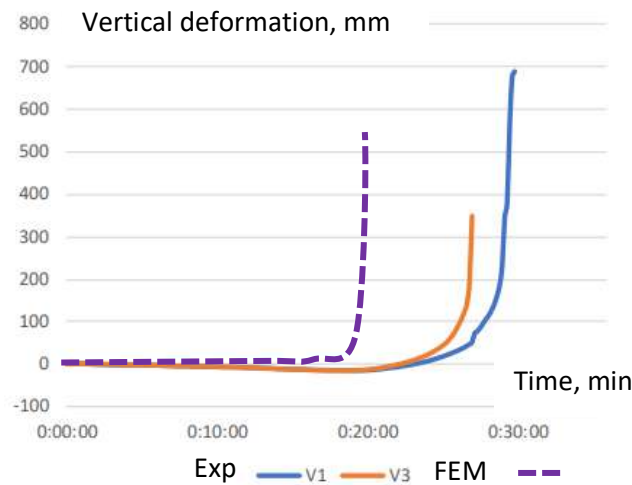


Figure 9. Comparison of predicted and measured vertical deformations of rafted 1

5 CONCLUSIONS

The experimental results and numerical design of the steel frame with connections are presented. The shell model is verified on the volume model and experimentally validated with the simplified frame with fusion connection and the sandwich panel fire wall.

The verification results of a simple supported beam show that the difference between the analytical model and CBFEM is less than 5% in all cases. According to EN1993-1-2:2005, the yield strength of steel has no reduction until 400°C. Therefore, the analytical model does not show any reduction in bending moment. The LBA module predicted the elastic critical moment resistance and the possible buckling shapes for lateral torsional buckling. Up to 700°C, the difference between the analytical model and CBFEM is less than 14% in all cases. As the length of the beam span or the cross-section size decreases, the CBFEM gives

about 20% higher results than the analytical model after 700°C. The degree of warping constraint changes with temperature because the end plate used to simulate boundary conditions is assumed to be at ambient temperature. The CBFEM is more conservative than the analytical model in calculating the lateral torsional buckling resistance at elevated temperatures. The most significant difference is 20% for the lateral torsional buckling resistance at 800°C. However, the results from the component-based finite element model were in agreement with the analytical results and showed that it is possible to predict the moment resistance of the beam at elevated temperature using a CBFEM.

The complex validation on experiment with simple frame shows the conservatism in the prediction of resistance by CBFEM shell model. The predicted resistance is about 75% of the experimental one. The fusion connection separates the walls well and has a noticeable effect on the calculation results.

ACKNOWLEDGMENT

This research is supported by the grant RFCS-RPJ 101034083 FISHWALL the preparation of this paper by Czech Technical University in Prague SGS22/144/OHK1/3T/11.

REFERENCES

1. EN 1993-1-2. Eurocode 3: Design of steel structures – Part 1-2: Design of members, 2005, Brussels, Belgium
2. DER, B., WALD, F. a Vild, M. Benchmark study for fire design of steel beam. In: Proceedings of the Applications of Structural Fire Engineering in Ljubljana, 10-11 June 2021. Lublaň: University of Ljubljana, Faculty of Civil and Geod, 2021. p. 394-399. 1. vydání. ISSN 2570-8074. ISBN 978-961-6884-71-6.
3. Liu, T. C. H., M. K. Fahad, and J. M. Davies. "Experimental investigation of behaviour of axially restrained steel beams in fire." *Journal of Constructional Steel Research* 58.9 (2002): 1211-1230.
4. A. Santiago, L. S. Da Silva, G. Vaz, P. V. Real, and A. G. Lopes, "Experimental investigation of the behaviour of a steel sub-frame under a natural fire," in *Steel and Composite Structures*, Techno Press, 2008, pp. 243–264. doi: 10.12989/scs.2008.8.3.243.
5. Y. C. Wang, X. H. Dai, and C. G. Bailey, "An experimental study of relative structural fire behaviour and robustness of different types of steel joint in restrained steel frames," *J Constr Steel Res*, vol. 67, no. 7, pp. 1149–1163, Jul. 2011, doi: 10.1016/j.jcsr.2011.02.008.
6. prEN1993-1-14, Eurocode 3: Design of steel structures – Part 1-14: Design assisted by finite element analysis, proposal of European Standard, 2022.
7. Šabatka, L.; Wald, F.; Kabeláč, J.; Kolaja, D.; Pospíšil, M. (2015) Structural Analysis and Design of Steel Connections Using Component-Based Finite Element Model. *Journal of Civil Engineering and Architecture* 9 895-901, doi: 10.17265/1934-7359/2015.08.002.
8. Der, B., Wald, F. and Vild, M. (2024), Fire design of steel member by component-based finite element method. *ce/papers*, 7: 36-44. <https://doi.org/10.1002/cepa.3020>
9. Vaněk J., Fire wall connected to an unprotected steel structure and penetrated by steel purlins, project FishWall RFCS-RPJ 101034083, Task 3.2, Fire resistance test report, No. Pr-23-2.086-En, PAVUS 2023.
10. EN1993-1-5: Eurocode 3 Design of steel structures - Part 1-5: General rules - Plated structural elements, CEN, Brussels 2006.
11. IDEA StatiCa Member 23.1. 2023, Product documentation. Retrieved from www.idea-rs.com.
12. EN 1993–1-2, Eurocode 3: Design of Steel Structures, Part1–2: General Rules, Structural Fire Design, European Committee for Standardization, Brussels, Belgium, 2005.

OPTIMISING AIRPORT STRUCTURAL FIRE DESIGN WITH FIRE SPREAD MODELS: A CASE STUDY ON INTEGRATING GOZONE WITH SAFIR

Jeremy Chang¹, Antonio Gamba², Linus Lim³, Peter Armstrong¹, Konstantinos Papaioannou¹

ABSTRACT

A significant upgrade of one of the main airports in New Zealand has been under planning for several years and the stakeholders are very aware of the benefits associated with structural fire engineering design. Considering the large compartments, defined use, and specific fuel loads in different areas, airports are the ideal projects for integrating fire spread models into the structural fire design. This paper discusses the application of structural fire engineering analysis for this project, specifically adopting the newly developed GoZone [1] program in predicting fire spread in large compartments, coupled with the thermal-mechanical software SAFIR [2] for forecasting structural behaviour during fires.

Keywords: GoZone; Travelling Fire; SAFIR; Finite Element Analysis; Airport

1 INTRODUCTION

Performance-based structural fire engineering design utilising finite element analysis has been adopted over the world in recent decades. The continuous evolution of computing power allows engineers to introduce diverse and more realistic fire scenarios into structural fire resistance designs. The key inputs for these analyses include parameters like fire size, structural dimensions, and material properties.

Although the idea of structural fire engineering is well-established in research, its practical application remains infrequent. Providing comprehensive explanation required for clients and approval authorities can be time consuming before a project is allowed to include performance-based structural fire design. Fortunately, the permission to use performance-based structural fire design for the proposed significant upgrade of a major airport aligns with the introduction of the GoZone program, providing a rare opportunity for immediate integration and utilization of a new engineering tool within the project timeline.

There are several unique characteristics in airports that make this type of structures ideal for carrying out performance-based structural fire design. Within most of the major airports, the compartments are mostly very big, the use of each area is well defined, subsequently, the available fuels within the compartments are also well defined. The presence of a reliable fire suppression system is also expected. With these characteristics, traditional structural fire design, which assumes an entire compartment experiencing a uniform temperature from either a standard fire or a parametric fire, would be overly simplistic and unrealistic. A more suitable approach for structural fire design involves considering localised fires, and in the ideal situation, incorporation of travelling fire scenarios would be the most appropriate choice.

¹ Holmes NZ, New Zealand

e-mail: jeremy.chang@holmesgroup.com, peter.armstrong@holmesgroup.com, and stan.papaioannou@holmesgroup.com

² ArcelorMittal Global R&D, Luxembourg

e-mail: antonio.gamba@arcelormittal.com, ORCID: <https://orcid.org/0000-0001-5937-577x>

³ Holmes Australia

e-mail: linus.lim@holmesgroup.com

2 CASE STUDY BACKGROUND

This case study is of a proposed significant expansion of an international airport situated in New Zealand. The envisaged extension comprises a three-storey structure: the ground floor encompasses a conveyor area alongside a baggage storage hall; the first floor includes retail area, food hall, and circulation areas; the top floor is designated for premium passenger lounges. In accordance with the New Zealand Building Code (NZBC) requirements and norms of design in New Zealand, the lightweight roof structure can remain unprotected, and therefore the top floor is not an area of interest in this design. For this paper, the example area is in the baggage storage hall.

The entire airport complex is provided with an automatic sprinkler system with dual water supply – a dedicated fire tanks and an alternative connection to the airport water main. In addition, the following fire safety systems are in the existing airport and will be extended into the expansion area – a double-knock smoke detection to prevent nuisance alarm, sounders with audible instructions, manual call points, smoke extraction in several areas. The complex also has its dedicated firefighting crew stationed on-site, and the customary implementation of heightened security protocols inherent to a major airport. These comprehensive safety provisions diminish the probability of a fire progressing to the fully developed stage, and are important information for performance-based structural fire design.

The process of the structural fire analysis can be broken down into the following steps: (1) identify the typical structural fire configurations for detailed analysis; (2) define credible design fires through the appropriate fire model; (3) determine the time-temperature development in the structural elements under exposure to the design fire; (4) undertake structural analysis of the structural system including columns above and below based on the outcomes from Step 3 and incorporating the physical loads on the structure.

3 SELECTION OF FIRE MODEL

Fires in large compartments tend to not burn across the entire space simultaneously; they will spread when the adjacent fuel is ignited and decay when the burning fuel is consumed. This is a phenomenon called travelling fire [3]. Over the years, several models were developed to simulate this phenomenon [3-8], however not all are suitable for design purposes.

For this project, various fire models were evaluated, with a specific emphasis on their suitability for performance-based structural fire design. The chosen model is expected to generate key outputs such as temperatures or heat flux to which the structural members will be exposed.

3.1 Fire Dynamics Simulator (FDS)

FDS [9] is a versatile and almost default fire dynamics program for fire engineers to use in design. It uses Large Eddy Simulation (LES) techniques to simulate the turbulent fluid motion in a fire compartment. The program will provide information at points of interest regarding temperatures as well as chemical species yield, layer height, air flow velocity, and visibility. FDS is also capable of handling irregular compartment size. Nonetheless, using FDS for the design application in large compartments has two significant drawbacks: CPU time and model complexity [6]. The long duration of each simulation hinders the ability to efficiently explore various ignition locations or different fuel loads. Additionally, the method of simulating fire spread within the compartment in FDS relies on user-defined approaches, such as using burners with a ramped heat release curve or assuming the ignition of adjacent fuel object once a certain temperature is reached. These user-defined approaches introduce additional parameters that requires agreement among all stakeholders involved in the process, and may require additional runs to reconfirm the parameters.

3.2 TRAFIR4SAFIR

The benefits and limitations of several recently developed tools on simulating travelling fires have been investigated [8,10] as part of the European research project TRAFIR, and the overall issues lie with the simplification of fire dynamics, lack of validation, and limited field of application. In addition to producing

a series of travelling fire test results, an analytical model has been developed [11]. The TRAFIR analytical tool can provide temperatures which vary along the height of the compartment. The model assumes a localised fire travelling at given speed velocity by neglecting contribution of smoke layer and taking account of the ventilation conditions by power reduction according to EN1991-1-2. This simple tool has been validated against test results in the framework of TRAFIR RFCS project. A module called TRAFIR4SAFIR has also been developed to compute the fire propagation based on the TRAFIR analytical model and write in a transfer file to feed into SAFIR for thermal and structural analyses. As TRAFIR4SAFIR was written for providing information for SAFIR, it does not consider chemical species or visibility and is significantly faster to run. However, TRAFIR analytical tool has simplified the fire spread to one-dimensional, and also it requires the compartment to be rectangular or square, which led us into choosing GoZone for this project.

3.3 GoZone

GoZone was developed in parallel with the TRAFIR project and was validated against the TRAFIR tests carried out in Ulster as well as the natural fire test carried out in Veselí [1,12]. GoZone is based on a cellular automata (CA) framework coupled with a zone model developed by Cadorin et al. [13]. Since the domain is described by CA, it can be theoretically of any shape. These models are typically characterised by the physical environment made of a discrete lattice of cells, the state of the individual cells being burning or not, a local transition rule to change the state of the cell, and the cells' neighbourhood influencing the cells through the transition rule. The fire dynamics and its evolution over time is processed by considering the interactions of discrete lattice of cells and the interaction with the environment. In particular, burning state of a cell is regulated by an ignition strategy based on concept of critical energy, which can be modified according to the ignitability of the fuel materials [14]. Therefore, fire spread velocity is not set a priori as an input parameter, instead it will be determined by the thermal exchange among fire, smoke and fuel cells. Information such as time-dependent smoke layer and the temperature of each zone is acquired by solving four ordinary differential equations to describe the mass and energy balance in each zone (zone model), whereas radiation heat flux from smoke layer using the smoke layer temperature, and radiation from the flames through a semi-empirical model known as the Point Source Model, which was considered more accurate than other semi-empirical models for the taking account of incident heat flux [15]. For a wood-based fuel, suggested parameters are a critical heat flux of 12.5 kW/m^2 and critical energy of 400 kJ/m^2 [1].

In comparison to other methods, GoZone aims to simulate the entire development of a fire in a compartment, from ignition, encompassing fire propagation and temperature development, in both fuel-controlled and ventilation-controlled scenario, but it can potentially also handle irregular compartment shape and two-dimensional fire spread. GoZone's outputs focus on predicting heat flux and gas temperatures. The simulations can be executed rapidly, allowing the convenient adjustment of input parameters to evaluate the effect of varying fuel characteristics or ignition locations. This speed of analysis enables the more effective selection of representative cases to use in subsequent structural analyses.

4 SELECTION OF THERMAL/STRUCTURAL ANALYSIS MODEL

Compared to the selection of fire development model, choosing the thermal and structural analysis model was relatively straightforward for this project. The performance-based structural fire design needs to be able to address irregular floor shape, look into global behaviour of the structure, and consider non-uniform heating across the compartment. Most importantly, as a design tool, it is essential that the outcomes are easily reviewable and replicable by peer reviewer and approval authority. To meet these criteria, SAFIR [2] became the obvious choice. In terms of fire scenarios, the radiant intensities [$\text{W/m}^2\text{Sr}$] from a specified domain in GoZone can be recorded into a transfer file for integration into SAFIR and to be used in the subsequent thermal and structural analysis. Therefore, structural analysis is done via weak coupling strategy which proved to be an effective means in structural fire safety problems [16].

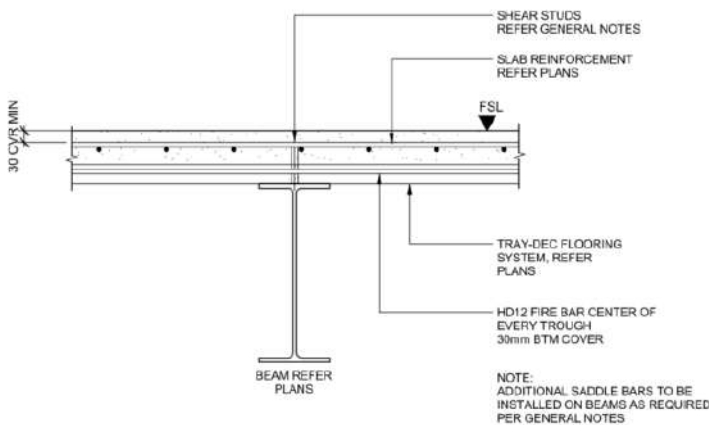
5 ANALYSIS INPUT INFORMATION

5.1 Structural system

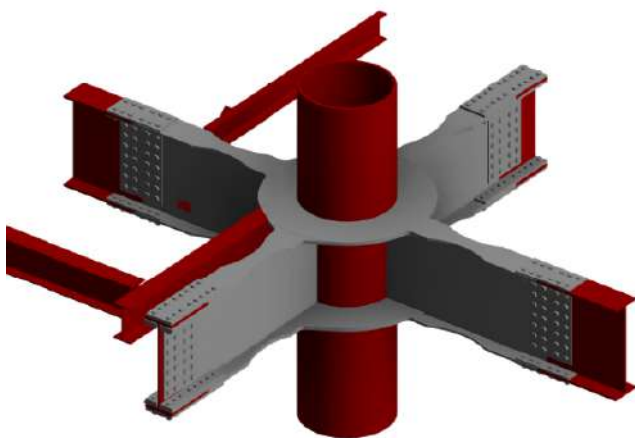
The structural system at the baggage storage hall consists of composite steel-concrete construction with 10 x 10 m square bays and 13 x 10 m structural bays. The flooring slab is the steel-composite Tray-dec 300 flooring system primarily 150 mm deep and spans continuously in one direction with reinforcing in both directions. The slab profile and a typical beam-slab connection with shear studs are shown in Figure 1(a).

The steel beams are designed in accordance with NZS 3404 [17] and are described here as primary and secondary beams, where primary beams span between columns and have reduced beam section (RBS) near the moment connections, and the secondary beams are connected to the primary beams with pinned connections. The examples of these connections are shown in Figure 1(b) and (c). Both the primary and secondary beam are welded beams as deep as 800 mm and acting compositely with the flooring slab above. The primary and secondary beams are made up of multiple penetrations along their mid-span, approximately covering the middle 35 % of the beams' length. The maximum penetration size is 300 mm in diameter.

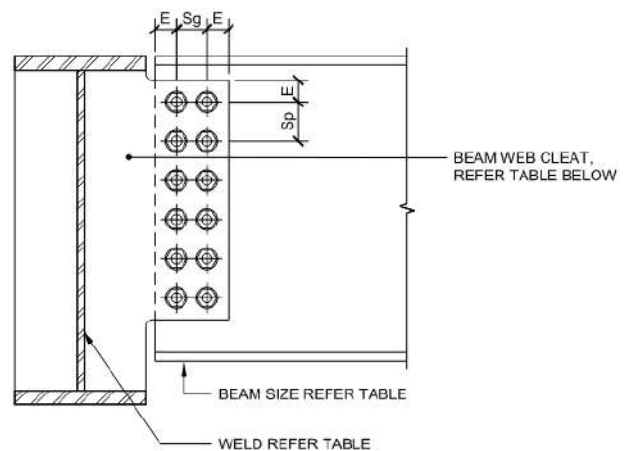
The design and detailing of structural connections for steel structures in New Zealand requires connections to accommodate potential inelastic ductile deformations for robustness in the event of an earthquake. The beams and floor slabs are detailed for ductility for participation as a floor diaphragm for seismic load resistance, which by default enables load sharing from the hotter areas to the cooler and lower loaded parts of the floor system in a severe fire. Simple and semi-rigid beam end connections are detailed to achieve minimum 30 milliradians rotation (at ambient temperature) without loss of load capacity.



(a) beam-slab connection



(b) moment connection between primary beams and a column



(c) pinned connection

Figure 1. Structural details (a) typical beam-slab connection, (b) example moment connection between primary beams and a column, (c) example pinned connection between secondary and primary beams

The columns in the baggage storage hall are concrete filled circular hollow sections (CHS) ranging in size up to 813x16 CHS. The CHS column infill concrete has a compressive strength of 50 MPa. The concrete infill is to act compositely with the CHS skin so that the concrete infill can be utilised to provide strength in fire scenarios.

The design load applied to the floor structure above the baggage storage hall is 7.72kPa which follows the load combination of (1.0 dead load + 0.5 live load) in accordance with NZS/AS 1170.0 [18].

5.2 Design fire characteristics

The baggage hall area is 7.5 m high consists of 6.4 m high of rack storage. The key inputs for the fire scenario are shown in Table 1, which are the values to be included in the GoZone model.

In terms of fire spread area, the spray zone of a single sprinkler head which is 8.5 m² is considered as we believe it is the most credible failure type of the sprinkler system for this building. If there is no presence of sprinkler system and the fire is to freely spread across the baggage area, considering the design fuel load and the conservatively low critical heat flux in comparison to the Ulster fire test results [11], the compartment will experience fire spread throughout before the fire in the area of ignition entering the decay phase. The design document in New Zealand “C/VM2” [19] prescribes a peak heat release rate of 20MW. This value was used to determine the heat release rate per unit area (HRRPUA) in the initial setup of the model, which is comparable to the values presented by Fleischmann [20].

According to Salminen et al. [21], for a sprinkler protected building considering a reduction in fire area and not taking the benefit of cooling effect from the sprinkler system is deemed extremely conservative. The sprinkler system redundancy in this building includes the dual water supply, dedicated zone isolation valve with additional isolations for the larger evacuation zones, separate fire main supplies for the area, additional tail end isolations for the small tenancies to minimise overall impact to overall zone.

Table 1. design fire characteristics as input to GoZone

Parameter	Value	Description
Critical heat flux	9 kW/m ²	based on ABS suitcase - the lowest value between plastics and rubber. [22]
Heat release rate per unit area (HRRPUA)	2350 kW/m ²	Prescriptive peak HRR of 20 MW over an area of sprinkler spray zone 8.5 m ² . Sensitivity was carried out checking 1500-2500 kW/m ² .
Growth rate (t _g)	150 s	Approximation of growth rate from an available rack storage fire experiment [23]
Total fuel load	5120 MJ/m ²	Prescriptive 800 MJ/m ² per metre of storage height from the verification document in New Zealand [19]

5.3 Acceptance criteria

Table 2 shows the acceptance criteria for the structural fire design of the baggage hall area. In this project we have not impose the maximum deflection limit of the floor slab. This is in reflection of the observations from the Cardington tests [24] where unprotected steel beams can undergo large deflections of up to 1/10 of the span and still maintain structural stability through load redistribution.

Table 2. Acceptance criteria

Columns	<ul style="list-style-type: none"> - Maintaining load carrying capacity for the duration of the design fire, including decay phase. - No buckling or runaway deflection to avoid global collapse.
Beams & Floor System	<ul style="list-style-type: none"> - Large deflections are acceptable provided runaway deflections do not occur and structural stability is maintained for the duration of the design fire including decay phase. - No global collapse is allowed. - Integrity is considered maintained if the mechanical strains in the reinforcing steel in the hogging regions of the protected beams and the central region of the slab bays do not exceed its maximum elongation limit of 10%.

5.4 Proposed fire protection strategy

It is necessary to develop a draft fire protection strategy first before carrying out the analyses, and this can be an iterative process if the proposed strategy does not meet the acceptance criteria. Table 3 outlines the proposed fire protection strategy for the structures in the baggage hall area which will be used as basis for building the thermal and structural models for SAFIR analyses.

Table 3. Proposed fire protection strategy

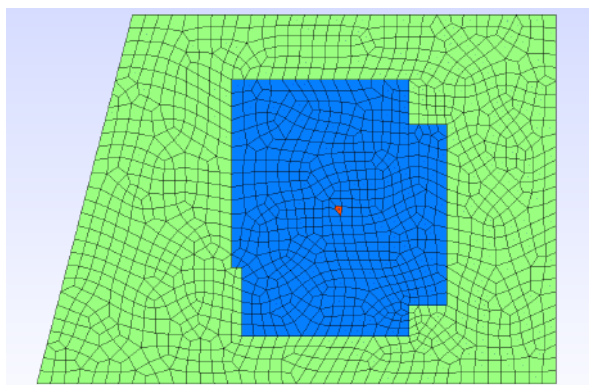
Columns	- Concrete filled CHS columns are proposed not to have additional fire protection covering the skin.
Beam-Column connections	- The collar connections to the columns are to be fire protected with passive fire protection to not exceed 550°C when exposed to 60 minutes of ISO 834 standard fire.
Beams	- Primary beams are to be fire protected with passive fire protection to not exceed 550°C when exposed to 60 minutes of ISO 834 standard fire. - Penetrations through the fire protected beams shall be kept at least 500 mm away from the connections.

For the thermal analysis the thermal properties of the passive fire protection were based on gypsum-based fire spray as it is not feasible to consider swelling in a SAFIR model to simulate intumescent paint, and the focus of this design is on the global behaviour of the structure with some members being protected instead of on the material details.

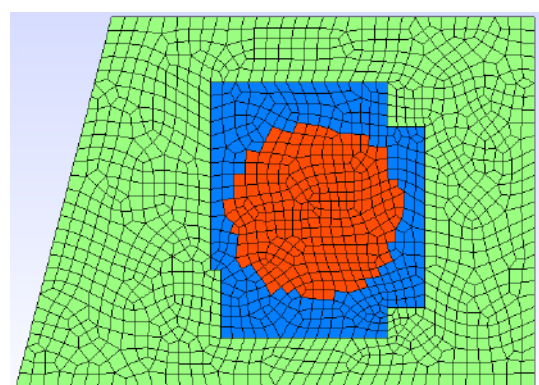
6 CASE STUDY RESULTS

6.1 Fire started at centre of the space

The first fire scenario carried out was with the fire started from the centre of the storage area, and at a centre of the 13 x 10 m structural bay. The 2-D flame spread and resultant gas temperature at the ceiling level that were output from the GoZone simulation are shown in Figure 2(a) and (b), where the blue zone representing areas with available unignited fuel, and the red zone indicating area with ignition. The domain of interest is within the large compartment shown in green, and details of openings were assigned at the model perimeter.



(a) point of ignition in red



(b) flame spreading beyond the spray zone of a failed sprinkler head

Figure 2. Visualization of the GoZone model for fire at the centre of the baggage storage area

The temperatures immediately above the flame and near the primary beams are shown in Figure 3. Noting that these temperatures are obtained from GoZone and were not used directly in the structural fire assessment. The thermal effect from the fire assessed by GoZone is captured as radiant intensity in the transfer file to be used in SAFIR for thermal analysis.

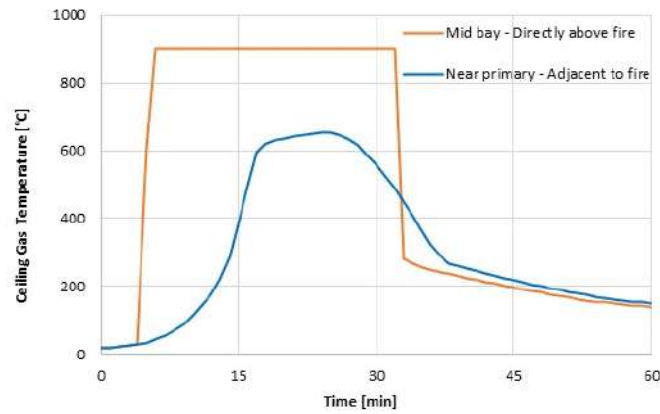


Figure 3. Ceiling gas temperatures at the mid-bay and near the primary beams for fire at the centre of the baggage storage area

Figure 4 illustrates the temperature distribution within the SAFIR model. The orientation of the structural members in relation to the heat source is more pronounced at the early stage of the fire before the smoke layer and ceiling jet travels across the space. The figures show that the columns and beams all have non-uniform heating at 600 seconds after ignition, with the area closer to the ignition source experiencing higher heat flux.

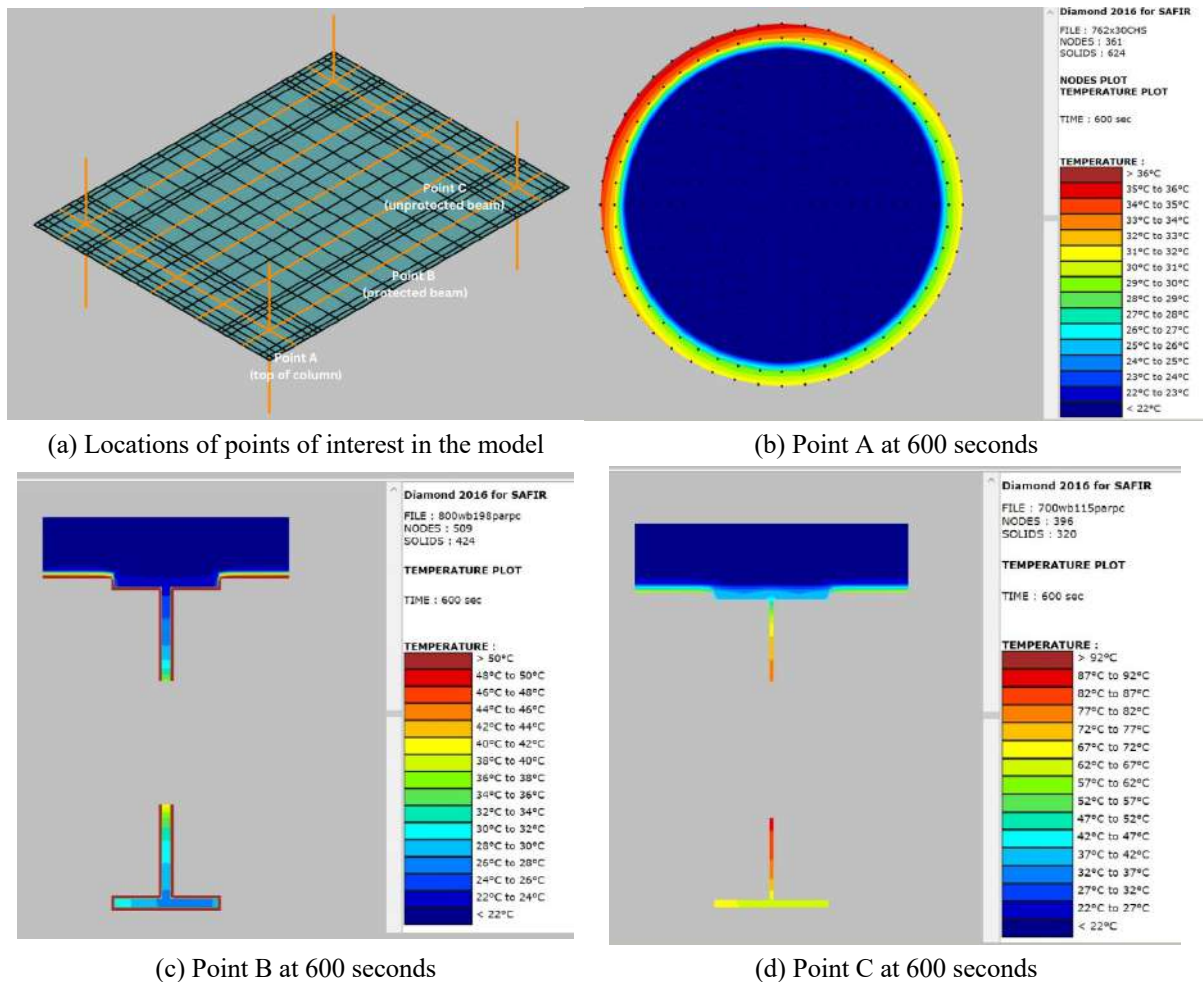


Figure 4. Ceiling gas temperatures at different locations at 600 seconds (note the scales are different)

The structural sub-model in SAFIR is shown in Figure 5(a). To allow for further flexibility to create penetrations in the project, all the beams are modelled as having 300 mm void at the web except in the area within 500 mm from the connections and where the RBS are located. Figure 4(b) shows the deformation shape of the structure.

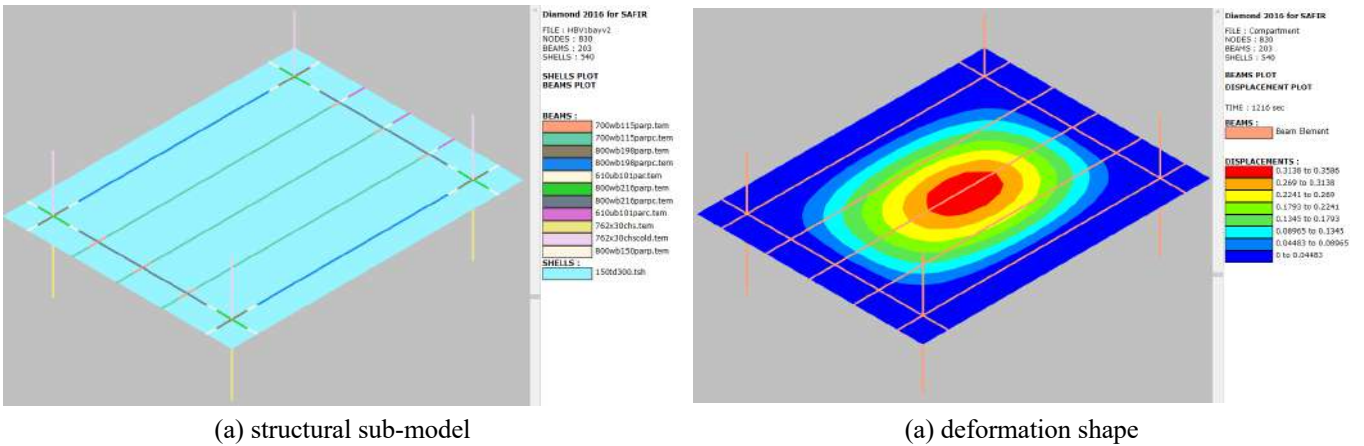


Figure 5. SAFIR model and deformation shape for fire at the centre of the baggage storage area

Figure 6 shows the results of the structural analysis and indicate the proposed fire protection strategy can satisfy the acceptance criteria. At the midspan the peak deformation of 425 mm was reached at 28 minutes, with a mechanical strain of 1.8%. It is evident that the structure was able to survive the design fire, but negligible recovery from the peak deflection could be observed after fire.

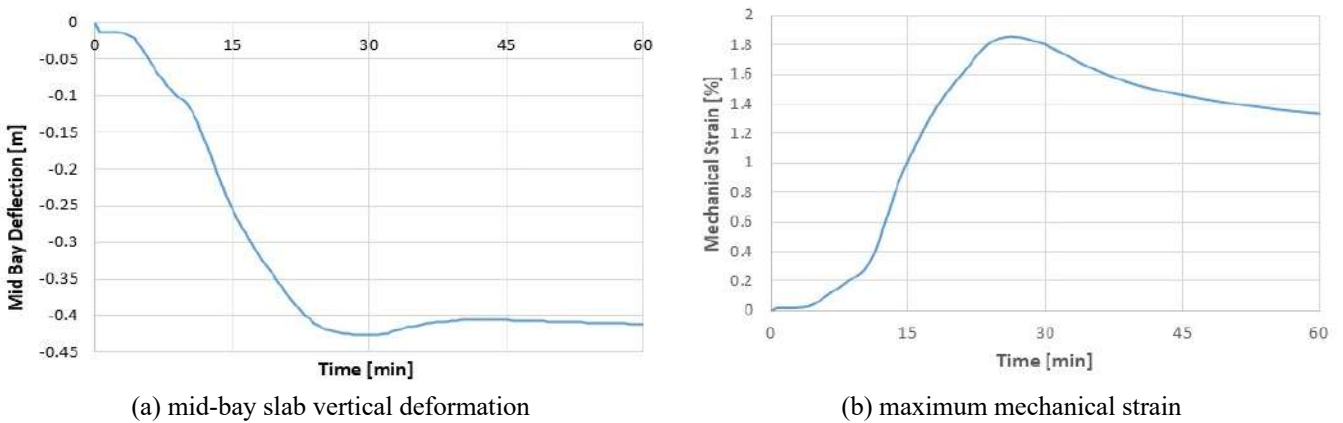


Figure 6. SAFIR model and results for fire at the centre of the baggage storage area

Sensitivity studies were carried out regarding HRRPUA. Figure 7(a) and (b) show the ceiling gas temperatures at the mid-bay and near primary beams respectively with different HRRPUA using GoZone. It can be observed that variation in this specific range of HRRPUA does not affect the temperatures significantly. This might be due to extraordinarily high HRRPUA, thus its variation is not changing fire dynamics.

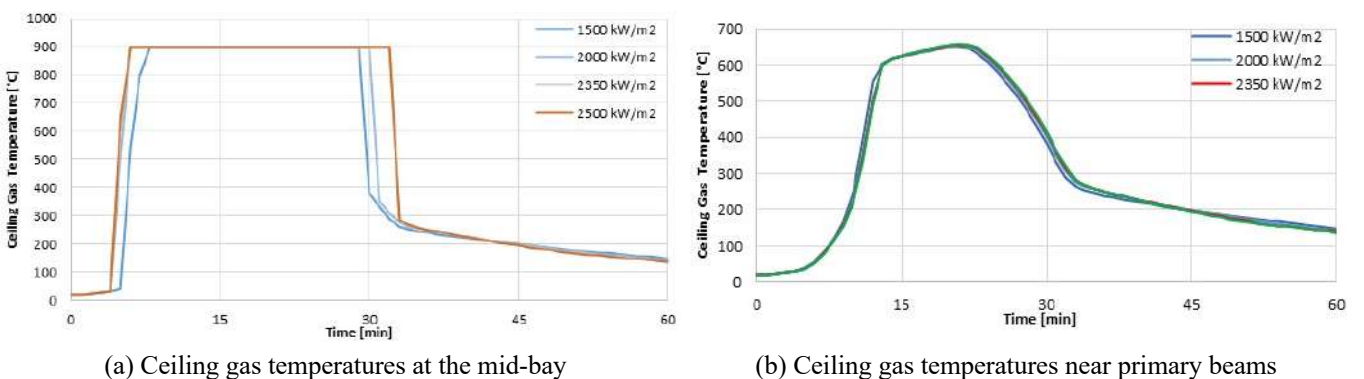


Figure 7. Ceiling gas temperatures with varying HRRPUA

Although the large compartment area, due to the high HRRPUA and the conservative assumption of a lack of ventilation available around the compartment, the fire goes to 1 zone situation in approximately 13 minutes regardless of the different HRRPUA tested. The 2500 kW/m² was shown to be within 3 °C of the 2350 kW/m². The 1500 kW/m² and 2000 kW/m² fires were shown to follow the same temperature curve as the design fire with the exception that the peak temperature of 900°C was maintained for a slightly shorter duration. This is due to the fact that fuel load is constant, thus high-power release leads to shorter cell duration. Threshold on the peak temperature is related to the non-local variable localised fire model [1]. Subsequent structural analysis showed the 2500 kW/m² case increased the maximum deflection by 0.7% (3 mm) and therefore is not sufficiently significant to cause concern.

Other than the fire protection strategy that got incorporated into the SAFIR models, the best practice details also need to be included in the final design, which include having coatback of fire protection below the bottom of the collar plate on the columns, providing vent holes in the concrete filled CHS, and having coatback of fire protection onto the secondary beams that are not nominated to have fire protection to limit heat transfer conducted from the exposed secondary beams to the primary beams.

7 ADDITIONAL CONSIDERATIONS

In addition to the technical aspect, tremendous effort was made in conveying the benefits and clarifying the misconception of performance-based structural fire engineering design to several parties. The fundamental ideas are obvious to the learnt researchers, but worthwhile to summarise below.

Questions have been raised regarding the maintenance of fire separations between evacuation zones, particularly concerning life safety, in buildings where performance-based structural fire engineering has been implemented, and a reduced level of passive fire protection for steel members in comparison to a conventional design. The selection of design fire in a performance-based structural fire design must account for a probable but highly unlikely scenario, thereby discounting the situation where fire is controlled by a fully functional sprinkler system within the building. In situations when the sprinkler system is compromised, it is imperative to adjust the evacuation strategy accordingly. Continuation of the defend-in-place strategy in a compartment immediately adjacent to the zone of fire origin should be avoided.

In the event of a fire incident within a building equipped with sprinkler protection, the likelihood of a threat to its structural integrity necessitates failure of multiple safeguards, including the building management systems and sprinkler itself. Under such a circumstance, albeit rare, property damage and operational disruptions in the vicinity of the fire origin are inevitable.

Optimising the passive fire protection to steel members in accordance with the potential fire severity, which is the focus of performance-based structural fire design, does not cause deflection. Increasing passive fire protections to structural members for eliminating property damage is a futile effort. The application of passive fire protection does not preclude the possibility of irreversible deformation in steel members when the fire reached to the fully developed stage. The deformation is attributed not only to the loss of material strength but also to non-uniform heating, leading to thermal bowing in the structure. Consequently, it is customary to replace steel members that have experienced irreversible deformation following a fire event.

8 CONCLUSIONS

This paper presents the performance-based structural fire engineering design for a major airport expansion in New Zealand. The timing of this project allowed the assessment to adopt the fire simulation model GoZone to simulate the fire in a large compartment. GoZone can handle various fuel types, different building geometries, requires short computational time for execution, and also provide only the essential information such as temperatures and radiation intensity to be used in the structural fire analysis, it is proven to be very useful to the advancement of performance-based structural fire design and allow the designers to carry out sensitivity studies while staying within the project budget and timeframe.

ACKNOWLEDGMENT

The authors would like to acknowledge the technical support from ArcelorMittal and its Secure with Steel network, in particular Dr Marion Charlier of ArcelorMittal and Professor Jean-Marc Franssen of the University of Liège. We would also like to extend our gratitude towards the design project team, in particular the structural and fire engineers and project management at Mott MacDonald and Holmes NZ.

REFERENCES

1. Gamba, A., Franssen, J-M., GoZone: A Numerical Model for Travelling Fires Based on Cellular Automata Concept, *Applied Sciences* 11(22):10679 (2021). <https://doi.org/10.3390/app112210679>.
2. Franssen, J-M., Gernay, T., Modelling Structures in Fire with SAFIR: Theoretical Background and Capabilities, *JSFE*, 8, 3, 300-323 (2017). <https://doi.org/10.1108/JSFE-07-2016-0010>.
3. Rein, G., Zhang, X., Williams, P. et al, *Multi-Storey Fire Analysis for High-Rise Buildings*, 11th Interflam, London, 605-616; 2007.
4. Clifton, G., *Fire Models for Large Firecells*, HERA, Auckland, 1996.
5. Stern-Gottfried, J., Rein, G., Travelling Fire for Structural Design – Part I: Literature Review, *Fire Safety J.*, 54, 74-85 (2012). <https://doi.org/10.1016/j.firesaf.2012.06.003>.
6. Dai, X. Welch S, Vassart, O. et al, An Extended Travelling Fire Method (ETFM) Framework for Performance-Based Structural Design, *Fire and Materials*, 44, 437-457 (2020). <http://doi.org/10.1002/fam.2810>.
7. Rackauskaite, E., Hamel, C., Rein, G., Improved Formulation of Travelling Fires and Application to Concrete and Steel Structures, *Composite Structures*, 3, 250-260 (2015). <https://doi.org/10.1016/j.istruc.2015.06.001>.
8. Charlier, M., Franssen, J-M., Dumont, F., Nadjai, A., Vassart, O., Development of an Analytical Model to Determine the Heat Fluxes to a Structural Element Due to a Travelling Fire, *Appl. Sci.*, 11, 9263 (2021) <https://doi.org/10.3390/app11199263>.
9. McGrattan, K., Hostikka, S., Floyd, J., McDermott, R., Vanella, M., Mueller, E., *Fire Dynamics Simulator Technical Reference Guide, Special Publication (NIST SP)*, NIST, Gaithersburg, MD; 2013. <https://doi.org/10.6028/NIST.sp.1018>.
10. Gamba, A., *A Numerical Model Based on Cellular Automata to Assess Travelling Fires*, PhD Thesis, University of Liège, 2021.
11. Charlier, M., Franssen, J-M., Temple, A., Welch, S., Nadjai, A., TRAFIR: Characterization of TRAVelling FIREs in Large Compartments, TS8/TGA4, European Commission, 2020.
12. Horová, K., Jána, T., Wald, F., Temperature Heterogeneity During Travelling Fire on Experimental Building, *Adv. Eng. Softw.* 62, 119-130 (2013). <https://doi.org/10.1016/j.advengsoft.2013.05.001>.
13. Cadornin, J F, D Pintea, J C Dotreppe, et J M Franssen. 2003. «A tool to design steel elements submitted to compartment fires - OZone V2. Part 2: Methodology and application.» *Fire Safety Journal* 38 (5): 429-451.
14. Welch, S, et N R Marshall. 2004. «Development and validation of a comprehensive model for flame spread and toxic products in full-scale scenarios.» (Proceedings 4th International Seminar on Fire & Explosion Hazards) 259-270.
15. Fleury, R., *Evaluation of Thermal Radiation Models for Fire Spread Between Objects*, Master's Thesis, University of Canterbury, 2011.
16. Tondini, N., & Franssen, J. (2013). Implementation of a weak coupling approach between a CFD and an FE software for fires in compartment. *Computational Methods for Coupled Problems in Science and Engineering V - A Conference Celebrating the 60th Birthday of Eugenio Onate*, COUPLED PROBLEMS 2013.
17. NZS 3404 Parts 1 & 2, *Steel Structures Standard*, Standards New Zealand, Wellington, 1997.
18. AS/NZS 1170 Part 0, *Structural Design Actions – Part 0: General Principles*, Standards New Zealand, Wellington, 2002.
19. C/VM2: *Verification Method: Framework for Fire Safety Design*, MBIE, Wellington, 2023

20. Fleischmann, C., Defining the Heat Release Rate per Unit Area for Use in Fire Safety Engineering Analysis, in book: Fire Science and Technology, 2015 https://doi.org/10.1009/978-981-10-0376-9_42
21. Salminen, M., Malaska, M., Jokinen, T., Ranua, R., Framework to Incorporate Sprinkler System in Structural Fire Engineering, Fire Technology, October 2023. <https://doi.org/10.1007/s10694-023-01503-7>.
22. Hurley, M.J. (ed.), SFPE Handbook of Fire Protection Engineering - Appendix 3: Fuel Properties and Combustion Data, Society of Fire Protection Engineers, London, 2016.
23. Lönnermark, A., Ingason, H., Fire Spread in Large Industrial Premises and Warehouses, SP Swedish National Testing & Research Institute, Borås, 2005
24. SCI, Fire Safe Design: A New Approach to Multi-Storey Steel Framed Building, SCI Publication P288, The Steel Construction Institute, Berkshire, 2000

PERFORMANCE-BASED ANALYSIS AND STRUCTURAL OPTIMIZATION OF EXISTING BUILDINGS: CASE STUDY AND DEVELOPMENTS

Julien Duboc¹, Eric Tonicello²

ABSTRACT

Retrofitting and refurbishment of existing infrastructures is an everyday challenge for fire safety engineers, and maybe even more for structural engineers that must deal with constructions made following old codes and practices. To respond to these subjects (verification of structural strength, reduction, or optimization of passive protection costs), engineering studies are increasingly using performance-based methods.

The first case study presents the thickness optimization of intumescent paint required to protect steel tubular columns filled with concrete. Based on the latest research in the field, an assessment of the minimum required paint thickness was carried out and validated with a numerical finite element simulation. This advanced analysis enabled the structure to be brought into compliance, while optimising passive protection requirements.

The second case study focus on the fire behaviour of the load-bearing systems, made of a composite steel-concrete floors and steel columns, in the luggage-handling facility building at Geneva airport. This advanced study, which combines an analysis of thermal solicitations with a CFD model and an assessment of deformations using finite elements, has made possible to optimise passive protection requirements. The existing and reinforced sprinkler system as well as and the membrane behaviour of the floor were considered.

Keywords: Computational fluid dynamics; Finite element modelling; Intumescent coat; Optimization; Sprinkler; Structures

1 CASE STUDY 1 – OPTIMIZATION OF PASSIVE PROTECTION

This case study concerns the renovation of a medium-rise administrative and commercial building, consisting of 5 underground levels and 5 above-ground levels, located in Sion, in the canton of Valais, Switzerland.

As part of the transformation, the building had to be brought into compliance with current fire protection standards and directives. The load-bearing systems, consisting of solid reinforced concrete slabs supported on columns, must comply with a fire resistance requirement of R(EI) 60.

1.1 Studied structures

The structure, which dates from 1984, is made up of solid reinforced concrete slabs and reinforced concrete columns for the above-ground levels, and tubular ROR columns filled with concrete for the basement levels. Soundings carried out on the reinforced concrete structures revealed a covering of at least 20 mm. In accordance with EN 1992-1-2, this covering is sufficient to guarantee the R60 of the structures.

¹ Risk assessment and fire safety engineer, ISI – Ingénierie et Sécurité Incendie Sàrl
e-mail: julien.duboc@incendie.ch ,

² Fire safety and civil engineer, ISI – Ingénierie et Sécurité Incendie Sàrl
e-mail: eric.tonicello@incendie.ch ,

As the requirement was met for the reinforced concrete structures, the engineering study focused on the composite columns in the basements.

There are different sections for each level, as shown in the table below:

Table 1: Section of composite columns

Type	Diameter [mm]	Thickness [mm]	Steel	Height [m]
ROR	406.4	12.5	S 355	3.10
ROR	457.0	20.0	S 355	3.10
ROR	406.4	16.0	S 355	3.10
ROR	457.0	20.0	S 355	3.10
ROR	419.0	20.0	S 355	2.90
ROR	508.0	20.0	S 355	2.90

For all the columns, a normal concrete representative of the period of construction, with a cement content > 250 kg/m³ and a characteristic compressive strength of 12.8 MPa were used as assumptions.

To take account of the increase in the compressive strength of concrete with age, an update of the characteristic value has been calculated based on the 2010 fib Model Code [2].

1.2 Fire resistance under the ISO fire curve

The various composite columns listed in There are different sections for each level, as shown in the table below:

Table 1 were studied using the advanced finite element (FEM) SAFIR[®] calculation code [1], in order to assess the evolution of deformations and stresses over time. The critical temperature of the various columns was also determined.

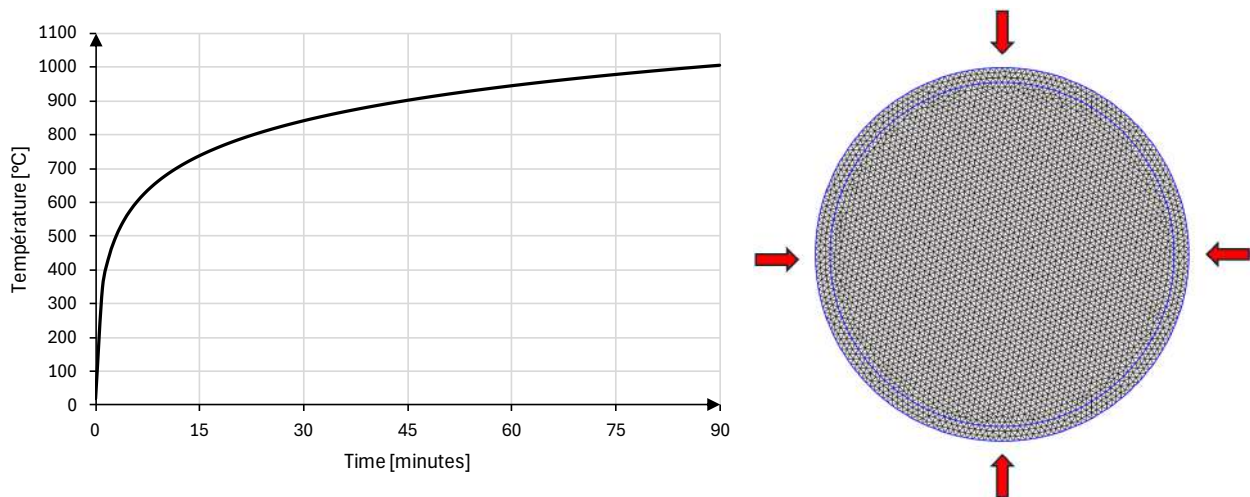


Figure 1: ISO fire curve (left) and finite element model of the ROR Ø 508 mm in SAFIR[®] (right)

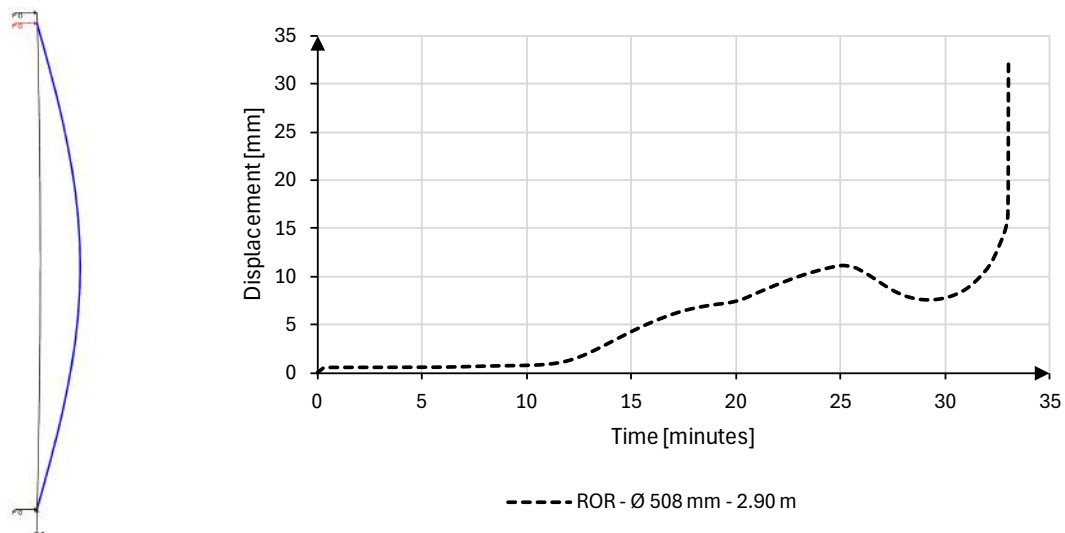


Figure 2: 2D structural model in SAFIR® with initial state in black and after 30 minutes in blue (left) and horizontal displacement of the ROR Ø 508 mm under ISO fire curve (right)

All the results for the different studied columns are given in Table 2.

For this type of section, where the concrete only acts as thermal insulation (unreinforced concrete), concrete has little contribution to the overall resistance of the column in fire situation. The order of fire resistance for such elements is R30, which is consistent with the results obtained.

Table 2: Fire resistance results for each composite column

Type	Diameter [mm]	Thickness [mm]	Steel	Height [m]	Critical temperature [°C]	Fire resistance
ROR	406.4	12.5	S 355	3.10	679	R 32
ROR	457.0	20.0	S 355	3.10	589	R 30
ROR	406.4	16.0	S 355	3.10	606	R 29
ROR	457.0	20.0	S 355	3.10	556	R 28
ROR	419.0	20.0	S 355	2.90	632	R 33
ROR	508.0	20.0	S 355	2.90	627	R 33

Based on the results obtained, the fire resistance is not sufficient to meet the requirements for the structure. Passive protection is thus required to meet the compliance.

1.3 Optimization of passive protection

By choice of the client, intumescent paint was chosen as the solution for bringing the composite columns into compliance, with an impact-resistant (epoxy based) product. This is a paint applied to the outer surface of the column, which swells when the temperature rises to form an insulating layer and slow down the heating of the steel.

With elements already R30 without protection, an advanced analysis was carried out to assess the possibility of reducing the thickness of the paint layer (layer thickness for 30-minute protection rather than layer thickness for 60-minute protection).

This analysis is based on research in the field [3]. Tests on this type of product have identified a correlation between incident heat flux and paint swelling speed.

$$\dot{d}_c = \begin{cases} 0 & \text{if } \dot{q}_{inc}'' < 20 \text{ kW/m}^2 \\ -0.0001 \cdot (\dot{q}_{inc}'')^2 + 0.0280 \cdot \dot{q}_{inc}'' - 0.3320 & \text{if } \dot{q}_{inc}'' \geq 20 \text{ kW/m}^2 \end{cases}$$

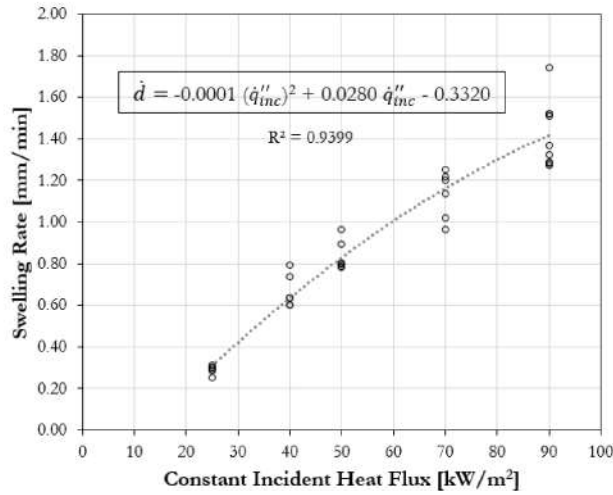


Figure 3: Swelling rate in function of the incident heat flux, according to [3]

Where:

\dot{d}_c is the swelling rate;

q_{inc} is the incident heat flux;

As the fire resistance analysis of the columns is carried out for an ISO fire scenario, the associated temperature curve must be expressed with the corresponding heat flow curve.

$$q = \sigma T^4 \quad (1)$$

Where:

$\sigma = 5.67 \times 10^{-8} \text{ W/(m}^2 \cdot \text{K}^4)$, the Stefan-Boltzmann constant

T, the gas temperature [K]

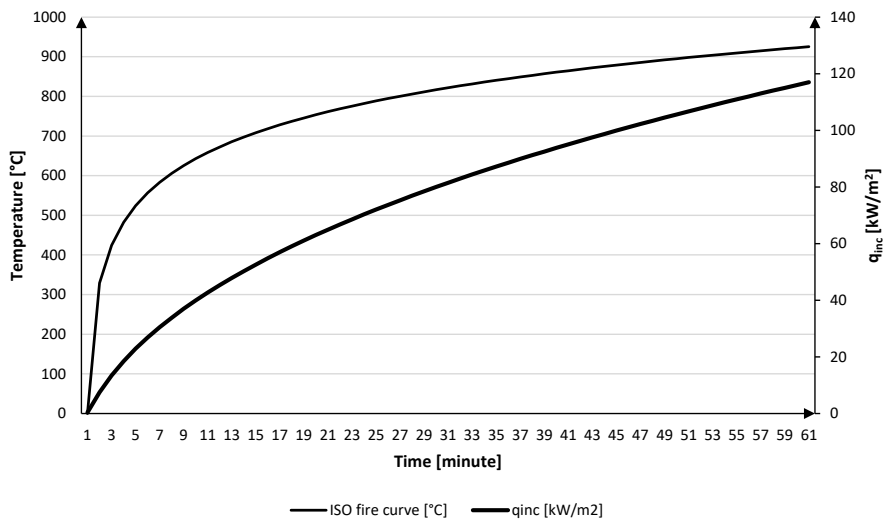


Figure 4: Incident radiant heat flux (ISO) and gas temperature (ISO)

Knowing the equivalent radiant heat flux of the ISO fire curve, it's easy to calculate the swelling rate of the intumescent coat. The second step consists in calculating the thickness of the insulating layer as a function of time, which depends on the dry layer, the swelling rate, and the duration.

$$d_c(t) = \begin{cases} DFT + \dot{d}_c \Delta t & \text{if } DFT + \dot{d}_c \Delta t \leq d_{max} \\ d_{max} & \end{cases}$$

Figure 5: Thickness of the intumescent coat in function of time, swelling rate and the initial thickness, according to [3]

Where

d_{max} is the maximum intumescent coat thickness under fire conditions.

DFT , the initial intumescent paint thickness.

The insulating layer increases until it reaches a maximum value, which depends on the thickness of the dry layer [3].

$$d_{max} = 17.7 DFT + 10.6 \tag{2}$$

The applicator of the chosen intumescent paint has calculated the minimum layer thickness required as a function of the fire resistance requirement; it is 0.974 mm for 30 minutes protection. The evolution of the layer thickness over time, with ISO fire exposure, is given in the following graph:

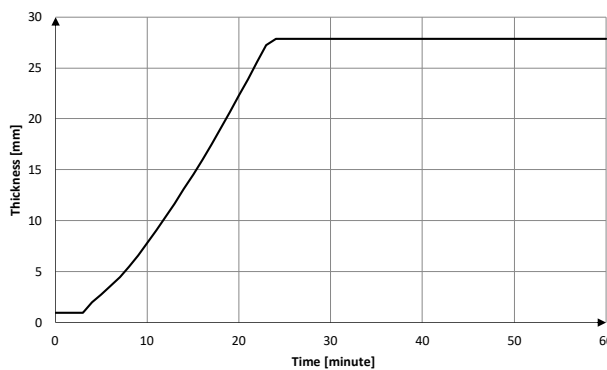


Figure 6: Intumescent coat thickness in function of time, under ISO fire exposure

Knowing the evolution of the protective insulating layer as a function of time, the idea is to repeat the calculation of heating in the section of the columns and to add a new layer of insulating material at each time interval.

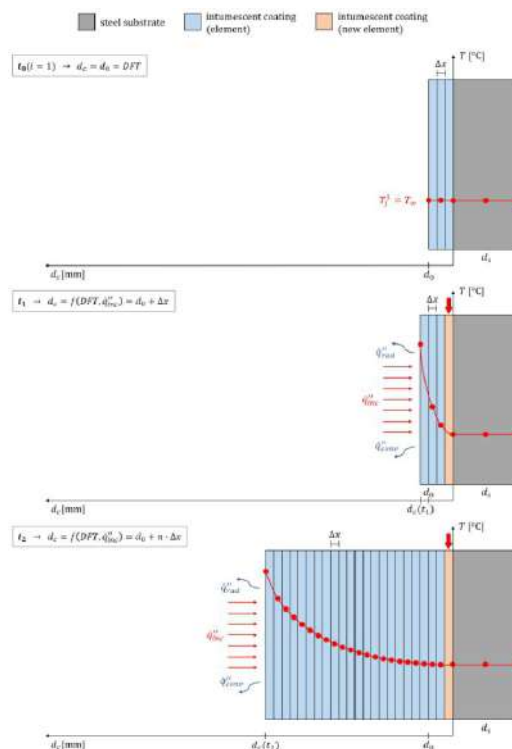


Figure 7: Finite element model with variation of the insulation material, according to [3]

This method, which approximates the heating of the column while considering the swelling of the paint, was applied using the RESTARTT function of the SAFIR® finite element calculation code.

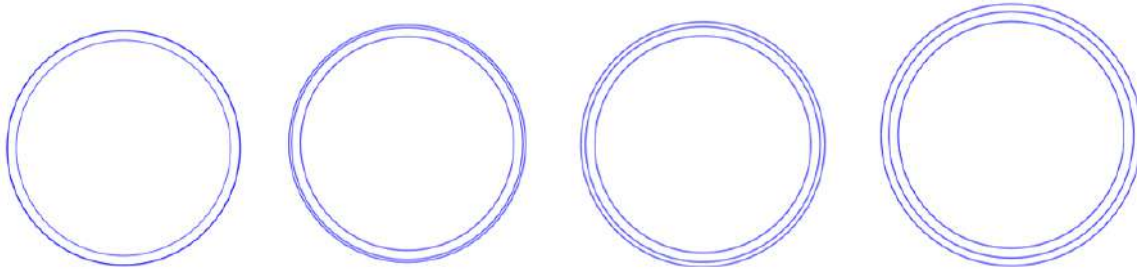


Figure 8: Evolution of the thermal model with intumescent paint swelling considered

1.4 Results

In this fire engineering study, an optimisation of passive protection was proposed, based on a thermal model that considers the evolution of the insulating layer formed by the intumescent paint as the temperature rises. This optimisation enabled the building to be brought into compliance, while making significant savings on the protection budget.

2 CASE STUDY 2 – OPTIMIZATION OF PASSIVE PROTECTION FOR COMPOSITE SLAB USING AN ADVANCED CFD MODEL

The second project presented deals with an existing building dedicated to luggage handling facility at Geneva airport in Switzerland. As part of the renovation of an existing structure, compliance with current fire protection standards and directives is required, particularly regarding the fire resistance of load-bearing systems.

The building is equipped with a sprinkler system, and a new system will be added to the existing one following the creation of mezzanines.

2.1 Studied structures

The structure is composed of a steel-concrete composite floor supported with steel columns. Soundings confirmed the presence of connectors between the steel beams and the composite floor, guaranteeing composite behaviour that is strongly beneficial in a fire situation, with the well-known tensile membrane effect.

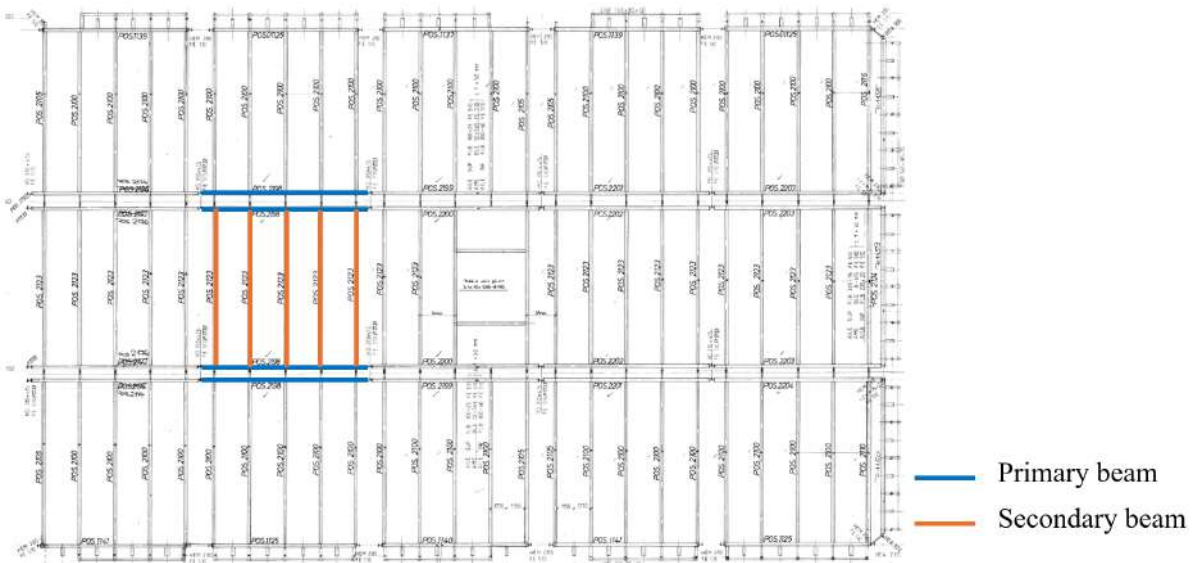


Figure 9: Extract of the studied structure

Primary and secondary beams are given below:

Primary beam (inner beam)	Primary beam (facade)	Secondary beam

The composite floor of 17 cm thick, is made with a Montarib MR 58 steel deck, with alternating rebars of $\text{Ø}10\text{-}12 / 800 \text{ mm}$ lengthways and $\text{Ø}8 / 200 \text{ mm}$ crossways.

The HEB 280 facade metal columns are already fire-protected, and additional fire protection will be in place for the inner ones.

For a mid-rise building with a total sprinkler system, a resistance requirement of $R(EI)30$ is required for all load-bearing systems.

2.2 ISO fire resistance study

The first stage of the study was to assess the behaviour of the floor under ISO fire thermal stresses. The floor was modelled in SAFIR[®].

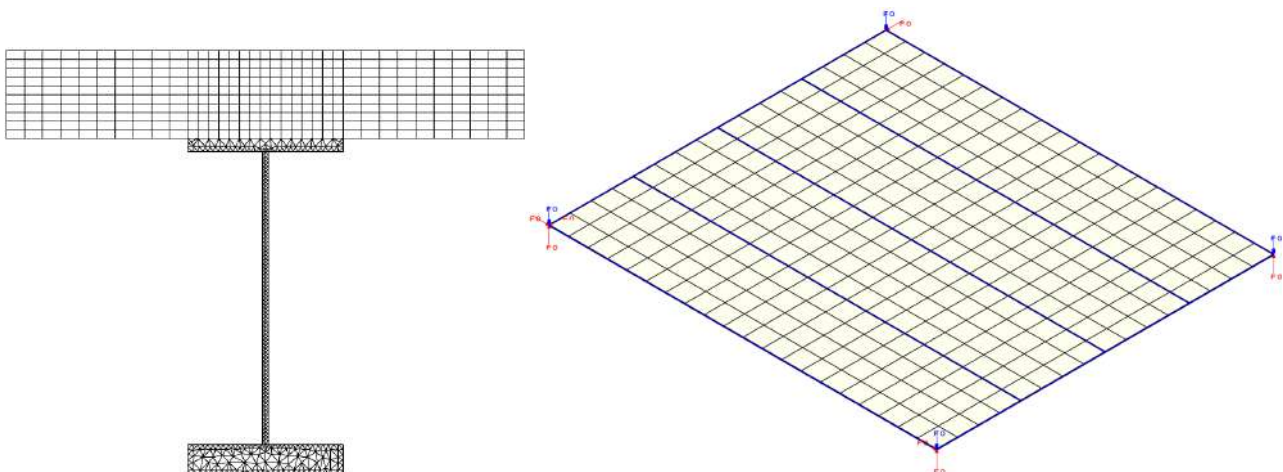


Figure 10: Finite element modelling of the primary beam section (left) and modelling of the slab field in a shell model with SAFIR[®] (right)

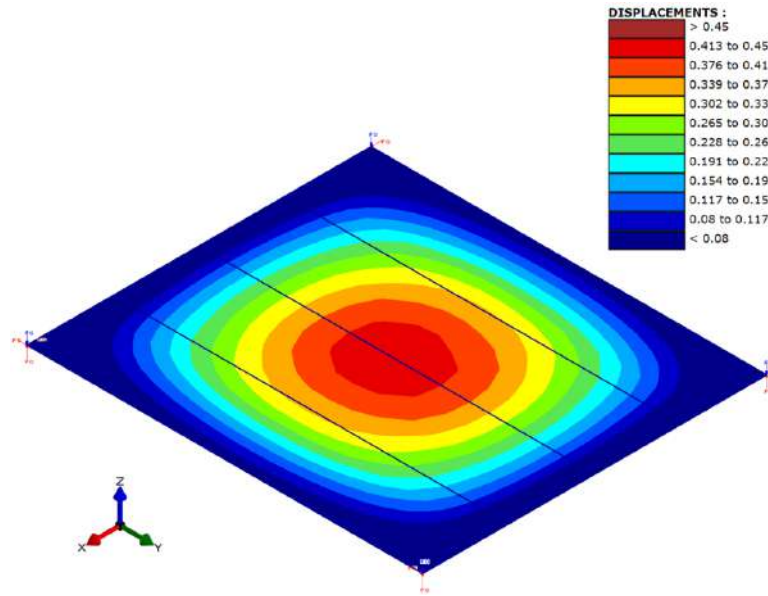


Figure 11: Vertical displacement field after 60 minutes under IFO fire

The ISO fire study confirmed that the composite floor could withstand R30, provided that the peripheral beams were protected by dale fields.

To assess the chances of suppressing the passive protection, a complete natural fire analysis was carried out. Considering the sprinkler installations and a localised thermal load, it is likely that the floor's behaviour would be more favourable with this approach than with the ISO fire.

2.3 Naturel fire scenarios analysis

As the building is dedicated to handling baggage for transport into aircraft for commercial flights, the thermal load present is represented by the baggage stored in the containers.



Figure 12: Layout of the premises with baggage containers at the drop-off points

The thermal load was calculated based on the composition of a standard baggage item, considering the literature [4] and tests carried out in the railway sector. The fire scenario used for this analysis is the combustion of a standard size baggage item in a full container, at a drop point, and close to other baggage containers.

The fire power curve was established accordingly to calorimetric cone test for a baggage fire. An ignition temperature of 300°C was specified for the surrounding baggage. This value is representative of cellulose and textile components.

Similarly, an ignition condition of 300°C has been specified for the conveyor belt [5] to take account of its contribution to the fire in the event of high thermal stress.

Finally, the double layered sprinkler installation was implemented in the model, via an aspersion model in the FDS calculation code, by setting the parameters specific to the installation (flow rate, position of the heads, covering surface, activation temperature, RTI, etc.). The model was validated using a set-up calculation to validate the parameters.

To stay on a safe side, and in agreement with the Swiss authorities, no influence of the sprinkler on the HRR fire curve is considered. If the temperature in the vicinity of a baggage item is high enough to allow it to ignite, then the fire will follow the implemented fire curve, even if the sprinkler is active. In other words, the sprinkler has only a cooling effect on the hot gases.

The objective of this analysis was to record the spatial thermal solicitations to use them as input data for the SAFIR® finite element calculation code. This will allow to assess the fire behaviour of the floor for a natural fire scenario. Adiabatic surface temperature sensors were positioned under the slab and at beam level.

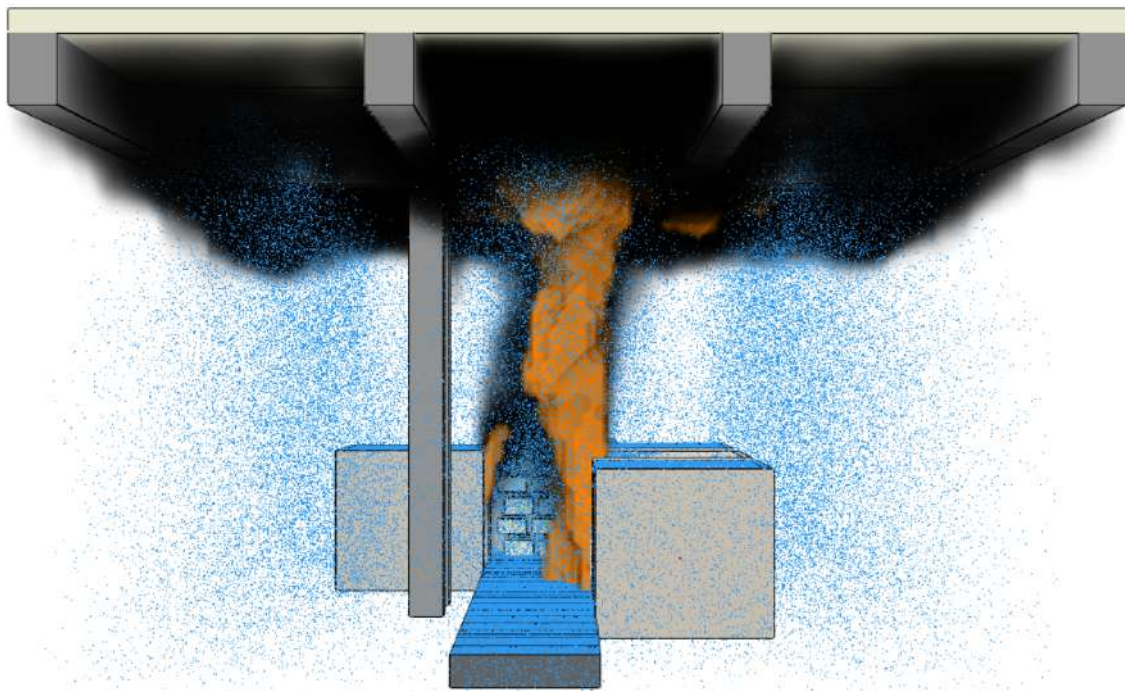


Figure 13: Fire and sprinkler installation modelling in the CFD calculation

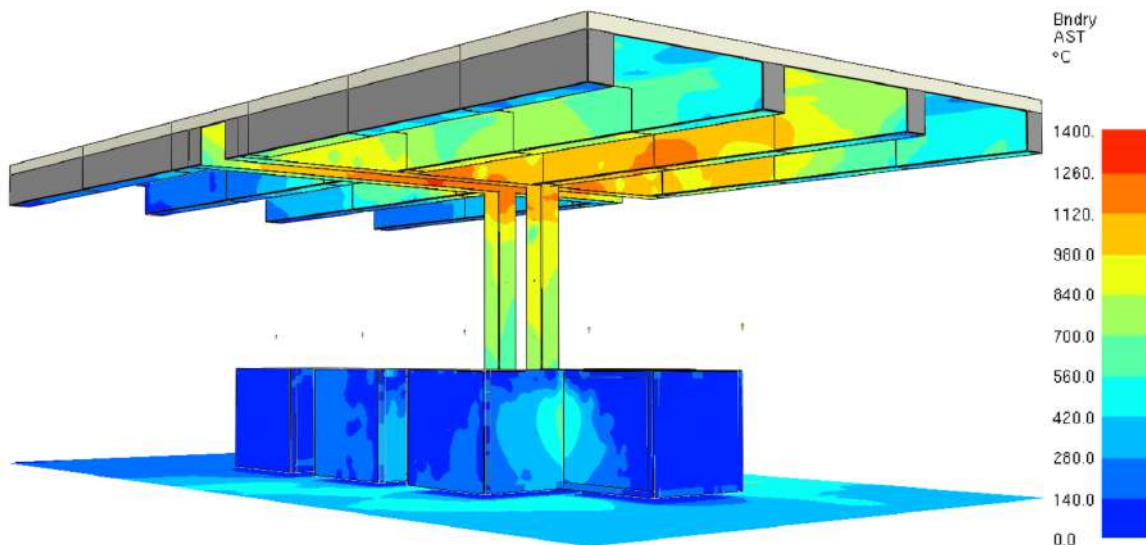


Figure 14: Thermal stresses (AST) as boundaries used for the FEM calculation

The model used to analyse the ISO fire is used to study the natural fire, by considering the heating of all floor elements as a function of the heat fluxes received over time. This approach makes it possible to consider the significant heating in the vicinity of the fire, and the more moderate temperatures away from the focus.

Two calculations were carried out, one with the primary beams exposed to the fire and the other with the primary beams protected. The evolution of the vertical deformation of the floor for the two configurations is shown in the graph below:

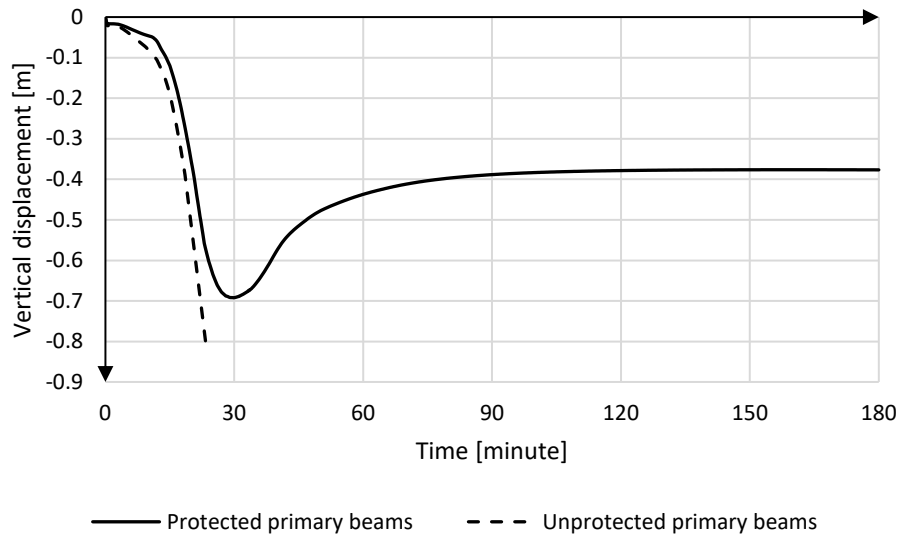


Figure 15: Vertical displacement of the composite slab.

The natural fire analysis confirmed that the floor would withstand the fire if the main beams were protected. As these beams carry a large proportion of the floor loads, combined with the high local thermal stresses, passive protection is then necessary.

The secondary beams behave more favourably and do not require protection.

3 CONCLUSIONS

Both practical studies presented here highlight the optimisation possibilities offered by advanced fire safety - performance-based - engineering studies. When the existing structural system needs to be made safe to current standards, optimisations are very often possible, enabling the customer to drastically reduce the protection costs thanks to few hours of hard-work calculation made by a good fire safety engineer.

REFERENCES

1. Modelling structures in fire with SAFIR®: Theoretical background and capabilities. Franssen et al. Journal of Structural Fire Engineering, 8(3), 300-323.
2. Fib, Model Code for concrete structures, 2010.
3. Fundamentals of thin intumescent coatings for the design of fire-safe structures, Andrea Lucherini, The University of Queensland, Australia, 2020.
4. Carried Fire Load in Mass Transport Systems, M. Kumm, Mälardalen University, Västerås.
5. Fire safety testing of conveyer belt, E. D. Yardley et L. R. Stace, Cerberus Ltd, 2002.

PROBABILISTIC FIRE ASSESSMENT OF BRIDGES: AN ITALIAN CASE STUDY

Patrick Covi¹, Nicola Tondini²

ABSTRACT

Fire is an action that can severely damage bridge structures, which are not generally designed with fire resistance criteria. However, the scientific literature highlights that the fire risk is not negligible. Although the likelihood of a fire affecting a bridge is typically lower than that of a building, the potential consequences remain significant. Indeed, high vulnerability to the fire of bridges can significantly impact the infrastructural network functionality. In this respect, the current study aims to assess the probability of occurrence of a fire on a bridge of an Italian highway based on actual data resulting from past fire vehicle accidents and the vulnerability of a steel-concrete composite bridge in the context of fire risk assessment. Different plausible fire scenarios caused by different vehicle types were considered below the bridge and were modelled using computational fluid dynamics (CFD). A series of thermomechanical analyses were then developed to identify the failure modes and times of collapse, as well as the deformative state that can cause the loss of functionality.

Keywords: Bridge fire probability; Steel-concrete composite steel bridge; CFD; Natural fire curves; GIS.

1 INTRODUCTION

Bridges are strategic infrastructures designed to withstand operating and exceptional load conditions. However, the current structural standards of bridges do not explicitly consider fire actions. This aspect can lead to a high vulnerability to the fire of bridges and in the event of a fire, a significant impact on the functionality of the infrastructural network can therefore be expected. In fact, bridge collapse or deformations that are too high can cause the loss of functionality of the structure, with severe repercussions on vehicular traffic. Examples of such fire events include the I-95 Overpass Collapses in Philadelphia (June 11, 2023) and the A21 Overpass in Italy (January 2, 2018). Several research works have reported past bridge fire accidents, especially in the United States [1-2].

In the United States alone, the estimated average annual losses from fire-damaged bridges amounted to \$1.28 billion in 2002 [REF]. Typically, the primary causes of fire ignition can be categorised as fires triggered by vehicle defects or collisions. Fires following collisions can be exceptionally intense, often due to rapid ignitions of highly flammable materials. Fires resulting from vehicle defects typically start in the engine, exhaust system, wheels, or brakes, seldom in the load. These fires often have slow initial development but may progress later on, allowing for extinguishment or containment using manual fire extinguishers or from the fire brigade. Fires after collisions are often accelerated by fuel leakage, resulting in faster development. Flammable liquid fires, such as pool fires with large amounts of flammable liquids, are rare occurrences requiring significant liquid release, typically following a collision or another major incident.

¹ Postdoctoral Researcher, Department of Civil, Environmental and Mechanical Engineering, University of Trento (Italy)
e-mail: patrick.covi@unitn.it, ORCID: <https://orcid.org/0000-0002-0570-4061>

² Associate Professor, Department of Civil, Environmental and Mechanical Engineering, University of Trento (Italy)
e-mail: nicola.tondini@unitn.it, ORCID: <https://orcid.org/0000-0003-2602-6121>

Bridges with steel girders or cables/stays, as well as steel-concrete composite structures, are particularly vulnerable because of the exposed unprotected steelwork. The load-bearing capacity of these structures diminishes quickly due to the rapid heating of steel elements during a fire, and they are frequently conceived with statically determined schemes lacking robustness in fire scenarios. Moreover, the closure of a bridge can have significant economic repercussions on the infrastructural network. The recent bridge collapses in Italy have highlighted the major disruption they can cause to the operation of nearby road networks and other indirect economic losses for prolonged periods. For example, the collapse of the Polcevera bridge (Morandi bridge) resulted in indirect losses of 359.1 m€ immediately after the incident, with estimated annual losses to the Italian economy approaching 1 bn€ [3,4].

Recently, there has been increased focus on investigating the structural behaviour of bridges under fire scenarios. Researchers analysed bridge failure causes [1,2,5-8], performed numerical simulations [9-14], conducted experimental tests [15,16], and investigated the fire risk applied to bridges [1,17].

In this context, the current study aims to assess the potential fire risk in bridges situated along critical road networks, such as highways, based on actual data resulting from past fire vehicle accidents that happened in Italy. Additionally, it aims to quantify the likelihood of structural member collapse in bridges resulting from fire scenarios.

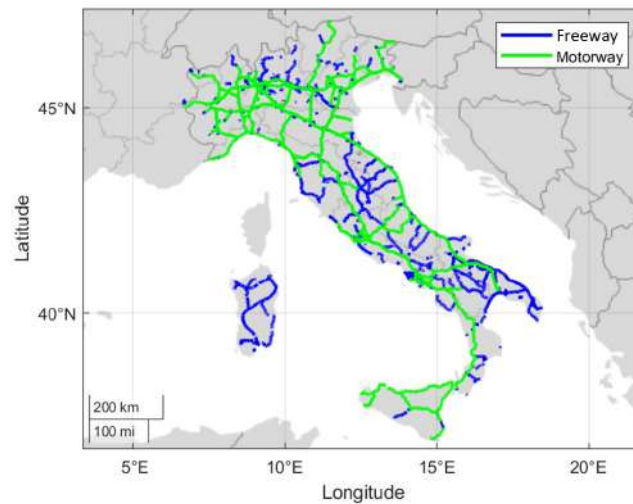


Figure 1. Italian highway networks (motorways and freeways)

2 PROBABILISTIC ANALYSIS OF FIRE IGNITION ON A BRIDGE

In this section, the probability of one vehicle fire occurring every year above or below a bridge of an important Italian highway is estimated by collecting actual data of the infrastructure. The main highways of Italy are reported in Figure 1. Overall, the length of the Italian motorway network is approximately 7043.2 km of motorway (2023) and 5515 km of freeways (2023).

Occurrences of fire incidents are random events governed by a stochastic approach and the Poisson distribution can be used to examine the likelihood of ignition and the occurrence of fire incidents in various scenarios [18]. In this respect, the estimated Italian fire mean intensity of highway vehicle fires in the last years is equal to 0.22 year^{-1} . This value is calculated using the vehicle fire data collected from the Italian fire brigade's annual reports [19-21]. Following the same approach, it is possible to compute the probability of one vehicle fire occurring every year on an Italian highway, which is equal to $P = 1 - e^{-\rho t} = 0.198$.

By comparison, the estimated fire intensity of highway vehicle fires in the United States reported by Naser and Kodur [18] based on NFPA is equal to $\rho=0.46 \text{ year}^{-1}$, and the probability of vehicle fire occurring on a highway every year is estimated as 0.37. Both of these values are higher compared to the Italian ones. This difference is mainly related to the higher number of U.S. highways and vehicles compared to the Italian highways and vehicles.

The following step was to determine the probability that a highway vehicle fire could happen on/under bridges. However, there is no available statistical information on the total number of fire incidents on/under bridges in Italy and in the United States. Therefore, statistical data from vehicle fires that occurred in the last 13 years along an important Italian highway were collected and analysed in terms of location, damage intensity, time, vehicle type, presence of an overpass or a bridge, distance from a fire station and, where possible, the type of fire load, ignition causes and multimedia files of the fire event. A geographic information system (GIS) was created to store all the data. For example, Figure 2 shows the vehicle fire accidents grouped by year and vehicle category extracted from the GIS. The vehicle fires observed between 2010 and 2023 mostly affected cars and HGVs. Figure 2 also shows some example of vehicle fires happened above, under or near a bridge.

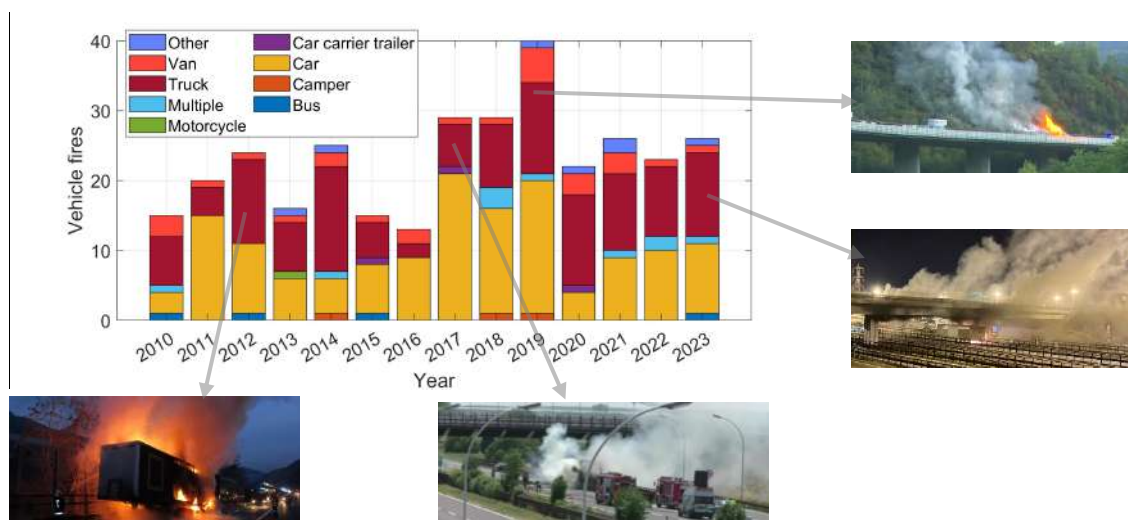


Figure 2. Vehicle fire accidents on an Italian highway extracted from the GIS

As a first step, the data stored in the GIS were also used to quantify the fire highway risk related to traffic intensity. Traffic data are needed in order to estimate the fire rate on highways per travelled vehicle kilometre. Figure 3a reports the traffic data regarding vehicle-kilometre of the case study grouped by vehicles up to 3.5 tonnes (Light vehicles: cars and motorcycles) and vehicles above 3.5 tonnes (heavy vehicles: HGVs, busses, etc.). Figure 3b shows the same vehicle fire values of as Figure 2 but is grouped by the heavy and light category previously explained. Figure 3c shows the fire rate expressed per billion vehicle kilometres. On average, 8.96 light vehicle fires and 7.54 heavy vehicle fires occurred every billion vehicle-km.

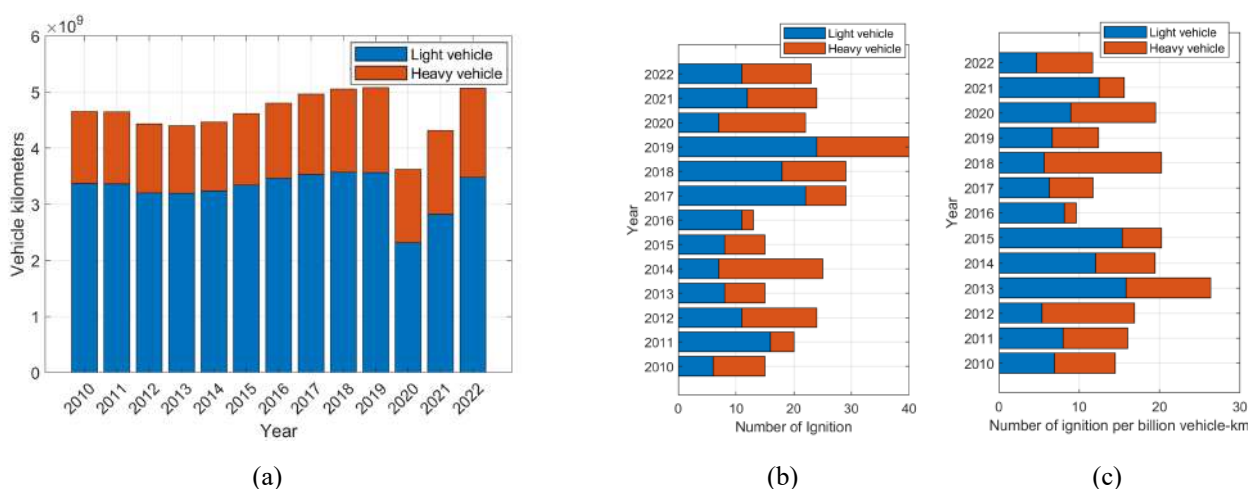


Figure 3. (a) traffic data in terms of vehicle-kilometers; (b) vehicle fire accidents; (c) frequency of the vehicle fire accidents per billion vehicle-kilometers

The data stored in the GIS were also used to quantify the fire bridge risk. In detail, 10.15% of the total highway fire accidents occurred above or below bridges on the highway, as shown in Figure 4.

Using the Poisson distribution, the probability of one vehicle fire occurring every year above or below a highway bridge was computed to be equal to 2.24%.

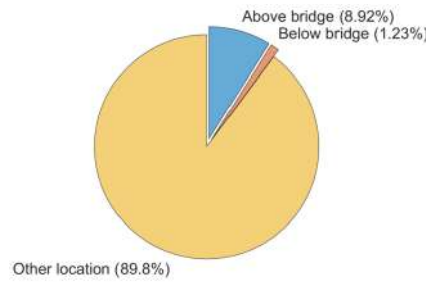


Figure 4. Vehicle fire locations

By comparison, Naser and Kodur assumed that 5% of total U.S. highway fire incidents were assumed to occur on/underneath bridges and estimated the probability of a fire breaking out on a bridge is 2.27% every year; that is a similar probability value obtained in this work.

3 VULNERABILITY OF A STEEL-CONCRETE COMPOSITE OVERPASS

Given the probability of occurrence of a fire on a bridge every year, it is worth evaluating the fire vulnerability of an overpass. In particular, a simply supported steel-concrete composite bridge was considered because of its potential high vulnerability.

3.1 Bridge characteristics

Figure 5 shows a 3D rendering of the overpass analysed in this paper. It is an unprotected simply supported made of steel-concrete composite girders. This overpass typology is one of the common ones that can be found along road networks, such as highways and primary and secondary roads. For this case study, it is located above a highway/motorway made up of 2 lanes per side.



(a)



(b)



(c)

Figure 5. 3D render details: (a) overview; (b) side view; (c) below view

The overpass is 45 m long and 16.1 m, and the deck consists of a concrete slab of 27 cm thick connected through welded studs to 6 double I-shape welded steel girders. Figure 6 illustrates the cross-section of the

deck and the girder detail. An S355 steel grade was used for the steel elements, while a concrete strength class C32/40 was employed for the concrete deck plate. The structural weight of the slab is equal to 6.75 kN/m², while the structural weight of one girder is 16.00 kN/m. The non-structural weight of a typical road and of the sidewalk are respectively 3.00 kN/m² and 6.25 kN/m². The weight of the guardrail and other barriers was estimated as 8.44 kN/m².

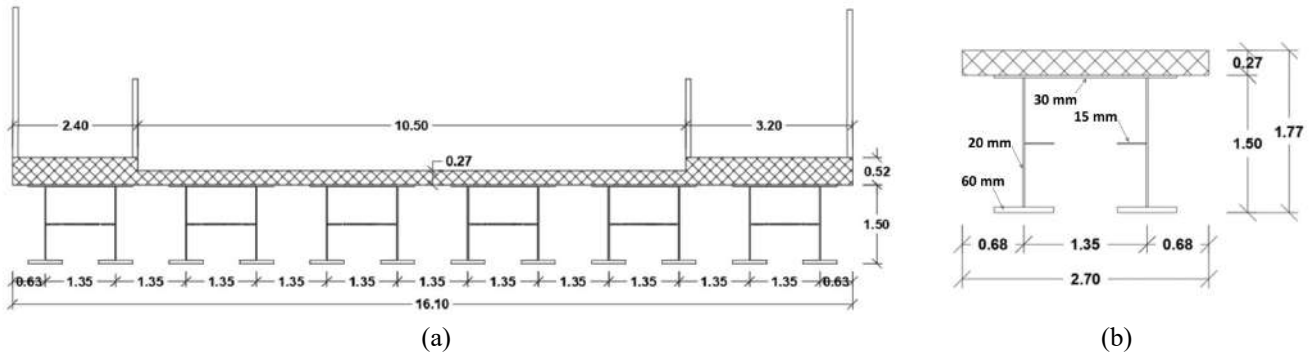


Figure 6. Section of the bridge

3.2 Finite element model

Typically, the restraints at the end of the bridge are considered as free or fixed end conditions. However, the presence of thermal joints introduces axial restraint conditions that are between these two boundary conditions. Consequently, a gap model simulating the thermal expansion joints of the bridge was devised, as illustrated in Figure 7. Notably, SAFIR [22] lacks a specific gap element for modelling expansion joints. Thus, the GAP model was developed using various existing elements within the software. The mechanical system operates like a Von Mises Planar Truss/Arch [23] and a pantograph. It comprises two straight hinges truss elements for the arch and a third horizontal truss element linking the arch to the bridge. To mitigate convergence issues and ensure minimal force for reopening the GAP model, a spring was installed at the crown of the arch. Specifically, a compressive gap of 0.2 meters was modelled to accommodate the thermal expansion of the bridge up to the end of the thermal joint. Beyond this point, any additional longitudinal expansion is entirely restrained. For a detailed description and validation of the GAP model the lectures are addressed to the papers of Covi et al. [24,25].

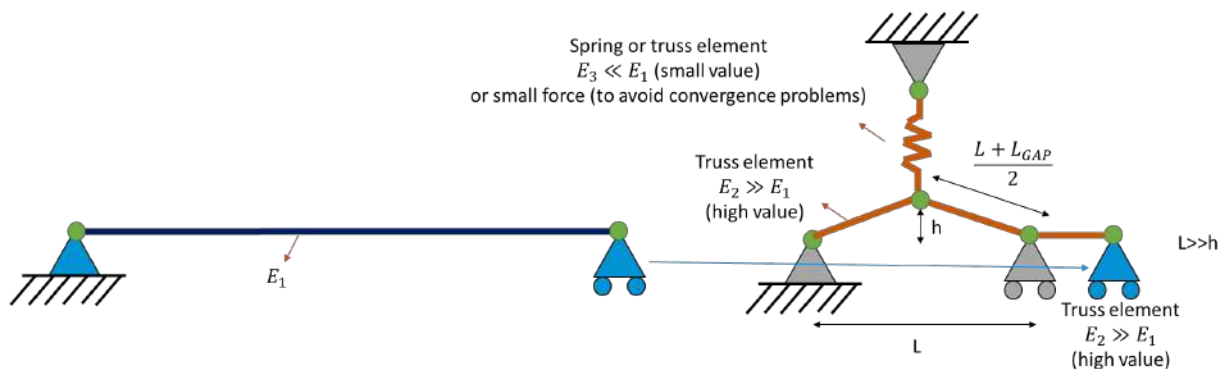


Figure 7. Mechanical configuration to simulate the bridge GAP

Two 3D thermomechanical models of the bridge were created in the SAFIR software using different types of elements:

- A 3D model using non-linear beam elements (BM), as shown in Figure 8.
- A 3D model using non-linear shell and beam elements (BSM), as shown in Figure 9.

In the beam model, the deck was subdivided into 45 elements as shown in Figure 8a. Figure 8b illustrates the thermal section model. In detail, the STEELEC3EN material was used for the girders, the STEELEC2EN for the reinforcing bars and the SILCON_ETC material for the concrete deck.

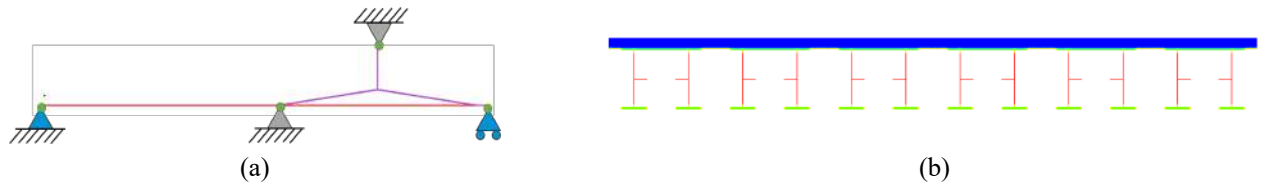


Figure 8. Beam model (BM): (a) Thermomechanical model; (b) Thermal section model

In the beam-shell model, the deck was modelled using three element types. Each girder was discretised using 45 beam elements and the concrete slab was modelled using 1125 shell elements, as shown in Figure 8a. Figure 9b illustrates the thermal section model for the girders, transversal beams and the concrete slab. In detail, the STEELEC3EN material was used for the girders, the STEELEC2EN for the reinforcing bars and the SILCOETC2D material for the concrete deck.

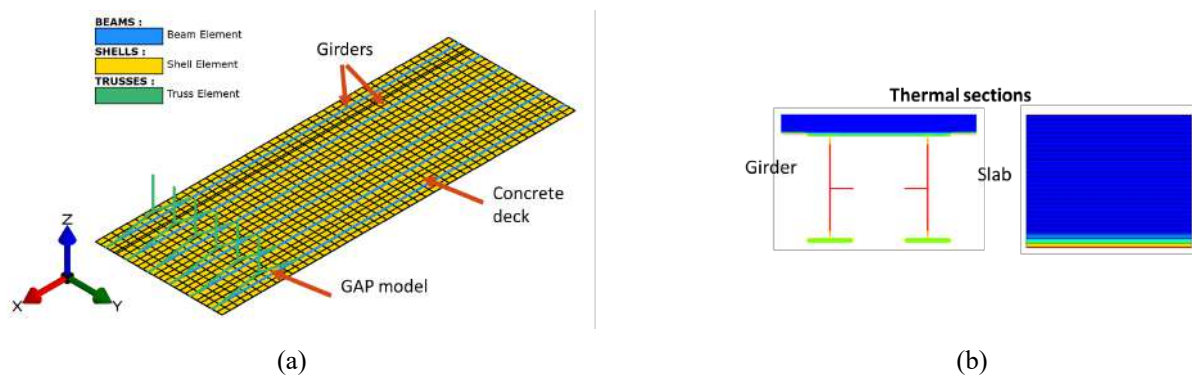


Figure 9. Beam-shell model (BSM): (a) Thermomechanical model; (b) Thermal section model

A series of thermomechanical analyses using natural fire curves was performed to investigate the structural fire behaviour, including the deformation behaviour that can cause the loss of functionality of the bridge.

3.3 Fire analysis

To model a real fire in a CFD analysis, an HRR (Heat Release Rate) thermal release curve can be applied, as described in the Italian Fire Prevention Code [26].

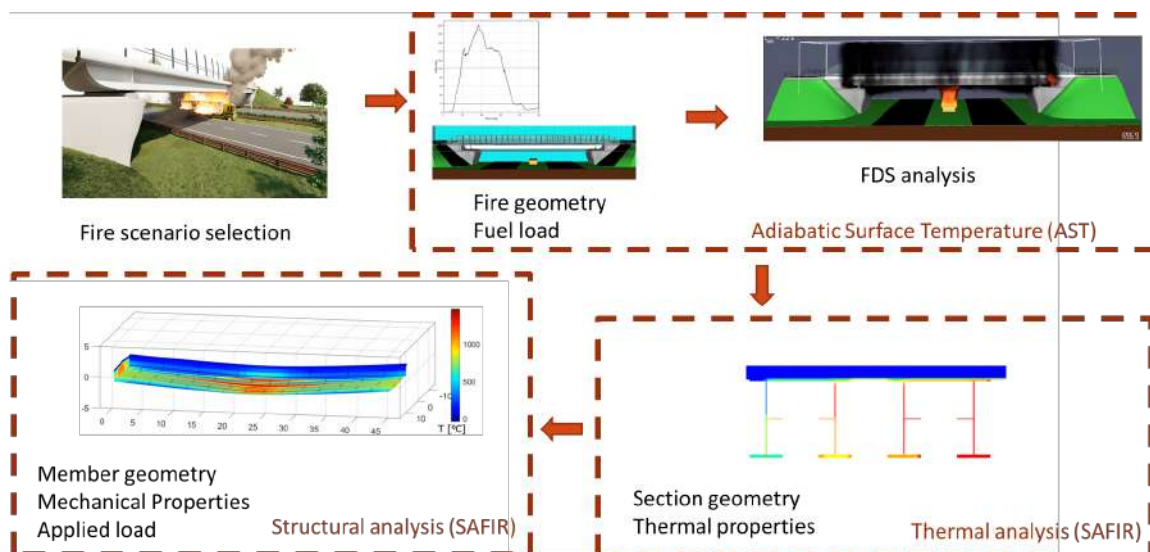


Figure 10. Fire analysis workflow

As illustrated in Figure 10, a 3D model of the overpass was imported into FDS. The model domain was 72 m wide, 26.0 m deep, and 15.0 m high to allow for sufficient volume for air entrainment and extension of flames. All boundaries were left open to ambient and the initial temperature was 20°C. The domain was subdivided into three parts with two different mesh sizes in order to optimise the computational time. In this respect, a mesh sensitivity analysis was performed and the size of the mesh was taken equal to 0.3 m for the area near the bridge deck and 0.5 m for the other part of the domain.

Three HRR curves were used for the simulations:

- Tank truck: A standard semi-trailer fuel truck full of petrol; the petrol tanker fuel fires can reach 200-300 MW [27-29]. For this case study an average value was chosen as maximum HRR ($HRR_{max} = 250$ MW).
- HGV (T1): the heavy goods vehicle loaded with wood and plastic pallets ($HRR_{max} = 201$ MW) [30].
- Bus: This vehicle represents a large passenger bus ($HRR_{max} = 39$ MW) [29].

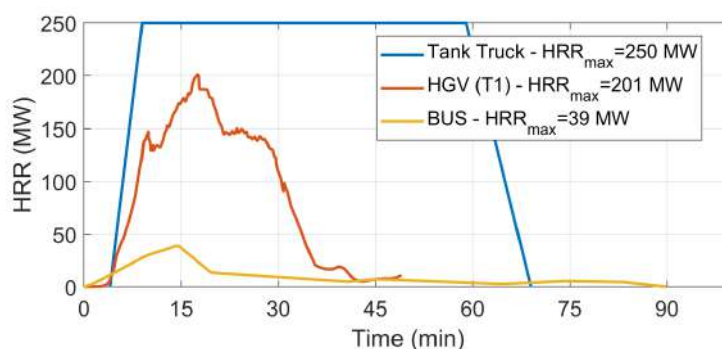


Figure 11. HRR of the three vehicle categories

The fires were placed in two different locations underneath the bridge:

- Middle location: the fire was centered at mid-span, both longitudinally and transversely (Figure 12)
- Side location: the fire location was moved from the center of the bridge near the end of the bridge.

A total of 7650 adiabatic surface temperature gas-phase devices were placed across the bridge deck in order to measure the gas temperature evolution. The output values from these devices were used for performing thermal-structural analysis in SAFIR.

For brevity, one simulation is selected as an example of scenario modelled in FDS that involved a standard semi-trailer fuel truck full of gasoline at mid-span of the domain. Figure 12a and b illustrate the development of fire and smoke respectively after 17 and 22 minutes from the beginning of one fire scenario as an example of the fire development stages.

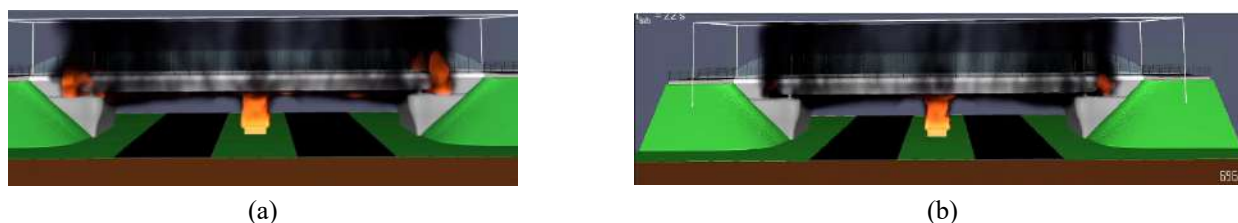


Figure 12. View of FDS results (a) after 17 min; (b) after 22 min

Figure 13 presents the FDS-thermomechanical results of the beam element model. Figure 13a and b show the deformed configuration and steel temperature 22 minutes after the beginning of the fire scenario. Figure 13c and d illustrate the horizontal and deflection time history of the bridge under the FDS fire load. Structural collapse was observed after 22 minutes due to failure of the mid-span part of the girders.

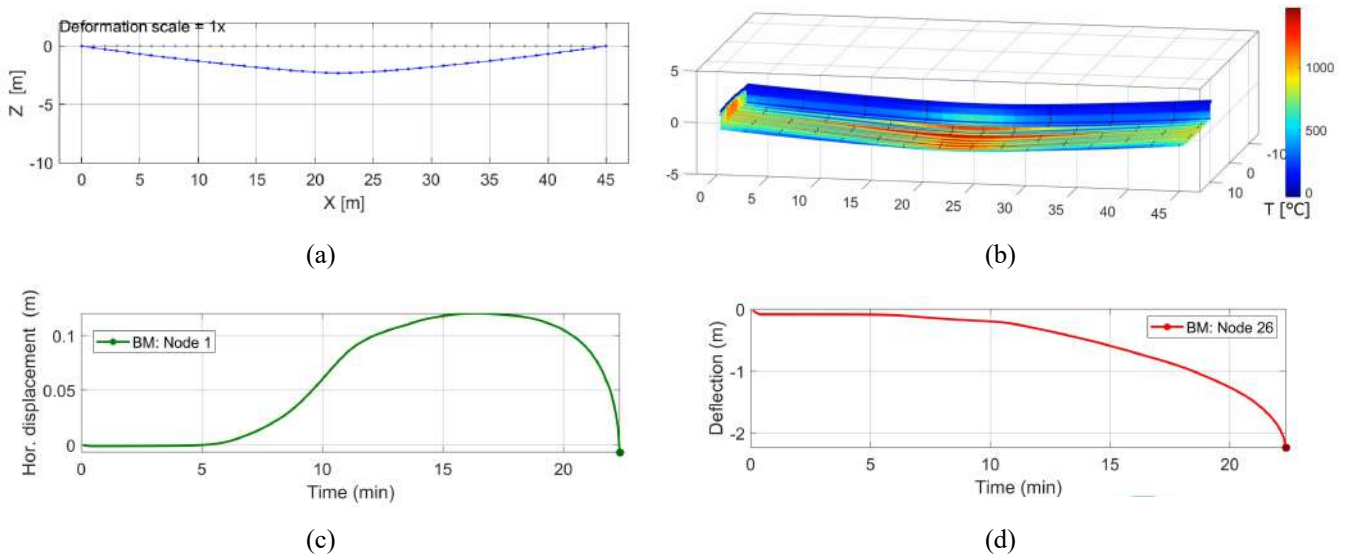


Figure 13. View of the bridge 22 min after the fire started: (a) Deformed shape of the beam model; (b) Deformed shape of the beam model and steel temperature of the deck

Figure 14 presents the FDS-thermomechanical results of the beam-shell element model. Figure 14a and b show the deformed configuration and steel temperature 21 minutes after the beginning of the fire scenario. Figure 13c and d illustrate the horizontal and the deflection time history of the bridge girders under the FDS fire load. Structural collapse was observed after 21 minutes due to failure of the mid-span girders. It is possible to notice that the GAP model of the 3rd and 4th girders reached the maximum thermal joint expansion capabilities after 14 minutes.

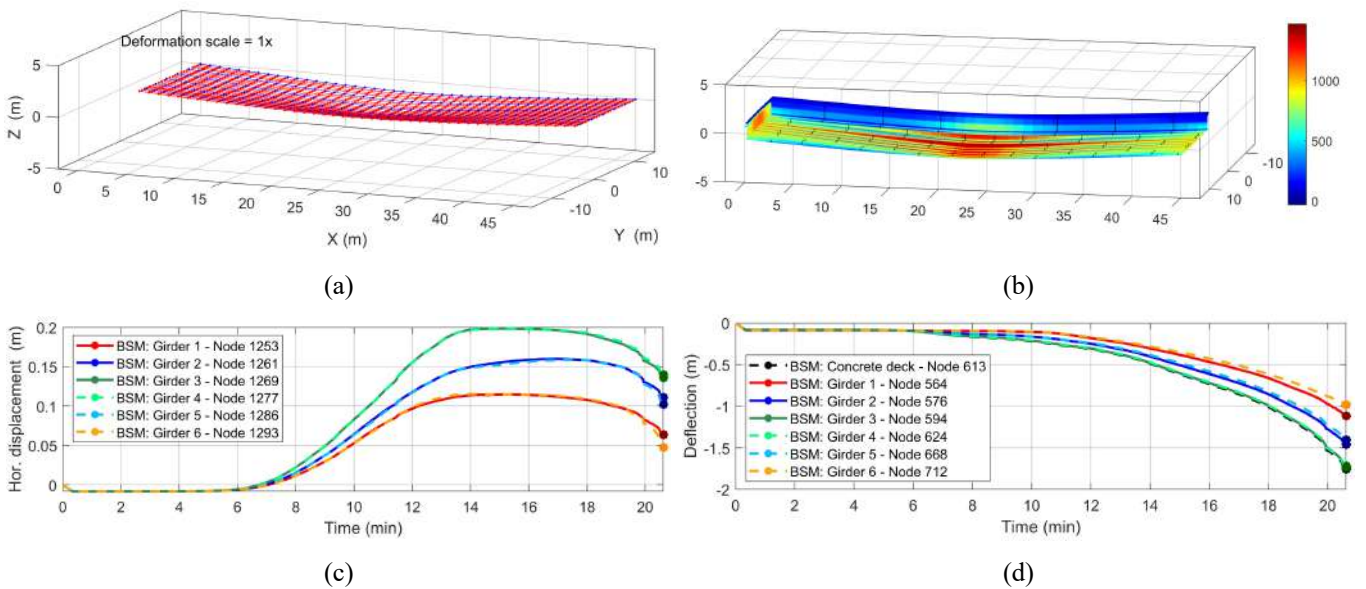


Figure 14. View of the bridge after 21 min after the fire started: (a) FDS results general view; (b) Deformed shape and steel temperature of the deck

As illustrated in Figure 15, the comparison between the beam and beam-shell models shows similar global behaviour. Overall, it is possible to observe a good agreement between the vertical displacement of the beam model and the middle girders of the beam-shell model. The beam-shell model better describe the single-girder and concrete deck behaviours.

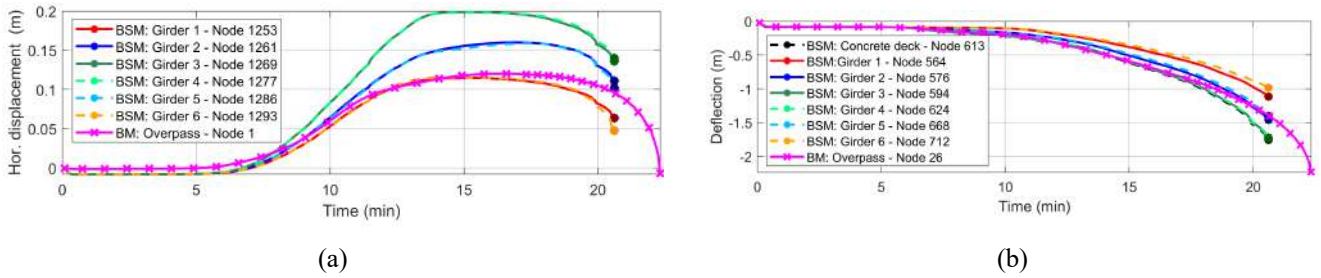


Figure 15. Comparison between the beam model and beam-shell model: (a) Horizontal displacements; (b) Deflection

The simulation results using the FDS scenarios of the beam-shell element, that involved some heavy vehicles, are summarised in Table 1. As previously calculated, on average, 7.54 heavy vehicle fires occurred on highways every billion vehicle-km, based on the data of a crucial Italian highway. The fire event occurred under a bridge in 1.23 % of the heavy and light fire vehicles. In the numerical simulation results, structural failure was observed in the Tank truck and HGV scenario caused by the girders failure. No structural failure happened considering the bus scenario with a maximum residual vertical displacement of around 12 cm, which means a value equal to about $L/375$ that considering a functional limit of $L/250$ might be deemed still functional [31]. However, the displacements are quite localised and careful judgements on a case-by-case basis should be provided.

Table 1. Results of the FDS scenarios

ID	Nominal curve	Fire location	Simulation stop time (min)	Maximum deflection (m)	Residual deflection (m)	Residual deflection over bridge's length
#1	Tank truck	Middle	21	Collapse	Not applicable	Not applicable
#2	Tank truck	Side	18	Collapse	Not applicable	Not applicable
#3	HGV	Middle	23	Collapse	Not applicable	Not applicable
#4	HGV	Side	22	Collapse	Not applicable	Not applicable
#5	Bus	Middle	End simulation	0.21	0.12	$L/375$
#6	Bus	Side	End simulation	0.18	0.11	$L/410$

4 CONCLUSIONS

The paper presented the derivation of the probability of occurrence of a fire on a bridge of an Italian highway based on actual data and the vulnerability analysis of a steel-concrete composite overpass in the context of fire risk assessment. The probability of one vehicle fire occurring every year on an Italian highway is equal to 19.8 %. By considering an important Italian highway, on average, 8.96 light vehicle fires and 7.54 heavy vehicle fires occurred every billion vehicle-km. In 10 % of the cases, it occurred above/under a bridge.

The paper also illustrated the thermomechanical analysis workflow and results of a numerical investigation of an unprotected simply supported steel-concrete composite bridge under fire in the context of the performance-based approach. Results showed that CFD analyses, despite being computationally demanding, provided a more realistic representation of the bridge fire scenario.

Both in the tank truck and HGV scenarios, the collapse occurred between 18 and 23 minutes, whilst in the analysed cases with bus on fire, the collapse did not occur. In the latter case, small residual deformations,

i.e., about L/410 - L/375, were observed for the CFD analyses, but were localised. In the tank truck scenario, the horizontal displacement of the overpass reached the maximum thermal joint expansion (GAP) capacity. Therefore, the modelling of the GAP in the numerical model allowed for obtaining a more realistic constraint condition than the boundary conditions frequently used in other studies, such as hinge-hinge or hinge-roller constraints.

Despite the probability of occurrence of a fire on/under a bridge is lower than for buildings, the consequences may be high given the vulnerability of simply supported steel-concrete composite bridge subjected to HGV fires. Thus, the evaluation of the fire risk may be useful for the decision-making process of the bridge. Indeed, future work will be based on the evaluation of the fire risk based on the strategic importance of the bridge in the infrastructure network.

ACKNOWLEDGMENT

This research has been supported by Fondazione CARITRO Cassa di Risparmio di Trento e Rovereto (grant number 2022.0228). The consortium RELUIS (DM 204 1/07/2022) and the Italian Ministry of Education Universities and Research (MIUR) in the framework of the project DICAM-EXC (Departments of Excellence 2023-2027, grant L232/2016) is also gratefully acknowledged.

REFERENCES

1. Kodur, V., & Naser, M. Z. (2021). "Fire hazard in transportation infrastructure: Review, assessment, and mitigation strategies". *Frontiers of Structural and Civil Engineering*, 15, 46-60.
2. Hu, Jiayu, Ricky Carvel, and Asif Usmani. (2021) "Bridge fires in the 21st century: A literature review." *Fire Safety Journal*.
3. di Genova, C. D. C. (2018). *Effetti economici indotti dal crollo del viadotto Morandi*. Confindustria Genova, Genova.
4. Abarca, A., Monteiro, R., & O'Reilly, G. J. (2022). Simplified methodology for indirect loss-based prioritisation in roadway bridge network risk assessment. *International Journal of Disaster Risk Reduction*, 74, 102948.
5. Diaz, E.E.M., Moreno, F.N., and Mohammadi, J. (2009). Investigation of Common Causes of Bridge Collapse in Colombia. *Practice Periodical on Structural Design and Construction*. 14(4): p. 194-200
6. Deng L, Wang W, Yu Y (2016) State-of-the-art review on the causes and mechanisms of bridge collapse. *J Perform Constr Facil*. [https://doi.org/10.1061/\(ASCE\)CF.1943-5509.0000731](https://doi.org/10.1061/(ASCE)CF.1943-5509.0000731)
7. Lee, G. C., Mohan, S., Huang, C., & Fard, B. N. (2013). *A study of US bridge failures (1980-2012)*. Buffalo, NY: MCEER.
8. Scheer, J. (2011). *Failed bridges: case studies, causes and consequences*. John Wiley & Sons.
9. Alos-Moya, J., Paya-Zaforteza, I., Hospitaler, A. and Loma-Ossorio, E., 2019. Valencia bridge fire tests: Validation of simplified and advanced numerical approaches to model bridge fire scenarios. *Advances in Engineering Software*, 128, pp.55-68.
10. Aziz, E. and Kodur, V., 2013. An approach for evaluating the residual strength of fire exposed bridge girders. *Journal of Constructional Steel Research*, 88, pp.34-42.
11. Dotreppe JC, Majkut S, Franssen JM. 2006. Failure of a tied-arch bridge submitted to a severe localised fire, structures and extreme events. *IABSE Symposium*; p. 272-273.
12. Payá-Zaforteza, I. and Garlock, M.E.M., 2012. A numerical investigation on the fire response of a steel girder bridge. *Journal of Constructional Steel Research*, 75, pp.93-103.
13. Song, C., Zhang, G., Kodur, V., Zhang, Y. and He, S., 2021. Fire response of horizontally curved continuous composite bridge girders. *Journal of Constructional Steel Research*, 182, p.106671.
14. Zhang, G., Song, C., Li, X., He, S. and Huang, Q., 2021. Fire performance of continuous steel-concrete composite bridge girders. *KSCE Journal of Civil Engineering*, 25(3), pp.973-984.
15. Alos-Moya, J., Paya-Zaforteza, I., Hospitaler, A. and Rinaudo, P., 2017. Valencia bridge fire tests: Experimental study of a composite bridge under fire. *Journal of Constructional Steel Research*, 138, pp.538-554.
16. Kaundinya, I., Bergerhausen, U. and Schmidt, J., 2017. Effects of extreme fire scenarios on bridges. *Bridge Structures*, 13(4), pp.159-167

17. Garlock, Maria, et al. "Fire hazard in bridges: Review, assessment and repair strategies." *Engineering structures* 35 (2012): 89-98.
18. Naser, M. Z., & Kodur, V. K. R. (2015). "A probabilistic assessment for classification of bridges against fire hazard". *Fire Safety Journal*, 76, 65-73.
19. Italian Ministry of the Interior (2022). "Statistical yearbook of the Italian fire brigade".
20. Civil Protection Agency Permanent fire brigade province of South Tyrol "Statistical annual report"
21. Fire and Civil Protection Service province of Trentino "S. BARBARA - Activity summary report"
22. Franssen, J-M, Gernay, T. (2017): Modeling structures in fire with SAFIR©: Theoretical background and capabilities. *Journal of Structural Fire Engineering*, 8 (3), 300-323.
23. R. von Mises, "Über die Stabilitätsprobleme der Elastizitätstheorie," *ZAMM*, vol. 3, pp. 406–422, 1923
24. Covi, P., Tondini, N., & Giuriati, E. (2022). Comparative analysis of the fire performance of a steel arch bridge. In *Proceedings of the 12 th International Conference on Structures in Fire* (pp. 37-48). The Hong Kong Polytechnic University.
25. Covi, P., & Tondini, N. (2023). Numerical investigation of a steel tied arch bridge under fire loading. *ce/papers*, 6(3-4), 2086-2091.
26. DM 3/08/2015 Italian Ministry of the Interior (2015), "Approvazione di norme tecniche di prevenzione incendi, ai sensi"
27. Kashkarov, S., Makarov, D., & Molkov, V. (2018). Effect of a heat release rate on reproducibility of fire test for hydrogen storage cylinders. *International Journal of Hydrogen Energy*, 43(21), 10185-10192.
28. Tarada, F. (2011). Fires in tunnels—can the risks be designed out?. *Eurotransport Magazine*, 9(4), 46-49.
29. Wright, W., Lattimer, B., Woodworth, M., Nahid, M., & Sotelino, E. (2013). Highway bridge fire hazard assessment draft final report. Virginia polytechnic institute and state university. TRB Project, (12-85).
30. Hurley, M. J., Gottuk, D. T., Hall Jr, J. R., Harada, K., Kuligowski, E. D., Puchovsky, M., and Wieczorek, C. J. (Eds.). (2015). *SFPE handbook of fire protection engineering*. Springer.
31. de Silva, D., Gallo, M., De Falco, L., & Nigro, E. (2023). Fire risk assessment of bridges: from state of the art to structural vulnerability mitigation. *Journal of Civil Structural Health Monitoring*, 1-20.

SMART PERFORMANCE-BASED STRUCTURAL FIRE DESIGN

Zhuojun Nan¹, Mhd Anwar Orabi^{2,*}, Xinyan Huang³, Asif Usmani⁴

ABSTRACT

Performance based structural fire engineering (PBSFE) is a necessary methodology for dealing with the complexities of modern structures which nuances have rendered them beyond the realm of prescriptive approaches. In addition, however, PBSFE often has the side-effect of reducing the costs associated with fire protection as it retargets the fire protection resources towards the parts of the structure for which they would be most impactful. In this paper, an enhanced open-source integrated simulation environment is used to attempt to improve the fire performance of a truss while reducing the amount of fire protection applied. This is done by generating a set of partial fire protection layouts that aim to prevent the failure mechanisms observed in unprotected structures, and then numerically analysing these layouts under different fire exposure scenarios and with different protection thicknesses. The results showed that the choice of fire protection layout is much more impactful than thickness of fire protection applied, and that suppressing selected failure mechanisms resulted in others manifesting leading to an equally catastrophic failure. This is likely due to the limited load-paths available within a simple structure such as the truss used for this study. Future work aims to better inform the fire protection layout generation to ensure that the potential solution space is covered sufficiently to enable smart performance-based structural fire design.

Keywords: Automation; smart design; structural fire; computer aided design; travelling fire; optimisation

1 INTRODUCTION

Modern structural-fire design problems have reached a level of complexity exceeding the limitations of traditional approaches. This has been shown repeatedly in the structural fire collapse of buildings that were, at some point in their lifetimes, designed up to the prescriptive standards of the day. Perhaps the most notable example of this is the World Trade Center building 7 (WTC7) [1]. This building actually exceeded prescriptive requirements of its time and was equipped with both passive and active fire protection measures. Since WTC7 was equipped with sprinklers, it only required a fire resistance rating of 2 hours for its columns and 90 minutes for its beams [2]. Instead, WTC7 members were reported to have had spray applied fire protection material equivalent to 3 hours for all columns and 2 hours for its floor members [2]. Despite this, WTC7 suffered a catastrophic collapse – one that should not befall a building of that scale regardless of fire resistance ratings. One could argue about the exact reasons for the collapse of WTC7, or Plasco [3] or

¹ Dr, Delft University of Technology, Department of Materials, Mechanics, Management & Design
e-mail: Z.Nan@tudelft.nl, ORCID: <https://orcid.org/0000-0001-8189-5448>

² Dr, The University of Queensland, School of Civil Engineering
e-mail: a.orabi@uq.edu.au, ORCID: <https://orcid.org/0000-0001-5083-3623>

³ Dr, The Hong Kong Polytechnic University, Department of Building Energy and Environment Engineering
e-mail: xy.huang@polyu.edu.hk, ORCID: <https://orcid.org/0000-0002-0584-8452>

⁴ Professor, The Hong Kong Polytechnic University, Department of Building Energy and Environment Engineering
e-mail: asif.usmani@polyu.edu.hk, ORCID: <https://orcid.org/0000-0003-2454-5737>

any other building for hours, but the common thread between these deadly unacceptable events is that they fall outside the scope of prescriptive design methodologies.

Performance-based structural fire design (PBSFD) is an essential methodology for ensuring the safety of the built environment and has emerged as a complement and sometimes a replacement for prescriptive design. Although this methodology is particularly needed to deal with structures outside the scope of design codes, it has also been used for reducing what may sometimes be prohibitively high fire protection costs. Lamont et al. [4] presented an impressively large-scale case study of a practical application of PBSFD in Mincing Lane. In this work, the authors used Abaqus to simulate the floor behaviour and established that leaving the secondary beams unprotected has very minor impact on the performance of the structure. Leaving the primary beams or columns unprotected, however, was not recommended. In this way, PBSFD was used to direct the resources used for passive fire protection towards where they would make the biggest impact rather than squander them where they would have little contribution to the overall fire performance of the structure. Around the same time as Lamont et al. [4], Green et al. [5] presented a similar case where an 11-storey hospital made with steel-concrete composite construction underwent PBSFD resulting in net savings of GBP 249,000. The main point made by Green et al in this work is that rigidly adhering to prescriptive standards for fire protection without considering actual performance is both expensive and potentially dangerous. In this way, and over 20 years ago, it was shown by example and evidence that PBSFD can reduce the costs of fire protection of structures all the while improving fire safety. More recently, Ma et al [6] presented a framework for evaluating the cost of fire protection in order to further enable the cost-benefit analysis of PBSFD. Amongst their findings was that the average cost of all passive fire protection in buildings is generally about 8%, while that of SFRM is less than 2%, and intumescent paint slightly more than that. Chaudhary et al [7] presented an optimisation framework, that in some ways compliments the work from Ma et al [6]. Among other objectives, the optimisation framework from [7] incorporates costs into the fire design objectives, thus enabling a more informed approach to PBSFD that holistically considers the risks, costs, and benefits involved with fire protection.

With that being said, it is often too expensive to perform the required analyses for PBSFD even when considering that, as a side effect, PBSFD may result in savings on fire protection. This is because representative and high-fidelity structural fire engineering simulations require hundreds of person-hours to design, build, execute, interpret, and action correctly. This means that while performance-based approaches are necessary from a technical standpoint, they are often far too expensive to perform to the required level from commercial and business perspectives.

As such, innovation in the design workflow focusing on the optimisation of the numerical simulation tools to optimise engineering design-time is a priority. The authors have dedicated significant efforts in the past in this direction ranging from developing open-source structural [8] and heat transfer solvers [9], to interface middle-ware [10], integrated simulation environments [11], and incorporating elements of automation [12] within the workflow. This paper presents builds upon these past endeavours by introducing a 'smart' approach that aims to enable the engineer to optimise fire protection design with minimal effort.

This paper explores using a newly developed fire protection design module in Gid+OpenSees [11], aimed at facilitating smart PBSFD, to test partial fire protection layouts that aim to provide an improved structural fire performance with less fire protection. The paper starts by introducing a 22.5-meter steel truss that was used as a test case for this design approach. The FEM model of the truss is first validated against experimental results using a small-scale truss based on the truss tested in the FireGrid project [13]. After that, the truss is subjected to the standard temperature-time curve and a selection of non-uniform fire scenarios without any fire protection applied. This allowed exploration of the failure mechanisms that manifested and then choosing fire protection layouts that are meant to suppress these failure mechanisms. Three optimised layouts were chosen in addition to a base uniform fire protection layout, and their performance under localised fire was then studied. The results of the analyses are then compared, and it was found that an optimal fire protection was never achieved for this truss, and that fire protection thickness was significantly less important than choice of fire protection layout.

2 METHODOLOGY

A steel truss was designed and built in Gid+OpenSees to demonstrate the smart performance-based structural fire design approach, aimed at optimising fire protection design by comprehensively considering potential fire scenarios, as shown in Figure 1.

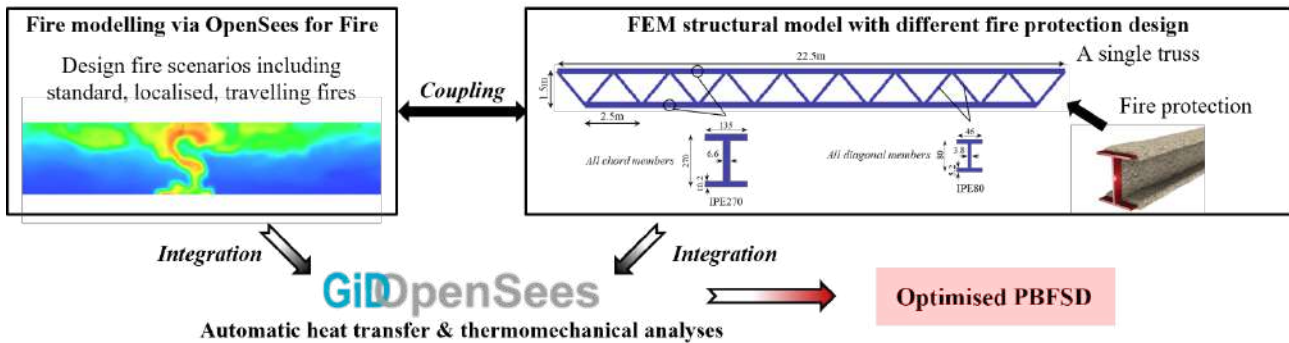


Figure 1. The smart PBSFD approach: a framework for optimising fire protection design

A new fire protection module, shown in Figure 2, was added to the existing Integrated Simulation Environment (ISE) – Gid+OpenSees [11]. This module forms the basis of the smart PBSFD approach introduced in this work and enables engineers to conduct fire, heat transfer, and thermomechanical analyses across hundreds of fire scenarios and fire protection configurations with only a few clicks.

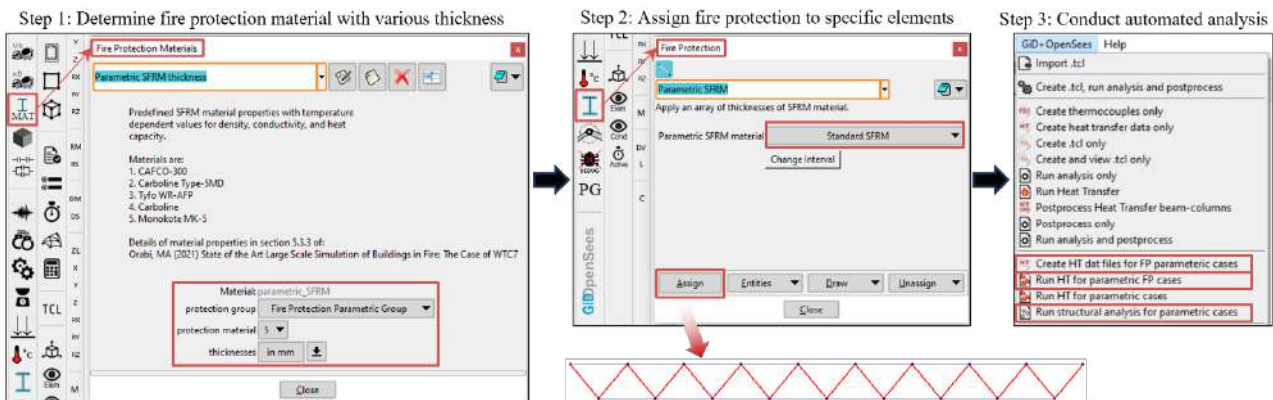


Figure 2. The fire protection design module in Gid+OpenSees

2.1 Structural model

Drawing inspiration from the small-scale truss of the FireGrid project [13], this study designed a full-scale steel truss, as shown in Figure 1. The truss spans 22.5 m, stands 1.5 m tall, with each zone spanning 2.5 m and a ceiling height of 4.5 m. It incorporates IPE270 and IPE80 for the chords and diagonals, respectively, using S355 grade steel. Following Eurocode [14], the truss was designed to resist an ambient design load of $1.983 \text{ kN/m}^2 = 1.35 \times 0.525$ (dead load) + 1.5×0.85 (live load), with the load evenly distributed to the bottom chord joints, assuming a 10 m longitudinal spacing between trusses.

The Finite Element Method (FEM) model of the small-scale truss, validated against FireGrid experimental results, indicated similar deflection trends as shown in Figure 3. Notably, the mid-span top deflection of the truss recorded in the test was attributed to the bending of its support frame under fire conditions, a factor not accounted for in the FEM model, where the truss was assumed to be simply supported. Employing the validated modelling approach, the full-scale truss FEM model utilised displacement-based beam-column elements with fiber-based sections for chords and diagonals, setting the cross-section integration points at 15 and assuming rigid beam-to-beam connections as per the experimental set-up. The thermal properties of steel were defined following Eurocode 3 [15]. Both mesh and time scaling sensitivity analyses were performed, leading to the discretisation of each structural member into 50 elements, totalling 1750 elements for 35 structural members. Fire duration was scaled down by a factor of 1/1000 for implicit dynamic

analysis in OpenSees. The analysis adopted load-controlled integration for both static and transient intervals; the latter yielded quasi-static responses prior to the buckling of the heated structural elements, followed by dynamic responses. Further details of interval data can be found in previous studies [1,16].

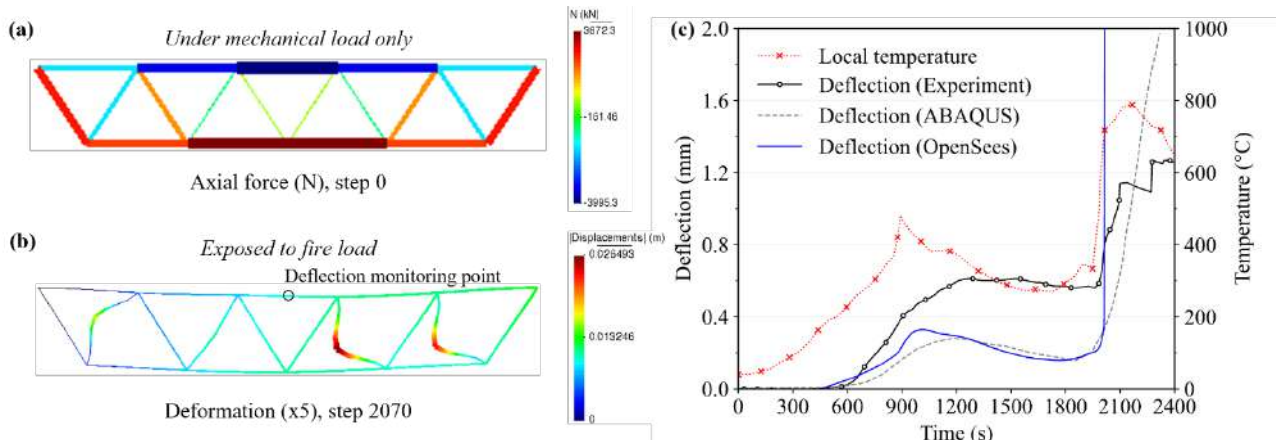


Figure 3. Simulation results of the truss in FireGrid (a - b) axial force and deflection, and (c) comparison between experimental measurement and predicted structural deflections

2.2 Design fire scenarios

This study considered various types of design fires, including the standard fire (ISO 834) [14], the Hasemi's localised fire model [17], and the natural fire model with travelling behaviour in OpenSees for fire [18]. Specifically, it adopted five design fire scenarios: the ISO 834 standard fire, three localised fires at different locations, and a travelling fire. Localised fire scenarios 1, 2, and 3 were placed at varying distance from the midspan of the truss, and the travelling fire was set to move from one end to the other along the longitudinal direction, as shown in Figure 4. These placements were later shown to have made a noticeable difference in the thermomechanical performance of the truss.

To examine the effectiveness of fire protection in preventing fire-induced structural collapse, extreme fire conditions, namely 10 MW fire, were designed for localised fires and the travelling fire to trigger structural collapse. It is worth mentioning that the Hasemi's localised fire model was also employed as near-field burning for the travelling fire. The fuel load density was set at 201.85 MJ/m², with a Heat Release Rate per Unit Area (HRRPUA) of 1000 kW/m². A total heat loss fraction of 0.85 and a radiative heat loss fraction of 0.35 were applied. The fire growth rate was classified as 'fast', with an α value of 0.0469 kW/s² and a duration of 30 min. For the travelling fire scenario, the fire spread rate was designed as 12.5 mm/s to maintain a consistent fire duration of 30 min. The locations of the three localised fires and the trajectory of the travelling fire are detailed in Figure 4.

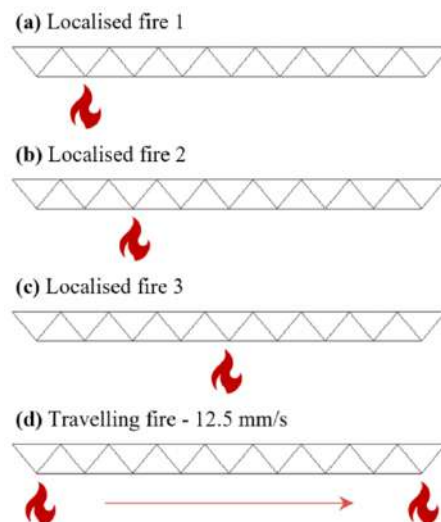


Figure 4. Demonstration of localised and travelling fire design scenarios

2.3 Fire protection design

Fire protection plays a pivotal role in structural fire design. In conventional design, the prescriptive approach entails the protection of all structural steel members to achieve the required Fire Resistance Rating (FRR), as shown in Figure 5(a). However, PBD offers room for alternative fire protection schemes. According to the structural response analysis under mechanical and fire loads, this paper proposed three optimised fire protection design schemes, as shown in Figure 5(b - d). CAFCO[®] 300, a widely used spray-applied fire protection coating, was applied in this study. The thickness of coating is calibrated based on the critical temperature of 550 °C (AS1530: Part 4) [19] to provide an equivalent FRR for structural elements. Considering the section factor (H_p/A) of diagonals (IPE80), thicknesses of CAFCO[®] 300 corresponding to $H_p/A = 400$ were selected as 16.8, 24.0, 31.9, 40.1, 54.5, and 70.1 mm, to achieve the required FRR of R30, R60, R90, R120, R180, and R240, respectively. A minimum fire protection thickness of 9.5 mm was applied, considering the section factor of 230 for chords (IPE270). To accommodate the challenges of construction in practical projects, a uniform thickness is maintained for the fire protection layers on both the chords and diagonals in each fire protection design case.

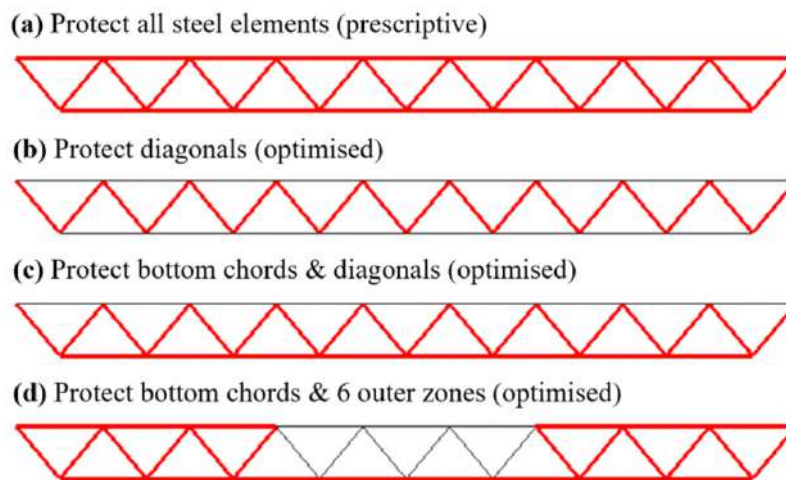


Figure 5. Demonstration of different fire protection design schemes

3 STRUCTURAL-FIRE RESPONSE

3.1 Without fire protection

This section presents the structural response of the unprotected truss to various design fire scenarios. These scenarios include the ISO 834 standard fire, three localise fire scenarios, and a travelling fire scenario. Figure 6 illustrates the different failure patterns of the truss exposed to these design fire scenarios. It is important to highlight the observation that a large deflection at the mid-span connection consistently accompanies the truss collapse. Therefore, this specific location, marked with black 'o' in Figure 6(a), has been chosen as the point for monitoring structural fire responses in subsequent discussions.

Figure 6(b) details the deflection development at the monitoring point under different design fire scenarios. In the standard fire, the intense heating across all steel components causes the temperature of all truss members to increase, experience significant restrained expansion, and ultimately collapse. Upon reaching an average beam temperature of around 480 °C across the cross-section, the combination of restrained-expansion stresses along with diminishing load-bearing capacity of the steel elements leads to buckling of some members. This, in turn, triggers progressive collapse approximately 430 seconds after the start of the fire exposure. Notably, collapse occurs earliest under the standard loads, attributed to the onerous assumption that all structural elements are uniformly exposed to intense fire loads.

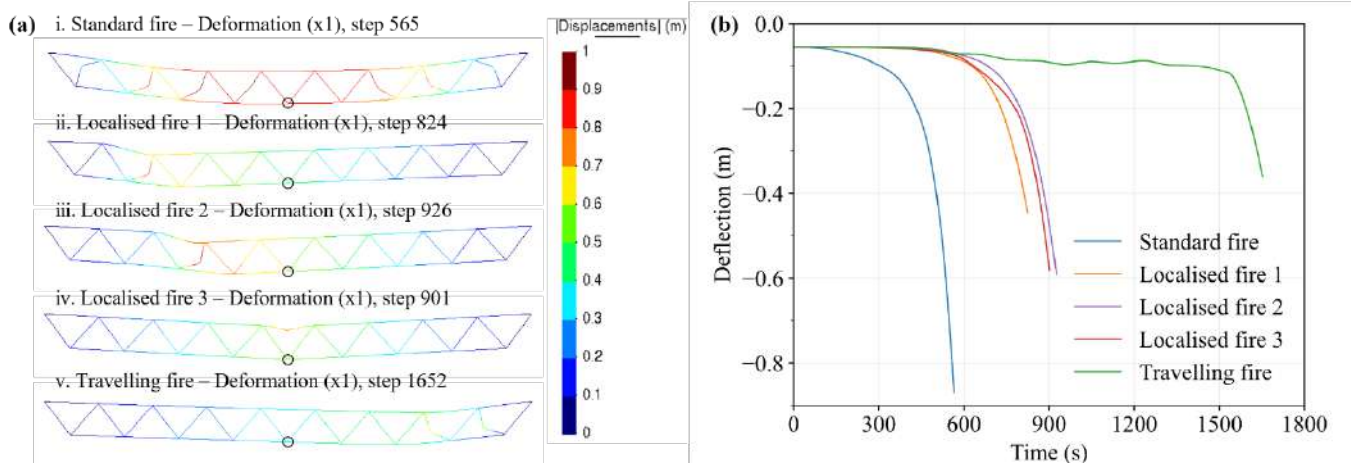


Figure 6. Truss displacement under different design fire scenarios without fire protection: (a) Displacement contour, and (b) Deflection of mid-span bottom connection

However, realistic fires rarely result in uniform gas-phase temperature distributions, particularly in modern architectural designs with open-plan layouts. Steel trusses are commonly used in large open spaces such as warehouses, shopping malls, exhibition centres, stadiums, and airports. Therefore, it is assumed that a steel truss ought to be subjected to more complex fire scenarios with non-uniform heating conditions as is the case for localised and travelling fire models. Under localised fires, as shown in Figure 6(a), the structural response of the truss varies with the fire location. Areas directly above localised fires experience significant deformation due to direct heat exposure. For example, under localised fire 1, the fourth diagonal member (from left to right) buckles triggering progressive collapse. The limited displacement observed in the first three spans (from left to right) of the truss is due to their proximity to the end support. The critical failure times for localised fires 1, 2, and 3 are 730, 800, 780 seconds, respectively. Yet, FireGrid observations and the simulations of structural fire responses presented in this section indicate that outer zone diagonals tend to buckle first under uniform gas-phase temperatures. This suggests these elements face the most adverse conditions under combined mechanical and fire loads, which might explain the collapse of the truss under localised fires.

Under the travelling fire, the truss undergoes ‘heating-cooling cycles’ [20–22], which results in a distinct structural-fire response when compared to localised fires. As the heat source moves, structural elements exposed to the ‘near-field’ fire are heated and then cool down as the fire ‘travels’ away. This dynamic effect contributed to the collapse of the truss at 1540 seconds when the fire spread 19.25 meters along the length of the truss and was located below the second-to-last bottom connection of the truss, as shown in Figure 6(b). Although the failure time under the traveling fire was found to be the longest, this does not imply that travelling fires are generally less severe. The ‘heating-cooling cycles’ induced by the travelling fire may result in ‘axial force reversal’ and a significant tensile force during the cooling phase, which could lead to unexpected structural failures [23,24]. However, this effect did not manifest in this simple 2D model, where the traveling fire scenario was not found to be particularly onerous.

3.2 Prescriptive fire protection designs

In this section, the investigation focuses on improvements in the fire performance of the truss by following prescriptive fire protection design. Specifically, the thickness of fire protection on all steel structural elements was varied from 9.5 mm to 70.1 mm, as detailed in Section 2.3.

According to AS1530: Part 4 [19], if a single steel beam with a section factor of 400 (e.g., IPE80) is coated with 24.0 mm of CAFCO® 300, and considering the critical temperature of 550 °C, then the beam could achieve an R60 rating, namely, a fire resistance rating of 60 minutes. However, and under one hour ISO 834 standard fire exposure, Figure 7(a), collapse takes place after 3300 seconds with a fire protection thickness of 24 mm, but is prevented with a protection thickness of 31.9 mm. This may be due to the restrained thermal expansion of the structure under the standard fire, causing the truss to collapse earlier

than expected. This indicates that merely adhering to prescriptive design for individual structural elements does not guarantee that the entire structure will achieve the expected fire resistance rating. This, of course, assumes that the expected performance in fire is based on standard fire exposure, which is widely accepted as a particularly intense loading scenario that does not necessarily represent the actual fire intensity a structure is expected to experience in its lifetime.

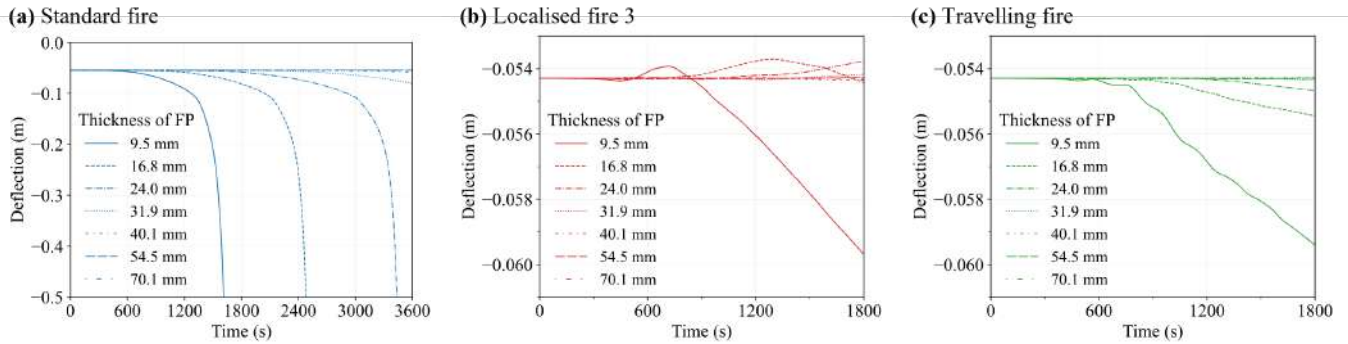


Figure 7. With prescriptive fire protection design, deflection of mid-span bottom connection under different fire scenarios: (a) Standard fire, (b) Localised fire 3, and (c) Travelling fire

Figure 8 further presents a summary of the maximum deflection among all connections in the truss when the truss is exposed to design localised and travelling fire scenarios with increasing thicknesses of fire protection coating. As shown in Figure 7(b - c) and Figure 8, under localised and travelling fire scenarios, protecting all steel elements, even with the minimum thickness of fire protection at 9.5 mm, prevents the failure of the truss. It also appears that increasing the thickness of fire protection until 31.9 mm improves the structural fire response although very marginally. Increasing the thickness beyond 31.9 mm, however, has no effect at all as shown in Figure 8. For example, the maximum deflection of the connections under the travelling fire decreased from -0.059 m to -0.055 m with an increase in the thickness of fire protection from 9.5 mm to 24.0 mm, due to the fire protection layers effectively slowing down heat transfer across the structural elements. This improvement is minuscule, however, and whether it is worth more than doubling the fire protection thickness should be addressed on a case-by-case basis.

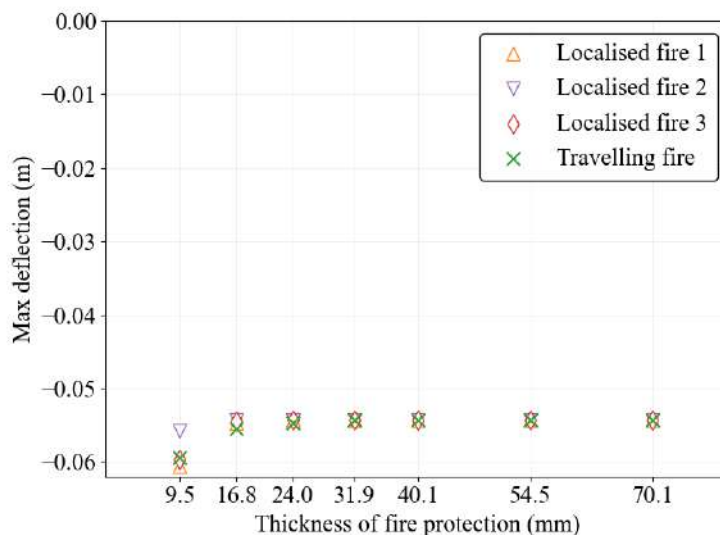


Figure 8. With prescriptive fire protection design, maximum deflections of truss connections under localised and travelling fire scenarios

3.3 Optimised fire protection designs

As discussed in Section 3.1, which investigated structural failure modes without fire protection, the diagonals in the outer zones are typically the first to buckle under combined mechanical and thermo-

mechanical stresses. This is primarily due to the smaller cross-sections of the diagonals, which not only lead to them heat up more rapidly but also have a limited load-bearing capacity. Likewise, the bottom chords are expected to be fully exposed to fire and are unlikely to be restrained from buckling unlike the top chords. Consequently, this study proposes three fire protection design layouts that aim to achieve the required structural fire performance while reducing the total amount of fire protection applied. These layouts are detailed in Figure 5(b - d) and are: (b) protect diagonal members only; (c) protect bottom chords and diagonals; and (d) protect bottom chords and six outer zones. The current paper presents the structural fire responses with the optimised fire protection designs under the three localised fire scenarios.

Figure 9 illustrates the development of mid-span bottom connection deflection in the truss with fire protection applied to all diagonals, observing the effect of increasing thickness of fire protection under localised fire scenarios. As shown in Figure 9 (a), under localised fire scenario 1, the application of the minimum thickness of fire protection (9.5 mm) prevents the collapse of the truss. This is indicated by the overall low deflection of 0.08 m which is less than $L/250$ (L represents the length of the truss, 22.5 m) and a low deflection rate of approximately 2.4 mm per minute. This is because the progressive collapse of the truss is triggered by the early buckling of diagonals located just above localised fire 1, thus by protecting them the collapse was prevented. This finding underscores the importance of applying fire protection to key structural elements to prevent fire-induced structural collapse. However, as depicted in Figure 9 (b - c), the truss collapses under localised fire scenarios 2 and 3, even with the thickest fire protection of 70.1 mm. This is due to the bulking of the top chord above localised fire scenarios 2 and 3. The issue arises not only because of the lack fire protection on the chords but also because localised fire scenarios 2 and 3 occur around/at the mid-span of the truss. As indicated in Figure 3(a), the top chords located closer to the mid-span are under greater compression compared to those near the supports, considering the mechanical loads. Therefore, when the fire occurs at locations 2 and 3, the top chord above the fire faces dangerous conditions due to both mechanical and fire loads. This outcome indicates that protecting only the diagonals is insufficient to ensure the survival of the truss under potential fire scenarios.

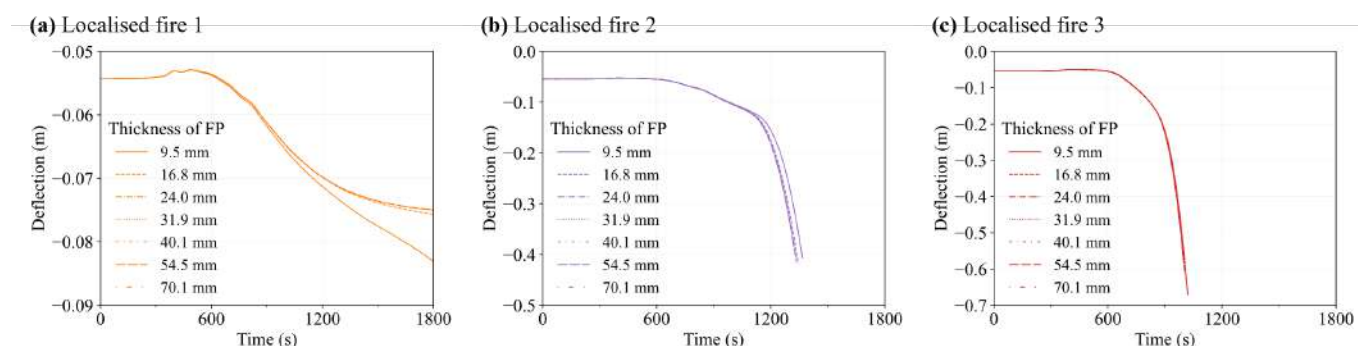


Figure 9. Protect diagonals, deflection of mid-span bottom connection under various localised fire scenarios

Figure 10 and Figure 11 show the recorded deflection at the monitoring point (i.e., the mid-span bottom connection) under the two fire protection schemes: (c) protecting bottom chords and diagonals, and (d) protecting bottom chords and six outer zones. Similarly, varying thicknesses of fire protection were applied, and the three localised fire scenarios were used. Compared to the scheme of protecting only the diagonals (see Figure 9), the fire performance of the truss improved. Notably, under localised fire scenario 2, the collapse of the truss has been prevented with fire protection thickness just above the minimum, as illustrated in Figure 10 and Figure 11. However, both protection schemes (c) and (d) result in collapse under localised fire 3 regardless of fire protection thickness.

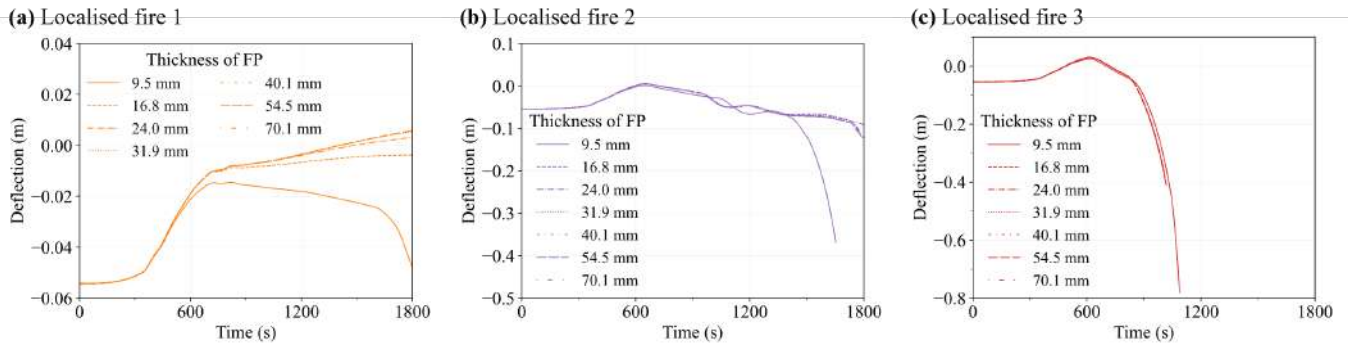


Figure 10. Protect bottom chords and diagonals, deflection of mid-span bottom connection under localised fire scenarios

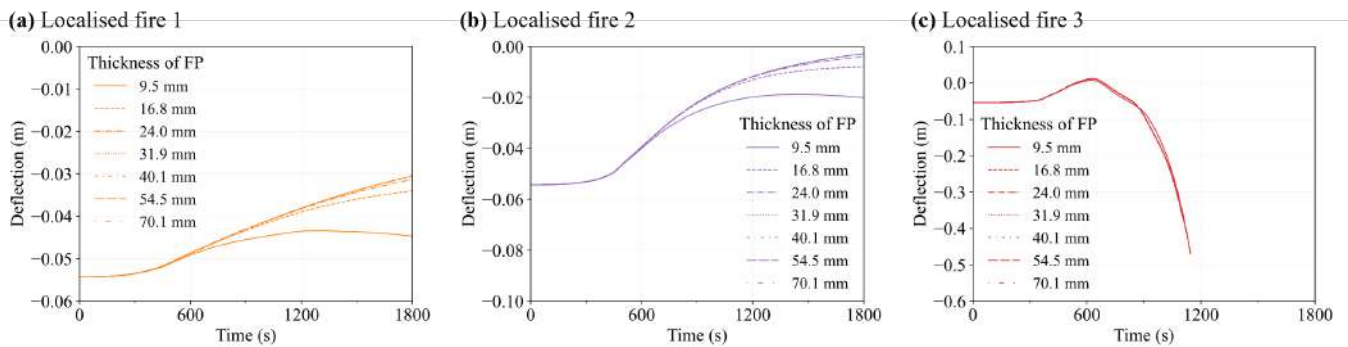


Figure 11. Protect bottom chords and six outer zones, deflection of mid-span bottom connection under localised fire scenarios

The results presented in Figure 9, Figure 10 and Figure 11 indicate that fire protection schemes developed to suppress the failure mechanisms obtained under the unprotected case are unable to provide required level of performance in fire. While schemes (c) and (d) were adequate for localised fire scenarios 1 and 2, they both failed to provide sufficient fire resistance when a fire is assumed to occur directly under the mid-span. So, while the thermomechanical analyses in section 3.1 showed that localised fire scenario 3 was not the fastest to reach failure, it turned out to be the most difficult to suppress with partial fire protection.

4 CONCLUSIONS

This paper presented an approach towards improving the structural fire performance of a truss subjected to different fire scenarios and protected with three unique fire protection layouts. Layout (b) provided fire protection only to the diagonals, layout (c) protected both the diagonals and the bottom chord, and layout (d) applied fire protection only to the bottom chord and diagonal members near the six zones adjacent to the support. These fire protection schemes aimed to suppress the failure mechanisms that took place, but once these mechanisms were prevented new ones took their place and resulted in collapse. Interestingly, if the fire protection layout was suitable for the fire exposure conditions, then the thickness was inconsequential and even a minimal amount of fire protection could prevent failure. This was observed for layout (b) with localised fire near the support, or layouts (c) and (d) with localised fires near the support and first third of the span. Likewise, if the layout was unsuitable for the exposure conditions, then no thickness of fire protection could prevent runaway collapse. This the case for all layouts with localised fire under the midspan; no thickness of fire protection could prevent this failure. For all non-uniform fire exposures, however, the ‘brute-force’ approach of applying fire protection to all members of the truss was able to protect against collapse. This indicates that while smart application of fire protection may work well on floor systems as whole, trusses simply do not have sufficient alternative load-paths to benefit from selective fire protection. That being said, however, only a few fire protection layouts were tested in this paper, and it is quite likely that they did not include the ‘optimal’ layout that optimises both cost and

performance. As such, there remains much to be done regarding generating the fire protection layouts - that is much to be done in ‘smart’ and data-enhanced design. From this work, it appears that using failure mechanisms of unprotected structure as a guide is not sufficient because new mechanisms quickly replace those suppressed by partial application of fire protection.

ACKNOWLEDGMENT

This work is funded by the Hong Kong Research Grants Council Theme-based Research Scheme (T22-505/19-N).

REFERENCES

- [1] M.A. Orabi, L. Jiang, A. Usmani, J. Torero, The Collapse of World Trade Center 7: Revisited, *Fire Technol* (2022). <https://doi.org/10.1007/s10694-022-01225-2>.
- [2] NIST, Final Report on the Collapse of World Trade Center Building 7, 2008.
- [3] M.A. Khan, A.A. Khan, A.S. Usmani, X. Huang, Can fire cause the collapse of Plasco Building: A numerical investigation, *Fire Mater* 46 (2022) 560–575. <https://doi.org/10.1002/fam.3003>.
- [4] S. Lamont, B. Lane Arup Fire, G. Flint, A. Usmani, Structural Behaviour in Fire and Real Design, (n.d.). <https://doi.org/10.1177/10423915060540388>.
- [5] M. Green, N. Butterworth, I. Burgess, R. Plank, Practical case studies in performance-based structural fire engineering design, in: *ASCE Specialty Conf.: Designing Structures for Fire, 2003*: pp. 259–266. <https://www.researchgate.net/publication/228496594>.
- [6] C. Ma, R. Van Coile, T. Gernay, Fire protection costs in composite buildings for cost-benefit analysis of fire designs, *J Constr Steel Res* 215 (2024). <https://doi.org/10.1016/j.jcsr.2024.108517>.
- [7] R.K. Chaudhary, T. Gernay, R. Van Coile, Multi-objective optimization of structural fire design, *Fire Saf J* 146 (2024). <https://doi.org/10.1016/j.firesaf.2024.104139>.
- [8] L. Jiang, M.A. Orabi, J. Jiang, A. Usmani, Modelling concrete slabs subjected to fires using nonlinear layered shell elements and concrete damage-plasticity material, *Eng Struct* 234 (2021). <https://doi.org/10.1016/j.engstruct.2021.111977>.
- [9] L. Jiang, Y. Jiang, Z. Zhang, A. Usmani, Thermal Analysis Infrastructure in OpenSees for Fire and its Smart Application Interface Towards Natural Fire Modelling, *Fire Technol* 57 (2021) 2955–2980. <https://doi.org/10.1007/s10694-020-01071-0>.
- [10] A.A. Khan, M.A. Khan, C. Zhang, L. Jiang, A. Usmani, OpenFIRE: An Open Computational Framework for Structural Response to Real Fires, *Fire Technol* 58 (2022) 1011–1038. <https://doi.org/10.1007/s10694-021-01184-0>.
- [11] M.A. Orabi, A.A. Khan, L. Jiang, T. Yarlagadda, J. Torero, A. Usmani, Integrated nonlinear structural simulation of composite buildings in fire, *Eng Struct* 252 (2022). <https://doi.org/10.1016/j.engstruct.2021.113593>.
- [12] M.A. Orabi, Z. Nan, A. Usmani, Automation of Structural Fire Resistance Design, in: X. Huang, W.C. Tam (Eds.), Springer, 2024: pp. 147–164. https://doi.org/10.1007/978-3-031-48161-1_7.
- [13] L. Han, S. Potter, G. Beckett, G. Pringle, S. Welch, S.H. Koo, G. Wickler, A. Usmani, J.L. Torero, A. Tate, FireGrid: An e-infrastructure for next-generation emergency response support, *J Parallel Distrib Comput* 70 (2010) 1128–1141. <https://doi.org/10.1016/j.jpdc.2010.06.005>.
- [14] EN 1991-1-2: Eurocode 1: Actions on structures - Part 1-2: General actions - Actions on structures exposed to fire, 1991.
- [15] EN 1993-1-2: Eurocode 3: Design of steel structures - Part 1-2: General rules - Structural fire design, 1993.

- [16] Z. Nan, M.A. Orabi, X. Huang, Y. Jiang, A. Usmani, Structural-fire responses forecasting via modular AI, *Fire Saf J* 140 (2023). <https://doi.org/10.1016/j.firesaf.2023.103863>.
- [17] Y. Hasemi, Y. Yokobayashi, T. Wakamatsu, A. Ptchelintsev, Modelling of heating mechanism and thermal response of structural components exposed to localised fires, 1996.
- [18] Z. Nan, A.A. Khan, L. Jiang, S. Chen, A. Usmani, Application of travelling behaviour models for thermal responses in large compartment fires, *Fire Saf J* 134 (2022) 103702. <https://doi.org/10.1016/j.firesaf.2022.103702>.
- [19] Standards Australia Limited., Methods for fire tests on building materials, components and structures. Part 4: Fire resistance tests of elements of building construction., in: Standards Australia, 2005: p. 160.
- [20] J. Stern-Gottfried, G. Rein, Travelling fires for structural design-Part I: Literature review, in: *Fire Saf J*, 2012: pp. 74–85. <https://doi.org/10.1016/j.firesaf.2012.06.003>.
- [21] J. Stern-Gottfried, G. Rein, Travelling fires for structural design-Part II: Design methodology, in: *Fire Saf J*, 2012: pp. 96–112. <https://doi.org/10.1016/j.firesaf.2012.06.011>.
- [22] X. Dai, S. Welch, A. Usmani, A critical review of “travelling fire” scenarios for performance-based structural engineering, *Fire Saf J* 91 (2017) 568–578. <https://doi.org/10.1016/j.firesaf.2017.04.001>.
- [23] X. Dai, S. Welch, O. Vassart, K. Cábová, L. Jiang, J. Maclean, G.C. Clifton, A. Usmani, An extended travelling fire method framework for performance-based structural design, in: *Fire Mater*, John Wiley and Sons Ltd, 2020: pp. 437–457. <https://doi.org/10.1002/fam.2810>.
- [24] Z. Nan, X. Dai, H. Chen, S. Welch, A. Usmani, A numerical investigation of 3D structural behaviour for steel-composite structures under various travelling fire scenarios, *Eng Struct* 267 (2022) 114587. <https://doi.org/10.1016/j.engstruct.2022.114587>.

THE FIRE ENGINEERING CHALLENGE ASSOCIATED WITH A STEEL BEAM PENETRATING A COMPARTMENT WALL

Edwin Ayala¹, Mark Davison², and Cristian Maluk³

ABSTRACT

Penetrations of steel beams through compartment walls pose a challenge in the building industry. Even though various regulatory and research bodies have recognised the issue, no practical recommendations are explicitly given. Past research has addressed the problem to an extent, but the application range of the findings remain constrained. To address this, our study employs Finite Element Method (FEM) modelling utilizing SAFIR to evaluate various scenarios. This study analyses the thermal behaviour of “I” steel beams passing through a compartment wall subjected to standard fire conditions at one side of the compartment. The study employs steel sections with a section factor ranging from 39 [m⁻¹] to 279 [m⁻¹]. It involves compartment walls of several materials (i.e., brick masonry, plasterboard cavity walls, or mass timber) with a fire resistance rating ranging from EI-30 to EI-240. Outcomes of the research show that the insulation of the system can be compromised when the steel beam is unprotected – meaning that in the event of a fire the wall and beam system is unable to prevent for the temperature at the other side of the wall to increase above a target temperature threshold. The outcomes of this study are shown as the length of the steel beam protruding from the compartment wall on the side not exposed to fire where the temperature threshold for the insulation criteria is exceeded.

Keywords: Compartmentation; steel beam; penetration; finite element modelling; SAFIR.

1 INTRODUCTION AND BACKGROUND

For a typical steel frame load-bearing building structure, there may be instances where the placement of an internal fire-rated compartment wall results in a steel beam passing through it, thereby connecting two compartments. The fire engineering challenge arises in scenarios where a fire originates in one compartment and spreads to an adjacent compartment due to heat being conducted via the steel beam connecting the two compartments. This scenario is commonly referred to as the “*failure of the insulation criteria of the compartment wall*”.

Currently, there is a lack of definitive guidance on the necessary protection measures when a steel beam penetrates a compartment wall. Nevertheless, various regulatory and research bodies have recognized this issue and provided general recommendations. For example, the Association for Specialist Fire Protection (ASFP) highlights in its guidelines that the insulation criteria (I) of the system may be the dominant feature when a steel beam passes through a fire compartment wall. Accordingly, additional protection thickness or measures will then be required for the steelwork in the proximity of the wall [1].

In the ASFP Advisory Note 18, titled ‘*ASFP Position on Installing Partitioning to the Underside of Structural Steel Sections Coated with a Reactive Fire Protection System*’ [2], it is suggested that boxing

¹ Fire Engineer, Semper
e-mail: edwinayala@sempergrp.com

² Director, Semper
e-mail: markdavison@sempergrp.com

³ Technical Director, Semper
e-mail: c.maluk@sempergrp.com, ORCID: <https://orcid.org/0000-0002-1662-6943>

out the beam with an independently tested system to provide the required level of protection, thereby ensuring the compartment's performance requirements are met. However, boarding the entire beam may not always be the preferred solution.

Additionally, the Building Research Establishment (BRE) emphasizes, in its report on '*The Integrity of Compartmentation in Buildings During a Fire*' [3] the importance of ensuring the deflection allowance of a steel beam passing through a compartment wall to prevent damage on the compartment wall and therefore loss of integrity (E) and insulation (I) of the compartment wall.

1.1 Past research

Bennetts and Goh (2001) [4] suggest that no protection is necessary when a steel member penetrates a concrete floor or slab, as the resulting temperature rise of the member is insufficient to cause ignition at the unexposed side of the compartment. Fire experiments utilized 20 and 2 [mm] steel plates to simulate the web of a hot rolled section and a purlin, respectively. Test samples were placed on a standard fire resistance wall furnace control to a standard temperature-time curve [5]. Maximum steel temperatures recorded on the unexposed side of the test specimens were less than 280°C for a 120 [mm] thick concrete wall (after 120 minutes of heating), and less than 185°C for a 200 [mm] thick concrete wall (after 180 minutes of heating). Non-fire-rated PVC cables and cardboard pieces were attached to the steel plate at the unexposed side to demonstrate the temperatures reached at the unexposed side were insufficient to cause ignition.

Bennetts and Moinuddin (2006) [6] conducted experiments demonstrating that the maximum temperature reached by a penetrating steel beam on the unexposed side of the cavity wall is significantly lower than that experienced on the heated side of the wall. This temperature appears to be influenced by various parameters such as the section factor of the penetrating steel beam, the size of the air cavity in the wall, the number and thickness of fire-resistant plasterboard layers, and the presence of steelwork inside the cavity. Findings from Bennetts and Moinuddin (2006) [6] concluded that the temperature of penetrating steel beams is unlikely to result in loss of insulation. However, it may be necessary for the compartment wall elements to be capable of accommodating vertical deflections at the wall to prevent loss of smoke integrity in the compartment wall. Conversely, a consultancy report detailing the penetration of compartment walls by steel purlins and beams, utilizing 500 [mm] insulation on both sides of the compartment wall [7], demonstrates successful attainment of the insulation criteria for the beam-fire compartment wall system. The study encompasses a range of steel sections, insulation materials, and compartment wall types. Nonetheless, it's important to acknowledge that the study focuses on specific products and protection systems.

1.2 Off-the-shelf solution

The industry has widely adopted a minimum insulation length of 500 [mm] for steel beams on both sides of the compartment to maintain compartmentation. This threshold is derived from guidance recommendations for similar circumstances and experiments conducted by passive protection manufacturers using specific materials [7]. The ASFP Technical Guidance Document (TGD) 08 – '*Code of Practice for Junctions between Different Fire Protection Systems when Applied to Load Bearing Structural Elements*' [8], emphasizes the importance of considering potential heat transfer from unprotected steel into protected structural steel. It is considered good practice to protect the adjoining 500 [mm] of 'unprotected' structural steel to limit unwanted heat transfer. Similarly, the ASFP Advisory Note (AN) 28 – '*Fire stopping of metal pipes, where flanges, valves or fittings fall within the insulation zone of a compartment wall penetration*' [9], recommends including insulation up to 500 [mm] from the wall for pipework services passing through compartment walls.

1.3 Failure Criteria

According to BS 476-20:1987 [5], insulation failure is identified by one of the following conditions:

- the mean unexposed surface temperature increases by more than 140°C above its initial mean value;
- the temperature at any location on the unexposed surface exceeds 180°C above the initial mean value;
- or
- integrity failure occurs.

Assuming an initial temperature of 20°C, the study described in this paper considers an insulation failure criteria of 160 °C. To simplify the assessment and adopt a conservative approach, the failure criteria is compared with the temperature recorded at any position on the unexposed surface of the steel beam and wall.

2 RESEARCH METHODOLOGY

2.1 Studied scenarios

This study examines several compartment wall materials and conditions (protected or unprotected) for penetrating load-bearing steelwork (more specifically steel beams) to offer a comprehensive understanding and propose broader and more effective solutions.

To achieve this objective, three types of compartment walls were modelled: masonry blockwork, mass timber, and plasterboard cavity walls. These materials were chosen due to their prevalence in the construction industry, as they are commonly used to construct compartment walls.

Furthermore, the study addresses both protected and unprotected steel beams penetrating the compartment walls. This serves two purposes: firstly, to confirm whether the compartment's insulation could be compromised, and secondly, to propose fire protection solutions for prevention and mitigation.

2.2 Approach

This study aims to utilize Finite Element Methodology (FEM) to determine the length at which the temperature insulation criteria are exceeded on the unexposed side of the steel beam penetrating a compartment wall. The objective is to recommend a minimum required insulation length necessary on the beam to prevent the failure of the insulation criteria. The study specifically addresses the heat transfer issue and operates under the assumption that the integrity of the compartment wall remains intact, at least for its own fire resistance. With this in mind, the study outlines the following methodology to address the problem.

Initially, a FEM model is executed with an unprotected steel beam passing through the compartment wall (Figure 1.a) to identify if the insulation of the system wall-beam is compromised. This step also aims to determine the length of the beam on the unexposed side of the compartment where the temperature failure criteria have been surpassed.

Once the compromised length is identified, a second model is executed (Figure 1.b). In this second model, the identified length is protected on both sides of the compartment wall using a plasterboard encasement. In the model, the encasement follows the shape of the steel beam. However, it is acknowledged that a box section with a fire stopping is most likely to be put in place. Lower temperatures on the steel section are expected with the boxing arrangement. Finally, temperatures on the unexposed side are verified in the second model to ensure they do not exceed the failure criteria.

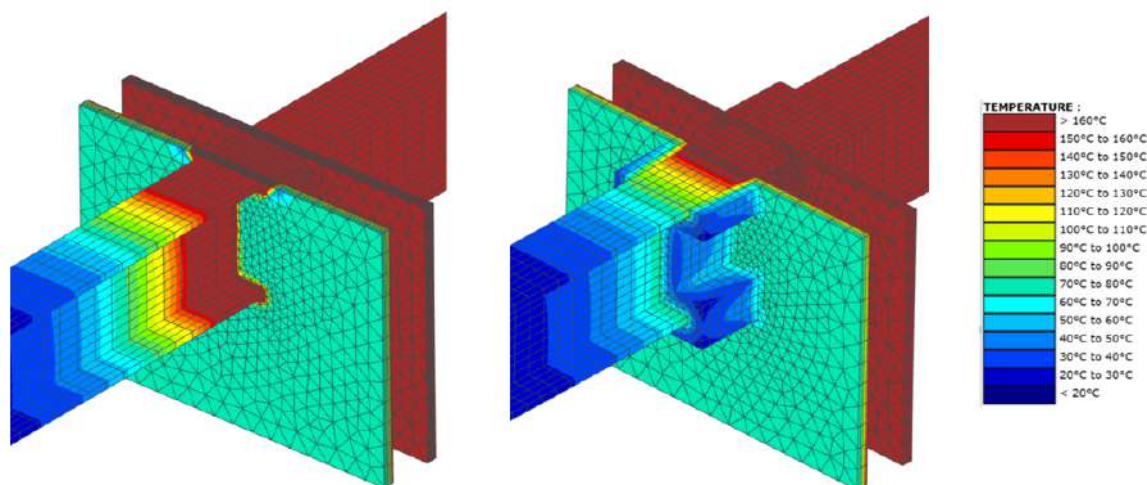


Figure 1. a) Model of unprotected steel beam penetrating a compartment wall b) Model of partially protected steel beam penetrating a compartment wall

3 DESCRIPTION OF THE MODEL

The finite element modelling (FEM) for this study has been performed employing SAFIR [10]. SAFIR is a nonlinear finite element software for structures in fire capable of calculating the temperature distribution within a building structure when it is exposed to fire. It takes into account various materials used in construction such as steel, concrete, timber, and insulating materials, allowing for analysis of both 2D and 3D structures. SAFIR provides detailed temperature data at each node of the structure over time, enabling users to estimate the transient thermal behaviour during a fire event.

3.1 Material properties

The thermal properties of the materials involved in the model are temperature dependent. Steel, timber, and masonry properties are sourced from Eurocode 3 [11], 5 [12], and 6 [13], respectively. It is worth noting that the values specified in the Eurocode represent effective values rather than physically measured values. Alternatively, plasterboard properties were derived from Thomas (2010) [14], where the specific heat values account for the gypsum ($\text{CaSO}_4 \cdot 2\text{H}_2\text{O}$) dehydration and decomposition of the calcium carbonate (CaCO_3) as recommended by Wakili et al. (2007) [15]. The thermal properties employed for plasterboard are illustrated in Figure 2.

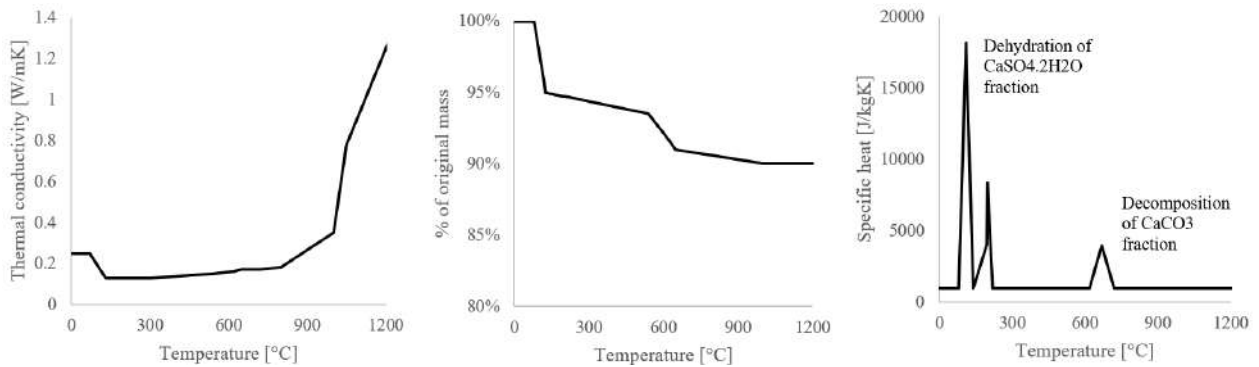


Figure 2. Thermal properties employed for plasterboard

3.2 Border conditions

Firstly, the compartment wall undergoes heating from a single side. The heating regime applied on the heated side of the compartment wall is assumed to be that of the standard temperature-time curve (BS 476) [5], while the boundary conditions at the unheated side assume losses by convection and radiation due to a constant ambient gas temperature of 20°C. The top flange is assumed to have adiabatic conditions at the top surface – simulating the presence of a floor slab in contact with the steel beam.

Thermal boundary conditions are defined by the temperature of the environment surrounding the surface (T_g). The heat flux (q''_{net}) at the boundary is calculated from the gas temperature (T_g) and the temperature at the surface (T_s) according to equation 1

$$q''_{net} = h(T_g - T_s) + \sigma \varepsilon (T_g^4 - T_s^4) \quad (1)$$

Where h is the convective heat transfer coefficient, σ is the Stefan-Boltzmann constant ($5.67\text{E-}8 \text{ W/m}^2/\text{K}^4$), and ε is the effective emissivity. The values for h and ε employed in this study and the reference for them are described in Table 1.

A sub-model is conducted to specifically gauge the thermal conditions inside the cavity – gas temperature (T_g) inside the plasterboard cavity wall. The command “VOID” [17] is employed to simulate the presence of the cavity. This tool involves two primary heat transfer mechanisms: linear convection between the cavity's internal surfaces and the air within the cavity, and radiation exchange among the internal surfaces of the cavity. The command simplifies the heat transfer calculation, operating on several assumptions: first, no heat conduction occurs within the cavity gas; second, the specific heat of the gas is disregarded; third, the gas is transparent to radiation. Based on the outcomes of the sub-model, the gas temperature inside the

cavity was determined. The thermal boundary conditions employed on the model and sub-model are illustrated in Figure 3.

Table 1. Heat transfer parameters employed in the models

Position	ε	h [kW/m^2]
Plasterboard [14]		
Fire side	0.8	25.0
Cavity	0.4	5.0
Ambient side	0.6	9.0
Steel [6,11]		
Fire side [6]	0.7	25.0
Cavity*	0.4	5.0
Ambient side*	0.4	5.0
Timber and Masonry [12,16]		
Fire side	0.8	25.0
Ambient side	0.8	4.0

*Heat transfer parameters on steel were calibrated based on the experimental results registered in Bennetts and Moinuddin (2006) [6].

3.3 Assumptions and limitations

The following assumptions are considered in the model:

- no gaps are considered between the steel beam and the compartment wall;
- integrity of the compartment wall remains intact;
- adiabatic conditions are assumed on the top surface of the top flange to simulate the presence of a floor slab in contact with the steel beam;
- temperature inside the cavity is assumed to be the average between the interior surface temperature for the cavity wall at the heated and unheated side;
- radiation and convection heat transfer are considered in the cavity employing the SAFIR VOID [17] tool. Therefore:
- no heat conduction occurs within the cavity gas;
- the specific heat of the cavity gas is disregarded; and
- gas in the cavity is transparent to radiation

The following limitations need to be considered when the model is applied:

- the model is constrained to the temperature domain;
- the convective heat transfer coefficient and emissivity assumed for the steel in the cavity and at the unexposed side of the compartment were calibrated based on Bennetts and Moinuddin (2006) [6] tests;
- material properties described in Eurocode are effective values rather than physically measured values; and
- the cavity sub-model does not consider more complex phenomena such as gravity's direction, the cavity's characteristic dimension, or the velocity of convective movements.

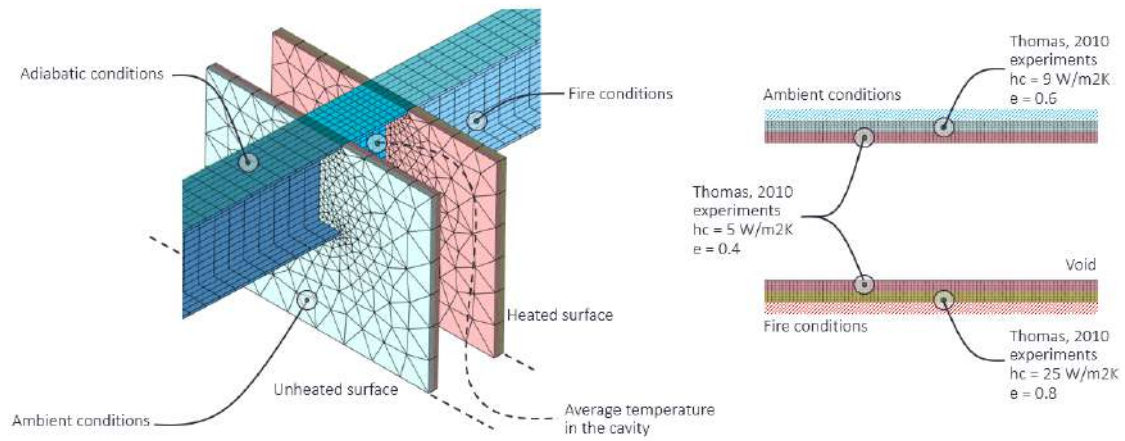


Figure 3. Frontier conditions for the 3D and 2D plasterboard cavity wall model

4 EMPIRICAL VALIDATION

4.1 Heat transfer in the cavity wall – temperature inside the cavity

The boundary conditions and material properties previously mentioned underwent validation against experiments conducted by Thomas (2010) [14], Kolarkar et al. (2012) [18], and Dias et al. (2019) [19]. Figure 4 to 6 demonstrates a strong agreement between the experimental results and the outcomes of the model - generally, the model tends to overpredict the experimental temperature. As anticipated and noted by Piloto et al. (2023) [20], a model that incorporates convection and radiation in the cavity yields a more precise approximation.

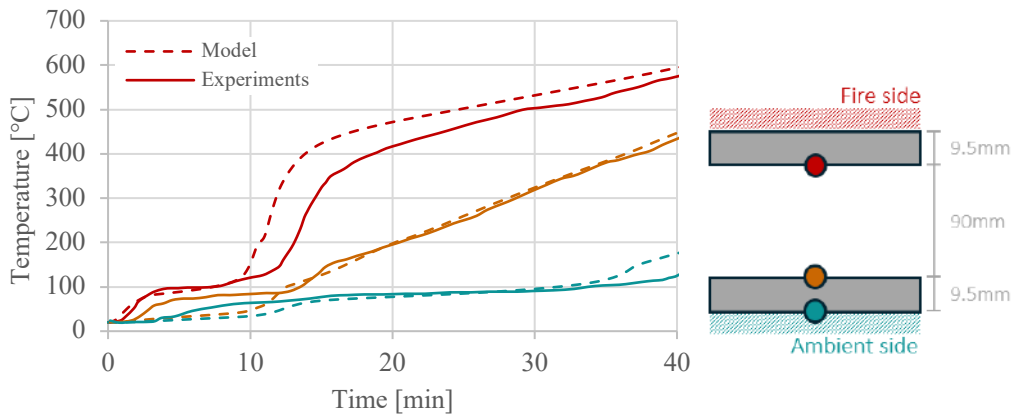


Figure 4. Comparison of model outcomes against experimental data from Thomas (2010) test 2 [14]

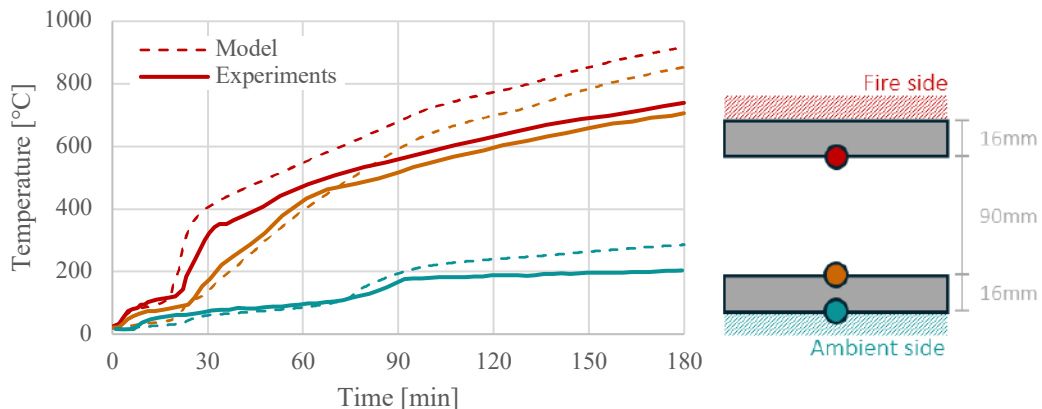


Figure 5. Comparison of model outcomes against experimental data from Kolarkar et al. (2012) test 2 [18]

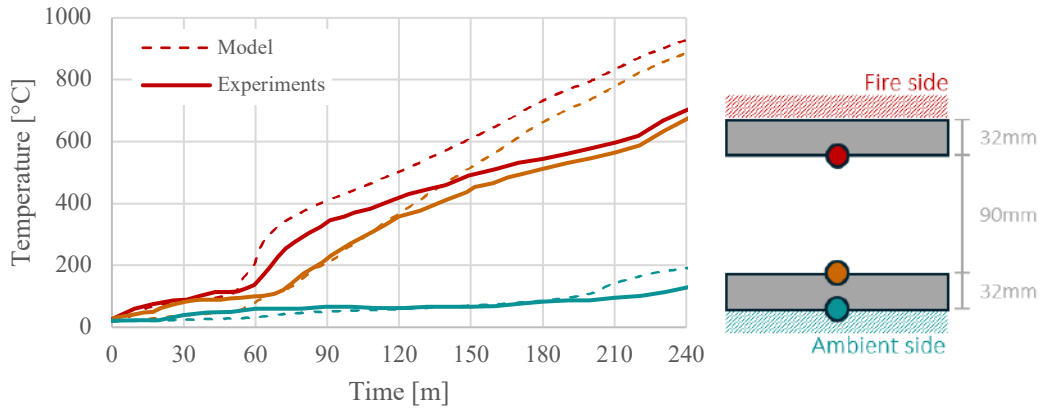


Figure 6. Comparison of model outcomes against experimental data from Dias et al. (2019) test 8 [19]

4.2 Steel temperature through the cavity wall

The thermal boundary conditions (i.e. h and ε values) for the length of the steel beam inside the cavity wall, utilizing the average temperature between the interior surface temperature at the heated and unheated side are calibrated using the experiments conducted by Bennetts and Moinuddin (2006) [6]. To encompass a broad spectrum of conditions, Bennetts and Moinuddin (2006) tested different plates' thicknesses ranging from 2 [mm] to 20 [mm]. These plate variations were selected to replicate structural elements such as a purlin (2 [mm]), a standard cleat plate (8 [mm]), a hot-rolled beam web (12 [mm]), and a combination of a cleat plate and hot-rolled web, or the flange of a hot-rolled section (20 [mm]).

Figures 7 and 8 show the comparison between the experiment results and the model for 2 [mm] and 12 [mm], respectively. It can be observed that by employing the convective heat transfer coefficient and emissivity values mentioned in Table 1, the model tends to overpredict the temperature of the steel at various locations (i.e., exposed side, cavity, and ambient side) but maintains a notable agreement between the experimental data and the model predictions.

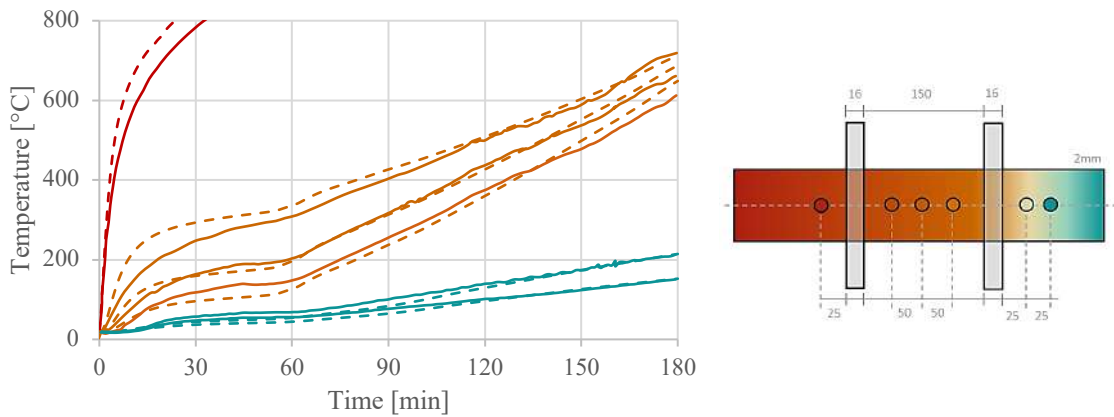


Figure 7. Comparison results for Bennetts and Moinuddin (2006) test VUT153 – 2mm [6]

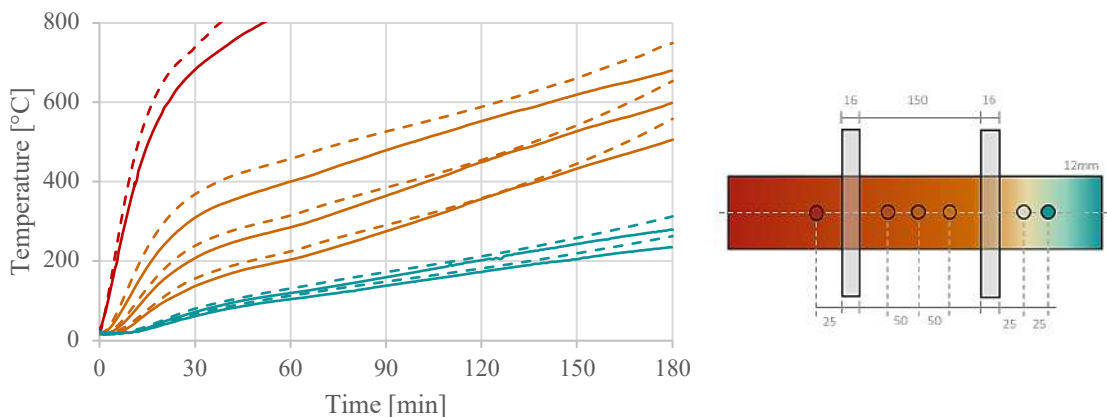


Figure 8. Comparison results for Bennetts and Moinuddin (2006) test VUT153 – 12mm [6]

5 RESULTS AND DISCUSSION

The outcomes of this study are shown as the length of the steel beam protruding from the compartment wall on the side not exposed to fire where the temperature threshold for the insulation criteria is exceeded.

The heat transfer mechanism of the steel beam penetrating a solid wall is illustrated in Figure 9. The heat transfer mechanism in cavity walls is more intricate (refer to Figure 10) than in solid walls, as the boundary conditions within the cavity significantly influence the temperatures of the steel beam on the ambient side. Numerous variables must be considered to estimate the steel beam temperature. For instance, factors such as the thickness and number of plasterboard layers on the wall, as well as the cavity width, determine the temperature within the cavity and subsequently affect the heat losses from the steel beams inside the cavity. The combination of the total thickness of the plasterboard and cavity width can vary in multiple ways, making the modelling more complex.

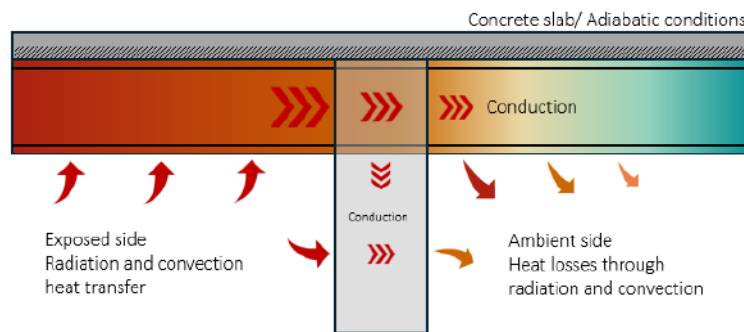


Figure 9. Heat transfer mechanism for a steel beam penetrating a solid wall

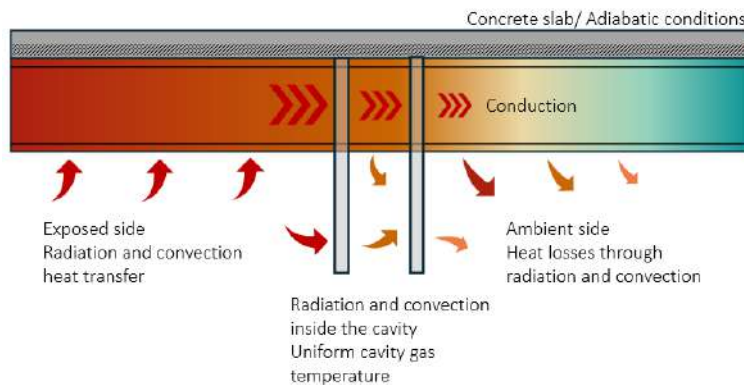


Figure 10. Heat transfer mechanism for a steel beam penetrating a cavity wall

5.1 Solid walls (Masonry and CLT)

Figure 11 and Table 2 and 3 illustrate the minimum length of beam protruding out that requires protection to prevent insulation loss in the compartment, considering different steel beam section factors on masonry walls and mass timber walls, respectively. Figure 11 shows the length of the steel exceeding the insulation criteria for section factors ranging from 39 [m⁻¹] to 279 [m⁻¹]. The fire-resistance rating of the solid walls ranges from EI-60 to EI-420 (65 to 205 [mm]) for masonry walls and from REI-90 to REI-300 (60 to 160 [mm]) for Mass Timber walls. The outcomes indicate that, in the modelled scenarios, the temperature threshold for the insulation criteria is exceeded for a length of 450 [mm] of the steel beam protruding from the compartment wall on the side not exposed to fire.

In both cases, the length of the steel where the insulation criteria are exceeded is inversely proportional to the section factor of the penetrating beam. Even though the steel beams with a lower section factor heat up faster on the exposed side of the compartment, they also lose heat more rapidly when exposed to ambient conditions. This behaviour is in accordance with the lumped mass heat transfer model which can be applied on steel elements surrounded by a gas at a uniform temperature.

The results also indicate that steel beams with a section factor exceeding 150 [m⁻¹], penetrating a solid wall (i.e. brick masonry or mass timber), exhibit a consistent length of the steel exceeding the insulation criteria,

regardless of the wall thickness. On the other hand, there is a similar length of the steel exceeding the insulation criteria when steel beams penetrate either mass timber or brick masonry walls. This can be explained by the low thermal conductivity of the wall material when compared to steel. This phenomenon can be attributed to the comparatively low thermal conductivity of the wall material compared to steel. The heat transfer via conduction within the wall is minimal compared to the heat losses through convection and radiation on the ambient side. However, this condition is not observed in bulkier sections (i.e., $>150 \text{ [m}^{-1}\text{]})$ due to a larger contact zone between the steel beam and the solid wall and because the heat losses at the ambient side take longer.

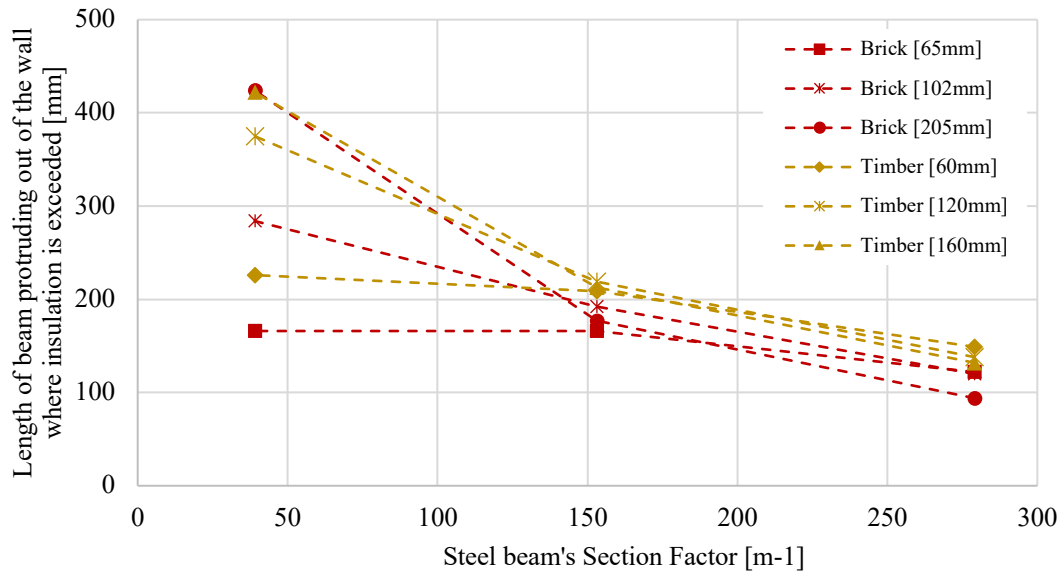


Figure 11. Length of the steel exceeding the insulation criteria for steel beams penetrating a brick masonry or Mass Timber wall

Table 2. Length of the steel exceeding the insulation criteria for steel beams penetrating a masonry brick compartment wall

		Time to reach 160 °C on the cold side [min]	60	120	420	
		Total depth [mm]	65	102	205	
		Section Factor (A/V)* [m⁻¹]				
Steel beam	Cross-section serial size	UB 127x76x13	279	122	120	94
	UB 457x191x74	153	166	192	177	
	UB 1016x305x584	39	166	284	424	

* Section factor for the steel beam heated from 3 sides.

Table 3. Length of the steel exceeding the insulation criteria for steel beams penetrating a Mass Timber compartment wall

		Time to reach 160 °C on the cold side [min]	90	210	300	
		Total depth [mm]	60	120	160	
		Section Factor (A/V)* [m⁻¹]				
Steel beam	Cross-section serial size	UB 127x76x13	279	149	138	132
	UB 457x191x74	153	209	219	213	
	UB 1016x305x584	39	226	375	422	

* Section factor for the steel beam heated from 3 sides.

5.2 Cavity wall

Figure 12 shows the length of the steel exceeding the insulation criteria for steel beams of several sections' factors penetrating a cavity plasterboard compartment wall of different fire resistances. The plot shows the length of the steel exceeding the insulation criteria for steel beams with a section factor between 39 m^{-1} and 279 m^{-1} . The fire resistance of the plasterboard cavity walls varies from EI30 to EI180. The cavity walls involved in the study employ several plasterboard layer configurations and cavity widths as detailed in Table 4. The results indicate that in all the modelled scenarios, the length of the steel exceeding the insulation criteria never exceeds 300 mm.

As observed with solid compartment walls, there exists an inverse relationship between the length of the steel exceeding the insulation criteria length and the steel beam section factor. However, in this case, some of the bulkiest sections penetrating compartment walls of lower fire resistance do not have sufficient time to get hot, resulting in lower length of the steel exceeding the insulation criteria compared to those with a higher section factor.

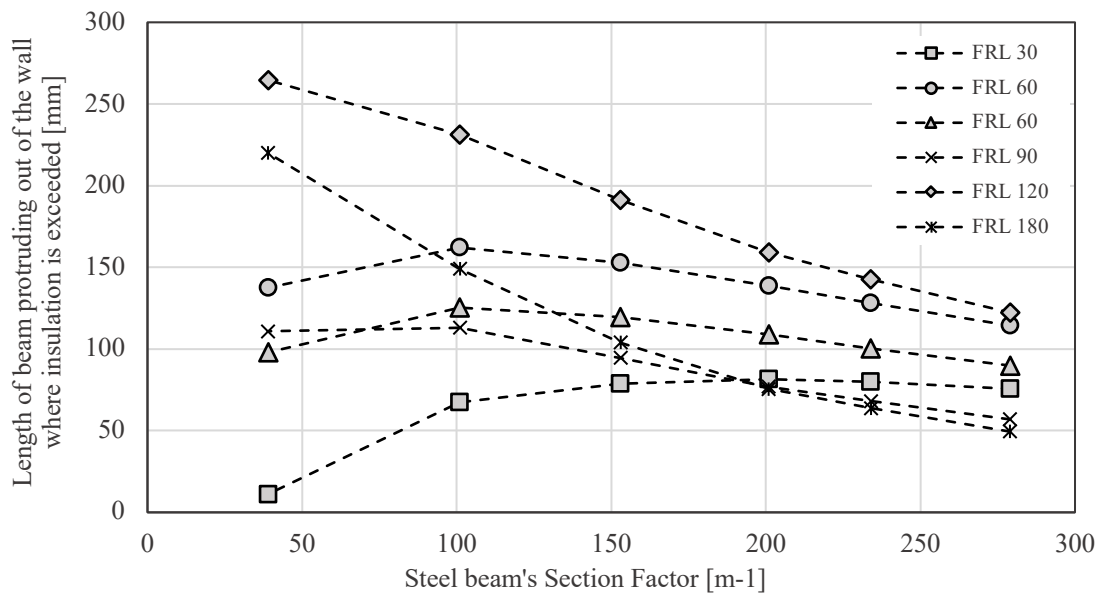


Figure 12. Length of the steel exceeding the insulation criteria for steel beams penetrating a cavity wall

Table 4. Length of the steel exceeding the insulation criteria for steel beams penetrating a cavity wall

		Fire resistance	30	60	60	90	120	180
		Gypsum board thickness per face [mm]	12.5	15.0	25.0	25.0	25.0	45.0
Cross-section serial size	Total depth [mm]	75	80	124	198	100	238	
	Section Factor (A/V)* [m^{-1}]							
Steel beam	UB 127x76x13	279	76	114	90	57	122	49
	UB 203x102x23	234	80	128	100	68	142	64
	UB 305x127x37	201	82	139	109	77	159	76
	UB 457x191x74	153	79*	153	120	94	191	104
	UB 838x292x194	101	67*	162	125	113	231	149
	UB 1016x305x584	39	11*	138*	98*	111*	265	220

*These values are lower because a larger cross-section of steel beams takes longer to heat up at the exposed side. Section factor for the steel beam heated from 3 sides.

6 CONCLUSIONS AND FUTURE WORK

6.1 Conclusions

This paper presented the heat transfer mechanism observed when a steel beam penetrates a compartment wall. The study's primary findings encompass:

- The penetration of a compartment wall with unprotected steel elements can result in the loss of insulation within the compartment.
- Solid walls exhibit similar behaviour regardless of the material comprising the compartment wall.
- Steel beams with a section factor above 150 m⁻¹, penetrating a solid wall (i.e., brick or Mass Timber), require a similar protection length, irrespective of wall thickness.
- Generally, the length of the steel exceeding the insulation criteria is inversely proportional to the section factor of the penetrating beam.
- Determining the adequate length of steel beams needing insulation fire protection for penetrations in cavity walls involves several variables, necessitating a careful analysis to ascertain the necessary protection level.

6.2 Future work

The findings of this study are based on a specific set of conditions. Subsequent research should aim to validate and generalize these findings through a wider experimental investigation. The current study focused primarily on “I” steel beams penetrating a compartment subjected to standard fire conditions at one side of the compartment. Future research should consider exploring with different heating regimes, other service penetrations and materials. Another important aspect to improve this research is related with the extrapolation to the mechanical domain and assess how the deflections of the steel beam could compromised the integrity of the compartment wall.

Additionally, conducting sensitivity analyses via modelling can elucidate the parameters governing the behaviour of the wall-beam system. Variables such as temperature threshold, type and thickness of beam protection, size of the cavity, compartment wall thickness, among others, warrant further exploration for a more comprehensive understanding.

REFERENCES

- [1] Association for Specialist Fire Protection – ASFP – Technical Questions [Technical questions - Association for Specialist Fire Protection \(asfp.org.uk\)](https://www.asfp.org.uk/technical-questions)
- [2] Association for Specialist Fire Protection – ASFP. (2022) Advisory Note 18 - ASFP Position on Installing Partitioning to the Underside of Structural Steel Sections Coated with a Reactive Fire Protection System. Available at www.asfp.org.uk.
- [3] Building Research Establishment – BRE (2005) The Integrity of Compartmentation in Buildings During a Fire [compartmentation.pdf \(bregroup.com\)](https://www.bregroup.com/compartmentation.pdf)
- [4] Bennetts, Ian & Goh, Chong. (2001). Fire behaviour of steel members penetrating concrete walls. *Electronic Journal of Structural Engineering*. 1. 10.56748/ejse.1131.
- [5] British Standard. (1987). BS 476-20:1987. Fire tests on building materials and structures – Part 20: Method for determination of the fire resistance of elements of construction (general principles).
- [6] Bennetts, Ian & Moinuddin, Khalid. (2006). Aspects of the Design of Fire-Resistant Plasterboard Walls in Fire. *Electronic Journal of Structural Engineering*. 6. 39-48. 10.56748/ejse.656.
- [7] Warrington fire – Trafalgar group (2022) Consultant advise report Steel purlins and beams penetrating wall separating elements [Steel beam and Purlin penetrations report \(tfire.com.au\)](https://www.tfire.com.au/steel-beam-and-purlin-penetrations-report)

- [8] Association for Specialist Fire Protection – ASFP. (2022) Technical Guidance Document 8 - Code of practice for junctions between different fire protection systems when applied to load bearing structural steel elements. ISBN: 978-1-870409-27-8. Available at www.asfp.org.uk.
- [9] Association for Specialist Fire Protection – ASFP. Advisory Note 28 - Fire stopping of metal pipes, where flanges, valves or fittings fall within the insulation zone of a compartment wall penetration'. Available at www.asfp.org.uk.
- [10] SAFIR - Nonlinear finite element software for modelling the behaviour of building structures subjected to fire. https://www.ucee.uliege.be/cms/c_6331644/en/safir
- [11] Eurocode 3. (2005). Design of steel structures - Part 1-2: General rules – Structural fire design. EN 1993-1-2.
- [12] Eurocode 5. (2004). Design of timber structures – Part 1-2: General rules – Structural fire design. EN 1995-1-2.
- [13] Eurocode 6. (2005). Design of masonry structures – Part 1-2: General rules – Structural fire design. EN 1996-1-2.
- [14] Thomas G. (2010). Modelling thermal performance of gypsum plasterboard-lined light timber frame walls using SAFIR and TASEF, *Fire and Materials*, 34:385–406. <https://doi.org/10.1002/fam.1026>
- [15] Wakili KG, Hugi E, Wullschleger L, Frank TH (2007) Gypsum board in fire—modelling and experimental validation. *Journal of Fire Sciences* 2007; 25(3): 267–282.
- [16] Eurocode 1. (2002). Actions on structures – Part 1-2: General actions – Actions on structures exposed to fire. EN 1991-1-2.
- [17] SAFIR (2016) Technical documentation [008_technical_reference_of_safir.pdf \(uliege.be\)](#)
- [18] P. Kolarkar, M. Mahendran (2012), Experimental studies of non-load bearing steel wall systems under fire conditions, *Fire Safety Journal*, Volume 53 <https://doi.org/10.1016/j.firesaf.2012.06.009>.
- [19] Y. Dias, P. Keerthan, M Mahendran (2019) Fire performance of steel and plasterboard sheathed non-load bearing LSF walls, *Fire Safety Journal*, Volume 103 <https://doi.org/10.1016/j.firesaf.2018.11.005>.
- [20] P. Piloto, S Gomes, L. Torres, C Couto, P Vila Real (2023) Accuracy of 2d numerical models towards the prediction of the fire resistance on LSF partition walls, *International Journal of Thermal Sciences*, Volume 193, <https://doi.org/10.1016/j.ijthermalsci.2023.108511>.

COMPOSITE STRUCTURES IN FIRE

A USER INTERFACE TO COMPARE THE LIFETIME COSTS OF PRESCRIPTIVE AND PERFORMANCE-BASED FIRE DESIGNS OF COMPOSITE BUILDINGS

Chenzhi Ma¹, Ruben Van Coile², Thomas Gernay³

ABSTRACT

The objective of this study is to develop a web-based interface tool to allow evaluating the economic impact of different structural fire designs for composite buildings. The economic assessment adopts a lifetime cost evaluation considering initial and maintenance construction costs, direct and indirect fire-induced losses, and co-benefits of the designs. A construction cost database with 130 prototypes of steel-framed composite buildings is built into the web interface to support the construction cost estimate. To estimate damage losses, fragility curves for composite floor systems are incorporated in the web interface based on probabilistic finite element simulations validated on full-scale fire tests. Variations in labor hours required for application of passive fire protection to steelwork and effects on construction time and rental revenues are estimated. Based on these cost components, the web interface generates the present value of the life-cycle cost for a cost-benefit comparison between alternative structural fire designs. A 16-story composite building is analyzed as a case study with comparison of the lifetime cost associated with prescriptive and performance-based designs. The methodology and its implementation in a user-friendly application can support assessment of the merits of performance-based structural fire designs for buildings.

Keywords: structural fire design; performance-based design; tensile membrane action; lifetime cost; cost-benefit analysis; web interface

1 INTRODUCTION

Statistics highlight the significant human and economic cost of fire, with more than a million building fires a year in the United States (U.S.) according to the National Fire Incident Reporting System (NFIRS). Structural fire design is an important layer of safety to mitigate fire risk. The cost of fire safety measures in building construction was estimated at 57 billion USD in 2014 in the U.S. [1], highlighting that changes in fire safety design methods can have considerable economic impact. For composite steel-concrete floor systems, fire protection materials are generally required for the steel members according to the building codes and specifications. However, research has shown that omitting fireproofing on selected steel members in composite slabs can result in the activation of tensile membrane action (TMA) under fire [2]. This TMA behavior can enhance the load-bearing capacity of the floors at large displacements, thereby

¹ Ph.D. student, Department of Civil and Systems Engineering, Johns Hopkins University,
e-mail: cma31@jhu.edu, ORCID: <https://orcid.org/0000-0002-1144-8033>

² Associate Professor, Department of Structural Engineering and Building Materials, Ghent University
e-mail: ruben.vancoile@ugent.be, ORCID: <https://orcid.org/0000-0002-9715-6786>

³ Assistant Professor, Department of Civil and Systems Engineering, Johns Hopkins University
e-mail: tgernay@jhu.edu, ORCID: <https://orcid.org/0000-0002-3511-9226>

achieving adequate fire integrity with reduced use of fire protection. This behavior was evidenced by several experimental fire tests [3]. As a result, performance-based structural fire design (PBSFD) has relied on TMA for the fire design of composite steel-concrete slabs with unprotected central beams in projects in multiple countries. As performance-based design (PBD) has become increasingly adopted by structural engineers, there is interest in assessing the economic impact of adopting PBD in lieu of a prescriptive approach for structural fire design.

Cost-benefit analysis (CBA) allows systematically evaluating and comparing design decisions in economic terms [4]. A recent study supported by the Fire Protection Research Foundation of the NFPA [5] conducted case studies on the economic impact of sprinkler systems, detection systems, and passive fire protection across various building types. Similarly, prior research has leveraged CBA to examine the cost effectiveness of different designs of elevators and exit stairs [6]. This approach can also be applied to estimate the economic impact of adopting a different structural design method instead of the prescriptive design. The American Society for Testing and Materials (ASTM) developed standards [7-11] to guide the CBA of investments in building design and building system decisions. These standards use various methods of evaluation, including the present value life-cycle cost analysis (PVLCC) [7], benefit-to-cost ratios (BCR) and savings-to-investment ratios (SIR) analysis [8], internal rate of return (IRR) and adjusted internal rate of return (AIRR) [10], and net present value (NPV) [11].

This paper focuses on the comparison of lifetime costs of prescriptive and performance-based fire designs for composite buildings. The approach adopts a PVLCC analysis implemented within a user-friendly web interface. This web-based tool allows integrating the cost components including the initial construction cost, lifetime maintenance cost, potential fire-induced lifetime damage loss, co-benefits, and environmental impact. Either user-provided or default parameters can be used. The interface includes a built-in construction cost database as well as estimates for the labor hours required for on-site work of applying passive fire protection to steel structures. This latter feature facilitates rent income analysis within the tool by accounting for variations in labor hours from different design. Besides, a set of fragility curves was developed to support the estimation of damage losses. By aggregating all cost components, the tool calculates the PVLCC, thereby enabling economic comparison between design choices. This provides stakeholders with an objective method for evaluating the economic impact of adopting PBSFD for buildings.

2 CONSTRUCTION COST DATABASE

The authors compiled a construction cost database that includes 130 building prototypes and eight building typologies consisting of four occupancy types [12]. The prototypes cover a range of occupancies and building sizes. The detailed costs for a prototype building are obtained from the RSMeans [13-16] database, an annually updated database of construction cost data that has been used in previous fire safety studies [6]. For each prototype, the cost of the substructure (e.g., foundations, basement walls), shell (e.g., floor system, roof, exterior windows), interiors (e.g., partitions, interior doors, stairs), services (e.g., elevators, sprinkler, electrical service), equipment (e.g., waste handling), and furnishings are obtained from the RSMeans square foot estimator. After collecting the cost details for the prototypes, some parameters are adjusted instead of using the default values for consistency in the type of steel-concrete composite systems considered. The default floor system is specified as a composite metal deck with shear connectors. The fire rating for the steel and composite structural members is adjusted based on the International Building Code (IBC) requirements.

The cost database includes cost breakdowns for the building fire safety measures. Results indicate that the total cost for fire safety measures in composite buildings ranges from 4% to 12% of the total construction cost of the building. The total cost for the sprayed fire-resistive material (SFRM) passive fire protection on the steelwork is between 0.00% and 1.23%. Additional insights, such as comparative costs of different fire protection materials, the effect of project location on construction costs, and more, are elaborated in [12].

3 LIFETIME COST ANALYSIS

The present value life-cycle cost (PVLCC) is used to evaluate the lifetime costs of prescriptive and performance-based fire designs of composite buildings. This approach aligns with the ASTM methods for economic assessments of building design investments [7, 9]. The PVLCC is estimated by Eq. (1):

$$PVLCC = C_I + C_M + D_D + D_{ID} - B \quad (1)$$

where C_I is the initial construction cost, C_M is the lifetime maintenance cost, D_D is the direct damage loss (including property and human loss directly caused by the fire), D_{ID} is the indirect damage loss, and B is the co-benefits. All future costs are converted to present value using a discount rate γ by Eq. (2).

$$P_0 = P_N \exp(-\gamma t) \quad (2)$$

When comparing the lifetime costs of prescriptive- and performance-based design, the cost difference can originate from all the cost components listed in Eq. (1).

3.1 Initial construction cost (C_I) and maintenance cost (C_M)

The construction cost database is used to support the development of a generalized method for estimating the cost of passive fire protection on steelwork in buildings. Figure 1 shows the detailed flowchart of three different approaches of assessing the construction cost of fire protection. The three approaches use the prototypes as baseline for calculating the fire protection costs but allow different levels of customization. The first method enables changing the fire design parameters of the building, such as omitting fire protection on some steel beams. The second method enables changing the building design, such as changing the story height and floor load. The third method estimates the fire protection cost based on user-defined steel component sizes and numbers. The construction cost database and the three described methods are incorporated in the web-based interface.

Figure 1 captures an on-site photograph showing a defective SFRM coating on the primary beam of a composite floor system. The defective fire protection may jeopardize the fire performance. This observation highlights the need for maintenance of passive fire protection systems to ensure their effectiveness during fire incidents. A common method for estimating maintenance costs is to consider them as a fixed percentage of the initial construction cost [5]. In this context, the lifetime maintenance cost C_M in the study period can be converted to present value by Eq. (3).

$$C_M = \frac{c_m}{\gamma} (1 - \exp(-\gamma t)) \quad (3)$$

where c_m is the annual maintenance cost, γ is the discount rate, and t is the number of years in the study period (further referred to as the “study year”).

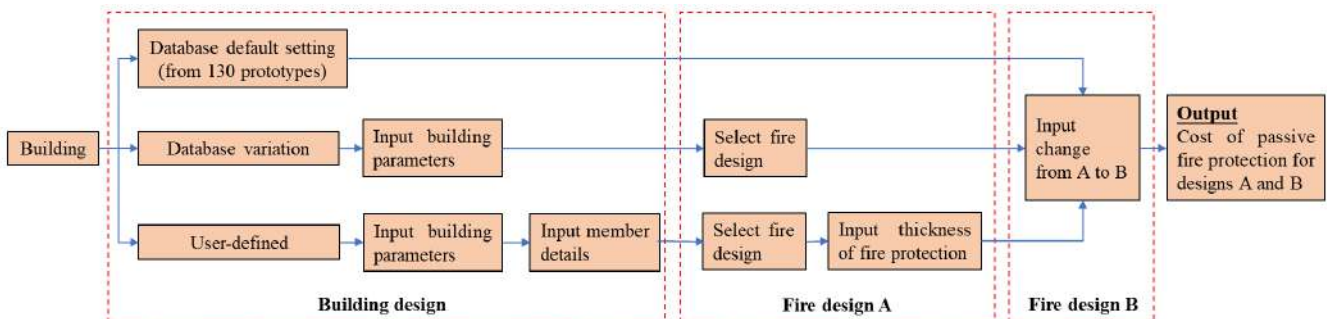


Figure 1 Flowchart of implemented methods for assessing the construction cost of fire protection in buildings



Figure 2 Illustration of defective SFRM on primary beam on the 1st floor of a high-rise residential building

3.2 Direct losses (D_D)

Direct damage losses are quantified using fragility curves. The curves relate the hazard intensity with the probability of reaching various damage states (DS). To generate the fragility points $P(DS = DS_i | q_m)$ for a specific DS_i under a given fire load q_m , advanced numerical analyses or on-site investigations are needed. The potential costs associated with each damage state are then inferred based on estimated repair costs, content losses, and potential human injuries associated with the respective damage state. For instance, if a composite slab reaches a major damage state, it is assumed that the entire floor system requires demolition and reconstruction [17], while under a minor damage state only the thermally damaged thickness of the slab needs repair. After establishing the costs associated with different damage states $C(DS = DS_i)$, a vulnerability curve $V(q)$ can be generated using Eq. (3). The vulnerability curve relates the hazard intensity with the probabilistic damage loss by combining the fragility curve with the damage costs for varying levels of damage [18].

$$V(q) = \sum_i^N P(DS = DS_i | q) \times C(DS = DS_i) \quad (4)$$

where N is the total number of damage states; $P(DS = DS_i | q)$ is the probability of the damage state i under fire load q ; and $C(DS = DS_i)$ is the estimated cost under damage state i .

3.3 Indirect losses (D_{ID}) and co-benefits (B)

Indirect losses include losses resulting from the impact of the fire on building functionality and people's well-being, such as business interruptions, evacuations, relocations, and losses associated with irreplaceable assets. Considering that steel-concrete composite construction is commonly used in mid-rise and high-rise office or residential buildings, the costs related to relocations and business downtime can be considerable. These indirect losses would depend on the structural fire design since the latter influences the performance of the building structure in the fire, and thus also its functional recovery.

On the other hand, various types of co-benefits can arise from modifying a building fire design. Here, the method accounts for the differential on-site labor requirements for applying passive fire protection on steel structures, which can affect the construction timeline and, consequently, potential rental income. The co-benefits can be considered as the reduction in rent loss due to the reduction in required labor hours. Labor hours associated with fire protection are obtained from unit labor cost of fire protection material and the corresponding labor daily cost. For example, crew G-2 as listed in [16] is used when considering the cost of applying the SFRM and its daily cost is about \$1140, and then the unit labor hour needed (i.e., the time needed for applying the fire protection on-site) is computed by dividing the unit fire protection labor cost by the labor daily cost.

The environmental impact of various building designs can also be incorporated into the co-benefits. For instance, adopting a PBSFD that leaves the central beam unprotected could result in a reduced global warming potential (GWP) for the building due to the lower amount of fire protection. A design with superior fire performance also offers reduction in GWP due to a reduced likelihood of requiring repair or reconstruction post fire. Which of these effects dominates will depend on the specifics of the case. The

holistic comparison of PBSFD and prescriptive design can therefore consider not only safety and resilience but also carbon footprint resulting from construction material usage and repair works.

4 IMPLEMENTATION IN A WEB INTERFACE

The construction cost database introduced in Section 2 and the lifetime cost analysis method introduced in Section 3 have been integrated into a web-based interface. The interface provides a stepwise procedure to conduct comparative lifetime cost analysis on different fire design methods, see Figure 3. Pre-defined unit costs, analysis methods, and parameters can be used for both the building and fire designs. User-defined values can be used instead of the default settings for conducting analysis of customized designs or projects.

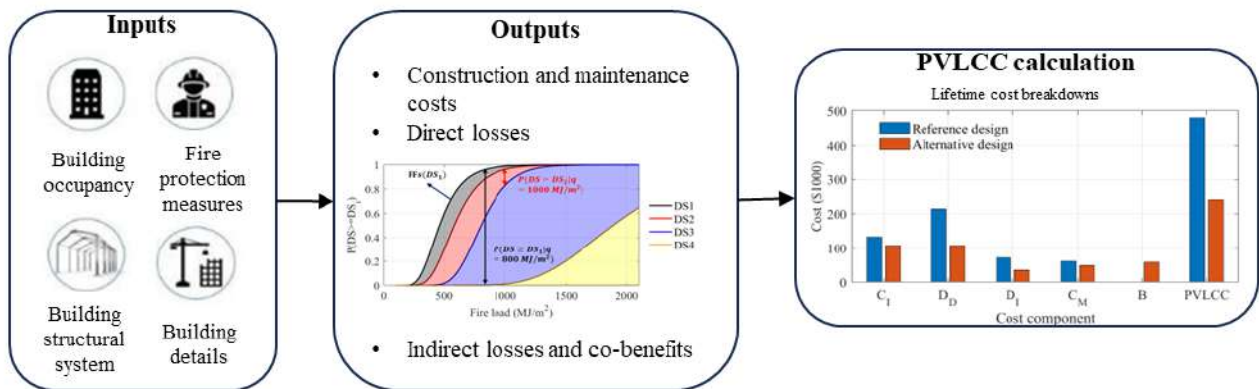


Figure 3 Web-based user interface to conduct the cost-benefit analysis of different designs

Here, the web interface is introduced along with a case study with two fire design methods. The case study considers a 16-story building with 10 ft. story height and total floor area of 233,063 sq. ft. Two fire design methods are considered, as listed in Table 1. Design 1 is based on the prescriptive method with all the central beams protected. Design 2 includes fire protection on half of the beams only, to represent a PBD with unprotected central beams and extra slab reinforcement to rely on tensile membrane action (TMA).

Table 1 Fire protection parameters of the five different scenarios

Design No.	Fire protection material	Percentage of protected Beams	Slab reinforcement cost
1 (Prescriptive)	SFRM	100 %	100%
2 (PBD)	SFRM	50 %	150%

4.1 Step-1 Construction and maintenance cost

When the tab of construction cost estimation within the web interface is activated, users are prompted to select a cost estimation method. It can be either modifying the existing building prototypes in the building database or inputting a user-defined building. In the case study, an existing building in the database is selected, with parameters shown in Figure 4 (a). The building index refers to the construction cost database which is accessible from the interface. The interface enables modifying both the building design parameters (e.g., story height, floor loads, typical bay size, etc.) and the fire design parameters (e.g., beam and column fire rating, fire protection material, and percentage of protected beams and columns). Besides, the interface allows users to replace the default material unit cost value with their own market-specific data to enhance the estimation accuracy. For the reference design (prescriptive) in this case study, default fire design parameters are set from IBC. For the alternative design, the percentage of protected beam is adjusted from

100% to 50%, illustrating a scenario with unprotected central beams, and the parameters for alternative design are shown in Figure 4 (b).

Once the necessary parameters have been input, the web tool can estimate the construction cost along with the required labor hours for applying passive fire protection, as shown in Figure 4 (c). In this case study, the unit cost of fire protection is based on RSMMeans 2022 national average value. The unit material cost typically includes both the bare material cost and the installation cost.

Current page: 1. Construction cost estimation

Choose a sub tool
Construction cost estimation: Modify datab... ▾

User Input Parameters

Analysis type
Start a new analysis ▾

clear all saved session state

Reset to default parameter (Construction cost)

The restored input parameter would not be applied

Input Building index (start from 1)
43 - +

Modify default building parameter

Modify default fire design paramter

Beam fire rating (hr) 2 - + Column fire rating (hr) 3 - +

Input beam fire protection material 1 - + Input column fire protection material 1 - +

Input beam fire protection percentage 1.00 - + Input column fire protection percentage 1.00 - +

Modify default fire protection cost value

Enable interpolation when the default building parameter is changed

Do you want to specify fire design parameters for alternative design?

Beam fire rating alt. (hr) 2 - + Column fire rating alt. (hr) 3 - +

Input beam fire protection material alt. 1 - + Input column fire protection material alt. 1 - +

Input beam fire protection percentage alt. 0.50 - + Input column fire protection percentage alt. 1.00 - +

(b) Fire design parameter input window for alternative design



(a) Design parameter input window for reference design

(c) Construction cost of passive fire protection on the steelwork for the two design methods

Figure 4 Sample of the construction cost estimation

To estimate the lifetime maintenance cost using the default method, users must input specific parameters such as the study year, the discount rate, and the annual maintenance cost as a percentage of the initial construction cost. The parameter input menu is shown in Figure 5 (a). This process allows for the customization of maintenance rates for alternative design methods, accommodating differences in fire protection materials. The tool then computes and displays the lifetime maintenance cost, as shown in Figure 5 (b).

Reset to default parameter (Maintenance)

Input study year of the building

50

How would you like to define maintenance cost

Constant percentage of total construction c... ▼

Input percentage as initial construction cost

3.00

Input the discount rate

3.00

parameters for alternative design

Input percentage as initial construction cost (alt.)

3.00

(a) Maintenance parameter input window

Results for reference design	Results for alternative design
Maintenance cost	Maintenance cost
245,711	174,192

(b) Maintenance cost of passive fire protection for the two design methods

Figure 5 Sample of the maintenance cost estimation

4.2 Step-2 Direct losses

Within the web interface, users have access to nine predefined fire fragility curves. The curves were developed based on numerical FE models that were calibrated against the full-scale fire tests on composite structures conducted by the NIST. These curves account for various design parameters of composite floor systems. Fragility curves 1-3 correspond to the prototypes that were tested at the NIST, while fragility curves 4-9 capture variations in parameters such as slab rebar areas, boundary conditions, and aspect ratios based on the NIST prototypes. To accommodate a wider range of scenarios and user needs, the interface also offers the capability to upload custom, user-defined fragility curves. In the case study, fragility curves one (based on NIST test #1 with protected central beam) and three (based on NIST test #3 with unprotected central beam and enhanced slab rebar) are chosen for Design 1 and Design 2, respectively.

Fire frequency in the case study is evaluated from the NFIRS fire event database (years 2012-2022) and the U.S. Census Bureau data on building stock. As composite floor systems are widely used in mid-rise and high-rise buildings, data in NFIRS is taken for buildings taller than four stories. The average building stock is determined using information from the U.S. Census Bureau for the years 2011 and 2021. Consequently, the frequency of structural significant fire, defined as fires with flame spreading beyond the origin, in multi-family dwellings is estimated as $2.97 \times 10^{-7}/sq. ft.$

The direct losses associated with damage states DS1 to DS3 are evaluated based on data in [17, 19]. These losses are mostly linked to repair needs within the affected compartment after the fire.

Damage state DS4, indicative of a structural integrity failure, encompasses a broader range of potential outcomes and is thus more challenging to quantify. A sensitivity analysis is conducted to explore the variations in direct damage losses associated with different assumed values for DS4 loss. The “g-value” is introduced as a metric, representing the loss at DS4 normalized by the initial construction cost of the floor system within the fire compartment. This g-value can take very large values if the integrity failure results in fire spread in multiple compartments and/or complete structural damage, since it is compared to the cost of the floor in a single compartment only (to make the analysis independent of the number of compartments in the building).

Figure 6 plots the relationship between the g-value and the ratio between the direct loss D_d respectively for the PBD and prescriptive design. A ratio below one means that the floor designed with the PBD approach (Test #3) has lower expected direct loss from fire compared to the one designed with the prescriptive method (Test #1). Higher g-values give more weight to integrity failure. It can be seen that

the PBD becomes increasingly superior to the prescriptive design as the g -value increases. This is because the PBD has a much lower probability of integrity failure than the prescriptive design, as the addition of steel reinforcement in the slab leads to a robust fire behavior. Since the estimated direct loss is conditioned to the fire load distributions (through the fragility functions), results are plotted for different building occupancies, themselves associated with different fire load statistics. The PBD leads to lower expected direct losses compared to prescriptive method for buildings with relatively large average fire load (e.g., dwelling, library) as long as the g -value larger than 3. However, since the activation of TMA relies on large deflections, the PBD tends to have higher direct losses for lower average fire load (e.g., school, hotel, theatre) until a large g -value (300 to 10,000) is applied. The results thus suggest that the most favorable design, in terms of direct fire losses, depends on the type of occupancy (because it influences the fire load) and the consequences of integrity failure (quantified through the g -value).

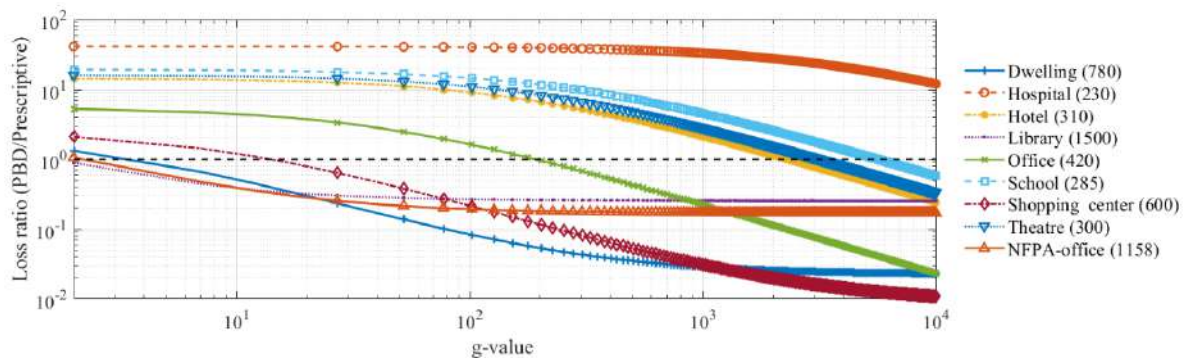


Figure 6 Ratio of direct damage loss for the two design approaches, considering different occupancies, as a function of the direct loss at DS4 quantified through g -value. (Mean values of the fire load are listed in brackets)

In this case study, the g -value is selected as 100 for illustration purposes. The selected fire load is based on residential buildings, which follows the Gumbel type 1 distribution with a mean value of 780MJ/m² and a standard deviation of 234MJ/m². Figure 7 (a) details all the input values utilized for the direct damage analysis within this case study, while Figure 7 (b) displays the resulting outputs. The results section provides the average loss per severe fire incident, the expected annual loss, the applied fragility curves, the distribution of the fire load, the distribution of damage losses, and the corresponding vulnerability curves. The outcomes indicate that Design 2 (PBD), tends to incur significantly lower fire losses per severe incident compared to Design 1 (Prescriptive). This observation aligns with the conclusions drawn from Figure 6, further substantiating the potential advantages of PBD in reducing fire-related direct losses.

Current page: 3.Direct damage estimation

User Input Parameter

Reset to default parameter (Direct damage)

Input probability of severe fire in a compartment (!*10⁻⁷)

25.60 - +

Input number of compartment

234 - +

How would you like to define the fragility curves

Use built-in fragility curves v

Input the index of the built-in fragility curves

1 - +

Enter your damage state value (comma-separated):

4932.393846153846,
18701.993333333336,
34115.724102564105,
2055164.1025641026

Input damage state cost value:

value
4,932.3938
18,701.9933
34,115.7241
2,055,164.1026

How would you like to define the fire load distribution

Use given distribution (gumbel distribution) v

Input mean value: 760 - + Input standard deviation: 234 - +

parameters for alternative design

Input the index of the built-in fragility curves (alt.)

3 - +

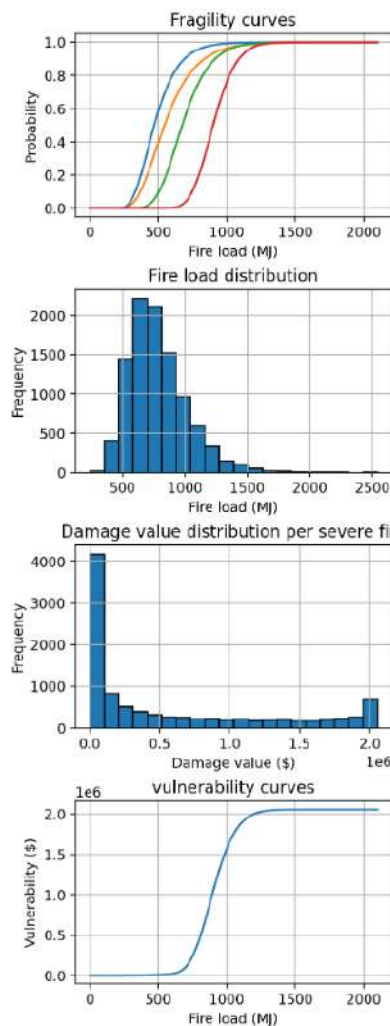
Enter your damage state value (comma-separated) alt.:

4837.973333333333,
18343.982222222225,
33462.648888888885,
7015877.77777777

Input damage state cost value for alt.:

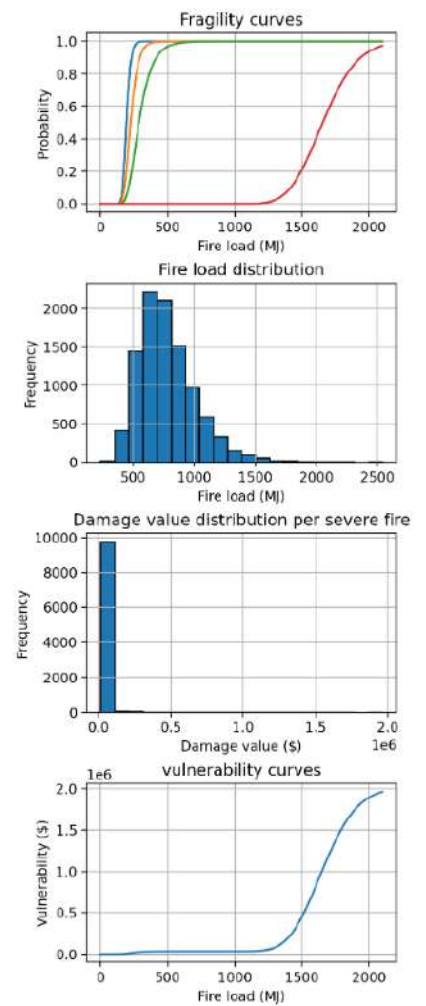
Results for reference design

Average loss per severe fire	Annual loss	Study year
583,243	3,493	50



Results for alternative design

Average loss per severe fire	Annual loss	Study year
47,993	287	50



(a) Direct damage parameter input window

(b) Direct damage for the two design methods

Figure 7 Sample of the direct damage estimation

4.3 Step-3 Indirect losses and co-benefits

The current version of the web tool does not provide a default method to estimate the indirect losses, but it offers users the capability to input their own estimates of indirect losses to facilitate further lifetime cost analysis.

For the co-benefit analysis, the built-in functions enable analysis of the variation in the rent income due to the changes in the construction schedule. It is important to note that the unit labor costs have been integrated into the overall construction material costs. Therefore, the analysis of labor hour primarily focuses on how reductions in labor hours might influence the construction schedule and, by extension, rental income.

The construction schedule can be significantly affected by the number of crews involved in applying the fire protection materials, with the default setting in the tool being two crews. This parameter can be adjusted to reflect different operational realities. The default rent rate is 3.6 USD per sq. ft per month (the average office rent rate is 5.0 USD in NYC). Users also have the option to specify what percentage of the area is considered when calculating rental income, with the default value set at 50%. This flexibility allows users to tailor the analysis to their specific project conditions and market environments.

The GWP associated with passive fire protection materials is estimated within the web tool based on data from the product's Environmental Product Declaration (EPD) reports. The default setting in the web interface assumes that two units of weight for SFRM result in the generation of one unit of CO₂ weight. This automatic estimation facilitates a preliminary assessment of the environmental impact during the construction phase. In the future, the module of lifetime GWP analysis will be added. This addition aims to provide a more comprehensive evaluation of the potential environmental impacts attributable to various damage states and building designs, contributing to more sustainable construction practices.

User Input Parameter

Reset to default parameter (Co-benefit)

The restored input parameter would not be applied

Run the rent loss analysis

Input rent rate month per sq.ft.

3.60 - +

Input number of crew G-2 working on applying fire protection on steelwork

5 - +

Input hours needed to cure the fire protection on steelwork (hr)

72 - +

Input the percentage of area that has been rented

0.50 - +

Run the global warming analysis

Analysis type

Default value ▾

Results for reference design		Results for alternative design	
Rent loss	GWP(CO ₂)	Rent loss	GWP(CO ₂)
358,449	101,218	266,273	71,757

(a) Co-benefit parameters input window

(b) Co-benefit for the two design methods

Figure 8 Sample of the co-benefit estimation

4.4 Step-4 Additional cost components

Section 4.1 to Section 4.3 detail the computation of cost components including construction, maintenance, direct damage, indirect losses and co-benefits. However, it is recognized that alternative design choices might incur additional costs under certain circumstances. For example, it is established [20] that the development of tensile membrane action highly relies on the amount of reinforcement in the concrete slab. Therefore, the web tool offers users the capability to input custom values for any extra costs associated with alternative designs. In the case study, an additional investment of 105,000 USD is applied to Design 2 to account for the increased amount of steel reinforcement. According to the cost data of welded-wire mesh in RSMMeans, increasing the welded mesh density from 60 mm²/m to 289 mm²/m entails a 55% additional cost, with 85% of this increase stemming from the material costs alone. Consequently, in the case study, the impact of altering the welded-wire mesh on the construction timeline is considered negligible.

5 RESULTS OF THE PVLCC CALCULATION

Once introducing all the cost components through the different steps is completed, the interface can automatically calculate and plot the breakdown lifetime costs and the PVLCC. These costs are provided side-by-side for both the reference design and one alternative design. This allows comparing, for a given building, two structural fire design approaches, for example based on prescriptive and PBD methods.

The results for the case study are shown in Figure 9. Design 2 (i.e., the PBSFD) has a significantly lower PVLCC in comparison to Design 1. This reduction is attributable to the savings in the construction cost, maintenance cost, damage losses and rent losses, which offset the additional expenditure on slab reinforcement in Design 2. It is important to emphasize that the results only refer to this specific case study with its specific design parameters, such as the mean fire load of 780 MJ/m², the fragility curves based on the NIST prototypes, etc. In the future, a range of situations will be studied with the tool to draw general conclusions for a range of buildings and design parameters.



Figure 9 Sample of the outputs of the life-cycle cost estimation for a composite building designed either with a prescriptive (Ref.) or a performance-based approach (Alt.)

6 CONCLUSION

Comparing the economic impact of different designs requires a holistic approach that incorporates not only upfront investment costs in fire protection measures but also estimates of lifetime costs associated with the expected fire performance. Evaluation of these different cost components relies on the combination of data and simulation results from probabilistic fire analysis. To streamline these evaluations and the economic impact assessment, we provided a stepwise procedure in a web interactive environment. The web interface provides data and a method to compare the lifetime costs of different fire design methods, which can support decisions by designers as well as evolution of building codes and standards.

The web interface provides an approach for evaluating different structural fire designs of composite buildings. It encompasses a cost database derived from the analysis of 130 prototypes, as well as fire fragility functions derived from FE analyses. It also allows user-defined adjustments to building and fire design parameters and the integration of user-defined data. The web interface is built to evolve with further data, for example to incorporate environmental impact assessments through the global warming potential (GWP) of fire protection materials. This will enable conducting economic evaluations with sustainable building practices, thereby supporting the construction industry's shift towards more environmentally responsible and cost-effective structural fire design methods.

A case study was conducted through the stepwise procedure in the web interface. The study compared the lifetime costs of a building designed according to prescriptive and PBD methods. The results indicate that the PBD design has an associated cost that is significantly lower than the prescriptive design, despite a

required additional upfront investment in steel reinforcement in the slab. The PBD offers savings in fire protection construction cost, maintenance cost, expected damage losses in case of fire, and rent loss which more than compensates for the extra cost in the slab reinforcement. This case study is based on specific inputs and should not be generalized before additional studies have been conducted, for example on building occupancies with lower average fire load.

ACKNOWLEDGMENTS

This work was performed under the following financial assistance award 60NANB22D110 from U.S. Department of Commerce, National Institute of Standards and Technology. This support is gratefully acknowledged. The statements, findings, conclusions, and recommendations are those of the authors and do not necessarily reflect the views of the NIST or the U.S. Department of Commerce.

REFERENCES

- [1] J. Zhuang, V.M. Payyappalli, A. Behrendt, K. Lukasiewicz, Total cost of fire in the United States, Fire Protection Research Foundation Buffalo, NY, USA, 2017.
- [2] C.G. Bailey, Membrane action of slab/beam composite floor systems in fire, *Engineering Structures* 26(12) (2004) 1691-1703.
- [3] Y. Zhang, J.X. Liu, K.H. Tan, Boundary continuity effect on performance of composite beam-slab sub-assemblages at elevated temperature, *Journal of Constructional Steel Research* 198 (2022) 107523.
- [4] J. Drèze, N. Stern, The theory of cost-benefit analysis, *Handbook of public economics*, Elsevier 1987, pp. 909-989.
- [5] R. Van Coile, A. Lucherini, R.K. Chaudhary, S. Ni, D. Unobe, T. Gernay, Economic Impact of Fire: Cost and Impact of Fire Protection in Buildings, Fire Protection Research Foundation, 2023.
- [6] D.T. Butry, R.E. Chapman, A.L. Huang, D.S. Thomas, A Life-Cycle Cost Comparison of Exit Stairs and Occupant Evacuation Elevators in Tall Buildings, *Fire Technology* 48(2) (2010) 155-172.
- [7] ASTM, Standard Practice for Measuring Life-Cycle Costs of Buildings and Building Systems, 2017.
- [8] ASTM, Standard Practice for Measuring Benefit-to-Cost and Savings-to-Investment Ratios for Buildings and Building Systems, 2010.
- [9] ASTM, Standard Guide for Selecting Economic Methods for Evaluating Investments in Buildings and Building Systems 1, 2020.
- [10] ASTM, Standard Practice for Measuring Internal Rate of Return and Adjusted Internal Rate of Return for Investments in Buildings and Building Systems, 2020.
- [11] ASTM, Standard Practice for Measuring Net Benefits and Net Savings for Investments in Buildings and Building Systems, 2020.
- [12] C. Ma, R. Van Coile, T. Gernay, Fire protection costs in composite buildings for cost-benefit analysis of fire designs, *Journal of Constructional Steel Research* 215 (2024) 108517.
- [13] Gordian, 2022 Square Foot Costs with RSMMeans Data (43th edition), Rockland, MA, 2022.
- [14] Gordian, 2022 Assemblies Costs Book with RSMMeans data (47th edition), Rockland, MA, 2022.
- [15] Gordian, 2022 RSMMeans Building Construction Costs Book (80th edition), Rockland, MA, 2022.
- [16] Gordian, RSMMeans Data Online, Rockland, MA, 2022.
- [17] R.K. Chaudhary, A. Lucherini, T. Gernay, R. Van Coile, Evaluation of anticipated post-fire repair cost for resilient design of composite slab panels, *Journal of Building Engineering* 52 (2022) 104460.
- [18] K. Porter, A beginner's guide to fragility, vulnerability, and risk, *Encyclopedia of earthquake engineering* 2015 (2015) 235-260.
- [19] S. Ni, T. Gernay, A framework for probabilistic fire loss estimation in concrete building structures, *Structural Safety* 88 (2021) 102029.
- [20] S. Lamont, M. Gillie, A.S. Usmani, Composite steel-framed structures in fire with protected and unprotected edge beams, *Journal of Constructional Steel Research* 63(8) (2007) 1138-1150.

BEHAVIOUR OF MODULAR BUILDING INCORPORATING CFST COLUMNS SUBJECTED TO COMPARTMENT FIRE

Lalita Lama¹, Thomas Gernay², Huu Tai Thai³, Tuan Ngo⁴, Brian Uy⁵

ABSTRACT

Modular construction has become increasingly popular in the construction industry due to its benefits such as cost-effectiveness, quicker construction time, reduced environmental impact, and flexibility in building sites with limited area. Adopting concrete-filled steel tubular (CFST) columns can further improve the performance of modular buildings. However, there is limited fire analysis research on modular buildings and none on composite modular buildings. This study delves into the fire behaviour of module compartments made of CFST columns and tubular beams, employing numerical analysis. The finite element (FE) model of CFST columns is validated against experiments, showing ability to capture temperature distribution, axial displacement, lateral displacement and failure modes. Then, a FE model of the composite module is developed to analyse the fire behaviour of the structural system. The design fire curve is determined using compartment zone models and considering a range of fuel loads, opening factors, and compartment properties. The thermal-structural response of the module structure is then analyzed. Parametric study is conducted to examine the influence of different sizes of columns, ceiling beams and floor beams on the fire behaviour of the module. The increase in member size in module can limit member expansion, delay global buckling formation and improve fire resistance. Based on the findings from the parametric analysis, recommendations are provided to improve the fire performance of the composite modules.

Keywords: CFST columns; compartment fire; composite building; modular building

1 INTRODUCTION

Modular construction involves the fabrication of prefabricated volumetric building units within factory settings. These units are then transported to the construction site and assembled to form the functioning structure [1]. Modular building has great potential because of its numerous advantages, such as structurally self-sufficient prefabricated units, adaptability to limited spaces, rapid on-site installation, high work safety and ability to be built for special applications requiring higher standards. Additionally, it offers minimal resource consumption, emissions, environmental impacts and ease of demolition [1]. Modular buildings have received a lot of attention from academics and engineers, who have been working to improve modular

¹ PhD student, Department of Infrastructure Engineering, The University of Melbourne,
e-mail: lalital@student.unimelb.edu.au,

² Assistant Professor, Department of Civil and Systems Engineering, Johns Hopkins University
e-mail: tgernay@jhu.edu, ORCID: <https://orcid.org/0000-0002-3511-9226>

³ Professor, Department of Infrastructure Engineering, The University of Melbourne,
e-mail: tai.thai@unimelb.edu.au,

⁴ Professor, Department of Infrastructure Engineering, The University of Melbourne,
e-mail: dtngo@unimelb.edu.au

⁵ Professor, School of Civil and Environmental Engineering, The University of New South Wales,
e-mail: b.uy@unsw.edu.au

buildings' structural performance and construction effectiveness [2]. Due to advancements in manufacturing and material technology, several modular highrise buildings have been constructed in recent years; notably, Australia is credited with erecting four of the ten tallest modular buildings [3]. However, structural fire can have detrimental effects on the modular buildings. Structure fires, in fact, have a high total number of incidents and high associated costs. Several incidents occurred due to structural fires, such as the partial collapse of the First Interstate Bank Building in 1988, Windsor Tower, Spain in 2005 and the Faculty of Architecture Building, Netherlands in 2009 as well as the entire collapse of the World Trade Centre Building 1, 2 and 7 in 2001 and Plasco Shopping Center, Iran in 2017. In addition to statistics and actual instances of building damage, numerous theoretical studies have demonstrated that prolonged fire exposure can result in the progressive collapse of structures. During an extended fire, a significant risk of global collapse exists in the building due to the extensive thermal expansion and subsequent catenary action of the heated floor system[4]. Therefore, the fire safety of the building is essential to preventing and protecting against fire-related damage. It is one of the crucial aspects of structural design.

Plenty of research has explored the collapse behaviour of steel modular buildings [5][6]. However, steel exhibits several drawbacks, including susceptibility to corrosion, low thermal resistance, higher maintenance requirements, and vulnerability to local buckling. Therefore, utilising composite components that combine concrete and steel, such as CFST columns, offers an ideal solution to mitigate these issues. The use of concrete-filled steel tubular (CFST) columns in modular buildings can provide higher ultimate strength capacity and superior fire resistance than steel columns. Due to the presence of infill concrete in the CFST column, when fire occurs, the outer steel tube has a reduction in temperature rise as the concrete absorbs heat from the steel. Also, the infill concrete retard the local buckling formation on the tube. Few studies have been found on composite modular buildings. A study was conducted by Gaurav et al. [7] on 10-storey composite modular buildings to evaluate their progressive collapse behaviour. Various methods of module removal were considered, and different values of dynamic application factors were suggested based on the module removal location. In thinner gusset plates, failure was initiated by shear failure, while in thicker plates, global buckling of adjacent columns occurred before gusset plate shear failure.

Limited research has been conducted on steel buildings exposed to fire scenarios, with even fewer studies focusing specifically on steel modular buildings. Agarwal et al. [8] investigated the overall performance of steel buildings subjected to real fire conditions. This study utilised two ten-story buildings: one featuring a perimeter moment-resisting frame, while the other incorporated an interior RC shear wall core. The findings highlighted the significance of gravity columns in maintaining structural stability during a fire. Additionally, it was observed that the slab's reinforcement plays a crucial role in transferring axial loads from failed columns to adjacent columns, thereby reducing the risk of additional failures and progressive collapse. Gernay et al. [9] conducted a nonlinear analysis of the steel-framed building under fire using performance-based analysis. The study focused on the structural stability of the building during severe fire scenarios, including compartment fires, fire spread across compartments, and events involving column loss followed by fire. Findings revealed that the performance-based fire designs of structures could be completed using a rigorous and systematic methodology. Additionally, the benefits of utilising performance-based designs are highlighted. Shan et al. [10] evaluated the collapse performance of steel modular buildings under fire scenarios. The influence of various parameters on the global performance of the building is investigated using parameters such as load ratios, cross-sectional dimensions of columns, fire locations and fire types. Subsequently, a practical design method was developed based on the findings. There has not been any research on the study of the failure mechanism of the composite modular building. In addition, experimental testing is not only time-consuming and expensive but also impossible to test complicated and massive constructions due to the size restriction of the furnaces. Therefore, this research will focus on the nonlinear finite element analysis of composite modular buildings under fire. Thus, it is necessary to get in-depth knowledge of the CFST columns' fire performance.

This study explores the response of compartments equipped with CFST columns to fire exposure through the application of advanced numerical analysis techniques. Initially, finite element (FE) models of CFST columns are developed and validated against experimental data, considering key parameters such as temperature distribution, axial and lateral displacements, and failure modes. Following this, an FE

composite module is constructed to conduct a comprehensive examination of the failure mechanisms inherent in different components. Through a sensitivity analysis, a design fire curve is selected, with parameters including fire loads, opening factors, and compartment properties being evaluated. Subsequently, parametric analysis is carried out with various sizes of columns, ceiling beams and floor beams. Based on the findings obtained from the parametric analysis, recommendations are developed to optimise both the design and performance of the module in fire scenarios.

2 DESIGN OF THE MODULE

A 10-storey modular building designed by Gaurav et al. [7] is utilised in this study. This building is designed for office building purposes according to the AS/NZS 2327 and is considered to be in Australia. The building features an overall plan dimension of 37m×15.83m, with one direction comprising 6 bays and the other side accommodating 5 bays. Each module measures 6 m×3 m and stands at a height of 3.3 m, aligning with the standard commercial sizes [3], as illustrated in Figure 1. The labels N and C in Figure 1(b) represent the node number and column number. The modules are made of CFST columns and steel beams. The dimensions of the components and the strengths of steel and concrete are adjusted slightly to align with the Australian Standard. The geometrical and mechanical characteristics of the ceiling beams, floor beams, slabs and columns are detailed in Table 1. The connections between the beams and columns are welded connections. The live load is taken as 2.5 kN/m² and the floor finish of 1kN/m² which is taken from the Eurocode. This model serves as the baseline for studying others.

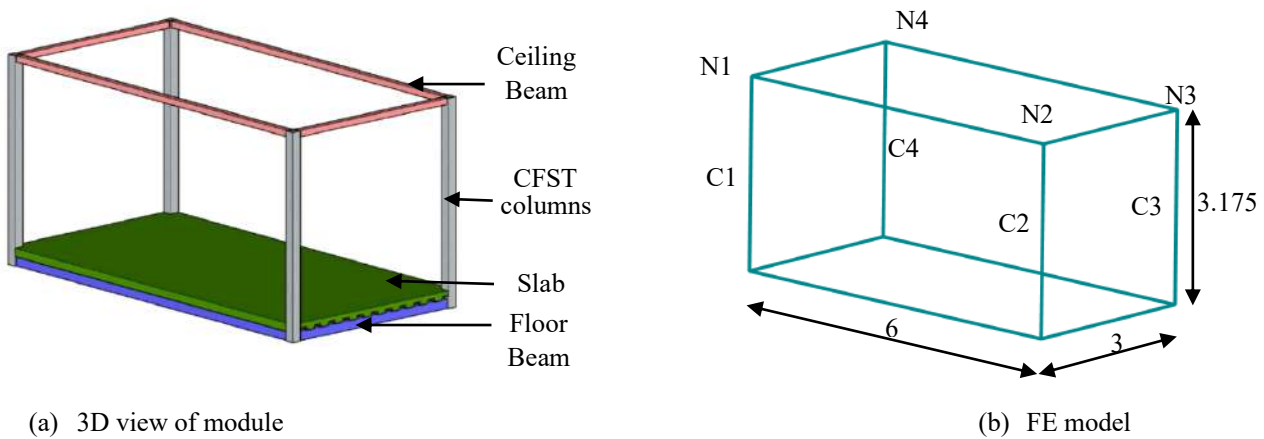


Figure 1. Module

Table 1 Module components

Components	Size (mm)	f_{ck} (MPa)	f_y (MPa)	Rebar mesh
Column	150×150×9	65	350	
Ceiling beam	100×100×5	-	350	
Floor beam	150×100×9	-	350	
Floor slab	6000×3000×130 & 0.9 (steel plate)	65	350	A252

3 FUEL LOAD AND DESIGN FIRES

The fire exposure assessment involves the development of a fire time-temperature history to evaluate the thermal response of the structure. The fire rating for the components of the office building is 120 minutes according to the Australian Building Code. The characteristic fire load density used for all fire scenarios is set at 511 MJ/m², corresponding to the 80% fractile value of fuel load density for an office according to Eurocode 1-2 [11]. For the generation of fire curves, the Ozone software is employed. This building is assumed to be equipped with sprinklers and automatic fire detection by smoke, utilizing a fire load of 193 MJ/m².

The sensitivity analysis is conducted to evaluate the nature of the fire curve with respect to different parameters such as fuel loads, compartment properties and ventilation openings. This analysis considers three cases: buildings with both automatic water extinguishing systems and automatic fire detection by smoke, only the automatic water extinguisher system and those without all the above systems which resemble the three design fire loads such as 193 MJ/m², 264.3 MJ/m², and 433.3 MJ/m² respectively. It also encompasses the consideration of two scenarios regarding wall materials such as gypsum board and shear walls along with various opening factors opening factors ranging from 0.03 to 0.2, corresponding to areas from 2.15 m² to 14.4 m². The several fire curves generated are presented in Figure 2(a), Figure 2(b) and Figure 2(c).

Overall, it can be observed that as the opening factor increases, the peak temperature decreases across all fire load cases. The maximum temperature fire curve, reaching 1050 °C, is illustrated in Figure 2(c) which also has a prolonged fire duration compared to other fire curves in Figure 2(a)-(c). In this study, the building has sprinklers and automatic fire detection by the smoke system (193 MJ/m²). In Figure 2(a), it is observed that the maximum fire temperature of 769 °C occurs for the 0.03 opening factor, hence it is selected for further investigation to account for the potential extreme fire scenario evolving within the compartment.

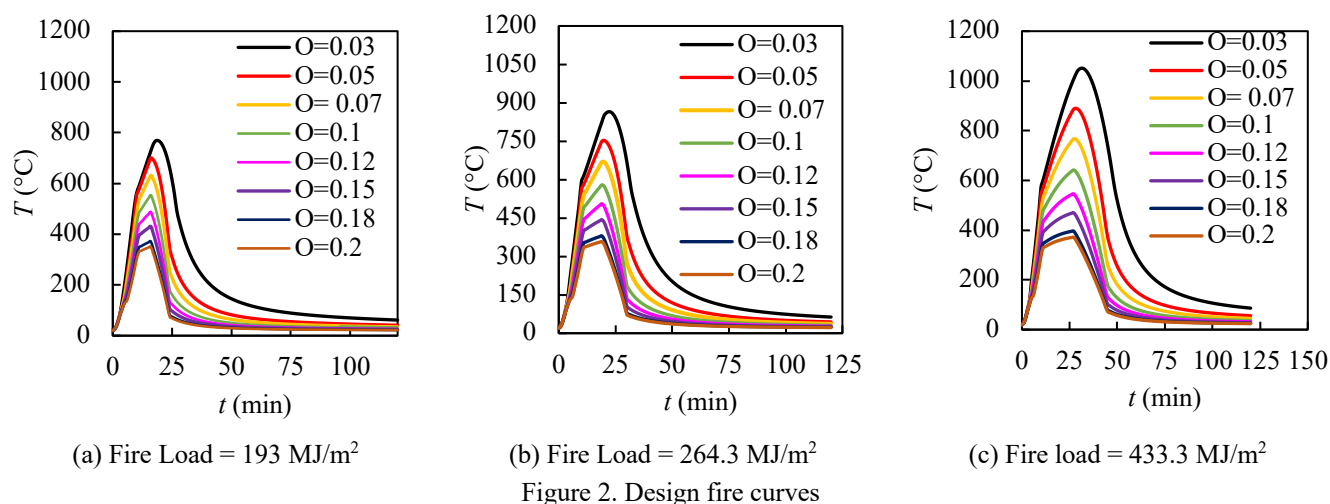


Figure 2. Design fire curves

4 PARAMETRIC ANALYSIS OF THE STRUCTURAL FIRE RESPONSE

The fire resistance of the modules can be enhanced by applying fire protection to the components and increasing the section sizes of the components. In this study, the fire resistance of the modules is investigated by altering the section sizes of different components. Initially, a module is developed with component details presented in Table 1. and thoroughly analyzed. This module is taken as the baseline for studying other modules. Subsequently, further study is conducted by changing parameters such as two different column sizes (200×200×6mm and 250×250×6mm), two ceiling beam sizes (150×150×5mm and 200×200×5mm) and a floor beam (200×100×9mm).

4.1 FE modelling

The thermal-structural response of the module is analysed through the nonlinear analysis software SAFIR. 2D thermal analysis is carried out for each component exposed to design fire curves. Fire is exposed to its surfaces. The floor beams are assumed to be at ambient temperature, as they are under the slab. Thermal and mechanical properties of the concrete and steel are taken from Eurocodes [12,13]. Siliceous concrete, featuring a convection coefficient of 25 W/m²K and an emissivity of 0.7 is employed. The concrete is characterised by a moisture content of 3% by weight and a density of 2300 kg/m³. The air gap of 0.005 Km²/W thermal resistance is adopted in this study. For the structural analysis, the FE modules are developed with 3D beam elements. The slab loads are directly applied to the beams. An initial sway imperfection of $L/500$ is applied to the compartment in the Y-direction. The connections between the beams and columns

are rigid as they are welded together. The bottom sections of the columns have fixed boundary conditions to prevent displacement while permitting rotation along the X and Y directions. However, the top corner nodes remain unrestricted during analysis. During the loading, the fire incident combination DL+0.3LL is taken according to Eurocode1-1-2[11]. The vertical load at the top of the columns is 30% of the capacity of the columns. The columns' sectional capacity is calculated according to the Eurocode [14] and found to be 1716 kN.

4.2 Validation of the FE modelling of the CFST columns

Before analysing a full compartment analysis, validation of the CFST columns has been conducted. Several FE models were developed in SAFIR software and validated against the experimental data, covering fire resistance time, time temperature curves, axial displacement time and lateral displacement time curves. One of the validations of the column can be observed in Figure 3 and Figure 4, where the predicted FE curves closely align with the test curves. Moreover, the predicted fire resistance time of 41 min closely matches the tested time of 43 min, indicating the columns' capability to accurately predict outcomes. Further comprehensive validation details and parametric study are available in [15].

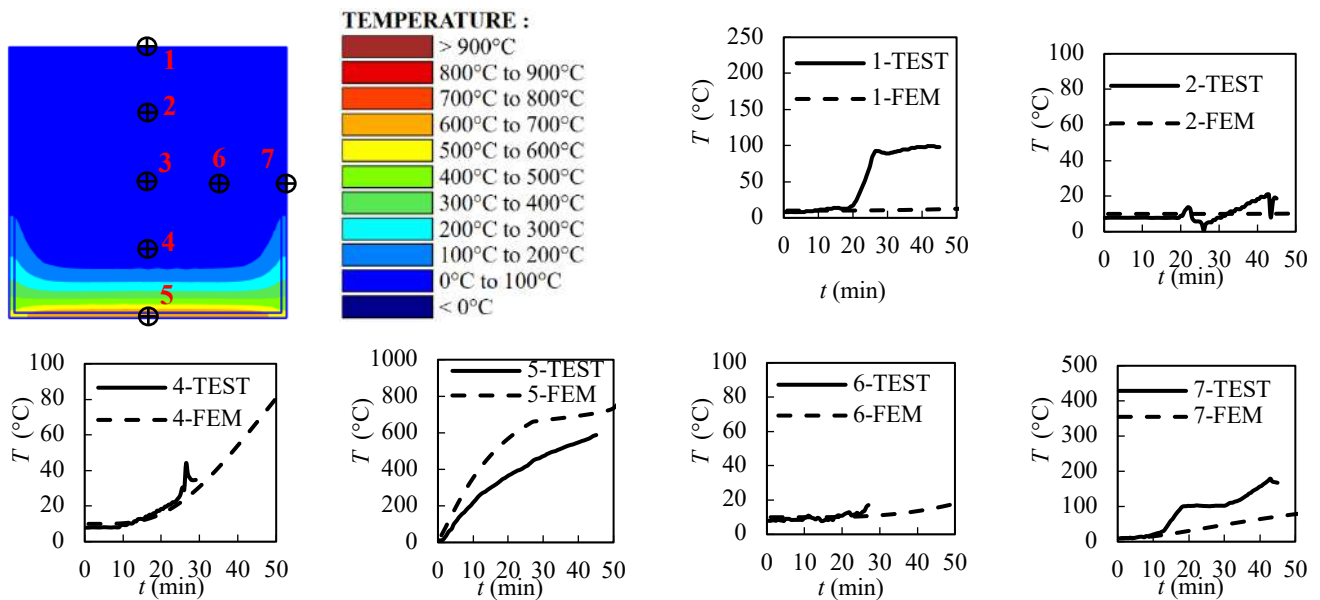


Figure 3. Comparison of predicted and measured time-temperature curves of specimen S5

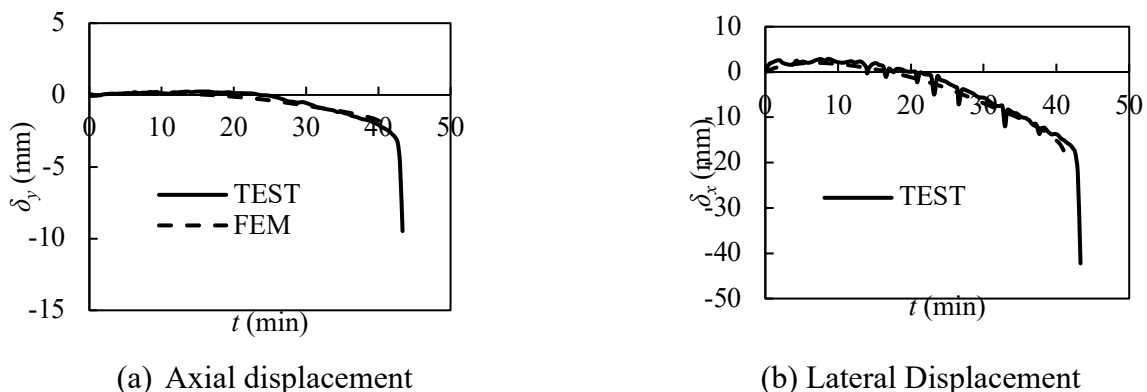


Figure 4. Comparison of predicted and measured displacement-time curves of specimen S5

4.3 Thermal Analysis of the baseline module

The thermal analysis is conducted on the baseline module and the resulting temperature profile of the columns and ceiling beams exposed to two-sided fire are shown in Figure 5. Because of the presence of walls, both the column and the ceiling beam are assumed to be exposed to two-sided fire. In columns, the

maximum temperature is observed at the exposed corner, with the minimum temperature found towards the opposite direction, as displayed in Figure 5(a). In a beam exposed to fire, the maximum temperature occurs at the exposed corner, with the minimum temperature found in the direction opposite corner to the maximum temperature in Figure 5(b). The maximum temperatures recorded are 533 °C and 707 °C while the minimum temperatures are 30 °C and 303 °C for columns and beams at 21 min respectively.

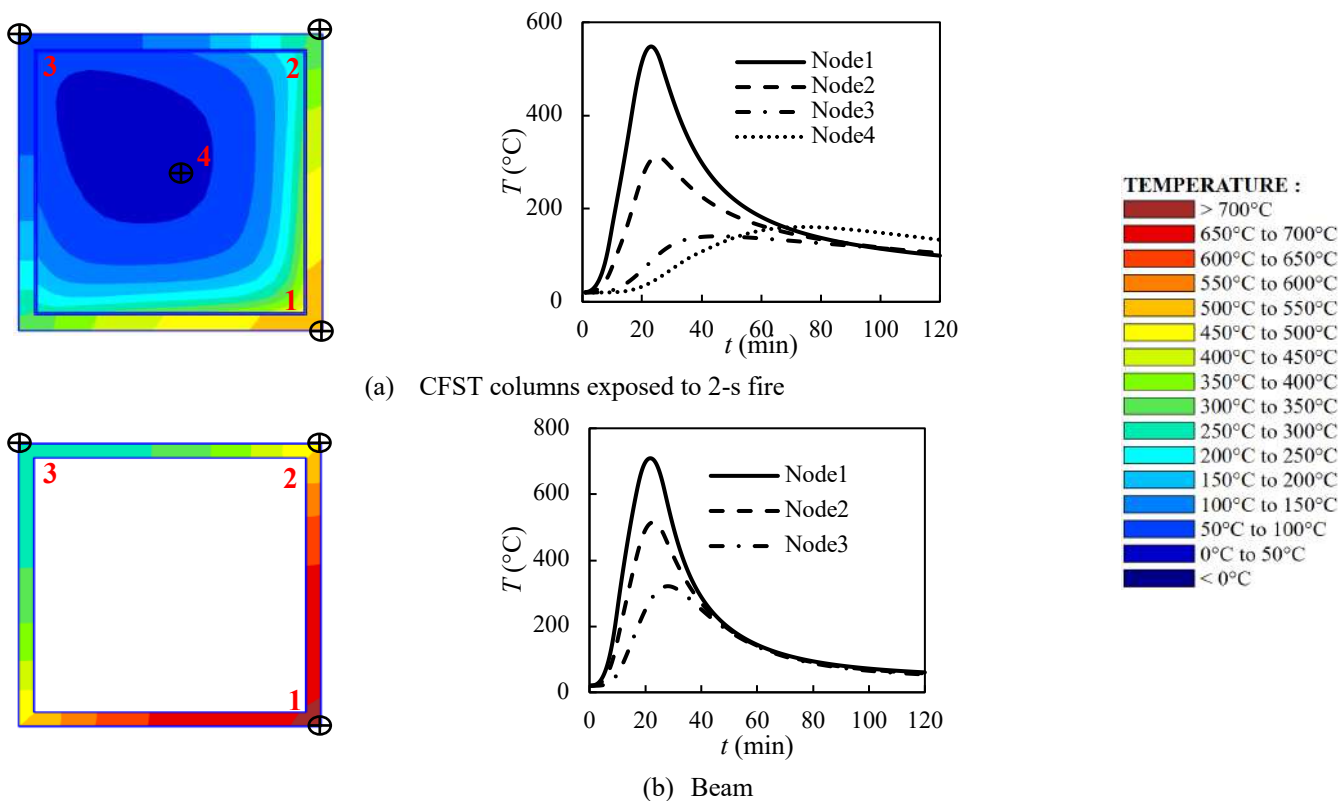


Figure 5. Temperature distribution and temperature curve at different locations of the section

4.4 Structural analysis of baseline model

The failure mechanism of the module with the columns and beams exposed to 2-s fire exposure is analysed. The failure of the module exposed to fire occurs around 34 min. At the moment of failure, the maximum temperature observed on the column is 384 °C at the exposed corner, with a minimum temperature of 74 °C at the opposite corner. Similarly, the ceiling beam reaches a maximum temperature of around 383 °C, while the minimum temperature observed is 293 °C at the opposite corner. The displaced module at different phases, displacement of the different locations and axial force on different components of the compartments are depicted in Figure 6, Figure 7 and Figure 8.

At the beginning stage, the columns experience a thermal contraction due to the applied load as shown in Figure 7(c) with an axial compression force of 515 kN as presented in Figure 8(a). Subsequently, a continuous expansion is observed as the temperature rises, with rapid contraction when the temperature decreases in the module. Simultaneously, a horizontal shift towards X and Y direction is noticed in the top nodes of the columns N1, N2, N3 and N4 as represented in Figure 1(b) and Figure 7 (a) and (b). The buckling phenomena in columns start around 13 min when the sudden drop in axial compression force occurs as shown in Figure 8(a). Then the rapid swaying of the columns towards the Y direction similar to the initial sway direction is observed as shown in Figure 6(c) and Figure 7(b).

Ceiling beams, on the other hand, are noticeably impacted by temperature variations. Initially, the beams are slightly in compression. As the temperature rises, the axial force shifts to tension and the beams are displaced with the sway of the frames as shown in Figure 8(b) and Figure 7(b). In Figure 8, the labels LB and SB denote the long and short beams respectively and the attached numbers indicate the node numbers. Together with the expansion the beam bends towards the fire area as shown in Figure 6(a). As the fire progresses, the beams bend opposite to the fire and rapid axial expansion towards the Y direction can be

observed inside the beams as displayed in Figure 6. The shorter beams expand along two opposite directions and with less value than the longer beams which only expand towards the positive Y direction as indicated in Figure 7(a) and (b). The initial sway direction and the longer beams higher expansion shift the upper parts toward the right direction. Conversely, the floor beams undergo gradual sagging, resulting in tensile axial forces.

Notably, the primary contributor to structural failure is the columns buckling as well as the ceiling beams, particularly the long beams as illustrated in Figure 6 and Figure 7. The heating and subsequent expansion of these beams lead to a pronounced expansion towards the Y direction, consistent with the initial sway direction as shown in Figure 6(c). This creates eccentricity in the columns. Then, the substantial moments generated at the bottom of columns due to the expansive sway of the ceiling beams and buckling of columns drag the upper structures towards the right, ultimately contributing to structural failure as displayed in Figure 6(c).

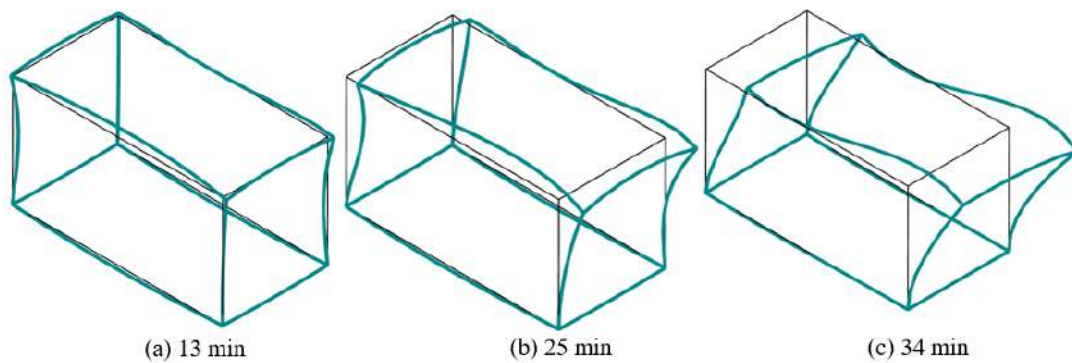
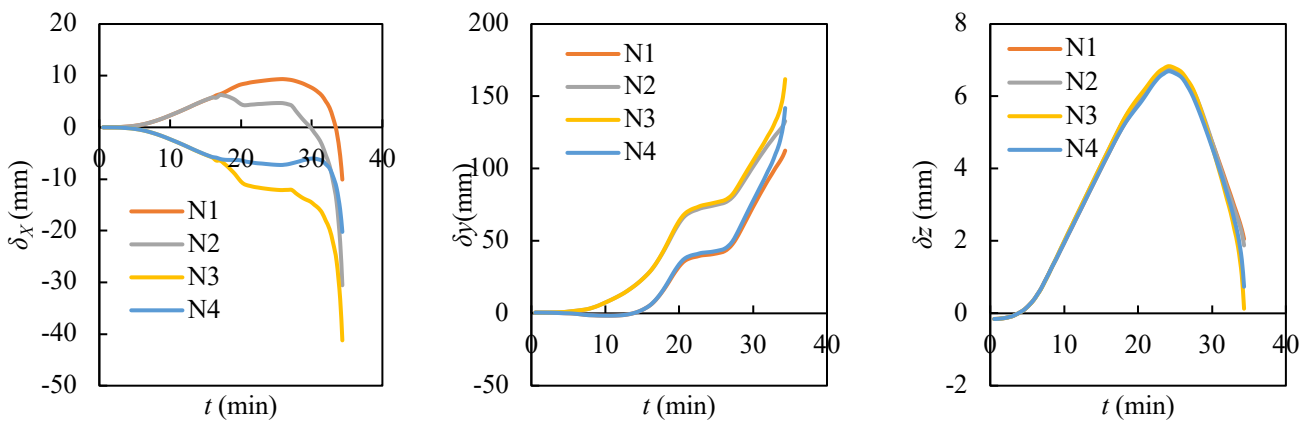
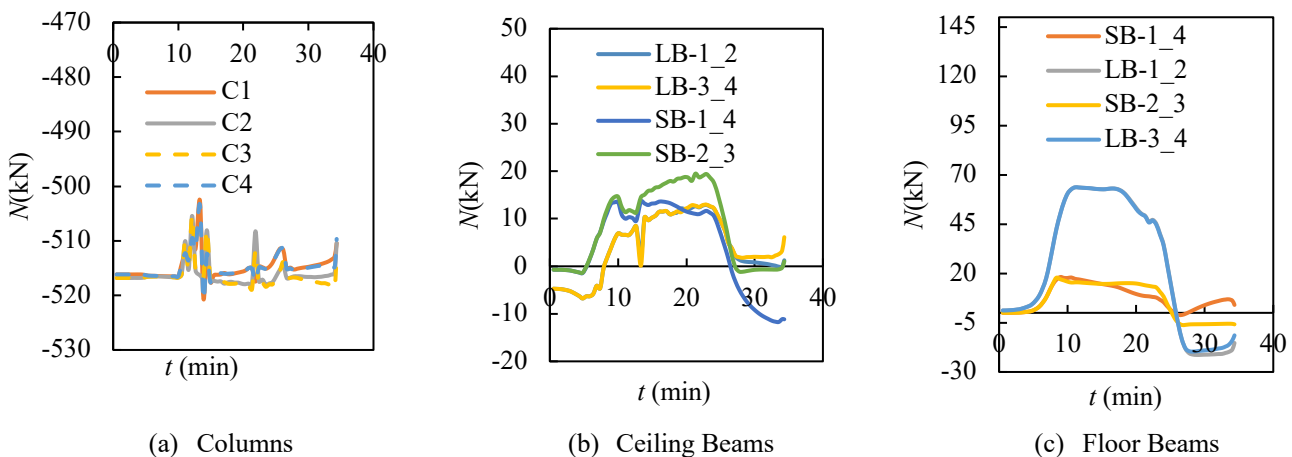


Figure 6. Different stages of module displacement (Scale:10)



(a) Displacement along X-direction (b) Displacement along Y-direction (c) Displacement along Z-direction

Figure 7. Displacement of the nodes along X, Y and Z-directions



(a) Columns (b) Ceiling Beams (c) Floor Beams

Figure 8. Axial force on different components

4.5 Parametric study

4.5.1 Effect of column sizes on fire resistance

The baseline model has a column size of $150 \times 150 \times 9$. Subsequently, two different column sizes are selected for this study $200 \times 200 \times 6$ and $250 \times 250 \times 6$ and the module used these columns labelled as C200 and C250. As the column sizes increase, the fire resistance of the model is observed to increase from 34 min to 54 min and 80 min as illustrated in Figure 9.

The displacement of nodes N1, N2, N3 and N4 along X, Y and Z directions are presented in Figure 1(b) and Figure 9. The displacement patterns are almost consistent across all three scenarios. The module C250 exhibits greater expansion in the x-direction compared to C200 at failure. Moreover, C250 demonstrates reduced sway in the Y direction, contributing to prolonged module stability. This reduced sway in C250 is advantageous for maintaining stability over an extended period. Additionally, C250 experiences more pronounced contraction during failure, attributed to its higher loading compared to the other configurations.

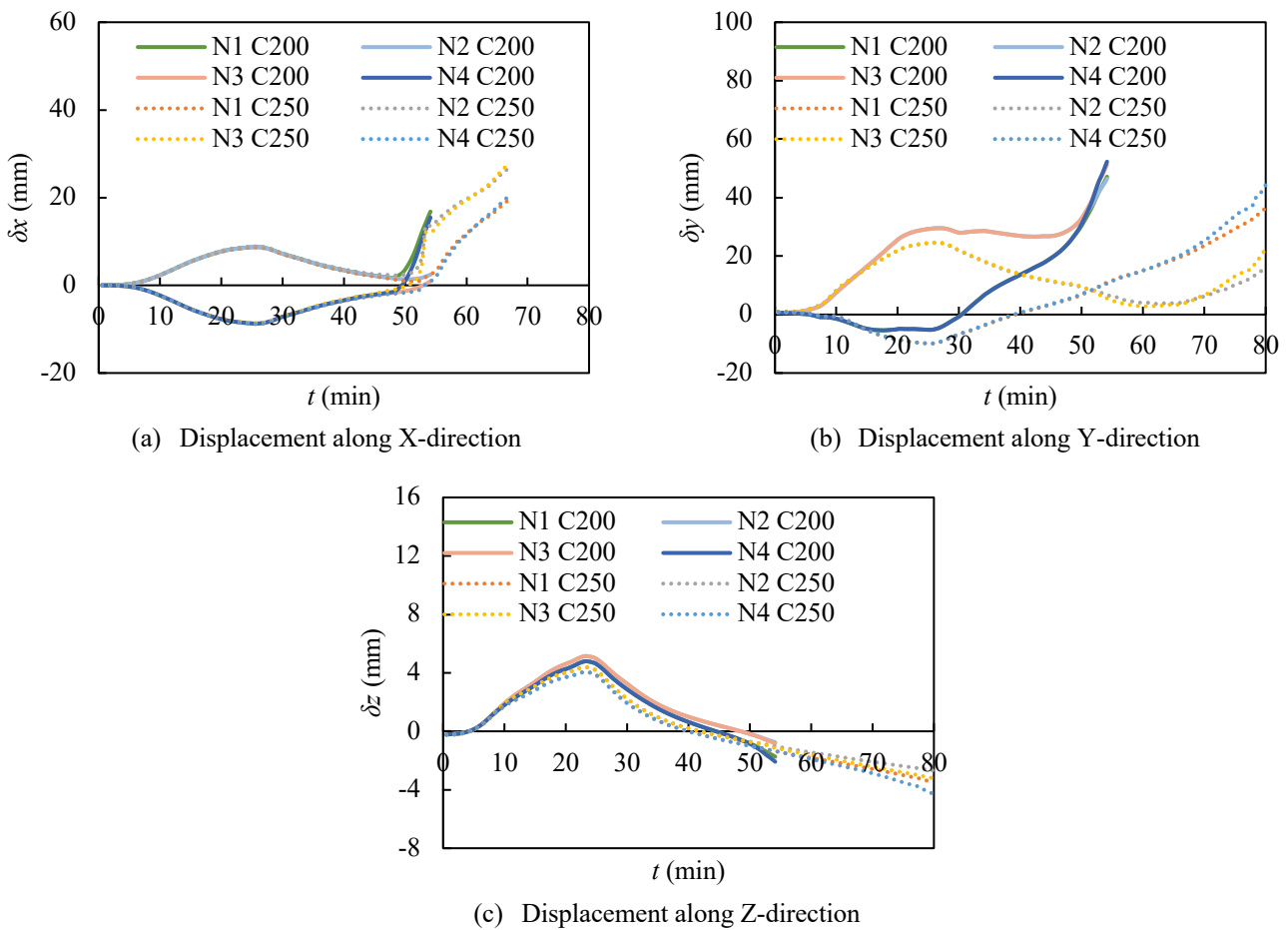


Figure 9. Displacement of the nodes along X, Y and Z-directions

4.5.2 Effect of ceiling beam sizes on fire resistance

The baseline model, featuring ceiling beams measuring $100 \times 100 \times 5$. Two variations in ceiling beam sizes are chosen for investigation such as $150 \times 150 \times 5$ and $200 \times 200 \times 5$ and labelled the modules with these ceiling beams as CB150 and CB200. When the ceiling beam sizes increase, the model's fire resistance is seen to progressively increase from 34 min to 46 min and 69 min respectively as shown in Figure 10. Figure 10 (b) demonstrates that the larger-sized ceiling beams experience decreased sway in the Y-direction. The slower lateral displacement along the Y-direction contributes to generating fewer moments at the bottom of columns, thus retraining overturning and increasing stability for a longer time.

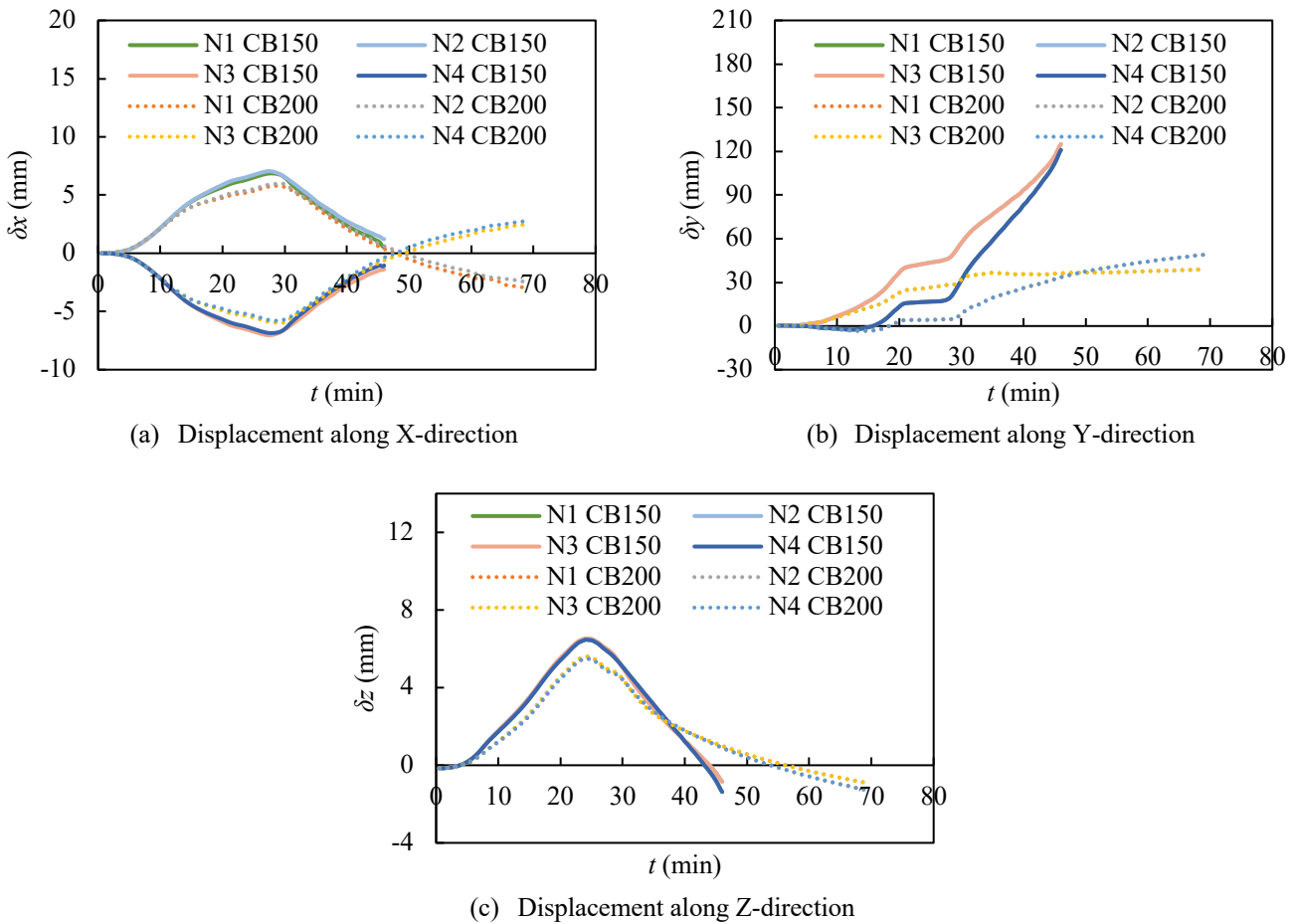
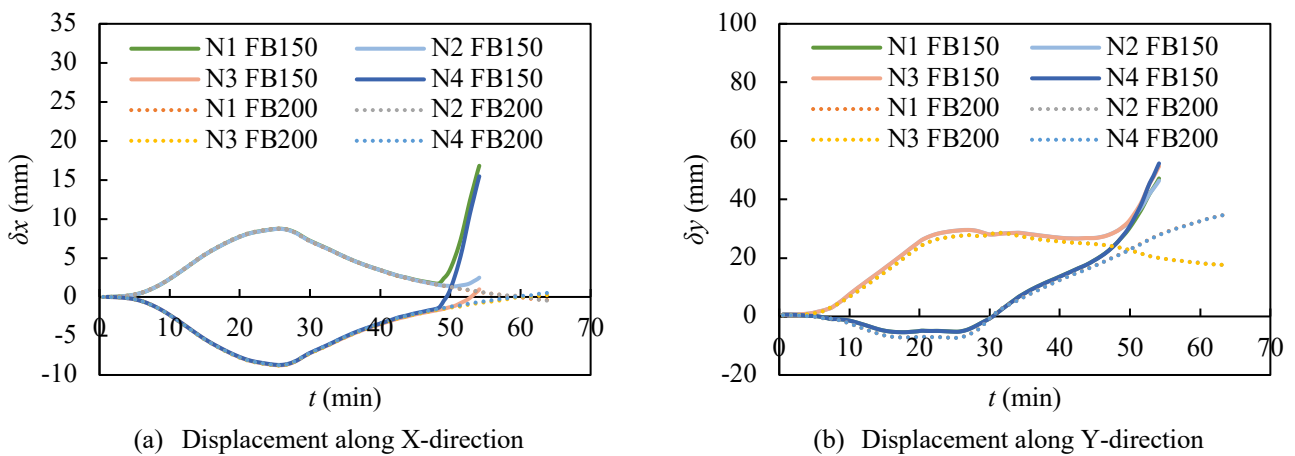
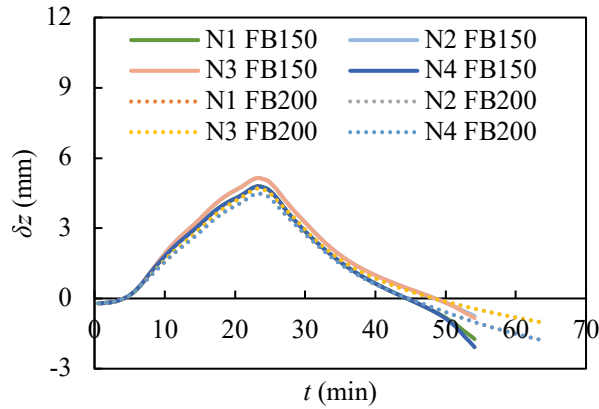


Figure 10. Displacement of the nodes along X, Y and Z-directions

4.5.3 Effect of floor beam sizes on fire resistance

The baseline model is altered with columns measuring 200x200x6, thereby named FB150. Subsequently, the model is analyzed. Then, an additional change is implemented by replacing the 150x100x9mm floor beam of the baseline model with one measuring 200x100x9, resulting module labelled as FB200. With this increase in floor beam size, the fire resistance is increased from 54 minutes to 63 minutes, as depicted in Figure 11. The displacements at the top nodes of the module appear to be slightly minimized by the floor beams.



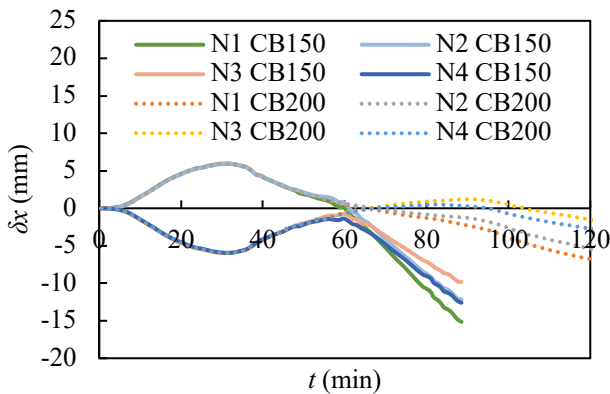


(c) Displacement along Z-direction

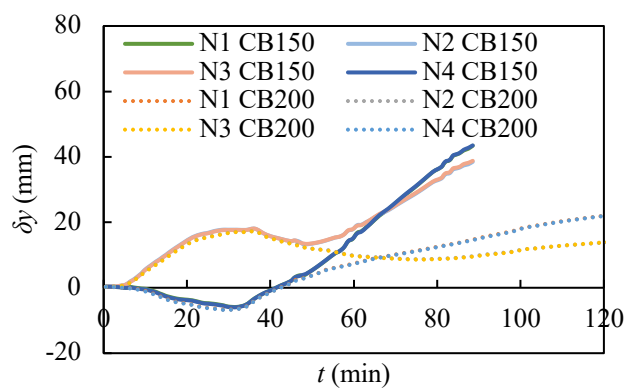
Figure 11. Displacement of the nodes along X, Y and Z-directions

4.5.4 Effect of changes in multiple component sizes on fire resistance

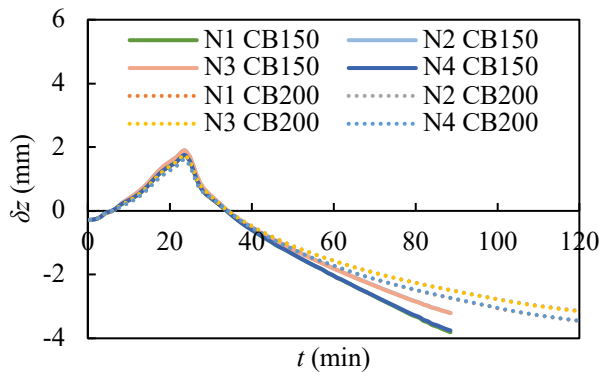
The investigation focuses on the effects of simultaneously altering multiple components within a module. Two distinct modules are examined: one characterized by increased column and ceiling beam dimensions compared to the baseline, with column and ceiling beam sizes of 250x250x6 and 200x200x9 respectively. In the other module, all component sizes are enlarged, including column (250x250x6), ceiling beam (200x200x9) and floor beam (200x100x9). These setups are labelled as CB150 and CB200 in Figure 12. Notably, fire resistance durations of 89 minutes and over 2 hours are exhibited by these configurations, respectively, highlighting the critical role of component sizes in ensuring structural stability during fire incidents. The comparatively low fire resistance of the baseline model can be significantly increased by altering the dimensions of columns, ceiling beams, and floor beams. The gradual increase in displacement can be observed in the CB200 module than others, as shown in Figure 12.



(a) Displacement along X-direction



(b) Displacement along Y-direction



(c) Displacement along Z-direction

Figure 12. Displacement of the nodes along X, Y and Z-directions

5 CONCLUSIONS

This study investigates the response of compartments equipped with CFST columns to fire exposure using advanced numerical analysis techniques. Initially, FE models of CFST columns are developed and validated against experimental data. Subsequently, an FE composite module is constructed to examine the failure mechanisms inherent in different components. Through sensitivity analysis, a design fire curve is selected. Parametric analysis is then conducted across a range of module configurations, varying in sizes of columns, ceiling beams and floor beams. The main conclusions are summarised as follows:

- The global buckling susceptibility is evident in columns when exposed to nonuniform fire exposure, higher in thinner size columns. Additionally, notable expansion of ceiling beams is observed.
- The increase in column size drastically enhances the fire resistance of the modules due to higher sectional capacity, low-temperature rise and observed delayed global buckling.
- The increase in ceiling beam size leads to an increase in fire resistance, with a significant delay in the instability by sway mode compared with the smaller beam size. The increase in floor beam size also improves fire resistance.
- The increment of multiple component sizes significantly enhances module fire resistance by collectively minimizing component expansion and maintaining structural integrity.

Future research will prioritize the integration of fire protection in modules to select the optimal module with reduced weight while ensuring high fire resistance and cost-effectiveness.

ACKNOWLEDGMENT

This research was supported by the Australian Research Council (ARC) under its Future Fellowship (FT200100024) and Discovery Project (DP230100018). In addition, the first author would like to acknowledge The University of Melbourne, the Melbourne Research Scholarship and the Building 4.0 CRC top-up scholarship for doctoral degree research support.

REFERENCES

1. Lawson, M., Ogden, R. & Goodier, C., Design in Modular Construction, 2014. <https://doi.org/10.1201/b16607>.
2. Peng, J., Hou, C. & Shen, L., Progressive collapse analysis of corner-supported composite modular buildings, *Journal of Building Engineering* 48, 103977 (2022). <https://doi.org/10.1016/j.jobbe.2021.103977>.
3. Thai, H.T., Ngo, T. & Uy, B., A review on modular construction for high-rise buildings, *Structures* 28, 1265–1290 (2020). <https://doi.org/10.1016/j.istruc.2020.09.070>.
4. Lange, D., Rößen, C. & Usmani, A., Tall building collapse mechanisms initiated by fire: Mechanisms and design methodology, *Engineering Structures* 36, 90–103 (2012). <https://doi.org/10.1016/j.engstruct.2011.10.003>.
5. Luo, F.J., Bai, Y., Hou, J. & Huang, Y., Progressive collapse analysis and structural robustness of steel-framed modular buildings, *Engineering Failure Analysis* 104, 643–656 (2019). <https://doi.org/10.1016/j.engfailanal.2019.06.044>.
6. Alembagheri, M., Sharafi, P., Hajirezaei, R. & Samali, B., Collapse capacity of modular steel buildings subject to module loss scenarios: The role of inter-module connections, *Engineering Structures* 210, (2020). <https://doi.org/10.1016/j.engstruct.2020.110373>.
7. Swami, G., Thai, H.T. & Liu, X., Structural robustness of composite modular buildings: The roles of CFST columns and inter-module connections, *Structures* 48, 1491–1504 (2023). <https://doi.org/10.1016/j.istruc.2023.01.052>.
8. Agarwal, A. & Varma, A.H., Fire Induced Progressive Collapse of Steel Building Structures: The Role of Interior Gravity Columns, *Engineering Structures* 58, 129–140 (2014). <https://doi.org/10.1016/j.engstruct.2013.09.020>.
9. Gernay, T. & Khorasani, N.E., Recommendations for performance-based fire design of composite steel buildings using computational analysis, *Journal of Constructional Steel Research* 166, 105906 (2020). <https://doi.org/10.1016/j.jcsr.2019.105906>.

10. Shan, S. & Pan, W., Collapse mechanisms of multi-story steel-framed modular structures under fire scenarios, *Journal of Constructional Steel Research* 196, 107419 (2022). <https://doi.org/10.1016/j.jcsr.2022.107419>.
11. EN 1991-1-2, Eurocode 1: Actions on structures - Part 1-2: General actions - Actions on structures exposed to fire, European Standard, (2011).
12. EN 1992-1-2, Eurocode 2: Design of concrete structures - Part 1-2: General rules - Structural fire design, European Standard, (2004).
13. EN 1993-1-2, Eurocode 3: Design of steel structures - Part 1-2: General rules - Structural fire design, European Standard, (2005).
14. EN 1994-1-1, Eurocode 4: Design of composite steel and concrete structures - Part 1-1: General rules and rules for buildings, European Standard, (2004).
15. Lama, L., Gernay, T., Thai, H.T., Ngo, T. & Uy, B., Nonlinear analysis and design of high-strength concrete filled steel tubular columns under nonuniform fires, *Journal of Constructional Steel Research* 217, 108633 (2024). <https://doi.org/10.1016/j.jcsr.2024.108633>.

CONCRETE-FILLED CLOSED BUILT-UP COLD-FORMED STEEL COLUMNS IN FIRE WITH RESTRAINED THERMAL ELONGATION

Hélder D. Craveiro¹, Rohola Rahnavard², Luís Laím³, Aldina Santiago⁴

ABSTRACT

The construction sector increasingly recognises the advantages of Cold-Formed Steel (CFS) products, highlighting their significant benefits in terms of speed, cost, versatility, return on investment and environmental impact. Pushing the boundaries of CFS products led to solutions incorporating multiple individual sections combined to create built-up members that are usually doubly symmetric, reducing the global slenderness and increasing the strength of individual members. Built-up members are usually recognised as the 2nd generation of CFS products. Further expanding the applicability of CFS products led to the investigation of a composite CFS-Concrete solution. This research investigated composite columns combining CFS and concrete in fire. The use of LWC either as fire protection material or as structural material significantly enhances the structural performance of closed-built-up CFS columns. Moreover, this research assessed the impact of restrained thermal elongation through experimental testing and numerical modelling. The experimental results and numerical models are discussed in detail, and the enhancements due to the use of concrete as infill are quantified. The innovative structural solution has inherent advanced structural fire performance and can be used effectively as a viable alternative structural solution.

Keywords: Buckling; cold-formed steel; composite; finite element modelling; restrained thermal elongation.

1 INTRODUCTION

Constructive solutions incorporating light gauge cold-formed steel (CFS) profiles are widely used in residential and industrial buildings. Due to their reduced thickness, high section factor and high thermal conductivity, these structural solutions usually exhibit reduced fire resistance, so it is often necessary to resort to additional passive fire protection solutions. A new generation of solutions has been recently investigated to enhance the performance of CFS products, focusing on built-up elements combining two or more individual shapes. Built-up members are usually symmetric, and combining multiple individual shapes will reduce global slenderness, increasing the strength of the individual elements [1-3]. However, their fire resistance is still relatively low.

Aiming to expand the applicability of CFS solutions further and address the limitations regarding fire resistance, it's crucial to promote synergies between different structural materials. One approach is combining the closed built-up sections with concrete or lightweight concrete, following the same strategy

¹ Researcher, University of Coimbra, ISISE, ARISE, Department of Civil Engineering, Coimbra, Portugal,
e-mail: heldercraveiro.eng@uc.pt, ORCID: <https://orcid.org/0000-0001-8590-5885>

² PhD Candidate, University of Coimbra, ISISE, ARISE, Department of Civil Engineering, Coimbra, Portugal,
e-mail: rahnavard@uc.pt, ORCID: <https://orcid.org/0000-0001-9399-104X>

³ Professor, University of Coimbra, ISISE, ARISE, Department of Civil Engineering, Coimbra, Portugal
e-mail: luislaim@uc.pt, ORCID: <https://orcid.org/0000-0002-8342-3695>

⁴ Associate Professor, University of Coimbra, ISISE, ARISE, Department of Civil Engineering, Coimbra, Portugal
e-mail: aldina@dec.uc.pt, ORCID: <https://orcid.org/0000-0003-3646-4926>

as traditional concrete-filled tubular composite columns. This solution is widely used in the construction sector for high-rise buildings, exploring the enhanced load-bearing capacity, increased stiffness, and structural fire performance [4-7]. However, traditional concrete-filled composite columns are not competitive for the residential market and mid-low-rise buildings. Aiming to address emerging issues related to prefabrication, versatility, ease of erection, demountability and reuse, a new structural system was proposed and developed at the University of Coimbra, using CFS products and lightweight concrete exclusively, resulting in an international patent application published under the patent cooperation treaty (PCT), with the international publication number WO 2024/009135 A1 [8]. The developed bespoke solutions for columns are presented in this investigation. The innovative composite columns combine CFS and concrete (either as fire protection material or as fire protection and structural material), minimising the susceptibility to local buckling phenomena due to the confinement provided by the concrete. Some relevant investigation has already been performed on this innovative solution at both ambient [8, 9] and fire conditions [11-12].

Rahnavard et al. [10] carried out experiments on concrete-filled closed built-up CFS-LWC (lightweight concrete) columns at elevated temperatures. Individual lipped channels, plain channels and sigma-shaped channels were used to fabricate the closed built-up sections that were subsequently filled with concrete. Based on the experimental campaign, numerical models were developed using the finite element software Abaqus [13] and considering the available experimental and numerical results, the available design guidelines according to EN 1994-1-2 [14] were assessed. A new proposal was presented based on the General Method of EN 1994-1-2 [14], considering the summation of the effective area of the individual cold-formed steel profiles determined according to EN 1993-1-3 [15]. It was also found that the fundamental failure mode of the square and rectangular composite built-up sections was local and distortional buckling. Craveiro et al. [12] reported the experimental investigation on closed built-up CFS-concrete columns in fire, considering the influence of restraint on thermal elongation. Comparisons were established with previous experimental results on bare steel closed built-up CFS columns, demonstrating the benefits of the explored synergies in terms of structural fire performance.

This research investigates innovative composite columns combining light gauge CFS profiles and concrete through experimental testing and numerical modelling. In this study, the numerical models were developed and calibrated against existing experimental results, focusing on the influence of restrained thermal elongation. Another relevant issue is related to the attained composite action between the individual CFS shapes, hence the spacing between fasteners [1, 3]. A parametric study focusing on the influence of restrained thermal elongation and fastener spacing was performed.

2 EXPERIMENTAL CAMPAIGN

2.1 Detailing the specimens and tests

The tested specimens comprised two individual cross-sections, namely lipped (C150×43 with $t = 1.5$ mm) and plain channels (U153×43 with $t = 1.5$ mm), arranged in different configurations to create two closed built-up cross-sections; one with 2 individual profiles (R) and the other with 4 individual profiles (2R) [12]. The dimensions of the individual shapes and composite cross-section are depicted in Figure 1. Also, the position of the self-drilling screws at the cross-section level is presented. The total length of the CFS profiles was 2950 mm, and the adopted longitudinal fastener spacing was 725 mm. It should be noted that the chosen spacing between fasteners does not preclude the possibility of local buckling events. The distinct profiles were secured with Hilti S-6.3×1.9MD03Z self-drilling screws. All individual profiles were manufactured with S280GD+Z steel; hot-dip galvanised with zinc on each side. The closed built-up sections were subsequently filled with C20/25 concrete. In this case, concrete was mainly considered a fire protection material; hence, in the definition of service load, only the load-bearing capacity of the bare steel columns was considered. The design of the built-up CFS members was performed according to EN 1993-1-1 [16] and EN 1993-1-3 [15]. The service load (P_0) adopted in the experimental tests corresponded to 50% of the design buckling load, $N_{b,Rd}$, at ambient temperature.

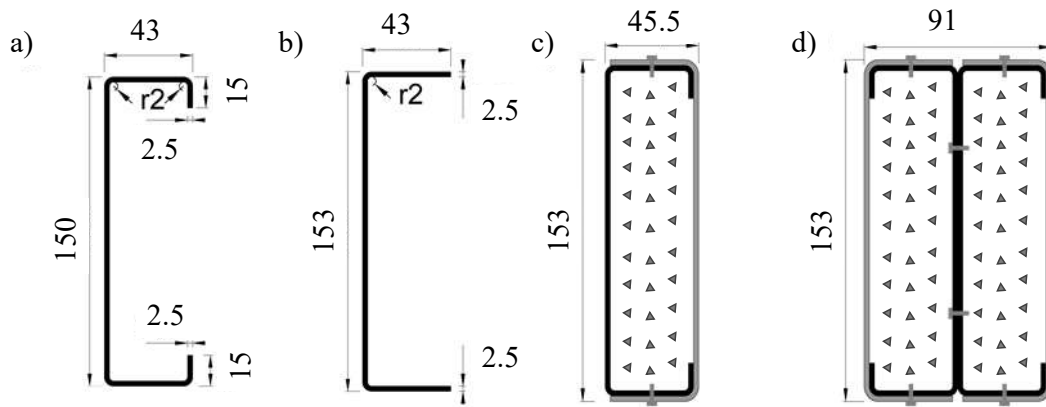


Figure 1. Dimensions of the individual profiles and composite closed built-up CFS-Concrete sections (c) and d)) [12]

The determined service loads (P_0) are presented in Table 1, considering both pinned and fixed boundary conditions.

Table 1. Estimated service load values as a function of the design buckling load ($N_{b,Rd}$) [12]

	R		2R	
	t=1.5 mm		t=1.5 mm	
	Pinned	Fixed	Pinned	Fixed
$N_{b,Rd}$ [kN]	45.35	81.58	159.06	203.82
P_0 [kN]	22.68	40.79	79.53	101.91

The innovative columns were tested in fire, considering explicitly the influence of restraint on thermal elongation. The test set-up comprised a main frame (1) and a secondary restraining frame (2), designed to simulate the influence of the surrounding structure to a column in fire (Figure 2).

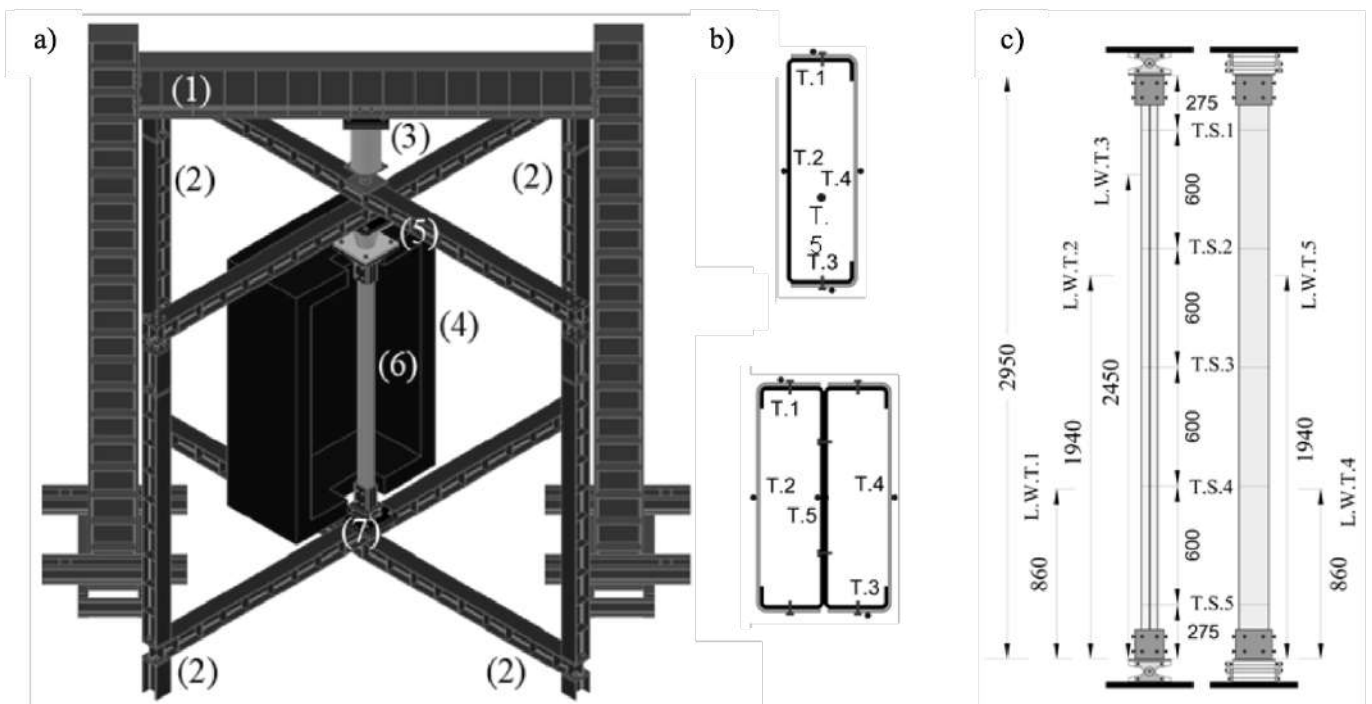


Figure 2. Experimental test set-up (a)) and details of the instrumentation (b) and c)) [12]

The theoretical imposed restraint to thermal elongation was approximately 3 kN/mm. The test procedure included the application of the service load, which was then maintained during the procedures of blocking the vertical rigid body-movement of the top orthogonal beams and during the fire test. With increasing temperature, the column in fire expands, but due to the imposed restraint, the column could not freely expand, and additional axial compressive forces would be gradually generated, up to the point where the column would no longer be able to withstand the applied axial compressive forces. The additional axial forces generated by the imposed restraint to thermal elongation were measured by a special device, including a load cell [12].

Details concerning the instrumentation used at both cross-section level and along the length of the columns are also presented in Figure 2 b) and c).

In the experimental campaign, the mechanical properties of the S280GD+Z steel were determined at both ambient and elevated temperatures [17], whereas for the concrete, only the mechanical properties at ambient temperature were determined [12].

3 DEVELOPMENT OF THE FINITE ELEMENT MODELS

3.1 Introduction

The finite element software Abaqus [13] was used, aiming to reproduce the observed experimental behaviour accurately. Several steps, including heat transfer analysis, linear buckling analysis and finally, geometrically and materially nonlinear analysis with imperfections (GMNIA), as explained in Figure 3, are required to reproduce the observed experimental behaviour involved. A sequentially coupled thermal-stress analysis was performed. Moreover, the complex composite action between the individual CFS shapes through the use of self-drilling screws and the interaction between the steel profiles and concrete was modelled in detail. In this chapter, the developed models are described, and all assumptions and modelling techniques are described.

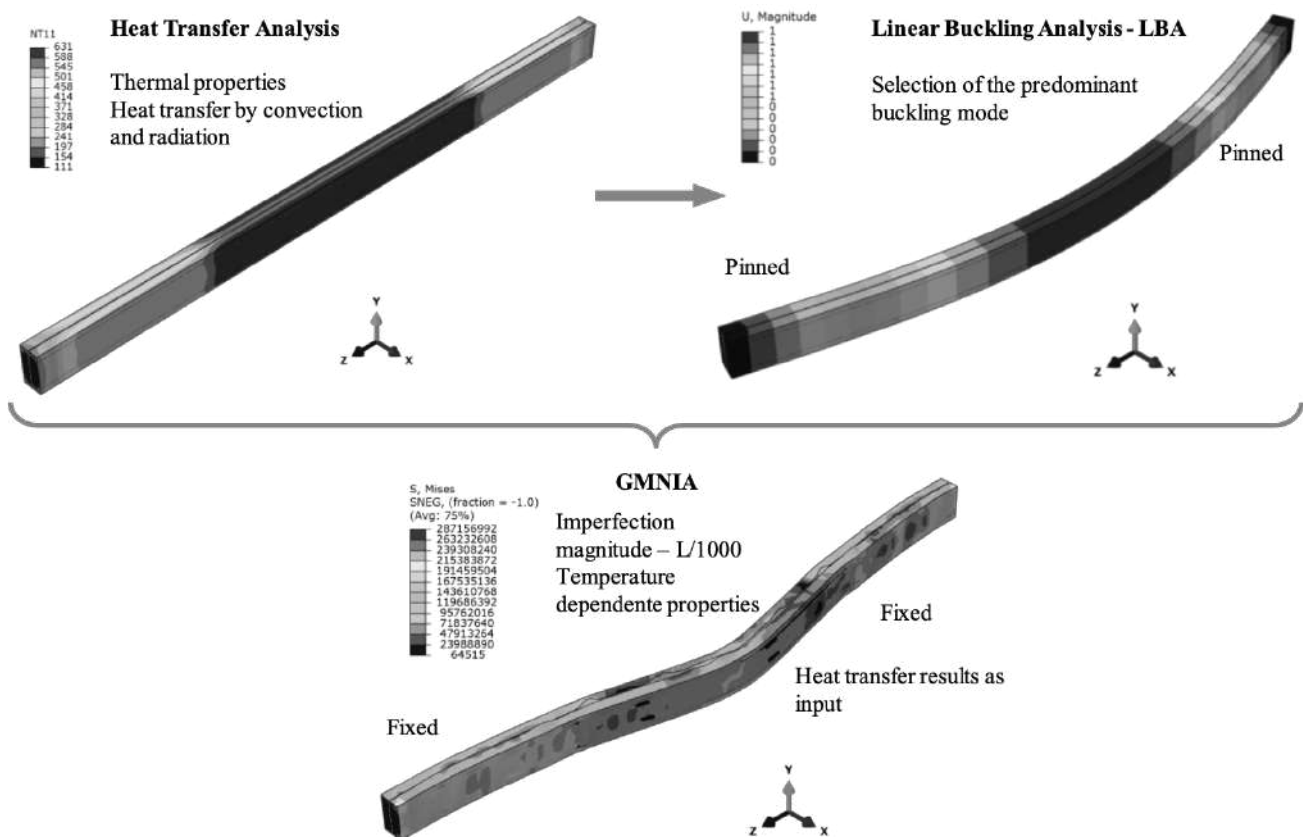


Figure 3. Key stages of the modelling of the composite columns in fire

3.2 Heat Transfer Analysis

Investigating the temperature distribution in the cross-section and along the length of the column requires performing a 3D heat transfer analysis, considering the thermal action monitored in the experimental tests (Time vs Temperature curves from the electric furnaces). The thermal properties considered were the thermal conductivity and the specific heat. Both were determined experimentally for the S280GD+Z steel using the transient plane source technique [17, 18], whereas, for concrete, the thermal properties models available in EN 1992-1-2 [19] were adopted.

Radiation was defined by the resultant emissivity of 0.16 (0.7 for the electrical resistances and 0.23 for the CFS profiles). Convection was defined by the coefficient of heat transfer by convection, which in this case was 15 W/m²K. Contact conductance between the CFS profiles and the CFS profiles and concrete was defined. The adopted values were 2000 and 200 W/m²K, respectively, for the contact conductance between CFS profiles and between CFS profiles and concrete. The physical constants, including absolute zero temperature and the Stefan–Boltzmann, were defined as –273.15 °C and 5.67×10^{–8} W/m² K⁴, respectively. In the parametric study, uniform temperature distribution along the length of the columns was considered, and the ISO 834 standard fire curve was selected as the thermal action. In this case, the selected coefficient of heat transfer by convection was 25 W/m²K, and the emissivity was 0.35.

The CFS profiles were modelled using heat transfer shell element DS4, whereas the solid concrete infill was modelled using heat transfer 8-node element type DC3D8. The outputs resulting from the heat transfer analysis were used as input in the GMNIA analysis.

3.3 Mechanical Analysis

For the geometrically and materially nonlinear analysis with imperfections (GMNIA), two basic steps are required, namely the linear buckling analysis and the nonlinear structural analysis with temperature increase and temperature-dependent mechanical properties, including the coefficient of thermal expansion for steel and concrete.

CFS was defined based on the study conducted by Craveiro et al. [17] on the S280GD+Z steel at both ambient and elevated temperatures (Figure 4 a)). The engineering stress vs strain curves were converted to true stress vs true strain and used as input to the finite element model. Thermal elongation for steel was defined according to the model proposed by Kaitila [20].

Concrete was modelled based on the specifications provided in EN 1992-1-1 [21] and EN 1992-1-2 [19]. The modulus of elasticity of concrete at ambient temperature ($E_{c,20}$) was determined using Eq. (1).

$$E_{c,20} = 22 \left(f_{c,20} / 10 \right)^{0.3} \quad (1)$$

Where

$f_{c,20}$ is the mean compressive strength at ambient temperature.

The Concrete Damage Plasticity model was adopted in the plastic range, considering the corresponding reduction factors for the mechanical properties established in the EN 1994-1-2 [14]. The compressive stress-strain curves for concrete at elevated temperatures were determined using Eq. (2).

$$\sigma_{c,\theta} = \frac{3\varepsilon f_{c,\theta}}{\varepsilon_{c1,\theta} \left[2 + \left(\frac{\varepsilon}{\varepsilon_{c1,\theta}} \right)^3 \right]} \quad \varepsilon \leq \varepsilon_{c1,\theta} \quad (2)$$

Where

$\sigma_{c,\theta}$ is the stress of concrete under compression at the temperature θ ;

ε is the strain;

$f_{c,\theta}$ is the characteristic value for the compressive cylinder strength of concrete in fire situation and temperature θ ;

$\varepsilon_{c1,\theta}$ is the concrete strain corresponding to $f_{c,\theta}$.

The obtained stress vs strain curves are plotted in Figure 4 b). Tensile behaviour was defined by considering tensile strength as a function of fracture energy at different temperature levels. The tensile strength of concrete was multiplied by an amplification factor of 1.2 to consider the strain rate effect, as recommended by the Abaqus manual [13]. The fracture energy was determined using Eq. (3) as defined by FIB-2010 [22].

$$G_F = 73 \times f_c^{0.18} \quad (3)$$

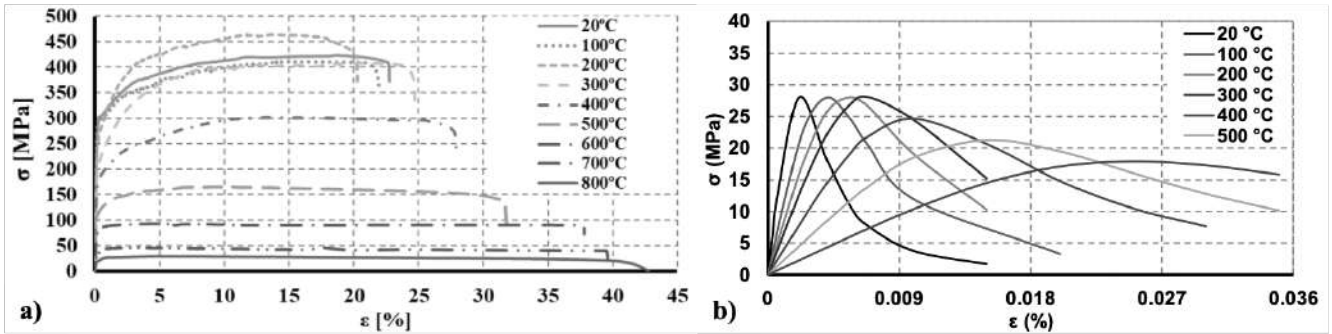


Figure 4. Material models used for both steel (a) and concrete (b) as input

The interaction between the components was defined using “General Contact”, considering normal hard contact and tangential penalty contact with a friction coefficient of 0.3 as the interaction properties. To connect the individual CFS cross-section shapes the fasteners were modelled using the “Beam connector and Fastener” tool available in Abaqus [13], defining the real radius of the self-drilling screws. The CFS and concrete infill were modelled using S4R shell finite elements and C3D8R solid finite elements.

Since restraint to thermal elongation was explicitly considered in the experimental tests, this indirect action was modelled by assuming a linear spring at the top of the composite columns, preventing its free expansion. Based on the information collected during the experimental tests, the stiffness of the linear spring was 2.3 kN/mm.

The structural analysis was conducted using a Dynamic Explicit procedure with mass scaling to speed up the simulation. The simulation was set by defining the initial geometric imperfections (magnitude of $L/1000$ for global and $h/200$ for local buckling modes) and importing the nodal temperature distribution obtained from the heat transfer analysis. The accuracy of the simulation, considering the Dynamic Explicit procedure, was assessed by comparing the kinetic energy with the internal energy. Kinetic energy remained below 3% of the internal energy.

3.4 Parametric Study

The parametric study is still in its infancy, and significant work is still needed to enhance the developed models and accurately define the optimum strategy, considering that even at ambient temperature, the design methodologies are still under validation. Consequently, at this stage, in terms of the definition of the service load, two strategies were used: i) design buckling load of the built-up CFS columns according to the EN 1993-1-3 [15], and ii) design buckling resistance of a composite column followed the design methodology presented in the EN 1994-1-1 [23], considering the steel gross cross-section area.

Also, the assessment of the influence of load level and level of restraint on thermal elongation is a critical topic by specifying different axial stiffness values to the springs simulating the surrounding structure. The axial restraint levels are determined as a function of the axial stiffness of the built-up CFS-concrete composite column. The axial stiffness ($K = (E_s A_s + E_c A_c)/L$) was determined, and the selected levels of axial restraint to thermal elongation corresponded to 0% and 10% of the axial stiffness of the column.

Still concerning the efficiency of the structural solution under development and verification, the fastener spacing may play a critical role in enhancing the composite action, both between CFS profiles and CFS and concrete, and the confinement to the concrete part; hence, this also becomes a key parameter to be assessed. Bear in mind that with an increasing number of fasteners, the influence of distortional buckling decreases.

4 RESULTS

4.1 Calibration of the numerical models – Heat Transfer analysis

Direct comparisons are established against experimental results (Figure 5) to validate the adopted assumptions and modelling strategies. In terms of temperature evolution, the critical cross-section (mid-height) is compared considering the instrumentation used and depicted in Figure 2.

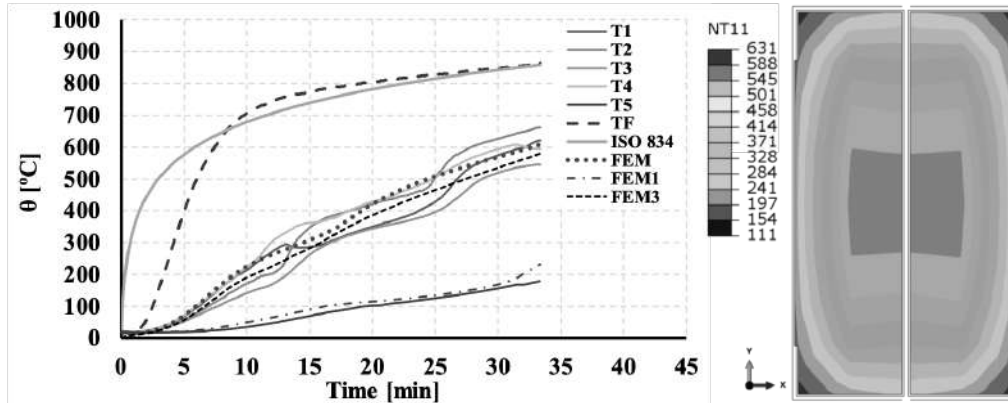


Figure 5. Comparison between experimental and FEM temperature evolution at mid-height of the composite column

In Figure 5, the monitored thermal action is presented and compared with the ISO 834 standard fire curve, as well as the temperature evolution in the external surfaces of the CFS individual profiles and the inner surfaces of the built-up CFS section, hence protected by the concrete infill. Overall, a very good agreement between experimental and numerical results can be observed, validating the adopted strategies and assumptions. As mentioned, the nodal temperatures calculated in the heat transfer analysis were subsequently imported into the mechanical model.

4.2 Calibration of the numerical models – Structural performance in fire

A comparison between the final deformed shapes of experimental specimens and finite element simulations is presented in Figure 6. A good agreement was observed, and the finite element model could accurately reproduce the observed global and local buckling modes.

In terms of the observed behaviour, the numerical model presented a good agreement with experimental results, both in terms of time and temperature (higher temperature monitored at the cross-section level), as can be observed in Figure 7. It is worth mentioning that the results are presented in terms of the P/P_0 ratio, relating the additional generated forces due to axial restraint to thermal elongation (P) and the initial service load level (P_0).

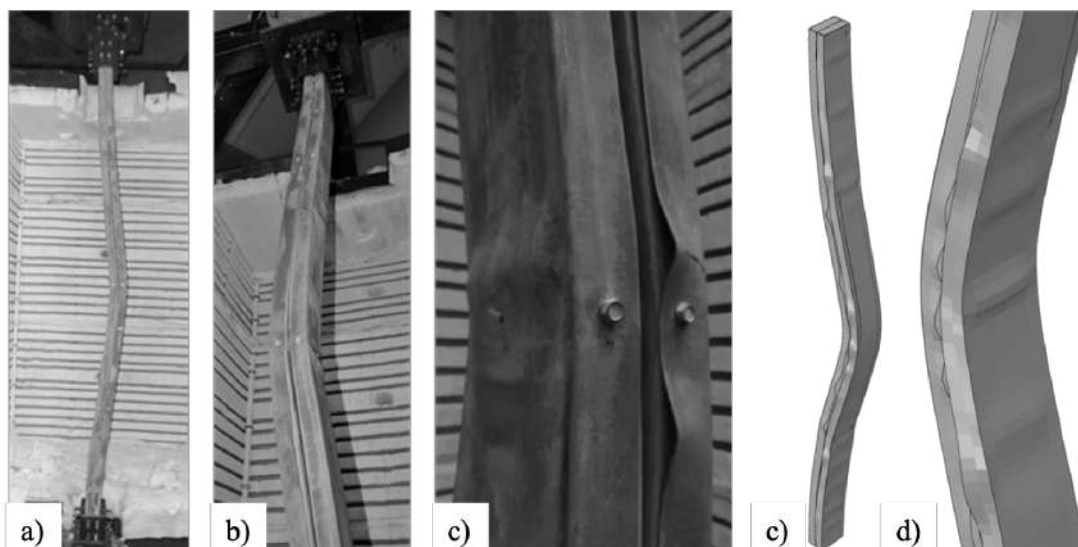


Figure 6. Comparison between experimental and numerical final deformed shape for 2R (Fixed-fixed) composite columns

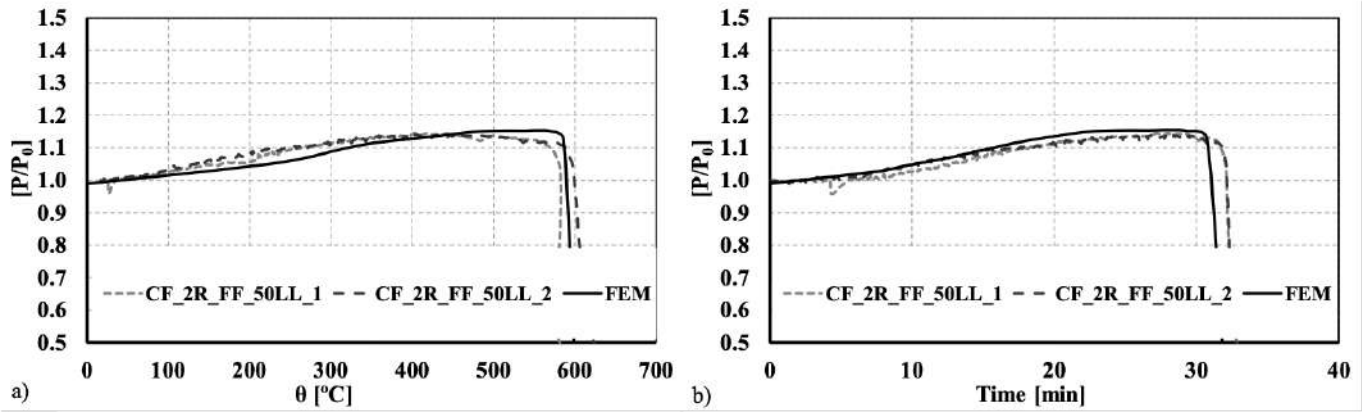


Figure 7. Evolution of axial forces due to restraint to thermal elongation and comparison with FEM results for 2R columns both in terms of time and temperature

4.3 Influence of load level and axial restraint to thermal elongation

Aiming to assess the influence of initial load level and axial restraint to thermal elongation, a set of numerical simulations was performed to identify the global trends for the tested composite cross-sections, namely the 2R section comprising 2C's and 2U's with the corresponding concrete infill.

In Figure 8 a), the Force vs Displacement (elongation and end shortening of the columns) curves are depicted for two different initial load levels and levels of axial restraint to thermal elongation. In Figure 8 b), Force vs Temperature curves are plotted, demonstrating the influence of restraint to thermal elongation, causing a significant decrease in the critical temperature of a composite column. Also, the impact of increasing the initial load level (in this case, determined according to EN 1993-1-3 [15]) can be observed. Increasing the load level from 50% to 70% led to a decrease in the critical temperature of approximately 28%.

As mentioned, no specific design methodologies exist for such columns in available design codes; hence, different assumptions may be adopted as an initial approximation to establish a lower and upper bound for the load-bearing capacity. In Figure 9, that comparison is performed by considering different load levels and different design buckling loads determined according to EN 1993-1-3 [15] (concrete simply as a passive fire protection material) and EN 1994-1-1 [23] (composite column considering the gross CFS cross-section area).

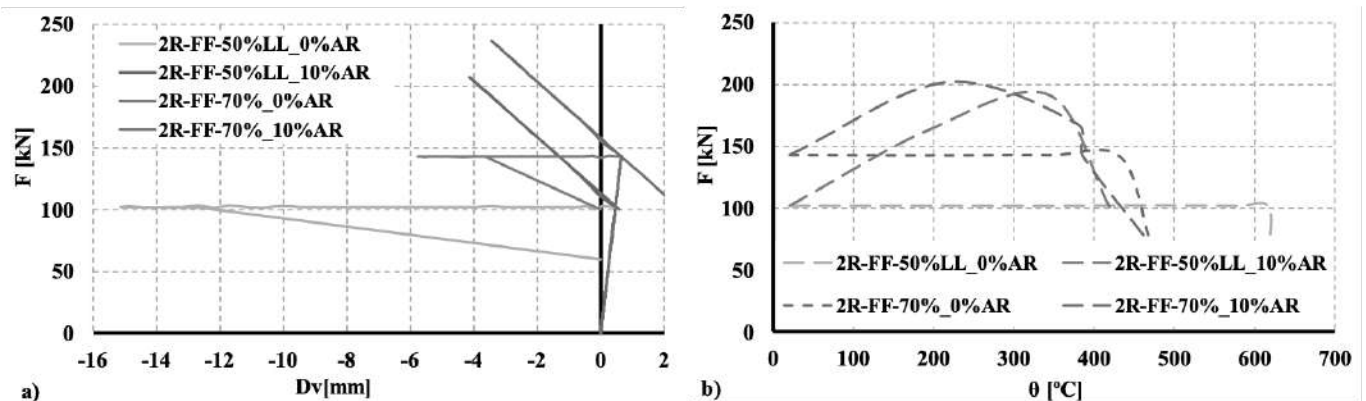


Figure 8. a) Force vs vertical displacement of the composite column. b) Evolution of axial forces due to restraint to thermal elongation

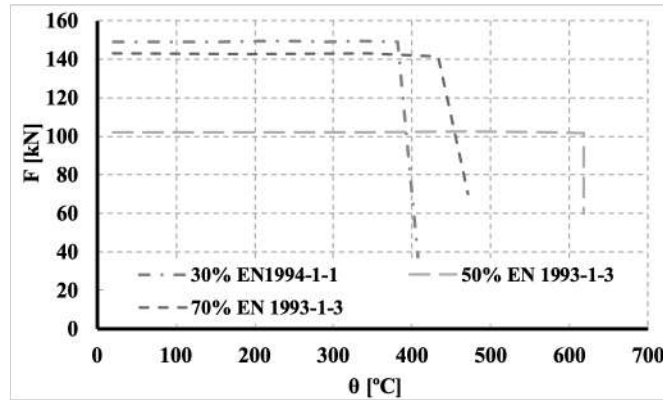


Figure 9. Influence of the initial load level, considering EN 1993-1-3 and EN 1994-1-4 for the design of the columns

Finally, the impact of fastener spacing was also assessed by reducing the fastener spacing from 712.5 mm to 356.25 mm. The same conditions as specified for the experimental test CF_2R_FF_50LL were considered in the simulation, and the only modification was the fastener spacing along the length of the column. With smaller spacing, specifically for the tested composite built-up cross-section, the susceptibility to distortional buckling is minimised, and concrete confinement is enhanced, contributing to the slight improvement of the load-bearing capacity of the column, demonstrating that the load-bearing capacity of built-up members strongly relies on the composite action between the individual components, as shown in Figure 10.

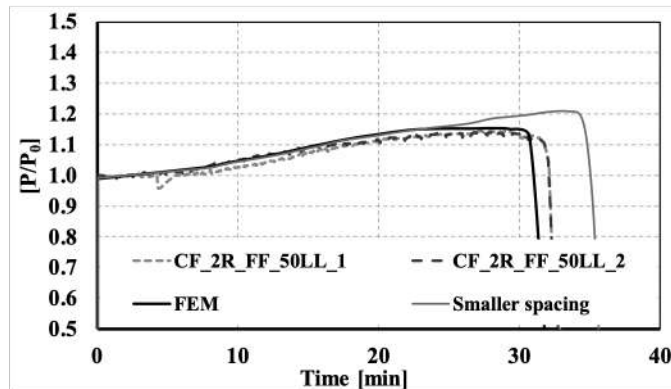


Figure 10. Influence of fastener spacing in the fire resistance of the 2R composite column

4.4 Comparisons with bare steel CFS columns

To evaluate the effectiveness and accuracy of the proposed solution, the results obtained were compared with those of similar solutions lacking the concrete infill and with a variation in the plate thickness of the cold-formed steel (CFS) profiles [12]. The composite sections used a thickness of 1.5 mm, while the bare steel configurations used a thickness of 2.5 mm. As shown in Figure 10 and Figure 11, the use of a 1.5 mm thick steel profile in the composite columns, when combined with concrete infill, significantly increased fire resistance times. For example, the fire resistance of the composite 2R columns increased by 153.8% to 33 minutes compared to the bare CFS 2R column with a 2.5 mm plate thickness. The concrete infill not only improves the fire performance of the CFS columns but also reduces the likelihood of local buckling in thin-walled CFS profiles, thus maximising the use of the steel's strength. This could also facilitate the use of higher-strength steel in composite structures.

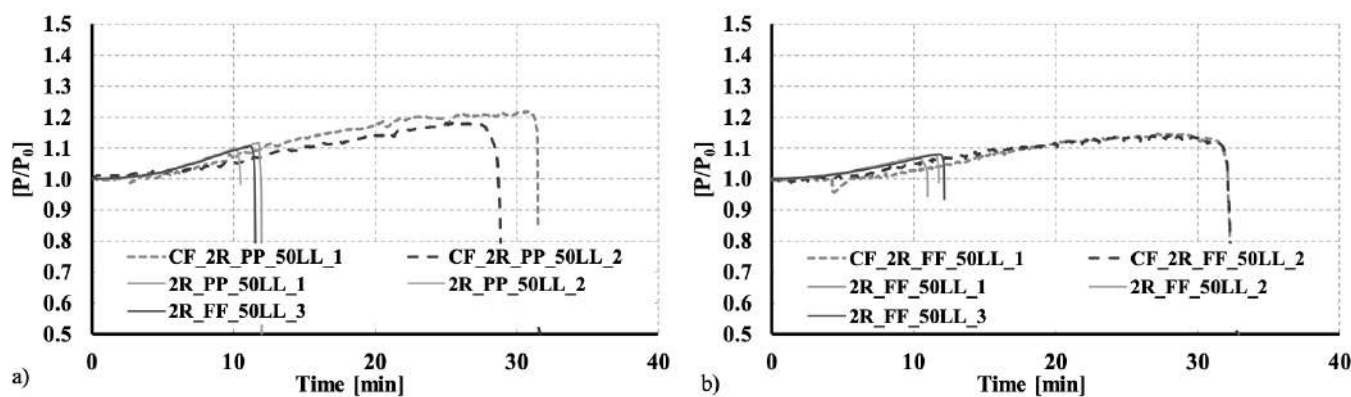


Figure 11. Comparison between bare steel and concrete-filled columns as a function of time [12]

5 CONCLUSIONS

The paper presents an experimental and numerical investigation on the behaviour of an innovative composite structural solution combining CFS and concrete and exploring the versatility of the individual CFS shapes.

Based on existing experimental results, it was found that combining CFS with concrete significantly enhances structural fire performance, demonstrating a 153% increase in fire resistance in some comparisons. Evaluation of the effect of restraint on thermal elongation revealed that restraint during heating generates additional axial forces, which reduce fire resistance and lower the critical temperature. This composite solution also helped prevent local buckling in thin-walled steel plates, further highlighting its benefits.

Then, advanced numerical models were developed to reproduce accurately the observed experimental results, detailing all the assumptions and techniques used. A parametric study assessed the influence of initial load level and axial restraint on thermal elongation, fastener spacing and design methodology based on existing recommendations. Nevertheless, further investigation is still required to understand the behaviour of this innovative composite structural solution.

ACKNOWLEDGEMENT

The first author gratefully acknowledges the Portuguese Foundation for Science and Technology (FCT) for its support under the framework of the individual Scientific Employment Stimulus (CEECIND – 3rd Edition) program with reference 2020.03588.CEECIND. The authors gratefully acknowledge the Portuguese Foundation for Science and Technology (FCT) for its support under the framework of the research project POCI-01-0145-FEDER-031858 – INNOCFSCONC – Innovative hybrid structural solutions using cold-formed steel and lightweight concrete" (<https://doi.org/10.54499/2020.03588.CEECIND/CP1609/CT0008>) financed by FEDER funds through the Competitvity Factors Operational Pro-gramme-COMPETE and by national funds through FCT, PCIF/AGT/0062/2018 – INTERFACESEGURA – Segurança e Resiliência ao Fogo das Zonas e Interface Urbana-Florestal (<http://doi.org/10.54499/PCIF/AGT/0062/2018>), financed by FCT through National funds. This work was partly financed by FCT / MCTES through national funds (PIDDAC) under the R&D Unit Institute for Sustainability and Innovation in Structural Engineering (ISISE), under reference UIDB/04029/2020 (<https://doi.org/10.54499/UIDB/04029/2020>).

REFERENCES

1. Kim J.R. Rasmussen, Mani Khezri, Benjamin W. Schafer, Hao Zhang, The mechanics of built-up cold-formed steel members, *Thin-Walled Struct.* 154 (2020), 106756, <http://dx.doi.org/10.1016/j.tws.2020.106756>.

2. D.K. Phan, K.J.R. Rasmussen, Flexural rigidity of cold-formed steel built-up members, *Thin-Walled Struct.* 140 (2019) 438–449, <http://dx.doi.org/10.1016/j.tws.2019.03.051>
3. Hélder D. Craveiro, Rohola Rahnavard, Luís Laím, Rui A. Simões, Aldina Santiago, Buckling behaviour of closed built-up cold-formed steel columns under compression, *Thin-Walled Structures*, Volume 179 (2022), 109493. <https://doi.org/10.1016/j.tws.2022.109493>
4. Q.Q. Liang *Analysis and Design of Steel and Composite Structures* CRC Press, Taylor & Francis Group, Boca Raton, FL, USA (2015)
5. M.L. Romero, A. Espinós, C. Renaud, G. Bihina, P. Schaumann, P. Kleiboemer, et al. Fire resistance of innovative and slender concrete filled tubular composite columns (FRISCC) Final Report, Catalogue Number KI-NA M.L. Romero, V. Moliner, A. Espinos, C. Ibanez, A. Hospitaler
6. V. Moliner, A. Espinos, M.L. Romero, A. Hospitaler, Fire behavior of eccentrically loaded slender high strength concrete-filled tubular columns, *J. Constr. Steel Res.*, 83 (2013), pp. 137-146.
7. L.H. Han, X.L. Zhao, Y.F. Yang, J.B. Feng, Experimental study and calculation of fire resistance of concrete-filled hollow steel columns, *J. Struct. Eng.*, 129 (2003), pp. 346-356.
8. Craveiro, Hélder D., Simões, R., Rahnavard, R. (2024), A prefabricated, modular, multi-material composite hybrid construction system, International Publication Number WO 2024/009135A1, World Intellectual Property Organization.
9. Rohola Rahnavard, Hélder D. Craveiro, Marco Lopes, Rui A. Simões, Luís Laím, Carlos Rebelo, Concrete-filled cold-formed steel (CF-CFS) built-up columns under compression: test and design, *Thin-Walled Struct.* (2022).
10. Rohola Rahnavard, Hélder D. Craveiro, Rui A. Simões, Luís Laím, Aldina Santiago, Fire resistance of concrete-filled cold-formed steel (CF-CFS) built-up short columns, *J. Build. Eng.* 48 (2022) 103854, <http://dx.doi.org/10.1016/j.jobe.2021.103854>
11. Rahnavard, R., Craveiro, Helder D., Simões, R.A., Santiago, A.(2023), Concrete-filled cold-formed steel (CF-CFS) built-up columns subjected to elevated temperatures: Test and design, *Thin-Walled Structures*, Volume 188, Article number [110792](https://doi.org/10.1016/j.tws.2023.110792). [10.1016/j.tws.2023.110792](https://doi.org/10.1016/j.tws.2023.110792)
12. Craveiro, Helder D., Rahnavard, R., Henriques, J., Simões, R.A., (2022), “Structural Fire Performance of Concrete-Filled Built-Up Cold-Formed Steel Columns”, *Materials*, Volume 15, Issue 6, Article number [2159](https://doi.org/10.3390/ma15062159). [10.3390/ma15062159](https://doi.org/10.3390/ma15062159)
13. Abaqus Analysis User’s Guide (2021), Dassault Systèmes Simulia, USA.
14. EN 1994-1-2. Eurocode 4. Design of Steel and Composite Structures, Part 1.2: Structural Fire Design. ENV 1994-1-2, British Standards Institution: European Committee for Standardization, London (2003).
15. EN 1993-1-3. Eurocode 3: Design of Steel Structures, Part 1–3: General Rules, Supplementary Rules for Cold-Formed Members and Sheeting. European Committee For Standardization, Brussels, Belgium (2004), p. 125
16. EN 1993-1-1, Eurocode 3: Design of steel structures. Part 1-1: General Rules and rules for buildings. Brussels, Belgium, European Committee for Standardization, 2005.
17. Craveiro, Hélder D., Rodrigues, João P., Santiago, A., Laím, Luís (2016). Review of the high temperature mechanical and thermal properties of the steels used in the cold-formed steel structures – The case of the S280GD+Z steel, *Thin-Walled Structures*, volume 98, Part A, pp. 154-168. <https://doi.org/10.1016/j.tws.2015.06.002>.
18. Craveiro, Hélder David da Silva Craveiro - Fire resistance of cold-formed steel columns. Coimbra: [s.n.], 2016. Tese de doutoramento. Disponível na WWW: <http://hdl.handle.net/10316/29612>
19. EN 1992-1-2, Eurocode 2: Design of concrete structures - Part 1-2: General rules - Structural fire design.
20. Kaitila Olli, *Finite Element Modelling of Cold-Formed Steel Members at High Temperatures*, Helsinki University of Technology Laboratory of Steel Structures Publications (2002).
21. EN 1992-1-1, Eurocode 2: Design of concrete structures - Part 1-1: General rules and rules for buildings.
22. Fib model code for concrete structures 2010, (2013), 10.1002/9783433604090.ch5
23. Eurocode 4. Design of Composite Steel and Concrete Structures, Part 1.1: General Rules and Rules for Building. BS EN 1994-1-1: 2004. British Standards Institution; London (UK) (2004)

ENHANCEMENT OF THE FIRE PERFORMANCE OF STEEL-REINFORCED CONCRETE-FILLED STEEL TUBULAR SLENDER COLUMNS WITH HIGH-PERFORMANCE MATERIALS

David Medall¹, Carmen Ibáñez², Ana Espinós³, Manuel Luis Romero⁴

ABSTRACT

Steel-reinforced concrete-filled steel tubular (SR-CFST) columns are a type of composite members where an inner steel profile is embedded into a conventional CFST section to enhance its compressive capacity. Moreover, the inner profile results thermally protected by the surrounding concrete, enhancing the performance of the columns also in a fire situation. The superior fire performance of this typology has been demonstrated in previous experimental campaigns, both available at the revised literature and from the own authors' previous works. Although the cross-sectional plastic capacity of stub SR-CFST sections under fire conditions has been well established, the available experimental results on slender columns are still scarce, being much needed for the calibration of numerical models and development of design rules applicable to this innovative typology of composite sections. To extend the available experimental database, a new set of fire tests on slender SR-CFST columns are presented in this paper. The known advantages of these composite sections are further exploited in this work with a more rational use of high-performance materials, combining the use of high strength steel at the inner profile and high strength concrete as infill, for a cost-effective fire design.

Keywords: Steel-reinforced concrete-filled steel tubular columns; slender members; fire resistance; high-strength steel, high-strength concrete

1 INTRODUCTION

The use of composite columns in the construction of high-rise buildings has been increasing in the recent years due to their reduced sections and improved mechanical capacities. One of the most popular type of composite columns is the Concrete Filled Steel Tubular (CFST) column, which consists of a steel tube filled with concrete, improving the load-bearing capacity of the member. Yet, a main drawback of these sections is their low performance under fire conditions as the outer tube quickly degrades when exposed to elevated temperatures, leading to the failure of the column. An innovative solution to this problem is the introduction of an embedded steel profile, resulting thermally protected by the surrounding concrete and greatly enhancing the mechanical capacity of the column. These sections are the so-called Steel-Reinforced CFST (SR-CFST) columns.

¹ PhD student, ICITECH, Universitat Politècnica de València, Valencia (Spain)

e-mail: damedmar@posgrado.upv.es, ORCID: <https://orcid.org/0000-0001-9212-5326>

² Associate Professor, ICITECH, Universitat Politècnica de València, Valencia (Spain)

e-mail: caribus@upv.es, ORCID: <https://orcid.org/0000-0002-9354-5637>

³ Associate Professor, ICITECH, Universitat Politècnica de València, Valencia (Spain)

e-mail: aespinos@mes.upv.es, ORCID: <https://orcid.org/0000-0001-7335-4676>

⁴ Full Professor, ICITECH, Universitat Politècnica de València, Valencia (Spain)

e-mail: mromero@mes.upv.es, ORCID: <https://orcid.org/0000-0001-5247-4767>

While the advantages of these sections under fire conditions are promising, the available experimental campaigns found in the literature are still scarce. One of the first works to appear in this topic is the research conducted by Dotreppe [1] at the University of Liege, Belgium. Ten SR-CFST slender columns with different embedded steel profiles were tested under fire conditions with both circular and square geometries. Meng et al. [2] conducted four thermo-mechanical tests on square SR-CFST columns to test their fire resistance. The investigation found that these typology greatly improves the fire resistance of the columns as compared to CFST sections. More recently, Mao et al. [3] tested eight innovative SR-CFST sections embedded with cruciform profiles. Non-uniform heating was also tested in the investigation with 1-side, 2-side, and 3-side exposure. The authors conducted a series of tests on the performance of SR-CFST stub columns under fire conditions for both circular and square geometries [4]. The columns were subjected to a constant load and an increasing temperature field until failure. The embedded section greatly increased the load-bearing capacity of the columns and improved the fire behaviour. High-strength materials were used both in the embedded profile and concrete infill of the columns and improved their performance at high temperatures.

Due to the lack of sufficient experimental investigations, some authors have focused on the analysis of the fire performance of SR-CFST by means of numerical models. Tan et al [5,6] studied the influence of stainless steel in the outer tube of SR-CFST sections. Espinós et al. [7] analysed several innovative sections (SR-CFST among them) to discern their fire performance and the effect of the use of high-strength steel. Other authors investigated the effect of the shape and size of the inner profile on the fire performance of the columns for SR-CFST sections [8].

After reviewing the available literature, further research is needed to fully understand the fire behaviour of SR-CFST sections and the effect of some relevant parameters over their performance under elevated temperatures. That is why, in this paper, an experimental campaign is presented to extend the available data of slender SR-CFST columns under fire. Additionally, a finite element model is developed to study the influence of introducing high-strength materials in the embedded steel profile and the concrete infill of the sections.

2 EXPERIMENTAL INVESTIGATION

2.1 Design of the experimental program

Four fire tests on slender SR-CFST circular and square columns were performed in this experimental campaign. The columns were designed to possess roughly the same steel area (steel profile + outer steel tube) with differences of less than 1% to adequately compare their fire behaviour. All the columns had a length of 3 m. The outer steel tubes of the circular sections consisted of $\phi 273 \times 6.3$ mm hollow tubes while the square specimens were #220x6.3 mm hollow steel tubes. The embedded steel profiles were HEB100 steel sections in all the specimens. The outer dimensions and embedded steel profile of the sections were kept equal for all the column specimens, instead the steel grade and concrete classes were varied following the recommendations of Liew and Xiong [9]. The columns were designated as follows: SR-CFST-X-TMLi (i.e., SR-CFST-S-TML1) where X stands for the cross-sectional shape of the column outer tube (S for square and C for circular) and TMLi denotes the test, each with a different combination of steel grade in the embedded profile and concrete class (1 for normal strength steel and concrete and 2 for high-strength steel and concrete). Table 1 summarizes the characteristics of the test specimens:

Table 1. Characteristics of the tested SR-CFST columns

No.	D or B (mm)	t (mm)	Inner profile	f_a (MPa)	f_y (MPa)	f_c (MPa)	Moist. (%)	$\bar{\lambda}_z$	Load (kN)	Load level	FT _{exp} (min)	FT _{num} (min)	FT _{exp} / FT _{num}
SR-CFST-S-TML1	220	6.3	HEB100	496	315	35.62	5.20	0.62	1348.97	33%	21	20	1.05
SR-CFST-S-TML2	220	6.3	HEB100	496	733	110.20	2.51	0.80	1402.44	21%	58	59	0.98
SR-CFST-C-TML1	273	6.3	HEB100	413	315	40.58	5.36	0.56	1369.30	31%	47	48	0.99
SR-CFST-C-TML2	273	6.3	HEB100	413	733	113.63	3.02	0.74	1559.84	21%	65	77	0.84

D = diameter (circular sections); B = width (square sections); t = steel tube wall thickness; FT: failure time.

2.2 Material properties

2.2.1 Steel

The square and circular hollow tubes were made from cold-formed carbon steel with a S355 steel grade while the embedded steel profiles were hot-rolled with a S275 grade in the TML1 specimens. For the high-strength steel profiles in the TML2, two 10 mm plates and one 6 mm plate of S700MC steel were used for the flanges and web of the section, respectively, to build up the fabricated sections.

The real strength of the outer tube steel (f_a) and embedded steel profile (f_y) was obtained by performing three coupon tests for each type of steel. The average values obtained are included in Table 1.

2.2.2 Concrete

For the concrete infill of the columns, two different types of concrete mixes were used. Normal strength concrete (30 MPa of nominal strength) was used in TML1 specimens while high-strength concrete (90 MPa of nominal strength) was used in TML2 specimens.

The real compressive strength of the concrete mixtures was determined by performing compressive tests on two sets of cylinder samples. The samples were prepared and cured in standard conditions for 28 days. The average compressive strength (f_c) obtained for each mixture is listed in Table 1.

2.2.3 Preparation of the column specimens

All the specimens were prepared at the laboratories of the Concrete Science and Technology Institute (ICITECH), Universitat Politècnica de València (Spain).

Firstly, a steel plate was welded to one end of the steel profile and the thermocouples were placed at three different heights. Then the steel tube, which had two ventilation holes previously drilled, was introduced and welded to the plate. The thermocouples were extracted from the hole located on the upper part of the column. The concrete mixture was then poured inside of the column and vibrated. Once dry, the concrete surface was smoothed to assure the planarity of this end of the column. Finally, a second steel plate was placed at the top end of the specimen and welded to the outer steel tube. Two sets of eight thermocouples were placed at 750 mm and 2250 mm of the column (TC1-TC8) while a set of ten was located at the centre of the specimens (TC1-TC10) to obtain the temperature distribution on the different elements along the column. A schematic view of the test setup and thermocouple locations is included in Figure 1.

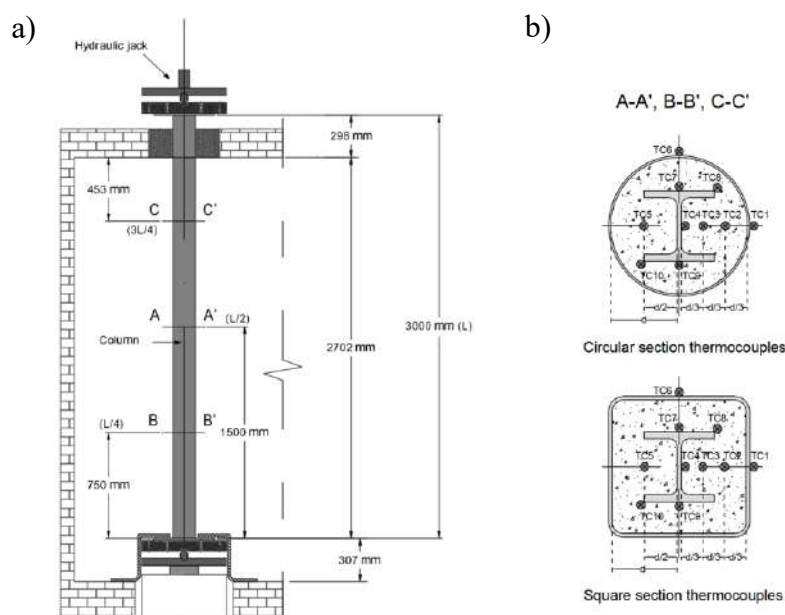


Figure 1: (a) Schematic view of the test setup; (b) thermocouple locations

2.3 Test set-up

The thermo-mechanical tests were conducted at the facilities of AFITI in Toledo, Spain. The specimens were placed inside a 4x4x3 m gas furnace and the load was applied by means of a hydraulic jack with a maximum capacity of 1600 kN attached to their top end. This limitation of the maximum capacity of the hydraulic jack limited the applied load levels for the columns to a 30% for the normal-strength specimens and a 20% for the high-strength ones.

The furnace temperature was controlled and recorded by a set of plate thermometers installed inside the furnace chamber. The boundary conditions for the tests were pinned-pinned (P-P) which were achieved by materializing two knife bearings at each column end. The axial displacement of the specimens was recorded by means of two LVDTs attached to the top end of the columns, outside of the furnace. The load was maintained during the test, while the temperature evolution inside the furnace chamber was set to follow the standard ISO-834 fire curve.

3 RESULTS

3.1 General results

The state of the four column specimens after the fire tests is shown in Figure 2. As can be seen, the primary failure mode observed in all the columns was overall buckling. In the particular case of specimen SR-CFST-S-TML2, a bulging deformation of the outer tube was observed, as well as a local folding at mid-height of the column (Figure 2b). This observation can be explained due to a combination of two factors: the low load applied, and the dilatation of the outer tube caused by the elevated temperature.



Figure 2: Interior of the furnace chamber: (a) SR-CFST-S-TML1, (b) SR-CFST-S-TML2, (c) SR-CFST-C-TML1, (d) SR-CFST-C-TML2

3.2 Thermal response

The temperature evolution at the mid-height of the column for each test is included in Figure 3. For most cases, the inner temperature of the sections did not reach 200 °C before the column failed. The square columns heating rate was faster, compared to the circular specimens due to their higher section factor (A_m/V), leading to shorter failure times for the same load level and steel usage.

The water evaporation effect can be observed as a plateau in the temperature measured at the inner thermocouples. This effect delayed the heating of the section, hence improving the fire-behaviour of the column. The temperature increase in specimens TML1 was less steep as compared to the TML2 specimens, probably due to the higher water content in the normal strength concrete (see Table 1). In the high-strength concrete, the reduced moisture of the concrete evaporates quickly, thus producing a faster heating of the inner parts of the section than their normal-strength concrete counterparts.

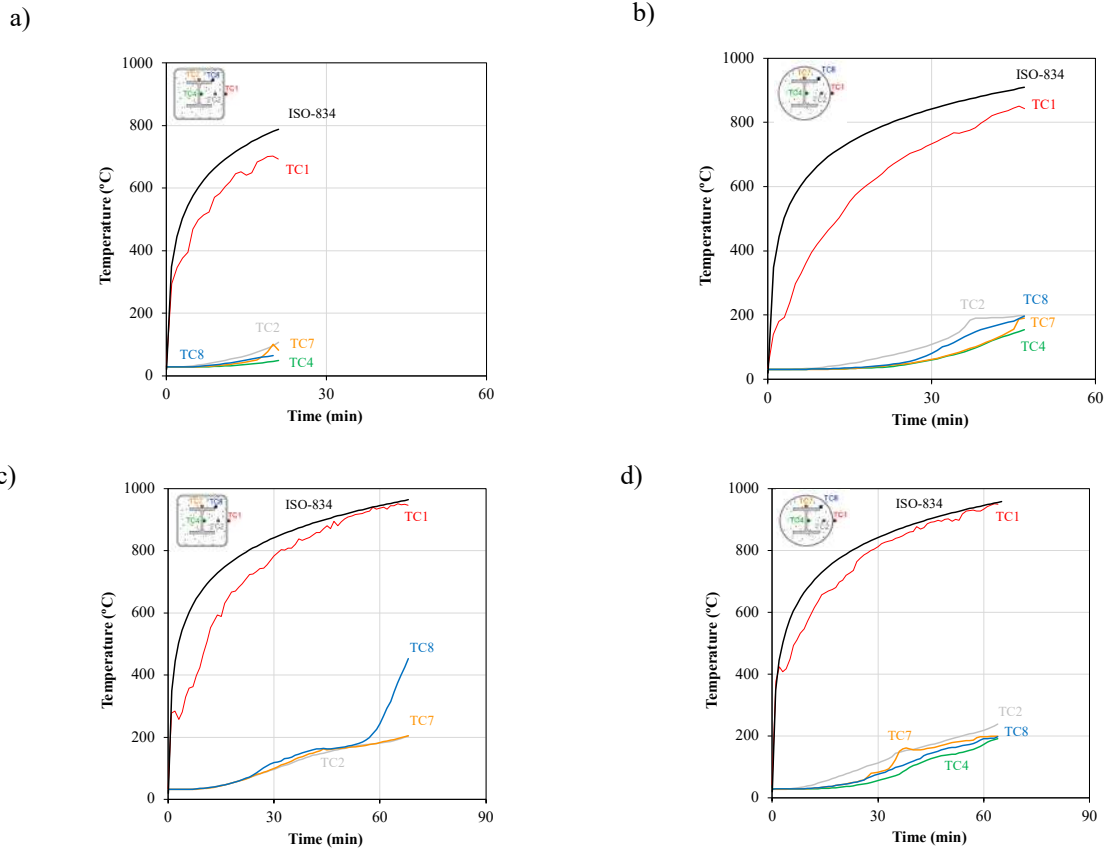


Figure 3: Temperature evolution at mid-height section registered at the fire tests: (a) SR-CFST-S-TML1, (b) SR-CFST-C-TML1, (c) SR-CFST-S-TML2, (d) SR-CFST-C-TML2

3.3 Mechanical response

Figure 4 includes the axial displacement at the top end of the columns along the fire exposure time for the four tested specimens. Four stages can be observed in all curves: an initial stage in which the outer tube bears a great percentage of the load and expands vertically, a second stage in which the steel tube loses its load bearing capacity due to the temperature exposure and shortens, a third stage where the load is transferred to the inner profile and concrete which bear the load during a significant amount of time, until eventually the column fails in the fourth stage due to overall buckling.

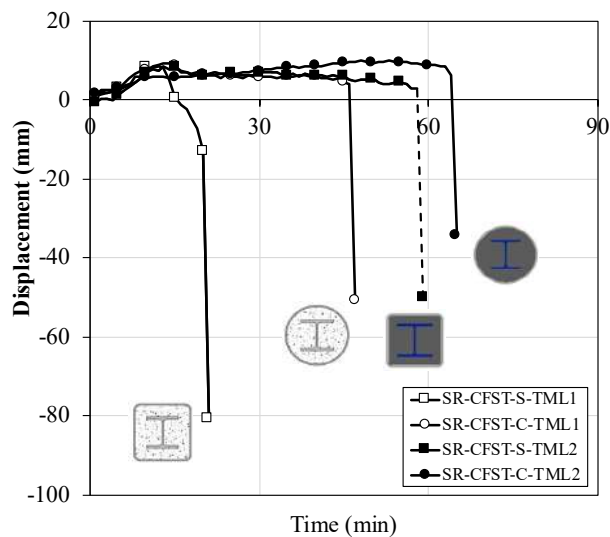


Figure 4: Axial displacement versus time curves for the four SR-CFST column specimens tested

The recommended criteria specified in EN 1363-1 Section 11.1(b) [10] were applied to determine the failure time (FT in Table 1) of the specimens. This standard establishes that the failure of vertical members in compression occurs when any of the following criteria is met:

- Vertical contraction limit: $h/100$ mm
- Contraction velocity limit: $3h/1000$ mm

where h is the column height in mm.

The failure time, for the same load level, was enhanced in the circular section as compared to square ones both in specimens TML1 (26 min) and TML2 (7 min). The higher section factor (A_m/V) of the square specimens, therefore higher amount of surface of the outer tube exposed to fire, resulted in a faster heating and degradation of the columns. The use of high-strength materials for the inner steel profile and the concrete infill increased the failure times of the columns as compared to normal-strength materials in both cases (37 minutes increase in the square sections and 18 minutes in the circular ones). Part of the increase observed in the failure time of the high-strength specimens (TML2) may be attributed to the lower load level applied as compared to the normal-strength specimens (TML1). Even so, the applied load was only a 10% lower, while the increase in failure time was of 38% in the case of circular columns and of 178% in the square ones. This outstanding improvement was caused by the ovalization of the square shape of the outer steel tube due to a combination of the effect of thermal expansion and a reduced applied load, which stabilized the column for a longer period of time. Therefore, only a portion of such enhancement can be attributed to the use of high-strength concrete and steel at the inner parts of the section.

4 DEVELOPMENT OF THE NUMERICAL MODEL

A three-dimensional (3D) finite element model was developed with the finite element analysis package ABAQUS [11], in order to extend the results of the experimental campaign and provide a framework to explore the influence of the variation of the main parameters of the studied typology.

4.1 Geometry and finite element mesh

The geometry of the model consisted of four parts: the outer steel tube, the embedded steel profile, the concrete infill, and the end plate used to distribute the load evenly at the column end (see Figure 5).

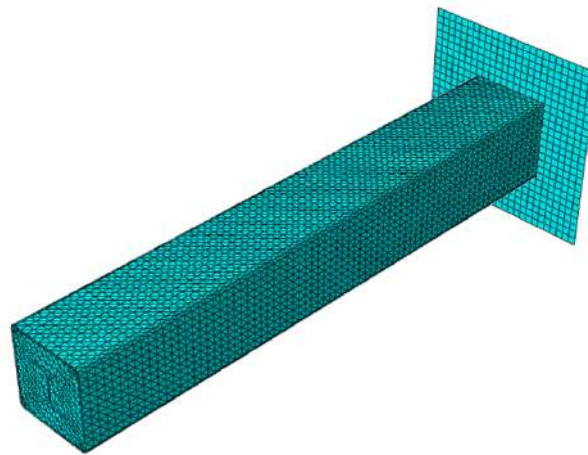


Figure 5: General view of the finite element mesh of the numerical model

In the thermal model, all the elements were modelled with 4-node linear heat transfer tetrahedrons (DC3D4) with nodal temperature degree of freedom, while in the mechanical model they were meshed with 4-noded tetrahedrons (C3D4). The loading plate was modelled as a discrete rigid element with 4-noded 3-d bilinear rigid quadrilateral elements (R3D4). The FE maximum size was set to 20 mm for the inner steel profile and concrete infill and to 15 mm to the outer steel tube, based on previous sensitivity studies by the authors [12,13].

4.2 Boundary conditions

On a first stage, a non-linear heat transfer analysis was conducted. In the validation of the numerical model, the measured temperature curve of the furnace chamber for each test was prescribed, while in the parametric studies the standard ISO-834 [14] fire curve was applied. The recommended values in EN1991-1-2 [15] for the heat transfer parameters were used: a convective coefficient of $\alpha_c = 25 \text{ W/m}^2\text{K}$ and an emissivity value $\varepsilon = 0.7$ were assumed at the exposed steel surface. The fire emissivity was set to $\varepsilon = 1$, and the Stephan-Boltzmann constant to $\sigma = 5.67 \cdot 10^{-8} \text{ W/m}^2\text{K}^4$. The concrete moisture content was assumed equal to a 4% in call cases, as per Clause 3.3.2 (7) of EN1994-1-2 [16].

The output of the thermal analysis (nodal temperatures, NT11) were subsequently imported to the mechanical model as a predefined temperature field to perform a sequentially coupled thermo-mechanical analysis. The boundary conditions at the end of the columns were set to Pinned-Pinned (P-P). Only a half of the column was modelled, using a symmetry boundary condition at the mid-section to reduce the computational cost of the simulations.

4.3 Steel-concrete interaction

Several thermal and mechanical interactions were defined between the concrete and steel parts. Regarding the thermal interaction, a perfect contact was defined between the inner steel profile and the concrete infill. In turn, a gap conductance was introduced between the outer steel tube and the concrete infill to simulate the effect of the expansion of the tube at elevated temperature, which creates a separation between the two elements, generating an “air gap” that delays the heat transfer. This conductance was set to $200 \text{ W/m}^2\text{K}$, based on previous research from the authors [12,13].

The mechanical contact between the steel and concrete parts was defined by means of an interaction property. The normal behaviour was modelled as a “hard contact” and the tangential behaviour was modelled by a friction coefficient of 0.3, as in previous investigations [12]. The tube was welded to the end plate; therefore, a “tie” contact was applied between both parts.

4.4 Material properties at elevated temperatures

The thermal properties of both concrete and steel were defined by considering the values recommended in EN1994-1-2 [16]. The density, conductivity and specific heat of both materials were introduced into the heat-transfer FE model as temperature dependent properties.

The mechanical properties of the materials were introduced in ABAQUS by using different plasticity models. For concrete, the Drucker Prager model was employed, while for steel, an isotropic elastic-plastic model with the von Mises yield criterion was used. For normal strength concrete and high-strength concrete, the elevated temperature reduction coefficients included in Table 3.1 and Table 6.1N of EN1992-1-2 [17] were used, respectively. In turn, for the reduction of the yield strength of steel at elevated temperature, the coefficients in Table 3.1 of EN1993-1-2 [18] were employed.

5 VALIDATION OF THE NUMERICAL MODEL

The presented model is validated in this section against the available data obtained from the previously presented thermo-mechanical experimental campaign for slender SR-CFST columns (see Table 1).

5.1 Thermal validation

The thermal response of the numerical model was validated by comparing the temperatures obtained at the thermocouple locations with the nodal temperature field extracted from the FE analysis. Figure 6 includes a comparison for the circular specimens C-TML1 and C-TML2.

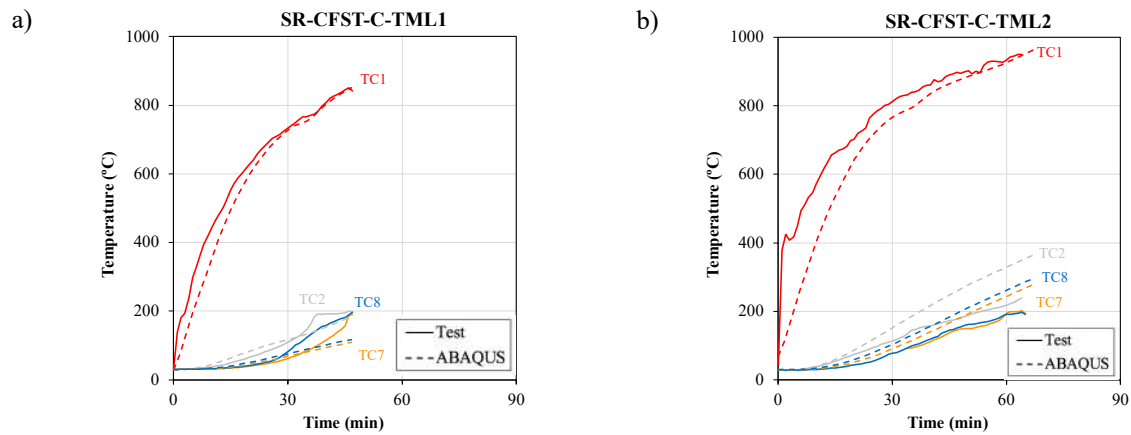


Figure 6: Comparison between measured and numerically calculated temperatures: (a) SR-CFST-C-TML1, (b) SR-CFST-C-TML2

As can be observed, a good agreement is found between the experimental and the numerically obtained temperatures both in the outer tube and at the inner parts of the sections (embedded steel profile and concrete core). Therefore, the thermal response of the model is considered accurate for conducting further numerical studies.

5.2 Mechanical validation

The thermo-mechanical model was validated by simulating the test conditions applied to the columns described at the previous experimental campaign. The numerically obtained time-displacement curves were compared to the experimentally recorded ones for the four column specimens tested; this comparison is shown in Figure 7.

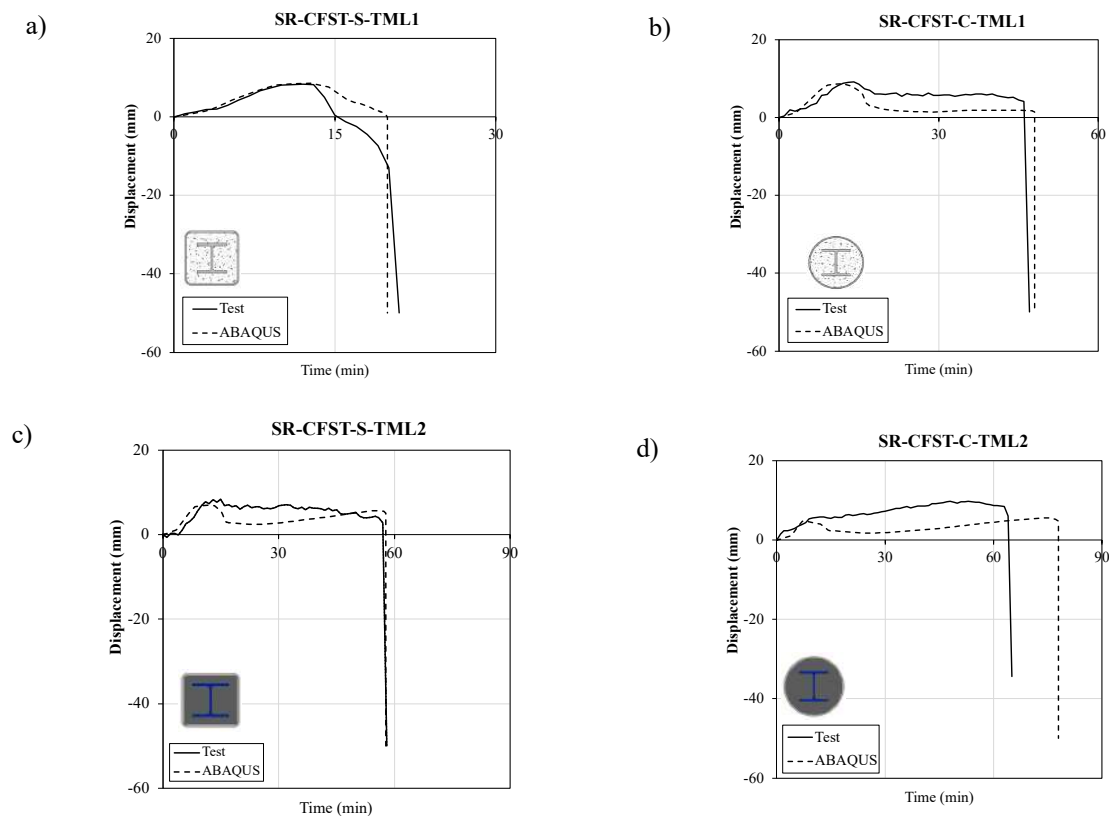


Figure 7: Comparison between measured and numerically calculated axial displacement-time curves for cases: (a) SR-CFST-S-TML1, (b) SR-CFST-C-TML1, (c) SR-CFST-S-TML2, (d) SR-CFST-C-TML2

The numerical predictions in terms of failure time (FT_{num}) are included in Table 1, together with the experimental results (FT_{exp}), as well as the relative error of the numerical predictions (FT_{exp}/FT_{num}). An average value of 0.97 and a standard deviation of 8.89% were obtained, which proves that the numerical model is capable to accurately simulate the fire behaviour of the SR-CFST columns.

6 PARAMETRIC STUDY

Once the numerical model was properly validated, a set of analysis cases was generated to study the influence of the use of high-performance materials on the fire behaviour of SR-CFST slender columns.

6.1 Analysis cases

The parameters varied for the generation of the case specimens to analyse in the parametric study were the yield strength of the embedded steel profile (f_y) and the compressive strength of the concrete infill (f_c). Five different grades were selected for the steel (S275, S355, S460, S550 and S690) while for the concrete four strength classes were studied (C30, C60, C90 and C120). Therefore, two sets of 20 analysis cases were generated – one group for the circular geometry and other group for the square shape – and in each group, the dimensions of the outer steel tube and inner profile, as well as the length of the column and boundary conditions remained constant. The applied load level was set to a 30% of the room-temperature capacity of the columns for all cases. Table 2 summarizes the analysis cases included in the parametric study.

Table 2. Combination of cases for the parametric study

	CIRCULAR CASES	SQUARE CASES
D or B (mm)	273	220
t (mm)	6.3	6.3
Load level	0.3	
f_y (MPa)	275 - 355 - 460 - 550 - 690	
f_c (MPa)	C30 - C60 - C90 - C120	
Inner profile	HEB100	

6.2 Evaluation of the results of the parametric study

6.2.1 General results

As an output from the conducted parametric study, a total of 40 axial displacement-time curves were obtained, one for each case analysis. Figure 8 shows a selection of these graphs, presenting the comparison between equivalent pairs of specimens by fixing the concrete class to C60 (Figure 8a and 8b) and by fixing the steel grade to S355 (Figure 8c and 8d), for clarity purposes.

As it can be observed in a first look to these graphs, the square cases (on the left) outperformed their circular counterparts (on the right), resulting in longer failure times. Although the circular cases have a more favourable thermal behaviour, given their lower section factor (A_m/V), what in turn delays the heating rate of the section and retains its mechanical properties for a longer time period, the square sections have a higher flexural stiffness due to their geometry – for the same amount of steel at the outer tube – as well as a lower applied load value for the same load level. These combined actions led to an enhanced fire performance for the square columns, as compared to their circular counterparts.

The specific influence of the use of the high-performance materials (high-strength concrete and steel) will be analysed in depth in the following subsections.

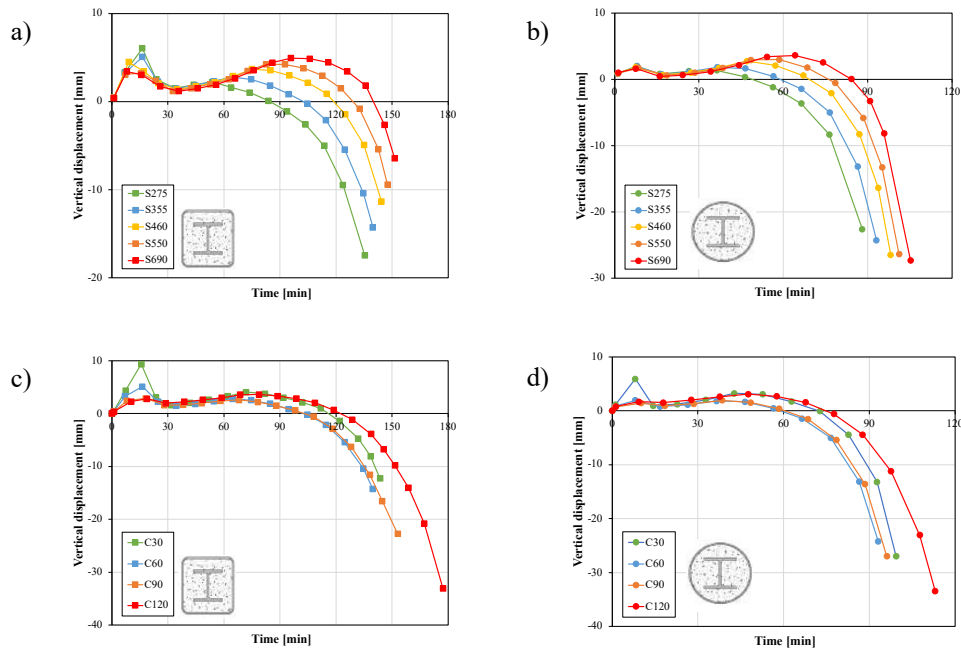


Figure 8: Comparison of the axial displacement-time curves for different steel grade combinations, with C60 concrete class (a and b) and for different concrete classes with S355 steel grade (c and d)

6.2.2 Influence of the concrete compressive strength

The influence of the concrete compressive strength is displayed in Figure 9. The parametric cases are divided in groups according to the steel grade used for the inner profile. Therefore, five groups are formed for each of the studied geometries and, in each one, the four compressive concrete strengths are listed. In this figure, the vertical axis represents the failure time (FT) of each specimen (expressed in minutes), while the concrete compressive strength (f_c) is represented in the horizontal axis.

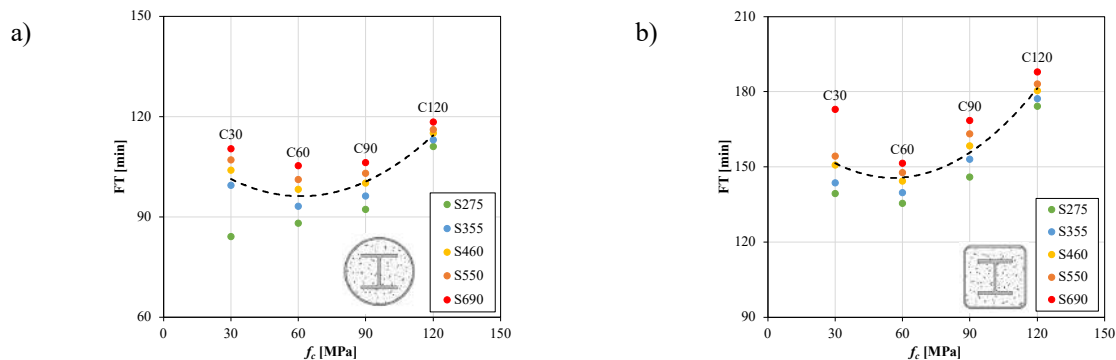


Figure 9: Influence of the concrete compressive strength (f_c) over the failure time of SR-CFST slender columns with circular (a) and square (b) geometries

As can be observed, the most favourable option was the one using the highest compressive strength (120 MPa) in both geometries. The increase in the failure time was more prominent in the square specimens as compared to the circular ones, given their improved flexural stiffness. A slight advantage can be observed when comparing the C30 cases to the C60 and C90 cases in the circular specimens (Figure 9a) and to the C60 in the square cases (Figure 9b). The reason is twofold: first, a higher compressive strength means a higher applied load to the column, as it depends on the properties of the materials of the section at room temperature; and second, high-strength concrete degrades faster at elevated temperatures (> 600 °C) as compared to normal strength concrete, in views of the elevated temperature reduction coefficients for concrete strength in Table 6.1N of EN1992-1-2 [17]. Therefore, the C30 concrete takes advantage of its reduced applied load and the more favourable reduction factors, thus lengthening its failure time.

It is worth mentioning that in this parametric study the moisture content was assumed to be a 4% in all cases. Usually, high strength mixtures (C90-C120) tend to have a lower water content than normal-strength ones (C30), leading to a faster heating and therefore a faster degradation of the mechanical properties in fire, aspect that has not been considered in this study.

6.2.3 Influence of the steel yield strength

The influence of the yield strength (f_y) of the inner steel profile is studied in Figure 10. Like in the previous section, the analysis cases are subdivided in four groups for each geometry, one for each of the studied concrete classes, to isolate and evaluate the effect of different yield strengths. In this figure, the vertical axis represents the failure time (FT) of each specimen (expressed in minutes), while the steel yield strength (f_y) is represented in the horizontal axis.

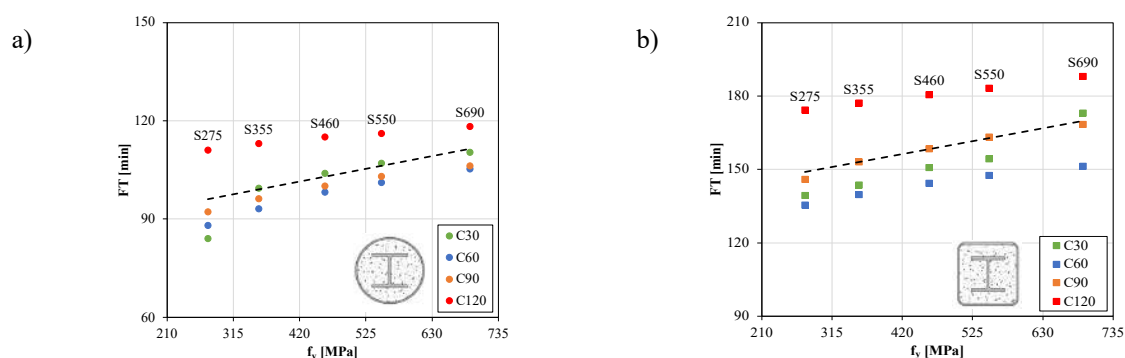


Figure 10: Influence of the steel yield strength (f_y) over the failure time of SR-CFST slender columns with circular (a) and square (b) geometries

The obtained results show that by increasing the grade of the steel of the embedded profile, the failure time of the columns increases in all cases, with a linear trend. As the steel profile results thermally protected by the outer steel tube and the concrete infill, it retains its mechanical properties unaffected by the temperature for a long period of time. Henceforth, a stronger steel grade at the inner profile provides an enhanced fire behaviour of the SR-CFST columns. A clear separation can be observed between the C30-C90 concrete groups and the C120 family, with a significant increase in failure time, proving that high-strength concrete provides the most beneficial fire behaviour, as commented in the previous section.

7 CONCLUSIONS

In this work, four slender SR-CFST columns with different shapes and material properties for the inner steel profile and concrete infill were tested under fire conditions. A finite element model was developed and validated against the results obtained from the conducted experiments, in order to extend these results. Several parametric studies were carried out to study the influence of the material strengths on the fire performance of this type of composite columns.

The use of high-strength materials at the inner parts of the sections proved to be favourable for the fire behaviour of the SR-CFST columns, as it improves their fire resistance. The use of high-strength steel at the inner profile was found beneficial for the column fire behaviour, as it improves its load-bearing capacity while being thermally protected by the surrounding concrete. The effect of the use of high-strength concrete was also found to improve the fire resistance of the columns. The combined effect of the two provides the best results as compared to the use of normal strength materials.

This study proved that the use of high-strength materials in slender SR-CFST columns is a good strategy to improve their fire performance. Notwithstanding, further research is necessary to properly characterize the fire behaviour of this typology, given to the reduced number of available experimental investigations. In future work, the authors intend to study the effect of other relevant parameters; such as the geometry of the section, the inner steel profile dimensions, the applied load level or the column slenderness, among others, to expand and complete the findings of this paper.

ACKNOWLEDGMENT

The authors would like to express their sincere gratitude for the help provided through the Grant PID2019-105908RB-I00 and for the first author's pre-doctoral contract through the Grant PRE2020-093106 funded by MCIN/AEI/10.13039/501100011033 and by "ESF Investing in your future". The authors are deeply grateful to Dr Enrique Serra for his help and assessment to prepare the experiments. The authors would also like to thank the Spanish Association for the Promotion of Research and Fire Safety Technology (AFITI) for providing their facilities and assisting with the setup and performance of the fire tests.

REFERENCES

1. Dotreppe J.C., Chu T.B., Eng R. & Franssen J.M., Steel hollow columns filled with self-compacting concrete under fire conditions. 3rd fib International Congress, Washington DC (USA); 2010.
2. Meng F-Q., Zhu M-C., Clifton G.C., Ukanwa K.U. & Lim JBP., Performance of square steel-reinforced concrete-filled steel tubular columns subject to non-uniform fire. *J Constr Steel Res* 166 (2020). <https://doi.org/10.1016/j.jcsr.2019.105909>.
3. Mao W.J., Wang W. Da & Zhou K, Fire performance on steel-reinforced concrete-filled steel tubular columns with fire protection. *J Constr Steel Res* 199, (2022). <https://doi.org/10.1016/J.JCSR.2022.107580>.
4. Medall D., Ibáñez C., Espinós A. & Romero M.L., Thermo-mechanical compression tests on steel-reinforced concrete-filled steel tubular stub columns with high performance materials. *Steel and Composite Structures* 49, 533–546 (2023). <https://doi.org/10.12989/scs.2023.49.5.533>.
5. Tan Q., Gardner L. & Han L., Performance of Steel-Reinforced Concrete-Filled Stainless Steel Tubular Columns at Elevated Temperature. *International Journal of Structural Stability and Dynamics* 19, (2019). <https://doi.org/10.1142/S0219455419400029>.
6. Tan Q., Gardner L., Han L. & Song T., Fire performance of steel reinforced concrete-filled stainless steel tubular (CFSSST) columns with square cross-sections. *Thin-Walled Structures* 143, (2019). <https://doi.org/10.1016/j.tws.2019.106197>.
7. Espinos A., Romero M.L. & Lam D., Fire performance of innovative steel-concrete composite columns using high strength steels. *Thin-Walled Structures* 106, 113–128 (2016). <https://doi.org/10.1016/j.tws.2016.04.014>.
8. Mao W.J., Wang W.D. & Xian W., Numerical analysis on fire performance of steel-reinforced concrete-filled steel tubular columns with square cross-section. *Structures* 28, 1–16 (2020). <https://doi.org/10.1016/j.istruc.2020.08.043>.
9. Liew J.Y.R., Xiong M. & Xiong D., Design of Concrete Filled Tubular Beam-columns with High Strength Steel and Concrete. *Structures* 8, 213–226 (2016). <https://doi.org/10.1016/j.istruc.2016.05.005>.
10. EN 1363-1. Fire resistance tests - Part 1: General requirements. Comité Européen de Normalisation; 2020.
11. Dassault Systèmes. Abaqus Unified FEA - SIMULIATM by Dassault Systèmes®. Dassault Systèmes Simulia; 2021.
12. Albero V., Espinos A., Romero M.L., Hospitaler A., Bihina G. & Renaud C., Proposal of a new method in EN1994-1-2 for the fire design of concrete-filled steel tubular columns. *Eng Struct* 128, 237–255 (2016). <https://doi.org/10.1016/j.engstruct.2016.09.037>.
13. Medall D., Espinós A., Albero V. & Romero M.L., Simplified proposal for the temperature field of steel-reinforced CFST columns exposed to fire. *Eng Struct* 237, (2022). <https://doi.org/10.1016/J.ENGSTRUCT.2022.115083>.
14. International Organization for Standardization. ISO 834-11 - Fire resistance tests — Elements of building construction. International Organization for Standardization, Geneva; 2014.
15. EN 1991-1-2, Eurocode 1: Actions on structures - Part 1-2: General actions - Actions on structures exposed to fire. Comité Européen de Normalisation, Brussels; 2002.
16. EN 1994-1-2, Eurocode 4: Design of composite steel and concrete structures. Part 1.2: General rules - Structural fire design. Comité Européen de Normalisation, Brussels; 2005.
17. EN 1992-1-2, Eurocode 2: Design of concrete structures, Part 1.2: General rules – Structural fire design. Comité Européen de Normalisation, Brussels; 2004.
18. EN 1993-1-2, Eurocode 3: Design of steel structures, Part 1.2: General rules – Structural fire design. Comité Européen de Normalisation, Brussels; 2005.

FIRE BEHAVIOUR OF CONCRETE-ENCASED CONCRETE-FILLED STEEL TUBE SLENDER COLUMNS UNDER CONCENTRIC AND UNIAXIAL ECCENTRIC LOAD

Nuoxin Wu¹, Kang Hai Tan²

ABSTRACT

Concrete-encased concrete-filled steel tube (CECFST) columns have become increasingly popular in mega construction structures in recent years owing to their superior structural performance. Despite extensive research under normal condition, limited attention has been given to their performance in fires. This paper aimed to fill in this research gap through experimental studies. Three CECFST slender columns, including one concentrically-loaded and two uniaxial eccentrically-loaded specimens, were tested in transient fire conditions under ISO 834 fire curve. Key test findings including the failure mode and process, temperature distribution, structural response and fire resistance were reported. It was found that CECFST generally attain superior fire ratings compared to concrete-filled steel tube (CFST) columns. Nonetheless, a potential risk of explosive spalling exists in the outer concrete layer, particularly when the moisture content is excessively high. The test results underscore the importance of employing proper concrete curing methods, especially during the early stages, to mitigate premature failures of these columns under elevated temperatures.

Keywords: Composite columns; Fire resistance; PP fibre reinforced concrete; Eccentric loading

1. INTRODUCTION

In recent years, concrete-encased concrete-filled steel tube (CECFST) columns have gained significant popularity in large-scale construction projects due to their exceptional structural performance. CECFST columns are characterised by their high compressive strength, excellent ductility and superior stiffness [1]. This innovative type of composite structures is composed of an outer reinforced concrete component and an inner concrete-filled steel tube (CFST) as shown in Figure 1(a). While extensive research has been conducted on their behavior under normal conditions, their performance in fire scenarios has received comparatively limited attention. Though it is widely presumed that the concrete encasement of CECFST columns provides enhanced fire protection, it is crucial to substantiate this belief through more comprehensive physical testing.

Abundant research works on fire performance of concrete-steel composite columns have been conducted in recent decades. Post-earthquake fire performance was investigated by Wang et al. [2] and design rules were proposed. Besides, Han et al. [3] investigated the fire performance of concrete filled stainless steel tubular (CFSST) columns under fire, and the test parameters included load level, sectional type and column dimensions. Lu et al. [4] explored the fire performance of self-consolidating concrete filled double skin tubular columns. Moreover, Moradi et al. [5] collected near 300 experimental data and used artificial neural networks to evaluate the impact of various parameters on fire resistance of CFST columns.

¹ PhD Candidate, School of Civil and Environmental Engineering, Nanyang Technological University
e-mail: nuoxin002@e.ntu.edu.sg, ORCID: <https://orcid.org/0000-0003-3056-3333>

² Professor, School of Civil and Environmental Engineering, Nanyang Technological University
e-mail: ckhtan@ntu.edu.sg, ORCID: <https://orcid.org/0000-0003-1500-6643>

In the existing literature on CECFST columns, Zhou and Han have shown that the CECFST columns exhibits higher fire resistance compared with CFST counterparts because of the excellent insulation provided by concrete encasement [6]. However, their study focused on the fixed-ended columns under concentric load, neglecting the effect of slenderness and load eccentricity. To bridge this research gap, current study aims to explore fire resistance of CECFST slender pin-ended columns under different load eccentricities.

2. EXPERIMENTAL PROGRAMME

2.1 Specimen design

In this study, three slender CECFST columns were designed and fabricated according to EC4-1-1 [7]. Table 1 lists the details of the test specimens, where B is the section size, D and t represent outer diameter and wall thickness of the steel tube, respectively. Three levels of load eccentricities (E) ranging from 0 to 80 mm were selected to study their effect on fire resistance. To evaluate the second-order effect, the effective length of each specimen exceeded 3000 mm. According to EC4-1-1 [7], their slenderness ratio, calculated as 0.659, falls beyond the scope of a stub column per Eurocode's definition. Besides, it is worth noting that P_c is ambient load capacity calculated considering second-order effect based on EC4-1-1 [7], while P_a represents applied load during fire test with a load ratio $n = P_a/P_c$ set as 0.35. It is important to highlight that two vent holes were pre-drilled at both ends of steel tube before casting concrete, which were located 100 mm away from the endplates. This step was necessary to release water vapour from the core concrete during fire exposure and prevent explosion of trapped vapour.

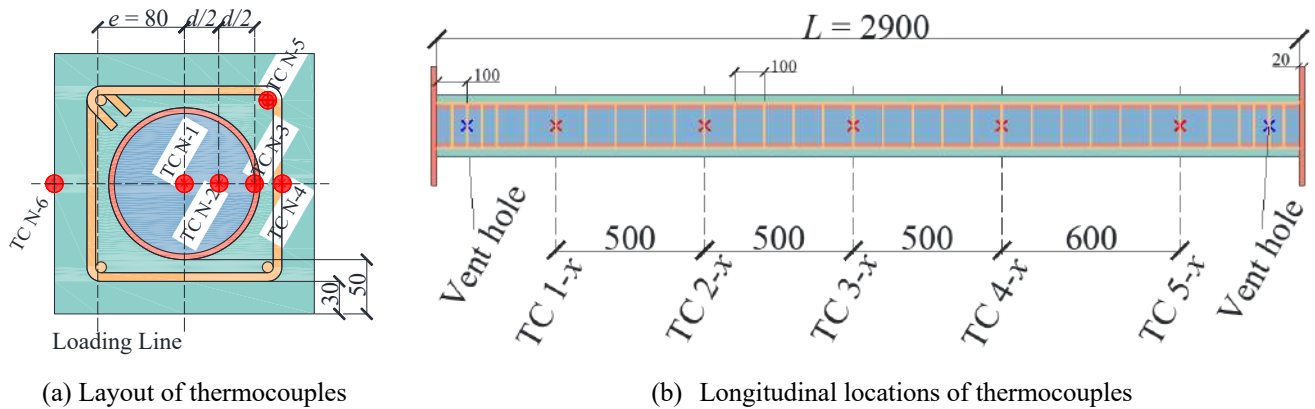


Figure 1. Test setup and instrumentations

Table 1. List of specimens

Specimen	Cross-section $B \times B$ (mm)	Steel tube $D \times t$ (mm)	Rebar No.-dia.(mm)	E (mm)	L_e (mm)	λ_{EC4}	P_c (kN)	P_a (kN)
L2900-E0	240 × 240	140 × 4.8	4Φ10	0	3220	0.659	2550	890
L2900-E40	240 × 240	140 × 4.8	4Φ10	40	3220	0.659	1300	455
L2900-E80	240 × 240	140 × 4.8	4Φ10	80	3220	0.659	800	280

2.1 Material properties

Tensile tests on steel coupons were performed following the procedures outlined in ASTM Standard E8/E8M-16a [8] for steel tubes, rebars and stirrups. Three coupons were fabricated for each component. Table 2 lists the mean results including the elastic modulus (E_s), yield strength and strain (f_y and ϵ_y) and ultimate strength and strain (f_u and ϵ_u). The coupons were elongated using a servo-hydraulic testing machine with a 100 kN capacity in displacement-controlled manner. The applied loading rates commenced at a speed

of 0.05 mm/min within the elastic range and increased to 0.8 mm/min after the material had yielded. Compression tests on concrete cylinders were conducted according to BS EN 12390-3 [9] for both inner and outer concrete. A total of fifteen concrete cylinders, each measuring 150 mm in diameter and 300 mm in height, were produced from the same concrete batch as the CECFST specimens. Inadequate curing time can compromise quality of concrete and make it susceptible to spalling. Therefore, a minimal of three-month curing process was executed to ensure competent structural performance. Additionally, 0.2 vol.% (1.94 kg/m³) polypropylene (PP) fibre was added to the outer concrete to prevent pre-mature explosive spalling of concrete during fire. Furthermore, the elastic modulus $E_{cm}=22(f_c/10)^{0.3}$ for both the inner and outer concrete was established in accordance with EC2-1-1 [10].

Table 2. Material properties

Steel					
	E_s (GPa)	f_y (MPa)	ε_y (%)	f_u (MPa)	ε_u (%)
Tube (4.8 mm)	214	360	0.194	501	13.0
Rebar (10 mm)	202	523	0.259	649	11.4
Stirrup (8 mm)	199	370	0.362	461	8.62
Concrete					
	f_c (MPa)	E_c (GPa)	PP fibre content (kg/m ³)		
Inner concrete	31.5	31	-		
Outer concrete	36.6	32.5	1.94		

2.3 Test setup

To record temperature variations across a specimen, 30 butt-welded chromel–alumel Type-K thermocouples were positioned at 6 points within the cross-section of CECFST columns as shown in Figure 1(a). Each thermocouple is labeled TC $N-x$ (with N ranging from 1 to 5 and x ranging from 1 to 6), denoting its placement on the N th cross-section at the x th location. Specifically, thermocouples TC N-1 and N-2 measured the temperature within the inner concrete. TC N-3 to N-6 were responsible for recording temperatures across different components: the steel tube (TC N-3), stirrup (TC N-4), reinforcement bars (TC N-5), and the outer concrete layer (TC N-6). The arrangement of instruments and fire test set-up are shown in Figure 2. Four LVDTs ($L1-L4$) were positioned at each end of the column to monitor thermal expansion, axial shortening and end rotation. Additionally, an LVDT ($L5$) was vertically placed at mid-point of the column with a ceramic rod for thermal insulation and displacement transmission. A load cell positioned between the actuator and knuckle bearing device was used to record the load applied to columns. ISO 834 standard fire curve was programmed as the temperature of electric furnace during transient fire tests, while applied load P_a was maintained by an actuator with capacity of 5000 kN.

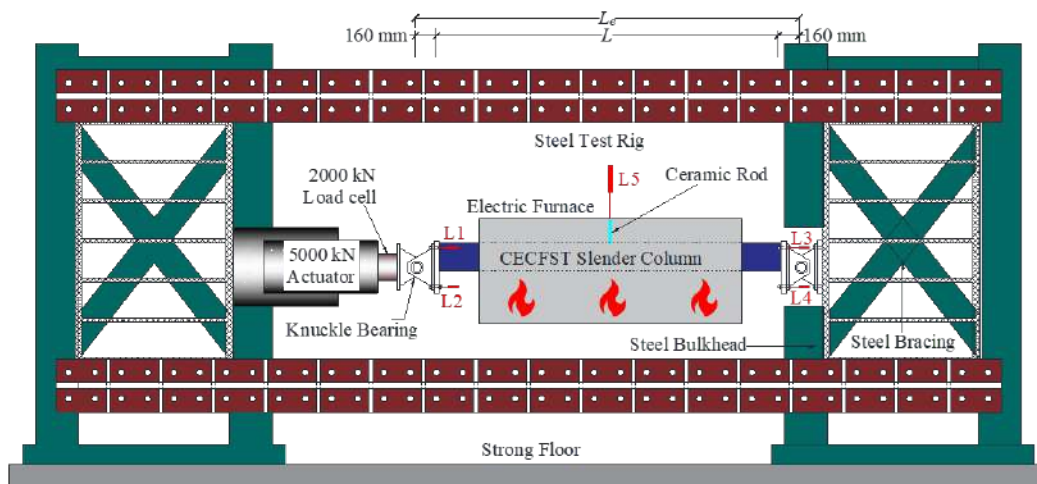


Figure 2. Test setup and instrumentations

2.4 Test procedure

To accurately replicate the CECFST columns in real-life conditions of a fire, fire resistance tests were performed under transient heating conditions, where the temperature varied over time. The test procedure shown in Figure 3 was executed compliant with EN 1363-1 [11]. Before testing, each specimen was preloaded to 10% of its load-bearing capacity. This preliminary step was essential to prevent potential equipment malfunctions and eliminate any existing slack. Following this, the pre-load was removed before initiating the formal test. The application of axial load to the columns was controlled in a displacement-driven approach. The actuator progressed at a constant rate of 0.3 mm/min until the intended load P_a . This load was maintained for 15 minutes to allow for the stabilization of both deflection and load.

Following this stabilization period, the electric furnace was engaged to replicate the ISO 834 standard fire curve, marking the commencement of the time axis in the fire test. Notably, the target load P_a was consistently upheld throughout the fire exposure. The tests concluded once the columns were unable to support P_a . The time from activating to deactivating the furnace determined the fire resistance of CECFST columns. After completing the tests, the specimens were left to cool naturally to room temperature. A detailed examination followed, focusing on failure mode, temperature distribution and structural response of the CECFST slender columns.

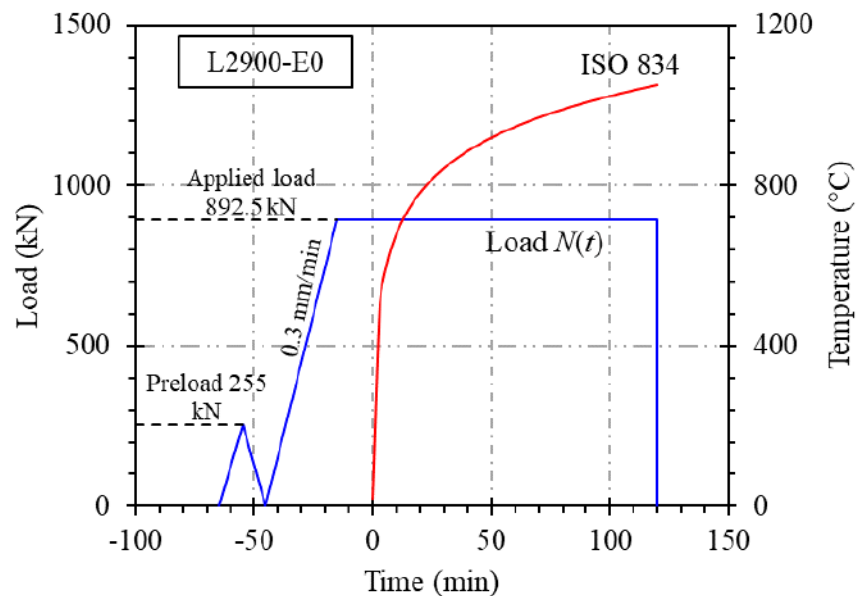


Figure 3. Test procedure

3. RESULTS AND DISCUSSIONS

3.1 Failure mode and failure process

After fire test, the residual deformation is shown in Figure 4, including both overall and localised failure patterns. A smooth, bow-shaped bending deformation was consistently observed across all specimens, accompanied by extensive tensile cracking along the bottom convex side. The observations indicated remarkable ductility and high participation of the whole column. This can be attributed to the inner steel tube, which significantly enhanced the ductility of the CECFST columns. All specimens exhibited a global buckling failure mode. This could be attributed to two reasons: 1) The tendency for slender columns to undergo global buckling under compression, specially evident in the tested specimens with a high λ_{EC4} value of 0.659; 2) The combined effects of eccentricity, initial imperfection and self-weight, which predefined the initial shape before exposure to fire, with the enduring fire exposure further amplifying the residual failure shape. Notably, the effect of initial imperfection and self-weight on load-bearing capacity is generally marginal, typically less than 1% based on calculation.

Despite the uniformity in buckling failure mode among the three columns, variations were observed in the damage extent of compression side. Figure 4 shows the localised damage pattern particularly in the middle region of the columns. Pronounced concrete crushing was evident in specimens L2900-E0 and L2900-E40, with the latter exhibiting more severe damage. Conversely, specimen L2900-E80 showed less apparent concrete crushing on the compression side. Furthermore, the concrete located at corners tended to sustain more extensive damage compared to the sides when exposed to fire. This type of deterioration, known as corner spalling, becomes increasingly significant with continued fire exposure [6, 12].

As for the failure process, water started to vaporise and was steadily released through the leakage at openings in the initial phase of testing. Moisture further escaped from both ends of the column through the surface of the outer concrete, evidencing as liquid water. This occurred as the water vapor from the inner concrete migrated through the vent holes and condensed upon contacting with the cooler external atmosphere. The first violent sound from specimen L2900-E40 was recorded after 38 minutes of heating, followed by four more clear sounds in the subsequent 42 minutes leading up to its failure. Considering the ultimate failure status of specimen L2900-E40, these sounds likely indicated explosive spalling. Although normal concrete is generally less prone to explosive spalling due to higher permeability, prior research has demonstrated the potential for normal concrete to undergo spalling at elevated temperatures [13]. Under the combined effects of compression, bending (especially on the concave side), and high temperatures, the concrete in L2900-E40 was subjected to significant stress, likely exacerbating microstructural deterioration. Accordingly, specimen L2900-E40 exhibited pre-mature failure resulting from the explosive spalling. It is noteworthy that, unlike L2900-E40, no such violent spalling was observed in the other two specimens. These test results highlight the critical importance of proper concrete curing practices, particularly in the early stages, to prevent premature failure of columns under high temperature conditions.

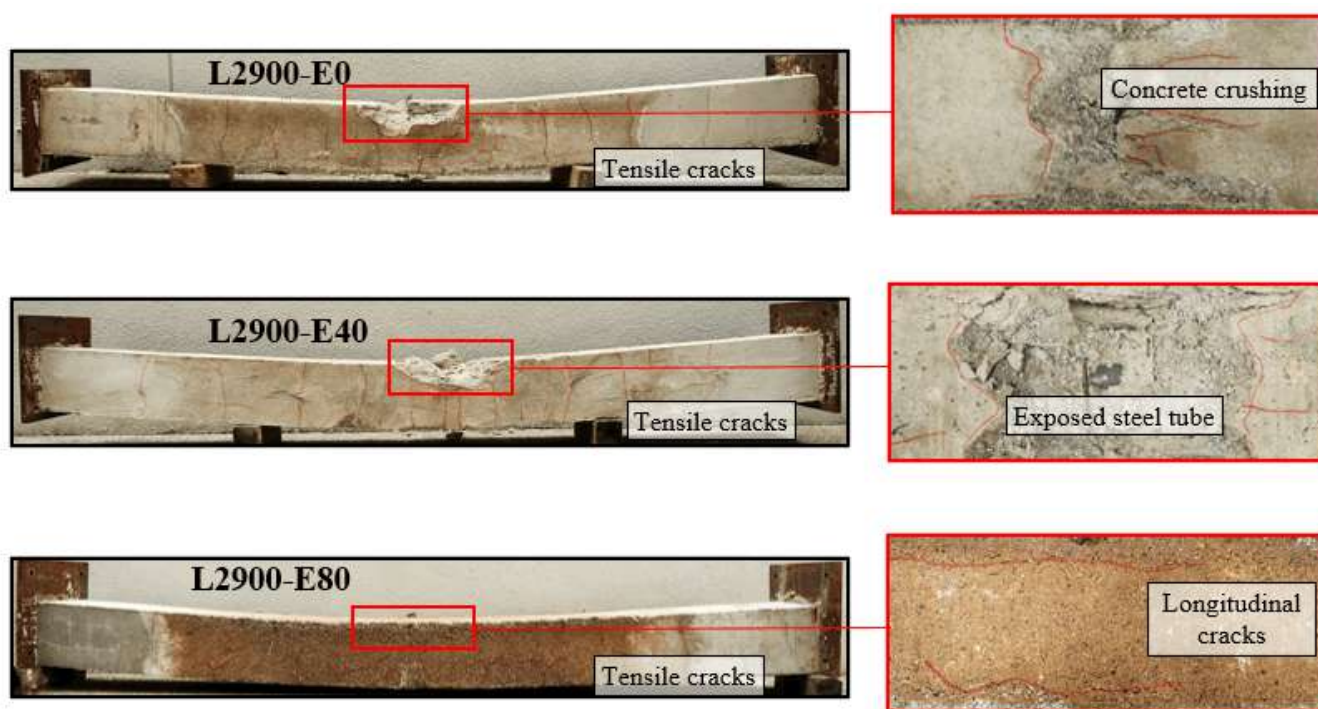


Figure 4. Failure patterns (overall and localised)

3.2 Temperature distributions

The objective was to conduct fire resistance tests on CECFST columns, following the ISO 834 fire curve. Figure 5 shows the temperature distribution within the furnace alongside the ISO 834 fire curve. The temperature readings, derived as an average from three type-K thermocouples strategically placed in the furnace, generally indicated a uniform temperature distribution. In the absence of a specimen, the electric

furnace could closely match the ISO 834 fire curve. However, introducing a large column specimen resulted in temperature deviations, likely due to the furnace's limited power capacity.

For specimens L2900-E40 and L2900-E80, the furnace temperature rise lagged behind the ISO 834 curve initially, with a maximum discrepancy of approximately 200°C in the early stages. After 70 minutes, the furnace temperature surpassed ISO 834, reaching a peak of 1300°C for specimen L2900-E80. The marginally lower temperature observed in specimen L2900-E0, as compared to the other specimens, was possibly a result of improper sealing of furnace opening. Despite using effective insulation materials like ceramic fiber cloth and mineral wool, it was possible they did not entirely seal the furnace.

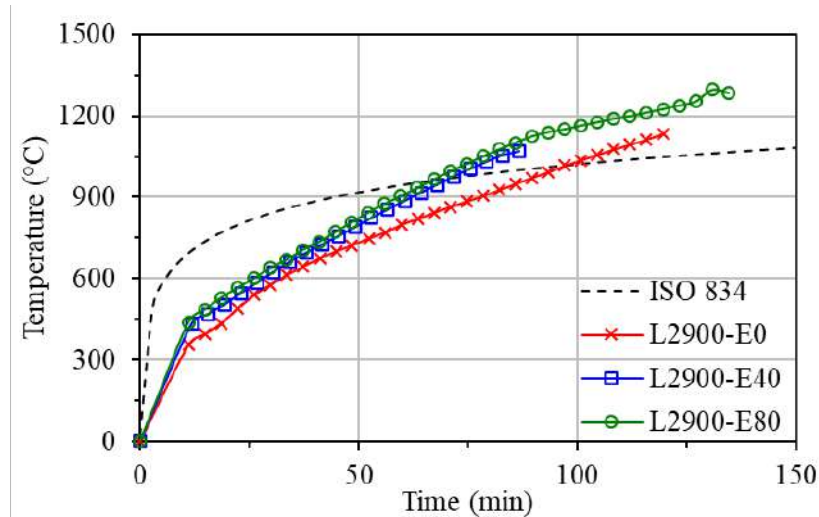


Figure 5. Furnace temperature

The thermal profile of concrete and steel reinforcement significantly influences performance of columns in fire scenarios. Thus, a precise assessment of temperature distribution, both longitudinally along the column and transversely within a cross-section, is crucial. As mentioned in Section 2.3, a 2000 mm central segment of the columns was exposed to heat, limited by the dimensions of furnace. Figure 6 presents the temperature development within the heated segment, focusing on cross-sections 2–4 of specimen L2900-E0. Six thermocouples were embedded at various points across each cross-section.

As can be found in Figure 6, thermocouples placed at identical locations across various cross-sections exhibited similar temperatures. This observation indicated a relatively uniform temperature distribution along the member length inside the furnace. Among the six thermocouples at each cross-section, the temperature variation of TC N-4 and TC N-5 (depicted in green and orange in Figure 6, respectively) is more significant compared to others. TC N-4 and TC N-5 measured the temperature of stirrups and rebars, respectively, both of which were encased in concrete cover. Therefore, the observed temperature difference could be attributed to progressive damage and delamination of the concrete cover at different cross-sections, which disrupted the heat conduction and affected the temperatures of rebars and stirrups.

Plateau stage as circled in Figure 6 was observed in TC N-1, N-2 and N-3 for all three specimens. This phenomenon occurred due to the endothermic process of water vaporisation. As moisture turns into vapor, it absorbed latent heat from its surroundings, creating a cooling effect that slows down the rise in surrounding temperature. Notably, this plateau stage happened at approximately 130 °C, slightly above the boiling point of water (100 °C). This elevation in the vaporization temperature could be explained by the higher pore pressure within the specimens, compared to atmospheric pressure, which raises the vaporization point.

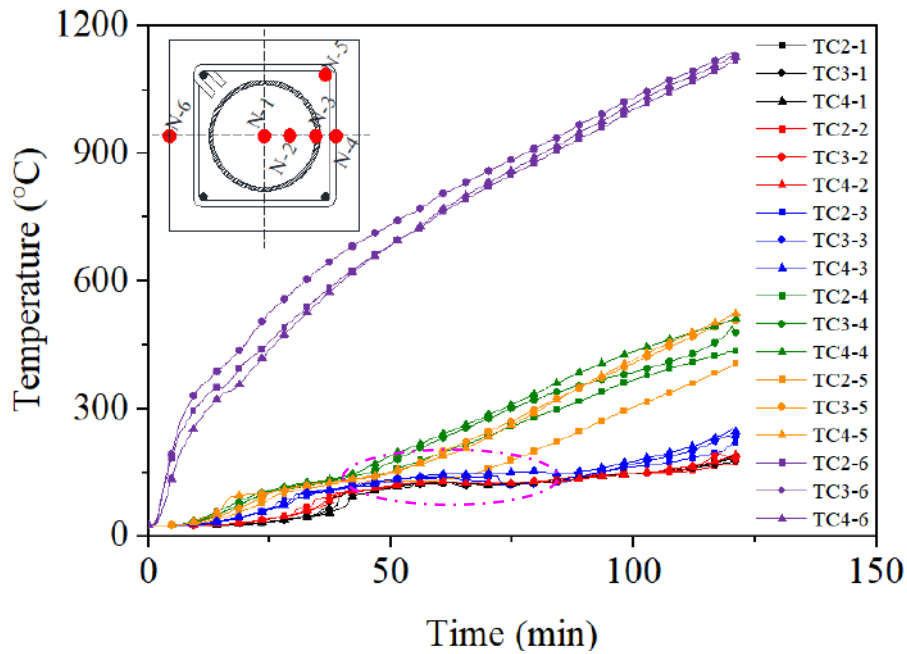


Figure 6. Temperature distribution on cross-sections 2, 3 and 4 of specimen L2900-E0

In relation to the temperature field of unheated column segment, Figure 7 depicts temperature–time relationship at cross-sections 1 and 5 of specimen L2900-E80. A significantly lower temperature distribution was observed for unheated segments, where the maximum temperature was below 200 °C until conclusion of the test except for TC 1-5. Notably, the temperatures at cross-section 1 (represented by solid lines in Figure 7) were slightly higher than those of cross-section 5 (depicted with dashed lines). This discrepancy was attributed to the challenges in completely sealing the furnace opening, and the leakage at opening led to a temperature imbalance between two sides. Furthermore, plateau stage was again detected for unheated segments as marked in Figure 7. Likewise, it was due to water vaporisation and occurred just above 100 °C.

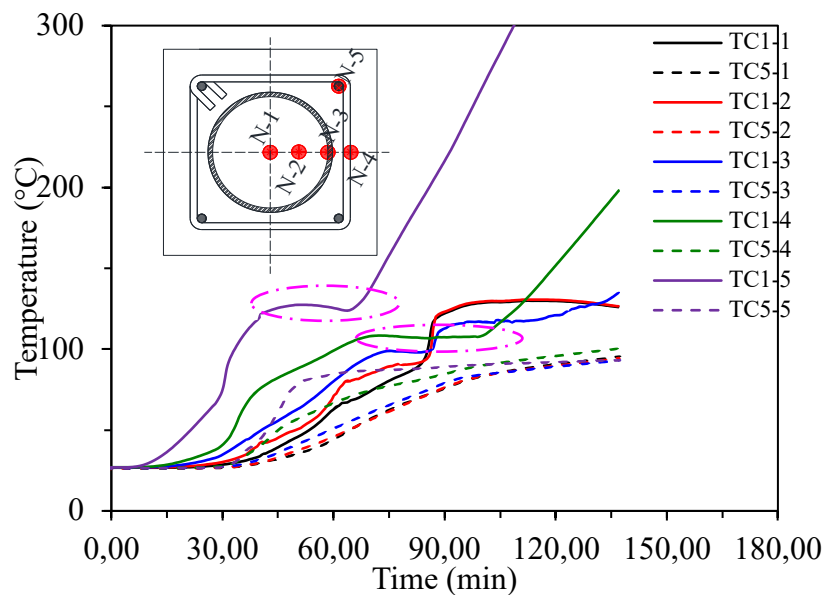


Figure 7. Temperature distribution on cross-sections 1 and 5 of specimen L2900-E80

The temperature histories measured at column middle cross-section of three specimens are shown in Figure 8. These temperature trends, upon analysis, can be categorized into three distinct groups: TC 3-6, which

recorded the temperature of the outer concrete surface; TC 3-4 and 3-5, which monitored the temperature of the reinforcing cage; and TC 3-1 to 3-3, which captured the temperature of the inner concrete and steel tube. The first group of curves, indicated in purple in Figure 8, demonstrated temperatures exceeding 1000 °C by the end of the tests. Since the central 2000 mm of the columns was subjected to fire on all sides, TC 3-6 in all tests basically aligned well with the measured furnace temperature as reported in Figure 5. Similar temperature distributions between TC 3-4 and 3-5, the second group of curves, are observed throughout the tests in all specimens. For CECFST specimens, the concrete cover effectively slowed down the heat transfer to the embedded steel reinforcements, leading to a thermal lag of approximately 700 °C compared to TC 3-6. During the fire tests, temperatures of inner components of CECFST, such as steel tube and inner concrete, were basically lower than 400 °C even after enduring an extended burning time of 130 min for specimen L2900-E80. This temperature level was considered insufficient to degrade the yield strength of structural steel, underscoring the significant protective role of concrete encasement. Relatively higher heat capacity and lower conductivity ensured concrete to absorb energy and delay temperature increase of steel tube. The concrete thickness, measuring 50 mm from the exterior surface of the steel tube to the outer concrete, acted as a physical barrier, shielding the steel tube from direct fire exposure. In engineering practice, this cover would be even thicker than in the scaled-down tests, ensuring that CECFST columns attain high fire ratings without the need for additional fire protection measures.

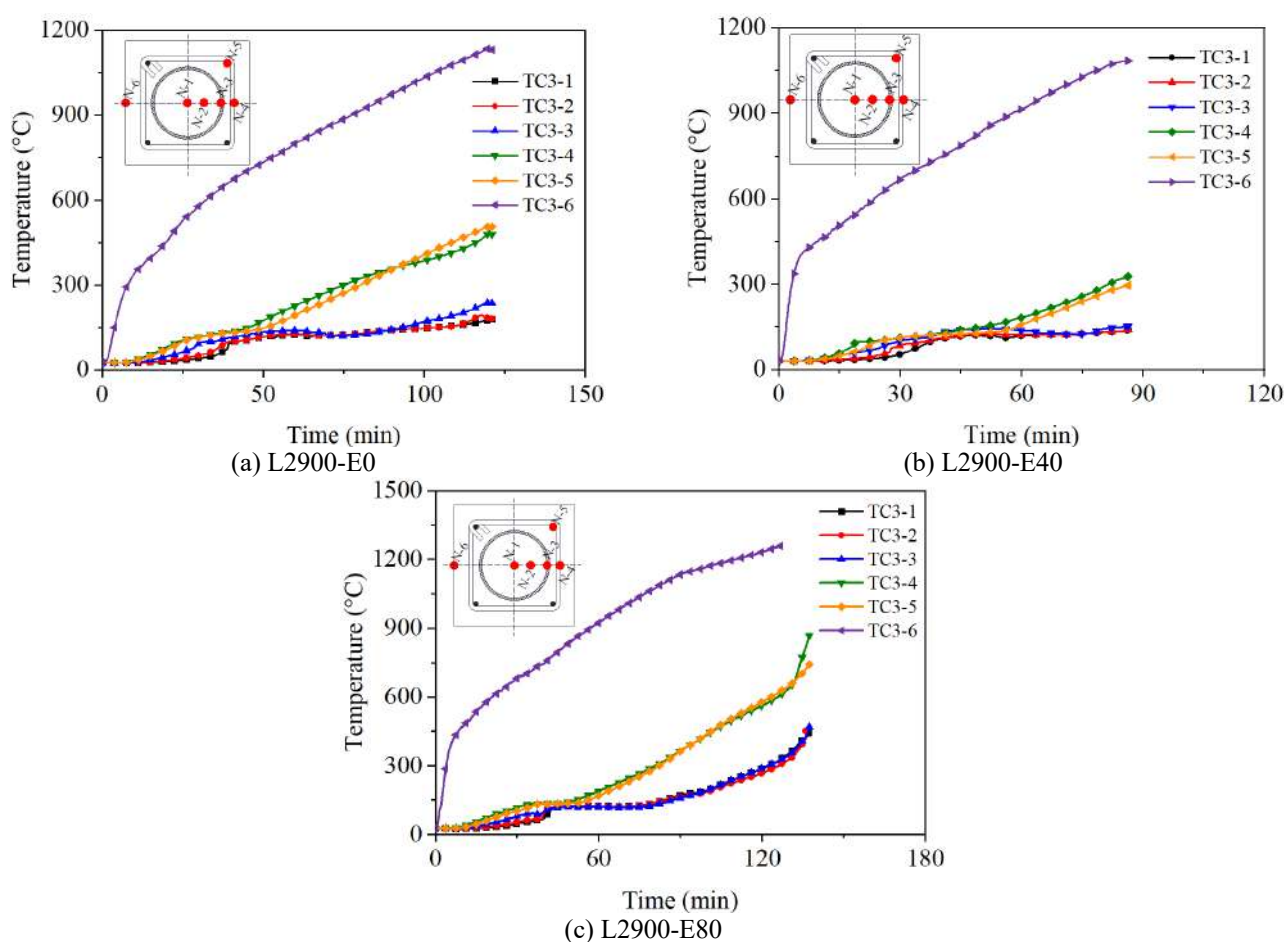


Figure 8. Measured temperature versus time relationship

3.3 Structural response

Axial deformation and lateral deflection are crucial in evaluating behaviour of CECFST columns at elevated temperatures. Axial deformation was gauged by taking average values from $L1$ to $L4$ mounted at both endplates. Figure 9(a) shows axial deformation for all columns. It should be noted that the axial deformation was initially set to zero at the onset of heating ($t = 0$). The adopted sign convention designated positive values for expansion and negative for shortening. Overall, the axial deformation pattern for all specimens could be

segmented into three distinct phases: OA (expansion phase), AB (shortening phase) and BC (failure phase). Typical anchor points were clearly marked in Figure 9(a). Phase OA was characterised by the thermal expansion of concrete and steel at elevated temperatures. This phase lasted until around 40 minutes, during which the column internal components were generally within 500 °C. Phase AB emerged when material stiffness deterioration at high temperatures counterbalanced the thermal expansion. This caused the columns to start shortening and axial deformation gradually reverted to 0 mm. In the failure phase BC, subjected to prolonged fire exposure, a significant reduction in the strength and stiffness of concrete and steel led to a pronounced contraction. Take specimen L2900-E80 as an example, phases OA and AB cumulatively lasted 117 minutes with a zeroed deformation. A sudden change in axial deformation occurred at the onset of anchor point B and specimens finally failed with a maximum deformation of 4 mm. Additionally, it was observed that specimen L2900-E80 with largest eccentricity exhibited the least shortening among the three specimens, possibly owing to the minimal applied load ($P_a = 280$ kN).

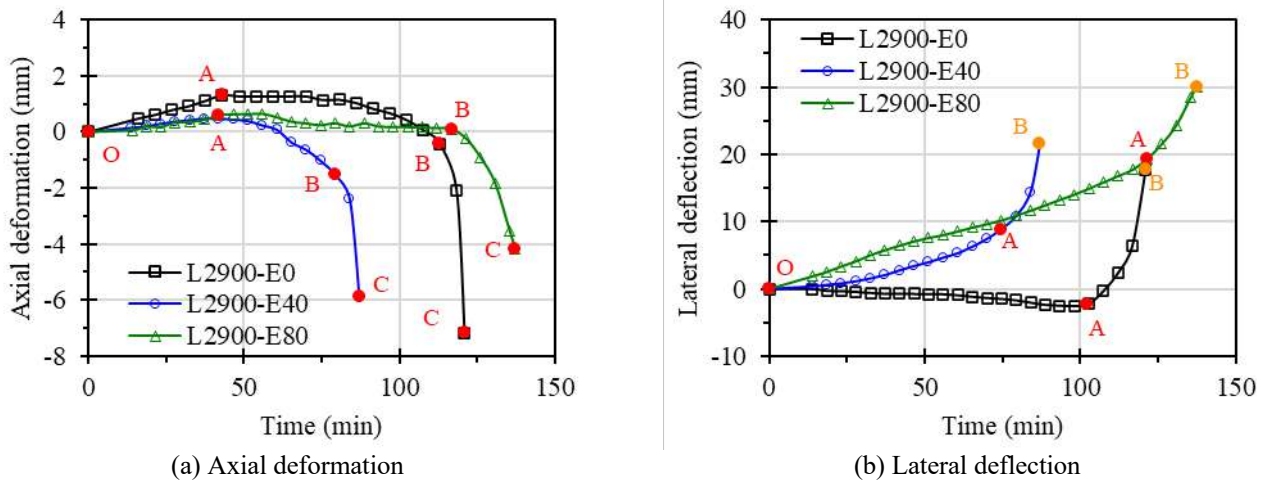


Figure 9. Axial/lateral deformation–time curves CECFST slender columns under fire condition

Mid-height lateral deflection was measured by $L5$ as specified in Figure 1. The lateral deflection versus time relationship of three specimens is shown in Figure 9(b). Unlike the three phases identified in axial deformation behaviour, lateral deflection curve can be segmented into two distinct phases. The first phase OA is a moderate-deformation phase characterised by a deflection rate below 0.5 mm/min, while the second phase AB is a rapid-deformation phase identified by a deflection rate exceeding 0.5 mm/min. Additionally, phase AB in lateral deflection–time curves nearly corresponded to those of phase BC in axial deformation–time curves. The maximum deflections for specimens with eccentricity $E = 0, 40$ and 80 mm were 17.7, 21.7 and 30.0 mm, respectively. Both the maximum deflection values and the initial deflection rates increased with the load eccentricity in CECFST slender columns, suggesting that the second-order effect was significant when the columns were subjected to fire. Furthermore, it was observed that the maximum deflections for all specimens were considerably lower than deflection limit ($L_e^2/(400B)=108$ mm) as stipulated in EN 1363-1 [11]. This could be attributed to the enhanced flexural stiffness imparted by the inner steel tube of the CECFST columns as compared to plain concrete columns.

3.4 Fire resistance

Fire resistance refers to the ability of structural members, the pin-ended CECFST slender columns herein, to withstand fire without significant impairment to their structural integrity. Figure 10 presents a comparison of fire resistance among three specimens, correlating with the duration of the distinct phases depicted in Figure 9(a). The comparison indicated that the duration of phase OA and BC was consistent, while the duration of AB for specimen L2900-E40 was significantly shorter than that of the other two. This discrepancy is likely due to the unexpected explosive spalling and premature failure of the outer concrete, as previously discussed in Section 3.1. Moreover, phase BC in all specimens generally spanned

approximately 10 minutes. The brevity of the failure phase can be attributed to two factors: (1) drastic degradation in the mechanical properties of the outer concrete led to a diminished confinement effect on the steel tube, and simultaneously (2) pin-ended CECFST slender columns under fire generally exhibited swift buckling failure mode.

The fire resistance for specimens L2900-E0, L2900-E40 and L2900-E80 were 121, 87 and 137 min, respectively. According to EN 1994-1-2 [14], the specified fire resistance for CECFST columns with the parameters outlined in this paper is 90 minutes. All specimens met or exceeded this benchmark, though the resistance of L2900-E40 fell short by three minutes. Furthermore, it seemed that an increase in fire endurance correlated with increasing eccentricity. Since the load ratio $n = P_a/P_c$ applied to all specimens was consistent, columns with larger eccentricities experienced lower applied loads, thereby increasing fire resistance. This observation aligned with previous studies [15, 16]. When compared with unprotected conventional CFST columns of similar dimensions and comparable load ratios, which typically exhibited fire resistance between 30 to 60 minutes, as referenced in [17, 18] the tested CECFST columns demonstrated significantly enhanced fire resistance without the need for additional protective measures.

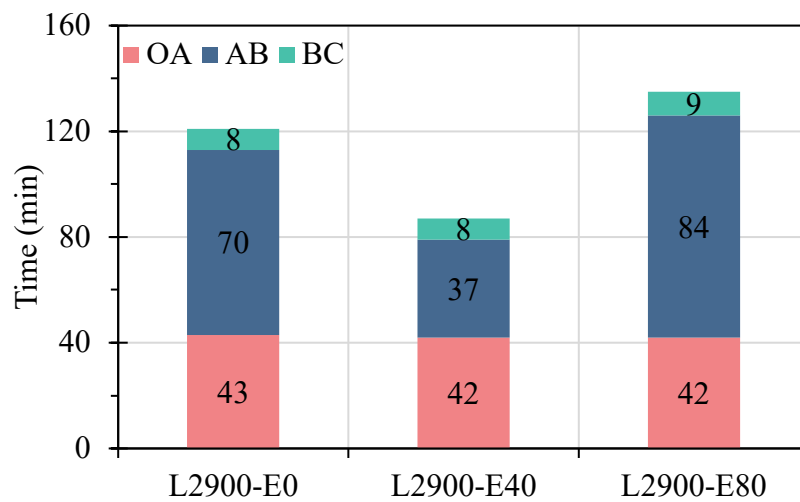


Figure 10. Duration of fire resistance at each phase

4. CONCLUSIONS

This study reported an experimental investigation into the fire behaviour of CECFST slender columns under eccentric loading. The test specimens underwent exposure to ISO 834 fire curves in transient heating conditions. Key test findings including the failure mode and process, temperature distribution, structural response and fire resistance were reported. The following summary can be concluded within the limitations of this paper:

- (1) All specimens failed with global buckling failure mode, while smooth bending deformation was observed. Widespread tensile cracks along the member indicated the whole columns were effectively engaged during heating. These characteristics suggested that CECFST columns exhibited desirable ductility, attributed to the inner steel tube.
- (2) Specimen L2900-E40 exhibited explosive spalling during fire test, as evidenced by the violent noises and the subsequent exposure of the inner steel tube. This led to its premature failure, occurring after just 87 minutes of heating. Despite incorporating PP fibers in the outer concrete layer to mitigate such issues, the specimen still underwent explosive spalling, presumably due to the high moisture content.
- (3) As the load eccentricity increased, there was a corresponding increase in both the maximum lateral deflection and the initial rate of deflection. Interestingly, fire resistance of CECFST columns demonstrated a positive correlation with the load eccentricity. This is likely owing to the relatively small magnitude of applied load P_a with a larger eccentricity.

- (4) Without additional coating treatment, CECFST columns exhibited significantly higher fire ratings compared to CFST columns with similar load ratios and dimensions.

ACKNOWLEDGMENT

The authors express their gratitude for the funding entitled ‘Singapore Ministry of National Development and National Research Foundation under CoT Award’ (COT-V3-2021-1). The authors are also grateful for the help from Mr Mohamad Nur Hafidz Bin Ahmad Fuaad from Nanyang Technological University during the tests.

REFERENCES

1. Han, L.-H., D.-Y. Ma, and K. Zhou, *Concrete-encased CFST structures: behaviour and application*, in *Proceedings 12th international conference on Advances in Steel-Concrete Composite Structures - ASCCS 2018*. 2018.
2. Wang, Y.-H., et al., *Post-earthquake fire performance of square concrete-filled steel tube columns*. *Thin-Walled Structures*, 2020. **154**: p. 106873.
3. Han, L.-H., et al., *Fire performance of concrete filled stainless steel tubular columns*. *Engineering Structures*, 2013. **56**: p. 165-181.
4. Lu, H., L.-H. Han, and X.-L. Zhao, *Fire performance of self-consolidating concrete filled double skin steel tubular columns: Experiments*. *Fire Safety Journal*, 2010. **45**(2): p. 106-115.
5. Moradi, M.J., et al., *The prediction of fire performance of concrete-filled steel tubes (CFST) using artificial neural network*. *Thin-Walled Structures*, 2021. **161**: p. 107499.
6. Zhou, K. and L.-H. Han, *Experimental performance of concrete-encased CFST columns subjected to full-range fire including heating and cooling*. *Engineering Structures*, 2018. **165**: p. 331-348.
7. *EN 1994-1-1, Eurocode 4: Design of Composite Steel and Concrete Structures - Part 1-1: General Rules and Rules for Buildings*, European Committee for Standardization (CEN), Brussels, 2004.
8. *ASTM Standard test methods for tension testing of metallic materials. E8/E8M-16a*. West Conshohocken, PA. USA: ASTM International. 2016.
9. *BS EN 12390-3, Testing Hardened Concrete - Part 3: Compressive Strength of Test specimens*, European Committee for Standardization (CEN), Brussels. 2009.
10. *EN1992-1-1, Eurocode 2: design of concrete structures-part 1-1: general rules and rules for building*, Brussels. . 2004.
11. European Committee for Standardization, B., *CEN. EN 1363-1:2012, Fire resistance tests. Part 1: General Requirements*. 2012.
12. Lo Monte, F. and P.G. Gambarova, *Corner spalling and tension stiffening in heat-damaged R/C members: a preliminary investigation*. *Materials and Structures*, 2015. **48**: p. 3657-3673.
13. Kanema, M., et al., *Spalling, thermal, and hydrous behavior of ordinary and high-strength concrete subjected to elevated temperature*. *Journal of Materials in Civil Engineering*, 2011. **23**(7): p. 921-930.
14. *EN 1994-1-2, Eurocode 4: Design of Composite Steel and Concrete Structures - Part 1-2: General Rules: Structural Fire Design*, European Committee for Standardization (CEN), Brussels, 2004.
15. Du, P., Y. Yang, and K.H. Tan, *Effects of Biaxial Bending and Axial Restraint on Hybrid Fiber Reinforced High-Performance Concrete Columns at Elevated Temperatures*. *Journal of Structural Engineering*, 2022. **148**(11): p. 04022185.
16. Espinos, A., et al., *Ambient and fire behavior of eccentrically loaded elliptical slender concrete-filled tubular columns*. *Journal of constructional steel research*, 2014. **100**: p. 97-107.

17. Han, L.-H., et al., *Experimental study and calculation of fire resistance of concrete-filled hollow steel columns*. Journal of structural engineering, 2003. **129**(3): p. 346-356.
18. Song, Q.-Y., et al., *Fire resistance of circular concrete-filled steel tubular (CFST) column protected by intumescent coating*. Journal of Constructional Steel Research, 2018. **147**: p. 154-170.

FIRE BEHAVIOUR OF TIMBER-CONCRETE COMPOSITE CONSTRUCTIONS UNDER FIRE EXPOSURE

Philipp Peifer¹, Catherina Thiele²

ABSTRACT

A research project was carried out at the RPTU Kaiserslautern, which focussed on the development of timber-concrete composite walls. During the project, further questions arose regarding the heating and charring behaviour of timber-concrete composite structures as a basis for the design of the components under fire exposure. A series of small-scale fire tests (48x48 cm) was used to quantify the start of charring and the charring rate of spruce timber structures initially protected by normal aggregate concrete exposed to fire on one side. Furthermore, measured concrete temperatures in composite components were compared with the temperature profiles of concrete components exposed to fire on one side. It was found that the correlations strongly correlate with the thickness of the concrete cross-section.

Keywords: timber-concrete composite; fire tests; fire behaviour; temperature distribution

1 INTRODUCTION

For timber structures exposed to standard fire, the charring depth can be calculated with the help of standardised charring rates from EN 1995-1-2 [1]. The temperature distribution in reinforced concrete components in case of fire can be estimated using temperature profiles in EN 1992-1-2 [2]. However, for timber-concrete composite structures the Eurocodes do not specify whether these approaches are applicable, nor do they provide alternative approaches. RPTU Kaiserslautern worked on a research project dealing with prefabricated timber-concrete composite walls under fire exposure. The fire tests performed in the project showed that the heating and charring behaviour of composite structures differs significantly from that of the individual construction methods. Further experimental investigations were therefore carried out to quantify these correlations.

2 RESEARCH PROJECT ON TIMBER-CONCRETE COMPOSITE WALLS

Between 2020 and 2023 a research project with the goal to develop timber-concrete composite walls was carried out at RPTU Kaiserslautern. The walls, shown in figure 1, consist of a core made of spruce cross-laminated timber and a shell made of normal aggregate concrete on both sides. On the one hand, the concrete should improve the fire resistance and, on the other hand, increase the load-bearing capacity against buckling and enable the walls to act as stiffening elements. Main objectives of the project were to dimension the concrete shells as a fire protection cladding and to evaluate the fire resistance of the construction under standard fire. The aim of a fire protection cladding classified in accordance with EN 13501-2 [3] is to protect the components behind it from charring for a defined period of time. The concrete shells were therefore not dimensioned as load-bearing elements in the first step. The main parameters

¹ M.Sc., Fachgebiet Massivbau und Baukonstruktion, RPTU Kaiserslautern-Landau, Germany
e-mail: philipp.peifer@rptu.de

² apl. Prof. Dr-Ing., Fachgebiet Massivbau und Baukonstruktion, RPTU Kaiserslautern-Landau, Germany
e-mail: catherina.thiele@rptu.de

influencing the design were the type and thickness of the concrete and the connectors. Screws and glued-in perforated plates were considered for the connection. A second project is currently in the application process. In this project, extensive load-bearing capacity tests are to be carried out, both at room temperature and in case of fire.

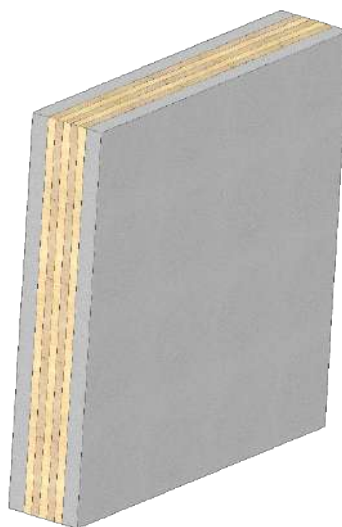


Figure 1. Timber-concrete composite walls from the research project

Some results of the first research project are summarised below. Detailed results are published in [4,5].

- Temperature measurements in the boundary layer between concrete and timber were used to quantify the start of charring. Minimum thicknesses to delay charring for 30 minutes (40 mm) and 60 minutes (65 mm) were derived for normal aggregate concretes. The use of lightweight aggregates can further delay the start of charring.
- The type and dimensions of the fasteners have a major impact on whether the concrete shells fall off during the fire exposure. It was found that the glued-in perforated plates favoured premature falling off of the cladding due to the low temperature resistance of the adhesive.
- First results indicate that the charring rate of timber members initially protected by concrete members is significantly reduced compared to direct fire exposure.
- It was found that the temperature profiles from EN 1992-1-2 [2] for reinforced concrete under fire exposure from one side may not be applicable for the composite components. Due to low thermal conductivity of the timber elements, the heat transfer through the composite components is reduced. This leads to higher temperatures in the concrete shell exposed to the fire and low temperatures for the non-exposed shell.
- Fire resistances REI90-M in accordance with [3] were verified for different versions of the construction.

3 DESIGN PRINCIPLES FOR TIMBER AND CONCRETE STRUCTURES IN CASE OF FIRE

In addition to tabulated design methods based on experience gained from fire tests, EN 1992-1-2 [2] provides temperature profiles for calculating component temperatures as the basis for simplified design methods for reinforced concrete components. Knowledge of the temperature profiles is also essential for composite components made of reinforced concrete and timber. The draft prEN 1995-1-2:2023 [6] refers to the draft prEN 1992-1-2 [7] with regard to the design of concrete in timber-concrete composite structures. However, in [7] no indication is given as to whether the temperature profiles for reinforced concrete cross-sections exposed to fire on one side are applicable to reinforced concrete cross-sections in composite structures with timber. The results of the research project indicate that flat timber constructions behind the concrete, as is common in timber-concrete composite floors for example, have a strong influence on the temperature distribution in the concrete and the temperature profiles may not produce reliable results.

The design of flat timber components in composite structures should be carried out according to the specifications of the effective cross-section method in prEN 1995-1-2 [6]. This is possible with the specifications for direct fire exposure, but there is no design basis for timber structures initially protected by concrete. In general, an encapsulated phase (phase 0 in Figure 2) is assumed for initially protected timber components. After the start of charring t_{ch} , the protected charring phase (phase 2 in Figure 2) follows with a reduced charring rate compared to direct exposure. After the protective layer falls off ($t_{f,pr}$), a charring rate increased by a factor of 2 is assumed until a char layer with a thickness of 25 mm has formed (phase 3 in Figure 2). From this point in time (t_a), the charring rate of an unprotected timber component can be assumed (phase 4 in Figure 2). Further processes of initially protected timber components are illustrated in [7]. These are not relevant in the context of this article.

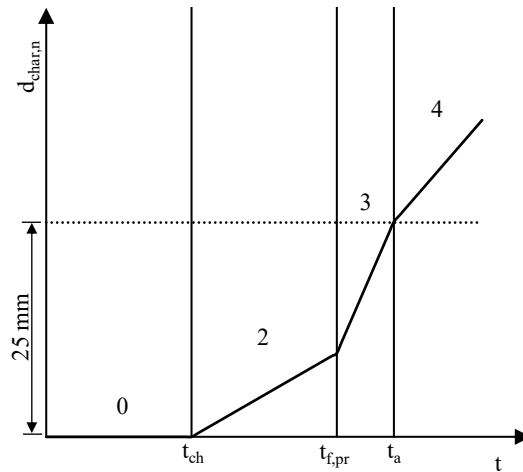


Figure 2. Initially protected timber components [6]

The charring rate is calculated using equation (1). For the protected charring phase, the tabulated charring rate must be reduced using the protection factor k_2 . Further modification factors are not taken into account in this article, as these reflect other influencing parameters. For the protection factor k_2 , prEN 1995-1-2 [6] provides mathematical correlations for gypsum-based boards, clay and mineral wool. This data is missing for concrete but is essential for determining the charring depth in the developed composite structures.

$$\beta_n = \prod k_i \cdot \beta_0 \quad (1)$$

where

β_n is the notional design charring rate within on charring phase, in mm/min,

β_0 is the basic design charring rate, in mm/min given in [6], $\beta_0 = 0,65$ mm/min for softwood,

$\prod k_i$ is the product of applicable modification factors for charring k_i given in [6].

4 FIRE TESTS

4.1 General

Based on the results of the research project and the design principles explained, several research questions were identified. In a test series of five small-scale fire tests, the heating and charring behaviour of flat timber-concrete components was further studied. The main objectives of the tests were to quantify the start of charring (t_{ch} according to [1,6]) and the reduced charring rate of timber elements behind cross sections of normal aggregate concrete. Both are strongly dependent on the thickness of the concrete shell [4]. Different thicknesses were analysed to determine the influence. Further points of interest are the temperature distribution in both cross sections.

4.2 Test specimens and temperature measurement

The test specimens, shown in Figure 3c, were 48x48 cm in size and consisted of spruce glulam and a shell of reinforced normal aggregate concrete attached to the side exposed to fire. Sand and gravel with a maximum diameter of 16 mm was used for the concrete. The thickness of the concrete varied between 40 mm and 100 mm. A Q188A structural reinforcement mesh was arranged in the centre of the concrete cross-section. The average compressive strength tested on concrete cubes was 48.2 MPa. The glulam had a thickness of 16 cm and the lamellas a thickness of 40 mm. The bulk density determined from the external dimensions was 457 kg/m³. The timber cross-sections consisted of two parts with a size of 24x48 cm, which were glued together after the thermocouples had been installed. Optical sorting was carried out to ensure that there were no knots or flaws in the measurement area. Four galvanised carbon steel pan head screws with a diameter of 6 mm and a length of 140 mm were used as fasteners. In order to exclude any influence on the heat transfer, the screws were positioned at a distance of at least 200 mm from the measuring points. Previous studies on the charring behaviour of wood, for example by Fahrni et al. [8], Lingens [9] and Brewer [10], have shown that the results can be influenced by many parameters. Important influencing parameters are, for example, the type and diameter of the thermocouples, and particularly the installation of these parallel to the isotherm. The findings from the literature were included in the standards EN 13381-7:2019 [11], prEN 13381-7:2024 [12] and prEN 1995-1-2:2023 [6], which formed the basis for the dimensioning of the test specimen, the installation of the thermocouples as well as the execution and evaluation of the tests. Information on the test specimens and the temperature measurements is summarised below.

Type K thermocouples with glass fibre insulated conductors were used. The thermocouples were tightly inserted into drilled holes with a diameter of 2 mm and a depth of 25 mm (Figure 3a). The boreholes were drilled with a stationary drilling machine, as inaccuracies in the positioning of the measuring points lead to large measurement uncertainties [9]. The thermocouples were laid parallel to the isotherm over a length of at least 50 mm to minimise heat conduction along the conductors (Figure 3b) [8,10]. Outside of the drilled holes, they were inserted into milled grooves so that the test specimen halves could be glued together over their entire surface. Single-component polyurethane adhesive was used. Cavities in the grooves were sealed with non-combustible acrylic. A distance of 20 mm to adjacent thermocouples and 160 mm to the edges of the test specimen was maintained to exclude mutual interference and edge influences.

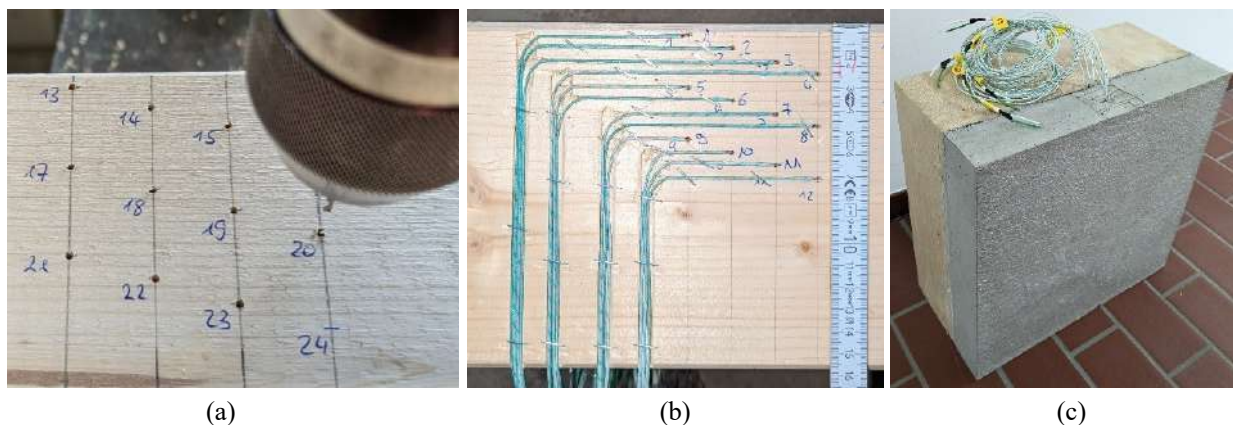


Figure 3. a) Drilled holes to insert the thermocouples. b) Laying the thermocouples outside of the drilled holes. c) Test specimen after installation of the thermocouples and concreting

The thermocouples were distributed in the cross-section of the timber at intervals of 6 mm up to a charring depth of 72 mm (Figure 4). Two identical measurement strings were set up. Due to a residual cross-section with a thickness of more than 80 mm, an influence of the unexposed surface can be ruled out [11,12]. In addition to the thermocouples inside the timber, four thermocouples were equally distributed in the boundary layer between the concrete and the timber to determine the start of charring t_{ch} . The number of thermocouples inside of the concrete varied depending on the thickness of the concrete.

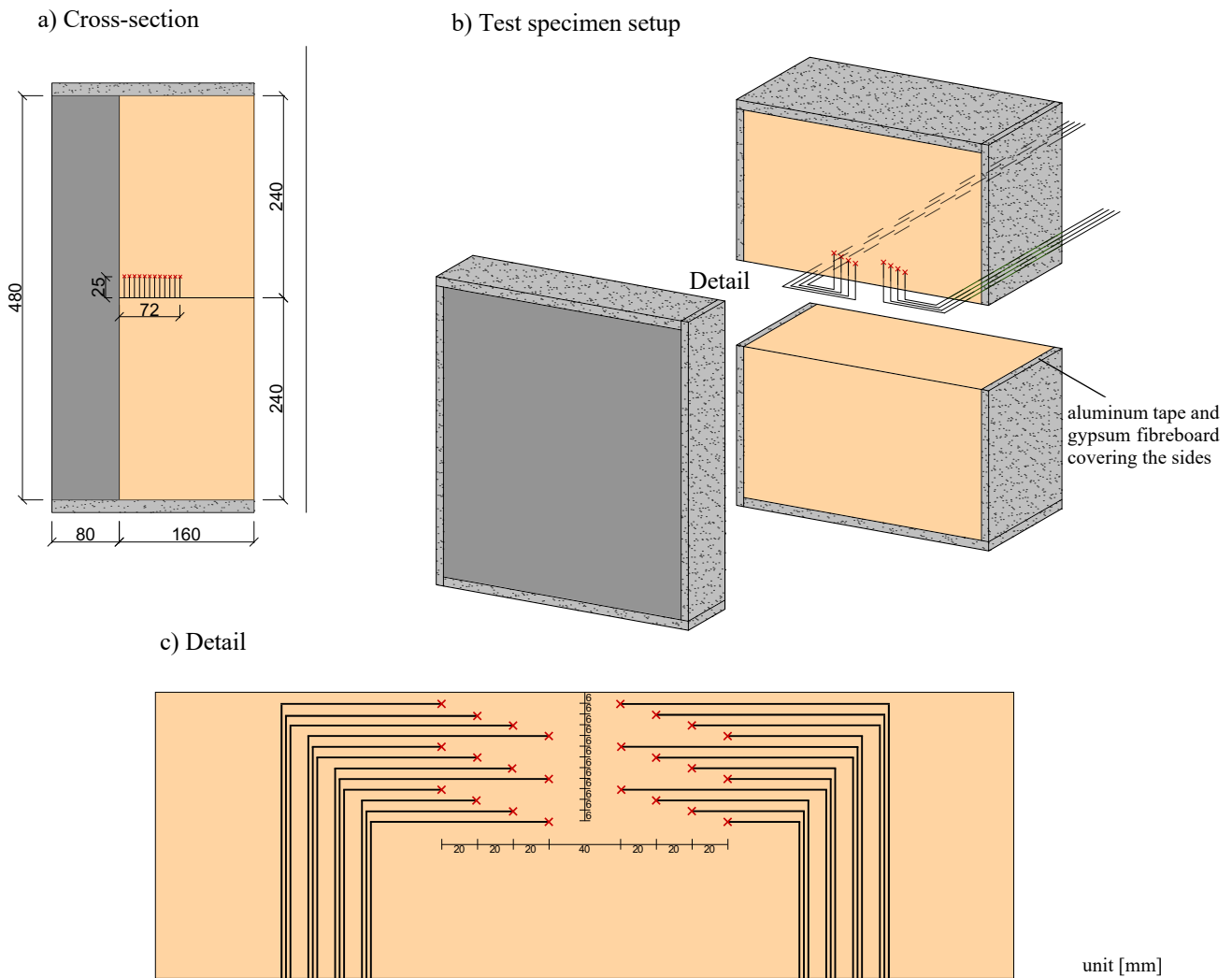


Figure 4. Design of the test specimens and positioning of the thermocouples in the timber cross-section [13]

In accordance with EN 1363-1 [14], the test specimens were conditioned for at least three months. Conditioning was carried out at a temperature of 20 °C and a relative humidity of 60 %. Under these boundary conditions, the expected moisture content of softwood is approximately 12 % and for normal aggregate concrete between 1 % and 5 % of the total mass [14, 15]. The moisture content was determined using three separate specimens with identical dimensions to the ones that were subjected to fire exposure. Drying was carried out at 105 °C in accordance with [14]. To determine the influence of the concrete cladding, the determination was carried out both for the pure spruce wood and for test specimens with concrete claddings (thickness 40 mm and 100 mm). For spruce wood, the moisture content varied between 12.8 % for the pure wood specimen and 13.6 % for the specimen with 100 mm thick concrete. The concrete moisture content was 2.45 % for a thickness of 40 mm and 3.35 % for a thickness of 100 mm. There was a slight influence of the thickness of the concrete cladding on the moisture content of wood and concrete.

4.3 Experimental setup and execution

The tests were performed in a small scale furnace according to DIN 4102-8 [16] using the standard fire curve. The test specimens were installed in a vertical opening on the side of the test furnace. The surface exposed to fire was approximately 45x45 mm. Aluminium tape and gypsum fibre boards with a thickness of 10 mm were provided around the edges of the test specimens. These serve to prevent lateral flow paths and moisture transport processes [17,18]. A non-combustible fire protection acrylic was also applied to counteract lateral burn-off due to the long test duration. The furnace temperature was controlled using a plate thermometer according to [14], which was positioned 100 mm in front of the flamed concrete surface. A schematic representation of the test setup is shown in Figure 5. Following the fire exposure, the test

specimens were directly removed from the test furnace, cooled down and the cladding and char layer were removed. This was intended to minimise further charring after the actual test. A total of five small scale fire tests were performed in this test series. The test specimens differed only in the thickness of the concrete cross-section. At first, an initially unprotected test specimen was tested in order to define the charring rate of the unprotected timber. Subsequently, test specimens with concrete cross-sections in thicknesses of 40 mm, 60 mm, 80 mm and 100 mm were subjected to fire exposure.

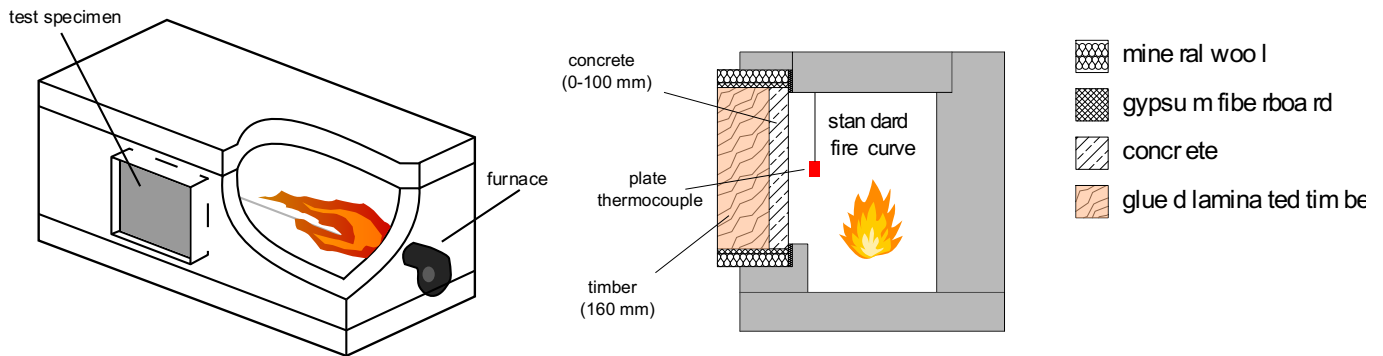


Figure 5. Schematic representation of the experimental setup [13]

5 EXPERIMENTAL RESULTS

5.1 Unprotected timber member

The measured charring depth, defined as the position of the 300 °C isotherm according to [1], of the initially unprotected glulam specimen as a function of time is shown in Figure 6a. The results show good agreement with the results of König & Walleij [17] as well as Werther [18]. The charring rate, shown in Figure 6b, was determined as the quotient of the burning depth and the fire duration. With increasing test duration, a slight decrease in the gradient can be observed, which is reflected in a decrease in the charring rate. The mean charring rate of the charring rates in Figure 6b was $\beta = 0.66$ mm/min for both measurement strings.

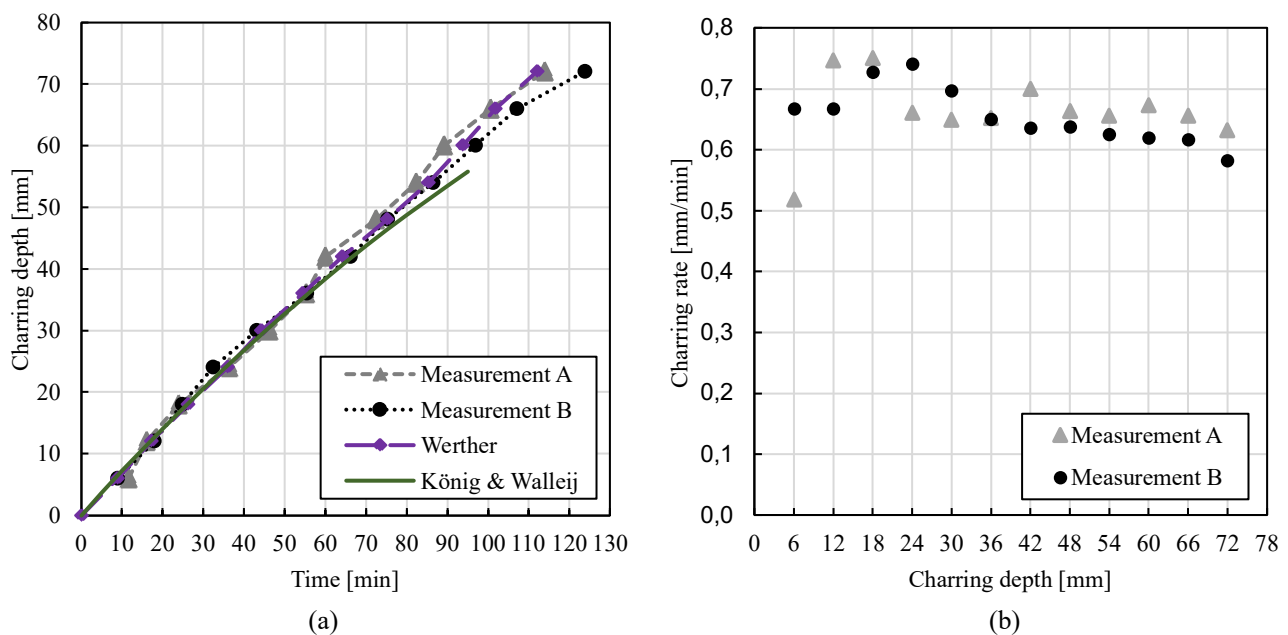


Figure 6. Results of unprotected timber member: a) Charring depth as a function of time. b) Charring rate as a function of the charring depth

The charring rate from the residual cross-sections was determined as the mean value of five measurements within the measuring range of the thermocouples. Measurements 1 and 5 were taken at a distance of 160 mm

from the edges, measurement 3 in the centre of the cross-section and measurements 2 and 4 in the middle between the other measuring points (Figure 7). The measured charring depths result in a charring rate of 0.66 mm and thus correspond exactly with the temperature measurements. The results obtained from the initially unprotected test specimen serve as confirmation of the tabulated charring rate of softwood of 0.65 mm/min in [1], which was derived from the results in [17]. The tabulated charring rate is therefore used as the basis for further analyses of the tests on the composite test specimens.

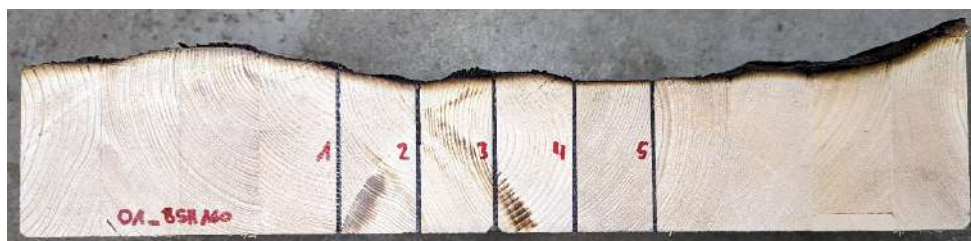


Figure 7. Residual cross-section of the initially unprotected test specimen

5.2 Timber-concrete composite members

The start of charring t_{ch} was analysed in accordance with the specifications of EN 13381-7:2019 [11] and prEN 13381-7:2024 [12] for charring specimens. The determination in [11] is based on equation (2) as the mean value of the measurement results. According to [12], the start of charring t_{ch} is defined, in contrast to [11], as the minimum of three charring test specimens with one measuring point each. As only one test was carried out for each concrete thickness, the minimum of the four measuring points on the timber surface was assumed as the start of charring. The evaluated start of charring for the performed fire tests is shown in Table 1 as well as Figure 8a.

$$t_{ch} = \sum_{i=1}^n \frac{t_{300,TC1,i}}{n} \quad (2)$$

where

t_{ch} is the start of charring of the charring, in min,

$t_{TC1,i}$ is the time the thermocouples on the initially protected surface detect 300 °C, in min.

Table 1. Start of charring t_{ch} according to [11] and [12] for timber structures initially protected by normal aggregate concrete

Test	concrete thickness d_c [mm]	EN 13381-7:2019 [11] t_{ch} [min]	prEN 13381-7:2024 [12] t_{ch} [min]
01	0	-	-
02	40	31.7	30.5
03	60	59.1	56.2
04	80	92.1	88.6
05	100	137.0	130.5

By assuming the minimum, the approach according to [12] results in an earlier start of charring and therefore more conservative results than [11]. The differences increase for greater concrete thicknesses. With the help of the test results in Table 1, the mathematical relationship between the concrete thickness and the start of charring shown in equation (3) and Figure 8a can be derived.

$$t_{ch} = 0,009 \cdot d_c^2 + 0,39 \cdot d_c \quad (3)$$

where

t_{ch} is the start of charring, in min,

d_c is the thickness of the normal aggregate concrete, in mm.

The assessment of the charring rate behind initially protected timber members also differs between EN 13381-7:2019 [11] and EN 13381-7:2024 [12]. According to [11], first the charring rates $\beta_{i,j}$ between two successive measuring depths “i” is determined for each temperature measuring point “j” (here measuring string) using equation (4). In the second step, the mean value β_j of the charring rates $\beta_{i,j}$ is calculated for each measurement string j according to equation (5). The maximum charring rate of the different measurement strings β_j is assumed to be the charring rate β_2 of the initially protected timber element and corresponds to the product of the basic design charring rate β_0 and the protection factor k_2 . As a comparison, the mean charring rates were also calculated from the charring depths determined using the temperature measurements. The start of charring t_{ch} according to equation (3) was taken into account. The complete results can be found in [19].

$$\beta_{i,j} = \frac{d_{i+1} - d_i}{t_{300,i+1} - t_{300,i}} \quad (4)$$

$$\beta_j = \sum_{i=1}^n \frac{\beta_{i,j}}{n} \quad (5)$$

where

- $\beta_{i,j}$ is the charring rate at depth i at temperature measuring string j, in mm/min,
- d_i is the measuring depth on point i, in mm,
- d_{i+1} is the measuring depth on point i+1, in mm,
- $t_{300,i}$ is the time at which a temperature of 300 °C is reached at measuring depth i, in min,
- $t_{300,i+1}$ is the time at which a temperature of 300 °C is reached at measuring depth i+1, in min,
- β_j is the mean charring rate at measuring string j, in mm/min.

In contrast to [11], in [12] the charring rate $\beta_{i,j}$ is not determined between two measuring points, but as the charring rate between the measuring depth i and the original wood surface according to equation (6). The charring rate β_2 is assumed as the second highest value of the charring rates $\beta_{i,j}$.

$$\beta_{i,j} = \frac{d_i - d_0}{t_{300,i} - t_{ch}} \quad (6)$$

where

- $\beta_{i,j}$ is the charring rate at depth i at temperature measuring string j, in mm/min,
- d_i is the measuring depth on point i, in mm,
- d_0 is the measuring depth on the timber surface, in mm, $d_0 = 0$ mm,
- $t_{300,i}$ is the time at which a temperature of 300 °C is reached at measuring depth i, in min,
- t_{ch} is the start of charring according to equation (2), in min.

Table 2 and Figure 8b summarise the results of the charring rates β_2 and the resulting protection factors k_2 from the tests for different concrete thicknesses. The results show a significant influence of the concrete thickness on the charring behaviour. The charring rate decreases with increasing concrete thickness. The results according to [11] are significantly higher than the mean test results and only reproduce them with bad accuracy. There are large differences, particularly for concrete thicknesses of 40 mm and 100 mm. These result from the charring rate between the measuring points $\beta_{i,j}$ according to equation (4). The evaluation according to prEN 13381-7:2024 [12] depicts the test results with good accuracy. By assuming the second largest measured value, one outlier in the measurement results is not considered and the results are still on the safe side, see Figure 8b. The protection factor k_2 according to [12] can be described mathematically using equation (7). It is shown in Figure 8b.

$$k_2 = 0,000042 \cdot d_c^2 - 0,104 \cdot d_c + 1 \quad (7)$$

where

- k_2 is the protection factor [-],
- t_c is the thickness of the normal aggregate concrete, in mm.

Table 2. Charring rates β_2 and protection factors k_2 . Mean test results and assessed test results according to EN 13381-7:2019 [11] and prEN 13381-7:204 [12] for timber structures initially protected by normal aggregate concrete

Test	concrete thickness d_c	Mean test results		Test results assessed according to [11]		Test results assessed according to [12]	
		β_2 [mm/min]	k_2 [-]	β_2 [mm/min]	k_2 [-]	β_2 [mm/min]	k_2 [-]
01	0 mm	0.65*	1.00	0.65*	1.00	0.65*	1.00
02	40 mm	0.39	0.60	0.54	0.83	0.42	0.65
03	60 mm	0.32	0.49	0.38	0.58	0.34	0.52
04	80 mm	0.25	0.38	0.31	0.48	0.28	0.43
05	100 mm	0.22	0.34	0.30	0.46	0.24	0.37

*Tabulated data from EN 1995-1-2 [1]

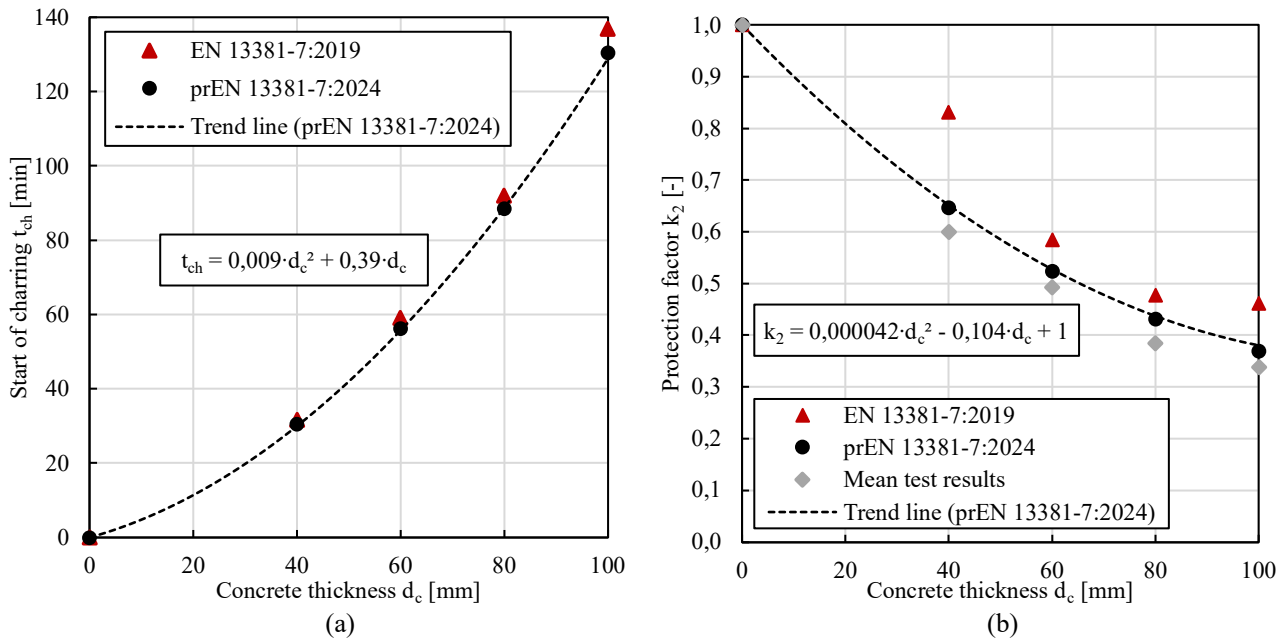


Figure 8. Results for timber member initially protected by normal aggregate concrete: a) Start of charring t_{ch} as a function of the concrete thickness d_c . b) Charring rate β_2 as a function of the concrete thickness d_c

A comparison of the measured mean charring depths and the charring depths calculated using the charring rate β_2 according to [12] is shown in Figure 9. The charring rate β_2 generates conservative charring depths for all concrete thicknesses. Differences between calculated and measured values increase for increasing concrete thicknesses. Overall, however, a good representation of the test results can be shown for all concrete thicknesses. Contrary to the observations for unprotected timber components, the charring rate of timber components initially protected by normal concrete increases with the duration of fire exposure, which is shown by an increasing slope of the charring depth graph. For long fire durations, the measurement results can therefore exceed the calculated charring depths. As this only occurs for fire durations significantly above usual fire resistances, it can be neglected. Measurements of the residual cross-sections confirmed the reduced charring rate compared to direct fire exposure. However, the results of the residual cross-sections are higher than the thermocouple measurements due to the additional charring that occurs during cooling and removal of the concrete. Therefore, these will not be analysed in more detail.

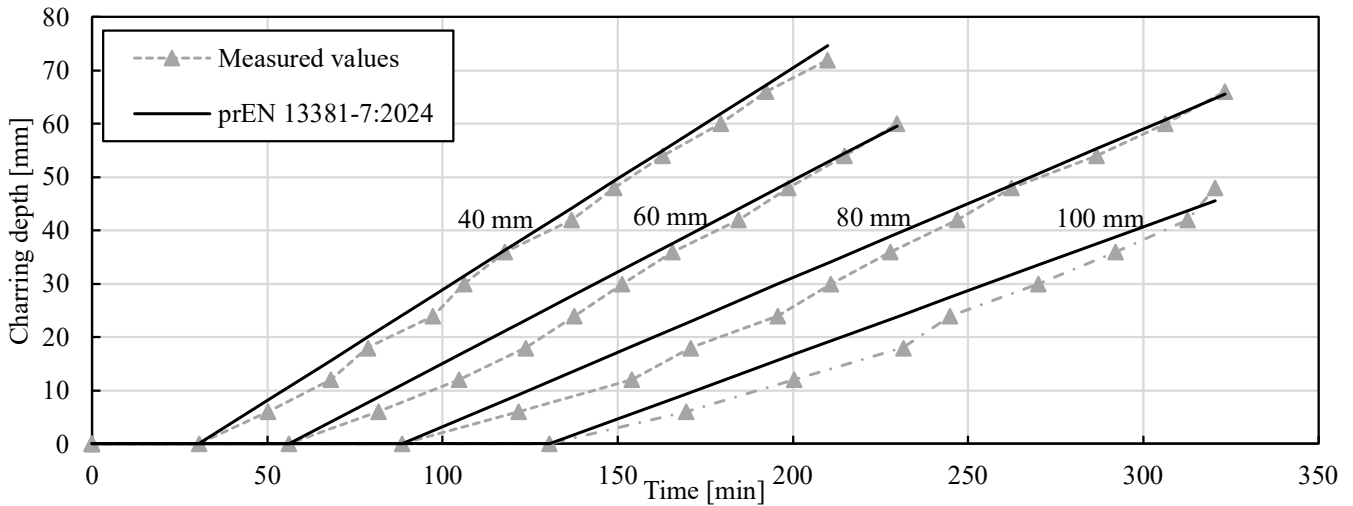


Figure 9. Charring depth as a function of time for timber member initially protected by normal aggregate concrete with thicknesses of 40 to 100 mm

The temperature profiles for concrete components exposed to fire on one side from [7] and the measured concrete temperatures within the composite specimens are shown in Figure 10 for fire durations of up to 120 minutes. Assuming concrete covers between 20 and 40 mm, a decent agreement of the temperatures in the area of the reinforcement can be determined for short fire durations of 30 minutes. In the boundary layer between concrete and timber, however, the measured values are significantly higher than the temperature profiles. The reason for this is the low thermal conductivity of the wood, which results in reduced heat transfer through the component. With increasing fire duration, the differences between the measured values of the composite members and the temperature profiles increase. After 60 minutes, the measured temperatures are already largely above the temperature profiles. The differences are larger for concrete cross-sections with low thicknesses (40 mm and 60 mm). Here too, the temperatures in the boundary layer should be emphasised, as this is where the greatest differences occur. For fire durations of 90 and 120 minutes, all measured temperatures are above those of the temperature profiles. Significant differences were found, particularly in the boundary layer. After 90 minutes, the temperature difference for a concrete thickness of 40 mm in the boundary layer was 308 °C. The differences decrease considerably with increasing concrete thickness and are increasingly closer to those of concrete components.

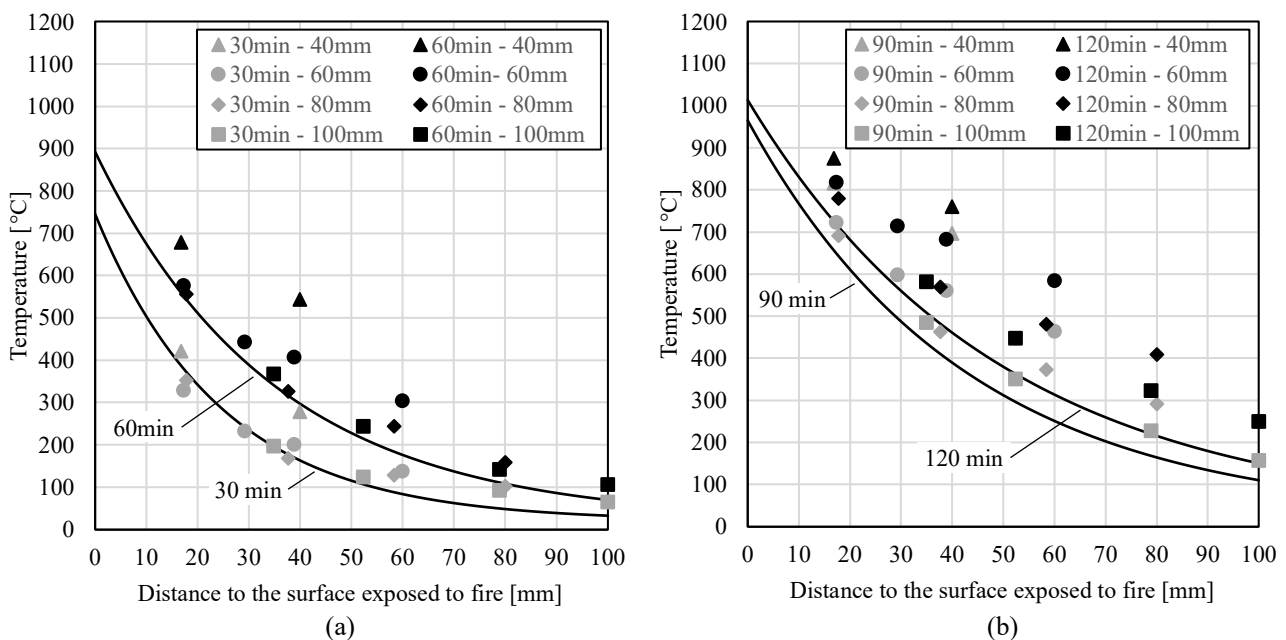


Figure 10. Comparison of the temperature profiles for concrete components exposed to fire on one side from [7] (solid lines) and the measured concrete temperatures in the composite members with concrete thicknesses of 40 to 100 mm (points)

6 CONCLUSIONS

The charring rate of a spruce timber member initially protected by normal aggregate concrete is reduced compared to an unprotected member. The charring rate decreases with increasing concrete thickness which can be described with protection factors k_2 . In contrast to unprotected timber members, composite members exposed to standard fire are characterised by an increasing charring rate over time. Measurements of the residual cross-sections confirm the reduced charring rate and the dependence on the concrete thickness.

The evaluations of the charring rate β_2 according to EN 13381-7:2019 [11] and prEN 13381-7:2024 [12] lead to significantly different results. The results according to [11] are strongly influenced by individual measurement results and reflect the measurement results badly. The charring rate β_2 assessed according to [12], on the other hand, reflects the measurement results better.

The temperature profiles for concrete components exposed to fire on one side from [7] cannot be transferred to timber-concrete composite components. The measured temperatures in composite components are above the temperature profiles from [7]. The differences increase with the fire duration. The biggest differences occur in the boundary layer between concrete and timber.

Further analyses on the heating and charring behaviour of timber-concrete composite structures will be carried out in [20].

ACKNOWLEDGMENT

The research project “Brandschutztechnisch separierende Wandfertigteile in Holz-Beton-Verbundbauweise” was supported by the Federal Ministry for Economic Affairs and Climate Action on the basis of a decision by the German Bundestag. The authors would like to express their gratitude for the support and thank the cooperation partners for the successful collaboration.

REFERENCES

1. DIN EN 1995-1-2:2010-12, Eurocode 5: Design of timber structures – Part 1-2: General – Structural fire design; German version EN 1995-1-2:2004 + AC:2009
2. DIN EN 1992-1-2:2010-12, Eurocode 2: Design of concrete structures – Part 1-2: General rules – Structural fire design; German version EN 1992-1-2:2004 + AC:2008
3. DIN EN 13501-2:2023-12, Fire classification of construction products and building elements – Part 2: Classification using data from fire resistance and/or smoke control tests, excluding ventilation services; German version EN 13501-2:2023
4. Peifer, P.; Thiele, C.: Brettsperrholzwände mit Brandschutzbekleidungen aus Beton. In: Kornadt, O.; Carrigan, S.; Hofmann, M.; Völker, C.: Bauphysiktag Kaiserslautern 2022 – Bauphysik in Forschung und Praxis. Technische Universität Kaiserslautern, Kaiserslautern, 2022, S. 33-35.
5. Peifer, P.; Brinnel, F.; Thiele, C.; Lorenz, D.: Temperaturen in Holz-Beton-Verbundkonstruktionen im Brandfall – Versuch und Simulation. In: Bautechnik (2023).
6. Draft DIN EN 1995-1-2:2023-09, Eurocode 5: Design of timber structures – Part 1-2: Structural fire design; German and English version prEN 1995-1-2:2023
7. Draft DIN EN 1992-1-2:2021-09, Eurocode 2: Design of concrete structures – Part 1-2: General rules – Structural fire design; German and English version prEN 1992-1-2:2021
8. Fahrni, R.; Schmid, J.; Klippel, M.; Frangi, A.: Correct temperature measurements in fire exposed wood, World Conference on Timber Engineering, August 20-23 2018.
9. Lingens, A.: Untersuchung des Abbrandes und der Brandgase ausgewählter Holzarten in Abhängigkeit vom chemischen und strukturellen Holzaufbau, Technische Universität München, Dissertation, 2003.
10. Brewer, W.D.: Effect of thermocouple wire size and configuration on internal temperature measurements in a charring ablator, NASA technical note D no. 3812, National Aeronautics and Space Administration, Washington, DC, 1967.
11. DIN EN 13381-7:2019, Test methods for determining the contribution to the fire resistance of structural members – Part 7: Applied protection to timber members; German version EN 13381-7:2019

12. Draft DIN EN 13381-7:2024, Test methods for determining the contribution to the fire resistance of structural members – Part 7: Applied protection to timber members; German and English version prEN 13381-7:2023
13. Klein, C.: Experimentelle und numerische Untersuchungen an Holz-Beton-Verbundbauteilen unter Brandbeanspruchung. Studienprojekt, RPTU Kaiserslautern, Fachgebiet Massivbau und Baukonstruktion, 2024, [unveröffentlicht].
14. DIN EN 1363-1:2020, Fire resistance tests – Part 1: General requirements; German version EN 1363-1:2020.
15. Hannoschöck, N.: Wärmeleitung und -transport. Springer Vieweg, Berlin, 2018.
16. DIN 4102-8:2003, Fire behaviour of building materials and components – Part 8: Small scale test furnace.
17. König, J.; Walleij, L.: One-Dimensional Charring of Timber Exposed to Standard and Parametric Fires in Initially Unprotected and Postprotection Situations – Rapport I 9908029. Swedish Institute for Wood Technology Research, Stockholm, 1999.
18. Werther, N.: Einflussgrößen auf das Abbrandverhalten von Holzbauteilen und deren Berücksichtigung in empirischen und numerischen Beurteilungsverfahren, Technische Universität München, Dissertation, 2016.
19. Peifer, P.; Thiele, C.: Holz-Beton-Verbund: Kleinbrandversuche zum Abbrand- und Erwärmungsverhalten. Versuchsbericht, RPTU Kaiserslautern, Fachgebiet Massivbau und Baukonstruktion, 2024, [unveröffentlicht].
20. Peifer, P.: Untersuchungen zum Erwärmungs- und Abbrandverhalten von Holz-Beton-Verbundkonstruktionen unter Brandbeanspruchung. Dissertation, RPTU Kaiserslautern, Fachgebiet Massivbau und Baukonstruktion. [unveröffentlicht]

FIRE PERFORMANCE OF PROTECTED HIGH STRENGTH CONCRETE-FILLED STEEL TUBULAR COLUMNS

Utsab Katwal¹, Zhong Tao², Qingtao Huang³, Maroun Rahme⁴

ABSTRACT

This paper presents the test results of high strength concrete-filled steel tubular (CFST) columns protected by a novel fly ash-based spray-applied fire resistive material (SFRM) recently developed by the authors. Five square CFST stub columns were tested, where the steel tubes had a nominal yield stress of 690 MPa and the concrete had a cylinder compressive strength of 99.8 MPa. One column was tested to determine the load-carrying capacity at ambient temperature, whereas the remaining four columns with or without protection were tested in fire. The unprotected columns failed within 30 min of fire exposure, whereas those protected with a nominal SFRM thickness of 20 mm resisted fire for 216 min and 201 min under load levels of 0.25 and 0.4, respectively. This proves that the developed SFRM is effective in protecting CFST columns made with high-strength materials. In addition, a finite element model was developed to predict the test results. Further research is required to adopt more accurate material models to improve the prediction accuracy.

Keywords: Fire protection coating, Spray-applied fire resistive materials, Concrete-filled steel tubes

1 INTRODUCTION

Concrete-filled steel tubular (CFST) columns made with high-strength concrete (HSC) and high-strength steel (HSS) are promising for use in modern high-rise buildings because of their large load-carrying capacity and relatively small cross-sections. Using such high-strength materials in CFST columns can reduce the column cross-section size to maximise the utilisation of valuable space. For example, ultra-high strength steel tubes ($f_y = 780$ MPa, where f_y is the yield stress of steel) and ultra-high strength concrete (UHSC) ($f'_c = 160$ MPa, where f'_c is the cylinder concrete strength) were used in the main columns in Techno Station, Tokyo, Japan, completed in 2010 [1]. Because of the utilisation of ultra-high strength materials, the diameter of the columns was successfully reduced from 800 mm (based on normal strength materials) to 500 mm. Similarly, f_y of 590 MPa and f'_c of 150 MPa have been used in CFST columns in the 300 m tall Abeno Harukas Building in Osaka, Japan, as reported by Liew et al. [2]. Several other examples of structures can be found in the literature, where high-strength CFST columns were utilised in the Latitude Tower (height 222 m) in Sydney, Australia;

¹ Postdoctoral Research Associate, Centre for Infrastructure Engineering, Western Sydney University, Australia
e-mail: : u.katwal@westernsydney.edu.au, ORCID: <https://orcid.org/0000-0002-8537-3505>

² Professor in Infrastructure Materials, Centre for Infrastructure Engineering, Western Sydney University, Australia
e-mail: : z.tao@westernsydney.edu.au, ORCID: <https://orcid.org/0000-0003-2117-2162>

³ PhD Candidate, Centre for Infrastructure Engineering, Western Sydney University, Australia
e-mail: 17172282@student.westernsydney.edu.au

⁴ Managing Director, Nu-Rock Technology Pty Ltd, Ryde, NSW 2112, Australia
e-mail: maroun.rahme@nu-rock.com

Two-Union Building (height 226 m), USA; SEG Plaza (height 356 m) in Shenzhen, China; Taipei 101 Tower (height 508m) in Taiwan; and Goldin Finance 117 (height 597 m) in Tianjin, China (Liew, 2015). These examples highlight the development and application of high-strength steel and concrete in CFST columns and the increasing use of such columns in the construction industry.

Despite the benefits of CFST columns made with HSC and HSS, there are concerns about the spalling of HSC [3] and the fast deterioration of strength and elastic modulus of HSS when exposed to fire [4]. Numerous fire tests have been conducted on CFST columns with NSC, but limited test data are available in the open literature for CFST columns made with HSS and/or HSC. The test conducted by Kodur [5] on a high strength circular CFST column ($\Phi 273.1 \text{ mm} \times 6.35 \text{ mm}$) with a load level of 0.26 and a f'_c of 90.6 MPa demonstrated lower fire resistance (48 min) compared to the counterpart column with a f'_c of 36 MPa (144 min). Similarly, a 200 mm square CFST column made with 12 mm thick Tata steel RQT 701 grade plates and HSC of 163 MPa, tested with a load level of 0.33, failed after 44 min of exposure to fire. In engineering practice, structural columns require a fire resistance level (FRL) between 90 min to 4 h, depending on the type of building [6]. Therefore, fire protection is usually required to meet the necessary FRL for CFST columns made with high-strength materials.

Spray-applied fire-resistive materials (SFRMs) are commonly used for fire protection due to their low thermal conductivity, lightweight, cost-effectiveness, and ease of application [7]. The SFRMs available in the market generally contain 50-75 wt% of gypsum or Portland cement, which significantly contributes to greenhouse gas emissions. Recently, the authors developed a novel fly ash-based SFRM, which is more cost-effective and can reduce greenhouse gas emissions by up to 68.4% compared to the available SFRMs in the market [8]. The thermal properties of the developed fly-ash based SFRM were comparable with the commercially available cementitious-based SFRM [8].

The authors have previously tested square steel hollow tubular columns with a nominal f_y of 690 MPa to investigate the performance of the novel fly-ash based SFRM. The unprotected tubes failed within 23 min of fire exposure, whereas those protected with SFRM resisted fire for 3 h 36 min and 2 h 47 min under the load levels of 0.3 and 0.5, respectively [9]. Based on our previous research, this work continues to assess the fire resistance of high strength CFST columns when protected by the novel SFRM.

This paper presents the test results of five short CFST columns made with HSC and HSS in this context. The effects of load level and efficacy of the SFRM in protecting CFST columns were investigated. Among them, one column was tested to determine the load-carrying capacity at ambient temperature, whereas the remaining four were tested in fire. Furthermore, a finite element (FE) model is developed to simulate the structural fire performance of the tested CFST columns.

2 TEST PROGRAM

2.1 Test specimens

The test specimens consist of five CFST columns with a length of 600 mm and a size of $150 \times 150 \times 5 \text{ mm}$. The control specimen CFST-A was tested at ambient temperature to determine the load-carrying capacity (N_u). The remaining four columns, presented in Table 1, were tested in fire. Out of these four fire test specimens, two of them (CFST-U1 and CFST-U2) were unprotected, whereas the remaining columns (CFST-P1 and CFST-P2) were protected by the fly ash-based SFRM developed by the authors [8]. Specimens CFST-U1 and CFST-P1 were tested at a load level [$n_f = \text{applied load } (N) / \text{ultimate capacity } (N_u)$] of 0.25, whereas the remaining specimens CFST-U2 and CFST-P2 had a n_f -value of 0.4.

2.2 Material properties

Bisalloy Structural Steel 80 plates were used to fabricate all specimens. Three tensile steel coupons were extracted and tested to determine the material properties of the steel tube. The measured yield stress (f_y) of the steel was 767.7 MPa. The average unconfined cylinder concrete strength (f'_c) was 99.8 MPa, which was measured at the time of testing. The density of the SFRM was 698 kg/m^3 , whereas its compressive strength

varied between 2343-3535 kPa. The measured thermal conductivity and specific heat of the SFRM are presented in Figure 1. More details of the SFRM can be found in [8].

Table 1: Fire test specimens

Specimen label	Section size (mm)	Column length (mm)	Load level n_f	Protection scheme	Fire resistance time (min)	Critical steel temperature (°C)
CFST-U1	150 × 150 × 5	600	0.25	Unprotected	28	790
CFST-U2	150 × 150 × 5	600	0.4	Unprotected	24	748
CFST-P1	150 × 150 × 5	600	0.25	Protected	216	598
CFST-P2	150 × 150 × 5	600	0.4	Protected	201	631

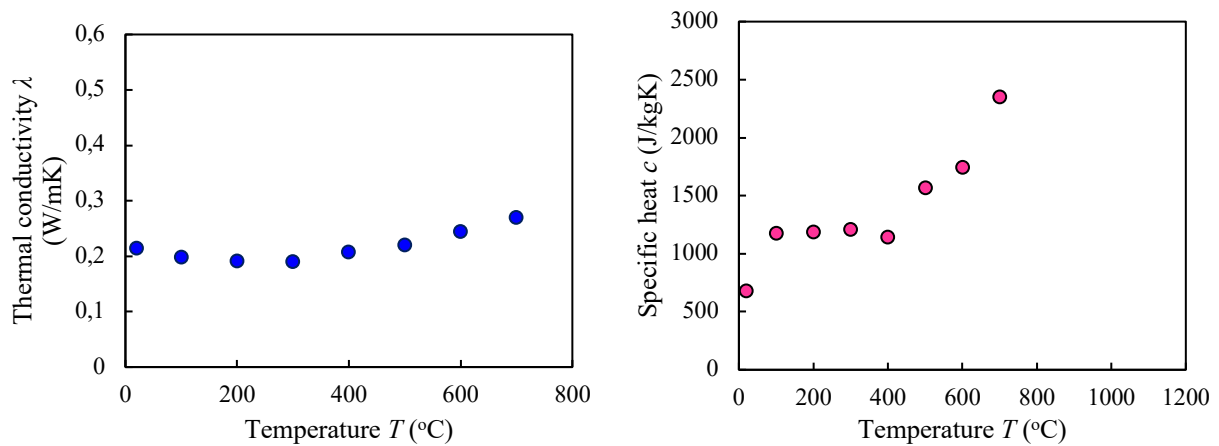


Figure 1. Thermal properties of fly ash-based SFRM [8]

2.3 Specimen preparation

The steel plates were cut as per the required dimensions and then welded to fabricate steel tubes. Welding consumables recommended in the Bisalloy manual for matching strength were used. Steel endplates with a thickness of 20 mm were then welded to both ends of a specimen. A 100 mm square hole was cut on the top endplate to facilitate concrete pouring. Two 10 mm vent holes were drilled in the steel tube to release water vapours during fire testing. All specimens were placed upright, and concrete was filled in layers. Each layer of concrete was compacted using a needle vibrator. After concrete placement, the top end of a specimen was sealed with plastic wraps to prevent moisture loss. Before testing, the surface of the top end was levelled using an angle grinder. The outer surfaces of the protected specimens (CFST-P1 and CFST-P2) were thoroughly cleaned to remove any rust using a wire wheel brush. These columns were then wrapped with steel wire mesh (0.7 mm diameter and 12.7 mm aperture) to ensure the successful coating of SFRM. Using a spray machine, the SFRM was sprayed to the columns' outer surfaces. The SFRM surface was finally levelled to achieve a target coating thickness of 20 mm.

2.4 Instrumentation and loading procedure

For the specimen CFST-A to be tested at ambient temperature, four strain gauges were attached to the mid-section of the outer steel tube to record the vertical strain development. Four linear variable differential transducers (LVDTs) were also used to record the axial deformation. The axial compression test was conducted using a Hongshan 10,000 kN machine at the Structures Laboratory of Western Sydney University (WSU), Australia. A displacement-based loading method was applied to test the column.

Three thermocouples were installed in the middle cross-section of the fire test specimens CFST-U1 and CFST-P1 before pouring concrete. One thermocouple was placed between the steel tube and concrete, and the second one was placed at the centre of the core concrete. The third one was placed between the first two

thermocouples. For specimens CFST-P1 and CFST-P2, only four thermocouples were installed on the four sides of a column, respectively, to monitor the surface temperature development. It was expected that CFST-U1 and CFST-U2 would have similar temperature distributions inside the columns. The same expectation was considered for CFST-P1 and CFST-P2. An LVDT was used to monitor the actuator's downward movement to represent the column's axial displacement.

The gas furnace and loading system in the Structures Laboratory at WSU, Australia, was used to conduct the fire resistance tests under axial compression. The entire length of a specimen was exposed to fire. Before the fire testing, an axial load was applied to the specimen at a predetermined load level (n_f), as presented in Table 1. A loading jack with a capacity of 2000 kN, located at the top of the furnace, was used to apply the load. The load was then kept constant, and the furnace temperature was increased to a target temperature of 800 °C at an average rate of 40 °C/min. The internal temperature of the furnace was monitored and recorded using three thermocouples. After reaching the target temperature, the furnace temperature was maintained until the column failed to support the applied axial load. The failure of the column in fire was identified based on the ISO 834 standard [10] failure criterion for axially loaded elements. Accordingly, the axial shortening exceeding $0.01L$ mm or the deformation rate exceeding $0.003L$ mm/min was considered the failure criterion, where L is the length of the specimen in mm. The elapsed time from the beginning of the temperature rise till the failure was considered as the fire resistance of the specimen.

2.5 Test results and discussion

2.5.1 Ambient test

Figure 2 shows specimen CFST-A before and after testing under axial compression. In the initial loading stage, the axial load was approximately proportional to the axial strain, as shown in the measured axial load versus axial strain ($N-\epsilon$) curve of the specimen in Figure 3. The axial strains are the averages of the strain readings of the four axial strain gauges. After reaching a peak load of 4271 kN, the column showed strength degradation and an initiation of local buckling. The local buckling of the steel tube was visible approximately after reaching an axial strain of $6600 \mu\epsilon$. Then, a continuous degradation in the load-carrying capacity was observed up to an axial strain of $26000 \mu\epsilon$. Beyond this limit, significant weld tearing was observed at a corner of the column. Upon completing the compression test, it was observed that the steel tube experienced significant local buckling and weld tearing. Meanwhile, concrete crushing was observed inside the steel tube.

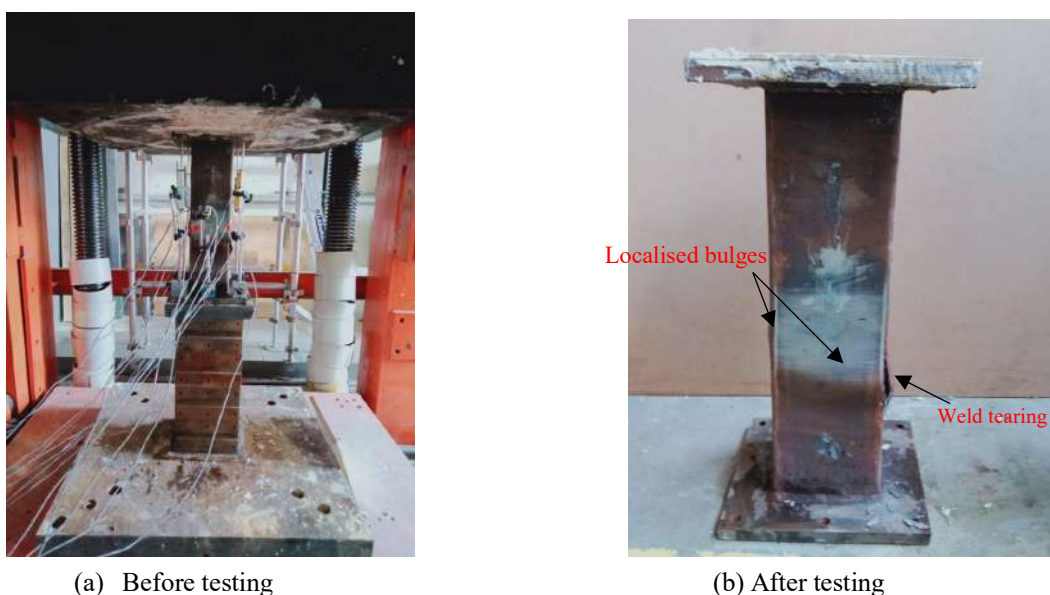


Figure 2. Specimen CFST-A before and after testing

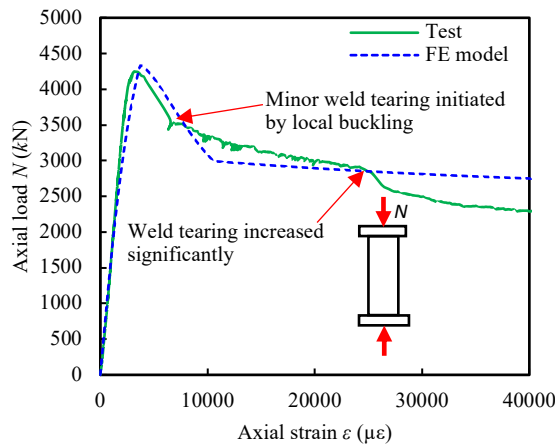


Figure 3. N - ε curve of specimen CFST-A tested at ambient temperature

2.5.2 Fire tests

Figures 4 and 5 present the failure modes of typical unprotected and protected specimens ($n_f = 0.25$), respectively. The unprotected specimen CFST-U1 showed a sudden failure with an explosive sound of concrete after exposure to fire for 28 min. Severe steel tube buckling, weld tearing, and concrete spalling occurred simultaneously at the time of failure (Figure 4b). Similar behaviour was observed in the other unprotected specimen CFST-U2 with an n_f of 0.4, which failed suddenly after exposure to fire for 24 min. For the protected CFST columns, minor cracks appeared on the SFRM surface after about 1 h of fire exposure (Figure 5b). This is due to the thermal contraction of SFRM observed at elevated temperatures [8]. Despite this, these protected columns survived fire for more than 3 h. At the end of the testing, sudden spalling of concrete with an explosive sound, steel tube buckling, and weld tearing were observed simultaneously.

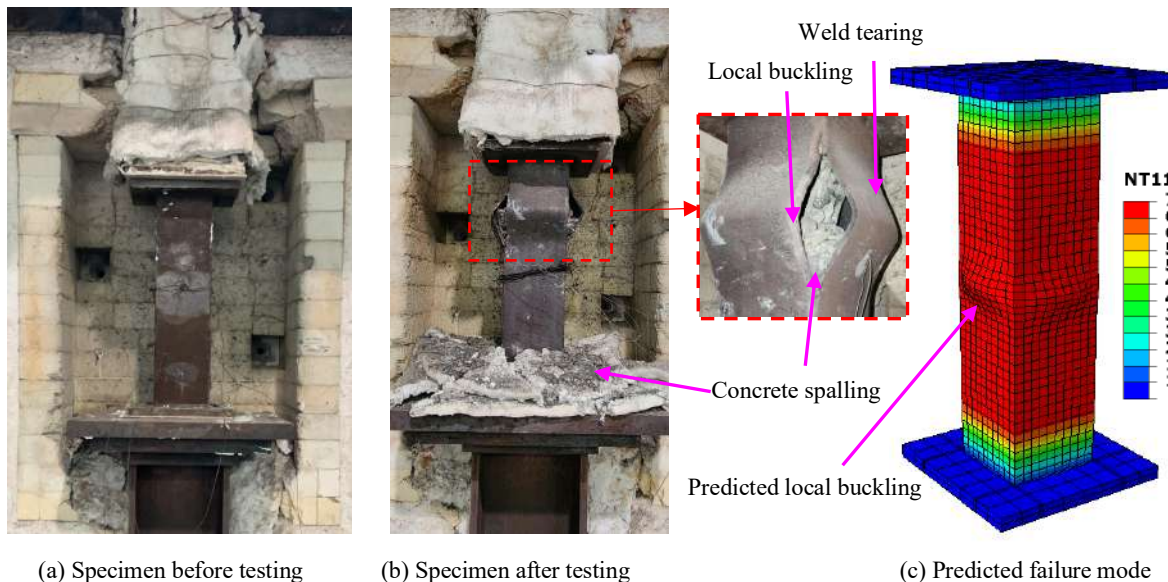


Figure 4. Unprotected specimen CFST-U1 tested in fire

Figure 6 shows the temperature (T) versus time (t) curves of the unprotected and protected specimens with an n_f of 0.25. The furnace temperature developments are also shown in this figure. The thermocouple installed to measure the temperature at Point 1 (steel tube-concrete interface) of the unprotected specimen CFST-U1 was broken while transporting it from the fabrication site to the fire test lab. Hence, this specimen's temperature at Point 1 could not be measured. CFST-U1 failed when the furnace temperature reached 795 °C at 28 min. At this moment, the concrete temperatures at Points 2 and 3 were 145 and 101 °C,

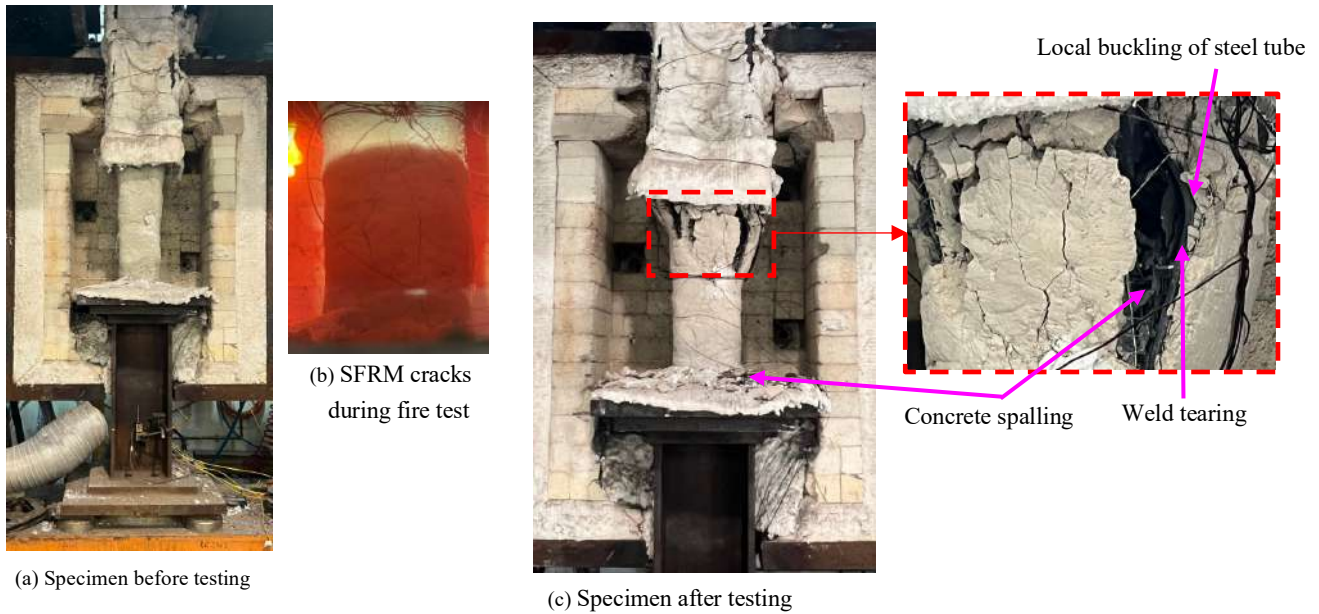


Figure 5. Protected specimen CFST-P1 tested in fire

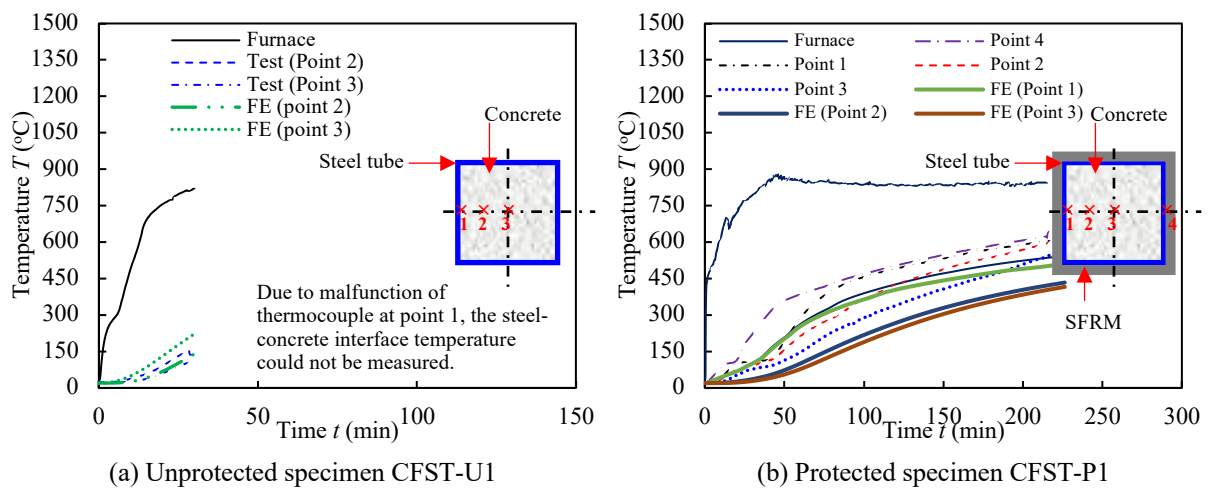


Figure 6. Temperature-time distribution in CFST columns

respectively (Figure 6a). For the protected specimen CFST-P1, the temperature developments in the steel tube and core concrete were much slower due to the SFRM protection. The temperature of the outer surface of the steel tube reached 100 °C at 24 min. It is also found that there was a temperature development delay at Point 1 (steel tube-concrete interface) compared with that at Point 4 (steel outer surface) when the fire exposure time was between 24 min and 83 min, which can be attributed to the evaporation of moisture trapped in the interface. However, after 83 min, the temperature difference between the two points disappeared, indicating complete moisture evaporation. This column resisted fire for 216 min, which was much longer than the fire resistance time (24 min) of the unprotected column. At the time of failure, the steel outer surface temperature was 604 °C, whereas the concrete temperatures at Points 2 and 3 were 599 °C and 544 °C, respectively. Prior to failure, the concrete in the protected column developed much higher temperatures than that in the unprotected column. However, the temperature of the steel outer surface (critical steel temperature) in the protected column was much lower than that in the unprotected column, which can be seen in Table 1. The SFRM provided effective fire protection to the HSS tube and allowed the concrete core to develop higher temperatures with a smaller temperature gradient.

The axial deformation (Δ) versus time (t) curves for all four specimens are shown in Figure 7. In general, a small thermal expansion was observed during the initial fire exposure. Then, a gradual axial shortening was observed, which can be attributed to the material degradation at high temperatures. Finally, a significant increase in axial shortening speed was observed when the column approached failure.

Figure 8 compares the fire resistance times of all four columns. The unprotected columns with n_f -values of 0.25 and 0.4 failed at 30 and 26 min, respectively; whereas the protected columns with n_f -values of 0.25 and 0.4 survived fire for 216 min and 201 min, respectively. Obviously, the SFRM protection led to a substantial improvement in fire performance of high strength CFST columns. Meanwhile, the fire resistance time of the columns decreased with increasing n_f . However, it seems that the influence of load level is not significant in the test range.

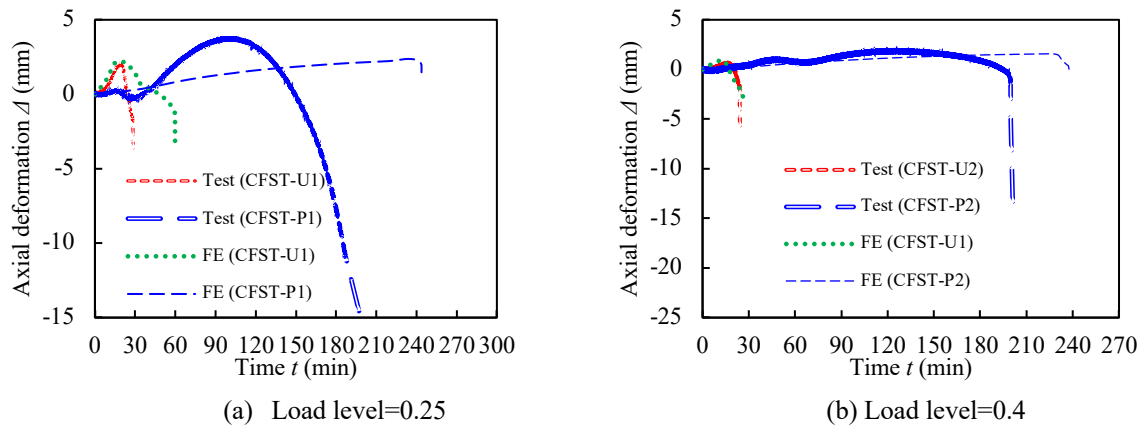


Figure 7. Comparison of measured $\Delta - t$ curves between protected and unprotected CFST columns

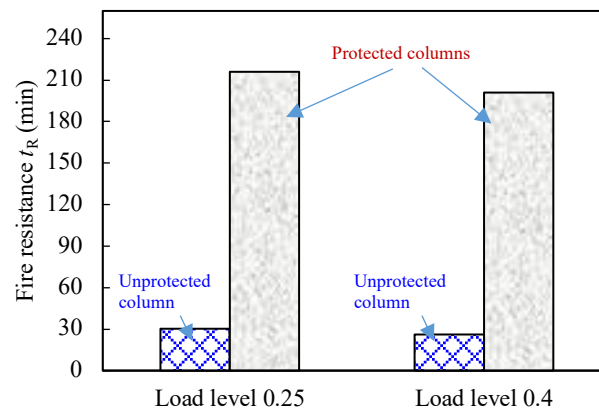


Figure 8. Comparison of fire resistance time of CFST columns with and without protection

3 FINITE ELEMENT MODELLING

A FE model was developed using the commercial software ABAQUS version 2021. The FE simulation for the fire tests was conducted in three stages. A buckling analysis was conducted first to include local imperfections of the steel tube, followed by sequentially coupled thermal and stress analyses. In simulating the steel tube, four-node quadrilateral heat transfer shell elements (DS4) were used for heat transfer analysis, and four-node homogeneous shell elements with reduced integration (S4R) were adopted for stress analysis. To simulate the concrete and SFRM, eight-node linear heat transfer brick elements with one degree of freedom per node (DC3D8) and eight-node solid brick elements with three degrees of freedom per node (C3D8) were adopted for heat transfer and stress analyses, respectively.

The simulation used a 14 mm mesh size. However, three elements were adopted along the thickness of the SFRM layer. Fixed boundary conditions were defined for the top and bottom ends in accordance with the

test conditions, except that the top end was allowed to move along the axial direction to simulate the column's expansion and shortening behaviour.

At ambient temperature, the stress–strain model proposed by Wang et al. [11] was used to simulate the HSS tube. Seif et al.'s model [12] was adopted at elevated temperatures. The thermal properties of HSS, such as the specific heat, thermal expansion, and thermal conductivity proposed by Xing et al. [13], were used. The longitudinal residual stresses were also considered initial stresses in the simulation using the predefined field feature of ABAQUS. The mechanical and thermal properties specified in Eurocode 2 [3] were tentatively used for concrete. The SFRM thermal properties reported by Huang et al. [8] were used in the heat transfer, but no strength contribution was considered.

The heat is transferred to the outer surface of the column through convection and radiation. For SFRM-protected columns, the heat is further transferred to the steel tube through conductance. In ABAQUS, heat flux to a surface due to boundary convection and radiation were modelled by defining a surface film condition and surface radiation interaction, respectively. For both thermal interactions, a history of furnace gas temperature adjacent to the fire-exposed surface was inputted into the program. For the fire-exposed surface of an unprotected steel column, the convective heat transfer coefficient (α_c) and radiative emissivity coefficient (ϵ_m) were defined as 25 W/m²K and 0.7, respectively, based on Eurocode 3 [14]. For SFRM-protected columns, the corresponding α_c and ϵ_m were specified as 60 W/m²K and 0.7, respectively. Surface-to-surface interaction was defined in both interfaces to consider thermal conductance between the interface of SFRM and the steel tube and that between the steel tube and concrete. The thermal contact conductance for both interfaces was defined as 104 W/m²K.

As the endplates were welded to the steel tube, a tie interaction was defined between an endplate and the adjacent end of the steel tube to simulate the welding between the endplate and the steel tube. The axial load was applied through a reference point located at the centre of the top endplate. The reference point was connected to the top end using the coupling option in ABAQUS. Surface-to-surface interaction was defined between the inner surface of the steel tube and the outer surface of the concrete core. Since the SFRM did not contribute to load load-carrying capacity, it was deactivated in the stress analysis using the “Modal change” interaction option available in ABAQUS.

To simulate the imperfections of the steel tube, an imperfection amplitude of $B/200$ [15] was defined based on the lowest local buckling mode, where B is the width of the cross-section. The stress analysis was conducted in two steps. In the first step, the “Static General” solver was used to analyse the column with the applied axial load, which was propagated to the second step. In the second step, the analysis was conducted using a “Dynamic Implicit” solver to simulate the fire exposure.

4 VALIDATION OF THE FE MODEL

The preliminary FE model developed in this study was used to predict the fire resistance of the tested CFST columns in this study. The load versus deformation curve of the ambient specimen was predicted very well (Figure 3). Meanwhile, the failure modes of both unprotected and protected columns tested in fire were also well captured (Figure 4). The predicted temperature developments of the steel tubes for protected and unprotected columns are compared with the measured temperatures in Figure 6. As can be seen, the temperature distribution in the unprotected specimen was reasonably predicted, but that in the protected specimen was underpredicted. A comparison of predicted and measured axial deformation versus time curves is shown in Figure 7. The expansion behaviour of the unprotected specimens was well captured, but the prediction accuracy for the failure stage of CFST-U1 can be improved. This could be attributed to the fact that the elevated temperature stress-strain model suggested in Eurocode 2 [3] is only valid for normal-strength concrete. For protected specimens, the fire resistance was overpredicted by 27 and 37 min for CFST-P1 and CFST-P2, respectively. Except for adopting the Eurocode 2 concrete model, the lower predicted temperatures might also be responsible for the prediction error. Further research is required to refine the FE model to improve its prediction accuracy.

5 CONCLUSIONS

This paper studied the fire performance of high-strength CFST tubular columns protected by a novel fly ash-based spray-applied fire resistive material (SFRM). It investigated the effects of load level and the efficacy of SFRM in protecting the columns. Furthermore, a finite element model was developed to predict the test results. The following conclusions can be drawn from this work.

- (1) The developed fly ash-based SFRM could effectively protect CFST columns with high-strength materials. All unprotected columns failed within 28 min of fire exposure, but the fire resistance of CFST columns protected by approximately 20 mm thick SFRM was greater than 3 h. This clearly demonstrated the efficacy of the developed SFRM.
- (2) The load level had a minor influence on the fire resistance of CFST columns. When the load level increased from 0.25 to 0.4, the fire resistance time of the unprotected column reduced from 28 min to 24 min. Similarly, the fire resistance time of the protected column reduced from 216 min to 201 min.
- (3) The developed FE model gave reasonable predictions of the thermal and structural responses of the tested CFST columns with or without SFRM protection. However, further research is required to refine the FE model to improve its prediction accuracy.

ACKNOWLEDGEMENTS

The authors are grateful for the financial support from the Australian Research Council (DP220100036). They are also thankful to the technical staff, Mr. Robert Marshall and Mr. Murray Bolden, at Western Sydney University, for their assistance in conducting the column tests. Finally, the authors acknowledge the assistance of undergraduate project students Mr. David Pola and Mr. George Gorgees in assisting with the column tests.

REFERENCES

1. Endo, F.; Watnabe, T.; Yoshida, O. & Takeshi, S. 2011. Advanced Technologies Applied at the New “Techno Station” Building in Tokyo, Japan, *Structural Engineering International*, 4: 508-513
2. Liew, J.Y.R.; Xiong, M.X., & Xiong, D.X. 2014. Design of high strength concrete filled tubular columns for tall buildings. *International Journal of High-Rise Buildings*, 3(3): 215-221.
3. European Committee for Standardization. Eurocode 2: Design of concrete structures - Part 1-2: General rules-structural fire design. EN 1992-1-2. 2004.
4. Xiong, M.X. & Liew, J.R., Fire resistance of high-strength steel tubes infilled with ultra-high-strength concrete under compression. *Journal of Constructional Steel Research* 176, 106410 (2021).
5. Kodur, V.R., 2006. Solutions for enhancing the fire endurance of HSS columns filled. *Engineering Journal*, 43(1), pp.1-7.
6. Australian Building Codes Board. (2022). National construction code volume one. <https://ncc.abcb.gov.au/editions/ncc-2022/adopted/volume-one>.
7. Zhang, Q. & Li, V.C., Ductile cement-based spray-applied fire-resistive materials,” *Journal of Structural Fire Engineering*. *Journal of Structural Fire Engineering* 7 (2), 114–125 (2016).
8. Huang, Q., Tao, Z., Pan, Z., George, L., Wuhner, R. & Rahme, M., Properties of fly ash-based spray-applied fire resistive materials,” *Journal of Cleaner Production* 425, 138894 (2023).
9. Tao, Z., Katwal, U., Huang, Q. and Rahme, M., Fire performance of high-strength steel tubular columns protected by sprayed fire-resistive material.
10. ISO 834-1, “Fire-resistance tests-Elements of building construction-Part 1: General requirements”, International Organization for Standardization, Geneva, 1999.
11. Wang X.Q., Tao Z., Katwal U. and Hou C., “Tensile stress-strain models for high strength steels”, *Journal of Constructional Steel Research*, **186**, 106879, 2021.

12. Seif, M., Choe, L., Gross, J., Luecke, W.E., Main, J.A., McColskey, D., Sadek, F., Weigand, J.M. and Zhang, C., 2016. Temperature-dependent material modeling for structural steels: formulation and application. Gaithersburg, MD, USA: US Department of Commerce, National Institute of Standards and Technology.
13. Xing Y., Wang W. and Al-azzani H., “Assessment of thermal properties of various types of high-strength steels at elevated temperatures”, *Fire Safety Journal*, **122**, 103348, 2021.
14. Eurocode 3, Design of steel structures, Part 1–2: General rules–structural fire design, European Committee for Standardisation, Brussels, 2005.
15. Meng X. and Gardner L., “Behavior and design of normal-and high-strength steel SHS and RHS columns”, *Journal of Structural Engineering*, **146**(11), 04020227, 2020.

FIRE RESISTANCE OF EARTHQUAKE-DAMAGED CFST COLUMNS FILLED WITH PLAIN AND FIBER-REINFORCED CONCRETE

Smita Singh¹, Anil Agarwal²

ABSTRACT

Past evidence has suggested that fire disasters often ensue after an earthquake catastrophe, perhaps resulting in much more severe damage than the earthquake itself. This research examines the fire resistance of concrete-filled steel tube (CFST) columns after an earthquake. Four CFST columns of the same dimensions (220*220 mm) were cast for this study. Three specimens were filled with fiber-reinforced concrete, and one specimen was filled with plain concrete. The experimental plan consists of two components: quasi-static testing (cyclic tests) and fire tests. During the cyclic tests, the CFST columns were subjected to a constant compressive force and cyclic horizontal force until they reached varying levels of seismic damage, replicating moderate and high earthquake damage. Subsequently, the columns that were already damaged were subjected to a constant axial compression force and then subjected to the fire load as per the ISO standard fire curve. One of the specimens underwent a direct test under fire to measure its fire resistance in an undamaged state. Columns were heated until they failed due to global buckling. The specimens also exhibited local buckling of the tubes because of the thermal expansion of the steel tubes and their separation from the concrete. The paper documented the duration of fire resistance and the specific ways in which these pre-damaged CFST columns failed.

Keywords: Fire resistance; Earthquake damage; Structural fire behaviour; Steel-concrete interface behaviour; fire tests

1 INTRODUCTION

The 1906 San Francisco and 1923 Tokyo earthquakes resulted in significant destruction as a result of ground shaking. However, the damage and losses caused by the ensuing fires were reported to be much greater than the damage caused by the shaking itself [1]. Following the 1989 Loma Prieta, 1994 Northridge, and 1995 Kobe earthquakes, other fires were recorded on a lesser scale [2]. To ensure robust structural design, it is crucial to have a better understanding of how seismic damage affects the fire resistance of structural elements, given the potential risks of fire at both local and widespread levels in structures after an earthquake.

Concrete-filled steel tubular (CFST) columns are becoming more globally used in construction due to their exceptional structural performance and simplicity of assembly. Several authors have studied the behaviour of CFST columns under axial compression, eccentric compression, flexural loading, and fire loading. Several previous research studies have shown the favourable seismic behaviour of CFSTs [3] [4], whereas other research has focused on CFSTs' fire resistance [5] [6] [7]. But very few researchers have studied the combined effect of both cyclic and thermal loading [8] [9].

¹ Research Scholar, Department of Civil Engineering, IIT, Hyderabad.
e-mail: ce17resch11007@iith.ac.in, ORCID: <https://orcid.org/0000-0003-2997-7651>

² Associate Professor, Department of Civil Engineering, IIT, Hyderabad.
e-mail: anil@ce.iith.ac.in, ORCID: <https://orcid.org/0000-0002-3902-4304>

Columns often undergo structural damage and subsequent thermal stress due to fire when exposed to multi-hazard loading conditions. This work further examines the behaviour of CFSTs when subjected to fire after an earthquake, building upon earlier research in this area. This study investigates the influence of cyclic damage on the fire resistance of CFST columns using a comprehensive experimental investigation.

2 EXPERIMENTAL PROGRAM AND RESULTS

An experimental study was done to test the behaviour of CFST columns under the combined effects of seismic damage and subsequent fire exposure. Four CFST columns of the same dimensions (220*220 mm) were cast for this study. Three specimens were filled with fiber-reinforced concrete, and one specimen was filled with plain concrete. The next sections explain the specimens and experimental settings used for cyclic and fire testing. The cyclic and fire tests were conducted at the Structural Engineering Lab at IIT Hyderabad, India.

Four CFST columns of the same dimensions (220*220 mm) were cast for this study. The specimens' height was 1080 mm. Two 20mm circular diameter holes were cut from the ends of the square hollow steel tube so that vapour pressure produced during the heating of the specimen could be released. During casting, four thermocouples were placed inside the tube. The cross-section's temperature was measured at various points using Type K chromel-alumel thermocouples. Concrete was filled inside a steel tube in the upright position, and a poker vibrator was used to compact the concrete.

All steel tubes were hot-rolled steel tubes with an 6 mm wall thickness. Three specimens were filled with fiber-reinforced concrete, and one was filled with plain concrete. The steel plate, which had a thickness of 20 mm, was welded at the bottom and top of the CFST columns. The material properties of steel and concrete are shown in Table 1. Table 1 shows a compilation of the experiments undertaken and a concise summary of the significant findings and observations.

Table 1. Summary of Specimens and Experimental Program

Specimen	L (mm)	D×t (mm)	f_c (MPa)	f_y (MPa)	Concrete Type	Drift (%)	Residual Drift (mm)	Fire Resistance (min)
S6-F-DR0	1080	220×6	32	365	Fiber	N/A	N/A	105
S6-F-DR4	1080	220×6	32	365	Fiber	4	23.11	34.2
S6-F-DR6	1080	220×6	32	365	Fiber	6	48	32.05
S6-P-DR6	1080	220×6	31	365	Plain	6	49.12	25.8

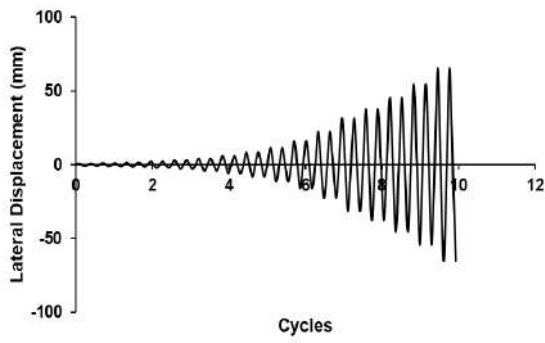
Legend: F-Fiber reinforced concrete; P-plain Concrete; DR-Drift Ratio; S-Steel

2.1 Cyclic Test Setup and Results

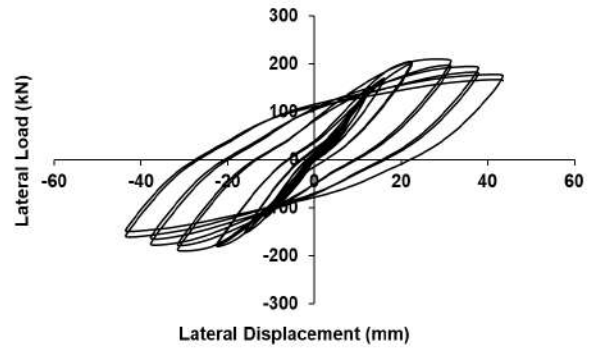
Figure 2 displays the test set-up used for quasi-static cyclic loading. The lower part of the specimen was fixed between two beams by pre-tensioning, while a hydraulic cylinder (capacity 2000 kN) exerted a consistent axial pressure on top of the specimen. Additionally, a horizontal actuator (capacity 500 kN) applied repetitive horizontal force to the upper part of the specimen.

The square CFST columns were subjected to cyclic horizontal force and a constant compressive force of 978 kN throughout the quasi-static tests until they sustained varying degrees of seismic damage. The applied compression load on the top of the specimen was selected to be 30% of the ultimate bearing capacity of the specimens (calculated as $f_{ck} \cdot A_c + f_y \cdot A_s$, where A_c is the cross-section area of concrete, f_{ck} is the compressive strength of concrete, f_y is the yield strength of steel, and A_s is the cross-section area of steel).

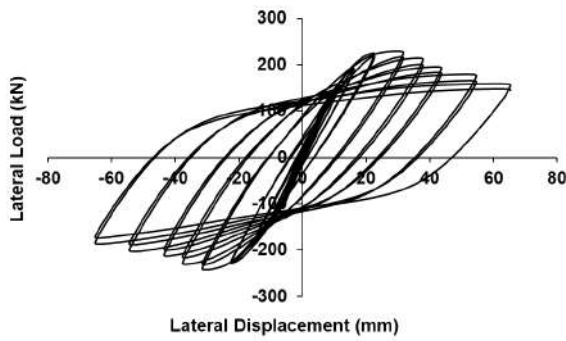
The FEMA 461 loading protocol was adopted to apply cyclic loading, as demonstrated in Figure 1(a). Specimen S6-F-DR4 were loaded to a 4% drift ratio, while specimens S6-F-DR6 and S6-P-DR6 were loaded to a 6% drift ratio. Specimen S6-F-DR0 was not subjected to any damage and was used as a reference.



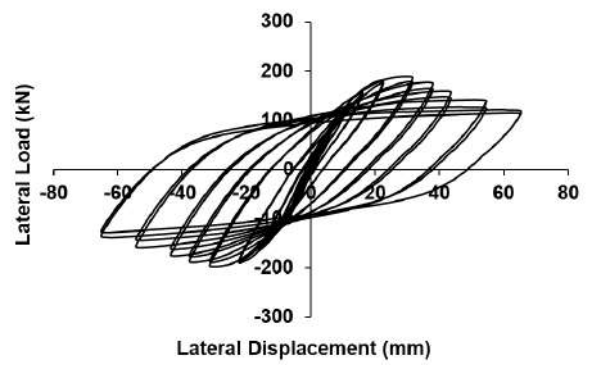
(a) FEMA 461 loading Protocol



(b) S6-F-DR4



(c) S6-F-DR6



(d) S6-P-DR6

Figure 1. Loading protocol and later displacement-force graphs



Figure 2. Quasi-static Cyclic Test setup



S6-F-DR4

S6-F-DR6

S6-P-DR6

Figure 3. Damage degree of columns after cyclic test

The Hysteresis curves for the CFST columns are shown in Figure 1. Test setup for the cyclic test, along with the respective failure modes for specimens, are shown in figures (2-3). Cyclic loading was done in the MTS actuator using multipurpose testware software by defining amplitudes of cycles according to the FEMA 461 loading protocol. Cyclic loading was terminated when the displacement was at its maximum, as shown in Figure 1(a), and then the actuator was moved manually until the force was zero.

2.2 Fire Test Setup and Results

Figure 4 displays the test set-up used for fire loading. Ceramic radiating panels of dimensions 470mm x 330mm were used to heat the CFST columns. A set of eight heaters was arranged in such a way as to create 4-side boundary conditions for heating the CFST columns. Heaters were assembled around the specimens and openings were closed by the glass wool. The portion of 950 mm of the specimen was subjected to heating. To measure the temperature of the chamber, eight thermocouples were placed inside the furnace cavity. Another set of seven thermocouples was used to measure the temperature distribution in the specimen.

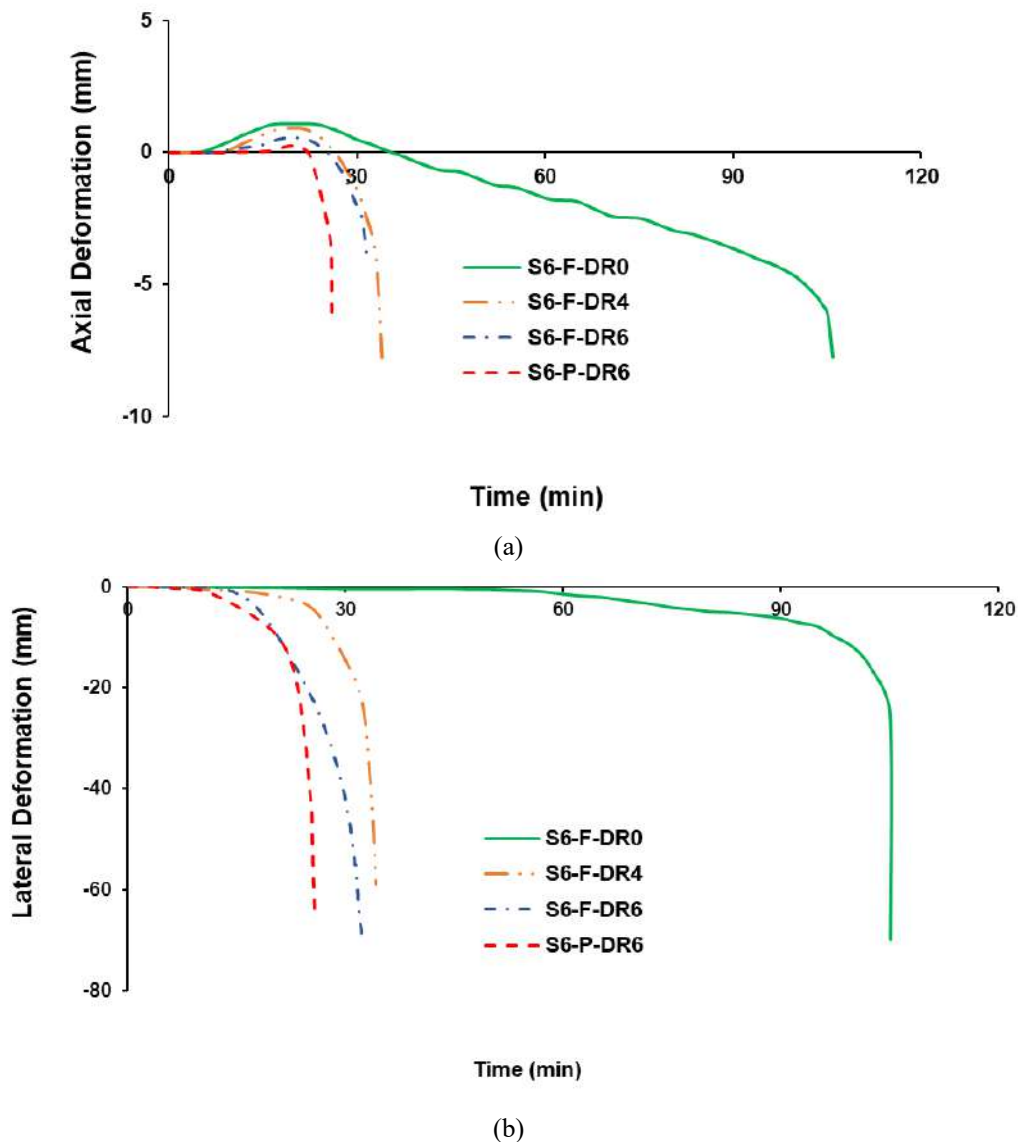
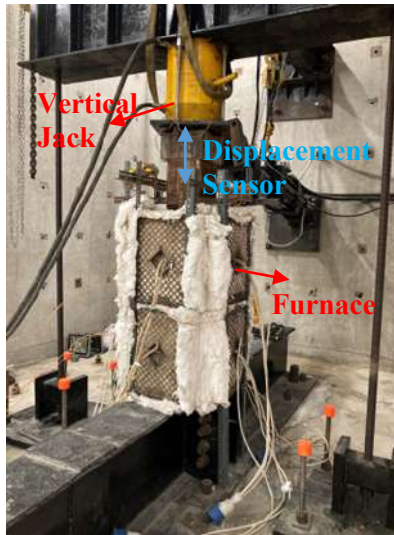


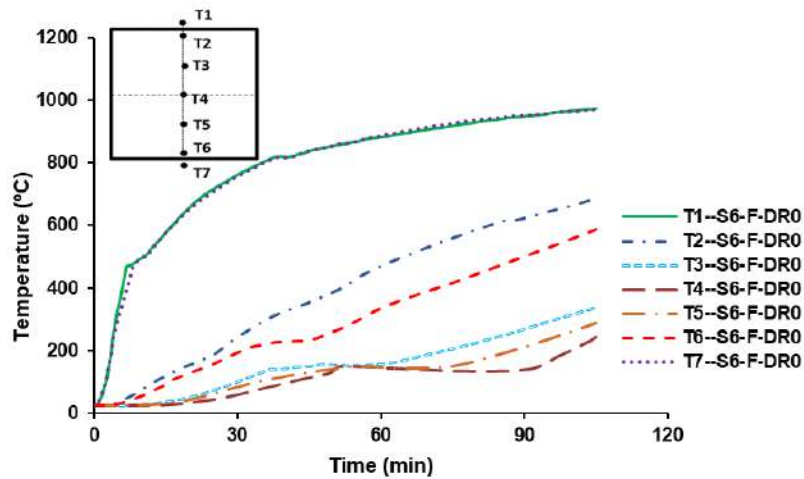
Figure 4. Displacement results from fire tests: (a) axial displacement results (b) lateral displacement results



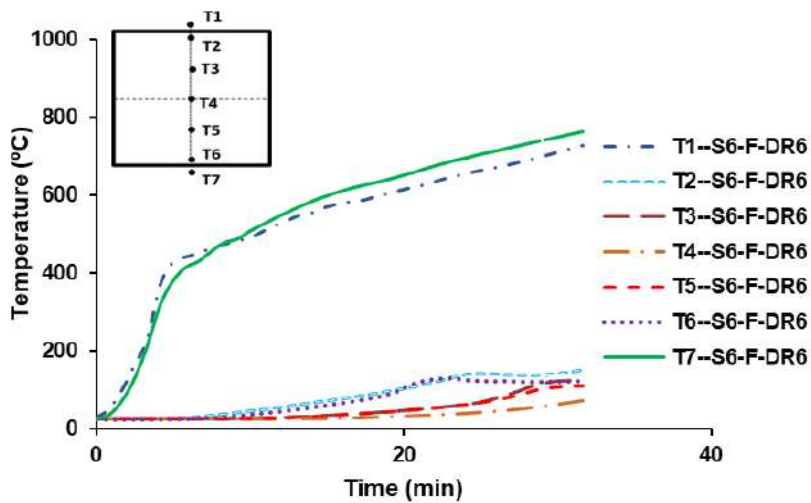
S6-F-DR0 S6-F-DR4 S6-F-DR6 S6-P-DR6

Figure 5. Heating Test setup

Figure 6. Failure of columns after fire test



(a)



(b)

Figure 7. Temperature distribution measured during fire tests in specimen: (a)S6-FC-Fire (b) S6-FC-DR6-Fire

The specimens were subjected to a continuous axial load throughout the testing. This load was managed by maintaining the necessary pressure for the hydraulic pumps to provide the correct degree of force. Heaters were then switched on, and the heating rate was followed as per ISO-834 standard fire curve[11]. Axial and lateral displacements of the columns, as well as the temperatures of the steel, concrete, and furnace, were all recorded throughout the test. Heating was continued till the column failed.

The columns are considered to have failed (i) when failure criteria are reached according to the specifications in ISO-834 [11]; (ii) when the hydraulic cylinder was not able to maintain the load anymore; (iii) when total drift of columns reached 10% DR, to prevent the damage to the furnace.

Figure 6 displays the failure modes of all four CFST columns. All columns failed in global buckling, as can be seen from the lateral deformation-time graphs shown in Figure 4 (b). A comparison of axial deformation and lateral deformation with time for CFST columns is shown in Figure 4(a) and 4(b), respectively.

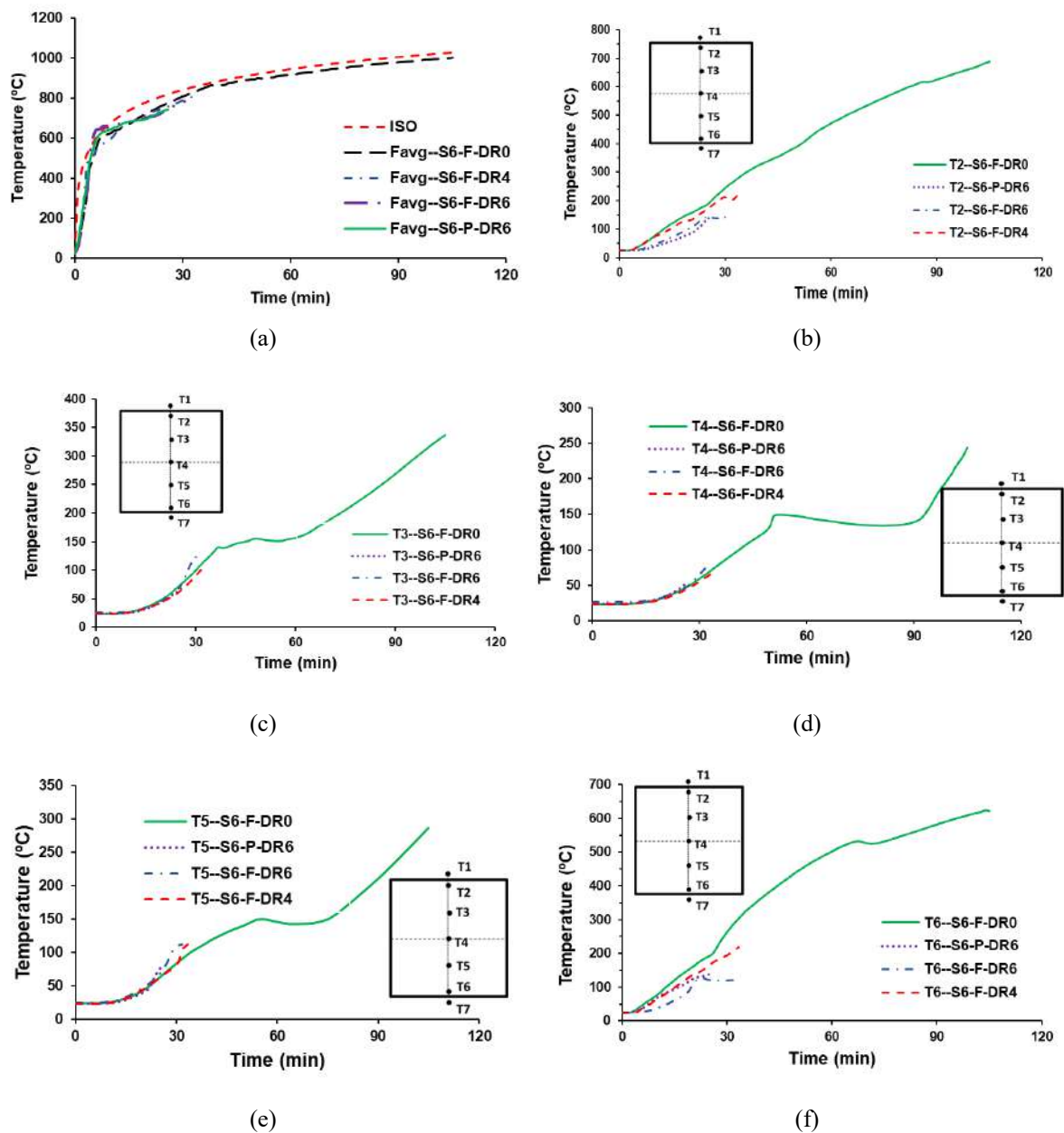


Figure 8. (a) ISO 834 fire curve along with average furnace temperature and temperature profile measured in fire test in all four specimens at locations (b) T2 (c) T3 (d) T4 (e) T5 (f) T6

Figures 7(a) and 7(b) show the temperature profile at the interface of steel and concrete for columns S6-F-DR0 and S6-F-DR6, respectively. The column labelled S6-F-DR6 experiences a slower increase in temperature compared to the undamaged column labelled S6-F-DR0 because of the gap created between the steel tube and the concrete core [12].

Figure 8(a) shows the average furnace temperature for all specimens, along with the ISO 834 fire curve. Figures 8(b) to 8(f) show the temperature distribution inside the specimens at various locations.

3 CONCLUSIONS

This research conducted experimental investigations on the fire resistance of square CFST columns with varying degrees of seismic damage.

When the results of three specimens filled with fiber-reinforced concrete were compared, the specimen that had been exposed to more seismic damage, that is, with a drift ratio of 6%, was found to have the lowest fire resistance duration. Specimen S6-P-DR6 had a lower level of fire resistance in comparison to specimen S6-F-DR6, despite the fact that both specimens were exposed to the same degree of earthquake damage. This S6-P-DR6 specimen has a lower fire resistance than other specimens since it is made of plain concrete.

REFERENCES

1. NOAA. (1972). "A study of earthquake losses in the San Francisco bay area—Data and analysis." Rep. Prepared for the Office of Emergency Preparedness, Washington, DC.
2. NIST. (1996). "The January 17, 1995 Hyogoken-Nabu (Kobe) earthquake; performance of structures, lifelines, and fire protection systems." NIST Special Publication 901, Gaithersburg, MD.
3. Han, L. H., and Yang, Y. F. (2005). "Cyclic performance of concrete-filled steel CHS columns under flexural loading." *J. Constr. Steel Res.*, 61(4), 423-452. doi:10.1016/j.jcsr.2004.10.004
4. Varma, A. H., Ricles, J. M., Sause, R., & Lu, L. W. (2004). Seismic behavior and design of high-strength square concrete-filled steel tube beam columns. *Journal of Structural Engineering*, 130(2), 169-179.
5. Hong, S., and Varma, A. H. (2009). "Analytical modelling of the standard fire behaviour of loaded CFT columns." *J. Constr. Steel Res.*, 65(1), 54-69. doi:10.1016/j.jcsr.2008.04.008
6. T.T. Lie, M. Chabot, 1992. Experimental studies on the fire resistance of hollow steel columns filled with plain concrete. National Research Council of Canada, Institute for Research in Construction.
7. Moliner, V., Espinos, A., Romero, M. L., & Hospitaler, A. (2013). Fire behavior of eccentrically loaded slender high strength concrete-filled tubular columns. *Journal of Constructional Steel Research*, 83, 137-146.
8. Imani, R., Mosqueda, G., and Bruneau, M. (2014) "Experimental Study on Post-Earthquake Fire Resistance of Ductile Concrete-Filled Double-Skin Tube Columns." *J. of Struct. Eng.*, 141 (8), 04015055. doi: 10.1061/(ASCE)ST.1943-541X.0001168.
9. Wang, Y. H., Tang, Q., Su, M. N., Tan, J. K., Wang, W. Y., Lan, Y. S., ... & Zhou, Y. (2020). Post-earthquake fire performance of square concrete-filled steel tube columns. *Thin-Walled Structures*, 154, 106873
10. FEMA. 2007. Interim testing protocols for determining the seismic performance characteristics of structural and nonstructural components. FEMA 461. Washington, DC: FEMA
11. ISO 834-1, Fire Resistance Tests-Elements of Building Construction, Part 1: General Requirements, International Organization for Standardization ISO 834, Geneva, Switzerland, 1999.
12. Singh, Smita, Prithvi Sangani, and Anil Agarwal. "Effect of structural damage on the thermal response of CFST columns. SiF2022 PolyU Hong Kong.

HEATING OF FIRE PROTECTED STEEL BEAMS WITH UNFILLED CAVITIES FORMED BETWEEN THE STEEL PROFILE AND OVERTOP STEEL DECK OF COMPOSITE SLABS - EXPERIMENTAL AND NUMERICAL STUDIES

Bin ZHAO¹ and Hoang-Tung VU²

ABSTRACT

This paper describes the current outcome of research works conducted at CTCIM to investigate the heating of fire protected steel beam supporting a composite slab with profiled steel deck under the condition that the cavities formed between the steel profile and the overtop steel deck are not filled. Within the scope of these research works, two specific fire tests have been carried out and allow to obtain solid experimental evidence about the heating behaviour of fire protected steel beam in this special case. Moreover, a specific numerical model has been developed to deal with the heating of fire protected steel beam under this situation on the basis of a simple empirical rule for hot gas temperature in the cavities. The comparison of this numerical model with fire tests show safe-sided and satisfactory correlation.

Keywords: Steel profile, steel sheet, fire protection, upper flange, cavity, fire test, numerical model

1 INTRODUCTION

To fire protect the steel profiles supporting a steel deck, in common cases, the cavities formed between the steel profile and the overtop steel deck has to be treated either by applying a fire protection to exposed part of top face of the steel profile or by filling the cavities with appropriate materials. However, this treatment could be challenging in practices due to very small spaces of these cavities. On the other side, these cavities with quite closed small spaces will reduce significantly the thermal actions in the event of a fire because the flow of hot gases and radiation effect from flames could be very limited. In consequence, even without any specific treatment of these cavities in terms of fire protection, the heating of upper flange of the steel profile will not be as high as a flange exposed to fire without any obstacle. Apparently, this reduced heating gives to a real possibility to leave these cavities without any specific treatment to ensure the necessary fire resistance of the steel profile. In current fire part of Eurocode 4 [1], this possibility is taken into account with a very simple rule. In one design document of SCI [2], it is clearly stated that it is necessary to increase the fire protection thickness of steel profile if these cavities are not filled. Another document dealing with this situation is the design recommendations published in one document of Steel Construction New Zealand Inc. [3]. However, above rules are either unrealistic or too limited to cover all the possible cases in practice. Recently, a research project combining both experimental investigation and numerical studies has been launched at CTCIM with the intention to provide more detailed design rules to deal with this specific situation.

In this paper, the research works conducted within the scope of this project as well as the results obtained up to now are described.

¹ Bin ZHAO, CTCIM

e-mail: bzhao@ctcim.com, CTCIM: <https://www.ctcim.com>

² Hoang-Tung VU, CTCIM

2 EXPERIMENTAL INVESTIGATION

2.1 Test set-up

Two fire tests with intentionally unfilled cavities formed between protected steel profiles and overtop steel deck of the composite slab were carried out in 2023 (see Figure 1) to obtain experimental data about the heating of steel profiles under this specific condition. In each of above tests, two specimens combining two different fire protected hot-rolled sections (HE300B and IPE300) and three types of steel sheet (Cofrastra40, Cofraplus60 and Cofraplus80) were used. These combinations allow the coverage of following parameters:

- Section factor of the steel beam,
- Geometry of the steel sheet (re-entrant et trapezoidal),
- Cavity depth (150 mm + 2 thickness of protection and 300 mm + 2 thickness of protection),
- Fire exposure duration: 60 minutes and 120 minutes.

For each specimen, the temperatures of twelve cross-sections, 4 cross-sections for each type of steel sheet were measured with a total of 78 thermocouples (see Figure 2). The temperature of the hot gas in the furnace was controlled to follow the standard fire (ISO 834 curve) using 8 plate thermometers installed 100 mm below the slab.

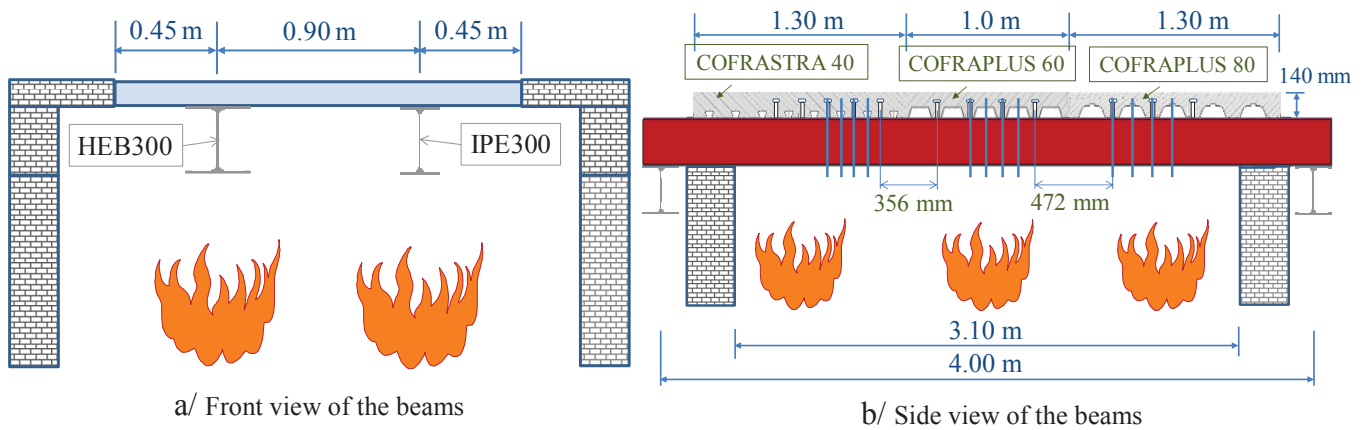


Figure 1: Test set-up

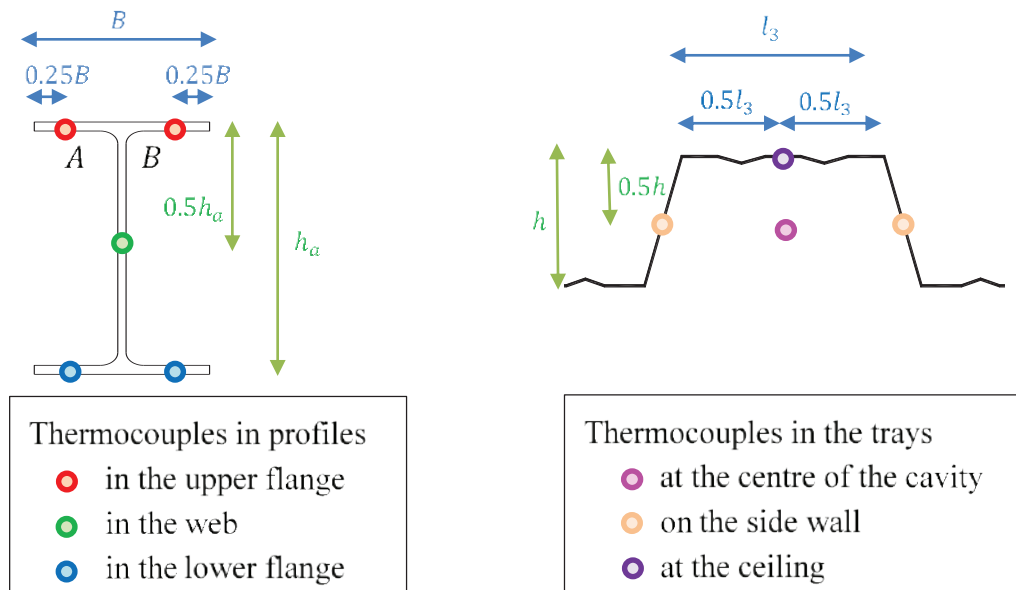


Figure 2: Position of the thermocouples on the cross-section

In order to better control the protection thickness, the mineral wool Superwool blanket is adopted to protection steel beams and the corresponding protection thicknesses are given in Table 1. These thicknesses

are selected with a target heating level of lower flange of steel profile at about 550 °C which is a common design value for critical temperature of steel beams under fire situation.

Table 1: Testing parameters

Steel profile	Steel sheet	Test 1 60 minutes fire exposure		Test 2 120 minutes fire exposure	
		Protection thickness	Total depth of cavities	Protection thickness	Total depth of cavities
HE300B	Cofrastra 40, Cofraplus 60 and Cofraplus 80	13 mm	326 mm	26 mm	352 mm
IPE300	Cofrastra 40, Cofraplus 60 and Cofraplus 80	19 mm	188 mm	44 mm	238 mm

2.2 Experimental results

The detailed test results can be found in [4]. In this paper, only the temperatures measured at key positions of the test specimens are provided. They correspond to the temperatures at the lower flange, mid-height of the web and at the upper flange of steel profiles. In addition, in order to have an accurate idea about the thermal actions around the cavities, the heating of the steel sheet at mid-height of cavity walls, at top of the cavities and the hot gas temperatures within the cavities are also measured during these tests.

For each fire test, the experimental results of six cavity configurations resulting from the combination of two steel profiles and three types of steel sheet (designated in the paper with the abbreviations cfr.40 for Cofrastra40, cfr.60 for Cofraplus60 and cfr.80 for Cofraplus80) are illustrated in Figures 3 to 10.

From the experimental results, the following general observations can be made:

- With the same steel profile, the temperatures of the upper flange increase according to following order: Cofrastra40, Cofraplus60, Cofraplus80, noting that the space of the cavities increases in the same order,
- With the same type of steel sheet, the hot gas temperatures in the cavity are lower with deeper cavity (HE300B) than those obtained with less deep cavity (IPE300).

With regard to steel profiles, more attention is paid to the heating of the upper flange which is the main target of our research project. In consequence, the measured temperatures of upper flange are provided in Figures 3 to 8 separately for the part under the cavities and for the part under the wave troughs of the steel sheet. On the contrary, the illustrated temperature of the web and the lower flange are not subject to this distinction since, according to the measurements, the heating of these parts is quite similar.

In addition to these graphical presentations, Table 2 summarises the average temperature values obtained at the target fire exposure times (60 and 120 minutes, respectively). It can be observed that:

- The measured temperatures of the upper flange vary significantly from re-entrant steel sheet (Cofrastra40) to trapezoidal steel sheet (Cofraplus60 and Cofraplus80): at the target fire exposure times, the steel sheet of Cofrastra40 leads to a heating less than 500°C, while the steel sheet of Cofraplus80 leads to a much higher heating, exceeding even 800°C after a fire exposure of 120 minutes;
- If the cavity is very narrow in terms of width (Cofrastra40), the temperature rise at mid-height of the web is more important than that of upper flange, but less important than that of lower flange;
- If the cavity is wider in terms of width (Cofraplus60 and Cofraplus80), the temperature rise at mid-height of the web is less rapid than that of the upper flange, but more speedy than that of the lower flange;

- The heating of the lower flange of the steel profiles is less affected with unfilled cavities but there is a temperature increase up to around 8% between re-entrant steel sheet (Cofrastra40) and trapezoidal steel sheets (Cofraplus60 and Cofraplus80).

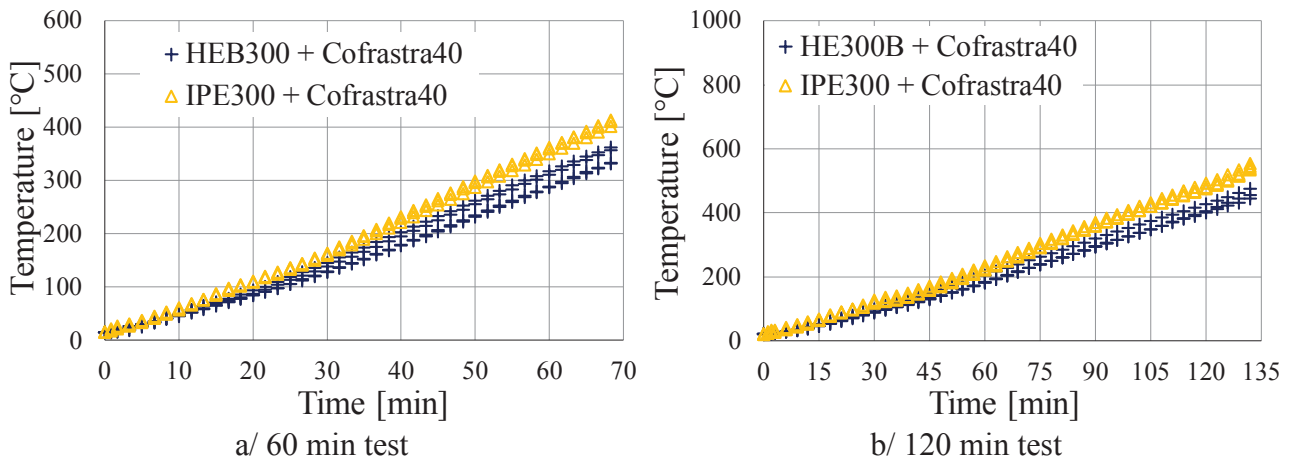


Figure 3: Temperatures of the upper flange of the profiles under the cavities - Case of Cofrastra40

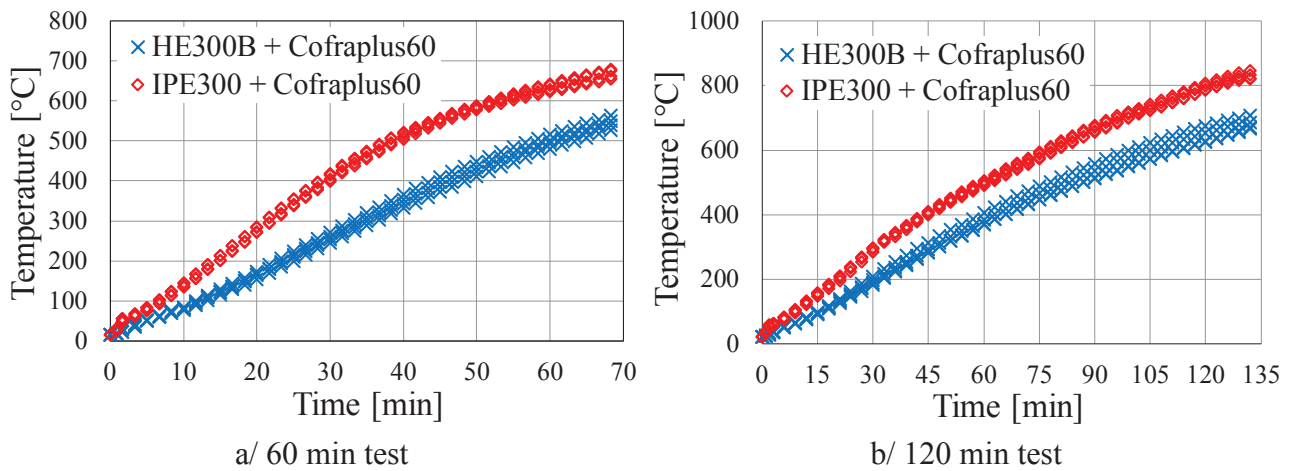


Figure 4: Temperatures of the upper flange of the profiles under the cavities - Case of Cofraplus60

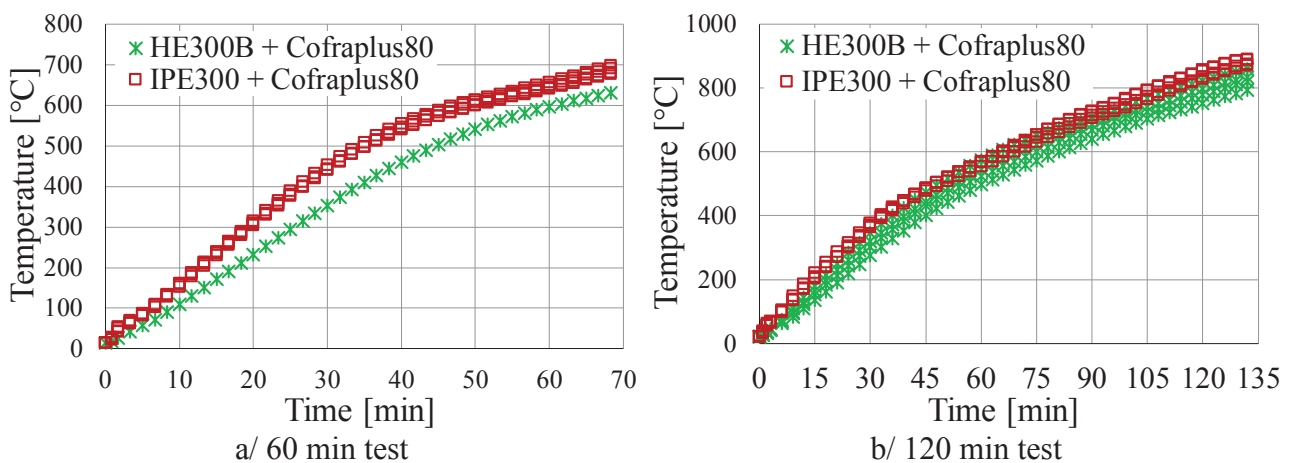


Figure 5: Temperatures of the upper flange of the profiles under the cavities - Case of Cofraplus80

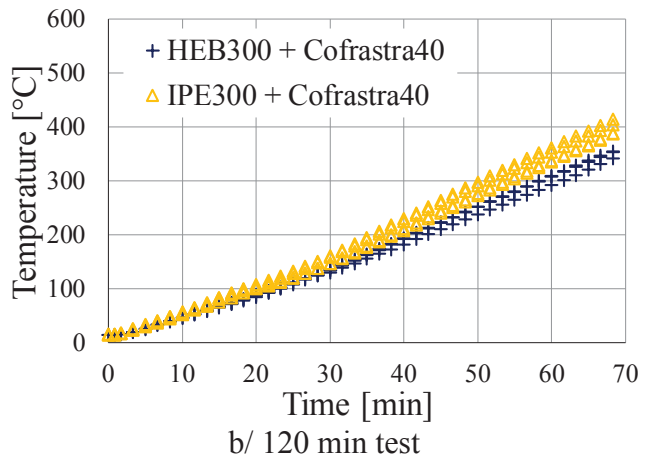
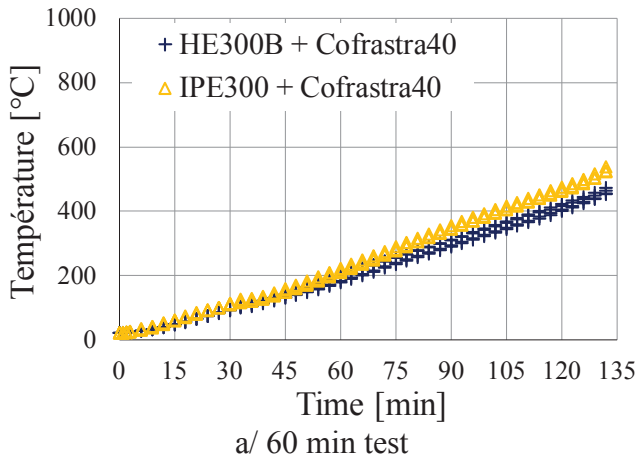


Figure 6: Temperatures of the upper flange of the profiles under the ribs - Case of Cofrastra40

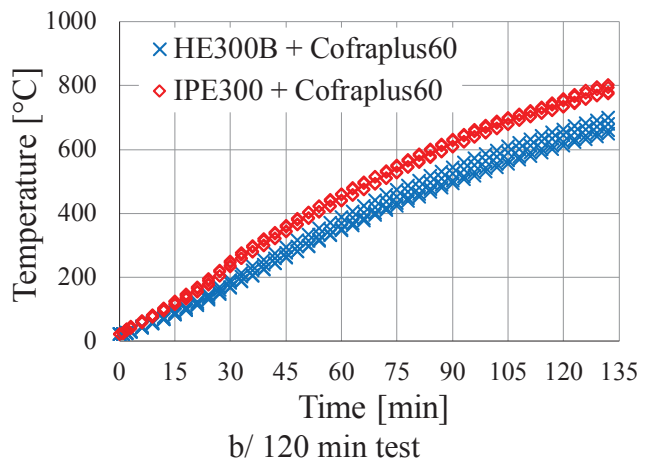
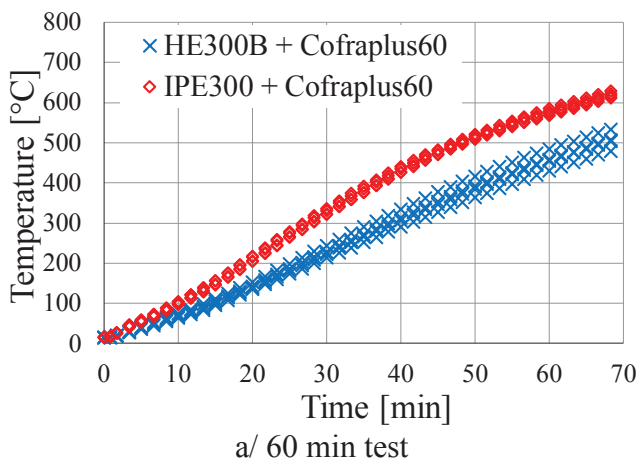


Figure 7: Temperatures of the upper flange of the profiles under the ribs - Case of Cofraplus60

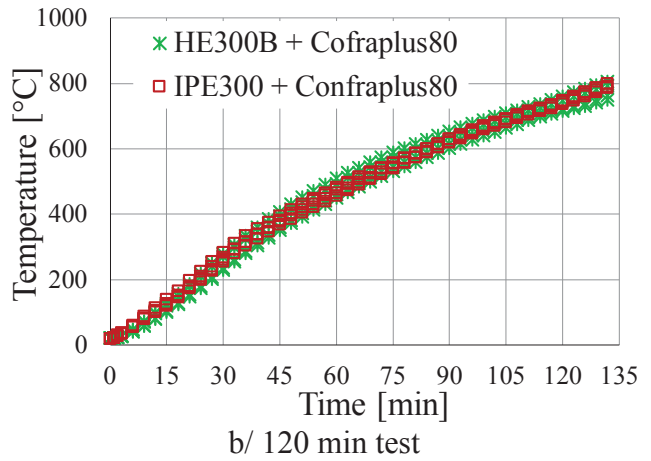
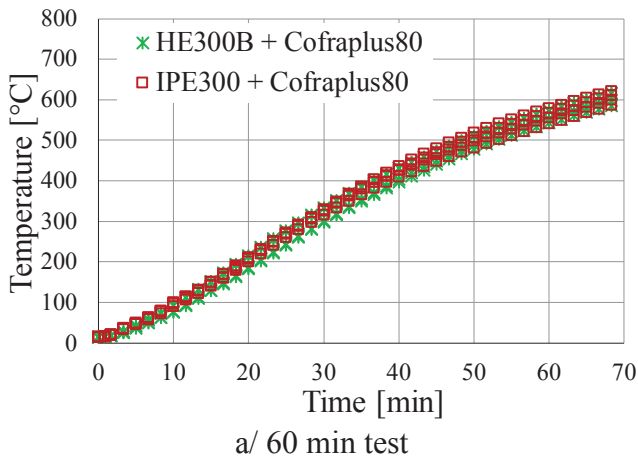


Figure 8: Temperatures of the upper flange of the profiles under the ribs - Case of Cofraplus80

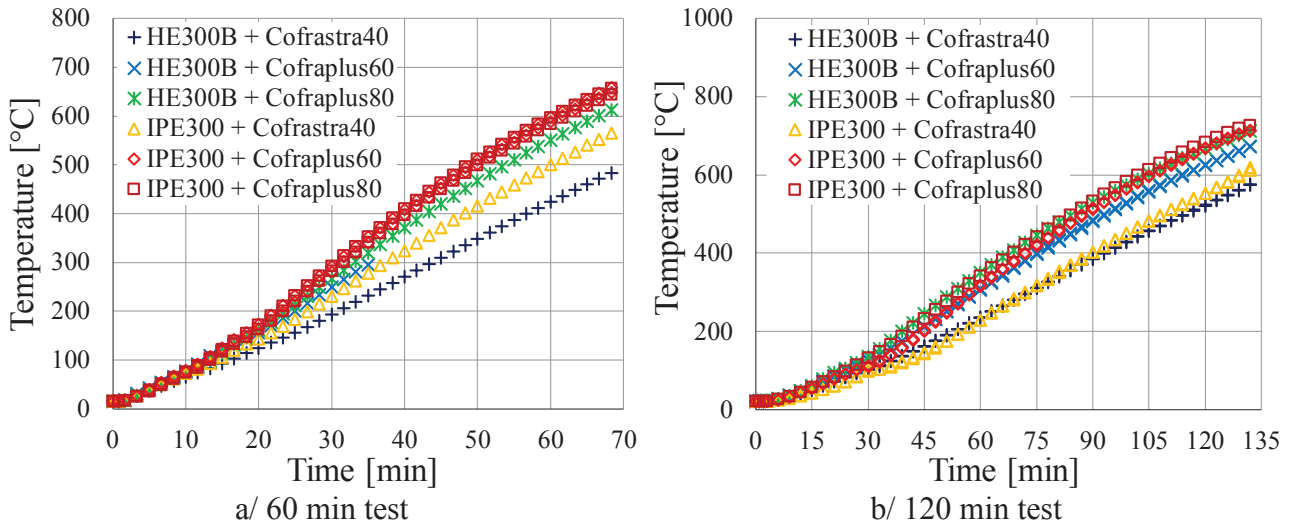


Figure 9: Temperatures at mid-height of the profiles for tested 6 configurations (3 steel sheets and 2 steel profiles)

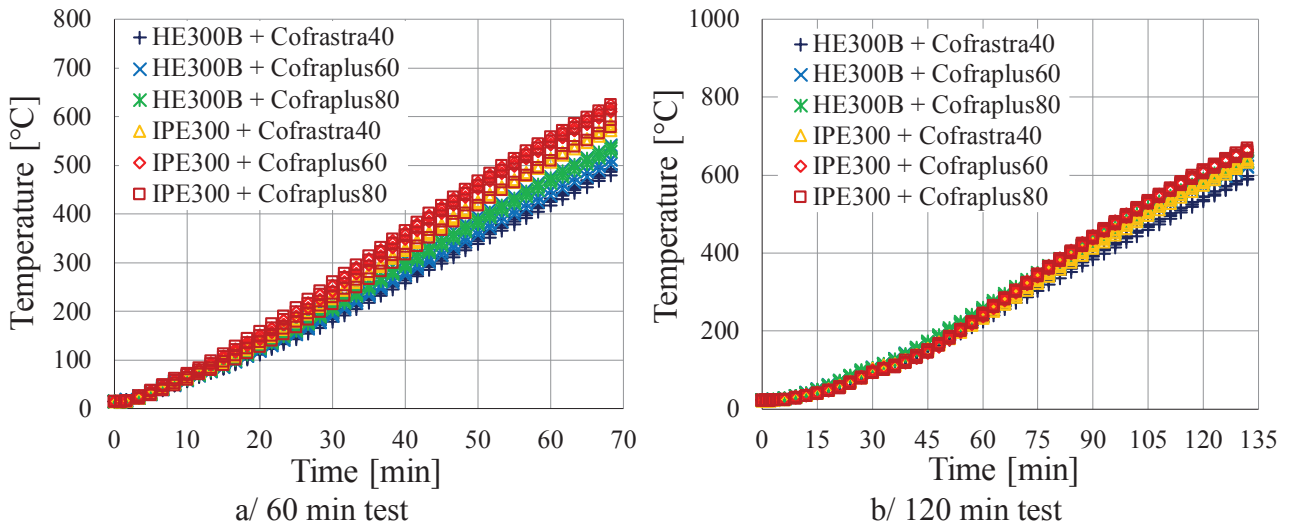


Figure 10: Temperatures of bottom flange of the profiles for tested 6 configurations (3 steel sheets and 2 steel profiles)

Table 2: Summary of measured heating of steel beams

Element considered	Time (min)	Configuration					
		HE300B +cfr. 40	HE300B +cfr. 60	HE300B +cfr. 80	IPE300 +cfr. 40	IPE300 +cfr. 60	IPE300 +cfr. 80
Upper flange under the cavities	60	315	509	597	362	641	654
	120	421	663	810	487	803	855
Upper flange under the wave troughs of steel sheet	60	311	471	573	358	582	585
	120	419	654	755	471	756	767
Web	60	424	—	551	500	597	597
	120	524	626	668	554	669	684
Lower flange	60	430	465	473	514	553	554
	120	545	578	588	584	611	612

The measured temperatures of the steel sheet at the ceiling and the walls of the cavities are shown in Figures 11 and 12. It can be found that the temperature of the steel sheet within this space is lower than that of the upper flange of steel profile, very possibly due to heat absorption of the concrete above the steel sheet.

The maximum temperature measured on the steel sheet is around 800°C after 120 minutes of exposure to fire. This is reached when the cavities formed between the steel profile and the steel sheet are more open and shallower (for example, steel sheet Cofraplus60 or Cofraplus80 combined with IPE 300 profile).

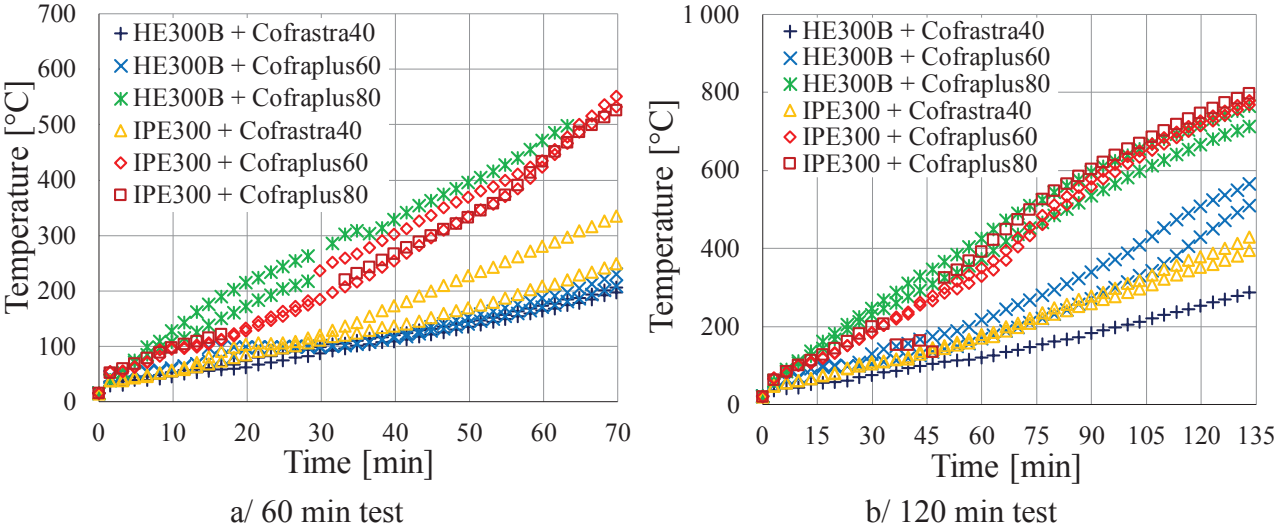


Figure 11: Temperatures obtained in the steel sheets at cavity ceiling

The temperature of the hot gas measured in the cavities formed between the steel profile and the steel sheet for the six configurations is shown in Figure 13. It can be observed that the temperature of the hot gas in this space is significantly lower than that in the common part of the furnace. This result confirms a reduced flow of hot gas in this narrow space and, consequently, lower thermal actions on the upper face of the steel profile.

Obviously, the geometry of the cavity plays an important role in the temperature of the hot gas within this space. In fact, for the same size of steel profile, the temperature of the hot gas in the cavity depends on the dimensions of the steel sheet and the depth of the cavity (i.e. the steel profile flange width and two protection thicknesses). In other terms, the hot gas flow inside the cavity increases from Cofrastra 40 to Cofraplus 60, then to Cofraplus 80 and decreases with the depth of the cavity. It is clear that the small cross-sectional area and important depth of the cavity create more obstacle for hot gas flow through this space.

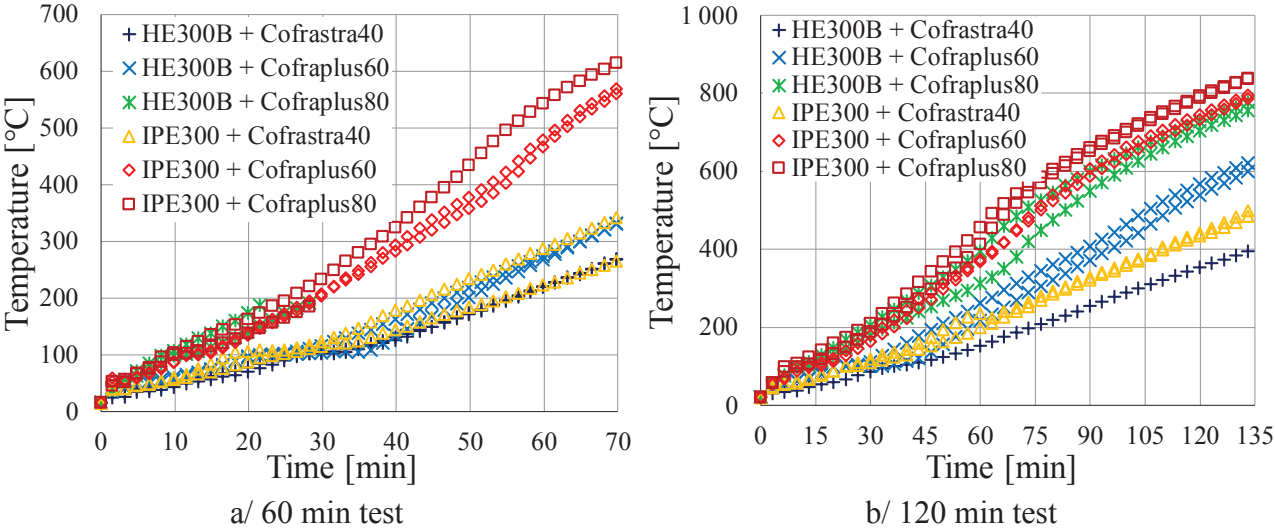


Figure 12: Temperatures obtained in the steel sheets at mid-height of the cavity walls

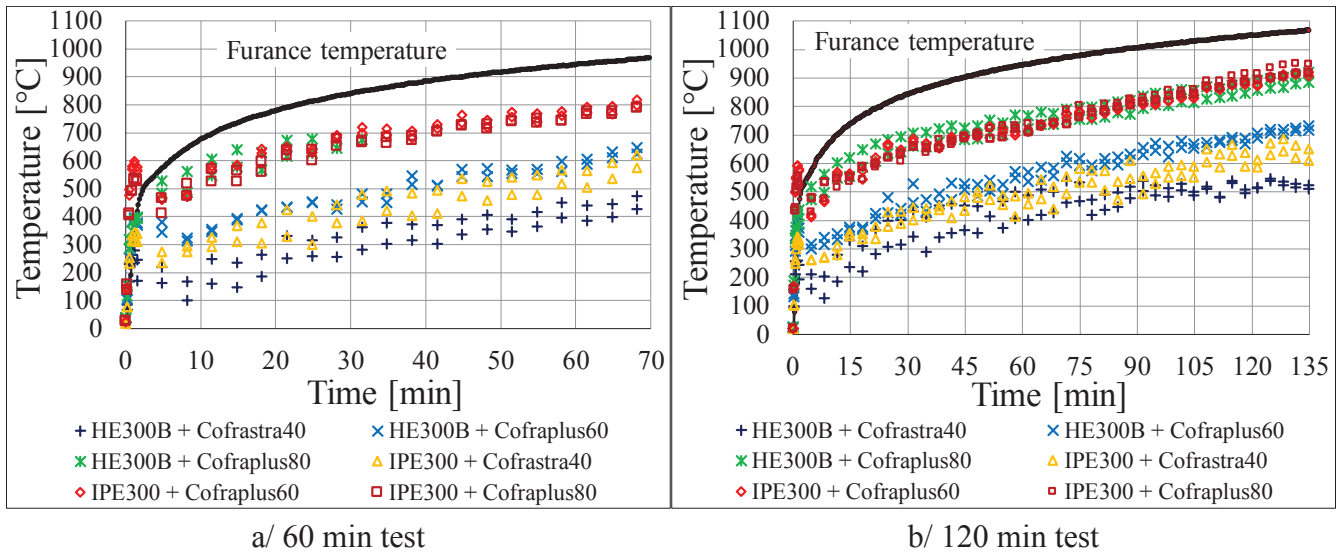


Figure 13: Hot gas temperatures in the cavities

3 NUMERICAL STUDY

3.1 Development of numerical modelling

In addition to experimental study to investigate the heating of steel beams with unfilled cavities formed between the steel deck and the upper flange of the steel beam, a specific numerical model using the computer code ANSYS is developed in order to analyse more efficiently the heating behaviour of steel beam under this specific situation (see Figure 14).

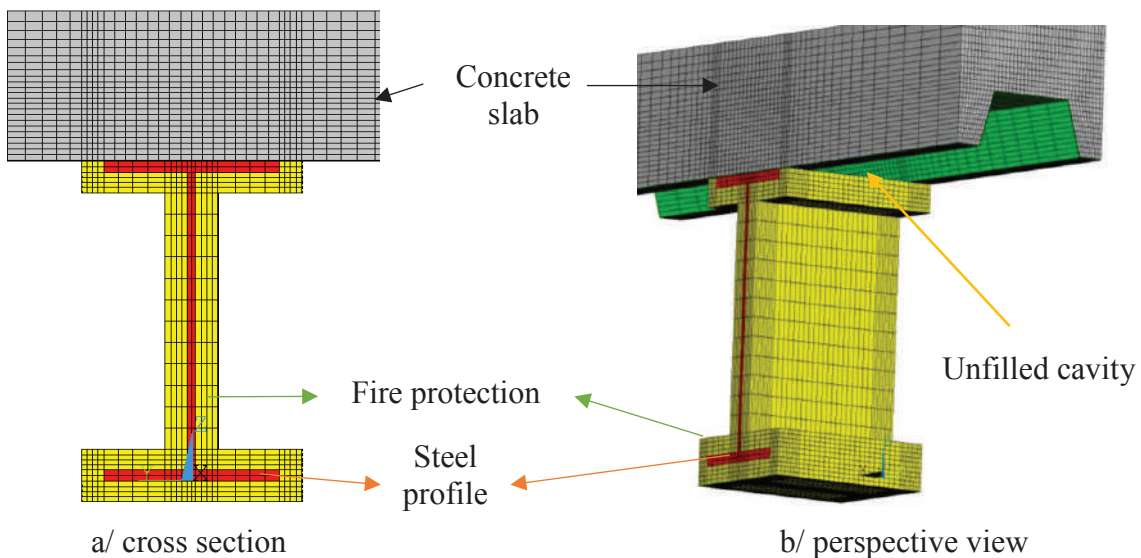


Figure 14: Illustration of numerical models

Following assumptions have been adopted for the numerical model:

- 8-node brick finite element for the 3D model were used,
- Heat exchange between the elements and their surroundings by convection and radiation according to EN1991-1-2,
- The shadow effect for the radiation inside the cavities formed between the steel profile and the steel sheet is explicitly taken into account,
- The thermo-physical properties (thermal conductivity, specific heat, density) of steel and normal density concrete are those given in Eurocode 4 part 1-2 and its French National Annex [1],

- The ambient temperature of 20° C is applied for heat exchanges on the top face of the slab, while the standard fire temperature (ISO 834) is applied for heat exchanges on the faces exposed to fire, except the faces of the cavity, namely, all the faces including unprotected top face of the upper flange as well as two protection thickness and all the walls of the steel sheet within this width,
- All the faces of the cavity formed between the steel profile and the steel sheet of the slab are considered to be subjected to convective heat exchange with a reduced hot gas temperature of which the value can be determined on the basis of a simple rule given in following paragraph (paragraph 3.2).

3.2 Simple rule for hot gas temperature in the cavities

The experimental results presented in the previous paragraph show clearly that the hot gas temperature within the cavities formed between the steel profile and the steel sheet is systematically lower than that of ISO standard fire curve. It is therefore more appropriate to use this reduced temperature to evaluate the heating of steel profile. On the basis of experimental results, a simple rule is proposed here to represent the hot gas temperature in the cavities. This rule is based on the geometric dimensions of the cavities to provide the hot gas temperature in these spaces according to following relationship:

$$\theta_{g,cav} = 20 + c_{eff} * t^{0,24}$$

Where

$\theta_{g,cav}$ is the temperature of the hot gas in °C in the cavities formed between the steel profile and the steel sheet;

t is the time in minutes;

$$c_{eff} = \min(300 ; 175 + 400\beta_{dim,cav})$$

with :

$$\beta_{dim,cav} = \frac{2hl}{(B+2e_p)^2}$$

B , e_p , h and l shown in Figure 15.

In fact, the parameter $\beta_{dim,cav}$ is an adimensional parameter to represent the open factor of the cavity. For tested six configurations, the resulting values of this parameter are given in Table 3.

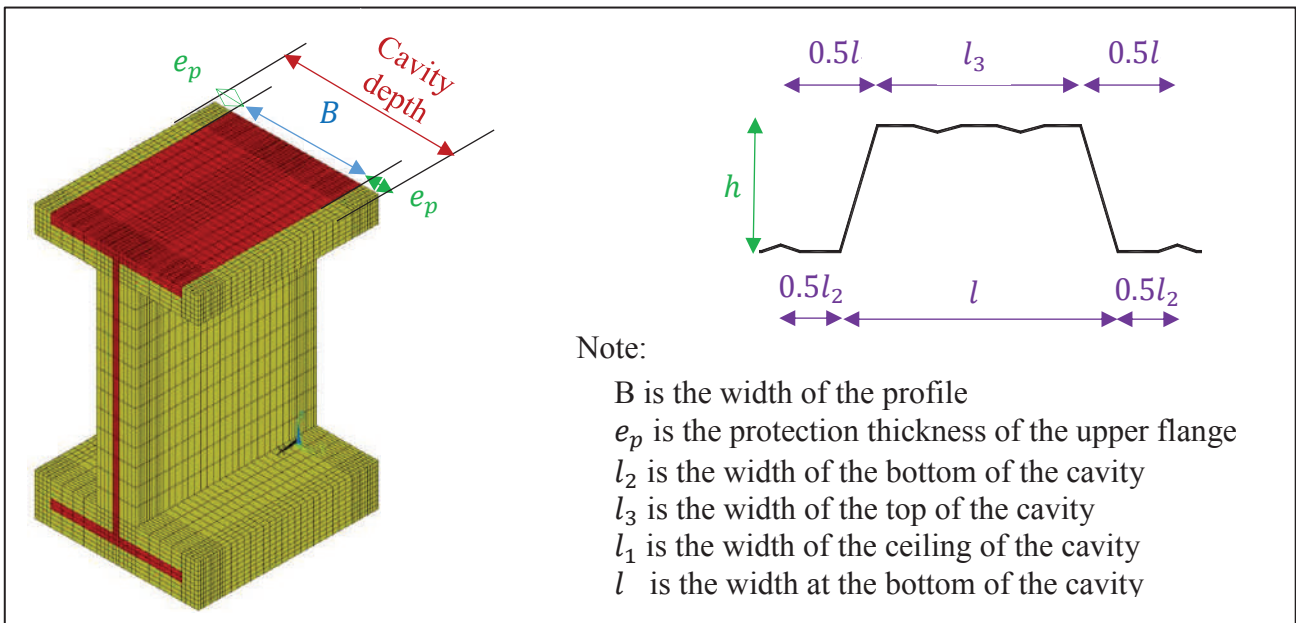


Figure 15: Illustration of the parameters for determination of $\beta_{dim,cav}$

This simple rule is then applied to all tested configurations in order to have an idea about its appropriateness with respect to reality. The corresponding results are shown in Figure 16 in which the lines represent the values derived from simple rule and the points illustrate the measured values from the tests.

It can be observed that the hot gas temperature of the cavities derived from this simple rule is quite close to experimental results but in general slightly higher than the latter.

Table 1 Values of the coefficient c_{eff} obtained for the configurations tested

Test	Configuration					
	HE300B Cofrastra40	HE300B Cofraplus60	HE300B Cofraplus80	IPE300 Cofrastra40	IPE300 Cofraplus60	IPE300 Cofraplus80
60 minutes	183	238,3	285,8	199	300	300
120 minutes	181,8	229,3	270	190	293,8	300

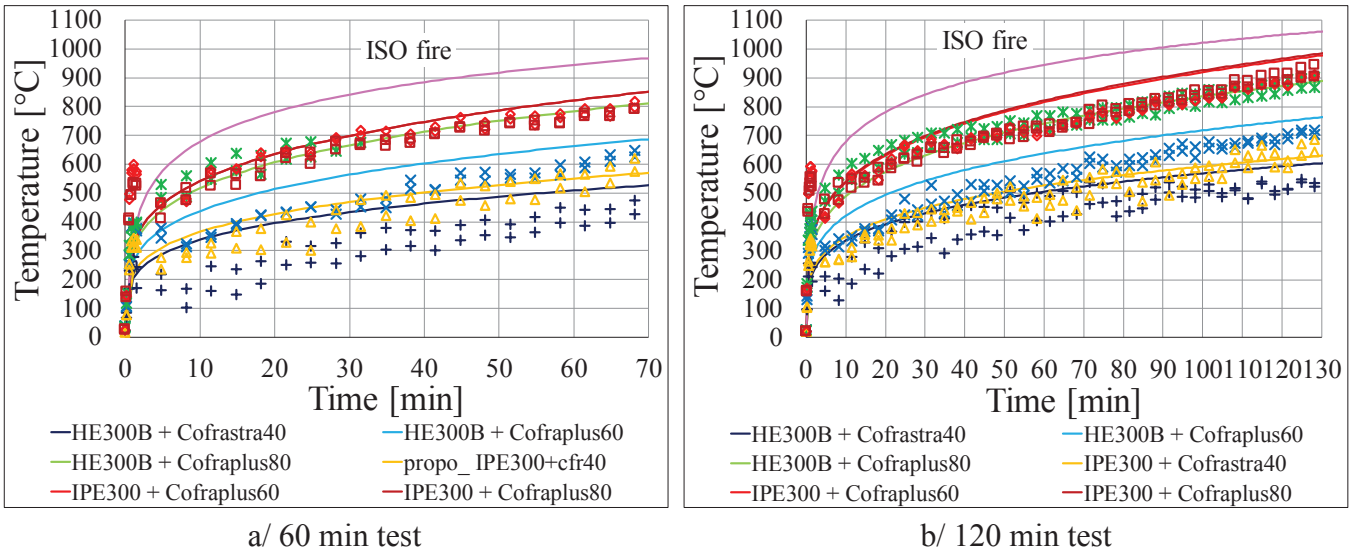


Figure 16: Hot gas temperatures in the cavities: comparison between the proposal and experimental results

3.3 Numerical analysis and comparison with experimental results

The numerical simulations with the help of the 3D numerical model explained above have been conducted for all tested configurations. Two typical examples are provided in Figure 17 to illustrate the numerical results of above simulations.

The results of these numerical simulations are systematically compared with the experimental measurements and, in order to avoid a heavy presentation, only four of these comparisons are given in Figures 18. To know the accuracy of above numerical approach, an overall comparison in terms of heating of the upper flange of steel profile between the experimental and numerical results is presented in Figure 19 for all tested configurations.

From this comparison, it can be observed that, in general, the numerical model overestimates the heating of the upper flange of the steel profile. However, this overestimation remains relatively modest and does not exceed 15%. In fact, this relative overestimation is higher in case of closed cavities (Cofrastra40 steel sheet) than in case of more open cavities (Cofraplus60 and Cofraplus80 steel sheets) for which the relative overestimation remains within the range of 10%.

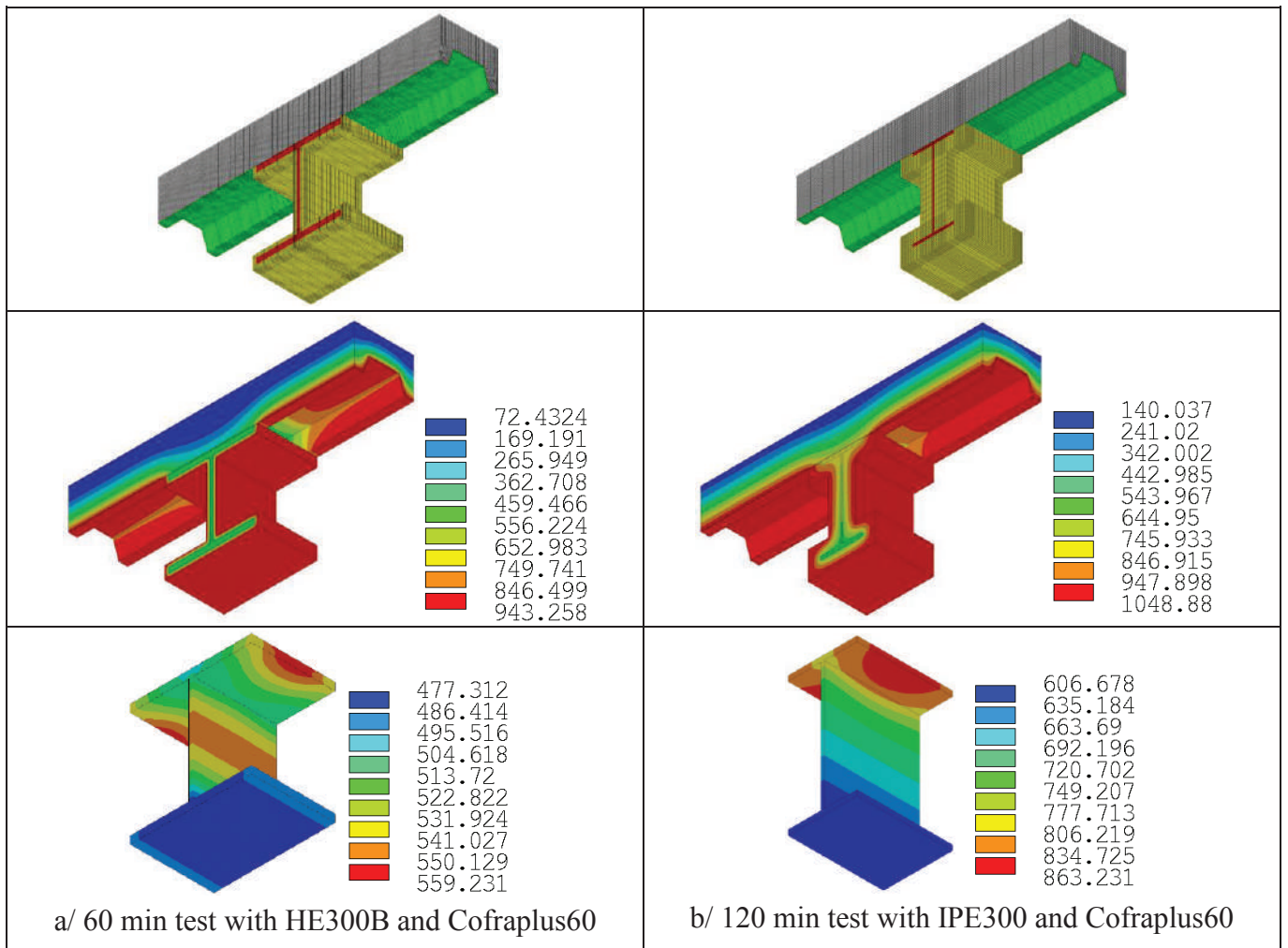


Figure 17: Two numerical modelling examples for thermal analysis of fire protected steel beam with unfilled cavities formed between the steel beam and overtop steel sheet

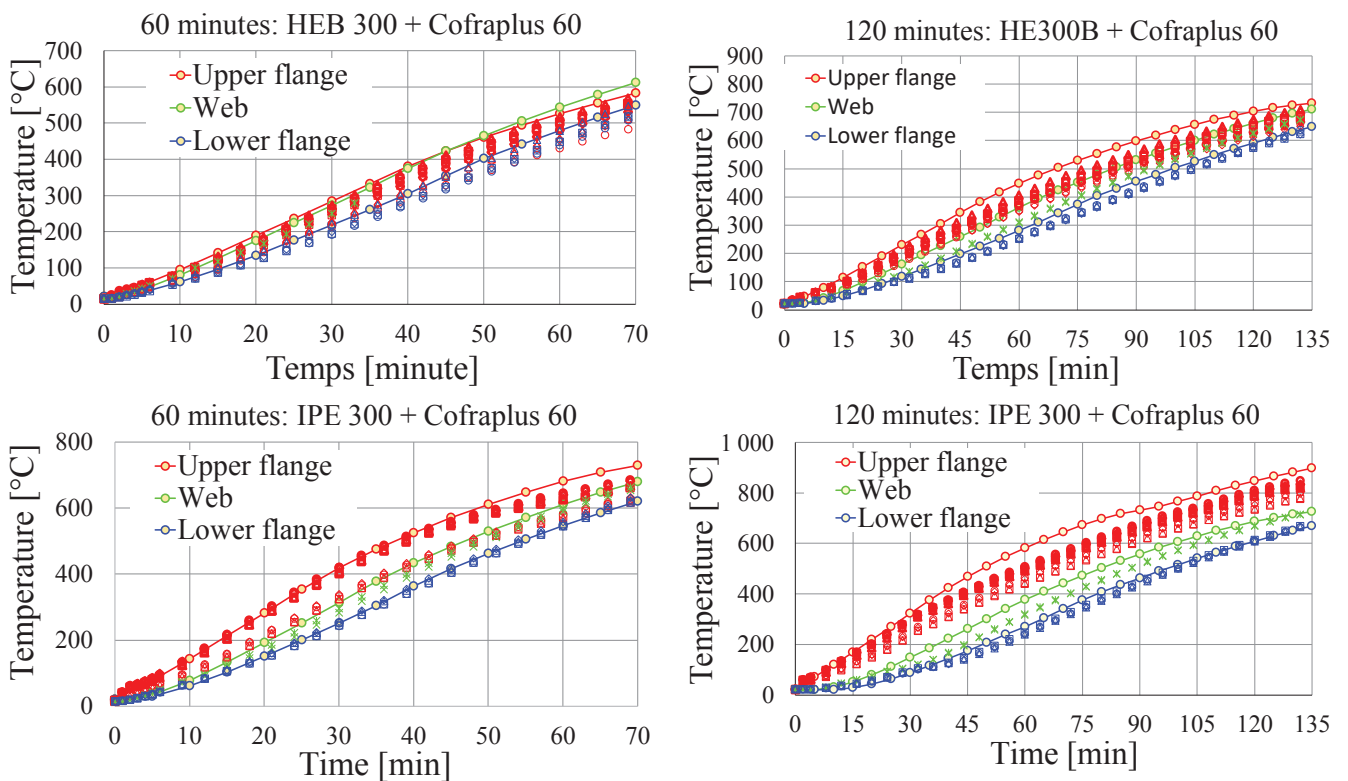


Figure 18: Comparison between experimental data (points) and numerical results (lines)

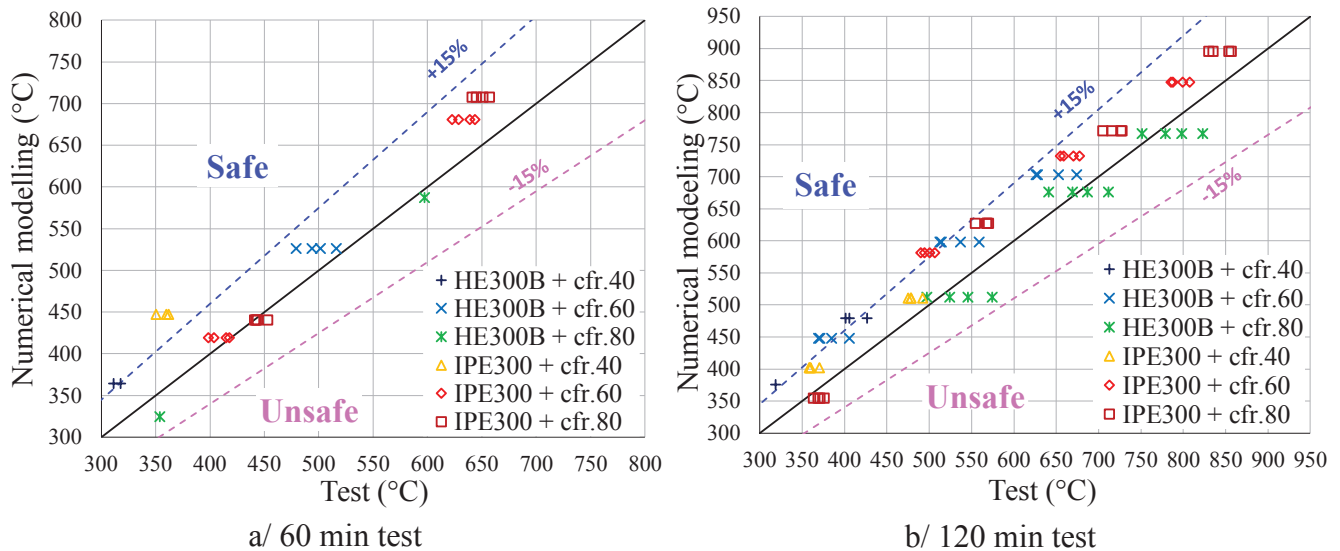


Figure 19: Comparison between experimental and numerical results in terms of heating of the upper flange

4 CONCLUSIONS

In this paper, the research works conducted recently at CTICM to investigate the heating of fire protected steel beams, in particular their upper flanges, in case where the cavities formed between the steel profile and the otop steel deck are not filled. The fire tests conducted specifically for this purpose show that the limited spaces of these cavities have a very important positive impact on the heating of steel beams under this specific case. The numerical approach proposed within the scope of these works is also described and compared with the experimental results. The accuracy of proposed numerical approach is satisfactory and will be used in the development of practical simple design rules, which will be the next tasks of these research works.

5 ACKNOWLEDGEMENTS

The authors would like to express their gratitude to ArcelorMittal for free delivery of all the steel members necessary for our fire tests.

6 REFERENCES

1. NF EN 1994-1-2, Eurocode 4: Design of composite steel and concrete structures, Part 1-2: General rules – Structural fire design (February 2006) and French National Annex (October 2007)
2. Newman, G.M., Fire Resistance of Composite Beams; SCI Technical Publication 109, The Steel Construction Institute, Ascot, England, 1991
3. Kevin Cowie, Fire Resistance of Composite Beams with Profiled Steel Decking, FIR1003, Steel Construction New Zealand Inc, 23 rd August 201
4. CTICM and ArcelorMittal, Heat transfer test on six configurations (HE300B, IPE 500 steel profiles + composite slabs with steel sheets Cofrastra40, Cofraplus60 and Cofraplus80), Fire test report EFR-22-001386, 2023, Efectis France

INFLUENCE OF LAPS ON THE BEHAVIOUR OF A COMPOSITE SLAB UNDER MEMBRANE ACTION IN FIRE

Moe Horie¹, Takeo Hirashima², Haruka Kanada³, Yusuke Shintani⁴

ABSTRACT

A simple design method for the composite slab under membrane action is proposed by ECCS. The composite slab must be able to transfer sufficient tensile stress at the laps to develop adequate load-bearing capacity under membrane action. In this paper, load-bearing fire test was conducted on a large-scale floor system consisting of steel beams and a composite slab with welded wire mesh of guaranteed weld point strength. The lap length of the meshes was their interval plus 50 mm (150 mm), which was less than the 250 mm specified by ECCS. The purpose of this study was to investigate whether tensile stresses were sufficiently transferred within the laps under the membrane action and to discuss the load-bearing capacity of the floor system. Two specimens were tested with either 2 or 2.67 times the load predicted by yield line theory. The test result showed that the floor system of the test specimens resisted the load not only during the 216-minute heating period, but also during the cooling period, although the second specimen experienced the integrity failure. Failure of the welded wire mesh adjacent to the lap was observed and the laps transferred sufficient tensile stress until the welded wire mesh yielded. Therefore, the lap length of the mesh interval plus 50 mm (150 mm) when using the welded wire mesh was adequate for transferring tensile stress. Furthermore, the test results indicated that the load-bearing capacity of the floor system based on ECCS was safe, taking into account the reduction in strength of the welded wire mesh at high temperature.

Keywords: Composite slab; Lap; Load-bearing fire test; Membrane action.

1 INTRODUCTION

Membrane action increases the load-bearing capacity of a two-way supported slab develops due to increased deflection. Composite slabs are generally designed as one-way supported slabs. In case of fire, the welded wire mesh within the slab bears the tensile forces instead of the steel deck plates. This causes the slab to behave a two-way slab under membrane action. Previous studies of membrane action include fire tests carried out at Cardington on an eight-storey steel building with composite slabs and unprotected beams [1], and a furnace fire test with composite slabs and unprotected secondary beams carried out undertaken as part of the FACOF project [2]. Membrane action occurred in both tests. Based on these fire tests, a simple design method was developed for the membrane action of composite structures in ECCS [3]. In this design method, the composite slab must be able to transfer sufficient tensile stress at the laps to develop adequate load-bearing capacity under membrane action.

¹ Master's Student, Graduate School of Science and Engineering, Chiba University
e-mail: horie2001@chiba-u.jp, ORCID: <https://orcid.org/0009-0009-3459-1244>

² Professor, Graduate School of Engineering, Chiba University
e-mail: hirashima@faculty.chiba-u.jp, ORCID: <https://orcid.org/0000-0003-1462-5370>

³ Master's Student, Graduate School of Science and Engineering, Chiba University
e-mail: chereeca5326@chiba-u.jp

⁴ Chief Researcher, Research & Development Institute, Takenaka Corporation
e-mail: shintani.yuusuke@takenaka.co.jp, ORCID: <https://orcid.org/0000-0002-5488-2761>

It is important that the laps of welded wire mesh can transfer tensile forces from the longitudinal wires in one sheet to the corresponding longitudinal wires in the other sheet to support the tensile forces under the membrane action. The lap length specified for ECCS with reference to Section 8.7.5 of EN1994-1-1 [4] is determined by the effect of the anchorage between the reinforcement and the concrete and requires an anchorage lap length of at least 250 mm. Meanwhile, in Japan, the lap length of the reinforcement is specified as the mesh interval (mesh size 100 mm or more) plus 50 mm [5]. The reason why this lap length is relatively short is assumed to be that the strength of the weld point is specified by JIS 3551 in the Japanese standard for welded wire mesh, which takes into account the effect of anchoring by the transverse wire. Kesler et al. [6] showed that tensile forces applied to the longitudinal wires at the laps are transferred by the bearing forces on the concrete in contact with the transverse wires. The strength of the weld point is important to ensure the bearing forces on the concrete. A fire test of a floor system with a composite slab and steel beams was conducted by Yoshida et al. in 2019 [7]. This test showed the failure of weld points at the lap due to insufficient transfer of tensile forces at the laps. This was due to the fact that the lap length of the reinforcement was only equal to the mesh interval (150 mm). Following this test, high-temperature loading tests were conducted on specimens with the lap length and temperature as test variables [8]. These were the small-scale tests on flat reinforced concrete slabs. The results showed that the lap with the length of the mesh interval plus 50 mm transfers tensile forces up to 550 °C after the welded wire mesh had yielded and prevents brittle failure.

In the paper, load-bearing fire test was conducted on a large-scaled floor system consisting of an unprotected secondary beam, primary beams, and a composite slab with welded wire mesh of guaranteed weld point strength. The lap length of the mesh was interval plus 50 mm (150 mm). The purpose of this study was to investigate, in a large-scale test, whether tensile forces were sufficiently transferred within the laps of the welded wire mesh up to the deflection limit under membrane action, even when plain welded wire mesh is used. In addition, the load-bearing capacity of the floor system was discussed following the design method proposed by the simple design method on ECCS.

2 TEST OUTLINE

2.1 Test parameters and specimens

Load-bearing fire tests were conducted on two identical specimens with different loads. The test loads (dead load plus live load) on specimens No.1 and No.2 were 9.48 kN/m² and 12.66 kN/m², respectively, as calculated from equation (1). These loads were 2.0 and 2.67 times, respectively, larger than the load strength at ambient temperature predicted by the yield line theory which was a high level of loading. The live loads were 6.96 kN/m² and 10.14 kN/m², respectively.

$$W = \frac{24 \times 0.9 \cdot d \cdot A_S \cdot \sigma_y}{l^2} \left(\frac{a}{\sqrt{1+3a^2}-1} \right)^2 \quad (1)$$

where

W is the load predicted by yield line theory (kN/m²)

a is the aspect ratio

l is the shorter span of slab (mm)

d is the effective depth (mm)

A_S is the cross-sectional area of reinforcement per unit width (282.7 mm²/m)

σ_y is the average tensile strength of the welded wire mesh on mill certification (kN/mm²)

Information on the components of the specimens is given in Table 1. The specimen is shown in Figure 1. The floor system consisted of four protected primary beams (PB), one secondary beam (SB), and a composite slab. The dimensions of the test specimen were 6.9 m x 4.6 m. The steel deck slab was simply supported on the top of the unprotected secondary steel beam. The laps of welded wire mesh were located in many places. The laps along the shorter span were located at the top of the secondary beam and at each quarter mark in the longer span, while the laps along the longer span were located at the half mark in the

shorter span (see Figure 1a). The cross-section of the slab is shown in Figure 2. The high-strength bolts were protected to prevent temperature rise in the centre of the primary beam due to heat bridge. Forty-two thermocouples were used to measure the temperature of the steel frame and the temperature distribution of the slab. The detail of the lap is shown in Figure 3. The slab thickness was 80 mm at the upper flange and 130 mm at the lower flange. The lap length was 150 mm (the mesh interval plus 50 mm). The welded wire mesh was located at 30 mm and 42 mm from the top of the slab. The effective depth of the welded wire mesh, which is the distance from the top surface to the intersection of the longitudinal and transverse wires, was either 36 mm or 48 mm (Figure 3). The thermocouples installed within the concrete slab are shown in Figure 4. The exposed surface temperatures were measured by attaching them to the top surface of the deck plate. The specification on the reinforcement is shown in Table 2. The reinforcement was a welded wire mesh WFP in accordance with JIS G 3551. Welded wire mesh WFP is a plain wire with a specified tensile strength but no specified yield stress and elongation. The reinforcing wires used in the welded wire mesh have a relatively high yield stress and yield ratio at ambient temperature. The welded wire mesh was formed from 6 mm -diameter wires spaced 100 mm apart in both directions. The average of the shear strength of welded point is 377 N/mm². The normal concrete mix design (for 1 m³) comprised of 323 kg normal OPC, 967 kg 5~20mm limestone, 842 kg 5mm sand, 170 kg water, 3.07 kg air entraining, and high-range water-reducing admixture. The concrete was mixed with pp fibres to prevent spalling in fire heating. The water-cement ratio of concrete is 52.6 %. Close to the day of the test, the measured average compressive cylinder strength of the concrete was 40.2 N/mm².

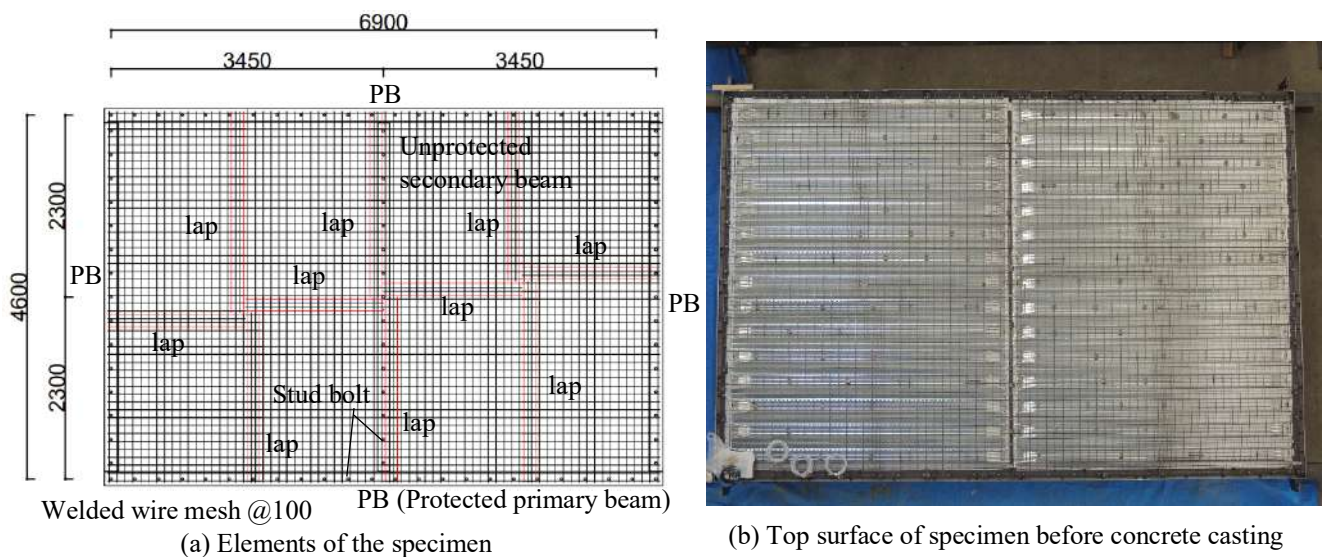


Figure 1. Outline of the specimen

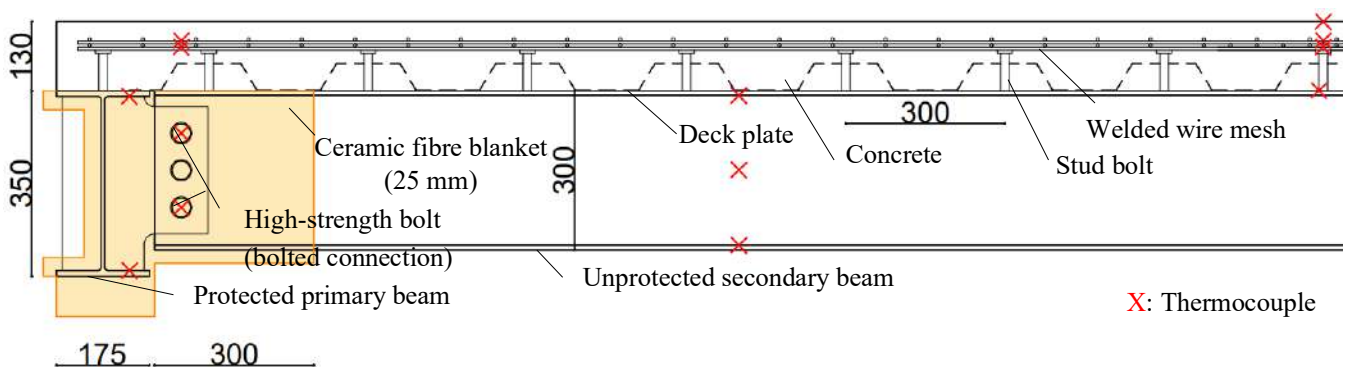


Figure 2. Cross section of the specimen

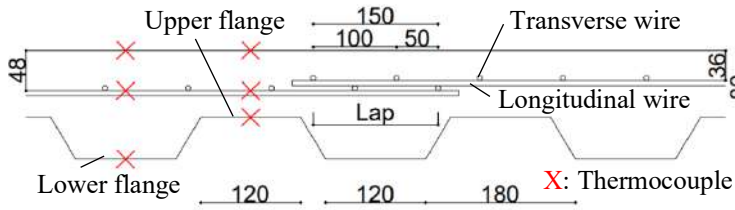


Figure 3. Details of the lap



Figure 4. Thermocouples inside the concrete slab

Table 1 Elements of the specimen

Components	Specification
Secondary beam	Dimension: H – 300 x 150 x 6.5 x 9 Steel grade: SS400 (JIS G 3101) Yield point: 338 N/mm ² (from mill certification)
Primary beam	Dimension: H – 350 x 175 x 7 x 11 Steel grade: SS400 (JIS G 3192) Yield point: 345 N/mm ² (from mill certification)
Reinforcement (welded wire mesh)	Grade: WFP, Diameter: 6 mm, Pitch: 100 mm Tensile strength: 642 N/mm ² (JIS G 3551)
Concrete	Type: normal weight concrete Design strength: f_c 24 N/mm ² Compressive strength: 31.9 N/mm ²
Stud bolt (shear connector)	Diameter: 15.88 mm, Length: 94.01 mm Yield point: 401 N/mm ² (JIS B 1198)
High-strength bolt (at beam end connection)	Grade: F10T, Diameter: 20 mm Design tensile strength: 1000 N/mm ² (JIS B 1186)

Table 2 Specification of the welded wire mesh

Inspection result dimensions [mm]						
Entry	Diameter		Spacing		Width of fabric	Length of fabric
	Longitudinal wire	Transverse wire	Longitudinal wire	Transverse wire		
Standard value	6	6	100	100	2000	4000
Allowable range	±0.1		±10		±5	±10
Measured value	5.98	5.96	100	100	1998	4002
Mechanical properties [N/mm ²]						
Entry	Shear strength of welded point		Tensile strength			
Standard value	Greater than the average 250 N/mm ²		Greater than 490 N/mm ²			
			Longitudinal wire		Transverse wire	
Measured value	367		649		656	
	375		647		648	
	382		631		643	
	383					
	Average 377		Average 642		Average 649	

2.2 Test setup and measurements

The test setup is shown in Figure 5. The test was carried out using a furnace at Takenaka Technical Research Institute. The mechanical load on the floor was applied to 24 load points connected to 4 hydraulic jacks. The load applied by the hydraulic jacks was the live load excluding the weight of the jig. This method simulated a uniformly distributed load. Vertical displacements were restrained under the primary beam at the corner. The furnace temperature was controlled according to the ISO standard fire curve. The specimen remained to apply the load during the cooling phase. Twenty-three displacement transducers were installed to measure the vertical deflection of the floor (see Figure 6).

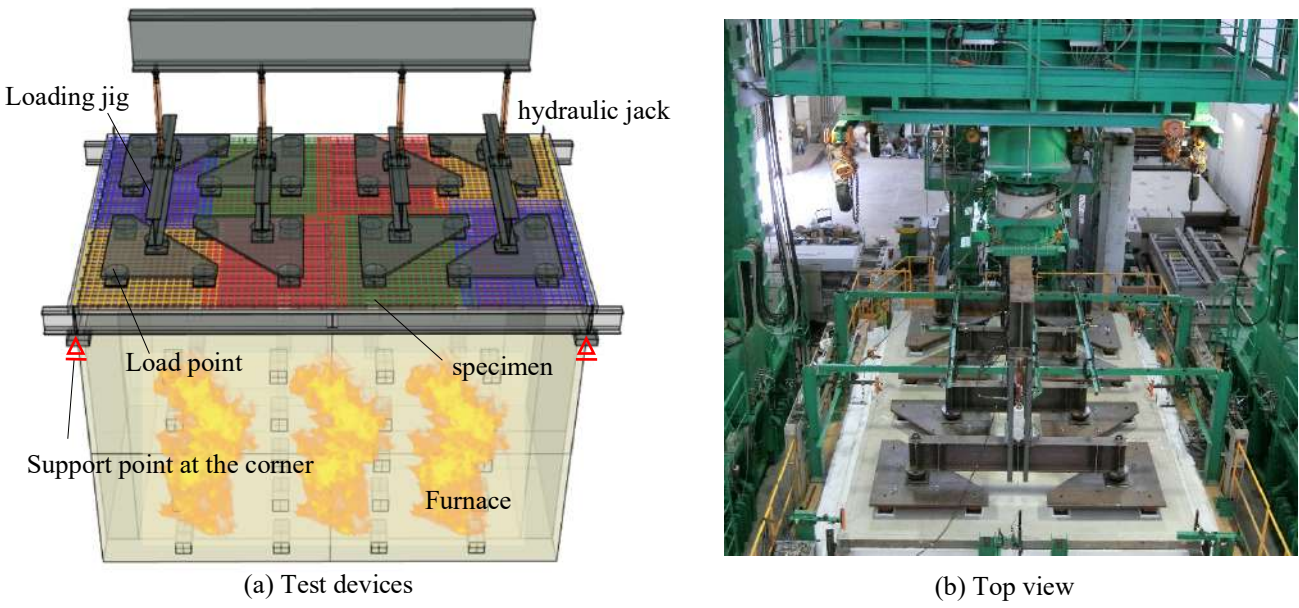


Figure 5. Test setup

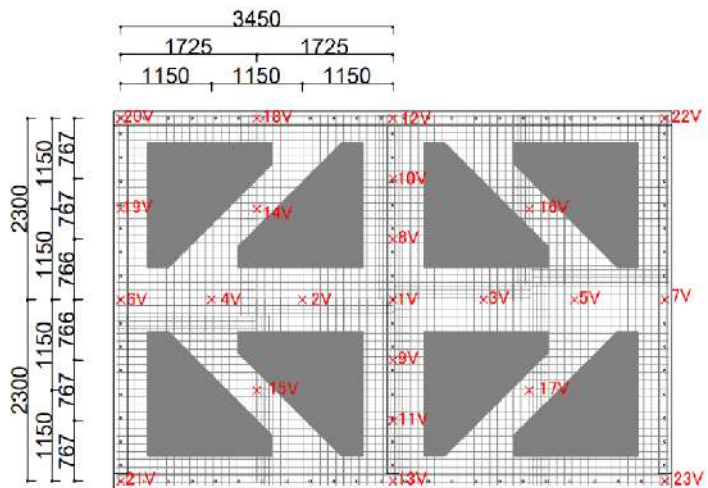


Figure 6. Measurement points of vertical displacement

2.3 High temperature properties of materials

Figure 7 shows the stress-strain curves of the welded wire mesh obtained from the high temperature coupon tests according to JIS G 0567. Figure 8 shows the effective yield stress of the welded wire mesh, which is the 0.2% offset yield strength. The stress of the welded wire mesh was similar to that at the ambient temperature before the temperature reached 200°C. The stress decreased after 200°C and was 400 N/mm² at 500°C. It decreased rapidly after 500°C. Figure 9 shows the compressive strength of the concrete obtained from the high temperature compression tests. The compressive strength at the ambient temperature obtained with this high temperature testing device was 38.9 N/mm². The strength of the concrete gradually decreased

when the temperature exceeded 200°C. Figure 10 shows the thermal strain of the concrete. The coefficient of thermal expansion α between 0°C and 400°C was 1.78×10^{-5} [1/°C].

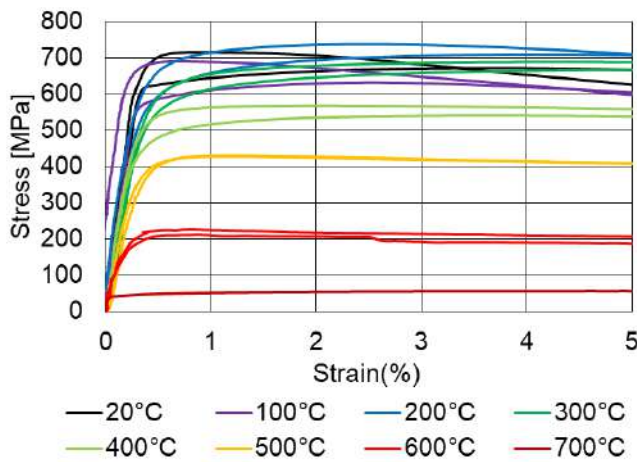


Figure 7. Stress-strain curve of the wire mesh

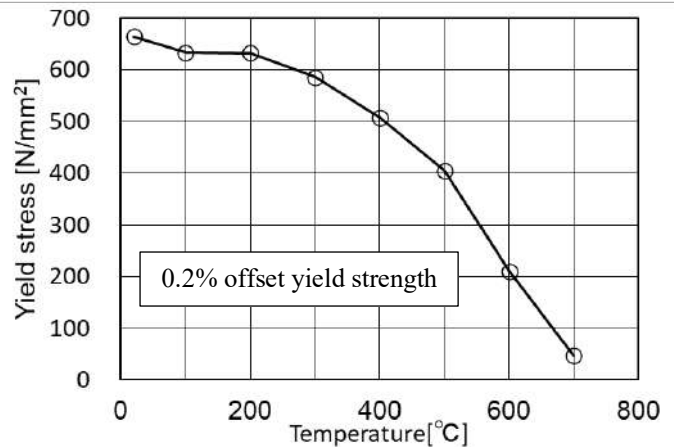


Figure 8. Yield stress of the wire mesh at high temperatures

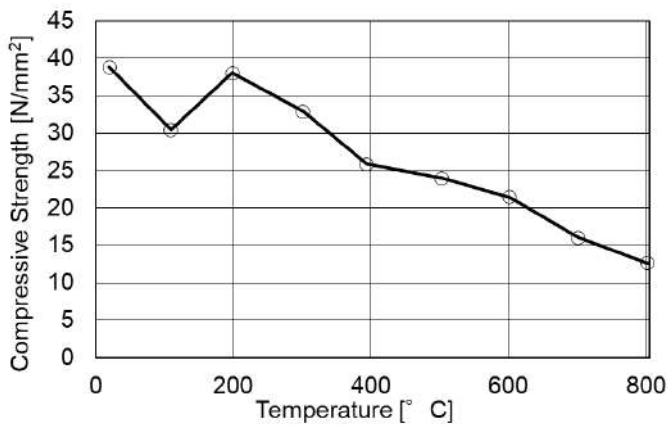


Figure 9. Compressive strength of the concrete at high temperatures

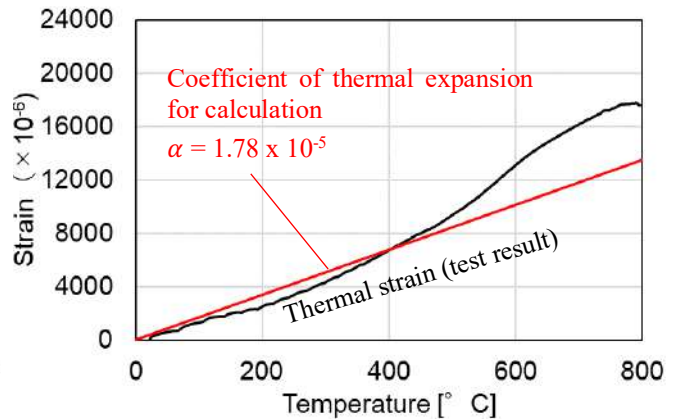


Figure 10. Thermal strain of the concrete

3 TEST RESULTS

3.1 Temperature of specimen

Heating of specimen No. 1 was stopped at 216 minutes to check the behaviour of the slab during the cooling phase. Meanwhile, heating of specimen No. 2 was stopped at 216 minutes due to integrity failure of the slab. Recording of specimen behaviour continued until 370 minutes. The temperatures of specimens No. 1 and No. 2 were very similar. This section shows the temperature of specimen No. 2.

Figure 11 shows the temperatures of the beams and the high strength bolts. The average temperatures on the unprotected secondary beam increased rapidly after heating, and reached 697°C at 30 minutes and 845°C at 60 minutes. After 60 minutes, this average temperature followed the ISO standard fire curve. Temperatures on the protected high-strength bolt connecting the primary and secondary beams reached 448°C at 120 minutes and 638°C at the end of heating. The temperature continued to increase after the end of heating, with a maximum temperature of 643°C. The maximum temperature of the protected primary beams was 350°C.

Figure 12 shows the temperatures of the concrete slab on the exposed and the unexposed surfaces. The temperatures of the exposed surface were higher at the lower flange of the deck plate than at the upper flange. One of the thermocouples on the concrete slab of the exposed surface above the upper flange was lower than the other thermocouples. The thermocouple may have been embedded in the concrete due to

faulty construction. The unexposed surface temperature remained at 100°C because the heat input was absorbed to evaporate water from the slab surface between 60 and 120 minutes. The maximum temperature difference between the exposed and unexposed surfaces of the slab was 866°C at 152 minutes.

Figure 13 shows the temperature of the welded wire mesh. The temperature of the welded wire mesh was higher on the upper flange of the deck plate, which was located closer to the exposed surface. The temperature of the welded wire mesh on the upper flange with an effective depth of 36 mm was 334°C at 120 minutes and 520°C at the end of heating. The temperature increased slightly after the end of heating to a maximum of 550°C at 220 minutes. The maximum temperature of the welded wire mesh on the upper flange with an effective depth of 48 mm was 637°C at 221 minutes.

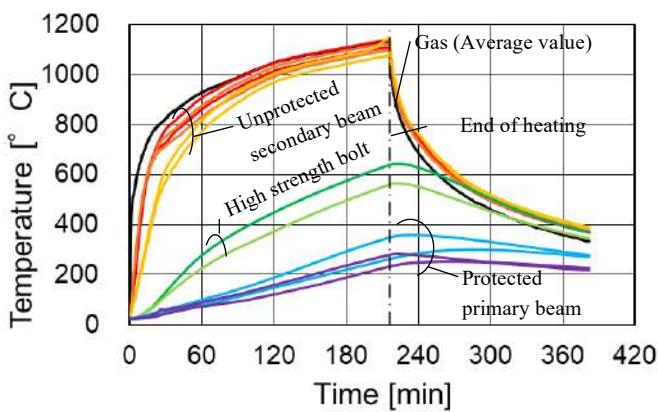


Figure 11. Temperatures of Steel beams (No.2)

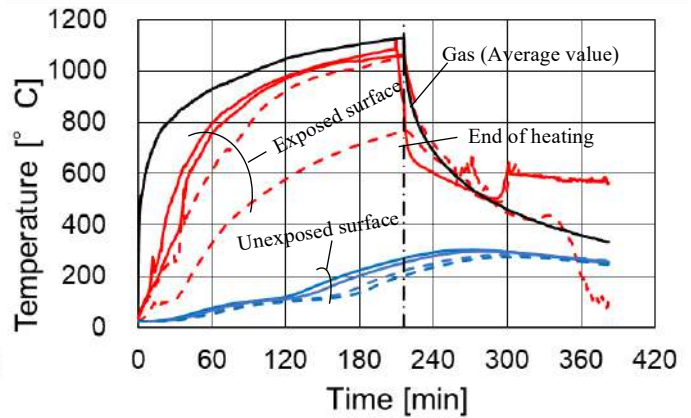
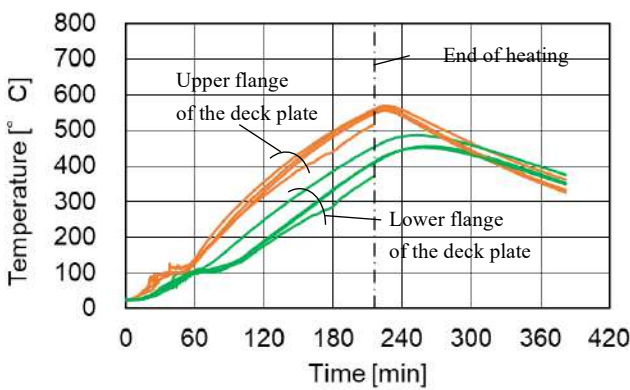
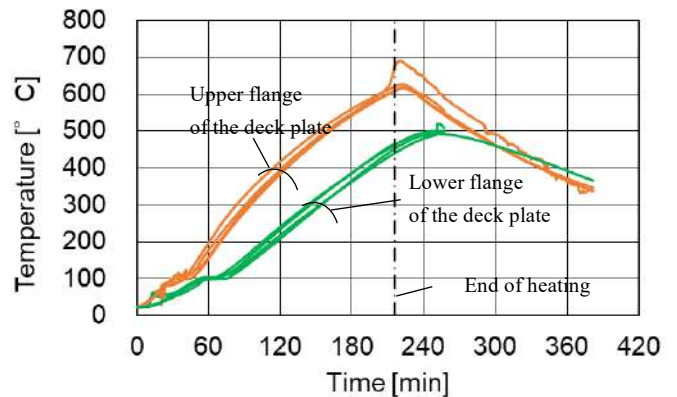


Figure 12. Surface temperatures of concrete (No.2)



(a) The effective depth: 36 mm



(b) The effective depth: 48 mm

Figure 13. Welded wire mesh temperatures (No.2)

3.2 Deflection

Figure 14 shows the deflections at the centre of the floor systems of specimen No.1 and No.2. These include deflection under loading before heating. The deflections before heating were 6 mm for specimen No.1 and 12 mm for specimen No.2. The deflection behaviour of specimen No.1 was almost similar to that of specimen No.2 up to 15 minutes from start of heating. At 15 minutes the deflections were 75 mm for specimen No.1 and 93 mm for specimen No.2. The increase in deflection was mainly caused by thermal deflection based on the temperature difference between the upper and lower flanges of the secondary beam. The increase in deflection became smaller after 30 minutes. This increase was due to the decrease in strength and stiffness of the unprotected secondary beam and the welded wire mesh with increasing temperature. The deflection rate of specimen No.2 after 30 minutes was generally similar to that of specimen No.1. Both specimens retained their load-bearing capacity not only during the heating phase but also during the cooling phase. The deflections of both specimens remained constant after approximately 240 minutes. The maximum deflection of No.1 and No.2 was 338 mm and 424 mm, respectively. This was approximately 1/14 and 1/11 of the shorter span, respectively.

Figure 15 shows the deflection curves connecting the vertical displacements measured on the long span of specimen No.2 (see Figure 6). The deflections are symmetrical up to 180 minutes. The integrity failure occurred at the point between 2V and 4V (1150-2300 mm from the centre) at 216 minutes. The deflection of 2V was larger than that of 3V at 216 and 250 minutes. During the cooling phase, the increase in the central deflection was less than in the other areas (2v,3V) because the temperature of the unprotected beam decreased. The curvature of the slab at the point of integrity failure developed intensively during the cooling phase.

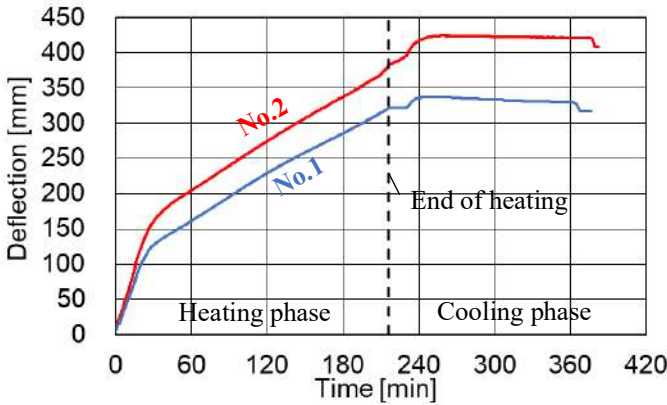


Figure 14. Deflections at the centre

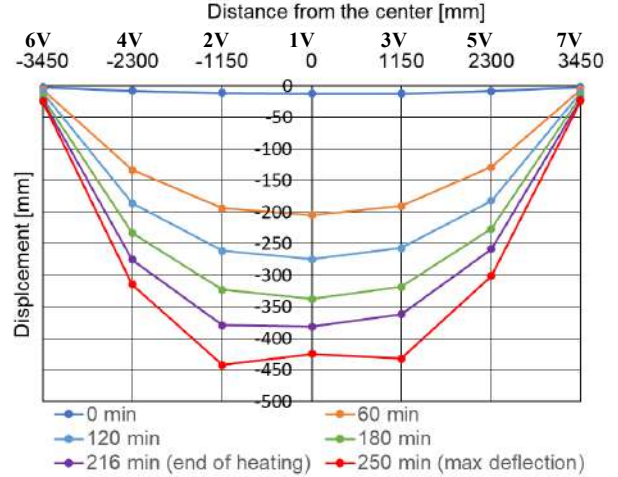
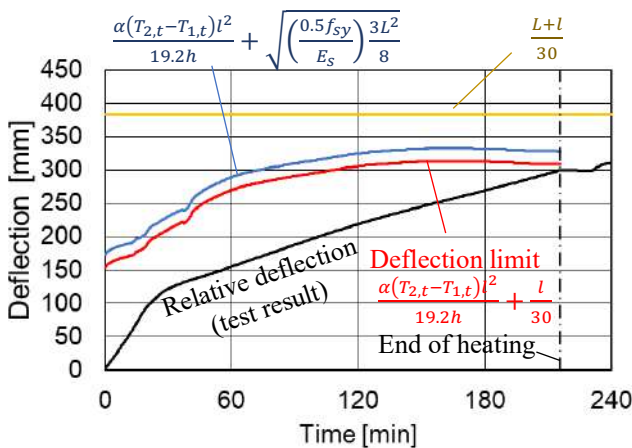
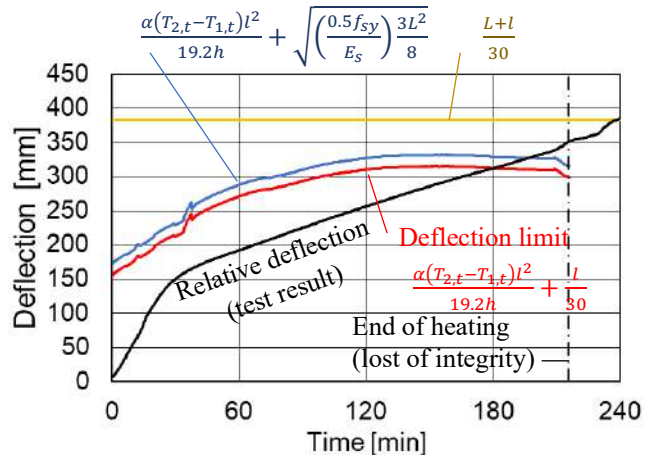


Figure 15. Deflection curves (long span, No.2)

Figure 16 shows the relative deflection and the deflection limit. The relative deflection is the vertical displacement of the centre reduced by the average vertical displacement of the centre of the four edge beams. ECCS [3] proposed a deflection limit for the design of composite slabs in fire. This deflection limit is used to predict the resistance of the slab. In this section, the deflection limit was calculated using the test result of the temperatures. The estimation of the slab deflection includes the thermal effect due to the temperature difference between the exposed and unexposed surfaces of the slab as well as the mechanical strains in the welded wire mesh. The thermal deflection was determined from the coefficient of thermal expansion of the concrete and the temperature difference of the slab. Baily and Moore [9] assumed the temperature difference to be 770°C. Due to the long heating time, the test result of the maximum temperature difference reached 886°C. The depth of the slab was 105 mm, which was the depth to the mid-height of the troughs of the slab. The effective yield stress f_{sy} is the value of the 0.2% offset yield strength at ambient temperature. In these tests, the mechanical deflection limit was determined based on the geometric limit of 1/30 times of the short span (equivalent to 153 mm). In addition, the deflection limit was less than 1/30th of the sum of the short and long spans. The relative deflection of specimen No.1 at the end of heating was 8 mm below the deflection limit. Meanwhile, the relative deflection of specimen No.2 exceeded the deflection limit at 180 minutes. At the end of heating, the relative deflection was 1.17 times larger than the deflection limit and was less than 1/30th of the sum of the short and long spans.



(a) Specimen No.1



(b) Specimen No.2

Figure 16. Relative deflection and the deflection limit

3.3 Failure

Figure 17 shows the fire penetration of specimen No.2 at the time of the integrity failure around the eastern quarter mark of the longer span. Figure 18 shows cracks on the top surface of specimen No.2. Many cracks were observed mainly along the direction of the short span of the slab (from the centre to 1775 mm in both longitudinal directions). The elliptical cracks formed around the tensile area under the membrane action. There was no failure of the crushing concrete in either specimen. Two large cracks occurred in the short span direction around the lap 1775 mm from the centre (Figure 18). The width of these cracks was approximately 30 mm. Figure 19 shows the damage to the exposed surface of specimen No.2. Debonding of the deck plate was observed and partial failure of the deck plate occurred. No buckling occurred in the secondary beam. Figure 20 shows the damage to the high-strength bolts. There was no shear failure of the high strength bolts. In specimen No.2, the concrete was removed from the area where cracks occurred to inspect the welded wire mesh. Figure 21 shows the welded wire mesh at the lap. Failure of the welded wire mesh occurred across the longer span with an effective depth of 48 mm. Figure 22 shows the location of the welded wire mesh failures. The failure of twenty welded wire meshes across the longer span and the failure of the two welded joints were observed. This failure could occur where the temperature increases rapidly with the development of cracks [10]. Most failures were observed in the welded wire mesh adjacent to the lap with an effective depth of 48 mm. The temperature of the welded wire mesh with an effective depth of 48 mm was higher than that of the welded wire mesh with an effective depth of 36 mm. And the strain of the mesh with an effective depth of 48 mm was larger than that of the mesh with 36 mm due to the development of curvature at the integrity failure point. There was no failure of the welded wire mesh within the laps. The test result indicated that the laps with the length of 150 mm (mesh interval plus 50 mm) continued to transfer tensile stress until the welded wire mesh had sufficiently yielded.



Figure 17. Fire penetration (No.2)

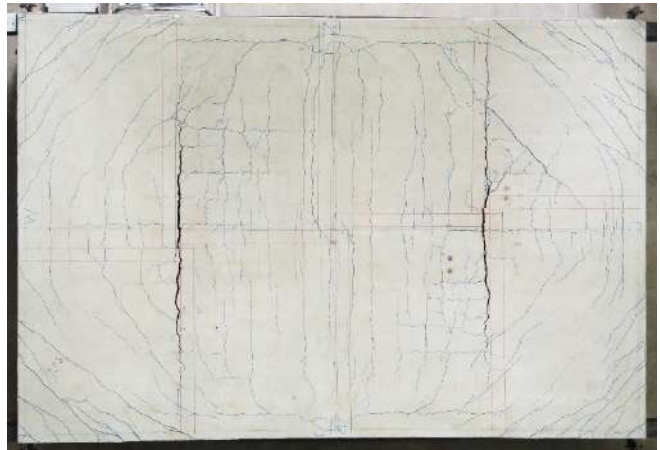


Figure 18. Cracks on the top surface (No.2)



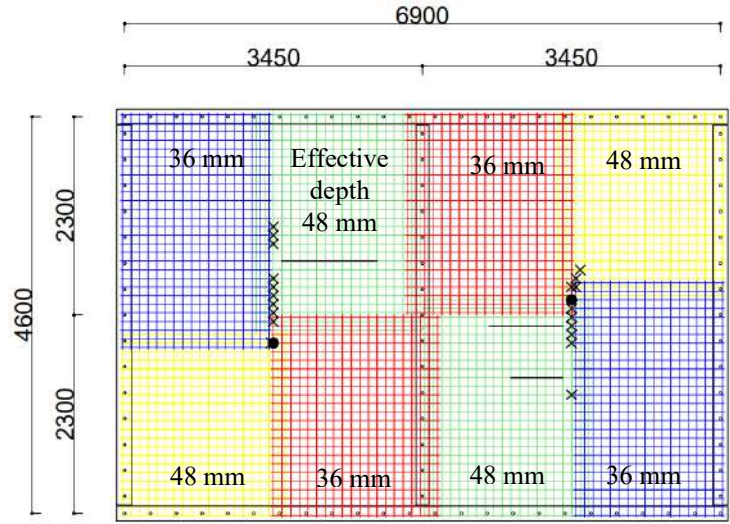
Figure 19. Damage to the exposed surface



Figure 20. Damage of the bolted connection



Figure 21. Failures of the welded wire mesh



x: welded wire mesh failure, •: welded joint failure
Figure 22. Location of the welded wire mesh failures

4 DISCUSSION ON LOAD BEARING CAPACITY IN FIRE

In the simple design method of ECCS [3], the load-bearing capacity of the floor system is calculated by the sum of the load bearing capacity of the composite slab and the unprotected beam as shown in equation (2). As shown in equation (3), the load-bearing capacity of the composite slab under membrane action is calculated by multiplying the load bearing capacity predicted by yield line theory by the enhancement factor (which takes into account the tensile membrane effects based on the deflection of the slab). The calculation of the enhancement factor in equation (4) depends on the ratio of the deflection to the effective depth of the slab, and its constant values were determined from factors of the aspect ratio and the depth of the compressive stress block. In calculating the load bearing capacity of the floor system, the temperature of the welded wire mesh and the secondary beam and the deflection at t minutes after the start of heating were obtained from the test results. The load-bearing capacity of Bailey and Moore [9] was based on the strength of the welded wire mesh at the ambient temperature, as the reduction in the effective strength of the reinforcement is slightly under the temperature below 400°C. Meanwhile, as results above 400°C were observed in the tests, the 0.2% offset yield strength obtained from the high temperature coupon tests of the welded wire mesh (see Figure 8) was applied to account for the reduction in strength. For the temperature of the welded wire mesh with an effective depth of 36 mm, the average value over the upper flange of the deck plate was used (see Figure 13). The deflection used in the calculations was the relative deflection as shown in Figure 16. The load bearing of the unprotected beam was calculated from equation (5) based on ECCS. The temperature of the unprotected secondary beam was the average temperature of the flanges and the web. The reduction in strength of the unprotected beam was based on the reduction factors given in EN 1994-1-2, 3.2.1 [11] and the yield strength at ambient temperature was 338 N/mm² from the mill certification of the steel.

$$W_{sys(t)} = W_{slab(t)} + W_{beam(t)} \quad (2)$$

$$W_{slab(t)} = e_{(t)} \times \frac{24 \times 0.9 \cdot d \cdot A_s \cdot \sigma_{y(t)}}{l^2} \left(\frac{a}{\sqrt{1+3a^2}-1} \right)^2$$

$$= e_{(t)} \times W_{(t)} \quad (3)$$

$$e_{(t)} = 0.23 \frac{v(t)}{d} + 0.93 \quad (4)$$

$$W_{beam(t)} = \frac{8}{l^2} \times \frac{2M_{fi,Rd}}{l} \quad (5)$$

where

$W_{sys(t)}$ is the load bearing capacity of the floor system at t minutes from the start of heating (kN/m²)

$W_{slab(t)}$ is the load bearing capacity of the composite slab at t minutes from the start of heating (kN/m²)

- $W_{beam(t)}$ is the load bearing capacity of the secondary beam at t minutes from the start of heating (kN/m^2)
- $\sigma_{y(t)}$ is the yield stress of the welded wire mesh at high temperature (kN/m^2)
- $W_{(t)}$ is the load bearing capacity of the slab predicted by yield line theory at t minutes from the start of heating (kN/m^2)
- $v_{(t)}$ is the relative deflection at the centre of the floor system (mm)
- $M_{fi,Rd}$ is the sagging moment resistance of the unprotected secondary beam (N/mm^2)
- L is length of the longer span of slab (mm)

For other parameters, see equation (1)

Figures 23 (a) and (b) show the changes in load-bearing capacity. The test load is the combined load of the dead and live load during the test. For both specimens, the load-bearing capacity of the floor system decreased rapidly after 10 minutes as the temperature of the secondary beam exceeded 400°C . The load-bearing capacity of the composite slab exceeded that of the secondary beam at 29 minutes for both specimens. As shown in Figure 14, the increase in deflection became smaller around 29 minutes. The load-bearing mechanism of the floor system could gradually change from the bending mechanism of secondary beam to the membrane mechanism of the slab after the load bearing capacity of the composite slab exceeded that of the secondary beam.

As shown in Figure 23 (a), the load bearing capacity of the floor system No.1 was close to the test load during the period from 60 to 180 minutes. During this period, although the strength of the welded wire mesh decreased (see the decrease of the value by the yield line theory), the deflection of the slab increased. This is the reason why the load-bearing capacity remained constant. This result can be seen as a validation of the floor system calculation method of Bailey and Moore [9]. The load bearing capacity of the floor system of specimen No.2 after 69 minutes was lower than the applied load of the test. This load bearing capacity was 0.58 times larger than the test load at the end of the heating. For specimen No.2, the difference between the test load (black line) and the load-bearing capacity of the floor system (purple line) developed at the end of the heating was much larger than in specimen No.1 because the deflection of the slab in specimen No.2 was lower than the predicted deflection. However, specimen No.2 maintained its load-bearing capacity until the end of the heating. In the case of the results from specimen No.2, this suggests that the load-bearing capacity of the floor system based on the simple design method on ECCS, taking into account the reduction in strength of the welded wire mesh at high temperature, was estimated on the safe side. In addition, the load-bearing capacity of the floor system increased after the end of the heating as the strength of the unprotected secondary beam was recovered. Although failure of the welded wire mesh occurred, it is assumed that the specimen continued to support the load-bearing capacity because the resistance of the secondary beam contributes to the resistance of the floor system during the cooling phase.

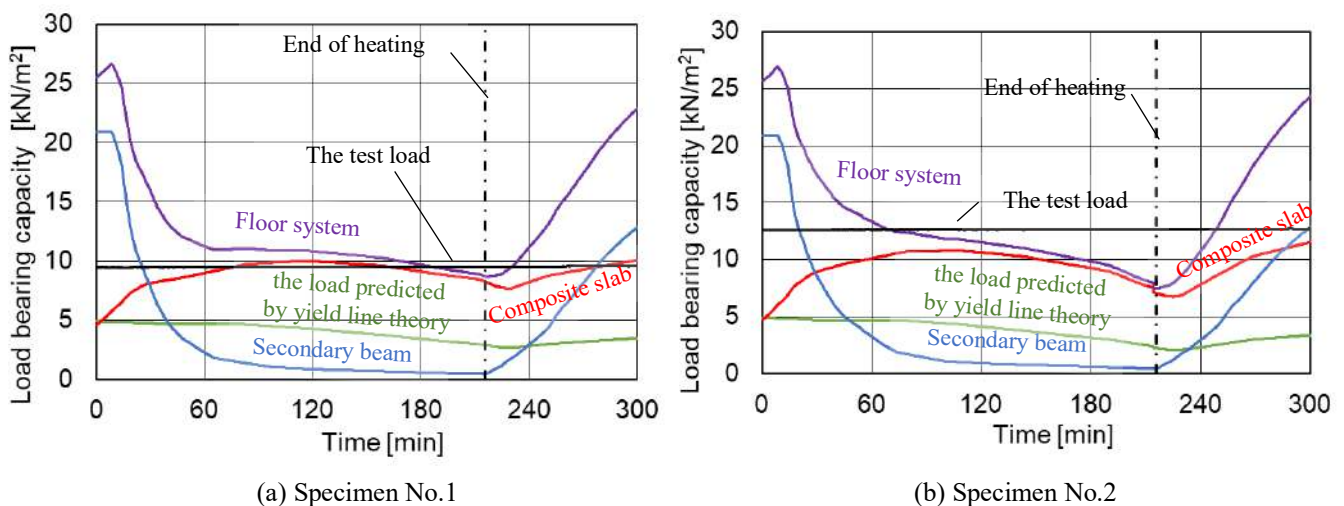


Figure 23. Change in the load bearing capacity with heating time

5 CONCLUSIONS

In this paper, load-bearing fire tests were conducted on the floor system on steel beams and a composite slab with welded wire mesh of the lap length of the mesh interval (100 mm) plus 50 mm. The floor system of the test specimen (No.2; with 2.67 times the load predicted by yield line theory) resisted the load not only during the 216-minute heating phase but also during the cooling phase, although it experienced the integrity failure. The maximum deflection of this specimen during the heating phase was 1/11 of the short span and exceeded the deflection limit of the simple design method on ECCS. Although there were few failures within the laps, the failures of the welded wire mesh adjacent to the lap were observed. The laps transferred sufficient tensile stress until the welded wire mesh adjacent to the lap yielded and failed. Therefore, the lap length of the mesh interval plus 50 mm (150 mm) when using welded wire mesh with guaranteed the weld point strength was sufficient to transfer tensile stress in the slab under membrane action. The load-bearing capacity was calculated taking into account the reduction in the strength of the welded wire mesh at high temperatures. When the test load was 2.0 times the load predicted by yield line theory, the load-bearing capacity of the floor system was generally close to the test load. Meanwhile, when the test load was 2.67 times the load predicted by yield line theory, the load-bearing capacity of the floor system was less than the test load. However, the specimens continued to maintain the load-bearing capacity. It is therefore considered that the load bearing capacity of the floor system based on ECCS was safe, taking into account the reduction in strength of the welded wire mesh at high temperature.

ACKNOWLEDGMENT

This research was funded under the Structural Research and Education Grant Programme by the Japan Iron and Steel Federation.

REFERENCES

1. Swinden Technology Centre: The Behaviour of Multi-Storey Steel Framed Buildings in Fire a European joint research programme, British steel plc, Swinden Technology Centre, 1999.
2. Zhao, B., Roosefid, M., Vassart, O.: Full scale test of a steel and concrete composite floor exposed to ISO fire and corresponding numerical investigation, Eurosteel 2008, Graz, Austria, 9.2008.
3. Vassart, O., Zhao, B.: Membrane Action of Composite Structures in Case of Fire, ECCS TC3, 2013.
4. CEN: EN 1994-1-1, Eurocode 4: Design of composite structures - Part 1-1: General rules and rules for buildings, European committee for standardization, Brussels.
5. Architectural Institute of Japan: AIJ standard for structural calculation of reinforced concrete structures, Architectural Institute of Japan, p.229 (2018).
6. Atlas, A., Siess, C., Bianchini, A. C., Kesler, C. E.: Behavior of Concrete Floor Slabs Reinforced with Welded Wire Fabric, T & AM Report No.260, Univ. of Illinois, 1964
7. Yoshida, T., Hirashima, T., Suzuki, J., Ozaki, F., Kimura, K., Murakami, Y.: Membrane action of floor slabs in fire (Part 2): Load-bearing fire tests of a flooring system composed of composed slabs and an unprotected steel beam, Journal of Structural and Construction Engineering (Transactions of AIJ), Vol. 87, No. 797, pp. 646-656 (2022). (in Japanese). <https://doi.org/10.3130/aijs.87.646>.
8. Horie, M., Mano, E., Kanada, H., Kikuchi, T., Totsuka, M., Hirashima, T., Kimura, K.: Bending resistance and deflection behavior of RC slabs with welded wire mesh lap joints at high temperatures, Summaries of technical papers of annual meeting, pp.221-224 (2023). (in Japanese).
9. Bailey, C. G., Moore, D. B.: The structural behaviour of steel frames with composite floor slabs subject to fire – Part 1 Theory, The Structural Engineer, vol. 78, No.11, pp. 19-27 (2000).
10. Burgess, I., Sahin, M.: Tensile Membrane Action of Lightly-reinforced Rectangular Composite Slabs in Fire, The Structural Engineers, vol. 16, pp. 176-197 (2018). <https://doi.org/10.1016/j.istruc.2018.09.011>.
11. CEN: EN 1994-1-2, Eurocode 4: Design of composite steel and concrete structures - Part 1-2: General rules – Structural fire design, European committee for standardization, Brussels.

INVESTIGATIONS ON HEADED STUDS IN PROFILED STEEL SHEETING AT ELEVATED TEMPERATURES

Kurt Tutzer ¹, Georg Knallinger ², Mohamad Mohamad ³, Martin Mensinger ⁴

ABSTRACT

Steel-concrete composite structures provide an economical and resource-efficient construction method. In addition, the use of trapezoidal sheeting can further optimise the construction method by reducing construction time and the need for additional formwork. Modern sheet geometries aim to maximise the height and slenderness of the ribs of the trapezoidal sheeting, reducing the amount of concrete required and increasing the span width during construction. However, when trapezoidal sheets are used with composite beams, their geometry has a significant influence on the load bearing behaviour of the headed studs. In recent years, extensive research has been carried out on the load bearing behaviour of headed studs in profiled sheeting. It has been found that the calculation approaches included in EN 1994-1-1 [1] partially overestimate the load-bearing capacity of headed studs when used in combination with modern profiled sheeting geometries that span transversely to the beam axis. For this reason, the design approaches in the new Eurocode generation prEN 1994-1-1 [2] have been adapted and extended. However, the design approaches for headed studs in profiled sheeting at elevated temperatures, as outlined in EN 1994-1-2 [3], have not been re-examined. To validate the formulations presented in [3], push-out tests at elevated temperatures were conducted at the Technical University of Munich. In combination with numerical investigations, the results of this research project aim to confirm the continued applicability of the approaches from EN 1994-1-2 [3]. This paper provides a first insight into the experimental procedures, their results, and the development of the numerical models.

Keywords: push-out; headed stud; numerical modelling; elevated temperature

1 INTRODUCTION

Steel composite structures, consisting of steel profiles and a concrete chord, have been used successfully for decades. To further optimize this construction method and workflow, the concrete chord can be executed as a composite slab. In this construction method, profiled sheeting is used, typically spanning perpendicular to the secondary beams. These profiled sheeting can act as permanent formwork and, through their composite action, they contribute as a reinforcement in the concrete slab. To improve structural efficiency while reducing concrete usage, manufacturers are increasingly offering modern trapezoidal sheet geometries characterized by slender and high ribs.

¹ Doctoral Candidate, Technical University of Munich, Chair of Metal Structures
e-mail: k.tutzer@tum.de

² M.Sc., Technical University of Munich, Chair of Metal Structures
e-mail: georgknallinger@gmail.com

³ M.Sc., Technical University of Munich, Chair of Metal Structures
e-mail: mohamad.raschad.1995@gmail.com

⁴ Professor, Technical University of Munich, Chair of Metal Structures
e-mail: mensinger@tum.de, ORCID: <https://orcid.org/0000-0001-5210-5400>

The composite action between the secondary beams and the perpendicular composite deck is usually ensured by the arrangement of headed studs. However, the placement of headed studs in trapezoidal sheeting also affects their load-bearing behaviour compared to those in solid concrete slabs. Recent studies carried out by several authors [4-8], some conducted as part of the DISSCO project [9], have found that existing normative approaches in some cases may overestimate the load-bearing capacity of headed studs in profiled sheeting. To address this discrepancy, new design approaches for headed studs placed in trapezoidal sheeting have been developed, intended to be incorporated into the ongoing revision of the Eurocodes. The final draft of the Eurocode 4 [2] includes the approach described by [5,7] as informative Annex G [2]. These new design formulas allow the determination of the load-bearing capacity of headed studs for specific trapezoidal sheet geometries, which cannot be reliably covered by the known approaches from [1] with an adequate level of safety.

The existing design formulas for the load-bearing capacity of headed studs at elevated temperatures from [3] are largely based on the work of Zhao and Kruppa [10]. Accordingly, the determination of the headed stud load-bearing capacity is done by applying material-specific, temperature-dependent reduction factors to the design formulas from [3]. The temperatures of the headed stud material and the surrounding concrete can thus be estimated based on [10] to be 80% and 40%, respectively, of the temperature of the upper flange of the steel profile. It's worth noting that [10] only included two push-out tests with an open trapezoidal sheet geometry. Although this database has been extended by studies from [11-14], the underlying data pool is still considered to be limited. The results of the studies mentioned are also contradictory in evaluating the safety level of the valid design approaches from [3].

A research project currently underway at the Technical University of Munich aims to expand the existing database of push-out tests, with a particular focus on modern profiled sheet geometries. This aims to help verify whether the calculation approaches from [3] remain applicable to these geometries. It also remains to be seen how compatible the new calculation approaches from Annex G [2] are with the formulations from [3]. Work by [11,13,15] has shown that numerically validated models from experimental push-out tests can help to extend the data base. This paper presents the results of an initial experimental series of push-out tests, used to calibrate numerical models. As a result of the finite element model calibration work, this will form the basis of a parameter study to evaluate the existing formulations of the expressions given in [1-3].

2 EXPERIMENTAL PROGRAMME AND RESULTS

2.1 Sheeting geometry and Test specimens

The overall project includes 19 push-out specimens tested both at room temperature and under ISO standard fire exposure. The purpose of this paper is to present the results of four of these push-out tests. For the tests reported below, push-out specimens were fabricated from Cofraplus60 trapezoidal sheets with a height h_p of 58 mm. The specimens were constructed according to the guidelines given in [2], which, in contrast to [1], also includes specifications for push-out specimens with profiled sheets. Due to the geometric constraints imposed by the size of the available furnace, the width of the concrete flange had to be limited to 550mm. The geometry of the specimens is shown in Figure 1.

2.2 Material properties

Material testing commenced 200 days post-casting, revealing an average concrete cube compressive strength ($f_{ck,cube}$) of 56.5 N/mm² and cylinder strength ($f_{cm,cylinder}$) of 49.8 N/mm². The concrete slab was reinforced with Q188 (Ø6/15) B500B mesh. A HE260B section as defined in [1, 2] was utilized, bisected along the centre of the web to facilitate horizontal casting as defined in [1, 2]. The headed studs used, 19 mm in diameter and 125 mm high, were made of S235J2+C470 steel. The yield strength of 483 N/mm² and the tensile strength of 521 N/mm² were recorded in the certification provided.

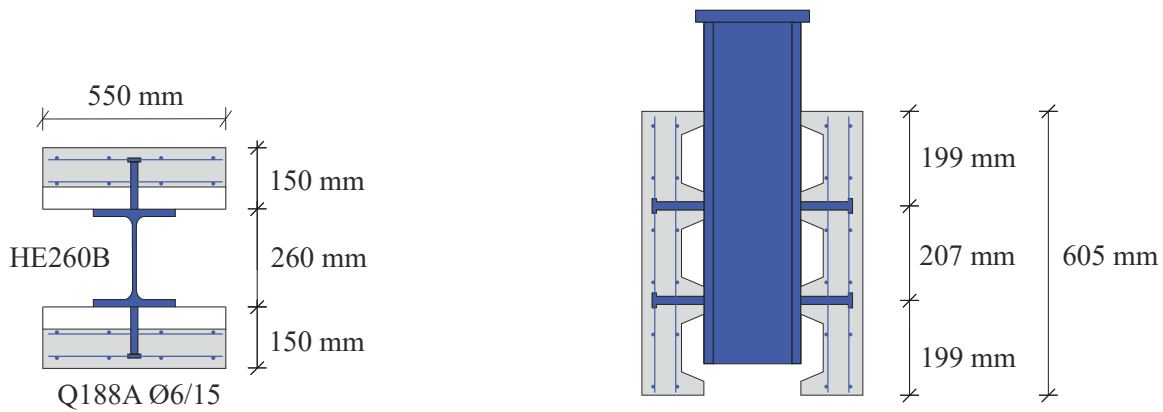


Figure 1. Test specimen with Cofraplus60 profiled sheeting

2.3 Instrumentations

The specimens were heated in a 660 x 660 x 700 mm electric furnace, which was designed with an open bottom and top, allowing it to encase the specimen. For load application in the experiments under elevated temperature, only the upper segment of the steel beam extended beyond the confines of the furnace. The electric heating elements of the furnace were installed only on two sides, perpendicular to the web of the steel section. To replicate the ISO fire curve given in [16], additional heat was provided by two gas burners installed in the concrete abutment. Parameters such as load, displacement, and slip were monitored throughout the test. A hydraulic cylinder applied the load, while deformations were measured using linear potentiometers. Due to the enclosure of the furnace during the fire tests, displacement transducers could only be mounted in limited areas. Quartz glass rods, known for their low thermal conductivity, low thermal expansion and high thermal resistance, were used to make measurements inside the furnace. This arrangement allowed displacement transducers to be placed on the tops of the rods. In addition, type K thermocouples with a glass fibre coating providing a temperature resistance of 800°C were used for all measurements on the specimens and in the concrete chord. Figure 2 below shows the test set-ups.

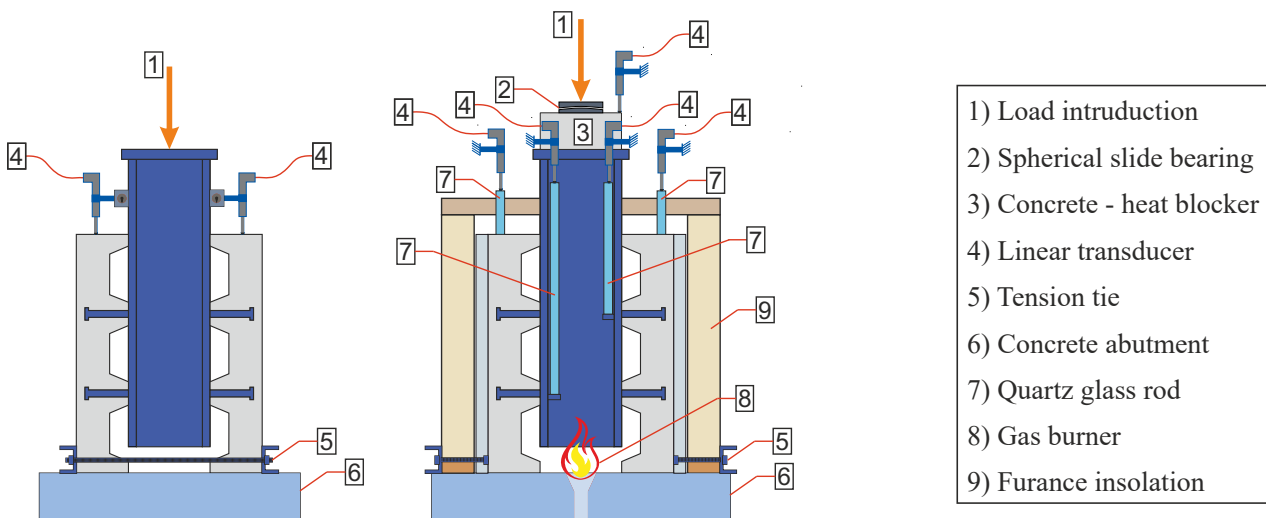


Figure 2. Visualization of the test setups; left at ambient temperature; right at elevated temperature

2.4 Testing procedure

The room temperature tests followed the guidelines set out in Annex B of [1] and [2]. In accordance with these guidelines, the initial phase of the test consisted of 25 load cycles, with overloads and underloads at 40% and 5% of the expected load respectively. The load was then increased at intervals to allow for short-term relaxation of the concrete (Figure 3, left). Due to the continuous heat transfer within the specimens during the fire test, a gradual load increase was considered inappropriate. Therefore, a constant load level

was maintained for the fire tests, and the thermal load, following the ISO standard fire curve, was introduced after a 5-minute stabilization period of mechanical loading only (Figure 3, right). This constant load approach, also used by Lim [11], corresponds well to a typical fire scenario. Load control was achieved by oil pressure until failure of the specimen. The load level for the present tests was set at approximately 75%, 65% and 40% of the shear resistance according to [2].

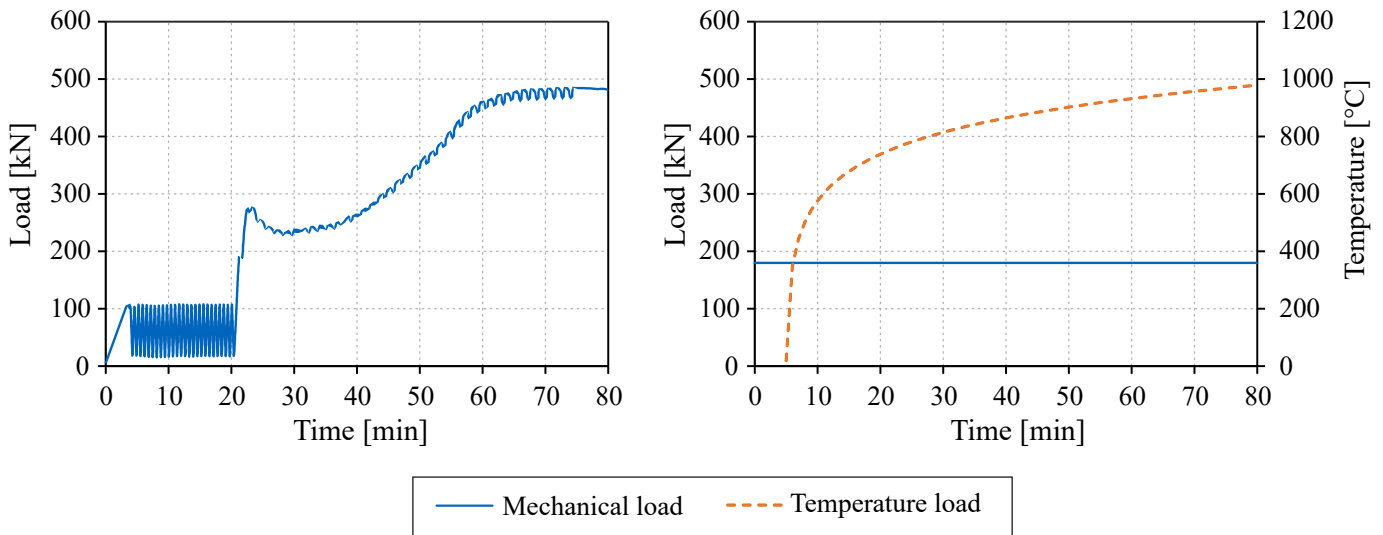


Figure 3. Test procedure; left at ambient temperature; right at elevated temperature

2.5 Results

The room temperature tests resulted in the load-slip curve shown in Figure 4, which is consistent with the results of previous studies [5-7]. In the test using a Cofraplus60 trapezoidal sheet, an initial peak load of 280 kN was observed within the first 6 mm of slip. After a small reduction in load due to concrete crushing at the base of the stud, a second peak load occurred. The test was stopped when the slip exceeded 47 mm, as no further results were expected at this time due to the advanced duration of the test.

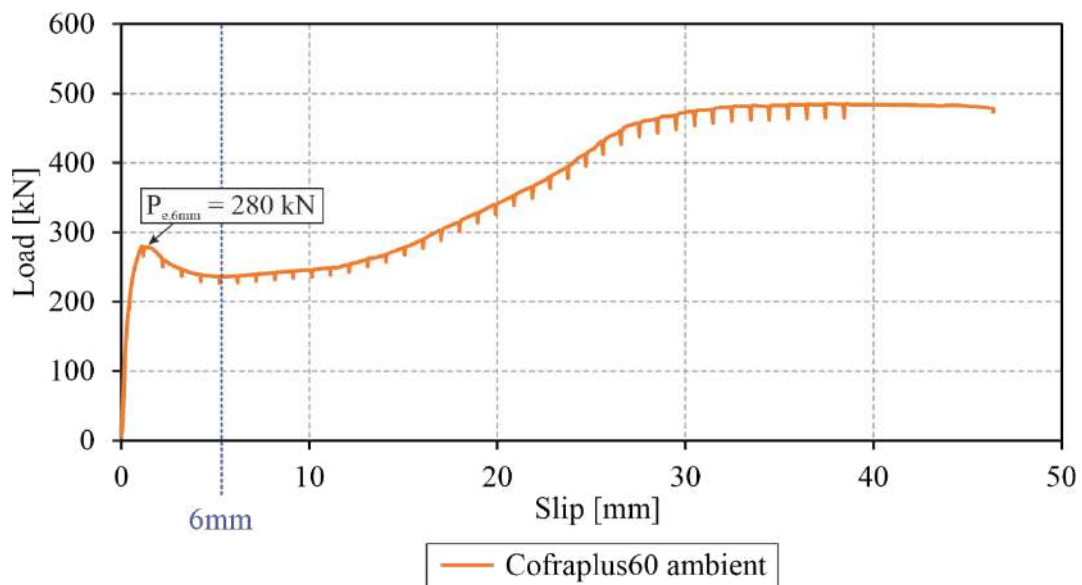


Figure 4. Experimental load-slip curve for the test specimen with Cofraplus60 at ambient temperature

Figure 5 shows the temperature development for the Cofraplus60 specimen subjected to a mechanical load of 110 kN. The furnace temperature was initially above target, but after 10 minutes of heating closely followed the ISO standard fire curve and was within the tolerances of EN 1363-1 [16]. Figure 6 (right)

shows the average temperatures at various measurement points on the steel section. The temperature of the flange was specifically measured in the vicinity of the shear stud, which was considered by the researchers to be critical in assessing the risk of failure of the stud. The shear stud's temperature was recorded 25 mm above the weld toe. This 25 mm measurement point aids the subsequent validation process of the numerical models, rather than directly determining the analytical load-bearing capacities for the headed studs. Measurements were stopped when specimen failure was observed after 77 minutes of fire exposure.

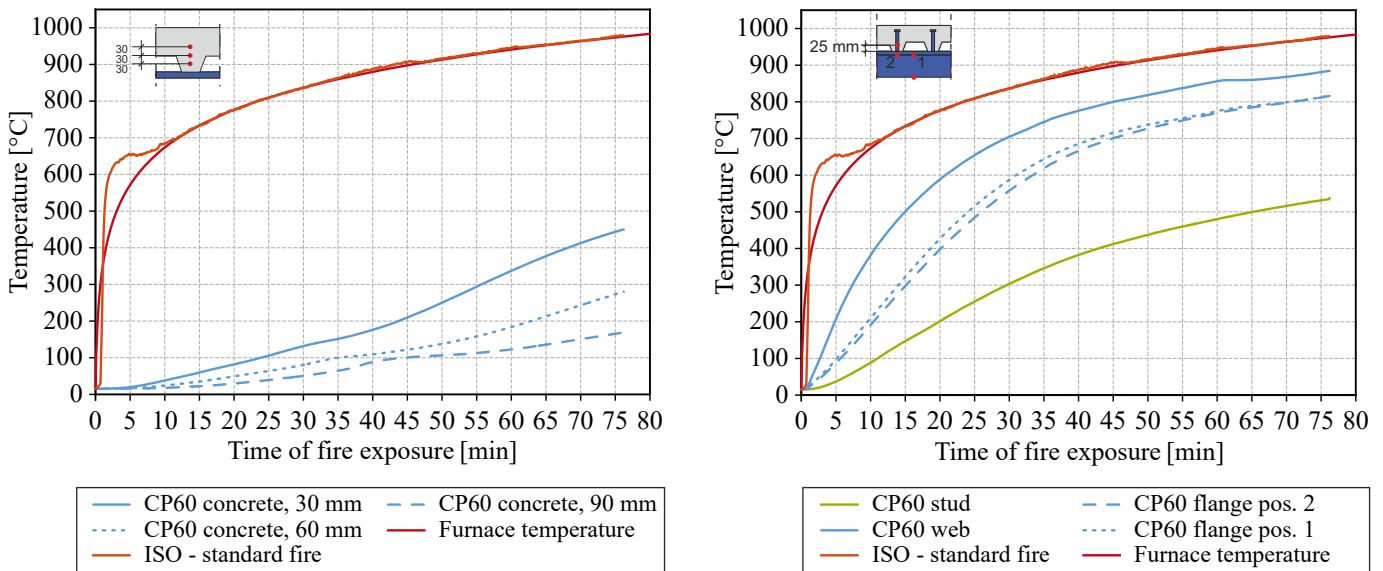


Figure 5. Measured temperature; left in the concrete chord; right on the steel section and in the headed stud

Figure 6 shows the progression of the measured mean slip values for the lower and upper headed stud for the three load levels tested with the Cofraplus60 sheet. Slip could be reliably measured due to the arrangement of the quartz glass rods. It should be noted that there are different slip values for the upper and lower headed studs due to thermal expansion. However, due to the ductility of the headed studs, it can be assumed that the ultimate loads are evenly distributed over the studs. It can also be seen that the measured slip of the headed studs decreases as the load level increases.

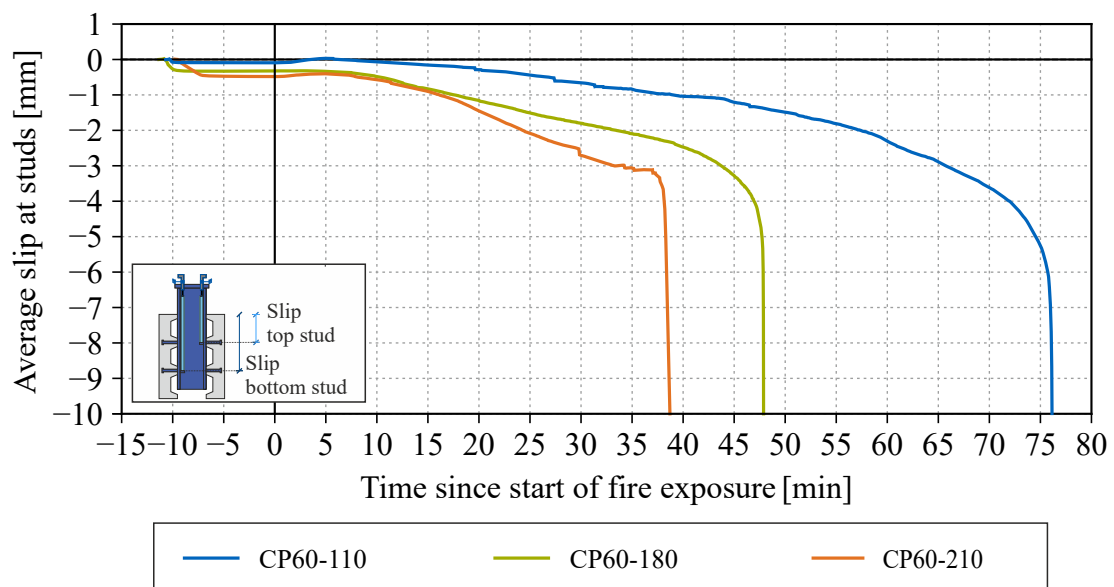


Figure 6. Slip behavior over the time of the experimental test at elevated temperature

3 NUMERICAL MODELLING AND VALIDATION

3.1 Development of the numerical model

Based on the results of recent research [6,11], which provided some guidance for modelling push-out tests, the FE software Abaqus CAE was selected to perform the simulations. The model was created as a 3D model using symmetry conditions. The model, which consists of individual "parts", is shown in Figure 7.

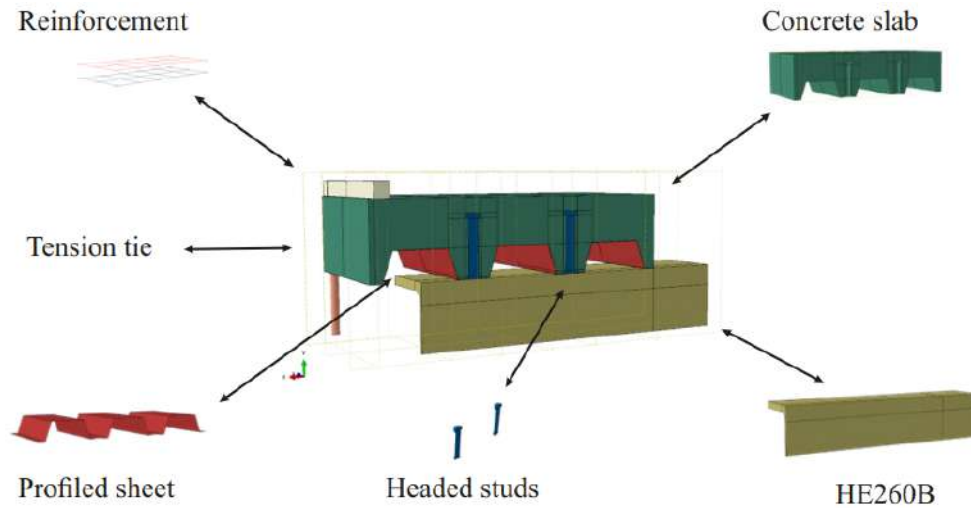


Figure 7. Configuration of the test specimen in Abaqus

Two separate models were created for the calculations in Abaqus. One model was used for thermal analysis only. The resulting temperature field was then transferred to a mechanical model to perform a simplified thermo-mechanical simulation. Table 1 gives an overview of the definitions used for the different parts and Abaqus elements.

Table 1. Element and shape definition in Abaqus

	Concrete chord	Reinforcement	Headed stud	Profiled sheet	Steel section
Shape type	Solid	Wire	Solid	Shell	Solid
Thermal	DC3D8	DC1D2	DC3D8	DS4	DC3D8
Thermomechanical	C3D8R	T3D2	C3D8R	S4R	C3D8R

3.2 Material Properties

For elevated temperatures, DIN EN 1994-1-2 [3] provides an approach for determining concrete compressive stresses. For numerical purposes, it is recommended to assume a linear decrease after reaching the maximum compressive strength of concrete. However, several studies dealing with similar issues have shown that the descending branch of the stress-strain relationship ($\sigma - \epsilon$) can also be modelled using the equation from [3], with good results [11,17,18]. For the tensile behaviour of concrete, a linear increase up to the tensile strength is proposed, following the slope of the corresponding modulus of elasticity. The temperature dependent decrease in tensile strength follows DIN EN 1992-1-2 [3]. However, [3] does not give details for the behaviour in the softening region after the tensile strength has been exceeded. One method of describing this softening behaviour is proposed by Hillerborg [19] and another by Hordijk [20], where the material behaviour is characterized by a stress-crack-opening relationship.

The required fracture energy, G_f , was determined using the Model Code 2010 [21] and extended for temperature dependence based on studies in [22]. The resulting stress-strain relationships for concrete, as shown in Figure 8, were implemented in the simulations using the Concrete Damaged Plasticity (CDP) model provided by Abaqus.

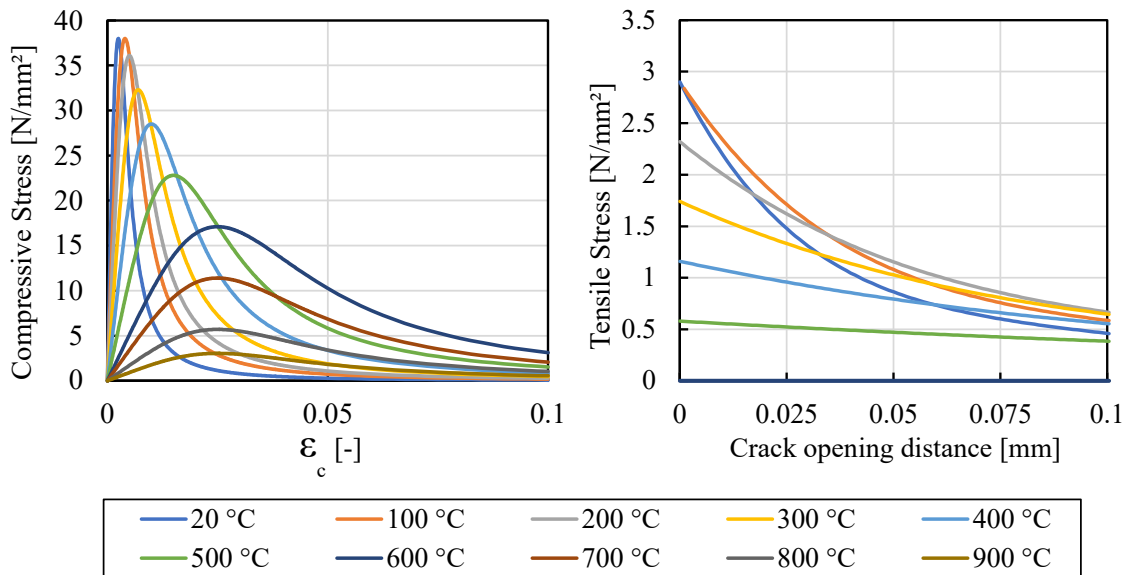


Figure 8. Stress-strain relationship for the concrete material model on the example of C30/37

For the steel material, definitions from DIN EN 1994-1-2 [3] were implemented in combination with the "Ductile Damage Model" available in Abaqus. Thermal material properties from [3] were used for the thermal simulation, using the upper limit of the thermal conductivity of concrete.

3.3 Mechanical Analysis

An initial purely mechanical finite element analysis (FE) was carried out on each specimen to validate the models based on tests at room temperature. This involved applying a displacement-controlled load to the top of the push-out specimen. As shown in Figure 9, there is a good correlation between the numerical results and the experimental tests for the specimen with the Cofraplus60 profiled sheet up to a displacement of 20 mm.

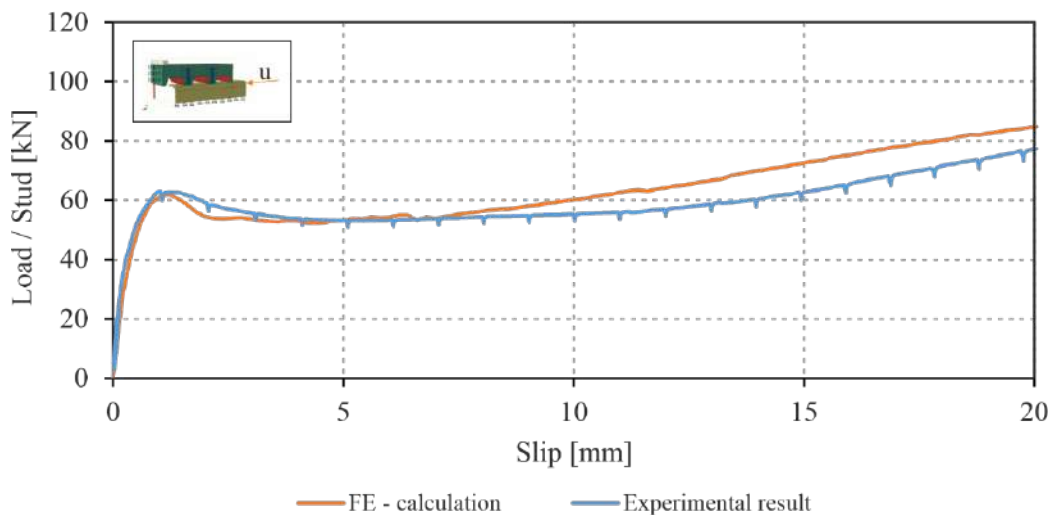


Figure 9. Comparison of the experimental load-slip behavior with the results of the numerical simulation

In addition to the analysis of the load-displacement curve, the observation of concrete damage and the formation of plastic hinges at the headed studs can provide further insight into the load bearing behaviour of the headed studs in profiled sheets. Figure 10 shows a comparison of the FE results with concrete cuts made on the specimens and subsequently scanned with a 3D scanner. These scans also include the undeformed headed studs which were recorded in a first scan prior to concreting. It can be seen that both the concrete damage and the development of plastic hinges are in good agreement with the experimental tests. Deviations are mainly due to the fact that the experiment was carried out up to a deformation of 47 mm, which exceeds the displacement applied in the FE model.

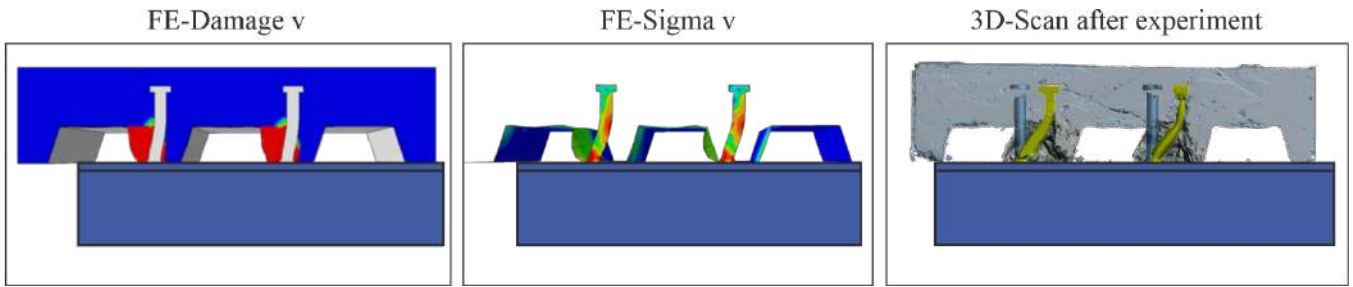


Figure 10. Comparison of numerical results with concrete cuts made subsequent the experimental tests

3.4 Thermal Analysis

As discussed in section 2.2, the material properties used for the thermal analysis were taken from [3]. The thermal loading, modelled using the ISO standard fire curve from [16], was applied as convection and radiation through the Abaqus interactions "surface radiation" and "surface film condition" to the relevant surfaces of the push-out test specimens. The initial focus was to validate the thermo-mechanical model, so the thermal models were calibrated by introducing additional shadow factors to make the temperature distribution in the specimen as close as possible to the temperatures from the corresponding experiments. It should be noted that during the heating of concrete protected by profiled sheeting, several significant influences on the temperature evolution occur during the duration of the fire event. This is attributed to overlapping effects influencing the heating behaviour, such as the release of pore water from the concrete matrix [23], the temperature-dependent emissivity of the galvanized profiled sheets [24], and the potential formation of an insulating air gap between the concrete and adjacent trapezoidal sheet [11]. Better agreement was obtained for measurements on the steel section, where the influences are more quantifiable. The main focus of the calibration was to match the flange temperature below the ribs of the profiled sheeting, as this temperature is considered to be critical to the load bearing behaviour of the headed studs. In general, it should be noted that the push-out tests, due to their vertical orientation and the resulting shadowing factors in the existing test furnace, exhibit a distinct heating behaviour that differs from that of horizontally oriented structural elements in composite construction. It is therefore planned to perform the final calibration of the thermal simulation models for the parametric study based on large scale beam tests. These tests have already been carried out as part of this research project in the slab test furnace at IBMB Braunschweig. Figure 11 shows a comparison between the experimental (EXP) and simulation-based (FE) temperature distributions for the specimen with Cofraplus60 sheet under a load of 110 kN.

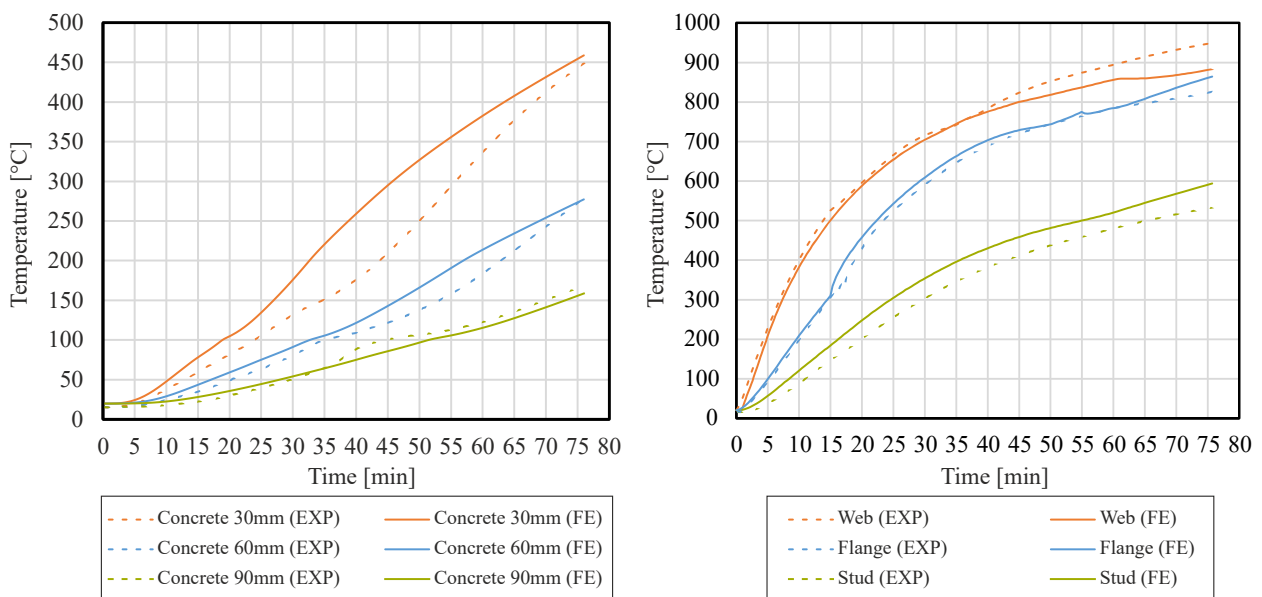


Figure 11. Comparison of the temperature development in Simulation and in the experiment; left for measurements in the concrete chord; right for measurements on the steel section and in the headed stud

3.5 Combined analysis

Following successful calibration of the thermal models, the generated temperature field was transferred to the mechanical model as a "predefined field". In the resultant simplified thermomechanical model, the mechanical load was first applied to the specimen. The time-dependent temperature field was then applied to this preloaded model until the model failed. Figure 12 shows a comparison of the load-slip curve from the experiment with the results from the FE calculations. It can be seen that there is a good agreement. Due to the known inaccuracies in the existing concrete models, discussed in [25] among others, the existing deviations are considered acceptable. This approach is now intended to be applied to further tested sheet geometries and will form the basis for an extensive parameter study.

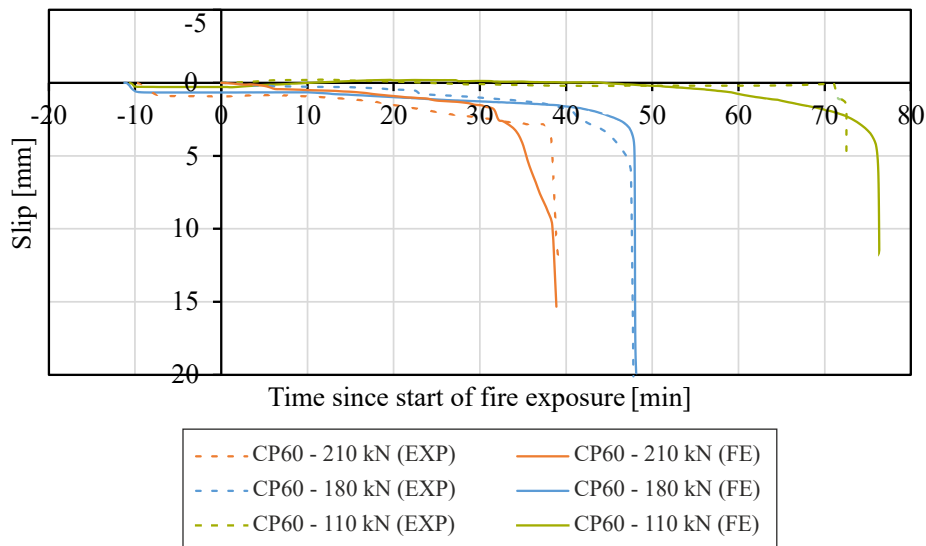


Figure 12. Comparison of the numerical slip behavior with the experimental results of the tests with Cofraplus60

4 CONCLUSIONS

This paper presents a series of push-out tests with Cofraplus60 profiled sheeting carried out as part of a research project at the Technical University of Munich. The chosen experimental approach allowed the determination of the temperature development and the load-slip behaviour of headed studs arranged in profiled sheeting. The tests carried out at room temperature showed good agreement with results from recent research projects. Due to the lack of sufficient data on push-out tests at elevated temperatures, no comparable experiments could be identified in the literature. Nevertheless, the results are considered reasonable and were used as a basis for the calibration of a numerical model. Simulations carried out using the FE software Abaqus CAE allowed for the creation of a calibrated thermal model, whose temperature field was subsequently transferred to a mechanical model. This allowed a simplified thermo-mechanical analysis to be performed, which showed good agreement with the experimental tests. The demonstrated approach to validating FE simulations will now be extended to the entire experimental database. Based on a parameter study carried out with these data and supported by the experimental results, a thorough validation of the design approaches for headed studs in profiled sheeting under elevated temperature from EN1994-1-2 [3] in combination with approaches from prEN1994-1-1 [2] and EN1994-1-1 [1] will be carried out.

ACKNOWLEDGMENT

All investigations were carried out as part of the research project "Shear studs in fire". The IGF-project 21403 N from the Research Association "German Committee on Steel Construction" (DAST e.V.), Düsseldorf, is supported by the Federal Ministry of Economic Affairs and Climate Action the German Federation of Industrial Research Associations (AiF) as part of the programme for promoting industrial cooperative research (IGF) on the basis of a decision by the German Bundestag. The project is carried out at Technical University of Munich.

REFERENCES

1. EN 1994-1-1:2004 + AC:2009. Eurocode 4: Design of composite steel and concrete structures - Part 1-1: General rules and rules for buildings.
2. prEN 1994-1-1 (2021) Eurocode 4: Design of Composite Steel and Concrete Structures Part 1-1, General Rules and Rules for Buildings. Entwurf Nov.2021.
3. EN 1994-1-2:2005 + AC:2008. Eurocode 4: Design of composite steel and concrete structures - Part 1-2: General rules - Structural fire design.
4. Konrad, M. (2011) Tragverhalten von Kopfbolzen in Verbundträgern bei senkrecht spannenden Trapezprofilblechen [Dissertation]. Universität Stuttgart.
5. Nellinger, S. (2015) On the behaviour of shear stud connections in composite beams with deep decking [Dissertation]. Université du Luxembourg.
6. Eggert, F. (2019) Einfluss der Verdübelung auf das Trag- und Verformungsverhalten von Verbundträgern mit und ohne Profilblech [Dissertation]. Universität Stuttgart.
7. Vigneri, V. (2021) Load bearing mechanisms of headed stud shear connections in profiled steel sheeting transverse to the beam [Dissertation]. Université du Luxembourg.
8. Degtyarev, V. Hicks, S. (2023) Shear resistance of welded studs in deck slab ribs transverse to beams, Engineering Structures.
9. Lawson, M. et al. (2017). Development of improved shear connection rules in composite. Final Report. Luxembourg: European Union.
10. Zhao, B. and Kruppa, J. (1997) Fire resistance of composite slabs with profiled steel sheet and of composite steel concrete beams Part 2: Composite beams. Final Report of Technical Steel Research Luxembourg: European Communities
11. Lim, O. (2020) Fire performance of shear studs in transverse deck slabs [Dissertation]. Ulster University
12. Chen, L. et al. (2015) Behaviour and design of shear connectors in composite slabs at elevated temperatures. Journal of Constructional Steel Research 115, p. 387-397.
13. Mirza, O. und Uy, B. (2009) „Behaviour of headed stud shear connectors for composite steel–concrete beams at elevated temperatures“. In: Journal of Constructional Steel Research 65.3, S. 662–674
14. Yasuda, S. et al. (2008) „Experimental study on shear strength of headed studs shear connectors at high temperature“. In: Journal of Structural and Construction Engineering (Transactions of AIJ) 73.630, S. 1417–1423
15. Wang, A. J. (2011). Numerical studies on shear connectors in push-out tests under elevated temperatures. Structural Engineering and Mechanics, 39(3), 317–338
16. DIN EN 1363-1:2020-05 (2020) Fire resistance tests - Part 1: General requirements; German version EN 1363-1:2020. Beuth, Berlin.
17. Dara, S. (2015) Behavior of the shear studs in composite beams at elevated temperatures [Dissertation]. University of Texas.
18. Meyer, P. D. (2022) „Schubtragverhalten von Verbunddübeln bei Stahlverbundträgern im Brandfall“. Dissertation. Gottfried Wilhelm Leibniz Universität Hannover.
19. Hillerborg, A., Modéer, M. und Petersson, P.-E. (1976) „Analysis of crack formation and crack growth in concrete by means of fracture mechanics and finite elements“. In: Cement and Concrete Research 6.6, S. 773–781.
20. Hordijk, D. A.: „Local approach to fatigue of concrete“. Dissertation. Technische Universität Delft, 1991.
21. CEB-FIP model code 2010. Berlin: Ernst & Sohn, 2013.
22. Zhang, B. et al. (2000) „Residual fracture properties of normal- and high-strength concrete subject to elevated temperatures“. In: Magazine of Concrete Research 52.2, S. 123–136.
23. Paliga, K. (2003). Entstehung und Vermeidung von Betonabplatzungen bei extremer Brandeinwirkung. Braunschweig.
24. Gaigl, C. (2019) Fire resistance of hot-dip galvanized steel structures, Dissertation, Technical University of Munich.
25. Kleibömer, I. (2018) Zum Verbundverhalten ausbetonierter Hohlprofilstützen mit massivem Stahlkern im Brandfall, Dissertation, Leibniz Universität Hannover.

LOAD-BEARING PERFORMANCE OF CONCRETE-FILLED STEEL TUBULAR COLUMNS WITH HIGH-STRENGTH STEEL SHEETS IN THE CORE EXPOSED TO FIRE

Shaghayegh Ameri¹, Michael Schäfers², Martin Mensinger³, Jochen Zehfuß⁴

ABSTRACT

Concrete-filled steel tubular (CFT) columns have long been acknowledged for their structural efficiency and their load-bearing performance has been standardized globally. This paper introduces an innovative method that leverages a composite system and high-strength steel to design more slender CFT columns for tall buildings. This method employs high-strength steel for the cladding tube to enhance the column's load-bearing capacity in ambient conditions and maintains concrete confinement during fire exposure. Additionally, high-strength steel sheets are incorporated into the core of the proposed columns, in order to increase load-bearing capacity and reduce internal residual stress by reducing steel element size, thereby minimizing imperfection leading to buckling. In order to achieve equivalent performance to a solid element in terms of load-bearing capacity, the optimized connection between the sheets in the core is investigated. This paper presents the findings from fire tests carried out on 5 columns with comparable outer diameters but differing core configurations, incorporating either 4 or 8 sheets. Steel grades 890 and 960 were employed for the tube and sheets, respectively and the sheets were connected either using bolts or welding methods. Developed advanced numerical models were described to simulate the thermo-mechanical behavior of the proposed columns under standard ISO fire, providing a basis for subsequent parametric analyses aimed at proposing a design concept for these composite columns.

Keywords: Composite column; High-strength steel; Experimental study; Numerical simulation;

1 INTRODUCTION

Various research groups have undertaken numerous investigations into the performance of CFT columns under ambient conditions and elevated temperatures. These studies have examined a multitude of parameters through both experimental methods and numerical simulations. The findings of these investigations have led to the development of design methodologies, which have subsequently been incorporated into various international standards. Examples of such standards include the Chinese Code DBJ13-51 [1], the National Building Code of Canada [2], ASCE/SFPE 29-99 [3], ACI 216 [4], and the European standard prEN1994-1-2 [5].

¹ Research Associate., Technische Universität Braunschweig, Institute of Building Materials, Concrete Construction and Fire Safety (iBMB), Braunschweig, Germany

e-mail: S.Ameri@ibmb.tu-braunschweig.de, ORCID: <https://orcid.org/0009-0001-8428-5175>

² Research Associate, Technical University of Munich, Institute of Metal Construction, Munich, Germany

e-mail: M.Schaefers@tum.de, ORCID: <https://orcid.org/0000-0003-0765-4640>

³ Professor, Technical University of Munich, Institute of Metal Construction, Munich, Germany

e-mail: Mensinger@tum.de, ORCID: <https://orcid.org/0000-0001-5210-5400>

⁴ Professor., Technische Universität Braunschweig, Institute of Building Materials, Concrete Construction and Fire Safety (iBMB), Braunschweig, Germany

e-mail: J.Zehfuss@ibmb.tu-bs.de, ORCID: <https://orcid.org/0009-0004-6547-2479>

The parameters under investigation encompass various geometrical aspects, including the utilization of circular [6], rectangular [7], and elliptical [8] cross-sections, while considering different sizes and column slenderness ratios. Additionally, the study explores a range of material properties employed in the construction industry. These materials include normal steel, high-strength steel [9], and stainless steel [10], alongside various concrete types such as normal concrete, high-strength concrete [11], with or without fiber reinforcement, and recycled aggregate concrete [12].

The CFT columns have a general performance in fire. During the initial phase of a fire, the steel tube heats up rapidly due to its higher thermal conductivity, expanding faster than the concrete core. This leads to a gradual loss of contact between the concrete core and the loading plate as the steel tube elongates axially and experiences slip at the steel-concrete interface. Consequently, the axial load ratio shifts towards the steel tube until it bears the entire load. Subsequently, as the steel tube reaches its critical temperature, local yielding occurs, causing it to shorten and re-establish contact with the concrete core. This initiates a transfer of load from the steel tube to the concrete core, resulting in an inversion of the axial force ratio. Eventually, as the concrete core degrades slowly due to its lower thermal conductivity, the column fails when the concrete loses its strength and stiffness entirely.

The latest strategies aimed at enhancing the performance of concrete-filled tubular section columns involve integrating additional embedded steel elements into the core. These elements can include another tubular steel [13], H-profiles, solid circular or square steel [14–17], and bundles of reinforcing bars [18].

Initially, the overall performance of the CFT columns with steel core in fire mirrors that of conventional ones. Following the failure of the steel cladding tube, the load reverts back to the core. Subsequently, both the concrete and steel within the core begin to longitudinally expand. This expansion persists until the material within the core can no longer withstand the load due to thermal degradation in shorter columns or buckling occurs in more slender columns. A comparison between the fire performance of CFT columns with different steel core was illustrated by Espinos [9].





The research team from the Technische Universität Braunschweig and the Technical University Munich, continuing their prior research on CFT columns with bar-bundle cores [19], has introduced the recent approach. This involves replacing the bar-bundle with steel sheets to enhance the potential for optimizing connections between the sheets and achieving increased load-bearing capacity under ambient conditions and during fires. This paper presents a five large-scale experimental tests on a novel composite column at elevated temperatures. These tests aim to explore the thermo-mechanical performance of the columns and validate a numerical model developed for the study, which reflects the observed fire behavior during fire exposure.

2 COLUMNS MANUFACTURING

Under the supervision of industrial partners, five columns were fabricated for the fire test. The process began by positioning the sheets and connecting them either through bolts or welding. To ensure full contact between the sheets and the head plate, both ends of the sheets were flattened, enabling proper force transmission through the head plate across the entire section. Spacers made of fibre-reinforced concrete were then affixed around the sheets with straps to centralize them inside the cladding tube. Subsequently, one end plate was welded to the cladding tube, and the column was vertically cast using flowable concrete with a maximum grain size of 8 mm (C30/37). Finally, the other end plate was welded to the cladding tube, and any empty spaces resulting from concrete shrinkage during curing were filled using expanding concrete injected through small holes on the end plate. Columns were stored for minimum 100 days to reach their highest strength.

Each column features a high-strength tube with a diameter of 244.5 mm and a thickness of 12.5 mm, constructed from steel grade 890. The core sheets, fabricated from steel grade 960, vary in configuration: two columns incorporate four sheets, each with a thickness of 40 mm, while the remaining three columns utilize eight sheets, each with a thickness of 20 mm. These sheets are interconnected using either welding (weld size 6) or bolting (M24 grade 8.8). Detail of columns geometry is listed in Table 1.

Table 1. Geometrical details of the columns

Configuration					
Column number	KH1	KH2	KH3	KH4	KH5
Tube Diameter [mm]	244.5				
Tube thickness [mm]	12.5				
Sheets width [mm]	150 , 127.5 (chamfer to 60)		165, 150, 120, 56		
Sheets thickness [mm]	40		20		
Sheet number	4	4	8	8	8
Column length [m]	4.09				
Connection type	bolted	welded	bolted	welded	welded
Connection size	5xM24 – distance 200 mm (each ends)	2x820mm (each ends)	5xM24 – distance 200 mm (each ends)	2x820mm (each ends)	8x205mm (distance 350 mm)

The investigation primarily focused on the configuration of the sheets and their method of connection. It is acknowledged that high-strength steels present challenges in workability, making welding a difficult and time-consuming process. Additionally, the brittleness of the material may affect the effectiveness of welded connections. Hence, it was imperative to thoroughly examine the performance of welded connections compared to the potential alternative of using bolts. To minimize the impact of other factors, all other geometric parameters were maintained constant.

The temperature measuring points were strategically placed at different locations within the section and across four levels in the height of the columns, aligning with the spacers intended for centering the core within the cladding tube. K-type thermocouples were affixed to the sheets using spot welding. To route the thermocouple cables between the sheets, small holes with a diameter of 12 mm were incorporated (Figure 1, 1). To prevent any damage to the thermocouple cables due to pressure between the sheets, small shears were cut on the surface of the sheets, allowing the cables to reach the holes without interference (Figure 1, 2). For measuring the temperature in the concrete some thermocouples with steel plate ends were installed on the spacers (Figure 1, 3).

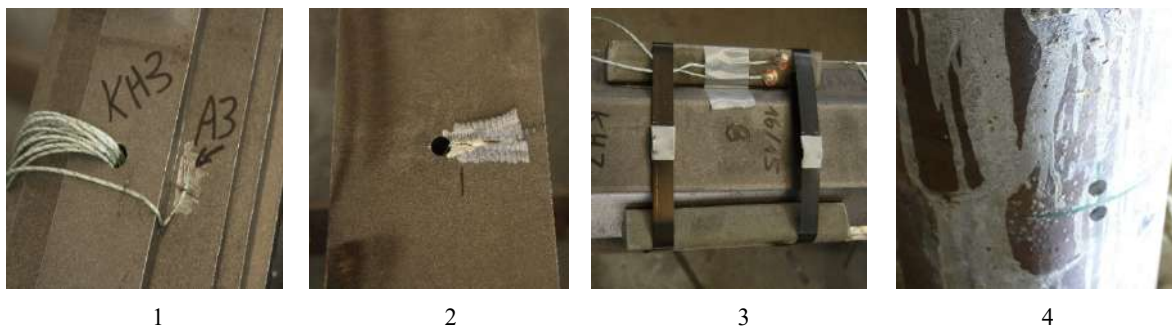


Figure 1. The hole to route the thermocouple cables (1), Shear cut on the sheet surface (2), Plate end thermocouples on spacers (3), and vapor outlets (4)

Vapor outlets, on top and bottom of the tube were considered to avoid explosive failure of the tube caused by the high vapour pressure building up by the heated concrete (Figure 1, 4). To facilitate the passage of thermocouples out of the columns, small cuts were made at the bottom of the columns.

3 CONDUCTING FIRE TESTS

3.1 Test details and set-up

The experiments were conducted at the Institute of Building Materials, Concrete Constructions and Fire Safety (iBMB) at the Technische Universität Braunschweig. The furnace has a floor area of $3.6 \times 3.6 \text{ m}^2$ and a module height of up to 5.6 meters with 6 oil burners. The load was applied from bottom by a hydraulic press, with a maximum load of 6.5 kN at 10 mm eccentricity. All fire tests were conducted with nominally pinned-fixed support conditions. The pinned end was realized by rocker bearing set-up using a half cylinder installed on the hydraulic jack (Figure 2, 3, bottom), while the fixed support was established using a reaction beam from the top (Figure 2, 3, top). For thermal protection of testing facilities, both ends were protected with a 20 cm thick layer of mineral wool (Figure 2, 4). Figure 2 (1, 2) shows an overall view of the column in the furnace with the corresponding schematic sketch.

The amount of the load and the vertical (axial) displacement of the supports were measured by the sensors of the hydraulic press. A linear variable differential transformer (LVDT) was used to measure the horizontal deformation, located at a height of approximately 1.7 meters from the bottom of the supports (Figure 2, 1). The furnace temperature measured using 6 plate thermocouples at various heights of the furnace near the supports to control the temperature inside the furnace and to check if the standard temperature-time curve according to ISO834 was maintained during the test.

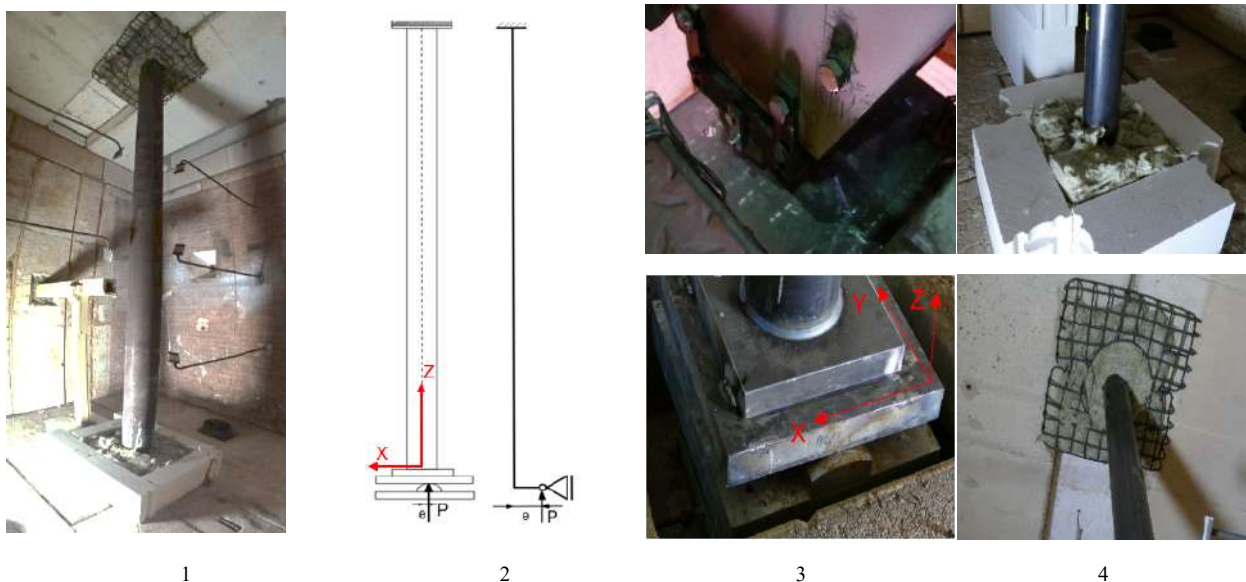


Figure 2. Overview of the column in furnace (1), Schematic sketch of the column and supports (2), The configuration of the fixed support (top) and pinned support (bottom) (3), Insulation of column ends (4)

In all tests, the mechanical load was initially applied at a speed of 8kN/s at room temperature and maintained constant for 30 minutes. Subsequently, the fire was ignited and continued until failure (buckling) occurred, except in the case of the KH5 column test, where the fire applied for 90 minutes. After this period, the mechanical load was increased to assess the fire resistance of the column after 90 minutes.

3.2 Result and discussion

The fire performance of the proposed columns exhibited unexpected variations during fire tests on columns KH1, KH2, KH3, and KH4. The observed fire resistance duration was significantly lower than expected for the initially calculated loads based on section capacity. Consequently, a recalculated load-bearing capacity was determined, considering new assumptions and hypotheses derived from post-fire test analyses of the columns. The amount of load applied at each column test and the fire resistance duration are listed in Table 2.

Table 2. Measured applied load and fire resistance duration of columns

Column number	KH1	KH2	KH3	KH4
Eccentricity [mm]	10			
Support condition	Pinned-Fixed			
Applied load [kN]	3100	3100	2000	1000
Fire resistance duration	44	46	64	122

Early buckling observed in the fire tests may be attributed to the high temperature in the steel sheets, as the primary contributing element to load-bearing capacity. Therefore, the temperature of the steel sheets was carefully monitored in the initial step. In the first test, the thermal results aligned with the initial calculations, and no unexpected occurrences, such as increased temperature in the section, were observed. Comparing the temperature of the steel core in each column (Figure 3) revealed consistent heating rates among the steel sheets, with no sudden increases that might indicate failure in the concrete cover. In the thermal analysis, a small plateau was observed at 100°C, attributed to the evaporation of moisture content within the concrete.

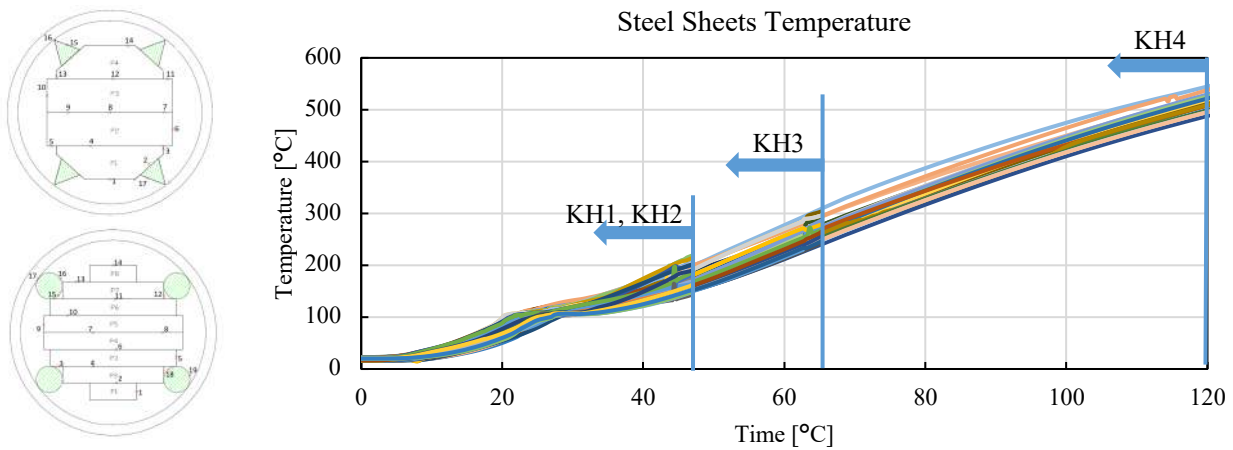


Figure 3. Location of measured points (left) Measured temperature by thermocouple in the sheets at 4 levels of column KH1, KH2, KH3 and KH4 (right)

The diagram legend in Figure 3 has been omitted due to the large number of measurement points (app. 80) in each column. The range of measured temperatures for the steel sheets is attributed to the difference of the sheets temperature in the middle and near the edge, difference of temperature in the height of the column and the slight difference in the concrete cover because of eccentricity of the core.

The thermo-mechanical behavior of the columns aligns with the typical response observed in concrete-filled hollow section columns with a steel core, which can be outlined as follows:

Cladding Tube: As the fire initiates, the temperature within the cladding tube rises, leading to radial and longitudinal expansion. Due to the weak contact between the cladding tube and concrete, radial expansion results in the formation of a thin air layer between them. This air layer delays the transfer of temperature to the core and allows the cladding tube to deform freely. Consequently, during longitudinal expansion, the cladding tube separates from the concrete and core, causing the entire load to be borne by the tube. However, as the temperature continues to increase over time, the cladding tube eventually reaches its critical temperature limit, leading to failure after a brief period of plastic deformation.

Core: Upon failure of the cladding tube, the temperature within the core increases, resulting in expansion of both the concrete and steel components. If the bond between them is weak, radial expansion may cause them to show separate longitudinal expansion. After the cladding tube fails, the load is transferred to the core. Given the significantly higher modulus of elasticity of steel compared to concrete, the main part of load is borne by the steel core. Longitudinal expansion continues in a semi-linear fashion from one side,

while the temperature rise within the core leads to degradation in the modulus of elasticity and yield strength of the steel. Ultimately, the load within the core reaches its critical point, leading to nonlinear geometric failure or buckling. The described behavior is evident in the vertical and horizontal deformation of the columns which is illustrated in Figure 4.

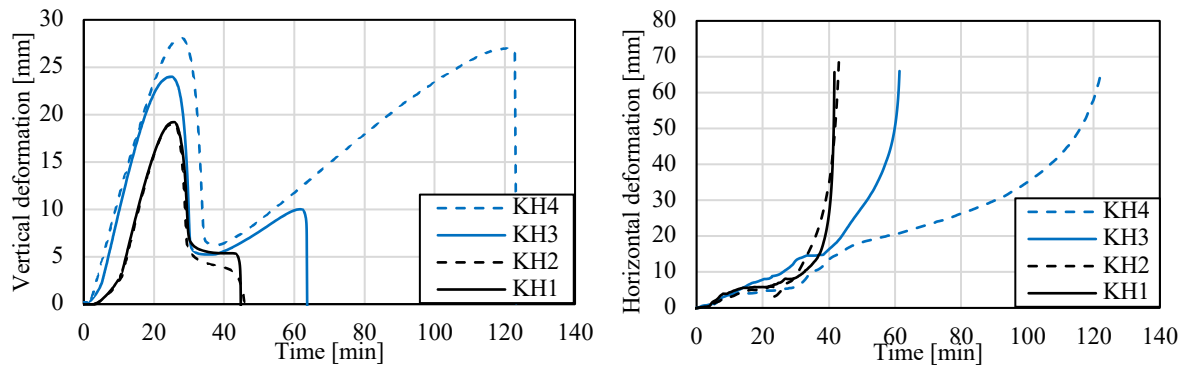


Figure 4. Comparison of Vertical deformation (left), Horizontal deformation (right) of the columns KH1, KH2, KH3 and KH4

The occurrence of early buckling during the initial fire test prompted the authors to investigate further by opening the columns to identify the underlying cause of this failure.

KH1: In KH1, for approximately 26 minutes, the load was carried by the cladding tube until its failure. Subsequently, when the load shifted to the core, it was unable to withstand it for an extended period. This transition is noticeable in the acceleration of horizontal deformation after 30 minutes, indicating the onset of buckling in the column in around 10 minutes before longitudinal expansion begins in the core.

- After the fire test, when the load was removed and the burners were turned off, a loud sound emanated from the furnace. Upon cooling down and opening the furnace, it was discovered that the weld between the tube and the end plate had fractured. During the fire tests, the steel sheets were in a linear phase, implying that after the load and fire were removed, they attempted to revert to their original straight form. However, the cladding tube, having undergone plastic deformation, retained some permanent deformation. This resulted in high tension on the weld line between the cladding tube and the end plate. Welds to high-strength steel are more susceptible to brittle break, and the tensile stress exerted on the weld line ultimately led to its fracture after the removal of the thermo-mechanical load
- Upon removing the end plate, it was observed that there was a slight slip of approximately 1 mm between the sheets (Figure 5, left). This slip was deemed reasonable, as the diameter of the holes drilled for the bolts was 2 mm larger than the bolt size. Sections of the cladding tube were cut to monitor the situation of the steel sheets and bolt connections. During the construction of the column, the bolts were initially tightened to a torque of 750 Nm, but the torque required to loosen them varied depending on their location (Figure 5, right). The torque needed to open the bolts increased as one approached the middle of the column, which experienced the highest level of horizontal deformation. However, since the difference in torque requirements was not significant, it is plausible that the concrete around the bolts may have also influenced the force needed to open the nuts.



Figure 5. The slip between the sheets of core (left), the torque load used to loose nuts (right)

- The measurement of concrete cover on each side of the core revealed that the core had a 5 mm eccentricity on the weaker side. While this may have had a minor effect on the load-bearing capacity of the column, it is unlikely to be the primary reason for the observed early buckling.
- No specific damage was observed in the concrete, only very small cracks that appeared randomly on the surface due to the significant deformation during

The observed slip between the sheets indicated poor interaction and inadequate load transfer between them. Consequently, it was necessary to evaluate the impact of the connection type on the load-bearing capacity of the columns. As a result, Since KH2 had similar section as KH1 only the connection between the sheets was weld; it was decided to conduct the second test under identical boundary conditions as the first test to specifically investigate the effect of the connection type.

KH2: According to the vertical deformations (Figure 4), the performance of the cladding tube in both columns KH1 and KH2 appears similar, which is expected given their same size and steel grade, as well as being subjected to identical loads. The marginal difference of 2 minutes in fire resistance, from 44 minutes in KH1 to 46 minutes in KH2, can mainly be attributed to the eccentricity of the core. Upon cooling down, the column KH2 was opened and the core was perfectly centered with no eccentricity, unlike KH1 where a 5 mm eccentricity was noted.

The diagrams (Figure 4) indicate that buckling commenced around 30 minutes, immediately after the failure of the cladding tube. The rate of horizontal deformation increased after 30 minutes, and the column began deforming even faster than KH1. However, the section managed to bear the load for a slightly longer period, possibly due to no eccentricity of the core and the type of connection between sheets. Nevertheless, overall, the results suggest that the connection type does not significantly affect the fire performance of the columns.

The observations in the column after the fire test are as follows:

- Once again, the weld between the cladding tube and the end plate on the side of the load was found to be broken after the removal of mechanical load and cessation of the fire
- Due to the welded connection between the sheets, no slip between the sheets was observed, and the concrete coverings were similar on opposite sides (no eccentricity of core).

The investigation into the contact between the concrete and the steel core was carried out more thoroughly this time. As depicted in Figure 6, the connection appeared tighter in the column opened after a buckling test in ambient conditions. However, after the fire tests, a very small space could be observed between the concrete and the core. This phenomenon aligns with observations made by Kleibömer [16] in concrete-filled tubular columns with a massive steel core. The discrepancy is linked to the surface characteristics of the steel in the core. Solid steel or steel sheets have very smooth and flattened surfaces, resulting in a poor connection between the concrete and the core. Therefore, during the fire, as the temperature increases beside the cladding tube, the concrete expanding radially. In this scenario, an air layer is generated between both the cladding tube and concrete, as well as between the concrete and the steel core. This phenomenon may not be perfectly visible in the photo since the elements return to their original size after cooling down. Consequently, these columns do not function as composite elements in fire, and there is either no or very little load transfer between the steel and concrete elements.



Figure 6. The connection between concrete and core in ambient condition (left), after fire (right)

Finally, this observation led to the hypothesis that in the event of fire and after the failure of the cladding tube, only the steel sheets carry the load. Based on this hypothesis, the load bearing capacity of the sheets for 90 minutes ISO-fire was calculated by InfoCAD software (2000 kN) and applied as the initial load on the column KH3.

KH3: In this test, the column was able to bear the load for 64 minutes, which was earlier than expected (90 minutes), indicating that the hypothesis stating the column doesn't function as a composite element is partly correct. However, there should be other factors influencing the fire performance of these types of columns.

The thermo-mechanical outcomes from this test highlight a significant improvement in the longitudinal expansion of the core following the failure of the cladding tube (Figure 4). Notably, the fire behavior of the cladding tube differed from previous test, due to a lower load on the column. This lower load facilitated greater expansion of the cladding tube, delaying the cladding tube reaching critical temperature. Consequently, even after the cladding tube failed, the core continued to expand for approximately 35 minutes until buckling occurred. Horizontal deformations indicate that buckling commenced around the 60-minute mark, evidenced by an increase in the slope of the diagram.

After the column cooled down, it underwent further examination, revealing several notable findings:

- In this test, no fracture observed in the weld between the cladding tube and end plate.
- The core was not perfectly centered, exhibiting a 5 mm eccentricity on the weaker side.
- Despite the sheets being connected by bolts this time, there was minimal slip between them (less than 1 mm).
- Once again, the connection between concrete and core was found to be poor, with observable space between them
- A new observation was made regarding the curvature of the column after cooling down. The location of maximum horizontal deformation indicated that the maximum deformation occurred at 0.82 column length. In other words, it was between location of maximum horizontal deformation at column with pinned-pinned buckling mode and pinned-fixed buckling mode.

The final observation stems from two factors: Firstly, the limited rotational possibility at the fixed support in the testing facilities. Secondly, since the sheets lack connection to the end plate, they have greater potential for rotation, thereby influencing the buckling curvature. Therefore, in the fourth test, the load-bearing capacity of the sheets was calculated, considering the worst-case scenario where the sheets act separately and behave like a pinned-pinned support. This capacity was determined to be 1000 kN for a 90-minute ISO fire.

KH4: In this fire tests, the column could bear the 1000 kN load for 122 minutes, which confirms the last hypothesis. The sheets had a buckling length of 1 (pinned-pinned support) and 0.7 (pinned-fixed support).

Again since the load was lower the behavior of the cladding tube was different and could expand and bear the load for longer time of app. 37 minutes until failure. Then the load transferred to the core and the expansion of core continued for more than 80 minutes. The observations made upon opening the columns reveal the following:

- No cracks were observed along the weld seam between the cladding tube and the end plate.
- The core exhibited approximately 5 mm eccentricity once again.
- There was minimal damage to the concrete, with only very small surface cracks being observed.
- A small gap between the concrete and the core was noted.

The results of the fire test indicate that while some hypotheses were partially correct, there was a need for a more comprehensive understanding of the factors influencing the fire behavior of the proposed columns. Therefore numerical simulations using Finite Element Method (FEM) software ABAQUS to gain deeper insights into the fire behavior of the steel-sheet columns were done. The goal was to develop a final optimized column based on these simulations.

Details of numerical simulations are presented in chapter 4. However, the key findings from the numerical simulations and parametric study lead to the subsequent test on the optimized column are as follows:

- The initial hypothesis regarding the individual functionality of each element was validated. The simulations revealed minimal participation of concrete in load-bearing during fire exposure, supporting the decision to focus primarily on the load-bearing capacity of the sheets in the core.

- The hypothesis concerning the buckling mode of the columns was partly confirmed. The mode shape was found to be closely related to the connection type between the sheets. Adjusting the length and number of welding seams along the column height resulted in variations in the buckling mode shape, thereby affecting the load-bearing capacity.
- Parametric studies on the columns demonstrated that the load transfer between the sheets strongly depends on the configuration of connections. Maintaining a consistent total length of weld but distributing it equally into multiple welding seams along the column height led to enhanced load-bearing behavior. Increasing the number of welding seams significantly improved the load-bearing capacity of the sheets.
- Based on the test results in ambient conditions and the outcomes of numerical simulations, it is recommended to avoid using bolted connections, or if utilized, design them to maximize shear capacity.

Given these findings, the last column manufactured exactly like column KH4. However, instead of 2 times 820 mm welds at both ends, 8 welding seams with 205 mm length, equally distributed along the length, were used to connect the sheets.

KH5: In this test the load bearing capacity of the column was calculated using numerical simulation with ABAQUS software considering the welding size and length as well as the definition of realistic fire test boundary conditions and connection between the sheets and concrete with sheets. The calculated load bearing capacity was app. 5500 kN for 90 minutes. In this test for having the possibility of comparison with previous tests and determination of the fire resistance of the column after 90 minutes standard fire, it was decided to apply 2000 kN as initial load with 10 mm eccentricity. The load increase on the column after 90 minutes and of the capacity measured was 5485.89 kN. This load was near to the numerical simulation which shows that the developed model reflects the fire test results in very good agreement.

The main finding highlights the significant impact of connections on the load-bearing behavior of the proposed columns. As a general recommendation for connection design, it is suggested that the required length of welding seams should be divided into smaller parts and distributed along the length of the column.

4 NUMERICAL SIMULATION

4.1 Model description

To examine the fire behavior of the proposed columns, a comprehensive three-dimensional model was developed, taking into account all boundary conditions and realistic connections between the composite column elements. These models, created using FEM software ABAQUS, were initially calibrated and then validated against the results of large-scale fire tests. Each element was meticulously generated as a three-dimensional component, precisely mirroring the dimensions of the constructed columns.

Material: The temperature-dependent mechanical properties of the steel grades 890 and 960, employed for the cladding tube and plates within the core, have been characterized in the software based on test results reported in [20]. The temperature-dependent thermal and mechanical properties of the concrete C30/37, utilized as filler in the constructed column, and the thermal properties of the steel were defined in accordance with prEN 1994-1-2 [5]. For definition of concrete behavior in Abaqus the concrete damage plasticity (CDP) model were used.

Thermal Contact: The effect of air layer between cladding tube and the outer surface of the concrete, as well as between sheets outer surface and the inner surface of concrete gap conductance of 200 W/(m²K) is considered between the surfaces. This value is defined according to the parametric analyses and comparison of test and simulation results.

Mechanical contact: For creation of a comprehensive model, the mechanical connection between the elements should be defined realistically. However, to avoid convergence problem some simplifications were considered.

- Cladding tube to end plates: They were tied together completely.
- Concrete and steel: Hard contact and friction with coefficient of 0.3.

- Between the sheets: Since the sheets were shot-blasted, the friction coefficient of 0.5 were defined between them, beside hard contact.
- Welding connection: welds were modeled as 3D elements and their surface tied to the sheets.
- Bolt Connection: For simplification, bolts were modeled as 3D rod inside the holes generated in the sheet. For considering this pre-tensioning effect, a circular partition was introduced at the location of the bolt holes, matching the size of the bolt heads, and the pre-tensioning force was applied as compression to the sheets, while the same load was applied as tension to the bolt rods.

Mesh: The mechanical model was meshed using three-dimensional 20-node quadratic (C3D20R) volume elements with reduced integration for all steel cladding tubes, concrete, steel sheets as well as weld or bolt elements. To reduce computation time, a mesh sensitivity analysis was performed, resulting in a maximum element size of 20 mm, which provided adequate accuracy of the results.

4.2 Thermo-mechanical analyses

The thermo-mechanical performance of the composite columns was analyzed using a sequential approach to avoid potential convergence issues that may arise from coupled temperature-displacement analysis. This method involves three distinct models:

- 1) Buckling analysis model: This model determines the deformation shape at the first buckling mode of the column.
- 2) Heat transfer analysis model: This model defines the temperature distribution in the column during the whole duration of the fire for fire exposure according to ISO 834 curve.
- 3) Mechanical model: This model contains mechanical loads with considering initial imperfections by incorporating a small factor of nodal deformation from the first buckling mode and with considering the effect of column temperature calculated with model 2.

At first, the thermal results from heat transfer analyses are compared with the measured temperatures in the fire tests and as example results in KH1 and KH 4 are depicted in Figure 7. The measured temperatures in the sheets as discussed in subsection 3.2 (Figure 3), are represented in gray, while the simulation results are shown in red. To succinctly present the findings, the temperatures calculated at the midpoint of the steel core were considered for the simulation results.

The plateau observed in the temperature results of the fire tests is attributed to the evaporation of moisture content present in the concrete. It's important to note that this study focused solely on the study of heat transfer, while neglecting the influence of moisture transfer. Despite this omission, the simulation results demonstrate a strong correlation with the experimental findings.

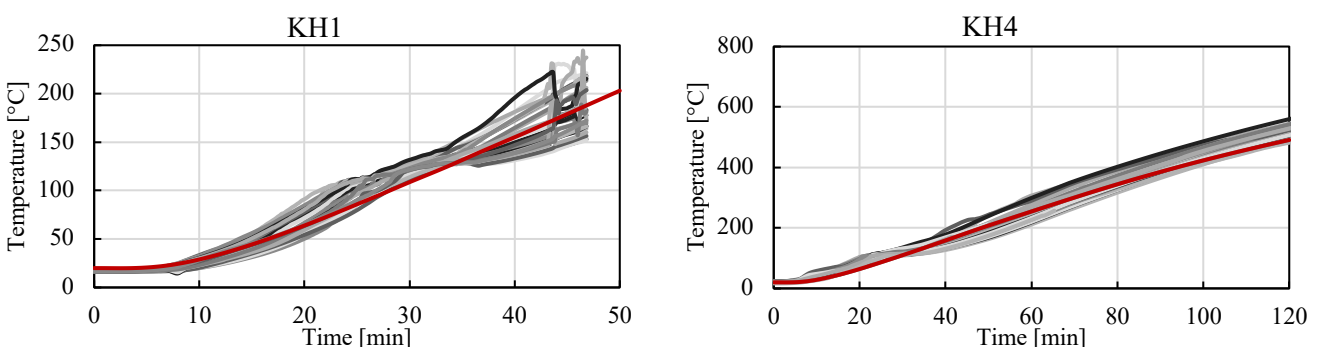


Figure 7. Comparison of the steel sheets temperature in fire test (gray) and simulation (red) in KH1 and KH4

In order to achieve the most comparable thermo-mechanical results in simulating with the fire tests, meticulous attention was paid to all details.

- The measured eccentricity of the steel sheets is considered in the model.
- As previously noted, there was a slight possibility of rotation in the fixed support. To account for this, the rotational stiffness in the weak direction of the columns was defined by a spring with a stiffness of 1000 Nm/mrad, which defined by calibration of numerical results.

- The measured air temperature in the furnace were applied on the cladding tube except 20 cm at both ends, which were insulated.
 - All calculations were conducted with considering L/1000 geometrical imperfection.
- Exemplary vertical deformations of the columns KH1, KH4 and KH5, as calculated through thermo-mechanical simulation, are compared with the measured values obtained from the fire tests, as illustrated in Figure 8.

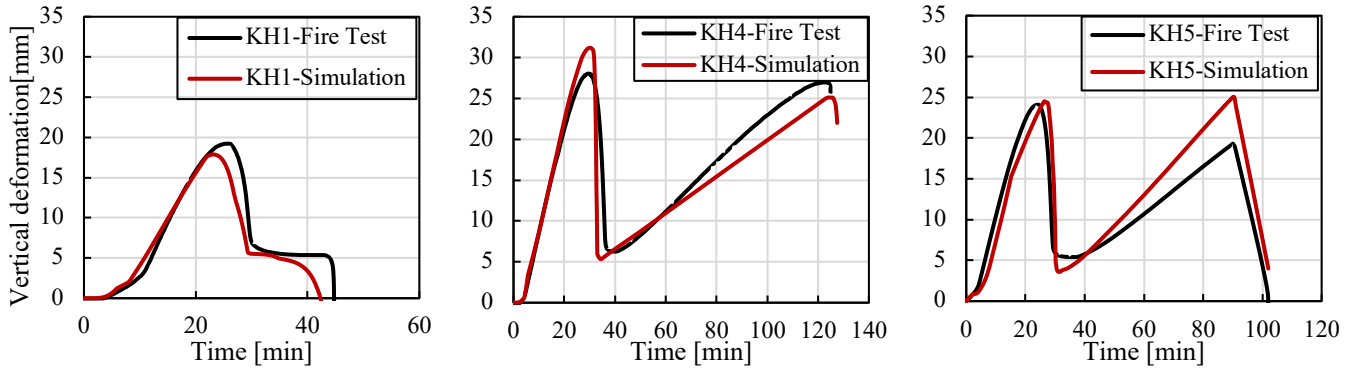


Figure 8. Comparison of the vertical deformation of the columns in fire test and simulation

The results demonstrate good agreement, indicating that the developed numerical model can reasonably predict the behavior of the columns in fire conditions. The overall performance of composite columns discussed in sub-section 3.2 was accurately observed in the simulations. Figure 9 illustrates the contribution of each element of the composite column KH2 to load-bearing during fire exposure.

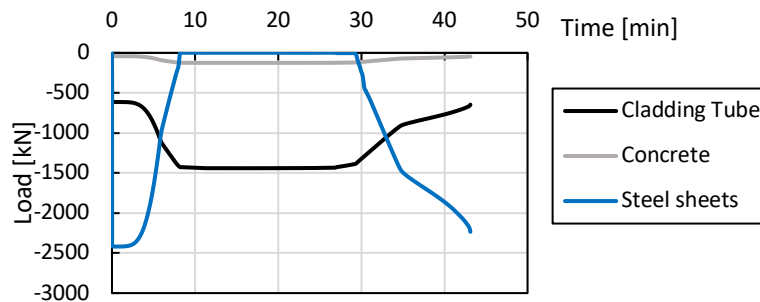


Figure 9. Load bearing contribution of the Tube, concrete and core during fire exposure (KH2)

As expected, the load distributes proportional to elements' stiffness and size. Initially predominantly the load is on the steel core and the tube. Throughout the duration of the fire, concrete exhibits minimal involvement in load-bearing. With the longitudinal expansion of the tube, the load is primarily transferred to it, while the steel core remains with no load until the tube fails, then the load gradually redistributing back to the core.

5 CONCLUSIONS

In summary, the paper presents a novel approach for enhancing the thermo-mechanical performance of CFS columns by incorporating high-strength steel sheets in the core. Experimental tests and numerical simulations demonstrate that the new approach achieves the project's initial objectives:

- Significant increase in the load-bearing capacity of the columns in fire by using high-strength steel sheets in the core. Highlighting the remarkable contribution of the high-strength cladding tube to the load-bearing capacity of the columns is only in ambient conditions.
- Optimizing the connection between the sheets as crucial factor for maximizing the load-bearing capacity and utilizing the full potential of the entire section. It is recommended to prioritize welded connections over bolted ones. Additionally, distributing the connection evenly along the length of the sheets, rather than concentrating it in specific regions, is paramount for achieving optimal performance.

- Ensuring that the high-strength steel tube maintains concrete confinement throughout fire exposure, preventing explosion failure or local buckling due to internal vapor pressure.
- Demonstrating that the developed numerical models can effectively predict the fire performance of the proposed columns, offering a cost-effective alternative to large-scale fire tests

ACKNOWLEDGMENT

The authors gratefully acknowledge the financial support of the German Federation of Industrial Research Associations (AIF), the scientific supervision of the Steel Application Research Association (FOSTA), and the technical support of industrial partners in the manufacture and provision of the test specimens.

REFERENCES

1. DBJ. DBJ13-51-2003: Technical specification for concrete-filled steel tubular structures (in Chinese). Fuzhou: The Construction Department of Fujian Province; 2003.
2. National Building Code of Canada. Ottawa, Canada: Canadian Commission on Building and Fire Codes; 2005.
3. ASCE/SFPE 29-99, Standard Calculation Method for Structural Fire Protection. Reston, USA: American Society of Civil Engineers; 1999.
4. ACI 216.1M-07, Standard Method for Determining Fire Resistance of Concrete and Masonry Construction Assemblies. Detroit, USA: American Concrete Institute; 2007.
5. European Committee for Standardization, prEN1994-1-2, Eurocode 4: Design of composite steel and concrete structures. Part 1-2: General Rules and Rules for Buildings, CEN, Brussels, prEN1994-1-2:2021.
6. Kodur, V. K. R., & Lie, T. T. (1996). Fire resistance of circular steel columns filled with fiber-reinforced concrete. *Journal of structural engineering*, 122(7), 776-782.
7. Yang, H., Liu, F., Zhang, S., & Lv, X. (2013). Experimental investigation of concrete-filled square hollow section columns subjected to non-uniform exposure. *Engineering structures*, 48, 292-312.
8. Espinos, A., Gardner, L., Romero, M. L., & Hospitaler, A. (2011). Fire behaviour of concrete filled elliptical steel columns. *Thin-walled structures*, 49(2), 239-255.
9. Espinos, A., Romero, M. L., & Lam, D. (2016). Fire performance of innovative steel-concrete composite columns using high strength steels. *Thin-Walled Structures*, 106, 113-128.
10. Gardner, L., Insausti, A., Ng, K. T., & Ashraf, M. (2010). Elevated temperature material properties of stainless steel alloys. *Journal of Constructional Steel Research*, 66(5), 634-647.
11. Kodur, V. R. "Solutions for enhancing the fire endurance of HSS columns filled." *Engineering Journal* 43, no. 1 (2006): 1-7.
12. Liu, W., Cao, W., Zhang, J., Wang, R., & Ren, L. (2017). Mechanical behavior of recycled aggregate concrete-filled steel tubular columns before and after fire. *Materials*, 10(3), 274.
13. Romero, M. L., Espinós, A., Portolés, J. M., Hospitaler, A., & Ibañez, C. (2015). Slender double-tube ultra-high strength concrete-filled tubular columns under ambient temperature and fire. *Engineering Structures*, 99, 536-545.
14. Neuenschwander, M., Knobloch, M., & Fontana, M. (2010). Fire behavior of concrete filled circular hollow section columns with massive steel core. *SDSS'Rio 2010-Stability and Ductility of Steel Structures*, 473-480.
15. Nonn, J., Janiak, T., Jalaeeyan, A., Wolters, K., Feldmann, M., Zehfuß, J., & Claßen, M. (2023). Universelle Hochleistungsstützen aus hochfesten Stählen ohne Schweißen. *Stahlbau*, 92(3), 119-131.
16. Schaumann, P., & Kleibömer, I. (2018). Experimental and numerical investigations of the composite behaviour in concrete-filled tubular columns with massive steel core at high temperatures. *Journal of Structural Fire Engineering*, 9(2), 147-160.
17. Schurgacz, P., & Knobloch, M. (2023). Betongefüllte Hohlprofil-Verbundstützen für Geschossbauten–Innovation und Bemessung. *Stahlbau*, 92(3), 155-172.
18. Ameri, S., Röß, R., Zehfuß, J., & Mensinger, M. (2024). Fire behavior of concrete-filled hollow section columns with high strength bar-bundle as core. *Journal of Fire Technology*.
19. Mensinger, M; Zehfuß, J. (2023) Stabbündelstützen mit hochfester Bewehrung (2023) – Schlussbericht zu IGF-Vorhaben Nr. 20352 N Berichtszeitraum: 01.02.2019-30.04.2022 - Bar bundle columns with high-strength reinforcement bars. Düsseldorf: Forschungsvereinigung Stahlanwendung e.V.
20. Mensinger, M; Zehfuß, J. (2024) Blechlamellenstützen aus hochfesten Stählen für den Hochbau (2024) - Schlussbericht zu IGF-Vorhaben Nr. 21366 N Berichtszeitraum: 01.10.2023 – 30.04.2024, Hybrid Columns Including Laminated High-Strength Plates Infilled in Hollow Sections for high-rised buildings. Düsseldorf: Forschungsvereinigung Stahlanwendung e.V. (will be Published in Jun).

MECHANICAL BEHAVIOUR OF VACUUM-INFUSED GFRP COMPOSITES AT ELEVATED TEMPERATURES – INFLUENCE OF FIBRE ARCHITECTURE

Eloísa Castilho¹, João P. Firmo², Mário Garrido³, João R. Correia⁴, Afonso Ataíde⁵, Marcos Roque⁶

ABSTRACT

This study addresses the influence of the fibre architecture on the mechanical properties of vacuum-infused glass fibre-reinforced polymer (GFRP) materials at elevated temperatures. Vacuum-infused laminates with three different fibre configurations (unidirectional, UD; bidirectional 0°/90° cross-ply, BI-D; and off-axis at ±45°) were subjected to tension and compression tests, under steady-state conditions, at temperatures up to 300 °C. The results were compared with data from previous tests performed on laminates with a multi-axial fibre lay-up. The research confirmed that the GFRP mechanical properties, especially the matrix-dominated ones, are highly temperature-dependent: at 100 °C, compressive strength underwent a major reduction (80%) due to the matrix glass transition, particularly for the UD configuration; conversely, at the same temperature, the reductions of tensile strength and tensile and compressive moduli (all fibre-dominated) were less pronounced, especially in the UD configuration (10%, 20% and 10%, respectively). For the multiaxial fibre architecture, the behaviour varied between that of the UD and BI-D configurations, thus emphasising the influence of the fibre architecture. Contrary to what was expected, the reduction of the tensile modulus was more pronounced than that of the tensile strength. The suitability of empirical and phenomenological analytical models to simulate the experimental results was also assessed. Finally, the experimental data was compared with a design-oriented temperature conversion factor proposed in the future Eurocode for the design of fibre-polymer composite structures: this factor seems to be appropriate and insights were obtained about its field of validity, namely in what concerns the fibre volume fraction in the load direction.

Keywords: vacuum infusion; fibre layup; elevated temperature; mechanical properties; degradation models; conversion factor.

1 INTRODUCTION

Fibre-reinforced polymer (FRP) composites are known for their high strength-to-weight ratio and improved durability when compared to conventional structural materials (*e.g.*, reinforced concrete, steel, timber). Also, their properties may be tailored to meet different types of loading conditions, by using and combining short, randomly oriented (for isotropic behaviour), or continuous and oriented fibres (for anisotropic

¹ PhD student, CERIS, Instituto Superior Técnico, University of Lisbon
e-mail: eloisa.castilho@tecnico.ulisboa.pt, ORCID: <https://orcid.org/0000-0001-5434-3357>

² Assistant Professor, CERIS, Instituto Superior Técnico, University of Lisbon
e-mail: joao.firmo@tecnico.ulisboa.pt, ORCID: <https://orcid.org/0000-0003-3449-3686>

³ Assistant Researcher, CERIS, Instituto Superior Técnico, University of Lisbon
e-mail: mario.garrido@tecnico.ulisboa.pt, ORCID: <https://orcid.org/0000-0003-2323-0776>

⁴ Full Professor, CERIS, Instituto Superior Técnico, University of Lisbon
e-mail: joao.ramoa.correia@tecnico.ulisboa.pt, ORCID: <https://orcid.org/0000-0001-5485-136X>

⁵ MSc, CERIS, Instituto Superior Técnico, University of Lisbon
e-mail: afonso.p.ataide@tecnico.ulisboa.pt

⁶ MSc, CERIS, Instituto Superior Técnico, University of Lisbon
e-mail: marcos.roque@tecnico.ulisboa.pt

properties) [1]. Notwithstanding these distinctive and interesting features, the polymeric nature of FRPs makes them vulnerable to elevated temperature (ET), which induces important reductions in their strength and stiffness properties. When the temperature approaches (and exceeds) the glass transition temperature (T_g) of the resin, its behaviour changes, affecting both the interlayer performance and the load transfer capacity between the fibres. Inevitably, this leads to a reduction in the mechanical properties of the composite. This concern has been addressed in a relatively limited number of studies, mostly focusing on pultruded composites (e.g., [2-4]), with fewer investigation efforts having been made for vacuum-infused composites (e.g., [5]). Such studies showed that the temperature increase has a detrimental effect on FRPs, especially on their matrix-dominated properties: (i) typically, for ET in the range of T_g , there is a slight decrease in tensile strength and in tensile and compressive moduli (for this last property, very little information is available), and (ii) a much more prominent impact on compressive strength [6] and in-plane shear strength and modulus [7]. Research focusing on compressive behaviour [4,5,8,9] has revealed that the compressive modulus is significantly less affected by ET than the compressive strength – such lower sensitivity of the compressive modulus to matrix-softening suggests it to be a more fibre-dominated property than compressive strength (which is clearly matrix-dominated). The tensile modulus and strength were observed to be fibre-dominated properties, with the former usually showing a higher retention capacity at ET than the latter [4,5,10-17]. It was also shown that reductions in fibre-dominated properties are typically lower with increasing fibre ratio along the load direction [18]. Nevertheless, most studies did not consider the influence of the fibre architecture on the degradation of the mechanical properties at ET [17,19,20]. Indeed, from the data collected by Shahabaz *et al.* [21], even though maximum retained strength was reported for laminates with unidirectional fibres (compared to laminates with woven and chopped strand mat fibres), the authors mentioned the lack of research on the effect of fibre orientation on the mechanical performance of FRP at ET. Despite some previous attempts to model this behaviour (e.g., [22]), the effect of (i) different fibre layup/architectures and (ii) the relative orientation between the main fibre directions and the load application (e.g., Zhang *et al.* [23]) on the degradation of mechanical properties at ET remains insufficiently reported and understood.

It is likely that different fibre layups experience distinct reductions of mechanical properties with temperature, especially for fibre-dominated properties; however, this has not yet been sufficiently investigated. In this context, the influence of the fibre architecture on the degradation of the mechanical properties of FRP at ET is considered a matter of considerable interest, especially for vacuum infused composites, for which multiaxial fibre configurations are common, and very little data is available. This paper aims at contributing to bridge these knowledge gaps by presenting experimental and analytical investigations about the mechanical performance of GFRP composites produced by vacuum infusion at ET.

2 MATERIALS AND METHODS

2.1 Material

The GFRP laminates used in the tests were produced by vacuum infusion using a urethane acrylate thermoset resin (*Crestapol* 1261, supplied by *Scott Bader*) and three different fibre layups: (i) unidirectional (UD), (ii) bidirectional $0^\circ/90^\circ$ cross-ply (BI-D) and (iii) off-axis ($\pm 45^\circ$), with respect to the load application direction. UD and BI-D laminates were produced with 14 unidirectional plies of E-glass fibres, each lamina with 529 g/m^2 of aerial weight (472 g/m^2 at 0° , 47 g/m^2 at 90° , and 10 g/m^2 of stitching fibres), respectively stacked with the following sequence: $[0/0/0/0/0/0]_s$ and $[0/90/0/90/0/90/0]_s$. Both laminates presented an estimated thickness of 6.2 mm and a fibre volume fraction of 45 %. The off-axis laminates consisted of 14 biaxial mats, $(\pm 45)_{14}$, with an aerial weight of 400 g/m^2 (200 g/m^2 in each direction), resulting in an estimated thickness of 4.3 mm (with a fibre volume fraction of 45 %). All laminates were cured at room temperature (RT) and their T_g was determined through dynamic mechanical analysis (DMA), as shown in Figure 1 for the neat resin and for the UD-laminates (as an illustrative example of the other laminates). The DMA was conducted according to ASTM E1640, from -30°C up to 150°C (heating rate of $2^\circ\text{C}/\text{min}$) in nitrogen atmosphere, at an oscillatory frequency of 1 Hz and a strain amplitude of 0.3 %, using a *Q800* dynamic mechanical analyser from *TA Instruments*. Based on the onset value of the storage

modulus curve (E') decay, the following T_g values were obtained: 109 °C for the neat resin, and 98 °C, 102 °C and 97 °C, for the UD, BI-D and off-axis lay-ups, respectively. The results of this study were compared with those of laminates with multiaxial layup $[0/0/0/90/\pm 45/\pm 45/0]_s$ and the same constituent materials, previously studied by the authors [5]. All GFRP configurations present an average inorganic content of 66 % (in weight), determined from calcination tests. The fibre volume fraction along the load direction is 45 % for UD laminates, 25 % for BI-D and multiaxial laminates and 0 % for off-axis laminates.

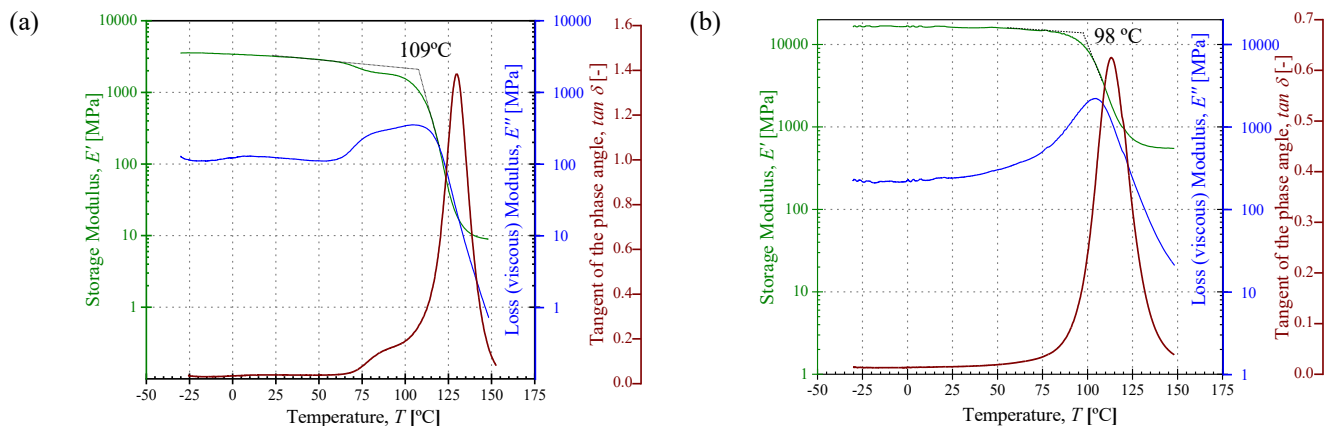


Figure 1. DMA results: (a) neat resin; (b) UD laminate

2.2 Overview of test programme

The tests were performed using a thermal chamber with a maximum operating temperature of 300 °C (from *Tinius Olsen*), coupled to a universal testing machine (*Instron 8800D*, with load capacity of 250 kN, or *Instron 5582D*, with a load capacity of 100 kN), as shown in Figure 2 and Figure 3. Tensile and compressive tests were performed in steady-state conditions, *i.e.*, the specimens were first heated up to the target temperatures and then the load was applied (while keeping a constant temperature). Temperatures were monitored using two type K thermocouples (0.25 mm of conductor diameter): one measuring the air temperature inside the thermal chamber, and another inserted in the centre of a dummy specimen (with the same cross-section as the tested specimen).

2.3 Tensile tests

The tensile properties of the GFRP laminates were determined according to the recommendations of ASTM D3039/D3039M standard, using specimens with $25 \times 1000 \times t$ mm³ (where t is the thickness, according to the laminate type), *cf.* Figure 2 (a). The specimen length was defined to allow “cold-grip” testing, thus preventing GFRP premature failures in the grips. The specimens were heated to the target temperature (20 °C - RT, 75 °C, 100 °C, 150 °C, 200 °C and 300 °C), and then a tensile load was applied up to failure, under displacement control, at a speed of 2 mm/min. The tensile strains were measured using a video extensometer (VE, *Sony* video camera, model XCG 5005E, with a *Fujinon* lens, model Fujifilm HF50SA-1), which monitored the position of 110 mm distanced target dots, along three longitudinal alignments. The average strain of these alignments was considered the reference value. The tensile modulus was calculated from the slope of the curves between strains of 1.0 ‰ and 3.0 ‰. To validate the strain measurements obtained with the VE, additional tests were performed on shorter specimens ($25 \times 210 \times t$ mm³) using a clip-on extensometer (*Epsilon*, Model 7642, gauge length of 50 mm) – Figure 2 (b). At least 3 replicate specimens were tested for each target temperature.

2.4 Compressive tests

For all types of laminates, the longitudinal compressive strength was determined according to the ASTM D6641/D6641 standard, using a combined loading compression (CLC) fixture (*cf.* Fig. 3a), at the following temperatures: 20 °C, 50 °C, 75 °C, 100 °C, 150 °C, 200 °C and 250 °C. The compressive strength was determined in specimens with rectangular cross section (25 mm \times t mm) with 140 mm of length. For all laminates except the off-axis ones, the compressive modulus was determined using slightly longer

specimens (210 mm long) – this extended length was needed to install a clip-on extensometer for measuring the axial strains. It is worth referring that, to prevent any possible buckling phenomenon on these longer (slenderer) specimens, the tests were performed only up to 50 % of the corresponding maximum load in compression. For off-axis laminates, due to their higher slenderness, a distinct procedure was implemented to prevent buckling: the compressive load was applied using wedge grips and slightly shorter specimens were used – 195 mm long, with a free length of 65 mm. Figure 3 illustrates the different setups adopted in these tests. The load was applied under displacement control, at a rate of 1.3 mm/min. The compressive modulus was estimated from the slope of the compressive stress vs. strain curves, between 25 % and 50 % of the maximum compressive stress. For each type of test, at least three specimens were tested.



(a)



(b)

Figure 2. Tensile tests – environmental chamber and universal testing machine (*Instron 8800D*):
(a) elastic properties, $L_{sp}=1$ m; (c) validation, $L_{sp}=0.21$ m



(a)



(b)

Figure 3. Compressive tests – Environmental chamber and universal testing machine (*Instron 5582D*):
(a) CLC fixture, $L_{sp}=140$ mm/210 mm;
(b) tensile wedge grips, $L_{sp}=195$ mm

3 EXPERIMENTAL RESULTS AND DISCUSSION

3.1 Tensile properties

Figure 4 shows the average values (and respective standard deviation) of the tensile properties as a function of temperature, including the previous results of the multi-axial laminates [5], as well as the storage modulus curves of the GFRP laminates and neat resin specimens. The absolute values are depicted in Figure 4 (a) and (c), whereas the normalised properties (*w.r.t.* to the corresponding values at RT) are shown in Figure 4 (b) and (d). The results show an overall reduction of both elastic modulus and tensile strength with increasing temperature, especially when temperature exceeds the T_g . The strength degradation is attributed to the softening of the matrix at temperatures around T_g . The consequent loss of integrity of the matrix and the degradation of the fibre-matrix interface compromises the load transfer capacity between fibres, leading to the observed steeper property degradation above T_g . In any case, it is noticeable the non-negligible residual strength (66 % for UD) at the maximum tested temperature (300 °C).

Regarding the influence of the fibre lay-up on the tensile properties, for the UD configuration, both tensile modulus and strength suffer a slight reduction up to T_g (retentions of respectively 80 % and 90 %), after which they present an almost linear reduction up to 200 °C (retentions of respectively ≈ 55 % and 70 %). Then, for higher temperatures, the tensile modulus continues to decrease up to 300 °C (retaining only ≈ 25 % of the RT value), whereas the tensile strength stabilizes (at 300 °C it presents a retention of ≈ 65 % of the RT value), meaning that for temperatures above 200 °C the tensile strength almost fully relies on the behaviour of the fibres, which, at this temperature range, are not significantly damaged. It is worth noting that the higher reduction of the tensile modulus compared to the tensile strength (*cf.* Figure 5) was not expected, since in UD laminates the stiffness is mostly dependent on the fibres' modulus, which, as mentioned, is not significantly affected for this temperature range. At this point, no clear reason could be identified for this higher degradation of the tensile modulus. The BI-D configuration showed almost constant tensile strength up to

100 °C (retention of $\approx 95\%$ of the RT value), after which it suffered a high degradation until 150 °C (retention of $\approx 70\%$), due to the glass transition process, and then stabilised. The tensile modulus, once again, showed higher reduction with temperature than the tensile strength. The results of the off-axis laminates highlight that the lack of fibre continuity along the load direction substantially reduces the effectiveness of the fibre reinforcement – for this laminate, the observed degradation is typical of a strongly matrix-dominated property. The multiaxial configuration exhibits absolute values of tensile properties that range between those of the UD and BI-D configurations. In the multiaxial laminates, the tensile strength degradation trend is generally similar to that of the BI-D, which is logical, as they both have the same fibre volume fraction along the load direction; however, the former presents lower tensile modulus reductions with temperature, which may be due to some stiffening provided by the $\pm 45^\circ$ plies, at least for lower load levels.

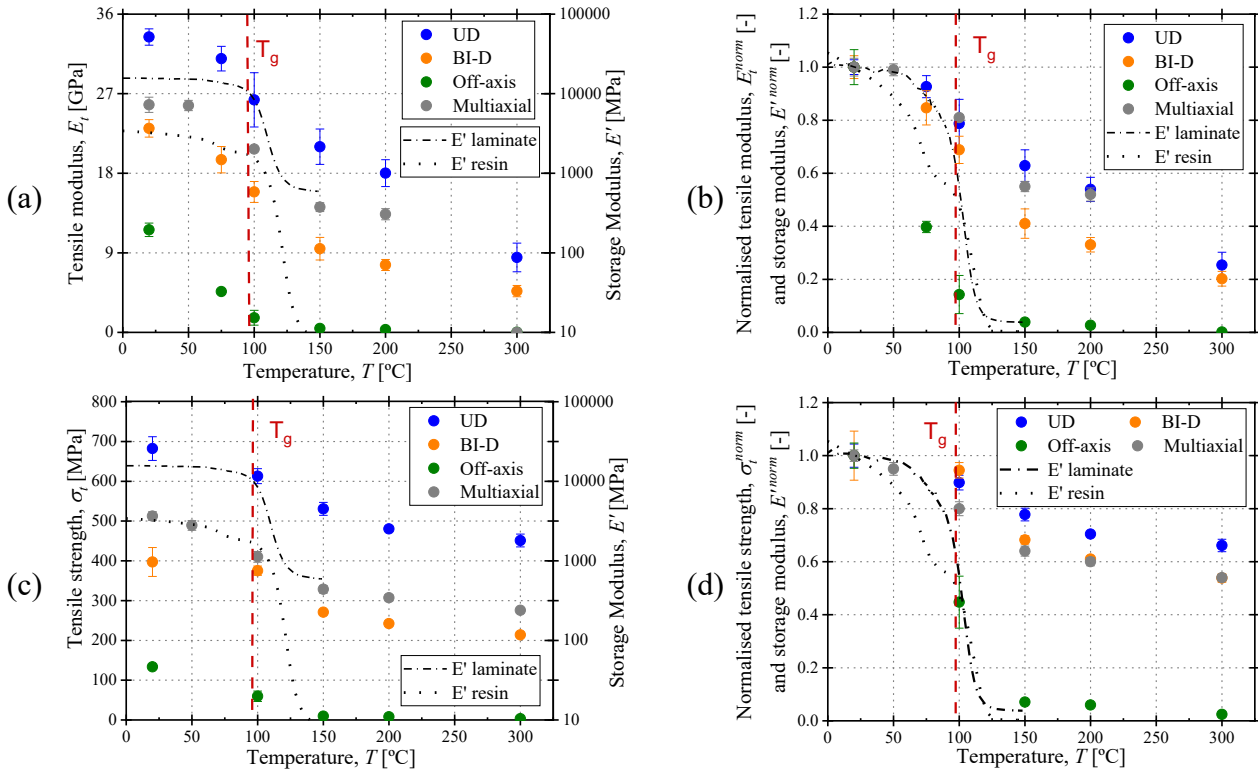


Figure 4. Tensile properties (average value and standard deviation) and storage modulus curves obtained from DMA vs. temperature: (a) modulus; (b) normalised modulus (c) strength; (d) normalised strength

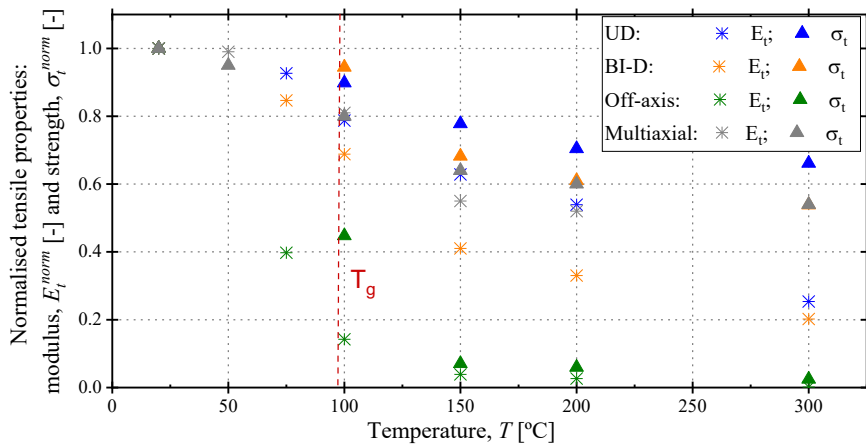


Figure 5. Tensile properties (modulus vs. strength) vs. temperature

The experimental results presented above confirm the obvious fibre dependence of tensile properties. As so, the fibre lay-up holds substantial importance: a lower quantity of fibres aligned with the load direction leads to greater matrix-dependence, therefore the mechanical properties are more prone to temperature degradation. Thus, the UD configuration is the upper bound of both tensile strength and modulus retention,

while the BI-D configuration (characterised by a higher matrix contribution) experiences a more pronounced and intermediate degradation. The off-axis configuration displays the lowest tensile properties retention, indicating that, when fibres are not continuous between the loaded extremities of the laminates, the mechanical behaviour at ET is essentially matrix-dominated.

3.2 Compressive properties

Figure 6 shows the average values (and the respective standard deviation) of the compressive properties evolution with temperature, together with the results of the multiaxial laminates and of the DMA tests. Absolute values are depicted in Figure 6 (a) and (c), while normalised values are shown in Figure 6 (b) and (d).

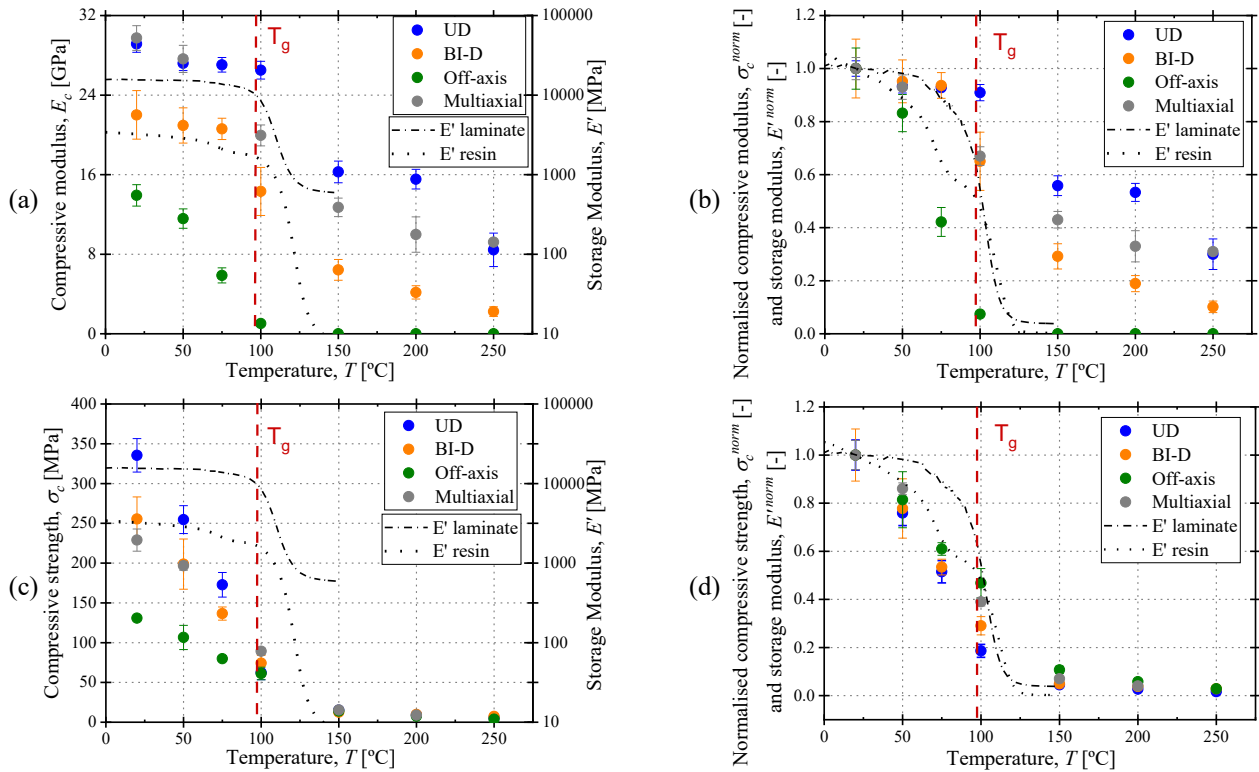


Figure 6. Compressive properties (average value and standard deviation) and storage modulus curves obtained from DMA vs. temperature: (a) modulus; (b) normalised modulus (c) strength; (d) normalised strength

Considering the observed degradation of the compressive modulus with temperature (Figure 6 (a) and (b)), it is clear that this property is also highly influenced by the fibre architecture: a more substantial degradation occurs for lower fibre volume fraction along the load direction (e.g., at 200 °C, reductions of the compressive modulus of $\approx 40\%$ and 80% were obtained for the UD and BI-D laminates, respectively). Once again, for the off-axis lay-up (where the fibres lack continuity between the loaded ends of the specimens), the effectiveness of the reinforcement was very low. On the other hand, the degradation with temperature of the compressive strength (Figure 6 (c) and (d)) was found to be more dependent on the resin integrity than on the fibre architecture, as it followed closely the storage modulus curve of the resin obtained from DMA (cf. Figure 6(d)) – these results highlight the substantial influence of temperature on matrix-dominated properties, such as the compressive strength. Due to the glass transition process of the matrix, the reduction of the compressive strength was particularly pronounced until 100 °C, especially for the UD configuration (20% retention) – note that at RT the compressive strength of this laminate configuration includes a major contribution from the fibres, which is lost when the confinement provided by the surrounding resin matrix is (remarkably) reduced. The overall influence of the fibre layup on the compressive strength reduction with temperature was not significant, with the largest differences being obtained at T_g , for which a higher experimental scatter is usually expected (since the reduction of mechanical properties for this temperature range is steeper, thus more affected by experimental uncertainties).

4 ANALYTICAL STUDY

4.1 Degradation models

The accuracy of various analytical models proposed in the literature to simulate the reduction with temperature of the tensile and compression properties was assessed. The results of the off-axis fibre architecture were not considered in this assessment, as it was not considered representative of a real laminate's behaviour due to the above-mentioned lack of fibre continuity.

4.1.1 Empirical degradation models

Several empirical models, based on curve fitting procedures, have been proposed to describe the temperature degradation of the mechanical properties of FRP materials, namely those developed by Bisby [24], Gibson *et al.* [22], Correia *et al.* [4], Wang *et al.* [25] and Mahieux *et al.* [17]. The corresponding fitting (for the normalised properties) is illustrated in Figure 7. All the mentioned models fitted reasonably well the experimental data from this campaign. The best fitting for the fibre-dominated properties was achieved with Correia's model, while Bisby's model provided the best adjustment for the matrix-dominated ones.

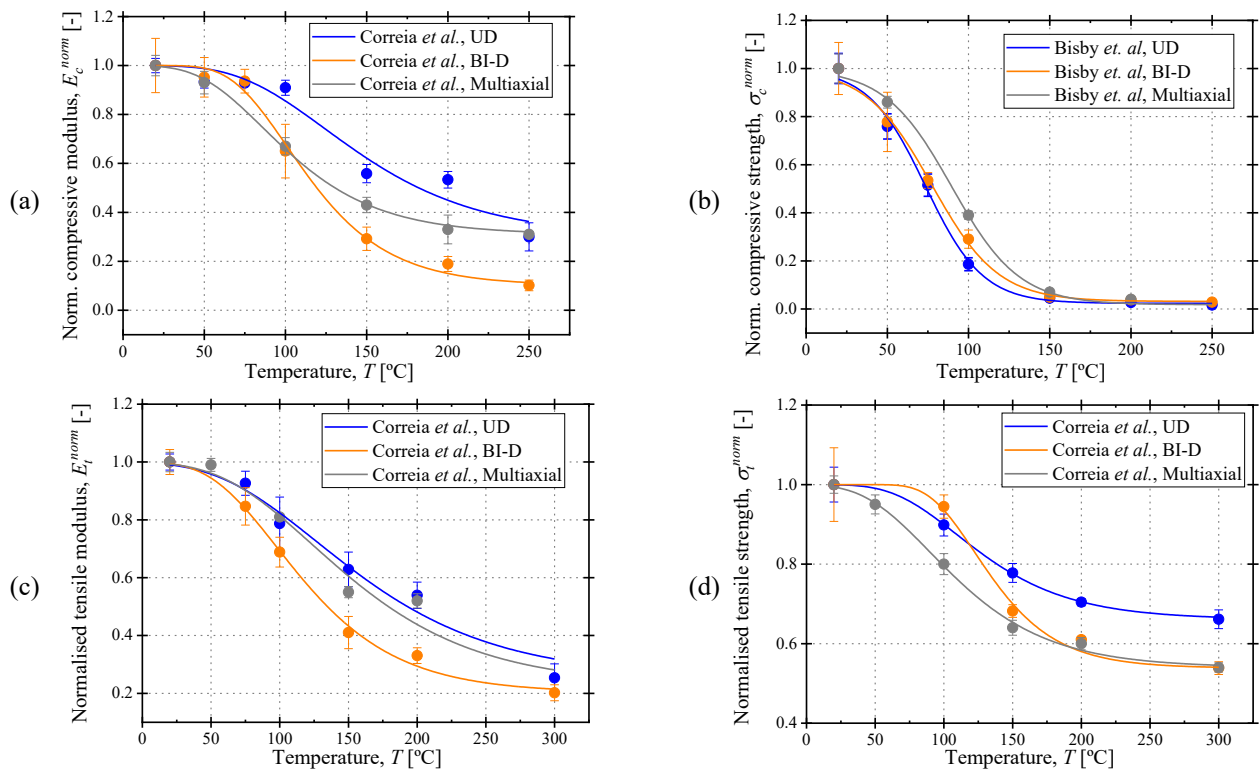


Figure 7. Best fit empirical models for normalised: (a) compressive modulus; (b) compressive strength; (c) tensile modulus; and (d) tensile strength

4.1.2 Phenomenological models

The phenomenological model proposed by Bai and Keller ([19,20]) considers that changes in the mechanical properties of FRP composites result from physical alterations in the polymer, which can be modelled assuming that the composite undergoes gradual changes in its state as a function of temperature (from solid to decomposed). The model is implemented by defining factors accounting for the conversion degrees associated with each state, estimated from kinetic theory. Results from DMA and TGA (thermogravimetric analysis) can be used to determine the conversion degrees, from 0 to 1, of glass transition (α_g) and decomposition (α_d), respectively, which are used to weigh the material properties (strength or modulus) in the glassy (P_g), leathery (P_l), rubbery (P_r), and decomposed (P_d) states, to obtain estimates of the material properties as a function of temperature. Bai and Keller's model for stiffness ([19]) follows the rule of mixtures (RM). As the moduli at the leathery and rubbery states are similar, the model may be simplified as follows:

$$P(T) = P_g \times [1 - \alpha_g(T)] + P_r \times \alpha_g(T) \times [1 - \alpha_d(T)] + P_d \times \alpha_g(T) \times \alpha_d(T) \quad (1)$$

The model was then extended to describe upper (rule of mixture) and lower (inverse rule of mixture, IRM) bounds of the strength degradation [20]. The lower bound of strength is therefore determined as:

$$\frac{1}{P(T)} = \frac{[1 - \alpha_g(T)]}{P_g} + \frac{\alpha_g(T) \times [1 - \alpha_d(T)]}{P_r} + \frac{\alpha_g(T) \times \alpha_d(T)}{P_d} \quad (2)$$

It is worth mentioning that, even though this model does not explicitly take into account the fibre layup, its influence is implicitly reflected by the mechanical properties determined experimentally for the above-mentioned degradation states. The agreement with experimental data is represented in Figure 8.

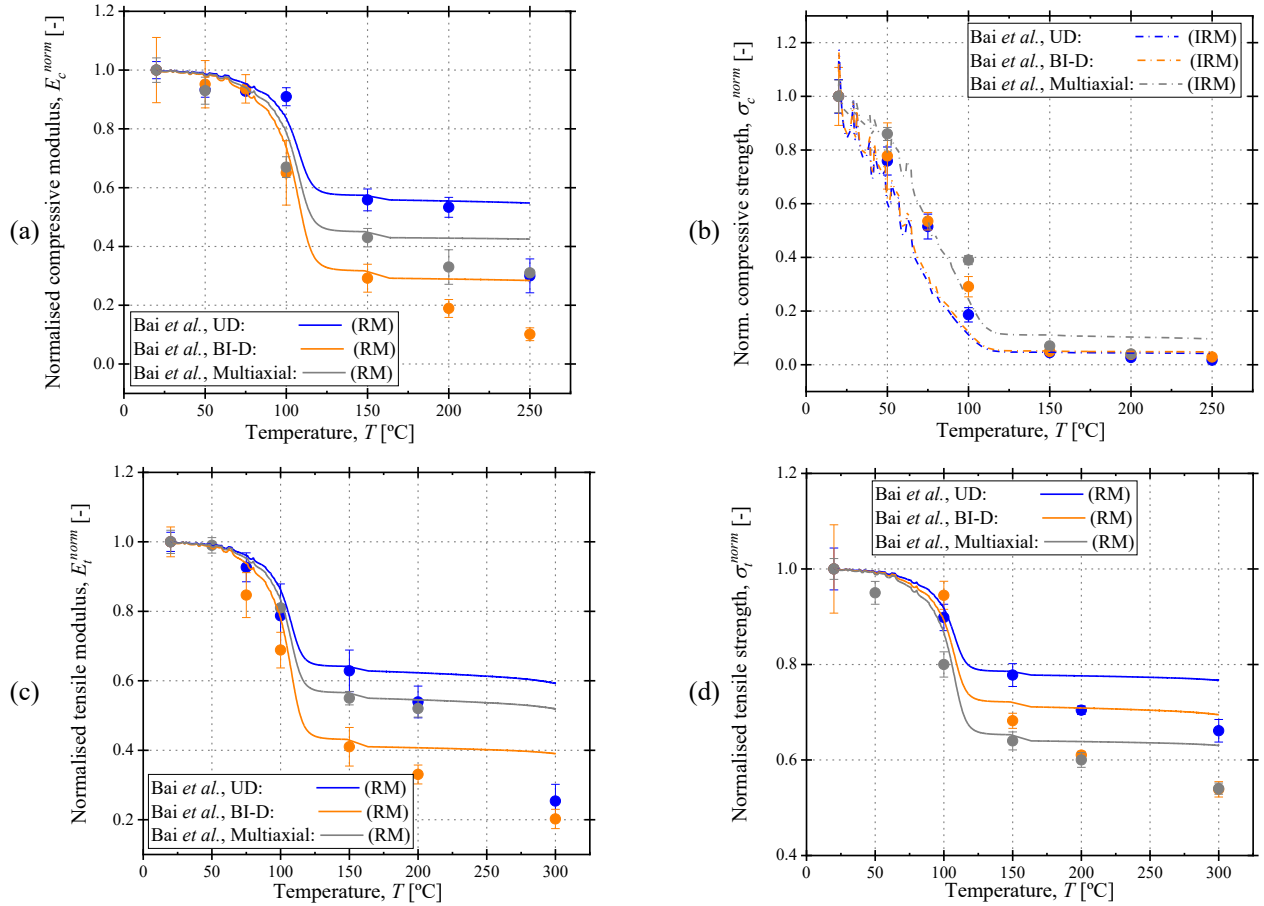


Figure 8. Phenomenological models for normalised: (a) compressive modulus; (b) compressive strength; (c) tensile modulus; and (d) tensile strength

As expected, the predictions based on the rule of mixtures provided a good fit to fibre-dependent properties, namely for the compressive and tensile moduli (Figure 8 (a) and (c)) and tensile strength (see Figure 8 (d)). The inverse rule of mixtures (*i.e.*, the lower bound) provided better fitting for the experimental values of compressive strength (see Figure 8 (b)), which indicates that it is more suitable to simulate the degradation with temperature of matrix-dominated properties; Bai and Keller [20] reported similar results for compressive strength, as well as Rosa [2], for in-plane shear strength (also matrix-dominated).

4.2 Assessment of a design-oriented temperature conversion factor

The experimental results reported above show that the fibre layup, namely the fibre content along the load direction, has significant influence on the temperature degradation of the mechanical properties. Consequently, it is a matter of interest to evaluate the temperature conversion factor defined in the recently developed European Technical Specification (TS) CEN/TS 19101:2022 “Design of Fibre-Polymer Composite Structures” for different fibre volume fraction values. The design-oriented temperature conversion factor is defined as follows [26]:

$$\eta_{ct} = \min \{1.0 - \alpha \cdot T_n; 1.0\} \quad (3)$$

where α is a parameter that depends on the sensitivity of a given material property to matrix softening, and T_n is the normalized temperature (ranging between 0 and 1), defined by $(T - 20)/(T_g - 20)$, where T represents the material temperature. It is worth highlighting that η_{ct} is only valid for temperatures up to $T_g - 20$ °C, therefore, it is not applicable for fire design, for which much higher temperatures are attained. The TS only distinguishes between fibre- and matrix-dominated properties, namely by adopting different values of α . A value of $\alpha = 0.25$ is proposed for fibre-dominated properties in directions with “high ratio of fibre reinforcement”; otherwise $\alpha = 0.80$ should be used. However, what can be considered as a “high ratio” is not explicitly defined. Therefore, there is a need to evaluate the minimum fibre fraction (in the load direction of the laminate) for which the conversion factor can be conservatively applied. To this end, the TS conversion factor for both fibre- and matrix-dominated properties was compared with the reductions obtained in the experimental campaign, as well as with data from the literature for various types of FRPs, with different types of fibres, fibre layouts and fibre volume fractions along the load direction.

4.2.1 Effect of temperature

Figure 9 compares the normalised experimental values obtained in the present study, for different types of laminates, with the conversion factor proposed in the TS (Equation 3) considering: $\alpha=0.25$ for compressive modulus (Figure 9 (a)), tensile modulus (Figure 9 (c)), and tensile strength (Figure 9 (d)); and $\alpha=0.80$ for compressive strength (Figure 9 (b)).

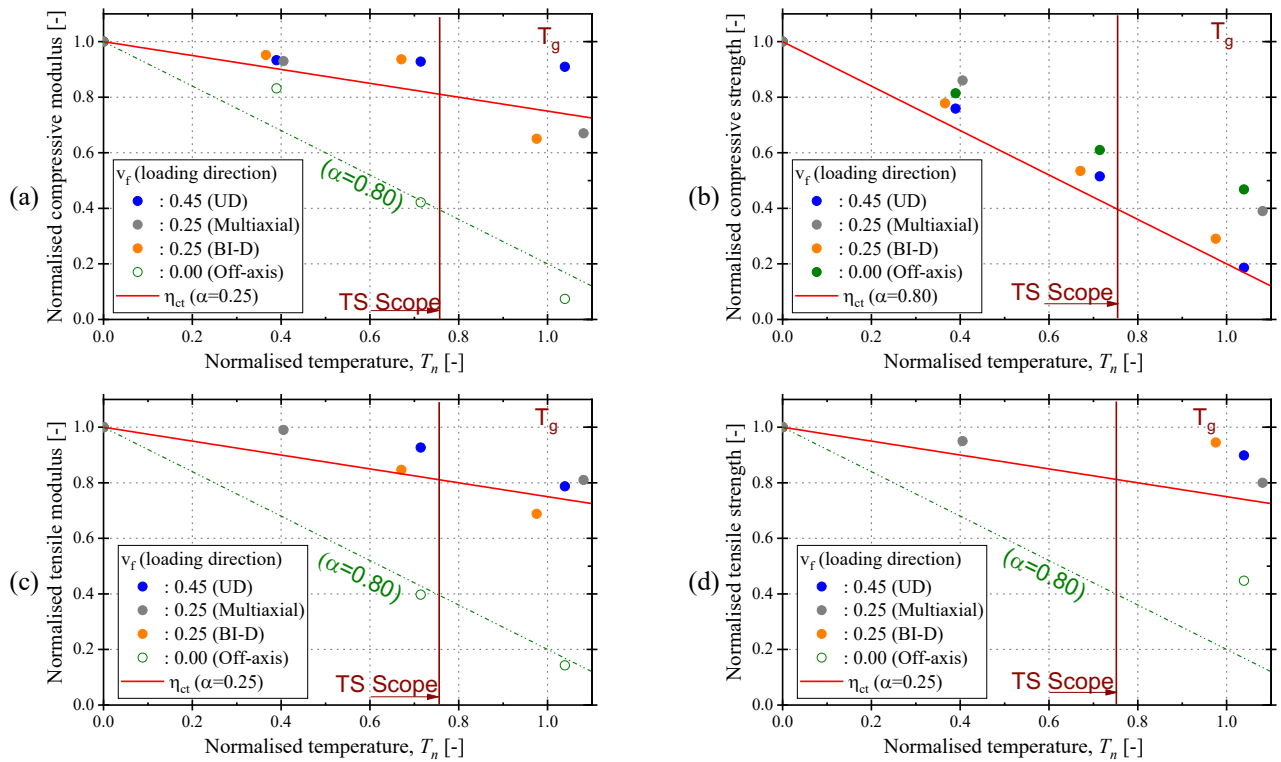


Figure 9. Experimental results vs. design-oriented conversion factor, η_{ct} , proposed in the CEN/TS 19101:2022 (scope for tested laminates marked with vertical line): (a) compressive modulus; (b) compressive strength; (c) tensile modulus; (d) tensile strength

The tested configurations are identified through their fibre volume fraction along the load direction (v_f). The off-axis architecture was analysed considering $v_f=0$, since the tested laminates had no fibre continuity between the loaded sections, as mentioned previously. Figure 9 (a) and (c) show that: up to $T_n = 0.76$ (the maximum scope of CEN/TS 19101:2022 for the laminates tested, considering $T_g = 102$ °C), for the compressive and tensile moduli, the conversion factor is always conservative, except in cases where there are no fibres in the load direction (off-axis layout, where in fact $\alpha = 0.25$ is not applicable, and $\alpha = 0.80$ should be considered instead); for the compressive strength, which is a matrix-dominated property, the conversion factor is consistently conservative, regardless of the fibre volume fraction – the same conclusion

applies to the tensile strength, *cf.* Figure 9 (d). For $T_n > 0.76$ (where η_{ct} is not applicable), predictions are still conservative for most cases and for data that is underestimated relative differences vary between 9 %-16 %. In summary, it can be concluded that the conversion factor proposed in CEN/TS 19101:2022 provides conservative estimates for the laminates and fibre layouts studied here.

4.2.2 Effect of fibre volume fraction along load direction

This section analyses the effect of the fibre volume fraction, along the load direction, on the reduction of the mechanical properties at ET with respect to the temperature conversion factor provided in CEN/TS 19101:2022. The main goal is to assess whether such factor should be defined based not only on T_g , but also on v_f . For this purpose, for all laminates tested in our study and using data reported in the literature ([4], [6], [13], [23], [27]–[33]), the ratio between experimental properties and the applicable conversion factor was determined (R). For the off-axis laminate tested in our study ($\pm 45^\circ$) and those tested in Zhang's [23] work ($30^\circ / 60^\circ$ and 90°), $v_f = 0$ was considered.

Figure 10 shows the results of this analysis, for compressive properties (v_f ranging from 0 and 0.52) and tensile properties (v_f ranging from 0.25 and 0.76), which prompt the following comments (applicable for the v_f ranges considered): (i) for the vast majority of cases where CEN/TS 19101:2022 applies, $R > 1$, *i.e.* conservative predictions are obtained for both fibre- and matrix-dominated mechanical properties; (ii) this is particularly the case of compressive strength, in which the R values present very high scatter (possible reasons for this scatter are provided in [26]) and quite high values (above 3); (iii) for all properties considered, it was not possible to identify a clear trend of variation of R with v_f . It is worth noting that the data available is relatively limited, especially for compressive modulus. Therefore, the findings above should be confirmed and possibly extended to lower values of v_f when additional experimental results are available.

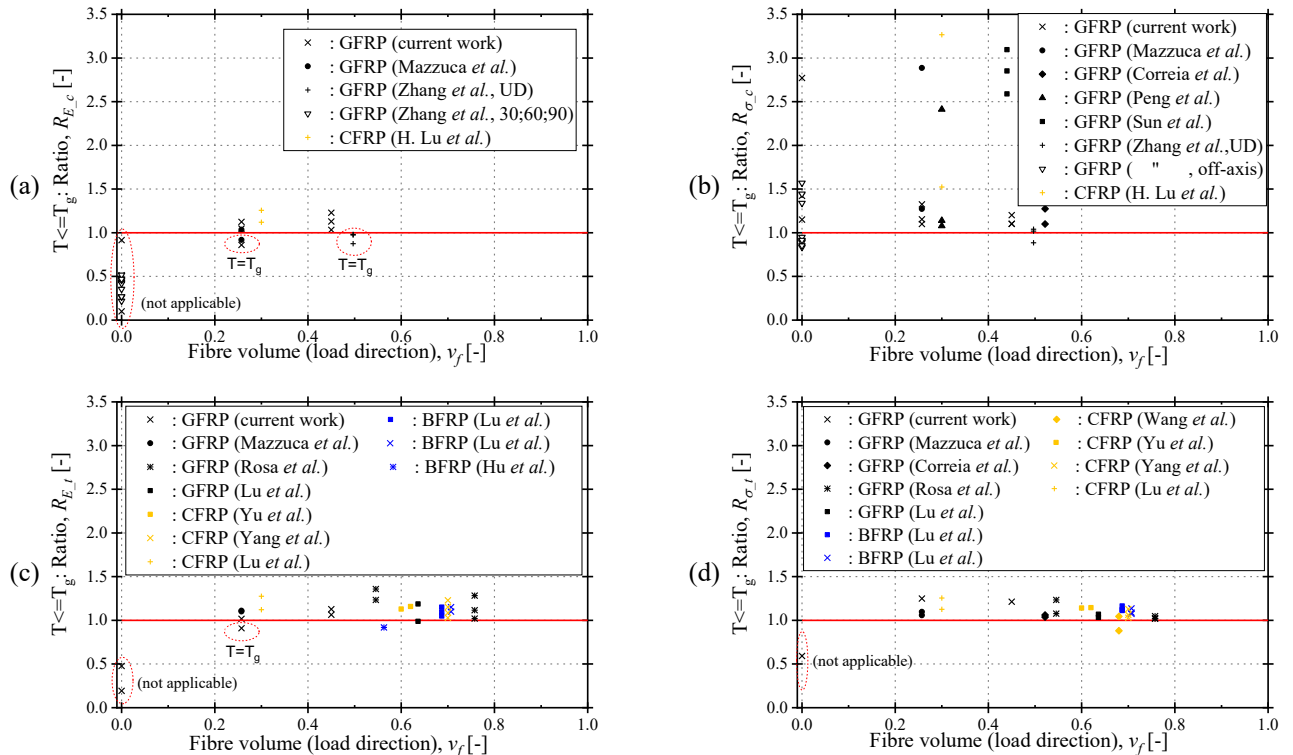


Figure 10. Ratios between the TS conversion factor and experimental values for different fibre volumes aligned with the load direction: (a) compressive modulus; (b) compressive strength; (c) tensile modulus; (d) tensile strength

5 CONCLUSIONS

The experimental results obtained in the present study confirmed that the mechanical properties of vacuum-infused GFRP laminates are highly affected by elevated temperature, especially those dominated by the matrix, namely the compressive strength – pronounced reductions occurred in the temperature range of

60 °C to 100 °C, due to the glass transition of the resin, with such reductions resembling the behaviour of the storage modulus curve of the resin obtained from DMA. The overall influence of the fibre layout on the temperature dependency of matrix-dominated properties was not significant. Conversely, the influence of the fibre layout was evident in the degradation of fibre-dominated properties (tensile strength and longitudinal tensile and compressive modulus). The reductions in fibre-dominated properties were generally less pronounced than for matrix-dominated properties, except for the off-axis configuration, for which the inevitably discontinuous and thus poorly anchored $\pm 45^\circ$ fibres did not constitute an effective reinforcement. This better performance of fibre-dominated properties was expected, since the mechanical properties of the glass reinforcement should not be significantly affected for the range of studied temperatures. In this context, the unidirectional configuration displayed the highest moduli and tensile strength retentions. Furthermore, it was observed that decreasing the fibre volume in the load direction led to higher reductions in fibre-dominated properties, especially for the highest studied temperatures. This is reflected in the property degradation for the multiaxial architecture (with intermediate fibre volume fraction along the load direction), which was also intermediate to that observed for the unidirectional and bi-directional configurations.

With respect to the temperature conversion factor defined in CEN/TS 19101:2022, it was confirmed that it generally provides conservative predictions of both matrix- and fibre-dominated properties, namely for $v_f > 0.25$. It was not possible to identify a clear trend of variation of the ratio between test data and the conversion factor with v_f . When more test data is available, including for a lower range of v_f ($v_f < 0.25$), it will be possible to further assess the temperature conversion factor provided in CEN/TS 19101:2022.

ACKNOWLEDGMENT

This work is part of the research activity carried out at *Civil Engineering Research and Innovation for Sustainability* (CERIS) and was funded by CERIS (project UIDB/04625/2020, DOI: 10.54499/UIDB/04625/2020), *Fundação para a Ciência e a Tecnologia* (FCT) in the framework of project PTDC/ECI-EGC/30611/2017(1801P.00776) *FireFloor – Fire Behaviour of GFRP Composite Panels for Rehabilitation of Building Floors*, the first author's PhD grant SFRH/BD/146632/2019, and PRR project R2UTechnologies (02-C05-i01.01-2022.PC644876810-00000019).

REFERENCES

- [1] D. R. Askeland and P. P. Fulay, *The science and engineering of materials*. Global Engineering, 2010.
- [2] I. C. Rosa, T. Morgado, J. R. Correia, J. P. Firmo, and N. Silvestre, "Shear behavior of GFRP composite materials at elevated temperature," *J. Compos. Constr.*, vol. 22, no. 3, p. 04018010, 2018.
- [3] K. Wang, B. Young, and S. T. Smith, "Mechanical properties of pultruded carbon fibre-reinforced polymer (CFRP) plates at elevated temperatures," *Eng. Struct.*, vol. 33, no. 7, pp. 2154–2161, 2011.
- [4] J. R. Correia, M. M. Gomes, J. M. Pires, and F. A. Branco, "Mechanical behaviour of pultruded glass fibre reinforced polymer composites at elevated temperature: Experiments and model assessment," *Compos. Struct.*, vol. 98, pp. 303–313, 2013.
- [5] P. Mazzuca, J. P. Firmo, J. R. Correia, and E. Castilho, "Influence of elevated temperatures on the mechanical properties of glass fibre reinforced polymer laminates produced by vacuum infusion," *Constr. Build. Mater.*, vol. 345, no. July, pp. 1–15, 2022.
- [6] H. Lu *et al.*, "Investigation on the mechanical properties and damage mechanisms of plain-woven composites at elevated temperatures through a newly-designed testing system," *Thin-Walled Struct.*, p. 111587, 2024.
- [7] J. R. Correia, Y. Bai, and T. Keller, "A review of the fire behaviour of pultruded GFRP structural profiles for civil engineering applications," *Compos. Struct.*, vol. 127, pp. 267–287, 2015.
- [8] P. M. H. Wong, J. M. Davies, and Y. C. Wang, "An experimental and numerical study of the behaviour of glass fibre reinforced plastics (GRP) short columns at elevated temperatures," *Compos. Struct.*, vol. 63, no. 1, pp. 33–43, 2004.
- [9] I. C. Rosa, "Mechanical Behaviour of FRP Composite Materials at Elevated Temperature," no. MSc dissertation in Civil Engineering, 2016.

- [10] L. P. Nguyen and H. Chi, "Experimental And Numerical Study On Thermo-Mechanical Behaviour Of Carbon Fibre Reinforced Polymer And Structures Reinforced With CFRP," vol. 36, no. 1, pp. 472–482, 2018.
- [11] M. Robert, P. Cousin, and B. Benmokrane, "Behaviour of GFRP reinforcing bars subjected to extreme temperatures," *Proceedings, Annu. Conf. - Can. Soc. Civ. Eng.*, vol. 3, no. August 2010, pp. 1587–1596, 2009.
- [12] A. Jafari, M. Bazli, H. Ashrafi, A. Vatani, S. Azhari, and X. Zhao, "Effect of fibers configuration and thickness on tensile behavior of GFRP laminates subjected to elevated temperatures," *Constr. Build. Mater.*, vol. 202, pp. 189–207, 2019.
- [13] I. C. Rosa, J. P. Firmo, and J. R. Correia, "Experimental study of the tensile behaviour of GFRP reinforcing bars at elevated temperatures," *Constr. Build. Mater.*, vol. 324, no. January, 2022.
- [14] E. U. Chowdhury, R. Eedson, L. A. Bisby, M. F. Green, and N. Benichou, "Mechanical Characterization of Fibre Reinforced Polymers Materials at High Temperature," *Fire Technol.*, vol. 47, no. 4, pp. 1063–1080, 2011.
- [15] M. Bazli and M. Abolfazli, "Mechanical properties of fibre reinforced polymers under elevated temperatures: An overview," *Polymers (Basel)*, vol. 12, no. 11, pp. 1–31, 2020.
- [16] M. Rezaei, V. Karatzas, C. Berggreen, and L. A. Carlsson, "The effect of elevated temperature on the mechanical properties and failure modes of GFRP face sheets and PET foam cored sandwich beams," *J. Sandw. Struct. Mater.*, vol. 22, no. 4, pp. 1235–1255, 2018.
- [17] C. A. Mahieux, K. L. Reifsnider, and S. W. Case, "Property modeling across transition temperatures in PMC's: Part I. Tensile properties," *Appl. Compos. Mater.*, vol. 8, no. 4, pp. 217–234, 2001.
- [18] H. Ashrafi, M. Bazli, A. Jafari, and T. Ozbakkaloglu, "Tensile properties of GFRP laminates after exposure to elevated temperatures: Effect of fiber configuration, sample thickness, and time of exposure," *Compos. Struct.*, vol. 238, no. November 2019, 2020.
- [19] Y. Bai, T. Keller, and T. Vallée, "Modeling of stiffness of FRP composites under elevated and high temperatures," *Compos. Sci. Technol.*, vol. 68, pp. 3099–3106, 2008.
- [20] Y. Bai and T. Keller, "Modeling of strength degradation for Fiber-reinforced polymer composites in fire," *J. Compos. Mater.*, vol. 43, no. 21, pp. 2371–2385, 2009.
- [21] S. M. Shahabaz, S. Sharma, N. Shetty, S. D. Shetty, and M. C. Gowrishankar, "Influence of Temperature on Mechanical Properties and Machining of Fibre Reinforced Polymer Composites: A Review," *Eng. Sci.*, vol. 16, pp. 26–46, 2021.
- [22] A. G. Gibson, Y. S. Wu, J. T. Evans, and A. P. Mouritz, "Laminate theory analysis of composites under load in fire," *J. Compos. Mater.*, vol. 40, no. 7, pp. 639–658, 2006.
- [23] L. Zhang, W. Liu, L. Wang, and Z. Ling, "On-axis and off-axis compressive behavior of pultruded GFRP composites at elevated temperatures," *Compos. Struct.*, vol. 236, no. January, p. 111891, 2020.
- [24] L. A. Bisby, "Fire behaviour of fibre-reinforced polymer (FRP) reinforced or confined concrete," p. 371, 2005.
- [25] S. T. S. Ke Wang, Ben Young, "Mechanical properties of pultruded carbon fibre-reinforced polymer (CFRP) plates at elevated temperatures," *Eng. Struct.*, vol. 33, no. 7, pp. 2154–2161, 2011.
- [26] J. R. Correia *et al.*, "Mechanical properties of FRP materials at elevated temperature – Definition of a temperature conversion factor for design in service conditions," *Constr. Build. Mater.*, vol. 367, no. January 2022, 2023.
- [27] K. Wang, B. Young, and S. T. Smith, "Mechanical properties of pultruded carbon fibre-reinforced polymer (CFRP) plates at elevated temperatures," *Eng. Struct.*, vol. 33, no. 7, pp. 2154–2161, 2011.
- [28] P. Feng, J. Wang, Y. Tian, D. Loughery, and Y. Wang, "Mechanical Behavior and Design of FRP Structural Members at High and Low Service Temperatures," *J. Compos. Constr.*, vol. 20, no. 5, 2016.
- [29] W. Sun, A. P. Vassilopoulos, and T. Keller, "Effect of temperature on kinking failure mode of non-slender glass fiber-reinforced polymer specimens," *Compos. Struct.*, vol. 133, pp. 178–190, 2015.
- [30] Z. Lu, G. Xian, and H. Li, "Effects of elevated temperatures on the mechanical properties of basalt fibers and BFRP plates," *Constr. Build. Mater.*, vol. 127, pp. 1029–1036, 2016.
- [31] Y. J. Hu, C. Jiang, W. Liu, Q. Q. Yu, and Y. L. Zhou, "Degradation of the in-plane shear modulus of structural BFRP laminates due to high temperature," *Sensors (Switzerland)*, vol. 18, no. 10, 2018.
- [32] B. Yu and V. Kodur, "Effect of temperature on strength and stiffness properties of near-surface mounted FRP reinforcement," *Compos. Part B Eng.*, vol. 58, pp. 510–517, 2014.
- [33] Y. Yang, Y. Jiang, H. Liang, X. Yin, and Y. Huang, "Study on tensile properties of CFRP plates under elevated temperature exposure," *Materials (Basel)*, vol. 12, no. 12, pp. 1–10, 2019.

NUMERICAL INVESTIGATION ON DIFFERENT FIRE PROTECTION SYSTEMS FOR STEEL-CONCRETE COMPOSITE BEAMS WITH DEMOUNTABLE SHEAR CONNECTORS

Vicente Albero¹, Ana Espinós², Andrés Lapuebla-Ferri³, Manuel Luis Romero⁴

ABSTRACT

The use of steel-concrete composite floor systems in construction has experienced a growing demand in recent years. In the particular case of composite downstand beams, welded studs have been predominantly used for connecting the steel beam to the concrete slab. In line with the current shift to a circular business model, demountable bolted connectors are being introduced into the market for enhancing the reusability of the composite floor systems. Even though the mechanical performance of composite beams with demountable shear connectors has been well established, the available knowledge on their fire performance is still scarce, hindering their practical application. In the event of a fire, the downstand steel beam would result directly exposed to the heat source from three sides, thus heating up fast and experiencing a rapid loss in terms of mechanical capacity. Therefore, it is needed to protect the steel beam with passive fire protection means. Traditional solutions such as intumescent paints, cementitious mortars or plaster boards have been commonly used for protecting the steel elements in case of fire. However, these fire protection materials do not fulfil the sustainability criteria in most cases. As an environmentally friendly alternative, timber panels can be used to cover the steel elements, offering them a certain degree of fire protection while achieving the environmental goals. Previous studies have demonstrated the potential of using timber as a fire protection material to provide additional fire resistance to the steel parts, proving the effective delay in the temperature development from which the steel profile can be benefited. In this investigation, a thermo-mechanical numerical model to represent the fire behaviour of steel-concrete composite beams with demountable shear connectors is developed by means of the FE software SAFIR, being used to analyse the effectiveness of different fire protection systems to delay the temperature rise of the steel beam.

Keywords: FE modelling; fire protection; timber; steel-concrete composite beams; demountable shear connectors

1 INTRODUCTION

Steel-concrete composite structural systems have become more popular in the building industry due to their multiple advantages including high flexibility, adaptability and reduction in self-weight compared to other structural systems. In the most common situations, a composite downstand beam is used, which consists of a steel profile connected to an in-situ reinforced concrete slab by mechanical shear stud connectors welded

¹ Associate Professor, Departamento de Ingeniería Mecánica y Construcción, Universitat Jaume I, Castellón de la Plana (Spain)
e-mail: valbero@uji.es, ORCID: <https://orcid.org/0000-0001-7193-9232>

² Associate Professor, ICITECH, Universitat Politècnica de València, Valencia (Spain)
e-mail: aespinos@mes.upv.es, ORCID: <https://orcid.org/0000-0001-7335-4676>

³ Assistant Professor, Dpto. Mecánica de los Medios Continuos y Teoría de Estructuras, Universitat Politècnica de València (Spain)
e-mail: anlafer0@mes.upv.es, ORCID: <https://orcid.org/0000-0001-9667-236X>

⁴ Full Professor, ICITECH, Universitat Politècnica de València, Valencia (Spain)
e-mail: mromero@mes.upv.es, ORCID: <https://orcid.org/0000-0001-5247-4767>

to the beam top flange [1]. However, one of the drawbacks of this type of construction method is its lack of reusability, which negatively impacts its life cycle assessment. By using replaceable bolted connectors instead, reusability can be enhanced, leading to a circular business model in the search of a sustainable, low-carbon and resource-efficient economy. The mechanical performance and ability for re-use of these type of connectors have already been investigated by researchers from the University of Luxembourg in the scope of the research project “REDUCE” [2] funded by the European Commission, however, the available research on its fire performance is still scarce. This aspect is currently under investigation in the framework of the ongoing project “FIREDUCE” [3] at the Polytechnic University of Valencia (Spain), which is as a continuation of the previous project. In the event of a fire at the lower compartment, the fact that the downstand steel beam results directly exposed to the heat source from three sides still compromises the fire performance of the composite member, losing its mechanical capacity after a short period of time. Therefore, it is crucial to protect the steel beam with passive fire protection means. Traditional passive fire protection systems such as intumescent paints, cementitious mortars or boards have been commonly used for protecting the steel elements in case of fire. Also, the option of combining concrete with steel has been regarded as good strategy for delaying the temperature rise of the steel element. However, these fire protection options do not fulfil the sustainability criteria in most cases, given the deficient demountability of the components and their unfavourable carbon footprint. As an environmentally friendly alternative, timber panels can be used to cover the steel elements, offering them a certain degree of fire protection while achieving the environmental goals. Previous studies have demonstrated the potential of using timber as a fire protection material to provide additional fire resistance to the steel parts [4-6]. Although timber is a combustible material, its favourable thermal properties and low charring rate can effectively delay the advance of the thermal front, and thus protect the steel parts during a certain time period.

In this work, a thermo-mechanical analysis of the different fire protection strategies for demountable steel-concrete composite beams under standard ISO-834 fire exposure will be performed by means of a finite element model developed in SAFIR [7], coupling a 2D-heat transfer model for the thermal analysis to a fibre beam model for the mechanical analysis. Based on the comparison between the thermo-mechanical performance of each option, detailed design recommendations will be provided to optimise the fire performance of demountable steel-concrete composite structures with the focus on sustainability.

2 DEVELOPMENT OF THE NUMERICAL MODEL

The finite element software package SAFIR [7] is used in this investigation to develop a sequentially coupled numerical model to represent the thermal response of the different fire protection options, which eventually influence the structural fire resistance of the steel-concrete composite beams. On a first step, the thermal response of the composite section is analysed by means of a two-dimensional heat transfer finite element model, which calculates the nodal temperatures across the cross-section under exposure to the ISO-834 standard fire curve. Subsequently, a thermo-mechanical analysis is performed with the help of a fibre beam model, where the nodal temperatures from the preceding thermal analysis are incorporated and cross-section integration is applied.

2.1 Thermal model

2.1.1 Geometry

All the studied solutions were modelled with the same base section for the demountable steel-concrete composite beam, consisting of three main parts: a concrete slab at the top, a downstand steel beam and the connection elements (Figure 1). The concrete slab elements consisted of two parts, with a thickness of 150 mm, connected to the top flange of an HEB 260 steel profile by the bolted connectors. A width of 500 mm for each slab element was employed to limit the size of the model whilst maintaining a representative part of the beam width which could influence the thermal response. Additionally, to have some extra clearance during the construction phase and room for elongation of the hardened concrete, a gap of 20 mm in between the two slabs was materialized. The fire protection parts are not displayed in Figure 1, but will be described in detail in the corresponding sections of the heat transfer analysis.

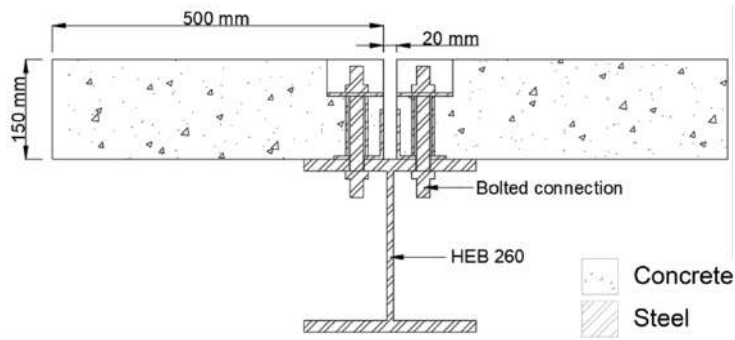


Figure 1. Geometry of the demountable steel-concrete composite beam

2.1.2 Finite element mesh

Particularly for the concrete slab and protection elements, 4-noded linear quadrilateral finite elements were used, with a maximum mesh size of 5 mm. A sensitivity analysis was performed on this mesh size to test its effect, leading to the conclusion that a mesh size of 5 mm gave the most accurate results, while using smaller mesh sizes would only lead to a higher computational cost without gain of precision. Additionally, for the steel elements, a finer mesh density was required due to the low thickness of the flanges and web of the profile, therefore 3-noded linear triangle finite elements with a mesh size of 3 mm were applied.

2.1.3 Thermal properties at elevated temperatures

The thermal properties for the different materials used in the studied configurations and their variation with temperature were defined in accordance with the corresponding Eurocodes, implemented in the SAFIR [7] material database. For concrete, steel and timber, Eurocodes 2, 3 and 5 were utilized as references, respectively. Based on EN 1992-1-2 [8], a recommended density value of 2400 kg/m³ and a moisture content of 3% was used for concrete. In turn, the suggested values for conductivity, specific heat and density given in EN 1993-1-2 [9] were utilized for steel. Lastly, EN 1995-1-2 [10] was employed for timber. Based on values from commercial glued laminated timber boards, a moisture content of 12% and a density of 450 kg/m³ were used for the timber panels.

2.1.4 Heat transfer analysis

At the bottom side of the composite beam, the standard ISO-834 fire curve was applied as a prescribed thermal load, while at the top side of the concrete slab, a constant initial temperature of 20 °C was considered to simulate ambient temperature. According to EN 1991-1-2 [11], on the fire exposed surfaces the thermal actions were modelled by means of the convection and radiation heat transfer mechanisms. On the fire exposed surface of the member, the coefficient of heat transfer by convection was set equal to 25 W/m²K, while at the unexposed surface, a value of 4 W/m²K was assumed. For the steel and concrete surfaces, the emissivity value was taken as 0.7, while for timber and gypsum plasterboard it was assumed equal to 0.8, as given in Clause 2.2(2) of EN 1995-1-2 [10].

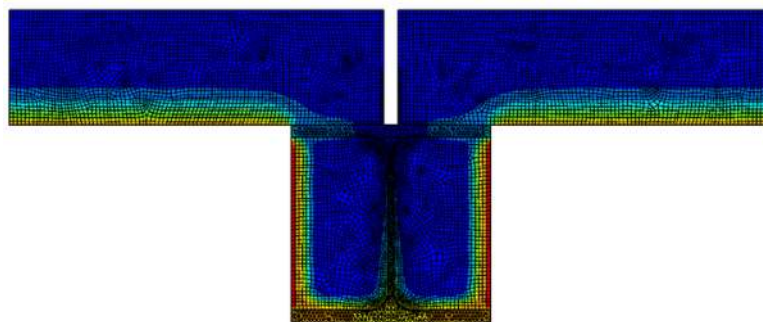


Figure 2. Thermal 2D finite element model developed in SAFIR

2.2 Thermo-mechanical model

To calculate the cross-section bending capacity at elevated temperatures of the composite beams, a structural finite element fibre beam model was implemented in SAFIR [7]. This software facilitates the consideration of large displacements, thermal strains, and non-linear temperature-dependent properties for the materials. The computer program manages these non-linearities through dynamic analysis.

2.2.1 Mechanical properties at elevated temperatures

The SAFIR [7] finite element software package incorporates all the relevant material properties at elevated temperatures, as established by the Eurocodes. For the purposes of this study, the material selection involves calcareous aggregate concrete with a compressive strength of 30 MPa and carbon steel with a nominal strength of 355 MPa. It is pertinent to note that the tensile strength of concrete is neglected in this work. Constitutive models in SAFIR are based on the hypothesis of strain decomposition in the frame of associate plasticity for metallic materials, and a combination of damage and plasticity theory for concrete that includes explicit transient creep.

2.2.2 Loading configuration and boundary conditions

Following the completion of the thermal analysis and the acquisition of nodal temperatures across the entire cross-section, these output results serve as input data for the structural model. Specifically, a four-point bending test was simulated by employing beam elements to represent a beam with a length of 6 meters, as illustrated in Figure 3. The beam elements were defined to have a maximum mesh size of 8 centimeters.

Regarding the boundary conditions, one end of the beam was modelled as pinned, while the other was configured as a roller in the longitudinal direction. Consequently, axial elongation resulting from elevated temperatures can be accommodated. In the structural analysis, the loading is initially applied, and subsequently, nodal temperatures obtained from the preceding thermal analysis are integrated across the cross-section and systematically imported into the beam elements in such a way that the section components progressively see their mechanical properties degraded by the thermal action.

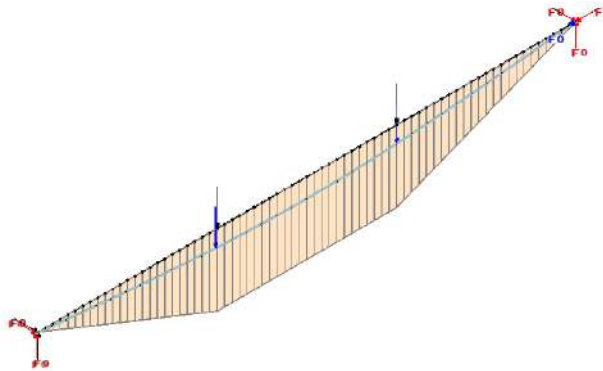


Figure 3. Thermo-mechanical fibre beam model

2.2.3 Failure criteria

Given the nonlinear properties of the materials at elevated temperatures, internal forces and displacements emerge along the beam as temperature increases due to fire exposure. Eventually, following the EN 1363-1 [12] standard for fire resistance tests, a maximum deflection of $L^2/(400 \times d)$ and a maximum deflection ratio of $L^2/(9000 \times d)$ are considered to define the standard fire resistance time. The structural analysis is iteratively performed for a set of values of the loading ratio, from where the corresponding bending capacity loss curve along the fire exposure time is subsequently derived (see section 4.3).

3 VALIDATION OF THE NUMERICAL MODEL

Before being able to investigate different strategies for protecting the steel-concrete composite beams at elevated temperature, it is needed to validate the numerical model to make sure that its thermo-mechanical response is reliable. In the absence of specific experimental fire tests results on the exact configuration investigated in this paper, other experimental results performed on similar composite beam configurations available in the literature are employed as a reference to validate the numerical model.

3.1 Unprotected steel-concrete composite beam

Zhao & Kruppa [13] performed an experimental analysis on the fire performance of an unprotected steel-concrete composite beam, with an in situ concrete slab of width 1200 mm and depth 120 mm attached to the upper flange of a downstand beam made of an IPE300 profile. This composite beam was reproduced in SAFIR for the validation of the thermal model, the comparison of the temperature evolution at different relevant points of the section between the numerical and experimental results can be seen in Figure 4.

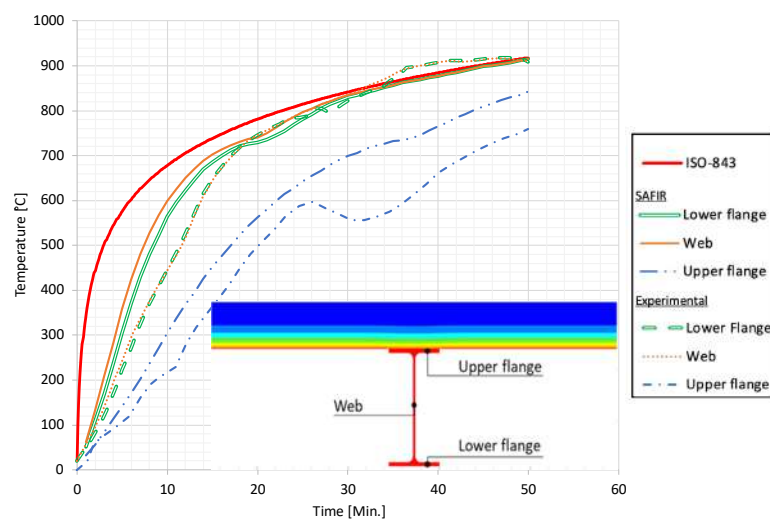


Figure 4. Validation of an unprotected steel-concrete composite beam, compared with reference [13]

As it can be seen, for both the web and the lower flange of the steel profile, the predicted temperature development followed closely the experimental measurements, reaching a maximum temperature of around 910°C. For the upper flange, higher deviations were obtained, since the experimental measurement became unstable after approximately 25 minutes, which can be attributed to the failure of the thermocouple attached in that position. Overall and despite that observation, it can be affirmed that the numerical model provides reasonable predictions in terms of temperature evolution for unprotected steel-concrete composite beams.

3.2 Protected steel-concrete composite beam

Nguyen et al. [6] conducted thermal experiments on hybrid steel-timber structures, using wood as a passive protective element for the steel components. In this context, test number 3 (steel beam partially encapsulated by timber) was selected for validation purposes, given its substantial similarity to the configuration under analysis in the present study. The steel beam employed for validation consisted of a welded steel section with dimensions of 240 mm in height and 120 mm in width. The steel beam was partially encapsulated by Douglas wood solid elements between the flanges and exposed to fire through three sides. The bottom flange was directly exposed to the fire, while the steel web and upper flange were protected by the surrounding wood. The Douglas wood used in the experiment had a density of 469 kg/m³ and a moisture content of 8%. These specific material characteristics were incorporated into the finite element model, aligning with the EN 1995-1-2 [10] thermal properties for timber at elevated temperatures, and were implemented in the SAFIR numerical model.

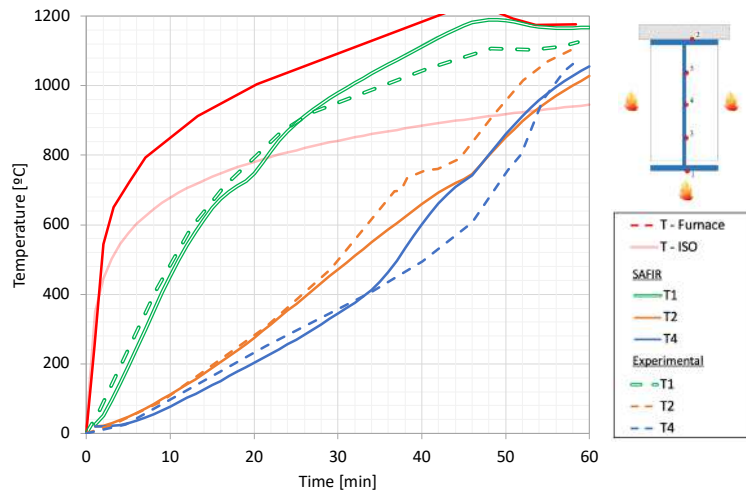


Figure 5. Validation of a steel-concrete composite beam partially encapsulated by timber, compared with reference [6]

The comparison between the reference test number 3 from Nguyen et al. [6] and the SAFIR model are presented in Figure 5, revealing precise predictions for the bottom flange (T1), top flange (T2) and web (T4) of the steel profile. It is noteworthy that temperature recordings were exclusively focused on the steel profile during the experiment, given that, in this particular beam configuration, timber serves only as a passive fire protection element without any contribution to the mechanical capacity of the beam at elevated temperatures. Moreover, it can be observed that the furnace temperature (T-Furnace) was clearly above the ISO-834 curve (T-ISO). This difference is attributed to the amount of fire load added by timber due to its combustion. Nonetheless, it is important to highlight that the SAFIR model utilized the actual furnace temperature curve as an input for the numerical simulations, guarantying the attainment of accurate results.

4 NUMERICAL STUDY AND DISCUSSION OF RESULTS

Once the numerical model developed in SAFIR was validated, it was used to simulate several alternatives to protect the downstand steel beam in case of fire and enhance the thermo-mechanical behaviour of the demountable steel-concrete composite beams. The effectiveness of different fire protection systems is assessed in this section and compared with the unprotected composite beam. Sustainable alternatives using timber are compared to other more conventional fire protection measures, such as gypsum boards or concrete encasement (see Figure 6).

The focus of these protection alternatives is put on protecting the bolts connecting the steel profile to the concrete slab, whilst maintaining the objective of reusability. Four options are studied:

- A: Timber boards around the HEB profile
- B: Concrete encasement in between the HEB profile flanges
- C: Timber encasement in between the HEB profile flanges
- D: Gypsum boards around the HEB profile

It is worth noting that, although it is not a demountable solution, option B was included in this comparison because it is a common solution used in downstand composite beams, which is covered in EN1994-1-2 [14]. As an alternative, timber encasement is proposed in option C to replace the concrete part, since the low carbon footprint of wood, together with its low thermal conductivity and slow charring rate make this one a good alternative and a sustainable option, in comparison with other encasement solutions. For the same reason, option A was considered to replace the commonly used gypsum boards (option D) by the more sustainable timber boards.

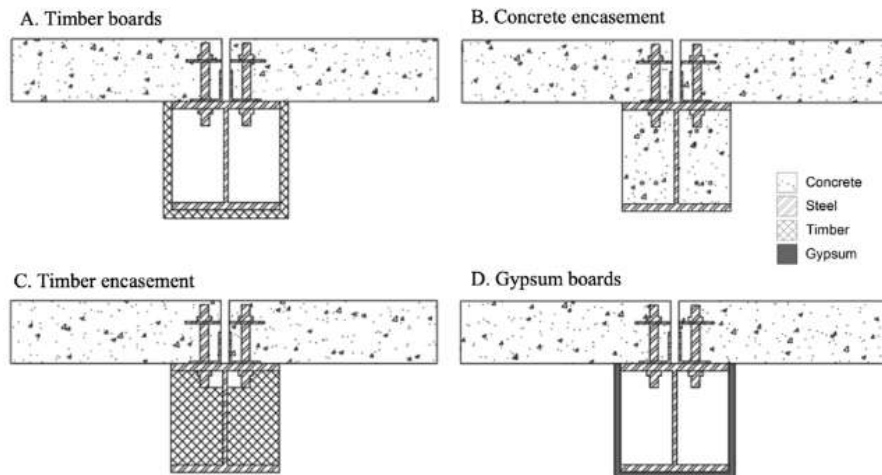


Figure 6. Case analyses considered in the numerical study

It is important to note that for options A and D, in between the HEB steel profile and the protection boards a gap exists, where cavity radiation emerges. Hence, radiative heat transfer occurs in the direction of the normal between the contact surfaces. This effect was considered in SAFIR [7] by applying void constraints on the surfaces where the cavity radiation arises. This software package allows for heat transfer by convection and radiation between the walls that make the cavity.

4.1 Thermal behaviour of unprotected steel-concrete composite beams

Before investigating the effect of the multiple fire protection methods, the thermal behaviour of an unprotected steel-concrete composite was examined. Figure 7 plots the temperature development in the lower flange, web and connection bolt of the unprotected beam in function of the fire exposure time.

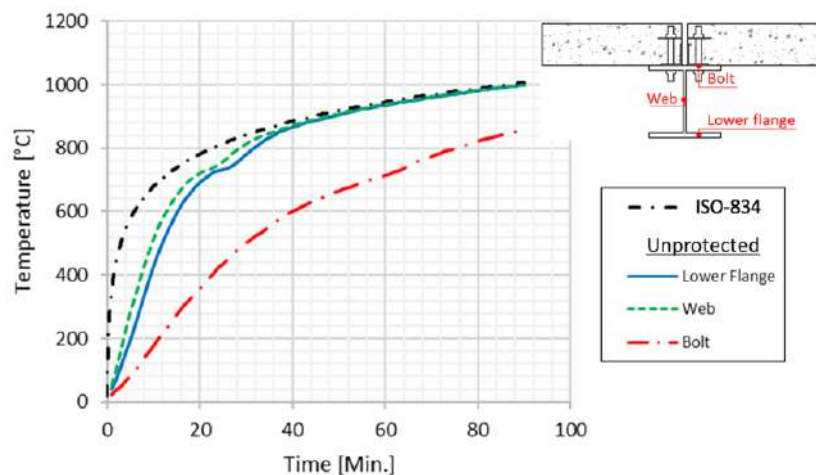


Figure 7. Thermal behaviour of an unprotected composite beam under ISO-834 fire

The overall behaviour in the steel profile under fire occurs in two stages. First, there is a quick increase in temperature proportional to the ISO-834 standard fire curve. The second stage starts once the fire curve flattens out, causing the heat evolution in the steel profile also to slow down. After 90 minutes, the lower flange and web reach a temperature of about 1000°C, while in the connection bolt it only goes up to 859°C. This noticeable difference of 141°C can be explained by the lower flange and the web being exposed to fire on both surfaces, hence heat convection from these fire exposed surfaces can occur. In the bolt on the other hand, only one side of the upper flange is subjected to fire, while the other side is in contact with the concrete slab. Therefore, since heat convection can only happen from one hot surface, the heat development is slower.

4.2 Study of the effectiveness of different fire protection systems

Now that the thermal response of the unprotected composite beam during a fire has been analysed, the effect of the different fire protection methods can be investigated and compared to the reference beam.

4.2.1 Timber boards

In the first place, the influence of attaching timber boards in the contour of the steel profile was analysed. As represented in Figure 8, timber boards of 20 mm thickness are applied closing the perimeter of the HEB profile. This way, the direct fire exposure of the steel beam parts is prevented. Initially, only cavity radiation and conduction along the web of the steel profile will cause heating of the composite beam. This boundary condition only applies until the charring of timber permeates the entire thickness of the boards. It is widely recognized that at 300°C, the physical structure of timber begins to deteriorate, and charring becomes evident. Consequently, thermal analysis was conducted upon reaching 300°C at the inner side of the timber boards. This occurred approximately after 30 minutes of fire exposure, considering the 20 mm thickness of the timber boards. Once this point was reached, the thermal analysis was restarted in SAFIR using the *RESTARTT command, excluding the presence of the timber boards since they would have lost their initial function due to complete charring. The thermal boundary conditions were then redefined, subjecting the entire contour of the steel profile (except its top flange) to radiation and convection from the fire.

Figure 8 shows the effectiveness of the timber board protection up to 30 minutes. After this point, there is a significant alteration in the overall thermal behaviour of the steel beam, with temperatures rapidly approaching the trend observed in the previously studied unprotected beam.

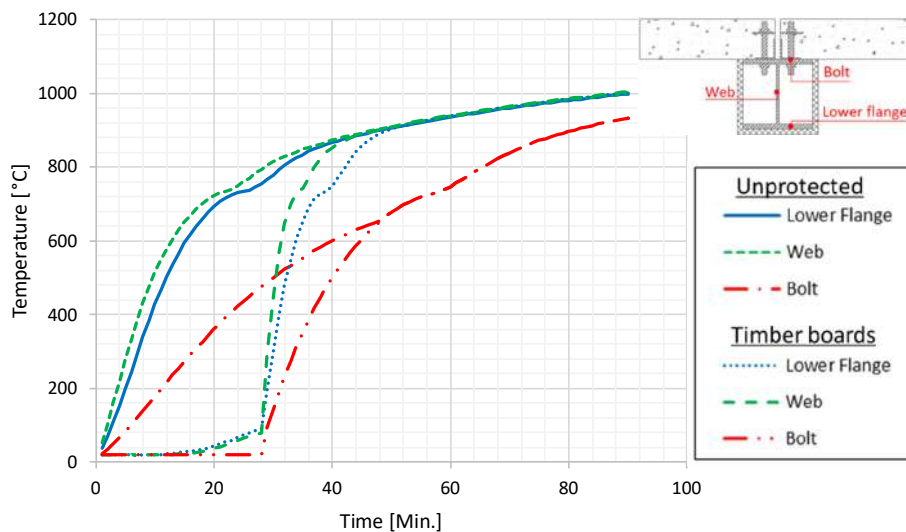


Figure 8. Effect of timber boards (option A) on the thermal behaviour of a composite beam

4.2.2 Concrete encasement

Using concrete encased in-between the steel profile flanges (Figure 9), is another method to enhance the fire resistance of the steel-concrete composite beam. It is important to mention that, in this case, the lower flange and the sides of the upper flange of the steel profile remain unprotected. Consequently, on these locations, direct exposure to the fire source is occurring. Especially in the lower flange, this issue becomes evident, since the temperature difference after 90 minutes between the unprotected and protected beam is only of 67°C (Figure 9). Even though a slower heat development is visible, the general thermal behaviour during fire exposure stays similar.

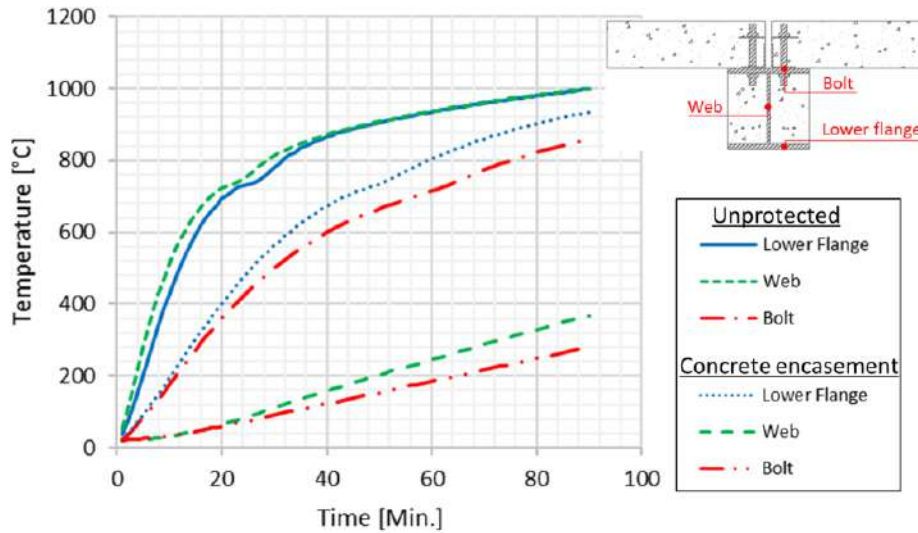


Figure 9. Effect of concrete encasement (option B) on the thermal behaviour of a composite beam.

On the other hand, the web and bolt are not directly exposed to fire, as they remain protected by the surrounding concrete. Thus, conduction from the lower flange of the steel profile is the responsible of the heating of these parts. This results in a significant temperature difference of 632°C (web) and 581°C (bolt) as compared to the unprotected beam, therefore this protection strategy is effective for these parts.

4.2.3 Timber encasement

Instead of concrete, timber can be used as encasement (Figure 10), for a more sustainable solution. As can be seen in Figure 10, timber encasement gives similar results as compared to concrete encasement, in light of the temperature evolution of the HEB profile parts. It can be seen that the lower flange reaches a maximum temperature of 966°C, while the web achieves a temperature of 449°C. Moreover, after 90 minutes the bolt goes up to 279°C, which justifies the effectiveness of this type of protection. It should be noted that the increase of fire load occurring in this case due to the combustion of timber has not been taken into account in the model, which could affect the results.

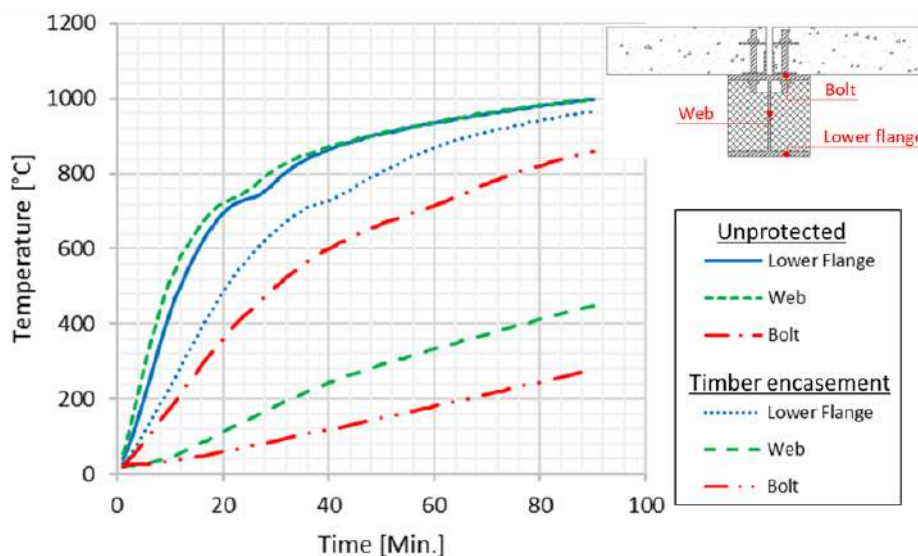


Figure 10. Effect of timber encasement (option C) on the thermal behaviour of a composite beam

4.2.4 Gypsum boards

The last thermal protection method discussed in this section are the traditionally used gypsum boards. As can be seen in Figure 11, these boards (with a thickness 15 mm) are applied around the HEB profile, closing

its perimeter, similarly to option A. Unlike the unprotected beam, by applying this option the temperature only starts to increase after the first 10 minutes. Afterwards there is an almost linear increase until reaching 90 minutes fire exposure. After this period, the difference of the maximum temperature with the unprotected steel-concrete composite beam temperature is obvious, being 498°C in the lower flange, 583°C in the web and 652°C in the bolt.

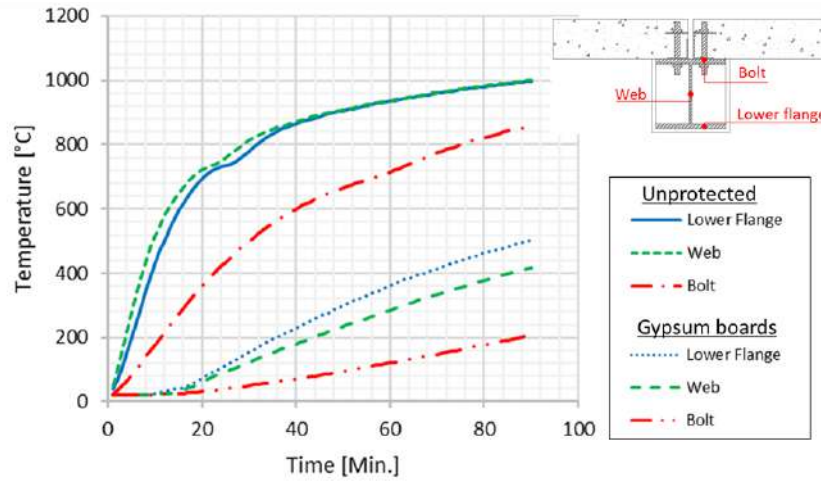


Figure 11. Effect of gypsum boards (option D) on the thermal behaviour of a composite beam

4.3 Thermo-mechanical analysis. Comparison of results

After analysing in depth the thermal response of the presented fire protection solutions, their thermo-mechanical response is simulated and discussed in this section. For each of the studied options, recurrent structural analyses were performed with the fibre beam model developed in SAFIR for a set of values of the loading ratio, from where the “bending moment capacity vs. fire exposure time” curve was derived by plotting the results of the multiple repetitions of the structural analysis. Figure 12 shows the loss of bending moment capacity of the steel-composite beam with the fire exposure time for the four options studied (A to D), in comparison with the unprotected steel beam. The horizontal lines in this figure correspond to control load levels set to $\mu_{fi} = 0.4$ and $\mu_{fi} = 0.6$, which are taken as a reference for comparison purposes.

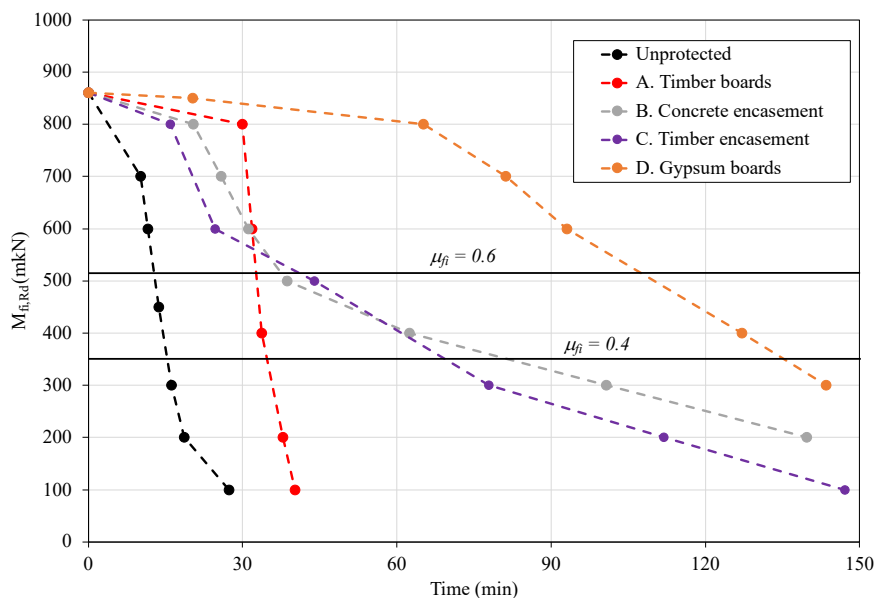


Figure 12. Reduction of the bending capacity at elevated temperatures, for the different protection options studied

The unprotected composite beam (black curve in Figure 12) shows a reduced fire resistance, which is around 15 minutes for intermediate load levels ($\mu_{fi} = 0.4 - 0.6$). The first fire protection solution studied, using timber boards (option A) provides up to 30 minutes fire protection even under high load levels (μ_{fi} above 0.6), but degrades fast once the timber board thickness is consumed upon charring, as explained in section 4.2.1. The timber encasement solution (option C) performs similarly to that with concrete encasement (option B), while being more environmentally friendly. Both options provide a substantial increment in terms of fire resistance time, surpassing 30 minutes for high load levels (μ_{fi} above 0.6) or 60 minutes for moderate load levels, even attaining 90 minutes for low load levels (μ_{fi} under 0.4). Finally, the solution with gypsum boards (option D) outperform this range, reaching 120 minutes for moderate load levels, although this solution would be penalized in terms of sustainability.

5 CONCLUSIONS

This paper presented a thermo-mechanical model developed in the finite element software package SAFIR to examine the performance of different fire protection solutions for steel-concrete composite beams with demountable shear connectors, with the focus on the reusability and sustainability of the system. The numerical model was validated by comparing its thermal response with available thermal test results for steel-concrete composite beams from the literature. Once the model was validated, it was extended to study the fire performance of four different fire protection options: timber boards, concrete encasement, timber encasement and gypsum boards. The conventional solutions using gypsum boards or concrete encasement showed significant enhancements in terms of fire resistance for the range of load levels studied. However, these options would not meet the sustainability requirements and would be penalized in a life cycle assessment of the structure, therefore alternative solutions were proposed. Using timber boards showed the potential to provide a certain delay to the heating of the steel beam, permitting the accomplishment of an R30 fire rating. In most building applications, however, a higher fire resistance rating is required, in which case using a timber encasement between the steel profile flanges may allow meeting R60 for moderate load levels or even R90 for low load levels, therefore this strategy can be deemed as an alternative solution to contribute in reducing the carbon footprint of these composite structural members.

ACKNOWLEDGMENT

The authors gratefully acknowledge the Spanish “*Agencia Estatal de Investigación*” for the help provided through the Project FIRSTIMB, carried out with a financial grant with reference TED2021-130580B-I00 funded by MCIN/AEI/ 10.13039/501100011033 and by the “European Union NextGenerationEU/PRTR”.

REFERENCES

1. Ahmed, I.M. & Tsavdaridis, K.D., The evolution of composite flooring systems: applications, testing, modelling and Eurocode design approaches. *Journal of Constructional Steel Research*, 155, 286–300 (2019). <https://doi.org/10.1016/J.JCSR.2019.01.007>.
2. Kozma, A., Odenbreit, C., Braun, M.V., Veljkovic, M. & Nijgh, M.P., Push-out tests on demountable shear connectors of steel-concrete composite structures. *Structures*, 21, 45–54 (2019). <https://doi.org/10.1016/j.istruc.2019.05.011>.
3. Mansilla, R., Espinós, A., Odenbreit, C., Payá-Zaforteza, I., Romero, M.L., Characterization of the elevated temperature behaviour of demountable shear connectors in steel-concrete composite beams through push-out tests. *Structures*, 59, 105810 (2024). <https://doi.org/10.1016/j.istruc.2023.105810>.
4. Šulc, S., Šejna, J., Šmilauer, V. & Wald, F., Steel elements with timber fire protection - experiment and numerical analysis, in: *Acta Polytechnica CTU Proceedings*, pp. 116–121 (2022). <https://doi.org/10.14311/APP.2022.34.0116>.
5. Le, T.D.H. & Tsai, M.T., Experimental assessment of the fire resistance mechanisms of timber-steel composites. *Materials*, 12 (2019). <https://doi.org/10.3390/ma12234003>.

6. Nguyen, M.H., Ouldboukhite, S.E., Durif, S., Saulnier, V. & Bouchair, A., Passive fire protection of steel profiles using wood. *Engineering Structures*, 275, 115274 (2023). <https://doi.org/10.1016/J.ENGSTRUCT.2022.115274>.
7. Franssen, J.M. & Gernay, T., User's manual for SAFIR 2022. A computer program for analysis of structures subjected to fire. Liege University; 2022.
8. EN 1992-1-2. Eurocode 2: Design of concrete structures - Part 1-2: General rules - Structural fire design. Comité Européen de Normalisation; 2004.
9. EN 1993-1-2. Eurocode 3: Design of steel structures - Part 1-2: General rules - Structural fire design. Comité Européen de Normalisation; 2005.
10. EN 1995-1-2. Eurocode 5: Design of timber structures - Part 1-2: General - Structural fire design. Comité Européen de Normalisation; 2004.
11. EN 1991-1-2. Eurocode 1: Actions on structures - Part 1-2: General actions - Actions on structures exposed to fire. Comité Européen de Normalisation; 2002.
12. EN 1363-1. Fire resistance tests - Part 1: General requirements. Comité Européen de Normalisation; 2020.
13. Zhao, B., Kruppa, J., Fire resistance of composite slabs with profiled steel sheet and of composite steel concrete beams: Part 2: Composite beams. European Commission; 1997.
14. EN 1994-1-2. Eurocode 4: Design of composite steel and concrete structures - Part 1-2: General rules - Structural fire design. Comité Européen de Normalisation; 2005.

PARAMETRIC NUMERICAL STUDY OF FIRE EXPERIMENTS ON STEEL- CONCRETE COMPOSITE FLOORS

Chenzhi Ma¹, Thomas Gernay²

ABSTRACT

Strategies for fire design of steel-concrete composite floors can rely either on fire protection of the individual elements or on alternate load path for structural integrity of the system. This study conducts numerical fire analyses of steel-concrete composite floors to advance understanding of the anticipated performance of the different fire designs. The numerical models were validated against three full-scale fire tests conducted at the NIST. In Test #1, built to prescriptive code for a 2-hour rating of the elements, large crack openings led to flame leak shortly after one hour. The finite element model captured the localized concrete damage and steel mesh fracture observed in the test, confirming the link between the integrity failure and the minimum amount of reinforcement ($60 \text{ mm}^2/\text{m}$) permitted in current U.S. practice. Test #2 and Test #3 both used $230 \text{ mm}^2/\text{m}$ of reinforcement, with the latter omitting the fire protection on the central steel beams. The numerical model captured the experimental behavior including stability under 2 hours of ASTM E119 fire and partial deflection recovery during the subsequent cooling phase. A parametric analysis on the slab rebar area shows that the floors with unprotected central beam need a minimum rebar area about 10% (based on S755) greater than those with protected beams. Further, a probabilistic analysis under natural fires indicates that the floors designed to harness system-level membrane behavior have a lower probability of failure than those designed via element-level prescriptive methods with minimum reinforcement.

Keywords: steel-concrete composite floor, full-scale fire test, performance-based fire design, concrete damage, tensile membrane action, fragility curve

1 INTRODUCTION

According to the National Fire Incident Reporting System (NFIRS), between 2012 and 2022, approximately 1.2 million building fires with flames spread beyond the origin of ignition were recorded in the United States (U.S.). These incidents resulted in around 70,000 fire-related injuries. These statistics highlight the significant human and economic cost of fire. Structural fire design is an important layer of safety to mitigate the fire risk. In the U.S., composite steel-concrete floor systems are widely used. Fire protection materials are generally required for the steel members according to the building codes and specifications. However, research over the last thirty years has shown that omitting fireproofing on selected steel members in composite slabs can result in activation of tensile membrane action (TMA) under fire [1]. Performance-based structural fire designs (PBSFD) have therefore relied on TMA for the fire design of composite steel-concrete slabs with unprotected central beams in projects in multiple countries [2]. However, relatively limited research has been conducted in the U.S. with the composite floor detailing specific to this country, and there is a lack of studies characterizing the probabilistic response of these designs.

¹ Ph.D. student, Department of Civil and Systems Engineering, Johns Hopkins University,
e-mail: cma31@jhu.edu, ORCID: <https://orcid.org/0000-0002-1144-8033>

² Assistant Professor, Department of Civil and Systems Engineering, Johns Hopkins University
e-mail: tgernay@jhu.edu, ORCID: <https://orcid.org/0000-0002-3511-9226>

The National Institute of Standards and Technology (NIST) recently conducted three full-scale experiments on steel-concrete composite floor systems under standard fire [3-5]. The goal was to test the full-scale performance of assemblies typically constructed in the United States and to compare a prescriptive and a performance-based design. The first experiment was designed per U.S. prescriptive provisions for a 2-hour fire rating, which includes thermal protection on the steel beams and 60 mm²/m of S755 reinforcement in the concrete slab. The floor slab developed a large crack along the protected secondary beam after about one hour and reached integrity failure well before the 2 hours of standard fire exposure. The second and third experiments were designed with 230 mm²/m of S480 reinforcement, with the third one omitting the fire protection on the central steel beams to develop tensile membrane action. These second and third experiments showed no failure within 2 hours. Cracks appeared starting at 132 mins in the third test.

The NIST fire tests provided valuable data on the performance of different design methods for composite floor systems in the U.S., and there is an opportunity for further investigation using these data to deepen the understanding and expand on the initial experimental findings. The experimental data can serve to validate the numerical models. These numerical models are then used to conduct detailed analyses, capture a wide range of data in the structure, such as the evolution of damage in concrete and internal forces over time, and conduct parametric analyses. Parametric analyses can serve to determine critical design parameters of the test prototypes, such as the minimum required slab rebar areas, and explore the effects of other design variables or fire exposures. Probabilistic numerical analysis can also be conducted to build fragility curves for the three test prototypes, for functional recovery and lifetime cost analysis.

This paper presents a comprehensive numerical investigation of the NIST full-scale fire experiments, supplemented by parametric and probabilistic analyses. The unique test data are used to validate nonlinear finite element (FE) models and gain further insights into the observed experimental behavior including early cracking and rebar failure of the prescriptive design. Then, the validated models are used to conduct parametric and probabilistic analyses including under natural fires. These numerical data can support improvement of design provisions in U.S. building codes for the fire design of steel-concrete floor systems.

2 NIST FULL-SCALE FIRE TEST

The tested structure was a two-story steel gravity frame with composite floors. It had two bays by three bays in plan, for a total floor area of 18 m × 11 m, see Figure 1. The fire compartment (9.14 m × 6.10 m) was subjected to a total gravity load of 5.2 kPa. The ASTM E119 fire was applied. Detailed information on structural design, construction, and mechanical properties is available in the NIST technical Notes [3-5].



Figure 1. Tested structure and observations during the test [4]

The first experiment with 60 mm²/m of welded wire mesh reinforcement (755 MPa strength) failed to maintain integrity for 2 hours of standard fire exposure though each individual element was designed per U.S. prescriptive provisions for a 2-hour fire rating. A full-depth crack appeared above the central beam after approximately one hour of exposure leading to integrity failure.

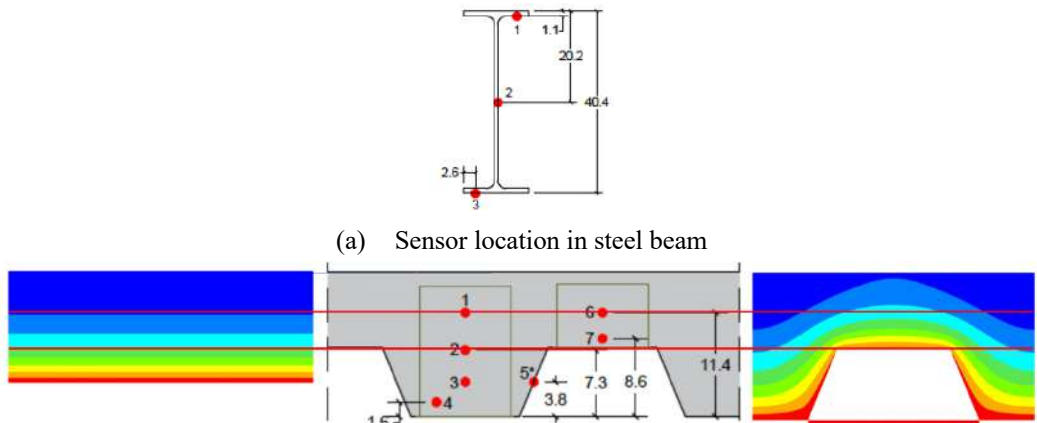
The second and third experiments were designed with 230 mm²/m of steel bars reinforcement (480 MPa strength) in the concrete slab in lieu of the minimum 60 mm²/m wire mesh, and the third experiment had no fire protection on the central steel beam. These second and third experiments showed no failure within 2 hours of exposure, and the third one had its first significant crack after 132 minutes.

3 NUMERICAL MODEL STRATEGY AND VALIDATION

A thermal-structural finite element (FE) model is developed using SAFIR [6] to simulate the behavior of the composite floor systems. Two-dimensional thermal analyses are performed on the sections of the beams and floors using the fire curves obtained from the average temperature of the upper layer in the tests as boundary conditions. Then, a 3D full building model is developed to conduct mechanical analysis.

3.1 Thermal analysis

The computed thermal analysis results for the steel beams and concrete slabs are compared with the test measurements. Temperature-dependent thermal properties of SFRM are adopted from Khorasani et al. [7] (details can be found in [8]). Temperature measurement locations for the beams are shown in Figure 2 (a). In the experiment, temperature readings along the beam length exhibited slight variations, in contrast to the one zone temperatures assumed in the simulation. Figure 3 (a) to (c) compare the steel beam temperature distributions between the test and the simulation for test #1. The temperature distributions in the steel beam computed by SAFIR agree well with the test. The variance in the thin lines, all the same color, represent the temperature measurements taken at different lengths of the beam but at identical sensor positions (e.g., the web), underscoring the spatial differences in the recorded temperatures during the test.



(b) Sensor location in concrete slab and two thermal analysis models (with temperature contour at 95 mins)

Figure 2. Location of thermocouples in the tests and the illustration of two concrete slab models

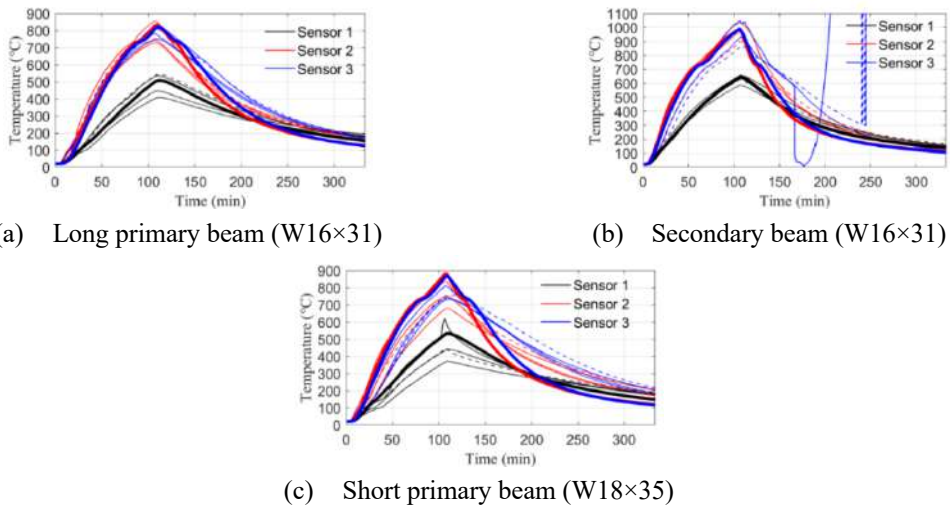


Figure 3. Comparison between measured and computed temperatures for Test #1 (model: bold lines)

Two modeling strategies are considered for the concrete slab: the first strategy uses the effective thickness approximation where the profiled shape of the slab is simplified based on the approach outlined in the Eurocode EN1994-1-2 Annex D [9]; the second strategy uses the actual geometry of the profiled slab, as shown in Figure 2 (b). The presence of the steel deck is disregarded in the thermal analysis.

3.1.1 Simplified shape concrete thermal analysis

The purpose of simplifying the profiled slab to a rectangular cross section is to facilitate its integration with the structural model, which uses constant thickness thin shell elements. The profiled concrete slab features depths of 158.75 mm and 82.55 mm for its deep and shallow sections, respectively. The effective thickness of the composite slab is 120.65 mm, including 82.55 mm of structural concrete and an additional 38.10 mm of thermal concrete. Figure 4 (a) to (c) compare the temperatures between the measurements and the computed values. The results indicate that the model successfully captured the overall temperature distribution of the slab. Some discrepancies in temperature are observed for the temperature of the reinforcement. In the test, the temperature at the reinforcement steel depth varies between the deep and shallow sections (based on the profiled shape of the deck). In the model, since a constant depth with an effective thickness is considered, the calculated rebar temperature is lower than the measurements taken at shallow sections but higher than those recorded at deep sections. For the same reason, the temperature at the location of sensor 2 is slightly overestimated by the model.

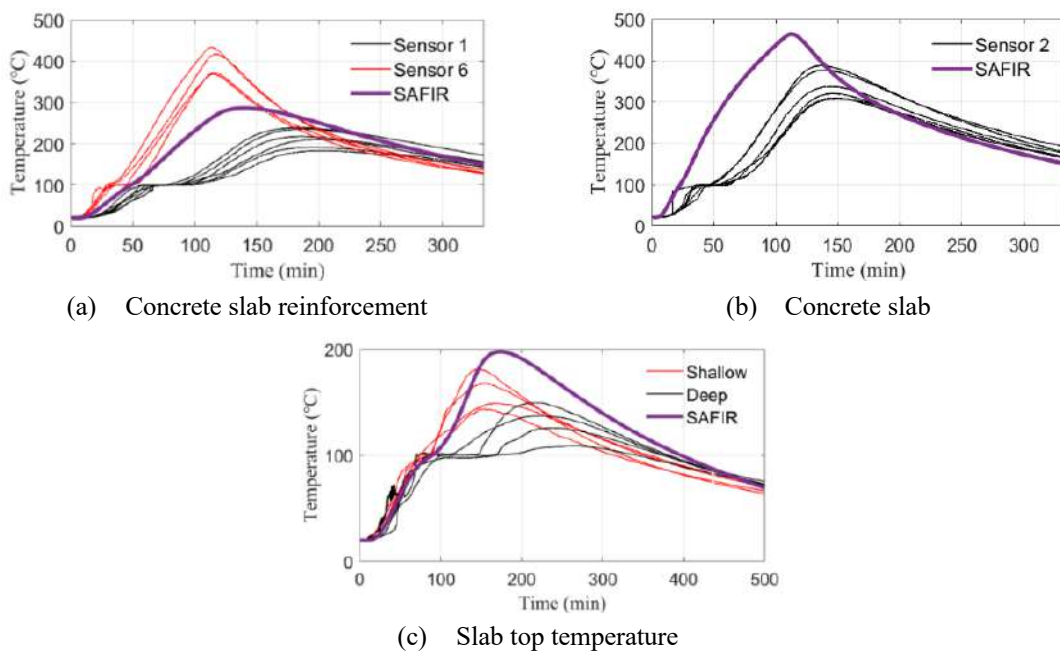


Figure 4. Comparison between measured and computed temperatures for Test #1 with simplified concrete shape (model: bold lines)

3.1.2 Profiled shape concrete thermal analysis

Agreement between computed and measured temperatures can be improved using a more detailed profiled concrete slab model in the thermal analysis [10] as shown in Figure 2 (b). The computed temperatures in the reinforcement are compared with the measured values in Figure 5 (a) The computed values agree with the measured values and the model captures the temperature difference between the shallow and deep sections. Figure 5 (b) and (c) compares the cross-sectional temperatures in both the deep and the shallow sections. The comparison reveals that the computed temperatures are slightly higher than the measured temperatures but still capture the overall temperature distributions.

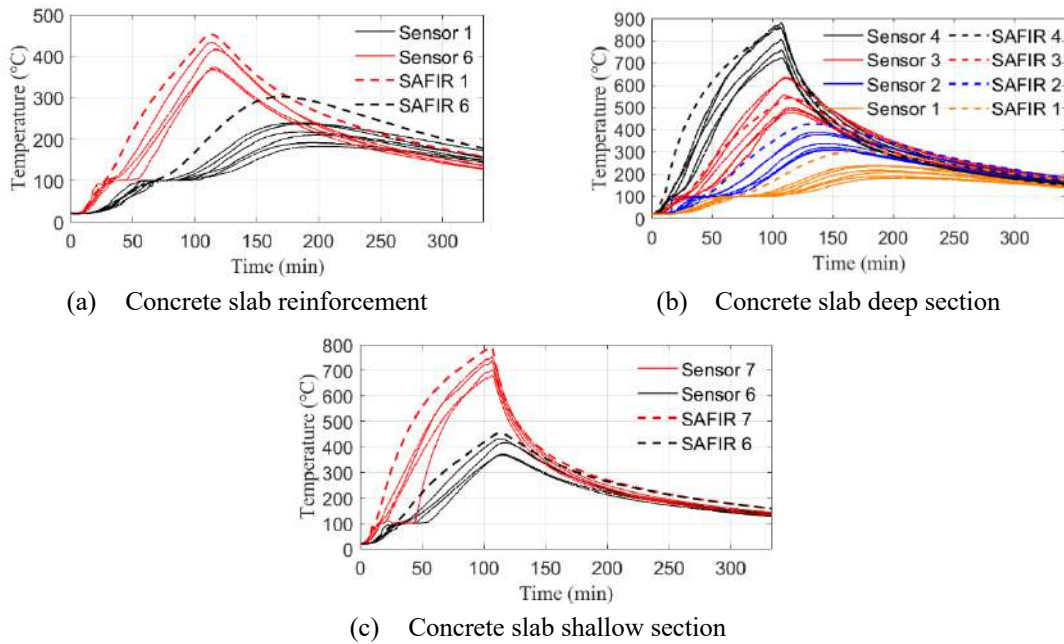


Figure 5. Comparison between measured and computed temperatures for Test #1 with profiled concrete shape (model: dashed lines)

3.2 Mechanical analysis

In the mechanical analysis, a three-dimensional full building model is established, as shown in Figure 6. The boundary conditions of the column ends and beam-column joints align with the test setup. Both the material and geometrical non-linearities and large displacements are considered. The steel deck is conservatively neglected as it is directly exposed to the fire and therefore quickly reaches high temperatures. The material properties used in the model are obtained from the test and their reduction factors at elevated temperatures is in accordance with the Eurocodes. The steel reinforcement is a hot rolled Class A reinforcement according to EN1992-1-2 [11]. The concrete model used with the shell elements is the elevated temperature plastic-damage model with explicit transient creep by Gernay et al. [12]. The reduction of strength with temperature is in accordance with Eurocode. A tensile strength of 1.5 MPa and tensile ductility of 6000 N/m², taking into account tension stiffening [13], are adopted. The numerical model is compared to experimental results and observations, focusing on vertical displacements, observed damage patterns within the concrete slab, and the observation at limit states.

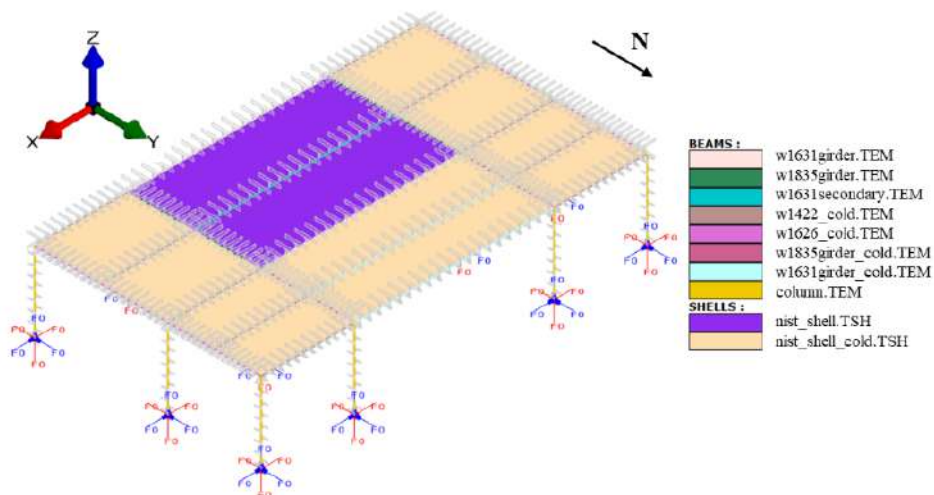


Figure 6. 3D FE model of the tested building in SAFIR (the fire-exposed part of the floor is in purple)

3.2.1 Vertical displacement

Figure 7 plots the vertical displacements at the center of the composite floor system of the three NIST tests, with measurements shown in solid lines and the computed results in dashed lines. The numerical model accurately reflects overall displacement trends and peak values. The model does not fully capture the sudden shifts in displacement rates due to damage, which develop more abruptly in the test. In Test #1, the displacement rose steadily until 69 mins of exposure, then a higher displacement rate was observed due to the development of the full-depth crack above the secondary beam. In the simulation of Test #1, the displacement increases at a constant rate until the peak value, and the simulation stops at 146 mins due to the steel reinforcement failure. Test #2 showed a constant displacement increase rate, captured in the simulation, likely stabilized by the larger rebar area facilitating load transfer across cracks. For Test #3, both test and simulation noted a displacement rate shift at 13 minutes. The initially faster displacements rate was due to the loss of strength of the metal deck and unprotected beam at high temperatures, followed by a slower displacement rate with the activation of tensile membrane action.

Test #2 showed the smallest maximum displacements among the three tests, owing to the enhanced rebar area and the protected central beam. Though Test #1 showed a smaller maximum displacement than Test #3 due to the protected central beam, it failed to survive the 2-hour standard fire in both the simulation and the test due to the inadequate rebar area. Once the crack initiated, it propagated rapidly since the inadequate rebar cannot transfer the load across the cracks, and resulted in integrity failure and stopping of the test.

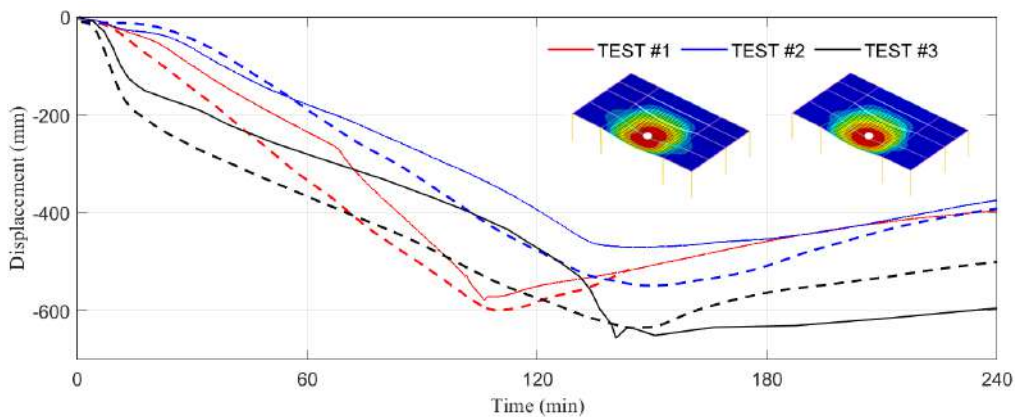


Figure 7. Comparison of vertical displacements at the center of the fire exposed composite floor for the three NIST experiments: measurements (solid lines) versus SAFIR model (dashed lines)

3.2.2 Damage distribution in concrete slab

The concrete shell model captures plasticity and damage. While it does not predict discrete crack openings, it computes a damage parameter in tension and compression at every point of integration in the shells. The damage parameter varies between zero and one, with one meaning that the material is fully damaged. In each shell element, there are 36 integration points (IP), distributed as four over the surface times nine across the thickness. Both the maximum value of the damage and the average over the 36 IP of the shell are plotted. The distribution of damage within the concrete slab at 69 mins from the numerical models is plotted in Figure 8. The damage in the simulation of Test #1 predominantly concentrates above the central beam and around the slab edges. The max damage distribution pattern indicates that the damage is not effectively transferred to other parts of the slab, which contrasts with the damage distribution in Test #2. The increased rebar area in Test #2 not only reduces the peak damage values but also enhances the load transfer capabilities along the rebar, illustrating the effectiveness of increased rebar in mitigating concentrated damage. The comparison between the simulation of Test #2 and #3 reveals that the unprotected central beam contributes to a more evenly spread damage pattern across the slab. Besides, the maximum damage value above the central beam is notably decreased compared to Test #2, indicating the critical role of central beam's fire protection on the concrete damage pattern.

In summary, the simulation of Test #1 exhibits a significant concentrated peak of damage near the central beam, aligning with the observed full-depth crack during the test. However, this is resolved by increasing the rebar area to spread the damage as evidenced by the simulated damage distribution of Tests #2 and #3.

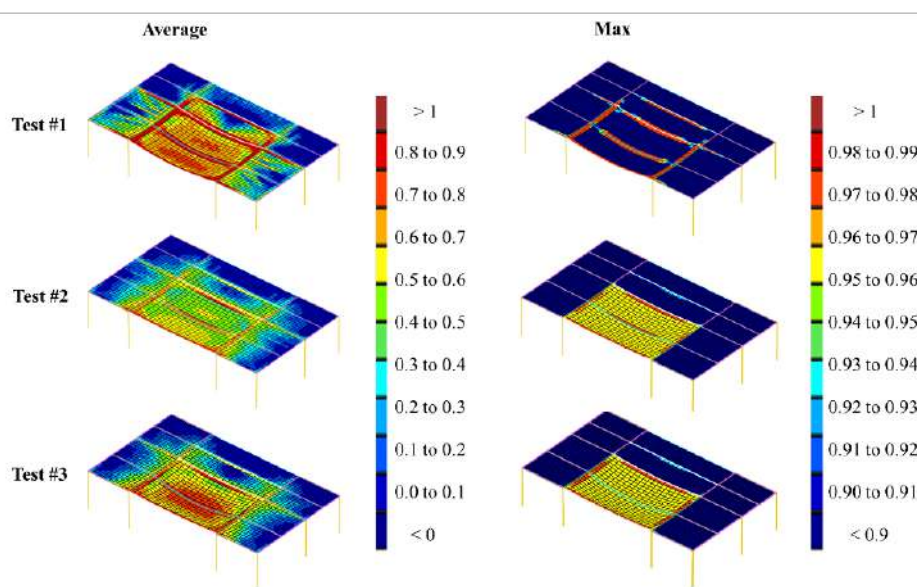


Figure 8. Computed distributions of damage (average and maximum values in each shell) in the concrete slab for the three tests at 69 mins. (Note: 69 min is the time of apparition of a large crack in Test #1)

3.2.3 Discussion on limit state

Figure 9 plots the computed concrete slab damage pattern at 2-hour and the post fire concrete crack patterns observed after the tests. The rebar failure pattern predicted by the simulation is also plotted. The simulation uses a stress-strain curve for the steel reinforcement that, after reaching the yield strength, plateaus up to a strain threshold of 0.05, beyond which the stress drops linearly to zero at 0.10 strain. Thus, failure of rebar is assumed once the strain in the rebars exceeds 0.05 (the steel is in the descending branch). For Test #1, the simulated concrete damage pattern aligns closely with the crack patterns observed in the test, and the simulation accurately predicts rebar failure locations above the central beam and at the north edge of the slab. For Test #2, a lot of small cracks (which closed upon cooling) were observed after the test but there was no rebar failure observed. Besides, more small cracks were observed at the south half of slab compared with the north half of the slab. This is also consistent with the observation in the numerical model. The simulation indicates a broader high damage zone (colored red) on the southern slab, with a maximum damage value significantly reduced from that of Test #1, suggesting effective load redistribution through the rebar network. For Test #3, the location of the observed concrete cracks correlates well with the high damage zone identified in the simulation. The consistency in the damage pattern between the test and simulation indicates that the numerical model can capture the concrete and rebar limit states of the tests.

Figure 10 plots the vertical displacement at slab center for the Test #1, with the black star marking the moment flame leakage was observed during the test, and a red star indicating the time of rebar failure in the simulation. It was noted during the test that the rupture of the steel rebar led to rapid expansion of the concrete crack, subsequently resulting in flame leakage. Therefore, rebar failure can serve as an indicator of potential flame leakage. The temporal alignment between the rebar failure and the onset of flame leakage underscores the effectiveness of the numerical model in accurately predicting the limit states, highlighting its potential as a predictive tool for assessing structural integrity under fire conditions.

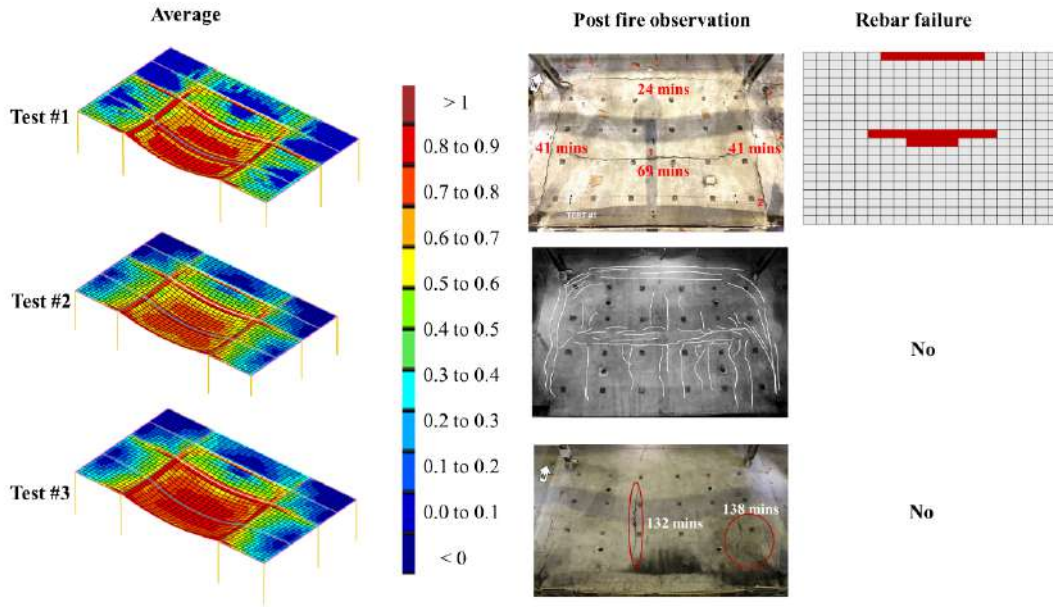


Figure 9. Comparison between observed cracks and computed distributions of damage (average and maximum values) in the concrete slab for the three tests at 2-hour. (Note: small cracks for test #2 are marked as white lines.)

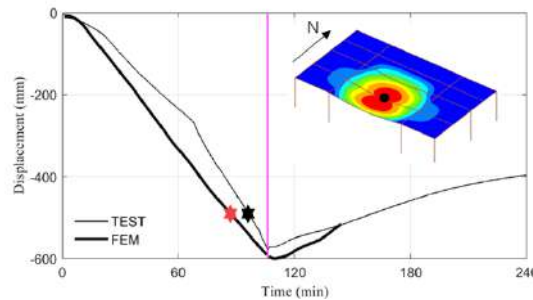


Figure 10. Vertical displacements at the center of the fire exposed composite floor for the Test #1. (Note: the pink line indicates the stop of the test.)

4 PARAMETRIC ANALYSIS

4.1 Minimum required slab rebar area

Both experimental and numerical findings highlight the critical role of slab rebar area in the fire response of the composite floor systems. A detailed analysis is performed to identify the minimum required rebar area for resisting 2-hour of standard ASTM E119 fire, focusing on avoiding reinforcement failure or simulation failures until the full cooling. Results are plotted in Figure 11. The analysis is conducted for the two different design approaches, namely the prescriptive (central beam protected, Test #1) and the performance-based design (central beam unprotected, Test #3). For Test #1, it is determined that increasing the rebar area from $60 \text{ mm}^2/\text{m}$ to $100 \text{ mm}^2/\text{m}$ allows the simulations to converge to the end without integrity failure. Although a rebar area of $80 \text{ mm}^2/\text{m}$ allowed the simulation to converge until 180 mins, rebar failure is observed during the cooling phase. Therefore, a rebar area of $100 \text{ mm}^2/\text{m}$ is identified as the minimum for the prescriptive design of this system (for the specific parameters considered here), which can distribute loads across cracks uniformly and avoid damage concentration at the existing cracks. It is important to note that the threshold of $100 \text{ mm}^2/\text{m}$ is determined based on the same welded wire mesh used in the test, characterized by a yield stress of 755 MPa.

For the floors with unprotected central beam, the determined minimum rebar area is $170 \text{ mm}^2/\text{m}$ to avoid integrity failure. Though the simulation with $150 \text{ mm}^2/\text{m}$ of rebar area can run to the end, rupture of steel reinforcement is observed during cooling phase, indicating that this rebar level was insufficient for ensuring structural resilience throughout the entire test, including the cooling period. The steel grade used in Test #3 was S480. Therefore, the minimum amount of steel reinforcement for the floor with unprotected central beam is slightly higher (8% more when the S480 used in Test #3 is converted to S755 used in Test #1) than for floors with protected central beams. This suggests that removing fire protection from central beams, while still ensuring structural integrity for two hours, could offer cost and sustainability advantages. These conclusions pertain to the context of the NIST floor prototypes and 2-hour ASTM E119 fire, which are based on U.S. design practices.

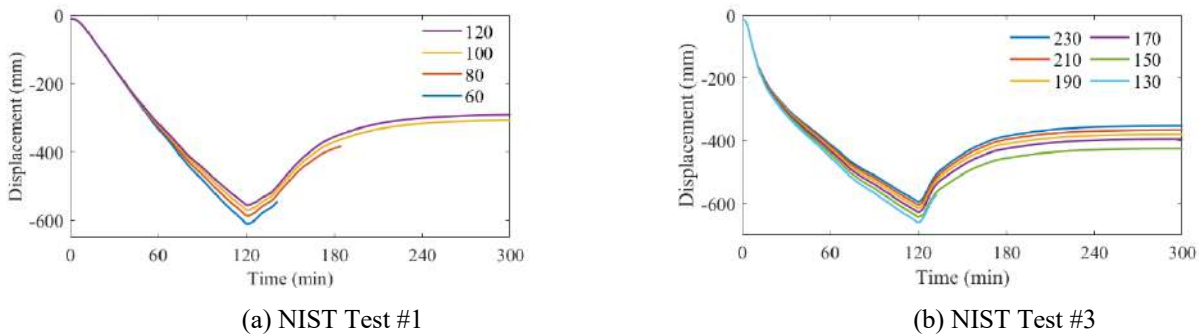


Figure 11. Central beam displacement as a function of the rebar areas (mm^2/m) in the slab, for the designs of (a) and (b)

4.2 Single slab model

The full building model in Section 3 accurately predicts the test observations but can be computationally expensive. This limits its application in probabilistic analyses, which requires running many simulations to account for variability and uncertainty in input parameters and conditions. For computational efficiency, an alternative model is developed, which excludes the surrounding slabs not exposed to the fire, as shown in Figure 12 (a). Translation in the x-direction is blocked to capture in a simplified manner the continuity of the concrete slab in that direction, which in the real structure restrains the thermal expansion.

The comparison of the vertical displacement between the single slab model and the test is shown in Figure 12 (b), indicating that the single slab model effectively captures the overall displacements. Unlike the full building model which shows an asymmetric response between the north and south beams due to surrounding bays, the single slab model shows a symmetrical displacement and damage pattern. Additionally, within the single slab model, the steel rebar and beams for Test #3 reach their limit strain, which is not observed in the full building model. This is expected to come from the beneficial effect of continuity at the boundaries in the full building model, known to improve the membrane action [14, 15].

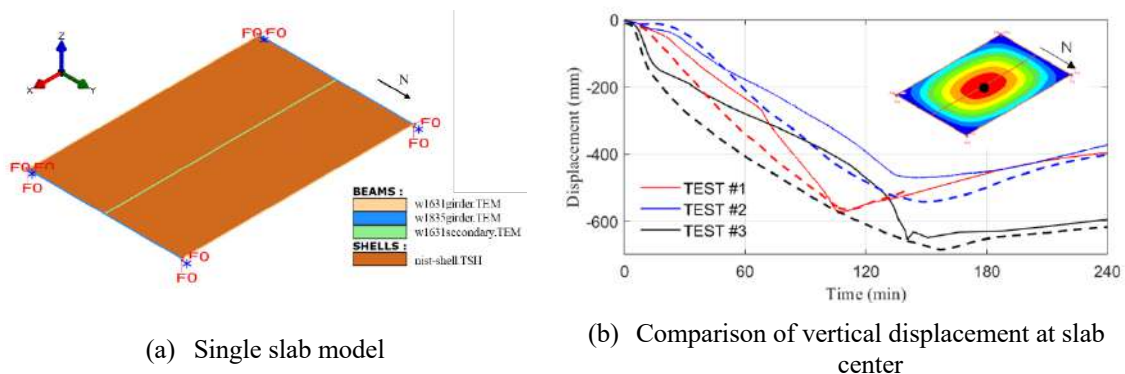


Figure 12. Single slab model and correspond response

While the single slab model may not achieve the same level of precision as the full building model in predicting the damage pattern, it provides a satisfactory prediction on the overall displacement response of the floor system. Crucially, the single slab model can reduce the computational cost significantly (for Test #1, the computation time of single slab model is 22% of the full building model), which is particularly advantageous for conducting probabilistic analyses.

5 PRELIMINARY STUDY ON THE FRAGILITY CURVES

5.1 Selection of Probabilistic Parameters

Probabilistic structural fire analyses are conducted under natural fires. Uncertainties in five parameters are considered. The opening factor is taken as a random variable. Uncertainties in temperature-dependent thermal properties (thermal conductivity, specific heat, density) of the sprayed fire resistive material (SFRM) and the mechanical properties of the steel for the beams are also considered based on the equations proposed in [7]. In addition, the fire load is varied in the range 100-2100 MJ/m², as the intensity measure.

5.2 Definition of Damage States

Five damage states are defined. The criteria for defining damage states zero to three are based on the residual vertical deflection Δ_s after the end of the fire [16], see Table 1. Damage state four is taken as the integrity failure of the floor. This is defined in the numerical model as lack of convergence due to either failure of the steel reinforcement or runaway vertical deflections.

Table 1 Definition of damage states for the composite floor system

Damage state	0	1	2	3	4
Criterion	$\Delta_s/l \leq 1/240$	$1/240 \leq \Delta_s/l < 1/120$	$1/120 \leq \Delta_s/l < 1/60$	$1/60 \leq \Delta_s/l$	$1/60 \leq \Delta_s/l$ and (non-convergence or steel failure)

Remark: Δ_s is the residual vertical deflection at the center of the slab. $l = \sqrt{l_1 l_2}$ where l_1 and l_2 are the spans of slab.

5.3 Development of Fragility Curves

The fragility curves are developed to depict the exceedance probability of the damage states and are conditional to the fire load. To generate the fragility points $P(DS = DS_i | q_m)$ for DS_i under a given fire load q_m , fire-thermo-mechanical analyses are conducted with the non-linear FE model. Between 10 to 30 simulations are run at each fire load level taken between 100 MJ/m² to 2100 MJ/m² with a step ranging from 50 MJ/m² to 200 MJ/m². Once the fragility points at different fire loads are generated, the fragility curves are fitted using a two-parameter lognormal distribution function, as given in Eq. (1).

$$FFs(DS_i | q) = P(DS \geq DS_i | q) = \Phi \left[\frac{\ln(\text{MinMaxScaler}(q)) - \mu}{\sigma} \right] = \frac{1}{2} \left[1 + \text{erf} \left(\frac{\ln \left(\frac{q - q_{min}}{q_{max} - q_{min}} \right) - \mu}{\sigma \sqrt{2}} \right) \right] \quad (1)$$

where Φ is the standardized cumulative normal distribution function, $\text{MinMaxScaler}(q)$ normalizes the fire load to range [0, 1], with $q_{min} = 100 \text{ MJ/m}^2$ and $q_{max} = 2100 \text{ MJ/m}^2$, erf is the Gauss error function, μ and σ are two parameters characterizing the fragility functions and are determined by maximizing the best fit with the data from the analysis.

5.4 Results

Fire fragility curves are established for the three NIST prototypes based on the single slab model introduced in Section 4.2. The curves are shown in Figure 13.

The comparison between the Test #3 and Test #1 indicates that the Test #3 (PBD) has a higher probability of reaching mild and moderate damage than the Test #1 (prescriptive) when the fire load ranges from 100 to 1000 MJ/m², but a much lower probability of reaching DS4 (integrity failure) when the fire load lies

between 700 to 2100 MJ/m^2 . This is because the development of TMA in Test #3 relies on large deflections, resulting in a higher likelihood of damage states 1-3 compared with the prescriptive design. Yet the development of TMA at large deflection successfully prevents excessive localized damage and wire rupture on the slab center, preventing the early development of full-depth cracks as observed in the NIST experiment, and therefore reducing the probability of integrity failure. The design based on TMA is thus more robust under natural fires than the current prescriptive design.

The comparison of the DS4 fragility curve for Test #2 and #3 reveals that, for the same rebar area, a composite floor with unprotected central beams is more likely to experience integrity failure than a floor with protected central beams once the fire load becomes higher than 1100 MJ/m^2 .

It is important to note that the above conclusions pertain to the context of the NIST floor prototypes, which are based on U.S. design practice.

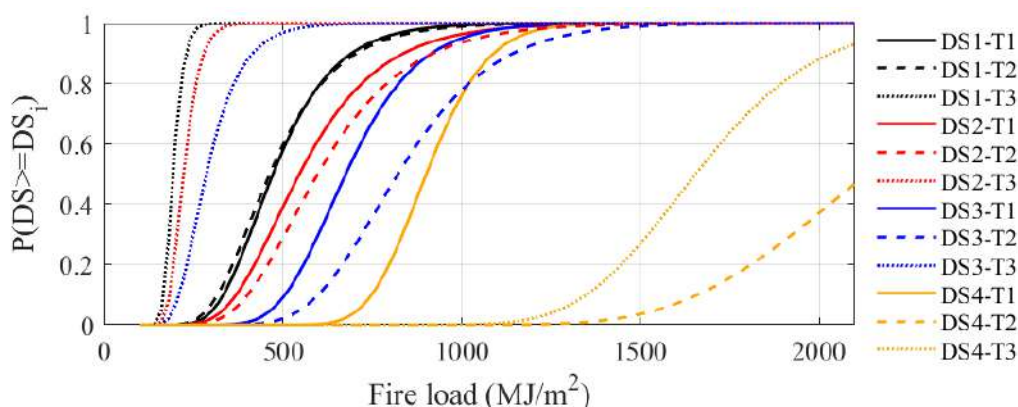


Figure 13: Fragility curves for the three prototypes of composite floors tested by the NIST

6 CONCLUSION

This study conducted a finite element (FE) analysis of steel-concrete composite floors, leveraging data from three full-scale fire tests at NIST to evaluate the U.S. prescriptive design and performance-based design methods. The three experiments included a prescriptive fire design (#1), a design with enhanced steel reinforcement in the slab (#2), and a design with enhanced reinforcement but without fire protection on the central steel beam (#3). The main conclusions are summarized below.

The study reveals that the minimum permitted rebar area of 60 mm^2/m in current U.S. prescriptive design codes may not be sufficient for two-hour fire resistance of the system, as evidenced by the observed integrity failure in both the experiment and the FE model. For designs with enhanced reinforcement (#2) and unprotected central beam (#3), both the experiment and FE model show the survival of the composite floor system until the end of the test. The FE models successfully predict the limit states and capture the beneficial effects of tensile membrane action and the importance of adequate steel reinforcement in composite floor systems.

The numerical study determined the minimum reinforcement necessary to avoid integrity failure until the full cooling. For the prescriptive design, an increase from 60 mm^2/m to 100 mm^2/m of the S755 mesh is required to survive the 2-hr ASTM E119 fire. For the performance-based design, the minimum amount of S480 rebars is 170 mm^2/m to develop tensile membrane action with unprotected central beam and survive the fire exposure. Using a consistent steel grade for comparison, the minimum amount for the performance-based design would be 108 mm^2/m of S755 mesh, thus only a limited increase from the prescriptive design to offset the removal of insulation on the central beam.

Additionally, a single slab FE model is established and shown to be a good trade-off between accuracy and computational efficiency for use in probabilistic studies. This single slab model is used for constructing fragility curves for the three NIST prototypes under physically based (i.e., natural) fires. The results indicate that Test #3 (PBD) with unprotected central beam has a higher likelihood of experiencing mild and moderate damage than Test #1 (prescriptive) but a lower probability of experiencing failure. This is because

the development of tensile membrane action relies on large deflections, but on the other hand offers a robust load path. The developed fragility curves will be used in future studies on lifetime cost analysis.

ACKNOWLEDGMENTS

This work was performed under the following financial assistance award 60NANB22D110 from U.S. Department of Commerce, National Institute of Standards and Technology. This support is gratefully acknowledged. The statements, findings, conclusions, and recommendations are those of the authors and do not necessarily reflect the views of the NIST or the U.S. Department of Commerce.

REFERENCES

- [1] C.G. Bailey, Membrane action of slab/beam composite floor systems in fire, *Engineering Structures* 26(12) (2004) 1691-1703.
- [2] T. Gernay, Performance-based design for structures in fire: Advances, challenges, and perspectives, *Fire Safety Journal* 142 (2024) 104036.
- [3] L. Choe, S. Ramesh, X. Dai, M. Hoehler, M. Bundy, R. Bryant, B. Story, A. Chakalis, A. Chernovsky, Fire resilience of a steel-concrete composite floor system: full-scale experimental evaluation for US Prescriptive approach with a 2-hour fire-resistance rating (test# 1), Technical Note (NIST TN), National Institute of Standards and Technology, Gaithersburg, MD, 2021.
- [4] L. Choe, M. Hoehler, M. Bundy, R. Bryant, B. Story, A. Chakalis, A. Chernovsky, S. Ramesh, X. Dai, Fire resilience of a steel-concrete composite floor system: full-scale experimental evaluation for influence of slab reinforcement (test# 2), Technical Note (NIST TN), National Institute of Standards and Technology, Gaithersburg, MD, 2022.
- [5] S. Ramesh, L. Choe, M. Hoehler, M. Bundy, R. Bryant, G.D.C. Torres, B. Story, A.R. Chakalis, A.A. Chernovsky, P. Deardorff, Fire Resilience of a Steel-Concrete Composite Floor System: Full Scale Experimental Evaluation for Influence of Slab Reinforcement and Unprotected Secondary Beam (Test# 3), Technical Note (NIST TN), National Institute of Standards and Technology, Gaithersburg, MD, 2023.
- [6] J.-M. Franssen, T. Gernay, Modeling structures in fire with SAFIR®: Theoretical background and capabilities, *Journal of Structural Fire Engineering* 8(3) (2017) 300-323.
- [7] N. Elhami Khorasani, P. Gardoni, M. Garlock, Probabilistic fire analysis: material models and evaluation of steel structural members, *Journal of Structural Engineering* 141(12) (2015) 04015050.
- [8] C. Ma, T. Gernay, Numerical analysis of full-scale structural fire tests on composite floor systems (Under review), *Fire safety journal* (2024).
- [9] EN1994-1-2, Eurocode 4: Design of composite steel and concrete structures - Part 1-2: General rules-Structural fire design, 2005.
- [10] J. Jiang, J.A. Main, J.M. Weigand, F. Sadek, Reduced-order modeling of composite floor slabs in fire. I: Heat-transfer analysis, *Journal of Structural Engineering* 146(6) (2020) 04020080.
- [11] EN1992-1-2, Eurocode 2: Design of Concrete Structures - Part 1-2: General rules - Structural fire design, 2004.
- [12] T. Gernay, A. Millard, J.-M. Franssen, A multiaxial constitutive model for concrete in the fire situation: Theoretical formulation, *International Journal of Solids and Structures* 50(22-23) (2013) 3659-3673.
- [13] S. Ni, T. Gernay, Considerations on computational modeling of concrete structures in fire, *Fire Safety Journal* 120 (2021) 103065.
- [14] T. Gernay, N.E. Khorasani, Recommendations for performance-based fire design of composite steel buildings using computational analysis, *Journal of Constructional Steel Research* 166 (2020) 105906.
- [15] J. Jiang, H. Qi, Y. Lu, G.-Q. Li, W. Chen, J. Ye, A state-of-the-art review on tensile membrane action in reinforced concrete floors exposed to fire, *Journal of Building Engineering* 45 (2022) 103502.
- [16] S. Ni, T. Gernay, A framework for probabilistic fire loss estimation in concrete building structures, *Structural Safety* 88 (2021) 102029.

SIMULATION OF BUILT-UP COLD-FORMED STEEL-LIGHTWEIGHT CONCRETE (CFS-LWC) COMPOSITE BEAMS SUBJECTED TO ELEVATED TEMPERATURES

Rohola Rahnavard¹, Hélder D. Craveiro², Rui A. Simões³, Luís Laím⁴, Aldina Santiago⁵, Leroy Gardner⁶

ABSTRACT

Cold-formed steel (CFS) products are extremely versatile and can be used in multiple applications. Recent experiments conducted by the authors have shown that mobilising composite action within systems comprising cold-formed steel beams and lightweight concrete is feasible and can lead to substantial improvements in structural performance; therefore, investigating their fire performance is essential. However, performing experiments on composite beams subjected to elevated temperatures is expensive and requires specialist equipment. An advanced finite element simulation can be used as an alternative means of studying their behaviour; this is, therefore, the focus of the present study. The aim is to develop a detailed numerical model to represent the fire behaviour of innovative built-up CFS-lightweight concrete (LWC) composite beams. The numerical modelling approach is described and validated against existing experimental data. The accuracy of the simulations and the key findings are discussed.

Keywords: Cold-formed steel; finite element modelling; fire tests; fracture; heat transfer analysis; lightweight concrete

1 INTRODUCTION

Composite steel beam-concrete slab systems are favoured in building construction for their reduced cost and shorter construction duration than conventional concrete beam-slab systems. The growing use of cold-formed steel (CFS) in construction relates to its versatility and high strength-to-weight ratio. Recently, researchers have turned their attention to incorporating CFS sections into composite systems, encompassing columns [1 – 9] and beams [10 – 16]. Rahnavard et al. [13– 16] recently examined the flexural behaviour of composite beams consisting of built-up cold-formed steel sections with various degrees of shear connections through tests and simulations. Many investigations have been carried out on the structural

¹ Ph.D. candidate, University of Coimbra, ISE, ARISE, Department of Civil Engineering, Coimbra, Portugal
e-mail: rahnavard@uc.pt, ORCID: <https://orcid.org/0000-0001-9399-104X>

² Researcher, University of Coimbra, ISE, ARISE, Department of Civil Engineering, Coimbra, Portugal
e-mail: heldercraveiro.eng@uc.pt, ORCID: <https://orcid.org/0000-0001-8590-5885>

³ Associate Professor, University of Coimbra, ISE, ARISE, Department of Civil Engineering, Coimbra, Portugal
e-mail: rads@uc.pt, ORCID: <https://orcid.org/0000-0002-1793-3291>

⁴ Assistant Professor, University of Coimbra, ISE, ARISE, Department of Civil Engineering, Coimbra, Portugal
e-mail: luislaim@uc.pt, ORCID: <https://orcid.org/0000-0002-8342-3695>

⁵ Associate Professor, University of Coimbra, ISE, ARISE, Department of Civil Engineering, Coimbra, Portugal
e-mail: aldina@dec.uc.pt, ORCID: <https://orcid.org/0000-0003-3646-4926>

⁶ Professor, Department of Civil and Environmental Engineering, Imperial College London, South Kensington Campus, London SW7 2AZ, UK
e-mail: leroy.gardner@imperial.ac.uk, ORCID: <https://orcid.org/0000-0003-0126-6807>

performance of composite beam-slab systems subject to elevated temperature [17– 19]. Zhang et al. [17] investigated the performance of composite beam-slab systems subjected to elevated temperatures using experimental and numerical tools. Nguyen et al. [19] tested three composite floor systems to examine the effect of the bending stiffness of the protected main beams on the fire behaviour of a single-storey building. Although some studies have been carried out to analyse the flexural behaviour of CFS-concrete composite beams at ambient and elevated temperatures, their fire performance is yet to be fully examined. Given the costs and challenges of conducting physical fire tests, development of a reliable numerical model of CFS-concrete composite beams at elevated temperatures to enable exploration of the response over a broad range of parameters is the focus of the present study. The thermal and mechanical properties of CFS and LWC at elevated temperatures are first explained. Heat transfer analysis of the CFS-LWC composite beam is then presented and discussed. Fire dynamics simulator (FDS) software was used to replicate the temperature development within the electric furnace virtually and extract the gas temperature on the surface of the composite beam to perform an accurate heat transfer analysis. Fire resistance simulations of the CFS-LWC composite beam were then conducted to replicate the structural behaviour, including fracture, of the CFS-LWC composite beams.

2 NUMERICAL SIMULATIONS

2.1 Geometry of the models

The results of a detailed experimental study conducted by Rahnavard et al. [20], featuring fire resistance tests on CFS-LWC composite beams at elevated temperatures, have been selected to validate the developed modelling approach. The geometry of the fire test specimens, corresponding samples of which were also tested at ambient temperature [16], are shown in Figure 1. The CFS built-up beams had a length of 4500 mm, while the distance between the supports was 3900 mm. The length and width of the steel deck were 4152 mm and 1075 mm. Two specimens were tested, namely 2C (two-lipped channels fastened back-to-back) and 2C+C (two-lipped channels fastened back-to-back with an additional lipped channel attached to the bottom of the CFS flange), as shown in Figure 2. In each specimen (2C and 2C+C), 40 bolted shear connectors were used in two rows along the lengths of the beams, each containing 20 connectors. According to [16,20], grade S280GD+Z275 steel and lightweight concrete with a compressive strength of 16 MPa and density of 1384 kg/m³ were used.

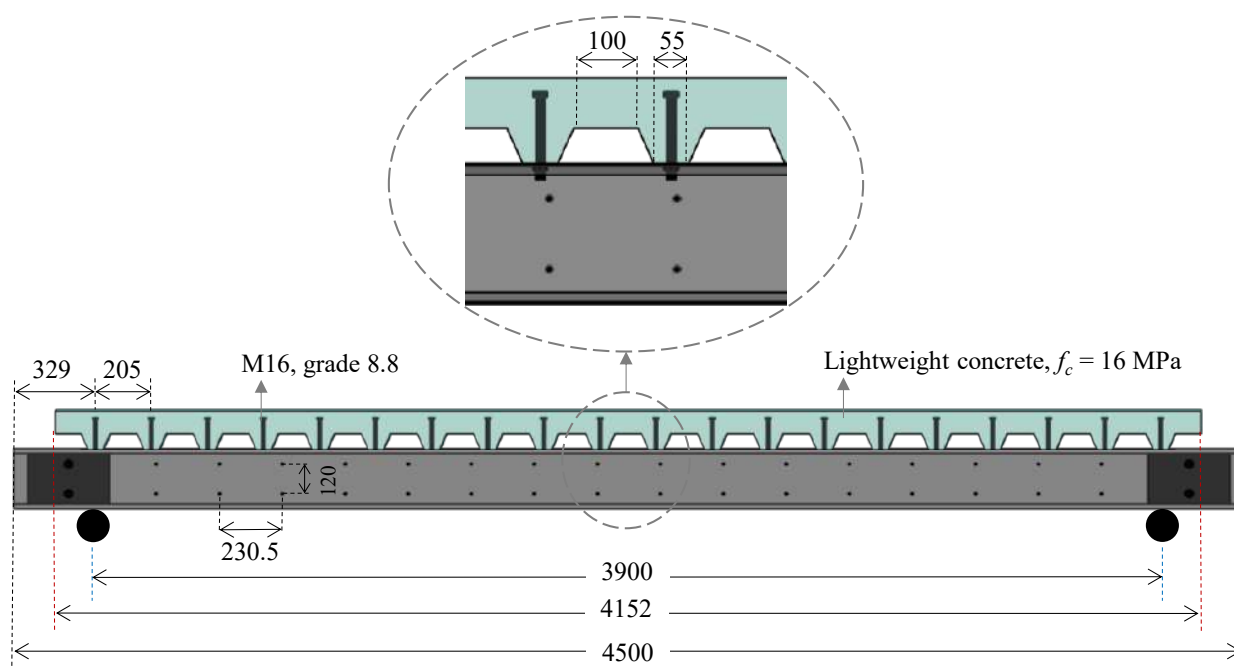


Figure 1. CFS-LWC test geometry [16,20], with dimensions in mm

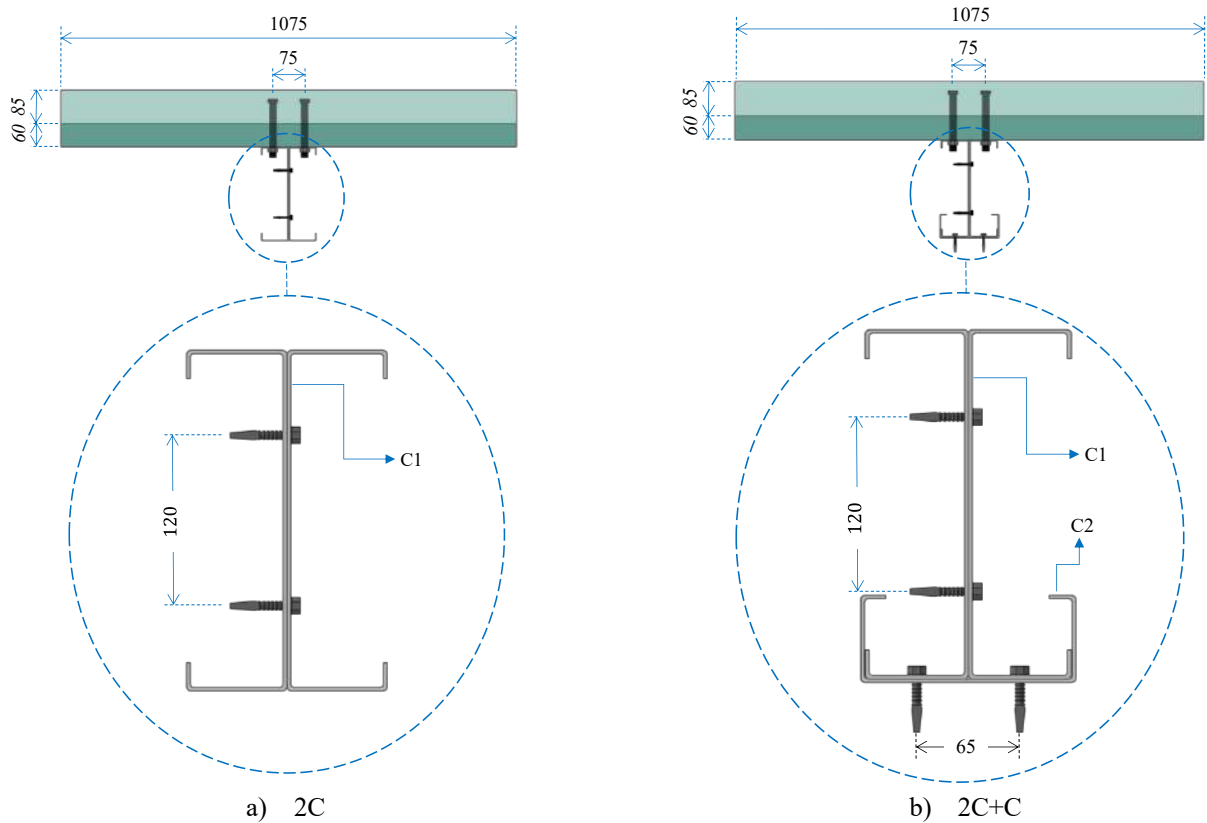


Figure 2. CFS-LWC composite beam cross-sections [16,20], with dimensions in mm

2.2 Simulation of electric furnace

A computational model of an electric furnace was developed using Fire Dynamics Simulator (FDS) software. Then, the model results were calibrated against the extracted air temperature from the electric furnace during the physical fire tests, as shown in Figure 3. A thermocouple was set up to measure the temperature history in both the test and simulation. Figure 3 shows excellent agreement between the results from the tests and FDS. The temperature distribution at different times is shown in Figure 4. The adiabatic surface temperatures (AST) output for different surfaces of the composite beam model that are exposed to direct heat were then extracted from the FDS and used as input to the finite element model (FEM) of the structural system.

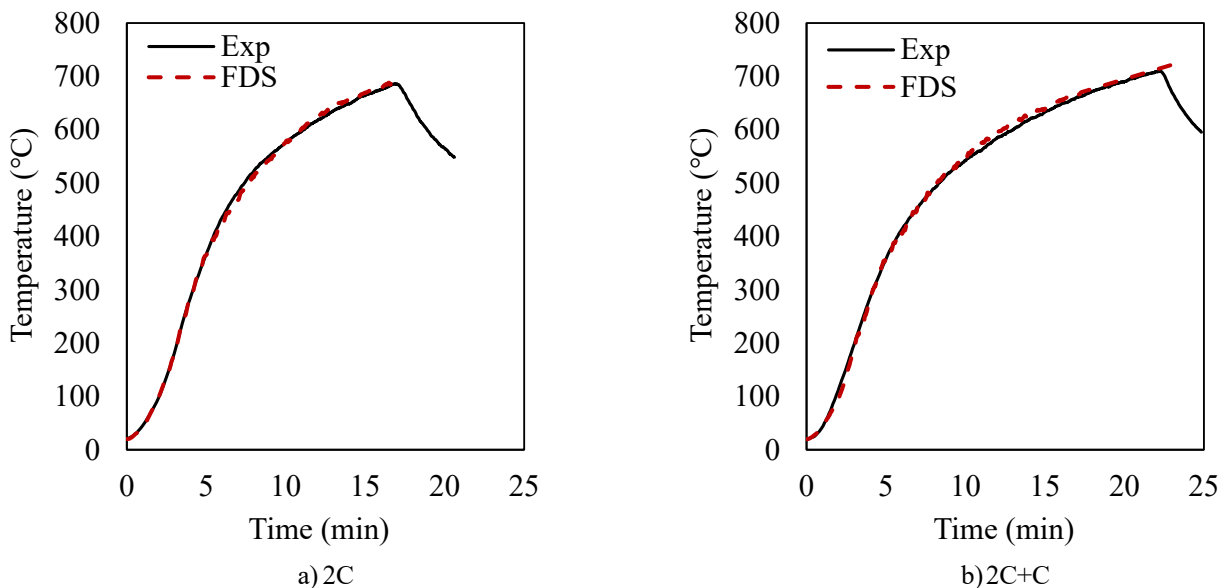


Figure 3. Comparison of air temperature from test and simulation

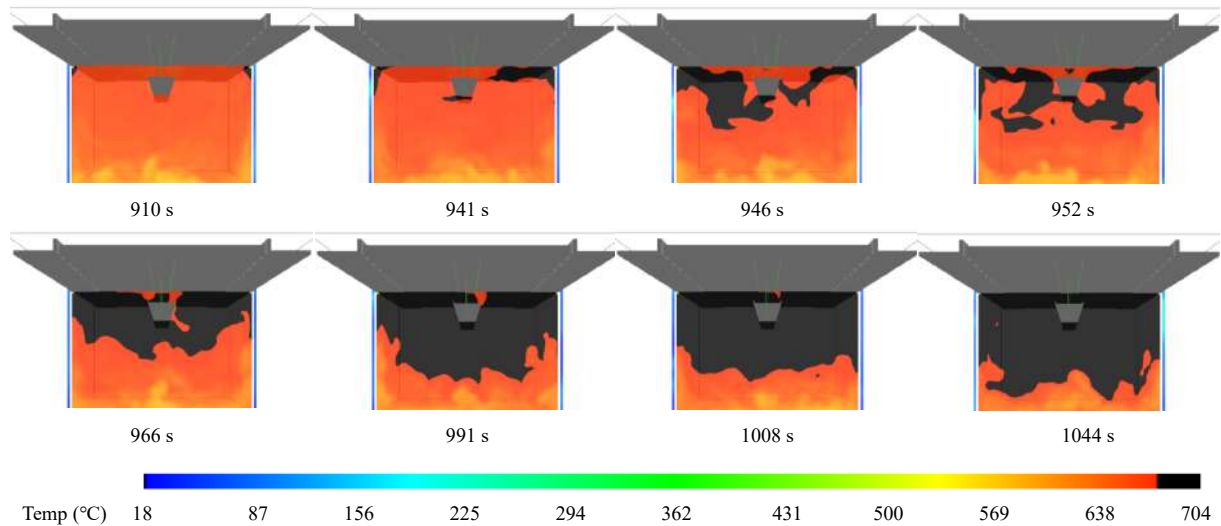


Figure 4. Simulated temperature field at different times

2.3 Heat transfer analysis

Transient heat transfer analyses were conducted using Abaqus [21] to obtain the temperature distribution within the CFS-LWC composite beams. The radiation and convection were defined to simulate the transfer of temperature from the fire to the external surface of the sections, hence determining the boundary conditions of the heat transfer analysis. Amplitudes were defined for different surfaces of the models according to the AST obtained from the calibrated models above, while the ambient temperature was defined as 20 °C. A resultant heat emissivity value of 0.16 was determined for the radiation. A value of 15 (W/m² K) was used for the convective heat coefficient. The heat resistance at the interface can be described using the heat contact conductance parameter. Heat contact conductances of 200 W/m² K and 2000 W/m² K were defined for the CFS-to-LWC and CFS-to-CFS contacts, respectively [8,9].

The CFS parts were modelled using DS4 heat transfer shell elements, while the concrete slab was modelled using DC3D8 heat transfer solid elements available in Abaqus [21]. Moreover, the shear connectors and reinforcement were modelled using DC1D2 heat transfer links.

The thermal properties of the steel and lightweight concrete materials were defined, including the specific heat of the steel c_a and concrete c_c , and the conductivity of the steel λ_a and concrete λ_c . Figures 5 and 6 show the adopted thermal properties of the steel and lightweight concrete, respectively.

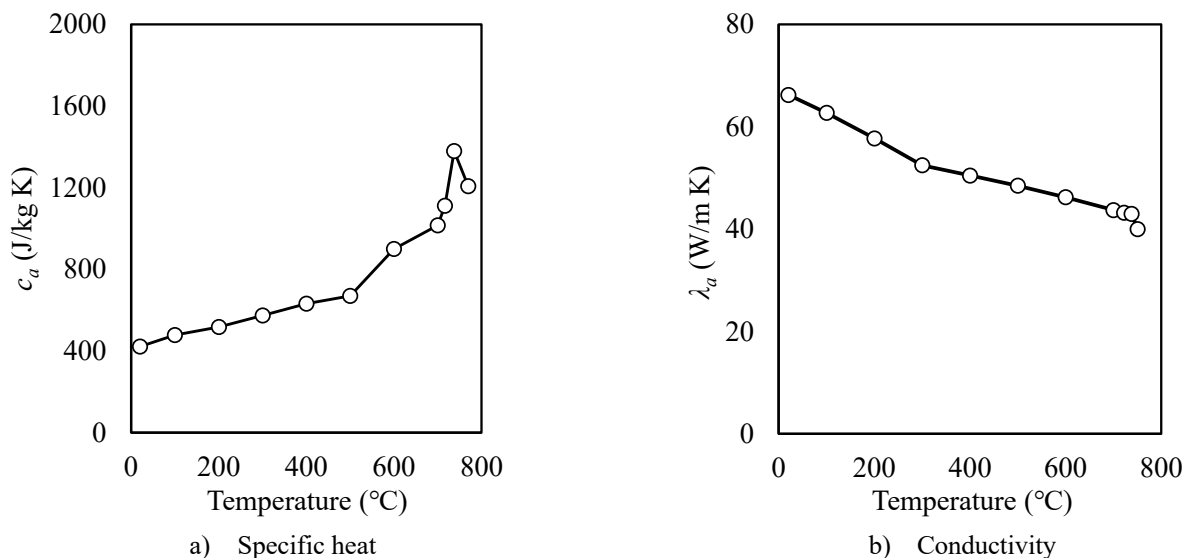


Figure 5. Thermal properties of modelled grade S280GD+Z275 steel [22]

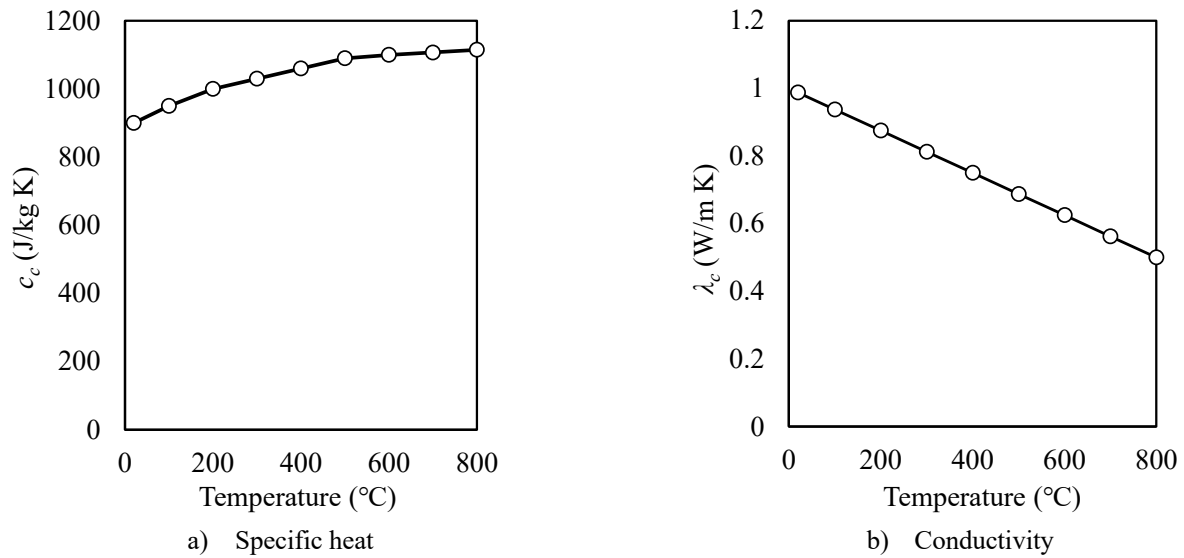


Figure 6. Thermal properties of modelled lightweight concrete [23]

2.4 Fire resistance structural analysis

Two analyses were performed for the structural analysis – a linear buckling analysis and a nonlinear structural analysis. The linear buckling analysis was used to define the initial imperfection. The structural analysis used the Dynamic Explicit Solver by defining the initial imperfection from the linear buckling analysis and importing the temperature distribution from the heat transfer analysis. The interaction between components was defined using “general contact”, with a contact property, including normal and tangential penalty contact with a friction coefficient of 0.3. The fasteners were modelled using the combined “Beam connector and fastener” available in Abaqus. In this technique, the connection between two nodes of two surfaces was defined by the “Beam connector”, and the real radius of the fasteners was defined using the “fastener” tool. The CFS and concrete slab were modelled using S4R shell elements and C3D8R solid elements, respectively.

The imperfection amplitude of $1/1000$ of the beam length was considered to define the initial imperfection, while the first buckling mode was considered for the imperfection shape.

The mechanical properties of CFS and LWC were defined as temperature-dependent. The ambient temperature modulus of elasticity E and the yield (0.2% proof) stress f_y were taken as the measured values of 204 GPa and 306.8 MPa, respectively [24]. The reduction factors for the elastic modulus $\frac{E_\theta}{E}$ and the yield stress $\frac{f_{0.2,\theta}}{f_y}$ at elevated temperatures are listed in Table 1, where E_θ is the elastic modulus and $f_{0.2,\theta}$ is the 0.2% proof stress at elevated temperature θ , respectively. The reduction factors were determined as the ratio between the values obtained at elevated and ambient temperatures. The plastic behaviour of CFS material was defined as temperature-dependent. The plastic true stress-strain curves at different temperatures were obtained by conversion of the engineering plastic strains and stresses following the procedure explained in [24], as shown in Figure 7.

Fracture was considered by defining the equivalent plastic strain at fracture versus average stress triaxiality relationship for S280GD+Z steel at different temperatures, as shown in Figure 8. Detailed procedures regarding the fracture of CFS materials subjected to elevated temperatures can be found in [24].

Table 1. Reduction factors for elastic modulus and 0.2% proof stress for grade S280GD+Z275 steel at elevated temperatures [22]

θ (°C)	20	100	200	300	400	500	600	700
$\frac{E_\theta}{E}$	1.000	0.980	0.841	0.703	0.593	0.414	0.305	0.108
$\frac{f_{0.2,\theta}}{f_y}$	1.000	0.962	0.898	0.728	0.592	0.370	0.253	0.118

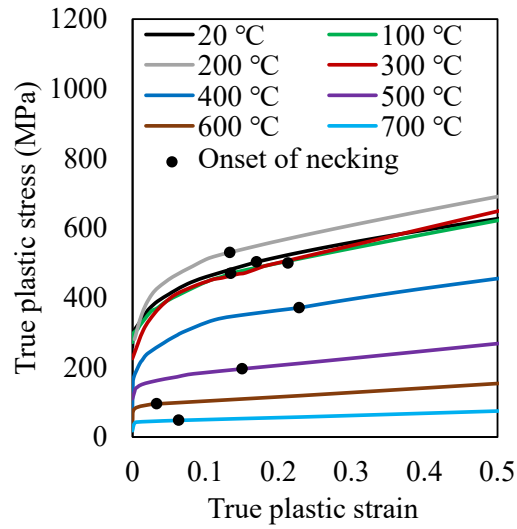


Figure 7. True plastic stress-strain curves of grade S280GD+Z275 steel at elevated temperatures [24]

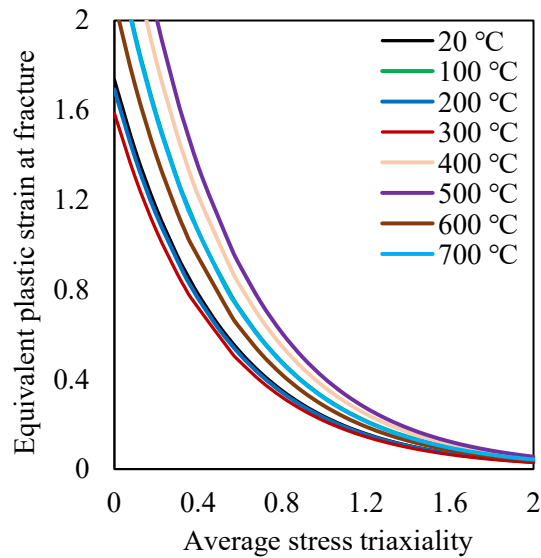


Figure 8. Equivalent plastic strain at fracture versus average stress triaxiality relationship for studied S280GD+Z steel at different temperatures [24]

The mechanical properties of the concrete in the elastic and plastic ranges were defined using a temperature-dependent concrete damage plasticity (CDP) model. The compressive plastic stress-strain curves for lightweight concrete at different temperatures were defined using Eq. 1, where $\sigma_{lc,\theta}$ is the lightweight concrete compressive stress, $f_{lc,\theta}$ is the lightweight concrete compressive strength and $\varepsilon_{c1,\theta}$ is the lightweight concrete ultimate strain at elevated temperature θ . Figure 9 shows the compressive stress-strain relationship of lightweight concrete with a compressive strength of 16 MPa at different temperatures. Note that the reduction factor for the compressive strength of the lightweight concrete was determined according to EN 1994-1-2 [23]. The tensile behaviour of the LWC was defined using tensile stress as a function of fracture energy at different temperatures, in which the tensile strength $f_{lct,\theta}$ and fracture energy of the lightweight concrete $G_{F,\theta}$ at elevated temperature θ were obtained using Eq.2 and Eq.3 [25], respectively.

$$\sigma_{lc,\theta} = \frac{3\varepsilon f_{lc,\theta}}{\varepsilon_{lc1,\theta} \left[2 + \left(\frac{\varepsilon}{\varepsilon_{c1,\theta}} \right)^3 \right]} \quad \varepsilon \leq \varepsilon_{lc1,\theta} \quad (1)$$

$$f_{lct,\theta} = 0.3 f_{lc,\theta}^{2/3} \times \left(0.4 + \frac{0.6\rho}{2200} \right) \quad (2)$$

$$G_{F,\theta} = 73 \times f_{lc,\theta}^{0.18} \quad (3)$$

where ρ is the density of concrete.

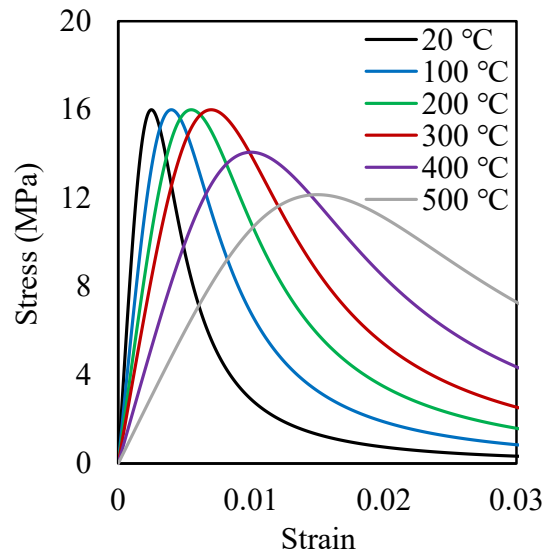


Figure 9. Compressive stress-strain relationship for studied LWC at different temperatures

3 RESULTS AND DISCUSSION

3.1 Heat transfer analysis

Figure 10 compares the temperature history obtained from the experiments and numerical heat transfer analysis. The temperature was measured at the mid-span of the beam at the bottom surface of the CFS and the top surface of the concrete slab. As can be seen, close agreement was achieved between the measured temperatures of the steel and concrete from the numerical and experimental results.

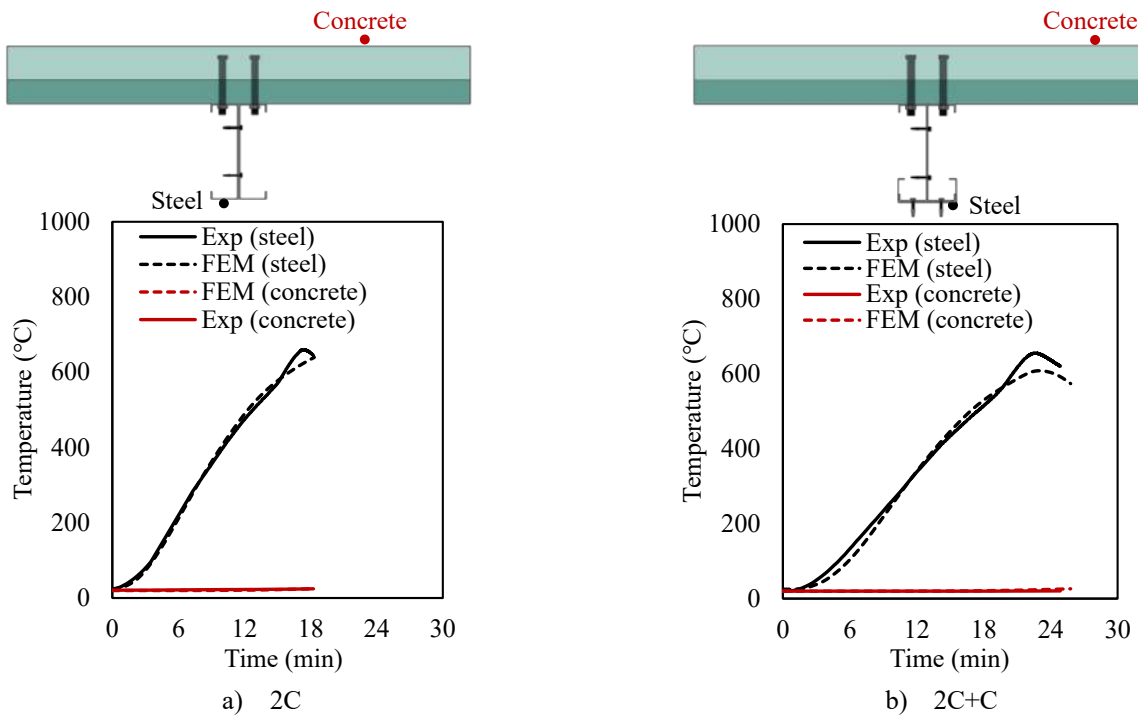


Figure 10. Comparison of steel and concrete temperature from test and simulation

3.2 Fire resistance

The load vs temperature relationship for the experiments and FE models is presented in Figure 11. As can be seen, the simulations represent the fire resistance of the experiments well. For the case of the 2C configuration, the steel temperature corresponding to failure was 653 °C and 640 °C for the test and simulation, respectively, showing a 2% difference. For the 2C+C configuration, the steel temperature corresponding to failure was 652 °C and 620 °C for the test and simulation, respectively, showing a 5% difference. Figure 12 presents a comparison of the fracture of the CFS-LWC composite beam (2C configuration) from the test and simulation, showing close agreement. Similarly, for the case of the CFS-LWC composite beam (2C+C configuration), close agreement was achieved for the occurrence of fracture from the test and simulation. Note that fracture of the steel beam in both the tests and simulations occurred during the cooling phase. The adopted modelling techniques were found to be suitable for predicting the load-bearing capacity of the CFS-LWC composite beams.

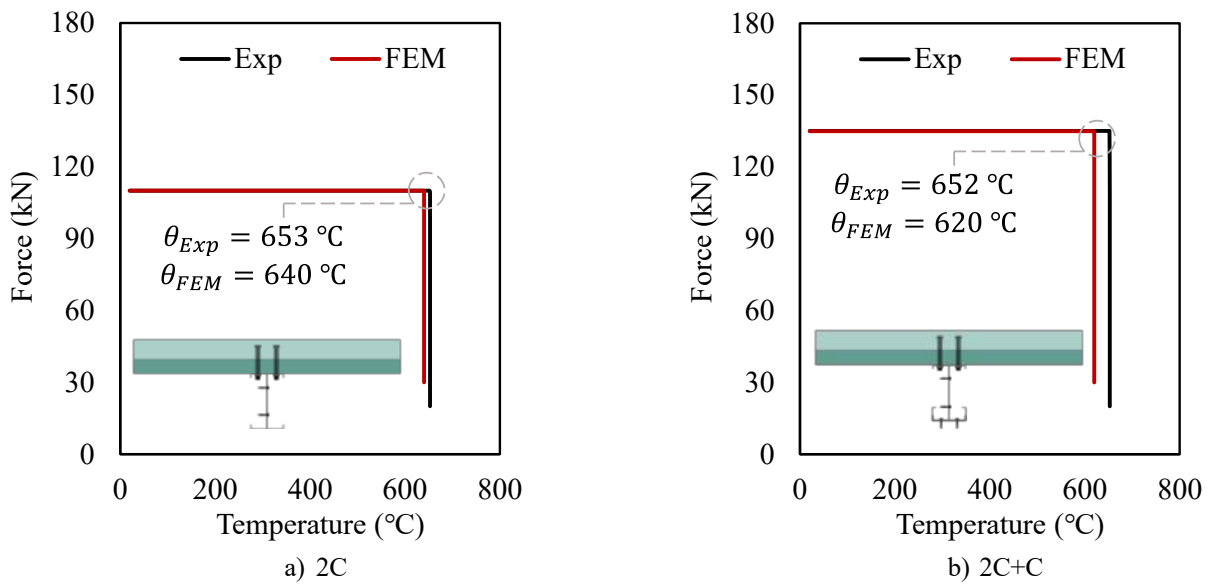


Figure 11. Comparison of fire resistance from tests and FE simulations

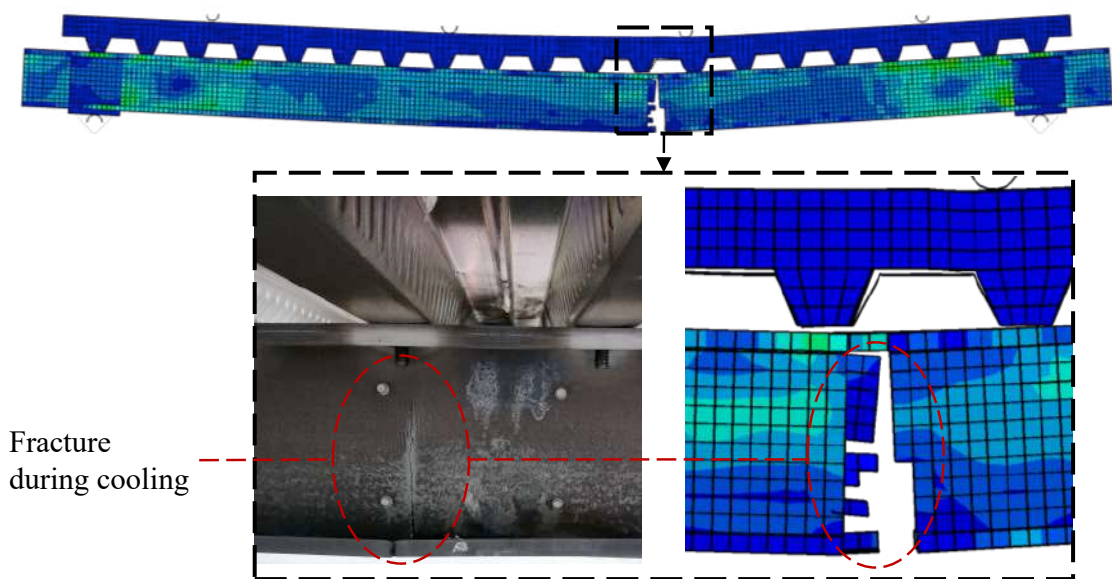


Figure 12. Comparison of observed fracture of CFS-LWC composite beam (2C configuration) from test and FE simulation

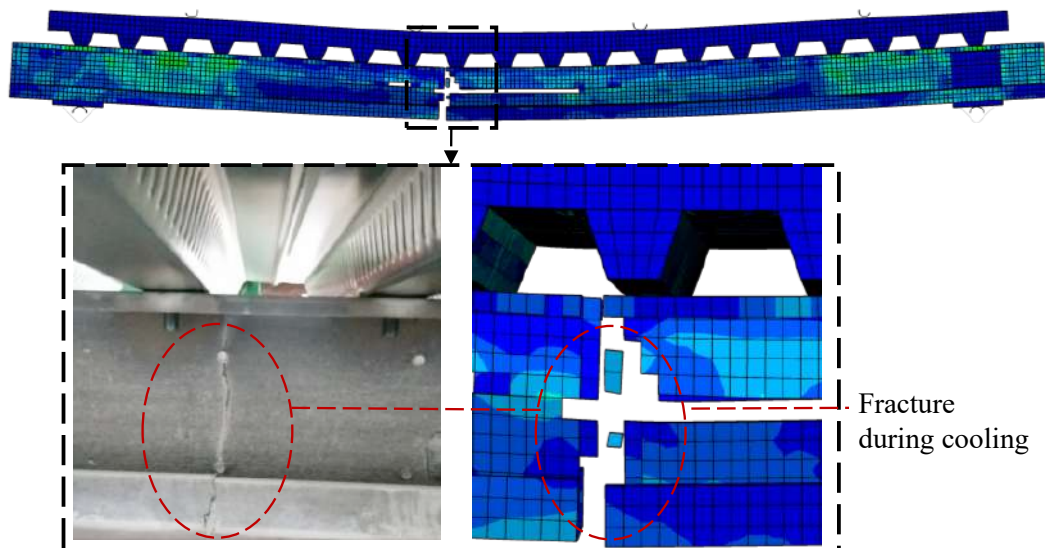


Figure 13. Comparison of observed fracture of CFS-LWC composite beam (2C+C configuration) from test and FE simulation

4 CONCLUSIONS

A numerical study into the simulation procedure to determine the fire resistance of CFS-LWC composite beams has been presented in this paper. A computational model of an electric furnace was first developed using Fire Dynamics Simulator (FDS) software. The results from the FDS were then used to simulate the temperature distribution in the CFS-LWC composite beams, using heat transfer analysis in Abaqus. Finally, the fire resistance of the CFS-LWC composite beams was simulated, considering the fracture behaviour of the CFS material at elevated temperatures; the obtained results were compared with the available test results. The simulations provided consistently accurate predictions of the temperature evolution, fire resistance and failure mode.

ACKNOWLEDGMENTS

This work is financed by national funds through FCT - Foundation for Science and Technology, under grant agreement 2021.06528.BD attributed to the 1st author (<https://doi.org/10.54499/2021.06528.BD>) and under the grant agreement 2020.03588.CEECIND attributed to the 2nd author.

The authors gratefully acknowledge the Portuguese Foundation for Science and Technology (FCT) for its support under the framework of the research project POCI-01-0145-FEDER-031858 - INNOCFSCONC - Innovative hybrid structural solutions using cold-formed steel and lightweight concrete" (<https://doi.org/10.54499/2020.03588.CEECIND/CP1609/CT0008>) financed by FEDER funds through the Competitvity Factors Operational Pro-programme-COMPETE and by national funds through FCT, PCIF/AGT/0062/2018 – INTERFACESEGURA.

REFERENCES

1. Rahnavard, R., Craveiro, H.D., Lopes, M., Simões, R.A., Laím, L., Rebelo, C. Concrete-filled cold-formed steel (CF-CFS) built-up columns under compression: Test and design, *Thin-Walled Structures*, Volume 179, 2022, 109603, <https://doi.org/10.1016/j.tws.2022.109603>.
2. Rahnavard, R., Craveiro, H.D., Simões, R.A., Torabian, S. and Schafer, B.W. CONCRETE-FILLED COLD-FORMED STEEL BUILT-UP COMPOSITE STUB COLUMNS. (2024), *ce/papers*, 7: 209-217. <https://doi.org/10.1002/cepa.3038>
3. Rahnavard, R., Craveiro, H.D. and Simões, R. (2023), New fire resistance design approach for concrete-filled cold-formed steel (CF-CFS) built-up composite column. *ce/papers*, 6: 181-186. <https://doi.org/10.1002/cepa.2428>
4. Rahnavard, R., Craveiro, H.D., Simões, R.A., Laím, L., Santiago, A. Fire resistance of concrete-filled cold-formed steel (CF-CFS) built-up short columns, *Journal of Building Engineering*, Volume 48, 2022, 103854, <https://doi.org/10.1016/j.jobbe.2021.103854>.

5. Rahnavard, R., Craveiro, H. D., Simões, R. A. Flexural resistance of Cold-formed steel-lightweight concrete (CFS-LWC) composite beam, *Thin-Walled Structures*, Volume 193, 2023, 111211, <https://doi.org/10.1016/j.tws.2023.111211>.
6. Craveiro, H.D., Rahnavard, R., Laím, L., Simões, R. A., Santiago, A. Buckling behavior of closed built-up cold-formed steel columns under compression, *Thin-Walled Structures*, Volume 179, (2022), 109493, <https://doi.org/10.1016/j.tws.2022.109493>
7. Rahnavard, R., Craveiro, H.D., Simões, R.A., Laím, L., Santiago, A. Buckling resistance of concrete-filled cold-formed steel (CF-CFS) built-up short columns under compression, *Thin-Walled Structures*, Volume 170, 2022, 108638, <https://doi.org/10.1016/j.tws.2021.108638>.
8. Rahnavard, R., Craveiro, H.D., Simões, R.A., Santiago, A. Equivalent temperature prediction for concrete-filled cold-formed steel (CF-CFS) built-up column sections (part A), *Case Studies in Thermal Engineering*, Volume 33, 2022, 101928, <https://doi.org/10.1016/j.csite.2022.101928>.
9. Rahnavard, R., Craveiro, H.D., Simões, R.A., Santiago, A. Equivalent temperature prediction for concrete-filled cold-formed steel (CF-CFS) built-up column sections (part B), *Case Studies in Thermal Engineering*, Volume 35, 2022, 102111, <https://doi.org/10.1016/j.csite.2022.102111>.
10. Kyvelou, P., Gardner, L., Nethercot, D. A. Design of Composite Cold-Formed Steel Flooring Systems, *Structures*, Volume 12, 2017, Pages 242-252, <https://doi.org/10.1016/j.istruc.2017.09.006>.
11. Kyvelou, P., Gardner, L. and Nethercot, D. A. (2018). Finite element modelling of composite cold-formed steel flooring systems. *Engineering Structures*. 158, 28-42. <https://doi.org/10.1016/j.engstruct.2017.12.024>.
12. Kyvelou, P., Gardner, L., Nethercot, D. A. Testing and Analysis of Composite Cold-Formed Steel and Wood-Based Flooring Systems. *Journal of Structural Engineering*, 2017, 143(11): 04017146
13. Rahnavard, R., Craveiro, H.D., Simões, R.A., Torabian, S. and Schafer, B.W. Understanding the behavior of built-up cold-formed steel lightweight concrete (CFS-LWC) composite beams. (2024), *Proceedings of the Annual Stability Conference Structural Stability Research*, Texas, USA.
14. Rahnavard, R., Craveiro, H.D. and Simões, R. (2023), Flexural resistance of Cold-formed steel-lightweight concrete (CFS-LWC) composite beam. *ce/papers*, 6: 176-180. <https://doi.org/10.1002/cepa.2479>
15. Rahnavard, R., Craveiro, H. D., Simões, R. A., Torabian, S., Schafer, B.W. Built-up cold-formed steel lightweight concrete (CFS-LWC) composite beams: simulation and design, 9th International Conference of Thin-Walled Structures, Sydney, 2023.
16. Rahnavard, R., Craveiro, H. D., Simões, R. A., Laím, L., Santiago, A. Test and design of built-up cold-formed steel-lightweight concrete (CFS-LWC) composite beams, *Thin-Walled Structures*, Volume 193, 2023, 111211, <https://doi.org/10.1016/j.tws.2023.111211>.
17. Zhang, Y., Liu, J.X., Tan, K.H. Boundary continuity effect on performance of composite beam-slab sub-assemblages at elevated temperature, *Journal of Constructional Steel Research*, Volume 198, 2022, 107523, <https://doi.org/10.1016/j.jcsr.2022.107523>.
18. Bailey, C.G., Toh, W.S., Small-scale concrete slab tests at ambient and elevated temperatures, *Engineering Structures*, Volume 29, Issue 10, 2007, Pages 2775-2791, <https://doi.org/10.1016/j.engstruct.2007.01.023>.
19. Nguyen, T.T., Tan, K.H. Behaviour of composite floors with different sizes of edge beams in fire, *Journal of Constructional Steel Research*, Volume 129, 2017, Pages 28-41, <https://doi.org/10.1016/j.jcsr.2016.10.018>.
20. Rahnavard, R., Craveiro, H.D., Simões, R.A., Santiago, A., Laím, L. and Gardner, L. BUILT-UP COLD-FORMED STEEL-LIGHTWEIGHT CONCRETE (CFS-LWC) COMPOSITE BEAMS SUBJECTED TO ELEVATED TEMPERATURES. (2024), *ce/papers*, 7: 202-208. <https://doi.org/10.1002/cepa.3037>
21. Abaqus 2021, *Analysis User's Guide*, Version 6.17 Dassault Systèmes Simulia USA.
22. Craveiro, H.D., Rodrigues, J.P.C., Santiago, A., Laím, L. Review of the high temperature mechanical and thermal properties of the steels used in cold formed steel structures – The case of the S280 Gd+Z steel, *Thin-Walled Structures*, Volume 98, Part A, 2016, Pages 154-168, <https://doi.org/10.1016/j.tws.2015.06.002>.
23. EN 1994-1-2, Eurocode 4: Design of steel and composite structures, Part 1.2: Structural fire design. ENV 1994-1-2, 2003.
24. Rahnavard, R., Craveiro, H.D., Simões, R.A., Gardner, L. Fracture behaviour of thin-walled cold-formed steel at elevated temperatures. (2024), *Construction and Building Materials*, (under review).
25. CEB-FIP model code. Fib model code for concrete structures 2010. Doc Competence Cent Siegmund Kästl eK, Ger 2010

CONCRETE STRUCTURES IN FIRE

A MODEL FOR THE EFFECT OF THERMAL SPALLING IN RC COLUMNS

David L. Peña¹, Carmen Ibáñez², Vicente Albero³, Antonio Hospitaler⁴, Andrés Lapuebla-Ferri⁵,
Héctor Saura⁶

ABSTRACT

Reinforced concrete (RC) members can lose part of their bearing capacity because of the phenomenon of spalling when the increase in the internal pore pressure due to water evaporation causes the loss of part of the concrete. Spalling is a stochastic phenomenon that usually occurs within the first 30 minutes of fire exposure and may affect any area of the exposed surface of a given RC member, making its occurrence hardly predictable. There are several models aimed at describing the mechanisms of spalling, but in this paper the occurrence of spalling is taken for granted and the focus is on how spalling may affect the behaviour of RC columns. To this end, an advanced numerical model is developed and experimental data coming from well-documented tests on slender RC columns subjected to axial force in fire conditions are used for the validation of the proposed model. The influence of the damage dimension at different parts of the cross-section (e.g. at the corners or along one of the sides) is investigated, together with the effect of the column slenderness or the location of spalling over the column length.

Keywords: reinforced concrete columns; thermal spalling; fire resistance; numerical model; SAFIR

1 INTRODUCTION

Due to water evaporation, the increase in the internal pore pressure of reinforced concrete (RC) members exposed to fire can result in the phenomenon of spalling, causing a loss of concrete and a subsequent loss of resistance of the cross-section. Parameters affecting the occurrence of spalling can be material, geometrical, or environmental related [1].

Conclusions about the possibility of spalling and the reasons producing it are generally circumstantial mostly due to the lack of instrumentation and consistent data results. In fact, most of the existing information comes from the observation of the event on buildings and other structures exposed to fire. As long as the proper conditions take place, any type of RC member can experience spalling, although, under identical circumstances, it is challenging to guess which will spall. Despite spalling being a stochastic phenomenon, the range of time occurrence seems to be reasonably well set for the worst case scenarios in which the reduction of the effective cross-section can have serious consequences on the fire resistance of RC elements ([1-3]). The worst case scenario tends to be when spalling results in the complete loss of the concrete cover, directly exposing the reinforcement to the heat source.

¹ Assistant Profesor, Civil Engineering Institute, Austral University of Chile, Valdivia (Chile)

e-mail: david.pena@uach.cl, ORCID: <https://orcid.org/0000-0003-2236-1774>

² Associate Profesor, ICITECH, Universitat Politècnica de València, Valencia (Spain)

e-mail: caribus@upv.es, ORCID: <https://orcid.org/0000-0002-9354-5637>

³ Associate Profesor, Department of Mechanical Engineering and Construction, Universitat Jaume I, Castellón (Spain)

e-mail: valbero@uji.es, ORCID: <https://orcid.org/0000-0001-7193-9232>

⁴ Full Profesor, ICITECH, Universitat Politècnica de València, Valencia (Spain)

e-mail: ahospitaler@cst.upv.es, ORCID: <https://orcid.org/0000-0001-7108-3104>

⁵ Assistant Profesor, Department of Continuum Mechanics and Theory of Structures, Universitat Politècnica de València, Valencia (Spain)

e-mail: anlafer0@mes.upv.es, ORCID: <https://orcid.org/0000-0001-9667-236X>

⁶ Associate Profesor, ICITECH, Universitat Politècnica de València, Valencia (Spain)

e-mail: hsaura@cst.upv.es, ORCID: <https://orcid.org/0000-0003-0620-2378>

Several approaches can be found with regard to experiments dealing with sensitivity to spalling of reinforced concrete members. Experimental programs can be performed on small, medium or full-scale tests, either on loaded or unloaded conditions. Temperature and pressure are usually monitored in unloaded prismatic RC specimens in small-scale investigations, such as the research conducted by Lo Monte and Gambarova [4] which focused on corner spalling. The authors found out that the thermal dilation along two converging planes was the dominant fracture mechanism. On the other hand, medium-scale tests typically consist in slabs or prismatic specimens heated on one side, again either loaded or unloaded. From the data coming from these two types of tests (small and medium scale) expected conclusions can be drawn: that spalling sensitivity rises from unloaded to loaded conditions; and that biaxial compression is a more critical condition than uniaxial loading [5].

Last of all, full scale investigations consist of testing structural members or substructures under conditions typical of the real ones. While this experimental level is, by far, the most representative of the actual structural behaviour, it is expensive and time demanding [6]. In accordance with this and specially regarding RC columns, Buch and Sharma [6] highlighted the importance of studying the fire resistance of structures subjected to eccentric loads combined with spalling. From the experimental results obtained by the authors, it was observed that load eccentricity increases the occurrence of spalling. Similarly to Khoury [8], they evidenced the effectiveness of reinforcing bars in limiting spalling, principally if these are distributed along the sides of the cross-section.

Some models focus on predicting the occurrence of spalling but given the stochastic nature of the phenomenon it is complicated to draw solid conclusions. Dwaikat and Kodur [9] developed a one-dimensional model based on pore pressure calculation. A model based on two coupled finite elements models was presented by Lottman et al. [10] where the first model finds the temperature and pore pressure evolution and the second one defines the fracture mechanism causing spalling.

On the other hand, Bajc et al. [11] proposed a new numerical procedure for simplified predictions of the effects of spalling on the fire resistance of RC columns based on the implementation of a macro-level hydro-thermal model for calculation of concrete temperatures and pore pressures, and a model for detection of structural response. However, when the spalled region is simulated at cross-sectional level, the whole edge is considered to be damaged, so the model cannot distinguish the modelling of corner and surface spalling. However, authors like Zhao et al. [12] pointed out that experiments have shown that thermal spalling can also occur to normal strength concrete and that a high moisture content increases the probability of the occurrence of spalling. The work conducted by Zhao et al. [12] revealed that in a normal concrete specimen, instead of explosive spalling, surface spalling induced by the vapor pressure occurs to the specimen. This fact was observed after analyzing the nonlinear mechanical effects of the vapor pressure and the thermal stress in the thermo-chemo-hydro-mechanical behavior of a normal strength cube specimen exposed to fire.

In contrast, the investigation presented in the current paper does not deal with modelling the mechanism of occurrence of spalling in reinforced concrete columns. It is implicit that spalling occurs, and its effects on the performance of RC columns are analysed after its occurrence. Besides, both types of spalling –the one affecting the corners of the cross-section and the one affecting one of the sides of the cross-section- are investigated.

The cross-sectional symmetry (both thermal and geometrical), that an undamaged RC column initially has, disappears when spalling occurs, due to the loss of part of the concrete cross-section (e.g. concrete cover). This non-symmetrical geometry may lead to what is, fundamentally, a biaxial bending problem. After the loss of part of the concrete cover, the concrete core and reinforcing bars may become exposed to fire. This may lead to a rapid increase in temperature and a reduction in the fire resistance of the column, resulting in a decrease in the level of safety of the column when designed using the prevailing fire resistance design framework [13].

Along these lines, the authors investigated at sectional level the influence of spalling in the fire resistance time of RC columns [14]. This sectional model developed in Matlab [15] was able to reproduce the conditions in the section after the occurrence of spalling. The manifestation of spalling adopted in this work consisted of a loss of concrete cover and assumed that the reinforcing bar affected was directly exposed to

the heat source after spalling. Both types of spalling, corner and surface, were investigated. Some key assumptions were made in the model presented by the authors, in absence of hard experimental evidence. Considering the assumptions made, it was found that from 45 minutes on, the spalling initiation time has no remarkable effect. Besides, the area of the cross-section affected was usually not large enough to influence the transmission of heat through the unspalled concrete of the cross-section. One of the main conclusions is that the negative effect of spalling in the RC cross-section resistance can be estimated by means of an additional fire exposure time (AFET), which ranges between 0-25 minutes for corner spalling and 0-35 minutes for surface spalling. However, the precise value of this additional time is determined by the column cross-section configuration, its dimensions and load level. Therefore, the results from a parametric study were used to build a proposal for a modified fire resistance time for the effect of spalling in RC sections, in situations in which the structural failure is not governed by buckling. Therefore, to continue with the previous research, it is the aim of the current paper to cover the analysis of slender RC columns affected by spalling by means of a numerical model developed to this end.

In the literature some interesting works related to numerical modelling of RC columns in the fire situation can be found [16-18]. Bamonte and Lo Monte [16] developed a one-dimensional numerical model for RC columns at high temperatures to underline the role of some critical aspects regarding RC members in fire, specifically second-order effects and transient and creep strains. The validation with experimental data confirmed that one-dimensional numerical modelling is generally consistent with the experimental evidence if transient and creep strains, as well as second-order effects are carefully taken into account. Four models for concrete behaviour in compression were investigated. EN 1992-1-2 model [19] proved to be the best in terms of agreement between numerical and experimental results. Nevertheless, in the research conducted by Bamonte and Lo Monte [16] spalling was not considered.

In the work presented by Ni and Gernay [18] an overview of different issues arising when modeling RC structures in fire is presented. Among others, the issues addressed were realistic thermal exposures including cooling phases on the material properties and deformations or the ability to capture shear failure modes. However, a number of important aspects affecting the numerical modeling of concrete exposed to fire were not covered, such as spalling and its effects on the fire resistance of RC columns.

Therefore, in the current paper an advanced one-dimensional numerical model for the fire resistance of RC columns is presented. The model is validated with experimental data of slender RC columns under bending subjected to fire published in the literature. Spalling can affect either the corner of the cross-section or one of the sides. In this work both types of spalling are covered to investigate the effect of a number of parameters, including the column slenderness, the location of spalling over the column length or the damage dimension.

2 NUMERICAL MODEL

2.1 Description

An advanced numerical model for simulating the fire behaviour of slender RC columns was developed employing the computer program SAFIR [20] for the analysis of structures, which enables modelling of the behaviour of structures at the accidental case of fire. The main parameters covered by the model were the column length, the cross-section dimensions, the load level and eccentricity, the end conditions, and the thermal and mechanical material properties. The one-dimensional numerical model consists of two parts: the concrete cross-section and the reinforcing bars. For both materials the thermal mechanical properties given by EN 1992-1-2 [19] were used since they proved to produce satisfactory results [16].

In the model, a sequentially-coupled thermal-stress analysis is conducted: first, a thermal analysis is carried out and then a mechanical problem is solved. For conducting the thermal analysis, the standard time-temperature curve ISO 834 is applied to the exposed surface through the convection and radiation heat transfer mechanisms. For validation, the actual furnace time-temperature curve reported in the literature was used. The cross-section is discretised (Figure 1) and each fibre is characterized by its position, temperature and corresponding material properties. Nodal temperatures are stored as a function of time and then implemented into the mechanical analysis from an input file.

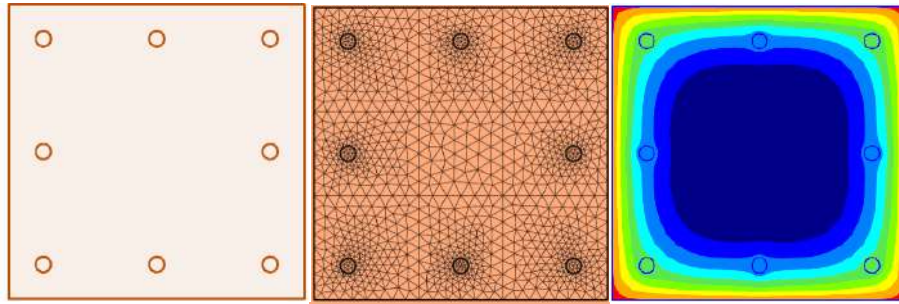


Figure 1. RC cross-section definition, mesh and temperature field after 60 min of fire exposure

As can be seen in Figure 2, the length of each column is discretised in several beam-column elements. The axial load is applied to the top node of the column. The initial imperfection of the column is considered by means of the first buckling mode shape of a pinned–pinned column which exhibits a sinusoidal shape. The value for the mid-height maximum deflection was set to $L/1000$. In Figure 2 the process of modelling for one of the columns modelled is shown as example.

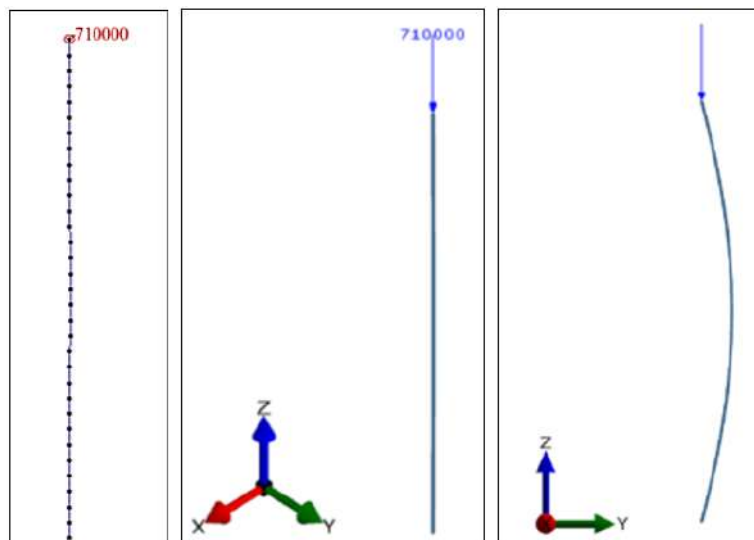


Figure 2. RC column modelling in SAFIR

2.2 Thermo-mechanical validation

The model was thermo-mechanically validated by comparing the numerical predictions with data from fire tests available in the literature. In total, the experimental results of 74 slender RC columns compiled by Gernay [21] were used. These columns were tested in different laboratories (at the Technical University of Braunschweig in Germany, the University of Ghent and the University of Liege in Belgium and the National Research Council in Canada). In each test, a loaded slender RC column was exposed to a standard time-temperature curve on its four sides. Some parameters varied between the tests: end conditions, length of the column, cross-section geometry, reinforcement ratio, mechanical properties of the materials, and magnitude and eccentricity of the load.

Each column was modelled and its behaviour was compared with the response registered in the corresponding test. Figure 3 shows the good agreement that exists between the tests and the predicted results in terms of fire resistance rating (FRR) for the 74 cases used in validation, with most of them lying on the safe side (with a value of the mean of 0.89 and a standard deviation of 0.27).

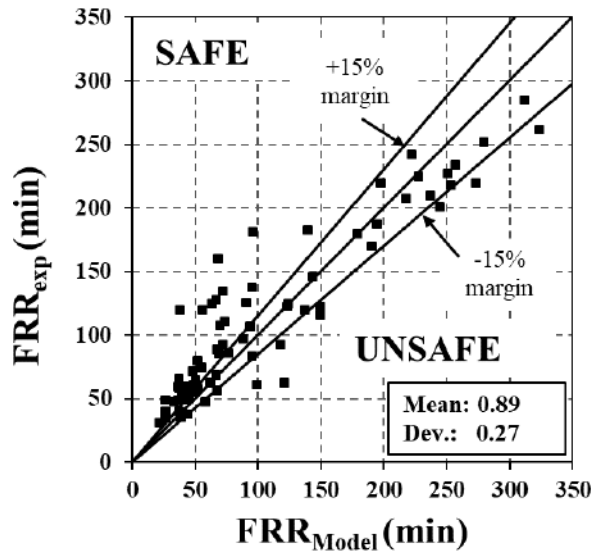


Figure 3. Model vs. experimental results in terms of FRR

In order to illustrate the satisfactory validation process, the comparison for four of the columns modelled is shown in detail below. In Table 1 the complete information for these columns is summarised together with the FRR registered in the experiment (FRR_{Exp}) and the FRR obtained in the numerical simulation (FRR_{Model}). In the last column, the error of the predictions for these four columns is calculated (FRR_{Model} / FRR_{Exp}) and the values obtained are very close to one, which proves the accuracy of the model. In Figure 4 the fire response of these columns in terms of axial displacement-time is presented. As can be clearly observed, the overall response predicted by the model reproduces with high precision the real behaviour of the columns.

Table 1. Details of four of the specimens used in validation

Description	FRR_{Exp} (min)	FRR_{Model} (min)	FRR_{Model} / FRR_{Exp}
Column a) 305x305 mm, 4 ϕ 25.5 mm, L = 3.81 m, ends = fixed-fixed, HR = 74%, f_c = 36.1 MPa, f_y = 444 MPa, u = 48 mm, N = 1067 kN (concentric) #60 [21]	208	218	1.05
Column b) 305x305 mm, 4 ϕ 25.5 mm, L = 3.81 m, ends = fixed-fixed, HR = 75%, f_c = 38.3 MPa, f_y = 444 MPa, u = 48 mm, N = 1333 kN (concentric) #62 [21]	187	195	1.04
Column c) 305x305 mm, 8 ϕ 25.5 mm, L = 3.81 m, ends = fixed-fixed, HR = --, f_c = 37.1 MPa, f_y = 444 MPa, u = 48 mm, N = 1333 kN (concentric) #68 [21]	225	227	1.01
Column d) 305x305 mm, 4 ϕ 25.5mm, L= 3.81m, ends = fixed-pinned, HR = 64%, f_c = 39.3 MPa, f_y = 444 MPa, u = 48 mm, N = 1000 kN (concentric) #72 [21]	220	197	0.90

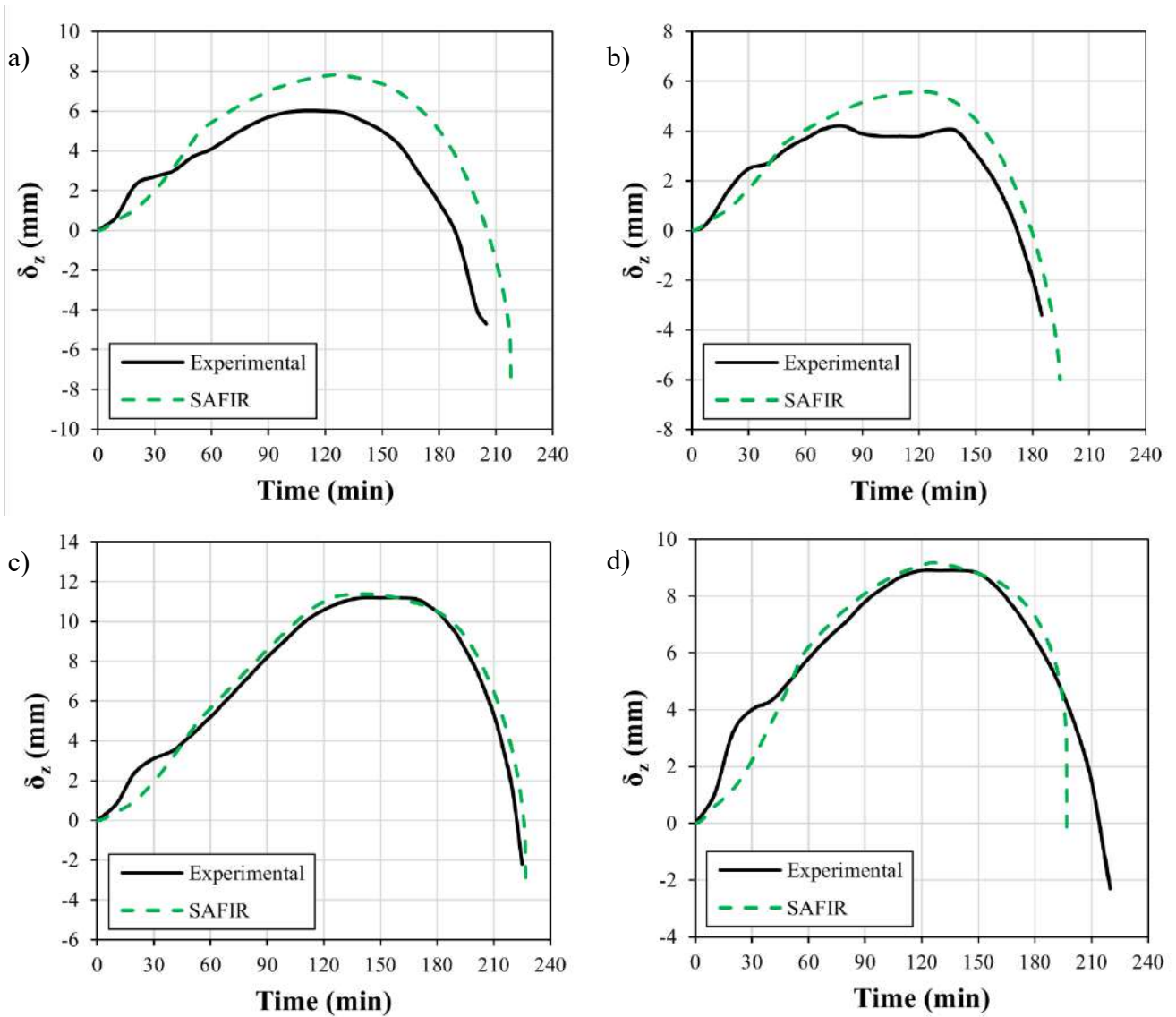


Figure 4. Axial displacement-time curves for four of the columns modelled

3 APPLICACION FOR THE EVALUATION OF THE EFFECT OF SPALLING

3.1 Description of the model

In this section, the proposed numerical model is applied to evaluate the effects of corner and surface spalling in slender RC columns (Figure 5). The times to the occurrence of spalling and the depth of spalling are set based on the conclusions obtained in previous works [14] and after the analysis of the reviewed literature. Thus, the times of occurrence of spalling once the heating has started are of 30 and 10 min respectively for corner and surface spalling respectively.

Regarding the depth of the damage, the most severe scenario with the reinforcement directly exposed to the heat source was modelled, considering the complete loss of the concrete cover. This approach is in line with the guidelines of EN 1992-1-2 [19] which states that, when the influence of spalling in the load-bearing capacity of a structural element is evaluated, the local loss of cover to one reinforcing bar or bundle of bars in the cross section should be assumed. Then, the reduced load-bearing capacity of the section should be checked. For this calculation, the temperature of the other reinforcing bars may be assumed to be that in an unspalled section.

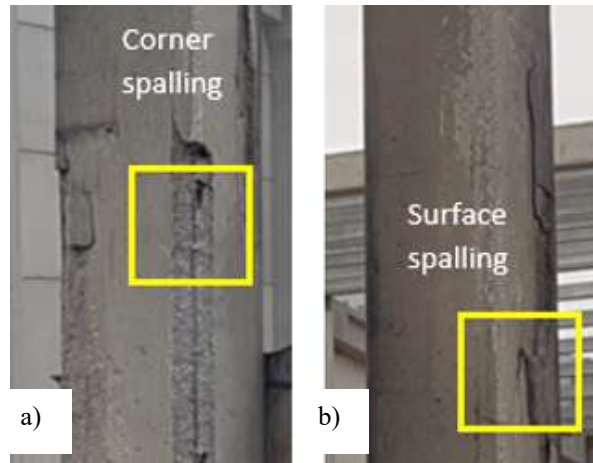


Figure 5. Detail of a) corner and b) surface spalling in a RC column

Consequently, in this work for both corner and surface spalling the local loss of the concrete cover is assumed. To be conservative, the geometry of the damage is set so that half of the perimeter of the affected reinforcing bar is directly exposed to fire (see corner bar in Figure 6a and side bar in Figure 6b). As can be seen in Figure 6, the geometry and shape of the spalled area varies between corner and surface spalling respectively.

In the current work, a cross-section measuring 300x300 mm with 8 ϕ 16 reinforcing bars and a concrete cover of 35 mm is taken as reference to illustrate the process of modelling and some of the obtained results. Grades C30 and B500S are used for concrete and reinforcing steel respectively. As can be seen in Figure 6, the column is 4-sided exposed to the standard curve ISO 834.

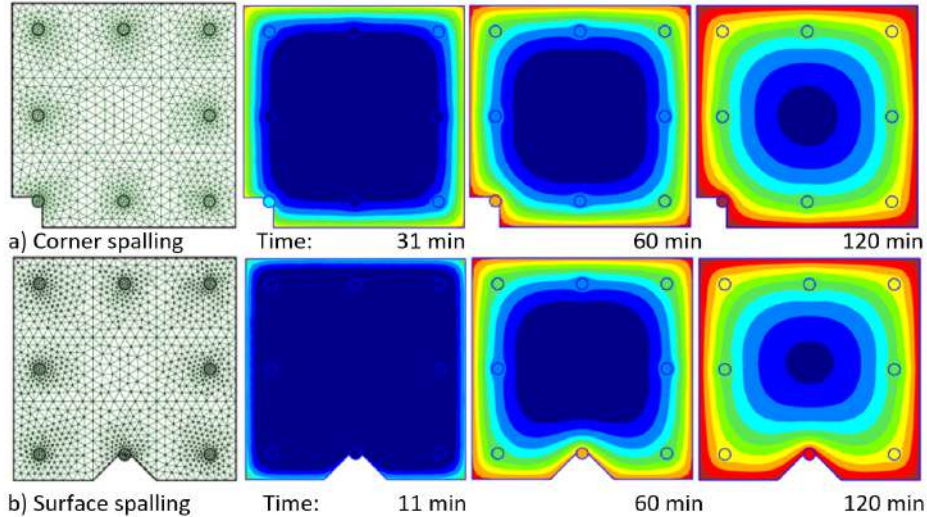


Figure 6. Cross-sectional mesh and temperatures for a) corner and b) surface spalling respectively

The way in which the occurrence of spalling is modelled is described hereafter. First, the thermal analysis is conducted as usual and when spalling is set to occur the fibres of concrete affected are eliminated. The cross-sectional temperatures must be updated for the new boundary conditions, as shown in Figure 6a and Figure 6b. A specific strategy implemented in SAFIR is used to that end. The new thermal file needed as an input for the mechanical analysis combines the temperatures of the section before and after spalling. This file must be created directly by the user keeping the SAFIR output file format. In order to neglect the contribution of the spalled fibres to the fire resistance of the RC column, they are assigned a very high

temperature (1200 °C as recommended in the technical documentation [20]). Once this is done, the thermal analysis continues in the cross-section considering the new boundary conditions.

3.2 Parametric study

With the proposed model of spalling, the influence of the column slenderness, spalling location over the column length or the damage dimension can be realistically described and analysed. To this end, a brief parametric study with a total of 32 cases is designed. In Table 2 the information about the parameters considered and the values adopted is summarised. The influence of the spalling location is shown in Figure 7 for a column slenderness of 60 as an example. In general, spalling at mid-length is more damaging and, in comparison with corner spalling, surface spalling results more harmful giving lower values of FRR for the RC columns.

Table 2. Details of the parameters considered

Parameter	Values
Type of spalling	Corner and surface
Column slenderness	60 and 120
Damage dimension [S] (cm)	0, 60, 120 and 180
Concrete moisture content (% weight)	3
Concrete moisture content (kg/m ³)	69
Load eccentricity [e ₀] (mm)	20
Load level [μ _{fi}]	0.5
Ends	Pinned-pinned
Time of occurrence for corner spalling (min)	30
Time of occurrence for surface spalling (min)	10
Damage location	Mid-length and top of the column

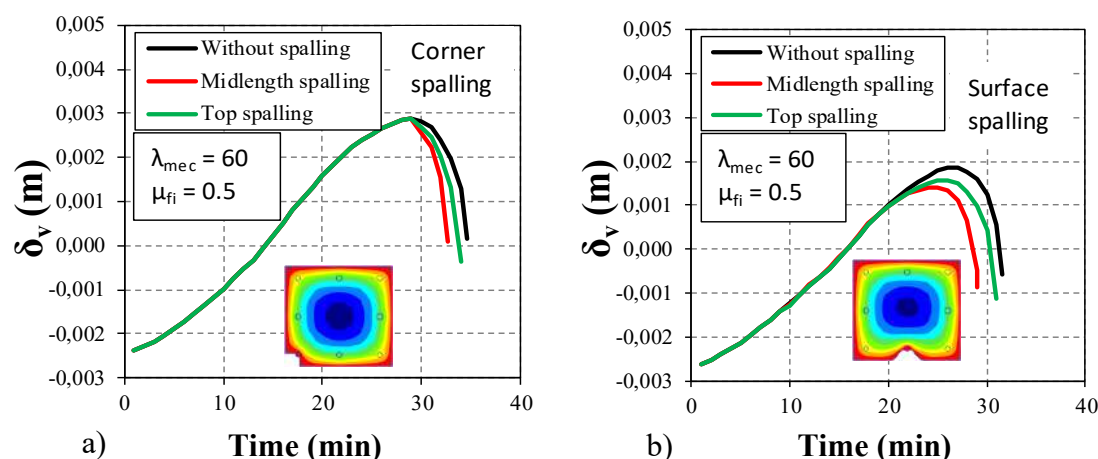


Figure 7. Influence of damage location for a) corner and b) surface spalling respectively

In Figure 8 the influence of the damage dimension is first shown for both types of spalling. Note that in this case the dimension of the damage is a magnitude expressed in cm, while the slenderness is a dimensionless value. In the other two graphs of Figure 8 the influence of the column slenderness for different damage dimensions and locations is represented. The values of the obtained FRR are practically the same in all of the cases displayed for the higher slenderness, for both corner and surface spalling. This lack of sensitivity obeys to the fact that this type of columns (e.g. in logistic buildings) fail due to global buckling. However, the effect of the damage dimension is more notable for the specimens with lower slenderness (e.g. columns in dwellings or in car parks).

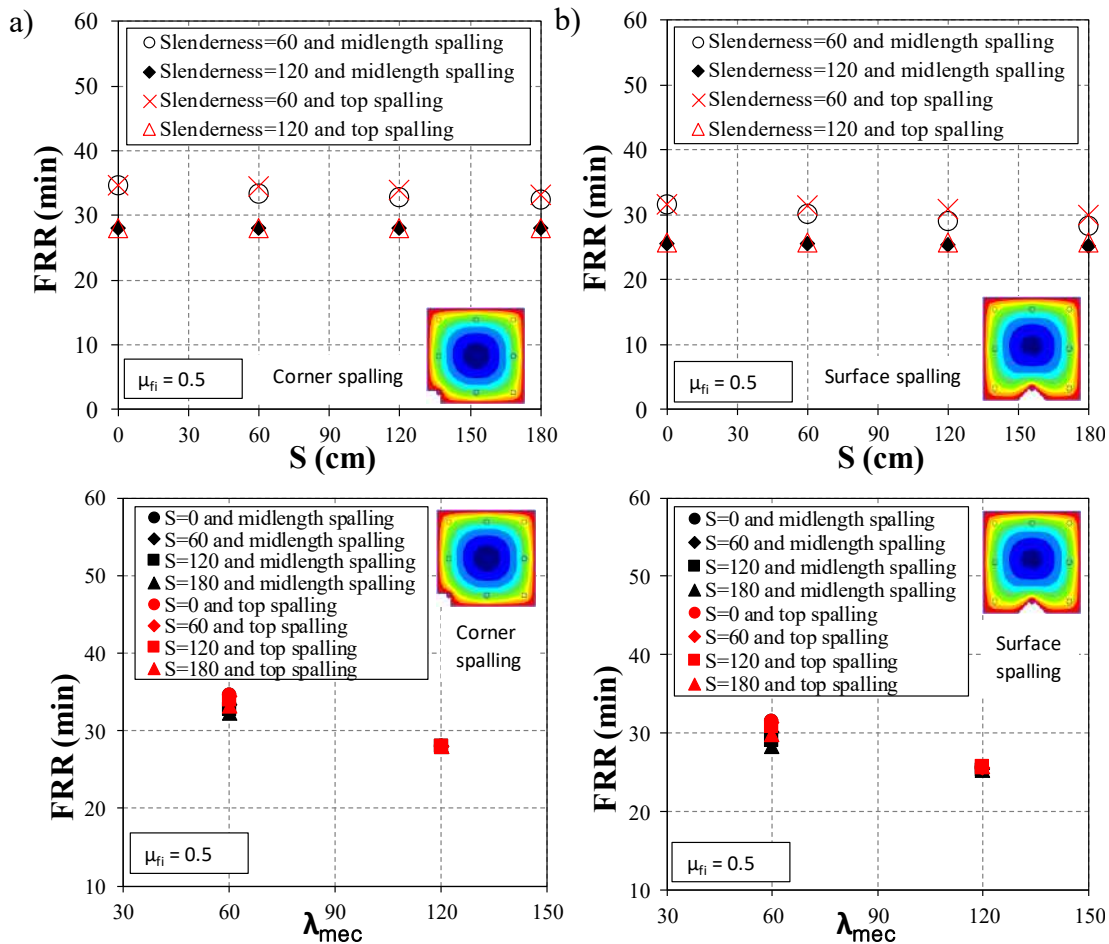


Figure 8. Influence of slenderness and damage dimension (S) for a) corner and b) surface spalling respectively

4 CONCLUSIONS

In this work, an advanced numerical model was developed in SAFIR for the effect of spalling in the fire response of slender RC columns. The numerical model was successfully validated with experimental data from the literature. The adopted model of spalling consisted of a loss of concrete cover and assumed that the reinforcing bar affected was left directly exposed to the heat source after spalling. Both types of spalling were considered, corner and surface spalling, in order to compare their different effects on the RC column. To assess the influence of different parameters on the effects of spalling, a parametric study was carried out. Considering all, the next conclusions can be drawn according to the model of spalling considered:

- When the damage due to spalling is located at mid-length of the column its negative effect is more remarkable. In the same way, surface spalling results more harmful giving lower values of FRR for the RC columns.
- For RC columns with higher slenderness, the effect of spalling can be neglected since, as expected, their failure is governed by global buckling. Note that values of slenderness between 90 and 120 correspond to RC columns that may be found in industrial buildings or logistics buildings.
- For RC columns with lower slenderness the effect is more significant. This fact is very important since RC columns with values of slenderness around 30 are those used within dwellings or in car parks. Note that, in particular, car parks are spaces with onerous fire requirements.

ACKNOWLEDGMENT

The authors would like to express their sincere gratitude to the “Conselleria d’Innovació, Universitats, Ciència i Societat Digital” of the Valencian Community (Spain) for the help provided through the project CIGE/2021/002.

REFERENCES

1. Dotreppe, J.C., Franssen, J.M., & Vanderzeipen, Y. Calculation method for design of reinforced concrete columns under fire conditions. *ACI Journal*, 96(1), 9-18 (1999).
2. Hertz, K.D. Limits of spalling of fire-exposed concrete. *Fire Saf J* 38, 103-116 (2003). [https://doi.org/10.1016/S0379-7112\(02\)00051-6](https://doi.org/10.1016/S0379-7112(02)00051-6).
3. Majorana, C.E., Salomoni, V.A., Mazzuccoa, G. & Khoury, G.A. An approach for modelling concrete spalling in finite strains. *Math Comput Simul* 80, 1694-1712 (2010). <https://doi.org/10.1016/j.matcom.2009.05.011>.
4. Lo Monte, F. & Gambarova, P.G. Corner spalling and tension stiffening in heat-damaged R/C members: a preliminary investigation. *Mater Struct* 48, 3657–3673 (2015). <https://doi.org/10.1617/s11527-014-0429-x>.
5. Miah, M.J., Lo Monte, F., Felicetti, R., Carré, H., Pimienta, P. & Borderie, C.L. Fire spalling behaviour of concrete: role of mechanical loading (uniaxial and biaxial) and cement type. *Key Eng Mater* 711, 549–555 (2016). <https://doi.org/10.4028/www.scientific.net/KEM.711.549>.
6. Lo Monte, F., Felicetti, R., Meda, A. & Bortolussi, A. Explosive Spalling in R/C Structures Exposed to Fire: Key Aspects in Experimental Testing. *Proceedings of Italian Concrete Days* 42, 372–384 (2020). https://dx.doi.org/10.1007/978-3-030-23748-6_29.
7. Buch, S.H. & Sharma, U.K. Fire resistance of eccentrically loaded reinforced concrete columns. *Fire Technol* 55, 1517-1552 (2019). <https://doi.org/10.1007/s10694-019-00823-x>.
8. Khoury, G.A. Effect of fire on concrete and concrete structures. *Prog Struct Eng Mater* 2, 429-447 (2000). <https://doi.org/10.1002/pse.51>
9. Dwaikat, M.B. & Kodur, V.K.R. Hydrothermal model for predicting fire-induced spalling in concrete structural systems. *Fire Saf J* 44(3), 425-434 (2009). <https://doi.org/10.1016/j.firesaf.2008.09.001>.
10. Lottman, B.B.G., Koenders, E.A.B., Blom, C.B.M. & Walraven, J.C. Spalling of concrete due to fire exposure: A coupled fracture mechanics and pore pressure approach. *MATEC Web Conf* 6(05002), 1-8 (2013). <https://doi.org/10.1051/mateconf/20130605002>.
11. Bajc, U., Kolšek, J.Č., Planinc, I. & Bratina, S. Fire resistance of RC columns with regard to spalling of concrete. *Fire Saf J* 130, 103568 (2022). <https://doi.org/10.1016/j.firesaf.2022.103568>.
12. Zhao, J., Zheng, J.-J., Peng, G.-F. & Wang, M.-Q. Numerical Investigation of Fire Induced Spalling of Normal Strength Concrete, *J Mater Civil Eng* 35 04023364 (2023). <https://doi.org/10.1061/JMCEE7.MTENG-15879>.
13. Fib-International Federation for Structural Concrete (2007) *Fib Bulletin 38: Fire design of concrete structures - Materials, structures and modelling*. Lausanne, Switzerland.
14. Peña, D., Ibáñez, C., Albero, V. & Hospitaler, A. Additional fire exposure time for the effect of spalling in reinforced concrete columns. *Fire Technol* (2023). <https://doi.org/10.1007/s10694-023-01401-y>.
15. MATLAB and Statistics Toolbox Release (2018) The MathWorks Inc. Natick, Massachusetts, United States.
16. Bamonte, P. & Monte, F. L. Reinforced concrete columns exposed to standard fire: comparison among different constitutive models for concrete at high temperature. *Fire Saf J* 71, 310-323 (2015). <https://doi.org/10.1016/j.firesaf.2014.11.014>.
17. Bamonte, P. A reappraisal of the nominal curvature method in the fire design of reinforced concrete columns. *J Fire Sci* 38(2), 106-121 (2020). <https://doi.org/10.1177/0734904119895436>.
18. Ni, S. & Gernay, T. Considerations on computational modeling of concrete structures in fire. *Fire Saf J* 120, 103065 (2021). <https://doi.org/10.1016/j.firesaf.2020.103065>.
19. CEN (2004). EN 1992-1-2, Eurocode 2: design of concrete structures, Part 1.2: General rules – structural fire design. Brussels, Belgium: Comité Européen de Normalisation.
20. Franssen, J.M. SAFIR: A thermal-structural program for modelling structures under fire. *Eng J* 42(3), 143-158 (2005).
21. Gernay, T. Fire resistance and burnout resistance of reinforced concrete columns. *Fire Saf J* 104, 67-78. (2019). <https://doi.org/10.1016/j.firesaf.2019.01.007>

A NEW TABULATED PROCEDURE TO FIRE-DESIGN RC RIBBED SLABS

Fabricio Longhi Bolina¹

ABSTRACT

Ribbed slabs are a solution for increasing bending capacity while reducing the total concrete consumption and the dead weight compared to conventional reinforced concrete slabs (RC) slabs. EN 1992-1.2 provides a tabulated method (TM) for the fire design of these structures, suggesting some combinations of section dimensions and concrete cover thickness to determine the fire resistance for each intended fire resistance rating (FRR). Using a finite element (FE) numerical model solved with Abaqus software, a thermal analysis of these slabs was performed, correlating the results with the standardized TM. To validate the FE models, two full-scale specimens were experimentally tested. It was found that the TM needs to be revised. A fire design of ribbed slabs based on EN 1992-1.2 shows that the reinforcement is heated beyond its critical temperature, but the flange thickness can be reduced. A completely new tabular procedure is proposed.

Keywords: ribbed slabs; reinforced concrete structures, finite element modelling; experimental analysis

1 INTRODUCTION

According to [1] and [2], 40-60 % of the total dead load of the concrete structures is accounted for by the slabs. In order to improve the performance of conventional slabs and reduce the total concrete consumption and dead load, small beams are often used as reinforced ribs of the reinforced concrete (RC) slabs, resulting in ribbed slabs. There are several types of ribbed slabs, which differ in the geometry and arrangement of the ribs [3]. Ribbed slabs are also an excellent solution to reduce the number of columns in buildings [4], [5], reducing concrete consumption and emphasizing the environmental aspect of ribbed slabs [6].

These slabs are formed by longitudinal and transverse ribs. It is a solution with a large cross-sectional inertia and a small total area. The ribs form a multiple rib arrangement, with the longitudinal ribs forming the main bending resistance [7]. The transverse ribs can be considered as discrete shear connectors along the length of the slabs, reducing the shear resistance of the longitudinal ribs and improving the bending resistance.

Research projects have attempted to optimize rib geometries in order to increase mechanical efficiency and at the same time reduce total concrete consumption [3, 5, 8, 9]. The use of alternative materials to improve the mechanical properties, such as ultra-high strength concrete or high strength steel, has been proposed to improve the reduction of the cross-sectional area [10-12]. Most of the full-scale experimental tests focused on analyses at room temperature without considering the effects of fire [1, 7, 13-16]. The same applies to the numerical researches [6, 17-20].

Reducing cross-sectional area increases the thermal field, making these slabs more susceptible to fire. However, it is clear that the study of ribbed slabs in fire is insufficient, implying that it has received little attention from researchers. Recent research on RC slabs (generally) in the event of fire has not focused on ribbed slabs [21-32].

High temperatures lead to physical, chemical and mechanical changes in building materials. This research focuses on mechanics. For steel reinforcement, fib Bulletin No. 38 [33] suggests 500°C as the critical

¹ PhD professor, UFSM (Federal University of Santa Maria), Brazil,
e-mail: fabriciobolina@gmail.com, ORCID: <https://orcid.org/0000-0002-0495-099X>

temperature. For concrete, there are divergences. Some studies [33] assume a critical temperature of 500°C from a mechanical point of view, but there are authors [34, 35] who suggest temperatures in the range of 250 to 500°C because of concrete spalling, and [36] suggest 300°C for the same reason. In fib Bulletin No. 38 [33], a critical temperature at the unexposed surface is also given. This temperature is on average 140°C or 180°C and is referred to as the thermal insulation criterion.

In the field of fire-design, EN 1992-1.2 [37] proposes a tabular method for the design of RC ribbed slabs based on critical temperatures. The EN 1992-1.2 [37] is based on DIN 4102-4 [38], which states that the tabulated data are based on experimental laboratory tests. After an extensive literature research, the origin of the tabular method proposed in the German standard cannot be clearly identified.

In this study, the fire behavior of RC ribbed slabs was investigated. To validate the-numerical model, two full-scale specimens were built and tested according to ISO 834 [39]. The experimental results are used to validate the numerical models. The results allowed a critical analysis of the tabulated method proposed by EN 1992-1.2. This investigation has shown that the standard tabular method needs to be revised and can sometimes be unsafe. A new tabular method was proposed.

2 EXPERIMENTAL RESEARCH

2.1 Specimens

Two identical specimens were built (named S1 and S2 slabs). The cross-section of which is shown in Figure 1. The experimental setup is shown in Figures 2a and 2b.

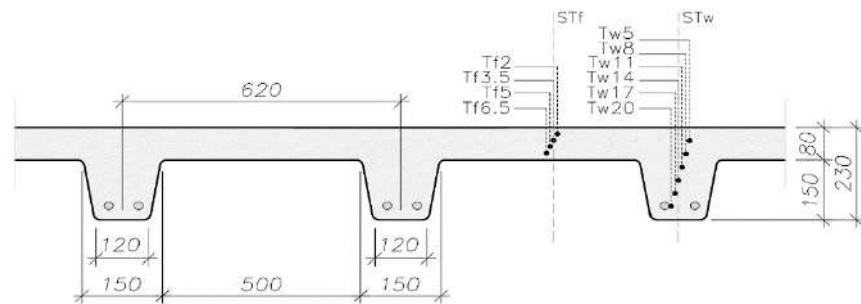
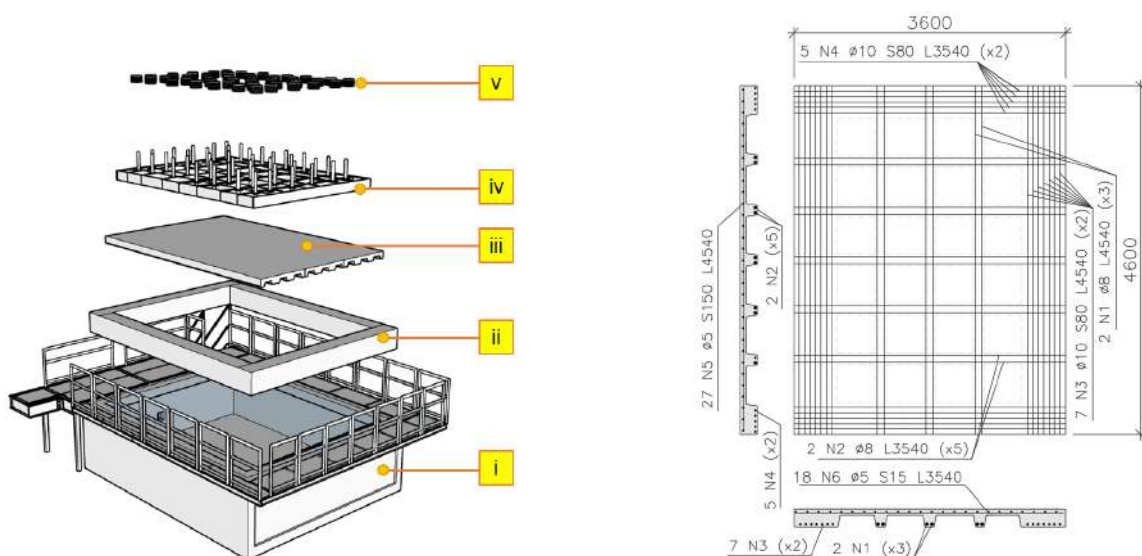


Figure 1. Cross section of the RC ribbed slab (dimensions in mm)



(a) horizontal furnace (i), RC auxiliary frame (ii), slab prototype (iii), auxiliary frame loading (iv), loading pistons and washers (v)

(b) structural design of the ribbed slabs

Figure 2. (a) Details of the testing set-up and (b) structural drawing of S1 and S2

The reinforcement and cross-section were designed at room temperature according to [40]. The specimen was loaded with steel washers placed in a rigid frame (auxiliary frame loading) producing a gravitational load of 2.5 (S1) and 3.0 kN/m² (S2). This is a conventional load used in the design of residential buildings [41]. The load was assumed to be constant throughout the fire test.

Figure 2b shows the structural drawing of the slab. N1 to N4 and N5 and N6 are the positive (tension) and the negative (compression) rebars, respectively, L is their length and S is the spacing between rebars. The slabs had a size of 3600 x 4600 mm. N1 and N2 had a diameter of Ø 8 mm, N3 and N4 had a diameter of Ø 8 mm, while N5 and N6 of Ø 5 mm. The thickness of the concrete cover was $c = 30$ mm.

2.2 Materials

A Portland Brazilian cement classified as Type III according to ASTM C 150 [43] was used. The gravel was dacite with plagioclase and quartz-base with maximum dimensions of 9.5- and 19-mm. Natural quartz and industrialized dacite sand were used in the concrete mixture. The compressive strength of the concrete at 540 days was 22.3 MPa. The tests were performed according to ASTM C39 [44]. Tension rebars were Ø 8 and Ø 10 mm in diameter. All specimens were constructed with anti-cracking welded steel mesh with a cross-sectional area of 92 mm²/m, Ø 5 mm in diameter and 15 cm spacing each other (both directions). The rebars had a tensile strength $f_y = 500$ MPa while the steel mesh $f_y = 600$ MPa.

2.3 Instrumentation

The cross-sectional temperatures were measured at the flange and the web. The flange is the thinnest part, while the web (rib) is the thickest part. The temperature control points at the flange were named STf (slab temperature flange) and at the web (rib) STw (slab temperature web). Type K thermocouples (Ø 1.65 mm) were placed in cross-sectional layers: four for alignment STf (named Tf20, Tf35, Tf50 and Tf65 at 20, 35, 50 and 65 mm from the top specimen surface, respectively) and six for STw (Tw50, Tw80, Tw110, Tw140, Tw170 and Tw200 at 50, 80, 110, 140, 170 and 200 mm from the top surface, respectively), according to Figure 1. Thermal insulation (Ti) was measured on the unexposed surface. The criterion was defined based on the average temperature of 4 points (Ti1-Ti4). These analyzes were based on the BS 476-20 [45].

2.4 Furnace temperature

The horizontal furnace has 8 gas burners that follow the ISO 834 [39]. The fire tests were made in the Fire Safety Laboratory of Unisinos University, in Brazil. The full-scale fire test was made according to ASTM E 119 [46], and BS EN 1363-1 [47].

3 NUMERICAL RESEARCH

3.1 Calibration and validation

The boundary conditions are shown in Figure 3. To reduce the time consumption, only the region of a rib was numerically tested. On their bottom surface, the [39] heating was applied assuming thermal convection (heat transfer $\alpha=25$ W/m².K) and radiation (thermal emissivity $\epsilon=0.70$ [37]). On the top surface (unexposed surface), a room temperature of 25°C was considered. The FE-model was developed in ABAQUS [48] software. The steel reinforcement was modelled as a truss with a 2-node link (DCC1D2) and the concrete as a 3D solid with 8-node linear isoperimetric (DC3D8) finite element. A mesh-sensitive analysis was performed, and the element size 0.5 mm for the DCC1D2 and 0.5 x 0.5 x 0.5 mm for the DC3D8 showing a good convergence with the experimental results proposed in this research. The thermal conductivity and density of the concrete were determined according to [37] and validated by the fire tests. The thermal conductivity and specific heat of the steel were taken from [37]. Reinforcements were considered with a density of 7850 kg/m³. FE model was validated in accordance with the experimental results.

3.2 Extrapolations

The thermal field analysis of the ribbed slabs was obtained assuming various cross-sectional characteristics. The width (b_w) and height (h_w) of the rib and the thickness of the flange (h_f) were considered as research

variables (see Figure 4). These cross-sectional dimensions (Tables 1 and 2) were selected in accordance to the EN 1992-1.2 [37]. Some of these dimensions are unusual, but are in accordance to the standardized TM. The parameters C and C' are the concrete thickness (distance between the axis of the reinforcements and the cross-section surface) in relation to the reinforcements placed in the ribs and flange, respectively.

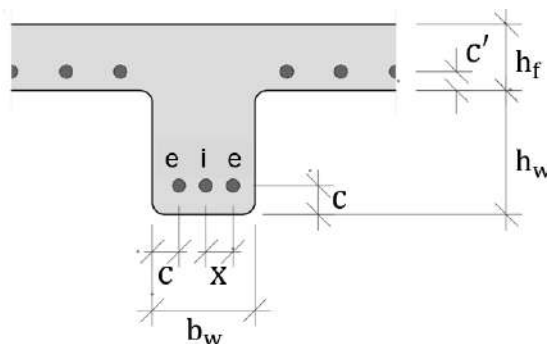
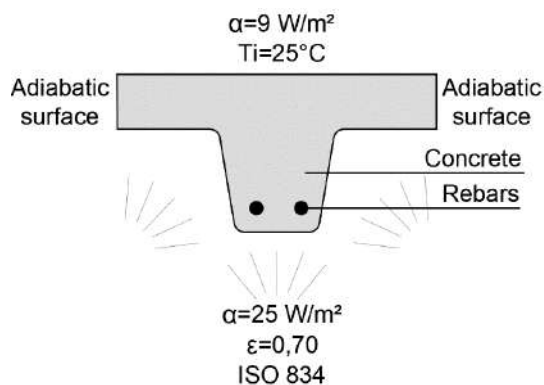


Figure 3. Boundary conditions of the FE-numerical model Figure 4. Cross-sectional data adopted in numerical research

In the case of the ribs, the “e” and “i” reinforcements are placed at the ends (corners) and in the intermediate position (between the two “e” reinforcements). The criterion aims to also analyse the temperatures of the “i” reinforcements, since they are more thermally protected than “e”. The distance between the “i” and “e” reinforcements is defined as “x”.

Tables 1 and 2 show the cross-sections used in the numerical study. In the case of reinforcements placed in the ribs, C values of 10 mm each were tested (see Table 1), with the minimum $C=10$ mm and the maximum being the geometrical capacity of the rib width. Regarding the flange, the C' thicknesses are given in Table 2, assuming $C'=5$ mm as the minimum and the limit of the neutral axis of the flange (around $0.5 \times h_f$) as the maximum thickness dimension.

Table 1. Dimensions of the cross section: study of the geometry of the ribs

Slab Nomenclature	Cross-section dimensions (mm)			
	b_w	h_w	h_f	C
80x300x100	80	300	100	10 to 40
100x300x100	100	300	100	10 to 50
120x300x100	120	300	100	10 to 60
160x300x100	160	300	100	10 to 80
190x300x100	190	300	100	10 to 90
220x300x100	220	300	100	10 to 90
250x300x100	250	300	100	10 to 90
260x300x100	260	300	100	10 to 90
300x300x100	300	300	100	10 to 90
350x300x100	350	300	100	10 to 90
410x300x100	410	300	100	10 to 90
500x300x100	500	300	100	10 to 90

Table 2. Dimensions of the cross section: study of the geometry of the flange

Slab Nomenclature	Cross-section dimensions (mm)			
	b_w	h_w	h_f	C'
100x300x80	100	300	80	5 to 40
100x300x90	100	300	90	5 to 45
100x300x100	100	300	100	5 to 50
100x300x110	100	300	110	5 to 55
100x300x120	100	300	120	5 to 60
100x300x130	100	300	130	5 to 65
100x300x140	100	300	140	5 to 70
100x300x150	100	300	150	5 to 75
100x300x160	100	300	160	5 to 80
100x300x170	100	300	170	5 to 85
100x300x175	100	300	175	5 to 85

4 RESULTS

4.1 Numerical model validation

Figure 5 shows the thermal field in the cross section. The experimental (exp) results are presented with the corresponding validation of the numerical model (num). The experimental cross-section characteristics of the specimens (see Figure 1) were used as the basis for the FE model. The temperatures in the flange and web are shown in Figure 5a and Figure 5b respectively.

Figure 5b show that the concrete becomes humid when the temperature reaches a plateau around 100°C in the thickest part of the cross-section. The phase change of the water causes constant temperatures between 20-60 min. The thicker section has more humidity than the thinner one, even a year after the specimen was built, as the prototype slab was kept outside the laboratory without any protection from the environment. In the first 30 min of the test, the difference between "num" and "exp" is about 20%. After 120 min, the difference is 17.9%. The difference decreases around the test. Considering the heterogeneity of the concrete (construction procedure, cracking, etc.), the differences are acceptable.

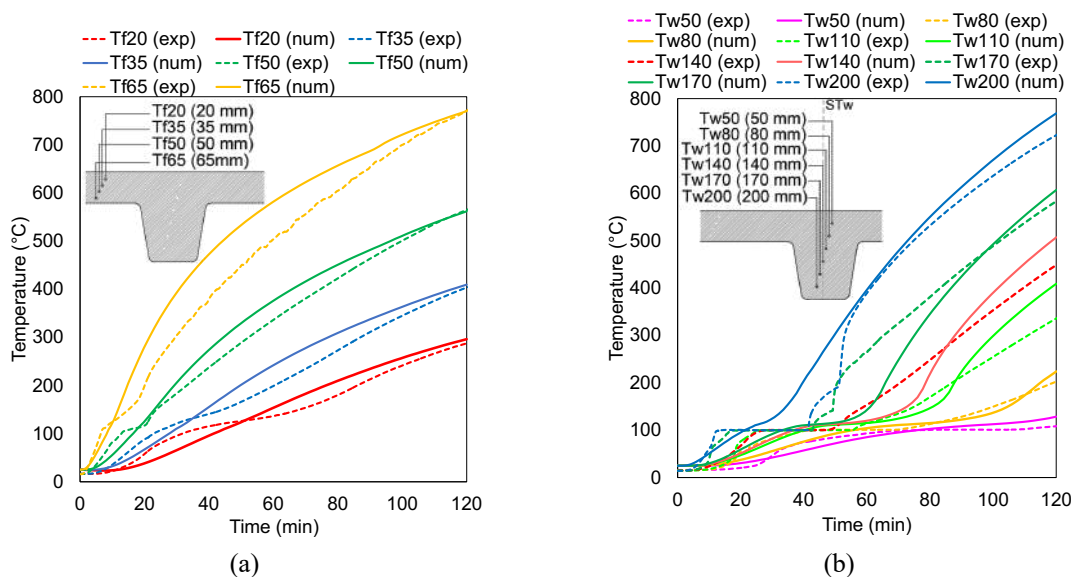


Figure 5. Validation of the FE-numerical models according to experimental results in (a) flange and (b) web of the slab

4.2 The influence of the rib of the slabs

Figure 6 shows the temperature of the reinforcement for some cross-sections. The corner reinforcement "e" and – as far as possible due to the width of the ribs and assuming at least 20 mm between the rebars – the intermediate "i" were taken into account. The average "av" between "e" and "i" is also given.

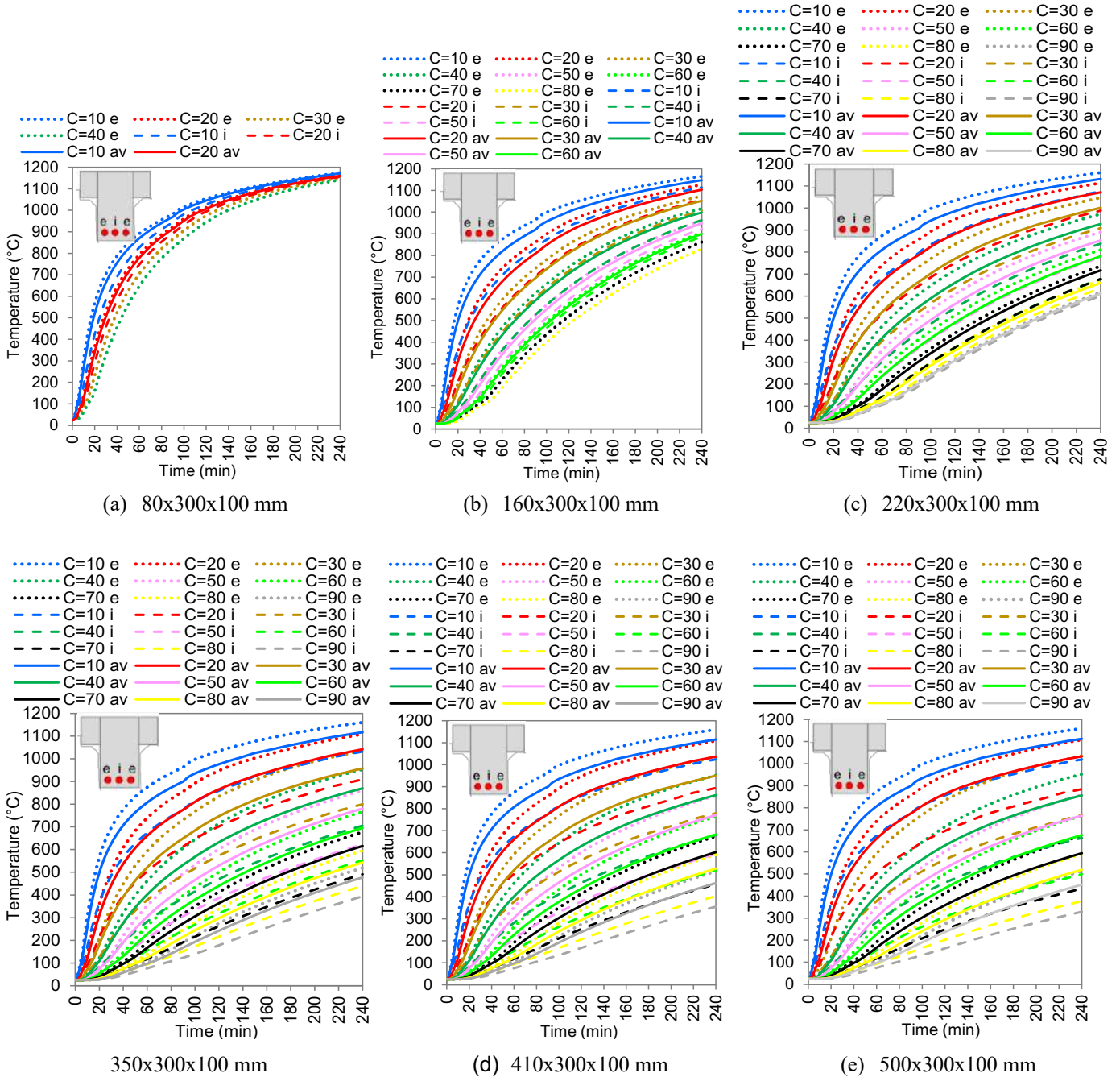


Figure 6. Temperature profile of the reinforcement located in the rib of the slab

Reinforcements placed at the corners of the ribs are more thermally affected and thus more mechanically damaged. The "e" rebars have an almost identical temperature profile. The width of the ribs has little effect. Insert a third rebar "i" is an intriguing solution, because produces lower temperature than the "e" and could be a solution to improve the average mechanical capacity of the reinforcement.

In the maximum condition (measured in the 500 mm wide rib), the "i" rebar had a 70% lower temperature than "e". The wider the rib, the greater the temperature difference between "i" and "e". These differences are small when the "C" thickness is small (10-20 mm) and when the rib widths are small (80-100 mm).

Regarding the temperature field of the "e", the thickness of the concrete cover proved to be more important than the width of the rib. The corner reinforcements are heated from both sides of the rib (i.e., lateral and bottom surfaces), so the width of the rib has little effect on these results. Increasing the rib width does have an effect on the temperatures measured in the rebars, but the critical factor for these results is the thickness of the "C". Increasing the rib width is therefore a necessary procedure to increase the thickness of the "C".

4.3 The influence of the flange of the slabs

Figure 7 shows the temperature profile of the rebars for some flange geometry, assuming different C' thicknesses. Due to their one-sided heating, these reinforcements are less affected by the temperatures than the rebars of the ribs. Increasing C' by 5 mm can reduce the temperature by more than 100 °C. As the rib is heated from three sides, its average temperature is higher than that of the flange. The flange directly above the rib showed a temperature of less than 200 °C in some cases. To optimize the position of the reinforcement on the flange, it can be concluded that the best position is above the rib, where the average temperatures are lower.

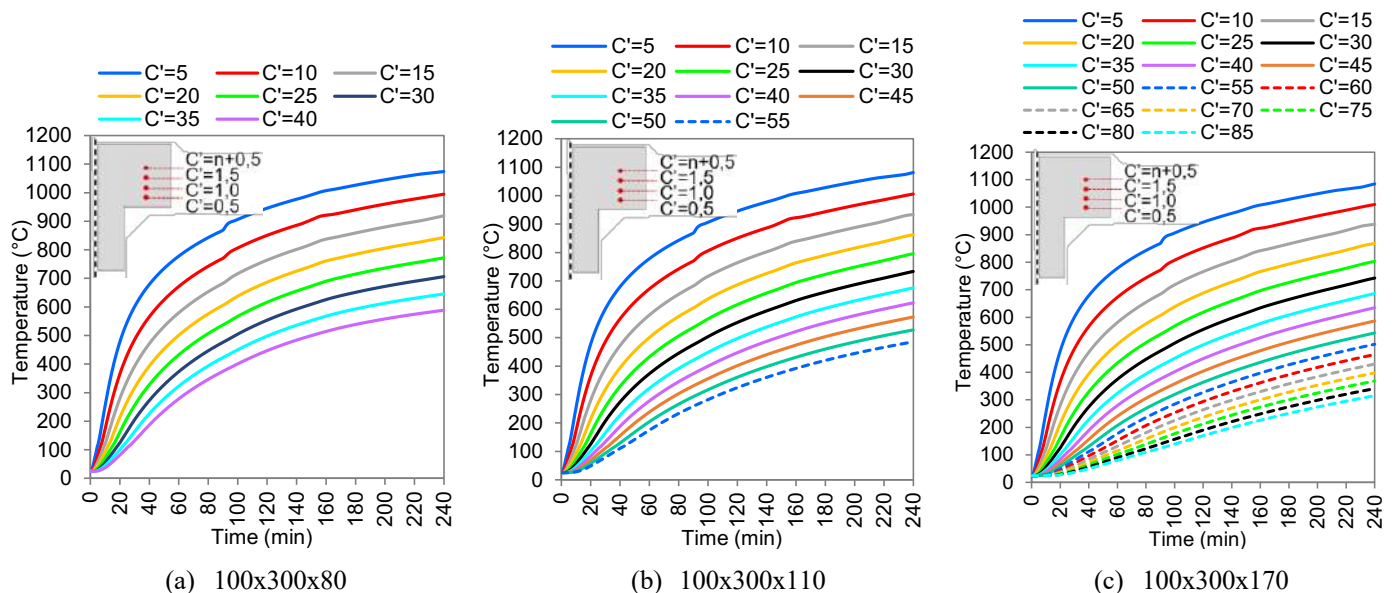


Figure 7. Temperature of the reinforcement located in the flange of the slab

4.4 EN 1992-1.2 validation

Table 3 compares the results with the tabular method proposed in EN 1992-1.2. The same applies to the Ti requirements in Table 4. The experimental and numerical results show that the "a" thickness proposed by EN 1992-1.2 differs from the values of this research. The required "a" thicknesses were greater than suggested in the standard. In all cases, the "a" should be between 15 and 20 mm greater than specified in the standard. The discrepancy could be related to the methodology used to produce the standardized TM (see the research carried out by the authors related to composite slabs [49]). However, no studies or data were found to indicate the origin of this standardized methodology. The analyses were based on the same rib width (bmin) proposed in the standard.

While maintaining the flange thicknesses (h) suggested in the standard, inconsistent results were obtained to the thermal insulation (Ti) requirements. This analysis also suggested that the "a" thickness should be increased to between 10 and 15 mm. The "h" can be decreased, even while "a" thickness must be increased.

Table 3. Comparison between the tabulated fire resistance parameters

FRR (min)	Reference	Alternative #1	Alternative #2	Alternative #3
30	EN 1992-1.2	$b_{\min} = 80$	X	X
		$a = 15$	X	X
	Research data	$a = 25$	X	X
60	EN 1992-1.2	$b_{\min} = 100$	$b_{\min} = 120$	$b_{\min} \geq 200$
		$a = 35$	$a = 25$	$a = 15$
	Research data	$a = 50$	$a = 40$	$a = 35$
90	EN 1992-1.2	$b_{\min} = 120$	$b_{\min} = 160$	$b_{\min} \geq 250$
		$a = 45$	$a = 40$	$a = 30$
	Research data	$a = 65$	$a = 55$	$a = 50$
120	EN 1992-1.2	$b_{\min} = 160$	$b_{\min} = 190$	$b_{\min} \geq 300$
		$a = 60$	$a = 55$	$a = 40$
	Research data	$a = 75$	$a = 65$	$a = 60$
180	EN 1992-1.2	$b_{\min} = 220$	$b_{\min} = 260$	$b_{\min} \geq 410$
		$a = 75$	$a = 70$	$a = 60$
	Research data	$a = 85$	$a = 80$	$a = 75$
240	EN 1992-1.2	$b_{\min} = 280$	$b_{\min} = 350$	$b_{\min} \geq 500$
		$a = 90$	$a = 75$	$a = 70$
	Research data	$a = 105$	$a = 95$	$a = 90$

Table 4. Comparison between thermal insulation (Ti) data

FRR min	Flange h/a (mm/mm)	
	EN 1992	Research data
30	80/10	80/10
60	80/10	80/20
90	100/15	100/30
120	120/20	110/35
180	150/30	140/45
240	170/40	160/55

4.5 A new tabulated method proposed

In place of the method suggested in EN 1992-1.2 [37] for the fire design ribbed slabs, this section proposes a new TM. The tables include a novel design principle: in addition to corner reinforcement, intermediate reinforcement (between corners) is assumed. When just two longitudinal reinforcements are considered (at the corners of the rib), a tabulated procedure is shown in Table 5 and Table 6 when additional intermediate reinforcements are provided. Table 7 suggests a new TM for thermal insulation.

The new tabular technique also suggests fire design parameters for the exposure durations of the ISO 834 curve that are not contained in EN 1992 (as 150 and 210 min), as well as novel combinations of the widths and thicknesses of flanges and ribs, respectively. It is important to emphasize that the standard provides only three combinations of ribs and concrete cover for each FRR intended. The proposed new tabular method suggests a total of eleven options for each required FRR. In some cases, it was not possible to find a solution, especially for thin ribs with high required FRR. This is due to the fact that high concrete cover thicknesses are required, making it impossible to place reinforcement in the thin rib sections.

The width of the rib affects the reinforcements temperatures up to a certain heating. Table 5 shows that for ribs larger than 100 mm with an FRR of 30 min, a minimum concrete cover thickness of 20 mm is required if only two longitudinal reinforcement is used. This thickness increases to 35 mm for ribs greater than 120 mm in length when 60 min is required. For ribs longer than 160 mm, the thickness increases to 50 mm at 90 min. For ribs longer than 220 mm, the thickness is 60 mm when the FRR is 120 min. For ribs wider than 220 mm, the thickness is 70 mm at 150 min, and for ribs wider than 220 mm, the thickness should be 80 mm at 180 min. For ribs wider than 250 mm, it is 85 mm at 210 min. In this sense, it is necessary to increase the width of the ribs to increase the thickness of the concrete cover and thus improve the thermal protection of the reinforcement.

When at least three rebars are used, Table 6 shows that for an FRR of 30 min and a width greater than 120 mm, the required concrete cover is 20 mm in all cases. For an FRR of 60 min and a rib thickness greater than 120 mm, the required concrete cover is 40 mm in all cases; for an FRR of 90 min, a concrete cover of 50 mm is used for all rib thicknesses greater than 190 mm. For an FRR of 120, 150, 180, 210 and 240 min and a rib width greater than 190, 250, 250, 300 and 300 mm, the concrete cover required in all cases is 60, 70, 80, 85 and 95 mm, respectively.

Regarding the thermal insulation criterion proposed in Table 7 and the thickness of the concrete cover of the flange, it can be seen that with the intended increase of the FRR, the thickness of the flange and the concrete cover also increases. As a general conclusion, an increase in FRR by 30 min requires an increase in flange and concrete cover thickness on the order of 10 mm. This suggested concrete cover thickness refers to the bottom side of the slab, since the fire heats the bottom side and not the top side. It is the same criterion proposed in EN 1992-1.2 [37]

The proposed tabular procedures provide a simple option for the structural engineer. Only the minimum thicknesses of concrete cover, rib width, and flange thickness are required for fire design of these slabs at any FRR times. The proposed tabular procedures correct several inconsistencies in the already recommended methodology in EN 1992-1.2 [37].

Table 5. A new tabular method for RC ribbed slabs (case 1: ribs with only two longitudinal rebars)

FRR	b_{min} (mm)										
	80	100	120	160	190	220	250	300	350	410	500
	C (mm)										
30	25	25	20	20	20	20	20	20	20	20	20
60	X	50	40	40	40	40	40	40	40	40	40
90	X	X	X	55	50	50	50	50	50	50	50
120	X	X	X	75	65	65	60	60	60	60	60
150	X	X	X	X	80	75	70	70	70	70	70
180	X	X	X	X	X	85	80	80	80	80	80
210	X	X	X	X	X	95	90	85	85	85	85
240	X	X	X	X	X	X	105	95	95	95	95

Table 6. A new tabular method for RC ribbed slabs (case 2: ribs with three longitudinal rebars)

FRR	b_{\min} (mm)										
	80	100	120	160	190	220	250	300	350	410	500
	C (mm)										
30	20	20	15	15	15	15	15	15	15	15	15
60	X	X	40	35	35	35	35	35	35	35	35
90	X	X	X	50	45	45	45	45	45	45	45
120	X	X	X	X	60	55	55	55	55	55	55
150	X	X	X	X	X	70	65	65	65	65	65
180	X	X	X	X	X	85	80	75	75	75	75
210	X	X	X	X	X	X	90	85	80	80	80
240	X	X	X	X	X	X	100	90	85	85	85

Table 7. A new tabular method for RC ribbed slabs (case 3: thermal insulation criterion)

Ribbed slab	FRR (min)							
	30	60	90	120	150	180	210	240
h (mm)	80	80	100	110	130	140	150	160
C' (mm)	10	20	30	35	40	45	50	55

5 CONCLUSIONS

The general conclusions of this paper are:

- The reinforcement at the rib corners is most affected by the fire. A third reinforcement (between the corner rebars) proved to be an interesting solution to mitigate their loss of mechanical strength;
- The temperature of the intermediate rebar can be 70.0% lower compared to the corner rebar.
- The most decisive factor was the concrete cover thickness.
- When thin ribs are exposed to fire for an extended period of time, their average temperature rises to 1000°C. This justifies the standard's proposal for atypical rib widths in the tabular method.
- The tabulated values proposed in the standard were sometimes insufficient. An increase in the concrete cover thickness proposed in EN 1992-1.2 is necessary. This increase is about 15 to 20 mm;
- In the case of the flange, the EN 1992-1.2 parameters were also insufficient and sometimes even excessive. This study shows that the thickness of the concrete cover must be increased by 10 to 15 mm. In some cases, the flange thickness proposed by EN 1992-1.2 can be reduced by 15 mm.
- The tabulated method suggest is an alternative to the one proposed by EN 1992-1.2.
- The new tabular method also expands the rib width and flange thickness options suggested by EN 1992-1.2, providing engineers with new combinations for fire design of these slabs.

REFERENCES

1. Huang, W. et al., Experimental Study on Flexural Behaviour of Lightweight Multi-Ribbed Composite Slabs. *Advances in Civil Engineering*, vol. 2019, p. 1093074, 2019, doi: 10.1155/2019/1093074.
2. Yardim, Y. et al, AAC-concrete light weight precast composite floor slab, *Constr Build Mater*, vol. 40, pp. 405–410, 2013, doi: <https://doi.org/10.1016/j.conbuildmat.2012.10.011>.
3. Ma, J. et al., Topology optimization of ribbed slabs and shells, *Eng Struct*, vol. 277, p. 115454, 2023, doi: <https://doi.org/10.1016/j.engstruct.2022.115454>.

4. Malviya, S. and Tiwari, V. K., Behaviour of flat slab, waffle slab, ribbed & secondary beam in a multistorey building under seismic response: A review, *Int. J. Res. Appl. Sci. Eng. Technol*, vol. 8, pp. 986–992, 2020.
5. Huber, T. et al., Structural design and testing of material optimized ribbed RC slabs with 3D printed formwork, *Structural Concrete*, vol. 24, no. 2, pp. 1932–1955, Apr. 2023, doi: <https://doi.org/10.1002/suco.202200633>.
6. Moyeda, A. & Fish, J., Multiscale analysis of solid, waffle, ribbed and hollowcore reinforced concrete slabs, *Comput Methods Appl Mech Eng*, vol. 348, pp. 139–156, 2019, doi: <https://doi.org/10.1016/j.cma.2019.01.022>.
7. Zheng, C., et al., Study on the flexural behavior of precast concrete multi-ribbed sandwich slabs under different boundary conditions, *Eng Struct*, vol. 291, p. 116342, 2023, doi: <https://doi.org/10.1016/j.engstruct.2023.116342>.
8. Favarato, L. F. et al. On the composite behavior of a rebar truss ribbed slab with incorporated shuttering made of lipped channel section, *Journal of Building Engineering*, vol. 55, p. 104663, 2022, doi: <https://doi.org/10.1016/j.jobe.2022.104663>.
9. Burger, J. et al., Design and fabrication of optimised ribbed concrete floor slabs using large scale 3D printed formwork, *Autom Constr*, vol. 144, p. 104599, 2022, doi: <https://doi.org/10.1016/j.autcon.2022.104599>.
10. Tan, C. et al., Study on Shear-Lag Effect of Steel UHPC Ribbed Slab Composite Structures Using Bar Simulation Method, *Buildings*, vol. 12, no. 11. 2022. doi: 10.3390/buildings12111884.
11. Martín-Sanz, H. et al, Shear-bending failure modeling of concrete ribbed slabs strengthened with UHPFRC, *Eng Struct*, vol. 222, p. 110846, 2020, doi: <https://doi.org/10.1016/j.engstruct.2020.110846>.
12. Rossi, P. et al., Bending and compressive behaviours of a new cement composite, *Cem Concr Res*, vol. 35, no. 1, pp. 27–33, 2005, doi: <https://doi.org/10.1016/j.cemconres.2004.05.043>.
13. Xiao, J. L. et al., Flexural behavior of steel-UHPC composite slabs with perfobond rib shear connectors, *Eng Struct*, vol. 245, p. 112912, 2021, doi: <https://doi.org/10.1016/j.engstruct.2021.112912>.
14. Liu, J., Flexural behavior of prestressed concrete composite slab with precast inverted T-shaped ribbed panels, *Eng Struct*, vol. 215, p. 110687, 2020, doi: <https://doi.org/10.1016/j.engstruct.2020.110687>.
15. Fodzi N. H. M. & Mohd Hashim, M. H., Structural Effect of Using Steel Fiber Reinforcement on the Punching Shear of Self-Compacting Fiber Reinforced Concrete (SCFRC) Ribbed Slabs, *Materials Science Forum*, vol. 972, pp. 99–104, 2019, doi: 10.4028/www.scientific.net/MSF.972.99.
16. Abdulhussein, S.S., & Alfeehan, A.A., Utilization of Iron Lathe Waste and Post-Tensioned Steel Reinforcement in Lightweight Concrete Ribbed Slabs, in 2020 2nd Al-Noor International Conference for Science and Technology (NICST), 2020, pp. 44–50. doi: 10.1109/NICST50904.2020.9280310.
17. Buka-Vaivade, K et al., Numerical Comparison of HPFRC and HPC Ribbed Slabs, *IOP Conf Ser Mater Sci Eng*, vol. 660, no. 1, p. 12054, 2019, doi: 10.1088/1757-899X/660/1/012054.
18. Mastali, M. et al, Development of innovative hybrid sandwich panel slabs: Advanced numerical simulations and parametric studies, *Compos Struct*, vol. 152, pp. 362–381, 2016, doi: <https://doi.org/10.1016/j.compstruct.2016.05.072>.
19. Ruggieri, S. et al, A numerical procedure for modeling the floor deformability in seismic analysis of existing RC buildings, *Journal of Building Engineering*, vol. 19, pp. 273–284, 2018, doi: <https://doi.org/10.1016/j.jobe.2018.05.019>.
20. He, Z. & Lin, P., Research on fatigue performance and optimal design of steel-UHPC composite slab, *Structures*, vol. 43, pp. 682–695, 2022, doi: <https://doi.org/10.1016/j.istruc.2022.06.067>.
21. Jin, L. et al., Evaluation of impact response of thermal-damaged FRP-RC slabs: Effects of FRP bar type and concrete cover thickness, *Journal of Building Engineering*, vol. 75, p. 107079, 2023, doi: <https://doi.org/10.1016/j.jobe.2023.107079>.
22. Bilotta, A. et al., Structural behaviour of FRP reinforced concrete slabs in fire, *Eng Struct*, vol. 221, p. 111058, 2020, doi: <https://doi.org/10.1016/j.engstruct.2020.111058>.
23. Wiesner F. et al., Structural Capacity of One-Way Spanning Large-Scale Cross-Laminated Timber Slabs in Standard and Natural Fires, *Fire Technol*, vol. 57, no. 1, pp. 291–311, 2021, doi: 10.1007/s10694-020-01003-y.
24. Xu, Q. et al., Comparative experimental study of fire resistance of two-way restrained and unrestrained precast concrete composite slabs, *Fire Saf J*, vol. 118, p. 103225, 2020, doi: <https://doi.org/10.1016/j.firesaf.2020.103225>.

25. Azevedo, A. S. et al., Fire behaviour of CFRP-strengthened RC slabs using different techniques – EBR, NSM and CREAtE, *Compos B Eng*, vol. 230, p. 109471, 2022, doi: <https://doi.org/10.1016/j.compositesb.2021.109471>.
26. Zhang, R. et al., Effect of elevated temperature on the low-velocity impact performances of GFRP reinforced concrete slabs, *Constr Build Mater*, vol. 395, p. 132285, 2023, doi: <https://doi.org/10.1016/j.conbuildmat.2023.132285>.
27. Hamzeh, H., GFRP-Reinforced Concrete Slabs: Fire Resistance and Design Efficiency, *Journal of Composites for Construction*, vol. 23, no. 2, p. 04019009, Apr. 2019, doi: [10.1061/\(ASCE\)CC.1943-5614.0000937](https://doi.org/10.1061/(ASCE)CC.1943-5614.0000937).
28. Coz-Díaz, J. J. et al., Comparative study of LightWeight and Normal Concrete composite slabs behaviour under fire conditions, *Eng Struct*, vol. 207, p. 110196, 2020, doi: <https://doi.org/10.1016/j.engstruct.2020.110196>.
29. Heo, I. et al, Experimental and Numerical Investigations on Fire-Resistance Performance of Precast Concrete Hollow-Core Slabs, *Applied Sciences*, vol. 11, no. 23, 2021, doi: [10.3390/app112311500](https://doi.org/10.3390/app112311500).
30. Sui, Z.-A. et al., Flexural Behavior of Fire-Damaged Prefabricated RC Hollow Slabs Strengthened with CFRP versus TRM, *Materials*, vol. 13, no. 11, 2020, doi: [10.3390/ma13112556](https://doi.org/10.3390/ma13112556).
31. Bolina F.L., & Rodrigues, J.P.C., Finite element analysis criteria for composite steel decking concrete slabs subjected to fire, *Fire Saf J*, vol. 139, p. 103818, 2023, doi: <https://doi.org/10.1016/j.firesaf.2023.103818>.
32. Flecknoe-Brown, K.W. & van Hees, P., Geometrical and environmental effect on fire behaviour of polyurethane foam slabs, *Fire Mater*, vol. n/a, no. n/a, Feb. 2023, doi: <https://doi.org/10.1002/fam.3133>.
33. FIB Bulletin 38, “Fire design of concrete structures – materials, structures and modelling – state of art report.” Fédération Internationale du Béton, Lausanne, Switzerland, 2007.
34. Qiao, R. et al, Explosive Spalling Mechanism and Modeling of Concrete Lining Exposed to Fire, *Materials*, vol. 15, no. 9, p. 3131, Apr. 2022, doi: [10.3390/ma15093131](https://doi.org/10.3390/ma15093131).
35. Khoury, G.A., Effect of fire on concrete and concrete structures, *Progress in Structural Engineering and Materials*, vol. 2, no. 4, pp. 429–447, Oct. 2000, doi: <https://doi.org/10.1002/pse.51>.
36. Tenchev R. & Purnell, P., An application of a damage constitutive model to concrete at high temperature and prediction of spalling, *Int J Solids Struct*, vol. 42, no. 26, pp. 6550–6565, 2005, doi: <https://doi.org/10.1016/j.ijsolstr.2005.06.016>.
37. EN 1992-1.2, Eurocode 2: Design of concrete structures - Part 1-2: General rules - Structural fire design, European Committee for Standardization, 2004.
38. DIN 4102, Fire behaviour of building materials and building components - Part 4: Synopsis and application of classified building materials Deutsches Institut für Normung, Berlin, 2016.
39. ISO 834, Fire-resistance tests — Elements of building construction — Part 1: General requirements, International Organization for Standardization. Geneva, 1999.
40. EN 1992-1.1, Eurocode 2: Design of concrete structures - Part 1-1: General rules and rules for buildings, 2004.
41. EN 1991-1.1, Eurocode 1: Actions on structures - Part 1-1: General actions - Densities, self-weight, imposed loads for buildings , European Standard. European Committee for Standardization, Brussels, 2004.
42. Bolina, F.L. et al., Experimental and numerical evaluation of RC ribbed slabs in fire conditions, *Structures*, vol. 51, pp. 747–759, 2023, doi: <https://doi.org/10.1016/j.istruc.2023.03.057>.
43. ASTM C 150, Standard Specification for Portland Cement. American Society for Testing and Materials, West Conshohocken, United States, 2007.
44. ASTM C39, Standard Test Method for Compressive Strength of Cylindrical Concrete Specimens, American Society for Testing and Materials, West Conshohocken, United States, 2022.
45. BS 476-20, Fire Tests on Building materials and structures – Part 20. Method of test for determination of the fire resistance of elements of construction (General principles), British Standard. London, 1987.
46. ASTM E119, Standard Test Methods for Fire Tests of Building Construction and Materials, American Society for Testing and Materials. West Conshohocken, United States, 2020.
47. BS EN 1363-1, “Fire resistance tests General requirements,” European standards. Geneve, 2020.
48. Abaqus, Abaqus analysis user’s guide. Simulia, 2016.
49. Bolina, F.L. & Rodrigues, J.P.C., Numerical study and proposal of new design equations for steel decking concrete slabs subjected to fire, *Eng Struct*, vol. 253, p. 113828, 2022, doi: <https://doi.org/10.1016/j.engstruct.2021.113828>.

APPLICATION OF THE METHOD OF PARALLEL SECTIONS (MPS) FOR THE ASSESSMENT OF THE THERMO-MECHANICAL PERFORMANCE OF PRECAST PRESTRESSED CONCRETE ROOF/FLOOR MEMBERS IN FIRE

Bruno Dal Lago¹, Matteo Mostachetti²

ABSTRACT

The structural check of prestressed concrete members in fire is typically carried out analytically, alternatively to simplified methods applicable to limited cases. The classical analytical check method consists in solving the thermal field on a cross-sectional basis employing a 2D finite element solver, later checking the safety margin based on stress integration, considering the material damage induced by the exposure to high temperature. This approach, however, does not consider the deformation behaviour of the member, as well as potential second order effects induced by compression, bending, or their combination, which may be of relevant importance especially for slender and long-span elements. More refined numerical methods able to evaluate such effects typically consist in 3D finite element (FE) solvers based on numerical models which are typically complex and highly time-consuming for their processing. Thus, they are typically restrained to the field of research, rather than practice design. This paper presents a series of applications of the Method of Parallel Sections (MPS) as a numerical tool for the simplified performance assessment of prestressed and reinforced concrete members in fire, to be intended as a design-oriented procedure alternative to explicit 3D FE solvers. The applications encompass horizontal prestressed members typical of the precast concrete market, evaluating moment-curvature diagrams, deflection and elongation profiles, and prestressing evolution over time exposure to the nominal standard ISO834 curve.

Keywords: Performance-based method; fire; structural design; precast concrete; prestressed beams

1 INTRODUCTION

Precast prestressed beam members are widely employed in the European construction heritage and current market for the construction of long-span industrial and commercial buildings. Such typology of slender elements indeed comprises members of very different cross-section and profile distribution. Their shape plays a crucial role over their fire performance [1], mainly since it determines the temperature rise rate in the reinforcement, and potential rise of second order effects induced by sectional distortion under large curvature (especially for thin-walled open section members [2,3]). Moreover, their behaviour in fire is not well-known, mainly due to the span limitations of the elements tested to far, due to the limited physical dimensions of the test setup furnaces [4-10].

The thermo-mechanical fire performance of a series of slab and beam members representative of the most recurrent elements employed was carried out based upon the recently proposed Method of Parallel Sections (MPS) [11-13]. This method is based on longitudinal stress integration along the cross section, following a sectional approach [14-18], although restraining it to plane bending. The material constitutive laws variable

¹ Associate Professor, Department of Theoretical and Applied Sciences, Università degli Studi dell'Insubria, 21100 Varese, Italy
e-mail: bruno.dallago@uninsubria.it, ORCID: <https://orcid.org/0000-0002-3088-8376>

² MSc Engineer, Department of Theoretical and Applied Sciences, Università degli Studi dell'Insubria, 21100 Varese, Italy
e-mail: mostachetti.matteo@gmail.com

with temperature described in Eurocode 2 [19] were implemented in a code written in Mathcad 15 [20] following the nominal characteristic material strengths. It is reminded that the Eurocode 2 [19] constitutive law formulations consider implicitly the effect of transient thermal creep [21].

It is worth recalling that the MPS does not currently include the possible effect of concrete loss in the cross-section during the exposure to fire, induced for example by concrete spalling or concrete delamination. However, it includes the effects of self-equilibrated thermally-induced stresses, although along the selected direction of the analysis, only. Nevertheless, it was extendedly demonstrated that self-equilibrated stresses are relevant for the deformation and local stress evaluation, while their contribution to the evaluation of the strength of the cross-section is practically negligible (unless a structural failure induced by self-equilibrated stress occurs, such as web explosion in I-beams with thin web and fire exposure on both sides). This study confirms this assumption by evaluating the performance of the analysed members both including and excluding thermally-induced self-equilibrated stresses.

This paper presents an extensive application of the MPS for the determination of the structural performance of precast prestressed concrete members in fire. In particular, five roof members typical of industrial buildings [22] spanning 25 metres, and five flat members typical of intermediate slabs of commercial buildings spanning 12 metres, were analysed.

The analysis was carried out in a Fire Safety Engineering framework, where (a) the fire was simply modelled considering nominal curves, (b) the non-linear thermal analysis was solved with the use of a numerical tool, (c) indirect actions are neglected due to the statically determined support scheme of the structural members at study and the typical relatively weak mechanical connections with the other structural members, and (d) the structural performance was evaluated based on the MPS in terms of non-linear moment-curvature diagrams, sectional stress diagrams, deformation profiles (both axial and transverse), and prestress evolution.

The results allow to carry out a general comparison of the performance of different slab and beam elements in fire, also highlighting the topics where further light must be shed in the near future.

2 METHOD OF PARALLEL SECTIONS

The MPS simplifies the actual 2D problem into a 1D problem of a series of sub-sections (Fig. 1 right) structurally acting in parallel, analysing their response under potential combined axial and uniaxial bending, thus expressing a system of two equilibrium equations, related to sectional translation (Eq. 1) and rotation (Eq. 2). This, indeed, is the typical solution employed for the design of beam members subjected to prevalent axial and uniaxial bending under static load. However, when dealing with thermal loads, the temperature-induced effects of both strain and damage are introduced, which change the condition of uniformity among the transverse chords of the cross-section. The MPS finds an approximate solution to this issue by introducing a discretisation among the chord width, formally by solving the problem by considering n cross-sections along the outer-inner direction acting in parallel. The equilibrium equations of each sub-cross-section is then included as a summatory in the solving system. The best criterion to select a proper number of cross-sections may be related with a variable width b_i defined on the basis of the expected thermal field to cover a similar temperature gradient. To a higher number n of cross-sections considered corresponds a higher accuracy, being the solution hypothetically exact given $n = \infty$. In such analysis, the thermal strain and damage are introduced for each chord according to the mean temperature along the chord width. The problem is defined by four variables, two of which are defined by the external loads (N, M) and the remaining two of which by the strain diagram (e.g. the curvature angle χ and the strain of the upper concrete chord $\varepsilon_{c,top}$). It is pointed out that this simplified procedure allows to fully account for the self-equilibrated stress generated by the non-linear thermal strain in the direction of the calculation, as well as the resulting global sectional curvature and mean elongation, whilst it neglects self-equilibrated strain/stress distribution in the transverse direction only. The MPS was positively subjected to check with the results from closed-source proprietary finite element software solving 2D cross-sectional calculations [23], with deviations of the order of few percentage points, similar to the expected magnitude of the numerical approximations. So far, the MPS has been applied for the structural assessment of many sorts of reinforced

concrete members in fire, including prestressed horizontal elements [11], barrel-vault-shaped completing shells [11], bi-directional waffle slabs [12], columns [13], and panels.

The workflow of the MPS is described in Fig. 1(right). Given a structural configuration, a set of static loads, and a member with assigned geometry, reinforcement, and material mechanical properties calculated from static analysis, the process starts with the definition of the thermal field analysis [24], providing temperature mapping for selected exposure times to the selected fire curve. Based on the distribution of parallel sections, the thermo-mechanical analysis is carried out by evaluating the non-linear moment-curvature diagram of the whole cross-section by setting progressive values of the curvature χ , assuming a constant external axial load N , evaluating through the two equilibrium equations the two remaining variables, both associated to the strain diagram per each imposed curvature. At this stage, in case the element is not transversally or longitudinally statically determined, the proper indirect actions can be evaluated by, for example, the flexibility method.

In case the performance at a given exposure time is not satisfied, the reinforcement layout (or the geometry or the material mechanical properties) is modified, and the workflow is carried out again up to convergence.

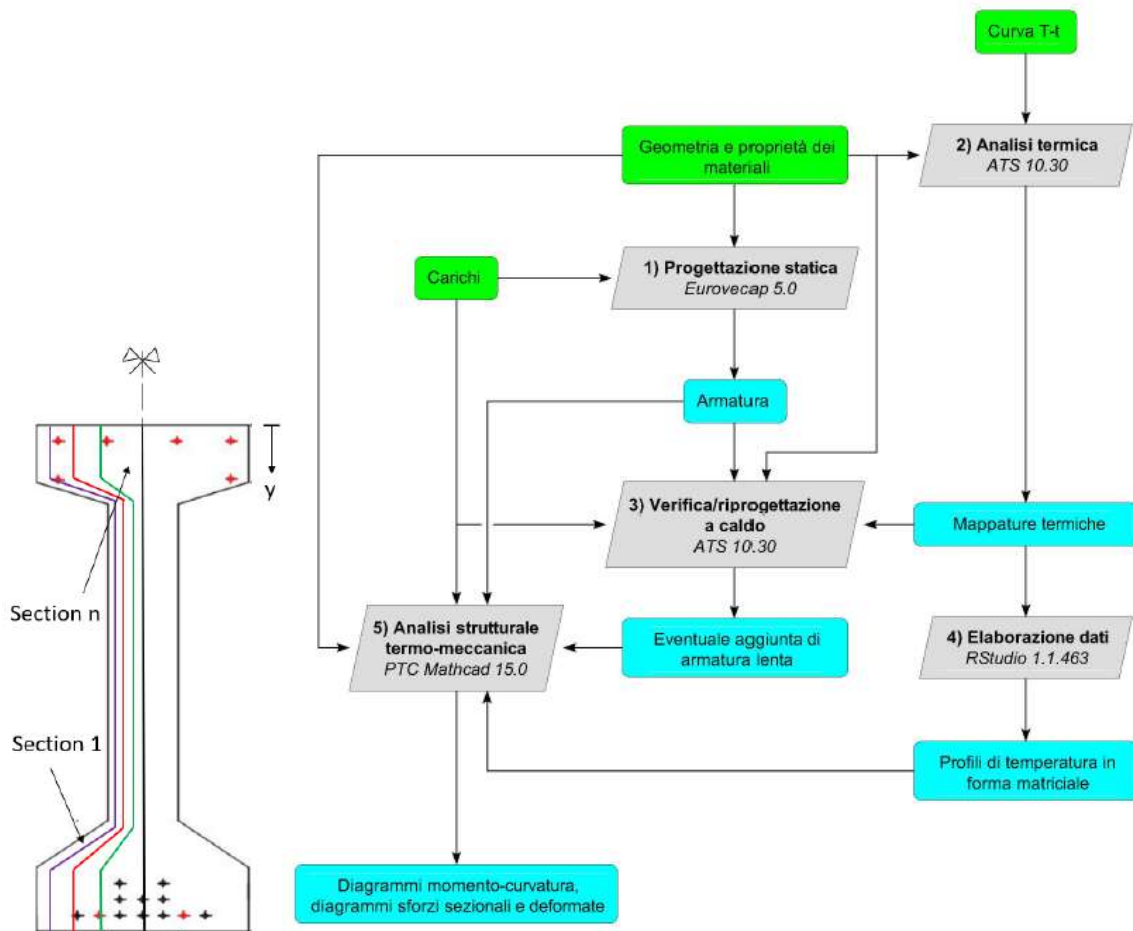


Figure 1. Example of definition of the parallel sections and logical workflow of the Method of Parallel Sections

$$\begin{aligned}
 N(\varepsilon_{ctop}, \chi) = & \sum_{i=1}^n \left(\int_0^H \sigma_c \left(\varepsilon(y, \varepsilon_{ctop}, \chi) - \varepsilon_{c\theta}(\overline{\Delta\theta}_i(y)), \overline{\Delta\theta}_i(y) \right) b_i(y) dy \right) \\
 & + \sum_{j=0}^{n_s} \sigma_s(\varepsilon(y_{sj}, \varepsilon_{ctop}, \chi) - \varepsilon_{s\theta}(\Delta\theta_{sj}), \Delta\theta_{sj}) A_{sj} \\
 & + \sum_{k=0}^{n_p} \sigma_p(\varepsilon(y_{pk}, \varepsilon_{ctop}, \chi) - \varepsilon_{p\theta}(\Delta\theta_{pk}) + \varepsilon_{p0k}, \Delta\theta_{pk}) A_{pk}
 \end{aligned} \quad (1)$$

$$\begin{aligned}
M(\varepsilon_{ctop}, \chi) = & \sum_{i=1}^n \left(\int_0^H \sigma_c \left(\varepsilon(y, \varepsilon_{ctop}, \chi) - \varepsilon_{c\theta} \left(\overline{\Delta\theta}_i(y) \right), \overline{\Delta\theta}_i(y) \right) b_i(y) (y - y_g) dy \right) \\
& + \sum_{j=0}^{n_s} \sigma_s (\varepsilon(y_{sj}, \varepsilon_{ctop}, \chi) - \varepsilon_{s\theta} (\Delta\theta_{sj}), \Delta\theta_{sj}) A_{sj} (y_{sj} - y_g) \\
& + \sum_{k=0}^{n_p} \sigma_p (\varepsilon(y_{pk}, \varepsilon_{ctop}, \chi) - \varepsilon_{p\theta} (\Delta\theta_{pk}) + \varepsilon_{p0k}, \Delta\theta_{pk}) A_{pk} (y_{pk} - y_g)
\end{aligned} \quad (2)$$

where:

N is the external axial load;

M is the external bending moment;

ε is the longitudinal strain;

ε_{ctop} is the longitudinal strain of the top concrete chord;

ε_{p0k} is the prestrain applied to the k_{th} prestressing strand/bar level;

χ is the sectional curvature;

$\sigma_{c,s,p}$ is the longitudinal stress of concrete, mild steel, and prestressing steel, respectively;

$\Delta\theta$ is the temperature gradient;

$\overline{\Delta\theta}$ is the mean temperature gradient;

n is the number of parallel sections in which the cross-section is divided;

$n_{s,p}$ is the number of mild steel rebar levels, and prestressing steel strand/bar levels, respectively;

H is the total depth of the concrete cross-section along the considered calculation direction;

y is the coordinate along the calculation direction of the element;

$\varepsilon_{c,s,p\theta}$ is the thermal strain of concrete, mild steel, and prestressing steel, respectively;

b is the chord width of the concrete cross-section;

y_g is the centre of gravity of the idealised cross-section;

$A_{s,p}$ is the area of the mild steel rebars, and prestressing steel strands/bars, respectively, for specific level.

The moment-curvature diagrams already provide important information not only strictly related to the ultimate resistance (e.g. cracking moment, stiffness degradation, etc.). Moreover, the deformation of the member can be evaluated both in the transverse direction, by double integration of the curvatures associated to the acting bending moment distribution along the span (Eq. 3), provided proper boundary conditions are set, and in the longitudinal direction, by calculating a mean elongation over the cross-section (Eq. 4).

To be noted that, if a homogeneous heat exposure occurs along the length of the element, the dependency of both moment-curvature diagram in Eq. 3 and thermal strain (and thus the whole integral argument) in Eq. 4 upon the coordinate x disappears simplifying the relative calculation.

$$v(x, \chi) = \iint_0^x \chi (M_{Ed,fire}(x), x) dx \quad (3)$$

$$\overline{\Delta L} = \int_0^L \frac{\sum_{i=1}^n \left(\int_0^H \varepsilon_{c\theta} \left(\overline{\Delta\theta}_i(x, y) \right) b_i(y) dy \right)}{\int_0^H b(y) dy} dx \quad (4)$$

where:

x is the coordinate along the longitudinal axis of the element;

v is the transverse deflection/camber;

$M_{Ed,fire}$ is the external design bending moment in exceptional fire load combination for a given position x ;

$\overline{\Delta L}$ is the mean elongation of the element.

3 APPLICATION TO ROOF ELEMENTS

The MPS has been applied to several roof elements, representative of the precast concrete industry for single-storey industrial buildings. In particular, the application encompasses elements having cross-sections as follows: wing-shaped [2,25] (Fig. 2), Omega-shaped (Fig. 3), TT with wide ribs (Fig. 4), TT with narrow ribs (Fig. 5), and Y-shaped (Fig. 6). TT elements with narrow ribs reflect the common practice of pre-80's elements, not conceived for fire resistance. TT elements with wide ribs are typical of a more modern production. All elements are assumed to have continuous cross-section along their whole span.

All members are assumed to be perfectly statically determined with double simple support static scheme over a calculation length of 25 m. All members were selected with depth of structural cross-section of 1 m.

The exceptional fire static load condition for all cases concerns uniformly distributed loads derived from a static scheme of spaced members with interaxis of 5 m, where the distance between each member is covered by reinforced concrete completing shell elements weighing 90 kg/m² of projected horizontal surface, including polypropylene skylights. A distributed non-structural dead load of 20 kg/m² is considered. For the static Ultimate Limit State (ULS) load condition, only, a uniformly distributed snow load of 120 kg/m² is considered. Standard safety coefficients of 1.4 for concrete produced in sophisticated batching plants, and of 1.15 for both mild and prestressing steel were considered, again for ULS static checks, only.

Concrete class C45/55, mild steel grade B450, and prestressing steel grade Y1860 were considered.

The thermal analysis was carried out by employing a dedicated software named ATS [23], based on the thermal-physical properties of concrete, mild steel, and prestressing steel provided by Eurocode 2 [19]. Hot surfaces were assigned to all the perimeter exposed to the bottom. Cold surfaces were assigned to the perimeter exposed to the top, assuming a low-melting temperature thermal insulation is installed in the building, and neglecting its contribution in the earlier stages of exposure to fire. The nominal standard ISO 834 [19] curve was employed as temperature time history of the gas (air) in the environment.

It is worth pointing out that the inner core of the wing-shaped roof element (Fig. 2) is made out of low-melting temperature polystyrene blocks which are discretely in contact with the top surface (i.e. the narrow top slab is not continuous, but alternated with polystyrene in contact with the surface). Thus, the presence of polystyrene in the core of that particular cross-section is ignored and replaced by air. The transmission of heat by convection and radiation within the core is considered in the calculation.

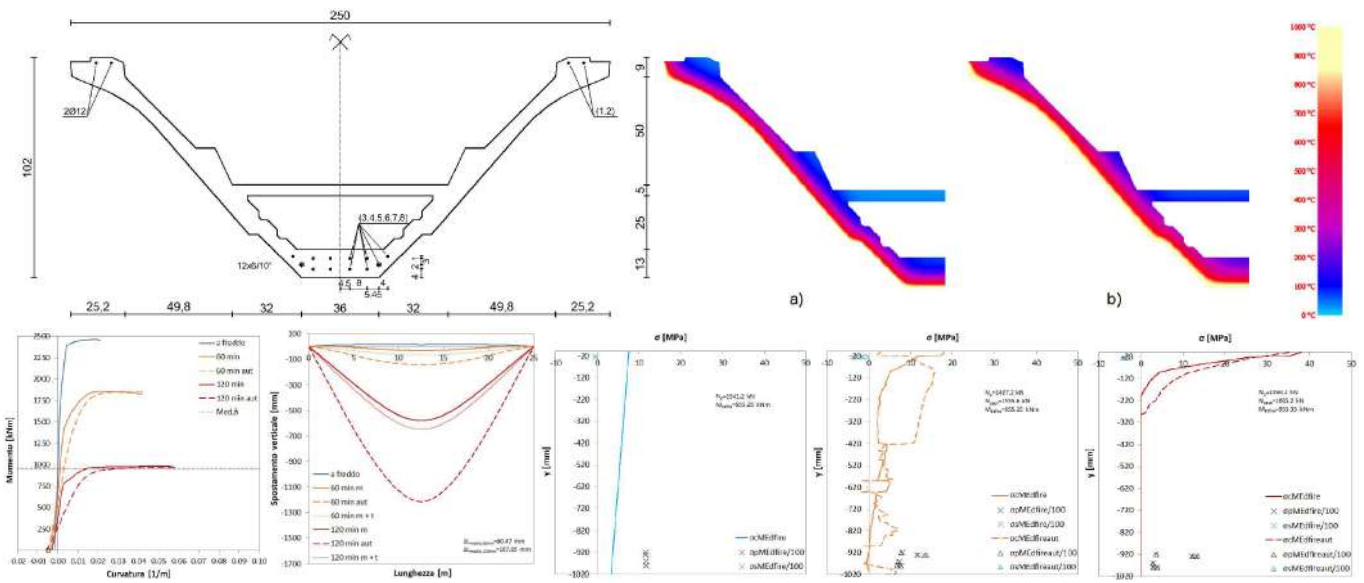


Figure 2. Wing-shaped roof element: (top left to right) cross-section and thermal field at a) 60 min and b) 120 min; (bottom left to right) moment-curvature and deformation diagrams, stress profile evolution at 0, 60, and 120 min of exposure to ISO834 fire

The results are provided in each figure in terms of the following:

- Drawing of the cross-section geometry with reinforcement details;
- Picture of the thermal fields at 60 and 120 minutes of exposure to ISO 834 curve;
- Non-linear moment-curvature of the midspan cross-section under exceptional load combination at 0 (blue line), 60 (orange lines), and 120 (red lines) minutes of exposure;
- Non-linear deflection profiles associated with the above time exposures;
- Non-linear stress profiles of concrete and reinforcement associated with the above time exposures;
- Value of the total prestressing N_p at the above time exposures.

In case additional mild steel is necessary to the checks at 120 or 60 minutes, the curves associated with the modified (increased) reinforcement layouts are indicated in purple.

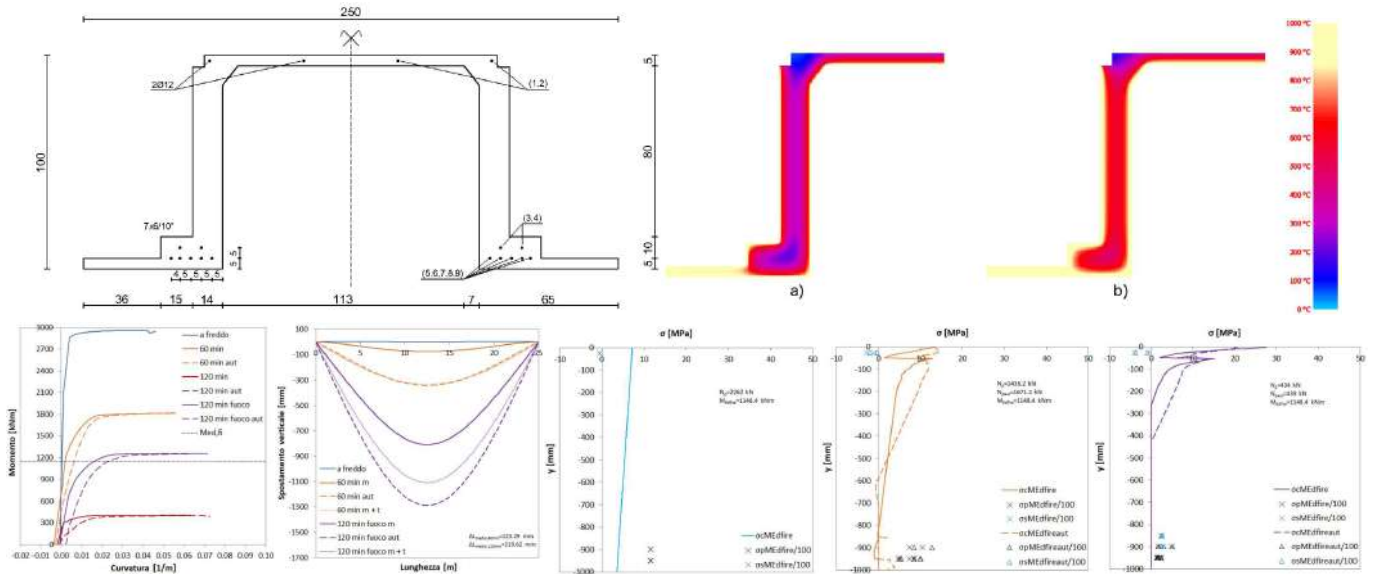


Figure 3. Omega roof element: (top left to right) cross-section and thermal field at a) 60 min and b) 120 min; (bottom left to right) moment-curvature and deformation diagrams, stress profile evolution at 0, 60, and 120 min of exposure to ISO834 fire

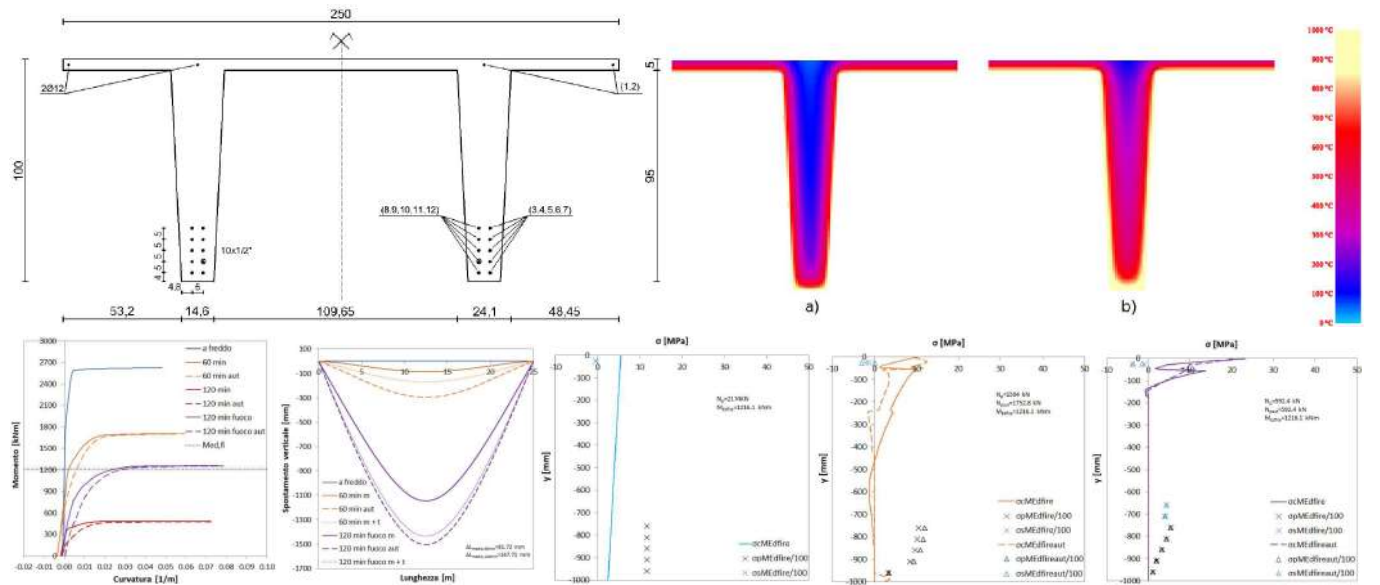


Figure 4. TT roof element with wide ribs: (top left to right) cross-section and thermal field at a) 60 min and b) 120 min; (bottom left to right) moment-curvature and deformation diagrams, stress profile evolution at 0, 60, and 120 min of exposure to ISO834 fire

To be noted that the checks are carried out under two assumptions: neglecting self-equilibrated stresses ($\epsilon_{c,s,p\theta} = 0$), and taking self-equilibrated stresses into account. The corresponding lines are solid and dashed, respectively.

For the evaluation of the deflection profile, only, a further light line is included as a representation of a tentative simplified method to consider the effect of self-equilibrated stresses in an uncoupled manner with respect to the thermo-mechanical full solution of the problem. This simplified methodology, which however proved to be grossly inaccurate, is not explicated in this paper for the sake of conciseness.

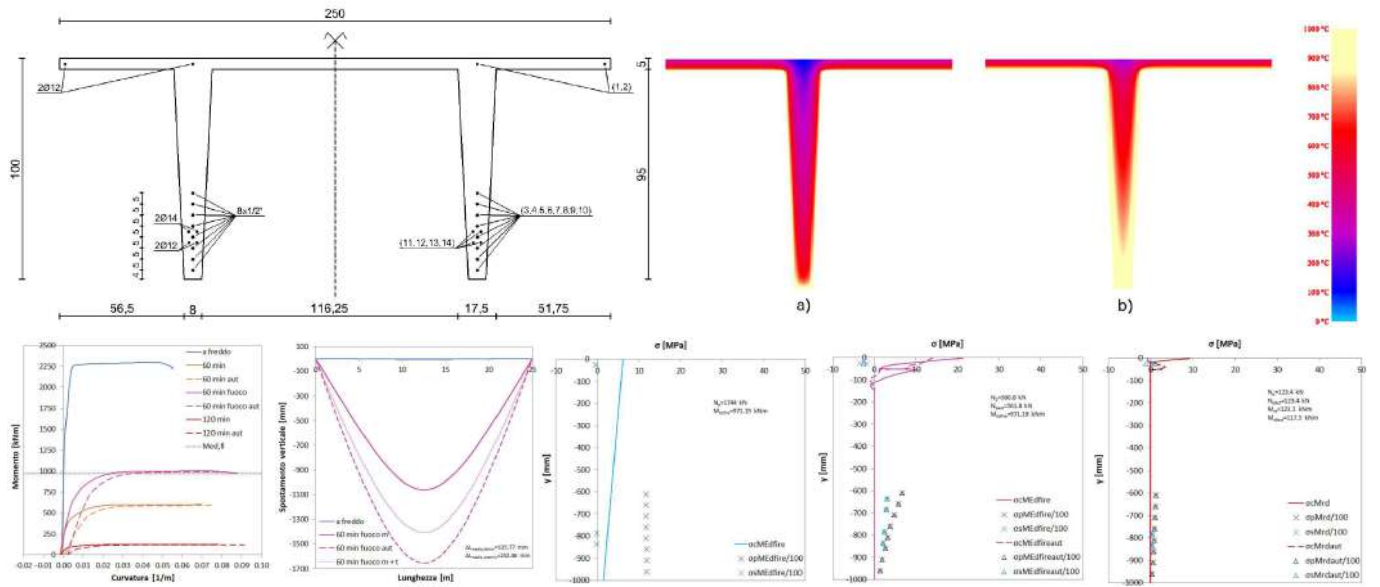


Figure 5. TT roof element with narrow ribs: (top left to right) cross-section and thermal field at a) 60 min and b) 120 min; (bottom left to right) moment-curvature and deformation diagrams, stress profile evolution at 0, 60, and 120 min of exposure to ISO834 fire

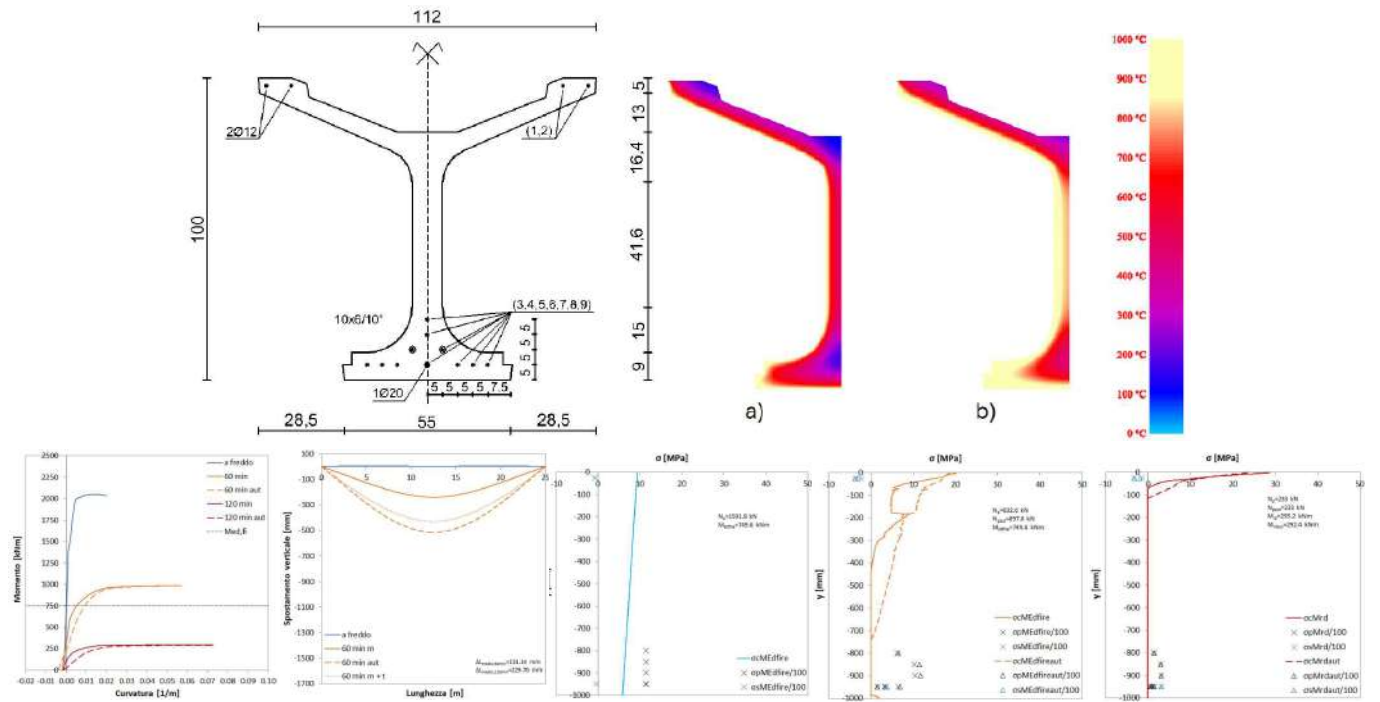


Figure 6. Y roof element: (top left to right) cross-section and thermal field at a) 60 min and b) 120 min; (bottom left to right) moment-curvature and deformation diagrams, stress profile evolution at 0, 60, and 120 min of exposure to ISO834 fire

4 APPLICATION TO FLOOR ELEMENTS

The MPS has been also applied to several floor elements, representative of the precast concrete industry for intermediate storeys of commercial buildings. In particular, the application encompasses elements having cross-sections as follows: hollowcore [26] (Fig. 7), Box-shaped with flat bottom flange [27] (Fig. 8), Omega-shaped (Fig. 9), TT with wide ribs (Fig. 10), and TT with narrow ribs (Fig. 11). Also for this application, TT elements with narrow ribs reflect the common practice of pre-80's elements, not conceived for fire resistance. TT elements with wide ribs are typical of a more modern production. All elements are assumed to have continuous cross-section along their whole span.

All members are assumed to be perfectly statically determined with double simple support static scheme over a calculation length of 12 m. All members were selected with depth of structural cross-section of 0.4 m. The exceptional fire static load condition for all cases concerns uniformly distributed loads derived from a static scheme of adjacent members with flat extrados, which is formed by additional reinforced concrete plate elements in case of cross-sections not having continuous top flange (box and omega sections). Apart from the completing plates, when present, non-structural dead loads of 250 kg/m² were considered, including finishing layers and non-structural partition walls. For the static Ultimate Limit State (ULS) load condition, a uniformly distributed live load of 300 kg/m² was considered, multiplied by the proper reduction coefficient ($\psi_2 = 0.3$) for the exceptional load combination used for fire checks.

All other parameters are assumed equal to those previously described for the roof elements.

Concerning both hollowcore and box sections, the inner core(s) is(are) indeed hollow, filled with air. The transmission of heat by convection and radiation within the core is considered in the calculation.

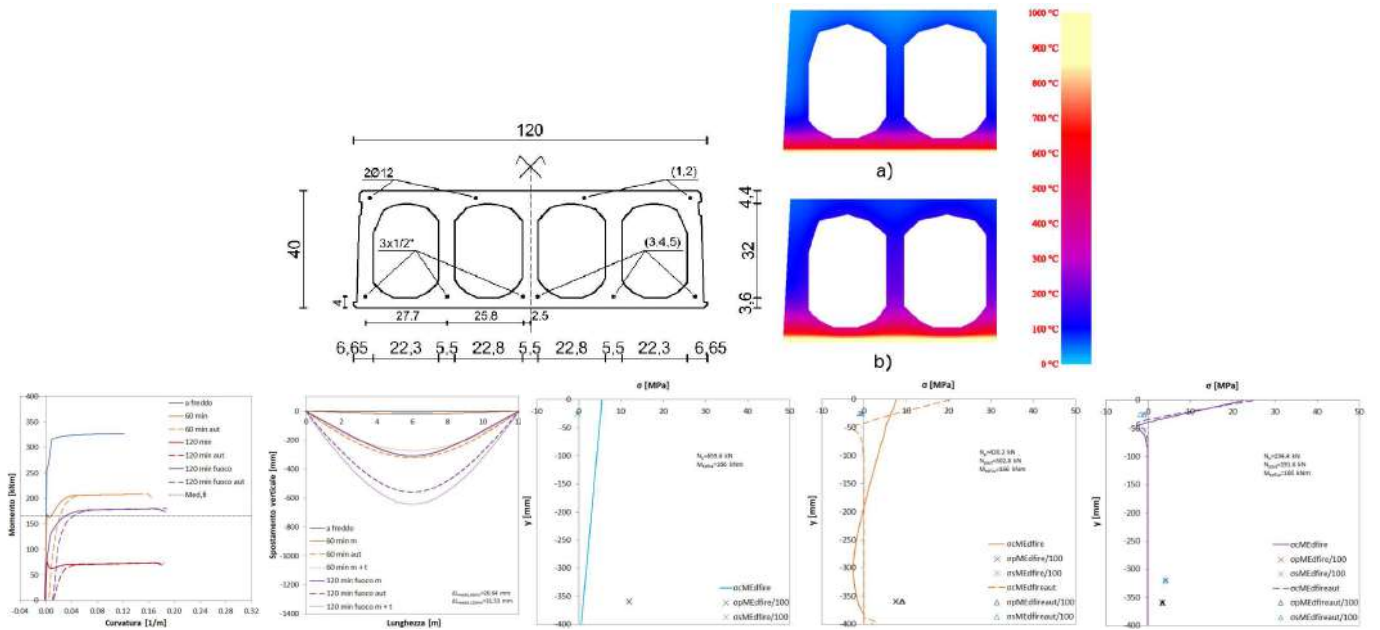


Figure 7. Hollowcore floor element: (top left to right) cross-section and thermal field at a) 60 min and b) 120 min; (bottom left to right) moment-curvature and deformation diagrams, stress profile evolution at 0, 60, and 120 min of exposure to ISO834 fire

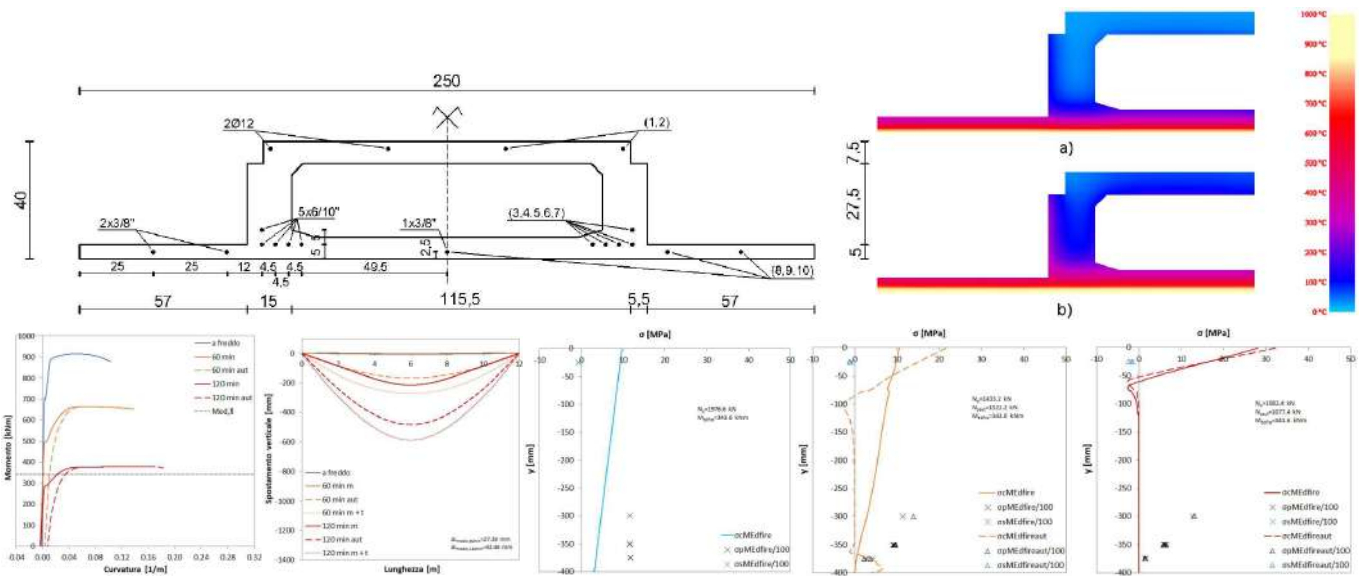


Figure 8. Box floor element with flat bottom flange: (top left to right) cross-section and thermal field at a) 60 min and b) 120 min; (bottom left to right) moment-curvature and deformation diagrams, stress profile evolution at 0, 60, and 120 min of exposure to ISO834 fire

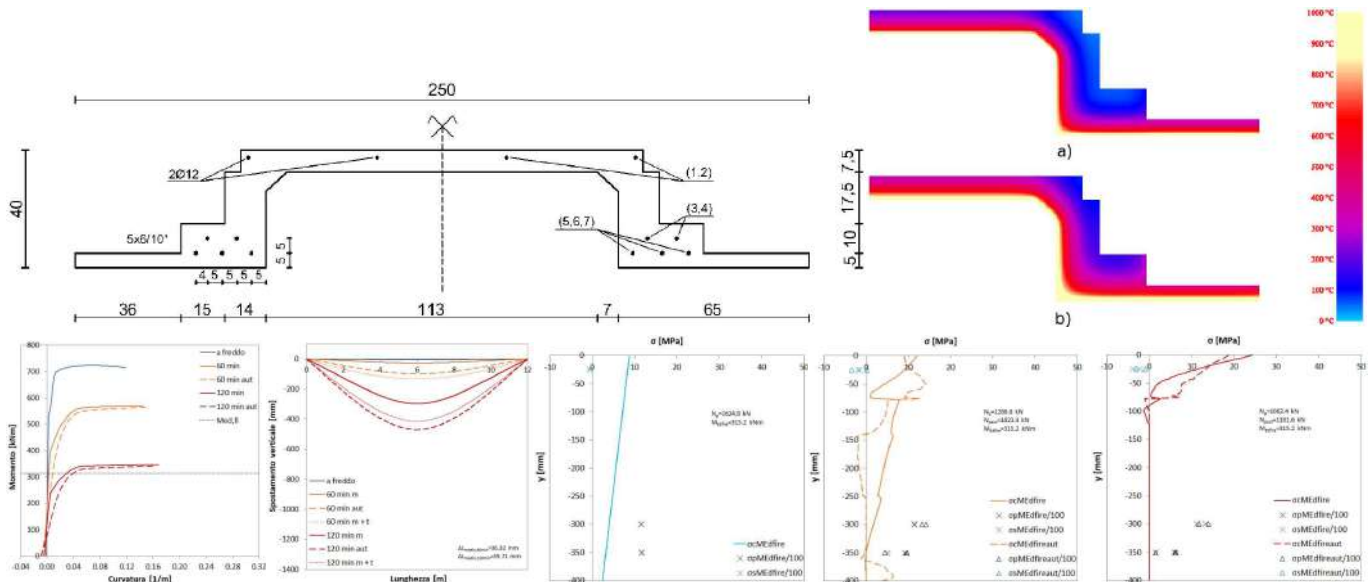


Figure 9. Omega floor element: (top left to right) cross-section and thermal field at a) 60 min and b) 120 min; (bottom left to right) moment-curvature and deformation diagrams, stress profile evolution at 0, 60, and 120 min of exposure to ISO834 fire

5 COMPARISON

The performance of the analysed elements in fire is resumed in Table 1.

Additional mild reinforcement to make the checks for fire resistance to 60 min of exposure to ISO 834 curve was necessary only for the TT roof element with narrow ribs, while all other elements designed according to static loads only automatically satisfied the requirement for R60.

Two elements, namely the TT roof element with narrow ribs and the Y roof element, resulted not proper to provide a fire performance of R120, not even adding a reasonable quantity of mild reinforcement. This is due to the heavy heating of the bulbs hosting the prestressing tendons, which are engulfed by fire from 3 sides for the TT element, and practically from all over for the Y element.

All other elements were capable to be designed to satisfy the R120 performance, despite TT roof element with wide ribs, both TT floor elements, omega roof element, and hollowcore floor element, with the need for additional mild or prestressing reinforcement with respect to what strictly needed for static checks. Only

three elements, namely wing-shaped roof element, omega floor element, and box floor element, were able to provide a R120 performance without the need for additional reinforcement. This is due to the peculiar shape of these elements, which turns out being particularly favourable in fire conditions, since the prestressing tendons are located closer to the cold side, rather than the hot side, which provides a smart passive resistance to their increase of temperature. It is worth noting that the omega profile falls in the group of high performance elements only in the flooring configuration: this is due to the fact that, when used for roofing, the elements are assumed to be distanced, and thus the prestressing bulbs are indeed exposed to fire from both sides, jeopardising the potential benefits of passive protection which only acts when they are installed in adjacency. Fig. 12 shows a schematic comparison of the various performance parameters associated with each analysed element. The performance is graphed in terms of deviation from the average value among each performance parameter for elements having the same function (roofing or flooring). The considered parameters are over-strength in case of fire, and consumption of concrete and steel.

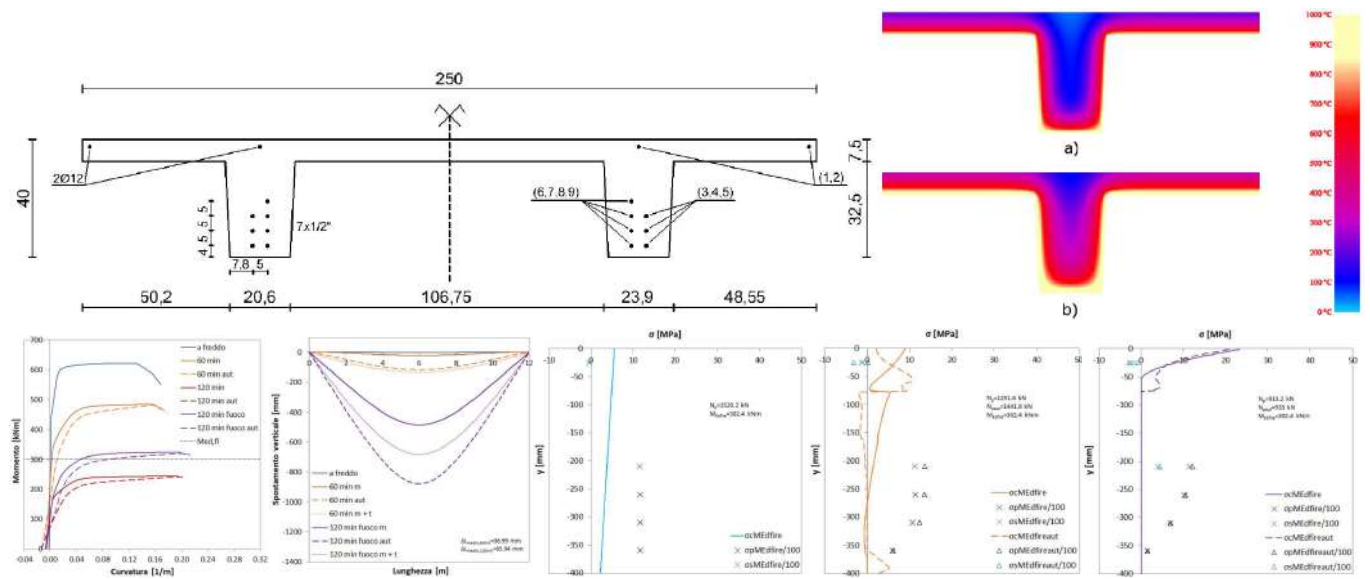


Figure 10. TT floor element with wide ribs: (top left to right) cross-section and thermal field at a) 60 min and b) 120 min; (bottom left to right) moment-curvature and deformation diagrams, stress profile evolution at 0, 60, and 120 min of exposure to ISO834 fire

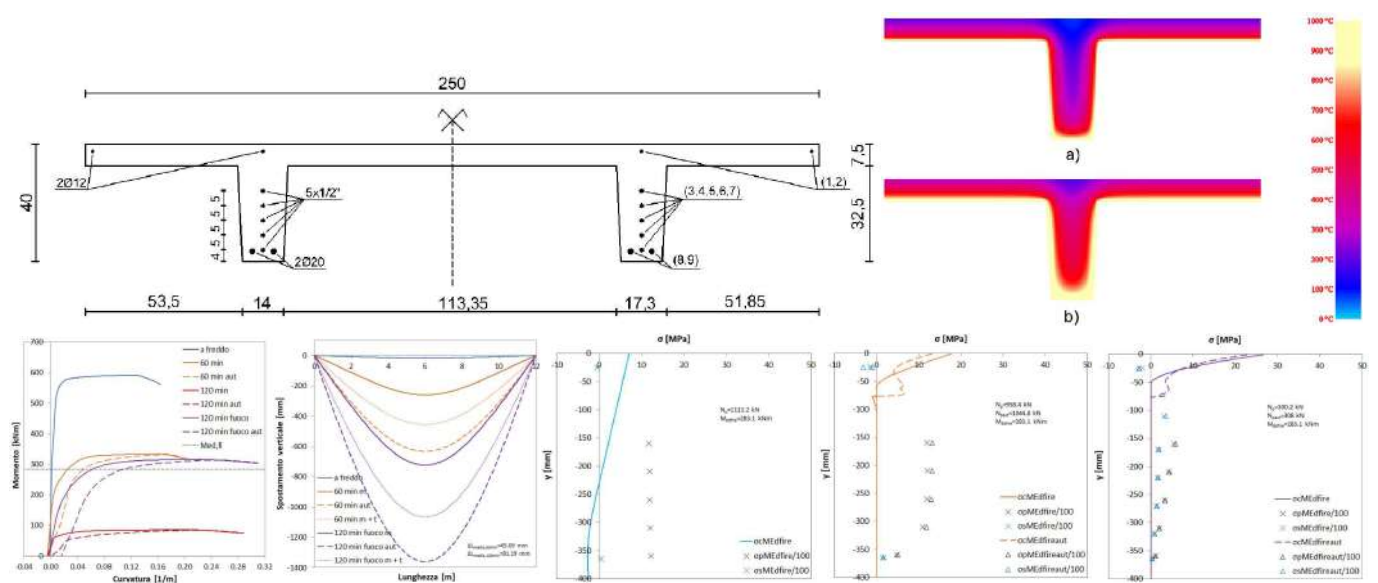
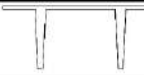
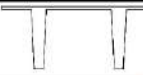
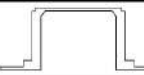


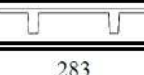
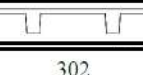


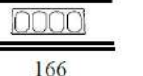


Figure 11. TT floor element with narrow ribs: (top left to right) cross-section and thermal field at a) 60 min and b) 120 min; (bottom left to right) moment-curvature and deformation diagrams, stress profile evolution at 0, 60, and 120 min of exposure to ISO834 fire

Table 1. Main structural performance parameters for the analysed (top) roof and (bottom) floor elements subjected to fire exposure

					
$M_{Ed,fire}$ [kNm]	971	1216	1148	955	750
$M_{Rd,0}$ [kNm]	2283	2617	2946	2427	2013
$M_{Rd,60}$ [kNm]	589	1697	1803	1837	967
$M_{Rd,60}/M_{Rd,0}$ [-]	0,26	0,65	0,61	0,76	0,48
$A_{s,60+}$ [cm ²]	20,36	-	-	-	-
$M_{Rd,60+}$ [kNm]	990	-	-	-	-
$M_{Rd,120}$ [kNm]	117	472	394	962	286
$M_{Rd,120}/M_{Rd,0}$ [-]	0,05	0,18	0,13	0,40	0,14
$A_{s,120+}$ [cm ²]	n/a	27,14	36,19	-	n/a
$M_{Rd,120+}$ [kNm]	n/a	1244	1244	-	n/a

					
$M_{Ed,fire}$ [kNm]	283	302	315	344	166
$M_{Rd,0}$ [kNm]	591	619	718	878	326
$M_{Rd,60}$ [kNm]	322	473	559	649	206
$M_{Rd,60}/M_{Rd,0}$ [-]	0,55	0,76	0,78	0,74	0,63
$A_{s,60+}$ [mm ²]	-	-	-	-	-
$M_{Rd,60+}$ [kNm]	-	-	-	-	-
$M_{Rd,120}$ [kNm]	77	230	336	374	70
$M_{Rd,120}/M_{Rd,0}$ [-]	0,13	0,37	0,47	0,43	0,21
$A_{s,120+}$ [cm ²]	67,04	9,05	-	-	7,70
$M_{Rd,120+}$ [kNm]	292	307	-	-	177

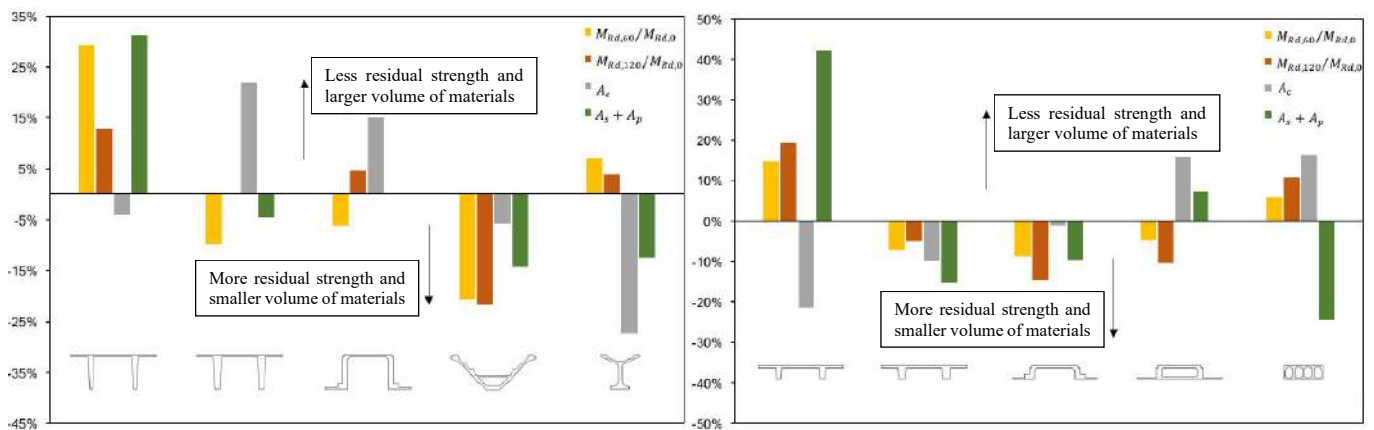


Figure 12. Comparison of the performance and design parameters of roof (left) and floor (right) elements

6 CONCLUSIONS

The application of the MPS provided valuable information about the actual performance of the analysed precast prestressed members in fire, pointing out the actual performance of the structural elements not only in terms of strength, but also in terms of deflection, stress, prestressing evolution, etc. This required a higher effort with respect to classical analytical methods based on cross-sectional strength checks only, although much limited with respect to advanced 3D modelling methods, in general not suitable for design activities. Future research will concern: (I) the study of the effects of thermal strain for thin-web elements exposed on both sides, which are characterised by a strong interaction of multi-axial strains, which cannot be tackled with the MPS; (II) the study of the 2nd order effects on columns and thin-walled open section elements; (III) the implementation of the effects triggering spalling; (IV) the characterisation of the heat transmission through joints and holes by CFD analysis.

REFERENCES

1. Jeyashree, TM, Kannan Rajkumar PR & Satyanarayanan, KS: Developments and research on fire response behaviour of prestressed concrete members – A review. *J Build Eng* 57, 104797 (2022).
2. Pedrani, L: Comportamento strutturale di tegoli alari precompressi soggetti a carico da incendio con effetti del secondo ordine. MSc thesis, Università degli Studi dell'Insubria (2023).
3. Pedron, A & Tondini, N: Fire behaviour of a prestressed thin-walled concrete v-beam. *Fire Tech* 58, 353–378, (2022).
4. Kumar, KP & Kodur, VKR: Response of prestressed concrete beams under combined effects of fire and structural loading. *Eng Struct* 246, 113025 (2021).
5. Acker, AV: Shear resistance of prestressed hollow-core floors exposed to fire. *Struct Conc* 4(2), 65-74 (2003).
6. Alimrani, N & Balázs, GL: Precast concrete hollow core slabs exposed to elevated temperatures in terms of shear deterioration – review article. *Conc Struct*, 19, 14-21 (2018).
7. Franssen, JM & Bruls, A: Design and tests of prestressed concrete beams. *Fire safety Science - Proceedings of the fifth international symposium*, 1081-1092 (1997).
8. Heo, I., Darkhanbat, K., Han, S.J., Choi, S.H., Jeong, H. and Kim, K.S. (2021), “Experimental and numerical investigations on fire-resistance performance of precast concrete hollow-core slabs”, *Applied Sciences*, 11(23), 11500.
9. Kodur, V.K.R. and Hatinger, N. (2011), “A performance-based approach for evaluating fire resistance of prestressed concrete double T-beams”, *Journal of Fire Protection Engineering*, 21(3), 185-222.
10. Venanzi, I., Breccolotti, M., D'Alessandro, A. and Materazzi, A.L. (2014), “Fire performance assessment of HPLWC hollow core slabs through full-scale furnace testing”, *Fire Safety Journal*, 69, 12-22.
11. Dal Lago, B & Tucci, P: Causes of local collapse of a precast concrete industrial roof after a fire event. *Comp Conc* 31(5), 371–384 (2023).
12. Dal Lago, B & Lo Monte, F: Structural performance of a large-span bi-directional partially precast waffle slab system under fire exposure. In proceedings of IFireSS2023, Rio de Janeiro, Brazil, 411–420 (2023).
13. Dal Lago, B, Nicora, A, Tucci, P & Panico, A: Precast concrete industrial portal frames subjected to simulated fire. In proceedings of the fib conference - Building for the Future: Durable, Sustainable, Resilient, Ed. A. Ilki, Istanbul, Turkey, 2, 13–23 (2023).
14. Riva, P & Franssen, JM: Non-linear and plastic analysis of RC beams subject to fire. *Struct Conc* 9(1), 31–43 (2008).
15. Felicetti, R, Gambarova, PG & Meda, A: Residual behaviour of steel bars and R/C sections after a fire. *Constr Build Mat* 23, 3546–3555 (2009).
16. Bamonte, P, Kalaba, N & Felicetti, R: Computational study on prestressed concrete members exposed to natural fires. *Fire Safety J* 97, 54–65 (2018).
17. El-Fitiany, SF & Youssef, MA: Assessing the flexural and axial behaviour of reinforced concrete members at elevated temperature using sectional analysis. *Fire Safety J* 44, 691-703 (2009).
18. Ellobody, E: Advanced analysis of prestressed hollow core concrete slabs exposed to different fires”, *Adv Struct Eng* 17(9), 1281-1298 (2014).
19. EN 1992-1-2. Eurocode 2 - Design of Concrete Structures - Part 1-2: General Rules - Structural Fire Design, European Committee for Standardization, Bruxelles, Belgium (2005).
20. Parametric Technology Corporation. Mathcad release 15.0, Needham, MA, USA (2010).
21. Franssen, JM & Gernay, T: A formulation of the Eurocode 2 concrete model at elevated temperature that includes an explicit term for transient creep. *Fire Safety J* 51, 1–9 (2012).
22. Bosio, M, Di Salvatore, C, Bellotti, D, Capacci, L, Belleri, A, Piccolo, V, Cavalieri, F, Dal Lago, B, Riva, P, Magliulo, G, Nascimbene, R & Biondini, F: Modelling and seismic response analysis of non-residential single-storey existing precast buildings in Italy. *J Earthq Eng* 27(4), 1047-1068 (2023).
23. Gaddi software. Manuale Introduttivo di Analisi Termica della Sezione (ATS). Version 12.0, (2013).
24. Bolina, FL, Dal Lago B & Martínez, EDR: The effect of experimental thermal-physical parameters on the temperature field of UHPC structures in case of fire. *Constr Build Mat* 411, 134254 (2024).
25. Dal Lago, B: Experimental and numerical assessment of the service behaviour of an innovative long-span precast roof element. *Int J Conc Struct Mat* 11(2), 261-273 (2017).
26. Shakya, AM & Kodur, VKR: Response of precast prestressed concrete hollowcore slabs under fire conditions. *Eng Struct* 87, 126-138 (2015).
27. Dal Lago, B, Martinelli, L & Foti, F: Slender precast voided slabs under walking-induced vibration. *Struct Conc* 23(6), 3416-3443 (2022).

CONFINED SLAB SPALLING TEST (CSST): A SCREENING TOOL TO ASSIST CONCRETE MIX DESIGN IN TUNNEL PROJECTS

Roberto Felicetti¹, Francesco Lo Monte², Umberto Cardu³, Federico Martellozzo⁴, Nicola Valiante⁵

ABSTRACT

Explosive spalling is one of the most challenging aspects in the design of segmental tunnel linings, due to the high concrete quality entailed by precast production, the severe design fire curves imposed by the design codes and the sustained compressive load borne by the tunnel vault. Since no established predictive models are yet available to account for the many variables governing the incidence of this phenomenon, experimental fire tests are generally regarded as the reference tool for optimizing the mix design and implementing the required mitigation measures (e.g. polypropylene fibre addition). A viable solution consists in testing square flat slabs under a biaxial confinement load. This symmetric configuration is more severe than uniaxial confinement and better replicates the isotropic effect of restrained thermal dilation in the central region of a lining segment. In the proposed Confined Slab Spalling Test setup (CSST), a 0.20 to 0.30 m thick slab is installed in the load frame and exposed to the prescribed fire curve on a 1.0 m side square area. The loading system comprises 8 hydraulic jacks restrained by a compact octagonal tense frame. The exerted load can range from 0 to 3 MN per axis, thus allowing to replicate the actual service conditions of most installations. Different sensors and monitoring systems can support a thorough analysis of the test results. In the paper, the testing setup is described together with the results of the validation tests performed.

Keywords: Explosive spalling, tunnel linings, fire tests.

1 INTRODUCTION

1.1 Fire performance and spalling sensitivity assessment in concrete

Tunnels can often be regarded as strategic infrastructures whose disruption may jeopardize the resilience of road and rail networks. In this context, structural fire safety is a pivotal requirement, which is frequently made demanding by the interaction of several aspects. Firstly, the geometrical layout, the type of combustible materials (mainly hydrocarbons) and the ventilation conditions promote the development of remarkably high temperatures (even higher than 1000° [1]). Secondly, the inherently redundant structural configuration and the compression-driven stress state in the lining bring in the formation of severe indirect actions during the development of a fire, with the consequent dramatic increase of the initial state of stress [2]. This may boost the incidence of explosive spalling, namely the expulsion of concrete chunks from the heated face of concrete due to the combined action of external force, thermal stress, and vapour pressure in the pores. The phenomenon is even more critical in the case of segmental tunnel linings, due to the high

¹ Department of Civil and Environmental Engineering, Politecnico di Milano, Milan (Italy),
e-mail: roberto.felicetti@polimi.it

² Department of Civil and Environmental Engineering, Politecnico di Milano, Milan (Italy),
e-mail: francesco.lo@polimi.it, ORCID: <https://orcid.org/0000-0003-4397-6591>

³ Webuild SpA, Centro Direzionale Milanofiori Strada 6, Rozzano (MI), Italy
e-mail: u.cardu@webuildgroup.com

⁴ Webuild SpA, Centro Direzionale Milanofiori Strada 6, Rozzano (MI), Italy
e-mail: f.martellozzo@webuildgroup.com

⁵ Webuild SpA, Centro Direzionale Milanofiori Strada 6, Rozzano (MI), Italy
e-mail: n.valiante@webuildgroup.com

early-age strength entailed by the precast production process, which in the long term translates into sizably higher concrete grades than required by the design.

Several numerical models have been developed in the last decades [3] aimed at simulating the heating process in concrete elements including mass transfer and, in a few cases, the effect of stress development and mechanical damage. However, the calibration of such multiphysics models is challenging, due to the combination of complex aspects such as the mutual interaction between pore pressure and concrete fracture behaviour [4] and the variation with temperature and saturation of concrete physical and mechanical properties, something very difficult to characterize in hot conditions. As a result, no design-oriented predictive models are yet available to determine the thickness of the spalled layer and the consequent reduction of cross-sections and rebar protection.

As an alternative, experimental testing allows to directly assess concrete sensitivity to spalling, even though great attention should be paid to the definition of the test setup, given the huge variety of specimen geometry and applied loading, restraint and heating that can be found in the literature. In this regard, tests can be grouped in small-, medium- or full-scale tests, either on loaded or unloaded specimens [5].

Small-scale investigations can be found where temperature and pressure were monitored in unloaded prismatic specimens made of plain or fibre-reinforced concretes [6, 7]. In these cases, relevant spalling was usually not obtained, since stress was caused just by thermal gradients occurring in limited volumes. On the other hand, sizeable spalling was obtained in other small-scale tests where specimens were loaded thanks to a steel casing or a ring restraining thermal dilation [8, 9] or by means of a steel ring loaded via hydraulic actuators [10].

Medium-scale tests generally consist in loaded or unloaded slabs or prismatic specimens heated on one side. External uniaxial compression can be applied in a rather easy way according to several setups, such as internal or external post-tensioning systems [11-14], and actuators [15, 16]. External biaxial compression, on the other hand, requires a more complex setup [10, 11, 17]. The common evidence is that loading increases the susceptibility to spalling and that biaxial compression is far more severe than uniaxial compression [13, 15, 18].

Full-scale tests, especially in the design phase of tunnels, led to the design of quite demanding setups [19, 20], where a real scale arched segment is installed on the test furnace and loaded to service conditions, involving independent transversal and chord loads in the range of meganewtons (Figure 1). Local equilibrium in case of a curved shape establishes a connection between the circumferential compressive stress σ_c due to restrained thermal dilation and the gradient of radial stress $d\sigma_r/dz$, whose ratio equals the radius of curvature of the lining. Due to the limited thickness of the involved cover (some centimetres) compared to the radius of curvature (some metres) the result is a minor stabilizing radial stress (less than 1 MPa) which wouldn't develop in a flat specimen (making this latter slightly conservative).

Despite the high representativeness of this scheme, it may be argued that loading and heating several square metres is not strictly required to represent a phenomenon whose scale is ruled by the thermal gradient and the consequent profiles of stress, moisture content, and pore pressure developing in the exposed cover. Moreover, the concrete mix has generally to be defined well before the construction of the segment formworks, requiring a simpler yet representative specimen geometry.

1.2 Fire testing on biaxially compressed slab - Confined Slab Spalling Tests (CSST)

In order to find a compromise between representativeness and cost/time effectiveness, a viable solution consists in testing square flat slabs under biaxial confining load [17], as hinted before in the case of intermediate-scale tests. Such symmetric configuration is more severe than uniaxial confinement and better replicates the isotropic effect of restrained thermal dilation in the central region of a tunnel segment.

Figure 2 shows the first version of the setup, aimed at testing small slabs (0.8x0.8m, with a heated area of 0.6x0.6m and a thickness ranging between 0.1 and 0.2m). As shown in the same figure, numerical studies were also performed via non-linear thermo-mechanical models to assess the influence of possible parasitic effects of confinement. In this regard, a key role is played by the unheated perimetral rim of the specimen, which acts as a thermal barrier for limiting the temperature of the actuators. This colder rim would restrain

the thermal dilation of the heated region of the specimen and take an unknown share of the applied load. Numerical analyses proved that the introduction of a set of perimetral slits minimizes the disturbance to the confining stress without affecting thermal protection of the load system. The actuators are also fitted with spherical seatings to accommodate the thermal curvature. The consistency with full-scale tests has been also ascertained via experimental tests [19].

Figure 3 shows that in a slab heated at the bottom face, the hot layer is characterized by compression, while tension arises in the cold core for translational equilibrium. Finally, compression again develops in the cold side due to rotational equilibrium. In absence of external confinement, the tensile strength would be exceeded in the core, leading to internal cracks parallel to the thermo-hygral flux, thus favouring the migration of vapour and the decrease of pressure in the pores, with consequent decrease of spalling severity. On the other hand, at increasing values of external confinement, cracking is prevented, and compression embraces the most hygrally-active zone (d_{ha}), thus keeping concrete sound and raising pressure in the pores, with an increased spalling severity [17]. Thus, in the plot of average spalling depth versus applied load, two regions can be defined: (I) low compression range, where at increasing external load a higher share of the hot layer undergoes compression and cracking in the core is reduced, and (II) high compression range, where increasing the external load leads only to higher mechanical stress in the hot layer, with minor effects on the thermo-hygral transient. In the first region the increase of spalling severity as a function of external compression is expected to be far higher than in the second region. This behaviour is evident in ordinary concrete, since its higher permeability makes d_{ha} larger. On the opposite, in (Ultra) High-Performance Concretes, the far lower permeability makes d_{ha} so small, that cracking in the cold core of the specimens does not significantly influence spalling severity. For this kind of concrete, therefore, just region (II) is recognized.

Starting from the above-discussed considerations, Webuild Group and PoliMi started a collaboration to develop this type of testing in the form of an in-house standard to support the optimization of concrete mixes in new tunnel projects. The main objective is to determine, for each investigated concrete mix, the amount of polypropylene fibre required to not exceed the acceptable spalling depth according to the structural design of the tunnel.

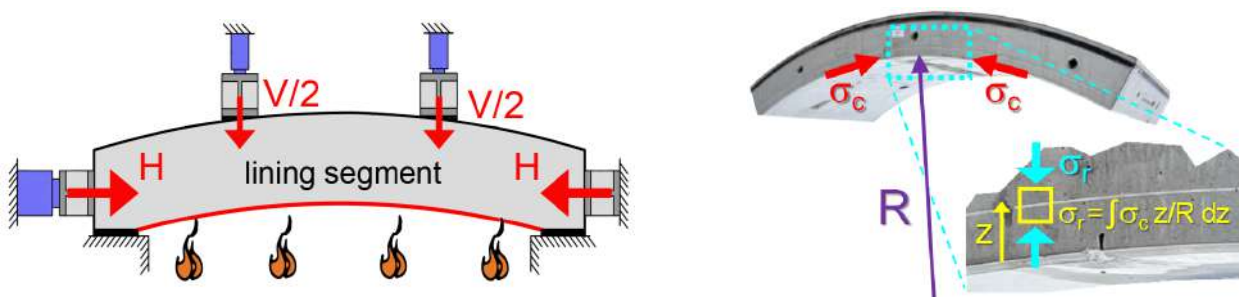


Figure 1. Arched segment load scheme and ensuing radial stabilizing stress

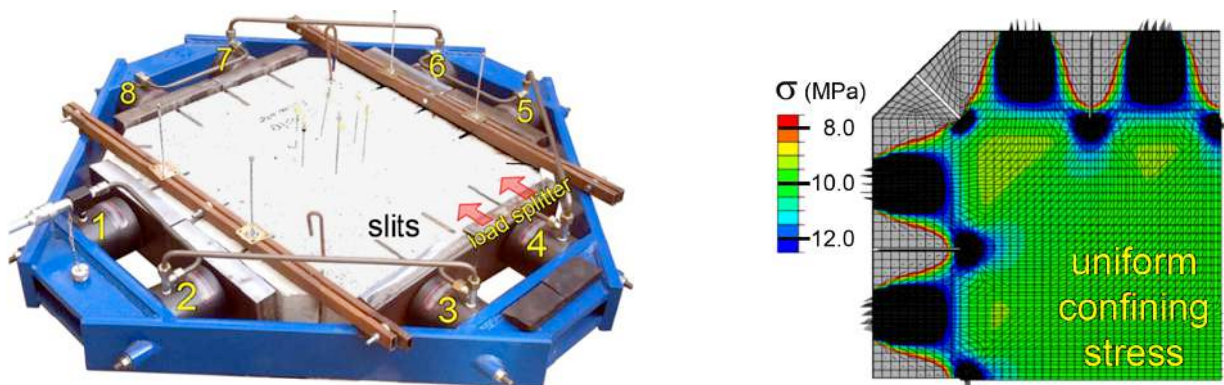


Figure 2. Original setup with the biaxially-loaded flat slab and stress uniformity allowed by the slitted rim

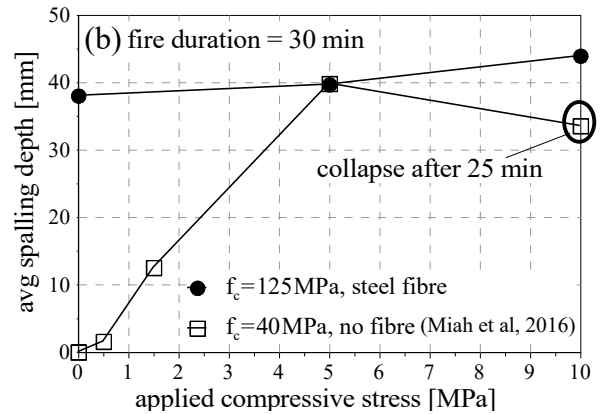
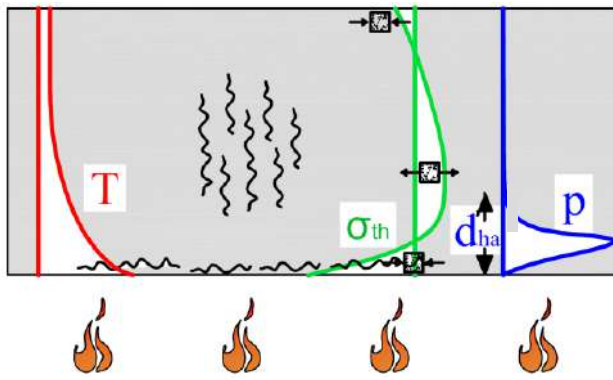


Figure 3. Schematic representation of temperature, thermal stress and pore pressure profiles across the lining thickness and dependency of spalling depth on the biaxial confining stress

2 EXPERIMENTAL SETUP

2.1 Design requirements

In the original proposal, the heated area (0.6x0.6m) and the slab thickness (0.1-0.2m) were oriented to the study of unreinforced elements undergoing limited spalling depth. To go beyond these limitations, the new project has been launched to further develop this approach in the following directions:

- scaling up the original setup to 1.0x1.0m heated area and thicknesses in the range 0.2-0.3m, allowing the reproduction of the intrados reinforcement layer;
- increasing the load capacity up to 3MN per axis so to allow the application of a membrane compression up to 15MPa for a specimen thickness of 0.2m;
- controlling the initial moisture content of samples to offset the detrimental effect of limited ageing;
- submitting the loaded sample to the RWS hydrocarbon fire curve in a vertical furnace;
- real-time monitoring of temperature profiles, concrete damage and reducing thickness.

As depicted in Figure 4, the specimen consists of a square slab with 1.3x1.3m in-plane dimension and a thickness ranging from 0.2 to 0.3 m. Considering the heated area is 1.0x1.0m, the cold rim has a width of 0.15 m. Its confinement effect is smoothed down by the realization of perimetral slits as already discussed in the previous section.

The loading system consists in an octagonal welded steel restraining frame. Thanks to load symmetry and positioning of the 1.5MN hydraulic jacks at the vertexes, the frame works mainly in tension, this allowing the design of a relatively light structure (recurring section 40x250mm). The jacks are connected to a hand operated pump ($p_{\max} = 700\text{bar}$) and the hydraulic circuit is fitted with an in-line flow control valve to allow smooth release of pressure when the load tends to increase due to the thermal dilation of the specimen.

According to the devised installation procedure, the frame is laid horizontally on the laboratory floor and the concrete slab is positioned between the loading platens. Then, the jacks are preloaded, and the whole system (about 3t weight) is lifted with an overhead crane and installed on a vertical stand facing the vertical test furnace (2.1x2.1m exposed area). A stainless-steel frame lined with ceramic fibre blankets reduces the furnace opening to the required exposed area (1.0x1.0m) as shown in Figure 4. The stand can be translated on its high-capacity wheels to press the specimen against the ceramic fibre screen and provide tightness to the exhaust smoke.

It has to be mentioned that the hottest stage of the RWS fire curve ($T_{\max} = 1350^{\circ}\text{C}$) often involves the incipient melting of the exposed concrete. In the case of a vertical furnace, gravity induces shear in the melted layer and more substantial flow compared to dripping from a horizontal surface. This effect, not addressed by fire testing standards, required to equip the insulating screen with a stainless-steel gutter to prevent tearing of the ceramic fibre.

The specimens are casted in plywood formwork panels and the perimetral slits are created by installing soft refractory panels (Millboard) which remain embedded in concrete. Different sensors and monitoring systems can support a thorough analysis of the test results [20,21]. Concerning temperature monitoring, 4 shielded “K-type” thermocouples were embedded in the slabs at 10, 50, 100 and 150mm depth from the exposed surface. A horizontal arrangement next to the measuring junction minimizes the possible disturbance to the thermal field.

The applied confining stress has been selected based on 3D Finite Elements analyses of the tunnel lining under the effect of sustained loads and thermal stress. The goal is to minimize the incidence of cracks parallel to the thermal flux and then prevent the anticipated drying of the exposed cover. Based on past experience, in this first series of tests a constant 5.0MPa biaxial confining pressure was maintained during fire exposure. This required releasing the actuators pressure a few times to balance the effect of thermal dilation. More advanced hybrid testing techniques may be implemented to simulate the structure to soil interaction, through deformation monitoring of the tested specimen and feedback into a numerical model of the lining ring embedded in the soil.

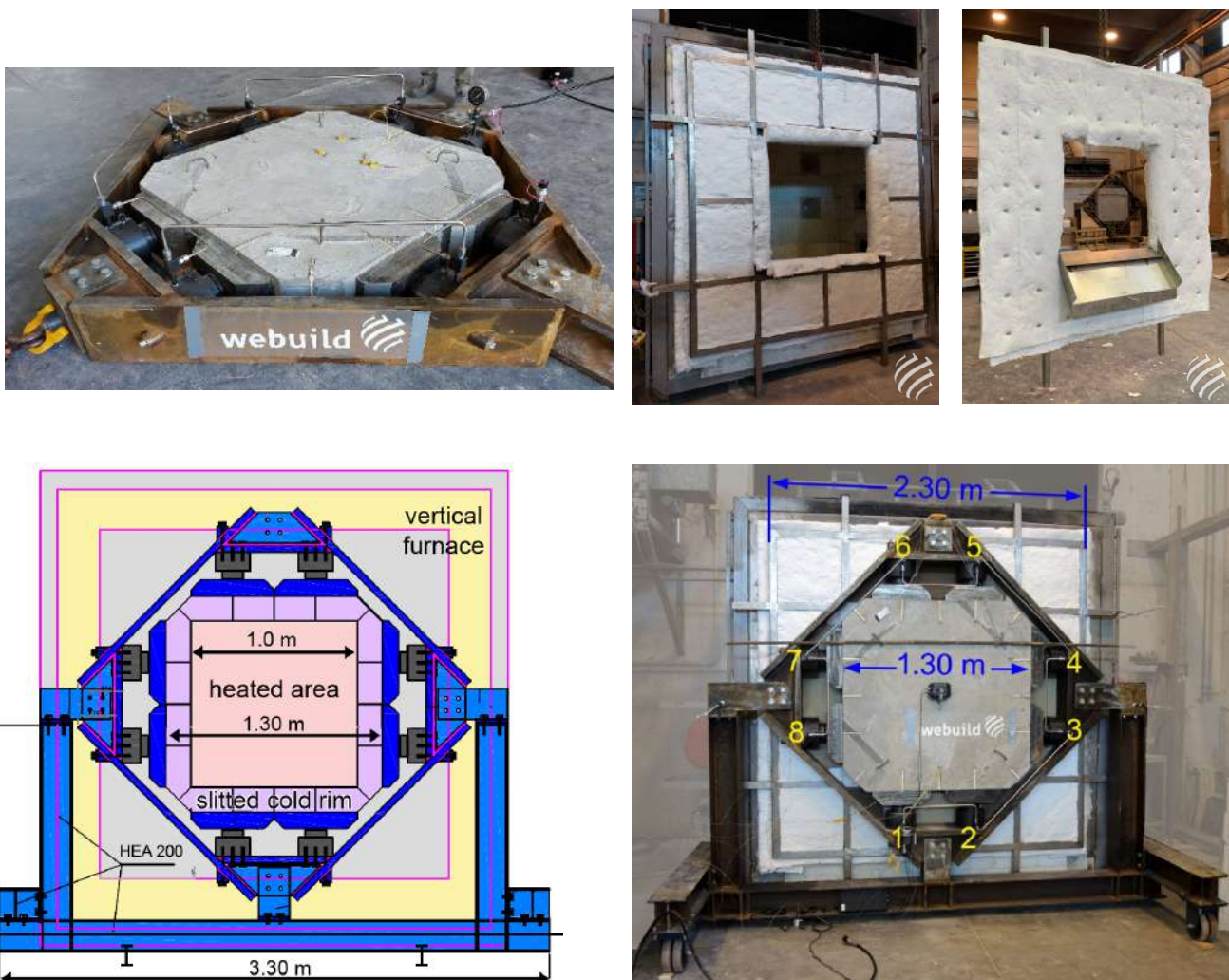


Figure 4. Specimen installation in the loading frame, insulating screen for reducing the exposed area, design sketch and final setup including the loaded specimen and the frame on the movable stand



Figure 5. Ultrasonic pulse-echo principle, sensor array (50kHz, shear waves) and wireless pulser/receiver for real-time monitoring of slab thickness and damage; 3D laser scanner for geometrical survey of the specimen after the tests

Concerning the real-time monitoring of spalling, the well-validated ultrasonic pulse-echo technique is implemented via a new wireless pulser and wave digitizer (Figure 5). Moreover, the total erosion undergone by the specimens is surveyed after the test by way of a 3D laser scanner.

One crucial point when relatively young specimens are being tested is the moisture content of concrete, since it is well known that spalling sensitivity tends to decrease with ageing and the consequent reduction of pore saturation. One future development for improving the representativeness of young specimens is the implementation of an accelerated drying system in which the slab is wrapped in a drainage geo-composite and enclosed in a sealed polyethylene envelope, to be connected to a two-stage vacuum pump. Compared to heating, vacuum drying is expected to minimize the internal stress due to meso-scale heterogeneity.

So far, a series of 6 tests have been performed, including different types of reinforcement (ordinary rebars or steel fibre), different amounts and types of polypropylene fibre, and two fire curves (RWS and fast raise to 450°C). Given the practicality of the proposed setup and the consistency of the results, this test method will be the reference for mix design optimization in many ongoing tunnel projects.

2.2 Real-time test survey

Concerning the real-time monitoring of spalling, the well-validated ultrasonic pulse-echo technique [22,23] was implemented via a new wireless pulser and wave digitizer (A1560 by Acoustic Control Systems, Figure 5). The test principle is based on the generation of a short pulse of ultrasonic waves via an ultrasonic sensor array installed on the cold side. The pulse propagates through the slab thickness and is back-reflected at the interface between the heated face and air. After crossing the thickness one second time, the pulse is detected at the unexposed face by the receiving stage of the same ultrasonic sensor. The initial propagation time (two times the thickness divided by the pulse velocity) is expected to smoothly increase because of thermal damage undergone by concrete. However, sudden reductions of the propagation time are observed in case of spalling, due to the stepwise thinning of the tested element.

Figure 6 shows several waves recorded in a former test [23]. By monitoring a reference feature of the wave (e.g. a negative peak) at different fire durations, a shift towards longer propagation times is observed (echo delay), due to material deterioration. It can be noticed that also the wave amplitude decreases, due to the higher attenuation in damaged concrete.

When spalling occurs, a sudden decrease in thickness is observed (at 36 minutes in Figure 6) due to the expulsion of a layer of hot concrete, this yielding to an anticipation of the reference feature of the wave (echo advance). Monitoring the echo delay, once known the temperature profile, can allow to real-time estimating the ultrasonic wave velocity variation with temperature thanks to inverse analysis.

An accurate assessment of the effect of thermal damage would require an inverse analysis in which the material decay with temperature (reduction of pulse velocity) is described via a parametric function whose coefficients are tuned so that the integral of the propagation time across the measured temperature profiles (Figure 7) matches the observed pulse delay [23]. Spalling events entail the loss of the most damaged layer, whose thickness can be determined based on the sudden echo delay reduction.

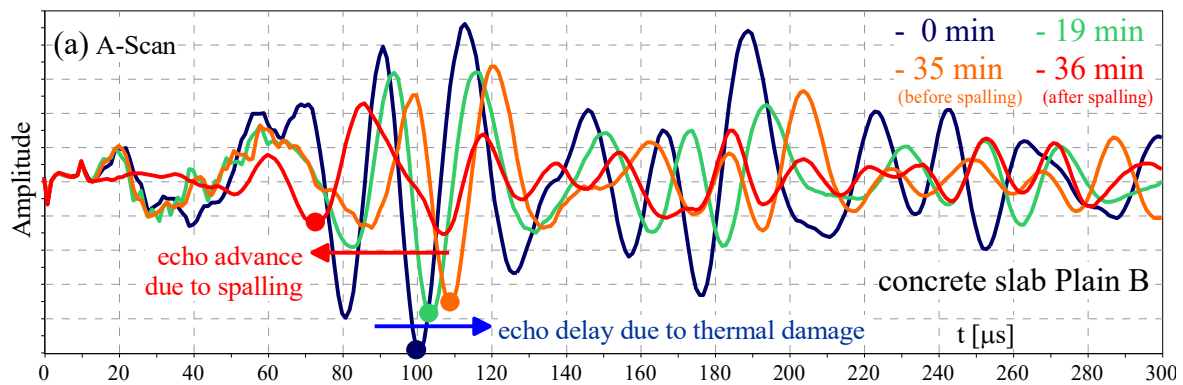


Figure 6. Ultrasonic Pulse-Echo method: waves at the receiver showing the echo delay increase due to heating and the sudden decrease due to spalling

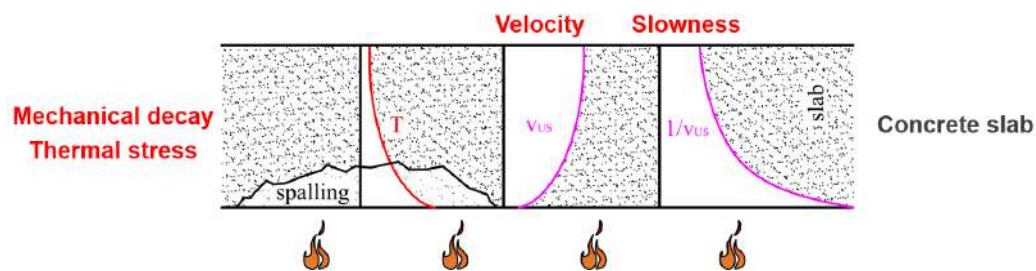


Figure 7. Concrete slab under heating: temperature and ultrasonic wave velocity and slowness profiles

3 INITIAL EXPERIMENTAL RESULTS

3.1 Spalling depth and exposed face at the end of testing

In this paper, the results are reported from the first 6 CSST fire tests aimed at investigating the sensitivity to spalling of one Steel Fibre Reinforced Concrete mix (SFRC) for precast tunnel lining applications. In particular, the effectiveness of different dosages and types of polypropylene (PP) fibers have been studied. The SFRC mix (characterized by CEM I type and steel fibre) is classified as C45/55 for compression (according to Eurocode 2) and 4C for tension (according to Model Code 10). Two different typologies of polypropylene fibres were considered, characterized by different geometry and Melt Mass-Flow Rate - MFR [24,25]: conventional PP fibre (CPP) with 12mm length, 34 μ m diameter and 25 MFR, and high-performance PP fibre (HPP) with 6mm length, 20 μ m diameter and 1000 MFR. One test has been performed on a reference specimen made of plain reinforced concrete (thus without any fibre).

Depending on the length of the tunnel for which the mix were intended, two different fire curves were considered according to the indications provided in [26]. The first one is the well-known RWS curve (Rijkswaterstaat, the Netherlands), also adopted by the Italian standard UNI 11076 [27] with 1350 $^{\circ}$ C maximum temperature, which applies to tunnels longer than 2000 m. On the other hand, a fast raise up to the 450 $^{\circ}$ C target temperature was considered for tunnels shorter than 2000 m. In all the cases, the duration of the fire test was 120 min.

In Table 1 the main information regarding the 6 tests is reported, together with the average spalling depth measured at the end of the test via the 3D laser scan. The heated face of the specimen at the end of the test is reported in Figure 8 (first column for the 450 $^{\circ}$ C-fire curve and second and third columns for the RWS fire curve).

Figure 9 shows a comparison of the specimen conditions right after the RWS fire test. Specimen SFRC F27 includes PP fibre, while specimens SFRC F03 and RC (Reinforced Concrete) F08 are both without PP fibre. The incremental beneficial effect of using steel fibre especially in combination with PP fibre appears evident if compared with traditional reinforced concrete.

Table 1. Main features and results of the tested specimens

	Test duration	Specimen	Fire curve	PP fibre	PP fibers dos. [kg/m ³]	Sample age [days]	Avg spalling depth [mm]
SFRC	120 min	F01	450°C	-	0.0	25	42
SFRC	120 min	F12	450°C	CPP	1.5	23	0
SFRC	120 min	F03	RWS	-	0.0	336	87
SFRC	120 min	V2	RWS	CPP	1.5	85	40
SFRC	120 min	F27	RWS	HPP	1.5	337	3
R/C	60 min	F08	RWS	-	0.0	366	>150

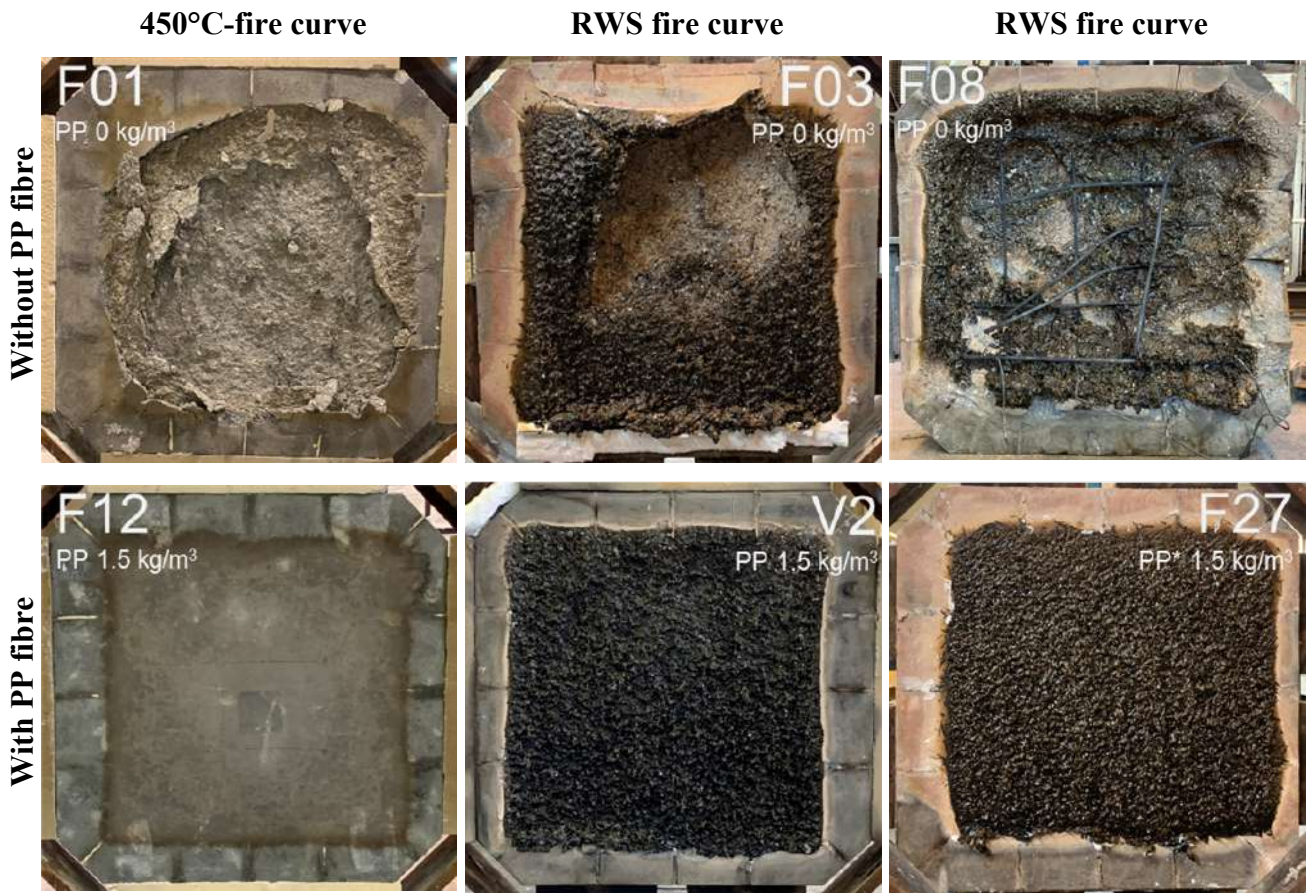


Figure 8. Exposed face of the specimens after testing (F08 is the reinforced-concrete specimen, the only with no steel fibre)

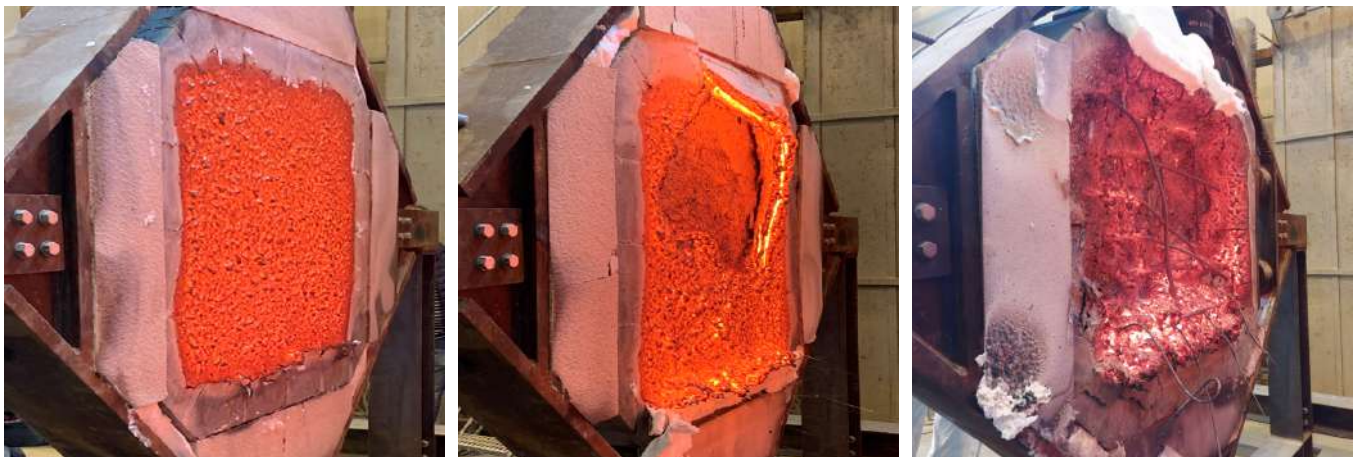


Fig. 9. Specimen SFRC F27 (left), SFRC F03 (center) and R/C F08 (right) as soon as they were extracted from the furnace

3.2 Real-time test survey

The results of pulse-echo monitoring are summarized in Figure 10. A good consistency is observed between the echo delay trends and the final depth of erosion of each specimen. Plain concrete with ordinary rebar reinforcement (test F08) showed a remarkable spalling sensitivity, with a continuous stream of “pop corn” events which translates into a constant rate of thickness reduction. Since in this case concrete spalls before experiencing a sizable damage, the initial wave velocity ($v = 2.65\text{mm}/\mu\text{s}$) can be used to transform the echo delay reduction ($140\mu\text{s}$) into the assessed thickness of the section erosion ($140\mu\text{s} \cdot 2.65\text{mm}/\mu\text{s} / 2 = 185\text{mm}$). This value is consistent with the final erosion (Table 1).

Steel fibre mitigates the impact of spalling, leading to less frequent events involving thicker splinters (test F03). In this case, the exposed face could reach higher temperatures before being detached, and the echo delay reduction should be multiplied by a smaller velocity ($2.3\text{mm}/\mu\text{s}$) to match the final thickness reduction observed via laser scans ($75\mu\text{s}$ correspond to 85mm erosion). It can also be noticed that a marginal benefit is allowed by the conventional polypropylene fibre (CPP), whereas the high-performance counterpart (HPP) prevents any detachment of splinters from the heated face.

In the case of the milder fire curve (450°C), spalling gets less critical and can be prevented already by the conventional PP fibre (test F12). In case of SFRC with no PP fibre (test F01), spalling is delayed by more than one hour, when a loud blast yields to a sudden reduction of the specimen thickness.

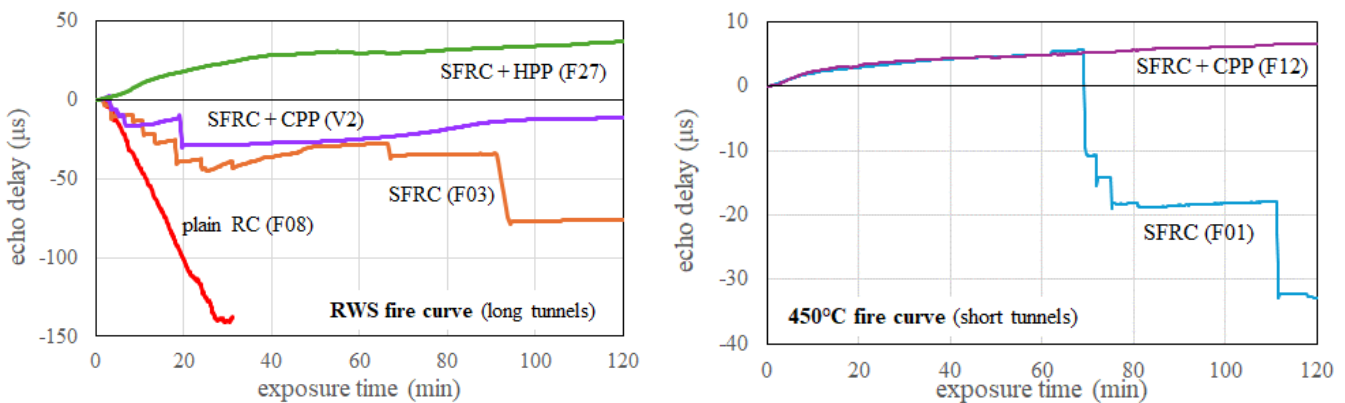


Fig. 10. Evolution of the delay of the ultrasonic pulse as a function of exposure time to the two adopted fire curves: progressive increase indicates thermal damage, stepwise decrease indicates a spalling event

4 CONCLUSIONS

The phenomenon of explosive spalling occurring in concrete exposed to fire is a tricky as well as important aspect to be taken into account, especially regarding strategic infrastructures as tunnels. Since not reliable predictive models are yet available in Standards or Guidelines to estimate a priori concrete spalling, experimental testing is generally agreed to be the most effective way to assess spalling sensitivity in concrete mixes and structural members.

Typically, full-scale testing is considered as a reference, this however being possible to be performed only once segment production has been organized (thus not at the design stage), thus not being feasible for the initial screening of mixes. An alternative is represented by testing on unconfined slabs, this however not being representative of the final application due to the lack of external compression.

An effective compromise is represented by the herein presented Confined Slab Spalling Test (CSST). This solution consists in testing square flat slabs under biaxial in-plane compression aimed at replicating the isotropic effect of restrained thermal dilation in the central region of a precast segment.

A first series fire tests was conducted on concrete mixes with and without polypropylene fibre, exposed to two different heating curves. The observation of the final average spalling depth confirmed the beneficial effect provided by the introduction of polypropylene fibre to the concrete mix, confirming their

effectiveness in reducing the likelihood of spalling in fire. Regarding the tests performed on a SFRC and on a R/C slabs with traditional reinforcement, both without PP fibers, a positive effect of steel fiber was observed, since spalling depth in SFRC specimen was significantly lower.

The role of PP fibers in preventing concrete fire spalling is well known and confirmed in the results herein presented, however there is a wide range of alternative in selecting PP fibers. Further tests are in progress to assess and evaluate the influences of different PP fiber parameters: geometry (length/diameter), quantity and melt viscosity (MFR).

ACKNOWLEDGMENT

The authors would like to thank Eng. Simone Centis and the team of Consorzio Dolomiti JV, for promoting and supporting the development of this study and solution.

REFERENCES

1. FIT, Technical Report - Part 1: Design Fire Scenarios, European Thematic Network FIT - Fire in Tunnels, Rapporteur A. Haack, supported by the European Community under the 5th Framework Programme 'Competitive and Sustainable Growth' Contract n° G1RT-CT-2001-05017, 2005.
2. Lo Monte F., Bamonte P., Beltrami C., Study on the Effects of Cooling Phase and Construction Technology on the Fire Performance of R/C Tunnels, Tunnelling and Underground Space Technology (132), 2023.
3. RILEM TC 227-HPB, Modelling of Concrete Behaviour at High Temperature, Millard A. and Pimienta P. (eds), State-of-the-Art-Report, Springer, 2019, 127 p.
4. Lo Monte F., Felicetti R. and Miah Md. J., The influence of pore pressure on fracture behaviour of normal-strength and High-Performance Concretes at high temperature, Cement and Concrete Composites, 104, 2017.
5. Krzemieña K., Hager I., Assessment of concrete susceptibility to fire spalling: A report on the state-of-the-art in testing procedures", Procedia Engineering 108, 2015, 285-292.
6. Kalifa P., Menneteau F.D. and Quenard D., Spalling and pore pressure in HPC at high temperatures, Cement and Concrete Research, 30, 2000, 1-13.
7. Mindeguia J. C., Pimienta P., Noumowé A. and Kanema M., Temperature, Pore Pressure and Mass Variation of Concrete Subjected to High Temperature - Experimental and Numerical Discussion on Spalling Risk, Cement and Concrete Research, 40, 2010, 477-487.
8. Hertz K. and Sørensen L., Test method for spalling of fire exposed concrete, Fire Safety Journal, 40, 2005, 466-476.
9. Tanibe T, Ozawa M, Lustoza RL, Kikuchi K, Morimoto H, Explosive spalling behaviour in restrained concrete in the event of fire, Proc. of the 2nd Int. RILEM Workshop on Concrete Spalling due to Fire Exposure, Delft (the Netherlands), October 5-7, 2011, 319-326.
10. Connolly R. The Spalling of Concrete in Fires, PhD Thesis, University of Aston in Birmingham, 1995.
11. Heel A. and Kusterle W., Die Brandbeständigkeit von Faser-, Stahl- und Spannbeton (Fire resistance of fiber-reinforced, reinforced, and prestressed concrete), Tech. Rep. 544, Bundesministerium für Verkehr, Innovation und Technologie, Vienna, 2004, in German.
12. Sjöström J., Lange D., Jansson R. and Boström L., Directional Dependence of Deflections and Damages during Fire Tests of Post-Tensioned Concrete Slabs, Proc. of the 7th Int. Conference Structures in Fire - SIF'12, Zurich (Switzerland), June 6-8, 2012, 589-598.
13. Boström, L., Wickström, U., Adl-Zarrabi B., Effect of Specimen Size and Loading Conditions on Spalling of Concrete, Fire and Materials, 31, 2007, 173-186.
14. Jansson R. and Boström L., Spalling of concrete exposed to fire, SP Technical Research Institute of Sweden, Borås, 2008.
15. Carré, H., Pimienta, P., La Borderie, C., Pereira, F., and Mindeguia, J. C., Effect of Compressive Loading on the Risk of Spalling, Proc. of the 3rd Int. Workshop on Concrete Spalling due to Fire Exposure, Paris (France), September 25-27, 2013, 01007-p1-9.
16. Rickard I., Bisby L., Deeny S. and Maluk C., Predictive Testing for Heat Induced Spalling of Concrete Tunnels - the Influence of Mechanical Loading, Proc. of the 9th International Conference Structures in Fire 2016 - SIF'16, Princeton (USA), June 8-10, 2016, 217-224.

17. Lo Monte F., Felicetti R., Heated slabs under biaxial compressive loading: a test set-up for the assessment of concrete sensitivity to spalling, *Materials and Structures/Materiaux et Constructions*, 50 (192), 2017.
18. Miah Md. J., Lo Monte F., Felicetti R., Carré H., Pimienta P., La Borderie C., Fire spalling behaviour of concrete: Role of mechanical loading (uniaxial and biaxial) and cement type", *Key Engineering Materials*, 711, 2016, 549-555.
19. Lo Monte F., Felicetti R., Meda A., Bortolussi A., Assessment of concrete sensitivity to fire spalling: A multi-scale experimental approach, *Construction and Building Materials*, 212, 2019, 476 - 485.
20. Pimienta P., Felicetti R., Rizos D., Rivillon P., Charuel S. and Amin T., Port Said Suez Canal tunnel segments - Laboratory fire spalling testing, *Proc. of the 7th Int. Workshop on Concrete Spalling due to Fire Exposure*, Berlin (Germany), October 12-14, 2022, 68-78.
21. Lo Monte F. and Felicetti R. (2015a), Experimental methods for spalling monitoring during and after fire test, *Proc. 4th International Workshop on Concrete Spalling due to Fire Exposure (IWCS)*, Leipzig, 8-9 October, 10p.
22. Lo Monte F., Felicetti R., Lualdi M. and Lombardi F., "Concrete Damage and Spalling Monitoring in Fire Tests via Ultrasonic Pulse-Echo and Ground-Penetrating Radar", *Proceedings of the International Symposium Non-Destructive Testing in Civil Engineering – NDT-CE*, Berlin (Germany), September 15-17, 2015b.
23. Felicetti R., Lo Monte F. (2016), Pulse-Echo Monitoring of Concrete Damage and Spalling during Fire, *Proc. of the 9th Int. Conference Structures in Fire 2016 – SIF'16*, June 8-10, 2016, Princeton (USA), p. 851-858.
24. EN ISO 1133-1:2022 – "Determination of the melt mass-flow rate (MFR) and melt volume-flow rate (MVR) of thermoplastics - Part 1: Standard method".
25. Knack I., 2011, "The use of PP fibers in tunnel construction to avoid explosive concrete spalling in case of fire. New test results for the clarification of the mode of action", *2nd Int. RILEM Work. on Concrete Spalling due to Fire Exposure*
26. RFI (Italian Railway Network), *Civil Works Design Manual, Part II - Section 4 Tunnels* (in Italian).
27. UNI 11076:2003 – "Test procedures for evaluation of the behaviour of protective materials, applied to ceilings of underground construction, under fire conditions" (in Italian).

EFFICIENT AND RELIABLE FIRE RISK ASSESSMENT OF RC COLUMN

Akshay Baheti¹, David Lange², Vasant Matsagar^{3*}

ABSTRACT

A suitably large number of simulations are expected to be carried out to provide a reliable estimate of structural risk against fire while employing a popular Monte Carlo procedure. It has been observed by many researchers in the earthquake engineering field that the use of an efficient intensity measure (IM) reduces the dispersion in the structural response for a random loading scenario, reducing the requirement of conducting a large number of simulations. This paper uses this hypothesis to present a methodology for a reliable and efficient estimate of the fire risk of a reinforced concrete (RC) column. Random time-temperature fire profiles are generated using popular fire frameworks – parametric fire and travelling fire. The random parameters associated with material and structural geometry uncertainties are not considered. The failure criteria are defined in terms of the limiting values of member deflection, rate of deflection, and 300 °C isotherm depth. The dispersion in the resultant fire fragility curves, hazard curves, and the consequent structural fire risk is observed with the number of fire profiles. The fire hazard and fragility curves are obtained for popular IMs, such as the fire load density and the most suitable IM for the RC column from a previous study, i.e., the maximum average reinforcement bar temperature. The results indicate that the fire risk is reliably and efficiently obtained when the most suitable IM is used in the analysis.

Keywords: Reinforced concrete; fire fragility; fire hazard curve; fire intensity measure; parametric fire; travelling fire.

1 INTRODUCTION

National building regulations around the world adopt an approach for structural fire design that relies on member resistance to a nominal design fire – commonly the ISO 834 fire or similar – as a means of specifying the required performance in the fire of a structure. Indeed, even in a performance-based regulatory environment, an often-prevailing means of verification is comparing performance when exposed to a fire or calculating an equivalent period of fire resistance to that expected in a standard fire resistance test [1]. However, this century-old practice may result in inefficient and potentially unsafe recommendations for structures or elements as the standard fire does not depict an actual fire scenario within practical building examples, especially in modern infrastructure [2]. Therefore, several researchers recommended conducting tests (experimental, numerical, or a combination of both) on structures and structural components under realistic worst-case natural fire conditions to gain a reliable understanding of how buildings respond to fires [3]. A relationship between the probability of exceedance of a damage state of a structure or structural component and hazard intensity is presented using the fragility curves. The

¹ PhD Research Scholar, The UQ - IIT Delhi Research Academy, India
e-mail: a.baheti@uq.net.au, ORCID: <https://orcid.org/0000-0002-8172-1103>

² Associate Professor, The University of Queensland (UQ), Australia
e-mail: d.lange@uq.edu.au, ORCID: <https://orcid.org/0000-0002-4551-1045>

³ Dogra Chair Professor, Indian Institute of Technology (IIT) Delhi, India

*Corresponding author e-mail: matsagar@civil.iitd.ac.in, ORCID: <https://orcid.org/0000-0002-7600-0520>

Monte-Carlo simulation technique is typically employed to derive the fragility curves for a structural system. A large number of simulations, encompassing uncertainties related to material and geometric properties of the structure and loading scenario, are carried out for a reliable estimate of the fragility curves and, thereby, risk assessment of structures to particular hazards, e.g., fire. Quite a few studies have been carried out on the structural fire fragility analysis.

Gernay et al. [4,5] conducted a steel building's fire fragility analysis by considering 200 random parametric fire profiles [6] generated by varying fuel load density and opening factor in the compartment. Rush and Lange [7] developed fragility curves for RC columns while considering the equivalent duration of ISO 834 standard fire as an IM for a real fire. They considered the IM variation at six different locations on the RC column. Memari and Mahmoud [8] developed fire fragility curves for steel columns using 100 random parametric fire profiles and considering uncertainty in thermal properties and structural loading. Roy and Matsagar [9] conducted a fragility analysis of RC slab and wall panels by subjecting them to varying ISO 834 standard fire duration and generating random scenarios by varying material properties and structural loading. Chaudhary et al. [10,11] recommended the use of a sufficiently large number of fire profiles and considering stochastic variation in material properties and structural loading for fragility curve development for reliable estimation of structural fragility to fire. Shrivastava et al. [12,13] developed fragility curves for an RC composite slab using 200 random parametric fire profiles by using the most appropriate fire intensity measure they realised from an efficiency analysis. Ni and Gernay [14] used five parametric fire profiles to illustrate a probabilistic loss framework; however, they highlighted that more fire profiles need to be generated for reliable estimation of losses. Randaxhe et al. [15] conducted a fire fragility analysis of steel pipe racks using 77 localised fire profiles generated using varying heat release rates for seven different fuels. Cardellino et al. [16] obtained fragility curves for a steel building by generating 36 random natural fire profiles through fire dynamics simulation. Possidente et al. [17] recommended the use of at least ten random fire profiles to obtain fragility curves when a cloud analysis procedure is adopted.

In all the studies mentioned above, there is no remark on the sufficiency of the number of fire profiles for obtaining reliable fragility curves. Therefore, a separate sensitivity analysis is conducted within the present study to find the least number of fire profiles for reliable estimation of the fire fragility. The decision about the necessary strengthening or retrofitting of a structure or structural component depends on the incident risk of a hazard. Risk can be quantitatively defined as the probability of consequences occurring. Thus, it needs a definition of probability considering uncertainties related to both – scenarios and consequences. The risk of a specific hazard can be evaluated by convolution of structural fragility and hazard curves, equation (1) [18].

$$P_f = \int P_{f|\lambda} \left| \frac{dH(\lambda)}{d\lambda} \right| d\lambda \quad (1)$$

where

λ is the hazard intensity parameter,

$P_{f|\lambda}$ is the fragility curve,

$H(\lambda)$ is the hazard curve.

The fragility of a structure is the conditional probability of the occurrence of specific consequences, whereas a scenario is quantified in terms of a hazard curve. Therefore, it is necessary to conduct a sensitivity analysis of a number of fire profiles to reliably estimate the fire hazard curve for reliable estimation of the fire risk. Thus, the objectives of the present study are: (i) to find the least number of fire profiles for reliable estimation of the fragility; (ii) to find the least number of fire profiles for reliable estimation of the fire hazard curve; (iii) to develop a methodology for an efficient fire risk analysis of a structure or structural member. All these three objectives are explored as a case study on a reinforcement concrete (RC) column. A similar procedure can be applied to other structures or structural elements before conducting a fire risk assessment.

2 FIRE FRAGILITY AND HAZARD ASSESSMENT FRAMEWORK

Fire-induced loss in RC structures is calculated through four steps – (a) hazard analysis, (b) structural analysis, (c) damage analysis, and (d) loss analysis [14,19]. Random variables associated with uncertainties of these four steps are (i) intensity measure (IM), (ii) engineering demand parameter (EDP), (iii) damage function, and (iv) cost function, respectively. Previous studies in structural fire engineering emphasised the necessity of the existence of a suitable correlation among all four steps [20].

2.1 Fire intensity measure and damage states

Fire intensity is most popularly presented in terms of fuel load density (f_d), as discussed in several fragility studies in the previous section. It was time and again brought by the researchers to use flux-based variables as IMs instead of time-temperature curve-based quantities [e.g., 19]. Therefore, a study was conducted on the RC column to check the correlation of all the plausible candidate IMs with EDPs through five test criteria a suitable IM should possess: efficiency, practicality, proficiency, sufficiency, and scaling robustness [21]. The candidate IMs were: (i) fuel load density (f_d); (ii) maximum temperature (T_{max}); (iii) time at peak temperature (t_{peak}); (iv) fire duration (t_{dur}); (v) cumulative incident radiation; (vi) average incident net heat flux ($\dot{q}_{net,avg}''$); (vii) maximum incident net heat flux ($\dot{q}_{net,max}''$). (viii) input heat energy (Q_i); (ix) area under time-temperature curve (AUC). More information about evaluating these candidate IMs from either time-temperature profile or heat transfer analysis can be referred to in the original study [22]. It was observed that the time-temperature-based variables did not suitably correlate to the EDPs in the RC column; instead, the average reinforcement bar temperature ($T_{r,avg}$) was the overall suitable fire IM for the RC column [21]. Although it seems to be a temperature-based quantity, it is, in actuality, a function of net heat flux on the surface of the element and, thus, is a heat energy-based quantity. The results, thus obtained from the cited study, provided another stimulus for considering flux-based intensity measures for checking correlation with the EDPs in a structure or structural component.

The efficiency attribute describes the degree of dispersion in the IM-EDP relationship. It was established in earthquake engineering that an efficient IM leads to lesser uncertainty in the correlation, leading to a reduced number of simulations for reliable estimation of structural fragility and risk assessment. Thus, it is hypothesised in the current study that the number of required fire simulations for reliable estimation of the structural fragility and risk is less for $T_{r,avg}$ as a fire IM than other candidate IMs. The present study compares the least number of simulations for $T_{r,avg}$ with those necessary for another popular candidate IM, i.e., f_d , to establish its overall effectiveness and encourage the use of efficient IMs for other structure/structural components for fire risk assessment.

RC column failure under fire is the only damage state considered in the present study based on the guidelines of several international standards. The RC column failure is defined in terms of limiting values of the maximum deflection (δ_{max}), equation (2), maximum rate of displacement ($\dot{\delta}_{max}$), equation (3), and maximum 300 °C isotherm depth ($dp300_{max}$), equation (4) [10,14].

$$\delta_{max} = \frac{h}{100} \quad (2)$$

$$\dot{\delta}_{max} = \frac{3h}{1000} \text{ (in mm/min)} \quad (3)$$

$$dp300_{max} = \frac{b}{4} \quad (4)$$

where

h is the column height in mm,

b is the column width.

2.2 Numerical modelling

An RC column of dimension 350 mm × 350 mm, having M25 concrete (characteristic compressive strength of concrete, $f_{ck} = 25$ MPa) and 8-16 mm diameter steel reinforcement bars of grade Fe500 (characteristic yield strength of steel, $f_y = 500$ MPa), is taken as a case study in the present work. The compartment height is taken to be 3.5 m. The schematic of the column cross-section is presented in Figure 1. The dimensions of the compartment are taken to be 15 m × 15 m. The column is subjected to fire from all four sides. The fire exposure is uniform across the height of the column. The clear cover to the longitudinal reinforcement is 40 mm from all sides. A random fire profile is generated using parametric fire and travelling fire framework, details of which are given in the next section.

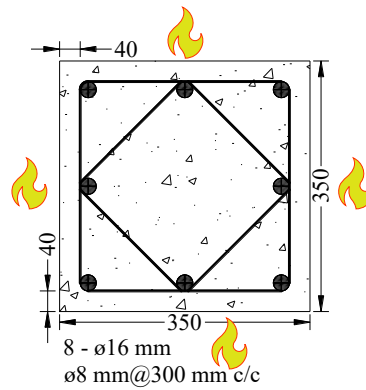


Figure 1. Schematic of the RC column section subjected to uniform fire over the height
(note: all dimensions are in 'mm')

The RC column is modelled as a 2D element in the 'OpenSees for fire' software framework [23]. The column section is divided into small elements of width and depth 5 mm while conducting the heat transfer analysis. The presence of steel reinforcement, both longitudinal and stirrups, is neglected while conducting the heat transfer analysis of the column section. This practice is acceptable owing to the negligible area of steel reinforcement compared to the surrounding concrete. The constituent concrete's thermal properties are modelled according to the material model in Eurocode 2 [24]. The output from the heat transfer analysis is obtained in terms of the temperature profile across the column section. The 300 °C isotherm depth, dp_{300} , is determined by observing the temperature profile across the column section and marking the boundary from the column edges where the temperature value is less than 300 °C.

It was observed in the previous studies that the correlation between RC column deflection and $T_{r,max}$ is invariant to the nature of the time-temperature profile of a fire hazard and therefore, semi-empirical equations were developed to calculate the column deflection, which eliminates the need for carrying out the nonlinear thermo-mechanical analysis of RC column [25]. The average temperature at each reinforcement location is obtained by taking the arithmetic mean of the temperature of all small elements parallel to the column's width. The $T_{r,avg}$ value is obtained by taking an average of the temperature of all reinforcement bars. This average value is further used to determine maximum deflection in the RC column using the relations in equations (5) and (6) [25].

$$\delta = -1 \times 10^9 \times \frac{h^2 A_{st}^{1.5} (T_{r,avg} - T_{rc})^3}{f_r^{2.5} E^{1.5} b^{1.5} D^3} \quad \forall f_r \geq 0.8 \quad (5)$$

$$\delta = -1 \times 10^9 \times \frac{h^2 A_{st}^{1.5} (T_{r,avg} - T_{rc})^3}{f_r^{(20f_r b D)} E^{1.5} b^{1.5} D^3} \quad \forall f_r < 0.8 \quad (6)$$

where

A_{st} is the area of the steel reinforcement in the column,

E is the modulus of elasticity of the reinforced concrete material,
 D is column depth,
 f_r is the force ratio on the column to be determined using equation (7),
 T_{rc} is the threshold temperature to be determined using equation (8).

$$f_r = \frac{P}{P_{cr}} \quad (7)$$

$$T_{rc} = (-350b - 250)f_r + 630b^{0.2}D^{0.09}f_{ck}^{0.03}A_{st}^{-0.03} \quad \forall 0.5 \leq f_r \leq 1.4 \quad (8)$$

where

P is the axial load on the column,

P_{cr} is the critical axial load-carrying capacity of the column to be determined using equation (9) [26].

$$P_{cr} = 0.4f_{ck}(bD - A_{st}) + 0.67f_yA_{st}. \quad (9)$$

The rate of deflection is determined in the relevant units from the deflection profile, thus obtained for checking the column failure. The critical reinforcement temperature, T_{rc} , is a temperature below which the column does not deflect in a downward direction, or it is a threshold value below which the column undergoes thermal expansion. Therefore, it is safe to assume that the column does not undergo failure from deflection and rate of deflection criteria. The current study focuses only on the axially loaded column with no or negligible bending moment on the column section, a case relatable to an internal column in a building. The corner or edge columns are generally subjected to uniaxial or biaxial moments. They are the subjects for the future study.

For the RC column shown in Figure 1, the critical load-carrying capacity, P_{cr} , is 1747.8 kN. The axial load on column P is varied to get the force ratio, with f_r values of 0.5, 0.8, 1.1, and 1.4, to record uniform results for the minimum required number of fire simulations for reliable estimation of fire fragility and risk for columns on all floors of the building. Even with the deterioration in material properties with service life, the observations recorded in this study are valid for the columns in the building. However, the readers must note that the results presented in this paper are limited to the column section in the building. Future researchers should adopt the methodology, not the results, to draw conclusions regarding the efficient way of conducting fire fragility and risk analysis. A load ratio value below 0.5 is not considered in the present study for two reasons: (i) the deflection equations are subject to the constraint of load ratio between 0.5 and 1.4; (ii) columns under lower load ratio have a typically lesser probability of failure under deflection or rate of deflection criterion. The credibility of the heat transfer analysis and the deflection equation is established in the cited study [25] and, therefore, is not reproduced in this paper. Readers are encouraged to refer to the cited research for more information.

2.3 Fire frameworks

There exist quite a few frameworks to obtain a time-temperature profile for a fire hazard. The limitation of using only temperature-based and not flux-based fire profiles is attributed to the limitation of the software framework currently used in the study. The random fire profile in a compartment is obtained using two frameworks in the present study: (i) parametric fire [6] and (ii) travelling fire [26]. The popular ISO 834 standard fire curve is not used in the current study because its time-temperature profile is independent of the material and geometric characteristics of the compartment. Parametric fire is an example of a fully developed compartment fire, and a random fire profile is obtained using equation (10).

$$T_g = T_a + 1325(1 - 0.324e^{-0.2t^*} - 0.204e^{-1.7t^*} - 0.472e^{-19t^*}) \quad (10)$$

where

T_g is the gas temperature in the compartment,

T_a is the ambient air temperature,

t^* is the modified time factor.

The modified time factor in the above equation depends on the compartment geometry, openings in the compartment, and compartment boundary. More details about the calculation of the modified time factor are not presented in this paper and may be referred to in the cited study. The maximum fire temperature is observed at t_{\max} , equation (11), which depends on the fuel load density and the compartment characteristics described previously.

$$t_{\max} = \max \left[\left(0.2 \times 10^{-3} q_{d,t} / O \right), t_{\lim} \right] \quad (11)$$

where

$q_{d,t}$ is the design value of the fuel load density,

O is the opening factor,

t_{\lim} is the threshold value dividing the fire regime into fuel-controlled and ventilation-controlled.

More details about the calculation of each term in the above equation are not presented in this paper and may be referred to in the cited study. Thus, the uncertainties associated with compartment material and geometry, fuel load density, and opening factor can affect the time-temperature profile of a random parametric fire. Similarly, the time-temperature profile in a travelling fire framework can be obtained using equations (12) and (13).

$$T_{\text{ng}} = T_a + \frac{T_{\text{nf}} (2r_{x_1} + L_f) - 2T_a r_{x_2}}{f} + \frac{32.28 \dot{Q}^{2/3}}{hf} (r_2^{1/3} - r_{x_2}^{2/3}) \quad (12)$$

$$T_{\text{fg}} = T_a + \frac{5.38}{h} \left(\frac{LL_t^* W \dot{Q}''}{x + 0.5LL_t^* - x_t^*} \right)^{2/3} \quad (12)$$

where

T_{ng} is the gas temperature in the near-field region,

T_{fg} is the gas temperature in the far-field region,

T_{nf} is the fixed peak value of near-field temperature, taken 1200 °C,

\dot{Q} is the total heat release rate,

f is the flame width,

L, W are the compartment length and width, respectively,

x is the location in the compartment at which the fire temperature is to be determined,

r^* are several parameters that control the compartment temperature profile.

More details about the calculation of various parameters may be referred to in the original study. The uncertainty associated with the time-temperature profile in a travelling fire can thus be attributed to the fuel load density, compartment geometry, heat release rate, and fire spread rate which controls the flame length. The travelling fire framework assumes the fire is in a fuel-controlled regime.

2.4 Thermal loading uncertainty

The sources of uncertainties in a fire profile are listed in the previous section. Variability in the compartment geometry, column geometry, or compartment boundary properties is relatively less [19] and, therefore, is not considered a source of uncertainty in the present study. The heat release rate is considered constant at the peak recommended value [6] for developing parametric and travelling fire profiles. Thus, variations in member material properties, fuel load density, and the compartment opening factor need to be considered for a reliable estimate of structural fragility. The uncertainty associated with the concrete and steel strength primarily affects the load ratio and marginalises other variables. Since a wide range of load ratio (0.5-1.4) is considered in the present study to base an inference about the efficient number of fire simulations,

uncertainty associated with material strength is not explicitly considered in the present study. Thus, considering the randomness of the fire profiles alone while considering a wide range of load ratios on the RC column will result in a generalised methodology.

The random fire profiles are generated using the parametric fire framework by varying compartment fuel load density and opening factor, whereas random travelling fire profiles are generated by considering random compartment fuel load density along with varying fire spread rates. The fuel load density varies as per the Gumbel type I distribution with a mean of 1409 MJ/m² and a standard deviation of 234 MJ/m², values recommended for residential buildings [27,6] from the Indian perspective. The compartment's opening factor varies with the lognormal distribution with a mean and standard deviation of 0.2 [28]. Different fire spread rates considered in the travelling fire framework are 0.5, 1, 1.5, 2, and 2.5 mm/s. 10,000 random fire profiles, thus generated, is deemed considerably a large number for accurate estimation of structural fragility in fire, and this number is reduced to check the least number at which deviation in the fire fragility curve is observed from that obtained for 10,000 fire simulations. The results of the fragility and hazard analysis are presented in the next section.

3 RESULTS AND DISCUSSION

3.1 Fire fragility analysis

The fire fragility curves for the RC column in Figure 1, obtained for a varying number of fire profiles and load ratios and generated while considering fuel load density (f_d) separately for parametric fire [6] and travelling fire [26], are presented in Figures 2 and 3. The number of fire profiles is reduced from 10,000 to 200. The data obtained for parametric fire profiles was relatively dispersed; therefore, smoothed curves are presented in Figure 2. It is observed from both figures that the fragility curves obtained for load ratios 0.5, 0.8, and 1.1 are identical to each other, indicating that the 300 °C isotherm depth (dp300) is the governing criterion among the three criteria considered in the present study. For load ratio 1.4, fragility

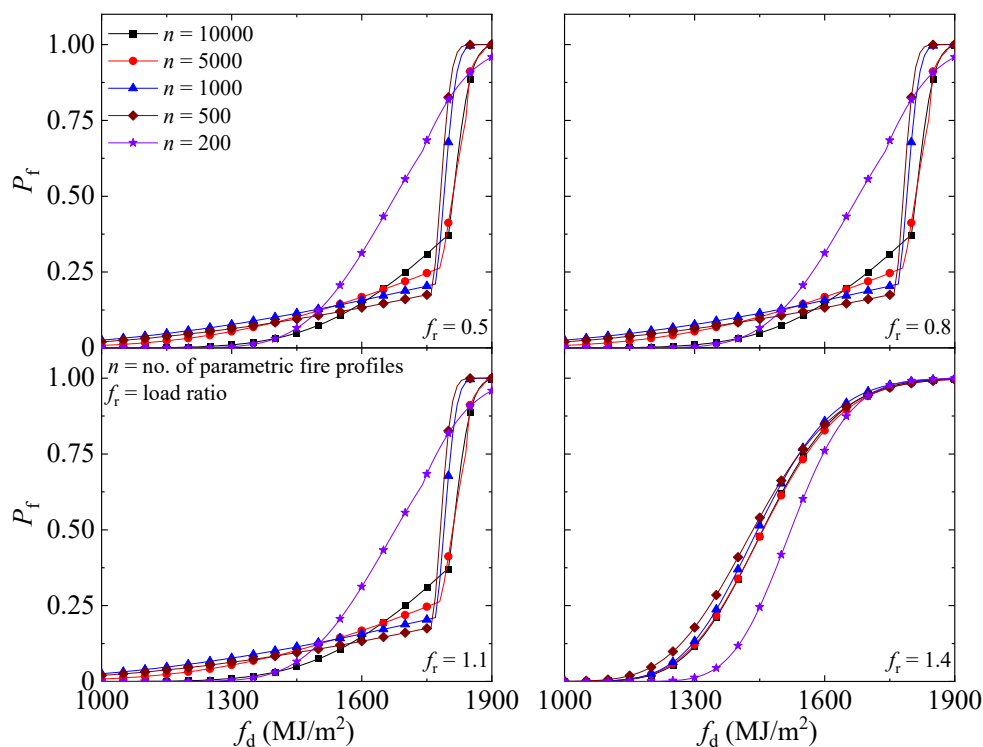


Figure 2. A comparison of the fragility curves was obtained for the RC column under different load ratios and subjected to random parametric fire profiles when the fuel load density (f_d) was taken for fire IM

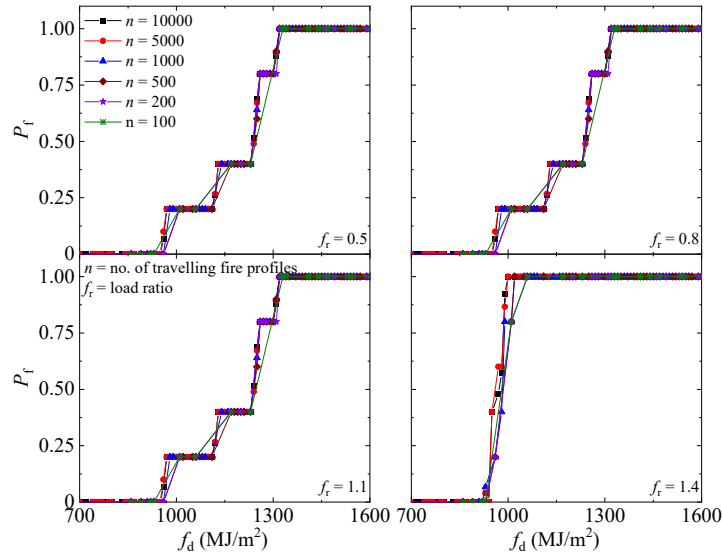


Figure 3. A comparison of the fragility curves was obtained for the RC column under different load ratios and subjected to random travelling fire profiles when the fuel load density (f_d) was taken for fire IM

curves have shifted to the left, indicating an increase in the fire fragility, which is acceptable. It is observed from the figures that the fragility curves obtained for 500 random fire simulations are quite close to those obtained by performing 10,000 random simulations. This observation is true for both fire frameworks. Therefore, it is concluded that the minimum number of fire simulations required for a reliable estimate of fire fragility of the RC column is 500 when considered f_d as an IM.

A similar analysis is carried out while considering the average reinforcement bar temperature ($T_{r,avg}$) as fire IM, and the results are presented in Figures 4 and 5, respectively, for parametric fire and travelling fire. A similar observation to the previous is recorded regarding dp300 being the governing criterion to define member failure among the considered criteria for load ratios 0.5, 0.8, and 1.1. It is observed from both figures that the fire fragility curves obtained by performing 50 random fire simulations are quite identical to those obtained from 10,000 random fire simulations. For the travelling fire framework, results obtained from 10 random fire simulations match those obtained from 10,000 fire simulations, indicating the necessity of using the most appropriate IM for efficient fragility analysis. Thus, it is concluded that reliable fire fragility curves can be obtained for the RC column by performing just 50 random fire simulations when $T_{r,avg}$ is taken as fire IM. In addition, there was no dispersion in the fragility data when $T_{r,avg}$ is taken as fire

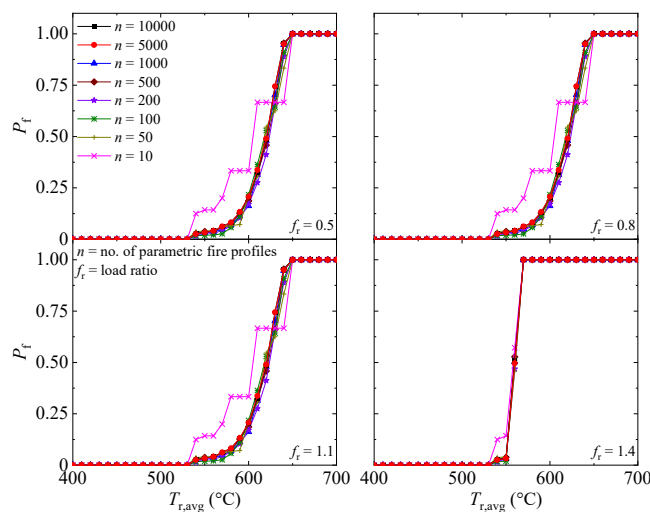


Figure 4. A comparison of the fragility curves was obtained for the RC column under different load ratios and subjected to random parametric fire profiles when the average reinforcement bar temperature ($T_{r,avg}$) was taken for fire IM

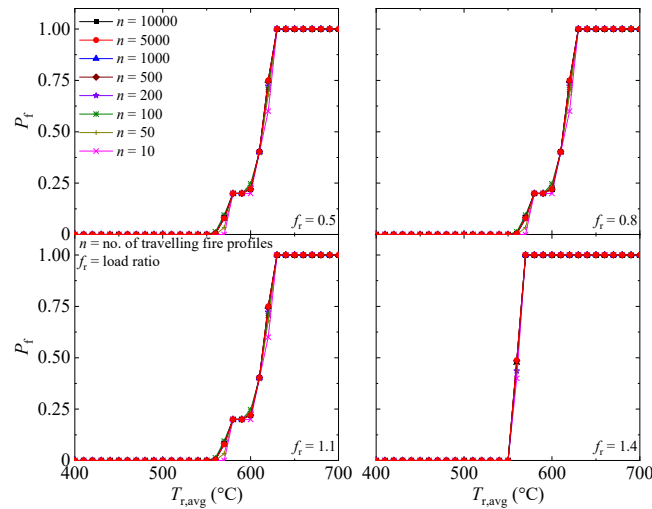


Figure 5. A comparison of the fragility curves was obtained for the RC column under different load ratios and subjected to random travelling fire profiles when the average reinforcement bar temperature ($T_{r,avg}$) was taken for fire IM

IM, unlike that for f_d . Additionally, the fire fragility curves for both – parametric fire and travelling fire are almost identical for the same load ratios; this observation is attributed to the excellent correlation between the IM and the EDPs, irrespective of the fire models. This reduces the necessity of considering random fire profiles from the available different frameworks, which reduces the computation efforts of practising engineers.

3.2 Fire hazard curve

Since the fire risk is a function of fragility and hazard, the fire hazard curves were obtained for varying numbers of fire simulations while considering the fuel load density (f_d) and the average rebar temperature ($T_{r,avg}$) as fire IMs are presented in Figures 6 and 7, respectively. While 50 random simulations are enough for predicting the fire hazard curve when parametric fire profiles are used, at least 500 random simulations are needed for predicting the fire hazard curve when travelling fire profiles are considered. This observation is applicable for both the fire IMs.

3.3 Fire risk assessment

The fire risk of the RC column was calculated using equation (1), and the results discussed in the previous section for varying numbers of fire profiles are presented in Table 1. The fire risk assessment is carried out for both IMs – f_d and $T_{r,avg}$. This exercise is carried out only for load ratios of 0.5 and 1.4 since the fire fragility curves for 0.8 and 1.1 were identical to those for 0.5, and the fire hazard curve does not change

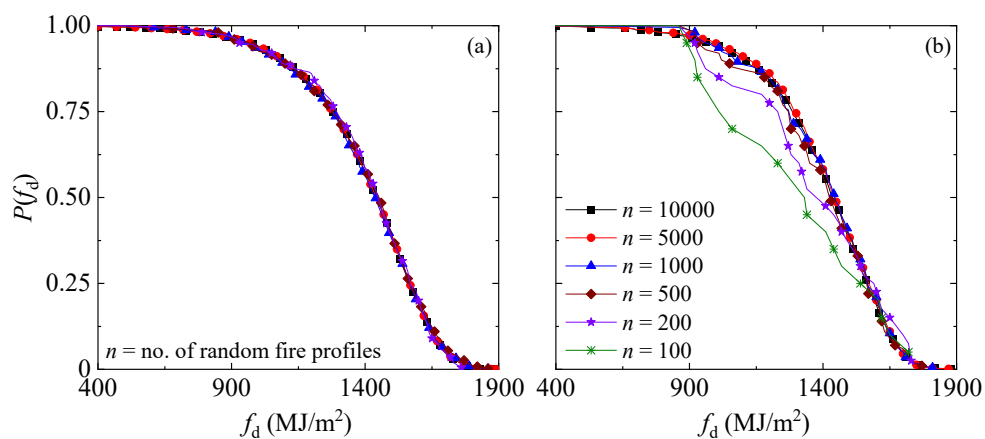


Figure 6. Fire hazard curves for random numbers of: (a) parametric fire and (b) travelling fire profiles considering fuel load density (f_d) as fire IM

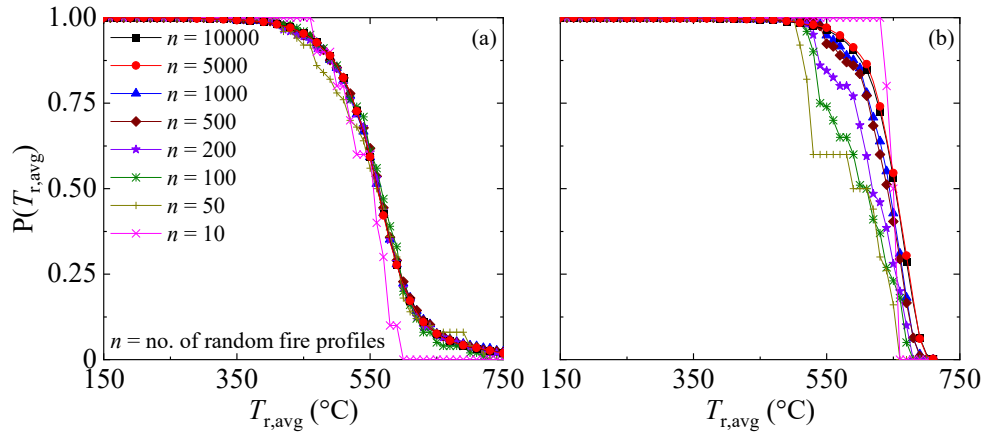


Figure 7. Fire hazard curves for random numbers of: (a) parametric fire and (b) travelling fire profiles considering average reinforcement bar temperature ($T_{r,avg}$) as fire IM

with change in column load ratio. It can be observed from the table that the fire risk value for travelling fire (TF) for 10,000 random fire simulations is almost the same, indicating that it is a sufficiently large number to get reliable results in any generalised IM. However, a similar observation is not recorded for parametric fire (PF); this is attributed to curve smoothing, as explained in Section 3.1, for a dispersed output when f_d is the fire IM. As expected, the least number of fire simulations to get a reliable estimate of fire risk is 500 for both IMs for any load ratio and fire framework. This is because fire hazards are reliably obtained for these many random simulations, although convergence in the fire fragility curve is obtained quickly for $T_{r,avg}$ as the candidate IM.

Table 1. Comparison of the fire risk for the RC column for two candidate IMs and varying number of simulations

Number of random fire simulations (n)	f_d as fire IM				$T_{r,avg}$ as fire IM			
	$f_r = 0.5$		$f_r = 1.4$		$f_r = 0.5$		$f_r = 1.4$	
	PF	TF	PF	TF	PF	TF	PF	TF
10,000	0.08	0.84	0.46	0.95	0.20	0.86	0.56	0.96
5,000	0.11	0.85	0.46	0.96	0.20	0.87	0.56	0.96
1,000	0.12	0.82	0.47	0.94	0.20	0.81	0.56	0.94
500	0.11	0.80	0.50	0.92	0.20	0.79	0.58	0.92
200	0.17	0.74	0.37	0.86	0.19	0.63	0.57	0.83
100	NA	0.62	NA	0.78	0.16	0.51	0.58	0.72
50	NA	NA	NA	NA	0.22	0.50	0.52	0.60

note: PF = parametric fire; TF = travelling fire; NA = results not available; f_i = load ratio.

4 CONCLUSIONS

The effect of the number of fire simulations on the resultant fire fragility and risk is analysed in the present paper. A large number of random fire profiles are generated using the popular parametric fire and travelling fire framework. The number of fire simulations is gradually reduced from 10,000 to 50, and its corresponding effect on the resultant fragility and risk of a reinforced concrete (RC) column is analysed to deduce the least number of fire simulations necessary for reliable estimation of the above-mentioned quantities. The results, thus obtained, are summarised below:

- At least 500 random fire simulations are required for a reliable estimate of structural fragility to fire when the popular choice of fire intensity measure (IM), i.e., fuel load density (f_d), is used. This observation is valid irrespective of the fire framework used to generate the random fire profile and a wide range of load ratio (0.5-1.4).
- The above number reduces to 50 when the most suitable IM for an RC column, i.e., the average reinforcement bar temperature ($T_{r,avg}$), is used. Additionally, the fragility curves are almost identical for both the fire frameworks used in the present study.
- The least number of fire simulations required for a reliable estimate of fire risk of an RC column is 500 for both f_d and $T_{r,avg}$.

Therefore, it is recommended that the most suitable IM should be used for reliable and efficient estimation of fire risk and fragility. This conclusion is in line with that of earthquake engineering. It is reiterated that future studies shall adopt the methodology, not the results, presented in this paper for estimation of the least number of fire simulations for a structure or structural members.

ACKNOWLEDGMENT

The research work presented herein is supported by the Government of India's Ministry of Education under its Scheme for Promotion of Academic and Research Collaboration (SPARC) for the project "Fire Safety in Underground Tunnels" (Project Code: P920). The PhD study of the first author is supported by a fellowship from the Indian Institute of Technology (IIT) Delhi, India and The University of Queensland (UQ), Australia, under their joint PhD program.

REFERENCES

1. Law, A., Stern-Gottfried, J. & Butterworth, N., A Risk Based Framework for Time Equivalence and Fire Resistance. *Fire Technol* 51, 771-784 (2015). <https://doi.org/10.1007/s10694-014-0410-9>.
2. Zhang, H. Y., Li, Q. Y., Kodur, V. & Lv, H. R., Effect of Cracking and Residual Deformation on Behavior of Concrete Beams with Different Scales under Fire Exposure. *Eng Struct* 245, 112886 (2021). <https://doi.org/10.1016/j.engstruct.2021.112886>.
3. Almand, K. H., Research Needs Identified Through Literature Review. In: *Structural Fire Resistance Experimental Research*, Springer, New York, 33-38 (2012). https://doi.org/10.1007/978-1-4614-8112-6_5.
4. Gernay, T., Khorasani, N. E. & Garlock, M., Fire Fragility Curves for Steel Buildings in a Community Context: A Methodology. *Eng Struct* 113, 259-276 (2016). <https://doi.org/10.1016/j.engstruct.2016.01.043>.
5. Gernay, T., Khorasani, N. E. & Garlock, M. Fire Fragility Functions for Steel Frame Buildings: Sensitivity Analysis and Reliability Framework. *Fire Technol* 55, 1175-1210 (2019). <https://doi.org/10.1007/s10694-018-0764-5>.
6. CEN, Eurocode 1 - Actions on Structures - Part 1-2: General Actions - Actions on Structures Exposed to Fire, EN-1991-1-2. European Committee for Standardization (CEN), Brussels; 2024.
7. Rush, D. & Lange, D., Towards a Fragility Assessment of a Concrete Column Exposed to a Real Fire-Tisova Fire Test. *Eng Struct* 150, 537-549 (2017). <https://doi.org/10.1016/j.engstruct.2017.07.071>.
8. Memari, M. & Mahmoud, H., Framework for a Performance-Based Analysis of Fires Following Earthquakes. *Eng Struct* 171, 794-805 (2018). <https://doi.org/10.1016/j.engstruct.2018.05.099>.
9. Roy, T. & Matsagar, V., Fire Fragility of Reinforced Concrete Panels under Transverse Out-of-Plane and Compressive In-Plane Loads. *Fire Saf J* 113, 102976 (2020). <https://doi.org/10.1016/j.firesaf.2020.102976>.
10. Chaudhary, R. K., Roy, T. & Matsagar, V., Member and Structural Fragility of Reinforced Concrete Structure under Fire. *J Struct Fire Eng* 11(4), 409-435 (2020). <https://doi.org/10.1108/JSFE-02-2019-0015>.
11. Chaudhary, R. K., Roy, T. & Matsagar, V., Framework for Fragility Assessment of Reinforced Concrete Portal Frame subjected to Elevated Temperature. *Struct* 28, 2785-2800 (2020). <https://doi.org/10.1016/j.istruc.2020.10.078>.
12. Shrivastava, M., Abu, A.K., Dhakal, R.P. et al. Severity Measures and Stripe Analysis for Probabilistic Structural Fire Engineering. *Fire Technol* 55, 1147-1173 (2019). <https://doi.org/10.1007/s10694-018-0799-7>.

13. Shrivastava, M., Abu, A. K., Dhakal, R. P., Moss, P. J. & Yeow, T. Z., Probabilistic Structural Fire Engineering using Incremental Fire Analysis and Cloud Analysis. *Proc Inst Civ Eng - Eng Comput Mech* 173(2), 47-58 (2020). <https://doi.org/10.1680/jencm.18.00001>.
14. Ni, S. & Gernay, T., A Framework for Probabilistic Fire Loss Estimation in Concrete Building Structures. *Struct Saf* 88, 102029 (2021). <https://doi.org/10.1016/j.strusafe.2020.102029>.
15. Randaxhe, J., Popa, N. & Tondini, N., Probabilistic Fire Demand Model for Steel Pipe-Racks Exposed to Localised Fires. *Eng Struct* 226, 111310 (2021). <https://doi.org/10.1016/j.engstruct.2020.111310>.
16. Cardellino, E., de Silva, D. & Nigro, E., Estimation of Structural Fire Vulnerability Through Fragility Curves. In: Pellegrino, C., Faleschini, F., Zanini, M. A., Matos, J. C., Casas, J. R., Strauss, A. (eds) *Proceedings of the 1st Conference of the European Association on Quality Control of Bridges and Structures. EUROSTRUCT 2021. Lecture Notes in Civil Engineering* 200. Springer, Cham; 2022. https://doi.org/10.1007/978-3-030-91877-4_67.
17. Possidente, L., Randaxhe, J. & Tondini, N. Fire Fragility Curves for Industrial Steel Pipe-Racks Integrating Demand and Capacity Uncertainties. *Fire Technol* 59, 713-742 (2023). <https://doi.org/10.1007/s10694-022-01358-4>.
18. Matsagar, V., Earthquake Engineering and Technology. In: Sitharam, T. G., Kolathayar, S., Jakka, R. S., Matsagar, V. (eds) *Theory and Practice in Earthquake Engineering and Technology*. Springer Tracts in Civil Engineering. Springer, Singapore; 2023. https://doi.org/10.1007/978-981-19-2324-1_1.
19. Lange, D., Devaney, S. & Usmani, A., An Application of the PEER Performance Based Earthquake Engineering Framework to Structures in Fire. *Eng Struct* 66, 100-115 (2014). <https://doi.org/10.1016/j.engstruct.2014.01.052>.
20. Baheti, A., Lange, D. & Matsagar, V., A Study to Determine Suitable and Robust Intensity Measures for Reinforced Concrete Slab subjected to Fire. In: Jiang, L., Real, P. V., Huang, X., Orabi, M. A., Qiu, J., Chu, T., Nan, Z., Chen, C., Wang, Z., Usmani, A. (eds) *Proceedings of the 12th International Conference on Structures in Fire*, 1219-1229, Hong Kong; 2022. <https://doi.org/10.6084/m9.figshare.22223968>.
21. Baheti, A., Lange, D. & Matsagar, V., Appropriate Fire Intensity Measures for RC Beam and Column. Manuscript submitted for publication. The UQ - IIT Delhi Research Academy, Indian Institute of Technology (IIT) Delhi.
22. Baheti, A., Lange, D. & Matsagar, V., A Framework to Determine Appropriate Intensity Measures for a Structure subjected to Fire. Manuscript submitted for publication. The UQ - IIT Delhi Research Academy, Indian Institute of Technology (IIT) Delhi.
23. Jiang, J., Jiang, L., Kotsovinos, P., Zhang, J., Usmani, A., McKenna, F. & Li, G. Q., OpenSees Software Architecture for the Analysis of Structures in Fire. *J Comput Civ Eng* 29(1), 04014030 (2015). [https://doi.org/10.1061/\(ASCE\)CP.1943-5487.0000305](https://doi.org/10.1061/(ASCE)CP.1943-5487.0000305).
24. CEN, Eurocode 2: Design of concrete structures - part 1-2: General rules - structural fire design, EN-1992-1-2. European Committee for Standardization (CEN), Brussels; 2023.
25. Baheti, A., Lange, D. & Matsagar, V., Semi-Empirical Equations to Evaluate Maximum Deflection in RC Beam and Column under Fire. Manuscript submitted for publication. The UQ - IIT Delhi Research Academy, Indian Institute of Technology (IIT) Delhi.
26. Rackauskaite, E., Hamel, C., Law, A. & Rein, G., Improved Formulation of Travelling Fires and Application to Concrete and Steel Structures. *Struct* 3, 250-260 (2015). <https://doi.org/10.1016/j.istruc.2015.06.001>.
27. Khan, N. A. & Srivastava, G., Enhanced Fire Severity in Modern Indian Dwellings. *Curr Sci* 115(2), 320-325 (2018). <https://doi.org/10.18520/cs/v115/i2/320-325>.
28. Vrouwenvelder, T., The JCSS Probabilistic Model Code. *Struct Saf* 19(3), 245-251 (1997). [https://doi.org/10.1016/S0167-4730\(97\)00008-8](https://doi.org/10.1016/S0167-4730(97)00008-8).

ENHANCING FIRE RESISTANCE OF GEOPOLYMER CONCRETE UTILIZING RECYCLED AGGREGATES, COPPER SLAG, AND GLASS SPHERES : A COMPREHENSIVE STUDY

Tawzia Manzoor¹, Asif H. Shah², Javed Ahmad Bhat³

ABSTRACT

Geopolymer materials are innovative and ecofriendly alternative to traditional Portland cement-based materials, harnessing industrial by products like fly ash and slag as binder materials. The behaviour of waste based geopolymer material at elevated temperatures is a crucial aspect of assessing its structural integrity and applicability in fire exposed conditions. The current study extensively examines and discusses the post high temperature exposure characteristics of geopolymer materials. The focus is on understanding changes in mechanical properties, microstructure and overall stability of geopolymer materials derived from waste products containing recycled aggregates, copper slag aggregates and comparing it with geopolymer concrete containing normal aggregates. Furthermore, this article explores the behaviour of such materials at elevated temperatures, considering varying additions of recycled Fibres, crumb rubber and glass powder. Experimental investigations involve subjecting waste-based geopolymer concrete specimens to controlled temperature regimes, simulating fire scenarios. Compressive strength is measured before and after exposure to elevated temperatures. Micro structural analysis, scanning electron microscopy (SEM) is conducted to observe any phase transformations, pore structure alterations, and the development of cracks.

Keywords: Fire resistance; copper slag; GGBS; Fly Ash; hollow glass microsphere

1 INTRODUCTION

Geopolymer concrete (GPC) has emerged as a sustainable substitute to conventional ordinary Portland cement (OPC) concrete which is the prime material used for infrastructure construction, demonstrating great potential owing to its strength and durability [1]. A common perception regarding concrete is that it is resistant to fire but in reality it does undergo alterations at high temperature which affects its strength and durability. While GPC exhibits commendable performance under standard conditions, it is crucial for this innovative material to showcase superior fire resistance compared to OPC concrete to ensure its long-term durability [2]. A comprehensive evaluation of GPC's response to high temperatures, including physical examinations for cracking, spalling, and strength loss during fires, serves as a crucial indicator of its resilience in this challenging environment [3].

¹ Ph. D Scholar, Dept. of Civil Engineering, National Institute of Technology Srinagar, Kashmir, India

Email: rathertawzia@gmail.com

² Assistant Professor, Dept. of Civil Engineering, Central University of Kashmir, Tulmulla Ganderbal Kashmir, India
mail: asif.shah@cukashmir.ac.in

³ Professor, Dept. of Civil Engineering, National Institute of Technology Srinagar, Kashmir, India

Email: bhat_javed@nitsri.ac.in

This study primarily focuses on assessing the performance of fibre reinforced GPC, specifically using ground granulated blast furnace slag (GGBS) and fly ash (FA) under elevated temperatures. The incorporation of GGBS not only improves compressive strength but also addresses a critical limitation in the form of heat curing, a challenge encountered by geopolymer concrete when relying solely on fly ash as the alumina silicate precursor [4,5]. Exploring the addition of recycled fibres (RFs) derived from tire wastes emerges as a strategic approach to enhance the behaviour of GPC at elevated temperatures. This not only promises improved performance but also results in resource conservation and waste reduction, thus alleviation of waste disposal issues in landfills. To further reduce reliance on natural aggregates, the research delves into the physical and micro structural characterization of GPC with the replacement of both coarse and fine aggregates. Recycled aggregates and copper slag in different ratios substitute normal coarse aggregates, while varying proportions of fine copper slag powder, rubber crumb, glass powder and hollow glass microspheres take the place of regular fine aggregates. The inclusion of copper slag not only contributes to thermal stability but also enhances the overall strength of GPC [6-8]. Simultaneously, the use of glass powder, melting at high temperatures, results in increased residual strength, thereby enhancing the material's resilience in adverse conditions [9-11]. The compressive strength of various GPC mixes incorporating normal aggregates with varying proportion of binders will be done. Optimal specimens, identified through preliminary tests, will undergo a detailed examination for the replacement of both fine and coarse aggregates. The new specimens formed will again be evaluated for compressive and residual compressive strength. The residual compressive strength test will be conducted after subjecting specimens to a temperature ranging from 200°C to 800 °C. Additionally, micro structural characterization of different mixes will be conducted using Scanning Electron Microscope (SEM) imaging.

2 EXPERIMENTAL PROGRAMME

The study subjected 100 mm × 100 mm geopolymer concrete cube specimens to varying temperature limited to 800°C, with rate of heating kept at 5°C per minute. The heat transfer within the specimens was monitored using K type thermocouples. The cubes were kept for 60 minutes at constant target temperature in order to uniformly heat the concrete up to core. Damages, including cracking and spalling, after exposure to varying temperatures were assessed. Mass loss was determined by weighing the specimens, and compression tests were conducted to ascertain the residual strength. Scanning electron microscopy images were utilized to examine the microscopic structure of the geopolymer concrete. Results suggest that geopolymer concrete exhibits lower spalling probability at high temperatures attributed to its unique properties and composition.

3 MATERIALS

Geopolymer concrete uses materials rich in aluminium and silica instead of Portland cement. The primary materials used in the current study of geopolymer concrete include:

- **FLY ASH (FA):** Fly ash is a powdered product derived from combustion of coal in power plants. It consists of the inorganic mineral residues left behind when coal is burned at high temperatures in boilers. Fly ash is carried from electrostatic precipitators of combustion chamber or bag filters before flue gas is released into the atmosphere. Fly ash primarily consists of spherical, glassy particles composed of silicon dioxide (SiO₂), aluminum oxide (Al₂O₃), iron oxide (Fe₂O₃), and small traces of other elements. The exact composition depends on the source of coal and the combustion process. To avoid lumps fly ash was passed through 1.12 mm sieve. The fly ash used had around 75% passing finer than 45 µm. FA was procured from MKB international exports, Nagpur. The chemical compositions of fly ash used is given in Table 1
- **GROUND GRANULATED BLAST FURNACE SLAG (GGBS):** GGBS is derived from the iron and steel industry, specifically from the production of iron in blast furnaces. GGBS is formed from rapid cooling of molten iron blast furnace slag in water, producing glassy granules. This

process results in a finely ground, pozzolanic material with chemical and physical properties that make it valuable in various construction and engineering applications. GGBS primarily consists of silicon dioxide (SiO₂), aluminum oxide (Al₂O₃), magnesium oxide (MgO) and calcium oxide (CaO). GGBS was procured from Gogga Minerals and Chemicals, Karnataka. The chemical composition of GGBS used is given in Table 1.

- **FIBRES:** Fibres enhance the tensile strength of geopolymer concrete. Two types of fibres were used nylon fibres and steel fibres. Nylon fibres used were virgin fibres while as steel fibres were obtained from discarded tires and procured from Earthman Rubber Industries Pvt Ltd. Both wavy and hooked steel fibres were used. Irregular geometry of steel fibres improves the bond of concrete and fibres and prevents explosive spalling of concrete, while as nylon fibres melt at high temperature and create voids [12,13].
- **COARSE AGGREGATE & FINE AGGREGATE:** Coarse aggregates consisted of aggregates with nominal sizes of 10 and 20 mm. River sand was used as fine aggregate, For recycled aggregates M20,M30,M40 concrete cubes were broken with hammer and crushed in crusher to obtain aggregates of around 10mm and 20 mm in size. Two types of coarse aggregates in saturated surface dry (SSD) condition were used. The specific gravity (SG) of NA was 2.6 while The SG of RCA was slightly lower at 2.3.
- **COPPER SLAG:** Copper slag emerges as a by-product in the process of smelting copper ore to obtain copper metal within refinery plants. Its composition primarily consists of iron silicate along with minor traces of elements like copper, zinc, lead, and arsenic. It was obtained locally from copper manufacturer.
- **RUBBER CRUMB:** Rubber crumb used was obtained from waste tyres and procured from Earthman Rubber Industries Pvt. Ltd. It was 3mm to 4mm in size. Rubber aggregates in the concrete reduce spalling of high-strength concrete at elevated temperature. The rubber particles create voids upon burning, thus permitting the release of water vapor and lowering of vapor pressure [14,15]. Rubber crumb was used in this study as partial replacement of sand.
- **GLASS POWDER:** Glass has a high percentage of SiO₂, and finely grounded glass can even substitute cement as a binder. Glass powder was used here as a partial replacement of sand. Glass powder used was of two types – fine granular and hollow microsphere type. The composition of glass powder used is given in Table 1.
- **ALKALINE SOLUTION:** Alkaline solution was made using solutions of sodium hydroxide and sodium silicate. Pellets of Sodium hydroxide with 99% purity were dissolved in distilled water to form a 12 M solution and were kept overnight to reduce its temperature. This was mixed with two types of sodium silicate solution, one having mass composition of 14.25% Na₂O, 32.9% SiO₂, and 2.3 specific gravity and the other having mass composition of 14.5% Na₂O, 31% SiO₂, and 2.0 specific gravity, procured from Shanti Chemical Works. These solutions were mixed together 1 hour minimum before addition to the fly ash and aggregates and were oven heated at a temperature of 40°C to avoid its crystallization. Adding hot alkaline solution results in quick setting of concrete, therefore temperature of 40°C is optimum.

Table 1: Chemical composition of oxides in % of Fly Ash and GGBS as per XRF

	SiO ₂	Al ₂ O ₃	CaO	MgO	Fe ₂ O ₃	SO ₃	Na ₂ O	K ₂ O	TiO ₂
Fly Ash	56.55	31.2	3.51	1.45	2.8	0.08	0.0	2.01	2.4
GGBS	32.7	24.2	34.94	5.3	0.4	0.99	0.21	0.6	0.66
Glass Powder	72.2	2.2	9.2	2.2	0.25	-	13.2	0.75	-

4 MIX PROPORTION

Nine variations of geopolymer concrete (GPC) incorporating normal aggregate, recycled aggregate, copper slag, rubber crumb, glass powder, and fibres were employed to assess the influence on fire endurance of geopolymer concrete in terms of residual compressive strength, mass loss and spalling of geopolymer concrete. An optimal mix was selected by varying the percentage of fly ash and GGBS as binder. 20% fly ash and 80% GGBS was considered as optimal proportion for binder. The mixture compositions for nine types, denoted as NF₂G₈, RF₂G₈, RCF₂G₈, RCRF₂G₈, RCGF₂G₈, RCFF₂G₈ as outlined in Table 2. At the age of 7 days, the tested compressive strengths for the respective batches of GPC were measured as 76 MPa, 58 MPa, 63 MPa, 48.3MPa, 55MPa and 64.8 MPa.

Table 2: Mix Proportion (Kg/m³)

Mix Name	NF ₂ G ₈	RF ₂ G ₈	RCF ₂ G ₈	RCRF ₂ G ₈	RCGF ₂ G ₈	RCFF ₂ G ₈
Fly Ash	108.5	108.5	108.5	108.5	108.5	108.5
GGBS	378	378	378	378	378	378
Sand	660	660	660	660	660	660
Glass powder	-	-	-	-	400	-
Glass Hollow sphere	-	-	-	-	40	-
Rubber crumb	-	-	-	13.5	-	-
Normal Aggregate 10mm	1250	-	-	-	-	-
Normal Aggregate 20mm	300	-	-	-	-	-
Recycled Aggregate 10mm	-	1100	550	550	550	550
Recycled Aggregate 20mm	-	265	132.5	132.5	132.5	132.5
Copper Slag10mm	-	-	750	750	750	750
Copper Slag 20mm	-	-	186	186	186	186
Steel Fibres	-	-	-	-	-	4.865
Nylon Fibres	-	-	-	-	-	4.865
Alkaline Solution	250	250	250	250	250	250
Super plasticizer	7.25	7.25	7.25	7.25	7.25	7.25
Additional water	55	55	60	60	65	65

5 SPECIMEN PREPERATION

A total of 90 Cubes measuring 100 mmx100mmx100mm were cast using the mixtures specified for geopolymer concrete (GPC) outlined in Table 2. The process was carried in two stages, dry mix and wet mix. Initially, aggregates, fly ash, GGBS, rubber crumb, glass powder and fibres was mixed in rotating type pan mixer for 2 minutes. 70% distilled water containing superplasticizer was poured and mixed for a minute. Alkaline solution was then mixed and poured into the wet material and mixing was continued for 2 minutes in pan mixer. It was then hand mixed to ensure homogeneity in the mixture. The concrete was

then casted in 100 mm cube moulds and table vibrator was used for compaction. A thermocouple was placed in centre of the cube to monitor temperature during the heating process inside the Vertical split furnace. Following casting the geopolymer concrete cubes were subjected to oven curing at around 70°C. The oven was kept on for alternate eight hours for three days. Among 90 cubic specimens casted, 18 specimens were allocated for compressive strength evaluations at room temperature while the remaining 72 specimens were employed for high-temperature tests.

6 TEST PROCEDURE AND RESULTS

The high temperature resistance of geopolymer concrete with varying mix proportion was examined by subjecting the specimens to different high temperatures. Specimens were heated to specified target temperatures (200, 400, 600, 800 °C) in a programmable electrical furnace at a heating rate of 5°C/min. The furnace door was shut simulating uniform heating of the concrete from all sides. Thermocouples mounted in the centre of specimens were used to assess temperature differentials during heating using data logger. On the achievement of target temperature, the specimens were maintained at that temperature for 60 minutes to achieve thermal stability before cooling naturally. After cooling specimens were checked for spalling. This was followed by mass loss check and compression test. A small piece of sample obtained from the crushed concrete after compression test was prepared for SEM analysis after gold coating.

7 RESULTS

▪ Compressive Strength Development

To assess strength development prior to fire exposure, tests for compressive strength were conducted on the concrete specimens. Fig.1 illustrates the compressive strength development of the five concrete types. Concrete specimens with natural aggregates showed maximum strength of 76 MPa, while the same reduced to 63 MPa with the use of 50% copper slag and 50% recycled aggregates and to 58 MPa with the use of 100% recycled aggregates. Addition of rubber crumb, glass powder further reduced the compressive strength while fibre addition slightly improved the strength.

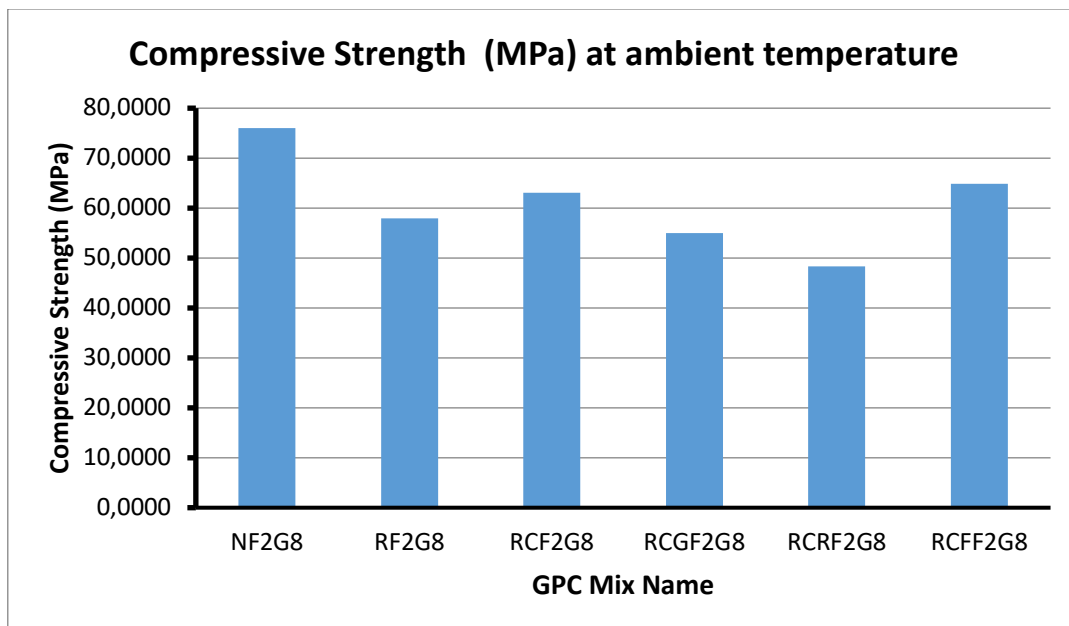


Figure1. Compressive strength of geopolymer concrete at ambient temperature

▪ *Color Changes, Surface Cracking and Spalling Tendency*

After exposure to various temperature ranges, noticeable color changes occurred in the geopolymer concrete samples. At 200°C, the color change was minimal while a slight light brown tinge appeared at 400°C. At 650°C, the color of the surface of geopolymer concrete specimens shifted to a light brown hue with small black areas in the specimens containing rubber and fibres which further darkened at 800°C. A clear difference in color was observed at 800°C in all specimens. Some red spots were also seen at 800°C in specimens containing glass powder and copper slag. These color changes were attributed to the high iron oxide content. Black spots and small pores were seen due to burning of rubbers and fibres. Red spots were also due to dehydration of geopolymer binders and micro structural changes within the aggregates. Slight thermal surface cracking was seen in specimens with normal aggregates but the specimens containing recycled aggregates at 800°C showed prominent surface cracking which again reduced in specimens containing rubber, fibres and glass powder. Burning of fibre and rubber at high temperature creates voids and finer channels which help in pore pressure dissipation while fibres increase tensile strength. No spalling was seen in any specimen revealing better resistance of spalling in geopolymer concrete. This resistance is attributed to geopolymer concrete's higher inherent tensile strength. However, number of burst bumps were seen at higher heating rates.

▪ *Residual Strength after Fire Exposure*

Residual compressive strengths of concrete specimens after subjection to different temperatures were evaluated. Strength in all specimens decreased after exposure to 200 °C while most of the specimens showed enhancement in strength in the range of 400 °C to 600 °C due to further geopolymerization during fire exposure. However, at higher temperature of 800°C all concrete types experienced significant strength loss except the one with glass powder which again showed improvement in compressive strength owing to sintering action of glass powder at high temperature. Fig. 2 depicts the residual compressive of geopolymer concrete as a function of the test temperature. As illustrated in Fig. 2, the compressive strength of geopolymer concrete experiences a rapid decline in NF₂G₈ and RF₂G₈ with increasing exposure temperature. With inclusion of copper slag, rubber crumb and fibres the rate of reduction decreased owing to thermal stability of copper slag and formation of pores by burning of rubber crumb and fibres.

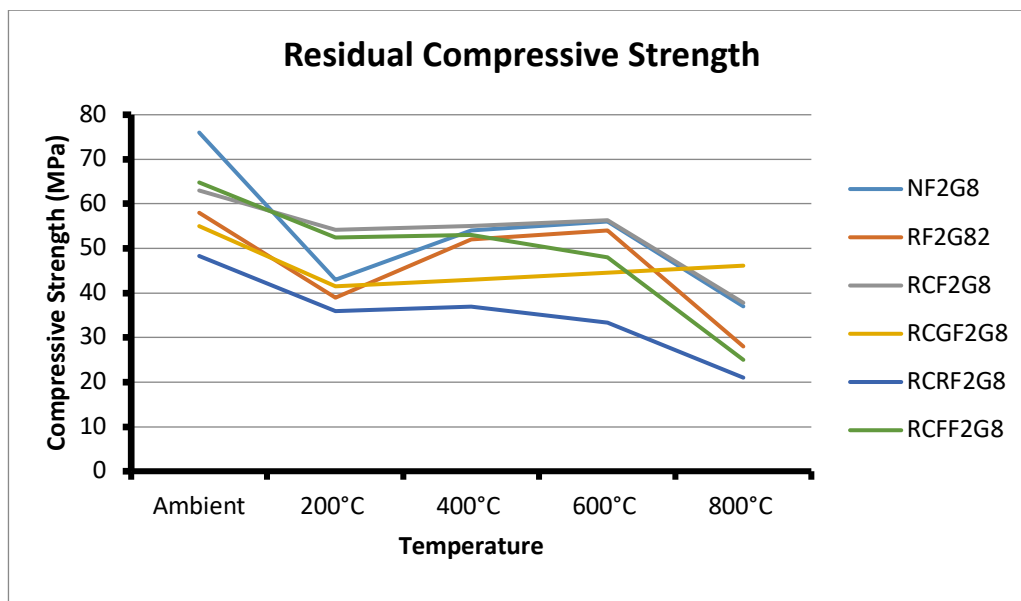


Figure 2. Residual Compressive strength with rising temperature in various mixes of GPC

▪ *Mass Loss And Sem Analysis*

The mass loss in concrete cubes after exposure to high temperature was determined by comparing the masses of the cubes before and after exposure. Fig. 3 illustrates the average mass loss in the six types of concrete after exposure to different temperatures. Increasing trend in mass loss can be observed at all temperatures. The majority of mass loss occurred at 600°C and 800°C. Maximum loss of 12.3% was seen in RF₂G₈ at 800°C, followed by 12.1% in RCGF₂G₈ at 600°C and 11% in RCF₂G₈ at 600°C. Minimum loss was seen in NF₂G₈ at all temperatures followed by RCF₂G₈ and RCRF₂G₈.

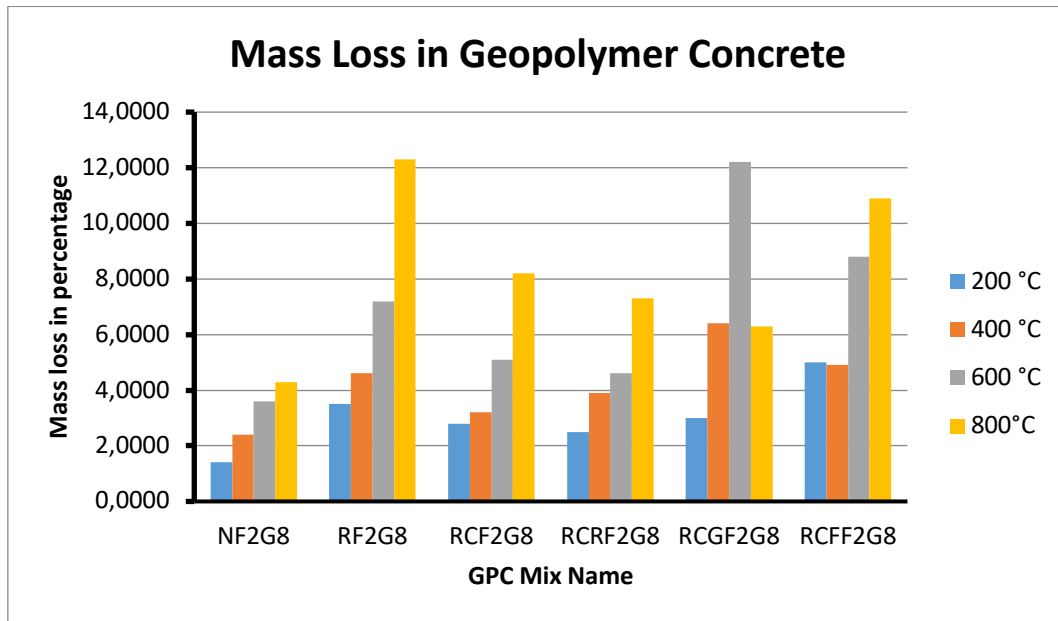
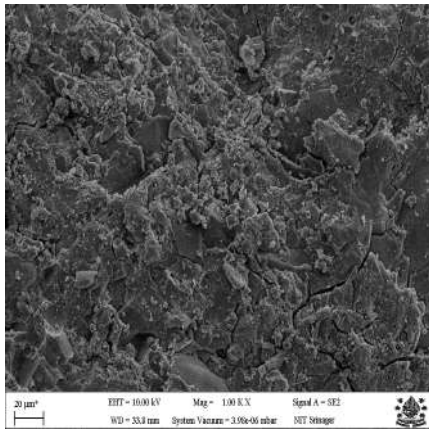
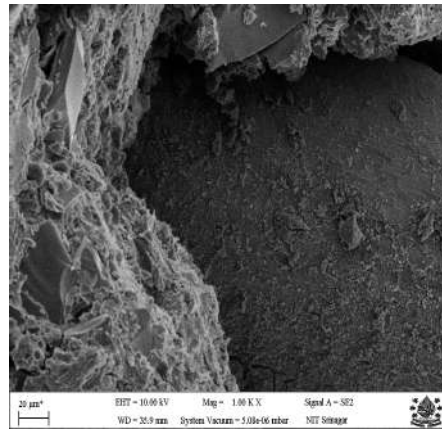


Figure 3. Mass loss with rising temperature in various mixes of GPC

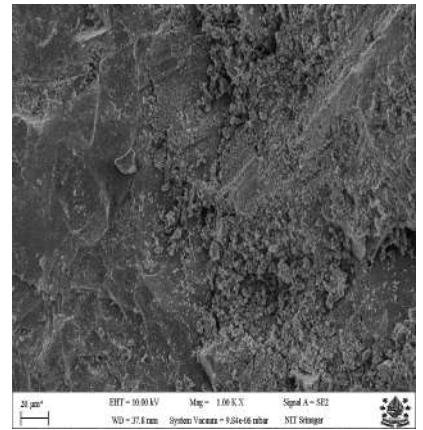
Scanning electron microscopy (SEM) was used to investigate the microstructures of geopolymer concrete. SEM images of Fig. 4A to 4L reveal densification of the geopolymer microstructures with increasing temperature up to 600°C. This densification occurs due to further geopolymerization and sintering action of fly ash with increasing temperature, resulting in a stable microstructure at high temperature. The increased denseness of the microstructure at this temperature correlates with the strength enhancement. Fig 4G, 4J shows pores formed by melting of rubber and nylon fibres while as steel fibres remain intact as shown in Fig 4I,4J 4K. Also sintering of glass powder can also be seen in Fig. 4D and 5L, Fig. 5B and 5H while cracks are shown in 4C, 4G, 4J, 4L. Copper slag in GPC is shown in 4A and 4C.



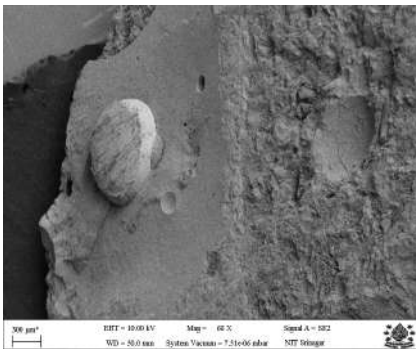
A



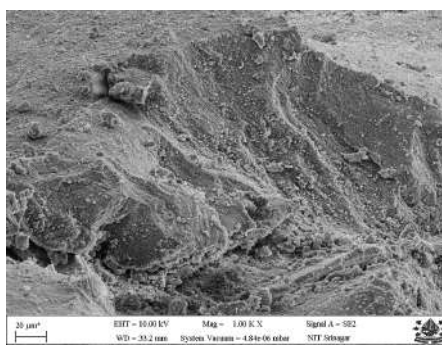
B



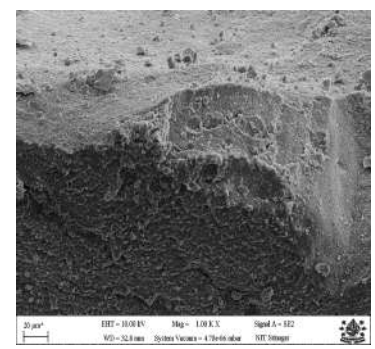
C



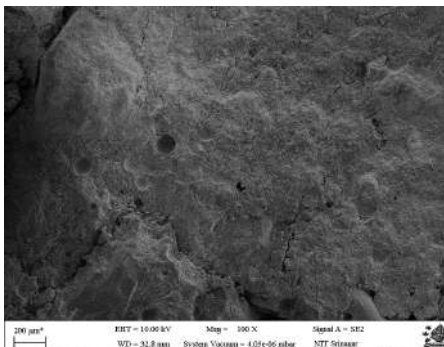
D



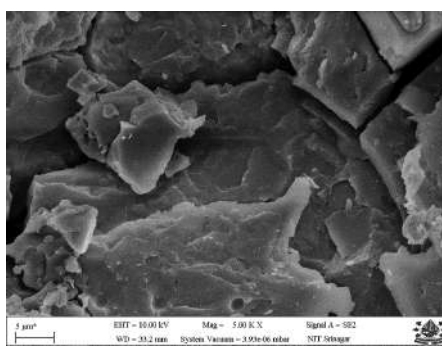
E



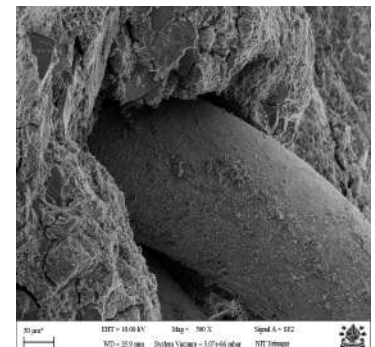
F



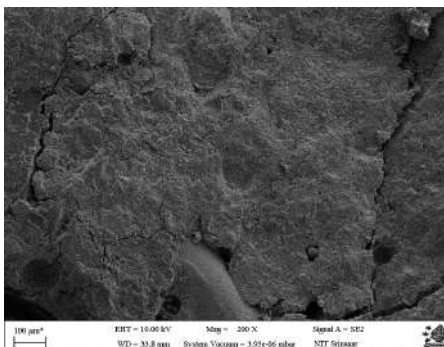
G



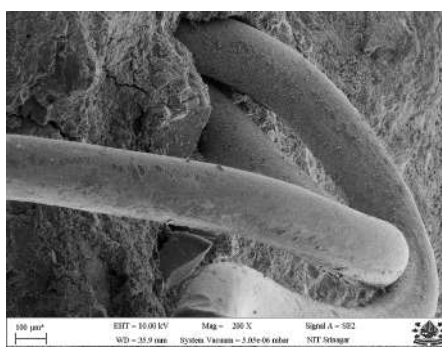
H



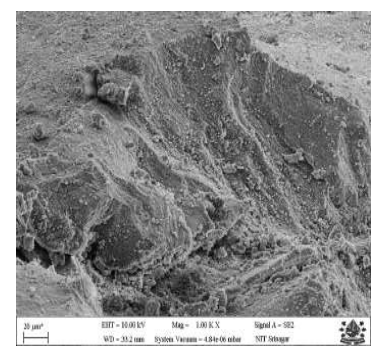
I



J



K



L

Figure 4. SEM images of various mixes of geopolymer concrete at varying temperature

8 CONCLUSION

To assess the performance of geopolymer concrete at high temperature, the influence of exposure temperature on the fire resistance in terms of residual strength of geopolymer concrete was examined. 72 cubes were subjected to high temperature profiles. The study compared the residual strength, mass loss and spalling of GPC specimens after exposure to various temperature. In addition microstructure of GPC was observed using SEM images. The conclusions reached from the test results are as follows:

- Geopolymer concrete demonstrates superior fire resistance. Out of the 72 geopolymer concrete specimens exposed to temp varying from 200°C to 800°C, none showed signs of spalling.
- Various temperature exposures induced color changes in geopolymer concrete samples, ranging from minimal at 200°C to noticeable shifts at 400°C and 650°C, with prominent changes observed at 800°C. Color alterations were attributed to binder content and structural transformations within aggregates. Thermal cracking and spalling resistance were noted, with enhancements attributed to rubber, fibre, and glass powder additives.
- Minor surface cracking was visible in GPC specimens exposed to temperatures up to 800°C. Specimens with recycled aggregates showed prominent surface cracking which further reduced with addition of copper slag, rubber and fibres.
- The mass loss of concrete samples due to high temperature was assessed by comparing pre and post exposure masses. Overall, an increasing trend in mass loss was observed across different temperatures, with the highest losses occurring at 600°C and 800°C. Maximum loss of 12.3% was seen in RF₂G₈ at 800°C, followed by 12.1% in RCGF₂G₈ at 600°C and 11% in RCFF₂G₈ at 600°C. Minimum loss was seen in NF₂G₈ at all temperatures followed by RCF₂G₈ and RCRF₂G₈.
- The residual compressive strength showed decrease at 200°C which was followed by enhancement between 400°C to 600°C due to further geopolymerization. At 800°C, significant strength loss occurred in all types except those with glass powder, which improved due to sintering. NF₂G₈ and RF₂G₈ exhibited rapid declines in strength with increasing temperature, while inclusion of copper slag, rubber crumb and fibres slowed down the reduction rate due to pore formation.

REFERENCES

1. Manzoor, T., Bhat, J.A. & Shah, A.H. Advancements in Geopolymer Concrete: A State-of-the-Art Analysis of Its Mechanical and Durability Features. *Iran J Sci Technol Trans Civ Eng* ; 2023
2. Tawzia Manzoor, Javed Ahmad Bhat, Asif H. Shah, Performance of geopolymer concrete at elevated temperature – A critical review, *Construction and Building Materials*, Volume 420, 2024, 135578, ISSN 0950-0618; 2024
3. A.H. Shah, U. K. Sharma, P. Kamath, P. Bhargava, G. R. Reddy, and T. Singh. ‘Fire performance of earthquake-damaged reinforced-concrete structures’, *Materials and Structures/Materiaux et Constructions*, vol. 49, no. 7, pp. 2971–2989; 2016
4. Jawahar, J. & Lavanya, D & Sashidhar, Chundpalle. Performance of Fly Ash and GGBS Based Geopolymer Concrete in Acid Environment. *International Journal of Research and Scientific Innovation*. 3. 101-104; 2016
5. Amran, Mugahed & Huang, Shan-Shan & Debbarma, Solomon & Rashid, Raizal. Fire resistance of geopolymer concrete: A critical review. *Construction and Building Materials*. 324. 126722. 10.1016/j.conbuildmat.2022.126722; 2022
6. Miltiadis, S.K., Giannopoulou, I., Tahir, M.F.M. et al. Upgrading Copper Slags to Added Value Fire Resistant Geopolymers. *Waste Biomass Valor* 11, 3811–3820 ; 2020.
7. Arunachalam, N.; Maheswaran, J.; Chellapandian, M.; Ozbakkaloglu, T. Effective Utilization of Copper Slag for the Production of Geopolymer Concrete with Different NaOH Molarity under Ambient Curing Conditions. *Sustainability*, 14, 16300. doi.org/10.3390/su142316300; 2022

8. Chakrawarthy, V.; Dharmar, B.; Avudaiappan, S.; Amran, M.; Flores, E.S.; Alam, M.A.; Fediuk, R.; Vatin, N.I.; Rashid, R.S.M. Destructive and Non-Destructive Testing of the Performance of Copper Slag Fibre-Reinforced Concrete. *Materials*, 15, 4536. doi.org/10.3390/ma15134536;2022
9. Ahmed M. Tahwia, Ashraf M. Heniegal, Mohamed Abdellatief, Bassam A. Tayeh, Mohamed Abd Elrahman, Properties of ultra-high performance geopolymer concrete incorporating recycled waste glass, *Case Studies in Construction Materials*, Volume 17, 2022, e01393, ISSN 2214-5095,
10. Levent Bostanci, Effect of waste glass powder addition on properties of alkali-activated silica fume mortars, *Journal of Building Engineering*, Volume 29, 2020, 101154, ISSN 2352-7102,
11. Mugahed Amran, Ali M. Onaizi, Diyar N. Qader, G. Murali, Innovative use of fly ash-finely powdered glass cullet as a nano additives for a sustainable concrete: Strength and microstructure and cost analysis, *Case Studies in Construction Materials*, Volume 17, 2022, e01688, ISSN 2214-5095,
12. Figueiredo, F.P., Huang, SS., Angelakopoulos, H. et al. Effects of Recycled Steel and Polymer Fibres on Explosive Fire Spalling of Concrete. *Fire Technol* 55, 1495–1516 ;2019.
13. Marija Jelcic Rukavina, Ana Baricevic, Marijana Serdar, Martina Grubor, Study on the post-fire properties of concrete with recycled tyre polymer fibres, *Cement and Concrete Composites*, Volume 123, 2021, 104184, ISSN 0958-9465,
14. F. Hernández-Olivares, G. Barluenga, Fire performance of recycled rubber-filled high-strength concrete, *Cement and Concrete Research*, Volume 34, Issue 1, 2004, Pages 109-117, ISSN 0008-8846.
15. Mehdi Mousavimehr, Mahdi Nematzadeh, Predicting post-fire behavior of crumb rubber aggregate concrete, *Construction and Building Materials*, Volume 229, 2019, 116834, ISSN 0950-0618,

EXPERIMENTAL INVESTIGATION ON THE CONCRETE BEHAVIOR IN THE COOLING PHASE OF THERMAL CYCLES AT HIGH TEMPERATURE

Jan Lyzwa¹, Jochen Zehfuss²

ABSTRACT

The application of natural fire models is an alternative to the use of the common ISO 834 standard fire in fire safety design, which requires the load-bearing capacity of structural components and entire structures to be designed for the entire fire duration, including the cooling phase. Due to the thermal inertia, concrete components undergo a delayed heating during the cooling phase of fire exposure.

The final draft of Eurocode 2-1-2 (FprEN 1992-1-2) [1] includes thermal and thermo-mechanical material properties for normal and high performance concrete. The included values were derived from experimental investigations of heated components based on the thermal exposure similar to the ISO 834 standard fire. However, the fire safety design of the concrete components and structures is more realistic and often more profitable when individual natural fires are considered instead of the standard fire. In addition to [2] in this paper pursued experimental investigations on thermo-mechanical material behaviour of normal (NSC) and high performance concrete (HPC) in the cooling phase after high temperatures are presented.

Keywords: Thermo-mechanical properties; natural fires; steady-state tests; transient creep tests; high performance concrete (HPC); residual mechanical properties

1 INTRODUCTION

In [2,3] thermo-mechanical properties of concrete during the cooling phase were investigated. In order to determine the temperature-dependent material behaviour, steady-state and transient creep tests were carried out. The steady-state tests showed that after cooling the strength of normal concrete (NSC) and of high performance concrete (HPC) is always lower than the strength at the maximum temperature as specified in FprEN 1992-1-2 [1]. Furthermore, some results showed that the strength continues to decrease during the cooling phase. In summary, the evaluation of the transient creep tests showed that up to a maximum temperature of 500 °C the derived stress-strain curves during the heating and cooling phases are only marginally different. In addition, the results showed that the stress-strain curves during the cooling phase significantly depend on the maximum temperature reached. Since the temperature range from 500 °C to 700 °C is relevant to the design of concrete members, further research efforts are required for this temperature range in order to formulate reliable design provisions. This is the objective of the paper, that is about an experimental campaign on concrete thermo-mechanical properties of NSC and HPC in the cooling phase.

¹ Dr.-Ing., Technische Universität Braunschweig, Institute of Building Materials, Concrete Constructions and Fire Safety (iBMB)
e-mail: j.lyzwa@ibmb.tu-bs.de

² Professor, Technische Universität Braunschweig, Institute of Building Materials, Concrete Constructions and Fire Safety (iBMB)
e-mail: j.zehfuss@ibmb.tu-bs.de

2 EXPERIMENTAL INVESTIGATION AND EVALUATION

2.1 Experimental Setup

The thermo-mechanical properties of a normal concrete with a target strength $f_c = 30$ MPa (C30/37) and of a high performance concrete with a target strength $f_c = 80$ MPa (C80/95) were investigated. The tests were carried out on concrete cylinders (approx. $\varnothing = 80$ mm and $h = 240$ mm).

The test procedure was developed on the basis of RILEM recommendations. In steady-state tests, the specimens are heated up to a maximum (reference) temperature and then they are progressively loaded until failure, while the axial deformation is recorded. In transient creep tests the specimens are subjected to a constant load and then they are heated until failure, while the axial deformation is measured. The general experimental setup for both test procedures is shown in Figure 1. With the results of the steady-state tests the strength at different temperatures can be determined. The transient creep tests are used to study concrete transient creep with the objective of deriving the stress-strain relationship during a heating and cooling process.



Figure 1. Experimental setup for steady-state and transient-creep tests

In order to investigate concrete behaviour in the cooling phase, the test procedures of RILEM recommendations were modified. In the steady-state tests the specimen were heated to a maximum temperature and subsequently cooled down to a lower temperature. After cooling, the load was increased until failure. In the transient creep tests, different load levels were introduced. At each load level, the specimen was heated to the specified maximum temperature and subsequently cooled down to 20 °C under the constant load. Afterwards the load was increased until failure. This procedure allows to determine the residual compressive strength as an additional material characteristic in the transient creep tests.

In a first step the compressive strength of two cylinders at ambient temperature for each concrete (NSC and HPC) was determined. The mean value of these tests is following referred as reference strength of the two concretes. For the NSC a reference strength of 38.92 MPa and for the HPC a reference strength of 64.10 MPa were determined. Although the target strength of the HPC was not reached, the concrete is still dedicated to the concrete class of high performance concrete. Compared to the conducted tests in [2] the compression facility was modified. While all specimen had to be clamped into the facility with a load of 20 kN, the specimen presented in this paper were clamped with a load of only approximately 5 kN. Thus, in both test series the clamping load is referred to as 0 % load utilization level α .

In all tests, the specimen were heated up with a rate of 4 K/min to a maximum temperature. Subsequently, the furnace kept this temperature for 120 minutes to guarantee a homogenous temperature distribution in

the cross-section of the cylinders. The cooling regimes differ between the steady-state and the transient creep tests. Following the evaluation of the steady-state and transient creep tests is presented.

2.2 Evaluation of the steady-state tests

In the steady-state tests, the specimen were investigated at a constant temperature and for an increasing mechanical load until failure, as described previously. As these tests do not take the transient creep of concrete into account, they can not represent the deformation behaviour of the components in case of fire. The steady-state tests provide the decrease in strength for a heating-cooling exposure. The temperatures of the thermal cycles in the steady-state tests are shown in Table 1.

Table 1. Temperature programs of steady-state tests

Concrete	Maximum temperature [°C]	Cooled level [°C]
NSC HPC	600	20
	600	300
	700	500
	800	300
	800	500

After reaching the maximum temperature and finishing the subsequent holding time (120 minutes) the furnace was cooled down to lower level as fast as possible (program controlled, with a closed furnace door). This (cooler) temperature was also kept constant for 120 minutes. Finally, the mechanical load was increased until failure. Due to test duration the temperature program 600 °C – 20 °C differs to the other four temperature programs. Here, after reaching the maximum temperature and finishing the subsequent holding time the furnace was completely turned off. From a furnace temperature of approximately 300 °C, the furnace door was opened and the specimen were exposed to natural cooling at room temperature. Finally, the mechanical load was increased until the test specimen failed. The time between opening the furnace door and the increasing of the load took approximately 1,010 minutes (\pm 16.8 hours). This cooling regime was also applied in the transient creep tests.

The temperature-dependent decrease in strength determined from the steady-state tests (SST) in [2] is shown in Table 2 and expanded to include the investigations carried out in this paper (highlighted in grey). The decrease in strength measured in the experiments when the lower temperature level was reached in the cooling phase is compared to the values in FprEN 1992-1-2 for normal-strength concrete ($f_{ck} < 70$ MPa) with siliceous aggregates and high-strength concrete ($f_{ck} \geq 70$ MPa) for the respective maximum temperature reached in the tests carried out. However, the investigated HPC in [2] reached a strength of 90.84 MPa. For verification purposes some tests were repeated. In [2] it was stated that steady-state tests have shown that:

- After reaching the maximum temperature, with a subsequent cooling phase, the strengths for both normal concrete and high-strength concrete are always below the values at maximum temperature specified in prEN 1992-1-2,
- In addition, the results tended to show that the strength continues to decrease during the cooling phase to a lower temperature level.

The investigations presented in this paper verify the first statement for NSC. For maximum temperatures up to 600 °C this seems also to account for HPC. For maximum temperatures between 700 °C to 800 °C the strength during the cooling phase seems to be on a level respectively above the given values in FprEN 1992-1-2 at maximum temperature. Doubtless, during the cooling phase down to the cooler level the strength of NSC and HPC does not regain the strength to given values at minimum temperature (e.g. HPC 800 °C – 300 °C: SST 0.27 < 0,75 FprEN 1992-1-2). Thus, the strength during the cooling phase significantly depends on the reached maximum temperature.

Table 2. Comparison of the decrease in strength in the cooling phase from steady-state tests (SST) at the lower temperature to FprEN EN 1992-1-2 at the maximum temperature based on strength at ambient temperature

Temperature [°C]		Related compressive strength $f_{c,t}/f_{ck}$ [-]			
		Normal-strength concrete (NSC)		High-strength concrete (HPC)	
SST	FprEN	SST	FprEN	SST	FprEN
20	20	1,00	1,00	1,00	1,00
100 – 20	100	0,82	1,00	0,72	1,00
300 – 200	300	0,78	0,85	0,71	0,75
500 – 200	500	0,54	0,60	0,40	0,60
700 – 500	700	0,28	0,30	0,28	0,30
700 – 300	700	0,23	0,30	0,26	0,30
600 – 20	600	0,33 0,31*	0,45	0,34	0,45
600 – 300	600	0,25 0,32*	0,45	0,38 0,35*	0,45
700 – 500	700	0,26	0,30	0,33	0,30
800 – 300	800	0,17 0,13*	0,15	0,27	0,15
800 – 500	800	0,10 0,11*	0,15	0,28	0,15

*Repeated Test

2.3 Evaluation of the transient creep tests

In the transient creep tests, first a clamping load of approximately 5 kN was applied. Subsequently, the mechanical load was increased to the target load utilization level α and kept constant for the entire temperature program. After the specimen reached ambient temperature again the load was increased until mechanical failure (see 2.4 Residual compressive strength). Based on the determined reference compressive strength at ambient temperature utilization levels of approximately 0%, 10 %, 15%, 20%, 30%, 40% and 45% were investigated. The resulting strain from the clamping load is neglected and set to zero. The scope of the experimental investigation is summarized in Table 3.

Table 3. Scope of the transient creep tests

NSC HPC	20 - 500 - 20 [°C]	0%	10%	20%	30%	45%
	20 - 600 - 20 [°C]	0%	10%	20%	30%	40%
	20 - 700 - 20 [°C]	0%	10%	20%	25%	-
	20 - 800 - 20 [°C]	0%	10%	NSC 15% HPC 20%	-	-

Exemplarily, in Figure 2 and Figure 3 the temperature program as well as the temperature-strain relation for HPC (20 - 600 - 20 [°C]) is illustrated. The deformation resulting from the determination of the residual strength is not included. The utilization level of 0% represents the almost unhindered thermal expansion ε_{th} of the specimen (blue curve). The solid curves show the deformation behaviour during the heating phase and the dotted curves during the cooling phase. The results demonstrate that due to the constant stress level a partial superposition of the mechanical strain terms ε_m occurred during the thermal expansion ε_{th} (see 2.5

Temperature-dependent stress-strain curves). With a load utilization level of 40% failure occurred during the cooling phase at approximately 145 °C. The results indicate that the mechanical strain terms ϵ_m at maximum temperature and after the cooling phase are almost the same and that the thermal expansion ϵ_{th} (blue line) completely returns to origin. Furthermore, the resulting strains from the load and the transient creep of the concrete depending on the maximum temperature reached remain.

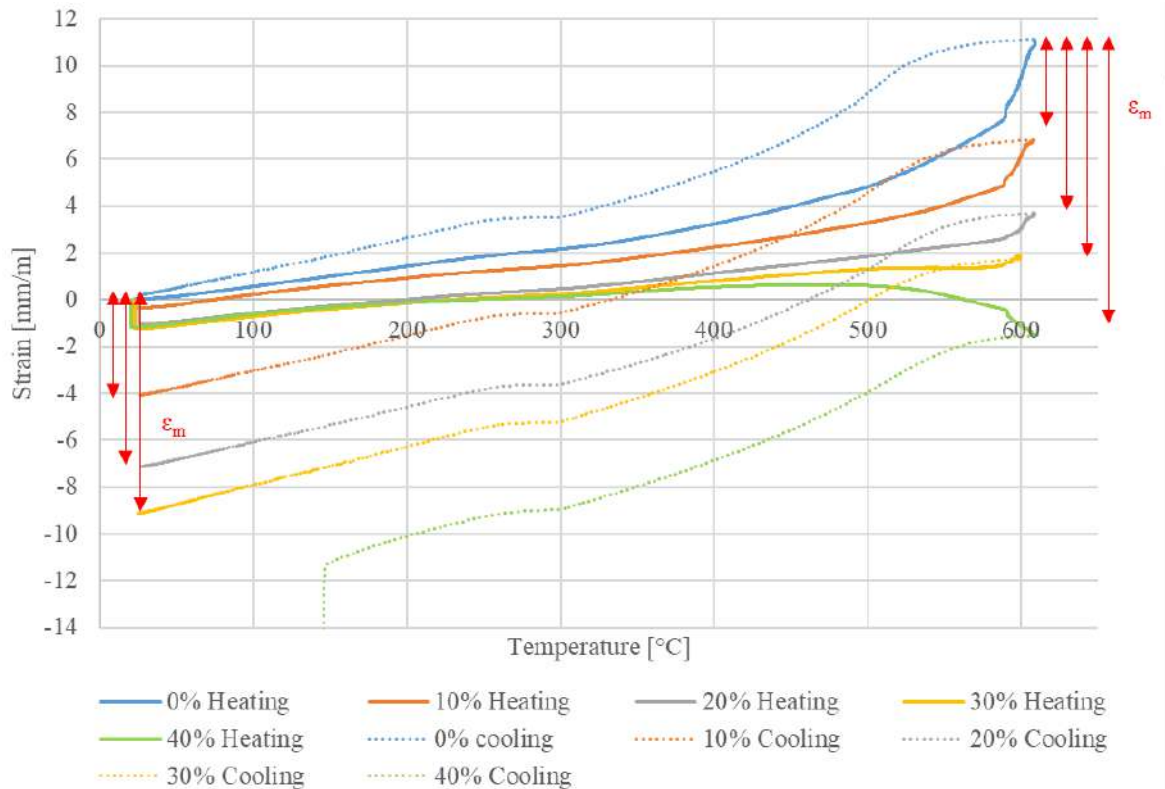


Figure 2. Temperature-strain relation in transient creep tests HPC 20 - 600 - 20 [°C]

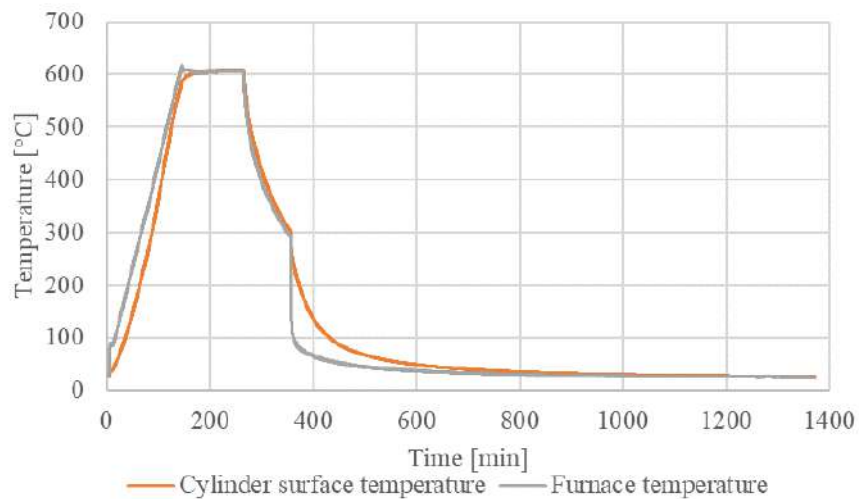


Figure 3. Temperature-strain relation in transient creep tests HPC 20 - 600 - 20 [°C], load utilization level 20%

2.4 Residual compressive strength

With regard to the residual compressive strength, a distinction must be considered as to whether it is regarded during or after the design period. For the application of natural fire the entire fire duration, including the cooling phase has to be considered. Thus, the residual strength can be examined at the last time step within the fire safety design or days, weeks or even months later. In [4] a literature review on residual strength of concrete is presented. It is specified that the time period of testing the specimen after

exposure to high temperatures has significant influence on the residual strength. Thus, after cooling due to the reaction of CaO to CH further decrease in strength can take place. Aside from that, due to the rehydration of unbounded cement particles a recovery in strength can occur.

In this paper the residual strength (transient creep tests, residual, TCTR) was determined within the time period of approximately 1,010 minutes between the door opening during the cooling phase at 300 °C and the load increase until mechanical failure. Therefore, different maximum temperatures as well as different load utilization levels were investigated. The related compressive strength (residual strength $f_{c,\theta,20^\circ C}$ / strength at ambient temperature f_{ck}) is summarized in Table 4 and compared to the given values in FprEN 1992-1-2. The results demonstrate that the residual strength of NSC is throughout below the given values in FprEN 1992-1-2 at maximum temperature (exception: 500 °C – 20°C, $\alpha = 20\%$ and 800 °C – 20°C, $\alpha = 10\%$). For maximum temperatures between 500 °C and 700 °C and a load utilization level of 0% during the thermal exposure this also seems to apply to HPC. With higher utilization levels ($\geq 10\%$) or a maximum temperature of 800 °C the decrease in strength is almost on a level or even above to the given values in FprEN 1992-1-2. This corresponds with statements in [5,6], that due to the thermal incompatibles between mortar and aggregate the residual strength is lower for unloaded specimen compared to loaded specimen during the thermal exposure.

Table 4. Comparison of the the residual strength from the transient creep tests (TCTR) to the decrease in strength according to FprEN EN 1992-1-2 at the maximum temperature based on strength at ambient temperature

Temperature [°C]		Related compressive strength $f_{c,\theta,20^\circ C}/f_{ck}$ [-] [-]											
		Normal-strength concrete (NSC)											
TCTR	FprEN	α	TCTR	α	TCTR	α	TCTR	α	TCTR	α	TCTR	FprEN	
500 – 20	500	0 %	0,43 0,56*	10 %	0,59	20 %	0,67 0,83*	30 %	0,55	45 %	0,49	0,60	
600 – 20	600	0 %	0,42 0,38*	10 %	0,34	20 %	0,41	30 %	0,40	40 %	0,40 ³	0,45	
700 – 20	700	0 %	0,27	10 %	0,21	20 %	0,22	25 %	0,25 ²	-		0,30	
800 – 20	800	0 %	0,13	10 %	0,20 0,20*	15 %	0,15 ¹	-		-		0,15	
		High performance concrete (HPC)											
TCTR	FprEN	α	TCTR	α	TCTR	α	TCTR	α	TCTR	α	TCTR	FprEN	
500 – 20	500	0 %	0,42	10 %	0,56	20 %	0,82 0,56*	30 %	0,82 0,51*	45 %	0,72	0,60	
600 – 20	600	0 %	0,44	10 %	0,48	20 %	0,52	30 %	0,53	40 %	0,40 ⁴	0,45	
700 – 20	700	0 %	0,34	10 %	0,36	20 %	0,37	25 %	0,38	-		0,30	
800 – 20	800	0 %	0,25	10 %	0,31	20 %	0,28	-		-		0,15	

*Repeated Test, ¹Failure during cooling phase 520 °C, ²Failure during cooling phase 330 °C, ³Failure during heating phase (holding time), ⁴Failure during cooling phase 145 °C

2.5 Temperature-dependent stress-strain curves

The temperature-dependent stress-strain curves can be derived from the transient creep tests, since this test procedure considers the transient creep of the concrete. According to FprEN 1992-1-2 the deformation behaviour (total strain ϵ) of heated concrete can be calculated by the sum of the thermal strain ϵ_{th} , the instantaneous stress-dependent strain ϵ_{θ} , the creep strain ϵ_{creep} and the transient state strain ϵ_{tr} . Due to the relatively short duration of fire tests, the classical material creep ϵ_{creep} is generally neglected. Thus, the total strain ϵ can be described by equation (1).

$$\varepsilon = \varepsilon_{th} + \varepsilon_{\theta} + \varepsilon_{tr} \quad (1)$$

In the transient creep tests, the thermal strain ε_{th} is determined from the non-loaded specimen (0 % load utilization). According to equation (2), the difference between the measured total strain ε and the thermal strain ε_{th} yields the mechanical strain ε_m , which contains the contributions of the instantaneous stress-dependent strain ε_{θ} and the transient state strain ε_{tr} . The stress-strain curves are derived from the mechanical strain ε_m . Here, for a given temperature the mechanical strains ε_m can be read from the temperature-deformation diagram (see Figure 2), transferred into a stress-strain diagram and connected to a temperature-dependent stress-strain curve. In this paper for each temperature program a stress-strain curve is created for the heating phase respectively for the cooling phase. Based on the transient creep tests, the mechanical strains ε_m are taken at the end of the heating phase (including the holding time of constant temperature) and at the end of the cooling phase (just immediately before the mechanical load is increased until failure). In Figure 4 and Figure 5 the developed stress-strain curve for NSC and HPC are shown.

$$\varepsilon_m = \varepsilon - \varepsilon_{th} \quad (2)$$

with

$$\varepsilon_m = \varepsilon_{tr} + \varepsilon_{\theta}$$

The evaluation of the stress-strain curves generally confirms the findings in [2], that up to a maximum temperature of 500 °C the stress-strain curves only slightly differ between the heating and the cooling phase. During the cooling phase, the material behavior of the concrete is significantly influenced by the damage of the specimen (maximum temperature). Transient state strain ε_{tr} is the difference in strain between concrete loaded at elevated temperature and concrete heated under load. This strain component arises during the first heating of concrete and is irreversible. In [7] it is stated that during the cooling process almost no further transient state strain ε_{tr} occurs.

In the well-known constitutive model in FprEN 1992-1-2 [1] according to equation (3) transient state strain ε_{tr} is included implicitly by the mechanical strain ε_m [8,9].

$$\sigma_c(\theta) = \frac{3\varepsilon_c f_{c,\theta}}{\varepsilon_{c1,\theta} \left(2 + \left(\frac{\varepsilon}{\varepsilon_{c1,\theta}} \right)^3 \right)} \quad (3)$$

where

$f_{c,\theta}$ is the compressive strength,
 $\varepsilon_{c1,\theta}$ is the strain corresponding to $f_{c,\theta}$.

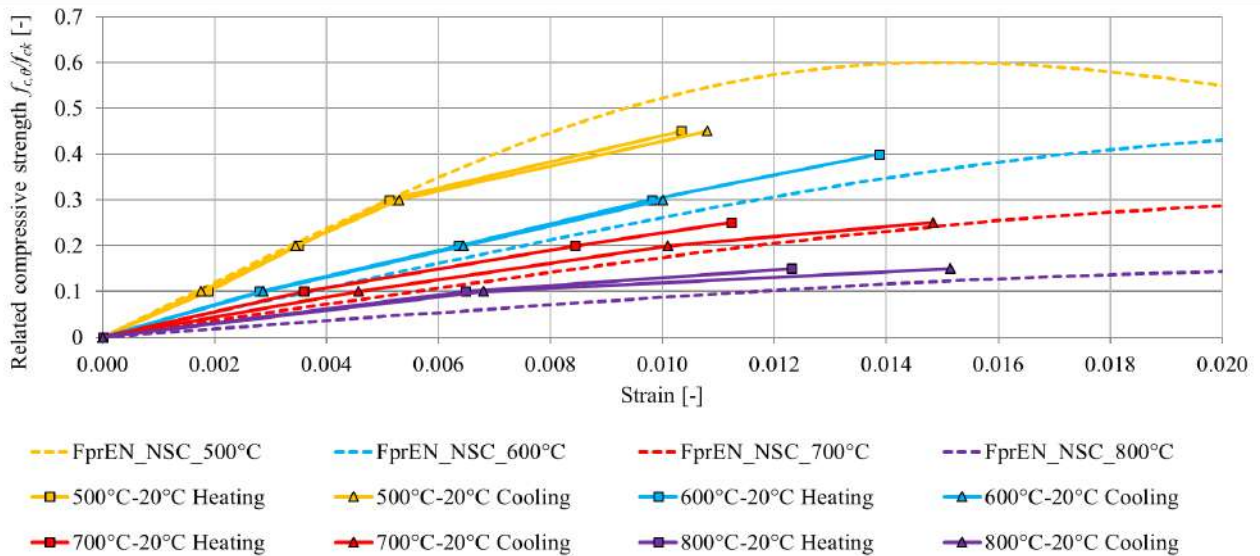


Figure 4. Derived stress-strain curves for NSC

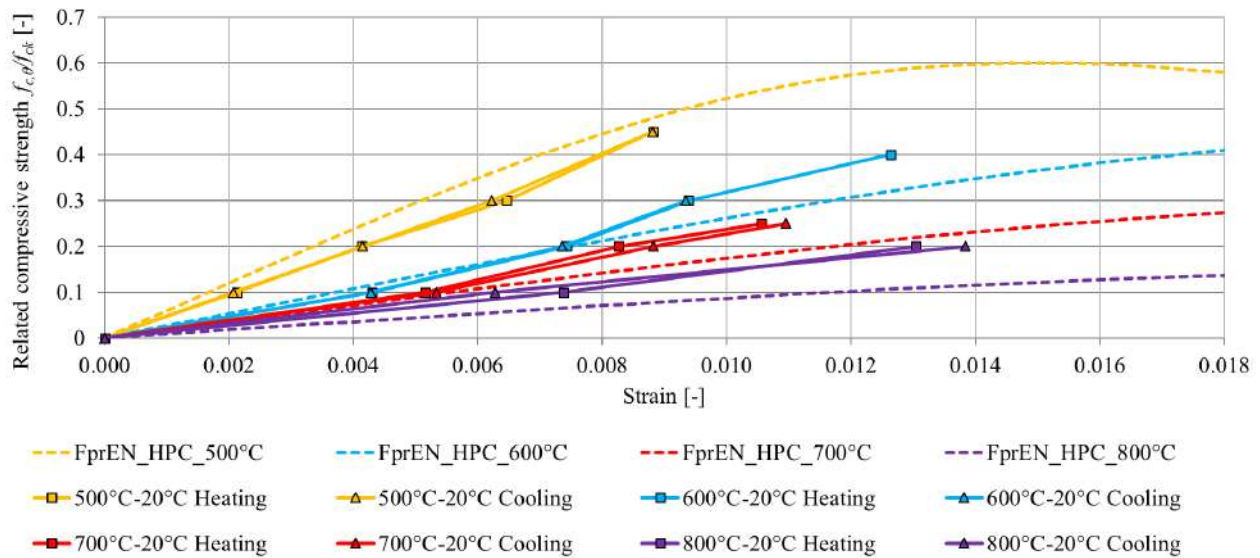


Figure 5. Derived stress-strain curves for HPC

Approach for the cooling phase in FprEN 1992-1-2

In FprEN 1992-1-2 [1] an approach is provided for the approximate consideration of the cooling behaviour of concrete. This approach has been transferred from EN 1994-1-2 [10]. Here, the basis is the stress-strain relationship for the maximum reached temperature. Based on the results of studies on the residual strength, the strength in the re-cooled state ($f_{c,\theta,20^\circ\text{C}}$) at $\theta = 20^\circ\text{C}$ is reduced by a factor φ , which ranges between 1.0 and 0.9, depending on the maximum temperature. Thus, the reduction in strength at maximum temperature is reduced again with a maximum of 10%. The values for the corresponding strain $\varepsilon_{c1,\theta}$ do not change, and the slope of the decreasing curve is also retained. In [5] it is specified that the residual strength can be even lower than 10% (up to 31%). However, the residual strength is not always determined immediately after the end of the cooling phase. Figure 6 shows an example of the temperature-dependent change in the stress-strain relationship for a concrete of strength class C40/50 with the subsequent transition to the cooling phase [1, 10].

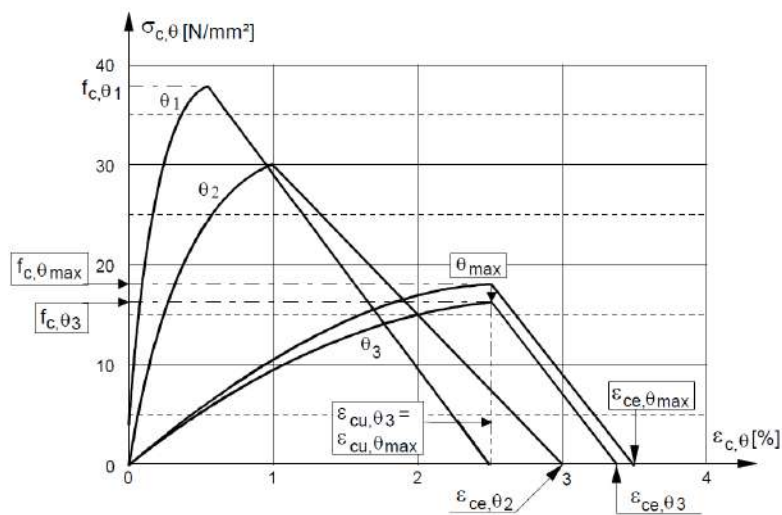


Figure 6. Stress-strain relationship for concrete C40/50; Heated to $\theta_1 = 200^\circ\text{C}$, $\theta_2 = 400^\circ\text{C}$, $\theta_{max} = 600^\circ\text{C}$ and subsequent cooling to $\theta_3 = 400^\circ\text{C}$ [10]

For $f_{ck} < 70\text{ MPa}$ for temperatures $< 100^\circ\text{C}$, there is no reduction in strength during the cooling phase. For temperatures between 100°C and 300°C , $\varphi = (0.0005 \cdot \theta_{max} + 1.05) \cdot (f_{c\theta_{max}}/f_{ck})$ is determined depending on the maximum temperature θ_{max} reached. From maximum temperatures $\geq 300^\circ\text{C}$, the compressive strength is reduced by 10% when the cooled again to 20°C . It should be noted that during the cooling

phases the strength is continuously reduced between the maximum temperature and the re-cooled state. For $f_{ck} \geq 70$ MPa and temperatures $20^\circ\text{C} \leq \theta_{max} < 1200^\circ\text{C}$ no further reduction during the cooling phase is considered [1]. Thus, the residual strength is assumed as at maximum temperature θ_{max} with $\varphi = f_{c\theta_{max}} / f_{ck}$. Based on the own carried out steady-state tests on NSC and HPC, a reduction factor $\varphi = 0.8 \cdot (f_{c\theta_{max}} / f_{ck})$ for temperatures $\geq 100^\circ\text{C}$ is recommend. The basic approach from FprEN 1992-1-2 is retained. The strength $f_{c,\theta,20^\circ\text{C}}$ after cooling to $\theta = 20^\circ\text{C}$ is considered. Furthermore, according to FprEN 1992-1-2 while the concrete is cooling, the strength is to be linearly interpolated between $f_{c,\theta,20^\circ\text{C}}$ and the strength $f_{c,\theta,max}$ at maximum temperature. Figure 7 and Figure 8 show the derived functions for the reduction factors $\varphi \cdot (f_{c\theta_{max}} / f_{ck})$ in the temperature range from 20°C to 800°C . Additionally the results from the steady-state tests (Table 2) and die residual strength for a load utilization level of 0 % (Table 4) are included in the Figures. Especially for the NSC the experimental results are in good accordance with the derived functions. Although, for a maximum temperature of 600°C the function considerable overestimates the strength during the cooling phase.

For the investigated HPC a reduction factor $\varphi = 0.8 \cdot (f_{c\theta_{max}} / f_{ck})$ overestimates the strength in the cooling phase for a maximum temperature of 100°C and a maximum temperature of 500°C . However, at a maximum temperature of 700°C , the strength during the cooling phase of HPC are covered very well with a reduction factor $\varphi = 0.8$. For a maximum temperature of 800°C the function underestimates the strength in the cooling phase. Furthermore, here the strength during the cooling phase is on a level with a maximum temperature of 700°C .

The residual strength ($f_{c,\theta,20^\circ\text{C}}$ after cooling to $\theta = 20^\circ\text{C}$) is covered quiet well for the NSC. Here, the strength is slightly underestimated. For maximum temperatures $\leq 500^\circ\text{C}$ the residual strength of HPC is overestimated. However, for maximum temperatures $\geq 600^\circ\text{C}$ the residual strength is underestimated when a reduction factor $\varphi = 0.8 \cdot (f_{c\theta_{max}} / f_{ck})$ is taken into account.

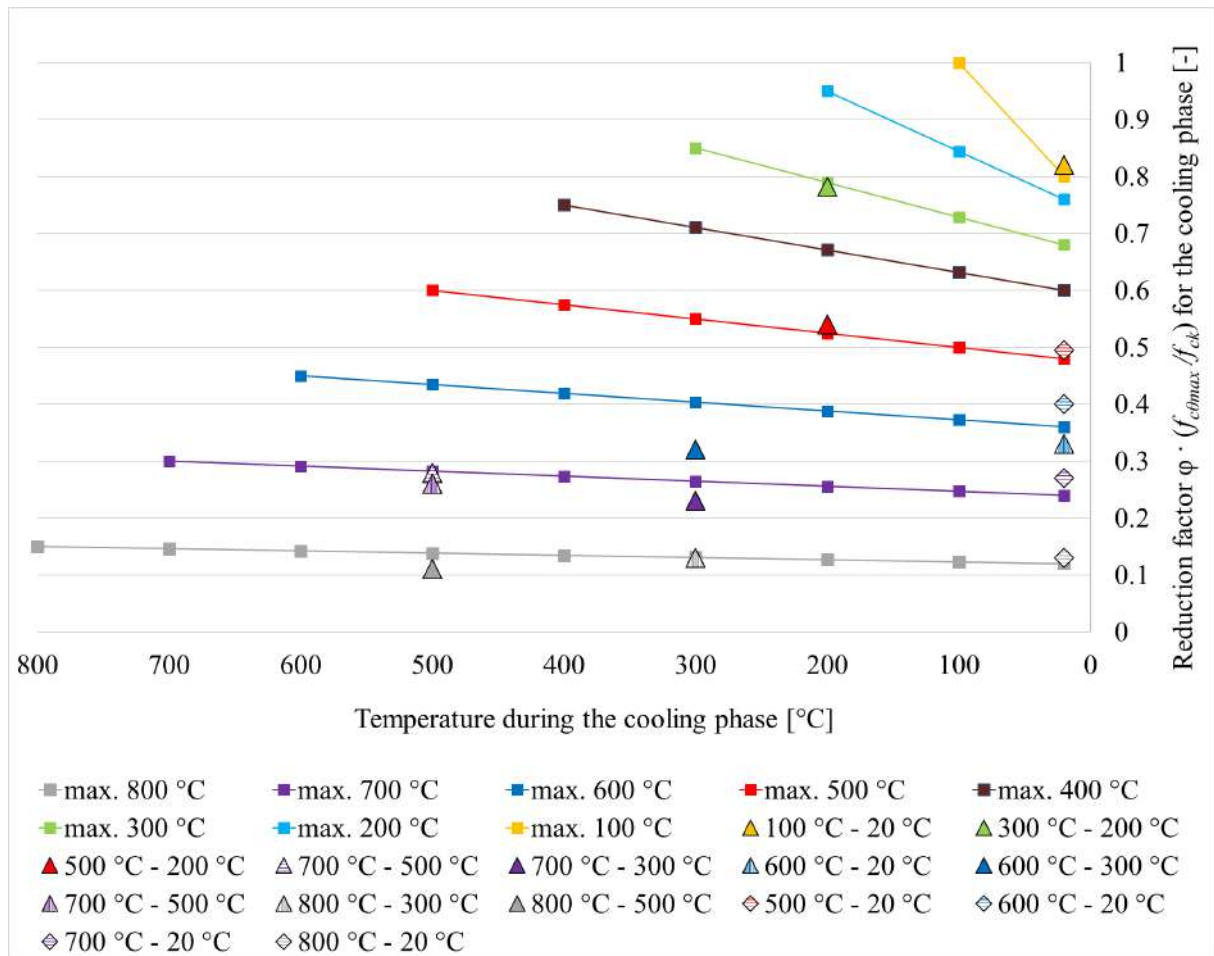


Figure 7. Reduction functions for the cooling phase up to the re-cooled state $f_{c,\theta,20^\circ\text{C}}$ depending on the maximum temperature θ_{max} and presentation of the experimental determined reduction factors $\varphi \cdot (f_{c\theta_{max}} / f_{ck})$ for NSC

The experimental investigations point out that the reduction factor φ in FprEN 1992-1-2 seems to overestimate the strength during the cooling phase. Therefore a reduction factor of at least $\varphi = 0.8 \cdot (f_{c\theta_{max}}/f_{ck})$ for maximum temperature ≥ 100 °C is recommended for NSC and HPC.

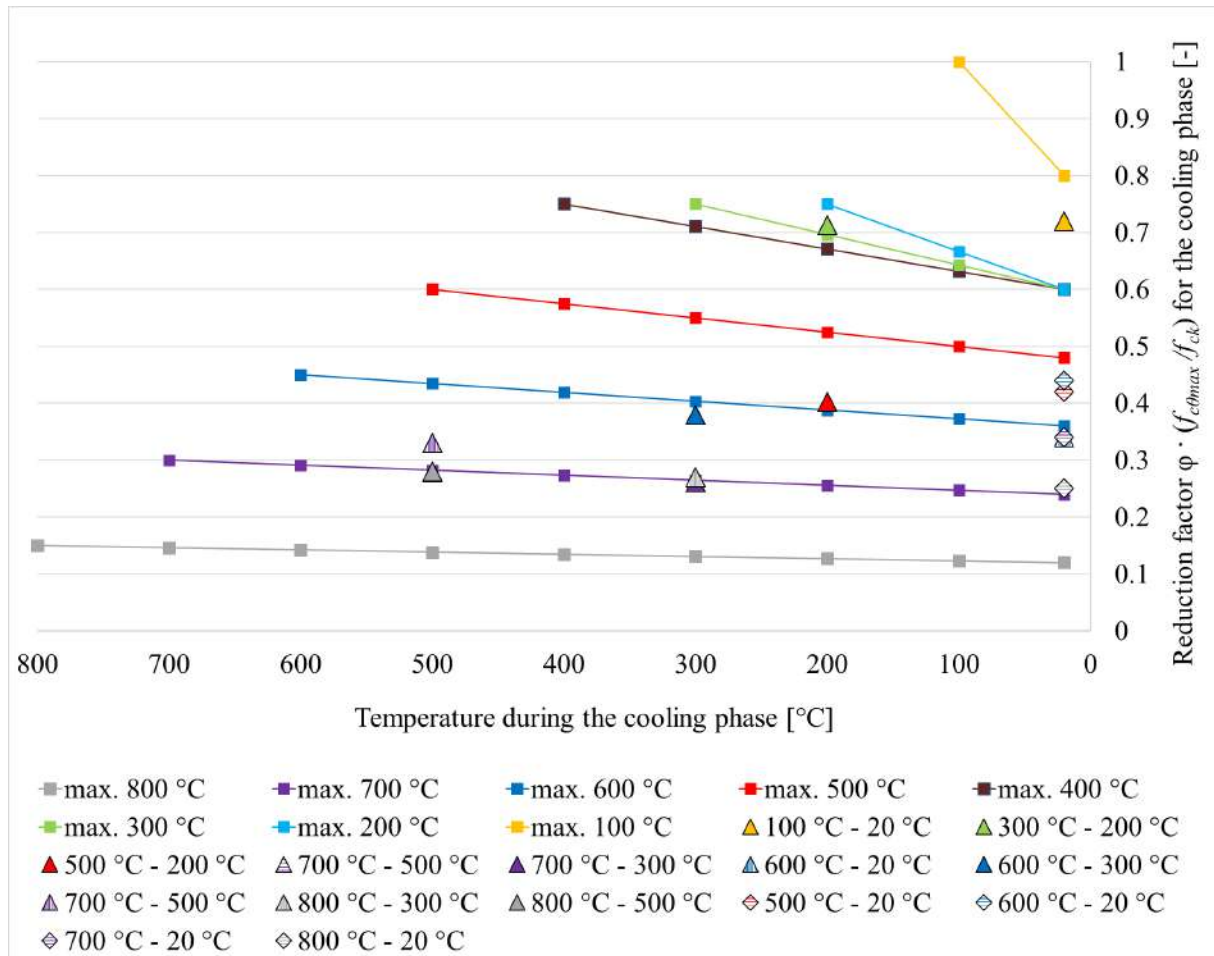


Figure 8. Reduction functions for the cooling phase up to the re-cooled state $f_{c,\theta,20^\circ\text{C}}$ depending on the maximum temperature θ_{max} and presentation of the experimental determined reduction factors $\varphi \cdot (f_{c\theta_{max}}/f_{ck})$ for HPC

3 CONCLUSIONS

In this paper, experimental investigations on the thermo-mechanical material behaviour of normal (NSC) and high performance concrete (HPC) in the cooling phase after high temperatures are presented. In order to determine the temperature-dependent material behaviour, steady-state and transient creep tests were carried out. The steady-state tests have shown for NSC that up to a maximum temperature of 800 °C the strength during the cooling phase is lower compared to the given values in FprEN 1992-1-2 at maximum temperature. This also applies to the investigated HPC up to a maximum temperature of 600 °. For higher temperatures, the measured values are on the same level or even above the standardized values at maximum temperature. The transient creep tests have shown that up to a maximum of 600 °C and utilization levels up to 45 % the stress-strain curves during the heating and cooling phases are only marginally different. For higher maximum temperatures, the difference in strain between the heating phase and the cooling phase increases. Here, additionally the difference in strain decreases as the utilization level below 45 % decreases. Additionally, at the end of the transient creep tests the residual strength at $\theta = 20$ °C has been determined. The lowest residual strengths have been measured on the unloaded specimen (0 % utilization).

The experimental results have been compared to the approach for the approximate consideration of the cooling behaviour of concrete according to FprEN 1992-1-2. The analysis indicates that for maximum

temperatures ≥ 100 °C the reduction factor φ should be modified (further reduced) for both NSC and HPC to ensure that the strength during the cooling phase is not overestimated. Further investigations are recommended, especially in the temperature range 500 °C to 600 °C, where quartz transformation processes of the aggregates occur.

ACKNOWLEDGMENT

The authors would like to gratefully acknowledge the German Research Foundation (DFG) for the financial support of the research project *Weiterführende Untersuchungen zur Beschreibung des Materialverhaltens von Beton in der Brandabkühlphase*, GZ: ZE 1053/3-1.

REFERENCES

1. FprEN 1992-1-2, Eurocode 2: Design of concrete structures. Part 1-2: General rules – Structural fire design, April 2023.
2. Zehfuß, J.; Lyzwa, J.: Theoretische und experimentelle Untersuchungen zur Erweiterung der Berechnungsgrundlagen unterschiedlicher Betone bei Naturbrandbeanspruchung (Theoretical and experimental investigation on the extension of basic calculations to different concretes under natural fires), DFG-Forschungsvorhaben (Research Project) GZ. ZE 1053/1-1, Final Report, 2019.
3. Lyzwa, J.; Zehfuß, J.: Experimental investigations of ultra-high performance concrete exposed to natural fires. *Fire Safety Journal*, Volume 125, 2021.
4. Botte, W. & Caspeele, R., Post-cooling properties of concrete exposed to fire. *Fire Safety Journal*, Band 92, pp. 142-150, 2017.
5. Klingsch, E. W., Frangi, A. & Fontana, M., Concrete Residual Strength in Compression: Blended Cements Versus Ordinary Portland Cement, Politecnico di Milano, Italy: Studies and Researches, Graduate School in Concrete Structures – Fratelli Pesenti, 2009.
6. Rao, C. B. K. & Kumar, R., A Study on Behaviour of Normal Strength Concrete and High Strength Concrete Subjected to Elevated Temperatures. *International Journal of Civil and Environmental Engineering*, 9(3), pp. 283-287, 2015.
7. Schneider, U., Concrete at High Temperatures - A General Review. *Fire Safety Journal*, Band 13, pp. 55-68, 1988.
8. Hosser, D. & Zehfuß, J., Brandschutz in Europa-Bemessung nach Eurocodes: Erläuterungen und Anwendungen zu den Brandschutzteilen der Eurocodes 1 bis 6. Berlin. Beuth Verlag, 2017.
9. Gernay, T. & Franssen, J.-M., A formulation of the Eurocode 2 concrete model at elevated temperature that includes an explicit term for transient creep. *Fire Safety Journal* 51: 1-9, 2012.
10. EN 1994-1-2, Eurocode 4 – Design of Composite Steel and Concrete Structures. Part 1–2: General Rules – Structural Fire Design, 2005.

EXPERIMENTAL INVESTIGATION ON THERMAL PERFORMANCE OF 3D PRINTED CONCRETE ELEMENTS SUBJECTED TO FIRE

Jin Qiu¹, Liming Jiang², Jinjin Wang³, Yiwei Weng⁴, Asif Usmani⁵

ABSTRACT

The application of 3D concrete printing (3DCP) technology to construction has been an overwhelming trend benefiting from its various advantages, such as its automation, construction precision, great potential on architectural aesthetics and so on. The layer-to-layer deposition manner characterised by the 3DCP technique renders it considerably different from the conventionally casted concrete construction method. To support the further widespread application of the 3DCP, building the knowledge base regarding to the structural safety of 3DCP structures is of paramount importance. This paper focuses on the thermal response of three types of candidate 3D-printed wall structure subjected to fire. The H-Tris system was deployed to apply localised thermal loads to seven reduced-scaled specimens. The temperature development in each specimen under the recorded heat flux was presented and discussed to showcase the heat transfer properties of 3DCP elements with different internal structural configurations.

Keywords: 3D concrete printing; Heat transfer; H-Tris; Fire testing; Cavity element

1 INTRODUCTION

Introducing Additive Manufacturing (AM) technology into the construction industry, i.e., 3D concrete printing (3DCP), has been an overwhelming trend. Apart from the obvious advantages of autonomous 3DCP on eliminating labour-intensive work, 3DCP also reduces the use of construction materials, shortens construction time, and facilitates innovative architectural designs [1]. Several real projects have been constructed with 3D printing technique, such as the Putuo Bridge in Shanghai, a two-storey villa in Beijing and an office building in the United Arab Emirates. However, the widespread application of the emerged 3DCP technique in the field of civil engineering confronts numerous challenges. For example, improving the printable and mechanical properties of 3D printing concrete materials and developing effective reinforcement methods to enhance the loading bearing capacity of 3D-printed concrete components are still in the research stage [2]. Besides, the absence of standardized industry protocols and performance evaluation research are also the limits to practical application of 3DCP technology in real practice. Particularly, the fundamental knowledge regarding structural safety including fire safety performance remains absent.

¹ Dr., Department of Building Environment and Energy Engineering, The Hong Kong Polytechnic University
e-mail: jijin.qiu@connect.polyu.hk, ORCID: <https://orcid.org/0000-0002-0603-854X>

² Dr., Department of Building Environment and Energy Engineering, The Hong Kong Polytechnic University
e-mail: liming.jiang@polyu.edu.hk, ORCID: <https://orcid.org/0000-0001-8112-2330>

³ Ms., Department of Building Environment and Energy Engineering, The Hong Kong Polytechnic University
e-mail: jinjwang@polyu.edu.hk

⁴ Dr., Department of Building and Real Estate, The Hong Kong Polytechnic University
e-mail: yiwei.weng@polyu.edu.hk, ORCID: <https://orcid.org/0000-0001-5637-1415>

⁵ Prof., Department of Building Environment and Energy Engineering, The Hong Kong Polytechnic University
e-mail: asif.usmani@polyu.edu.hk, ORCID: <https://orcid.org/0000-0003-2454-5737>

While traditional furnace fire testing remains a commonly adopted method to evaluate the fire performance of concrete structures, a more quantifiable testing approach for testing small-size structural elements has been proposed using controllable radiant panels. It is known as the H-Tris system, which is capable of applying radiant heat on the exposed surface of the test specimens [3]. Recently, an H-Tris system has been built at the Hong Kong Polytechnic University by the authors, which achieves computer control of radiant heat flux by adjusting the air intake volume and the distance between the panel and the specimen using servo motors. This testing system can approximate real fire conditions and greatly facilitate the observation of fire responses of specimens, such as the behaviour of 3DCP specimens.

Concrete materials would experience mechanical performance degradation, cracking and even spalling when they are exposed to fire heating as a result of physical change of cement paste and aggregate as well as thermal expansion owing to elevated temperatures [4]. 300°C is usually regarded as the critical point when the conventional siliceous concrete strength begins to lose, while for the modern concrete structures, the critical temperature can be higher [5]. The fire-induced material degradation of concrete could result in the structural instability and even collapse [6, 7]. Unlike the conventionally casted concrete manner, 3DCP extrudes printable materials via a nozzle and prints the designed shape in a layer-to-layer deposition manner. The denser concrete extruded under high pressure and the lack of fusion between the filaments induced by the layer grooves would lead to different performance of 3D printed concrete at elevated temperatures compared to casted concrete in the same scenario [8] given that the porosity and density are the two main factors that dominate the thermal behaviour of concrete material [9]. To date, rather limited studies regarding to the fire performance of 3D-printed concrete elements have been performed. D'hondt et al. [10] adopted the ISO 834 furnace fire [11] to study the mechanical properties and fire resistance of cut 3D printed single-layer solid test blocks. A preliminary study on the thermal behaviour at high temperatures and the mechanical properties of the interlayer structure on a series of traditional cast specimens and cut single-layer solid 3D printed specimens was conducted by Cicione et al. [8] using the radiant panels. Kruger et al. [12] employed the same testing method to explore the material properties of printed concrete containing steel fibre materials. These studies primarily focus on the heat transfer characteristics of printing materials. Recently, some research efforts have begun to be devoted to the thermal response of candidate 3D printed wall panels with cavities. Compared with the solid elements, the existence of internal cavities in the 3DCP elements leads to more complex heat transfer properties [13] considering the cavity radiation and convection. Nevertheless, these 3DCP components with cavities may show unique advantages and potential in terms of fire resistance. Currently, the research associated with the heat transfer analysis on 3DCP elements with different types of cavities are primarily limited to the numerical simulation. Based on the test results by Cicione et al. [8], Suntharalingam et al. [14, 15] performed numerical simulation to imitate the heat transfer performance of 3DCP elements with cavities subjected to ISO 834 standard fire using the commercial software of MATLAB and ABAQUS. The lack of physical tests on the thermal properties of 3DCP elements with cavities results in the absence of the benchmark datasets which could be adopted to validate the development of numerical models. Also, it may hinder the optimization on the structural design of 3DCP concrete walls.

This study aims to fill the above-mentioned research gap by experimentally investigating the thermal response of seven 3DCP elements of different section shapes. The H-Tris testing system was utilized to apply the localised thermal loads to the specimens. The temperature development at different locations, heat flux at the fire exposed surface were collected and presented to show the thermal response of 3DCP elements with without cavities as a result of different types of internal toolpaths. The test results obtained in this research not only provide valuable test data to advance the application of 3DPC technology to structural engineering, but also help understand the fire safety performance of 3DCP structural members.

2 SPECIMEN DESIGN AND PRINTING

A total of seven reduced-scaled candidate 3DCP wall structures were designed and tested. To compare the influence of different types of cavities on the thermal performance of 3DCP elements, three different cross-sections (see Figure 1) were selected. The three specimens with internal U-shaped toolpath were designated

with SC1, SC2 and SC3. The two specimens with complete rectangular cavity were named as CR1 and CR2. In specimens CW1 and CW2, the internal toolpath was V-shaped. Note that compared with the other two groups of specimens, the specimens with internal U-shaped toolpath were closer to the solid elements, which can be taken as the reference group to reveal the influence of cavity on the thermal response of 3DCP elements. However, owing to the inherent challenges of maintaining control over small-scaled 3DPC in the material preparation and printing stages, the final printed specimens may have little difference in terms of geometrical details compared with the design parameters. The actual geometries as well as the details related to the filament layer in each specimen are summarized in Table 1.

The specimens were printed in the Industry Centre in The Hong Kong Polytechnic University using a desktop-type 3D concrete printer (NELD-3D736) manufactured by NELD Limited in Beijing, China. The 3D concrete material was composed of 40 % - 50 % Ordinary Portland Cement (OPC), 0 % - 10 % Calcium Sulfoaluminate (CSA), and 40 % - 60 % sand. To improve its printable and mechanical properties, 0 - 0.5 % superplasticizer (powder), 0 % - 0.5 % emulsion powder, 0.1 % - 0.5 % Hydroxypropyl methylcellulose (HPMC) and fibres were added to the mix material at a rate of 0-2 kg per ton.

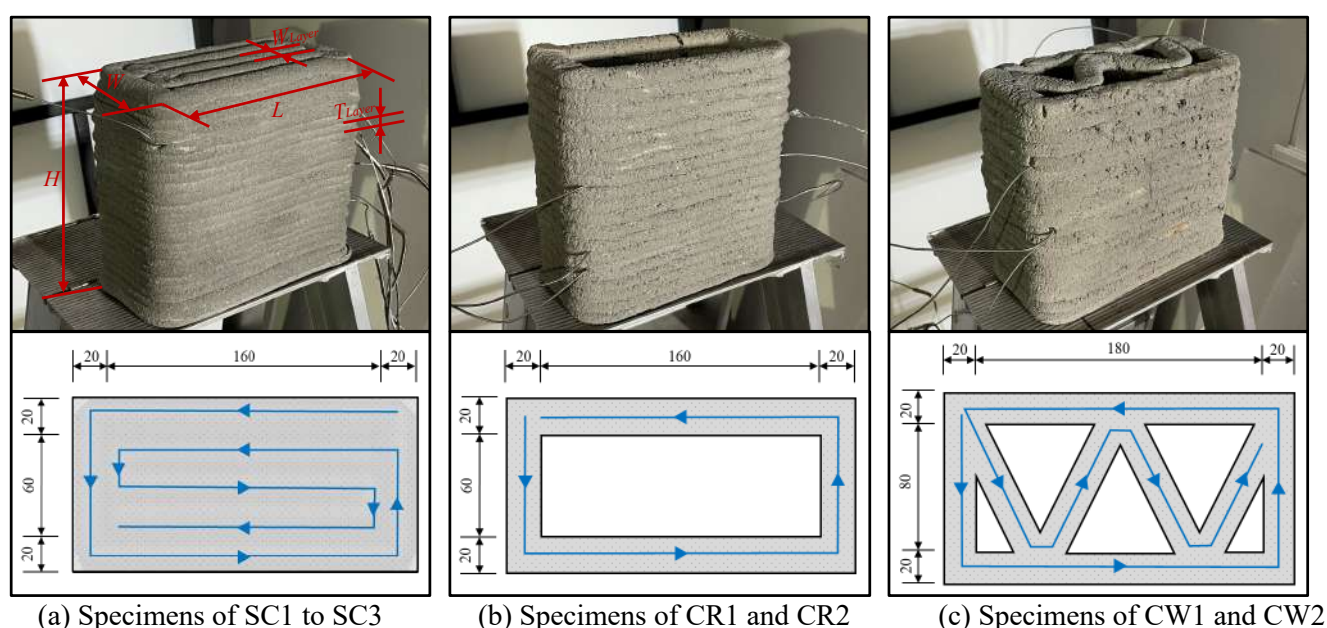


Figure 1. Design of the 3DCP specimens

Table 1. Summary of measured specimen details

Specimen	Internal toolpath	L	W	H	$T_{layer} (mm)$	$W_{layer} (mm)$
SC1	U-Shaped	205	100	182	7	20
SC2		190	100	188		
SC3		190	95	184		
CR1	None	200	100	205	10	20
CR2		202	100	220		
CW1	V-shaped	225	125	195	10	20
CW2		220	120	200		

3 TEST SETUP AND INSTRUMENTATION

The test was conducted in the Fire Laboratory in The Hong Kong Polytechnic University utilizing the H-Tris testing system. The test setup is shown in Figure 2. A radiant panel was employed to apply thermal

load to one surface of the specimens to ensure the simplicity and reliability of subsequent analysis and simulation of the internal time histories of heat transfer, the two sides of the specimen were wrapped with asbestos to isolate the heat exchange between the sides surface and the surrounding environment, while the non-fire surface was directly exposed to the ambient temperature. As the focus of this paper is on the heat transfer characteristics of 3DCP elements with different types of cavities to the elevated temperatures, only the temperature development the 3DCP specimens with different internal configurations was consider.

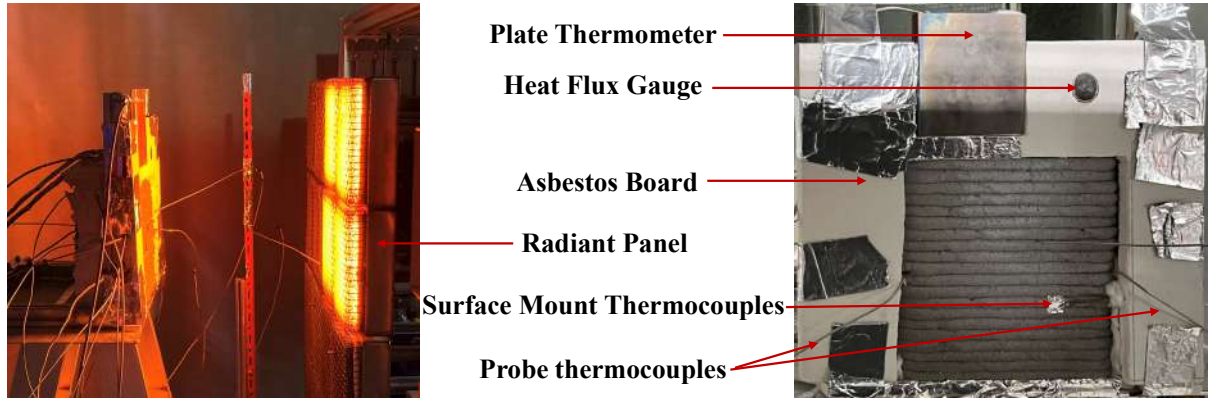


Figure 2. Test setup

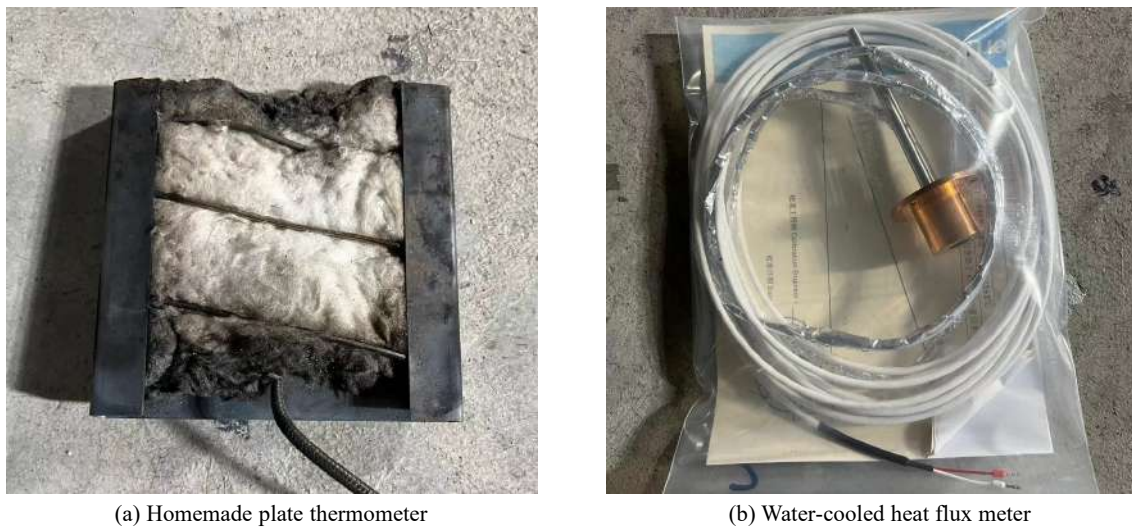


Figure 3. Equipment for measuring the applied heat flux

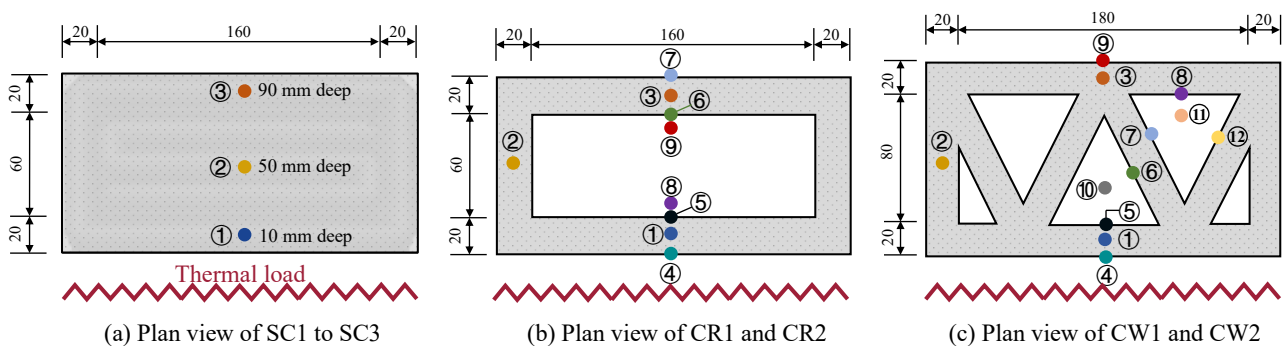


Figure 4. Installed locations of the thermocouples

In this test, the temperature evolution at different locations inside the specimens and the gas temperatures near the non-fire exposed surface were monitored using the probe-type thermocouples (WRNK-16X), while a surface thermocouple (XS-K-20) was utilized to measure the temperatures of fire-exposed surface. The

applied thermal loads on the fire exposed surface were measured by using a water-cooled heat flux meter (see Figure 3(b)) for all specimens. Additionally, for specimens CR2 and CW2, a homemade plate thermocouple (see Figure 3(a)) was installed to quantify the thermal load by measuring the adiabatic temperatures of the surface exposed to fire. The detailed installation of thermocouples is shown in Figure 4. The thermocouples were distributed at mid-plane of the specimens. The specific installation locations of thermocouples for each group of specimens are shown in Figure 4. In specimens SC1-SC3, three thermocouples at a distance of 10 mm, 50 mm and 90 mm from the fire exposed surface were arranged. More thermocouples were arranged in the specimens with cavities with the aim of demonstrating the effect of cavities on the heat transfer of 3DCP elements. A total of nine and twelve thermocouples were installed in the groups of CR and CW respectively, including the temperature measurement inside the concrete and the in the cavities.

4 TEST RESULTS

4.1 Test observations

All the specimens with different internal toolpaths behaved similarly in the tests. At the early stage of heating, the steam was observed at the top of the specimens resulting from the evaporation of water within the 3D concrete material, which indicated a relatively high moisture content in these specimens. Along with the rising temperatures in the specimens, the heated surfaces of 3DCP exhibited varying degrees of spalling and the minor spalling could be found in the non-exposed surfaces. This is because the evaporation of water inside the concrete increases the porosity and internal pressure within the concrete microstructure, leading to the microscopic cracks and spalling [16]. The heating continued until the temperature of the fire-exposed surface reached a stable state and then the heated specimens entered into natural cooling stage.



(a) Interlayer cracks in specimen



(b) Vertical cracks in the specimens

Figure 5. Cracks in the specimens

After being cooled down, each specimen exhibited several vertical cracks in the direction perpendicular to the layer grooves in the fire-exposed surface. As shown in Figure 5(b), vertical cracks penetrated from the top to the bottom of the specimens. This is out of expectation as the interlayer delamination in 3DCP elements is more common. However, due to the high temperature during heating and the cracks were very fine, determining the exact time of crack formation was challenging. Herein, two possibilities were given: 1) these cracks may be induced by the changes of internal temperature and pressure gradients during heating stage 2) This crack may form in the cooling stage as a result of inconsistent thermal expansion and contraction among different internal parts. It has been found that the disparity in contraction coefficients may induce temperature gradients and thermal stresses, leading to the cracks inside or on the surface of the concrete, thereby relieving internal stress [17]. After longer post-fire duration, one 3DPC specimen with U-shaped internal toolpath exhibited interlayer cracks (see Figure 5(a)). This phenomenon is correspond to the previous study on the thermal performance of 3DCP solid elements [8] which can be attributed to the lack of fusion between layers.

4.2 Temperature development in 3DCP elements with internal U-shaped toolpath

In practice, when 3D-printed solid components are required, the U-shaped toolpath is often deployed to fill the internal space. Therefore, conducting tests on 3D-printed concrete elements with U-shaped toolpath can provide valuable information on evaluating the fire safety of 3DCP elements.

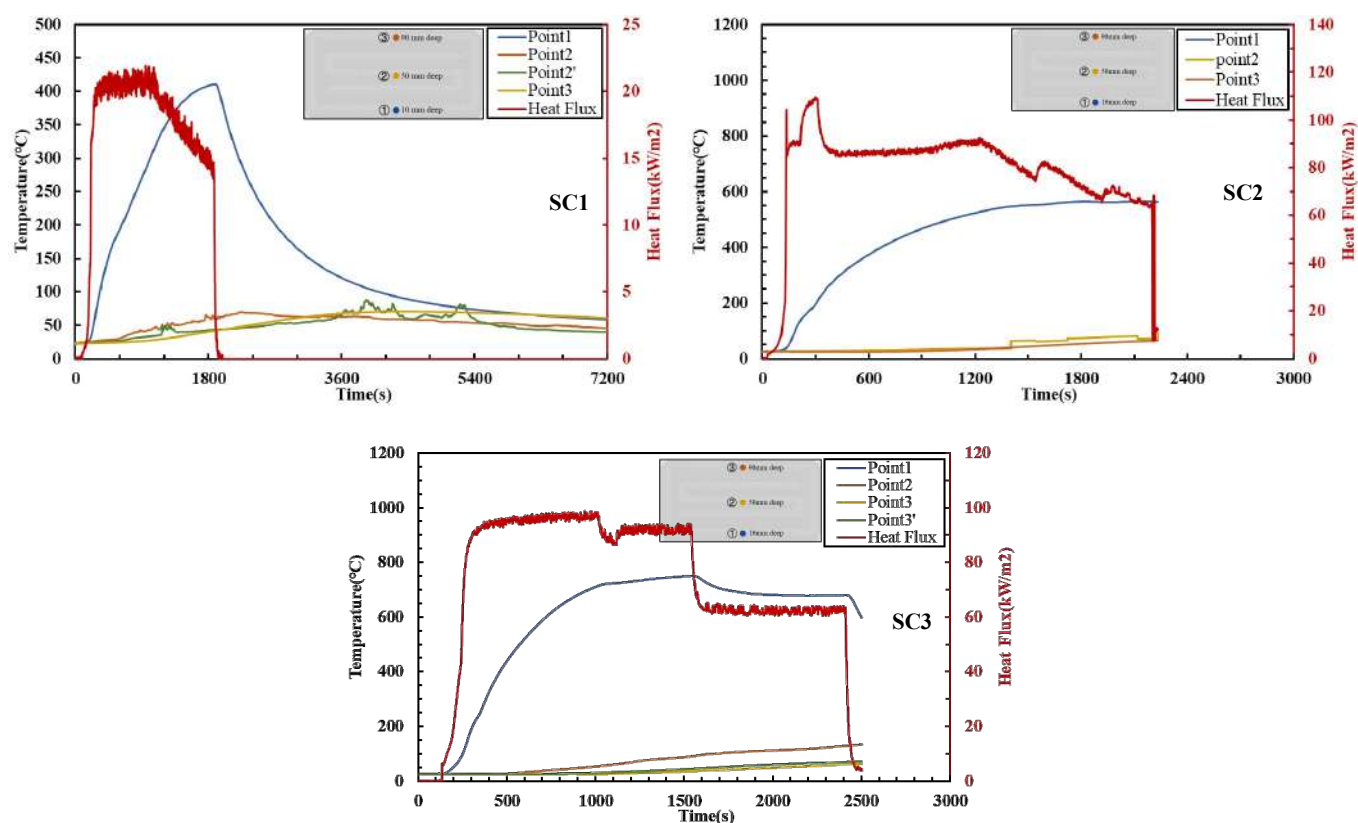


Figure 6. Incident heat flux and temperature evolution in specimens SC1 to SC3

Figure 6 shows the applied heat fluxes on the fire-exposed surface and the temperature development inside the specimens SC1-SC3. The heat flux applied on the specimens of SC2 and SC3 reaches 100 kW/m^2 , which is significantly larger than that applied in specimen SC1, which is about 20 kW/m^2 . It is expected that the larger heat flux leads to the higher peak temperatures as the peak temperature in specimens SC2 and SC3 at point 1 is about $550 \text{ }^\circ\text{C}$ and $700 \text{ }^\circ\text{C}$ respectively, while the peak temperature at the same measurement location in specimen SC1 is about $400 \text{ }^\circ\text{C}$. Compared to specimen SC2, the longer duration of the heat flux in specimen SC3 results in the higher peak temperature. For point 2 and point 3, which are further away from the fire source, only the peak temperature at point 2 in specimen SC3 is around $100 \text{ }^\circ\text{C}$, while the other measurement points in these three specimens are lower than $100 \text{ }^\circ\text{C}$.

4.3 Temperature development in 3DCP elements with cavities

The applied heat flux and the temperature development in the specimens with complete rectangular cavity, i.e., specimens CR1 and CR2 are shown in Figure 7. The heat flux in specimen CR1 is about 35 kW/m² and it lasts for about 25 min. Though the heat flux applied to specimen CR2 is 5 kW/m² higher than that applied to the specimen CR1, the heat flux does not maintain and then it begins to decrease. For specimens CW1 and CW2, the applied heat flux is up to 45 kW/m². However, in specimen CW1, the heat flux enters into a fast-decreasing stage while the heat fluxes were maintained longer for specimen CW2.

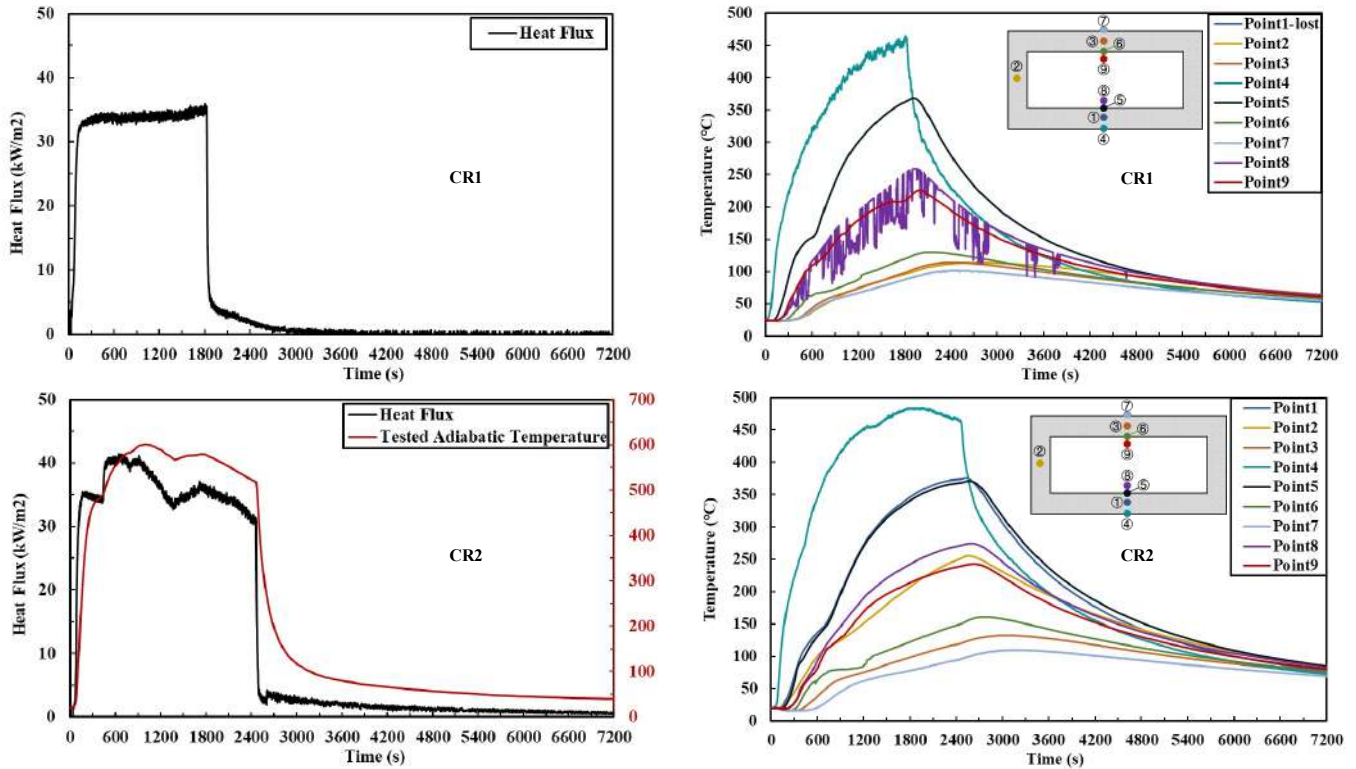


Figure 7. Fire-exposed surface heat flux and temperature evolution in specimens CR1 and CR2

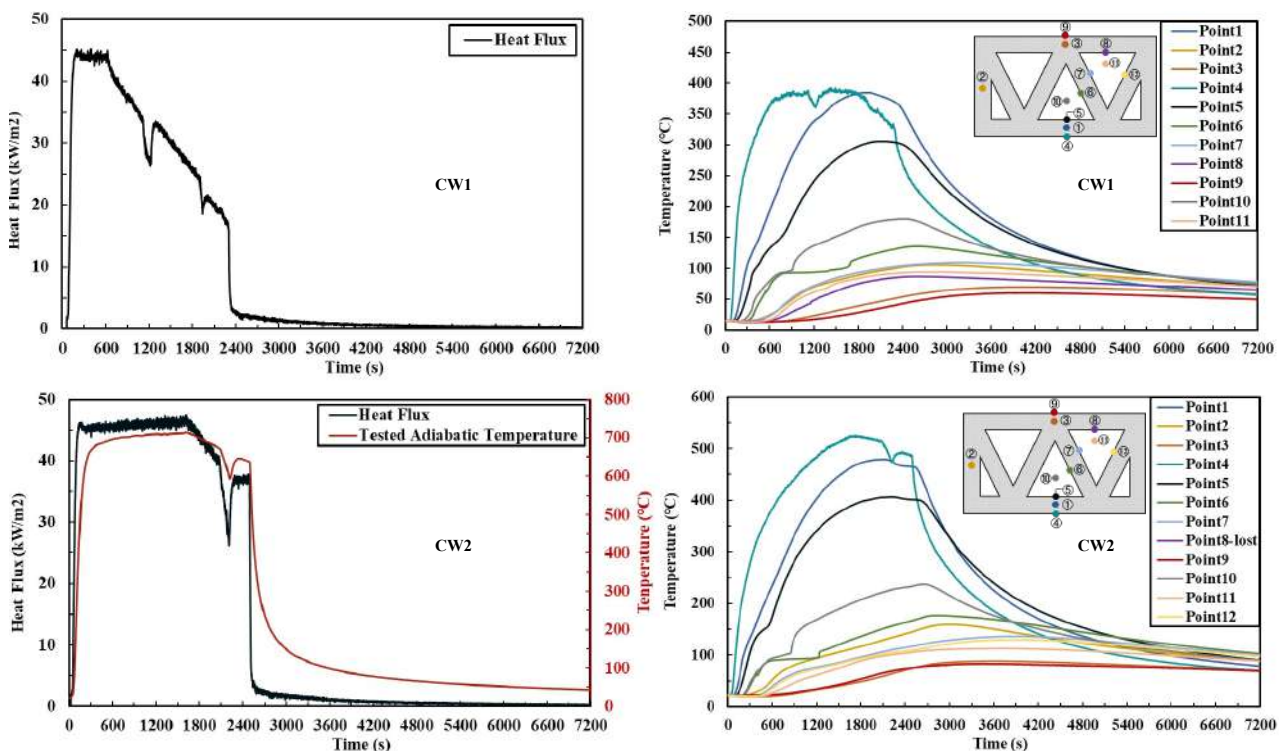


Figure 8. Fire-exposed surface heat flux and temperature evolution in specimens CW1 and CW2

During the heat transfer process from the fire-exposed surface to the unexposed surface, the location of point 6 in the specimen groups of CR and CW is the first cavity wall that the heat energy would encounter after passing through the cavity. The temperatures at this measurement point in these specimens present a stable period after about 10 minutes of heating load, and then continue to increase, at which the temperature at point 5 reaches approximately 300 °C. It may be attributed to the dominant heat transfer way in the cavity shifts from thermal convection and thermal conduction to radiation. Point 5 is exactly at the inner wall that radiates heat to the cavity during the heat transfer process. Moreover, the point 5 itself also presents a shorter temperature plateau at around 150 °C which may also be caused by the existence of cavities. For specimen CW2 which was exposed to the longer duration of heat flux of approximately 40 kW/m², the temperatures at multiple measurement points approaching 400 °C at which the concrete material starts to fail. Hence, in real fire scenarios which means a significantly higher heat flux, the fire safety performance of 3DCP structural buildings necessitates more careful consideration.

5 CONCLUSIONS

This study investigated the thermal response of three types of 3DCP wall sections subjected to fire heating. The H-Tris testing system was deployed to apply thermal load to the 3DCP elements with different internal cross sections. The results derived from this paper would enrich the knowledge on the heat transfer properties of 3DCP elements. More importantly, it provides the benchmark test results for the further development of numerical model for heat-transfer analysis on 3DCP elements.

It is worth to note the observed cracks in the direction perpendicular to the layer grooves in addition to the interlayer delamination, which suggests a high possibility of the occurrence of vertical cracking when the 3DCP elements are subjected to a room fire. Further analyses on the formation mechanism of these vertical cracks propagating from the top to the bottom of the 3DCP walls should be conducted as it may influence the overall fire performance of 3DCP structures.

The existence of cavities in the 3DCP elements increases the complexities of heat transfer within the structures. When the temperature at the surrounding concrete structure reaching 300 °C, the dominant heat transfer manner to the inner structure may shift from thermal convection and conduction from the cavities to radiation from the concrete with higher temperatures. Besides, the 30 min exposure at a constant heat flux of 45 kW/m² resulted in the concrete material at various parts of the 3DCP elements enters into the failure stage.

REFERENCES

- [1] J. J. del Coz-Díaz, J. E. Martínez-Martínez, M. Alonso-Martínez, and F. P. Álvarez Rabanal, "Comparative study of LightWeight and Normal Concrete composite slabs behaviour under fire conditions," *Engineering Structures*, vol. 207, 2020, doi: 10.1016/j.engstruct.2020.110196.
- [2] A. Siddika, M. A. A. Mamun, W. Ferdous, A. K. Saha, and R. Alyousef, "3D-printed concrete: applications, performance, and challenges," *Journal of Sustainable Cement-Based Materials*, vol. 9, no. 3, pp. 127-164, 2019, doi: 10.1080/21650373.2019.1705199.
- [3] C. Maluk, L. Bisby, M. Krajcovic, and J. L. Torero, "A Heat-Transfer Rate Inducing System (H-TRIS) Test Method," *Fire safety journal*, vol. 105, pp. 307-319, 2019, doi: 10.1016/j.firesaf.2016.05.001.
- [4] J. Qiu, L. Jiang, and A. Usmani, "Post-fire Repair of Concrete Structural Members: A Review on Fire Conditions and Recovered Performance," *International Journal of High-Rise Buildings*, 12/31 2021, doi: 10.21022/IJHRB.2021.10.4.323.
- [5] G. A. Houry, "Effect of fire on concrete and concrete structures," *Progress in Structural Engineering and Materials*, vol. 2, no. 4, pp. 429-447, 2001, doi: 10.1002/pse.51.
- [6] J. Qiu, L. Jiang, X. Cai, G.-q. Li, and A. Usmani, "Reconstruct the 3D load redistribution paths of framed structures subjected to local column failure and multi-floor fire," *Structures*, vol. 58, 2023, doi: 10.1016/j.istruc.2023.105668.
- [7] M. A. Orabi, L. Jiang, A. Usmani, and J. Torero, "The Collapse of World Trade Center 7: Revisited," *Fire Technology*, 2022, doi: 10.1007/s10694-022-01225-2.

- [8] A. Cicione, J. Kruger, R. S. Walls, and G. Van Zijl, "An experimental study of the behavior of 3D printed concrete at elevated temperatures," *Fire Safety Journal*, vol. 120, 2021, doi: 10.1016/j.firesaf.2020.103075.
- [9] A. H. Buchanan and A. K. Abu, *Structural design for fire safety*. John Wiley & Sons, 2017.
- [10] M. D'Hondt, S. Rémond, P. Leblond, B. Iea, E. Hynek, and N. Pinoteau, "Fire Behavior of a Printed Sample for Building," (RILEM Bookseries. Cham: Springer International Publishing, 2020, pp. 428-438.
- [11] *Fire tests – Calibration and Use of Heat Flux Meters – Part 4: Guidance on the Use of Heat Flux Meters in Fire Tests (ISO 14934-4:2007)*, I. O. f. Standardization, 2007.
- [12] J. Kruger *et al.*, "Facilitating Ductile Failure of 3D Printed Concrete Elements in Fire," (RILEM Bookseries. Cham: Springer International Publishing, 2020, pp. 449-458.
- [13] H. Marais, H. Christen, S. Cho, W. De Villiers, and G. Van Zijl, "Computational assessment of thermal performance of 3D printed concrete wall structures with cavities," *Journal of Building Engineering*, vol. 41, 2021, doi: 10.1016/j.job.2021.102431.
- [14] T. Suntharalingam *et al.*, "Fire resistance of 3D printed concrete composite wall panels exposed to various fire scenarios," *Journal of Structural Fire Engineering*, vol. 12, no. 3, pp. 377-409, 2021, doi: 10.1108/jsfe-10-2020-0029.
- [15] T. Suntharalingam *et al.*, "Finite Element Modelling to Predict the Fire Performance of Bio-Inspired 3D-Printed Concrete Wall Panels Exposed to Realistic Fire," *Buildings*, vol. 12, no. 2, 2022, doi: 10.3390/buildings12020111.
- [16] H. Mohammed, H. Ahmed, R. Kurda, R. Alyousef, and A. F. Deifalla, "Heat-Induced Spalling of Concrete: A Review of the Influencing Factors and Their Importance to the Phenomenon," *Materials (Basel)*, vol. 15, no. 5, Feb 24 2022, doi: 10.3390/ma15051693.
- [17] L. Li, A. Dabarera, and V. Dao, "Evaluation of zero-stress temperature and cracking temperature of high performance concrete at early ages," *Materials and structures*, vol. 55, no. 7, 2022, doi: 10.1617/s11527-022-02019-2.

EXPERIMENTAL STUDY ON THERMO-HYDRAL RESPONSE OF CRACKED CONCRETE SUBJECTED TO ELEVATED TEMPERATURES

Yu-Qing Ge¹, Chao Jiang², Hao-Chuan Zhang³, Xiang-Lin Gu⁴, Xiao-Bin Song⁵

ABSTRACT

This paper investigated experimentally the thermal-hydral responses, i.e., the temperatures and pore pressures, at different depths into unilaterally heated cracked concrete plates subjected to elevated temperatures. Based on the test results, the effects of crack width and the effects of interactions between cracks on the distributions of temperatures and pore pressures were explored. Results showed that when the crack width was less than 1 mm, the crack width had delayed effects on the heat transfer in the cracked sections of the concrete plates, and when the crack width was larger than 1 mm, the crack width had accelerated effects on the heat transfer in the cracked sections of the concrete plates. The crack width had no obvious effects on the temperature distributions over the uncracked sections of the concrete plate specimens. The interactions between cracks had accelerated effects on the heat transfer in both the cracked and uncracked sections of the concrete plates. The crack width had no obvious effects on the maximum pore pressures in the concrete plates except that the maximum pore pressures of measuring points at 15 mm depth in the uncracked sections of the concrete specimens decreased with the increase of the crack width. The interactions between cracks had no obvious effects on the maximum pore pressures in the cracked sections but reduced the maximum pore pressures in the uncracked sections of the concrete specimens.

Keywords: Cracked concrete; elevated temperature; thermo-hydral response; pore pressure

1 INTRODUCTION

Reinforced concrete structures account for the vast majority of existing residential buildings in China [1]. Existing concrete structures usually work with cracks due to occasional overloading and/or reinforcement corrosion. On the other hand, building fires frequently occur in recent years [2]. Structural concrete usually undergoes complex coupled thermal, hydraulic, mechanical and chemical processes under elevated temperatures [3 - 5]. During a fire, cracks are able to make the high temperature vapor inside the concrete easy to escape and take away the heat, which further affect the thermo-hydral response of concrete and finally affect its fire resistance [6]. Experimental results provided by Ervine et al. [7] and Wu et al. [8] indicated that the temperatures in the cracked regions of cracked concrete are usually lower than that in the

¹ PhD Candidate, Department of Structural Engineering, College of Civil Engineering, Tongji University,
e-mail: 1910272@tongji.edu.cn

² Associate Professor for Research, Key Laboratory of Performance Evolution and Control for Engineering Structures (Ministry of Education),
Tongji University,

e-mail: cjiang@tongji.edu.cn, corresponding author, ORCID: <https://orcid.org/0000-0002-2414-3968>

³ PhD Candidate, Department of Structural Engineering, College of Civil Engineering, Tongji University,
e-mail: 2011132@tongji.edu.cn

⁴ Professor, Department of Structural Engineering, College of Civil Engineering, Tongji University,
e-mail: gxl@tongji.edu.cn

⁵ Professor, Department of Structural Engineering, College of Civil Engineering, Tongji University,
e-mail: xiaobins@tongji.edu.cn

uncracked regions at the same depth from the heated surface during the heating process. However, the experimental study conducted by Ba et al. [9,10] found the opposite results. The contradictory experimental results may be due to that these tests did not control the moisture conditions of cracked concrete specimens before heating [11]. Although the temperature distributions of specimens were measured in all above experiments, the data of hydraulic responses were not collected to make further analysis. Therefore, based on the test set-up designed and developed by the authors [12], this paper investigates experimentally both the thermal and hydraulic responses, i.e., the temperatures and pore pressures, at different depths into unilaterally heated cracked concrete plates subjected to elevated temperatures.

2 EXPERIMENTS

2.1 Materials and specimens

Six concrete plate specimens with dimensions of 100 mm×290 mm×390 mm, were designed and cast. Five specimens (B1 ~ B5) with pre-made cracks and one reference specimen (B0) without crack. Meanwhile, three prism concrete specimens with dimensions of 150 mm×150 mm×300 mm were cast to test the strength of concrete. The mix proportion of concrete is shown in Table 1. The water-cement ratio was 0.5. Ordinary Portland cement (OPC # 425) and tap water were used. ISO standard sand and granite gravels were used as fine and coarse aggregates, respectively. Coarse aggregates were within sizes ranging from 5 to 20 mm. The tested strength of the designed concrete was 35 MPa after 28 days of moisture curing at a room temperature.

Table 1. Mix proportion of concrete

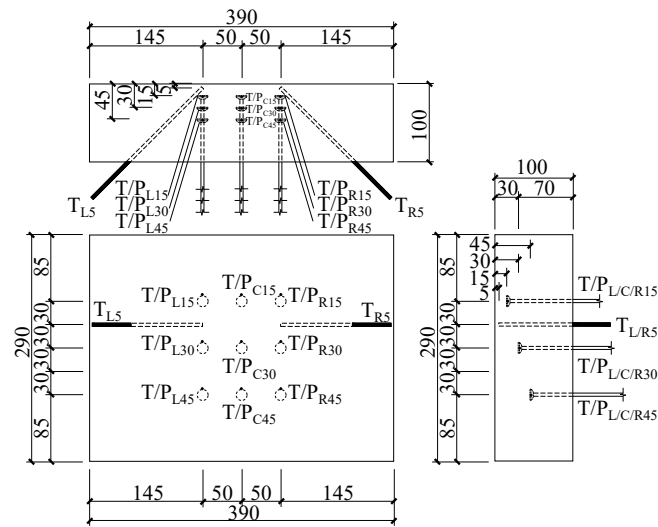
Water (kg/m ³)	Cement (kg/m ³)	Fine aggregate (kg/m ³)	Coarse aggregate (kg/m ³)
195	390	664.1	1180.6

The crack parameters design of single-side cracked concrete specimens is shown in Table 2. The crack shape of the specimens was set as rectangle for simplification. Specimens B1 ~ B4 were designed to explore the effects of crack width on the distributions of temperatures and pore pressures in concrete under elevated temperatures. Specimen B2 and B5 were designed to explore the effects of interactions between cracks on the distributions of temperatures and pore pressures in concrete under elevated temperatures. Specimen B0 was reference specimen without crack.

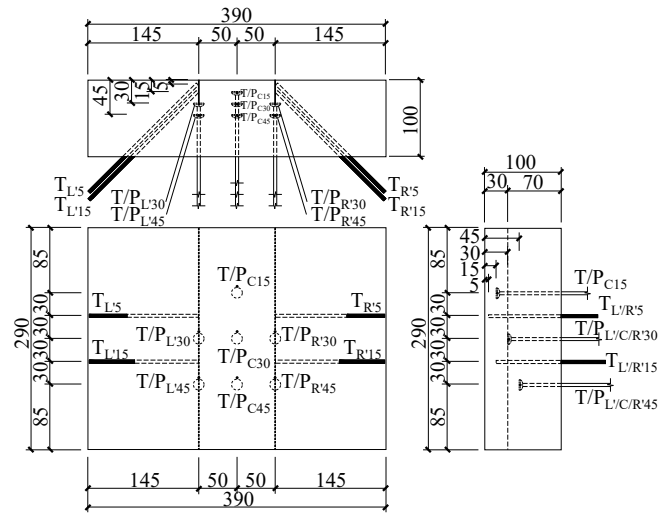
Table 2. Crack parameters of specimens

Specimen	Crack width (mm)	Crack depth (mm)	Crack spacing (mm)	Crack depth to width ratio
B0	0	0	0	0
B1	0.5	30	100	60
B2	1	30	100	30
B3	3	30	100	10
B4	10	30	100	3
B5	1	30	0	30

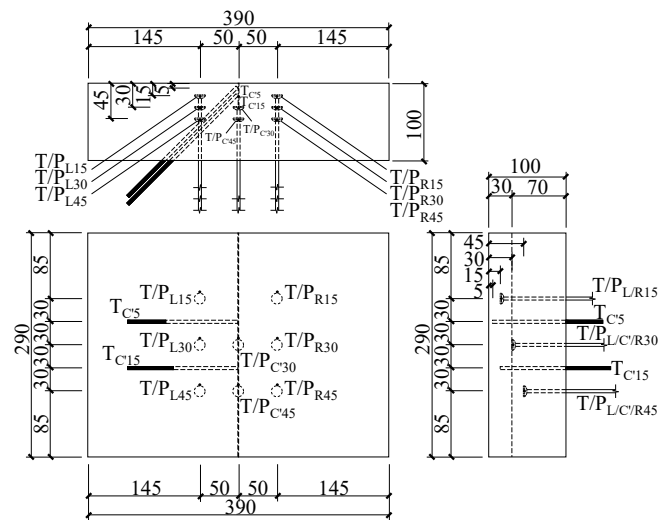
For concrete plate specimens B1 ~ B4, seven metal tubes were embedded for pore pressure measurements and eleven thermocouples were embedded for temperature measurements at different depths within cracked and uncracked sections. For concrete plate specimen B5, eight metal tubes and ten thermocouples were embedded. For concrete plate specimen B0, nine metal tubes and eleven thermocouples were embedded only in uncracked sections. The overviews and side views of specimens mentioned above are illustrated by Figure 1. Details for the metal tubes could be found in Ref. [12].



(a) B0



(b) B1 ~ B4



(c) B5

— Thermocouple - - - Metal tube - - - Metal tube with thermocouple

Figure 1. Overviews and side views of concrete plate specimens with embedded metal tubes and thermocouples (mm)

2.2 Mould design

Different crack arrangements were obtained by inserting steel plates of different thicknesses and positions into the plywood mould. Several slots were pre-cut on the plywood moulds. The dimensions of the slots were equal to the width, depth and length of the designed cracks. The spacing of the slots was equal to the designed crack spacing. The greased steel plates were inserted into the slots, and should be removed after the final setting of concrete. The thickness and width of the steel plates were equal to the width and depth of the designed cracks. Both the thermocouples and the metal tubes were fixed on the plywood mould by two parallel boards and two auxiliary boards with a certain spacing. Two days after the concrete had been poured, the steel plates and plywood moulds were removed. On the one hand, the concrete had finally set so that the crack shape can be maintained. On the other hand, the steel plates and the concrete are not bonded and easy to remove. Before the heating tests, the measured crack width, depth and spacing are listed in Table 3. The measured values of crack parameters are close to the pre-set values.

Table 3. The measured crack width, depth and spacing of specimens

Specimen	Nominal crack width (mm)	Actual crack width (mm)	Nominal crack depth (mm)	Actual crack depth (mm)	Nominal crack spacing (mm)	Actual crack spacing (mm)
B0	0	0	0	0	0	0
B1	0.5	0.57	30	30	100	100.5
B2	1	0.95	30	30.5	100	99.5
B3	3	3.14	30	30	100	100
B4	10	10	30	30	100	100
B5	1	0.94	30	30	0	0

2.3 Test set-up

The temperature and pore pressure responses at different depths into the heated concrete plates were measured by the test set-up designed and developed by the authors [12]. Each specimen was sealed by aluminium foil and insulated by ceramic fibre cotton peripherally to achieve sealing and heat insulation of four sides of the concrete plate specimen. Before the heating test, thermocouples were embedded in the cracks of specimens B1, B2, B3 and B5 to obtain the temperatures of the air in the crack. The thermocouple probes were located at 5, 15 and 30 mm away from the heating surface of each cracked specimen respectively. Then each specimen was partially inserted into a furnace so that the concrete plate specimen could be heated unilaterally, as illustrated in Figure 2.

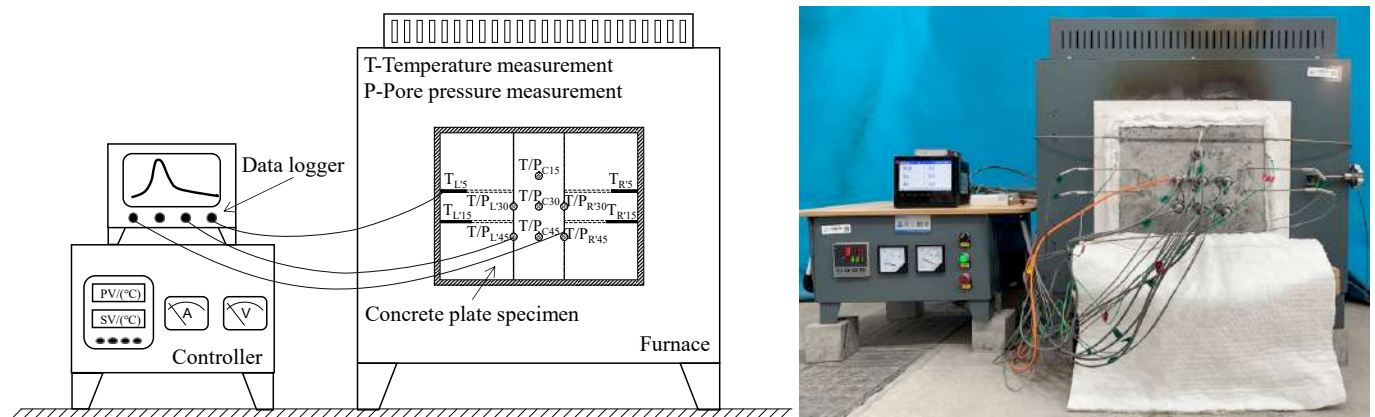


Figure 2. Test set-up

2.4 Heating programs

The temperature in furnace increased linearly at a heating rate of 10 °C/min up to the target temperature 800 °C and maintained for 3 hours. After that, the furnace underwent a natural cooling to the ambient temperature. During the heating and cooling process, the temperatures and pore pressures occurring at the pre-set depths were automatically monitored and recorded by the data logger.

3 RESULTS AND DISSCUSION

3.1 Temperatures

The temperature developments at different depths into the concrete plate specimens are illustrated in Figure 3. As shown in Figure 3, the measuring points at the same distance from the heating surface in the cracked and uncracked sections of each concrete plate specimen were relatively close. The air temperatures inside the cracks were slightly higher than the temperatures inside the concrete at the same distance from the heating surface.

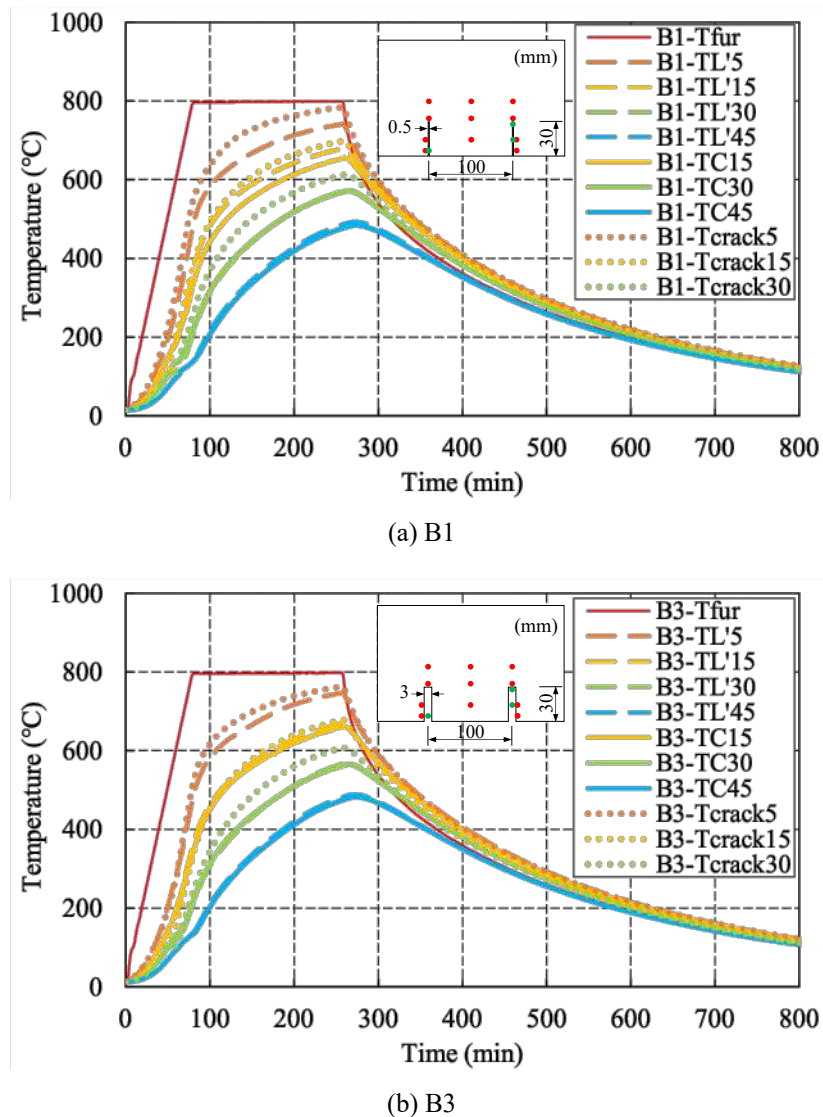


Figure 3. Temperature developments at different depths into the concrete plate specimens

The temperature distributions on the cracked sections of the concrete plate specimens with different crack widths, i.e., specimens B0 ~ B4, at different times are shown in Figure 4. The whole heating process lasted for 260 minutes. The specimens were in the heating process at 130 min and in the cooling process at 390 min. When the specimens were heated for 130 min, the temperature distributions of the specimens showed that with the increase of the crack width, the temperatures of measuring points at the same depth in the

cracked sections of the concrete plates first decreased and then increased. When the crack width was less than 1 mm, the crack width had delayed effects on the heat transfer in the cracked sections of the concrete plates. When the crack width was larger than 1 mm, the crack width had accelerated effects on the heat transfer in the cracked sections of the concrete plates. Comparing the temperature distributions of the specimens at 260 min and 390 min, it could be found that with the increase of the crack width, the temperature reductions of the measuring points at the same depth in the cracked sections of the concrete plates first decreased and then increased. This showed that the effects of crack width in the cooling process was similar to that in the heating process. When the crack width was less than 1 mm, the crack width had delayed effects on the heat transfer in the cracked sections of the concrete plates. When the crack width was larger than 1 mm, the crack width had accelerated effects on the heat transfer in the cracked sections of the concrete plates.

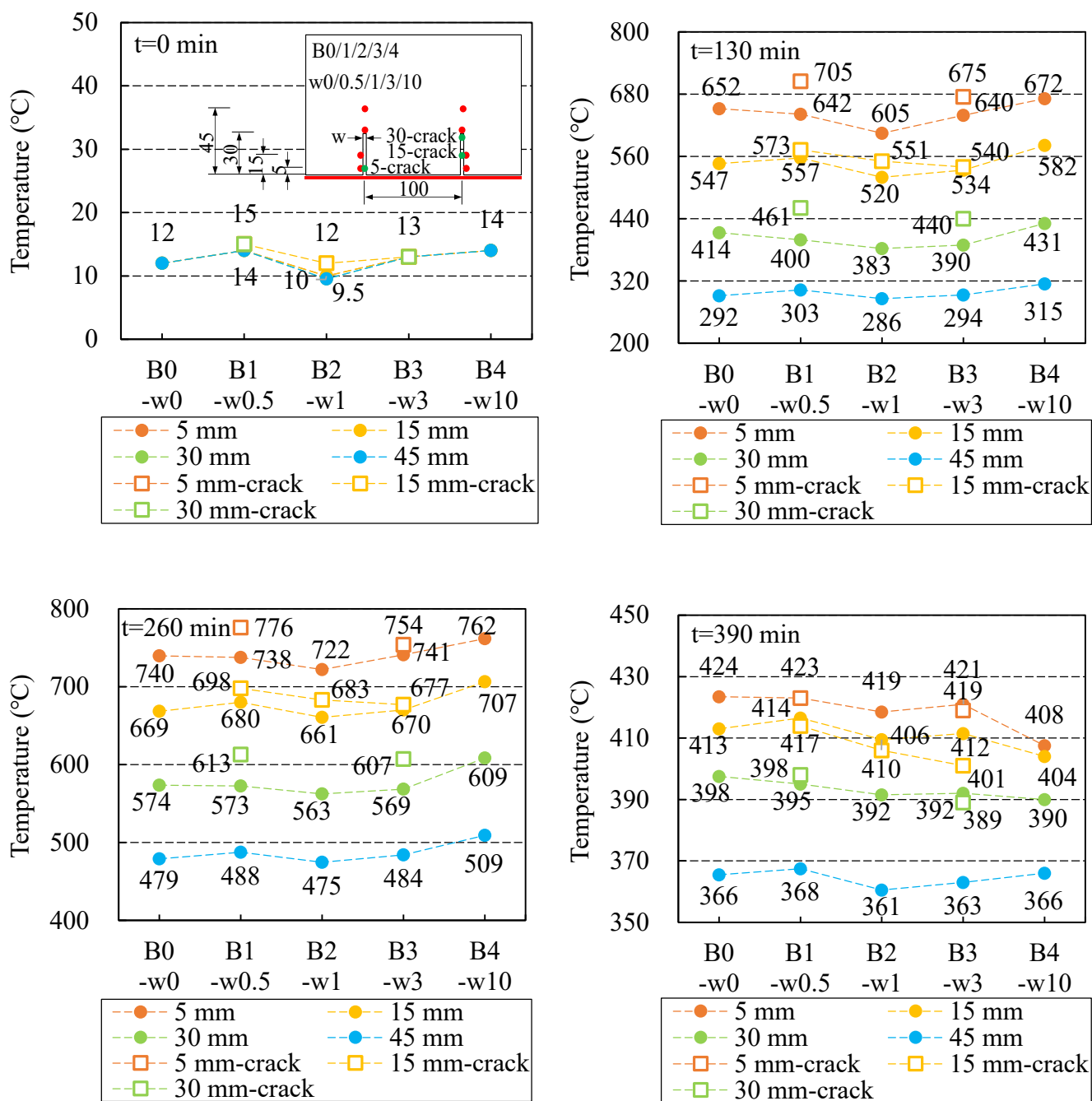


Figure 4. Temperature distributions on the cracked sections of the specimens with different crack widths

As illustrated in Figure 5, the crack width had no obvious effects on the temperature distributions over the uncracked sections of the concrete plate specimens.

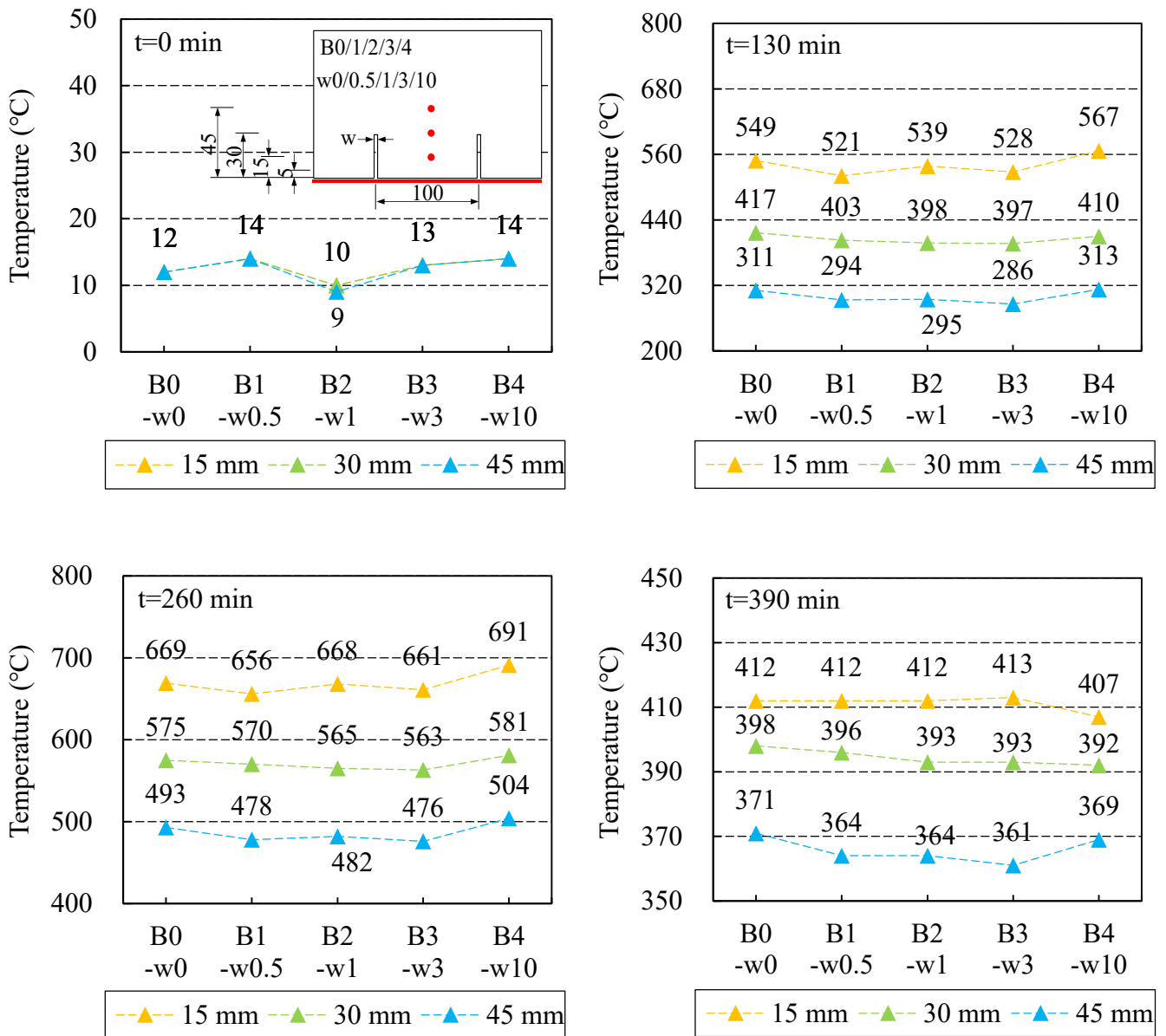


Figure 5. Temperature distributions on the uncracked sections of the specimens with different crack widths

The temperature distributions on the cracked and uncracked sections of the concrete plate specimens with 1 and 2 cracks, i.e., specimens B5 and B2, at different times are shown in Figure 6 and Figure 7, respectively. When the specimens were heated for 130 min, the temperature distributions of the specimens showed that the interactions between cracks had accelerated effects on the heat transfer in the concrete plates. The temperatures of measuring points at the same depth in the cracked and uncracked sections of specimen B2 with 2 cracks were higher than that of specimen B5 with 1 crack. Comparing the temperature distributions of the specimens at 260 min and 390 min, it could be found that the interactions between cracks had accelerated effects on the heat transfer in the concrete plates. The temperature reductions of the measuring points at the same depth in the cracked and uncracked sections of specimen B2 with 2 cracks were higher than that of specimen B5 with 1 crack.

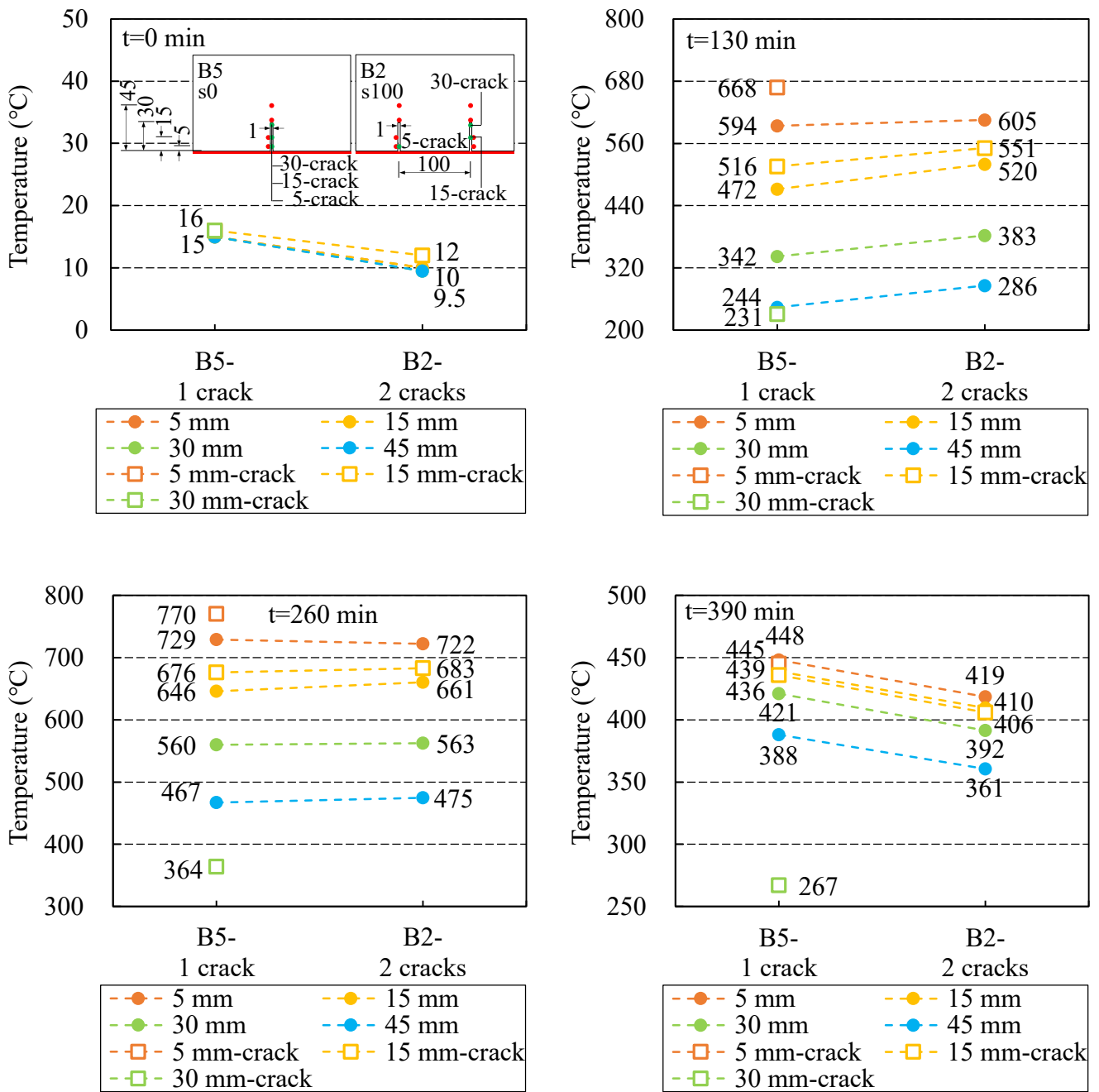


Figure 6. Temperature distributions on the cracked sections of the specimens with 1 and 2 cracks

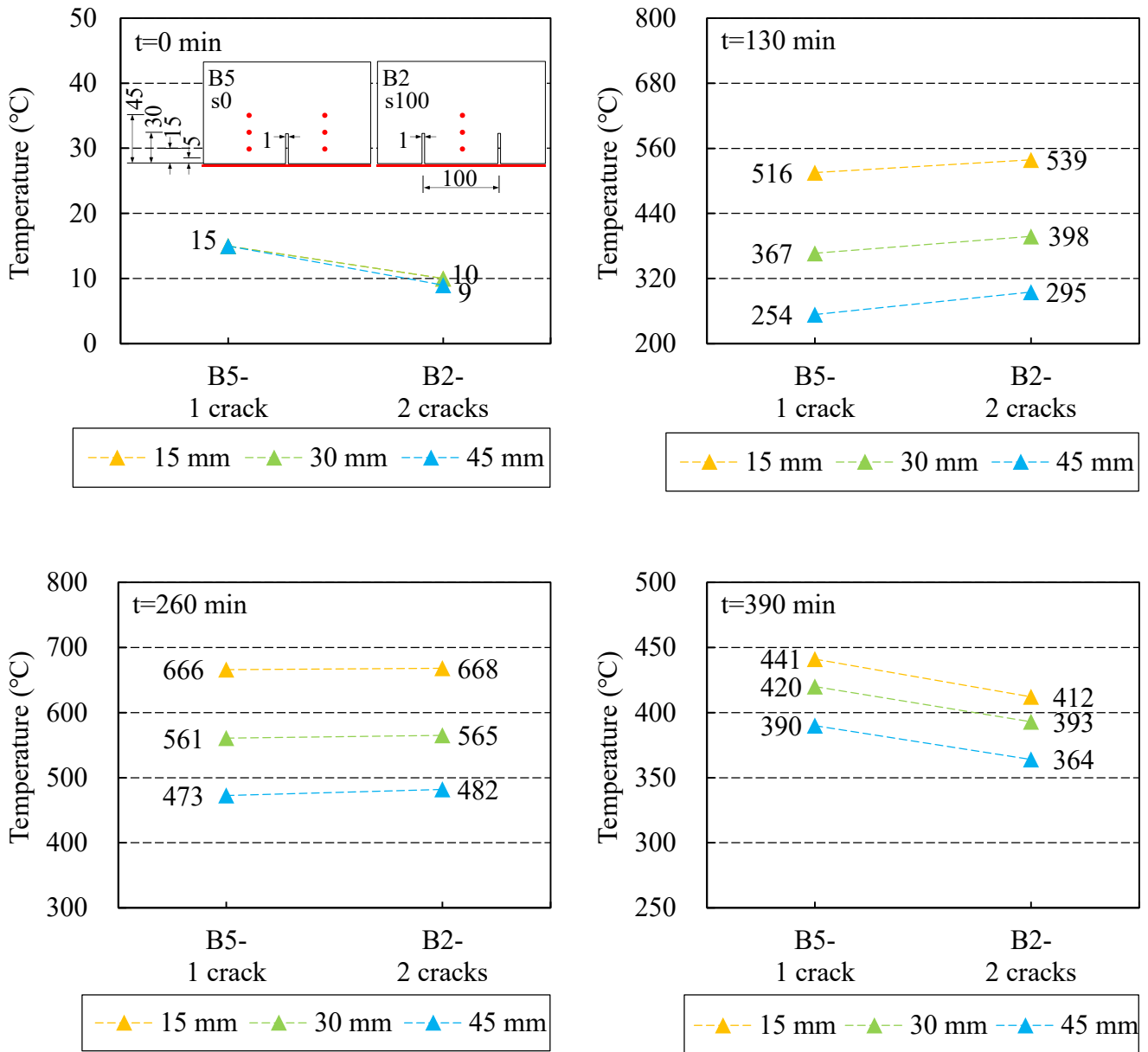


Figure 7. Temperature distributions on the uncracked sections of the specimens with 1 and 2 cracks

3.2 Pore pressures

For concrete plate specimens with cracks, except specimen B3, the maximum pore pressures of measuring points in the cracked sections were higher than that of measuring points at the same depth in the uncracked sections, as illustrated in Figure 8. As shown in Table 3, the maximum pore pressures of most measuring points at 30 mm and 45 mm depths in the cracked sections of specimens B1 ~ B4 were very small, and the crack width had no obvious effects on the pore pressure developments at different depths into the concrete plate specimens. The maximum pore pressures of measuring points at 30 mm depth were between 0.017 and 0.034 MPa except that B3-PR'30 was 0.143 MPa. The maximum pore pressures of measuring points at 45 mm depth were between 0.034 and 0.078 MPa except that B1-PL'45 was 0.143 MPa. In the uncracked sections of specimens B1 ~ B4, the maximum pore pressures of measuring points at 15 mm depth decreased with the increase of the crack width. The crack width had no obvious effects on the maximum pore pressures of measuring points at 30 and 40 mm depths in the uncracked sections of the concrete specimens.

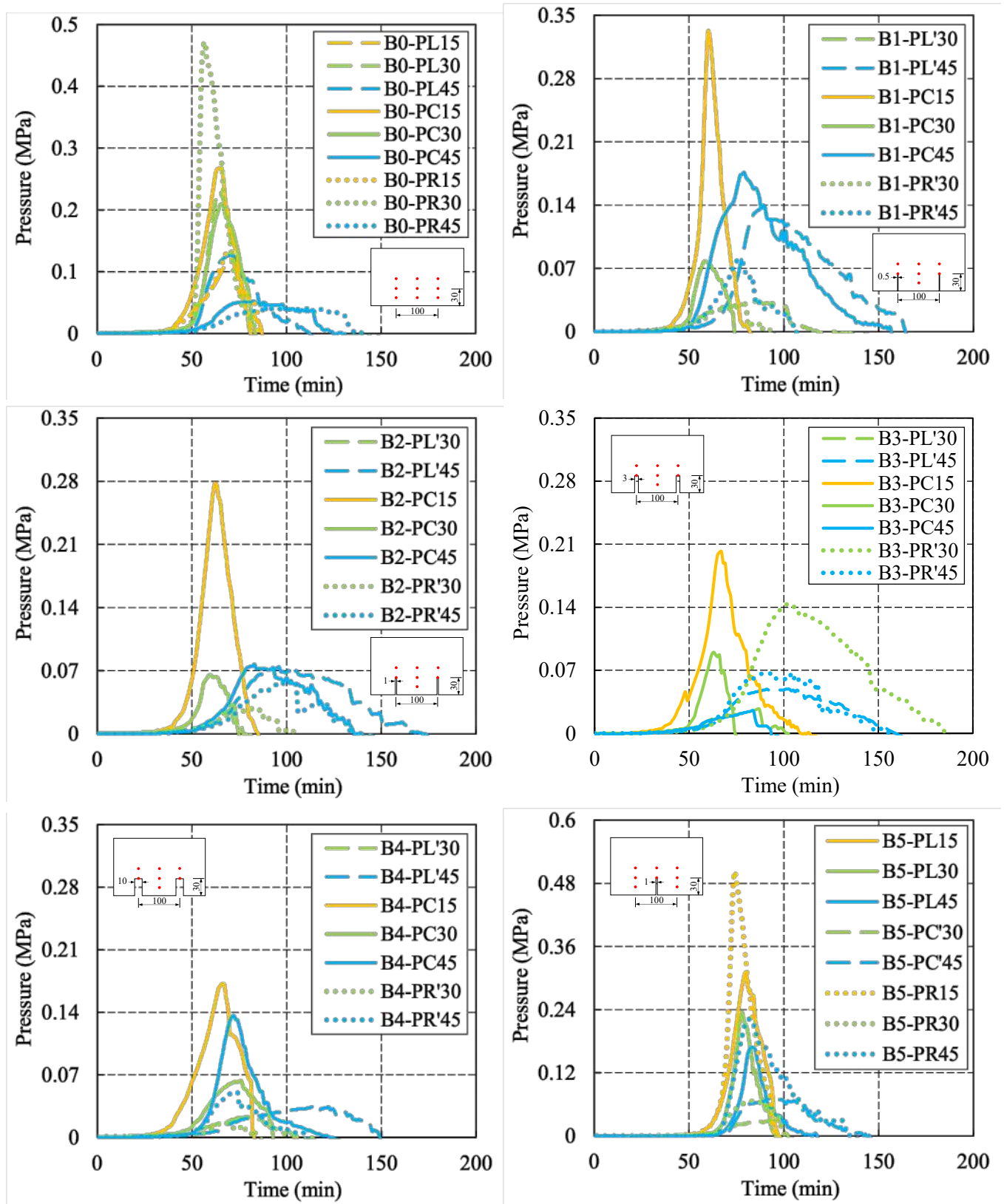


Figure 8. Pore pressure developments at different depths into the concrete plate specimens

As shown in Table 4, the maximum pore pressures of measuring points at 30 mm and 45 mm depths in the cracked sections of specimen B2 with 2 cracks were close to specimen B5 with 1 crack, and the interactions between cracks had no obvious effects on the pore pressure developments at different depths into the concrete plate specimens. The maximum pore pressures of measuring points at 30 mm depth were between 0.026 and 0.030 MPa. The maximum pore pressures of measuring points at 45 mm depth were between

0.059 and 0.076 MPa. The maximum pore pressures of measuring points at different depths in the uncracked sections of specimen B2 were lower than that of specimen B5, indicating that the interactions between cracks reduced the maximum pore pressures in the uncracked sections of the specimens.

Table 4. The maximum pore pressures of specimens with different crack widths

Tubes	Maximum Pressures (MPa)	Time (min)	Temperatures (°C)
PL'30 (B0/B1/B2/B3/B4)	0.230/0.034/0.026/0.027/0.024	65/88/71/87/82	155/240/146/237/244
PR'30 (B0/B1/B2/B3/B4)	0.472/0.030/0.028/0.143/0.017	58/80/83/102/66	136/216/207/319/131
PL'45 (B0/B1/B2/B3/B4)	0.126/0.138/0.074/0.050/0.034	70/91/97/96/114	129/180/189/188/277
PR'45 (B0/B1/B2/B3/B4)	0.041/0.078/0.059/0.067/0.050	114/76/101/90/73	246/128/199/173/121
PC15 (B0/B1/B2/B3/B4)	0.267/0.332/0.277/0.202/0.172	65/61/63/68/67	236/193/221/247/262
PC30 (B0/B1/B2/B3/B4)	0.209/0.078/0.065/0.090/0.063	67/59/60/64/76	159/133/126/135/191
PC45 (B0/B1/B2/B3/B4)	0.052/0.176/0.077/0.025/0.136	81/80/84/84/73	150/136/145/140/131

Table 5. The maximum pore pressures of specimens with 1 and 2 cracks

Tubes	Maximum Pressures (MPa)	Time (min)	Temperatures (°C)
PL'30 (B2)/PR'30 (B2)/PC'30 (B5)	0.026/0.028/0.030	71/83/95	146/207/163
PL'45 (B2)/PR'45 (B2)/PC'45 (B5)	0.074/0.059/0.076	97/101/96	189/199/122
PC15 (B2)/PL15 (B5)/PR15 (B5)	0.277/0.310/0.503	63/80/74	221/225/196
PC30 (B2)/PL30 (B5)/PR30 (B5)	0.065/0.235/0.067	60/78/84	126/142/172
PC45 (B2)/PL45 (B5)/PR45 (B5)	0.077/0.168/0.222	84/83/82	145/120/115

4 CONCLUSIONS

This paper investigated experimentally the thermal-hydral responses, i.e., the temperatures and pore pressures, at different depths into unilaterally heated cracked concrete plates subjected to elevated temperatures. Based on the test results, the effects of crack width and the effects of interactions between cracks on the distributions of temperatures and pore pressures were explored. Results showed that:

- (1) When the crack width was less than 1 mm, the crack width had delayed effects on the heat transfer in the cracked sections of the concrete plates; when the crack width was larger than 1 mm, the crack width had accelerated effects on the heat transfer in the cracked sections of the concrete plates; the crack width had no obvious effects on the temperature distributions over the uncracked sections of the concrete plate specimens.
- (2) The interactions between cracks had accelerated effects on the heat transfer in both the cracked and uncracked sections of the concrete plates.
- (3) The crack width had no obvious effects on the maximum pore pressures in the concrete plates except that the maximum pore pressures of measuring points at 15 mm depth in the uncracked section of the concrete specimens decreased with the increase of the crack width.
- (4) The interactions between cracks had no obvious effects on the maximum pore pressures in the cracked sections but reduced the maximum pore pressures in the uncracked sections of the concrete specimens.

More experiments to explore the effects of moisture content, crack depth, crack spacing and heating rate on the distributions of temperatures and pore pressures in cracked concrete plate specimens subjected to elevated temperatures are underway in the authors' group and will be reported in the near future.

ACKNOWLEDGEMENTS

This research work was financially supported by the National Natural Science Foundation of China with Grant No. 52278524.

REFERENCES

1. National Bureau of Statistics, "Report 19 on Economic and Social Development Achievements Since the 18th National Congress of the Communist Party of China [EB/OL]," 2022, https://www.stats.gov.cn/sj/sjjd/202302/t20230202_1896697.html (in Chinese).
2. Y. Luo, Q. Li, L. Jiang and Y. Zhou, "Analysis of Chinese fire statistics during the period 1997–2017," *Fire Saf. J.*, vol. 125, p. 103400, 2021, doi: 10.1016/j.firesaf.2021.103400.
3. C. Jiang, H.C. Zhang, Y.Q. Ge, X.L. Gu and X.B. Song, "Experimental study on thermo-hydro-mechanical responses of concrete plates subjected to in-plane compressive loading and one-side heating," *Fire Saf. J.*, vol. 144, pp. 104108, 2024, doi: 10.1016/j.firesaf.2024.104108.
4. C. Jiang, J. Fang, J.Y. Chen, X.L. Gu, "Modeling the instantaneous phase composition of cement pastes under elevated temperatures," *Cement Concr. Res.*, vol. 130, pp 105987, 2020, doi: 10.1016/j.cemconres.2020.105987.
5. C. Jiang, H.C. Zhang, Y.Q. Ge, X.L. Gu, "Effects of carbonation on fire spalling behaviour of concrete: a preliminary experimental study," in: L. Jiang, P.V. Real, X. Huang, Z. Nan, A. Usmani (Eds.), *Proceedings of the 12th International Conference on Structures in Fire*, Hong Kong, China, 2022.
6. E. Vejmelkova, P. Padevet, and R. Cerny, "Effect of cracks on hygric and thermal characteristics of concrete," *Bauphysik*, vol. 30, no. 6, pp. 438-444, 2008.
7. A. Ervine, M. Gillie, T.J. Stratford and P. Pankaj, "Thermal Propagation through Tensile Cracks in Reinforced Concrete," *ASCE J. Mater. Civil Eng.*, vol. 24, no. 5, pp. 516-522, 2012, doi: 10.1061/(ASCE)MT.1943-5533.0000417.
8. B. Wu, W. Xiong and B. Wen, "Thermal fields of cracked concrete members in fire," *Fire Saf. J.*, vol. 66, pp. 15-24, 2014, doi: 10.1016/j.firesaf.2014.04.003.
9. G.Z. Ba, J.J. Miao, W.P. Zhang and L.N. Ji, "Influence of crack on temperature field of concrete at elevated temperature," *J. Build. Mater.*, vol. 19, no. 04, pp. 730-736, 2016, doi: 10.3969/j.issn.1007-9629.2016.04.021 (in Chinese).
10. G.Z. Ba, J.J. Miao, W.P. Zhang and C.W. Liu, "Influence of Cracking on Heat Propagation in Reinforced Concrete Structures," *J Struct. Eng.*, vol. 142, no. 7, 2016, doi: 10.1061/(ASCE)ST.1943-541X.0001483.
11. Y. Liu, J. Miao, J. Liu, G. Ba and C. Liu, "Calculation of Thermal Fields of Cracked Concrete at Elevated Temperatures," *KSCE J Civ. Eng.*, vol. 25, no. 1, pp. 153-161, 2021, doi: 10.1007/s12205-020-2057-z.
12. C. Jiang, Y.Q. Ge, H.C. Zhang and X.L. Gu, "Effects of thermal expansion of enclosed medium and direction of pressure bearing plane of metal tubes on pore pressure measurements in cement-based materials under elevated temperatures," *Fire Saf. J.*, vol. 130, pp. 103599, 2022, doi: 10.1016/j.firesaf.2022.103599.

FIRE BEHAVIOUR OF REINFORCED CONCRETE BEAMS STRENGTHENED IN SHEAR USING EMBEDDED THROUGH-SECTION (ETS) STEEL OR CFRP BARS – FIRE RESISTANCE TESTS AND NUMERICAL THERMAL MODELLING

Adriana S. Azevedo¹, João P. Firmo², João R. Correia³

ABSTRACT

The first part of this paper presents an experimental study about the fire behaviour of reinforced concrete (RC) beams strengthened in shear according to the embedded through-section (ETS) technique using different strengthening materials (CFRP or steel bars), bonded to concrete with an epoxy adhesive. The RC beams were simultaneously subjected to the ISO 834 standard fire curve and a service loading in a three-point bending configuration. The results confirmed the vulnerability of ETS strengthening systems to fire: the mechanical contribution of the ETS-CFRP system was lost after only 12 min of fire exposure, whereas the fire resistance of the ETS-steel system was 48 min. At these instants, the average temperatures measured along the anchorage length of the ETS systems were respectively 64 °C and 221 °C. In the second part of the paper, three-dimensional finite element thermal models were developed to assess the influence on the fire resistance of ETS-strengthened RC beams of (i) the concrete cover thicknesses of the ETS bars and of (ii) applying fire protection systems composed by calcium silicate boards. The numerical results showed that with ETS-CFRP bars it is possible to attain fire resistances of 32 min or 121 min by adopting, respectively, a concrete cover of 30 mm (for the ETS bars), or a U-shaped fire protection with 24 mm and 48 mm of thickness, respectively, at the beam's side and bottom faces. For ETS-steel bars, adopting a concrete cover of 30 mm or applying a U-shaped fire protection with a constant thickness of 12 mm allowed attaining fire resistances of 87 min or 140 min, respectively.

Keywords: RC beams; shear strengthening; embedded through-section (ETS) technique; fire resistance tests; numerical thermal modelling.

1 INTRODUCTION

Carbon fibre reinforced polymer (CFRP) systems have been successfully used during the last two decades for strengthening existing reinforced concrete (RC) structures due to their advantages over the more conventional strengthening solutions (e.g. concrete jacketing or steel plate bonding). These advantages include high strength-to-weight ratio, resistance to corrosion and ease of application. For shear strengthening of RC beams, the most common CFRP strengthening technique consists of bonding CFRP laminates or sheets directly on the lateral surface of beams. Although the structural effectiveness of this technique (known as “externally bonded reinforcement” - EBR) has been thoroughly studied and demonstrated, premature failure modes due

¹ PhD student, CERIS, Instituto Superior Técnico, University of Lisbon
e-mail: adriana.azevedo@tecnico.ulisboa.pt, ORCID: <https://orcid.org/0000-0001-6525-8748>

² Assistant Professor, CERIS, Instituto Superior Técnico, University of Lisbon
e-mail: joao.firmo@tecnico.ulisboa.pt, ORCID: <https://orcid.org/0000-0003-3449-3686>

³ Full Professor, CERIS, Instituto Superior Técnico, University of Lisbon
e-mail: joao.ramoa.correia@tecnico.ulisboa.pt, ORCID: <https://orcid.org/0000-0001-5485-136X>

to CFRP debonding can occur, preventing the full exploitation of the CFRP's strength. To overcome this issue, a new technique named embedded through-section (ETS) has emerged, which consists of bonding CFRP or steel bars inside predrilled holes in the concrete section. Various studies (e.g. [1,2]) have shown the higher effectiveness of the ETS technique for shear strengthening of RC beams (at ambient temperature conditions) when compared to that provided by EBR-CFRP strengthening. However, when exposed to elevated service temperatures or fire, the mechanical contribution of CFRP strengthening techniques is highly affected, as it relies on the bond behaviour to concrete ensured by polymeric adhesives, which undergo a glass transition process when heated – the glass transition temperature (T_g) of typical polymeric adhesives is within the 45-80 °C range, and is normally considered as a “critical” temperature, above which the mechanical and bond properties of the systems are highly compromised.

The susceptibility of EBR-CFRP strengthening systems to fire is unanimously recognised and a significant number of studies have addressed this issue (e.g. [3]), however, no information is available in the literature about the effects of elevated temperatures/fire exposure on ETS-strengthened RC structures. The authors have recently started an investigation that aimed at contributing to fill this knowledge gap; as a first step, the bond behaviour to concrete of ETS-bars at elevated temperatures was experimentally evaluated through direct pull-out tests on CFRP and steel bars bonded to concrete cylinders using an epoxy adhesive ($T_g = 65.5$ °C) [4]. The results confirmed that both ETS-CFRP and -steel systems are susceptible to high temperatures, with the CFRP bars presenting a steeper bond strength reduction with temperature compared to the ETS-steel counterparts (e.g. reductions of $\approx 75\%$ and $\approx 45\%$ at 50 °C, respectively).

Following the above-mentioned study that confirmed the vulnerability of ETS-bars bonded to concrete when exposed to elevated temperatures, the present paper describes a second step of that investigation, with the main goal of understanding the effects of such bond strength reduction on the fire resistance behaviour of ETS-strengthening systems installed in RC beams. To this end, an experimental study was performed about the fire behaviour of RC beams strengthened in shear using ETS-CFRP and -steel bars (similar to those used in [4]). Then, three-dimensional (3D) finite element (FE) thermal models of the ETS-strengthened beams were developed to evaluate the efficacy of different strategies to improve the fire resistance of the ETS strengthening systems, namely by (i) adopting different concrete cover thicknesses for the ETS bars, or (ii) applying different fire protection systems.

2 DESCRIPTION OF THE FIRE RESISTANCE TESTS

2.1 Test series and materials

The experimental programme comprised fire resistance tests on 3 beams with a cross-section of 200 × 300 mm (width × height) and length of 1500 mm long (1400 mm span, cf. Figure 1): one reference RC beam (hereafter identified as “Ref” - unstrengthened), one beam strengthened with vertical ETS-steel bars (beam Steel-90) and one beam strengthened with vertical ETS-CFRP bars (beam CFRP-90). All beams were cast with ready-mixed concrete using Portland cement type CEM II/A-L 42.5R with the following average properties at the age of testing (1100 days): compressive strength of 35 MPa (cubes), and splitting tensile strength of 2.5 MPa. The internal steel reinforcement (average yield stress of 603 MPa) was designed to promote shear failure in the shorter shear span (610 mm long, cf. Figure 1a), where the ETS strengthening systems were installed.

Two types of ETS bars were adopted: (i) conventional ribbed steel bars with 10 mm of diameter (steel A500, average yield stress of 565 MPa; elastic modulus of 191 GPa) and (ii) sand-coated CFRP bars with 8 mm of diameter (BASF MasterBrace Bar 165/2500), composed by 68% of unidirectional carbon fibres (in volume) embedded in an epoxy resin matrix, with a ≈ 1 mm thick sand coating (cf. Figure 1) and the following average properties: tensile strength of 2522 MPa and elastic modulus of 167 GPa. The T_g of the CFRP bars was determined from dynamic mechanical analysis (DMA) performed according to ASTM E1640, resulting in $T_g = 75.8$ °C, defined based on the onset value of the storage modulus curve decay. Both types of ETS-bars were bonded inside pre-drilled vertical holes in the central alignment of the beams (diameters of 16 mm and 18 mm for CFRP and steel bars, respectively) using a two-component epoxy-based adhesive (S&P Resin 55), with a T_g of 65.5 °C, determined according to the same method used for the CFRP bars.

The ETS bars were designed to provide high shear strength increases, thus simulating a scenario in which the strengthening system is needed to withstand the design load for a fire (design) situation. Preliminary tests performed at ambient temperature conditions on similar beams [5] showed that the ETS-steel and -CFRP strengthening systems provided shear strength increases of 47% and 58%, respectively, when compared to the shear capacity of the reference RC beam.

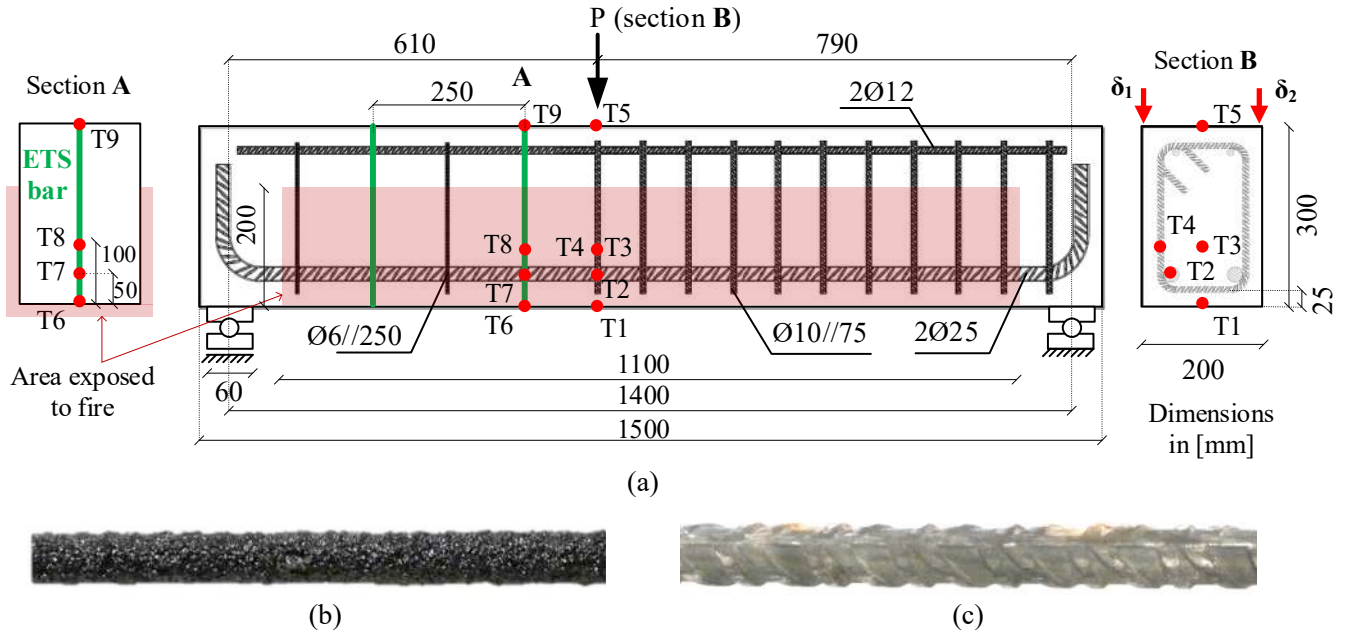


Figure 1. (a) Geometry of beams, position of thermocouples (T) and displacement transducers (δ); (b) sand-coated CFRP bars; (c) ribbed steel bars

2.2 Test setup, instrumentation and procedure

The beams were placed at the top of an intermediate scale furnace and loaded in a three-point bending configuration (Figure 2a). The applied load, defined as 70% of the design load at ambient temperature, was 51% (95.5 kN), 55% (149.3 kN) and 53% (157.6 kN) of the experimental shear load capacity at ambient temperature conditions (determined in [5]) of beams Ref, Steel-90 and CFRP-90, respectively. As shown in Figure 2, the load was transmitted to a distribution beam at one end through a steel bar fixed to a hydraulic jack (capacity of 500 kN), and reacted on the loaded section of the RC beam and on the reaction frame through hinged-steel plates.

To simulate the typical fire exposure of a RC beam, the top surface was exposed to ambient temperature and the upper 100 mm of the lateral faces were protected with ceramic wool (to simulate the presence of a slab); with this insulation scheme, only the bottom face and 200 mm of the beams lateral faces were exposed to fire (figure 2b).

Temperatures were measured using thermocouples type K (external diameter of 1 mm) distributed in the concrete, internal steel reinforcement and strengthening system, in two cross sections of the beams (cf. Figure 1). At the load application section (section B), three thermocouples were placed at different heights of the concrete (T1, T3 and T5) and two thermocouples were placed at the internal steel reinforcement (T2 at the tensile steel rebar and T4 at the steel stirrups); the ETS bars were instrumented with four thermocouples at different heights (T6, T7, T8 and T9 at the strengthening bar in section A, cf. Figure 1). The vertical displacement at the loaded section was also measured with two displacement transducers placed at the top of the RC beams (cf. δ_1 and δ_2 in Figure 1).

The test procedure consisted of two stages: (i) application of the above-mentioned point loading and, after 10 min (to ensure displacements' stabilization), (ii) exposure to the standard ISO 834 fire curve. The tests were stopped some minutes after the mechanical contribution of the strengthening system was lost (the identification of those instants is discussed in section 3.2).

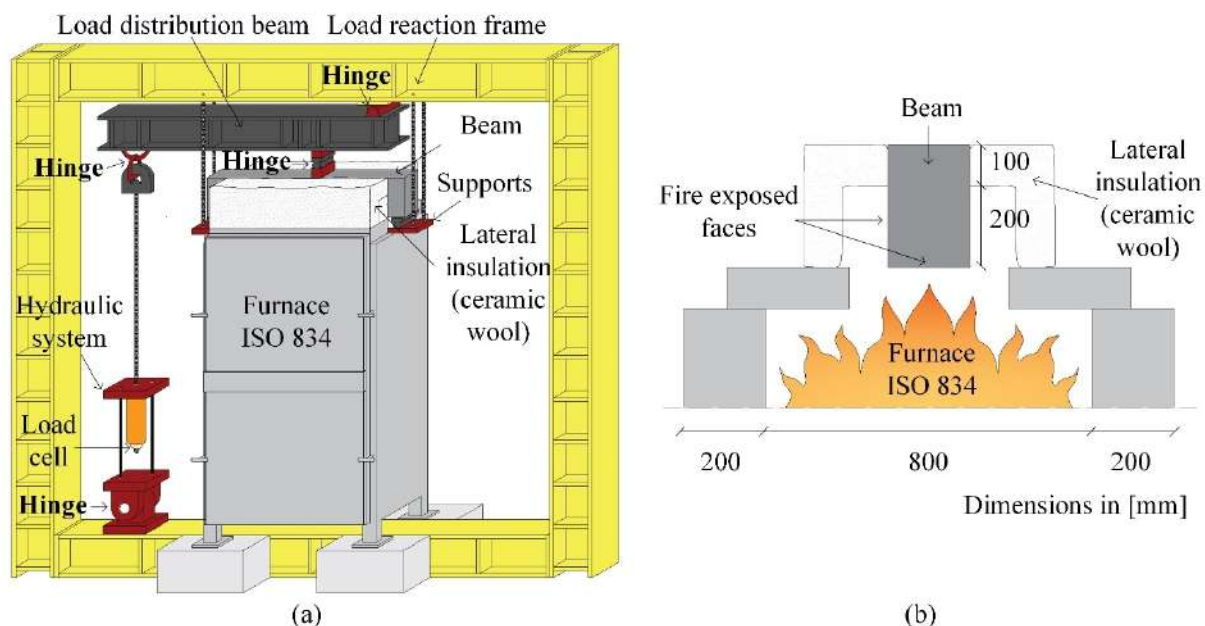


Figure 2: (a) Schematic overview of fire resistance test setup; (b) scheme of lateral fire insulation

3 EXPERIMENTAL RESULTS

3.1 Temperature distributions

Figure 3 shows the evolution of the temperatures in different locations of the tested beams at sections A (with strengthening system) and B (load application). The furnace temperature (T_{furnace} , cf. Figure 3b) followed very closely the ISO 834 standard time-temperature curve, with maximum relative differences ($\pm 48^\circ\text{C}$) well within the allowed limits of that standard ($\pm 100^\circ\text{C}$). The temperatures at the bottom steel rebars and steel stirrups (respectively thermocouples T2 and T4, Figure 3b) presented a similar behaviour in all beams: they increased almost linearly up to 100°C , exhibiting a small plateau at this temperature (due to concrete's water evaporation), and then increased up to the end of the fire tests, reaching maximum temperatures of 321°C (T2) and 265°C (T4) in beam Steel-90, when the strengthening system debonded (those instants are identified in Figure 4b, as discussed in section 3.2) – for those temperatures, the reductions on the mechanical properties of steel can be considered negligible (e.g. according to EN 1992-1-2). As expected, the temperatures in the concrete (thermocouples T1, T3 and T5) and in the ETS bars (thermocouples T6, T7, T8 and T9) increased at higher rates next to the exposed faces.

Figures 3 (c) and (d) show that temperatures attained in the strengthening systems at the debonding instants can be significantly higher than the adhesive's T_g (65.5°C), especially at the bottom part of the strengthening bars (thermocouple T6) in beam Steel-90.

Figure 4 (a) presents the temperatures in the strengthening bars along the beam's height at the debonding instants (identified in Figure 4 (b) and discussed in section 3.2). As expected, temperatures increased from the top faces towards the bottom faces (exposed to fire) of the beams, regardless of the type of ETS bar. However, it is noted that the temperatures attained at the debonding instant in the ETS-steel bars are higher than those attained in the CFRP counterparts. Figure 4 (a) also shows that, in beam CFRP-90, the temperature attained at the debonding instant in thermocouple T8 (at 1/3 of the beam's height, i.e. 100 mm , cf. Figure 1) is close to ambient temperature; this result shows that even though most of the bonded length was kept approximately at ambient temperature, the strengthening system debonded, confirming the major influence of moderately elevated temperatures in the structural behaviour of ETS-CFRP strengthening systems. On the other hand, significantly higher temperatures were attained at the debonding instant in the same location (thermocouple T8) in beam Steel-90 (128.6°C) – these results show that the steel-concrete bonded interface can resist much higher temperatures than the CFRP-concrete counterpart, due to the lower

bond strength reduction of the latter, which is consistent with results of bond tests previously reported by the authors using the same materials/systems [4].

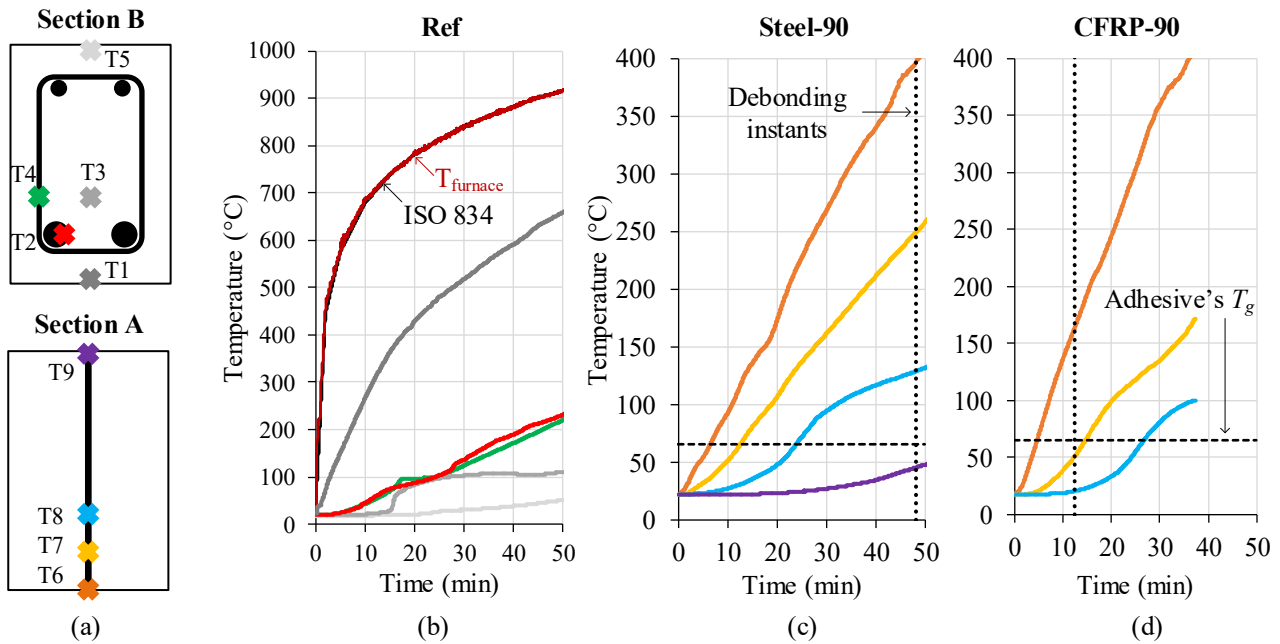


Figure 3. (a) Position of thermocouples in sections A and B (see Figure 1); temperatures vs. time of fire exposure at section B in beam (b) Ref, and at “section” A in beams (c) Steel-90, (d) CFRP-90 (vertical dashed lines mark debonding instants)

3.2 Structural response in fire and failure modes

Figure 4b shows the vertical displacement increase at the load application section with the time of fire exposure; the debonding instants of the ETS bars (i.e. when the mechanical contribution of strengthening systems was lost) were identified through the sudden displacement increases in these curves. In beam CFRP-90, the strengthening system debonded after 12 min of fire exposure, whereas in beam Steel-90 debonding occurred after a significantly longer period of fire exposure (48 min) – the better performance of the latter beam was attributed to the lower bond strength reduction of steel-ETS bars when compared to that of CFRP counterparts (again, in agreement with [4]).

After the strengthening systems debonded, the beams exhibited similar behaviour, with increasing displacement due to the effects of high temperatures on the stiffness and strength of all materials, followed by shear failure that occurred after 37 min and 85 min, respectively in beams CFRP-90 and Steel-90. These differences in time to failure are explained by the better performance of the steel-ETS system (as mentioned above) and by the fact that different fire (mechanical) loads had been imposed (higher for CFRP-90, cf. section 2.2); in fact (and as expected), after the debonding of the strengthening systems, the RC beams with higher fire loads failed after shorter periods of fire exposure.

Post-fire observations (Figure 5) showed that, as intended, the strengthened beams failed in shear after the debonding of the strengthening system - the ETS-steel bars lost their contribution due to adhesive failure at the bar-adhesive interface, whereas on ETS-CFRP bars the sand coating was ripped off from the bar’s core (similar failure modes had been observed in [4]). Regardless of the material of the ETS bars; the failure mode of all beams involved tensile rupture of the steel stirrups and shear failure of concrete with the formation of a (main) shear crack. These critical shear cracks crossed the ETS bars at about half of their bonded length; therefore, based on this observation, it was concluded that the strengthening bars were anchored along approximately half of their length (i.e. 150 mm). Based on this observation, a “critical” average temperature along the bottom anchorage length of ETS bars was calculated at the debonding instants – resulting in “critical” temperatures of 221 °C and 64 °C, respectively for the ETS-steel and -CFRP bars. These figures confirm, again, that the ETS-steel strengthening system used in the present study outperforms the ETS-CFRP system, being able to keep its mechanical contribution for higher temperatures

than those attained in the CFRP counterpart. It is important to mention that the anchorage length/critical temperatures may vary with the relative position between the shear cracks and the ETS bars; therefore, additional studies about ETS-strengthened RC members with different geometries (and materials) are needed to validate the above-mentioned findings and assumption.

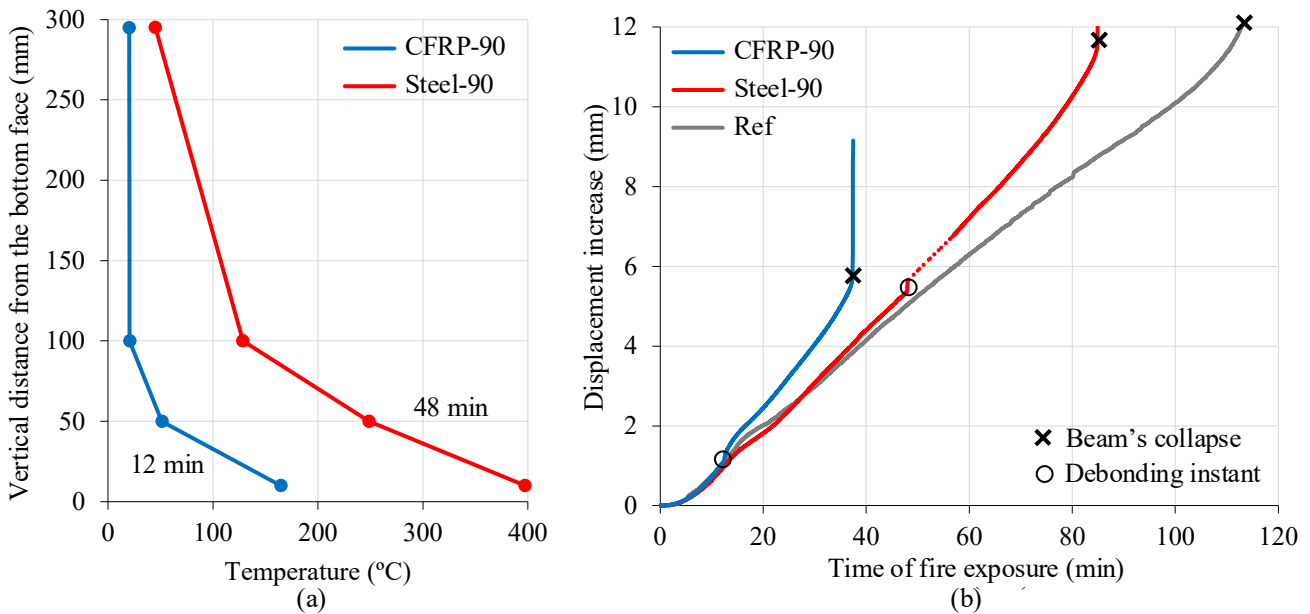


Figure 4. (a) Temperatures along the height of ETS systems (measured in adhesive) at debonding instants, and (b) increase of vertical displacement at load application section (section B) with time of fire exposure

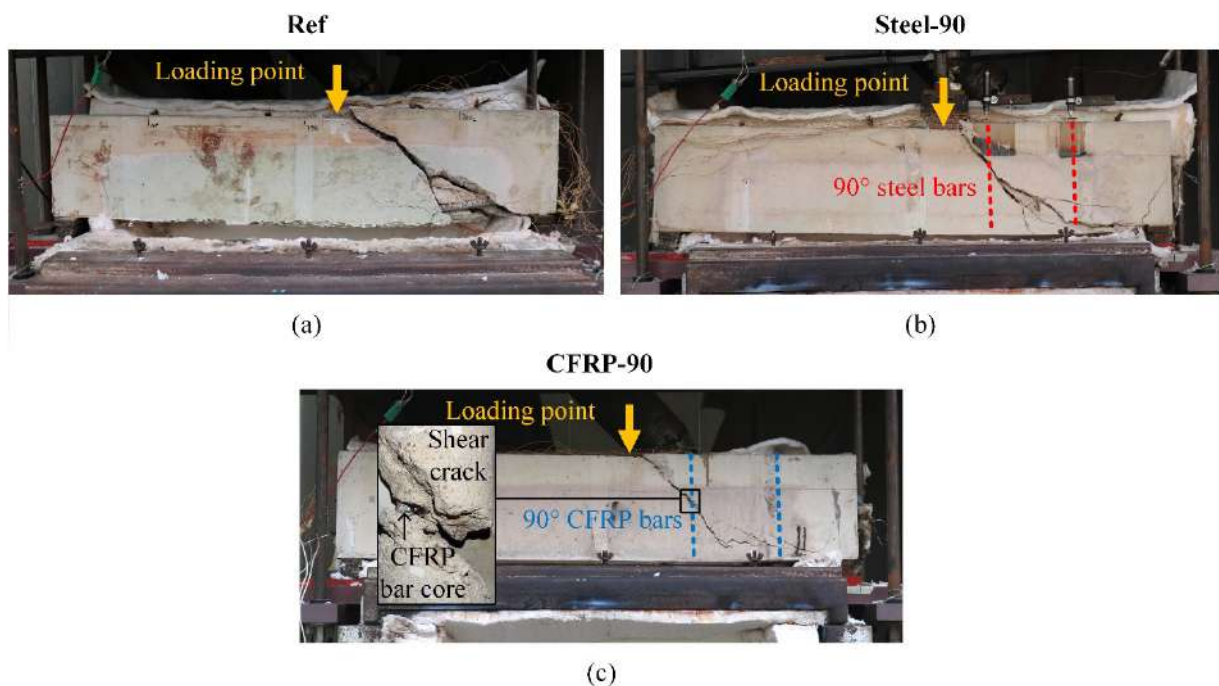


Figure 5. Post-fire assessment of tested beams: (a) Ref, (b) Steel-90, (c) CFRP-90 [fire (mechanical) load marked in yellow and strengthening bars marked as dashed lines]

4 NUMERICAL THERMAL MODELS

4.1 Objectives, description and validation

The main objective of the numerical thermal study was to assess the efficacy of different strategies to improve the fire resistance of RC beams strengthened with ETS-CFRP or -steel bars, namely the use of

(i) thicker concrete cover on the ETS bars, or (ii) fire protection systems composed by calcium silicate (CS) boards. The “concrete cover thickness” of the ETS bars is considered as the distance between the bottom (i.e. fire-exposed) surface of the beams and the lower extremity of the ETS bars, which was null in the tested beams (cf. Figure 1).

The numerical study was divided into two stages. Firstly, three-dimensional (3D) finite element (FE) thermal models of the tested beams were developed using Abaqus software and validated with the experimental temperature distributions. Then, the validated models were used to assess the influence of applying different fire protection geometries/thicknesses and concrete cover thicknesses on the fire resistance of the ETS strengthening systems, assumed here as the fire exposure period for which the average critical temperatures (cf. section 3.2) are attained along the ETS bars’ anchorage length (more details are given in section 4.2).

As shown in Figure 6, only half of the beams’ width (100 mm) and a length of 200 mm around the strengthened section were modelled to reduce computational costs. Twenty-node brick elements (DC3D20) were used to simulate the concrete, strengthening bars and calcium silicate boards, and three-node link elements (DC1D3) were used to model the internal steel reinforcement (all with maximum FE dimensions of 10 mm). The bonding adhesive layer was not modelled due to its negligible influence on the thermal distribution along the ETS bars. Figure 6 also illustrates the thermal boundaries considered in the models. As mentioned in section 2, only a height of 200 mm of the beam’s lateral face was exposed to fire, while the remaining 100 mm were insulated with ceramic wool to simulate the presence of a slab. The top face was exposed to ambient temperature through radiation and convection (adopting a constant convection coefficient of $5 \text{ W}/(\text{m}^2 \cdot ^\circ\text{C})$), whereas the bottom face and the remaining 200 mm of the beam’s side face were exposed to the ISO 834 fire curve, considering radiation and convection, with a constant convection coefficient of $25 \text{ W}/(\text{m}^2 \cdot ^\circ\text{C})$, defined according to EN 1992-1-2. Adiabatic boundaries were considered for the remaining faces.

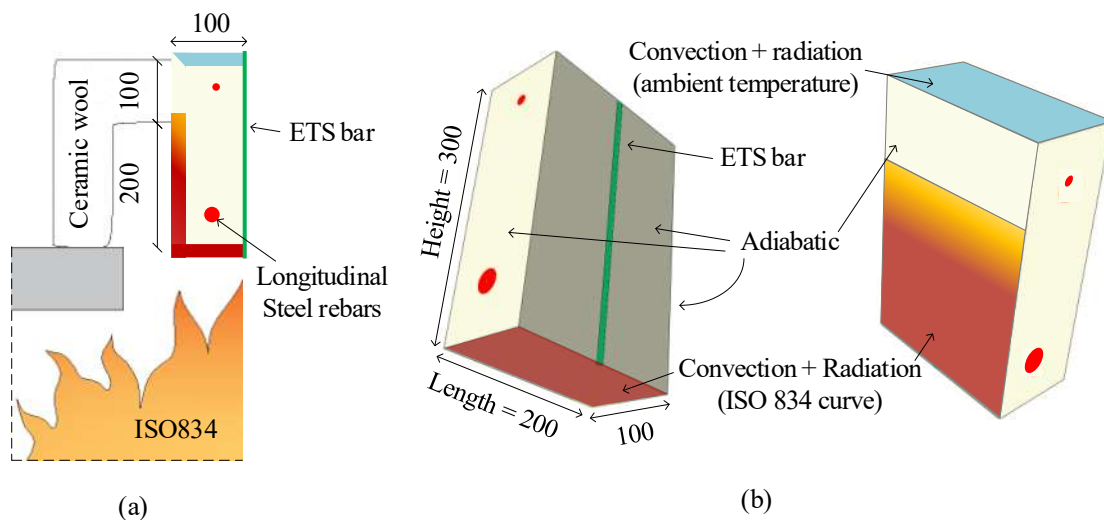


Figure 6. Thermal boundary conditions: (a) scheme of thermal boundaries in fire tests, and (b) thermal boundary conditions assumed in FE models (all dimensions in [mm])

The temperature-dependent thermophysical properties of all materials were considered - the concrete’s density, specific heat and thermal conductivity were defined according to EN 1992-1-2; the concrete’s emissivity was considered as 0.7 and constant with temperature (also according to EN 1992-1-2); the variation with temperature of the thermophysical properties of steel (internal reinforcement and ETS bars) was defined according to EN 1993-1-2; the properties of CFRP bars were defined as in [6] for CFRP pultruded laminates; the thermophysical properties of the CS boards were defined as in [7].

Figure 7 compares the experimental (dashed lines) and numerical (full lines) temperatures as a function of the time of fire exposure at different locations of the load application section in the concrete (section B, cf. Figure 1) for the ETS-steel strengthened beam, and at the strengthened section (section A, cf. Figure 1) for both ETS-CFRP and -steel strengthened beams. The numerical curves present smoother temperature increases with the time of fire exposure when compared to the experimental ones – this might be due to differences between the thermal properties considered in the models (most from the literature) and the actual material properties. Notwithstanding these differences, the models predicted with reasonably good accuracy the corresponding experimental temperatures, thus validating the numerical strategy adopted.

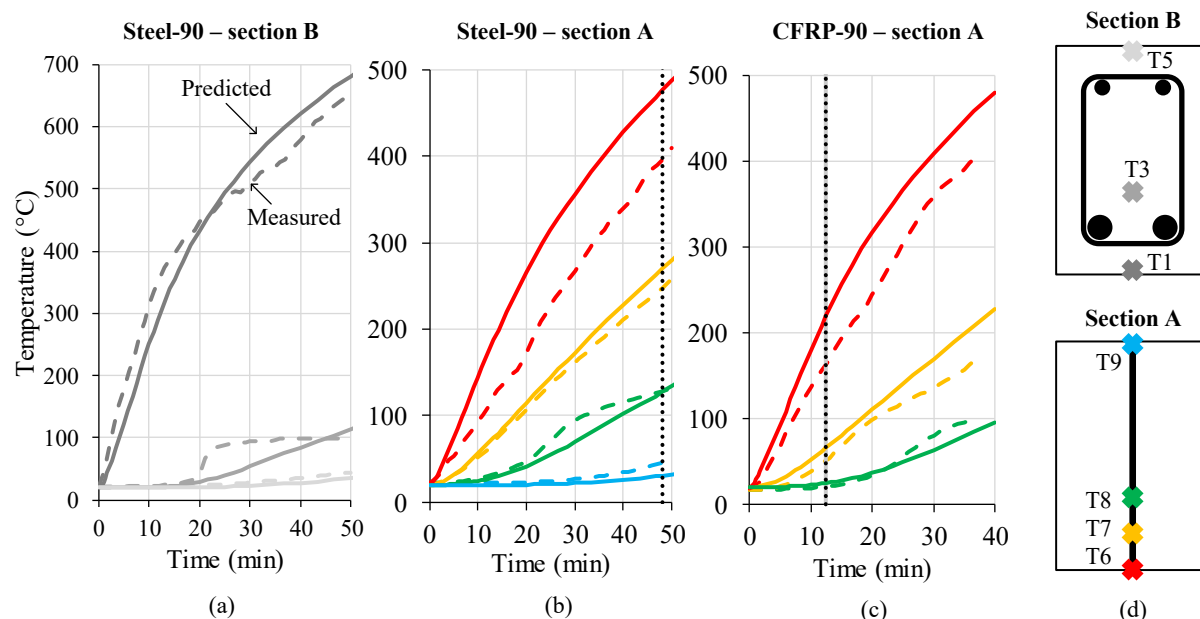


Figure 7. Comparison between predicted temperatures (thermal models, full lines) and measured temperatures (experimental data, dashed lines) in concrete (section B) of beam (a) Steel-90 (as an example), and in the interface (section A) of beams (b) Steel-90 and (c) CFRP-90; (d) thermocouples location (debonding instants presented in black)

4.2 Effects of the concrete cover thickness and fire protection

Different concrete cover thicknesses were considered for the ETS bars: (i) 0 mm (as in the experimental tests), (ii) 10 mm, (iii) 20 mm, and (iv) 30 mm (cf. Table 1); it is worth noting that the length of the ETS bars decreased with the corresponding concrete cover thickness (as exemplified by the FE meshes presented in Figure 8). Assuming that the critical shear crack intersects the ETS bars at approximately the mid-height of the beams' cross-section (as observed in the tests – cf. section 3.2), increasing the concrete cover thickness for the ETS bars results in a reduction of the available anchorage length (with this length corresponding to the distance between the mid-height of the cross-section and the end of the ETS bar closest to the bottom surface of the beam, cf. Figure 8). It is important to mention that this reduction in the anchorage length can affect the overall efficacy of the strengthening system; however, this effect was not considered in the numerical thermal models developed in the present study - additional investigations should be performed to assess this effect by conducting tests and/or developing thermomechanical models.

The fire protection system considered in the numerical study comprised the following geometries/thicknesses of CS boards: (i) 12 mm thick boards applied only at the beams' bottom face, (ii) U-shaped 12 mm thick boards (i.e. 12 mm thick both in the bottom and lateral faces of the beams) (iii) 24 mm thick U-shaped boards, and (iv) U-shaped geometry, with thickness of 24 mm at the beam's side faces and 48 mm at the bottom face (cf. Table 1 and Figure 9). The last two geometries were only simulated for the CFRP-ETS-strengthened beams, as in steel-ETS-strengthened beams satisfactory fire resistance estimates (i.e. above 120 min) were obtained with thinner fire protections.

Table 1. Nomenclature and variables of the developed thermal FE models

Model	ETS material	Concrete cover of the ETS bars	Fire protection geometry
C-0	CFRP	0	-
S-0	Steel	0	-
C-10	CFRP	10	-
C-20	CFRP	20	-
C-30	CFRP	30	-
S-10	Steel	10	-
S-20	Steel	20	-
S-30	Steel	30	-
C-12	CFRP	0	12 mm, Bottom surface
C-U12	CFRP	0	12 mm, U-shape
C-U24	CFRP	0	24 mm, U-shape
C-U24/48	CFRP	0	24 mm side/48 mm bottom, U-shape
S-12	Steel	0	12 mm, Bottom surface
S-U12	Steel	0	12 mm, U-shape

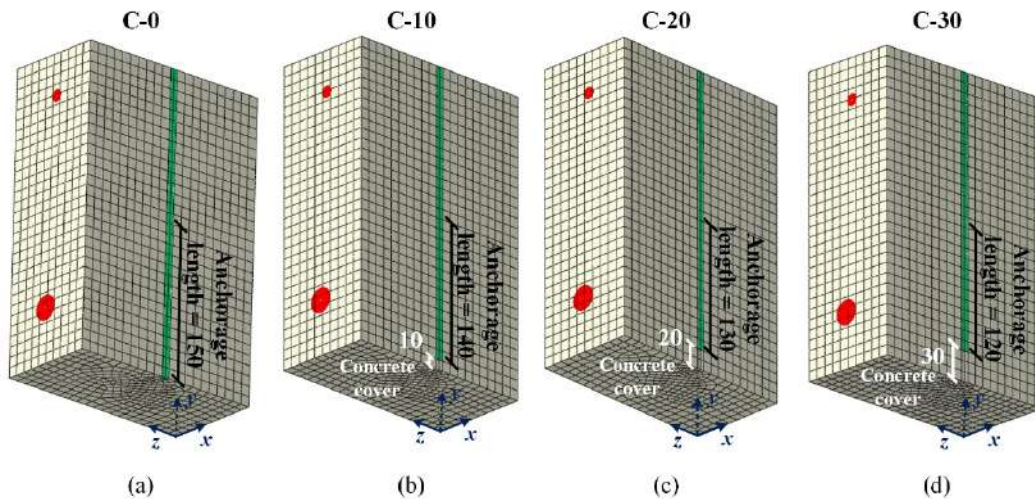


Figure 8. Examples of FE meshes of developed models with different concrete cover thicknesses for ETS-CFRP strengthened beams: (a) C-0, (b) C-10, (c) C-20, (d) C-30 (dimensions in mm)

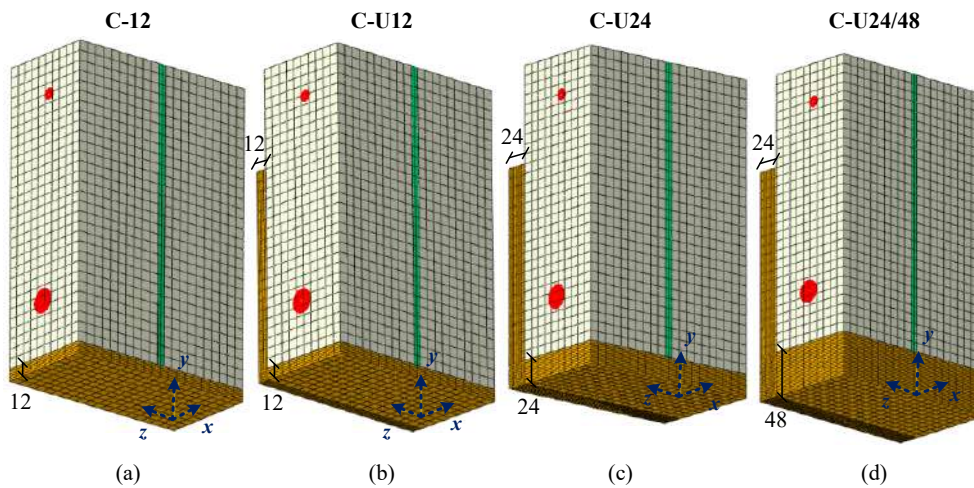


Figure 9. Examples of FE meshes of developed models with different fire protection geometries for CFRP-ETS-strengthened beams: (a) C-12, (b) C-U12, (c) C-U24, (d) C-U24/48 (dimensions in mm)

To assess the influence of the above-mentioned strategies to increase the fire resistance of the ETS strengthening system, a (simplified) thermal criterion was assumed based on a “critical” average temperature along the anchorage length of the ETS bars (considered as the distance between the mid-height of the beams and the bottom end of the ETS bars, cf. section 3.2) related to the debonding of strengthening systems⁴: 286 °C and 94 °C, respectively for ETS-steel and -CFRP bars. Next, when these average temperatures were attained in the different numerical models, the corresponding time of fire exposure was assumed as the predicted fire resistance of the ETS systems.

Figure 10(a) presents the predicted time of fire resistance, i.e. the instant when the above-mentioned “critical” average temperatures were attained along the anchorage lengths (cf. Figure 10b). This figure shows that, as expected, the (predicted) time of fire resistance increased with the concrete cover, resulting in 64 min, 76 min and 87 min, respectively for the beams strengthened with ETS-steel bars, adopting 10 mm (S-10), 20 mm (S-20) and 30 mm (S-30) of concrete cover, respectively, and in 19 min, 26 min and 33 min for the ETS-CFRP-strengthened beams C-10, C-20 and C-30, respectively.

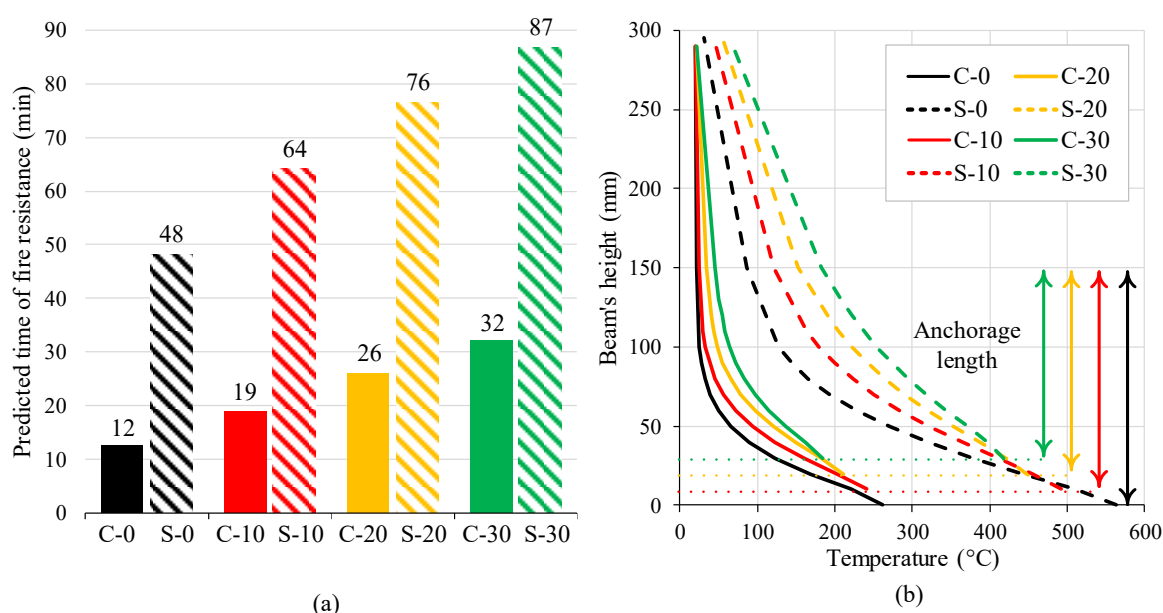


Figure 10. (a) Predicted fire resistance of ETS strengthening system for different concrete cover thicknesses (experimental results available indicated); and (b) Calculated distribution of temperatures along CFRP and steel 90°-ETS bars at debonding instants

Regarding the effect of the fire protection systems, as presented in Figure 11(a), the predicted fire resistance of the strengthening systems increased for both ETS-CFRP and -steel strengthened beams when thicker fire protections were adopted, resulting in 95 min and 140 min for beams S-12 and S-U12, respectively, and 39 min, 51 min, 86 min and 121 min for beams C-12, C-U12, C-U24 and C-U24/48, respectively. Comparing these results with those obtained with the models considering different concrete covers (Figure 10), it was concluded that applying fire protection systems composed by CS boards is more effective in increasing the fire resistance of ETS systems than increasing the concrete cover of ETS bars.

The numerical results presented in Figure 11(a) show that when applying 12 mm thick U-shaped calcium silicate boards on ETS-steel-strengthened beams it is possible to attain (and exceed) 120 min of fire resistance

⁴ The “critical” average temperatures considered in the numerical study were calculated based on the numerical temperature distributions obtained for the fire exposure durations corresponding to the debonding instants; therefore, these “critical” temperatures are different (and higher) to those measured in the fire resistance tests (221 °C and 64 °C, respectively for ETS-steel and -CFRP bars). An alternative approach would be to consider the temperatures measured in the fire resistance tests – at least for beams C-0 and S-0, this assumption would provide conservative estimates of fire resistance of the ETS strengthening systems.

for the ETS systems (which would fulfil the requirements for most building applications), whereas in ETS-CFRP counterparts, CS boards with thickness of 24 mm at the beam's side faces and 48 mm at the beam's bottom face would be needed to attain such fire resistance threshold. It is worth reminding that these conclusions were obtained based on simplified thermal criteria; therefore, additional experimental and numerical studies (namely involving the development of thermomechanical models) are needed to investigate in further depth the fire resistance behaviour of ETS-strengthened RC members and to validate the above-mentioned assumption (thermal criterion) for the loss of effectiveness of ETS strengthening systems in fire.

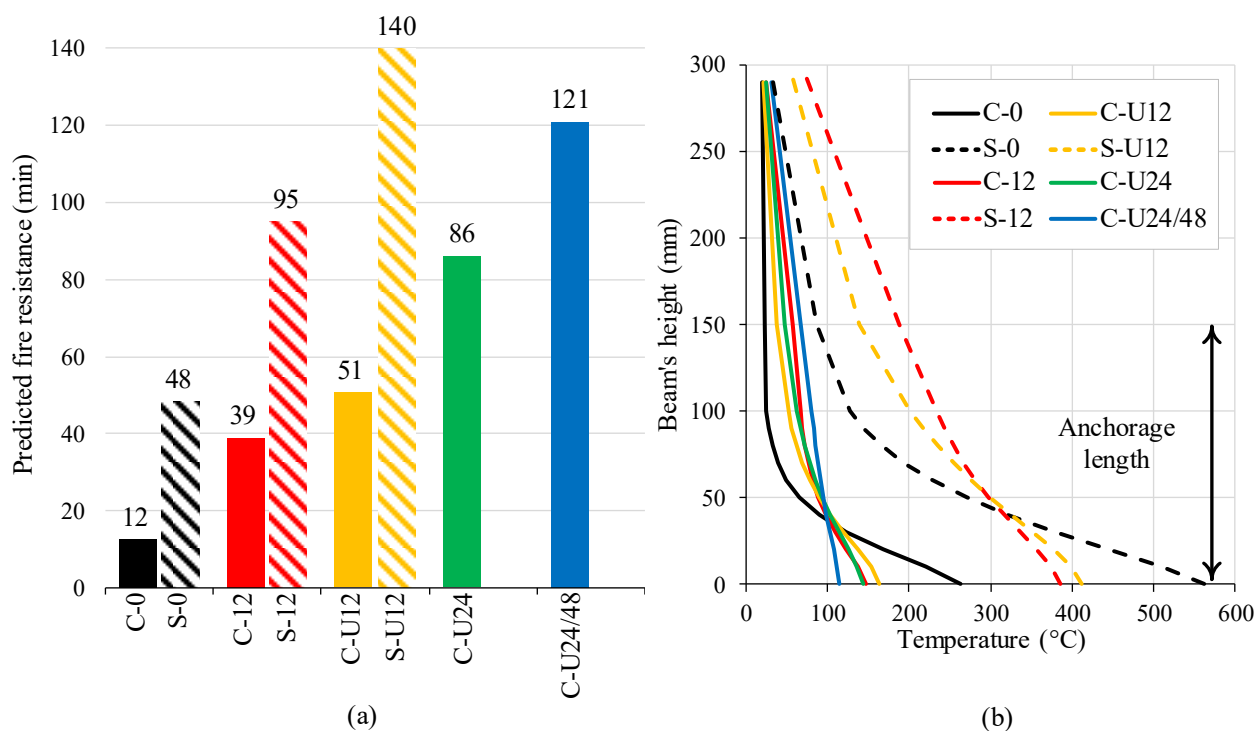


Figure 11. (a) Predicted fire resistance of ETS strengthening system with different fire protection geometries, and (b) temperature distribution along CFRP and steel 90°-ETS bars at debonding instants

5 CONCLUSIONS

This paper presented experimental and numerical studies about the fire resistance behaviour of RC beams strengthened in shear using ETS-CFRP and -steel bars. The following main conclusions are drawn:

- The experimental tests confirmed the susceptibility of the ETS strengthening technique to fire exposure, regardless of the strengthening material adopted: in RC beams strengthened with ETS-CFRP bars and ETS-steel bars, the strengthening system lost its structural effectiveness after respectively 12 min and 48 min of fire exposure. In these beams the cover of ETS bars was null and there was no fire protection.
- The critical average temperature along the anchorage length of the ETS bars at the debonding instants was much higher in the ETS-steel strengthened beam (221 °C) than in the ETS-CFRP counterpart (64 °C). The worse performance of ETS-CFRP bars was attributed to their lower bond strength at elevated temperature compared to the ETS-steel bars, which is supported by previous bond tests.
- The thermal FE models, validated with experimental results, showed that when the concrete cover of the ETS bars increases to 10 mm, 20 mm and 30 mm, the critical temperatures at the anchorage length are attained after longer periods of fire exposure, namely 19 min, 26 min and 32 min in ETS-CFRP strengthened beams, and 64 min, 76 min and 87 min in ETS-steel strengthened beams.
- The FE models showed that the use of fire protection systems composed by calcium silicate boards can increase significantly the fire resistance of the strengthening systems: 121 min in an ETS-CFRP-strengthened beam when using U-shaped fire protection with thicknesses of 24 mm and 48 mm,

respectively at the lateral and bottom faces of the beam; and 140 min in an ETS-steel-strengthened beam when using 12 mm thick U-shaped fire protection.

- Applying calcium silicate boards with U-shaped geometry (between 12 mm and 48 mm thick) in ETS-steel and -CFRP strengthened beams is significantly more effective in extending the fire resistance of the ETS strengthening system than increasing the concrete cover of the ETS bars up to 30 mm.

Some of the findings reported above, namely concerning the effects of fire protection and concrete cover thickness on the fire resistance of ETS strengthening systems, should be confirmed through full-scale experimental tests and/or thermo-mechanical models accounting for the actual bond vs. slip behaviour of ETS bars. These further investigations should also allow validating some of the assumptions that were made in the present study, namely regarding the anchorage length and “critical” average temperatures considered.

ACKNOWLEDGMENT

The authors wish to acknowledge FCT for the funding provided through project FireComposite PTDC/ECM-EST/1882/2014 and CERIS project UIDB UIDB/04625/2020 (DOI: 10.54499/UIDB/04625/2020); Secil and Unibetão for supplying the concrete; and S&P Clever Reinforcement for supplying the epoxy adhesive. The first author also wishes to thank the financial support of FCT through the scholarship SFRH/BD/145256/2019.

REFERENCES

1. Chaallal, O., Mofidi, A., Benmokrane, B., Neale, K., Embedded Through-Section FRP rod method for shear strengthening of RC beams: performance and comparison with existing techniques, *Journal of Composites for Construction*. 15, 374–383 (2011). [https://doi.org/10.1061/\(ASCE\)CC.1943-5614.0000174](https://doi.org/10.1061/(ASCE)CC.1943-5614.0000174).
2. Breveglieri, M., Aprile A., Barros, J.A.O., Embedded Through-Section shear strengthening technique using steel and CFRP bars in RC beams of different percentage of existing stirrups, *Composite Structures* 126, 101–113 (2015). <https://doi.org/10.1016/j.compstruct.2015.02.025>.
3. Firmo, J.P., Correia, J.R., Bisby, L., Fire behaviour of FRP-strengthened reinforced concrete structural elements: a state-of-the-art review, *Composites Part B: Engineering* 80, 198-216 (2015). <https://doi.org/10.1016/j.compositesb.2015.05.045>
4. Azevedo, A.S., Firmo, J.P., Correia, J.R., Bond behaviour at high temperatures between concrete and CFRP or steel strengthening bars applied according to the Embedded Through-Section (ETS) technique, *Cement and Concrete Composites* (submitted in February 2023, under review).
5. Azevedo, A.S., Firmo, J.P., Correia, J.R., Almeida, J., Embedded through-section (ETS) technique for shear strengthening of reinforced concrete beams – experimental and analytical study, *Cement and Concrete Composites* (submitted in March 2024, under review).
6. Firmo, J.P., Arruda, M.R.T., Correia, J.R., Rosa, I.C., Three-dimensional finite element modelling of the fire behaviour of insulated RC beams strengthened with EBR and NSM CFRP strips, *Compos. Struct.* 183, 124-136 (2018). <https://doi.org/10.1016/j.compstruct.2017.01.082>.
7. Azevedo, A.S., Firmo, J.P., Correia, J.R., Three-dimensional finite element modelling of the fire response of passive and prestressed near-surface mounted (NSM)-CFRP-strengthened reinforced concrete slab strips, *Composite Structures* 331, 117872 (2024) <https://doi.org/10.1016/j.compstruct.2023.117872>.

FIRE-INDUCED SPALLING OF NORMAL STRENGTH CONCRETE WITH DIFFERENT TYPES OF BLENDED PORTLAND CEMENT

Tim Pittrich¹, Ludwig Stelzner², Frank Weise³

ABSTRACT

The cement industry is looking to reduce its overall CO₂ footprint. Greener manufacturing can be achieved by the introduction of more clinker-reduced cements. Concrete exposed to fire tends to show explosive spalling caused by thermomechanical and thermohydraulic processes. It is therefore essential to determine how concretes with clinker-reduced cements behave under fire exposure, especially for concretes containing calcined clays, as these are expected to be the supplementary cementitious material of the future. In this paper, normal strength concretes with four different cements (CEM I, CEM II/A-LL, CEM III/A and CEM II/B-Q) were examined for their fire-induced spalling behaviour. In addition, a mix with PP fibres was investigated for each concrete. The experiments were conducted on ring-restrained cylindrical specimens exposed to the hydrocarbon fire curve. The results showed that the cement type influences spalling behaviour. Samples with CEM I spalled the least, followed by CEM II/A-LL and CEM III/A. Finally, samples with CEM II/B-Q showed the most severe damage. It was found that the spalling behaviour of different concretes correlates with the moisture content before exposure to fire, meaning that higher moisture content leads to higher spalling susceptibility. The use of 2 kg/m³ PP fibres completely inhibited spalling regardless of the cement type used and therefore remains a successful avoidance strategy.

Keywords: Fire-induced concrete spalling; normal strength concrete; blended Portland cement; SCM; PP-fibres

1 INTRODUCTION

Cement is the most used material in the world, and as the world's population grows, so does the demand for more buildings and infrastructure rise [1]. However, cement clinker production is associated with high CO₂ emissions that are mainly caused by the decomposition of limestone and the use of fossil fuels for rotary kilns. In total, the cement industry is responsible for approximately 8% of the global CO₂ emissions [2]. One strategy for lowering cement's CO₂ emissions is to reduce the clinker factor. This is achieved by replacing cement clinker with supplementary cementitious materials (SCMs) such as fly ash (FA), granulated blast furnace slag (GBFS) or calcined clays. The utilisation of calcined clays in particular is expected to increase, as reduced availability of slag and fly ash is forecast for Europe [2]. Therefore, blended cements with a reduced clinker factor will become an increasingly important aspect for the construction industry.

Concrete structures exposed to fire can experience heavy damage due to explosive spalling. This results on the one hand in reducing the load-bearing cross-section and on the other hand in exposing reinforcement [3]. The reasons behind explosive concrete spalling are not yet fully understood. Concrete is a

¹ Bundesanstalt für Materialforschung und -prüfung
e-mail: tim.pittrich@bam.de, ORCID: <https://orcid.org/0009-0003-4397-1958>

² Bundesanstalt für Materialforschung und -prüfung
e-mail: ludwig.stelzner@bam.de, ORCID: <https://orcid.org/0009-0007-3955-7841>

³ Bundesanstalt für Materialforschung und -prüfung
e-mail: frank.weise@bam.de, ORCID: <https://orcid.org/0000-0001-6441-0058>

multicomponent material consisting of cement paste and aggregates; however, the individual components behave in contrasting ways during heating. The aggregates dilate while the hardened cement paste shrinks from a temperature of approx. 150 °C, resulting in stresses and the formation of microcracks. Additionally, concrete's low thermal diffusivity leads to high thermal gradients between the hot, fire-exposed side and the cool interior. This causes restrained thermal dilation, the obstruction of which results in high compressive stresses close to the fire-exposed surface [4]. These compressive biaxial thermal stresses parallel to the heated surface produce tensile stress perpendicular to the heated surface according to [5], [6]. Exceeding the tensile strength causes brittle fracture of the concrete, described as spalling. Another approach to describing concrete spalling originated with the so-called "moisture clog" theory by Shorter and Harmathy [7], later developed in more depth by [8]. The authors state that pore pressure inside concrete rises when exposed to fire. Subsequently, water vapour moves out of the specimen towards both the heated surface and the concrete's cooler interior. The lower temperatures further inside the specimen lead to the condensation of water vapour. The ongoing accumulation of liquid water continues until an impermeable fully saturated zone has developed. This impermeable layer prevents any further moisture transport, causing a rapid rise in pore pressure. If the pore pressure exceeds the transversal tensile strength of the concrete, the material starts to crack and spall. The measurement of pore pressure at fast heating rates proved to be difficult, as induced cracks lead to a rapid pressure drop [9]. Therefore, the relation between pore pressure and explosive concrete spalling is not yet totally clarified. Another approach is the boiling liquid expanding water explosion theory (BLEVE). The theory states that when water is heated above 100 °C, it remains liquid as long as a certain pressure is present. When the pressure suddenly drops, the liquid water turns into steam, releasing all the stored energy and thus causing an explosion [10]. The heat-induced moisture transport and the existence of the "moisture clog" were experimentally confirmed in studies by [11-13].

An effective strategy to avoid spalling is the addition of polypropylene fibres (PP fibres) [14, 15]. After the fibres melt at around 170 °C, expansion space is available in the form of empty fibre beds connected through mechanically induced microcracks. This induced network of canals supports the release of water vapour to the outside, reducing the overall moisture content and steam pressure in the system and thus minimizing the spalling risk [14].

The information available in the literature does not provide clear insights into the relation of cement type to the susceptibility to concrete spalling. Hager et al. [16] investigated concretes containing CEM I 42,5 R and CEM III/A 42,5 N under the ISO 834 fire curve. The experiments showed greater spalling for concretes containing CEM I, even though higher permeability and lower compressive strength were measured for those types of concretes [17]. The authors suggested no explanation for these contrary results. Extensive studies by Reiners [18] using the ISO 834 fire curve showed the following results: the most severe spalling was observed for concretes containing CEM III/A 42,5 N, followed by CEM II/B-V 42,5 R. Concretes containing CEM II/A-LL 42,5 N and CEM I 42,5 R exhibited only comparatively low amounts of spalling under restrained conditions. Equal experiments without restraint showed similar results, except that concrete with CEM I or CEM II/A-LL did not spall [18]. Miah [19] investigated the spalling behaviour of concretes containing CEM II/A-LL 42,5 R and CEM III/A 42,5 N under different applied loads using ISO 834 fire exposure. While unloaded specimens did not spall in both cases, uniaxial loaded samples with CEM II/A-LL showed spalling. In the case of biaxial loading, it was not clearly distinguishable which cement type led to more spalling on average [19]. Lublóy et al. [20] studied concretes with CEM I 42,5 N and CEM II/A-P 42,5 N as well as CEM II/A-V 42,5 R. At temperatures of 500°C, spalling of the cube corners was noticed for CEM I concrete. Concretes with other types of cement experienced no spalling. Kirnbauer et al. [21] investigated the spalling behaviour of CEM I 42,5 N, CEM II/A-LL 42,5 R and a sulphate slag cement concrete by applying the ISO 834 curve. Summarized, concretes with sulphate slag cement and CEM II/A-LL led to more intense spalling than concretes with CEM I [21]. Research on the high temperature behaviour of concretes with metakaolin was carried out by Poon et al. [22]. The authors replaced 5%, 10% and 20% by weight of Portland cement in normal and high-strength concrete with metakaolin. The researchers observed more spalling with increasing metakaolin content in both cases when heating the specimens up to 800 °C [22].

This paper presents the results of fire spalling tests of normal strength concretes (NSC) containing different types of blended cement with and without PP fibres. The aim of the research was to identify how different SCMs influence the spalling behaviour of concretes. Of special interest here was cement containing

calcined clays. Up to this point, no in-depth research concerning the spalling behaviour of calcined clay cement concrete has been carried out. Furthermore, the performance of PP fibres in concrete mixes with different binders was also investigated.

2 RAW MATERIALS AND MIX DESIGN

Table 1 displays the chosen cements classified according to DIN EN 197-1 [23] and their composition. All cements contained Portland cement clinker from the same manufacturing batch and only differed in the type and quantity of SCM. The kaolinitic-illitic clay was calcined at 700 °C to generate pozzolanic properties. Quarzitic aggregates with a grain size up to 16 mm were used in all concrete mixtures. The superplasticizer used throughout the work was a polycarboxylate ether-based product. Lastly, PP fibres of $l = 6$ mm and $\varnothing = 15.4$ μm were used.

Table 1. Composition of the cements used

	CEM I 42,5 N	CEM II/A-LL 42,5 N	CEM III/A 42,5 N	CEM II/B- Q 42,5 N
Portland cement clinker [wt.%]	95.7	85.7	55.8	71.6
Limestone [wt.%]	4.3	14.3	3.8	3.4
Blast furnace slag [wt.%]	-	-	40.4	-
Calcined clay [wt.%]	-	-	-	25.0

Eight different mix designs were tested in total: for each cement one mix without and one mix with PP fibres (Table 2). The water to cement ratio (w/c) was kept equal in all formulations at 0.47. Superplasticizer was not needed in the formulations without PP fibres, except for the one with calcined clays. In the further mixes, 2 kg/m³ PP fibres were added, as recommended in the Eurocode (EN 1992-1-2:2004) [24]. The mix designs with PP fibres contained superplasticiser in different amounts to ensure comparable workability in the fresh concrete state. The compressive cube strength was determined after 28 d and on the day of fire testing (at least 90 d).

Table 2. Concrete mix designs and properties [kg/m³]

	CEM I		CEM II/A-LL		CEM III/A		CEM II/B-Q	
	PC	PC_pp	LC	LC_pp	SC	SC_pp	CC	CC_pp
cement	420		420		420		420	
water (w/c)	197 (0.47)		197 (0.47)		197 (0.47)		197 (0.47)	
superplasticiser	0	1.5	0	3.4	0	2.1	2.5	5.0
PP fibres	0	2	0	2	0	2	0	2
quarzitic aggregates								
0 / 2 mm	646	640	646	634	646	637	634	628
2/ 4 mm	153	152	153	150	153	151	150	149
4/ 8 mm	221	219	221	217	221	218	217	215
8/ 16 mm	679	675	679	668	679	669	666	661
compressive cube strength [MPa]								
28 d	46	46	51	54	57	65	57	60
> 90 d	50	52	55	61	59	73	56	62

3 METHODOLOGY

3.1 Sample preparation

For the fire test two cylindrical samples ($h = 29$ cm; $\varnothing = 47$ cm) of each concrete mix were prepared. The samples were demoulded one day after casting and subsequently placed under water for 6 more days. Afterwards, the samples were stored in a climate chamber at (20 ± 2) °C and (65 ± 5) % RH until the day of testing. Additionally, the lateral surface was covered to provide a 1D moisture transport.

To generate restraint testing conditions, the cylindrical specimens were grouted into a steel ring (outer $\varnothing = 51$ cm) after Klimek et al. [25], a methodology based on the work of Ozawa et al. [26]. Both the steel ring and the outer boundary of the concrete remain insulated during the fire test. Therefore, the reduced thermal dilation of the steel ring leads to restraint stresses. The restrained set up and the disabled moisture transport were chosen to simulate the conditions in the centre of a large-scale concrete wall.

3.2 Experimental set-up

The fire tests were conducted in an oil burner furnace running the hydrocarbon fire curve for 1 h under unloaded conditions. The fire room had a volume of 1 m³ and the samples were placed at a furnace opening of 0.25 m². The fire exposed area measured 0.14 m², thus the remaining specimen was insulated by a vermiculite board and high temperature mineral wool. The temperature inside the concrete samples was measured with embedded thermocouples Type K, at depths of 5, 15, 30, 50 and 100 mm from the fire-exposed surface. Acoustic signals of spalling events were recorded with a microphone placed outside the furnace. The moisture content was determined according to the recommendation of RILEM TC 256-SPF [23], by drying two cylindrical samples ($h = 30$ cm; $\varnothing = 10$ cm) at (105 ± 5) °C until mass equilibrium. Mass equilibrium was reached when the mass difference between two consecutive weight intervals within 24 h was less than 0.1 %. Moisture distribution and content were additionally determined on equally treated accompanying concrete cylinders ($h = 29$ cm; $\varnothing = 7$ cm) by means of ¹H-NMR relaxometry. The technique can detect water content ranging from water bound in gel pores to free water in coarse pores, which distinguishes it from the method above. The topography of the concrete specimens was measured before and after fire exposure with a handheld 3D laser scanner. In addition, the spalled volume was calculated by defining an assessment area equal to 90% of the fire exposed surface and the corresponding spalling depths according to [27]. Figure 1 shows the set-up of the spalling experiments as well as a sketch of the test specimen.

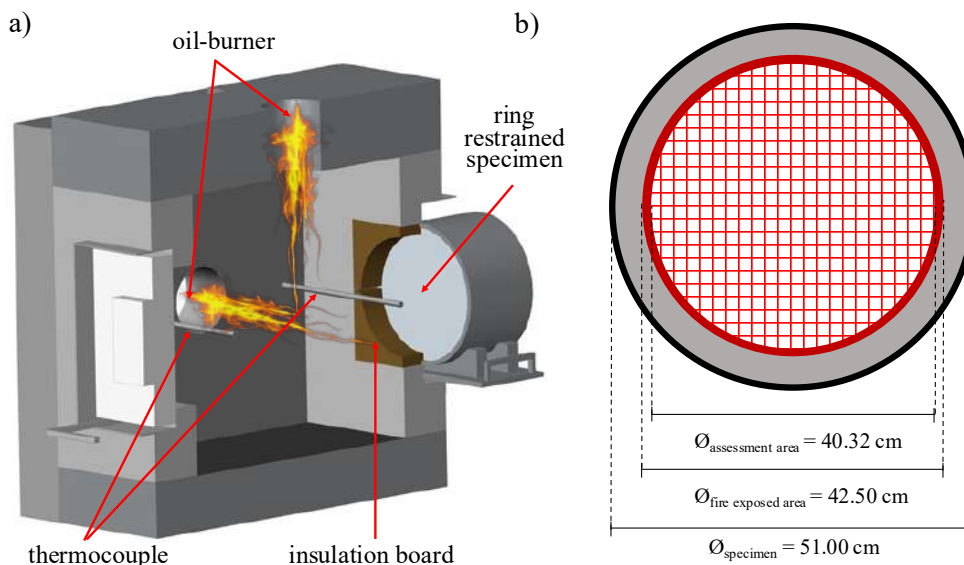


Figure 1. a) Oil-burner furnace with ring restrained concrete specimen b) sketch of cylindrical concrete specimen

4 RESULTS

4.1 Initial moisture content and distribution

Table 3 gives an overview of the moisture content determined by mass loss as stated above. As the addition of PP fibres showed no drastic influence on the initial moisture content, it was assumed that the moisture content of CC and CC_pp was comparable. The captured data showed that PC had the overall lowest moisture content and mix CC_pp the highest.

Table 3. Moisture content

	PC	PC_pp	LC	LC_pp	SC	SC_pp	CC	CC_pp
[wt.%]	5.43	5.66	5.67	5.46	5.60	5.44	-	6.08

Figure 2 presents the initial detectable water content of the concrete cylinders after 90 d up to a depth of 116 mm, measured in 2 mm steps. It shows that all concretes displayed a drying gradient from the concrete centre to the surface. The gradient extended to similar depths in all cases but differed in its absolute moisture content. The mean moisture content for PC was 8.41 Vol.% and for LC 9.05 Vol.%. SC concrete showed slightly higher moisture with an average of 9.59 Vol.%. Concrete mix CC showed the overall highest moisture content with an average value of 10.39 Vol.%. The moisture content for the fibre mixes follows the same sequence, as PC_pp presented the lowest amount of water with 8.60 Vol.% followed by LC_pp and SC_pp with 8.98 Vol.% and 9.29 Vol.% respectively. Lastly, CC_pp contained the most water with 10.58 Vol.%. No significant differences between the mixes with and without fibres were observed.

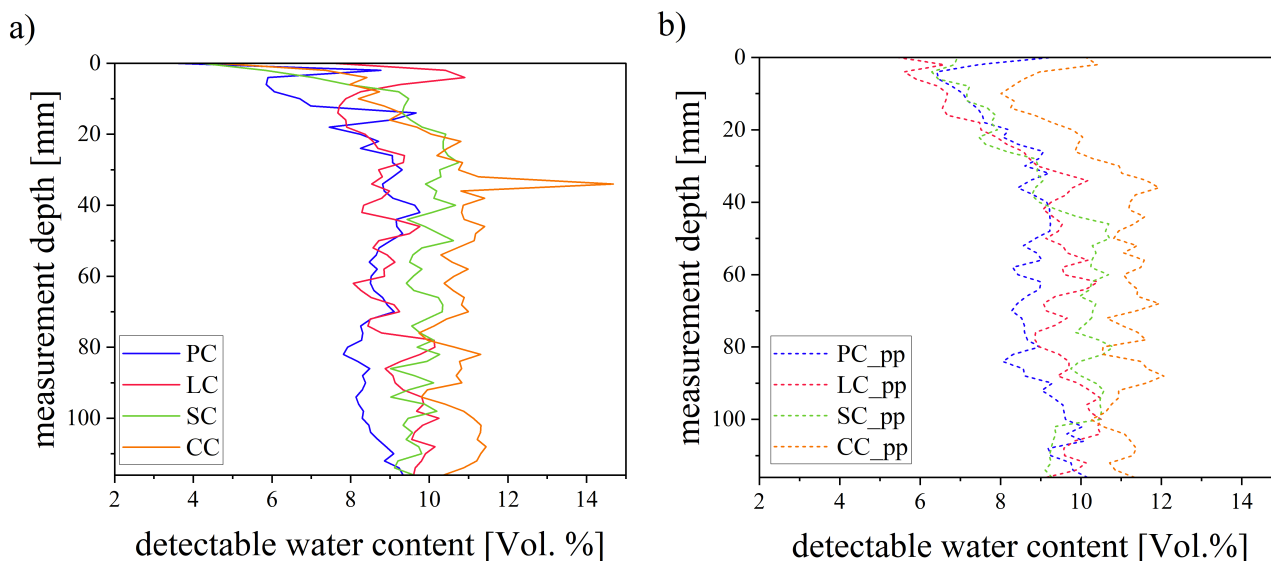


Figure 2. Detectable water content measured by ^1H -NMR relaxometry a) mixes without fibres b) mixes with fibres

Both results show that with the same amount of water during preparation, different moisture states occur after 90 days of curing, depending on the binder used.

4.2 Temperature propagation and acoustic registered spalling events

The temperature profiles of the different concretes are shown below in Figures 3 and 4 for one test specimen per cement type. Explosive spalling was observed in each test specimen without PP fibres. The concrete with PC showed a rapid increase in temperature at the depths of 5 and 15 mm around minute 3 after test begin. This increase in temperature is associated with spalling events, uncovering the designated thermocouples, and therefore indicating the approximate depths of spalling. Five spalling events were recorded for each of the specimens tested. Concrete LC exhibited a heavy temperature increase beginning

after 2 mins at the thermocouples embedded at 5, 15 and 30 mm from the fire exposed surface. In total, 70 spalling events for specimen one and 96 for specimen two were counted. Concrete mix SC also showed a rapid temperature rise in minute 3 measured by the first three thermocouples. 88 spalling events were recorded for specimen one and 134 for specimen two. Mix design CC also experienced a high temperature increase after roughly 2 mins. The spalling of the concrete exposed the top four thermocouples. Additionally, 134 and 216 spalling events were counted, respectively. The appearance of temperature plateaus was recorded in all specimens, particularly with the thermocouple located at 100 mm depth. This phenomenon is associated with the evaporation of liquid water, an endothermic process consuming energy. No spalling events were recorded for any sample with PP fibres, leading to a much lower temperature development inside the specimens. Again, temperature plateaus were observed caused by the evaporation of water. It is notable that the plateaus occur at lower temperatures compared to the non-fibre mixes, which indicates lower pressure during phase transition.

Of further interest are the temperatures measured at 50 mm depth, where the reinforcement is usually located. Concrete PC showed a maximum temperature of 400 °C, mix LC and SC showed maximum temperatures of approximately 650 °C and 600 °C, respectively. Mix CC showed a maximum temperature of above 1000 °C. The maximum recorded temperature for PP fibre concretes was around 200 °C, independent of the cement type utilized. The results show that the use of PP fibres would effectively reduce the heating of a potential steel reinforcement.

Furthermore, the temperature of the steel ring was measured at three different locations at a depth of 30 mm for one of each sample. The results always displayed lower temperatures for the steel ring compared to the concrete member (after 30 mins maximum steel temperature 270 °C), confirming the idea of a restraint testing regime by differing thermal dilations. This is consistent with the findings of Klimek et al. who used a similar test setup [25].

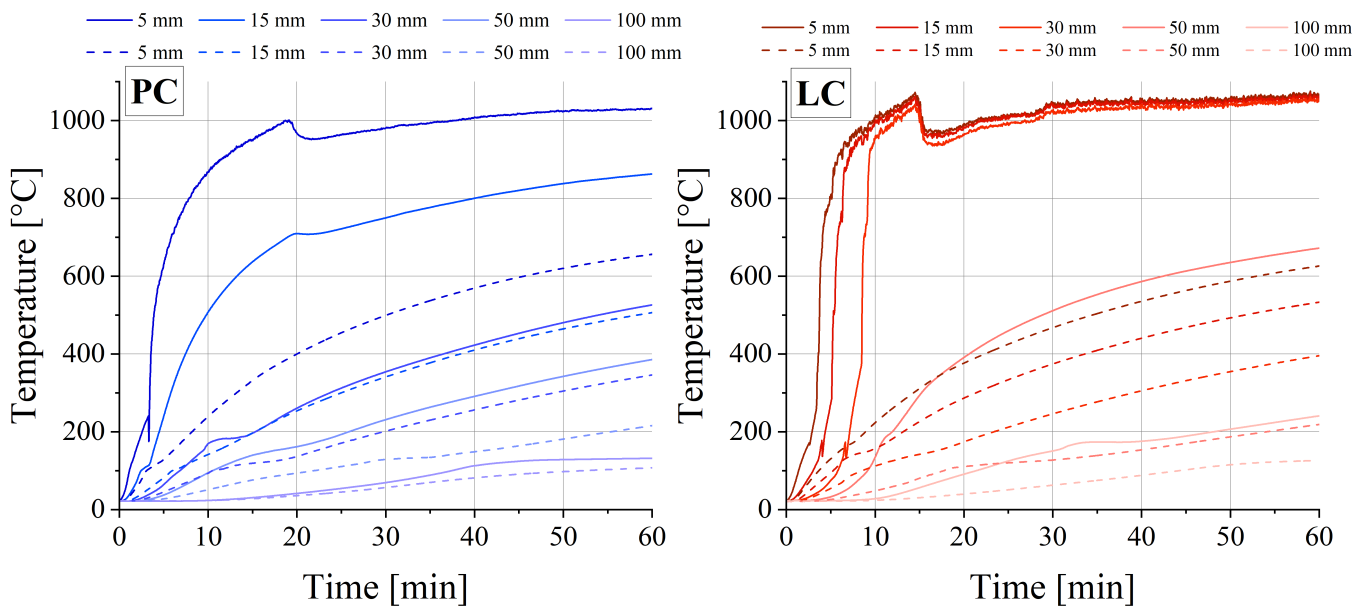


Figure 3. Concrete temperatures of mix PC and LC with applied HC curve (without PP—) (with PP ----)

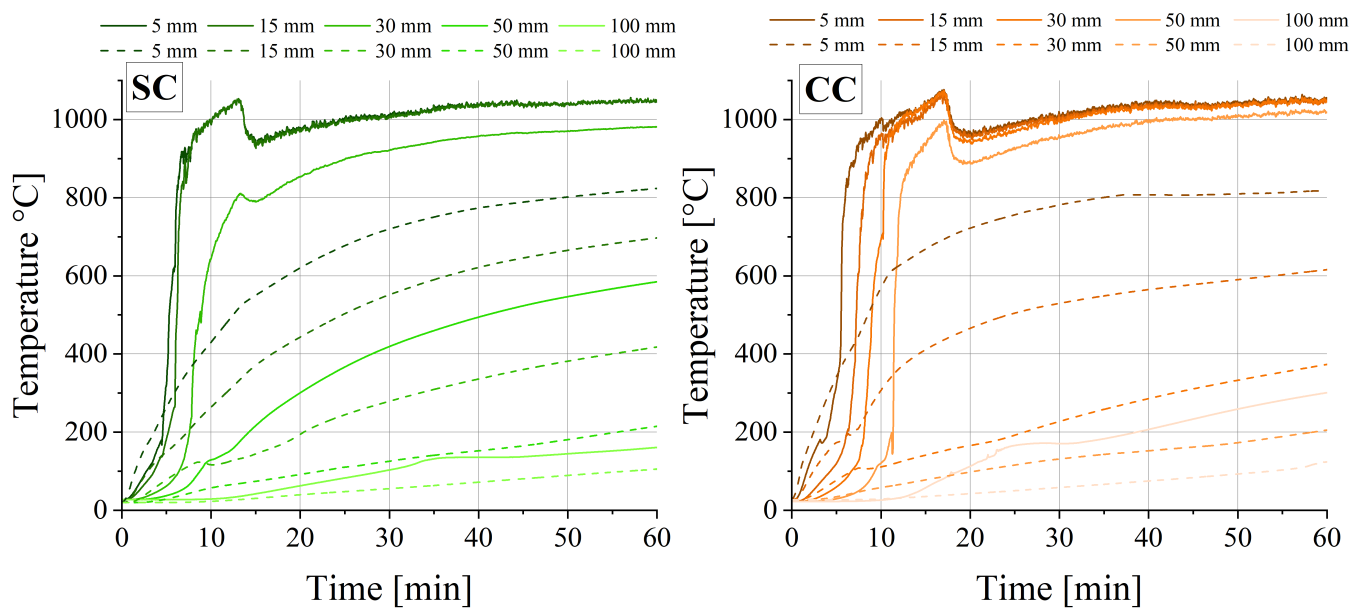


Figure 4. Concrete temperatures of mix SC and CC with applied HC curve (without PP—) (with PP ----)

4.3 3D surface analysis

The results of the 3D surface analysis are summarized in Figure 5 as locally resolved colour coded spalling depths. The different concretes containing various types of cements exhibit different spalling behaviour. PC showed the lowest amount of damage with a spalling volume of 786.83 cm³ and 321.71 cm³. Maximum spalling depths of 15 and 13 mm were recorded. While sample one showed a homogeneous spalled surface, only about half the area of sample two spalled. The residual area showed slight local expansions. Mix LC experienced heavier spalling with a spalled volume of 2385.21 cm³ and 3025.23 cm³. The recorded maximum spalling depth was 46 and 53 mm, respectively. Similar results could be observed for concrete SC. The specimens' entire fire exposed surface spalled and a volume loss of 2302.6 cm³ and 2856.15 cm³ was measured. The maximum spalling depths were 50 and 52 mm, respectively. Samples of mixture CC were most prone to spalling with recorded volumes of 2798.86 cm³ and 4084.07 cm³; their maximum spalling depths sat at 56 and 72 mm. Both the mean spalling depth and the mean spalling volume are given in Table 4 below.

Concretes containing PP fibres did not spall, regardless of the cement type used. Slight damage in the form of cracks and expansions up to 5 mm were determined for every specimen. A change in colour from grey to whitish and reddish colours on the concrete surface was visible. According to Hager [3] the colour change to white is caused by the transformation of CaCO₃ to quicklime and the reddish colours appear due to the oxidation of iron-containing mineral composites in the quarzitic aggregates. It should be noted that during the fire test of SC_pp_1 the top oil- burner failed and therefore, the desired HC fire curve was not reached.

Table 4. Mean spalling depth and mean spalling volume of concretes without PP fibres

	PC	LC	SC	CC
depth _{mean} [mm]	4.34	23.54	22.45	26.96
V _{mean} [cm ³]	554.27	2705.22	2579.38	3441.47
V _{mean} [Vol. %]	1.49	7.28	6.94	9.26

Concrete specimens	
without PP-fibres	with PP-fibres

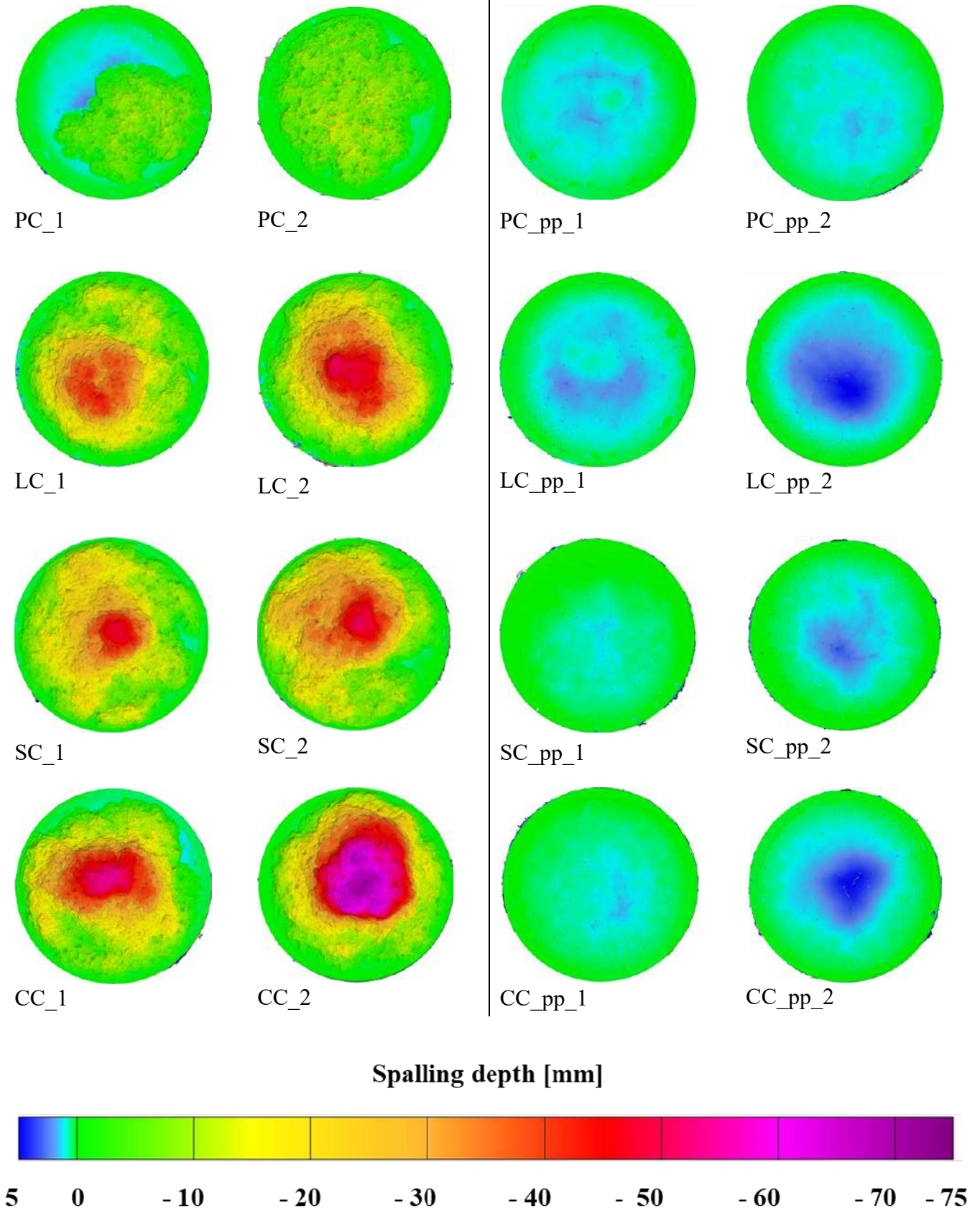


Figure 5. Ring restrained specimens after fire exposure

5 DISCUSSION

Although cements with the same strength class were provided by the same manufacturer and an equal mix design was applied for all concretes, differences in compressive strength appeared. This should be kept in mind when referring to the spalling experiments, since a higher compressive strength leads to more spalling. Also, in this study the concrete mix with CEM I exhibited the lowest strength and the lowest amount of spalling. The problem, however, seems to be unavoidable since an adaption of strength would suggest a change of mix design, most probably affecting the water content. Moreover, the adjustment of the water content to obtain equal compressive strength values would essentially influence the spalling behaviour of the concretes. Furthermore, it is seen that the addition of 2 kg/m³ PP fibres lead to an increase of the compressive strength compared to the mixtures without fibre addition. Mixture SC_pp in particular experienced a heavy strength gain of 24 %. Results in literature show that fluctuations and changes of strength appear dependent on the fibre properties and dosage [28, 29]. The effectiveness of PP fibres was proven in every concrete, as no spalling was observed in any case even though compressive strengths increased. Since the fibres primarily affect internal moisture transport, this further emphasises that thermohydraulic processes are decisive for explosive spalling.

The experiments presented here clearly showed the influence of cement type on the spalling behaviour of NSC. The maximum spalling depths in concretes with blended cements reached values where steel reinforcement could be uncovered and directly exposed by the fire. Direct heat exposure of the steel member can be critical for the residual stability of a building during a fire. The study also shows the relationship between moisture content and spalling intensity, as increasing spalling was observed with increasing moisture content. While all specimens were prepared with the same w/c ratio of 0.47, the water content varied on the day of testing. This is even more emphasised when looking at the ¹H-NMR Relaxometry data, which provides insights into the amount of water beyond the free water content. Therefore, the influencing water content must consist of the amount of chemical, physical and free water predetermined by the mineral phase composition of the cements used. For example, an increasing change in the morphology of outer product C-S-H from a fibrillar to a denser foil-like structure is seen in systems containing slag and pozzolana [30]. A denser microstructure with possibly lower permeability would slow the drying process during conditioning as well as disabling the water release at fire exposure. The high availability of water plus the impossibility for it to escape consequently lead to increased explosive spalling of concretes with blended cements. The findings are in agreement with the literature, where it can be found that high moisture content is responsible for heavy spalling [31].

For further understanding of the moisture influence on the fire spalling behaviour of concretes with blended cements, pore size-specific moisture distribution studies will be carried out on specimens before and after heat exposure. In addition, porosity and permeability experiments are planned to finalise the picture.

6 CONCLUSIONS

This paper provides new insights into the spalling behaviour of normal strength concrete containing different types of blended Portland cement. The above-mentioned results of this study can be summed up as follows:

- The cement type influences the explosive spalling susceptibility of NSC. Concretes with CEM I only experienced minimal spalling with an average depth of 4 mm. Concretes containing CEM II/A-LL and CEM III/A already showed deeper spalling with an average depth of 23.5 and 22.5 mm, respectively. The highest average spalling depth was recorded for concrete made with CEM II/B-Q with a value of 27 mm.
- There is a relation between moisture content and spalling amount, as increasing spalling was observed with increasing initial moisture. The respective free water content, determined by drying cylinders at 105 °C, was 5.43 wt.% for CEM I concrete, 5.67 wt.% for CEM II/A-LL concrete, 5.60 wt.% for CEM III/A concrete and 6.08 wt.% for CEM II/B-Q concrete. The results were confirmed by the ¹H-NMR relaxometry measurements.

- Spalling occurred between minute 2 and 15 in all concrete mixes without fibre addition. The number of acoustically recorded spalling events correlates with the intensity of damage.
- It was proven that 2 kg/m³ PP fibres inhibit explosive spalling regardless of the cement type in NSC.

Under the given conditions every concrete with a clinker-reduced cement showed worse fire-induced spalling behaviour than concrete with OPC. Above all, concrete with calcined clay-containing binder was damaged the most. This should be taken into consideration when thinking about the utilization of these cements in cases where fire resistance is crucial. However, the problem can be avoided by adding PP-fibres.

ACKNOWLEDGEMENT

We gratefully acknowledge the support and extend our gratitude to the German Research Foundation (DFG) for their financial support, which has been instrumental in conducting the investigations presented in this paper. We also express our sincere appreciation to our colleagues, specifically acknowledging the collaborative efforts of BAM divisions 7.1 “Building Materials”, 7.3 “Fire Engineering”, and 7.4 “Technology of Construction Materials”. Their expertise and resources have significantly enriched the scope and depth of our study.

REFERENCES

1. Schneider, M., The cement industry on the way to a low-carbon future, *Cement and Concrete Research* 124 (2019).
2. Favier, A., De Wolf, C., Scrivener, K., Habert, G., A sustainable future for the European Cement and Concrete Industry - Technology assessment for full decarbonisation of the industry by 2050, ETH Zurich, Zurich (2018).
3. Hager, I., Behaviour of cement concrete at high temperature, *Bulletin of the Polish Academy of Sciences, Technical Sciences* 61(1) (2013).
4. Fu, Y., Li, L., Study on mechanism of thermal spalling in concrete exposed to elevated temperatures, *Materials and Structures* 44 (2011) 361-376.
5. Bazant, Z.P., Analysis of pore pressure, thermal stresses and fracture in rapidly heated concrete, in: Phan, L.T., Carion, N.J., Duthinh, D., Garboczi, E., (Eds.) *Int. Workshop on Fire Performance of High-Strength Concrete*, National Institute for Standards and Technology, Gaithersburg, (1997) 155-164.
6. Ulm, F.J., Coussy, O., Bazant, Z.P., The “Chunnel” fire I: chemoplastic softening in rapidly heated concrete, *Journal of Engineering Mechanics* 125(3) (1999) 272-282.
7. Shorter, G.W., Harmathy, T.Z., Discussion on the Fire-resistance of prestressed concrete beams, *Institute of Civil Engineers* (1961).
8. Harmathy, T.Z., Effect of moisture on the fire endurance of building elements, *ASTM Special Technical Publication No. 385* (1965).
9. Stelzner, L., Analyse des thermisch induzierten Feuchtetransports in gefügedichten Beton, *Werkstoffe im Bauwesen*, Universität Stuttgart (2021).
10. Ichikawa, Y., Prediction of Pore Pressures, Heat and Moisture Transfer Leading to Spalling of Concrete during Fire, Department of Civil and Environmental Engineering, University of London, 2000.
11. van der Heijden, G.H.A., van Bijnen, R.M.W., Pel, L., Huinink, H.P., Moisture transport in heated concrete, as studied by NMR, and its consequences for fire spalling, *Cement and Concrete Research* 37 (2007) 894-901.
12. Jansson, R., Fire Spalling of Concrete, KTH Architecture and the Built Environment, KTH Royal Institute of Technology, Stockholm (2013).
13. Stelzner, L., Powierza, B., Oesch, T., Dlugosch, R., Weise, F., Thermally-induced moisture transport in high-performance concrete studied by X-ray-CT and 1H-NMR, *Construction and Building Materials* 224 (2019) 600-609.
14. Pistol, K., Weise, F., Meng, B., Schneider, U., The mode of action of polypropylene fibres in high performance concrete at high temperatures, *2nd International RILEM Workshop on Concrete Spalling due to Fire Exposure*, (2011), 289-296.

15. Poon, C-S., Shui, ZH., Lam, L., Compressive behaviour of fibre reinforced high-performance concrete subjected to elevated temperatures, *Cement and Concrete Research* 34 (2004) 2215-2222.
16. Hager, I., Mróz, K., Tracz, T., Concrete propensity to fire spalling: Testing and observations, *MATEC Web of Conf.* 163 (2018).
17. Hager, I., Tracz, T., Choinska, M., Mróz, K., Effect of Cement Type on the Mechanical Behaviour and Permeability of Concrete Subjected to High Temperatures, *Materials* 12(18) (2019).
18. Reiners, J., The Influence of the Physical and Chemical Properties of Hardened Cement Paste on the Fire-Induced Spalling of Concrete *Technische Universität Carolo-Wilhelmina zu Braunschweig* (2023).
19. Miah, M.J., The Effect of Compressive Loading and Cement Type on the Fire Spalling Behaviour of Concrete, *Université de Pau et des Pays de l'Adour-Laboratoire SIAME* (2017).
20. Lublój, É., Kopecskó, K., Balázs, G.L., Restás, Á., Szilágyi, I.M., Improved fire resistance by using Portland-pozzolana or Portland-fly ash cements, *Journal of Thermal Analysis and Calorimetry* 129 (2017) 925-936.
21. Kirnbauer, J., Schneider, U., Influence of cement type and aggregate shape on explosive concrete spalling, *2nd International RILEM Workshop on Concrete Spalling due to Fire Exposure, Delft*, (2011), 432-439.
22. Poon, C-S., Azhar, S., Anson, M., Wong, Y-L., Performance of metakaolin concrete at elevated temperatures, *Cement & Concrete Composites* 25 (2003) 83-89.
23. D.I.f.N. DIN, Cement – Part 1: Composition, specifications and conformity criteria for common cements, *Beuth Verlag GmbH, Berlin* (2011).
24. D.I.f.N. DIN, Eurocode 2: Design of concrete structures Part 1-2: General rules – Structural fire design, *Beuth Verlag GmbH, Berlin*, (2010).
25. Klimek, A., Stelzner, L., Hothan, S., Zehfuß, J., Influence of thermal strain on concrete spalling, *Materials and Structures* 57(15), (2024).
26. Ozawa, M., Tanibe, T., Kamata, R., Uchida, Y., Rokugo, K., Parajuli, S.S., Behaviour of ring-restrained high-performance concrete under extreme heating and development of screening test, *Construction and Building Materials* 162 (2018) 215-228.
27. Pimienta, P. et al., Recommendation of RILEM TC 256-SPF on the method of testing concrete spalling due to fire: material screening test, *Materials and Structures* 56(164) (2023).
28. Maluk, C., Bisby, L., Terassi, G.P., Effects of polypropylene fibre type and dose on the propensity for heat-induced concrete spalling, *Engineering Structures* 141 (2017) 584-595.
29. Mashrei, M.A., Sultan, A.A., Mahdi, A.M., Effects of Polypropylene Fibres on Compressive and Flexural Strength of Concrete Material, *International Journal of Civil Engineering and Technology (IJCIET)* 9(11) (2018) 2208-2217.
30. Richardson, I.G., The nature of C-S-H in hardened cements, *Cement and Concrete Research* 29 (1999) 1131-1147.
31. Hertz, K., Limits of spalling of fire-exposed concrete, *Fire Safety Journal* 38 (2003) 103-116.

FROM XAI INTO CAUSAL INFERENCE: A QUANTIFICATION OF POLYPROPYLENE FIBERS EFFECT IN MITIGATING FIRE-INDUCED SPALLING ACROSS CONCRETE GRADES

Mohammad Khaled Gazi al-Bashiti¹, M.Z. Naser²

ABSTRACT

Conventional machine learning (ML) methods excel at identifying patterns to make predictions but often struggle to quantify them. This highlights a critical research gap and the need for methodologies to overcome such limitations, especially in high-dimensional phenomena like fire-induced concrete spalling. We argue that the gap between domain knowledge and traditional ML approaches could be bridged by adopting a causal inference methodology. In this spirit, we leverage the largest compiled spalling database to date to predict the occurrence of spalling and then estimate the causal effect of utilizing polypropylene (PP) fibers to mitigate spalling. Several causal inference estimators were employed, namely, matching techniques, meta-learners, double machine learning approach, and ordinary least squares, to quantify the effectiveness of PP fibers. To our knowledge, our analysis is the first to quantify the average causal effect of adding PP fibers in reducing the spalling propensity by about 31%. More specifically, the effect of PP fiber in high-performance concretes (i.e., HSC, UHPC) is shown to be more pronounced in reducing the spalling by up to 36%. To complement this analysis, we present a state-of-the-art, user-friendly tool capable of predicting spalling with over 90% accuracy enhanced by explainability insights.

Keywords: Fire; concrete; spalling; causal; inference; prediction; software: explainable AI.

1 INTRODUCTION

One of the most critical elements of modern construction is the resilience of concrete structures. However, the fire-induced spalling of concrete phenomena represents a severe threat to that resilience [1]. Spalling can be generally described as the explosive or gradual chipping away of concrete under thermal stress, which might amplify a catastrophic failure. Spalling occurs due to the physical manifestation of material failure or structural degradation and complex interactions of multiple factors that significantly influence its occurrence [2, 3]. Positioning it as a complex phenomenon due to its reliance on many influencing factors, the literature presents a contrasting view about [2, 3]. Still, we lack a unified theory that can better capture spalling mechanisms, as well as quantified recommendations for existing mitigation techniques [4].

Extensive work has been put into the spalling domain, resulting in proposing various theories [5]. One of the earliest explanations of spalling stated that spalling occurs due to the rising pore pressure of evaporating moisture during heat, also known as the thermo-hygral process. The tensile strength is the threshold limit; once the pore pressure bypasses this limit, chunks of concrete will disintegrate from the concrete bulk. However, some experimental studies have demonstrated occasions where insufficient pore pressure caused spalling [6]. Other theories have attributed spalling to the triaxial mechanical stresses induced by high thermal gradients on heated surfaces, also called thermo-mechanical [7]. However, experimental results showed that spalling may still occur at low heat gradients [8]. Lastly, the also-called thermo-chemical mechanism states that some chemical degradation of concrete composites during heat temperatures above

¹ Ph.D Student, ¹School of Civil and Environmental Engineering, and Earth Sciences, Clemson University, USA
e-mail: malbash@g.clemson.edu, ORCID: <https://orcid.org/0000-0002-3889-2564>

² Assistant Professor, School of Civil and Environmental Engineering, and Earth Sciences, Clemson University, USA
e-mail: mznaser@clemson.edu, ORCID: <https://orcid.org/0000-0003-1350-3654>

700°C might weaken concrete [7]. However, it has been well documented that explosive spalling can occur at early fire age, well below such temperatures [9].

As one can see, these many theories and inconsistent reasoning of spalling have been a burning issue for assessing structures under fire. Specifically with the emerging higher-performance concrete types, such as high-strength concrete (HSC) and ultra-high-performance concrete (UHPC). Higher-performance concretes are more prone to spalling due to their lower permeability and denser microstructure. One way to mitigate the effect of spalling is by incorporating polypropylene (PP) fibers. The low melting temperature of fibers (between 160°C-170°C) provides channels for moisture to travel inward without developing a higher pore pressure or forming a micro-cracks.

There is a broad consensus among existing work on some of the primary factors that influence the spalling of concrete under fire [10]. These include the compressive strength of concrete, moisture content levels, rate of heating, peak temperature exposure, silica fume to binder ratio, and the addition of PP fibers, among others. Evidently, whilst considering mitigation strategies and risks, the essence of investigating into the interactions between influencing factors becomes crucial. Unfortunately, the literature mainly highlights such factors in qualitative terms [3]. Despite the hard work implemented on the spalling domain using traditional approaches (i.e., experimental and numerical analysis), they fall short in measuring the individual effect of factors. This might affect the adopted recommendations and guidelines on mitigating fire-induced concrete spalling.

The evolution of Artificial intelligence (AI) and machine learning (ML) in the structural fire engineering domain has experienced substantial growth, promising to enhance our ability to predict and potentially mitigate the adverse effects of spalling. Indeed, AI models have successfully been able to predict a wide range of real-world problems. Regardless, such a model is often built on complex architecture, further amplifying the perception of a black box. This showed the need for eXplainable AI (XAI) to enhance the potentiality of the AI model as it can implement explainable techniques to 'partially' open the black box and provide a transparent view "to some degree" model's prediction route. Fortunately, it has been newly implemented in the fire spalling domain, and we verified the literature-contributed factors and provided some limits to mitigate spalling [10]. Still, the imposed effect of these factors on concrete under fire remains amorphous, and the complex interaction between such factors plays a critical role in addressing their impact. Thus, this paper aims to quantify the estimated causal effect of factors influencing fire-induced concrete spalling through the application of causal inference principles.

2 CAUSAL INFERENCE

2.1 Overview

Causal inference has been used widely across various domains, such as medical trials and social sciences. Its utilization in these fields is driven by the need to understand the impact of interventions, policies, or treatments in systems where controlled experiments may be difficult to control, costly, or unethical to conduct [11]. A major challenge to the validity of causal conclusions from observational studies is the issue of unmeasured confounding factors. This occurs when differences exist between treatment and control groups before the application of the treatment, which could influence the outcome. Such unmeasured confounding factors can question the true effect of the treatment and lead to a potential misleading of the causal effect. Some domains, such as engineering, require a deep understanding of cause-effect relationships. The necessity arises from the inability of predictive models to distinguish between correlation and causation. On the other hand, causal inference can help overcome this complexity by identifying causal pathways and isolating the effects of individual factors within the system. Therefore, causal inference connects between quantifying the causal effect of a treatment factor on a target label while controlling for other influencing factors [12]. Providing a potential framework for understanding complex causal relationships.

Some related terminologies need to be clarified in causal inference — see Figure 1. Confounders are factors that influence both the treatment (i.e., PP fibers) and the outcome (e.g., spalling occurrence) [13]. In this

case, it is the PP fibers that influence the spalling of concrete. The treatment group consists of samples that received PP fibers, while the control group consists of those without PP fibers. The control group serves as a baseline for researchers to estimate the effect of the treatment by comparing outcomes between the treatment and control groups.

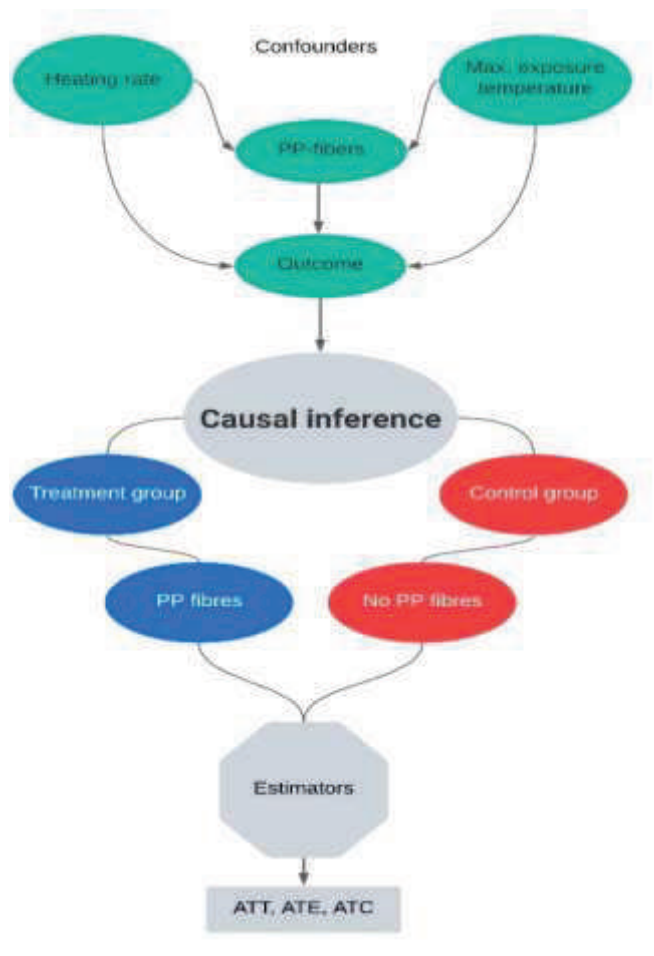


Figure 1: Causal inference

Along the same lines, several key measures are commonly used to quantify the impact of a treatment. The Average Treatment Effect (ATE) measures the expected outcome difference between the treatment and control groups across the entire population. Alongside the ATE, the Average Treatment Effect on the Control group (ATC) assesses the effect of the treatment on the control group, only showing the benefit if it had been used. Alternatively, the Average Treatment Effect on the Treated group (ATT) focuses specifically on samples that received the treatment, highlighting the effect of the treatment among this group alone. The effectiveness of the treatment for those who receive it is highlighted, compared to an average effect across all groups, given the confounders.

In this work, we base our analysis on the strong assumption that all relevant confounders are observed; we operate under the condition known as 'un-confoundedness.' This is challenging because the diversity between controlled and treated groups can break this assumption. The secondary challenge arises from the idea of receiving treatment and the difficulty in controlling the characteristics of the other confounders, leading to difficulty in identifying the treatment's true effect. This allows for the application of various sophisticated estimation methods designed to overcome these difficulties and, hence, quantify causal effects [14].

These methods include a range of statistical techniques and ML predictive models/models. In this section, we will review some popular estimation methods within the causal inference framework: matching techniques, meta-learner approaches, the double machine learning (DML) method, and ordinary least squares (OLS).

2.2 Matching techniques

Matching is a statistical method that aims to pair each sample in the treatment group with one or more samples in the control group that are similar in terms of observed confounders [15]. This method helps satisfy the un-confoundedness assumption, meaning that all confounding factors that could influence both the treatment and the outcome have been satisfactorily controlled for and are now independent [16]. Other matching methods exist, but the universal aim is to quantify the effect of the treatment on the outcome. One limitation of matching techniques is that they tend to discard some of the data that were not matched. This can be resolved by using Inverse Probability Weighting (IPW), which assigns a probability of receiving treatment to each sample.

2.3 Meta learners

The meta-learners leverage a wide variety of supervised ML models to predict the causal effect of treatments. S-learning uses a single ML algorithm to predict the outcome while controlling for all the factors, including the treatment. In the second stage, the variation is measured among the estimated values when the treatment assignment indicator is changed from control to treatment [17]. X and T-learning approaches train a double ML model, one model for each of the treatment and control groups. The T-learner then compares the predictions from the two models and concludes the estimated effect per group. In the case of imbalanced treatment and control groups, the T-learner is more likely to overfit the treatment group. To overcome this limitation, X-learning is particularly useful when there is an imbalance between the treatment and control groups. X-learner is a more complicated approach as it uses information from the control group to develop better estimators for the treatment group or vice versa. In the second step, the X-learner predicts the outcome of the treatment group using the control group model, and the control group is imported into the treatment model for prediction. In a subsequent step, both predictions are compared using a third model to capture the variation in the predictions. Simply put, an X-learner is similar to a T-learner but uses each observation training set in an X-like shape; hence, it is called an X-learner. It is worth noting that in meta-learning, the goal is to estimate the average effect of the treatment among the two groups, which is a continuous variable, despite the fact that the outcome and the treatments are binary.

2.4 Double Machine Learning (DML)

DML is a method that deals with the biases in traditional ML causal effect estimators [18]. The DML method is especially powerful when the relationships between treatment, covariates, and outcome are complex and possibly nonlinear. It works by employing two ML algorithms to predict the outcome and the treatment factor separately. Hence, classification models are used for the first step. Then, the DML combines the models in a final stage estimation to create a model of the heterogeneous treatment effect.

Non-parametric DML uses various ML algorithms, while linear DML uses linear models (i.e., linear regression). This approach can control for confounders by modelling the treatment and outcome separately, and then a less flexible model (often a linear model like LassoCV) is used in the final stage to estimate the treatment effects. It is worth noting that DML can be implemented using parametric or non-parametric algorithms based on the complexity of the task at hand.

2.5 Ordinary Least Squares (OLS)

OLS provides a fundamental method of estimating the treatment effect by employing regression analysis assuming linear relationships among variables. In other words, the OLS weights are optimal for predicting the effect on the target label based on the original data, which addresses the "*what is*" question. Instead, we are interested in predicting "*what if*"-scenarios, that is, hypothetical changes in the treatment-assigned samples. Such simplicity might limit our capabilities of capturing complex, nonlinear causal effects [19].

3 DATASET

This section describes the largest collected spalling database to date, consisting of more than a thousand fire tests [20]. This work will focus on the top 6 key factors identified as critical factors from the literature

[10]. Namely, compressive strength of concrete, moisture content levels, heating rate, peak temperature exposure, the silica fume to binder ratio, steel fiber quantity, and the addition of polypropylene (PP) fibers. Table 1 demonstrates the statistical insights, such as the minimum, maximum, median, skewness, mean, data distribution, and standard deviation of each factor.

Table 1. Statistical insights of the utilized database

Parameter	Min	Max	Median	Skew	Std	Mean	Distribution
Maximum exposure temperature (°C)	75	1200	600	-0.05	226.9	577.23	Normal
Heating rate (°C/min)	0.1	200	10	1.94	35.62	25.96	Lognormal
Moisture content (%)	0	0.09	0.03	0.04	0.02	0.04	Normal
PP fiber quantity (Kg/m ³)	0	16	0	4.07	2.55	1.03	Lognormal
Silica fume/binder ratio (%)	0	0.23	0	0.83	0.08	0.06	Gumbel
Compressive strength (MPa)	20	214	84.1	0.53	40.44	91.05	Normal

4 CAUSAL INFERENCE RESULTS AND DISCUSSION

In this study, we evaluated the impact of adding PP fibers on fire-induced concrete spalling. Adding PP fibers to concrete mixtures helps mitigate spalling by forming a network of channels within the concrete by the melted PP fibers at a temperature of around 160oC [21]. These channels allow for the escape of steam generated under high temperatures, which, in return, reduces the buildup of internal pressure, which can lead to spalling. Studies have shown that concrete mixes containing PP fibers exhibit significantly lower rates of spalling [22–24]. However, the literature lacks a quantification of the effect of including PP fibers in a concrete mix.

To address this gap, advanced statistical methods were employed to rigorously analyze the data and quantify the impact of PP fibers on reducing spalling. The linear DML method employed a linear regression model for the treatment group, while LassoCV was used for the control group. In addition, non-parametric DML utilized eXtreme Gradient Boosting (XGBoost) regressor and classifier. Similarly, meta-learner models employed XGBoost regressor to estimate the ATE on the outcomes with the addition step attributed to T and X-leaners by employing LassoCV as the final model.

4.1 The effect of PP fibers on different concrete grades

PP fibers are used in concrete to enhance its mechanical properties and resistance to spalling [25]. Findings details of the employed estimators — see Table 2, quantify the estimated treatment effect of incorporating PP fibers into concrete regarding its resistance to spalling under elevated temperatures. The treatment group was selected based on the inclusion of PP fibers, while the control group used samples that did not contain PP fibers. Our analysis selected the maximum exposure temperature and the heating rate as confounders, given that they are the driving forces of degrading the fibers. One can see that the treatment effects are all negative, indicating there is a reduced propensity of spalling risk in adding PP fiber into a concrete mix.

Quantitatively, the presence of PP fibers in the concrete mix reduces the spalling propensity by approximately 17-30%. This gives a broad picture of the effectiveness of PP fibers in reducing spalling across all types of concrete, regardless of whether they were specifically treated with PP fibers or not. More specifically, the *matching* estimator shows a strong effect of PP fibers, with an ATE of -25.9%, showing a reduction of spalling chances.

Furthermore, the reduction was significantly lower among the treated group (ATT -32.9%), but less pronounced within the control group, where ATC stood at -22.5% reduction in propensity. *OLS regression* Offered a conservative estimate compared to other methods, with an ATE of -0.184. Similar results can be seen for the *linear DML*, showing an even lower effect at a 17.7% reduction in the spalling probability. These low estimates may be due to the limitations of such methods in fully accounting for nonlinearity in the confounding factors, even though they controlled for maximum exposure temperature and heating rate. Alternatively, *non-parametric DML* gives more substantial estimates than the *linear DML* form and the *OLS* model, demonstrating the strongest effect, with an ATE of 31.9% reduction. Additionally, ATT and

ATC accounted for -35% and -30% spalling propensity reduction by incorporating PP fibers into the concrete mix. Such results are more likely to be accurate, benefiting from the ability to better handle complex causation and nonlinearities in the data as well as mitigating the overfitting.

Looking at the *meta-learners'* estimators, one can see that the *S-Learner* displayed a moderate overall effect (ATE at -0.239). Also, the *T-Learner*, which models treated and control units separately, indicated an even stronger effect ATE at -25.7%, possibly reflecting how PP fibers perform under varying conditions of exposure and heat. Lastly, the *X-Learner*, designed to enhance estimations in cases of treatment effect heterogeneity and preventing overfitting, results show almost similar effects to those of the *T-Learner*, particularly noting substantial benefits in treated scenarios at ATE of 28%.

Below are Here are the detailed outcomes for each estimator:

1. **Matching:** ATE of -29.2% indicates that the treatment reduces spalling outcomes by this percentage across the entire population. The effect is slightly less pronounced for the control group with an ATC of -25.7% and a more substantial effect with an ATT of -34.9% for the treated group.
2. **OLS:** The ATE of -18.4% suggests a moderate reduction in spalling rates overall. The control group sees a nearly equivalent effect with an ATC of -17.9%, and the treated group observes a similar effect with an ATT of -19.5%.
3. **Linear DML:** This estimator provides an ATE of -17.7%, demonstrating a moderate impact on spalling reduction. The control group's effect (ATC) is -17.1%, closely aligned with the overall effect, while the treated group shows a slightly higher effect at -19.1%.
4. **Non-parametric DML:** Showcasing the most significant effects, this estimator records an ATE of -31.9%. The control group experiences an ATC of -30.2% and the treated group has a higher impact with an ATT of -35.5%.
5. **S-Learner:** An ATE of -23.9% indicates a noticeable reduction in spalling rates. The controls have a reduced effect at -19.7%, and the treated group sees a substantial reduction with an ATT of -32.8%.
6. **T-Learner:** The ATE is -25.7%, indicating a significant mitigation effect on spalling. The control group has an ATC of -20.0%, while the treated group benefits more significantly with an ATT of -37.8%.
7. **X-Learner:** This estimator suggests a strong treatment effect with an ATE of -28.0%. The effect on the control group (ATC) is -22.2%, and the treated group experiences a pronounced reduction in spalling rates with an ATT of -36.9%.

Table 2. Causal treatment effects

Estimator	ATE	ATC	ATT
Matching	-0.259	-0.225	-0.329
OLS	-0.184	-0.179	-0.195
Linear DML	-0.177	-0.171	-0.191
Non-parametric DML	-0.319	-0.302	-0.355
S-Learner	-0.239	-0.197	-0.328
T-Learner	-0.257	-0.200	-0.378
X-Learner	-0.280	-0.222	-0.369

A cross-examination of the tabulated results — see Table 2, shows a consistently higher effect of PP fibers on the treated groups (ATT). In our case, the PP fibers are likely to be added to HSC and UHPC mixtures. These concrete types are prone to spalling primarily due to their low permeability, which restricts the movement of the evaporated moisture, increasing the internal pressure and risk of spalling.

4.2 PP fibers effect on the HSC/UHPC dataset

Modern concrete types are known for their compressive strengths exceeding 55 MPa and 80 MPa for HSC and UHPC, respectively. Furthermore, they are particularly susceptible to spalling due to their dense microstructure and low permeability [26]. This part of the analysis builds upon the outcomes of the previous subsection and quantifies the ATE, ATT, and ATC for higher-grade concretes. We analyzed the impact of PP fibers on the spalling of concrete using the same set of estimators.

Table 3 presents the calculated causal effects for HSC and UHPC, showing a similar trend of higher impacts across all average effect groups compared to those observed in the full population examined in the previous subsection. All estimators show negative ATE, ATC, and ATT values, indicating that the inclusion of PP fibers in concrete significantly reduces the propensity for spalling across all groups. Across the range of utilized estimators' effects, a reduction trend was seen in spalling propensity, typically between 22-36%(ATE). Highlighting PP fibers' effectiveness as a mitigation material for various concrete formulations. The overall results of each of the employed estimators are as follows:

1. **Matching:** ATE of -29.2%, indicates that the treatment reduces the outcome by this percentage across the entire population. For the control group, the effect is slightly less pronounced with an ATC of -25.7%, while the treated group experiences a more substantial effect with an ATT of -34.9%.
2. **OLS (Ordinary Least Squares):** ATE of -22.8%, the effects are nearly uniform across groups, with an ATC of -22.2% and an ATT of -23.8%, suggesting a consistent impact of the treatment across both treated and control groups.
3. **Linear DML (Double Machine Learning):** This estimator reports a minimal variation in treatment effects across different groups: an ATE of -22.9%, an ATC of -22.6%, and an ATT of -23.2%, indicating a uniform efficacy of the treatment across all participants.
4. **Non-parametric DML:** Showing the strongest effects among the estimators, Non-parametric DML reports an ATE of -36.0%, an ATC of -33.2%, and an ATT of -40.7%. This suggests a significantly higher effectiveness of the treatment in the treated group compared to the overall and control groups.
5. **S-Learner:** The S-Learner finds a general treatment effect (ATE) of -27.7%. It indicates a lesser effect on the control group with an ATC of -21.5% and a higher impact on the treated group with an ATT of -38.1%, highlighting a substantial benefit for those receiving the treatment.
6. **T-Learner:** This model calculates an ATE of -30.8%, with a relatively lower effect on the control group (ATC of -26.6%) compared to a more pronounced effect on the treated group (ATT of -37.8%), demonstrating enhanced benefits for the treated participants.
7. **X-Learner:** The X-Learner estimates an ATE of -29.5%, with an ATC of -26.0% and an ATT of -39.8%. This indicates a notable increase in treatment effectiveness when applied to the treated group compared to the control group.

Table 3. Causal treatment effects (higher concrete grades)

Estimator	ATE	ATC	ATT
Matching	-0.292	-0.257	-0.349
OLS	-0.228	-0.222	-0.238
Linear DML	-0.229	-0.226	-0.232
Non-parametric DML	-0.360	-0.332	-0.407
S-Learner	-0.277	-0.215	-0.381
T-Learner	-0.308	-0.266	-0.378
X-Learner	-0.295	-0.260	-0.398

Similarly, the ATT values are the most pronounced against the other groups, indicating that PP fibers are especially effective in concrete mixtures where they are applied, reducing spalling propensity by up to 40%. The higher ATT scores in HSC and UHPC reinforce the idea that PP fibers are particularly effective in

environments where strength amplifies spalling risks. Our analysis also observed that the effect is more pronounced in treated groups (ATT), even with simpler estimators such as OLS, linear DML, and S-learner. For robust estimators, the reduction in spalling is the most significant, often exceeding 35% in the treated groups (ATT), where PP fibers are added to the concrete mix. This highlights the fibers' critical role in enhancing high strength concretes' resilience. For the control groups (ATC), the hypothetical addition of PP fibers could potentially reduce spalling risks by up to 33%. It is worth noting that advanced models like Non-parametric DML, X-Learner, and T-Learner provide higher estimates of treatment effects, suggesting their greater sensitivity to complex dynamics in data involving treatment interactions.

5 FIRE-INDUCED SPALLING OF CONCRETE PREDICTION TOOL

To complement this work, an XAI predictive tool has been developed to predict fire-induced spalling of concrete accurately. Utilizing three advanced machine learning models—XGBoost, Random Forest, and Light Gradient Boosting Machine (LGBM). Trained on the above-discussed database and configured with multiple factors, as detailed in Figure 2-a. Each model consistently achieves an accuracy rate exceeding 90%. Additionally, the SHAP local explainability tool is employed to provide transparent insights into the decision-making process of each prediction, illustrating how specific factors contribute to the outcomes — see Figure 2-b. We are hoping that, in future work, we will incorporate a causality section in the software.



a. Fire-induced spalling of concrete predictive tool



b. SHAP explainability tool

Figure 2 Illustration of the proposed tool

6 CONCLUSIONS

This section outlines the main findings and outcomes of this work.

- The analysis across a number of causal inference techniques quantifies and reinforces the understanding of the effectiveness of PP fibers mitigates spalling in various concrete grades.
- Maximum exposure temperature and heating rate factors were selected as the confounders in our causal analysis due to their significant influence on the activation of the degradation process of PP fibers. Furthermore, controlling for such confounders provides a more accurate estimate of the true effect of PP fibers.
- This analysis used a wide range of causal estimators, with S-learner and OLS being the simplest and the non-parametric DML being the most robust due to its ability to capture complex and nonlinear causal effects.
- The average causal effect of adding PP fibers in concrete is that it reduces the propensity of concrete spalling by up to 31%.
- The focused analysis on HSC and UHPC confirms that PP fibers significantly mitigate the risk of spalling in high-strength concretes by up to 36%.
- The conducted analysis demonstrated a consistently higher ATT, which reinforces the benefit of PP fibers in higher grades of concrete and opens up avenues for further research.

REFERENCES

1. Amran, M., Huang, S.-S., Onaizi, A.M., Murali, G., Abdelgader, H.S.: Fire spalling behavior of high-strength concrete, A critical review. *Constr Build Mater.* 341, 127902 (2022). <https://doi.org/10.1016/j.conbuildmat.2022.127902>
2. Gil, A., Banerji, S., Kodur, V.: Factors influencing pore pressure measurements in concrete during heating and its influence on fire-induced spalling. *Cem Concr Compos.* 142, 105228 (2023). <https://doi.org/10.1016/J.CEMCONCOMP.2023.105228>
3. De Domenico, D., Khan, M., Cao, M., Farooqi, M.U., Mohammed, H., Ahmed, H., Kurda, R., Alyousef, R., Deifalla, A.F.: Heat-Induced Spalling of Concrete: A Review of the Influencing Factors and Their Importance to the Phenomenon. *mdpi.com.* (2022). <https://doi.org/10.3390/ma15051693>
4. Mcnamee, R.J.: Fire spalling theories-Realistic and more exotic ones. (2019)
5. Kannangara, T., Joseph, P., Fragomeni, S., Guerrieri, M.: Existing theories of concrete spalling and test methods relating to moisture migration patterns upon exposure to elevated temperatures – A review. *Case Studies in Construction Materials.* 16, e01111 (2022). <https://doi.org/10.1016/J.CSCM.2022.E01111>
6. Jansson, R., Boström, L.: The influence of pressure in the pore system on fire spalling of concrete. *Fire Technol.* 46, 217–230 (2010). <https://doi.org/10.1007/S10694-009-0093-9/TABLES/3>
7. Liu, J.C., Tan, K.H., Yao, Y.: A new perspective on nature of fire-induced spalling in concrete. *Constr Build Mater.* 184, (2018). <https://doi.org/10.1016/j.conbuildmat.2018.06.204>
8. Hertz, K.D.: Limits of spalling of fire-exposed concrete. *Fire Saf J.* 38, (2003). [https://doi.org/10.1016/S0379-7112\(02\)00051-6](https://doi.org/10.1016/S0379-7112(02)00051-6)
9. Sanjayan, G., Stocks, L.J.: Spalling of High-Strength Silica Fume Concrete in Fire. *Materials Journal.* 90, 170–173 (1993). <https://doi.org/10.14359/4015>
10. al-Bashiti, M.K., Naser, M.Z.: Verifying domain knowledge and theories on Fire-induced spalling of concrete through eXplainable artificial intelligence. *Constr Build Mater.* 348, (2022). <https://doi.org/10.1016/j.conbuildmat.2022.128648>
11. Yao, L., Chu, Z., Li, S., Li, Y., Gao, J., Zhang, A.: A Survey on Causal Inference. *ACM Transactions on Knowledge Discovery from Data (TKDD).* 15, (2021). <https://doi.org/10.1145/3444944>

12. Subramanian, A., Huang, Y., Pinto, M.D., Downs, C.A., Rahmani, A.M.: Estimating the Impact of Pre-Exposure Prophylaxis (PrEP) on Mortality in COVID-19 Patients: A Causal Inference Approach. <https://doi.org/10.1101/2023.03.16.23287365>
13. Hernán MA, Robins JM (2020). *Causal Inference: What If*. Boca Raton: Chapman & Hall/CRC.
14. Pearl, J.: Causal inference in statistics: An overview. *Stat Surv.* 3, 96–146 (2009). <https://doi.org/10.1214/09-SS057>
15. Stuart, E.A.: Matching methods for causal inference: A review and a look forward. *Stat Sci.* 25, 1 (2010). <https://doi.org/10.1214/09-STS313>
16. Kuang, K., Li, L., Geng, Z., Xu, L., Zhang, K., Liao, B., Huang, H., Ding, P., Miao, W., Jiang, Z.: Causal Inference. *Engineering.* 6, 253–263 (2020). <https://doi.org/10.1016/J.ENG.2019.08.016>
17. Zhao, Y., Liu, Q.: Causal ML: Python package for causal inference machine learning. *SoftwareX.* 21, 101294 (2023). <https://doi.org/10.1016/J.SOFTX.2022.101294>
18. Fuhr, J., Berens, P., Papies, D.: Estimating Causal Effects with Double Machine Learning -- A Method Evaluation. (2024)
19. Słoczyński, T.: Interpreting OLS Estimands When Treatment Effects Are Heterogeneous: Smaller Groups Get Larger Weights. *Rev Econ Stat.* 104, 501–509 (2022). https://doi.org/10.1162/REST_A_00953
20. Khaled al-Bashiti, M., Naser, M.Z.: What can we learn from over 1000 tests on fire-induced spalling of concrete? A statistical investigation of critical factors and unexplored research space. *Constr Build Mater.* 403, 133200 (2023). <https://doi.org/10.1016/j.conbuildmat.2023.133200>
21. Bilodeau, A., Kodur, V., Composites, G.H.-C. and C., 2004, undefined: Optimization of the type and amount of polypropylene fibres for preventing the spalling of lightweight concrete subjected to hydrocarbon fire. Elsevier.
22. Liu, J.C., Zhang, Z.: Neural network models to predict explosive spalling of PP fiber reinforced concrete under heating. *Journal of Building Engineering.* 32, 101472 (2020). <https://doi.org/10.1016/J.JOBE.2020.101472>
23. Li, Y., Tan, K.H., Yang, E.H.: Influence of aggregate size and inclusion of polypropylene and steel fibers on the hot permeability of ultra-high performance concrete (UHPC) at elevated temperature. *Constr Build Mater.* 169, 629–637 (2018). <https://doi.org/10.1016/J.CONBUILDMAT.2018.01.105>
24. Khoury, G.A.: Polypropylene fibres in heated concrete. Part 2: Pressure relief mechanisms and modelling criteria. *Magazine of Concrete Research.* 60, (2008). <https://doi.org/10.1680/mac.2007.00042>
25. Liu, J.C., Huang, L., Tian, Z., Ye, H.: Knowledge-enhanced data-driven models for quantifying the effectiveness of PP fibers in spalling prevention of ultra-high performance concrete. *Constr Build Mater.* 299, 123946 (2021). <https://doi.org/10.1016/J.CONBUILDMAT.2021.123946>
26. Ko, J., Ryu, D., Noguchi, T.: The spalling mechanism of high-strength concrete under fire. *Magazine of Concrete Research.* 63, (2011). <https://doi.org/10.1680/mac.10.00002>

HIGH-TEMPERATURE BOND STRENGTH OF GFRP REINFORCING BARS FOR INFORMING DESIGN RECOMMENDATIONS

Bronwyn Chorlton¹, Naeim Roshan², Hamzeh Hajiloo³, Mark Green⁴

ABSTRACT

Glass fibre reinforced polymers (GFRP) bars can be used as a corrosion-resistant alternative to steel bars, however, there remain limitations in their use induced by challenges in assessing their fire performance. Standard tests such as ASTM E119 fire tests are often still required by regulatory bodies, in which the members are loaded based on ultimate strength only without considering the actual loads that will be applied in service on a GFRP reinforced member. In addition, previous studies have shown the bond strength to be the critical factor governing the failure of GFRP reinforced concrete slabs in fires. The purpose of this study is to outline challenges in establishing the fire performance of GFRP reinforced concrete beams and slabs, and to present new pullout test results. Given the load levels to which GFRP reinforced members are expected to be subjected, the applied service moment ensuring midspan deflection compliance should be set by deflection-based calculation, which would require current standards to update fire loading requirements for GFRP reinforced concrete members.

Keywords: Fibre reinforced polymers; standard fire tests; practical approaches; pullout tests

1 INTRODUCTION

Glass fibre reinforced polymer (GFRP) bars are a viable replacement for corrosion-prone steel bars in reinforced concrete structures. However, the fire performance of GFRP reinforced concrete has been a major concern because of the degradation of GFRP material properties at high temperatures. Bond interaction between concrete and GFRP has been highlighted as considerably different than that of steel bars [1]. Fire resistance in GFRP reinforced concrete has progressed significantly from not recommending GFRP internal reinforcement for structures, in which fire resistance is essential to maintain structural integrity, to moving towards providing specific design provisions to achieve the desired fire resistance (e.g., ACI CODE-440.11-22 [2]). Additionally, Canadian standard CSA-S806-12 [3] provides a semi-empirical approach for determining the fire performance of FRP-reinforced concrete slabs based on the minimum concrete cover, which is due for an update to incorporate recent advances in the field.

To have confidence in the fire resistance of a member, standard fire tests such as ASTM E119 [4] (or ISO 834 [5]) are often required by regulatory bodies. The standard ASTM fire test of reinforced concrete beams or slabs requires the application of loads on a reinforced concrete member based on the ultimate capacity of the member; this was initially developed based on the moment resistance of steel reinforced flexural members. In steel reinforced members, strength is the governed design criterion while GFRP reinforced

¹ Postdoctoral Fellow, Queen's University,
e-mail: b.chorlton@queensu.ca, ORCID: <https://orcid.org/0000-0003-2840-9679>

² PhD student, Carleton University
e-mail: NaeimRoshan@cmail.carleton.ca, ORCID: <https://orcid.org/0000-0002-0531-7117>

³ Assistant Professor, Carleton University
e-mail: hamzeh.hajiloo@carleton.ca, ORCID: <https://orcid.org/0000-0002-5932-2640>

⁴ Professor, Queen's University
e-mail: greenm@queensu.ca, ORCID: <https://orcid.org/0000-0002-6610-0325>

concrete members are designed for service loads they typically have much higher flexural capacity than is needed to carry the loads based on strength because deflection limitations and service stress limits (e.g., 25 to 30% of ultimate strength [2-3]) govern their design. Section 8.8.3.1 of ASTM E119 requires the application of a superimposed load to simulate a maximum load condition. This load can be reduced when a national design code specifies limited design criteria.

The main purpose of this paper is to outline the challenges in establishing fire resistance for GFRP reinforced concrete beams and slabs. This will be complemented by a new experimental series considering the bond strength of GFRP reinforced concrete, further informing the high-temperature performance of the technology.

2 CHALLENGES IN FIRE TESTING OF GFRP REINFORCED MEMBERS UNDER FULL LOAD

2.1 Superimposed loading according to ASTM E119

The superimposed load (w_s) for the simulation of maximum load conditions on reinforced concrete floors and roofs during the fire-resistant test can be found in ASTM E119 [4] and CAN/ULC S101[6]. Fire resistance tests of floor and roof specimens (reinforced with steel bars) are normally conducted using strength limit state criteria to simulate a specified load condition. Introducing fibre reinforced polymer (FRP) bars in such members, serviceability criteria (e.g. deflection) may govern the ultimate state in design [7]. To compute the moment resistance and midspan deflection of the specimen reinforced with FRP, design codes and standards such as ACI 440.11 [2] and CSA S806 [3] can be utilized. According to ASTM E119 [4] and assuming the ratio of dead load (DL) to live load (LL) equal to 1.00 ($r=1$), also given the corresponding load factor α_D and α_L (respectively for DL and LL), the applied service load, w_s , for each specimen can be calculated based on strength or serviceability criteria per Equation 1:

$$\begin{cases} w_{s,1} = \frac{1}{\alpha s} \cdot \frac{8(\phi M_n \text{ or } M_r)}{L^2} - w_d \\ w_{s,2} = \frac{384EI_d \Delta}{s5L^2} \end{cases} \rightarrow w_s = \min(w_{s,1}, w_{s,2}) \quad (1)$$

where the load factor, α , can be calculated as $\alpha=(r\alpha_D+\alpha_L)/(1+r)$, s is the width of the test specimen, L is the span length, and w_d reflects the dead load of the test specimen, M_n is the nominal moment capacity, M_r is the factored moment capacity, and ϕ is the resistance factor. Also, Δ and I_d are the maximum permissible deflection and corresponding moment of inertia of the specimen, respectively. If sustained applied moment (M_{sus}) contains the effects of both dead and live loads during the fire test, for a unit width ($s=1$) of the test specimen, M_{sus} can be calculated accordingly. Using the strength limit approach in ASTM E119 and CAN/ULC S101, which were originally developed for steel reinforced concrete (steel-RC) members, $M_{sus}/\phi M_n$ or M_{sus}/M_r (both called load ratio here) is roughly equal to 60-70% of ultimate load capacity of the specimen. However, for reinforced concrete members incorporating GFRP bars (GFRP-RC), the serviceability criteria should be used instead which is categorized as a “restricted” load condition [4]. Additionally, because of the sudden rupture of FRP bars at the ultimate state, the desirable failure mode for FRP-RC members normally initiates with the crushing of concrete in the compressive zone of the section ($\rho>\rho_b$). In light of this issue, most experimental tests on FRP-RC structural members cannot provide the ASTM E119 [4] specifications regarding the strength-based load ratio during the fire test. As can be seen from the details of various full-scale fire tests on GFRP-RC beams [8–10] and GFRP-RC slabs [11–14], the applied load ratio during the fire test was between 20% and 50% of the ultimate flexural capacity of the specimens reinforced with GFRP bars through the fire test [15]. The reason for lowering the load ratio during the fire test is the serviceability criteria (especially midspan deflection) to be met by GFRP-RC beams or slabs. In most cases, the serviceability criteria such as stress in FRP, crack width, and maximum deflection exceed their permissible values by applying the load ratio computed based on the flexural capacity of the member. As mentioned by Hajiloo et al. [11], during the design process of GFRP-RC

members, the criteria related to the serviceability state often take precedence over those concerning the ultimate state. The lower stiffness of FRP bars, particularly Glass FRP (GFRP) bars, poses challenges in employing traditional design methods similar to steel-RC members. Additionally, GFRP bars are more prone to creep and fatigue effects, which could influence the design approach during a fire. These modifications predominantly affect serviceability criteria such as crack width, deflection, creep, and fatigue considerations. The following sections provide detailed information regarding the serviceability of GFRP-RC flexural members.

2.2 Calculation of Service Stress in FRP Bars

FRP reinforcement has higher strength, f_{frp} , than the specified yield strength, f_y , of common steel bars. However, due to the lower modulus of elasticity of FRP bars compared to steel reinforcement, the higher strength cannot be fully utilized in reinforced concrete structures [7]. According to ACI 440.11 [4], the sustained stress in FRP bars under unfactored service load is limited to 30% of the ultimate strength of the bars. The sustained service stress can be calculated assuming an elastic cracked section hypothesis. On the other hand, ISIS Design Manual No. 3 [7] uses 25% FRP's ultimate tensile strength (based on the Canadian design code [3]) as the permissible stress in FRP reinforcement. The calculation for finding the service stresses and their permissible values in FRP bars based on both standards are carried out here and the results are shown in Figure 1. For better comparison, relative values including the load ratio ($M_a/\phi M_n$ or M_a/M_r) of each specimen and the ratio of calculated stress to allowable stress ($f_{frp,cal}/f_{frp,allow}$) are implemented. As can be perceived from the results, using the ISIS manual M3 [7], in most cases, the calculated stress in GFRP bars exceeds their permissible limit by applying the strength-based load ratio recommended by ASTM E119. However, based on ACI 440.11 assumptions, the calculated stresses in GFRP bars are within the limited stresses for the recommended load ratio.

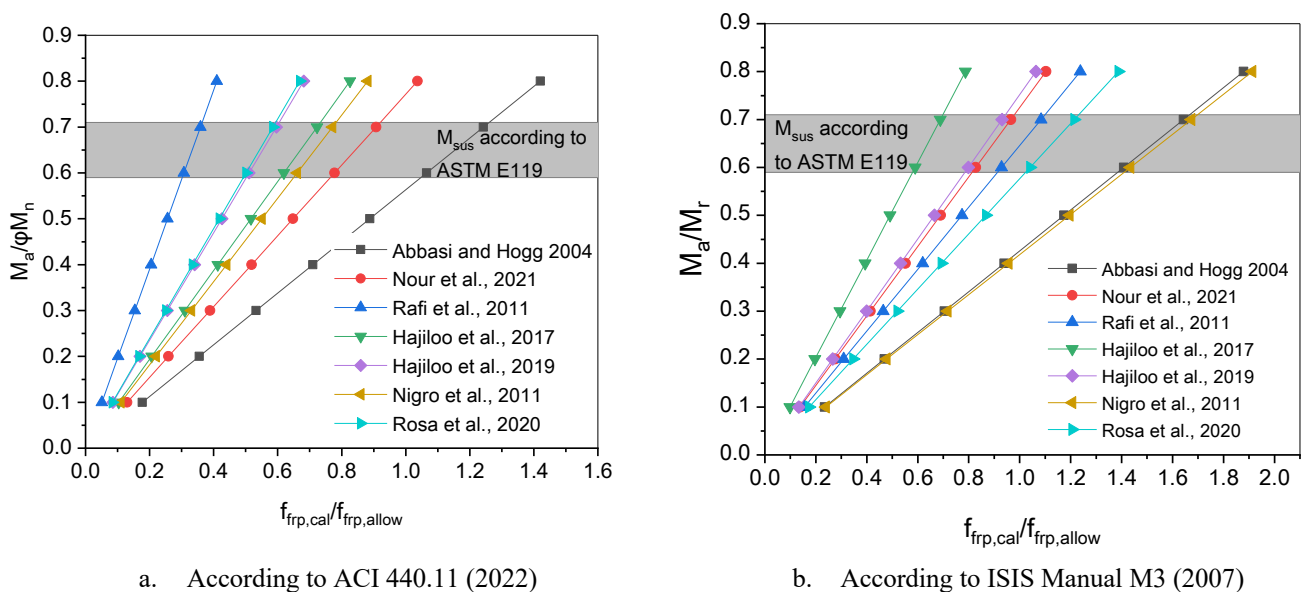


Figure 1. Calculated stress in GFRP bars under varying applied moments

2.3 Cracking in GFRP-RC Beams or Slabs

In accordance with ISIS manual M3 [7], the crack width can be computed using a modified formula, which is based on the original work by Gergely and Lutz [16]. This empirical formula is based on the effective area of concrete in tension, the strain gradient from the level of the reinforcement to the tensile face, the number of bars, the reinforcement cover, and the stress in the flexural reinforcement. Here, the crack width is calculated for different studies found in the literature [8–14] and the results are obtained as shown in Figure 2. Regarding the obtained results, the calculated crack width for load ratios recommended by strength-based approach in ASTM E119 exceeds the limit provided by ISIS manual M3 [7] by 2 to 5 times.

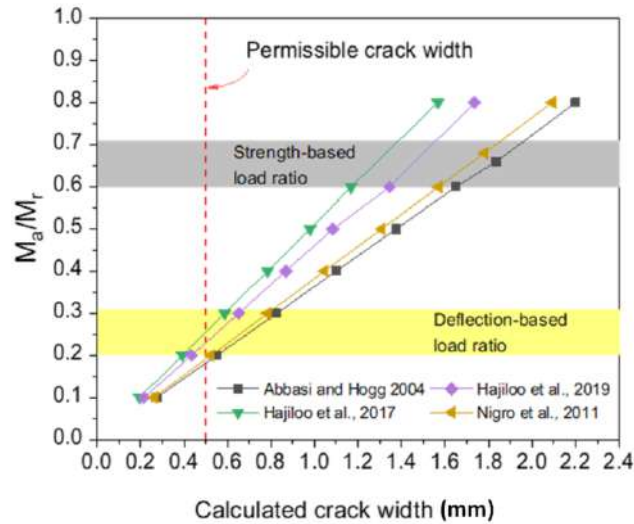
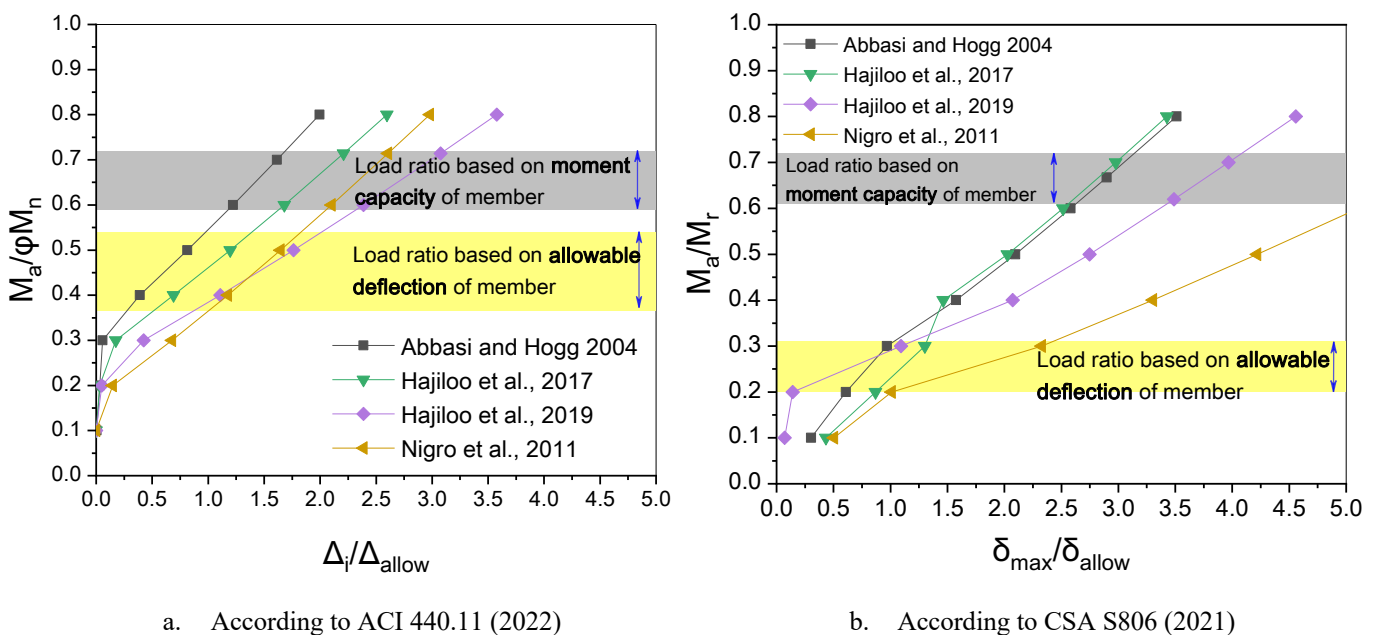


Figure 2. Calculated crack width under applied moments

2.4 Midspan Deflection in GFRP-RC Beams or Slabs

When computing immediate deflections in beams or one-way slabs reinforced with GFRP bars, it is essential to account for both the impact of cracking and the influence of reinforcement on the stiffness of the structure. Based on ACI 440.11, the overall flexural stiffness of a cracked member varies between gross member stiffness ($E_c I_g$) and cracked member stiffness ($E_c I_{cr}$), depending on the magnitude of the applied service moment and the extent of cracking along the member. On the other hand, the Canadian standard [3] uses a trilinear moment-curvature behaviour with the slope of the three segments being $E_c I_g$, zero, and $E_c I_{cr}$. The calculation (as shown in Figure 3) illustrates the exceedance of relative midspan deflection (relative to allowable value) due to the strength-based load ratio (to moment capacity) suggested by ASTM E119 for GFRP-RC beams and slabs, with higher severity for full-scale specimens [8,11–13]. For short specimens tested by Nour et al. [9] and Rafi et al. [10], lower values for the midspan deflection are obtained. Applying load ratios consistent with deflection-based load ratio for a full-scale test of GFRP-RC slabs or beams is 40% and 30% of the moment capacity of the specimen, respectively according to ACI 440.11 and CSA S806 standards. This calculation proves the consistency of meeting serviceability criteria with load ratio accounting for the allowable deflection values.



a. According to ACI 440.11 (2022)

b. According to CSA S806 (2021)

Figure 3. Midspan deflection for a varying applied moment

3 GFRP PULLOUT TESTS

3.1 Method

The experimental testing of the GFRP pullout tests was conducted to quantify the bond strength of the GFRP reinforcing bars. Two test series were conducted, considering either steady state or transient temperatures. A summary of the tests conducted is shown in Tables 1 and 2. The temperatures for these tests range from room temperature to 200 °C. Although temperatures in a fire test are much higher (over 1000 °C), temperatures inside reinforced concrete members are much lower (e.g., below 600 °C) because of concrete cover. In the anchorage zones where bond is critical, the temperatures at the level of the reinforcement are typically below 200 °C [17].

With regards to the procedure for the steady state tests, the specimen was heated to a specified temperature, held at that temperature until the temperature at the reinforcing bar reached a steady state temperature, and was then loaded to failure at that temperature. A constant load of 2 kN was applied during heating, to maintain the position of the specimen. For the transient temperature tests, the specimens were loaded to a specified load and then exposed to continuously increasing temperature until failure.

The average bond stress was calculated by dividing the pullout load over the surface area of the bars, as seen in Equation 2.

$$\tau = \frac{F}{(\pi * d_b * L_{em})} \quad (2)$$

Where the bond stress is represented by τ , F is the pullout load, d_b is the diameter of the bar, and L_{em} is the embedment length of the specimens.

The average compressive strength of the concrete at the time of testing was 28.5 MPa (from 18 cylinders). The recommended cube size, per CSA S806 [3], is 150 mm with an embedment length of 4d (where d is the nominal diameter of the bar). One type-K thermocouple was attached to each bar. The thermocouple was installed in a square shape to avoid altering the concrete-to-bar interface by the thermocouple (Figure 4). Testing was done using an INSTRON SATEC apparatus. The test setup was customized for this test series, with a 20 mm thick steel fixture with a groove cut out of the bottom, to accommodate the concrete cube and rebar. A furnace was then mounted around the fixture, such that heating and loading can occur simultaneously. The furnace provided uniform heat around the cube, at a controlled rate of heating. A heating rate of 5 °C/min and a loading rate of 1.0 mm/min were chosen to align with previous tests [17].

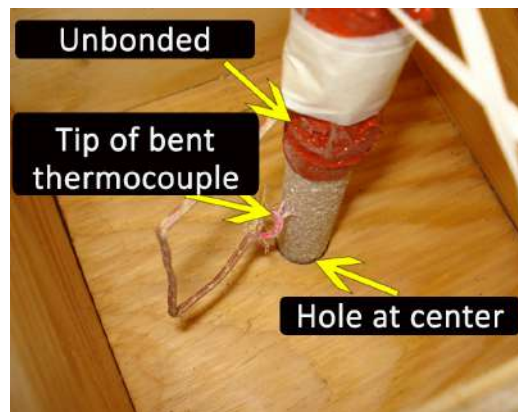


Figure 4. Thermocouple configuration

The pullout tests considered either a steady state temperature while the mechanical load was applied (denoted as ‘steady-state’ herein), or loaded after heating (denoted as ‘residual’) herein. For the steady-state tests, the samples were placed in the apparatus and the furnace was turned on. Once the furnace reached its set temperature, the samples were allowed to continue heating for 120 minutes, until a fairly stable temperature condition was met. At this time, with the furnace still turned on, the sample was mechanically loaded to failure. For the residual tests, a similar procedure was followed in bringing the samples to a stable temperature, however, instead of loading to failure, the oven was turned off and the sample was allowed to cool for 24 hours at room temperature. After this time, the sample was mechanically loaded to failure at room temperature.

3.2 Results and Discussion

Table 1 summarizes the results of the steady-state tests. The second column, T_{bar} , denotes the temperature of the bar when loading is stated. The third column, T_{fur} , denotes the set temperature of the furnace. The fourth column shows the pullout load of each specimen. The bond stress was calculated per Eq. 2. The last column, R , represents the retained strength of the sample compared to the control tests conducted at 25 °C. The failure modes are denoted as either 1 or 2. Failure mode 1 represents a core-to-surface failure, in which the core of the reinforcing bar detaches from the surface of the reinforcing bar. Failure mode 2 represents a surface-to-concrete failure mode, in which the failure involves the interface between the surface of the reinforcing bar and the concrete. These failure modes are shown in Figure 5. Figure 6 shows the failure loads of the tests according to the temperature of the bar.

Table 1. Steady-state test results

Specimen	T_{bar} (°C)	T_{fur} (°C)	Failure Load (kN)	Bond (MPa)	Failure Mode ¹	R (%)
GFRP - 25 ²	25	25	71.0	18.5	2	100
GFRP - 80	77	80	50.5	13.1	2	72
GFRP - 100	98	100	45.7	11.9	2	65
GFRP - 125	116	125	30.0	7.8	M	43
GFRP - 150	134	150	26.4	6.7	1	37
GFRP - 200	170	200	14.7	3.8	1	21

¹ - Failure Mode 1 – Core-to-surface; Failure Mode 2 – Surface-to-concrete; M – Mix of failure modes

² – Average of three tests

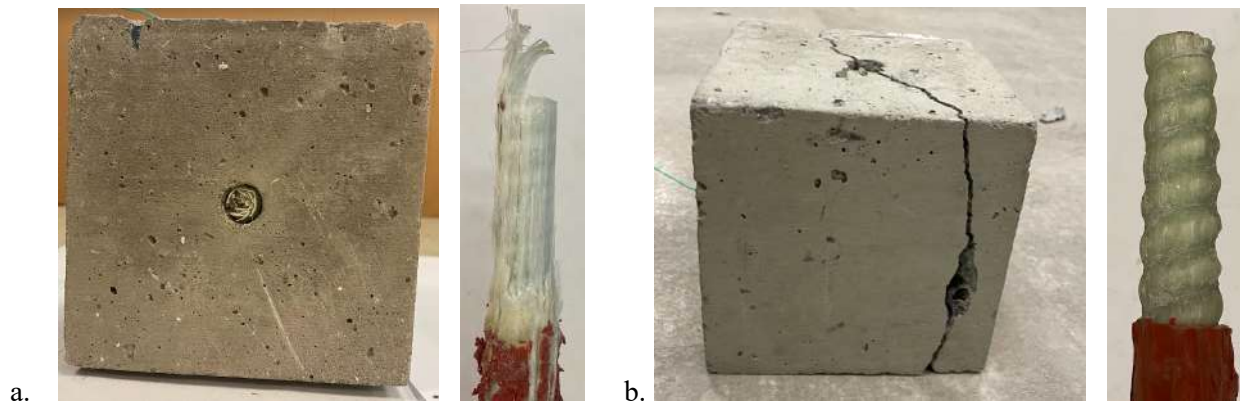


Figure 5. a. Core-to-surface failure mode. b. Surface-to-concrete failure mode

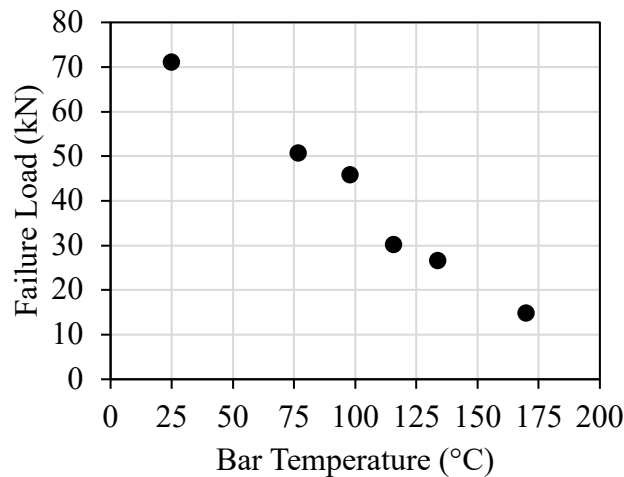


Figure 6. The failure load of steady-state tests

Figure 6 shows an approximately linear degradation of failure load with bar temperature. At a bar temperature of 170 °C, the failure load is only 21% that of the control tests. CSA S807 [18] defines for a minimum bond strength of 10 MPa at room temperature. For the bars in consideration, they fell below this threshold at a furnace temperature of 125 °C (bar temperature of 116 °C). As seen in Figure 6, this corresponds with a relatively sharp drop in failure load in comparison to its surrounding temperatures. This is also in line with previous research on similar bars [17].

Figure 7 shows the load vs. stroke displacement of the tests. Stroke displacement includes effects other than slip, however, the test setup does not allow for more accurate measurements of slip within the furnace, without damaging instrumenting equipment. The load vs. stroke curves provide an idea of the deterioration of bond at high temperatures.

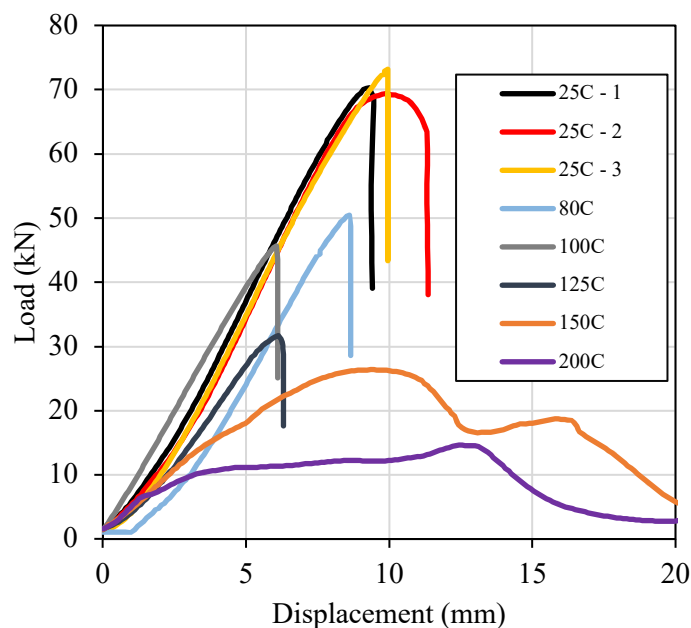


Figure 7. Load vs. stroke displacement of steady-state temperature tests

In terms of failure modes, at room temperature, the bars failed at the interface of the surface of the rebar to the concrete. At a bar temperature of 134 °C (furnace 150 °C), failure mode 1 was observed – failure between the core of the bar to surface of the bar. Thus, there is evidence to support that though the bar’s core and surface remain strong below 125 °C furnace temperature, above this point, the primary weak point shifts to the bond between the bar core and surface treatment. The sample tested at a furnace temperature of 125 °C showed a mixed failure mode, where initially failure mode 2 – surface to concrete – was observed, however upon closer inspection, there was some (minimal) deterioration of the surface treatment of the bars.

The performance of the bars can be compared to previous tests by Hajiloo and Green, 2018 [17], which were done using the same setup and procedure. However, each manufacturer used a different method of achieving bond with concrete – the GA series having a sand coating, the GB series having a helical braid, and the GC series having indentations cut into the bar. The new tests presented in this manuscript considered bars that are similar to the GB bars, but that instead use an integral rib to mechanically lock with the concrete. Figure 8 shows the retained ratio of the novel test series presented in this manuscript, relative to the GB bar test series presented by Hajiloo and Green, 2018 [17]. However, the new test series presented for the first time in this manuscript shows promise in the quantity of surface deterioration observed on the bars after testing. Limited damage was observed on the bars below a furnace temperature of 125 °C (at which temperature damage was minimal) – more significant deterioration was noticed at 150 and 200 °C.

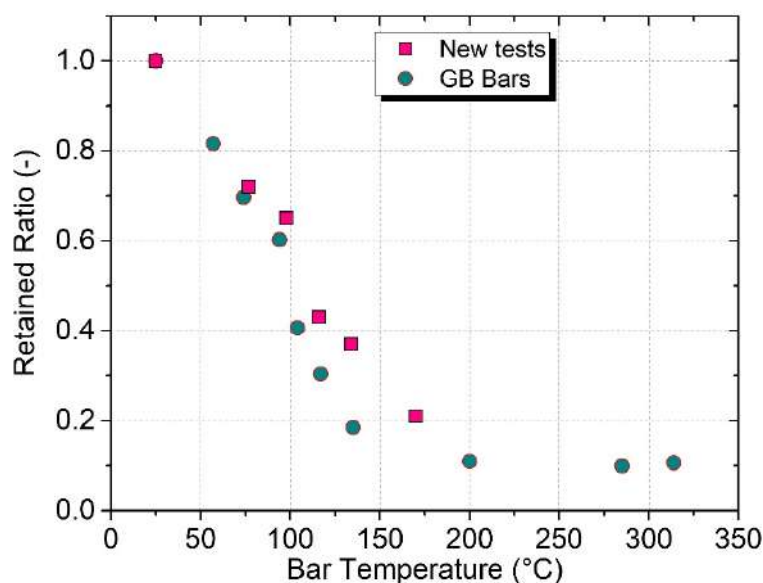


Figure 8. Retained ratio vs bar temperature of the novel test series, relative to the series by Hajiloo and Green, 2018 [17].

4 CONCLUSIONS

The experimental test results showed that the bond strength remained at or above 10 MPa at bar temperatures up to 98 °C, thus meeting the minimum bond strength for service conditions as set by CSA S807 [18] Thus, the bond strength of the reinforcing bars has the potential to be sufficient under mildly elevated temperatures. Because the bond strength of the GFRP bars can be a critical aspect of evaluating a GFRP reinforced structural member in a fire, these test results provide insight into the performance of GFRP reinforced concrete members at high temperatures. The results of this test series are relatively well aligned with past tests, showing some potential improvement in the quantity of surface damage of the reinforcing bars. This will be explored further in full-scale tests.

The application of full load of GFRP reinforced concrete members based on strength requirements as per ASTM E119 and CAN/ULC S101 remains a challenge for achieving fire ratings. Under load levels calculated based on strength limit, serviceability criteria such as crack width and maximum deflection cannot be satisfied. In experimental studies, lower load levels, which are consistent with deflection-based calculation, are applied on GFRP-RC slabs or beams. Consequently, as previously indicated by many research findings, the highest applied service moment (M_a) ensuring maximum midspan deflection compliance for full-scale testing of GFRP-RC slabs or beams should be set by deflection-based calculations. This requires standards such as ASTM E119 and CAN/ULC S101 to update the fire loading requirements for GFRP reinforced concrete members.

REFERENCES

- [1] Cosenza E, Manfredi G, Realfonzo R. Behavior and Modeling of Bond of FRP Rebars to Concrete. *Journal of Composites for Construction* 1997;1:40–51. [https://doi.org/10.1061/\(ASCE\)1090-0268\(1997\)1:2\(40\)](https://doi.org/10.1061/(ASCE)1090-0268(1997)1:2(40)).
- [2] ACI CODE-440.11-22: Building Code Requirements for Structural Concrete Reinforced with Glass Fiber-Reinforced Polymer (GFRP) Bars. 2022.
- [3] CSA S806-12: Design And Construction Of Building Structures With Fibre-Reinforced Polymers. 2012.
- [4] ASTM International. ASTM E119: Standard Test Methods for Fire Tests of Building Construction and Materials 2022.
- [5] International Organization for Standardization. ISO 834-11: Fire resistance tests -Elements of building construction - Part 11: Specific requirements for the assessment of fire protection to structural steel elements 2014.

- [6] Standards Council of Canada. CAN/ULC-S101-14: Fire Endurance Tests of Construction and Materials 2014.
- [7] Intelligent Sensing for Innovative Structures Canada. Design Manual No. 3: Concrete Structures with Fibre Reinforced Polymers. Winnipeg, Manitoba: 2007.
- [8] Abbassi A, Hogg P. Fire testing of concrete beams with fibre reinforced plastic rebar. *Advanced Polymer Composites for Structural Applications in Construction* 2004;445–56.
- [9] Nour O, Salem O, Mostafa A. Experimental fire testing of large-scale glass fibre-reinforced polymer - reinforced concrete beams with mid-span straight-end bar lap splices. *Fire Mater* 2022;46:360–75. <https://doi.org/10.1002/fam.2960>.
- [10] Rafi M, Nadjai A, Ali F, O'Hare P. Evaluation of Thermal Resistance of FRP Reinforced Concrete Beams in Fire. *Journal of Structural Fire Engineering* 2011;2:91–107. <https://doi.org/10.1260/2040-2317.2.2.91>.
- [11] Hajiloo H, Green MF, Noël M, Bénichou N, Sultan M. Fire tests on full-scale FRP reinforced concrete slabs. *Compos Struct* 2017;179:705–19. <https://doi.org/10.1016/j.compstruct.2017.07.060>.
- [12] Hajiloo H, Green MF, Noël M, Bénichou N, Sultan M. GFRP-Reinforced Concrete Slabs: Fire Resistance and Design Efficiency. *Journal of Composites for Construction* 2019;23. [https://doi.org/10.1061/\(ASCE\)CC.1943-5614.0000937](https://doi.org/10.1061/(ASCE)CC.1943-5614.0000937).
- [13] Nigro E, Cefarelli G, Bilotta A, Manfredi G, Cosenza E. Fire resistance of concrete slabs reinforced with FRP bars. Part I: Experimental investigations on the mechanical behavior. *Compos B Eng* 2011;42:1739–50. <https://doi.org/10.1016/j.compositesb.2011.02.025>.
- [14] Rosa IC, Santos P, Firmo JP, Correia JR. Fire behaviour of concrete slab strips reinforced with sand-coated GFRP bars. *Compos Struct* 2020;244:112270. <https://doi.org/10.1016/j.compstruct.2020.112270>.
- [15] Rosa IC, Firmo JP, Correia JR, Bisby LA. Fire Behavior of GFRP-Reinforced Concrete Structural Members: A State-of-the-Art Review. *Journal of Composites for Construction* 2023;27. <https://doi.org/10.1061/JCCOF2.CCENG-4268>.
- [16] Gergely P, Lutz L. Maximum Crack Width in Reinforced Concrete Flexural members. SP-20: Causes, Mechanism, and Control of Cracking in Concrete, Farmington Hills, Michigan: American Concrete Institute; 1968.
- [17] Hajiloo H, Green MF. Bond Strength of GFRP Reinforcing Bars at High Temperatures with Implications for Performance in Fire. *Journal of Composites for Construction* 2018;22. [https://doi.org/10.1061/\(ASCE\)CC.1943-5614.0000897](https://doi.org/10.1061/(ASCE)CC.1943-5614.0000897).
- [18] CSA S807:19 Specification for fibre-reinforced polymers. 2019.

INFLUENCE OF DESIGN MOMENT REDISTRIBUTION TO THE FIRE RESISTANCE OF FIBRE-REINFORCED LIGHTWEIGHT AGGREGATE CONCRETE CONTINUOUS SLABS

Christopher Kevinly¹, Panwei Du², Bak Koon Teoh³, Kang Hai Tan⁴

ABSTRACT

Designing continuous slabs with redistributed design moments is commonly done to prevent reinforcement congestion in joint areas. Given that this practice is common, it is urgent to assess its potential effects on the structural behaviour under fire, which up to this point is largely unknown. Moreover, the raising environmental awareness has increased the interest in fibre-reinforced lightweight aggregate concrete (FRLWAC) implementations in structural slabs for its improved insulation and lower weight. However, studies on FRLWAC slabs under fire have not been widely available. This study is done to address the knowledge gap by investigating the structural behaviour of three FRLWAC slabs, one simply-supported and two continuous, under ISO 834 fire. The two continuous slabs were designed with different levels of moment redistribution to study their effect on fire resistance. The structural behaviours of these slabs are presented in this paper, along with the effect of design moment redistribution and continuity on their fire resistance. A recommendation regarding the design of FRLWAC continuous slabs is also presented in this paper.

Keywords: Moment redistribution; fire exposure; fibre reinforcement; continuity;

1 INTRODUCTION

Designing beams and slabs with continuity greatly benefits the behaviour of structures, mainly due to reduced deflection and improved structural safety resulting from the presence of multiple load paths, provided the ductility requirements are met [1]. However, reinforcement congestion might occur in cases where a significant amount of hogging reinforcement is present in the joint region, leading to workability issues during construction. Engineers circumvent this issue by redistributing the design moments of the beam and slabs, where the hogging design moment is redistributed towards the sagging area, resulting in lesser reinforcement in the hogging area.

Eurocode 2 (EN 1992-1-2) [2] allows for design moment to be redistributed up to 15% in continuous beams and slabs. Despite having this prescription, there is no recent study investigating the effect of design moment redistribution in continuous slabs. This is particularly true in the case of beams and slabs made of fibre-reinforced lightweight aggregate concrete (FRLWAC), which has been gaining mainstream appeal due to its enhanced mechanical properties and improved sustainability aspects over conventional concrete [3–4].

¹Research Associate, Ir., Nanyang Technological University
e-mail: christop012@e.ntu.edu.sg ORCID: <https://orcid.org/0000-0002-4845-0188>

²Research Fellow, Dr., Nanyang Technological University
e-mail: pwdu@ntu.edu.sg ORCID: <https://orcid.org/0000-0003-3838-2705>

³Senior Lecturer, Dr., Nanyang Technological University
e-mail: bakkoon.teoh@ntu.edu.sg ORCID: <https://orcid.org/0000-0002-7513-4279>

⁴Professor, Dr., Nanyang Technological University
e-mail: ckhtan@ntu.edu.sg ORCID: <https://orcid.org/0000-0003-1500-6643>

Lightweight aggregate concrete is generally perceived to perform well under fire due to its good insulation properties [5]. However, its poor toughness in compression hindered its wide adoption in the construction industry. Moreover, modern lightweight aggregate concrete with high mortar density tends to spall under fire conditions. FRLWAC containing both steel and polypropylene (PP) fibres are developed to address the aforementioned issues, with steel fibre improving compression toughness [6] and PP fibre preventing fire-induced spalling [7–8]. Despite its great potential, studies involving FRWLAC under fire have been few and far between. Therefore, this study was conducted to study the effect of design moment redistribution on the structural behaviour of FRLWAC slabs under fire.

2 EXPERIMENTAL PROGRAMME

2.1 Specimen design and reinforcement configuration

Three specimens, listed in Table 1, were designed and tested in this study. The first specimen (SSS-FIRE) was designed as a simply-supported one-way slab, while the second and third specimens (CS(+15)-FIRE and CS(0)-FIRE) were designed to have a cantilever at one end to emulate continuity effect, with the other end being simply-supported. All of the specimens were designed to fulfil the 2-hour fire resistance prescriptive requirement of EN 1992-1-2 for lightweight concrete structures. The two continuous specimens were designed with different design moments: Specimen CS(+15)-FIRE was designed with a positive moment redistribution of 15%, which is the limit allowable by EN 1992-1-2, while specimen CS(0)-FIRE was designed based on the design moment obtained through elastic structural analysis. The simply-supported specimen was used as the reference. All the specimens were designed to support the same uniformly distributed load.

Table 1. List of specimens

Variation	Layout	Design moment redistribution
SSS-FIRE	Simply-supported	-
CS(+15)-FIRE	Continuous	15% to Sagging
CS(0)-FIRE	Continuous	No design redistribution

The side view and the cross-sections of the specimens are shown in Figure 1 and Table 2, respectively. The main span was 2200 mm long, which corresponded to the outer length of the furnace. The thickness of the main span was 140 mm, while the cantilevers of the continuous specimens had a higher thickness of 170 mm to prevent shear failure due to the restraining force. The slabs were 650 mm wide, which aligned with the width of the furnace opening. Steel plates with a thickness of 10 mm were cast at the loading and supporting points to prevent local concrete crushing.

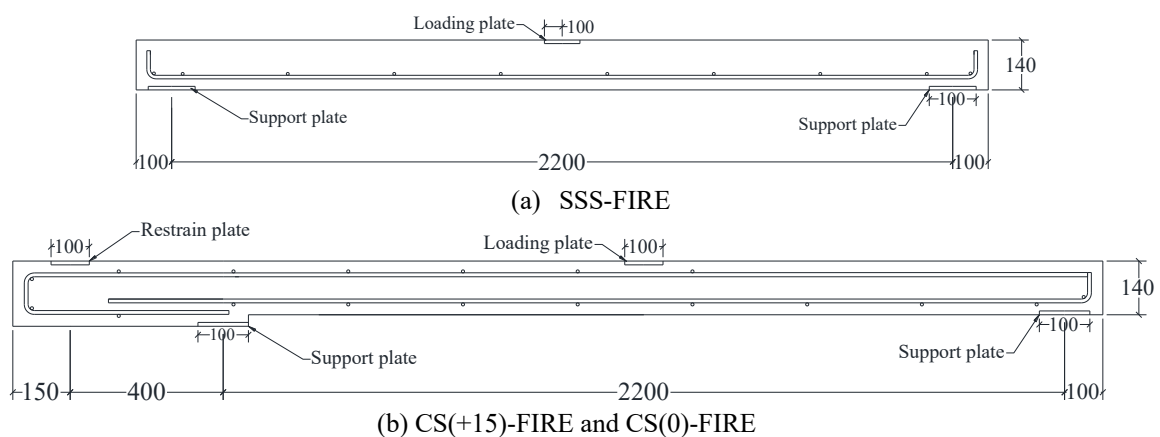
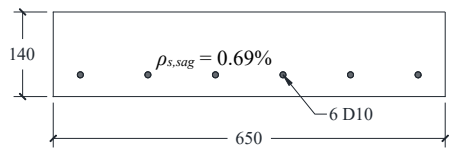
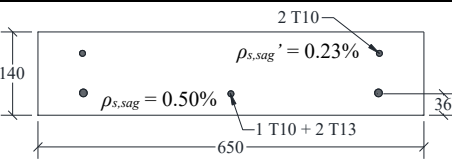
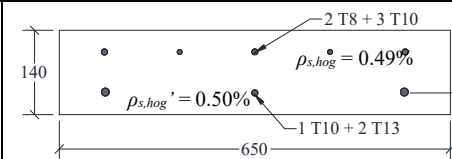
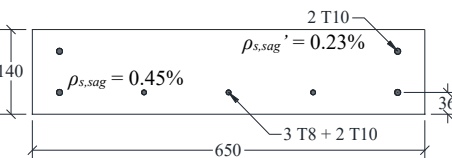
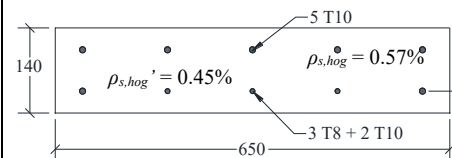


Figure 1. Side view of the specimens (dimensions in mm)

The reinforcement configurations of the slabs are shown in Table 2. The bottom reinforcements were designed to be continuous throughout the main span of the slabs in all three specimens, which means the sagging tension reinforcement ratio $\rho_{s,sag}$ is the same as the hogging compression reinforcement ratio $\rho_{s,hog}$. No top reinforcement was designed on the simply-supported specimen, while the full top reinforcements were only added to the hogging area of the main span in continuous slabs, which ended at 900 mm from the continuous end of the main span. Specimens with design moment redistribution had lesser hogging tension reinforcements ($\rho_{s,hog}$) compared to the one designed with no moment redistribution. The concrete cover to the centroid of the bar was designed to be 36 mm, in line with the EN 1992-1-2 prescriptive design provision for lightweight aggregate concrete slabs with a 2-hour fire rating.

Table 2. Specimen cross-sections (dimensions in mm)

Variation	Sagging	Hogging
SSS-FIRE		-
CS(+15)-FIRE		
CS(0)-FIRE		

2.2 Mechanical properties of concrete and steel reinforcement

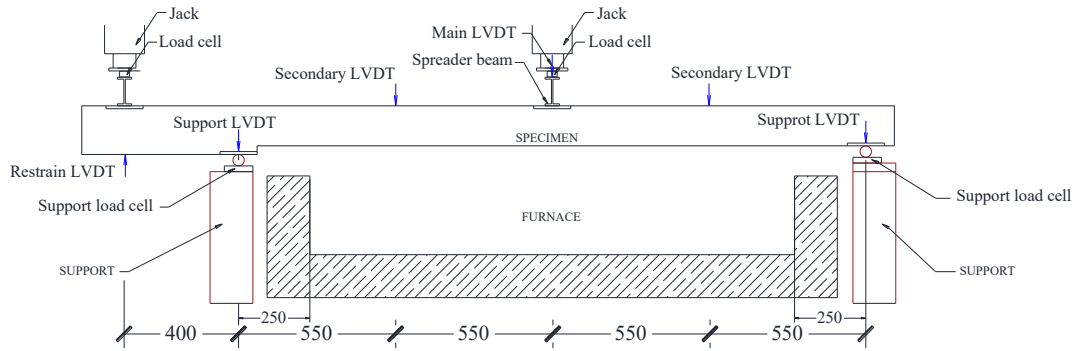
The low density of the FRLWAC used in this study was achieved by using LECA as its coarse aggregates and a mix of silica sand and fly ash cenosphere as its fine aggregates. The FRLWAC had a water-to-binder ratio of 0.24, with high-strength cement (CEM II 52.5R) and silica fume chosen as binders and high-range water reducer added to improve workability. The use of lighter aggregates, high-strength binders and a low water-to-binder ratio allowed a mix with a dry density of 1789 kg/m³ and a strength of 47.9 MPa to be cast. Hooked steel fibre (0.5% by volume) was also incorporated into the mix to improve the compression toughness and post-crack tensile strength, along with 0.2% of PP fibre to prevent fire-induced explosive spalling.

Deformed reinforcing bars with three different diameters (8 mm, 10 mm and 13 mm) were used as longitudinal reinforcement. The yield strength of the 8 mm, 10 mm and 13 mm bars were 503 MPa, 533 MPa and 543 MPa, respectively. These bars had ultimate strengths of 668 MPa, 622 MPa and 635 MPa, respectively, which fulfilled the requirement for reinforcement class B500B in Singapore Standard SS 560:2016 (the yield strength should be more than 500 MPa and the ultimate strength should be more than 1.08 times the yield strength).

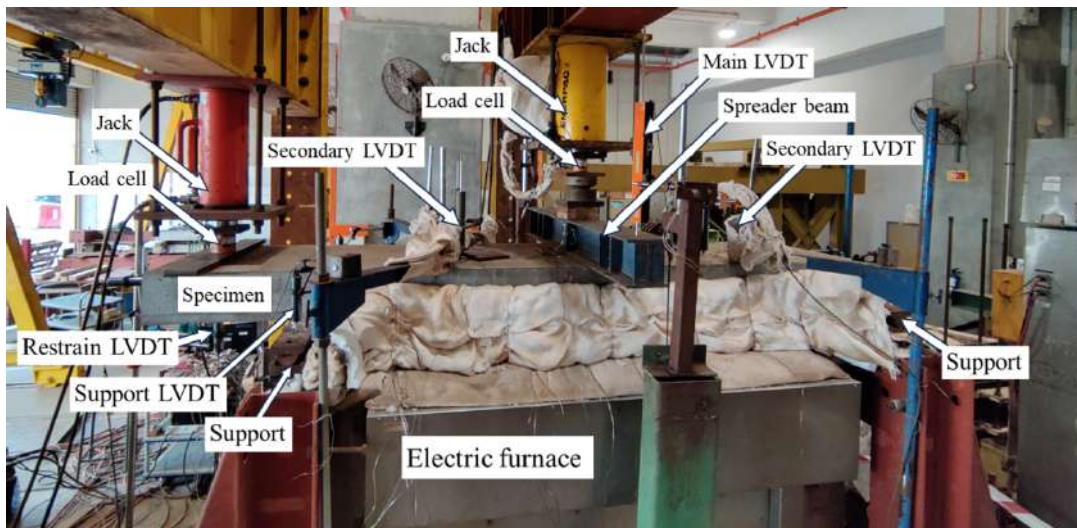
2.3 Test setup, instrumentation and procedure

The schematic of the test setup is shown in Figure 3a, while the implementation of the setup is shown in Figure 3b. The specimen was placed over an electric furnace capable in replicating ISO 834 fire curve that had a heating area of 1700 mm by 700 mm. Support pedestals were installed next to both long ends of the furnace to maximise the relative exposed area of the slab. As the slab was exposed to a one-side heating on its soffit, the sides of the slab were insulated using mineral wool and ceramic fabric. Two hydraulic jacks were employed: the first hydraulic jack was used to apply the load at the midspan of the slab, while the

second one (only present in continuous specimens) was used to apply restraining force at the cantilever. Compression load cells were installed at all both loading and supporting points to monitor changes in internal forces during the test. Spreader beam was placed on top of the loading points to distribute the load along the width of the slab. The deflection profile of the slab was monitored by LVDTs installed at the loading point (main LVDT) and at the middle of both half-spans of the slab (Secondary LVDTs). Support LVDTs were installed to monitor the support settlement, and Restrain LVDT was installed to control the restraining force applied by the second jack.



(a) Schematic (dimensions in mm)



(b) Implementation

Figure 2. Experimental setup and instrumentation

K-type thermocouples were used to monitor the furnace gas temperature and the cross-sectional temperatures. The placement of the internal thermocouples at the midspan of the slab is depicted in Figure 3. Three thermocouples were installed: two were placed at the top and bottom reinforcement levels, respectively, and another at the mid-depth of the slab.

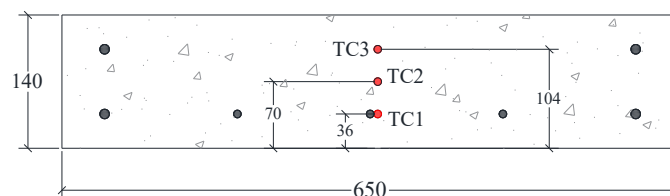


Figure 3. Internal thermocouple placements (dimensions in mm)

At the start of the test, the load was gradually applied at the midspan to reach 40% of the ambient strength of the slab. The ambient strength was determined through a series of tests of similar specimens [9]. As the load progressed, the restraining load was added and adjusted to ensure minimal displacement at the cantilever. Upon reaching the target load, the load was maintained for 30 minutes before the furnace was

ignited. The load was kept constant during the fire exposure, with the restraining force was adjusted as necessary to maintain minimal displacement at the restraining point. The test was terminated once the applied load could no longer be maintained.

3 EXPERIMENTAL RESULT

3.1 Temperature measurements

The readings from the furnace and internal thermocouples are shown in Figure 4. The furnace temperatures generally resembled ISO 834 curve, with slightly lower temperatures observed during the first hour of exposure. This variation could be attributed to the lower initial heating rate of the electric furnace and possible gaps in the insulation. The temperature of the bottom reinforcement at the failure of Specimen SSS-FIRE was 591 °C, at which point only 47% of the initial yield strength remained according to EN 1992-1-2 [2]. On the other hand, the bottom steel temperatures of the continuous specimens CS(+15)-FIRE and CS(0)-FIRE reached 730 °C and 742 °C, respectively. Although the reinforcement was expected to retain only around 20% of its resistance at these temperatures, the continuity effect in these specimens facilitated moment redistribution. This allowed the hogging section to take-up additional bending moments as the sagging section lost its moment capacity.

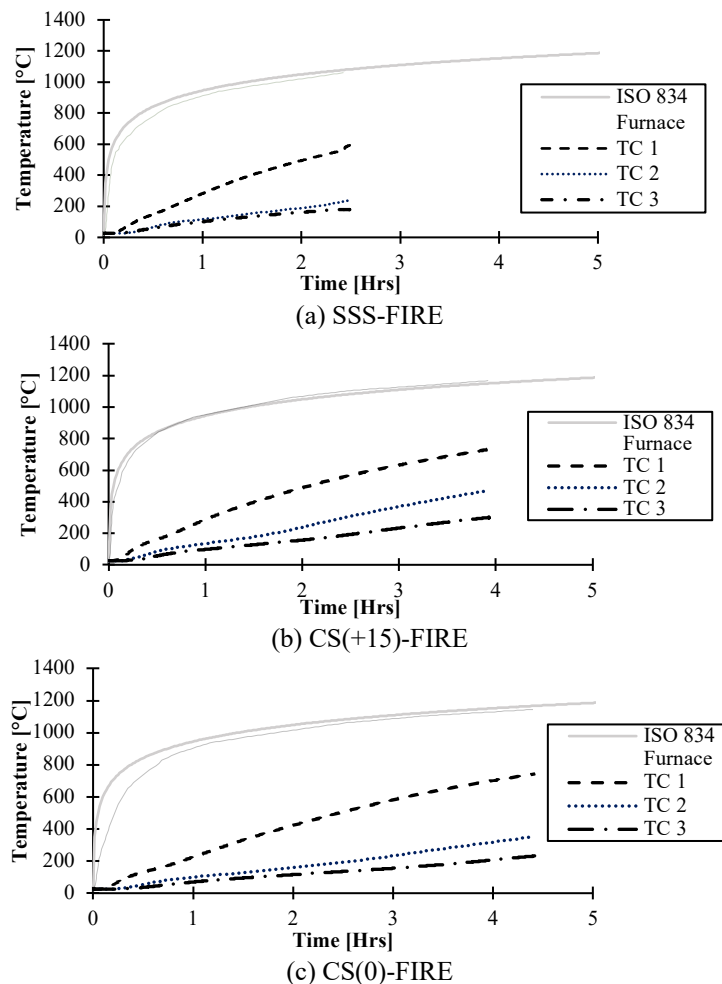


Figure 4. Measured temperatures

3.2 Fire resistance and specimen deformation history

The midspan displacement histories of the specimens throughout the exposure are shown in Figure 5. All the specimens lasted more than its prescribed fire rating of 2 hours. It is observed that the simply-supported specimen (SSS-FIRE) failed much earlier at 2.38 hours compared to the two continuous specimens

(CS(+15)-FIRE and CS(0)-FIRE) that failed at 3.89 hours and 4.36 hours, respectively. The specimen designed without redistribution also lasted longer than the one designed with redistributed moment. The superior fire resistance of specimen CS(0)-FIRE over CS(+15)-FIRE can be attributed to the higher hogging moment capacity in the former. As the sagging moment capacity was degraded due to fire exposure, the moments were forced to be redistributed towards the hogging areas. This moment redistribution could not occur in the simply-supported specimen SSS-FIRE, thus the loss of sagging moment resistance resulted in the complete failure of the specimen.

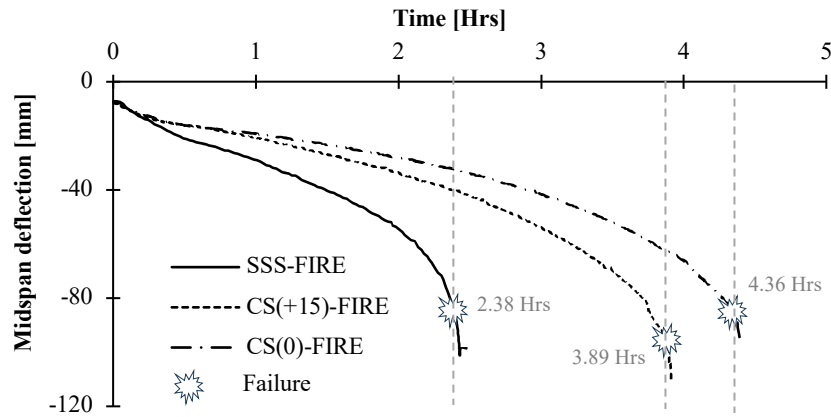


Figure 5. Time-displacement history

Figure 6 shows the deformations of the specimens at different stages of the fire exposure. The deformed shape of the slab formed relatively smooth curves throughout the fire exposure. However, clear discontinuity at both the midspan and the continuous end of the specimens were observed at failure, indicating the formation of plastic hinges at these areas.

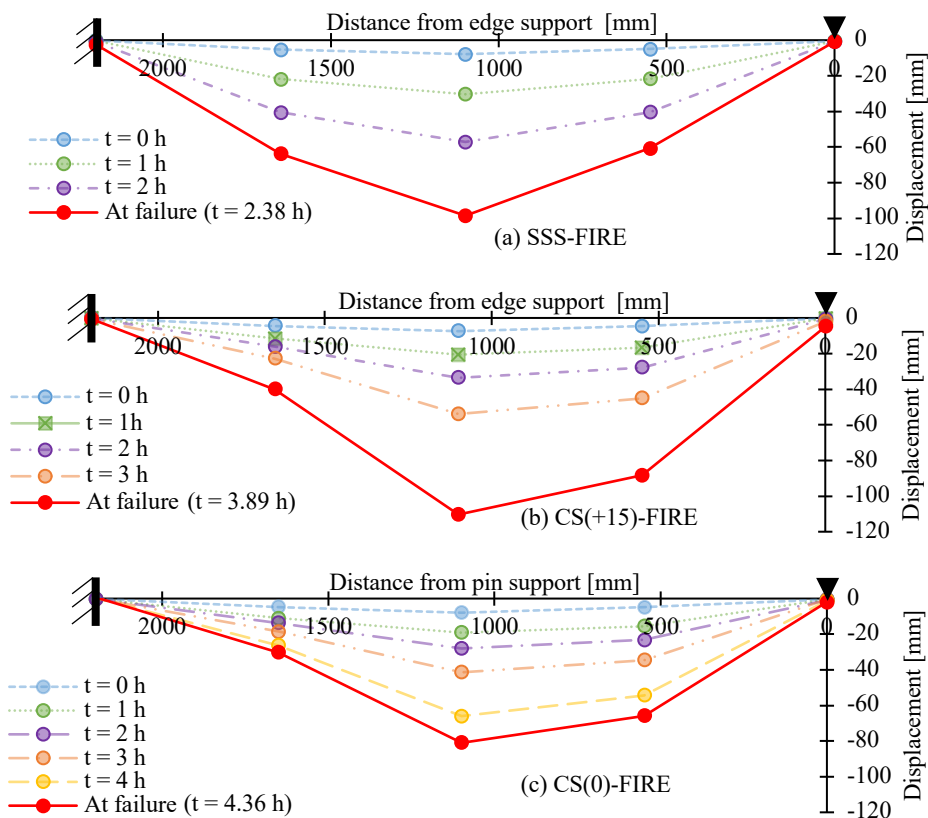


Figure 6. Slab deformed shape during test

3.3 Visual observations of specimens after test

The sides of the specimens after fire tests are shown in Figure 7, with major cracks highlighted in red. No spalling was observed on the specimens, which confirmed the efficacy of PP fibre in preventing fire-induced explosive spalling in FRLWAC. The visual observations confirmed the presence of plastic hinges at both the midspan and the continuous end of the slabs, as shown in Figure 8. It was also observed that most of the hinge rotation was concentrated in a single or two cracks, in contrast to more distributed cracks commonly observed in conventional concrete after fire [10–11]. This observation is consistent to the ones made on fibre-reinforced concrete with low reinforcement ratios at ambient conditions [12–13].

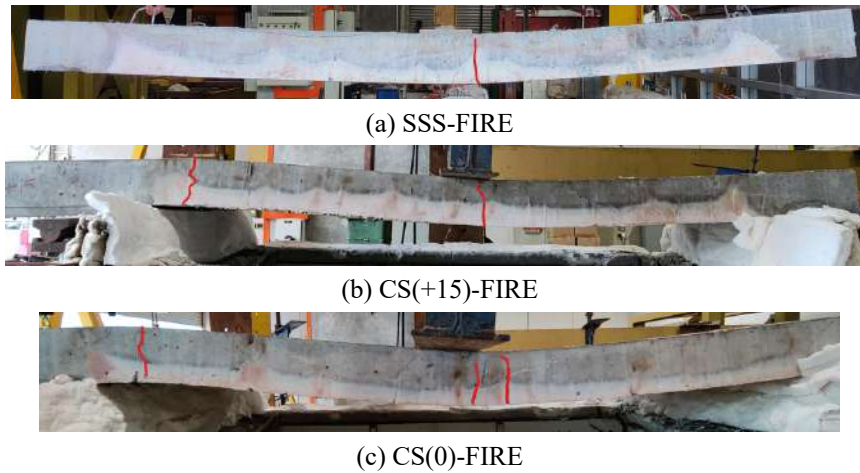


Figure 7. Side view of the specimens after testing

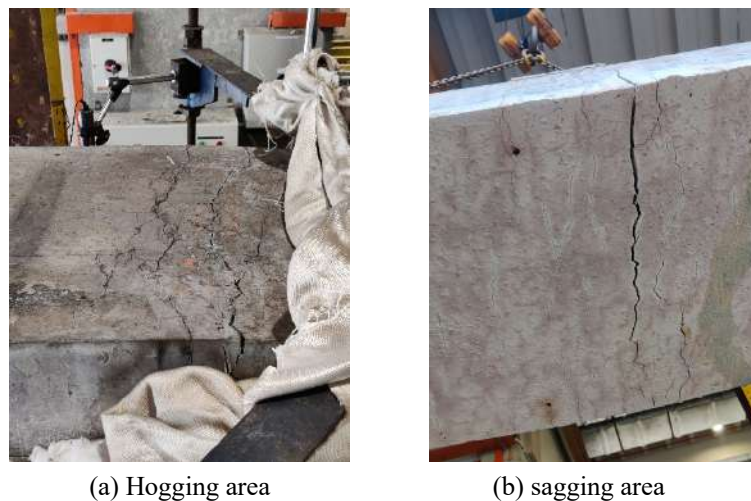


Figure 8. Major flexural cracks at the plastic hinge areas

3.4 Fire-induced moment redistribution

Figure 9 shows the changes in hogging and sagging moments of the continuous specimens throughout the test. A significant amount of sagging moment were redistributed towards the hogging area in the first 30 minutes of the fire exposure (from the start of the fire exposure to point A in the figures), after which the bending moments of both specimens were mostly similar. Another significant moment redistribution was observed around 30 minutes before the specimen failed, indicated by point B in the figures, where the sagging moment was redistributed even further towards the hogging area. These two moment redistribution events were governed by different mechanisms, the first event was due to the restrained thermal bowing effect, while the second was due to the loss of the moment resistance in the sagging region.

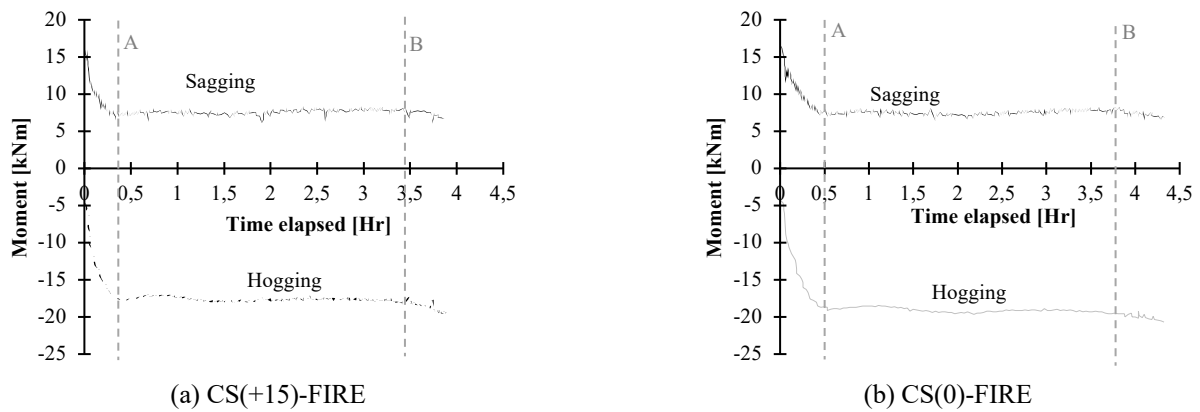


Figure 9. Changes in bending moments during the tests

The mechanism responsible for the first moment redistribution event is illustrated in Figure 10. The aggressive heating of the soffit of the slab led to significant temperature gradients throughout its thickness. In unrestrained situations as in specimen SSS-FIRE, this thermal gradient resulted in thermal bowing due to the linear equivalent thermal strain caused by the thermal gradient. This was also reflected in the deflection rate in the first 30 minutes observed in Figure 5. In the continuous specimens, this thermal bowing was restrained due to the continuity effect. This restraint resulted in additional bending moment $M_{T,Res}$ forming at the continuous end of the beam. This restraint hogging moment resulted in the reduction of the sagging moment. While the thermal gradient tended to be leaner at the later phase of the exposure, the stiffness and the moment resistance of the sagging region would have been degraded from the fire exposure, thus preventing the moment to be redistributed back to the sagging area. Moreover, this sagging moment capacity degradation also resulted in further moment redistribution towards the hogging area, as reflected in the second moment redistribution event. The slabs failed once their hogging moment resistance was reached.

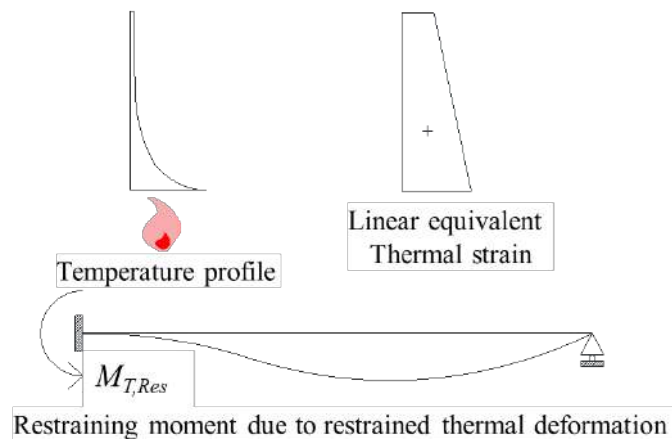


Figure 10 Mechanism of early moment redistribution

4 PRACTICAL IMPLICATIONS AND RECOMMENDATIONS

In this study, it was found that the EN 1992-1-2 prescriptive design provision for simply-supported lightweight aggregate slab can be extended to the design of FRLWAC slabs, with the test result outlasting the predicted fire resistance from the code. However, it was found that the prescriptive design provision was too conservative in predicting the fire resistance of FRLWAC continuous slabs, with the actual slabs surviving for around twice as long as predicted. While conservative, this underestimation of the fire resistance of FRLWAC slabs may lead to unoptimised and expensive design. Therefore, it is suggested that

the prescriptive design provision of EN 1992-1-2 for continuous slabs to be re-evaluated, mainly in cases where fibre-reinforced concrete is implemented.

Another possible improvement on the prescriptive code is to include the effect of design moment redistribution. At its current state, the fire resistance of continuous slabs with up to 15% of design moment redistribution are assumed to have similar fire resistance with slabs designed with no moment redistribution. In this test series, it was apparent that the design moment redistribution affected the fire resistance of continuous slab noticeably.

The addition of PP fibre has been proven to be effective in preventing explosive spalling from taking place in FRLWAC slabs. Therefore, an addition of 0.2% of PP fibre is recommended when designing FRLWAC slabs with enhanced fire resistance in mind.

5 CONCLUSIONS

A series of fire tests involving three FRLWAC slabs were conducted and presented in this paper. This work highlighted the importance of continuity effect and design moment redistribution to the fire resistance of FRLWAC slabs. Recommendations on FRLWAC slab design and implementation is also proposed based on the experimental results. Based on the works done in this paper, the following conclusions can be made:

- All FRLWAC slabs tested exceeded the prescriptive fire rating based on EN 1992-1-2, demonstrating FRLWAC suitability to be implemented in cases where adequate fire resistance is required.
- The continuity effect greatly enhanced the fire resistance of FRLWAC slabs. The continuous slab without design moment redistribution (CS(0)-FIRE) lasted more than twice as long as it was rated for. Therefore, the prescriptive design code of EN 1992-1-2 for continuous slabs should be evaluated for more efficient designs.
- Designing continuous slabs with design moment redistribution towards the sagging moment resulted in lower fire resistance compared to the slabs designed with no moment redistribution. This was due to lower design moment in the hogging area, which resulted in less reinforcement being designed there. This lower hogging moment resistance affected the fire resistance, where significant moment redistribution towards the hogging area occurred.

ACKNOWLEDGMENT

This material is based on research supported by the Singapore Ministry of National Development and National Research Foundation under CoT Award No. COT-V3-2021-1. Any opinions, findings, conclusions or recommendations expressed in this material are those of the author(s) and do not necessarily reflect the views of CoT. The authors also would like to thank the Construction Technology and Protective Engineering laboratories of NTU for facilitating the tests.

REFERENCES

1. R. Scott & R. Whittle, Moment redistribution effects in beams. *Magazine of Concrete Research*, **57** (2005) 9–20.
2. CEN, *EN 1992-1-2. Eurocode 2: Design of concrete structures, Part 1-2: General rules - Structural fire design* (Brussels: European Committee for Standardization, 2004).
3. B. F. Bender, Economics and Use of Lightweight Concrete in Prestressed Structures. *PCI Journal*, **25** (1980) 62–67. <https://doi.org/10.15554/pcij.11011980.62.67>.
4. Y. H. Lee, N. Chua, M. Amran, Y. Yong Lee, A. B. Hong Kueh, R. Fediuk, N. Vatin, & Y. Vasilev, Thermal Performance of Structural Lightweight Concrete Composites for Potential Energy Saving. *Crystals*, **11** (2021) 461. <https://doi.org/10.3390/cryst11050461>.
5. D. J. L. Clarke, ed., *Structural Lightweight Aggregate Concrete*, 0 ed (CRC Press, 1993). <https://doi.org/10.1201/9781482269307>.

6. M. Zhao, M. Zhao, M. Chen, J. Li, & D. Law, An experimental study on strength and toughness of steel fiber reinforced expanded-shale lightweight concrete. *Construction and Building Materials*, **183** (2018) 493–501. <https://doi.org/10.1016/j.conbuildmat.2018.06.178>.
7. D. Zhang, A. Dasari, & K. H. Tan, On the mechanism of prevention of explosive spalling in ultra-high performance concrete with polymer fibers. *Cement and Concrete Research*, **113** (2018) 169–177. <https://doi.org/10.1016/j.cemconres.2018.08.012>.
8. J.-C. Liu, K. H. Tan, & Y. Yao, A new perspective on nature of fire-induced spalling in concrete. *Construction and Building Materials*, **184** (2018) 581–590. <https://doi.org/10.1016/j.conbuildmat.2018.06.204>.
9. C. Kevinly, P. Du, B. K. Teoh, & K. H. Tan, Experimental study and modelling of flexural behaviour of continuous fibre-reinforced lightweight aggregate concrete one-way slab at ambient and elevated temperatures. *Engineering Structures*, **307** (2024) 117924. <https://doi.org/10.1016/j.engstruct.2024.117924>.
10. Q. Xu, C. Han, Y. C. Wang, X. Li, L. Chen, & Q. Liu, Experimental and numerical investigations of fire resistance of continuous high strength steel reinforced concrete T-beams. *Fire Safety Journal*, **78** (2015) 142–154. <https://doi.org/10.1016/j.firesaf.2015.09.001>.
11. G. L. Albuquerque, A. B. Silva, J. P. C. Rodrigues, & V. P. Silva, Behavior of thermally restrained RC beams in case of fire. *Engineering Structures*, **174** (2018) 407–417. <https://doi.org/10.1016/j.engstruct.2018.07.075>.
12. A. Caratelli, A. Meda, & Z. Rinaldi, Monotonic and cyclic behaviour of lightweight concrete beams with and without steel fiber reinforcement. *Construction and building materials*, **122** (2016) 23–35.
13. D. C. T. Cardoso, G. B. S. Pereira, F. A. Silva, J. J. H. Silva Filho, & E. V. Pereira, Influence of steel fibers on the flexural behavior of RC beams with low reinforcing ratios: Analytical and experimental investigation. *Composite Structures*, **222** (2019) 110926. <https://doi.org/10.1016/j.compstruct.2019.110926>.

INVESTIGATING THE HIGH-TEMPERATURE BEHAVIOR OF POLYMER CONCRETE

Srishti Banerji^{1*}, Venkatesh Kodur², Ahmed Almaadawy³, Manish Sah⁴, David Unobe⁵

ABSTRACT

This paper presents findings from a series of mechanical and thermal property tests to characterize the behavior of polymer concrete (PC) and polymer-modified concrete (PMC) at high temperatures. This study also investigates the effectiveness of different solutions for improving the fire performance of PC and PMC, including the addition of fire flame retardants, such as alumina trihydrate (ATH) and the addition of fibers, like basalt fibers (BF). The results showed that the thermal conductivity of PC and PMC specimens at room temperature was higher than normal strength concrete with values ranging from 1.59 to 2.27 (W/mK) compared to typical values 1.3-1.5 (W/mK) for NSC, while specific heat was lower than normal strength concrete. Furthermore, it was observed that all epoxy-based PC specimens could only withstand temperatures up to 100°C in hot condition. At 200°C, excessive smoke release occurred, leading to failure of the specimen. Conversely, polyester-based PC specimens sustained temperatures up to 200°C in hot condition but failed at 400°C, while some specimens flamed and disintegrated completely at 500°C. However, PMC specimens were able to withstand temperatures up to 600°C. Furthermore, incorporating ATH flame retardant or combining ATH with BF in PMC specimens resulted in retaining 28% of its initial compressive strength at room temperature, while using BF alone led to a 20% retention of initial compressive strength at room temperature.

Keywords: Polymer concrete; polymer-modified concrete; high-temperature behavior; fire resistance; thermal and mechanical properties.

1. INTRODUCTION

Polymer concrete is a type of concrete that uses polymer (resin) as the binder, instead of cement as in the case of conventional concrete. When the polymer completely substitutes the cement in the mixture, it is termed polymer concrete (PC), and when the polymer partially replaces cement, it is called polymer-modified concrete (PMC). The typical components of PC include aggregates (sand and gravel), polymer resins (such as epoxy, vinyl ester, polyester, and methyl methacrylate), and a curing agent (polyamine hardener). Whereas a typical mixture of PMC consists of the traditional concrete components (cement, sand, gravel) in addition to polymer in the form of latex, emulsion, or powder. Due to the several limitations of normal strength concrete (NSC) such as low flexural strength, low tensile strength, low failure strain, highly sensitive to low temperature, and frost, all this led to a search for new materials i.e., polymer that

1* Assistant Professor, Dept. of Civil & Environmental Engineering, Utah State University, Logan, UT, USA.
email: srishti.banerji@usu.edu

2 University Distinguished Professor, Dept. of Civil & Environmental Engineering, Michigan State University, East Lansing, MI, USA.
email: kodur@egr.msu.edu

3 Graduate Research Assistant, Dept. of Civil & Environmental Engineering, Utah State University, Logan, UT, USA.
e-mail: ahmed.almaadawy@usu.edu

4 Graduate Research Assistant, Dept. of Civil & Environmental Engineering, Michigan State University, East Lansing, MI, USA.
email: sahmanis@msu.edu

5 Assistant Professor, Schreiner University, Memorial Blvd, Kerrville, TX, USA.
email: dunobe@schreiner.edu

could be used to replace Portland cement to fix these drawbacks. Early references to polymer concrete date back to the mid-20th century when researchers began exploring the use of polymers as binders in concrete. In the 1950s, researchers investigated the mechanical properties of polymer concrete and its potential applications [1]. Afterwards, polymer concrete gained popularity by the mid-1970s. Then, in 1975, the application of precast polymer concrete structures started for underground facilities. Due to further increase in applications some designed standards were implemented for the manufacturer to implement while manufacturing polymer concrete. In 1970s and 1980s U.S. Federal Highway Administration, the Department of Energy, the Bureau of Reclamation, and chemical companies performed numerous investigations in polymer concrete fabrication. They finally made it available for commercial production after improving and expanding polymer binder implementation [2,3]. As compared to conventional concrete, PC and PMC at ambient temperatures exhibit high flexural strength (14–28 MPa) and improved durability against chemicals, acids, and harsh environmental conditions. Due to its enhanced durability properties, the use of polymer concrete is gaining momentum in civil infrastructure applications such as bridge deck overlays, industrial flooring, and chemical storage tanks [4].

The ability of any structural member to withstand fire without failure in terms of structural integrity, stability, and heat transmission is referred to as fire resistance [5]. The fire resistance in any structural member can be evaluated according to the ASTM E119 standard test [6]. In the last few decades, previous studies developed a numerical model to predict the fire resistance of the structure. However, temperature dependent thermal and mechanical properties must be taken into consideration into the numerical model to predict the fire resistance predictions. A few studies have shown that these properties can significantly vary with the type of concrete, batch mix proportion, specimen shape and size [6–9]. Additionally, when concrete is used for fabricating structural members, the members are required to satisfy code-specified fire resistance ratings. At present, there is a good amount of information on temperature dependent thermal and mechanical properties for different types of cement concrete but there is no such information for polymer concrete or polymer-modified concrete.

To embark on, unlike conventional concretes, polymer concrete comprises of polymer which softens at low glass transition temperatures (T_g) between 70–110°C; T_g is the temperature at which polymer transitions from a hard, glassy state to a softer, rubbery state. Thus, the fire performance of polymer concrete is expected to be poor, which currently limits its applications in structural members. Only a handful of studies in the literature have investigated the high-temperature behavior of PC by conducting material property tests in 20–250°C temperature range [10–13]. Moreover, all existing tests were carried out at residual conditions following cooling of heated specimens, which leads to the re-hardening of the polymer and is not representative of hot condition tests. Different solutions for improving the fire performance of polymer concretes were used in previous studies, such as flame retardants and fibers.

Concerning the flame retardants, Haurie et al. [14] studied the effect of addition different types of flame retardants on the thermal and mechanical properties of epoxy-based polymer concrete. Four types of flame retardants were used: synthetic hydromagnesite (HyM), magnesium hydroxide (MH), melamine polyphosphate (Mel), and ammonium polyphosphate (APP). The results showed that all the flame retardants showed efficient fire-retardant activity in polymer concrete. Another study conducted by Elalaoui et al. [11] investigated the influence of two types of flame retardants, ammonium polyphosphate (APP) and aluminium hydroxide (ATH), on the mechanical properties of epoxy-based polymer concrete. The outcomes showed that at high temperature of 250°C, PC-APP experiences a reduction of approximately 73% in flexural strength and 74% in compressive strength compared to room temperature, whereas PC-ATH experiences a decrease of 26% in flexural strength and 10% in compressive strength after exposure to 250°C. Furthermore, different types of fibers were utilized in the previous studies to improve the fire performance of PC at elevated temperatures. Elalaoui [12] studied the effect of two types of fibers, carbon fibers were used in two batches (1% and 2% by total weight) and polypropylene fibers were used in one batch (1% by total weight), on the mechanical properties of epoxy-based polymer concrete exposed to high temperatures. The results showed that the flexural strength of PC with 2% carbon fibers increased by approximately 20%, while the compressive strength decreased by 25.9%, compared to PC with 1% carbon fiber. In addition, the polypropylene fibers showed weak binder-fiber contact, which led to a decrease in the performance of PC. Furthermore, another type of the most important fibers used to enhance the fire

performance of PC is basalt fiber which has been studied by Niaki et al. [13]. The findings indicated that increasing the fiber content to 2% resulted in a 10% improvement in compressive strength compared to plain PC. However, surpassing the 2% fiber content led to a decrease in compressive strength (using 3% fiber content decreased the compressive strength by 20%).

On the other hand, the fire performance of PMC at elevated temperatures was investigated in previous studies without using any additions such as flame retardants or fibers. Previous studies have shown that the addition of polymers to concrete improves bond strength, flexural and tensile strengths, reduces modulus of elasticity, and decreases water permeability [15–17]. These improvements in properties enhance the durability of the concrete [18], impact and abrasion resistance [16,19], corrosion resistance [16], and resistance to extreme environmental conditions [15]. At high temperatures, Muthadhi and Kothandaraman [20] studied experimentally the mechanical properties of PMC with four polymer content ratios: 0, 5, 10, and 20%, subjected to temperatures 200-800°C for 1-3 hour. It was found that PMC and conventional concrete can be exposed to 400°C for 3 hours without any adverse effect on strength properties. The addition of 20% polymer was detrimental to concrete subjected to elevated temperatures. The duration of exposure does not have much influence on the residual compressive strength properties of conventional concrete and PMC. To address these knowledge gaps for PC and PMC, the presented study undertakes compression strength and thermal properties tests to characterize the behavior of PC and PMC at high temperatures in the range of 20-600°C at hot state. This study also investigates the effectiveness of different solutions for improving the fire performance of PC and PMC, including optimization of mix proportions, and addition of fire retardants and basalt fibers.

2. EXPERIMENTAL PROGRAM

2.1. Materials

Three different types of resins were used in the current study. In polymer concrete (PC) batches, epoxy and polyester resins were used. The epoxy resin (E-BOND 105) is a two-component resin A and B with a mixing ratio of 1:1 by volume, while the polyester resin is used along with the methyl ethyl ketone peroxide (MEKP-9) catalyst, which was used with a ratio of 1% of the resin weight. In polymer-modified concrete (PMC) batches, styrene butadiene rubber latex (SikaLatex SBR) was used, which is a superior modified styrene butadiene emulsion with a milky white liquid appearance. In addition, the PMC batches were made using QUIKRETE® Portland Cement, which is a high-quality portland cement that complies with ASTM C150 specifications. In all casted batches, crushed rock was utilized as coarse aggregates with an average particle size of 4–12 mm, whereas the natural sand was used as fine aggregates with an average particle size of 0–4 mm. Figure 1 shows the grain size distribution of the coarse and fine aggregates used in the current study. Moreover, two different types of fire performance-enhancing solutions were used: alumina trihydrate (ATH) flame retardant and basalt fiber (BF). Alumina trihydrate (ATH), also known as aluminum hydroxide, is a widely used flame retardant. At approximately 220°C, ATH decomposes into aluminum oxide and releases water in an endothermic reaction. The heat energy from the flaming plastic is absorbed, and the released water molecules suppress flame smoke. The chopped basalt fiber is a promising solution for applications that require high temperature resistance, and the basalt fiber used in the current study has an approximately cut length of 19 mm.

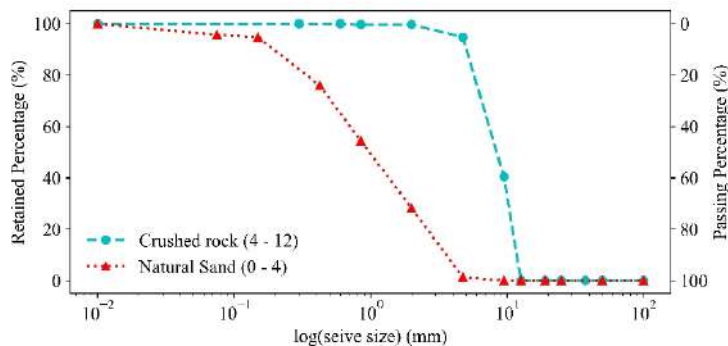


Figure 1. Particle size distribution of fine and coarse aggregates

3. BATCHES MIX PROPORTIONS

Five polymer concrete batches and three polymer-modified concrete batches were considered in the current study. Epoxy resin (EP) was used for fabricating three PC batches (plain batch-PLAIN, batch with flame retardant-ATH, and batch with basalt fiber-BF), while polyester resin (PO) was the polymer for two PC batches (plain batch-PLAIN and batch with basalt fiber-BF). The SBR latex is used as polymer in all three PMC batches, but the fire performance-enhancing solution used in each batch differs: basalt fiber (BF), aluminum hydroxide (ATH), or both BF and ATH together. The composition of each batch is listed in Table 1.

Table 1. Mix proportions of PC and PMC batches

Batch ID	Mix proportions (kg/m)								
	Resin			Aggregates		Cement	Water	Basalt fiber	Flame Retardant
	Epoxy	Polyester	SBR	C	F				
PC-PO-PLAIN	----	326	----	1298	639	----	----	----	----
PC-PO-ATH	----	326	----	1298	639	----	----	----	60
PC-EP-PLAIN	260	----	----	600	1100	----	----	----	----
PC-EP-ATH	260	----	----	600	1100	----	----	----	60
PC-EP-BF	260	----	----	600	1100	----	----	40	----
PMC-BF	----	----	78	1183	625	390	67	47	----
PMC-ATH	----	----	78	1183	625	390	67	----	71
PMC-BF-ATH	----	----	78	1183	625	390	67	47	71

3.1. Casting and curing

The PC and PMC mixtures were cast into 75 mm x 150 mm cylindrical molds instrumented with a K-type thermocouple for high-temperature testing, as shown in Figure 2a. Casting of PC and PMC batches needs to follow a distinct procedure from conventional concrete casting. For the PC casting, the first step is to mix the aggregates (gravel and sand). After that, in a bucket, the two parts of resin and the initiator were mixed, and the flame retardant or fibers were added in this step. Next, this mixture is gradually added to the aggregates and mixed further until the concrete reaches the appropriate consistency. On the other hand, the first step in the PMC casting process is also to mix the aggregates. Next, the cement is to be added to the aggregates for over two minutes and mixed for five minutes. In a bucket, the SBR latex was mixed with water, and the flame retardant was added in this step. After that, 50% of this mixture was added to the cement and aggregates, and they were left to mix for five minutes. Afterwards, 30% was added, and let them mix until the cement accumulated and started to form little balls. Eventually, the final 10% was added, and the concrete was mixed to the appropriate consistency.



(a) Casted cylindrical specimen instrumented with Type K- thermocouple



(b) Specimen insulated in a thermal blanket to maintain its hot state while testing

Figure 2. Thermocouple instrumentation and specimen insulation

Compared to normal strength concrete and polymer-modified concrete, the polymer concrete specimens have a different curing process. Hence, PC takes 7 days only to achieve the full strength, whereas both NSC and PMC need 28 days to reach their strengths due to time associated with cement hydration reactions. In addition, both NSC and PMC can be cured in air or water, but higher strengths can be achieved using water curing [21]. On the other hand, PC can be only air-cured at a temperature 20°C and humidity of 50% [22].

3.2. Testing procedure

The current study includes a set of thermal and mechanical properties tests on PC and PMC. The relevant thermal properties of concrete include thermal conductivity, specific heat, mass loss, thermal expansion, and thermal diffusivity. The current study presents results on thermal conductivity, thermal diffusivity, and specific heat at room temperature, whereas the tests for measuring thermal properties at high temperatures are currently underway. Thermal properties were measured following ISO 22007-2 standard procedures at room temperature. The Kapton sensor shown in Figure 3a was placed in between two concrete specimens of dimensions $50 \times 50 \times 25$ mm. The thermal property measurements were carried out using the Hot Disk TPS 2500 S instrument shown in Figure 3b. To achieve a good reading the specimen must be properly in contact with the sensor. For each testing procedure sensor measurement power and measuring time was taken as 0.9W and 40 second [5]. The mechanical properties such as compressive strength tests which were performed by a Tinius Olsen universal strength testing machine. These strength tests were carried out at temperatures of 20 (ambient), 100, 200, 400, and 600°C. For each batch, three repeat specimens were tested at room temperature and two repeat specimens were tested at each high temperature. For high-temperature testing, the specimens were heated at a rate of 2°C/min up to the specified target temperature and held for an hour for uniform temperature distribution in the specimen. Thereafter, the hot specimen is wrapped in an insulation casing, as shown in Figure 2b, to minimize heat loss and transferred to the strength test machine for evaluating high-temperature compressive strength [23].



(a) Kapton sensor



(b) Hot disk TPS 2500 S

Figure 3. Instruments that are used to measure thermal properties

4. RESULTS AND DISCUSSION

The results of thermal properties tests at room temperature in addition to the mechanical properties tests at room and high temperatures are presented in this section. All the compressive strengths at high temperatures were observed in the hot state. Hence, it was important to measure the temperature distribution throughout the heating process for all tested specimens. The furnace temperature, the temperatures at the surface, as well as the internal temperatures, were measured and recorded using K-type thermocouples during heating the specimen. Figure 4 shows the temperature distribution of one of the PMC specimens at 600 °C.

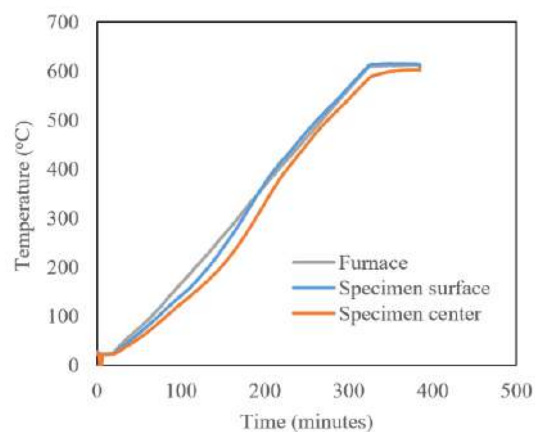


Figure 4. Temperature distribution of one of PMC specimens at 600°C

3.1 Thermal properties

A comparison of thermal conductivity, thermal diffusivity, and specific heat room temperature for normal strength concrete (according to Lie et al. [24]), epoxy-based polymer concrete, and polymer-modified concrete are shown in Table 2. In addition, the calculated density of these specimens, which is the ratio of the specimen weight to its volume is also shown in Table 2. It can be noted that all the density of PC and PMC specimens were lower than NSC. In addition, incorporating basalt fiber in epoxy-based PC led to a decrease in the density compared to the plain epoxy specimen. In PMC specimens, the specimen which includes basalt fiber only showed the lower density among the other PMC specimens. The thermal conductivity of plain epoxy polymer concrete (PC-EP-PLAIN) and epoxy-based polymer concrete with basalt fiber (PC-EP-BF) are 1.75 and 1.43 W/mK, respectively which represents a higher thermal conductivity than that of NSC, ranging between 1.-1.5 W/mK. Moreover, the thermal diffusivity, which is the ratio between thermal conductivity to the volumetric specific heat was also higher in PC than NSC. The volumetric specific heat is the product of density and specific heat of the test specimen. On the other hand, the specific heat of NSC was higher than those of epoxy-based polymer concrete specimens whether plain or with basalt fiber. Regarding the polymer-modified concrete, the thermal conductivity of PMC specimens with ATH or with BF or with a combination of ATH and BF at room temperature is 2.27, 1.92, and 2.03 W/mK, which also represents an increase of 62%, 37%, and 45% compared to NSC. Additionally, the specific heat of PMC specimens was also lower than NSC, especially PMC with ATH specimens showed the lower value of specific heat (209 J/kgK) among the other specimens. It is better to have a lower value of thermal conductivity and higher value of specific heat because the lower value of thermal conductivity slows the conduction of heat within the specimen and the higher value of specific heat enhances the capacity to absorb heat before transferring into the specimen. This includes that NSC has better thermal properties than PC and PMC at room temperature. The thermal properties tests of polyester-based polymer concrete specimens are currently underway.

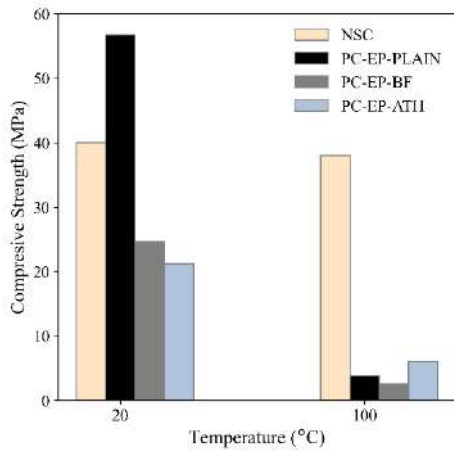
Table 2. Thermal properties of PC and PMC batches compared to NSC

Batch ID	Thermal conductivity (W/mK)	Thermal diffusivity (mm ² /s)	Volumetric specific heat (MJ/m ³ K)	Density (kg/m ³)	Specific heat (J/kgK)
NSC [24]	1.3-1.5	0.75-0.77	1.68-2.0	2400	700-833
PC-EP-PLAIN	1.75	1.38	1.26	2320	547
PC-EP-BF	1.59	1.43	1.11	2036	545
PMC-ATH	2.27	4.53	0.50	2385	209
PMC-BF	1.92	1.65	1.03	2325	443
PMC-ATH-BF	2.03	1.52	1.33	2348	566

3.2 Mechanical properties

3.2.1 Polymer concrete

A comparison between the NSC results obtained by Ma et al. [25] and the current study results of the three epoxy resin batches, namely PC-EP-PLAIN, PC-EP-ATH, and PC-EP-BF are presented in Figure 5a. The epoxy plain (PC-EP-PLAIN) specimen had a compressive strength of 57 MPa at room temperature, which is more than the NSC by 42%. Incorporating the basalt fiber (PC-EP-BF) and flame-retardant ATH (PC-EP-ATH) led to a reduction in compressive strength at room temperature by 57% and 63%, respectively, compared to PC-EP-PLAIN specimen. It is observed that using the ATH flame retardant at 100°C led to retain 28.4% of the room temperature strength, while using the epoxy plain and basalt fiber was only able to retain 6.8% and 10.3% of their room temperature strengths. Conversely, the NSC shows a retention in compressive strength at 100°C of about 95% of its initial strength at room temperature. Furthermore, all the epoxy-based PC specimens were not able to sustain temperatures above 100°C, and Figure 5b shows the state of one of the epoxy specimens with ATH addition inside the furnace at 200°C.



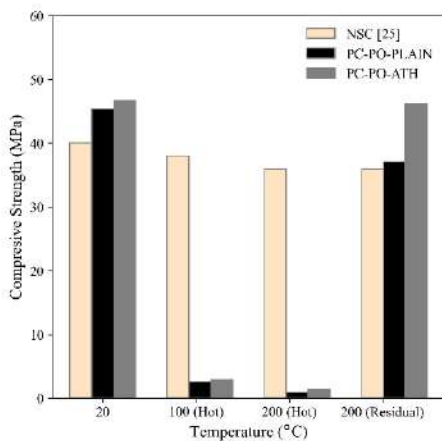
(a) Compressive strength of epoxy PC specimens



(b) PC-EP-ATH specimen inside the furnace at 200°C

Figure 5. Test results of epoxy-based polymer concrete specimens

Utilizing the polyester resin, two batches were tested, one is plain without any addition (PC-PO-PLAIN) and one with ATH flame retardant (PC-PO-ATH). Figure 6a shows a summary of the measured compressive strengths of polyester resin specimens compared to the NSC results provided by Ma et al. [25]. It can be noticed that the compressive strengths of both the PC-PO-PLAIN and PC-PO-ATH specimens at room temperature are 45 MPa and 46 MPa, respectively, which are quite similar and higher than NSC by 12.5% and 15%, respectively. The PC-PO-PLAIN samples retained compressive strengths of approximately 5.7% and 1.9% at 100°C and 200°C, respectively, whereas the PC-PO-ATH samples exhibit slightly better strength retention, with values around 6.3% and 3% at the same temperatures. Conversely, the NSC shows a retention in compressive strength at 100°C and 200°C of about 95% and 90%, respectively of its initial strength at room temperature. Moreover, residual strength tests were conducted alongside heating tests for polyester resin specimens. In these tests, specimens were heated to 200°C and then cooled down to room temperature before compressive strength tests were performed to evaluate residual strength. The residual strength results indicate that both PC-PO-PLAIN and PC-PO-ATH retained a significant portion of their original strength with values of 81.7% and 98.9%, respectively, whereas the NSC retained 90% of its initial strength. This suggests that incorporating the fire-retardant additive ATH shows promise for enhancing residual strength. While ATH doesn't notably improve the strength during heating, its addition significantly enhances the material's ability to maintain its initial compressive strength after cooling from 200°C. The compressive tests at 400°C could not be performed because the polyester resin specimens were not able to sustain this temperature. Figure 6 shows the status of one such polyester resin specimen when heated to 400°C inside the furnace. Heating at 500°C led to the specimen bursting into flames and severely damaged the furnace. Due to the specimens' inability to withstand such high temperatures, no testing was conducted at 600°C.



(a) Compressive strength of polyester PC specimens

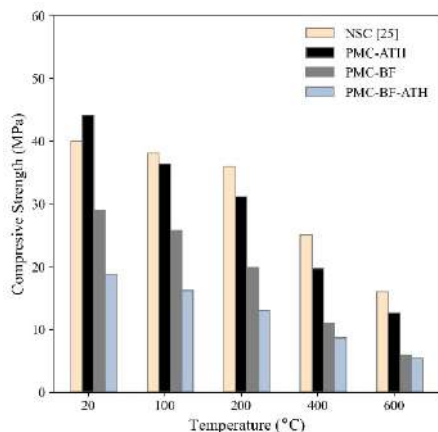


(b) PC-PO-ATH specimen inside the furnace at 400°C

Figure 6. Test results of epoxy-based polymer concrete specimens

5. 3.2.2 Polymer-modified concrete

Test results for three PMC batches, namely PMC-BF, PMC-ATH, and PMC-BF-ATH, are presented in this section and compared to NSC results in Ma et al. [25]. Figure 7a shows a comparison between compressive strength for all PMC batches and NSC. It can be noted that the compressive strength of the PMC specimen with flame retardant ATH only (PMC-ATH) at room temperature was 44 MPa compared to 40 MPa of NSC. The addition of basalt fiber only (specimen PMC-BF) or both basalt fiber and ATH (PMC-BF-ATH) decreased the compressive strength at room temperature by about 34% and 57%, respectively, compared to the specimen PMC-ATH, which has ATH only. At a temperature of 100°C, the PMC-ATH and NSC had a little difference in compressive strength around 4.2%. Furthermore, at 100 °C, the PMC-ATH, PMC-BF, and PMC-BF-ATH retained 82.5%, 88.8%, and 86.5%, respectively of their initial compressive strength, while NSC retained 95% of its original strength. At a temperature of 200°C, the NSC retained 90% of its original strength. In addition, there was no significant difference between the percentage of retention of compressive strength for the three PMC specimens. All PMC specimens retained at 200°C about 68.6-70.4% of their initial room temperature strengths. At a temperature of 400°C, the NSC concrete retained about 62.5% of its initial strength at room temperature. Moreover, the specimen PMC-BF with basalt fiber retained 37.8% of its room temperature strength, while the other two specimens PMC-ATH and PMC-BF-ATH nearly retained 44.7% and 45.9% of their strengths, respectively. The same scenario happened at 600°C. The NSC retained 40% of its room temperature strength, while PMC-BF specimen only retained 20.4% of its strength, and the other two specimens PMC-ATH and PMC-ATH-BF retained about 28% of their strength. The sharp degradation in compressive strength of PMC compared to NSC is due to the presence of polymer resin (SBR latex) which has a low glass transition temperature of about 50°C according to Backfolk et al. [26]. It can be noted that all PMC specimens were able to sustain temperatures till 600°C showing a large number of surface fine cracks due to the evaporation of the moisture from the specimen's surface, and Figure 6c shows the status of one such PMC with ATH specimen after heating to 600°C.



(a) Compressive strength of PMC and NSC

(b) PMC-ATH specimen after heating to 600°C

Figure 7. Test results of polymer-modified concrete specimens

6. CONCLUSIONS

The current study presents a set of thermal and mechanical tests to study the behavior of polymer concrete and polymer-modified concrete at high temperatures in the range of 20–600°C in hot state. Based on the findings obtained from the experimental tests, the following conclusions can be inferred:

- The thermal conductivity of PC and PMC is higher than NSC, while the specific heat of PC and PMC is lower than NSC. This infers that NSC exhibits better thermal behavior than PC and PMC since the lower thermal conductivity slows the conduction of heat within the specimen and the higher value of specific heat enhances the capacity to absorb heat before transferring into the specimen.

- Epoxy-based polymer concrete specimens failed to sustain temperatures exceeding 100°C, releasing excessive smoke, whereas polyester-based polymer concrete specimens remained stable up to 200°C, At about 400°C, the polyester-based specimens failed inside the furnace and when heated further to 500°C the specimen burst into flames, and this severely damaged the furnace.
- Incorporating alumina trihydrate (ATH) flame retardant in epoxy-based polymer concrete specimens at 100°C resulted in retaining 28.4% of the room temperature strength but it was not able to sustain 200°C, whereas, incorporating ATH in polyester-based polymer concrete specimens resulted in slightly improved strength retention, with values hovering around 6.3% and 3% at 100°C and 200°C the temperatures. Conversely, NSC specimens retained about 95% and 90% at 100°C and 200°C, respectively of their original room temperature strength.
- After being heated to 200°C and subsequently cooled back to room temperature (residual tests), both the plain polyester-based polymer concrete specimens and those incorporating polyester resin with ATH retained a substantial portion of their room temperature strength, with values of 81.7% and 98.9%, respectively. This shows that incorporating the ATH flame-retardant is a promising for enhancing residual strength after exposure to high temperature.
- Incorporating ATH flame retardant in polymer-modified concrete (PMC) specimens increased the compressive strength at room temperature by 10% compared to NSC. In addition, when basalt fibers were incorporated into PMC specimens, they retained 20.4% of their strength at 600°C, whereas utilizing ATH or a combination of ATH and BF retained approximately 28% of their room temperature strength. Conversely, the NSC can retain about 40% of its original room temperature strength at 600°C.

REFERENCES

- [1] Reis JML dos. Effect of temperature on the mechanical properties of polymer mortars. *Materials Research* 2012;15:645–9.
- [2] Taha MMR, Genedy M, Ohama Y. *Polymer concrete. Developments in the Formulation and Reinforcement of Concrete*, Elsevier; 2019, p. 391–408.
- [3] Niaki MH, Ahangari MG. *Polymer concretes: advanced construction materials*. CRC Press; 2022.
- [4] Sprinkel MM. Polymer concrete bridge overlays. *Transp Res Rec* 1993;1392:107.
- [5] Kodur VKR, Banerji S, Solhmirzaei R. Test methods for characterizing concrete properties at elevated temperature. *Fire Mater* 2020;44:381–95.
- [6] Kodur V. Properties of concrete at elevated temperatures. *Int Sch Res Notices* 2014;2014.
- [7] Chang Y-F, Chen Y-H, Sheu M-S, Yao GC. Residual stress–strain relationship for concrete after exposure to high temperatures. *Cem Concr Res* 2006;36:1999–2005.
- [8] Khaliq W, Kodur V. Thermal and mechanical properties of fiber reinforced high performance self-consolidating concrete at elevated temperatures. *Cem Concr Res* 2011;41:1112–22.
- [9] Felicetti R, Gambarova PG, Bamonte P. Thermal and mechanical properties of light-weight concrete exposed to high temperature. *Fire Mater* 2013;37:200–16.
- [10] Elalaoui O, Ghorbel E, Mignot V, Ouezdou M Ben. Mechanical and physical properties of epoxy polymer concrete after exposure to temperatures up to 250 C. *Constr Build Mater* 2012;27:415–24.
- [11] Elalaoui O, Ghorbel E, Ouezdou M Ben. Influence of flame retardant addition on the durability of epoxy based polymer concrete after exposition to elevated temperature. *Constr Build Mater* 2018;192:233–9.
- [12] Elalaoui O. Effect of Short Fibers on Fracture Properties of Epoxy-Based Polymer Concrete Exposed to High Temperatures. *Polymers (Basel)* 2023;15:1078.

- [13] Niaki MH, Fereidoon A, Ahangari MG. Experimental study on the mechanical and thermal properties of basalt fiber and nanoclay reinforced polymer concrete. *Compos Struct* 2018;191:231–8.
- [14] Haurie L, Lacasta AM, Ciudad A, Realinho V, Velasco JI. Addition of flame retardants in epoxy mortars: Thermal and mechanical characterization. *Constr Build Mater* 2013;42:266–70.
- [15] Walters DG, Bartholomew JJ, Bolton DJ, Butler WB, Cain RR, Carter PD, et al. Guide for polymer concrete overlays. *ACI Mater J* 1993;90:499–522.
- [16] Hare CH. Trouble with coating structural concrete: part II. *Journal of Protective Coatings & Linings* 1999;16.
- [17] Wang J, Zhang S, Yu H, Kong X, Wang X, Gu Z. Study of cement mortars modified by emulsifier-free latexes. *Cem Concr Compos* 2005;27:920–5.
- [18] Shaker FA, El-Dieb AS, Reda MM. Durability of styrene-butadiene latex modified concrete. *Cem Concr Res* 1997;27:711–20.
- [19] Wong WG, Fang P, Pan JK. Dynamic properties impact toughness and abrasiveness of polymer-modified pastes by using nondestructive tests. *Cem Concr Res* 2003;33:1371–4.
- [20] Muthadhi A, Kothandaraman S. Experimental investigations on polymer-modified concrete subjected to elevated temperatures. *Mater Struct* 2014;47:977–86.
- [21] Chen ZY, Zhong SY. Research and development of polymers in concrete in China. *Polymers in Concrete* 1997;3.
- [22] Rebeiz KS. Time-temperature properties of polymer concrete using recycled PET. *Cem Concr Compos* 1995;17:119–24.
- [23] Banerji S, Kodur V. Effect of temperature on mechanical properties of ultra-high performance concrete. *Fire Mater* 2022;46:287–301.
- [24] Lie TT, Kodur VKR. Thermal and mechanical properties of steel-fibre-reinforced concrete at elevated temperatures. *Canadian Journal of Civil Engineering* 1996;23:511–7.
- [25] Ma Q, Guo R, Zhao Z, Lin Z, He K. Mechanical properties of concrete at high temperature—A review. *Constr Build Mater* 2015;93:371–83.
- [26] Backfolk K, Holmes R, Ihalainen P, Sirviö P, Triantafillopoulos N, Peltonen J. Determination of the glass transition temperature of latex films: Comparison of various methods. *Polym Test* 2007;26:1031–40.

LOAD-INDUCED THERMAL STRAIN OF HIGH-STRENGTH CONCRETE AT ELEVATED TEMPERATURES

Dinh Ba Le¹, José L. Torero², Vinh Dao³

ABSTRACT

Deformational characteristics of concrete exposed to elevated temperatures are required for fire performance assessment of resulting concrete structures. However, despite substantial previous research, a comprehensive understanding of the deformational change of high-strength concrete subject to elevated temperatures under loading conditions has not yet been established. In this paper, the load-induced thermal strain (LITS) of high-strength concrete exposed to temperatures up to 500°C is investigated based on innovative experiments that more closely reflect the nature of concrete exposed to realistic fires. Several key factors affecting the evolution of LITS are explored in-depth, including imposed heat flux levels (which are directly related to heating rates), average target temperatures and load levels. For concrete subject to different heat fluxes: LITS for specimens exposed to a lower heat flux of 20 kW/m² is found to be higher than that for heat flux of 30 kW/m². It is noted that LITS evolves approximately linearly as the concrete temperature increased up to ~350°C, above which the development of LITS tends to accelerate. The reliable full-field deformation data enabled by the newly developed test setup using an optimised 3D digital image correlation technique allow to extract the transverse LITS, which is shown to have an essentially linear relationship with the corresponding longitudinal LITS. LITS during cooling is also reported and shown to be significant, highlighting the need for such LITS during cooling to be properly accounted for in assessing concrete performance in fire.

Keywords: Load-induced thermal strain; high-strength concrete; elevated temperatures; deformation

1 INTRODUCTION

Thermal deformation at elevated temperatures is a critical part of thermal performance of concrete. Proper understanding of and model for the thermal deformation characteristics of concrete subjected to elevated temperatures is thus required for fire performance-based designs of concrete structures. In the literature, the deformational characteristics of concrete subjected to elevated temperatures have been widely investigated. It has been recognized that there exist an evident difference in the thermal deformation of concrete elements when heated with and without axial compression load [1, 2]. Essentially, such a difference in the thermal deformation comes mainly from the Load-induced Thermal Strain (LITS). In theory, LITS includes various strain components which change according to loading and heating conditions [3-5]: transitional thermal creep, drying creep, strain induced by the degradation of Young's modulus, and strain induced by thermal cracking, among others. Generally, for concrete heated up to

¹ PhD Graduate, School of Civil Engineering, The University of Queensland, Australia
Lecturer, Faculty of Civil Engineering, Danang University of Science and Technology, The University of Danang, Vietnam
e-mail: badinh.le@uq.net.au, ORCID: <https://orcid.org/0000-0001-6999-7265>

² Professor, Department of Civil, Environmental & Geomatic Engineering, University College London, UK
e-mail: j.torero@ucl.ac.uk, ORCID: <https://orcid.org/0000-0001-6265-9327>

³ Associate Professor, School of Civil Engineering, The University of Queensland, Australia
e-mail: v.dao@uq.edu.au, ORCID: <https://orcid.org/0000-0002-1036-1446>

600°C and subjected to a sustained compressive load less than 50% of the compressive strength at ambient temperature, LITS drives mainly from the transitional thermal creep [4-6].

Unfortunately, despite substantial previous research, the reliable data on LITS of concrete remains rather limited, due mainly to the poorly defined thermal boundary conditions and the difficulty in capturing deformation of test specimens during testing at elevated temperatures. To generate reliably measured LITS data and thereby explore the mechanisms behind the evolution of LITS, a recent study using a new testing system with advanced thermal boundary control and deformation measurement has been conducted and some of the initial outcomes are reported in this paper. On that basis, LITS of hardened concrete under varied loading and heating conditions is examined, with a special focus on the influence of imposed heat flux levels (which are directly related to heating rates), average target temperatures level, and load levels on LITS of high strength concrete cylinders under axial compression load. Particularly, values of both longitudinal and transverse LITS of the concrete cylinders are presented, and on that basis, the ratio between transverse LITS and longitudinal LITS upon heating is evaluated. The negative value of this ratio is called as “LITS Poisson’s ratio” (strictly not the same definition as the traditional Poisson’s ratio) in literature [7] to recognise the multiaxial direction of LITS.

2 EXPERIMENTAL STUDY

2.1 Raw materials and concrete mixtures

Two high strength concrete mixes with water-to-cement ratio of 0.41 and 0.33, commercially available in Australia, were investigated in this study. Their mix designs (named Mix A and Mix B, respectively) are given in Table 1. At the age of 28 days, the compressive strength of the two concrete mixtures were determined at 67.6 and 82.4 MPa, respectively, in accordance with the relevant Australian Standard (AS 1012-2014) [8].

Table 1. Mix designs of concrete studied (Unit: kg/m³)

Constituents	Mix A	Mix B
Portland cement	472	580
Fly ash	88	0
Water	195	193
Fine sand	366	140
Coarse sand	472	600
10 mm aggregate	855	925
Superplasticiser	4.65	4.87
Retarder	1.53	0

2.2 Preparations of concrete specimens

After concrete mixing, concrete cylinders with dimensions of $\Phi 100$ mm \times 200 mm were cast for experimental studies. At an age of 24 hours after mixing, all concrete cylinders were demolded and immediately cured in a water tank with a constant temperature of 23°C for 7 days. After the water curing, all specimens were stored in an environmental room with the temperature around 23 \pm 1.5°C and relative humidity approximately 50 \pm 3% for more than 13 months. To provide information on the temperature profile of concrete cylinders upon heating and cooling, reference specimens with nine Type-K thermocouples embedded (Figure 1) were also prepared. For the same concrete mixture, all specimens with and without thermocouples were cast at the same time and cured at the same condition. Therefore, the average temperature profiles of specimens subjected to the same heating/cooling conditions can be reasonably assumed identical.

Based on the raw data given by thermocouples, a 4th degree polynomial curve was used for fitting temperatures along the specimen's diameter ($T(x)$, in Equation 1). Four-degree polynomial functions were chosen to reflect the symmetry of expected temperature distributions. They were also able to adapt the change of temperature profiles during the transition period from the end of heating to the initial period of cooling, when surface temperatures quickly dropped but inner sections' temperatures followed the trend with delays. The coefficients of the 4th degree polynomial functions were determined by regression analysis using MATLAB. Then, the average temperature of the specimen (T_{ave}) at a given time point was calculated by Equation 1. The obtained average temperature was then used in the current study for deformation-temperature relationships and related discussions (see Section 3).

$$T_{ave} = \frac{\int_0^{50} T(x)(2\pi x dx)}{A} \quad (1)$$

where $T(x)$ represents the 4th degree polynomial function. A is the cross-sectional area of the specimen ($A = 7854 \text{ mm}^2$). 50 mm is the radius of the specimens, and x is the radial distance from the centre.

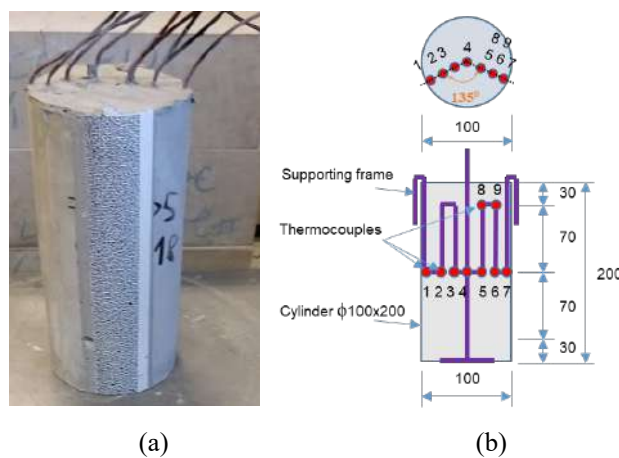


Figure 1. Reference concrete cylinder with thermocouples embedded (a) a photo and (b) location of thermocouples

In addition, prior to experiments, speckle patterns for deformation capturing of DIC were painted onto the specimens' surface. The speckle pattern dimension was 30 mm × 200 mm to cover the entire height of concrete cylinders. The width of 30 mm was chosen so that it was three times of aggregate size, which aims to reliably measure the transverse strain of concrete cylinders. Besides, to facilitate the painting of the speckle pattern with diameter of 0.5 mm and density of 50%, a powerful and precise laser cutting machine was utilised to fabricate speckle stencils. Detailed information on speckle stencils and painting on specimens can be found in [4, 9].

2.3 Test setup for thermal-mechanical loading and deformation capturing

Being inspired by the advantages of radiant panels system relative to conventional furnaces [10-12], in the current study, a system of four radiant panels symmetrically arranged around a test concrete cylindrical specimen was used to create reliable thermal boundary conditions for studying the fire performance of high strength concrete (Figure 2). The mid-height levels of the panels were the same and equalled that of the test specimen. The distances from the panels to the specimen's surface were adjustable to reach a specific pre-determined incident heat flux level.

Mechanical loads were provided by an actuator attached to a steel portal frame. Through precise closed-loop controls, this actuator could offer both force control and displacement control for a pre-set load path. The portal frame included two steel columns and one steel beam with a 1.0 MN actuator attached. The frame's stability was ensured by inclined braces with one end anchored to the strong floor. The actuator's head was attached to a top block including water-cooling system. The top block was in the vertical alignment with the base block on which the specimen was located during testing. Like the top block, the base one had a water-cooling system as well. For the measurement of LITS of concrete at a pre-set stress

level, shortly after a constant compressive stress was applied on specimens, the four radiant panels were turned on to apply the intended predetermined incident heat flux level.

Using DIC technique, the displacement field on the visible surfaces of test specimens was obtained by comparing and tracking the locations of subsets of pixels in digital images. During heating, the radiant panels emit a large amount of radiated energy within regions of visible wavelengths that can be reflected on the specimen surface and transmitted to the DIC cameras. The heated specimen itself also releases a quantity of radiation in the visible spectrum. These sources of light negatively affect the quality of captured images, making them overexposed. To address this issue, a Midopt BP470 filter and an EFFI-Lase-Power-CM-C02-465 blue light were employed. While the filter limited the amount of thermal radiation transmitted to the cameras, the blue light enhanced the illumination condition, as shown in Figure 2. Prior to the start of experiments, the effectiveness of DIC at ambient conditions and at elevated temperatures was carefully verified and calibrated, as reported in [9, 13].

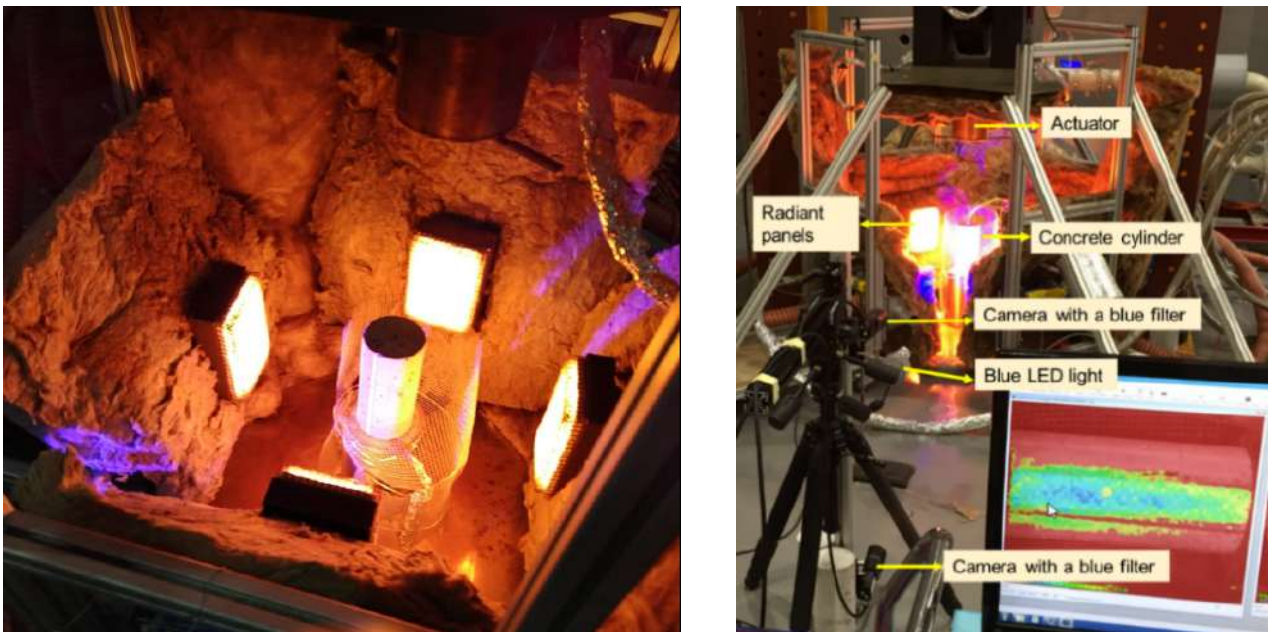


Figure 2. Test setup with radiant panels and DIC with blue light and filters

2.4 Other test parameters

In this study, two incident heat flux levels (HF of 20 kW/m² and 30 kW/m²) were employed during heating of concrete cylinders with or without loading. The pre-set target temperature of specimens investigated was 200°C, 300°C and 450°C for the first heating, respectively.

For the loaded concrete cylinders, the applied compressive stress level was pre-set at 20% and 40% of the corresponding ambient compressive strength of concrete at the time of testing. Typically, specimens were exposed to elevated temperatures condition only once, except Test Series 5 in which the specimens were heated up twice. During the first heating phase, the Series 5 specimens (A-HF30-SR40-T300-Stressed40-T500) were heated up to 300°C and then naturally cooled down to the room temperature. After 4-7 days since the first heating, these specimens were heated again up to 500°C. Details of series of specimens tested are presented in Table 2. [In Table 2, the Series ID “A-HF20-Stressed40-T300”, for example, indicates that the tested concrete cylinders are from Mix A, subjected to a compressive stress of 40% of ambient compressive strength while being heated up to the average target temperature of 300°C by an incident heat flux of 20 kW/m².]

The LITS of concrete at elevated temperatures can be determined by the difference between the strains of concrete specimens with and without axial compression load since the start of heating (or cooling) [5, 6], as given by Equation 2:

$$\varepsilon_{LITS}(t) = \varepsilon_{stressed}(t) - \varepsilon_{unstressed}(t) \quad (2)$$

where, t is the time, $\varepsilon_{stressed}$ is the total strain of the stressed concrete specimen, and $\varepsilon_{unstressed}$ is the total strain of corresponding reference unstressed specimen.

Moreover, through DIC data analysis, the deformations of specimen in both longitudinal and transverse directions could be captured. Based on the measured longitudinal and transverse LITS, the ratio between transverse LITS and longitudinal LITS can be determined (refer to the concept of Poisson's ratio [14]), as given by Equation 3.

$$\vartheta(t) = -\frac{\varepsilon_t(t)}{\varepsilon_l(t)} \quad (3)$$

where, ϑ is the ratio between transverse LITS (ε_t) and longitudinal LITS (ε_l).

Besides, the mass loss of concrete upon heating is also determined, as given below.

$$\omega = \frac{m_0 - m_h}{m_0} \times 100\% \quad (4)$$

where, m_0 is the initial weight (g) of the specimen immediately before heating tests, and m_h is the weight (g) of the specimen at hot conditions immediately after heating tests.

Table 2. Details of series of specimens tested

Series No.	Series ID	Number of specimens	Concrete mix	Heat fluxes (kW/m ²)	Stress (%)	Temperature (°C)
1	A-HF20-Stressed40-T300*	3	A	20	40	300
2	A-HF30-Stressed40-T300	9	A	30	40	300
3	A-HF20-Unstressed-T300	3	A	20	0	300
4	A-HF30-Unstressed-T300	3	A	30	0	300
5	A-HF30-Stressed40-T300-Stressed40-T500	3	A	30	40	300/500**
6	A-HF30-Stressed40-T300-Unstressed40-T500	3	A	30	0	300/500**
7	A-HF30-Stressed40-T450		A	30	40	450
8	A-HF30-Unstressed-T450		A	30	0	450
9	B-HF20-Stressed40-T300	3	B	20	40	300
10	B-HF20-Unstressed-T300	3	B	20	0	300
11	B-HF20-Stressed20-T200	3	B	20	20	200
12	B-HF20-Stressed40-T200	3	B	20	40	200
13	B-HF20-Unstressed-T200	3	B	20	0	200

* A-HF20-Stressed40-T300: Series was from Mix A, compressed at a stress of 40% of ambient compressive strength while being heated up to average temperature of 300 °C by an incident heat flux of 20 kW/m².

** 300/500: target temperatures were 300°C and 500°C for the first and second heating.

3 RESULTS AND DISCUSSION

3.1 Longitudinal LITS during heating

Figure 3 presents the evolution of the total concrete strain with temperature for four sets of concrete cylinder specimens (namely, *A-HF20-Unstressed40-T300*, *A-HF20-Stressed40-T300*, *A-HF30-Unstressed40-T300* and *A-HF30-Stressed40-T300*) and the resulting corresponding LITS. For each set

(Figure 3), the evolution of the measured strain with temperature is displayed by an average curve and a shaded region with its width equal to two times the corresponding standard deviation of the strain. The recorded heating times for reaching the pre-set target temperatures and the corresponding mass loss are shown in Figure 4.

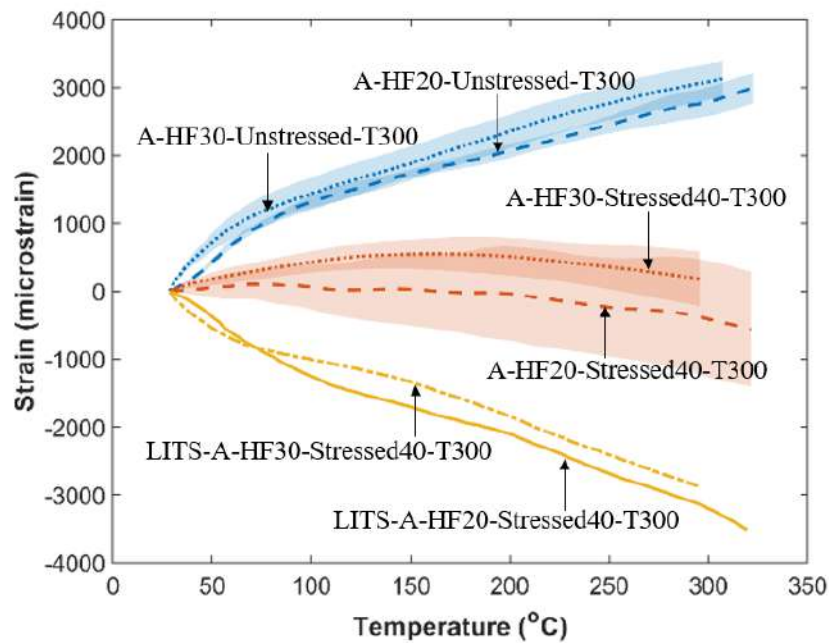


Figure 3. LITS of concrete cylinders during heating by different incident heat flux levels

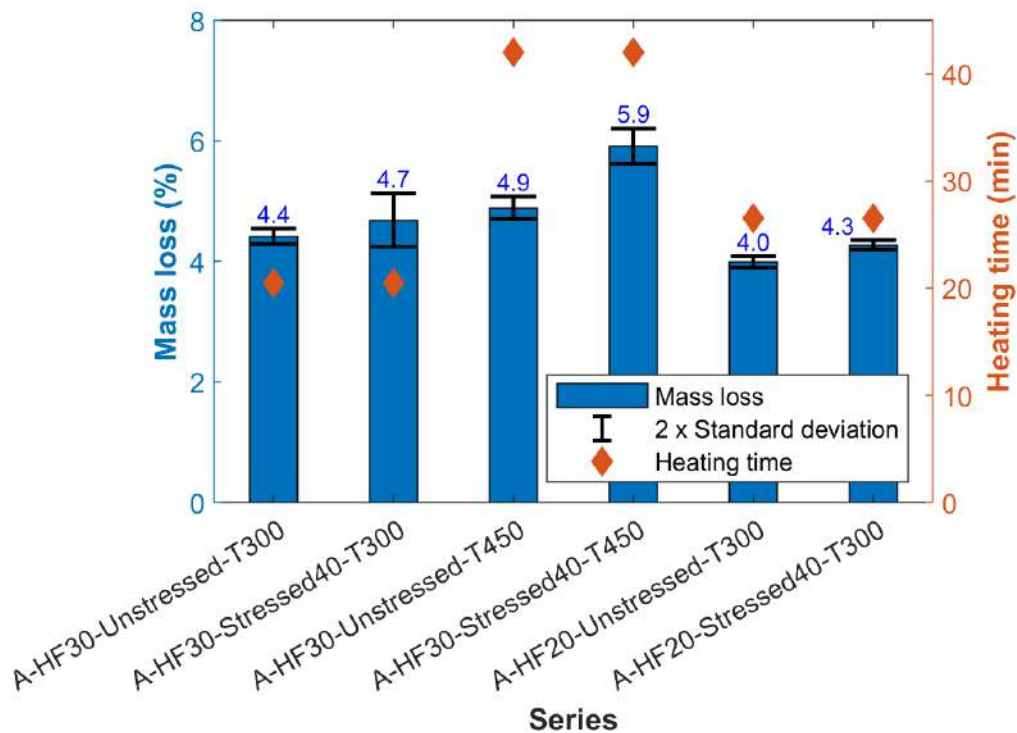


Figure 4. Mass loss of specimens subjected to different heating and loading conditions

It can be observed that the measured free thermal strains (FTS) of unstressed concrete specimens exposed to a heat flux of 30 kW/m² are slightly higher than that of specimens subjected to a heat flux of 20 kW/m², particularly for average temperatures lower than 100°C (Figure 3). At temperatures lower than 100°C, FTS mostly comprises (i) the expansion of cement paste due to dilation of physically-bound water and (ii) microcracks caused by non-uniformity of thermal deformation and of drying shrinkage [15]. Higher heat

fluxes likely resulted in more extensive microcracking near the specimens' surface, which in turn caused higher mass loss, as evidenced in Figure 4.

While the FTS and mass losses were higher for specimens exposed to 30 kW/m², the measured total strains of stressed specimens under heat flux of 20 kW/m² were more compressive (Figure 3), due possibly mainly to the longer heating times to reach the same target average temperature (see Figure 4). As a result, more time-dependent transient creep develops [5], leading to a slightly higher LITS of concrete exposed to the heat flux of 20 kW/m², as shown in Figure 3.

Specimens of the two series *A-HF30-Stressed40-T300* and *A-HF30-Stressed40-T450* were subject to the same incident heat flux (of 30 kW/m²) and the same loading level, but were heated to different target average temperatures. The obtained LITS of the two series are plotted in Figure 5. It can be clearly observed that the evolution of LITS with the average temperature for both series followed essentially identical curves, as expected. This is another strong evidence for the reliability and repeatability of the adopted experimental set-up and procedure.

As evidenced in Figure 5, the obtained LITS evolved approximately linearly with increasing concrete temperature up to ~350°C. Above ~350°C, the LITS evolution became faster, which is generally consistent with reported outcomes in previous studies [16, 17]. Possible reasons for such increased rate of LITS evolution after ~350°C include: (i) the accelerated dehydration of C-S-H, which promotes the concrete contraction and lowers elastic modulus of concrete [18-20]; (ii) the decomposition of Ca(OH)₂ at temperature over 400°C [5, 20, 21]; and, (iii) the likely increased sliding between C-S-H layers in compressively-stressed specimens caused by additional moisture released from the decomposition of C-S-H and Ca(OH)₂ [22-25].

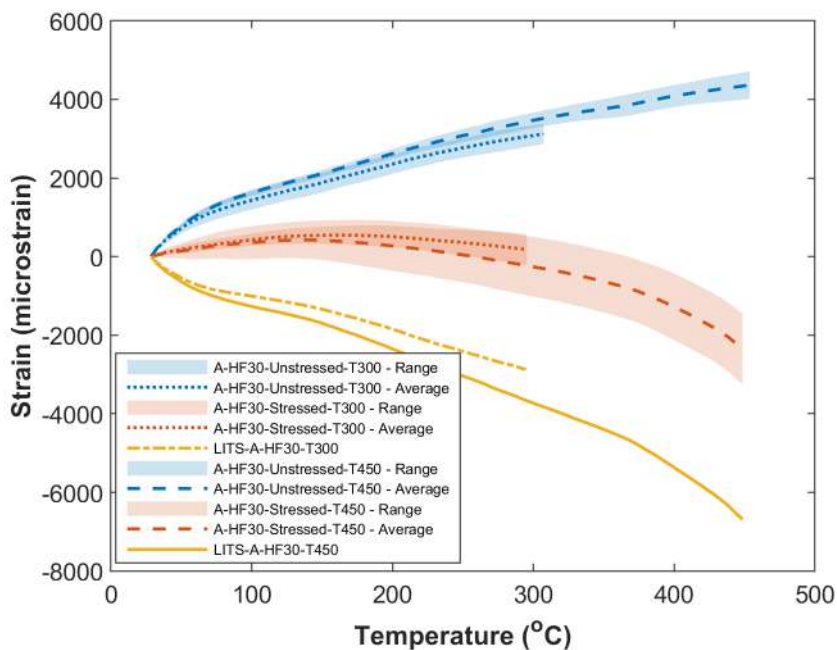


Figure 5. LITS during heating to different target average temperatures

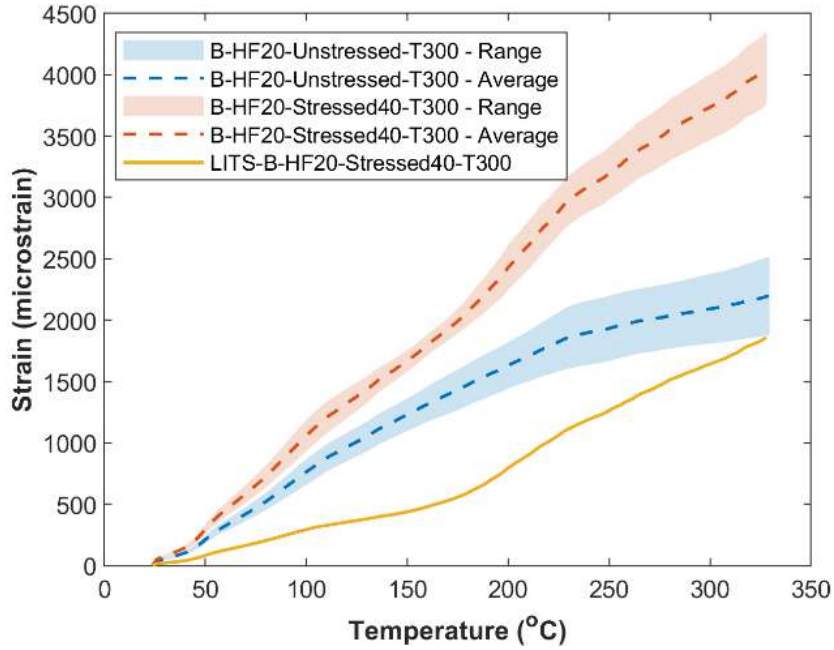
3.2 Transverse LITS during heating

The transverse LITS was measured following the same experimental procedure used for determining the longitudinal LITS of concrete cylinders. The measured transverse and longitudinal LITS of specimen *B-HF20-Stressed40-T300* are plotted in Figure 5. The evolutions of both transverse and longitudinal LITS are found to follow a similar pattern, which is possibly due mainly to their sharing of the same thermomechanical origination (although transverse LITS is also influenced by thermomechanical longitudinal cracks).

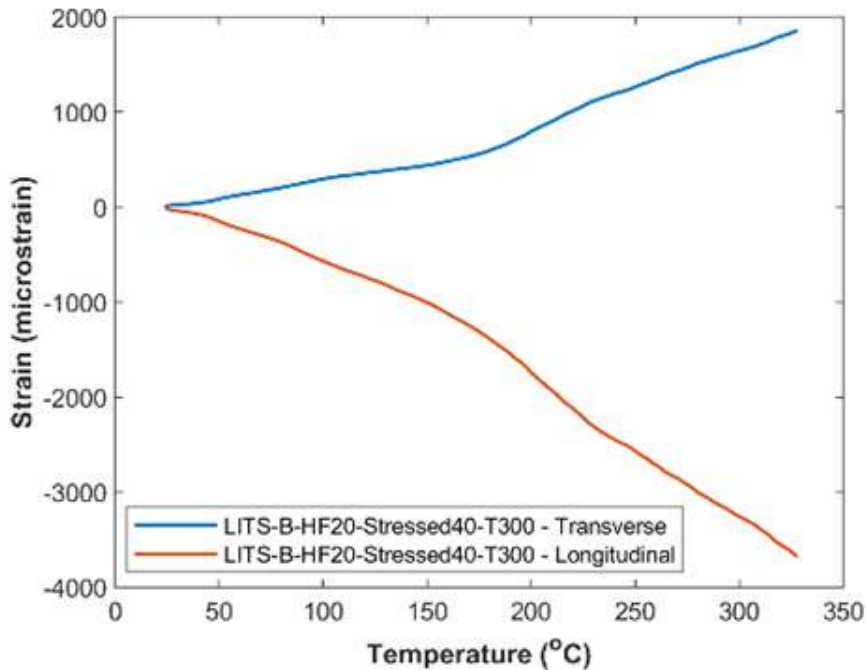
Figure 6 presents the development of transverse LITS with temperatures of concrete specimen during heating up to 200°C under load levels of 20% and 40%. It can be noted that the higher the load level, the

larger the transverse LITS, which is also consistent with the influence of loading levels on the longitudinal LITS.

The transverse and longitudinal LITS for specimens of *B-HF20-Stressed20-T200* and *B-HF20-Stressed40-T300* series are plotted in Figure 8, indicating an essentially linear relationship between them. However, the slopes (i.e. “LITS Poisson’s ratios”) are different for the two cases (i.e. of 0.23 for *B-HF20-Stressed20-T200* and 0.50 for *B-HF20-Stressed40-T300*), possibly due to the effects of different load levels.



(a) Transverse LITS



(b) Comparison of transverse and longitudinal LITS

Figure 6. Transverse and longitudinal LITS of *B-HF20-Stressed40-T300*

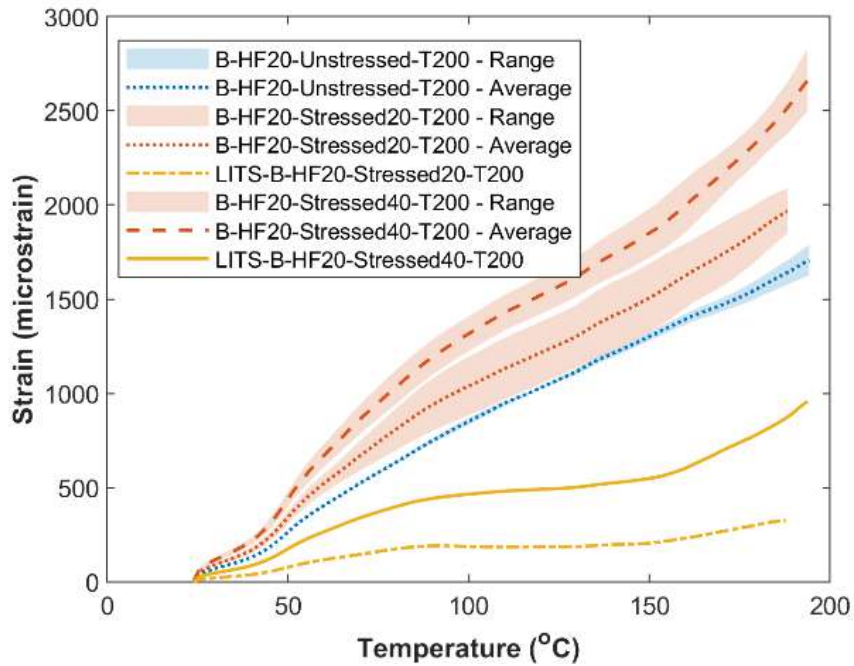


Figure 7. Transverse LITS of concrete under different load levels

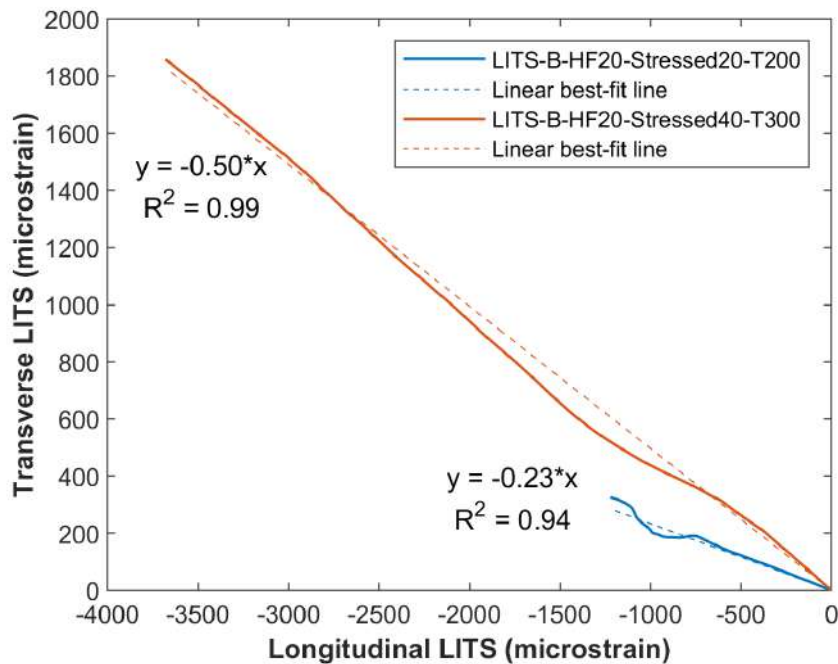


Figure 8. Transverse LITS and longitudinal LITS

3.3 LITS during cooling

The longitudinal LITS during natural cooling of *A-HF20-Stress40-T300* and *B-HF20-Stress40-T300* specimens are plotted in Figure 9. The longitudinal LITS during cooling is clearly shown to be significant (albeit being less than LITS during heating, see Figure 3) – This is contrary to the widely adopted assumption of LITS being negligible or non-existence during cooling [15, 26]. Such conventional understanding seems a result of long heating times combined with low heating rates during conventional testing, which have effectively exhausted the relevant transformation and moisture movement processes –

However, such heating rates and time do not realistically reflect the nature of real fires. Accordingly, the potential significant LITS during cooling in real fires should be recognised and properly accounted for in assessing concrete performance in fire.

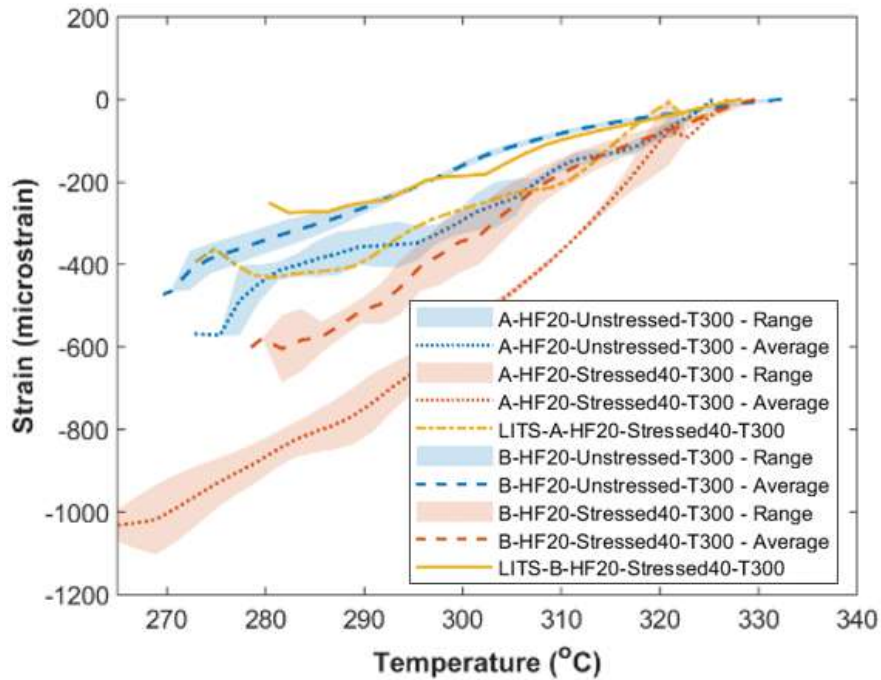


Figure 9. Longitudinal LITS during cooling

4 CONCLUSIONS

In this paper, the deformational characteristics of concrete (with and without loading) exposed to elevated temperatures up to 500°C are presented, with a special focus on the determination of LITS under different combined loading and heating conditions. On the basis of reliable data generated using innovative experiments that more closely reflect the nature of concrete exposed to realistic fires, the following key findings can be drawn:

- The reliability and repeatability of the adopted experimental set-up and procedure are further confirmed by the reliable and consistent obtained data, including (i) the essentially identical LITS curves for *A-HF30-Stressed40-T300* and *A-HF30-Stressed40-T450* (subject to the same incident heat flux and loading level, but heated to different target average temperatures) and (ii) the consistent evolution of transverse and longitudinal LITS.
- LITS evolves approximately linearly with increasing concrete temperature up to ~350°C, above which the LITS evolution became faster.
- While the free thermal strains and mass losses are higher for specimens exposed to 30 kW/m², the measured total strains of stressed specimens under heat flux of 20 kW/m² are more compressive, resulting in slightly higher LITS of concrete exposed to the heat flux of 20 kW/m² compared to that for 30 kW/m².
- The reliable full-field deformation data enabled by the newly developed test setup using an optimised 3D digital image correlation technique allow to extract the transverse LITS, which is shown to have an essentially linear relationship with the corresponding longitudinal LITS. However, the slopes for such linear relationships are different for the two reported cases (of 0.23 for *B-HF20-Stressed20-T200* and 0.50 for *B-HF20-Stressed40-T300*), possibly due to the effects of different load levels.

- LITS during cooling is shown to be significant and thus should be properly accounted for in assessing concrete performance in fire.

ACKNOWLEDGMENT

The financial support from the Australia Research Council (DP180103160 and DP220103362) is gratefully acknowledged.

REFERENCES

1. Khoury, G.A., et al., *Fib bulletin 38: Fire design of concrete structures—materials, structures and modelling. State-of-the art report*. Federation internationale du beton, Lausanne, Switzerland, 2007.
2. Pimienta, P., R.J. McNamee, and J.-C. Mindeguia, *Physical Properties and Behaviour of High-Performance Concrete at High Temperature: State-of-the-Art Report of the RILEM Technical Committee 227-HPB*. Vol. 29. 2019: Springer.
3. Pan, Z., J.G. Sanjayan, and F. Collins, *Effect of transient creep on compressive strength of geopolymer concrete for elevated temperature exposure*. Cement and Concrete Research, 2014. **56**: p. 182-189.
4. Le, B.-D., *Fire Performance of High Strength Concrete using Novel Fire Testing*. PhD Thesis. 2022, The University of Queensland.
5. Tao, J., et al., *Transient strain of self-compacting concrete loaded in compression heated to 700 °C*. Materials and Structures, 2013. **46**: p. 191-201.
6. Khoury, G.A., *Strain of heated concrete during two thermal cycles. Part 1: Strain over two cycles, during first heating and at subsequent constant temperature*. Magazine of Concrete Research, 2006. **58**: p. 367-385.
7. Petkovski, M. and R.S. Crouch, *Strains under transient hygro-thermal states in concrete loaded in multiaxial compression and heated to 250°C*. Cement and Concrete Research, 2008. **38**: p. 586-596.
8. Standards Australia, *AS1012-2014 - Methods of testing concrete*. Standards Australia Limited: Sydney.
9. Le, D.B., et al., *Deformation capturing of concrete structures at elevated temperatures*. Procedia Engineering, 2017. **210**: p. 613-621.
10. Maluk, C., et al., *Novel fire testing methodology: Why, how and what now?* 2012.
11. Maluk, C. and L. Bisby. *A Novel Test Method for Materials and Structures in Fire*. Proceedings of the 8th International Conference on Structures in Fire (SiF'14). 2014.
12. Le, Q.X., et al., *Effects of temperature and temperature gradient on concrete performance at elevated temperatures*. Advances in Structural Engineering, 2018. **21**(8): p. 1223-1233.
13. Le, D.B., et al., *Application of digital image correlation system for reliable deformation measurement of concrete structures at high temperatures*. Engineering Structures, 2019. **192**: p. 181-189.
14. Aili, A., et al., *Time evolutions of non-aging viscoelastic Poisson's ratio of concrete and implications for creep of C-S-H*. Cement and Concrete Research, 2016. **90**: p. 144-161.
15. Khoury, G.A., B.N. Grainger, and P.J. Sullivan, *Transient thermal strain of concrete: literature review, conditions within specimen and behaviour of individual constituents*. Magazine of Concrete Research, 1985. **37**(132): p. 131-144.
16. Alogla, S.M. and V. Kodur, *Temperature-induced transient creep strain in fiber-reinforced concrete*. Cement and Concrete Composites, 2020. **113**: p. 103719.
17. Gernay, T. and J.M. Franssen, *A formulation of the Eurocode 2 concrete model at elevated temperature that includes an explicit term for transient creep*. Fire Safety Journal, 2012. **51**: p. 1-9.

18. Hager, I. and P. Pimienta. *Transient thermal strains of high performance concretes*. Proceedings of Concreep7 - The International Conference on Creep, Shrinkage and Durability of Concrete and Concrete Structures. 2005.
19. Lee, J., et al., *A multiscale model for modulus of elasticity of concrete at high temperatures*. Cement and Concrete Research, 2009. **39**: p. 754-762.
20. Ahn, Y.B., J.G. Jang, and H.K. Lee, *Mechanical properties of lightweight concrete made with coal ashes after exposure to elevated temperatures*. Cement and Concrete Composites, 2016. **72**: p. 27-38.
21. Zhang, Q. and G. Ye, *Dehydration kinetics of Portland cement paste at high temperature*. Journal of Thermal Analysis and Calorimetry, 2012. **110**: p. 153-158.
22. Bažant, Z.P. and M. Jirásek, *Creep and hygrothermal effects in concrete structures*. Vol. 225. 2018: Springer.
23. Sinko, R., et al., *Transient effects of drying creep in nanoporous solids: understanding the effects of nanoscale energy barriers*. Proceedings of the Royal Society A: Mathematical, Physical and Engineering Sciences, 2016. **472**(2191): p. 20160490.
24. Thelandersson, S., *Mechanical Behaviour of Concrete under Torsional Loading at Transient, High-temperature Conditions*. Bulletin of Division of Structural Mechanics and Concrete Construction, Bulletin 46, 1974.
25. Torelli, G., et al., *Concrete strains under transient thermal conditions: A state-of-the-art review*. Engineering Structures, 2016. **127**: p. 172-188.
26. Mindeguia, J.-C., et al., *Parametrical study of transient thermal strain of ordinary and high performance concrete*. Cement and Concrete Research, 2013. **48**: p. 40-52.

NUMERICAL ANALYSIS OF LOAD-BEARING FIRE TESTS OF A COMPOSITE SLAB WITH LAPS

Haruka Kanada¹, Shimono Kisei², Moe Horie³, Takeo Hirasima⁴, Kei Kimura⁵, Yusuke Shintani⁶

ABSTRACT

In load-bearing fire tests of composite slabs conducted in 2023, after withstanding fire heating for more than three hours, the welded wire mesh in the long span fractured near the laps due to membrane action. The behaviour of the tests was investigated through numerical analysis of composite slabs with laps using software SAFIR. First, it was shown that the deflection behaviour of the centre of the slab in fire can be roughly traced by the analysis. It was also shown that the tensile membrane force of the slab in lap areas was slightly greater than that in non-lap areas and the stress in the welded wire meshes near the laps was slightly greater than that in other areas. The tensile stress of the welded wire mesh at the larger effective depth was larger than the proportional limit after 180 minutes of heating. In addition, the model with two welded wire meshes of different depths showed a decrease in tensile stress from the centre to the edge of the slab.

Keywords: membrane action; composite slab; numerical analysis; fire; laps

1 INTRODUCTION

The experimental works at Cardington [1] demonstrated that the membrane action improved the load-bearing capacity of composite slabs in fire and allowed the use of unprotected secondary steel beams. Subsequently, a number of tests, including FRACOF project tests [2], were carried out to further validate membrane action.

Following these tests, the membrane action was investigated by means of numerical analyses.

Huang et al. carried out an analytical study [3] of the Cardington Corner Test and proposed a model based on the Mindlin/Reissner (thick plate) theory, which takes into account both geometric and material nonlinearities [4], and showed the distribution of membrane forces of the slab in membrane action [5].

¹ Graduate student, Graduate School of Science and Engineering, Chiba University,
e-mail: chereeca5326@chiba-u.jp

² Graduate student, Graduate School of Science and Engineering, Chiba University,
e-mail: 24wm3126@student.gs.chiba-u.jp

³ Graduate student, Graduate School of Science and Engineering, Chiba University,
e-mail: horie2001@chiba-u.jp, ORCID: <https://orcid.org/0009-0009-3459-1244>

⁴ Professor, Graduate School of Engineering, Chiba University,
e-mail: hirashima@faculty.chiba-u.jp, ORCID: <https://orcid.org/0000-0003-1462-5370>

⁵ Chief Researcher, Research and Development, Nippon Steel Corporation,
e-mail: kimura.ze8.kei@jp.nipponsteel.com, ORCID: <https://orcid.org/0000-0002-7808-3585>

⁶ Chief Researcher, Research & Development Institute, Takenaka Corporation,
e-mail: shintani.yuusuke@takenaka.co.jp, ORCID: <https://orcid.org/0000-0002-5488-2761>

Vassart et al. carried out an analytical study for the FRACOF project with a flat slab model using SAFIR and showed that a flat slab model using effective thickness can approximate the deflection behaviour of a ribbed slab [6].

Mano et al. carried out an analytical study for the load-bearing fire tests of composite slabs in 2019 and showed that the difference in the effective depth of welded wire meshes has little effect on the deflection behaviour [7].

In 2023, the load-bearing fire tests of composite slabs were conducted (the test results were presented by Horie et al. in the SiF2024 conference [8]). In the tests, after withstanding fire heating for more than three hours of fire heating due to membrane action, the welded wire meshes near the laps failed across the longer span.

In the present study, the behaviour of the tests was investigated through numerical analysis of composite slabs with laps using software SAFIR [9]. Generally, in SAFIR, welded wire mesh was modelled as a single sheet in a concrete slab. However, in the present study, the structural analysis model had eight sheets and their laps. After comparing the results of the tests and the analysis, the stress distribution in the slab was discussed.

2 THERMAL ANALYSIS

2.1 Outline of thermal analysis

Figures 1 (a) – (c) show the cross-section of the members on which the thermal analysis was carried out. As shown in Figure 1 (a), the primary beam was sufficiently protected by insulation. As shown in Figure 1 (b), the secondary beam was unprotected and directly exposed to the fire heating. The slab of the test specimens had steel decks and the composite slab was a ribbed slab. The thickness from the top of the slab to the lower flange and to the upper flange of the steel deck was 130mm and 80mm, respectively. Referring to EUROCODE4 [10], the effective thickness of the flat concrete slab for the analysis model was 105 mm as shown in Figure 1 (c). The thickness of the slab was divided into 10 for the mesh. Moreover, the thermal model of the slab had no welded wire mesh.

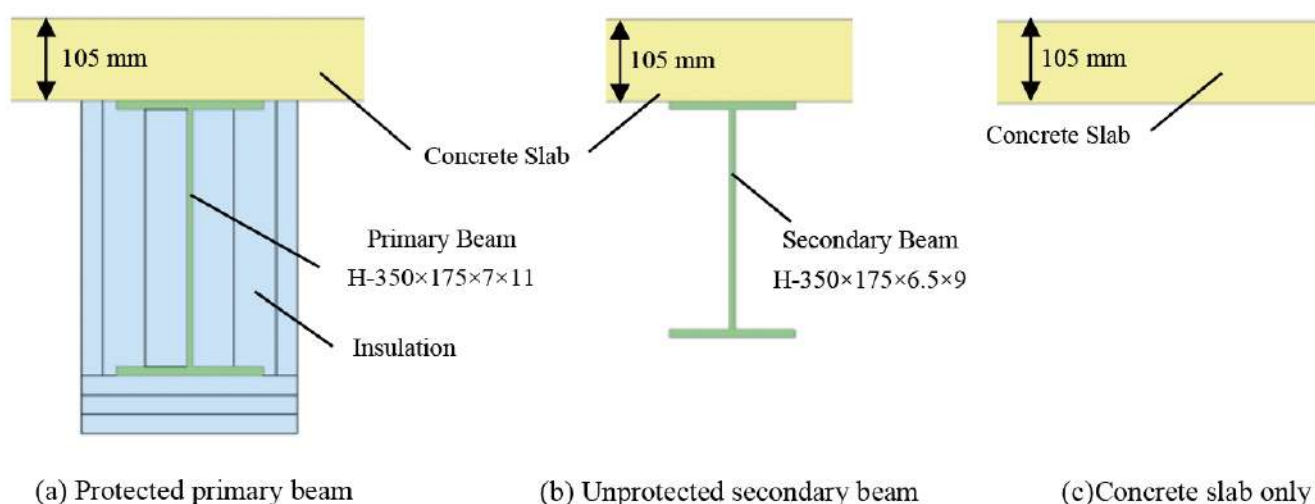


Figure 1. Cross – section of the members

Table 1 shows the thermal properties of the concrete, steels and ceramic wool. The specific heat and thermal conductivity of concrete and steel were given according to EUROCODE4 [10]. The moisture content of the concrete was 6.9 % and the specific mass was 2273 kg/m^3 based on the material tests.

The boundary conditions for the thermal analysis are shown in Table 2. The value of relative emission 0.2 was set so that the temperature at the bottom of concrete slab matched the test value. The value of

convection heat transfer coefficient $23 \text{ W}/(\text{m}^2\cdot\text{K})$ was determined so that the temperature at the top surface of the concrete slab matched the test value. The gas temperature at the heated surface was based on the standard fire heating temperature specified in ISO834. The temperature at the unheated surface was 20°C .

Table 1. Thermal properties

Thermal property	Concrete (Normal weight)	Steels	Insulation
Specific mass	$2273 \text{ kg}/\text{m}^3$	$7850 \text{ kg}/\text{m}^3$	$128 \text{ kg}/\text{m}^3$
Moisture content	6.9 %	-	0.0 %
Specific heat	EUROCODE4	EUROCODE4	$800 \text{ J}/(\text{kg}\cdot\text{K})$
Thermal conductivity	EUROCODE4 (upper limit)	EUROCODE4	$0.06 \text{ W}/(\text{m}\cdot\text{K})$

Table 2. Boundary conditions

Type	Value
Convection heat transfer coefficient at heated surface	$23 \text{ W}/(\text{m}^2\cdot\text{K})$
Convection heat transfer coefficient at non-heated surface	$23 \text{ W}/(\text{m}^2\cdot\text{K})$
Relative emission of concrete	0.2

2.2 Results of temperature

Figure 2(a) shows the results of the temperatures of the slab. The analytical values were compared with the test values for specimen No. 1. The temperature of the welded wire mesh for the analysis was related to the concrete temperature at the location of the welded wire mesh.

The temperature of the concrete at the heated surface was close to the test value of the lower flange of the slab. Up to about 60 minutes, the difference in temperatures between the and bottom of the slab for the analysis was larger than that for the test. Thereafter, the analysis values were close to the test values.

The temperature of the welded wire mesh of the analysis was close to the values above the lower flange of the test. At 180 minutes after heating ignition, the temperature of the welded wire mesh at an effective depth of 36 mm was 442°C for the upper flange of the test, 337°C for the lower flange of the test, and 342°C for the analysis. Also at 180 minutes after heating, the temperature of the welded wire mesh at an effective depth of 48 mm was 556°C for the upper flange of the test, 339°C for the lower flange of the test, and 408°C for the analysis.

Figure 2(b) shows the results of the beams temperatures. The temperatures of the upper and lower flanges of the protected primary beam for the analysis were almost the same as those for the test. The temperature values of the upper and lower flanges of the unprotected secondary beam for the analysis were larger than those for the test, while the difference in temperatures between the upper and lower flanges for the analysis was similar to that for the test.

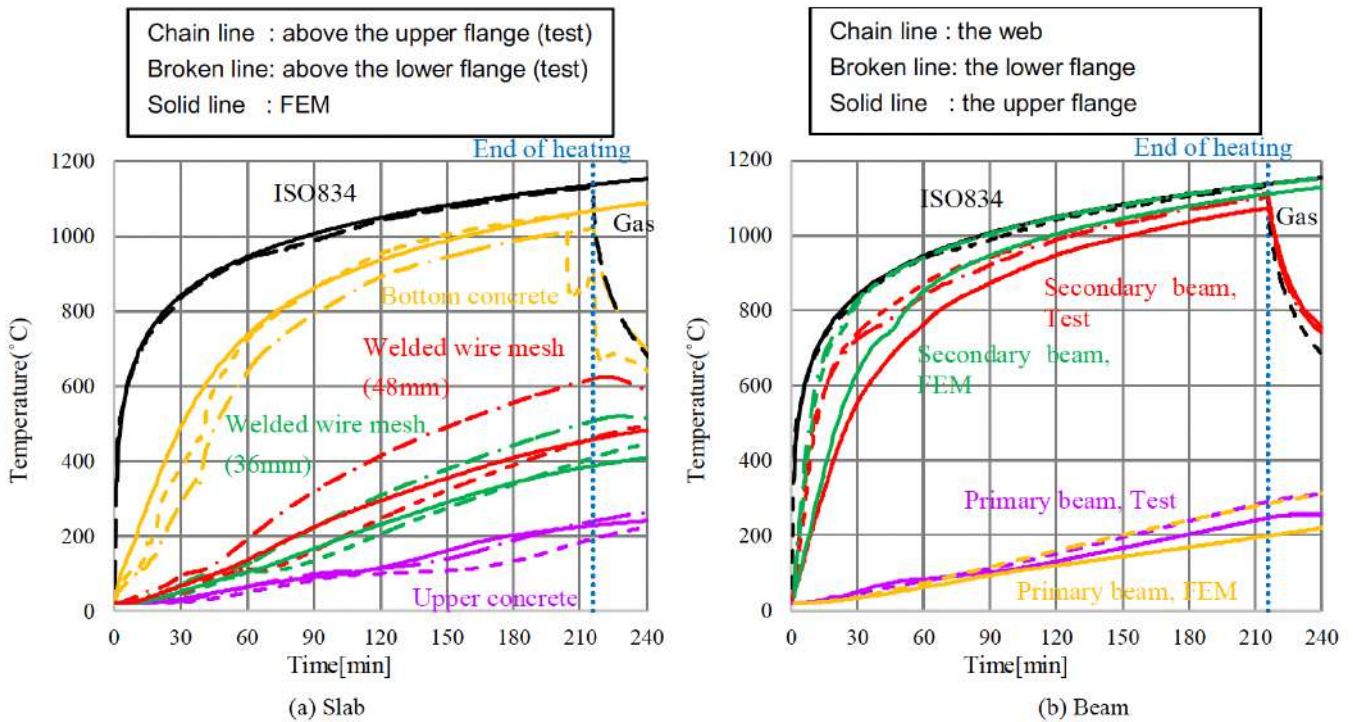


Figure 2. Result of temperatures

3 STRUCTURAL ANALYSIS

3.1 Structural analysis model

After performing the thermal analysis, the temperature results were input into the structural analysis using SHELL elements for the slab and BEAM elements for the beams.

Figure 3 shows the structural analysis model of the floor considering of beams and a composite slab with laps (Lap Model). The size of the slab was 4.6 m × 6.9 m and the secondary beam was located at the middle of the slab. The connection between the end of the secondary beam and the primary beam was modelled in the analysis as a pin connection. Vertical displacements were constrained at the corners of the floor system, and rotations were constrained at its centre. The live loads were 6.964 kN/m² (specimen No. 1) and 10.142 kN/m² (specimen No. 2) based on the applied loads of the tests, respectively. The dead loads of the slabs were 2.52 kN/m² (both specimens). Similar to the test specimen used in the experiment, the effective depth of the welded wire mesh differs depending on the location in the analysis model, and the area where the welded wire mesh overlaps was defined as the lap area.

Figure 4(a) shows the cross sections of the slabs for the Lap Model at the laps. Referring to EUROCODE4 [10], the thickness of the concrete slab for the analysis model was 105 mm (see Section 2.1). The lap length was 150 mm based on the test specimen. The temperature of the welded wire mesh was input for each of the different effective depths of the thermal analysis. Stress was transmitted at the lap by perfect adhesion. In order to compare the results of the Lap Model, the analysis was also carried out using the Normal Model without laps as shown in Figure 4(b).

The properties of the concrete are shown in Table 3. The compressive strength of the concrete at ambient temperature was 38.86 N/mm² based on the material tests. The stress-strain curve of the concrete at high temperatures in the analysis was in accordance with EUROCODE2 [11]. The tension ductility of the concrete for the analysis in SAFIR was 2500 N/mm².

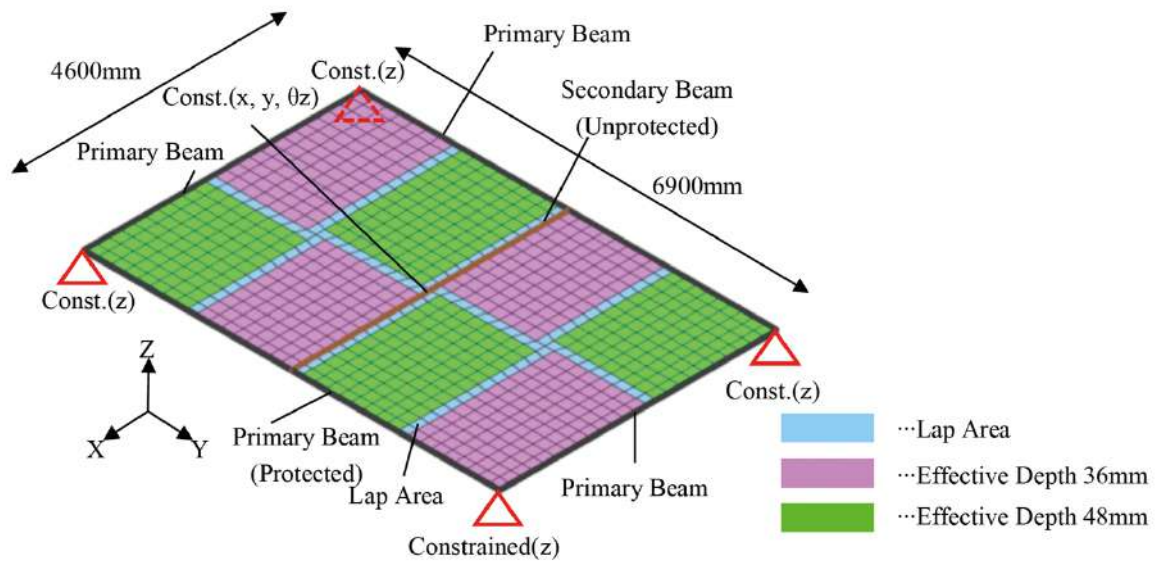


Figure 3. Structural analysis model (Model A)

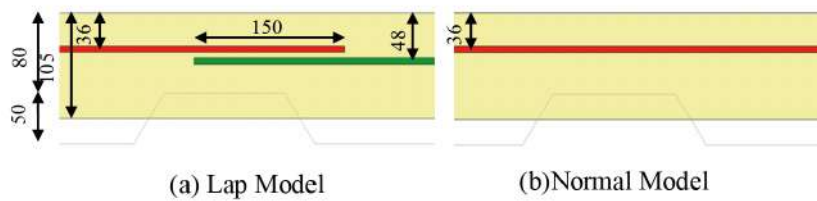


Figure 4. Cross section of slabs of analysis models at the lap

The properties of the steels were given in Table 4. The yield strength of the primary beam was 344.5 N/mm^2 and that of the secondary beam was 338.0 N/mm^2 at ambient temperature based on the inspection certificate. The strength and stiffness of the beams at high temperatures in the analysis were in accordance with EUROCODE3 [12].

Figure 5 shows the yield strength of the welded wire mesh at high temperatures. The yield strength for the test was the stress at 2% strain based on the high temperature coupon tests of the welded wire mesh. The strength and stiffness of the welded wire mesh at high temperatures in the analysis were in accordance with EUROCODE2 [11]. The yield strength of the welded wire mesh at ambient temperature for the analysis was 633.3 N/mm^2 , which was determined so that the yield strength from $500 \text{ }^\circ\text{C}$ coupon test result matched that of the value used in the analysis. Figure 6 shows the stress-strain relationships of the welded wire mesh at high temperatures used in the analysis.

Table 3. Properties of concrete

Type	Value
Material type	Calcareous
Compressive strength	38.86 N/mm^2
Tensile strength	4.12 N/mm^2
Poisson ratio	0.2
Tension ductility	2500 N/mm^2

Table 4. Mechanical properties of steels at ambient temperature

Type	Primary beam	Secondary beam	Welded wire mesh
Yield strength	344.5 N/mm ²	338.0N/mm ²	633.3 N/mm ²
Young's modulus	2.05 × 10 ⁵ N/mm ²	2.05 × 10 ⁵ N/mm ²	2.05 × 10 ⁵ N/mm ²
Poisson ratio	0.3	0.3	0.3

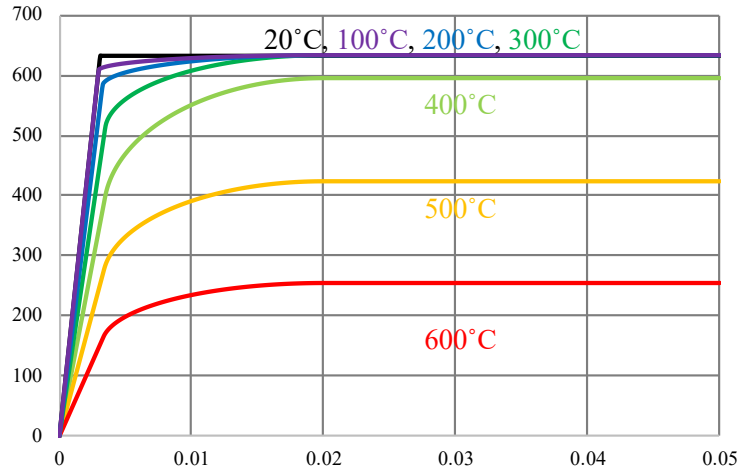
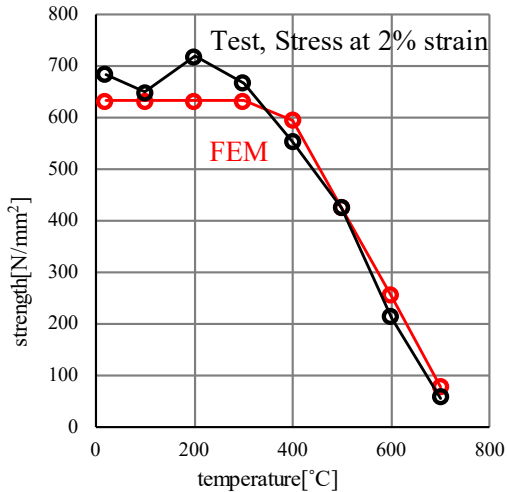


Figure 5. Yield strength of the welded wire mesh Figure 6. Stress-strain relationships of the welded wire mesh for the analysis

3.2 Results of deflection behaviour

Figure 7 shows the deflection at the centre of the slab. The deflection at the centre of the slab and the failure time for the Lap Model were almost identical to those for the Normal Model, because the difference in the effective depth of the welded wire meshes in the slab does not have a significant effect on the deflection behaviour [7]. The deflection in the analysis was less than that in the test from 20 minutes to 90 minutes. This may be due to differences in the coefficient of thermal expansion of the concrete and the mechanical properties of the welded wire mesh at lower temperatures. After 90 minutes, the deflection at the centre of the slab under membrane action for the analysis agreed well with that for the tests.

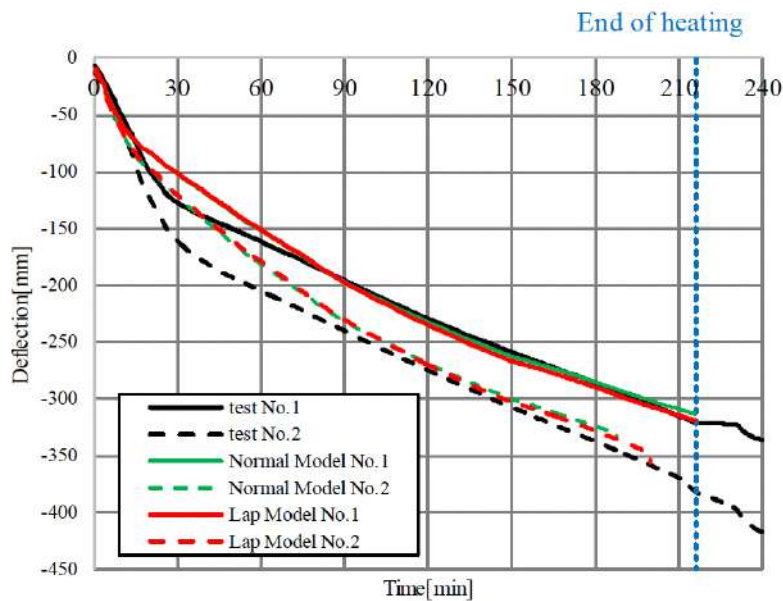


Figure 7. Deflection curve of the centre of the slabs

Figure 8 shows the deflection curve of the slab at the middle of the short span and long spans. The deflection curves of the slabs for the analysis were almost the same as those for the tests in both spans. In the long span, the deflection near the laps, where the axial stiffness was larger than that in other areas, was slightly bent and not a smooth curve in the analysis results using the Lap Model as shown in figures 8 (b) and (d). In the short span, such a bend in the deflection was not observed.

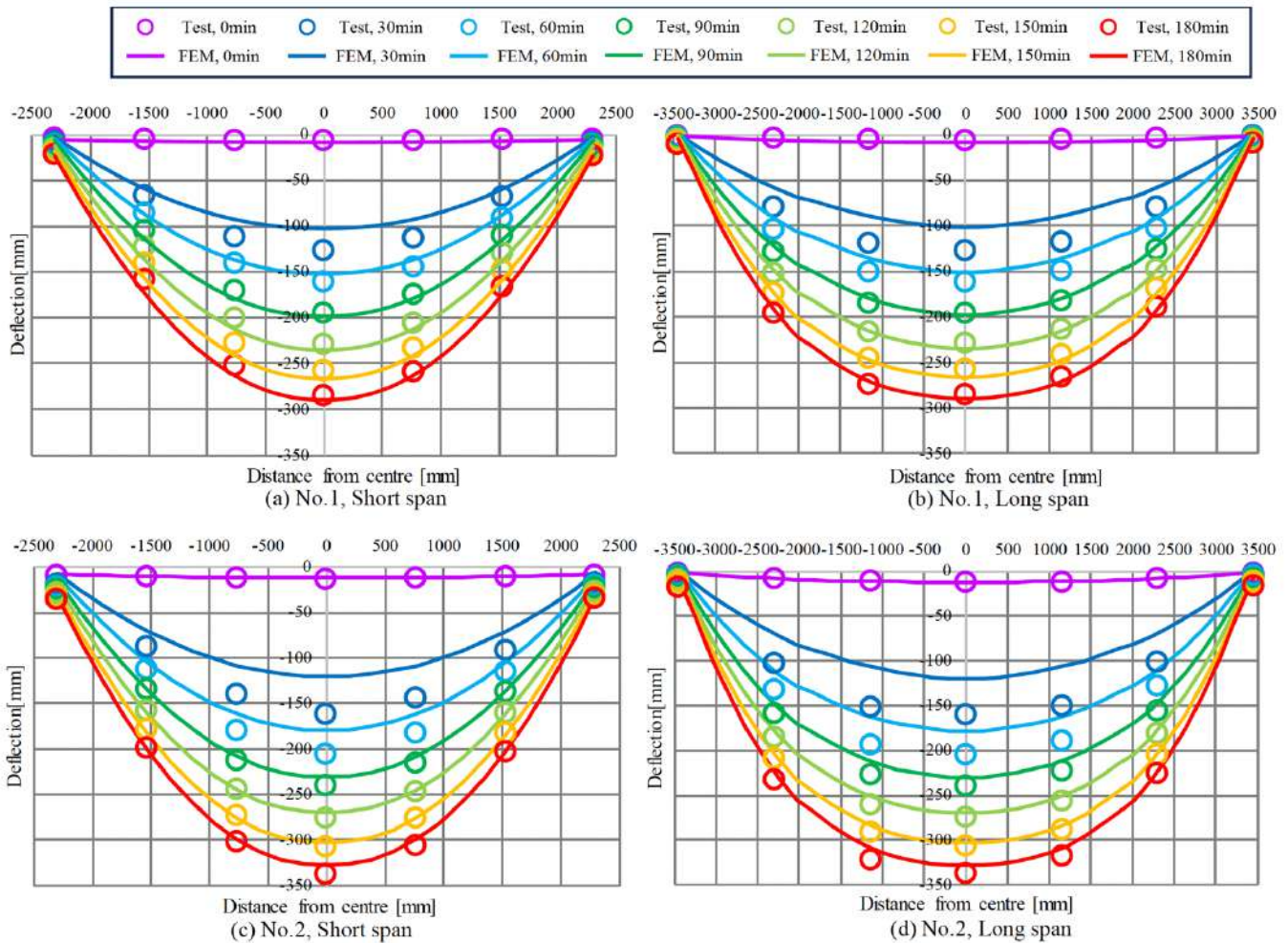


Figure 8. Deflection curve of the slabs

3.3 Results of principal membrane force and stress in welded wire meshes

Figure 9 shows the principal membrane force of the slab obtained from the analysis of the Lap Model (specimen No.2). The red lines represent the tensile membrane force, and the blue lines represent the compressive membrane force. At 15 minutes of heating, the compressive area covered most of the slab, and the tensile area was connected around the unprotected secondary beam in the centre as shown in Figure (a). After 60 minutes of heating, the membrane force distribution was characteristic of the membrane action, with the area in the centre of the slab being the tensile area and with the area around the tensile area being the compressive area as shown in Figure (b). After 60 minutes, the elliptic tensile area gradually expanded. The principal membrane forces in the lap areas were slightly larger than those in the non-lap areas. The distribution of membrane force in Normal model was similar to that in the Lap Model but the characteristic distribution in the lap areas was not found in the Normal Model as shown in Figure 9 (f).

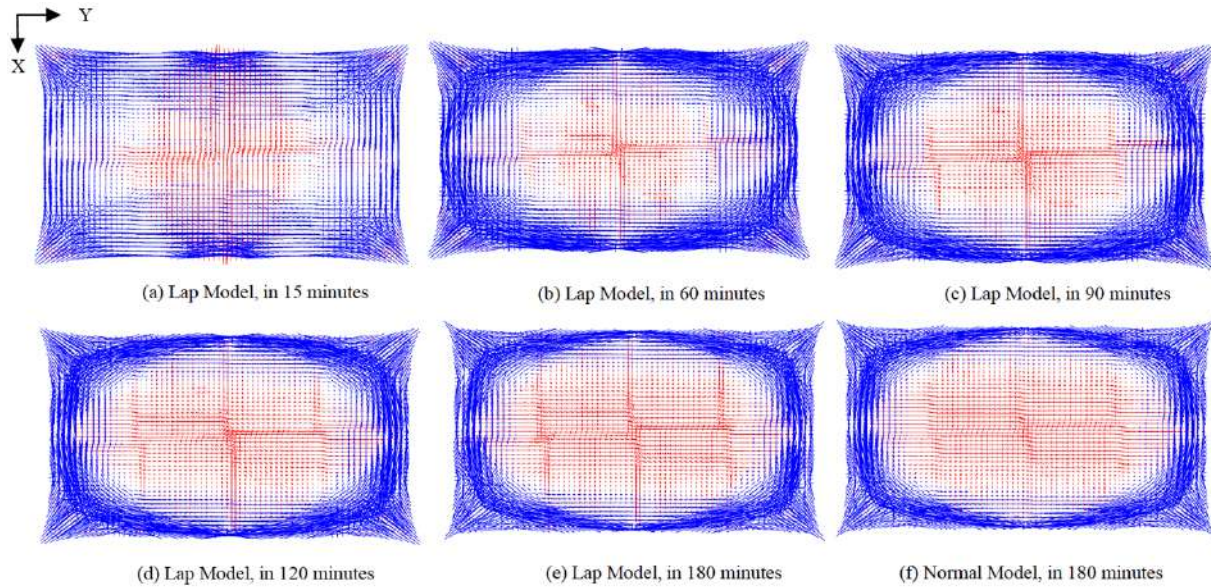


Figure 9. Principal membrane force of the slab (No.2)

Figure 10 shows the normal stresses in the welded wire meshes in the X and Y directions for specimen No.2. In Figure 10 (a)-(d), the stress in the lap areas was described as the stress at the effective depth of 48 mm because both the stresses at the effective depth of 36mm and 48mm were similar values. The effective depth of the welded wire mesh was the distance from the top surface to the intersection of the longitudinal and transverse wires (see Figure 4). Between 60 and 180 minutes, the tensile stress in the X-direction was decreased as shown in Figures 10 (a) and (c). On the other hand, the tensile stress in the Y-direction was increased as shown in Figures 10 (b) and (d). At 180 minutes, the maximum stress in the X-direction (short span) in the elliptical tensile area was 246 N/mm², recorded at an effective depth of 36 mm near the middle lap (Point A as shown in Figure 10 (c)). The maximum stress in the Y-direction (long span) in the elliptical tensile area was 477 N/mm², recorded at an effective depth of 48 mm near the middle lap (Point B as shown in Figure 10 (d)). With regard to the tensile stress within the elliptical area, the stress in the longitudinal direction (Y – direction) tended to increase as the deflection increased with the heating time. In both directions, the stress in the lap areas was significantly lower. Meanwhile, the stress near the lap areas was slightly larger than that in the other areas.

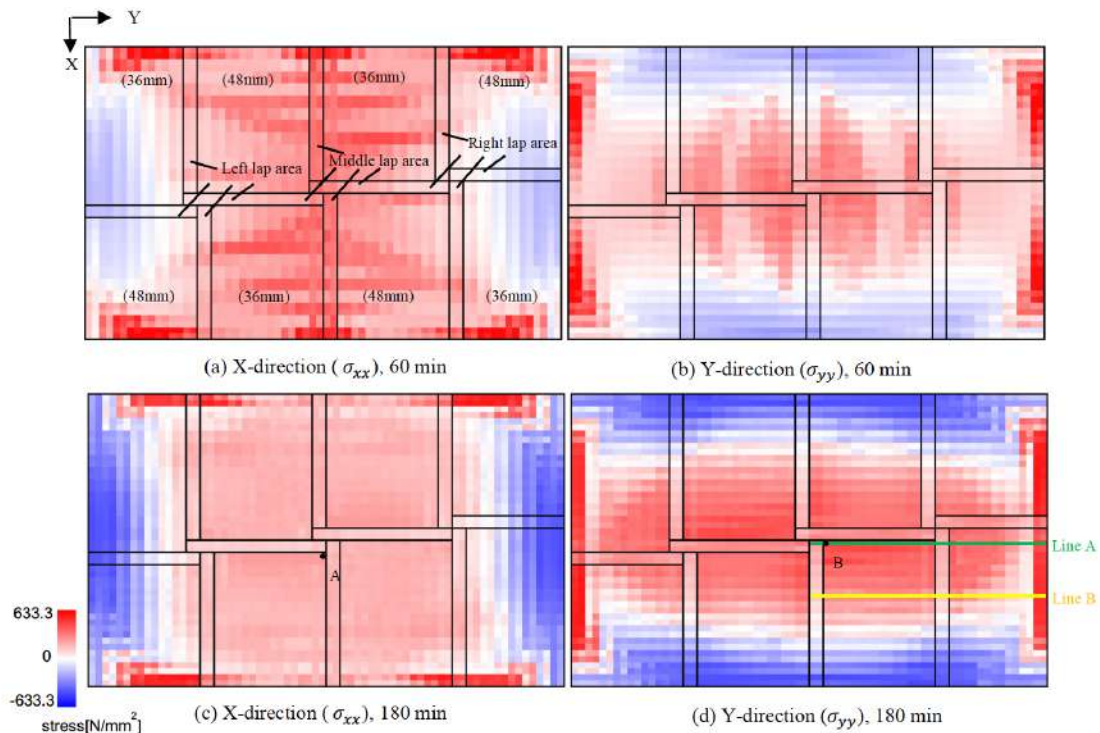


Figure 10. Stress in welded wire mesh (Specimen No.2)

Figure 11 shows the distributions of the stress in welded wire meshes in the Y- direction on the two lines (Line A, B) in Figure 10 (d) at 180 minutes. The yield strength of welded wire meshes at 180 minutes in the analysis was 617 N/mm^2 (effective depth of 36 mm, $342 \text{ }^\circ\text{C}$) or 581 N/mm^2 (effective depth of 48 mm, $408 \text{ }^\circ\text{C}$). The tensile stress in the welded wire meshes was quite lower than the yield strength at that time.

On the other hand, as shown in Figure 11 (a), on Line A in the middle of the short span, the stress of the welded wire mesh at an effective depth of 48mm was larger than the proportional limit. The tensile stress at an effective depth of 36 mm outside the right lap area was the proportional limit except at the end of the slab. In addition, the Lap Model with two welded wire meshes of different depths showed a decrease in tensile stress from the centre to the edge of the slab, while the Normal Model did not show this feature as shown in Figure 11 (b).

On Line B, away from the middle of the short span, the tensile stress was below the proportional limit in all areas except the end of the slab. In addition, unlike on Line A, the tensile stress on Line B at an effective depth of 48mm was almost constant regardless of the distance from the centre, and it became almost the same as the tensile stress on Line A near the right lap area.

On both lines, the stress in the welded wire meshes in the lap areas was almost half of that in the other areas. The stress near the laps was slightly larger than that in the areas away from the laps. The stress at an effective depth of 48 mm near the right lap on both lines was almost equal to the proportional limit. This place was location where the reinforcing bars failed in specimen No. 2, which lost its integrity at 216 minutes. In the test, the welded wire meshes failed at effective depth of 48 mm near the both the right and left laps, and two large cracks were observed across the short span.

However, in the analysis, the stress in the welded wire mesh near the middle lap was larger than that near the right and left laps. In fact, although the some large cracks were observed near the middle lap in both specimens No. 1 and No. 2, their widths were smaller than those near the right lap, and there was no failure of the reinforcing bar near the middle lap. There were two possible reasons for the discrepancy between the location where the reinforcing bars failure occurred in the test and location where the maximum stress was recorded in the analysis. Firstly, the live load in the analysis was given as a uniformly distributed load, whereas the live load in the tests was given as concentrated load at 24 points (in 6 rows and 4 columns). The middle lap area was away from those load points, while the left and right lap areas were located very close to the load points. If the concentrated load was applied somewhat unevenly at the load points in the test, the curvature of the slab could become larger at the point where the load was larger. The second reason was that more than one failed reinforcing bars could occur during the cooling phase after heating. During the cooling phase, the temperature of the unprotected steel beam decreased rapidly, which could change the stress distribution within the slab. The experimental report by Horie et al. showed that the deflection curve of the slab in the long span changed the cooling process. The factors contributing to this discrepancy will be investigated in the additional analysis in the future.

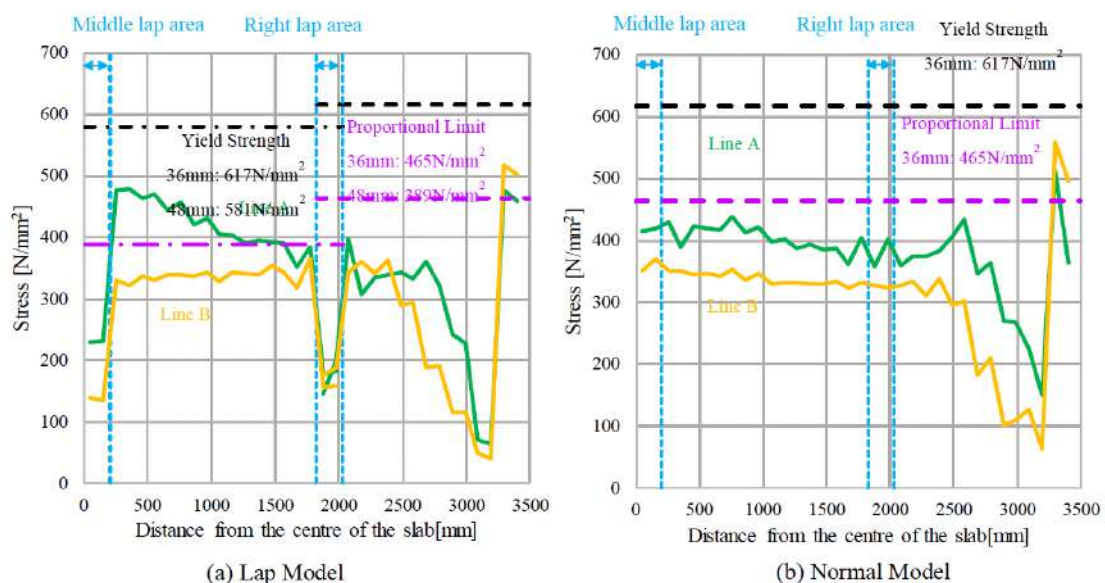


Figure 11. Stress in welded wire mesh (No.2, 180min, σ_{yy})

4 CONCLUSIONS

In the present study, the analysis was carried out for the load-bearing fire tests of a floor system consisting of steel beams and a composite slab with welded wire meshes and their laps. In the structural analysis model, shell elements were used for the floor slab, and welded wire meshes with different effective depths and their laps were considered. The results of the analysis were described below.

The analysis result of the deflection behaviour at the centre of the slab under membrane action approximately agreed with the test result after 90 minutes of fire heating. The deflection behaviour and the failure time for the Lap Model were almost identical to those for the Normal model.

After about 60 minutes of heating, the membrane force distribution was characteristic of the membrane action, with the central area of the slab being the tensile area, after which the elliptic tensile area gradually expanded. In addition, the tensile membrane force of the slab in the lap areas was slightly larger than that in the other areas. In term of the tensile stress within the elliptical area, the longitudinal stress tended to increase as the deflection increased with the heating time.

The tensile stress of the welded wire mesh at an effective depth of 48mm was larger than the proportional limit after 180 minutes of heating. In addition, the Lap Model with two welded wire meshes of different depths showed a decrease in tensile stress from the centre to the edge of the slab. The location where the reinforcing bars failure occurred in the test differed from the location where the maximum stress was recorded in the analysis. The factors contributing to this discrepancy will be investigated in the additional analyses in the future.

ACKNOWLEDGMENT

This research was funded under the Structural Research and Education Grant Programme by the Japan Iron and Steel Federation.

REFERENCES

1. British Steel plc, Swinden Technology Centre: A European Joint Research Programme, The Behaviour of Multi-Storey Steel Framed Buildings in Fire, 1999.
2. Zhao. B, Roosefid M, and Vassart O, "Full Scale Test of a Steel and Concrete Composite Floor Exposed to ISO Fire", Proceedings of the Fifth International Conference on Structures in Fire, pp.539-550, 2008.9
3. Huang Z, Burgess IW, and Plank RJ, "Three-Dimensional Analysis of Composite Steel-Framed Buildings in Fire", Journal of Structural Engineering, Vol.126, No.3, pp.389-397, 2000.3.
4. Huang Z, Burgess IW, and Plank RJ, "Modeling Membrane Action of Concrete Slabs in Composite Buildings in Fire. I: Theoretical Development", Journal of Structural Engineering, Vol.129, No.8, pp.1093-1102, 2003.8.
5. Huang Z, Burgess IW, and Plank RJ, "Modeling Membrane Action of Concrete Slabs in Composite Buildings in Fire. II: Validations", Journal of Structural Engineering, Vol.129, No.8, pp.1103-1112, 2003.8.
6. Vassart O, Bailey. CG, Hawes M, Nadjai A, Simms WI, Zhao B, Gernay T, and Franssen JM, "Large-Scale Fire Test of Unprotected Cellular Beam Acting in Membrane Action", Journal of Structural Fire Engineering, Vol.2, No.4, pp.259-268, 2011.12.
7. Mano E, Hirashima T, Kimura K, "Membrane Action of Floor Slabs in Fire (Part 3): Numerical Analysis of Load-Bearing Fire Tests of A Flooring System Composed of Composite Slabs and An Unprotected Steel Beam", Journal of Structural and Construction Engineering, AIJ, Vol.88, No.810, pp.1294-1305, 2023.8.
8. Horie M, Hirashima T, Kanada H, Shintani Y, "Influence of the Behaviour of a Composite Slab Under Membrane Action in Fire", SiF 2024, The 13th International Conference on Structures in Fire, University of Coimbra, Portugal, 19 to 21 June 2024.
9. Gerna T, and Franssen JM, "Modeling structures in fire with SAFIR®: Theoretical background and capabilities", Journal of Structural Fire Engineering, Vol. 8, No. 3, pp.300-323, 2017.8.
10. CEN-EN1994-1-1, Eurocode 4: Design of composite steel and concrete structures - Part 1-1: General rules and rules for buildings. European standards, 2004.
11. CEN-EN1992-1-2, Eurocode 2: Design of concrete structures - Part 1-2: General rules - Structural fire design. European standards, 2004.
12. CEN-EN1993-1-2, Eurocode 3: Design of steel structures - Part 1-2: General rules - Structural fire design. European standards, 2005.

POST-FIRE BOND STRENGTH OF STEEL REINFORCING BARS TO CONCRETE USING BEAM-END SPECIMENS

Nima Tajik¹, Negar Elhami-Khorasani², Ravi Ranade³, Anthony Tessari⁴

ABSTRACT

This study examines the residual bond strength between rebar and concrete after exposure to high temperatures. The tests use a beam-end setup to replicate realistic loading conditions in structural members and cover temperatures ranging from 20°C to 400°C. The selected temperatures represent moderately damaged reinforced concrete structures that may require repair. Two heating protocols are applied, one with slower but more uniform heating and one that results in a thermal gradient within the concrete cover. Results show a decrease in bond strength and slip with increasing temperature and a greater reduction in bond strength than concrete's compressive strength. The measured residual bond strength using beam-end tests with induced temperature gradient in the cover is lower than the median of data from existing measurements in the literature with pull-out tests. The heating protocol may influence the bond strength, with uniform heating resulting in slightly higher strengths compared to shorter, but more intense fire exposure, likely due to greater damage to the concrete cover. A systematic heating protocol is essential for the proper quantification of bond strength.

Keywords: Specimen type; heating protocol; residual bond strength; slip; furnace tests.

1 INTRODUCTION

Concrete structures may perform adequately at high temperatures and avoid collapse when subjected to moderate fires. Yet, these structures experience damage and require repair after a fire to resume their function. Repair and replacement of reinforcement in a damaged reinforced concrete structure is generally more complex and takes longer compared to restoring or replacing concrete alone. In addition to the loss of strength at high temperatures, existing studies confirm that the interfacial bond between reinforcement and concrete influences the response of reinforced concrete structures under fire and their post-fire capacity. Therefore, it is important to characterize the post-fire residual bond strength between rebar and concrete.

The bond between rebar and concrete is typically characterized using stress-slip behavior, with a flat plateau at the maximum strength in the case of a pull-out failure or a distinct and sharp peak in the case of a splitting failure [1]. The bond strength can be influenced by various factors, including concrete's compressive strength, concrete cover thickness, diameter of reinforcing bars, surface coating, etc. Existing studies on bond behavior at elevated temperatures suggest that the decrease in bond strength at high temperatures is comparable to the reduction in concrete compressive strength [2]. However, Lubl6y and Bal6z [3] and

¹ Graduate Student, Department of Civil, Structural and Environmental Engineering, University at Buffalo
e-mail: nimataji@buffalo.edu, ORCID: <https://orcid.org/0009-0006-5228-9223>

² Associate Professor, Department of Civil, Structural and Environmental Engineering, University at Buffalo
e-mail: negarkho@buffalo.edu, ORCID: <https://orcid.org/0000-0003-3228-0097>

³ Associate Professor, Department of Civil, Structural and Environmental Engineering, University at Buffalo
e-mail: ranade@buffalo.edu, ORCID: <https://orcid.org/0000-0001-6030-8371>

⁴ Associate Professor, Department of Civil, Structural and Environmental Engineering, University at Buffalo
e-mail: atessari@buffalo.edu, ORCID: <https://orcid.org/0000-0003-0231-345X>

others noted that the degradation in bond strength after exposure to elevated temperatures (i.e., residual state) is greater than that of the degradation in compressive strength of concrete.

Existing studies have utilized different test setups to study the bond behavior between rebar and concrete after exposure to high temperatures, including four-point bending test, beam-end test, and pull-out test. In a pull-out test setup, a rebar is embedded in a concrete cylinder or cube, which is then extracted by applying a tension force at a slow rate while the surrounding concrete is subjected to compression. Among the existing configurations, the pull-out test is the least representative of the stress state in realistic concrete structures. In a beam-end bond test (or modified cantilever beam), the test rebar is subjected to an axial tensile load while the specimen is tied down at the opposite end, leading to the development of tensile stresses within the concrete. As per ACI 408R-03 [4], the bond strength obtained using beam-end specimens closely correlates with that achieved in specimens designed to represent full-scale reinforced concrete members.

A review of existing data in the literature by the authors led to a collection of more than 770 data points [5,6]. However, more than 90% of the collected data were based on small-scale pull-out tests (cylinders and cubes) to obtain the residual bond strength between steel reinforcing bars and concrete. Among the existing studies, Bosnjak et al. [7] used a modified beam-end test setup to examine the post-fire bond behavior between reinforcement and concrete using two specimens and after exposure to the standard ISO 834 fire for 30 minutes. The study concluded that the results fell below the lower bound of the available data on residual bond strength.

The objective of this study is to quantify the residual bond strength using the beam-end bond test and compare the test results with data in the literature. The paper presents the results of tests conducted on 12 beam-end specimens with target temperatures of 20°C, 150°C, 200°C, 300°C, and 400°C and heated using two different protocols to evaluate the residual bond strength. The selected temperature range is for moderately damaged reinforced concrete structures that may require repair.

2 METHODOLOGY

The study involved 12 reinforced concrete blocks with dimensions of 610 mm x 230 mm x 355 mm constructed in accordance with the ASTM A944-22 standard [8]. Test rebar with a diameter of 19 mm (US rebar No. 6), nominal yield strength of 420 MPa (US Grade 60), clear cover of 60 mm, and a bonded length of 133 mm ($7d_b$) was used in all cases. The specimens were heated in a furnace located at the University at Buffalo's Structural Engineering and Earthquake Simulation Laboratory, as illustrated in Figure 1a. Thermocouples were used to track temperature changes both inside the specimen and within the furnace. Two thermocouples were placed inside each specimen on the stirrups at the level of the test bar to keep the bonded length of the rebar intact. Additionally, concrete cylinders were cast to measure the concrete's compressive strength and moisture content.

The residual bond strength, after cooling down each specimen to room temperature, was evaluated using the test setup in Figure 1b, which features an actuator, a reaction block, and string potentiometers. A compression reaction plate was positioned at a clear distance of 240 mm from the center of the test bar. This distance exceeds 0.9 times the embedded length of the rebar, following ASTM A944 guidelines. The tests proceeded at an average loading rate of 12.7 mm/min, with the bar failing in less than 10 minutes. String potentiometers were used to measure the slip in rebar as well as track the displacements (if any) of the components in the test setup (e.g., reaction block, coupler, actuator). It was ensured that the reaction block against which the rebar in the concrete specimen was pulled in tension did not move during the tests. It should be noted that small-scale pull-out tests are typically repeated with results reported for an average of three tests. However, in this study, two specimens were tested for five of the seven scenarios to evaluate the repeatability and consistency in the results of beam-end tests, considering the size of specimens and the setup configuration.

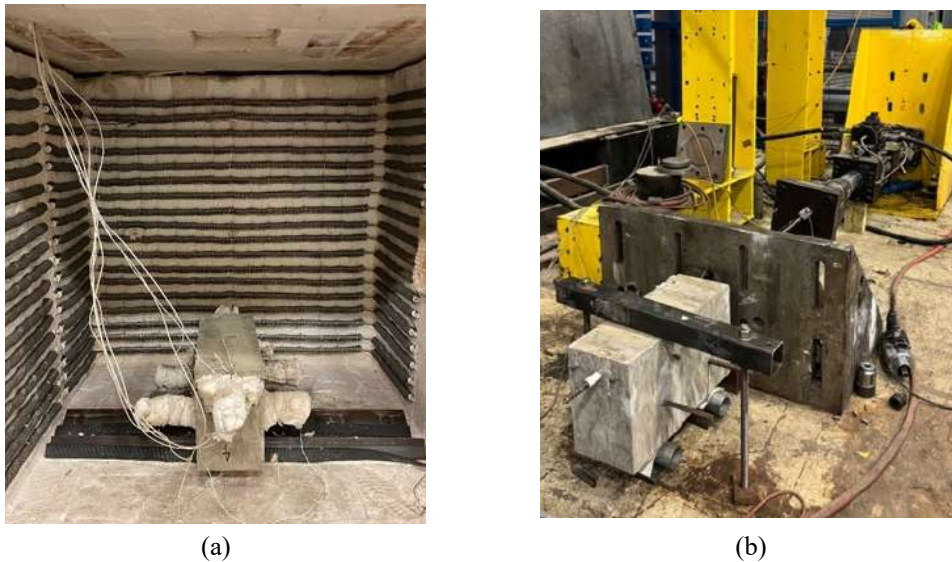


Figure 1. (a) Sample specimen inside the furnace, and (b) the beam-end test setup for bond strength

2.1 Heating protocol

Specimens were subjected to two heating protocols to reach the target temperature, both utilizing a consistent heating rate of $12^{\circ}\text{C}/\text{min}$ while varying the maximum temperature. The protocols were as follows:

(1) The maximum furnace temperature was set to 50°C above the target temperature at the rebar and concrete interface, as shown in Figure 2a. This protocol mirrors the approach of small-scale pull-out tests reported in the literature. The specimens tested with this protocol were marked with “U” (where “U” stands for uniform), indicating a uniform temperature distribution.

(2) The maximum furnace temperature was set to 450°C , as shown in Figure 2b. This approach induces a temperature gradient in the concrete cover and reduces the time needed to achieve the target temperature at the rebar and concrete interface. The specimens tested with this protocol were designated with “G” (where “G” stands for gradient), reflecting the temperature gradient.

The concrete mix was prone to spalling, suggesting that exposure to realistic fire temperatures could have led to significant damage, including the loss of concrete cover. Thus, the maximum furnace temperature was kept below 450°C .

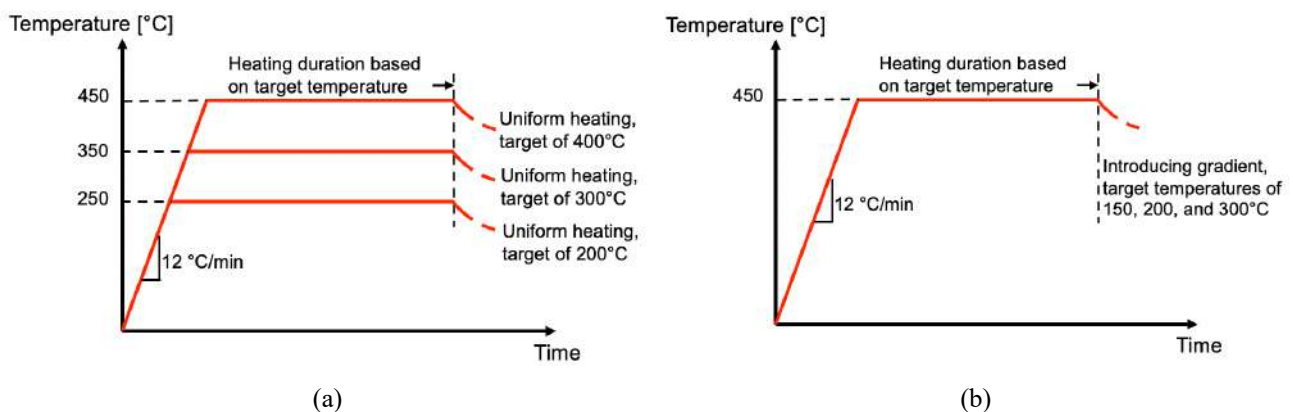


Figure 2. Heating protocol inside the furnace for (a) target temperatures of 200°C , 300°C , and 400°C with relatively uniform temperature profiles in the concrete cover, and (b) target temperatures of 150°C , 200°C , and 300°C with temperature gradient inside the cover

Two methods were implemented to determine the required heating duration and verify that the desired temperature at the interface between the rebar and concrete was reached: (1) temperature observations using

thermocouples attached to the stirrups at the rebar's level, and (2) a pre-test heat transfer analysis using SAFIR [9]. The use of modelling was especially important for the second heating protocol as the temperature in a concrete section could continue to rise after the furnace was turned off. In such cases, relying only on the thermocouple readings during the test might have resulted in exceeding the target temperature. The furnace was turned off once it was confirmed that the desired temperature would be reached at the concrete-rebar interface. To avoid the risk of inducing cracks in the concrete through rapid cooling, both the furnace and the specimens were left to cool to room temperature naturally. Following their complete cooling, mechanical testing was conducted to determine the residual bond strength.

2.2 Material-scale tests

Concrete cylinders were tested to determine the ambient compressive strength, the residual compressive strength after heating, and the moisture content. The heating of the cylinders to measure the residual compressive strength after being subjected to high temperatures was carried out in an oven, following the heating curve in Figure 3. The heating protocol was developed through a heat transfer analysis performed using SAFIR, aiming to ensure a uniform temperature distribution across the entire cylinder cross-section [10]. After returning to room temperature, the compressive strength of the cylinders was measured in accordance with ASTM C39 [11]. The moisture content in the cylinders was derived from the weight loss after being heated to 105°C for a period of 72 hours. The results for an average of three cylinders were recorded for all measurements.

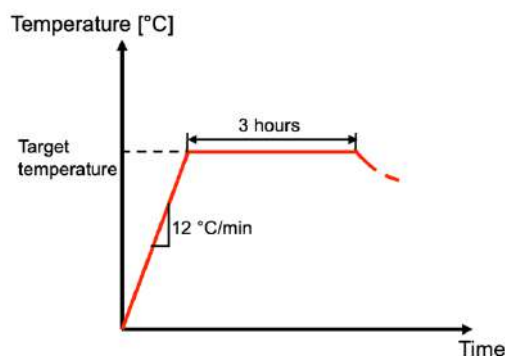


Figure 3. Heating protocol for cylinder samples

2.3 Summary of bond strength tests

Table 1 provides a summary of the conducted tests. In addition to the benchmark tests carried out at room temperature, the residual bond strength was assessed at target temperatures of 150°C, 200°C, 300°C, and 400°C. The initial furnace test was conducted 122 days after the casting of the concrete. The specimens were subjected to heating within the furnace to reach the designated target temperatures, using the two specified heating protocols.

3 RESULTS

This section provides the results on the obtained temperatures within specimens during heating in the furnace, residual bond strength tests, and the comparison of residual bond strength with existing data.

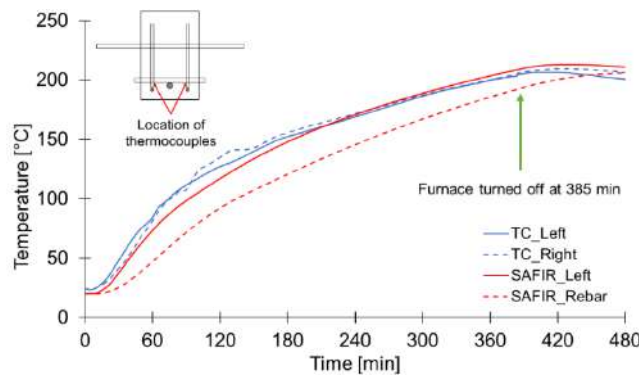
3.1 Temperature observations

Figure 4 compares the SAFIR results with thermocouple measurements from the stirrups for two sample cases (200_U and 300_G). The two thermocouples (TC_Left and TC_Right) were placed on the stirrups at equal distances from the test rebar; thus, they should have read approximately the same temperature. It was expected that the temperature of the test rebar, placed at the center of the section, would lag behind the

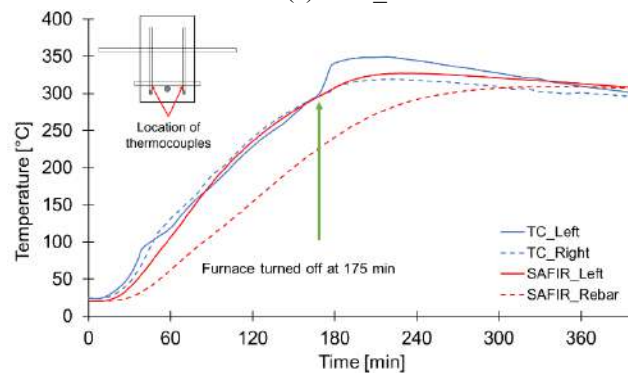
Table 1. Summary of completed tests

Specimen	Target temperature [°C]	Heating rate [°C/min]	Max. furnace temperature [°C]	Total duration of heating [min]
S1_20	Ambient	N/A	N/A	N/A
S2_20	Ambient	N/A	N/A	N/A
S1_200_U	200	12	250	385
S1_300_U	300	12	350	252
S2_300_U	300	12	350	252
S1_400_U	400	12	450	320
S2_400_U	400	12	450	320
S1_150_G	150	12	450	45
S1_200_G	200	12	450	60
S2_200_G	200	12	450	60
S1_300_G	300	12	450	175
S2_300_G	300	12	450	175

temperature of the stirrups. The presented results from SAFIR assumed the lower limit for concrete's thermal conductivity in the Eurocode 2 model [12]. The SAFIR results match the thermocouple measurements well. The results confirmed the delay in heat progression inside the concrete section for the test 300_G. The results also confirmed that the target temperature at the interface of the rebar and concrete was reached in both cases.



(a) 200_U



(b) 300_G

Figure 4: Comparison of SAFIR results and thermocouple (TC) measurements during the tests

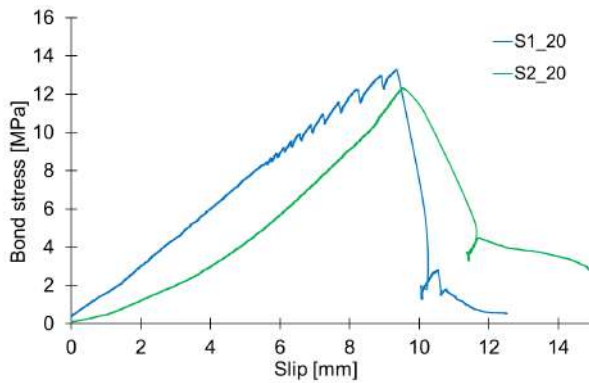
3.2 Bond strength

Table 2 provides a summary of the bond strength with the corresponding slip at peak bond value, and Figure 5 shows the measured residual bond stress versus slip based on the maximum temperature reached at the rebar and concrete interface and the applied heating protocol. The bond stress (and bond strength) is the average stress transferred between the rebar and concrete, calculated by dividing the pull-out load by the embedded area of the rebar.

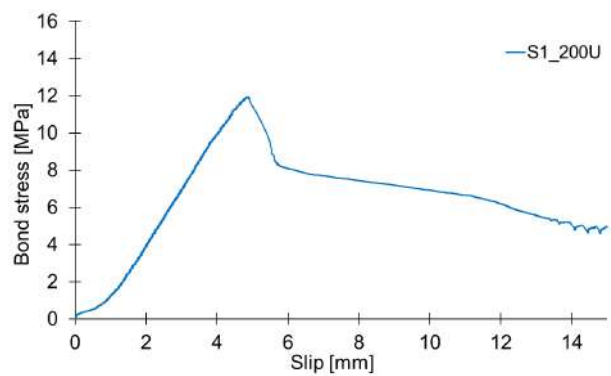
Table 2. Summary of results for bond strength

Specimen	Target temperature [°C]	Bond strength [MPa]	Slip at peak bond strength [mm]
S1_20	Ambient	12.3	9.6
S2_20	Ambient	13.3	9.4
S1_200_U	200	11.9	4.9
S1_300_U	300	7.7	5.2
S2_300_U	300	8.2	1.7
S1_400_U	400	6.3	4.5
S2_400_U	400	7.0	2.8
S1_150_G	150	8.4	3.4
S1_200_G	200	11.2	4.6
S2_200_G	200	11.1	3.6
S1_300_G	300	7.7	3.4
S2_300_G	300	6.3	3.1

The results show that both residual bond strength and the corresponding slip decreased with an increase in target temperature, except for the noticeable drop in strength at 150°C. Splitting behavior was consistently observed at the point of failure across all samples. The above results also suggest that the heating protocol may influence the residual bond strength and slip behavior. In cases where the maximum furnace temperature was limited to 50°C above the target temperature at the interface, which resulted in slow and uniform heating of the specimen, the residual bond strength was slightly larger than those with faster heating (200U vs. 200G and 300U vs. 300G). The clear concrete cover thickness to the rebar was 50 mm with a bar diameter of 19 mm. Assuming that the area within $3d_b$ of the rebar (i.e., ~60 mm) influences the bond strength, the temperature distribution and consequently the residual concrete strength within the cover impacts the bond strength.



(a) Ambient temperature



(b) 200_U

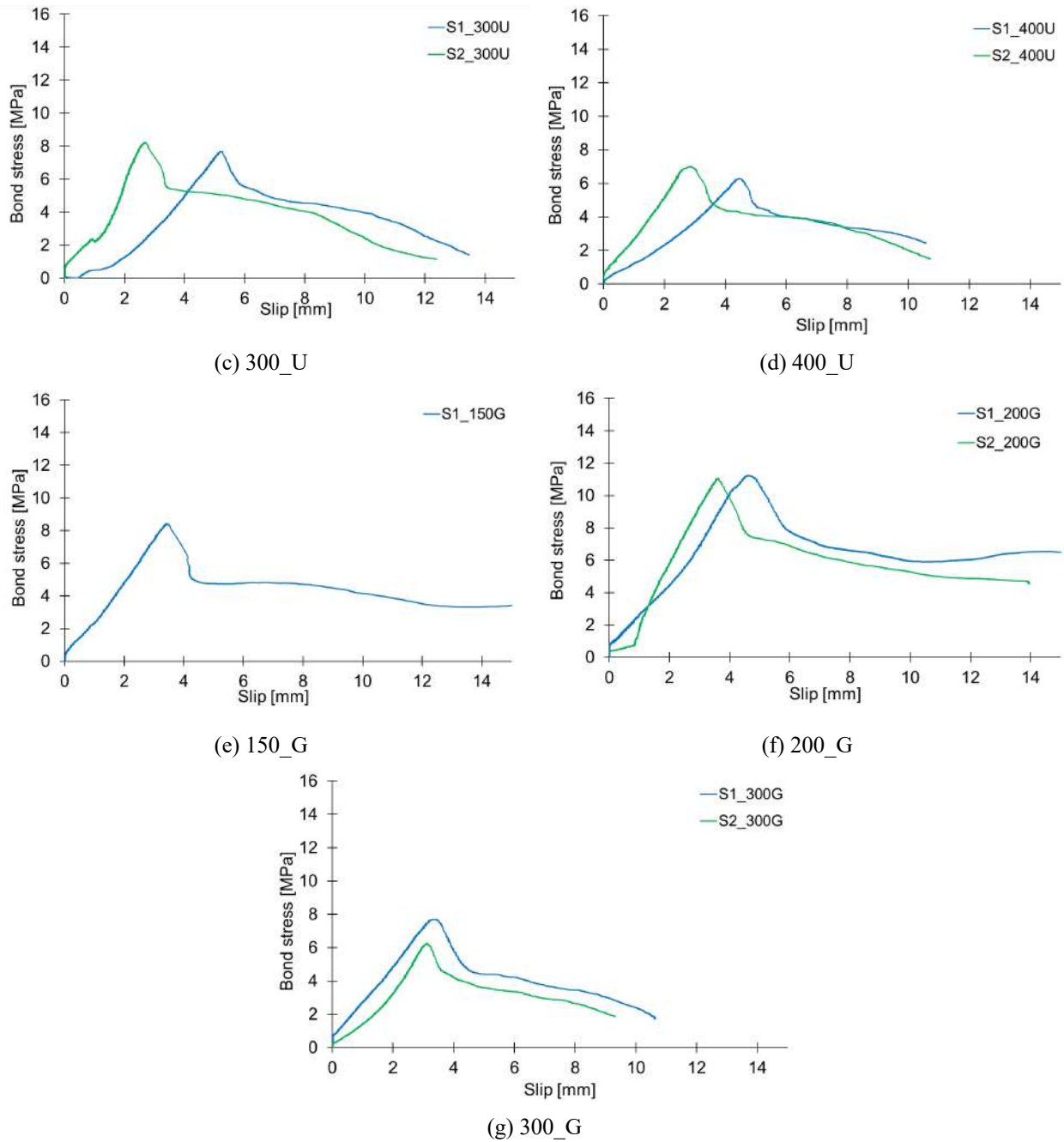


Figure 5. Residual bond stress-slip behavior at various maximum (rebar-concrete) interface temperatures (20, 150, 200, 300, 400°C) and heating protocols (G/U)

Figure 6 provides a comparison between the observed reductions in bond strength from experiments in this study and the data collected from the literature. The plot includes more than 750 data points, with 230 points for temperatures at or below 400°C. More than 90% of the collected data were based on pull-out tests. Details of the collected data can be found in [5, 6]. The bond strength measured from beam-end tests in this study at 150, 300, and 400°C were towards the lower bound of the literature data. The measured bond strength at 200°C was close to the median of the literature data. Overall, the test results from this study were close to or below the median of the literature data. This trend aligns with findings from two beam-end specimens previously examined by Bosnjak et al. [7].

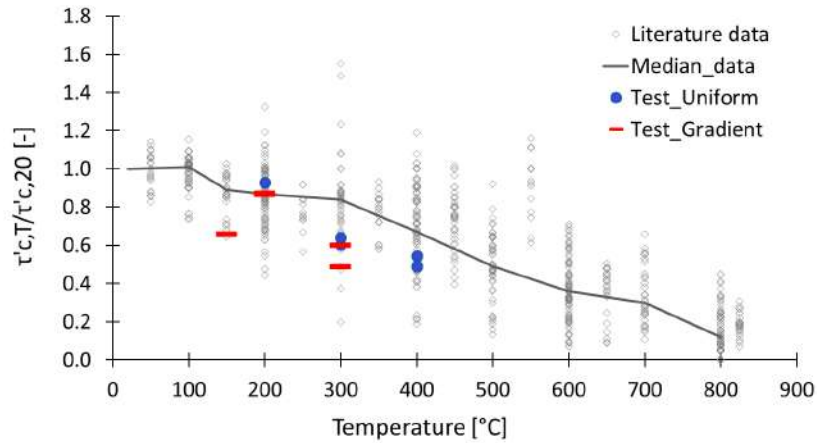


Figure 6. Comparison of degradation in residual bond strength from experiments in this study and literature data

3.3 Material-scale properties

Figure 7 compares the residual concrete compressive strength at various target temperatures with recommended values from Eurocode 4 [13] for calcareous (EC4_Ca) and siliceous aggregates (EC4_Si). The plot includes the minimum, maximum, and mean of the measured values for all cylinders at each target temperature. Note that separate sets of cylinders were tested for each beam-end specimen. At ambient temperature, the compressive strength of the specimens varied between 46 and 61 MPa, with an overall average of 55 MPa. The decrease in residual strength at 150°C for the cylinder tests corresponding to the one specimen tested was more significant compared to the Eurocode 4 recommendation. The observed reductions in strength at 200 and 300°C were within expected ranges, while the strength was higher than expected at 400°C. Two beam-end specimens were tested at 400°C with three cylinders tested at ambient temperature and three cylinders heated to 400°C for each beam-end specimen. The reduction in average residual concrete compressive strength at 400°C (from three cylinders) for one of the beam-end specimens was 0.86, while the reduction in average residual compressive strength of the cylinders made with the second specimen was 0.94.

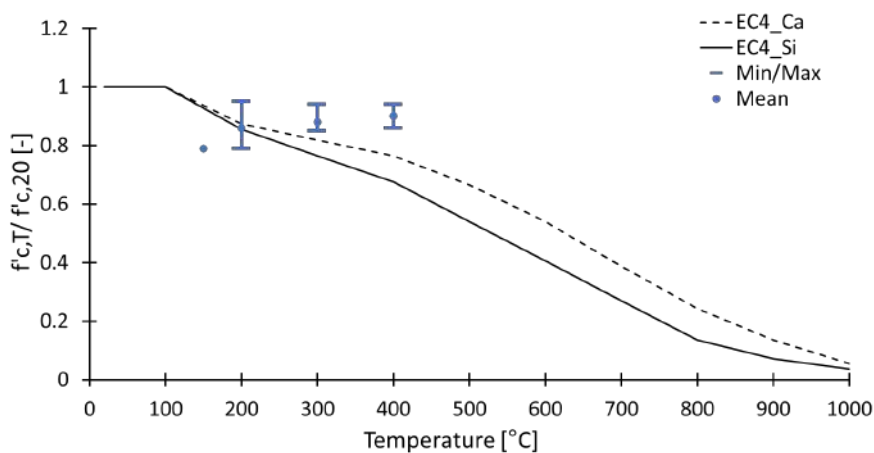


Figure 7. Comparison of the residual concrete compressive strength from cylinder tests with Eurocode 4 recommendations [13]

Figure 8 compares the reductions in residual bond strength with degradation in concrete compressive strength. As stated in the introduction section, previous studies suggested that the decrease in bond strength of specimens tested mechanically at high temperatures is similar to the reduction in concrete's compressive strength [2], whereas the degradation in residual bond strength (determined at room temperature) after

exposure to elevated temperatures is greater than that of the degradation in compressive strength of concrete [3]. The median of the collected data on bond strength from the literature follows the reduction in concrete compressive strength. However, as mentioned earlier, the majority of the collected data are based on pull-out tests that may overestimate bond strength. The measured bond strengths in this study fall below the compressive strength of concrete, except at 200°C, which is close to the median.

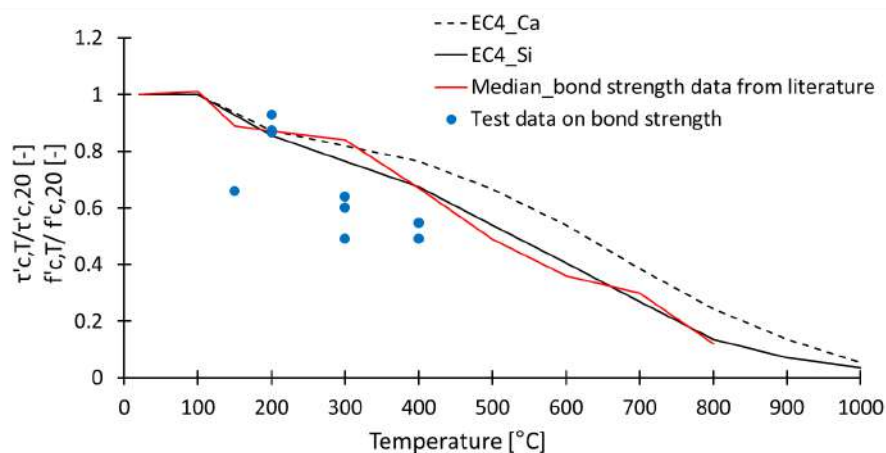


Figure 8. Comparison of residual bond strength from tests with residual concrete compressive strength based on Eurocode 4 recommendation [13]

4 CONCLUSIONS

This study investigated the residual bond strength between rebar and concrete after exposure to high temperatures, using beam-end specimens in accordance with ASTM A944 guidelines. The research targeted rebar-concrete interface temperatures of 20°C, 150°C, 200°C, 300°C, and 400°C, mirroring the conditions in moderately damaged reinforced concrete structures requiring repair to restore functionality. Experiments quantified the degradation of the bond between rebar and concrete as a function of the maximum temperature reached at the rebar. The specimens underwent heating in a furnace following two different protocols to explore the impact of the heating protocol on residual bond strength.

The results showed that both the bond strength and the slip at the peak bond value decreased with an increase in temperature. The reduction in residual bond strength was greater than the degradation in concrete compressive strength. Furthermore, the results from the beam-end specimens consistently had lower values when compared with those reported in existing studies. The majority of existing experiments have used pull-out tests. The difference is mostly related to how pull-out tests using cylindrical or cubic specimens lead to unfirm compression in concrete and do not resemble realistic stress conditions that exist in structural members. The beam-end bond test generates tensile and compressive stresses within concrete due to bending, which correlates well with realistic loading conditions in a structure.

The heating protocol could influence the measured residual bond strength. In this study, temperatures in the furnace were controlled to not exceed 450°C to prevent concrete spalling. However, specimens that underwent uniform heating (a method commonly referenced in the literature) were found to have a slightly higher bond strength than those subjected to shorter durations of higher heat exposure. This could be explained by the greater extent of damage experienced by the concrete cover under a fast and intense heating protocol, which negatively impacts the bond strength. Finally, it is necessary to develop a systematic heating protocol for bond strength tests, considering that the temperature gradient within the concrete cover affects the bond strength.

ACKNOWLEDGMENT

The authors thank the ACI Foundation, research grant number CRC 2022 P0053, and the Institute of Bridge Engineering at the University at Buffalo for their generous support. Any opinions, findings, conclusions, or recommendations expressed in this paper are those of the authors and do not necessarily reflect the views of the funding agencies.

The authors are thankful to their colleagues at the Structural Engineering and Earthquake Simulation Laboratory (SEESL) at the University at Buffalo, without their contributions, this work would not have been possible.

REFERENCES

1. International Federation for Structural Concrete (fib). (2010). *fib Model Code for Concrete Structures*. Lausanne, Switzerland: Fédération Internationale du Béton.
2. Diederichs, U., Schneider, U. (1981). "Bond strength at high temperatures." *Magazine of Concrete Research*, 33(115), 75-84.
3. Lublóy, É., György, B. L. (2014). "Temperature effects on bond between concrete and reinforcing steel." *Zbornik radova Građevinskog fakulteta*, Subotica, (26), 27-35.
4. ACI. (2003). ACI 408R-03: Bond and development of straight reinforcing bars in tension. Technical Document, American Concrete Institute, Farmington Hills, MI.
5. Tajik, N., Elhami-Khorasani, N., Ranade, R., Tessari, A., Szasdi-Bardales, F. (2024). *Post-fire damage classification of reinforced concrete structures using thermal analysis*. The 13th International Conference on Structures in Fire, University of Coimbra, Portugal, June.
6. Elhami-Khorasani, N., Ranade, R., Tessari, A., Tajik, N., Koli, K. S. (2024). *Damage Classification of Reinforced Concrete Structures for Fire: Rebar Temperature*. Project CRC 2022 P0053. American Concrete Institute, Farmington Hills, MI, USA.
7. Bošnjak, J., Sharma, A., Öttl, C. (2018). Modified beam-end test setup to study the bond behavior of reinforcement in concrete after fire. *Materials and Structures*, 51, 1-10.
8. ASTM A944-22. (2022). Standard Test Method for Comparing bond strength of steel reinforcing bars to concrete using beam-end specimen. ASTM International, West Conshohocken, PA.
9. Franssen, J. M., Gernay, T. (2017). "Modeling structures in fire with SAFIR®: Theoretical background and capabilities." *Journal of Structural Fire Engineering*, 8(3), 300-323.
10. Hua, N., Khorasani, N. E., Tessari, A., Ranade, R. (2022). "Experimental study of fire damage to reinforced concrete tunnel slabs." *Fire Safety Journal*, 127, 103504.
11. ASTM C39/C39M-17b. (2017). *Standard Test Method for Compressive Strength of Cylindrical Concrete Specimens*. West Conshohocken, PA.
12. CEN. (2004). *Eurocode 2: Design of Concrete Structures - Part 1-1: General Rules and Rules for Buildings*. European standards, 1992-1-1 -E.N. Brussels, Belgium.
13. CEN. (2005). *Eurocode 4: Design of Composite Steel and Concrete Structures - Part 1-2: General Rules - Structural Fire Design*. 1994-1-2 -E.N. Brussels, Belgium.

POST-FIRE DAMAGE CLASSIFICATION OF REINFORCED CONCRETE STRUCTURES USING THERMAL ANALYSIS

Nima Tajik¹, Negar Elhami-Khorasani², Ravi Ranade³, Anthony Tessari⁴, Fernando Szasdi-Bardales⁵

ABSTRACT

Post-fire assessment of reinforced concrete structures involves deciding whether to repair or demolish a structure, particularly after moderate fires where an immediate decision cannot be made based on observations. This paper proposes a damage classification that considers the distribution of temperature inside reinforced concrete sections, post-fire material properties, and residual bond strength. Heat transfer analysis can be conducted quickly after a fire event if information on the fuel characteristics, ventilation, and fire scenario is obtained. The result of this heat transfer analysis can be mapped to the level of damage. The proposed damage classification can also be used as part of the performance-based design of reinforced concrete structures. The paper describes the heat transfer analyses of a set of reinforced concrete slabs and beams exposed to ASTM E119 to evaluate potential damage. The results suggest that damage state 2 can be expected after 30 minutes of fire exposure, with damage states 3 and 4 occurring at and beyond 60 minutes of fire, indicating major damage and the need for repair or replacement. The analyses suggest that adjustments to design dimensions and concrete cover to control the level of damage may be needed depending on the performance objectives.

Keywords: Temperature thresholds; material properties; bond strength; slabs; beams.

1 INTRODUCTION

Concrete structures typically behave well at high temperatures and do not collapse when subjected to moderate fires. The superior performance of concrete structures under fire, compared to other materials, is related to the low thermal conductivity of the material and the large mass of the structural components. Nonetheless, these structures sustain damage that necessitates repair after the fire to restore functionality. Post-fire assessment of a structure involves deciding whether a structural member or the whole structure needs to be demolished or repaired. This is most important for moderate fires, where an immediate decision based on observations cannot be made.

¹ Graduate Student, Department of Civil, Structural and Environmental Engineering, University at Buffalo
e-mail: nimataji@buffalo.edu, ORCID: <https://orcid.org/0009-0006-5228-9223>

² Associate Professor, Department of Civil, Structural and Environmental Engineering, University at Buffalo
e-mail: negarkho@buffalo.edu, ORCID: <https://orcid.org/0000-0003-3228-0097>

³ Associate Professor, Department of Civil, Structural and Environmental Engineering, University at Buffalo
e-mail: ranade@buffalo.edu, ORCID: <https://orcid.org/0000-0001-6030-8371>

⁴ Associate Professor, Department of Civil, Structural and Environmental Engineering, University at Buffalo
e-mail: atessari@buffalo.edu, ORCID: <https://orcid.org/0000-0003-0231-345X>

⁵ Ph.D. Candidate, Department of Civil, Structural and Environmental Engineering, University at Buffalo
e-mail: fszasdib@buffalo.edu, ORCID: <https://orcid.org/0000-0002-9643-5919>

The available guidelines on damage assessment of concrete structures after a fire are limited [1-5]. Post-fire damage assessment and repair classifications in the current guidelines rely on visual inspection, non-destructive testing (NDT), and sampling of material for laboratory testing. Visual inspection provides recordings of concrete color, concrete spalling, cracking, surface crazing, distortion, and deflections. Visual inspections serve as the most direct assessment, but numerous NDT techniques such as the rebound (Schmidt hammer) test and the ultrasonic pulse velocity test are used to provide a more reliable evaluation of damage. Samples of damaged material, along with undamaged benchmarks, can be extracted for laboratory investigation using compression tests and petrographic examination to evaluate the depth of microcracking, paste alteration, and carbonation. Overall, most post-fire damage evaluations are performed on a case-by-case basis, which could result in missing crucial damage inside a structural element.

Distinct temperature gradients develop during a fire in reinforced concrete sections due to the low thermal conductivity of concrete, impacting the level of damage and residual capacity. Previous work of the authors has argued that advanced modeling can be used to simulate the distribution of temperatures within sections if the information on the fire scenario during the event (e.g., fuel type, ventilation) can be collected [6]. Heat transfer analysis can be conducted quickly and efficiently to evaluate the distribution of temperatures inside structural elements during the event. Concrete core sampling can support the model results for temperature distribution within the section. Thus, the proposed idea is to define post-fire damage classifications and the associated repair categories not only based on the results of observations and non-destructive testing but also using the results of modeling. In doing so, damage classifications can include information beyond the color, level of spalling, and cracks. For example, the temperature of reinforcement and level of heat penetration within the section can be used as indicators for the level of damage.

A detailed damage classification that incorporates the effect of temperature distribution inside concrete sections can be a valuable tool for both post-fire damage assessment and performance-based design of concrete structures under fire. Predicting the level of damage for pre-defined fire scenarios during the design phase allows for mapping potential downtime and associated costs. The design can be adjusted to meet the resilience goals set by the project stakeholders, taking into account the criticality of the structure and potential economic and social losses from a fire event.

This paper has two objectives:

- (1) To propose temperature thresholds for damage states considering temperature distribution inside a concrete section as well as the reduction in post-fire material properties (concrete and steel rebar) and bond strength (between rebar and concrete). The consideration of bond strength is an important damage indicator and a novel approach in this paper.
- (2) To conduct heat transfer analysis to obtain the temperature distribution for a series of reinforced concrete slabs and beams designed according to ACI 216.1 [7] and exposed to different durations of ASTM E119 [8] to evaluate potential damage in elements that follow the minimum code requirements.

2 METHODOLOGY

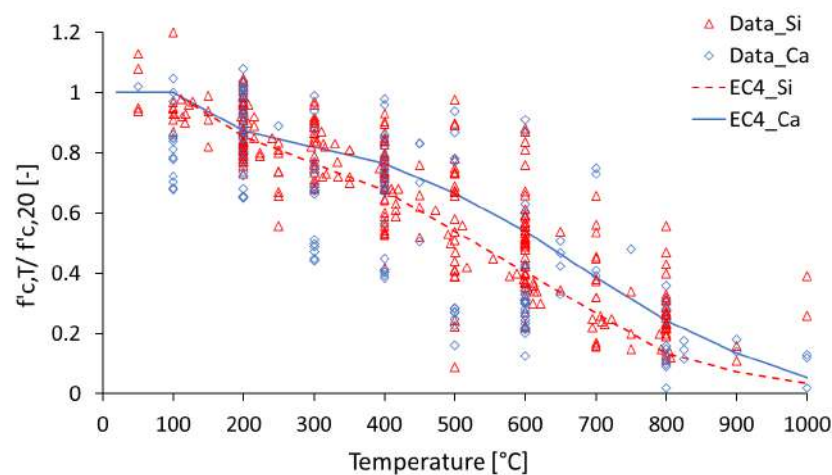
2.1 Temperature thresholds for damage classification

This section proposes temperature thresholds for damage classifications of concrete members. The temperature thresholds are determined based on the residual strength of concrete, steel, and the post-fire degradation of the bond between concrete and steel. Aside from temperature-dependent concrete strength, the temperature of the reinforcement is a key indicator of the level of damage and residual strength, as the rebar temperature can be related to both residual bond strength and the reduction in yield strength of steel. Reinforced concrete slabs and beams are typically heated from one or three sides during a fire, leading to a reduction in the strength of positive steel reinforcement while the concrete in compression is less exposed. Concrete columns in compression may or may not be heated on all sides depending on the location (interior versus exterior columns) and fire scenario. The residual capacity of a concrete column after a fire depends on the strength reduction in both concrete and rebar.

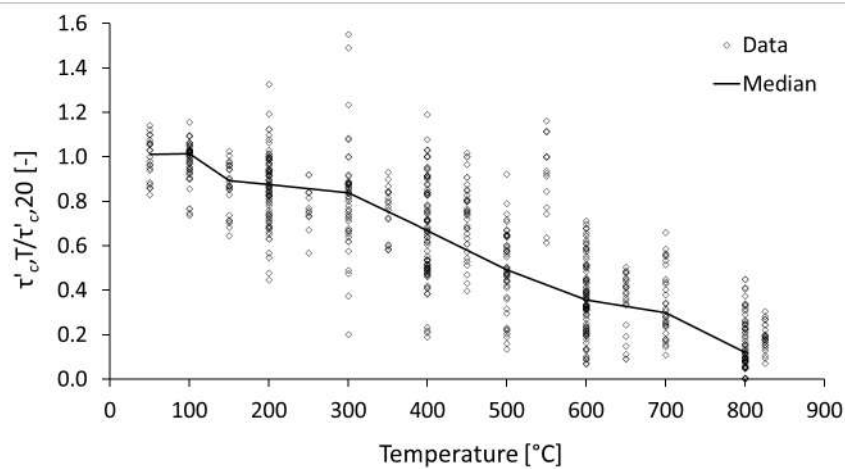
Figure 1a shows collected data on residual concrete strength based on previous work of the authors [9], where $f'_{c,T}$ is the residual concrete strength after being heated to temperature T [°C] and $f'_{c,20}$ is the measured concrete strength at 20°C. About 340 and 150 data points were collected for concrete with siliceous and calcareous aggregates, respectively. The collected data covered normal-strength concrete with a characteristic compressive strength of less than 55 MPa. The plot also includes the Eurocode 4 (EC4) [10] recommended reduction factors for post-fire residual concrete strength. The EC4 recommendation is close to the median of the collected data from the literature.

Figure 1b shows the collected data on normalized residual bond strength, where $\tau'_{c,T}$ is the residual bond strength of a specimen after being heated to temperature T [°C] and $\tau'_{c,20}$ is the bond strength at 20 °C. The plot includes about 770 data points from 13 studies published between 2004 and 2022 [11-23]. Available tests covered temperatures up to 825 °C. The range of considered concrete compressive strength was limited to normal-strength concrete (less than or equal to 55 MPa).

Most of the collected data in Figure 1b were generated using the pull-out test with cylinders or cubes. Around 47% of the test specimens in the dataset were cubes, 45% were cylinders, and the remaining 8% were square prismatic and beams. The reason for a higher percentage of pull-out may be attributed to the easier and more manageable test setups for these specimen types compared to square prismatic and beams. However, it is important to note that the pull-out test does not fully represent the stress state in a reinforced concrete element that experiences both tensile and compressive stresses.



(a)



(b)

Figure 1. Collected data (a) on residual concrete strength and (b) residual bond strength between concrete and rebar

Table 1 summarizes the residual compressive strength of concrete with siliceous and calcareous aggregates, the residual yield strength of steel, and the residual bond strength between rebar and concrete after exposure to high temperatures. Temperature refers to the maximum temperature reached during the fire. The residual compressive strength of concrete is based on the recommendation by EC4. The median of the collected data in Figure 1b is listed for residual bond strength. Finally, it is assumed that steel recovers strength if heated up to 500°C with a 10% reduction for every 100 degrees of heating beyond 500°C [24].

Table 1. Residual material and bond properties

Temp [°C]	Residual $f'_{c,T}/f'_{c,20}$ Si from EC4	Residual $f'_{c,T}/f'_{c,20}$ Ca from EC4	Residual $\tau'_{c,T}/\tau'_{c,20}$ from literature	Residual $F_{y,T}/F_{y,20}$
20	1.00	1.00	1.00	1.0
100	0.90	0.90	0.99	1.0
150	0.88	0.89	0.88	1.0
200	0.86	0.87	0.87	1.0
300	0.77	0.82	0.82	1.0
400	0.68	0.77	0.68	1.0
500	0.54	0.67	0.49	1.0
600	0.41	0.54	0.36	0.9
700	0.27	0.39	0.34	0.8
800	0.14	0.24	0.16	0.7
900	0.07	0.14	-	0.6
1000	0.04	0.05	-	0.5

Table 2 proposes four damage states based on temperature thresholds inside a section considering the residual material and bond properties of Table 1: Damage state 1 requires cosmetic repair, damage state 2 requires minor repair, damage state 3 requires major repair, and damage state 4 requires evaluation for major strengthening or replacement. The following criteria were considered in developing the damage thresholds:

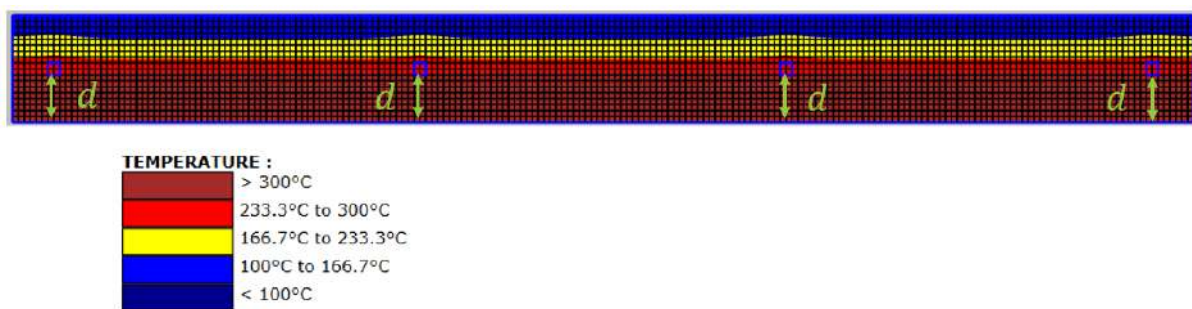
- Post-fire reduction in concrete compressive strength and bond strength at the rebar level remains within ~15% for temperatures below 150°C. The threshold is selected conservatively considering uncertainties in the datasets.
- Several standards, experiments, and observations in the literature recommend 300°C as the threshold for discoloration and a reduction in the residual strength of the concrete [2-3, 25-29] at which point the concrete may be replaced.
- The reduction in concrete compressive strength and bond strength is reduced to about ~50% for rebar temperatures approaching 500°C. The structure will likely experience significant damage and require major strengthening or replacement if the rebar temperature exceeds 500°C.

In determining the damage states, both the temperature of reinforcement and the depth of concrete with temperatures above 300°C, indicated as d in Table 2, are evaluated. The condition corresponding to the higher level of damage is the controlling one. The thresholds in Table 2 should be supplemented with other metrics (such as surface color or cracks) to assess structural safety and guide the decision process.

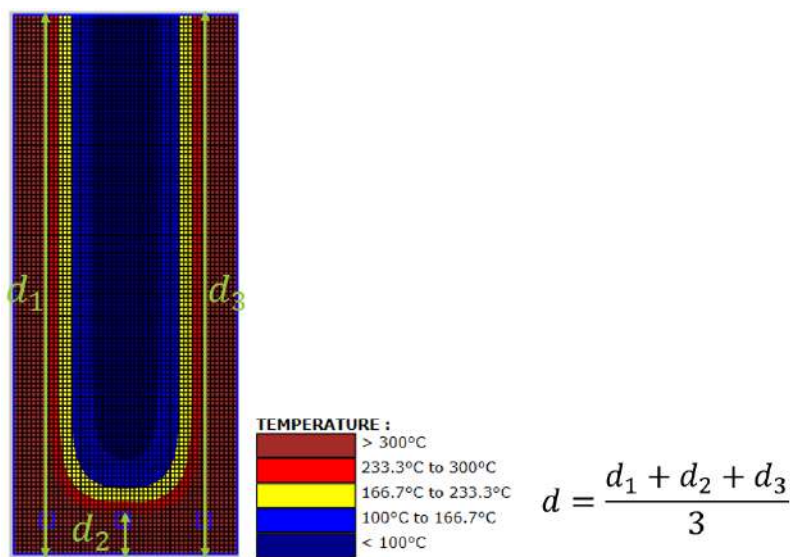
The term d in Table 2 is the average depth of concrete with temperatures above 300°C. Slabs are typically heated from one side; thus, d can be measured at any location along the length of the slab, as shown in Figure 2a. Beams subjected to uneven heating (e.g., 3-sided fire) experience a non-uniform distribution of temperature within the section. Thus, d in Table 2 is calculated as the average depth of concrete with temperatures above 300°C at the locations of rebars, as shown in Figure 2b. This measurement indicates the extent of concrete that would need to be replaced in the section.

Table 2. Proposed damage classification based on temperature thresholds within a concrete section

Damage state	Depth of concrete with temperatures > 300 °C	Temperature of reinforcement	Note
1	$d < \text{half cover depth}$	$T < 150 \text{ }^\circ\text{C}$	Reductions in concrete and bond strength at the rebar level are within ~15%
2	$\text{half cover depth} \leq d < \text{cover depth}$	$150 \text{ }^\circ\text{C} \leq T < 300 \text{ }^\circ\text{C}$	Concrete beyond rebar remains below 300°C
3	$\text{cover depth} \leq d < \text{half section depth}$	$300 \text{ }^\circ\text{C} \leq T < 500 \text{ }^\circ\text{C}$ or partially exposed	Reductions in concrete and bond strength at the rebar level are within ~50%, steel strength starts to degrade
4	$d \geq \text{half section depth}$	$T \geq 500 \text{ }^\circ\text{C}$ or significantly exposed	Large reductions in material and bond properties



(a)



(b)

Figure 2. Determining d , the average depth of concrete with temperatures above 300 °C, for (a) a slab and (b) a beam

2.2 Thermal analysis of slabs and beams

Two slabs and four beams with varying section dimensions, rebar configuration, and cover thickness were designed as listed in Tables 3 and 4. Different durations of ASTM E119 up to the fire rating of the structural member were used as the fire curve. A total of six scenarios for the slabs and twelve scenarios for the beam were considered. Provisions in ACI 216.1 were used to select the minimum dimensions and concrete cover based on specified fire ratings. Heat transfer analysis was performed in SAFIR [30]. Slabs were heated on one side and beams were heated on three sides.

Table 2.3 of ACI 216.1 was used as a guide to select the minimum cover for solid cast-in-place floor slabs with siliceous aggregate and unrestrained conditions. Clear spacing between the rebars was calculated based on the minimum spacing requirement between the rebars.

Table 2.4 of ACI 216.1 was used as a guide to select the beam width and the cover in non-prestressed and unrestrained beams. Cases with both minimum cover, as well as those larger than minimum, were studied to evaluate the effect of cover depth on the level of damage. The number and size of rebars were selected to satisfy the minimum and maximum reinforcement ratios according to ACI-318-19 [31]. The required cover for cases with two corner rebars or three rebars considered the effect of heating from multiple sides. According to ACI 216.1, clause 2.3.1.2, “the concrete cover for an individual bar is the minimum thickness of concrete between the surface of the bar and the fire-exposed surface of the beam. For beams in which several reinforcing bars are used, the cover, for the purpose of Table 2.4, is the average of the minimum cover of the individual bars. For corner reinforcing bars (that is, reinforcing bars equidistant from the bottom and side), the minimum cover used in the calculation shall be 1/2 the actual value.”

Table 3. Summary of analyzed slabs

Slab thickness [mm]	No. of rebars per meter	Rebar diameter [mm]	Cover [mm]	Fire resistance rating
90	4	12.7 mm (#4 US rebar)	40	1 hour
125	4	12.7 mm (#4 US rebar)	40	2 hours

Table 4. Summary of analyzed beams

Beam size [mm x mm]	No. of rebars	Rebar diameter [mm]	Cover in vertical direction [mm]	Cover in horizontal direction [mm]	Fire resistance rating
175 x 400	2	19.05 (#5 US rebar)	40	40	1 hour
175 x 400	2	19.05 (#5 US rebar)	50*	50*	1 hour
175 x 400	2	19.05 (#5 US rebar)	60*	40	1 hour
250 x 600	3	19.05 (#5 US rebar)	30	30	1 hour
250 x 600	3	19.05 (#5 US rebar)	40*	40*	1 hour
250 x 600	3	19.05 (#5 US rebar)	50*	40*	1 hour

* Cover is larger than the minimum requirement

SAFIR was selected to conduct the numerical analyses as the finite element program is developed specifically for the analysis of structures subjected to fire. The boundary temperature of the concrete section at the surface was calculated through convection and radiation heat transfer modes. The temperature distribution within the concrete section was then obtained by heat conduction analysis at each time step. Convective heat transfer coefficients of $25 \text{ W/m}^2\text{°C}$ and $9 \text{ W/m}^2\text{°C}$ were taken for the fire-exposed and unexposed surfaces, respectively. The emissivity value for radiative heat transfer on the exposed surfaces of the concrete member was assumed to be 0.8. Relationships for high-temperature thermal properties of concrete were determined according to Eurocode 2 [32]. The modeling approach was validated using the results of experiments conducted at the University at Buffalo [33].

The temperature distributions within the slab and beam sections were summarized for different fire exposure times and mapped to the proposed damage states to evaluate the potential level of damage for structural members designed according to the ACI 216.1 provisions. The next section will provide the results.

3 RESULTS

Figure 3 shows a sample heat transfer result for a slab in SAFIR and Table 5 summarizes the damage states for example slabs based on the proposed thresholds. The 90 mm and 125 mm slabs have fire-resistance

ratings of 1 hour and 2 hours, respectively. The slabs were heated from one side, and it took time for the heat to distribute within the section. Both damage indicators d and the temperature of the rebar indicate that the slabs experienced damage state 2 after being exposed to 30 minutes of the ASTM E119 fire curve. Subsequently, the slabs progressed to damage state 3 after 60 and 90 minutes of ASTM E119 for the 90 mm and 125 mm slabs, respectively. Finally, the 125 mm slab reached damage state 4 after 120 minutes of ASTM E119, with damage indicator d being the controlling factor.

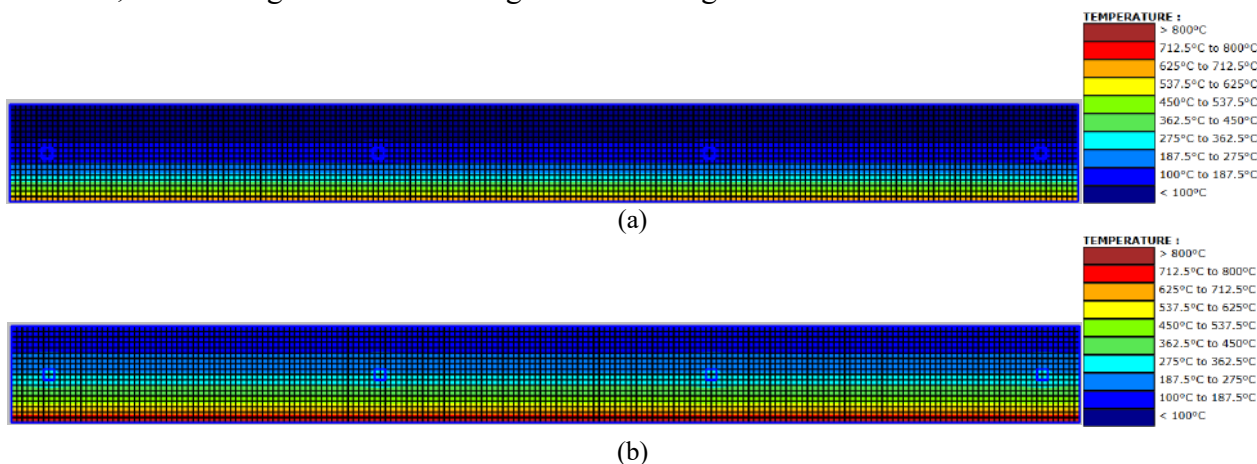


Figure 3. Slab (90mm x 1000mm) with a cover of 40 mm after (a) 30- and (b) 60-min exposure to ASTM E119, models have a mesh size of 5 mm

Table 5: Damage states for considered slabs

Slab size [mm x mm]	Rebar diameter [mm]	Cover [mm]	Exposure time [min]	$d > 300$ °C [mm]	Temp. of rebar [°C]	Damage state
90 x 1000	12.7 mm (#4 US rebar)	40	30	20	140°C	2
			60	40	285°C	3
125 x 1000	12.7 mm (#4 US rebar)	40	30	25	135°C	2
			60	40	270°C	3
			90	60	365°C	3
			120	70	435°C	4

Figure 4 shows a sample heat transfer result of a beam in SAFIR and Table 6 summarizes the damage states for example beams based on the proposed thresholds. The beams were heated from three sides, having either two or three rebars. Overall, the beams mostly experienced damage state 2 after 30 minutes and damage state 3 after 60 minutes of exposure to the ASTM E119 fire curve. The increase in the cover helped with one of the beams, switching the level of damage to a lower state. The 250x600 beam with a cover of 30 mm had a damage state 4 after a 60-minute fire. The damage level was reduced to 3 after increasing the cover by 10 mm in both directions.

The heat distribution inside the concrete section is mainly a function of the section size, material properties, and exposure time. Increasing the cover does not influence the heat distribution within the concrete section much. That is, the total volume of concrete within the section that requires replacement (concrete experiencing temperatures beyond 300°C) does not change by much. However, the calculated average depth of concrete above 300°C in this study is at the locations of the rebar. Thus, an increase in the cover leads to a decrease in the level of concrete damage at the location of the rebars since the rebars are placed further inside the concrete. This can be seen in the case of the 175x400 beam: the beam with a 40 mm cover in both directions had a d of 100 mm and rebar temperature of 425°C after a 60-min fire; the same beam with a 50 mm cover in both directions had a d of 75 mm and rebar temperature of 325°C after the same duration of the fire. The reduction in the level of damage at the rebar location reduces the amount of repair work and associated losses.

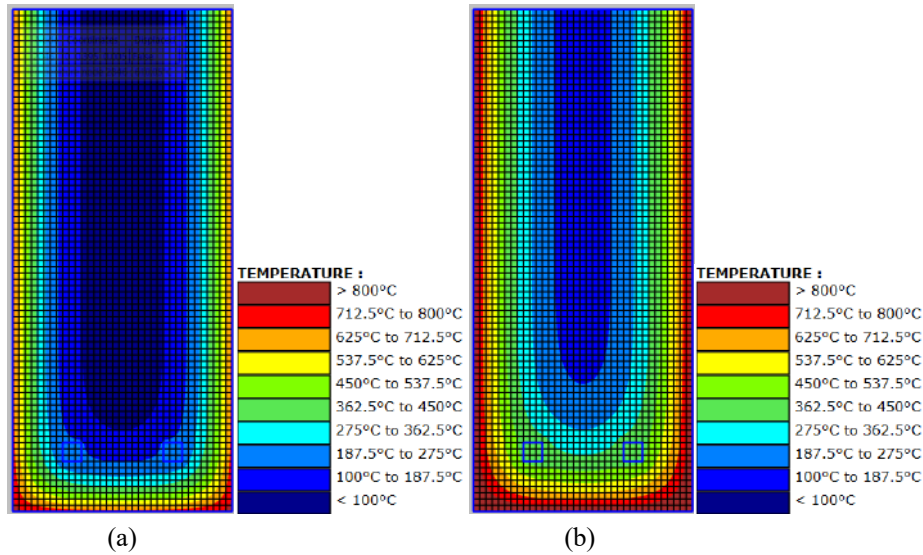


Figure 4. Beam (175mm x 400mm) with a cover of 40mm after (a) 30-min and (b) 60-min exposure to ASTM E119, models have a mesh size of 5 mm

Table 6: Damage states for considered beams

Beam size [mm x mm]	No. of rebars	Rebar diameter [mm]	Cover [mm]	Exposure time [min]	d > 300 °C [mm]	Temp. of rebar [°C]	Damage state
175 x 400	2	15.87 (#5 US rebar)	40×40	30	30	210°C	2
		15.87 (#5 US rebar)	40×40	60	100	425°C	3
	15.87 (#5 US rebar)	50×50	30	30	145°C	2	
	15.87 (#5 US rebar)	50×50	60	75	345°C	3	
	15.87 (#5 US rebar)	60×40	30	30	160°C	2	
	15.87 (#5 US rebar)	60×40	60	100	355°C	3	
250 x 600	3	15.87 (#5 US rebar)	30×30	30	25	260°C	2
		15.87 (#5 US rebar)	30×30	60	415	460°C	4
	15.87 (#5 US rebar)	40×40	30	30	180°C	2	
	15.87 (#5 US rebar)	40×40	60	75	370°C	3	
	15.87 (#5 US rebar)	50×40	30	30	150°C	2	
	15.87 (#5 US rebar)	50×40	60	75	320°C	3	

* Cover is larger than the minimum requirement

4 CONCLUSIONS

This paper presented quantitative thresholds to assist with damage diagnosis for post-fire assessment of structural conditions as well as performance-based design of concrete structures. Four damage states were defined, and the temperature thresholds were selected based on the reduction in material strength (steel and concrete) and bond strength between rebar and concrete. The residual reduction in concrete compressive

strength and bond strength at the rebar level remains within about 15% for temperatures below 150°C (damage state 1). Based on several standards and experiments in the literature, concrete that reaches temperatures beyond 300°C may be replaced. Minor repair can be expected if the temperature within the cover remains below 300°C (damage state 2). The reduction in concrete compressive strength and bond strength is reduced to about 50% for rebar temperatures close to 500°C (damage state 3). The structure most likely experiences significant damage and requires major repair or replacement if the rebar temperature exceeds 500°C (damage state 4).

Analyses of two slabs and four beams, which were designed following the ACI 216.1 guidelines and studied under eighteen scenarios, showed that damage state 2 can be expected after 30 minutes of the ASTM E119 fire curve with damage states 3 and 4 occurring at and beyond 60 minutes of fire exposure. The results indicated that adjustments to the minimum dimensions and covers may be needed to control the level of damage and improve the resilience of the design, especially for beams, if performance objectives beyond safety requirements are imposed.

This study did not consider the cooling phase of fire, during which temperatures inside the concrete section may continue to increase after the peak fire temperature. Future work will include the effect of cooling on the level of damage.

ACKNOWLEDGMENTS

The authors thank the ACI Foundation, research grant number CRC 2022 P0053, and the Institute of Bridge Engineering at the University at Buffalo for their generous support. Any opinions, findings, conclusions, or recommendations expressed in this paper are those of the authors and do not necessarily reflect the views of the funding agencies.

The authors would like to thank, Ms. Kalyani Sudam Koli and Mr. Billy Grippi, students at the University at Buffalo, who helped with developing the SAFIR models.

REFERENCES

1. National Codes and Standards Council of the Concrete and Masonry Industries. (1994). *Assessing the condition and repair alternatives of fire-exposed concrete and masonry members*. Fire protection planning report.
2. Concrete Society. (2008). *Assessment, design and repair of fire-damaged concrete structures*. Concrete Society, Camberley, UK.
3. International Federation for Structural Concrete (fib). (2008). *Fire design of concrete structures - structural behavior and assessment*. International Federation for Structural Concrete, Lausanne, Switzerland.
4. ACI. (2013). *Report on nondestructive test methods for evaluation of concrete in structures*. American Concrete Institute Committee 228, Farmington Hills, MI.
5. ACI. (2016). *ACI 562-16: Code requirements for assessment, repair, and rehabilitation of existing concrete structures and commentary*. American Concrete Institute, Farmington Hills, MI.
6. Hua, N., Elhami-Khorasani, N., Tessari, A. (2023). "Utilizing advanced modelling for fire damage assessment of reinforced concrete tunnel linings," *IABSE Structural Engineering International*, 33(4): 586-595, doi.org/10.1080/10168664.2022.2161440.
7. ACI. (2007). *ACI 216.1: Code requirements for determining fire resistance of concrete and masonry construction assemblies*. American Concrete Institute, Farmington Hills, MI.
8. ASTM Designation (2020), *ASTM E119-20: Standard test methods for fire tests of building construction and materials*. Am. Soc. Test. Mater.
9. Shahraki, M., Hua, N., Elhami-Khorasani, N., Tessari, A., Garlock, M. (2023). "Residual compressive strength of concrete after exposure to high temperatures: A review and probabilistic models." *Fire Safety Journal*, 135, 103698.
10. CEN. (2005). *Eurocode 4: Design of Composite Steel and Concrete Structures - Part 1-2: General Rules - Structural Fire Design*. European standards, 1994-1-2 -E.N. Brussels, Belgium.
11. Sharma, A., Bošnjak, J., Bessert, S. (2019). "Experimental investigations on residual bond performance in concrete subjected to elevated temperature." *Engineering Structures*, 187, 384-395.

12. Haddad, R. H., Al-Saleh, R. J., Al-Akhras, N. M. (2008). "Effect of elevated temperature on bond between steel reinforcement and fiber reinforced concrete." *Fire Safety Journal*, 43(5), 334-343.
13. Bingöl, A. F., Gül, R. (2009). "Residual bond strength between steel bars and concrete after elevated temperatures." *Fire Safety Journal*, 44(6), 854-859.
14. Xiao, J., Hou, Y., Huang, Z. (2014). "Beam test on bond behavior between high-grade rebar and high-strength concrete after elevated temperatures." *Fire Safety Journal*, 69, 23-35.
15. Lublóy, É., György, B. L. (2014). "Temperature effects on bond between concrete and reinforcing steel." *Zbornik radova Građevinskog fakulteta*, Subotica, (26), 27-35.
16. Ergün, A., Kürklü, G., Başpınar, M. S. (2016). "The effects of material properties on bond strength between reinforcing bar and concrete exposed to high temperature." *Construction and Building Materials*, 112, 691-698.
17. Abdallah, S., Fan, M., Cashell, K. A. (2017). "Bond-slip behaviour of steel fibres in concrete after exposure to elevated temperatures." *Construction and Building Materials*, 140, 542-551.
18. Bošnjak, J., Sharma, A., Bessert, S. (2017). *Bond performance of reinforcement in concrete after exposure to elevated temperatures*. Proceedings of the 3rd International Symposium on Connections between Steel and Concrete, Stuttgart, Germany.
19. Hlavička, É. L. V. (2017). "Bond after fire." *Construction and Building Materials*. 132, 210-218.
20. Li, X., Bao, Y., Xue, N., Chen, G. (2017). "Bond strength of steel bars embedded in high-performance fiber-reinforced cementitious composite before and after exposure to elevated temperatures." *Fire Safety Journal*, 92, 98-106.
21. Varona, F. B., Baeza, F. J., Bru, D., Ivorra, S. (2018). "Evolution of the bond strength between reinforcing steel and fibre reinforced concrete after high temperature exposure." *Construction and Building Materials*, 176, 359-370.
22. Yusuf, M., Sarhat, S., Hajiloo, H., Green, M. F. (2022). "Bond strength between steel reinforcement and RCA concrete during and after exposure to elevated temperatures." *Construction and Building Materials*, 345, 128362.
23. Bošnjak, J., Sharma, A., Öttl, C. (2018). "Modified beam-end test setup to study the bond behavior of reinforcement in concrete after fire." *Materials and Structures*, 51, 1-10.
24. Kodur, V. K. R., Agrawal, A. (2016). "An approach for evaluating residual capacity of reinforced concrete beams exposed to fire." *Engineering Structures*, 110, 293-306.
25. Federal Highway Administration. (2015). *Tunnel operations, maintenance, inspection, and evaluation (TOMIE) manual*. Washington DC, USA.
26. Fire Safety Committee of the Concrete and Masonry Industry. (1994). *Assessing the condition and repair alternatives of fire-exposed concrete and masonry members*. Skokie, Illinois.
27. Du, S., Zhang, Y., Sun, Q., Gong, W., Geng, J., Zhang, K. (2018). "Experimental study on color change and compression strength of concrete tunnel lining in a fire." *Tunnel Underground Space Technol.* 71:106–114.
28. Hager, I. (2014). "Colour change in heated concrete." *Fire Technology*, 50, 945-958.
29. Khoury, G. A. (2000). "Effect of fire on concrete and concrete structures." *Progress in Structural Engineering and Materials*, 2(4), 429-447.
30. Franssen, J. M., Gernay, T. (2017). "Modeling structures in fire with SAFIR®: Theoretical background and capabilities." *Journal of Structural Fire Engineering*, 8(3), 300-323.
31. ACI. (2019). ACI 318-19: Building Code Requirements for Structural Concrete and Commentary. American Concrete Institute, Farmington Hills, MI, USA.
32. CEN. (2004). Eurocode 2: Design of Concrete Structures - Part 1-1: General Rules and Rules for Buildings. European standards, 1992-1-1 -E.N. Brussels, Belgium.
33. Elhami-Khorasani, N., Ranade, R., Tessari, A., Tajik, N., Koli, K. S. (2024). *Damage Classification of Reinforced Concrete Structures for Fire: Rebar Temperature*. Project CRC 2022 P0053. American Concrete Institute, Farmington Hills, MI, USA.

POST-FIRE STRUCTURAL PERFORMANCE OF CORRODED CONCRETE BEAMS

Ethan Phillion¹, Kathryn Chin², Austin Martins-Robalino³, John Gales⁴

ABSTRACT

Reinforced concrete is a well-researched material; however, there are a lack of studies addressing the effects of corrosion on the post-fire structural performance of concrete beams. Concrete structures such as overpasses can be exposed to potential frequent fires and environments which promote corrosion. Within this study, five 30 MPa and five 60 MPa reinforced concrete beams were cast and corroded in a controlled process to result in a mass loss of steel ranging from 0 – 30%. The beams were then exposed to a 30-minute methanol pool fire at the centre span. Finally, the concrete beams were loaded in a four-point bending test to examine the bending capacity of the beams post-fire. Deflection and crack growth were monitored during the fire and bending tests with the use of narrow spectrum illumination and digital image correlation. Preliminary findings show that all concrete beams reached a negative camber at the end of monitoring. During the bending tests, the corroded beams exhibited yielding behaviour. The more severely corroded beams reached higher peak loads but would begin to show yielding behaviour at lower midspan deflections.

Keywords: Concrete; corrosion; fire performance; structural performance; Digital Image Correlation – DIC; narrow spectrum (in DIC)

1 INTRODUCTION AND MOTIVATION

The subject of reinforced and normal concrete in fire has been extensively studied since the material has been proposed for structural use. Its behaviour has been well qualified from the earliest papers by Ira Woolson on the subject where distinct strength loss can occur in addition to factors which promote the degradation and spalling of concrete in structures [1-2]. While there have been many contemporary studies which rationally attempt to quantify its performance, see NIST 1188 [3] as an example for a summary of large-scale and material testing, there have not been many studies that consider deteriorated and corroded reinforced concrete in and after a fire.

Concrete structures are often considered to perform well in a fire due to their insulative properties for their tensile and compressive reinforcement. However, with aging or unmaintained infrastructure, it is not guaranteed that there is still sufficient concrete cover to the reinforcement due to effects such as corrosion. As steel corrodes, the tensile strength of concrete can be affected which can lead to defects such as cracking,

¹ PhD. Student, Department of Civil Engineering, York University (Canada)
e-mail: ephillion@yorku.ca, ORCID: <https://orcid.org/0009-0001-7116-6935>

² MAsC. Student, Department of Civil Engineering, York University (Canada)
e-mail: kchin01@yorku.ca, ORCID: <https://orcid.org/0000-0002-5903-741X>

³ PhD. Student, Department of Civil Engineering, York University (Canada)
austinmr@my.yorku.ca, ORCID: <https://orcid.org/0000-0002-2041-445X>

⁴ Associate Professor, Department of Civil Engineering, York University (Canada)
e-mail: jgales@yorku.ca, ORCID: <https://orcid.org/0000-0001-8025-3902>

spalling or delamination of concrete. It can also reduce the steel reinforcing capability. This study forms a component of the IC-IMPACTS program, Fire Performance of Aged Reinforced Concrete Structures: Applications for Occupant Survivability During Fires research program. Within this study, the impact of corrosion on the post-fire bending capacity of reinforced concrete beams is examined.

2 SOCIO-CONTEXT

The authors provide a short illustrative study herein to exemplify the fire risk to corroded structures to provide a socio-context to the fire problem identified herein.

The research program herein was established in 2018 and principally sought to consider the aging reinforced concrete infrastructure which had experienced corrosion and was meant to be applied internationally. After the initiation of the study, there has been more focus recently on the type of fire exposure expected on these types of infrastructure. Commonly, one would immediately conclude a vehicular fire to be the expected incident, and in turn the fire to be a rare occurrence. While a vehicular fire is of probable cause, it is not the only fire exposure these structures will experience nor is fire rare in all cases for structures with advanced corrosion deterioration.

Following COVID-19 pandemic conditions in 2020, there has been a pronounced increase in the number of informal settlements in developed countries as unemployment, inflation and the cost of living grow. Informal settlements are a collection of impoverished shelter areas typically built without building or planning regulation; they have strong tendencies to pose a fire risk wherever they are formed. For example, Toronto (Canada) had over 200 documented settlement fires last year (2023). Typical fire sources include gas fires from heating units and electric batteries. The resulting ignition is fuelled by the shelters and contents themselves. These settlements have been observed to develop under high-volume transit bridge overpass infrastructure (see Figure 1). From a perspective in the event of fire under these bridges, this can cause concern if the infrastructure already shows signs of deterioration, such as would be seen in corroded concrete (Figure 2). Since the fuel load under the roadway from informalized settlements is not well understood, this exuberates the risk to the structure. There exists limited information available regarding how deteriorated infrastructure can respond to any severity of fire [4]. The authors studied the number of fires caused by settlements under a transitway road system in Toronto over 2020-2023 (Figure 3). The system was primarily made of reinforced concrete undergoing a range of deterioration from corroded reinforcement. The authors also quantified the number of dispersals of settlements over the same time. Despite the city's efforts to remove these settlements they re-establish. Figures 4 and 5 illustrate the damage caused by the fire which necessitated a portion of the transitway to be closed for several months.



Figure 1. Visible encampment under expressway during summer 2020 (Author's photo)



Figure 2. Corroded concrete beams and columns on an expressway in 2020 (Author's photos)

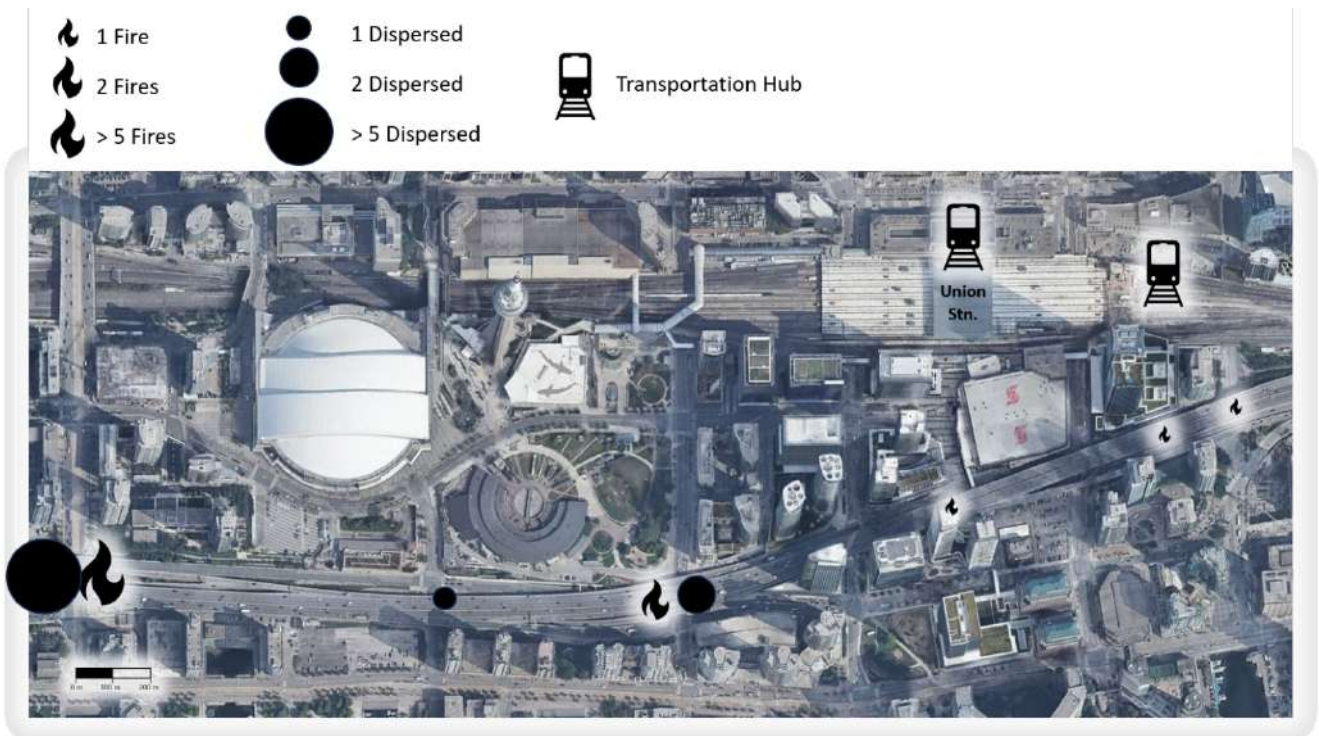


Figure 3. Frequency of fires on expressway between 2020 and 2023



Figure 4. Post-fire photo of an expressway in February 2020 (Author's photos)



Figure 5. Post-fire photo of an overpass in August 2020 with fire occurring in March of 2020 (Author's photos)

3 LITERARY BACKGROUND

One primary mode of degradation of reinforced concrete is corrosion of the steel rebar, which can occur through a Redox reaction. If there is a sufficient number of wet-dry cycles, concrete can act as the electrolyte for the reaction while the steel rebar can act as both the anode and cathode [5]. During this process, the anode portion of steel will have its iron oxidized to a ferrous state where it is further oxidized to form an iron oxide on the cathode. The presence of chlorides (present in de-icing salts or salt water) can increase the potential of steel corrosion by making the steel exposed to chloride more anodic [5].

During the process of corrosion, several mechanisms weaken a concrete member. One of which is the breakdown of the steel material as it returns to iron oxides. As this occurs, the remaining effective steel cross-section decreases resulting in higher stress being transferred through the steel. While the effective cross-section is decreasing, the corroded steel expands through this process. The expansion of the corroded steel can cause several consequences to the structural performance of the concrete. As the steel expands it can apply tensile stresses to the concrete itself. This can cause the formation of cracks, and potentially cause or promote spalling of the concrete cover. Both the cracking and spalling can introduce additional means for moisture to reach the steel rebar and expedite corrosion.

Several studies have been conducted to better understand the effects corrosion has on the fire performance of reinforced concrete. Chandra et al. [6] considered the effect on load-bearing columns. Their investigation studied two normal and two high-strength columns. Accelerated corrosion of 20% to uncorroded counterparts was specified. The columns were tested with an axial load at 33% capacity and followed a standard time and temperature exposure following ISO 834 [7]. They found a significant decrease in the performance of high-strength columns (31.4% decrease in fire resistance) and a subtle enhancement in normal strength performance (6.7% increase in fire resistance). Their research pointed to a need to further understand the effects of corrosion and spalling. Subsequently, this study furthers this investigation with consideration of beams and variable accelerated corrosion levels.

Ba et al. [8] loaded concrete beams in four-point bending during a furnace fire to determine the fire performance of corroded concrete beams. One of the primary findings of the study was that lower corroded concrete beams had similar failure modes to unreinforced concrete beams, whereas the severely corroded beams had a brittle failure [8]. This is due to the corrosion reducing the yield strength of the steel, which in turn results in larger crack formation during loading and allowing heat to reach the steel [8].

Zhang et al. [9] studied the effects of impressed current density on corrosion induced cracking of concrete cover. Zhang et al. [9] exposed 150 x 150 x 550 mm concrete prisms to current densities ranging from 50 to 300 $\mu\text{A}/\text{cm}^2$. While the prisms corroded through an impressed current, crack progression was measured with smart aggregate and digital image correlation (DIC) techniques. Results showed that as the impressed current density increased, the expansion coefficient of the steel corrosion products decreased [9]. This caused an increase in the corrosion degree at the inner and outer surface cracking of the concrete cover.

While it is promising to see studies addressing the effects of corrosion on the fire performance of reinforced concrete, structures such as overpasses exist where severely corroded concrete elements may be exposed to fire scenarios. The structures can remain intact through the fire and after investigation be put back in service. Therefore, it is critical to understand how these structures are impacted by corrosion in their post-fire structural performance.

4 METHODOLOGY

4.1 Specimen preparation

Five 1.5-meter long and 200 mm deep reinforced-concrete beams were cast with a target 30 MPa compressive strength (tested on average cylinder strength of 35 MPa). Five 1.5-meter long and 200 mm deep reinforced-concrete beams were also cast at a 60 MPa compressive strength (tested on average cylinder strength of 56.7 MPa). The reinforcing strength was 15M ultimate strength 500 MPa grade (tested on average rebar strength of 647.6 MPa)

All reinforced concrete beams were cast with the tensile longitudinal steel protruding from the concrete in order to facilitate the corrosion process. As described in Figure 6, the corrosion of the concrete was performed following an impressed current accelerated corrosion process. This process involved submerging the soffits of the concrete beams in a saline solution of 3.5% NaCl to mimic sea water and applying an electrical current (see Chandra et al. [6]). The tensile longitudinal rebar (anode) was wired to a power supply at 0.379 Amps. Following Faraday's law, with this current, approximately every 55 days would result in a 10% mass loss of steel due to corrosion. Stainless steel rods were also wired to the power supply to be the cathode of the redox reaction. One concrete beam was not exposed to corrosion or fire to be the control specimen. The remaining concrete beams were corroded to the following levels and would also be exposed to fire: 0%, 10% (estimated 55 days), 20% (estimated 110 days), and 30% (estimated 165 days).

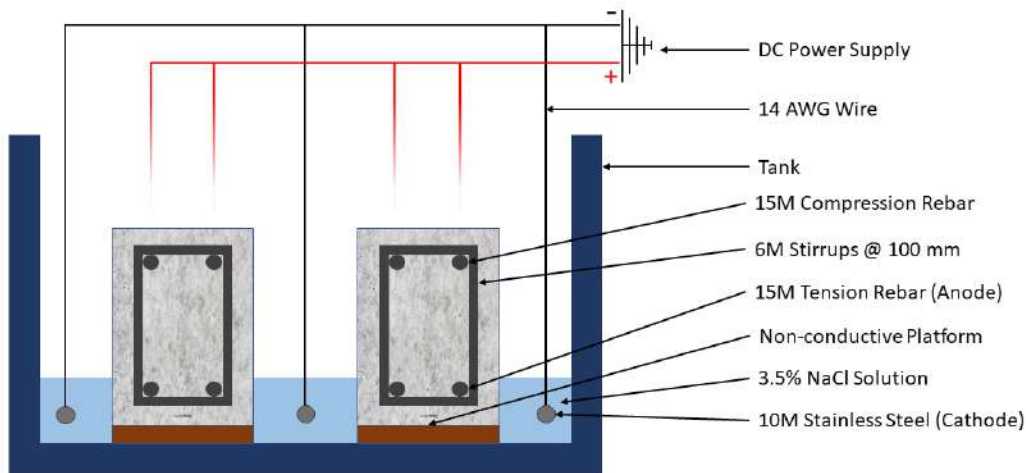


Figure 6. Diagram of specimens in accelerated corrosion tank

4.2 Fire testing

Fire exposure of the concrete beams consisted of a 30-minute methanol pool fire. A pool fire was selected as the thermal exposure as it is a consistent and easily replicable method of applying a known fire to specimens of this scale (see Nicoletta et al. [10] and Harun et al. [11]). The tray which held the methanol had an opening of 500 mm by 280 mm and was placed under the midspan of the concrete beams. In this configuration, 8 L of methanol was used in each test to reach a 30-minute exposure. A safety mesh was placed over the fuel tray as a preventative and necessary safety measure against concrete splashing the fuel during testing. It is important to note the mesh may impact the degree of applicability of a direct pool fire equation for future modelling exercises. Note that the authors currently feel modelling is premature until a study with sufficient sample size can be conducted where phenomena can be more rationally explained qualitatively. A burn was conducted with a thermocouple tree to ensure that the presence of the mesh did not impact the temperature. These beams were supported by concrete masonry units (CMU) to form a 120 mm gap between the soffit of the concrete beams and the lip of the fuel pan was used for all tests. A 120 mm gap was used as prior testing indicated that the temperatures at this distance for this pool fire set-up would be in the range of 700-750 °C. Below, Figure 7 summarizes the experimental set-up for the fire testing.

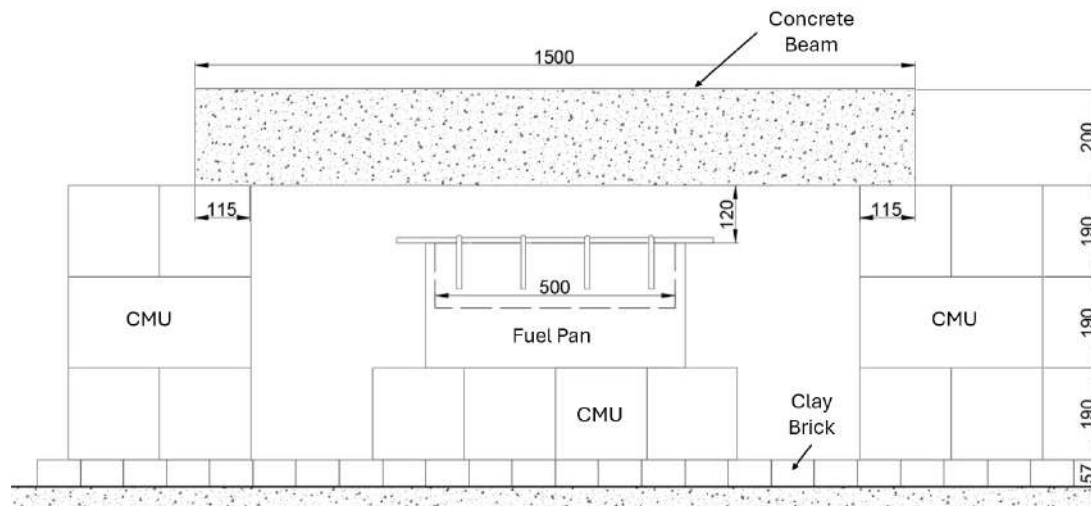


Figure 7. Diagram of experimental set-up for fire testing (dim in mm)

During the fire testing, data was collected for the temperature of the longitudinal rebar (tension and compression steel), crack growth, and midspan deflection. The data was collected during the fire and as the specimen cooled down post-fire until the intact concrete was approximately 100 °C. The crack growth and midspan deflection measurements were collected with digital image correlation (DIC) using narrow spectrum illumination.

For DIC, the flames of a fire pose an issue as they can obscure the area of interest in a photo. Narrow spectrum illumination can effectively remove the flames from the view of a camera. The technology works through the illumination of a material in a high degree of blue light. This is achieved through the use of high intensity theatre style blue LED. Alike to image correlation procedures, high resolution cameras (Canon 5D Mark IV) are placed to view the material undergoing deformation, images are sequenced and compared to a reference image. Only in the case of this technique, the sample is under a fire load, and the camera contains a unique filter piece which removes colours above the blue spectrum. This allows materials to be studied under high temperature exposure with deformation able to be quantified. Below, Figure 8 shows an image of a concrete beam exposed to a fire and how the blue light and filter remove the flames from the image. The drawback is the intensity of the fire is usually less than one would see in an enclosed furnace. A full description of the technique and other uses can be found in Smith and Hoehler [12], and Gatien et al. [13]. The technique has successfully been used on steel and timber samples in the past [10-11]. The analysis tool used for the DIC was GeoPIV (RG) adapted from camera settings seen in Gatien et al. [13].

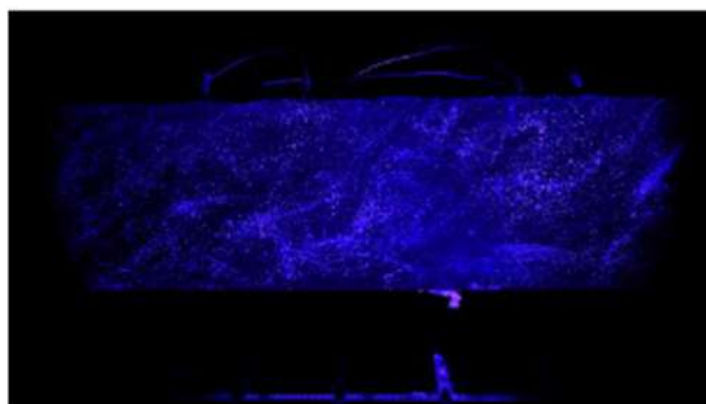


Figure 8. Image of a concrete beam during fire testing using narrow spectrum illumination to be used for DIC analysis

4.3 Four-point bending testing

Four-point bending was chosen as the loading procedure to ensure the centre third of the beam was in pure moment and reached the maximum moment. This is important as it was the longitudinal tension side steel which was corroded. Figure 9, summarizes the experimental setup for a four-point bending test. To provide a level surface for the point loads, the tops of the beams were coated with a layer of gypsum cement and sanded until level. A load rate of 0.167 mm/min was used. As the load rate was low, tests were typically concluded prior to experiencing a significant drop in load as post-peak softening occurred. Midspan deflection and flexural crack growth were monitored while the load was applied. Similar to the fire testing, DIC was used to collect this data. GeoPIV was applied to the data with the same settings as Section 4.2.

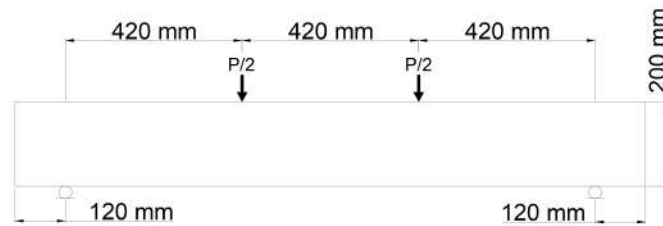


Figure 9. Diagram of four-point bending test set-up

5 RESULTS AND DISCUSSION

5.1 Corrosion observations

Although 30% mass loss due to corrosion is not as severe as a structure could experience, a significant difference between 10% and 30% was observed. In Figure 10 it can be seen that while at 10% mass loss, there are spots with minor staining. Whereas the 30% specimen it can clearly be seen where each stirrup is located, indicating corrosion of the stirrups. Future work would entail the removal of the steel to determine the extent of corrosion for each portion of the steel (i.e., tension steel, compression steel, and stirrups). It should be noted that the pictures in Figure 10 were taken after being loaded and the cracking was not due to corrosion.



Figure 10. Visual impact of corrosion to 60 MPa beams at 10% mass loss (top) and 30% mass loss (bottom)

5.2 Fire testing

Throughout all eight fire tests (0% - 30% corroded for 30 MPa and 60 MPa concrete), no cracking or spalling was observed during the heating or cooling of the reinforced concrete beam. Below, Table 1 summarizes the deflection of the concrete beams once the fire had extinguished (approximately 30 minutes) and the recovery of the deflection at the end of monitoring the specimen noting the beams were unrestrained during fire testing. There is no value provided for the final deflection of the 60 MPa 30% corroded beam. This is because the duration of the test was longer than the camera's battery at full charge and data was not collected for the entire test duration. Within Table 1, it can be seen that all concrete beams recovered from their fire-induced deflections, which is expected as the beams were unloaded. In fact, several ended with a

slight, negative camber after cooling. A potential reason for this is as the concrete beam cools down, a temperature gradient forms where the temperature increases towards the top of the beam resulting in a negative camber. However, an analysis of the recorded temperatures would be required to confirm this.

Table 1. Summary of deflections during fire testing

Beam Strength and Corrosion Level	Deflection at end of fire (mm)	Deflection at end of monitoring (mm)
30 MPa 0%	3.20	-0.14
30 MPa 10%	3.63	-0.21
30 MPa 20%	3.62	-0.38
30 MPa 30%	3.80	-0.44
60 MPa 0%	1.67	0.41
60 MPa 10%	4.33	-0.36
60 MPa 20%	3.91	0.12
60 MPa 30%	4.92	-

5.3 Four-point bending testing

When comparing the data collected for the control beams and non-corroded beams an assumption for the impact of the fire exposure on the structural performance can be made. Figures 11 and 12 display the midspan deflection and crack growth, respectively, of the control and non-corroded beams during the four-point bending test. It should be noted that flexural cracks were not observed for the 30 MPa beams at lower corrosion levels. From the data collected, it appears that the fire exposure had minimal impact on the midspan deflection of the 60 MPa concrete beams and both appear to begin yielding at the same point. However, for the 30 MPa concrete beams, the non-corroded beam subjected to fire reached a higher peak load (similar to that of the 60 MPa beams). It should be noted that the 30 MPa control beam was one of two beams to have considered failing in the four-point bending test. The 30 MPa control beam had failed in shear and the test was concluded when there was no continuity of concrete throughout the length of the beam. The other beam which failed was the 30 MPa 10% corroded. At 48 min and 40 s into the test, the beam failed in shear.

Below, Figures 13 and 14 display the midspan deflection and crack growth of the more severely corroded beams during the four-point bending tests. One of the first observations made was that all beams still achieved yielding as evident in the plateaus in Figure 13. Impacts of the level of corrosion can also be observed from Figures 13 and 14. In Figure 13, it can be observed that the more severely corroded beams achieved higher peak loads and have a greater stiffness than the less corroded beams of equal strength. Additionally, in Figure 14, it can be observed that the crack width grew more rapidly for the beams with a lower corrosion level than the more severely corroded beams. It should be noted that the levels of corrosion used in this study are not extreme but were used to examine the impact of lower levels of corrosion on the post-fire performance of concrete beams. Therefore, it is reasonable that the beams still exhibited ductile behaviour. Additionally, the rebar used for the concrete beams was tested for their yield strength by following an adapted ASTM E8 [14] procedure. It was found that the rebar had an average yield strength of 465 MPa which was 16% greater than the nominal yield strength of 400 MPa. Therefore, the reduction in the cross-sectional area should not have caused a significant loss of strength in the rebar when assuming a yield strength of 400 MPa.

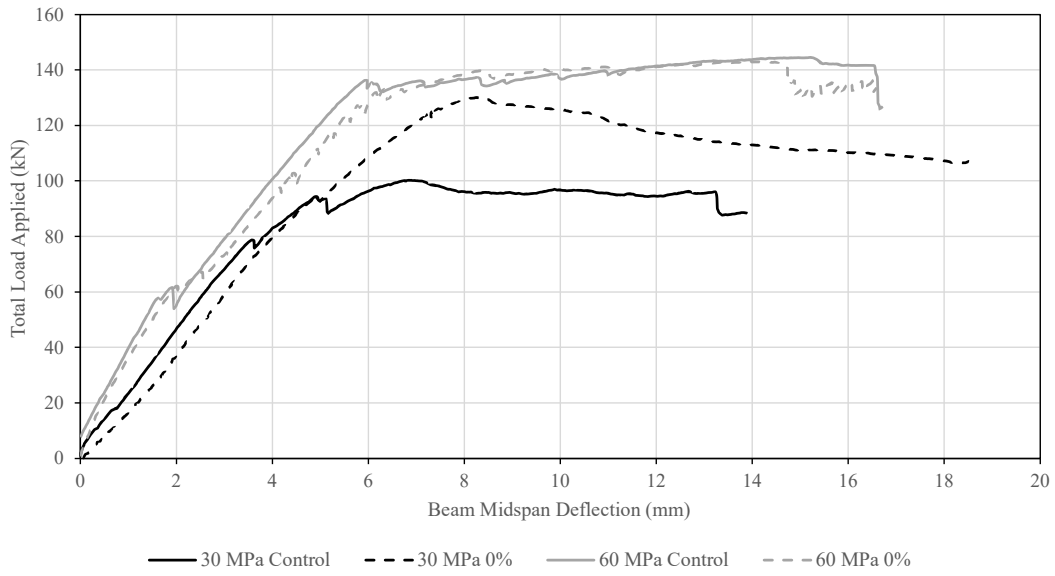


Figure 11. Midspan deflection of concrete beams with no corrosion during four-point bending tests

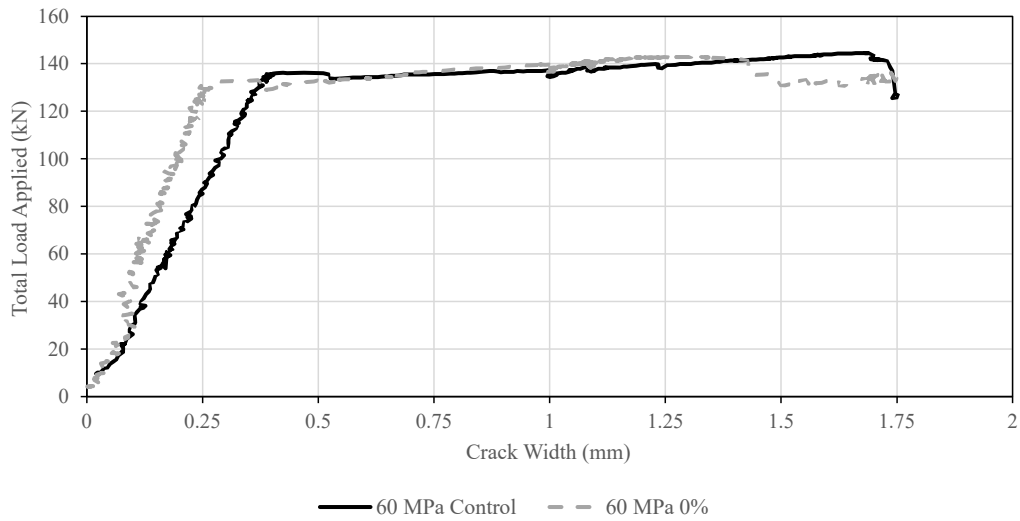


Figure 12. Crack width of concrete beams with no corrosion during four-point bending tests

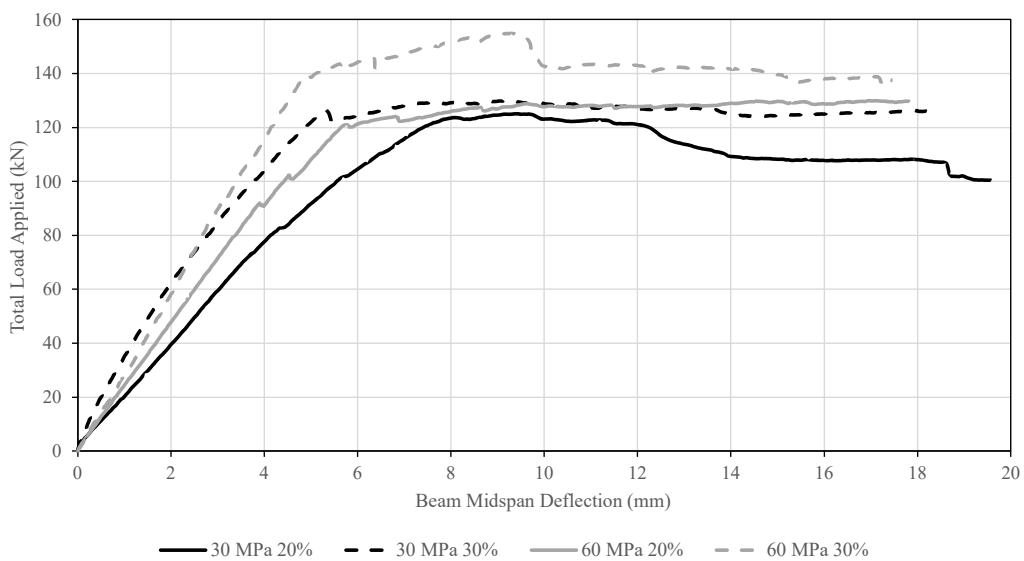


Figure 13. Midspan deflection of highly corroded concrete beams during four-point bending tests

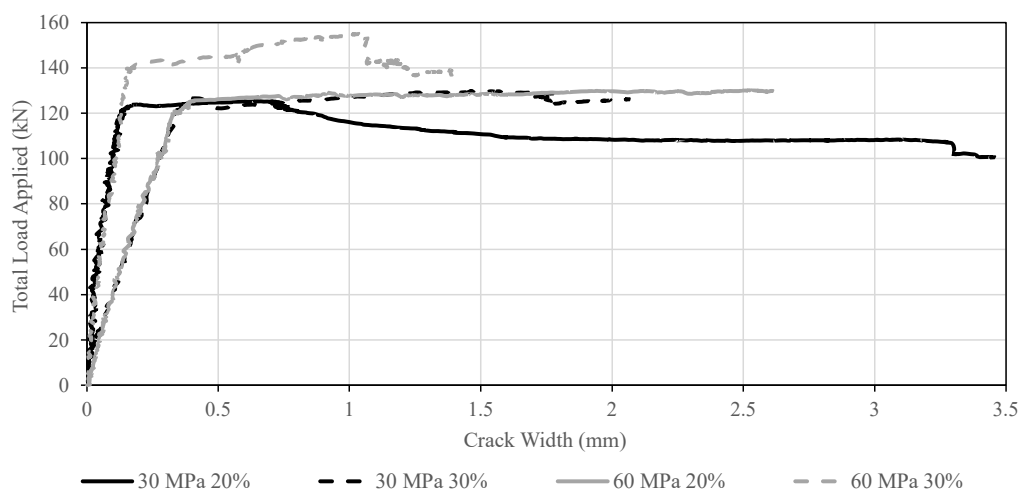


Figure 14. Crack width of highly corroded concrete beams during four-point bending tests

5.4 Limitations and future research

It is important for the authors to remark on the timing of the study presented herein and believe it beneficial to provide context of the difficulties in performing experimental tests during the height of the COVID-19 pandemic. Half of the specimens were cast at the beginning of March 2020. About two weeks prior to the universal shutdown of most Canadian universities due to the escalating COVID-19 pandemic. Apart from the limited time to cast, this complicated assessment of concrete quality at 28 days, and further compounded the testing of instrumentation on the casted specimens. Due to the nature of the lockdown, limited access to the laboratory was restricted until the Fall of 2020 upon which it was found that the intended concrete strength of the first batch of beams was higher than the strength targeted as part of the research plan necessitating the knowledge a second cast would be required to achieve the intended targeted strength. The target strength was to match strengths being used by other researchers in the research program (30 MPa). While it was possible to corrode the beams artificially in Fall of 2021 it was not possible to perform a second concrete cast until several members of the research team could work in a group on campus – where full lab access would be permitted. At that time, researchers were limited in number in lab space. Further pandemic-related lockdowns and significant restrictions on campus access interrupted the possibility of further specimen preparation until the Fall of 2022 upon which it was decided to test and report the values herein based on the sample conditions that had occurred. A second series of samples was prepared to expand the scope of the study to include a second and proper graded strength for direct comparison. Making further samples was not practical as mix conditions would not be identical, and it was deemed testing the samples made in 2020 would provide scientific value.

The authors recommend a further replication study that tests more samples in replicate to statistically study the effect corrosion has on samples. Such a study needs careful consideration to the strength of the reinforcing steel being provided. New testing should also consider a more severe fire exposure and of longer duration so as to further exacerbate the effects of corrosion damage to study them. While the conclusions here should be taken with reservation, they are useful for those attempting to study the effect of corrosion and fire in greater detail.

The results of the current study are in alignment with results from other corrosion of reinforced concrete studies [6] and may be used to support those findings. Due to the resource-intensive nature of this type of study, it is not feasible for many labs to undertake concrete corrosion studies with enough samples to be statistically significant. Therefore, future studies can build upon this work and lead toward fully understanding of the effects of corrosion on the fire performance of reinforced concrete.

Currently, further work is required to obtain a stronger understanding of the impact corrosion has on the post-fire structural performance of concrete beams. The first step would be to retrieve rebar samples from the concrete beams to verify the level of corrosion based on mass loss. Following this, several additional

studies would need to be performed. One study would be to replicate the tests performed in the current study to provide more samples and data to determine statistically significant trends. The following studies would be to expand the dataset. This would include examining the post-fire structural performance when concrete beams are exposed to more severe levels of corrosion, or corroded concrete beams which are exposed to fires for various durations and intensities. Finally, the scope of this study was on the bending capacity of the concrete beams; further studies are required to examine the impact of corrosion on the shear capacity of concrete beams. Lastly, many corroded concrete structures contain a range of rehabilitation or technologies to maintain their service life. These retrofit strategies should also be studied under fire scenarios.

6 CONCLUSIONS

While it is known that corrosion affects the strength of concrete members, there has been limited research into the effects of corrosion on the post-fire performance of concrete beams. Within this study, ten concrete beams were corroded to various levels and exposed to a 30-minute methanol pool fire. From the fire tests, it was found that the beams would recover their deflection and often would reach a slight negative camber at the end of monitoring. During the bending tests, it was found that as the level of corrosion increased, the beams were able to reach a higher peak load and would enter a yielding phase earlier than the specimens at a lower corrosion level. Additionally, it was observed that the presence of corrosion increased the width of the flexural cracks, however crack width was not proportional to corrosion level. Finally, it was observed that the exposure to the 30-minute methanol pool fire did not have a significant impact on the post-fire structural performance of the concrete beams. Future testing has been recommended to confirm the severity of corrosion in the concrete beams as well as to expand the scope of testing to include the impact of heat exposure on the post-fire structural performance of concrete beams.

ACKNOWLEDGMENT

The authors thank the IC Impacts program Fire Performance of Aged Reinforced Concrete Structures: Applications for Occupant Survivability During Fires for providing financial student support for the research herein. Yutaro Fukuhara is thanked for his assistance in corroding the concrete beams and helping with the second phase of the concrete cast. Kiara Mavalwala is thanked for her work on illustrative study figures.

REFERENCES

1. Woolson, IH.: Investigation of the Effect of Heat Upon the Crushing Strength and Elastic Properties of Concrete, vol. 5. in Proceedings of the American Society for Testing Materials, vol. 5. Philadelphia, 1905.
2. Woolson, IH.: Fire in a Reinforced Concrete Warehouse at Far Rockaway, New York, U.S.A, vol. No. 214. in Red Books, vol. No. 214. The British Fire Prevention Committee, 1918.
3. Yang, JC., Bundy, MF., Gross, JL., Hamins, AP., Sadek, FH. & Raghunathan, A., International R and D Roadmap for Fire Resistance of Structures Summary of NIST/CIB Workshop. National Institute of Standards and Technology, NIST SP 1188, Jun. 2015. doi: 10.6028/NIST.SP.1188.
4. Nicoletta, B., Kotsovinos, P., & Gales, J. Review of the fire risk, hazard, and thermomechanical response of bridges in fire. *Can. J. Civ. Eng.* 47 (4), 363–381 (2020). doi: 10.1139/cjce-2018-0767.
5. Smith, JL. & Virmani, YP. Materials and Methods for Corrosion Control of Reinforced and Prestressed Concrete Structures in New Construction. FHWA-RD-00-081. Southern Resource Center and Office of Infrastructure R&D; 2000.
6. Chandra, S., Sharma, UK., Green, M., Gales, J., & Bhargava, P. Fire Performance of Corroded Reinforced Concrete Columns. *Fire Technol* (2023). doi: 10.1007/s10694-023-01472-x.
7. International Organization for Standardization: ISO 834-11: Fire resistance tests - Elements of building construction - Part 11: Specific requirements for the assessment of fire protection to structural steel elements. 2014.

8. Ba, G., Miao, J., Zhang, W., & Liu, J. Influence of reinforcement corrosion on fire performance of reinforced concrete beams. *Construction and Building Materials* 213, 738–747 (2019). doi:10.1016/j.conbuildmat.2019.04.065.
9. Zhang, W., Chen, J., & Luo, X. Effects of impressed current density on corrosion induced cracking of concrete cover. *Construction and Building Materials* 204, 213–223 (2019). doi:10.1016/j.conbuildmat.2019.01.230.
10. Nicoletta, B., Gales, J., Kotsovinos, P., & Weckman, B. Experimental Thermal Performance of Unloaded Spiral Strand and Locked Coil Cables Subject to Pool Fires. *Structural Engineering International* 32(3), 392–410 (2022). doi: 10.1080/10168664.2021.1881943.
11. Harun, G., Chorlton, B., Richter, F., & Gales, J. The effects of radial cracks on the fire performance of heritage timber. *Fire and Materials* 47(3), 386–399 (2023). doi: 10.1002/fam.3104.
12. Smith, CM., & Hoehler, MS. Imaging Through Fire Using Narrow-Spectrum Illumination. *Fire Technol* 54(6), 1705–1723 (2018). doi: 10.1007/s10694-018-0756-5.
13. Gatién, S., Young, T., Hoehler, MS., & Gales, J. Application of narrow-spectrum illumination and image processing to measure surface char formation in lateral ignition and flame spread tests. *Fire and Materials* 43(4), 358–364 (2019). doi: 10.1002/fam.2706.
14. ASTM: E8 Standard Test Methods of Tension Testing of Metallic Materials. 2022.

QUANTIFYING THE LINK BETWEEN IN-DEPTH TEMPERATURE GRADIENTS AND ONSET OF FIRE-INDUCED CONCRETE SPALLING

Ho Yin Lam¹, Kai Teng Eunice Lim², and Cristian Maluk³

ABSTRACT

Numerous efforts have historically been devoted to investigating the variables that influence concrete spalling during fire incidents. However, to date, empirical data categorically quantifying the governing variables and conditions underlying this phenomenon remains lacking. While certain key variables, such as internal moisture content, are widely acknowledged to influence spalling, their precise quantitative impact and critical thresholds remain poorly defined. This study aims to address this gap by investigating the influence of heating conditions (and in-depth temperature gradients) on the occurrence for heat-induced concrete spalling. Utilizing the H-TRIS test method, the experimental study ensures well-controlled experiments that are both relatively simple and easily replicable, while maintaining strict control over all relevant variables. The findings reveal that, regardless of the heating condition and time-to-spalling, the in-depth temperature gradient close to the heated surface (<25 mm) consistently exhibits similar characteristics. This suggests the existence of a critical in-depth temperature gradient threshold for concrete spalling occurrence.

Keywords: concrete spalling; heating conditions; in-depth temperature gradients; H-TRIS.

1 INTRODUCTION AND BACKGROUND

Fire-induced concrete spalling is a phenomenon where heated concrete detaches or flakes away in a more or less violent manner from the surface (or surfaces) exposed directly to heat during a fire. Spalling is known to occur during growing stages, fully developed stages, or decay stages of a fire. The consequences of spalling are a reduction of the concrete cover to the internal reinforcement and a reduction in the load-bearing cross section of the concrete elements; both having detrimental effects in the structural stability during or after fire.

The current method for evaluating the propensity of fire-induced concrete spalling and the fire resistance of load-bearing concrete structures is centred in the use of a standard fire resistance furnace test; widely used for scientific knowledge growth, although conceived for regulatory approval testing more than a century ago. The fire resistance furnace test is known to have relatively poor repeatability of test outcomes (e.g., time-to-spalling), and comparatively high economic and temporal costs associated with its use [1,2]. Studies in available literature which report the occurrence of concrete spalling during fire resistance tests show a large scatter in test results; such that the research community argues to some extent that fire-induced concrete spalling is an apparently random phenomenon [2].

¹ The University of Queensland, St Lucia, Australia
e-mail: hoyn.lam@uq.edu.au

² The University of Queensland, St Lucia, Australia
e-mail: kaitengeunice.lim@uq.edu.au

³ Technical Director, Semper, UK
e-mail: c.maluk@sempergrp.com, ORCID: <https://orcid.org/0000-0002-1662-6943>

Based on past research (both experiment and modelling), fire-induced concrete spalling is believed to be driven by a combination of thermal-induced stresses, internal pore pressure build up, and reduction of the mechanical properties of concrete at elevated temperatures [2]. Spalling is known to be influenced to some degree, at least by the following: concrete strength, internal moisture condition, age, aggregate type and grading, certain admixtures, mechanical loads, mechanical restraint, heated area, element thickness, severity of thermal exposure, inclusion of steel and/or polypropylene fibres, and others [3]. The number of factors known to influence spalling make its prediction difficult, if not impossible, in practice. Within scientific and engineering communities, is currently challenging to state with confidence which phenomena or mechanisms primarily influence the occurrence of spalling [4].

Although hundreds of experimental studies have been performed in recent decades, there is yet no empirical data that has been able to categorically quantify the governing variables and conditions which underpin the scientific nature of concrete spalling during a fire. The motivation for this research study is to move knowledge on heat-induced concrete spalling forward in a direction where the governing variables and critical thresholds resulting in concrete spalling during a fire are quantified.

1.1 Research need

Heat-induced concrete spalling is without a doubt driven by fire and the internal heating conditions (of concrete due to the fire – bottom line, the fire is “what gets the ball rolling”). Despite the incredible amount of experimental, theoretical, and numerical research studies on concrete spalling, there is no well-defined thresholds which can give an answer to “what is the ‘critical’ heating condition resulting in spalling for any given concrete mix.”

There is relative consensus around the scientific and engineering communities that rapid growing fires result in a higher likelihood of concrete spalling – outcomes of work in this remain qualitative in nature, without quantifiable thresholds for a ‘critical’ heating conditions.

Within the scope of this study, the aim of is to investigate the likelihood of concrete spalling for a very wide range of heating scenarios. This comprehensive experimental study will evaluate four different heating conditions experienced by concrete when tested in a fire resistance furnace test (standard, hydrocarbon, modified hydrocarbon, and RABT-Rail).

2 RESEARCH METHODOLOGY

2.1 Test setup

The Heat-Transfer Rate Inducing System (H-TRIS) fire test method was used within the scope of this experimental work. Thoroughly described elsewhere [8-9], H-TRIS carefully quantifies and controls the thermal boundary conditions imposed on the target heated surface of test samples; the time-history of incident radiant heat flux at its exposed surface [10]. The testing equipment controls the relative position between the exposed surface of the test sample and an array of high-performance radiant heaters coupled with a mechanical linear motion system (see Figure 1).

Using this test method enables the visual inspection of the test samples during fire testing, which is technically very challenging during a furnace test. Although done in past studies using H-TRIS, within the scope of the study described herein concrete samples were left unloaded and unrestrained; therefore, the influence of sustained external loads or restraint during heating was not investigated.

Sixteen high-performance radiant heaters were mounted on a frame, creating a 600 x 800 mm² radiant source of heat. This configuration enables a heating system with a high and stable operational temperature and outstanding thermal homogeneity at the emitting surface. The computer-controlled linear motion system controls the relative position between the array of radiant panels and the exposed surface of the test sample; programmed to impose potentially any time-history of incident radiant heat flux, limited by the maximum proximity to the test sample.

The maximum possible incident radiant heat flux that could be achieved using the H-TRIS at The University of Queensland is >250 kW/m². Essentially, with H-TRIS the time-history of incident radiant heat flux at

the exposed surface of test samples can be precisely controlled (refer to Figure 4). Since the main aim of this research study described herein is to examine the fire behaviour (including the potential occurrence of progressive spalling), tests with H-TRIS were continued for a duration of 2 hours.

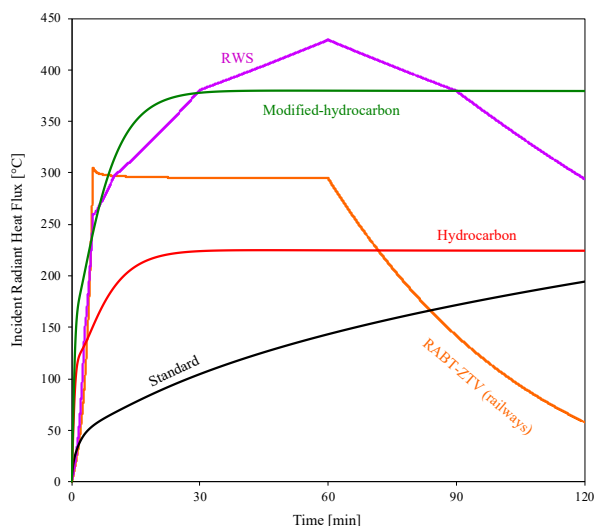


Figure 1. Time-history of incident radiant using H-TRIS for heating conditions tested and example of outcomes of high-speed camera showing the moment of spalling

2.2 Quantifying the heating conditions

To understand the need for the novel fire testing approach described herein, a brief description of key heat transfer principles is shown in this section. Regardless of the design fire selected, the heat transferred from the fire to the exposed surface of a concrete structure (e.g. concrete lining) is normally expressed in terms of a net heat flux, \dot{q}''_{net} [12]:

$$\dot{q}''_{net} = -k_c \cdot \left. \frac{\partial T}{\partial x} \right|_{x=0} \quad (1)$$

Where k_c is the thermal conductivity of concrete, and $\left. \frac{\partial T}{\partial x} \right|_{x=0}$ represents the in-depth time dependent temperature distribution at the exposed surface. For simplicity, in the current analysis heat conduction through the surface is taken only in the direction of the principal heat flow.

Within the scope of this study, H-TRIS was programmed to impose a thermal boundary condition equivalent to that experienced by a concrete sample of equivalent depth under idealised conditions during a standard fire resistance tests (controlled to follow the standard Hydrocarbon time-temperature curve). Figure 4 shows the time-history of incident radiant heat flux yielding an equivalent time-history of net heat flux, and hence equivalent in-depth temperature distributions as experienced during the fire resistance tests. Every test lasted for 120 minutes.

It is worth highlighting that within the work described herein, incident radiant heat flux refers to the rate of thermal energy imposed (per unit of exposed surface and per unit of time) at the exposed surface of test specimens during testing.

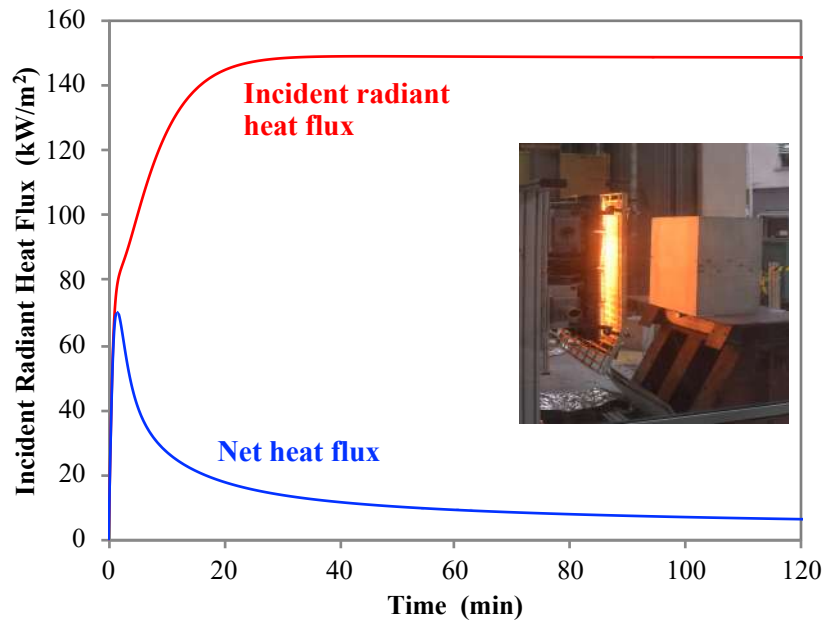


Figure 2. Time-history of incident radiant using H-TRIS for heating conditions tested and example of outcomes of high-speed camera showing the moment of spalling

2.3 Concrete mixes

Concrete mixes were chosen to reflect nominal mixes used in the current Australian construction industry using three types of aggregates. The concrete mix included general purpose cement and fly ash. Concrete mixes were defined by the coarse aggregates included: limestone, granite, and basalt (all of them less than 10mm diameter). Fine aggregate for all mix types contained an even blend of manufactured sand and natural fine sand. Commercially available water reducer was used to obtain the conditions shown in the table below. The curing conditions remained constant for all concrete test samples; (1) kept in the casting moulds for 24 hours, (2) demoulded, (3) placed under water for 7 days, and then (4) kept in a control environment at 20°C and 50% RH until before testing. Measured moisture content at the time of testing was in average 4.9% (by mass). Concrete test samples were tested at an age of 2 to 2.5 years.

For practical considerations, a concrete mix was chosen to reflect a nominal shotcrete mix used in the current Australian construction industry. Although not detailed herein, the concrete mix included general purpose cement, fly ash, silica fume, 10 mm basalt aggregates, normal and fine sand, and a commercially available water reducer. The concrete mix was designed to achieve a cylindrical compressive strength of 50 MPa at 28 days.

The curing conditions remained constant for all concrete test samples; (1) kept in the casting moulds for 36 hours, (2) demoulded, (3) placed under water for 7 days, and then (4) kept in a control environment at 20°C and 50% RH until before testing.

Table 1. Fresh and hardened properties of the concrete mixes

Concrete Mix	Properties of fresh concrete		Properties of hardened concrete		
	Slump (mm)	Air Content (%)	Compressive strength at 28 days (MPa)	Compressive strength at testing* (MPa)	Moisture content at testing* (mass/mass)
Plain concrete	220	3.0	54.1	79.5	4.9%

* These measurements were completed at the same time as when the spalling tests were performed.

2.4 Preparation of concrete test samples

Concrete from a single mixing truck containing one concrete mix type was used for casting all test samples prepared within the scope of the research described herein (see Figure 2). Additionally, standard cylindrical

concrete samples (100 mm diameter, 200 mm height) were casted for monitoring compressive and tensile strength, and non-standard small cylindrical samples (25 mm diameter, 100 mm height) were casted for monitoring internal moisture content of concrete.

The dimensions of the concrete samples casted for the spalling testing were 300 x 300 mm², with a depth of 200 mm. This dimensions of the samples where defined based on past experiments conducted [7] which have demonstrated that, for the expected transient heating conditions, for the concrete sample will behave as a semi-infinite solid. Three samples were casted for each concrete heating condition – therefore, three identical repeat test will be carried for each heating condition. Moulds incorporated thermocouples, precisely placed at thirteen depths from the target exposed surface (2, 5, 10, 15, 20, 25, 50, 75, 100, 150, and 200 mm).

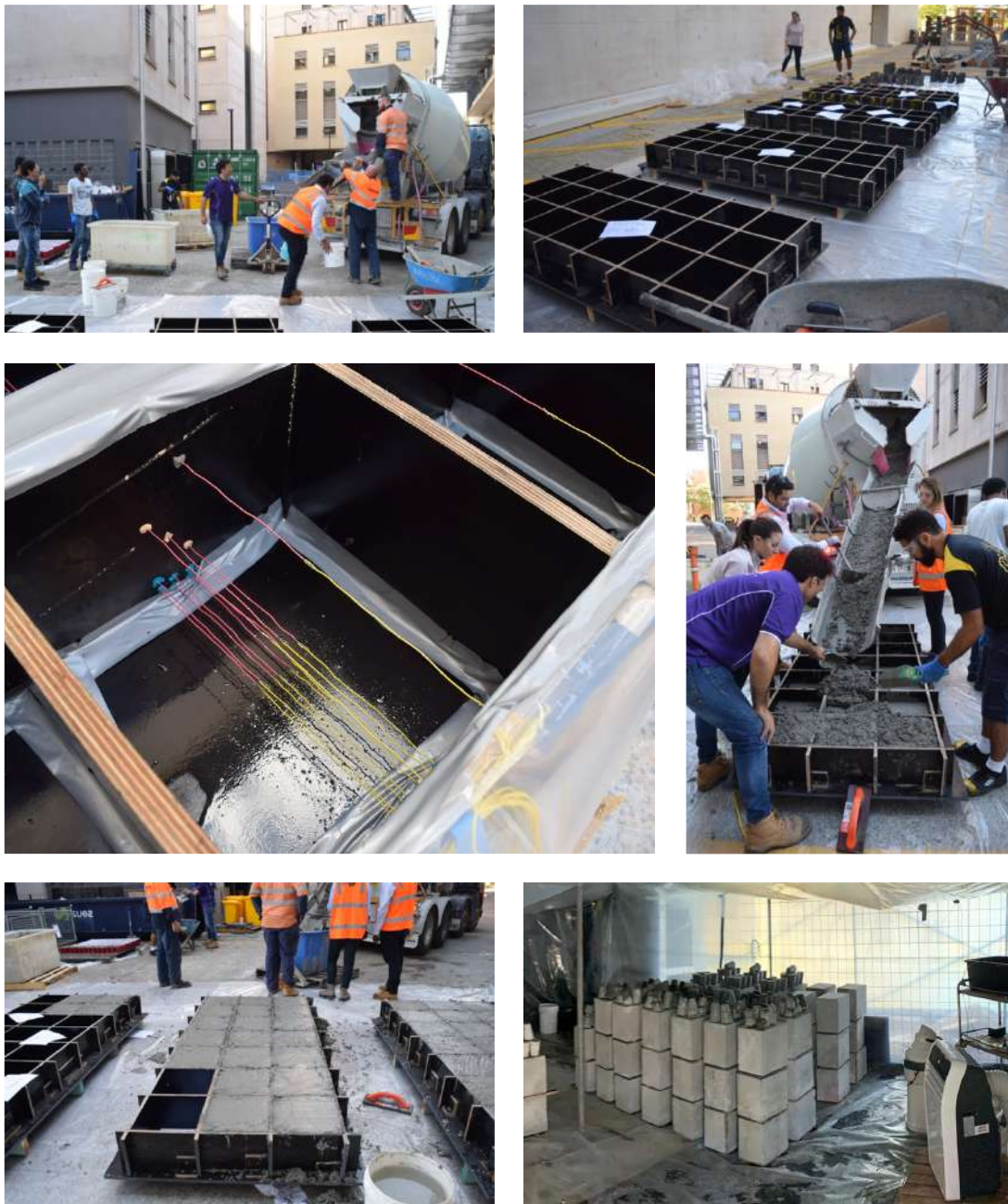


Figure 3. Photographs of casting setup and concrete moulds prior to concrete casting, close-up view of moulds with thermocouples, pouring of concrete, and concrete sample during curing inside a room conditioned with controlled temperature and humidity

3 TEST RESULTS

Precisely controlled and repeatable spalling tests were performed at one test per day which in itself demonstrated the low cost and relative ease of using the H-TRIS method. It is noteworthy that contrary to

variability expectations based on prior fire-induced concrete spalling experimental studies [13], when spalling occurred for a given mix it occurred for both repeat tests at very similar times from the start of heating (refer to Section 3). When tested, concrete samples had an age between 2 and 2.5 years.

In-depth temperature was measured for each of the samples tested; thermocouples were positioned at 13 locations in moulds prior to casting (using distance to the heated surface as a reference; see Section 2). Temperature was recorded during heating and cooling. Figure 8 shows the in-depth temperature between the start of the test and completion of the heating regime (120 min, refer to Section 3.1). The Figure below shows the in-depth temperature for each of the heating conditions tested.



Figure 4. Photograph for each spalled sample after testing

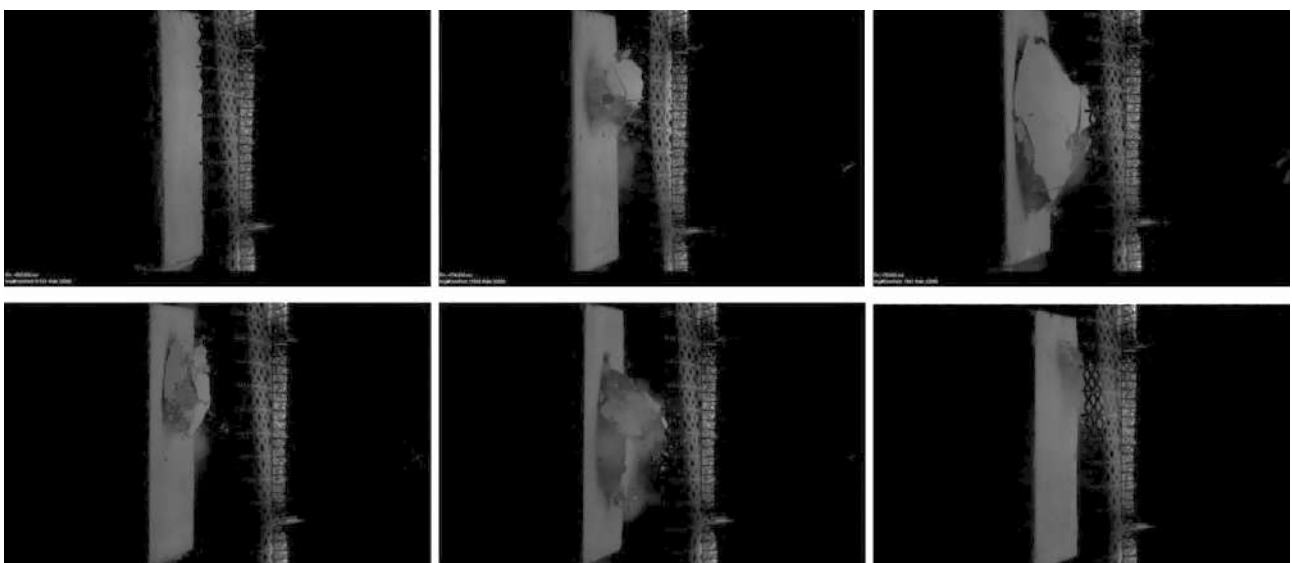


Figure 5. High-speed camera showing the moment of spalling for one exemplar fire test

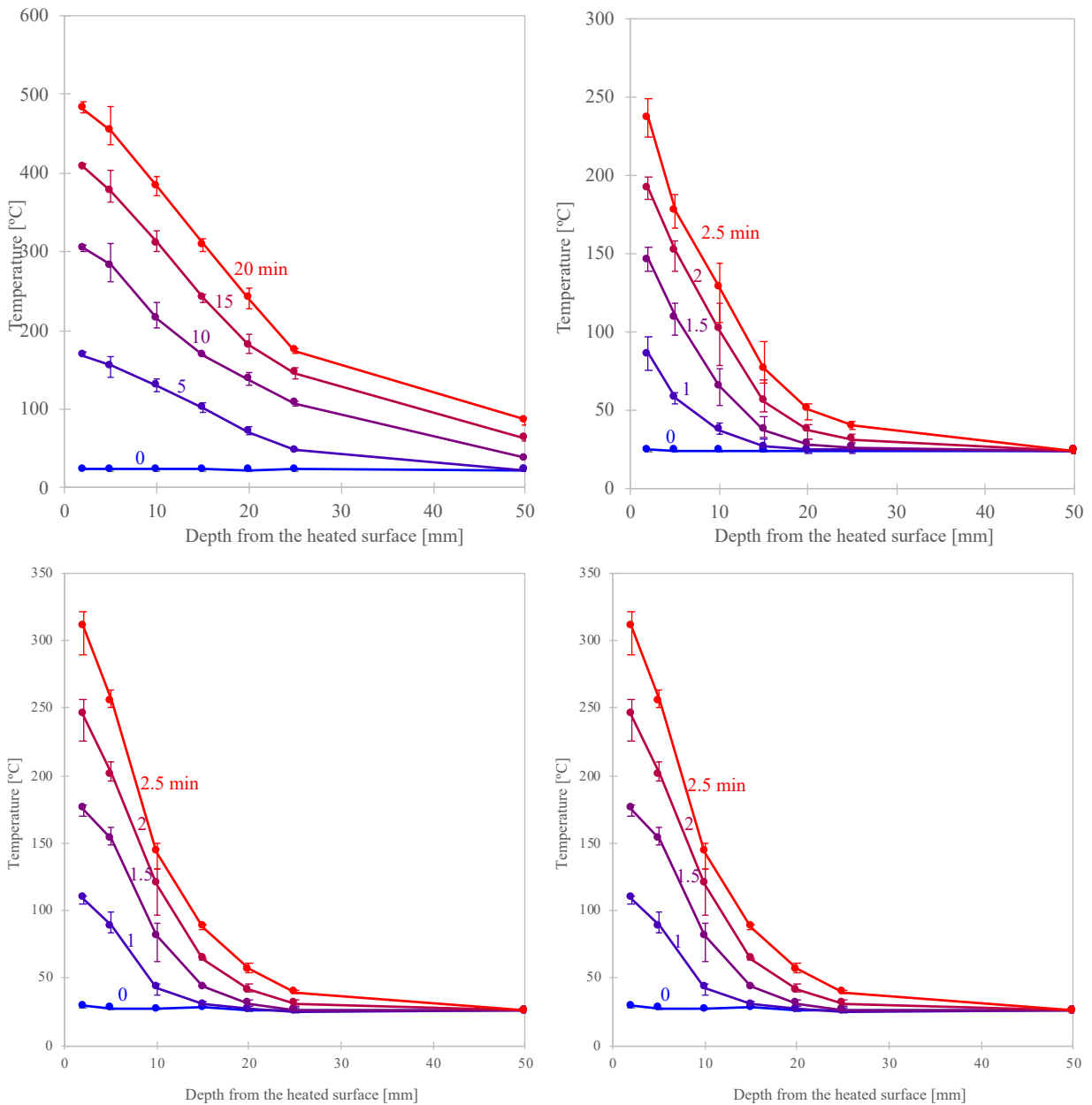


Figure 6. Exemplar in-depth temperature gradient for four spalled test samples

4 ANALYSIS AND DISCUSSION

Each average temperature result presented in this section were demonstrated with various curve representing the temperature profile with every 30 seconds after the first minute into the test. As such, temperature curves presented in each plot will only display the average temperature profile before time-to-spalling under the corresponding heating condition.

The major differences between the six heating condition curves affecting the temperature of concrete specimens, is primarily due to the heating gradient and magnitude of the imposing heat flux over time. Despite that fact that majority of specimen spalled at 1 – 4 minutes into the test, the average temperature measured from the exposed surface were observed to decrease exponentially as depth towards the opposite side of exposed surface increase. This is due to high-strength concrete consisted with low thermal conductivity and thermal inertia, heat is unlikely to penetrate 200mm depth of concrete specimen thoroughly before spalling occurred. Hence, except for Standard fire curve, the average temperature profile tested under all five remaining heating condition curves were observed to varied only from the

heat-exposed surface to typically 25 mm into the specimen, towards the opposite side of exposed surface (Figure 10 to Figure 12).

By combining the temperature profile of each tested result at their corresponding time-to-spalling except for specimens heated under Standard Fire curve, it can be surprisingly found that the temperature at different depth into the concrete specimen, as well as the temperature gradient at their moment of spalling contained with very high likelihood, as illustrated in Figure

Except for specimen heated under Standard Fire curve, all experimental temperature result were displayed in Figure 8 with a typical time-to-spalling range of 1 – 4 minutes into the test. Though, It is believe that this experimental finding has not been verified with any existing literature, it is confident to state that the temperature threshold of plain concrete specimen that exposed under the remaining five heating condition curves was found, as the majority of specimen were observed to spalled when temperature gradient reached approximately 200 [C] at 2mm, 150 [C] at 5mm and 100 [C] at 10mm depth into exposed specimen surface, given the specimen geometric and material condition stated in previous section can further illustrated that due to the short timeframe of specimen has been heated, temperature rise was not considered significant beyond 25mm depth into the heat-exposed surface of specimen. Therefore, it can be summarised that by considering the concrete specimen with 200mm thickness, the influence of heating conditions only affecting temperature profile from the heat-exposed surface to 25mm depth into the concrete specimen by the time-to-spalling, which is 12.5% thickness of the entire specimen at the heat-exposed side.

This experimental result could be valuable for global tunnel fire safety design, as the heating condition presented herein were often studied and referred to when considering tunnel structural safety under threat of fire. However, there are room of potential improvement including numerical correlation to be compute or alternative verification approach in future development.

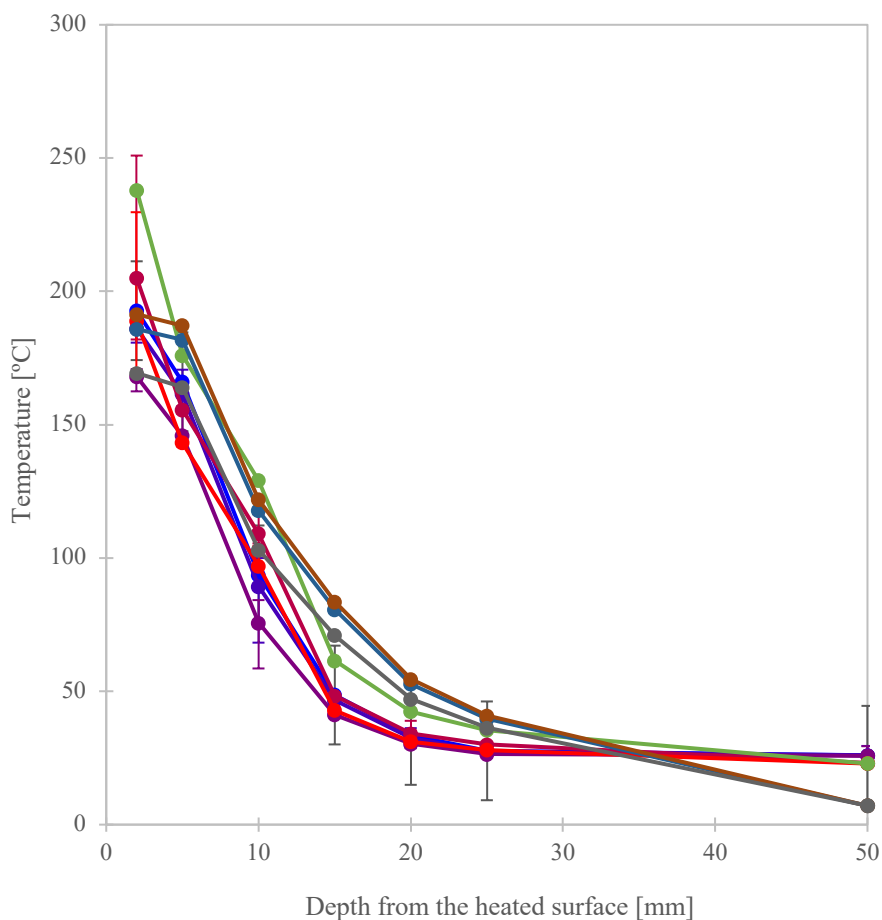


Figure 7. In-depth temperature for all samples that experienced spalling, at the precise moment of spalling.

5 CONCLUSIONS AND FUTURE WORK

5.1 Conclusions

This paper describes the outcomes of a study investigating the influence of heating conditions on the propensity and severity of concrete spalling during fire. Experiments here conducted for four different heating conditions with varying growth at the beginning of the experiment – with test conducted in triplicate. Based on the outcomes of the experiments and analysis of the test data, the following may be concluded:

- Regardless of the heating condition and the time-to-spalling, when spalling occurred, the in-depth temperature gradient close to the heated surface (<25 mm) was always very similar –concluding that there is a critical in-depth temperature gradient for which concrete spalling will occur.
- For the concrete type used in this study, the critical in-depth temperature gradient was found to be between -10.1 and -11.7 °C/mm. This in-depth temperature gradient was found to happen for the Hydrocarbon, Modified-Hydrocarbon, and RABT-Rail heating conditions and therefore spalling occurred for these concrete samples.
- The temperature at the mean depth of spalling measured after the test, at the moment in which spalling occurs, was estimated for each sample, for the mean depth of spalling measured as measured after cooling. For the concrete type used in this study, the temperature was estimated between 111 and 191 °C.

The outcomes of the study described herein is a leap forward in better understanding the likelihood of concrete spalling during a fire. There is still significant work ahead if we (scientific and engineering communities together) are ever to understand the governing variables in the propensity, severity, and consequences of heat-induced concrete spalling.

ACKNOWLEDGEMENTS

The authors are grateful for the support of the School of Civil Engineering at The University of Queensland, Hanson Australia, Propex, Twincon, and The University of Sheffield, and in particular to (in alphabetical order) Dr Harris Angelakopoulos, Stephen Boyle, Jeronimo Carrascal, Martin Chow, Hannah Davidson, Ruth Donohoe, Davi Fagundes Leal, Michael Gunn, Dr Mateo Gutierrez Gonzalez, Thanh Nhat Hoang, Andrew Hockey, Dr Shan-Shan Huang, Manikandan Iyngaran, David Lashin, Dr Andrea Lucherini, Dr Martina Manes, Stewart Matthews, Van Thuan Nguyen, Sam Nothard, Sung Won Park, Fraser Reid, Chris Russ, Jake Savins, Aayush Sharma, Mark Stewart, Charlie Stoneman, Jason Van der Gevel, Shane Walker, Ho Sum Andre Wu, and Tengzheng Zhang.

REFERENCES

- [1] Maluk C, Bisby L, Krajcovic M, and Torero JL. (2019). The Heat-Transfer Rate Inducing System (H-TRIS) Test Method. *Fire Safety Journal*. 105, pp. 307-319
- [2] Maluk C. (2014). Development and Application of a Novel Test Method for Studying the Fire Behaviour of CFRP Prestressed Concrete Structural Elements. PhD Thesis, The University of Edinburgh, UK, 473 pp.
- [3] Arup Fire. Fire Resistance of Concrete Enclosure – Work Package 3 and 4 (RevA). Elaborated for the Nuclear Safety Directorate of the Health and Safety Executive, London, UK, 2005, 52 pp.
- [4] Maluk C, Bisby L., and Terrasi GP. (2017). Effects of polypropylene fibre type and dose on the propensity for heat-induced concrete spalling. *Engineering Structures*, 131, pp. 584-595.

- [5] Maluk C, Terrasi GP, Bisby L, Stutz A, and Hugi E. (2015). Fire resistance tests on thin CFRP prestressed concrete slabs, *Construction and Building Materials*, 101(1), pp. 558-571.
- [6] Falkner H, Huang Z, and Teutsch M. (1995). Comparative Study of Plain and Steel Fiber Reinforced Concrete Ground Slabs. *Journal of Concrete International*, 17(1), pp. 45-51.
- [7] Kukreja CB, Kaushik SK, Kanchi MB, and Jain OP (1980) Tensile strength of steel fibre reinforced concrete, *Indian Concrete Journal*, July, pp.184-188.
- [8] Aufmuth, R.E., Naus, D.J., Williamson, GR (1974). Effect of aggressive environments on steel fiber reinforced concrete, *Construction Engineering Research Laboratory, Technical Report M-113*, Champaign, Illinois, November.
- [9] Nordström E. (2000). Steel fiber corrosion in cracks – Durability of sprayed concrete, *Licentiate Thesis*, Lulea University of Technology.
- [10] Nordström E. (2001). Durability of steel fiber reinforced shotcrete with regard to corrosion, *Shotcrete: Engineering Developments*, Bernard (ed.), pp. 213-217, Swets & Zeitlinger, Lisse.

RESPONSE OF STRUCTURAL CONCRETE ELEMENTS TO THERMO-MECHANICAL LOADS

Biswajit Pal¹, Ananth Ramaswamy²

ABSTRACT

In reinforced concrete (RC) structures, the mechanical properties of both concrete and steel deteriorates with rise in temperature. In addition, concrete subjected to elevated temperature shows two kinds of spalling, namely, explosive spalling and thermal spalling. In the present study a three-dimensional (3D) finite element (FE) model that accounts for not only the hygral and thermal effects (in a homogenized macro-scale concrete material) but also the bond-slip and transient thermal strains for accurate prediction of the behavior of RC assemblages under combined mechanical and thermal loads is presented. The model considers the degradation of material properties (and the uncertainty associated with their values) with increase in temperature. A hygro-thermal analysis is included for the estimation of temperature and pore pressure variations. Specific attention is paid in explicitly modelling the interfacial bond-slip behavior between steel reinforcement and the surrounding concrete. The strength of the model is evaluated through the simulation of benchmark problems that includes axial members, flexural members, and a RC frame assembly. A comparison of the fire resistance values obtained from the model against those determined from the code-based approaches shows that the code-based values are un-conservative in most cases, especially when it involves high strength concrete or very high/low load ratios. To account for the heterogeneous nature of concrete and the contrasting nature of the constituents to high temperature, the work has been extended to a meso-scale hygro thermos mechanical model in an equivalent 2D frame work that enables the distribution of aggregates of varying size randomly in the cement concrete paste. Examples illustrating the benefits of this approach are also presented.

Keywords: Thermal Loads, Degradation, Vapour Pressure, RC assemblages, Coupled model.

1 INTRODUCTION

Research on behavior of concrete subjected to high temperature started over a century back. In the 1910s, Gary [1] observed high internal stresses in concrete due to evaporation of water and thermal gradients and construed those as the primary factors resulting in spalling of concrete at elevated temperature. Studies were carried out on plain concrete and reinforced concrete specimens to ascertain the factors that affect spalling such as the type of aggregates [2], mineral and chemical admixtures in concrete [3], heating characteristics [4], strength-related parameters, loading [5], etc. Aslani and Bastami (2011)[6] presented the constitutive relationships developed for normal-strength concrete and high-strength concrete subjected to fire to provide efficient modeling and specify the performance criteria for concrete structures exposed to fire. Khaliq and Kodur (2011)[7] reported the strength and stiffness properties of concrete deteriorate with an increase in temperature as encountered during exposure to fire. Studies [8] shows that the moisture content, type of aggregate and mix proportions have a significant influence on

¹ Scientist, Central Building Research Institute, Roorkee, India.

e-mail: biswajitjgce.1992@gmail.com , ORCID: <https://orcid.org/0000-xxxx-xxxx-xxxx>

² Professor, Indian Institute of Science, Bangalore, India

e-mail: ananth@iisc.ac.in , ORCID: <https://orcid.org/0000-0003-0391-8952>

the thermal conductivity and several equations to estimate the values of thermal conductivity at high temperature have been proposed. For conventional concrete with granite aggregate, the thermal conductivity ranges between 1.4 and 3.6 W/m degree K at ambient temperature (20°C) [9]. Studies in the literature [10] have found that the specific heat of concrete is affected by the moisture content and the composition of concrete; the specific heat of concrete not only increases with temperature but also increases with a decrease in density of concrete. Aggregates have a slight influence on specific heat up to a temperature of 800°C. Compressive and tensile strength of concrete (both NSC and HSC) show a range of variations at elevated temperature. Reported data by Kodur et al. (2008) [11], Eurocode [12] and ASCE manual [13] and ACI [14], show a large variation in compressive strength of NSC between temperatures of 20 - 800°C. However, the variation in HSC is more in the temperature range of 20 - 500°C, and lesser beyond 500°C. The tensile strength of concrete is a crucial parameter in the purview of high temperature loading as it determines the occurrence of spalling in concrete members and several studies have been undertaken to determine its variation with rise in temperature [15]. The decrease in tensile strength of NSC is attributed to the weak microstructure that allows for growth of micro-cracks [16]; whereas in the case of HSC, the high internal stresses developed on account of pore pressure results in rapid loss of tensile strength [17].

In concrete, the thermal expansion is a net result of differential expansion of its individual constituents (aggregates and cement paste) resulting in high internal stresses. The phenomenon is further complicated by the volume changes due to moisture loss, chemical processes (like dehydration and change in composition), creep and micro-cracking. The values of coefficient of thermal expansion reported in the literature increases from 0 to 1.3 % at 700°C and then remains constant up to 1000°C [18]. Permeability and porosity of concrete are the two crucial parameters that are closely related to explosive spalling. In terms of permeability, it is mentioned by Harmathy [19] that spalling is unlikely to occur if the permeability of the concrete exceeds $k = 5:0 \times 10^{-15} \text{m}^2$. However, recent tests [20] have shown that no spalling was noticed, even with a permeability of the concrete below this value, hence it is difficult to assess the risk of spalling by permeability alone. Although spalling can occur in all types of concrete, HSC is most susceptible to spalling due to its very low permeability and they form the focus of studies [21] pertaining to permeability and porosity. Addition of polypropylene (PP) fibers in HSC has been shown to improve the permeability of concrete in high temperature conditions; as PP fibers have a low melting point of around 170°C. The melting of these fibers creates channels in hardened concrete through which the vapors may escape [21]. The variation of porosity with temperature is equally important for predicting spalling performance of HSC members [21].

Beginning with Shorter and Harmathy in 1965 [22], several analytical models to capture spalling resulting from either of the two mechanisms have been proposed: (1) Development of pore pressure within concrete leading to high bursting stresses (explosive spalling) and (2) Development of thermal stresses due to high thermal gradients resulting in net stresses exceeding the degraded strength of concrete (thermal spalling). These models adopt a coupled transport phenomena involving heat and moisture to tackle these problems. Bazant (1978) [23] has pointed out that for concrete structures exposed to environment, to obtain realistic stresses for prediction of cracks, the associated moisture and heat transport problem must be solved. Studies [24], indicate that when concrete is subjected to sustained compressive stresses and high temperature, the time-dependent deformations such as creep and transient strains become significant.

Creep strain in concrete is caused due to dislocation of microstructures of the material [25]. When stress and temperature are held constant, the creep strain evolves with time. Transient creep strains in concrete at high temperature is mainly caused by the two following reasons: (1) moisture movement and dehydration of concrete due to high temperatures and (2) acceleration in the process of breakage of bond. Unlike thermal strains, the creep and transient strains are dependent not only on temperature, but also on time and stress level, which makes it difficult to distinguish between these strains in experiments. Experimental investigation in steel-concrete bond at high temperature was first carried out [26]. It was found that the bond strength of ribbed steel bars increased until 250°C and then dropped.

The primary focus of most of the existing meso-scale studies (includes coarse aggregates distributed spatially in a cement matrix) focused on characterizing the concrete behaviour under mechanical (M) load

only, either in 2D [27] or 3D [28] framework using coupled damage-plasticity [29] or cohesive-zone [30] based constitutive behaviour for ITZ and under different loadings, e.g., monotonically increasing compressive load [31] or under creep deformation [32] etc. A coupled thermo-mechanical (TM) model at meso-scale, focused on analysing concrete under freeze-thaw cycles [33] or at ultra-low [34], ambient [35] and high temperature [36]. Very few studies included the hygral (H) aspects in the meso-scale model of concrete and performed the analysis in a hygro-mechanical (HM) [37] or thermo-hygro-mechanical (THM) [38] framework. In [38], various critical simplifications or assumptions were made, such as, pore-pressure evolution was considered as a function of temperature only. Further, other THM based meso-scale at high temperatures studies, e.g., [39], lack in terms of one or more of the following aspects or have not considered explicitly: the process of dehydration and thermo-chemical damage, the convective flow of heat through moisture inside pores, separate consideration of capillary and adsorbed water, transport of liquid phases, etc.

In the first part of the present study, a three-dimensional (3D) finite element (FE) model is extended to include effects of bond-slip and transient thermal strain for accurate prediction of the behaviour of RC assemblages under combined mechanical and thermal loads. Calculation of transient thermal strains is included along with mechanical and thermal strains in the analysis. Specific attention is paid in explicitly modelling the interfacial bond-slip behaviour between steel reinforcement and the surrounding concrete that leads to more realistic predictions of stresses, strains, and displacements. Further, the work evaluates the uncertainty associated with the material properties used in the model through a stochastic framework. Explicit consideration of various coupled multi-physical processes and heterogeneity are crucial in a mathematical model in assessing the structural safety of a concrete structure subjected to high temperatures. To the best of our knowledge, such a detailed description of hygro-thermo-chemical-mechanical processes at the meso-scale where they originate in a numerical modelling framework at elevated temperature has not been attempted. The developed model is then used to simulate the thermo-mechanical behaviour of both plain and reinforced concrete structural elements. In the second part of the study the simulated predictions for examples chosen are then validated with the corresponding available experimental data reported in the literature to highlight the developed meso-scale model's general applicability.

2 METHODOLOGY

High temperature induced concrete spalling serves as one of the crucial factors in estimating the thermo-mechanical behaviour of any concrete members that is subjected to fire. However, in the case of normal strength concrete, spalling phenomena might not play the critical role. Whereas, owing to the lower permeability of high-strength concrete, spalling could be one of the critical factors in assessing the structural capacity of a fire exposed concrete structure made with high strength concrete. Depending on the thermo-mechanical loading and boundary conditions, high-temperature induced spalling can be explosive. As a result of spalling, the effective area of cross-section of a concrete member reduces and thus, in the case of reinforced concrete, reinforcement bars exposed to more heat which resulted in the reduction in load carrying capacity of the concrete. The various factors that influence spalling are heating rate, specimen type, permeability of concrete, structural restraint, composition of aggregate, presence of fibres etc. The first theory said that when the effective pore pressure crosses the tensile strength of concrete, concrete spall. Here, effective pore pressure means the pore pressure multiplied by the Biot's coefficient [41]. In contrast to normal strength concrete, high strength concrete is thought to be more prone to the development of pore pressure under the exposure to high temperature owing to its lower permeability value. In the present study a Hygro-thermo-chemo mechanical model (based on [8]) is suitably modified and implemented to estimate gaseous pressure, capillary pressure, temperature, and displacements that are treated as the state variables which intern varies with the extent of hydration completed and the dehydration process when concrete is exposed to high temperature. Concrete is treated as a deformable, multiphase porous material. The model is developed based on a state of thermodynamic equilibrium being established locally (slow phenomena). Phase changes and chemical reactions (hydration-dehydration) are considered in the model development. The model is a fully coupled hygro-thermo-mechanical and chemically coupled process (accounting for the extent of dehydration). The model accounts for various moisture, energy, and transport phenomena (Characteristic of the various phases

of concrete). Evolution of material properties (porosity, permeability, strength properties) with the extent of dehydration of concrete is considered in the model. Material nonlinearities due to temperature, gas pressure, moisture content and material degradation are included in this development. The model considers a representative elementary volume to describe the micro scale processes and a volume averaging [8] to develop the macroscopic (space averaged) balance equations (conservation of Mass, enthalpy and momentum as explained a little later in this section). Assuming the concrete being exposed to high temperature is only undergoing dehydration (no further concrete hydration), and using the conservation of mass, energy and momentum principles, a coupled set of equations of the form (equation 1):

$$C \left(\frac{dX}{dt} \right) + KX = F \quad (1)$$

Where X is the set of state variables (capillary pressure, gaseous pressure, temperature, and displacements) and C, K and F are the nonlinear coefficient matrices of appropriate size described in [8]. MATLAB [42] and COMSOL® [43] platform is used to solve the above equations with appropriate boundary conditions in a time marching scheme. Details of how to specify the boundary conditions is discussed [8]. The equations are solved spatially in a finite element domain and in a temporally through a finite difference backward scheme.

In refining the upscale homogenized macro-scale model to account for the heterogeneous nature of concrete, a meso-scale modelling of concrete in a multi-physics (hygral-thermal-mechanical) based framework involves two important steps. The first involves the generation of the aggregate configuration in the concrete domain. In a mesoscopic model of concrete, the various mesoscopic parameters are the volume fraction, gradation and shape of aggregate, consideration of ITZ thickness, establishment of mesoscopic configuration etc. In all the simulations, volume fraction and gradation of aggregate is taken in accordance with the experiment that is simulated. Whereas, with respect to the shape of the aggregate particle, it is taken as spherical [44, 45] due to the requirement of one shape control parameter, called radius, in its numerical generation. In addition to shape, placing a numerically generated spherical shape aggregates in the concrete space (i.e, to check its intersection with any pre-generated particle or with concrete boundary) can be done from its centroid coordinates and radius data unlike ellipsoidal or random polyhedral particles that need several shape control parameters. Issues of non-interference of the particles is discussed in [45]. Following particle generation, the second step of the multi-physics-based meso-scale model involves defining the governing physics of the problem inside the three constituents of concrete (coarse aggregate, ITZ, and cement mortar) along with different constitutive relations of the constituents. In the context of a multi-phase description of concrete at the meso-scale, the mortar part is assumed to be composed of solid, liquid, and gaseous phases. The liquid phases of mortar are further divided into free water in capillary pores and gel or adsorbed water that is physically bounded to the solid surface [45]. In the context of thermodynamic equilibrium, the phase change that occurs between water and vapor (e.g., water converts to vapor) is considered. However, at high temperatures, owing to the negligible contribution of dry air in the total gaseous pressure compared to water vapor pressure [9], in the present study, the dry air effect is neglected in calculating total pore pressure. Water and vapor transportation are assumed to be governed by Darcy's advection and/or Fickian's diffusion. The temperature distribution and mechanical analysis are modelled using a modified classical heat transfer equation and linear momentum balance. Several physical, thermal, and mechanical properties of the constituents (aggregate, ITZ, and mortar) at the meso-scale vary as a temperature function. The mass balance equation of *i*th phase (e.g., *i*=w, v etc., represents water, vapor, respectively) in its general form can be written as [45] (over a representative volume element in a multi-phase system) the combined equation of mass balances of liquid water (w) and water vapor (v) can be written as (equation 2):

$$\frac{\partial(n_s s_{tw} \rho_w)}{\partial t} + \frac{\partial(n(1-s_w) \rho_v)}{\partial t} + \nabla \cdot (J_w) + \nabla \cdot (J_v) = \dot{M}_{dehy} \quad (2)$$

Contrary to mortar, most of the commonly used aggregates in concrete have porosity and permeability are much lesser than the corresponding cement paste, except the aggregates such as lightweight aggregates or highly porous aggregates [46]. In such a situation, one can consider aggregate as hygrally inert [45]. However, at high temperatures, aggregates can also thermally decompose, creating pores inside aggregates

and degradation of mechanical properties. Therefore, it would be more realistic to consider such a decomposition of aggregates in a meso-scale model. However, bringing such factors about aggregates not only makes the problem complex but also explicit consideration of such factors requires the details about the formation of pores at high temperature inside aggregates. Hence, such thermal decomposition of aggregates is implicitly considered through a total damage variable. This total damage variable is then, in a multiplicative manner, dependent on the degradation that occurs owing to restrained thermal dilatation and thermo-chemical decomposition.

Energy conservation in the case of a porous material like concrete is obtained by adding the energies over all the phases present within an elementary volume. Further, it is assumed that the thermodynamic equilibrium of all the phases presents within an elementary volume also must be held. Therefore, at high temperatures, by ignoring some of the energy contributions like energy lost due to viscous dissipation, etc., the energy balance equation inside the mortar domain can be written as [45] (equation 3):

$$(\rho C_p)_{eff} \frac{\partial T}{\partial t} - \nabla \cdot (\lambda_{eff} \nabla T) + (n S_{tw} \rho_w C_{p,w} v_{w,s} + n(1 - S_w) \rho_v C_{p,v} v_{v,s}) \cdot \nabla T = -H_{vap} \dot{M}_{vap} + H_{dehy} \dot{M}_{dehy} \quad (3)$$

The two terms on the right-hand side of Eq. (3) are the heat effects associated with vaporization and dehydration. In Eq. (3), $(\rho C_p)_{eff}$ and λ_{eff} are the effective specific heat capacity and thermal conductivity of the porous material (i.e., contribution of water, vapor and solid components are considered). In this study, the following form of relation is used to describe the variation of effective heat capacity of mortar with temperature [84] (equation 4):

$$(\rho C_p)_{eff} = n S_{tw} \rho_w C_{p,w} + n(1 - S_{tw}) \rho_w C_{p,w} + (1 - n) \rho_s C_{p,s} \quad (4)$$

In Eq. (4), the volume average approach is used to calculate the temperature-dependent heat capacity of elementary mortar volume, where $C_{p,i}$ represents the specific heat of *i*th species (*i*=w, v, s stands for water, vapor, and solid).

In the field of poro-mechanics, the mechanical behaviour of a material can be described by adding the linear momentum balance equation of each phase present inside an elementary volume of interest. By neglecting the inertial forces etc., the linear momentum balance of a porous medium can be obtained as [45] (equation 5):

$$\nabla \cdot \sigma_t + \rho g = 0 \quad (5)$$

Where, σ_t is the total stress tensor that depends on both fluid pressure and mechanical load. At high temperatures within the mortar domain, this total stress can be described as $\sigma_t = \sigma - \alpha^b p^v \mathbf{I}$, where σ represents the effective stress that is associated with deformations of the solid skeleton. Whereas, in the case of aggregate, these total and effective stress are equal owing to the non-consideration of hygral aspects explicitly inside the aggregate domain. Temperature-dependent Biot's coefficient of the mortar, as presented in [91] based on the multi-scale homogenization technique, is taken in this study. On the other hand, the density (ρ) of the mortar is calculated based on the variant phases present within an elementary volume at a particular time, which is $\rho = (1 - n) \rho_s + (S_{tw} \rho_w + (1 - S_{tw}) \rho_v) n$. Whereas, in the case of aggregate, density ρ can be taken equal to the temperature-dependent density of the solid phase of the aggregate (ρ_{agg}). A coupled set of equations connecting the hygral, thermal and mechanical response is developed having the structure of equation 1 above.

A realistic mechanical representation of a cementitious composite quasi-brittle material, which displays strain-softening characteristics, needs a non-linear theory. Therefore, in the present study, fracture and the associated reduction in material stiffness are described through an isotropic damage-based model, as proposed by Mazars [44], through which the stress-strain relation is expressed as (equation 6):

$$\sigma = (1 - d) \mathbf{D} : \varepsilon_m \quad (6)$$

Where \mathbf{D} represents the initial stiffness tensor, d stands for the total scalar damage variable. When a concrete structure is exposed to high temperatures, mechanical properties deteriorate due to mechanical load and several thermal-chemical-physical processes that occur within the different concrete constituents at high temperatures. Total damage parameter (d) is defined based on the multiplicative combination of the individual damages (due to mechanical load and thermo-chemical degradation), as follows [39] (equation 7):

$$1 - d = (1 - d_{cm})(1 - d_c) \quad (7)$$

The procedure adopted in this study for uncertainty evaluation consists of three steps: (1). Sampling from the set of uncertain material parameters. (2) Repeating the deterministic FE analysis discussed for the entire sample of input parameters. (3) Evaluating the mean and 95 % confidence bounds on the response.

The material parameters considered in the stochastic study are partially specified, correlated set of non-Gaussian random variables and hence, a transformation procedure needs to be adopted to sample from such a set of parameters. Nataf transformation [47] is adopted in this study to transform the set of correlated non-Gaussian random variables to a set of correlated Gaussian variables. Samples of correlated Gaussian random vector can be generated by Eigenvalue decomposition. The mean response and 95 % confidence bounds are obtained through the Monte Carlo simulation (MCS) technique. The complete stochastic model is coded in MATLAB [42].

3 RESULTS AND DISCUSSION

The model is first implemented for the analysis of axial column members subjected to a combination of mechanical and thermal loading. For this purpose, the experiments conducted by Kodur and McGrath (2003) [3] on HSC columns are simulated. The column HSC6 is provided with 8-15 mm main rebars symmetrically placed around the cross-section and 6 mm ties at 76 mm spacing. The confinement is further enhanced by providing two cross-ties of 6 mm at 76 mm spacing. The FE mesh and fire exposed sides of the column used in the analysis are shown in Fig. 1. The concrete used had a compressive strength of 120MPa, an initial water content of 72 kg/m³, a water cement ratio of 0.223, an aggregate cement ratio of 3.364, density 2220 kg/m³, specific heat 1020 J/(kg deg K), an initial pore pressure of 2028.4MPa corresponding to a relative humidity of 64%, initial temperature of 298.2 deg K, and steel rebars having a yield strength of 420MPa and a Young's modulus of 200GPa. The column was initially subject to an axial compressive load of 2964kN while the ends were thermally insulated. The lateral four faces were then exposed to an ASTM time temperature curve. Figure 2 shows the comparison of measured and predicted temperatures across the cross-section. Figure 3 shows a comparison of the measured and predicted axial deformations with the load held constant while the thermal load is applied. The effect of transient strain is seen to be significant in capturing the prediction. Table 1 shows the fire performance of the column, showing that the model and codal procedures are quite close to the experimental results.

A two-story RC frame that involves the study of beam, column and the beam-column joint under thermo-mechanical loading is analyzed. For this purpose, the experiment conducted by Raouffard and Nishiyama [48,49] is simulated. In most of the studies that consider isolated RC members subjected to thermo-mechanical loading, the ends are insulated and the degradation of joint stiffness is not studied. To get a realistic evaluation of the response, the end boundary conditions must mimic the constraints present in a real RC system.

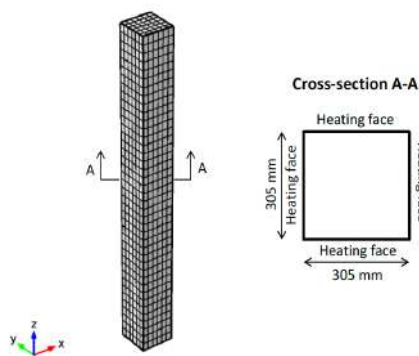


Figure 1. FE mesh and fire exposed sides of HSC6 column (305 x 305 x 3810 mm) [Ends thermally insulated. Axial compression followed by lateral heating, Kodur and McGrath [3]]

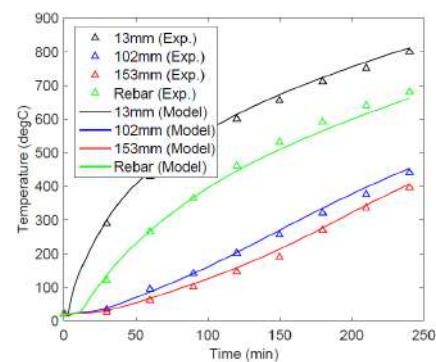


Figure 2. Comparison of measured and predicted temperature versus time at different cross section depth with time, Kodur and McGrath [3]

Figure 4 shows the modelling (symmetry considered) of one column and the joint detail showing the heated face (the beam column joint, the bottom portion of the beam and the column experiences heating).

The concrete used has a compressive strength of 31.3MPa, a Young’s Modulus of 25.3 GPa, an initial water content of 5% by volume, a water cement ratio of 0.63, an aggregate cement ratio of 3.364, an overall density of concrete of 2300 kg/m³, specific heat 1020 J/(kg deg K), an initial pore pressure of 2219.4MPa corresponding to a relative humidity of 70%, initial temperature of 293.15 deg K, and steel rebars having a yield strength of 408, 351, and 377MPa and a Young’s modulus of 188, 191, and 200 GPa in the beams, columns and ties respectively. An ASTM time temperature curve was applied on all exposed faces. The top of the column had an axial load of 30.9kN and a moment M of 3.86 kN-m. The beam had a downward load of 30.9kN at a distance 0.8m from the face of the column. The comparisons of temperatures measured inside the joint region together with the predictions are seen in figure 5 indicating good comparison. Figure 6 shows a comparison of the mid-span beam deflection from the model prediction along with the experimental results. Table 2 gives a comparison of the experiment [48, 49] model predictions and codal predictions of the fire resistance for the beam.

Table 2 clearly indicates that the exposure of the joint to temperature results in an overly un-conservative resistance prediction for the RC elements from the codal based methods, while the prediction from the present model is quite close.

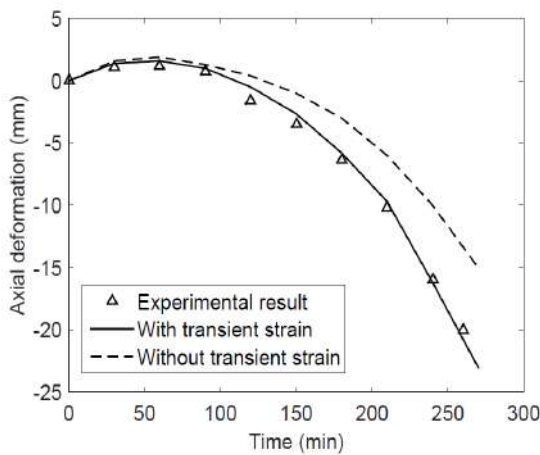


Figure 3 Axial deformation of column HSC6 predicted by model with and without transient strain plotted against experimental deformation reported in [3]

Table 1. Fire resistance based on failure criteria for HSC6

	Temperature	Strength	Deformation	Rate of deformation
Experimental [3]	175	-	>260	>260
Deterministic	182	210	320	340
Stochastic	180	225	310	310
ASCE [13]	210	220	-	
ACI [14]	180	-	--	
500 Isotherm [12]	190	-	-	
Zone Method [12]	190	-	-	
Eurocode 2 [12]	120	-	-	

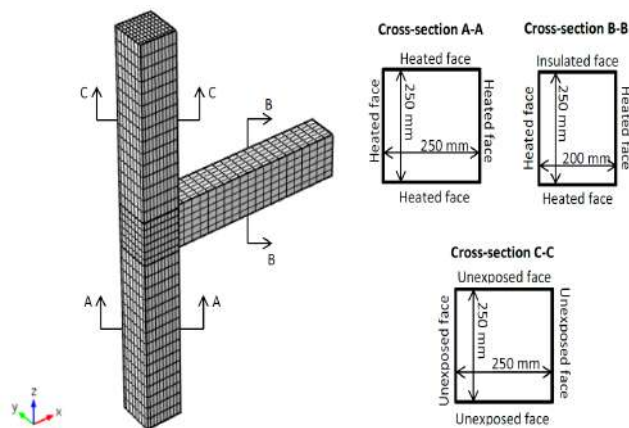


Figure 4. FE mesh and fire exposed sides of RC frame – [Details of test in 48,49]

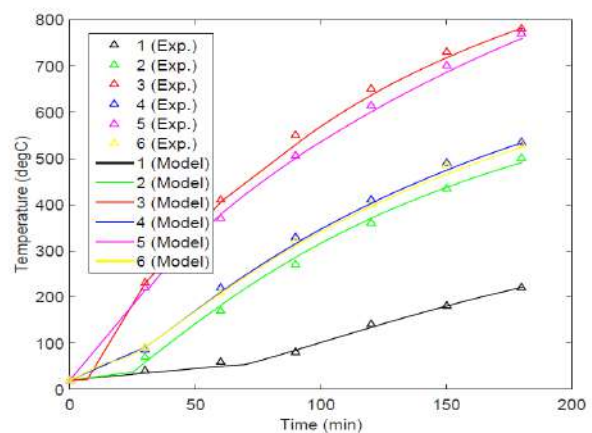


Figure 5 Comparison of model temperature prediction on vertical cross-section at joint center with experimental values [48,49]

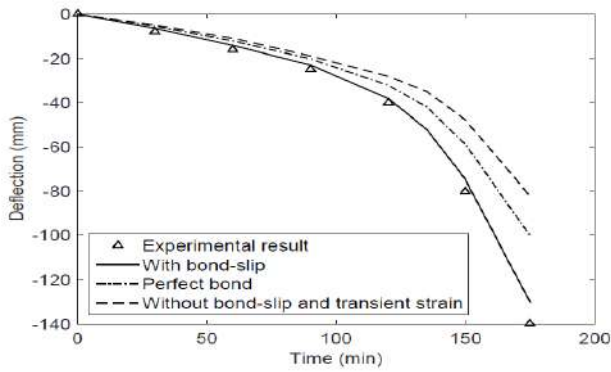


Figure 6. Comparison of Mid-span deflection of the beam, experimental [48,49] and model predictions

Table 2. Fire resistance based on failure criteria for the beam member

	Temperature	Strength	Deformation	Rate of deformation
Experimental [48, 49]	65	-	120	140
Deterministic	68	55	125	140
Stochastic	64	-	140	150
ASCE [13]	240	-	-	-
ACI [14]	180	-	--	-
500 Isotherm [12]	90	100	-	-
Zone Method [12]	90	90	-	-
Eurocode 2 [12]	90	-	-	-

The thermo-mechanical behaviour of a one-way reinforced concrete slab of size 4.9 m x 1.9 m x 0.15 m subjected to mechanical load and followed by heating is studied in a meso-scale framework. The chosen example follows the experiment performed in [50]. In the experiment, the slab was simply supported on the shorter edge (where support is at 0.2 m from the end); see Fig. 7 for details. The slab is first loaded over its entire width and then subjected to heating from the bottom face following the time-temperature curve used in the experiment. The amount of reinforced steel is 1178mm², 15mm bottom cover, an applied load value of 5.4 N/mm² is prescribed. Other values of mechanical, thermal, and hygral properties of the concrete constituents are from [39] [E 42.5GPa, σ_c 43MPa, σ_t 4.3MPa G_f 165J//m² C_p 1070J/kg/K]. Whereas in the case of steel, the modulus of elasticity and yield strength at ambient temperature are taken as 215 GPa and 504 MPa (as reported in the experiment [50]). A linear elastic perfectly plastic material model is used to represent steel. The relative degradation of the above-mentioned mechanical properties of steel with temperature is taken based on the experimental data reported in [39]. Variation of other thermo-physical properties of steel e.g., thermal conductivity, specific heat, coefficient of thermal expansion, and mass density with temperature are taken according to ASCE standard [13] and their values at ambient temperature are 47 W/(m-K), 435 J/(kg-K), 12.1 1/K and 7850 Kg/m³, respectively. In terms of the interaction of reinforcement bar and concrete, temperature-dependent linear bond-stress slip relationship up to peak value (bond-strength) and followed by complete slip with no stress increase is considered. The degradation of steel-concrete bond strength with temperature is taken in this study following the experiment conducted in [45]. Moreover, the experimental study of [51] showed that the variation of the slip value (corresponding to peak bond stress) with temperature can be approximately fitted by a horizontal linear relation with the corresponding slip value of 1 mm. When a mechanically loaded concrete specimen is heated for the first time, the resulting strain is higher the non-loaded specimen at a particular temperature. The additional strain is known as the load induced thermal strains (LITS) or transient creep strain [24]. However, as stated in [30, 52], a major part of the transient thermal strain in concrete occurs owing to the thermal degradation of its constituents, thermal incompatibility of cement pastes and aggregate, etc. This additional strain increases with the increase in the temperature owing to the increase in the thermo-chemical strain and thermo-mechanical damage induces strain. Since, the various governing mechanism of transient creep strain are inherently considered in the developed HTM based meso-scale model, hence, it is expected that analysis of concrete at the meso-scale does not require this transient creep strain to be defined explicitly [30].

Based on the analysis performed, the simulated vertical deflection of the slab at mid-span with heating duration is shown in Fig. 8. The same plot (Fig. 8) shows available experimental data [50]. A reasonably good agreement between the simulated deflection and the experimental results can be observed without defining any additional transient creep strain for the mortar matrix. the reinforced concrete specimen

is further chosen to show the effect of including the damage model, thermo-chemical strain, and geometric non-linearity on the deformation of the specimen during the heating phase. For the various conditions mentioned above, separate simulations have been conducted for different cases (Figure 8). For instance, in case 1, all the conditions: temperature-dependent elastic properties, damage model, thermo-chemical strain, and geometric non-linearity, are considered. Whereas, in case 4, the latter three conditions are suppressed in the simulation. Here, suppressing the damage model implies a non-consideration of material failure at any temperature that includes both thermo-mechanical and thermo-chemical damage contributions. However, in all the cases, temperature-dependent elastic properties of the constituents (aggregates, cement paste, and ITZ) are taken. In the simulation, geometric non-linearity is modelled through the total Lagrangian formulation available in COMSOL [43]. Fig. 8 shows the simulated mid-point vertical deformation of the reinforced concrete slab for the four cases. Experimental data [50] are also presented in the same plot (Fig. 8). It can be observed (Fig. 8, case 4) that non-consideration of the damage model, thermo-chemical strain, and geometric non-linearity in the model could lead to a significant underestimation of the predicted deformation. As the different contributing factors (damage, thermo-chemical strain, and geometric non-linearity) are included in the model (i.e., moving from case-4 to case-1), the simulated results advance toward the experiment. For the example chosen here, the underprediction amount in the vertical deformation with case 2, case 3, and case 4 are 7.4%, 16.3%, and 36.4%, respectively, after 25 minutes of fire, compared to case 1. Further, one can see (Fig. 8) that the simulations have not converged for the whole 35 minutes of fire duration in case 2 (where geometric non-linearity is ignored) and case 3 (where geometric non-linearity and thermo-chemical strain is ignored), unlike case 1 (where problem complexity is even more). By changing the solver settings like its type (e.g., implicit, or explicit method) or relaxing the tolerance, one could run the simulation for up to 35 minutes. In this study, our intention here is not only to show the relative variation of the simulated deformation for the various cases considered but also to highlight how different conditions (e.g., damage model, thermo-chemical strain, and geometric non-linearity) influence the numerical convergence rate.

4 CONCLUSIONS

The HTCM macroscopic model used in the first part of the present study captures the thermos mechanical response of different structural elements accurately. The nodal based methods provide good predictions in instances where the joints are not exposed to thermal loads. However, the predictions from code-based methods are un-conservative when the joint is exposed to thermal loads. A novel methodology of investigating the high temperature behaviour of concrete in a coupled mesoscopic hygro-thermo-mechanical based continuum framework has then been developed. In the second part of this study the proposed methodology brings newness with respect to the characterisation of concrete, as follows:

- HTCM at a scale where aggregate and mortar is considered explicitly,
- Inclusion of various contrasting chemical-physical-hygral-thermal processes that occurs inside.

The developed continuum based HTM meso-scale model is then employed to simulate the high-temperature behaviour of both plain and reinforced concrete structural elements in terms of temperature evolution, pore pressure, damages, deformation, etc. The simulated results are then validated with the corresponding experimental data. Based on the numerical studies performed, the following conclusions can be drawn:

- Localization of damage and subsequently a more realistic failure pattern during spalling (where random parts spall out at a different time as observed in experiments) can be reproduced only through a meso-scale-based model,
- Validation of the developed meso-scale model in terms of various hygral, thermal and mechanical responses in case of a wide variety of heating conditions, is obtained.

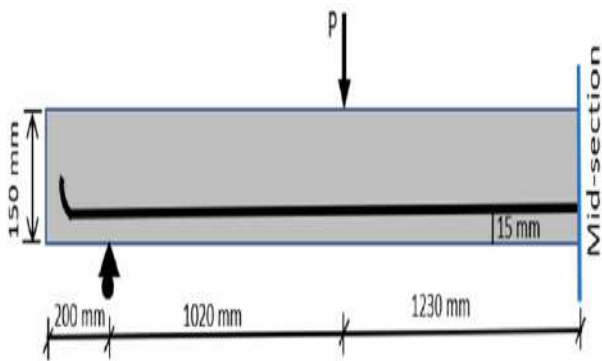


Figure 7 Details of RCC Beam [50]

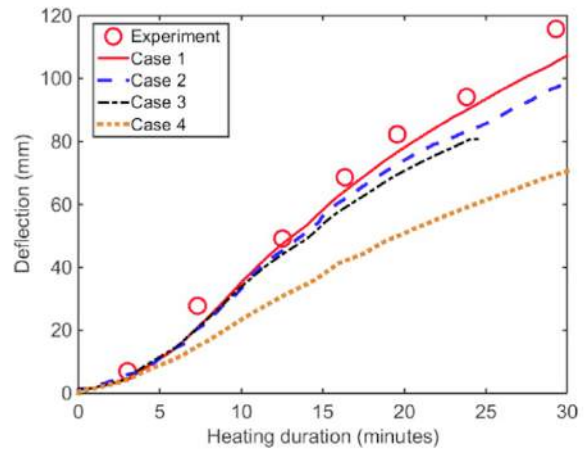


Figure 8 Effect of damage model, thermo-chemical strain, and geometric non-linearity on the deformation of reinforced concrete specimen and comparison with experimental data [50]

5 REFERENCES

- [1] Gary, M. (1917). Properties of concrete. German Committee on Iron Concrete, Wilhelm Ernst and Sohn, Berlin.
- [2] Khoury, G. A. and Anderberg, Y. (2000). Concrete spalling review. *Fire Safety Design*, 60:5(12)
- [3] Kodur, V. K. and McGrath, R. (2006). Effect of silica fume and lateral confinement fire endurance of high strength concrete columns. *Canadian journal of civil engineering*, 33(1), 93-102.
- [4] Klingsch, E. W., Frangi, A., and Fontana, M. (2011). High-and ultrahigh performance concrete: A systematic experimental analysis on spalling. *Special Publication*, 279, 1-50.
- [5] Kodur, V. and Phan, L. (2007). Critical factors governing the fire performance of high strength concrete systems. *Fire Safety Journal*, 42(6), 482-488.
- [6] Aslani, F. and Bastami, M. (2011), "Constitutive relationships for normal- and high-strength concrete at elevated temperatures:" *ACI Materials Journal*, pp 355-365
- [7] Khaliq, W. and Kodur, V.K.R. (2011) Effect of High Temperature on tensile strength of different types of high strength concrete, *ACI Materials Journal*, pp. 394-402
- [8] Gawin, D., Pesavento, F., and Schreer, B. A. (2006). Modelling damage processes of concrete at high temperature with thermodynamics of multi-phase porous media. *Journal of theoretical and applied mechanics*, 44(3), 505-532.
- [9] Bazant, Z. P. and Kaplan, M. F. (1996). *Concrete at high temperatures: material properties and mathematical models*. Longman, UK.
- [10] Harmathy, T. (1970). Thermal properties of concrete at elevated temperatures. *Journal of Materials*, 5(1), 47-74
- [11] Kodur, V. and Dwaikat, M. (2008). A numerical model for predicting the fire resistance of reinforced concrete beams. *Cement and Concrete Composites*, 30(5), 431- 443.
- [12] Eurocode-2 (2004). *Design of Concrete Structures*. British Standards Institution, London.
- [13] ASCE Manual (1992). *Structural fire protection, manuals and reports on engineering practice*, No. 78. New York, NY.
- [14] ACI-216.1 M-07 (2007). *Standard Method for Determining Fire Resistance of Concrete and Masonry Construction Assemblies*. American Concrete Institute, Detroit, USA.
- [15] Felicetti, R., Gambarova, P., Rosati, G., Corsi, F., and Giannuzzi, G. (1996). Residual mechanical properties of high-strength concretes subjected to high temperature cycles. In *Proceedings of 4th International Symposium on Utilization of high-strength concrete*, pages 579-588.
- [16] Cengel, Y. A. (2003). *Heat transfer: A practical approach*. McGraw Hill, New York.

- [17] Chan, Y., Peng, G., and Anson, M. (1999). Residual strength and pore structure of high-strength concrete and normal strength concrete after exposure to high temperatures. *Cement and Concrete Composites*, 21(1), 23-27.
- [18] Kodur, V. (2014). Properties of concrete at elevated temperatures. *ISRN Civil engineering*, 2014.
- [19] Harmathy, T. (1965). Effect of moisture on the re-endurance of building elements In *Moisture in Materials in Relation to Fire Tests*. ASTM International
- [20] Klingsch, E. and Frangi, A. (2013). Explosive Spalling of Concrete in Fire: Test Report. Institute of Structural Engineering and Construction, ETH Zurich.
- [21] Hertz, K. D. (2003). Limits of spalling of fire-exposed concrete. *Fire safety journal*, 38(2), 103-116.
- [22] Shorter, G. and Harmathy, T. (1965). Moisture clog spalling. *Proceedings of institution of civil engineers*, 20, 75-90.
- [23] Bazant, Z. P. and Thonguthai, W. (1978). Pore pressure and drying of concrete at high temperature. *Journal of the Engineering Mechanics Division*, 104(5), 1059-1079.
- [24] Khoury, G. A., Grainger, B. N., and Sullivan, P. J. (1985). Strain of concrete during first heating to 600 c under load. *Magazine of concrete research*, 37(133), 195-215.
- [25] Terro, M. J. (1998). Numerical modeling of the behavior of concrete structures in fire. *ACI Structural Journal*, 95(2), 183-193.
- [26] Milovanov, A. and Salmanov, G. (1954). The influence of high temperature upon the properties of reinforcing steels and upon bond strength between reinforcement and concrete. *Issledovanija po zharoupornym betonu i zhelezobetonu*, pages 203-223
- [27] X.F. Wang, Z.J. Yang, J.R. Yates, A.P. Jivkov, C. Zhang, Monte Carlo simulations of mesoscale fracture modelling of concrete with random aggregates and pores, *Constr. Build. Mater.* 75 (2015) 35–45, <https://doi.org/10.1016/j.conbuildmat.2014.09.069>.
- [28] L. Zhang, X. Sun, H. Xie, J. Feng, Three-dimensional mesoscale modeling and failure mechanism of concrete with four-phase, *J. Build. Eng.* 64 (2023), <https://doi.org/10.1016/j.job.2022.105693>.
- [29] Z. Yu, Z. Chen, P. Chen, X. Liu, Y. Wu, C. Wang, Factors affecting uniaxial compressive strength and ultrasonic pulse velocity of meso-scale heterogeneous concrete, *Constr. Build. Mater.* 389 (2023) 131680.
- [30] J. Geng, C. Liu, A methodology for parameter identification and calibration of the cohesive element based meso-scale concrete model, *Constr. Build. Mater.* 393 (2023) 132075.
- [31] T. Wang, R. San Nicolas, T.N. Nguyen, A. Kashani, T. Ngo, Mechanical behaviour of glass-mortar under uniaxial compression loading based on a meso-scale modelling approach, *Constr. Build. Mater.* 359 (2022) 129499.
- [32] F. Bernachy-Barbe, B. Bary, Effect of aggregate shapes on local fields in 3D mesoscale simulations of the concrete creep behavior, *Finite Elem. Anal. Des.* 156 (2019) 13–23.
- [33] H. Miao, C. Guo, Z. Lu, Z. Chen, 3D mesoscale analysis of concrete containing defect damages during different freeze-thaw cycles, *Constr. Build. Mater.* 358 (2022) 129449.
- [34] Y. Cai, Y. Zhang, Y. Liu, J. Li, Predictive method for the macroscopic mechanical properties of concrete at ultra-low temperatures, *Constr. Build. Mater.* 357 (2022), <https://doi.org/10.1016/j.conbuildmat.2022.129276>.
- [35] A. Taibi, T.T. Chimoto, F.K. Maradzika, M. Matallah, Mesoscale investigation of mass concrete temperature control systems and their consequences on concrete mechanical behaviour, *Frat. Ed. Integrita Strutt.* 16 (2022) 416–437, <https://doi.org/10.3221/IGF-ESIS.60.29>.
- [36] L. Jin, R. Zhang, X. Du, Computational homogenization for thermal conduction in heterogeneous concrete after mechanical stress, *Constr. Build. Mater.* 141 (2017) 222–234, <https://doi.org/10.1016/j.conbuildmat.2017.03.016>.
- [37] S. O'zbolt, S.Zadran Gambarelli, Coupled hygro-mechanical meso-scale analysis of long-term creep and shrinkage of concrete cylinder, *Eng. Struct.* 262 (2022), <https://doi.org/10.1016/j.engstruct.2022.114332>.
- [38] A. Caggiano, D.S. Schicchi, G. Etse, M. Ripani, Meso-scale response of concrete under high temperature based on coupled thermo-mechanical and pore-pressure interface modelling, *Eng. Fail Anal.* 85 (2018) 167–188.

- [39] J. Bosnjak, Explosive spalling and permeability of high-performance concrete under fire-numerical and experimental investigations, Dr. Diss., Inst. F. üR. Werkst. Im. Bauwes. der Univ. Stuttgart. (2014), <https://doi.org/10.18419/opus-529> accessed March 13, 2022.
- [40] V.K.R. Kodur, Spalling in High Strength Concrete Exposed to Fire: Concerns, Causes, Critical Parameters and Cures, Structures Congress 2000, Adv. Technol. Struct. Eng. 103 (2004) 1–9, [https://doi.org/10.1061/40492\(2000\)180](https://doi.org/10.1061/40492(2000)180).
- [41] J. Zhao, J.J. Zheng, G.F. Peng, K. van Breugel, A meso-level investigation into the explosive spalling mechanism of high-performance concrete under fire exposure, Cem. Concr. Res 65 (2014) 64–75, <https://doi.org/10.1016/j.cemconres.2014.07.010>.
- [42] MATLAB U2014) User's Manual, The Math works USA
- [43] COMSOL (2016) User's Manual, COMSOL, Ltd.
- [44] Mazars, J. and Pijaudier-Cabot, G. (1989). Continuum damage theory application o concrete. Journal of Engineering Mechanics, 115(2), 345-360.
- [45] B. Pal, A. Ramaswamy, A multi-physics-based approach to predict mechanical behavior of concrete element in a multi-scale framework, Mech. Mater. 176 (2023) 104509, <https://doi.org/10.1016/J.MECHMAT.2022.104509>.
- [46] M. Alexander, S. Mindess, Aggregates in Concrete, 1st Edition, CRC Press, London, 2005.
- [47] Der Kiureghian, A. and Liu, P.-L. (1986). Structural reliability under incomplete probability information. Journal of Engineering Mechanics, 112(1), 85-104.
- [48] Raouffard, M. M. and Nishiyama, M. (2015). Fire resistance of reinforced concrete frames subjected to service load: Part 1. Experimental study. Journal of Advanced Concrete Technology, 13(12), 554-563.
- [49] Raouffard, M. M. and Nishiyama, M. (2016). Residual load bearing capacity of reinforced concrete frames after fire. Journal of Advanced Concrete Technology, 14(10), 625-633.
- [50] R. Minne, M. Vandamme, Resistance of reinforced concrete floor slabs against fire, Cement 34 (1982) 642–646.
- [51] W. Botte, R. Caspeelee, Post-cooling properties of concrete exposed to fire, Fire Safety J. 92 (2017) 142–150, <https://doi.org/10.1016/j.firesaf.2017.06.010>.
- [52] A.F. Bingöl, R. Gül, Residual bond strength between steel bars and concrete after elevated temperatures, Fire Saf. J. 44 (2009) 854–859, <https://doi.org/10.1016/j.firesaf.2009.04.001>.

SPALLING TESTS OF ULTRA-HIGH PERFORMANCE CONCRETE: INFLUENCE OF POLIPROPYLENE FIBERS, DRYING AND HEATING RATE

V. Albero¹, D. Hernández-Figueirido², L. Reig³, M. Roig-Flores⁴, A. Melchor-Eixea⁵, A. Piquer⁶,
A. Pitarch⁷

ABSTRACT

This study investigates the efficacy of incorporating polypropylene fibres (PPF) into ultrahigh-performance concrete (UHPC) to mitigate spalling. This research work explores the impact of different PPF doses (up to 2 kg/m³), heating rates (2°C/min, 5°C/min, 15°C/min) and drying methods (natural and accelerated) on the spalling phenomenon in UHPC. Four UHPC formulations with increasing PPF contents were prepared, along with a reference mixture without PPF. The results proved that the specimens containing 2 kg/m³ of PPF exhibited spalling resistance under all the conditions, regardless of the heating rate and drying condition. This is consistent with Eurocode 2 recommendation, which promotes including 2 kg/m³ of PPF to mitigate fire-induced spalling. The specimens dried at 80°C, for both 3 and 14 days showed spalling resistance when containing at least 0.5 kg/m³ of PPF. The results revealed that adding 2 kg/m³ PPF, and combining accelerated drying at 80°C for 3 days and adding a minimum of 0.5 kg/m³ PPF, are effective ways of avoiding explosive spalling and its negative effects, enhancing the fire resistance of UHPC structures.

Keywords: Ultrahigh-performance concrete; high temperature; fire; concrete spalling; polypropylene fibres.

1 INTRODUCTION

Ultrahigh-performance concrete (UHPC) has been paid considerable attention in civil engineering due to its exceptional mechanical properties: compressive strength of approximately 150 MPa [1]; tensile strength ranging from 7 to 15 MPa [2] and low permeability [3]. Well-designed UHPC structures offer enhanced structural efficiency, small member dimensions and a long service life. Yet despite these remarkable attributes, UHPC is susceptible to spalling, a phenomenon in which concrete fragments suddenly eject or detach from the structure's surface under fire conditions. Spalling poses a significant threat to UHPC structures' safety and integrity in the event of fire, and potentially endangers occupants and firefighters [4].

¹ Associate Professor, Department of Mechanical Engineering and Construction, Universitat Jaume I, 12071 Castellón de la Plana, Spain, valbero@uji.es, ORCID: <https://orcid.org/0000-0001-7193-9232>

² Associate Professor, Department of Mechanical Engineering and Construction, Universitat Jaume I, 12071 Castellón de la Plana, Spain, hernandd@uji.es, ORCID: <https://orcid.org/0000-0002-3728-513X>

³ Associate Professor, Department of Mechanical Engineering and Construction, Universitat Jaume I, 12071 Castellón de la Plana, Spain, reig@uji.es, ORCID: <https://orcid.org/0000-0001-5683-2779>

⁴ Associate Professor, Department of Mechanical Engineering and Construction, Universitat Jaume I, 12071 Castellón de la Plana, Spain, roigma@uji.es, ORCID: <https://orcid.org/0000-0002-1067-1276>

⁵ Research Assistant, Department of Mechanical Engineering and Construction, Universitat Jaume I, 12071 Castellón de la Plana, Spain, amelchor@uji.es, ORCID: <https://orcid.org/0009-0006-5352-7916>

⁶ Associate Professor, Department of Mechanical Engineering and Construction, Universitat Jaume I, 12071 Castellón de la Plana, Spain, ana.piquer@uji.es, ORCID: <https://orcid.org/0000-0003-1601-0310>

⁷ Associate Professor, Department of Mechanical Engineering and Construction, Universitat Jaume I, 12071 Castellón de la Plana, Spain, pitarcha@uji.es, ORCID: <https://orcid.org/0000-0002-1091-8283>

Spalling is a complex process that is influenced by various factors: the UHPC microstructure, thermal gradients, pore pressure development and the presence of internal moisture [5,6]. UHPC's susceptibility to spalling is strongly influenced by its low permeability and porosity, which lead to water pressure accumulating in pores when exposed to fire, resulting in explosion or fragmentation [4,7,8]. This phenomenon can also lead to loss of protective cover, exposing the underlying reinforcement to high temperatures and over-reducing the structure's load-carrying capacity [9]. Understanding UHPC behaviour at high temperatures is, therefore, crucial for mitigating spalling risks. However, as the mechanisms that underlie explosive spalling in UHPC are not fully understood [10], further exploring UHPC behaviour when exposed to high temperatures is essential.

Various strategies have been proposed to address spalling in UHPC, including the addition of non-structural fibres, the application of protective coatings, the incorporation of mineral additives and the optimisation of mix designs [11,12]. This study focuses on combining metallic and polymeric fibres in UHPC development to enhance spalling resistance. While previous research works have highlighted that the effectiveness of steel fibres alone is insufficient, combining them with polypropylene fibres (PPF) can alleviate vapour pressure and prevent spalling [3,12]. In line with this, previous studies have observed that UHPC permeability and, consequently, its spalling resistance, can improve by not only the melting of PPF, but also by the different thermal expansions between PPF and the binding matrix [3]. Using PPF in UHPC has successfully prevented spalling by increasing permeability, especially when combined with steel fibres and larger aggregates. Then, drying or preheating UHPC reduces spalling by creating a network of capillary pores and microcracks that allows water vapour to evaporate from the concrete structure during a fire. This method is effective to protect existing structures from fire because it prevents the formation of macrocracks and larger pores, which can rapidly lead to not only the reduction of compressive and tensile strengths, but also to decreased resistance to aggressive substances and frost [13]. The greater permeability resulting from PPF addition reduces the maximum pore pressure in UHPC, further mitigating the spalling risk [14]. This is consistent with Eurocode 2 recommendation, which promotes including 2 kg/m³ of PPF to mitigate fire-induced spalling [15].

As for the heating rate that should be applied to simulate fire, as Kodur and Banerji [7] highlight, currently there are no standardised procedures to evaluate the variation in UHPC mechanical properties when exposed to high temperatures, being different heating rates, specimen dimensions or drying processes used. In this sense, Amran et al. [12] observed that the heating rate of Standard ISO 834 fire [16] (average of 67.8°C/min for the first 10 minutes) is too fast to be directly applied in UHPC. Then different UHPC properties have been reported depending on the parameters such as test procedures, specimen dimensions or mix proportions. Aiming to provide further information on the spalling behaviour of UHPC, exposed to high temperatures, this study essentially focused on the influence of increasing amounts of PPF, the followed drying method, and varying heating rates on spalling phenomena. Compression tests were also included to assess the effect of PPF content on the room temperature strength of the developed UHPC.

In short, although UHPC is a promising material with good strength and durability, aspects like susceptibility to spalling, lack of design codes or variability in reported properties reduce its broad practical applicability. This study aims to complement existing knowledge of UHPC exposed to high temperatures by complementing scarce and variable existing data, and providing recommendations for designing and constructing fire-resistant UHPC structures. To do so, this research work aimed to assess the effectiveness of incorporating varying amounts of PPF, and the influence of the drying method (natural or accelerated) and increasing heating rates on the spalling propensity of UHPC.

2 EXPERIMENTAL PROCESS

2.1 Sample preparation

A reference sample without PPF and four distinct UHPC formulations with increasing PPF contents (Table 1) were prepared to investigate the influence of PPF on UHPC when exposed to fire. Twelve UHPC 100 mm cubes were produced for each concrete mixture. Three were employed to determine the compressive strength at room temperature and the remaining nine to assess the spalling phenomenon. Samples were developed in a pan concrete mixer at Preffor's facilities (Vilamarchante, Spain), a company renowned for

its expertise in constructing prefabricated structures using UHPC. CEM I 42.5SR, according to UNE EN 197-1:2011 specifications [17], was utilised in all the concrete mixes. UHPC samples were covered with a plastic sheet to prevent water evaporation in the initial curing phase. After 24 hours, samples were demoulded and transported to the Universitat Jaume I (UJI; Castellón, E Spain). They were then immersed in temperature-controlled water for 28 days at 20°C.

Table 1. UHPC mixture proportions

ID	Polypropylene fibres (kg/m ³)	Cement (kg/m ³)	Fine aggregates (kg/m ³)	Silica fume (kg/m ³)	Steel fibres (% vol.)	Water		Superplasticiser (% mass cement)
						Effective water (L/m ³)	Effective (w/c)	
PP0.0	0.0	800	1182	135	2.5	160	0.2	1.1
PP0.5	0.5							
PP1.0	1.0							
PP1.5	1.5							
PP2.0	2.0							

2.2 UHPC compressive strength

The influence of PPF on the compressive strength of the developed UHPC was assessed in 10 cm cubes cured for 28 days at 20°C. Three cubes per mixture were tested until failure in a hydraulic press of 3000 kN capacity at 6 KN/s following Standard UNE-EN 12390-3 [18]. The mean values and standard deviations were determined.

2.3 Preliminary drying tests

Three specimens with each PPF content were subjected to natural drying under ambient conditions for 14 days and three were oven-dried at 80°C for the same period. This specific temperature was chosen considering the onset of PPF degradation at 82°C. As shown in Figure 1, the accelerated-dried samples exhibited a change in the humidity loss rate trend around drying day 3. Consequently, drying at 80°C for 3 days was selected in this research work to investigate the impact of humidity and to assess whether this drying period was sufficient to prevent spalling.

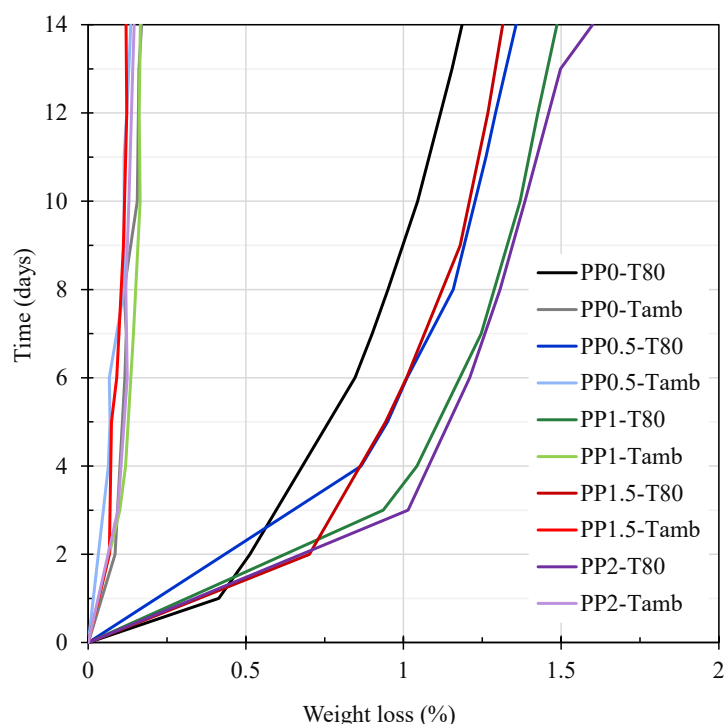


Figure 1. Weight loss recorded during UHPC drying at room temperature and 80°C

2.4 Spalling tests

The UHPC specimens were dried at room temperature for 14 days, at 80°C for 3 days and at 80°C for 14 days (three samples per PPF content and drying condition). Spalling assessments were made for each composition and drying condition at three distinct heating rates: 2°C/min, 5°C/min and 15°C/min. The furnace was programmed for every heating rate up to a temperature of 600°C, which was maintained for 1 hour to allow the entire specimen to reach the desired temperature. Three more specimens (one per heating rate), with a thermocouple placed in their geometrical centre, were prepared to monitor the temperature profile at the core of the UHPC samples. This procedure helps to determine the temperature gradient between the surface and specimens' exterior. Figure 2 plots the programmed temperatures and those recorded in the embedded thermocouples. As expected, there was a gap between them.

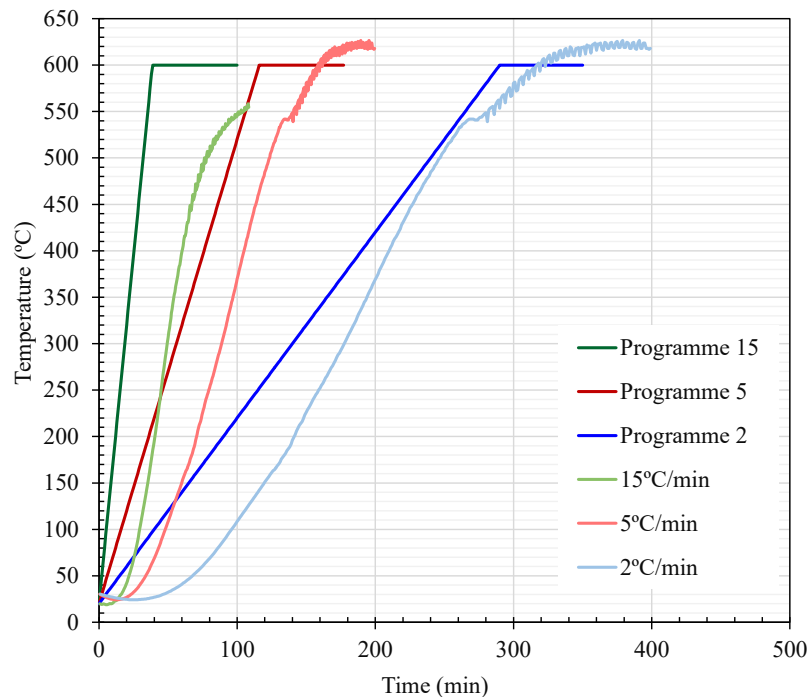


Figure 2. Temperature cycle – Programmed temperature-time heating ramps and temperatures recorded in the embedded thermocouples

To prevent furnace deterioration due to the projection of concrete fragments during spalling, a protective metal cage surrounding the UHPC specimens (see Figure 3) was employed during the spalling tests.



Figure 3. Metallic cage to protect the furnace from explosive spalling

2.5 UHPC permeability

The potential for PPF to melt during fire exposure and to generate a network of pores inside UHPC, which facilitates steam release, was also investigated. For that purpose, three more specimens were prepared for each PPF content previously defined in Table 1. Their water absorption was determined before and after exposure at 200°C for 3 hours. This temperature was selected based on the PPF melting point, which occurs at approximately 160°C. These samples' water absorption was evaluated following Standard EN 12390-8 [19]. To do so, samples' weight was measured before and after immersion in a water tank for 3 days.

3 RESULTS

3.1 UHPC compressive strength

Figure 4 illustrates the impact of increasing amounts of PPF on the compressive strength of the UHPC cured at 20°C for 28 days. Although this research focused mainly on spalling phenomena, compression tests were also conducted to monitor strength variation depending on PPF content. The graph below presents the mean values and standard deviations of three specimens per mixture. The results evidenced that the compressive strength of the developed UHPC remained within the 145-155 MPa range, which indicates that including PPF did not significantly alter UHPC compressive strength at room temperature. The slightly lower strength and wider dispersion observed for mix PP2.0 were attributed to its high fibre content, which difficulties achieving uniform distribution in the cementitious matrix. These findings are consistent with those reported by Du et al. [20], who found that incorporating PPF and air-entraining agents effectively reduces explosive spalling in high-strength concrete, albeit with a minor decrease in mechanical strength.

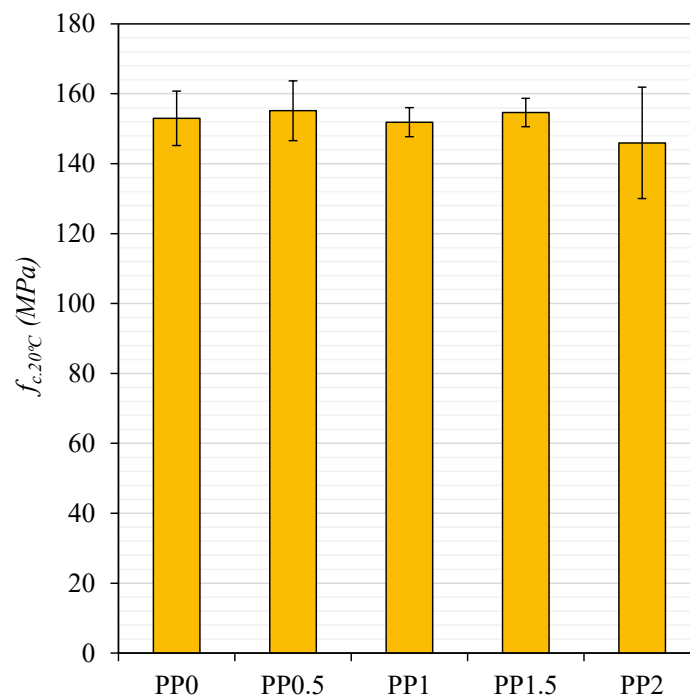


Figure 4. Compressive strength of the UHPC containing up to 2 kg/m³ PPF

3.2 UHPC samples' permeability

The weight loss of the UHPC containing up to 2 kg/m³ PPF, recorded after exposure to 200°C for 3 hours, progressively increased with PPF, as depicted in Figure 5a. Consequently, the weight gain observed in Figure 5b after immersing these specimens in water for 3 days also progressively rose. Although PPF generally enhanced UHPC permeability, no significant variation occurred between 1.5 and 2 kg/m³. These results fall in line with Zhu et al.'s review [3], who observed that the melting of PPF creates microchannels that interconnect isolated pores in UHPC, enabling accumulated vapour pressure release.

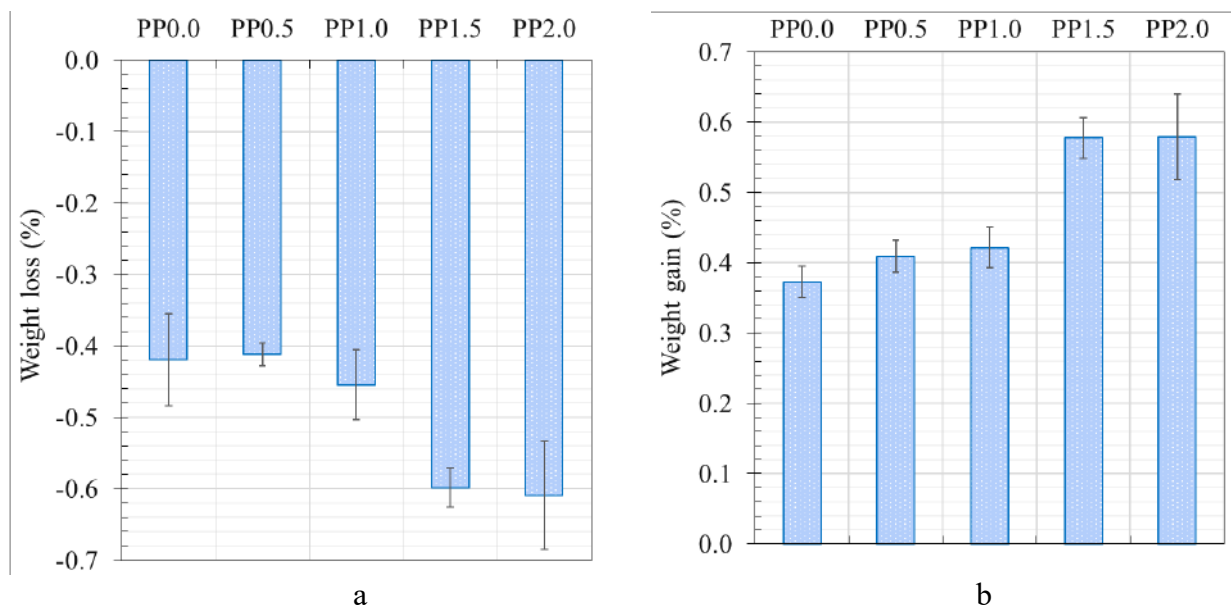


Figure 5. Weight variation of UHPC with increasing PPF contents: a) after drying at 200°C for 3 hours; b) after drying at 200°C and water immersion for 3 days

3.3 Spalling phenomenon

Table 2 summarises the spalling results after applying the heating protocols specified in Section 2.4. A red cross denotes spalling and a green tick indicates successful spalling prevention. A double mark means that the test was repeated. As observed, no spalling occurred in the oven-dried specimens that contained PPF, not even with small amounts (0.5 kg/m³). This conclusion is very significant because it implies that 3 days of accelerated drying at 80°C may successfully prevent spalling when combined with small amounts of PPF. Our results also highlight that steel fibres alone do not prevent spalling, and must necessarily be combined with a PPF content of at least 0.5 kg/m³.

Although minor differences were recorded between the water absorption measured with 1.5 kg/m³ and 2 kg/m³ PPF (Figure 5), one of the PP1.5 UHPC samples underwent spalling, but this phenomenon did not occur for the samples prepared with 2 kg/m³ PPF, regardless of the drying conditions or heating rates. These results are consistent with the Eurocode 2 recommendation (Section 6.1) [15] of adding 2 kg/m³ PPF to lower the spalling risk in high-strength concrete.


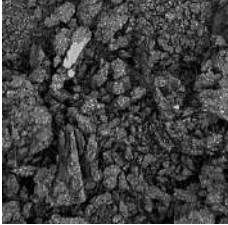


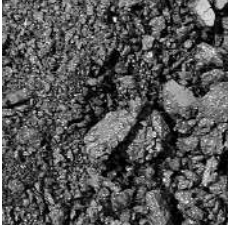
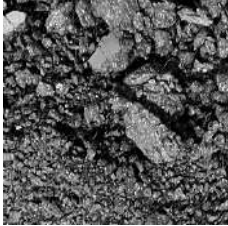

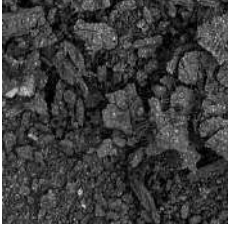

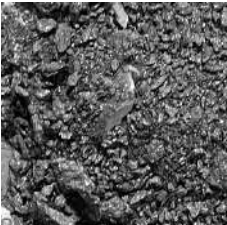







Table 2. Spalling results in the UHPC containing up to 2 kg/m³ PPF

Heating 2°C/min				Heating 5°C/min				Heating 15°C/min			
PP	ND	OV3	OV14	PP	ND	OV3	OV14	PP	ND	OV3	OV14
0	×	×	×	0	×	×	×	0	×	×	×
0.5	×	✓	✓	0.5	×	✓	✓	0.5	×	✓	✓
1.0	✓	✓	✓	1.0	×	✓	✓	1.0	×	✓	✓
1.5	✓	✓	✓	1.5	×	✓	✓	1.5	✓	✓	✓
2.0	✓	✓	✓	2.0	✓	✓	✓	2.0	✓	✓	✓

ND: Naturally-dried; OV3: Oven-dried for 3 days; OV14: Oven-dried for 14 days.

The images of the UHPC cubes that underwent spalling are shown in Table 3, together with the recorded weight loss. The specimens that completely disintegrated (90% to 100% weight loss) are labelled as 'DIS'. As observed, damage was generally severer with lower PPF contents. Thus, the samples with no PPF usually disintegrated or registered a mass loss above 70 %, and those containing 0.5 kg/m³ PPF normally reduced to powder. Additionally, when spalling occurred, it affected the entire thickness of the 10 cm cubes.

Table 3. Images of the UHPC cubes with different PPF contents that underwent spalling after being subjected to different drying conditions and heating rates

	2°C/min	5°C/min	15°C/min
0.0 PPF kg/m³			
ND	 DIS	 DIS	 60.19%
OV3	 DIS	 DIS	 DIS
OV14	 87.43%	 DIS	 69.91%
0.5 PPF kg/m³			
ND	 DIS	 46.67%	 39.58%
		 DIS	 DIS
1.0 PPF kg/m³			
ND	No spalling	 48.14%	 91.32%
1.5 PPF kg/m³			
ND	No spalling	 41.48%	No spalling

4 CONCLUSIONS

Although UHPC offers remarkable mechanical and durability characteristics, ensuring its safety under fire conditions requires thoroughly understanding its behaviour at high temperatures. This study aimed to assess fire-induced spalling in UHPC by analysing the influence of PPF doses, heating rate and drying conditions. The following conclusions were reached:

- Regardless of the applied heating rate or followed drying methodology, the specimens incorporating 2 kg/m³ of PPF demonstrated spalling resistance under all the studied conditions. This aligns with Eurocode 2 recommendations, which promote including 2 kg/m³ of PPF to mitigate the fire-induced spalling risk
- The UHPC specimens dried at 80°C for 3 and 14 days exhibited spalling resistance if they contained at least 0.5 kg/m³ of PPF
- The spalling phenomenon led to a fragmented structure or complete sample disintegration, with weight losses within the 40-100% range
- Minor variations in the 28-day compressive strength values were noted at room temperature when up to 2 kg/m³ PPF were incorporated

This study illustrates that incorporating PPF and exposing samples to a brief accelerated-drying period prove effective in preventing explosive spalling when exposing UHPC to high temperatures.

ACKNOWLEDGEMENT

The authors are grateful to the “Generalitat Valenciana” regional government for supporting this study with Project INVEST/2022/243, and to the UJI for its support with Project UJI-B2021-34. They also thank the company PREFFOR S.L. for providing the UHPC required to conduct this research.

REFERENCES

1. Xiong, M.X., Liew, J.Y.R., Mechanical behaviour of ultra-high strength concrete at elevated temperatures and fire resistance of ultra-high strength concrete filled steel tubes. *Mater Des* 104, 414–427 (2016). <https://doi.org/10.1016/j.matdes.2016.05.050>.
2. Kusumawardaningsih, Y., Fehling, E., Ismail, M., & Aboubakr, A. A. M. (2015). Tensile strength behavior of UHPC and UHPFRC. *Procedia Engineering*, 125, 1081–1086. <https://doi.org/10.1016/j.proeng.2015.11.166>
3. Zhu, Y., Hussein, H., Kumar, A., Chen, G., A review: Material and structural properties of UHPC at elevated temperatures or fire conditions. *Cem Concr Compos* 123, (2021). <https://doi.org/10.1016/j.cemconcomp.2021.104212>.
4. Qin, H., Yang, J., Yan, K., Doh, J.H., Wang, K., Zhang, X., Experimental research on the spalling behaviour of ultra-high performance concrete under fire conditions. *Constr Build Mater* 303, (2021). <https://doi.org/10.1016/j.conbuildmat.2021.124464>.
5. Zhang, D., Liu, Y., & Tan, K. H. (2021). Spalling resistance and mechanical properties of strain-hardening ultra-high performance concrete at elevated temperature. *Construction and Building Materials*, 266. <https://doi.org/10.1016/j.conbuildmat.2020.120961>
6. Kodur, V. K. R., & Phan, L. (2007). Critical factors governing the fire performance of high strength concrete systems. *Fire Safety Journal*, 42(6–7), 482–488. <https://doi.org/10.1016/j.firesaf.2006.10.006>
7. Banerji, S., & Kodur, V. (2022). Effect of temperature on mechanical properties of ultra-high performance concrete. *Fire and Materials*, 46(1), 287–301. <https://doi.org/10.1002/fam.2979>
8. Chen, H. J., Yu, Y. L., & Tang, C. W. (2020). Mechanical properties of ultra-high performance concrete before and after exposure to high temperatures. *Materials*, 13(3). <https://doi.org/10.3390/ma13030770>
9. Missemer, L., Ouedraogo, E., Malecot, Y., Clergue, C., & Rogat, D. (2019). Fire spalling of ultra-high performance concrete: From a global analysis to microstructure investigations. *Cement and Concrete Research*, 115, 207–219. <https://doi.org/10.1016/j.cemconres.2018.10.005>

10. Mohammed, H., Ahmed, H., Kurda, R., Alyousef, R., & Deifalla, A. F. (2022). Heat-Induced Spalling of Concrete: A Review of the Influencing Factors and Their Importance to the Phenomenon. In *Materials* (Vol. 15, Issue 5). MDPI. <https://doi.org/10.3390/ma15051693>
11. Lu, J. X., Shen, P., Sun, Y., & Poon, C. S. (2022). Strategy for preventing explosive spalling and enhancing material efficiency of lightweight ultra high-performance concrete. *Cement and Concrete Research*, 158. <https://doi.org/10.1016/j.cemconres.2022.106842>
12. Amran, M., Murali, G., Makul, N., Kurpińska, M., & Nehdi, M. L. (2023). Fire-induced spalling of ultra-high performance concrete: A systematic critical review. In *Construction and Building Materials* (Vol. 373). Elsevier Ltd. <https://doi.org/10.1016/j.conbuildmat.2023.130869>
13. Nováková, I., Diederichs, U., & Bodnárová, L. (2014). Usage of Heat Pretreatment for Reduction of Explosive Spalling of High Performance Concrete. *Advanced Materials Research*, 1054, 37–42. <https://doi.org/10.4028/www.scientific.net/amr.1054.37>
14. Ye, Li., Pierre, Pimienta., Nicolas, Pinoteau., Kang, Hai, Tan. (2019). Effect of aggregate size and inclusion of polypropylene and steel fibers on explosive spalling and pore pressure in ultra-high-performance concrete (UHPC) at elevated temperature. *Cement & Concrete Composites*, 99:62-71. <https://doi.org/10.1016/J.CEMCONCOMP.2019.02.016>
15. EN 1992-1-2: Eurocode 2: Design of concrete structures - Part 1-2: General rules - Structural fire design. The European Union Per Regulation 305/2011, Directive 98/34/EC, Directive 2004/18/EC, 2004.
16. ISO 834-11:2014 - Fire resistance tests — Elements of building construction — Part 11: Specific requirements for the assessment of fire protection to structural steel elements.
17. UNE-EN 197-1:2011 Standard; Cement - Part 1: Composition, specifications and conformity criteria for common cements. Asociación Española de Normalización y Certificación (AENOR): Madrid, Spain, 2020.
18. UNE-EN 12390-3:2020 Standard; Testing hardened concrete - Part 3: Compressive strength of test specimens. Asociación Española de Normalización y Certificación (AENOR): Madrid, Spain, 2020.
19. UNE-EN 12390-8 Standard; Testing hardened concrete - Part 8: Depth of penetration of water under pressure. Asociación Española de Normalización y Certificación (AENOR): Madrid, Spain, 2020.
20. Du, Y., Qi, H. H., Huang, S. S., & Richard Liew, J. Y. (2020). Experimental study on the spalling behaviour of ultra-high strength concrete in fire. *Construction and Building Materials*, 258. <https://doi.org/10.1016/j.conbuildmat.2020.120334>

STRUCTURAL FIRE ASSESMENT OF AN EXISTING TUNNEL USING PERFORMANCE BASED APPROACH AND DESIGN

Eric Tonicello¹, Julien Duboc²

ABSTRACT

Retrofitting and refurbishment of existing infrastructures is an everyday challenge for fire safety engineers, and maybe even more for structural engineers that must deal with constructions built according to old codes and practices. To challenge the verification of structural strength, reduction, or optimization of passive protection costs, engineering studies are increasingly using performance-based methods. This article describes a real case study on an existing road tunnel that will receive a new tramway line. In this context of tunnel transformation, the structure needs to be upgraded. A fire safety engineering study was carried out to assess the tunnel's current resistance to standardised and natural fire scenarios. The results, obtained using simplifying assumptions to take account of prestressing, were used to make choices regarding the tunnel's compliance.

Localised passive protection combined with a new water mist installation were the solutions chosen for the project.

Keywords: Computational fluid dynamic; concrete structures; finite elements modelling; tunnel fire; water mist

1 INTRODUCTION

As part of a project to extend Geneva's urban mobility infrastructure, the authorities required that the existing road tunnel under the Geneva airport runway be upgraded to accommodate a tramway extension.

The tunnel has a pre-stressed reinforced concrete structure dating from 1960, part of which is located under Geneva airport's main runway. In such an environment, the requirements for the tunnel's behaviour in the event of fire are very high and sensitive. Structural deformations are unacceptable, as they would require the airport to be closed while the road structure is repaired. An advanced analysis of the fire scenarios in the tunnel and monitoring of residual deformations were essential to our approach.

It was against this backdrop that an advanced fire safety engineering study was carried out to propose appropriate solutions for securing the structure, without the risk of interrupting airport operations.

¹ Fire safety and civil engineer, ISI – Ingénierie et Sécurité Incendie Sàrl
e-mail: eric.tonicello@incendie.ch ,

² Risk assessment and fire safety engineer, ISI – Ingénierie et Sécurité Incendie Sàrl
e-mail: julien.duboc@incendie.ch ,

2 DESCRIPTION OF THE STRUCTURE

2.1 Load-bearing systems

The tunnel analysed in this article consists of a 2-bays frame made of reinforced concrete, which slabs uses prestressing in transversal direction, under the runway of Geneva Airport. A cross-section of the structure is shown below:

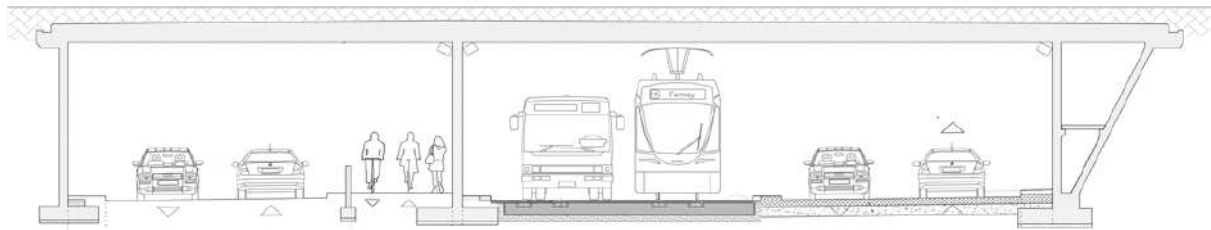


Figure 1. Geometry of the tunnel with tramway project

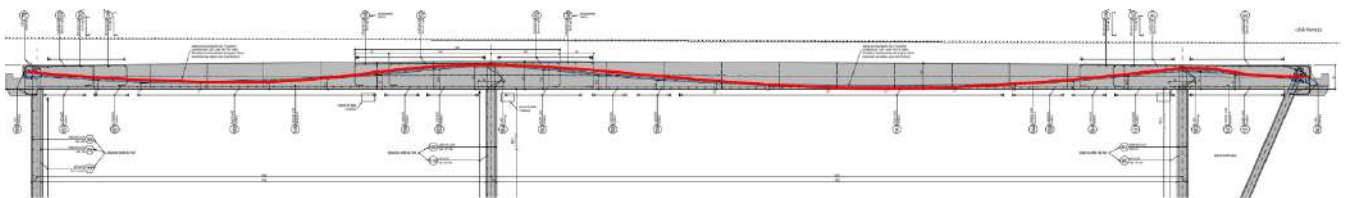


Figure 2. Structure of the tunnel with identification, in red, of the prestress cable

2.2 Assumption and simplification

To assess the structural behaviour of the tunnel, simplifications were done regarding the prestressing behaviour. In accordance with the civil engineering team of the project, prestressing was simply modelled with replacement forces q_{p1} , q_{p2} , q_{p3} and q_{p4} (Figure 3).

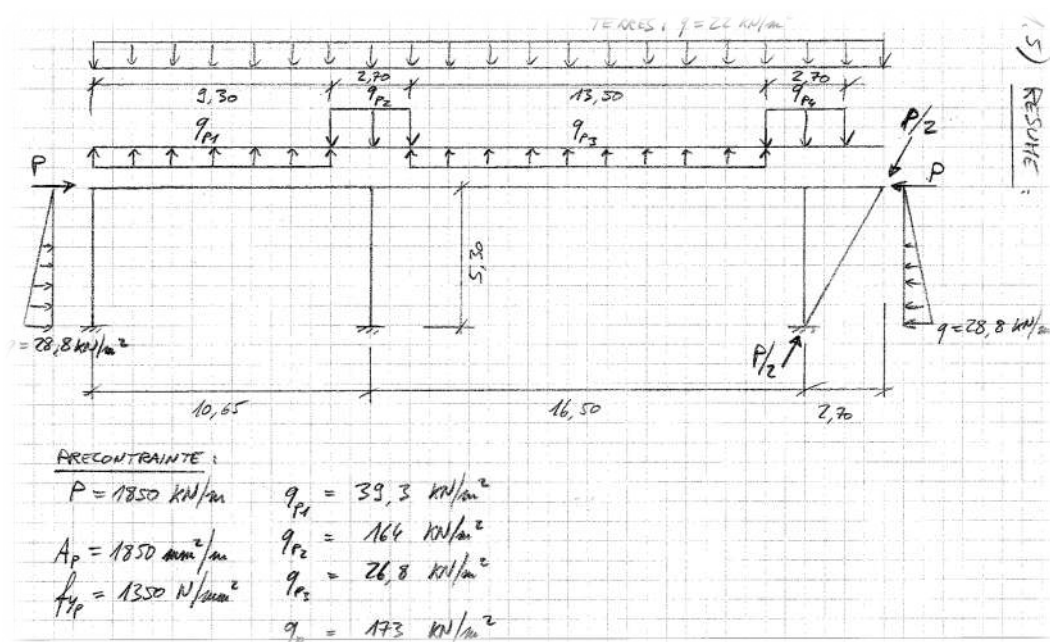


Figure 3. Loads applied on the structure

Materials were defined in accordance with the structural standards at the construction date:

- Steel (rebars): $f_{sk} = 345 \text{ N/mm}^2$;
- Steel (prestressing): $f_{yp} = 1'350 \text{ N/mm}^2$;
- Concrete: $f_{ck} = 19.7 \text{ N/mm}^2$

The characteristic value of the compressive resistance of concrete was calculated considering the resistance increase with time, according to the fib Model Code [7].

3 ANALYSIS UNDER STANDARD FIRE CURVES

3.1 Selection of standard fire scenarios

In a first approach, an analysis is carried out with standard fire curves to assess the structural behaviour of the tunnel in severe scenarios. Unlike studies of building structures, where the ISO fire curve is often adapted, different scenarios must be considered for tunnel structures. Standard fire curves have been developed specifically for tunnels following several fire tests.

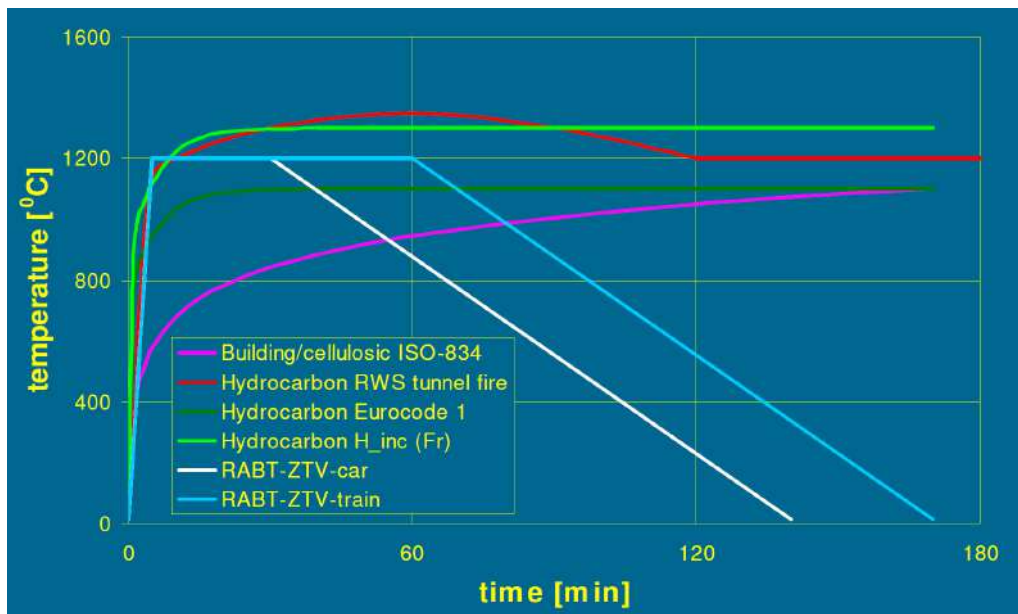


Figure 4. Different standard fire curves used in structural fire engineering analysis

In this study, the RWS fire curve is used to analyse the slab. This is a standardised curve representative of heavy vehicle fires (HGVs with highly calorific goods or the transport of hazardous materials). To assess the behaviour of the slab in the event of a light vehicle fire, the ISO fire curve is also used.

3.2 Prestressing and thermal stresses

Since prestressing is considered in a simplified way with the introduction of replacement forces, it is necessary to evaluate the influence of temperature rise on prestressing and therefore on the evolution of replacement forces.

In the event of fire, prestressing tendons are affected in two different ways. Firstly, the increased temperature of the steel reduces the material's modulus of elasticity (Figure 5).

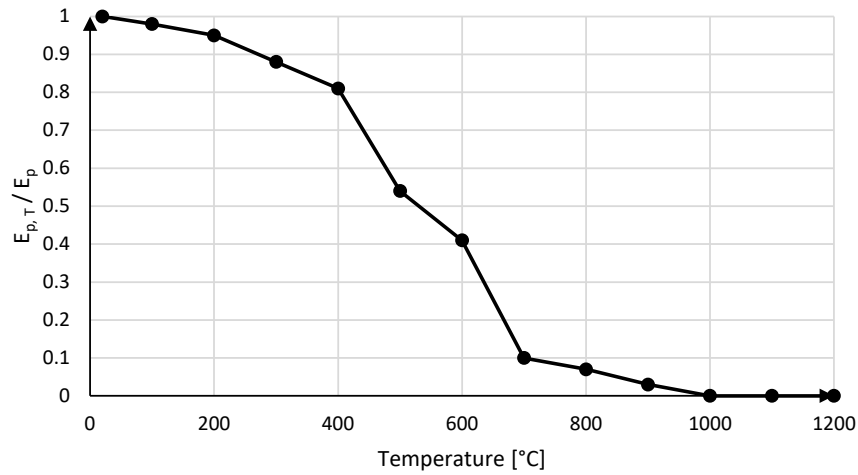


Figure 5. Young modulus evolution of prestressed steel in function of temperature

Secondly, thermal expansion of the cable under high temperatures will lead to a reduction in prestressing and therefore a reduction in replacement forces during the fire scenario.

$$L_{i+1} = \alpha L_i (T_{i+1} - T_i) + L_i \quad (1)$$

Where :

α is the coefficient of thermal expansion of steel;

L_i is the length of the prestressed cable at time i ;

T_i is the prestressed cable temperature at time i ;

The prestressing steel is affected as soon as the temperature exceeds 100°C. A finite element calculation of the thermal heating of the slab using SAFIR[®] was used to assess the depth to which a temperature in excess of 100°C is reached in the slab after 120 minutes of RWS fire (Figure 6).

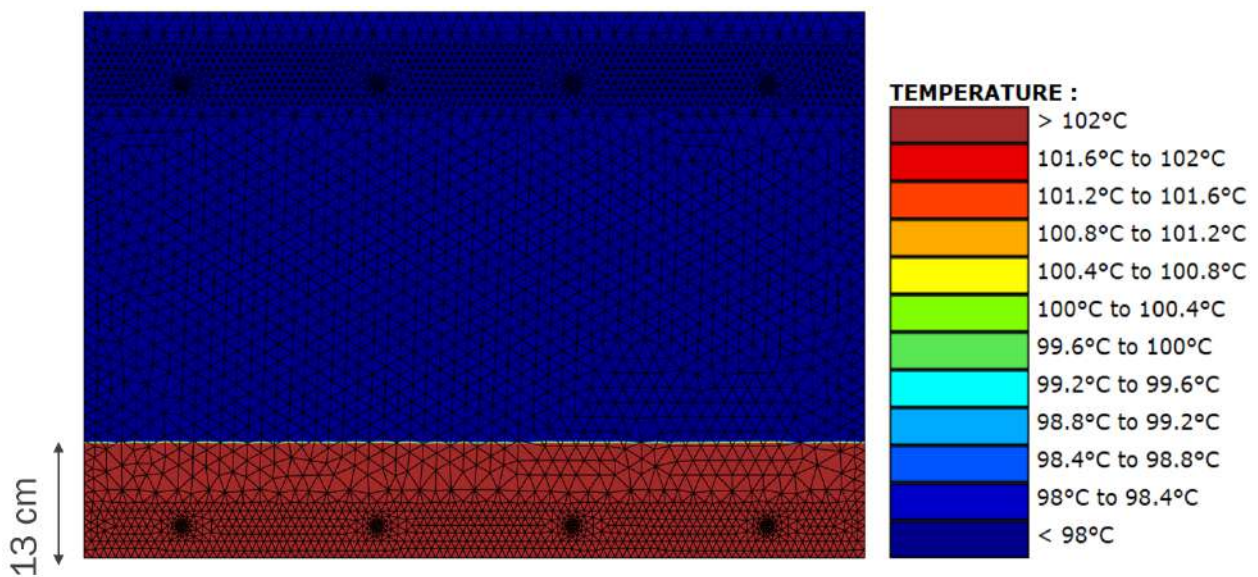


Figure 6. Temperature in the slab after 120 min of RWS fire

Based on onsite soundings, the critical zone for the prestressing cable in the event of fire was identified (Figure 7).

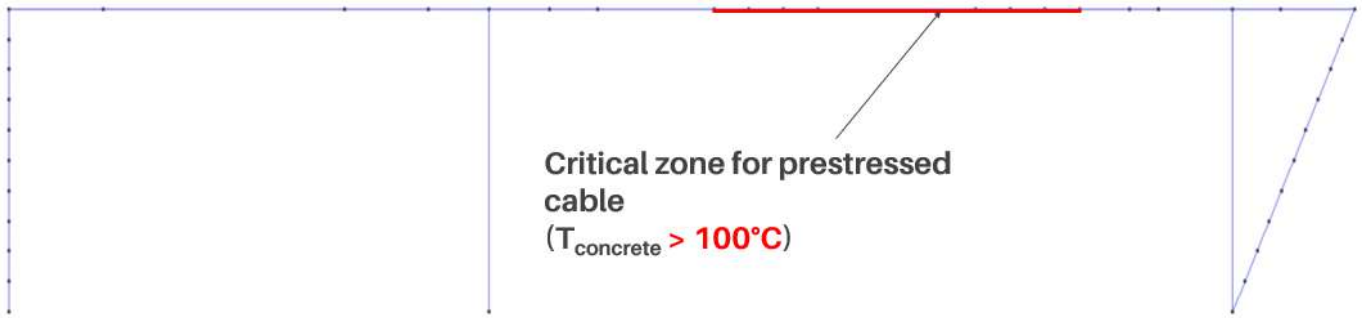


Figure 7. Critical zone in the slab where prestressing is impacted

Knowing the position of the prestressing cable in the slab (Figure 8), an evaluation of the steel temperature was calculated (Figure 9) using finite elements with a thermal calculation in SAFIR®.

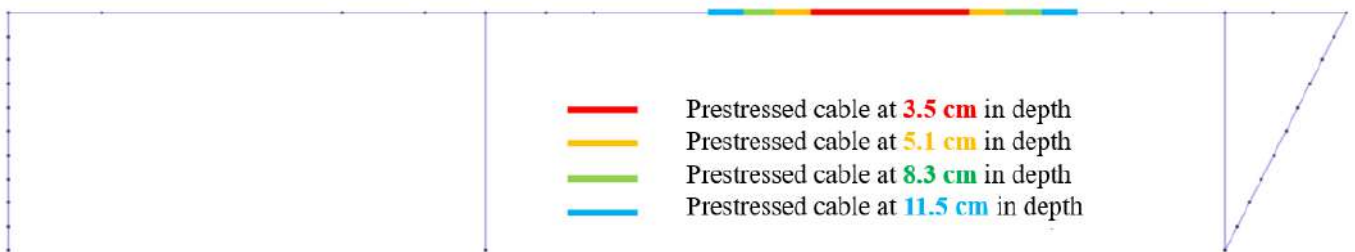


Figure 8. Prestressing position in the slab

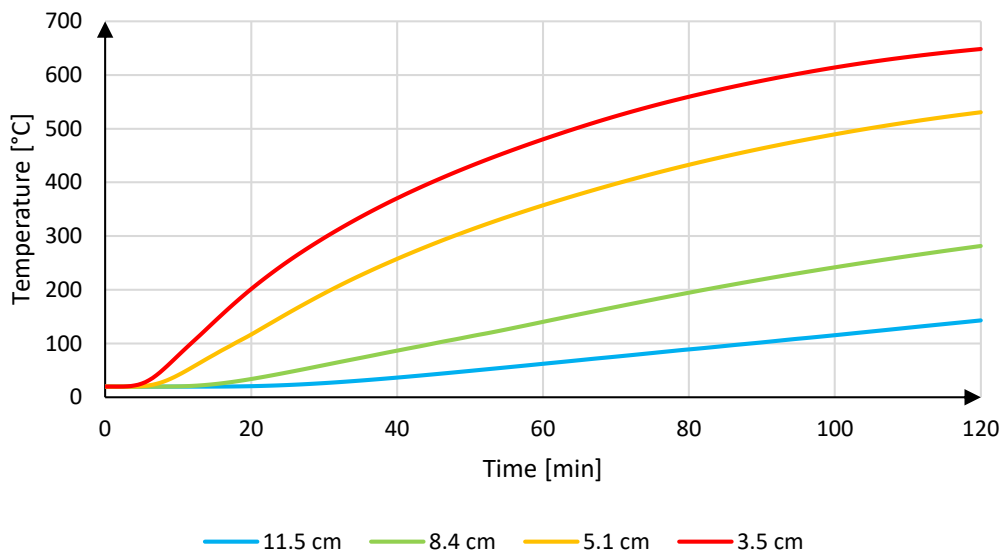


Figure 9. Prestressed cable temperature in function of its depth in concrete slab, under RWS fire curve

Precisely knowing the temperature of the prestressing steel in the slab over time, the evolution of the replacement forces q_{p1} , q_{p2} , q_{p3} and q_{p4} can be calculated (Figure 10).

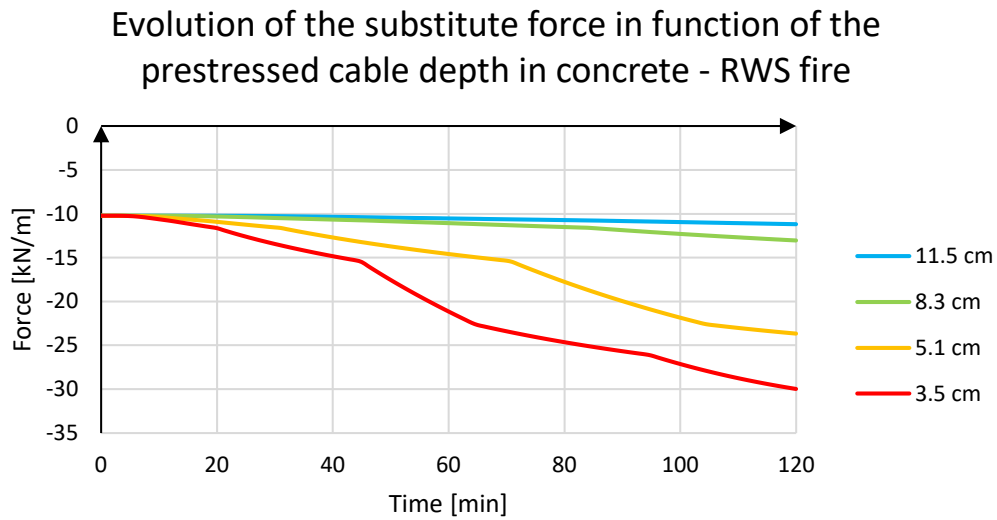


Figure 10. Forces evolution due to thermal elevation around the prestressed cable

3.3 Fire resistance under standard fire curves

To assess the fire behaviour of the tunnel structure, a simple frame-type model was used (Figure 11). As the 2 directions of traffic in the tunnel are separated by a solid reinforced concrete wall, it is assumed that the fire will only affect one side of the tunnel.

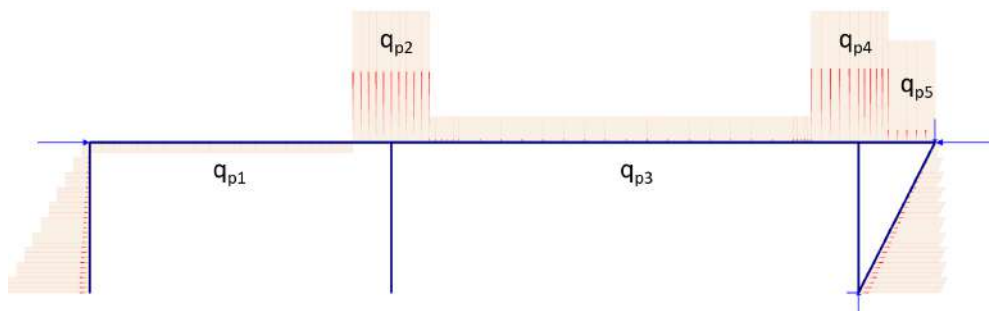


Figure 11. Structural model of the tunnel studied with SAFIR®

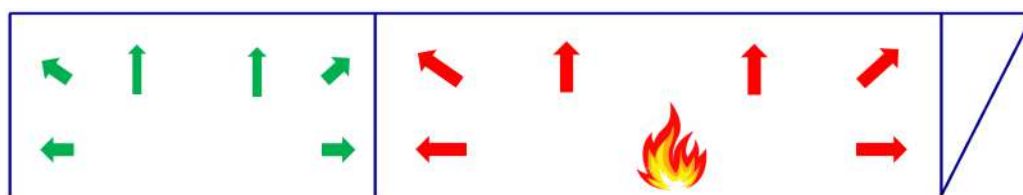


Figure 12. Heating model studied

Results of the analysis are given in Table 1.

Table 1. Structural fire resistance under standard fire curves

Tunnel resistance – Standard fire scenarios	Fire resistance [minute]	Maximum displacement [mm]	Residual displacement [mm]
ISO	36	Collapse	
RWS	27	Collapse	

The structure can only withstand fire scenarios (ISO or RWS) for 30 minutes. After 30 minutes, very significant deformations, up to and including localized slab collapse, are highly probable. Given the stringent requirements in terms of fire resistance and behaviour due to the presence of the runway on the surface, these results are not acceptable (heavy repairs lasting several weeks with a major interruption to airport activities).

4 ANALYSIS UNDER NATURAL FIRE SCENARIOS

To assess whether an analysis using real fire scenarios would be more favourable than the standardised fire approach, an advanced study was carried out. The most unfavourable scenarios were selected for analysis based on book 4 of the CETU guide [5].

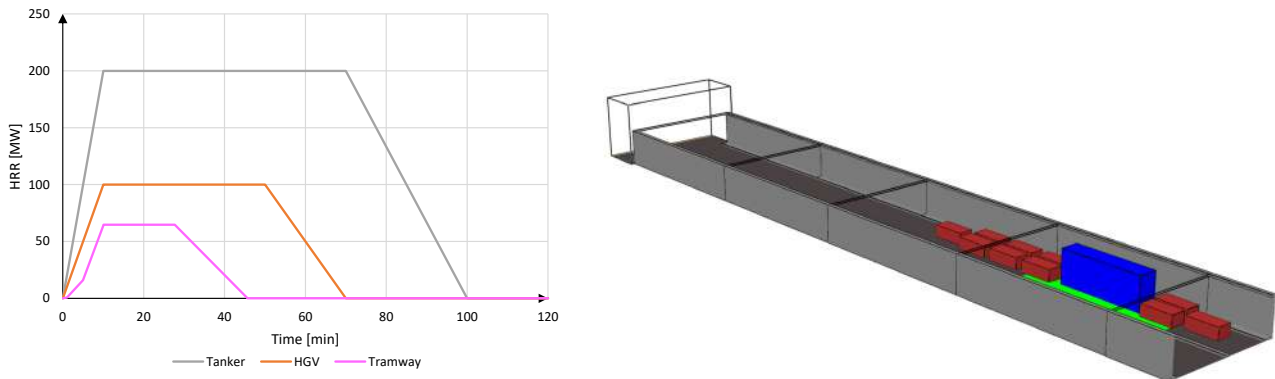


Figure 13. Standard HRR curves for vehicles (left) and FDS model with the HGV fire (right)

Thermal stresses are assessed using the FDS calculation code to record temperatures and heat flows over time at any point in the structure. This data was used as input to the fire resistance calculations to assess the behaviour of the frame.

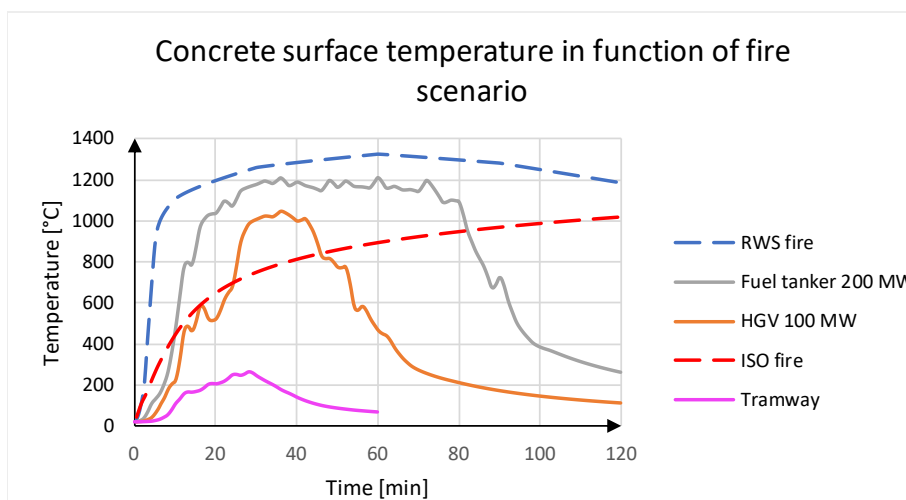


Figure 14. Comparison of the thermal stressed between standard curves and natural fire scenarios

Table 2. Structural fire resistance under natural fire scenarios

Tunnel resistance – Natural fire scenarios	Fire resistance [minute]	Maximum displacement [mm]	Residual displacement [mm]
Tramway	OK	25	13 - 15
HGV	28	Collapse	
Tanker	27	Collapse	

Except for the tramway fire scenario, the results obtained for the HGV and tanker fires are like those obtained with the standardised fire approach. Protective measures are needed to improve the existing situation and ensure that airport operations can continue in the event of a fire in the tunnel.

5 PROTECTION MEASURES

An analysis of the existing structure revealed its strong vulnerability in the event of a major fire. Major damage is likely, with a significant risk to airport operations.

To improve the existing situation, protective measures have been proposed. Given the context, and the importance of being able to guarantee very minimal deformations, a solution combining both passive and active protection has been chosen. Passive protection ensures the protection of the most vulnerable structural elements (prestressing cable and vertical bearers), while active protection, via a water-mist extinguishing system, limits the risk of a major fire developing within the structure. This combination will also limit damages to the technical infrastructure and ensures that the airport can be reopened after only a few hours following the fire, with no impact on airport operations.

The passive protection was designed with the most unfavourable natural fire scenarios (HGV and tanker) using SAFIR® heating and structural calculations (Figure 15).

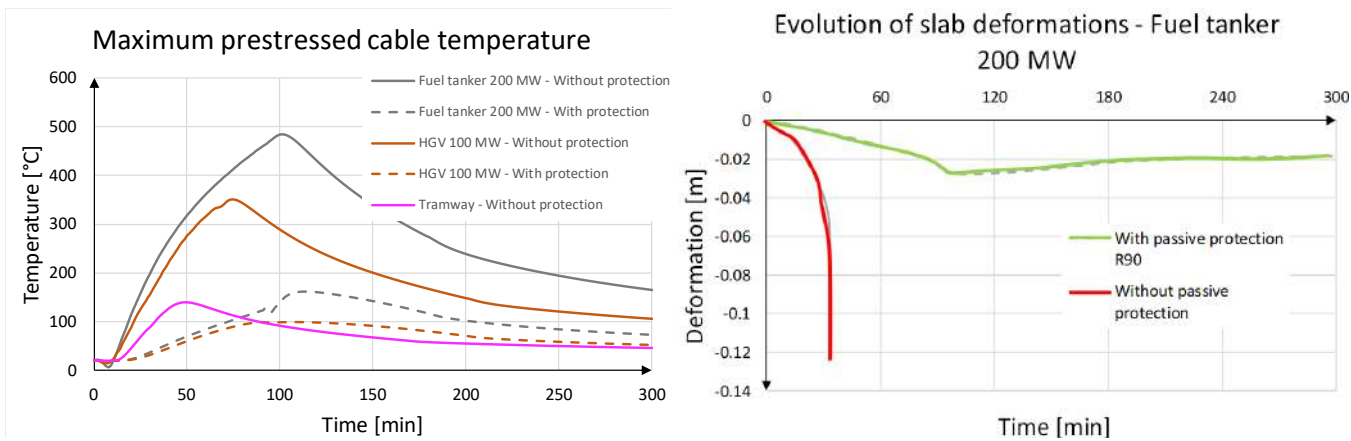


Figure 15. Comparison of the structural behaviour without passive protection and with 90 minutes passive protection

Fire protection of the slab in the areas where the prestressing cable is closest to the intrados of the slab, combined with protection of the load-bearing walls, means that deformation of the slab can be limited to post-fire values of the order of 20 mm.

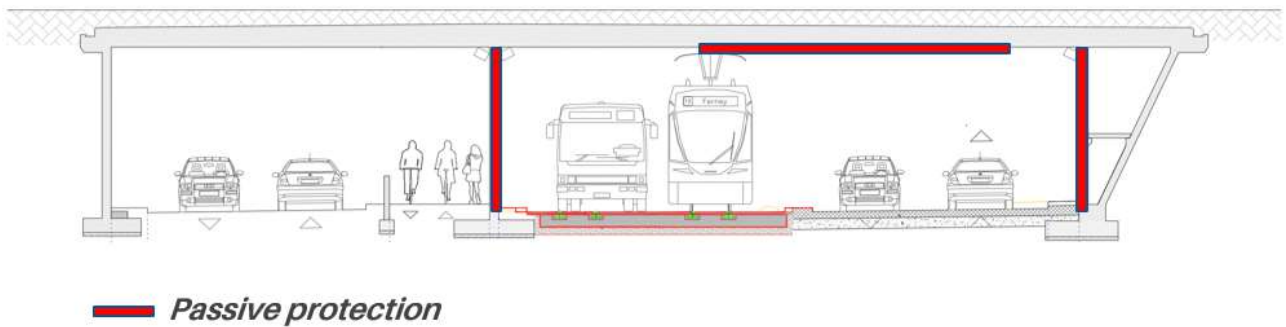


Figure 16. Identification of the areas protected with passive measures

6 CONCLUSION

The engineering study highlighted the high vulnerability of the structure, which in the event of fire would cause major damage and force the airport to close for repairs, which could take several weeks.

Based on this analysis, safety measures have been proposed to improve the existing situation and ensure that airport operations can continue, even in the event of a major fire in the tunnel.

REFERENCES

1. Modelling structures in fire with SAFIR®: Theoretical background and capabilities. Franssen et al. *Journal of Structural Fire Engineering*, 8(3), 300-323.
2. Fire Dynamics Simulator - Technical Reference Guide EN 1991-1-2, Action on structures submitted to fire, NIST, 2019.
3. Performance based Fire Safety Design, Hurley, Rosenbaum, SFPE, 2015.
4. Risk-based design for fire spalling of concrete, Borgogno et al., Zürich, 2017.
5. Guide des dossiers de sécurité des tunnels routiers – Fascicule 4, Les études spécifiques des dangers (ESD) – Centre d’Etudes des Tunnels, Septembre 2003.
6. CFD Modelling of High-Pressure Water Mist System in Road Tunnels, Paulína Magdolenová, <https://doi.org/10.1016/j.trpro.2021.07.184>.
7. Fib, Model Code for concrete structures, 2010

STRUCTURAL FIRE DESIGN OF BLAST DAMAGED CONCRETE COLUMNS

Kevin Mueller, PhD, PE, PSP¹, Daksh Patel, EIT², Kyle Root, PE³

ABSTRACT

High-profile private developments are routinely incorporating protective design measures into their design. One of the most common threats considered are vehicle-borne improvised explosive devices (VBIED) located at the site perimeter, unscreened at-grade parking areas, and within under-building parking garages. In addition to the explosive threats, the parking of petrol vehicles and charging of electric vehicles (EV) within the under-building parking garage is unavoidable. This multi-hazard environment is especially critical to primary columns of high-rise towers, as they routinely have under-building parking and are subjected to the VBIED and subsequent fire, including thermal runaway from electrical vehicle batteries.

This paper discusses a high-rise office tower above a 4-story below-grade parking structure, with a concrete structural system that includes tower columns, parking level columns, full height core (shear) walls, PT band beams, 1-way and 2-way slabs. The threat, vulnerability, and risk assessment (TVRA) identified over 50 threats, ranging from hostile vehicles to ballistics to civil unrest, including a VBIED threat within the parking levels. This paper focuses on the primary tower columns as there is no redundancy should one fail under either the explosive or subsequent fire threat.

Keywords: Structural fire engineering; Blast-damage; Spalling; Finite element modelling

1 INTRODUCTION

A high-profile private development, consisting of a central 50+ story high-rise tower above a 4-story basement parking structure, is under design by the authors. The threat, vulnerability, and risk assessment (TVRA) for the project identified over 50 threats, ranging from active shooter to improvised explosive devices (IED), arson, and chemical biological radiological nuclear (CBRN) threats. The IED threats are taken at the site perimeter and at any legal parking space within the 4-story below-grade parking structure. The parking structure consists of the following structural members: Tower Columns, Parking Columns, Core Wall, Foundation and Sea Walls. Only the Tower Columns are reported herein.

1.1 Tower Columns

The primary tower columns within the parking structure (Figure 1) are rectangular with overall cross-section dimensions of 1524 mm by 1372 mm x 3048 mm (span). Embedded reinforcement includes two (2) W14x730 (American standard shape) steel columns with associated shear studs, sixteen (16) #10 vertical rebar, and #4 hoops/ties at 450 mm on center. Concrete compressive strength is 110 MPa. Due to the marine environment at this building's location, A1035 Grade 100 (ChromX 9100) steel is used for vertical reinforcement, whereas A767 Grade 60 (Galvanized) steel is used for the hoops and ties.

¹ Senior Associate, Thornton Tomasetti, Inc.
e-mail: KM Mueller@ThorntonTomasetti.com

² Senior Engineer, Thornton Tomasetti, Inc.
e-mail: DPatel@ThorntonTomasetti.com

³ Project Engineer, Thornton Tomasetti, Inc.
e-mail: KRoot@ThorntonTomasetti.com

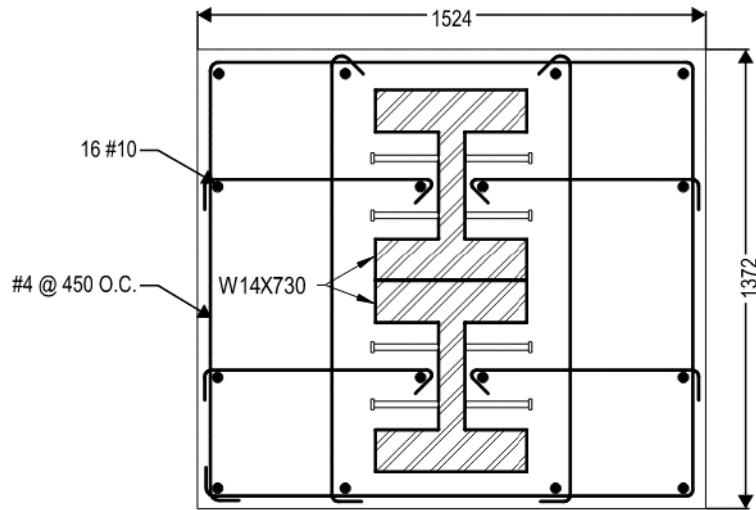


Figure 1. Tower Column Cross Section

2 RESPONSE TO INITIAL EXPLOSIVE THREAT

2.1 Security Threat Environment

The threats at the parking levels varied from person-borne (PBIED = 22.7 kg) to vehicle-borne (VBIED = 136 kg) improvised explosive devices. The PBIED threat was designed to be placed within 50 mm of the structural member (i.e., near contact charge). While a small fire may result from this size charge, it is likely to develop only localized damage. The VBIED threat was designed to be placed at the nearest legal parking spot (Figure 2), where the attacker utilizes a time-delay for safe passage out of the building prior to detonation. This threat is likely to cause a large fire post-blast and cause widespread damage on the nearest tower column.

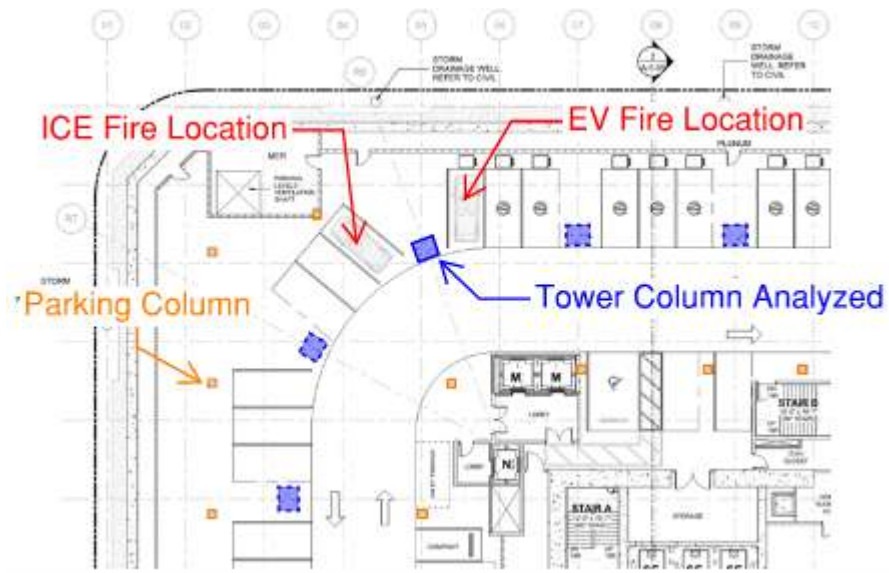


Figure 2. Typical Parking Level Layout

2.2 Modeling and Design Assumptions

Airblast and structural models of the tower column was constructed to investigate damage levels resulting from close-in detonation of the VBIED. The airblast CFD model generated the blast wave from the VBIED and calculated the load on the tower column. The structural model was then used to evaluate the possibility

of collapse of the column from the blast loading. The detonation of the explosives and propagation of the resulting shock waves were modeled using the MAZ computational fluid dynamics (CFD) code [1]. The pressure loads generated by MAZ were applied to a structural model of the column. NLFLEX [2], a large deformation, explicit, transient analysis, finite element code, was used to analyze the response of the column subjected to the explosive environment generated by MAZ. NLFLEX was used to model the structural response of the column and its stability after the blast event.

MAZ, an adaptive zoning finite element computational fluid dynamics code developed by Thornton Tomasetti under a Defense Threat Reduction Agency (DTRA) sponsorship, was used to model the detonation of a sphere of TNT in contact with the column and the floor. The explosive charge was located at the base of the column above the floor level. The model contains the column of interest and bounding floor slabs. The detonation was assumed to take place in a large room over a short duration, so reflections off walls were not considered. Pressure time histories were saved on the column surface at a refined enough spacing to resolve the gradients in the shock. This pressure loading was then applied to the structural model of the column.

2.3 Analysis Results

The NLFLEX model was run with the VBIED adjacent to either side of the cross-section. Both models showed extensive damage to the concrete cover that exposed the vertical reinforcement (Figure 3). As shown in Table 1, even with the loss of concrete cover the tower columns have adequate residual capacity to carry the required axial load post-blast event.

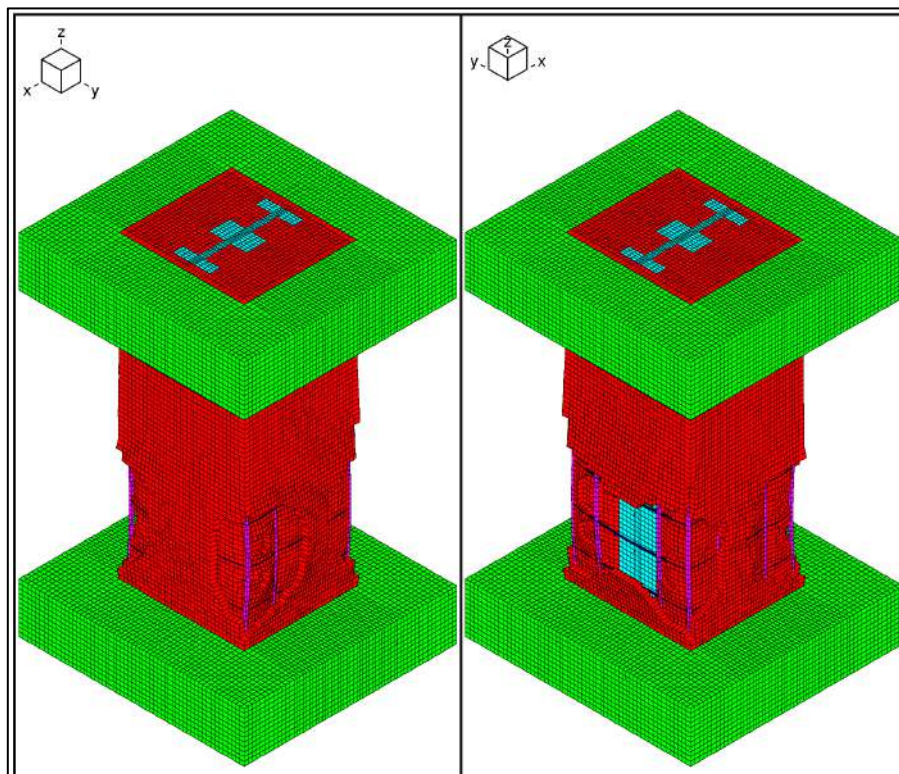


Figure 3. Tower Column Post-Blast Damage

Table 1. Tower Column Post-Blast Axial Capacity

Threat	Width (mm)	Depth (mm)	Span (m)	Column Capacity	
				Residual (kN)	Required (kN)
VBIED	1524	1372	3048	818000	126116
	1372	1524	3048	807000	126116

3 RESPONSE TO SUBSEQUENT FIRE THREAT

3.1 Threat Environment

Two fire scenarios [3] were simulated to understand the resulting surface temperatures at the tower column faces: a standard internal combustion engine (ICE) and an electric vehicle (EV). Each fire scenario was modeled using Pyrosim [4], which is a graphical wrapper for the NIST Fire Dynamics Simulator (FDS) [5]. FDS is a large-domain computation fluid dynamics model that numerically solves the conservation equations of mass, momentum, and energy that govern low-speed, thermally driven flows with an emphasis on smoke and heat transport from fires.

The FDS model (Figure 4) uses default inert and open surface assignments to replicate the tower column and parking garage geometry identified in Figure 2. A burner surface is assigned a peak heat release rate per unit area (HRRPUA) and a custom ramping function to create the HRR time history of the two fire scenarios based on the total burner area (Figure 5). The ICE fire is assumed to be focused on the front of the vehicle (due to the geometry of the parking garage reversing into the parking spot will be difficult) and uses a burner surface equivalent to half the length of a standard parking space. The EV fire is assumed to be spread over the entire length of the vehicle and uses an area equivalent to one standard parking space.

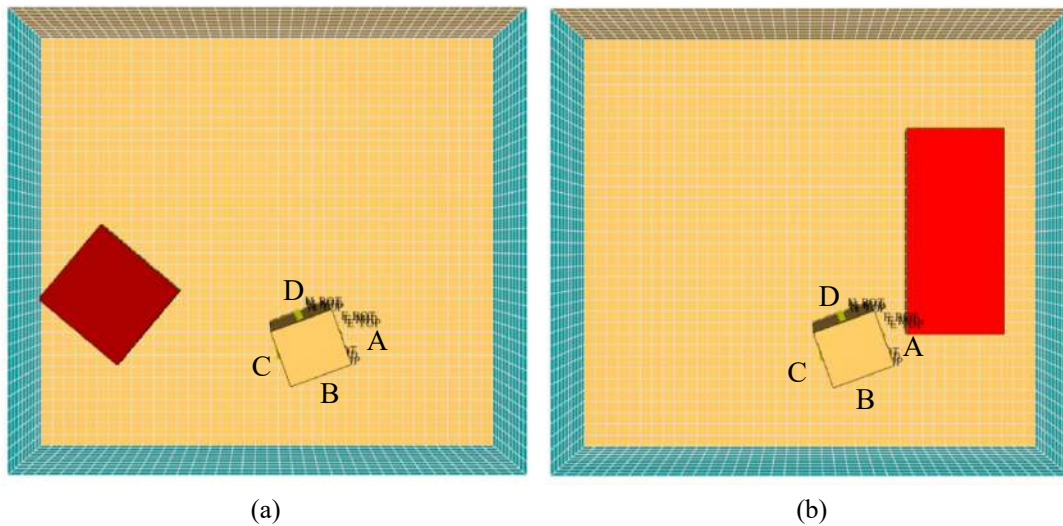


Figure 4. FDS Fire Scenarios
(a) ICE (b) EV

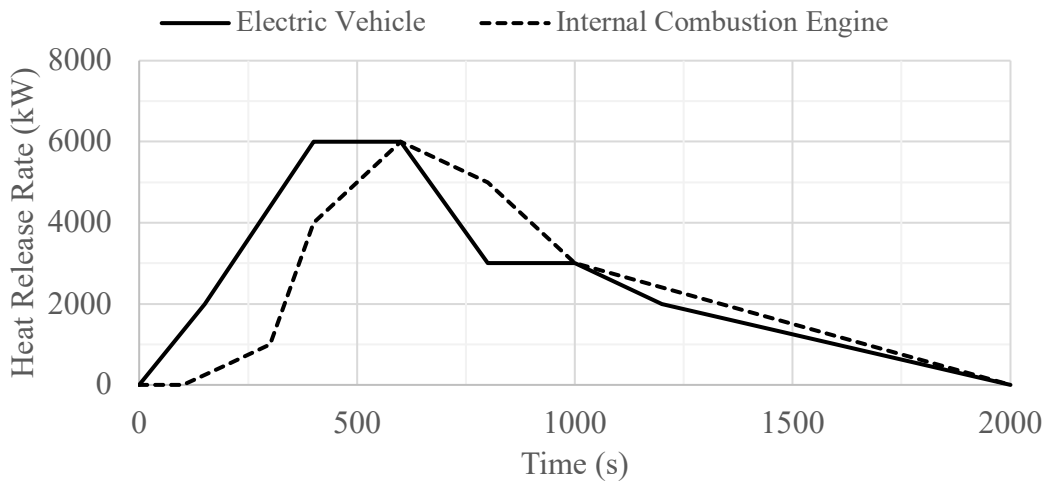


Figure 5. Heat Release Rates of ICE and EV Fires

The adiabatic surface temperature (AST) was measured at three locations along the column span on each of the rectangular concrete column faces (Figure 6). Maximum AST on each face (Table 2) was utilized in the subsequent heat transfer and structural analyses. Given the open boundary conditions in the simulation, maximum temperatures spread along the ceiling above the source of the fire and primarily heated the structural members at the ceiling. The tower column was heated through radiation and did not become engulfed in the fire. It is likely that the fire from this EV could subsequently ignite adjacent vehicles (ICE or EV); however, those fire threats would be located further from the tower column and result in smaller temperature increases due to the radiation dominated heat transfer.

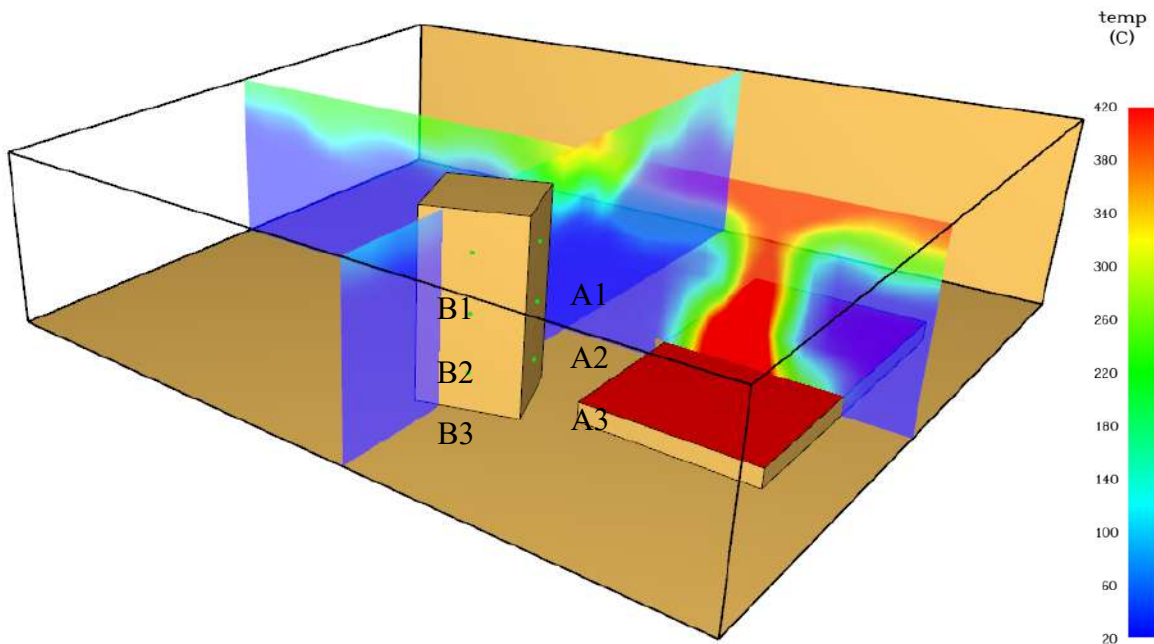


Figure 6. FDS EV Fire Model Temperature Distribution at Peak Heating (600s)

Table 2. Maximum Adiabatic Surface Temperature (°C)

FDS AST Probe	Fire Threat	
	ICE	EV
A1	52	264
A2	26	310
A3	24	324
B1	65	88
B2	26	31
B3	24	28
C1	218	57
C2	220	30
C3	208	28
D1	143	181
D2	92	183
D3	86	179

3.2 Modeling and Design Assumptions

Ansys Mechanical [6], a finite element analysis program, was used to model the heat transfer from the fire on the column cross section. The temperature dependent thermal properties of concrete and steel (Table 3) were derived through the methods outlined in Section 2.4 of Eurocode 2 [7] and Section 3.4 of Eurocode 3 [8], respectively. An emissivity of 0.7 and convection coefficient of 25 W/m² K was used.

Table 3. Thermal Material Properties

Temp	Steel				Concrete			
	Specific Heat	Density	Thermal Conductivity	Coefficient of Thermal Expansion	Specific Heat	Density	Thermal Conductivity	Coefficient of Thermal Expansion
°C	J/(kg K)	lb/ft ³	W/(m K)	/°C	J/(kg K)	lb/ft ³	W/(m K)	/°C
20	440	490	53.33	0.000014	900	2400	1.64	0.000018
200	530	490	47.34	0.000014	1000	2352	1.33	0.000018
400	606	490	40.68	0.000014	1100	2280	1.05	0.000018
600	760	490	34.02	0.000014	1100	2238	0.83	0.000018
800	803	490	27.36	0.000014	1100	2196	0.68	0.000018
1000	650	490	27.30	0.000014	1100	2154	0.59	0.000018
1200	650	490	27.30	0.000014	1100	2112	0.57	0.000018

The mechanical properties of concrete (Figure 7) and steel (Figure 8) at elevated temperatures were obtained from the stress-strain relationship and reduction factors defined by Section 3.2.2 of Eurocode 2 and Section 3.2.1 of Eurocode, respectively. It is important to note that the reduction in strength for steel was taken as A992, even though ChromX 9100 was used for the vertical reinforcement, as temperature-dependent properties of ChromX 9100 has not been measured.

3.3 Analysis Results

The adiabatic surface temperatures from the FDS model were applied to the column cross-section as radiation and convection heat transfer on all 4 sides. The post-blast damage model revealed that the concrete cover in portions of the column had spalled, exposing the vertical reinforcement. Thus, two cross sections were analyzed during the heat transfer analysis: one with full concrete cover and a second without the concrete cover (Figure 9).

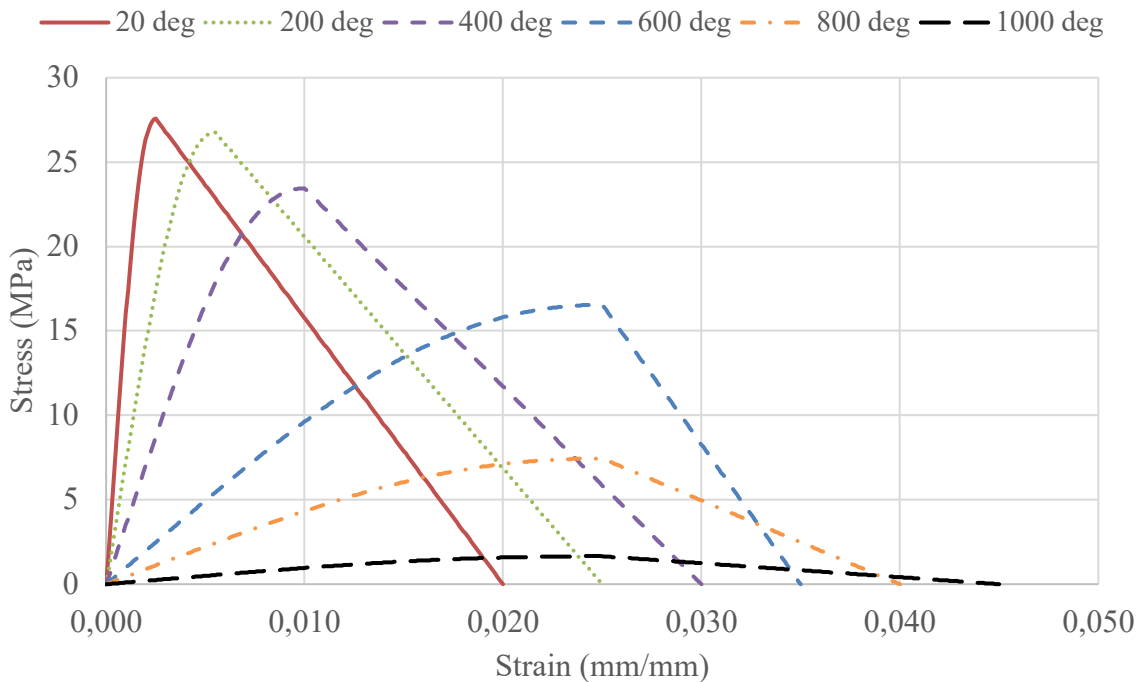


Figure 7. Mechanical Material Properties at Elevated Temperatures of Calcareous Concrete

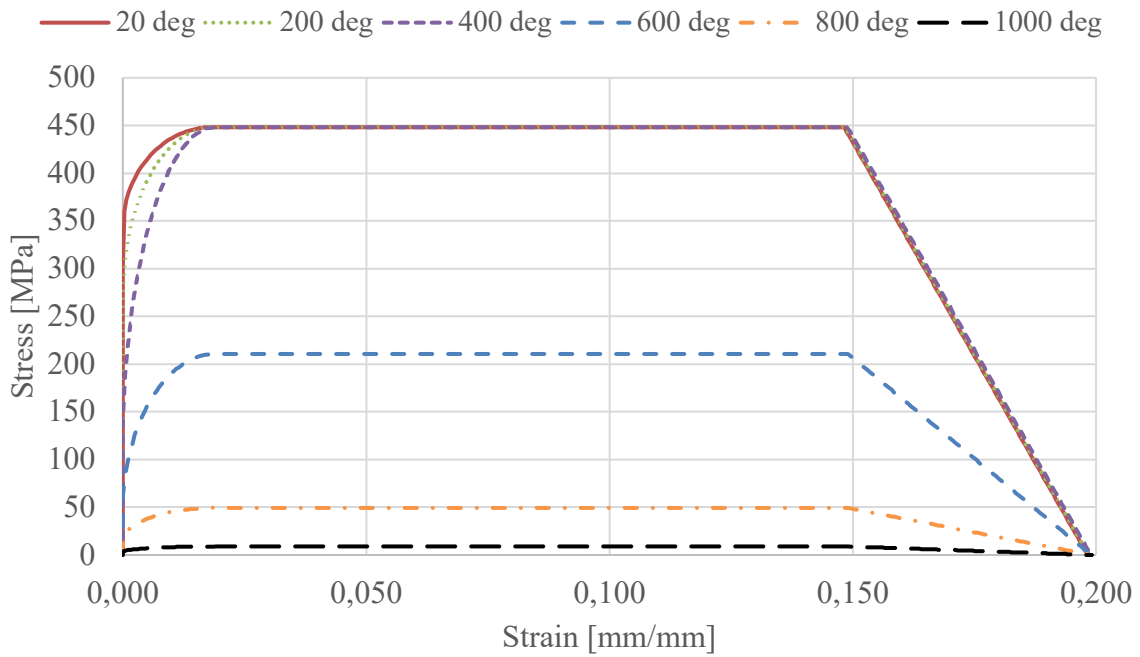


Figure 8. Mechanical Material Properties at Elevated Temperatures of A992 Steel

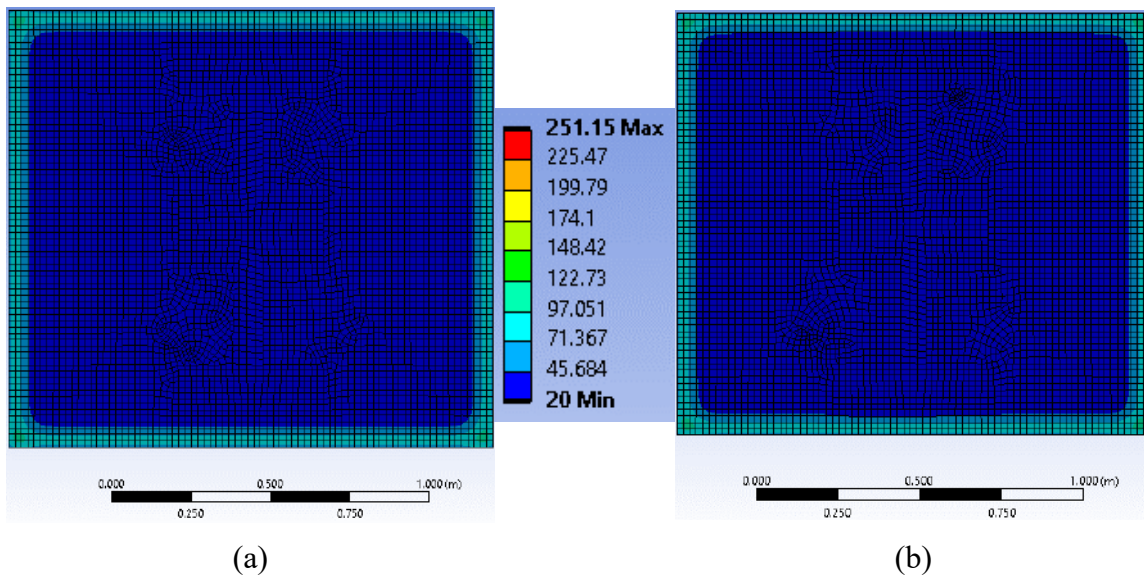


Figure 9. Ansys Cross-Section Heat Transfer
(a) Column with Full Cover; (b) Column with No Cover

The cross-section temperatures at peak fire were then mapped to the FLEX model to analyze the post-blast column under elevated temperatures. As shown in Figure 9, the maximum concrete and steel temperature reaches approximately 250°C, which results in minor reduction in compressive strength of the concrete and no reduction in strength of the steel. However, both the concrete and steel are expected to experience minor softening due to the small reduction in stiffness.

Figure 10 shows the axial load versus displacement of the column after the fire event in relation to the post-blast capacity. The residual capacity of the column decreases from 183700 kN post-blast to 172500 kN post-blast + fire, resulting in an approximately 6% reduction in axial strength due to fire. For comparison,

the tower column has an undamaged, ambient axial capacity of 301000 kN and must maintain an axial capacity of 126116 kN to prevent failure under service-level loads.

Figure 11 shows the damaged state of the tower column post-blast + fire, highlighting that the vertical reinforcement softening allowed the concrete core to expand and reduce the residual axial capacity. The embedded W14x730 structural steel members are still intact, although exposed due to continued concrete cover loss. Additional fires due to adjacent vehicle spread may cause additional damage to the column.

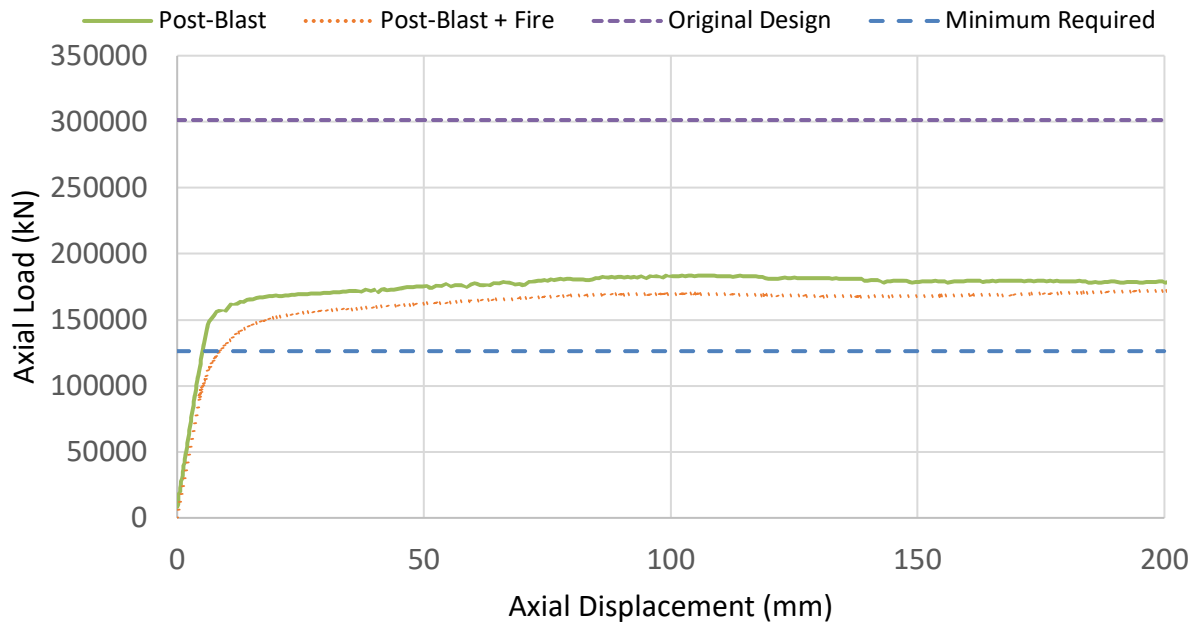


Figure 10. Tower Column Post Blast + Fire Axial Capacity

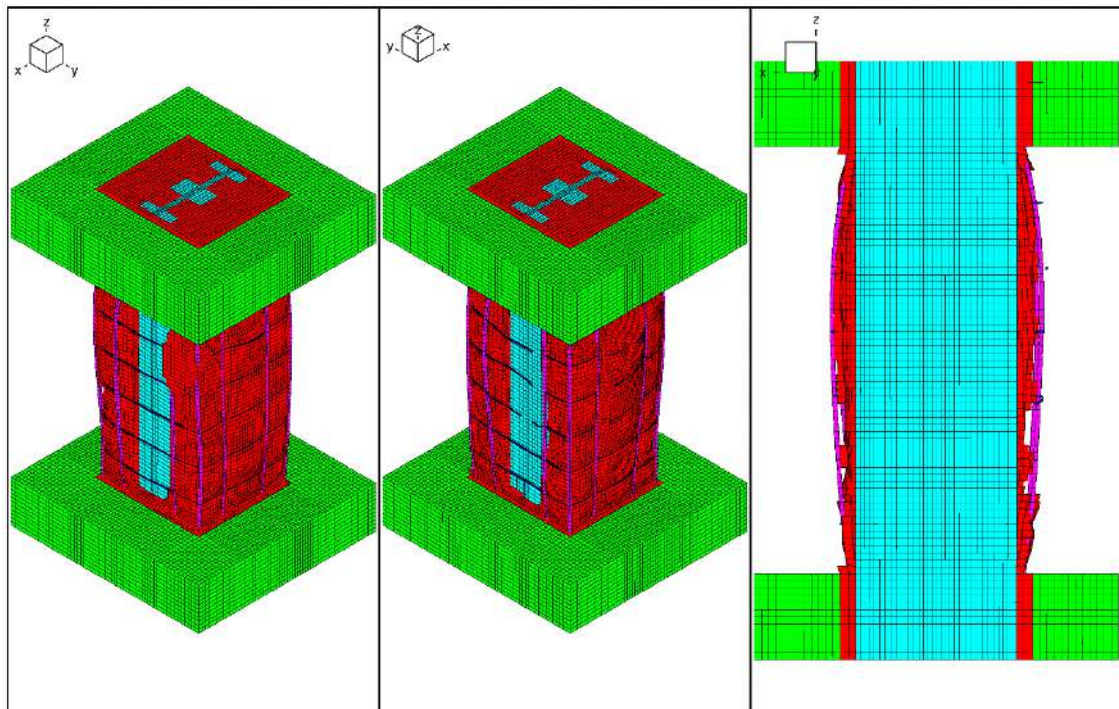


Figure 11. Tower Column Post-Blast + Fire Damage

4 DESIGN SUMMARY AND CONCLUSIONS

4.1 Close-In Explosive Threats

The damage due to the VBIED located nearly adjacent to the tower column is typical of a close-in explosive threat. Instead of a flexural response, where end rotation of the concrete column would govern the allowable damage, a close-in threat causes localized shear, breach, and spalling damage. In this project, the embedded W14x730 structural steel members provide adequate resistance to direct shear and breach. Concrete cover spalling is widespread over the cross-section, reducing the axial capacity but precluding failure. This level of damage is considered repairable and acceptable by the owner.

4.2 Extreme Fire Loading

Unlike the standard ASTM E119 fire, the threats within the parking garage have a more severe rise in temperature and complicated emergency response procedures. Electrical vehicles and their charging stations have a rapid rise in temperature, the potential for thermal runaway, and could cause adjacent vehicles to combust. Traditional fire sprinklers may unintentionally spread the fire unless they are able to completely smother the vehicle. While this paper only reported on a single EV or ICE fire, multiple vehicles need to be considered for a proper structural fire engineering design.

4.3 Residual Axial Capacity

As discussed herein, the performance of the tower column was determined using the axial capacity at each stage of the analysis. First the undamaged, ambient column axial capacity was calculated as the baseline design. This axial capacity is significantly higher than what is required to support the structure post-extreme event (i.e., reduction in live load and safety factors). Working with the Structural Engineer of Record, the required residual capacity of the column was calculated to determine the level required to support the structure and preclude failure.

ACKNOWLEDGMENT

The authors would like to thank Eric Hansen (Principal, Thornton Tomasetti) for assisting with the MAZ and NLFLEX analyses. Funding for this research was provided by the Thornton Tomasetti Protective Design & Security Practice research and development program.

REFERENCES

1. P. Hassig, "VCFD User Manual". Cupertino, California, USA: Thornton Tomasetti. 2017.
2. D.K. Vaughan, "FLEX User's Guide," in Report UG8298, Cupertino, California, USA: Thornton Tomasetti, May 1983 plus updates through 2023.
3. P. Sun, R. Bisschop, H. Niu, X. Huang, "A Review of Battery Fires in Electric Vehicles," Fire Technology, 2020.
4. PyroSim, <https://www.thunderheadeng.com/pyrosim>
5. Fire Dynamics Simulator (FDS), <https://pages.nist.gov/fds-smv/>
6. Ansys Mechanical (Ansys), <https://www.ansys.com/products/structures/ansys-mechanical>
7. Eurocode 2. EN 1992-1-2: Design of concrete structures - Part 1-2: General rules - Structural fire design. Brussels, Belgium, 2004.
8. Eurocode 3. EN 1993-1-2: Design of steel structures - Part 1-2: General rules - Structural fire design. Brussels, Belgium, 2005.
9. Carlton, A., Guo Q., Ma S., Quiel, SE., Naito CJ., Experimental Assessment of Explosive Spalling in Normal Weight Concrete Panels Under High Intensity Thermal Exposure. Fire Safety Journal Vol 134, 2022.

STRUCTURAL MODELLING COUPLED WITH LARGE-SCALE FIRE TESTS FOR DETERMINING SPALLING OF CONCRETE STRUCTURES: A REAL APPLICATION CASE TO THE MONT-BLANC TUNNEL VAULT

Dorjan DAUTI¹, Julien VIALE², Jos BIENEFELT³, Maïkel LOPEZ⁴, Clifford CHINAYA⁵, Xavier DUPONCHEL⁶, Nicolas ROGES⁷, Jean Noel PONTAROLLO⁸

ABSTRACT

Concrete structures can be vulnerable to fire-induced spalling. The physics behind the phenomenon is complex and theoretical spalling models cannot yet provide reliable predictions. Large-scale fire testing in the laboratory therefore remains the most reliable method for determining the spalling behaviour of concrete structures, under the condition that the tested element is representative of the real structure.

This paper deals with the challenges encountered when performing a large-scale fire test in laboratory conditions on an element, chosen and designed, to be representative of the real structure. For a given concrete composition, the stress state has proven to be one of the most important parameters influencing spalling. This paper presents a method where structural modelling is coupled with large-scale fire tests for determining the spalling behaviour of concrete structures. In this method, finite element modelling is used to reproduce the same stress state evolution in the tested element as in the real structure during fire.

The application of this method is illustrated via a real case, i.e. Mont-Blanc Tunnel Vault, where structural modelling has proven to be indispensable for determining the loading and boundary conditions during the test. The model results are compared with experimental measurements for validation. Different case studies are presented in order to analyse the impact of thermomechanical properties on the model predictions.

Keywords: Spalling; structural modelling; large-scale test; stress profile; fire resistance

¹ Dr.Ing., Efectis France, Saint Aubin Cedex, France,
e-mail: dorjan.dauti@efectis.com, ORCID: <https://orcid.org/0000-0001-7052-799X>

² Ing., Efectis France, Saint Aubin Cedex, France
e-mail: julien.viale@efectis.com

³ Ing., Efectis Nederland, NL 2665 NZ Bleiswijk, The Netherlands
e-mail: jos.bienefelt@efectis.com

⁴ Ing., Efectis France, Saint Aubin Cedex, France
e-mail: maikel.lopez@efectis.com

⁵ Ing., Efectis France, Saint Aubin Cedex, France
e-mail: clifford.chinaya@efectis.com

⁶ Ing., Efectis France, Saint Aubin Cedex, France
e-mail: xavier.duponchel@efectis.com

⁷ Ing., Spie batignolles génie civil, Nanterre CEDEX, France
e-mail: nicolas.roges@spiebatignolles.fr

⁸ Ing., TMB-GEIE, P.le Sud Traforo Monte Bianco - 11013 Courmayeur
e-mail: jn.pontarollo@tunnelmb.com

1 INTRODUCTION

Several catastrophic fires in tunnels (Channel tunnel fire in 1996, Mont-Blanc tunnel fire in 1999, St. Gotthard tunnel in 2002, among others) but also other structures such as bridges, closed car parks and high-rise buildings, which have caused a large economical and social damage, and even loss of life, have emphasized the vulnerability of concrete to fire-induced spalling. A lot of research has been dedicated on developing methods to prevent spalling and on determining the parameters that have an influence on it. In addition, extensive research has been dedicated to numerical modelling as well as material-scale-experiments of heated concrete for being able to predict spalling. A non-exhaustive review of such models and experiments is given in [1].

Several spalling theories have emerged, but explanations are mostly qualitative and no consensus on a single theory has been reached yet. Due to the complex nature of spalling (combined thermal stresses and pore pressure, heterogeneous material, evolving pore structure etc.), theoretical models are not able to provide realistic predictions. For this reason, the most reliable method for determining spalling of real structures remains large-scale fire testing in the laboratory [21]. The main challenge when performing such testing in laboratory conditions is being representative of what happens with the structural element on site, especially with respect to the factors that influence spalling. These main factors are: moisture content [2], heating rate [3,4], mineralogical character and size of aggregates [7,12], geometry [8,9], concrete age [10], cement type [11], the concrete's permeability (for example, concrete with polypropylene fibres added to the mix are less likely to spall) and the stress state [5,6]. Of all these parameters, only the last can vary for a given concrete composition and a given temperature curve.

According to the recommendation of RILEM TC 256-SPF on fire spalling assessment [13] the high compressive stress is one of the most influential parameters. It is therefore essential to reproduce, the stress state on the fire-exposed face.

This paper presents a method, which consists in coupling structural modelling with large-scale fire tests for determining the spalling depth of concrete structures. The method is described in chapter 2. Then in chapter 3, the application of this method to a real case, the Mont-Blanc Tunnel Vault, is presented.

2 METHOD DESCRIPTION

The two principal mechanisms behind spalling phenomenon are: (i) the pore pressure build-up, also known as moisture clog [16] (ii) and thermomechanical processes due to thermal gradients [14,15]. Explosive spalling generally occurs under the combined action of pore pressures and thermal stresses in the fire-exposed zone. The pore pressure build-up is related to the moisture transport in concrete and is directly related to parameters that concern the concrete composition such as moisture content and permeability. The second mechanism is related to the thermo-mechanical processes. The exposure of a face of a concrete member to high temperature gives rise to a considerable temperature gradient, which provokes significant thermal dilation. The major effect of the thermal expansion is the significant compressive stress ensuing in the cover, notably when the structural element is restrained. The restrain of this expansion, induces thermal stresses in deeper layers of the material. Fractures induced by the thermo-mechanical processes can contribute to spalling. The sudden unstable release of the potential energy of thermal stresses stored in the structure can cause the brittle fracture. In [15] it was also noted that high pore pressure can only be assumed as a "trigger" to a crack but cannot drive the explosion. It is therefore essential to reproduce, as faithfully as possible, the stress state of the real structure when testing a representative concrete element. The main challenge is linked to the method of applying the boundary conditions and the loading within the laboratory conditions (i.e. on the representative specimen).

This paper presents the method for evaluating the spalling sensitivity of concrete structures in laboratory conditions. The method consists of three phases:

- Phase 1: Designing the test set up for loading and/or constraining the structural element in the furnace
- Phase 2: Structural modelling in the scope of reproducing the stress state
- Phase 3: Large-scale fire test of the representative test element

2.1 Phase 1: Experimental set up for loading and/or constraining the structural element

In a real-life situation, the fixed connections between elements, the phenomena of restrained expansion and the curvature of elements generates important stresses in the sections subjected to thermal action over time. In order to reproduce these stresses as closely as possible, it is necessary to apply external mechanical load to the test body, generating internal stresses of the same order of magnitude.

The objective of this phase is having an experimental set up which allows loading or constraining the structural element. Two common testing setups that are used at Efectis are presented below:

1. Reverse bending moment setup: This method consists in applying a vertical load through hydraulic jacks at each cantilever end of a concrete element, which induces compressive stresses in the fire-exposed side (intrados). Figure 1a shows the test configuration and loading. This method can be used for flat concrete elements (zero curvature).
2. Bi-axial loading frame: Figure 1b shows the biaxial loading frame. This method consists in applying simultaneously a vertical load and a horizontal load through hydraulic jacks. The method is often used for testing curved elements such as tunnel linings.

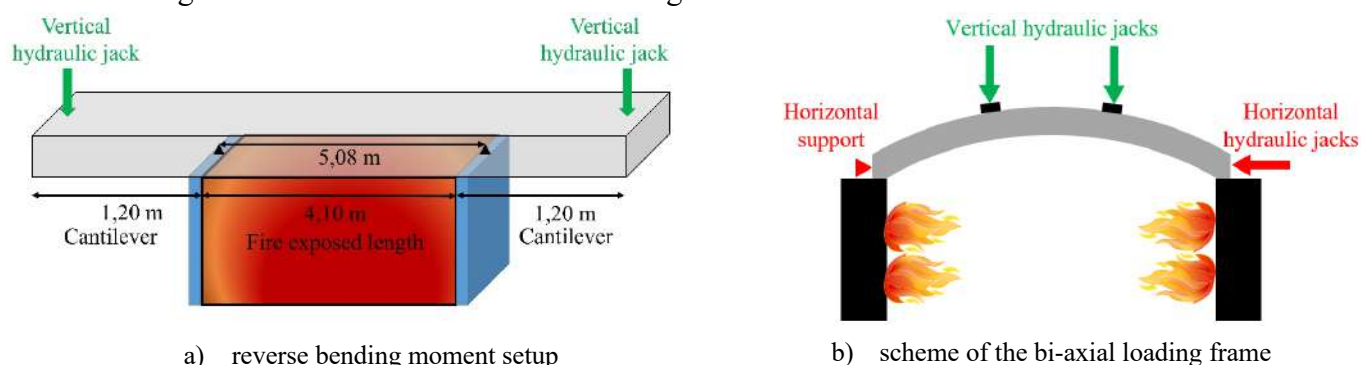


Figure 1. Experimental setups used at Efectis for large scale spalling tests

2.2 Phase 2: Structural modelling for reproducing the stress state of the real structure

Phase 2 is thus essential for determining the geometry, reinforcement and loading conditions of the tested element. This phase consists in making advanced thermomechanical calculations, using the finite element method (FEM) to ensure that the stress level of the tested element is representative of the actual structure. This requires two steps:

1. Step 1: Determining the stress state evolution in time at the fire exposed side of the real structure

The 1st step is the development of a thermomechanical model that corresponds to the real structure considering realistic boundary conditions (soil-structure interaction, load, etc.) . The model allows identifying the zones with highest compressive stresses and retrieving the stress-state evolution at this area.

2. Step 2 : Determining the loading conditions to be applied during testing such that the stress state of the tested element fits to the stress state of the real structure.

The 2nd step is the development of a thermomechanical model that corresponds to the experimental set up. Figure 2 presents the numerical models of the concrete elements tested at Efectis using the experimental setups presented in Phase 1 (see chapter 2.1). The loading curve is determined such that the stress state in the tested element is as close as possible to the stress state of the real structure exposed to the same fire condition. When considering the rapid heating (ex. hydrocarbon fires) of an unprotected concrete element, the reproduction of the stress state is particularly important during the first part of the fire resistance test (spalling phenomena generally occur during the first few minutes of exposure). The thermomechanical model of the tested element is also used for verifying the safety of the fire test.

The thermomechanical calculations in both steps take into account:

- The variation with temperature of thermomechanical properties of concrete
- Thermal stresses due to nonlinear temperature profile and 2nd order effects due to large displacements
- The elastoplastic behaviour of concrete with a constitutive behaviour that is temperature dependent
- Complete cross section (no spalling)

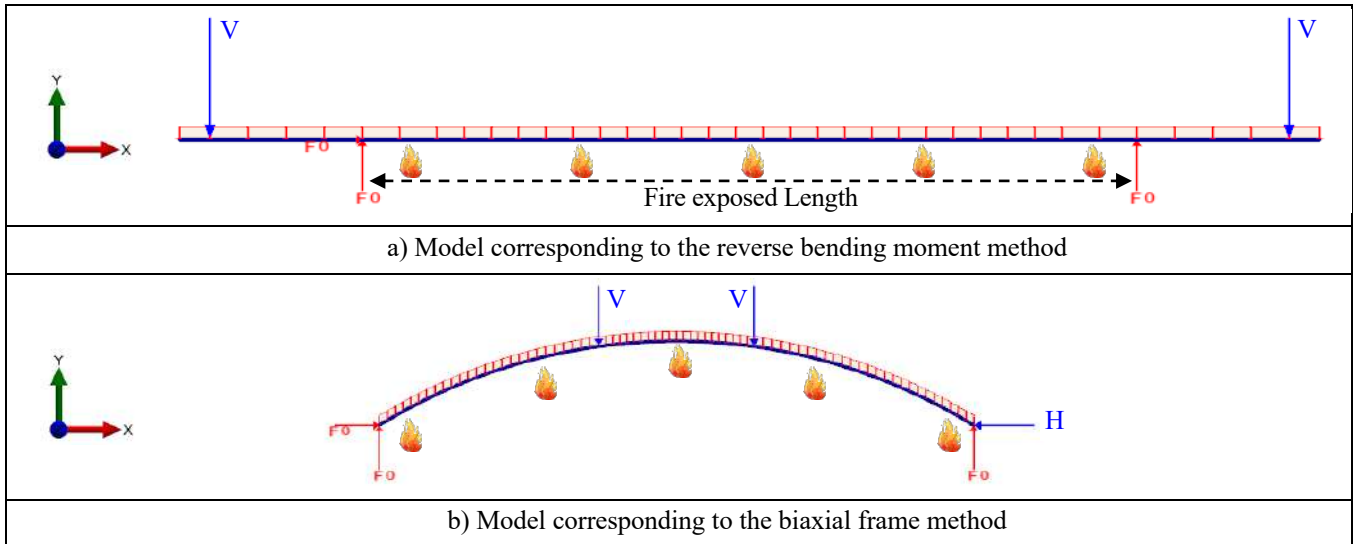


Figure 2. Thermomechanical model for the tested element

2.3 Phase 3: Large scale fire test of the representative test element

The concrete elements designed in phase 1 are heated with the required fire curve in the large-scale furnace. While the specimen is being heated, the concrete element is loaded mechanically. The loading curve, which has been determined during phase 2, is often evolving with the time to achieve the required stress level. Figure 3 shows illustrations from tests performed at Efectis using the designed experimental setups.



a) Inverse moment setup



b) Biaxial loading frame

Figure 3. Large-scale fire test setup (Efectis Laboratory)

3 APPLICATION CASE TO MONT-BLANC TUNNEL VAULT

A real case application is presented here to illustrate the previously described method, which involves modelling and testing. As part of the refurbishment of the Mont-Blanc tunnel vault and at the request of our customer SPIE BATIGNOLLES, Efectis carried out laboratory fire tests to determine the spalling depth of the concrete structure.

3.1 Thermomechanical model

The stress state of the real structure and its evolution in time obtained through a thermomechanical finite element model (Step 1 in §2.2). The results are shown in Figure 4.

The focus of this chapter is Step 2 in §2.2, which consists in determining the loading conditions to be applied during testing such that the stress state of the tested element fits to the stress state of the real structure shown in Figure 4. In order to achieve this, a thermomechanical model that corresponds to the testing concrete element has been developed in the finite element software SAFIR [20]. The simulations are performed in two runs:

1. Heat transfer calculation on a 2D section to determine the heating of the element
2. Thermomechanical calculation to determine the stress state evolution inside the concrete element.

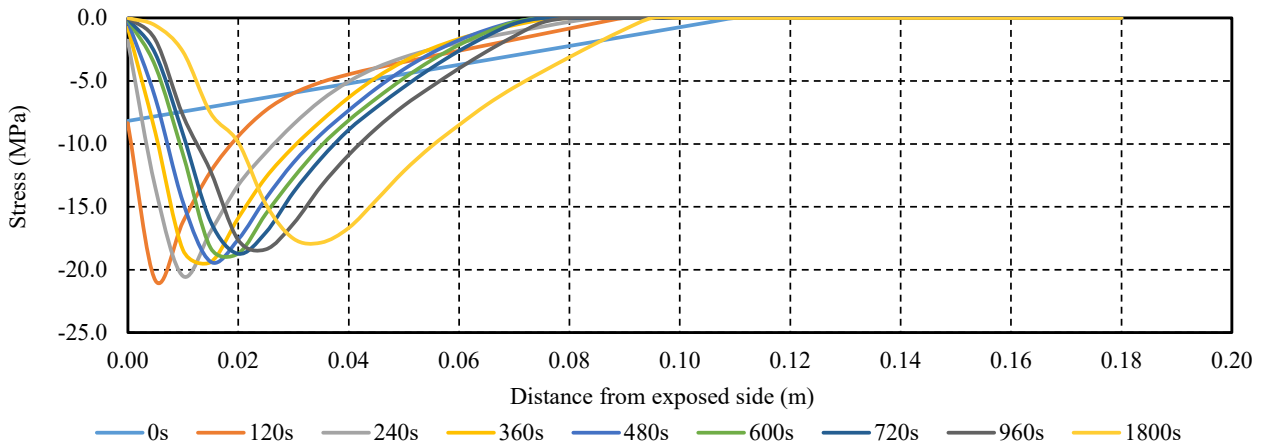


Figure 4. Stress state evolution in the real structure

3.1.1 Heat transfer calculation

The heat transfer calculation is performed on a 2D section of concrete. The sections are modelled using triangular and rectangular elements. The thermal properties of concrete and reinforcing steel are considered temperature-dependent, as defined in Eurocode 2 part 1-2 and its French national annex [18]. The moisture content of the concrete is assumed 1.5%. The density of the concrete is assumed 2300 kg/m³.

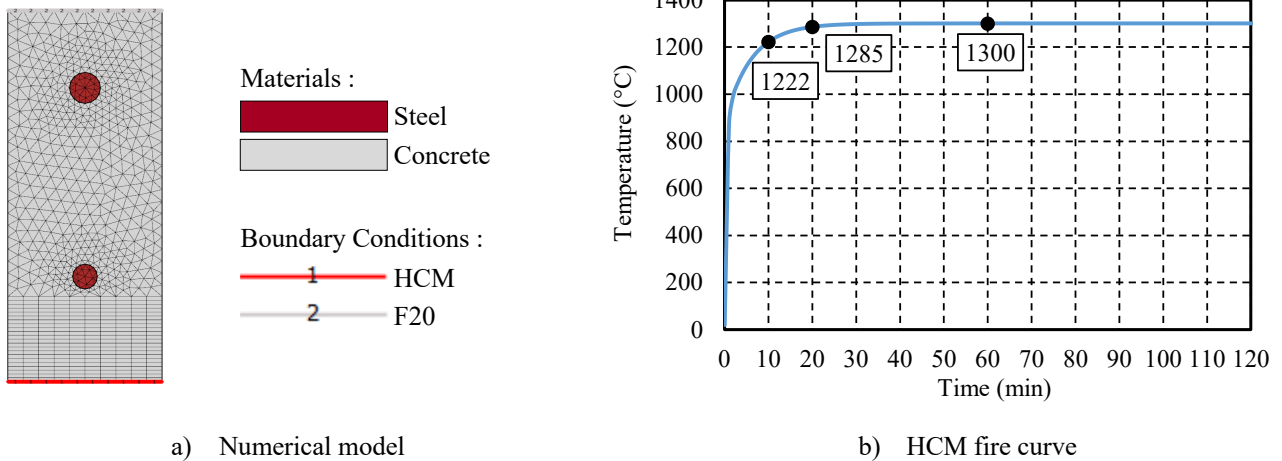


Figure 5. Heat transfer model

The applied thermal action corresponds to the modified hydrocarbon curve (HCM) as defined in [21], which is governed by the following equation, where θ is the temperature in °C and t is the time in min:

$$\theta(t) = 1280(1 - 0.325e^{-0.167t} - 0.675e^{-2.5t}) + 20 \quad (1)$$

Following the recommendations of Eurocode 1 Part 1-2 and those of Eurocode 2 Part 1-2, the convective heat transfer coefficient is $h = 50 \text{ W/m}^2\text{K}$ on the exposed face and $h = 4 \text{ W/m}^2\text{K}$ on the unexposed face. The emissivity is $\epsilon_c = 0.7$. The following figure gives the temperature distribution at different time instants:

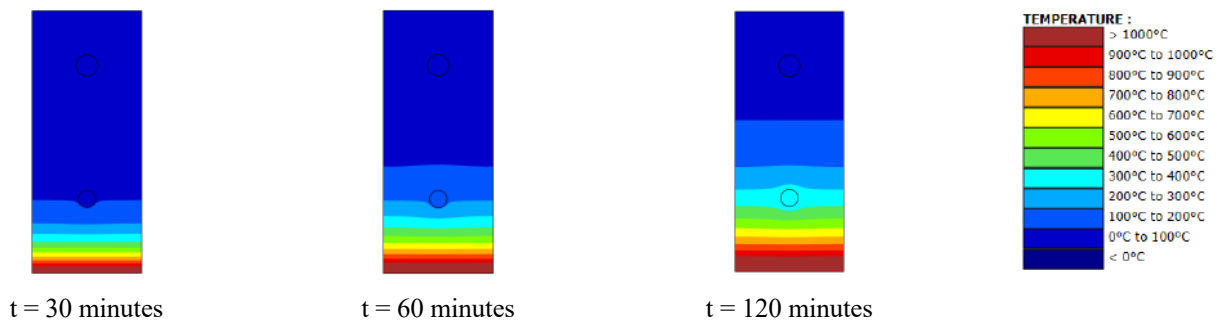


Figure 6. Temperature distribution in the cross section at different time instants

3.1.2 Stress state evolution

The thermomechanical model developed for reproducing the stress state in the tested element is illustrated in Figure 2b. The mechanical properties of steel and concrete are considered to evolve with temperature as prescribed in Eurocode 2, part 1-2 [18]. Vertical supports are considered in both extremities as boundary conditions. Horizontally, the displacements are blocked only one side (on the left of the model). Vertical and horizontal loads corresponding to the positions of the hydraulics jack are considered in the model. In this configuration, the curved element will be loaded with an axial force and negative moment in order to have the bottom fibres of the exposed concrete compressed by the effect of the moment and axial load. This model therefore makes possible to reproduce the thermomechanical conditions (stresses) on the exposed face of the vault in the real configuration.

Figure 7 shows the final geometry of the tested element whose properties are presented in Table 1. The curvature of the lower surface is identical to that of the structure. The thickness of the tested element (i.e. 24 cm) is higher than the real structure (i.e. 18 cm) in order to ensure the safety during the test.

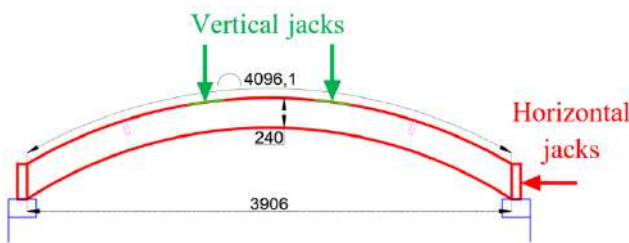


Figure 7. Geometry and configuration of the testing element (dimensions in mm)

Table 1: Properties of the tested element

Length/Width/Thickness Design concrete grade:	3.9m ; 2.4m; 0.24m; C35/45
Transversal reinforcement (Non-exposed side):	Ø=10mm@150mm, cover=30 mm, B500B
Longitudinal reinforcement (Non-exposed side):	Ø=20mm@100mm, cover=40 mm, B500B
Transversal reinforcement (Exposed side):	Ø=16mm@100mm, cover=60 mm, B500B
Longitudinal reinforcement (Exposed side):	Ø=10mm@150mm, cover=50 mm, B500B

The loading applied to the test specimen makes it possible to obtain a stress state similar to that calculated in a real situation. However, for safety reasons during the test, the forces and therefore the load applied must be limited so as not to risk brittle failure of the element in the event of excessive spalling. This means limiting the length of time during which the stresses are the same on the fire exposed face in the real situation and in the test (concordance of stresses obtained over the first 30 minutes only). Given the current state of knowledge of spalling phenomena in concrete structures, for a given concrete composition, the stresses on the first few centimetres of the exposed face are an essential parameter to reproduce during the test to ensure that the results are sufficiently representative to real conditions. It was therefore ensured that the stresses developed in the first few centimetres of concrete on the exposed face were sufficiently representative of those on the actual structure.

Figure 8 shows the applied load during the test, which made it possible to reproduce the stresses as closely as possible during the first 30 minutes.

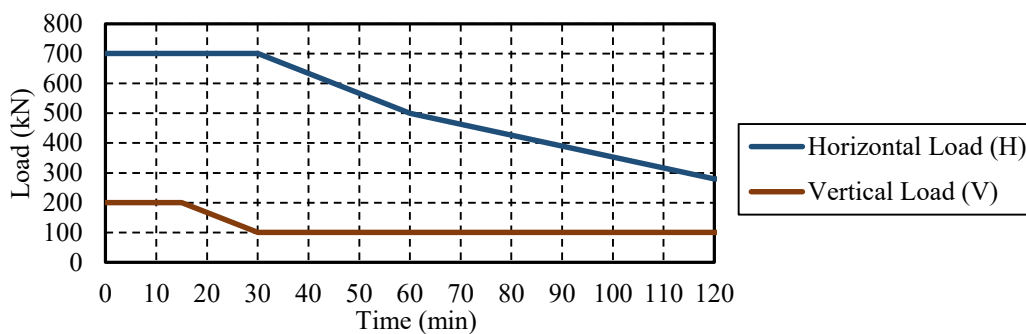


Figure 8. Horizontal and vertical loading conditions

Figure 9 illustrates the normal longitudinal stress profile obtained in the section at several instants of exposure to the HCM fire, in the most critical zone of the prefabricated vault in the real structure (solid line) and of the concrete element during the test (dotted line). Given the objective in the current project of demonstrating spalling of less than 5 cm, the stresses are presented for the first 6 cm.

It can be seen that up to 30 minutes the stress level on the exposed side of the tested element is very similar to that calculated in the real structure. The maximum stress deviation is around +5% at 10 minutes and around -3% at 30 minutes. Note that this deviation applies to the maximum stress value. The averaged stress deviation at different instants during the first 30 minutes is around 0.1%.

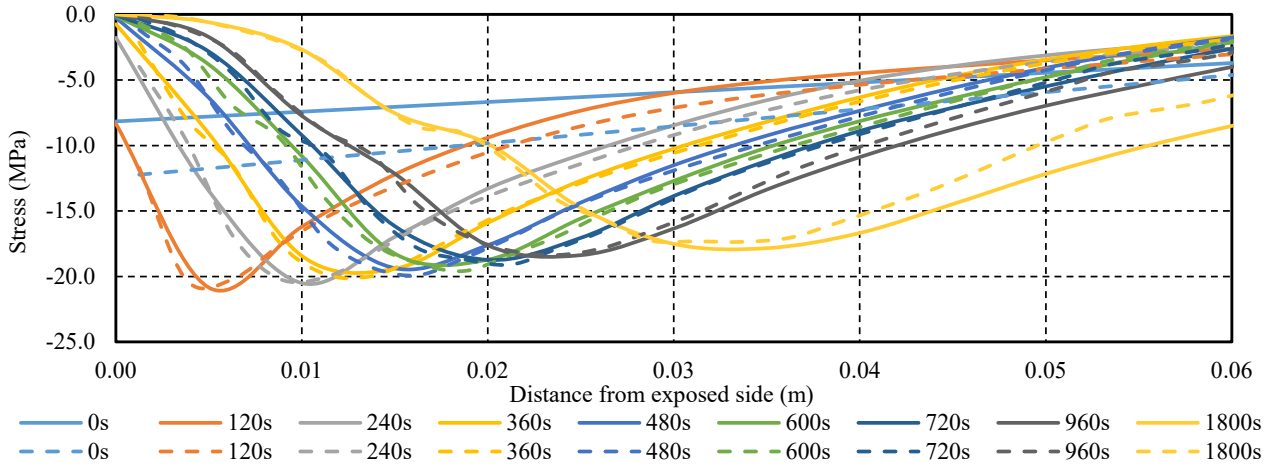


Figure 9. Stress state evolution in the first 6 cm: testing element (dashed lines) vs. real structure (continuous lines)

Figure 10 shows the complete diagram (over the entire height of the section). The compressed height was between 7 and 10 cm during the test, whereas in reality it was between 7 and 11 cm on the exposed side over the first 30 minutes.

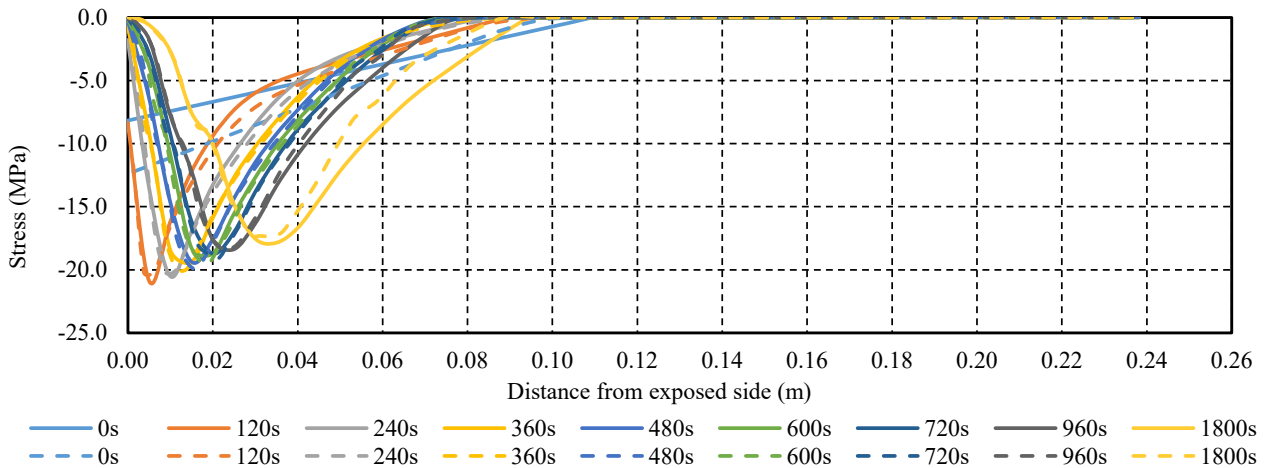


Figure 10. Stress state evolution over the whole thickness: testing element (dashed lines) vs. real structure (continuous lines)

It is important to emphasize the difference in the stress state at room temperature between the real structure and the tested element (light blue curves at $t=0s$). Fitting the stress state at ambient temperature requires an important evolution of loading during the first instants of the spalling tests. For practical and feasibility reasons, this situation has been avoided and the loading conditions are merely based on the objective of fitting the stress state after the heating begins (first fitting is at $t=2$ min), given that spalling is a phenomenon that occurs during heating.

Other approaches are based on stress-state-fitting at ambient temperature. This is discussed more in detail in the next chapter.

3.1.3 Discussion on stress-state reproduction of the testing element

According to the method for stress-state-reproduction described in chapter 2.2 and illustrated in chapter 3.1.2, the loading conditions are determined such that stress-state in the tested element coincides with stress state of the real structure during at least 30 min of heating. Another existing alternative approach for spalling tests consists in determining the loading conditions based on the stress-state fitting at ambient temperature only. Then the loading condition are maintained constant during the test. The real case application presented in the previous chapter has been used here to verify whether this approach is conservative or not.

The loading conditions are determined such that, the stress state in the real structure fits the stress state of the testing element at ambient temperature (see dashed and continuous light blue curves at $t=0$ s in Figure 11). The necessary loads for the stress fitting at ambient temperature are: 850 kN in horizontal direction and 425 kN in vertical direction. These loads are then maintained constant during 2h of numerical simulation. When comparing the stress states at other instants in time, important discrepancies between the two models (real structure vs. tested element) are observed. The stress level in the tested element is lower that the stress level in the real structure. The stress deviation is around -6% at 2 minutes and around -18% at 30 minutes. Note that this deviation applies to the maximum stress value. The averaged stress deviation at different instants during the first 30 minutes is around -10%. The results obtained here are strongly linked with the type of structure that is studied. However, they demonstrate that the ambient-temperature-stress-fitting approach may lead to loading conditions, which give lower compressive stresses in the tested element compared to the real structure. Consequently, the obtained spalling may be underestimated and a test under these conditions would not be conservative.

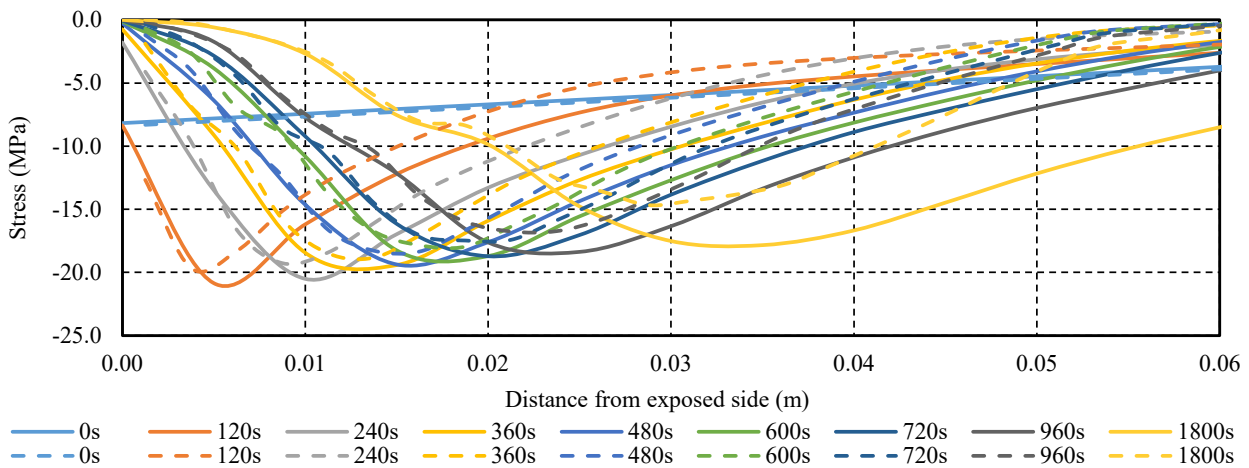


Figure 11. Alternative approach for stress-state fitting: testing element (dashed lines) vs. real structure (continuous lines)

3.2 Large-scale fire test

The test specimen representative of the prefabricated vault is shown in the Figure 7 (3.91 m long by 2.4 m wide). The specimen has been instrumented with type K thermocouples, which were installed throughout the depth of the specimen. During concrete casting, small samples were made for monitoring the compressive strength, the density and the water content. The sample has been tested at the Efectis furnace in Netherlands using the biaxial loading frame shown in Figure 3. The loading and the boundary conditions are shown in Figure 1b.

3.2.1 Ablation phenomenon

Ablation of concrete in the exposed phase was observed, giving it a very granular appearance (see Figure 12c and Figure 12d). Certain components of concrete begin to melt from a temperature of around 1150-1200°C, but the literature contains little information about the process itself and the phases that form in connection with melting. It would appear that the liquefaction of concrete begins with the melting of the hardened cement paste matrix, and that the melting of the aggregates only takes place afterwards [19].



Figure 12. Photos before and after the test

The melting of the cement paste depends essentially on the chemical composition of the cement used. An ordinary cement composition (60% C3S, 20% C2S) results in a cement paste melting temperature of around 1200°C [20]. The melting temperature of the aggregates obviously depends on their nature, e.g. 1060°C for basaltic rock, 1210°C for granitic rock and 1700°C for quartzite. The concrete of the prefabricated vault was made up of exclusively siliceous aggregates and cement of the CEM IV/A V 42.5R type, which is a pozzolanic cement with 65-79% clinker, the rest was made up of pozzolan, fly ash and possibly other secondary constituents. The presence of the secondary constituents lowers the melting point further, so that the appearance of the first melting zones can be expected at around 1100°C [19]. The black colour observed on the exposed surface (Figure 12d) could be explained by the severity of the vitrification that took place during the HCM fire test. The vitrification is probably linked to the secondary constituents of the cement (i.e. constituents other than clinker such as pozzolan, fly ash or others) or to the nature of the fines (sand) used in the concrete mix.

3.2.2 Spalling measurements

Manual measurements of spalling are summarised in the figure below (in red the areas with the most spalling and in blue the areas with the least spalling). The maximum value is 26 mm, the average spalling is 16 mm and the fractile 95% is 22 mm.

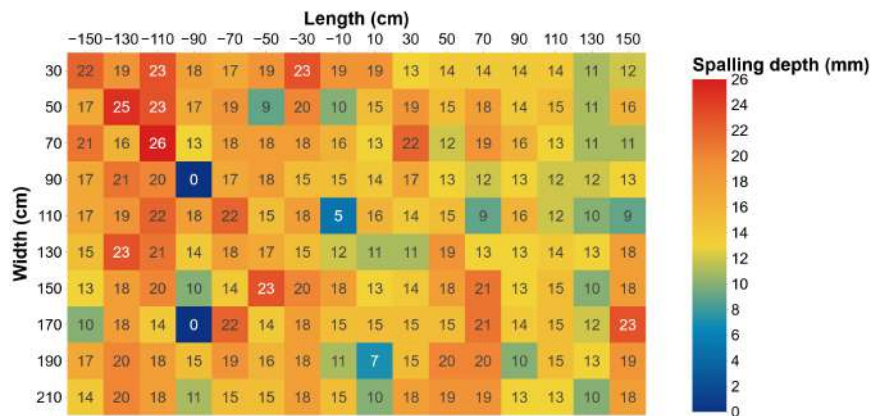


Figure 13. Measured spalling depth

3.2.3 Displacements: Tests vs. Modelling

Four displacement sensors have been used for monitoring the horizontal and vertical displacements during the test (2 strain gages for each direction). The horizontal displacements are taken at the end of the arch, and the vertical displacements at mid-span of the arch. The positive horizontal displacement corresponds to an elongation of the test body at the level of the horizontal jacks at the end of the vault. The positive vertical displacement corresponds to a downward descent of the test body at mid-span of the vault. Figure 14 shows in continues lines the measured vertical and horizontal displacements (2 strain gages in each direction). Displacements measurements are compared to the results given by the numerical model. A numerical investigation has been conducted for analysing the impact of different concrete properties on the deformation of the concrete element.

The numerical investigation has been conducted through four case studies:

1. Case study 1: The design thermomechanical properties presented in chapter 3.1.1 and 3.1.2 have been used in the model. The transient creep strain is taken into account implicitly as in EN1992-1-2 [18].
2. Case study 2: The thermomechanical properties measured in small concrete samples (compressive strength, water content and density) have been used in the model. The transient creep strain is taken into account implicitly as in EN1992-1-2 [18].
3. Case study 3: The thermomechanical properties measured in small concrete samples and a reduced cross section in order to consider spalling have been used in the model. The transient creep strain is taken into account implicitly as in EN1992-1-2 [18]. The following assumptions have been made:
 - a. An average spalling depth of 16 mm (as measured after the tests) has been considered by reducing the cross section of exposed face evenly
 - b. Spalling has been considered starting from the beginning of the test ($t=0s$)
4. Case 4: The thermomechanical properties measured in small concrete samples (compressive strength, water content and density) have been used in the model. An explicit transient creep (ETC) formulation of the Eurocode model has been used. The formulation is detailed in [22].

The thermomechanical properties for each case study are shown in Table 2.

Table 2. Thermomechanical properties for different numerical case studies

	Case Study 1	Case Study 2	Case Study 3	Case Study 4
Compressive strength f_c (MPa)	35	61	61	61
Tensile Strength f_t (MPa)	0	4.5*	4.5*	4.5*
Water Content w (%)	1.5	5.5	5.5	5.5
Density ρ (kg/m ³)	2300	2225	2225	2225
Spalling (mm)	0	0	16	0
Transient Strain Model	EN1992-1-2 [18]	EN1992-1-2 [18]	EN1992-1-2 [18]	ETC formulation [22]

*Calculated following NF EN1992-1-2 [18]

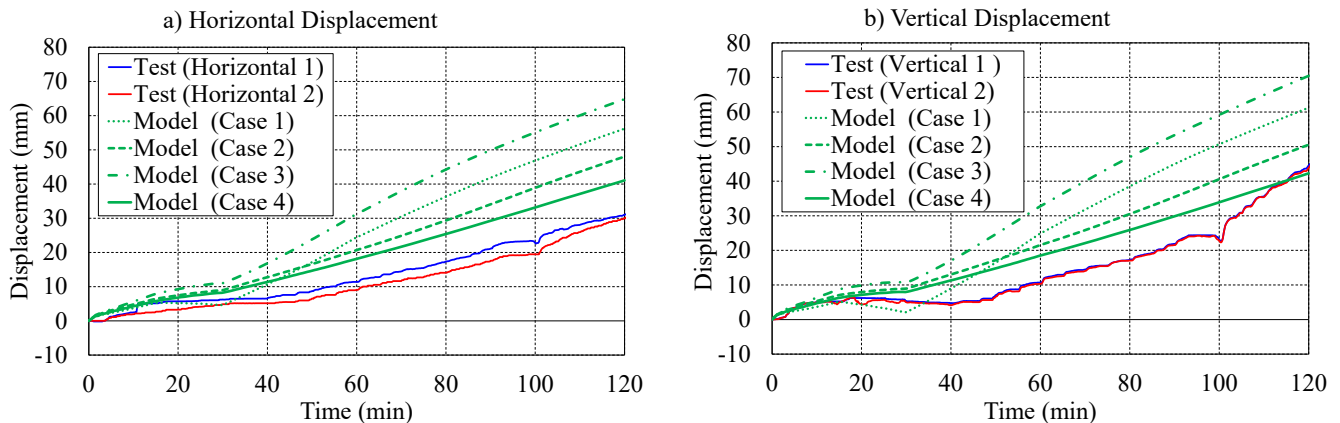


Figure 14. Vertical and horizontal displacements (Test vs. Modelling)

The numerical investigation shows that:

- When using the design properties (Case Study 1), the deformation of the concrete element (see dotted lines) during the test is well predicted by the numerical model for at least 30 min. At around 30-40 minutes, the change of slope in the displacement graph observed in the experiments is also captured by the numerical model. However, the final displacements given by the numerical model are higher.
- When using the measured properties (Case Study 2), the model results are improved (see continuous lines). In addition to the good prediction of the deformation behaviour at the first stage (before 30 min), the model displacements get closer to the measured values during the 2nd stage (after 30 min).
When analysing the adjusted thermomechanical properties of Case Study 2 one-by-one, the following conclusions can be made when comparing to Case Study 1:
 - An increase of the compressive strength (from 35 MPa to 61 MPa), increases the vertical and horizontal displacements
 - Considering the tensile strength in the simulations decreases the vertical and horizontal displacements
 - An increase of the water content (from 1.5% MPa to 5.6%) decreases further the vertical and horizontal displacements
- When using the measured properties with a reduced cross section (Case Study 3), the displacements in the numerical model are higher, increasing the gap with the measured values. This can be explained by assumptions taken into account in the numerical mode with respect to spalling (reduction of cross section all over the exposed surface, spalling starting from $t=0s$) which are probably not realistic and over conservative. It is also important to highlight that the reduced cross section is mostly due to spalling but part of it can also be related to flakes of concrete that may fall down after the test during cooling or specimen removal from the furnace.
- Case Study 4, which considers an explicit transient creep formulation with adjusted thermomechanical properties as measured in experiments, gives the best match with the actual behaviour. The differences with the results obtained with the implicit strain model (Case Study 2), are linked with the computation of the concrete material stiffness during unloading. Considering the transient creep strain as reversible in the implicit model, leads to an overestimation of the final horizontal elongation of the curved element.

4 CONCLUSIONS

This paper deals with one of the main challenges when performing large-scale spalling tests in laboratory conditions, which is the determination of a test set up and associated loading conditions such that the tested element is representative of the real structure. The proposed method for spalling determination using large-scale fire testing can be split in three phases, which are strongly related: (i) Design of the test set up (ii) Structural modelling for reproducing the stress state of the real structure (iii) Large scale test of the representative element.

In order to illustrate the proposed method, a real application case to Mont-Blanc Tunnel Vault has been presented. A thermomechanical model has been developed and used for fitting the stress state of the tested element to the stress state of the real structure at different instants of fire exposure. An additional numerical analysis has shown that fitting the stress state at ambient temperature only may lead to lower compressive stresses in the tested element compared to the real structure and, consequently, to a potential underestimation of spalling during the test.

Finally, a numerical analysis where the displacements given by the numerical model using different parameter sets were compared to the experimental measurements has been presented. The analysis has shown that the model gives a good prediction of the displacements when the measured thermomechanical properties are used.

REFERENCES

1. Dauti, D., PhD Thesis, A combined experimental and numerical approach to spalling of high-performance concrete due to fire. Mechanics of materials. Université Grenoble Alpes, 2018. English. (NNT : 2018GREAI062). (tel-01950731)

2. Harmathy, T., Effect of Moisture on the Fire Endurance of Building Elements. Research paper 385. ASTM Special Technical Publication, 74 –95 (1965)
3. Hertz, K., “Danish investigations on silica fume concrete at elevated temperatures”. In: ACI Materials Journal 89, pp. 345–347 (July 1992).
4. Anderberg, Y , “Spalling phenomena of HPC and OC”. In: Proceedings of International Workshop on Fire Performance of High-Strength Concrete, pp. 69–73 (Jan. 1997).
5. Boström, L., Wickström, U., and Adl-Zarrabi, B, “Effect of specimen size and loading conditions on spalling of concrete”. In: Fire and Materials 31, pp. 173 –186 (Apr. 2007)
6. Carré, H., Pimienta, P., La Borderie, C., Pereira, F., and Mindeguia, J.-C. , “Effect of compressive loading on the risk of spalling”. In: MATEC Web of Conferences 6, p. 01007. (2013).
7. Ingberg, S., Griffin, H., Robinson, W., and Wilson, R., “Fire tests of building columns”. In: Journal of The Franklin Institute-engineering and Applied Mathematics 191, pp. 823–827 (Jan. 1921).
8. Guerrieri, M. and Fragomeni, S., “An experimental investigation into the influence of specimen size, in-situ pore pressures and temperatures on the spalling of difference size concrete panels when exposed to a hydrocarbon fire”. In: MATEC Web of Conferences 6, p. 01002 (Sept. 2013)
9. Werner, S. and Rogge, A., “The effect of various fire-exposed surface dimensions on the spalling of concrete specimens”. In: Fire and Materials 39.5, pp. 545–556 (2015).
10. Jansson, R. and Boström, L., “Factors influencing fire spalling of self compacting concrete”. In: Materials and Structures 46.10, pp. 1683–1694 (2013).
11. Iravani, A. and Anders, S., “Effects of cement type, aggregate type and concrete age on the mass loss of concrete exposed to elevated temperature”. In: 5th International Workshop on Concrete Spalling due to Fire Exposure in Borås, Sweden, pp. 63–72 (2017).
12. Dauti, D., Tengattini, A., Dal Pont, S., Toropovs, N., Briffaut, M., Weber, B., Analysis of moisture migration in concrete at high temperature through in-situ neutron tomography, Cement and Concrete Research, Volume 111, 2018, Pages 41-55 (2018) <https://doi.org/10.1016/j.cemconres.2018.06.010>
13. Pimienta, P., McNamee, R., Robert, F. et al. Recommendation of RILEM TC 256-SPF on fire spalling assessment during standardised fire resistance tests: complementary guidance and requirements. Mater Struct 57, 3 (2024). <https://doi.org/10.1617/s11527-023-02248-z>
14. Saito, H., “Explosive Spalling of Prestressed Concrete in Fire”. In: Bulletin of Japan Association for Fire Science and Engineering 15, pp. 23–30 (Jan. 1966)
15. Bažant, Z. P., “Analysis of pore pressure, thermal stresses and fracture in rapidly heated concrete”. In: International Workshop on Fire Performance of High-Strength Concrete, pp. 1487–1499 (1997).
16. Harmathy, T., Effect of Moisture on the Fire Endurance of Building Elements. Research paper 385. ASTM Special Technical Publication, pp. 74 –95 (1965).
17. SAFIR – Logiciel de simulation du comportement mécanique des structures soumises à un incendie – User’s Manual – J.M. Franssen, T. Gernay, Janvier 2019 ;
18. NF EN 1992-1-2 et Annexe Nationale : « Eurocode 2 – Calcul des structures en béton – Partie 1-2 : Règles générales – Calcul du comportement au feu », Octobre 2005 et NF EN 1992-1-2/NA, Octobre 2007 ;
19. RILEM TC 227-HPB: STAR 1 - Physical Properties and Behaviour of High-Performance Concrete at High Temperature
20. Jean-Christophe Mindeguia. Contribution expérimentale à la compréhension des risques d'instabilité thermique des bétons. Matériaux. Université de Pau et des Pays de l'Adour, 2009. Français. (NNT :). (tel-00418218)
21. Circulaire interministérielle n° 2006-20 du 29 mars 2006 relative à la sécurité des tunnels routiers d’une longueur supérieure à 300 mètres (annule et remplace la circulaire n° 2000-63 tout en maintenant le renvoi à l’Instruction Technique qui y est annexée), NOR : EQU0610841C
22. Gernay, T., Franssen, J.-M., A formulation of the Eurocode 2 concrete model at elevated temperature that includes an explicit term for transient creep, Fire Safety Journal, Volume 51, pp 1-9 (2012)

TEMPERATURE EFFECTS ON THE BOND BEHAVIOUR OF REINFORCEMENT IN FIBRE-REINFORCED LIGHTWEIGHT AGGREGATE CONCRETE

Christopher Kevinly¹, Panwei Du², Kang Hai Tan³

ABSTRACT

The growing importance of sustainable and mechanically superior construction materials has increased the interest in fibre-reinforced lightweight aggregate concrete (FRLWAC) for its enhanced structural performance over conventional lightweight aggregate concrete, while preserving sustainability aspects of the latter. There is an urgent need for investigating the bond behavior of reinforcing bars in FRLWAC under elevated temperatures due to its significance for the safety of FRLWAC structures in fire scenarios. This paper presents a study on the bond behavior of FRLWAC with varying steel fibre contents, concrete cover depths, and temperature exposures. It was found that exposure to elevated temperatures caused a shift in bond failure towards more brittle modes. However, the incorporation of steel fibres helped mitigate the occurrence of brittle bond failure. Furthermore, the test data was compared with predictions from the *fib* Model Code, revealing that the Model Code provided overly conservative estimates of bond strength for FRLWAC at both ambient and fire conditions.

Keywords: Bond-slip; lightweight concrete; fire behaviour; fibre reinforcement

1 INTRODUCTION

Lightweight aggregate concrete (LWAC) is becoming more lucrative in recent years due to the global drive towards a more sustainable construction industry. The use of LWAC in beams and slabs allows for smaller columns and foundations to be designed and constructed, thus reducing concrete usage [1] and the overall carbon footprint of the building. Furthermore, LWAC is known to possess good insulating properties [2–3], which may improve the operating efficiency of climate-control systems of buildings with LWAC.

Despite its apparent benefit, one of the reasons for the slow adoption of LWAC in the industry is the belief that it possesses inferior bond strength compared to conventional concrete. This raises concerns among engineering practitioners as bond behaviour governs the deflection [4] and rotational capacity [5] of flexural members. Moreover, modern LWAC tend to have higher mortar density to compensate for the low aggregate strength, which may lead to explosive spalling when exposed to fire [6]. Steel fibre has been proven to improve the bond behaviour in LWAC in ambient temperature [7–8], while polypropylene (PP) fibre is proven to effectively mitigate fire-induced explosive spalling [9]. For this reason, both steel and polypropylene fibres were introduced to improve both the bond strength and spalling resistance of LWAC.

¹Research Associate, Ir, Nanyang Technological University
e-mail: christop012@e.ntu.edu.sg ORCID: <https://orcid.org/0000-0002-4845-0188>

²Research Fellow, Dr, Nanyang Technological University
e-mail: pwdu@ntu.edu.sg, ORCID: <https://orcid.org/0000-0003-3838-2705>

³Professor, Dr, Nanyang Technological University
e-mail: ckhtan@ntu.edu.sg, ORCID: <https://orcid.org/0000-0003-1500-6643>

Despite the superior performance of fibre-reinforced lightweight aggregate concrete (FRLWAC) over LWAC in ambient temperature, its behaviour under elevated temperature is still largely unknown. Moreover, the effect of fibre addition to the bond strength of FRLWAC with different concrete cover is not well-understood yet. Therefore, this study attempts in tackling these research gaps by presenting a series of tests studying the bond-slip behaviour of FRLWAC with and without steel fibre with various concrete covers and temperature exposures.

2 EXPERIMENTAL PROGRAMME

2.1 Test parameters

Table 1 shows the variations of the specimens tested in this study. Each variation was cast twice to ensure the consistency of the specimens. The chosen variables were the steel fibre content, concrete cover and temperature exposures. Two steel fibre contents, 0.0% and 0.5%, were designed to highlight the effect of steel fibre on the bond behavior of FRLWAC, with 0.5% being the commonly used steel fibre content in the Singapore construction industry. Two specimen diameters, 100 mm and 200 mm, were chosen, resulting in concrete covers of 43.5 mm and 93.5 mm, respectively. The smaller concrete cover equated to a clear-cover-to-bar-diameter ratio (c_c/d_b) of 3.34 (representing longitudinal bars in beams and slabs), while the larger one corresponded to a c_c/d_b of 7.19 (representing anchored bars in beam-column joints). The specimens were also exposed to four different temperature levels: ambient temperature, 200 °C, 400 °C and 600 °C. The upper limit of 600 °C was chosen as it is the temperature where the bond between steel bars and concrete is considered to be completely lost according to *fib* Model Code 2010 [10]. The first part of the specimen nomenclature in Table 1 indicated the steel fibre content, while the second and third parts of the nomenclature denoted the specimen diameter and temperature exposure, respectively.

Table 1. List of specimens

Variation	Steel fibre	Concrete clear cover	c_c/d_b	Temperature
0-100-A	0.0 %	43.5 mm	3.34	Ambient
0-100-200	0.0 %	43.5 mm	3.34	200 °C
0-100-400	0.0 %	43.5 mm	3.34	400 °C
0-100-600	0.0 %	43.5 mm	3.34	600 °C
0-200-A	0.0 %	93.5 mm	7.19	Ambient
0-200-200	0.0 %	93.5 mm	7.19	200 °C
0-200-400	0.0 %	93.5 mm	7.19	400 °C
0-200-600	0.0 %	93.5 mm	7.19	600 °C
0.5-100-A	0.5 %	43.5 mm	3.34	Ambient
0.5-100-200	0.5 %	43.5 mm	3.34	200 °C
0.5-100-400	0.5 %	43.5 mm	3.34	400 °C
0.5-100-600	0.5 %	43.5 mm	3.34	600 °C
0.5-200-A	0.5 %	93.5 mm	7.19	Ambient
0.5-200-200	0.5 %	93.5 mm	7.19	200 °C
0.5-200-400	0.5 %	93.5 mm	7.19	400 °C
0.5-200-600	0.5 %	93.5 mm	7.19	600 °C

2.2 FRLWAC mix and mechanical properties

The mix design of the FRLWAC is shown in Table 2. The binders used in this study are CEM II 52.5 R cement from Asia Cement Corporation and grade 940U silica fume from Elkem Microsilica. The water-binder ratio (w/b) of this mix was 0.24, with superplasticiser from SIKA used to improve the workability as the w/b is low. The coarse aggregates used in this study were lightweight expanded clay aggregates

(LECA) with a dry density of 972.7 kg/m^3 and maximum and minimum diameters of 12 mm and 3mm, respectively. Two types of fine aggregates were used: silica sand and fly-ash cenosphere grade QK300. The cenosphere was used to partially replace the sand to reduce the mortar density of FRLWAC. Hooked steel fibre (3D65/35) from Dramix with a diameter of $55 \mu\text{m}$ and a length of 35 mm was used along with PP fibre with a diameter of $30 \mu\text{m}$ and a length of 13 mm.

Table 2. FRLWAC mix design (units are in kg/m^3)

Cement	Silica fume	Water	Superplasticiser	LECA	Cenosphere	Silica sand	PP fibre	Steel fibre
548	78	150	20	180	83	750	2	0 or 40

The mechanical properties of FRLWAC are presented in Table 3. The concrete compression strength was obtained through compression tests on three cylinders with 100 mm diameter and a height of 200 mm, while the mortar strength was obtained through compression tests on three 50 mm cubes without LECA for each mix. Tensile properties of the FRLWAC with 0.5% steel fibre were obtained through 3-point bending tests following EN 14651 [11], while the one without steel fibre was assumed to share the limit-of-proportionality tensile strength with the mix with 0.5% steel fibre, but without the residual tensile strength.

Table 3. Mechanical properties of FRLWAC (*denotes the assumed value)

Properties	0% Steel fibre	0.5% steel fibre
f_c	45.6 MPa	38.9 MPa
$f_{c,mortar}$	88.2 MPa	82.7 MPa
$f_{ct,lop}$	3.99 MPa*	3.99 MPa
$f_{ct,1}$	0.00 MPa*	5.32 MPa
$f_{ct,2}$	0.00 MPa*	4.30 MPa
$f_{ct,3}$	0.00 MPa*	2.83 MPa
$f_{ct,4}$	0.00 MPa*	2.22 MPa
ρ_c	1773 kg/m^3	1752 kg/m^3

2.3 Specimen design and fabrication

The bond-slip specimens were 195 mm tall FRLWAC cylinders with a specimen diameter (d_s) of 100 mm or 200 mm and with embedded H13 reinforcing bars in the centre. These specimens were designed to have a bonded length (l_b) of 65 mm, which corresponded to five times the bar diameter ($5d_b$), aligned with the tests done by Eligehausen [12] and the provision of EN 10080:2005 [13]. The areas before and after the bonded length were debonded using PVC tubes to prevent conical failure during the pull-out tests. The drawing of the specimen is shown in Figure 1. The specimens were cast vertically in cylindrical moulds made of PVC tubes, with the reinforcement bar protruding towards the loaded face for testing purposes. Acrylic plates were installed on the loaded face to flatter the surface during casting, which reduced the risk of premature failure due to the crushing of the loaded face in the tests.

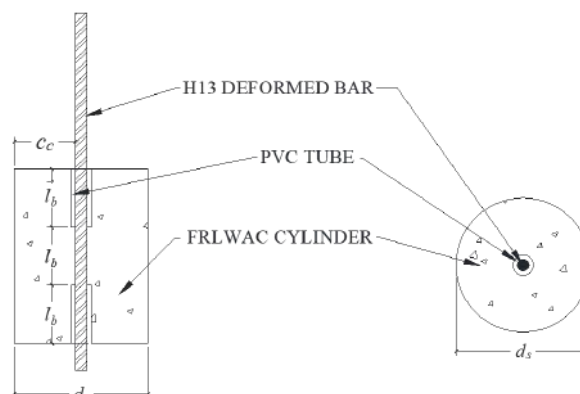


Figure 1. Side and top view of the specimen

2.4 Specimen conditioning

The specimens were air-cured for 28 days in an indoor tropical environment. After curing, the specimens were then heated in an electric furnace as shown in Figure 2. The exposed reinforcing bars were wrapped with ceramic cloth to prevent significant temperature gradients between the steel bar and the surrounding concrete. The heating curves of the furnace are shown in Figure 3, where the target temperatures were held for 12 hours to ensure uniform temperature distribution within the specimens. The furnace was then turned off and the specimens were cooled naturally inside the furnace before being set-up for testing.



Figure 2. Specimens in the electric furnace

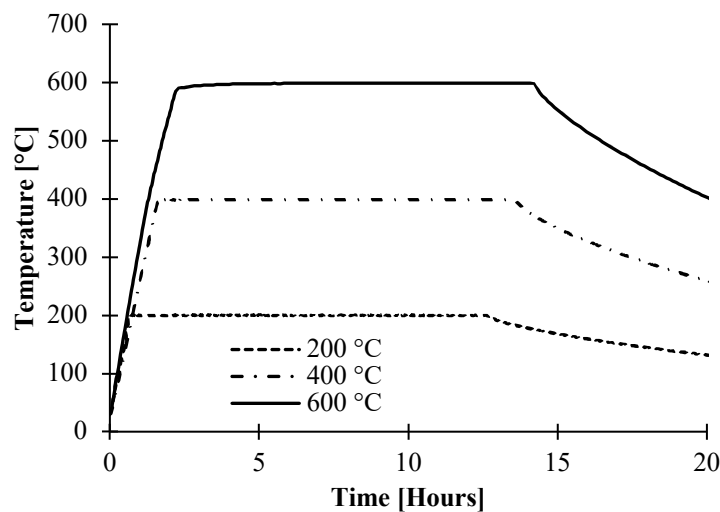


Figure 3. Temperature history of the electric furnace

2.5 Test setup and procedure

The test setup was assembled following a schematic shown in Figure 4. The specimen was set into the universal testing machine (UTM) by securing it between two plates. The bottom plate was anchored to the bottom clamp of the UTM using the steel fin welded to the bottom plate, while the top plate was connected to the bottom plate using threaded bars, screwed tight to ensure that the specimen face made full contact to the top bar. Both the top and bottom bars have holes in the middle to accommodate the protruding reinforcing bar. The reinforcing bar was clamped at the top clamp jaw of the UTM for loading. A spreader bar was attached on reinforcing bar for displacement measurement.

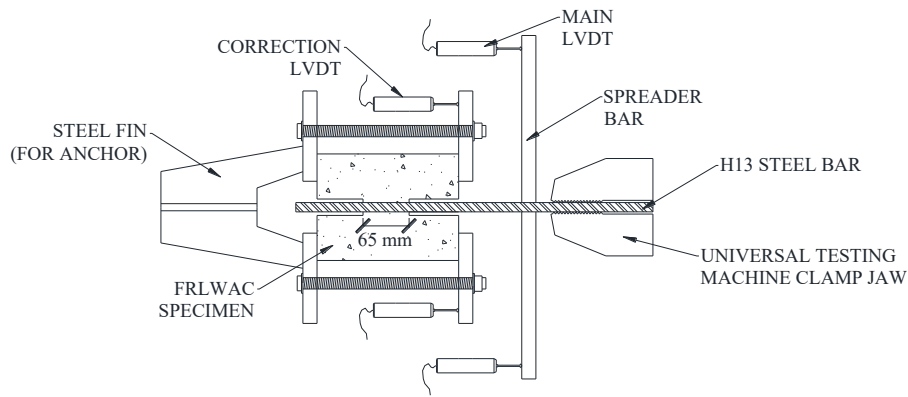


Figure 4. Test setup schematic

The bar is pulled out monotonically with a rate of 1.7 mm/min, in line to the test of Eligehausen [14]. During the pull-out test, the load was measured using the built-in load cell within the UTM, while the bar displacement was measured using two LVDTs attached to the spreader bar and corrected by additional two LVDTs attached to the top plate. The test was terminated when the force measured by the UTM load cell was lower than 10% of the peak force, and the bar was removed from the specimen so that the bonded area can be visually inspected.

3 EXPERIMENTAL RESULT

3.1 Typical bond-slip curves and failure modes

The bond strength of the specimens can be calculated by equation (1). The typical bond-slip curves of the tested specimens are shown in Figure 5, where three distinct types of bond-slip curves corresponding to three different failure modes (brittle splitting, ductile splitting and pull-out) were observed. Brittle splitting failures were characterised by sudden and catastrophic loss of bond strength just after the peak bond was reached. A sudden drop in bond strength was also seen in ductile splitting failure, but no complete loss of bond strength occurred and a more gradual decrease in bond strength was observed after the initial drop. In pull-out failure, there was no sudden drop in bond strength, instead only gradual decline in bond strength was observed as the slip increased.

$$\tau_b = \frac{F_b}{l_b \pi d_b} \quad (1)$$

where

- τ_b is the bond strength,
- F_b is the peak force recorded during the test,
- l_b is the bonded length of the reinforcement,
- d_b is the reinforcement diameter.

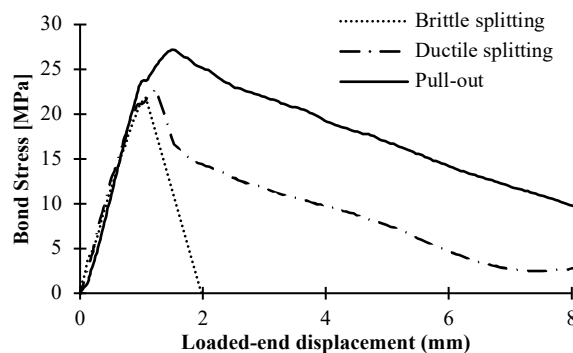


Figure 5. Typical bond-slip curves

The visual observations of the specimens with different failure modes are also shown in Figure 6. Specimens with brittle splitting mode exhibit wide longitudinal splitting crack that went through the whole length of the specimen, while the ones with ductile splitting only exhibit thin longitudinal crack. Specimens with pull-out failure did not have any crack appearing on its surface.

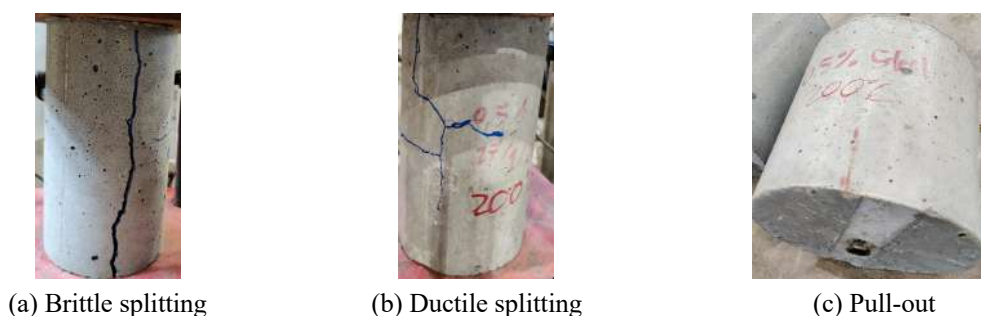


Figure 6. Failure mode visual manifestations

The complete list of failure modes of the specimens were listed in Table 4. It is clear that the presence of steel fibre prevented the brittle splitting failure mode in favour to the more ductile variation. Moreover, it is also clear that temperature exposure shifted the failure mode from pull-out to splitting.

Table 4. Failure modes of the specimens

Variation	Specimen 1 failure mode	Specimen 2 failure mode
0-100-A	Brittle splitting	Brittle splitting
0-100-200	Brittle splitting	Brittle splitting
0-100-400	Brittle splitting	Brittle splitting
0-100-600	Ductile splitting	Ductile splitting
0-200-A	Pull-out	Pull-out
0-200-200	Brittle splitting	Pull-out
0-200-400	Pull-out	Brittle splitting
0-200-600	Ductile splitting	Ductile splitting
0.5-100-A	Ductile splitting	Ductile splitting
0.5-100-200	Ductile splitting	Ductile splitting
0.5-100-400	Ductile splitting	Ductile splitting
0.5-100-600	Ductile splitting	Ductile splitting
0.5-200-A	Pull-out	Pull-out
0.5-200-200	Pull-out	Ductile splitting
0.5-200-400	Ductile splitting	Ductile splitting
0.5-200-600	Ductile splitting	Ductile splitting

3.2 Temperature effect on bond strength

The effect of temperature exposure to FRLWAC bond strength is shown in Figure 7. The first notable impression is that the bond strength at ambient temperature is significantly higher at around 28 MPa than the predicted bond strength according to *fib* Model Code [10] (15.8 MPa for C40/50 concrete). Another notable observation is that the bond strength of the specimens with c/d_b of 7.19 degraded faster compared to specimens with c/d_b of 3.34. This degradation was also affected by steel fibre content, with specimens with no steel fibre had larger bond strength drop from ambient to 400 °C compared to the ones with steel fibre. At 600 °C, the specimens with different concrete covers had practically similar bond strength.

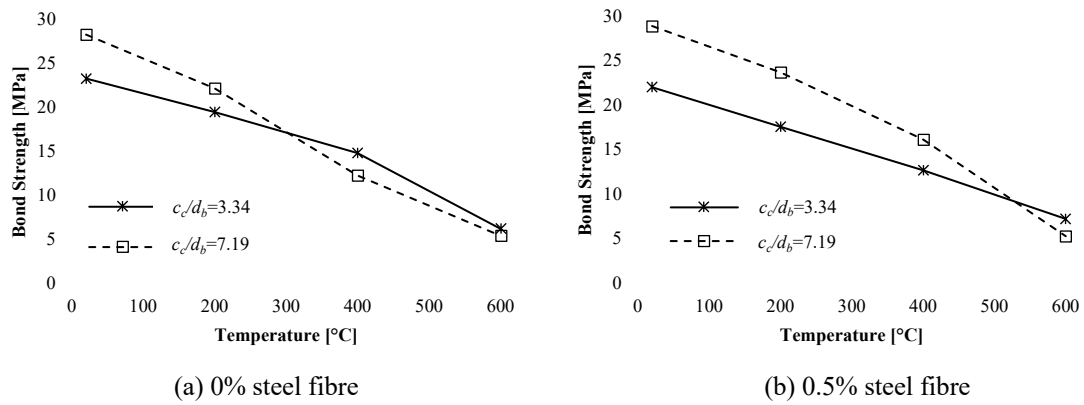


Figure 7. Mean bond strength of specimens with different steel fibre dosages at different temperatures

The bonded region of the bar after testing is shown in Figure 8. It was observed that mortar shear-off occurred in specimens failing in pull-out, while mortar crushing was observed on the rib-faces of the steel reinforcement in specimens failing in either ductile and brittle splitting. This observation implied that the pull-out strength is mostly influenced by mortar strength instead of the concrete strength as prescribed in *fib* Model Code [10]. The differences between the two are particularly notable in LWAC, where the mortar strength tend to be higher compared to the concrete strength (as listed in Table 3).

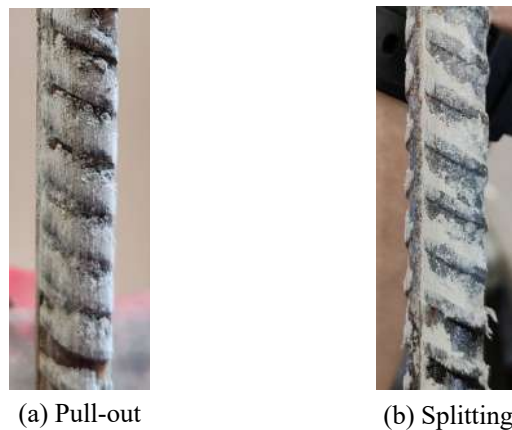


Figure 8. Reinforcement ribs after failure

It is known that splitting bond failure is governed by the tensile strength of concrete [15], and tensile strength of concrete is more sensitive to high temperature compared to compression strength that governs pull-out failure [16]. Therefore, the more significant bond degradation in larger specimens was due to the shift of failure mode from the more ductile pull-out to the more brittle splitting modes (either the more brittle or ductile variations, depending on the presence of steel fibre).

3.3 Bond toughness

The bond toughness presented in Figure 9 was calculated by integrating the post-peak bond-slip curve over the distance equal to the spacing between the ribs of the bar. It is apparent that the presence of steel fibre provided toughness in smaller specimens with c/d_b of 3.34, as well as reduced the temperature-induced toughness loss in larger specimens with c/d_b of 7.19. This improvement in toughness was contributed by the bridging effect of steel fibre that prevented a complete concrete cover splitting from occurring, thus maintaining residual bond-strength as observed in the specimen with ductile splitting failure illustrated in Figure 5. As temperature progressed, the toughness differences between larger and smaller specimens with steel fibre diminished, as the steel fibre lost its efficacy at elevated temperatures [17].

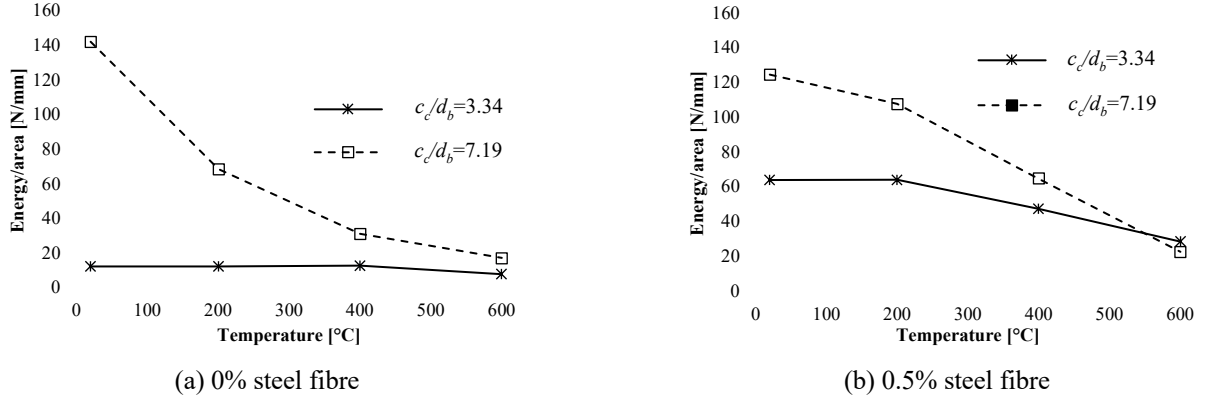


Figure 9. Mean bond toughness of tested FRLWAC specimens

4 COMPARISON WITH CODE PREDICTIONS

The *fib* model code 2010 [10] provides a provision to predict the bond strength of reinforcing bars in concrete with different failure modes. After considering the parameters of this study, the Model Code bond strength prediction of specimens failing in pull-out is shown in Equation (2), while the bond strength prediction of specimens failing in splitting is shown in Equation (3). The Model Code also provisioned that the bond strength degradation follow the tensile strength degradation of concrete, as expressed in Equation (4). From this provisions, it was implied that the Model Code did not consider the bond failure mode shift due to elevated temperatures.

$$\tau_{b, fibPO} = 2.5 \sqrt{f_c} k_{b,T} \quad (2)$$

$$\tau_{b, fibS} = 6.5 \left(\frac{f_c}{25}\right)^{0.25} \left(\frac{25}{d_b}\right)^{0.2} \left(\frac{c}{d_b}\right)^{0.33} k_{b,T} \quad (3)$$

$$k_{b,T} = 1 - \frac{T - 100 \text{ }^\circ\text{C}}{500 \text{ }^\circ\text{C}} \text{ for } 100 \text{ }^\circ\text{C} < T \leq 600 \text{ }^\circ\text{C} \quad (4)$$

where

$\tau_{b, fibPO}$ is the predicted pull-out bond strength,

$\tau_{b, fibS}$ is the predicted splitting bond strength,

f_c is the concrete cylinder strength,

$k_{b,T}$ is the temperature modification factor,

T is the interface temperature between steel and concrete.

The comparisons between the Model Code prediction and the test results are presented in Figure 10. The Model Code predictions provided overly-conservative predictions in all cases, underestimating the test results by more than half of the actual strength in most cases. Furthermore, it also observed that the bond strength was not zero at 600 °C, thus resulting in the overestimation of thermal-induced bond degradation in the predictions. This conservative predictions occurred due to the Model Code provisions were calibrated to predict the bond strength of conventional concrete. As previously discussed, the pull-out bond strength of FRLWWAC depends on the mortar strength instead of the concrete strength. Moreover, the bond prediction in the Model Code does not incorporate the effect of steel fibre contribution.

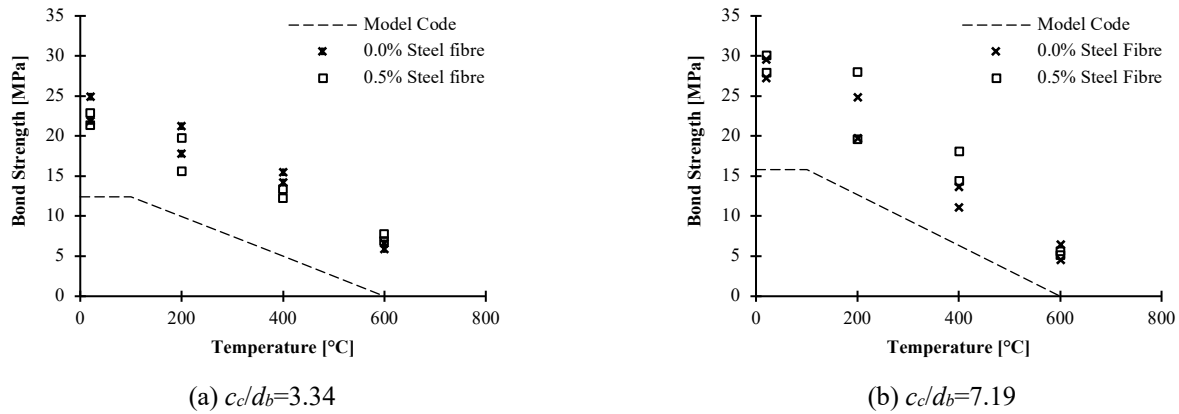


Figure 10. Model Code bond strength prediction versus test results

5 CONCLUSIONS

An experimental study on 32 FRLWAC bond-slip specimens with different steel fibre contents, concrete covers and temperatures were presented. From this study, several conclusions can be made regarding the bond behaviour of FRLWAC at ambient and fire exposures:

- The fire-induced bond strength degradation of FRLWAC occurred not only due to the compression strength degradation of concrete, but also the failure mode change from pull-out to splitting failure.
- Steel fibre enhanced the bond behaviour of FRLWAC by improving the post-peak bond-slip strength in cases where splitting failure are expected.
- The bond strength predictions made using the *fib* Model Code 2010 is overly conservative at both ambient and elevated temperatures.

ACKNOWLEDGMENT

This material is based on research supported by the Singapore Ministry of National Development and National Research Foundation under CoT Award No. COT-V3-2021-1. Any opinions, findings, conclusions or recommendations expressed in this material are those of the author(s) and do not necessarily reflect the views of CoT. The authors also would like to thank the Construction Technology and Protective Engineering laboratories of NTU for facilitating the tests.

REFERENCES

1. B. F. Bender, Economics and Use of Lightweight Concrete in Prestressed Structures. *PCI Journal*, **25** (1980) 62–67. <https://doi.org/10.15554/pcij.11011980.62.67>.
2. T. L. Cavalline, J. Gallegos, R. W. Castrodale, C. Freeman, J. Liner, & J. Wall, Influence of Lightweight Aggregate Concrete Materials on Building Energy Performance. *Buildings*, **11** (2021) 94. <https://doi.org/10.3390/buildings11030094>.
3. Y. H. Lee, N. Chua, M. Amran, Y. Yong Lee, A. B. Hong Kueh, R. Fediuk, N. Vatin, & Y. Vasilev, Thermal Performance of Structural Lightweight Concrete Composites for Potential Energy Saving. *Crystals*, **11** (2021) 461. <https://doi.org/10.3390/cryst11050461>.
4. M. A. Abed, Z. Alkurdi, A. Kheshfeh, T. Kovács, & S. Nehme, Numerical Evaluation of Bond Behavior of Ribbed Steel Bars or Seven-wire Strands Embedded in Lightweight Concrete. *Periodica Polytechnica Civil Engineering*, (2020). <https://doi.org/10.3311/PPci.16689>.
5. C. Kevinly, P. Du, B. K. Teoh, & K. H. Tan, Experimental study and modelling of flexural behaviour of continuous fibre-reinforced lightweight aggregate concrete one-way slab at ambient and elevated temperatures. *Engineering Structures*, **307** (2024) 117924. <https://doi.org/10.1016/j.engstruct.2024.117924>.
6. J.-C. Liu, K. H. Tan, & Y. Yao, A new perspective on nature of fire-induced spalling in concrete. *Construction and Building Materials*, **184** (2018) 581–590. <https://doi.org/10.1016/j.conbuildmat.2018.06.204>.

7. G. Campione, C. Cucchiara, L. La Mendola, & M. Papia, Steel–concrete bond in lightweight fiber reinforced concrete under monotonic and cyclic actions. *Engineering Structures*, **27** (2005) 881–890. <https://doi.org/10.1016/j.engstruct.2005.01.010>.
8. E. Güneyisi, M. Gesoğlu, & S. İpek, Effect of steel fiber addition and aspect ratio on bond strength of cold-bonded fly ash lightweight aggregate concretes. *Construction and Building Materials*, **47** (2013) 358–365. <https://doi.org/10.1016/j.conbuildmat.2013.05.059>.
9. D. Zhang, A. Dasari, & K. H. Tan, On the mechanism of prevention of explosive spalling in ultra-high performance concrete with polymer fibers. *Cement and Concrete Research*, **113** (2018) 169–177. <https://doi.org/10.1016/j.cemconres.2018.08.012>.
10. Fédération Internationale de la Précontrainte, FIP, *fib model code for concrete structures 2010* (Berlin: Ernst & Sohn, 2013).
11. CEN, *EN 14651:2005. Test method for metallic fibre concrete - Measuring the flexural tensile strength (limit of proportionality (LOP), residual)* (Brussels: European Committee for Standardization, 2005).
12. R. Eligehausen, E. P. Popov, & V. V. Bertero, Local bond stress-slip relationships of deformed bars under generalized excitations. *Earthquake Engineering Research Center, Berkeley*, (1982).
13. CEN, *EN 10080:2005. Steel for the reinforcement of concrete. Weldable reinforcing steel. General* (Brussels: European Committee for Standardization, 2005).
14. R. Eligehausen, E. P. Popov, & V. V. Bertero, Local bond stress-slip relationships of deformed bars under generalized excitations. *Earthquake Engineering Research Center, Berkeley*, (1982).
15. C. Kevinly, P. Du, & K. H. Tan, Local bond-slip behaviour of reinforcing bars in fibre reinforced lightweight aggregate concrete at ambient and elevated temperatures. *Construction and Building Materials*, **377** (2023) 131010. <https://doi.org/10.1016/j.conbuildmat.2023.131010>.
16. CEN, *EN 1992-1-2. Eurocode 2: Design of concrete structures, Part 1-2: General rules - Structural fire design* (Brussels: European Committee for Standardization, 2004).
17. Y. Li, E.-H. Yang, & K. H. Tan, Flexural behavior of ultra-high performance hybrid fiber reinforced concrete at the ambient and elevated temperature. *Construction and Building Materials*, **250** (2020) 118487. <https://doi.org/10.1016/j.conbuildmat.2020.118487>.

TEST OF A FULL-SCALE CONCRETE SLAB WITH STEP EXPOSED TO A LONG-DURATION ISO FIRE

Mami Saito¹, Yusuke Shintani², Toshihiko Nishimura³, Kei Kimura⁴

ABSTRACT

To evaluate membrane action on a concrete slab during a fire, a full-scale fire test on a stepped concrete floor specimen and numerical analyses were conducted. For the fire test, a reinforced concrete slab with a 270 mm step in the unprotected secondary beam section was exposed to ISO834 heating for 8 h under the vertical load-bearing condition. The experimental results indicated that the step section, which was thicker than the general section, exhibited a higher stiffness and lower concrete temperature than the general area, leading to an increased load-bearing capacity in the step section, even after the unprotected secondary beam had lost its load-bearing capacity. Therefore, the membrane effect in the upper and lower slabs was separated by a step during a fire. However, owing to cracking at the inside corner of the step, which weakened the fixity of the slab edge, the lower slab was deformed more than the upper slab. The deformation of a reinforced concrete slab with a step on numerical analyses, which utilized a simplified shell model, were in good agreement with the experimental results by applying an appropriate thickness setting to the shell for the step region.

Keywords: Full-scale fire test; Stepped concrete slab; Membrane action

1 INTRODUCTION

Many buildings have floors with steps, especially the sink and basin areas in hotels have floor slabs with steps to tie in with the levels of other rooms while accommodating drainage pipes and maintaining waterproofing. In Japan, it is common to have steps of around 200 to 300mm, so it is often planned to install secondary beams in the step section.

Since the real-scale experiments in Cardington [1], many studies have been conducted on the membrane action of reinforced concrete slabs under fire conditions [2~5]. However, none of the previous studies including full-scale fire tests considered the membrane action of stepped concrete slabs, and it is not possible to evaluate the fire resistance performance of floors with steps considering the membrane action. Therefore, in this study, a full-scale fire test on a concrete floor specimen with a step and numerical analyses were conducted to investigate the load-bearing mechanism of a slab with unprotected secondary beams at the step.

¹ Chief Researcher, Research & Development Institute, Takenaka Corporation,
e-mail: saitou.mamia@takenaka.co.jp, ORCID: <https://orcid.org/0000-xxxx-xxxx-xxxx>

² Chief Researcher, Research & Development Institute, Takenaka Corporation,
e-mail: shintani.yuusuke@takenaka.co.jp, ORCID: <https://orcid.org/0000-0002-5488-2761>

³ Senior Chief Researcher, Research & Development Institute, Takenaka Corporation,
e-mail: nishimura.toshihiko@takenaka.co.jp, ORCID: <https://orcid.org/0000-xxxx-xxxx-xxxx>

⁴ Senior Researcher, Steel Structures Research Lab., Nippon Steel Corporation
e-mail: kimura.ze8.kei@jp.nipponsteel.com, ORCID: <https://orcid.org/0000-0002-7808-3585>

2 EXPERIMENTAL METHODS

2.1 Specimen

For the fire test, a reinforced concrete slab specimen was fabricated. The configuration of the specimen is shown in Figure 1. The specimen comprised a concrete slab supported by four protected primary beams (H-450×200×9×14 (SS400)) and an unprotected secondary short-span beam (H-400×200×8×13 (SS400)). The primary beams were protected by a ceramic fibre blanket. The dimensions of the specimen were 6550 mm × 3800 mm, measured centre-to-centre between the primary beams. The primary beams in the X-direction were extended and pin-supported 100 mm from their ends, as shown in Figure 1. The right half of the slab, with an area of 2875 mm × 3400 mm (grey area in Figure 1) was 270 mm lower than that of the left half. The lower slab was constructed as a flat deck slab, and the upper and lower reinforcement (D10 rebars) were installed in a two-way direction with a pitch of 200 mm. The flat deck slab was fixed in place using angles welded to the web of the beams and then spot welded in place. The upper slab was constructed as a truss deck, and only the upper reinforcement was installed in a two-way direction. The specifications for the deck upper and lower slabs differed to simulate those commonly adopted in Japan. “Z-shaped” rebars (D10 rebar) were installed in the step at a pitch of 200 mm to transfer the tensile forces, as shown in Figure 2. At the step in the primary beams, the head-side ends of the “Z-shaped” rebars were bent downward. The “Z-shaped” and slab rebars were spaced at 100 mm centre-to-centre. The rebars were manufactured from SD295 steel. The concrete slabs were connected to the primary and secondary beams via shear studs, as indicated by the small circles in Figure 1. Both slabs had a depth of 140 mm and were constructed using light-weight concrete ($\sigma_c = 34.5 \text{ N/mm}^2$) with PP (poly propylene) fibres added at a rate of 1 kg/m^3 to prevent the concrete from exploding. The moisture content of the concrete was 5.6%.

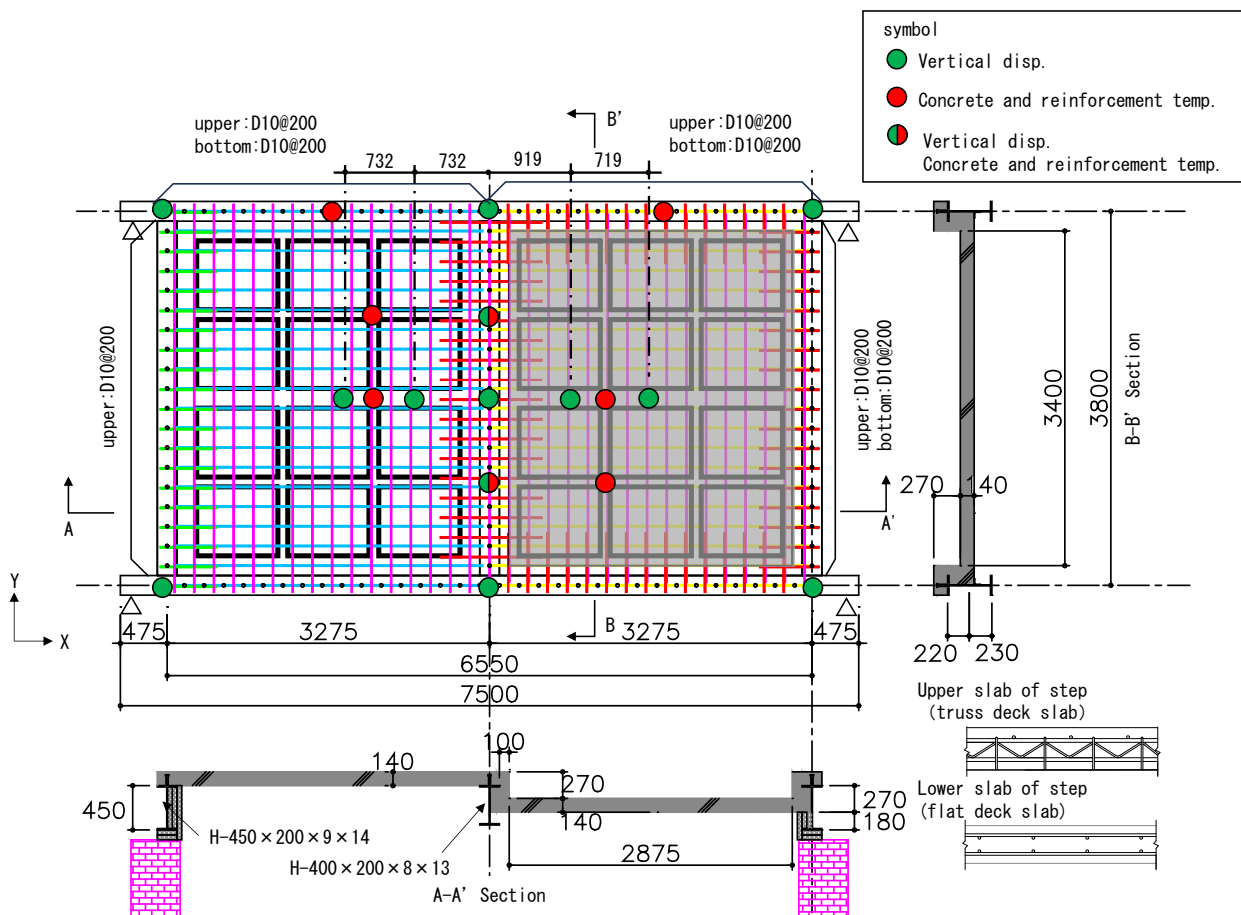


Figure 1. Configuration of the specimen

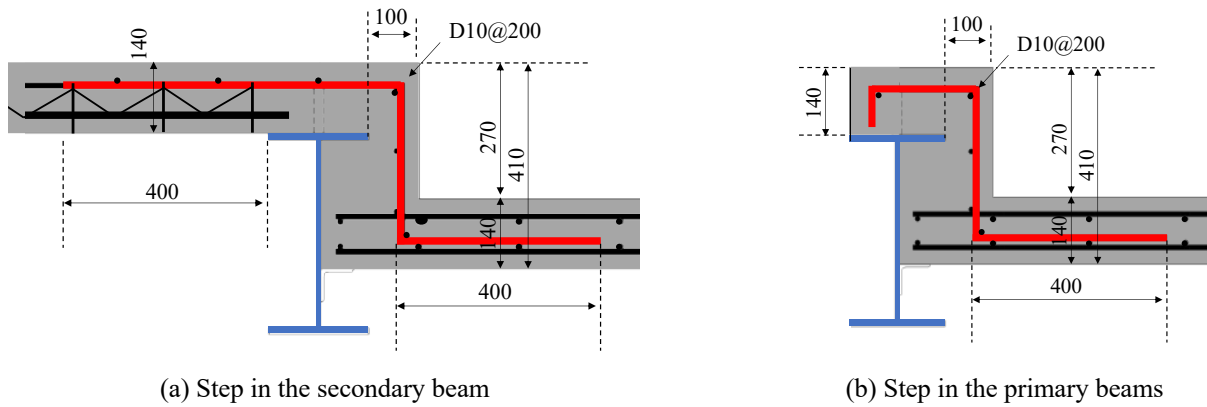


Figure 2. Reinforcement details of the concrete step

2.2 Experimental setup

The specimen was placed on a fire-test furnace to heat the bottom surface, as shown in Figure 3. To allow vertical deformation, the primary beams were placed 100 mm above the furnace. This gap between the primary beams and furnace was filled with ceramic fibre blankets. Twenty-four concrete weights (10.4 kN per unit), indicated as rectangular blocks in Figure 1, were used to load the specimens, as shown in Figure 4. The total load was 12.5 kN/m². Three pieces of calcium silicate board (100 mm × 100 mm × 25 mm) were placed between each weight and the top surface of the specimen to ensure that the weight did not come into direct contact with the slab. The weights were suspended by wires, which were maintained in a slack position during the test to prevent them from falling into the furnace once the specimen collapsed. The specimen was exposed to an ISO fire for 8 h and subjected to loading for a further 13 h to determine their load-bearing capacity in both the heating and cooling phases.

The concrete and steel temperatures and vertical displacements were measured at the positions shown in Figure 1.



Figure 3. Bottom heated surface of the specimen



Figure 4. Experimental setup

3 NUMERICAL ANALYSIS

The nonlinear finite-element software SAFIR [6] was used to conduct the heat transfer and thermal stress analyses, similar to that in earlier studies [7,8]. The numerical analysis results were then compared with the experimental results.

3.1 Heat transfer analysis

Figure 5 shows the heat transfer analysis model of the (a) unprotected secondary beam, (b) protected primary beam, and (c) slab. The secondary beam was H-400×200×8×13 to replicate the conditions under

which the Z-shaped slab was attached. The primary beam was H-450×200×9×14 and protected by 55-mm-thick ceramic wool. The depth of both slabs was 140 mm. To simulate the condition of heating from below, the ambient temperature on the heating surface was set to the ISO heating curve temperature, and the unexposed surface was maintained at 20 °C. The convection heat transfer coefficients of the heated and non-heated surfaces were set to 23 and 4 W/(m²·K), respectively. The emissivity of the specimen and flame was 0.7 and 1.0, respectively. The rebars in the slab above beams, steel decks, and shear studs were not modelled, thus, the effects of these elements on the member temperature were not considered in the analysis. Figure 6 shows the heat transfer analysis model of the step. To simplify the thermal stress analysis, the concrete and rebars in the slab at the step were modelled using shell elements. However, limited knowledge is available regarding the effective thickness of the Z-shaped concrete at the slab step. Therefore, the step was modelled using a shell element, and an effective depth of 210 mm was considered, as shown on the right side of Figure 6(a), considering the point symmetry of the heating and non-heating surfaces, as shown by the left image of Figure 6(a). For comparison, an analysis model with a slab depth of 410 mm at the step was created, as shown in Figure 6(b). The validity of the effective depth setting was confirmed by comparing the analysis results of the full model shown in Figure 5(a) with those of the simplified model shown in Figure 6(a).

The thermal properties of the concrete and steel prescribed in Eurocode 4 [9] were applied. The moisture content of the concrete was set to 5.6% based on the material test results. The thermal properties of the ceramic wool were based on those of calcium silicate boards. The moisture content of the ceramic wool was set to 10.0%.

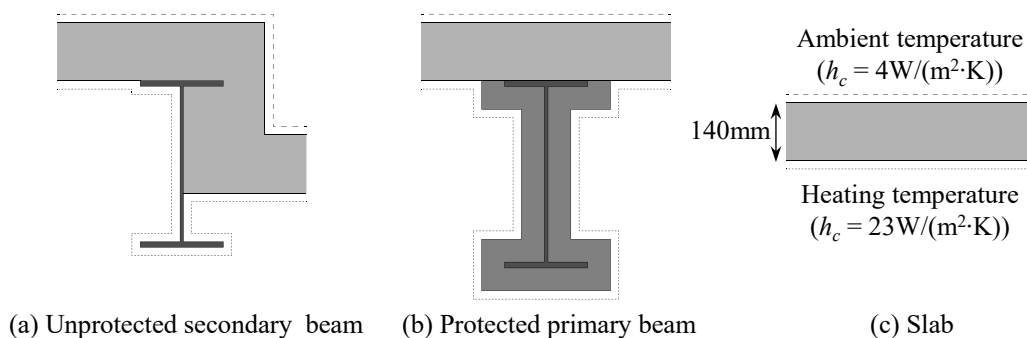


Figure 5. Heat transfer analysis model

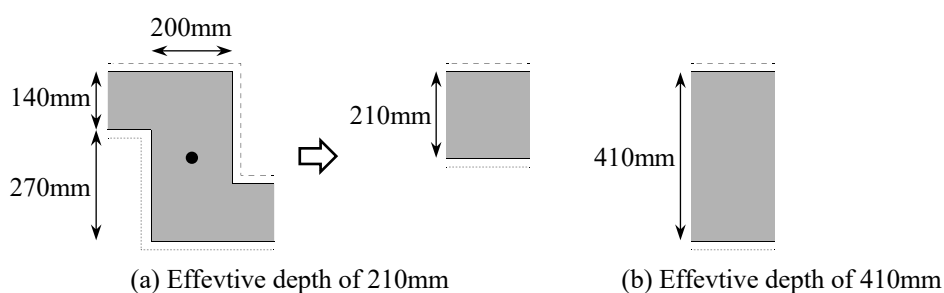


Figure 6. Heat transfer analysis model of the step

3.2 Thermal stress analysis

Figure 7 shows the thermal stress analysis model. The unprotected secondary and protected primary beams were modelled using beam elements. The primary beam support span in the X-direction was set at 7500 mm, and the vertical displacement at the support was constrained. The secondary beam support span in the Y-direction was set at 3800 mm. A vertical load was applied uniformly to the surface of the concrete slab. The concrete slab, including the reinforcing bars, was modelled using a shell element. For the truss deck slab on the upper slab, only the upper reinforcing bars were modelled because the lower X-direction rebars were discontinued in the secondary beam. For the flat deck in the lower slab, both the upper and lower rebars were modelled in the X- and Y-directions. The slab at the step was also modelled using shell elements to

simplify the analysis model. Figure 7(a) and (b) show the model with steps having effective depths of 210 and 410 mm, respectively. Figure 7(c) shows a model in which the same shell elements were used for both the step and slab, which is equivalent to a case without a step. The numerical results for the three cases were compared with the experimental results. The step in the slab at the primary beam was not modelled. The stress–strain relationships of the concrete and reinforcement at high temperatures reflected those published in Eurocode 4 [9]. The compressive and tensile strengths of the concrete at ambient temperature were set to 34.5 and 0 N/mm², respectively. The yield points of the reinforcement and primary and secondary steel beams were 369, 325, and 330 N/mm², respectively, based on the material test results.

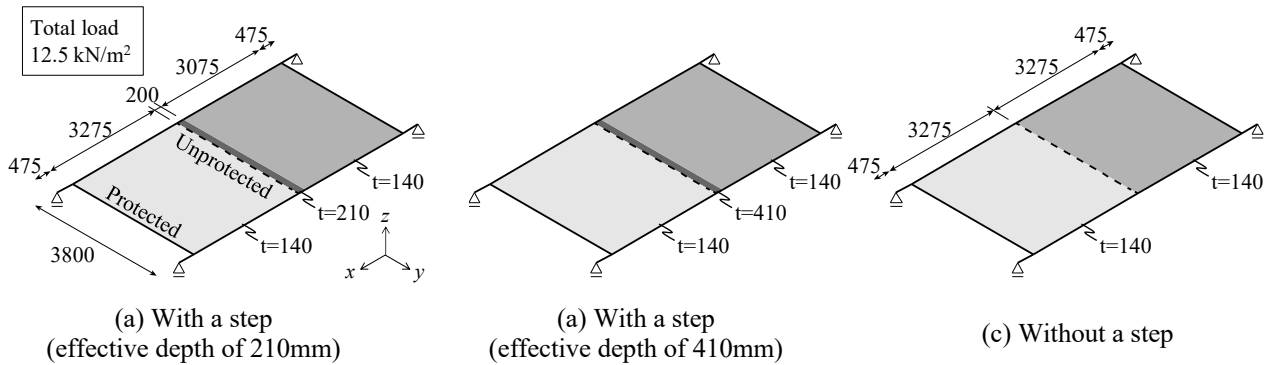


Figure 7. Thermal stress analysis model

4 RESULTS AND DISCUSSION

4.1 Temperature of the specimen

The temperature history of the specimen obtained from the experiment and numerical analyses are shown in Figure 8. The solid and dashed lines represent the experimental results for the upper and lower sides of the step, respectively. Circles indicate the calculated results. The reason for the experiment results stopping at heating is owing to a break in the thermocouple. Figure 9 shows the temperature distribution at 480 min of the analysis.

Figure 8(a) shows the temperature history of the primary beams. In the experiment, the web and top flange on the lower side of the step (right-hand side in Figure 1) were covered by concrete at the step, resulting in lower temperatures compared to the upper side of the step. Because the numerical analyses did not replicate the slab at the side of the primary beams, these analyses result closely resemble the experimental result on the upper side of the step.

Figure 8(b) shows the temperature history of the secondary beams. In the experiment, the temperature of the heated side of the upper flange of the unprotected secondary beam is approximately equal to the heating temperature. However, the temperature of the unheated side of the upper flange is lower than that of the heated side. The temperature of the heated and unheated sides of the web are nearly equal. The calculated temperatures of the upper and lower flanges are in good agreement with the experimental results. The temperature distribution at the step follows the Z-shape of the step as shown in Figure 9(a).

Figure 8(c) shows the temperature history of the slab. The detachment of the deck caused an increase in temperature at the lower slab at approximately 4.5 h and the upper slab at approximately 7.5 h. The flat deck at the lower slab began to detach after 3.5 and was completely detached by 4.5 h. The truss deck at the upper slab started detaching at 6 h and was fully detached at 7.5 h. The unheated surface of the reinforced concrete slab remains below 300 °C, even after exposure to an ISO fire for 8 h.

Figure 8(d) shows the temperature history of the reinforcement. Although the specifications of the decks differed for the upper and lower slabs on either side of the step, in general, the temperatures of the concrete and reinforcement measured at the same height are observed to be similar. As shown in Figure 8(c) and (d), the analytical and experimental results of the upper reinforcement temperature, which is the main contributing factor to membrane action during a fire, are closely matched.

Figure 8(e) and (f) shows the temperature history in the Z-shaped rebar and concrete temperatures measured around the unprotected secondary beam. The bottom corner of the Z-shaped rebar exhibits a temperature

history was similar to that of the bottom rebars located immediately below. The upper corner of the Z-shaped rebar shows a lower temperature compared to that of the top rebar in the general area. The temperature difference the bottom and upper corner of Z-shaped rebar was 630 °C at 8 h. The concrete temperature at the centre between the upper and lower surfaces is 380 °C at 8 h.

Figure 8(e) and (f) show the temperature analysis results for the slab step section with effective depths of 210 and 410 mm, respectively. The analysis results of the upper rebars for the step section with an effective depth of 210 mm correspond well with the experimental results for the upper corner of the Z-shaped rebar. However, the temperature associated with depth of 410 mm is approximately 200 °C lower than that of the experimental results of the upper corner of Z-shaped rebar.

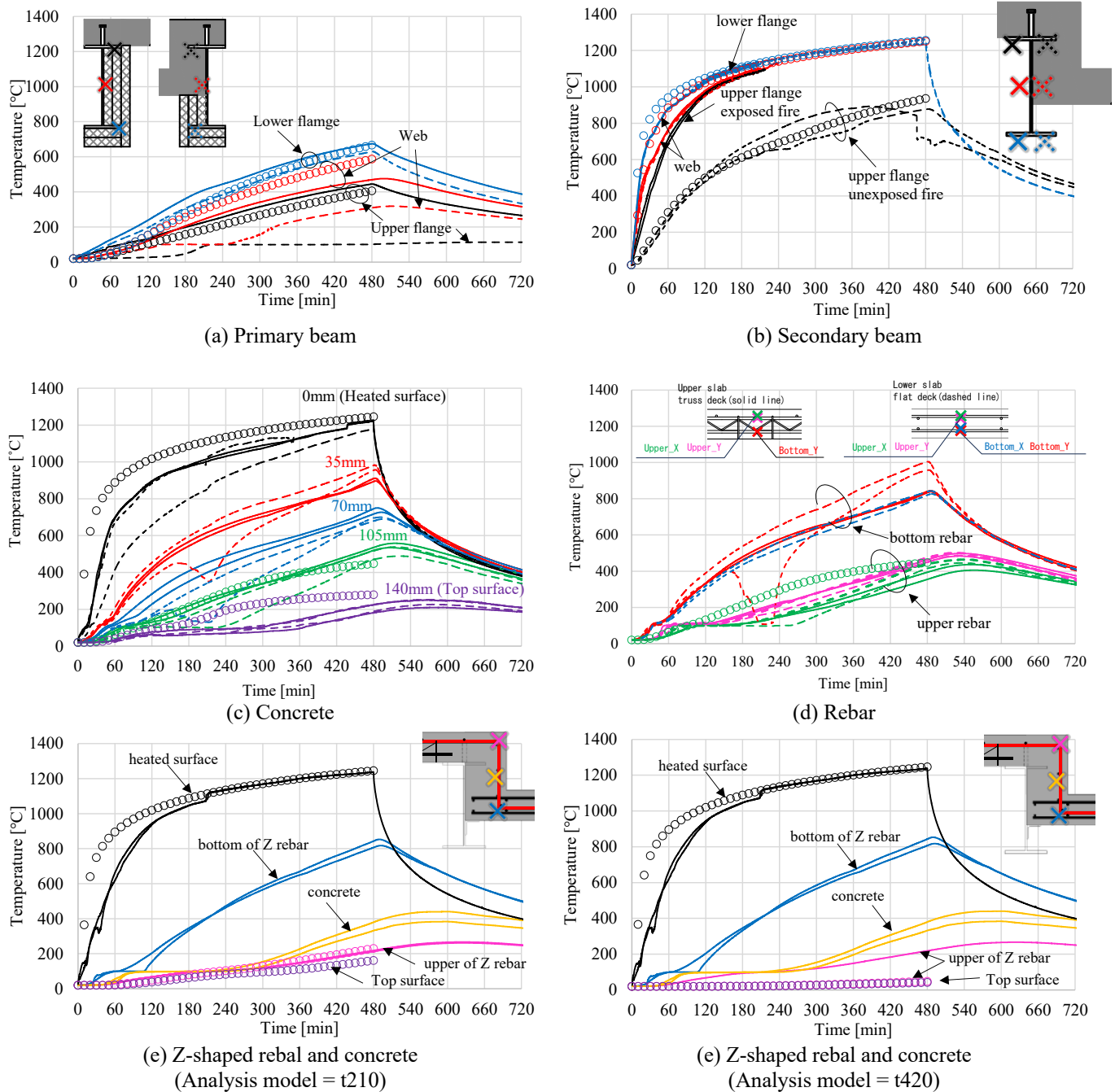


Figure 8. Temperature of the specimen

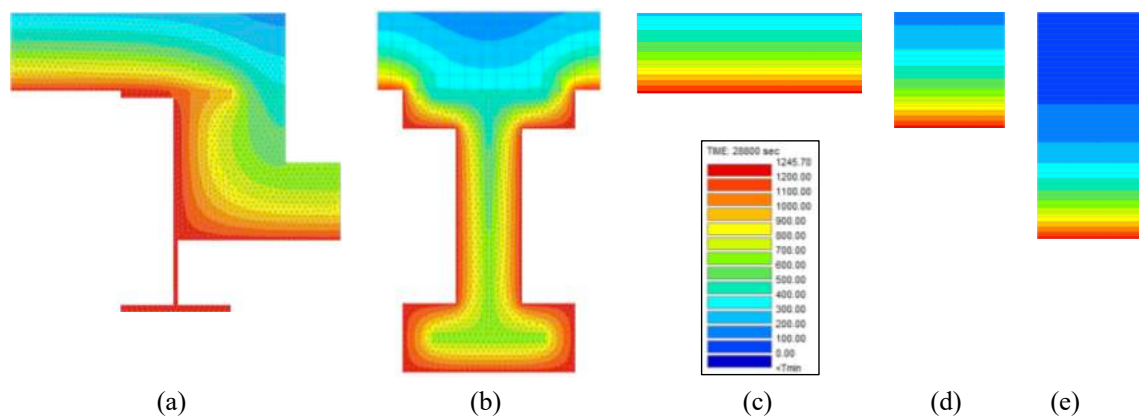


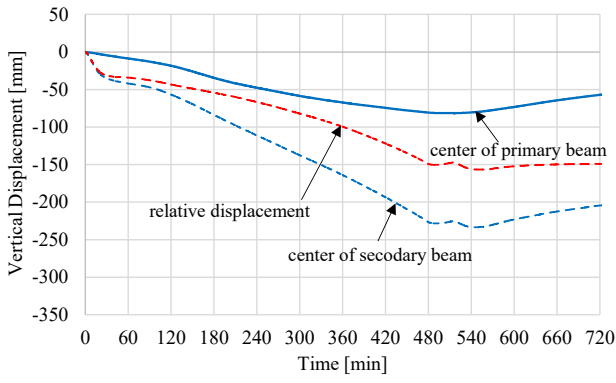
Figure 9. Temperature distribution at 480 min

4.2 Deformation of the specimen

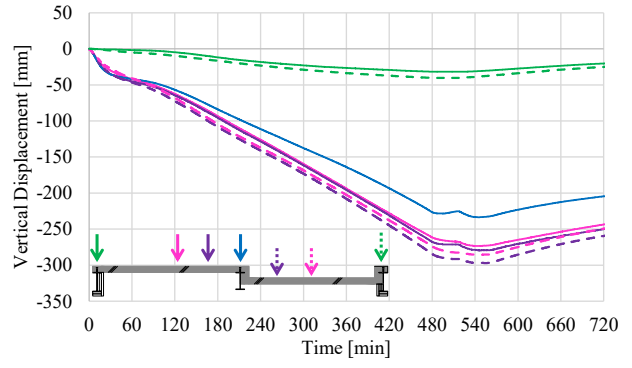
Figure 10 shows the vertical displacements of the protected primary beam in the X-direction (solid line) and unprotected secondary beam (dashed line), as well as the relative displacement, which is the difference between the displacement of the primary beam and secondary beam. The primary beam exhibits an almost linear downward displacement with increasing temperature. The increase in relative displacement of the secondary beam decreases after 30 min. Figure 10(b) shows the vertical displacement at the centre of the slab. Figure 11(a) shows the vertical displacement of the slab at each time step. The X-axis in Figure 11 represents the distance from the centre of the secondary short-span beam, with positive values representing the lower step and negative values representing the upper step. During the initial heating, deformation progressed in the central area (at the secondary beam position), however, after 34 min, the deformation at the adjacent measurement point became maximum, transitioning into “W” shaped deformation. The gradual decrease in the deformation of the secondary beam may result from the membrane action exerted on both the upper and lower slabs. The “W” shaped deformation continues to progress until the heating ceases.

As shown in Figure 1, the vertical displacement of the slab measured during the experiment is not symmetrical. Therefore, to facilitate the comparison of the vertical displacement difference upper and lower the step, the distances from the secondary beam to the measurement points were considered positive both upper and lower the step, as shown in Figure 11(b). The solid line shows the deformation of lower slab, and the dashed line shows the deformation of upper slab. Despite the lower amount of reinforcement resisting tension in the upper slab, deformation of upper slab was smaller than lower slab after 120 min.

Figure 12(a)–(c) shows the numerical analysis results for the vertical displacement of the slab at each time step. Figure 12(d) shows a comparison of the deformation at 8 h based on the numerical analysis results of the three cases modelled. The analysis modelling reveals that for the slab step (a) with an effective depth of 210 mm and (b) with a depth of 410 mm, vertical displacement decreases at the unprotected secondary beam, similar to the experimental results. In contrast, for the analysis case without a step, the floor deflection reaches its maximum at the unprotected secondary beam position. Using thicker shell elements for the step section was found to result in a smaller overall slab deflection. In this study, the results of the analysis case with an effective depth of 210 mm were the closest to the experimental results. This is thought to be due to the temperature of the upper rebar and the difference in slab temperatures between the heated and unheated surfaces which cause an overestimation of the stiffness when the thickness of the shell elements in the step section is increased. The analysis revealed that the deformation of lower slab was smaller than upper slab, because the lower amount of reinforcement resisting tension in the upper slab.

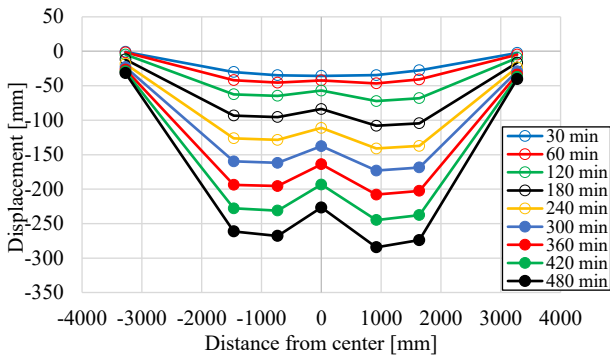


(a) Beam

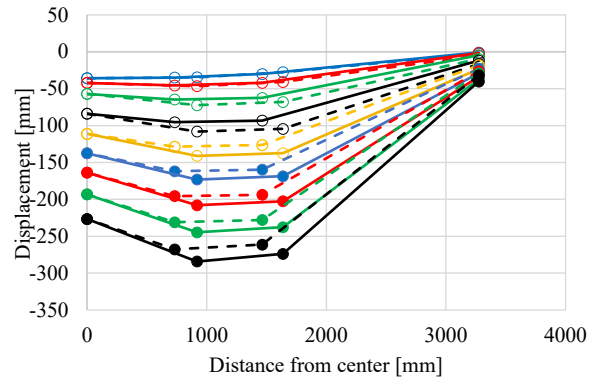


(b) Slab

Figure 10. Vertical displacements

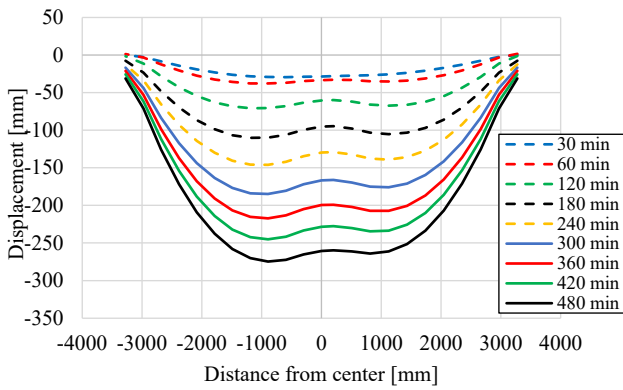


(a)

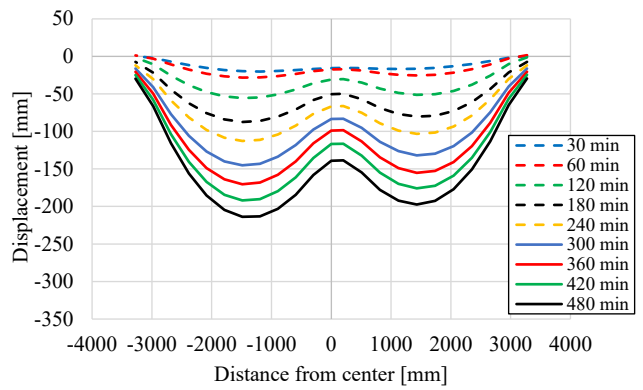


(b)

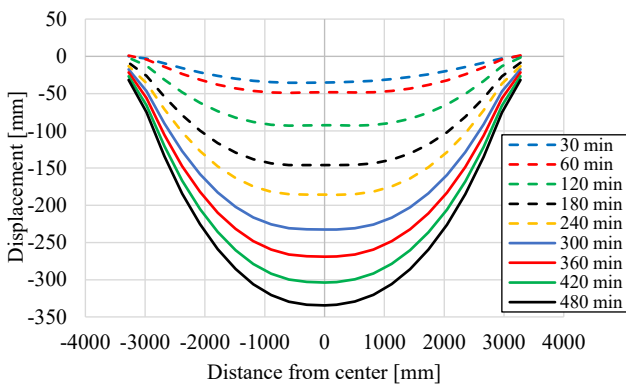
Figure 11. Vertical displacement of the slab in the experiment



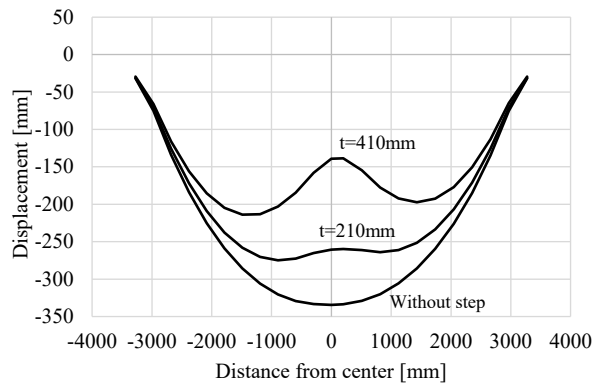
(a) Withe a step (effective depth of 210mm)



(a) Withe a step (effective depth of 410mm)



(c) without a step



(d) Comparison between the deformation of the three cases modelled at 8 h based on the analysis results

Figure 12. Vertical displacement of the slab in the numerical analysis

4.3 Cracks on the concrete surface

Figure 13 shows the test specimen after the experiment. Cracks in the X-direction occurred centrally in both the upper and lower sides of the step, with larger cracks observed on the lower side of the step. The presence of bottom rebars in the lower side of the step likely resulted in greater tensile forces in the slab compared with the upper side without bottom bars in the Y-direction. As shown in Figure 13(a), oval-shaped cracks typical of membrane action were observed in both the upper and lower sides of the step during the experiment. Therefore, membrane mechanisms are likely involved in both the upper and lower slabs.

Figure 13(b)–(d) shows different views of the step section from the top. Figure 14 shows a cross-section of the step section after the experiment. The observations indicate the occurrence of cracks at the corner of the step section during heating. The cracks extended from the surface deep into the slab. The increased vertical deformation in the experiment in the lower slab after 120 min, as shown in Figure 11, can be attributed to the progression of cracks at the corner of the step, which weakened the fixity of the slab edge.

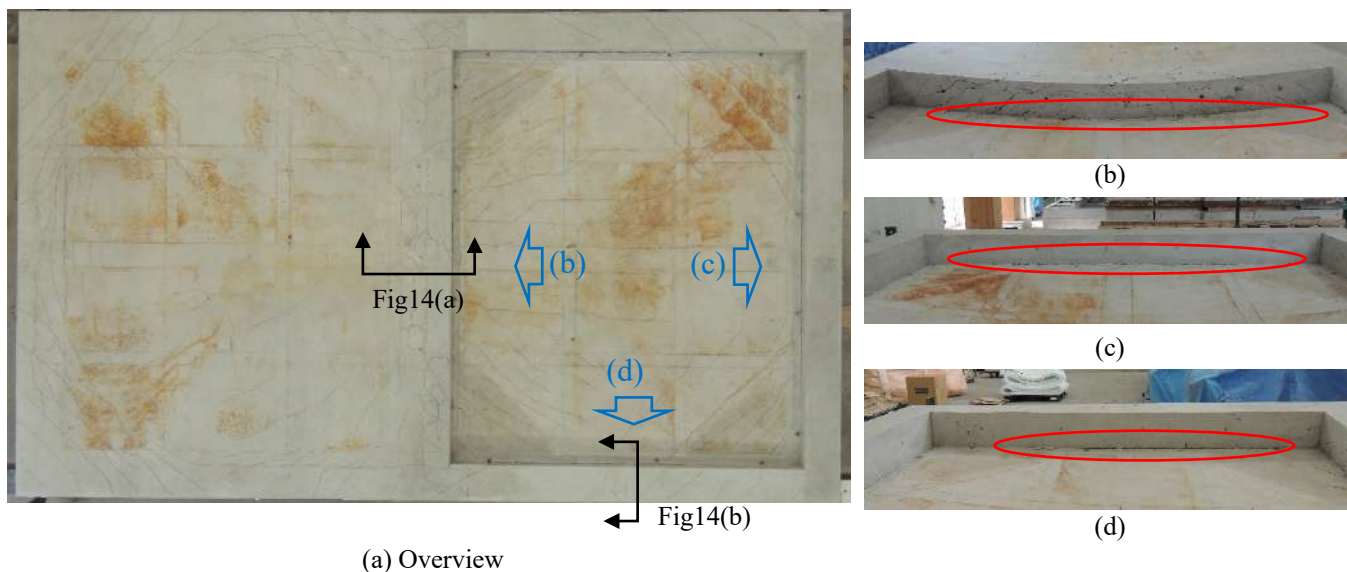


Figure 13. Cracks in the unheated surface



Figure 14. cracks at the step

5 CONCLUSIONS

Loaded heating tests and numerical analyses were conducted on a full-scale floor slab with a step to investigate the membrane effect in the upper and lower slabs separated by a step during a fire. This effect enables slabs to maintain their load-bearing capacity even during prolonged fires of 8 h.

The step section, which was thicker than the general section, exhibited a higher stiffness and lower concrete temperature than the general area, leading to an increased load-bearing capacity in the step section. Consequently, an effect resembling lifting of the deformation of the entire slab occurred at the step section, potentially resulting in smaller deformations compared to slabs without steps. However, excessive deformation of lower slab occurred due to decreased fixity at the slab edge on the lower side caused by concrete cracking at the corner of the step.

The deformation of slabs with steps can generally be evaluated through analysis by appropriately modelling the slab thickness at the step section.

To assess the deformation of slabs with steps, the proper evaluation of concrete cracking at the corner of the step and the load-bearing capacity at the step section during the design phase is essential.

Further studies are necessary to establish methods to evaluate the fire resistance of floors by considering steps with the aim of developing a comprehensive method to evaluate the fire resistance performance of floors with steps.

REFERENCES

1. C. C. Bailey, T. Lennon, D. B. Moore, "The behaviour of full-scale steel framed buildings subjected to compartment fires," *The Structural Engineer*, 77(8), pp.15-21, 1999
2. Linus C. S. Lim, "Membrane action in fire exposed concrete floor systems," Ph D thesis, University of Canterbury, 2003.4
3. B. Zhao, M. Roosefid, O. Vassart, "Full scale test of a steel and concrete composite floor exposed to ISO fire and corresponding numerical investigation," *Eurosteel 2008*, 2008
4. T. Hirashima, K. Kinoshita, T. Yoshida, J. Suzuki, F. Ozaki, K. Kimura, Y. Murakami, "Membrane action of floor slabs in fire (Part 1): Load-bearing fire tests of a composite flooring system composed of RC slabs and an unprotected steel beam," *Journal of Structural and Construction Engineering (Transactions of AIJ)*, 86(785), pp.1106-1116, 2021. doi:10.3130/aijs.86.1106
5. Y. Shintani, T. Nishimura, K. Kimura, "Full-scale test and numerical analysis of composite flooring system exposed to a long-duration ISO fire," *The 12th International Conference on Structures in Fire*, 2022.
6. J.-M. Franssen, T. Gernay, "Modelling structures in fire with SAFIR: Theoretical background and capabilities", *Journal of Structural Fire Engineering*, 8(3), pp.300-323, 2017
7. K. Kimura, T. Hirashima, F. Ozaki, T. Yoshida and J. Suzuki, "Numerical analysis of load-bearing fire test for reinforced concrete slab", *9th International Conference on Composite Construction in Steel and Concrete*, 2021
8. K. Kimura, "Membrane actions of reinforced concrete floor slabs exposed to fire", *Steel Construction Today & Tomorrow*, 60, pp.9-12, 2020
9. EN 1994-1-2, Eurocode 4: Design of composite steel and concrete structures, Part 1.2: General rules – Structural fire design, 2005

UNRAVELLING THE DYNAMICS OF FIRE-INDUCED CONCRETE SPALLING: A FOCUS ON THERMAL ENERGY IN A TWO-STAGE MECHANISM

Ramin Yarmohammadian¹, Roberto Felicetti²

ABSTRACT

Explosive spalling in concrete during fire incidents is a complex phenomenon, involving the detachment and projection of fragments from heated surfaces. While existing literature outlines pore pressure and thermal stress as primary driving mechanisms, their individual roles fail to explain the violent expulsion of concrete fragments. This paper proposes a new framework, combining these factors synergistically, to reassess the mechanism underlying spalling. The first stage involves incipient crack formation, where thermal gradients and external loads induce tensile stress in small convex samples or high compressive stress in large heated faces, interacting with hydrostatic tension ensuing from pore pressure. High-Performance Concrete (HPC) and Ultra-High-Performance Concrete (UHPC) exhibit diffuse cracking due to their homogeneous nature and low permeability. The second stage involves rapid crack propagation, leading to particle projection at high velocity, fuelled by accumulated thermal energy. A novel small-scale spalling test is developed to explore the influencing parameters, supporting spalling risk assessment and suggesting insights into mitigation strategies. The study provides a comprehensive understanding of spalling dynamics, highlighting factors such as concrete composition, element shape, and pore pressure effects. Future research lines are suggested for enhancing spalling prevention and mitigation strategies.

Keywords: Fire-induced spalling; Concrete structures; Thermal energy

1 INTRODUCTION

Spalling, namely the detachment of fragments from the heated surface of concrete elements during a fire, is a multifaceted phenomenon influenced by thermal, mechanical, and hygral factors. The existing literature suggests two primary driving mechanisms—pore pressure and thermal stress—each tied to distinct conditions and material attributes. However, none of them can alone explain how concrete could be fractured and the ensuing pieces be accelerated and violently projected at a distance. The synergistic combination of these two factors is most probably the reason behind concrete failure. Many times, extensive but stable cover delamination is observed in concrete elements surviving a fire, which means that incipient crack formation is not necessarily followed by the rapid expulsion of the fragments. A process organised in two chained stages seems to fit better with this evidence when a crack initiation is followed by crack instability, collectively termed as explosive spalling.

Based on this new framework, in which thermal stress and pore pressure cooperatively drive a two-stage process, the paper aims to reassess the mechanism underlying explosive spalling through a critical discussion of significant results from the literature and some recent findings by the authors [1, 2]. The scope is to provide a consistent interpretation of sometimes puzzling indications and to identify new lines for future research.

¹ PhD student, Politecnico di Milano

e-mail: ramin.yarmohammadian@polimi.it, ORCID: <https://orcid.org/0000-0003-4912-2095>

² Full professor, Politecnico di Milano

e-mail: roberto.felicetti@polimi.it, ORCID: <https://orcid.org/0000-0001-8658-0461>

2 FIRST STAGE (INCIPIENT CRACK FORMATION)

Starting with the first stage, the inquiry arises about how concrete's tensile strength is surpassed at elevated temperatures. Felicetti et al. could partially answer this question when, by monitoring the pore pressure in the mid-section of splitting cubes, they concluded that pore pressure alone is not able to trigger a crack [1]. The effectiveness of pore pressure is linked to the connectivity of the pore structure at the fracturing plane, which can be lower in high-performance concrete and higher in normal-grade concrete. However, the development and coalescence of microcracks (e.g. due to external loading) is expected to bridge the pores and boost the mechanical effects of vapour pressure.

Then, there should be a supplementary triggering force which can help pore pressure overcome the tensile resistance of concrete. In small-scale laboratory specimens (cylinders, prisms), the heated skin expands more than the colder core leading to triaxial tensile stress in the latter. Since there is a small interaction among the three tension stresses in the material (the Rankine criterion applies), the maximum tensile component can be added to the effective stress due to pore pressure in that region. Therefore, in convex shape samples, the tensile strength of the material is overcome by the combination of pore pressure and tensile thermal stress due to temperature gradients, smoothed by transient creep effects.

In the case of High-Performance Concretes (HPCs) or Ultra-High-Performance Concretes (UHPCs), crack initiation does not necessarily occur significantly earlier than the following unstable propagation. These concretes exhibit fewer defects or weak interfaces, making them more homogeneous and resistant to higher loads. Instead of cracking at localized weak interfaces, a region in HPCs or UHPCs may reach its threshold for cracking diffusely. Moreover, due to their low permeability, these mixes may retain water in the pores even beyond 300°C, considerably boosting the role of pore pressure. Then, the accumulated driving forces can release a substantial amount of energy when stability is lost in the material.

The term "regional or intrinsic instability" is suggested when the criterion for instability is met extensively in a region of concrete at the same time. The observation following this event would result in pulverized material or small pieces of concrete with densely cracked regions. This nuanced perspective helps capture the intricacies of spalling in different types of concrete materials.

A new experimental campaign was planned to study the spalling sensitivity of a UHPC mix in a controlled way. The mechanical properties of that mix are presented in the Table 1. Concrete disks (D=100mm, h=60mm), with the same geometry as the samples illustrated in Figure 1, were obtained by drilling cores from UHPC beams. A protective box was developed to hold the sample and provide additional safety to the furnace. As shown in Figure 1, a tube-shaped steel cage (150 inner diameters, 10 mm thickness and 80 mm height) is devised to accommodate the sample and enclose it between the top and bottom bolted plates. This rather heavy protective box was designed to retain concrete pieces inside and release pressure through drilled holes. Two K-type thermocouples were installed to measure the temperature during the test. One was located on the protective cage and the other one was installed tightly on the surface of the sample. These tests aimed to understand the role of size, heating rate and initial moisture in the instability of such an explosive event. Then, by considering different heating rates and initial moisture, their influences on the spalling were investigated more deeply.

Table 1. Material properties of UHPC used for different heating and drying conditions

material properties	units []	D1-V2	D1-V1
Steel fibre by volume	[%]	2%	0
Compressive strength	[N/mm ²]	135	128
Tensile strength *	[N/mm ²]	6.8	6.6
Density	[kg/m ³]	2411	2318
Expansion coefficient	[]	1.5e-5	1.5e-5
Young modulus	[N/mm ²]	42,000	42,000

* Direct tensile test with notch

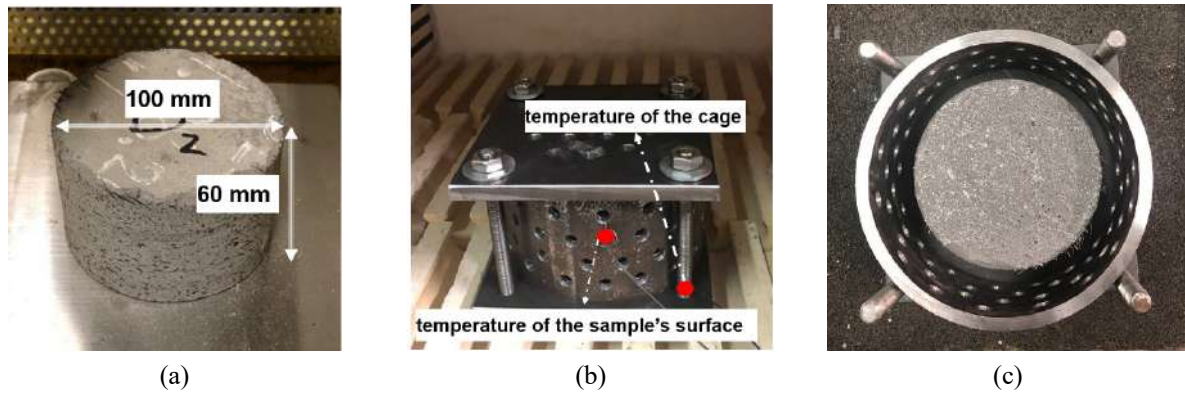


Figure 1. (a) Samples' dimensions; (b) Location of temperature measurements; (c) The sample positioned in the protective cage before its closure

Disk samples were exposed to different heating rates (0.3, 1.5, 5, 10°C/min) and the blasting time and temperature were recorded. The sample exposed to 0.3°C/min did not experience instability. For higher heating rates, the material got unstable with rather loud noise and dust clouds coming out of the furnace, whose door was not locked to mitigate the impact of the pressure wave. Although there was a protective cage to reduce the shock to the furnace, the door of the furnace could be moved when the blast happened. For 1.5°C/min, one out of two samples experienced an unstable situation. A of single loud blast could be heard in that case, with a cloud of dust coming out the of furnace (Figure 2). Multiple explosions were also witnessed at higher heating rates (smaller bangs followed by more explosions), as the stronger thermal stress could trigger the splitting of coarser fragments which later blasted due to the increasing temperature and pressure.

Table 2. Concluding results from different heating rates and initial moisture content.

test	pre-dried mass loss [%]	heating rate [°C/min]	spalling	type of spalling	spalling temperature [°C]		saturation pressure in core [MPa]	
					surface	core* ¹		
D1-V2 moist	1	-	0.3	no	-	-	-	
	2	-	1.5	no	-	-	-	
	3	-	1.5	yes	single	322	306	9.1
	4	-	5	yes	multiple	340	276	6
	5	-	5	yes	single	340	273	5.7
	6	-	10	yes	multiple	340	223	2.4
D1-V2 dried	7	1.7%	1.5	no	-	-	-	
	8	1.8%	5	yes	multiple	338	220	2.3
	9	1.8%	10	yes	multiple	350	226	2.6
	10	6%* ²	10	no	-	-	-	

*¹ Calculated temperature at the middle of disk samples by FEM ABAQUS model (EC2 material properties)

*² Using the survived sample in test number 2 heated up to 400°C (no crack observed on the sample)

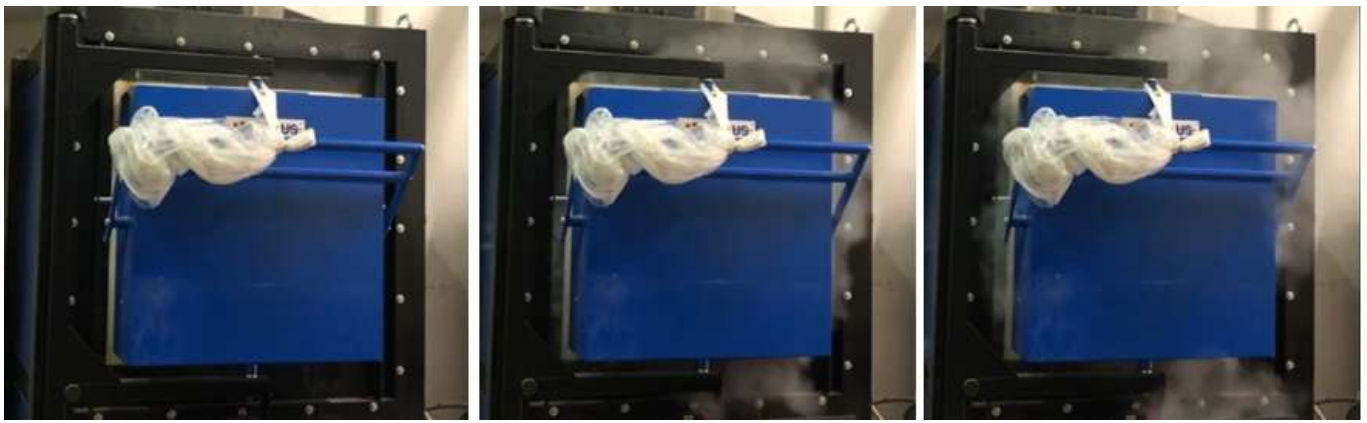


Figure 2. The explosion of disk samples inside the protective cage and the built-up pressure with a cloud of dust coming out of the furnace

The intrinsic instability was also witnessed in the work of authors like Klingsch when cylindrical concrete samples blasted while heated at different heating rates [3]. Installed thermocouples in the core and the surface of the samples were measuring temperature during heating. The material properties of the investigated concrete mixes are described in Table 3.

The summary of test results is presented in Table 4. Similar to the previous tests, by increasing the heating rate the explosion changes from a single event to multiple ones. In case of slow heating and rather uniform temperature, the whole core of the sample gets unstable due to a combination of high pore pressure and mild thermal stress, leading to a single destructive blast.

Conversely, thermal stress has a pivotal role in the case of fast heating, leading to the fracturing of coarse pieces, which in turn will blast once their internal pressure and stress reach a critical condition, in the form of multiple spalling events.

Table 3. Material properties of 4 different mixes used by Klingsch for spalling tests [3], the sample geometry of cylinders

Material properties	units []	M1-V2	M1-V1	M2-V2	M2-V1
Steel fibre by volume	[%]	2.5%	0	2.5%	0
Compressive strength	[N/mm ²]	151.3	153.1	120	91.1
Density	[kg/m ³]	2411	2318	2447	2274
Young modulus	[N/mm ²]	46,600	47,700	41,478	43,749
Initial moisture by mass	[%]	1.03%	1.22%	2.31%	3.17%
Expansion coefficient	[]	1.5e-5	1.5e-5	1.5e-5	1.5e-5
Tensile strength	[N/mm ²]	5.2	7.1	5.3	4.2

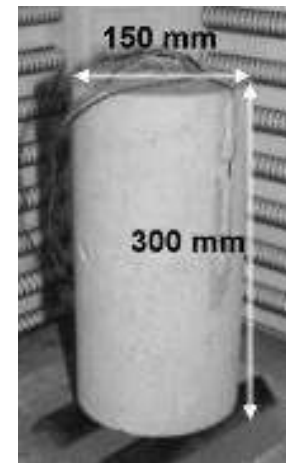
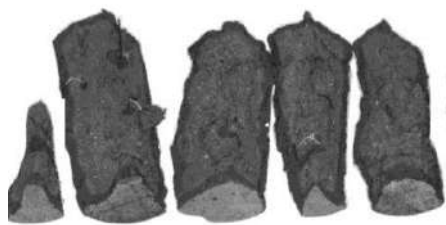


Table 4. The spalling results of different concrete mixes at different heating rates

	test	heating rate [°C/min]	spalling	type of spalling	spalling temperature [°C]		saturation pressure in core [MPa]
					surface	core	
M1-V2	1'	0.25	no	-	-	-	-
	2'	0.5	no	-	-	-	-
	3'	0.75	yes	single	368	304	9.1
	4'	1	yes	multiple	297	256	4.4
M1-V1	5'	0.25	no	-	-	-	-
	6'	0.5	yes	single	300	282	6.6
M2-V2	7'	0.5	no	-	-	-	-
	8'	1	no	-	-	-	-
	9'	1.75	yes	single	366	-	-
	10'	2	yes	single	357	267	5.25
	11'	2.5	yes	single	371	260	4.7
	12'	3	yes	multiple	357	-	-
M2-V1	13'	0.5	no	-	-	-	-
	14'	1	no	-	-	-	-
	15'	1.5	no	-	-	-	-
	16'	2	yes	single	427	296	8.1
	17'	2.5	yes	single	433	277	6.1
	18'	4	yes	multiple	411	-	-



M1-V2, 0.75°C/min (# 3')



M1-V1, 0.5°C/min (# 6')

Figure 3. Concrete pieces after the spalling event in the cylinders

An axisymmetric finite element model was created in ABAQUS to analyse the heat transient and the mechanical effects of thermal gradients. A thermo-mechanical model is introduced incorporating material properties from Eurocode 2. A reduced value of Young's modulus was introduced to equivalently account for the smoothing effect of transient creep which gives more reasonable stress values, consistent with the frequent observation that slowly heated samples don't crack macroscopically. This parameter was determined so as to give the same thermal stress in a perfectly restrained heated element:

$$\epsilon_{therm} + \epsilon_{mech} + \epsilon_{trans} = \alpha T + \sigma/E + k_{tr} \cdot \alpha T \cdot \sigma/f_c = 0 \quad (1)$$

$$\sigma = -\frac{1}{\frac{1}{\alpha T \cdot E} + \frac{k_{tr}}{f_c}} = -\alpha T \cdot E_{eq} \quad (2)$$

where k_{tr} is the transient strain coefficient, taken equal to 2 in these analyses [4].

Measured temperatures in the core of the samples may be disturbed by the vapour leakage through the textile insulation of thermocouples, which entails a clear plateau while moisture is vaporised at environmental pressure. The plateau indicates that the measured temperature is lower than the actual undisturbed temperature because the vaporization of free water near the thermocouple's tip reduces the temperature of its surrounding area.

In the case of exploded samples, the sum of the reduced thermal stress in the core of the samples and the effective tensile stress due to the saturation pressure at the blasting temperature gives a substantially constant total stress at all heating rates.

Within each concrete mix, the increase in the heating rate corresponds to an increase in the thermal stress contribution, ultimately leading to anticipation of spalling (lower temperature and concurrent pore pressure). Notably, in concrete mix D1-V2, the slowest heating rate is corresponding to lower combined driving force than the other two. Under these conditions, just one out of two samples in the experiment experienced spalling, which could be attributed to a lower combination in this case compared to the other scenarios.

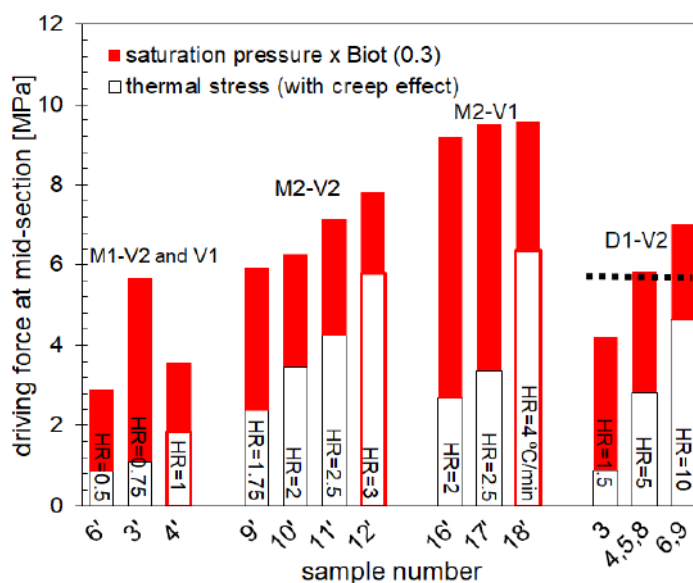


Figure 4. Driving force and instability threshold for different samples

To comprehensively consider the combined effect of a restrained section and effective pore pressure, it is necessary to examine how bi-axial compression can influence the tensile failure criteria of concrete perpendicular to the heated surface. As the outer layer expands more than the inner regions, biaxial compression parallel to the heated surface is created (Figure 5). At the same time, hydrostatic tensile stress due to pore pressure acts in three directions. Since the magnitude of confinement stress is generally predominant with respect to the effective stress generated by pore pressure, their combination results in a stress field characterized by biaxial compression plus orthogonal tension, which has a higher probability of meeting the multiaxial failure criteria of concrete. In the study by Pichler et al [5, 6], the perpendicular evolution during fire exposure of the stress profile across the lining thickness, was evaluated showing the development of high biaxial stress (Figure 5).

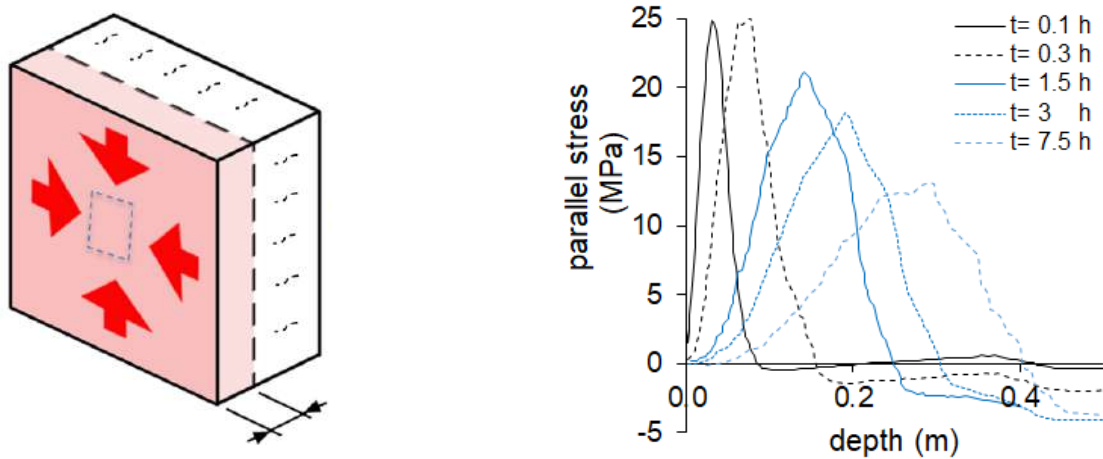


Figure 5. Stress in superficial and deep layers of heated tunnel linings [5]

A closer examination of Kupfer's failure criteria in concrete reveals a significant impact of compression on tensile strength (Figure 6). In a study by A. Hussein et al. [7], it has been shown that the effect is exacerbated in the case of high-performance concrete (Figure 6). It is confirmed that the development of compressive thermal stress weakens the tensile response of concrete in the orthogonal direction.

The difference between different types of concrete is more evident if the interaction diagram is represented in normalized terms. Zhukov in 1976 also provided a failure tensile criteria for the material which can be reached by “the steam permeation stress” [8]. This criterion (with compression less than 0.4) matches the failure criteria by A. Hussein for HPC. The only disparity between this failure criterion and reality lies in the biaxial compression force, which could further decrease tensile resistance. The higher reduction in tensile resistance might be attributed to the constraints on strain in the second compression axis.

The max thermal stress assessed [9, 10] via the Eurocode equations for thermal dilation and stress-strain relation (fully restrained material, nil total strain) is about 60% of the original strength (Figure 5 left). The saturation pressure at the typical spalling temperature may be in the 4-6 MPa range for HPC (250-275°C), but the poor interconnection of pores limits the effective stress to 30%, namely 1/3 of the tensile strength [1]. Both values alone are less than their respective limits, but their combination lies on the limit curves of this diagram, proving that the synergistic effect of thermal stress and pore pressure has a higher chance to initiate a fracture in the fire exposed cover.

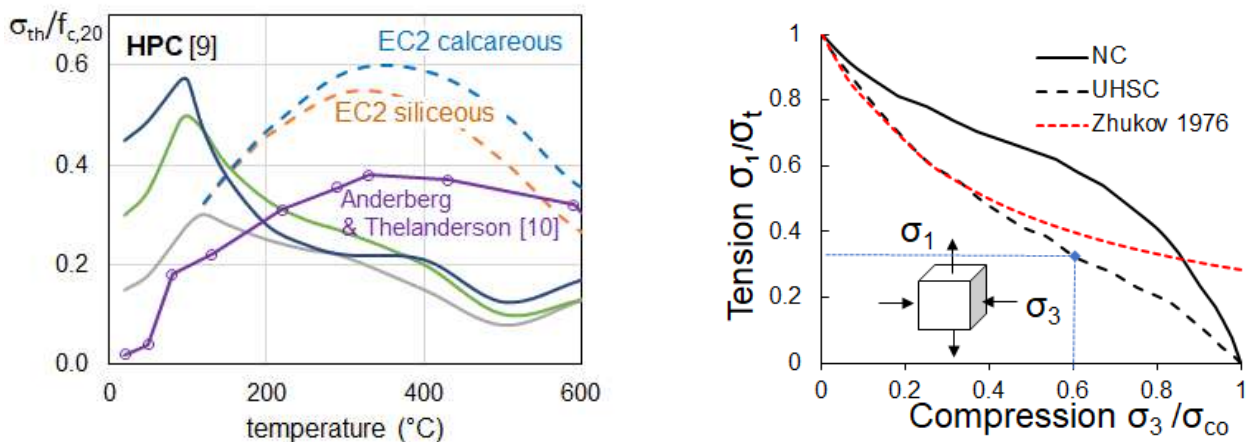


Figure 6. Restraint stress trends and normalized failure criterion for interaction between compression and tension.

3 SECOND STAGE (CRACK INSTABILITY)

Regarding the second stage of the spalling phenomena, elastic energy alone cannot justify the explosive nature of the process [11]: accumulated thermal energy serves as a supplementary source, together with the water in the pores, which can generate kinetic energy through vaporization [2].

Therefore, a novel small-scale spalling test was developed to explore the influencing parameters in the second stage of spalling, observing mass loss and fast crack opening during the instability onset (see Figure 8-left). The crack is initiated in the sample by means of higher thermal dilation of a polymeric insert. The shape and dimension of both the concrete sample (a 100x60mm disk) and the polymeric insert (a 60/46mm ring) were optimized by means of a FEM modelling in ABAQUS. Then the polymer thickness (0.5 mm) was calibrated to generate the crack in the mid-section at the typical spalling temperature range.

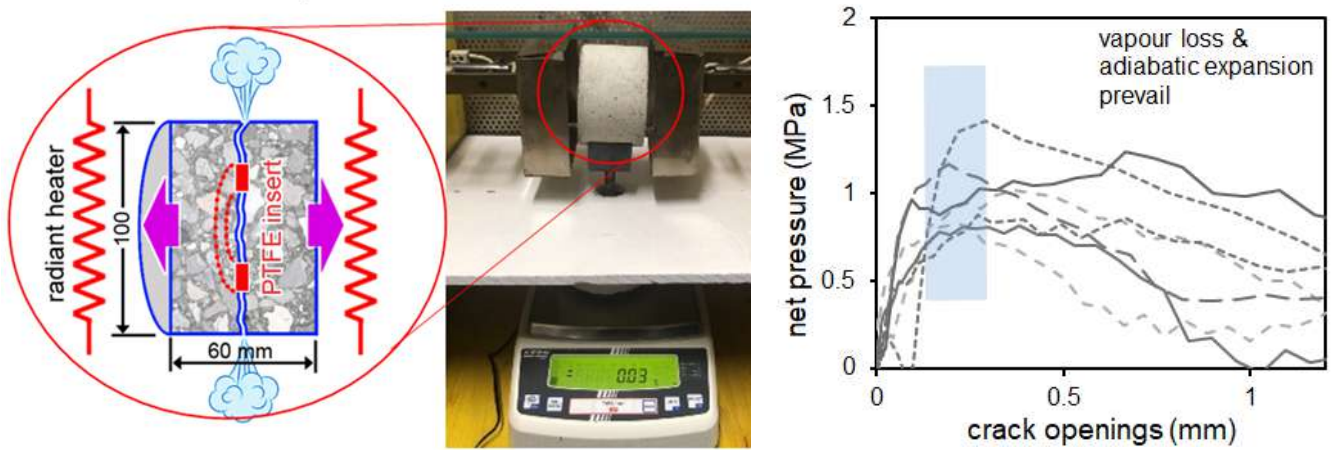


Figure 7. scheme of screening spalling test, results of photosensors in net pressure versus crack opening

The relative displacement between the two separating halves of the breaking disk was monitored by means of reflective photosensors mounted astride the potential fracturing plane. The internal force separating the two parts was assessed through acceleration by way of the second Newton's law of motion under the assumption of splitting the sample into equal masses $M/2$. That force results from the difference between the pressure within the crack and the residual cohesive tensile stress borne by the fracturing concrete. To switch from the net force to the net pressure, the constant nominal cross-section area is here considered, despite the presence of the ring and the progressively extending fractured area. The net pressure versus crack opening in different samples is presented in Figure 7. The maximum net pressure calculated is comparable to the saturated pressure at about 200°C (11 bar or 1.1 MPa).

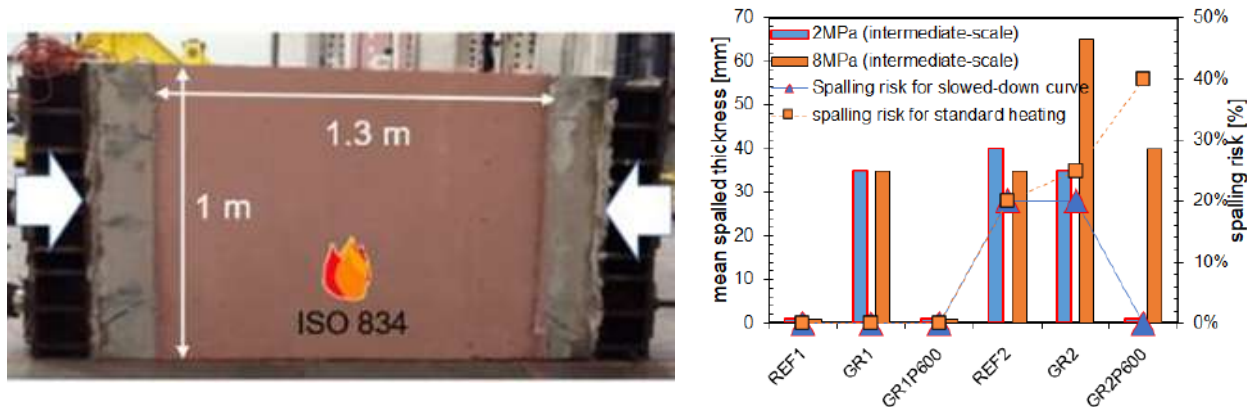


Figure 8. (left) Intermediate-scale spalling test, (right) Cross-comparison between two different scales

The same setup was considered also for its ability to screen different concrete mixes and conditioning procedures in terms of spalling risk. This was validated through intermediate-scale tests on the same concrete mixes (see Figure 8). To mitigate excessive natural drying of small samples during curing, specific measures should be implemented. This highlights the potential of the new test to reduce the need for intermediate-scale tests, streamlining the process of screening mixes, and ultimately cutting costs. The main key findings allowed by the new setup are:

- Mass losses correlate with crack instability, attributed to water vaporisation.
- Acceleration of separating parts corresponds to substantial pressurization within the crack, with calculated net pressure approaching the equilibrium saturation value.
- Crack initiation timing is crucial, with early and late cracks exhibiting greater stability. High-temperature concrete with significant moisture impairs spalling severity. Polypropylene fibre proves effective in mitigating spalling by releasing pressure and speeding up the drying of pores, to the point that the large amount of available thermal energy cannot be effectively transformed into mechanical work.

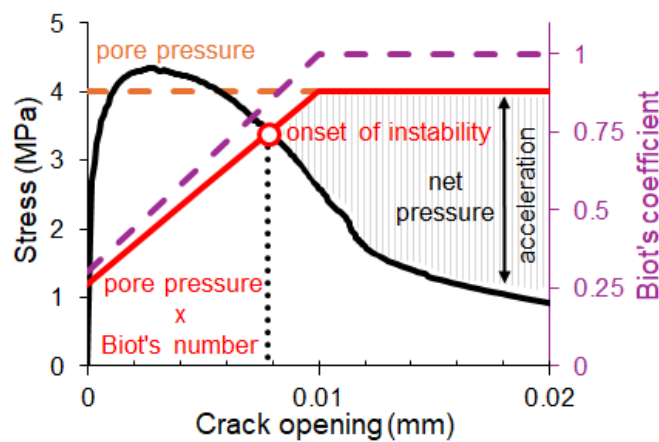


Figure 9. Evolution of effective pore pressure in two stages mechanism

Several processes impact effective stress from pore pressure in the transition between the two stages: increase in Biot's coefficient due to bridging of pores, flash vaporization of liquid water from pores facing the incipient crack, adiabatic expansion of the vapour injected in the opening crack and vapour leakage from the open edge of a separating splinter.

- Biot's coefficient (effectiveness of pore pressure)

As it is mentioned before, the pore pressure alone cannot trigger the crack due to the low connectivity of pores and damage in the fracturing plain. With the further help of thermal stress, the micro damages leads to higher connectivity and effectiveness of the same pore pressure. The Biot's coefficient increases as the crack propagates through the entire section, potentially escalating effective pore pressure.

- Flash Vaporization

Crucial in mitigating substantial pressure drop by feeding vapour to the incipient crack. This process is viable when a very superficial and highly saturated layer, known as the influencing region, is engaged in a rapid process (timing of transport phenomena go with the distance squared). Moisture near the crack undergoes vaporization, converting thermal energy and reducing the pressure drop due the increasing volume of a crack propagating across the pores.

- Adiabatic Expansion and Vapour Leakage

Expansion occurs when pressure decreases on an adiabatically expanding isolated system.

Vapour leakage also prevails when a pathway is provided by a propagated crack to the surface. In the Figure 9, the effective pore pressure is depicted in red, initially not surpassing the tensile resistance of concrete. However, due to explained reasons in the crack initiation part (concurrent tensile or compressive stress due to thermal gradients), the concrete can reach the falling branch where the effective pore pressure and the resistance of the section can potentially intersect—a crucial moment for crack instability. The difference

between these two forces represents the instability force, also known as net pressure, with the maximum measurement in the tests proving comparable to the saturation pressure in the crack (see Figure 9). This unbalance is responsible for the sharp acceleration of the fractured splinter, which can reach velocities in the range of 5-15 m/s in a matter of 0.1ms.

4 CONCLUSION

The proposed study unfolds a two-stage mechanism to elucidate the complexity of spalling. In the first stage – incipient crack formation – external loads induce tensile stress or high compressive stress parallel to the heated face, interacting with hydrostatic tension from pore pressure. This stage sets the foundation for understanding the conditions that lead to the second stage.

4.1 Influencing parameters in incipient crack formation

- Cracks in restrained or loaded sections: Thermal expansion induces compressive stress, affecting concrete’s integrity. Biaxial restrained dilation tests showed significant damage in the unloaded direction [4].
- Cracks due to mesoscale heterogeneity: Thermal dilation differences between mortar and coarse aggregates generate micro-cracks at their interface.
- Cracks due to element shape: Convex shapes at the section corners or in small laboratory samples (e.g. cylinders) entail significant radial tensile stress, which easily exceeds the material strength.
- Weak planes and strain incompatibility of rebars: Reinforcing bars determine preferential fracture planes, especially in the case of two-way reinforcement. Differential thermal dilation between concrete and reinforcement may exacerbate this effect, especially in the case of polymeric rebars.
- Cracking fostered by pore pressure: UHPC samples heated at different rates exploded with different shares of thermal stress and pore pressure giving the same total effective tensile stress.

4.2 Unstable crack propagation (second stage)

The second stage involves the rapid propagation and opening of cracks, leading to the projection of particles at high speed. Seeking for the driving energy source, the high potential of the thermal energy accumulated by the heated concrete can be proved by simple hand computations [2]. A compact screening test was developed where cracks in hot concrete are triggered with the limited contribution of thermal stress [12], casting new light on the fundamental mechanisms behind explosive spalling.

The following table summarizes the influencing factors for the above-listed mechanisms.

Table 5. Summary of influencing factors in spalling

stage	mechanism	Influencing factors
Incipient crack formation	thermal stress	heating rate, thermal dilation, material stiffness, element thickness, boundary conditions, applied load
	mesoscale heterogeneity	mix design, coarse aggregate
	pore pressure	heating rate, permeability*, pore saturation*
	tensile stress at corners and edges	element geometry
	stress concentration due to rebars	reinforcement geometry and material
Crack instability	elastic energy	heating rate, thermal dilation, material stiffness*, element thickness, boundary conditions, applied load
	thermal energy	heating rate, pore saturation*
	inherent material brittleness	concrete grade, coarse aggregate

* factors being mitigated by PP fibre

REFERENCES

1. Felicetti R, Lo Monte F, Pimienta P (2017) A new test method to study the influence of pore pressure on fracture behaviour of concrete during heating. *Cem Concr Res* 94:13–23. <https://doi.org/10.1016/j.cemconres.2017.01.002>
2. Felicetti R, Yarmohammadian R, Dal Pont S, Tengattini A (2024) Fast Vapour Migration Next to a Depressurizing Interface: A Possible Driving Mechanism of Explosive Spalling Revealed by Neutron Imaging. *Cem Concr Res*. <https://doi.org/10.2139/SSRN.4597427>
3. Klingsch EW (2014) Explosive spalling of concrete in fire. *IBK Bericht* 356:. <https://doi.org/10.3929/ETHZ-A-010243000>
4. Torelli G, Mandal P, Gillie M, Tran VX (2016) Concrete strains under transient thermal conditions: A state-of-the-art review. *Eng Struct* 127:172–188. <https://doi.org/10.1016/J.ENGSTRUCT.2016.08.021>
5. Pichler C, Lackner R, Mang HA (2006) Safety Assessment of Concrete Tunnel Linings under Fire Load. *J Struct Eng* 132:961–969. [https://doi.org/10.1061/\(asce\)0733-9445\(2006\)132:6\(961\)](https://doi.org/10.1061/(asce)0733-9445(2006)132:6(961))
6. Zhang Y, Zeiml M, Pichler C, Lackner R (2014) Model-based risk assessment of concrete spalling in tunnel linings under fire loading. *Eng Struct* 77:207–215. <https://doi.org/10.1016/j.engstruct.2014.02.033>
7. Hussein A, Marzouk H (2000) Behavior of High-Strength Concrete under Biaxial Stresses. *Acı Mater J* 97:27–36. <https://doi.org/10.14359/802>
8. Zhukov V V. (1976) Reasons of explosive spalling of concrete by fire. *Concr Reinf Concr*
9. Diederichs U, Jumppanen U-M, Penttala V (1989) Behavior of high strength concrete at high temperatures
10. Anderberg Y, Thelandersson S (1976) Stress and Deformation Characteristics of Concrete at High Temperatures. 2. Experimental Investigation and Material Behaviour Model
11. Gawin D, Pesavento F, Schrefler BA (2006) Towards prediction of the thermal spalling risk through a multi-phase porous media model of concrete. *Comput Methods Appl Mech Eng* 195:5707–5729. <https://doi.org/10.1016/j.cma.2005.10.021>
12. Yarmohammadian R, Felicetti R, Robert F, Izoret L The role of moisture on crack instability of spalling concrete. In: 7th International Workshop on Concrete Spalling due to Fire Exposure. p 108

**EXPERIMENTAL RESEARCH OF
STRUCTURES IN FIRE**

A NEW APPROACH TO THE ASSESSMENT OF THE FIRE RESISTANCE OF STRUCTURES

Tom Lennon¹, Octavian Lalu², Diana Duma³

ABSTRACT

This paper introduces a novel methodology for assessing the fire resistance of structures, emphasising realistic conditions of fire exposure and applied load. Developed to address limitations of standard fire tests in meeting Building Regulations, the approach incorporates large-scale fire testing to examine structural element interactions. Tailored for Modern Methods of Construction (MMC), especially volumetric modular and mass timber systems, this methodology offers a robust assessment tool for ensuring compliance and safety in diverse construction applications. The paper discusses the conceptual background, rationale, and practical implications of this innovative approach.

Keywords: Fire resistance, Large-scale fire testing, Assessment

1 INTRODUCTION

This paper sets out a new methodology for the assessment of the fire resistance of structures. The background to the development of the new approach is presented. The approach is based on a concept of large-scale fire testing, which considers the interaction between structural elements under realistic conditions of fire exposure and applied load when subjected to a natural post-flashover fire, the severity of which is related to the end-use application. The methodology is appropriate for those construction systems or materials where reliance on the results from standard fire tests may be insufficient or inappropriate to demonstrate compliance with the requirements of National Building Regulations. The methodology has been developed with the specific aim of providing a means of assessing the structural behaviour for various types of Modern Methods of Construction (MMC), particularly volumetric modular and mass timber construction, under a realistic fire scenario.

2 BACKGROUND

The approach set out in this paper has been developed through a current UK government research project led by the Building Research Establishment (BRE) entitled *Structural Fire Resistance and Fire Resisting Elements*. However, the methodology is derived from a long history of involvement in large-scale fire testing, including European research projects focused on steel, concrete, and timber construction, as well as commercial projects for clients responsible for the manufacture and supply of modular systems designed for permanent residential and temporary site accommodation [1,2]. This paper is focused on the

¹ Principal Fire Engineer, Building Research Establishment,
e-mail:tom.lennon@bregroup.com, ORCID: <https://orcid.org/0000-0002-2786-0591>

² Senior Fire Engineer, Building Research Establishment,
e-mail:octavian.lalu@bregroup.com, ORCID: <https://orcid.org/0000-0003-0461-6526>

³ Senior Fire Engineer, Building Research Establishment,
e-mail:diana.duma@bregroup.com, ORCID: <https://orcid.org/0000-0002-6121-3099>

development and rationale for the methodology rather than presenting the detailed experimental results. The results will be disseminated more widely once the current project is complete.

Concerns about the performance in fire of innovative forms of construction are nothing new. Following the programme of large-scale fire testing undertaken on the 8-storey composite steel framed building in the BRE's Large Building Test Facility (LBTF) in Cardington in 1995 and 1996, a number of additional research projects were carried out. One such project was focused on the fire safety of light steel framed houses with two full-scale fire tests undertaken on two different steel framing systems supplied by different manufacturers in 2002 (Figure 1). The results are provided in a BRE Information Paper [3], and the principal outcomes are summarised below:

- The tests demonstrated that detailing and workmanship issues are of crucial importance in ensuring that the performance of the whole building is not compromised by a local failure.
- Modes of failure that cannot be predicted from reliance on standard fire resistance test data should be considered in terms of the fire performance of the whole building. This is particularly important where light steel framed structures are used for multi-occupancy residential buildings.



Figure 1. Full-scale fire test of light steel framed house

The work identified potential issues with combustible insulation within the external walls leading to fire spread from one compartment to another, bypassing mitigation measures designed to inhibit the spread of fire and smoke within concealed spaces in the structure (cavity barriers). Another important aspect of performance is the interaction of the individual elements and the effect of the large deformations associated with the fire limit state. In one application, large deflections of the floor joists following failure of the plasterboard linings led to the failure of the connections between the floor joists and the edge beams, leading to a disproportionate collapse of the compartment floor in the latter stages of the fire (Figure 2). Such phenomena are not considered in standard fire resistance testing.



Figure 2. Collapse of floor slab in latter stages of fire experiment

The approach to full-scale fire testing of three-dimensional structures was developed through the work undertaken on the steel-framed building at Cardington and later extended to cover multi-storey concrete and timber buildings. However, the work conducted to investigate the fire safety of light steel framed buildings was also informed by previous attempts to create a methodology for large-scale fire testing. In the UK, BS 476-32 [4] was published in 1989. This document provided recommendations on the conduct of full-scale experiments simulating fires in buildings. It was acknowledged that the document was providing advice for an experimental setup that could be used as a basis for an agreement for the execution of ad hoc work. The document was explicitly focused on an examination of the pre-flashover behaviour and contribution to the fire growth of the products under consideration. As such, it would never be appropriate for evaluating structural response where the post-flashover phase is of primary importance. Similarly, BS 476 Part 33 [5], which reproduces ISO 9705, simulates a fire that, under well-ventilated conditions, starts in a corner of a small room with a single open doorway. A test performed in accordance with this method provides data for the early stages of a fire, from ignition to flashover.

The fact that these methods (despite the titles) are restricted to the early stages of fire development is potentially a recognition of the difficulties in codifying an approach to evaluating whole-building behaviour. It is potentially also an indication that, for many people, structural fire issues are covered by the standard fire resistance test methods and approaches. Where required (based on data relating to property protection), the insurance industry sometimes requires a level of performance over and above that is specified in relation to ensuring compliance with the mandatory requirements of the Building Regulations. Documents such as the Loss Prevention Standard (LPS) 1195 [2] set out an approach to assessing the performance of complete structures (in this case, temporary site accommodation) when subject to a fully developed post-flashover fire scenario.

This approach provides guidance on the choice of the parameters that impact on post-flashover fire behaviour, notably fire load density, ventilation conditions, and specification of compartment lining materials. The intention is that work undertaken to this standard would form a major part of a certification scheme that would enable specific products to be “listed” in a manner that is commonplace for passive and reactive fire protection products and suppression systems. However, many manufacturers choose to go

through the test, but not the full certification process, to demonstrate the performance of a particular system, and this approach has been influential in determining a suitable means of assessment and assurance for modular construction. Figure 3 shows the layout of the fuel load within a typical system subject to testing in accordance with LPS 1195.



Figure 3. Typical fuel load for a site accommodation unit

The subject of structural fire engineering is now an established discipline with centres of expertise across a number of specialist consultancies and academic institutions. However, there remains a lack of understanding of structural behaviour among “fire scientists” whose academic background is often in chemistry or physics. This helps them to deal with the complexities of fire dynamics and to explain the contribution to the fire growth of specific products and materials. Such knowledge is essential in looking at cause and effect in relation to forensic science and in providing the data required to control products and systems on the market and ensure their application is based on the potential risk of ignition, likely fire growth, and consequence of unmitigated fire spread. However, in many cases, there is an in-built assumption among professionals and regulators that structural performance can be assumed based on achieving the required level of performance in standard fire resistance tests. This assumption has been questioned recently, particularly in relation to the proliferation of Innovative Construction Products and Techniques [6].

Large-scale fire experiments such as those conducted at the BRE’s Cardington laboratory have identified issues that cannot be addressed through reliance on standard fire testing. On the one hand, there are failure mechanisms (such as connection failure) that are not covered by the fire resistance test standards, and on the other hand, there are alternative load-carrying mechanisms (such as tensile membrane action), which cannot be predicted based on the results from fire resistance tests. These issues are independent of the potential differences between the standard fire exposure and the temperatures achieved in real fires and can only be dealt with by those with an understanding of structural fire engineering.

Over the last few decades, there has been a growth in innovative forms of construction that attempt to provide sustainable solutions to a housing shortage and a skills shortage within the construction industry while minimising the environmental impact of such developments. Ironically, the introduction of Modern

Methods of Construction (MMC) is nothing new. Prefabricated housing and panelised systems, including Large Panel Systems for multi-storey residential construction, were part of the solution to the same issues that followed the end of the Second World War in the UK. In some cases, their introduction led to systemic problems that formed a large part of the focus of the work of the Building Research Establishment throughout the 1970s and 1980s [7]. Many of these earlier systems incorporated traditional construction materials, which were largely incombustible. The current generation of MMC has been designed to provide good thermal as well as structural performance, as priorities have changed in relation to regulatory requirements over the years [8]. In many cases, this has led to either incorporating combustible materials within the walls and floors of modular or panellised systems or using combustible materials as the principal load-carrying members.

Given the experience with systemic faults in the previous generation of prefabricated buildings, the absence of a database from real fire incidents, and concerns among key stakeholders as to how modern systems will behave in a natural fire situation, there is a demand for additional means of assurance. One approach is to utilise structural fire engineering approaches to predict the anticipated behaviour in the event of a fire. Such techniques would include advanced design methods often based on Finite Element Analysis (FEA). An alternative approach is to consider the behaviour under realistic conditions of load and fire exposure using established experimental methods to demonstrate performance. Although the former may be widely used in the future, numerical techniques require validation. Therefore, at the present time, there is a growing demand for full-scale fire experiments that will demonstrate adequate performance under the specified design conditions and provide the assurance required for key stakeholders such as the regulators and building control professionals, the insurance industry, the Fire and Rescue Service and mortgage providers among others.

3 EXPERIMENTAL METHODOLOGY AND RATIONALE FOR THE EXPERIMENTAL PROGRAMME

The experimental methodology that forms the basis of the experimental programme currently underway has been developed based partly on existing methods of large-scale fire testing [1]. The authors believe the approach described in this paper represents the most rational and logical approach to assessing the fire performance of modern forms of construction currently available.

The primary purpose of the experimental programme is twofold:

1. To assess those aspects of system behaviour that cannot be evaluated using a standard fire test procedure predicated on isolated elements and with no cooling phase.
2. To provide a means of assessment that is consistent and reproducible for all systems where, for whatever reason, reliance on the results from standard fire testing is insufficient to demonstrate compliance with the mandatory requirements of the Building Regulations in relation to performance in fire.

The performance criteria adopted are those of the standard fire test system (loadbearing capacity (stability), integrity, and insulation), and the fire design is based on a standard fire exposure equivalent to the level of fire resistance recommended for the specific system under consideration. In this way, performance can be assessed and understood by a range of construction professionals in a language with which they are already familiar. It also means that the individual experiment can be tailored to the specific application in terms of the required minimum recommended period of fire resistance.

The results from the large-scale fire experiments need to be put into context. In many cases, a temperature rise above the criteria for insulation failure on the unexposed face of the construction may not be critical. Similarly, localised integrity failure around the joints of external panels may not be a major concern.

In general, the reason for conducting the large-scale test will often be to assess the ability of the structure to maintain overall stability and to exhibit restricted deflections such that damage is limited in extent and a fire in a single compartment of a multi-storey building does not lead to disproportionate damage or disproportionate collapse.

Global stability can be assessed in two ways. Firstly, by incorporating a representative (fire limit state) load on the upper surface of the structure by replicating both the ceiling of the fire compartment and the floor of the unit above and ensuring the building can support the applied load for the entire duration of the fire including the cooling phase. It is also possible to determine the load-bearing capacity and potentially the ability of the structure to support loads over and above the fire limit state load by measuring the temperature of critical structural members, such as corner posts or columns, for the entire duration of the fire, including the cooling phase. Although the proposed approach is much closer to reality than the current standard fire test procedures, there are several constraints that limit the approach.

The most obvious limitation is related to the size of the units that can be incorporated within currently available fire test facilities. Although the Large Building Test Facility at Cardington could accommodate large buildings, this facility is no longer available for undertaking fire tests, and routinely constructing such buildings would not be economically viable. The performance of modular systems may be influenced by restraint to thermal expansion provided by adjacent units. In general, structural continuity is likely to be beneficial in reducing deflections and potentially in redistributing forces from areas of the building directly impacted by fire to undamaged areas remote from the ignition source. Ideally, it would be beneficial to incorporate additional units above and adjacent to the fire compartment. However, logistical, economic, and environmental constraints mean that such an approach is unlikely. However, it is feasible to investigate global stability and potential breaches of compartmentation whilst limiting the scale to something which is economically viable and logistically feasible.

Within the period of the fire test, the ability of the structure to prevent fire spread from compartment to compartment is important. This would generally be assessed by visual means supported by temperature measurements on the unexposed surface of any critical components, such as the unexposed surface of the floor above the fire compartment or the unexposed surface of any party wall detail providing separation between apartments. The concept is illustrated schematically in Figure 4.

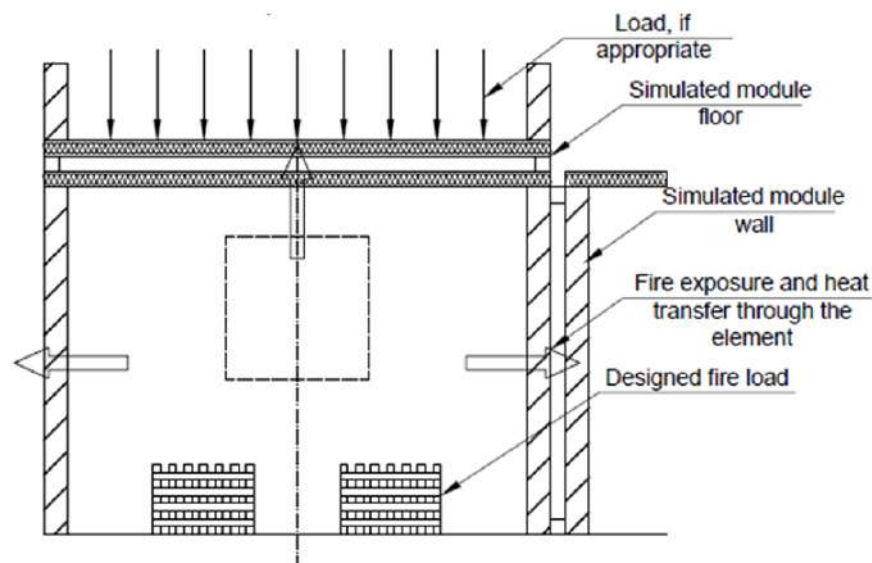


Figure 4. General arrangement of test module showing fire load and potential routes for fire spread

For practical purposes, the maximum module size that can be accommodated within our current available test facility is approximately 6 m wide by 4 m long. The approach set out in LPS 1501 [1] specifies a fire load density based on the general approach set out in Annex E of BS EN 1991-1-2 [9]. However, this approach has been modified in the current project to provide a nominal fire load based on the end use of the building system. The final choice of the fire load density is based on the concept of time equivalence to provide a natural fire exposure with an equivalent fire severity to the design fire resistance for the specific application. To aid comparative assessment and promote reliability and repeatability, a number of

parameters are fixed. As far as possible, the ventilation conditions are standardised, and the primary variable will be the fire load density. The choice of the appropriate fire load density is based on the intended end-use application provided by the manufacturer, which will be related to the recommended minimum fire resistance period.

The concept of time equivalence, as set out in Annex F of the fire part of the Eurocode for Actions [9], is used to relate severity to an equivalent period of exposure to the standard fire test. In this way, performance can be related to a metric familiar to many construction professionals.

Part of what the Project team is trying to assess is whether there is anything specific to the system (such as sensitivity to the rate of heating) that may make reliance on standard fire test results potentially inappropriate. The approach can also determine if the mode of failure associated with the system is something that cannot be assessed or predicted based on the results from standard fire resistance tests on isolated elements. Examples would include failures associated with restrained thermal expansion, connection failure because of large deformations, or failures associated with the cooling phase of the fire or hidden seats of smouldering combustion.

The proposed methodology also allows for a consideration of the performance of cavity barriers, fire-stopping, and penetration seals (as they will be installed) under realistic conditions of thermal exposure. In many cases, products and systems are used in conditions that differ significantly from the direct field of application covered by the fire test reports. It is also possible to account for the potential impact of suppression systems by reducing the design fire load by a factor derived from a consideration of Annex E in the Eurocode [9] based on the information set out in the UK National Annex [10].

The research is focused on understanding the failure mechanisms of structures within a real fire scenario, which traditional means of fire testing cannot assess due to the single-element methodology or the inability of the current testing methodology to adequately represent real fire scenarios. Although there are geometrical constraints to what can be included in the experimental programme, the focus of the research relevant to MMC concerns is listed below:

- Volumetric systems are often reliant on 3D interaction for structural performance, with design load paths reliant on connection stability between vertical and horizontal members.
- Both volumetric and panellised light gauge steel systems rely on connections which may be critical in a fire situation and are not assessed within a standard fire test.
- Mass timber systems could potentially contribute to the fire load should the fire protection linings fail (either within the heating or cooling phase of the fire), increasing the severity of the fire and the speed and likelihood of flashover. They may also be susceptible to smouldering and hidden seats of combustion, which may reignite many hours or even days after the initial fire.

4 PROCEDURE

In the research project, the primary objective is to determine if specific forms of construction can maintain overall stability for the entire duration of the natural fire exposure, including the cooling phase, without any external intervention. In this way, one of the principal objectives is to determine if the structure can survive burn-out of the anticipated combustible fire load when this load is related to the recommended period of fire resistance stipulated by regulatory guidance [11].

The methodology developed during the current research project funded by the UK government and based on the earlier attempts to provide a robust means of assessment based on large-scale three-dimensional structural behaviour in fire incorporates a number of specific steps as discussed below:

1. Discussion with the potential supplier to determine overall geometry, potential end-use application, and method of construction. This information will be used to derive the fire design as set out below but will also inform decisions on the type and position of instrumentation used to assess performance and the inclusion of additional items such as cavity barriers, fire stopping, and penetration seals.

2. Determine the appropriate fire load density to provide a design fire exposure based on information derived during step 1 above and informed from Annex A and Annex F of EN 1991-1-2. The critical parameters here are the overall geometry, ventilation conditions, and linings of the fire compartment.
3. Deliver or erect (depending on whether volumetric or panellised) the unit to the fire test facility, considering restrictions in relation to overall geometry and incorporating provisions for loading the floor above the fire compartment.
4. Install all relevant instrumentation to enable an assessment of performance to be made. As a minimum, this would include temperature measurements to record the gas temperature within the compartment and the temperature of the unexposed faces of the separating elements but may also include instruments to record deflection at critical locations and potentially measurements to record the radiant heat flux opposite the ventilation openings. Build the fire load from timber cribs based on calculations undertaken in step 2 above in relation to the specified design fire resistance period.
5. Expose the unit to a fire representative of the likely end-use application and record all instruments for the duration of the fire, including the cooling phase. Where there is the potential for smouldering combustion, the data acquisition period may need to be extended to cover any reignition of the structure.

The starting point for the project is that, for traditional forms of construction, a reliance on the results from standard fire resistance tests is both a sufficient and generally conservative approach. In order to “calibrate” this assumption, the initial experiment was undertaken within a compartment constructed from loadbearing masonry blocks for the walls and precast concrete planks for the floor. Both the walls and the floor were lined with a single layer of plasterboard to simulate anticipated insulation within a dwelling, but there was no specific level of fire resistance provided. The results will provide a baseline level from which to judge the performance of other systems incorporating steel and concrete modular construction, panellised steel frame units, and mass timber construction.

To date, several systems have been through this process as part of the government research project, including light steel frame volumetric and panellised systems and mass timber panellised systems. The complete results will be disseminated once the project is finished.

The basic layout of the compartment geometry for the project is illustrated in Figure 5, while Figure 6 shows flames emerging from the opening immediately following flashover for the initial fire experiment involving traditional forms of construction. The measured compartment temperatures are compared with both the standard fire curve and the predicted compartment response based on the parametric approach from Annex A of EN 1991-1-2 in Figure 7.

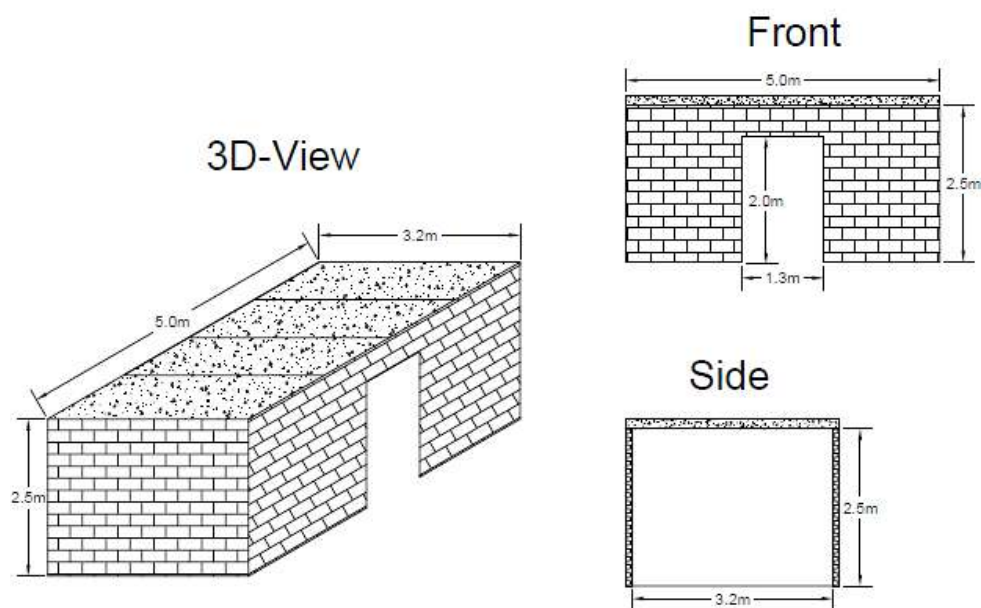


Figure 5. Overall geometry for the compartments included in the research project



Figure 6. External flaming shortly after flashover

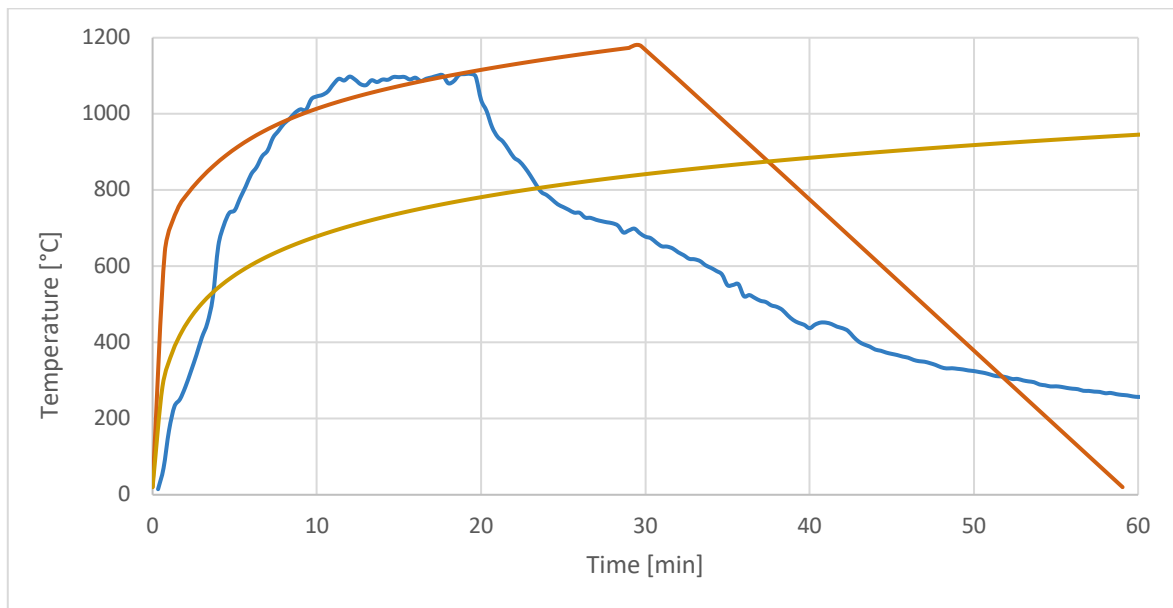


Figure 7. Compartment time-temperature response compared with standard fire exposure and predicted values based on the parametric approach in EN 1991-1-2

In this case, the design fire resistance for the form of construction being assessed was 60 minutes, and the fire design and choice of design fire load were based on this value. Although there is not a direct relationship between the measured values for the natural fire and the equivalent period represented by the area under the curve of the 60-minute fire exposure, the results do show a reasonable correlation and suggest that this is a suitable approach for the research project.

The fire experiment was allowed to continue until all the fire load was consumed, and no attempt was made to intervene at any stage. The results confirmed that traditional forms of construction designed on the basis

of the standard fire resistance test are capable of surviving burn-out of all combustibles within a reasonable worst-case fire scenario and confirm the initial assumption that, for traditional forms of construction, a reliance on the results from standard fire resistance tests is both a sufficient and generally conservative approach. This approach has been adopted for the other systems included in the research project and will provide the basis of the methodology developed.

5 CONCLUSIONS

This research has been designed to provide answers to questions currently arising in industry and government regarding the fire performance of innovative forms of construction. Therefore, the focus has been mindful of reflecting industry systems and building applications that are most used, serving high-risk scenarios as a priority.

The methodology described also allows for the study of additional issues of relevance to modern forms of building construction. Those issues identified thus far include the potential for failure because of downward fire spread, not currently considered in regulatory guidance, the issue of loadbearing walls within a fire compartment exposed to fire on two sides but currently assessed on the basis of one-sided exposure, issues around penetrations and fire stopping and cavity barriers in modern forms of construction where tested and certified solutions may be used outside of their scope of application.

The proposed methodology will provide a means of assurance for stakeholders that innovative forms of construction can achieve the mandatory requirements of the Building Regulations in relation to Fire Safety, particularly where there are concerns that such assurance cannot be provided through reliance on the results from standard fire resistance tests. How such a methodology may be utilised or adopted by the construction industry is outside the scope of the current research, but initial results have confirmed the need for alternative means of assessment over and above that provided by the standard fire resistance test procedures.

REFERENCES

1. Loss Prevention Standard LPS 1501 Issue 1.1., Fire test and performance requirements for innovative methods of building construction, BRE Global Limited, (2014).
2. Loss Prevention Standard LPS 1195 Part 1 Issue 4.1., Fire test and evaluation requirements for the LPCB approval and listing of temporary buildings for use on construction sites, BRE Global Ltd, (2014).
3. Lennon, T., and Hopkin, D., Fire performance of light steel-framed buildings, BRE Information Paper IP 6/11, IHS BRE Press, (2011).
4. BS 476 Fire tests on building materials and structures – Part 32: Guide to full scale fire tests within buildings, BSI, London, (1989).
5. BS 476 Fire tests on building materials and structures – Part 33 Full-scale room test for surface products, BSI, London, (ISO 9705: 1983).
6. Communities and Local Government, Innovative Construction Products and Techniques, BD 2503, (2008).
7. Currie, R.J., Reeves, B.R., and Moore, J.F.A., The structural adequacy and durability of large panel system dwellings Part 1 Investigations of construction, Building Research Establishment Report, Crown Copyright (1987).
8. Gaze, C., Ross, K., Nolan, E., Novakovic, O., and Cartwright, P., Modern methods of construction (MMC) in housing: Drivers and barriers to their use, BRE Information Paper IP 3/07 Part 1, IHS BRE Trust, (2007).
9. BS EN 1991-1-2, Eurocode 1: Actions on structures – Part 1-2: General actions – Actions on structures exposed to fire, BSI, London, (2002).
10. National Annex UK National Annex to Eurocode 1: Actions on structures – Part 1-2: General actions – Actions on structures exposed to fire, BSI, London, (2007).
11. HM Government, The Building Regulations 2010, Approved Document B Fire Safety, Volume 2: Buildings other than dwellings, (2019). Edition incorporating 2020 amendments – for use in England.

APPARATUS FOR ASSESSING THE LOAD-INDUCED THERMAL STRAIN OF CONCRETE AT ELEVATED TEMPERATURE

Kajanan Selvaranjan¹, Maurizio Guadagnini², John L. Provis³, Giacomo Torelli⁴

ABSTRACT

This paper discusses the development of a test rig to measure the deformation of concrete under constant load and transient high temperatures, while taking into account laboratory constraints and critical safety issues. A bespoke two-part load-maintaining solution was developed. The system combines the use of a self-reacting load frame equipped with a 1 MN cylinder at the high end of a hydraulic force multiplier and a lever arm system, enabling the application of a sustained constant compression load at temperatures up to 600 °C. The loading platens were designed to minimise their impact on both the thermal performance of the furnace and the temperature distribution along the longitudinal axis of the test specimens. The platens were fitted with ultra-high performance fibre reinforced concrete thermal breaks. The load application system was calibrated using a reference load cell. Additionally, a non-contact measuring technique based on 2D-point tracking was used to monitor the axial deformation of the concrete specimen. The accuracy of the 2D-point tracking was validated against data obtained via conventional contact methods and was found to be 1 µm. Additional technical challenges for the development of a safer and more cost-effective test setup to assess load-induced thermal strain (LITS) are also discussed and commented upon.

Keywords: Concrete; Deformation; High temperature; Constant load; 2D-point tracking

1 INTRODUCTION

Accurate measurement of concrete deformation at high temperatures is crucial for developing and verifying constitutive models that can capture creep phenomena, transient effects induced by elevated temperatures, and the mechanical damage experienced by concrete over time. Thermal strain of concrete is significantly important in understanding the behaviour of concrete structures subjected to high temperature heating–cooling cycles under sustained compressive loads. However, the reliability of data obtained using traditional testing methods for assessing concrete deformation under load at elevated temperatures (Load Induced Thermal Strain - LITS) can be affected by various sources of error [1] and only limited recommendations are available (e.g.[2]).

Load application and strain measurements are affected by various sources of uncertainty. Many test setups have been proposed in the literature to analyse the LITS of concrete at high temperatures [3]–[5]. To date, there is a notable lack of information on the consistency of load maintenance throughout experiments. The degree of load variation over time necessarily influences the measured LITS; however, no clear guidelines

¹ Department of Civil and Structural Engineering, The University of Sheffield, UK
e-mail: k selvaranjan1@sheffield.ac.uk

² Department of Civil and Structural Engineering, The University of Sheffield, UK
e-mail: m.guadagnini@sheffield.ac.uk

³ Paul Scherrer Institut, Laboratory for Waste Management, Forschungsstrasse 111, 5232 Villigen PSI, Switzerland
e-mail: john.provis@psi.ch

⁴ Department of Civil and Structural Engineering, The University of Sheffield, UK
e-mail: g.torelli@sheffield.ac.uk

exist for ensuring constant-load conditions during testing. The load can be applied in different ways. The usual practice is to use a universal testing machine equipped with a load cell positioned in the top moveable cross head [3]. The main disadvantage of this configuration is that the load cell may be exposed to elevated temperatures, which can affect measurement accuracy. Another practical challenge in employing a servo-hydraulic or electromechanical universal testing machine is the long duration of operation and various safety measures that should be implemented to minimise the required user interaction. An alternative approach is manual loading, which involves the use of a loading jack or chain system [6]. None of these methods considered the issues in guaranteeing the application of a constant load over time. Maintaining constant load conditions is critical to ensure the reliability and reproducibility of the results.

In addition to load application methods, the choice of the strain measurement technique introduces another layer of uncertainty in LITS testing. Various methods such as extensometers, LVDTs, and digital image correlation (DIC) systems are employed for measuring strains in concrete under elevated temperatures. However, each technique comes with its own set of limitations and sources of error, complicating the accurate determination of concrete deformation. Furthermore, the compatibility of these measurement techniques with high-temperature environments adds another dimension to the challenge. In the majority of studies available in the literature, the axial deformation of a uni-axially loaded specimen at high temperatures was assessed based on the relative displacement between the two loading platens [6]–[8]. The other technique to measure the deformation is the use of specially designed platens, which allow for the use of a glass tube or rod to measure transfer deformations outside the furnace [9]. However, the relative displacement between two loading platens includes the deformation of the platens and end effects of the specimen, and quartz tubes are susceptible to misalignment affecting the precision of the displacement measurements.

In order to overcome these issues, this paper proposes a new test setup designed to effectively evaluate the LITS of concrete while ensuring safety of operation. The proposed setup uses a two-part load-maintaining system, integrating a hydraulic mechanism with a lever arm to apply sustained loads for an extended period of time (10 hours). Furthermore, 2D-point tracking is adopted for strain measurement. This technique is shown to be a reliable way to measure the axial deformation along a given gauge length, thus providing a valid and more practical alternative to the above-mentioned traditional techniques. Additionally, the design of the load application system incorporates custom perforated platens with thermal breaks to minimise axial temperature differentials within the specimen throughout the test.

The primary objective of this study was to evaluate the accuracy of both the applied load and strain measurements, and to validate the reliability of the developed test apparatus. To ensure consistency of the applied load, a load cell was integrated into the setup, and a comparative study was conducted. The reliability of the strain measurements was verified through comparison with traditional contact-based measurement devices.

2 DEVELOPMENT OF THE TEST SETUP

The aim of the transient thermal experiments was to investigate the strain behaviour of unsealed cylindrical concrete specimens subjected to constant load levels and a steady rate of heating for temperatures up to 600 °C. Therefore, the test rig should be capable of applying constant loads and rates of temperature increase to the specimen, while simultaneously minimising the axial temperature differential within the specimen throughout the thermal transient test. In this section, the design of the test rig, which is used to evaluate both the free thermal strain and load-induced thermal strain of concrete specimens, is discussed. This test rig has been developed from scratch, considering several technical challenges and safety concerns.

2.1 General design of the test rig

A simple and effective experimental setup for assessing the LITS of concrete at high temperatures is necessary to address practical experimental challenges, reduce measurement uncertainties, and address operational safety. Based on design requirements, the most unfavourable conditions are generally specified as the prolonged duration (10+ hours) required to apply and maintain the load in a high-temperature

environment, the strain measuring technique at high temperatures, and the heat sink issues in the furnace, all of which are crucial for ensuring safety and providing reliable tests.

The apparatus for the uniaxial compression of concrete at elevated temperatures was designed to satisfy three key criteria:

- a) The loading system should be able to maintain the target load level with high accuracy for the entire duration of the test (10+ hours) and with minimal user interaction.
- b) The deformation of the specimen should be measured in a practical and reliable manner. A non-contact point-tracking technique was used to measure the deformation of the specimen along its middle third portion and mitigate any uncertainties related to the use of extension rods to mount LVDTs outside the oven. The gauge length was selected as this region of the test specimen is considered to be unaffected by the restraining action of the loading platens, and with a primarily uniform axial temperature.
- c) The heat sink effect introduced by using large steel loading platens should be minimised to avoid any significant axial temperature gradient along the test specimen. To this end, the use of bespoke perforated platens with thermal breaks is proposed.

2.2 Design of the loading frame

Mechanical loading is applied using a two-part load-maintaining system and a self-reacting steel frame equipped with perforated loading platens and thermal breaks. A conceptual diagram of the test setup is shown in Figure 1.

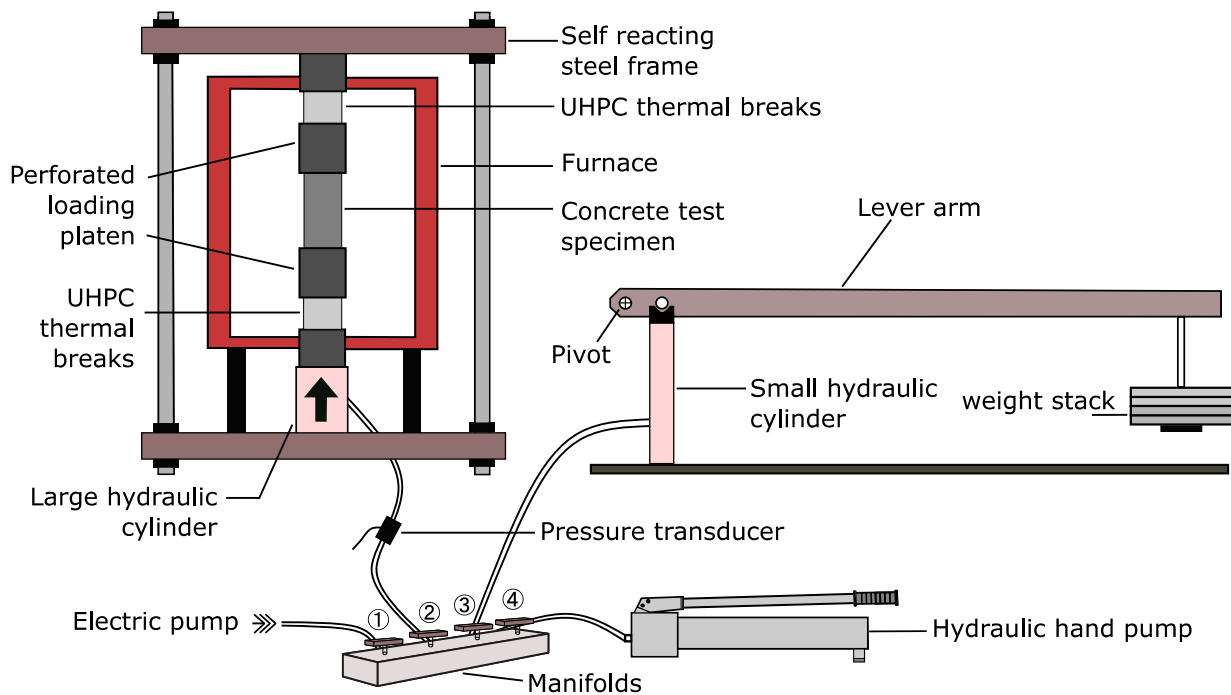


Figure 1. Overview of the test rig and complete setup with the two-part load maintaining system

The main frame of the LITS test setup comprises four solid steel columns, each with a diameter of 60 mm and a length of 1700 mm, and two rectangular steel hollow sections (RHS) welded together as shown in Figure 2. The cross section of the RHS is 300 mm × 200 mm and 16 mm thick. The high stiffness of the frame was achieved by having a 1000 mm × 1000 mm and 100 mm thick solid steel plate at the base of the frame.

A vertical split furnace is used to apply the target thermal load at selected heating rates. This furnace is housed in the loading frame and is equipped with two 125 mm holes, positioned at the top and bottom,

allowing for the insertion of the loading platens. The front segment of the furnace is equipped with a window to enable visual access to the specimen and facilitate the monitoring of deformation through non-contact methods. The efficiency of the furnace is enhanced by the addition of one layer of Vermiculite board and a layer of ceramic fibre blanket.

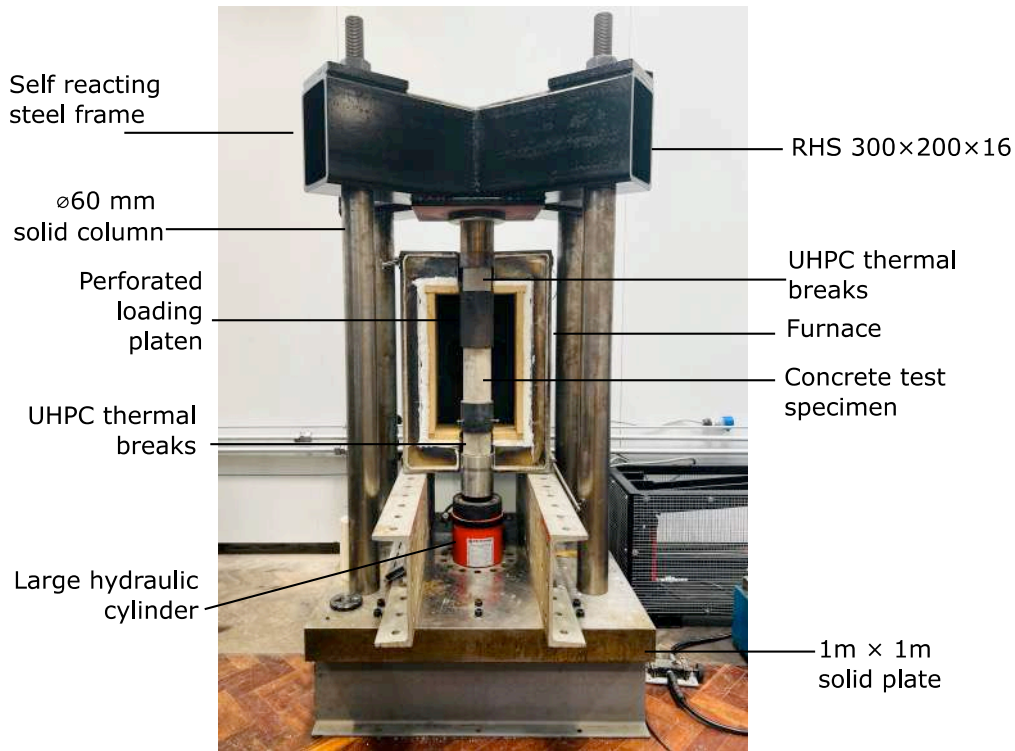


Figure 2. The test rig frames and supports

The test setup was designed to evaluate standard-sized cylindrical concrete specimens, measuring 100 mm in diameter and 200 mm in height. To ensure uniform load application during testing, a 120 mm diameter loading platen was chosen. Initially, a solid steel section was used for the platens. However, this setup caused a heat-sink effect, potentially leading to a significant temperature gradient along the length of the test specimen. To overcome this challenge, thermal breaks (produced from ultra-high performance concrete, UHPC) were incorporated, and perforated platens were used to reduce the overall mass of the steel components inside the heated volume. By implementing these modifications, it was possible to minimise the heat transfer through the platens, thereby mitigating the undesirable temperature gradient experienced by the test specimen.

2.3 Design of two-part load maintaining system

The system was designed to apply a maximum load of 1 MN using a combination of a lever arm system and a closed hydraulic system equipped with two single-acting cylinders as shown in Figure 3. The distance between the pivot and the small hydraulic cylinder fitted within the mechanical lever arm is 180 mm, while the load, comprising a series of 20kg weights, is applied at a distance from the hydraulic cylinder yielding a force multiplier ratio of 25:1. Rolling bearings are integrated in the pivot to mitigate frictional forces. The maximum degree of rotation of the lever arm during testing was also considered in the design of the system to ensure safe operation and a dead stop is fitted to prevent the lever arm from hitting the floor in case of brittle failure of the test specimen

The small hydraulic cylinder has a surface area of 6.4 cm² and a total capacity of 4.5 tonnes and transfers the load to a larger cylinder with a surface area of 153.4 cm² and a total capacity of 109 tonnes, giving a load ratio of 24:1.

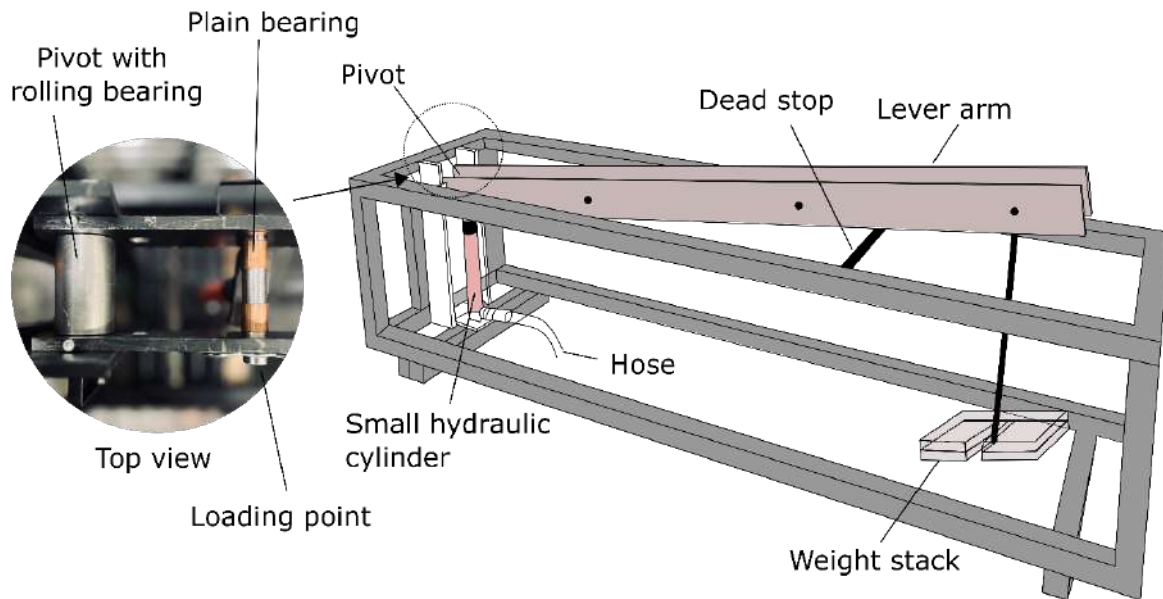


Figure 3. Structure of mechanical loading system of test rig with a bespoke lever arm and weight stack

A 4-way manifold is used to control the various phases of load application (Figure 1). One end (1) of the manifold is connected to an electric pump. This pump is used to displace the large hydraulic cylinder and move the concrete specimen until it comes in contact with the top platen. The fourth port (4) of the manifold is connected to a hand pump for fine tuning of the hydraulic pressure. This also allows to operate the system without the need of an electrical power source. The remaining two ports on the manifold are connected to the large (2) and small (3) hydraulic jacks. The following are the steps to apply the load:

- a. Specimen setup - Begin the experimental procedure with valves 3 and 4 fully closed, and valves 1 and 2 open. Activate the electric pump to displace the large hydraulic cylinder until the specimens comes in contact with the top platen.
- b. Loading - When near the above step is completed, close valve 1. Subsequently, open valves 3 and 4 to allow for the expansion of the system. Weights are added to attain the desired output load. The hand pump is used to regulate the internal pressure and bring the lever arm in a horizontal position. Once the lever arm reaches the horizontal level, promptly close valve 4 to stabilise the system.
- c. Testing - Throughout the experimental duration, maintain valves 2 and 3 in an open position, while ensuring that valves 1 and 4 remain closed to uphold the integrity of the experimental setup.

Using a pressure transducer connected to valve 2, the hydraulic pressure within the large cylinder is continuously measured. This pressure data is seamlessly integrated into a PC-based solution built around National Instruments hardware and a dedicated LabVIEW program for data acquisition. The LabVIEW software provides real-time monitoring of load variations, allowing prompt adjustment of the hydraulic system as needed. This allows for precise adjustment of weights and lever arm distances to achieve any required load level.

2.4 Displacement and strain measurement

2.4.1 Overview

The measurement of deformation of concrete under load at high temperature typically involves transferring the displacement of the specimen mechanically out of the furnace, so it can be gauged by a displacement transducer. This method, however, ignores the deformation of the end platens at high temperatures (Figure 4a) and includes the local deformation of the specimen due to end-platen effects. The use of non-contact

deformation methods can effectively address these issues and provide a more practical solution (Figure 4b). When only axial deformation is of interest, point tracking techniques, which involve monitoring the movement of specific points or markers on the surface of the material, can be simpler to implement and the acquired images are faster to post-process than performing full field digital image correlation (DIC) [10].

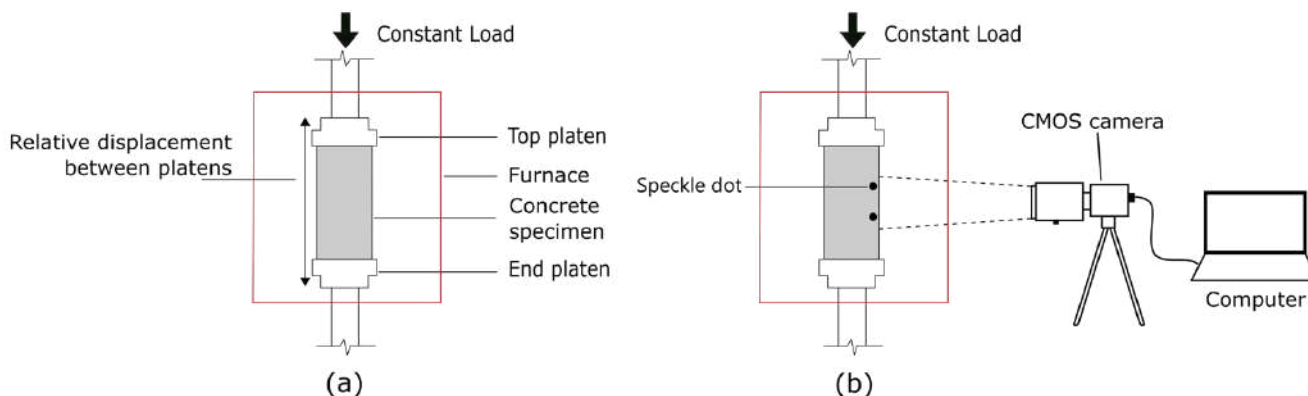


Figure 4. (a) Conventional technique for measuring the axial displacement of the concrete specimen inside the furnace under loading, (b) 2D point tracking for measuring the axial displacement using image-processing technique.

2.4.2 2D point tracking principles

Point tracking involves the detection and tracking of specific features or points over time on a surface. One common approach is to utilise a different intensity feature on a background, then track the outline (i.e. edges) of that feature. The concept of tracking a dot on a concrete surface is depicted in Figure 5. As previously discussed, it involves an image processing technique aimed at tracking the outline of black dots within images of concrete surfaces.

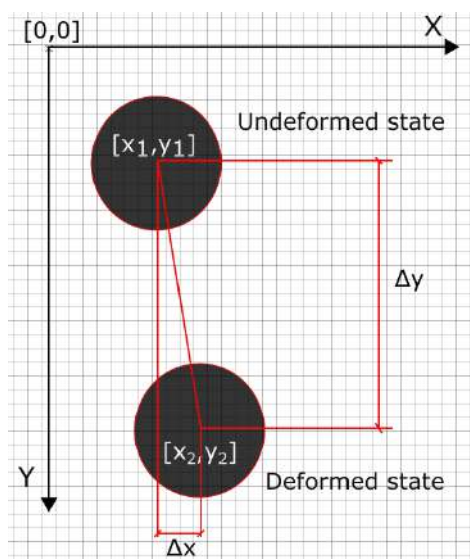


Figure 5. Schematic illustrations of the principle of tracking the relative position of subset before deformation and a deformed subset after deformation

Once the outline of the black dot is detected, the next step is to determine its centre. This is achieved by calculating the centroid of the detected outline. The centroid represents the geometric centre of the shape. Before outline detection, the input image is pre-processed by binary thresholding to enhance accurate detection. A binary image consists of only two intensity levels: black (usually represented by 0) and white (usually represented by 255). After the outline is detected, the algorithm iterates through each pixel within the outline. The coordinates of these pixels are recorded, and the average x-coordinate and average y-coordinate are calculated. These average coordinates represent the centre of the dot within the image. The

distance (d) between the centre coordinates (x_1, y_1) and (x_2, y_2) can be found using Equation 1. The distance can be calculated in physical units (e.g. mm) by calibrating the image using a known scale.

$$d = \sqrt{(x_2 - x_1)^2 + (y_2 - y_1)^2} \quad (1)$$

3 EXPERIMENTAL VALIDATION

3.1 Materials

The experiments were performed on cylindrical concrete specimens having a diameter of 100 mm and a height of 200 mm. Concrete specimens were produced using the mix composition reported by Petkovski & Crouch [11], cured in water for 3 months and then oven dried for 30 days at 65 °C. A heating rate of 1 °C/min was selected to minimise thermal stresses.

3.2 Sample preparation

Circular markers are created using a 3.97 mm hole punch on adhesive aluminium strips, which are then affixed to the (cleaned and sanded) concrete surface. A gauge length of 70 mm between two markers was selected to capture average strains along the middle-third region of the specimen (the region of interest -ROI) and over a distance that can be considered to be representative, while also mitigating end-platens effects.

Heat-resistant spray paint [12], specifically VHT FLAMEPROOF SP102, capable of withstanding temperatures of up to 1000°C, was utilised to spray the markers on the surface of the concrete specimens. The markers were sprayed following a first coating of heat-resistant white spray paint to create a background with high contrast.

3.3 2D-point tracking

A CMOS digital camera having a 5472 × 3648-pixel resolution (BFS-U3-200S6M-C USB 3.1 Blackfly® S, Monochrome) was used to capture images at a frequency of one image per minute. The camera was equipped with 75 mm fixed focal length lens. The camera was connected to a computer and controlled by the Spinnaker SDK software. Two light-emitting diode (LED) lamps were used to illuminate the targeted field of view. The camera lens was situated at a distance of approximately 550 mm enabling the coverage of the ROI. Image processing is carried out using ImageJ software [13].

Concerns arose regarding the potential degradation of image quality attributed to the presence of hot air and radiation within the furnace [14]. In response, a Midpot BP470 band-pass filter was integrated into the lens system for investigation. No substantial issues were observed during experimentation. It has been reported that thermal radiation of the specimen beyond 600 °C is a major challenge associated with the application of this method [10], [15]. This experiment specifically targeted temperatures up to 600 °C, and there was no observable deterioration in the image quality. This system is capable of measuring displacements with an accuracy of 10⁻⁶ m.

3.4 Load calibration

In this study, the load measurement system was calibrated with reference to standards provided by the National Physical Laboratory (NPL), UK. By aligning the system with the NPL standards, a robust framework for precise load measurement was established. The calibration procedure involves subjecting the hydraulic jack to known loads under controlled conditions, while concurrently recording the hydraulic pressures measured by the pressure transducer. The recorded pressures were then compared with the corresponding known loads provided by the NPL standards. Through this comparison, calibration curves were generated to establish a direct correlation between the applied loads and measured pressures. To account for potential nonlinearities or system variations, a calibration process was performed across a range of load levels. By adhering to the NPL standards, the hydraulic system undergoes rigorous calibration, ensuring that the measured loads conform accurately to internationally recognised guidelines.

To ensure the long-term accuracy of the load measurements, a 500 kN load cell was positioned in place of the concrete specimen for a trial run, allowing for continuous monitoring of the applied load. This load cell

served as an independent means of verifying the load applied by the hydraulic system. A comprehensive analysis of the load accuracy over an extended duration was conducted by comparing the load measurements obtained from the load cell with those recorded by the pressure transducer. The results of this comparison are shown graphically in Figure 6. The measurement yielded for the deviation a mean value of -0.31 kN with a standard deviation of 0.27 kN.

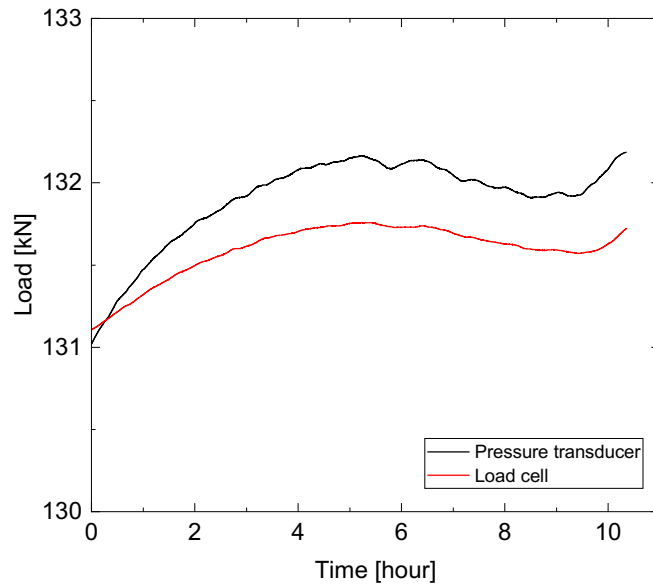


Figure 6. The comparison of load measured by the pressure transducer with the load cell

3.5 Temperature gradient within the test specimen

In the experiment, a furnace with dimensions of 800 mm in height and internal dimensions of 500 mm in height, 300 mm in length, and 350 mm in width served as the primary heating source. Temperature regulation of the furnace was achieved using an automatic programming device. Real-time temperature data were recorded using thermocouples and LabVIEW software. The furnace's maximum operating temperature was 700 °C; however, for this experiment, it was limited to a maximum of 600 °C. The heating rate was set at 1 °C/min. Temperature was measured at both the surface and centre of the test specimens using thermocouples. Figure 7a shows the thermocouple readings for a specimen heated at 1 °C/min to 600 °C. A maximum temperature difference of 23.5 °C is reached along the radius of the concrete specimen (Figure 7b).

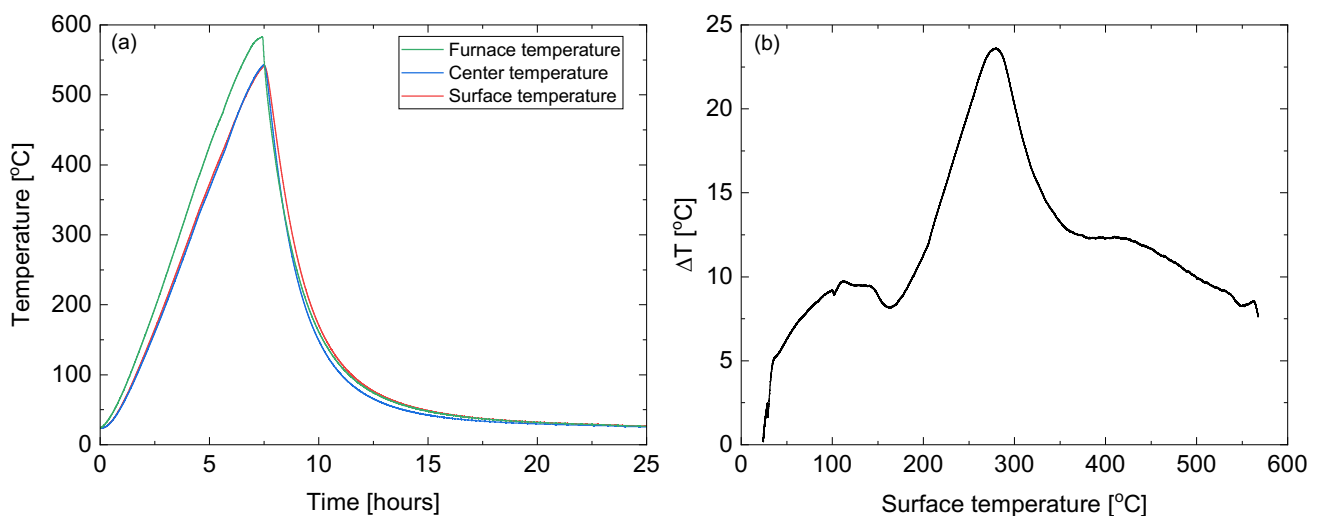


Figure 7. (a) Measured temperature in a cylindrical specimen heated at 1 °C/min; (b) temperature difference between the centre and surface

3.6 Strain measurement validation

The accuracy of the 2D-point tracking method was evaluated by comparing the obtained measurements with those obtained from conventional contact measurement devices under ambient conditions. This evaluation was further extended to check the accuracy at high temperature conditions by comparing the deformation of steel specimens.

3.6.1 At ambient temperature

In this study, the accuracy of the deformation of concrete captured by 2D-point tracking at ambient temperature was assessed by comparing the axial deformation recorded by conventional contact measurement devices such as strain gauges and LVDTs. The specimen was loaded up to a stress level equal to 30% of its compressive strength (which was approximately equivalent to a load of 200 kN in the current setup) (Figure 8). Three cycles of loading and unloading were performed as shown in Figure 9b. LVDT with a gauge length of 70 mm was used to measure the axial deformation of the concrete cylinders. The two LVDTs were placed diametrically opposite and centrally aligned. The strain gauges were positioned on the surface of the specimen along its longitudinal axis and at 120 degrees along its circumference. The markers were attached near the strain gauges and LVDT at a gauge length of 70 mm, as shown in Figure.

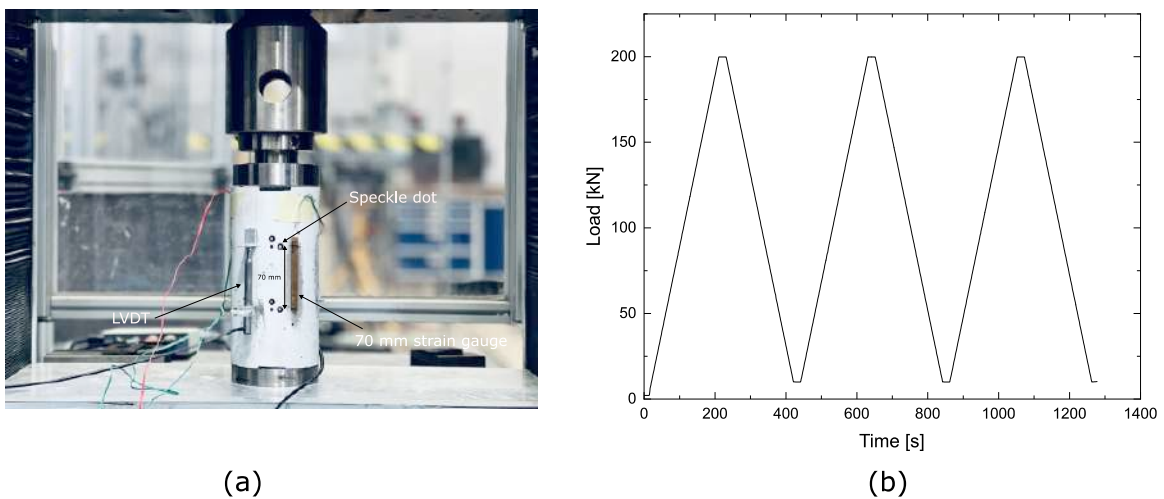


Figure 8. (a) Concrete cylinders with applied speckle dots, strain gauges and LVDTs, (b) loading profile used

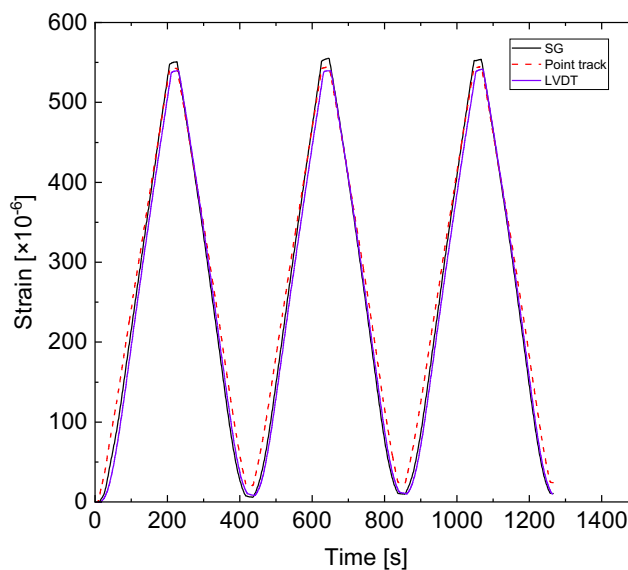


Figure 9. Comparisons between deformations captured by strain gauges (SG), point tracking, and LVDT

The variation in the axial displacements over time between the 70 mm gauge length of the test sample determined by the strain gauges, LVDT, and point tracking are plotted in Figure 9. From the comparison, it can be observed that the strain values obtained by point tracking exhibit good agreement with the strain values measured by the strain gauges and LVDT. This validation proves that point tracking can be utilised as a suitable tool to analyse the axial displacement.

3.6.2 At elevated temperature

The reliability of 2D-point tracking at high temperatures was evaluated through experimentation with steel specimens. A steel sample with dimensions of 10 mm × 10 mm in cross section and 200 mm in length was employed. Markers were applied with a gauge length of 70 mm. The specimen was heated at a rate of 2 °C/min up to 500 °C, and images were captured at a frequency of 1 image per minute. To validate the outcomes, a specimen made of the same steel and with a cross-section of 10 mm × 10 mm and a height of 25 mm, was tested in a DIL 402 Expedis Thermomechanical Analyzer (TMA). This involved measuring thermal dilation under conditions of constant heating at 2 °C/min, a constant load of 0.2 N, and a nitrogen purge rate of 50 mL/min.

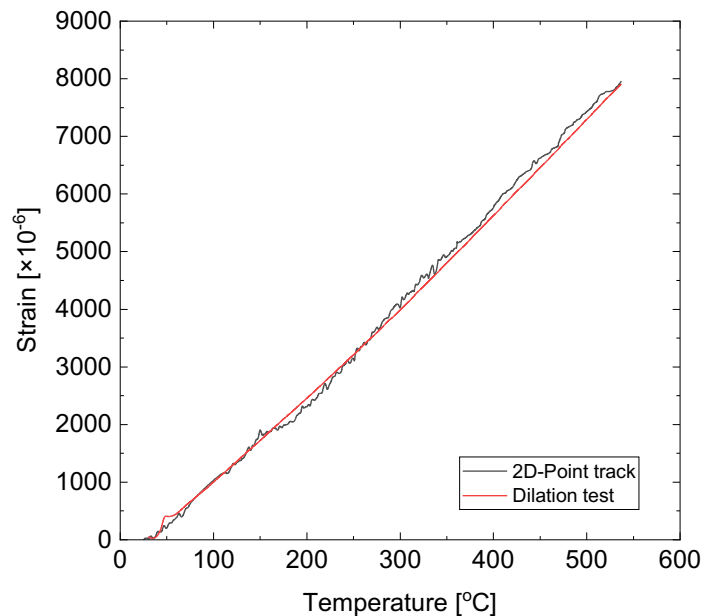


Figure 10. Comparisons between the deformation determined by 2D-point tracking and dilation testing

The overall strain of the steel specimens given by 2D-point tracking and by the TMA are shown to exhibit a good fit (Figure 10), with an overall error of 46 micro strains. This confirms the reliability of employing 2D-point tracking as strain measurement technique also at high temperature.

The above discussion attests to the capability of the 2D-point tracking method in accurately capturing the axial deformation of concrete at both ambient and elevated temperatures.

4 CONCLUSIONS

This study addresses the significant challenges associated with constant-load application and strain measurement in high-temperature environments to assess the thermal strain of concrete. Promising results were achieved through the development of a new test setup employing a two-part load-maintaining system and 2D-point tracking technique for strain measurements. The comparison of prolonged load measurements with conventional load cell methods demonstrated good agreement, indicating the effectiveness of the approach as a simple, cost-effective, and safety-oriented technique for load application. Additionally, the validation of 2D-point tracking at both ambient and elevated temperatures,

in comparison with conventional contact methods, highlights its potential as a reliable tool for studying the axial deformation of concrete in high-temperature environments. This work lays the foundation for improved methodologies for assessing concrete behaviour under thermal stress, offering more accurate experimental data.

ACKNOWLEDGMENT

The authors wish to thank Engineering and Physical Sciences Research Council (EPSRC) and EDF Energy for funding the PhD project of KS at the University of the Sheffield.

REFERENCES

- [1] S. M. Alogla and V. Kodur, "Temperature-induced transient creep strain in fiber-reinforced concrete," *Cem. Concr. Compos.*, vol. 113, 103719, 2020, doi: <https://doi.org/10.1016/j.cemconcomp.2020.103719>.
- [2] RILEM TC 129-MHT, "Recommendations of RILEM TC 129-MHT: Test methods for mechanical properties of concrete at high temperatures. Part 7: Transient Creep for service and accident conditions.," *Mater. Struct.*, vol. 31, pp. 290–295, 1998.
- [3] S. Huismann, F. Weise, B. Meng, and U. Schneider, "Transient strain of high strength concrete at elevated temperatures and the impact of polypropylene fibers," *Mater. Struct.*, vol. 45, no. 5, pp. 793–801, 2012, doi: [10.1617/s11527-011-9798-6](https://doi.org/10.1617/s11527-011-9798-6).
- [4] G. Torelli, M. Gillie, P. Mandal, and V. X. Tran, "A multiaxial load-induced thermal strain constitutive model for concrete," *Int. J. Solids Struct.*, vol. 108, pp. 115–125, 2017, doi: [10.1016/j.ijsolstr.2016.11.017](https://doi.org/10.1016/j.ijsolstr.2016.11.017).
- [5] J. Tao, X. Liu, Y. Yuan, and L. Taerwe, "Transient strain of self-compacting concrete loaded in compression heated to 700 °C," *Mater. Struct.*, vol. 46, no. 1, pp. 191–201, 2013, doi: [10.1617/s11527-012-9894-2](https://doi.org/10.1617/s11527-012-9894-2).
- [6] G. A. Khoury, B. N. Grainger, P. J. E. Sullivan, G. A. Khoury, P. J. E. Sullivan, and B. N. Grainger, "Strain of concrete during first heating to 600°C under load," *Mag. Concr. Res.*, vol. 37, no. 133, pp. 195–215, 1985, doi: [10.1680/mac.1985.37.133.195](https://doi.org/10.1680/mac.1985.37.133.195).
- [7] S. Huismann, F. Weise, B. Meng, and U. Schneider, "Influence of Polypropylene Fibres on the Thermal Strain of High Strength Concrete at High Temperatures," *J. Struct. Fire Eng.*, vol. 2, no. 3, pp. 173–180, Jan. 2011, doi: [10.1260/2040-2317.2.3.173](https://doi.org/10.1260/2040-2317.2.3.173).
- [8] T. Lee, K. Jeong, and H. Choi, "Effect of Thermal Properties of Aggregates on the Mechanical Properties of High Strength Concrete under Loading and High Temperature Conditions," *Materials*, vol. 14, no. 20, 2021, doi: [10.3390/ma14206093](https://doi.org/10.3390/ma14206093).
- [9] Y. Anderberg and S. Thelandersson, "Stress and deformation characteristics of concrete: experimental investigation and material behaviour model," *Bull. Div. Struct. Mech. Concr. Constr.*, vol. 54, pp. 1–86, 1976.
- [10] D. B. Le, S. D. Tran, J. L. Torero, and V. T. N. Dao, "Application of digital image correlation system for reliable deformation measurement of concrete structures at high temperatures," *Eng. Struct.*, vol. 192, pp. 181–189, 2019, doi: <https://doi.org/10.1016/j.engstruct.2019.05.009>.
- [11] M. Petkovski and R. S. Crouch, "Strains under transient hygro-thermal states in concrete loaded in multiaxial compression and heated to 250 °C," *Cem. Concr. Res.*, vol. 38, no. 4, pp. 586–596, 2008, doi: <https://doi.org/10.1016/j.cemconres.2007.10.008>.
- [12] G. T. Bellamy, M. J. DiDomizio, M. K. Patel, and M. B. McKinnon, "Characterization of high-temperature paints for infrared thermography in fire research," *Fire Saf. J.*, vol. 137, 103775, 2023, doi: <https://doi.org/10.1016/j.firesaf.2023.103775>.
- [13] A. B. Schroeder, E. T. A. Dobson, C. T. Rueden, P. Tomancak, F. Jug, and K. W. Eliceiri, "The ImageJ ecosystem: Open-source software for image visualization, processing, and analysis.," *Protein Sci.*, vol. 30, no. 1, pp. 234–249, 2021, doi: [10.1002/pro.3993](https://doi.org/10.1002/pro.3993).
- [14] L. Wang, Y. Zhao, and Y. Xing, "Investigating high-temperature deformation evolution of concrete under sustained loading using DIC technology and a temperature-mechanical coupled damage constitutive model," *Constr. Build. Mater.*, vol. 324, 126638, 2022, doi: <https://doi.org/10.1016/j.conbuildmat.2022.126638>.
- [15] L. Yu and B. Pan, "Overview of high-temperature deformation measurement using digital image correlation," *Exp. Mech.*, vol. 61, no. 7, pp. 1121–1142, 2021, doi: [10.1007/s11340-021-00723-8](https://doi.org/10.1007/s11340-021-00723-8).

ASSESSMENT OF BURNOUT PERFORMANCE OF A CONCRETE BEAM USING A NOVEL ELECTRIC RADIANT PANEL

Balša Jovanović¹, Robby Caspeele², Edwin Reynders³, Geert Lombaert⁴, Florian Put⁵, Andrea Lucherini⁶,
Ruben Van Coile⁷

ABSTRACT

This study investigates the behaviour of a concrete beam exposed to a natural fire by means of experiments using a novel electric radiant panel and simulations using Finite Element Modeling (FEM). In the experimental program, a reinforced concrete beam was tested for deflection, deformation, and temperature changes considering exposure to a heat flux as given by the Eurocode Parametric Fire Curve. The radiant panel enabled precise heat flux control and accurate application of the intended exposure, also in the cooling phase. FEM simulations corroborated experimental data, demonstrating accurate prediction of thermal effects and beam behaviour during fire exposure. It is concluded that the novel test method offers a practical approach for studying the fire response of concrete elements. The results highlight the electric radiant panel's effectiveness in fire simulation and the value of FEM in assessing the structural performance in fire scenarios.

Keywords: Fire testing, Radiant panel, Concrete beam, Numerical modelling

1 INTRODUCTION

Because the traditional fire resistance paradigm does not consider structural performance in the decay and cooling phases, it does not provide direct insight into the performance of structures in real fires [1] [2]. This lack of understanding can be addressed through experimental testing, where structures are examined under full-scale fire conditions, including heating and cooling phases. Although large-scale testing offers deep insights into the damage caused by fire, such tests are generally costly and logistically challenging. The repeatability of these tests is hard to ensure due to the complexity of controlling the fire exposure precisely. Additionally, adhering to specific cooling phases can be problematic, which limits the tests' applicability [3].

¹ PhD student, Department of Structural Engineering and Building Materials, Ghent University, Belgium
Department of Civil Engineering, Structural Mechanics Section, KU Leuven, Belgium,
e-mail: Balsa.Jovanovic@ugent.be, ORCID: <https://orcid.org/0000-0001-5200-5848>

² Professor, Department of Structural Engineering and Building Materials, Ghent University, Belgium,
e-mail: Robby.Caspeele@ugent.be, ORCID: <https://orcid.org/0000-0003-4074-7478>

³ Professor, Department of Civil Engineering, Structural Mechanics Section, KU Leuven, Belgium,
e-mail: Edwin.Reynders@kuleuven.be, ORCID: <https://orcid.org/0000-0002-1042-0282>

⁴ Professor, Department of Civil Engineering, Structural Mechanics Section, KU Leuven, Belgium,
e-mail: Geert.Lombaert@kuleuven.be, ORCID: <https://orcid.org/0000-0002-9273-3038>

⁵ PhD student, Department of Structural Engineering and Building Materials, Ghent University, Belgium
e-mail: Florian.Put@UGent.be, ORCID: <https://orcid.org/0000-0002-4522-9015>

⁶ PhD, Senior Researcher, Slovenian National Building and Civil Engineering Institute (ZAG), Slovenia
e-mail: Andrea.Lucherini@zag.si, ORCID: <https://orcid.org/0000-0001-8738-1018>

⁷ Professor, Department of Structural Engineering and Building Materials, Ghent University, Belgium,
e-mail: Ruben.VanCoile@ugent.be, ORCID: <https://orcid.org/0000-0002-9715-6786>

Consequently, there is a growing interest in developing techniques to directly manage the thermal conditions applied to test samples. An example is the H-TRIS system [4], which employs a gas-powered radiant panel that can precisely control the applied heat flux to the sample by adjusting the distance between the panel and the sample. Fire testing using electrical pads have been recently presented in [5], however, the electrical pads highlighted shortcomings related to the maximum temperature that could be accurately controlled and therefore the range of the heat flux that could be applied on the test sample. This study utilizes a similar approach but with a very high intensity and fast response electric radiant panel. The panel is designated as the HIFREP (High-Intensity Fast-Response Electric Panel) and enables to cover the typical range of heat flux for fire testing. Its composition and capabilities are presented in [6]. More specifically, the feasibility of performing large-scale structural (i.e., loaded) tests using the HIFREP is demonstrated in the following, in a case study of a concrete beam. The objective is to monitor the structural behaviour of the beam, such as deflections, deformations, and temperature variations, during the heating and cooling phase. Complementing this experimental approach, Finite Element Modeling (FEM) is employed to offer a detailed analysis of the structural responses, enhancing the insights obtained experimentally.

2 EXPERIMENTAL PROGRAM

2.1 Beam description

The beam measures 3.8 meters in length, with a cross-sectional height of 290 mm and a width of 200 mm. Reinforcement includes five steel rebars, each 16 mm in diameter. Of these, three rebars are placed in the beam's tension zone, with the remaining two situated in the compression zone. The concrete cover is 20 mm. This limited cover is chosen intentionally to enhance the structural effect of the thermal loading while limiting the total exposure time to a manageable duration. For shear reinforcement, 8 mm stirrups are utilized, arranged at intervals of 200 mm over the beam's length. The concrete used has a C30/37 concrete class and the reinforcement is B500B grade steel. The constituents of the concrete mix used for the beam are listed in Table 1. The design moment capacity is 61.6 kNm, determined in accordance with [7].

Table 1. Concrete mix constituents

Materials	Weight [kg/m ³]	Ratio to cement [-]
Cement	340	1.00
Aggregate	1780	5.23
Water	187	0.55

The mean compressive strength result for the sample concrete cubes is $f_{c,cube} = 45.7 \text{ MPa}$ with a standard deviation of 2.0 MPa. The measured mean yield strength of the reinforcement is $f_y = 565 \text{ MPa}$ and the mean value of the modulus of elasticity is $E_s = 213 \text{ GPa}$.

2.2 Panel description

To simulate the conditions of fire exposure for this experiment, a novel electric radiant panel with high-intensity output is utilized, i.e., the HIFREP. The panel is made up of 21 emitters, each 500 mm long, which emit high-intensity, short-wavelength infrared radiation. Together, these emitters span an area of about 900 mm by 500 mm and are shielded by a detachable transparent quartz glass panel. At full power, the panel is capable of producing a nearly uniform radiative heat flux of 100 kW/m² over a targeted area of 200 mm by 700 mm, located 100 mm away from the glass protector. The variation in radiative heat flux across this area, relative to that at the central position, is depicted in Figure 1.

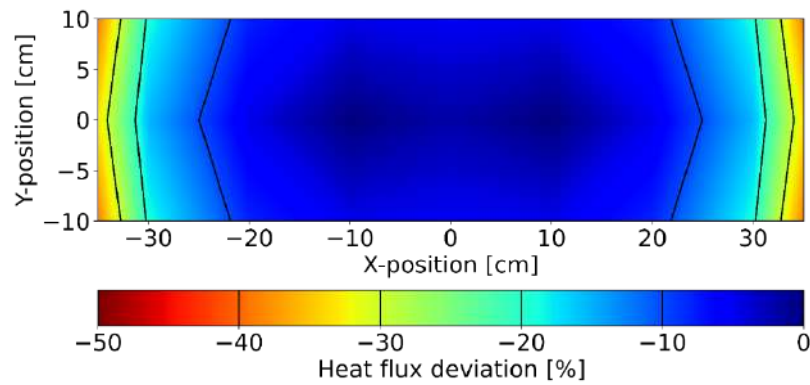


Figure 1. Received heat flux deviation compared to the central position over the exposed beam area, for the panel positioned at a 100 mm distance

Precise control of the panel's radiation intensity is managed by adjusting the voltage as an input signal. This precise control enables the fine adjustment of the radiative heat flux experienced by the specimen, mirroring the total heat flux a specimen would face in a fire scenario, encompassing the heating, decay and cooling phases [8]. This control is implemented via a custom Python program on a computer, facilitating the real-time modification and tracking of the radiant heat flux.

2.3 Setup description

A reversed four-point bending setup was employed to apply mechanical loading, inverting the usual configuration for enhanced safety during the heating phase (Figure 2). The beam supports were symmetrically placed from the beam's centre, spaced 2100 mm apart. Loads were applied 100 mm from the beam's edges, which translates to 750 mm from where the supports were positioned. This inverted arrangement offered multiple benefits. It positioned the beam's tensioned side upwards, optimizing the exposure to the radiant panel's heat flux for safety and efficacy. Moreover, this setup maintained the displacements caused by the heat in proximity to the panel to a low level, reducing the need for adjustments due to beam bending.

The central section of the beam, spanning 700 mm, was directly subjected to the panel's radiative heat flux. This specific section is characterized by a uniform bending moment, aside from the effects of the beam's own weight. To isolate the heating effect within this zone, insulation boards were placed over the top sections of the beams not intended for heating. Additionally, the beam's lateral surfaces were shielded with insulation boards to minimize thermal losses in these areas, as illustrated in Figure 3. This setup was designed to create conditions approximating one-dimensional heat transfer over the beam's height, as much as possible eliminating lateral heat losses. This then allows for a simple adiabatic surface condition at the beam's sides in a thermal analysis of the beam.

2.4 Instrumentation

Vertical displacements were recorded using Linear Variable Differential Transformers (LVDTs) placed beneath the load application points and at the beam's midpoint, specifically on the side shielded from the radiant panel. Additionally, Digital Image Correlation (DIC) was employed for capturing displacement data in the beam's central region. The use of insulation boards and the radiant panel's intense illumination meant that displacement measurements through DIC were confined to the beam's lower half, i.e. the side under compression, as depicted in Figure 4. For processing these images, VIC-3D software by Correlated Solutions was utilized [9].

Temperature variations within the beam were measured by casting 18 type-K thermocouples. These sensors were distributed across three key areas along the beam's length: the centre and two neighbouring sections, each 300 mm from the midpoint, as indicated in Figure 7. At these points, six thermocouples were installed at varying depths from the surface facing the heat: at 12 mm (in the middle of the shear reinforcement), 20 mm (connection of the main and shear reinforcement in the tension zone), 50 mm, 100 mm, 150 mm and

278 mm. These thermocouples were fixed using 2 mm thick steel wires attached to the reinforcement cage, ensuring their stability throughout the casting process.

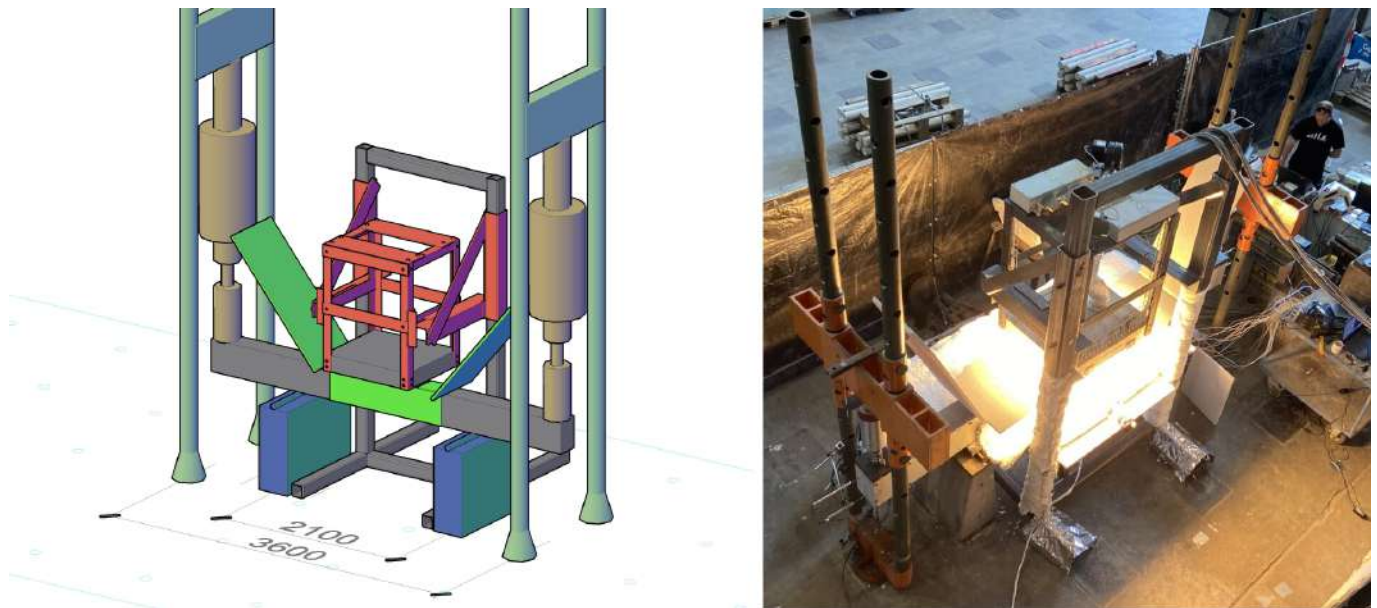


Figure 2. Test setup schematic overview (left); picture of the actual test set-up (right)

2.5 Fire exposure

The experiment replicated natural fire conditions by adhering to the Eurocode Parametric Fire Curve (EPFC) [10]. Specifically, an EPFC variant with a Γ value of 0.45 and a heating phase set to last 1 hour was adopted. This specific EPFC variant predicts a peak “gas” exposure temperature of 826 °C and a total fire exposure duration of 233 minutes. The radiant panel's heat flux was calculated to mirror the EPFC's total heat impact on the beam's surface. Achieving a maximum radiative heat flux of 85.75 kW/m², the application of heat was discontinued at the 155-minute mark, coinciding with the moment when the needed panel intensity is lower than 10% of its maximum power. Illustrations of the targeted temperature-time trajectory and the heat flux applied are provided in Figure 5.



Figure 3. Insulation protection on the beams



Figure 4. The compressed side of the beams monitored using the Digital Image Correlation (DIC)

Throughout the testing process, the beam's surface heat flux was measured using a water-cooled Schmidt-Boelter heat flux meter. This device was placed next to the beam, aligned with the surface at the central part of the heat exposure area. To accommodate the beam's potential deformation, the heat flux meter was attached in a manner that maintained its alignment with the beam's surface. The outcome of this measurement is detailed in Figure 6. Notably, the recorded heat flux values exceeded the predetermined target. This discrepancy is largely ascribed to convective heat transfer from the surrounding warm air impacting the heat flux meter. By estimating the convective heat transfer coefficient at approximately $20 \text{ W}/(\text{m}^2\text{K})$ and assuming that the air temperature near the meter approximately matches the targeted concrete surface temperature, an adjustment was made to the measured heat flux values. This adjusted comparison suggests that the beam's surfaces indeed were subject to the planned radiative heat flux levels.

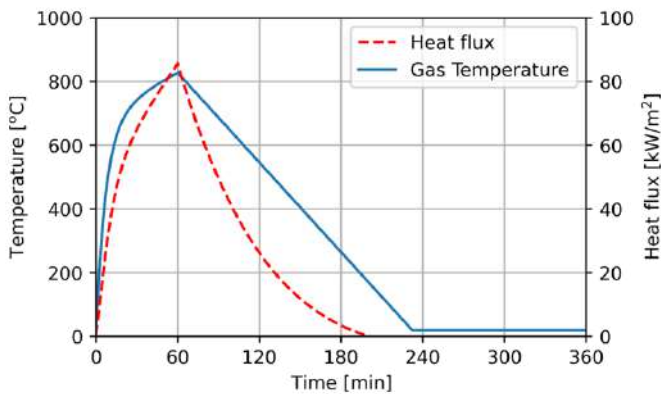


Figure 5. Eurocode Parametric Fire Curve temperature-time curve and equivalent radiant heat flux from the panel

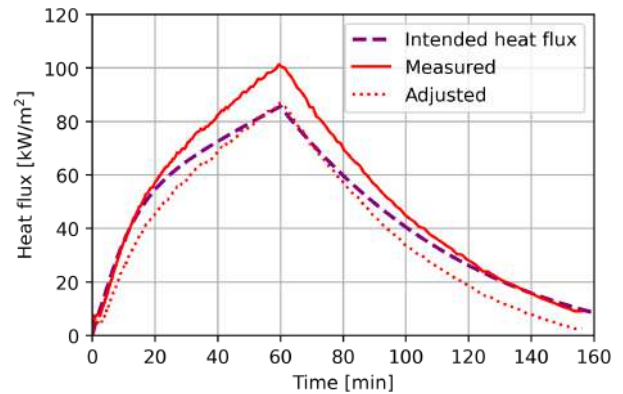


Figure 6. Measured and intended radiative heat flux during the tests. After 155 min, the panel was shut down and the beam was allowed to cool naturally

3 EXPERIMENTAL RESULTS

As outlined in Section 2.4, the internal temperatures of the beam were monitored at three longitudinal points along their length, employing six thermocouples embedded within the beam at each location depicted in Figure 7. The temperatures recorded at depths of 20 mm, 50 mm, and 150 mm from the beam's surface that faced the heat are showcased in Figure 8. This figure reveals that the heating effect was evenly distributed, as indicated by the nearly identical temperatures on both the left and right sides of the zone subjected to heat. Nevertheless, temperatures at the central part were observed to be higher, attributed to the radiative heat flux's imperfect uniformity over the exposed area (as seen in Figure 1) and the greater impact of heat conduction towards the beam's cooler sections. This pattern of temperature distribution was consistently observed at every depth measured by the thermocouples.

Figure 9 provides a visual representation of the temperature variations within the beam's core over time, achieved through linear interpolation of temperature data from various depths. This approach aids in

illustrating the temperature gradient throughout the beam. Notably, the data also indicate that temperatures within the beam continue to rise beyond the 60 minutes of the heating phase, penetrating deeper into the beam as anticipated. It highlights that the temperature readings at all three monitored positions remain relatively consistent with one another. The most notable variances occur near the beam's surface, particularly at a depth of 12 mm, where the thermal gradient is most pronounced. Minor shifts in the placement of thermocouples at this shallow depth can markedly influence the recorded temperatures. Despite this sensitivity, the disparity in temperature readings remains within a 10% margin, underscoring the precision of the measurements. For deeper positions within the beam, the temperature differences become virtually inconsequential, indicating uniform thermal behaviour throughout the structure's cross-section under fire exposure conditions.

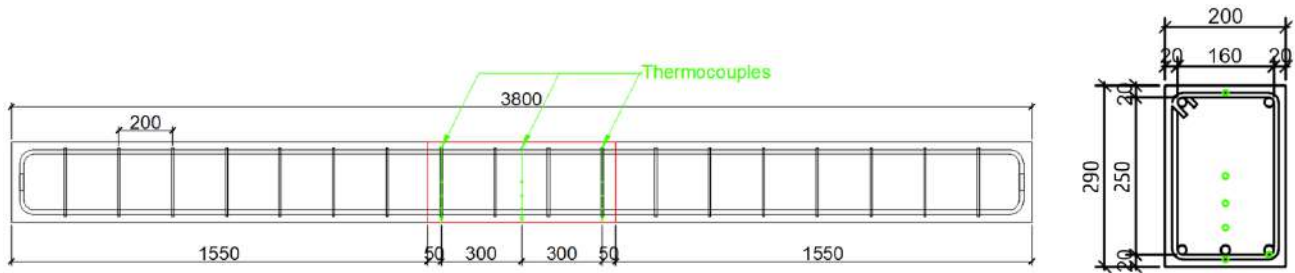


Figure 7. Position of the thermocouples cast inside the beams in the longitudinal direction and in the cross-section (red box represents the heated area) (dimensions in mm)

The panel was deactivated after 155 minutes, and the radiative heat flux dropped to below 10% of its peak value. This transition is visible in Figure 13 as the shutdown marks a change in thermal boundary conditions: with the end of radiative heat, the surface begins to cool through convection. This quasi-immediate cooling effect is particularly noticeable at shallower depths of 12 and 20 mm, whereas at greater depths, its impact is minimal.

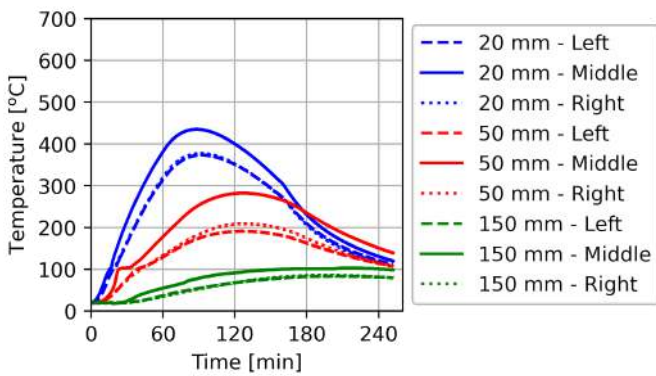


Figure 8. Measured temperatures at different depths and positions during the test

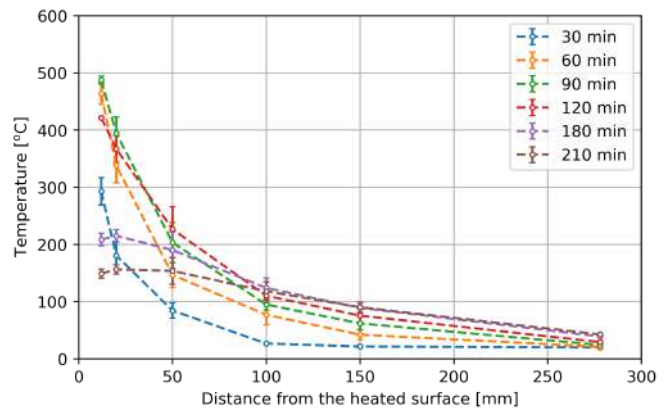


Figure 9. Thermal gradient inside of the beam at different points in time (error bar represents the standard deviation between three positions)

Figure 10 illustrates the midspan deflection recorded during the testing. These deflections are depicted relative to their initial state at the onset of the heating phase, with a baseline (0 mm) representing the deflection under the serviceability load before heating commenced. In the initial 60 minutes, correlating with the period of increasing heat flux, the deflections display an almost linear rise. This upward trend in deflections decelerates but persists until about 95 minutes, at which point the beam achieves its peak deflection. Following this peak, the deflections maintain a near-constant level for around 15 minutes before

gradually declining. This reduction pattern in deflections mirrors the temperature behaviours observed; notably, the deflection decrease rate alters once the heating panel is deactivated at 155 minutes.

Figure 11 displays the average displacements occurring under the points where loads were applied during the tests. The pattern of deformation observed under the load application points mirrors that of the midspan deflections. Employing Digital Image Correlation (DIC) allowed for the detailed assessment of curvature across the zone subjected to a uniform moment. The resulting curvature changes within the heated zone are documented in Figure 12.

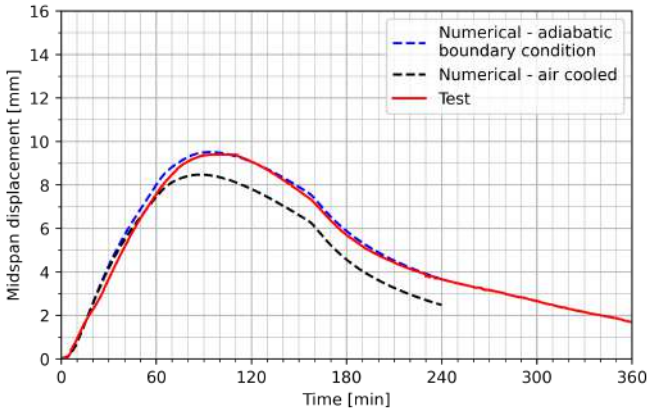


Figure 10. Midspan displacement during the tests compared to the results of numerical simulations

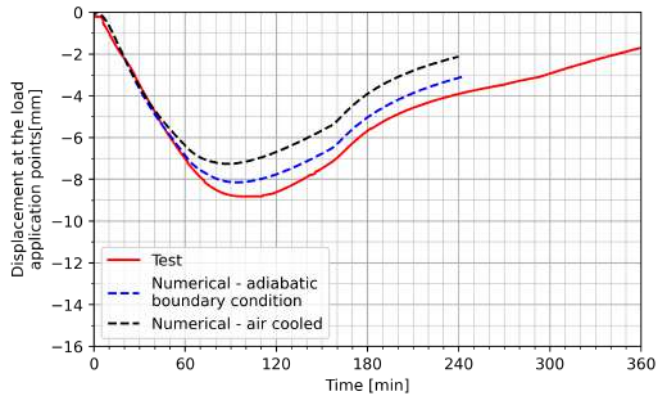


Figure 11. The average displacement at the load application points during the tests compared to the results of numerical simulations

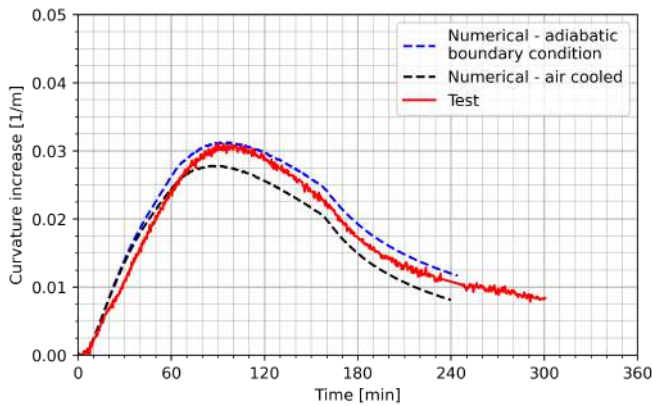


Figure 12. Midspan curvature change observed during the test and numerical simulations

4 NUMERICAL MODELING

A finite element model for the beam was created using the SAFIR [11] software. This analysis consists of two distinct phases. Initially, a heat transfer analysis was undertaken to produce the temperature-time history of the beam. Subsequently, this temperature-time data serves as an input for the structural analysis, enabling an evaluation of the beam’s structural behaviour during the natural fire exposure.

4.1 Heat transfer

The heat transfer analysis employed a two-dimensional model to simulate the temperature changes within the beam's cross-section. The cross-section was segmented into 1320 rectangular elements, their sizes ranging from 4 to 8 mm. To represent the concrete and its steel reinforcement within the model, the materials SILCON_EN for concrete and STEELEC2EN for steel were utilized with their default parameters

as stated in EN 1992-1-2 [12]. The model's thermal boundary conditions at the tensioned edge are modelled as both radiative and convective heat transfer from a singular temperature-time profile. Specifically, from an EPFC characterized by a Γ value of 0.45 and a heating duration of 1 hour, as detailed in Section 2.5 and illustrated in Figure 5.

Upon the panel's deactivation at the 155-minute mark, adjustments were made to the EPFC's cooling trajectory: the EPFC was followed until 155 minutes after which the temperature-time curve was abruptly transitioned to a stable 20 °C. This approach to modelling radiative heat transfer assumed a concrete surface absorptivity/emissivity of 0.7, with convection being modelled with a coefficient of 35 W/(m²K) in accordance with Eurocode guidelines [10, 12]. For the beam's compressed side, where both convective and radiative heat losses were projected against a steady 20 °C ambient temperature, the parameters were set to an emissivity of 0.7 and a reduced convection coefficient of 4 W/(m²K), consistent with Eurocode's recommendations [10, 12]. The described modelling approach thus starts from the exposure intended to be applied with the panel, and not from the measured exposure. It thus constitutes an a priori modelling.

As previously noted, the beam sides were safeguarded against direct radiation through the application of insulation boards. Nonetheless, an air gap of about 15 mm was present between the board and the beam to facilitate instrumentation. This air gap was manually sealed with insulation material at the top. Thus, the air gap was intended to effectively act as an insulator, rendering the boundary condition of the beam's sides akin to perfect insulation. Consequently, this scenario was modelled as an adiabatic boundary condition, assuming no heat transfer through these surfaces.

In Figure 13 the outcomes of the heat transfer analysis are illustrated and compared with the in-situ thermocouple readings from the testing phase. This comparison reveals a strong agreement between the simulated heat transfer behaviours and the empirical temperature measurements across various depths within the beam, underscoring the model's accuracy in replicating the thermal dynamics experienced by the beam under test conditions. The alternative “air-cooled” modelling approach presented in the figure is outlined below in Section 5.

4.2 Structural analysis

In the structural phase of the analysis, the beam was conceptualized as a two-dimensional fibre model spanning 3600 mm, i.e., the distance between points where loads were applied. This model was segmented into 72 elements, each measuring 50 mm in length. Specifically, the central 14 elements were assigned the temperature-time profiles derived from the heat transfer analysis, while the remaining segments of the model were maintained at a constant temperature of 20 °C for the duration of the simulation. The simulation's mechanical boundary conditions mirrored those utilized in the experimental setup, incorporating both roller and pin supports to replicate the test conditions accurately. Loading was simulated by applying two vertical forces, each fixed at 55 kN, positioned at the beam's extremities.

The analysis utilized the SILCON_ETC concrete model, which incorporates the explicit transient creep model introduced in [13]. This model's parameters were aligned with empirically determined material properties, setting the concrete's compressive strength to $f_c = 45.7$ MPa and its tensile strength $f_t = 2.9$ MPa. The reinforcement was represented through the STEELEC2EN model, as outlined in EN 1992-1-2:2004, with a specified yield strength $f_y = 565$ MPa and a modulus of elasticity $E_s = 213$ GPa, reflecting the actual material characteristics measured.

Figure 10 compares the simulated midspan deformations against those observed during experimental testing, showcasing the model's precision in reflecting the beam's experimental behaviour.

5 DISCUSSION

The heat transfer within the model was initially assumed to occur under conditions of perfect insulation. However, the presence of an air gap during experimental testing complicates the accurate modelling of the actual heat loss, due to the complex interaction and cavity effects between the concrete, air and insulation. To investigate this discrepancy, an alternative model was adopted with different boundary conditions at the

beam's vertical edges. In this revised model, these edges were considered to be exposed to ambient air, mirroring the cooling conditions applied to the compressed edge of the beam, as depicted in Figure 14. The comparison of experimental results with the simulation indicates a closer alignment when the side edges are assumed to be adiabatically insulated, particularly within the initial 120 minutes of testing. A noticeable transition towards the conditions simulating exposure to ambient air becomes evident thereafter. This observation could be attributed to the temperature dynamics within the air gap: during the heating phase, the air within this gap warmed up together with the beam, but likely remained colder than the air at the top of the gap. Thus there was no buoyancy-driven air replacement, mitigating any cooling effect on the beam's side. As the beam's temperature began to decrease, the air within the gap became more hot than the air at the top of the gap. Thus, a buoyancy-driven flow likely developed, enhancing the cooling effect on the beam's sides. The impact of these differing boundary conditions on the side edges appears to be minimal at greater depths within the beam.

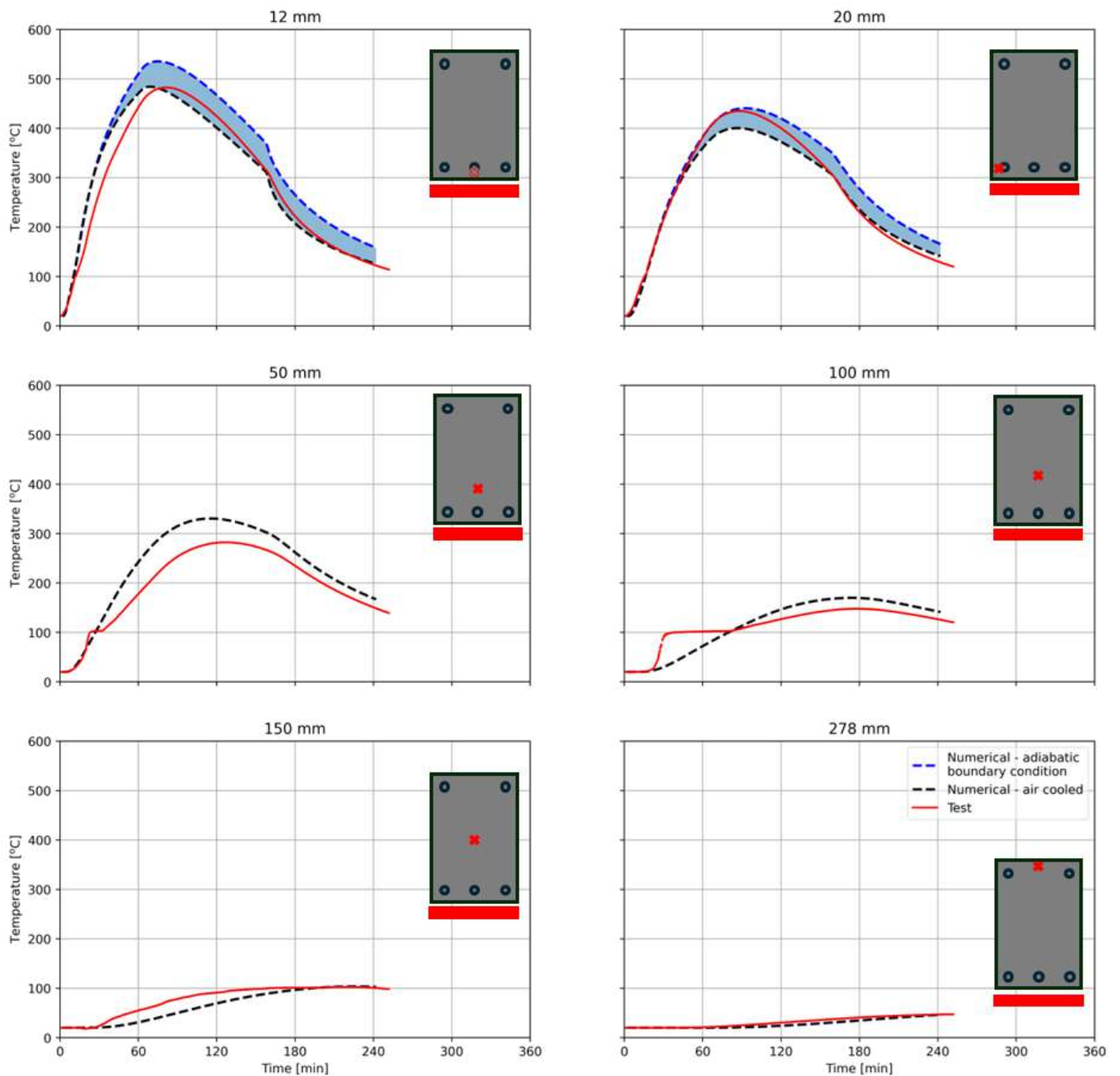


Figure 13. Temperatures at the midspan section measured during the test at different depths compared to the numerical results. A distinction is made between (i) adiabatic and (ii) air-cooled numerical results related to the modelling of the boundary condition for the side of the beam

When looking at Figure 10, it can be concluded that the correspondence between the numerical simulations and the empirical results of midspan deformations is significantly better when the boundary conditions along the beam's side edges are assumed to be adiabatic. This pattern of similarity extends to the behaviours depicted in Figure 11, which charts the deflection variations at the load application points—essentially, the beam's extremities—throughout the heating and cooling stages. Further, an examination of the mid-span curvature in Figure 12 reveals a very close agreement between the experimental outcomes and the simulation predictions.

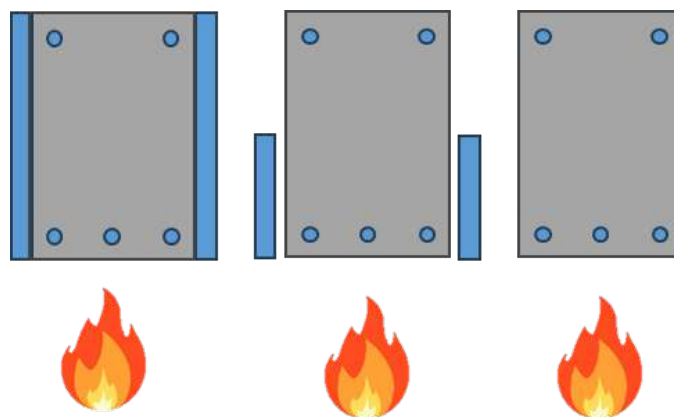


Figure 14. Different cases for modelling boundary conditions on the side edges of the concrete beam: full insulation (left), real scenario during the test (middle; this case is not directly modelled) and ambient air contact (right)

6 CONCLUSIONS

A novel electric radiant panel was employed to replicate the effects of natural fire on a concrete beam. Despite constraints regarding the size of the heated area and the peak heat flux attainable, the panel's performance excelled in terms of control accuracy and the consistency of test conditions.

During the heating phase, the structural behaviour of the beam transitioned through several stages. Initially, deflections increased in a linear fashion, then progressed at a diminished rate until reaching a peak. Following this peak, the beam exhibited a period of stability, maintaining its maximum deflection before the deflections gradually decreased as the beam cooled. This pattern of response is in line with the anticipated behaviour of concrete structures subjected to fire, evidencing a predictable reaction to increasing temperatures.

The Finite Element Method (FEM) analysis that takes into account both the heat transfer and elevated temperature material behaviour, using the SAFIR software, has shown to be a very accurate means of simulating the behaviour of the simply supported concrete beam under natural fire conditions. The model's predictions of how the beam would respond structurally to thermal stress were closely aligned with empirical observations. The difference between the simulated results and the test data was minimal.

The strong correlation between observed temperature measurements and the results from numerical simulations highlights the effectiveness of the experimental setup in accurately replicating conditions as in the Eurocode Parametric Fire Curve's temperature-time profile.

This study contributes to the field of fire engineering by showcasing a novel and environmentally friendly methodology for replicating fire-induced damage in concrete elements. Employing the novel electric radiative panel to mimic real fire conditions accurately presents a viable path for examining how concrete structures behave during exposure to a natural fire with cooling regime.

ACKNOWLEDGEMENTS

The authors wish to thank the Research Foundation of Flanders (FWO) for the financial support on the research project (Grant number 3G010220) “Vibration-based post-fire assessment of concrete structures using Bayesian updating techniques”. Andrea Lucherini is funded by the FRISSBE project within the European Union’s Horizon 2020 research and innovation program (GA 952395) and Florian Put is funded by Research Foundation of Flanders (FWO) within the scope of the research project (Grant number 1137123N) “Characterization of the thermal exposure and material properties of concrete during the fire decay phase for performance-based structural fire engineering”.

REFERENCES

1. Gernay, T.: Fire resistance and burnout resistance of reinforced concrete columns. *Fire Safety Journal*. 104, 67–78 (2019). <https://doi.org/10.1016/j.firesaf.2019.01.007>
2. fib, Fédération International du Béton: fib Bulletin 108. Performance-based fire design of concrete structures. (2023)
3. Gernay, T., Franssen, J.-M., Robert, F., McNamee, R., Felicetti, R., Bamonte, P., Brunkhorst, S., Mohaine, S., Zehfuß, J.: Experimental investigation of structural failure during the cooling phase of a fire: Concrete columns. *Fire Safety Journal*. 134, 103691 (2022). <https://doi.org/10.1016/j.firesaf.2022.103691>
4. Maluk, C., Bisby, L., Krajcovic, M., Torero, J.L.: A Heat-Transfer Rate Inducing System (H-TRIS) Test Method. *Fire Safety Journal*. 105, 307–319 (2019). <https://doi.org/10.1016/j.firesaf.2016.05.001>
5. Seweryn, A., Lucherini, A., Franssen, J.-M.: An Experimental Apparatus for Bench-Scale Fire Testing Using Electrical Heating Pads. *Fire Technol.* (2023). <https://doi.org/10.1007/s10694-023-01514-4>
6. Put, F., Jovanović, B., Evelien, S., Lucherini, A., Merci, B., Van Coile, R.: High-Intensity Fast-Response Electric radiant Panel (HIFREP) for increased accuracy on thermal boundary conditions during fire testing. 4th European Symposium on Fire Safety Science – ESFSS 2024. (in press)
7. CEN: EN 1992-1-1:2004: Eurocode 2: Design of concrete structures - Part 1-1: General. rules and rules for buildings, (2004)
8. Lucherini, A., Torero, J.L.: Defining the fire decay and the cooling phase of post-flashover compartment fires. *Fire Safety Journal*. 141, 103965 (2023). <https://doi.org/10.1016/j.firesaf.2023.103965>
9. Correlated Solutions: Vic-3D, www.correlatedsolutions.com/supportcontent/VIC-3D-8-Manual.pdf, (2010)
10. CEN: EN 1991-1-2:2002 Actions on structures - Part 1-2: General actions - Actions on structures exposed to fire, (2002)
11. Franssen, J.-M., Gernay, T.: Modeling structures in fire with SAFIR®: theoretical background and capabilities. *Journal of Structural Fire Engineering*. 8, 300–323 (2017). <https://doi.org/10.1108/JSFE-07-2016-0010>
12. CEN: EN 1992-1-2:2004: Eurocode 2: Design of concrete structures - Part 1-2: General rules. Structural fire design, (2004)
13. Gernay, T., Franssen, J.M.: A formulation of the Eurocode 2 concrete model at elevated temperature that includes an explicit term for transient creep. *Fire Safety Journal*. 51, 1–9 (2012). <https://doi.org/10.1016/j.firesaf.2012.02.001>

CHARACTERIZATION OF THE CHANGE IN POLYMER CONCRETE OVERLAYS DUE TO VEHICLE FIRE EXPOSURE

Ikwulono David Unobe^{1,2}, Shuna Ni³

ABSTRACT

Polymer concrete has found increasing use in construction over recent decades, notably as overlays on bridges and highways. This popularity stems from its advantageous properties, such as rapid curing, high resistance to salt and water, and strong compressive strength. However, PC is prone to degradation when subjected to high temperatures, necessitating a thorough understanding of its behavior in such conditions. This study conducted a vehicle fire test on a reinforced concrete slab overlaid with PC. Various performance metrics of the PC overlay, including skid resistance, surface hardness, resistance to water and chloride penetration, abrasion resistance, bond strength and resistance to delamination, were evaluated before and after exposure to the fire. The results show a notable decline in performance across all parameters following heat exposure. These findings offer insights for improving the fire resistance of PC in the future.

Keywords: Polymer concrete; Vehicle fire; Material properties; Elevated temperatures

1 INTRODUCTION

Polymer concrete (PC) has become a prevalent material for highways and bridges, primarily as an overlay, owing to its impressive attributes such as rapid curing, high compressive strength, and resistance to salt and water. The binders used in PC, are commonly composed of thermoset polymers [1], which, due to their cross-linked structure, generally exhibit higher thermal stability than thermoplastics. However, it is important to note that thermoset polymers are still susceptible to decomposition under elevated temperatures [2], resulting in property changes. It should be noted that the decomposition temperatures of polymer resins are typically well above their glass transition temperatures. Research indicates that the mechanical properties of epoxy and polyester polymer concrete are more influenced by the heat distortion temperatures of resins than by their glass transition temperatures [3–6], as the heat distortion temperatures of resins are lower than their glass transition temperatures. When temperatures go above the heat distortion points of resins, the mechanical strengths of both types of PC concrete drop quickly.

Vehicle fires pose a significant risk to PC overlays, particularly on highways where such incidents are relatively common. In 2022 alone, 222,000 vehicle fires were reported in the U.S., caused by various factors including mechanical or electrical failures, collisions, or exposure to other fires. These fires often occur on highways, subjecting surfaces to elevated temperatures. Although the NFPA 1710 [7] established a criterion that requires the first engines to arrive on the scene within 240 seconds for 90% of incidents, a study [8] has shown that the actual response time typically exceeds the recommended duration. Tests in [9–11] reveal that vehicle fire durations vary from less than 300 seconds to over 6000 seconds. Peak Heat Release Rate

¹ Postdoctoral Research Associate, Utah State University,

² Assistant Professor, Schreiner University,

e-mail: dunobe@schreiner.edu, ORCID: <https://orcid.org/0000-0001-7145-5027>

³ Assistant Professor, University of Maryland, College Park,

e-mail: shunani@umd.edu, ORCID: <https://orcid.org/0000-0002-8795-176X>

(HRR) can span from under 1000 kW to about 4700 kW, with the time to reach peak HRR ranging from 250 to 4000 seconds [9–11]. Additionally, peak temperatures can reach up to 1200°C [9–13].

This study investigates how PC overlays, commonly used in road infrastructure, respond to vehicle fire exposure. A realistic vehicle fire test was carried out on a concrete slab with PC overlay. The examined PC overlay is a polyester polymer mix, widely used in bridges and roads. Performance tests of the PC overlay before and after the vehicle fire exposure were measured and the change of PC overlay will guide enhancements in the design and construction of PC overlay.

2 DESIGN AND IMPLEMENTATION OF TESTS

This study includes 1) vehicle fire tests on a concrete slab with PC overlay to replicate realistic vehicle fire exposure conditions, and 2) pre-fire and post-fire performance tests of the PC overlay.

2.1 Construction and instrument of the test slab

The first step of this study is to design and construct a concrete slab with PC overlay. The slab (36 ft x 20 ft x 8 in.) was designed to replicate a bridge deck with similar cross-sectional properties. The reinforcements in the concrete slab were designed and constructed aligning with the specifications of the Utah Department of Transportation (UDOT) [14]. Class AAA concrete with a compressive strength of 4.5 ksi was used. A polyester polymer concrete (PPC) mix was used for the overlay, and placed to an average thickness of 0.94 in. over the concrete slab. The PPC mix employed consists of a polyester-type polymer resin (unsaturated isophthalic polyester-styrene), with a methyl ethyl ketone peroxide (MEKP) initiator, and graded silica-quartz aggregate, both approved for application in PC overlays by UDOT.

The slab was instrumented with Type K thermocouples distributed evenly, as shown in Figure 1. These thermocouples were placed at both the surface of the PC overlay and at the interface between the overlay and the substrate concrete to capture the temperature variation across the surface and also across the cross-section.

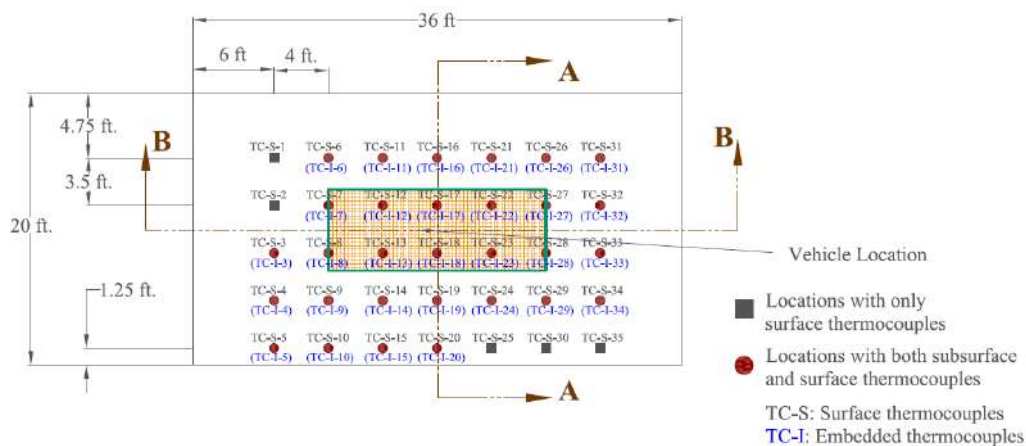


Figure 1. Layout of Thermocouples on the overlay surface and at the overlay-concrete interface

2.2 Design of the vehicle fire test

Rear-end collisions are notably dangerous among vehicle accidents, primarily due to their propensity for causing gasoline leaks that can swiftly escalate into fires. In this study, a vehicle fire, typically following a rear-end collision, was replicated on the constructed concrete slab. The vehicle used for testing was a 2007 Subaru Outback. To replicate a vehicle fire started by a rear-end collision and the ignition of leaking gasoline, a 3 mm hole was drilled in the gas tank, similar to previous studies [15]. This was to ensure that gas leaked onto the slab surface as can happen during a car crash. In addition, the vehicle had broken rear and trunk windows, an open driver's door, and a slightly open left passenger door, to replicate ventilation conditions expected with a fire in a vehicle that had just crashed. The vehicle was equipped with thermocouples, as shown in Figure 2, positioned both internally and externally. Some thermocouples were

hung to capture gas temperatures inside the vehicle. Two heat flux sensors were placed at the side and back of the vehicle, at distances of 12 ft and 18 ft respectively from the center of the vehicle. Both sensors were placed at a height of 4 ft from the slab surface. These heat flux sensors were positioned to capture the heat from the vehicle fire to the surrounding infrastructure. To record the burning process of the vehicle, four cameras were placed around the slab.

Before the test, 2.4 gallons of gasoline were added to the tank to mimic a scenario where a vehicle in use wouldn't have a full tank. Initially, a plug covering the predrilled hole in the gas tank was removed, allowing the gasoline to leak for 90 seconds. The leaked gasoline on the slab was then ignited with a handheld flare, and the vehicle was allowed to burn freely before firefighters extinguished the fire.

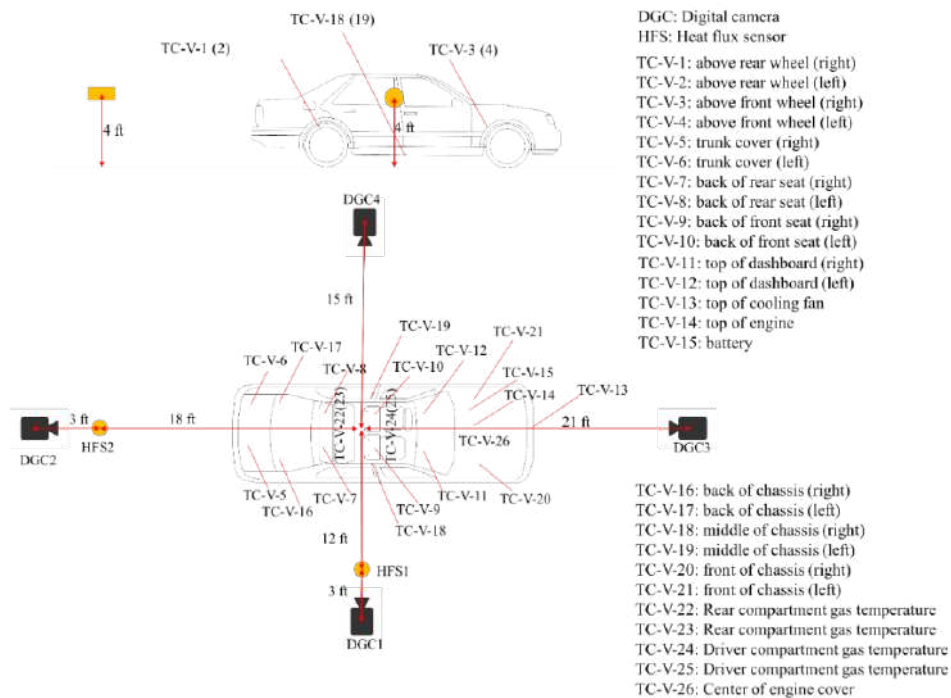


Figure 2. Locations of thermocouples, cameras and heat flux sensors placed in and around the test vehicle

2.3 Pre-fire and post-fire tests of the PC overlay

Assessments for the PC overlay, including skid resistance, surface hardness, delamination, bond strength, abrasion resistance, water permeability, and rapid chloride penetration tests, were planned across the slab and near thermocouple positions (shown in Figure 3). These tests are described below.

Skid resistance: Skid resistance tests, following ASTM E303 [16], use a British pendulum tester to measure surface friction through the British Pendulum Number (BPN). Skid resistance is calculated by averaging several BPN readings from the same spot.

Surface hardness: Surface hardness tests, crucial for assessing the PC overlay's integrity and usability according to ASTM C805 [17], were conducted using a rebound hammer. The highest value from multiple tests on one spot represents the hardness of that spot.

Delamination: The notable thermal conductivity differences between PC overlay and substrate concrete expose the slab to the risk of delamination at the bonding surface under high temperatures. A non-destructive thermal imaging method, following ASTM D4788 [18], detects potential delamination by identifying temperature variances over 0.5°C between adjacent areas.

Bond strength: Bond strength tests, following ASTM C1583 [19], evaluate the adhesion between a PC overlay and concrete substrate. This involves applying tensile force to a drilled core on the slab surface

until failure occurs. If failure occurs in the substrate concrete, it suggests that the bond strength surpasses the substrate concrete's tensile strength. Conversely, failure in the bonding surface indicates the opposite.

Water permeability: Water permeability tests, adhering to ASTM D5084 [20], assess the resistance of a material to water ingress by measuring the water permeation rate. The permeability of concrete varies with its composition, making it challenging to evaluate permeability changes post-vehicle fire exposure when using different samples for pre-fire and post-fire tests. To circumvent this, relative permeability is assessed for the same samples before and after heat exposure using the falling head method.

Abrasion resistance: Abrasion resistance tests evaluate the resistance of a material to wear, indicating long-term durability. Conducted per ASTM C944 [21], this involves running a rotating cutter across the surface of a sample and measuring the weight of the material removed after two minutes.

Rapid chloride penetration: Rapid Chloride Penetration tests evaluate the resistance of material to chloride ingress, which is crucial for preventing corrosion of embedded reinforcing steel. It follows the AASHTO T358 [22] and employs a Wenner probe array to pass an electrical charge through the material, estimating its resistivity. The material's chloride penetration classification is determined by this resistivity.

While some tests (skid resistance, surface hardness, delamination) were non-destructive and could be repeated in the same spots for pre- and post-vehicle fire tests, others were destructive and could not be repeated in the same spots. Thus, for the pre-fire properties requiring destructive testing, a test section matching the slab's specifications was added to the main slab, and cores extracted from this section were used in assessing the PC's pre-fire properties. Given the substantial influence of concrete composition on water permeability, the same concrete cores were used for both pre-fire and post-fire permeability tests (See Section 3.3 for more details). The numbers of tests carried out for each property are shown in Table 1.

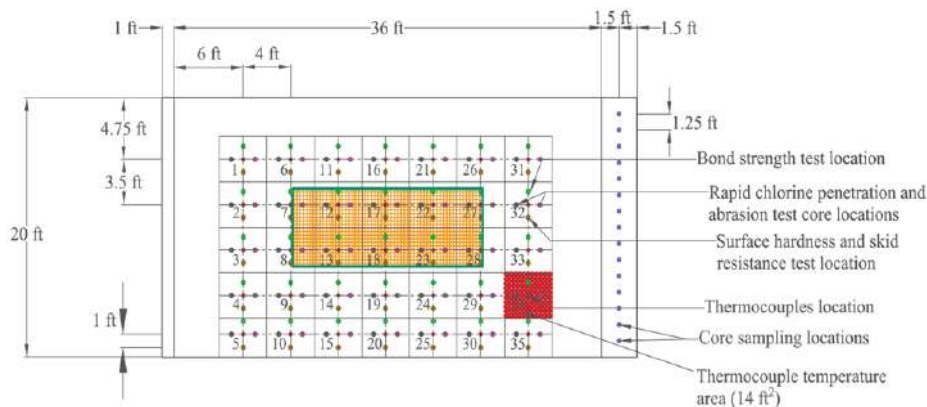


Figure 3. Locations of testing sampling for the PC performance tests

Table 1. Number and sizes of specimens for each experiment

Test	Specimen size	No. of pre-fire tests	No. of post-fire tests	ASTM Standards
Skid resistance test	N/A	35	35	ASTM E303 [16]
Surface hardness test	N/A	35	35	ASTM C805 [17]
Delamination test	N/A	N/A	N/A	ASTM D4788 [18]
Bond strength test	Disc size 2 in.	5	20	ASTM C1583 [19]
Water-penetration test	4 in dia. with 4 in height	6	6	ASTM D5084 [20]
Abrasion resistance test	4 in dia. with 4 in height	5	20	ASTM C944 [21]
Rapid chloride penetration test	4 in dia. with 4 in height	5	20	AASHTO T 358 [22]

3 RESULTS AND DISCUSSIONS

3.1 Vehicle fire test results

The burning process of the vehicle is shown in Figure 4. The fire started with the ignition of the leaking gasoline. About 57 seconds into the test, flames engulfed the interior of the vehicle; melted plastic fell to the surface of the slab and burned directly on the slab, raising the temperatures of these areas. Within the first 90 seconds of the test, the rear left window shattered, and the flames spread outwards, emerging at the top of the vehicle. The flames spread to the front interior of the vehicle engulfing it after 169 seconds except the engine compartment and more parts of the slab were directly exposed to flames due to the continuous falling of melted plastic from the vehicle. Subsequently, 213 seconds into the test, a jet flame from the gas tank was observed and the vehicle was covered in flames except the engine compartment. The firefighters then started the extinguishing process 225 seconds after the ignition, before the anticipated time to guarantee that the fire remains under control.

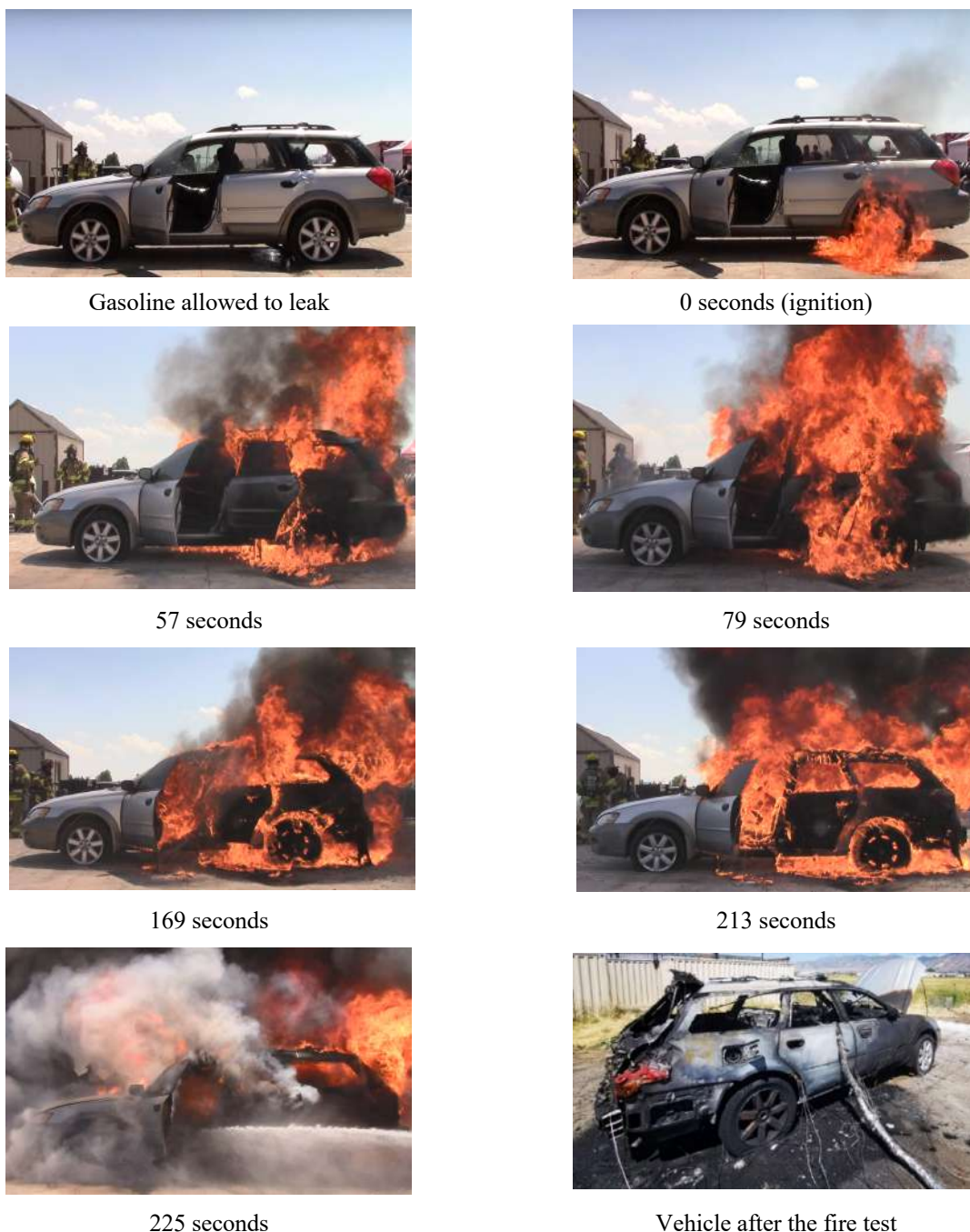


Figure 4. Burning process of the vehicle fire

Figure 5a shows the heat exposure of the surroundings due to the vehicle fire, captured by heat flux sensors positioned at the side and the rear of the vehicle. Both the heat flux sensors recorded two peaks. For the sensor placed 12 ft from the side of the vehicle, the first (16.9 kW/m^2) occurred at around 92 seconds and corresponds to the time when the flame engulfed the exterior. The second peak (47.5 kW/m^2) occurring at 225 seconds, occurred right after the jet flame from the gas tank and the vehicle was almost engulfed in the flames. The sensor placed a little further away (18 ft) from the rear of the vehicle recorded its first peak (18.1 kW/m^2) 199 seconds into the test at the moment when the flames had significantly engulfed the exterior of the vehicle. The second peak also occurred at the moment right after the jet flame was emitted from the gas tank. Such intense heat flux can pose significant risks to surrounding infrastructure and even increase the risk of sparking wildfires if the vehicle fire occurs in Wildland-Urban Interface (WUI) regions. Figure 5b shows the temperatures recorded in the vehicle. Initially, a consistent rise in temperatures could be observed in the vehicle's interior space, spanning from the trunk to the dashboard, as the fire progressed and consumed the vehicle's interior. The interior of the vehicle suffered significant damage as the fire progressed towards the vehicle's front. Conversely, minimal temperature increases were noted in the regions surrounding the vehicle's engine, as this area was the farthest from the ignition point and remained unignited until the fire was extinguished. The gas temperature inside the vehicle reached approximately 1200°C while the lowest peak temperature, slightly above 40°C , was measured at the top of the battery in the engine compartment. Some specific locations, such as the back chassis near the slab, experienced temperature peaks around 160 seconds into the test, maintaining a relatively steady temperature until the fire was extinguished. In contrast, temperatures inside the vehicle continued to rise, peaking at the moment when the jet flame was emitted from the gas tank.

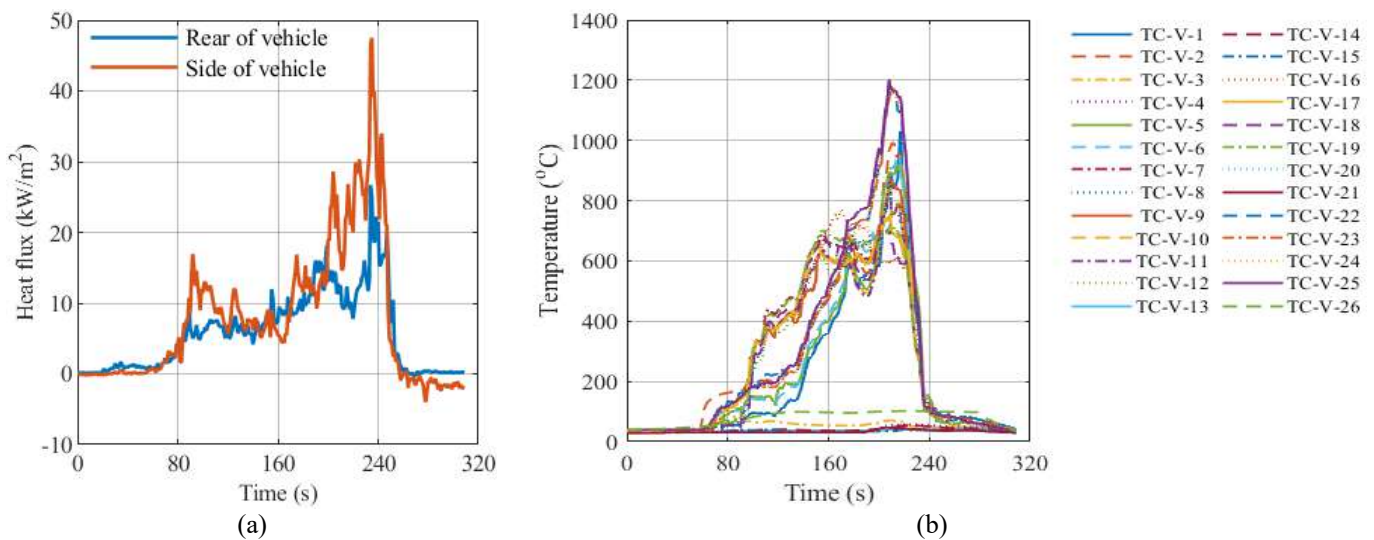


Figure 5. a) Heat flux from vehicle during test with maximum heat fluxes recorded at 224 seconds and 225 seconds at the back and side of the vehicle respectively and b) Temperature evolution at different locations inside the vehicle

3.2 Heat exposure of the PC overlaid slab

After the fire test, the burnt vehicle was removed from the slab, and the surface was cleaned of debris using water and a brush. The slab surface after the fire test is shown in Figure 6. Considerable burn marks were found on the slab surface directly below where the test vehicle was located, with the PC overlay significantly damaged. This damage included the peeling of finishing sand and the surface charring due to the thermal degradation of polymer resin. At a greater distance from the vehicle, the slab surface showed minimal to no visible damage.



Figure 6. Post-fire surface of the slab

Figure 7 shows the temperature evolution over time across the surface of the PC overlay and Figure 8 shows the peak temperatures recorded at each location. Areas with notable temperature changes generally exhibited two peaks correlated with events during the vehicle fire test: the first due to the ignition of the leaked gasoline and the burning of falling plastic on the slab. The second peak was between 188 seconds and 247 seconds due to the fire engulfing the vehicle and the jet flame emitted from the gas tank. Some peaks persisted after firefighting commenced, emphasizing the non-instantaneous nature of extinguishing such fires. A maximum temperature of 744°C was recorded around the vehicle location, and post-fire analysis of the PC overlay prioritized these areas and their surroundings, circled in Figure 8. Core samples collected from these locations were tested to assess the impact of vehicle fire on abrasion resistance and rapid chloride penetration. However, non-destructive tests on skid resistance, surface hardness and delamination were conducted across the entire slab, irrespective of fire exposure levels.

Figure 9 shows the temperature changes at the interface during the vehicle fire test. In contrast to surface temperatures, the interface temperatures remained relatively unchanged throughout the test and started to increase near the end of the vehicle fire test, indicating that the heat was starting to transfer through the overlay and onto the substrate concrete. The results indicate that PC overlays offer a degree of thermal insulation to structural concrete in highways and bridge decks when exposed to high temperatures, thereby slowing down the detrimental transfer of heat to the concrete.

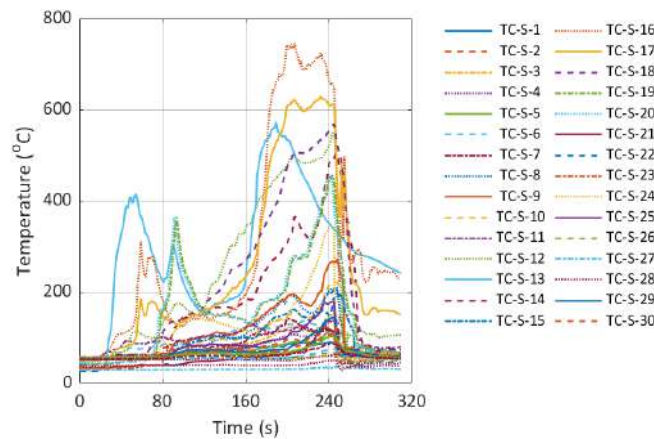


Figure 7. Temperature evolution at the surface of the PC overlay during the vehicle fire test



Figure 8. Maximum recorded temperature at different locations over the surface (circles show the locations for post-fire test sampling)

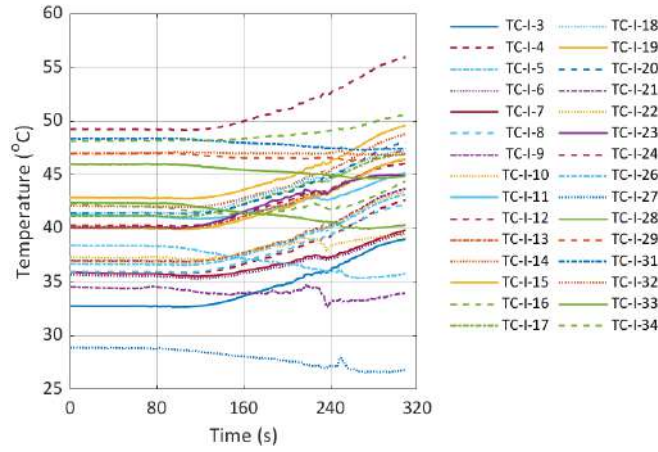


Figure 9. Temperature evolution at the interface between overlay and concrete during the vehicle fire test

3.3 Change of PC properties after fire exposure

A series of performance tests were conducted on the slab both before and after the vehicle fire. These tests varied in nature, being either non-destructive or destructive. Non-destructive tests could be conducted at each designated location marked in Figure 3 before and after the vehicle fire test. However, destructive tests were only feasible in the designated locations after the vehicle fire. To establish representative pre-fire exposure values for the properties, multiple cores were collected from a location away from the main test area on the slab. The changes in properties are shown in Figures 10~12 and summarized in Tables 2~3. On average, in the area significantly exposed to high temperatures and its immediate surroundings (locations from #6 to #25 in Figure 8), the skid resistance was reduced by 23.6%, the surface hardness by 10.7%, the abrasion resistance by 10.6%, and the chloride penetration resistance by 9.8%. The maximum changes in these properties were 34.7%, 31.6%, 30.2%, and 45.6% for skid resistance, surface hardness, abrasion resistance, and chloride penetration resistance, respectively. The results indicate that even with a relatively short vehicle fire exposure, PC could experience a notable performance decrease, compromising its effectiveness as a protection layer for roadways.

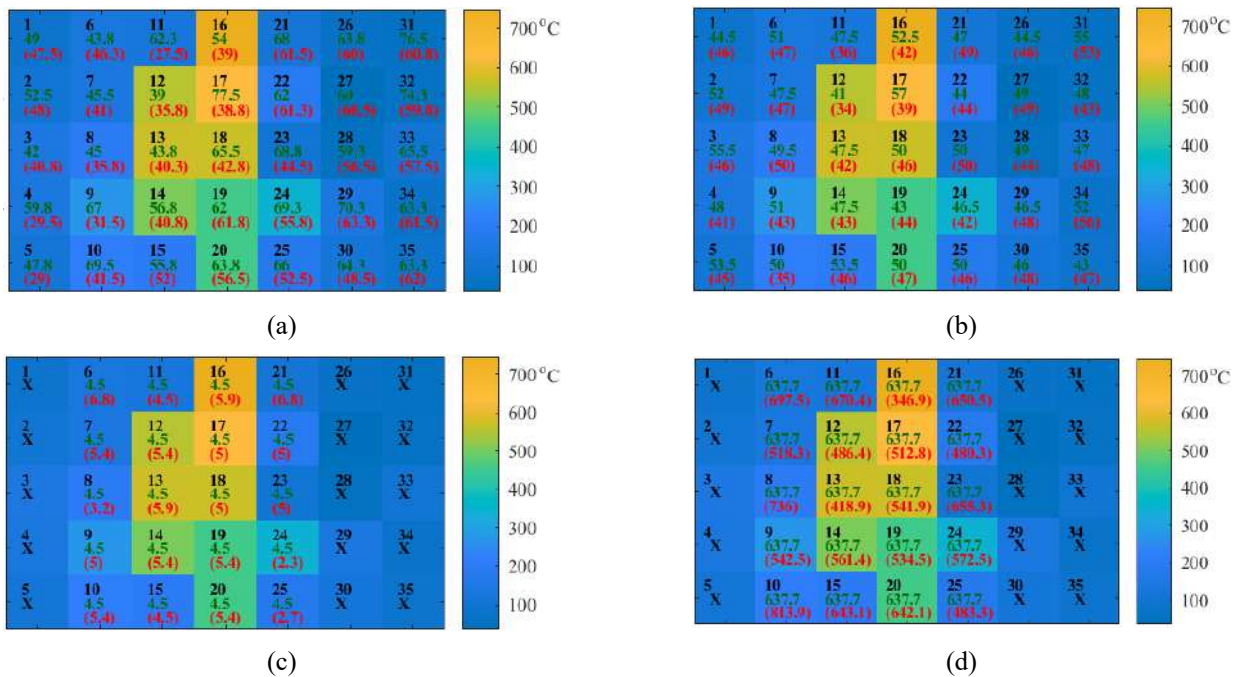


Figure 10. Evaluation of PC properties before and after vehicle fire for a) skid resistance (British pendulum number), b) surface hardness (rebound number), c) abrasion resistance (unit: grams) and d) chlorine penetration resistance (unit: kΩ-cm). Values in green indicate pre-fire properties and those in red indicate post-fire properties

Table 2. Percentage change in properties after the vehicle fire test

Tests	Average change over the entire slab (%)	Average change in locations #6 to #25 (%)	Maximum change in high-temperature locations (%)
Skid resistance	19.3	23.6	34.7
Surface hardness	7.5	10.7	31.6
Abrasion resistance	-	10.6	30.2
Chloride penetration resistance	-	9.8	45.6

Water permeability tests were conducted separately from other property tests. Anticipating significant differences in the values of water permeability across different samples, both pre-fire and post-fire water permeability tests were performed on the same cores collected before the vehicle fire test. The falling head tests were conducted on core samples before heating. Then the cores were heated in a furnace at a heat rate of 3 °C/s to mimic the exposure of the slab to high temperatures during the vehicle fire test. This study examined two specific target temperatures: 350 °C and 700 °C, across three varied exposure durations: 60 seconds, 180 seconds, and 300 seconds. The falling head tests were conducted on the same core samples again after they returned to ambient temperature. Table 3 shows the changes in the water permeability of those tested samples. The test results showed a clear link between PC overlay permeability and high-temperature exposure. At 350°C, permeability increased by 57.1% after 60 seconds and 115.3% after 300 seconds. Similarly, at 700°C, 60-second heat exposure raised permeability by 108.0%, which jumped to 370.8% after 300 seconds.

Table 3. Change in Water Permeability

Temperature	Duration of exposure (s)	Percentage change (%)
350°C	60	57.1
	180	68.5
	300	115.3
700°C	60	108.0
	180	290.8
	300	370.8

The bond strength tests assess the bond between the PC overlay and substrate concrete. A test either causes the bond failure (separation between the overlay and substrate concrete) or the fracture of concrete substrate. Concrete fracture typically indicates excellent bond strength between the overlay and concrete, with bond strength exceeding concrete tensile strength. Initially conducted on cores drilled into the added section of the slab, all the pre-fire tests failed in substrate concrete, indicating strong overlay-concrete bonding. Post-fire, the tests were carried out in areas exposed to elevated temperatures and their immediate surroundings (locations #6 to #25 in Figure 8). Results diverged from pre-fire tests, with 75% (15 out of 20 locations) exhibiting bond failure, suggesting reduced bond strength of the PC overlay after the vehicle fire exposure. Figure 11 shows locations where this failure pattern occurred.

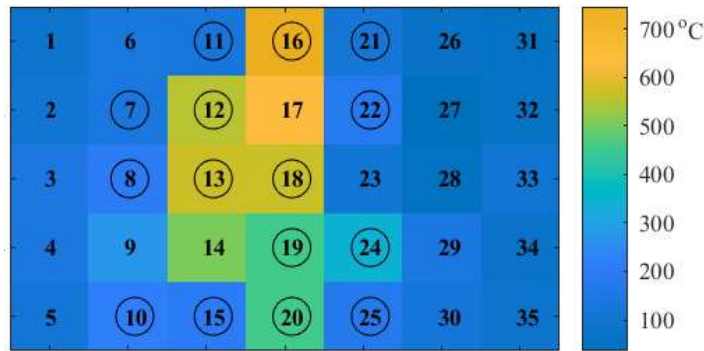


Figure 11. Failure mode in bond strength test (colors represent the maximum recorded temperatures, and the circles around numbers represent locations with bond failure)

The marked difference in thermal expansion coefficients between concrete and PC can lead to the delamination of PC overlay at high temperatures. A FLIR T640 thermal imaging camera captured the surface temperature distribution of the PC overlay to assess delamination. Before testing, the surface underwent sunlight exposure for a minimum of 3 hours per ASTM D4788 guidelines. Due to equipment limitations, instead of a single infrared image for the entire slab, separate IR images for each region (from #1 to #35) were recorded. Thus, capturing thermal images of the entire slab surface is a process usually extending beyond an hour. The environmental shifts during the process impact the surface temperature of the slab, which makes the data processing challenging.

To address variability, post-processing steps were implemented. Thermal images were initially enhanced using a Gaussian filter. These images for each region were then stitched together to generate maps for the entire slab. Figure 12 identified the hot spots by comparing the temperature of each pixel in hot regions (from #6 to #25) with the average temperature of the surrounding cool regions, at least 0.5°C hotter than the surroundings. It was noted that the regions exposed to high temperatures during the vehicle fire test exhibited more hotspots after the fire test, which could potentially indicate delamination. While no additional tests confirmed the presence of delamination, bond failure in the bond strength tests in these areas supported this conclusion (shown in Figure 11). Ideally, to eliminate the effects of environmental conditions and variability in thermal images, UAVs can be utilized to capture the entire surface in a single thermal image, enhancing the reliability of delamination assessment.

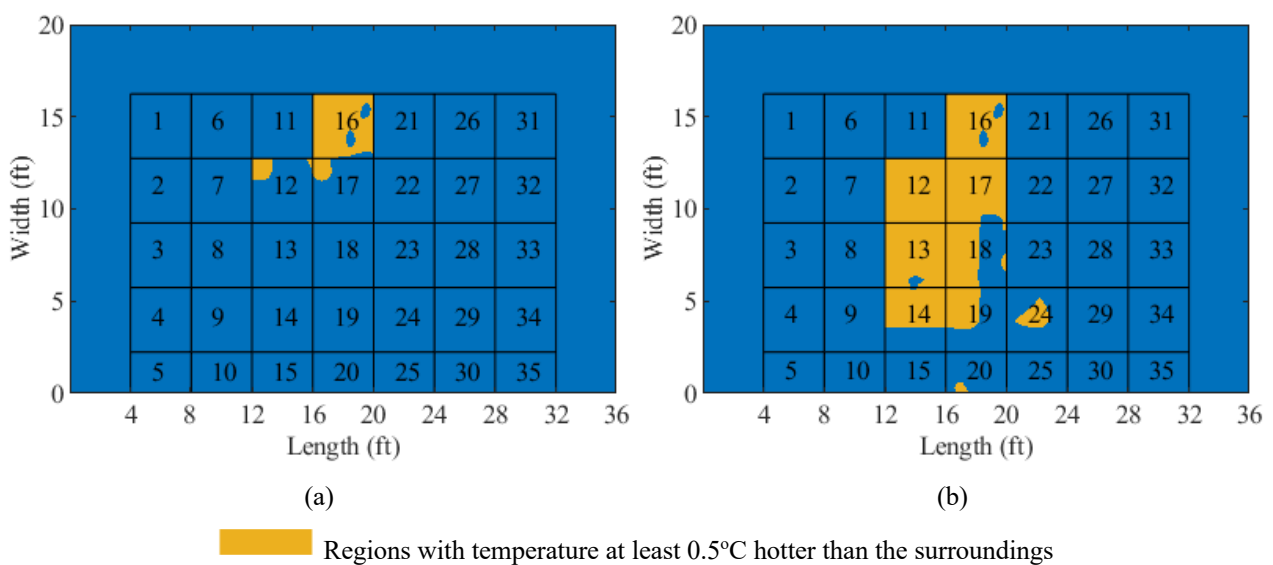


Figure 12. Slab surface a) hotspots before fire exposure identified by comparing hot areas with cool areas, and b) hotspots after fire exposure identified by comparing hot areas with cool areas

4 CONCLUSION

This study aimed to assess the impact of elevated temperatures, particularly from vehicle fires, on PC overlays and civil infrastructure. A realistic vehicle fire test was carried out on a concrete slab with PC overlay. The examined PC overlay is a polyester polymer mix, widely used in bridges and roads. Performance tests of the PC overlay before and after heat exposure were measured. Heat flux sensors recorded peak fluxes of 26.7 kW/m² and 47.5 kW/m², highlighting the threat to surrounding infrastructure. Thermocouples recorded peak temperatures of around 1200°C inside the vehicle and 744°C on the surface of the slab, while the interface between the PC overlay and the substrate concrete showed minimal temperature change. Despite the vehicle fire lasting just 225 seconds, the PC overlay exhibited a notable decline in post-fire performance. Tests showed significant reductions in skid resistance, surface hardness, abrasion resistance, and chloride penetration resistance—decreasing by up to 34.7%, 31.6%, 30.2%, and 45.6% respectively from pre-fire levels. Water permeability resistance, tested using a different routine, also showed significant changes (up to 370.8%) after exposure to elevated temperatures. Tests for delamination and bond strength further demonstrated the adverse effects of vehicle fire heat on the PC overlay. As PC becomes more prevalent in road and bridge overlays, understanding how temperature affects its degradation is vital. The importance of this issue is heightened by the rise of electric vehicles, whose fires present considerable challenges to extinguishing. Measures should be developed to limit the exposure of PC overlay to high temperatures or slow down the degradation of their performance under such conditions.

ACKNOWLEDGMENT

The authors gratefully acknowledge the support of the U.S. Department of Transportation through the Mountain Plains Consortium (MPC-663) for providing the necessary funding to complete this work. Additionally, the authors would like to thank Jinghui Jiang for assisting with the slab construction and for the initial literature review of historical vehicle fire incidents and tests, Dr. James Bay and Dr. John Rice for valuable advice on designing the water penetration tests, as well as Dr. Andrew Sorensen for providing support in the experimental preparation. The authors would also like to extend their sincere thanks to Granite Construction for their invaluable assistance with placing the overlay, and to the Cache County Fire Department for generously providing a safe and suitable location for conducting the vehicle fire test, as well as for providing the necessary resources to carry out the test.

REFERENCE

1. Marschall J, Frederick M (1987) Thermal degradation of polymer concrete. *Constr Build Mater* 1:14–18
2. Xue-gui S, Xian-jie D, Hong-hu Y, Ben-kui L (2016) Research of the thermal stability of structure of resin anchoring material based on 3D CT. *Int J Adhes Adhes* 68:161–168
3. Ribeiro MCS, Nóvoa PR, Ferreira AJM, Marques AT (2004) Flexural performance of polyester and epoxy polymer mortars under severe thermal conditions. *Cem Concr Compos* 26:803–809
4. Reis JML dos (2012) Effect of temperature on the mechanical properties of polymer mortars. *Materials Research* 15:645–649
5. Shokrieh MM, Heidari-Rarani M, Shakouri M, Kashizadeh E (2011) Effects of thermal cycles on mechanical properties of an optimized polymer concrete. *Constr Build Mater* 25:3540–3549
6. Hayashi F, Oshima M, Koyanagi W (1996) Structural materials. Thermal properties and temperature dependence of mechanical properties of resin concretes for structural Use. *Journal of The Society of Materials Science, Japan* 45:1014–1020
7. National Fire Protection Agency (NFPA) (2009) NFPA 1710, Standard for the organization and deployment of fire suppression operations
8. Upson R, Notarianni KA (2010) *Quantitative Evaluation of Fire and EMS Mobilization Times*, 1st ed. Springer Science +Business Media, Worchester, MA
9. Okamoto K, Otake T, Miyamoto H, et al (2013) Burning behavior of minivan passenger cars. *Fire Saf J* 62:272–280. <https://doi.org/10.1016/j.firesaf.2013.09.010>

10. Okamoto K, Watanabe N, Hagimoto Y, et al (2009) Burning behavior of sedan passenger cars. *Fire Saf J* 44:301–310. <https://doi.org/10.1016/j.firesaf.2008.07.001>
11. Tewarson A, Quintiere JG, Purser DA (2005) *Post Collision Motor Vehicle Fires*. Charlottesville, VA
12. Jiang X, Zhu G, Zhu H, Li D (2018) Full-scale Experimental Study of Fire Spread Behavior of Cars. *Procedia Eng* 211:297–305. <https://doi.org/10.1016/j.proeng.2017.12.016>
13. Zhu H, Gao Y, Guo H (2020) Experimental investigation of burning behavior of a running vehicle. *Case Studies in Thermal Engineering* 22:100795. <https://doi.org/10.1016/j.csite.2020.100795>
14. Utah Department of Transportation (UDOT) (2017) *Structures Design and Detailing Manual*
15. A. Tewarson, J.G Quintiere, D.A. Purser (2005) *Post collision motor vehicle fires*. Charlottesville, VA
16. ASTM E303 (2022). Standard test method for measuring the surface frictional properties using the British Pendulum tester, American Society for Testing and Materials, West Conshohocken, PA.
17. ASTM C805/C805M (2018). Standard test method for Rebound Number of hardened concrete, American Society for Testing and Materials, West Conshohocken, PA
18. ASTM D4788 (2022). Standard Test Method for Detecting Delaminations in Bridge Decks Using Infrared Thermography, American Society for Testing and Materials, West Conshohocken, PA.
19. ASTM C1583/C1583M (2020). Standard test method for tensile strength of concrete surfaces and the bond strength or tensile strength of concrete repair and overlay materials by direct tension (pull-off method), American Society for Testing and Materials, West Conshohocken, PA
20. ASTM D5084 (2016), Standard test methods for measurement of hydraulic conductivity of saturated porous materials using a flexible wall permeameter, American Society for Testing and Materials, West Conshohocken, PA
21. ASTM C944/C944M (2019). Standard test method for abrasion resistance of concrete or mortar surfaces by the rotating-cutter method, American Society for Testing and Materials, West Conshohocken, PA
22. AASHTO T 358 (2019). Standard method of test for surface resistivity indication of concrete's ability to resist chloride penetration, American Association of State Highway and Transportation Officials, Washington DC

CONCRETE SPLITTING OF POST INSTALLED REBARS AT HIGH TEMPERATURES: EXPERIMENTAL INVESTIGATION

Fatima Ben Mouhou¹, Nicolas Pinoteau², Omar Al Mansouri³, Roberto Piccinin⁴, Kresimir Nincevic⁵, Sébastien Rémond⁶, Dashnor Hoxha⁷

ABSTRACT

Post-installed rebars (PIRs) are installed using a structural adhesive to bond a reinforcing bar into an existing concrete structure. They are used in various construction applications due to the technical and architectural solutions they provide. Their behaviour has been investigated thoroughly under different loads in the literature (static, seismic, fire, and post-fire loadings). When exposed to extreme temperatures (i.e., a fire event), the mechanical properties of concrete, steel and adhesive significantly decay leading to a competition between bond, steel, and concrete related failure modes.

This paper presents an experimental investigation of the splitting resistance of PIRs at high temperatures, with different concrete covers (c_{min} =40 mm, 60 mm, 80 mm, and 100 mm). 21 tests were carried out at CSTB on beam-end test specimens (L800 × H600 × W300 mm³) under two different heating scenarios (using electrical and gas heating). Initially, reference tests were conducted at ambient temperature, followed by tests at high temperatures using an electrical heating system to investigate the influence of temperature increase on the degradation of the splitting resistance. Subsequently, to validate the equivalence between electrical and gas heating, validation tests were carried out in a gas furnace under standard ISO 834-1 fire conditions. The results revealed that splitting failure occurs at temperature levels that are relatively lower than temperatures at which pull-out failure occurs. The temperature transition from splitting to pull-out failure depends on the concrete cover. The investigation also revealed that this transition temperature between splitting and pull-out failure, shifts towards lower temperatures with increased cover, until pull-out failure governs for both ambient and high temperature at large concrete covers.

Keywords: Bond-splitting; post-installed rebars; beam-end tests; resistance to fire

¹ PhD Candidate, Centre Scientifique et Technique du Bâtiment (CSTB); Univ Orléans, Univ Tours, INSA CVL, LaMé, EA.France
e-mail: fatima.benmouhou@cstb.fr, <https://orcid.org/0009-0007-4843-1036>

² Research Coordinator, Centre Scientifique et Technique du Bâtiment (CSTB)
e-mail: nicolas.pinoteau@cstb.fr, ORCID: <https://orcid.org/0000-0001-9569-9835>

³ Research and Expertise Engineer | R&D Project Manager, Centre Scientifique et Technique du Bâtiment (CSTB)
e-mail: omar.almansouri@cstb.fr, ORCID: <https://orcid.org/0000-0002-4458-9182>

⁴ Group Manager Code Development, Hilti Corp.
e-mail: roberto.piccinin@hilti.com

⁵ ARC Code Development Research | Project Manager, Hilti Corp.
e-mail: kresimir.nincevic@hilti.com, ORCID: <https://orcid.org/0000-0002-7740-7891>

⁶ Professor, Univ Orléans, Univ Tours, INSA CVL, LaMé, EA.France
e-mail: sebastien.remond@univ-orleans.fr, ORCID: <https://orcid.org/0000-0001-7700-9319>

⁷ Professor, Univ Orléans, Univ Tours, INSA CVL, LaMé, EA.France
e-mail: dashnor.hoxha@univ-orleans.fr, ORCID: <https://orcid.org/0000-0001-7868-5466>

1 INTRODUCTION

PIRs are increasingly being used in strengthening and rehabilitation projects, as well as in specific applications in new construction. These bars are installed in holes drilled into hardened concrete with an adhesive product (structural resin or mortar) that ensures the bond between the steel bar and the concrete. Their tension behavior under static and quasi-static loading is governed by four potential failure modes: concrete cone failure, pull-out failure, steel failure and concrete splitting failure. Each failure mode is associated with exceeding the ultimate capacity of the respective material (concrete, steel, mortar). Splitting failure occurs with insufficient concrete confinement when the tensile resistance associated with the surrounding concrete is not enough to equilibrate the splitting forces generated by the bond. The forces spread from the sides of the ribs at an angle α due to the dense transverse cracking in the form of funnel-shaped compression cone, in the surrounding concrete as described in. These forces are transmitted by adhesion and micro interlock due to the roughness of the borehole surface between the adhesive mortar and concrete. The radial components of these forces are equilibrated by rings of tensile stress in the concrete around the bar. When the force exerted by the bonding action exceeds the tensile capacity of the ring, the splitting of the concrete cover occurs manifested by a longitudinal crack parallel to the bar axis [1-3].

The existing studies on the bond behavior of PIRs highlighted the role of bond strength and stiffness in improving the tensile capacity of PIRs. Since the earliest experimental study conducted by Spieth et al. [4] using several adhesive mortars at different edge distances, it has been demonstrated that, for large concrete covers, PIRs with high-bond adhesive products provide higher bond strength compared to cast-in rebars. These products have also presented equivalent or higher bond-splitting resistances in the extreme conditions of concrete confinement (rebar installed in the corner) and the absence of transverse reinforcement. As the performance of adhesive mortars has developed over time, Rex and al. [5] conducted a recent comparison study by means of pull-out tests performed in more realistic boundary conditions (i.e., relatively small concrete covers) using the beam-end specimen, to assess tensile capacity of PIRs realistically. The results presented a higher bond-splitting strength for PIRs with high-bond adhesive products than cast-in rebars, which can be explained by the beneficial effect of the adhesive in redistributing the radial stresses from the ribs of the rebar to the surrounding concrete [5].

Since the previous studies have shown that PIRs installed with qualified products can achieve equivalent or higher performances compared to cast-in rebars, the European Organization for Technical Assessment (EOTA) has issued a technical report TR023 [6] for the evaluation of PIR connections to fully exploit the potential of the bond strength of PIRs, which was later transformed into the European Assessment Document - EAD 330087 [7]. This procedure allowed PIR products to be designed in accordance with the cast-in reinforcement provisions in EN 1992-1-1[8]. EAD 332402 [9] was developed a few years later to allow the PIR products that go beyond the performance of a cast-in rebar to be designed based on their qualified characteristic resistance using a product-specific bond-splitting equation. EOTA has developed their design provisions in a Technical Report - TR 069 [10] that combines the design provisions of anchors in concrete in accordance with EN 1992-4 [11] with the assessed bond-splitting equation (see Equation 1). The constant A_k and exponents $sp1$ to $sp4$ and $lb1$ depend on the performance of the product and they can be found in its European Technical Assessment (ETA). They are obtained through an extensive test program in accordance with the EAD [9] to quantify the influence of all the different parameters involved in the bond-splitting strength (concrete strength f_{ck} , rebar diameter ϕ , concrete cover c_d , anchorage length l_b).

$$\tau_{Rk,sp} = A_k \left(\frac{f_{ck}}{25}\right)^{sp1} \left(\frac{25}{\phi}\right)^{sp2} \left[\left(\frac{c_d}{\phi}\right)^{sp3} \left(\frac{c_{max}}{c_d}\right)^{sp4} + K_m \cdot K_{tr}\right] \left(\frac{7\phi}{l_b}\right)^{lb1} \quad \text{Equation 1}$$

K_m factor for the effectiveness of transverse reinforcement defined according to the fib Model Code 2010 [12] and fib Bulletin 72 [13]

K_{tr} normalized ratio to consider the amount of transverse reinforcement crossing a potential splitting surface defined and calculated according to the fib Model Code 2010 [12]

The bond capacity of PIRs under fire conditions has been analyzed by several researchers [14-17]. The existing research has primarily focused on pull-out failure driven by the mechanical performance of the

adhesive products, as most adhesives are composed of polymeric resins that are highly sensitive to temperature increase. A method for assessing the product-specific bond strength of PIRs under fire conditions has been established through confined pull-out tests at high temperatures[7]. Furthermore, fire design provisions of PIRs as equivalent to cast-in rebars are being debated at the European level. However, when using PIR products that go beyond the performance of cast-in rebars, their static and seismic behavior are well-known and documented, but their actual bond-splitting behavior under fire conditions is scarce in the literature. In concrete-to-concrete connections, relatively small concrete covers are involved which could make their fire design the governing load case. The aim of the paper is to experimentally evaluate the bond-splitting strength of PIR products at high temperatures. The presented work considers different conditions of concrete cover by carrying a series of tension tests on beam-end specimens heated using two different protocols: electrical heating and standard ISO 834-1 gas fire conditions.

2 EXPERIMENTAL PROCEDURE AND MATERIALS

2.1 Beam end specimen

Tests were conducted on beam-end specimen as originally prescribed in the ICC-ES AC308 [18], and adopted in EAD 332402 [9] to assess PIR connections with improved bond-splitting behaviour under static load. Figure 1 presents the details of the beam-end test specimen. It consists of reinforced beams of (L800 × H600 × W300 mm) casted horizontally as shown in Figure 2. The specimens were equipped with a post-installed rebar with an embedment length consisting of two zones. An initial de-bonded length of 200 mm (ten times the diameter of the bar) using a PVC tube with a nominal diameter corresponding to the diameter of the drilled hole (25 mm) to prevent contact with the surrounding concrete and undesired localized cone failure of concrete in this zone, followed by the bonded length of 140 mm (seven times the diameter of the bar) to characterize the localized bond-splitting resistance as a function of the tested parameters.

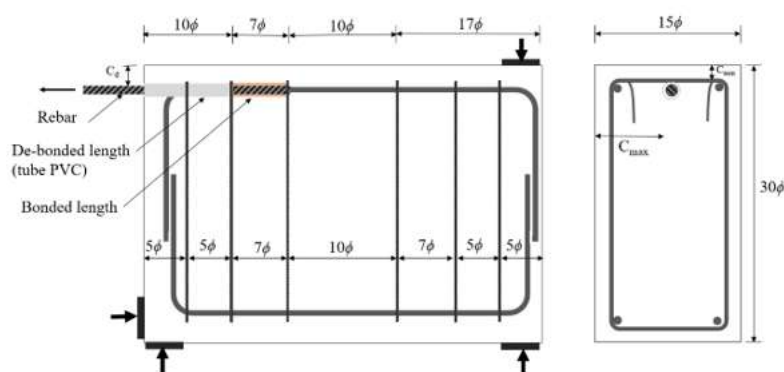


Figure 1. Beam-end test specimen dimensions



Figure 2. Formwork of the beam-end tests specimen

2.2 Materials

The tests were conducted with C20/25 concrete class. The mix design of the concrete is reported in the Table 1. The mean compressive cubic strength of the concrete after 28 days was $f_{c,cube} = 21.7 \text{ N/mm}^2$, and $f_{c,cube} = 24.2 \text{ N/mm}^2$ at the day of the test (after 90 days from the casting day). The used rebars are of Gewi type with a diameter of 20 mm, a relative rib area of $f_R = 0.08$ and a yield limit characterized at 560 N/mm^2 . The steel rebars were post-installed using a hybrid adhesive in accordance with the Manufacturer's Product Installation Instructions (MPII). The holes were drilled using hammer drilling with a nominal cutting diameter of 25 mm and cleaned using compressed air and steel brushes.

Table 1. Mix design of concrete

Constituent	Quantity (kg/m ³)
Cement CEM II / B-LL 32.5 R	320
Sand 0/8 mixte	880
Graval 4/14 A lluvial	792
Graval 4/22.4 A lluvial	88
Water	227

2.3 Test program and procedure

Table 2 outlines the tests program performed in this work. Reference tests were conducted at normal ambient temperature ($20 \pm 3^\circ\text{C}$) on different concrete cover values (c_d): 40, 60 and 80 mm to assess the reference bond-splitting resistance of the product. $c_d = 40$ mm corresponds to the minimum concrete cover allowed for PIRs with a diameter of 20 mm. Consequently, the tests were conducted at high temperatures using an electrical heating system for concrete cover values (c_d) of 40, 60, 80 and 100 mm to quantify the degradation of the bond-splitting resistance with temperature increase. More tests were conducted on specimens with small concrete cover values to capture the bond-splitting performance on the cases where the occurrence of this failure mode is most favorable. For $c_d = 40$ mm, six tests were carried out at different load levels. For $c_d = 60$ mm, four tests were conducted. For $c_d = 80$ and 100 mm, three and two tests were performed, respectively.

Additional tests were later executed in a gas furnace under ISO 834-1 [19] fire conditions for concrete cover values (c_d) of 40, 50 and 60 mm to compare the results using two heating scenarios (electrical heating vs. 834-1 ISO 834-1) and their representativity of the bond-splitting behavior of PIRs at high temperatures.

Table 2. Test program

Test type & thermal conditions	Tests Serie ID	Minimum clear concrete cover c_d [mm]	Number of repeatability tests
Beam-end tests at normal ambient temperature	BET-Ref- c_d 40	40	× 1
	BET-Ref- c_d 60	60	× 1
	BET-Ref- c_d 80	80	× 1
Beam-end tests at high temperatures using electrical heating	BET-T- c_d 40	40	× 6
	BET-T- c_d 60	60	× 4
	BET-T- c_d 80	80	× 3
	BET-T- c_d 100	100	× 2
Beam-end tests under standard ISO 834-1 fire conditions	BET-ISO- c_d 40	40	× 1
	BET-ISO- c_d 50	50	× 1
	BET-ISO- c_d 60	60	× 1

The reference tests were conducted by applying a monotonic tension load on the rebar at normal ambient temperature, using a displacement-controlled hydraulic jack with a rate of 0,8 mm/s until failure. The tests at high temperatures were conducted under constant tension load. The rebar is loaded in tension until a target load level shortly before the fire test. Once the target load is reached, it is maintained throughout the exposure to high temperature. The target loads were chosen to cover a large range of failure temperatures as will be described in part 3.2.2. The specimen is progressively subjected to thermal loading (furnace or electrical heating system) until failure of the PIR. The thermal loading is applied on the surrounding concrete of the rebar from one side of the beam, as shown in Figure 3. Figure 4 shows the used electrical heater that consists of radiant panels assembled in a metal framework of (300 × 300

mm²), which sufficiently covers the concrete surrounding the bonded area of the PIR and allows uniform application of the heating conditions. The temperature during the test was measured on the exposed surface of the beam using five disc-type thermocouples, and on the surface of the rebar using two wire-type thermocouples as shown in Figure 5. The temperature measurements were recorded every 1 second allowing relatively precise temperature measurements at the failure moment. As presented in Figure 3, a PVC tube was used to break adhesion between the bar and the concrete near the surface of the beam-end test specimen. This allows to ensure concrete longitudinal confinement while avoiding any load transfer to the concrete in this area.

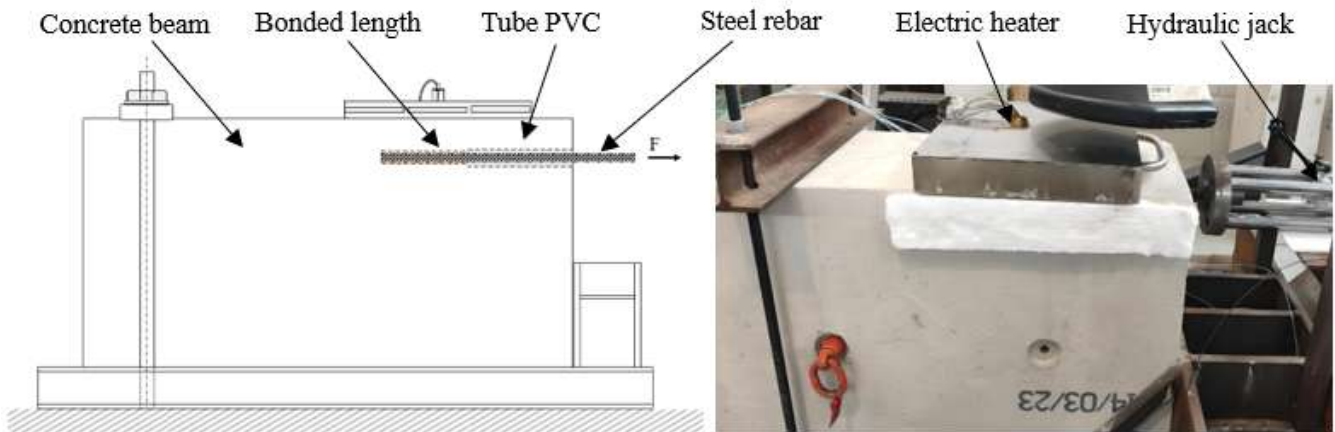


Figure 3. Electrical heating test setup



Figure 4. Radiant panels

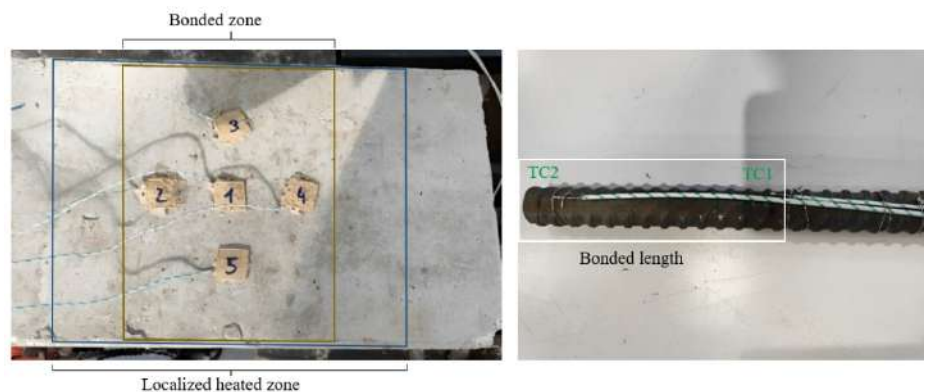


Figure 5. Temperature measurement on the exposed surface of the beam and on the surface of the rebar

For the 3 beam-end tests subjected to ISO 834-1 fire conditions, the specimens were placed on the framework support of the gas furnace as displayed in Figure 6. One side of the beam was exposed to fire conditions while the other sides were exposed to normal ambient air temperature. The closure of the furnace was ensured using mineral-based ceramic wool. For the sake of comparability, tests on different specimens were repeated according to the same test procedure. Rebars were kept loaded in tension during exposure to fire conditions. All tests (reference and high temperature) were performed on an identical specimen geometry, concrete batch, rebar specifications, and adhesive batch. For comparison purposes between electrical heating and ISO 834-1 fire conditions.

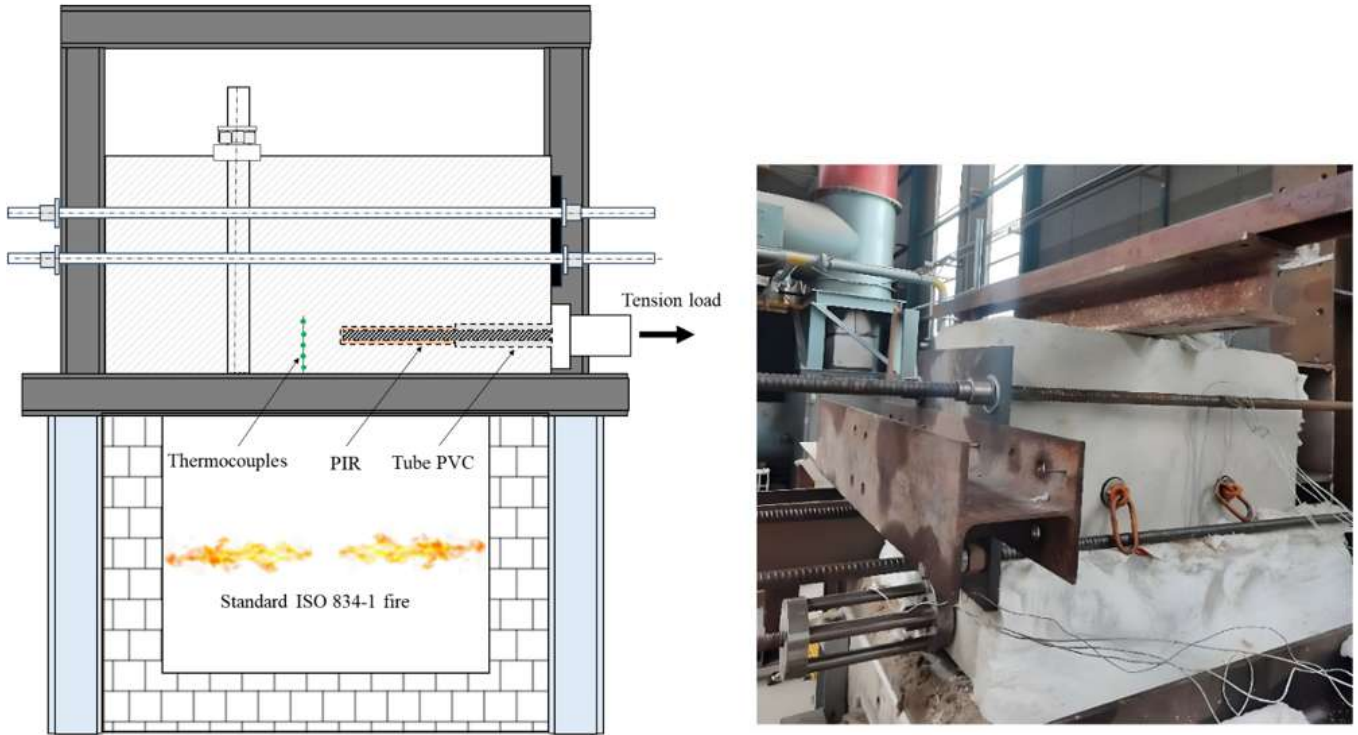


Figure 6. Standard ISO 834-1 fire test setup

2.4 Bond strength

The uniform bond stress model was assumed in this study since the embedment length is situated between 4 and 20 times the diameter, and the temperature along the embedment length is quasi-homogeneous. The tested bond strength is calculated by dividing the tension load by the contact area:

$$\tau = \frac{F_u}{\pi \cdot \phi \cdot l_b} \quad \text{Equation 2}$$

Where: τ = bond or bond-splitting strength, F_u = maximum reached load in the reference tests (or applied sustained load in the heated tests), ϕ = rebar diameter, and l_b = embedment length (without taking into account the unbonded zone with the PVC tube).

3 RESULTS AND DISCUSSION

3.1 Reference tests at ambient temperature

Figure 7 presents the failure mode obtained for each specimen at normal ambient temperature. All three tests failed by splitting manifested by the formation of typical longitudinal splitting cracks. The longitudinal cracks are initiated from the loaded end of the bonded zone and propagate, where the bond stresses are concentrated, towards the unloaded end, crossing the deboned zone as well. Failure is reflected by the rapid drop of resistance observed in the load-displacement curves presented in Figure 8. The contribution of concrete cover to the bond-splitting resistance was clearly observed in the load-displacement curves, i.e., the larger the cover, the higher the bond-splitting resistance. For $c_d = 40$ mm, the peak load was 120 kN with a rebar displacement of 1.11 mm. For $c_d = 60$ mm, the resistance increased to 146 kN with a corresponding displacement of 1.52 mm. For $c_d = 80$ mm, to the resistance increased to 167 kN with a corresponding displacement of 2.02 mm.

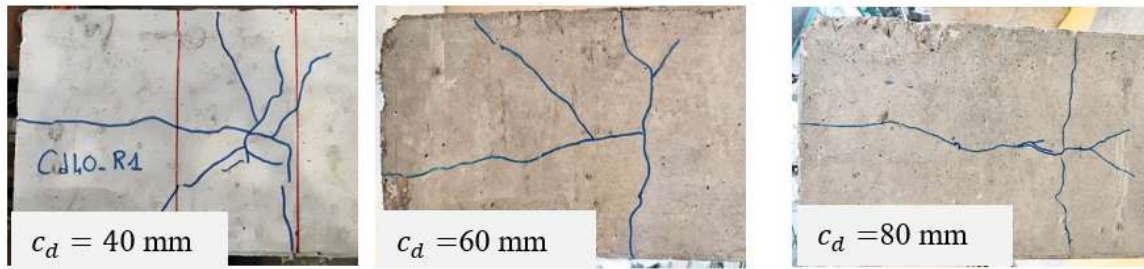


Figure 7. Crack patterns of specimens showing splitting failure

The obtained bond splitting resistances were normalized to the nominal C20/25 concrete strength using the following equation:

$$N_{u,sp} = N_{t,sp} \left(\frac{f_{ck}}{f_{c,t}} \right)^{sp1}$$

Where $N_{t,sp}$ = Failure (peak) load of the test; $f_{c,t}$ = concrete compressive cylinder strength of the test specimen (obtained by converting the compressive strength obtained from cubes, where $f_{c,t} = 0.8 f_{c,cube}$); f_{ck} = Nominal cylinder concrete strength of concrete according to EN 206 [20].

A bond splitting equation exists for the qualified product and has been evaluated according to EAD 332402. Results at normal ambient temperature were compared with the equation to verify its representativity (Figure 9). The coefficient of variation between the tested and calculated splitting resistance is 1~4%, confirming the representativity of the equation.

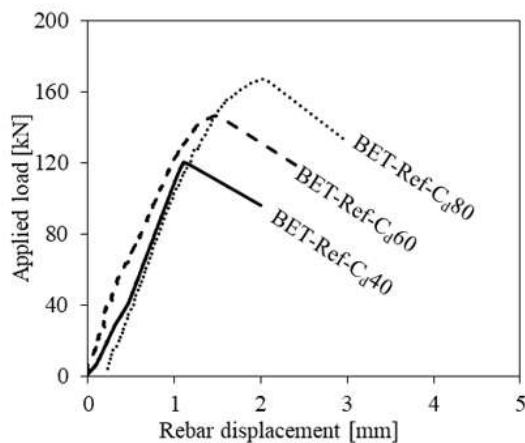


Figure 8. Load-displacement curves of the reference tests

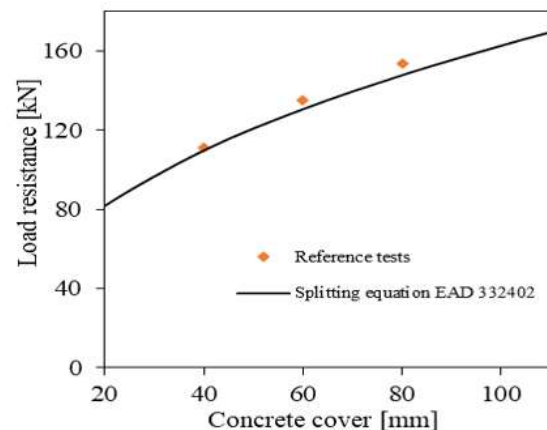


Figure 9. Bond-splitting strength vs. concrete cover

3.2 Beam-end tests at high temperatures

3.2.1 Failure modes

At high temperatures, both pull-out and concrete splitting failures were observed depending on the failure temperature during the test. The rise in temperature degrades both the mechanical properties of the concrete and the bond strength of the mortar, leading to a competition between the two failure modes. Concrete splitting failure occurred at temperatures that are relatively lower than those at which pull-out failure occurred. Splitting failure at high temperatures is characterized by the formation of longitudinal splitting cracks along the bonded zone, which do not, cross the deboned zone. Pull-out failure was reported in this study when no longitudinal splitting cracks were observed in the surface of the specimen at the moment of collapse and slippage of the bar out of the borehole was observed.

3.2.2 Bond-splitting strength at high temperatures

The tests were conducted at the anchor laboratory of the Scientific and Technical Center for Building (CSTB) in Champs-sur Marne, France. All test equipments were calibrated and subjected to regular inspection for

measurement precision. The measured bond-splitting strength is represented by the failure temperature and the bond strength calculated by Equation 2. The failure temperature corresponds to the mean value of the temperatures measured at the surface of the rebar with thermocouples referenced TC1 and TC2. Figure 10 presents the experimental test results showing the degradation of the bond-splitting strength vs. temperature for the investigated concrete cover values. For $c_d = 40$ mm, only splitting failures occurred up to the maximum tested temperature of 279°C. This is due to the fact that splitting failure, which may be linked to the strength of the concrete, degrades faster than pull-out which is linked to the bond properties of the adhesive product, For the tested concrete cover. This can be explained by the inadequacy of the tested concrete cover in equilibrating the splitting forces due to the degradation of concrete tensile strength with the temperature increase. The bond-splitting strength was reduced from 13,8 N/mm² at normal ambient temperature to 7 N/mm² at 67°C which represents a reduction of 51% compared to reference resistance at ambient temperature, and to 3 N/mm² at a failure temperature of 171°C corresponding to a reduction of 21%. For $c_d = 60$ mm, $c_d = 80$ mm and $c_d = 100$ mm, splitting failure occurs as well prior to pull-out failure. However, at a certain temperature level it switches to pull-out failure. At higher temperatures, the bond layer can neither resist to the applied bond stress nor transmit the radial stresses to the surrounding concrete, resulting in a bond pull-out failure. It was observed that the “transitional temperature” describing the temperature level at which the failure mode shifts from splitting to pull-out with increasing temperature, decreases with the increase of concrete cover. For $c_d = 60$ mm, the first pull-out failure was observed at 150°C, and for $c_d = 80$ the first pull out failure occurred at 124°C and at 100°C for $c_d = 100$.

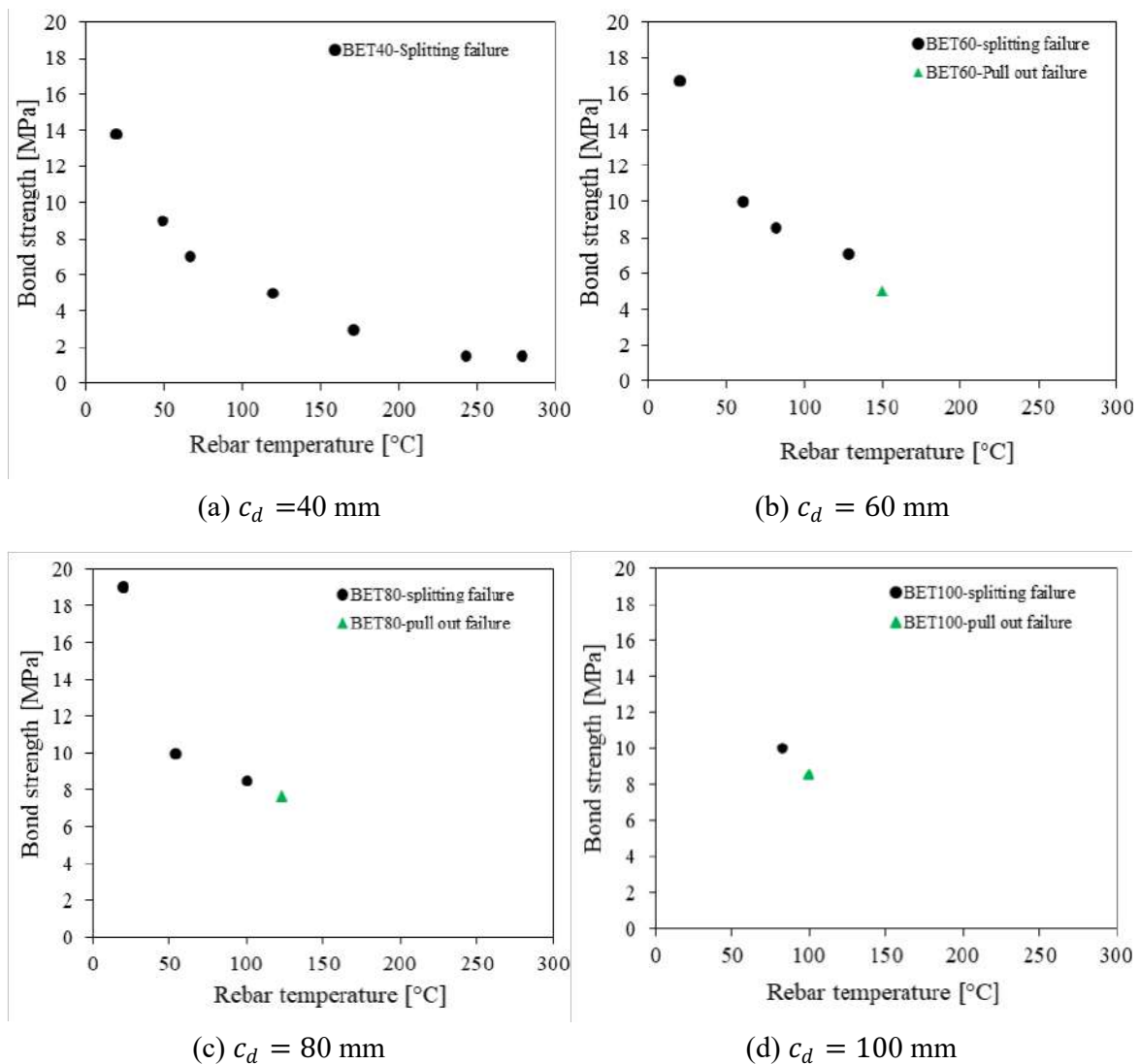


Figure 10. Bond-splitting degradation for different concrete cover values vs. temperature at the rebar/adhesive interface in the bonded zone (a) $c_d = 40$ mm, (b) $c_d = 60$ mm, (c) $c_d = 80$ mm and (d) $c_d = 100$ mm

3.3 Beam-end tests under standard ISO 834-1 fire conditions

The tests were conducted at the fire resistance laboratory of the Scientific and Technical Center for Building (CSTB) in Champs-sur Marne, France. All test equipments were calibrated and subjected to regular inspection for measurement precision. The furnace satisfies the requirements for fire resistance tests in the international standard ISO 834-1 [19]. Three beam-end test specimens were tested on the furnace with different concrete cover values: $c_d = 40$ mm, $c_d = 50$ mm, and $c_d = 60$ mm. Figure 11 presents the evolution of the applied gas temperature in the furnace during the three tests. The three tests were performed at a bond stress of 8,53 N/mm². It was chosen within the range of bond stresses that induces splitting failure, based on the results obtained with the electrical heating. Splitting failure occurred in all three tests (Figure 12). The recorded failure temperatures were measured in the same as the electrical heating tests, i.e., at the rebar/adhesive interface with two thermocouples along the bonded zone. The obtained failure temperatures at the surface of the rebar increase with the increase of concrete cover. The splitting failure for $c_d = 40$ mm occurred after 15 min of exposure to fire conditions at a failure temperature of 58°C. For $c_d = 50$ mm the temperature failure was 67°C after 21 min, and for $c_d = 60$ mm at 78°C after 39 min.

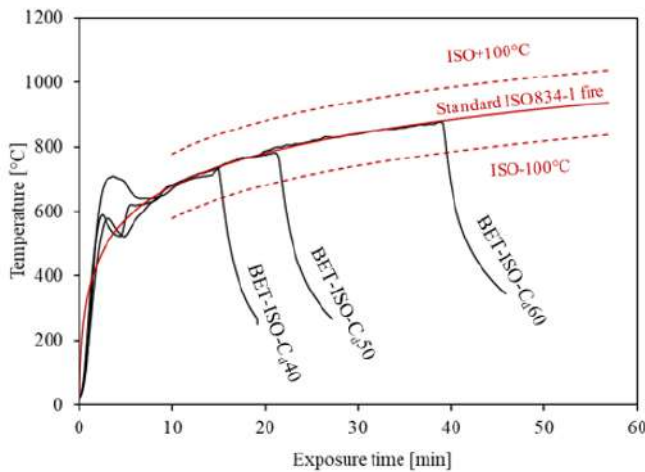


Figure 11. Evolution of gas temperature in the furnace

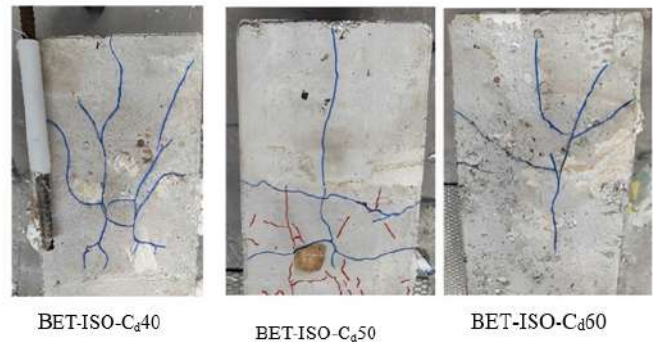


Figure 12. Splitting failures under ISO 834-1 fire conditions

The comparison between the bond-splitting strengths obtained under ISO 834-1 fire conditions and under electrical heating is presented in Figure 13. It can be observed that the two heating scenarios lead to similar failure temperature levels for a given applied bond stress. For $c_d = 60$ mm with an applied bond stress of 8,53 N/mm², the failure temperature was 82°C with electrical heating and 78°C with ISO 834-1 fire conditions. This may be related to the efficiency of the radiant panels constituting the used electrical heater to generate a nearly identical temperature gradient throughout the concrete cover compared to gas heating. Figure 14 presents the temperature evolution at 10 mm from the exposed surface recorded for the ISO 834-1 fire tests, compared to the temperature obtained with electrical heating. Within the first 15 to 20 min, the temperature approximately increases with the same rate. Then the difference is noticeable around 20 min. This can be attributed to the slower heating rate of the used radiant panels after 20 minutes. Despite the fact that radiant panels simulate a localized quasi-uniform heating, the radiation temperature of the used panels is limited to 530°C which slows down the temperature evolution in the concrete for long exposure durations compared to ISO 834-1 fire heating in a gas furnace. Nonetheless, the heating capacity of the used panels was deemed sufficient for these exposure durations. Yet, with the significant difference in the temperature gradient throughout the concrete cover for $c_d = 60$ mm at collapse moment for both electrical and fire heating, the splitting failure occurred at the same temperature in the surface of the rebar as described previously.

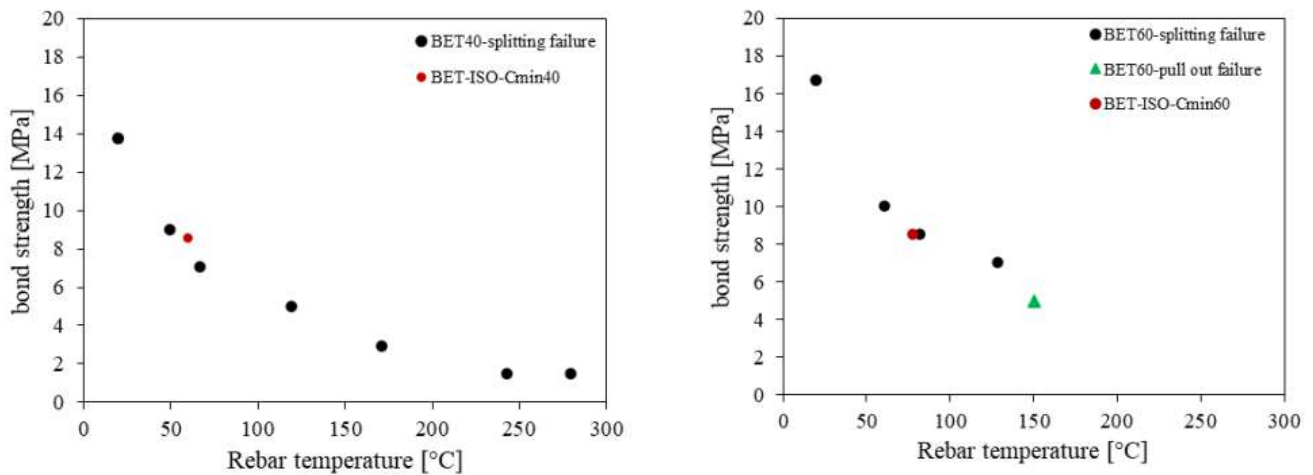


Figure 13. Comparison of bond splitting strength obtained under ISO fire and electrical heating (in the right Cmin40 and Cmin60 in the left)

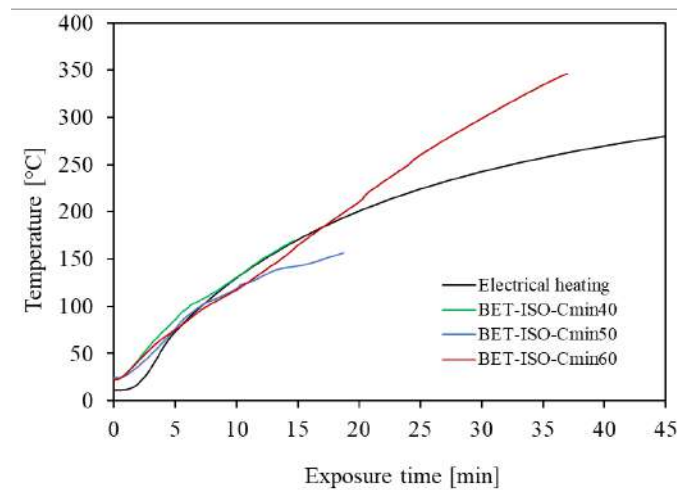


Figure 14. Temperature evolution at 10 mm from the exposed surface (electrical heating vs. ISO 834-1 fire conditions)

4 CONCLUSION

This paper presents an experimental study focused on the bond-splitting resistance of PIRs at normal ambient and high temperatures using two different heating scenarios (electrical heating and ISO 834-1 fire conditions). Tests were performed on beam-end test specimen with different concrete cover values c_d (40, 60, 80 and 100 mm). Reference tests were conducted at normal ambient temperature to assess the bond-splitting strength as a function of concrete cover and validate the prediction of the product-specific bond-splitting equation (assessed in accordance with EAD 332402).

Tests were then conducted at high temperatures to assess the degradation of bond-splitting resistance of PIRs and verify the consistency of the failure mode at different failure temperature levels. The temperature increase reduces the splitting capacity of PIRs, where splitting failure governs the tested configuration at normal ambient temperature, it was found that bond-splitting failure occurs at temperatures relatively lower than those at which pull-out failure governs. Moreover, it was found that the transitional temperature from splitting to pull-out failure depends on the concrete cover value. For concrete cover $c_d = 40$ mm, splitting failure governed up to a temperature of 279°C (in the surface of the rebar). However, for $c_d = 60$ mm, $c_d = 80$ mm and $c_d = 100$ mm, the failure transitions from splitting to pull-out decreasingly from 150°C to 124°C and 100°C respectively. The larger the concrete cover, the more pull-out failure tends to govern the tensile behavior at high temperatures. It has also been noticed that the two heating scenarios applied in this

work (electrical vs. ISO 834-1 fire conditions) lead to similar bond-splitting strength values at relatively the same temperature levels. Both observations: i) trend of decay in splitting capacity and ii) the failure transition zone (from splitting to pull-out) will be used to establish a product qualification procedure and design method for PIRs under fire.

ACKNOWLEDGEMENT

The experimental campaign was carried out in the anchor and fire laboratories of CSTB (Centre Scientifique et Technique du Bâtiment) in collaboration with Hilti. The authors would like to thank the teams of both laboratories and Hilti Corp. for providing the necessary material and for their great contributions to this work.

REFERENCES

- [1] R. Tepfers, “Cracking of concrete cover along anchored deformed reinforcing bars,” *Magazine of Concrete Research*, vol. 31, no. 106, pp. 3–12, Mar. 1979, doi: 10.1680/mac.1979.31.106.3.
- [2] S. Lettow, “Ein Verbundelement für nichtlineare Finite Elemente Analysen - Anwendung auf Übergreifungsstöße,” 2006.
- [3] J. Cairns and K. Jones, “Influence of rib geometry on strength of lapped joints: an experimental and analytical study,” *Magazine of Concrete Research*, vol. 47, no. 172, pp. 253–262, Sep. 1995, doi: 10.1680/mac.1995.47.172.253.
- [4] H. A. Spieth, “Tragverhalten und Bemessung von eingemörtelten Bewehrungsstäben,” 2002, doi: 10.18419/OPUS-160.
- [5] J. Rex, A. Sharma, and J. Hofmann, “A new test specimen to investigate the bond behavior of post-installed reinforcing bars,” Apr. 2019.
- [6] EOTA TR 023, “Assessment of post-installed rebar connections.” Nov. 2006.
- [7] EOTA, “EAD 330087-00-0601 - Systems for post-installed rebar connections with mortar.” Dec. 2020.
- [8] NF EN 1992-1-1, “Eurocode 2: Design of concrete structures. Part 1-1 : General rules and rules of buildings,” Afnor EDITIONS.
- [9] EOTA, “EAD-332402-00-0601-Post-Installed reinforcing bar (rebar) connections with improved bond-splitting behaviour under static loading.” Jun. 2021.
- [10] EOTA TR 069, “Design method for anchorage of post-installed bars (rebars) with improved bond-splitting behavior as compared to EN 1992-1-1.” Oct. 2019.
- [11] EN 1992-4, “Eurocode 2- Design of concrete structures - Part 4: Design of fastenings for use in concrete.” Accessed: Apr. 05, 2024. [Online].
- [12] *Model Code 2010. 1*. in Bulletin / Fédération Internationale du Béton, no. 55. Lausanne : International Federation for Structural Concrete (fib), 2010.
- [13] Fib Bulletins: “Bond and anchorage of embedded reinforcement.” Accessed: Jan. 19, 2024.
- [14] N. Pinoteau, P. Pimienta, T. Guillet, P. Rivillon, and S. Rémond, “Effect of heating rate on bond failure of rebars into concrete using polymer adhesives to simulate exposure to fire,” *International Journal of Adhesion and Adhesives*, vol. 31, no. 8, pp. 851–861, Dec. 2011, doi: 10.1016/j.ijadhadh.2011.08.005.
- [15] J. Hofmann, H. Lakhani, and J. Aggarwal, “POST INSTALLED REBARS – PULL-OUT CAPACITY DURING FIRE,” vol. 18, 2019.
- [16] M. A. Lahouar, J.-F. Caron, N. Pinoteau, G. Forêt, and K. Benzarti, “Mechanical behavior of adhesive anchors under high temperature exposure: Experimental investigation,” *International Journal of Adhesion and Adhesives*, vol. 78, pp. 200–211, Oct. 2017, doi: 10.1016/j.ijadhadh.2017.07.004.
- [17] F. Ben mouhou, O. Al-Mansouri, N. Pinoteau, S. Remond, and D. Hoxha, “A parametric study on the influence of steel diffusivity on Pinoteau’s Resistance Integration Method for post installed rebars in concrete under fire.” 2022.

- [18] AC308, "Acceptance criteria for post-installed adhesive anchors in concrete elements," *ICC Evaluation service*.
- [19] International Organization for Standardization, "ISO 834-1 Fire-resistance tests - Elements of building construction-." 2012.
- [20] EN 206, "Concrete - Specification, performance, production and conformity," Afnor EDITIONS.

DYNAMIC RESPONSE ASSESSMENT OF RC STRUCTURE EXPOSED TO NATURAL FIRE

Muhammad Noman^{1*}, Muhammad Yaqub², Salman Khan¹

ABSTRACT

The holistic and dynamic response of reinforced concrete (RC) structures exposed to natural fires is still an unsolved mystery for the research and regulatory community. In an effort to address this gap, this paper investigates the dynamic response of a scaled down RC structure exposed to short duration (SD) and long duration (LD) natural fires. A well instrumented scaled-down two storey RC structure was constructed and tested in natural fires generated using wooden logs. The SD fire had a flashover time of 20 minutes whereas the long duration fire had a duration of 100 minutes. Dynamic characteristics of the structure, including natural frequencies and mode shapes, were examined by applying a gentle impact using a mass source. This generated an impulse, initiating free vibrations within the structure for assessment. The structural integrity was further assessed through non-destructive tests (Ultrasonic Pulse Velocity and Schmidt hammer), and load tests, before and after each fire exposure. The results indicated a decrease of 14.71% in the natural frequencies of the structure when subjected to SD. However, a significant decrease of 49.5% was noted in natural frequencies following exposure to LD, signifying a substantial loss of global structural stiffness. The findings from the NDT and dynamic tests offer valuable insights for establishing correlations between fire-induced material changes and the resulting alterations in the structure's dynamic behaviour, potentially enabling NDT to predict these dynamic changes in real-world fire scenarios.

Keywords: Dynamic characteristics, Natural Fire, Frequency, Mode Shapes, NDT

1 INTRODUCTION

Recent criticism from both research and regulatory bodies has targeted the conventional approach of single-element standard fire testing [1–3]. This testing method forms the basis for the current structural fire design, operating under the assumption that structures will replicate the behavior of individual elements during these tests. The actual response of the structure could not be accurately represented in standard elemental fire tests due to impractical loading and support conditions, unrealistic load transfer mechanisms, as well as the unrealistically intense and prolonged nature of the fire, coupled with the absence of a decay phase in the fire simulation [4–6]. Due to these limitations, there is a growing trend towards shifting from conventional testing methods to real fire testing. Nevertheless, actual fire tests conducted on concrete structures are very few, with only few tests are reported thus far [2].

The majority of fire assessments, whether conducted through standard furnace trials or actual fire simulations [2,4,6–10] usually occur under high thermal stress to replicate worst-case scenarios. In most instances, the fuel present in a room is inadequate to sustain a 900 °C fire for over 30 minutes. As far as the authors are aware, there hasn't been any real-world testing utilizing short, naturally occurring fires. It's imperative to evaluate how structures perform in both short duration (SD) and long duration (LD) natural fires under realistic conditions.

¹ Department of Civil Engineering, Faculty of Engineering & Technology, International Islamic University, Islamabad

² Department of Civil Engineering, University of Engineering and Technology, Taxila

* Correspondence to: muhammad.noman@iiu.edu.pk

The critical property of stiffness in concrete significantly deteriorates at elevated temperatures [11]. This loss of stiffness directly manifests in altered dynamic properties of the structure, such as its natural frequencies, damping ratios, and mode shapes [12]. These dynamic characteristics play a vital role in how a structure responds to seismic events [13,14]. However, despite their importance for earthquake resistance, the behavior of these dynamic properties under fire conditions remains an under-explored area of research [13,14]. This highlights a critical knowledge gap that this study aims to address by investigating the influence of fire exposure on the dynamic response of reinforced concrete structures.

Given the preceding discussion, this paper deals with investigating the holistic and dynamic behavior of a scaled RC structure in SD and LD natural fire tests. This research offers valuable insights into the behavior of reinforced concrete (RC) structures during both short and long-duration real fires. The findings will not only improve our understanding of fire's impact on these structures but also serve as a crucial database for developing and validating numerical modeling techniques for RC structures in fire scenarios.

2 EXPERIMENTAL WORK

The experimental work undertaken in this study is presented in the form of flow chart in Figure 1. The sizing of the frame components was established through an analysis of typical construction methodologies employed in office building projects across Pakistan. The design assumed material properties of ASTM 615 grade 60 steel with a yield strength (f_y) of 60 ksi and ordinary Portland cement concrete with a 28-day compressive strength (f_c') of 4000 psi. The structure is considered to be constructed on firm soil/rock conditions, eliminating the need to account for soil interaction or settlement in the design considerations. The live load was taken as 50 psf per the load requirements for offices as per ASCE 7-10. The structure was assumed to be located in the seismic zone 2B of Pakistan (PGA 0.16 - 0.24). The $\frac{1}{2}$ scaled structure was constructed following the geometric similitude laws (see Figure 2). The structural details of columns, beams, and slab are presented in Figure 3. $\frac{2}{8}$ " diameter bars are used as positive & negative reinforcement in both directions of the slab. To create the compartment behavior of the fire, a masonry enclosure was built around the structure. Nonetheless, this enclosure was detached from the structure to prevent it from bearing any structural forces during load testing and vibration testing (see Figure 2b).

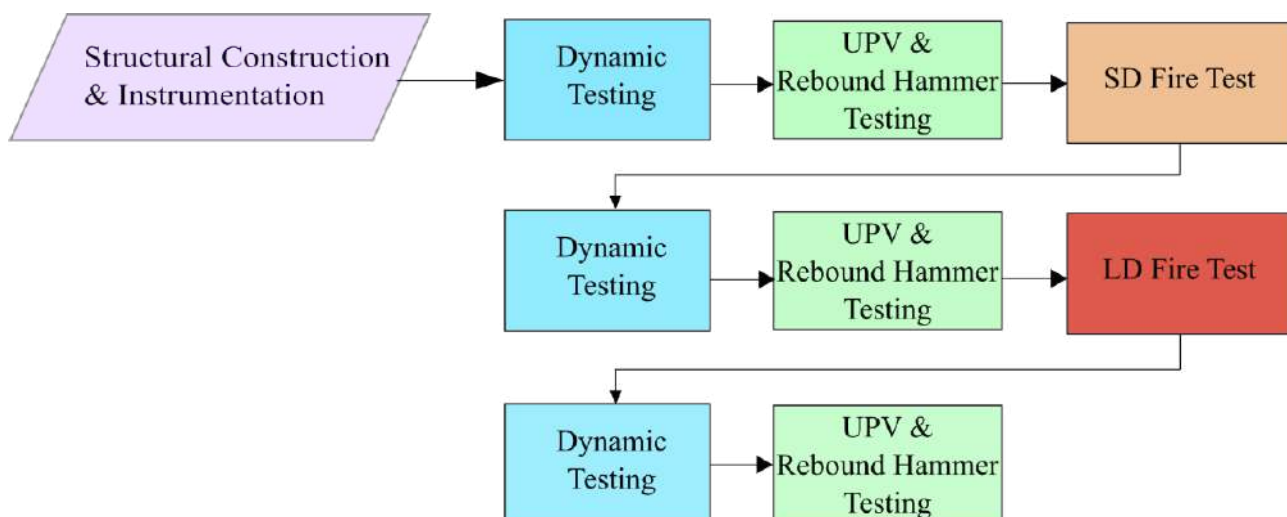


Figure 1: Flow chart for structural testing

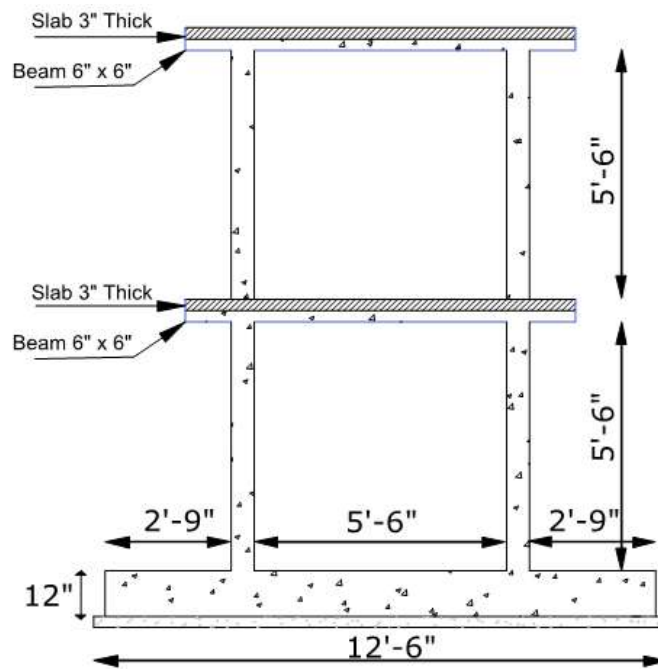


Figure 2: Model structure's broad cross-sectional view

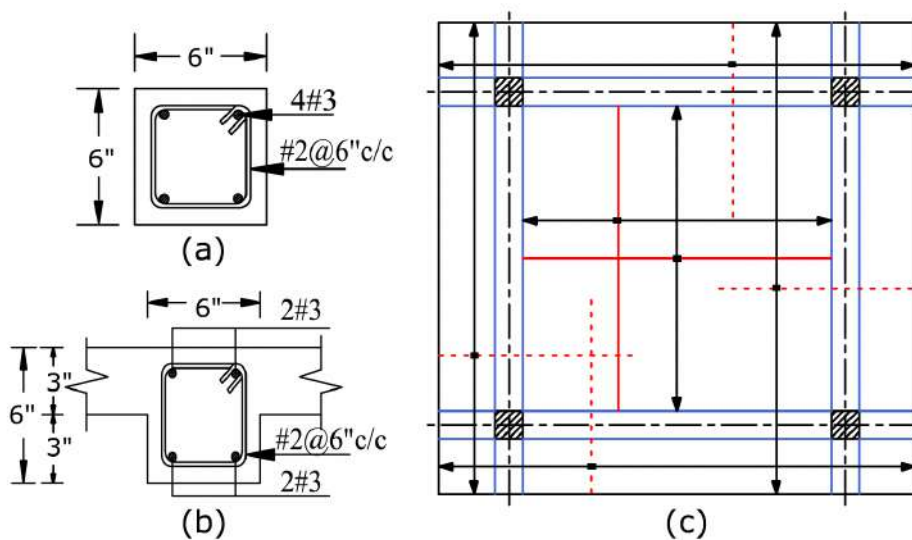


Figure 3: Reinforcement details (a) Column, (b) Beam, and (c) Slab (all #2 bars @ 9" c.c.)

2.1 Arrangement of Thermocouples

A complex network of K-type thermocouples was provided to determine the thermal behaviour inside the structure and the thermal gradient inside the cross-sections of various structural members. Temperature measurements were facilitated by the AT4532 data acquisition system from Applent Technology. Initially equipped with 32 channels, the capacity was expanded to 80 channels by adding six modules, each capable of supporting eight channels. Fire test data was continuously monitored in real time.

Thermocouples were strategically placed within each column: six positioned across the cross-section, four affixed to stirrups, two at the midpoint, and two situated equidistant between the midpoint and the stirrup. Within each beam, three thermocouples were installed at the midpoint, two fastened to stirrups at opposite ends, and one positioned at the centre to monitor core temperature. For comprehensive temperature monitoring, thermocouples were strategically positioned at three designated locations along the length of the slab (detailed in Figure 4). Prioritizing the safety of personnel and equipment, a dedicated control room was established on-site.

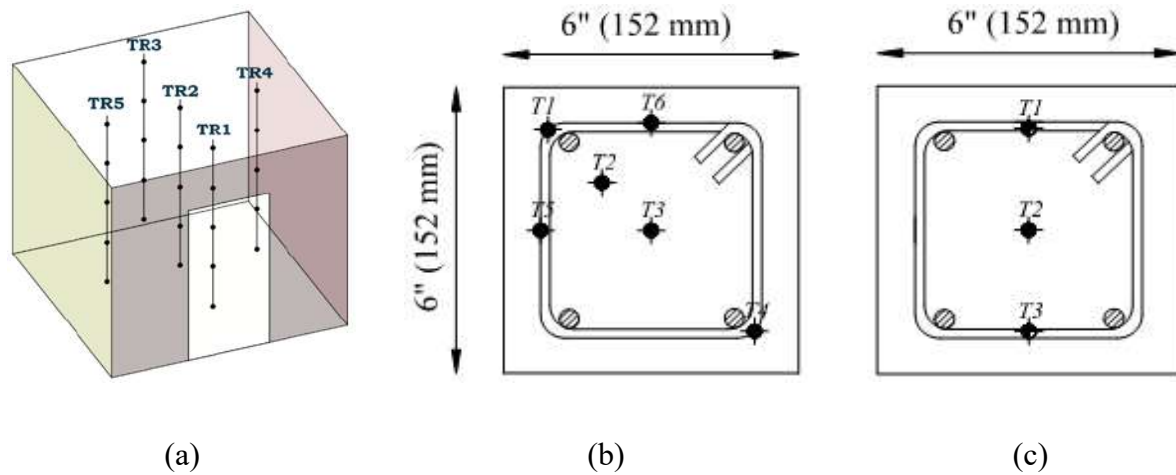


Figure 4: Locations of thermocouples for temperature measurement: (a) Compartment trees, (b) Columns, (c) Beams.

2.2 Dynamic Testing

Dynamic testing was carried out to identify the fundamental dynamic characteristics of the structure, including natural frequencies, damping, and mode shapes, across various levels of damage. Fundamental natural frequency outcomes are presented in terms of variations in fundamental periods and normalized lateral stiffness. A mass source was used to gently impact the structure, generating an impulse that induced free vibration in the structure and allowed for the derivation of its dynamic properties (see Figure 5). Four accelerometers, positioned in a zigzag pattern on each floor (two per floor), were affixed to the structure to assess its response in three dimensions (refer to Figure 6).

To guarantee data consistency and minimize the possibility of errors arising from instrumentation or human factors, the data acquisition system employed a high sampling rate of 256 Hz. Additionally, the impact testing procedure involved repeated strikes to ensure data reliability. Acceleration histories, recorded with a data logger, were analyzed using the advanced technical data analysis and display software DADiSP [15]. The tests were conducted on the structure before the fire test, after the low-duration fire test, and after the high-duration fire test.

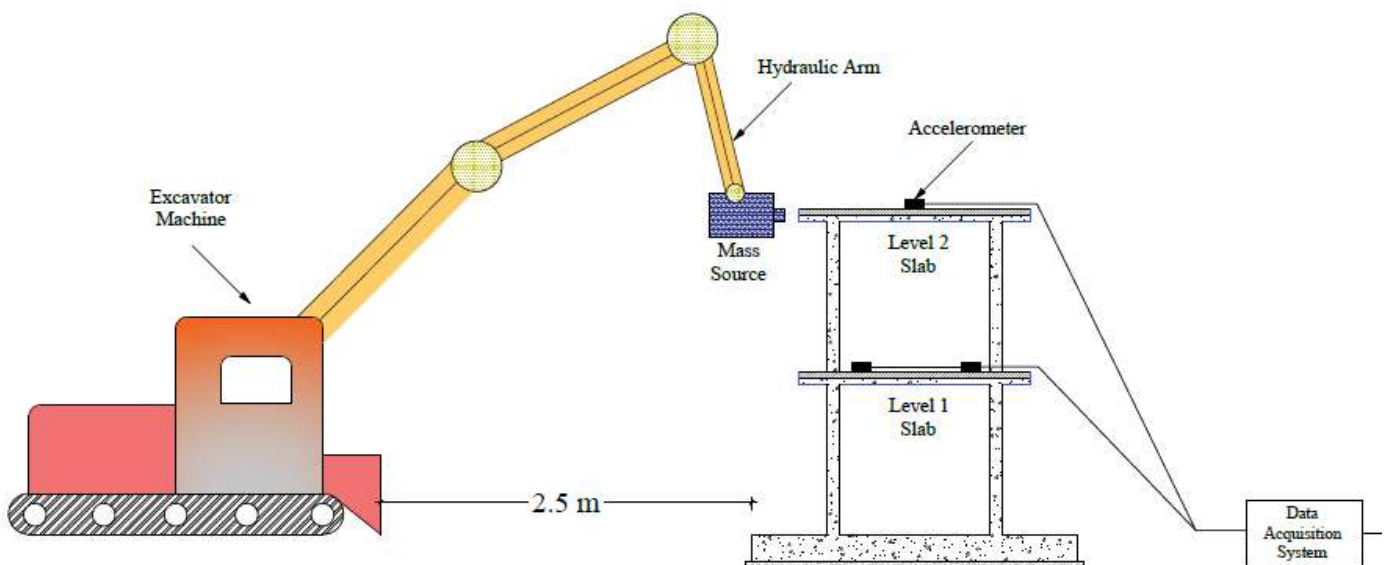


Figure 5: Dynamic testing of the structure

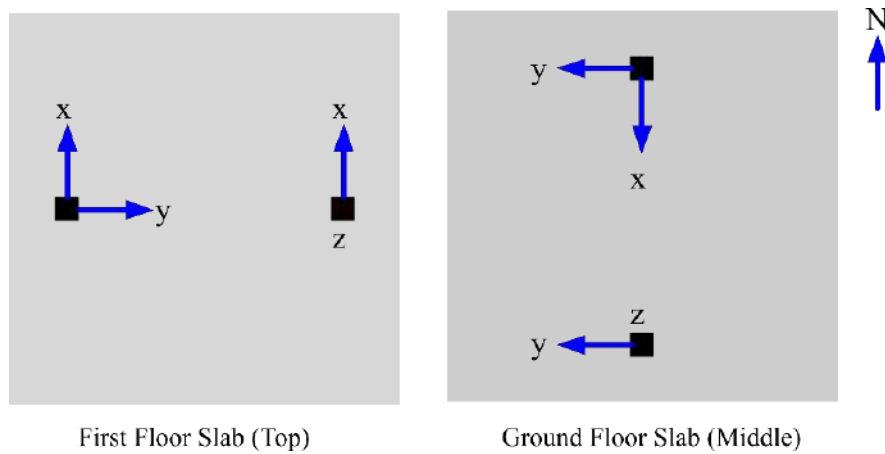


Figure 6: Accelerometers positioning on the structure

2.3 Non Destructive Testing (NDT)

Throughout the structural testing, Non-Destructive Testing (NDT), including ultrasonic pulse velocity (UPV) and Schmidt hammer rebound testing, was conducted at various stages. Concrete column strength was evaluated at mid-height, beams were tested for pulse readings at critical bending and shear points, and slab were assessed at different locations.

2.4 Fire Test

The initial SD test used 150 kg (22 kg/m^2) of Eucalyptus wood (having calorific value 19.10 MJ/Kg, and density 495 kg/m^3), whereas the LD test utilized 320 kg (48 kg/m^2) of Mulberry wood (having calorific value 17.62 MJ/Kg, and density 610 kg/m^3) within the compartment. The selection of different wood types aimed to create fires with varying time-intensity characteristics. Four equally spaced wooden log piles, each consisting of 2 ft (610 mm) logs with diameters ranging from 2-2.5 inches (50.8-63.5 mm), were utilized in both of the tests. Kerosene oil was used to ignite the fire. Additionally, the compartment's slab was loaded with 16 evenly distributed concrete cylinders, each weighing an average of 13.4 kg (29.5 lbs.), resulting in a total slab load of 215 kg (472 lbs.), equivalent to 15.6 lb/ft^2 (refer to Figure 7). The SDF design aimed for a flashover duration of 20 minutes whereas the LDF aimed for a flashover of 100 minutes. Figure 8 shows the fuel burning at the flashover point during the SD fire test.

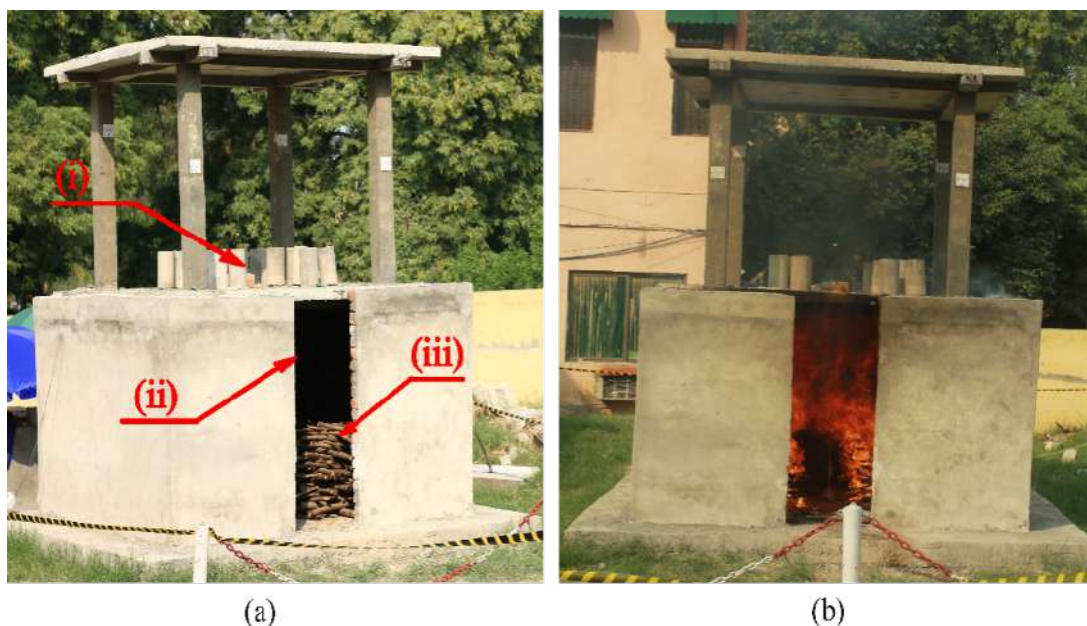


Figure 7: (a) Test setup (i) Superimposed load (ii) Opening of compartment (iii) Fuel for fire (b) SD fire test



Figure 8: Flashover of SD fire test

3 RESULTS

3.1 Results from Fire Testing

3.1.1 Thermal Response from SD Fire Test

Temperature variations within the compartment were monitored using thermocouple arrays positioned at five distinct locations. Figure 9 illustrates the temperature distribution within the compartment throughout a 20-minute fire test. Three thermocouple arrays were strategically placed, spanning from the south (near the opening) to the north. As expected, the highest temperature of 852 °C was recorded at the uppermost thermocouple on the southernmost array, closest to the compartment opening. This location likely received the brunt of the heat due to its proximity to the fire source and unrestricted airflow. Conversely, temperatures measured by the thermocouple arrays further north displayed a significant decrease, reaching a maximum of 690 °C. This substantial difference can be attributed to the limited oxygen availability farther from the opening, hindering combustion and overall heat generation in those areas.

The temperature profile indicates a vertical heat flow, with higher elevations (C1 and C2) registering higher temperatures during the flashover phase compared to lower elevations (C3, C4, and C5). As the fire subsided (decay phase), thermocouples near the compartment floor measured the highest temperatures. This indicates ongoing combustion of fuel that settled at the bottom.

Each beam within the compartment was equipped with three embedded thermocouples. During the decay phase, Beam B12 closest to the opening recorded the highest temperature (258 °C) at the bottom clear cover, while its core reached 132 °C [Figure 10 (a)]. This pattern was consistent with side beams (B13, B24). Beam B34, farthest from the opening, exhibited lower temperatures, indicating a link between reduced oxygen supply and lower temperature rise.

Similarly, temperature trends observed in the slabs mirrored those of the beams. The bottom concrete cover of the slabs registered a maximum temperature of 260 °C [see Figure 10 (b)]. Interestingly, minimal disparity was observed between the core temperature and the temperature at the outermost surface of the slabs, likely due to their thinness. Of particular note, the thermocouple on the top clear cover near the opening exhibited significantly greater temperatures compared to the core. This spatial difference in temperature points towards the opening as a source of radiant or convective heat affecting the exposed clear cover.

Each column's middle section was equipped with six thermocouples. Figure 10 (c) showcases the thermal response of columns C1 and C4. The maximum core temperature for both columns was recorded at 142 °C. The figure might also include data points for other locations within the columns, such as near the surface, providing a more comprehensive understanding of the temperature distribution.

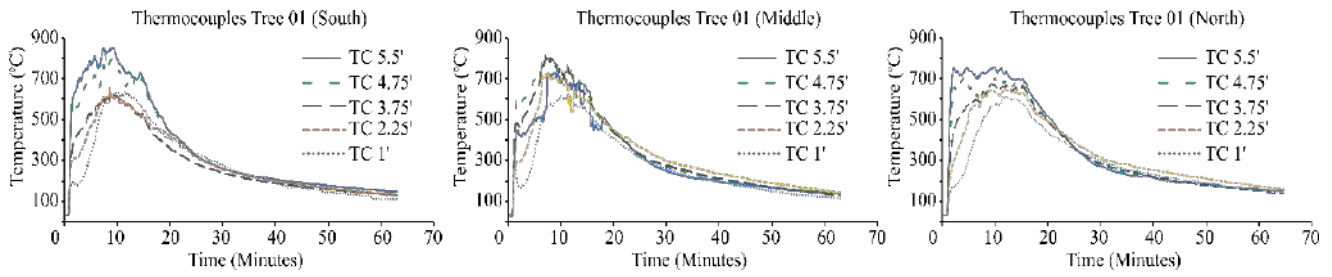


Figure 9: Chronological temperature data recorded at different points within the compartment

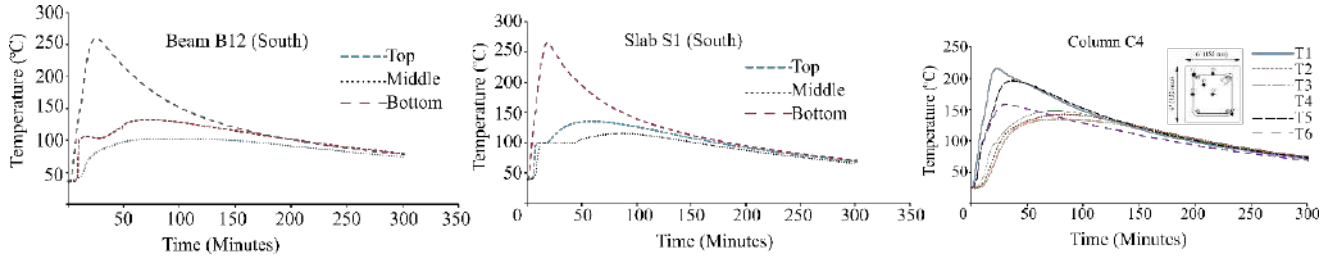


Figure 10: Variations in temperature over time across beam sections

3.1.2 Thermal Response from LD Fire Test

The distribution pattern of fire from the LD fire test within the compartment bears resemblance to SD fire, affirming the heat flow within the compartment under specified opening conditions. The highest temperature recorded in the compartment reached 813 °C, detected by thermocouple T1 positioned nearest to the opening and at the topmost point. In contrast to SD, LD fire exhibited an extended flashover period lasting nearly 100 minutes, accompanied by a comparatively slower fuel decay rate.

Regarding core temperatures, beams, columns, and the slab registered maximum temperatures of 240 °C, 326 °C, and 190 °C, respectively. Figure 11 provides comprehensive data on fire recording. It's worth mentioning that there's a significant temperature contrast of around 100 °C between thermocouples near the compartment opening and those placed farthest from it.

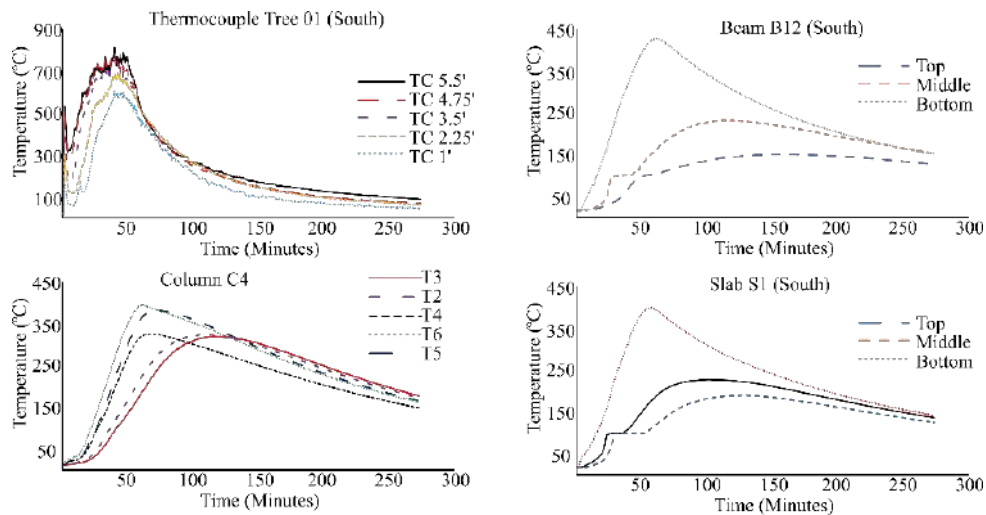


Figure 11: Compartment and sectional temperature data for the LD fire

3.2 Results from NDT

3.2.1 Schmidt Hammer Test Results:

The compressive strength of the columns was reduced after SD exposure to fire. On average, there was a 27 % reduction, as depicted in Figure 12. After LD fire tests the compressive strength was further declined, resulting in an overall reduction of 45 % from their original strength. Notably, this reduction was consistent across all columns due to their symmetrical design.

Conversely, the reduction in strength for the beams was uneven. Those in close proximity to ventilation, notably B12, experienced significant reductions. Following the SD fire, there was a 49.5 % reduction, which escalated to 54.6 % after the second fire. This increase in loss of strength is likely attributed to the elevated temperatures increase from the oxygen supply outside the compartment. Beams positioned in the East (B13) and West (B24) directions showed similar patterns of strength reduction. After the SD fire, reductions of 37.2 % and 39.4 % were observed, respectively, followed by further reductions to 48.8 % and 44.8 % after the LD fire. Conversely, beams in the north direction, receiving the least oxygen supply, sustained the least damage, experiencing reductions of 32.8 % and 44.8 % after the first and second fires, respectively.

Slabs in the middle section incurred more substantial damage compared to those adjacent to columns and beams. After the SD fire test, there was an average loss of 41 % in strength, which increased to 45 % after the exposure to LD fire test.

The results of the Schmidt hammer tests indicated notably low values. This can be attributed to the fact that the rebound hammer solely measures the surface strength of concrete. In compartment fires, external temperatures elevate rapidly, while the core temperature remains relatively low until prolonged exposure to heat. Consequently, surface concrete easily loses strength, manifesting in the Schmidt hammer rebound tests.

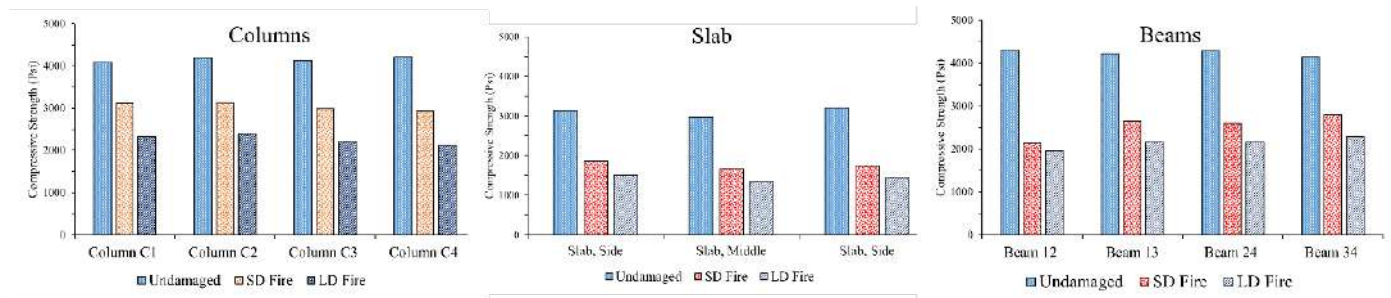


Figure 12: Strength of slab using rebound hammer testing

3.2.2 Ultrasonic pulse velocity test

The ultrasonic pulse velocity testing results do not provide information about the compressive strength of concrete. However, they do offer insights into concrete quality by detecting cracks, voids, honeycombs, and other non-homogeneities. This method involves measuring the time taken by a wave pulse to travel through concrete from the transmitter to the receiver.

Figure 13 indicate that columns and beams sustain damage after the SD and LD fires, with more significant damage occurring in the latter. The decrease in velocity suggests micro-structural damage due to heat exposure. Column symmetry results in a uniform strength reduction across all columns, as observed in Schmidt hammer rebound testing. Unlike columns, beam damage varies. Figure 13 show higher velocity reductions in beams, especially those near ventilation. The substantial loss in velocity may be attributed to elevated temperatures from external oxygen supply. Beams in the East and West directions exhibit similar strength reductions, while those in the North direction, with lower oxygen supply, experience less damage.

Slabs endure more damage in the middle portion compared to areas near columns and beams, with an average strength loss of 20.4 % after the SD fire and 41.5 % after the LD fire. The UPV results from slab tests before the fire and after the SD and LD fire tests are shown in Figure 14. A comparison between rebound hammer, and ultrasonic pulse velocity in form of percentage is presented in the Table 1.

Schmidt hammer test results are low, indicating surface strength loss due to rapid external temperature increase during compartment fires, despite core temperatures remaining low initially. This emphasizes the test's limitation in assessing core concrete strength.

Table 1: Comparison of Rebound hammer strength and UPV in SD and LD fires

	Rebound hammer strength (%)		UPV (%)	
	SD	LD	SD	LD
Average of all Columns	73	54.4	87	75.1
Average of all Beams	59.9	50.5	77.9	66.7
Average of Slab	56.6	46.1	79.6	41.5

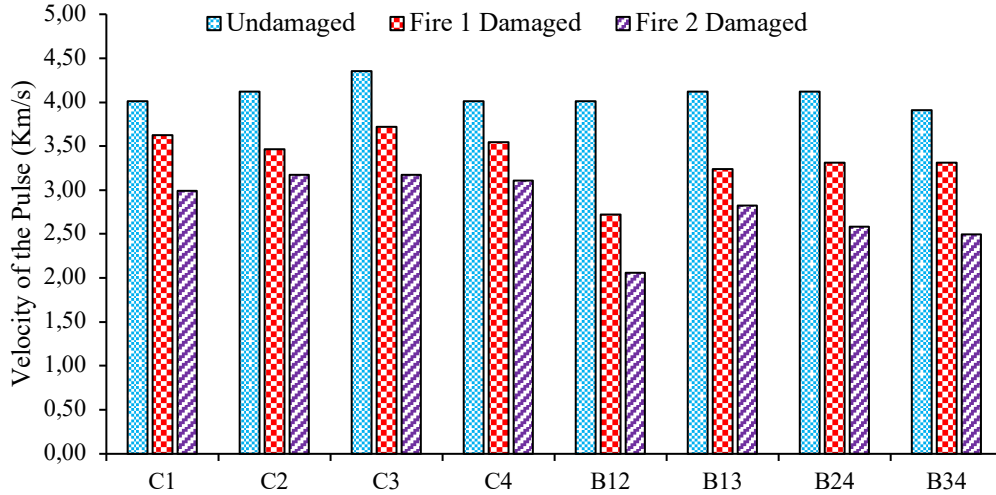


Figure 13: Strength evaluation of columns and beams using UPV

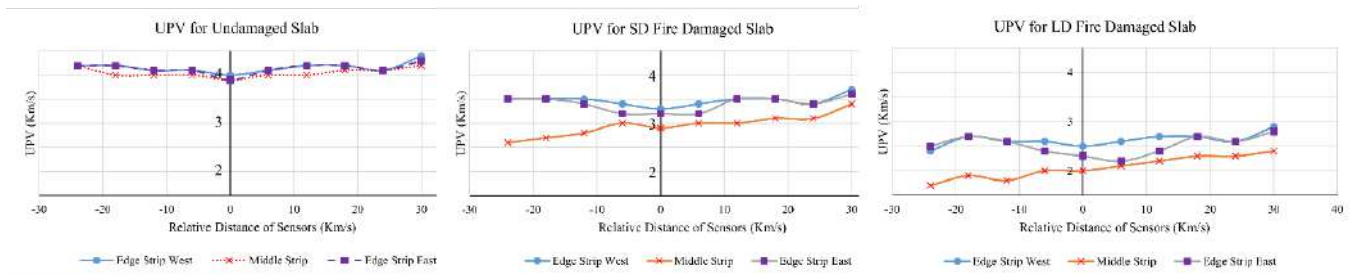


Figure 14: UPV for slabs before fire and after SD & LD fire tests

3.3 Results from Dynamic Testing

Figure 15 displays the Power Spectral Densities (PSDs) of the undamaged structure, acquired from four accelerometers in both North-South and East-West directions, showing consistent frequencies. However, an increase in temperature results in decreased natural frequencies of the structure due to SD and LD fire tests as depicted in Figure 15 and Figure 16 respectively. After SD fire test, frequencies dropped from 4.38 Hz & 4.35 to 3.96 Hz & 3.71 Hz, while after LD fire test, they further decreased to 2.23 Hz & 2.21 Hz. These changes in natural frequencies, influenced by parameters like mass & stiffness, suggest damage from high-intensity fires. LD fire test exhibits more significant frequency alterations (50.5 % of undamaged structure) compared to SD fire test (85.29 % of undamaged structure), as illustrated in Figure 16.

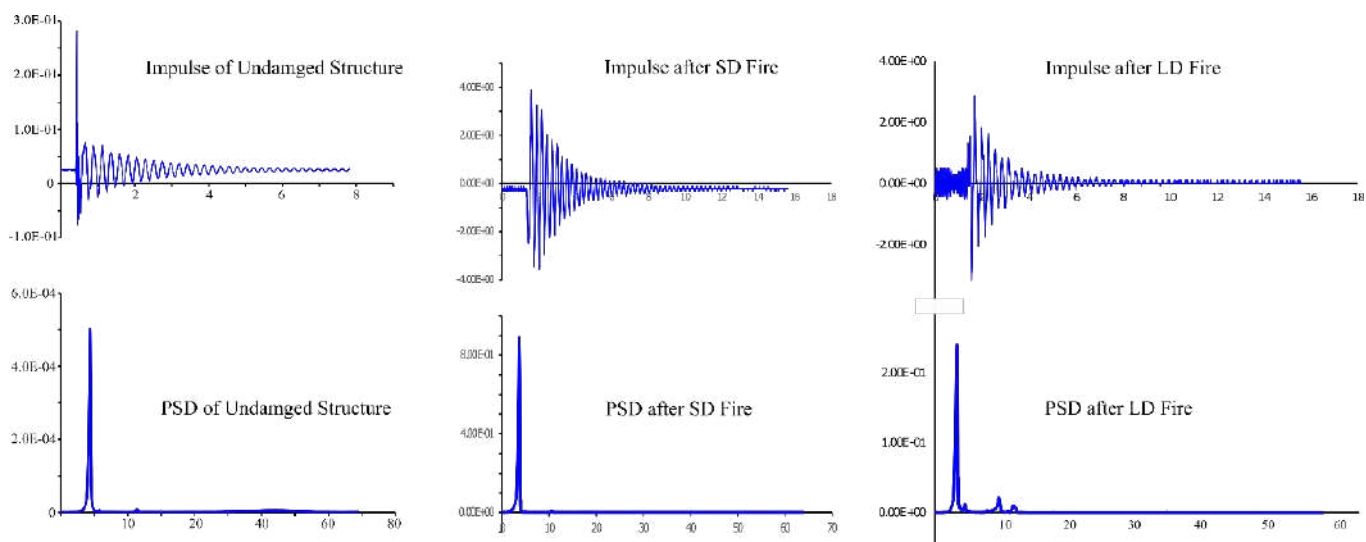


Figure 15: The vibration response and power spectral density of an undamaged structure under excitation in the north-south direction

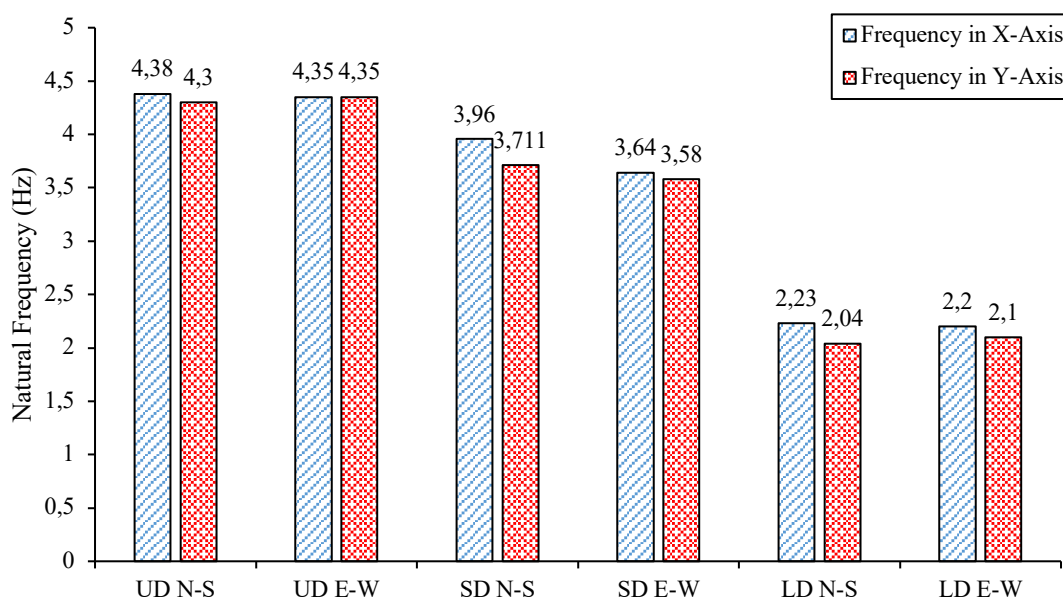


Figure 16: Evaluating the structural natural frequencies comparatively

During structural impact tests, data from accelerometers was employed to derive transfer functions (TF), which depict the normalized structural response in relation to the Fourier transform of the imposed base motion across frequency domains. Utilizing these TFs, mode shapes corresponding to fundamental natural frequencies were computed, leveraging accelerometer data mounted on the test structure. Particular attention was given to assessing relative slab motion between the two floors of the structure, with accelerometers strategically positioned for mode shape analysis. Figure 17 showcases the average TFs across frequency domains for both ground floor and first floor levels.

Due to minimal structural impact, only the initial two mode shapes could be discerned. The mode shapes of the undamaged structure was extracted by normalizing the amplitude of the transfer function as illustrated in Figure 18. Correspondingly, mode shapes for the structure following SD and LD fire tests were also determined. Although exhibiting slight behavioral deviations compared to the undamaged structure following the SD fire test, the alterations became more conspicuous post LD fire test (refer to Figure 18).

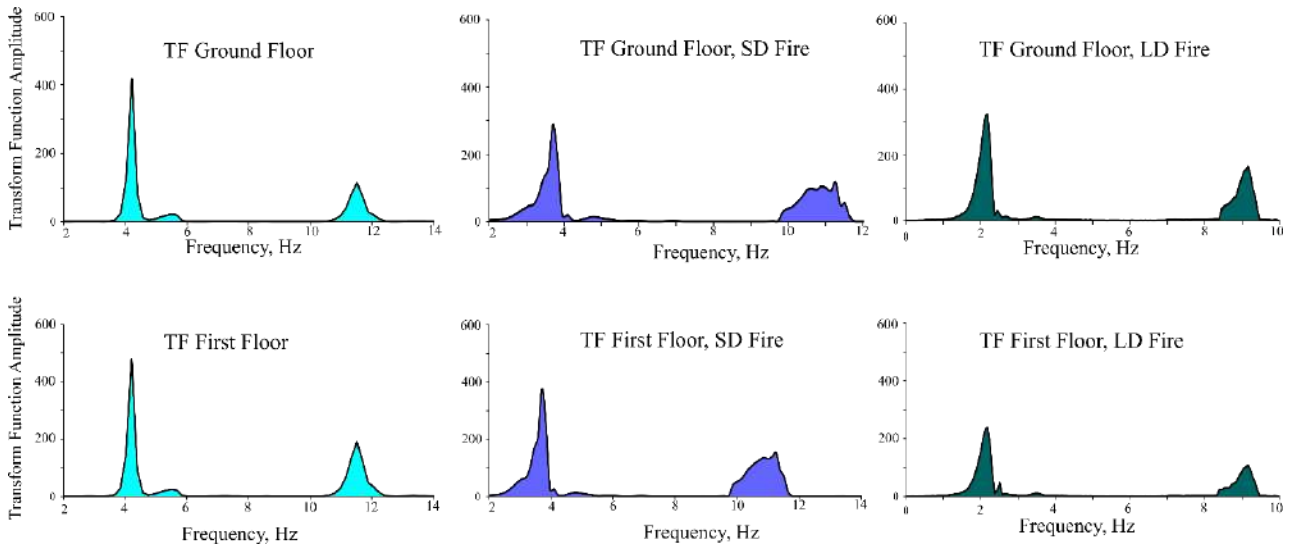


Figure 17: Amplitude of Ground and First Floor Transfer Functions for Undamaged Conditions, SD fire test, and LD fire test

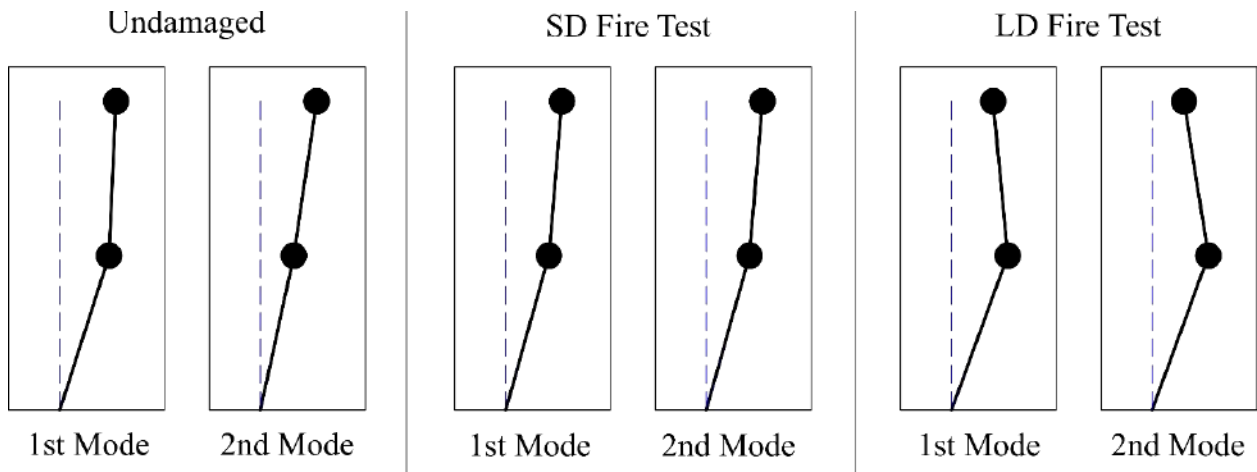


Figure 18: Mode shapes of the structure at different fire durations

4 CONCLUSIONS

This paper discusses the experimental findings regarding changes in the dynamic properties of a reduced-scale two-story reinforced concrete (RC) building following exposure to real fires of both short and long durations. The conclusions drawn from these results are as follows:

1. A 20-minute short-duration (SD) fire test subjected the compartment to peak temperatures of 852 °C. Despite this intensity, the test failed to cause substantial damage to the three-dimensional structure's components. Beam, column, and slab core temperatures during the SD fire test remained relatively low, reaching maximums of 132 °C, 142 °C, and 133 °C, respectively.
2. The 100-minute long-duration (LD) fire test produced a peak compartment temperature of 813 °C, comparable to the SD test. However, the extended duration in the LD test resulted in significant damage, evident through NDT and vibration testing. Core temperatures in beams, columns, and slabs during the LD test reached substantially higher values compared to the SD test, with peaks of 240 °C, 326 °C, and 190 °C, respectively.
3. The experiment revealed a substantial decline in the structure's natural frequency as fire temperatures intensified. Following the short SD fire test, the natural frequency dropped to 85.29 % of its initial value. This decline became even more pronounced after the LD fire test, with a

frequency reduction of 50.5 %. These observations highlight the significant influence of elevated temperatures on the structural dynamics of the three-dimensional structure.

4. Fire exposure demonstrably altered the structure's dynamic behaviour, evident through significant changes in its mode shapes. These changes were particularly pronounced after the LD fire test compared to the SD test. This suggests a stronger correlation between sustained high temperatures and the degree of structural transformation.
5. The UPV results shows present good agreement with the dynamic characteristics as compared to the rebound hammer test results which shows only the result of the surface damage of the structure.

ACKNOWLEDGEMENT

We gratefully acknowledge the financial support provided by the Higher Education Commission (HEC) Pakistan through the National Research Program for Universities (NRPU) grant number NRPU/10607.

REFERENCES

- [1] M. Law, Designing fire safety for steel–recent work, in: Proc. ASCE Spring Conv. Am. Soc. Civ. Eng., 1981.
- [2] L. Bisby, J. Gales, C. Maluk, A contemporary review of large-scale non-standard structural fire testing, *Fire Sci. Rev.* 2 (2013) 1. <https://doi.org/10.1186/2193-0414-2-1>.
- [3] D. Drysdale, An introduction to fire dynamics, 3rd ed., 2011.
- [4] V.K.R. Kodur, M. Garlock, N. Iwankiw, Structures in Fire: State-of-the-Art, Research and Training Needs, *Fire Technol.* 48 (2012) 825–839. <https://doi.org/10.1007/s10694-011-0247-4>.
- [5] L. Bisby, J. Gales, C. Maluk, A contemporary review of large-scale non-standard structural fire testing, *Fire Sci. Rev.* 2 (2013) 1–27. <https://doi.org/10.1186/2193-0414-2-1>.
- [6] J. Gales, C. Maluk, L. Bisby, Large- scale structural fire testing- How did we get here, Where are we, and where are we going?, 15th Int. Conf. Exp. Mech. Fire Symp. (2012) 1–22.
- [7] C. Bailey, Holistic behaviour of concrete buildings in fire, *Proc. Inst. Civ. Eng. - Struct. Build.* 152 (2002) 199–212. <https://doi.org/10.1680/stbu.2002.152.3.199>.
- [8] P. Kamath, U.K. Sharma, V. Kumar, P. Bhargava, A. Usmani, B. Singh, Y. Singh, J. Torero, M. Gillie, P. Pankaj, Full-scale fire test on an earthquake-damaged reinforced concrete frame, *Fire Saf. J.* 73 (2015) 1–19. <https://doi.org/10.1016/j.firesaf.2015.02.013>.
- [9] M. Usman, M. Yaqub, M. Auzair, W. Khaliq, M. Noman, A. Afaq, Restorability of strength and stiffness of fire damaged concrete using various composite confinement techniques, *Constr. Build. Mater.* 272 (2021) 121984. <https://doi.org/10.1016/j.conbuildmat.2020.121984>.
- [10] B. Li, Y.-L. Dong, D.-S. Zhang, Fire behaviour of continuous reinforced concrete slabs in a full-scale multi-storey steel-framed building, *Fire Saf. J.* 71 (2015) 226–237. <https://doi.org/10.1016/j.firesaf.2014.11.021>.
- [11] Q. Xing, J. Liao, Z. Chen, W. Huang, Shear behaviour of fire-damaged reinforced-concrete beams, *Mag. Concr. Res.* 72 (2020) 357–364.
- [12] A.C. Altunışık, F.Y. Okur, V. Kahya, Modal parameter identification and vibration based damage detection of a multiple cracked cantilever beam, *Eng. Fail. Anal.* 79 (2017) 154–170.
- [13] M. Noman, M. Yaqub, M. Fahad, F. Butt, B. Khalid, Dynamic Characteristics of RC Structures in Short and Long Duration Real Fires, *Case Stud. Constr. Mater.* 16 (2022) e01058. <https://doi.org/10.1016/j.cscm.2022.e01058>.
- [14] M. Noman, M. Yaqub, Restoration of dynamic characteristics of RC T-beams exposed to fire using post fire curing technique, *Eng. Struct.* 249 (2021) 113339. <https://doi.org/10.1016/j.engstruct.2021.113339>.
- [15] DADiSP, The DADiSP TM Worksheet Data Analysis and Display Software, 2003.

EXPERIMENTAL STUDY OF THE LOADBEARING PERFORMANCE OF LIGHT GAUGE STEEL FRAME (LSF) WALLS EXPOSED TO FIRE ON TWO SIDES

Iziengbe Inerhunwa¹, Danny Hopkin², Grzegorz Kimbar³, Michael Spearpoint⁴,
Georgios Kanellopoulos⁵, Piotr Turkowski⁶

ABSTRACT

Concerns have been raised by UK industry regarding the expected fire performance of buildings that employ light gauge steel frame (LSF) walls as a solution for their structural loadbearing system. There is a level of uncertainty arising from the potential exposure of internal and external loadbearing walls to heating conditions on both sides. This study investigated the performance of loadbearing LSF walls exposed to fire on two sides to determine whether their loadbearing performance is likely affected by the number of faces simultaneously exposed to fire. A total of four wall specimens were tested, two each (with and without cavity insulation) for one- and two-sided fire exposure conditions under the ISO 834 heating regime. The main findings from the experiments are that exposure of LSF walls to fire on two sides markedly intensifies heating compared to one-sided exposure, evidenced by higher stud temperatures and accelerated rates of increase particularly at higher fire resistance periods. The loadbearing capacity of LSF walls is considerably reduced under two-sided fire, dropping to 44% for non-insulated walls and 62% for cavity-insulated walls, relative to one-sided exposure. While cavity insulation precipitates a notable temperature gradient and subsequent early failure in one-sided exposure, its impact is negligible in two-sided scenarios. Furthermore, the results showed that fire resistance classifications for single-sided exposure should not be extrapolated to two-sided exposure.

Keywords: Light gauge steel frame (LSF); loadbearing walls, two-sided exposure; standard fire test

1 INTRODUCTION

Light gauge steel frame (LSF) walls are commonly used in modern building construction [1], consisting of cold-formed steel studs, sheathing material, and may include insulation [2]. LSF walls may be used as fire-separating walls to mitigate fire and smoke spread from one compartment to another and limit temperature

¹ Fire Engineer, OFR Consultants, UK

e-mail: iziengbe.inerhunwa@ofrconsultants.com, ORCID: <https://orcid.org/0000-0001-8029-6478>

² Director, OFR Consultants, UK

e-mail: danny.hopkin@ofrconsultants.com, ORCID: <https://orcid.org/0000-0002-2559-3581>

³ Professor, Fire Research Department, Building Research Institute (ITB), Poland

e-mail: g.kimbar@itb.pl, ORCID: <https://orcid.org/0000-0003-0500-4062>

⁴ Research Leader, OFR Consultants, UK

e-mail: michael.spearpoint@ofrconsultants.com, ORCID: <https://orcid.org/0000-0002-3632-4870>

⁵ Fire Engineer, OFR Consultants, UK

e-mail: yorgos.kanellopoulos@ofrconsultants.com, ORCID: <https://orcid.org/0009-0009-0020-9692>

⁶ Assistant Professor / Head of Fire Resistance and Fire Protection Systems of Structural Elements Division, Fire Research Department, Building Research Institute (ITB), Poland

e-mail: p.turkowski@itb.pl, ORCID: <https://orcid.org/0000-0002-0020-0091>

increase on the unexposed surface for a specified period [3]. LSF walls also find application as both loadbearing and non-loadbearing walls which may not have a fire-separating function.

Concerns have been raised by UK industry regarding the expected fire performance of internal loadbearing LSF wall systems [4]. There is a level of uncertainty arising from the potential exposure of internal loadbearing walls to heating conditions on both sides. These walls may be architecturally separating elements, but not fire-separating elements, e.g., they do not form part of a compartment boundary. This means that where a compartment is fully involved in a fire, these walls can be exposed to fire on both sides and may not perform as expected in terms of loadbearing capacity compared to when heated from just one side. A similar concern has also been raised by industry [5] for external loadbearing walls afforded non-fire-resisting cladding, where flames emanating from an enclosure fire can heat the external surface of an LSF wall, with the internal face simultaneously heated by the internal fire. However, current design guidance in England [6] does not explicitly identify a need to test for two-sided exposure.

Extensive experimental and numerical studies have been carried out to understand the performance of LSF walls exposed to fire. However, almost all of the studies have only focused on the loadbearing performance of LSF walls exposed to fire on one side only (e.g., [7 – 16]).

At the time of carrying out this study, the authors found only two existing studies that investigated the performance of LSF walls exposed to fire on two sides [17,18]. The two-sided existing studies had limitations in that they employed only numerical (finite element) models without validating against any experimental/test results of two-sided fire exposure as noted by Vy et al. [18]. Finite element modelling (FEM) may be a valid means of understanding the performance of LSF walls exposed to fire on two sides. However, given a lack of experimental/test data necessary for validation, the assessment of such modelling remains a cause for concern as there is a limited basis for benchmarking. Consequently, there is currently a knowledge gap regarding the expected structural performance of LSF elements that are exposed to heating conditions on both sides.

To resolve the uncertainty that arises from the lack of test data, and to improve confidence in future FEM studies, an experimental investigation of the loadbearing performance of LSF walls with both one- and two-sided fire exposure has been carried out. The aim of the experiments was to determine how the loadbearing performance of LSF walls are likely affected by the number of faces simultaneously exposed to fire.

2 EXPERIMENTAL PROGRAMME

A total of four wall specimens were tested, two each for single- and two-sided fire exposure conditions. Previous studies (i.e., for one-sided exposure [14 – 16]) have shown that the insulation between the studs has a significant impact and, therefore, the tested specimens in this study included cases with and without cavity insulation. A summary of the test cases are: (Test 1) Two-sided fire exposure, no insulation; (Test 2) One-sided fire exposure, no insulation; (Test 3) Two-sided fire exposure, with cavity insulation; (Test 4) One-sided fire exposure, with cavity insulation.

The test methods adopted for the testing of the LSF walls were as per BS EN 1365-1:2012 [19] for the one-sided fire exposure test, and BS EN 1365-4:1999 [20] for the two-sided test. Both test methods expose the sample to the standard time-temperature curve in accordance with BS EN 1363-1:2020 [21].

2.1 Description of specimens

The tested LSF wall system comprised cold-formed steel studs and sheathing boards, with the addition of insulation material within the cavity for the insulated wall specimens. The tested wall build-up was 3 m wide by 3 m high with 6 studs spaced at 600 mm centres. Evidence from other materials (i.e., masonry and concrete [22 – 24]) suggests that the difference between one-sided and two-sided exposure is more significant at higher fire resistance demands. Therefore, to elucidate the difference between single- and two-sided fire exposure of LSF walls, the tested walls were designed to achieve a minimum of 90-minute fire resistance rating under one-sided fire exposure when afforded cavity insulation. Figure 1 (a and b) show a section of the tested wall specimen with no insulation and with cavity insulation provided, respectively.

The steel stud section used was a lipped channel section (C89×1.2) with nominal dimensions being 89 mm, 41 mm, 1.2 mm for depth, width, and thickness, respectively. The stiffener depth was 11 mm. The specific mass of steel was 1.75 kg/m; the steel grade was S350GD. The sheathing material was 2 layers (nominal thickness of 15 mm each) of fire rated gypsum board with a measured surface density ranging from 12.6 kg/m² to 13.0 kg/m² per board for the four different tests, ambient temperature thermal conductivity of 0.2 W/mK and measured moisture content of between 0.2% and 0.3%. The gypsum boards were attached to the studs with self-drilling screws at 300 mm centres at each board edge and each board mid-width over a stud. The screws used were 3.5×35 mm for the first layer and 3.5×55 mm for the second layer. The free vertical side edges of the wall were covered with two layers of the boards, the same as the ‘wall’ surfaces. Gypsum filler was used as the jointing compound to seal the joints between plasterboards. The insulation material used (for the cavity insulated wall specimens) was mineral wool insulation completely filling the cavity between the studs and the sheathing boards, with density of 35.1 kg/m³, ambient temperature thermal conductivity of 0.036 W/mK and 0.8% moisture content.

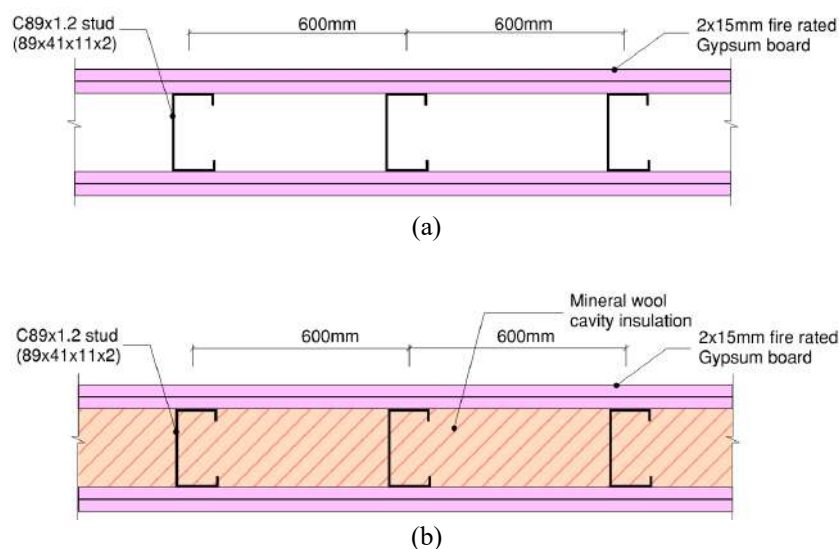


Figure 1. Section of tested LSF wall (a) without insulation (b) with cavity insulation

2.2 Experimental setup

Tests were conducted in a furnace with dimensions able to accommodate the wall specimen. Internal dimension of the furnace chamber was 3.3 m × 4.3 m × 3.7 m. For the one-sided test, the wall was placed at the end of the furnace and heated on one side only. For the two-sided test, the wall was placed at the centre of the furnace along the longer side (resulting in approximately 0.65 m of free space at both ends of the wall) and heated on both sides simultaneously. In both cases, the wall was fixed to a 700 mm high masonry plinth at the bottom and loaded at the top. The furnace followed the ISO standard heating regime, which was achieved through the use of propane gas burners. Figure 2 shows a sketch of the plan and elevation of the wall specimen inside the furnace for both exposure conditions.

The load was applied axially to the wall specimen by means of a beam and actuator at the top edge of the wall. The total load applied to the wall was 80 kN i.e., 13.3 kN per stud. Before the commencement of fire exposure, the load on the test specimen was increased gradually from 0 kN to 80 kN in 10 minutes and then sustained at the full test load (80 kN) for 20 minutes.

The test was conducted until failure of the steel studs occurred, with failure defined as a loss in loadbearing capacity, indicated by runaway vertical / lateral deflection. This is similar to failure criteria used in previous studies on one-sided fire exposure (e.g. by Chen et al. [9]). All measurements (temperature, applied load, deflection, furnace pressure and furnace power) were recorded at 15 s intervals for the duration of the test.

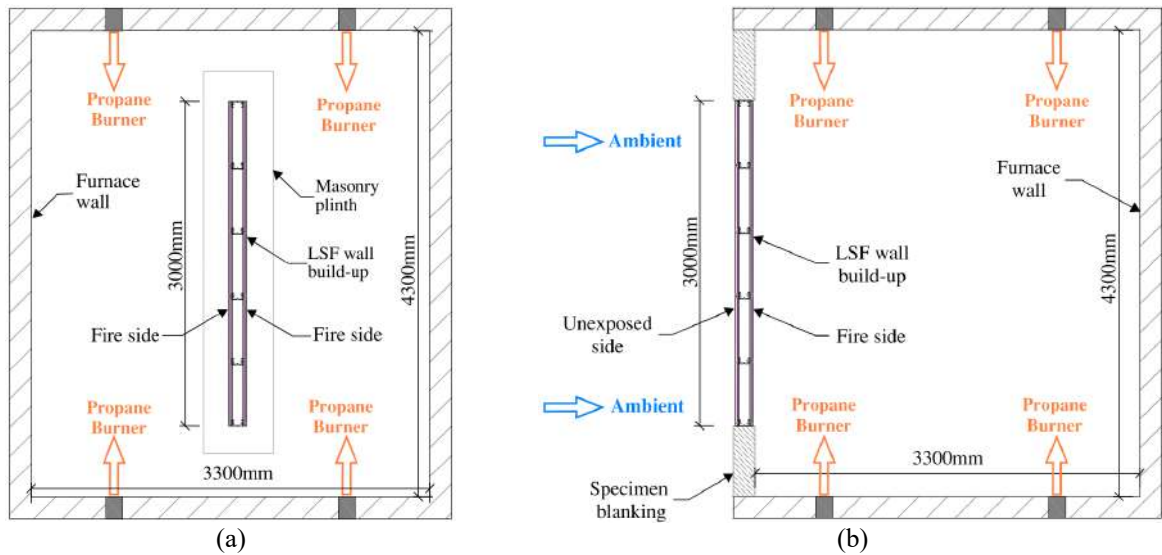


Figure 2. Sketch plan of test setup for (a) two-sided exposure and (b) one-sided exposure

2.3 Instrumentation

2.3.1 Furnace temperature measurements

The furnace was provided with plate thermometers to record gas temperature during the experiments. The plate thermometers were distributed to give a reliable indication of the average temperature in the vicinity of the test specimen and positioned so that they were not in contact with flames from the burners and that they are at least 450 mm away from any wall, floor, or roof of the furnace. Figure 3a) and Figure 3b) show a picture of the test setup and the location of the plate thermometers, for the two sided and one-sided fire exposure tests, respectively.

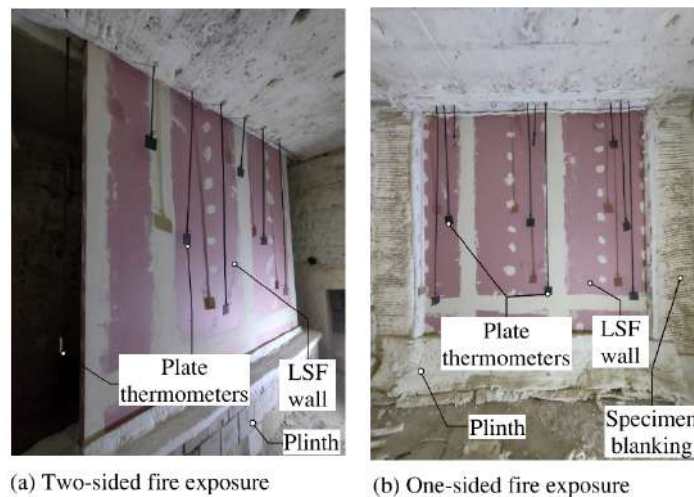


Figure 3. Picture of test setup showing location of plate thermometers for gas temperature measurements

2.3.2 Steel stud temperature measurements

Each wall specimen was provided with 20 internal thermocouples mounted on the flanges and web of the steel studs at different locations (the two middle studs and adjacent studs) to record the temperature rise of the steel. For the two middle studs, thermocouples were provided at three different locations along the height of each stud at the top $\frac{1}{4}$ height, mid-height, and bottom $\frac{1}{4}$ height (thermocouple group TE1 to TE6). The adjacent studs were provided with thermocouples at mid-height of the stud (thermocouple group TE7 and TE8). Each of the TE1 to TE6 groups had three thermocouples provided (at the two flanges – Flange 1

and Flange 2, and the web) at each stud location. Groups TE7 and TE8 had one thermocouple located at the web of the section. Figure 4a is a section drawing of the wall showing the location of the internal thermocouples. For the one-sided test, Flange 2 was the flange near the unexposed face of the wall.

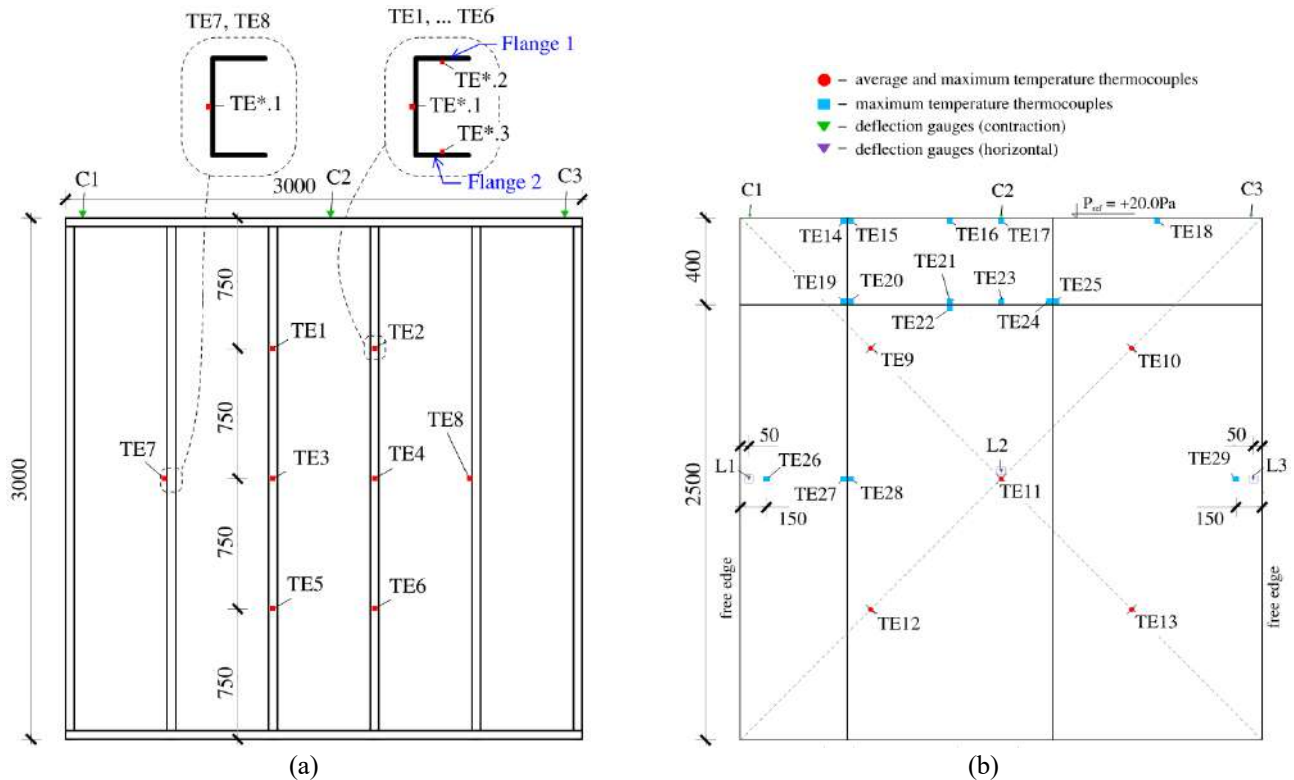


Figure 4. Section drawing showing location of (a) internal thermocouples and deflection gauges (b) external thermocouples and deflection gauges

2.3.3 Unexposed surface temperature (one-sided test)

For the one-sided test, the unexposed wall surface temperature was also measured. Thermocouples (21 nos. – group TE9 to TE29) were attached to the unexposed face to measure the average (TE9 to TE14) and the maximum (TE15 to TE29) temperature rise. The purpose of the average unexposed face temperature measurement was to determine the general level of insulation performance while disregarding hotspots. The average temperature rise on the unexposed surface was thus based upon measurements obtained from surface thermocouples located at or near the centre of the test specimen and at or near the centre of each quarter section of the wall. The purpose of maximum unexposed face temperature measurement was to determine the level of insulation performance at those locations where higher temperatures were expected to occur. Figure 4b is an elevation drawing showing the location of the external thermocouples.

2.3.4 Deflection measurements

The axial deflection of the wall was measured by gauges suitably arranged to measure the vertical deflection (contraction) and horizontal (lateral) deflection of the wall during the test. The zero point for the deflection was measured after applying the (full) load at the beginning of the test and before the commencement of heating. Horizontal deflection was only measured and recorded for the walls exposed to fire on one side. Horizontal deflection was not measured for the two-sided tests because the instrumentation would have been exposed directly to furnace heating and damaged in the process, as it involved fixing a wire and transducer to the mid-height of the wall inside the furnace. The locations of the deflection gauges (contraction gauges – C1, C2, and C3; horizontal deflection gauges – L1, L2 and L3) are shown in Figure 4 (a and b).

3 RESULTS

3.1 Failure times

The failure criteria of the wall specimens were based on observation of runaway vertical / lateral deflection. The results of vertical and lateral deflection are presented in detail in Section 3.3. The loadbearing failure times for the wall specimens are summarised in Table 1. For the cavity-insulated walls, times to failure were recorded at 68 min and 156 min, for the two-sided and one-sided exposure, respectively. For the non-insulated walls, failure times were 72 min and 116 min, for the two-sided and one-sided exposure, respectively. The ratio of time to failure of two-sided to one-sided is therefore 0.44 for the no insulation case and 0.62 for the cavity-insulated case.

Table 1. Summary of time to failure for one-sided vs two-sided fire exposure conditions

Test ID	Fire exposure condition	Cavity insulation	Time to failure [minutes]	Ratio of two-sided to one-sided
LZP01	Two-sided	No	68	0.44
LZP02	One-sided		156	NA
LZP03	Two-sided	Yes	72	0.62
LZP04	One-sided		116	NA

3.2 Steel stud temperature distribution

Figure 5 shows the temperature distribution across the central steel stud section at the mid-height of the wall for the four test cases. The graph shows that the two-sided test generally results in a higher temperature across all parts of the stud section (Flange 1, web, Flange 2) compared to the one-sided test. In the experiments both with and without insulation, the two-sided fire exposure had a higher rate of stud temperature increase compared to the one-sided experiment, leading to a quicker time to failure. However, the difference in temperature rise across the section for two-sided vs one-sided exposure is greater at higher exposure times. The maximum flange temperature at mid-height of the wall section observed (prior to failure of the wall specimen) is c. 546 °C and 697 °C for two-sided and one-sided fire exposure, respectively, with no insulation. For the insulated walls, the maximum flange temperature is 614 °C and 985 °C for two-sided and one-sided fire exposure, respectively. Furthermore, Figure 5 shows that the temperature gradient across the stud section (from Flange 1 through the web to Flange 2) is greater for the one-sided fire exposure condition and cases where insulation is present.

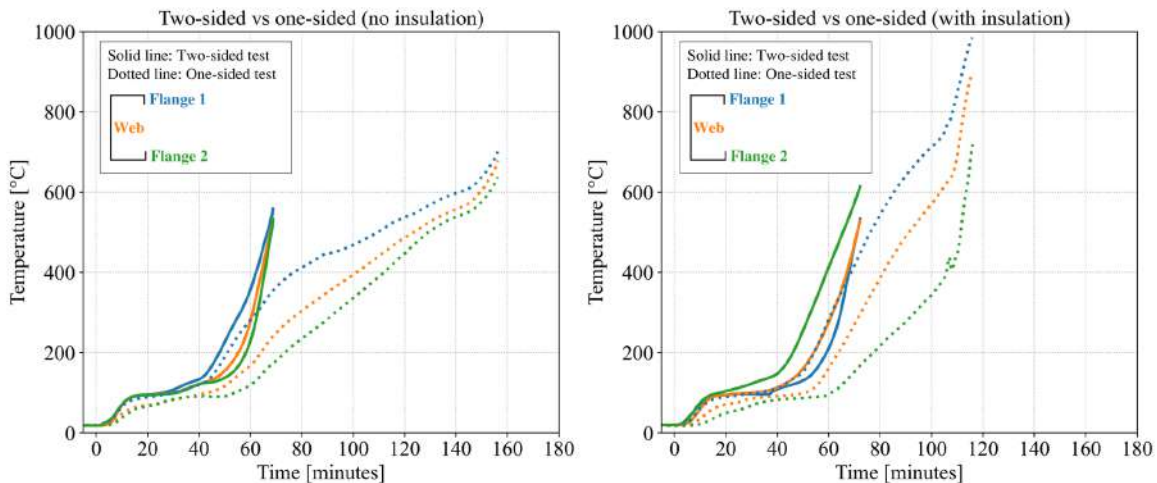


Figure 5. Stud temperature distribution at mid-height section (central stud – group TE3 in Figure 4)

Figure 6 compares the stud section temperature variation at different points along the height of the wall (top ¼ height, mid-height, and bottom ¼ height). The results show that the temperature distribution along the height of the stud can be described as uniform. As observed in Figure 5, Figure 6 also shows that the temperature gradient across the section of the stud at a particular height is higher for LSF walls exposed to fire on one side only vs two-sided fire exposure and higher for insulated LSF walls vs non-insulated LSF walls.

Figure 7 compares the stud web temperature variation along the (horizontal) length of the wall. Four locations were considered as shown in Figure 4 (the two central studs and adjacent studs i.e., TE3, TE4, TE7 and TE8). The results show that there is no significant variation along the length of the wall for all the wall specimens tested with temperature variation not exceeding 50 °C across the four locations for the two-sided test. The temperature variation was higher for the one-sided test with insulation with a maximum temperature variation of approximately 150 °C.

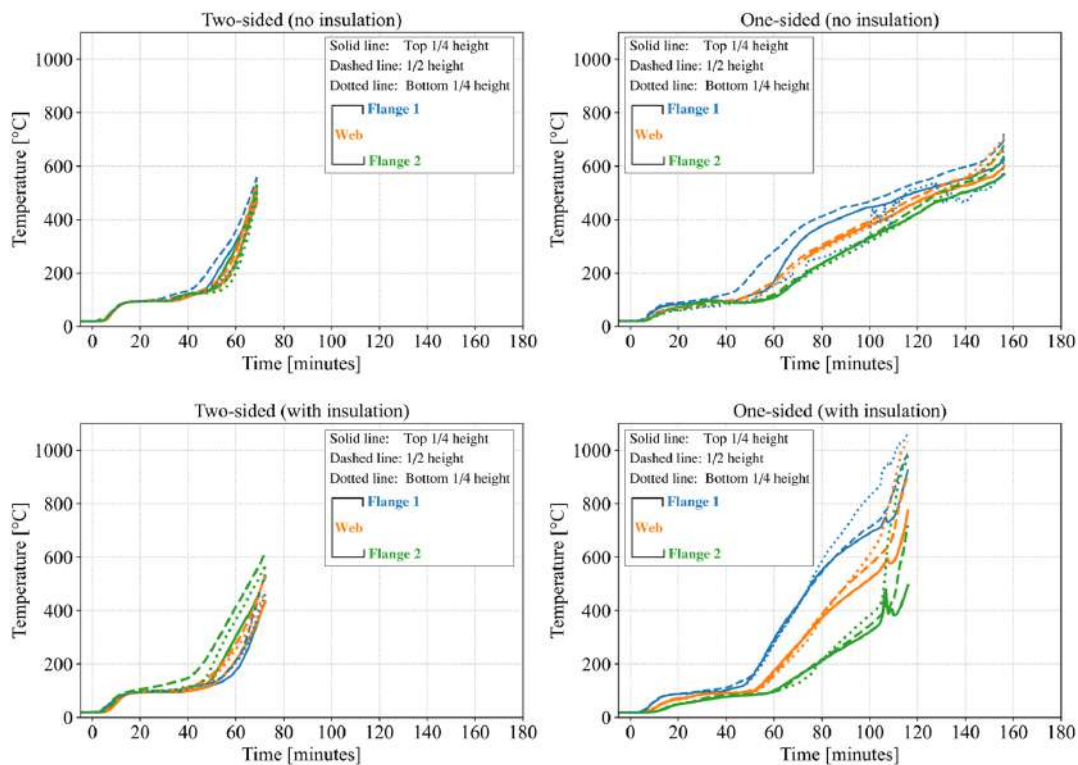


Figure 6. Comparison of stud temperature distribution at different points along the height of the stud (central stud – TE1, TE3 and TE5 in Figure 4)

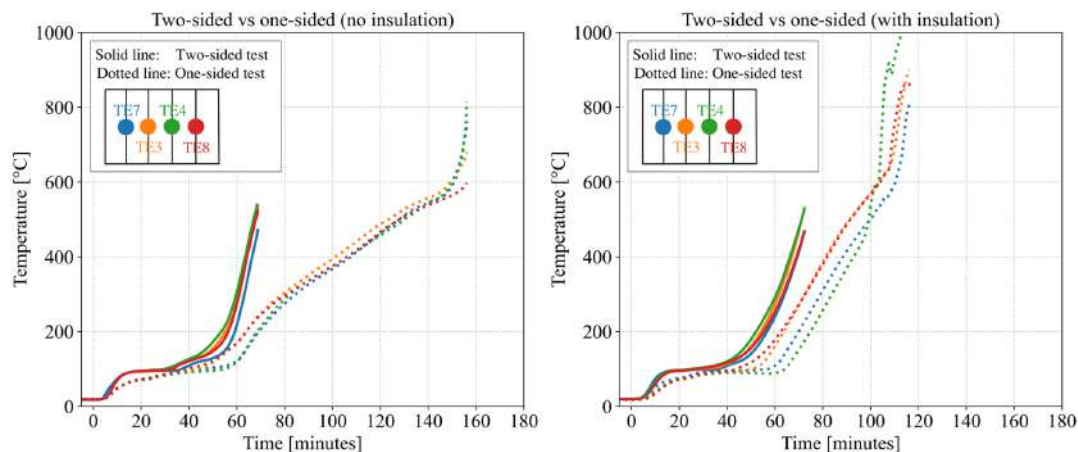


Figure 7. Comparison of stud web temperature variation along the length of the wall (TE3, TE4, TE7 and TE8 in Figure 4)

3.3 Deflection

Figure 8 compares the vertical deflection of the wall specimens at three locations at the top of the wall i.e., near both ends – C1 and C3, and at the centre – C2 (Figure 4). The results show that, for all the tested scenarios, the vertical deflection (contraction) across the top of the wall was approximately uniform irrespective of heating condition and presence of insulation.

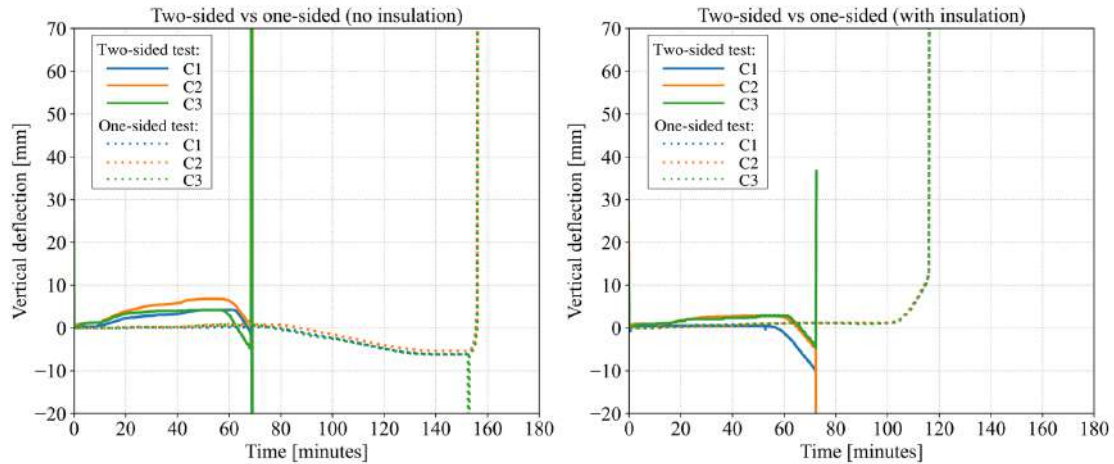


Figure 8. Vertical deflection of wall specimen (positive values = contraction; negative values = expansion)

Figure 9 shows the lateral deflection on the unexposed face of the wall (for the one-sided heating) at three locations at the mid-height of the wall i.e., near both ends – L1 and L3, and at the centre – L2 (Figure 4b) for both no insulation and with insulation scenarios. The result show that the lateral deflection at the centre of the wall was higher than that observed near the ends of the walls. The results also show that the wall with no insulation, exposed to fire on one side, had a greater capacity to resist lateral deflection compared to the wall with cavity insulation. This indicates that the temperature gradient across the wall section, which is amplified by the presence of insulation, significantly contributed to the lateral deflection of the wall.

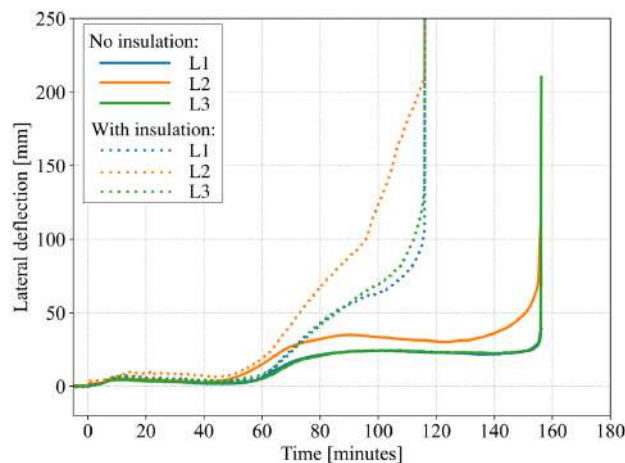


Figure 9. Lateral deflection (into the furnace) of unexposed face of walls exposed to fire on one side (no insulation vs with insulation)

From Figure 8 and Figure 9, for the LSF walls without insulation, runaway vertical / lateral deflection was observed at 68 min and 156 min for the two-sided and one-sided fire exposure, respectively. For the cavity-insulated wall specimens, this was observed at 72 minutes and 116 minutes for the two-sided and one-sided fire exposure, respectively. Figure 10 shows photographs of the wall specimens after the test indicating the extent of vertical and lateral deflections of the walls, with the walls bowing towards the hotter side.

Significant sheathing material fall-off was observed during the test following the runaway deflection which likely caused the failure in the jointing material and screws used for fixing the sheathing boards to the stud. Complete wall collapse was observed at the end of the test for the two-sided fire exposure and one-sided fire exposure, with more damage observed in the two-sided scenario.



Figure 10. Pictures of LSF wall under testing showing extent of deflection for the one-sided fire exposure condition

3.4 Unexposed surface temperature

Figure 11 plots the average and maximum temperature readings on the unexposed face of the LSF wall (with and without insulation) exposed to fire on one side. The plots are presented in the form a range graph of readings of all the average thermocouple elements (TE9 to TE14) and maximum thermocouple elements (TE9 to TE29). The result of TE16 for the scenario with cavity insulation was not included as the temperature measurements were significantly different from those of the other thermocouples, likely due to fall-off of the thermocouple during the test.

As expected, temperatures at unexposed face of the wall were lower and with a more gradual increase for the wall with cavity insulation than for the wall without insulation due to delayed heat transfer associated with the insulation. At 90 minutes of fire exposure, the upper bound of average and maximum temperatures observed were 74 °C and 78 °C, respectively, for the scenario with no insulation; and 50 °C and 55 °C, respectively, for the scenario with cavity insulation. Through the duration of the test, the maximum unexposed surface temperature did not exceed 100 °C for both cases.

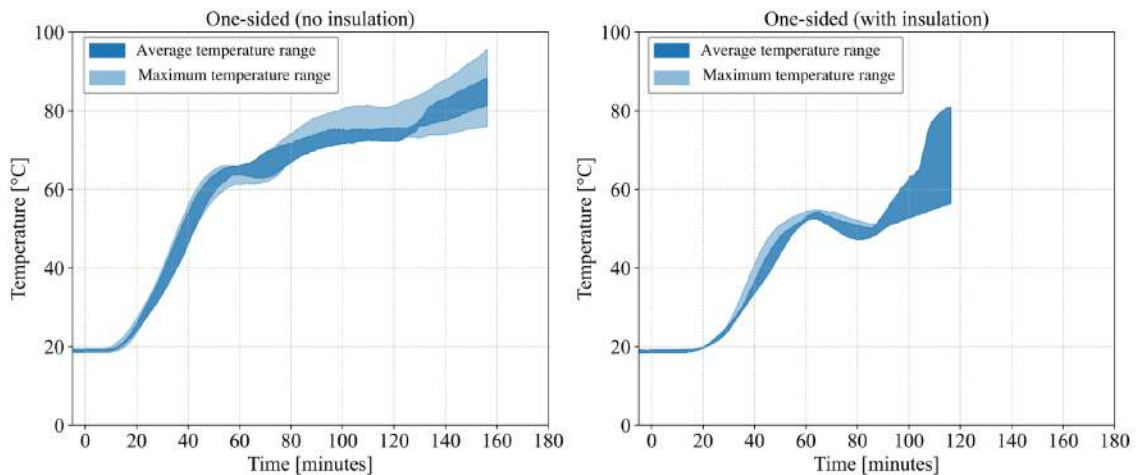


Figure 11. Average and maximum temperature on unexposed face of wall (one-sided fire exposure)

4 DISCUSSION

The results of the tests presented in Section 3 demonstrate that two-sided fire exposure generally results a more severe heating condition on the LSF walls. This is evidenced by the earlier failure times, higher ultimate temperatures and rate of temperature rise recorded across all components of the stud section – flanges and web – when compared to one-sided exposure. However, the impact of two-sided fire exposure is more significant at higher exposure times (around 45 – 50 minutes and above) as shown in Figure 5 to Figure 9. Previous studies on numerical modelling of two-sided fire exposure by other researchers also produced similar trends [17 – 18].

The experimental results show that one-sided fire exposure creates a thermal gradient within the stud cross-section, which is heightened when the cavities of the wall are insulated. Similar observations have been made in previous experimental and numerical studies on cavity-insulated LSF walls exposed to fire on one side [10 – 13]. This suggests that non-uniform heating is a significant characteristic of one-sided exposure, especially when insulation is present. Conversely, the experimental results show that two-sided exposure tends to promote more uniform heating across the stud section. Uniform distributions were also reported in the numerical (FE) analysis of two-sided fire exposure [17 – 18], suggesting that FE models are able to simulate the temperature distribution across the studs when the wall is exposed to fire on two sides.

The deflection results reveal that, for all tested scenarios, vertical deflection at various locations atop the wall were uniform. In contrast, lateral deflection (only measured for the one-sided fire exposure scenarios) was greater at the wall's centre compared to its ends. The higher central lateral deflection was more pronounced in insulated walls. This was expected as the results from the experiments have shown that insulation amplifies the temperature gradient, contributing to the lateral deflection of LSF walls.

The main findings from the experiments as summarised in Table 1 is that the loadbearing performance of LSF walls is reduced to 44% of the no insulation case and 62% of the cavity insulation case, when exposed to fire on both sides compared to one-sided exposure. This can have notable implications for the design of loadbearing LSF walls, particularly those with high utilisation ratios. The difference in percentage reduction between the non-insulated wall and cavity-insulated case further show that for one-sided exposure, the temperature gradient created by cavity insulation induces thermal bowing and earlier failure. Similar observations have been made in previous studies on cavity-insulated LSF walls exposed to fire on one-side where it was observed that the thermal gradient created due to the presence of cavity insulation reduces the loadbearing performance of LSF walls [2,10]. For two-sided exposure, the results indicate that the impact of cavity insulation is not significant as there is not a substantial deviation in time to failure. Furthermore, it is shown that the reduction in loadbearing performance due to two-sided heating is greater than the reduction caused by the thermal gradient created by the presence of cavity insulation for one-sided heating. Noting that the cavity-insulated wall specimens were designed to achieve a minimum loadbearing capacity of 90 minutes under one-sided fire exposure, the one-sided test results show that the walls achieved this fire rating and that the wall build-up (and material selection) were adequately designed. On the other hand, the experimental results demonstrated that for the same wall construction, when exposed to fire on two sides (with and without cavity insulation), the fire resistance rating achieved were lower than that the walls were designed to achieve under one-sided fire exposure, as the wall failed prior to 90 minutes. This implies that loadbearing classifications achieved for one-sided exposure should not be extrapolated to two-sided exposure.

5 CONCLUSIONS

The current work has presented the results of experiments conducted to assess the impact of the exposure condition (one- or two-sided) on the fire resistance performance of LSF walls. A total of four wall specimens were tested (under load), two each (with and without cavity insulation) for one- and two-sided fire exposure conditions under the ISO fire regime.

The main findings / conclusions from the experiments are as follows:

- Two-sided fire exposure results in a more severe heating condition on LSF walls than one-sided fire exposure, as indicated by higher temperatures and rates of temperature increase, particularly beyond 45 – 50 minutes of exposure.
- The loadbearing capacity of LSF walls decreased significantly when exposed to two-sided fire: down to 44% of the one-sided exposure capacity for non-insulated walls and 62% for insulated walls.
- One-sided fire exposure leads to a significant thermal gradient within the stud section, especially when insulation is present, resulting in non-uniform heating. In contrast, two-sided exposure generally promotes a more even temperature distribution across the stud section. The former typically results in reduced load-bearing fire resistance, however, the reduction due to two-sided heating is greater.
- Cavity insulation in one-sided fire exposure creates a significant temperature gradient, leading to thermal bowing and earlier structural failure compared to non-insulated walls. For two-sided fire exposure, the influence of cavity insulation on the performance was not significant versus non-insulated walls.
- The cavity-insulated walls were designed to achieve at least 90 minutes fire resistance for one-sided exposure. Given walls exposed on two-sides failed to achieve this, fire resistance classifications for one-sided exposure should not be extrapolated to two-sided exposure.
- The temperature distribution along the height of the stud is largely uniform, regardless of whether the exposure is one-sided or two-sided, due to the uniform furnace temperatures. Temperature variations along the length of the wall are minimal for two-sided fire exposure but can be substantial for one-sided exposure with insulation, reaching variations of up to 150 °C.
- Vertical deflection of wall specimen is uniform across various top locations of the wall under all test scenarios, while the centre of the wall exhibits greater lateral deflection, particularly for insulated walls under one-sided exposure.

From the findings of the study listed above, the following broader design implications arise:

- The test samples are considered to be representative of common LSF construction practices and, therefore, it is probably that the findings are broadly applicable to the technology.
- Where there is the potential for two-sided exposure, there is a sufficient reduction in performance that elements should be specifically designed to address such an exposure condition.
- In guidance, there is justification to explicitly request test evidence for two-sided exposure and this research shows how testing such a configuration is achievable.

ACKNOWLEDGMENT

The authors would like to acknowledge the Building Safety Regulator (BSR) at the Health and Safety Executive (HSE), for funding this study as part of the ‘Real Fires Project’ (CPD/004/122/039). The authors would also like to acknowledge colleagues at OFR Consultants for their insights and discussions while carrying out this work, particularly Ian Fu and Chris Mayfield.

REFERENCES

1. H. Rajanayagam *et al.*, ‘Thermal performance of LSF wall systems with vacuum insulation panels’, *Buildings*, vol. 11, no. 12, 2021, doi: 10.3390/buildings11120621.
2. S. Kesawan and M. Mahendran, ‘A Review of Parameters Influencing the Fire Performance of Light Gauge Steel Frame Walls’, *Fire Technology*, vol. 54, no. 1, pp. 3–35, Jan. 2018, doi: 10.1007/s10694-017-0669-8.
3. S. Kesawan and M. Mahendran, ‘Fire tests of load-bearing LSF walls made of hollow flange channel sections’, *Journal of Constructional Steel Research*, vol. 115, pp. 191–205, Dec. 2015, doi: 10.1016/j.jcsr.2015.07.020.
4. CROSS-UK, ‘Fire protection to light gauge steel frame walls’, CROSS-UK, CROSS Safety Report 1116, Jun. 2022. Accessed: Feb. 26, 2022. [Online]. Available: <https://www.cross-safety.org/uk/safety-information/cross-safety-report/fire-protection-light-gauge-steel-frame-walls-1116>

5. CROSS-UK, 'Fire protection to structure by cavity barriers', CROSS-UK, CROSS Safety Report 1231, Nov. 2023. Accessed: Dec. 21, 2023. [Online]. Available: <https://www.cross-safety.org/uk/safety-information/cross-safety-report/fire-protection-structure-cavity-barriers-1231>
6. HM Government, 'The Building Regulations 2010, Approved Document B (Fire Safety) Volume 2: Buildings other than dwellinghouses (2019 edition incorporating 2020 and 2022 amendments)'. Dec. 2022.
7. T. Abey Siriwardena and M. Mahendran, 'Numerical modelling and fire testing of gypsum plasterboard sheathed cold-formed steel walls', *Thin-Walled Structures*, vol. 180, Nov. 2022, doi: 10.1016/j.tws.2022.109792.
8. D. Perera *et al.*, 'Novel conventional and modular LSF wall panels with improved fire performance', *Journal of Building Engineering*, vol. 46, Apr. 2022, doi: 10.1016/j.jobbe.2021.103612.
9. W. Chen, J. H. Ye, Q. Y. Zhao, and J. Jiang, 'Full-scale experiments of gypsum-sheathed cavity-insulated cold-formed steel walls under different fire conditions', *Journal of Constructional Steel Research*, vol. 164, Jan. 2020, doi: 10.1016/j.jcsr.2019.105809.
10. Y. X. Tao and M. Mahendran, 'Fire tests and thermal analyses of LSF walls insulated with silica aerogel fibreglass blanket', *Fire Safety Journal*, vol. 122, Jun. 2021, doi: 10.1016/j.firesaf.2021.103352.
11. M. Peiris and M. Mahendran, 'Numerical modelling of LSF walls under combined compression and bending actions and fire conditions', *Thin-Walled Structures*, vol. 182, Jan. 2023, doi: 10.1016/j.tws.2022.110132.
12. P. Samiee, S. E. Niari, and E. Ghandi, 'Thermal and structural behavior of cold-formed steel frame wall under fire condition', *Engineering Structures*, vol. 252, Feb. 2022, doi: 10.1016/j.engstruct.2021.113563.
13. A. D. Ariyanayagam and M. Mahendran, 'Fire resistance of cavity insulated light gauge steel framed walls', presented at the Wei-Wen Yu International Specialty Conference on Cold-Formed Steel Structures 2018, R. A. LaBoube and W. W. Yu, Eds., St. Louis, 2018, pp. 879–893.
14. D. Perera *et al.*, 'Fire performance of cold, warm and hybrid LSF wall panels using numerical studies', *Thin-Walled Structures*, vol. 157, Dec. 2020, doi: 10.1016/j.tws.2020.107109.
15. N. Soares, P. Santos, H. Gervásio, J. J. Costa, and L. Simões da Silva, 'Energy efficiency and thermal performance of lightweight steel-framed (LSF) construction: A review', *Renewable Sustainable Energy Rev*, vol. 78, pp. 194–209, 2017, doi: 10.1016/j.rser.2017.04.066.
16. D. Perera *et al.*, 'Fire performance of modular wall panels: Numerical analysis', *Structures*, vol. 34, pp. 1048–1067, Dec. 2021, doi: 10.1016/j.istruc.2021.06.111.
17. A. D. Ariyanayagam and M. Mahendran, 'Behaviour of LSF walls exposed to fire on both sides', in *Proceedings of the 3rd International Fire Safety Symposium*, Ottawa, Ontario, Jun. 2019, pp. 137–145. [Online]. Available: <https://cibworld.org/wp-content/uploads/2022/05/IFireSS-2019-Proceedings.Updated.pdf>
18. S. T. Vy, A. Ariyanayagam, and M. Mahendran, 'Behaviour and design of CFS stud walls under both sides fire exposure', *Thin-Walled Structures*, vol. 197, p. 111619, Apr. 2024, doi: 10.1016/j.tws.2024.111619.
19. BSI, 'BS EN 1365-1:2012 Fire resistance tests for loadbearing elements. Walls', BSI, London, 2012.
20. BSI, 'BS EN 1365-4:1999 Fire resistance tests for loadbearing elements. Columns', BSI, London, 1999.
21. BSI, 'BS EN 1363-1:2020 Fire resistance tests. General requirements', BSI, London, 2020.
22. BSI, 'BS EN 1996-1-2:2005 Eurocode 6. Design of masonry structures. General rules. Structural fire design', BSI, London, 2005.
23. BSI, 'NA to BS EN 1996-1-2:2005 UK National Annex to Eurocode 6. Design of masonry structures. General rules. Structural fire design', BSI, London, 2007.
24. BSI, 'BS EN 1992-1-2:2004+A1:2019 Eurocode 2. Design of concrete structures. General rules. Structural fire design', BSI, London, 2005.

HYBRID FIRE TEST ON A CONCRETE-FILLED STEEL TUBE (CFST) COLUMN

Majid Hamidi Iravani¹, Masoud Adelzadeh², Hamzeh Hajiloo³

ABSTRACT

This paper investigates a hybrid fire test of a concrete-filled steel tube (CFST) column following ASTM E119 [1]. This study involves conducting a hybrid fire test on a concrete-filled steel tube (CFST) column fabricated in 1992 to evaluate its fire resistance under realistic boundary conditions. The column is assumed to be a part of a three-story 3D structure. The experimental setup involves exposing the column to fire in a standard furnace while concurrently simulating the rest of the structure. To ensure continuous communication between the components of the hybrid test, a communication platform has been developed to transfer data at each time step of the test. Through meticulous experimentation and analysis, the study addresses critical aspects such as load redistribution, thermal expansion, and material degradation. The findings contribute to enhancing the understanding of CFST column behavior and inform the development of more resilient structural systems for fire safety in building design and construction.

Keywords: concrete-filled steel tube; sub-structuring method; hybrid fire test; finite element modeling; fire resistance test.

1 INTRODUCTION

In recent years, concrete-filled steel tube (CFST) columns have been widely used, especially in high-rise building construction. These columns offer significant advantages, including high load-barring capacity, easy construction, high ductility, and cost-effectiveness [2-4].

The degradation of the steel material at high temperatures may lead to failure of the column. The interaction between the concrete and tubular steel improves the fire resistance of a CFST column due to the low thermal conductivity and thermal expansion of the concrete. During the fire and compared to hollow steel tubes or reinforced concrete columns, the steel tube functions as a protective shield and limits the radiation exposure to the concrete core resulting in a lower temperature rise within the concrete cross-section. The steel tube loses its strength and stiffness, and then, the load is effectively transferred to the concrete core [5, 6]. Additionally, the concrete core prevents the buckling and the collapse of the column [3], and on the other hand, the steel section provides confinement for the concrete and significantly enhances its compressive strength [7].

Lu et al. [8], Ding and Wang [9], and Espinos et al. [10] generated numerical models to explore the behavior of axially loaded CFT columns in fires. The previous studies described the progression of the

¹ Title, affiliation,

e-mail: majidhamidiiravani@cmail.carleton.ca , ORCID: <https://orcid.org/0000-xxxx-xxxx-xxxx>

² Title, affiliation

e-mail: Masoud.Adelzadeh@nrc-cnrc.gc.ca , ORCID: <https://orcid.org/0000-xxxx-xxxx-xxxx>

³ Title, affiliation

e-mail: Hamzeh.Hajiloo@Carleton.ca , ORCID: <https://orcid.org/0000-0002-5932-2640>

CFST column axial displacement over time across four distinct stages, which is depicted in Figure 1. The steel tube's temperature increases faster than the concrete core due to its higher conductivity and direct exposure to fire. This results in greater expansion of the steel tube compared to the concrete core, leading to the loss of contact between the concrete core and the loading plate. Consequently, the axial load of the steel tube progressively rises until it reaches a point where the steel tube sustains the entire applied load (stage 1). This state continues until the local yielding of the steel tube (stage 2). Subsequently, the steel tube contracts, leading to the return of contact between the loading plate and the concrete core, and the applied load sustained by the steel tube is transferred gradually to the concrete core (stage 3). As the temperature rises within the concrete cross-section, the mechanical properties of the concrete core undergo progressive degradation. After a considerable duration, the concrete core experiences loss of strength and stiffness, ultimately failing (stage 4).

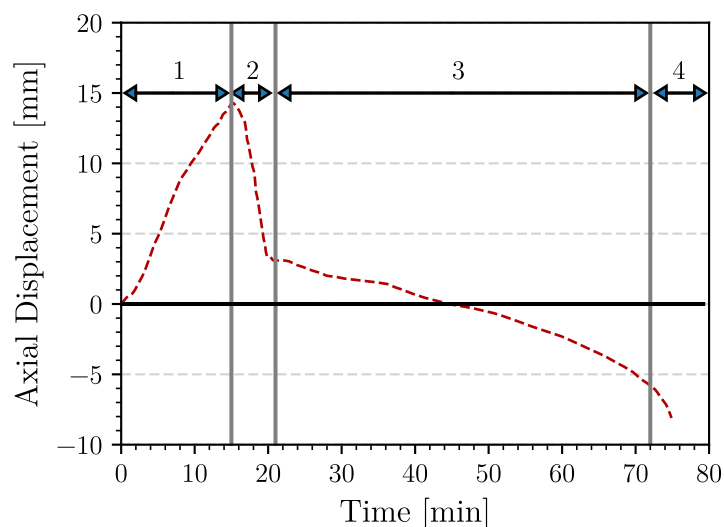


Figure 1. Axial displacement versus time for CFST element in a fire condition, from Espinos et al. [10]

The current study focuses on the fire behavior of CFST columns that act compositely with a steel structure. One of the most comprehensive experimental studies into concrete-filled steel tube columns in the fire was conducted by Lie and Chabot [11] at the National Research Council of Canada (NRC). This project included a series of large-scale experimental tests, subjecting several CFST columns exposed to the ASTM E119 [1] standard fire. The experiments aimed to assess the fire resistance of both circular and square hollow structural steel columns filled with plain concrete. In total, 44 full-scale fire resistance tests were conducted, varying parameters such as column dimensions, steel section wall thickness, concrete strength, type of concrete aggregate, effective length, load intensity, and eccentricity. Due to the complex nature of fire conditions and the behavior of the CFST columns, the research tends to concentrate on the behavior of individual structural elements without considering the interaction between the column and the rest of the structure [12]. While previous studies have established a foundation for modeling the behavior of CFST columns in fires, understanding the broader system-level structural response to fire conditions remains essential. Standard fire resistance tests often overlook critical factors such as global stiffness, load distribution, and structural redundancy. Particularly, they struggle to accurately represent boundary conditions, especially when fire-affected structural elements interact with the overall system [13]. In response to this challenge, Hybrid Fire Testing (HFT) emerges as a promising solution. HFT integrates experimental fire tests with numerical simulations, continually adjusting boundary conditions during a fire test based on the response of a Numerical Substructure (NS) derived from a finite element model [14]. HFT aims to establish accurate restraints, continuity, and realistic boundary conditions for experimentally tested members, making it well-suited for capturing authentic structural behavior [15, 16]. This method offers a cost-effective means of evaluating overall building performance, providing more dependable results compared to traditional approaches that neglect the interactions between building elements and the entire structure [17-19].

This paper aims to investigate this behavior using a hybrid fire test approach. This method involves dividing the structure into two sub-structures: the CFST column is subjected to experimental testing within a furnace as Physical Substructure (PS), which is expected to experience significant deformations due to the fire; the surrounding structure, which is expected to exhibit elastic behavior, is modeled using beam-column elements in a separate assembly at a reduced cost as the Numerical Substructure (NS). A middleware or interaction software is developed to connect the two assemblies at the interface. This innovative approach offers a highly effective and adaptable tool for the efficient and precise testing of large structural systems exposed to complex fire scenarios.

The column test C-28 for the current study is selected from the Lie and Chabot [11]. The column was analysed using OpenSees for fire [20] to validate the finite element analysis results with the results obtained from the experimental test. This study involves conducting a hybrid fire test on column C-28 to assess its fire resistance in realistic boundary conditions. The purpose is to compare these results with the fire resistance test of a single-column element.

2 METHODOLOGY

To conduct a hybrid fire test, multiple components must be coordinated and interact during the test. The primary aim of the hybrid test is to assess the structural system's behaviour by integrating experimental testing with numerical analysis. It's imperative to ensure continuous interaction between the experimental and numerical components throughout the test to attain equilibrium and compatibility at the interface. This integration allows for a comprehensive understanding of the structural response to various conditions, providing valuable insights into the system's performance under different scenarios [21].

The primary components of a hybrid fire test include:

- Physical Substructure (PS): The PS constitutes the part of the structure subjected to fire and tested experimentally within the furnace. It represents the part of the structure with unknown behaviour, where real-world conditions are applied and observed.
- Numerical Substructure (NS): The NS encompasses the surrounding structure, which can be represented either through a finite element (FE) model or a predetermined matrix.
- Communication Platform: The communication system facilitates continuous data exchange between the PS and NS, ensuring seamless coordination throughout the test. A dedicated software application has been developed for this purpose, utilizing TCP/IP protocols to transfer data between the NS and PS interfaces.

In the current study, a 3-story steel building with the moment-resisting frame system is selected for testing. The central CFST column of the base story considered the PS, while the surrounding structure is modelled using OpenSees for Fire [20, 22]. This setup enables a comprehensive evaluation of the structural response to fire, offering insights into the performance and behaviour of the entire building system.

The test methodology incorporates a convergence function and iterative process to ensure equilibrium and compatibility at the interface of the CFST column and the rest of the structure during the hybrid fire test. The convergence function continuously adjusts boundary conditions based on the response of the NS derived from a finite element model. The flowchart of the proposed method for conducting HFT is shown in Figure 2. Through iterative steps, the displacement and reaction forces of the NS are updated to match those of the PS subjected to fire. This iterative process aims to achieve convergence, where the numerical simulation accurately reflects the real-world behaviour of the CFST column under fire conditions. By iteratively adjusting boundary conditions, the hybrid test methodology ensures that the numerical model closely aligns with the experimental observations, providing reliable insights into the structural response of CFST columns to fire exposure.

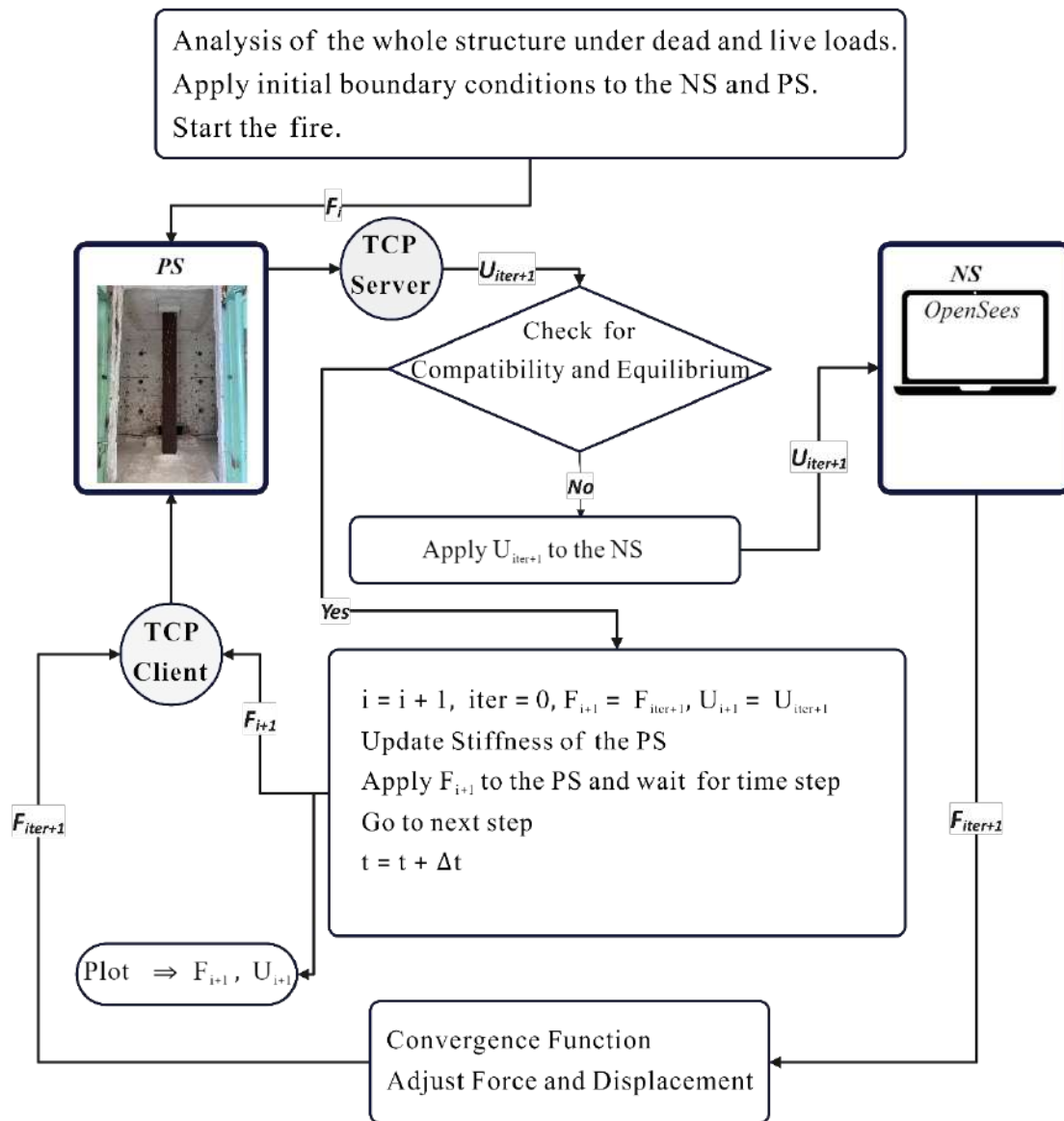


Figure 2. The flowchart of the methodology employed for hybrid fire testing

3 REFERENCE STRUCTURE

The reference structure considered for this hybrid fire test, shown in Figure 3. The 3-story reference structureFigure 3, was a symmetric 3-story steel building consisting of 2-bay moment-resisting frames with a span of 6 m. The height of each story was 4.2 m, and the CFST section profile was assigned to all column members. In this study, as illustrated in Figure 3, the middle column of the base story was exposed to the fire and tested experimentally as the physical specimen, while the surrounding structure remained at room temperature as the numerical model. To design the reference structure, the load combination was adjusted to match the axial load applied to the center column of the middle frame, aligning with the constant load used in the fire-resistance test of the single column conducted by Lie and Chabot [11].

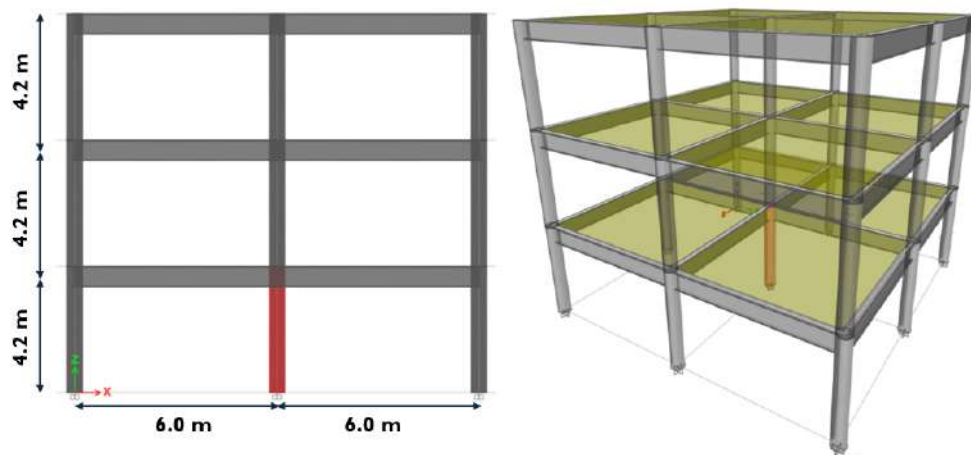


Figure 3. The 3-story reference structure

As described above, an experimental test was conducted on a CFST column under a constant load. For comparative purposes, the PS element in the current hybrid test was selected to mirror these properties. The column specimen, measuring 4.3 meters in length, featured the cross-section shown in Figure 4. The compressive strength of the concrete core was 23.8 MPa, while the steel had a yield strength of 350 MPa. The entire section had a diameter of 355.6 mm, with a steel wall thickness of 6.35 mm. The column furnace dimensions permitted exposure of 3810 mm of the column to the fire.

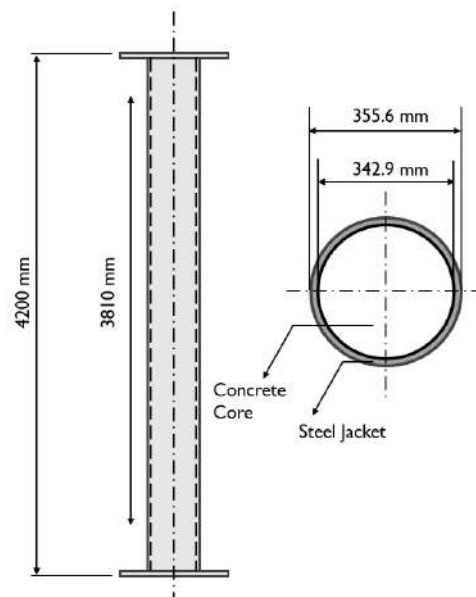


Figure 4. The column specimen used as the physical substructure of the hybrid test

4 EXPERIMENTAL SETUP

The experimental test involved subjecting the CFST column to ASTM E-119 fire within the NRC's unique column furnace. As shown in Figure 5, the furnace chamber is located inside a steel framework supported by four steel columns. The furnace chamber measured 2600x2600 mm in floor area and had a height of 4300 mm. To protect the test apparatus, the top and bottom of the column specimens are insulated, ensuring that only 3200 mm of the column is directly exposed to the fire during testing. Throughout the test, the column was exposed to controlled heat, ensuring that the average temperature in the furnace followed the ASTM-E119 [1] standard temperature-time curve. To measure the temperature of the furnace during the test, eight Type K thermocouples were employed at different heights 305 mm away from the column specimen.

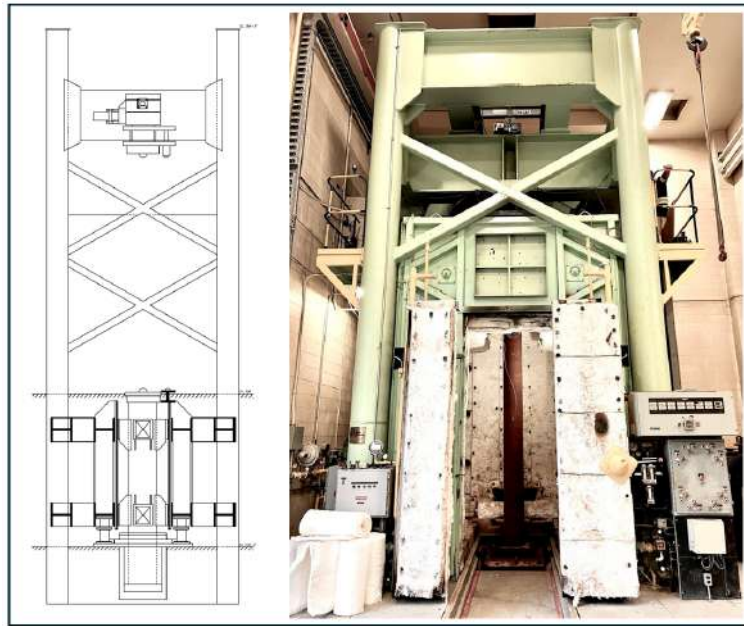


Figure 5. The column furnace and test specimen

The hydraulic jack placed at the bottom of the chamber applied the axial load to the column. The load was adjusted and measured through pressure transducers, and the axial deformation of the test specimen was recorded by tracking the displacement of the jack that supports the column. Displacement measurements were conducted using transducers with a high degree of accuracy, capable of detecting movements as small as 0.002 mm [11].

The CFST column element considered as the PS in this test was subjected to an axial load of 600kN. The applied load is 16% of the factored compressive resistance of the column determined based on CSA Standard CSA/CAN-S16.1-M89 [23]. The load was applied about 30 minutes before the test began and continued until no further increase in axial deformation could be observed. This state was considered the initial condition of the hybrid fire test.

5 RESULTS AND DISCUSSION

Figure 6 illustrates the axial deformation and axial load at the interface node of the column during the test. As the axial deformation of the column specimen varied throughout the test due to thermal expansions, an analysis was conducted on a numerical model using the current axial deformation value and time to determine the axial load of the column specimen for the subsequent step. When the fire started, the CFST column experienced a significant increase in axial load, rising from 600 kN to 1145 kN, primarily due to thermal expansion and interaction with the surrounding structure, which resisted the column's expansion. At this stage, the entire axial load was sustained by the steel tube. However, with increasing temperature and axial load, the stiffness of the steel material degraded, leading to local yielding. Subsequently, the steel tube began to shorten, allowing the loading plate to make contact with the concrete core. As the column shortened, the load previously sustained by the steel tube gradually transferred to the concrete core as the steel tube lost its load-bearing capacity. Concurrently, the mechanical properties of the concrete core progressively degraded with increasing temperature. Consequently, the load on the column decreased due to load redistribution by the surrounding structure to adjacent elements. Figure 6 shows a comparison between the outcomes derived from the hybrid fire test conducted on the CFST column and the results from the fire resistance test of the same column performed by Lie and Chabot [11]. In the single-column test, a constant axial load of 1050 kN was applied throughout the test duration. Contrasting the standard test results on the individual column with those of the hybrid fire test reveals that the interaction between the column and the surrounding structure within

the HFT led to the column experiencing a higher axial load and lower axial deformation. These findings underscore the constraints of conducting fire tests on individual members, as they may not consistently yield a conservatively safe solution.

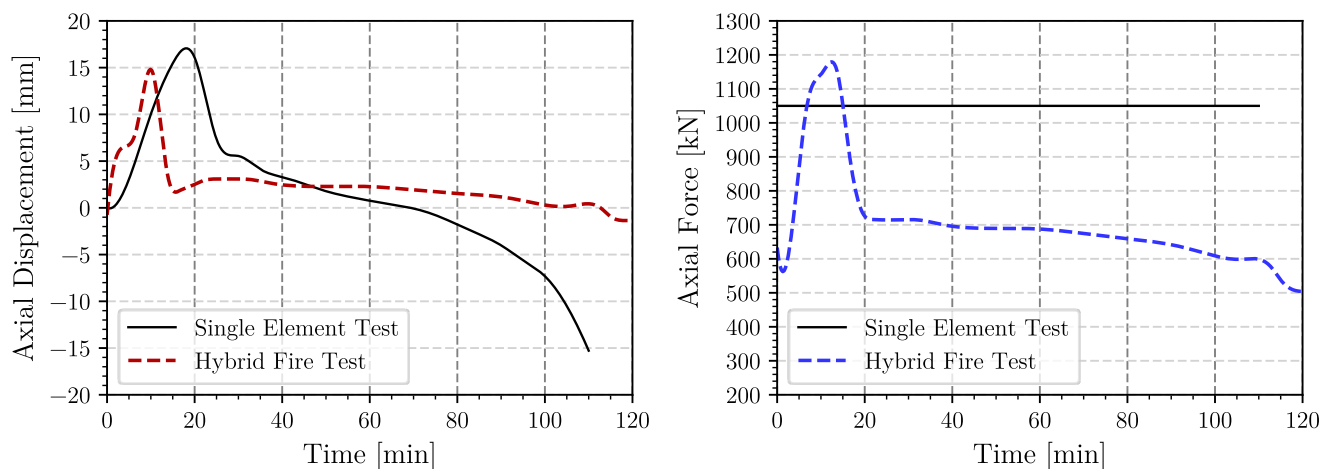


Figure 6. The axial displacement and axial force of the column versus time for the hybrid fire test and single element test

6 CONCLUSION

This study presents a comprehensive analysis of the fire resistance of a CFST column using a hybrid fire testing approach. The results obtained from the hybrid tests indicated that due to the interaction of the column with the surrounding structure, it experienced higher axial forces and lower deformation than the same isolated column tested under a routine standard fire test protocol. Because the maximum load experienced by the column during the HFT was significantly lower than its strength, the column's behaviour was primarily governed by displacement. In contrast to a standard fire test, the column under HFT did not fail once it was tested as a part of a real structure under practical service loads. The results highlight the effectiveness of the HFT in providing a realistic assessment of structural performance in fires. By comparing the findings with traditional fire resistance tests, the limitations of isolated member testing were identified, emphasizing the importance of considering structural interaction in fire evaluations. This research contributes to an advanced understanding of CFST column behavior in fire and presents the significance of hybrid fire testing in structural fire engineering.

ACKNOWLEDGMENT

The research is financially supported by the Fire Engineering Department of the National Research Council of Canada (NRC). The authors would like to thank Mr. Patrice Leroux, Mr. Pier-Simon Lafrance, Mr. Daniel Lefebvre, Mr. Eric Gibbs, Mr. Mark Weinfurter, Mr. Karl Gratton and Mr. Andrew Frade for their assistance and contribution to implementing the HFT.

REFERENCES

1. ASTM, A., *E119: Standard Test Methods for Fire Tests of Building Construction and Materials*. 2007, West Conshohocken, USA.
2. Han, L.-H., W. Li, and R. Bjorhovde, *Developments and advanced applications of concrete-filled steel tubular (CFST) structures: Members*. 2014. **100**: p. 211-228.
3. Wang, J., J. He, and Y. Xiao, *Fire behavior and performance of concrete-filled steel tubular columns: review and discussion*. 2019. **157**: p. 19-31.
4. Moradi, M., K. Daneshvar, D. Ghazi-Nader, and H. Hajiloo, *The prediction of fire performance of concrete-filled steel tubes (CFST) using artificial neural network*. 2021. **161**: p. 107499.
5. Twilt, L., *Design guide for structural hollow section columns exposed to fire*. 1994.
6. Romero, M.L., V. Moliner, A. Espinos, C. Ibañez, and A. Hospitaler, *Fire behavior of axially loaded slender high strength concrete-filled tubular columns*. 2011. **67**(12): p. 1953-1965.

7. Rahnavard, R., H.D. Craveiro, R.A. Simões, L. Laim, and A. Santiago, *Fire resistance of concrete-filled cold-formed steel (CF-CFS) built-up short columns*. 2022. **48**: p. 103854.
8. Lu, H., X.-L. Zhao, and L.-H. Han, *Fire behaviour of high strength self-consolidating concrete filled steel tubular stub columns*. *Journal of constructional steel research*, 2009. **65**(10-11): p. 1995-2010.
9. Ding, J. and Y. Wang, *Realistic modelling of thermal and structural behaviour of unprotected concrete filled tubular columns in fire*. *Journal of Constructional Steel Research*, 2008. **64**(10): p. 1086-1102.
10. Espinos, A., M.L. Romero, and A. Hospitaler, *Advanced model for predicting the fire response of concrete filled tubular columns*. 2010. **66**(8-9): p. 1030-1046.
11. Lie, T.T. and M. Chabot, *Experimental studies on the fire resistance of hollow steel columns filled with plain concrete*. 1992: National Research Council Canada, Institute for Research in Construction.
12. Khan, M.A., *Analysis of perforated beams in fire using a virtual hybrid simulation approach*. 2019, Brunel University London.
13. Wang, X., R.E. Kim, O.-S. Kwon, and I. Yeo, *Hybrid simulation method for a structure subjected to fire and its application to a steel frame*. *Journal of Structural Engineering*, 2018. **144**(8): p. 04018118.
14. Mergny, E., T. Gernay, G. Drion, and J.-M. Franssen, *Hybrid fire testing in a non-linear environment using a proportional integral controller*. *Journal of Structural Fire Engineering*, 2019.
15. Saouma, V. and M. Sivaselvan, *Hybrid simulation: Theory, implementation and applications*. 2014: CRC Press.
16. Sauca, A., C. Zhang, A. Chernovsky, and M. Seif, *Communication framework for hybrid fire testing: Developments and applications in virtual and real environments*. *Fire safety journal*, 2020. **111**: p. 102937.
17. Sauca, A., E. Mergny, T. Gernay, and J.-M. Franssen, *A method for Hybrid Fire Testing: Development, implementation and numerical application*, in *Applications of Fire Engineering*. 2017, CRC Press. p. 225-234.
18. Sauca, A., C. Zhang, A. Chernovsky, and M. Seif. *Hybrid fire testing of a single degree-of-freedom linear system*. in *Proceedings of the 10th International Conference on Structures in Fire, Belfast*. 2018.
19. Mergny, E. and J.-M. Franssen, *Real-time multi degrees of freedom hybrid fire testing using Pi control*. 2020.
20. Usmani, A., J. Zhang, J. Jiang, Y. Jiang, and I. May, *Using openses for structures in fire*. *Journal of Structural Fire Engineering*, 2012.
21. Sauca, A., *Development and implementation of a methodology for hybrid fire testing applied to concrete structures with elastic boundary conditions*. 2017, Université de Liège, Liège, Belgique.
22. Jiang, Y.-Q., *Development and application of a thermal analysis framework in OpenSees for structures in fire*. 2013, University of Edinburgh.
23. Association, C.S., *Limit states design of steel structures—CAN/CSA-S16. 1-94*. 1994.

INTRODUCTION TO THE JET FIRE AND FORCE LOADING COUPLED TEST DEVICE

Yanhong Zhang¹, Guobiao Lou², Guoqiang Li³, Mengjie Wang⁴, Honghui Qi⁵

ABSTRACT: Petroleum and natural gas account for more than 50% of global energy structure, making their safety crucial for overall economic and social development. Leaks during the production and transportation of petroleum and gas can easily lead to fires, with jet fires accounting for approximately 50% of all fire incidents. Addressing the critical frontiers of fire prevention and control in the petroleum and gas energy production and transportation infrastructure, it's pressing to develop a jet fire test device that capable of simultaneously simulating jet fires, mechanical loading, and firefighting water spray. The upcoming construction of jet fire and force loading coupled test device will facilitate research on the combustion characteristics and action models of jet fires, the damage mechanisms of fire protection materials under jet fire, the evolutionary mechanism of engineering structures under jet fire, and the theoretical design of fire protection. Furthermore, it will support research on the development of fire protection materials and the enhancement of jet fire resistance in petroleum and gas energy infrastructure, providing crucial experimental means for innovation. This apparatus holds significant practical significance for effectively preventing jet fire disasters, reducing casualties, and ensuring the safety of petroleum and gas energy production and transportation facilities.

Keywords: Fire test equipment; Propane Jet Fire; The jet fire and force loading coupled test device

1 INTRODUCTION

The energy and chemical industry serves as the foundation for driving operations across various sectors, such as industry, transportation, and daily life. It stands as a crucial pillar of national economic development, integral to national security. Petroleum and natural gas hold significant positions in global energy structure, comprising more than 50% of the total. Petroleum and gas, being flammable and explosive, pose significant risks. Leaks during production, transportation, or storage can lead to major fire accidents, resulting in substantial casualties and economic losses. The increasing demand for petroleum and gas energy, along with the expansion of related industries, has heightened the challenge of ensuring fire safety in their production, storage, and transportation infrastructure.

¹ PhD Candidate, School of Civil Engineering, Tongji University, Shanghai 200092, China
e-mail: 2210319@tongji.edu.cn

² Associate professor, School of Civil Engineering, Tongji University, Shanghai 200092, China
e-mail: gblou@tongji.edu.cn

³ Professor, School of Civil Engineering, Tongji University, Shanghai 200092, China
e-mail: gqli@tongji.edu.cn

⁴ PhD Candidate, School of Civil Engineering, Tongji University, Shanghai 200092, China
e-mail: mengjiewang@tongji.edu.cn

⁵ PhD Candidate, School of Civil Engineering, Tongji University, Shanghai 200092, China
e-mail: hhqi@tongji.edu.cn

Common petroleum and gas fires (also known as hydrocarbon fires) can be divided into pool fires, jet fires, ball fires, and flash fires (as shown in Figure 1). Jet fires refer to jet flame caused by leaks during the production, storage, and transportation of flammable fuels under high pressure. About 50% of serious fire incidents are primarily characterized by jet fires in their initial stage. Statistical analysis from authoritative accident information databases by Giovanni et al. [1] reveals that jet fires comprise approximately 54.3% of all fire accidents. Compared to fiber fires and pool fires, jet fires ignite when fuel and air are fully mixed under pressure, resulting in more severe fires and greater harm[2]. Jet fires exhibit a faster heating rate, higher peak temperature, and greater thermal radiation intensity. As can be seen in Figure 2, within 5 minutes of ignition, the temperature peak can reach 1300°C, with a thermal radiation flux reaching 350kW/m². Additionally, jet fires exhibit significant momentum in the spraying direction. As shown in Figure 3, fire protective coatings are susceptible to damage and peeling under the high-temperature impact of flames, leading to direct exposure of protected components or equipment to flame radiation, exacerbating damage and resulting in more significant disasters.

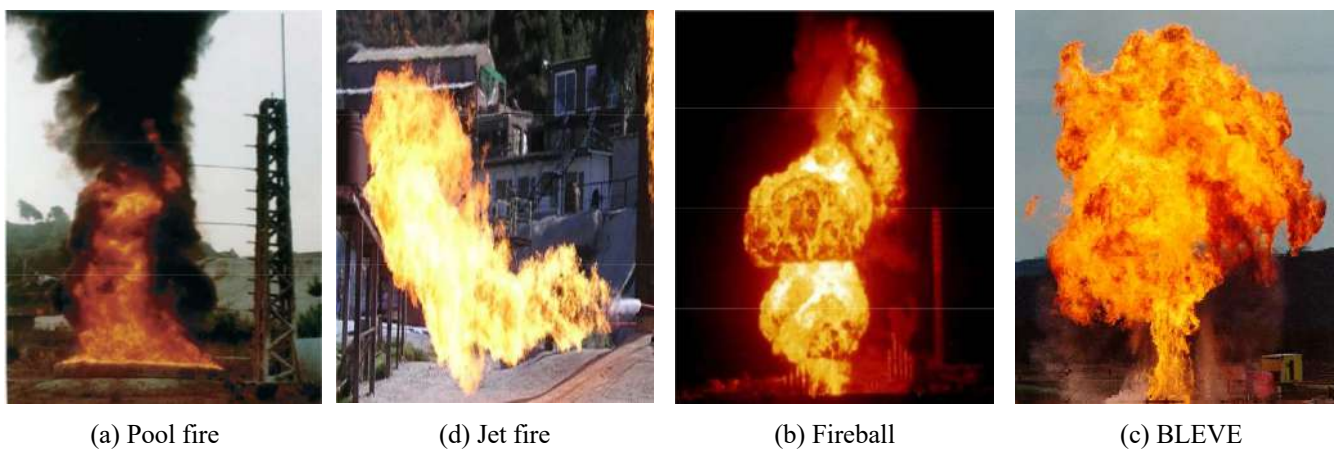


Figure 1. Common types of hydrocarbon fires

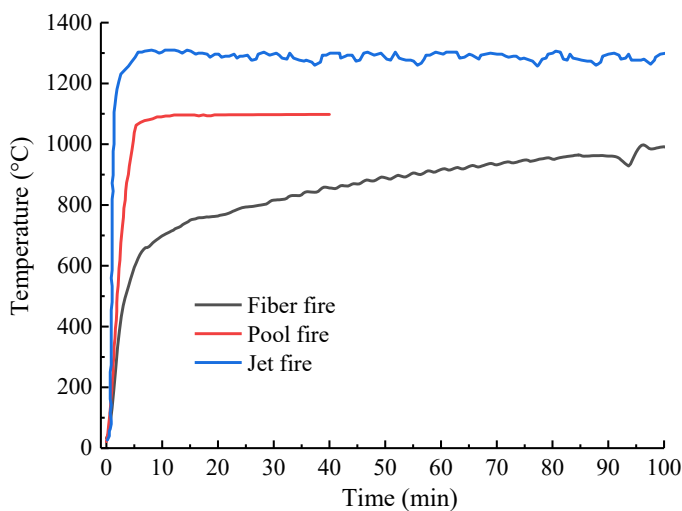


Figure 2. Heat-up curves for fibre fires, hydrocarbon pool fires, hydrocarbon jet fires



Figure 3. Impact of jet fires on fire protection

Following a jet fire, materials, structures, pipelines, valves, and equipment with insufficiently fire-resistant may fail under prolonged exposure to the fire. This failure can exacerbate petroleum and gas leakage, escalating the severity of fires and potentially resulting in flash fires and explosions, culminating in catastrophic fire and explosion accidents. In 1988, a jet fire occurred on the Piper Alpha offshore petroleum

production platform (Figure 4(a)), leading to 167 deaths. Subsequently, the platform sank to the sea floor, resulting in direct economic losses amounting to \$2 billion^[3]. In 2007, a liquid propane jet leak occurred at the Valero McKee refinery in Texas, USA (Figure 4(b))^[4], where a high-pressure propane jet fire caused damage to structural steel supports, collapse of the pipeline corridor. This accident resulted in extensive equipment damage, and, ultimately, more than \$50 million in direct economic losses and 14 burn injuries. In 2020, operators at the Olefins Plant of China Petroleum & Chemical Corporation's Qilu Branch used non-explosion-proof tools (such as shovels and grinders), inadvertently generating sparks^[5]. These sparks ignited the gas mixture overflowing from the vent, resulting in jet fires. Subsequently, the tank roofs tore off and caught on fire, tragically leading to the deaths of two people.



(a) Fire accident on the Piper Alpha offshore oil recovery platform



(b) Fire accident at Valero McKee refinery

Figure 4. Jet fire accident cases

Considering the hazards of jet fires, some codes specify criteria for the fire resistance of load-bearing structures, fire barriers, and more against jet fire, necessitating performance testing for offshore production facilities in the petroleum and gas industry, such as ISO13702^[6] and GB/T 20660-2006^[7]. However, the jet fire testing facilities are primarily located in Europe and the United States, with no such facility currently existing in the Asia-Pacific region. Consequently, research, product development, and testing related to jet fires must rely on these laboratories. This dependence proves not only costly and time-consuming but also increasingly problematic as foreign organizations have started imposing restrictions or outright prohibitions on certain product and research tests.

Addressing the critical frontiers of fire prevention and control in the national petroleum and gas energy production and transportation infrastructure, research and development of a jet fire test system capable of responding to jet fire characteristics while considering external loads is imperative. This paper introduces the jet fire and force loading coupled test device proposed by the group, that capable of simultaneously simulating jet fires, mechanical loading, and firefighting water spray. It will facilitate research on the combustion characteristics and action models of jet fires, the damage mechanisms of fire protection materials under jet fire, the evolutionary mechanism of engineering structures under jet fire, and the theoretical design of fire protection. This device can support research on basic theory and fire design methods related to jet fire resistance, promote product research and development, ensure the fire safety of petroleum and gas facilities.

2 DEVELOPMENT OF THE JET FIRE TEST

2.1 Full-scale jet fire

In 1988, a major fire accident occurred on the Piper Alpha offshore petroleum production platform in the North Sea of the United Kingdom, resulting in 167 deaths and \$2 billion in direct economic losses. The British government conducted an in-depth investigation into the accident for two years and released a detailed accident investigation report^[3]. The accident report showed that the jet fire caused by high-pressure gas leakage caused serious harm to the offshore petroleum production platform, which triggered the international attention to the jet fire test.

Conventional fire tests are mainly based on temperature-time curves and are conducted in a closed test furnace. Although the total heat flux of the furnace test can achieve to be similar to that generated in an actual jet fire, it cannot reproduce fire variables such as the balance of radiation and convection, high gas velocities, and thermal shock in an actual jet fire. Therefore, when evaluating the fire response and stability, thermal insulation, and thermal adiabatic properties of fire protection materials, structures and components, fire barriers, pipes and valves, equipment and components, etc. in a jet fire scenario, the best way is to use a high-intensity jet flame to directly impinge on the specimen. For this reason, a number of full-scale jet fire test (Figure 5) research projects have been carried out internationally.

In 1985, the Isle of Grain tests studied releases of propane (1-10 kg/s) impacting onto copper plate targets at a distance of 7 to 10 m^[8]. Water cooled calorimeters recorded heat fluxes of 50-250 kW/m².

The Shell and British Gas tests provided a far more extensive insight into the heat flux distribution across impinged targets^[9]. A series of 170 tests were conducted over s1989 to 1991, in order to characterise a range of sonic and subsonic releases of natural gas (up to 10 kg/s) and propane (up to 22 kg/s). The impinged target was either a 0.9 m diameter pipe or a 13 tonne vessel. A total of 41 tests with an instrumented target were identified as giving reliable data. The time-averaged maximum total heat flux values reported in these tests is 150-350kW/m².

To assess the ability of passive fire protection materials to withstand the combination of high erosive forces and highly localised heat flux values, Shell conducted a programme known as “SOFIPP” in 1990^[10], to study the thermal response of steel under two types of protection system that were commercially available at the time. A 3 kg/s sonic natural gas release was chosen for the tests with the targets set at a distance of 9 m. This release had been well characterised in the CEC funded work described above and was chosen to give a severe, yet representative, combination of erosion and heat fluxes in a long duration test. The targets were I-sections, instrumented with thermocouples and coated with the protection systems.

These tests, which involved different fuels, flow rates and construction types, provided the basis for the development of subsequent standardized jet fire test procedures.



Figure 5. Full-scale jet fire test

2.2 Standard jet fire test

Conducting a full-scale jet fire test is costly, of significant potential hazard, and affected by numerous environmental factors, leading to low repeatability and challenges in accurately reproducing test conditions. Therefore, to develop a manageable and reproducible jet fire test procedure featuring desirable flame characteristics, SINTEF embarked on simulating jet fire tests in 1986^[11]. A laboratory-scale jet fire test procedure was proposed by investigating heat fluxes, temperatures, and gas velocities across various configurations. The test procedure included injecting a propane jet flame at a release flow rate of 0.3 kg/s into a 1.5 m × 1.5 m × 0.5 m flame recirculation chamber. The chamber, with the test panel comprising its back wall of the chamber, is specifically designed to minimize flame escape. The test program successfully

replicated the high heat flux, thermal convection, and flame impingement characteristics that were observed in the full-scale jet fire test.

In 1993, the Interim Jet Fire Resistance Test procedure (IJFT) was developed by Health and Safety Executive (HSE) drawing upon the foundation established by SINTEF's procedure^[12]. The test method extends the scope of the test specimen, encompassing a central vertical web specimen with edge features and a separate panel system incorporating joint features, beyond the traditional plate specimen. To evaluate the reproducibility of the test procedure, SINTEF Laboratory in Norway, Southwest Research Institute (SwRI) in the USA and the Health and Safety Executive (HSE) in the UK all conducted two jet fire tests^[13]. The test results demonstrated remarkable consistency among the various laboratories, thereby validating the IJFT method's viability for conducting jet fire tests in different laboratory environments.

Due to the IJFT's lack of coverage of tubular sections, SwRI conducted a study to ascertain the essential parameters needed to simulate full-scale jet fire testing of tubular sections^{[14],[15]}. Eight IJFT scale jet fire tests were conducted on specimens, each with an inner diameter of 203mm^[16]. In 1996, HSE revised the IJFT test method and published the Jet Fire Resistance Test Method for Fire Protection (JFRT)^[17], which consists of four test configurations, namely panel test, planar steelwork test, structural steelwork test and tubular section test, as shown in Figure 6. British Gas carried out a full-scale jet fire test on fire-protected H-sections^[18] and tubular^[19] specimens with a release flow rate of 3kg/s, to verify the suitability of the JFRT Scale Jet Fire Test. The comparison between the full-scale jet fire test and the JFRT jet fire test demonstrates that the latter can effectively replicate the characteristics of the former, such as heat flux and thermal shock^[20]. In 2007, ISO adopted the JFRT jet fire test method as ISO 22899-1^[21], now acknowledged globally as the primary means for verifying passive fire protection material performance under jet fire exposure.

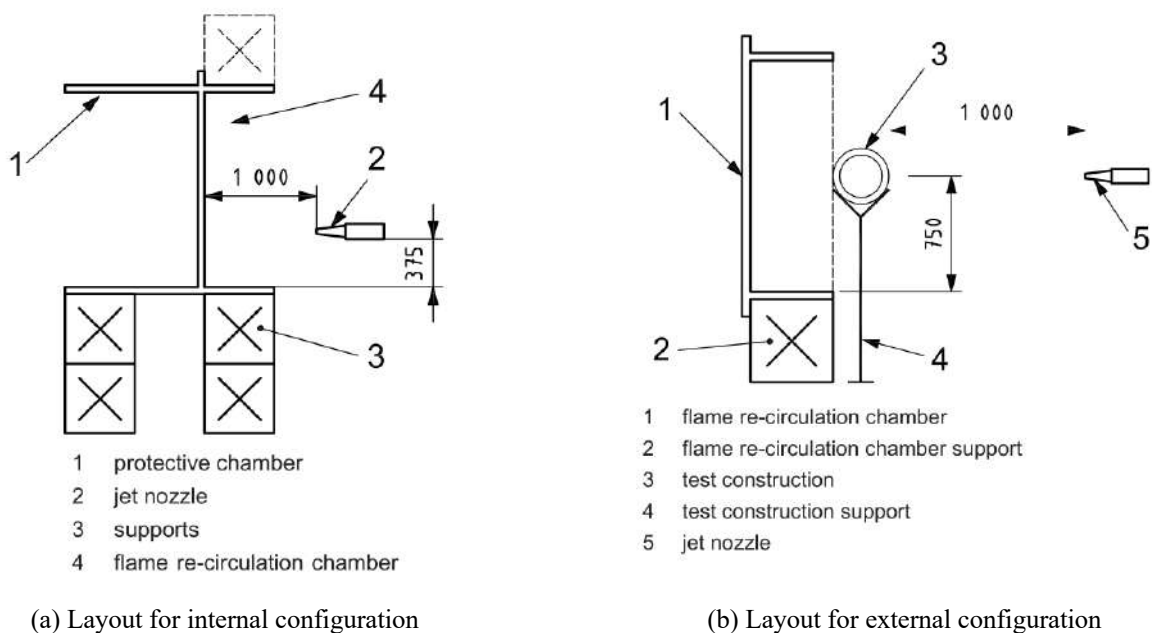


Figure 6. Standard jet fire test

In accordance with the requirements of ISO22899-1, several jet fire organizations have been established internationally. These institutes possess specialized experimental conditions and technical capabilities, enabling them to conduct jet fire resistance performance tests and issue inspection and assessment reports, which are used to guide the fire protection design of petroleum and gas energy production, storage and transportation infrastructures. However, these jet fire testing facilities are primarily located in Europe and the United States, with no such facility currently existing in the Asia-Pacific region.

2.3 Future Development of Jet Fire Test Equipment

There are still some improvement for current standard jet fire test device, which also represent the technological breakthroughs and future development directions for the new generation of jet fire test devices.

- (1) Current standard jet fire test device fails to consider force loading effects. This omission is unrealistic and unscientific in the context of load-bearing structures in practical engineering applications, as the primary fire resistance property of load-bearing structures under fire is their stability (load-bearing capacity). Therefore, the next generation of jet fire test devices should incorporate loading devices, such as actuators, reaction frames, with stringent cooling and thermal insulation measures to ensure normal loading and bearing of the specimen under the jet fire.
- (2) The next generation of jet fire test device should consider the effects of water cooling. In the event of a fire, water spray or fire water guns are often utilized for fire suppression. The rapid cooling will cause additional thermal shock, potentially interfering with the foam reaction of intumescent fireproofing coatings and leading to the detachment of the fire protection layer, consequently compromising the component's fire resistance. Therefore, the next generation of jet fire test device should be capable of simulating fire extinguishing sprinkler, fire water gun and water cannon. Moreover, the water cooling function in the next generation of jet fire devices can compensate for the inability of traditional test furnaces, thereby offering a more realistic testing method to reproduce the entire fire and fire suppression process (including fire after the fire spray cooling, fire and spray cooling at the same time, as well as spray cooling after the fire re-ignition of the fire).
- (3) To simulate different fire scenarios, the next generation of jet fire test devices should be capable to simulate fire combustion based on a pre-set heat flux time curve. Conducting tests under multiple fire scenarios enables a more comprehensive assessment of fire response and resistance of material, structure, and equipment across various fire conditions, thus providing a more reliable benchmark for fire safety testing. Solenoid valves, self-adaptive control technology, and other means are required to achieve automatic feedback of heat flux, and automatic control of fuel flow rate.

3 JET FIRE AND FORCE LOADING COUPLED TEST DEVICE

3.1 Main function

To address the critical fire prevention and control needs of petroleum and gas energy production, storage, and transportation infrastructure, the jet fire and force loading coupled test device, compliant with ISO 22899-1 and featuring novel force action loading and fire extinguishing sprinkler functionalities, has been developed. This test device's application can address the following significant scientific and technical challenges.

- (1) Modelling the combustion characteristics and mechanism of action of jet fires.

The jet fire and force loading coupled test device enables accurate control of fuel flow and adjustment of jet speed, angle, and other flame parameters, to simulate flame characteristics under various fire conditions. Additionally, it incorporates a large calorimeter for precise measurement of transient heat release rates, offering robust testing capabilities for investigating the combustion mechanism and physical properties of jet fires. It facilitates exploration of jet flame stability, combustion product behavior, heat transfer, propagation characteristics, impact dynamics, and more. Building upon experimental studies of jet fire, fire dynamics, and Computational Fluid Dynamics (CFD) simulations, research is conducted to unveil the combustion characteristics and mechanism of jet fires. This includes establishing models for morphology, temperature distribution, and heat radiation of jet fires, aimed at providing a comprehensive fire field model for investigating the evolutionary mechanism for engineering structures under jet fire exposure, and disaster control and prevention.

- (2) Evaluation methods for fire resistance and breakdown mechanisms of fire protection materials under jet fire exposure.

Fire protection materials are the crucial technical measures for enhancing the fire resistance of engineering structures and industrial equipment when subjected to jet fire. The mechanical properties of fire protection

materials and its bonding strength with the substrate significantly degrade under the ultra-high temperatures and the kinetic energy impact of jet fire flames, thus posing a risk of damage, failure, or detachment. The jet fire and force loading coupled test device enables erosion tests on fire protection materials under various jet fire scenarios. The chemical reaction thickness, carbonized layer thickness and characteristics, degree of breakage and length of detachment, as well as temperature rise curves of steel specimen, can be obtained. Combined with numerical and theoretical analysis, it enables to reveal the fire resistance and breakdown mechanisms of fire protection materials under jet fire exposure, establish the evaluation method of jet fire resistance based on the critical temperature.

(3) Evolutionary mechanism and fire protection design methods for carrying pipelines and engineering structures under jet fire exposure.

Engineering structures primarily serve to bear external loads. Their stability and load-bearing capacity under fire is crucial for structural fire safety, fire spread control, and fire rescue. The jet fire and force loading coupled test device enables the simultaneous application of jet fire and force action on engineering structures worldwide for the first time. This resolves a significant limitation of existing test devices, which cannot handle loads, and accurately reproduces the entire thermal response of engineering structures to jet fire. Consequently, it facilitates the establishment of theory and methods for calculating the temperature increase of engineering structures exposed to jet fire in open environments, revealing the evolution of evolutionary and failure mechanisms under such conditions. Furthermore, it enables the development of fire protection design methods for engineering structures against jet fire, guiding project design and construction to mitigate fire disasters.

3.2 Overall structure and main indicators

According to the modular and intelligent design concept, the jet fire and force loading coupled test device consists of five major systems: jet fire system, high-temperature loading and reaction frame support system, spray cooling system, control and analysis system, and test safety guarantee system. The 3D diagram of the jet fire and force loading coupled test device is shown in the Figure 7.

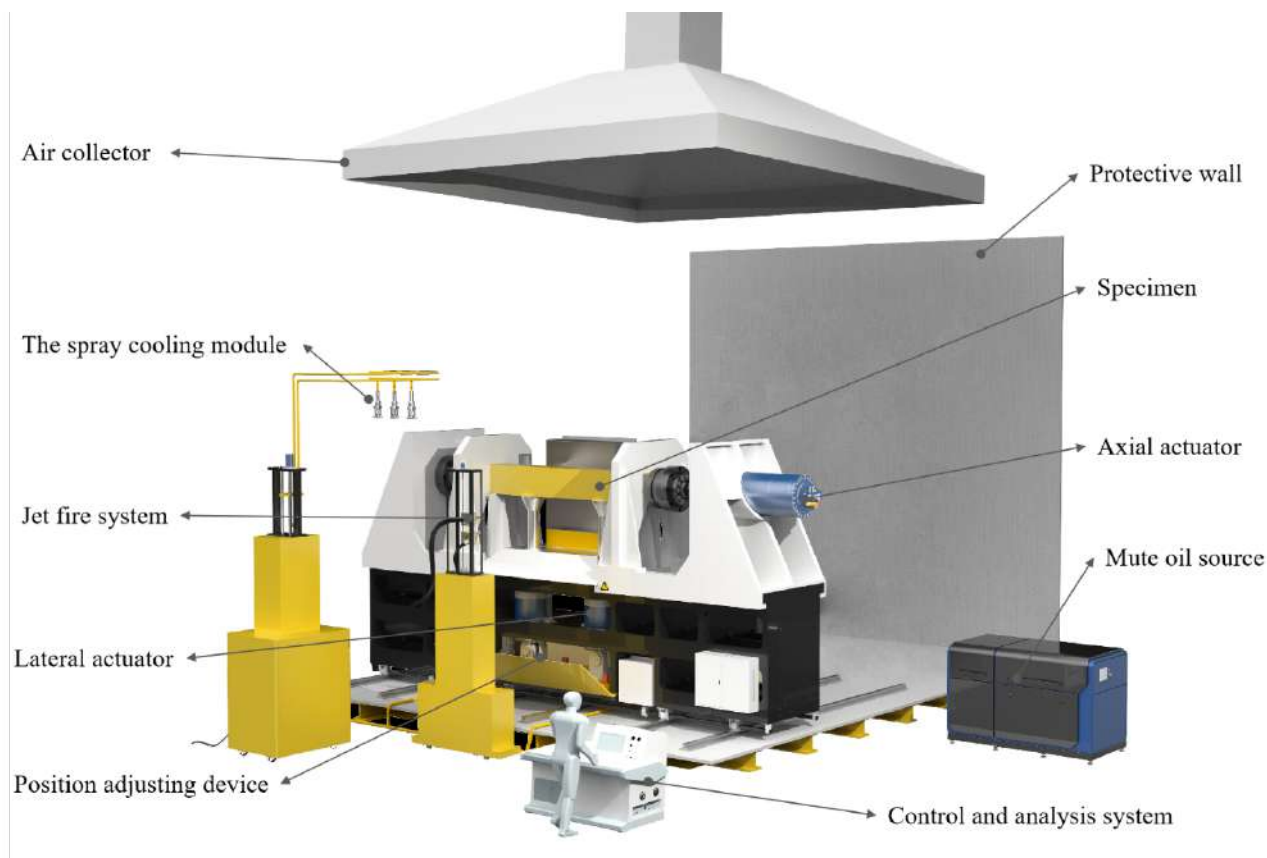


Figure 7. The 3D diagram of the jet fire and force loading coupled test device

(1) Jet fire system

The primary purpose of the jet fire system is to apply propane jet fire to the specimen. The jet fire system is combined with a fuel supply module, a jet fire combustion module, and a large calorimeter test module. Among them, the fuel supply module vaporizes the liquid propane fuel and provides fuel for jet fire combustion, with a gas supply volume reaching 1600kg/h. The large-scale calorimeter module is used to detect the heat release rate of a jet fire with a maximum range of 20 MW. The jet fire combustion module, as shown in Figure 8, ejects and ignites pressurized propane gas from the nozzle at a predetermined flow rate to form a jet fire. According to the ISO22899-1, the propane flow rate is 0.3 kg/s. To ensure stability and durability of the test device, its maximum propane flow rate is designed to be 0.4 kg/s. For precise flow control, the device can adjust to varying flow requirements via the control valve. Additionally, the position and angle of the nozzle can be adjusted according to test requirements.

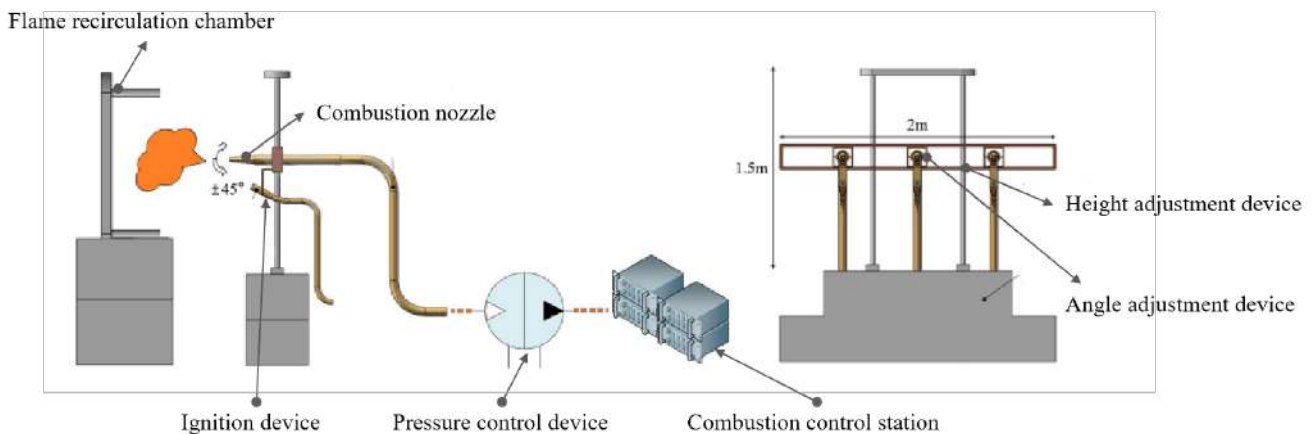


Figure 8. The composition of the jet fire combustion module

(2) High-temperature loading and reaction frame support system

The primary function of the high temperature loading and reaction frame supporting system is to apply force to the specimen at elevated temperature. The system comprises actuators, a mute oil source and a reaction frame module, as shown in Figure 9. The system applies an axial loading force of 5000 kN and a lateral loading force of 1000 kN (2-point loading). It accommodates specimens with maximum dimensions of 350 mm in width, 500 mm in height, and 4000 mm in length, meeting the majority of test requirements.

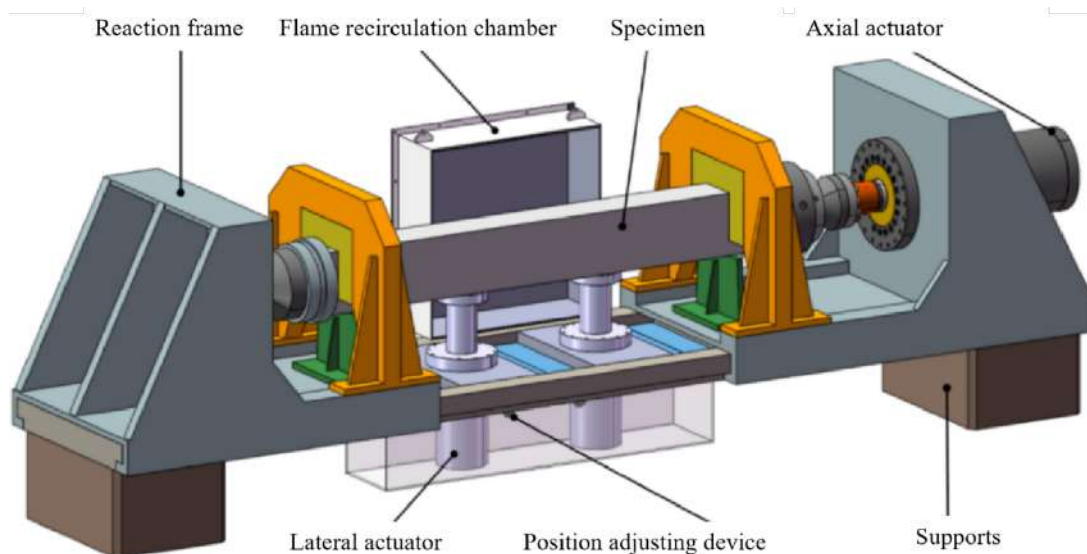


Figure 9. The high-temperature loading and reaction frame support system

During jet fire tests, the high temperature and intense thermal radiation around the specimen necessitate stringent fire protection and heat insulation measures for critical components like actuators and reaction frames in the testing apparatus. Furthermore, the firefighting process exerts considerable impact and erosion on the loading device, necessitating advanced waterproofing measures to ensure the device functions properly under high temperature environments and spray cooling, without compromising the accuracy and reliability of the tests. Simultaneously, the repetitive exposure to fire and water during multiple tests imposes increased demands on the stability and durability of the test device. The loading technology must exhibit high stability and reliability to ensure the accuracy and repeatability of the test data. The system employs both simulation analysis and experimental verification to precisely assess the thermal stress and thermal fatigue status of the equipment in elevated temperature environments, thereby offering a scientific foundation for thermal protection design. Additionally, a composite protection system is created utilizing new materials with outstanding thermal insulation and water erosion resistance, along with multi-layer structural design, to guarantee the stability and reliability of the loading device in extreme environments.

(3) Spray cooling system

The water spray cooling system comprises two modules: the spray cooling module and the spray water column cooling module. It can conduct spray fire extinguishing from both spray and fire water guns, to simulate the thermal shock and water gun pressure shock to the specimen. The strength of the spray cooling ranges from 4 to 16 L / (min·m²), the flow rate of the spray water column cooling module is 5 L/s, and the injection pressure is 0.35 MPa, meeting the requirements of most projects.

(4) Control and analysis system

The primary function of the control and analysis system is to regulate the output of jet fire parameters, force actions, and water spray, measure fire action parameters and specimen reactions, analyze test results, monitor test site conditions, and trigger automatic alarms. The system comprises a digital control module and a test analysis and monitoring module. Specifically, the digital control module interfaces with the combustion controller, actuator controller, and water spray cooling system controller to centrally manage and regulate the output parameters of the jet fire, force, and water spray. The test analysis and monitoring module is utilized for monitoring equipment status, specimen response, and test site conditions, encompassing fuel pipeline temperature, pressure, jet velocity, jet pressure, heat flux, flame temperature, specimen deformation, and temperature, as well as recording high-definition video footage of the test site.

The ultra-high temperature of the jet flame imposes stringent requirements on measurement methods and sensors. Sensors must possess high temperature, oxidation, and corrosion resistance, among other characteristics, to ensure stable operation in harsh environments. Consequently, the test device enhances sensor high temperature resistance through the utilization of special materials and coating technology, while concurrently optimizing sensor structure to mitigate the impact of thermal stress on measurement accuracy.

(5) Test safety guarantee system

The primary function of the test safety guarantee system is to collect and purify exhaust gas, monitor system operating parameters and test site environmental parameters in real time, and automatically alert and respond to emergencies when safety thresholds are exceeded. It comprises exhaust gas collection and purification modules, equipment safety assurance modules, and environmental safety assurance modules. Among these modules, the exhaust gas collection and purification modules primarily employ mechanical forced exhaust to promptly channel exhaust gases into purification equipment for treatment, with an effective exhaust volume of 120,000 m³/h. The equipment safety assurance system primarily monitors equipment and test operation status, whereas the environmental safety assurance system focuses on monitoring and alarming regarding the safety of the surrounding environment during testing.

To mitigate the impact of environmental changes on the loading device and minimize potential losses, the jet fire and force loading coupled test device is situated in the laboratory, where safety concerns are of utmost importance. Inadequate combustion of propane generates significant amounts of black smoke, requiring purification of the resulting exhaust gas prior to its release into the atmosphere. This device intends to utilize a combination process comprising a water film cyclone washing tower, a high-voltage electric field separator, an activated carbon adsorption box, and a fan. The exhaust gases are permitted for

release into the atmosphere via the exhaust stack only after undergone treatment and comply with the required standards. Additionally, in consideration of the high temperature, intense heat, and toxic gases produced during jet fire testing, as well as the risk of detonation from propane-air mixtures, this project intends to employ on-site real-time detection of gas concentration and temperature. If safety thresholds are exceeded, alarms will be triggered, appropriate measures taken, and exhaust gas collection devices and waste gas treatment equipment installed above the test area. Additionally, protective walls will be installed behind the combustion chamber, along with reflective walls within the thermal radiation range, to safeguard the building structure, surrounding equipment, and personnel, thus ensuring laboratory safety.

4 CONCLUSION

To address the critical fire prevention and control needs of petroleum and gas energy production, storage, and transportation infrastructure, a jet fire and force loading coupled test device will develop. The developed experimental apparatus is capable of simultaneously simulating jet fires, mechanical loading, and firefighting water spray. The device consists of five major systems, namely jet fire system, high-temperature loading and reaction frame support system, spray cooling system, control and analysis system, and test safety guarantee system. It will facilitate research on the combustion characteristics and action models of jet fires, the damage mechanisms of fire protection materials under jet fire, the evolutionary mechanism of engineering structures under jet fire, and the theoretical design of fire protection. This device can support research on basic theory and fire design methods related to jet fire resistance, promote product research and development, ensure the fire safety of petroleum and gas facilities.

REFERENCES

- [1] Ramírez, J., Carbone, F., Pastor, E., Bubbico, R. & Casal, J., Assessing the Consequences of Pipeline Accidents to Support Land-Use Planning. *Safety Science*, 2017, 97: 34-42.
- [2] Wang, J., Zhang, R., Wang, Y., Shi, L., Zhang, S. & Liu, J., Experimental Study on Combustion Characteristics of Pool Fires in a Sealed Environment. *Energy*, 2023, 283: 128497.
- [3] Cullen, L., The Public Inquiry into the Piper Alpha Disaster. Health and Safety Executive, 1990.
- [4] What Exactly Happened When a Liquid Propane Leak Caused a Fire and Injured 14 People? (2017-08-14). https://www.sohu.com/a/164522694_656055
- [5] Investigation Report on The "6.9" Fire Accident at the Olefin Plant of Qilu Branch of China Petroleum and Chemical Corporation. (2020-12-01). https://ajj.zibo.gov.cn/gongkai/channel_c_5f9fa491ab327f36e4c1305e_n_1605682601.5791/doc_5fc59f02d4c7016cbf09b909.html
- [6] ISO 13702: 2015 Petroleum and natural gas industries—Control and mitigation of fires and explosion on offshore production installations—Requirements and guidelines
- [7] Standardization Administration of the People's Republic of China, GB/T20660-2020. Petroleum and Natural Gas Industries - Control and Mitigation of Fires and Explosions on Offshore Production Installations - Requirements and Guidelines, Beijing, 2020.
- [8] Tam, V., Cowley, L., Consequences of Pressurized LPG Releases: The Isle of Grain Full Scale Experiments//GASTECH '88Gastech Exhibitions Limited. 1988.
- [9] Bennett, J., Cowley, L., Davenport et al. Large-Scale Natural Gas and LPG Jet Fires - Final Report to the CEC, TNER.91.022, Shell Research Limited, 1991.
- [10] Bennett, J., Cotgreave, T., Cowley, L. & Shirvill, L., Shell Offshore Flame Impingement Protection Programme. 1990.
- [11] Wighus, R., Shirvill, L., A Test Method for Jet Fire Exposure: 251561. SINTEF NBL, 1992.
- [12] The Jet Fire Test Working Group. Interim Jet Fire Test for Determining the Effectiveness of Passive Fire Protection Materials: OTO93028. Health and Safety Executive, 1993.
- [13] Road, A., Assessment of the Uniformity of the Interim Jet Fire Test Procedure: OTH 95477. Health and Safety Executive, 1996.

- [14] Parker, A., Dodge, F., Investigation of Critical Parameters Necessary to Simulate Large-Scale Jet Fire Events Involving Tubular Sections: No. 01-9841. 1995.
- [15] Parker, A., Wenzel, A., AL-Hassan, T., Characterization of The Laboratory-Scale Jet Fire Environment Involving Tubular Sections//4th International Conference of Offshore Structures - Hazards. London, UK: Safety & Engineering Working in the New Era, 1995.
- [16] HSE Offshore Safety Division. Characterisation of the Laboratory-Scale Jet Fire Around 203-mm Inside Diameter Tubular Geometries: OTO 96 048. Health and Safety Executive, 1996.
- [17] The Jet-Fire Test Working Group. Jet Fire Resistance Test of Passive Fire Protection Materials: OTI 95634. Health and Safety Executive, 1996.
- [18] White, G., Campbell, D., Validation of the Jet Fire Resistance Test Procedure - Large Scale Jet Fire Tests on Fire Protected I-Section Beams: OTO 96 055. Health and Safety Executive, 1996.
- [19] White, G., Campbell, D., Validation of the Jet Fire Resistance Test Procedure - Large Scale Jet Fire Tests on Fire Protected Tubular Members: OTO 96 054. Health and Safety Executive, 1996.
- [20] Mather, P., Smart, R., Large Scale & Medium Scale Jet Fire Tests: OTO 97 079. Health and Safety Executive, 1996.
- [21] ISO Copyright office, ISO 22899-1 Determination of the Resistance to Jet Fires of Passive Fire Protection Materials. Part 1: General Requirements, Switzerland, 2021.

PERFORMANCE OF FREEDAM JOINTS UNDER FIRE – EXPERIMENTAL ASSESSMENT

Ana Francisca Santos¹, Aldina Santiago², Hélder Craveiro³, Luís Simões da Silva⁴

ABSTRACT

In this paper, the results from an experimental campaign aimed to assess the behaviour under elevated temperatures of a dissipative beam-to-column connection, currently named FREEDAM connection, are presented. This connection has the particularity of having a sliding mechanism given by a friction damper with slotted holes located at the lower beam flange, which proved to be quite efficient in dissipating high amounts of energy during extreme seismic events, ensuring that the remaining components of the connection and structure remain within the elastic range. Furthermore, even for column loss scenarios, these connections allowed great vertical deformations without inelastic deformations of the structure and premature failure of the structure. This last point motivated the study presented in this paper since the sliding mechanism inherent in these connections provides significant ductility to the system and delays the development of great axial forces in the beam, that appear due to the expansion of the members under elevated temperatures.

Keywords: FREEDAM connection, fire structural behaviour, experimental tests

1 INTRODUCTION

Beam-to-column connections are considered key elements in steel structures since they control the stability of structures and facilitate the transmission of internal forces between the members, especially after accidental events, such as the World Trade Center disaster in 2001, where the thermal loading from the fires which occurred after the explosions induced the final collapse of the buildings [1]. When exposed to high temperatures, the members tend to expand, which, when restrained by cooler members (e.g. beams of the adjacent compartment), they experience significant compression forces along with additional bending moments that were not presented at ambient temperature. This additional set of loads, combined with the degradation of material properties due to heating, can result in local buckling of the beam flange near the connection and the reduction of the stiffness of this region which is typically manifested by a sudden development of tensile actions (catenary actions) [2] [3]. In addition, the failure modes can deviate from those observed under ambient temperature, due to the interaction between bending moments, tying forces (catenary actions) [3, 2] and shear forces [4, 2, 5, 6].

¹ Dr, University of Coimbra, ISISE, ARISE, Department of Civil Engineering, Coimbra, Portugal
e-mail: francisca.santos@uc.pt, ORCID: <https://orcid.org/0000-0002-7448-8876>

² Prof, University of Coimbra, ISISE, ARISE, Department of Civil Engineering, Coimbra, Portugal,
e-mail: aldina@dec.uc.pt, ORCID: <https://orcid.org/0000-0003-3646-4926>

³ Dr, University of Coimbra, ISISE, ARISE, Department of Civil Engineering, Coimbra, Portugal,
e-mail: heldercraveiro.eng@uc.pt, ORCID: <https://orcid.org/0000-0001-8590-5885>

⁴ Prof, University of Coimbra, ISISE, ARISE, Department of Civil Engineering, Coimbra, Portugal,
e-mail: luiss@dec.uc.pt, ORCID: <https://orcid.org/0000-0001-5225-6567>

Concerning the abovementioned behaviour, an important characteristic of a connection under fire is its ductility or rotation capacity, which allows the development of high deformations and rotations without failing. In this sense, it was thought that the use of innovative connections such as the *free from damage* connection could be advantageous. These connections, developed during the previous RFCS FREEDAM project have a sliding mechanism which proved to be quite efficient in dissipating high amounts of energy during extreme seismic events [7], while keeping the remaining components of the connection and structure free from damage. In addition, studies on buildings using this connection as beam-to-column connections under column loss scenarios have shown that using these connections allowed great vertical deformations without inelastic deformations of the structure and early failure [8, 9].

This last point motivated the investigations of the performance of the Freedom connection under fire actions, since under elevated temperatures, the beams tend to present high vertical deformations, and the connections must be able to sustain these rotations without failing. In this paper, the experimental campaign carried out to assess the behaviour of the Freedom connection under fire is presented.

2 EXPERIMENTAL SETUP

2.1 Connection details

The connection used in the experimental campaign is part of the 3-storey steel building in construction on the Campus of the University of Salerno, within the scope of the pilot RFCS project (RFCS-2020-101034015). The building is 11.9 m in height and the floors have a plan area equal to 344 m², each with a different occupancy activity, namely a basement with parking, a medical laboratory on the 1st floor and offices on the 2nd floor. FREEDAM connections are implemented as beam-to-column connections of the seismic-resistant external frames. The fire resistance (R) of the structural elements and connections, according to the Italian fire code [10] and the EN 1991-1-2 [11], is reported in Table 1.

Table 1. Minimum fire resistance criteria

Floor	Activity	Fire resistance (min)
Ground floor	Car park/plant room	R30/R60 (<i>depending on the materials of the plant room</i>)
1st floor	Medical labs	R45
2nd floor	Offices	R30

For the experimental campaign, the FREEDAM connection adopted on the 2nd floor was chosen. This connection is composed of a beam IPE 400, a column HEB 400, an upper T-stub connecting the beam upper flange to the face of the column and the friction device D1 located at the lower beam flange (Figure 1). The friction device D1 is composed of a couple of L-stubs connecting the device to the face of the column, a couple of friction plates (i.e., steel plates with a coating surface providing a high friction coefficient) between the L-stubs and the haunch, and the haunch, composed by a steel grade S355 plate bolting the haunch to the lower beam flange and a stainless-steel part with long horizontal slotted holes. The sliding of the joint is provided by the relative movement of the haunch plate in the friction plates and L-stubs. All these parts are connected through the use of M16 10.9 HV preloaded bolts.

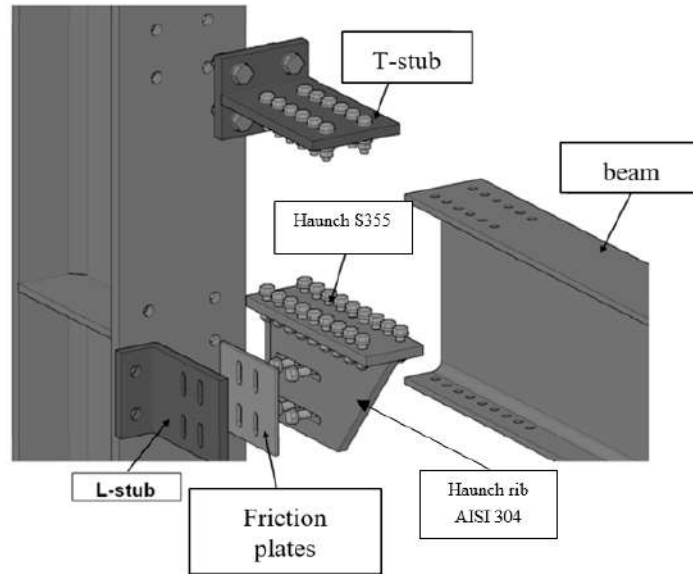


Figure 1. FREEDAM connection

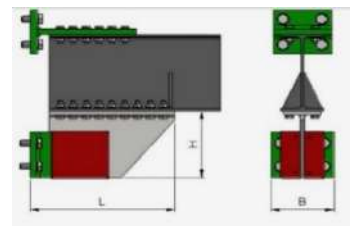
The flexural resistance of the connection is given by the friction resistance of the device by the lever arm of the connection, whereas the rotation capacity is controlled by the size of the slotted holes. The resistance force of the friction damper, $F_{D,Rd}$, should be at least equal to:

$$F_{D,Rd} = \frac{\mu_{st,k} n_s n_b F_p}{\gamma_{creep}} \geq F_{D,Ed} = \frac{M}{z} = \frac{m M_{pl,Rd,b}}{z} \quad (1)$$

Where, $\mu_{st,k}$ is the characteristic dynamic friction coefficient for the friction device given in [12, 13] ($\mu_{st,k} = 0.53$), n_s is the number of shear planes ($n_s = 2.0$), n_b is the number of bolts of the device ($n_b = 4.0$), γ_{creep} the safety factor accounting for the loss of initial preload due to short-term and long-term relaxation phenomena according to [14] ($\gamma_{creep} = 1.15$), F_p is the design preloaded force which can take values between 40%-60% of the preload proof load according to EN 1933-1-8, $F_{p,C}$ [12, 13] (for the study case, $F_p = 0.6 F_{p,C} = 65.9$ kN) and m is the utilisation factor of the joint, which can be in the range 0.3-0.6 [7]. For the joint under consideration, $m = 0.3$. The resistance values of the friction damper for the analysed case are depicted in Table 2.

Table 2.. Main properties of friction device D1

Friction Device D1 – properties			
$F_{slip,Rd}$ [kN]	244.2	L [mm]	515
$M_{j,Rd}$ [kNm]	141.6	H [mm]	265
n_b [-]	4	B [mm]	226
n_b [-]	2		
F_p [kN]	66.2		



2.2 Experimental layout, instrumentation and test procedure

The testing layout is schematically reported in Figure 2. The column is pinned at the base, whereas at the top the vertical restraint is free, allowing the column to expand at high temperatures. The beam end is free to rotate and slide horizontally. i.e. no axial restraint is applied. The decision to leave the beam end axially free was made after conducting preliminary FEM analysis carried out in Abaqus software for the connection under study. As reported in [15], even when fully restrained under elevated temperatures, the axial forces applied to the beam due to the restraint decreased rapidly to almost until zero once the connection began to slip. Therefore, the experimental layout was simplified and no axial restraint was considered.

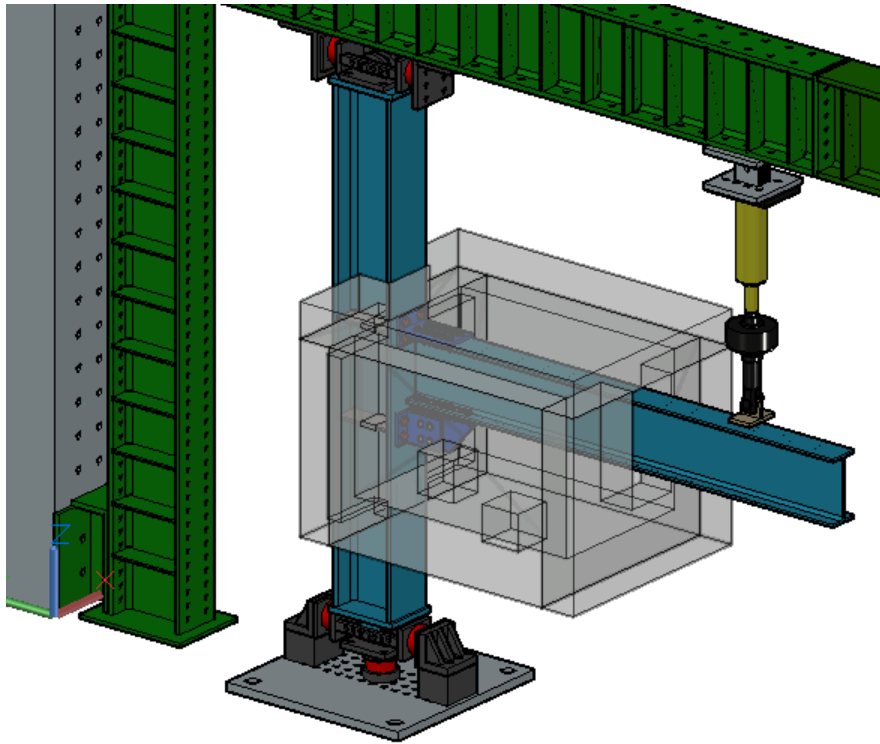


Figure 2. Test layout scheme

The tests follow 3 steps:

- i. Application of a mechanical load as a vertical load at the beam end: 1 test with a force to subject the connection to a hogging moment equal to $60\%M_{j,Rd}$ ($M = 83 \text{ kNm}$) and two tests with a force to subject the connection to a hogging moment equal to $80\%M_{j,Rd}$ ($M = 112 \text{ kNm}$)
- ii. Heating the connection and keeping the mechanical load constant throughout the heating process. The connection was heated using an electrical furnace following the ISO 834 heating curve (dashed line in Figure 3). The furnace module used has electrical resistance on three faces, below the joint and on both sides. However, due to the use of only one furnace module, the temperatures inside in furnaces were consistently lower than the ISO 834 curve, as observed in Figure 3). The heating process ended once the maximum beam displacement was achieved, i.e. when the beam touched the edge of the furnace window.
- iii. Cooling: the natural decrease of the temperatures was measured during +/- 17 hours.

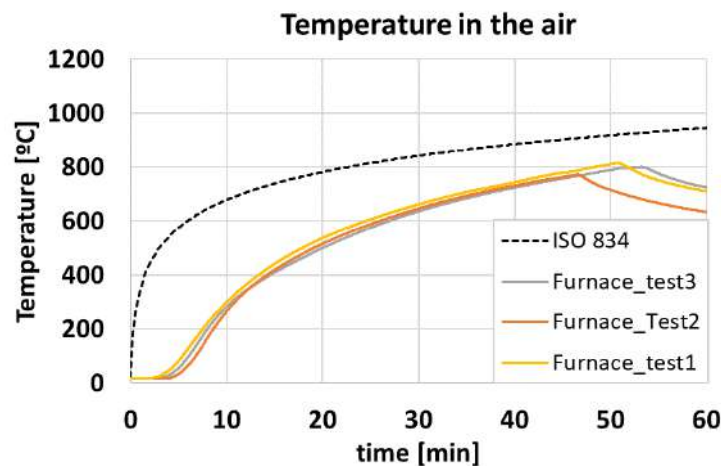


Figure 3. Heating curves ISO 834 and temperature in the air inside the furnace

Regarding instrumentation, temperatures through thermocouples and a thermal camera, deformations (outside the furnace) with LVDTs and forces with load cells have been measured, as the schematic shown in Figure 5.

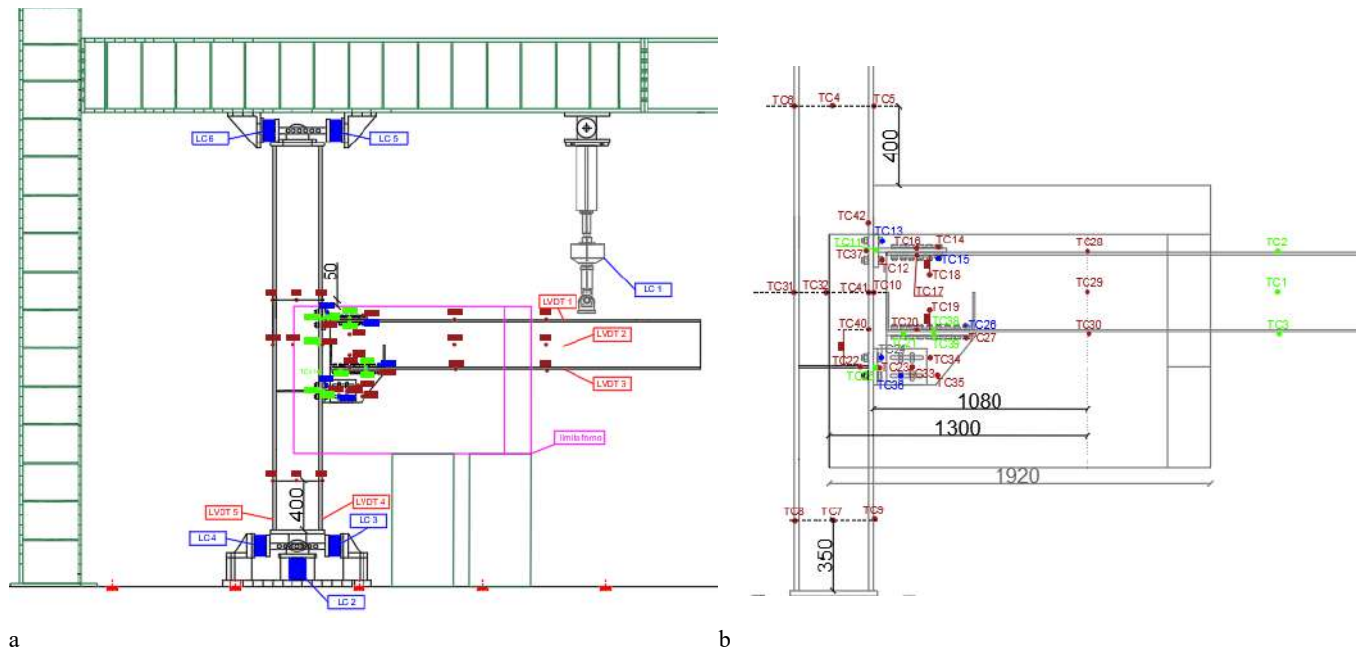


Figure 4. Instrumentation: a. Position of all instrumentation, b. Thermocouples

3 EXPERIMENTAL RESULTS

3.1 Temperatures in the connection

The evolution of temperatures in different parts of the specimen is shown in the following figures for test 1 (similar evolution was observed for tests 2 and 3). Inside the furnace, two distinct zones can be highlighted: a) the beam outside the connection zone (TC 28 – TC 30 in Figure 4b) and b) the connection zone comprising b.1) upper part (T-stub) and b.2) lower part (haunch).

In the beam outside the connection zone (Figure 5), temperatures initially rise at a slower rate compared to the furnace temperature, but, in the end, the temperatures in the member reach the same value as those within the furnace, which was expected since the member is not protected, and the massivity in this zone is low.

In the upper and lower parts of the connection (Figure 6 and Figure 7, respectively) the evolution of temperatures, was measured in the face and thickness of the column, beam web, bolts and T-stub and friction dampers. The highest temperatures recorded reached around 750°C at the beam web (TC18 and TC19), whereas the coolest zones are the column face, T-stub and L-stub face connected to the column, with a maximum temperature of around 500°C, because these zones are located at the edge of the furnace and are not directly heated by the electric resistances. The friction damper zone, composed of the L-stub face, friction plates and haunch, showed higher temperatures than the column flange but were not as high as those observed at the beam web due to the greater massivity of this zone.

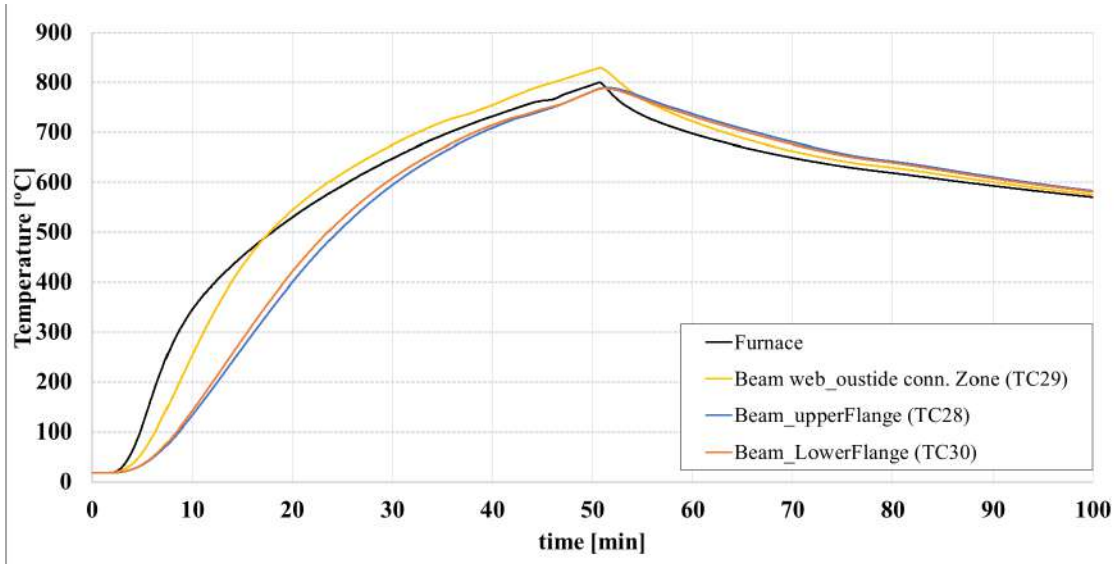


Figure 5. Temperature in the beam outside the connection zone

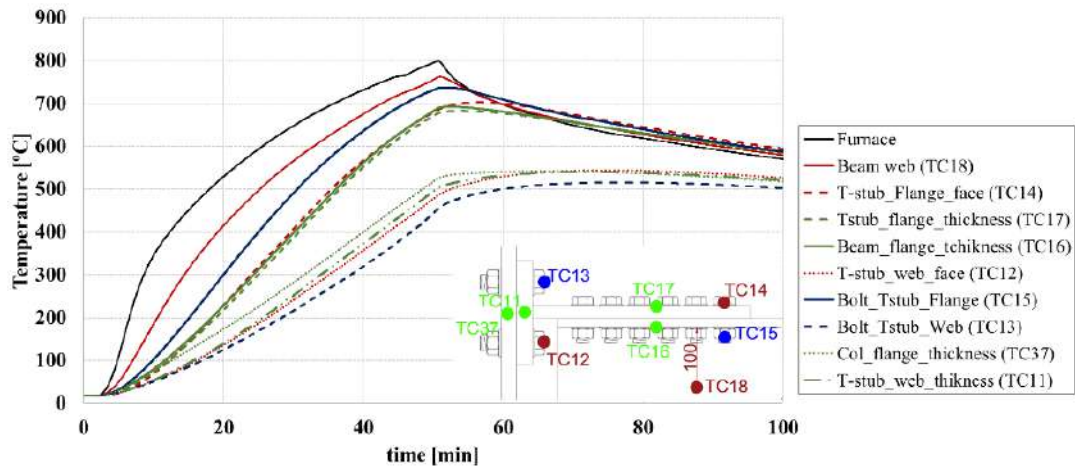


Figure 6. Temperature in the upper part of the connection (T-stub)

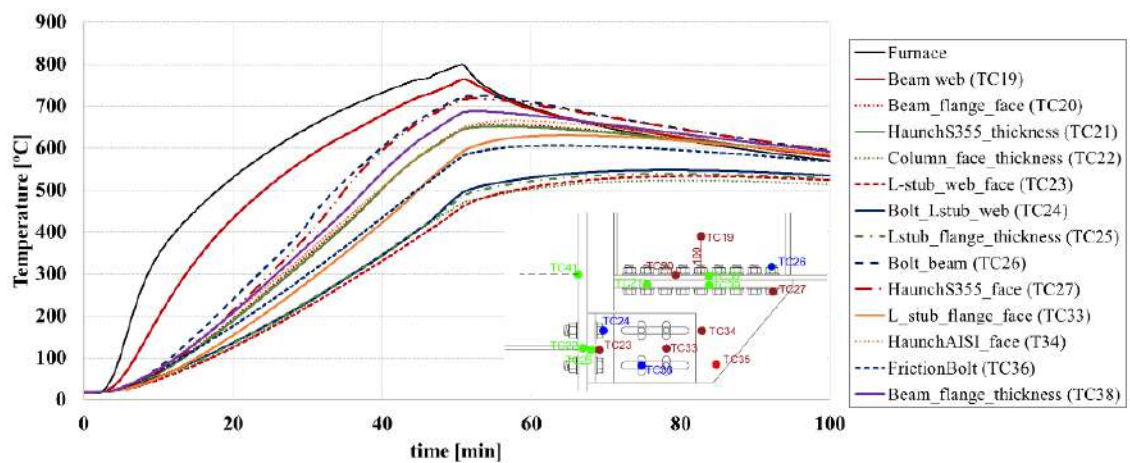
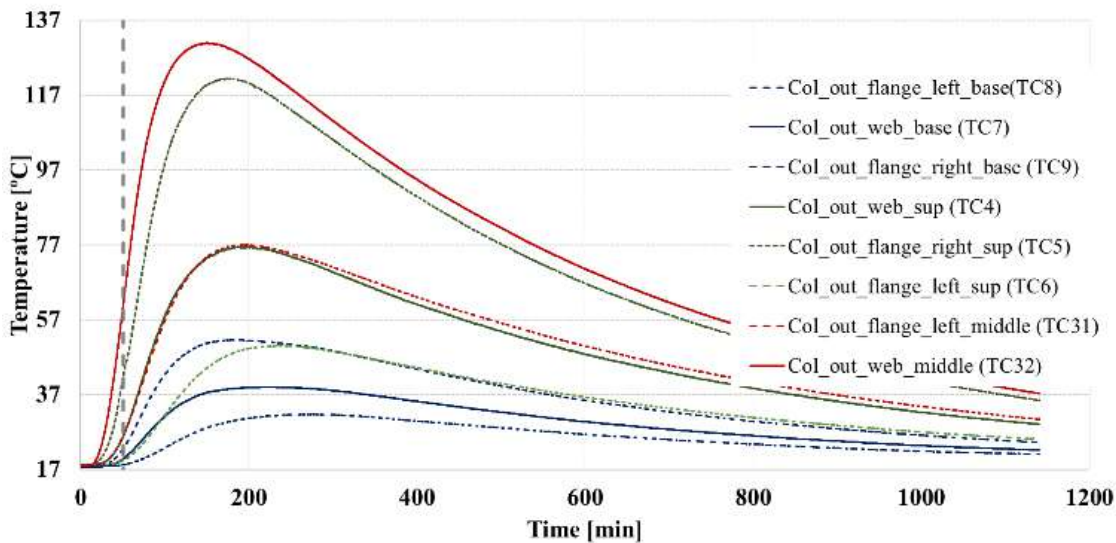


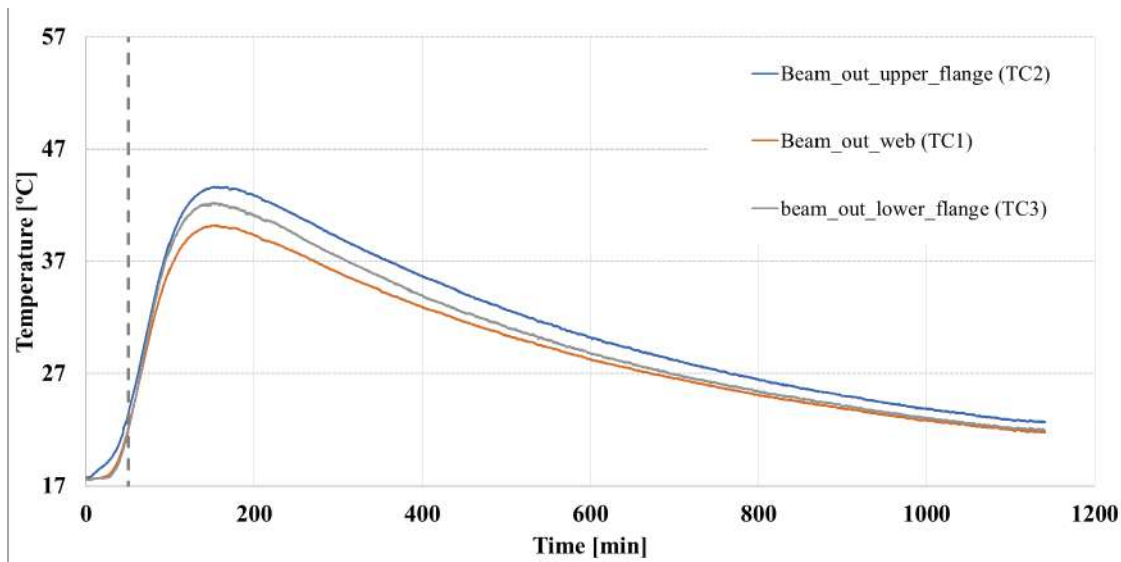
Figure 7. Temperature in the lower part of the connection (friction damper)

In addition, temperatures in the column and beam outside the furnace were also recorded to assess the thermal conductivity of the members and potential heat losses (Figure 9). During the heat process, temperatures remained consistently below 20°C, except in two thermocouples placed right in the vicinity

of the furnace, where 60°C was registered (dashed line in Figure 9). The maximum temperatures in these zones were recorded during the cooling phase due to the conductivity of the members, with a maximum of 120°C.



a)



b)

Figure 8. Temperature outside the furnace a) in the column and b) beam

3.2 Rotational capacity and deformation

The connection deformation was registered by a couple of LVDTs placed at the actuator zone and column base. The rotation of the beam versus temperature at the friction bolt (TC36 in Figure 4b) for each test.

The rotation of the beam was assessed by dividing the vertical displacement recorded by the LVDT near the actuator by the distance between the LVDTs and the column face. As observed, in all tests, the joint exhibited rigid behaviour until the beginning of the slip of the damper, which happens when the flexural friction resistance provided by the damper equals the applied bending moment in the connection, due to the loss of the preload caused by elevated temperatures in the bolts (+/- 450 °C when the slip occurs). The slip occurred at a slightly lower temperature and duration in test 2, which was due to the application of a higher initial load. Conversely, in test 3, even applying the same load as in test 2, slip initiation took longer, indicated it happened at higher temperature in the bolt.

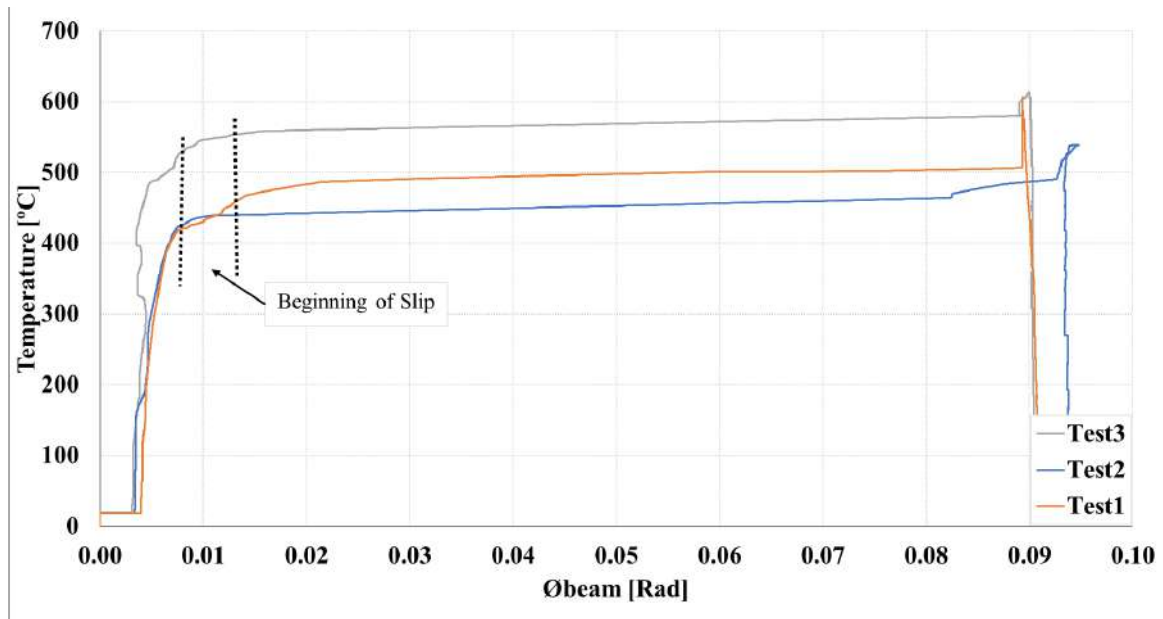


Figure 9. Beam rotation vs time and temperature

The local deformations were checked only after disassembling the furnace. In general, a global deformation with the complete slip of the connection was noticed (Figure 10). Locally, the lower bolt of the damper experienced shear deformation (Figure 11, left), as well as bearing within the holes of the L-stubs webs and haunch. The friction plates did not suffer excessive wearing of the coating material even with the elevated temperatures recorded (Figure 11, right).



Figure 10. Deformation of the connection after the test (after cooling)



Figure 11. Shear of the bolts (left), wearing of the friction plates (right)

4 CONCLUSIONS

This paper presents the results of the experimental campaign carried out to assess the behaviour of the Freedom connection under elevated temperatures. A total of three tests were carried out on an external beam-to-column Freedom connection, varying the initial applied load. No horizontal beam restraint was considered in the tests, focusing solely on assessing the influence of elevated temperatures on the component's strength and ductility along the initial applied load. From the tests, the following conclusions could be withdrawn:

- The web of the beam seems to be the weaker element of the connection, as it reaches higher temperatures much sooner than the plates/bolts of the friction device and upper T-stub. One potential solution can be to apply fire protection only in this zone;
- The connection initially deforms as rigid until the flexural friction resistance of the device is similar to the service bending moment applied. This happens due to the loss of preload with the loss of strength properties of the bolts and expansion due to the increase in temperature;
- After the slip, there is visible engagement of the bolts in shear and plates in bearing, giving an additional resistance to the connection.
- Overall, the slip mechanism of the connection seems to be an advantage in a fire situation, offering an extra “elastic” rotation capacity to the connection before the yielding of the steel parts.

The test results presented in this paper serve as the calibration tests for a parametric finite elements analysis of these connections under fire, which will consider “real” beam axial restraints, to study deeper into the M-N interaction of these particular connections.

ACKNOWLEDGEMENT

This work was partly financed by FCT / MCTES through national funds (PIDDAC) under the R&D Unit Institute for Sustainability and Innovation in Structural Engineering (ISISE), under reference UIDB / 04029/2020 (doi.org/10.54499/UIDB/04029/2020), and under the Associate Laboratory Advanced Production and Intelligent Systems ARISE under reference LA/P/0112/2020. This work was also financed by the European Commission's Research Fund for Coal and Steel through the research project RFSR-CT-2020-101034015.

REFERENCES

- [1] Federal Building and Fire Safety Investigation of the World Trade Center Disaster, “Final Report of the National Construction Safety Team on the Collapses of the World Trade Center Tower,” September, 2005.
- [2] A. Santiago, *Behaviour of beam-to-column steel joints under natural fire*, Ph.D. Thesis, Department of Civil Engineering, University of Coimbra, 2008.
- [3] T. Jána, T. Heistermann and F. Lopes, “Design of composite joints for improved fire robustness (COMPFIRE) : final report,” European Commission, Directorate-General for Research and Innovation, Publications Office, 2014.
- [4] H. Yu, I. W. Burgess, J. Davison and R. Plank, “Numerical simulation of bolted steel connections in fire using explicit dynamic analysis,” *Journal of Constructional Steel Research*, vol. 64, no. 5, pp. 515-525, 2008.
- [5] R. Rahnavard and R. J. Thomas, “Numerical evaluation of the effects of fire on steel connections; Part 1: Simulation techniques,” *Case Studies in Thermal Engineering*, vol. 12, pp. 445-453, 2018.
- [6] A.-J. K.S., D. J.B. and B. I.W., “Performance of beam-to-column in fire - A review,” *Fire Safety Journal*, vol. 43, pp. 50-62, 2008.
- [7] R. Tartaglia, M. D'Aniello, A. Campiche and M. Latour, “Symmetric friction dampers in beam-to-column joints for low-damage,” *Journal of Constructional Steel Research*, vol. 184, p. 106791, 2021.
- [8] A. F. Santos, A. Santiago, M. Latour and G. Rizzano, “Robustness analysis of steel frames subjected to vehicle collisions,” *Structures*, vol. 25, pp. 930-942, 2020.
- [9] T. Golea, A. Santos, J.-P. Jaspart, A. Santiago and J.-F. Demonceau, “Design for robustness of steel structures with dissipative freedom joints,” *Ingegneria Sismica*, vol. 39, no. 2, pp. 40-55, 2022.
- [10] Ministero dell'Interno, DPR 1 Agosto 2011, n.151 -Regolamento Recante Semplificazione Della Disciplina Dei Procedimenti Relativi Alla Prevenzione Dgli Incendi., 2011.
- [11] EN 1991-1-2, Eurocode 1: Actions on structures - Part 1-2: General actions - Actions on structures exposed to fire, Brussels, Belgium: European Committee for Standardization, 2002.
- [12] G. F. Cavallaro, A. Francavilla, M. Latour, V. Piluso and G. Rizzano, “Cyclic response of low yielding connections using different friction materials,” *Soil Dynamics and Earthquake Engineering*, vol. 114, p. 404–423, 2018.
- [13] A. B. Francavilla, M. Latour, V. Piluso and G. Rizzano., “Design criteria for beam-to-column connections equipped with friction devices,” *Journal of Constructional Steel Research*, vol. 172, p. 106240, 2020.
- [14] G. F. Cavallaro, M. Latour, A. B. Francavilla and G. R. Vincenzo Piluso, “Standardised friction damper bolt assemblies time-related relaxation and installed tension variability,” *Journal of Constructional Steel Research*, vol. 141, pp. 145-155, 2018.
- [15] A. Santos, A. Santiago, H. Craveiro and L. Simões da Silva, “Finite element study on the behaviour of free from damage connections under fire.,” in *ce/papers*, 6: 2178-2183. , 2023.

TEMPERATURE DISTRIBUTION AND RESIDUAL STRENGTH OF MORTAR INFILLED MODULAR RECTANGULAR STEEL COLUMNS EXPOSED TO STANDARD FIRE

Seulgi Han¹, Junyoung Gwak², Sunhee Kim³, Inrak Choi⁴, Sungmo Choi⁵

ABSTRACT

Modular construction offers superior constructability, quality, and affordability. In Korea, high-rise modular buildings are required to have a 3-hour fire resistance rating. Currently, a total of 57 mm of gypsum board has been used to meet this requirement, but it is economically impractical considering the dimensions of the modular columns (\square -200×100×9). Therefore, a mortar infill of rectangular steel tube was applied to ensure 3 hours of fire resistance. To verify the fire resistance of the mortar-infilled steel tube column, a fire test was conducted using a standard fire curve. In addition, a residual strength test was conducted after the fire test to evaluate the structural performance of the columns. The test results show that the temperature slowly increased by about 57% when the mortar infilled the steel tube. In addition, the residual strength after exposure to standard fire was about 87% compared to the column not exposed to fire. It shows that the fire resistance was improved when the mortar was infilled inside the steel tube of modular structure.

Keywords: Temperature distribution; mortar infill; modular rectangular steel tube columns; standard fire; residual strength

1 INTRODUCTION

Modular construction has the advantage of reducing construction time and improving construction quality by utilizing a factory fabrication process and on-site installation (Kim, et al. 2015; An et al. 2015; Park, 2022). While some countries, such as Europe, evaluate fire resistance through performance-based design, which considers fire scenarios and fire loads, Korea requires fire resistance based on prescriptive design, which considers occupancy or building height (number of floors). In Korea, rectangular steel tube columns used in modular structures must be certified to meet a 3-hour fire resistance rating, which is typically achieved by applying three layers of gypsum board (total thickness of 57 mm). However, this method becomes economically impractical due to the increased self-weight of the building. Therefore, a fire-resistant cladding method for high-rise modular buildings has been proposed as an alternative (Dashdemberel, 2024).

¹ Seulgi Han, University of Seoul
e-mail: seulgihan94@naver.com

² Junyoung Gwak, University of Seoul
e-mail: kjy7119159@naver.com

³ Sunhee Kim, University of Seoul
e-mail: sun@uos.ac.kr

⁴ Inrak Choi, Hoseo University
e-mail: irchoi@hoseo.edu, ORCID: <https://orcid.org/0000-xxxx-xxxx-xxxx>

⁵ Sungmo Choi, University of Seoul
e-mail: smc@uos.ac.kr, ORCID: <https://orcid.org/0000-0002-9391-528x>









In this study, mortar filling inside the rectangular steel tube was proposed as a way to ensure 3 hours fire resistance to apply high-rise modular construction. In order to verify the fire resistance of the modular steel tube column, an unloaded fire resistance test was conducted to determine the temperature distribution characteristics of the cross-sectional area for 3 hours with and without mortar filling on a steel tube column with a Spray-applied Fire Resistive Material (SFRM) thickness of 30 mm. Compressive strength tests were then performed on the steel tube columns after fire exposure. By comparing and analyzing the load-displacement relationship between fire-exposed and non-exposed columns, the fire resistance performance of the fire-exposed rectangular steel tube columns was investigated.

2 LITERATURE REVIEW

2.1 Modular Construction in Korea

Early modular construction in Korea (2003-2007) was initially applied to public buildings, such as schools and military barracks, and later expanded to dormitories and offices (Kim, 2014). From 2008 to 2012, the industry experienced growth in international markets, including Russia, Australia, and Guam. The period from 2013 to 2019 saw the emergence of a modular public housing sector, most notably with the construction of the Pyeongchang Media Residence. In the 2020s, modular construction of high-rise buildings of 12 stories or more expanded, exemplified by projects such as the Gwangyang Living Center and the Yongin Yeongdeok Apartment Building. This development is summarized in Table 1.

Table 1. Development of modular construction in Korea

2003~2007	2009~2013	2014~2019	2020~present
School Military Barracks	Dormitories Exports to Guam, Russia	Offices, Hotels Residential	High-rise buildings
			
Shingi Elementary School	Gwangyang Apartment House (4F)	Ganyangdong Apartment House (4F)	Gwangyang Residential (12F)
			
Daejeon Elementary School	ELGA Mining Accommodation Russia(3F)	Pyeongchang Media Residences Hotel (4F)	Yongin Yeongdeok Happy House (13F)

A typical modular building under construction in Korea is shown in Figure 1. Each modular unit measures $7,000 \times 3,340 \times 3,100$ mm. The column size is \square - $200 \times 100 \times 9$, the beam size is \square - $150 \times 100 \times 4.5$, and the brace size is \square - $100 \times 50 \times 3.2$. In addition, bracing within the modular unit was used to resist lateral forces.

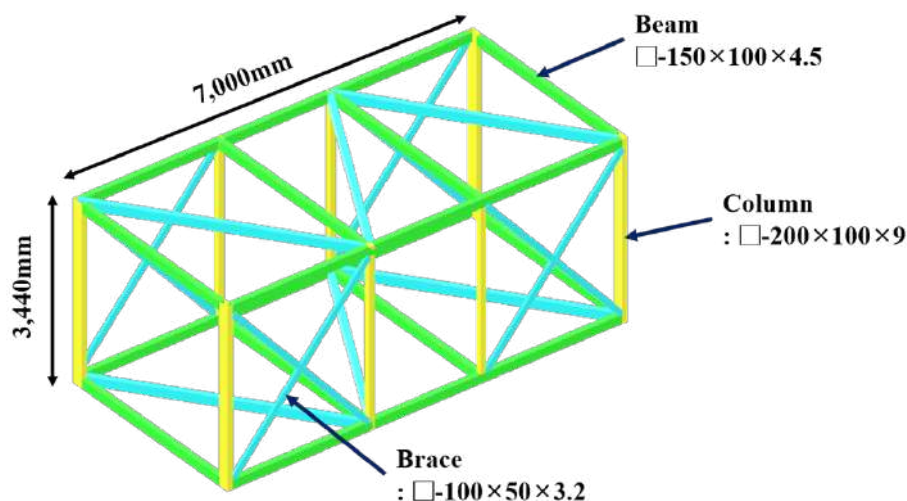


Figure 1. Modular units in South Korea

2.2 Fire resistance certification of modular columns in Korea

In Korea, fire resistance is required for each type of major structural component based on the use and size of the building, according to the rules of the Standards for Evacuation and Fireproof Structure of Buildings. Since it does not take into account the fire load of each building or the material of the major structural parts, it is essential to use fireproof board, spray paint and fireproof paint to meet the fire resistance time of 1-3 hours. To meet the 3-hour fire resistance of beams and columns used in modular buildings, three gypsum boards (57mm) are required as shown in Table 2. This significantly increases the weight of the modular building, making transportation and on-site construction uneconomical, and significantly reduces the interior area of the room because the gypsum board is applied with a thickness of 57mm.

Table 2. Status of 2 and 3 hours fire resistance certifications for modular columns in Korea

Fire-resistant section(mm)	Gypsum board thickness(mm)	Fire Resistance Time
□-100×100×6	38mm over (2 sheets)	2h
□-125×125×6	57mm over (3 sheets)	3h

2.3 Residual Strength of CFT Columns

Lin, (2002) conducted compressive strength experiments on □-100×75×2.86 and □-130×85×2.86 columns heated to 100, 200, 300, 400, 500, 600, 700, 800, and 900°C, respectively, and left at ambient temperature for 2 hours. The results showed that the columns exposed to high temperatures showed mostly ductile behavior, and the columns exposed to 300, 500, and 900°C retained 78, 55, and 35% of their residual strength, respectively.

Kim, (2012) confirmed that the residual strength of single CFT columns (□-460×9) exposed to a standard fire for 3 hours had a residual strength approximately 60% higher than that of columns not exposed to fire.

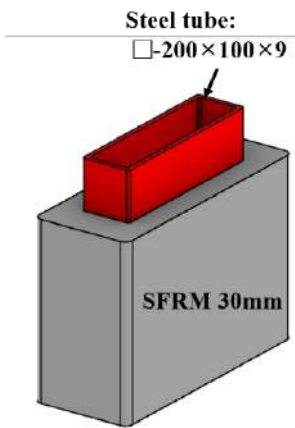
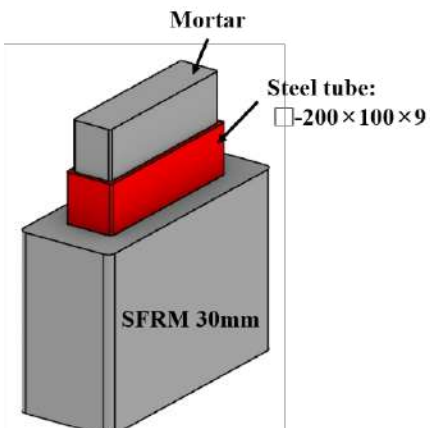
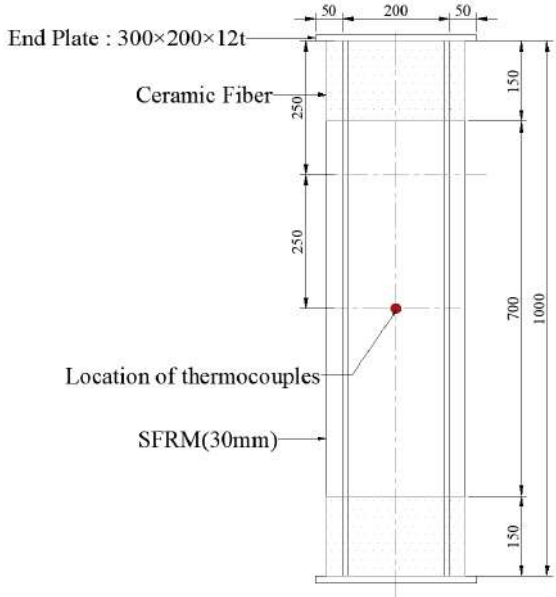
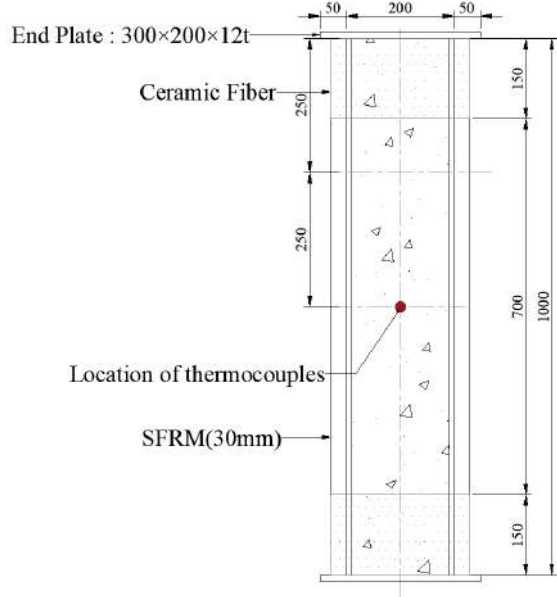
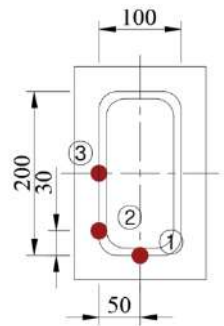
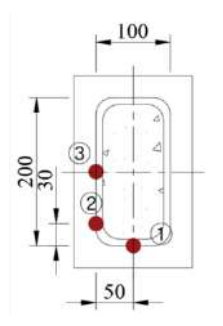
3 FIRE TEST OF RECTANGULAR STEEL TUBE COLUMNS EXPOSED TO STANDARD FIRE

3.1 Test Plan

The specimen cross-section is 200 mm wide, 100 mm long, 9 mm thick, and 1,000 mm high, as shown in Table 3. The number of specimens is 2 with and without mortar filling inside the rectangular steel tube with

30 mm SFRM. Since this study is about the fireproofing method for high-rise modular buildings, the standard fire exposure condition was set to 3 hours. The nominal yield strength (F_y) of the steel is 275 MPa, and the compressive strength (f_{ck}) of the mortar is 20 MPa. The temperature measurement locations of the specimen are three locations on the surface of the steel as shown in Table 3. The fire resistance performance is evaluated by whether the average temperature of the three temperature measurement locations exceeds 538°C and the maximum temperature exceeds 649°C according to the Korean standard.

Table 3. Section of test specimens and location of thermocouples

	Without Mortar Infill	With Mortar Infill
3d Model		
Section		
Location of Thermocouples		

The unloaded fire resistance test was conducted at KTR in Hongseong using a furnace measuring 4 m in width, 3 m in depth, and 1.5 m in height. The furnace is shown in Figure 2.

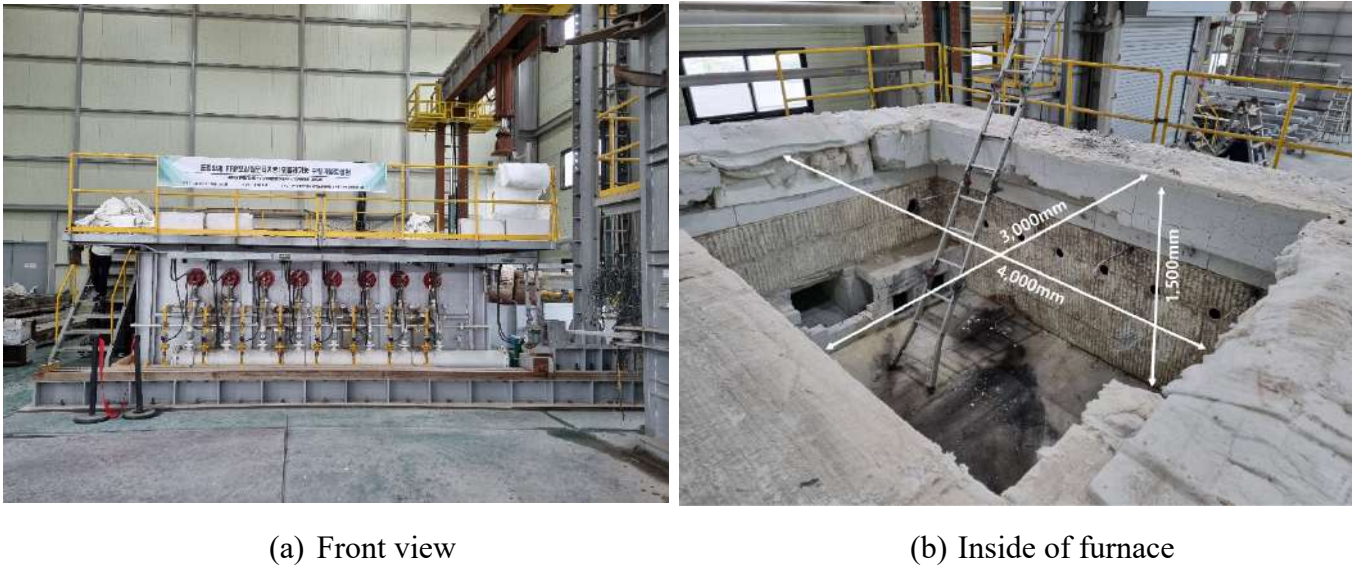


Figure 2. Horizontal fire furnace

3.2 Test Results

The temperature increase trend over time was observed for modular square steel tube columns with and without mortar infill, each specimen applied with a 30 mm thickness of SFRM. As shown in Figure 3, the temperature of the mortar-filled specimen showed a linear increase, while the temperature of the unfilled specimen gradually increased until 30 minutes, remained relatively constant, and then increased sharply. The mortar-filled specimen exceeded the limit temperature of the steel of 538°C at about 106 minutes, while the specimen without mortar infill reached only 78% of the limit temperature at 180 minutes. This indicates that the heat storage of the mortar inhibits the rise in surface temperature of the steel. The surface temperatures of the steel at 1, 2, and 3 hours are summarized in Table 4.

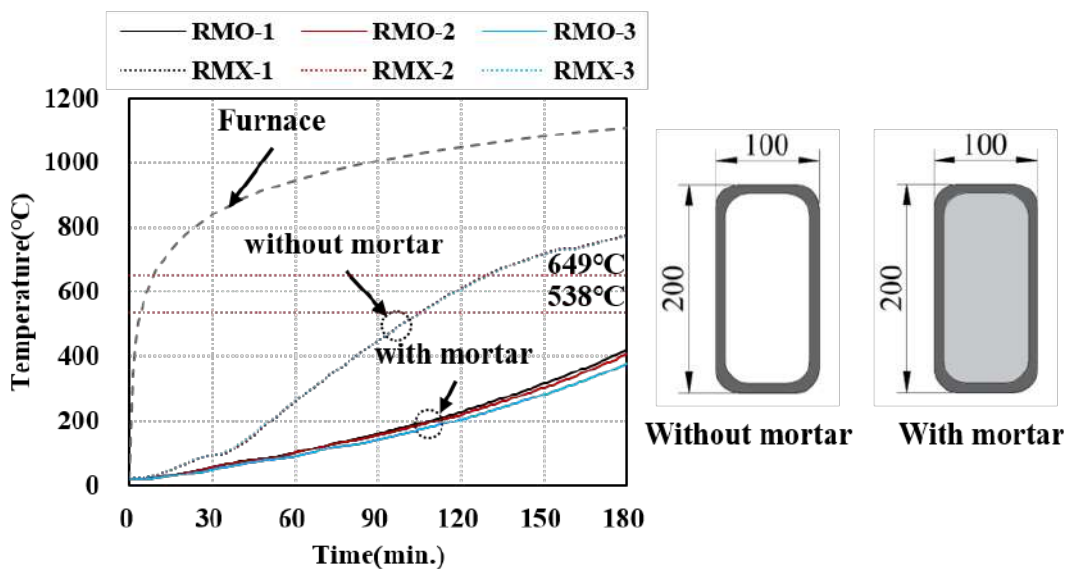


Figure 3. Temperature distribution of steel tube over time

Table 4. Temperature of the steel surface of specimens after 1, 2, and 3 hours

Time (min.)	Without Mortar Infill (°C)	With Mortar Infill (°C)
60	262.4	98.7
120	610.8	218.5
180	778.9	402.3

4 RESIDUAL STRENGTH OF MODULAR RECTANGULAR STEEL COLUMNS

In Chapter 3, the temperature distribution of a modular rectangular steel tube column exposed to a standard fire for 3 hours was studied. The specimen was then kept at ambient temperature for approximately 40 days. Since the modular rectangular steel tube column exposed to fire for 3 hours was kept at ambient temperature, the changes in the mechanical properties of the steel were checked and the residual strength was examined.

4.1 Test Plan

The residual strength was evaluated by conducting a compressive strength experiment of the modular rectangular steel tube columns and the rectangular steel columns not exposed to fire under the same conditions. The cross-sectional dimensions of the specimen are 200 mm width, 100 mm depth, 9 mm thick, and 1,000 mm height. The nominal yield strength (F_y) of the steel is 275 MPa, and the compressive strength (f_{ck}) of the mortar is 20 MPa. The experimental equipment was a 3,000 kN UTM (Universal testing machine), as shown in Figure 4, and the displacement control method was used at a speed of 0.02 mm/sec. The list of test specimens is summarized in Table 5.



Figure 4. Test set-up of axial loading test

Table 5. List of test specimen

Specimen	Mortar infill	Fire exposure
RXA	X	X
RXF	X	O
ROA	O	X
ROF	O	O

- 1) Nominal Strength: Steel (F_y) = 275MPa(SM275), Mortar (f_{ck}) = 20MPa
- 2) SFRM Thickness: 30mm

4.2 Test Results

4.2.1 Material Test Results

The compressive strength of the mortar was tested according to ASTM C109/109M. The results showed an average of 8.8 MPa for three specimens. The steel tensile strength test was performed in accordance with ASTM A370. The results showed Young's modulus of 212,988 MPa, yield strength of 433 MPa, and tensile strength of 518 MPa.

4.2.2 Load-Displacement Relationship

The fire-exposed specimen without mortar infill (RXF) exhibited approximately 60% of the peak load of the specimen without fire exposure and mortar infill (RXA), as shown in Figure 5. The fire exposed mortar filled specimen (ROF) exhibited a peak load of approximately 84% of the peak load of the mortar filled specimen (ROA) that was not exposed to fire, as shown in Figure 5. The peak load and displacement of each specimen are summarized in Table 7. It can be seen that the mechanical properties of the steel change even after remaining at ambient temperature, because the temperature of the unloaded steel column increases by about 700°C or more after 3 hours of standard fire. The temperature of the steel surface increases slowly due to the heat storage of the mortar, and accordingly, it is judged to be applicable to high-rise modular construction because it shows sufficient strength even after 3 hours of exposure to standard fire.

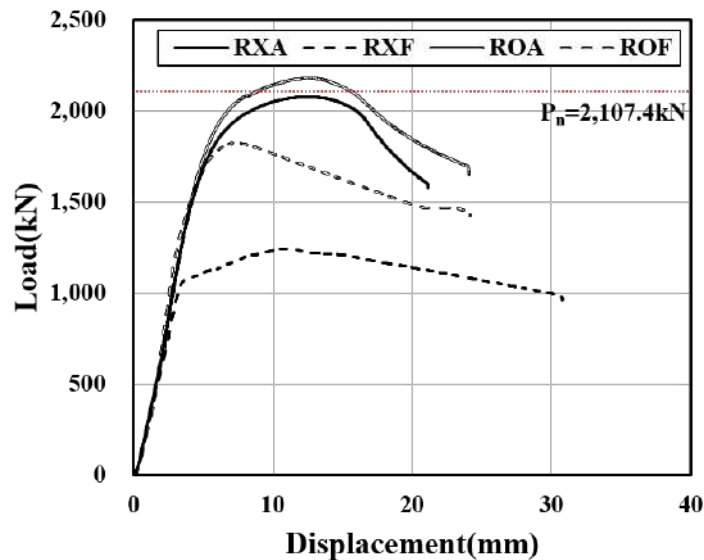


Figure 5 Axial load – displacement relationship

Table 6. Maximum axial load and displacement of test specimens

Mortar Filling	Without Mortar Infill		With Mortar Infill	
Fire exposure conditions	X	O	X	O
Maximum load (kN)	2,079.8	1,245.1	2,183.6	1,825.7
Maximum displacement (mm)	21.3	30.8	24.1	24.1

4.2.3 Failure Mode of the Specimens

The failure modes of the modular rectangular steel tube columns after the compressive strength test are shown in Figure 6. Local buckling occurred at the top and bottom of the modular rectangular steel tube columns that were not exposed to the fire, while the fire-exposed rectangular steel tube columns exhibited local buckling at the center of the column.

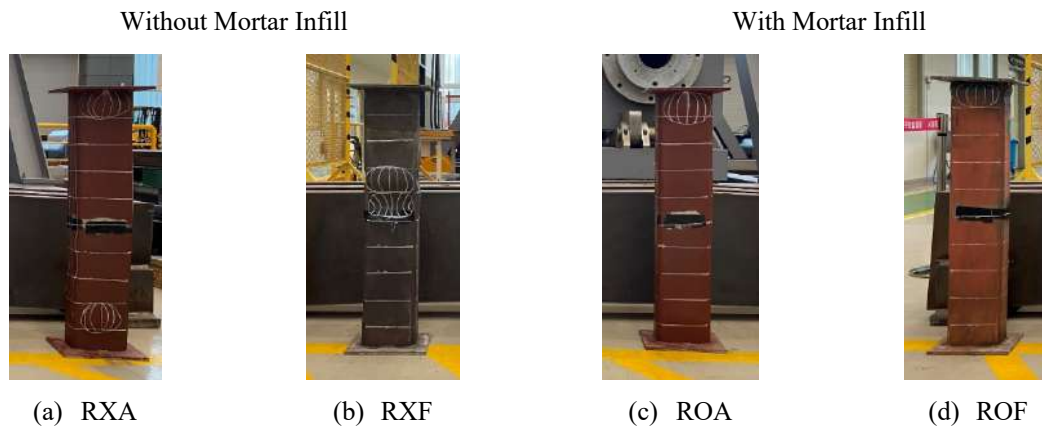


Figure 6. Failure Mode of test specimens

5 CONCLUSIONS

In order to propose a solution to ensure the 3-hour fire resistance performance for high-rise modular buildings, the temperature distribution of the column cross-section was evaluated by an unloaded fire resistance test and the residual strength experiment was conducted after standing at ambient temperature. The following conclusions were obtained by analyzing the effect of mortar filling or not on the residual strength under the same conditions with a 30mm SFRM thickness.

- 1) The maximum temperature of the modular rectangular steel tube column exposed to a standard fire for 3 hours was 402.3°C in the case of mortar filling and 778.9°C in the case of without mortar filling. From this, it can be concluded that the temperature of the steel surface slowly increases due to the heat storage effect in the case of mortar filling, which improves the fire resistance performance.
- 2) The residual strength of the mortar-filled steel tube column was about 84% of the residual strength without fire exposure, while the residual strength of the steel tube column without mortar infill was about 60% of the residual strength without fire exposure.
- 3) The heat storage provided by the mortar filling effectively suppresses the temperature rise of the steel surface of the rectangular steel tube. As a result, under standard fire exposure conditions for 3 hours, the temperature of the steel surface does not exceed the 538°C limit temperature when using 30mm SFRM and mortar filling.

ACKNOWLEDGMENT

This work was supported by the National Research Foundation of Korea(NRF) grant funded by the Korea government(MSIT)(RS-2023-00273519).

REFERENCES

1. Kim, SH, Ok, CY and Choi, SM, Clarification of the Thermal Properties of Intumescent Paint and Suggestion of the Required Fire Protection Thickness for Steel and Composite columns, *Journal of the Korean Society for Advanced Composite Structures*, 11(6), pp. 21-29 (2015). <https://doi.org/10.11004/kosacs.2015.6.1.021>.
2. An, J. H., Yeo, I. H. and Park, J. S. A Experimental Study on Fire Resistance Performance of Board Encased Steel Frame Used in Modular House. *Journal of Korean Society of Steel Construction*, 15(1), pp. 223-229(2015). <http://dx.doi.org/10.9798/KOSHAM.2015.15.1.223>.
3. Park, SI, A study on the High-Rise Modular Apartment Housing by Performance-Based Fire Resistance Design, Master Thesis, University of Seoul, (2022).
4. Dashdemberel, N, A Study of the Fire Resistance Performance of Rectangular Steel Tube Columns in High-rise Modular Houses Exposed to Standard Fire, Master Thesis, University of Seoul, (2024).
5. Kim, JY, and Lee, JK, A Basic Study on the Application of Modular Construction-Focused on the Analysis of Case Study, pp. 39-46 (2014). <http://doi.org/10.6107/JKHA.2014.25.4.039>.

6. Lin, HH, Hua Y, and Shu, LC, Residual Strength of Concrete Filled RHS Stub Columns after Exposure to High Temperatures, *Advances in Structural Engineering*, (2002).
7. Lin, HH and Jing, SH, Concrete-Filled Hollow Structural Steel Columns after Exposure to ISO-834 Fire Standard, *Journal of Structure Engineering*, (2003). [http://doi.org/10.1061/\(ASCE\)0733-9445\(2003\)129:1\(68\)](http://doi.org/10.1061/(ASCE)0733-9445(2003)129:1(68)).
8. Kim, SH, Won, YA and Choi, SM, A Study on the Evaluation of Residual Strength of Double Concrete Filled Tube Column by Unstressed test, *Journal of Korean Society of Steel Construction*, Vol. 24(1), pp. 81-89 (2012). <http://doi.org/10.7781/KJOSS.2012.24.1.081>.
9. ASTM A370, Standard Test Methods and Definitions for Mechanical Testing of Steel Products, (2024).
10. ASTM C109/C109M, Standard Test Method for Compressive Strength of Hydraulic Cement Mortars (Using 2-in. or [50-mm] Cube Specimens), (2008).
11. EN 1991-1-2, Eurocode 1: Actions on Structure – part 1-2: General actions-Actions on Structures exposed to Fire, CEN, (2005).
12. Dashdemberel, N, Han, SG, Shin, JW, Choi, IR and Choi, SM, Fire Resistance for Modular Rectangular Steel Tube Columns to ISO 834 Standard Fire, *International Conference on Civil Engineering and Architecture*, (2022).
13. Dashdemberel, N, Han, SG, Shin, JW, Choi, IR and Choi, SM, Compressive and flexural performance of spallation clad modular square steel columns exposed to a standard fire for 3 hours, *Korean Institute of Fire Science & Engineering Conference*, (2022).
14. Dashdemberel, N, Han, SG, Shin, JW, Choi, IR and Choi, SM, Modular Rectangular Steel Tube Columns with Standard Fire During 3 Hours exposure of SFRM Thickness and Mortar Filling by Unstressed Experiment, *Korean Society of Steel Construction*, (2023).
15. Han, SG, Dashdemberel, N, Kim, SH, Choi, IR and Choi, SM, Structural Performance of Modular Rectangular Steel Tube Columns with SFRM after exposed to 3 hours Standard Fire, *The 12th International Symposium on Steel Structures*, (2023).

THERMAL PERFORMANCE OF FIRE PROTECTION MATERIALS UNDER NON-STANDARD HEATING REGIMES: AN EXPERIMENTAL PARAMETRIC STUDY

Antonio Cibelli¹, Donatella de Silva², Francesco Dionisio³, Emidio Nigro⁴

ABSTRACT

In civil engineering, passive protection is generally adopted to hinder the mechanical performance decay that fire-induced high temperature yields on bare steel. The fire-resistance of protective materials is affected by several factors, relevant to inherent properties, such as microstructure, chemical composition, free and chemically bound water content, as well as external aspects, like input flux, heating rate, and installation methods. In modern codes, worldwide, the increased awareness about the behaviour of structures in fire has allowed to enable the use of a performance-based approach, in which a reliable characterisation of the complex thermo-physical behaviour of all materials, including fire protection, at elevated temperatures is of utmost relevance. The research project PROSYSSIF (chemo-physical of PROtective Systems for Steel Structures in Fire) aims to contribute to the settlement of guidelines for allowing to accurately account for the beneficial effects of passive protective systems in structural analyses. The experimental work presented in this contribution aims to provide insights in the above-mentioned field. To properly identify the thermal properties of four different fire protection materials, cone calorimeter tests have been conducted. The experimental outcomes have allowed to draw useful insights about the effect of some governing parameters, i.e. section factor, input flux, and thickness of the protection layer, resulting in a valuable design-oriented experimental parametric study.

Keywords: Thermal conductivity; passive protection; experimental campaign; steel structures

1 INTRODUCTION

A significant proneness to heat conduction together with structural members typically featuring high section factors make steel structures particularly vulnerable to fire. During and after fire exposure, both stability and integrity of structural systems may be compromised due to the loss of strength and stiffness, as well as thermally induced forces and displacements. Therefore, the protection of the structural elements is crucial to prevent structural failure and ensure the occupants safety [1].

In civil engineering, a passive protection is generally adopted to limit the mechanical performance decay that fire-induced high temperatures yield on bare steel. Within the broad family of the fire protective materials, the latter are divided into two categories: (a) non-reactive (e.g., gypsum plasterboards and spray plaster), and (b) reactive, among which the intumescent coatings are the most widely used. The fire-resistance

¹ PhD, Research Fellow, Department of Structures for Engineering and Architecture, University degli Studi di Napoli “Federico II”
e-mail: antonio.cibelli@unina.it, ORCID: <https://orcid.org/0000-0002-7331-2086>

² PhD, Assistant Professor, Department of Structures for Engineering and Architecture, University degli Studi di Napoli “Federico II”
e-mail: donatella.desilva@unina.it, ORCID: <https://orcid.org/0000-0001-6638-1983>

³ M.Eng., Research Fellow, Department of Structures for Engineering and Architecture, University degli Studi di Napoli “Federico II”
e-mail: fr.dionisio@studenti.unina.it, ORCID: <https://orcid.org/0009-0009-8110-0938>

⁴ PhD, Full Professor, Department of Structures for Engineering and Architecture, University degli Studi di Napoli “Federico II”
e-mail: eminigro@unina.it, ORCID: <https://orcid.org/0000-0002-3848-7454>

of such materials is affected by several factors, relevant to the inherent material properties, such as micro-structure, chemical composition, free and chemically bound water content, as well as external aspects, like input flux, heating rate, and installation methods.

In modern codes, worldwide, the increased awareness about the behaviour of structures in fire has allowed to enable the use of a performance-based approach, alternative yet equivalent to the classical prescriptive one. Whereas the latter refers to standard fire curves and deemed-to-satisfy structural systems, the performance-based approach allows to model both fire scenarios and structural behaviour with higher flexibility and accuracy [2]. However, the path towards the implementation of modern Fire Safety Engineering principles within the common practice is still littered with open issues to address. As an example, Eurocodes do not provide any general rule to design passive protective systems or include their beneficial effects on the structural response against natural fires.

In the performance-based approach, a reliable characterisation of the complex thermo-physical behaviour of all materials, including fire protection, at elevated temperatures is of utmost relevance. The research project PROSYSSIF (chemo-physical of PROtective Systems for Steel Structures in Fire) aims to contribute to the settlement of guidelines for allowing to accurately account for the beneficial effects of passive protective systems in structural analyses. The simulation of how protected steel structures behave in fire require the knowledge of the thermo-chemo-physical properties of the adopted protective material, which generally vary with temperature. A painstaking literature survey has revealed that only few works are available on this topic, and they mainly refer to intumescent coatings [3-6], whereas for plasterboards and sprayed fire-resistant materials (SFRMs) the consolidated knowledge seems to be even more limited [7]. Within the framework of the project PROSYSSIF, both experimental and modelling approaches are being adopted to deliver (i) a combined numerical-experimental methodology to identify the correlation between effective thermal conductivity and temperature, and (ii) a proof-of-concept of the use of such correlations to assess the structural safety of protected steel structures.

The experimental work presented in this contribution aims to provide insights in the above-mentioned field. To properly identify the thermal properties of four different fire protection materials, cone calorimeter tests have been conducted. Such low-scale laboratory test has been used by several authors to investigate the insulating properties of intumescent coatings, proving to be an effective tool for the assessment of the insulating properties under different heating regimes [3-6]. For plasterboards and SFRMs, instead, other tests are generally adopted [7]. For the sake of consistency and results' comparability, in the present activity all the investigated materials have been tested by adopting the same testing approach. The temperature recorded at the exposed and protected faces have been used to derive the effective thermal conductivity according to EN 13381-4,8 [8]. The procedure aims to deliver normalised effective thermal conductivity vs. temperature curves, by means of which the influence of governing parameters, e.g. section factor, input flux, and thickness of the protection layer, can be assessed, resulting in a valuable step towards the proper application of Fire Safety Engineering (FSE) principles to protected steel structures.

2 EXPERIMENTAL INVESTIGATIONS

The cone calorimeter tests discussed in this work are framed into a wider experimental campaign, aiming to fully characterise the thermo-chemical behaviour of four fire-protective materials, selected as representative of the most widely used classes of materials to ensure the safety of steel structures in case of fire: (i) gypsum-based plasterboards (XS); (ii) cement-based plasterboards (H); (iii) sprayed fire-resistant materials (SP); (iv) waterborne intumescent coatings (IC). Therefore, the tests have been carried out on:

- plasterboards type XS of thickness 25 mm;
- plasterboards type H of thickness 20 mm;
- spray-applied lightweight gypsum-based plaster (hereinafter referred to as SP) of thickness 15 and 25 mm;
- water-based intumescent coating (IC) of thickness 1.0 and 1.5 mm.

2.1 Setup and specimen instrumentation

The cone calorimeter tests have been conducted at the University of Naples “Federico II”, by employing a Dual Cone Calorimeter, produced by Fire Testing Technology. The machine presents a conical heater, rated 5000 W at 230 V with a heat output of 100 kW/m², whose temperature is measured, by three K-type thermocouples, and controlled, through three-term PID controller. A split shutter mechanism protects the sample area before the test. The specimen is placed below the heater, at a distance ranging between 25 and 60 mm, depending on the type of protective material is being tested (i.e. reactive materials like intumescent coatings need a larger distance to properly expand), in compliance with ISO 5660 prescriptions [9].

The exposed face of the specimen has dimensions 100 mm x 100 mm. At the protected face two holes have been realised to locate two K-type thermocouples: one in the centre, and one at a distance of 25 mm from the first one. The specimen holder has been realised to limit as much as possible the heat losses and boundary effects. To this purpose, rock wool has been placed underneath the sample, whereas plasterboard carters are used to limit the dispersion along the lateral faces. The specimen-to-carter gap has been sealed with rock-wool. Finally, the temperature of the exposed face has been monitored by means of a K-type thermocouple placed at 1 mm above the specimen face. A four-channel data logger has been used as acquisition system. The setup and specimen instrumentation are shown in Figure 1.

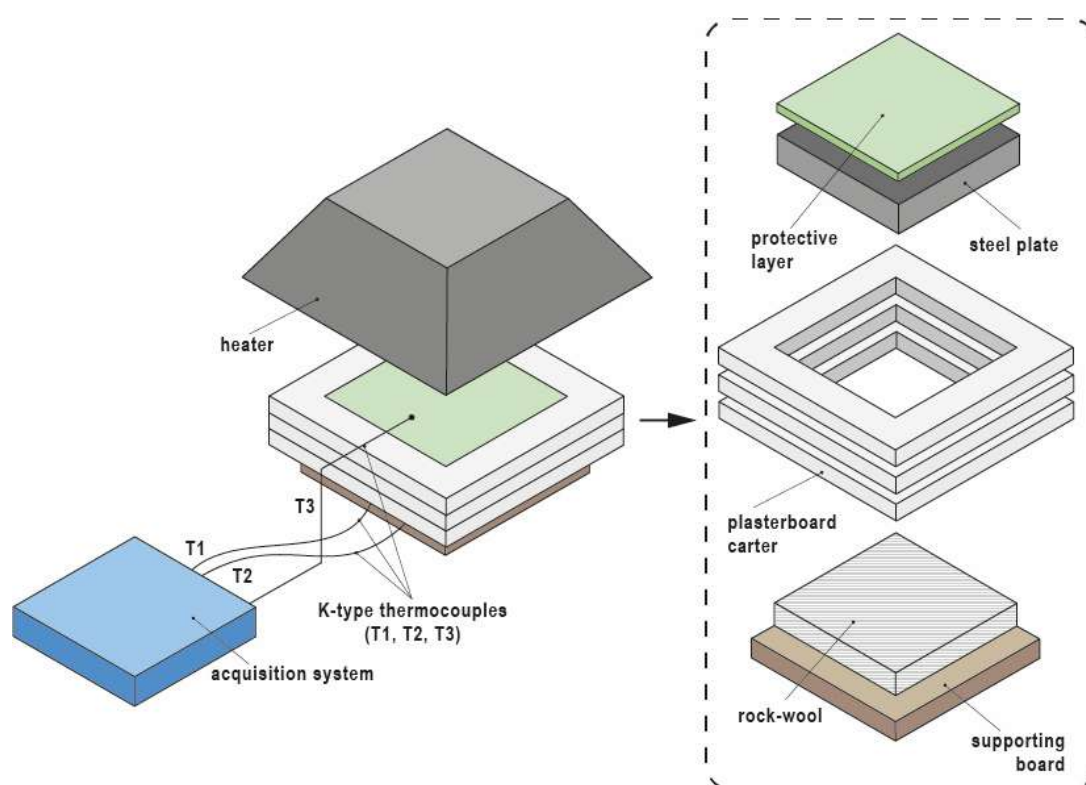


Figure 1. Test setup and specimen instrumentation

2.2 Test programme

The test programme consists of investigating the thermal behaviour under two heat fluxes, namely 50 and 70 kW/m². To assess the effect due to the section factor (A/V), the protective layer has been applied on steel plates featuring three different A/V values, namely 250, 125 and 67 m⁻¹, with exception of plasterboards XS and H, which have been tested with a 1 mm metal sheet underneath, to ensure a more stable temperature reading. As a reference the unprotected (bare) steel plates have been tested as well. All the tests have been repeated two times, and stopped when the temperature increase is equals to 0.2°C/min. In Table 1 the synopsis of the test programme is reported. The setup has been validated by testing bare steel plates and comparing the temperature recordings with the analytical solution of the thermal analysis.

Table 1. Synopsis of the test programme

sample	A/V [1/m]	t _{prot} [mm]	q̇ [kW/m ²]
bare steel (ref.)	67, 125, 250	-	50, 70
XS plasterboard	-	25	50, 70
H plasterboard	-	20	50, 70
SP sprayed plaster	67, 125, 250	15, 25	50, 70
IC intumescent coating	67, 125, 250	1.0, 1.5	50, 70

3 EXPERIMENTAL RESULTS AND PARAMETRIC STUDY

In this section the experimental results are presented in terms of (i) temperature vs. time and (ii) effective thermal conductivity vs. temperature curves. Each curve is labelled as “material”_ “section factor”_ “protective thickness”_ “heat flux”, and refers to the average between the results obtained on identical specimens tested against the same boundary conditions.

3.1 Gypsum- and cement-based plasterboards

In Figure 2 the comparison between the temperature evolution detected in XS and H samples are shown, with respect to the two investigated fluxes. The two materials experience a different behaviour in terms of insulating performance. The cement-based plasterboards are thinner, which might be the cause of the better protection they exert on the steel sheet underneath. However, what differs the most between XS and H plasterboards is the duration of the first plateau at approximately 100°C, due to the drying associated to the moisture phase transition. An interesting point is also represented by the effect due to the heat flux: a higher flux seems to not yield a substantial change of the initial branch for H specimens below 200°C, whereas it shortens the plateau at 100°C on XS samples. Finally, in terms of exposure time, from Figure 2 it stands out clearly that XS 25 mm thick specimens ensure that the temperature in the steel profile stays below 400°C for approximately 90 minutes, whereas for H 20 mm thick samples this temperature threshold is reached in one third less time, i.e. 60 minutes.

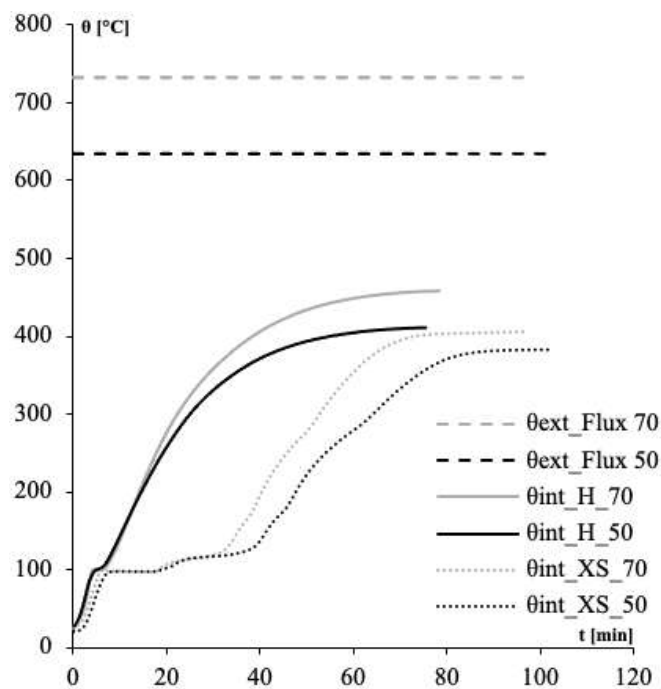


Figure 2. Temperature vs. time for gypsum- (XS) and cement-based (H) plasterboards under 50 and 70 kW/m² heat flux

The effective thermal conductivity has been derived by employing the formula (EN 13381-4):

$$\Delta\theta_{s,t} = \left[\frac{\lambda_{p,t}/t_p}{c_s \rho_s} \cdot \frac{A_p}{V} \cdot \left(\frac{1}{1 + \phi/3} \right) \cdot (\theta_{g,t} - \theta_{s,t}) \cdot \Delta t \right] - \left[(e^{\phi/10} - 1) \cdot \Delta\theta_{g,t} \right] \quad (1)$$

where $\theta_{g,t}$ and $\theta_{s,t}$ are the temperature of exposed and protected face, whereas $\Delta\theta_{g,t}$ and $\Delta\theta_{s,t}$ are the temperature increments over the time interval Δt . c_s and ρ_s are, respectively, the steel specific heat and density, whereas those of the protective material are included in the definition of the model parameter ϕ , which reads:

$$\phi = \frac{c_p \cdot \rho_p}{c_s \cdot \rho_s} \cdot t_p \cdot \frac{A_p}{V} \quad (2)$$

in which c_p and ρ_p are the specific heat and density of the protective material, t_p the thickness of the protective layer and A_p/V the section factor of the element exposed to the heat flux. Regarding the variability of specific heat and density, the results presented in this study have been obtained by assuming that ϕ is constant over the range of temperature investigated, while in Eq. 1 c_s is assumed to vary with temperature. Finally, the effective thermal conductivity has been calculated by assuming a constant value for $\theta_{g,t}$. The value adopted corresponds to the average temperature in steady conditions, which are typically reached after few minutes. In order to validate this assumption, the temperature on the exposed face, monitored through the thermocouple T3, has been compared to the analytical value determined through the balance equation:

$$\varepsilon\sigma\theta_g^4 + h_c(\theta_g - \theta_\infty) = Q_e - Q_{loss} - \frac{(\Delta\theta_g + \Delta\theta_s)}{2\Delta t} \rho_p C_p d_p - \frac{\Delta\theta_s}{\Delta t} \rho_s C_s d_s \quad (3)$$

where σ is the Stefan-Boltzmann constant, whereas ε and h_c are, the emissivity and convection heat-transfer coefficient of the protective material. C_p and C_s are the heat capacity of protective material and steel element, respectively. Finally, θ_∞ is the temperature away from the heat source, assumed equals to 20°C, and Q_e is the incoming flux, i.e. the heat flux incident under the calorimeter cone. In Eq. 3, within the right-hand term, the heat loss Q_{loss} and the terms referred to the heat capacity are assumed to be negligible with respect to the other terms of the equation. Though this assumption surely represents a debatable point when referred to heavily protected steel profiles [10,11], the comparison between analytical and experimental results, shown in Figure 3, demonstrates that a good agreement between them holds.

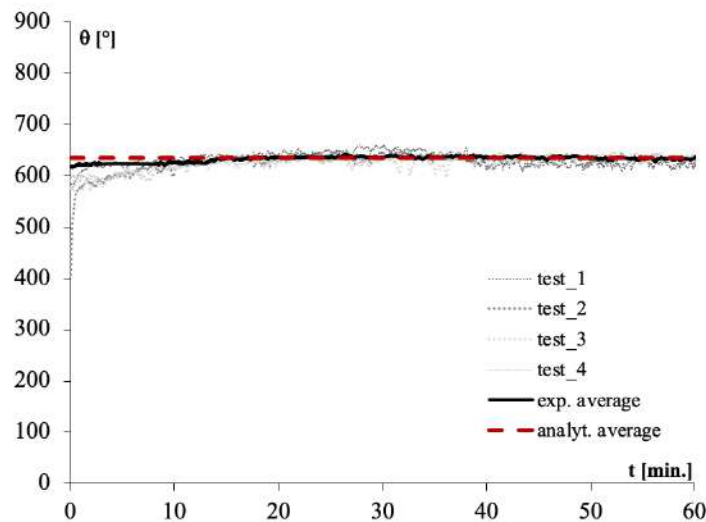


Figure 3. Comparison between experimental and analytical temperature of the exposed face under 50 kW/m² heat flux

The effective thermal conductivity, derived as described above, has been then plotted against temperature (Figure 4). The results show that the overall response of the two materials is comparable, justifying the assumption of a constant thermal conductivity of 0.075 W/mK.

The cement-based plasterboards (H) experience a more stable behaviour, with a discontinuity lumped at approximately 100°C. On the contrary, the gypsum-based boards (XS) show a more fluctuant trend, most likely because they experience a step-by-step chemo-physical degradation as temperature grows. A confirmation might be provided by dedicated chemo-physical analyses at lower scale, such as thermogravimetry, differential scanning calorimetry and scanning electron microscopy at different temperatures. The latter are currently being executed in the framework of the research project PROSYSSIF. Finally, for H and XS specimens the heat flux seems to not affect the thermal conductivity, meaning that this parameter can be assumed regardless the heating rate of interest.

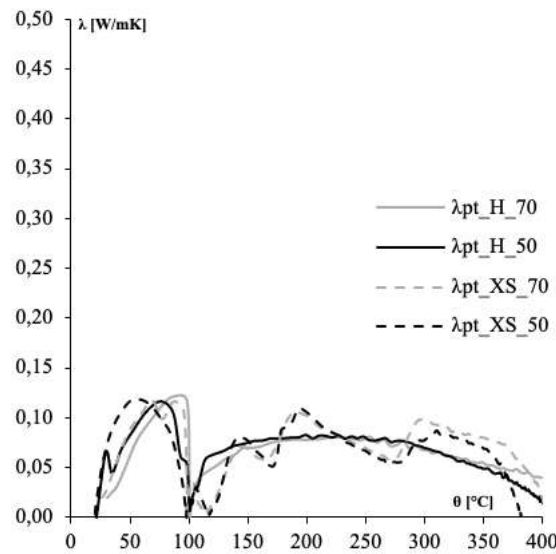


Figure 4. Effective thermal conductivity vs. temperature for gypsum- (XS) and cement-based (H) plasterboards under 50 and 70 kW/m² heat flux

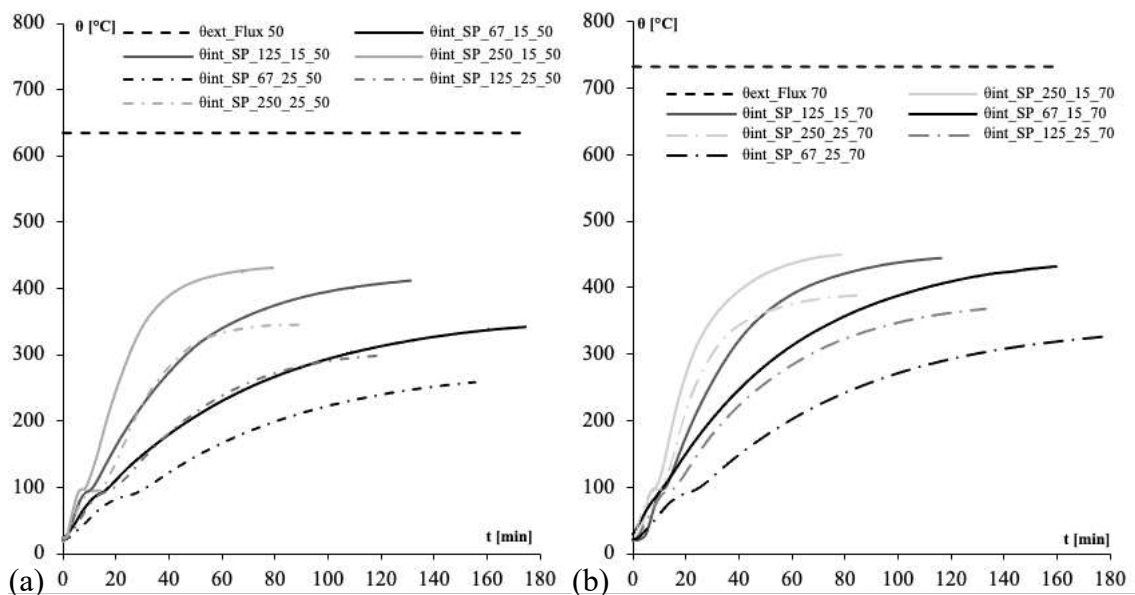


Figure 5. Temperature vs. time for sprayed plaster (SP) under (a) 50 and (b) 70 kW/m² heat flux

3.2 Spray-applied plaster

The tests carried out on SP specimens have shown that both thickness and entity of the heat flux play a crucial role on the insulating performance (Figures 5 and 6). As a matter of fact, the results permit to clearly

identify a direct correlation between the two above-mentioned parameters and the temperature within the steel profile, assumed to be coincident with the temperature of the protected face. In addition, the evidence apparently prove that thicker protective layers partially limit the growth that heat flux may cause. For a given section factor, the curves relevant to 50 and 70 kW/m² are closer to each other when 15 mm layer is used. This aspect is quite evident for small section factors (e.g. 250) as standing out from Figures 6 and 7.

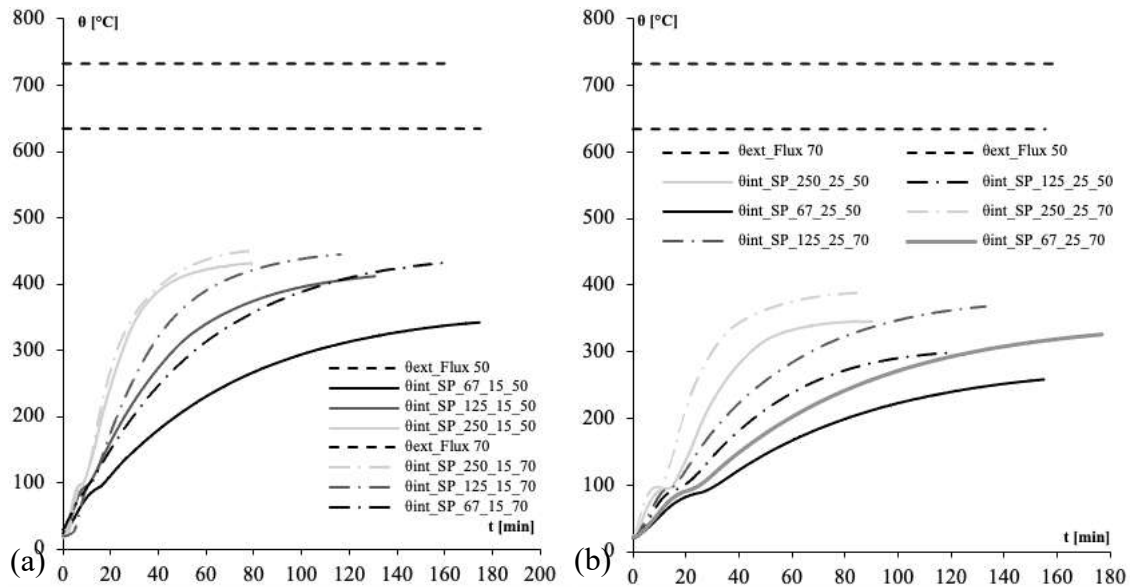


Figure 6. Temperature vs. time for sprayed plaster (SP) featuring (a) 15 mm and (b) 25 mm of protective thickness

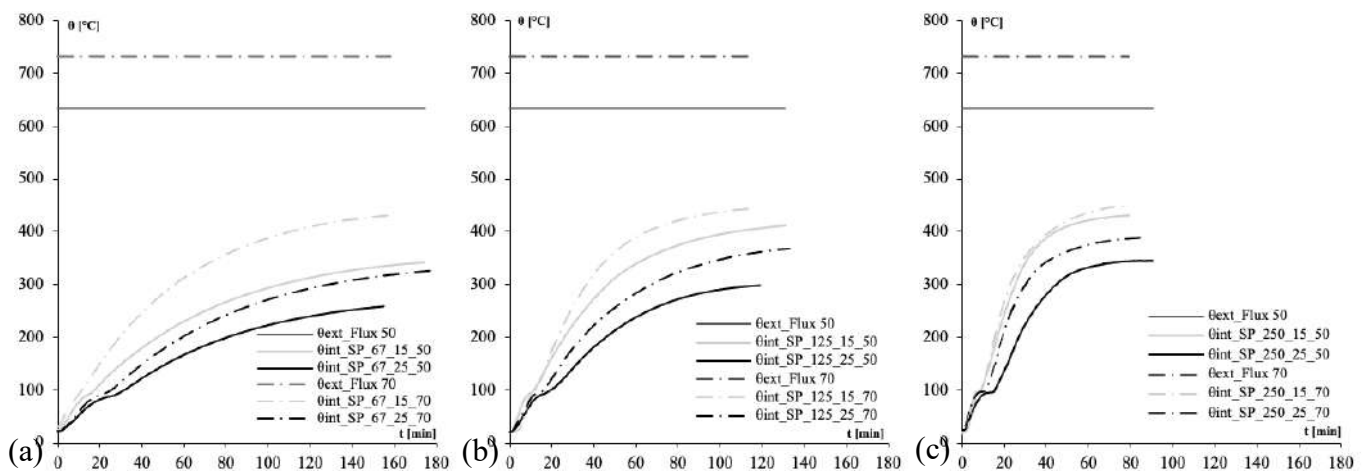


Figure 7. Temperature vs. time for sprayed plaster (SP) with A/V equals to (a) 67 m⁻¹, (b) 125 m⁻¹ and (c) 250 m⁻¹

The plots thermal conductivity vs. temperature confirm, as expected, the trends previously detected, as the thermal conductivity has been derived from temperature recordings. However, Figures 8, 9, and 10 represent a useful tool for drawing considerations to deploy in structural analyses at larger scales. As a matter of fact, for the spray-applied plaster at issue a constant value for effective thermal conductivity seems to not capture the actual thermal behaviour. This parameter, in addition, shows a non-negligible correlation with (i) section factor, i.e. higher A/V results in higher λ , (ii) heat flux and (iii) thickness of the protective layer, i.e. λ decreases slower at higher heat flux and thickness. This last phenomenon is partially mitigated when high section factor profiles are adopted.

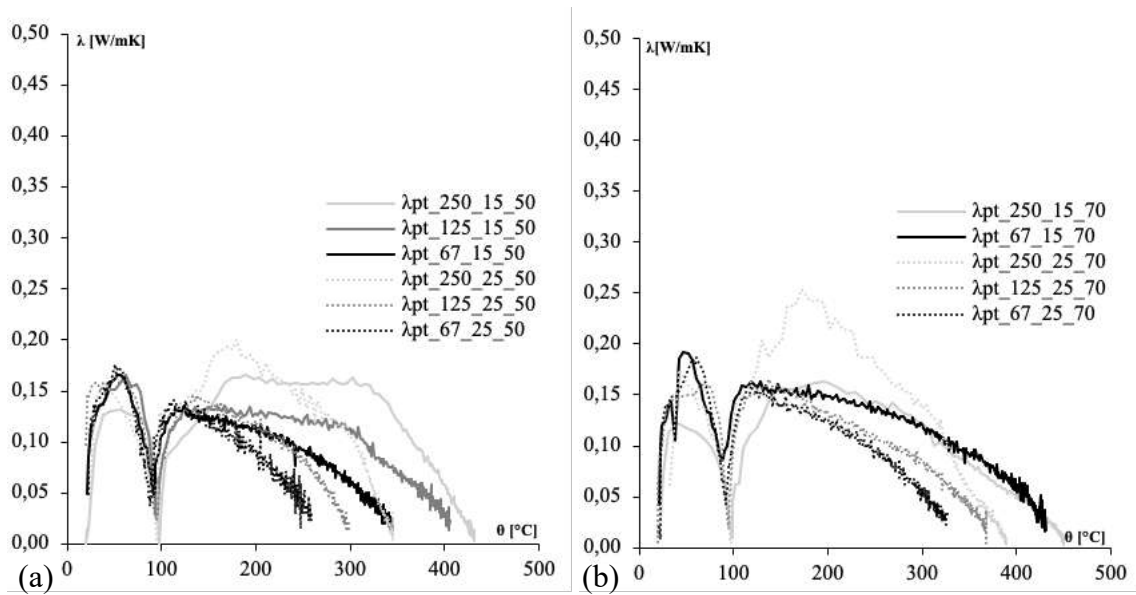


Figure 8. Effective thermal conductivity vs. temperature for sprayed plaster (SP) under (a) 50 and (b) 70 kW/m² heat flux

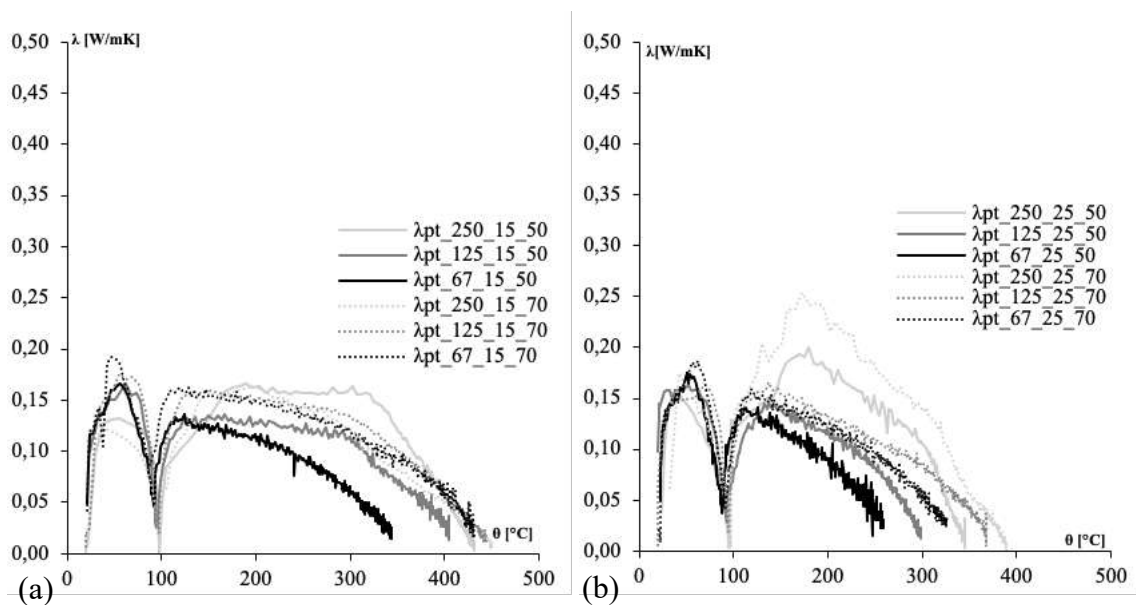


Figure 9. Effective thermal conductivity vs. temperature for sprayed plaster (SP) featuring (a) 15 mm and (b) 25 mm of protective thickness

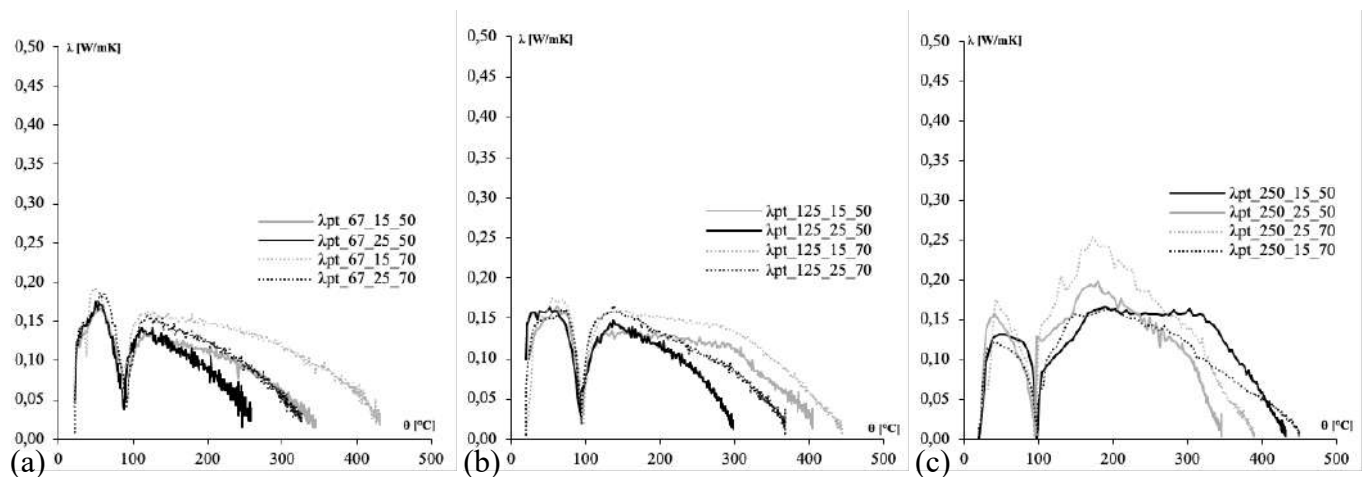


Figure 10. Effective thermal conductivity vs. temperature for sprayed plaster (SP) with A/V equals to (a) 67 m⁻¹, (b) 125 m⁻¹ and (c) 250 m⁻¹

3.3 Intumescent coating

The temperature profiles in time allow to deliver some useful insights. In Figure 11, for a given heat flux, the heating rate of the protected steel plate grows with section factor, with a more consolidated trend when 70 kW/m² are applied, whereas thickness act as delayer parameter. However, a thinner layer seems to be more effective when high A/V holds. Figures 12 and 13 also confirm the afore-mentioned trends.

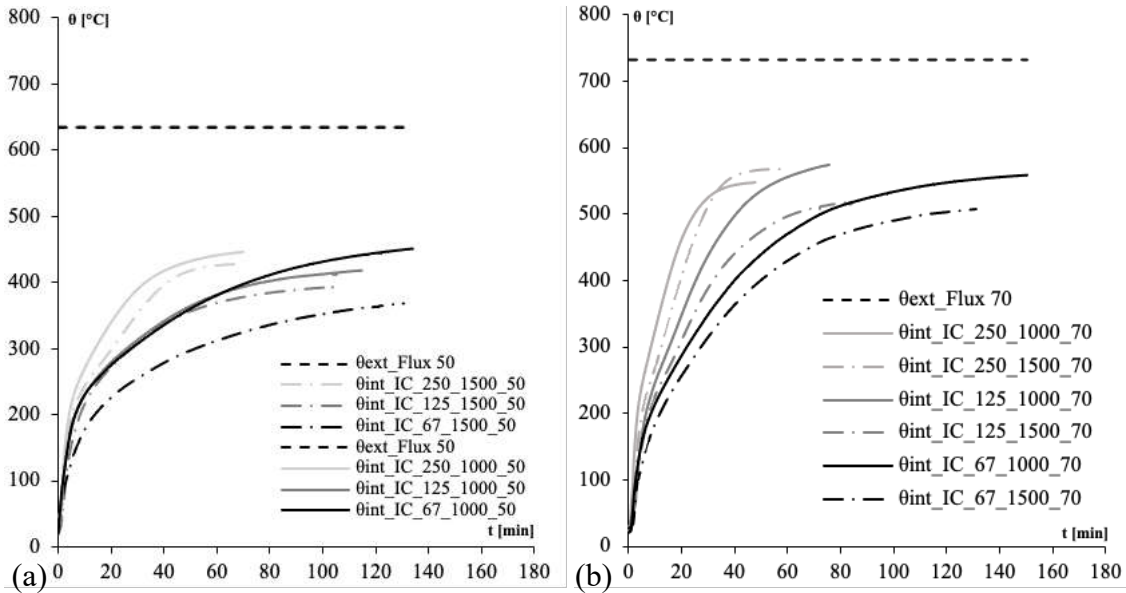


Figure 11. Temperature vs. time for intumescent coating (IC) under (a) 50 and (b) 70 kW/m² heat flux

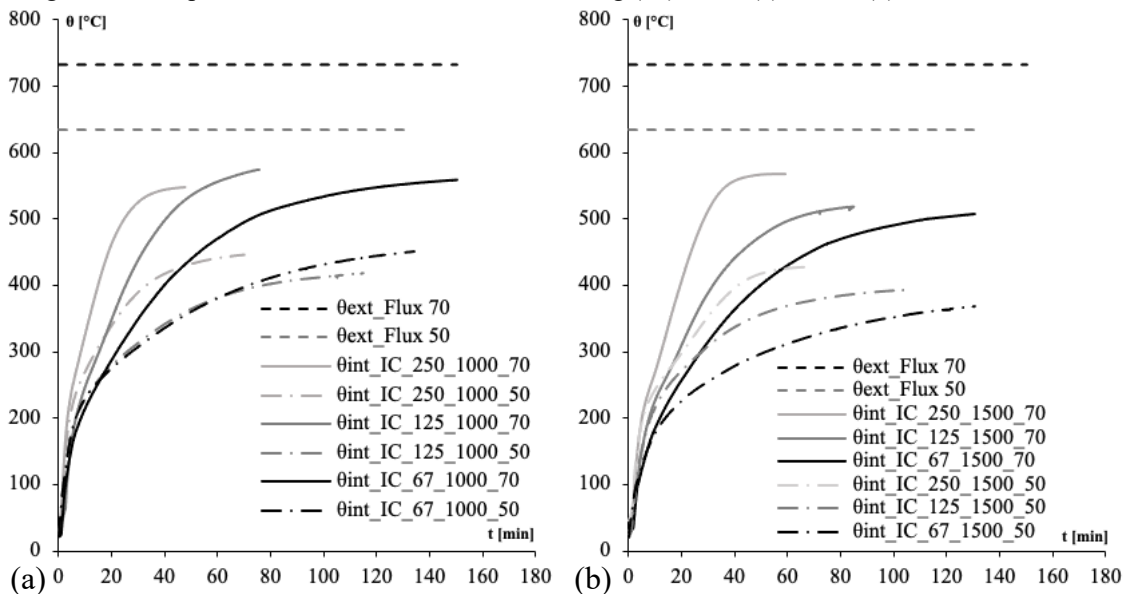


Figure 12. Temperature vs. time for intumescent coating (IC) featuring (a) 1.0 mm and (b) 1.5 mm of protective thickness

In this case, the effective thermal conductivity, derived through the calculation based on EN 13381-8 prescriptions, is quite lower with respect to that one detected for spray-applied plaster and plasterboards. In addition, its value tends to stabilise above 150°C. Significant larger and scattered values are, instead, derived below this threshold. In particular, the variability seems to be governed by the section factor, mostly, and protective thickness. Indeed, from the results shown in Figures 13, 14 and 15, it is possible to state that the temperatures at which the IC thermal conductivity reaches the minimum are very similar for both the investigated fluxes.

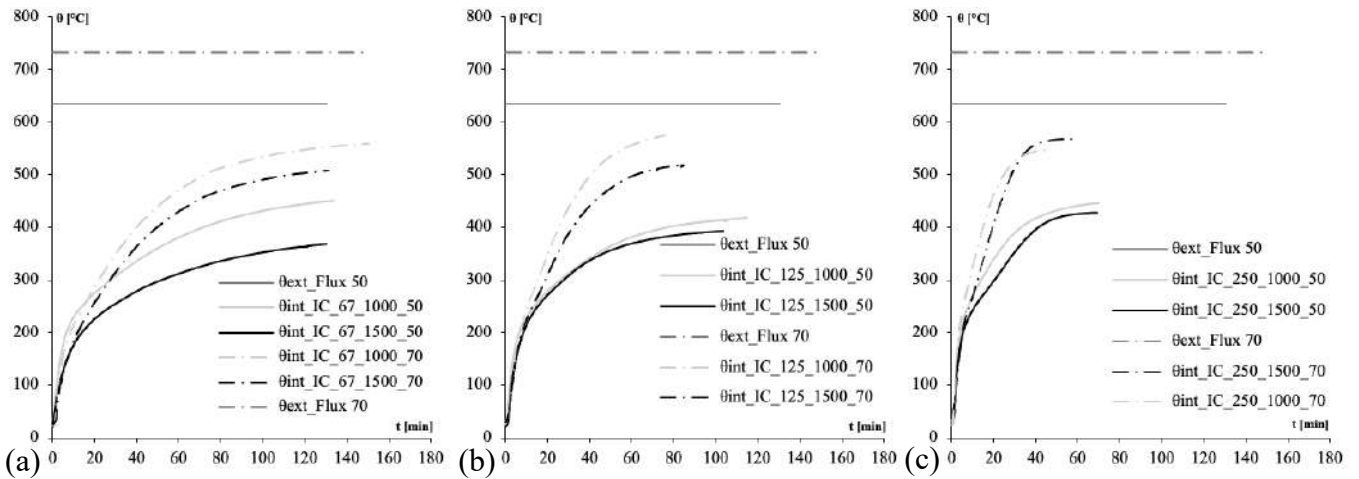


Figure 13. Temperature vs. time for intumescent coating (IC) with A/V equals to (a) 67 m⁻¹, (b), 125 m⁻¹ and (c) 250 m⁻¹

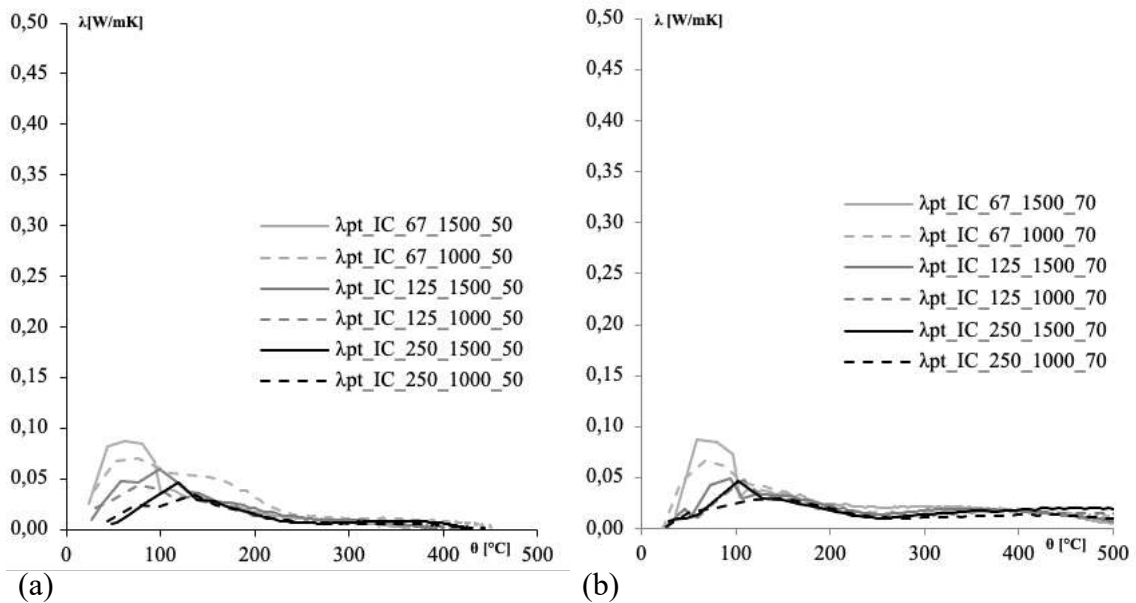


Figure 14. Effective thermal conductivity vs. temperature for intumescent coating (IC) under (a) 50 and (b) 70 kW/m² heat flux

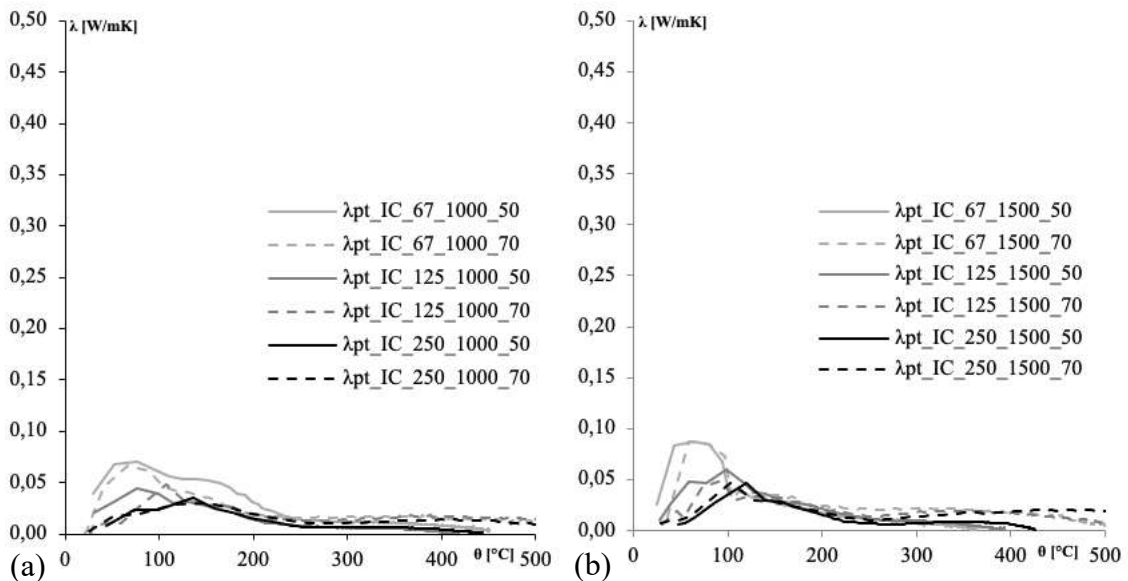


Figure 15. Effective thermal conductivity vs. temperature for intumescent coating (IC) featuring (a) 1.0 mm and (b) 1.5 mm of protective thickness

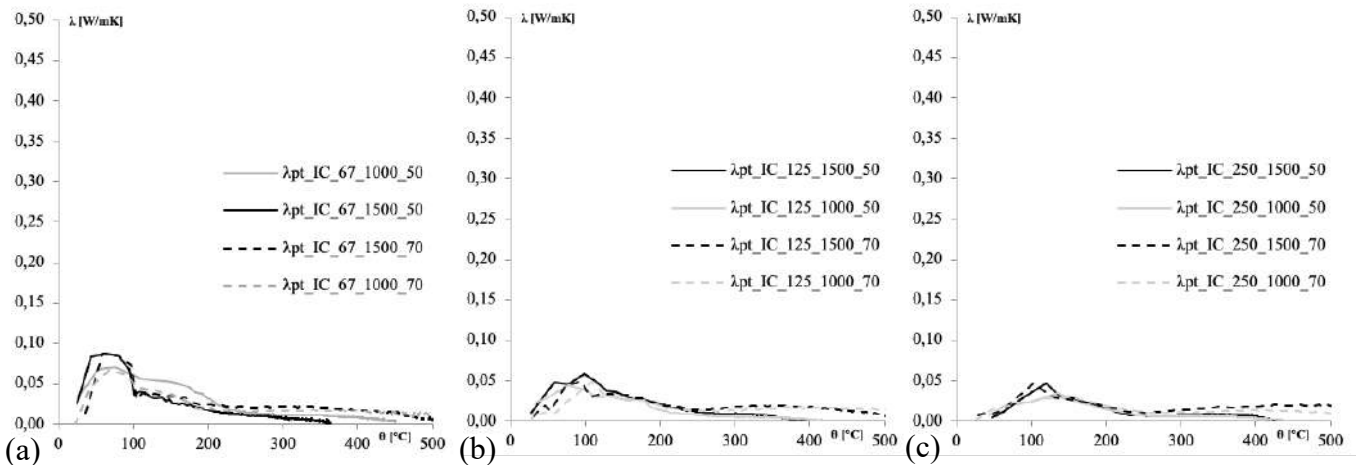


Figure 16. Effective thermal conductivity vs. temperature for intumescent coating (IC) with A/V equals to (a) 67 m^{-1} , (b) 125 m^{-1} and (c) 250 m^{-1}

4 CONCLUSIONS

In this paper an experimental parametric study is presented, consisting of cone calorimeter tests on four different passive fire-protective materials: gypsum- and cement-based plasterboards, sprayed fire-resistant material and intumescent coating. The tests have been conducted to investigate the effect of three parameters on the thermal behaviour of the protected steel plates. Test setup and specimen instrumentation have been calibrated by running reference tests on bare steel plates, whose temperature rise under a given heat flux can be easily calculated analytically. The results have been reported in terms of temperature vs. time and effective thermal conductivity vs. temperature. The effective thermal conductivity has been derived in compliance with EN 13381-4 and EN 13381-8 for passive and reactive protection materials respectively.

The analysis of the results allows the authors to draw the following conclusions:

- the study has confirmed that (i) heat flux, (ii) section factor, and (iii) thickness of the protective layer play a key role on the thermal performance of the protected steel elements;
- gypsum- and cement-based plasterboards behave quite similarly, regardless the governing parameter is being investigated. The cement-based one seems to have a more stable response during the exposure;
- for the spray-applied plaster, the effective thermal conductivity grows with the section factor, whereas a higher protective layer thickness and a higher heat flux make it decrease, even if at a lower rate;
- the intumescent coating has shown to be the most performing protective material. Their response is mainly affected by section factor and coating thickness when $\theta < 150^\circ\text{C}$. As overall trend, it seems to not significantly depend on the input heat flux. The effective thermal conductivity might be assumed constant above 150°C .

The experimental campaign, in which the activities presented in this work are framed, is wider and includes also the chemo-physical characterisation of the investigated protective materials. It is currently ongoing. All the experimental evidence will be eventually analysed to assess the role played by each governing parameter (i.e. heat flux/fire curve, steel section factor, thickness of the protective layer, type of protection system), and calibrate reliable models for capturing the evolution of the effective thermal conductivity. Notably, the research activity aims to weigh the effect that a simplified effective thermal conductivity vs. temperature law has on the resulting temperature profiles within protected structural steel members and their structural response during fire.

ACKNOWLEDGMENT

This work was carried out within the project STAR PLUS 2020 - LINEA 1. N. Prog. 21-UNINA-EPIG-136- PROSYSSIF - Chemo-physical properties of PROtective SYstems for Steel Structures in Fire.

REFERENCES

1. Usmani, A.S., Rotter, J.M., Lamont, S., Sanad, A.M., Gillie, M.: Fundamental principles of structural behaviour under thermal effects. *Fire Saf. J.* 36, 721–744 (2001). [https://doi.org/10.1016/S0379-7112\(01\)00037-6](https://doi.org/10.1016/S0379-7112(01)00037-6)
2. Franssen, J.-M., Real, P.V.: *Fire Design of Steel Structures: EC1: Actions on structures; Part 1-2: Actions on structure exposed to fire; EC3: Design of Steel Structures; Part 1-2: Structural fire design*, John Wiley & Sons, 2016.
3. Schaumann, P., Waldemar, W.: Effect of heating rates in natural fires on the thermal performance of a solvent-borne intumescent coating. In *Proceed. of the 2nd Int. Fire Safety Symp. IFireSS 2017*.
4. Han, Z., Fina, A., Malucelli, G., Camino, G.: Testing fire protective properties of intumescent coatings by in-line temperature measurements on a cone calorimeter. *Progress in Organic Coatings* 69, 475–480 (2010) <https://doi.org/10.1016/j.porgcoat.2010.09.001>
5. Lucherini, A., Giuliani, L., Jomaas, G.: Experimental study of the performance of intumescent coatings exposed to standard and non-standard fire conditions. *Fire Safety Journal* 95, 42–50 (2018). <https://doi.org/10.1016/j.firesaf.2017.10.004>
6. de Silva, D., Bilotta, A., Nigro, E.: Effect of the thermal input on the behavior of intumescent coatings. *Applications of Fire Engineering*, 325–334 (2017).
7. Kodur, V.K.R., Shakya, A.M.: Effect of temperature on thermal properties of spray applied fire resistive materials. *Fire Safety Journal* 61, 314–323 (2013). <http://dx.doi.org/10.1016/j.firesaf.2013.09.011>
8. EN 13381-8 - Test Methods for Determining the Contribution to the Fire Resistance of Structural Members – Part 8: Applied Reactive Protection to Steel Members, European Committee for Standardization, Brussels, 2013.
9. ISO 5660 – Reaction to fire tests: Heat release, smoke production and mass loss rate, International Organization for Standardization, Geneva, 2015.
10. Possidente, L., Tondini, N.: Validation of a New Analytical Formula to Predict the Steel Temperature of Heavily Insulated Cross-Section. *Fire Tech.*, 1–23 (2023). <https://doi.org/10.1007/s10694-023-01511-7>
11. Possidente, L., Tondini, N., Wickström, U.: Derivation of a new temperature calculation formulation for heavily fire insulated steel cross-sections. *Fire Safety Journal* 141, 103991 (2023). <https://doi.org/10.1016/j.firesaf.2023.103991>

UPDATING FRENCH CAR PARK FIRE SCENARIOS FOR MODERN VEHICLES: HRR EXPERIMENTAL STUDY

Jean-Baptiste Tramoni¹, Mathieu Suzanne², Gildas Auguin³, Christophe Thauvoye⁴

ABSTRACT

The purpose of this paper is to assess the real fire scenarios currently used in fire safety engineering studies of open car parks in France. In French studies two kind of vehicles are considered: light commercial vehicles (LCV) and passenger vehicles of 1,250 kg. For LCV, the heat release rate (HRR) was estimated by expert judgment while it was measured for passenger cars. Both curves originate from the 1990s without being updated since. For this purpose, two tests on LCV and two tests on modern passenger cars have been conducted.

Experiments took place under a calorimetric hood allowing the measurement of HRR over time. Focusing only on heat released, tests showed that the theoretical HRR of LCV greatly overestimates the peak and underestimates the fire duration. On another hand, results on modern cars showed that the increase in amount of plastic in cars design has little influence on the combustion. Indeed, equivalent peak HRR, total heat released and combustion duration were recorded.

Keywords: Open car park; calorimetry; modern vehicle fires; fire tests

1 INTRODUCTION

Since the early 2000s, in France, fire safety engineering studies have been performed to assess the fire resistance of open car park structures. These studies consider two kinds of vehicles: passenger cars and Light commercial vehicles (LCV). The combustion of passenger vehicles was studied in the 1990s [1]. An experimental campaign was performed on 15 internal combustion engine (ICE) cars, either individually or in pairs. Fire scenarios were developed based on the measured data. At the same time, the purely analytical heat release rate (HRR) of LCV was established by INERIS, considering a 1,250 kg passenger car loaded with 250 kg of highly flammable paint, equivalent to a 10,000 MJ load [2]. Together, these data are used in a calculation method developed by the CTICM and validated by the CECMI (Committee for the study and classification of materials according to their fire hazard - chaired by the Ministry of the Interior). This method allows the safe and economical design of open carparks in steel [2]. Two issues have arisen in the recent years.

The first is the age of the vehicles tested in the 1990s. Indeed, authors such as Boehm *et al.* [3] report an increase in the amount of plastic used in newer car designs, which could affect the kinetics of fire growth. However, to date there is little experimental data [4-5] to confirm this statement.

The second issue concerns the combustion of LCV. The HRR curve used for LCV seems questionable in terms of its shape and the amount of energy released: the maximum HRR is very high (18 MW for 10

¹ Research project manager, CTICM

e-mail: jbtramoni@cticm.com, ORCID: <https://orcid.org/0000-0002-5054-4669>

² Head of the fire modelling, research and experimentation department, LCPP

e-mail: mathieu.suzanne@interieur.gouv.fr, ORCID: <https://orcid.org/0009-0005-0891-2025>

³ Technical Director, Efectis

e-mail: gildas.auguin@efectis.com ORCID: <https://orcid.org/0000-0002-5037-4671>

⁴ Fire Research Department Manager, CTICM

e-mail: cthauvoye@cticm.com, ORCID: <https://orcid.org/0000-0002-0201-8461>

minutes, see Figure 7). This can be explained by the assumptions made. Indeed, a theoretical total heat release (THR) of 9,500 MJ is considered for the unladen LCV. Joyeux et al. [6] showed that an equivalent passenger car releases about 6,800 MJ during its combustion. Therefore, this value seems to be greatly overestimated. In addition, the paint load is too important for this type of fuel. The effective heat of combustion is closer to that of solvents than to that of solvent-based paints, resulting in a paint load that is 1.6 time higher than that of a passenger car [6]. Furthermore, most paints sold today are water-based.

For these two reasons, an experimental campaign was performed on two modern ICE vehicles and two modern LCVs with an additional fuel load. This campaign was conducted by CTICM at Efectis France facilities, involving ArcelorMittal, GagnePark and LCPP as partners. It was supported by the Renault Group for the supply of vehicles.

This paper first presents the vehicles studied and the experimental configuration. It then presents the combustion dynamics of the four vehicles in relation to the HRR measurements over time. The results obtained are also compared for the same type of vehicle. Finally, a comparison with existing literature concludes the discussion.

2 MATERIAL AND METHODS

2.1 Vehicles

Four vehicles were provided by the Renault Group. Two Renault Talismans (2020-2022), successors to the Renault Laguna tested in the 1990s, were studied to verify the evolution of the combustion in passenger cars. It should be noted that the two vehicles had different equipments, the top model (PV1) having a full-length sunroof. An aluminium plate was added to limit the influence of this additional opening during the fire growth. It melts completely during the full development of the fire.

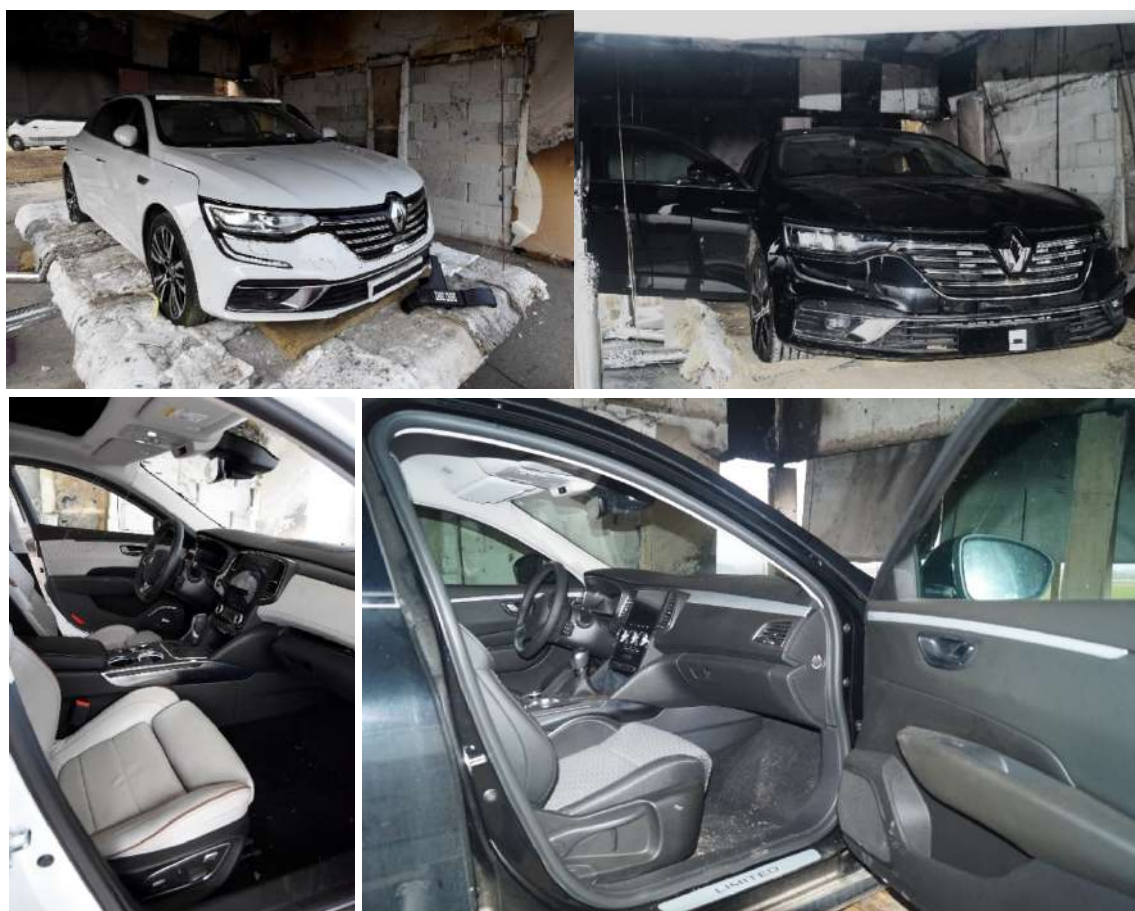


Figure 1. Exterior and interior photos of PV 1 (left) and PV 2 (right)

With regard to LCV, the assumptions made by INERIS do not appear to be representative of reality in terms of THR, as exposed above. Furthermore, the solvent paints considered by INERIS are not common today. Therefore, two types of additional fuel loads were selected: a mixture of combustible and non-combustible solid fuels (representative of a craftsman’s load) and another with pots of paints. Details of both loads are given in Table 1. A Renault Kangoo and a Mercedes Citan (based on Kangoo) (2012-2021) were considered. As for passenger cars, the two vehicles had significant differences in the presence of rear windows on LCV 1. In order to reduce the differences between LCVs and to approach what can be observed on craftsman LCVs, wooden panels were fitted over the rear windows of LCV 1. As for the aluminium plate for passenger cars, the panels are designed to limit the influence of additional windows during the fire growth.



Figure 2. Exterior and load arrangement photos of LCV 1 (left) and LCV 2 (right)

Table 1. Solid and liquid loads characteristics

Load	Materials	Total weight [kg]	Theoretical total heat released [MJ]
Solid	Wood and Polyethylene pallets, concrete block, steel, White spirit (aliphatic hydrocarbon)	372.7	4 428
Liquid	Acrylic paint, solvent paint, epoxy paint, White spirit	331.4	3 438

Details on the four vehicles are shown in Table 2.

Table 2. Details on the tested vehicles

Fire test	Model	Year model	Dimensions (m × m × m)	Unladen mass (kg)	Total mass (kg)	Fuel tank (L)
LCV 1	Kangoo	2012-2021	4.3 × 1.6 × 1,8	1 398	1771	40
LCV 2	Citan	2012-2021	4.3 × 1.8 × 1,8	1 315	1646	40
PV 1	Talisman	2020-2022	4.8 × 1.9 × 1,5	1 580	1 580	0
PV 2	Talisman	2020-2022	4.8 × 1.9 × 1,5	1 540	1 540	33

2.2 Experimental configuration

The four tests were conducted using a 7.7 m x 5.3 m Large Scale Heat Release (LSHR) apparatus. This apparatus allows the estimation of HRR over time and the total heat released during the fire based on oxygen consumption calorimetry. The chimney duct is equipped with McCaffrey probes, thermocouples, and a gas sampling probe to measure smoke flow rate, temperature, and molar fractions of O₂, CO₂, and CO. These data were combined with measurements of gas temperatures, radiative and total heat fluxes all around the vehicles. In addition, load cells were used to record mass loss over time. To prevent flames from reaching the measurement section in the duct and to simulate a car park ceiling, a ceiling was suspended 2.6 m above the ground.



Figure 3. Calorimetric hood (left) and ceiling (right) photos

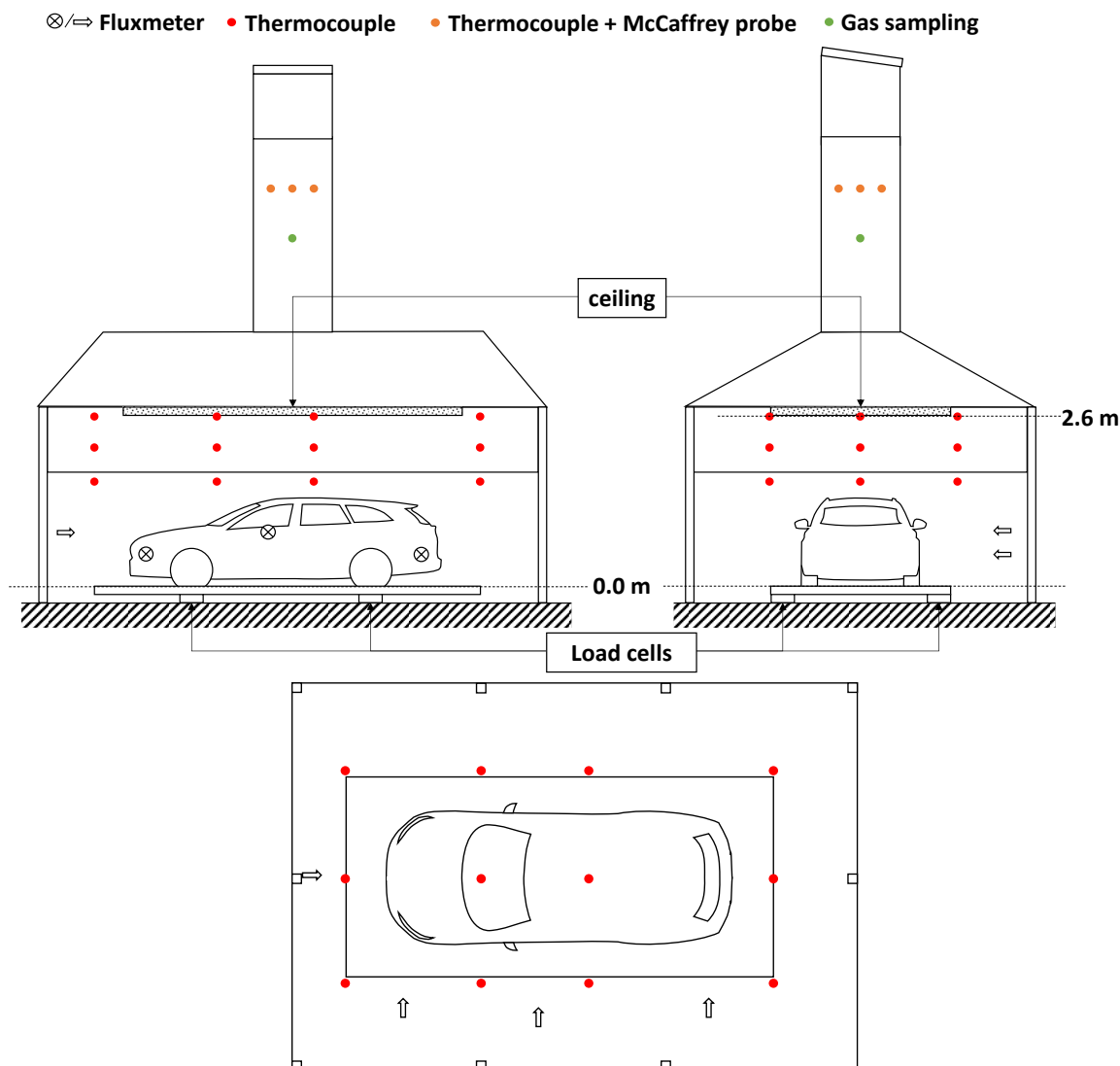


Figure 4. Experimental set-up

Ignition was carried out under the front passenger seat and the dashboard using a pan filled with heptane. During the Talisman tests, a heptane-soaked cloth was placed in the pan for safety. This method was estimated to produce 12 kW for 20 minutes. To aid fire growth, the left rear window was opened $\frac{2}{3}$ for the two Talisman tests, the passenger window was opened $\frac{1}{2}$ during the LCV 1 and the two front windows were opened for the LCV 2 test. These changes were due to a ventilation problem observed during the first test (LCV1).

The PV 2 and LCV fuel tanks were $\frac{2}{3}$ full of diesel, while the PV 1 test was performed with an empty tank. To prevent diesel leakage from spreading outside the hood, the vehicles were placed on a tray placed on the load cells.

Finally, the pressure vessels and batteries were removed from both vehicles for safety reasons, with the exception of the airbags.

This test protocol was designed to be as close as possible to that used by Daniel Joyeux in the 1990s, both in terms of vehicle preparation and test configuration.

3 RESULTS

This section presents the events observed during the four tests, and their effect on HRR. The HRR and THR results are then compared for the same vehicle type.

3.1 Phenomenology and HRR

All tests are divided into four main phases, which occur in parallel:

- combustion of the passenger compartment,
- combustion of the front of the vehicle (bumpers, tyres, engine compartment and exterior trim)
- combustion of the rear of the vehicle (bumpers, tyres and exterior trim),
- tank failure and diesel combustion (for PV 2, LCV 1 and LCV 2).

There is a tarpaulin to channel the smoke (see Figure 3), the presence of which makes it difficult to identify the end of the various phases.

3.1.1 Light commercial vehicles

The four major phases are shown in Figure 5 for the two LCV tests.

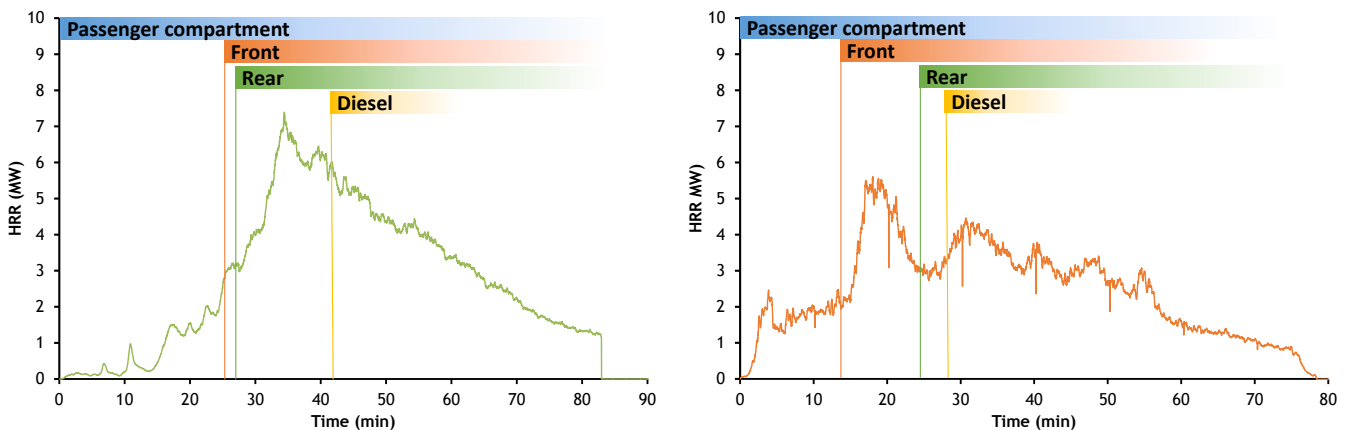


Figure 5. HRR over time and major events for LCV 1 (left) and LCV 2 (right)

Regarding the test on LCV 1, the fire grows slowly inside the cabin. The passenger door is opened several times before it is finally closed at 11 minutes. Just before the door is closed, the fire penetrates the windscreen. From 14 minutes, the intensity of the fire increases, reaching 7.3 MW at 34 minutes. As the fire grows, the plywood boards and windows are perforated one by one between 21 and 32 minutes. At the same time, the fire spreads to the front and rear elements of the vehicle, at 25 minutes and 27 minutes respectively. Full development of the fire is observed at the front and the rear at 34 and 40 minutes respectively. Fuel tank failure is observed at 41 minutes. The test is stopped at 83 minutes and the end of the combustion is estimated at 108 minutes.

In the LCV 2 test, the front windows were opened before the fire started. The fire grows in the passenger compartment without any intervention. The windscreen breaks after 2 minutes, resulting in a slightly rising plateau of about 1.8 MW. The fire then spreads to the front of the vehicle at 13 minutes. The HRR increases significantly and reaches a peak of 5.6 MW. This value is recorded at 18 minutes, during the full development of the fire at the front. The intensity of the front fire decreases 3 minutes later. A further increase in HRR is observed at 23 minutes, as the fire spreads to the rear. The fuel tank finally fails at 27 minutes. The joint combustion of the rear elements and the diesel fuel of the vehicle leads to a second peak in HRR of 4.4 MW at 33 minutes. The test is stopped at 76 minutes. A total fire duration of 89 minutes is estimated.

Two fire growths are obtained. In the LCV 1 test, it was observed that each window break resulted in an increase in HRR. The same phenomenon was observed for bodywork components. The absence of rear windows on the LCV 2 seems to have slowed down the fire growth and its spread to the rear of the vehicle. Thus, the parts of the LCV 1 burned simultaneously, while the parts of the second LCV burned sequentially.

During the two tests, 14 857 MJ (LCV 1) and 11 953 MJ (LCV 2) were released. This is a difference of 2,904 MJ. Based on the heat loads shown in Table 1, the first test can release 935 MJ more than the second test, based on two identical vehicles. The experimental difference is greater, which can be explained by:

- differences between the vehicles, particularly in terms of the plastic finishes,
- the degree of uncertainty in the fuel load of the liquid test. The exact composition of the paints is not fully known,
- the combustion efficiency of the test with the liquid load, partly related to ventilation. Even if a combustible material pyrolyses, the release of energy is lower if combustion takes place in an under-ventilated environment.

3.1.2 Passenger vehicles

As for the LCV tests, the four main phases are shown in Figure 6. It should be noted that as there is no fuel in the PV 1 tank; the tank combustion phase is not shown in the figure.

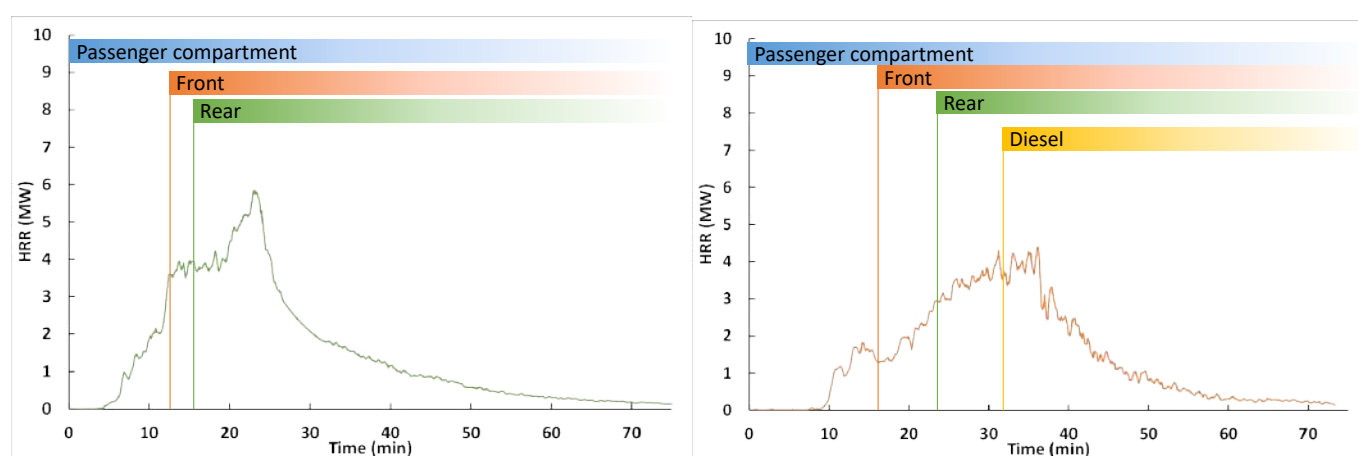


Figure 6. HRR over time and major events for PV 1 (left) and PV 2 (right)

In the PV 1 test, as in the LCV 1 test, it is difficult for the fire to grow in the cabin after the ignition. The front door is opened for 4 minutes before it is finally closed. Before the door was closed, the windscreen was partially pieced. When it breaks completely, a large column of flame reaches the ceiling. All the windows break between 9 and 11 minutes. As a result of these various breakages, the HRR increases until it reaches a plateau of 4 MW, with maximum ventilation of the passenger compartment. Between 10 and 20 minutes, the fire spreads to the front parts of the vehicle. The full development of the fire at the front is observed after 20 minutes. The fire spreads to the rear of the vehicle, 5 minutes after the front, to reach its full development at 23 minutes, corresponding to the peak HRR of 6,1 MW. The net increase in HRR at 20 minutes seems to be partly caused by the fire penetrating the rear door, which leads to an increase in air income. The fire then decays to complete extinction at 100 minutes.

In the PV 2 test with diesel, the fire grows slowly in the cabin until the windscreen breaks at 11 minutes. All windows break between 16 and 31 minutes. However, the breakage of the rear window occurs too late after the main combustion of the cabin. So, there is no real peak observed. There is a maximum of 4,6 MW around 33 minutes. Meanwhile, the fire spreads to the front of the car after 17 minutes. The fire is fully developed at the front at 28 minutes. A little earlier, the fire spreads to the rear of the vehicle at 22 minutes and is fully developed at 33 minutes. Finally, the tank fails at 31 minutes. Although an increase in intensity can be seen during the test, it is not visible on the HRR curve. The complete extinction of the fire is estimated at 105 minutes.

As with the LCV tests, two fire growths are observed. In the PV 1 test, all window breakages occur during the fire growth inside the cabin. Each break increases the amount of air income until a plateau in HRR of 4 MW is reached. The fire then spreads to both the front and rear bumpers of the vehicle, with the HRR

peaking at 6.1 MW as most of the fuel parts of the vehicle burn simultaneously. During the tests, the modern vehicles released 6,894 and 6,291 MJ for PV 1 and PV 2, respectively.

In contrast, the test on PV 2 shows a different combustion dynamic. The side window failures coincide with the bumper propagation, but are staggered in time, with some occurring after the bumper propagation. Consequently, there is no abrupt increase in HRR. Although the front bumper propagation is consistent with the first test, rear propagation is slightly delayed due to late rear window breakage, which mitigates temperature increase at the rear of the vehicle. The diesel tank rupture is delayed and coincides with a plateau in the HRR at 4.6 MW.

4 DISCUSSIONS

In this section, the experimental results obtained during the four tests are compared with the previous data available in [2,6].

4.1 Light commercial vehicles

The HRR curve developed by INERIS is compared with those measured during the tests in Figure 7. Both the maximum HRR and the fire duration are very different. The value of the plateau and the total duration of the INERIS theoretical curve are 2.45 times higher and 3.6 times shorter than the values measured during the first test. This shows that the analytical curve based on expert judgement is not in agreement with the experimental data.

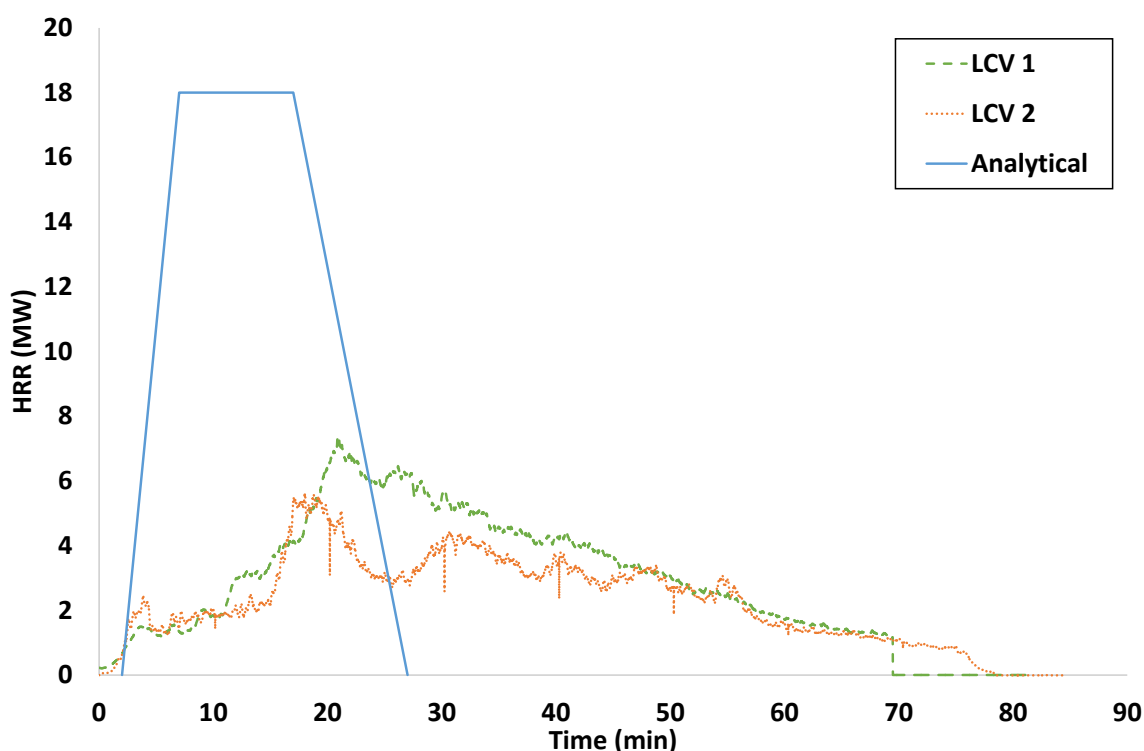


Figure 7. Measured HRR of LCV and analytical HRR over time

Compared to the vehicle tested in the 1990s, the duration of the plateau after ignition is close to that observed in the LCV 2 test. The increase after the plateau is similar to that of the LCV 1 test. However, there is a more significant increase for the 1990s passenger car, with a peak HRR slightly above 8 MW. The duration of this peak is short. The fire behaviour during the three tests remains similar up to this peak. For the 1990s test, the fire decreases sharply after the HRR peak, whereas for the LCV tests it is much more gradual. The total heat released by the loaded LCV is approximately 2 times greater than that of the 1990s

passenger cars (6,800MJ) and 20% less than the theoretical LCV. These tests show that a high fire load does not imply a high HRR peak: ventilation control plays an essential role.

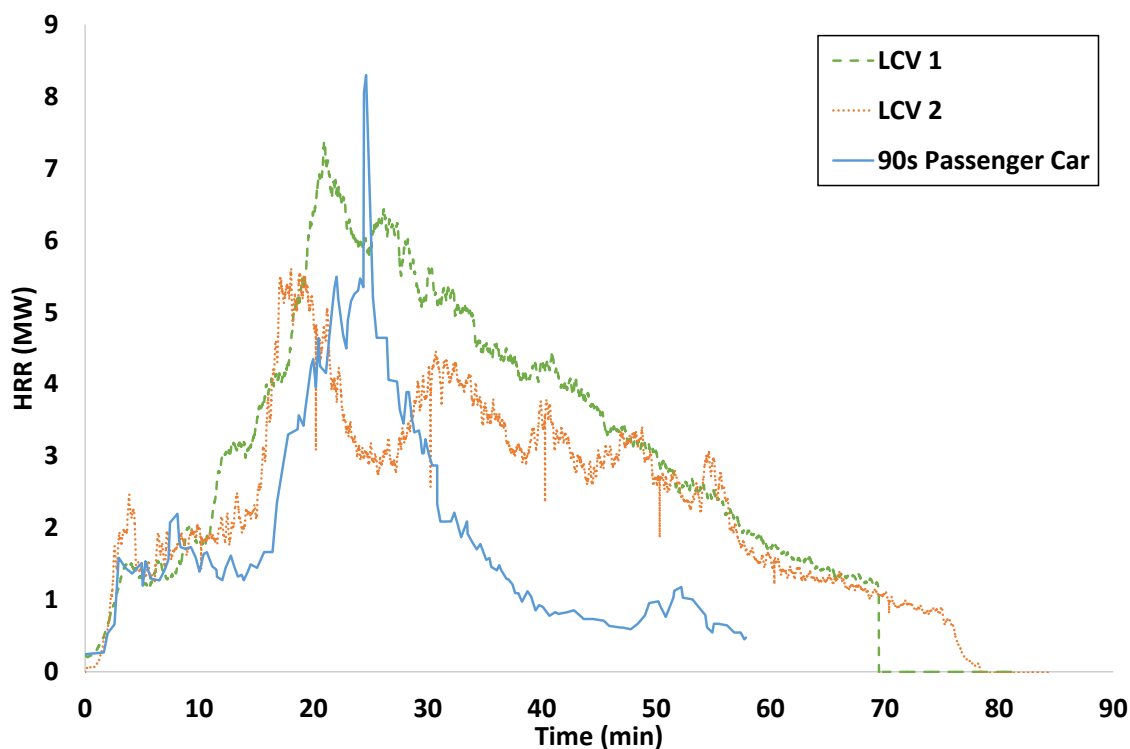


Figure 8. Measured HRR of LCV and 90s passenger vehicle over time

4.2 Passenger vehicles

The measured HRR versus time of the two passenger cars and during the 1990s are shown in Figure 9. The combustion times are similar for the three tests.

After ignition, it is observed a HRR plateau of 1 minute for PV 1, 5 minutes for the PV 2, and 14 minutes for the 1990s, with a value of approximately 1.5 MW. The duration of this plateau correlates with the time of window breakages in the vehicles. A similar phenomenon was observed in the 1990s test, where the rear window breakage occurred at 17 minutes, coinciding with a sudden increase in the flame flow and HRR. The peak HRR values are lower in the current vehicle tests compared to the older vehicle, 6.1 MW and 4.6 MW for the PV 1 and PV 2 tests, compared to 8.3 MW for the 1990s vehicle. The main combustion (HRR > 2 MW) lasts slightly longer for the newer vehicles, lasting 20 minutes compared to 16 minutes for the 1990s vehicle.

During the main combustion phase, 4,980 MJ and 4,135 MJ are released in the PV 1 and PV 2 tests respectively, compared to 3,740 MJ in the 1990s test. Despite the lower maximum HRR values in the modern vehicle tests, a greater amount of heat is released during the main combustion phase. Focusing on the first 48 minutes of the fire, PV 1 and PV 2 released 6,216 and 5,798 MJ respectively, compared to 6,085 MJ for the 1990s car. Relative to the 90s THR, the PV 1 test released 2.1% more heat, while the PV 2 test released 4.7% less. These values are close enough to suggest that the heat available in the vehicles has remained relatively stable over time.

Different combustion dynamics were observed in the two 2/3 full tank tests (PV 2 and 1990s). In the 1990s test, the diesel tank failure precedes full propagation to the rear bumper, resulting in diesel spillage to the ground and subsequent combustion, increasing the HRR. Conversely, in the modern car test, tank failure occurs after full propagation to the rear bumper and during the decay phase of front combustion. The spilled diesel spreads over a smaller area, possibly due to the absorbent nature of the tray under the vehicle. Despite

the advanced combustion of the rear bumper and the decay phase of other vehicle parts, no significant increase in HRR is observed. Rather, the heat produced seems to cancel each other, resulting in the plateau shown in the HRR figure.

It should be noted that the “1990s test” is the only test that gave such significant peak HRR and THR results during this campaign. This is the reason why this curve was chosen as the reference curve for the engineering studies (and is still used). The average results for all the single car tests were 4 ± 2 GJ and 4.5 ± 2.6 MW for THR and peak HRR, respectively. In contrast to the previous paragraphs, THR values are given over the entire combustion time. For the two car tests, the mean THR is 7.7 ± 1.8 GJ and the mean peak HRR is 6.2 ± 3.4 MW. However, 1,250 kg vehicles were mainly tested in the two cars configuration. Tohir *et al.* [7] collected the HRR and THR results available in 2014. These tests mainly include vehicles from the 1990s. Compared to 1,180 to 1,360 kg passenger cars, the average peak HRR and THR, excluding the tests by Joyeux *et al.* are 3.5 ± 0.9 MW and 5.0 ± 1.60 GJ, respectively. According to the same review, the test considered in engineering studies is closer to 1,380 to 1,470 kg vehicles (6.8 ± 2.8 MW and 6.5 ± 0.5 GJ on average). This safety curve therefore includes the results obtained in other tests on 1990s vehicles weighing around 1,300 kg. Based on the results obtained during PV 1 and PV 2 tests, the reference curve for passenger cars is still safe for modern cars.

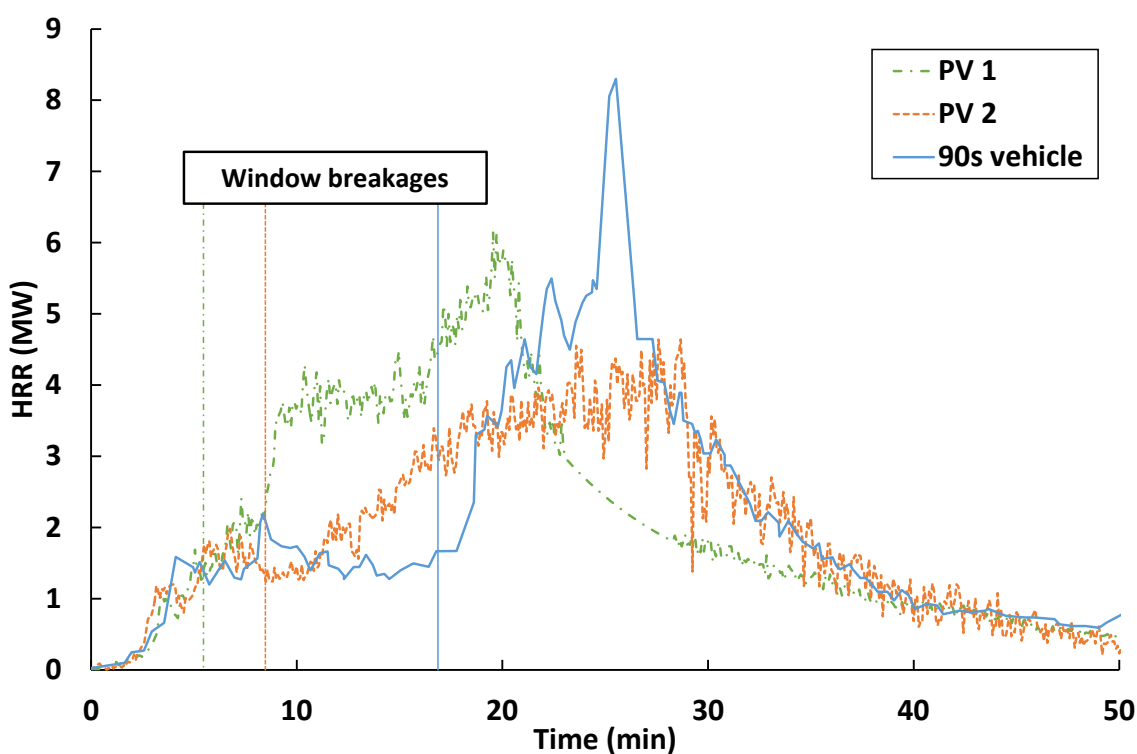


Figure 9. Measured HRR of modern and 90s passenger vehicles over time and first window breakage time associated

5 CONCLUSIONS

This paper presents the combustion of two modern passenger cars and two loaded LCVs. In order to compare these tests with the data used in French engineering studies, HRR over time were obtained using a calorimetric hood. Other physical quantities such as temperatures, heat fluxes and mass loss over time were also recorded but not presented.

Overall, it was observed that the ventilation conditions of the vehicle (glass elements) play an important role in the dynamics of fire growth. The more windows there are and the faster they break, the greater the intensity of combustion in the passenger compartment. As a result, the fire spreads more quickly throughout the vehicle, resulting in higher peak HRR.

For the LCV tests, despite the additional fuel load, the HRRs obtained over time are closer to those of passenger cars. The peak HRR is only slightly affected, but the fire slowly decreases in intensity, resulting in longer combustion times. Therefore, the theoretical HRR over time does not seem to be representative of a realistic configuration. In comparison, the fires released 14,857 MJ (LCV 1) and 11,953 MJ (LCV 2) compared to 18,000 MJ for the theoretical HRR. This amount of heat is much greater than that of a passenger car.

With regard to modern passenger cars, the two tests carried out show lower HRR peaks than the one used in engineering study. The combustion dynamics of PV 2 do not allow such peaks to be reached. However, the addition of diesel to the tank of PV 1 could have resulted in a higher peak. In addition, the THR results remain similar during the 48 first minutes of the tests with $6,007 \pm 209$ MJ released for modern vehicles versus 6,085 MJ for the 1990s car test. It should be emphasised that the HRR used in engineering studies corresponds to the test where HRR and THR measured were maximum. During the 1990s campaign, other tests results on equivalent vehicles showed much lower values. The increase in the use of plastics seems to be leading to more intense combustion of vehicles, but remains lower or equivalent to the reference curve currently in use. Thus, HRR over time used in engineering study remains valid.

Finally, the vehicle fleet has changed significantly over the last 30 years. Vehicles have become heavier and bigger with the emergence of SUV. This type of vehicle has an approximate weight of 1400 kg. A further study would enable us to check whether SUV fires are equivalent to those of 90s vehicles of equivalent weight.

In addition to the experimental study mentioned above, an experimental campaign on electric vehicles will be carried out in France in the near future, as this type of vehicle is becoming increasingly popular and is being called into question by the emergency services.

ACKNOWLEDGMENT

The authors are grateful to Renault Group for providing the vehicles and to GagnePark and ArcelorMittal for their contribution to the funding of the project.

REFERENCES

1. Joyeux, D., Kruppa, J., Cajot, L.-G., Schleich, J.-B., Van De Leur, P., Twilt, L., Demonstration of real fire tests in car parks and high buildings, EUR 1–171, (2002).
2. Cwiklinski, C., Parcs de Stationnement en Superstructure Largement ventilés – Avis d’expert sur les scénarios d’incendie. Rapport final, INERIS DRA-CCw/MCh-2001-cgr22984 26, (2001).
3. Boehmer, H., Klassen, M., Olenick, S., Modern vehicle hazards in parking structures and vehicle carriers. Fire Protection Research Foundation FPRF-2020-07, (2020).
4. Lam, C., MacNeil, D., Kroeker, R., Lougheed, G., Lalime, G., Full-scale fire testing of electric and internal combustion engine vehicles, in: 4th International Conference on Fire in Vehicle, Baltimore, (2016).
5. Truchot, B., Fouillen, F., Collet, S., An experimental evaluation of toxic gas emissions from vehicle fires. Fire safety journal 97, 111–118, (2018).
6. Joyeux, D., Car fire tests n° 7 : rate of heat release of a large car made in 1995 (test 96-S-251 No. INC-96/300-DJ/VG). CTICM, (1996).
7. Mohd Tohir, M.Z., Spearpoint, M. Distribution analysis of the fire severity characteristics of single passenger road vehicles using heat release rate data. Fire Sci Rev 2, 5 (2013). <https://doi.org/10.1186/2193-0414-2-5>.

MASONRY STRUCTURES IN FIRE

SIMPLIFIED VERIFICATION METHOD FOR THE CLASSIFICATION OF THERMALLY INSULATING VERTICALLY PERFORATED BRICKS IN CASE OF FIRE

Heiner Kruse¹, Catherina Thiele²

ABSTRACT

The fire resistance of thermally insulating brick masonry is currently defined in accordance with DIN EN 1365-1 [1] for specification in approvals or type approvals on the basis of large-format fire tests in which the test specimen is 3,0 m in height and length. Currently, DIN EN 1996-1-2 [2] does not include any design values for the temperature-dependent stress-strain curve for thermally insulating vertically perforated bricks in Annex D, which are required for calculation models. Also, the more precise calculation method for the fire case described there is excluded according to the German national annex, just like the simplified calculation method in Annex C. Tables in Annex B, whereby brick masonry can be classified into fire resistance classes taking into account various material properties. However, the table values given in the standard can only be applied when the bricks are standardized. Thermally insulating vertically perforated bricks are therefore excluded. For a rapid classification into fire resistance classes according to the current state of the art there are no calculation methods or simplified table values. By specific fire tests, data on fire resistance for thermally insulating brick masonry with different utilization factors are to be defined, which can be used in future without fire resistance testing. Special attention is paid to the possibility of defining increased fire resistance durations at lower utilization factors or higher utilization factors for lower fire resistance durations.

Keywords: Masonry; bricks; fire; simplification, classification

1 INTRODUCTION

According to statistics, an average of around 187.000 residential fires broke out in Germany between 2002 and 2015 [3]. Converted, this means that there is a fire approximately every 3 minutes. The top priority in fire protection is to save people, animals and property [4]. For this reason, buildings must be constructed and maintained in such a way that the development and spread of fire is prevented [4].

Brick is the most commonly used building material for residential construction [5]. When choosing bricks, increasing emphasis is being placed on sustainability, whereby it is not only the ecological balance of wall-building materials that plays a decisive role. Energy and heating costs can be reduced by using thermally insulating bricks.

¹ M.Sc., Fachbereich Bauingenieurwesen, Fachgebiet Massivbau und Baukonstruktion, Rheinland-Pfälzische Technische Universität Kaiserslautern-Landau,

e-mail: heiner.kruse@rptu.de

² apl. Prof. Dr.-Ing., Fachbereich Bauingenieurwesen, Fachgebiet Massivbau und Baukonstruktion, Rheinland-Pfälzische Technische Universität Kaiserslautern-Landau

e-mail: catherina.thiele@rptu.de

In response to the high demand for brick products for masonry construction described above, the brick industry must react promptly with market-driven products that meet the constantly increasing building physics requirements for thermal, sound and fire protection. It is also important to save resources in brick production and limit carbon dioxide emissions to a minimum. For this reason, the innovation cycles for bricks are very short and new products are developed and launched on the market at short intervals. This includes not only targeted adjustments to the geometric hole pattern and web design and the use of fillers as highly insulating components, but also innovative measures to optimize raw materials and firing technology in order to produce bricks in a more carbon-neutral way. Changes in standards are associated with a great deal of time and effort. For this reason, short-term and permanent changes cannot be recorded promptly, which is why the majority of all processed bricks are regulated by approvals. The largest group of these bricks are vertically perforated bricks or generally planar perforated bricks. These are usually made using the thin-bed mortar method. [6]

The improvement of just one physical building property interacts in different ways with the other physical building properties. For example, improved thermal conductivity usually reduces sound insulation or the permissible mechanical load-bearing capacity due to an increase in porosity caused by the raw material. With regard to fire protection, brick masonry is divided into fire resistance classes. The state of the art is that very time-consuming and cost-intensive fire resistance tests are carried out selectively for a product in accordance with the European harmonized standards DIN EN 1363-1 [7], DIN EN 1363-2:1999 [8] and DIN EN 1365-1 [9] on storey-high walls in order to classify the fire resistance duration.

2 STATE OF THE ART

2.1 Thermally insulating vertically perforated bricks

Due to constantly increasing building physics requirements with regard to thermal insulation, thermally insulating vertically perforated bricks are often used in energy-efficient new buildings or energy-efficient renovations. These are mainly defined by their thin webs and many cavities. As a rule, thermally insulating vertically perforated bricks are not standard bricks because, among other things, the total perforation cross-section is greater than 50 %. On the one hand, trapped air is a good insulating material due to its low thermal conductivity, on the other hand, the cavities can also be filled with insulating materials. This further minimizes heat loss. Mineral wool or perlite fillings are mainly used as insulating materials. To reduce the gross density, additional porosity is achieved by adding fine cellulose fibers such as untreated sawdust or paper pulp and/or polystyrene as well as coal dust [10].

Thermally insulating vertically perforated bricks are usually processed with thin-bed mortar. One reason for this is the good thermal conductivity of mortar compared to thermally insulating vertically perforated bricks. The thinner the mortar layer, the better the insulating properties of the masonry. The bed joint is usually capped (full-surface mortar application). The butt joints are generally not mortared. In view of the product range of thermally insulating vertically perforated bricks, they can be classified into three types.

Large-chamber bricks without insulation do not currently exist on the market because, among other things, they cannot be designed with a capped bed joint. Figure 1 shows an example of the hole pattern structures of thermally insulating vertically perforated bricks. On the left is a filled thermally insulating large-chamber vertically perforated brick (MZ70) and in the middle a small-perforated brick, also with mineral wool filling (W07 V). On the right, the same brick as in the center is shown without insulation filling (W07 UV).

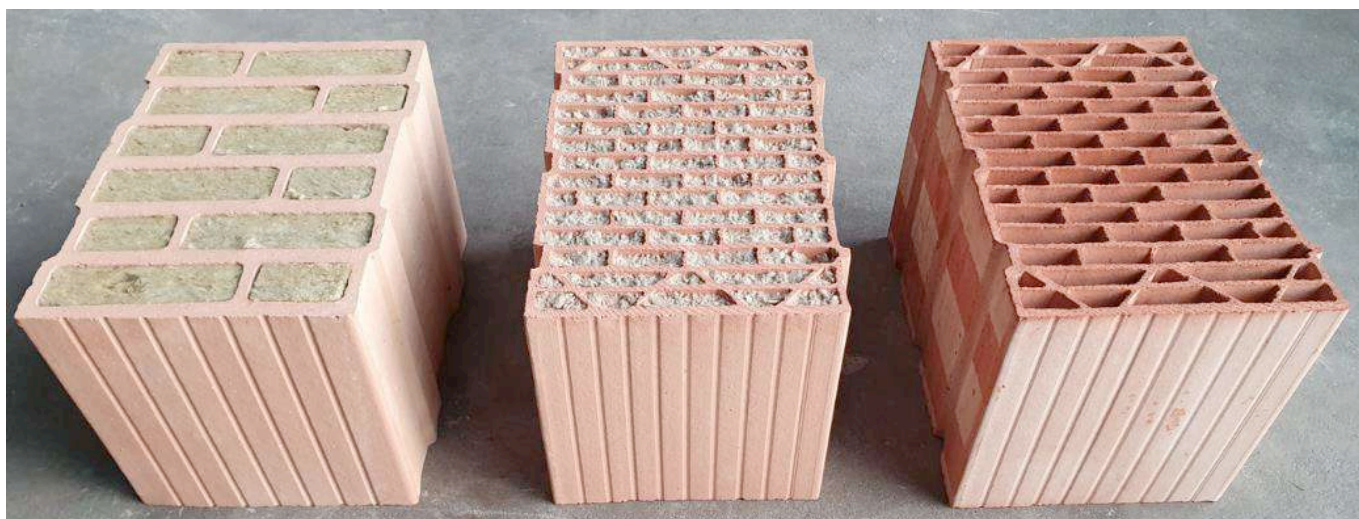


Figure 1. Exemplary hole pattern structures of thermally insulating vertically perforated bricks

Another characteristic of thermally insulating vertically perforated bricks is that they generally have a gross density of less than 0.8 kg/dm^3 . Gross density is defined as the mass of a body in relation to its volume. In comparison, solid bricks generally has a gross density of around 1.1 kg/dm^3 to 1.6 kg/dm^3 . In terms of thermal conductivity, also known as the thermal conductivity coefficient, bricks specially developed for good thermal insulation generally have a lambda of $\lambda_R = 0.10 \text{ W/mK}$ to 0.07 W/mK . In general, the lower the λ_R , the better the insulating capacity of a building material. The thermal conductivity for solid bricks is $\lambda_R = 0.69 \text{ W/mK}$ to 0.48 W/mK . This illustrates once again how good the thermal insulation properties of thermally insulating vertically perforated bricks are. [11]

The heat transfer coefficient (U-value) is the quotient of the heat flow density in the stationary state and the temperature difference between the environments on each side of a system [11]. The lower the heat transfer coefficient, which depends on the wall thickness, the better the insulating effect. Walls made of thermally insulating vertically perforated bricks with a thickness of 365 mm and additionally plastered usually have a heat transfer coefficient in the range of $0.18 \text{ W/m}^2\text{K}$ to $0.30 \text{ W/m}^2\text{K}$ [12].

Due to their low thermal conductivity, thermally insulating vertically perforated bricks are used for their intended purpose as external wall bricks where high demands are placed on thermal insulation. This is the case, for example, in detached houses and apartment buildings as well as in multi-storey residential buildings. Here, the building physics requirements can generally be met with wall thicknesses of 300 mm or 365 mm. The bricks mentioned can also be used in passive or low-energy houses with the appropriate wall thickness without additional thermal insulation. Walls made of thermally insulating vertically perforated bricks are usually plastered on both sides, which can also improve the thermal insulation. The compressive strength classes of bricks generally range from 6 to 12, whereby characteristic masonry compressive strengths of $f_k = 1.8 \text{ N/mm}^2$ to 4.5 N/mm^2 are achieved [12].

2.2 Production of the test specimens

For the following investigations to define simplified table values for fire resistance classification, masonry walls with dimensions of 3.0 m in height and 1.0 m in length were made and plastered on both sides. Walls of different thicknesses were produced. Information on the wall thicknesses resulting from the tile dimensions used can be found in the following tables 1 and 2. Table 1 contains information on the large-chamber tile ThermoPlan MZ70 used.

Table 1. Large-chamber tile ThermoPlan MZ70

Name	ThermoPlan MZ70 (filled)
Approval number	Z-17.1.1084
Tile widths tested	190 mm; 240 mm; 365 mm; 490 mm
Characteristic masonry compressive strength f_k	2.7 N/mm ² ; 2.2 N/mm ² ; 2.7 N/mm ² ; 2.1 N/mm ²
Thermal conductivity λ_R	0.07 W/(m·K) [13]
Insulation material	Brickrock®, Building material class A1 [13]

The following table 2 contains information on the small-perforated brick UNIPOR W07 CORISO with and without mineral wool filling.

Table 2. Small-perforated brick UNIPOR W07 CORISO with and without mineral wool filling

Name	UNIPOR W07 CORISO (filled)	UNIPOR W07 CORISO (not filled)
Approval number	Z-17.1.1056	-
Tile widths tested	175 mm, 365 mm	175 mm, 365 mm
Characteristic masonry compressive strength f_k	2.4 N/mm ² ; 2.4 N/mm ²	2.4 N/mm ² ; 2.4 N/mm ²
Thermal conductivity λ_R	0.07 W/(m·K) [14]	> 0.07 W/(m·K)
Insulation material	UNIPOR CORISO mineral wool, building material class A1 [14]	-

The thermally insulating vertically perforated bricks were mortared with maxit mur 900 d thin-bed mortar [15]. The thickness of the exterior and interior plaster is 15 mm. Mineralpor lightweight plaster MP 69 Speed from Baunit was used for the exterior plaster [16]. On the inside, the side facing the fire, Baunit's Klima KP 36 W lime plaster was used [17].

2.3 Fire test setup

The walls were tested in accordance with DIN EN 1363-1 [7] and DIN EN 1365-1 [1]. Deviations from the standards are that the walls were not 3.0 m in height and 3.0 m in length. They were reduced to 1.0 m in length. Due to the test structure, the lower 0.15 m of the 3.0 m high wall was not directly exposed to flames. Reducing the length of the test specimen to 1.0 m not only saves bricks. It also allows the test series to be completed more quickly due to shorter conversion times. The reduced test specimen length results in other temperature and deformation measuring points than in the standards. In the fire resistance tests, the temperatures and deformations on the wall surface were measured in accordance with DIN EN 1365-1 [1]. The following figure 2 shows the test setup and the positions for the measuring device.

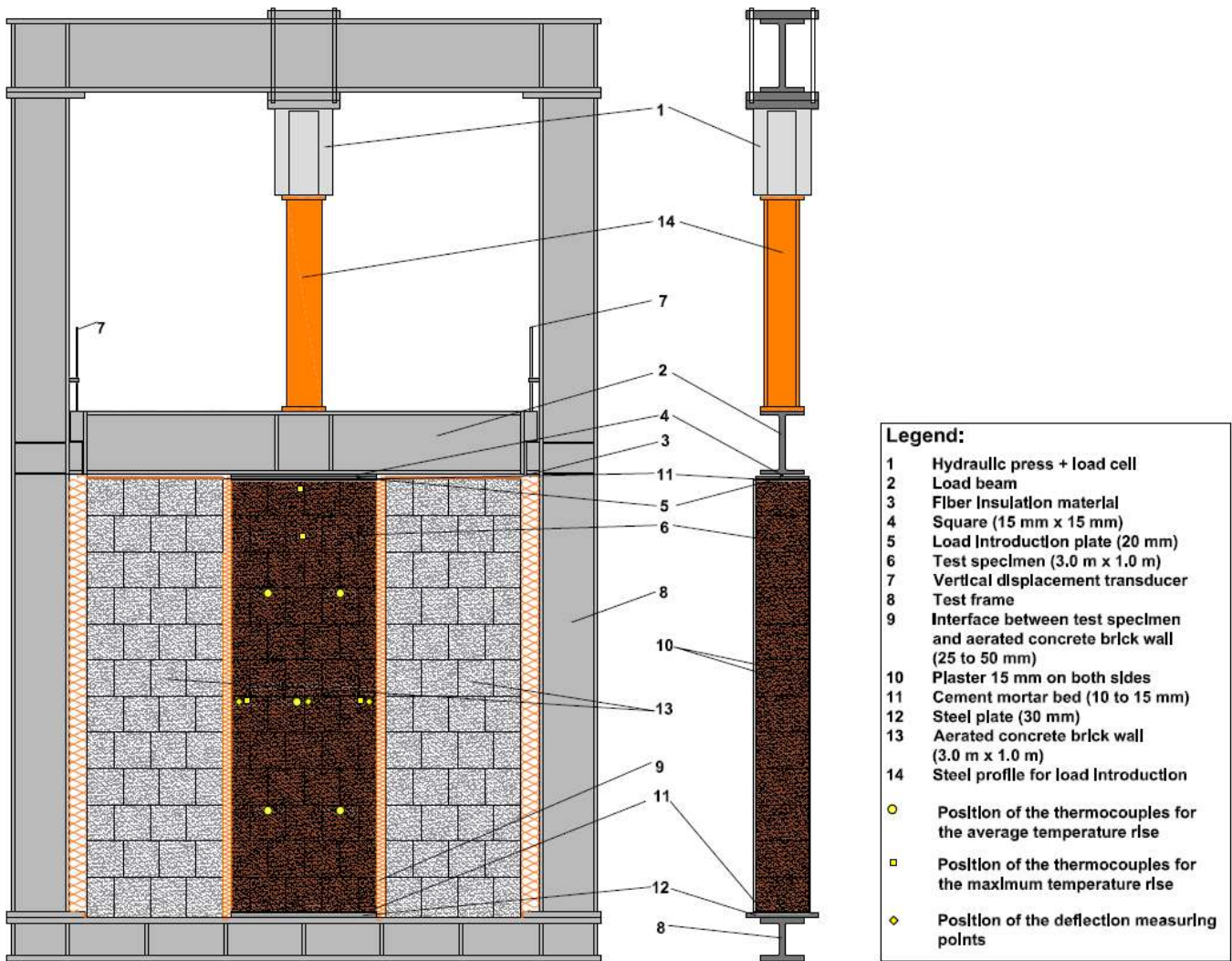


Figure 2. Fire test setup [20]

Only the wall in the middle is loaded. The walls to the left and right of the test specimen, made of aerated concrete bricks in combination with fire protection cladding, did not have to be replaced during the test series.

3 DETERMINING THE FIRE RESISTANCE OF MASONRY WALLS

3.1 Classification by fire resistance tests

The most relevant test criteria for the fire resistance tests for a classification of fire resistance duration are presented below. Since 2000, a classification system (REI) in accordance with DIN EN 13501-2 [18] has been introduced at European level. This system differentiates the individual criteria in the designation much more than the German system according to DIN EN 4102-2 [19], which only specifies a fire resistance duration depending on the component (F for walls, ceilings, building columns and beams as well as stairs). A visual inspection of the components and a note of any anomalies during the entire test procedure is essential for all tests. In accordance with DIN EN 13501-2 [18], load-bearing and room-enclosing walls must be tested for the following three properties that describe the fire resistance:

1. load-bearing capacity (R)
2. room closure (E)
3. insulation (I)

A loss of load-bearing capacity is defined by the fact that the component is no longer able to absorb the applied normal force load. This is usually applied centrally to the test specimen. If a failure of the wall is detected, it must be recorded with the corresponding time. Failure of the room closure is verified by means of a absorbent cotton test, gap leakage and visual inspection for flame formation on the side of the wall facing away from the fire. The insulation effect is checked via the temperature rise on the side of the wall facing away from the fire. This criterion is used to limit the transfer of fire or heat to the side of the wall facing away from the fire. For compliance, the temperature rise must not exceed a required level. The last two properties result from the function of the walls in the event of fire. They are intended to seal off escape routes from fire and smoke and must therefore prevent the transmission of hot gases and temperatures. [18]

The test procedure stipulates that the wall is subjected to the test load 15 minutes before the start of the fire resistance test. After the 15 minutes have elapsed, the burners in the combustion chamber of the furnace are ignited and the actual fire resistance test begins. The maximum test duration is either specified by the client or limited by failure of the wall. [1]

The temperature curve in the furnace is regulated in accordance with DIN EN 1363-1 [7]. The unit temperature-time curve specified there, also known as ETK, is used for all fire resistance tests of the investigations. The following equation describes the temperature curve of the ETK.

$$T = 345 \cdot \log_{10} \cdot (8 \cdot t + 1) + 20 \quad (1)$$

Where:

T is the mean oven temperature [°C]

t is the time [min]

Certain limit values must be observed for the temperature curve for each fire resistance test. These are defined as follows: [11]

For $5 < t \leq 10$	15 %
For $10 < t \leq 30$	$(15 - 0.5(t - 10))$ %
For $30 < t \leq 60$	$(5 - 0.083(t - 30))$ %
For $t > 60$	2.5 %

The fire resistance duration in minutes resulting from a fire resistance test is always rounded down to the nearest value divisible by 30 for classification into a fire resistance class. Fire resistance requirements for building components usually range from 30 minutes to 120 minutes.

3.2 Fire resistance tests series A

A total of nine fire resistance tests were carried out on walls with a nominal thickness of 0.365 m. The test program included three tests each with the filled large-chamber brick ThermoPlan MZ70, three tests with the small-perforated filled brick UNIPOR W07 CORISO and three tests with the unfilled brick UNIPOR W07 CORISO. The aim of the tests was to induce a failure of the 1.0 m long and 3.0 m high walls over a period of 30 minutes to 120 minutes. This is related to the fire protection requirements for exterior walls of residential buildings. To achieve the time periods, the centrally applied test load (P_{selected}) was individually adjusted after each fire resistance test.

Different wall thicknesses and characteristic masonry compressive strengths f_k result in different design values for the vertical load-bearing resistance N_{Rd} , for which the wall slenderness λ is taken into account via the reduction factor Φ_m . Depending on the design value for the vertical load-bearing resistance N_{Rd} , different utilization factors α_{fi} result for the same selected test load P_{selected} , which influence the fire resistance duration. Due to fluctuating test loads P_{selected} of approximately ± 1.0 kN during all fire resistance tests, the design value for the vertical load-bearing resistance N_{Rd} is also rounded to whole numbers. The following table provides information on the fire resistance tests.

Table 3. Data of the fire resistance tests of test series A [20]

Brick	Wall thickness t [mm]	f_k [N/mm ²]	Φ_m [-]	N_{Rd} [kN/m]	$P_{selected}$ [kN/m]	α_{fi} [-]	Fire resistance duration [min]
MZ70	364	2.7	0.99	650	375	0.58	82
MZ70	364	2.7	0.99	650	240	0.37	72
MZ70	364	2.7	0.99	650	200	0.31	105
W07 V	362	2.4	0.99	574	509	0.89	39
W07 V	362	2.4	0.99	574	375	0.65	70
W07 V	362	2.4	0.99	574	280	0.49	69
W07 UV	362	2.4	0.99	574	375	0.65	47
W07 UV	362	2.4	0.99	574	280	0.49	65
W07 UV	362	2.4	0.99	574	200	0.35	89

$$\Phi_m = 1.14 \cdot \left(1 - 2 \cdot \frac{e_{mk}}{t_{ef}}\right) - 0.024 \cdot \lambda \leq 1 - 2 \cdot \frac{e_{mk}}{t_{ef}}$$

$$f_d = \frac{\zeta \cdot f_k}{\gamma_M} \quad \text{with } \zeta = 1.0; \gamma_M = 1.5$$

$$N_{Rd} = \Phi_m \cdot t \cdot l \cdot f_d \quad \text{with } l = 1.0 \text{ m}$$

$$\alpha_{fi} = \frac{P_{selected}}{N_{Rd}}$$

As can be seen from the table, some of the tests show large variations in the fire resistance duration in relation to the utilization factor in comparison with other tests.

3.3 Fire resistance tests series B

The following fire resistance tests are identical to those of series A. The only difference is that the test specimens are not walls with a thickness of 0.365 m. Two tests each were carried out on walls made of the filled and unfilled brick UNIPOR W07 CORISO with a width of 0.175 m and on 0.190 m thick walls consisting of the brick ThermoPlan MZ70. These dimensions were achieved by sawing the 0.365 m wide bricks, whereby care was taken to ensure that the cut brick still had webs on both sides on the outside. Due to the different thicknesses of the inner and outer webs of the small-perforated brick UNIPOR W07 CORISO, different outer web thicknesses were obtained after sawing. In the subsequent fire resistance tests, the side of the wall with the thicker outer web faced the one-sided fire exposure. The inner and outer webs of the large-chamber bricks have the same dimensions, meaning that the outer webs remained the same thickness after the bricks were sawn.

In addition, a 3.0 m high and 1.0 m long masonry wall with nominal thicknesses of 0.240 m and 0.490 m was produced using the large chamber brick ThermoPlan MZ70 and tested in a fire resistance test. The component behavior of walls with a thickness of 0.175 m, 0.190 m, 0.240 m, 0.365 m up to 0.490 m is investigated.

Table 4. Data of the fire resistance tests of test series B [20]

Brick	Wall thickness t [mm]	f_k [N/mm ²]	Φ_m [-]	N_{Rd} [kN/m]	$P_{selected}$ [kN/m]	α_{fi} [-]	Fire resistance duration [min]
MZ70	190	2.7	0.86	293	200	0.68	129
MZ70	190	2.7	0.86	293	200	0.68	86
MZ70	239	2.2	0.91	320	200	0.63	48
MZ70	497	2.1	1.00	696	375	0.54	80
W07 V	175	2.4	0.83	233	200	0.86	58
W07 V	175	2.4	0.83	233	154	0.66	72
W07 UV	175	2.4	0.83	233	200	0.86	62
W07 UV	175	2.4	0.83	233	82	0.35	184*

* No failure after 180 minutes. Load then increased until failure at 176.3 kN.

$$\Phi_m = 1.14 \cdot \left(1 - 2 \cdot \frac{e_{mk}}{t_{ef}} \right) - 0.024 \cdot \lambda \leq 1 - 2 \cdot \frac{e_{mk}}{t_{ef}}$$

$$f_d = \frac{\zeta \cdot f_k}{\gamma_M} \quad \text{with } \zeta = 1.0; \gamma_M = 1.5$$

$$N_{Rd} = \Phi_m \cdot t \cdot l \cdot f_d \quad \text{with } l = 1.0 \text{ m}$$

$$\alpha_{fi} = \frac{P_{selected}}{N_{Rd}}$$

The masonry walls consisting of the 0.190 m wide large chamber bricks ThermoPlan MZ70 were loaded with a centrally applied normal force of 200 kN, which corresponds to a utilization factor of $\alpha_{fi} = 0.68$ according to table 4. The fire resistance tests show very different failure times of 129 minutes and 86 minutes. The factor between the fire resistance durations is therefore 1.50 and the percentage difference is 40.0 %.

4 SIMPLIFIED VERIFICATION METHOD FOR THE CLASSIFICATION

4.1 Evaluation variant

Due to the large scatter and the small number of tests, no significant difference between the different wall thicknesses can be identified. The slenderness of the walls is taken into account when calculating the utilization factor α_{fi} . For this reason, the test data from test series A and B are evaluated together. Due to the small number of tests, no evaluation was carried out with regard to the different bricks tested.

As can be seen from the tables, no results are available for fire resistance durations < 39 minutes. For this reason, the fire resistance class REI 30 is determined on the safe side using a reduction based on the evaluation for fasteners in concrete in the event of fire in accordance with EAD 330232-01-0601 [21]. The selected procedure for the evaluation of the fire resistance tests follows step by step.

1. Calculation of N_{Rd} (DIN EN 1996-1-1 [22])
2. The load-bearing resistances resulting from step 1) represent the cold case ($\cong 0$ minutes fire resistance duration) with a utilization factor $\alpha_{fi} = 1.0$.
3. The test loads of the tests are divided by the load-bearing resistances from step 2) to determine the utilization factor α_{fi} .
4. Presentation of the test results from steps 2) and 3) in a coordinate system. The fire resistance duration is plotted on the vertical diagram axis and the utilization is plotted on the horizontal diagram axis.
5. An exponential function is created on the basis of all data points displayed in the coordinate system.

6. The exponential function is shifted by the furthest data point below.
7. The functional equation of the shifted exponential function is used to determine the utilization for the fire resistance durations of 60, 90 and 120 minutes.
8. The fire resistance durations for 60 and 90 minutes defined in step 7) are used to create a regression grade.
9. The functional equation for the degrees of regression from step 8) is used to determine the fire resistance duration for 30 minutes.

4.2 Classification values and validation with test reports

Figure 3 shows the test data from test series A and B in black. The evaluation procedure described in chapter 4.1 is used for these. The yellow data points come from test reports of different testing institutes and are used for validation. With a few exceptions, there were no failures in these tests. The fire resistance tests were stopped after a defined time. [20]

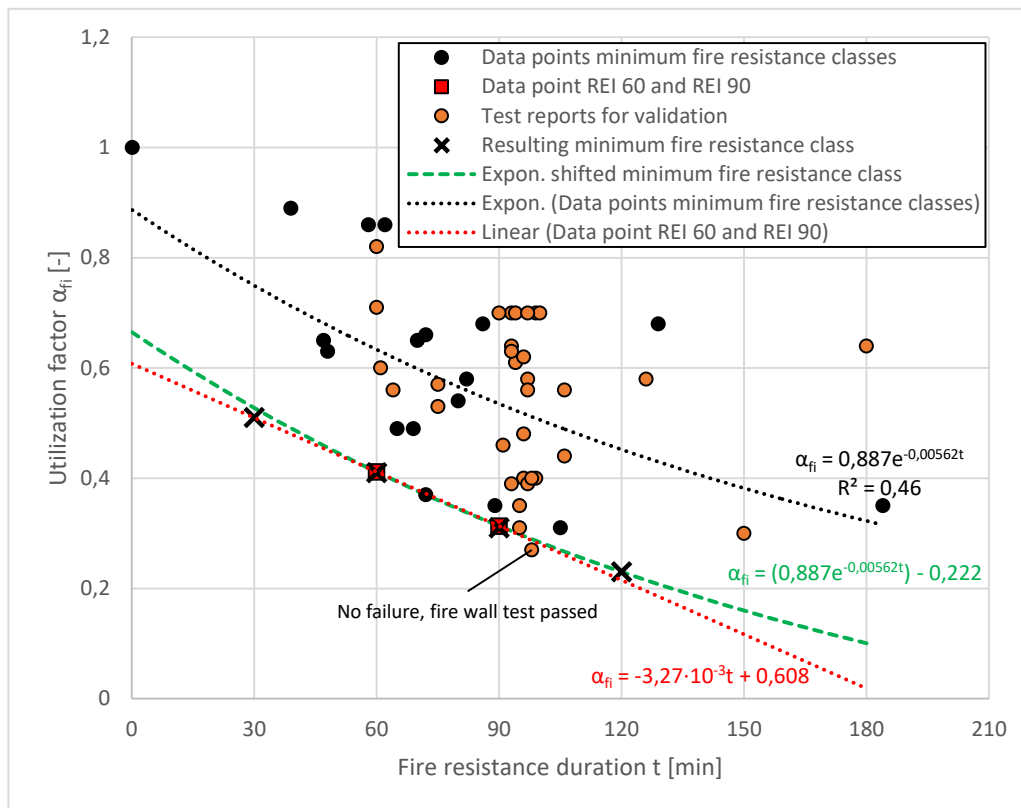


Figure 3. Specification of the minimum fire resistance classes for thermally insulating vertically perforated bricks [20]

Figure 3 shows a trend of how the fire resistance duration of masonry walls consisting of thermally insulating vertically perforated bricks behaves as a function of utilization. These findings apply regardless of European standards.

The test data show that 1.0 m long masonry walls tend to have shorter failure times than the 3.0 m long masonry walls. An exact factor could not be determined. This would have to be determined by further tests. In general, the data basis for the creation of table values for the classification of fire resistance is on the safe side.

Table 5 shows the defined minimum fire resistance classes (according to European standard) based on figure 3. The minimum wall thickness of 175 mm corresponds to the smallest tested wall thickness in the fire resistance tests carried out, which must be complied with as a minimum.

Table 5. Minimum fire resistance classes [20]

Minimum wall thickness for thermally insulating vertically perforated bricks for classification into fire resistance classes with centric load application and one-sided fire exposure				
Utilization factor α_{fi}	REI 30	REI 60	REI 90	REI 120
$\alpha_{fi} \leq 0.51$	(≥ 175 mm)	-	-	-
$\alpha_{fi} \leq 0.41$	(≥ 175 mm)	(≥ 175 mm)	-	-
$\alpha_{fi} \leq 0.31$	(≥ 175 mm)	(≥ 175 mm)	(≥ 175 mm)	-
$\alpha_{fi} \leq 0.23$	(≥ 175 mm)	(≥ 175 mm)	(≥ 175 mm)	(≥ 175 mm)
Wall thicknesses in (): Plastered on both sides with a ≥ 15 mm thick fire-resistant plaster layer				

In table 5, the fire resistance durations are indicated with the letters REI. The R here means that the masonry wall has a load-bearing capacity of the number in minutes behind it. The tests have shown that smoke did not penetrate through the masonry wall plastered on both sides at any time during a test (criterion E). Similarly, the temperature increase on the back of the wall was so low due to the good insulating effect of the bricks that the insulation criterion was also met in every fire resistance test (criterion I). The design value of the vertical load-bearing resistance N_{Rd} of the masonry in the cold case, which is required for the calculation of the utilization factor α_{fi} , must be calculated in accordance with the general verification method (DIN EN 1996-1-1 [22]). The application conditions for the table values are currently still being coordinated.

5 CONCLUSIONS

The fire resistance of thermally insulating brick masonry walls was investigated. These findings have general applicability. Table values have been defined which can be used to classify the fire resistance of thermally insulating brickwork quickly and easily according to the European standard. The classification values can be found in table 5. The application conditions for the use of the table values created for the classification of fire resistance still need to be defined. The influence of the reduced wall length must also be investigated to be able to define the factor in relation to safety more precisely.

REFERENCES

1. Feuerwiderstandsprüfungen für tragende Bauteile: Teil 1: Wände, 1365-1, DIN Deutsches Institut für Normung e.V., Berlin, Aug. 2013.
2. Eurocode 6: Bemessung und Konstruktion von Mauerwerksbauten: Teil 1-2: Allgemeine Regeln – Tragwerksbemessung für den Brandfall, 1996-1-2, DIN Deutsches Institut für Normung e.V., Berlin, Apr. 2011.
3. Statista. „Anzahl der Brände in Deutschland von 2002 bis 2015.“ <https://de.statista.com/statistik/daten/studie/155263/umfrage/entwicklung-der-gesamtanzahl-der-braende-in-deutschland-seit-2002/> (Zugriff am: 14. März 2024).
4. Musterbauordnung: Fassung November 2002, Beschluss der Bauministerkonferenz, Feb. 2019.
5. Statistisches Bundesamt, Bauen und Wohnen: Baugenehmigungen von Wohn- und Nichtwohngebäuden nach überwiegend verwendetem Baustoff (Lange Reihen z. T. ab 1980) (2021). Statistisches Bundesamt (Destatis), 2021.
6. M. Pröll, Ziegellexikon Mauerwerk 2020, 2020. Aufl. München: G. Peschke Druckerei GmbH, 2020.
7. Feuerwiderstandsprüfungen: Teil 1: Allgemeine Anforderungen, 1363-1, DIN Deutsches Institut für Normung e.V., Berlin, Mai. 2020.
8. Feuerwiderstandsprüfungen: Teil 2: Alternative und ergänzende Verfahren, 1363-2, DIN Deutsches Institut für Normung e.V., Berlin, Okt. 1999.
9. Feuerwiderstandsprüfungen für tragende Bauteile: Teil 1: Wände, 1365-1, DIN Deutsches Institut für Normung e.V., Berlin, Aug. 2013.

10. S. Wagner, B. Harr und U. Meyer, "Ökologisches Bauen mit Ziegeln", Mainz, Jan. 1998. Zugriff am: 14. März 2024. [Online]. Verfügbar unter: https://ziegel.de/sites/default/files/2018-10/O_01__Ziegel-Oekobilanz-Broschuere_2002%5B1358%5D.pdf
11. Verband Österreichischer Ziegelwerke. „Wärme – ziegel.at.“ <https://www.ziegel.at/ziegeltechnik/bauphysik/waerme> (Zugriff am: 14. März 2024).
12. August Lücking GmbH & Co. KG, "Produktbandbuch 2023: Technische Daten und Ausschreibungstexte", Warburg-Bonenburg, Bausteine für eine gesunde Welt, Dez. 2022.
13. August Lücking GmbH & Co. KG, "Lücking Produktbandbuch 2021: Produktdatenblatt ThermoPlan MZ70 HLZ B 8-0,55", August Lücking GmbH & Co. KG, 2021.
14. Ziegelwerk Otto Bergmann gmbH, "Produktdatenblatt UNIPOR-W07 CORISO", Ziegelwerk Otto Bergmann gmbH.
15. Franken maxit GmbH & CO., "maxit mur 900 D: Deckelnder Dünnbettmörtel", Franken maxit GmbH & CO., Kasendorf, Dez. 2013.
16. Baunit GmbH, "MineralporLeichtputz MP 69 Speed: Beschleunigt abbindender Kalk-Zement-Leichtputz Typ II für die manuelle und maschinelle Verarbeitung. Leichtputzmörtel LW und CS II nach DIN EN 998-1.", Baunit GmbH, Bad Hindelang, Mai. 2020.
17. Baunit GmbH, "Kalkputz Klima KP 36 W: Naturweißer Kalkputz für die manuelle und maschinelle Verarbeitung im Innenbereich. Normalputzmörtel GP und CS II nach DIN EN 998-1.", Baunit GmbH, Bad Hindelang, Mrz. 2020.
18. Klassifizierung von Bauprodukten und Bauarten zu ihrem Brandverhalten: Teil 2: Klassifizierung mit den Ergebnissen aus den Feuerwiderstandsprüfungen, mit Ausnahme von Lüftungsanlagen, 13501-2, DIN Deutsches Institut für Normung e.V., Berlin, Dez. 2016.
19. Brandverhalten von Baustoffen und Bauteilen: Bauteile, Begriffe, Anforderungen und Prüfungen, 4102-2, DIN Deutsches Institut für Normung e.V., Berlin, Sep. 1977.
20. H. Kruse: Untersuchungen an Mauerwerkswänden hergestellt aus wärmedämmenden Hochlochziegeln bei einseitiger Brandbeanspruchung, Dissertation RPTU Kaiserslautern -Landau, bisher unveröffentlicht.
21. Mechanical fasteners for use in concrete, 330232-01-0601, EOTA, Dez. 2019.
22. Eurocode 6: Bemessung und Konstruktion von Mauerwerksbauten: Teil 1-1: Allgemeine Regeln für bewehrtes und unbewehrtes Mauerwerk, 1996-1-1, DIN Deutsches Institut für Normung e.V., Berlin, Feb. 2013.

THE COMPREHENSIVE STUDY OF THE THERMO-MECHANICAL BEHAVIOUR OF MASONRY WALLS

Armita Obaei¹, Javad Eslami², Anne-Lise Beaucour³, Dashnor Hoxha⁴, Albert Noumowe⁵,
Pierre Pimienta⁶

ABSTRACT

Fires can cause catastrophic damage to buildings, and masonry structures are not exempt from this threat. Despite the potential for a significant loss, the number of studies investigating the behaviour of masonry in fire situations especially at the structural level is limited. In this context, a portion of the ANR POSTFIRE project adopts an approach that integrates experiments and numerical simulations to analyse the thermomechanical behaviour of three different limestone masonry walls exposed to high temperatures. The experimental results show symmetrical out-of-plane deformations with a deflection oriented towards the heat source for all walls during heating. This approach also highlighted the effect of the presence of the mechanical load on the thermal bowing of the walls which leads to a decrease in the wall's deflection. Thermomechanical modelling using the finite element method, considering the evolution of the physical and mechanical properties of the stones as a function of temperature, highlights the crucial importance of mechanical properties such as the modulus of elasticity as well as boundary conditions on the deformed wall pattern and displacement intensity.

Keywords: Masonry; Limestone; Fire resistance; Thermo-mechanical behaviour; Numerical modelling.

1 INTRODUCTION

Masonry is an ancient and widely used construction system that involves the assembly of blocks or individual masonry units, typically made of stone, brick, or concrete, with or without the use of mortar. Limestone, a sedimentary rock primarily composed of calcium carbonate, has historically been employed in masonry due to its availability and ease of shaping.

While masonry structures have been well studied under static and dynamic loading conditions [1, 2], both on the material and structural scale, the understanding of the behaviour of stone masonry exposed to fire is limited [3]. Fire poses a significant threat to buildings, necessitating an understanding of thermal damage and the mechanical behaviour of stone masonry at high temperatures.

During a fire, masonry walls undergo thermal bending due to heating on one face, creating a thermal gradient across their thickness [4-6]. As a result, a thermal bending phenomenon occurs due to the difference in thermal expansion between the two faces of the wall. Because the face exposed to heat expands

¹ CY Cergy Paris University, Laboratoire de Mécanique et Matériaux du Génie Civil,
e-mail: armita.obaei@cyu.fr

² CY Cergy Paris University, Laboratoire de Mécanique et Matériaux du Génie Civil,
e-mail: javad.eslami@cyu.fr

³ CY Cergy Paris University, Laboratoire de Mécanique et Matériaux du Génie Civil,
e-mail: anne-lise.beaucour@cyu.fr

⁴ Orleans University,
e-mail: dashnor.hoxha@univ-orleans.fr

⁵ CY Cergy Paris University, Laboratoire de Mécanique et Matériaux du Génie Civil,
e-mail: albert.noumowe@cyu.fr

⁶ CSTB - Centre Scientifique et Technique du Bâtiment,
e-mail: pierre.pimienta@cstb.fr

more rapidly than the opposite face remaining cold, the wall tends to bend towards the fire. This thermal curvature, combined with material degradation, can lead to wall instability. At high temperatures, physical and chemical transformations affect the properties of masonry units and mortars. In the case of limestone, the decarbonisation of calcite causes them to contract beyond 700°C, which leads to reducing the mechanical properties of the exposed face and potentially causing damage even after the fire [7].

Various authors have employed experimental methods to assess the fire resistance of masonry. Byrne provided the first experimental evidence of thermal bending in clay brick masonry walls, conducting diverse experiments on walls of different dimensions [8]. Shields et al. [9] studied the thermomechanical response of concrete brick masonry walls exposed to fire according to the BS-476 standard [10]. Lavery et al. [11] tested scaled-down concrete brick masonry walls subjected to various levels of load and fire exposure, explaining thermal deformation and reverse thermal deformation phenomena.

Regarding masonry walls constructed of natural stone, research in this area is relatively limited. A recent study conducted by Pham et al. [12] focused on investigating the thermo-mechanical behaviour of a specific type of natural stone masonry wall known as Saint-Vaast limestone. The study involved two fire tests, revealing the occurrence of thermal bowing in the walls, which is influenced by mechanical loading. Additionally, the researchers examined cracking patterns in these walls, which typically initiate in vertical joints and propagate vertically through blocks, which can indicate compression failure. Building on this work, Donval [13] further emphasized the impact of compression loading during fire tests, elucidating a significant loss in wall resistance. She also correlated these findings with numerical modelling and propositions.

Few numerical investigations have addressed the simulation of the thermomechanical response of masonry structures subjected to fire. Gnanakrishnan et al. developed a simplified finite element model in plane deformation with overestimated results due to the omission of geometric nonlinearity, material cracking, and transient deformation components [14]. Dhanasekar et al. presented a 2D finite element model highlighting thermal buckling in masonry walls, with satisfactory validation compared to experimental tests [15]. However, the transient deformation component was neglected. This may lead to inappropriate results in the analysis of masonry walls under load. Nadjai et al. developed a 2D micro model based on the finite element method considering geometric and material nonlinearities, thermal gradients, and temperature-dependent material properties [16]. Nguyen and Meftah numerically validated a hollow clay block masonry subjected to fire with a nonlinear 3D micro model in Cast3M. Their model accounted for spalling criteria based on crushing, detachment, and buckling and was successfully validated against experimental observations [17].

Among the studies, existing literature lacks comprehensive data on the thermo-mechanical responses of natural limestone walls to fire exposure. This knowledge gap underscores the critical need for systematic investigations to understand how these materials behave under such conditions. Therefore, the primary objective of this study is to bridge this gap by examining the thermo-mechanical behaviour of different natural limestone walls during fire incidents combined with the comparison of numerical simulations with experimental data which contributes to a better understanding of thermomechanical behaviour. By doing so, we aim to provide valuable insights into the behaviour of masonry structures under fire conditions. Furthermore, a detailed exposition of the experimental part of this work is presented in another article [18].

2 EXPERIMENTAL PROGRAM

2.1 Materials and walls construction

The experimental part of this study explores the behaviour of limestone masonry during fires through six fire resistance tests conducted at the CSTB (Scientific and Technical Centre for Building). Three types of limestone, with different strengths, were examined. Two walls were constructed for each type of limestone, with mortars tailored to each stone resistance, and subjected to the two hours of the heating period, with and without mechanical loading during heating. This study also investigates the impact of mechanical loading during the fire, examines wall displacements in three directions, and analyses the post-fire behaviour of the walls.

The limestone used comes from the quarries of Saint-Leu, Tervoux, and Massangis, with compression strengths of 7.3, 37.2, and 102 MPa respectively ([Table 1](#)). For each type of stone, a suitable mortar was formulated following the NF DTU 20.1 2020 standard [[19](#)]. This standard defines, for natural stone masonry, the binder dosage of the mortar based on the compression strength of the stone. The mortar mix aims to replicate historical mortars with low hydraulicity, using natural hydraulic lime NHL 2, NHL 3.5. And also Super White Cement CEM II/42.5 N is also used to achieve the desired compressive strength. The mortars were made using a yellow plastering silica sand with a granular class of 0-1 mm. The strength of the mortars from Saint-Leu, Tervoux, and Massangis was measured respectively after 4, 2, and 3 months.

Table 1. Characteristics of tested walls including the limestone stones and mortars

Wall	Stone	Stone compressive strength (MPa)	Mortar	Curing time	Mortar compressive strength (MPa)	Compressive load	Residual load
1	Saint-Leu	7.3 ± 1	350 kg NHL2	4 months	0.5 ± 0.05	Not-loaded – 14 tones (0.23 MPa)	105 tones (1.75 MPa)
2						Loaded – 36.3 tones (0.61 MPa)	102 tones (1.75 MPa)
3	Tervoux	37.3 ± 1	250 kg NHL3.5 + 100 kg Cement	2 months	1.5 ± 0.15	Not-loaded – 30 tones (0.5 MPa)	>200 tones (3.3 MPa) No rupture
4						Loaded – 141 tones (2.35 MPa)	200 tones (3.3 MPa)
5	Massangis	102.4 ± 6	200 kg NHL3.5 + 150 kg Cement	3 months	7 ± 3	Not-loaded – 26 tones (0.43 MPa)	>375 tones (6.25 MPa) No rupture
6						Loaded – 375 tones (6.25 MPa)	>375 tones (6.25 MPa) No rupture

To study the influence of mechanical loading at high temperatures, tests were conducted on walls with and without mechanical loading during heating. The vertical compression load for the loaded tests was set at 50% of the masonry's allowable load, proposed by the Eurocode, taking into account the compression strength of the stone, its mortar, and the wall geometry. After the fire, to assess the residual strength, all walls were subjected to mechanical loading until failure one day after cooling. The imposed load on the walls, representing the residual load, is presented in [Table 1](#).

The walls were constructed using stone blocks (or half-blocks) measuring 0.72 (0.36) m in length, 0.36 m in height, and 0.2 m in thickness, bonded together by a 0.01 m layer of mortar. The walls have a width of 2.92 m, a height of 2.97 m, and a thickness of 0.2 m. The walls were placed within a reinforced concrete frame, which comprises the frame's top beam affixed to the furnace's top beam and a U-shaped frame (According to the NF EN 1363-1 [[20](#)]). The U-shaped part of the frame has the possibility of moving in the vertical direction. The walls fitted into the frame with a 0.06m-wide rock wool strip on their lateral sides to ensure thermal insulation. A 0.02 m layer of mortar was applied to the bottom, while a 0.055 m layer was applied on top of the wall ([Figure 1](#)). The walls were exposed to a temperature rise according to the ISO 834-1 [[21](#)] curve for 120 minutes, reaching 1050°C in the furnace.

Temperature monitoring during heating was conducted using nine thermocouples inside the furnace situated 10 cm away from the exposed surface of the wall, five thermocouples on the unexposed surface, and six

thermocouples embedded in the blocks. Three blocks (named Block A, B, and C) were instrumented with these six thermocouples each, at different depths from the exposed side, at 1 cm, 2 cm, 5 cm, 8 cm, 12 cm, and 17 cm. These thermocouples are positioned within holes measuring 50 mm in length and 3 mm in diameter which have been drilled at different depths on opposite lateral faces of the blocks and filled with crushed stone powder to maintain consistent thermal measurement conditions. Five Linear Variable Differential Transformers (LVDTs) were placed on the unexposed side to measure the out-of-plane displacement of the wall, and two wire sensors recorded the vertical displacement of the wall between the top beam and the frame. The Digital Image Correlation (DIC) technique was also employed to obtain displacement fields in three directions.

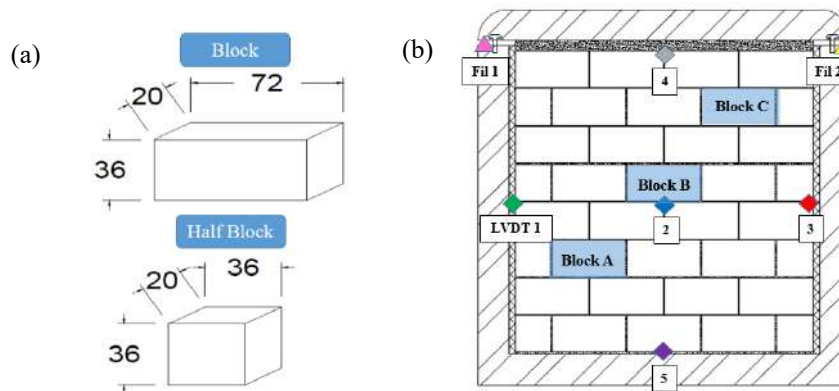


Figure 1. (a) Dimension of the block and half block; (b) The wall in the reinforced concrete frame with instrumented blocks by the thermocouples and LVDTs position

2.2 Experimental results

[Figure 2-a](#) illustrates the temperature evolution within the thickness of the wall obtained by the real exact position of thermocouples during heating tests for both loaded and not-loaded walls made of Tervoux stone. A relative dispersion, around 100°C, was observed for the temperatures recorded at one and two cm from the heated surface. This may be attributed to differences in the exact positions of the thermocouples in comparison to their theoretical positions. It also highlighted that due to the very high thermal gradient near the heated surface, a variation of one or two mm in the thermocouples' positions near to the heated surface can significantly impact the results. This behaviour and results were observed for all six walls. Furthermore, upon comparing the temperature profiles of the walls, it was noted that the temperature across the thickness of the walls made of Massangis stone was higher than that of the walls made of Tervoux and Saint-Leu stone ([Figure 2-b](#)). These findings are consistent with the thermal conductivity values of each type of stone [22].

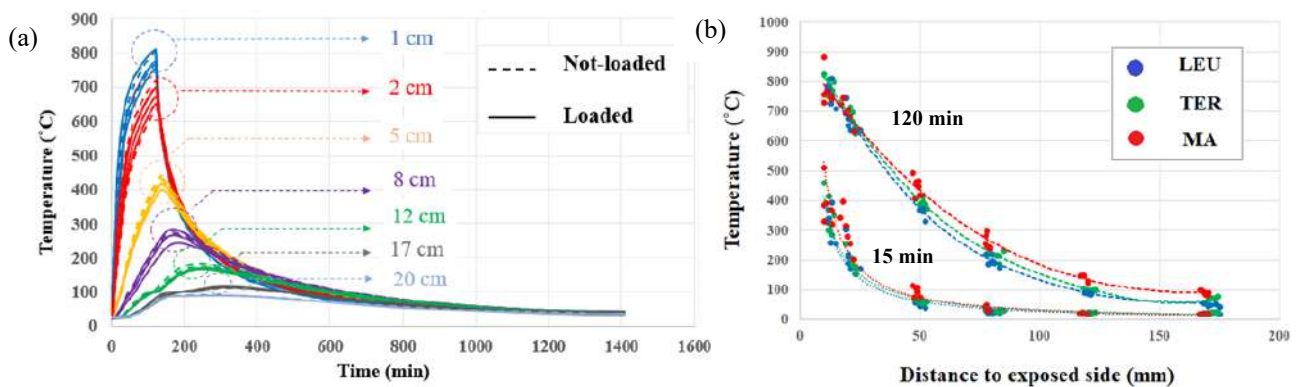


Figure 2. (a) The evaluation of temperatures in the thickness of the wall (example of the Tervoux walls); (b) The profile of temperature of the three studied limestones at different times of the heating

[Figure 3-a](#) illustrates the out-of-plane deformations for the not-loaded Tervoux wall determined on the non-exposed surface after 120 minutes of heating using the DIC technique. The results reveal symmetrical

displacement towards the fire, with two axes of symmetry along the X and Y axes passing through the centre of the wall. The most significant displacement occurs at the centre of the wall, decreasing towards the edges. The exact position of the LVDTs is presented in [Figure 1](#), and the results indicate that the LVDT placed in the middle of the wall recorded the maximum out-of-plane displacement ([Figure 3-b](#)). This symmetrical behaviour was observed for all 6 walls. [Figure 3-b](#) illustrates the time-dependent evaluation of out-of-plane displacement obtained by the LVDTs and the approximate positions of the LVDTs indicated by the DIC. It's important to note that while the values obtained by the DIC may not precisely correspond to the exact positions of the LVDTs due to limitations in the calculated area of the DIC, there is a strong correlation between the results of these two methods.

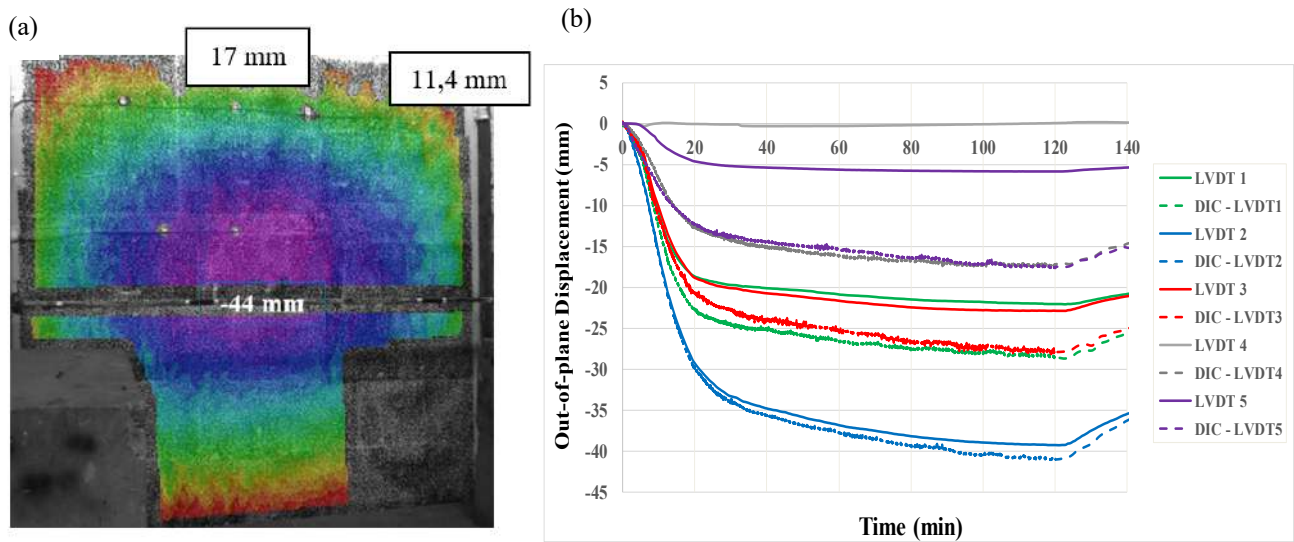


Figure 3. (a) The contour of out of plane displacement on the unexposed side of wall after 120 min of heating in Not-Loaded Tervoux wall; (b) The evaluation of the out-of-plane displacement on the same wall during the heating phase obtained by LVDTs and DIC

Moreover, results indicated that the not-loaded walls generally exhibit a higher out-of-plane displacement compared to the loaded walls ([Figure 4-a](#)). An exception is observed with the Saint-Leu wall, where the difference in the value of load between not-loaded and loaded tests is minimal. Corresponding to the ISO curve, the rapid initial heating leads to a higher rate of increase in out-of-plane displacement at the beginning of the heating process. At the end of the heating phase, the maximum deflection is observed for the not-loaded Tervoux wall (39 mm), followed by the not-loaded Massangis wall (32.7 mm), while the loaded Massangis wall shows the smallest deflection (6 mm). These observations also indicate the formation of bowing towards the heat source ([Figure 4-b](#)).

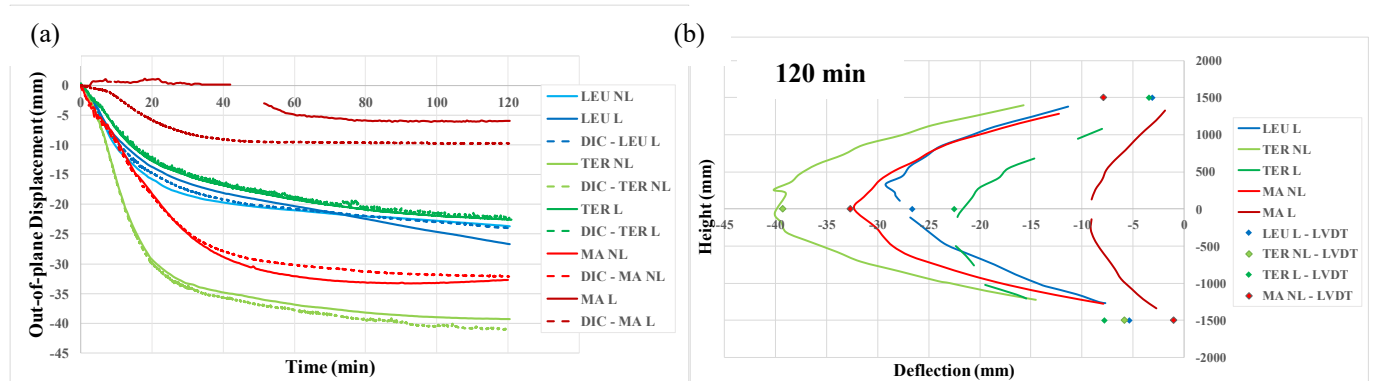


Figure 4. (a) The evaluation of the out-of-plane displacement in the middle of the wall during the heating in all six walls; (b) Deflection profiles along the height at mid-width of all the tested walls with the comparison to the LVDT values after 120 minutes of heating

During the early cooling phase, the walls experience a reduction in out-of-plane displacement, with varying degrees of reversibility observed. The not-loaded Tervoux wall exhibited the lowest reversibility at 45%, followed by 61.45% for the loaded Saint Leu wall, 64.87% for the loaded Tervoux wall, and 69.43% for the loaded Massangis wall. Meanwhile, the not-loaded Massangis wall demonstrated nearly complete reversibility at 94%.

In summary, upon observing the walls for two weeks' post-test, the observed cracking and the degradation on the exposed side of the walls can be explained by the section of the wall that experienced temperatures exceeding 730°C, as evidenced by [Figure 2](#) (and [Figure 5](#)). Approximately 10 mm of the wall reached temperatures over 730°C, triggering a decarbonation reaction that released CO₂ and CaO. Upon contact with moisture, these substances reacted to form portlandite, Ca(OH)₂, causing material expansion and potentially leading to cracks. This phenomenon is gradual and develops over several days following the test. This degradation, along with the reversibility of out-of-plane displacements observed in the walls, highlights the complex interplay between thermal effects, material properties, and structural behaviour under fire conditions.

3 NUMERICAL SIMULATION

The conducted numerical modelling aims to investigate the influence of the thermomechanical properties of the stones as well as the boundary conditions on the out-of-plane displacement of the walls during heating tests. Therefore, thermomechanical calculations using the finite element method were performed using Code-Aster (www.code-aster.org), a structural mechanics simulation software developed by EDF (Electricité de France). The presented thermomechanical modelling was carried out only for the loaded and not-loaded Tervoux stone walls.

3.1 Thermal modelling

The thermal modeling process relies on maintaining an energy balance, where the application of Fourier's law leads to the general equation of heat conduction in a presumed homogeneous body:

$$\vec{\nabla} \cdot [\lambda(T) \vec{\nabla} T] + P(\vec{r}) = \rho(T) C_p(T) \frac{\partial T}{\partial t} \quad (1)$$

Where T: temperature in K; λ : thermal conductivity in W.m⁻¹.K⁻¹; ρ : density in kg/m³; P: energy produced within the material in W/m³ (not considered in this study); and C_p: specific heat capacity in J.kg⁻¹.K⁻¹.

The thermal parameters used in the modelling (specific heat capacity and thermal conductivity) are considered as a functions of temperature [\[23\]](#).

Regarding the thermal boundary conditions, a convection boundary condition has been applied to both exposed and unexposed surfaces. The heated surface is exposed to the heating curve recorded in the furnace with a convection coefficient H = 200, and the unheated surface is exposed to a constant temperature of 25° with a corresponding convection coefficient of H = 5.

[Figure 5](#) illustrates the comparison between experimentally measured average temperatures and numerically predicted temperatures among the wall thickness during heating for the two walls made of Tervoux stone. Overall, the predicted temperatures closely align with the measured temperatures throughout the entire exposure duration. With the inclusion of the convection condition, the numerical model successfully obtained the temperature distribution across the exposed surface during the test. Additionally, given that the experimental data represent average values and the thermocouple positions were not consistently fixed, the numerically obtained temperature values for the 12mm thickness correlate better with the maximum experimental values for the 10mm thickness, which effectively represents the mean temperature for the 12mm thickness.

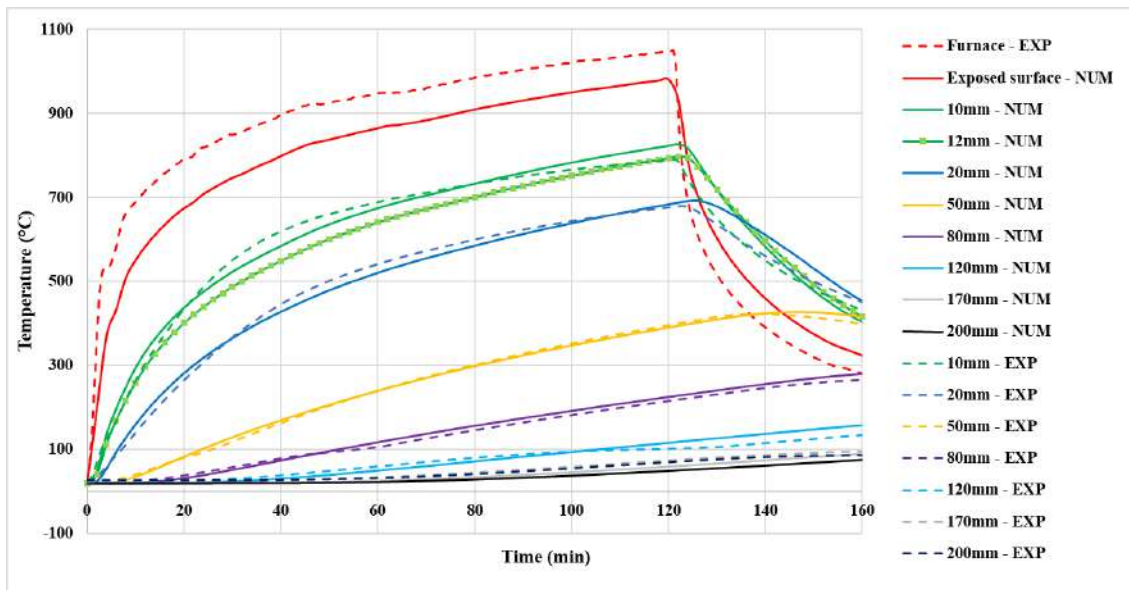


Figure 5. Temperatures measured within the thickness of the wall in Tervoux tests and with the numerical modelling

3.2 Mechanical modelling

In order to assess the influence of boundary conditions and the thermomechanical properties of stones on the overall behaviour of walls exposed to high temperatures, a thermo-elastic behaviour law was considered. The impact of mortar joints on the overall behaviour of walls was initially evaluated by considering two models: one taking into account stone blocks and mortar along with perfect contact and their temperature-dependent properties (heterogeneous), and the other model considering only the properties of the stone for the entire wall (homogeneous) (Figure 6). With symmetry conditions in mind, only a quarter of the wall was modelled in order to reduce the mesh's numbers.

Both models considered the same boundary conditions and simulated the not-loaded Tervoux wall. The out-of-plane displacement results showed no significant difference between the two models. Therefore, it can be concluded that the presence of a one-centimetre mortar joint between blocks in a three-meter wall has no notable influence on the overall behaviour of the wall in the context of thermo-elastic modelling.

To examine the effect of boundary conditions further, the subsequent modelling considered the homogeneous model.

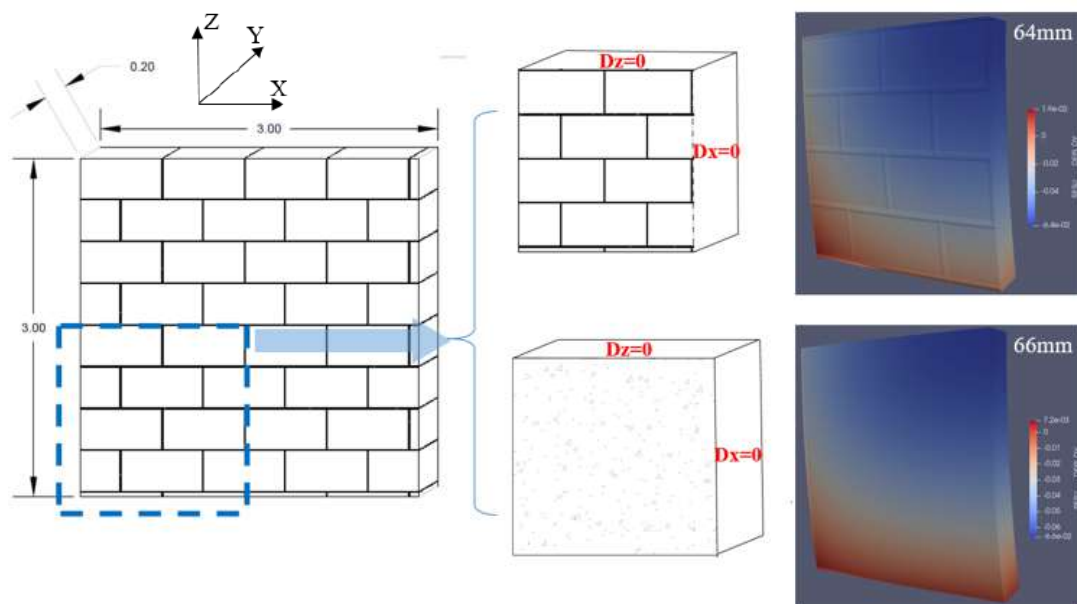


Figure 6. Modelling one-quarter of the wall with and without mortar joints to assess the effect of mortar joints

The walls were assembled within a U-shaped frame, with a beam placed on the upper surface of the wall. The upper beam was fixed in all three directions, while the U-shaped frame had the ability to move vertically. To assess the impact of boundary conditions, three configurations were compared by modelling half of the wall with symmetry conditions imposed on the vertical surface in the middle of the wall:

- Configuration I: The top surface of the wall was fixed in all three directions (X, Y, and Z), while the bottom surface was fixed only in the X and Y directions (to prevent the sliding of this surface) and free in the Z direction.
- Configuration II: Displacements were fixed in all three directions along the central line of the top surface of the wall, as well as in the X and Y directions along the central line of the bottom surface.
- Configuration III: The same boundary conditions as the second configuration were imposed on the two front lines (the lines common between the surfaces and the heated surface).

The objective of considering these three configurations (see [Figure 7](#)) is to evaluate the impact of boundary conditions on the distribution and the value of maximum out-of-plane displacement of the wall.

Furthermore, the influence of the loss of elasticity modulus of the stone with temperature on the thermomechanical behaviour of the walls was assessed by considering two different distributions of Young modulus depending on temperature, E1 determined at residual and E2 at high temperatures. The decrease in elasticity modulus with temperature is more significant for tests at high temperatures.

The diagrams illustrating the deformation of the not-loaded wall at the end of the heating phase for the different configurations are presented in [Figure 7](#). Configuration I shows an eccentric deformation pattern deviating from the symmetrical pattern observed experimentally.

[Table 2](#) shows the values of maximum out-of-plane displacement of the wall at the end of the heating phase for the three configurations with the two Young's modulus evolution curves along with the tests' results. It is noteworthy that the values for configuration I significantly underestimate the out-of-plane displacement recorded during the heating tests. For the other two configurations, the deformation patterns are almost similar and correspond to the pattern observed experimentally. However, the out-of-plane displacement is overestimated by these two configurations. These results indicate that to reproduce the deformation pattern obtained experimentally, it would be necessary to allow rotations at both the top and bottom contact surfaces. However, the overestimation of displacement by configurations II and III suggests that this rotation is not entirely free. Indeed, the presence of the mortar layer between the wall and the frame could contribute to adhesion between the wall and frame, thus partially preventing rotation of the contact surfaces.

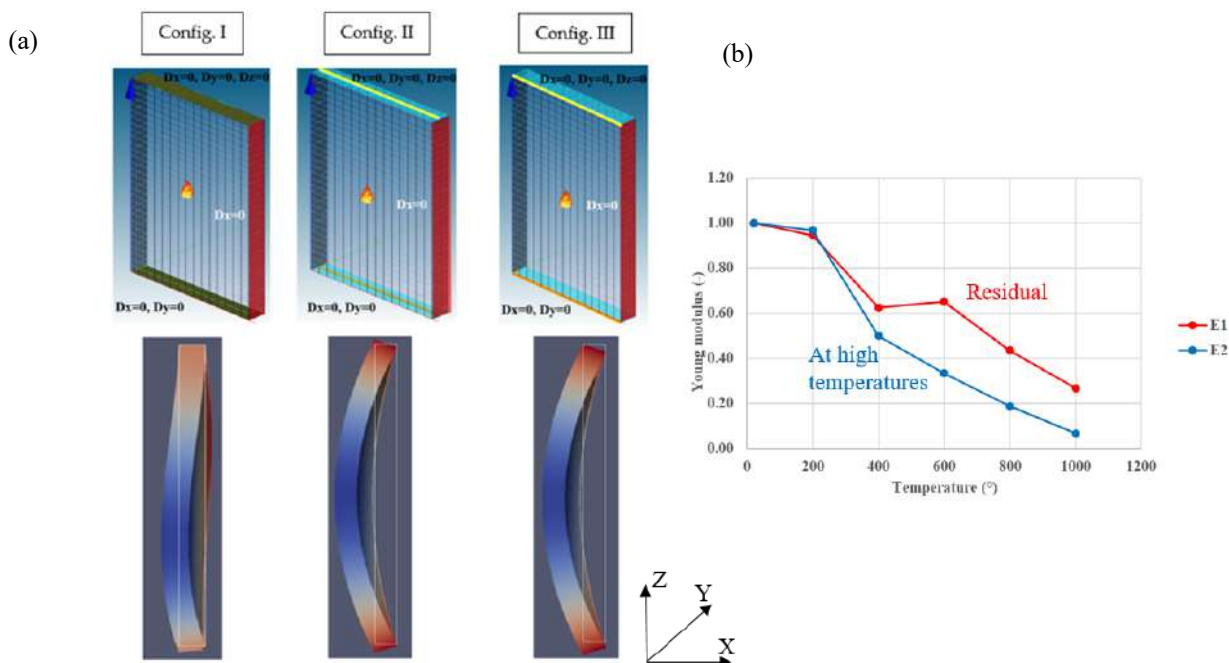


Figure 7. (a) The 3 configurations and the deformed shape of the wall after heating; (b) Evolution of residual Young's modulus (E1), and high temperature Young's modulus (E2) as a function of temperature

To model the loaded wall in Tervoux stone, configuration III was considered with a stress of 2.35 MPa applied directly to the bottom surface of the wall, simulating the load imposed by jacks positioned beneath the frame's lower beam. Despite efforts, the significant difference in out-of-plane displacement between loaded and not-loaded walls couldn't be replicated in the model. This divergence between experimental and numerical results can be partly explained by the fact that the mechanical load is applied numerically over the entire contact surface throughout the heating process despite its rotation. Indeed, due to the rotation of the lower surface of the wall during heating, the contact area between the frame and the wall diminishes. In other words, there is a progression of detachment of the wall from the frame, from the side of the unexposed surface to the heated surface. This leads to an eccentricity of load and consequently to an increase in stress on the heated side of the wall.

To model both the adhesion between the wall and the frame and the eccentricity of mechanical loading during heating, a system of springs was utilized (see [Figure 8](#)) and the bottom beam of the frame was modelled. The 336 springs on the upper surface of the wall, simulate the top mortar layer. Each spring is modelled as a discrete element with a length of 2 cm and with one end fixed in the X, Y, and Z directions and the other end attached to the upper surface of the wall. Additionally, there are 336 springs on the bottom surface, each to simulate the mortar layer between the wall and the lower beam. It's important to note that the modelled beam is a rigid beam capable of vertical movement (see [Figure 1-b](#)).

Table 2. Comparison of displacements between experimental testing and modelled configurations

Boundary conditions	Out-of plane displacement (mm)
Not-loaded Tervoux (Exp)	39
Loaded Tervoux (Exp)	22.5
Config I , not-loaded – E1	19
Config II , not-loaded – E1	53
Config II , loaded – E1	51
Config III , not-loaded – E1	52
Config I , not-loaded – E2	15
Config II , not-loaded – E2	42
Config III , not-loaded – E2	42

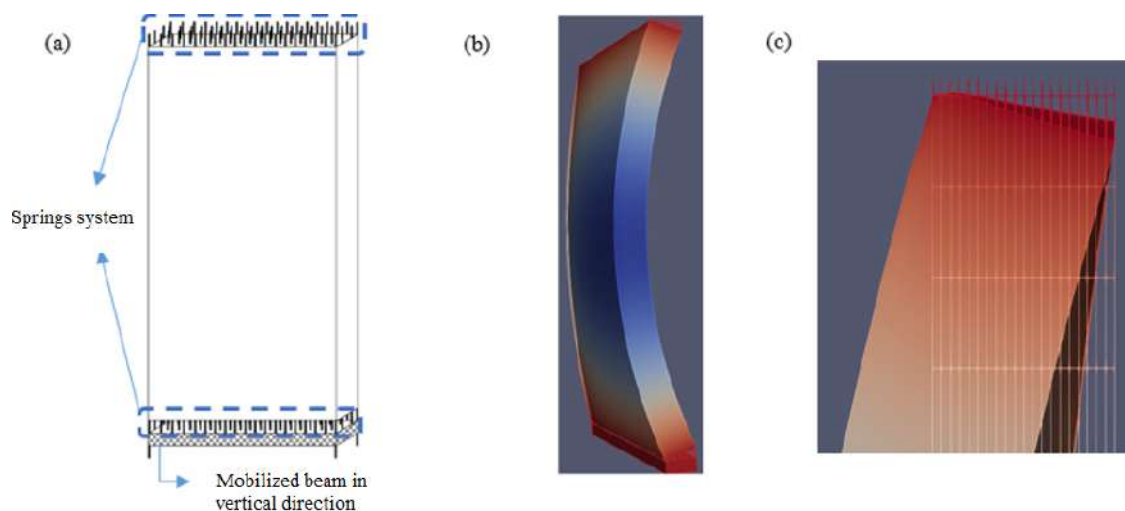


Figure 8. (a) Schematic of the wall modelled with the spring system; (b) deformed shape of the wall; (c) the rotation of the wall's top surface during the heating

The stiffness of the springs (discrete elements) is determined by considering the thickness of each mortar layer and the Young's modulus of the mortar. As a part of the parametric study, an elastic behavior in compression and perfectly plastic behavior in tension were considered for all springs (Figure 9-b). It should be noted that due to the deformed shape of the walls, the springs located on the exposed side of the wall work in compression, while the other springs work in tension.

Considering a tensile strength of 2 MPa, Figure 9-a compares the evolution of the experimental and numerical out-of-plane displacement at the center of the unexposed surface for a loaded and not-loaded Tervoux stone wall. Taking into account the spring system, the numerical results approximate the experimental results in the case of the not-loaded wall, and we could obtain a more significant difference between the loaded and not-loaded walls. However, the out-of-plane displacement in the case of the loaded wall is still overestimated by the model. This discrepancy between the numerical and experimental results could be reduced by considering transient strain which can play a considerable load specially in the loaded cases.

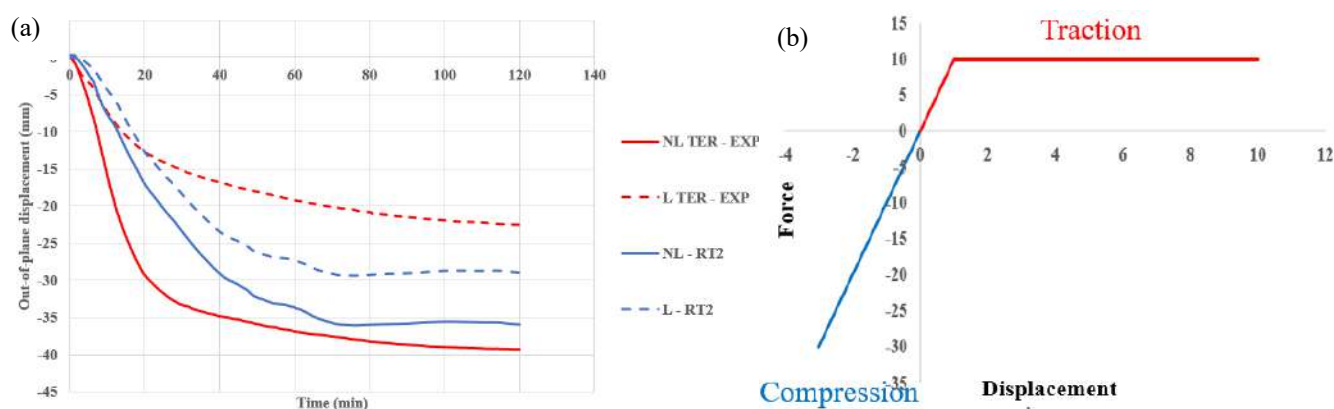


Figure 9. (a) Comparison of out-of-plane displacement at the centre of the wall between experiments and modelling; (b) Spring's behaviour model

4 CONCLUSIONS

This study deepens our understanding of the thermo-mechanical behaviour of limestone walls during fires by combining full-scale experimental tests and numerical simulations. The experimental phase sheds light on the influence of loading and the Young's modulus of limestone on the magnitude of thermal deformation. It is noteworthy that all six tested walls withstood two hours of heating without rupture; only material degradation due to temperature was observed. Additionally, for all six walls, only a portion of the out-of-plane displacements was reversible, which is crucial information for designing the residual load-bearing capacity of structures after a fire.

Furthermore, the 3D finite element modelling of masonry walls emphasizes the importance of boundary conditions during thermal testing simulations as well as the values of mechanical properties as a function of temperature. Our future research will integrate the interactions between mortar and stone to enhance understanding of damage mechanisms as well as impact of transient strain, thereby enriching our knowledge of stone masonry behaviour under high-temperature conditions.

ACKNOWLEDGMENT

The authors extend their gratitude to the partners of the POSTFIRE project for fruitful technical discussions, notably ROCAMAT for providing the limestone blocks and constructing the walls, as well as the CSTB team involved in conducting the tests. Special thanks are extended to Mr. Charuel, Mr. Cruz, and L. Gontier. We also acknowledge the financial support from the French National Research Agency (ANR), which has paved the way for scientific collaboration with CY Cergy Paris Université, CTMNC, ROCAMAT, LRMH, CSTB, and the University of Orléans.

REFERENCES

1. Lourenço PB, M. G. (2007). Analysis of masonry structures: Review of and recent trends in homogenization techniques. *Can J Civ Eng*, 34:1443–57.
2. PB., L. (2013). Computational strategies for masonry structures: multi-scale modeling, dynamics, engineering applications and other challenges. *Congr. Métodos Numéricos En Ing*, (pp. 1–17). Semni, Bilbao.
3. Salvatore Russo, F. S. (2013). Masonry exposed to high temperatures: Mechanical behaviour and. *Fire safety journal* 55, 69-86.
4. Cooke, G. (1988). Thermal bowing and how it affects the design of fire separating constructions. *Fourth Int. Fire Conf.* 22–24, March (pp. pp. 230-236). Church College Cambridge: Interflam 88.
5. A. Nadjai, M. O. (2006). Compartment Masonry Walls in Fire. *Fire Technology*, 211-231.
6. Lawrence S, G. N. (1987). The fire resistance of masonry walls, an overview. *First Natl Struct Eng Conf Melb*, (pp. pp. 8-26).
7. Martin Vigroux, J. E.-L. (2021). High temperature behaviour of various natural building stones. *Construction and Building Materials*.
8. Byrne. (1979). Fire resistance of load-bearing masonry walls. *Fire Technology*, 15:180-8.
9. Shields T, O. D. (1988). Thermal bowing of a model brickwork panel. Dublin. *Int. Brick/Block Mason. Conf.*, (pp. 846-56). Dublin
10. BS. (1987). *Fire tests on building materials and structures; Methods for determination of the fire resistance of load bearing elements of construction*
11. Laverty D, N. A. (2000). Modelling of thermo-structural response of concrete masonry walls subjected to fire. *Appl Fire Sci*, pp. 10:3–19.
12. Pham, D. T., Donval, E., Pinoteau, N., Pimienta, P., Pallix, D. (2022). Test of loaded and unloaded natural stone masonry walls exposed to fire, *Materials and Structures/Materiaux et Constructions*, 55/9, November 2022, art. 229
13. Donval, É. (2024). *Résistance au feu des murs de maçonnerie en pierre naturelle*. PhD thesis.
14. Gnanakrishnan N, L. R. (1989). Some aspects of the fire performance of single leaf masonry construction. *International Symposium on Fire Engineering for Building Structures and Safety*, 89/16, (pp. pp. 93–99). Melbourne.
15. Dhanasekar M, C. V. (1994). A numerical model for thermal bowing of masonry walls. *Tenth Int. Brick/Block Masonary Conf.* Calgari.
16. Nadjai A, O. M. (2003). Finite element modelling of compartment masonry walls in fire. *Computer Structure*, ;81:1923–30.
17. Nguyen T-D, M. F. (2014). Behavior of hollow clay brick masonry walls during fire. Part 2: 3D finite element modeling and spalling assessment. *Fire Safty*, pp. 66:35–45.
18. Pierre Pimienta; Armita Obaie; Elodie Donval; Duc Toan Pham; Albert Noumowe; Javad Eslami; Dashnor Hoxha. (2023). FIRE BEHAVIOUR OF LIMESTONE MASONRY DURING AND AFTER FIRE. *IFireSS 2023 – International Fire Safety Symposium*. Rio de Janeiro, Brazil.
19. NF DTU 20.1. (2020). *Ouvrages en maçonnerie de petits éléments – parois et murs*.
20. NF EN 1363-1 (2020) *Essais de résistance au feu-Partie 1'exigences générales*.
21. EN 1991-1-2. (2002). *Eurocode 1: Actions on structures -Part 1-2: General actions Actions on structures exposed to fire*.
22. Ayoub Daoudi, J. E.-L. (2023). High-temperature behaviour of various limestone used in heritage buildings at material and block scales. *ADVANCES IN FRACTURE AND DAMAGE MECHANICS*, (pp. Volume 2848, Issue 1). Spain.

23. Ayoub Daoudi, J. E.-L. (2024). EXPERIMENTAL CHARACTERISATION OF PHYSICAL, THERMAL, TRANSPORT AND MECHANICAL PROPERTIES OF 13 FRENCH LIMESTONES. *Building Engineering*

**NUMERICAL MODELLING OF
STRUCTURES IN FIRE**

A COMPUTATIONAL MODELING APPROACH FOR STEEL GRAVITY FRAMES WITH COMPOSITE FLOOR SYSTEMS SUBJECTED TO FIRE

Mohammed A. Morovat¹, Joseph A. Main², Jonathan M. Weigand³, Fahim H. Sadek⁴, Long T. Phan⁵

ABSTRACT

This paper describes the development and validation of a computational methodology to predict the behavior of steel gravity frames with composite floor systems subjected to fire. A full-scale compartment fire test conducted on a two-story steel gravity frame structure with a composite concrete floor slab on steel decking was used in the validation process. The experiment was conducted under combined gravity (self-weight plus external load) and fire loading in the National Fire Research Laboratory at the National Institute of Standards and Technology. The objective of the computational study, summarized in this paper, was to validate the adequacy of the computational modeling approach to capture the primary structural behavior and failure modes observed during the fire test and to provide additional insights into the structural performance. The computational model of the composite floor system was developed using the LS-DYNA finite element software and incorporated detailed modeling of the system components. The model adequately predicted the large deformations observed in the fire test of the composite floor assembly and captured its predominant deformation mechanisms, including lateral distortional buckling of the steel beams supporting the composite floor. Results from this study can further the implementation of performance-based design approaches for structural-fire safety in the U.S. and worldwide.

Keywords: Steel-framed buildings; composite floor systems; simulation and validation; thermal restraint; membrane action

1 INTRODUCTION

The applicability of standard fire resistance ratings in predicting the complex behaviors of steel frames with composite floor systems in fire has been a subject of ongoing research for decades. These research studies stemmed from observations in building fires where the performance of steel-framed buildings with composite floors differed from that prescribed by standard fire resistance ratings (e.g., the Broadgate Phase 8 fire [1]). These differences were attributed to system-level behaviors, including the development of tensile membrane action in the composite slab related to restraint of thermal expansion and the role of connections in the overall stability of steel frames with composite floors in fire. Such system-level behaviors are not captured in standard fire resistance tests of individual structural components or sub-assemblies.

¹ Guest Researcher, National Institute of Standards and Technology
e-mail: mohammed.morovat@nist.gov, ORCID: <https://orcid.org/0000-0002-2691-6151>

² Research Structural Engineer, National Institute of Standards and Technology
e-mail: joseph.main@nist.gov, ORCID: <https://orcid.org/0000-0003-0621-3137>

³ Research Structural Engineer, National Institute of Standards and Technology
e-mail: jonathan.weigand@nist.gov, ORCID: <https://orcid.org/0000-0002-6938-6197>

⁴ Research Structural Engineer, National Institute of Standards and Technology
e-mail: fahim.sadek@nist.gov, ORCID: <https://orcid.org/0000-0002-0424-5799>

⁵ Leader, Structures Group, National Institute of Standards and Technology
e-mail: long.phan@nist.gov, ORCID: <https://orcid.org/0009-0009-4322-6193>

To address the potential shortcomings of the standard fire resistance rating tests to adequately represent the performance of steel-framed buildings with composite floors in fire, sub-assembly and large-scale structural fire tests have been conducted around the world. One such experimental program included a series of three full-scale fire tests conducted at the National Institute of Standards and Technology (NIST) National Fire Research Laboratory (NFRL) on composite floor systems subjected to compartment fires. The main objective of this experimental program was to study the system behavior of the composite floor systems (with different slab reinforcement details and different schemes of spray-applied fire-resistive materials on supporting beams) subjected to large enclosure fires that closely resemble the standard fire exposure. The single-plate shear beam-to-column, beam-to-girder, and girder-to-column connections were the same in the three tests conducted at the NIST NFRL. The two-story steel gravity frame in the NIST NFRL experiments was designed based on U.S. practices with a 2-hour fire-resistance rating. A detailed description of the composite floor system tested in the NIST NFRL experiments can be found in NIST Technical Note 2165 [2].

To validate the adequacy of the computational methods in modeling the structural behavior and failure modes of steel frames with composite floor systems in fire, and to extend the scope of large-scale fire tests beyond their inherent limitations (such as the specimen size and the fire exposure type), a computational study was performed to develop validated analytical tools capable of modeling the complex behavior of multistory composite steel-framed structures in fire. This paper provides a summary of this study where the development and validation of the adopted modeling approach using the Composite Floor Test #2 (CF2 Test) of the NIST NFRL experiments are described and major findings are presented. First, important features of the CF2 Test are summarized. This is followed by an overview of the development of the computational model of the composite steel-framed structure. Representative results highlighting the validation of the modeling approach are then provided. The paper concludes with a summary of major observations, limitations of the current study, and recommendations for future work.

2 DESCRIPTION OF THE CF2 TEST

2.1 Composite steel frame: structural components

A two-story composite steel frame, two by three bays in plan, was tested in the NFRL. This composite steel frame consisted of a lightweight concrete floor slab on steel deck, W16×31 beams, W18×35 girders, and W12×106 columns. The composite floor system was reinforced with No. 3 deformed reinforcing bars spaced at 305 mm on center (230 mm²/m) in orthogonal directions. Figure 1 shows the details of the composite W16×31 beam and composite W18×35 girder sections for the CF2 test specimen. The composite floor assembly was designed based on the 2-hour fire-resistance rating requirement for steel-framed structures in the International Building Code [3]. Further, as seen in Figure 2, all the beam-to-column, beam-to-girder, and girder-to-column connections in the test bay were single-plate shear connections.

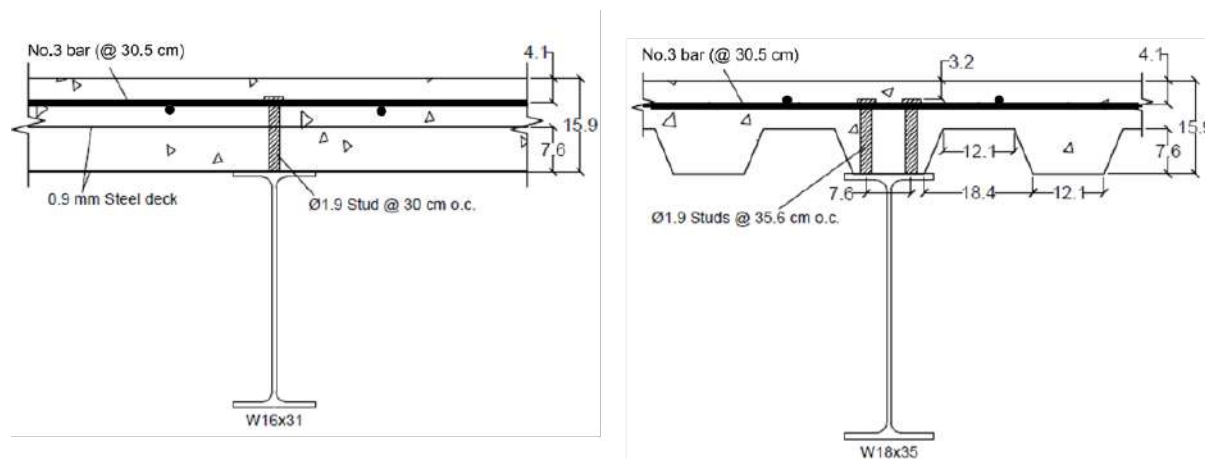


Figure 1. Composite beam and girder sections in the CF2 Test [4] (units in cm; W-shapes in U.S. customary units)



Figure 2. (a) Beam- and girder-to-column and (b) beam-to-girder single-plate shear connections in the CF2 Test [4] (W-shapes in U.S. customary units)

2.2 Composite steel frame: compartment fire exposure

The composite floor with plan dimensions of 9.1 m \times 6.1 m was subjected to a compartment fire during the CF2 Test. As shown in Figure 3, this fire tested slab was in the south middle bay of the composite steel frame.

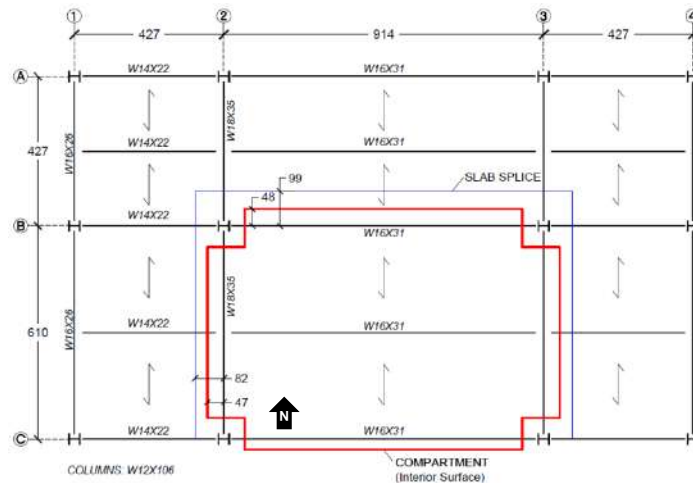


Figure 3. Plan view of the fire-tested slab in the CF2 Test [4] (units in cm; W-shapes in U.S. customary units)

3 COMPUTATIONAL MODEL: DEVELOPMENT

3.1 Material

Successful modeling of the behavior of composite steel-framed structures in fire depends on employing material models that accurately capture their stiffness and strength degradation when subjected to the elevated-temperatures induced by fire. This section briefly describes the material models used in the finite element simulation of the composite steel-framed structure subjected to the fire in the CF2 Test. Detailed information on material modeling can be found in NIST Technical Note 2269 [5].

The *MAT_ELASTIC_VISCOPLASTIC_THERMAL (MAT_106) material model in LS-DYNA [6] was used to represent the mechanical behavior of structural steels (ASTM A992 and ASTM A36), bolts, and shear studs by defining curves governing the elastic and viscoplastic behavior of structural steel for temperatures ranging from 20 °C (ambient temperature) to 1200 °C (beyond the maximum temperatures measured in the CF2 Test). The true stress-true strain curves developed in this study for the ASTM A992 and ASTM A36 steels were enhanced models originally described by Seif et al. [7 – 8] with improved capability to model low- or high-strength steels. Representative stress-strain curves for the material models of ASTM A992 and ASTM A36 steels are shown in Figure 4(a), and Figure 4(b), respectively.

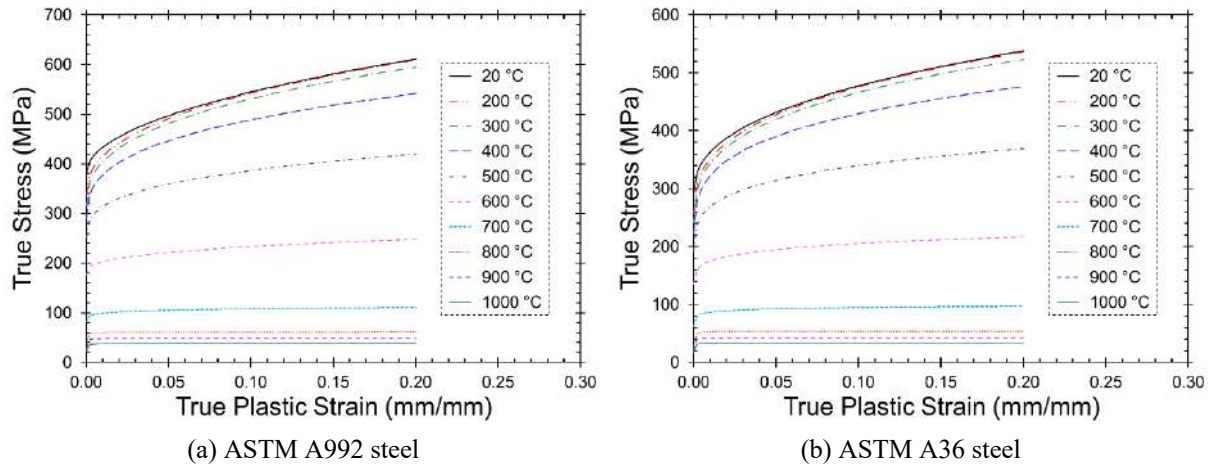


Figure 4. True stress-true strain models for structural steels: (a) A992 steel; (b) A36 steel [5]

A reduced-order modeling approach was used for the bolted connections, in which a temperature-dependent load-displacement relationship was defined for each bolt row of the connection (see Figure 5), based on a component-based connection model for single-plate shear connections at ambient temperatures developed by Weigand [9]. The temperature-dependence was included by incorporating temperature-dependent mechanical properties for the shear plate steel, the beam web steel, and the bolt steel directly into the mechanical equations used to capture the connection response. The resultant load-displacement relationships for the connection component spring at various temperatures, obtained by integrating the force-deformation relationships for the various connection components, are shown in Figure 5(b). The load-displacement curves shown in Figure 5(b) were implemented in the model of the composite floor system by representing each bolt row in a connection using a single hexahedral solid element, with the force-displacement relationships converted to stress-strain relationships by scaling based on the element's cross-sectional area and length [5].

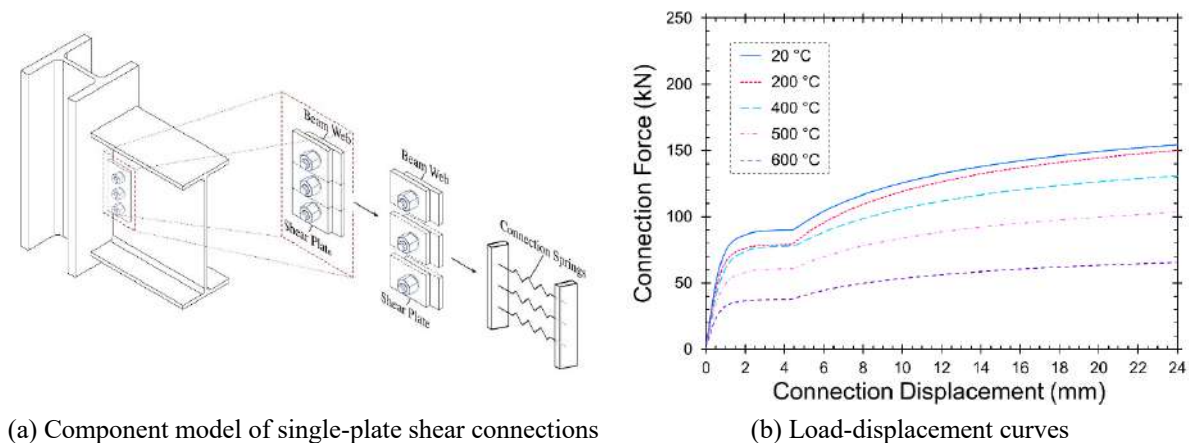


Figure 5. Force-displacement model for the connection component spring at elevated temperatures: (a) Load-displacement curves; (b) Discretization of single-plate shear connection into connection springs [5]

Similar to the bolt rows of the single-plate shear connections, a reduced-order modeling approach was used for the shear studs, in which each shear stud was represented using a temperature-dependent load-displacement relationship intended to capture the resultant shear force versus slip behavior of a shear stud embedded in a composite concrete floor slab. The temperature-dependent load-displacement model for shear studs was developed using the empirical load-slip relationship proposed by Ollgaard et al. [10] at

ambient-temperature (shown as a dashed line in Figure 6(a)). Based on experimental measurements from ambient-temperature testing of a composite beam [11], a new load-slip model was developed for shear studs at ambient temperature (shown as a solid line in Figure 6(a)). As shown in Figure 6(a), this new model follows the model proposed by Ollgaard et al. [10] up to a maximum shear strength (Q_{max}) of 85% of the ultimate shear strength of the shear stud (Q_u) with the shear force remaining constant at this maximum value until a slip of 3 mm is reached, at which point the shear force drops linearly to zero at a slip of 5 mm. The temperature-dependent load-slip curves for the shear studs shown in Figure 6(b) were then developed by scaling the ambient-temperature load values at each temperature level using the reduction factors determined for the yield strength of high-strength structural bolts by Weigand et al. [12].

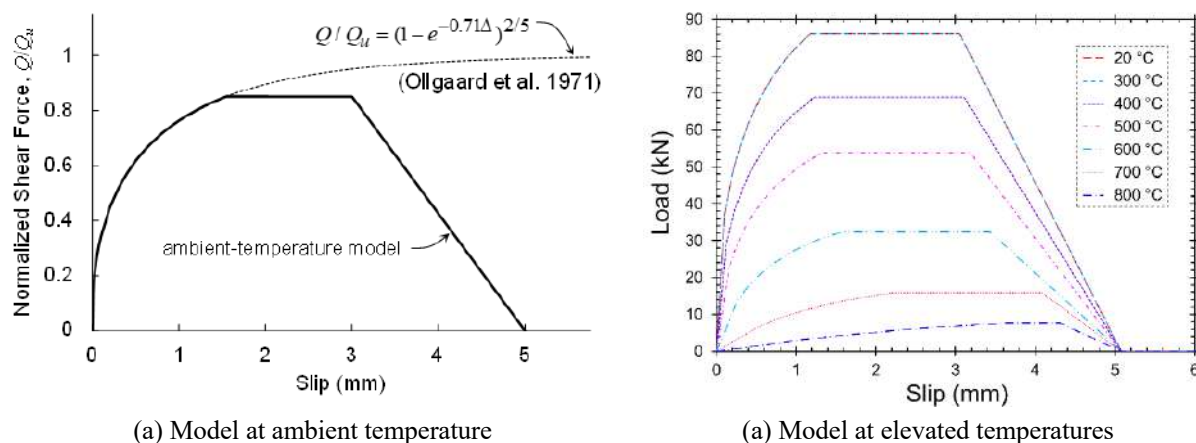


Figure 6. (a) Ambient temperature and (b) temperature-dependent load-slip models for shear stud at elevated temperatures

Similar to the bolted single-plate shear connections, the load-displacement relationships in Figure 6(b) were implemented in the model of the composite floor system by representing each shear stud using a single solid hexahedral element, with stress-strain relationships obtained by scaling the target load-displacement relationships based on the element's cross-sectional area and length.

Finally, the *MAT_CONCRETE_EC2 (MAT_172) material model in LS-DYNA [6] was used to capture the material behavior of concrete in the composite slab at elevated temperatures. The stress-strain curves in this material model for concrete and reinforcing bars at ambient and elevated temperatures were based on the Eurocode 2 (EC2) [13]. The MAT_172 material model was used to model concrete, steel decking, and embedded steel reinforcement as distinct layers in a composite shell element formulation. Using the MAT_172 model, the influences of crushing of concrete in compression and cracking of concrete in tension were specifically captured. The potential for spalling of concrete at elevated temperatures was not considered in this model.

3.2 Geometry

Elements of the composite steel-framed floor system in the NIST NFRL CF2 Test were explicitly modeled in LS-DYNA. Specifically, Belytschko-Tsay four-node shell elements [6] were utilized to discretize the steel plates, angles, beams, girders, and columns. Eight-node hexahedral solid elements were used for reduced-order modeling of bolts and shear studs. The composite slab was modeled in LS-DYNA adopting the reduced-order approach previously developed and validated by NIST researchers [14]. In this approach, the composite slab (the concrete slab, steel reinforcement, and profiled steel decking) was modeled using alternating strips of shell elements representing the thick and thin portions of the composite slab. Using the *PART_COMPOSITE feature in LS-DYNA, a four-node layered composite shell formulation with distinct structural material, thermal material, and thickness was specified for each layer. Distinct layers were specified for the steel decking and the steel reinforcement, with multiple layers representing concrete specified through the thickness of the slab. Detailed information on modelling the geometry of composite steel-framed floor system is provided in NIST Technical Note 2269 [5].

3.3 Mechanical and thermal loads

The applied loads and temperatures in the computational model of the composite floor test followed the mechanical and thermal loads used in the NIST NFRL CF2 Test. Specifically, a total gravity load of 5.2 kPa was applied to the test-bay floor slab. This total gravity load included the floor self-weight and the 2.5 kPa external load applied using hydraulic jacks (24 point loads of 6.2 kN). Additionally, measured temperatures in different components of the composite floor system due to exposure to the compartment fire during the CF2 Test were used as input temperatures in lieu of a thermal analysis. This approach eliminated the need to consider uncertainties associated with the heat transfer analysis and their influence on the overall capability of the model in capturing the structural response to the fire environment, allowing for a simplified validation of the modeling approach by conducting structural analysis only. Representative temperature assignments in the model are shown in Figure 7, where the temperature histories for the web of the middle W16×31 beam of the tested slab are plotted. In this case, the measured temperatures at the mid-height of the web (location TB6_3) were selected as prescribed temperatures for the web of the middle W16×31 beam.

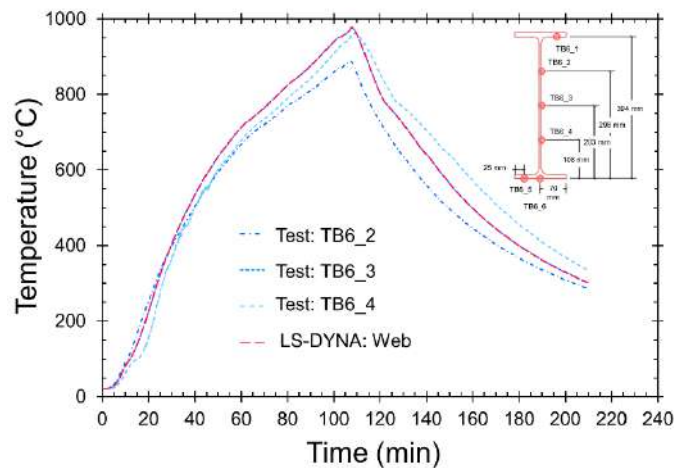


Figure 7. Measured and applied temperature histories at the web of the middle W16×31 beam

4 COMPUTATIONAL MODEL: RESULTS AND VALIDATION

4.1 Displacements

The structural response of the composite floor system to the fire exposure was used to compare the analysis and the experimental results. Particularly, displacements, including vertical displacements of the composite slab of the fire-tested floor, vertical and horizontal (lateral) displacements of the supporting steel beams, and horizontal (lateral) displacements of steel columns of both the fire-tested floor and the surrounding floors were used in validating the model. The computational results were only validated for the heating stage, up to the maximum gas temperature in the fire compartment, while the results and observations from the fire experiment corresponded to a temperature-time exposure that included an uncontrolled cooling stage after halting the fire application.

Figure 8 shows sample results of the validation where experimental and finite element predictions of the slab displacements are compared throughout the fire exposure and up to the maximum fire temperature. Despite some differences in the displacement rate at the beginning of the fire test, good agreement is generally observed between the measured and computed slab displacements. Specifically, the percent deviation between the experimental and computational slab displacements corresponding to the maximum fire temperature was about 0.3 %.

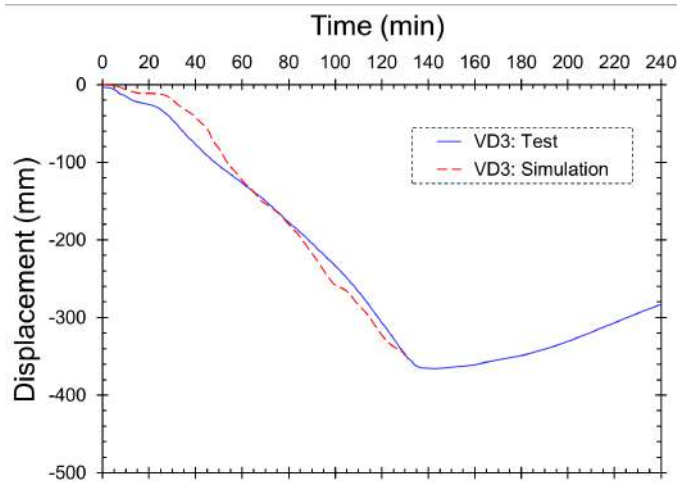


Figure 8. Simulated and measured vertical displacement histories at the center of north half of the tested slab

Figure 9 shows further results of the validation where measured and computed vertical displacements at the midspan of the middle W16×31 beam of the fire-tested floor are shown. As seen in the figure, good agreement is observed between the measured and computed beam displacements. Specifically, the percent deviation between the experimental and computational beam displacements corresponding to the maximum fire temperature was about 0.4 %.

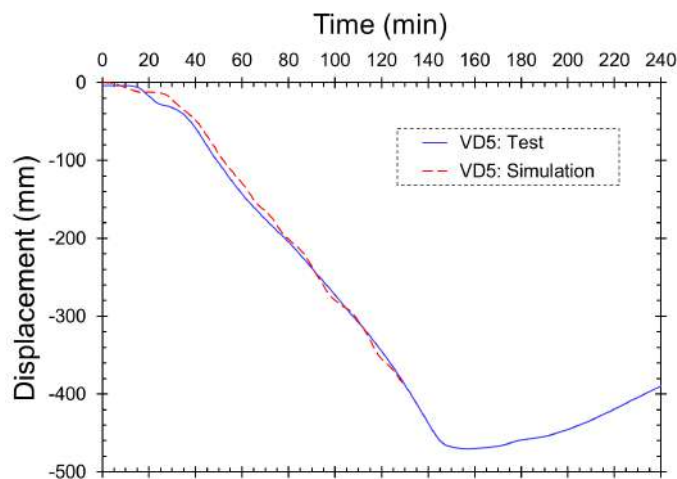


Figure 9. Simulated and measured vertical displacement histories at the midspan of the middle W16×31 beam

4.2 Deformation-related failure mechanisms

The computational model was also validated based on the deformation mechanisms observed in the experiment, including the lateral distortional buckling of W16×31 beams of the fire-tested slab. A sample result is provided in Figure 10, where the predictions of the lateral displacement of secondary beams are compared with those from the experiment. As can be seen in Figure 10, due to the significant lateral displacements of their lower flanges, the north and south beams exhibited lateral deformation resembling that of lateral distortional buckling. As seen clearly in Figure 10, the computational model could predict the lateral deformation mechanism of the W16×31 beams caused by the applied load and the restrained thermal expansion corresponding to the maximum fire temperature.



Figure 10. Simulated and observed lateral displacement of bottom flanges of the north, and south W16×31 beams (test pictures are from Choe et al. [4])

Formation of cracks in composite slabs results in direct exposure of slab reinforcement to fire temperatures that can impact the tensile membrane action of the composite slab and compromise the overall stability of composite steel-framed structures in fire. Therefore, the ability of the computational model to capture concrete damage in the composite slab was of particular interest. In the analysis of composite steel-framed structure, the effective plastic strain was adopted to predict damage (indicative of crack formation) in the composite slab under the applied load and increasing temperatures.

Figure 11 illustrates the observed crack pattern from the experiments and the damage pattern obtained from the computational model. As can be observed from Figure 11, the model could predict the development of concrete damage in the composite floor slab with acceptable accuracy.

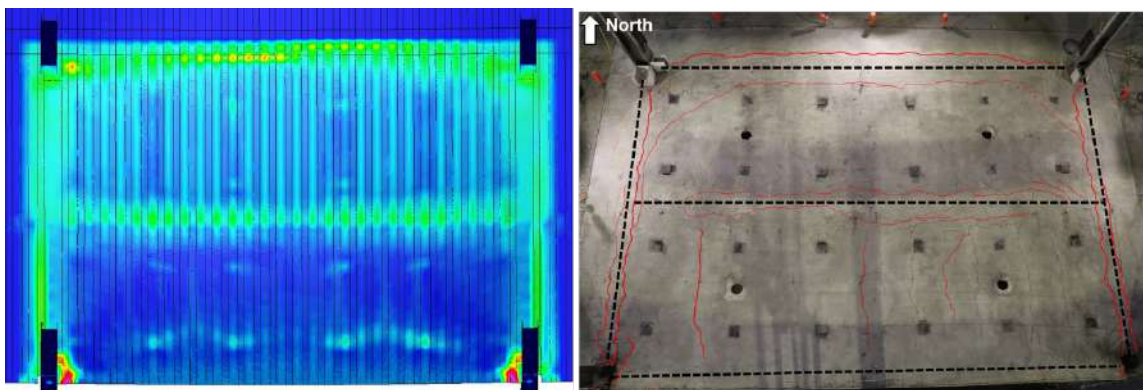


Figure 11. Simulated and observed damage and cracking in the composite slab of the test bay (test pictures are from Choe et al. [4])

4.3 Forces

The validated model was further used to examine the forces in secondary beams that were not directly measured in the test. Figure 12 shows a plot of axial force histories for the north, middle, and south beams obtained at beam ends in the simulation. As seen in Figure 12, the north beam with the highest degree of thermal restraint exhibited significant axial load levels during the exposure to elevated temperatures. The high axial force demand for the north beam also explains the significant twist in the cross section and lateral distortional behavior of this beam as discussed in the previous section and illustrated in Figure 10.

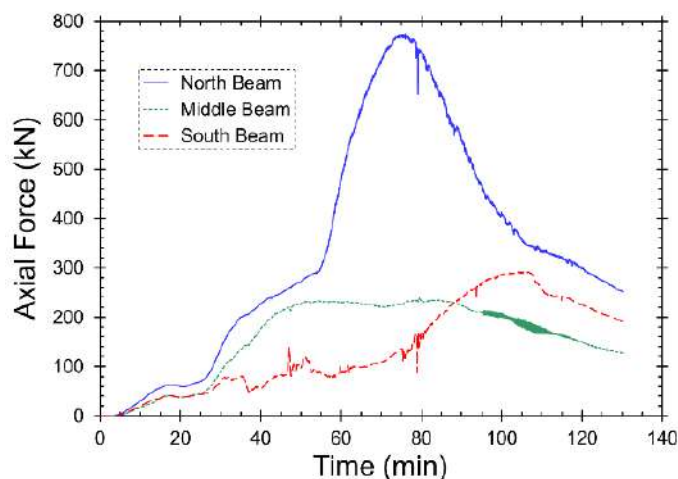


Figure 12. Simulated axial force histories for the north, middle, and south beams

5 CONCLUDING REMARKS

Using the results from the validated computational approach presented in this paper, the following key observations can be made:

- The simulation adequately captured the deformations (displacements) of different components of the composite floor assembly (i.e., steel beams and composite slab). The accuracy of the model was quantified as the percentage difference between the computed and measured displacements at the end of the simulation, which occurred after 130 minutes of fire exposure, corresponding to the maximum fire temperature reached in the CF2 Test. For example, the vertical displacement at the middle of the fire-tested slab obtained from the computational model agreed with that observed in the NFRL CF2 Test with a maximum percent deviation of 7 %.
- The computational model captured the deflections of the W16×31 beams of the fire-tested composite floor within 12 %. The model further captured the deformation-related stability failure mechanisms observed in the experiment, such as lateral distortional buckling of steel beams.
- Additional research is needed to better understand how behavior of connections might affect the overall behavior of steel-composite frame buildings, especially in the cooling phase of the fire.

Moreover, the developed computational approach to model the behavior of composite floor systems in fire has the following limitations:

- Rather than performing a coupled thermal-structural analysis, this study used a temperature-dependent structural analysis approach in which measured temperature-time histories obtained from the fire experiment were prescribed as nodal temperature histories in the finite element model. However, the computational modeling approach presented in this study is suitable for coupled thermal-structural analysis, and future modelling efforts can consider heat transfer analysis in conjunction with the structural analysis.
- The results and observations from the validated computational model are limited to fire conditions with rising temperatures. Consequently, the computational approach has not been validated for the cooling phase of the fire exposure.
- The results and observations from the validated computational model are limited to the specific type of connections used in the full-scale experiment. Specifically, the computational approach was validated for a steel frame with single-plate shear connections.
- The steel columns in the composite steel frame of the CF2 Test were not subjected to thermal loads. Therefore, the model is validated for conditions where only the slab, steel beams, and connections are exposed to fire, not the supporting columns.

REFERENCES

1. Mwangi, S., Why Broadgate Phase 8 composite floor did not fail under fire: Numerical investigation using ANSYS® FEA code. *Journal of Structural Fire Engineering* 8(3), 238–257 (2017). <https://doi.org/10.1108/JSFE-05-2017-0032>.
2. Choe, L, Ramesh, S, Dai, X, Hoehler, M, Bundy, M, Bryant, R, Story, B, Chakalis, A, Chernovsky, A: Fire Resilience of a Steel-Concrete Composite Floor System: Full-Scale Experimental Evaluation for U.S. Prescriptive Approach with a 2-Hour Fire-Resistance Rating (Test #1), NIST Technical Notes (TN) 2165. National Institute of Standards and Technology, Gaithersburg; 2021. <https://doi.org/10.6028/NIST.TN.2165>.
3. International Code Council IBC 2021 – International Building Code, International Code Council, Washington, DC, 2021.
4. Choe, L, Hoehler, M, Bundy, M, Bryant, R, Story, B, Chakalis, A, Chernovsky, A, Ramesh, S, Dai, X: Fire Resilience of a Steel-Concrete Composite Floor System: Full-Scale Experimental Evaluation for Influence of Slab Reinforcement (Test #2), NIST Technical Notes (TN) 2203. National Institute of Standards and Technology, Gaithersburg; 2022. <https://doi.org/10.6028/NIST.TN.2203>.
5. Morovat, M, Main, J, Weigand, J, Ammons, M, Sadek, F, Phan, L: Analysis of a Steel Gravity Frame with Composite Floor System Subjected to Compartment Fire (Test #2), NIST Technical Notes (TN) 2269. National Institute of Standards and Technology, Gaithersburg; 2023. <https://doi.org/10.6028/NIST.TN.2269>.
6. LSTC (Livermore Software Technology Corporation) LS-DYNA Keyword User’s manual, R9.0, Livermore Software Technology Corporation, Livermore, CA, 2016.
7. Seif, M, Choe, L, Main, J, Zhang, C, Weigand, J, Gross, J, Sadek, F, McColskey, D, Luecke, W: Temperature-Dependent Material Modeling for Structural Steels: Formulation and Application, NIST Technical Notes (TN) 1907. National Institute of Standards and Technology, Gaithersburg; 2016. <https://doi.org/10.6028/NIST.TN.1907>.
8. Seif, M., Main, J., Weigand, J., McAllister, T. & Luecke, W., Finite element modeling of structural steel component failure at elevated temperatures. *Structures* 6(5), 134–145 (2016). <https://doi.org/10.1016/j.istruc.2016.03.002>.
9. Weigand, J., Component-Based Model for Single-Plate Shear Connections with Pretension and Pinched Hysteresis. *Journal of Structural Engineering* 143(2), 04016178 (2017). [https://doi.org/10.1061/\(ASCE\)ST.1943-541X.0001662](https://doi.org/10.1061/(ASCE)ST.1943-541X.0001662).
10. Ollgaard, J., Slutter, R. & Fisher J., Shear strength of stud connectors in lightweight and normal-weight concrete. *Engineering Journal, American Institute of Steel Construction* 8(2), 55–64 (1971).
11. Ramesh, S, Choe, L, Seif, M, Hoehler, M, Grosshandler, W, Sauca, A, Bundy, M, Luecke, W, Bao, Y, Klegseth, M, Chen, G, Reilly, J, Glisic, B: Compartment Fire Experiments on Long-Span Composite-Beams with Simple Shear Connections Part 1: Experiment Design and Beam Behavior at Ambient Temperature, NIST Technical Notes (TN) 2054. National Institute of Standards and Technology, Gaithersburg; 2019. <https://doi.org/10.6028/NIST.TN.2054>.
12. Weigand, J., Peixoto, R., Vieira, L., Main, J. & Seif, M., An empirical component-based model for high-strength bolts at elevated temperatures. *Journal of Constructional Steel Research* 147(8), 87–102 (2018). <https://doi.org/10.1016/j.jcsr.2018.03.034>.
13. CEN EN 1992-1-2 Eurocode 2, Design of Concrete Structures – Part 1-2: General Rules – Structural Fire Design, European Committee for Standardization, Brussels, Belgium, 2004.
14. Jiang, J, Main, J, Sadek, F, Weigand, J: Numerical Modeling and Analysis of Heat Transfer in Composite Slabs with Profiled Steel Decking, NIST Technical Notes (TN) 1958. National Institute of Standards and Technology, Gaithersburg; 2017. <https://doi.org/10.6028/NIST.TN.1958>.

A NUMERICAL INVESTIGATION ON FIRE RESISTANCE OF STEEL WAREHOUSE BASED ON FIRE PROTECTION OPTIMIZATION

Pegah Aghabozorgi¹, Aldina Santiago², Luís Laím³

ABSTRACT

This study focuses on enhancing fire resistance in steel warehouses by optimizing fire protection design. Firstly, using thermal properties previously established for gypsum-based board insulation coatings, numerical models for heat transfer and thermomechanical analyses are developed using Abaqus finite element software. The main objective is to determine the optimal thickness of fire protection boards to ensure fire safety within the portal frame under elevated temperatures, assuming a frame fire resistance rating of R60. Following this, a parametric study is conducted to assess how various factors, including thermal actions and portal frame dimensions, influence the optimal thickness of fire protection and overall fire resistance of the frame. This iterative process contributes to refining optimized fire protection design strategies and enhancing overall fire safety protocols for steel warehouses.

Keywords: Steel warehouses; Fire protection mortars; Numerical analysis; Fire protection optimization, Fire design.

1 INTRODUCTION

Industrial steel warehouses play a pivotal role in various industries, facilitating storage, manufacturing, and distribution. However, their vulnerability to fire poses a significant risk, potentially jeopardizing the structural integrity of steel elements when exposed to elevated temperatures. To address this concern, this study focuses on enhancing the fire performance of steel portal frame elements within warehouses by applying gypsum-based board insulation coatings known for their exceptional thermal insulation capacity [1].

The thermal properties of these fire protection (FP) boards have been previously evaluated through thermal analysis tests conducted at the ISISE laboratory at the University of Coimbra [2,3]. Previous studies has confirmed the efficacy of these materials in providing the thermal protection for structural steel elements and improving their fire resistance [4–6].

This research specifically aims to assess the effectiveness of this gypsum-based fire protection boards when applied to the primary structural elements of the portal frame. The objective is to determine the maximum allowable thickness (or the optimal thickness) for these fire protection boards, ensuring the portal frame's resistance to elevated temperatures and during 1-hour exposure to fire (R60). This assessment involves comprehensive heat transfer and thermomechanical analyses using finite element (FE) software, Abaqus [7]. Therefore, two industrial warehouses with different heights were selected as case studies. FE models were developed in Abaqus (version 2021) [7] for each case. To begin with, identical thicknesses of FP material

¹ Ph.D. Researcher, University of Coimbra, ISISE, ARISE, Department of Civil Engineering, Coimbra, Portugal
e-mail: pa@uc.pt, ORCID: <https://orcid.org/0000-0002-9041-5693>

² Associate Professor, University of Coimbra, ISISE, ARISE, Department of Civil Engineering, Coimbra, Portugal
e-mail: aldina@dec.uc.pt, ORCID: <https://orcid.org/0000-0003-3646-4926>

³ Assistant Professor, University of Coimbra, ISISE, ARISE, Department of Civil Engineering, Coimbra, Portugal
e-mail: luislaim@uc.pt

(gypsum-based fire protection mortar with perlite) were applied to both rafters and columns across a range of values for the case with smaller height (Case 1). This aimed to identify the optimal FP thickness for a one-hour fire resistance (R60) under the ISO-834 standard fire curve [8] and vertical loadings. The optimal FP thickness for rafters and columns was determined through an iterative process in Abaqus.

Then, a parametric analysis is conducted to consider previously unaddressed factors in optimizing fire protection for steel warehouses. Firstly, a natural fire curve was generated using CFAST software (version 7.7.0) [9] for comparison with the standard fire scenario. CFAST (Consolidated Model of Fire and Smoke Transport) [10] used a two-zone model approach, requiring key compartment features such as fire load, openings, and the compartment dimensions for calculating the temperature evolution. In this scenario, the fire was located at the center of a compartment with the dimension of 25m×25m for the floor area and a floor-to-ceiling height of 8.9m. Two 3m×3m openings were included in the façade, while the roof remained sealed with no opening. Given the industrial nature of the structure, a rapid fire growth rate was assumed, with a fire load density (FLD) of 1755 MJ/m², a maximum heat release rate (HRR) of 35 MW (according to EN 1991-1-2 [11]), a fire load area of 36 m², and wood as the primary combustion material, with a heat combustion value of 17500 kJ/kg.

Secondly, the impact of roof openings on fire protection requirements for a steel portal frame in an industrial warehouse was investigated. In this regard, two fire scenarios were considered, both with a compartment floor area of 25m×25m with two façade openings with the area of 3m×5m, and a characteristic fire load density of 1755 MJ/m². The maximum heat release rate (HRR) was 90 MW, and the fire was located in the center of the compartment. The first scenario had a 12m floor-to-ceiling height with no roof opening, while the second had the same dimensions with a 5% roof opening area.

Lastly, a more advanced fire model, Computational Fluid Dynamics (CFD), was employed using Fire Dynamic Simulator (FDS) software (version 6) [13] for the comparison with the optimization results based on CFAST fire curve. This allowed for a detailed time-temperature curve compared to CFAST as it simulates fire behaviour with greater detail, but requires more user input to define the fire and compartment geometry, making it more time-consuming [12]. The results are then compared to elucidate the impact of each parameter change on fire resistance and the optimal FP thicknesses required for steel warehouses.

2 DEVELOPMENT OF FINITE ELEMENT NUMERICAL MODELS

This section details the development of finite element (FE) models used for evaluating the fire resistance of protected steel components within the portal frame of an industrial warehouse, with a focus on fire protection (FP) optimization. Abaqus software version 2021 [7] was used to create these FE models. The development process involved subjecting each model to a series of three analyses:

1. Linear buckling analysis: This initial analysis assessed the buckling susceptibility of the beams and columns.
2. Heat transfer analysis: This analysis aimed to predict the temperature distribution throughout the member under fire conditions.
3. Thermo-mechanical analysis: This final analysis investigated the structural response of the member under fire exposure, using the temperature distribution obtained from the heat transfer analysis as an input.

To simulate real-world condition, an initial global imperfection of L/1000 was introduced to both the beams and columns during the linear buckling analysis. In the following, the failure mode and critical temperature at which failure would occur were determined in the non-linear stress analysis by applying combined thermal and mechanical loads to the imperfect column.

2.1 Model Description

The case study investigated and compared the fire resistance of two single-story steel industrial sheds located in Figueira da Foz, Portugal, under different natural fire scenarios simulated using software like CFAST and FDS. The goal was to find the optimal thickness required for the structural elements, particularly to the rafters and columns. This optimization was based on the predicted temperature profiles

obtained from fire simulation software using different fire compartment models. A scheme of the portal frame geometry used in Finite Element (FE) simulation of the first case study is depicted in Figure 1. Both sheds had portal frames with a span of 25.0 meters and a roof slope of 10%. The portal frames were considered pinned at the column bases and horizontally braced in both case scenarios. However, the mid-span column heights were different: 8.9 meters in the first case and 12 meters in the second.

Each shed spanned 100 meters, with portal frames spaced 6.25 meters apart ($L/4$) in both case studies. According to design standard, the beam-to-column connections included 2.5-meter-long haunches ($L/10$) with an approximate height of 0.714 meters ($L/25$). Purlins on the rafters were spaced every 2.5 meters, while facade rail beams were positioned equidistantly at 1.875 meters above the exterior column face in both cases.

Both the sheds were constructed from hot-rolled profiles: HEB 260 for the columns and IPE 450 for the rafters. Besides that, both the columns and rafters were protected against fire with a coating layer of gypsum-based fire protection mortar with perlite.

For this study, the ULS load combination was considered, with the maximum utilization factor calculated according to EN 1990 [14] and with the dominant vertical load (i.e., $1.35G + 1.5Q + 0.75S$), being G the dead load (self-weight of the frame), Q the variable imposed load (based on EN1991-1-1:2003 [15]), and S the variable snow load.

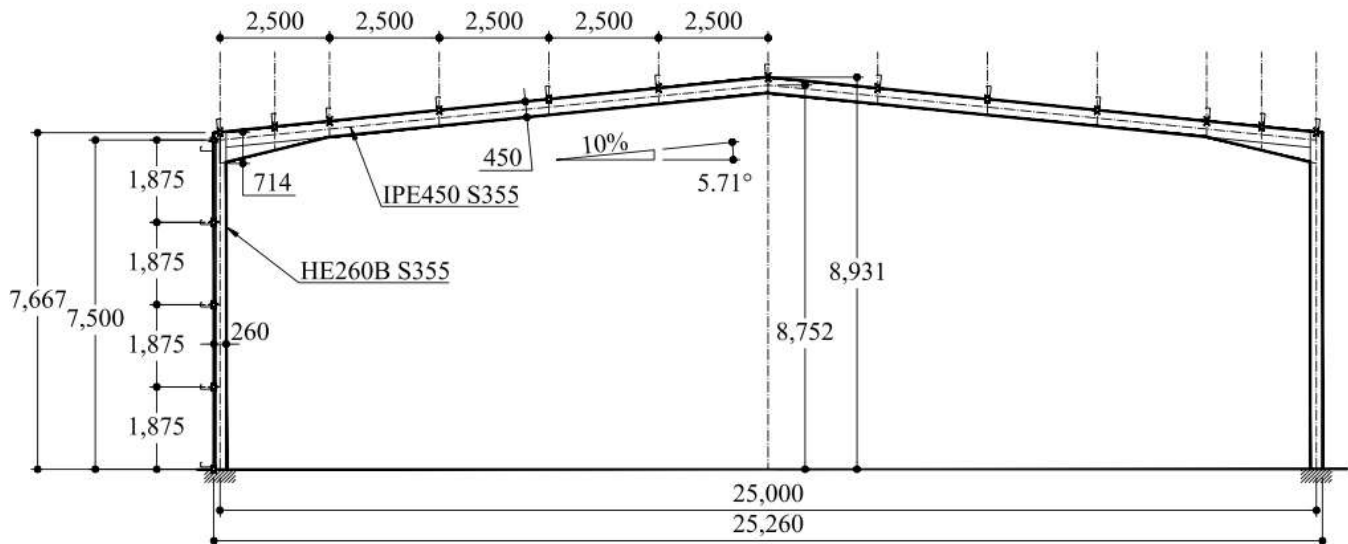


Figure 1. Schematic view of prototype industrial shed for Case 1 [16]

2.2 Finite Element Models

The development of finite element model (FEM) for an industrial metal shed protected with gypsum-based mortar boards, followed a symmetric approach. Figure 2 shows a 3D finite element model (FEM) of half of the portal frame developed using advanced FE program ABAQUS. Structural elements (rafters and columns) were represented using shell elements, with finite element mesh sizes set at 25mm for cross-section and 50mm along the length.

Vertical loads were distributed on the rafters at 2.5m intervals, aligning with the placement of purlins, as shown in Figure 2. In order to define the boundary conditions in the finite element model, a reference point was created at the centroid of each column base and the frame's peak. These points were then kinematically coupled to their corresponding cross-sections, effectively constraining the degrees of freedom of the element. At the peak, only vertical movement was allowed (all translational and rotational degrees of freedom were prevented), while at the column base, four degrees of freedom were constrained (all translational and longitudinal-axis rotational degrees).

In addition, the effect of purlins and façade rails was indirectly accounted for by applying lateral restraints to the outer flange of the rafters and columns. Therefore, both the rafters and columns were fully restraint against lateral movement at the connection points (see Figure 2). To assess the impact of different fire scenarios on the metal shed, the time-temperature fire curves were applied to all sides of both the rafters and columns. A multi-step analysis was then performed. This included buckling analysis, heat transfer thermal analysis, and nonlinear geometric and material static analysis, conducted sequentially to assess the overall structural response of the industrial metal shed, where structural elements were protected with enhanced gypsum-based mortars.

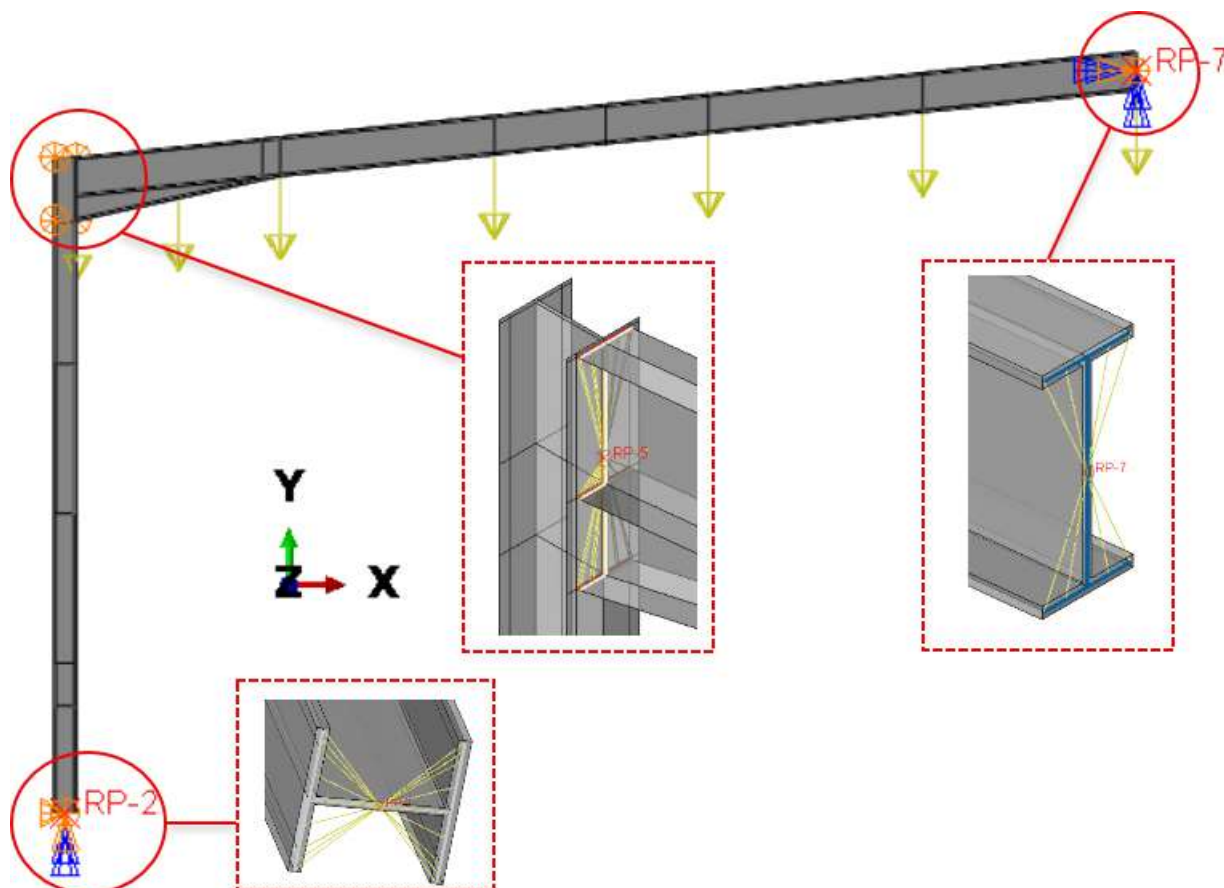


Figure 2. The FE model of half of the portal frame with protection (Case 1)

2.3 Material Properties

The main elements of the portal frame were made of S355 steel (yield strength of 355 MPa). At ambient temperature, a nonlinear isotropic material model was assumed, considering Von Mises yield criterion with a Young's modulus of 200 GPa and the specified yield stress of 355 MPa; while at elevated temperature, temperature-dependent material properties were incorporated in the FE model according to Eurocode 1993-1-2:2005 [17]. Note that, true stress-strain curves were included within the material definition to capture the behaviour of steel at large deformations experience during fire events. A constant density of 7850 Kg/m³ was assigned to the steel with the Poisson's ratios equal to 0.3.

In contrast to the steel, the fire protection mortar properties were assumed to remain constant with varying temperatures. The values used were based on previous thermal analysis test conducted at the ISISE laboratory at the University of Coimbra (UC) laboratory (refer to Table 1) and represent the material's behaviour at ambient temperature. Poisson's ratios were defined as 0.2 for the developed fire protection material: gypsum-based fire protection mortars with perlite (DFPM).

Table 1. The measured thermal properties of gypsum-based fire protection materials at ambient temperature [16]

DFPM	Thermal properties at ambient temperature		
	Conductivity (W/mK)	Mass density (Kg/m ³)	Specific heat(J/KgK)
	0.2309	860.186	861.79

3 THERMO-MECHANICAL RESULTS

3.1 ISO-834 standard fire curve (Case1)

In Figure 3 (a), the non-linear thermo-mechanical analysis results in terms of the evolution of vertical displacement at the top of the rafter are presented. This analysis considered various FP thicknesses applied to both the rafter and column. Figure 3 (a) highlights a significant increase in vertical displacement at the top of the rafter, leading to the frame failure, when the FP thickness reached 5mm. As shown in this figure, the optimal thickness is achieved through an iterative process.

Analysing different FP thicknesses for columns and rafters revealed an optimal FP thickness of 5mm for column and 6mm for the rafter. The deformed configuration of the portal frame FE model for a 5mm FP thickness of the rafter is depicted in Figure 3 (b).

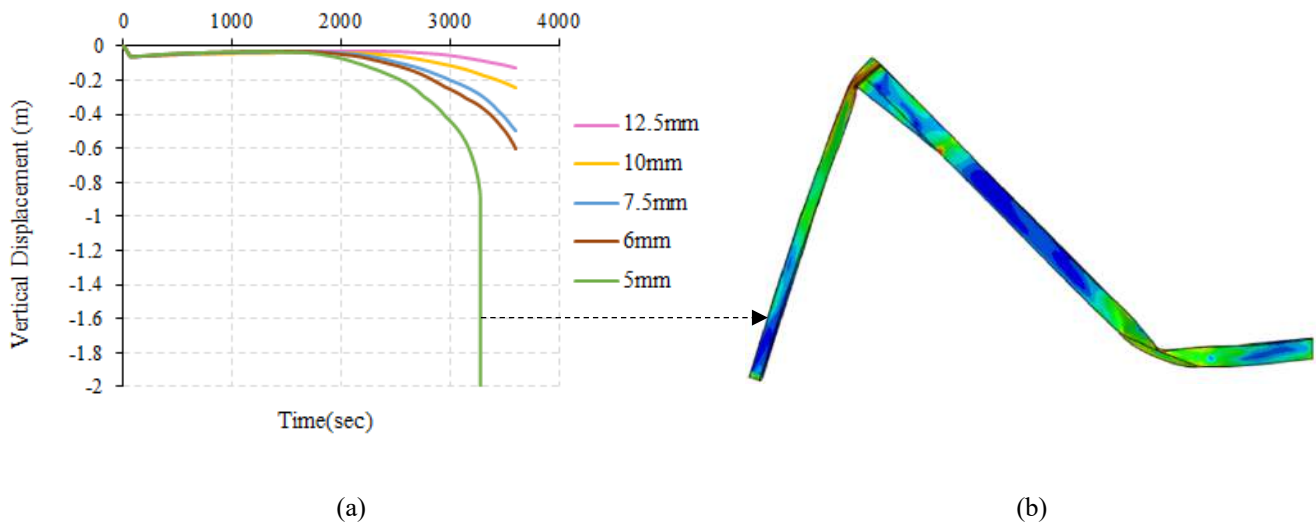


Figure 3. (a) Rafter displacement evolution for different thicknesses of fire protection mortar under 1-hour ISO fire exposure (b) Nonlinear static analysis results-Deformed configuration of the portal frame protected with 5mm FP board

4 PARAMETRIC STUDIES: NATURAL FIRE CURVES FOR FIRE PROTECTION OPTIMIZATION IN INDUSTRIAL METAL WAREHOUSES

This section deviates from the standard ISO-834 fire curve, which assumes a rapid and continuous rise in temperature surrounding the structure. Instead, it employs more realistic natural fire curves generated by fire simulation software like CFAST and FDS for evaluating the fire resistance of the industrial metal sheds. These natural fire curves provide a more accurate representation of real-world fire scenarios with realistic heating and cooling phases.

By analysing the results, an iterative optimization process is then implemented to identify the most suitable thickness of gypsum-based FP boards for each case study (Case 1 and Case 2), by considering factors like failure time and fire resistance rating during exposure to the different natural fire curves.

The goal is to design the fire protection that allows the structure to maintain stability during the fire until it burns out completely. By analysing how different fire scenarios influence fire protection requirements, this approach seeks to identify the most effective fire safety measures for each situation.

4.1 Natural fire curve (Case 1): Localized fire scenario

Following the evaluation of fire resistance and identification of the optimal fire protection thickness for the rafters and columns of the portal frame (Case 1) under standard fire exposure, this section explores an optimized fire protection design based on a more realistic localized fire scenario.

Figure 4 (a) shows the evolution of gas temperature within the compartment for different zones, as computed by CFAST software. Since the fire is centered, the distribution of the heat on the steel elements is based on their zone location (Figure 4 (b)). To clarify, the lower column section is in the cold air zone, while the upper column section is in the hot air zone. The rafter is divided into two parts, the part close to the center was exposed to plume air time-temperature curve, while the one close to the column was exposed to the hot air time-temperature curve. The hot and cold zone boundaries are defined by the temperature-height profile obtained from CFAST.

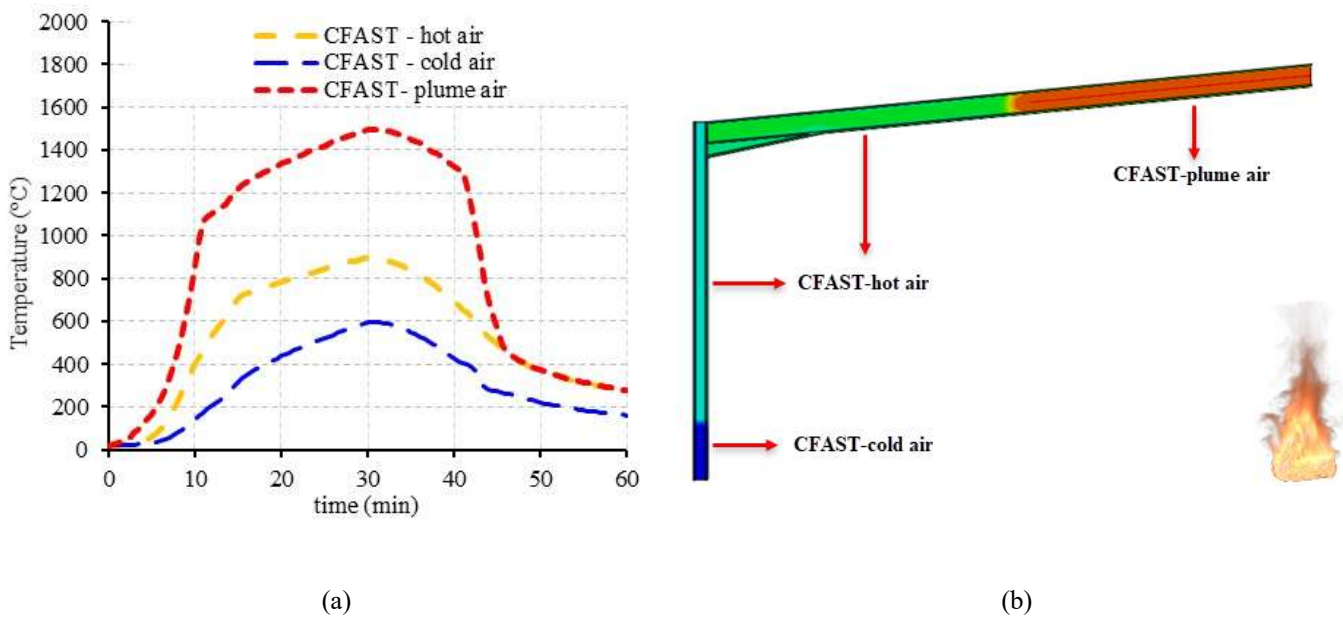


Figure 4. (a) Evolution of the gas temperature in the compartment center from fire simulation of a steel warehouse (CASE 1) using CFAST software (b) Schematic illustration of steel frame configuration with specified fire scenario applied to each section of steel elements

Figure 5 presents the thermo-mechanical results concerning the optimization of FP thickness on the main structural elements of the industrial compartment (columns and rafters). It can be found out that when the structural elements within the industrial compartment are exposed to the natural fire curve, simulated by CFAST, the required FP thickness for rafter is 1mm higher (7mm) compared to the exposure to the standard time-temperature fire curve from Eurocode 1993-1-2 [17].

The analysis results clearly indicate that relying solely on the standard fire curve for fire safety design in large space compartments might underestimate the actual fire resistance needed for metal structures, depending on the existing fire scenario.

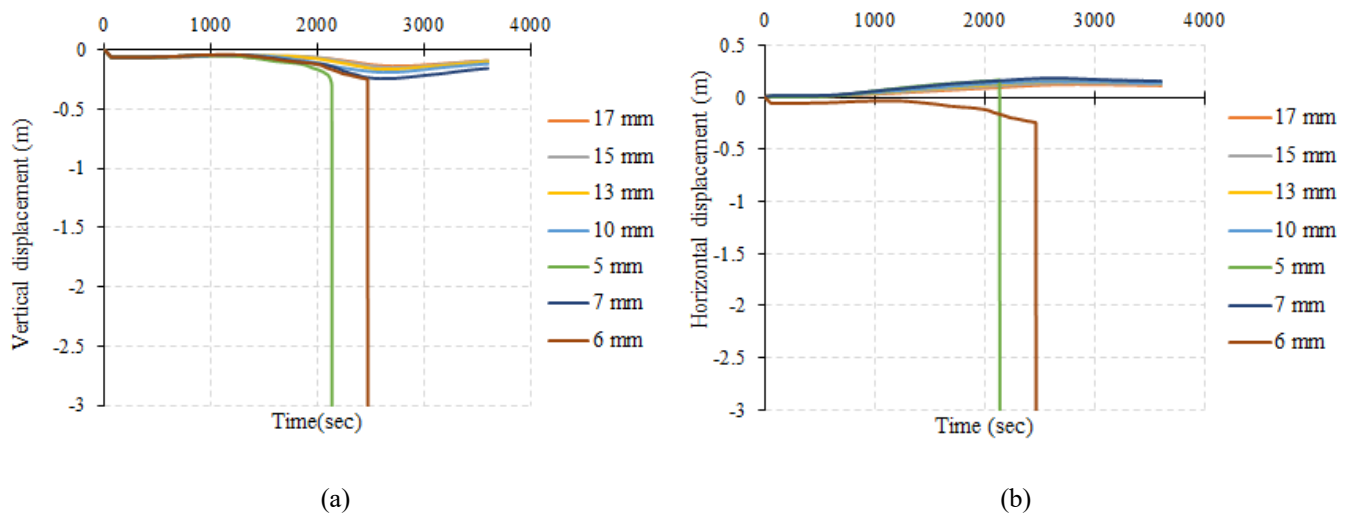


Figure 5. (a) Evolution of vertical displacement at frame top (Case 1) and (b) Maximum horizontal displacement at the column with 5mm FP thickness applied, for different FP thicknesses on the rafter, under one-hour exposure to natural fire curve (CFAST)

4.2 Natural fire curve (Case 2): Localized fire scenario

In this section, CFAST software (version 7.7.0) is used to simulate the gas temperature inside the compartment in both scenarios. Figure 6 shows the resulting natural fire curves (cold air, hot air, and plume air temperature profiles) in both scenarios.

Figure 7 shows the optimal FP thickness for the rafter element under the exposure to the CFAST fire curve considering the first scenario (no roof opening). As expected, the scenario with no roof opening requires a thicker FP layer (by 9 mm) for the rafters compared to the scenario with a 5% roof opening. This difference is because trapped hot gases and smoke inside the compartment without a roof opening significantly increase the temperature experienced by the structure, especially the roof elements. While roof openings act as vents, allowing heat and smoke to escape, reducing the overall temperature within the warehouse, and decreasing the thermal load on the structural elements. Consequently, less fire protection is needed when roof opening is present.

This highlights the importance of roof openings in fire safety designs and fire protection optimization in in large-space compartments such as industrial warehouse.

Furthermore, Figure 8 shows the gas temperature-time curves obtained from the FDS simulation in different height level inside the compartment with 5% roof opening of the total roof area. The time-temperature curves corresponding to each height level as shown in the figure below is associated to different height level sections of the column as well as rafter. These curves are applied to all four sides of the structural elements of the portal frame.

Analysis of the thermo-mechanical response of the steel portal frame (Case 2) under combined vertical loads and thermal actions (FDS natural fire curve) revealed an optimal FP thickness of less than 5 mm for both rafters and columns. This finding closely aligned with the results obtained from the fire simulation in CFAST under similar conditions. This could be due to a short high temperature duration experienced by the columns because the FDS fire stays mostly at higher temperatures when oxygen concentrations are high (see Figure 8).

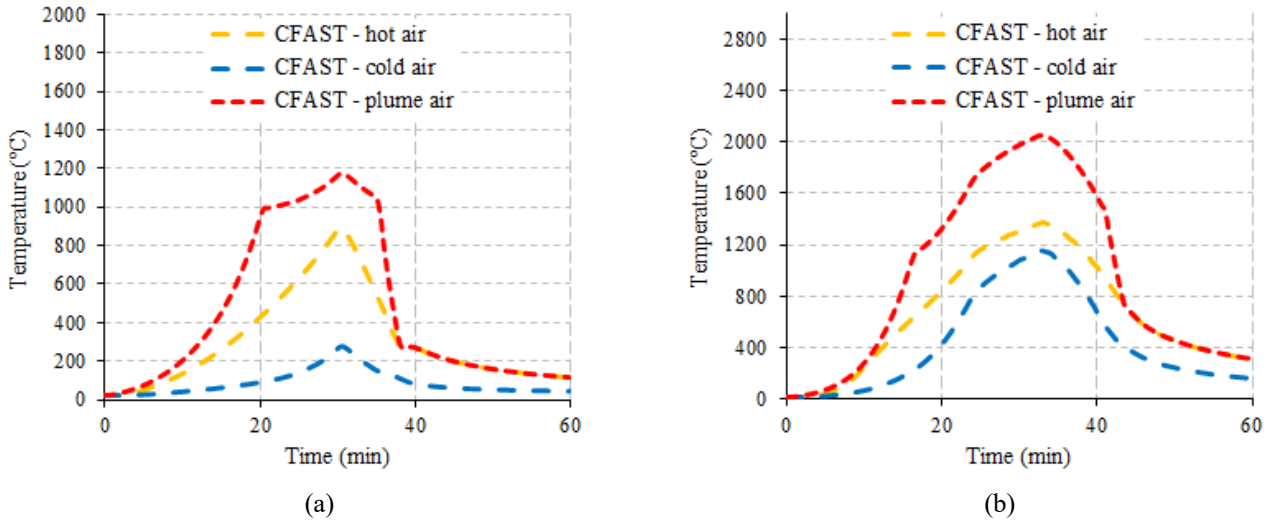


Figure 6. A comparison of the gas temperature in the compartment center derived from fire simulation in CFAST software for a steel warehouse (case 2) with (a) 5% roof opening and (b) no roof opening

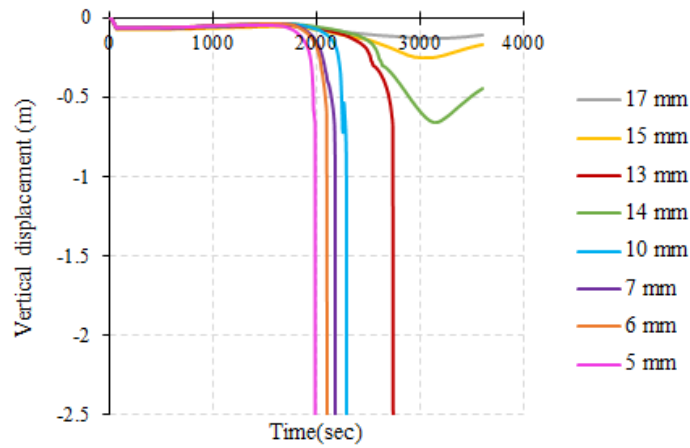


Figure 7. Evolution of vertical displacement at frame top (Case 2) without roof opening when different FP thicknesses are applied to the rafter, under one-hour exposure to natural fire curve (CFAST)

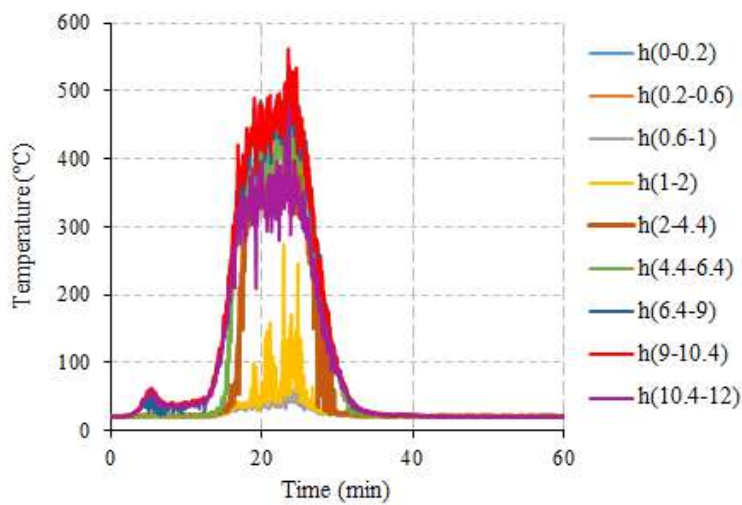


Figure 8. Evolution of the gas temperature inside the compartment of an industrial warehouse (CASE 2) using CFD fire simulation software, FDS (version 6)

5 CONCLUSIONS

In this paper, numerical simulations were employed to investigate the fire resistance and optimize fire protection thicknesses for structural elements in industrial steel warehouses under different thermal loads. Two case studies with different column heights for an industrial shed were analysed.

From the thermo-mechanical analysis results, it can be concluded that FP thickness requirements is increased by approximately 20% when considering natural fire curves (CFAST and FDS) compared to the standard ISO 834 curve for the first case study (the portal frame with shorter columns). This highlights the potential underestimation of actual fire resistance when using the standard fire curve in the fire safety design for large spaces, depending on the specific fire scenario.

Furthermore, different factors like building size, openings, fire load, and fire location can significantly impact flashover risk and optimal fire protection requirement. For instance, removing the roof opening resulted in a threefold increase in required fire protection thickness compared to a 5% roof opening scenario. Besides that, the analysis results from the second case study portal frame demonstrated that usually the optimal FP thickness from the FDS fire simulation is trivial (5mm) due to the short duration of high temperatures experienced by the columns.

This study contributes to a deeper understanding of fire performance in steel-framed structures, particularly warehouses. By considering a comprehensive set of parameters, it enables a more precise evaluation of fire resistance.

These findings are crucial for developing optimized fire design approaches, ensuring the structural integrity and safety of industrial steel warehouses under diverse fire conditions. Ultimately, the study's insights offer valuable guidance for enhancing fire safety strategies in steel-framed structures.

ACKNOWLEDGMENT

This work is financed by FCT / MCTES through national funds (PIDDAC) under the R&D Unit Institute for Sustainability and Innovation in Engineering Structures (ISISE), under reference UIDB / 04029/2020, and under the Associate Laboratory for Advanced Manufacturing and Intelligent Systems (ARISE) under reference LA/P/0112/2020. We acknowledge their support.

REFERENCES

1. Laím L, Caetano H, Santiago A. Review: Effects of nanoparticles in cementitious construction materials at ambient and high temperatures. *J Build Eng* [Internet] 2021;35(November 2020):102008. Available from: <https://doi.org/10.1016/j.jobe.2020.102008>
2. Caetano H, Santiago A, Shahbazian A. Cement mortar as passive fire protection in steel columns. *Proc 7th Int Conf Appl Struct Fire Eng ASFE' 21, Ljubljana, Slov 2021;(June):9–11.*
3. Caetano H, Laím L, Santiago A, Durães L, Shahbazian A. Development of Passive Fire Protection Mortars. *Appl Sci* 2022;12(4):2093.
4. Laím L, Santiago A, Caetano H, Craveiro D, Shahbazian A. Numerical analysis and structural fire design of protected SHS steel columns with thermally enhanced gypsum-based mortars. 2022;54.
5. Aghabozorgi P, Santiago A, Laím L, Cândido N. A parametric study of tubular steel columns protected with gypsum-based mortars under fire load using finite element modelling. In: *Proceedings of the 12th International Conference on Structures in Fire (SiF 2022).* 2022. page 693–702.
6. Aghabozorgi P, Laím L, Santiago A, Cândido N. STRUCTURAL FIRE BEHAVIOUR OF PROTECTED TUBULAR STEEL COLUMNS IN INDUSTRIAL WAREHOUSES UNDER STANDARD AND SIMULATED FIRE CONDITIONS. In: *Proceedings of IFireSS 2023-International Fire Safety Symposium.* 2023.
7. ABAQUS/CAE. ABAQUS/CAE, Stand. User's Manual, Version 2021, Dessault Syst. Simulia Crop.2021;
8. ISO. ISO 834-1 Fire resistance tests -Elements of building construction, Part 1: General requirements. *Int Organ Stand Geneva, Switz* 1999;
9. Jones W, Forney G, Peacock R, Reneke P. A technical reference for CFAST: an engineering tool for

estimating fire and smoke transport. NIST Tech Note [Internet] 2000; Available from: <http://fire.nist.gov/bfrlpubs/fire00/art004.html>

10. Peacock RD, Reneke PA, Forney GP. CFAST-Consolidated Model of Fire Growth and Smoke Transport (Version 7) Volume 2 : User ' s Guide. Nist 2017;2(Version 7).
11. 1991-1-2 E. Eurocode 1 : Actions on structures - Part 1-2: General actions - Actions on structures exposed to fire. 2002.
12. Molkens T, Rossi B. On the Simulation of Real Fire for Post Fire Resistance Evaluation of Steel Structures [Internet]. Springer US; 2021. Available from: <https://doi.org/10.1007/s10694-020-01025-6>
13. McGrattan K, Hostikka S, McDermott R, Floyed J, Weinschenk C, Overholt K. Fire Dynamics Simulator (FDS) (version 5), technical reference guide, National Institute of Standards and Technology, U.S. Department of Commerce. 2007.
14. En BS. BS EN 1990: 2002. Eurocode - Basis of structural design. Bs En 19902002 2002;3.
15. Eurocode - BS EN, Schwind W. BS EN 1991-1-1-1: Eurocode 1 - Actions on structures - Part 1-1: General actions - Densities, self-weight, imposed loads for buildings. Bauingenieur 2011;86(JULY-AUGUST).
16. Aghabozorgi P, Santiago A. A NUMERICAL INVESTIGATION ON FIRE PERFORMANCE OF INDUSTRIAL STEEL WAREHOUSES PROTECTED WITH GYPSUM-BASED BOARDS. 2024;7(1):175–85.
17. CEN. EN 1993-1-2. Eurocode 3 : Design of steel structures - Part 1-2 : General rules -Structural fire design. Brussels, Belgium, European Committee for Standardization.

CHEMO-THERMO-HYGRO-MECHANICAL ANALYSIS OF BLENDED CONCRETES UNDER FIRE LOADING

Simon Peters¹, Günther Meschke²

ABSTRACT

A computational analysis of chemo-thermo-hygro-mechanical behaviour of concrete structures at high temperature is presented, investigating blended concretes regarding the pore pressure developments and moisture flow, addressing the different dehydration characteristics. Based on known stoichiometric dehydration formulas and kinetics of each hardened cement paste constituent, the dehydration characteristics at elevated temperatures are determined in terms of water release and porosity increase. Hydration models are used to predict the initial volume fractions of the individual cement paste constituents. According to the numerical chemo-thermo-hygro-mechanical simulations, the investigated cement blends, blast furnace slag and calcined clay, increase the induced pore pressures within the concrete structures compared the ordinary Portland cement.

Keywords: Multiscale modelling; finite element modelling; chemo-thermo-hygro-mechanical analysis

1 INTRODUCTION

Minimising the global carbon footprint and the increasing demand for engineering infrastructures worldwide pose great scientific challenges towards sustainable building materials. Blended Portland cement compositions with supplementary cementitious materials such as limestone, fly ash, blast furnace slag or calcined clays represent a suitable solution reducing the climate impact of the most used building material, concrete, significantly. However, concretes with these blended cements show higher explosive spalling risks under fire loading in experiments [1]. It proves challenging to study explosive concrete spalling through experimental means alone. Therefore, numerical models offer a possible solution to provide additional insights into the specifics of the problem with its multi-physical nature.

Chemo-thermo-hygro-mechanical (CTHM) models on macro scale are already well developed [2] but suffering from some drawbacks while investigating concrete at elevated temperatures. For instance, not all input parameters of these models can be captured by experiments sufficiently. One important example is the dehydration characteristic of concrete at elevated temperatures.

During the dehydration process at elevated temperatures chemically bound and pore water will be released [3]. This dehydration process affects all the material properties, such as Young's modulus, permeability, or diffusivity. Moreover, the induced pore pressures inside the concrete are affected which may lead to explosive spalling at elevated temperatures [4]. Therefore, water release should be captured within the numerical investigation.

Within a thermogravimetric analysis (TGA) the dehydration behaviour of a concrete composition can be experimentally determined with the following drawbacks as input in a macroscopic chemo-thermo-hygro-

¹ M.Sc., Institute for Structural Mechanics, Ruhr University Bochum
e-mail: simon.peters@rub.de, ORCID: <https://orcid.org/0009-0007-4368-3832>

² Prof. Dr., Institute for Structural Mechanics, Ruhr University Bochum
e-mail: guenther.meschke@rub.de, ORCID: <https://orcid.org/0000-0003-2277-1327>

mechanical model. First, concrete compositions are varying according to the fields of application, resulting in a TGA for each composition. Second, the dehydration characteristics is time depended and these dehydration kinetics cannot be captured easily by TGA experiments. To overcome these drawbacks Wang et al. [5] proposed a computational framework assuming an intrinsic kinetic and equilibrium dehydration characteristic separately for each hardened cement paste constituent.

Motivated by existing models as a point of departure, a developed multiscale model able to describe the dehydration characteristics of CO₂-reduced blended concretes (blast furnace slag and calcined clay) [6,7] is embedded into a chemo-thermo-hygro-mechanical model, connected with the following main objectives:

- Investigation of pore pressure development in concrete made from blended Portland cement compositions with supplementary cementitious materials in comparison to ordinary Portland cement (OPC) compositions.
- Evaluation of the influence of the heating rate according to the pore pressure development.
- Assessment of the initial moisture state on the pore pressure development and moisture flow in concretes pore space.

2 CHEMO-THERMO-HYGRO-MECHANICAL MULTISCALE MODEL

As pictured in Figure 1, before the macroscopic finite element simulation starts, the cement composition is inputted in a hydration model to get the initial hydrate volume fractions of the hardened cement paste. Based on these volume fractions the dehydration characteristic is calculated in each time step in the finite element simulation. The dehydration behaviour is captured by two dehydration parameters, $\xi_{w,dehyd}$ and $\xi_{\phi,dehyd}$ representing the water release and capillary pore growth of the concrete, respectively. The latter is subsequently transferred in a micromechanical framework calculating the Young's modulus, diffusivity and permeability increase according to the thermo-chemo induced porosity, see Section 2.3.

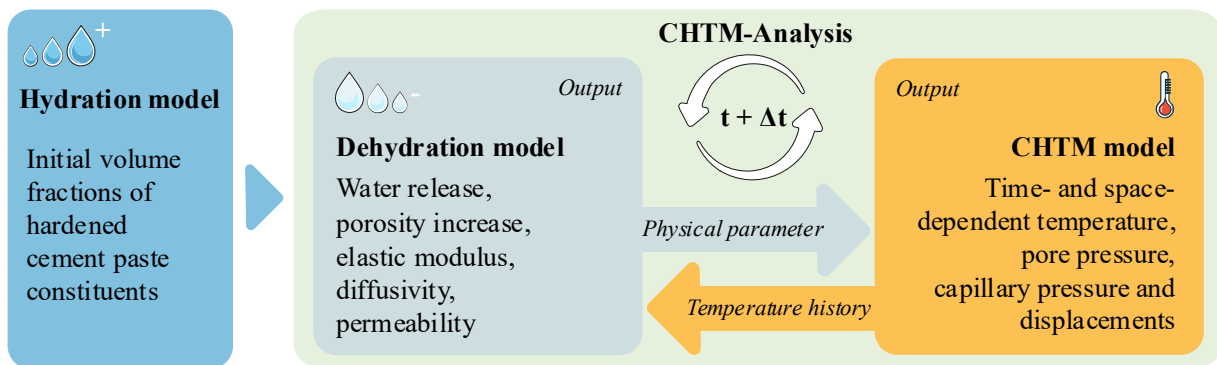


Figure 1. Framework of the coupled CHTM model for concrete under elevated temperatures

2.1 Chemo-thermo-hygro-mechanical model on macro scale

Inspired by [8], the model considers four primary state variables, i.e. temperature T , gas pressure p_g , capillary pressure p_c , displacement u and two internal variables on the micro scale, i.e. dehydration degree ξ_{tot} and chemo-thermo-mechanical damage d_{ctm} . The final form of the model equations are listed below and the full development of the equations is presented in [9]:

The enthalpy balance equation of the multi-phase medium (energy equation) accounts for the conductive heat flow and heat effects of phase changes and dehydration process and can be written as follows:

$$(\rho C_p)_{eff} \frac{\partial T}{\partial t} - \text{div}(\tilde{\mathbf{q}}) = -\dot{m}_{vap} \Delta H_{vap} + \dot{m}_{dehyd} \Delta H_{dehyd} \quad (1)$$

where

$(\rho C_p)_{eff}$ is the effective specific heat capacity of concrete.

$\text{div}(\tilde{\mathbf{q}})$ is the conductive heat flow.

$\dot{m}_{vap}\Delta H_{vap}$ is the heat effect of phase change.

$\dot{m}_{dehydr}\Delta H_{dehydr}$ is the heat effect of dehydration.

The linear momentum conservation equation of the multi-phase medium can be written as

$$\text{div}[(1 - d_{ctm})K : (\boldsymbol{\varepsilon}_{tot} - \boldsymbol{\varepsilon}_{th} - \boldsymbol{\varepsilon}_{tr})] = 0 \quad (2)$$

where

d_{ctm} is the chemo-thermo-mechanical damage parameter.

K is the stiffness tensor.

$\boldsymbol{\varepsilon}_{tot}$ is the total strain tensor.

$\boldsymbol{\varepsilon}_{th}$ is the thermal strain tensor.

$\boldsymbol{\varepsilon}_{tr}$ is the load induced thermal strains.

Mass balance equation of the dry air (continuity equation) considers the diffusive and advective air flow as well as variations of porosity caused by the dehydration process and has the following form:

$$-\frac{\partial}{\partial t}(\varphi(1 - S)\rho_a) + \nabla(\rho_a v_a) = 0 \quad (3)$$

where

$\varphi(1 - S)\rho_a$ is the air gas density.

$\rho_a v_a$ is the gas flux of air.

Mass balance equation of the dry air (continuity equation) considers the diffusive and advective air flow as well as variations of porosity caused by the dehydration process and has the following form:

$$-\frac{\partial}{\partial t}(\varphi(S\rho_l + (1 - S)\rho_v)) + \nabla(\rho_v v_v + \rho_v v_l) = \dot{m}_{dehyd} \quad (4)$$

where

$\varphi(S\rho_l + (1 - S)\rho_v)$ is the fluid density of water in gas and liquid state.

$\rho_v v_v + \rho_v v_l$ is the fluid flux of water in gas and liquid state.

2.2 Hydration model

Free hydration models online can calculate initial volume fractions of all hardened cement paste constituents, e.g. CemGEMS web app [10] by the international Nanocem consortium, PHREEQCC [11] by the U.S. Geological Survey, CEMHYD3D or VCCTL Software by the National Institute of Standards and Technology (NIST). For OPC, CEM III/B and CEM IV CemGEMS web app was utilized because its models were calibrated by experiments, resulting in high accuracies for these specific cement compositions. All initial volume fractions of hydration products are summarized in Table 1.

Table 1. Initial volume fractions f_i of the investigated hardened cement pastes (w/b = 0.3)

Phase	CEM I	CEM III/B	CEM IV/A
Clinker	0.0898	0.0251	0.0736
CSH	0.4019	0.4135	0.4011
CH	0.2210	0.0626	0.0000
AFt	0.1268	0.0859	0.0913
AFm	0.0301	0.1115	0.2580
TCA	0.0932	0.0904	0.0189
inert	0.0289	0.1727	0.1439
Cap. Porosity	0.0083	0.0383	0.0132

2.3 Dehydration model on micro scale^{3†}

Using the calculated volume fractions and a given heating rate, the dehydration model predicts the mass loss, porosity, and volume fractions of the dehydration products, which are subsequently input to the micromechanical model calculating the actual Young's modulus, diffusivity, and permeability. The full model for Young's modulus, water release and porosity increase is described in detail in [7].

The coupling of the dehydration model on micro scale with the CHTM model on macro scale takes place in two ways. First, the material properties are changed according to the micro mechanical model induced by the change of moisture, chemically induced porosity, and micro cracks. Second, \dot{m}_{dehyd} is calculated by the dehydration model using equation (5) [5,7,12].

$$\dot{m}_{dehyd} = - \sum_j Q_j^W \cdot \dot{\xi}^j \quad (5)$$

where

$\dot{\xi}^j$ is the dehydration degree for hydrate j,

Q_j^W is the chemically bound water contained in the hydrate j.

This quantity of chemically bound water Q_j^W contained in the hydrate j at the beginning of the dehydration process can be calculated from the hydration degree of the anhydrous phases by the dehydration model, see Section 2.2, e.g. for OPC the main hydrates are CH, C-S-H and AFm⁴, so the calculation of Q^W would have to be performed for these three hydrates with

$$Q_j^W = f_j \cdot N_j^W \cdot \frac{M_j}{M_w} \text{ with } j \in \{\text{hydrate phases}\} \quad (6)$$

where

f_j is the volume fraction of hydrate j,

N_j^W is the amount of released molecules of water due to dehydration,

M_j is the molar mass of hydrate j,

M_w is the molar mass of water.

To capture the dehydration kinetics for each hardened cement paste constituent j, the mass loss kinetics for each cement paste constituent j is calculated using

$$\dot{\xi}^j = H(T - T_0^j) \cdot (\xi_{eq}^j(T) - \xi^j) \frac{1}{\tau^j} \exp\left(\frac{E_a^j}{R} \left(\frac{1}{T} - \frac{1}{T_0^j}\right)\right) \quad (7)$$

where

$H(T - T_0^j)$ is the Heaviside function,

$\xi_{eq}^j(T)$ is the final dehydration degree at a given temperature,

T_0^j is the temperature from which the hydrate j begins to dehydrate,

τ^j is the characteristic time [s] associated with hydrate j, and

E_a^j is the activation energy associated with hydrate j.

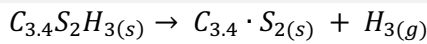
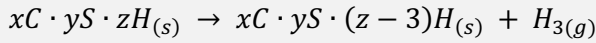
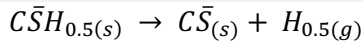
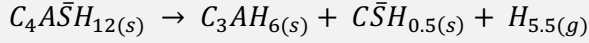
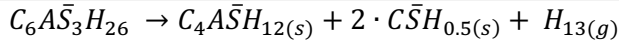
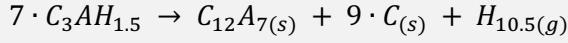
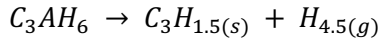
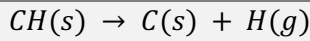
The kinetic dehydration parameters for equation (7) respective dehydration curves are contained in Figure 2 for a heating rate of 5°C/min.

³ This model written in Matlab is freely available on <https://github.com/SimPeterz>

⁴ Cement chemistry abbreviations will be used in this paper: C = CaO; S = SiO₂; A = Al₂O₃; F = Fe₂O₃; S = SO₃; H = H₂O

Table 2. Stoichiometric dehydration reactions and reaction types of hydrate constituents in cementitious notation

Stoichiometry of reaction



All considered chemical reactions regarding dehydration processes are listed in Table 2, with more detailed explanations in [6,12]. Finally, the dehydration induced porosity is calculated by [13]

$$\phi_T = 0.72 \cdot 10^{-3} m_{dehyd} \quad (8)$$

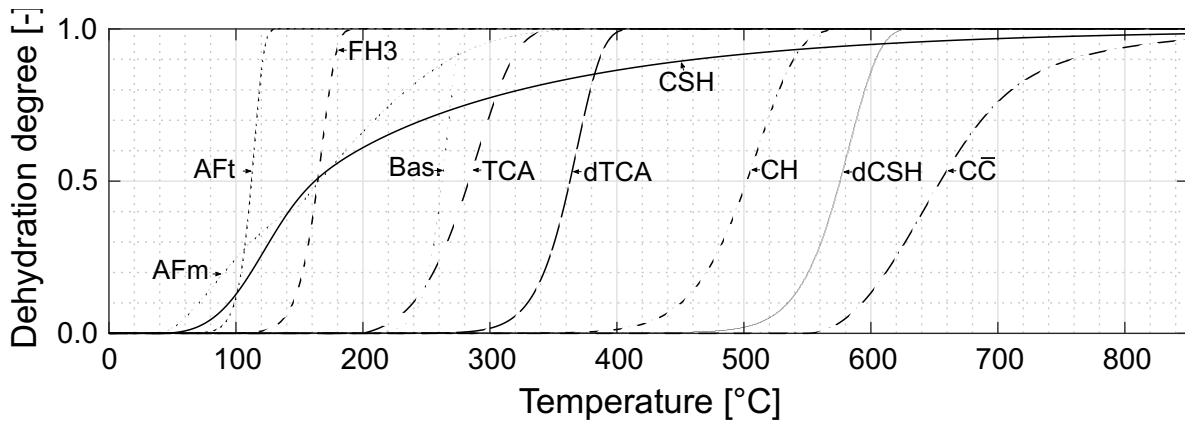


Figure 2. Illustration of the dehydration characteristics of the hydrate phases contained from [7] in the temperature range up to 850°C for a heating rate of 5°C/min

2.4 Constitutive parameters of concrete at elevated temperatures

The relationship between permeability and the pore structure of hardened cement paste is expressed by the following relationship [14,15]

$$K_{eff} = \left(\frac{p_g}{101325} \right)^{0.368} \cdot (K_0 10^\delta + K_d) \text{ with } \delta = \frac{6(\phi - \phi_0)}{0.3 - 0.4\phi_0} \text{ and } K_d = d_{ctm} \cdot 10^{-16} \quad (9)$$

where

K_0 is the intrinsic permeability at reference temperature equal to $1.7 \cdot 10^{-19} [m^2]$,

K_d permeability increase due to cracking,

a mean crack aperture,

p_g gas pressure in pore space.

The coupling of the diffusivity of the cement paste is utilized via [16]

$$D_{eff} = D_0 \frac{p_g}{101325} \phi^{4/3} (1 - S)^{10/3} \left(\frac{T}{T_0} \right)^{1.667} \quad (10)$$

where

D_0 diffusion coefficient of vapour species in the air at T_0 equal to $2.58 \cdot 10^{-5} [m^2 s^{-1}]$,

ϕ is the capillary porosity.

The gas properties are defined according to Daltons law

$$p_a = p_g - p_v \text{ with } p_v = p_{sat} \cdot \exp\left(\frac{-p_c M_w}{\rho_l R T}\right) \quad (11)$$

where

p_a is the air pressure,

p_v is the vapor pressure,

p_{sat} is the sat. pressure with $p_{sat} = \max(\exp(23.5771 - (4042.9/(T - 37.58))), 22842472.79)$,

ρ_l is the water density with $\rho_l = \max(1011.5 - 0.740T + 0.00873T^2 - 9.6971 \cdot 10^{-5}T^3 + 3.6733 \cdot 10^{-7}T^4 - 5.0775 \cdot 10^{-10}T^5, 350) [kg/m^3]$

R is the universal gas constant with $R = 8.314 [J/mol \cdot K]$,

M_w is the molar mass of water with $M_w = 0.01802 [kg/mol]$,

And the density of gases is calculated by

$$\rho_\pi = \frac{M_\pi}{RT} p_\pi \quad (12)$$

where

p_π is the partial pressure of the gas phase,

M_π is the molar mass of gas.

The isotherm is assumed to be temperature depended with the following formula by van Genuchten [17]

$$S = \left[1 + \left(\frac{|p_c|}{10^6} \right)^{1/(1-0.49)} \right]^{-0.49} \quad (13)$$

The expressions of the relative permeability of liquids k_{lg} and gases k_{rg} , the dynamic viscosity of liquid water μ_l and moist air μ_g and the enthalpy of evaporation are taken out of [18]. For the thermal conductivity and specific heat, the following simple relationships were used, respectively:

$$\lambda_T = 2 - 0.2451 \cdot \frac{T}{100} + 0.0107 \cdot \frac{T}{100}^2 \left[\frac{W}{mK} \right] \quad (14)$$

and

$$c_p = 900 + 80 \cdot (T/120) - 4 \cdot (T/120)^2 \left[\frac{J}{m^3K} \right]. \quad (15)$$

3 CHEMO-THERMO-HYGRO-MECHANICAL ANALYSIS

3.1 Application to the PTM test by Kalifa et al.

Kalifa's experiments [19] have been accepted as a benchmark problem by many authors focused on modelling of concrete subjected to high temperatures. Within this experiment, see Figure 3, the specimens were subjected to a unidirectional heating up to e.g. 600°C using a radiant heater. For the numerical investigation this set up can be idealised by an 1D problem. On the heated side, the temperature is set as a heat flux and on the unexposed side a convective boundary condition is set as done in [20]. If not specified, all other boundary conditions are assumed as zero flux conditions. For the mechanical problem the actual stress state can be expressed by $\sigma_2 = -E(\alpha\Delta T - \varepsilon_{tr})$.

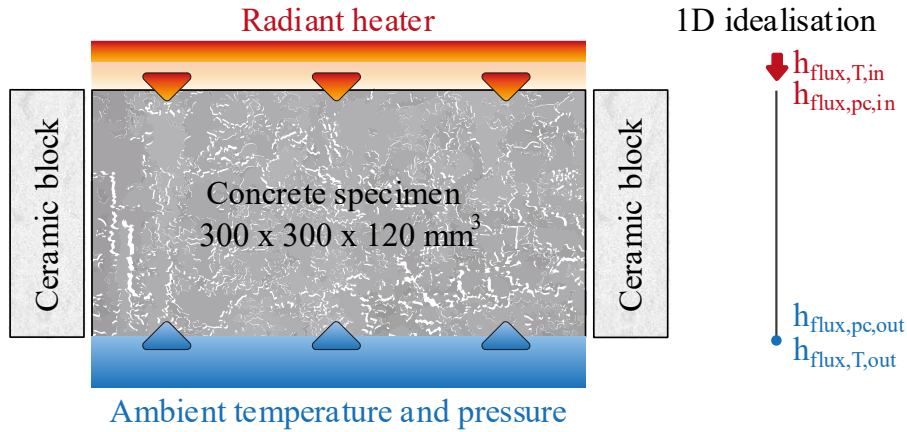


Figure 3. Scheme of the test set up and idealised numerical problem

3.2 Pore pressure development at elevated temperatures for different cement compositions

In the first numerical investigation, different the pore pressure developments of OPC, CEM III/B and CEM IV are compared. The initial saturation is set to 77% which is the reported value by Kalifa et al., the initial temperature is set to 20°C and the initial pore pressure to 101325 Pa. The boundaries on the exposed and outer part were set to [20]

$$h_{flux,T,in/out} = \alpha_{c,in/out}(T - T_{\infty}) + e\sigma_{SB}(T^4 - T_{\infty}^4), \quad (16)$$

$$h_{flux,pc,in/out} = \beta_{c,in/out}(\rho_v - \rho_{v\infty}), \quad (17)$$

where

$\alpha_{c,in}$ is set to 20, $\alpha_{c,out}$ is set to 4, $e\sigma_{SB}$ is set to $0.7 \cdot 5.67 \cdot 10^{-8}$, $\beta_{c,in}$ is set to 0.028, $\beta_{c,out}$ is set to 0.0009, and

$$T_{\infty} = \mathbf{1}_{0:300 [s]} \cdot (20 + t \cdot 1.3667) + \mathbf{1}_{300:\infty [s]} \cdot (430 + (t - 300) \cdot 0.00164) \quad (18)$$

The resulting pore pressures and temperatures at 2, 10, 20, 30, 40, 50 mm from the heated side are investigated. The simulation was carried out with Comsol Multiphysics and took about 100s calculation time. The domain was discretised with 1715 finite elements.

Figure 4 a) shows the different pore pressure evolutions of the investigated blended concretes in comparison with an ordinary Portland cement (CEM I) concrete. Only the temperature evolution of the CEM I concrete is shown because no mentionable differences between the blended and ordinary concrete was determined. The pore pressure developments of the different concretes are very similar in its shape and varying only in its maximal amplitudes, e.g. the maximal pore pressures of CEM I is 3.3 MPa, for CEM III/B is 3,7 MPa and for CEM IV 4 MPa.

Within this model, there are two main reasons for the higher induced pore pressures. First, higher pore pressures are induced, if more water is released at in a certain temperature range. Secondly, the pore pressures are generally higher when more water is released at lower temperatures as the permeability of concrete is increasing significantly at the onset of cracking. Table 1 shows that CEM III/B and CEM IV have more earlier dehydrating constituents in comparison to CEM I according to the hydration of the blast furnace slag and the pozzolanic reaction. In CEM I, the portlandite (CH) is not consumed during the hydration process, leading to a late water release in comparison with other hardened cement paste constituents, see Figure 2. CEM IV has the highest AFm content of the investigated concretes and has fewer late dehydrating constituents, leading to the highest pore pressures.

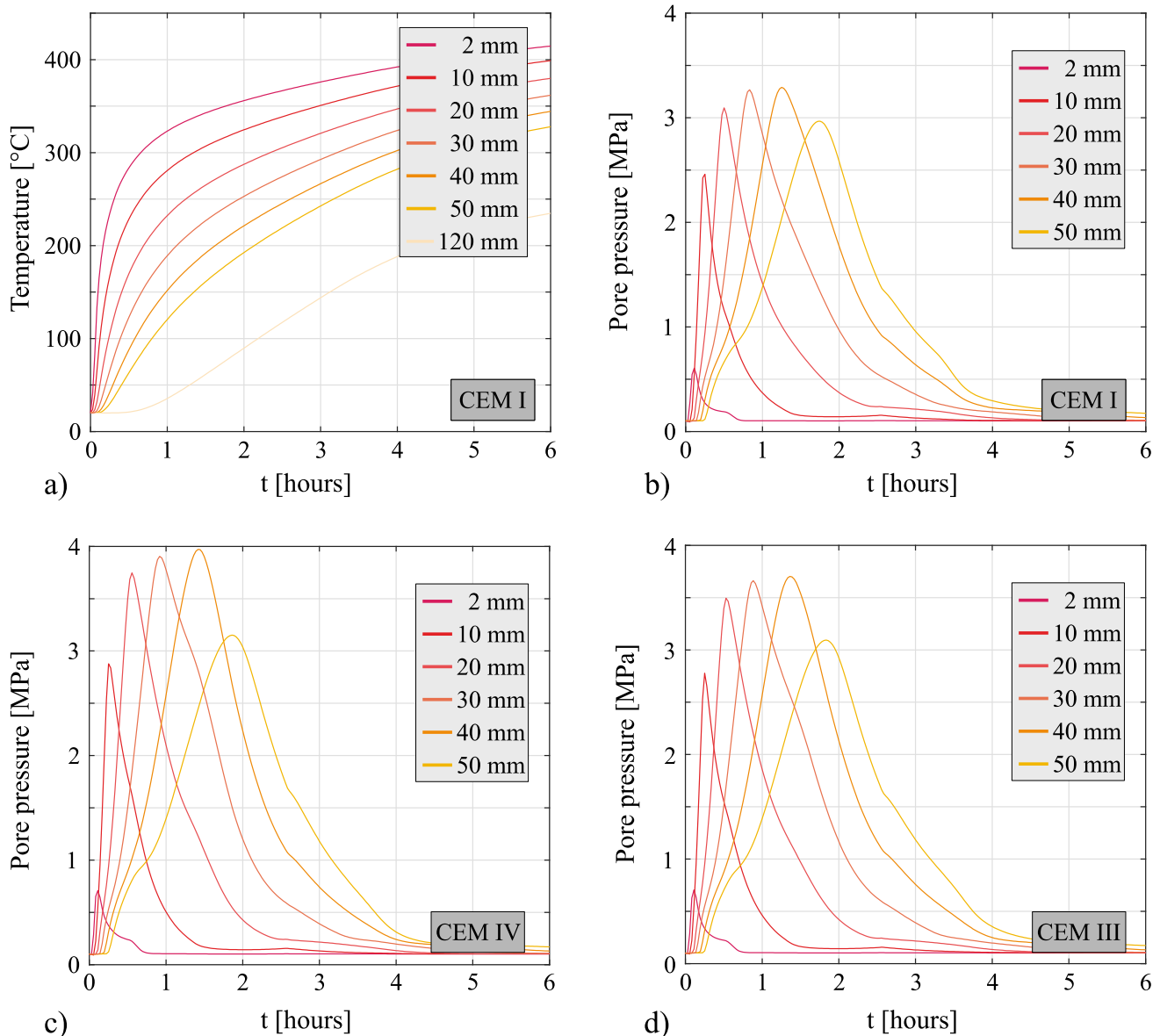


Figure 4. Comparison of the pore pressure developments of blended cement compositions with a CEM I. a) Determined temperature evolution by the presented model for concrete made of CEM I. b) Determined pore pressure evolution of a CEM I concrete by the presented model. c) Determined pore pressure evolution of a CEM VI concrete with calcined clay by the presented model. d) Determined pore pressure evolution of a CEM III concrete with blast furnace slag by the presented model.

3.3 Pore pressure development within a low initial moisture state

The next numerical analysis determines the pore pressure developments of the investigated blended concretes within a low initial moisture state. All boundary conditions remaining similar to the last example except the initial saturation at all points is set to 5%.

Figure 5 a) shows the different pore pressure evolutions of the investigated blended concretes in comparison with an ordinary Portland cement (CEM I) concrete. The pore pressure developments of the different concretes are varying in its maximal amplitudes and general shape. As in the last numerical example, CEM IV induces the highest pore pressures and CEM I the lowest for the same reasons discussed above. On the other hand, the general shape of the pore pressure developments is different. For CEM IV and CEM III the highest amplitude is at 40 mm from the heating exposed surface and for CEM I at 50 mm.

In this regard, more investigations are needed because the isotherms for concrete are poorly investigated for saturations below 10% and higher than 90%. This can lead to the relatively high induced pore pressures for the dried conditions.

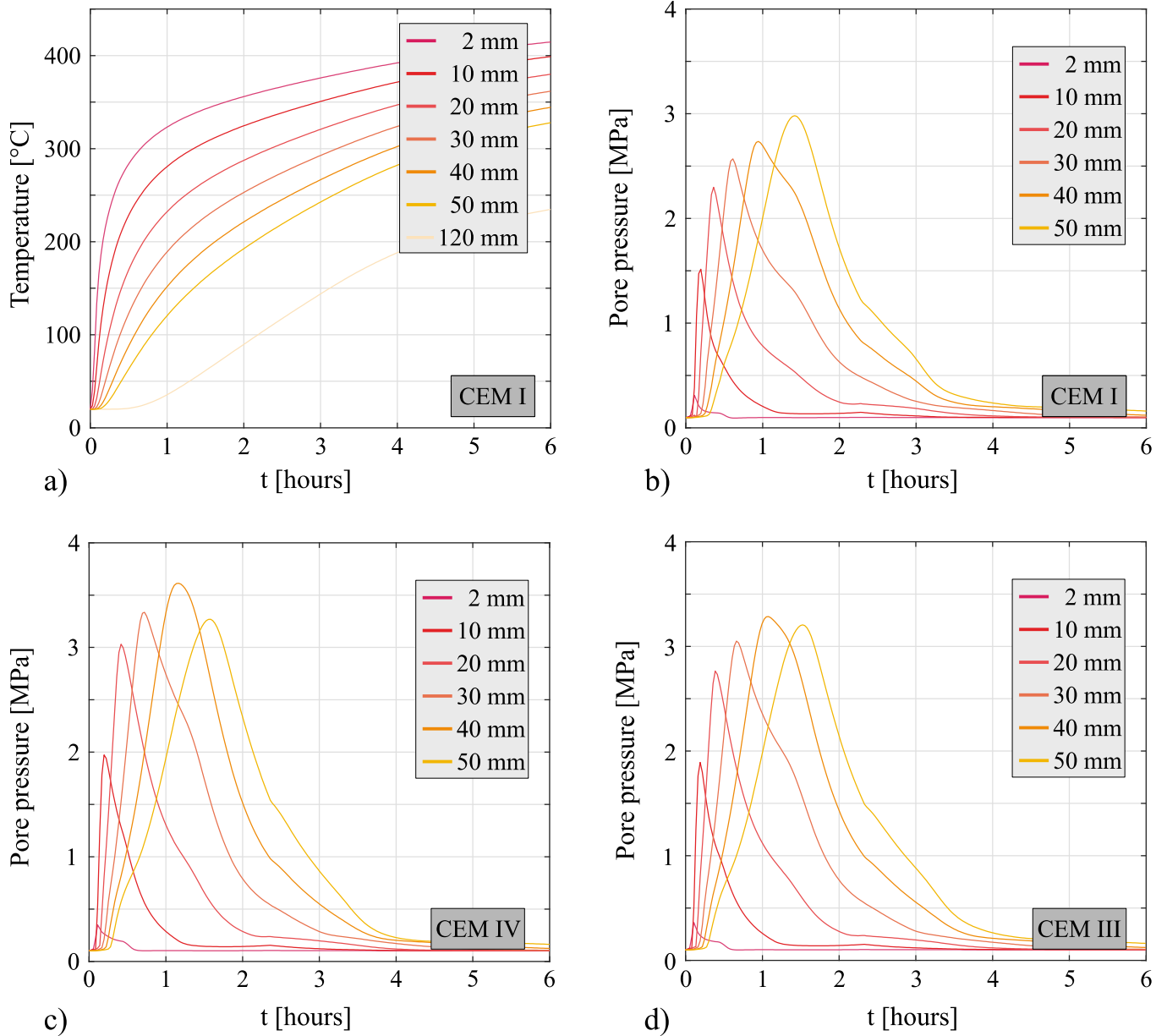


Figure 5. Comparison of the pore pressure developments of blended cement compositions with a CEM I. a) Determined temperature evolution by the presented model for concrete made of CEM I. b) Determined pore pressure evolution of a CEM I concrete by the presented model. c) Determined pore pressure evolution of a CEM VI concrete with calcined clay by the presented model. d) Determined pore pressure evolution of a CEM III concrete with blast furnace slag by the presented model.

3.4 Pore pressure development at elevated temperatures for different cement compositions with ISO fire loading.

The third numerical analysis investigates the pore pressure and saturation development within ISO fire loading, since the dehydration behaviour is time depended. All boundary conditions remaining like the first example except T_{∞} is defined as the ISO curve as

$$T_{\infty} = 20 + 345 \cdot \log(8t + 1). \quad (19)$$

Figure 6 a) shows the different pore pressure evolutions of the investigated blended concretes in comparison with an ordinary Portland cement (CEM I) concrete. The pore pressure developments of the different concretes are varying in its maximal amplitudes and general shape. As in the first numerical example, CEM IV induces the highest pore pressures and CEM I the lowest and the general shape of the pore pressure developments are similar.

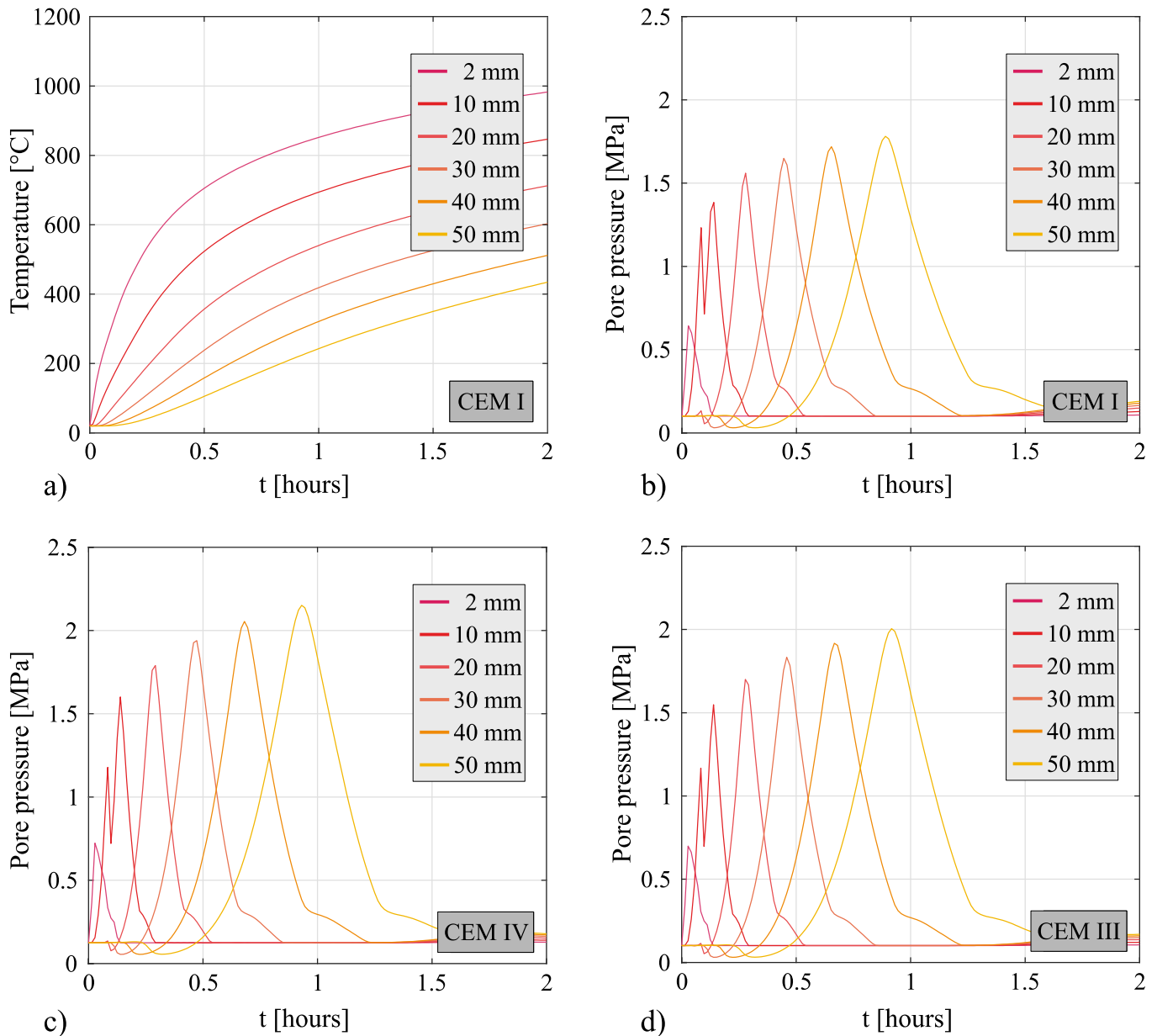


Figure 6. Comparison of the pore pressure developments of blended cement compositions with a CEM I under ISO fire loading. a) Determined temperature evolution by the presented model for concrete made of CEM I. b) Determined pore pressure evolution of a CEM I concrete by the presented model. c) Determined pore pressure evolution of a CEM VI concrete with calcined clay by the presented model. d) Determined pore pressure evolution of a CEM III concrete with blast furnace slag by the presented model.

Figure 7 shows the saturation development of a CEM I and a CEM IV concrete in a) and b) respectively. According to the different dehydration characteristics, a small moisture clog is created in the CEM IV saturation profile. As in the previous examples, the CEM III/B develops a saturation profile in which the plateau is higher than the CEM I and lower than CEM IV.

4 OUTLOOK

Further investigations will focus on the isotherms of the different blended concretes and a detailed multiscale implementation of a macroscopic damage law. In addition, a developed micromechanical framework [7] will be extended to further material parameters such as thermal conductivity and diffusivity, see e.g. [21].

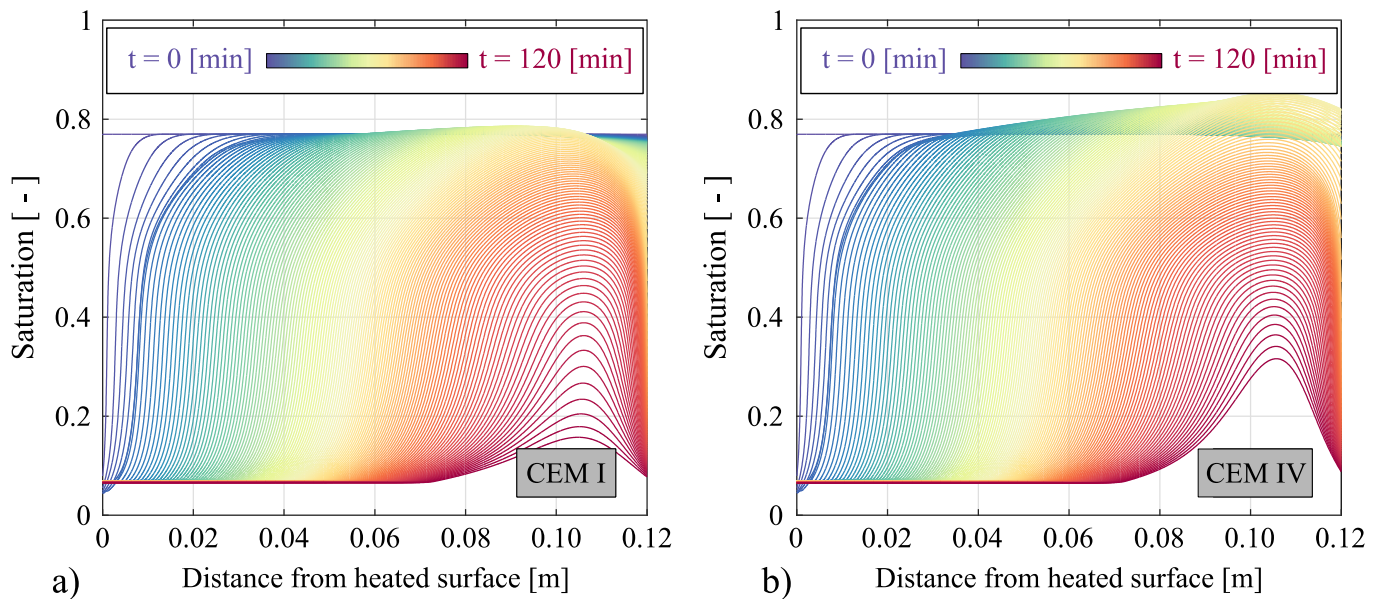


Figure 7. Comparison of the saturation profiles of the blended cement composition CEM IV b) with a CEM I a) under ISO fire loading

5 CONCLUSIONS

A chemo-thermo-hygro-mechanical multiscale model was proposed to investigate the pore pressure and saturation development of blended concretes (CEM III/B and CEM IV) at elevated temperatures under different heating rates and moisture conditions. The numerical investigations are summarised as follows:

- If a blended concrete contains more cement paste constituents dehydrating at lower temperatures, this results in lower pore pressure developments.
- More early dehydrating cement paste constituents within a concrete lead higher saturation plateaus.
- The dehydration kinetics do not affect the general trends of the saturation and pore pressure developments of the investigated blended concretes in comparison with a CEM I.
- The initial moisture condition significantly influences the shape and amplitudes of the pore pressure development.

ACKNOWLEDGMENT

Financial support was provided by the German Research Foundation (DFG) in the framework of the project “Thermohydraulic spalling mechanisms in concretes with different binders with and without PP-fibres under fire exposure: An experimental and numerical analysis” (Grant ME 1848/11-1). This support is gratefully acknowledged.

REFERENCES

1. Reiners, J, The Influence of the Physical and Chemical Properties of Hardened Cement Paste on the Fire-Induced Spalling of Concrete, Technische Universität Carolo-Wilhelmina zu Braunschweig, vol. 85, 2023.
2. Gawin, D, Pesavento, F, Schrefler, B.A., What physical phenomena can be neglected then modelling concrete at high temperature? A comparative study. Part 2: Comparison between models. *Int J Solids Struct* 49(13), 1945-1961 (2011). <https://doi.org/10.1016/j.ijsolstr.2011.03.003>
3. Zhao, J, Zheng, J, Peng, G., Breugel, K, Prediction of thermal decomposition of hardened cement paste, *J. Mater. Civ. Eng.* 24, 592-598 (2012). [http://dx.doi.org/10.1061/\(ASCE\)MT.1943-5533.0000423](http://dx.doi.org/10.1061/(ASCE)MT.1943-5533.0000423)
4. McNamee, R, Fire spalling of concrete: theoretical and experimental studies, KTH Architecture and Built Environment, (2013)
5. Wang, J, Lacarriere L, Sellier, A, Multicomponent modelling of cement paste dehydration under different heating rates, *Mater. Struct.* 52(1), (2019) 6. <https://doi.org/10.1617/s11527-018-1306-9>

6. S. Peters, G. Meschke, “Dehydration model of cement paste for predicting the material properties at elevated temperatures,” In: Proceedings of the 7th International Workshop on Concrete Spalling due do Fire Exposure, 2022
7. Peters S, Meschke, G, Computational multiscale modelling of thermally induced dehydration of blended hardened cement paste, *Cem. Concr. Res.* 180, (2024). <https://doi.org/10.1016/j.cemconres.2024.107485>
8. Gawin, D, Pesavento, F, Schrefler, B.A, Towards prediction of the thermal spalling risk through multi-phase porous media model, *Comput. Methods Appl. Mech. Engrg.* 195, 5707-5729 (2006). <https://doi.org/10.1016/j.cma.2005.10.021>.
9. Gawin, D, Pesavento, F, Schrefler, B.A., Modelling of hygro-thermal behaviour of concrete at high temperature with thermo-chemical and mechanical material degradation, *Comput. Methods Appl. Mech. Engrg.* 192, 1731-1771 (2003). [https://doi.org/10.1016/S0045-7825\(03\)00200-7](https://doi.org/10.1016/S0045-7825(03)00200-7)
10. Kulik D.A., Winnefeld, F, Kulik, A, Miron, G.D., Lothenbach, B., Cemgems – an easy-to-use web application for thermodynamic modelling of cementitious materials, *RILEM Tech Lett* 6, no. 1, 21–39 (2021). <https://doi.org/10.21809/rilemtechlett.2021.140>
11. Holmes, N., Tyrer, M, West, R, Lowe, A, Kelliher, D., Using PHREEQC to model cement hydration, *Constr. Build. Mater.* 319 (2022) 126129. <https://doi.org/10.1016/j.conbuildmat.2021.126129>
12. Wang, J, Modeling of concrete dehydration and multiphase transfer in nuclear containment concrete wall during loss of cooling accident, *Génie civil nucléaire, Université Paul Sabatier – Toulouse III*, (2016).
13. Feraille, A, Le rôle de l’eau dans le comportement a haute temperature des bétons, Thèse de doctorat, ENPC, France, 186p (2000).
14. Meschke, G, Grasberger, S, Numerical modelling of coupled hygro-mechanical degradation of cementitious materials, *J. Eng. Mech.* 129 (4), 383-392 (2003). [https://doi.org/10.1061/\(ASCE\)0733-9399\(2003\)129:4\(383\)](https://doi.org/10.1061/(ASCE)0733-9399(2003)129:4(383))
15. Rastiello, G, Boulay, C, Dal Pont, S, Tailhan, J, Rossi, P, Real-time water permeability evolution of a localized crack in concrete under loading, *Cem. Concr. Res.* 56(2), 20-26 (2014). <https://doi.org/10.1016/j.cemconres.2013.09.010>
16. Millard, A, Pimienta, P, Modelling of concrete behaviour at high temperature, *RILEM State-of-the-Art Reports*, Springer Cham, Basel. 2019. <https://doi.org/10.1007/978-3-030-11995-9>
17. Van Genuchten, MTh, A closed-form equation for predicting the hydraulic conductivity of unsaturated soils, *SSSAJ* 44, 892-898 (1980). <https://doi.org/10.2136/sssaj1980.03615995004400050002x>
18. Gawin, D, Majorana, CE, Pesavento, F, Schrefler, B.A., Numerical analysis of hygro-thermal behaviour and damage of concrete at high temperature, *Mech. Cohes. Frict. Mater.* 4, 437-74 (1999)
19. Kalifa, P, Chéné, G, Gallé, C, High-temperature behaviour of HPC with polypropylene fibres from spalling to microstructure, *Cem. Concr. Res.* 31, 1487-1499 (2001). [https://doi.org/10.1016/S0008-8846\(01\)00596-8](https://doi.org/10.1016/S0008-8846(01)00596-8)
20. Benes, M, Stefan, R, Hygro-thermo-mechanical analysis of spalling in concrete walls at high temperatures as a moving boundary problem, *Int. J. Heat Mass Transf.* 85, 110-134 (2015). <https://doi.org/10.1016/j.ijheatmasstransfer.2015.01.050>
21. Damrongwiriyapap, N, Scheiner, S, Pichler, B, Hellmich, C, Self-consistent channel approach for upscaling chloride diffusivity in cement pastes, *Transp. Porous Med.* 11, 495-518 (2017) <https://doi.org/10.1007/s11242-017-0867-3>

EXPERIMENTAL AND ANALYSIS OF PRECAST CONCRETE SANDWICH PANELS FAÇADE (PCSPF) SYSTEMS AT ELEVATED TEMPERATURES

Ali Nadjai¹, Donatella De Silva², Gabriella De Rosa³, Naveed Alam⁴, Faris Ali⁵

ABSTRACT

Like most structural members, the physical characteristics and resistance of the precast concrete sandwich panels deteriorate at elevated temperatures. These changes promote a considerable loss in the stiffness of the structural system and compromises the integrity of the stainless-steel ties which is a major concern. Therefore, it is imperative to investigate the precast concrete sandwich panels under the fire condition. To understand this concern and to propose an engineering solution, finite element modelling was conducted to simulate the behaviour of precast concrete sandwich panel system under fire conditions using SAFIR which is an advanced computational tool. The mechanical and thermal material nonlinearities of the structural members, such as the concrete walls and reinforcing bars were included in the model. The model used is based on the frame analogy considering a strip of wall to investigate the fire performance focusing on the integrity of the stainless-steel ties of the external wall cladding. The reinforcement stainless-steel tie connectors are considered based on the publication [1] to check the minimum satisfaction of the PCSPF system existing in construction. The model used demonstrated encouraging results for different cases considered during the study and the results from the computational modelling were well aligned with the experimental results.

Keywords: Experimental tests; fire and structures; finite element modelling; precast façade panels

1 INTRODUCTION

Precast concrete sandwich panels Façade (PCSPF) systems are known for their good inherent thermal and acoustic insulating properties. This technology allows the fast construction of energy-efficient and durable buildings. Due to these advantages and the growing need for sustainable solutions, sandwich panels have gained in popularity in industrial and residential construction. Precast concrete sandwich panels are usually composed of two steel-reinforced concrete walls and an insulation layer in between. The outer concrete layer usually does not play any structural role and serves solely as a form of aesthetic protection for the insulating layer. On the other hand, the inner layer concrete layer is load-bearing. The inner and the outer concrete walls are mechanically linked together by means of connectors. The connectors and insulation together constitute the so-called core layer. The inner, load-bearing concrete wall is designed to carry all

¹ Professor/Director, FireSERT Ulster University, UK

e-mail: a.nadjai@ulster.ac.uk, ORCID: <https://orcid.org/0000-0002-9769-7363>

² Lecturer, University of Naples Federico II,

e-mail: donatella.desilva@unina.it, ORCID: <https://orcid.org/0000-0002-4058-902>

³, Lecturer, University of Naples Federico II,

e-mail, ing.gabrieladerosa@gmail.com,

⁴ Lecturer, FireSERT Ulster University, UK

e-mail: n.alam@ulster.ac.uk, ORCID: <https://orcid.org/0000-0003-3637-1113>

⁵ Professor, FireSERT Ulster University, UK

e-mail: f.Ali@ulster.ac.uk, ORCID: <https://orcid.org/0000-0002-9807-6251>

the vertical and bending loads. The design of the connectors in the PCSPF system must be robust and checked at ultimate limit state to satisfy strength, stability, stiffness, serviceability, soundness.

In fire situation, the insulation layer should first ensure the thermal protection of the load-bearing inner layer, stay firm during the fire, and not contribute to fire spread. Further, especially for sandwich walls, the effectiveness of shear transfer during fire, provided by the insulation and connectors, should be assessed, since this gives information about their contribution to the PCSPF system action. Additionally, since the concrete precast walls are produced with different thicknesses, the side of the wall being exposed to fire could potentially impact the behaviour of the connectors.

1.1 Assumptions and objectives

To obtain comprehensive information on the fire resistance of the PCSPF systems used in construction, the worst-case scenario is considered with the following assumptions:

- 1) The base of the study is the experimental test conducted by FireSERT on the heat transfer of a thinner bearing PCSPF wall with 80 mm thickness.
- 2) The representative limiting insulation layer thickness of 200mm is considering based on the heat transfer test conducted at FireSERT and the computational modelling is conducted for a period of 120minutes for a bearing wall with 80mm concrete thickness (FireSERT fire test simulation, figure 10).
- 3) Thicker thermal insulation, as shown in figure 10, can expose larger lengths of the connector to high temperatures. Such exposure conditions result in the deteriorated mechanical properties over longer lengths in connectors which can lead to more severe damage to the shear connection between the inner and the outer concrete precast walls. Hence for longer connector ties with higher thickness of the insulation, more server damage may be encountered as compared to the case with short connectors resulting from lesser thickness of the insulation.
- 4) Due to the wide range of connector types available on the market [1,2], the minimum reinforcement steel tie connectors [1] are considered to check the minimum satisfaction of the PCSPF system existing in practice.

To solve this problem finite element model is proposed to simulate the PCSPF system behaviour under fire conditions using SAFIR, an advanced computational modelling tool [3]. The mechanical and thermal material nonlinearities of the structural members, such as the concrete walls and steel reinforcement, insulation are included in the model. The model is validated at the early stages by conducting a comparative analysis of the numerical modelling results with the precast panel test conducted at FireSERT. The methodology used in this work is listed below as:

- Objective 1: Analysis of fire resistance test precast concrete facade system conducted FireSERT, Ulster University, using ISO834 fire curve.
- Objective 2: Computational studies on the tested façade systems from Objective 1 using SAFIR software to validate the computational (finite elements, FE) models to further understand their fire and structural performance focusing on the stainless-steel ties integrity.
- Objective 3: To extend the thermal and structural models from Objective 2 to other potential parametric study to cover an analysis based on worst case scenario with assumptions discussed previously with the goal to verify the fire safety level of the stainless-steel tie integrity using the ISO834 Fire curve.

The analyses conducted during this research is based on the recommendations and principles from the Eurocodes [4,5] listed as references.

2 GENERAL EXPERIMENTAL ON PRECAST SANDWICH PANEL

The experimental details of the fire test conducted at FireSERT Ulster University are shown in Figure1. This experimental investigation was aimed at assessing the fire resistance of reinforced concrete sandwich walls with thermal insulating materials (see Figure 2). The adopted dimensions (1500mm by 1500mm – width by height) of the half scale sandwich walls followed by the BS EN 1363-1, 2012 [7]. The testing

specimen was constructed out of three layers: internal reinforced precast wall exposed to elevated temperature, a core layer of mineral wool thermal insulating non-combustible material and the external concrete layer. The furnace internal temperature was monitored and regulated with four standard- plate thermocouples placed approximately 100 mm away from the fire-exposed surface of the specimen. The fire test provided a useful data set on the recorded thermal distribution across the cross-section of the wall system which will be used to achieve objectives 2 and 3 mentioned in the previous section.



Figure 1. Precast sandwich Panel tested at Ulster University using ISO834 for 1 hour fire resistance

Figure 2 illustrates the cross-sectional details of the sandwiched concrete wall panel used during the experimental fire test. The instrumentation comprised of 3 thermocouples in the Structural Face side (SF) exposed to the fire, 2 thermocouples in the unexposed Architectural Face side (AF), and an additional TC at the cooler face.

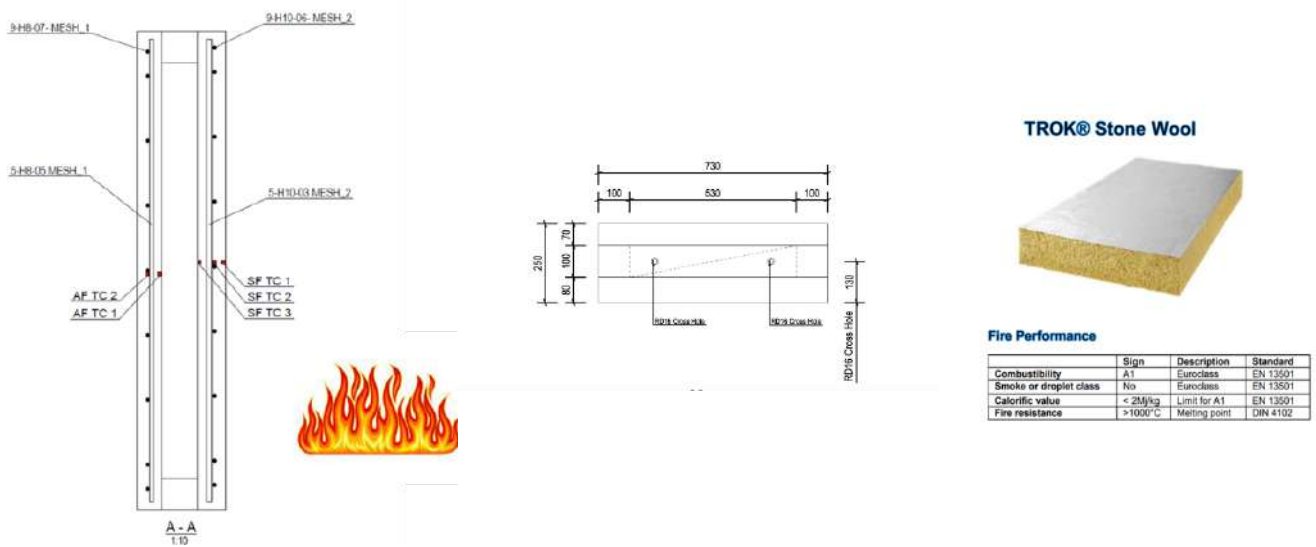


Figure 2. Details of the PCSPF system used during the experimental work

3 COMPUTATIONAL VALIDATION OF THE EXPERIMENTAL FIRE TEST USING SAFIR

3.1 Experimental test results

The fire exposure conditions during the test were in accordance with the standard temperatures time curve. This is seen in Figure 3 where the furnace temperatures recorded by all 6 thermocouples used have been provided. Further, the average temperatures recorded in the furnace have been presented as a thick black line which are on accordance with ISO834 curve, which is presented as a thick red line in Figure 3. The

data presented in Figure 3 shows that the heating conditions during the test were in accordance with the standard temperatures time curve, ISO834.

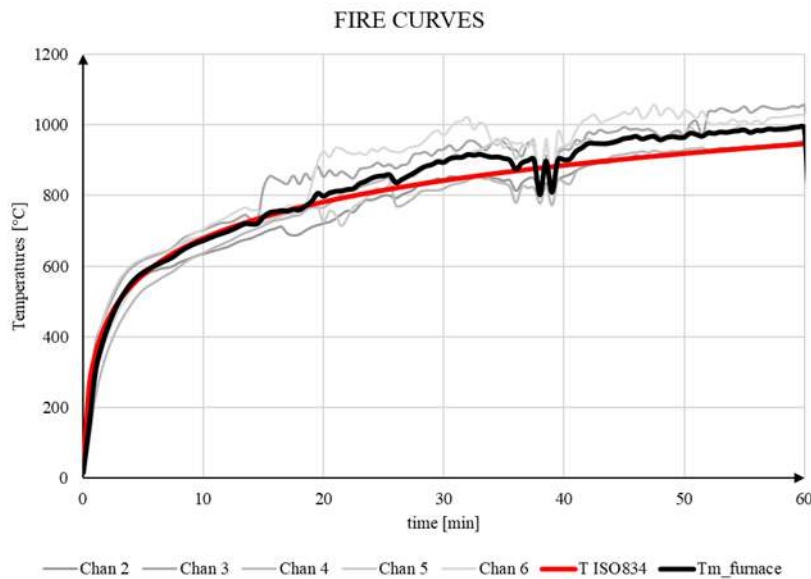


Figure 3. ISO fire curve and comparison with furnace temperatures

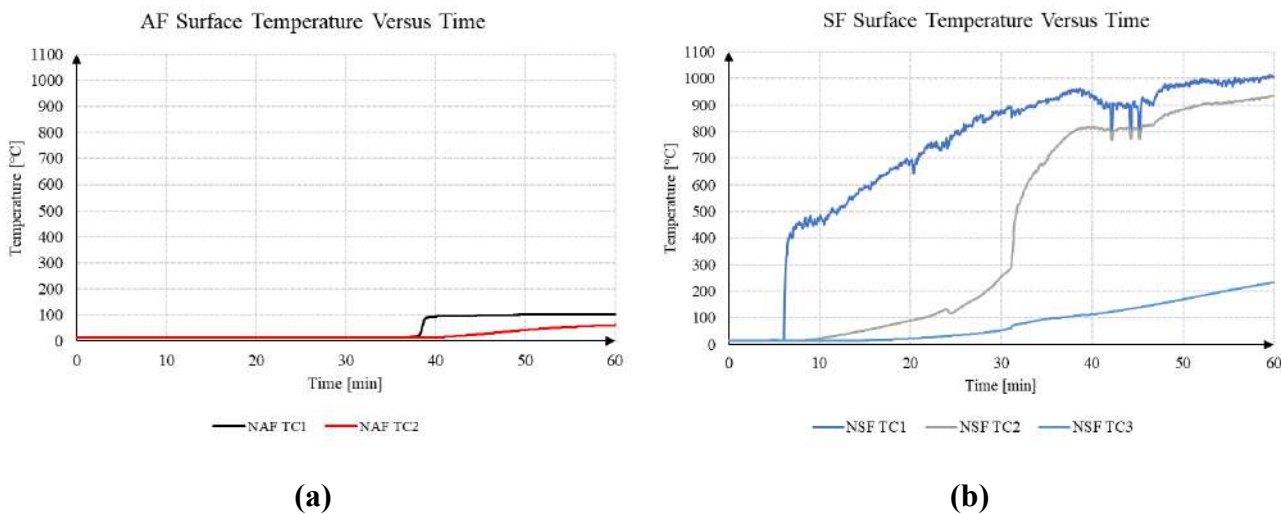


Figure 4. Temperatures recorded during the fire test in the unexposed (AF) and exposed (SF) concrete walls

The thermal data recorded in the insulated concrete wall panel is presented in Figure 4 for both unexposed and exposed sides. It is seen in Figure 4 (a) that the temperatures in the exposed concrete wall (AF) remain below or around 100°C for the while duration of the fire test. On the other hand, temperatures recorded in the exposed concrete wall are significantly higher reaching around 1000°C in some thermocouples. Further, the results in Figure 4 (b) show that the results near the exposed surface (TC1) are highest and with the increase in the distance from the exposed surface, recorded temperatures reduce (TC2 and TC3).

The average temperatures recorded on the unexposed surface have been presented in Figure 5 which are around 15°C. Considering the insulation requirements of structural members which should serve as fire walls, the mean temperature on the unexposed side must not exceed 180°C [8].

Although testing standards do not set requirements for the temperature increase within the cross sections of the wall to the side not exposed to fire enables a better understanding of the thermal and mechanical performance of insulation and the steel tie connectors.

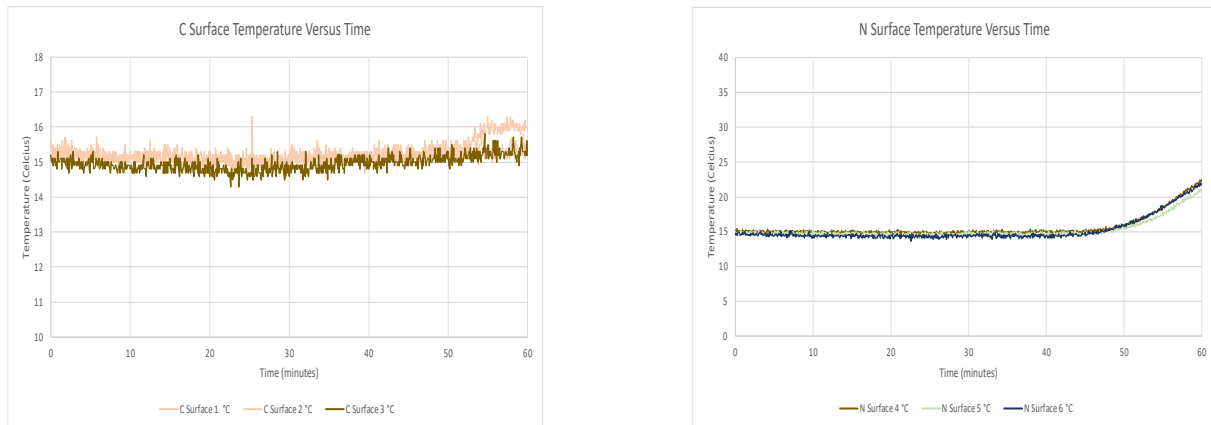


Figure 5. Temperatures recorded at the surface of the unexposed side

3.2 Validation of the Experimental fire test with SAFIR

As mentioned earlier, SAFIR is a computer program that models the behaviour of buildings and structures subjected to fire. The structure can be made of a 3D skeleton of linear elements such as beams and columns, in conjunction with planar elements such as slabs and walls. Volumetric elements can be used for analysis of details in the structure such as connections. Different materials such as steel, concrete, timber, aluminium, gypsum, or thermally insulating products can be used separately or in combination in SAFIR for numerical studies. Keeping in view the advantages, SAFIR software was employed to conduct the finite-element simulation of the temperature field of PCSPF system cross sections (see Figure 6). This was done through the validation of the test conducted by FireSERT and later the validated model was used to conduct further studies. During the FE analysis, nonlinear elements were considered, taking in account mechanical and geometrical non linearities.

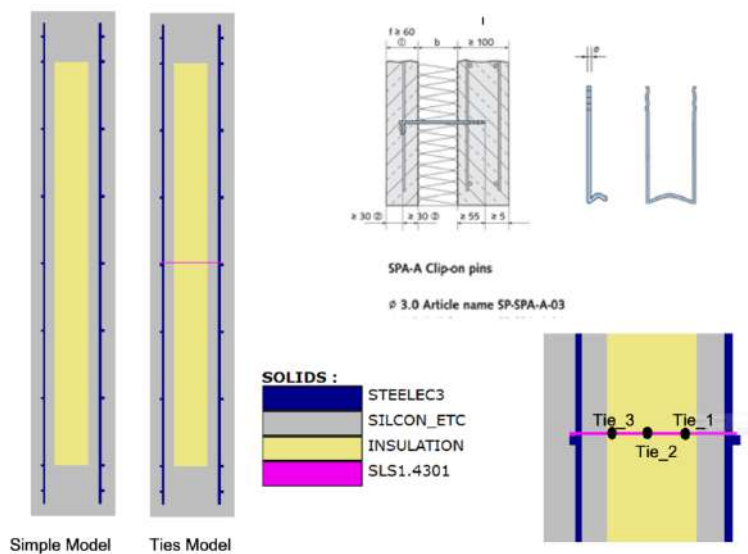


Figure 6. Computational modelling details (SAFIR Models)

The computational modelling was conducted for two PCSPF systems:

- 1) The precast wall with wool rock insulation.

2) The precast wall with wool rock insulation with steel ties element.

Details of both models can be seen in Figure 6 where simple and the tie model are shown adjacent to each other. Further, the elements of the models in terms of the clip-on pins, details of ties and materials have also been shown.

The results from the computational modeling are presented against the test data in Figures 7 and 8. The results presented are in terms of temperatures and there is a good agreement between the test and the analysis results from SAFIR modelling. As the computational model applied is efficient and can replicate the test conducted by FireSERT, it will be employed to conduct further studies in the proceeding sections.

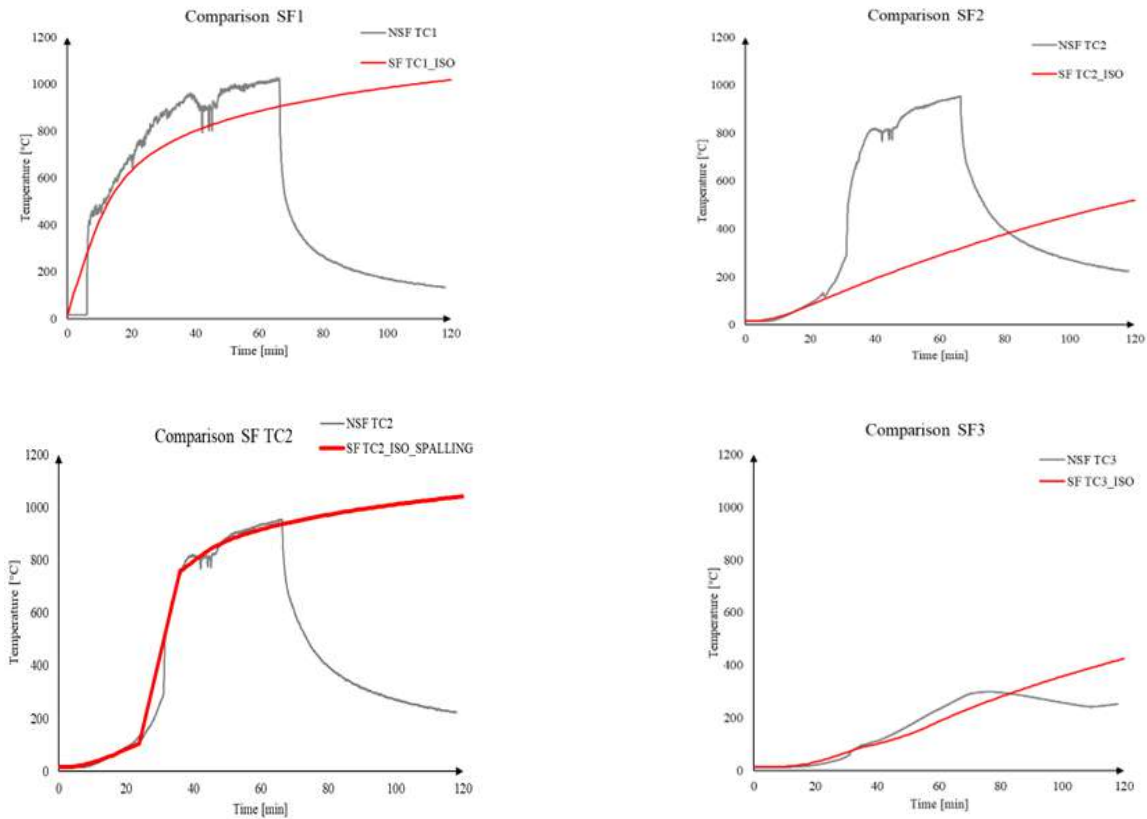


Figure 7. Comparison between computational and experimental temperatures for PCSPF panel exposed to the ISO834

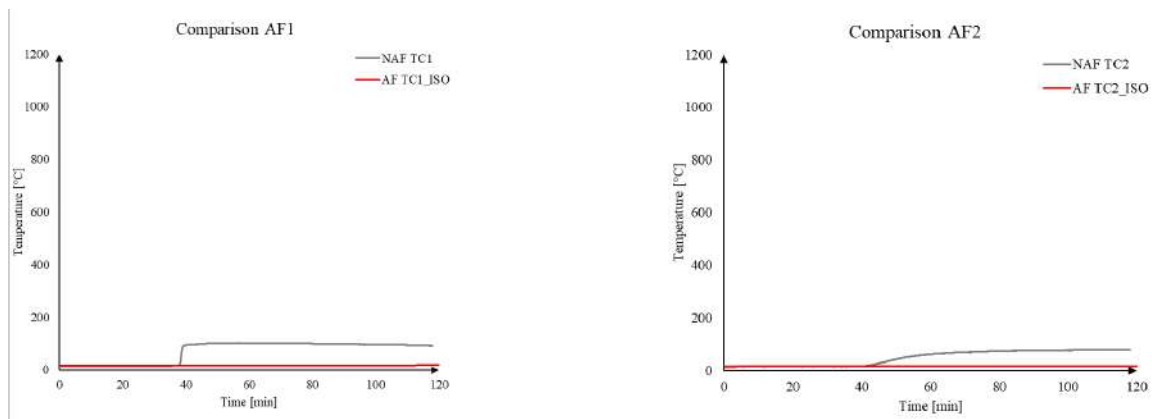


Figure 8. Comparison between SAFIR and experimental temperatures in an exposed panel to the ISO834

3.3 Connectors Behaviour

The validated analyses approach was repeated to study a case which considered the connected element between the two parts (inner and outer walls) of the concrete to investigate the influence of heat transfer on the steel tie connectors between the two walls. As shown in Figure 10, on the unexposed surface, the temperatures given by the ties model (dashed black line) are generally higher than the ones obtained for the simple model (red line). Also, in Figure 9, the influence of concrete spalling on recorded temperatures can be seen clearly.

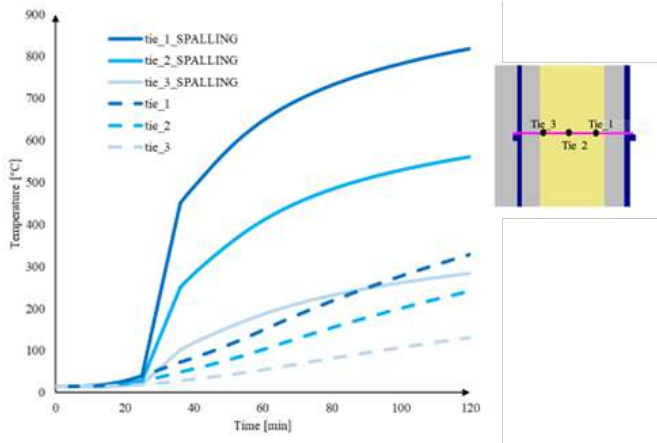


Figure 9. Steel Ties influenced by the concrete spalling

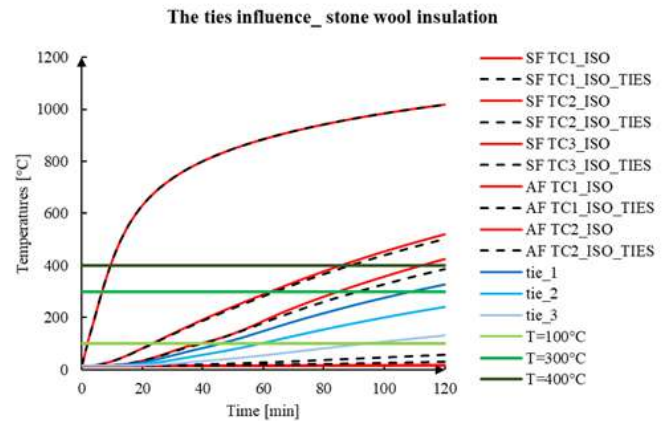


Figure 10. Maximum temperature recorded at steel ties is between 160°C- 330°C for 2 hours fire resistance ISO834

Eurocodes, BS EN 1993-1-2: 2005 [9], propose the reduction factors at elevated temperatures related to strength and stiff as presented in Table 1. This if compared to the FE analysis results where the temperatures in the steel ties was around 300°C or less, it can be concluded that the stiffness and strength are almost at its full capacity, 88% and 73% as evident from Table 1 below.

Table 1. Factors for determination of stain and stiffness steel at elevated temperatures

Steel Temperature θ_a	Reduction factor (relative to E_a) for the slope of the linear elastic range $k_{E,\theta} = E_{a,\theta}/E_a$	Reduction factor (relative to f_y) for proof strength $k_{0.2p,\theta} = f_{0.2p,\theta}/f_y$	Reduction factor (relative to f_u) for tensile strength $k_{u,\theta} = f_{u,\theta}/f_u$	Factor for determination of the yield strength $f_{y,\theta}$ $k_{2\%,\theta}$
Grade 1.4301				
20	1,00	1,00	1,00	0,26
100	0,96	0,82	0,87	0,24
200	0,92	0,68	0,77	0,19
300	0,88	0,64	0,73	0,19
400	0,84	0,60	0,72	0,19
500	0,80	0,54	0,67	0,19
600	0,76	0,49	0,58	0,22
700	0,71	0,40	0,43	0,26
800	0,63	0,27	0,27	0,35
900	0,45	0,14	0,15	0,38
1000	0,20	0,06	0,07	0,40
1100	0,10	0,03	0,03	0,40
1200	0,00	0,00	0,00	0,40

4 ANALYSIS OF FULL-SCALE PRECAST SANDWICH PANEL FAÇADE

With the full satisfaction with the validation, the computational study was extended to model a real scale PCSPF system (see Figure 11) with the external panel subjected to gravity loading which facilitated a

possibility of vertical deflection. In a situation where the PCSPF is exposed to fire, the insulation layer should first ensure the thermal protection of the load-bearing layer, stay firm during the fire, and not contribute to fire spread. Further, the effectiveness of shear transfer during fire provided by the insulation and connectors should be assessed, especially for sandwich walls, since these are one of the core elements of PCSPF system and contribute to their functionality as a construction element.

The thickness of the insulation between the concrete walls is one of the key aspects in the design of PCSPF systems as it influences the temperature development along their cross-section, therefore, different mechanical performances. Additionally, since the concrete precast walls in any PCSPF system have different thickness, the side of the wall being exposed to fire could potentially impact the behaviour of connectors. In case of higher thickness of insulation, longer length of the connector will be outside concrete and may expose to fire which may result in achieving higher temperatures. As the mechanical properties deteriorate at higher temperatures, longer connectors can lead to more severe damage to the shear connection between the precast concrete walls of a PCSPF system as compared to the case with short connectors. To study the response of a critical PCSPF system, the worst scenario was considered during this study with assumptions discussed before.

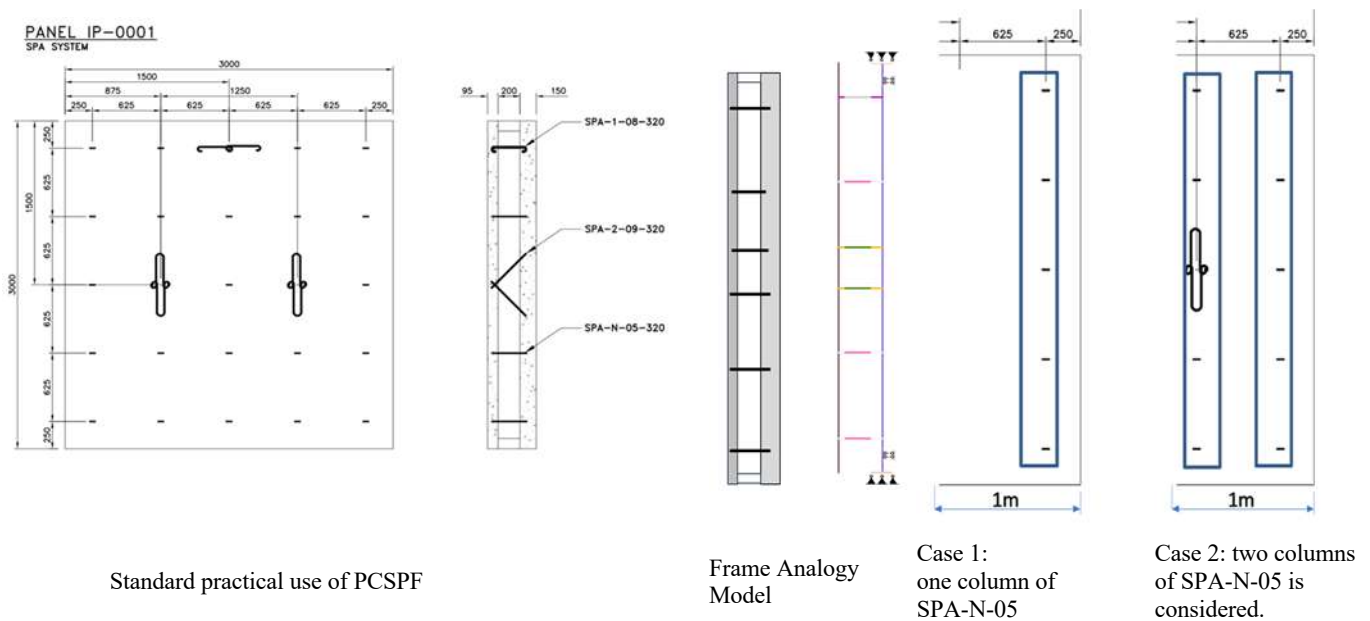


Figure 11. Detailing of PCSPF and model used with two scenarios using minimum steel tie reinforcement

4.1 SAFIR 2D and 3D computational models

Before proceeding with further studies, a benchmark study was conducted using 2D and 3D modelling approaches. The purpose of this benchmark study was to find the most economical modelling approach in terms of computational time. Figure 12 demonstrates the temperature distribution in the PCSPF system by comparing the 2D and 3D modelling results. It can be seen that the 2D modelling results are in a good agreement with the 3D results, hence, the 2D modelling approach will be used to study further cases of PCSPF systems.

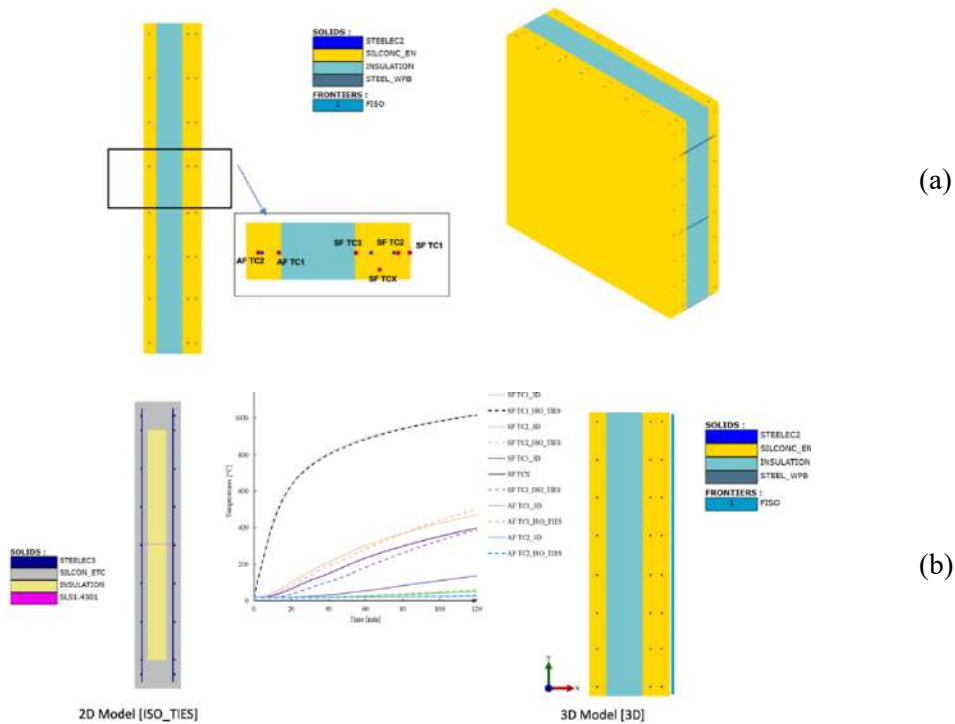


Figure 12. Comparison 2-D with 3-D modelling results, (a) 3D, (b) 2D

4.2 SAFIR Model for a possible worst-case scenario

4.2.1 FE Modelling Approach

The FE modelling was conducted for a worst-case scenario (the critical case) by modelling a 1m band with minimum steel reinforcement of one column of reinforcement considering only the SPA-N-05-320. In particular, the SAFIR thermo-mechanical analyses were performed by considering each part of the wall (e.g. external wall and structural wall) as beam elements, connected by the ties (see Figure 13), developed by Nadjai [6]. The software SAFIR works in a decoupled way, by means thermal analyses of all the structural section in the first step and the thermo-mechanical analyses in the second step. Therefore, in the next sections the results of both thermal (STEP 1) and thermo-mechanical (STEP 2) analyses are reported, by including all the assumptions and thermal conditions.

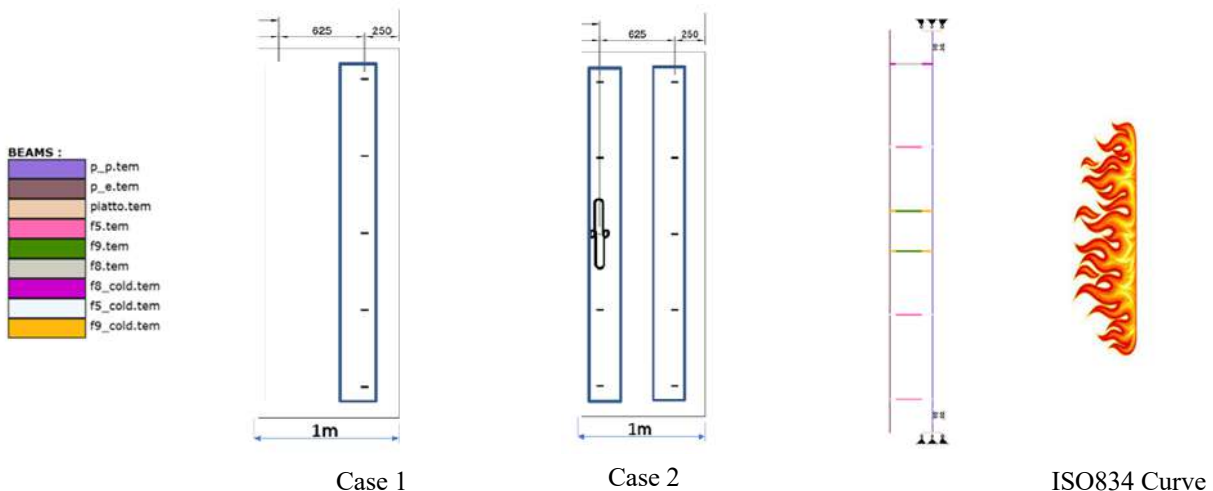


Figure 13. Minimum reinforcement used the 1m band with wall constraints are hinged

4.2.2 STEP1: Sectional thermal analyses

The temperature distribution in each part of the PCSPF system were calculated starting from the results of the detailed thermal analyses explained before which yielded a good agreement between the experimental and numerical results. The details of thermal analyses for each component of the PCSPF section are given in the following.

External wall: The F20 frontier has been imposed to the unexposed architectural face, to permit the heat exchange with the external ambient. While, on the other face, the temperature distribution called “myfire.fct” (see Figure 14), which is the temperatures curve reached in the nondimensional analysis (as seen before in Figure 8), to better reproduce the real thermal field reached during the experimental test was assigned. This frontier is assigned to the face on the insulation side.

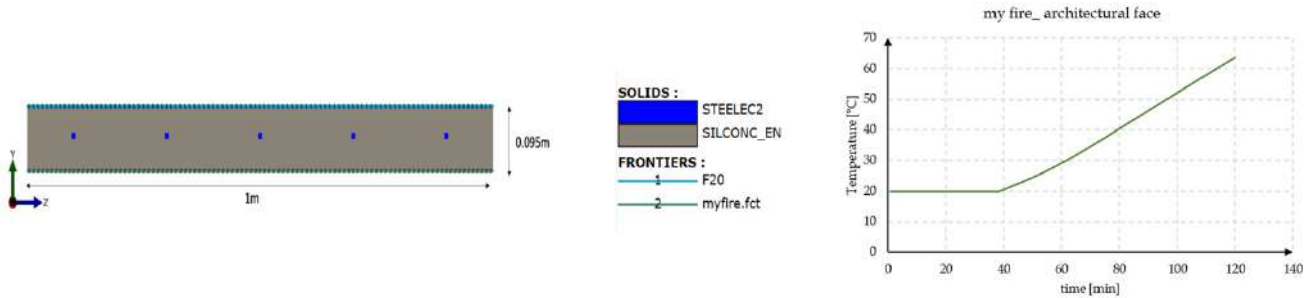


Figure 14. The external wall and temperature curve used

Structural Wall: The structural wall is exposed to the standard fire curve, ISO-834.

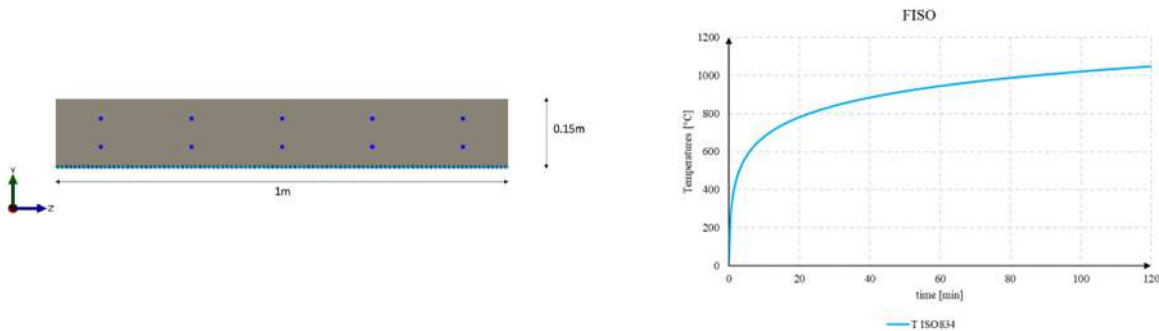


Figure 15. Bearing wall exposed of ISO fire curve

Ties Temperatures: For better reproduce the real condition, the temperature frontier for the ties sections was directly taken from the 3D thermal model, as shown in the following Figure 16.

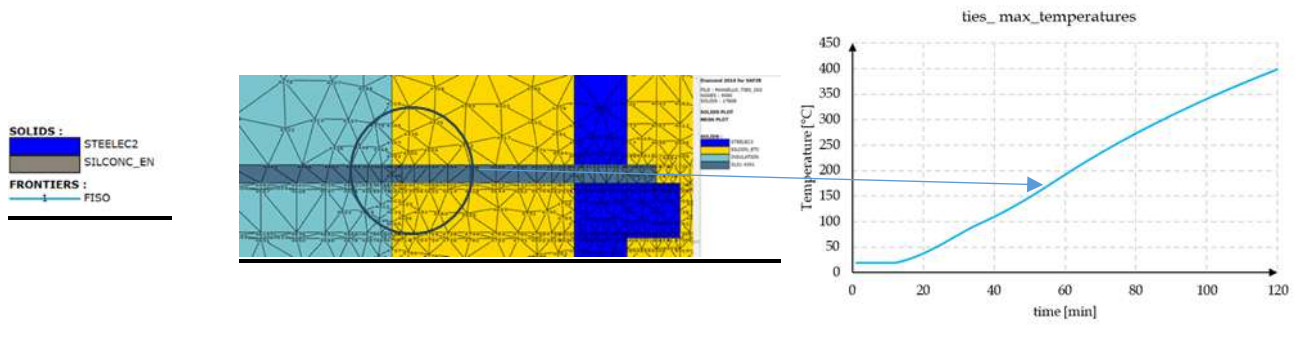


Figure 16: The temperatures given by the mono-dimensional analysis (Node 4545) were assigned as frontier (1) to the tie’s boundary

4.2.3 Thermo-mechanical Analyses Results

In this section the results of the performed thermo-mechanical analyses were reported. The loading applied on the structural internal wall is 50 kN/m on a strip of 1m band of walls considering the self-weight of both internal and external walls. Considering the same boundary conditions as in practice where the top and bottom parts are restrained by the side walls and slabs above and below at the level of each intermediate floor. The deflection of the external cladding between each level should not exceed the practical gap of 15mm. It can be seen from Figure 17 that the deflections of the external wall in both case is not exceeding the 15 mm. Therefore, the stainless-steel ties integrity of the external wall cladding is well satisfied for both cases.

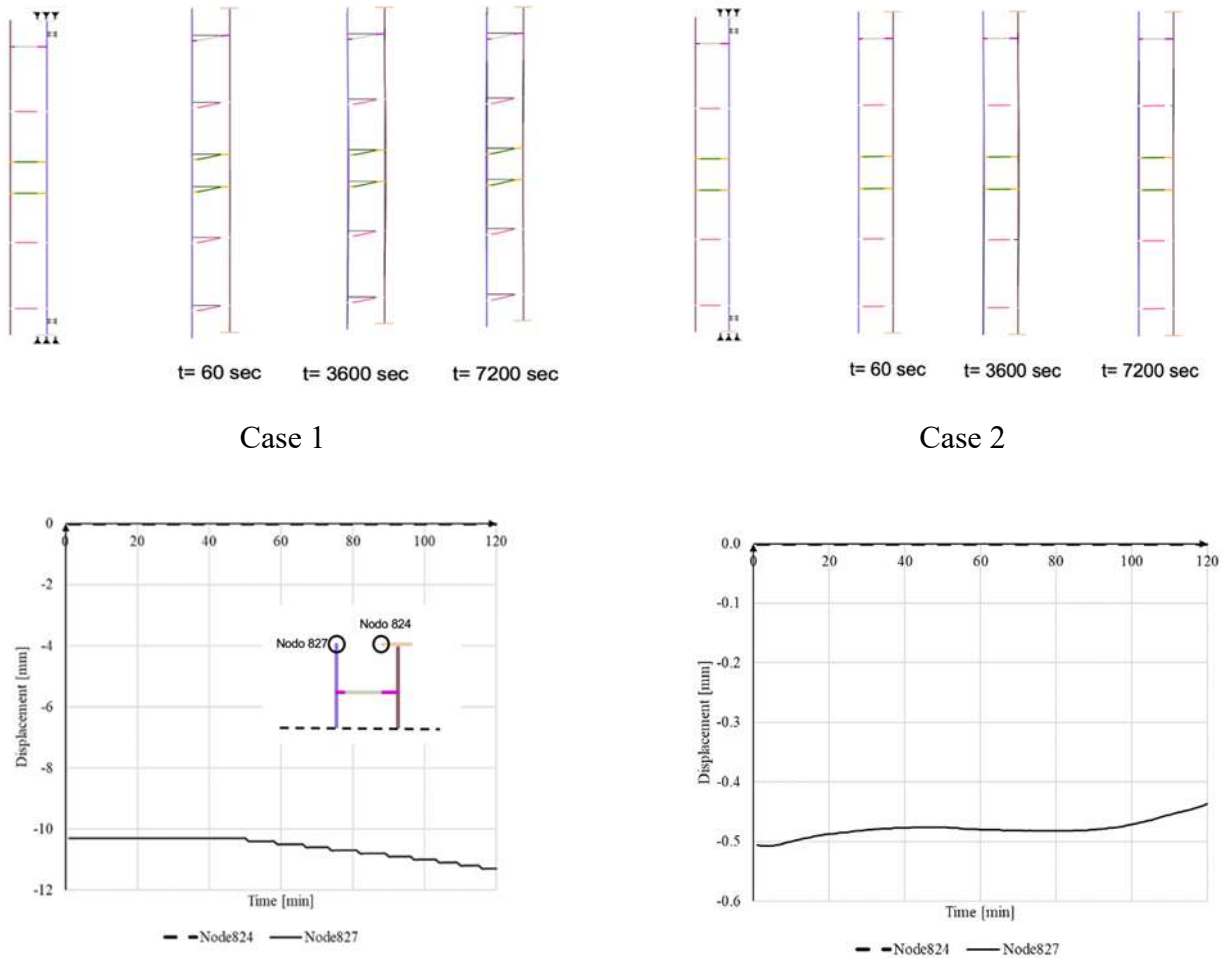


Figure 17: deflection of the external wall for both cases are less than 15mm provided in the gap between walls of each floor level

5 DISCUSSION ON RESULTS

Following the frame analogy model process and the obtained results by considering the worst-case scenarios in the absence of real fire full scale, and with the assumption discussed in the core it can be summarised that: The model provided an excellent validation with the experimental conducted by FireSERT at Ulster University, the thermal and structural performance of the insulation and connectors under high temperatures were analysed. Following the BS EN 1993-1-2: 2005, it can be concluded that the stiffness and strength are almost at its full capacity. The displacement of the unsupported facing wall is very small for case 1 and negligible for case 2 using the minimum reinforcement as the critical benchmark.

- In case 1, the deflection of the external wall is already 10.2 mm at the early stage and next increase beyond 50min and achieve 11.3 mm in 120min. This case can represent a PCSPF left with minimum tie connectors reinforcement in actions.
- In case 2, with the increase of the tie connectors reinforcement area the deflection of the external wall is reduced at 0.5mm at early stage but next moved upwards to 0.45mm for a duration of 120min. This indicates that the displacement of the edge resulting from the rotation caused by the heat induced bowing that the potential sagging of the wall under its weight supported by the core layer.

6 CONCLUSIONS

It can be concluded that with the minimum reinforcement connectors maintain their mechanical properties throughout the fire resistance of 120 minutes and are able to maintain a constant distance between the concrete precast walls, coupling them together for a typical external wall 95mm, insulation 200mm and internal wall 150mm. Increasing the thickness of the internal wall over 150mm will increase the fire resistance of the system and with the additional connectors as designed in the system will maintain their mechanical properties throughout the fire resistance of 120 minutes even with the increase of the insulation thickness over 200mm, and the deflection of the external will be very small by moving upward and behave like case 2 as discussed above. On the other hand, if the internal wall thickness is reduced than 150mm, for example 130mm with less insulation thickness as 100mm, the PCSPF system can achieve 120min fire resistance as the assumptions used are the most critical. Further experimental tests of the PCSPF system are under consideration to be conducted in the near future in FireSERT at Ulster University.

REFERENCES

1. Leviat A CRH Company (2020), Halfen Sandwich Panel Anchors, Technical Product Information, 2020 SP 19.1-E. (Available at: https://downloads.halfen.com/catalogues/de/media/catalogues/precastsystems/SP_Leviat_19-1-E.pdf)
2. Fédération Internationale du Béton. Fib Bulletin No. 84. Precast Insulated Sandwich Panels; International Federation for Structural Concrete: Lausanne, Switzerland, 2017.
3. J.M. Franssen & T. Gernay, User's manual for SAFIR 2016c - A computer program for analysis of structures subjected to fire, 2017.
4. Eurocode 1. "Actions on Structures, Part 1-2: General Actions - Actions on Structures Exposed to Fire," 2002.
5. Eurocode 4. "Design of Composite Steel and Concrete Structures, Part 1-2: General Rules - Structural Fire Design." Commission of European Communities, Brussels, Belgium, 2005.
6. A. Nadjai, & D. Johnson, Analysis of spatial real buildings by discrete force method, The structural Design of Tall Buildings, Vol 5, Nre3: pp183-204, 1996.
7. British Standards Institution. (2012). BS EN 1363-1:2012 Fire resistance tests - Part 1: General requirements. BSI Standards Limited.
8. British Standards Institution, "BS 476-21 - Fire tests on building materials and structures. Methods for determination of the fire resistance of loadbearing elements of construction," 1987.
9. British Standards Institution. (2005). Eurocode 3: Design of steel structures - Part 1-2: General rules - Structural fire design. BSI Standards Limited.

FIRE FRAGILITY ASSESSMENT FOR BRIDGE STRUCTURES

Donatella de Silva¹, Andrea Miano², Gabriella De Rosa³, Francesco Di Meglio⁴, Andrea Prota⁵, Emidio Nigro¹

ABSTRACT

Italy is strongly interested by seismic and hydrogeological hazards and, in addition, degradation and obsolescence phenomena are common on infrastructures approaching the end of their nominal life. Furthermore, during their service life these infrastructures can be subjected also to extreme actions such as the fire. In particular, the past examples of damages on infrastructures as consequence of fire accidents and the high dependency on uncertain factors of fire have inspired the study for developing methodologies to estimate the possible consequences that this phenomenon can cause on infrastructures. In particular, the paper sets a procedure to assess the structural fire fragility of infrastructures, based on fire hazard scenarios, developed specifically for bridges. Then, two existing typological case studies (a reinforced concrete bridge and a composite steel-concrete one) are modelled, by deriving the structural response under different natural fire scenarios. By means of Cloud Analysis, a linear regression about the key parameters in the fire action definition and the structural response is assessed, by considering different performance levels, specifically proposed for bridges. Finally, the fragility curves are obtained, measuring the capacity of the case study bridges under the selected fire scenarios. The study also shows which of the fire scenarios parameters can be better correlated to the structural response of the bridge, that is useful for a proper fire resistance assessment and design.

Keywords: Fragility curves; fire resistance; numerical simulations; damage levels, bridges

1. INTRODUCTION

In recent years, the risk of fire in transportation infrastructure has significantly increased, mainly due to the rapid development of urban ground transportation systems and the increase in transportation of hazardous materials 1. These fires can cause significant losses both economically, due to the costs of maintenance/reconstruction of structures and diversion of traffic to alternative routes, where available, and in terms of human lives 2. Literature studies have shown that the probability of a fire occurring on a bridge is not as often believed compared to other risks. In particular, Lee et al. 3 demonstrated that the number of bridges damaged by fires is greater than the number of bridges damaged by earthquakes. A similar survey was conducted by the New York Department of Transportation 4.

¹ PhD, Assistant Professor, Department of Structures for Engineering and Architecture, University degli Studi di Napoli “Federico II”
e-mail: donatella.desilva@unina.it ORCID: <https://orcid.org/0000-0002-4058-902X>

² PhD, Assistant Professor, Department of Structures for Engineering and Architecture, University degli Studi di Napoli “Federico II”
e-mail: andrea.miano@unina.it, ORCID: <https://orcid.org/0000-0001-6638-1983>

³ M.Eng., Research Fellow,, Department of Structures for Engineering and Architecture, University degli Studi di Napoli “Federico II”
e-mail: ing.gabrielladerosa@gmail.com ORCID: <https://orcid.org/0009-0008-7884-6037>

⁴ M.Eng., Research Fellow,, Department of Structures for Engineering and Architecture, University degli Studi di Napoli “Federico II”
e-mail: francesco.dimeglio@unina.it ORCID: <https://orcid.org/0009-0007-6214-7891>

⁵ PhD, Full Professor, Department of Structures for Engineering and Architecture, University degli Studi di Napoli “Federico II”
e-mail: a.prota@unina.it, ORCID: <https://orcid.org/0000-0003-3820-663X>

⁶ PhD, Full Professor, Department of Structures for Engineering and Architecture, University degli Studi di Napoli “Federico II”
e-mail: emidio.nigro@unian.it, ORCID: <https://orcid.org/0000-0002-3848-7454>

Despite the increasing importance of the issue, in bridge design, unlike risks such as earthquakes, wind, and snow, the fire risk is not included in current codes and regulations. Furthermore, buildings codes are not directly applicable due to significant differences in fire conditions. In fact, fires that occur in buildings are often limited by ventilation, and the material involved in the fire is cellulose-based, whereas fires involving transportation infrastructure such as bridges occur in open environments and are not limited by ventilation, with predominantly hydrocarbon materials involved. This means that fires involving transportation infrastructure are often highly intense and explosive. Therefore, in the event of a fire, these structures could be particularly vulnerable to fire-induced damage. In the past, fire fragility analyses were mainly conducted with reference to structures, such as in 5. Given the growing importance of this issue, this study proposed a methodology for evaluating the structural response of bridges under fire conditions, determining fragility curves based on specific performance levels proposed by de Silva et al. 6 as a function of the vertical displacement of the bridge deck midspan. In order to compare the behavior between multiple typological structures, two bridges were analyzed in this study, the first one representative of a prestressed reinforced concrete bridge and the second one is representative of a composite bridge.

Once the geometric and mechanical characteristics of the bridges to be analyzed were determined, a literature review was conducted to identify heat release rate (HRR) curves related to the most probable fire scenarios that bridges could be subjected to during their lifetime. After obtained the heat release rate curves, thermo-mechanical analyses of the structures were conducted using SAFIR software 7. Based on the results of these analyses, fragility curves were determined considering two different measures of fire intensity: the fire load and the peak of the heat release rate curves.

2. METHODOLOGY

Fragility curves describe the probability that a structure will be damaged beyond a certain damage level for a given intensity measure. The starting point for developing the fragility curves of a structure is to identify the performance levels against which to construct these curves. In this study, the performance levels considered were established following the guidelines provided by se Silva et al. 6, including both the maximum vertical displacement of the bridge deck's midspan and its residual vertical displacement, as reported in Table 1.

Table 1. Performance levels for bridge

PL	Description
I	The bridge must hold for the time required for evacuation
II	The bridge must withstand the duration of the fire
III	Max displacement should be limited to $L/100$ for the duration of the fire and residual displacement should be limited to $50\% \Delta_{in}$
IV	Max displacement should be limited to $L/250$ for the duration of the fire and residual displacement should be limited to $20\% \Delta_{in}$

Generally, fragility curves provide a graphical representation of the probability that a structure will reach or exceed a specific level of damage or performance under the influence of a given intensity measure (IM). To assess the fragility of a structure, it is necessary to establish the relationship between the intensity measure of the action to which the structure is exposed and the probability exceeding a certain limit state or predefined performance level. To do this, a series of consequently phases must be followed. Firstly, the geometric and mechanical parameters of the structure for which fragility curves need to be determined are defined. Potential fire scenarios to which the structure may be subjected throughout its lifetime are identified. These scenarios are characterized based on a representative measure, in this study, the peak thermal release (W this parameter which can have a good fit with the structural materials with a high thermal conductivity) and fire load (GJ have a good fit with the structural materials with a high thermal inertia) were considered. Then the thermo-mechanical analyses are conducted. Once the analyses are completed

and the response parameter of the structure is chosen, in this case, the maximum and residual vertical displacement of the point located at the center of the bridge span, this response parameter is used to determine the maximum demand-to-capacity ratio as a function of the specific performance level considered (see Table 1). After obtaining the demand-to-capacity ratio for each fire scenario, a logarithmic linear regression of these values is performed, providing the necessary value to construct the fragility curves. In fact, a fragility analysis is done, conceptually equivalent to the seismic field in which Cloud Analysis based fragility curves are derived, based on a procedure in which a structure is subjected to a set of ground motion records of different first-mode spectral acceleration $S_a(T)$ values 8-10.

3. CASE STUDIES

In this study, two typological bridges representative of Italian bridges was considered. The first one is made of reinforced concrete (R.C. bridge), and the second one has a composite steel-concrete deck (composite bridge). These bridges, built between 1970's and 1990's, mostly feature a statically determinate scheme with simply supported decks and circular section piers. Specifically, concerning reinforced concrete bridges, given the large number of such bridges in Italy and the significant geometric and mechanical characteristics of materials, it was decided to study a single span of median bridge derived by Zelaschi et al. 11, which analyzed approximately 500 reinforced concrete bridges in Italy. Therefore, only one span of this median bridge was investigated. The second bridge analyzed is a typological bridge with a composite steel-concrete deck. This bridge consists of 4 isostatic spans, but in this study, similar to the previous case, only the longest span was considered. The geometrical properties of these bridge analyzed are illustrated in Table 2.

Table 2. Geometrical properties

Dimensions of concrete bridge		Dimension of steel bridge	
Variable	Value	Variable	Value
Pier Haight (m)	7.03	Pier Height (m)	7.05-8.85 (average 7.95)
Pier circular section diameter (m)	12.06	Pier circular section diameter (m)	2.00
Span length (m)	31.18	Span length (m)	32.23
Deck thickness (m)	0.2	Deck thickness (m)	0.25
Deck width (m)	12.06	Deck width (m)	8.50

The mechanical properties of the bridge analyzed in this study are illustrated in Table 1.

Table 3. Mechanical properties of the bridges analysed

Mechanical properties of concrete bridge		Mechanical properties of steel bridge	
Bars tensile strength (MPa)	544.4	Steel	Fe510/ S355
Reinforcing bars Young Modulus (GPa)	210	Concrete	Rck > 40 / C32/40
Concrete compressive strength (MPa)	40	Steel bars	Feb44k/ B450C

To determine the tensile strength of the strands used for prestressing beams and to determine the cross-sectional area of the bridge deck, average value from structures of similar dimensions were considered. In particular, the tensile strength of the strands are 1820 MPa. For the bridge in prestressed reinforced concrete, the cross-sectional of the bridge consists of 8 simply supported straight beams in prestressed

concrete equally spaced. The beams are reinforced with $\phi 12$ bars and $\phi 3/8$ stands. At the ends of the section, there are two curb beams with a base width of 0.5m and height of 0.25m, while the deck slab has a thickness of 0.2m. As for the piers, there are $42\phi 24$ bars present. The concrete cover for both the beams and piers is 0.05m. The geometry of the cross-section is shown below in Figure 1 and in Figure 2.

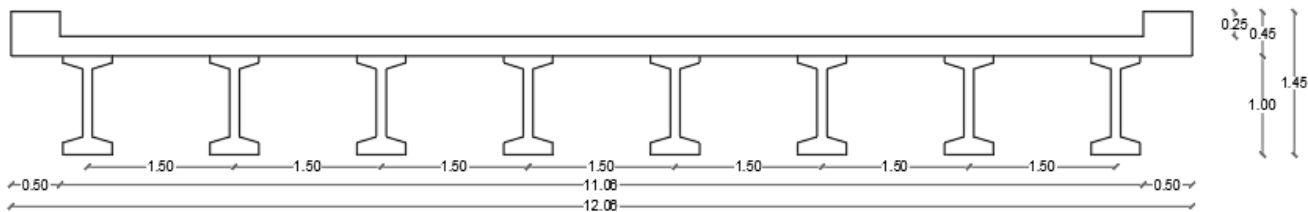


Figure 1. R.C. bridge deck cross-section

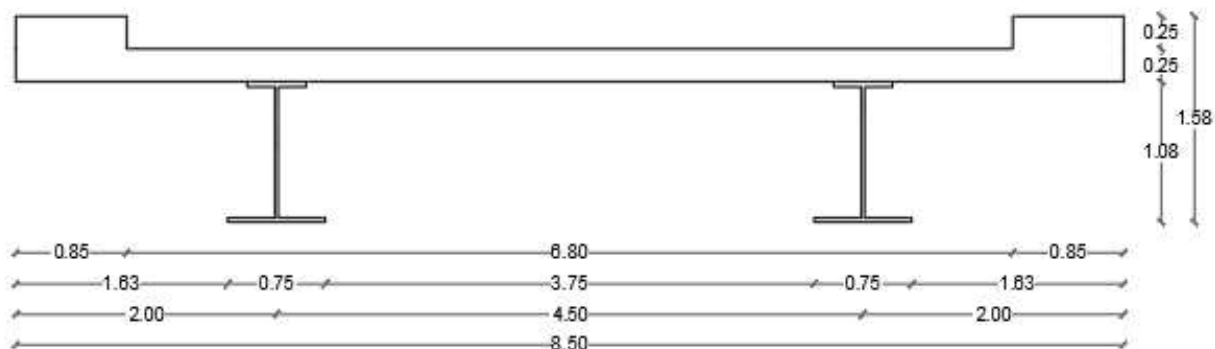


Figure 2. Composite bridge deck cross-section

For the loads acting on the bridges, these have been determined according to the combination of exceptional load specified by the Italian code. These loads are shown in Table 4.

Table 4. Distribution load of the analysed bridges

Concrete bridge		Steel bridge	
$G_{1,k}$ [kN/m ²]	12.5	$G_{1,k}$ [kN/m ²]	6.0
$G_{2,k}$ [kN/m ²]	5.2	$G_{2,k}$ [kN/m ²]	14.1

4. FIRE SCENARIOS

The selection of potential and realistic fire scenarios for a bridge is crucial for accurately assessing how it might respond in fire situations. In this study, various fire scenarios involving either a single vehicle or multiple vehicles have been considered. Each of these fire scenarios is characterized by flame diameter and a specific Heat Release Rate (HRR) curve, which represents the rate of thermal energy release per unit time, typically expressed in kW. In particular, the vehicles HRR curves (12-13-14) adopted were: semi-trailer with palletized flammable cargo (S1), a large passenger bus (S2), a car (S3), a standard semi-trailer fuel truck full of gasoline (S4), a semi-trailer truck that is half full of palletized flammable cargo (S5), a motorcycle (S6), and another type of car (S7).

Starting from the fire scenarios involving single vehicle, scenarios involving multiple vehicles catching fire simultaneously have also been determined. These scenarios have been obtained as a linear combination of the scenarios involving single vehicles. By doing so, a total of 31 fire scenarios have been determined starting from seven single vehicles. The trend of all HRR curves for the 31 scenarios considered is reported in Figure 3.

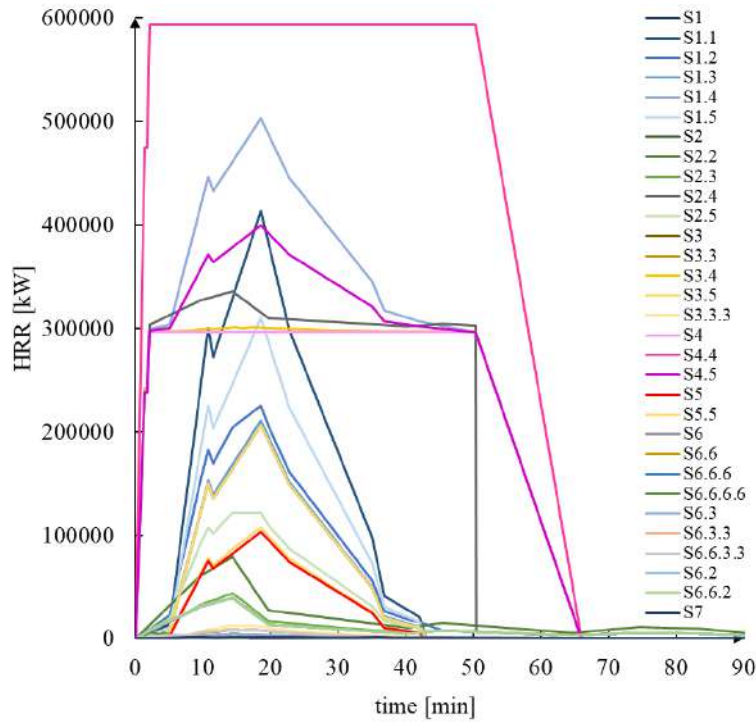


Figure 3. Fire scenarios heat release rate curves

Finally, the position of the fire relative to the bridge geometry was established. In particular, it was assumed that the fire is located at the midpoint of the bridge span for all the considered fire scenarios.

5. FIRE MODELLING

In cases where fire occurs in open compartments such as bridges, it is rare to reach the flash-over point 13, therefore the fire is not generalized but localized. In generalized fires, the gas temperature remains constant, while in localized fires, temperatures vary greatly. To assess the thermal impact of a localized fire on structural elements, various models can be adopted, such as the Hasemi model 15 described in Annex C of the standard EN 1991-1-2 (2002) 16, which was used in this study. The Hasemi model provides structure temperature based on fire position, fire source diameter, ceiling height, and HRR of each vehicle. However, the Hasemi model has applicability limits 17, so when the considered fire scenarios exceed these limits, it was necessary to perform a Computational Fluid Dynamics (CFD) analysis. Dynamic flow simulations were performed using the Fire Dynamics Simulator (FDS) software 18, which allowed determining gas temperature values around the structural elements. The result of these analyses is the natural fire curves, i.e., the trend of gas temperatures around the structural elements. These curves are then used as input data to perform thermal analyses in order to determine temperatures within the structural elements 19.

6. STRUCTURAL ASSESSMENT RESULTS

The thermal analysis were conducted by SAFIR software for a duration of 360 and 180 minutes respectively for reinforced concrete bridge and composite bridge, allowing the heated structure to cool down temperature once the fire scenario was completed. In Figure 4 is represented the temperature trend, in particular in 4.a) for the most exposed steel bar for the prestressed reinforced concrete bridge, while in 4.b) for the steel section of the composite bridge.

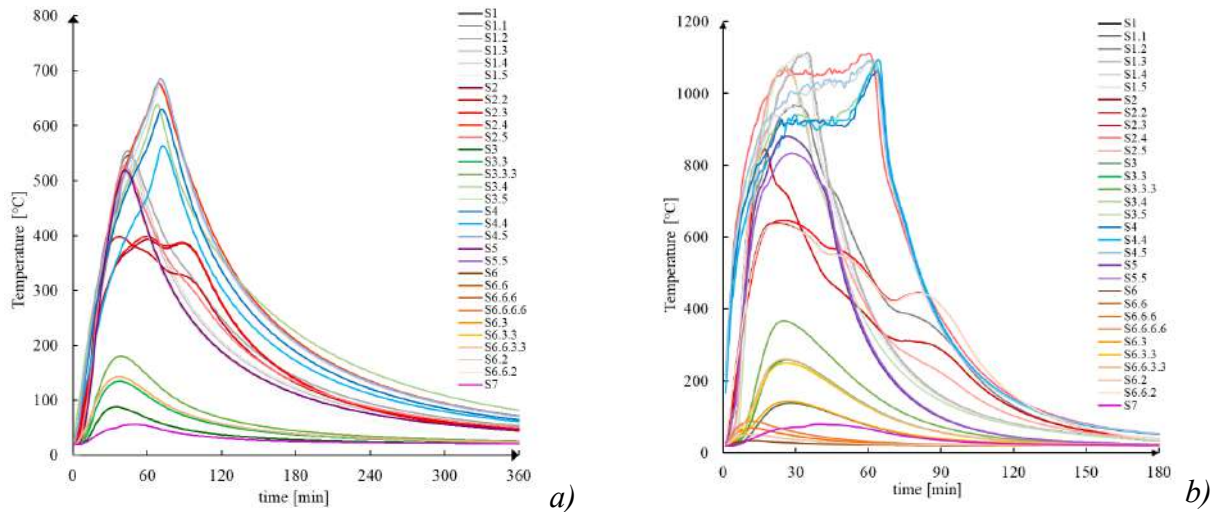


Figure 4. a) temperature in the most fire-exposed reinforcement bar in the prestressed reinforced concrete bridge; b) the mean temperature of the steel beam for the steel-concrete composite bridge.

It can be observed that the maximum temperature reached by the steel beam of the composite bridge is higher than the maximum temperature reached by the most exposed steel bar of the reinforced concrete bridge. Additionally, the steel beam cools down more quickly than the steel bar of the reinforced concrete bridge. This difference, both in the heating and cooling phases, is due to the concrete covering that the steel bar has in the reinforced concrete bridge. After the thermal analyses were completed, mechanical analyses of the analyzed structures were carried out. The response parameters considered were the maximum vertical displacement at the midspan of the bridge deck and the residual vertical displacement. These displacement values were normalized with respect to limit displacements based on the considered performance level. Using the obtained values, a fragility analysis was performed, determining fragility curves based on data analysis through Cloud Analysis.

7. FRAGILITY CURVES FOR BRIDGES IN CASE OF FIRE

At the end of the Cloud Analyses, a fragility curve is determined for each of the chosen performance levels based on the adopted intensity measure and the selected response measure (both for maximum vertical displacement and for residual vertical displacement of the midspan of the bridge deck). An example of the Cloud Analysis results is reported in the Figure 5 for the prestressed reinforced concrete bridge, considering the peak of heat release rate for characterized fire scenarios. In this case, once the fire scenarios are applied to the structure, the maximum demand-to-capacity ratio for the chosen performance level is determined.

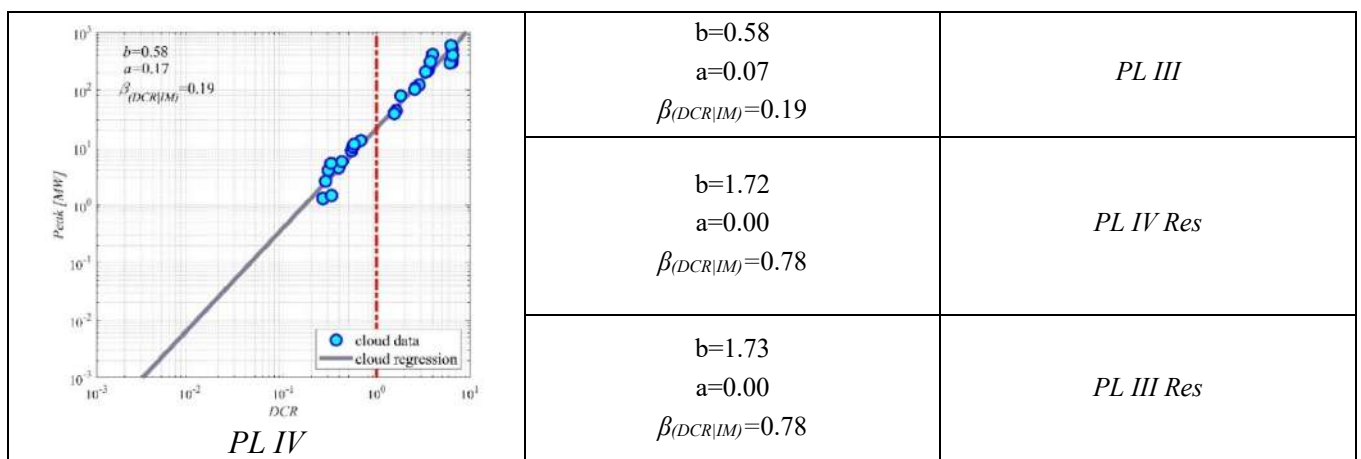


Figure 5. Linear regression for peak heat release rate

In Figure 5, a it's the regression intercept, b is slope coefficient on the line regression, β is the standard deviation, the blue line represents the line regression, the red vertical line represents unitary DCR; each blue point represents a fire scenario characterized by a certain DCR value and certain IM value. In Figure 6 the fragility curves obtained as a function of the peak thermal release rate are represented for both the reinforced concrete bridge and the composite bridge, considering both performance level III and performance level IV. In case a), the maximum vertical displacement was considered, while in case b) the residual vertical displacement was considered.

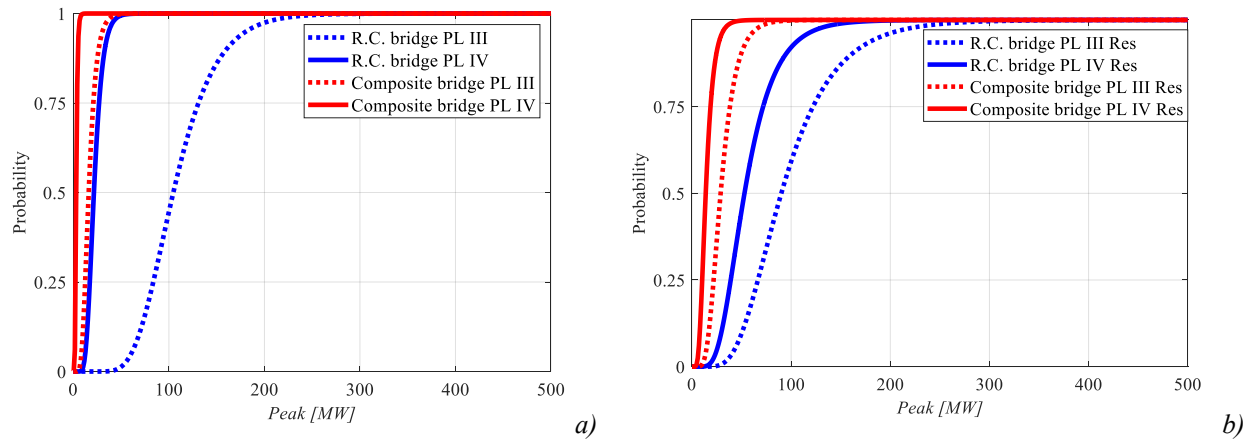


Figure 6. Fragility curves as a function of peak of heat release rate for performance level III and performance level IV: a) maximum displacement; b) residual displacement

Similarly, in Figure 7, but considering the peak of heat release rate instead of the fire load.

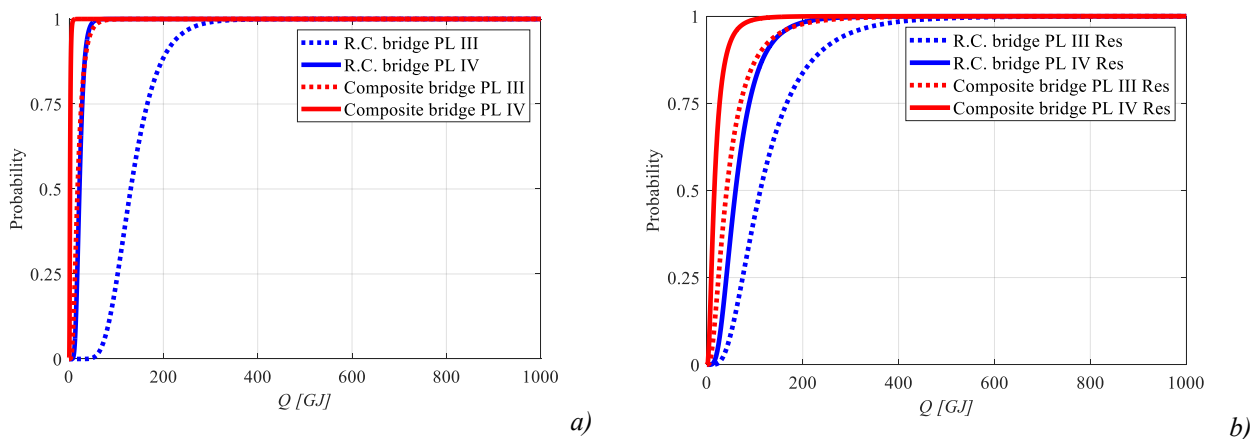


Figure 7. Fragility curves as a function of fire load Q for performance level III and performance level IV: a) maximum displacement; b) residual displacement

8. CONCLUSIONS

The study presented in this paper provides a methodology for estimating the fragility curves of bridges under fire conditions. In particular, the proposed methodology has been developed considering two types of bridges with similar geometrical properties, the first representing the family of R.C. bridge, and the second representing the family of composite bridges, to evaluate their structural performance under fire actions. Therefore, after defining the geometrical and mechanical properties of the analyzed bridges, the most probable fire scenarios have been determined and simulated. Then, the advanced thermo-mechanical analyses have been conducted and the maximum and residual vertical displacements of the bridges have

been considered as response parameters for determining the fragility curves, that link the probability of exceeding performance levels III and IV to some parameters characterizing the fire, such as the peak heat release rate and the fire load.

The main conclusions of this study can be summarized as following:

- to assess structural fire behaviour, it is essential to accurately evaluate the possible natural fire scenarios to which the infrastructure is subjected, because its response can be significantly different;
- the natural fire curves are strongly dependent on the combination of the vehicles involved in the fire, as demonstrated from the curves shown for the overall set of the considered scenarios;
- in most of the cases, it is necessary to perform advanced thermo-fluid dynamic analyses, instead of using simplified models, to obtain consistent natural fire input in bridges.

Moreover, focusing on the fragility analyses for two cases, the main conclusions are:

- even if a direct comparison in terms of fragility curves is not possible since the different input structural parameters, the composite bridge with steel beams has been found to be more vulnerable than the R.C. one because of its intrinsic material higher fire vulnerability;
- the presence of concrete cover, in the R.C. bridge, helps in reducing the temperature inside the steel reinforcements with the consequent reduction of the fire vulnerability.

In conclusion, the proposed methodology constitutes an operational tool for engineers to assess the fire resistance of these structures both in the design phase for new bridges and in the assessment phase for existing ones.

KNWOLEDGMENTS

This study was carried out within the RETURN Extended Partnership and received funding from the European Union Next-Generation EU (National Recovery and Resilience Plan – NRRP, Mission 4, Component 2, Investment 1.3 – D.D. 1243 2/8/2022, PE0000005) and within the project P2022NCY5B Estimation of the combined earthquake-fire risk and optimization of interventions for structures and infrastructures in the context of metropolitan areas (SaFeBIMAs) CUP: E53D23017360001.

REFERENCES

1. M. Garlock, I. Paya-Zaforteza, V. Kodur, L. Gu, Fire hazard in bridges: review, assessment and repair strategies, *Eng. Struct.* 35 (2012) 89–98
2. Naser, M. Z., & Kodur, V. K. R. (2015). A probabilistic assessment for classification of Bridges Against Fire Hazard. *Fire Safety Journal*, 76, 65–73
3. Lee GC, Mohan SB, Huang C, Fard BN. A study of US bridge failures (1980-2012). Buffalo: 2013
4. New York State Department of Transportation, Bridge Fire Incidents in New York State, New York State Department of Transportation, USA, 2008
5. Miano, A., de Silva, D., Compagnone, A., & Chiumiento, G. (2020). Probabilistic seismic and fire assessment of an existing reinforced concrete building and retrofit design. *Struct. Eng. Mech.* 74, 481-494.
6. de Silva, D., Gallo, M., De Falco, L., & Nigro, E. (2023). Fire risk assessment of bridges: From State of the art to structural vulnerability mitigation. *Journal of Civil Structural Health Monitoring*. <https://doi.org/10.1007/s13349-023-00670-z>
7. Franssen, J.M., Gernay, T. (2017), Modeling structures in fire with SAFIR®: Theoretical background and capabilities, *Journal of Structural Fire Engineering*, 8(3):300-323
8. Jalayer, F., Ebrahimian, H., Miano, A., Manfredi, G., & Sezen, H. (2017). Analytical fragility assessment using unscaled ground motion records. *Earthquake Engineering & Structural Dynamics*, 46(15), 2639-2663.
9. Jalayer, F., Ebrahimian, H., & Miano, A. (2020). Intensity-based demand and capacity factor design: A visual format for safety checking. *Earthquake Spectra*, 36(4), 1952-1975.
10. Jalayer, F., Ebrahimian, H., & Miano, A. (2021). Record-to-record variability and code-compatible seismic safety-checking with limited number of records. *Bulletin of Earthquake Engineering*, 19(15), 6361-6396.
11. Zelaschi, C., Monteiro, R., & Pinho, R. (2016). Parametric characterization of RC bridges for Seismic Assessment purposes. *Structures*, 7, 14–24. <https://doi.org/10.1016/j.istruc.2016.04.003>

12. Wright W., Lattimer B., Woodworth M., Nahid M., Sotelino E. Highway Bridge Fire Hazard Assessment – Draft Final Report. NCHRP Program Transportation Reserarah Board of The National Academies. Virginia Polytechnic Institute; 2013.
13. SFPE Handbook of Fire Protection Engineering, Fifth Edition. Springer; 2016
14. Chen, C. J., Tsai, M. J., Ji, B. C., Wu, C. W., Pu, J. Y., & Lin, T. H. (2005). Burning analysis of motor scooters. *Fire Safety Science*, 671-680. <https://doi.org/10.3801/IAFSS.FSS.8-671>
15. Pchelintsev A, Hasemi Y, Wakarnatsu T, Yokobayashi Y. Experimental and numerical study on the behavior of a steel beam under ceiling exposed to a localized fire. In *Fire Safety Science-Proceedings of the 5th International Symposoum*. Melbourne: IAFSS, 1997.
16. EN 1991-1-2 (2002). Eurocode 1: Actions on Structures—Part 1-2: General Actions—Actions on Structures Exposed to Fire. Brussels: European Committee for Standardization, 2002.
17. Alos-Moya J, Paya-Zaforteza I, Hospitaler A, Loma-Ossorio E. Valencia bridge fire tests: Validation of simplified and advanced numerical approaches to model bridge fire scenarios. *Adv Eng Softw* 2019;128:55–68.
18. McGrattan K., Hostikka S., Floyd J., Baum H., Rehm R., Mell W., McDermott R., 2010a, *Fire Dynamics Simulator (Version 5)*. Technical Reference Guide, NIST Special Publication 1018-15, US Government Printing Office, Washington, USA.
19. de Silva, D.; Sassi, S.; De Rosa, G.; Corbella, G.; Nigro, E. Effect of the Fire Modelling on the Structural Temperature Evolution Using Advanced Calculation Models. *Fire* 2023, 6, 91.

INTEGRATED ANALYSIS OF LOADING ECCENTRICITY ON RESPONSE OF A COLUMN UNDER TRAVELLING FIRE

Rabinder Kumar¹, Naveed Alam², Ali Nadjai³

ABSTRACT

Columns are crucial structural elements designed to carry axial loads. When these loads are applied off the column's central axis, it results in eccentric loading, introducing both axial stress and bending moments in the column. This complexity becomes even more pronounced under transient heating conditions, such as those encountered during travelling fires. Understanding these interactions is vital for designing structures that can withstand unusual loading and heating scenarios, ensuring their safety and resilience. In consideration of this, the present study undertakes nonlinear analyses to explore the effects of eccentricities due to load positioning and also the effects of transient heating on columns and beams exposed to traveling fires. The analysis is conducted in two phases: initially, an isolated steel column is subjected to full-scale traveling fires, considering axial loading with eccentricity ratios (e/h) of 0, 0.25, and 0.5. Subsequently, a two-bay frame is exposed to the combined effects of traveling fires and imposed loads. The computational modelling for this investigation is done using Abaqus software. Findings from the analysis reveal that increased eccentricity significantly enhances lateral deformation and triggers local buckling in flanges. Columns under higher eccentricity also display lower temperatures at which buckling occurs. Additionally, for steel frames, the combination of transient heating and imposed loads brings about both axial and flexural deformations in structural members. As eccentricity escalates, there's a notable reduction in critical load, precipitating premature section failure and significant lateral displacement. Furthermore, critical stresses are observed at beam-column junctions, and a twisting phenomenon occurs when beams are subjected to transient heating while columns remain at ambient temperatures.

Keywords: Travelling Fires; Steel Columns; Fire Resistance; Computational modelling

1 INTRODUCTION

The ability of buildings to withstand fire is crucial for the safety, and well-being of the occupants and the protection of the building's contents. Due to large open-plan layouts in modern building designs, one of the most challenging scenarios for building safety is a travelling fire. During travelling fires, structural elements are exposed to a complex thermal environment and high temperatures for prolonged durations. Such fire exposures may compromise the integrity of the structure leading to failure [1-2]. In structural fire design, the standard fire exposure conditions (ISO-834) are considered which assume a post-flashover fire scenario with uniform temperatures within the compartment. This assumption may stand true for small compartments, however, for larger floor areas, the assumption of uniform temperatures within compartments has been found to be inaccurate [3-4]. Since the beginning of the century, there have been

¹ PhD Researcher, FireSERT, Ulster University, UK
e-mail: kumar-r6@ulster.ac.uk,

² Lecturer, FireSERT, Ulster University, UK
e-mail: n.alam@ulster.ac.uk,

³ Professor/Director, FireSERT, Ulster University, UK
e-mail: a.nadjai@ulster.ac.uk,

several well-documented cases of traveling fire incidents, including the 2001 World Trade Center Twin Towers in New York City, the 2005 Windsor Tower in Madrid, and the 2008 Faculty of Architecture Building at Delft University of Technology in the Netherlands [6-7]. In terms of fire incidents in the UK, the tragic Grenfell Tower fire incident in London in 2017 remains one of the most recent and impactful fire incidents in the country [8]. These large fire incidents have attracted the interest of researchers from different parts of the world to study large open plan fires and their impact on the surrounding structural frames during such fires. Generally, the response of structural elements is temperature dependent as their strength and stiffness are compromised at higher temperatures. In case of fire exposure, the structural elements may achieve temperatures as high as 1000°C which significantly reduces their resistance to external loads. Two main factors impact the mechanical properties of structures during a fire: a) thermal elongation and b) the decrease in modulus of elasticity and yield strength of materials. The thermal elongation results in the generation of compressive forces within the structural members due to the restraining effect from the surrounding structure which may lead to the buckling of the structural member [9]. Furthermore, the decrease in modulus of elasticity and yield strength of materials due to fire exposure leads to strength loss and has profound consequences on the safety, integrity, and functionality of structures.

In any structural skeleton, a column is a fundamental element and plays a critical role in the overall resistance, support, stability, and integrity of buildings. The importance of columns is magnified when they are directly influenced by the fire dynamics often being engulfed in flames [10]. When a steel column in a building is exposed to fire, several consequences can occur including thermal expansion leading to distortion and potential buckling. In addition, the combination of axial load, eccentricity (e), and high temperatures can elevate the risk of buckling in the column. This introduces higher bending stress, lateral-torsional buckling, P-Delta effect, and causes a reduction in the effective area of the column [11]. This phenomenon can be observed in travelling fires even for centric loads due to transient heating of the structure. For instance, the position of the travelling fire at a point may compromise the strength of the nearby structural elements, including the columns. On the other hand, the structural elements away from the travelling fire will still offer support and resistance to the external loads. The beams supported on the hotter side transfer loads to the column in a different way as compared to the beams supported on the cooler side. This temperature difference in the beams creates eccentricity in the column which is encountered during a travelling fire event (or in a large compartment fire event) and is irrelevant to the loading conditions of the column.

Yao et al., [12] conducted a computational analysis to assess the behaviour of concrete-filled steel tubular (CFST) slender columns subjected to eccentric loads and exposed to ISO-834 standard fire. Their model incorporated parameters like concrete tensile strength and stirrup ratio which yielded reasonable accuracy compared to experimental results. The computational modelling approach was further used to conduct parametric studies to investigate the impact of various factors such as eccentricity ratio, yield strength of steel, compressive strength of concrete, and the reinforcement ratio on the fire resistance of CFST columns. In another study, Du et al., [13] investigated the behaviour of eccentrically loaded pin-ended concrete-encased steel (CES) composite columns under heating and cooling conditions. Du et al (2013) [13] developed and validated a nonlinear 3D finite element analysis (FEA) model using ANSYS. The findings from their study revealed that CES columns undergo temperature increases at different rates and positions, emphasizing the need to consider full fire exposure until temperatures decrease uniformly. They observed significant lateral deformation during the cooling phase. Detailed FEA studies by Du et al (2013) identified key parameters such as load ratio, slenderness ratio, duration time, depth to width ratio, and steel ratio influencing lateral deformation and residual deformation ratio, providing insights for structural design considerations. An experimental study conducted by Al-Talqani et al., [14] examined the response of normal-weight concrete encased steel (CES) columns under eccentric loading and varying elevated temperatures, using an electrical furnace. The findings from the experiments demonstrated that all CES columns experienced failure due to flexural buckling, with concrete crushing occurring at the middle third of the compression side of the column, accompanied by local buckling of the steel section flange.

The existing literature [15–18] predominantly focuses on concrete columns under eccentric loading during standard fire conditions, with limited attention given to steel columns subjected to eccentric loading due to traveling fire scenarios. Understanding the behaviour of eccentrically loaded columns under traveling fire

conditions is crucial for ensuring structural safety considering modern designs and open-plan layouts. To understand the influence of temperature-induced eccentricities, it is vital to initially study the response of eccentrically loaded columns in travelling fires. The combination of non-uniform temperature and loading eccentricity could profoundly impact the behaviour of columns, a scenario that has not yet been explored in detail as evident from the existing literature. The integrated analysis presented in this study provides valuable insights into the response of columns, aiding in achieving better design and fire-resistant construction practices.

2 NUMERICAL ANALYSIS

Computational analysis during this research is conducted using ABAQUS software [19], a robust tool renowned for finite element analyses and computer-aided engineering tasks. The numerical analysis encompasses two phases. During the initial phase, the first eigenmode is determined through a linear perturbation frequency analysis procedure. This eigenmode is subsequently utilized in the stress analysis phase (the second phase) to induce the necessary initial imperfection of the column set as $L/1000$ in all cases [20]. In the stress analysis phase, the column is partitioned into five levels, as illustrated in Figure 2, with temperatures applied through predefined fields. For structural investigation, a distinct set of analysis elements are employed for steel. The steel material is modelled using incompatible mode elements, specifically C3D8I elements, as done previously by other researchers while performing computational modelling on steel structures [21]. The 40 mm average element size mesh was compatible with the procedures in all cases. The mechanical properties of materials during structural analysis have also been taken from the Eurocodes [22].

2.1 Validation with experimental data

To confirm the accuracy of the FE analysis method, the numerical predictions were compared with the key results from experiments conducted by Faris and Conner [23] on axially loaded restrained columns. The details of the experiment are reported in the publication listed as reference [23]. The numerical predictions were compared with the key results from experiments which included the axial deformation and lateral displacement in a column. The numerical findings exhibited a notable concurrence with the experimental outcomes. In this study, both dynamic explicit and nonlinear static analyses were executed to validate the method's accuracy, yielding consistent results across both approaches. To mitigate computational expenses and keeping in view the scope of this paper, the static analysis is considered to simulate the column behaviour under prescribed loads subjected to a traveling fire. The results of axial and lateral displacements are shown in Figure 1.

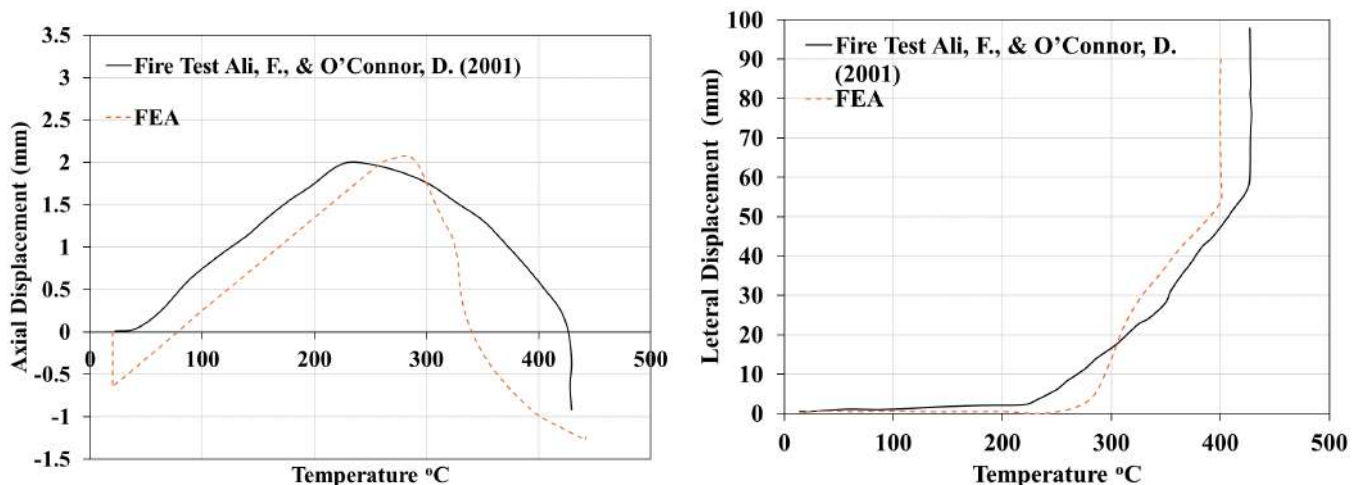


Figure 1. Axial and lateral deformation

3 CASE STUDIES

3.1 Investigated Cases

The methodology consisted of computational analysis conducted in two phases as explained above. The computational analysis is initially performed for isolated HEA200 steel columns subjected to travelling fires. The selected column sections are the same as the ones used during the tests performed at Ulster University [1, 24]. The columns were subjected to axial loading with consideration for the following eccentricity cases: 1) $e/h = 0$, 2) $e/h = 0.25$, and 3) $e/h = 0.5$, as illustrated in Figure 2. In these cases, "e" represents the eccentricity, and "h" denotes the depth of the section. The variations in loading eccentricity were applied along the minor axis on the web of the section. The imposed load on the column in this case is 50% of the minimum design buckling resistance ($N_{b,rd}$) of a column section about minor axes.

In the second phase, eccentricity was induced through the transient heating of structures. For example, as illustrated in Figure 2(b), a section of the frame was exposed to fire, potentially compromising the strength of elements, reducing stiffness, and altering the load transfer path compared to the sections at ambient temperatures. This induced eccentricity in the column, regardless of any variations in eccentricities induced due to the position of the external loads applied. In the second phase, four distinct scenarios as listed in Table 1. In case 1, only the column is subjected to transient heating while in case 2, along the column, one beam is also exposed to elevated temperatures as seen in Figure 2(b). In cases 3 and 4, additional loads of 20% and 30% are applied, respectively, based on the load-carrying capacity of the beam (see Table 1). *Note. In the text thermal load, temperature load, and transient heating refer to travelling fire scenarios.*

Table 1: Details of frame cases selected for computational investigation

Frame Cases	Details
Case 1	Only middle column exposed to travelling fire.
Case 2	Middle column and one beam exposed to travelling fire (see Figure 2(b)).
Case 3	Same as Case 2 but with 20% external loads.
Case 4	Same as Case 3 but with 30% external loads.

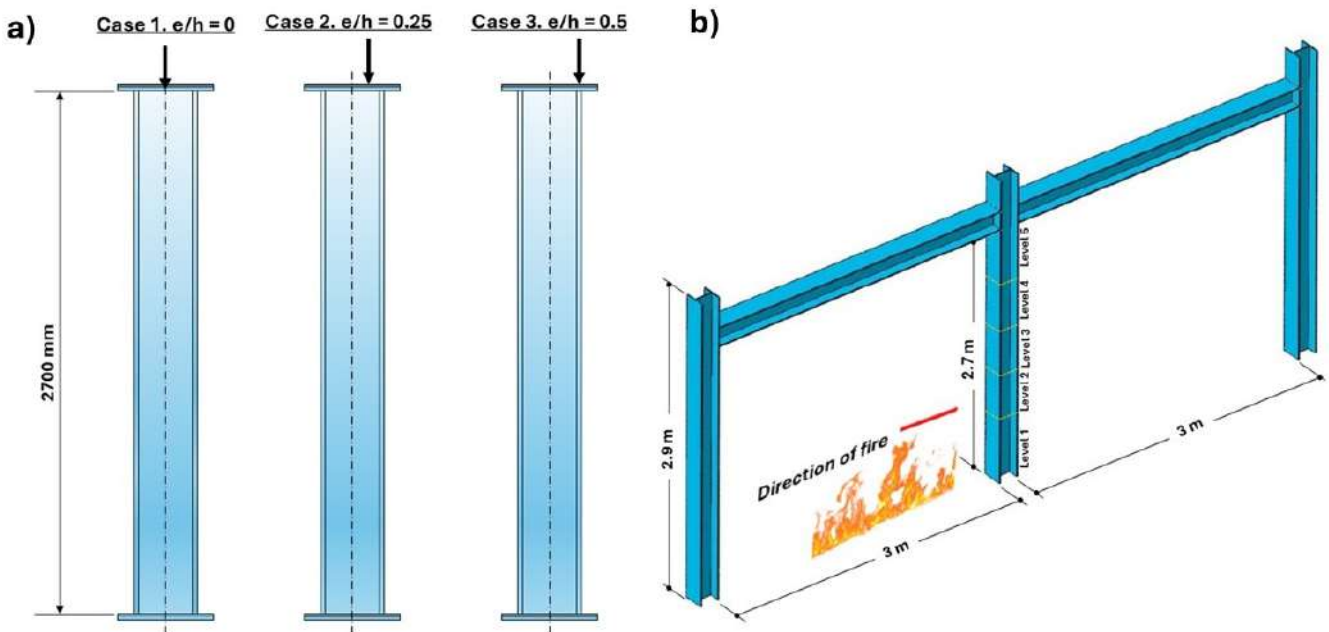


Figure 2. a) Analysis phase I, eccentricity scenarios with respect to axial loads, b) Analysis phase II, eccentricity scenarios according to transient heating (the travelling fires)

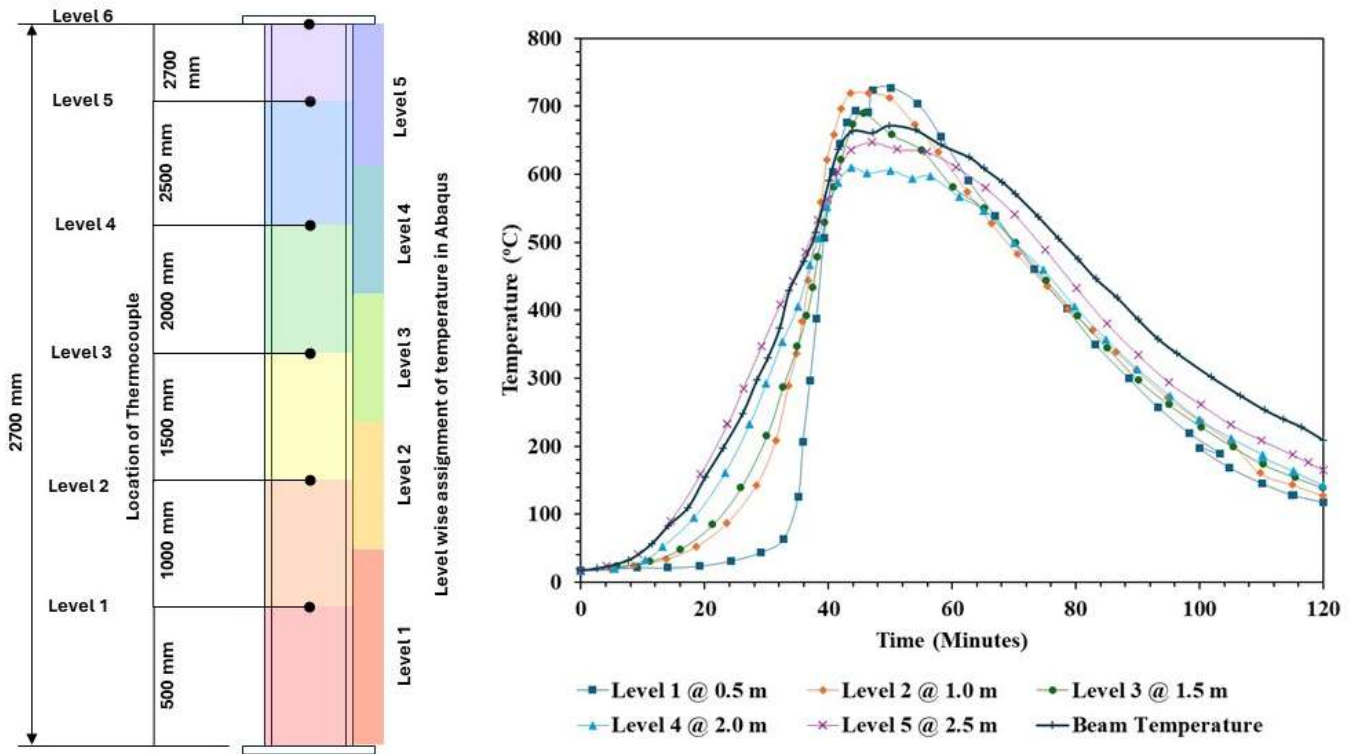


Figure 3. Recorded temperature in columns at different levels extracted from [2]

4 RESULTS

4.1 Column under travelling fire scenario

Since no external loading was considered in the real fire test [2], initially, the computational simulation of the model was exclusively under thermal loading considering the temperature data obtained for the test, with no external loads to evaluate deformations. The boundary conditions at the column's base were set as fixed while allowing translational movement in the vertical direction and rotational movement about the z and x axes at the top of the column. The results describing displacements of the column under thermal loading along all three axes are illustrated in Figure 4.

The displacements are measured at various levels in all three directions due to the temperature being applied incrementally across levels as shown in Figure 3. The deformation along the x, y, and z axes are shown as U1, U2 and U3 respectively in Figure 4. Notably, Figure 4 reveals that the maximum displacement occurs in the vertical direction (U2), which defines axial displacement, whereas displacements in the other two directions (U1 and U3) are observed to be negligible. As the temperature was applied transiently, upon reaching maximum temperature, the deformation peaks; correspondingly, as the temperature decreases, the deformation reduces. Specifically, the maximum axial deformation of 23 mm is observed at the top level of the column during peak temperature. Subsequent cooling results in reduced deformation, with the residual deformation in the column recorded at 5 mm. Overall, no severe deformation is observed as per the results. This was also observed during the full-scale experiments by Ulster University as no damages were reported during the fire test [2].

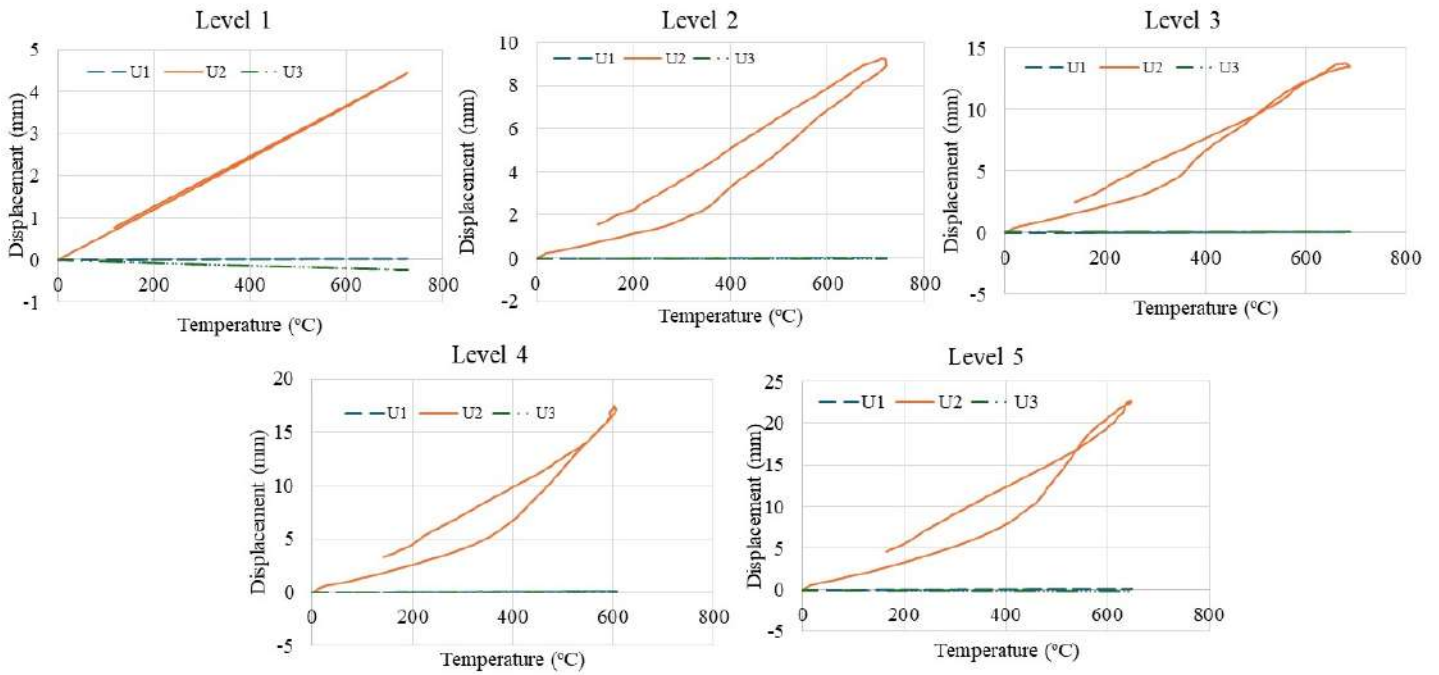


Figure 4. Deformation on the unloaded isolated column under thermal load at different heating zones

4.2 Eccentricity through position of axial loading

The deformation of the column under various eccentricity ratios is depicted in Figure 5. Figure 5(a) illustrates the buckling mode for the scenario of concentric axial loading, occurring along the axis of lower flexural rigidity. In cases of eccentric loading (Figure 5(b) and (c)), the deformation mode shifts to the weak axis (z-axis), where the load is applied at varying distances.

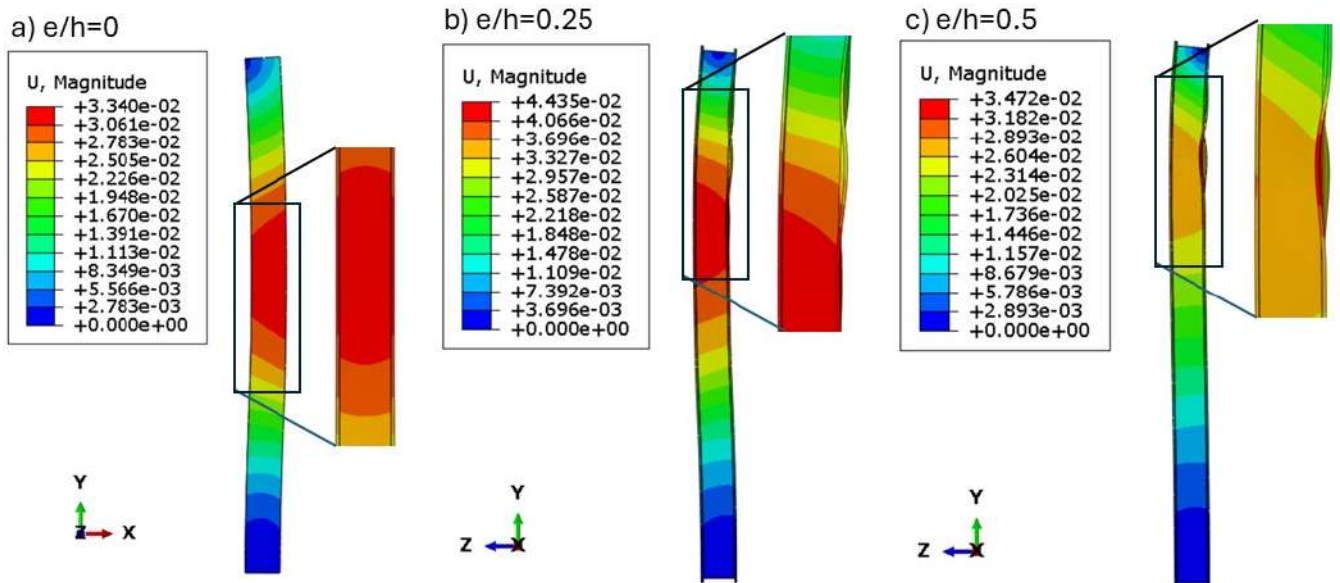


Figure 5. Column deformation at different eccentricities

Figures 6 and Figure 7 showcase the lateral displacement and axial deformation of the column when subjected to eccentric loading under a traveling fire scenario. As shown in Figure 6, that lateral deformation increased significantly with increasing temperatures, particularly at higher eccentricities. For the case when $e/h=0$, the lateral displacement remains constant regardless of temperature changes. A rapid increase in

displacement occurs after reaching 500°C, resulting in an overall lateral displacement of 32 mm. For the case of $e/h=0.25$, a slight increase in lateral displacement is observed as the temperature rises. At 500°C, the lateral displacement reaches approximately 5 mm. Beyond 500°C, deflections increase exponentially, developing a final displacement of 42 mm. Notably, in both scenarios, the section fails to support the load at approximately the same time. Additionally, the start of local buckling in the flanges is observed due to eccentric loading, and the initiation of material yielding at the flanges is observed (refer to Figure 5(b)).

For the case of $e/h=0.5$ significant deformation begins immediately after the material is exposed to temperatures above 200°C, with lateral deformation increasing sharply beyond 400°C. The section begins to exhibit local buckling in the flanges and starts to fail before reaching 500°C. In the eccentric cases, it is observed that higher stresses develop in the section's flange, leading to failure in further load-carrying capacity of the section. Increasing the loading eccentricity significantly amplifies lateral deformation, with the most pronounced effect observed for $e=b/4$, indicating a higher susceptibility to deformation at elevated temperatures.

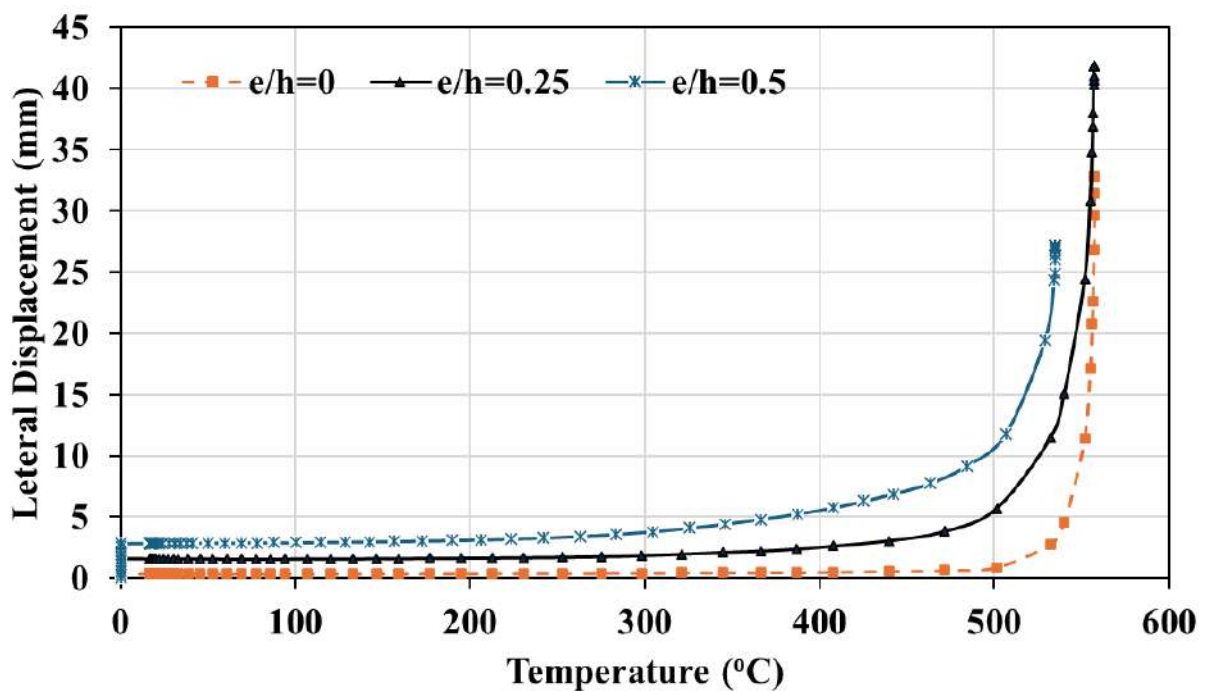


Figure 6. Lateral displacement in the isolated columns under different eccentricities

Figure 7 presents the results of axial deformation as a function of temperature for different eccentricity ratios. The temperature at which a column's axial deformation peaks is termed the buckling temperature; this temperature marks the onset of significant lateral deflection and buckling due to the column shortening under temperature [25]. As depicted in Figure 7, the buckling temperature for a column in the concentric case ($e/h=0$) is 530°C. For eccentricity ratios of $e/h=0.25$ and $e/h=0.5$, the buckling temperatures are 528°C and 504°C, respectively. Wang [26] defines the failure temperature of a restrained column as the point where the axial force in the column returns to its initial value. According to this definition, the failure temperatures for columns with eccentricity ratios of $e/h=0$, $e/h=0.25$, and $e/h=0.5$ are 568°C, 567°C, and 534°C, respectively. It is observed that increasing eccentricity reduces the buckling temperature, indicating that columns under eccentric loading fail earlier than those under concentric loading. Overall, the higher eccentricity ratio showed lower buckling temperature and the difference between failure temperature and buckling temperature was varied between 30°C to 40°C among considered eccentric ratio cases.

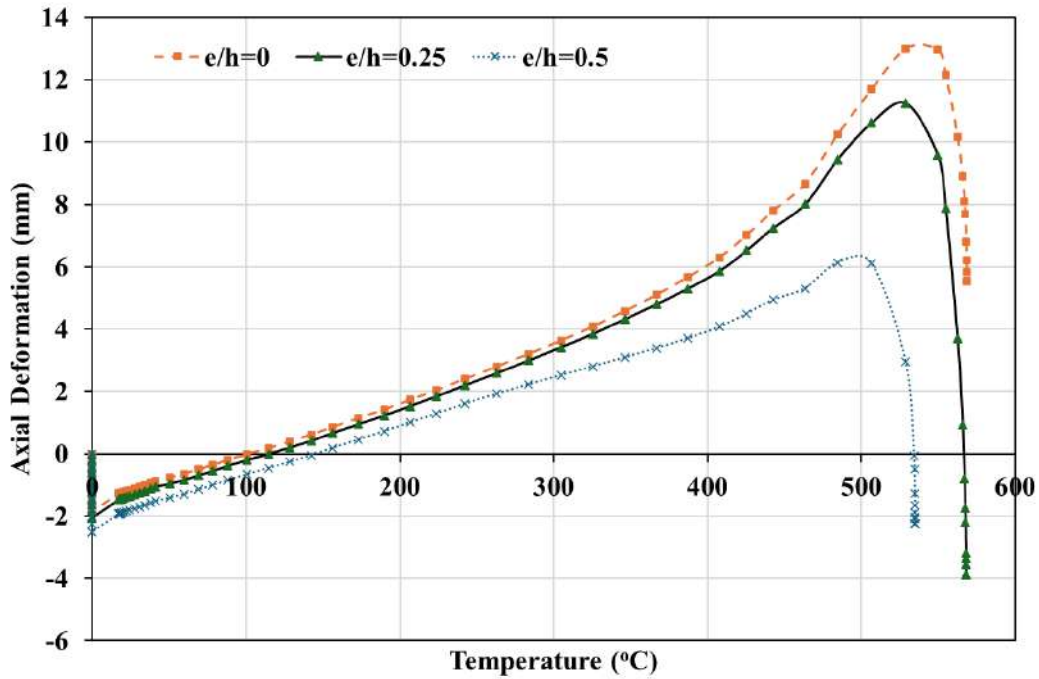


Figure 7. Axial deformation in the isolated columns under different eccentricities

4.3 Eccentricity through transient heating

4.3.1 Deformations in Column

Figure 8 illustrates the stress distribution in structural members under various eccentricity scenarios induced by transient heating. In Figure 8(a), the stress distribution in the members is depicted when the thermal load is exclusively applied to the column (Case 1, Table 1). Figure 8(b) showcases the stress levels when transient heating affects both the column and the beam along the left side (Case 2, Table 1). Figures 8(c) and 8(d) showcase the structural response at 20% and 30% of imposed loads combined with thermal load, respectively (Case 3 and Case 4, Table 1). Figure 9 depicts deformation in a frame frame under 30% imposed load in a travelling fire scenario. Deformation results for the column and beam are presented in Figure 10 and Figure 11, respectively. In Figure 10(a-d), the deformation under different scenarios outlined in Figure 8 is displayed. For Case 1, where the column is subjected to transient heating (Refer to Figure 10(a), the governing mode of deformation is along the axial direction, with minimal displacement (U1 and U3) along the orthogonal axes (x and z axes). The structure remains undamaged in this case, exhibiting no plastic deformation. Notably, the critical point where stresses are generated is at the beam-column connection. The final axial displacement (U2) in this case is recorded as 3mm. Conversely, in Case 2 where both the beam and columns are subjected to thermal load alone, as shown in Figure 10(b), vertical deformation (U2) occurs during the temperature rise, alongside deformation along the axes of lower flexural rigidity is developed in the z-direction (U3). This indicates combined axial and flexural deformations. Upon cooling, residual axial deformation in the column is observed as 3mm, similar to case 1, returning to its original position after temperature reduction.

For Case 3, where a 20% imposed load on the beam is applied along with the transient thermal load on the column and beam, the structures can sustain the load throughout the temperature duration, exhibiting elastic deformation. Additionally, deformation along the x-axis (U1) is observed alongside U2 and U3. After temperature reduction, final deformations occur primarily in the vertical direction and along the z-axis. In Case 4, with a 30% imposed load applied to the beam as shown in Figure 10(d), it becomes evident that the section starts to fail, resulting in deformation corresponding to the temperature rise. The maximum lateral displacement observed in a column is recorded as 10mm.

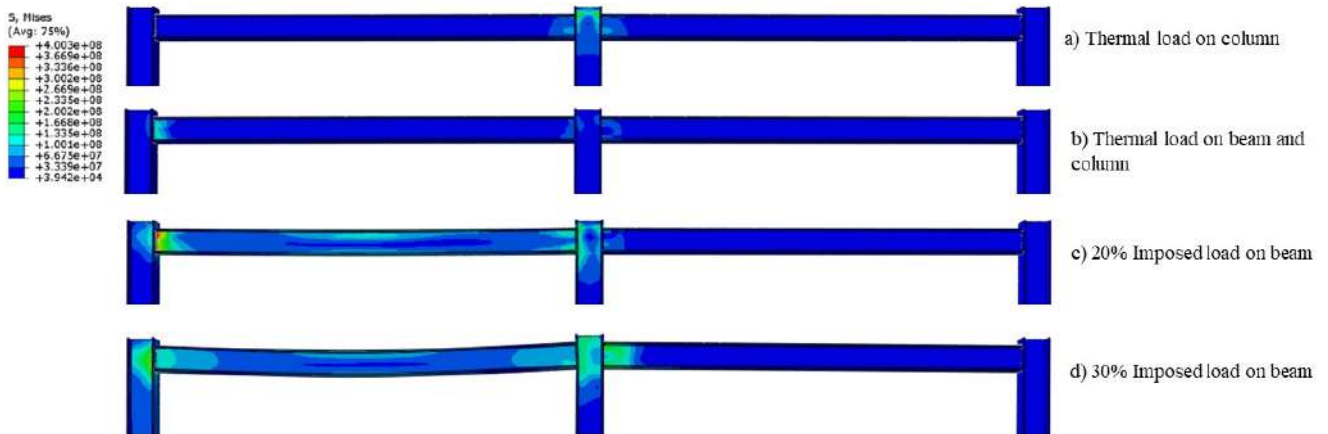


Figure 8. Stress distribution across members due to imposed load and thermal load

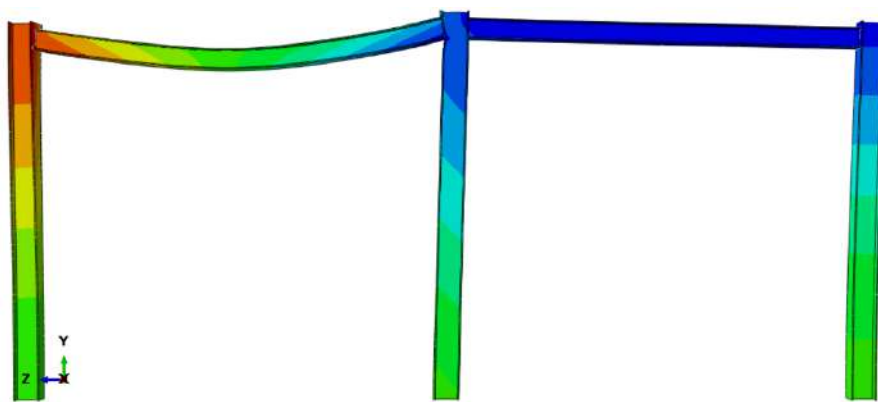


Figure 9. Deformation in a frame under 30% imposed load in a travelling fire scenario

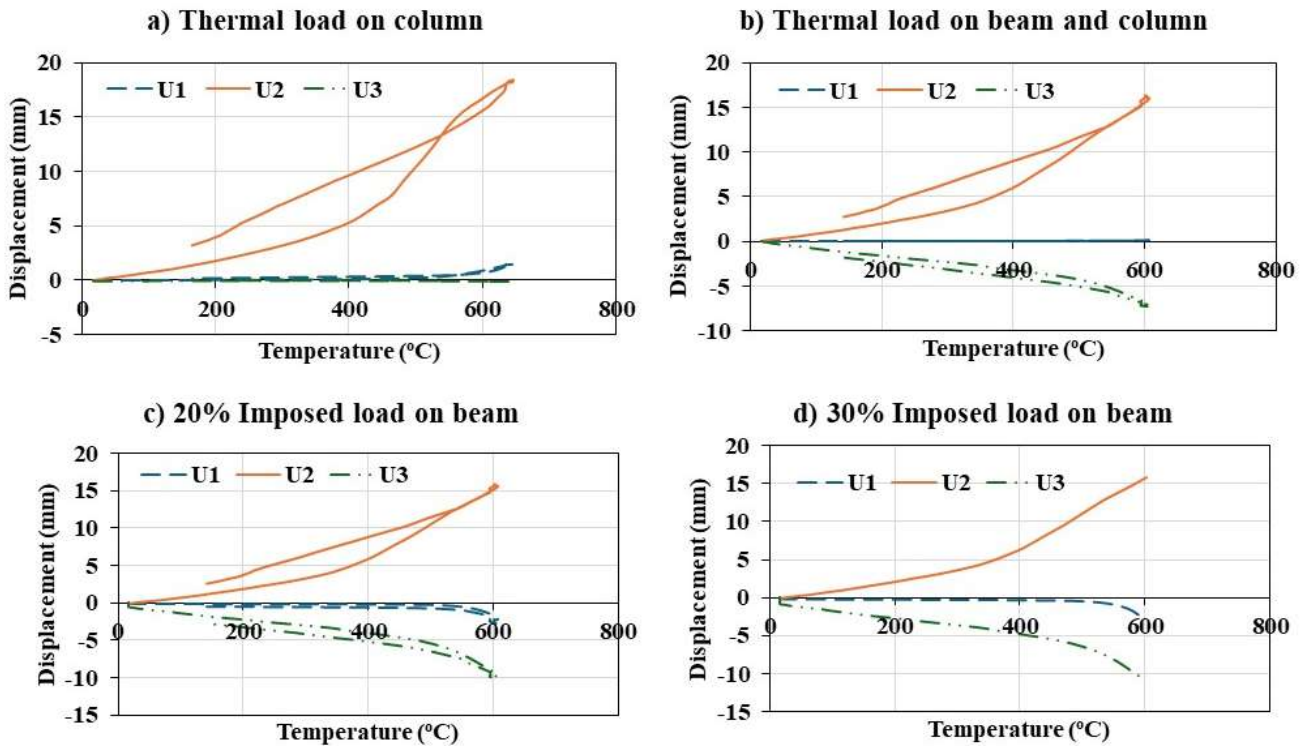


Figure 10. Deformation on a column in case of frame under thermal load with a combination of imposed load

4.3.2 Deformations in a beam

Furthermore, the response of deflection in the beam under imposed load in combination with transient thermal load is presented in Figure 11. For the unloaded case, in which only thermal load is applied, the section responds elastically by showing a deflection of merely 2 mm. It can be seen in Figure 8(a-d), that in all the loading cases the beam-column interactions are critical one which experiences higher stresses relative to other locations along the members. At 20% imposed load, the frame section can carry the load with temperature. Overall deflection produced in this case is 8mm. However, increasing the load by 30%, the sections start failing after 40 minutes of the thermal load. The maximum deflection recorded in this case is 10 mm. The adjacent column presented a slight twisting when a beam is subjected to transient heating and imposed load as shown in Figure 8. This could be attributed to the differential thermal environment of the beam and column, as the beam was subjected to temperature load, and the column was exposed to ambient conditions. It must be noted that the perfect connection between the beams and columns was modelled using the “Tie-Constraint” option available in ABAQUS.

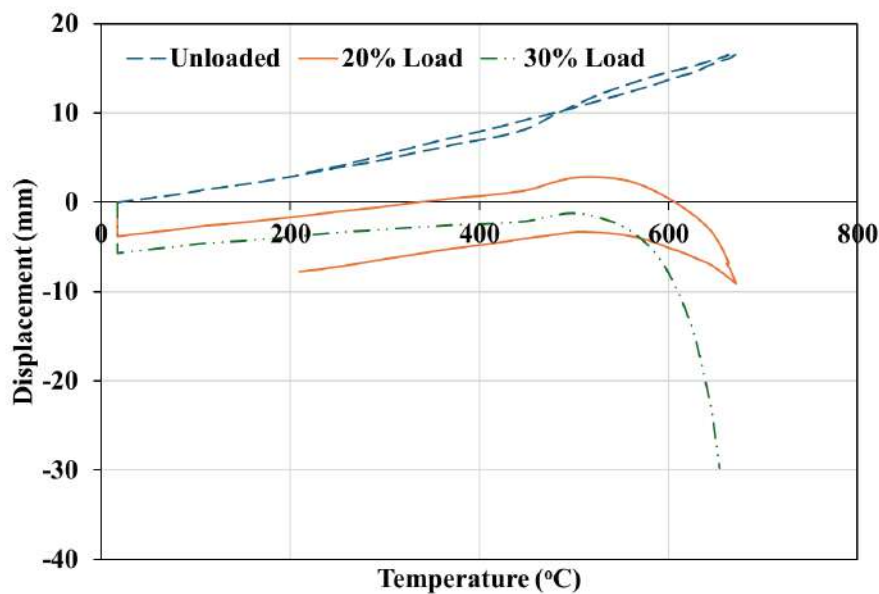


Figure 11. Beam Deformation under different loading

5 CONCLUSIONS

The study employed nonlinear analyses to explore the effects of eccentricities resulting from the applied loads and transient heating of columns during travelling fires. Abaqus software was utilized to simulate column buckling behaviour, accounting for geometric imperfections and material nonlinearity. The investigation focused on analysing stress distribution and deformation behaviour of structural members under transient heating scenarios with varying eccentricities. The key findings from the study are given below:

- Higher loading eccentricities intensify deformation, with local buckling observed in the flanges and initiation of material yielding. Temperature elevation, especially beyond 500°C, leads to substantial lateral displacement, ultimately resulting in section failure. Moreover, columns with higher eccentricity exhibited lower buckling temperatures. The variance between the failure temperature and the buckling temperature varied in the range of 30°C to 40°C.
- In case of steel frames, where transient heating affects both the column and frames, the structure remains intact without experiencing plastic deformation. It is noteworthy that the critical stress point occurs at the beam-column connection, with a residual axial displacement of 3mm.
- Transient heating with a 20% imposed load on the beam showed the structure withstands the load during the entire temperature duration, displaying elastic deformation. Upon cooling, the final

deformations primarily apparent in the vertical direction and along the weak axis. However, when a 30% imposed load is applied to the beam, the section begins to fail, leading to deformations corresponding to the temperature rise. The maximum lateral displacement observed in a column is recorded at 10mm.

- Thermal loads induce additional forces and moments on the structure, leading to load redistribution within the beam-column interactions. This redistribution results in increased stresses at critical points within the beam column interaction.

ACKNOWLEDGMENT

The authors would like to express their gratitude to Ulster University for generously providing access to research facilities, which have been instrumental in the successful completion of this study.

REFERENCES

1. A. Nadjai *et al.*, “Large scale fire test: The development of a travelling fire in open ventilation conditions and its influence on the surrounding steel structure,” *Fire Safety Journal*, vol. 130, 2022, doi: 10.1016/j.firesaf.2022.103575.
2. N. Alam *et al.*, “Large scale travelling fire tests with open ventilation conditions and their effect on the surrounding steel structure--the second fire test,” *Journal of Constructional Steel Research*, vol. 188, p. 107032, 2022, doi: <https://doi.org/10.1016/j.jcsr.2021.107032>.
3. X. Dai, S. Welch, and A. Usmani, “A critical review of ‘travelling fire’ scenarios for performance-based structural engineering,” *Fire Safety Journal*, vol. 91, pp. 568–578, 2017, doi: <https://doi.org/10.1016/j.firesaf.2017.04.001>.
4. A. A. Khan, A. Usmani, and J. L. Torero, “Evolution of fire models for estimating structural fire-resistance,” *Fire safety journal*, vol. 124, p. 103367, 2021, doi: <https://doi.org/10.1016/j.firesaf.2021.103367>.
5. A. Law, J. Stern-Gottfried, M. Gillie, and G. Rein, “The influence of travelling fires on a concrete frame,” *Engineering Structures*, vol. 33, no. 5, pp. 1635–1642, 2011, doi: 10.1016/j.engstruct.2011.01.034.
6. M. D. Engelhardt *et al.*, “Observations from the fire and collapse of the faculty of architecture building, delft university of technology,” in *Structures Congress 2013: Bridging Your Passion with Your Profession*, 2013, pp. 1138–1149, doi: <https://doi.org/10.1061/9780784412848.101>.
7. R. G. Gann *et al.*, “Reconstruction of the fires and thermal environment in World Trade Center buildings 1, 2, and 7,” *Fire technology*, vol. 49, pp. 679–707, 2013, doi: <https://doi.org/10.1007/s10694-012-0288-3>.
8. E. Guillaume, V. Dréan, B. Girardin, F. Benameur, and T. Fateh, “Reconstruction of Grenfell Tower fire. Part 1: Lessons from observations and determination of work hypotheses,” *Fire and Materials*, vol. 44, no. 1, pp. 3–14, 2020, doi: 10.1002/fam.2766.
9. P. Dias Simão, J. P. C. Rodrigues, and R. L. G. Oliveira, “Simple analytical models for restrained steel columns in fire,” *Engineering Structures*, vol. 236, no. February, 2021, doi: 10.1016/j.engstruct.2021.112119.
10. K. H. Tan and W. F. Yuan, “Buckling of elastically restrained steel columns under longitudinal non-uniform temperature distribution,” *Journal of Constructional Steel Research*, vol. 64, no. 1, pp. 51–61, 2008, doi: 10.1016/j.jcsr.2007.02.003.
11. Y. Bai, Y. Shi, and K. Deng, “Collapse analysis of high-rise steel moment frames incorporating deterioration effects of column axial force – bending moment interaction,” *Engineering Structures*, vol. 127, pp. 402–415, 2016, doi: 10.1016/j.engstruct.2016.09.005.
12. Y. Yao, H. Li, H. Guo, and K. Tan, “Fire resistance of eccentrically loaded slender concrete-filled steel tubular columns,” *Thin-Walled Structures*, vol. 106, pp. 102–112, 2016, doi: 10.1016/j.tws.2016.04.025.
13. E. F. Du, G. P. Shu, and X. Y. Mao, “Analytical behavior of eccentrically loaded concrete encased steel columns subjected to standard fire including cooling phase,” *International Journal of Steel Structures*, vol. 13, no. 1, pp. 129–140, 2013, doi: 10.1007/s13296-013-1012-y.
14. N. A.-H. Al-Talqani and H. Al-Thairy, “Behavior of eccentrically loaded normal weight concrete encased steel columns at elevated temperature,” *IOP Conference Series: Materials Science and Engineering*, vol.

- 1076, no. 1, p. 012124, 2021, doi: 10.1088/1757-899x/1076/1/012124.
- [15. Y. Du, H. Qi, J. Jiang, J. Y. R. Liew, and S. Li, "Thermo-mechanical behaviour of ultra-high strength concrete encased steel columns in standard fires," *Engineering Structures*, vol. 231, p. 111757, 2021.
- [16. S. Li, J. Y. R. Liew, and M.-X. Xiong, "Fire performance of composite columns made of high strength steel and concrete," *Journal of Constructional Steel Research*, vol. 181, p. 106640, 2021.
17. F. Liu, H. Yang, and W. Wang, "Behaviours of concentrically and eccentrically loaded square steel tube confined reinforced concrete slender columns after fire exposure," *Thin-Walled Structures*, vol. 158, p. 107155, 2021.
18. X. Wei, Y. Yang, J. Liu, W. Yang, Y. F. Chen, and H. Zhang, "Experimental and numerical study of fire performance of L-shaped concrete-filled steel tubular columns under eccentric compression," *Journal of Building Engineering*, vol. 50, p. 104149, 2022.
19. ABAQUS, "Finite Element Modelling Programme and Standard User's Manual. Version 6.14. SIMULIA.," <http://130.149>, vol. 89, no. 2080, p. v6, 2018.
20. H. A. A. model for predicting the fire re-sponse of concrete filled tubular columns. J. C. S. R. 2010;66:1030–46. Espinos A, Romero ML, "No Title."
21. N. Alam, A. Nadjai, F. Hanus, C. Kahanji, and O. Vassart, "Experimental and numerical investigations on slim floor beams exposed to fire," *Journal of Building Engineering*, vol. 42, no. May, p. 102810, 2021, doi: 10.1016/j.job.2021.102810.
22. B. Eurocode 1: Actions on structures – Part 1–2: General actions – Actions on Structures Exposed to Fire, European Standard EN 1991-1-2, 2002. CEN, "No Title."
23. F. Ali, I. Sirmms, and D. O'connor, "Behaviour Of Axially Restrained Steel Columns During Fire," *Fire Safety Science*, vol. 5, pp. 1105–1116, 1997, doi: 10.3801/iafss.fss.5-1105.
24. A. Nadjai, N. Alam, M. Charlier, J. McGillighan, and O. Vassart, "Experimental and Numerical Investigations on Steel Columns Compartment Subjected to Travelling Fires," *Ce/Papers*, vol. 4, no. 2–4, pp. 1429–1436, 2021, doi: 10.1002/cepa.1441.
25. G. Q. Li, P. Wang, and Y. Wang, "Behaviour and design of restrained steel column in fire, Part 1: Fire test," *Journal of Constructional Steel Research*, vol. 66, no. 8–9, pp. 1138–1147, 2010, doi: 10.1016/j.jcsr.2010.03.017.
26. Y. C. Wang, "Postbuckling behavior of axially restrained and axially loaded steel columns under fire conditions," *Journal of structural Engineering*, vol. 130, no. 3, pp. 371–380, 2004.

NUMERICAL ANALYSIS OF STEEL-CONCRETE COMPOSITE SHEAR WALL AT ELEVATED TEMPERATURE

Bhatt Nav Raj¹, Mahbub Khan², Huu Tai Thai³, Tuan Ngo⁴, Brian Uy⁵

ABSTRACT

Steel-concrete composite shear walls (SCCSW) are gaining popularity in various building applications because of their benefits, such as modular design and accelerated construction times. Since fire safety is paramount in building design, evaluating the fire performance of SCCSW is essential. A more profound comprehension of its fire behaviour can help modular construction become more sustainable and effective. The study investigates the thermal and structural response of SCCSW exposed to combined fire and gravity loading conditions using an extensive FE model created using ABAQUS. Validated models exhibit strong alignment in terms of temperature distribution, axial displacement, and failure time when compared to experimental data from earlier research. The impact of different factors like load ratio, eccentricity, steel strength, concrete strength, and fire exposure scenarios on the fire performance of SCCSW is further investigated using parametric studies. The results offer insights to improve the structural integrity and fire safety of SCCSW and throw light on essential aspects impacting their fire resistance. The parameters that affect the SCCSW's behaviour are examined, and suggestions are made for creating design guidelines.

Keywords: Composite structures; steel-concrete composite shear wall; fire performance; numerical analysis

1 INTRODUCTION

Shear walls are structural elements designed to withstand lateral forces in the same plane through shear and bending resistance while bearing vertical loads simultaneously. Although traditional reinforced concrete (RC) walls have been extensively employed in high-rise buildings and have proven effective in supporting forces along both compressive and lateral loads, they are susceptible to surface cracks due to seismic and environmental factors, such as thermal effects [1]. Additionally, in tall buildings, the increase in axial compressive forces can necessitate excessively thick RC shear walls, which is not economical and space-efficient. Steel-concrete composite shear wall (SCCSW) presents a viable option for RC walls, overcoming many limitations.

¹ Doctoral Student, University of Melbourne,
e-mail: navraj@student.unimelb.edu.au

² Postdoctoral Researcher, University of New South Wales
e-mail: mahbub.h.khan@unsw.edu.au

³ Professor, University of Melbourne
e-mail: tai.thai@unimelb.edu.au

⁴ Professor, University of Melbourne
e-mail: dtngo@unimelb.edu.au

⁵ Professor, University of New South Wales
e-mail: b.uy@unsw.edu.au

SCCSW, also referred to as composite plate shear wall or concrete-filled composite shear wall, has been used in structural engineering due to several advantages, such as modularity and the ability to accelerate the construction timeline. In an SCCSW, steel plates are stiffened together with tie bars and concrete is poured between the two steel plates, as shown in Figure 1. Shear studs are also used to enhance shear transfer and promote composite action between steel and concrete. SCCSW can fully harness the benefits of both steel and concrete, enabling them to resist horizontal and vertical loads collaboratively. As a result, SCCSW is lighter and thinner compared to traditional RC walls, which reduces the load on the foundation system and offers additional benefits such as improved space efficiency and cost-effectiveness.

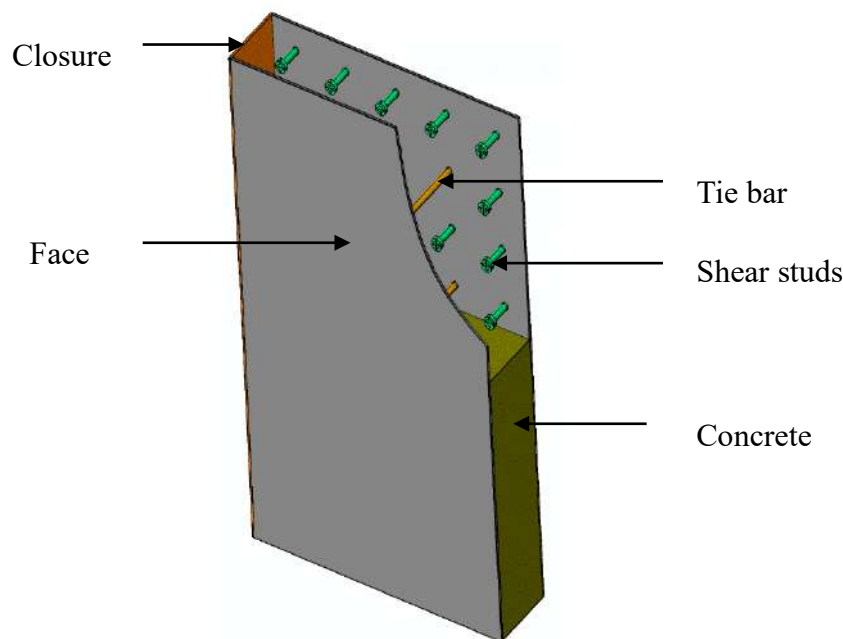


Figure 1. Steel-concrete composite wall

The idea for the composite wall draws inspiration from the composite flooring system, as demonstrated in the work by Wright et al. [2]. This system comprises outer steel plates attached to the filled concrete through a range of connections, such as shear studs, truss connectors, and diaphragms. Initially, SCCSW was explored and implemented in nuclear plants to withstand horizontal earthquake loads, demonstrating exceptional structural performance, as evidenced by research conducted by Varma et al. [1]. Subsequently, its application extended to steel frame systems in multi-storey buildings, as documented in different studies [3,4]. Zhang et al. [5] developed equations for stud spacing in SCCSW to prevent local buckling before yielding and to guarantee an adequate development length for steel faceplates. Mo et al. [6] conducted an experimental and numerical study on the axial performance of SCCSW walls under axial compression, providing design recommendations.

High-rise structures experience extreme loading conditions, such as fire incidents, that affect their structural integrity and safety. A critical component of assessing the suitability of SCCSWs for commercial construction involves investigating how these walls perform and maintain stability when subjected to fire loading. Without fire protection, the exterior steel plates of SCCSW would be directly subjected to direct fire loads, resulting in increased and uneven temperature distribution across the wall's cross-section. These elevated temperatures can degrade the mechanical properties of both steel and concrete, potentially leading to local or global buckling. Furthermore, the increased temperatures of these walls can trigger failure at lower axial load levels than what they can withstand at normal ambient temperatures. Consequently, it is crucial to assess the stability of SCCSW under fire-loading conditions.

A design method based on fire performance tests on rib-stiffened steel plate concrete (SSC) walls was proposed by Moon et al. [7] to ensure the required fire resistance rating. The research tested loaded 300 mm thick SCC walls with a cross-sectional size of 3000 × 3000 mm under the ISO 834 standard fire curve.

At 40% and 63 % axial ratios, the specimens failed after 180 minutes and 89 minutes, respectively. Failures in the specimens were attributed to local buckling of steel plate, spalling of concrete and weld failures of studs and tie bars.

Wei et al. [8] performed twelve experiments on SCCSW, including eight tests with four-sided exposure and the rest with single-sided fire exposure. They investigated the influence of slenderness ratio, shear stud spacing, steel ratio and wall thickness on the performance of SCCSW walls at elevated temperatures. The findings from the experiments revealed that the slenderness ratio of the specimens exerts a notable impact on wall behaviour. As the slenderness ratio of the specimens increases, the fire resistance decreases. Moreover, an increase in wall height can induce global instability, with the tallest specimen (1850 mm height) experiencing failure due to this instability. For specimens exposed to uniform heating, they either failed due to global instability or crushing. The tests demonstrated that the composite interaction between the outer steel and infilled concrete weakens with increasing temperature regardless of the spacing of shear studs.

In their study, Hu et al. [9] investigated how the lateral stiffness of SCCSW is affected when subjected to fire. They found that the reduction in stiffness is associated with both the duration and surface temperature of the fires and put forward equations for estimating the lateral stiffness of SCCSW when subjected to fire loads. Fire tests validated the precision of the proposed equations.

In their comprehensive analysis, Anvari et al. [8,9] conducted experimental and numerical investigations to address the gaps in the prior experimental investigations. Specimens were exposed to simultaneous fire and loading along the axis in five separate tests to study the effect of axial compression ratio, exposure condition and stud spacing. Numerical simulations were performed using ABAQUS to investigate the thermal and structural behaviour of SCCSW when exposed to both fire and gravity loads. The findings shed light on how the applied vertical force is distributed between steel and concrete, as well as the impact of the critical components of the wall on fire resistance.

Du et al. [12] performed an experimental study to investigate the fire resistance of SCCSW with truss connectors. Four walls were subjected to one-sided ISO-834 standard fire [13]. The test demonstrated that reducing the load ratio from 0.5 to 0.3 shifted the wall's vertical deformation from being predominantly compressive to primarily expansive. Additionally, a greater truss spacing resulted in a more pronounced buckling of the steel plate towards the heated side. The test samples were able to withstand the applied axial load for approximately three hours during the heating process.

In summary, prior studies contributed immensely to understanding the behaviour of SCCSW walls under varying loading conditions, wall thickness and wall slenderness. However, there is still a need for more research that focuses on the performance of SCCSW under eccentric load, varying fire exposures, and varying steel and concrete strengths at increased temperatures. Eccentric loads may be anticipated in an SCCSW due to factors such as asymmetrical loading, irregular wall geometry, connection details, and so on. High-strength materials are overly used in high-rise construction, necessitating research into their fire performance. This research aims to bridge that gap by exploiting FE to investigate the behaviour of SCCSW during fire situations and enhance their fire resistance and structural robustness.

2 FINITE ELEMENT MODELLING

Numerical models were developed using ABAQUS to predict the behaviour of SCCSWs under combined axial load and fire conditions. A sequentially coupled transient thermo-stress approach was utilised. Sequential coupled thermal-stress analysis in Abaqus involves a two-stage process where the thermal and stress analyses are carried out one after the other in sequence. It offers advantages such as flexibility in solution methods and computational efficiency compared to fully coupled thermos-stress analysis. Wei et al. used test specimens comprising steel plates, concrete, studs and tie bars. In the heat transfer analysis, eight-node linear heat transfer bricks (DC3D8) were employed for discretising all the wall elements. For stress analysis, the wall elements were segmented into eight-node linear brick elements (C3D8R). The accuracy of the FE results was confirmed against the fire test results. A thorough exposition of the model development is provided herein.

2.1 Steel and concrete material properties

Concrete and steel's mechanical and thermal properties go through substantial changes at increased temperatures. Thermal properties, including density, specific heat, and conductivity, and mechanical properties, including elastic modulus, stress-strain relations, and thermal expansion, are affected. The thermal and mechanical characteristics of both steel and concrete were established in accordance with Eurocode 4 [14] and Eurocode 2 [15]. Figure 2 shows the relative strength reduction of different types of concrete and steel at high temperatures per Eurocode. The upper limit thermal conductivity of normal concrete was assumed, and 3 % concrete was considered when calculating its specific heat. The heat transfer coefficient due to convection was also set at 25 W/m²K for surfaces exposed to fire. A thermal emissivity of 0.7 was assigned to the exposed faces of steel.

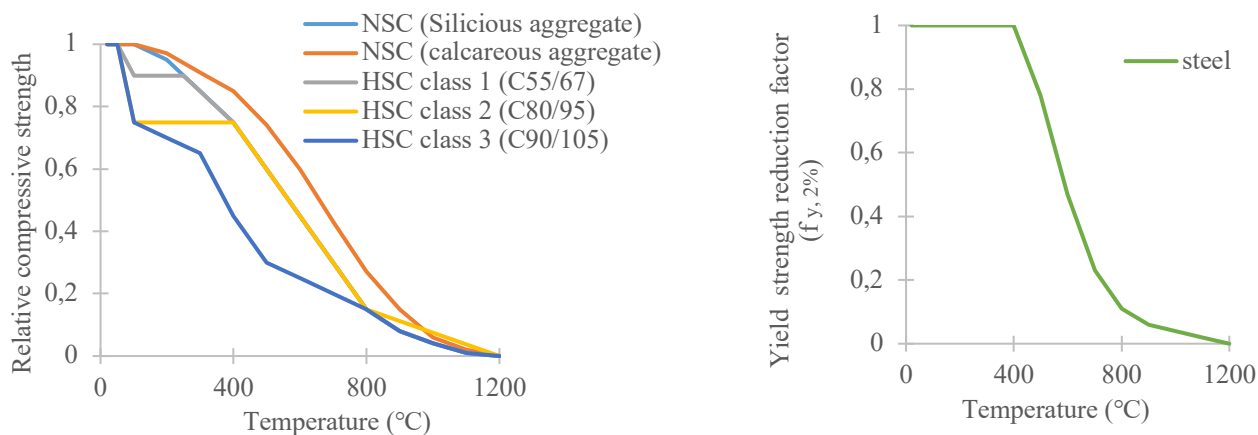


Figure 2. Relative strength of concrete and steel at elevated temperatures [15]

2.2 Thermal analysis

During the first stage, a thermal analysis was conducted to establish the temperature distribution within the structure. The initial temperature of the specimen was set at 20 °C. The temperature applied to the wall surface followed the standard ISO834 curve. The 'surface film condition' and 'surface radiation' subroutines in ABAQUS were used to simulate heat transfer between the furnace and the steel. These subroutines use gas temperatures to compute the temperatures of the heated regions of the specimen, taking into consideration convection and radiation parameters [13]. The thermal conductance between steel and concrete was determined based on a study conducted by Ghojel [16], which establishes a relationship between conductance and temperature. To ensure the thermal conductance remains largely unaffected by the distance between closely positioned surfaces, minimal values were assigned to the clearance between them.

2.3 Stress Analysis

In the second stage, stress analysis was carried out. The axial load was initially applied in increments up to the desired level. Subsequently, while keeping the load constant, temperatures at regular time intervals obtained from the thermal analysis were applied to the corresponding nodes of the wall. The Dynamic Implicit solver was used to execute the stress analysis. The behaviours of the steel and concrete materials were characterised using the 'elastic-plastic' and 'concrete damaged plasticity model', respectively. Tie interactions were defined for the connections between the steel plate and stud, the steel plate and tie bar, and between the two steel plates. The shear studs and tie bars were modelled as embedded in concrete. Both ends of the wall were fixed, permitting rotation about the major axis at each end and vertical displacement at the top end.

3 MODEL VALIDATION

The accuracy of the developed FE model in predicting SCCSW's behaviour under fire was assessed by comparing its predictions with data presented in Wei et al.'s fire tests on SCCSW [8]. Thermal and structural domains of the experimental results were used in the evaluation.

3.1 Description of validated wall

The experiments were carried out in a gas furnace where the wall specimens were loaded with uniform axial loads, and fire was applied simultaneously. The furnace temperature was controlled to follow the ISO 834 curve. In the experiment, the width of the wall was standardised at 1000 mm. The heights of the specimen range between 850 mm and 1850 mm. The wall thickness was selected as either 150 mm or 200 mm, while the steel plate thicknesses varied between 2mm and 5mm. Loads were applied to maintain a load ratio from 0.26 to 0.4. For composite action, 2 mm diameter studs with a length of 20 mm were employed, along with 10 mm width tie bars spaced at intervals of 160 mm to hold the face plates together. Moreover, to mimic real scenarios, two extra inner steel plates of identical thickness were inserted 150 mm away from the closure plates, establishing boundary columns at both ends of the wall.

3.2 Thermal response

Figure 3(a) and (c) illustrate the comparisons of FE and experimental temperature profiles along the concrete's surface centre for the uniformly heated specimens SC4 and SC7. Figure 3(c) and (d) show the FE temperature distribution across the wall. Overall, the FE results align well with the experimental output. The plateaus observed may be due to some heat loss or inconsistencies in measurement.

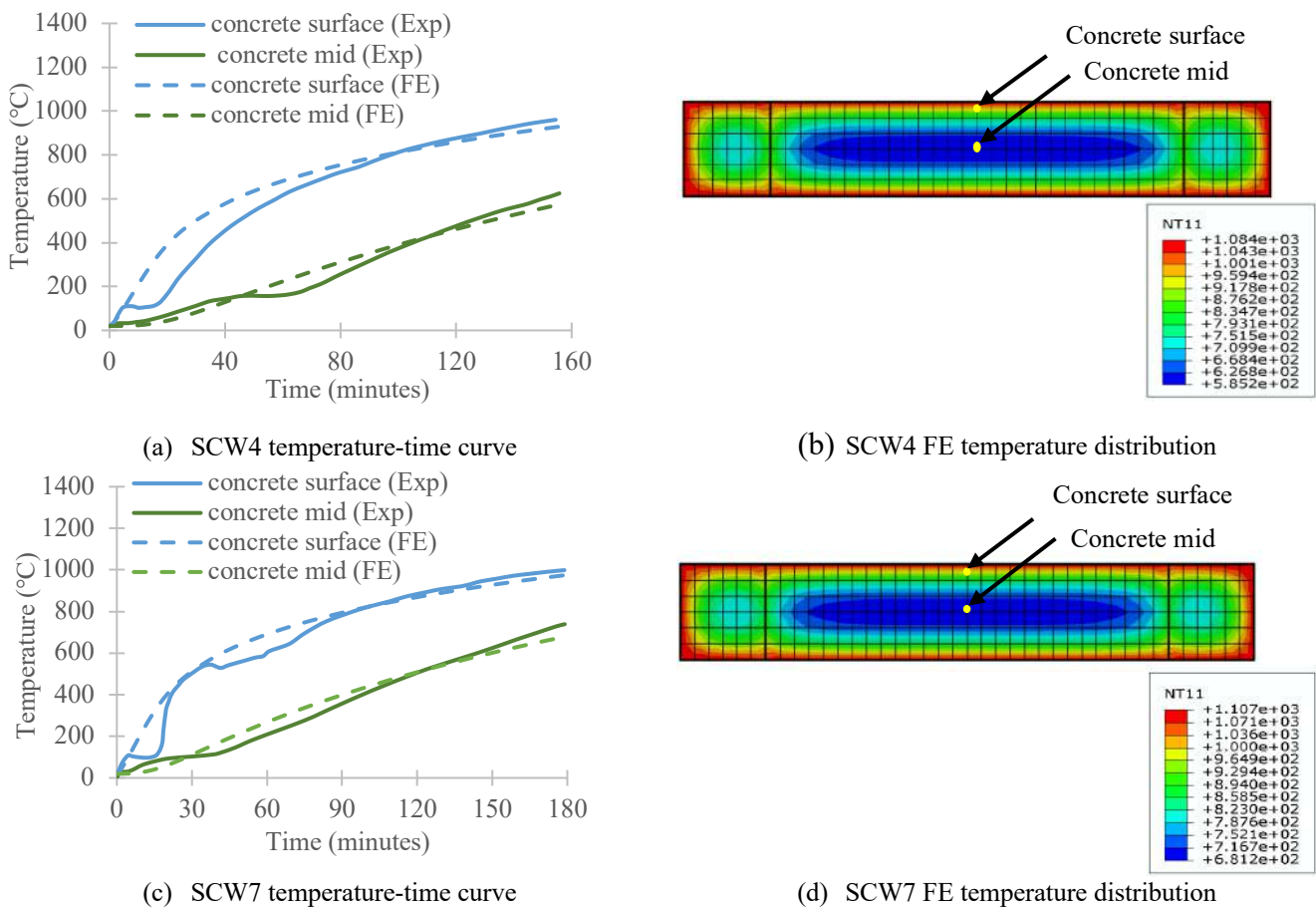


Figure 3. Comparison of experimentally measured and FE-predicted temperature for specimens SCW4 and SCW7 [8]

3.3 Structural response

Figure 4(a) and (b) present the comparative analysis of FE axial deformation against the experimental axial deformation for walls SCW4 and SCW7 that were uniformly heated from all sides. During the initial phase, the walls exposed to four-sided fire experienced thermal expansion, followed by a period of axial compression. As the steel and concrete temperatures rose, resulting in decreased material strength, the axial compressive deformation surpassed thermal expansion. This axial compression intensified gradually,

culminating in rapid axial contraction and specimen failure. The FE analyses reasonably estimated the deformation-time response. Discrepancies in axial deformation during the initial stages of fire exposure likely stem from the displacement measurement method used for the specimens. Instead of measuring displacements directly at the specimens' ends, the measurements were taken at the ends of the RC loading beams. This approach may have caused some of the displacements to be absorbed by the thermal expansion of the steel plates. It's important to note that the FE analyses did not incorporate the loading beams in their modelling, and thus, the reported displacements pertain solely to the specimens themselves.

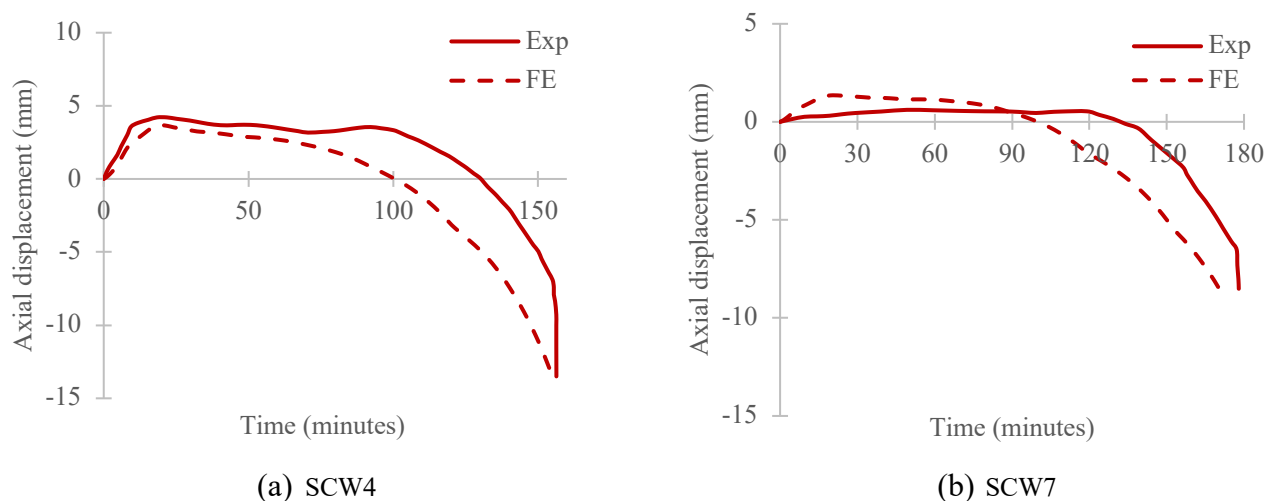


Figure 4. FE-predicted axial deformation vs experimentally measured axial deformation for walls SCW4 and SCW7 [8]

4 PARAMETRIC STUDY AND DISCUSSION

A set of parametric studies was selected to analyse the behaviour of the SCCSW subjected to fire loading. The variable parameters included load ratio, eccentricity ratio (e/t), steel strength, concrete strength, and fire exposure condition. The thickness of the wall was 200 mm, including 6 mm of steel plates on both ends. The wall had a height-to-thickness ratio of 10 and a width of 800 mm. Employed for shear connection were 19 mm diameter studs and tie bars. The baseline concrete and steel strengths used for the analysis were 32 MPa and 350 MPa, respectively. The parameter values considered are listed in Table 1.

Table 1. List of parameters

Parameters	Values
Axial load ratio (L_r) %	20, 35, 50, 70
Fire exposure condition	1-sided, 2-sided, 4-sided
Eccentricity ratio (e/t) %	0, 5, 10, 15, 20
Steel strength (MPa)	350, 690
Concrete strength (MPa)	32, 120

4.1 Effect of load ratio

The behaviour of the SCCSW under four different load ratios, 0.20, 0.35, 0.50 and 0.70, was studied. The axial displacement response of the wall under one-sided and four-sided exposures is shown in Figure 5. The results indicate that the fire resistance is higher for the walls with smaller loads. The fire resistance of the walls with 0.2, 0.35, 0.5 and 0.7 load ratios were 246 minutes, 137 minutes, 72 minutes, and 34 minutes for four-sided fire. For one-sided fire, the respective fire resistance times were over 360 minutes, 241 minutes, 132 minutes, and 56 minutes. It was observed that during the initial phase, a lower load ratio on the walls allowed more axial expansion. The fire resistance time was roughly halved with an increase in the load ratio from 0.2 to 0.35, while it decreased nearly threefold when the load ratio elevated to 0.5.

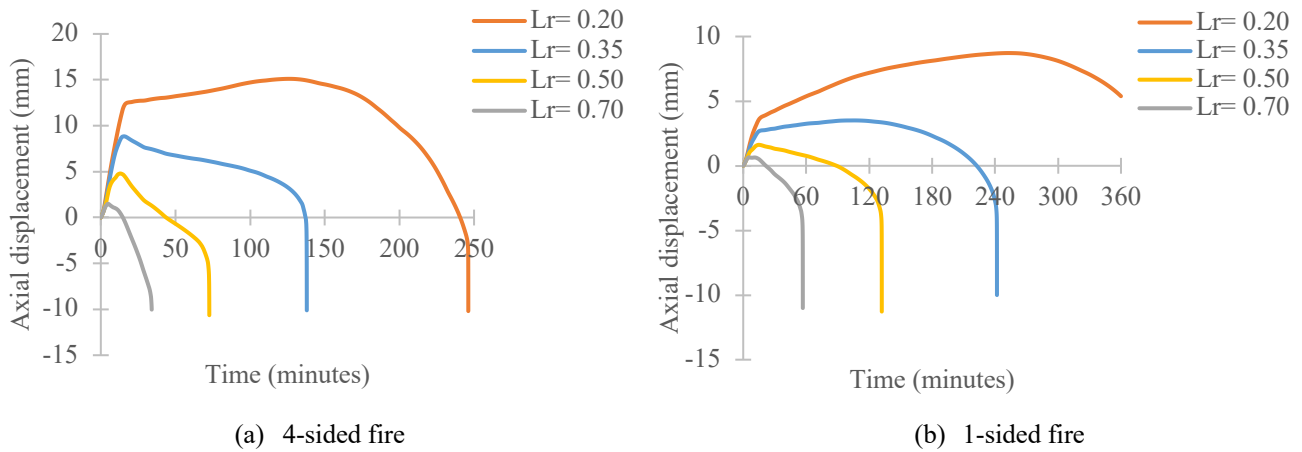


Figure 5. Axial displacement of SCCSW with varying load ratio

4.2 Effect of eccentricity

Growing eccentricity leads to a substantial reduction in the fire resistance of SCCSW, as shown in Figure 6. Eccentric loads can amplify second-order effects. The second-order effects can lead to additional deformations and stresses, further compromising the fire performance of the wall. For all studied load eccentricities, walls displayed a buckling response. As shown in Figure 6(a), with a mere 5 % eccentricity ratio, the fire resistance under 4-sided fire conditions was nearly halved. Figure 6(b) and (c) illustrate the vertical deformation response of walls with height-to-thickness ratio (H/t) 10 and 20 under single-sided fire exposure. In the case of SCCSW ($H/t = 10$), as the load eccentricity shifted towards the heated side ($e < 0$), the wall exhibited a more pronounced vulnerability. Conversely, for $H/t = 20$, SCCSW experienced a notable decline in failure time when the load eccentricity increased towards the unexposed side ($e > 0$). The reason may be attributed to the significant thermal bowing of the $H/t = 20$ wall towards the heated side compared to $H/t = 10$ wall.

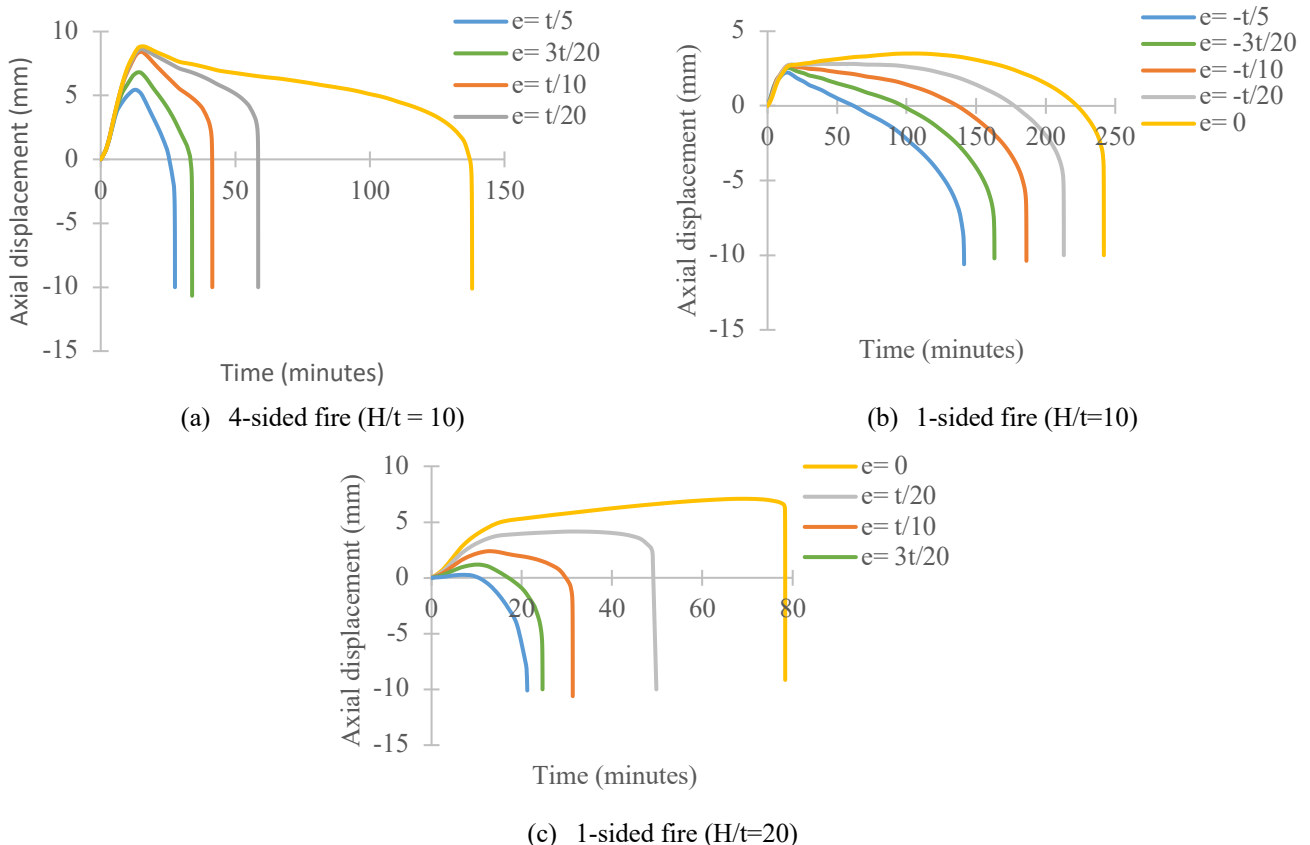


Figure 6. Axial displacement of SCCSW with varying eccentricity

4.3 Effect of steel strength

Figure 7 illustrates the axial deformation response of SCCSWs with varying steel strengths under 4-side and 1-side heat exposure scenarios. Two different steel grades were assessed: 350 MPa and 690 MPa. The result indicates that as the steel strength increases, the fire resistance of the wall diminishes when maintaining a constant load ratio. This is because steel, being directly exposed to heat, has high thermal conductivity, which causes it to heat up more rapidly and lose strength more quickly. Also, high-strength steel exhibits a faster rate of strength degradation than low-strength steel [17]. These factors significantly contribute to the reduced fire resistance of walls with high-strength steel compared to low-strength steel, provided that the load ratio remains the same.

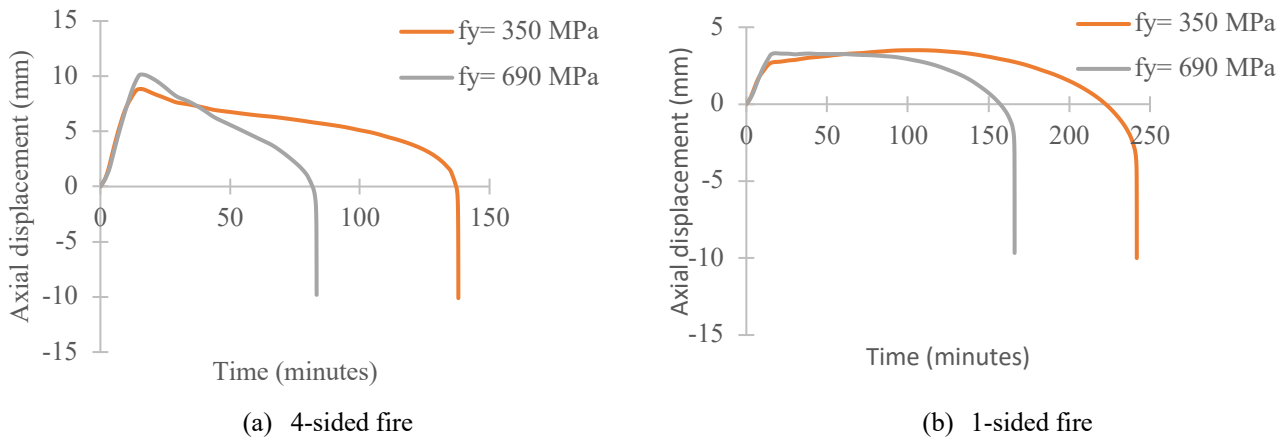


Figure 7. Axial displacement of SCCSW with varying steel strengths

4.4 Effect of concrete strength

The fire resistance capacity of SCCW is significantly affected by the strength of the concrete. In this study, two different grades of concrete, 32 MPa and 120 MPa, were examined to assess their impact on the fire resistance of SCCSW. Figure 8 demonstrates that, for 4-side and 1-side exposure conditions, an increase in concrete strength decreased the fire resistance time of SCCSW. For four-sided exposure, grade 32 MPa showed a fire resistance duration of 137 minutes compared to 105 minutes for grade 120 MPa, and for single-sided exposure, grade 32 lasted 241 minutes while grade 120 lasted 194 minutes. All other parameters, including the load ratio, were kept constant, indicating that the actual load applied was higher for the SCCSW with concrete grade 120 MPa. The reason is that high-strength concrete degrades faster than normal-strength concrete at elevated temperatures, as shown in the graph in Figure 2.

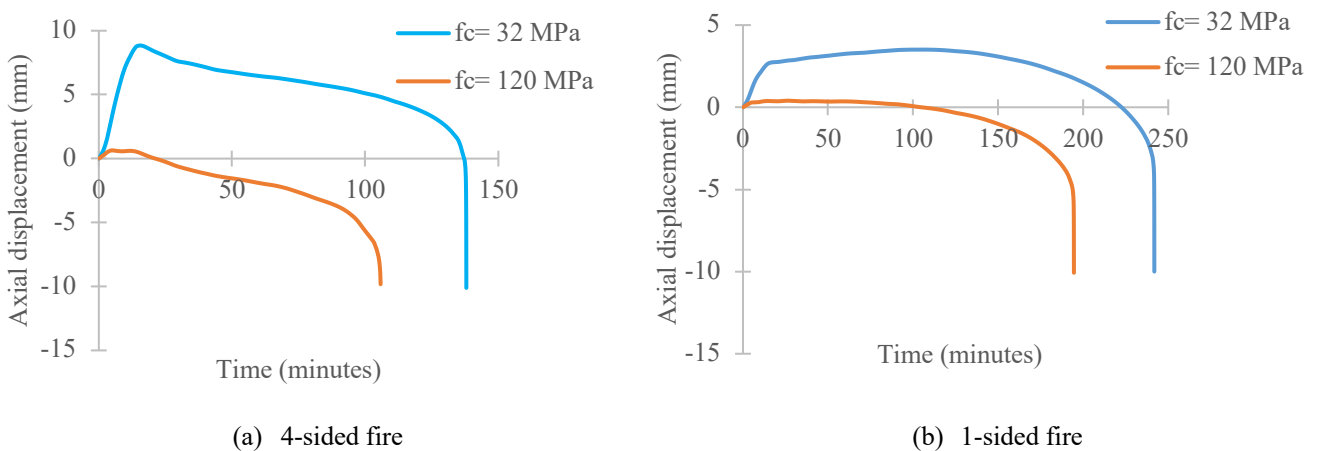


Figure 8. Axial displacement of SCCSW with varying concrete strengths

4.5 Effect of fire exposure

The research examined three fire scenarios: 1-side, 2-side, and 4-side, with findings displayed in Figure 9. The results suggest that the extent of fire exposure directly affects the SCCSW's ability to withstand load during a fire. The fire resistance notably improves with 1-side fire exposure compared to 2-side and 4-side exposures. Given that the thickness of the wall is less compared to its width, the difference in the fire resistance between 4-sided and 2-sided scenarios is lesser. This enhanced fire resistance could be due to the lower temperature rise on the unexposed side. The fire-induced degradation of material towards the unexposed side is slow; thus, the wall can withstand load for a prolonged period.

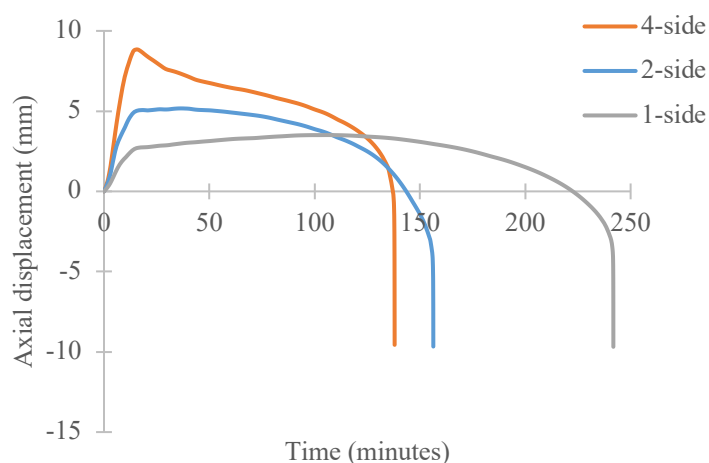


Figure 9. Axial displacement of SCCSW with different fire exposures

5 CONCLUSIONS

This study performed a numerical investigation of SCCSW variable fire loads. FE models were created using ABAQUS for the SCCSW and cross-checked with previous experimental results on temperature distribution, axial displacements, and fire resistance. Afterwards, a thorough examination was conducted on a number of variables, such as the fire-exposed sides, the strengths of steel, eccentricity and the load ratios, to determine their influence on the fire behaviour of SCCSW. The following are the main conclusions:

- The fire endurance of SCCSW is significantly decreased by an increase in the load ratio and the amount of section surfaces exposed to fire. The fire boundary considerably impacts the temperature distribution. A large area of fire exposure results in an early failure of SCCSW.
- Under the same fire conditions and load ratios, low-grade steel and concrete demonstrate superior fire resistance than their high-grade counterparts.
- The eccentricity of the load substantially reduces the fire performance of SCCSW. For single-sided fire exposures, the critical scenario arises in short walls when the load is applied towards the exposed side. In contrast, the critical scenario occurs in slender walls when the load is applied on the unheated side.

ACKNOWLEDGEMENT

This research was supported by the Australian Research Council (ARC) under its Discovery Projects (DP230100018).

REFERENCES

1. Zhao Q, Astaneh-Asl A. Cyclic behavior of steel and composite shear walls. 8th US National Conference on Earthquake Engineering 2006. 2006;1(February):142–51.

2. Wright, Howard and Evans, Roy and Gallocher S. Composite walling. In: *Composite Construction in Steel and Concrete II*. 1992. p. 783--797.
3. Huang Y, Young B. The art of coupon tests. *J Constr Steel Res*. 2014;96:159–75.
4. Guo L, Wang Y, Zhang S. Experimental study of rectangular multi-partition steel-concrete composite shear walls. *Thin-Walled Structures*. 2018;130(June):577–92.
5. Zhang K, Varma AH, Malushte SR, Gallocher S. Effect of shear connectors on local buckling and composite action in steel concrete composite walls. *Nuclear Engineering and Design*. 2014;269:231–9.
6. Mo J, Uy B, Li D, Thai HT, Wang Y. Behaviour and design of composite walls under axial compression. *J Constr Steel Res*. 2022;199(October):107635.
7. Hwan I, Yong N, Ki W, Seon C, Tae S. Performance-based Design of Stiffened Steel Plate Concrete Wall in Fire. *Power Engineering*. 2009;4618(SMiRT 20):1–9.
8. Wei F, Fang C, Wu B. Fire resistance of concrete-filled steel plate composite (CFSPC) walls. *Fire Saf J*. 2017 Mar 1;88:26–39.
9. Hu B, Huang JQ, Lou G biao. Degradation of Out-of-plane Initial Stiffness of Steel-concrete Walls Exposed to Fire. *International Journal of Steel Structures*. 2018;18(1):51–67.
10. Anvari AT, Bhardwaj S, Wazalwar P, Varma AH. Structural Fire Engineering and Design of Filled Composite Plate Shear Walls (SpeedCore). 2020;203.
11. Taghipour Anvari A, Bhardwaj SR, Sharma S, Varma AH. Performance of Composite Plate Shear Walls/Concrete Filled (C-PSW/CF) Under Fire Loading: A Numerical Investigation. *Eng Struct*. 2022;271(September):114883.
12. Du E feng, Shu G ping, Qin L, Lai B lin, Zhou X liang, Zhou G gen. Experimental investigation on fire resistance of sandwich composite walls with truss connectors. *J Constr Steel Res*. 2022;188(September 2021):107052. <https://doi.org/10.1016/j.jcsr.2021.107052>
13. Standard I, Preview TS. *Iso 834-1*. 1999;1999.
14. Eurocode 4-Design of composite steel and concrete structures-Part 1-2: General rules-Structural fire design. 1994.
15. EN 1992-1-2: Eurocode 2: Design of concrete structures - Part 1-2: General rules - Structural fire design. 1992.
16. Ghojel J. Experimental and analytical technique for estimating interface thermal conductance in composite structural elements under simulated fire conditions. *Exp Therm Fluid Sci*. 2004;28(4):347–54.
17. Xiong MX, Liew JYR. Mechanical properties of heat-treated high tensile structural steel at elevated temperatures. *Thin-Walled Structures*. 2016;98:169–76.

NUMERICAL DESIGN CALCULATION OF THE CARDINGTON FRAME JOINTS

Batuhan Der¹, František Wald², Petr Červinka³, Martin Vild⁴

ABSTRACT

The main objective of this paper is to present the validation of the Component-Based Finite Element Method (CBFEM) for predicting the resistance of endplate and fin-plate connections in fire. The model is the most widely used numerical design calculation in steel structures. It is a combination of the analytical component method and the numerical finite element method (FEM) and is code independent and can be used to calculate according to any standard. To predict the behavior at elevated temperature, the heat transfer based on the mass of plates and connections and the multilinear material degradation curves of steel according to the EN1993-1-2:2005 model have been prepared. The fire behavior of the connections is studied based on standard design specifications to verify the numerical calculation. The validation of this model is done using experimental results in terms of failure modes in joints and buckling modes of steel members.

Keywords: Steel structure; Cardington fire test; fire design; numerical calculation; end plate joint; fin plate joint

1 INTRODUCTION

The fire behavior of steel connections is an important topic in structural fire engineering. The behavior of steel connections has been studied experimentally by many researchers [1-4]. However, experimental studies cannot test every type of connection due to the cost of fire testing and the lack of furnace size. Therefore, many numerical studies can be found in the literature [5-8]. The mechanical response of steel members and connections at elevated temperatures is significantly influenced by temperature changes, boundary conditions and large displacements [9]. Previous experimental and numerical studies of steel frames at elevated temperatures [10-14] have highlighted the importance of global structural behavior in understanding the fire response of steel connections. The primary objective of the structural integrity fire test on the Cardington frame was to obtain test data on the fire behavior of typical beam-to-column and beam-to-beam frame joints [10].

¹ Ph.D. Student, Czech Technical University in Prague,
e-mail: batuhan.der@fsv.cvut.cz, ORCID: <https://orcid.org/0000-0003-1091-9101>

² Prof. Ing., Czech Technical University in Prague
e-mail: wald@fsv.cvut.cz, ORCID: <https://orcid.org/0000-0003-2416-8951>

³ Ph.D., IDEA RS s.r.o.
e-mail: petr.cervinka@ideastatica.com, ORCID: <https://orcid.org/0009-0000-4435-7106>

⁴ Ph.D, Brno University of Technology
e-mail: vild.m@fce.vutbr.cz, ORCID: <https://orcid.org/0000-0002-2327-3162>

Wald et al [10] conducted an experimental program to investigate the global structural behavior of a compartment on the 8-story steel-concrete composite frame building at elevated temperatures to investigate the response of the composite slab, beams, columns and connections. Al-Jabri [11] studied the influence of fire on the mechanical behavior of multi-story steel frames and emphasized that the behavior of steel members is very different from the response of isolated members due to structural integrity. Santiago et al [12] conducted a numerical study to investigate the response of the structural subframe. The numerical model used 3D shell elements considering geometric imperfections and temperature changes over the section. Parametric studies showed the importance of beam end restraints on the force distribution over the joints. Jiang and Usmani [13] conducted benchmark studies to evaluate the performance of steel frames at elevated temperatures. This study includes nonlinear thermo-mechanical analysis using the OpenSees framework. Silva et al [14] analyzed the use of simplified design methods to evaluate the fire resistance of steel frames exposed to natural fires. They compared simple and advanced calculation models for buckling analysis in fire.

Finite element models is divided into two types: Numerical Simulation (NS) and Numerical Design Calculation (NDC), prEN1993-1-14 [15]. Simulation generally uses volume models and geometric and material nonlinear analysis with imperfections and gives results like experimental results. A validated simulation is used to generate numerical experiments for sensitivity studies of significant parameters. However, the generation of the simulation is very time consuming and costly. Shell elements are recommended for modeling plates in the finite element model design of the structural connection in the numerical calculation. In steel connection design, curve fitting, analytical and finite element models are used to model stiffness, resistance, and deformation capacity. CBFEM [16] is a method for analyzing and designing connections and members of steel structures. It is a combination of the component method and the finite element method. The stresses, strains and internal forces are calculated using the advantages of the finite element method to check the individual components according to the design specifications [17] and [18]. Der et al [19] to [21] verify and validate the model to design the steel members and connections at elevated temperatures.

In this study, the numerical model is prepared to numerically investigate the behavior of joints from Cardington tests. The proposed model evaluates the internal forces using global analysis of the steel frame at ambient temperature. Then, the steel connections are analyzed under the calculated loads at elevated temperature. The failure modes obtained from the model are compared with the test results. The main objective of the study is to validate the model based on Cardington fire tests.

2 EXPERIMENTAL STUDY

2.1 Test Specimens

A detailed description of the test setup and measurements can be found in the study [10]. Therefore, only a brief description is given in this chapter. The tested steel structure consisted of two primary beams (356x171x51UB section, steel grade S350), two secondary beams (305x165x40UB section, steel grade S275), edge beam (356x171x51UB section) and four columns (inner columns are 305x305x198UC section, outer column is 305x305x137UC section, steel grade S350). Flexible end plates and fin plates were designed for the beam-to-column joints and the beam-to-beam joints, respectively. In both cases the plates were made of S275 steel, and M20 grade 8.8 bolts were used. All columns were fully fire rated. Figure 1 presents the Cardington fire tests on steel structure. The steel beams were supported by a composite slab with overall depth of 130mm and the steel decking has a trough depth of 60 mm.

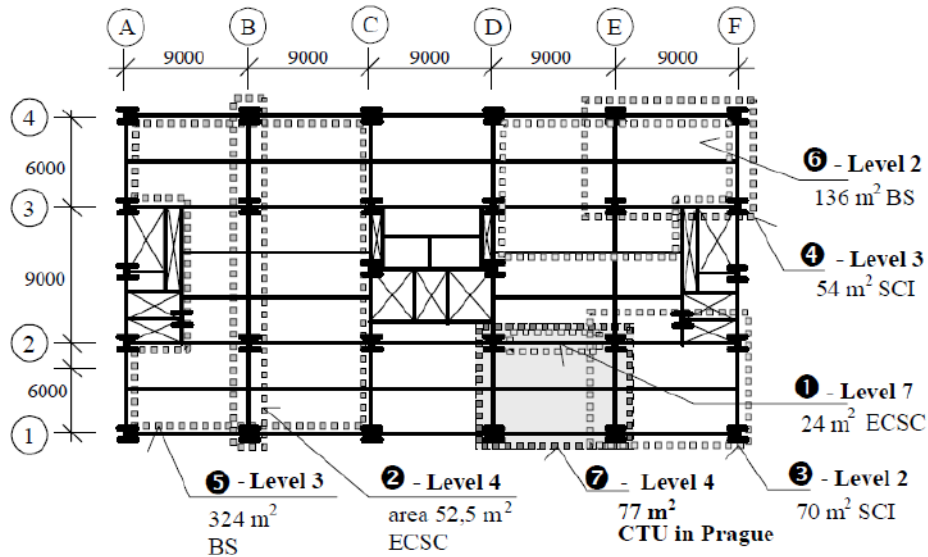


Figure 1. The Cardington fire tests on steel structure

2.2 Test Description

1 100 kg sandbags were used to simulate the applied load over an area of 18 m by 10,5 m on the floor immediately above the fire compartment. The instrumentation used included thermocouples, strain gauges and displacement transducers. Thermocouples were used to record the temperature of the connections and the steel beams within the compartment. High and ambient temperature strain gauges were used to measure the strain in the elements. In Figure 2 the arrangement of steel frame is shown. Transducers were utilized to measure the vertical deformation of the concrete slab. Wooden cribs were taken as the fuel load.

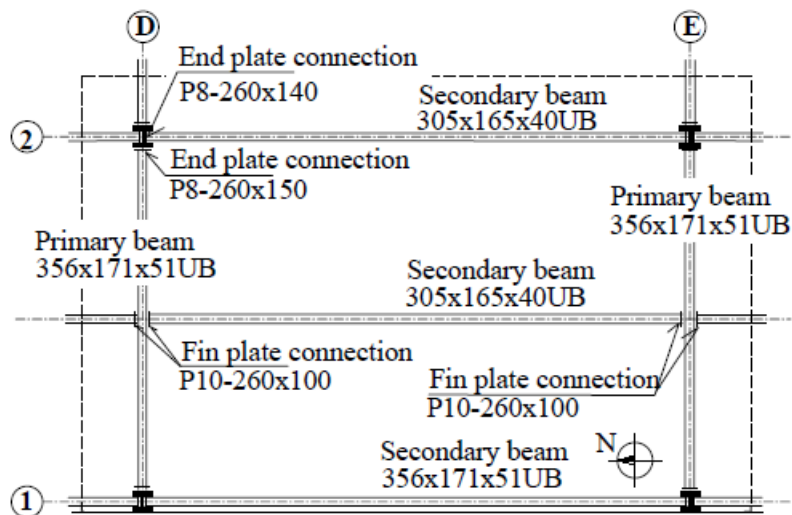


Figure 2. Arrangement of members in fire compartment

3 NUMERICAL DESIGN CALCULATION

3.1 CBFEM

The component-based finite element method is a combination of the component method and the finite element method for analyzing steel connections, anchors, and steel members at ambient and elevated temperatures. This method is an example of numerical design. The model checks the behavior of welds and bolts using the resistance equations presented in EN 1993-1-8. The plastic limit strain, recommended as 5% in EN 1993-1-5, is used to evaluate the resistance of steel plates. The model is generated using the

commercial software IDEA StatiCa [22] and [23] to study the behavior of the Cardington frame and connections [10]. IDEA StatiCa Member can perform three types of analysis: material nonlinear analysis, linear buckling analysis, and geometric and material nonlinear analysis with imperfections.

3.2 Model Description

Figure 3 indicates the geometric configuration of the steel frame based on the study [10]. The steel frame consists of I-shaped UB and UC beams and columns. The material properties of the steel members are considered as nominal values. Rigid supports were added at the ends of the columns. Displacements in X, Y, and Z directions were restrained at the bottom of the column, while the top of the columns was restrained only in X and Y directions. The length of the secondary beam (L) is 9 m and the distance between two secondary beams (b) is 3 m. Since L/b is greater than 2, the load transfer can be assumed as a one-way slab. All slabs are meshed with 4-node quadrangle shell elements.

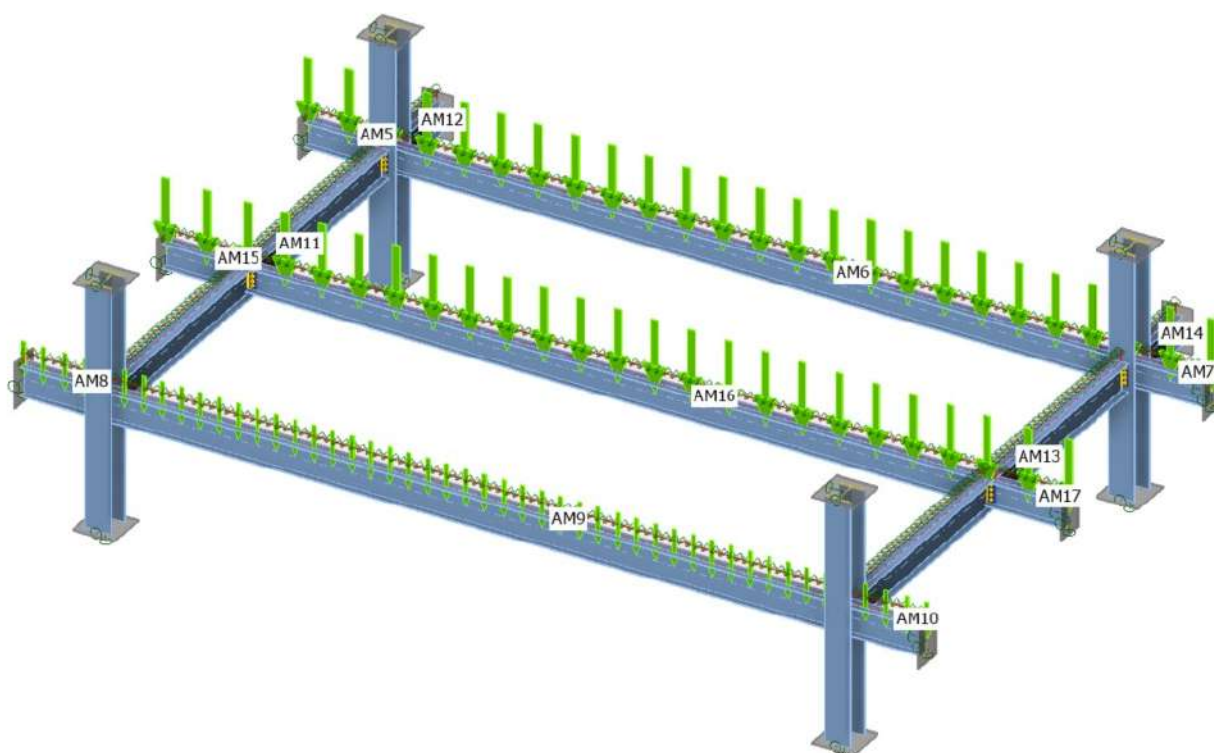


Figure 3. The CBFEM model

To simulate the fire behavior of steel, it is necessary to assign the temperature-dependent mechanical properties of the structural material. For steel and bolts, the reduction factor of strength and modulus of elasticity of steel and bolts at elevated temperatures proposed by EN 1993-1-2:2005 [17] are adopted. To evaluate the internal forces induced by the Cardington frame joints, the steel frame is analyzed using the loads obtained from the experimental study at ambient temperatures. Later, these calculated loads are applied to the joints at elevated temperature. To simulate the influence of the composite slab, lateral and torsional restraints are applied to the top flange of the steel beams.

3.3 Material Properties

Models use simplified material curves based on the design specifications. The models the plates with an elastic-plastic material with a nominal yield plateau slope $\tan^{-1}(E/1000)$ according to EN 1993-1-5:2005 [24]. The von Mises yield criterion governs the response of the material under load. It is assumed that the material behaves elastically until it reaches the design yield strength, f_{yd} . EN 1993-1-5:2005 recommends the value of 5 % plastic strain limit to simulate the behavior of plates. Figure 4 displays the theoretical true and engineering stress-strain curves as well as the material model used in the CBFEM model.

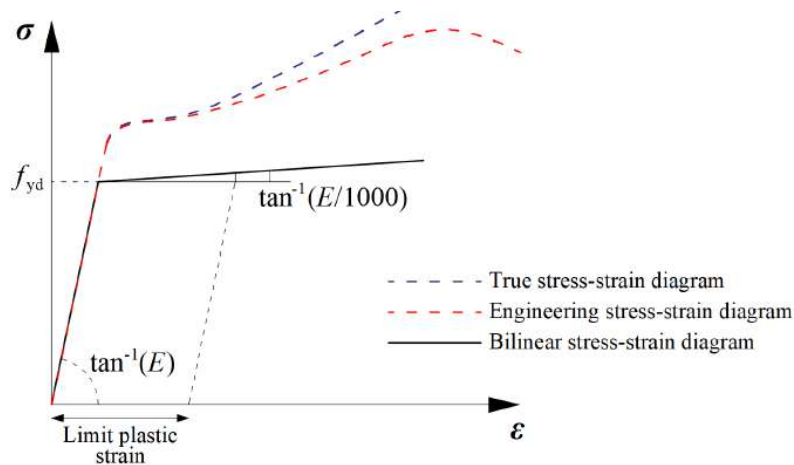


Figure 4. Material model for numerical design calculation

Bolts are represented by nonlinear springs with properties based on design codes. The bolt in tension is described by the spring with its initial axial stiffness, design resistance, yielding initialization, and deformation capacity, as shown in Figure 5. More details on the generation of the load-deformation relationship for bolts in shear and tension can be found in this paper [25].

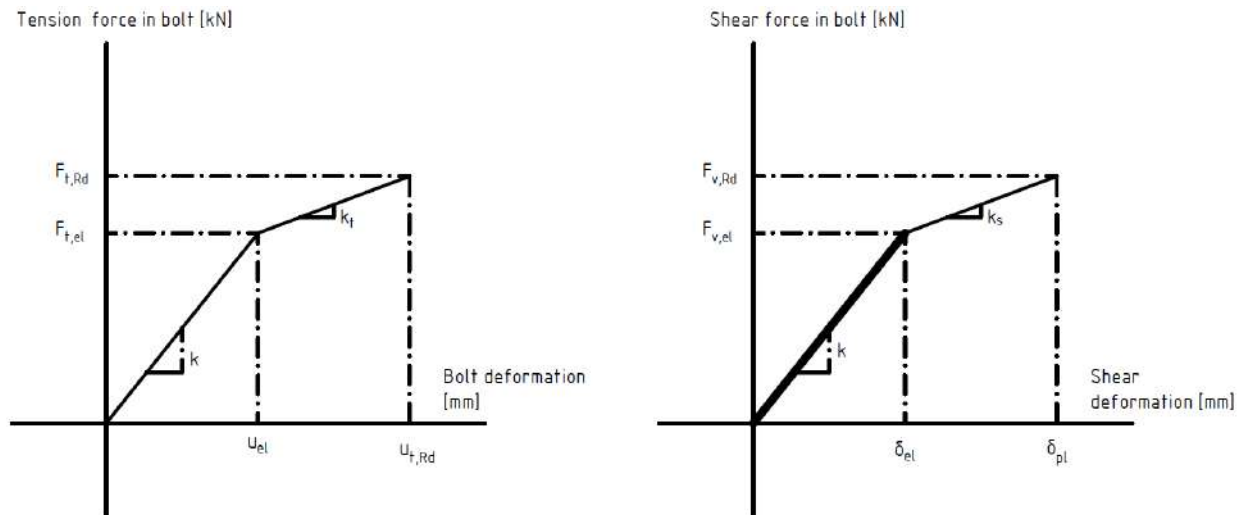


Figure 5. The load-deformation behavior of bolts in tension (left) and in shear (right)

4 RESULTS

4.1 Global Analysis of Steel Frame

The applied loads include the self-weight of the composite slab and the weight of the sandbags. The dead load of the steel structure is considered automatically. The steel frame is analyzed under the calculated loads at ambient temperature to calculate the internal forces for evaluating the fire performance of the steel connection. The model considers geometric and material imperfections (GMNIA) Therefore, LBA and GMNIA analyses were performed. Linear Buckling Analysis (LBA) allows the visually buckling mode shapes in a 3D view and the correct introduction of imperfections into system.

The CBFEM model is generated to predict the fire behavior of steel members and connections. It includes displacements, strains, and failure modes. Figure 6 shows the deformed shape of the steel frame at elevated temperatures. The maximum deformation was calculated to be 83 mm at the center of the steel beam (AM16) at ambient temperature. During the experimental study, the maximum deflection in the composite panel was measured to be 96 mm in 10 mins. It can be seen that the plastic strain induced in the steel plates

exceeds the recommended strain limit. Therefore, the model predicts a conservative deformation value compared to the test results.

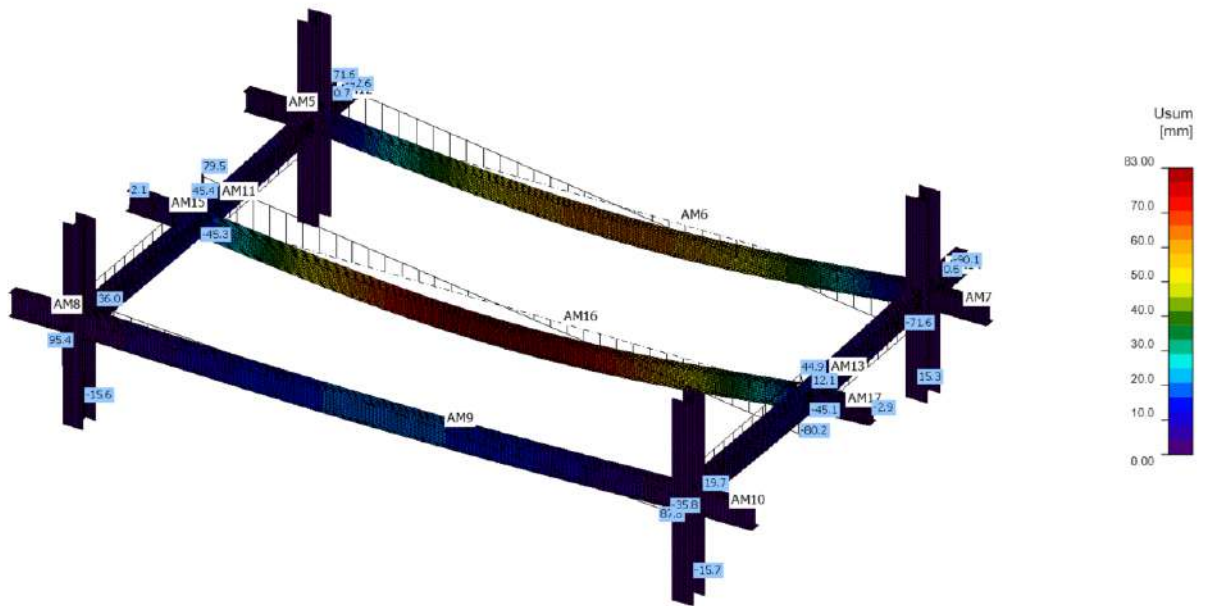


Figure 6. Global analysis of steel frame at ambient temperature

The most critical buckling mode from LBA analyses for the steel beam is shown in Figure 7. The imperfection amplitude $d/200$ was used to consider the local buckling effect on the analyzed steel members into the direction selected by LBA. The results obtained from the model captured the relevant mechanics well, such as lower flange buckling and beam web in shear.

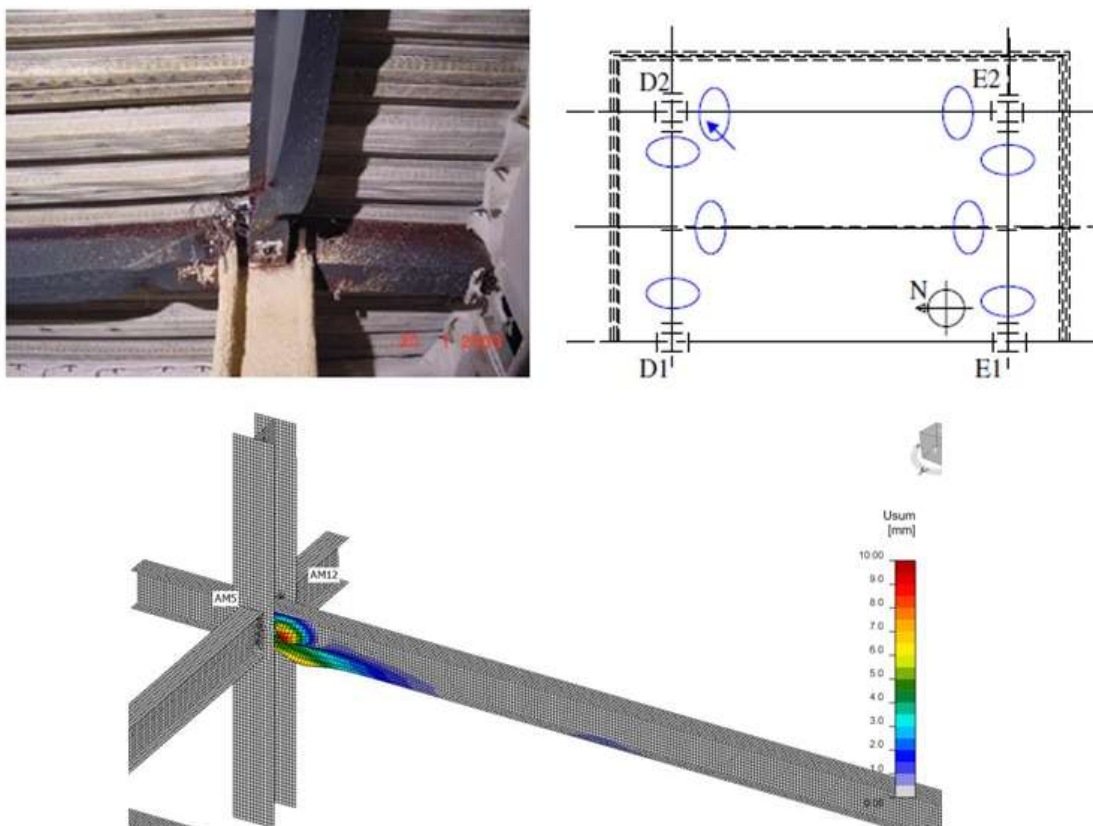


Figure 7. The lower flange buckling at the elevated temperature in experiment and in the CBFEM

4.2 Connections

There were two typical joint types in Cardington test: beam-to-column flexible endplate and beam-to-beam fin plate joints. To investigate the fire behavior of these joints, the CBFEM models were generated. This study aims to propose a numerical design calculation for joints at elevated temperatures. Therefore, a uniform temperature was applied to the joint. Since the columns were fully protected, the material properties of steel columns in the CBFEM were not degraded. The global frame analysis at ambient temperature determined the internal force values that influence the steel joints. Figure 8 depicts the behavior of beam-to-beam fin plate joints at elevated temperatures. The study [10] observed the elongation of holes in the beam web in fin plate connection. As can be seen, the CBFEM also predicts the failure mode as the bearing in plate. Welds and plates did not reach the full capacity.

The second failure mode observed in joints was fracture of the endplate along the welds. The CBFEM model decided failure mode as weld failure along the endplate. The plastic strain induced in the plate was 2.6% as seen in Figure 9. The heat transfer was also conducted in the CBFEM using the standard fire curve presented in EN 1993-1-2. The CBFEM model uses the step-by-step method [17] to calculate the temperature values of each component in the joint. Since it is not possible to insert the user-defined fire curves in IDEA StatiCa yet, the temperature prediction is conservative. The temperature of joints reaches 860° at 30 mins, whereas the measured temperature is approaching this value around 60 mins. Therefore, it is applied the uniform temperature to the joint except for steel columns.

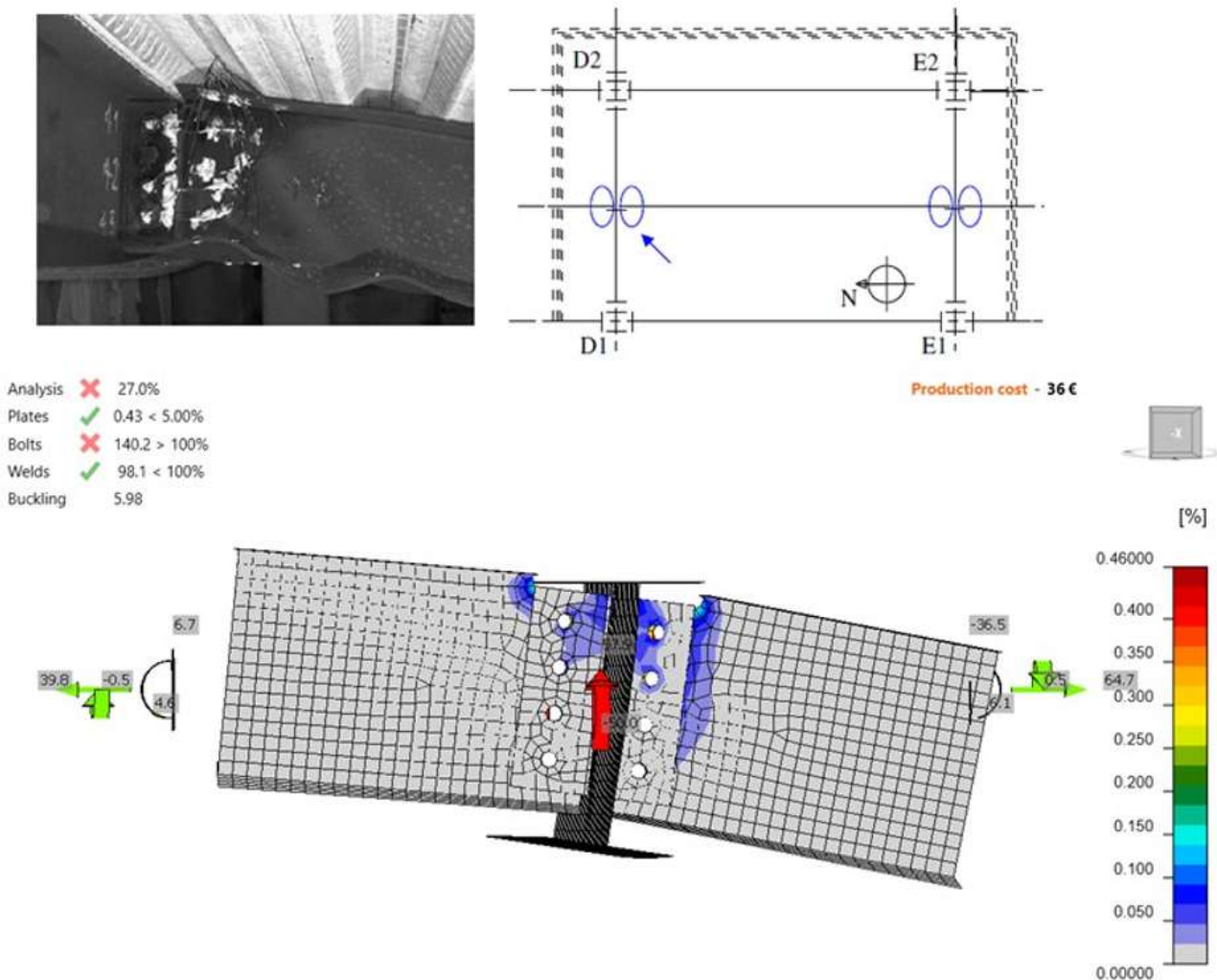


Figure 8. Beam-to-beam fin plate joints at elevated temperatures

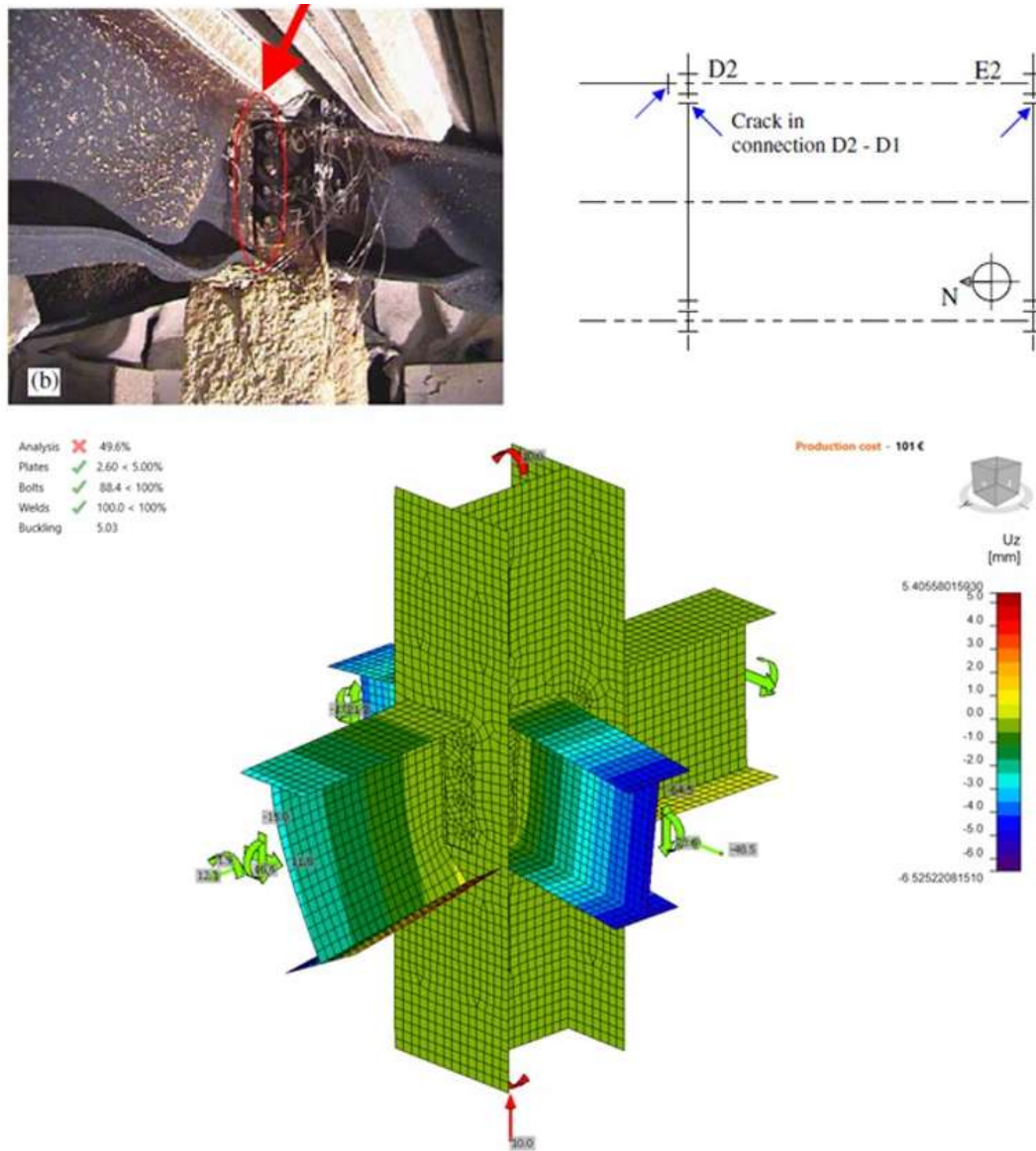


Figure 9. Beam-to-column endplate joints at elevated temperatures

5 CONCLUSIONS

This study presents a numerical design calculation using the numerical calculation model to investigate the mechanical response of flexible end plates and fin plate connections at elevated temperatures. The fire design of steel structures is very complex due to several reasons, including temperature distribution, thermal constraints, and material degradation. Numerical simulations can deal with these difficulties; however, it is not practical for fire design engineers. Therefore, this paper uses several simplifications to design steel members and joints at elevated temperatures.

The proposed model evaluated the global response of the steel frame at ambient temperature to understand the internal forces acting on the connections. The geometrical imperfection was considered by linear buckling analysis. Then, the beam-to-beam fin plate joints and the beam-to-column flexible end plate joints were investigated at elevated temperatures. The model was able to predict the similar failure modes observed in the experimental studies. Therefore, it can be concluded that the model is a safe and fast tool to analyze and design steel members and joints at elevated temperatures as an alternative to analytical models and numerical simulations.

ACKNOWLEDGMENT

The paper was prepared under grant GAČR no. 24-14577L and supported no. SGS22/141/OHK1/3T/11 from Czech Technical University in Prague.

REFERENCES

1. Hu Y, Davison JB, Burgess IW, Plank RJ. Experimental study on flexible end plate connections in fire. In: The 5th European conference on steel structures. 2008.
2. Yu HX, Burgess IW, Davison JB, Plank RJ. Experimental investigation of the behaviour of fin plate connections in fire. *Journal of Constructional Steel Research*. 2009. 65. 723–36.
3. Y.C. Wang, X.H. Dai, C.G. Bailey, An experimental study of relative structural fire behaviour and robustness of different types of steel joint in restrained steel frames, *J. Constr. Steel Res.* 67. 7. 2011. 1149–1163, <https://doi.org/10.1016/j.jcsr.2011.02.008>.
4. Santiago, A. Da Silva, Luis S., Real, Paulo V., Vaz, G., Lopes, Antonio G., (2009). "Experimental Evaluation of the Influence of Connection Typology on the Behavior of Steel Structures Under Fire," *Engineering Journal*, American Institute of Steel Construction. 46. 81-98.
5. Garlock, Maria & Selamet, Serdar. (2010). Modeling and Behavior of Steel Plate Connections Subject to Various Fire Scenarios. *Journal of Structural Engineering-asce - J STRUCT ENG-ASCE*. 136. 10.1061/(ASCE)ST.1943-541X.0000179.
6. Seif, Mina & Main, Joseph & Weigand, Jonathan & Mcallister, Therese & Luecke, William. (2016). Finite element modeling of structural steel component failure at elevated temperatures. *Structures*. 6. 134-145. 10.1016/j.istruc.2016.03.002.
7. R. Rahnvard, R.J. Thomas, Numerical evaluation of the effects of fire on steel connections; Part 1: simulation techniques, *Case Stud. Ther. Eng.* 12. 2018. 445–453.
8. T. Gernay, J.M. Franssen, The introduction and the influence of semi-rigid connections in framed structures subjected to fire, *Fire Safety Journal*. 11. 2020. 103007.
9. Benes M, Wald F, Sokol Z, Pascu HE. Numerical study to structural integrity of multi-story buildings under fire. In: Lamas A, Simoes da Silva L, editors. *Proceedings of the third European conference on steel structures—Eurosteel 2002*. Coimbra, Portugal: cmm Press. 2002. 1401–11
10. F. Wald, L. Simões da Silva, D.B. Moore, T. Lennon, M. Chladná, A. Santiago, M. Beneš, L. Borges, Experimental behaviour of a steel structure under natural fire, *Fire Safety Journal*. 41. 7. 2006. 509-522. <https://doi.org/10.1016/j.firesaf.2006.05.006>.
11. Al-Jabri K. S., Behavior of Steel-framed Buildings in a Fire, *Steel Structures*. 7. 2007. 227-237.
12. Santiago, A., Simões da Silva, L., Vila Real, P., Veljkovic, M., Numerical study of a steel sub-frame in fire, *Computers & Structures*. 86. 15–16. 2008. 1619-1632, doi.org/10.1016/j.compstruc.2008.01.006.
13. Jiang J, Usmani A. Modeling of steel frame structures in fire using OpenSees. *Comput Struct*. 2013.118:90–9. <https://doi.org/10.1016/j.compstruc.2012.07.013>.
14. Thiago Silva, Martina Carić, Carlos Couto, Paulo Vila Real, Nuno Lopes, Davor Skejic, Buckling Analysis of Steel Frames Exposed to Natural Fire Scenarios, *Structures*. 10. 2017. 76-88. ISSN 2352-0124, <https://doi.org/10.1016/j.istruc.2017.02.003>.
15. prEN1993-1-14, Eurocode 3: Design of steel structures – Part 1-14: Design assisted by finite element analysis, proposal of European Standard, 2022.
16. Šabatka, L.; Wald, F.; Kabeláč, J.; Kolaja, D.; Pospíšil, M. (2015) Structural Analysis and Design of Steel Connections Using Component-Based Finite Element Model. *Journal of Civil Engineering and Architecture* 9 895-901, doi: 10.17265/1934-7359/2015.08.002.
17. EN 1993–1-2, Eurocode 3: Design of Steel Structures, Part1–2: General Rules, Structural Fire Design, European Committee for Standardization, Brussels, Belgium, 2005.
18. EN 1993–1-8, Eurocode 3: Design of steel structures–Part 1–8: Design of joints, CEN, Brussels, 2005.
19. Der B, Wald F, Vild M., Modelling of bolted joints in fire using the component-based finite element method. *ce/papers*. 2023, 6:2103-2107, <https://doi.org/10.1002/cepa.2485>.

20. Wald, F., Vild, M., Kabeláč, J. and Der, B., Component based finite element method for steel joints at ambient and elevated temperatures, 2023, <https://doi.org/10.59382/pro.intl.con-ibst.2023.keynotes-2>
21. Der, B., Wald, F. and Vild, M. (2024), Fire design of steel member by component-based finite element method. *ce/papers*, 7: 36-44. <https://doi.org/10.1002/cepa.3020>
22. IDEA StatiCa Member 23.1. 2023, Product documentation. Retrieved from www.idea-rs.com.
23. IDEA StatiCa Connection 23.1. 2023, Product documentation. Retrieved from www.idea-rs.com.
24. EN1993-1-5: Eurocode 3 Design of steel structures - Part 1-5: General rules - Plated structural elements, CEN, Brussels 2006.
25. IDEA StatiCa Connection, Bolts and preloaded bolts connections, <https://www.ideastatica.com/support-center/bolts-and-preloaded-bolts>, 2023, accessed 13 October 2003.

NUMERICAL INVESTIGATION OF THE STRUCTURAL FIRE RESPONSE OF TUNNEL STRUCTURES WITH RECTANGULAR CROSS-SECTIONS

Thomas Thienpont¹, Florian Put², Balša Jovanović³, Ranjit Kumar Chaudhary⁴, Ruben Van Coile⁵

ABSTRACT

In the present paper, the structural fire performance of a reinforced concrete road tunnel with two rectangular tubes is studied, taking into account the effect of spalling. Using numerical simulations in SAFIR in combination with a custom Python script, the study explores the effect of various spalling rates and spalling locations on the internal forces, the deformations and the possible collapse mechanism of the tunnel in case of a two-hour RWS fire. The results showcase the critical role of spalling in determining the tunnel's structural fire performance. The tunnel is shown to rapidly lose stability when a uniform spalling rate is assumed. Conversely, when no spalling is assumed, the tunnel is able to survive two hours of RWS fire. The analyses also show that the tunnel structure is most vulnerable to spalling in the roof slab, as this can lead to a loss of stability early on in the fire. Additionally, the study highlights the significant damage incurred by the tunnel due to the formation of plastic hinges at different locations on the unexposed side of the tunnel roof and walls, also when the structure survives the full fire exposure.

Keywords: Tunnel fire; finite element modelling; spalling

1 INTRODUCTION

Tunnel fires can sometimes lead to devastating consequences, including loss of life, property damage, prolonged service interruptions, and significant socioeconomic repercussions [1]. Spalling can severely affect the structural fire performance of reinforced concrete tunnel structures, as it leads to a reduction of the cross-section and potentially complete removal of the thermal protection of the steel reinforcement [2]. Severe spalling of the tunnel linings has been observed in several historical large tunnel fires (e.g. Mont Blanc Tunnel, Tauern Tunnel) although collapse or local failure of tunnel structures is rare [1]. Whilst several studies have been carried out on the structural fire performance of (deep) circular tunnels [2–5], there have been few investigations into the fire response of (shallow) rectangular tunnels. The latter are often applied in urban areas in major cities, to move large traffic streams underground.

¹ Postdoctoral researcher, Ghent University, Ghent, Belgium

e-mail: Thomas.Thienpont@ugent.be, ORCID: <https://orcid.org/0000-0003-1466-3377>

² PhD student, Ghent University, Ghent, Belgium

e-mail: Florian.Put@UGent.be, ORCID: <https://orcid.org/0000-0002-4522-9015>

³ PhD student, Ghent University, Ghent, Belgium

e-mail: Balsa.Jovanovic@ugent.be, ORCID: <https://orcid.org/0000-0001-5200-5848>

⁴ PhD, Ghent University, Ghent, Belgium

e-mail: RanjitKumar.Chaudhary@ugent.be, ORCID: <https://orcid.org/0000-0002-1104-5859>

⁵ Associate professor, Ghent University, Ghent, Belgium

e-mail: Ruben.VanCoile@UGent.be, ORCID: <https://orcid.org/0000-0002-9715-6786>

This paper explores the complex structural behaviour and possible collapse mechanisms of a shallow road tunnel with two rectangular tubes, taking into account the effect of spalling. To this end, a 2D model of the tunnel cross-section is numerically analysed using the finite element software SAFIR in combination with a custom Python script, which handles the spalling of the concrete. The numerical model is then used to study the effect of different spalling rates, as well as different spalling locations on the structural fire response of the tunnel.

2 NUMERICAL MODEL

Sequentially coupled numerical analyses are performed using the finite element software SAFIR [6], considering both cases with and without spalling. The heat transfer analyses for cases without spalling were performed using the standard approach, while for the cases with spalling, a custom Python script was used which enables the removal of the concrete cover at a constant rate. The following section presents the properties of the studied tunnel, as well as the details on the heat transfer and the mechanical analyses.

2.1 Tunnel geometry and model assumptions

The effect of spalling on the structural fire response of a reinforced concrete tunnel is investigated for reference cross-section as depicted in Figure 1.a. The cross-section is taken from an existing road tunnel with two large rectangular tubes, which can accommodate four lanes of traffic. The roof slab and outer walls are designed to withstand a 60 minute RWS fire. The evacuation path between the tunnel tubes is designed to remain stable for at least 120 minutes of RWS fire. The structural behaviour of the tunnel is analysed in a simplified way, by considering a 0.5 m wide cross-section slice and analysing it as a two-dimensional (2D) frame structure. This frame consists of 20 different sections, see numbering in Figure 1.b. For each change in the cross-section (geometry and/or reinforcement layout), a different section is considered.

While analysing the structural fire response of concrete tunnels using 2D models is commonly applied in literature (e.g. [1, 7, 8]), it is noted that this approach has some limitations. For example, a 2D analysis neglects the force redistribution in the longitudinal direction of the tunnel. As such, the 2D model may predict a (local) collapse of the structure, while an equivalent 3D model could still be able to find equilibrium. Hence, a 2D analysis is deemed a conservative approach and can be considered as a lower bound for the structural response.

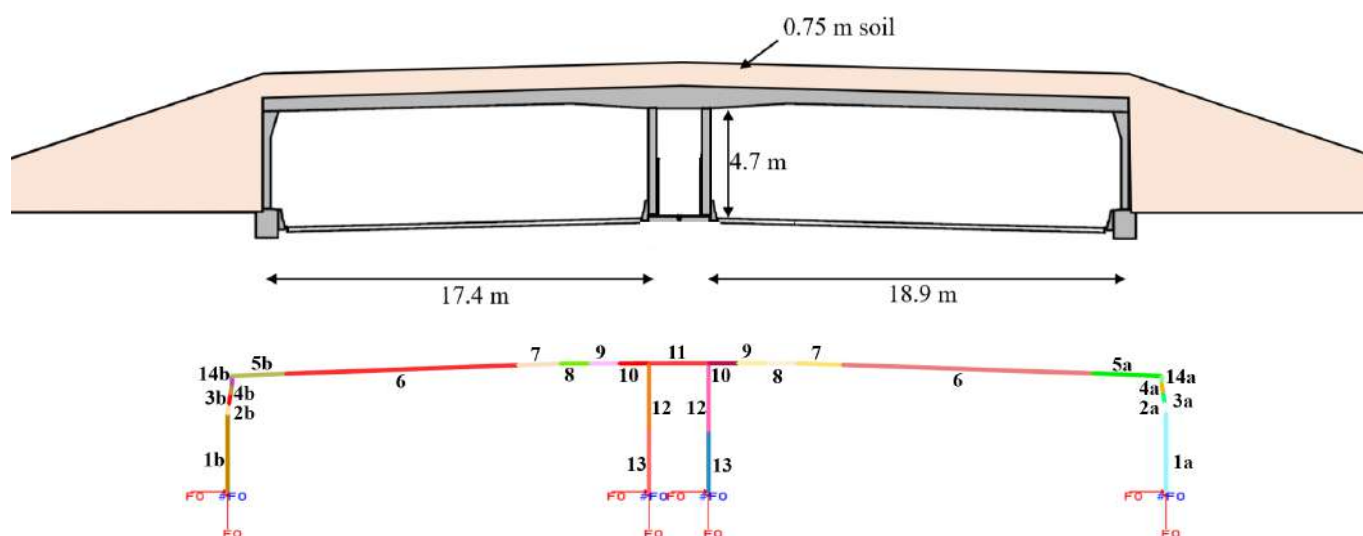


Figure 1. (top) Tunnel cross-section; (bottom) Representation in SAFIR model, including numbering sections

2.2 Fire scenarios

The fire exposure is modelled using the RWS fire curve, considering different durations of the heating phase and an exponential cooling phase defined by Eq. (1), see Figure 2. The latter is based on the

experimental observations reported in [9] and a series of numerical analyses of the cooling phase in compartment fires [10]. As in [11], a value $b = 0.025 \text{ min}^{-1}$ is assumed, based on the data reported in [9].

$$\theta_c = \theta_{ref} + (\theta_{RWS} - \theta_{ref}) \cdot e^{-b(t-t_{RWS})} \quad (1)$$

where

θ_c is the (adiabatic) surface temperature during cooling,

θ_{ref} is the reference temperature (20°C),

θ_{RWS} is the temperature at the end of the heating phase according to the RWS fire curve definition,

b is the cooling rate parameter,

t is the time in minutes since the onset of the cooling phase,

t_{RWS} is the duration in minutes of the exposure to the RWS curve.

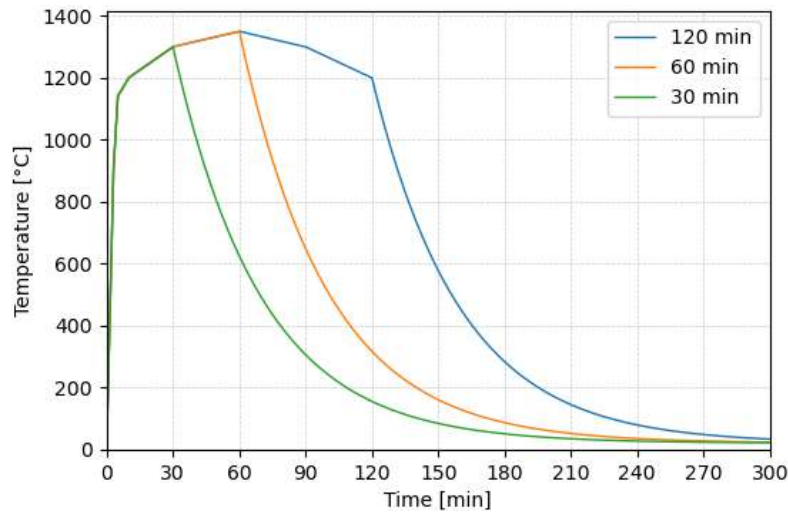


Figure 2. RWS fire curves with exponential cooling phase

2.3 Heat transfer analysis, accounting for spalling

The temperature development in the different sections of the walls and the roof slab is evaluated using a 2D heat transfer analysis. In the cases where spalling is considered, a predefined constant spalling rate is applied, which starts after a predefined period of time after the start of the fire exposure. As such, spalling is taken into account through an explicit modelling assumption, rather than a more complex calculation. This approach is in line with the recommendations in the *fib* state-of-the-art bulletin on performance-based design of concrete structures [12].

The heat transfer analysis with a constant spalling rate is implemented based on a methodology proposed by Hua et al. [1]. First, the cross-section is discretized in rectangular mesh elements, see Figure 3. The area between the fire-exposed surface and the bottom rebars is discretized in a large number of layers with very thin elements. These layers of elements can be removed at fixed timesteps, in accordance with a predefined spalling rate (e.g. 5 mm/min). Each time a layer of elements is removed, the boundary conditions are updated and the heat transfer analysis is restarted.

In the analyses, it is assumed that spalling starts after 1 minute of fire exposure, and stops when either the entire concrete cover is spalled off (i.e. when the first layer or rebars is reached), or when the fire scenario enters the cooling phase. The assumption that spalling starts after 1 minute is deemed conservative, as corroborated through the database of spalling tests reported in [1]. The assumption that spalling stops when the first layer of rebars is reached is based on the experimental observations reported in [13] which provide some justification that a dense reinforcement can be deemed to limit further reduction in concrete cross-section. The principle of the spalling code is depicted in Figure 3, for a reinforced concrete cross-section with a 70 mm concrete cover, exposed to fire at the bottom, with a constant spalling rate of 5 mm/min.

In all cases, the temperature-dependent material properties (thermal conductivity, specific heat and density) governing the heat transfer inside the concrete and the boundary conditions governing the heat transfer at the concrete-air interface are taken from EN 1992-1-2:2004 [14] and EN 1991-1-2:2002 [15] respectively. The thermal properties are assumed to remain constant during cooling. The convective heat transfer coefficients at the fire-exposed side and unexposed side are taken as 50 W/m²K and 4 W/m²K, respectively, with a concrete emissivity $\varepsilon_c = 0.7$. Due to the thickness of the tunnel linings, the boundary condition at the unexposed side is not consequential. The convective cooling coefficient has been adopted for convenience. It is considered that conductive cooling to the surrounding soil could be implemented or an adiabatic boundary condition applied without inducing a significant change in results.

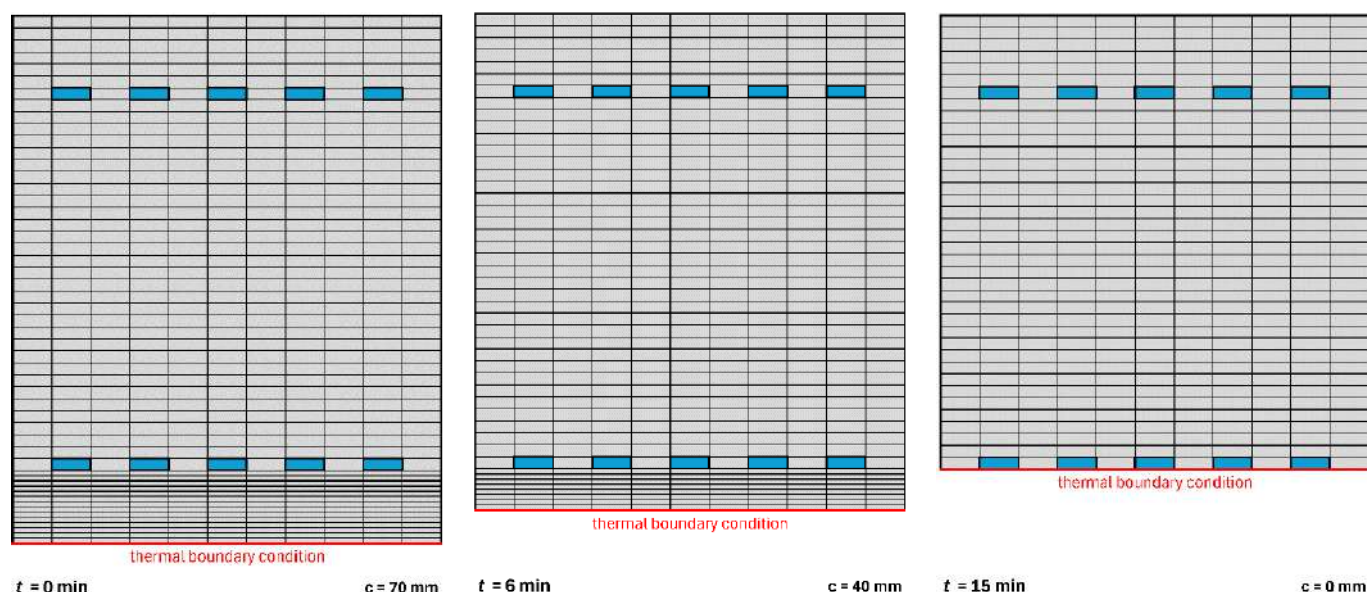


Figure 3. Principle of the concrete spalling model in SAFIR

2.4 Mechanical analysis

The mechanical response of the tunnel structure is simulated using the 2D frame structure depicted in Figure 1. The loads on the roof sections include the self-weight, the loads due to the soil and a 1.5 kN/m² variable load (expected value). The loads on the outer walls include the self-weight and the horizontal soil pressure which increases linearly with the depth below the ground level. The boundary conditions at the bottom of the inner and outer walls are modelled as clamped supports, assuming rigid foundations.

The mechanical properties of the concrete and steel are presented in Table 1. These properties correspond to expected values. In the analyses with spalling, the temperatures of the elements which have spalled are overwritten to a value of 1200°C. As such, these elements have zero strength and do not contribute to the strength of the section. Also during cooling, these elements are modelled not to have any strength recovery.

Table 1. Material properties mechanical analysis

Property	Value	Strength retention model
Concrete compressive strength $f_{c,20^\circ\text{C}}$	38 MPa	EN 1992-1-2:2004 (irrecoverable properties in cooling)
Concrete tensile strength $f_{ct,20^\circ\text{C}}$	2.9 MPa	EN 1992-1-2:2004 (irrecoverable properties in cooling)
Steel yield strength $f_{s,20^\circ\text{C}}$	550 MPa	EN 1992-1-2:2004 (partially recoverable properties in cooling)

3 NUMERICAL RESULTS

3.1 Heat transfer analyses

The results from the heat transfer analyses of the roof slab and the bottom section of the outer wall are depicted in Figure 4, for a 120 min RWS fire with exponential cooling phase. The graphs depict the results for a case without spalling, as well as for spalling rates of 2 mm/min and 5 mm/min. Due to the thick sections (600 mm for the walls, 700 mm for the roof), the temperature of the top rebars barely increases throughout the two-hour heating phase. The temperature in the bottom rebars is highly affected by the spalling: both in the case of 5 mm/min and 2 mm/min, the temperature in the rebar exceeds 1200°C.

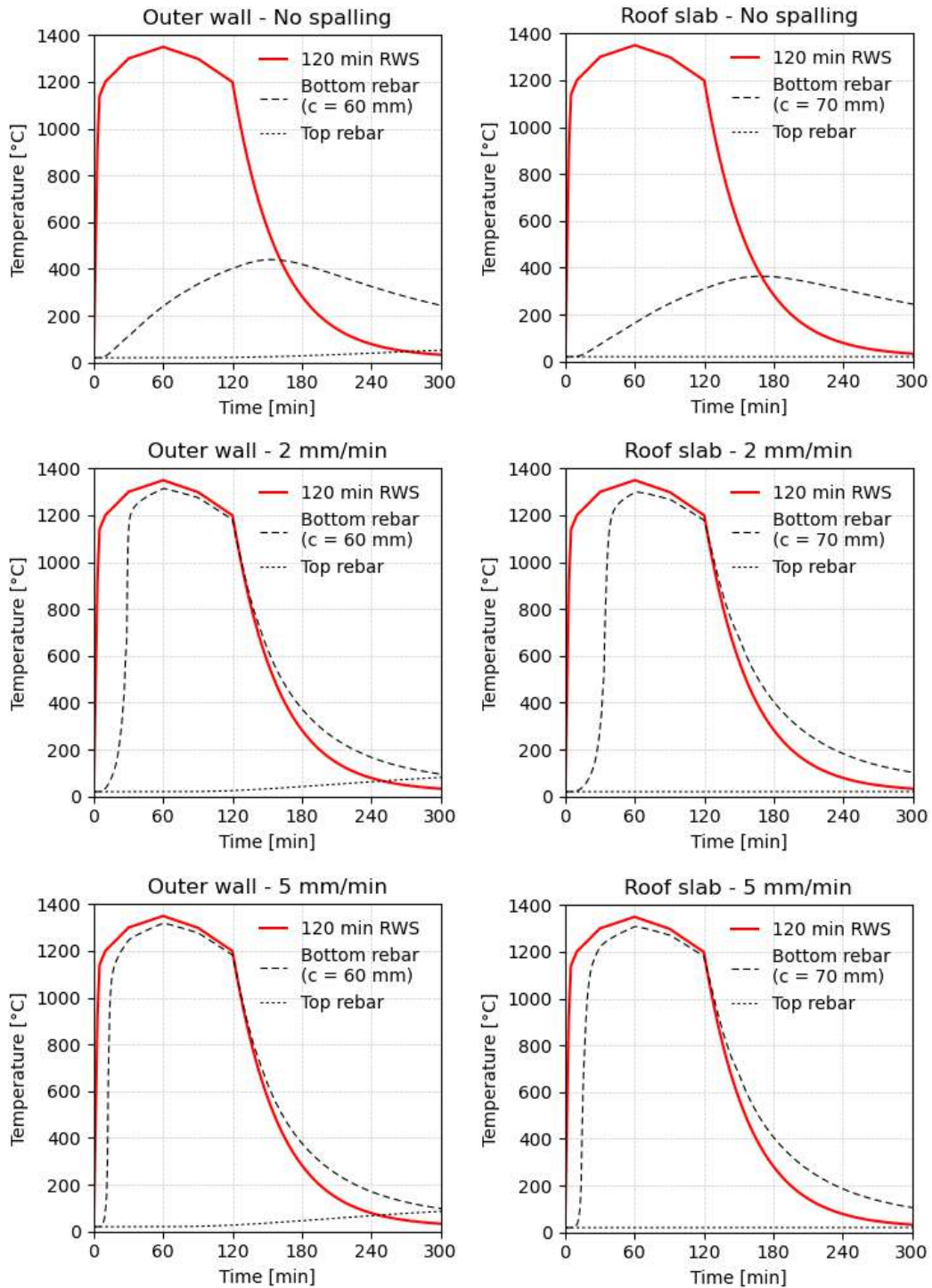


Figure 4. Heat transfer analyses for the outer walls and roof slab, considering a 120 RWS fire curve with exponential cooling (red curve), and different spalling rates

3.2 Mechanical analyses: Moments and forces

The mechanical response of the tunnel structure is evaluated for the three spalling cases, assuming a severe RWS fire scenario in the left tube of the tunnel. Herein, it is assumed that both the walls and the ceiling of the tunnel are exposed to the fire. Initially, it is also assumed that spalling occurs for all lining surfaces in the exposed tube, i.e., for all fire-exposed sections listed in Figure 1.

From the analyses, it is clear that the mechanical response of the tunnel significantly depends on the spalling rate. In the absence of spalling, the tunnel is able to survive the entire duration of the fire including the cooling phase (calculation up to 24 hours), thanks to the thick concrete cover. The cases with 2 mm/min and 5 min/min spalling collapsed after 34.2 and 14.7 minutes since the start of the exposure respectively, following the formation of plastic hinges (see further).

Figures 5 through 7 depict the displacements and the development of the bending moments and axial forces in the structure at different points in time, for each of the considered cases. The figures clearly illustrate how the forces inside the roof and the walls change throughout the fire. In the case without spalling (Figure 5), an upward shift of the moment line can be observed, due to the restrained thermal expansion of the roof slab and the walls of the fire-exposed tunnel tube. During the heating phase, the field moment in the middle of the span of the fire-exposed roof slab changes from 567 kNm/m (bending) to 121 kNm/m (hogging) after 55 minutes. During and after the cooling phase, the moment line partially returns to its initial shape, but the model clearly indicates permanent changes in the internal forces: the bending moment in the midspan of the fire-exposed roof slab remains at -742 kNm/m. A similar conclusion can also be drawn from the graphs with the axial forces. During the heating phase, the compression force at the bottom of the fire-exposed inner wall increases significantly from 353 kN/m (ambient conditions) to 827 kN/m after 55 minutes, while the compression force in the inner wall next to the unaffected tube drops from 520 kN/m to a mere 64 kN/m. After cooling (24 hours) the axial force in the inner walls remains at 534 kN/m (exposed tube) and 370 kN/m (unaffected tube).

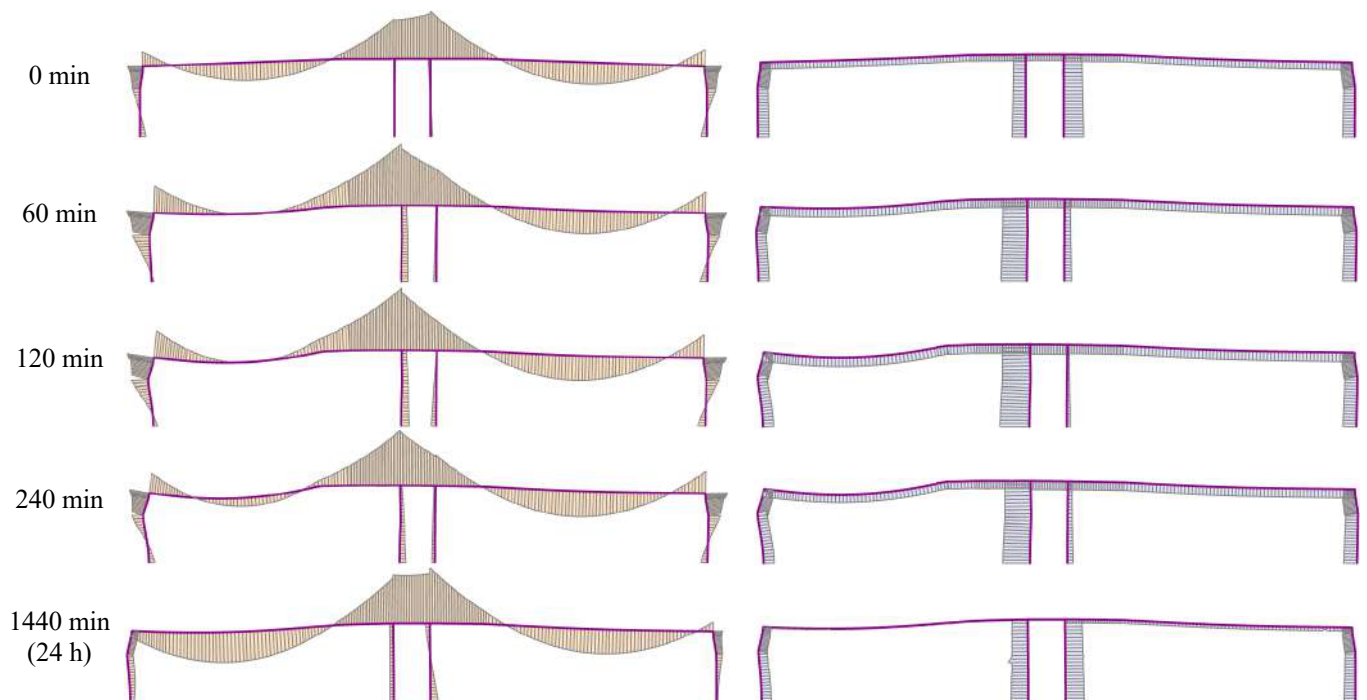


Figure 5. Deformations (5x scaling) and development of bending moments and axial forces for a 120 min RWS fire in the left tunnel tube, no spalling

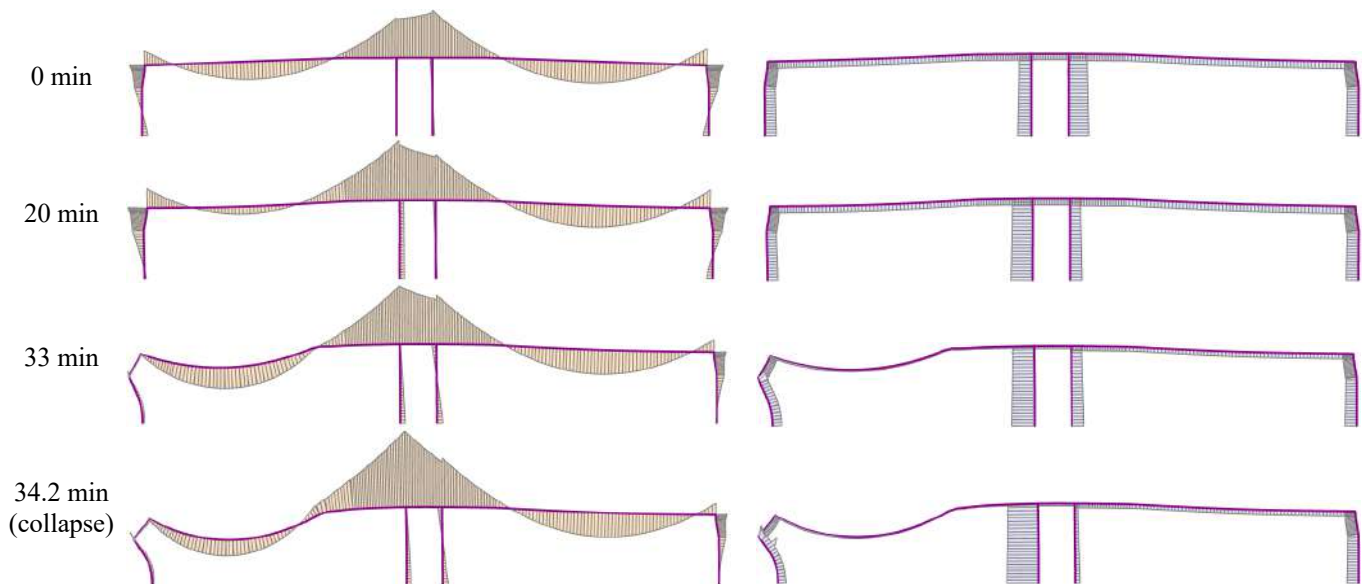


Figure 6. Deformations (5x scaling) and development of bending moments and axial forces for a 120 min RWS fire in the left tunnel tube, 2 mm/min uniform spalling

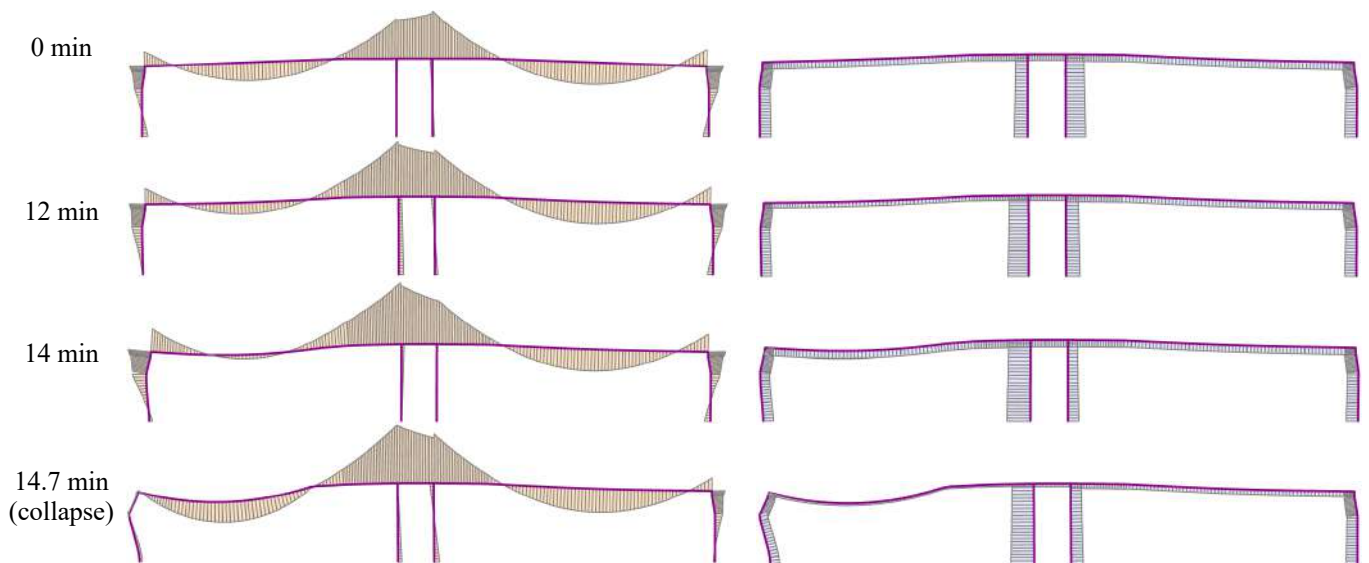


Figure 7. Deformations (5x scaling) and development of bending moments and axial forces for a 120 min RWS fire in the left tunnel tube, 5 mm/min uniform spalling

In the cases with spalling, a similar behaviour is observed in the period prior to the failure of the left tunnel tube. The moment line first rises, but then drops down again upon the formation of plastic hinges in the fire-exposed roof and the outer wall. In both cases also an increase in the axial force in the inner wall is observed. In the case of 2 mm/min spalling, the rise in the axial force is more pronounced, as in the case of 5 mm/min spalling the fast removal of heated concrete effectively precludes the generation of fire-induced forces and later on failure of the roof slab occurs before a significant rise in the axial force can develop.

3.3 Mechanical analyses: Deflections and failure mechanisms

Figure 8 depicts the vertical deflections of the roof slab over the fire-exposed tunnel tube, at the location of maximum displacement (6.7 meter from the outer wall). In the case without spalling, the deflection of

the roof slab increases steadily in the first three hours, and then slowly returns to a value of 57.6 mm after 24 hours, thus indicating significant residual deformations in the structure. Additionally, the mechanical analysis indicates that the stress in the steel reinforcement exceeds the yield strength at three different locations. As a result, three plastic hinges are identified, see Figure 9. After approximately 45 minutes into the fire, the first plastic hinge develops in the outer wall of the fire-exposed tube, due to the significant increase in the bending moment (see also Figure 5). The 2nd and 3rd plastic hinges develop in the roof slab and the inner wall, after 60 minutes and 95 minutes respectively. The formation of these plastic hinges allows for a redistribution of the bending moment in the roof slab and the outer wall. In all hinges, the steel at the unexposed side develops significant plastic tensile strains but does not reach the ultimate strain. As such, despite the formation of three plastic hinges, the tunnel does not collapse. The tunnel is however permanently damaged, since at the location of the plastic hinges, the concrete at the unexposed side of the roof and outer wall is severely cracked, which could lead to durability issues in the long term.

The deflections of the roof slab for both the cases with spalling indicate a rapid increase shortly after the entire concrete cover is spalled off. Shortly after, the numerical model for these analysis no longer converges due to loss of stability of the fire-exposed tunnel tube. Also here, the development of plastic hinges is observed. Figure 10 depicts the location of the plastic hinges for the case of 2 mm/min spalling, at the moment of failure, i.e. when the model is no longer able to find equilibrium for the structural members making up the roof and outer wall of the fire-exposed tube. In the last iterations, before the model stops converging, three plastic hinges are observed: one in the outer wall and two in the roof slab. A similar behaviour is observed in the case with 5 mm/min spalling, see Figure 11. Here, the third hinge develops at the bottom of the outer wall, due to crushing of the concrete at the unexposed side.

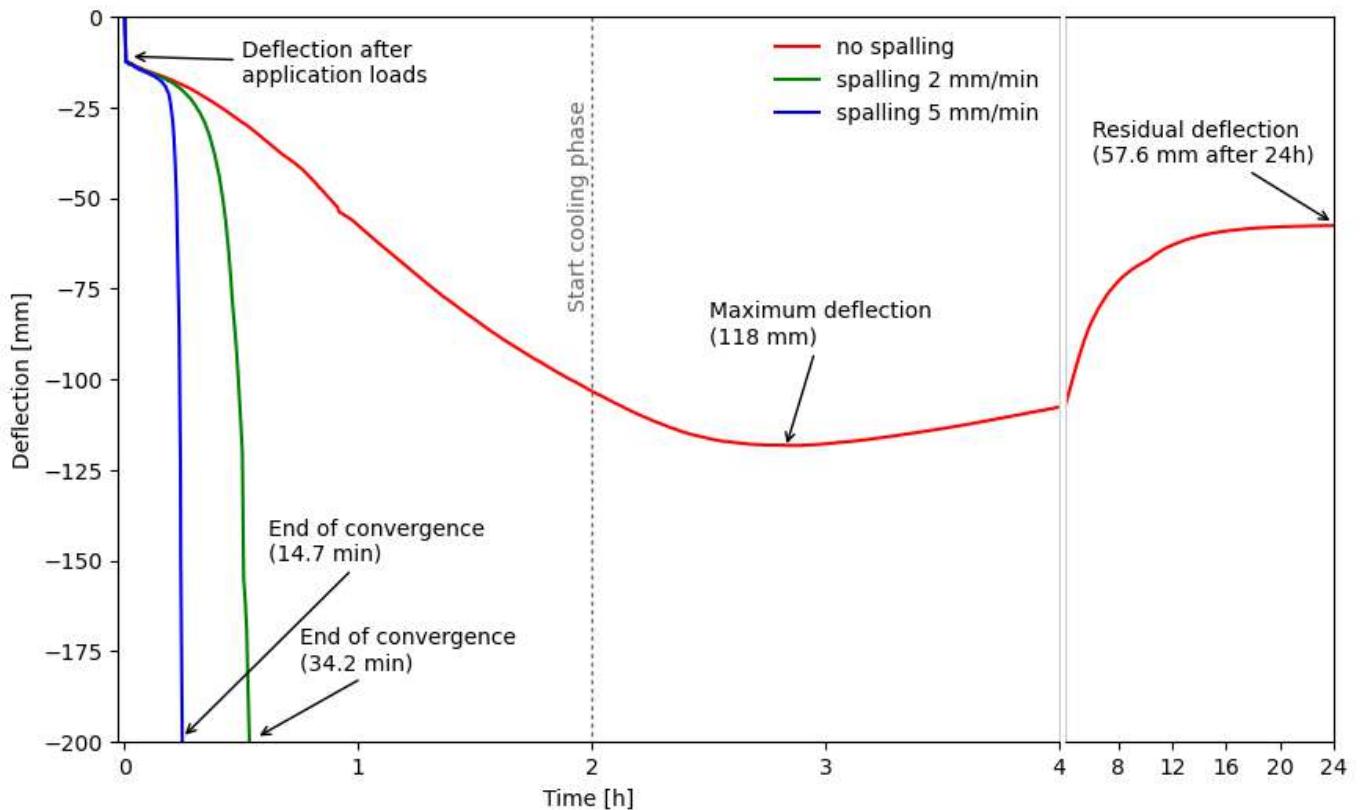


Figure 8. Vertical deflection of the fire-exposed roof slab, 120 min RWS fire in left tunnel tube

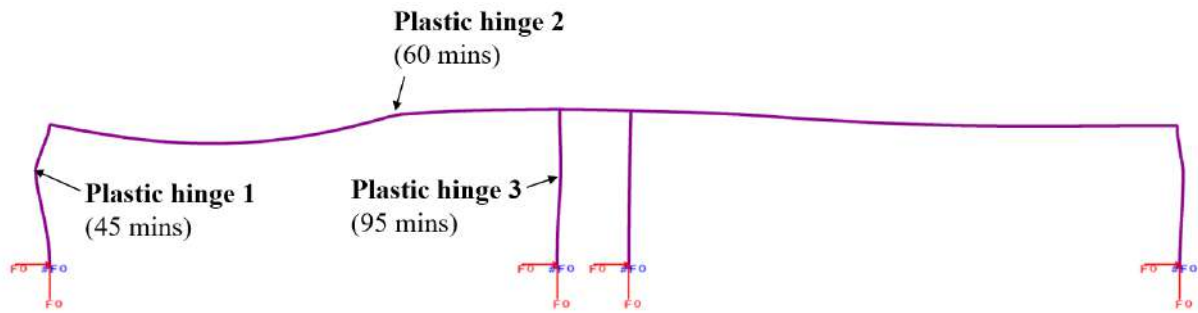


Figure 9. Location of plastic hinges and indication of time at which they develop, for case without spalling. Indicated on deformed structure (10x scaling), at 95 minutes of fire exposure

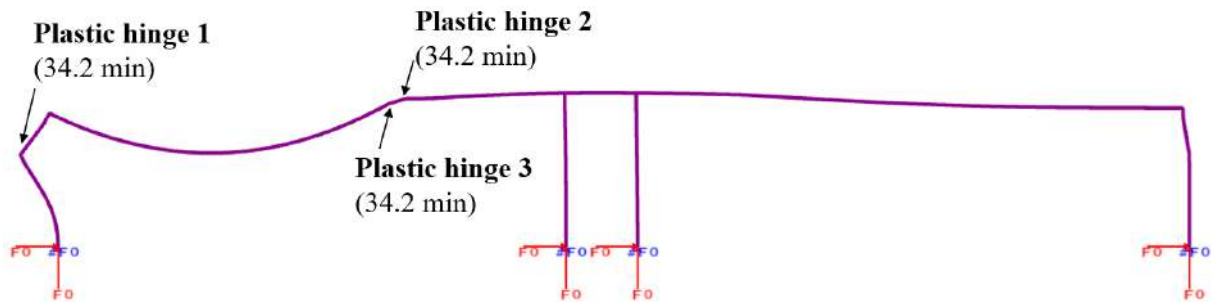


Figure 10. Location of plastic hinges and indication of time at which they develop, for case with 2 mm/min uniform spalling. Indicated on deformed structure (10x scaling), at the moment of failure

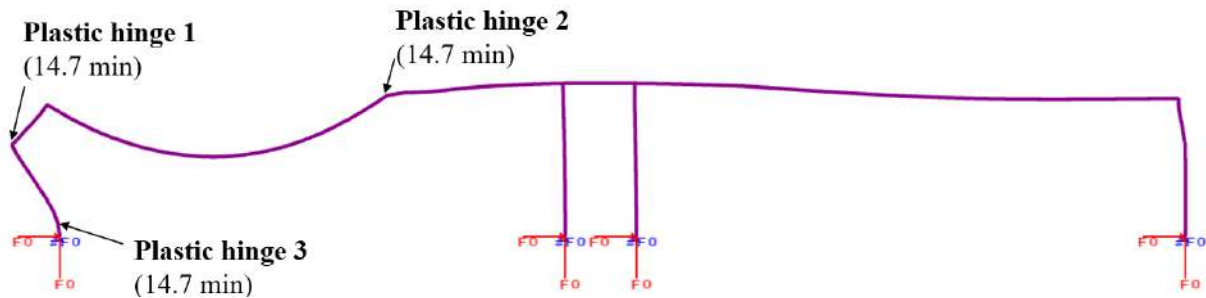








Figure 11. Location of plastic hinges and indication of time at which they develop, for case with 5 mm/min uniform spalling. Indicated on deformed structure (10x scaling), at the moment of failure

4 EFFECT OF SPALLING LOCATION

In an additional set of analyses, the effect of localized spalling on the structural fire response of the tunnel is explored, see Table 2. Six cases are considered, where each time only a limited region of the tunnel is assumed to suffer from spalling, while the other sections are modelled with non-spalling concrete. The results show that the tunnel is highly sensitive to the location where spalling occurs. The tunnel is prone to collapse in cases where spalling occurs in the roof slab near the middle of the span or near the outer wall (cases A and C). In these cases, the structure is unable to redistribute the applied loads to the parts of the structure that are not experiencing spalling. When spalling occurs only in the outer wall (cases B and D) or near the inner wall (cases E and F), the analysis indicates that the tunnel is able to survive the entire fire scenario including the cooling phase. In all these cases, plastic hinges develop at various locations, which allows the structure to redistribute the applied loads. In all cases, the structure remains permanently deformed and suffers from cracking at the unexposed side of the outer wall and the roof slab. Overall, these results illustrate that the damage to the tunnel in case of fire highly depends on the parts of the tunnel where the concrete suffers from spalling, as some cases lead to rapid loss of stability, while others are able to survive 2 hours of RWS fire.

Table 2. Effect of spalling at different locations on the structural fire response of the tunnel for a 120 minute RWS fire

Sections with 5 mm/min spalling	Structural response
<p>Case A</p>  <p>Central roof slab</p>	<p>Collapse after 17 minutes. Forces and bending moment similar to the case with uniform spalling (see Figure 7).</p>
<p>Case B</p>  <p>Top side outer wall</p>	<p>Structure survives full fire scenario (calculation up to 24 hours). Redistribution of forces similar to the case without spalling (see Figure 5).</p>
<p>Case C</p>  <p>Roof slab near outer wall and top side outer wall</p>	<p>Collapse after 85 minutes. Failure occurs due to the section of the roof slab with spalling being unable to take up a significant field moment.</p>
<p>Case D</p>  <p>Entire outer wall</p>	<p>Structure survives full fire scenario (calculation up to 24 hours). Redistribution of forces similar to the case without spalling (see Figure 5).</p>
<p>Case E</p>  <p>Roof slab near inner wall</p>	<p>Structure survives full fire scenario (calculation up to 24 hours). Redistribution of forces similar to the case without spalling (see Figure 5).</p>
<p>Case F</p>  <p>Roof slab near inner wall and inner wall</p>	<p>Structure survives full fire scenario (calculation up to 24 hours). Redistribution of forces similar to the case without spalling (see Figure 5), except no plastic hinge formation in the inner wall.</p>

5 CONCLUSIONS

This paper explored the structural fire response of a reinforced concrete road tunnel with two large rectangular tubes. Numerical analyses were performed in SAFIR, for different spalling rates (5 mm/min, 2 mm/min and no spalling). The results highlight the critical impact of spalling on the structural fire response of shallow rectangular tunnels. The results for the reference case without spalling showed that the tunnel is able to survive the full two-hour RWS fire curve, including the cooling phase, but that the unexposed surfaces of the tunnel suffer significant damage due to the formation of plastic hinges at three different locations. The numerical analyses on tunnels where uniform spalling is assumed demonstrate that spalling, even at moderate rates, can lead to rapid structural failure. A series of analyses on tunnels with spalling in some specific regions highlighted that the studied tunnel structure is most vulnerable to spalling in the roof slab.

REFERENCES

1. Hua, N., Tessari, A., Elhami Khorasani, N.: Characterizing damage to a concrete liner during a tunnel fire. *Tunnelling and Underground Space Technology*. 109, 103761 (2021). <https://doi.org/10.1016/j.tust.2020.103761>
2. Lo Monte, F., Bamonte, P., Beltrami, C.: Study on the effects of cooling phase and construction technology on the fire performance of R/C tunnels. *Tunnelling and Underground Space Technology*. 132, 104838 (2023). <https://doi.org/10.1016/j.tust.2022.104838>
3. Hua, N., Tessari, A.F., Elhami-Khorasani, N.: Damage assessment framework for tunnel structures subjected to fire. In: *Proceedings of the 11th International Conference on Structures in Fire (SiF2020)*. The University of Queensland, Online (2020)
4. Lilliu, G., Meda, A.: Nonlinear Phased Analysis of Reinforced Concrete Tunnels Under Fire Exposure. *Journal of Structural Fire Engineering*. 4, 131–142 (2013). <https://doi.org/10.1260/2040-2317.4.3.131>
5. Stucchi, R., Amberg, F.: A Practical Approach for Tunnel Fire Verification. *Structural Engineering International*. 30, 515–529 (2020). <https://doi.org/10.1080/10168664.2020.1772697>
6. Franssen, J.: SAFIR. A thermal-structural program for modelling structures under fire. *Engineering Journal*. 3, 143 (2005)
7. Shen, Y., Zhu, H., Yan, Z., Zhou, L., Zhang, T., Men, Y., Lu, Y.: Thermo-mechanical analysis of fire effects on the structural performance of shield tunnels. *Tunnelling and Underground Space Technology*. 132, 104885 (2023). <https://doi.org/10.1016/j.tust.2022.104885>
8. Feist, C., Aschaber, M., Hofstetter, G.: Numerical simulation of the load-carrying behavior of RC tunnel structures exposed to fire. *Finite Elements in Analysis and Design*. 45, 958–965 (2009). <https://doi.org/10.1016/j.finel.2009.09.010>
9. Ingason, H., Gustavsson, S., Dahlberg, M.: Heat release rate measurements in tunnel fires. Swedish National Testing and Research Institute (1994)
10. Lucherini, A., Jovanovic, B., Merci, B., Van Coile, R.: Numerical analysis on the characterisation of the fire decay phase of post-flashover compartments. In: *Proceedings of the 12th Asia-Oceania Symposium on Fire Science and Technology (AOSFST 2021)*. The University of Queensland, Online (2021)
11. Van Coile, R., Jovanović, B., Chaudhary, R.K., Deckers, X., Lucherini, A.: Simplified modelling of the performance of concrete tunnels during fire and post-fire damage classification. *APP*. 36, 253–260 (2022). <https://doi.org/10.14311/APP.2022.36.0253>
12. Gernay, T., Coile, R. van, International Federation for Structural Concrete eds: *Performance-based fire design of concrete structures: state of the art-report*. Fédération internationale du béton (fib), Lausanne, Switzerland (2023)
13. Lindlbauer, W., Zeiml, M., Mai, A., Heel, A., Kusterle, W.: *Forschungsvorhaben Brandbeständigkeit von Faser-, Stahl- und Spannbeton – Aufgabenstellung und Versuchsdurchführung*.
14. CEN: EN 1992-1-2. Eurocode 2 – design of concrete structures. Part 1–2: general rules – structural fire design., (2004)
15. CEN: EN 1991-1-2. Eurocode 1: actions on structures – Part 1–2: general actions – actions on structures exposed to fire., (2002)

ON THE FIRE DEVELOPMENT AND MODELLING FOR AUTOMATED RACK SUPPORTED WAREHOUSES

Margherita Autiero¹, Donatella de Silva², Emidio Nigro³

ABSTRACT

Automated Rack-Supported Warehouses (ARSWs) are a particular type of steel racks that combines the structural efficiency of steel constructions with automated machines for handling stored products. This work has addressed the fire modelling of ARSW, by investigating the fire modelling which can be used in a multi-depth ARSW structure, by adopting localized fire models, zone models, and Computational Fluid Dynamics models. A fire model that allows vertical and horizontal propagation, starting from a localized fire, evaluated and validated against experimental results available in the literature, is proposed. Also, a criterion to evaluate the vertical and horizontal propagation times is provided.

Keywords: Fire propagation; steel racks; fire modelling; advanced analyses.

1 INTRODUCTION

Automated Rack Supported Warehouses (ARSW) are a particular type of steel racks (SRs) that combine the structural efficiency of steel construction with automated machines for handling stored products. A fundamental difference exists between traditional SRs and ARSWs. SRs are designed to carry on the structural self-weight and the weight of the stored goods. ARSW are self-bearing rack structures committed to support, besides self-weight and weight of products, also environmental loads (i.e., wind, snow, and seismic action) and all the other non-structural elements such as clads, equipment, etc. A typical structure during its construction is shown in the following Figure 1a. The traditional structural steel racking system is characterized by a regular sequence of frames composed of several shoulders, made of two uprights (the vertical members), connected in the Down Aisle (DA) direction by pallet beams devoted to bringing the goods and, in the Cross-Aisle (CA) direction by horizontal beams and by a bracing system to provide lateral stability of the structure in this direction.

In the ARSW the handling of the pallets can be done by using two systems, AS/RS, and shuttle systems. In the case of AS/RS, a stacker crane moves on a rail back and forth along the DA direction. The shuttle system is composed of two parts: a shuttle carrier and a shuttle, the shuttle carrier moves back and forth on the aisle along the DA direction, and when it has reached the unit load, the shuttle starts moving on rail beams underneath pallets to reach these ones. Three building types of ARSW can be defined depending on the pallet disposal: single-depth, double-depth, and multi-depth. Where there is one unit load line or two unit loads per frame, respectively. In this work, the focus is given to Automated Multi-Depth Shuttle Warehouses (AMSWs), which are compact systems providing large surface occupation and maximum storage density, where the handling of unit loads is realized by a system of shuttles that move goods along rails in the warehouse DA and CA directions.

¹ M.Eng., PhD candidate Department of Structures for Engineering and Architecture, University of Naples Federico II (Italy), e-mail: margherita.autiero2@unina.it.

² PhD, Assistant Professor Department of Structures for Engineering and Architecture, University of Naples Federico II (Italy), e-mail: donatella.desilva@unina.it, ORCID: <https://orcid.org/0000-0002-4058-902X>

³ PhD, Full Professor Department of Structures for Engineering and Architecture, University of Naples Federico II (Italy), e-mail: emidio.nigro@unina.it, ORCID: <https://orcid.org/0000-0002-3848-7454>

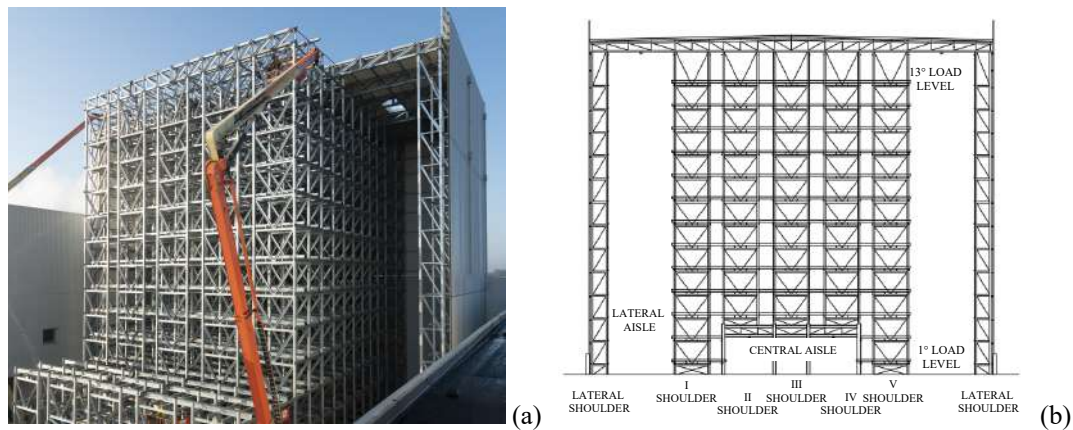


Figure 1. (a) an ARSW during its construction. (b) cross-aisle direction (Source: ROSSS s.p.a.)

The new Italian fire regulation [1] establishes five performance levels (PL), with PLI potentially applicable to ARSWs due to their limited human occupancy, typically involving only occasional and short-term activities by highly trained workers. Different design solutions can be chosen to comply with the PL, based on prescriptive or performance-based approaches, PA, and PBA respectively.

In ARSWs, opting for the PBA over the PA is crucial due to the PA's requirement for minimum fire resistance in structural elements. These structures mainly consist of thin-walled sections obtained by cold-forming thin metal sheets that, on the one hand, optimize the structural performance by reducing the steel weight, the costs, and the assembly time. On the other hand, under fire conditions, the thinness of CFS profiles and the high thermal conductivity of steel causes a rapid rise in steel temperature, resulting in a substantial loss of material stiffness and strength. Applying traditional passive fire protection systems to CFS elements is challenging due to their high section factors (A_m/V) and low critical collapse temperatures. For instance, intumescent paints would require impractically thick applications exceeding $1,000\mu$ for fire resistance. Applying such coatings post-construction is difficult, leading to significant costs. Since their fire vulnerability, these structures are typically protected by active fire protection measures to limit any structural damage. At the same time, the fire protection of an ARSW can be challenging due to their high fire load, moreover, of the variety of goods which can be stored, the choice of active fire protection could be different. Moreover, installing a significant number of sprinklers with related pipes inside a rack could be difficult for space reasons. In addition, the use of active fire protection can lead to losing the stocked goods, and in any case, they could fail their job, therefore the study of the fire scenario without these systems should be analysed. Moving in the context of PBA, the first step is the selection of the design fire scenarios and the definition of the natural fire curves, according to the fire models. The number of possible fire scenarios is usually too large and the analysis of each one is not practicable. Therefore, the design fire scenarios should be chosen, to analyse the most severe cases for the structure. As analysed in [2] fire scenarios for ARSW will consider primarily the chance of an electrical malfunction that causes the burning of the stacker crane. Moreover, the malfunction is considered at the lower building level; because rack uprights are more stressed at the lower level, so the fire possibility is considered riskier. Since they are large and high structures a fully developed fire seems unrealistic and for this reason the fire model that better fits in this case could be the localized fire model. All these considerations lead to affirm that for the ARSW single or double depth the fire scenario at the base within the aisles for stacker cranes can be modelled by considering the localized fire (LOCAFI model). On the other hand, in the case of multi-depth ARSW because of their configuration and the presence of the shuttle systems, the fire could start like a localized fire also within the load levels and could develop into a traveling fire both in horizontal and vertical directions.

The first researcher who attempted an analysis of fire spread in compartments was Clifton in 1996 [3] assessing that in large compartments (called firecells) without any partitions, fires could move across the floor. Clifton proposed a model, the Large Firecell Method (LFM) where each Firecell at a defined time, was divided into four design areas. Each of these could be in the following states – fire, pre-heat, smoke

logged and burned-out, being then subjected to time-temperature curves, (parametric fire curves [1]). This model for localised fire moving throughout the enclosure and generating non-uniform heating in the compartment was not widely used, due to insufficient experimental validation [4]. Stern-Gottfried and Rein [5] developed a Travelling Fire Methodology (TFM), which considers that the fire-induced thermal field is divided into two regions: the near field and the far field, these regions are relative to the fire, which travels within the compartment following a one-dimensional path. The methodology is independent of the fire model selected and can utilise simple analytical expressions or sophisticated numerical simulations. Indeed, the first version of this methodology used the CFD code Fire Dynamics Simulator (FDS) as the fire [6]. However, both models neglect some aspects of the fire dynamics, such as the accumulation of a hot smoke layer, which was partially later improved with the travelling fire methodology (iTFM) [7]. In 2016, Dai et al. [8] proposed the ETFM (Extended Travelling Fire Method) framework, based on a “mobile” version of Hasemi’s localized fire model [8]. Such methodology also considers that the fire-induced thermal field is divided into two regions: the near field, for which a mobilized version of the Hasemi model is considered, and the far field, for which a calculation of a smoke layer based on the FIRM zone model. This combined fire model enables the analysis to capture both spatial and temporal changes of the thermal field and also accounts for the accumulation of a hot smoke layer, and variable fuel load distribution along the fire path, thus addressing more fire dynamics than previous models. However, the ETFM framework still considers a predetermined localized fire path, and it has some limitations in terms of zone model compared to other existing ones such as (OZone [10] CFAST [11]), and Hasemi’s localized fire model, which provides heat fluxes only at the ceiling level when the fire affects the ceiling. Furthermore, this methodology sums the results (thermal impact) obtained with the localised fire and of the zone model, while the Annex D of the EC1 part 1-2 [9] states that in the case of a localised fire, a combination of results may be considered, considering the maximum effect at each location given by the two fire models. Nevertheless, the ETFM is described as a framework, implying users may modify the localised fire and zone models depending on their specific design fire conditions.

Fire design methods for vertically traveling fires are not as developed as for horizontal ones. Vertically traveling fires have been analysed like multi-floor fires in high-rise buildings, which represent a different condition than the ARSWs one. In 2009 Usmani et al. [12], analysed the problem and faced it up for structural fire analysis by recognizing that post-flashover fires can develop at different time intervals for different floors. Therefore, a simple yet important parameter, time delay (Δt , delay) has been introduced to study the structural performances in vertical traveling fires.

Finally, to study the fire behaviour of the ARSW, it is necessary to obtain a fire model that allows the vertical and horizontal propagation of localized fires to be considered. The paper proposes a multi-cells and zones fire model for ARSW structures, validated by some experimental results on steel racks available in the literature. Also, a criterion to evaluate the vertical and horizontal propagation times is provided.

2 FIRE MODELLING FOR STEEL RACKS

In order to obtain a fire model considering the vertical propagation of localized fires, some experimental results were looked for in the scientific literature. Since, no one has carried out an experimental campaign on ARSW, it was necessary to consider works regarding usual steel racks. In particular, the work used as principal references for validating the fire model was the one carried out by Lönnermark and Ingason [13], which performed several fire scale tests (1:5), to investigate the fire spread in rack storages without any suppression system. Indeed, that most of the large-scale tests with rack storage carried out worldwide include tests with sprinkler systems [14], but no large-scale tests have been performed without the interference of a sprinkler system, such tests would be too difficult to perform due to the risk of damaging the test facilities and of course due to their high costs. For these reasons, Ingason has performed several tests [15], both large scale and model scale, where the effects of the geometry and type of fuel on the fire growth in rack storages, have been investigated. The results have shown that there is a good correlation between the large-scale tests and the model scale tests in a scale 1:3. Therefore, the authors decided to perform the tests in a model scale, in particular, the most appropriate scale was found to be 1:5, for practical reasons related to the dimensions of the fire hall used. When carrying out tests on the model scale, the

measured values of the various parameters must be scaled up to a large scale using various physical scaling laws [15]. The technique means that it is possible to investigate fire behaviour in larger stores i.e., with more and higher racks relatively cheaply. The test program presented in the report, consisted of five different test series:

- Test series 1: Cone calorimeter tests of the cardboard boxes used in the rack storage tests;
- Test series 2: Fire spread tests with one small rack;
- Test series 3: Free burning tests (without ceiling) with four racks;
- Test series 4: Study of the influence of the size of the enclosure;
- Test series 5: Fire spread tests with four racks.

The tests carried out by Lönnermark and Ingason [13] and described in the previous paragraphs have been simulated numerically by using the software CFAST [11] developed by NIST. In this way, it was possible to validate a fire model that allows studying the vertical propagation of localized fires in a multi-depth ARSW.

2.1 Test series 1 (Cone calorimeter tests) and Test series 2 (Fire spread tests with one small rack)

During the test series 1, the cardboard material of the boxes was tested in a cone calorimeter to obtain information about the flammability and thermal response properties of the material. Specimens with dimensions equal to 100×100 mm and with a thickness of one layer equal to 6 mm, were tested horizontally and by exposing them to radiation of 50 kW/m². Test Series 1 included 4 tests in total, by varying the thickness of the box and by using more than one layer of the cardboard. These test series allowed evaluation: the time to ignition, time to extinction, heat release rate (HRR), developed energy, smoke production, mass loss rate, total mass loss, and heat of combustion. At the end of these tests, the authors decided that reference in the following tests would be made to the double-thick cardboard box. The test series 2 consisted of the analysis of the vertical propagation of the fire within one rack, filled with 4 boxes in an 2x2 configuration, while the flue width (*w*), the height of the rack (number of levels), and the wall thickness of the boxes (single, double, or triple boxes) were varied. Six tests were carried out, in total. The experimental set-up of test series 2 is shown in Figure 2a. In tests 2.1 - 2.3 and 2.5 four levels of boxes were used, and gas temperatures were measured by using thermocouples of type K (0.25mm) in two positions: x2 and x3. In tests 2.6 five levels of boxes were used and gas temperatures were measured in positions: x 1 and x 2. In addition, in each test the heat release rate (HRR) was measured by oxygen calorimetry (ISO 9705). The tests' results showed that the fire behaviour of the case with five levels of double boxes and a flue width (*w*) of 50 mm best suited the purposes of the tests with large racks and therefore the authors decided to use these dimensions in all the other test series.

To validate the CFAST models the Test series 1 and 2, which provide the necessary input data, were modelled. In particular, Test series 2.2 was modelled first, since this one refers to boxes with a double thickness, the Heat Release Rate (HRR) curve was set starting from results of the test series 1.2 and by doing some considerations: The Maximum Heat Release Rate (HRR_{max}) was considered equal to 247 kW/m², like the test results. The total developed energy (*q_f*) for a single box was equal to 23.9 MJ/m², but to consider 4 boxes per level, this value was amplified obtaining a value of *q_f* equal to 95.6 MJ/m². The value of *t_α* was considered equal to 250 s, which is the value between the ones that the Eurocode provides for bookshops (150 s) and offices (300 s), therefore similar uses of paper and paperboard. The fire area *A_f* was calculated as the floor area of the shelves containing the boxes multiplied by 4 to represent the 4 levels of boxes. The fire area *A_f* was calculated as the load level area equal to 0.53x0.45x4 equal to 0.954 m². By knowing these parameters, it was possible to evaluate the HRR curve, which was compared with the experimental one, see Figure 2b. From this comparison, it is possible to realize that the calculated HRR curve and the experimental one, are very similar to each other in terms of pattern and duration, and therefore the HRR curve calculated can be considered representative of fire test 2.2 and can be used like the HRR input curve for the CFAST model.

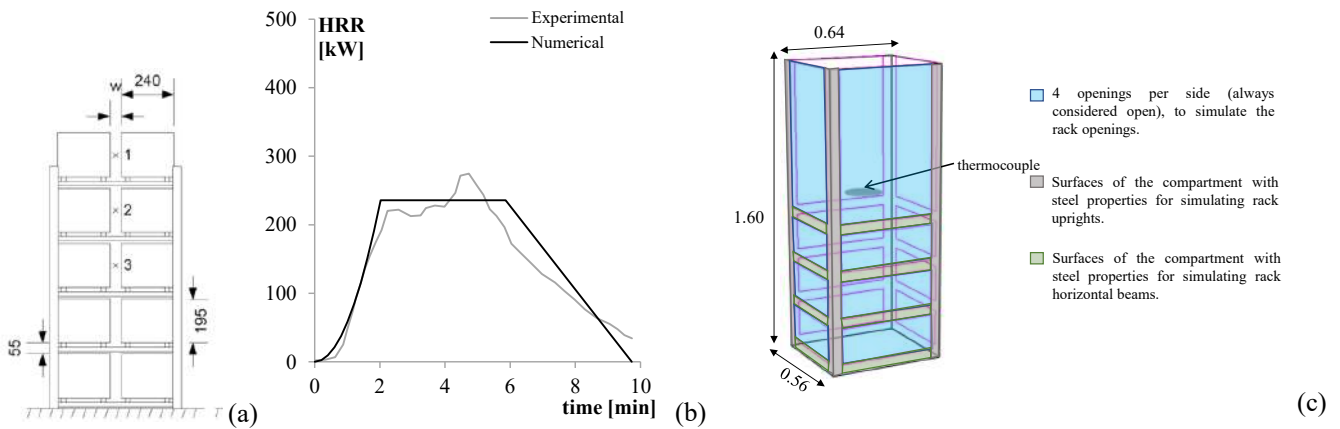


Figure 2. Test 2.2: (a) Experimental setup. (b) CFAST model. (c) Comparison between numerical and experimental HRR curves

To model Test 2.2 setup a single compartment with the rack dimensions of 0.64x0.56 m in plan and 1.60 m in height was modelled in CFAST. Since this compartment represents a single rack, each surface was characterized by the thermal properties of the steel. Along the walls 4 openings per side (always considered open), were defined to simulate the rack openings. The compartment modelled is shown in Figure 2c. A single type of fire has been defined, characterized by the previously calculated HRR curve, which was placed in the middle of the compartment at the height of the bottom shelf. A steel target in the middle of the rack was modelled, such as the thermocouple 2 in test 2.2. Figure 3b shows the comparison between the experimental temperatures and the numerical ones.

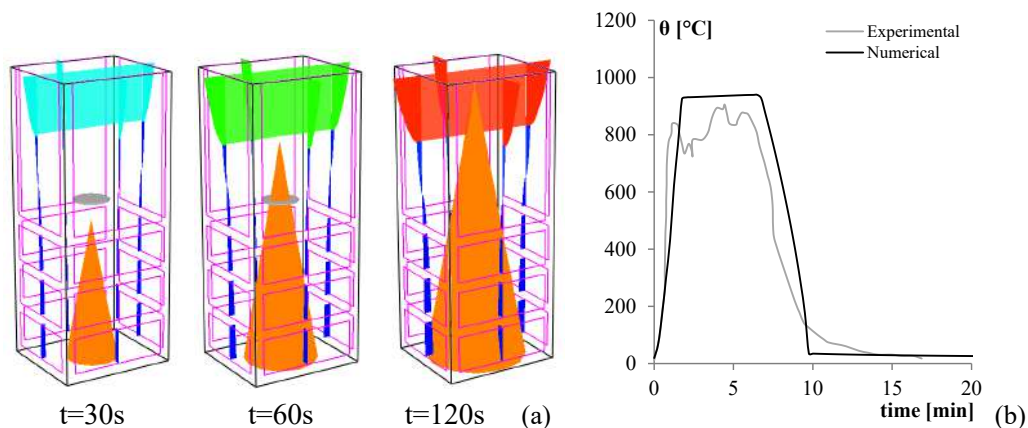


Figure 3. Test 2.2 results: flame development (a). Comparison between numerical and experimental results in terms of temperatures (b)

The temperature calculated in CFAST, regards the fire durations and the temperatures range can be considered coherent with the one recorded experimentally. In conclusion, by modelling the test 2.2 it was possible to validate the CFAST model for a single rack. The test with double and triple boxes (Test 2.2 and 2.3, respectively) burned similarly at the beginning of each test.

2.2 Test series 5 (Fire spread tests with four racks)

In test series 5 four racks were placed next to each other and under a ceiling to study the effect of the distance between the commodities and the ceiling. In this test series, two main results were investigated, such as the time for fire spread from one rack to the next and the gas temperature and flow rate near the ceiling. For this reason, temperatures were the main measurement with thermocouples placed in 24 different positions beneath the ceiling. Moreover, the times when the fire spread to the different racks were registered together with the time for the flame to reach the ceiling. Each of the four racks was filled with $2 \times 12 \times 5$ boxes with flue width (w) of 50 mm, with a single wall thickness of the boxes in racks 1,3, and 4 and, the

double wall thickness of the boxes in rack 2. In each test the ignition took place at the bottom of 2nd rack (first ignition to I level), with vertical propagation up to the other V levels and horizontal propagation to the other three racks (see Figure 5b). Fire test 5 was simulated in CFAST, considering the fire propagation as time delays applied to the HRR curve of a single level. The HRR curve of the single levels of the 2nd rack was evaluated by using the same procedure used to evaluate the HRR curve of the entire rack for test 2.2, i.e., starting from the test series results 1.2 and by considering that the 2nd rack of test 5.3 was characterized by 24 double thickness boxes for each level. Therefore, starting from HRR curves of a single level, these were then summed moment by moment, referring to the exact time delays provided in [13], and obtaining the HRR curve of the whole 2nd rack, shown by the red curve in Figure 4a.

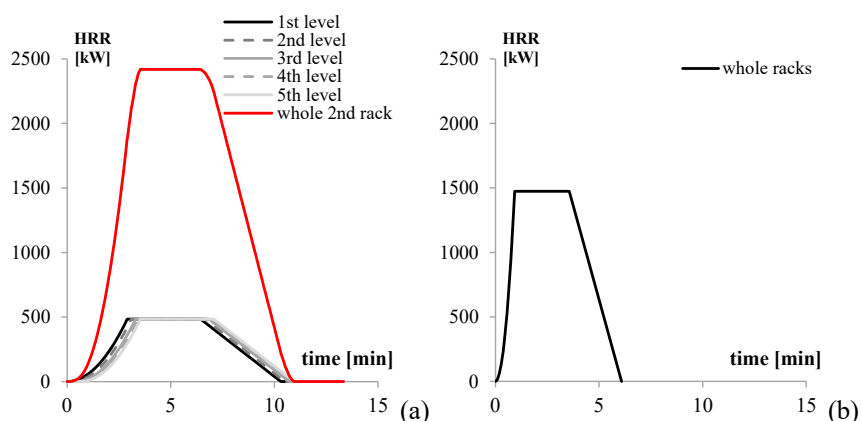


Figure 4. Test 5.3: HRR curves of the 2nd rack (a) and of the lateral ones (b)

For the other three racks, the test results in [13] didn't provide the vertical time delays, in this case, the HRR curve of the whole rack was directly evaluated, starting from the results of the test 1.1. The HRR curve obtained is shown in Figure 4b. These HRR curves provided the input of the CFAST program.

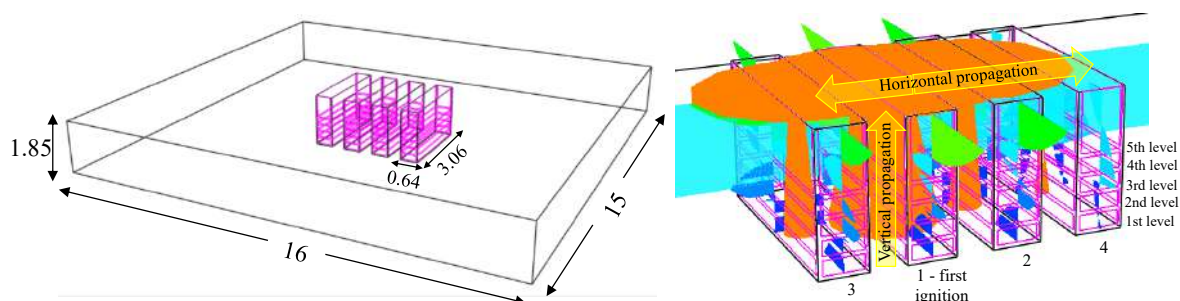


Figure 5. Test 5.3: CFAST model, dimensions are in meters

To model the test 5 setup a large compartment of 16x15 m in plan and 1.85 m in height, was modelled, its dimensions were not provided by authors [13], and for this reason, they were defined to guarantee proper ventilation to reach the decay phase of the fire test. Within this one, 4 compartments representing the 4 racks were modelled (see Figure 5a). The surfaces of the large compartment were plasterboard to simulate the walls of the test setup, while the 4 compartments representing the racks were characterized by the thermal properties of the steel. Along the walls, 5 openings per side (always considered totally open), were defined to simulate the rack openings. For each rack, the corresponding fire was placed at the base, in the middle of the compartment. In particular, the fire of the 2nd rack was modelled by the red HRR curve as shown in Figure 4a. As regards the lateral racks, the fire of the 1st, 3rd, and 4th racks was modelled using the HRR curve shown in Figure 4b applied at 129 seconds, 130 seconds and 150 seconds respectively as defined by authors. The following Figure 6 shows the comparison between the experimental results and the numerical ones, in terms of temperature. The temperature calculated in CFAST regarding the maximum temperature, is coherent with the one recorded experimentally. The heating phase is not too different, indeed

only a time delay is observed in the numerical temperature. The same is true for the first part of the cooling phase, while, after 8 minutes, the temperatures are very similar.

To define a generalized model for the vertical propagation, it was necessary first to validate the propagation times of Test 5.3. It was found that these are equal to the times for the flame to reach the upper level of the racks calculated by using the flame lengths L_f for a localized fire proposed in the Annex C of the EN1991-1-2 [9] and given by:

$$L_f = -1.02 D_{fire,eq} + 0.0148 HRR(t)^{0.4} \quad (1)$$

Where; $HRR(t)$ is the heat release rate of the fire in [W], $D_{fire,eq}$ is the equivalent diameter in [m]; which can be evaluated by using the expression, given in [16].

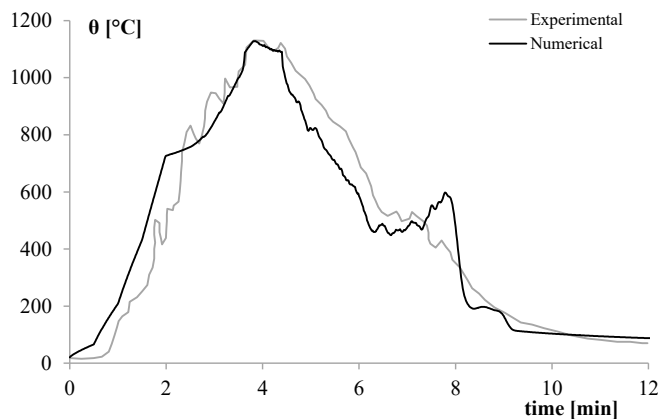


Figure 6. Test 5.3: Comparison between numerical and experimental results

From the results obtained and shown in Table 1 it is possible to observe that the calculated times are in good agreement with the time provided by the experimental test and for this reason it is possible to affirm that the vertical propagation of the fire can be modelled like the time for the flame to reaches the following load level along its vertical. In particular, it is worth saying that the values are all the more consistent at the first levels compared to the following ones, this is because the formula was calibrated to consider only one fire and not the overlapping of more fires, moreover the exponential leads to an asymptote at a certain time, which doesn't allow to reach a higher fire length.

Table 1 Comparison between experimental and calculated propagation times

Load Level	Experimental time [s]	Calculated time [s]
1 st	0	0
2 nd	12	13
3 rd	24	25
4 th	32	38
5 th	38	50

3 APPLICATION OF THE FIRE MODEL TO A TYPOLOGICAL ARSW

3.1 Description of the structure

Starting from these considerations, one typological self-supporting automated warehouse was studied, the structure object of this study is shown in Figure 1 and consists of a steel-supporting structure and equipped with infill panels and roofing with sandwich panels. This AMSW has a rectangular plan with a total length of 52 m and a width of 35m, it consists of a central block, used for the storage of the reels, and two side lanes served by stacker cranes for handling the reels. In the down-aisle direction, the central block consists of a succession of frames, while at either end of the warehouse, the first two spans of the structure host the bracing towers. In this direction, the frames are joined with pallet beams with open section cold formed profiles. For each span, a unit load (a paper reel) is stored; the UDCs are supported by particularly designed channels resting on the principal

beams. The handling of unit load (UDC) is realized by a system of shuttles and satellites that move goods along rails in the warehouse cross and down aisle directions. In the CA direction each frame is composed of five shoulders with V-shaped braces (see Figure 1b), and it is characterized by 13 load levels placed at 2 m, with a total height of 29.8 m. The nomenclature adopted in the following analyses and consideration is also reported in the Figure 1b. The warehouse structural system consists of hot-rolled tubular columns with hollow square (HSS) cross section and cold formed horizontal and diagonal elements with C cross-sections.

3.2 Proposed fire model for ARSW - CFAST

Thanks to the simulation and validation of the fire tests carried out by Lönnermark and Ingason [13] by using the software CFAST it was possible to obtain the parameters that define the design fire, together with the method to calculate the times for the vertical propagation, can be applied to obtain a fire model for the ARSW structure. Since the fire tests carried out by the authors were small-scale fire tests, the following step to obtaining a real fire model is to scale up these fire parameters in a way that they can be representative of a full-scale fire configuration by using various physical scaling laws. Physical scaling has been widely used in the fire safety science community, allowing a better understanding of fire dynamics. Li and Ingason provided a general scaling method for pallet fires presented in [15] modelled ad hoc on cellulosic material fires that develop in steel racks structures. This method is based on the Froude scaling technique in particular, these coefficients can be used for scaling the parameters that define a fire in terms of HRR value, volumetric flow, propagation speed, time, energy released, mass, and temperature, concerning the geometric ratio between the full-scale dimensions L_f (in real scale) and the model scale dimensions L_m (in reduced scale). Considering the case study, it was obtained a geometrical ratio equal to 11.76, which leads to different scale factors used for the time and the HRR values. Regarding the value of α , firstly the same value of the fire test equal to 250s was considered, but by carrying out a critical analysis of the HRR obtained, it was observed that the HRR for paper material was not consistent with the value according to Italian regulation that for paper material proposes a α equal to 150s. For this reason, it was decided to modify the HRR curve by applying only to the parabolic section the suggestion of the code, leaving unchanged the peak, the duration, and the descending phase of the HRR curve. The HRR curve modified in this way is shown in Figure 7a. The vertical fire propagation times were then calculated for the ARSW structure according to the method validated before, by placing the first ignition at the base of the central shoulder and considering that the height of the load cell is equal to 2.04 meters, the ignition time was the time at which the flame length reaches this height, and its multiples. In this way it was possible to obtain the vertical propagation times from the instant $t=0$ s the vertical propagation times are: 107s for the flame to reach the 2nd level, 244s for the 3rd level, 368s for the 4th level, 515s for the 5th level and finally 691s for the 6th level and 800 s for the 7th level. It is worth saying that since the flame length fails to reach the height of the 7th level equal to 12.24 m it was supposed that there was no ignition of the 7th load level, and therefore the proposed fire model will consider a vertical fire propagation within the first six load levels. Regarding the study of the horizontal fire propagation, a time delay between the ignition of the first shoulder and the ignition of the adjacent ones was evaluated. In particular, the time required for the combustible material stored in the adjacent load cells to reach a temperature of 230 °C that is the paper auto-ignition temperature [20] was considered, obtaining a time equal to 506 seconds e.g., 8.4 minutes.

In CFAST, a first large compartment that represents one transversal cross section was modelled. Within this one, 5 compartments representing the 5 racks shoulder and 1 steel compartment representing the bottom steel frame, were modelled. In this way, 7 compartments were modelled, in total (see Figure 7b). The lateral shoulders were not modelled as a compartment because they were considered cold. It is worth saying that once the compartment is characterized by openings and the fire can travel from one compartment to another one, the meaning of the compartment is lost, so in the following descriptions, the term “cell” will be used to refer to this type of zones modelling. Thanks to the time delays calculated previously, it is possible to affirm that for this fire model, the ignition took place at the bottom of the central shoulder (first ignition to 1st level), with vertical propagation up to the other six levels and horizontal propagation to the other two shoulders. For this reason, in the CFAST model, for each shoulder, 6 HRR curves were assigned at the middle height of each load level with the corresponding time delays, defined previously. In this way, 18 HRR curves were assigned.

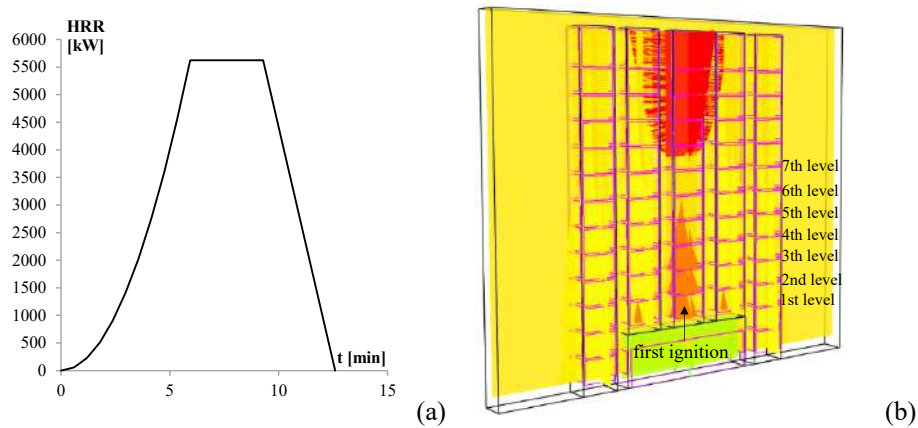


Figure 7. (a) HRR curve. (b) First CFAST model of the ARSW structure

Figure 8 shows the temperature distributions recorded by the CFAST thermocouples placed at the first four levels near the horizontal and upright elements.

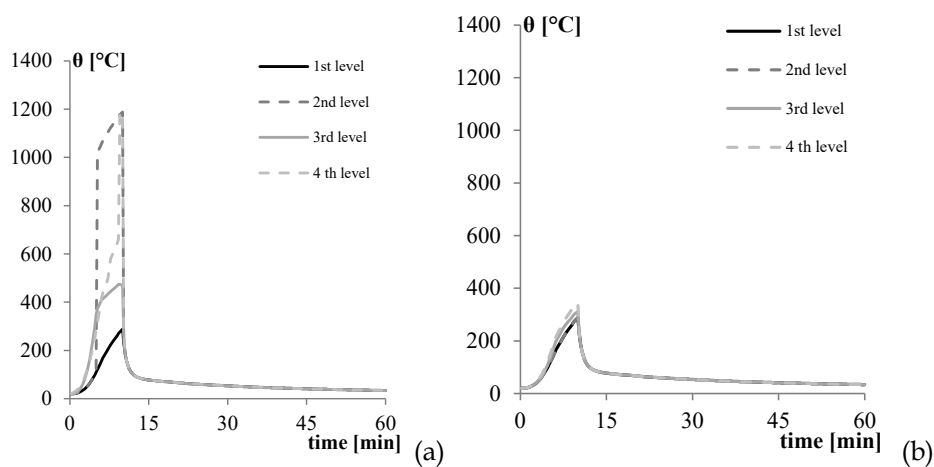


Figure 8. Temperatures recorded in the CFAST model for the horizontal elements (a) and uprights one (b)

By analysing the results, it is possible to see that a strong discontinuity characterizes the heating phase and that different temperatures are reached for the 3rd level compared to the others. Moreover, since in this type of model, there is only one hot zone at the upper level of each compartment (i.e., shoulder), it was not possible to compare the temperature of the hot zone with the temperature recorded by the thermocouple, to see if the thermocouples work properly. In conclusion, this type of model didn't work properly and for this reason, different modifications were made. The first modification that was made in the CFAST model to better represent the fire scenario, concerned the different modelling of each shoulder. Every single unit of the load was modelled as a single cell but communicated between them thanks to horizontal openings (ceiling/floor vent). In this way a model with different compartments/cells allowed comparing the temperatures recorded by the thermo-couple with the temperatures of the hot zone and cold zone. Indeed, such a model allowed dividing each load level into two zones instead of the entire shoulder. The second modification that was made concerned the ventilation condition, the first large compartment that represented one transversal cross section was modified by referring to the dimension of the entire volume of the ARSW representing the entire ARSW, but since it was noted that even this condition underestimated the oxygen supply, a bigger volume was considered to provide more oxygen to the fire. The result was, a fluid dynamics model too complex for processing by using CFAST. Therefore, it was decided to achieve a good compromise between the complexity of the model, the potential of the software, the processing time and the amount of data generated. The fluid dynamic model that met these requirements consists of an extremely large external compartment capable of providing the amount of oxygen necessary for the full development of all the HRR curves. For the central three shoulders, the first six load levels which were directly affected by the presence of a fire, were modelled as a single compartment but communicated among them. The result was a model with seven compartments

for each shoulder in particular: six single compartments related to the first six levels where, with several delays, the fire develops and the seventh compartment grouping the remaining load levels where no fire was defined. Figure 9a shows the temperature distributions recorded by the CFAST thermocouples placed at the first seven levels near the horizontal elements, while Figure 9b shows the temperature of the hot zone.

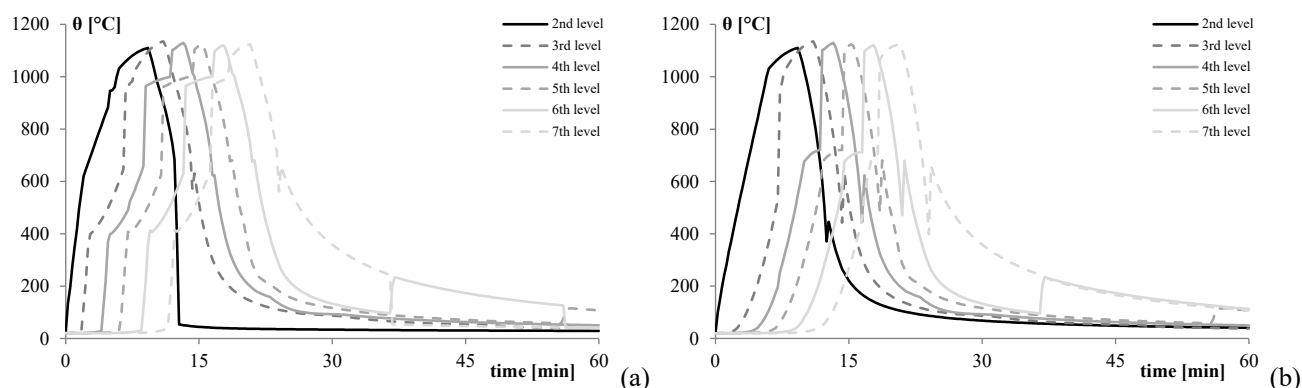


Figure 9. Temperature distributions recorded by the thermocouples placed at the first 7 levels near the horizontal elements (a) and temperature of the hot zones (b) of the central shoulder

By analysing temperature results, it is possible to appreciate, how the time delay imposed for the HRR curves was found also in the natural fire curves. All the curves reach a maximum temperature equal to about 1120 °C. The results confirm that the measurements of the thermocouples near the transverse elements are in good agreement with the temperatures recorded in the hot zone of each compartment where a fire is present. Moreover, the new modelling allows also overcoming the problem of the strong discontinuity that characterized the heating phase in the previous modelling. In the new modelling, the thermocouple near the generic transverse is always in the hot zone, during all the thermal transients. Thus, it heats up in the same way as the gases that are concentrated there, with slower heating but reaching the same peak of temperature. The new modelling didn't sort out the problem regarding the other thermocouples placed outside the hot zone; therefore, to define the heating curves for the diagonals and the uprights elements, a temperature curve evaluated as the average of the temperatures recorded in the hot zone and in the cold zone was considered at each level.

3.3 Proposed fire model for ARSW - FDS

The computational fluid dynamics model of the ARSW structure was created also in FDS software developed by NIST [6] to simulate the gas temperature distributions and compare them to CFAST measurement results. In Pyrosym, a large volume that represents the whole compartment was defined as 52 m x 35m x 29.8 m in a model domain of 58.8m x 35.4m x 30m. Into FDS environment, the geometry is described in terms of rectangular obstructions (OBS) that can heat up, burn, conduct heat, etc.; and VENTS from which air or fuel can be either injected into or drawn from the flow domain. A boundary condition needs to be assigned to each obstruction and vent, describing its thermal properties. For this reason, firstly, in the computational domain the steel frame was modelled as shown in Figure 10a, it is worth saying that the diagonal bracings belonging to the shoulder and the truss were not modelled because of the type of modelling that this type of program request, where it is only possible to model rectangular OBS. The boundary conditions were defined as close as possible to the ones of the reality. Boundary conditions for obstructions and vents are prescribed by an attached surface (SURF) where most parameters must be defined. In FDS software, solids are assumed to consist of layers that can be made of different materials, the thermal properties of each material required are designated via the MATL name list group. In this context, the floor and the ceiling were set as INERT which is the default FDS boundary condition representing a smooth wall with a fixed temperature, equal to the ambient temperature, and emissivity equal to 0.9, where radiative and convective heat transfer is calculated. The walls were considered made of 0.15 m of gypsum, the surface attached was set as a “layered” type, with a layer of 0.15 m of material “gypsum”. The same type of “layered” surface was assigned to the structural steel elements, it was set that the steel elements are not allowed to participate in combustion and whose physical surface characteristics are

calculated during the thermal transient with the incident flow. The specified ignition of the fire was modelled as the ejection of gaseous fuel from a solid surface, this is essentially a burner, with a specified Heat Release Rate per Unit Area, HRRPUA, in units of kW/m².

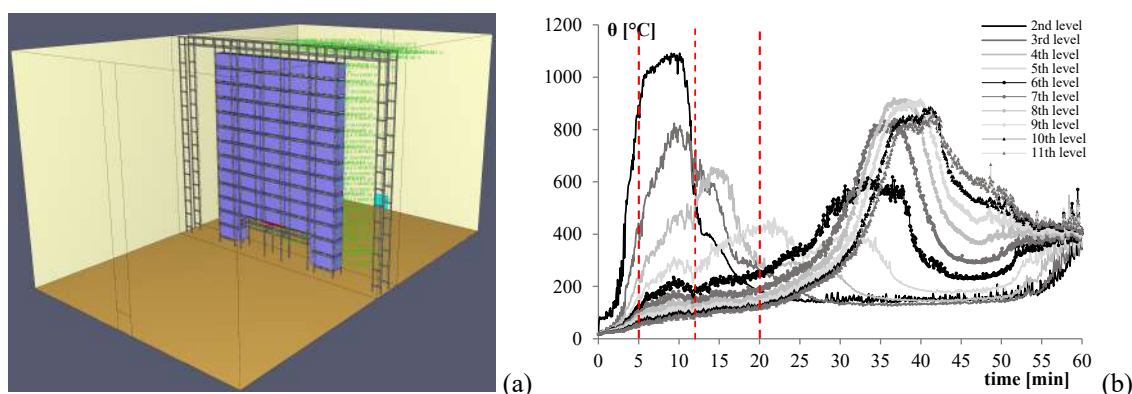


Figure 10. (a) FDS model of the ARSW structure with AST devices positions. (b) Temperature distributions computed by FDS at the horizontal beams of the central shoulder

The solid burner was modelled with dimensions equal to 4.05m x 1.65m x 0.15 m, and to obtain the same HRR used in the CFAST model, the HRRUA for this surface was set equal to 670.2 kW/m², and a time ramp for volumetric heat source was specified. The paper constituting the cubes is assumed to be pine wood type with the same chemical composition specified for the zone model. All the other unit loads were modelled as solid cubes with dimensions equal to 4.05m x 1.65m x 1.65 m, i.e., the real dimensions of the unit loads. To obtain the same HRR, the HRRUA for this surface was set equal to 174.81 kW/m², with a specific time ramp for this volumetric heat source. Since one of the aims of this simulation was to analyse the fire propagation without the predefined delay times, all the unit loads were not modelled as BURNERS but as surfaces with an ignition temperature set equal to 230 °C which is the paper autoignition temperature. When the threshold temperature of 230°C is met on at least one face of the volume, then the six surfaces are set to start burning following the prescribed HRRPUA curve. Two openings were placed along the length of the compartment, on both walls parallel to the DA direction of the compartment, always considered open. Figure 10b shows the temperature distributions recorded by the AST placed at the eleven seven of the horizontal beams of the central shoulder, (third shoulder as represented in Figure 1). The first thing that it is possible to observe is that by using the CFD model it is possible to observe vertical and horizontal propagation without the pre-defined delay times. The second aspect is that the temperature doesn't reach the same peak for all the structural elements like the CFAST temperature. In the case of the first heated element, the horizontal beam at the 2nd level, is possible to observe a very similar behaviour to CFAST. At 5 minutes, the first cube is heated and the flame reaches the 2nd level, at 12 minutes all the first cube is consumed by the fire which means that all the HRR of this level is used, this is the reason why the temperature distribution for the 2nd level is very similar to the CFAST one. At 20 minutes going to the 3rd and 4th levels the temperature peak decreases because the fire starts to propagate within the aisle between the two shoulders, like a chimney effect, confirming that the ventilation effect may play a very important role, in changing the fire traveling trajectory. At 35 minutes, it is possible to observe that due to this type of propagation, the fire reaches the upper levels very fast going to heat also all the truss elements, indeed all the horizontal beams from the 6th to the 11th levels are heated at the same times, with only a little delayed time among them.

4 CONCLUSIONS

This study evaluates a self-supporting automated multi-depth warehouse's response to fire scenarios. Specifically, it examines how fires originating within the load levels can spread horizontally and vertically. In the last decade, vertically traveling fires have been analysed like multi-floor fires in high-rise buildings, which represent a different condition than the ARSWs one. Thus, a key goal is to develop a fire model capable of accurately simulating both vertical and horizontal propagation of localized fires. To achieve this goal some experimental results on steel racks available in the literature were considered. In this way, it was possible to obtain a multi-cells and zones fire model for ARSW structures. It was found that since the main assumption of

the zone model is that the temperature is uniform in each compartment, it was necessary to divide the whole geometry into different cells as the load level of structure, i.e., where the combustion material is present. Therefore, a CFAST model characterized by cells communicating among themselves through horizontal openings was obtained in the examined case study. In each cell, the horizontal and vertical propagation was considered by assigning time delays to the HRR curves. It was found that vertical time propagation is equal to the time for the flame to reach the upper level of the racks, calculated by using the flame lengths L_f proposed in EC1 part 1-2. Regarding the horizontal fire propagation, a time delay equal to the time required for the combustible material stored in the adjacent load cells to reach its own auto-ignition temperature was considered. The same fire scenario was modelled also by using FDS software, which allows the analysis of the fire propagation without the predefined delay times. The CFD model in this case underlines on one hand the ventilation effect, which may play a very important role in changing the fire traveling trajectory, but on the other hand, allows the validation of the fire propagation times calculated analytically and used in the zone model.

REFERENCES

1. D.M. 3 agosto 2015 Approvazione di norme tecniche di prevenzione incendi, ai sensi dell'articolo 15 del decreto legislativo 8 marzo 2006, n. 139, GU n. 192 del 20/8/2015 – S.O. n. 51 (in Italian).
2. A. Mei, "Robustness of Automated Rack supported Warehouses in Fire", PhD thesis, Faculty of Architecture, Civil Engineering and Environmental Sciences University of Braunschweig - Institute of Technology and the School of Engineering, University of Florence, 2023.
3. G. C. Clifton, "Fire models for large firecells", HERA Report R4-83, 1996.
4. Y. Wang, I. Burgess, F. Wald, M. Gillie, "Performance-Based Fire Engineering of Structures", London, CRC Press, 2012.
5. J. Stern-Gottfried, "Travelling fires for Structural Design", PhD thesis, University of Edinburgh, 2011.
6. K. McGrattan, S. Hostikka, R. McDermott, J. Floyd, C. Weinschenk, K. Overholt, "Fire Dynamics Simulator User's Guide (Sixth Edit)", National Institute of Standards and Technology (NIST), Special Publication 1019, 2017.
7. E. Rackauskaite, C. Hamel, A. Law, G. Rein, "Improved formulation of travelling fires and application to concrete and steel structures", *Structure*, vol.3, pp. 250-260, 2015.
8. X. Dai, S. Welcha, A. Usmani, "A critical review of "travelling fire" scenarios for performance-based structural engineering", *Fire Safety Journal* vol. 91, pp. 568–578, 2017.
9. EN 1991-1-2, "Eurocode 1: Actions on structures - Part 1-2: General actions - Actions on structures exposed to fire", 2002.
10. J.F. Cadorin, J.M. Franssen. "A tool to design steel elements submitted to compartment fires - OZone V2. Part 1: pre- and post-flashover compartment fire model", *Fire Safety Journal*, vol. 38 (5), pp. 395-427, 2003.
11. W. W. Jones, G. Forney, R. D. Peacock, and P.A. Reneke "A Technical Reference for CFAST: An Engineering Tool for Estimating Fire and Smoke Transport", Technical Note, (NIST TN), National Institute of Standards and Technology, Gaithersburg, MD, May 2, 2003.
12. A. Usmani, C. Roben, A. Al-Remal, A. "A Very Simple Method for Assessing Tall Building Safety in Major Fires." *International Journal of Steel Structures*, vol. 9(1), pp. 1-15, 2009.
13. A. Lönnermark, H. Ingason, "Fire Spread in Large Industrial Premises and Warehouses", in BRANDFORSK project 630-021, 2005.
14. H.C. Kung, H.-Z. Yu and R. D. Spaulding, "Ceiling Flows of Growing Rack Storage Fires", *Twenty-First Symposium (International) on Combustion*, PP. 121-128, 1986.
15. Y. Z. Li, H. Ingason, "Scaling of wood pallet fires", SP Technical Research Institute of Sweden SP Report 2014:57. 2014
16. O. Vassart, F. Hanus, M. Brasseur, R. Obiala, J.-M. Franssen, A. Scifo, , B. Zhao, C. Thauvoye, A. Nadjai, and H Sanghoon, "Temperature assessment of a vertical steel member subjected to localised fire, acronym LOCAFI", Report RFSR-CT-2012-00023, European Commission, 2016.
17. SFPE Handbook of Fire Protection Engineering, 5th edition, 2016, ISBN: 978-1-4939-2564-3.

OPTIMISING DIAGRID DESIGN FOR FIRE RESISTANCE IN HIGH-RISE BUILDINGS

Zhiruoyu Wang^{1*}, Mhd Anwar Orabi², Zhunjun Nan³, Matthew Mason⁴ Weiyong Wang⁵, David Lange^{6*}

ABSTRACT

This paper introduces a methodology for the optimisation of the fire resistance of diagrid structural systems in high-rise buildings, balancing material efficiency with fire safety. The used approach adapts existing stiffness-based design principles, traditionally used to optimize structural performance under ambient conditions, to the specific challenges posed by various fire scenarios. The innovation of this research lies in the integration of these design principles to simultaneously optimize the use of steel and fire protection materials. By employing Python scripting, Grasshopper, Rhino, and OpenSees in Fire, the methodology facilitates the evaluation of various diagrid layouts under different fire conditions. This approach allows for a refined determination of diagrid element layouts and sizes that achieve an optimal balance between material efficiency and fire resilience.

The methodology is demonstrated through empirical findings that identify diagrid angles between 75° and 82° as optimum for a particular case. These configurations not only optimize steel usage but also enhance the effectiveness of fire protection measures, thereby bolstering the structural integrity under fire. This research is an advancement in diagrid design, providing a framework that effectively marries structural efficiency with fire safety considerations, enabling the design of safer, more efficient high-rise buildings.

Keywords: Diagrid Structural System, Layout Optimisation, Fire Structural Resistance, Computational Structural Analysis

1 INTRODUCTION

The diagrid structural system, characterised by its diagonal grid design, has become a prominent feature in medium to high-rise buildings, offering architectural elegance and resource efficiency. This popularity arises from the flexibility in topology, enabling innovative and aesthetically pleasing designs[1].

Since 2005, there has been significant research into optimising diagrid structures. This study follows the methodology outlined in Figure 1, which focuses on designing the diagrid structural system [2]. This work implements diagrid's layout based on two key approaches: stiffness-based and strength-based design [3].

¹ PhD Candidate, The University of Queensland, Brisbane, Queensland, Australia,
e-mail: zhiruoyu.wang@uq.edu.au, ORCID: <https://orcid.org/0000-0003-4149-8477>

² Dr, The University of Queensland, Brisbane, Queensland, Australia,
e-mail: a.orabi@uq.edu.au, ORCID: <https://orcid.org/0000-0001-5083-3623>

³ Dr, Delft University of Technology, Delft, Netherlands,
e-mail: Z.Nan@tudelft.nl, ORCID: <https://orcid.org/0000-0001-8189-5448>

⁴ Dr, The University of Queensland, Brisbane, Queensland, Australia,
e-mail: matthew.mason@uq.edu.au, ORCID: <https://orcid.org/0000-0003-4622-693X>

⁵ Prof, Chongqing University, Chongqing, China
e-mail: wywang@cqu.edu.cn, ORCID: <https://orcid.org/0000-0002-8607-3379>

⁶ Assoc. Prof, The University of Queensland, Brisbane, Queensland, Australia,
e-mail: d.lange@uq.edu.au, ORCID: <https://orcid.org/0000-0002-4551-1045>

This approach enables a determination of both the required layout and the required size of the diagrid elements. These studies are based on an understanding of the diagrid's response to fire, leading to more optimal designs. However, this optimisation research is fundamentally based on the principle of maximising material efficiency within structural systems considering ambient temperature response.

This study aims to extend the optimisation methodology to the structural fire resistance field. Building on an existing approach to optimisation, the research will focus on the response and performance of the diagrid in various fire sizes and stages. The objective is to identify a methodology for determining optimal overall diagrid layout among several representative layouts, as shown in Figure 1, by considering the local and global response of the system. Studies are planned to explore the effects of varying fire sizes and locations on diagrid systems. The research will also investigate the relationship between local and global collapse, as well as redundancy, providing insights into the behaviour of diagrid systems in fire. A key aspect of this research will be the examination of different overall layouts of the diagrid system. This exploration aims to discover optimal trends in angle variation between the diagrid element and beam, with a focus on performance in fire.

These findings could lead to design solutions that balance material efficiency and fire safety. This work aims to contribute to provide new methodologies for designing safer and more efficient diagrid systems in the face of fire challenges.

2 METHODOLOGY

2.1 Structural Model Approach

The methodology to understanding the fire safety performance of diagrid systems in high-rise buildings incorporates a Python script within the Grasshopper environment. This integration allows to model the topology of the diagrid structure. Inspired by the iconic 30 St Mary Axe building, the initial models are defined using Rhino and Grasshopper, with the Python script used to define the element geometry based on the angle of the diagrid. These models were then imported into GiD for finite element analysis via OpenSees in Fire for structural and heat transfer analysis. OpenSees for fire has been validated in previous studies by teams at the University of Edinburgh and Hong Kong Polytechnic University [4-6], and has been used effectively in hybrid simulations [7-9]. A novel aspect of the model presented in this work is the inclusion of a representative floor structure that incorporates outrigger beams extending from diagrid nodes to the central core, modelled with 500 mm x 500 mm x 70 mm rectangular hollow sections (RHS) and I-section floor beams. This design choice allows for an analysis of the diagrid's independent response. By omitting the columns of the core, the core primarily functions in transferring horizontal loads to the diagrid, emphasizing the role of the external structure [10].

All beam elements were modelled with the OpenSees displacement-based Beam-column element, and the steel was modelled using the Steel01Thermal material model in OpenSees, with a yield stress of 500 MPa, an initial elasticity of 200 GPa, and a strain-hardening ratio of 0.15. The density was set at 7850 kg/m³. For the concrete slab, the shell elements employed were ShellNLDKGQThermal with the CDPPlaneStressThermal concrete damage plasticity material. This choice is suitable for concrete structures in OpenSees, incorporating reduction factors and thermal expansion properties as defined in Eurocode 2. The concrete material has a density of 2400 kg/m³. The slab thickness is 160 mm for all models.

The structural analysis of the diagrid system encompassed both static and dynamic intervals. During the static interval, a load-controlled integration employing the Band General system of equations was utilized for mechanical load analysis. This approach incorporated the reverse Cuthill-McKee numbering technique, a transformation constraints handler, and the Full Newton-Raphson algorithm for solving equations. In the dynamic interval, a comparable load-controlled method was applied, but with the UmfPack system of equations. The same numberer and constraint handler were used for both mechanical and thermomechanical dynamics analyses. For the thermal mechanical analysis, the Newmark method, using parameters $\gamma=0.5$ and $\beta=0.25$ [6], was employed for integration, alongside the Krylov Newton algorithm for equation solving. The time of for the fire scenario was scaled by a factor of 1/1000 for implicit dynamic analysis in OpenSees [11].

2.2 Layout Approach

The structure is based on the 30 St Mary Axe building, with various layouts of diagrid defined based on stiffness-based design method [2, 3], with angles of 62°, 69°, 75°, and 82° for the diagrid configuration as shown in Figure 1 [10]. This allowed for a comprehensive analysis of diagrid performance under different geometric conditions.

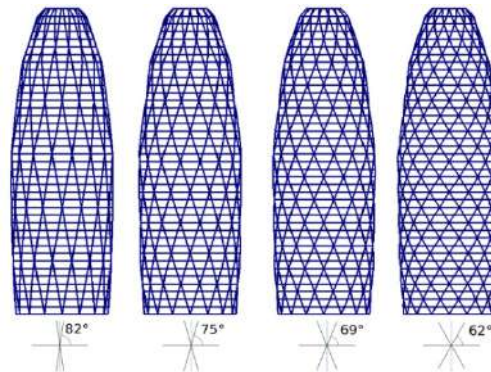


Figure 1. Structural layout with various diagonal angles

The parametric model built represents a 40-story structure, with dimensions adjusted to capture the building's narrowing profile from base to top. The implementation of a Python script within the Rhino+Grasshopper environment allowed modelling the diagonal elements of the diagrid, ensuring representation of each layout's characteristics. This included varying dimensions and mechanical properties across different heights, as well as the integration of a representative floor structure for a more realistic analysis of the diagrid system under various loading conditions, including fire scenarios.

2.3 Fire Scenarios

The diagrid was exposed to various localized fire scenarios. The locations of the fire were chosen to analyse the response of the diagrid to heating of one or more members on a single floor, as well as scenarios involving five, eight, or twelve members plus chords on multiple floors. These combinations of heated elements were considered on either the 19th or 20th floor. The heating of the composite floor system in these models was ignored, focusing instead on the external grid itself. Given that the model is composed of steel, its behaviour will not be significantly influenced by the rate of heating. Therefore, the results are presented as a function of the average steel temperature.

Table 1. Table of fire cases

Fire scenario case	Description
000	Five diagrid members span on 19F
001	Five diagrid members span on 20F
002	Eight diagrid members span on 19F
003	Eight diagrid members span on 20F
004	Twelve diagrid members span on 19F

2.4 Optimisation Approach

Figure 2 shows a flow chart that describes the process employed in the methodology to balance material efficiency with fire resistance. This methodology integrates a multi-objective optimization approach that encompasses variables including the diagrid angles, the dimensioning of structural elements, and the assimilation of passive fire protection measures.

Central to this methodology is the function $C(m, n)$, representing the core computational analysis for a set of m fire scenarios applied to n diagrid angles, leading to the determination of critical temperatures and

informing subsequent material efficiency analysis. This sequential approach supports the development of the final design, optimizing for both safety and material efficiency. As input, the approach requires the overall design, including the architectural topology. Based on this design, m scenarios are defined which represent the different exposure conditions in terms of heated members. Different diagrid structural layouts (n) are also defined, and then all combinations of m and n are subject to structural fire analysis. Based on this analysis, the critical temperature is identified for the diagrid angles. Finally, based on this critical temperature, for any design fire, passive protection can be specified such that based on a heat transfer analysis the diagrid temperature does not exceed that critical value. It is important to highlight that the critical temperature evaluated and used for specifying the fire protection is not a predefined value but one that emerges as an *output of the structural fire analysis* as explained next.

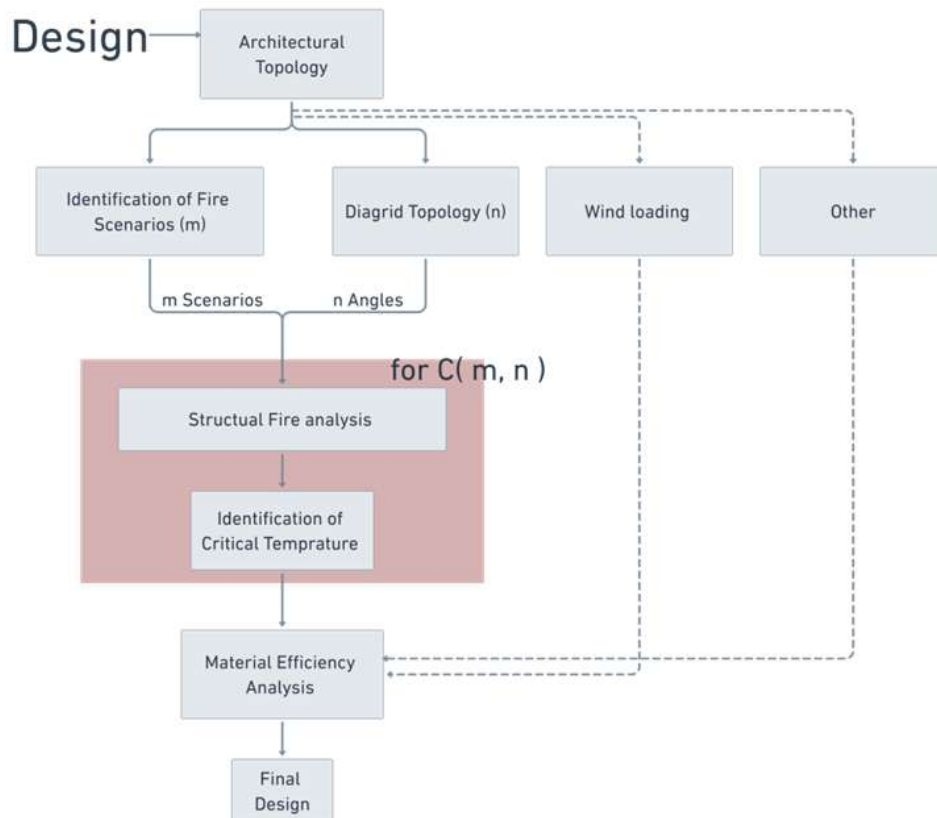


Figure 2. Overall Flow Chart of Optimizing Diagrid Design for Fire Resistance in High-Rise Buildings

As illustrated in Figure 3, Step 1 involves analysing the Z-axis displacement in response to increased steel temperatures, considering different nodes marked A, B, C, and D on a set of diagrid models inspired by the topology of the 30 St Mary Axe building. These nodes provide a measure of the diagrid's structural response to different fire scenarios listed in Table 1. The graph detailing this represents the core of the performed optimization, where the distinct diagrid layouts 62°, 69°, 75°, and 82° are evaluated for their thermal mechanical loading performance under different fire scenarios.

Proceeding to Step 2, the critical temperatures corresponding to peak Z-displacements for each layout angle are plotted, showing the temperature thresholds that result in a downwards translation of the overall structure. Finally, Step 3 extends this analysis across different fire scenarios, allowing the relationship between diagrid angles and the critical temperatures for various fire scenarios to be explored. This stage allows the determination of which layouts provide the most effective fire resistance capabilities. Considerations of steel and fire protection material efficiency are not included at this stage, as we are focusing on identifying the critical temperatures for further specification following heat transfer analysis. Together, these steps allow an assessment to be made of diagrid behaviour under fire, specifically through the identification of a critical temperature of a diagrids elements for varying fire exposures.

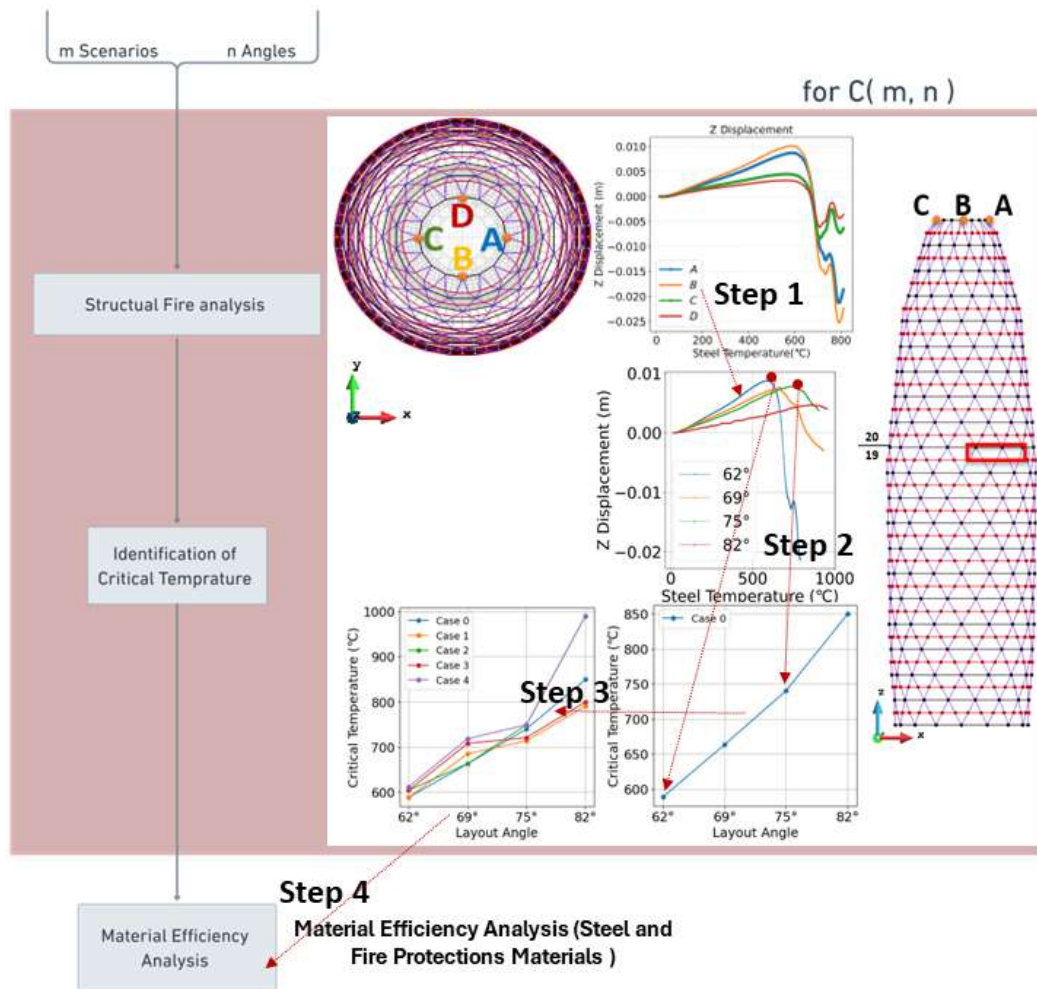


Figure 3. Detailed Flow Chart of Diagrid Structural Analysis and Optimization for Varied Fire Scenarios

3 RESULTS AND OPTIMISATION ANALYSIS

3.1 Evaluation of Diagrid System Under Thermal Mechanical Loading Conditions

The discussion in Section 3.1 lays the groundwork for the optimization approach detailed in Step 1 of Section 2.4 by conducting an evaluation of the diagrid system under thermal mechanical loading conditions. In the discussion of results, the focus is on how fire scenarios affect the displacements along the X, Y, and Z axes at the top of structure. These nodes serve as indicators of the response of the whole diagrid system under thermal load.

The analysis is illustrated using the 62° layout. Fire scenarios ranging from Case 000 to Case 004 were considered, with Case 000 serving as the baseline against which other cases were evaluated.

Central to this analysis are two primary factors: the individual node displacements along the Z-axis at the top of the structure, and the average Z-axis displacements across different cases, which are illustrated in Figure 4 (a) and (b), respectively. Examining these parameters across Cases 000 to 004 reveals critical details about the load-bearing behaviours and the resultant structural reactions of the diagrid system when subjected to fire.

The analysis reveals a progressive increase in the average Z-axis displacements as the number of diagrid members under fire load increases. This trend is clearly discernible when comparing the lower number of members impacted in Cases 000 and 001 with the greater number in Cases 002 and 003. Particularly, the effects of fire become more pronounced at the higher levels of the diagrid. When comparing Cases 002 and 003, the upper portions of the diagrid, being less stiff, show a more significant reaction to fire exposure. This heightened response can be attributed to the reduced mechanical loads and the decreased size of diagrid elements towards the top of the structure. The escalation in response intensity reaches its peak in Case 004,

where 12 diagrid members are exposed to fire, pushing the structure to the brink of failure. This is depicted in Figure 3 (b), which illustrates the critical displacement levels that are indicative of structural collapse.

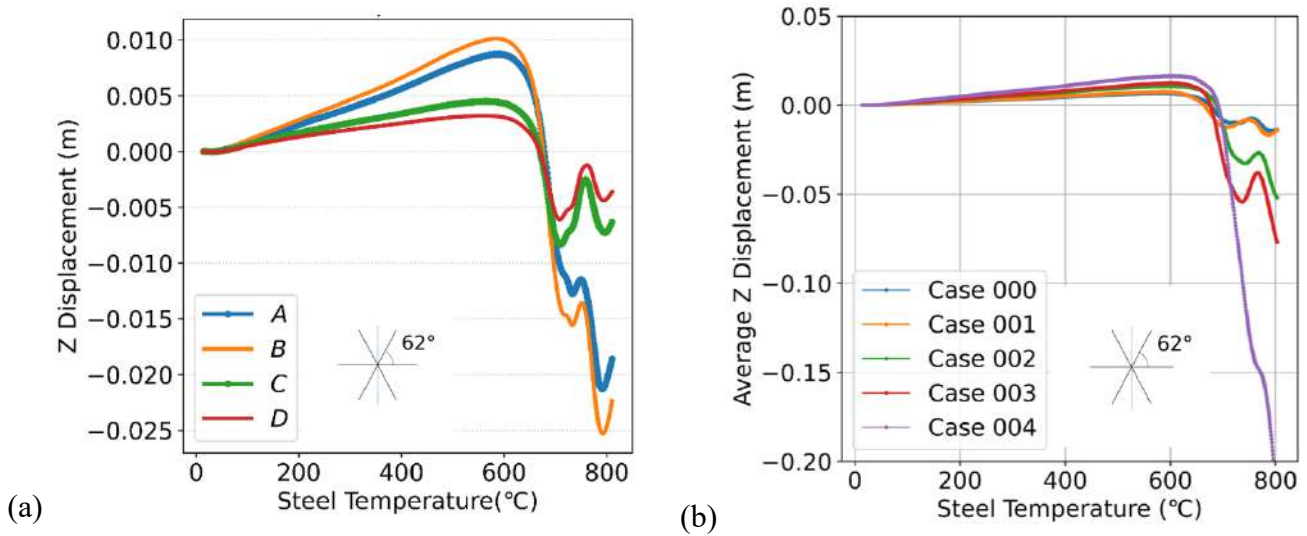


Figure 4. Comparative Analysis of Z-Axis Displacements in 62° Diagrid Structure Layouts under Fire Scenario Case 0 (a) Displacement of Individual Nodes at the Building's Top (b) Average Z-Axis Displacement Across Cases 0-4

3.2 Comparative Analysis of Structural Responses in Varied Fire Scenarios cross different layouts

Building upon the evaluation from Section 3.1, which shows the thermal mechanical loading conditions of the 62° layout, the scope of the analysis is extended to include a broader array of diagrid layouts. This examination facilitates the identification of critical temperature thresholds as a function of the diagrid angle, directly informing the optimization strategies of Steps 2 and 3 as discussed in Section 2.4.

In Figure 5, the Z-axis displacement responses for diagrid layouts at 62°, 69°, 75°, and 82° angles are shown for fire scenarios ranging from Case 0 to Case 4. These graphs expand on the initial analysis by comparing the reactions of these angles to increasing fire scenario intensities.

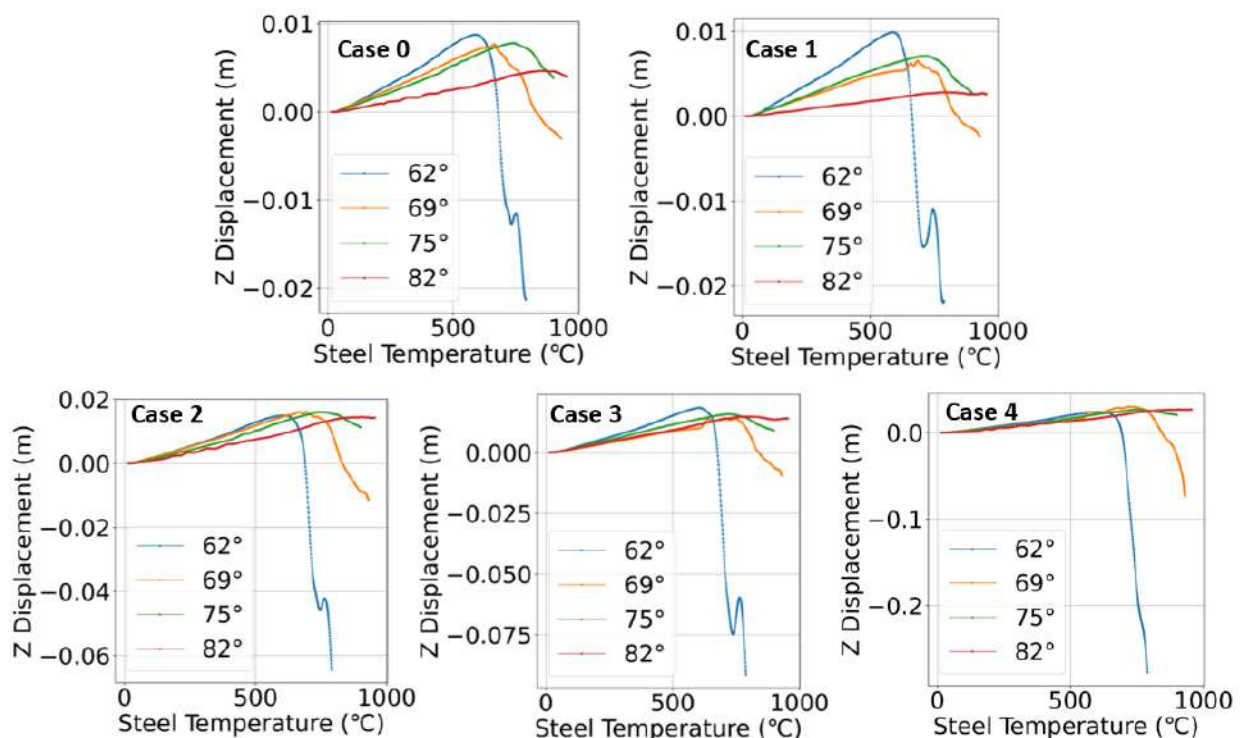


Figure 5. Z-Axis Displacement Responses of Diagrid Structures for Angles 62° to 82° Across Fire Scenarios Case 0 to Case 4

Figure 6 shows the critical temperatures that correspond to peak Z-displacements for each diagrid layout angle. These temperatures mark the thresholds at which structural integrity may be compromised as indicated by the reduction in vertical displacement of the top of the diagrid. From this analysis, two key observations emerge:

- Firstly, the plots clearly demonstrate that as fire scenarios intensify, the critical temperatures associated with peak displacements increase. This observation not only supports the findings from Section 3.1 but also contributes to an improved understanding of how diagrids respond to heat. Specifically, the simultaneous expansion of multiple structural members leads to a reduction in the overall stiffness of the structure, which in turn, results in buckling at higher temperatures.
- Secondly, the analysis of the 82° layout during fire scenarios (Cases 2 and 4) reveals that no failure seems to occur at up to 1000 °C steel temperatures.

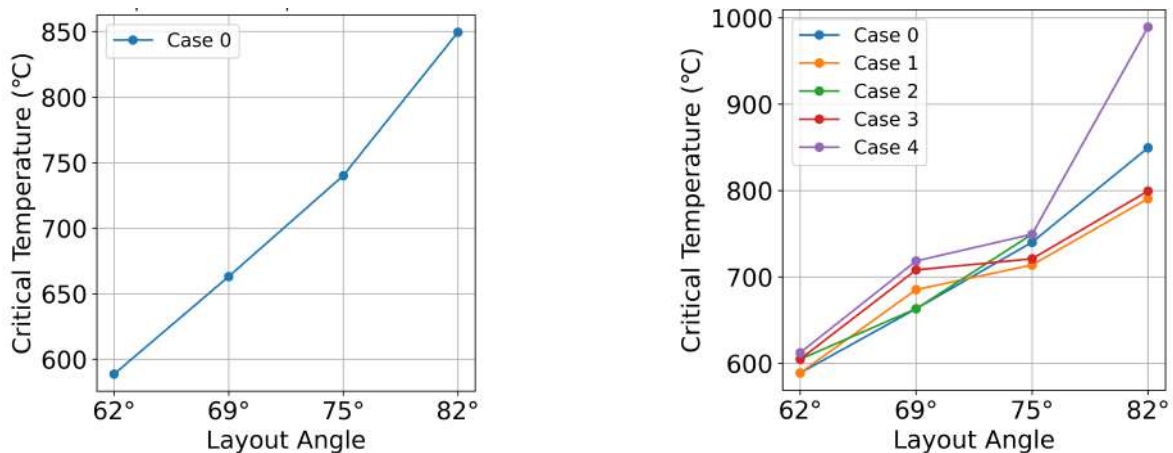


Figure 6. Critical Temperature Thresholds for Peak Z-Axis Displacements Across Diagrid Layout Angles in Fire Scenarios

3.3 Optimisation Analysis

Building upon the analysis of critical temperatures identified for each diagrid layout angle in Figure 6, Figure 8 proceeds to the final optimization phase. This phase incorporates a detailed evaluation of the efficiency of steel materials in relation to the thickness of applied fire protection layers, specifically taking into account the heat transfer characteristics of the protective material.

Figure 8 illustrates a series of heat transfer analyses conducted using OpenSees in fire for diagrid layouts at 62°, 69°, 75°, and 82°. Each graph represents the temperature evolution over a standardized ISO 834 fire exposure period of 120 minutes (while the ISO fire was chosen to illustrate the process, this could include any other definition of a fire suitable for structural analysis), demonstrating how different thicknesses of Cafco300 fire protection material impact the average temperature rise in the steel members. The reason Cafco300 was chosen is because its material properties were clearly provided in and is readily accessible in OpenSees for Fire [12].

The dotted lines in Figure 8 indicate the critical temperatures at which structural integrity becomes compromised for each layout. These critical thresholds allow an optimization of the fire protection strategy. The analysis indicates that optimal fireproofing thicknesses are 25 mm for the 62° layout, 15 mm for the 69° layout, 9 mm for the 75° layout, and 2 mm for the 82° layout. This approach to fire protection upholds the structural safety of each configuration and also maximizes the use of protective materials, allowing for a balance between cost, safety, and structural performance under fire conditions.

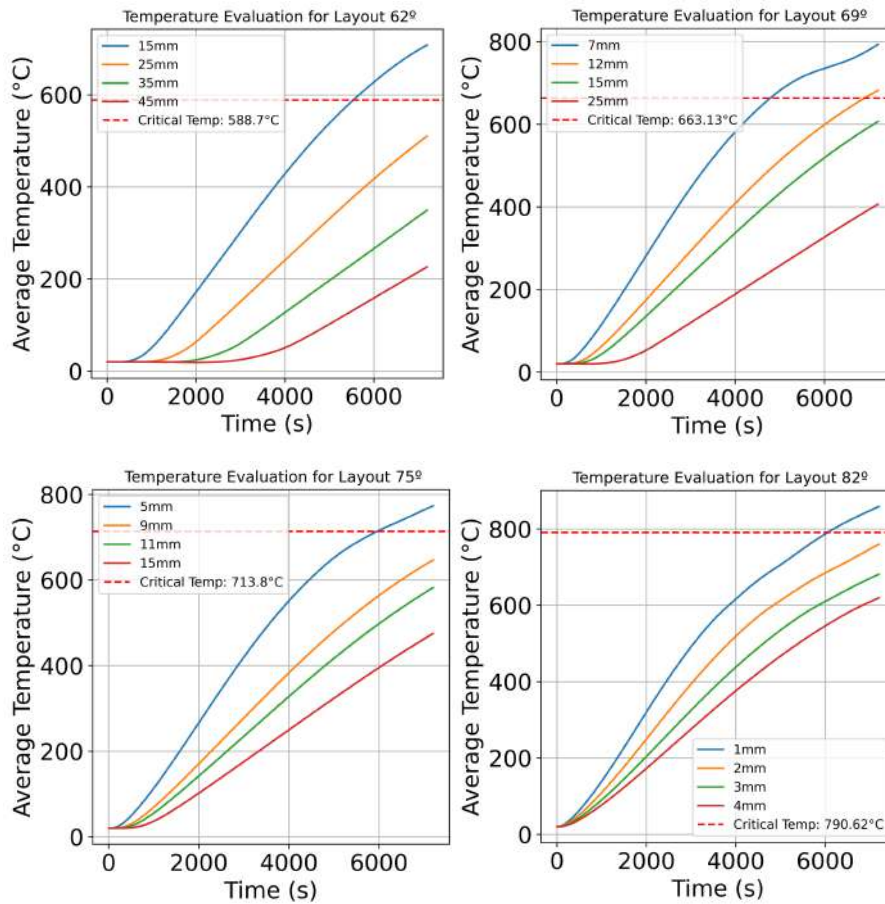


Figure 7. Heat Transfer Analysis of Diagrid Layouts with Variable Cafco300 Fire Protection Thicknesses During a 120-Minute ISO 834 Fire Duration

Continuing from the thermal and structural considerations detailed in Figure 8, the subsequent step in the optimization analysis is visualized in Figure 9, which shifts focus to the material aspects of diagrid construction. This figure presents an evaluation of the volumes of steel (S-Values) and fire protection material (P-Values) for the respective diagrid angles. Notably, a material efficiency trend emerges when comparing the steep increase in steel volume with the declining volume of fire protection material needed as the layout angle increases, with the most significant changes occurring between the 75° and 82° layouts.

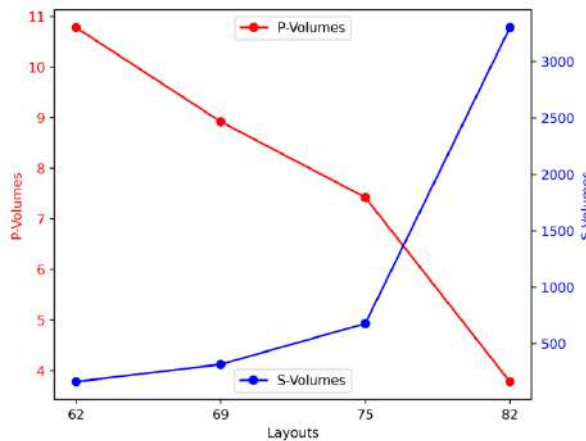


Figure 8. Material Efficiency Analysis: Comparative Volume of Steel and Fire Protection Across Different Diagrid Angles

As noted in the analysis, while there was a direct jump from examining four-floor spans (75°) to seven-floor spans (82°), not all intermediate angles were explored. However, this does not prevent the identification of the 75° to 82° layouts as potentially optimal in terms of material usage. The absence of data for certain angles does not detract from the conclusion that, within this range, a point of efficiency exists, which could inform future research and design of diagrid structures.

4 CONCLUSIONS

An innovative modelling approach, utilizing Grasshopper, Rhino, and Python scripting, has enabled relatively straightforward simulations to be conducted for analysing fire behaviours in diagrid structures. This approach has led to the identification of configurations that optimize material efficiency while ensuring fire safety.

The findings underscore the role of diagrid geometry in thermal response, providing insights for designing fire-resilient buildings. It has been demonstrated that diagrid angles influence structural outcomes under fire loading, with optimized designs achieving a balance between material efficiency and structural integrity. The investigation presented identified configurations that maximize material efficiency and sustain structural integrity when subjected to fire.

Although the focus has primarily been on material volume, the introduction of cost considerations and diverse fire models is viewed not as limitations, but as opportunities to enhance the applicability of the optimization approach. The core success of this optimization strategy remains intact. Looking ahead, it is anticipated that continuing to build on this foundation will further advance the fire safety of diagrid structures, emphasizing the effectiveness and adaptability of the strategy.

REFERENCES

- [1] K. Al-Kodmany and M. M. Ali, "An overview of structural and aesthetic developments in tall buildings using exterior bracing and diagrid systems," *International Journal of High-Rise Buildings*, vol. 5, no. 4, 2016.
- [2] K. S. Moon, J. J. Connor, and J. E. Fernandez, "Diagrid structural systems for tall buildings: characteristics and methodology for preliminary design," *The structural design of tall and special buildings*, vol. 16, no. 2, pp. 205-230, 2007.
- [3] E. Mele, M. Torenio, G. Brandonisio, and A. De Luca, "Diagrid structures for tall buildings: case studies and design considerations," *The Structural Design of Tall and Special Buildings*, vol. 23, no. 2, pp. 124-145, 2014.
- [4] T. Yarlagadda, H. Hajiloo, L. Jiang, M. Green, and A. Usmani, "Preliminary modelling of Plasco Tower collapse," *International Journal of High-Rise Buildings*, vol. 7, no. 4, pp. 397-408, 2018.
- [5] J. Jiang and A. Usmani, "Modeling of steel frame structures in fire using OpenSees," *Computers & Structures*, vol. 118, pp. 90-99, 2013.
- [6] M. A. Orabi, L. Jiang, A. Usmani, and J. Torero, "The collapse of world trade center 7: revisited," *Fire Technology*, pp. 1-28, 2022.
- [7] X. Cai *et al.*, "Dual-3D hybrid fire simulation for modelling steel structures in fire with column failure," *Journal of Constructional Steel Research*, vol. 197, p. 107511, 2022.
- [8] M. A. Khan, L. Jiang, K. A. Cashell, and A. Usmani, "Virtual hybrid simulation of beams with web openings in fire," *Journal of Structural Fire Engineering*, vol. 11, no. 1, pp. 118-134, 2020.
- [9] M. A. Khan, L. Jiang, K. A. Cashell, and A. Usmani, "Analysis of restrained composite beams exposed to fire using a hybrid simulation approach," *Engineering Structures*, vol. 172, pp. 956-966, 2018.
- [10] Z. Wang, M. A. Orabi, Z. Nan, W. Wang, M. Mason, and D. Lange, "The response of diagrid structures to fire," *Fire Safety Journal*, vol. 141, p. 103924, 2023.
- [11] Z. Nan, M. A. Orabi, X. Huang, Y. Jiang, and A. Usmani, "Structural-fire responses forecasting via modular AI," *Fire Safety Journal*, vol. 140, p. 103863, 2023.
- [12] V. Kodur and A. Shakya, "Effect of temperature on thermal properties of spray applied fire resistive materials," *Fire safety journal*, vol. 61, pp. 314-323, 2013.

RESPONSE OF COMPOSITE BRIDGE GIRDERS EXPOSED TO REALISTIC FIRE SCENARIOS USING A DEEP LEARNING BASED APPROACH

Mustesin Ali Khan ¹, Aatif Ali Khan ², Nan Zhuojun ³, Ghazanfar Ali Anwar ⁴, Katherine Cashell ⁵,
Asif Usmani ⁶

ABSTRACT

This paper presents an accurate and predictive framework for evaluating composite bridge performance under realistic fire scenarios by exploiting CFD-FE coupling and advanced ANN modelling capabilities. A series of realistic fire scenarios are developed by conducting CFD simulations. Various parameters affecting the fire behaviour are included in CFD model such as bridge soffit height, fire intensity, and fire location along the bridge span. The time-temperature history obtained from CFD simulations is coupled with Finite Element (FE) model to analyse the structural performance of composite bridges with different thicknesses of fire protective coatings. While performing CFD and FE simulations is a tedious and computationally expensive task, an ANN model is trained on simulation data to provide rapid predictions of structural fire response of composite bridges. The ANN model proposed in this study predicts crucial parameters such as failure time, failure temperature and vertical displacement behaviour for assessing structural performance and safety of composite bridges during fire events. This enables fire safety engineers to quickly evaluate the structural response under numerous fire scenarios and corresponding design alternatives, resulting in an efficient decision-making tool in bridge fire design and fire safety assessment.

Keywords: Bridge fire; machine learning; CFD-FEM coupling, failure forecasting, ANN

1. INTRODUCTION

One of the greatest potential risks to the structural integrity and safety of composite bridges is a fire event. In order to understand the structural fire response of bridges, the majority of previous studies employed prescriptive fire scenarios [1–8]. Almost all international engineering regulations and guidelines recommend utilising standard fire curves, including the Hydrocarbon (HC) [9] and ISO 834 [10] fire curves. This has historically been regarded as a conservative depiction of a real fire scenario [11]. Xu and Mao [12] performed a numerical study to understand the fire resistance of steel-concrete composite girders, under ISO834 and HC fire conditions. Paya et al. [13] also assumed non-realistic fire exposures such a HC fire and also Stoddard's fire in their numerical analysis. These fire scenarios are highly conservative in terms of peak temperatures and the extent of application because they assume that the entire bridge span was exposed to a uniform temperature. Aziz et al [14] combined experimental and numerical methods to

¹ Lecturer, Ras Laffan Emergency and Safety College, University of Central Lancashire

e-mail: makhan21@uclan.ac.uk, ORCID: <https://orcid.org/0000-0003-2562-9916>

² Lecturer, University of Canterbury,

e-mail: aatif.khan@canterbury.ac.nz, ORCID: <https://orcid.org/0000-0001-9181-4795>

³ Post-doctoral, TU Delft

e-mail: z.nan@tudelft.nl, ORCID: <https://orcid.org/0000-0001-8189-5448>

⁴ Post-doctoral, Hong Kong Polytechnic University

e-mail: ghazanfar-ali.anwar@connect.polyu.hk, ORCID: <https://orcid.org/0000-0002-2499-0999>

⁵ Associate Professor, University College London

e-mail: k.cashell@ucl.ac.uk, ORCID: <https://orcid.org/0000-0003-2804-4542>

⁶ Professor, Hong Kong Polytechnic University

e-mail: asif.usmani@polyu.edu.hk, ORCID: <https://orcid.org/0000-0003-2454-5737>

evaluate the fire behaviour of standard steel girders that are frequently used in bridge construction. Three steel-concrete composite girders were tested for simultaneous loads and ASTM E119 fire exposure as part of the investigation. However, the standard fire scenario employed was shown to not offer an appropriate solution because of the fact that bridge structures are situated in open spaces, which bear no resemblance to the compartments with limited ventilation upon which the “standard fire” is based. In another study, Song et al. [8] investigated how prestressed concrete box bridge girders behaved when exposed to fire. They developed a 3D nonlinear finite element model of the prestressed concrete box bridge girder using the ANSYS software.

There are advantages to prescriptive fires including their simplicity for use and large data base of existing analysis for comparison. However, they do not realistically reflect real-world situations when used for bridges. These fires offer regulated testing environments but fall short of accurately simulating the dynamic nature and unpredictability of real fires. There are various factors which makes real bridge fires significantly different from prescriptive fires. Prescriptive bridge fires generally assume uniform heating of the entire bridge component(s) which is rarely the case in reality i.e., the part of the bridge girder in the vicinity of a burning vehicle experiences higher temperatures compared to other locations [15]. Prescriptive fires also ignore parameters that govern fire behaviour such as the location of the fuel along the span and the bridge geometry (mainly height). Placing the fuel load at different locations along the span may result in completely different fire scenarios and corresponding structural responses. If the fuel is placed near the abutment, for example, it may result in lower temperatures as the released fuel vapours travel away from the source seeking sufficient air for burning as there is less air for fuel vapour to burn near the abutment [15]. The detailed analyses of bridge performances under these uniform or prescriptive fires are potentially unrealistic and can be over conservative. A heterogeneous fire model is therefore needed to develop a performance-based design approach. This can be achieved using fire inputs from Computational Fluid Dynamics (CFD) models. Nevertheless, few studies have employed CFD modelling to estimate the fire loads in bridge structures in a realistic manner. A common CFD software for fire is the Fire Dynamics Simulator (FDS) [16], which is an open-source package developed by NIST.

Xu et al.[12] performed a study by coupling a thermomechanical finite-element model (FEM) with a CFD fire model to determine the structural fire response of steel box bridges. The numerical results represented the localized thermomechanical response of the fire exposed segments as well as the global response. Timilsina et al. [17] studied the post-fire behaviour of a concrete bridge in Irving, Texas. CFD analysis was performed to estimate the peak temperature and a generalised fire curve similar to a HC fire was proposed and used as the thermal boundary condition for the heat transfer analysis. However, the temperatures obtained using the CFD simulations were not used for the heat transfer analysis; instead, the entire span was exposed to the same temperature as a generalised fire. A performance-based framework for designing bridge structures under vehicle-induced fire was proposed by Rujin et al. [18]. CFD based fire scenarios were used to analyse the fire response of a cable stayed bridge. It was demonstrated that additional fire protective measures are required to reduce the burning time and associated fire maintenance costs. A realistic fire scenario was also developed by Moya et al. [19] for the I-65 overpass in Birmingham, USA using CFD simulations. The influence of a realistic fire versus a standard fire was studied. It was observed that prescriptive fires do not accurately represent a realistic fire owing to their uniform application along the whole length and also because they neglect fire decay.

Although CFD simulations can generate realistic fire scenarios, performing CFD simulations is a complex and computationally expansive process. Using the results obtained after performing CFD simulations as thermal boundary conditions in FE models to understand the structural fire response is also a challenging problem. Therefore, in this paper, a computationally cost-effective framework, “OpenFIRE” [20], which can couple CFD and FEM, is utilised to generate a database for training an artificial intelligence (AI) model capable of predicting the structural response of composite bridges under realistic fire scenarios.

2. MODEL VALIDATION

In this paper, the I-65 Birmingham bridge fire incident is considered as a case study. A simplified geometrical model of the I-65 Birmingham bridge is generated in the Fire Dynamics Simulator (FDS) software (a widely

used CFD based fire simulation tool) as shown in Fig. 1. The input parameters, such as material properties and soot yield are adopted from the values given by Moya et al. [21]. Additional information regarding the CFD model, such as mesh sizes and boundary conditions, can be found in [22]. To capture the temperature profiles along the bridge span, adiabatic surface temperature (AST) devices are installed at regular 1m intervals. Fig. 2 shows the AST temperature profiles in the near field (location of girder which was engulfed in flames) and far-field (15 m away from the fire location, where the girder was heated mainly by smoke). It is clear that there is a significant difference in temperature between these two locations.

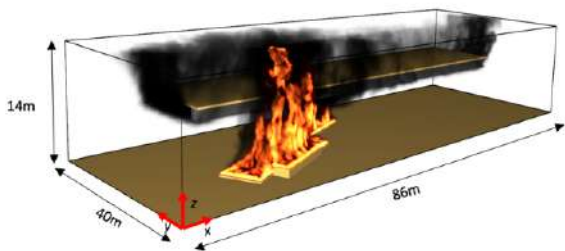


Figure 1. Computational domain for CFD simulation

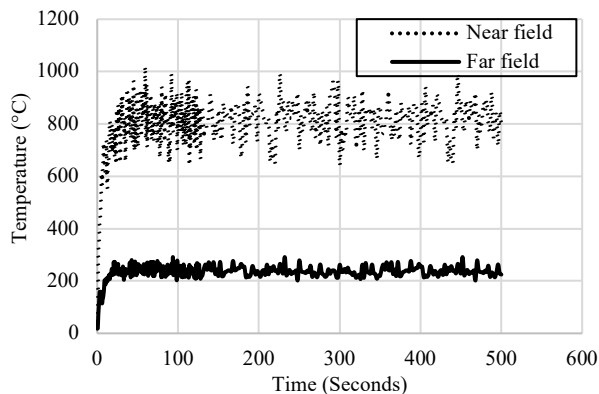


Figure 2. AST temperatures obtained from FDS at the near field and far-field

After establishing realistic fire scenarios using FDS simulation, a finite element (FE) model of the bridge is developed using the Abaqus software to predict the thermomechanical response. The 37m central span of the bridge is mainly exposed to the fire during the incident. The yield strength of the steel is 350 N/mm^2 . The concrete slab is 170mm in thickness and has a compressive strength of 40 N/mm^2 [21]. The thermal properties of the steel and concrete are assigned in accordance with the Eurocode [23]. The AST obtained from FDS simulations are applied at different locations along the bridge span as thermal boundary conditions in the FE model using a middleware “OpenFIRE” developed by Khan et. al. [20].

Fig. 3 illustrates the resulting midspan deflections of the bridge span. After approximately 12mins, there is a sudden increase in deflection followed by failure of the bridge; this is mainly attributed to the loss of strength of the steel girder which has reached a temperature of $800 \text{ }^\circ\text{C}$ at this point; this observation is in agreement with the literature [21]. Moreover, the deflected shape of the bridge is also in agreement with the real fire accident as shown in Fig. 4. Therefore, it is shown that a realistic fire scenario can be developed using CFD simulations, and these can then be used predict a reasonable estimation of the fire resistance of bridge structures.

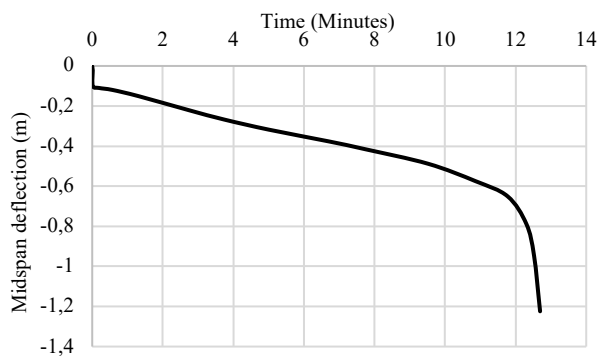


Figure 3. Maximum span deflection-time behaviour with HRRPUA of 2500 kW/m^2

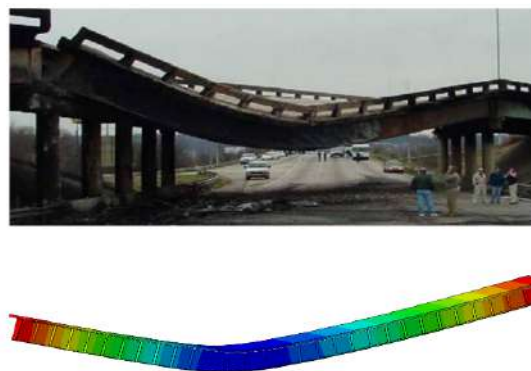


Figure 4. Deformed shape of the bridge in the real fire accident [21] and the FE simulation[22]

3. DATABASE FOR TRAINING THE ANN

In this study, a numerical database is generated to train an Artificial Neural Network (ANN) model which can predict the thermomechanical response of composite bridges exposed to realistic fire scenarios. The process involves conducting a series of FDS simulations and Finite Element (FE) simulations, to generate a comprehensive database for training the ANN. In the first step, FDS simulations are performed to generate different fire scenarios by varying heat release rates (HRRs), bridge soffit heights, and fuel placements along the bridge span. Table 1 shows all the perimeters considered to generate the database. Considering all the parameters used to generate the database, a total of 108 cases are modelled. The parameter values are selected in order to represent realistic fire scenarios associated with oil tanker fires under bridges. This study demonstrated the tanker fire, however in further studies different vehicles sizes such as cars, light goods vehicles, and heavy goods vehicles would also be included. The 60 MW, 80 MW, and 100 MW of HRRs are derived from average HRR values for fires involving tanker trucks that transport gasoline or diesel fuel [15,24]. These fire intensities range from fire sizes that are large to those that are extremely large. The height of bridge soffit from top surface of the fuel can vary significantly depending upon the size of the tanker and the height of the bridge. The soffit height represents the distance between the top of fuel source (e.g., fuel tanker) to the soffit of the bridge. The potential soffit heights from top surface of the fuel used in this study are of 2m, 3.5m, and 5m. The mid-span, quarter-span, and end-span fuel placements are selected to capture the effects of fire location on the bridge girders' structural response. As the most crucial location in terms of possible damage level, the fire location has been set at mid-span to measure the heat flux resulting from the fire exposure caused by an accident below the centre of span (maximum bending moment location). The fire location closest to the abutment (end-span) is anticipated to test the bridge superstructure's decreased shear capacity as end-span is the location of maximum shear force. As a middle case, the quarter point under span is also examined. In the next step, these fire scenarios are coupled with a FE heat transfer model using the OpenFIRE framework [20]. There are four fire protection levels included in the finite element model: 0mm, 5mm, 8mm and 12 mm. The effectiveness of various insulation strategies under extreme tanker fire scenarios can be evaluated by evaluating multiple protection levels. CAFCO 300 has been used as the fire protection as various researchers have found that CAFCO 300 is an excellent fire protection material [25][26] Temperature-dependent thermal properties of CAFCO 300 such as conductivity and specific heat are utilised as recommended by Bentz and Prasad [26]. Subsequently, sequentially coupled thermomechanical analyses are performed to evaluate the structural fire response of the composite bridge girders.

A comprehensive dataset is generated by conducting simulations for all combinations of these parameters. Table 2 shows the details of the first 27 cases with no fire protection (0mm). The subsequent cases with fire protection levels of 5mm, 8mm, and 12mm follow a similar pattern with 27 cases for each protection level. Using this large dataset, an ANN can be trained to predict the structural fire response of composite bridges under different fire scenarios and protection levels without the need for computationally expensive CFD and FE simulations. The use of the generated ANN model in the design and assessment of fire-resistant composite bridge structures results in increased safety and resilience in infrastructure.

Table 1. Parameters used to generate the database for the AI model

Fire Size (HRRPUA) MW/m ²	60, 80, 100
Height of bridge from top surface of fuel (m)	2, 3.5, 5
Location of the fire	Mid-span, quarter-span, and end-span
Fire resistive ratings (mm)	0, 5, 8, 12

Table 2. Detailed parameters for the first 27 cases with 0 mm fire protection

Cases	HRR MW/ m ²	Height (m)	Location	Fire Protection	Cases	HRR MW/ m ²	Height (m)	Location	Fire Protection
1	60	2	Mid	0mm	15	80	3.5	End	0mm
2	60	2	Quarter	0mm	16	80	5	Mid	0mm
3	60	2	End	0mm	17	80	5	Quarter	0mm
4	60	3.5	Mid	0mm	18	80	5	End	0mm
5	60	3.5	Quarter	0mm	19	100	2	Mid	0mm
6	60	3.5	End	0mm	20	100	2	Quarter	0mm
7	60	5	Mid	0mm	21	100	2	End	0mm
8	60	5	Quarter	0mm	22	100	3.5	Mid	0mm
9	60	5	End	0mm	23	100	3.5	Quarter	0mm
10	80	2	Mid	0mm	24	100	3.5	End	0mm
11	80	2	Quarter	0mm	25	100	5	Mid	0mm
12	80	2	End	0mm	26	100	5	Quarter	0mm
13	80	3.5	Mid	0mm	27	100	5	End	0mm
14	80	3.5	Quarter	0mm					

3.1 Structural fire responses obtained from the FE models

In this section, effect of various parameters such as HRR, bridge height, fuel location and fire protection thickness on the structural fire response of composite bridge girders have been studied. In bridges subjected to fire conditions, the occurrence of runaway vertical displacement is a crucial sign of potential structural failure. A sudden and uncontrollably increasing vertical displacement resulting from reduction in load carrying capacity is known as runaway vertical displacement. It is observed that the structural response in the form occurrence of runaway displacement, time and temperature at the onset of runaway displacement is influenced by the interplay of multiple factors.

3.1.1 Effect of heat release rate and bridge soffit height

The three different HRR values that are taken into account in the simulations were 60 MW, 80 MW, and 100 MW. These values ranges from moderately large to extremely large fire sizes, which are typical of tanker truck fires that carry either gasoline or diesel fuel. As expected, higher HRRs have resulted in more severe fire scenarios and rapid reduction in the load carrying capacity of the composite bridge. This is shown in the results, where cases with higher HRRs (80 MW and 100 MW) showed earlier runaway occurrences and higher temperatures at the onset of runaway displacement than cases with lower HRRs (60 MW). For example, in cases with 0mm fire protection, the runaway for Case 4 (60 MW), happened at 732 seconds, compared to 466 seconds for Case 22 (100 MW) at the mid-span location as shown in Fig.5. Moreover, a noteworthy distinction in performance is observed between cases with higher fire protection (12 mm) and those with lower HRRs. Throughout the simulation period of 5400 seconds, no runaway displacement failure is observed for the 60 MW HRR (Case 85). On the other hand, runaway failure happened at 4405 seconds for the 100 MW HRR (Case 103) as shown in Fig.5, suggesting that intense 100 MW fire eventually overwhelmed the protective insulation, resulting in a structural failure.

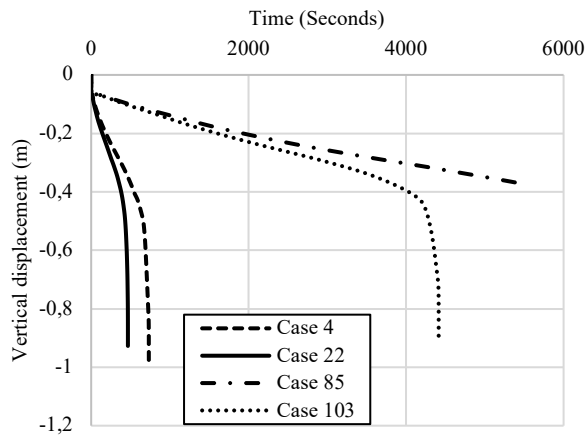


Figure 5. Vertical displacement variation of composite bridge under different HRRs in cases with and with 0mm protection

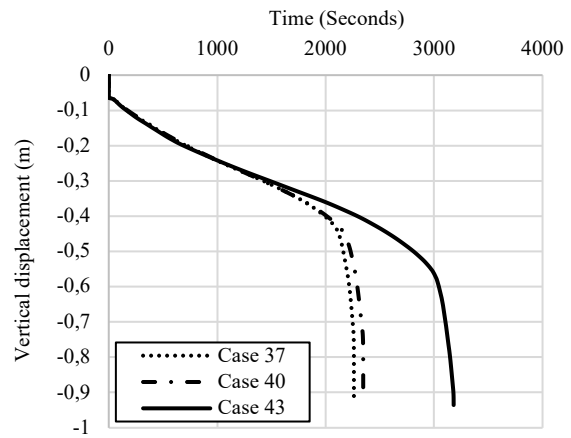


Figure 6. Vertical displacement variation of composite bridge for different bridge soffit heights

The soffit height represents the distance between the top of fuel source (e.g., fuel tanker) to the soffit of the bridge. Three heights are considered: 2m, 3.5m, and 5m. The higher soffit heights from the fuel top surface tended to result in lower temperature and delayed failure (runaway displacement) compared to lower heights. For lower soffit heights, flames can reach and impinge the beam and slab directly, whereas for higher soffit heights, the flame might not reach directly or have less impact. This has resulted in a reduced thermal exposure on the bridge structure for larger soffit heights, ultimately leading to delayed runaway and lower temperatures. For example, in the case of 80 MW HRR (Case 37), the runaway occurred at 2255 seconds for a height of 2m, and 3176 seconds for (Case 43) with soffit height of 5m, as shown in Fig.6.

3.1.2 Effect of fuel placement and fire protection level

The structural response is also influenced by the location or placement fuel source (mid-span, quarter-span, or end-span) along the bridge span. When compared to fires at the end-span, those at the mid-span or quarter-span typically produced an earlier start to runaway. For example, in the case of 80 MW HRR with 5mm fire protection and soffit height of 3.5m, the runaway occurred at 2344, 2369 and 4973 seconds for Case 40, Case 41 and Case 42 (mid-span, quarter-span and end-span) respectively as shown in Fig.7.

The vertical displacement profiles and stress distributions along the span provide an explanation for this. In comparison to end-span fires, mid-span fires usually expose a greater area of the bridge girders to direct heat and burn more effectively. Because of the confined space near the end supports, less area of the bridge is heated compared to the mid-span and quarter span cases. Additionally, mid-span being the region of maximum bending moment, when the fuel is placed at the centre of the span, a reduction in flexural load carrying capacity results in accelerated runaway failure.

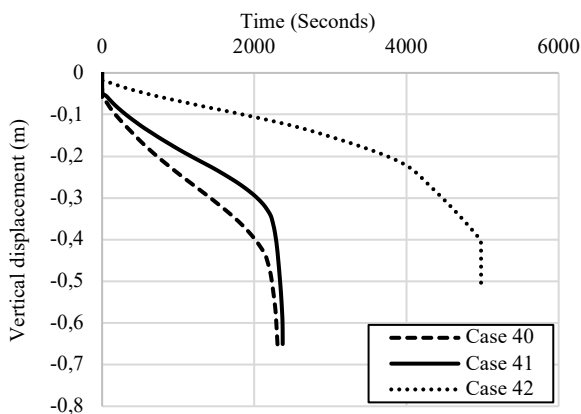


Figure 7. Vertical displacement variation of composite bridge for different fuel placements along the bridge span

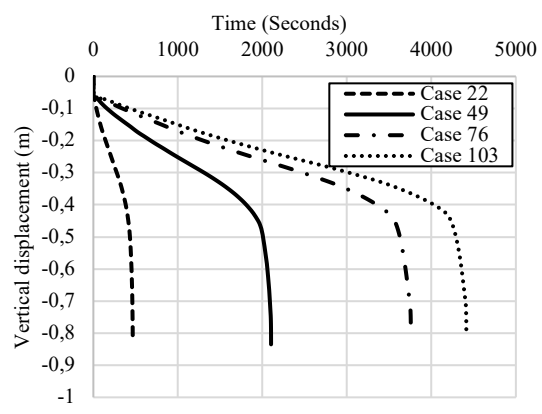


Figure 8. Vertical displacement variation of composite bridge for different level of fire protection

With an increase in fire protection thickness, the onset of runaway is delayed in all the cases and there are fewer instances of runaway failures. Runaway displacement is observed in the majority of cases with either no fire protection (0mm) or lower protection levels (5 mm and 8 mm), indicating that the composite bridge is unable to maintain stability due to its reduced load-carrying capacity under severe thermal exposure. However, the onset of runaway deflection is significantly delayed, or even prevented, within the simulation time frame, as the fire protection thickness increased to 12mm. For example, in the case of 100 MW HRR at the mid-span location with bridge soffit height of 3.5m, runaway displacement happened in 466, 2102, 3749 and 4404 seconds for 0mm protection, 5mm, 8mm, and 12mm fire protection (Case 22, Case 49, Case 76 and case 103), respectively as shown in Fig.8.

4. DEVELOPMENT OF THE MACHINE LEARNING (ML) MODEL

4.1 Overview of ML models

Given the catastrophic consequences of bridge failures, early-warning systems play a crucial role in preventive measures and emergency planning. This study introduces ANNs for forecasting fire-induced bridge collapses. It develops two interconnected machine learning models as a two-step predictive framework, as presented in Fig. 9.

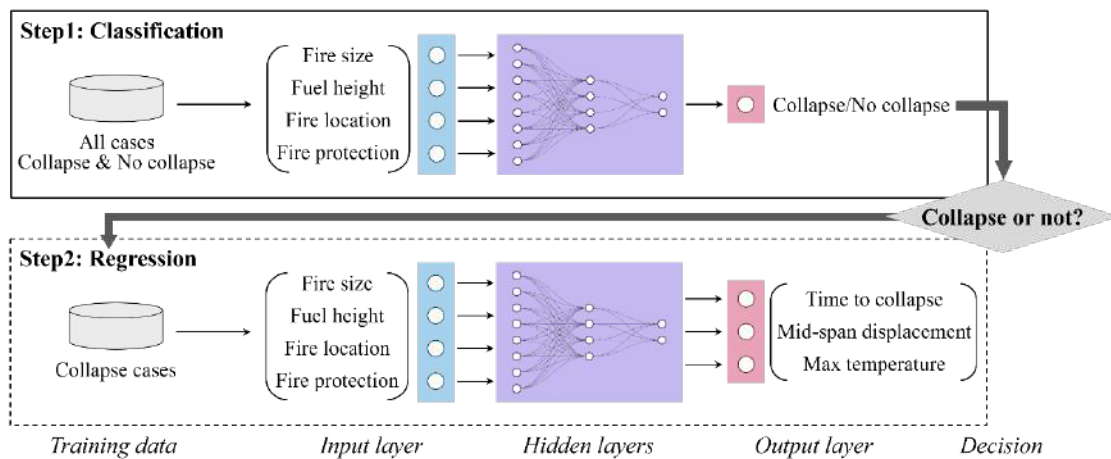


Figure 9. Schematic of the interconnected ML models for classification and regression tasks

The models, constructed using PyTorch, share a similar architectural design but are tailored for different objectives: classification and regression tasks. First, the binary classification model predicts the likelihood of bridge collapse, specifically, whether the bridge will collapse or not under fire. Subsequently, activated by a positive collapse prediction, a regression model estimates the critical failure time (i.e., when a collapse is imminent) and critical failure indicators, including mid-span vertical displacement of the bridge and maximum temperature at the time of collapse. The dataset comprises 108 cases, each characterised by four input features related to fire characteristics and structural parameters: fire size (i.e., HRR), soffit height, fire location, and thickness of fire protection layers. These features serve as inputs for both models. The dataset undergoes preprocessing with standard normalisation techniques to scale the input features, ensuring effective model training. Both ANN models adopt similar architectures, comprising three fully connected layers with decreasing units of 128, 64, and 32, following the input layer. Rectified Linear Unit (ReLU) and dropout layers with a rate of 0.1 are employed for each hidden layer. The dataset is then divided into training, validation, and testing sets, with allocations of 60%, 20%, and 20%, respectively. During the training process, separate loops are established for each model, incorporating loss tracking and early stopping based on validation loss to prevent overfitting. Binary Cross Entropy (BCE) loss and Mean Squared Error (MSE) loss are used for tracking the validation loss for the classification and regression models, respectively. As shown in Fig. 10, the performances of the ML models during training are evaluated. It was found that 185 epochs with a learning rate of 0.0001 and 570 epochs with a learning rate of 0.001 are sufficient for the classification and regression models, respectively.

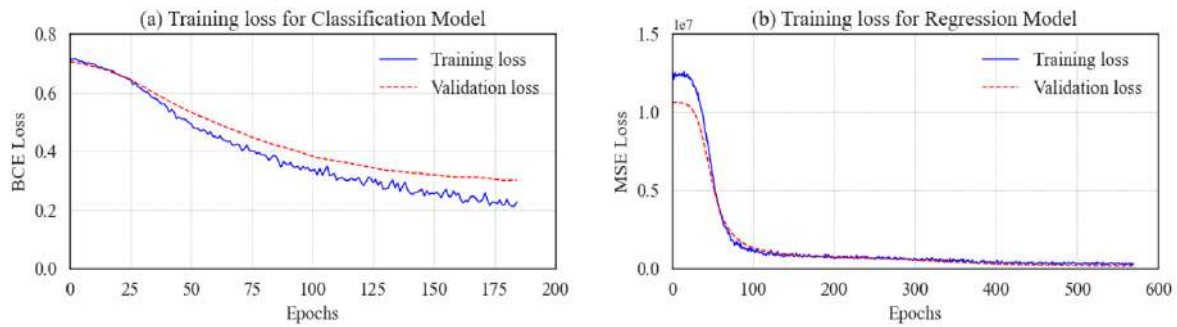


Figure 10. Evaluating the performance of ML models during training

4.2 Performance Evaluation of FE-based ML models

The performance of the two-step ML models was evaluated using a hold-out testing set, highlighting their potential as reliable predictive tools for fire-induced bridge collapses. As shown in Fig. 11, the classification model achieved good accuracy in distinguishing between ‘collapse’ and ‘no collapse’ cases, with accuracy and precision of 0.86 and 0.83, respectively. A recall value of 1 indicates that no collapse cases were missed, meaning our classification model successfully predicted all dangerous bridge collapse cases. However, there were three false predictions where collapses were forecasted, but no collapses occurred according to the simulation results. Such discrepancy could affect the performance of the subsequent regression models.

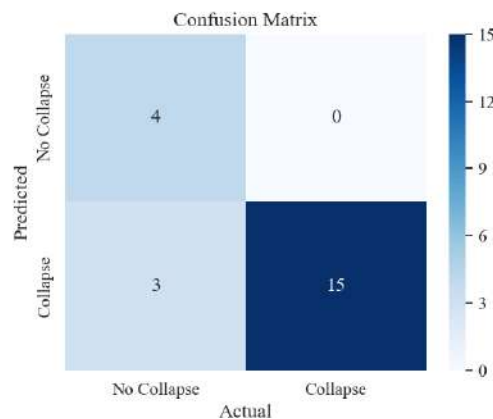


Figure 11. Confusion matrix of prediction results for fire-induced bridge failure, distinguishing between ‘Collapse’ and ‘No Collapse’ cases

The regression model provided good estimates of failure times. Fig. 12(a) shows that the predicted failure times closely align with the dashed line that representing the ideal fit, with an average prediction error of only 248 seconds. An R-square value of 0.96 suggests that the model captures a significant proportion of the variance in the data, indicating its effectiveness in predicting the critical failure time of fire-induced bridge collapses. However, the performance of the regression model in predicting the mid-span vertical displacement trigger for collapse and the maximum temperature at collapse was poor. Figs 12(b) and (c) indicate that the predictions significantly deviate from the actual values, potentially resulting in misleading conclusions. The previously mentioned false collapse predictions, where simulations indicated no collapse, likely introduced noise into the training dataset for the regression model. This issue highlights the need for further research to refine the models.

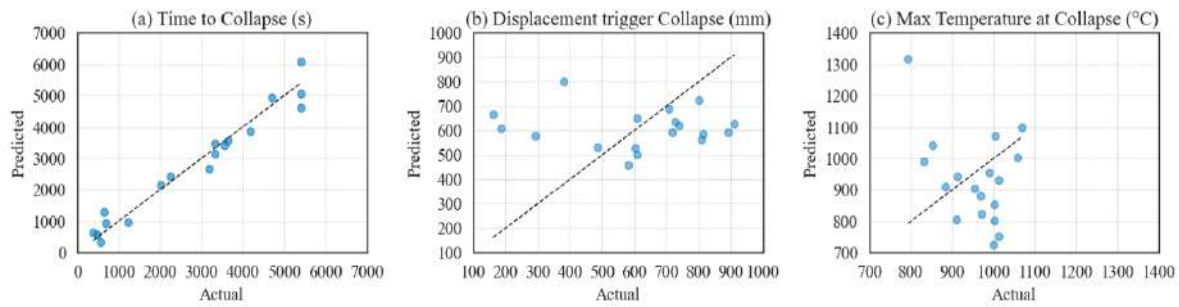


Figure 12. Regression model predictions vs. simulation results for (a) critical failure time, (b) mid-span vertical displacement triggering collapse, and (c) maximum temperature at collapse

This study is an initial step towards applying AI in the research of bridge fires. By predicting bridge failures under fire conditions, the developed two-step predictive framework, which consists interconnected ML models, contributes to the enhancement of public fire safety and infrastructure resilience. Future work will aim to include more complex fire scenarios and structural designs, expand the input feature set and database, and refine the models to improve prediction accuracy. Furthermore, efforts will be made to broaden the applicability of the models to a wider range of structures under natural fires.

5. CONCLUSION

A novel data-driven framework that makes use of machine learning and computational modeling techniques to predict the thermomechanical response of composite bridges under realistic fire scenarios is presented in this study. This is an issue that is crucial for public safety and resilient infrastructure design. With the use of FE analyses and CFD simulations, an extensive numerical database is generated by considering crucial parameters such as HRR, bridge soffit height, fuel location along bridge span, and fire protection level. The influence of these parameters on structural response of composite bridge is investigated. Two interconnected ANN models are created for classification and regression tasks using this database. The classification model predicts the likelihood of bridge collapse with reasonable accuracy, precision, and recall. The regression model is also capable of estimating critical failure time and temperature accurately. The proposed method overcomes limitations of conventional approaches that rely on simplified fire scenarios. It enables a quick evaluation of bridge performance across a wide range of plausible fire scenarios and design alternatives providing a decision-making tool for enhancing fire resilience of composite bridges. However, further refinement in ANN model is still required by training and including more input parameters such as different span length and vehicle types in order to broaden the applicability of the framework to a wide range of composite bridges.

REFERENCES

- [1] Payá-Zaforteza I, Garlock MEM. A numerical investigation on the fire response of a steel girder bridge. *J Constr Steel Res* 2012;75:93–103. <https://doi.org/10.1016/j.jcsr.2012.03.012>.
- [2] Kodur VK, Aziz EM, Naser MZ. Strategies for enhancing fire performance of steel bridges. *Eng Struct* 2017;131:446–58. <https://doi.org/10.1016/j.engstruct.2016.10.040>.
- [3] Kodur V, Aziz E, Dwaikat M. Evaluating fire resistance of steel girders in bridges. *Journal of Bridge Engineering* 2013;18:633–43. [https://doi.org/10.1061/\(ASCE\)BE.1943-5592.0000412](https://doi.org/10.1061/(ASCE)BE.1943-5592.0000412).
- [4] Aziz E, Kodur V. An approach for evaluating the residual strength of fire exposed bridge girders. *J Constr Steel Res* 2013;88:34–42. <https://doi.org/10.1016/j.jcsr.2013.04.007>.
- [5] Astaneh-Asl A, Noble CR, Son J, Wemhoff AP, Thomas MP, McMichael LD. Fire protection of steel bridges and the case of the macarthur maze fire collapse. *TCLÉE 2009: Lifeline Earthquake Engineering in a Multihazard Environment* 2009;357:69. [https://doi.org/10.1061/41050\(357\)69](https://doi.org/10.1061/41050(357)69).
- [6] Aziz EM, Kodur VK, Glassman JD, Moreyra Garlock ME. Behavior of steel bridge girders under fire conditions. *J Constr Steel Res* 2015;106:11–22. <https://doi.org/10.1016/j.jcsr.2014.12.001>.

- [7] Wu X, Huang T, Au FTK, Li J. Posttensioned Concrete Bridge Beams Exposed to Hydrocarbon Fire. *Journal of Structural Engineering* 2020;146:04020210. [https://doi.org/10.1061/\(asce\)st.1943-541x.0002791](https://doi.org/10.1061/(asce)st.1943-541x.0002791).
- [8] Song C, Zhang G, Hou W, He S. Performance of prestressed concrete box bridge girders under hydrocarbon fire exposure. *Advances in Structural Engineering* 2020;23:1521–33. <https://doi.org/10.1177/1369433219898102>.
- [9] EN 1991-1-2. Eurocode 1: Actions on structures - Part 1-2: General actions - Actions on structures exposed to fire. European Committee for Standardization 2005.
- [10] Eurocode I. BS EN 1991-1-2:2002. Eurocode 1: Actions of Structures - Part 1-2: General Actions - Actions on Structures Exposed to Fire. 2002.
- [11] Khan AA, Usmani AS, Torero JL. Evolution of fire models for estimating structural fire-resistance. *Fire Saf J* 2021.
- [12] Xu K, Mao X. Study on the behaviour of steel box girder bridge under fire condition. *Journal of Suzhou University of Science and Technology (Engineering and Technology)* 2018;31:13–8.
- [13] Payá-Zaforteza I, Garlock MEM. A numerical investigation on the fire response of a steel girder bridge. *J Constr Steel Res* 2012;75:93–103. <https://doi.org/10.1016/j.jcsr.2012.03.012>.
- [14] Aziz EM, Kodur VK, Glassman JD, Moreyra Garlock ME. Behavior of steel bridge girders under fire conditions. *J Constr Steel Res* 2015;106:11–22. <https://doi.org/10.1016/j.jcsr.2014.12.001>.
- [15] Hu J. Highway Bridges in Fire: Characterisation of Fire Loading and Structural Behaviour. The University of Edinburgh 2018.
- [16] McGrattan K, Hostikka S, McDermott R, Floyd J, Weinschenk C, Overhold K. Sixth Edition Fire Dynamics Simulator User's Guide (FDS). NIST Special Publication 1019 2016;Sixth Edit. <https://doi.org/10.6028/NIST.SP.1019>.
- [17] Timilsina S, Yazdani N, Beneberu E. Post-fire analysis and numerical modeling of a fire-damaged concrete bridge. *Eng Struct* 2021;244:112764. <https://doi.org/10.1016/j.engstruct.2021.112764>.
- [18] Ma R, Cui C, Ma M, Chen A. Performance-based design of bridge structures under vehicle-induced fire accidents: Basic framework and a case study. *Eng Struct* 2019;197. <https://doi.org/10.1016/j.engstruct.2019.109390>.
- [19] Alos-Moya J, Paya-Zaforteza I, Garlock MEM, Loma-Ossorio E, Schiffner D, Hospitaler A. Analysis of a bridge failure due to fire using computational fluid dynamics and finite element models. *Eng Struct* 2014;68:96–110. <https://doi.org/10.1016/j.engstruct.2014.02.022>.
- [20] Khan AA, Khan MA, Zhang C, Jiang L, Usmani A. OpenFIRE: An Open Computational Framework for Structural Response to Real Fires. *Fire Technol* 2021;Under Revi.
- [21] Alos-Moya J, Paya-Zaforteza I, Garlock MEM, Loma-Ossorio E, Schiffner D, Hospitaler A. Analysis of a bridge failure due to fire using computational fluid dynamics and finite element models. *Eng Struct* 2014;68:96–110. <https://doi.org/10.1016/j.engstruct.2014.02.022>.
- [22] Khan MA, Khan AA, Domada R, Usmani A. Fire hazard assessment, performance evaluation, and fire resistance enhancement of bridges. *Structures* 2021;34:4704–14. <https://doi.org/10.1016/j.istruc.2021.10.080>.
- [23] EN-1994-1-2. Eurocode 4: Design of composite steel and concrete structures - Part 1-2 General rules - Structural fire design. European Committee for Standardization 2005.
- [24] Hu J, Carvel R, Sanad A, Usmani A. New Design Fires for Performance Based Engineering of Highway Bridges. *Proceedings of the Ninth International Conference (Structures in Fire)* 2016:768–75. <https://doi.org/10.3929/ethz-a-007050197>.
- [25] Kodur V, Shakya A. Effect of temperature on thermal properties of spray applied fire resistive materials. *Fire Saf J* 2013;61:314–23.
- [26] Bentz DP, Prasad KR. Thermal Performance of Fire Resistive Materials I. Characterization with Respect to Thermal Performance Models. Rep No BFRL-NIST 7401, NIST, Gaithersburg, Md 2007:1–9.

STRUCTURAL BOLT HEATING AND COOLING: NUMERICAL STUDY

Gordon Chen¹, Anthony Abu², Gregory MacRae³

ABSTRACT

An approach to obtain the plastic stress-strain curve of high strength steel at any given temperature, after it has been heated to a peak temperature, is developed for use in the software ABAQUS. A software routine stores the maximum temperature, and current temperature, at each node to obtain the temperature history dependent plastic stress-strain curve at a given temperature. Numerical modelling is used to illustrate the application of the approach to unloaded high strength structural steel bolts during seven individual heating and cooling cycles. Peak temperatures were 20 °C, 400 °C, 600 °C, and 800 °C, and the final temperatures to which the bolts were cooled were either 20 °C or 400 °C. The bolts are then subject to tension, or double shear. It is shown that the process reproduced behaviour which matched experimental stresses at the ultimate strain to an accuracy better than 6% for most of current/maximum temperature pairs investigated. The proposed model is used in an analysis of a previous experiment in literature consisting of an end plate joint subassembly heated to 550 °C then cooled to ambient temperature. The moment-rotation response of the analysis showed good agreement with the experimental study.

Keywords: connection, structural fire, high-strength steel, decay phase, post-fire

1 INTRODUCTION

Common high-strength structural bolts, such as Grade 8.8 or Grade 10.9 bolts, may have yield and tensile strengths exceeding 640 MPa [1]. Under ambient temperature conditions, their high strength allows: (i) only a few bolts to connect structural elements, and (ii) connection inelastic demands to be moved from the bolts or welds to weaker components with greater inelastic deformation capacity. These high-strength bolts are often produced from a type of heat-treated high-strength steel known as “tempered martensite” with improved ductility over that of untempered martensite.

The response of a structure under fire conditions depends on the physical properties of the individual members and joints. As steel increases in temperature, its mechanical properties degrade. The ratio of a steel property (e.g. strength or stiffness) at elevated temperature, divided by that prior to fire exposure, is referred to as the “reduction factor (k_b for bolts)”. Parts made from heat-treated high-strength steels are particularly vulnerable to fire conditions. For high-strength steel parts heated to more than 600 °C, the crystalline structure undergoes a phase change from heat-treated tempered martensite to pearlitic grains, resulting in characteristics similar to those of non-heat treated mild steel [2]. The decreases in yield and tensile strengths of high-strength steels are more drastic than that of mild steel at the same temperature. At high temperatures, the low k_b may lead to bolt strength reducing below that the connected parts, potentially leading to a shift in failure mode to bolt fracture. This has been observed in end plate, fin plate, and web

¹ Title, Department of Civil and Natural Resources, University of Canterbury, Christchurch, Canterbury, New Zealand
e-mail: gordon.chen@pg.canterbury.ac.nz, ORCID: <https://orcid.org/0009-0002-6857-0424>

² Associate Professor, Department of Civil and Natural Resources, University of Canterbury, Christchurch, Canterbury, New Zealand
e-mail: anthony.abu@canterbury.ac.nz, ORCID: <https://orcid.org/0000-0001-6237-3361>

³ Professor, Department of Civil and Natural Resources, University of Canterbury, Christchurch, Canterbury, New Zealand
e-mail: gregory.macrae@canterbury.ac.nz, ORCID: <https://orcid.org/0000-0002-3011-5146>

cleat, bolted joint experimental studies [3-5] subject to different temperatures. When temperatures exceeded about 650 °C, failure occurred in the bolts (by shear or tension) regardless of the ambient temperature failure mode. For lower temperatures, bolt failure did not necessarily occur.

On cooling from a high temperature where the high-strength heat treatment is lost, strength and stiffness do not fully recover to their ambient temperature values [6]. Instead, the residual mechanical properties may resemble those of mild steel. Thus, the behaviour of a high-strength steel part, such as a structural bolt, may be drastically different between heating and cooling phases. The material properties observed during and after cooling may be considered by a “residual reduction factor (k_{nr})” [7], calculated as the property (e.g. stiffness or strength) at a certain temperature T_f on cooling from the peak temperature T_u , divided by the strength at the same temperature on initial heating. There is a greater reduction (i.e. smaller k_{nr}) for larger maximum temperature and for current (lower) and maximum temperatures which are further apart. Together, k_b and k_{nr} model the reduction of yield strength from ambient conditions to the current steel temperature considering the cooling effect. This is illustrated in Figure 1.

Experiments on the post-fire behaviour of high-strength steels indicate significantly different behaviour before and after exposure to temperatures above 600 °C. Hanus et al. [7], Qiang et al. [8], Kodur et al. [9], Rezaeian et al. [10] indicate that for coupons cut from bolts exposed to a heating (up to 900 °C) and cooling to as low as ambient temperature, (i) yield and tensile strength reductions were as much as 60% of ambient, (ii) the fracture strain increased by up to 100%, (iii) the increase in the strain at tensile strength increased from 2% to 10%, (iv) the failure mode changed from brittle to ductile, and (v) the elastic modulus decreased by as much as 50% of ambient. Steels exposed to temperatures less than about 500 °C, roughly corresponding to typical annealing temperatures of tempered martensite, showed residual reduction factors close to unity.

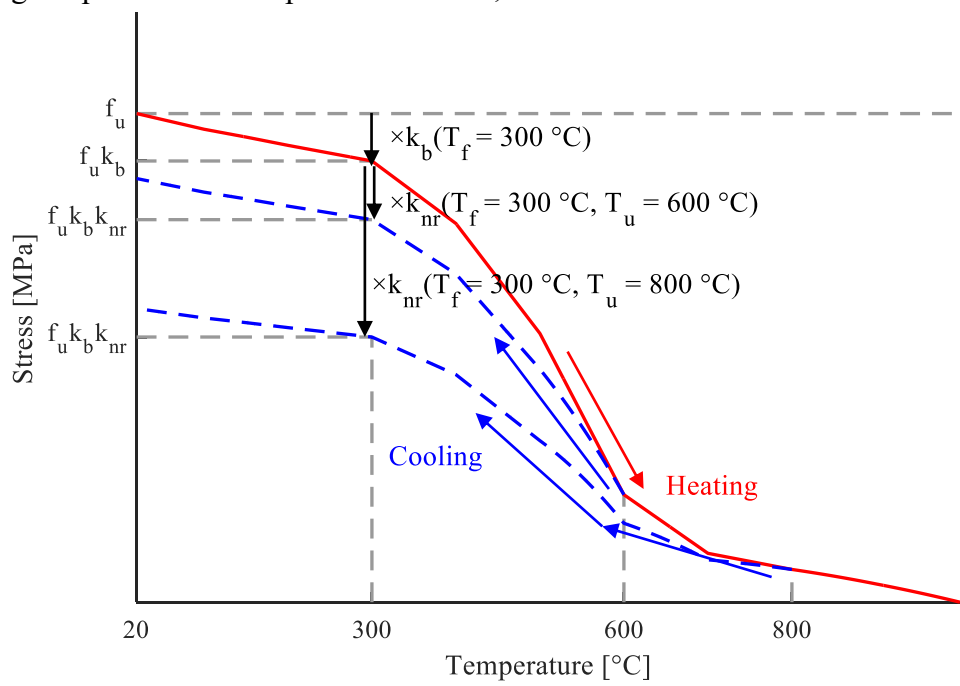


Figure 1. Diagrammatic representation of traditional reduction factor k_b and residual reduction factor k_{nr}

Due to the degradation of mechanical properties, bolts may become the weakest parts of a joint even after the structure has cooled completely. Large tensile forces on beams, due to catenary action and/or thermal contraction from cooling, may lead to bolt failure. Fischer et al. [11] conducted a review of nominally pinned joints under fire conditions and found that bolt shear, and weld fracture, were the predominant failure modes on bolted joints during the cooling phase of a fire. Santiago et al. [12] found similar results for flush and extended end plate joints. Thus, the analysis of bolted joints, which can use many high-strength steel bolts, that have reached temperatures exceeding 600-650 °C should consider this degradation once the fire and steel begin to cool. Numerical modelling is an appropriate tool as interpreting this behaviour is

complex due to the combined effect of gravity and thermal demands imposed on structural joints, and the variability in factors such as peak temperature and duration of real fires.

Hanus et al. [7] introduced stress-strain models incorporating both the traditional Eurocode reduction factors and the residual reduction factors for both heating and cooling phases. However, such stress-strain models have not been used in state-of-the-art numerical analyses of structures against fires undergoing both heating and cooling because current versions of finite element analysis software (such as ABAQUS) determine plastic stress based only on plastic strain and current temperature T_f at each integration point and do not account for temperature history. Specific finite element software such as SAFIR may only account for user-defined residual yield strength reductions and may not consider different yield and ultimate strains under heating and cooling that can significantly alter the stress-strain curve. Analyses therefore often use either the same stress-strain-temperature relationships under both heating and cooling, thereby neglecting the impact of the residual strength phenomenon, or analyse the structure during the cooling or post-fire phase only, thereby neglecting the impact of preexisting plastic deformations that may have developed before this phase. Since bolt failure modes often govern the response of bolted joints under high temperatures, it is important to have a complete understanding of the material behaviour under all conditions that the bolts may reasonably experience. To ensure future numerical models are realistic, it is important to ensure that the material definitions used in numerical analyses consider this phenomenon.

2 SCOPE

It can be seen from the above discussion that there is a need to develop a methodology to account for the temperature-history dependence of high-strength steels under exposure to natural fires. This will help ensure that future numerical models produce more realistic results, particularly during the cooling phase, thereby aiding fire related structural engineering decisions. To address this need, answers are sought to the following questions:

1. Can temperature history effects for heat-treated steels be incorporated in finite element analysis?
2. How do these considerations compare to previous test results of high-strength steel bolts?
3. How does the stress–strain–temperature–history relationship compare to observed behaviour of bolted joints under isothermal conditions exposed to high temperatures?

3 NUMERICAL PROCESS

A stress-strain relationship was written for ABAQUS using FORTRAN to model the temperature-history dependent behaviour of high-strength steel bolts comprised of 3D elements in decoupled thermo-mechanical analyses under transient fire conditions. This solution consists of three components: (i) a UFIELD subroutine for ABAQUS/Standard which stores the maximum temperature during the thermal analysis; (ii) a utility program 'fFVtoNT' that converts the stored maximum temperatures into a format readable into the mechanical analysis; and (iii) a VUHARD subroutine for ABAQUS/Explicit that outputs the plastic stress of the material based on the current and maximum temperature. The software code and instructions for use in an analysis are available on the corresponding author's GitHub [13].

The UFIELD subroutine implements a simple algorithm to record the maximum temperature reached. The maximum temperature is stored in a user-defined 'field variable', which is an additional parameter available in ABAQUS that can be generated, stored and used in user-defined functions. During a thermal analysis, the UFIELD subroutine compares the temperature reached at each integration point at the current increment with the field variable stored in each point from the previous increment. The field variable at the integration point for the current increment is then set as the greater of the two. Afterwards, the field variables at the integration points are extrapolated to the nodes of each element. This nodal value is then averaged across adjacent elements to obtain the average nodal value. These nodal field variables are then stored in an accompanying 'results file (.fil)' at the end of each increment. This results file, combined with the output

database (.obd) file, provides the temperature history information required to model the high-strength steel during the cooling phase.

The utility program fFVtoNT reads the results file and converts the nodal field variable records to nodal temperature records. This conversion is done as ABAQUS cannot read field variable data from one analysis directly into another, but can read nodal temperature output data into field variable input data [14]. Each record in the results file is transcribed to a new results file (.fin).

In the mechanical analysis, both the nodal temperature data from the output database and field variable data from the new results file are read into the model. This provides each node with both the current (T_f) and maximum (T_u) temperature at each timestep. Both temperatures as well as the true plastic equivalent strain are used to calculate the true plastic stress at each integration point according to the stress-strain relationship implemented in the VUHARD subroutine. The stress-strain curve implemented in the software is a modified version of the relationship in as included in Eurocode 3 Part 1.2 [15] and by Hanus et al. [7] and is shown in Figure 2. The equations defining the curve are:

$$\sigma(\varepsilon, T_f, T_u) = \begin{cases} E\varepsilon & \varepsilon_p > \varepsilon \geq 0 & \text{Elastic} \\ f_p - c + ab\sqrt{a^2 - (\varepsilon_y - \varepsilon)^2} & \varepsilon_u > \varepsilon \geq \varepsilon_p & \text{Nonproportional} \\ \frac{f_t - f_u}{\varepsilon_t - \varepsilon_u}(\varepsilon - \varepsilon_u) + f_u & \varepsilon_t > \varepsilon \geq \varepsilon_u & \text{Post - ultimate} \\ \frac{-f_t}{\varepsilon_{ult} - \varepsilon_t}(\varepsilon - \varepsilon_t) + f_t & \varepsilon_{ult} > \varepsilon \geq \varepsilon_t & \text{Post - limiting} \\ 0 & \varepsilon \geq \varepsilon_{ult} & \text{Fracture} \end{cases} \quad (1)$$

Each parameter in these equations is defined as follows:

f_u : temperature-history dependent tensile strength of the high-strength steel

$$f_u(T_f, T_u) = f_{u,amb} \cdot k_b(T_f) \cdot k_{nr}(T_f, T_u) \quad (2)$$

f_p : proportional limit

$$f_p(T_f, T_u) = f_u(T_f, T_u) \cdot k_p(T_u) \quad (3)$$

f_t : limiting stress

$$f_t = \min(500 \text{ MPa}, f_u(T_f, T_u)) \quad (4)$$

ε_u : strain at tensile strength, $\varepsilon_u = 0.02$

ε_t : limiting strain, $\varepsilon_t = 0.1$

ε_{ult} : ultimate strain, $\varepsilon_{ult} = 0.15$

k_{nr} : residual strength reduction factor [7]:

$$k_{nr}(T_f, T_u) = \frac{f_u(20^\circ\text{C} \rightarrow T_u \rightarrow T_f)}{f_u(20^\circ\text{C} \rightarrow T_f)} = 1 - 1.33 \times 10^{-3} \cdot (T_u - \max(T_f, 500^\circ\text{C})) \quad (5)$$

k_b : bolt reduction factor as defined in Eurocode 3 Part 1.2

$$k_b(T_f) = f_u(T_f)/f_u(20). \quad (6)$$

k_p : proportional limit factor, linearly interpolated between the values in Table 1.

The preceding equations are modified where $T_u > 800^\circ\text{C}$ such that $\varepsilon_{ult} = 0.25$, $\varepsilon_u = 0.1$, and $f_u = f_t$, and f_t and f_p are then determined from the new values. Between 600°C and 800°C , the values of ε_{ult} , ε_u , and f_u are linearly interpolated between these two cases.

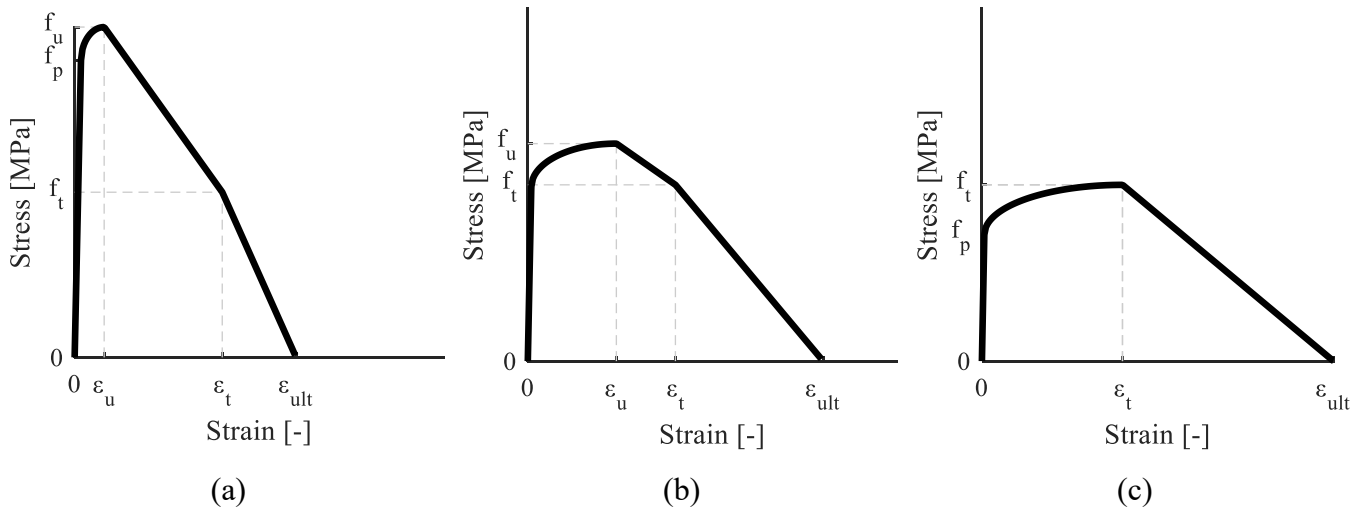


Figure 2. Stress-strain relationship for (a) $T_u \leq 600 \text{ }^\circ\text{C}$, (b) $600 \text{ }^\circ\text{C} < T_u \leq 800 \text{ }^\circ\text{C}$ and (c) $T_u > 800 \text{ }^\circ\text{C}$

Table 1. Proportional limits at different maximum temperatures [7]

$T_u \text{ [}^\circ\text{C]}$	$k_p(T_u)$
20	0.9
200	0.8
400	0.75
600	0.75
800	0.6

4 MODEL VERIFICATION

4.1 Material Tensile and Shear Testing

To verify the material model, simple tensile and shear tests on dog-bone and double-shear specimens were modelled and compared against experimental data in the literature. A decoupled thermo-mechanical analysis process was used. In the thermal analysis, the modelled specimens were first heated to a peak temperature T_u until steel temperatures stabilised, then cooled to the testing temperature T_f and allowed to stabilise again. In these analyses, the final testing temperature and current nodal temperature (as previously defined in Section 3) are the same value. The resulting final temperature and maximum temperature from the thermal analysis was then read into the mechanical analysis. Tensile tests were conducted on a model of a dog-bone sample of 10 mm diameter and 100 mm length, shown in Figure 3a. One end of the dog-bone model was fully restrained and the opposite end pulled at 0.25 mm/s. Shear tests were conducted on a 10 mm diameter rod in double shear between three plates of 10 mm thickness shown in Figure 3b, pulled at 0.25 mm/s. Seven temperature regimes were investigated, where peak temperatures were 20 °C, 400 °C, 600 °C, or 800 °C, and the final temperatures were 20 °C or 400 °C. Engineering stress and strain was converted from von Mises stress and equivalent plastic strain from the most deformed element.

For the temperature regimes studied, the material model was found to produce adequate results compared to experimental data from Hanus et al. [7] and Kodur et al. [9], as shown in Figure 4 and Figure 5. The difference in ultimate stress at the model's ultimate strain between the model and the plotted results was less than 6%, except for the case $T_f = 400 \text{ }^\circ\text{C}$, $T_u = 600 \text{ }^\circ\text{C}$ where the difference was 11%. Both the tensile and shear tests produced the same stress-strain relationships for each temperature regime. Numerical instabilities at strains greater than $\varepsilon_t = 0.1$ were observed for models where the maximum temperature was

up to 600 °C, resulting in a sudden loss of strength and simulating fracture of the material. This simulated fracture occurred at a similar strain as the fracture observed in the referenced experimental studies.

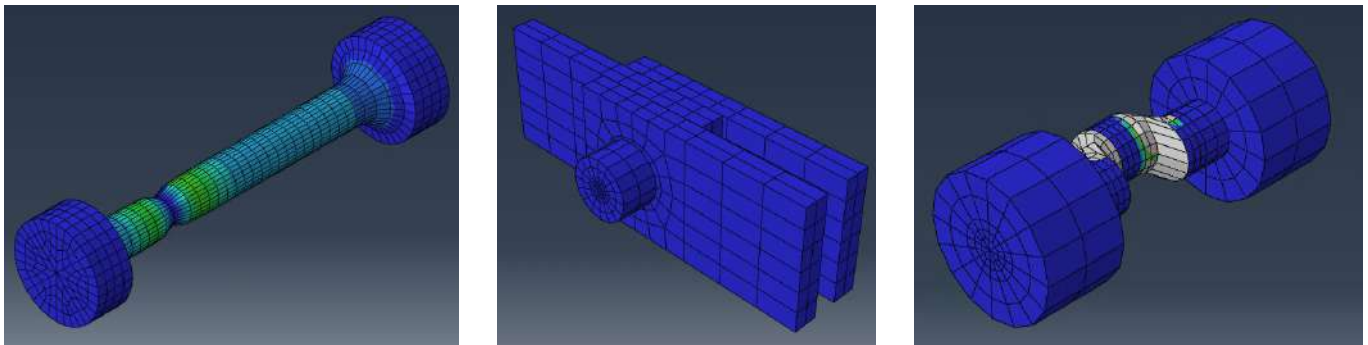


Figure 3. (a) Dog-bone model, and (b) double-shear model before and (c) after mechanical loading

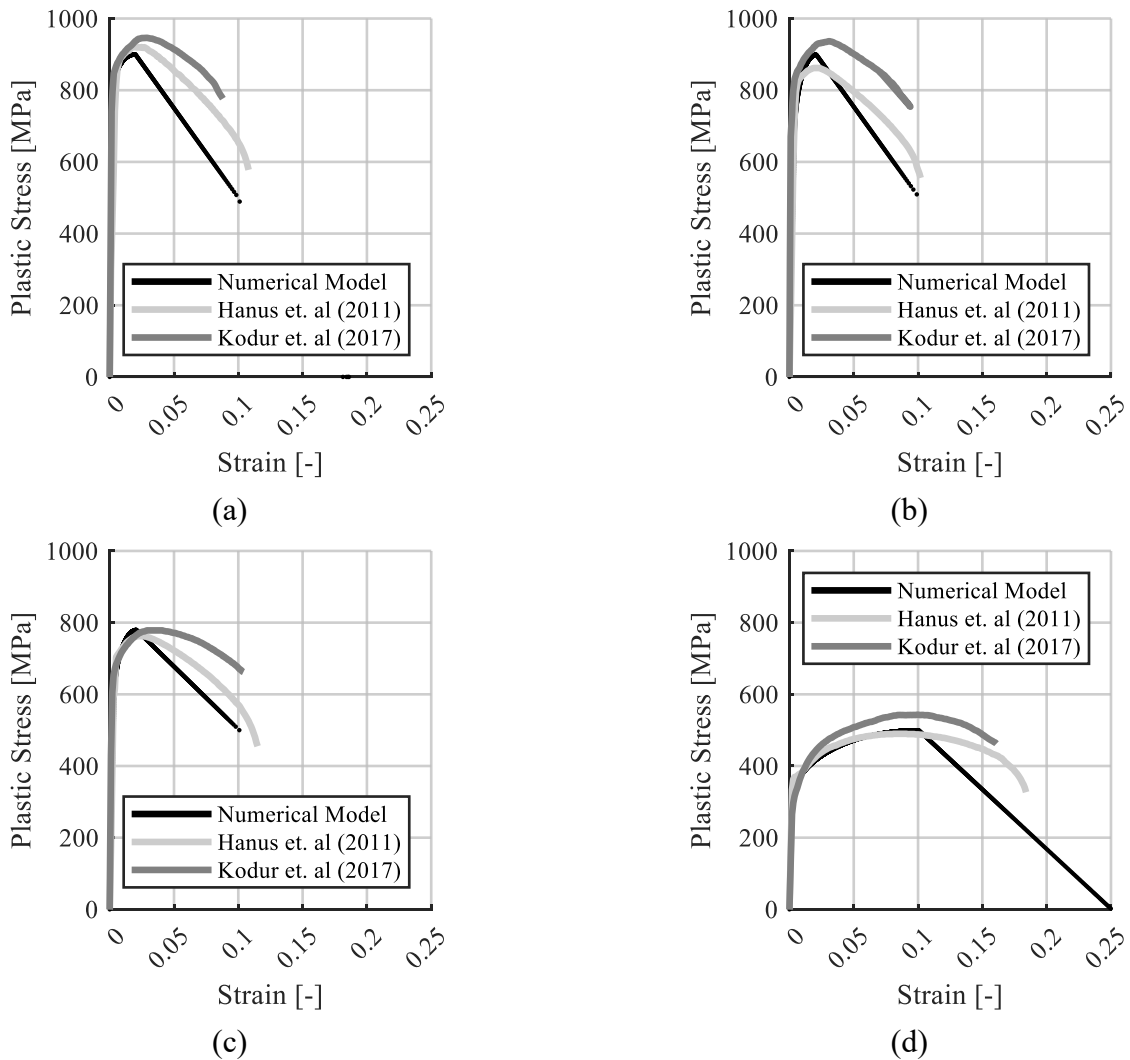


Figure 4. Stress-strain curve of the numerical model compared to experiments in literature, $T_f = 20\text{ }^\circ\text{C}$ from T_u of (a) 20 °C, (b) 400 °C, (c) 600 °C and (d) 800 °C

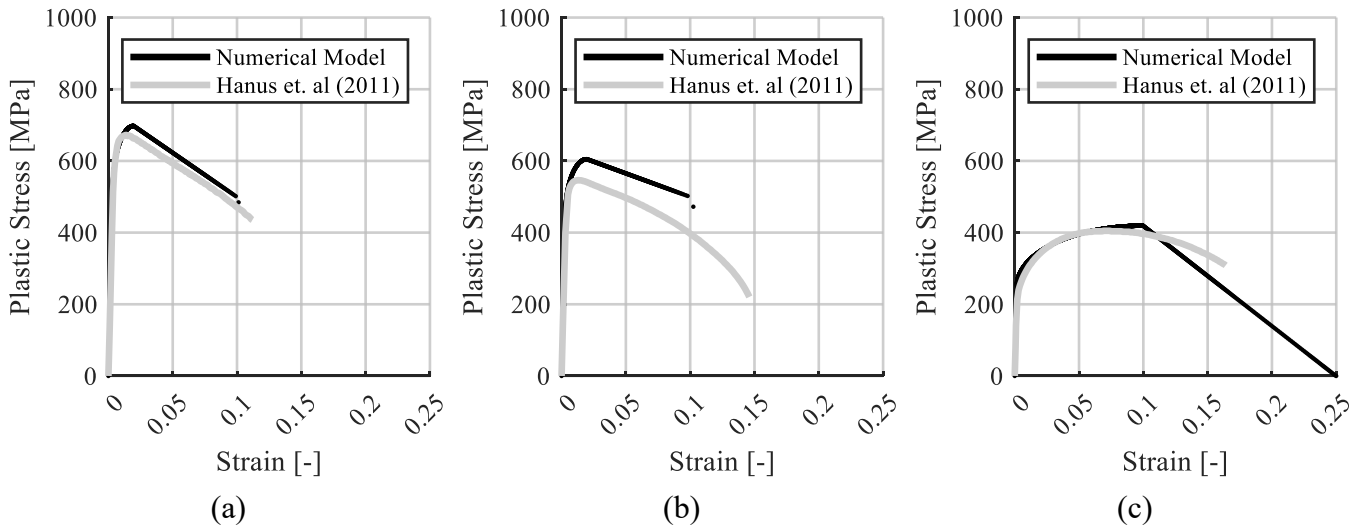


Figure 5. Stress-strain curve of the numerical model compared to experiments in literature, $T_f = 400\text{ }^\circ\text{C}$ from T_u of (a) $400\text{ }^\circ\text{C}$, (b) $600\text{ }^\circ\text{C}$ and (c) $800\text{ }^\circ\text{C}$

4.2 Isothermal Model of Joint subassembly

To verify the applicability of the material model to full-scale numerical modelling, a simple joint supporting a cantilevered beam stub was analysed under post-fire conditions. This was compared to an experimental study on bolted end plate connections by Qiang et al. [16]. The numerical model of the joint consisted of a Q345 HW300×300 beam stub connected to a Q345 HW 400×400 column through an end plate joint. The top and bottom of the column were fixed against displacement. A tie constraint joined the beam stub and end plate, and all other interactions between parts were defined through contact pairs. The joint was comprised of a full-depth Q235 end plate with three rows of Grade 8.8 M27 bolts. A schematic of the joint is shown in Figure 6. The numerical model is shown in Figure 7. The model was analysed three times using different ultimate stress and elastic modulus for the high-strength steel bolts:

- (i) the material properties as recorded in Qiang et al. [17]
- (ii) the proposed high-strength steel model as implemented in the FORTRAN code
- (iii) the proposed FORTRAN model, where ϵ_u is changed from 0.02 to 0.05 to better match the observed ultimate stress of the tested high-strength-steel bolts

The residual elastic modulus of the high-strength steel in analysis (i) was 195 MPa, whilst analyses (ii) and (iii) used the ambient temperature elastic modulus of 210 GPa since the proposed model does not account for degradation of residual elastic modulus of the high-strength steel. The ambient temperature ultimate stress of the bolts was 950 MPa. The stress-strain curves of the materials used in the analyses are shown in Figure 8. To reduce numerical instabilities, the proposed model did not allow the stress to reduce to zero at large strains; instead, the stress was held constant beyond ϵ_T for analyses (ii) and (iii). A decoupled thermal-mechanical analysis was used. The joint was heated to $550\text{ }^\circ\text{C}$ and the temperature allowed to stabilise, then cooled to $20\text{ }^\circ\text{C}$ and allowed to stabilise again. In the mechanical analysis, the beam was loaded by a monotonically increasing point load at a stiffener near the free end of the beam stub.

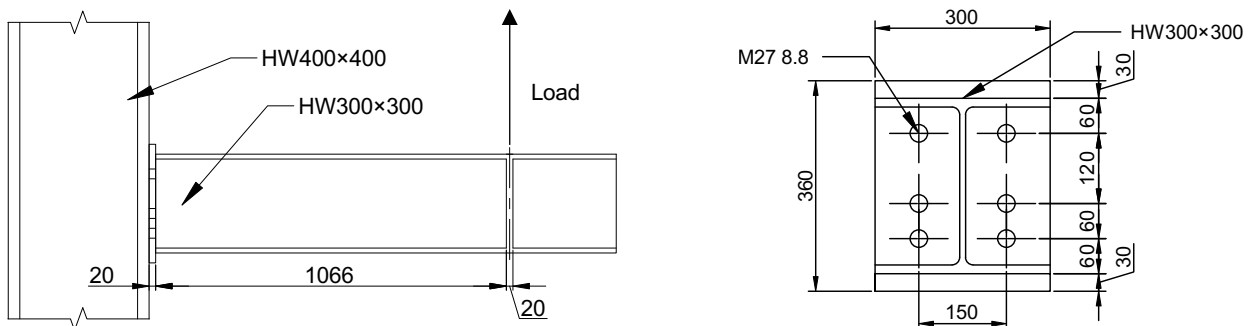


Figure 6: Modelled test setup of the experiment by Qiang et al. [16]

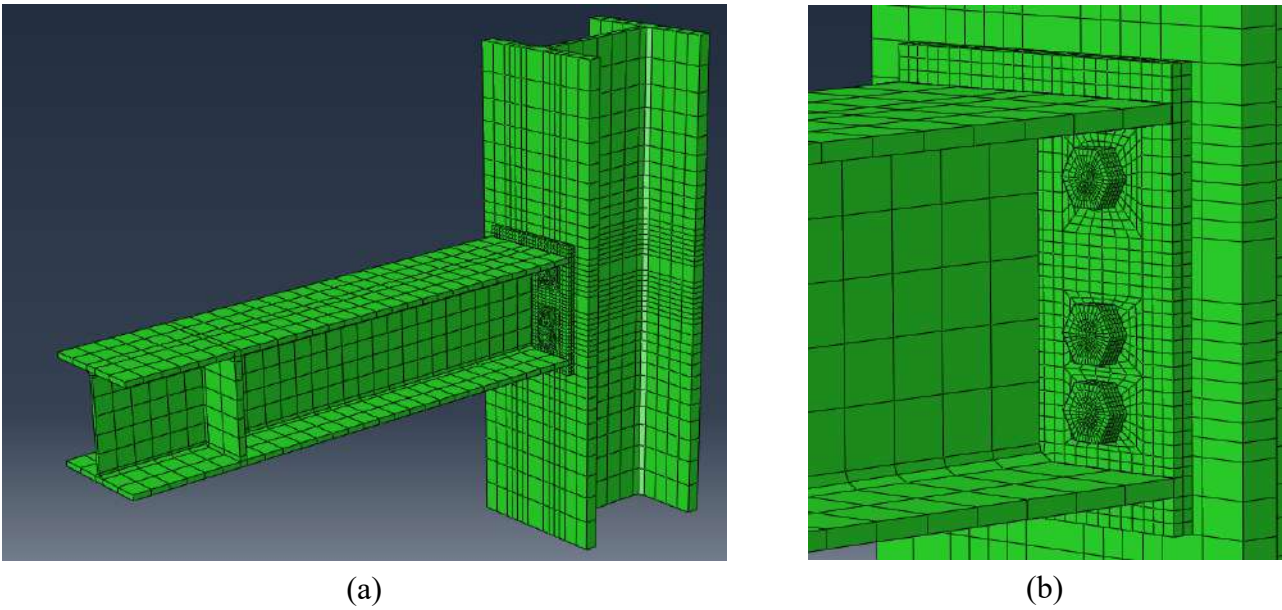


Figure 7: (a) Modelled assembly, (b) close-up of joint region

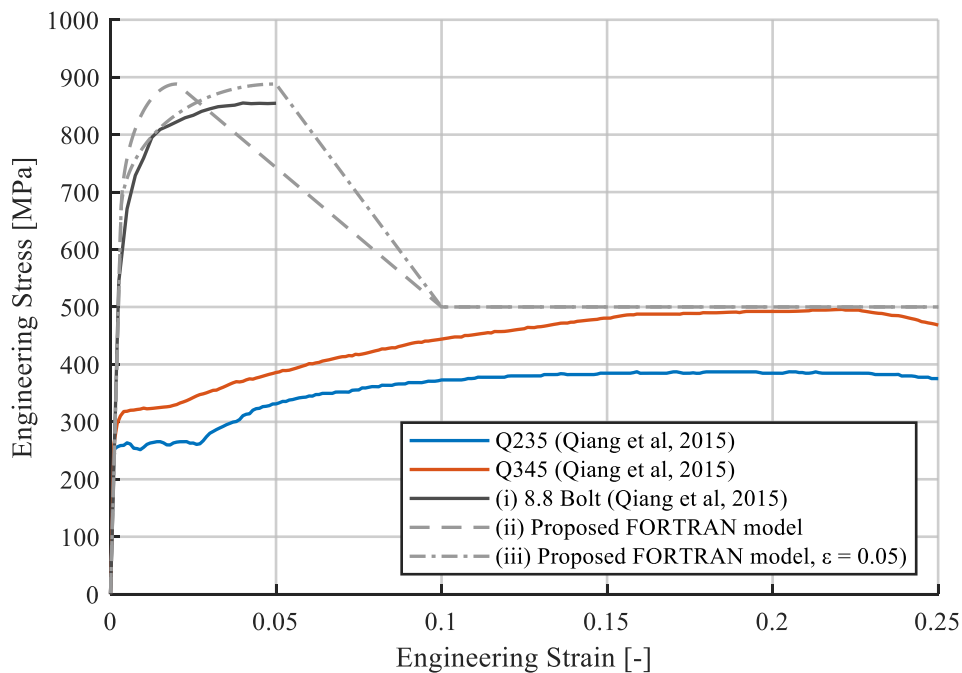


Figure 8. Stress-strain curves used for modelling the isothermal joint subassembly

The results were compared against the experimental data presented in the referenced study [16, 17]. The subassembly following the analysis is shown in Figure 9. The moment-rotation plot of the experiment is compared against the three analyses in Figure 10. This showed that the proposed model produced good agreement with the experimental results of the referenced study. The analyses using the proposed model initially predicted a greater moment resistance than both the experiment and the analysis using the measured bolt properties, which was likely a result of both the greater residual ultimate stress predicted by the proposed model compared to the experimental stress-strain data and the elastic modulus remaining at the ambient temperature value. At rotations above 60 mrad, the proposed model produces a reasonably close match to the experimental data. When ϵ_u was adjusted to better match the experimental high-strength steel bolt stress-strain curve, the proposed model performed better than the other two analyses at rotations between 120 to 150 mrad. In all analyses, both rows of tension bolts showed large strains exceeding ϵ_t (0.1) and reaching 1.0, as shown in Figure 11, which would likely result in the fracture of the bolts.

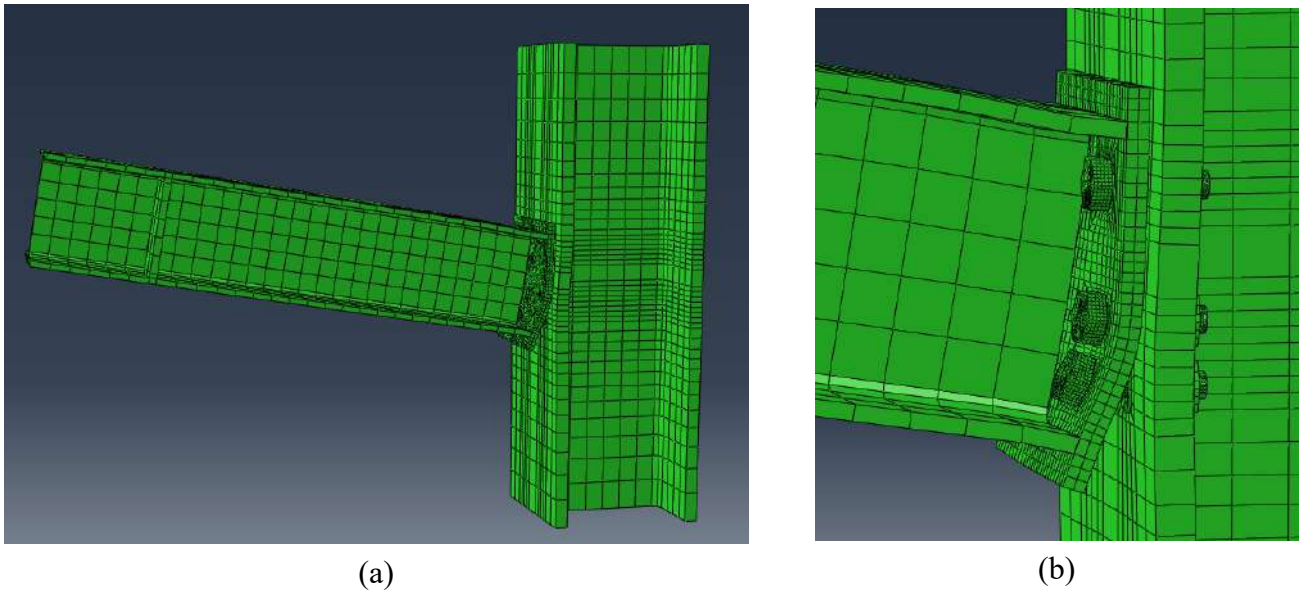


Figure 9. Isothermal joint subassembly after loading

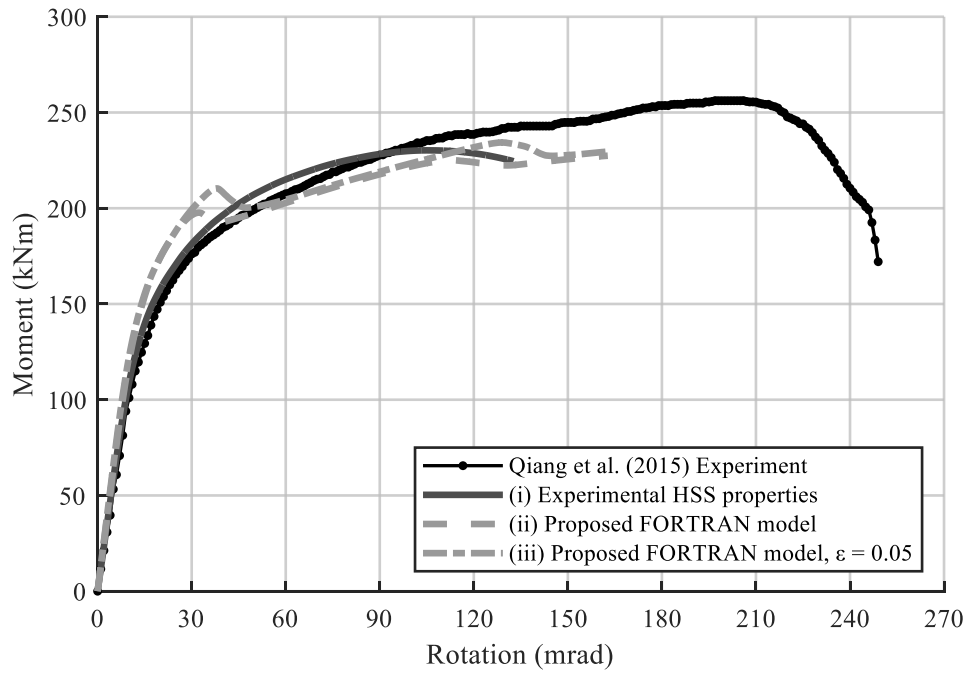


Figure 10. Comparison between experiment conducted by Qiang et al. [16] and a finite element model including the proposed high-strength steel model

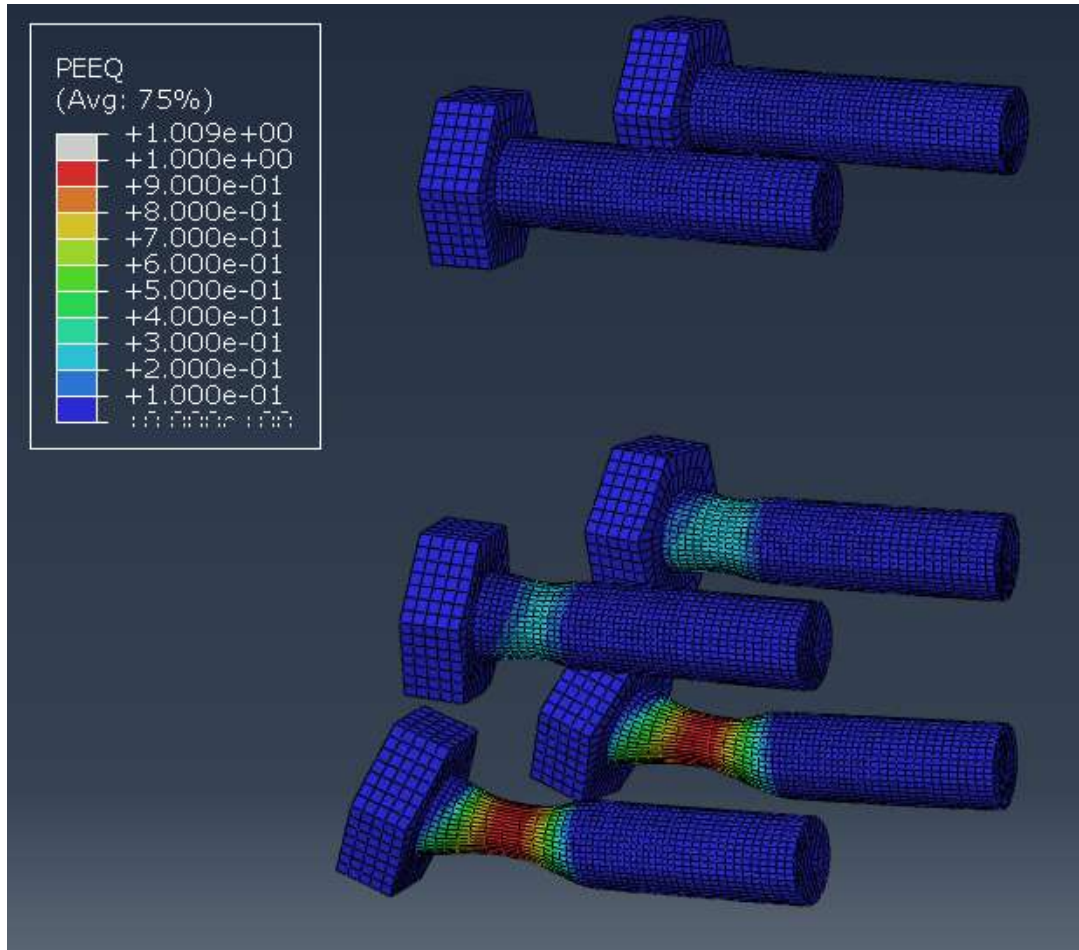


Figure 11. Strains in the bolts of the isothermal joint subassembly considering the proposed model at a rotation of 162 mrad

5 CONCLUSIONS

A process for modelling the temperature-history-dependence of high-strength steel in ABAQUS was presented and appraised in this paper. In answer to the questions presented in the Scope:

1. A material model was produced for ABAQUS/Explicit using FORTRAN that accounts for temperature-history dependent effects on the stress-strain relationship of high-strength steel bolts. The modelling process is comprised of three software components that together store the maximum temperature reached at each node and calculates a plastic stress based on the current and maximum temperature.
2. The model produces a stress-strain relationship comparable to studies in the literature of high-strength steels exposed to a heating and cooling cycle. The model produces the same stress-strain relationship under both tensile and shear loading.
3. The high-strength steel model was used in an isothermal analysis of a steel end plate joint subassembly utilising high-strength steel bolts, based on an experiment conducted by Qiang et al. [16] undergoing an isothermal heating and cooling temperature regime. The proposed model provided good agreement with the experimental results above 60 mrad.

REFERENCES

1. International Organization for Standardization, *ISO 898-1*, in *Mechanical properties of fasteners made of carbon steel and alloy steel Part 1: Bolts, screws and studs with specified property classes - Coarse thread and fine pitch thread*. 2013, International Organization for Standardization: Geneva, Switzerland.
2. Król, P.A. and M. Wachowski, *Effect of Fire Temperature and Exposure Time on High-Strength Steel Bolts Microstructure and Residual Mechanical Properties*. 2021. **14**(11): p. 3116.
3. Qiang, X., F.S.K. Bijlaard, H. Kolstein, and X. Jiang, *Behaviour of beam-to-column high strength steel endplate connections under fire conditions – Part 1: Experimental study*. *Engineering structures*, 2014. **64**: p. 23-38.
4. Yu, H., I.W. Burgess, J.B. Davison, and R.J. Plank, *Tying capacity of web cleat connections in fire, Part 1: Test and finite element simulation*. *Engineering Structures*, 2009. **31**(3): p. 651-663.
5. Yu, H., I.W. Burgess, J.B. Davison, and R.J. Plank, *Experimental investigation of the behaviour of fin plate connections in fire*. *Journal of constructional steel research*, 2009. **65**(3): p. 723-736.
6. Kirby, B.R., *The behaviour of high-strength grade 8.8 bolts in fire*. *Journal of Constructional Steel Research*, 1995. **33**(1): p. 3-38.
7. Hanus, F., G. Zilli, and J.M. Franssen, *Behaviour of Grade 8.8 bolts under natural fire conditions—Tests and model*. *Journal of constructional steel research*, 2011. **67**(8): p. 1292-1298.
8. Qiang, X., F.S.K. Bijlaard, and H. Kolstein, *Post-fire mechanical properties of high strength structural steels S460 and S690*. *Engineering structures*, 2012. **35**: p. 1-10.
9. Kodur, V., M. Yahyai, A. Rezaeian, M. Eslami, and A. Poormohamadi, *Residual mechanical properties of high strength steel bolts subjected to heating-cooling cycle*. *Journal of Constructional Steel Research*, 2017. **131**: p. 122-131.
10. Rezaeian, A., M. Shafiei, and M. Eskandari, *Effect of Temperature on Mechanical Properties of Steel Bolts*. *Journal of Materials in Civil Engineering*, 2020. **32**(9): p. 04020239.
11. Fischer, E.C., R. Chicchi, and L. Choe, *Review of Research on the Fire Behavior of Simple Shear Connections*. *Fire Technology*, 2021. **57**(4): p. 1519-1540.
12. Santiago, A., L. Simões Da Silva, and P. Vila Real, *Numerical Modelling of the Influence of Joint Typologies on the 3D Behaviour of a Steel Sub-Frame Under a Natural Fire*. *Fire Technology*, 2010. **46**(1): p. 49-65.
13. Chen, G., *HSS SUB v1.0*. 2023, GitHub: https://github.com/gChen-structFire/HSS_SUB/releases/tag/v1.0.
14. Dassault Systèmes, *Predefined Fields*, in *Abaqus 2022 Documentation*. 2022, Dassault Systèmes.
15. British Standards Institute, *BS EN 1993-1-2:2005: Eurocode 3. Design of steel structures. General rules. Structural fire design*. 2005, CEN: Brussels, United Kingdom.
16. Qiang, X., X. Jiang, F.S.K. Bijlaard, H. Kolstein, and Y. Luo, *Post-fire behaviour of high strength steel endplate connections — Part 1: Experimental study*. *Journal of Constructional Steel Research*, 2015. **108**: p. 82-93.
17. Qiang, X., X. Jiang, F.S.K. Bijlaard, H. Kolstein, and Y. Luo, *Post-fire behaviour of high strength steel endplate connections — Part 2: Numerical study*. *Journal of Constructional Steel Research*, 2015. **108**: p. 94-102.

THERMO-MECHANICAL ANALYSIS AND VALIDATION OF SAFIR FOR HISTORIC FORMS OF CONSTRUCTION

Octavian Lalu¹, Tom Lennon², Diana Duma³, Thomas Gernay⁴

ABSTRACT

This paper presents a comprehensive investigation into the thermo-mechanical analysis and validation of advanced numerical techniques for assessing the fire performance of historic forms of construction. The primary focus is on filler joist floors and hollow pot floors, two significant historical floor types commonly found in structures in the UK dating from the 19th and early 20th centuries.

Keywords: Historic forms of construction, thermo-mechanical analysis, standard fire exposure, SAFIR

1 INTRODUCTION

The main objective of structures-in-fire (SiF) analysis is to determine the thermo-mechanical behaviour of a structure during a fire until failure. The software SAFIR was developed to allow numerical modelling of the behaviour of structures subjected to fire [1]. The software enables thermal analysis, and the information obtained on the temperature distribution can be used to estimate the load-bearing capacity of the members. For existing historical forms of construction undergoing refurbishment or change of use, it is often necessary to determine the fire resistance of the structural components. The standard fire resistance procedures involve testing individual elements such as columns, beams and floors [2]. Historic buildings often exhibit structural characteristics distinct from modern construction, posing challenges for traditional fire testing approaches [3]. Computational methods may provide an appropriate means to demonstrate compliance with the mandatory requirements of the Building Regulations. The Eurocodes governing structural fire engineering design highlight the need to validate advanced numerical models using relevant experimental data [4,5].

The advanced finite element software SAFIR has been extensively validated and benchmarked against the cases set out in the German National Annex for EN 1991-1-2 (2010) [6-11]. The existing validation studies focus on recent forms of construction and are not necessarily relevant to historic structures.

This paper explores the use of advanced numerical techniques to estimate the anticipated fire behaviour of existing floor systems used in historic buildings in the UK. The main objective is to benchmark the numerical model against standard fire resistance test data for historic floor constructions.

¹ Senior Fire Engineer, Building Research Establishment,
e-mail: octavian.lalu@bregroup.com, ORCID: <https://orcid.org/0000-0003-0461-6526>

² Principal Fire Engineer, Building Research Establishment,
e-mail: tom.lennon@bregroup.com, ORCID: <https://orcid.org/0000-0002-2786-0591>

³ Senior Fire Engineer, Building Research Establishment,
e-mail: diana.duma@bregroup.com, ORCID: <https://orcid.org/0000-0002-6121-3099>

⁴ Assistant Professor, Johns Hopkins University
e-mail: tgermay@jhu.edu, ORCID: <https://orcid.org/0000-0002-3511-9226>

2 METHODOLOGY

The methodology involves using SAFIR software to validate the thermo-mechanical behaviour of historic types of floors using standard fire resistance test evidence.

The numerical analysis is based on two steps. In the first step, a heat transfer analysis is performed to determine the heat distribution through the floor section. The heat transfer by conduction is based on the Fourier Law (equation 1). [1].

The Fourier equation is expressed in equation 1.

$$\frac{\partial}{\partial x} \left(k \frac{\partial T}{\partial x} \right) + \frac{\partial}{\partial y} \left(k \frac{\partial T}{\partial y} \right) + \frac{\partial}{\partial z} \left(k \frac{\partial T}{\partial z} \right) + Q = c_p \rho \frac{\partial T}{\partial t} \quad (1)$$

Where $k_{(\theta)}$ is the thermal conductivity (W/mK), $c_{p(\theta)}$ is the specific heat (J/kgK), $\rho_{(\theta)}$ is the density (kg/m³), and Q is the internal heat generation (W/m³). The thermal properties are temperature-dependent.

In the second step, the mechanical analysis is performed based on the temperature output from the thermal analysis, which considers a reduction of the material properties at elevated temperatures. The mechanical problem can be solved in a quasi-static manner using equation 2 or a dynamic formulation.

$$\Delta F = K \cdot \Delta u \quad (2)$$

Where K is the structure's stiffness matrix, ΔF is the vector of incremental applied nodal forces, and Δu is the vector of incremental nodal displacements.

3 PERFORMANCE OF FILLER JOIST FLOORS IN FIRE

Filler joist floor systems are a typical form of construction used in the 19th century. The term "*filler joist*" is a generic one used for certain types of building floors dating from the late Victorian era to World War II. The floors comprise metal beams completely embedded in concrete. The floors can have wrought iron sections or even cast-iron tees in the early period. Usually, they span one way between the supports, and they are encased in concrete made with coke-breeze, clinker, broken brick, or conventional aggregates [12]. The concrete provides mainly insulation for the steel joists. The joists act as the main load-bearing members and are usually spaced at a centre distance ranging from 600mm to 900mm. The joists can rest either on solid masonry walls or on steel beams. The typical overall depth can range from 100mm to 300mm based on the steel joist size. General sections through proprietary historic floor systems are shown in Figure 1 [13].

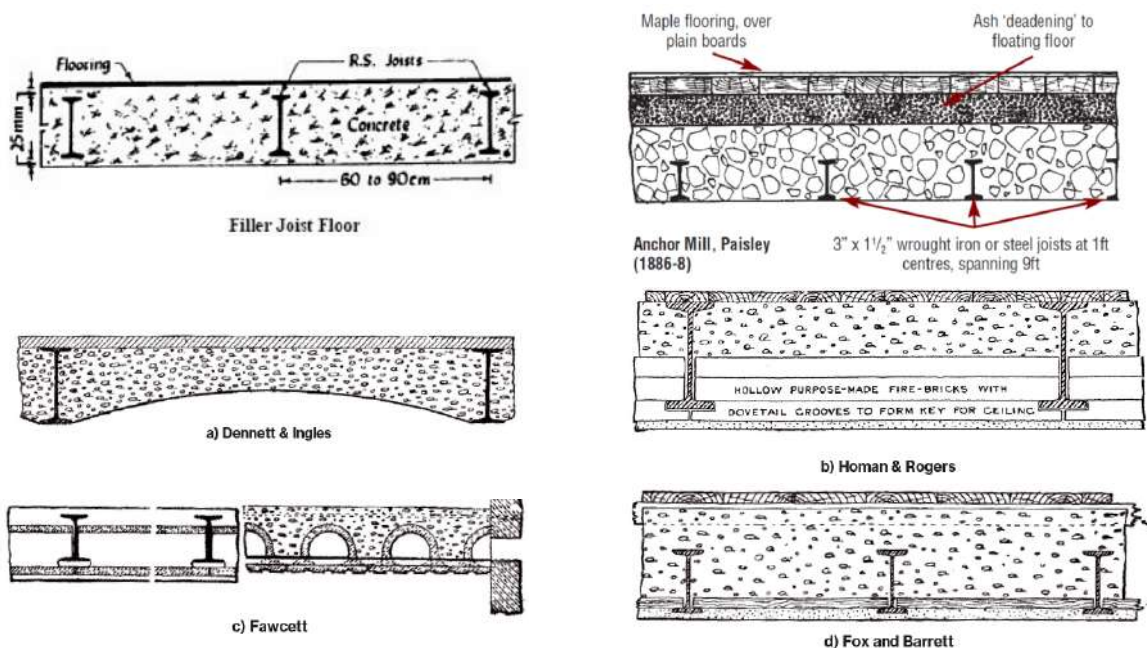


Figure 1. Typical section through a filler joist floor

The concrete cover governs the fire resistance by reducing the heat transfer to the steel section in the event of a fire. The fire resistance of the structure can be compromised if the cover to the joists has been lost by material falling off the soffit. If the soffit cover is missing, it needs to be reinstated. This applies to all filler joist floor systems or jack arches as they have evolved as "fire-proof" solutions [14].

The performance of many innovative floor systems would have been established through fire testing, particularly where reinforced concrete was used alongside other materials to provide the required level of performance. It is improbable that the test data were publicly accessible, and often, the details necessary to validate the fire-resistance performance of these systems are no longer accessible. Some information from standard fire tests, including results from a range of in-situ and precast concrete flooring systems, is available in the literature [16-18].

Figure 2 shows a section through the filler joist floor system used in the standard fire testing and the positions of the instruments. Table 1 summarises the historic test data for filler joist floors.

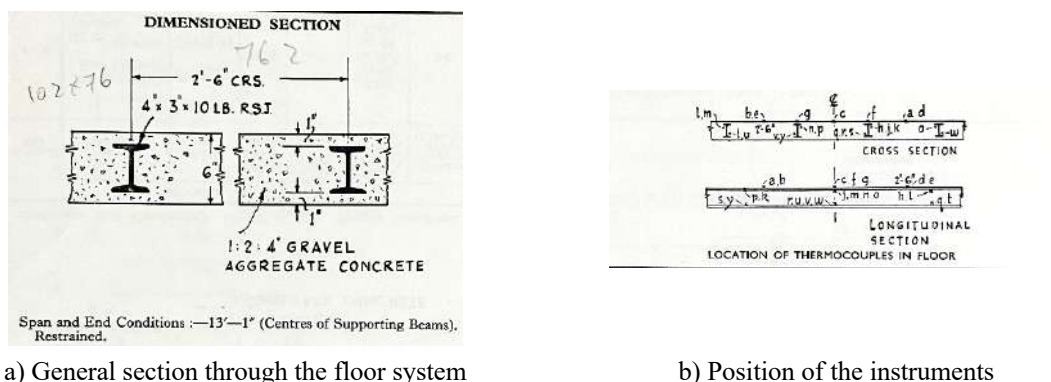


Figure 2. Section through a filler joist floor subjected to standard fire testing [15]

Table 1. Historic test data for filler joist floors [15]

Test Ref.	Depth of floor (mm)	Joist size (mm)	Cover (mm)	Span (mm)	Test duration (min)	Comments
F30	152	102 × 76	26	762	29	Limited spalling. The test was continued for 180 min. Local integrity failure.
FR1	152	102 × 76	26	762	228	Spalling after 5 min up to 20 min
F62	178	102 × 76	38	762	360	-
F8	184	102 × 76	20	762	240	13mm plaster
F9	184	102 × 76	20	762	120	13mm plaster
F10	159	102 × 76	20	914	240	13mm plaster
F11	159	102 × 76	20	914	240	13mm plaster
F12	159	102 × 76	20	914	150	Limited spalling
F28	152	102 × 45	26	610	270	-
F29	152	102 × 45	26	762	215	-

The tested specimens incorporated granite or crushed brick aggregate and clinker concrete inserts. In all cases, the test duration was limited due to either integrity or insulation failure, often initiated through crack

formation or localised temperature rise. None of the tests in the table above had a load-bearing capacity (R) failure mode.

4 PERFORMANCE OF HOLLOW POT FLOORS IN FIRE

Hollow clay pots were first used in the early part of the 20th century as a means of constructing fire-proof floors while reducing the dead load of the building. A typical section is shown in Figure 3 [18].

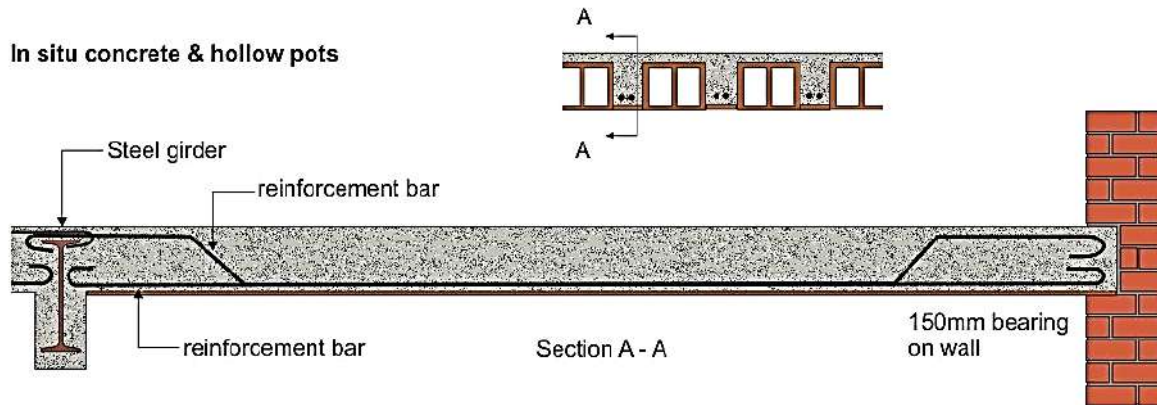


Figure 3. Hollow clay pot floor construction [18]

In general, the hollow pot floor system is one-way, spanning on beams or load-bearing walls. Overall approximate depths vary from 150mm to 300mm with downstand concrete ribs at 400mm-500mm centres. They generally incorporate some form of aesthetic finish to the underside of the soffit (often gypsum plaster) and may have a structural topping or other floor systems on the upper surface. Hollow pot floors are included as a form of plain soffit floor in BS8110-2 [19] and BR128 [20]. However, in many cases, the fire resistance achievable is derived from considering the contribution of the various components to the system, which may well include a plaster finish to the underside of the soffit and any non-combustible structural topping or levelling screed. The anticipated performance when exposed to fire for an existing structure will depend on several factors, including the presence and nature of any defects, the cover to the reinforcement may be insufficient, or the clay pots may be damaged.

Figure 4 and Table 2 below summarise the principal parameters for a number of hollow clay pot floors tested between 1936 and 1945.

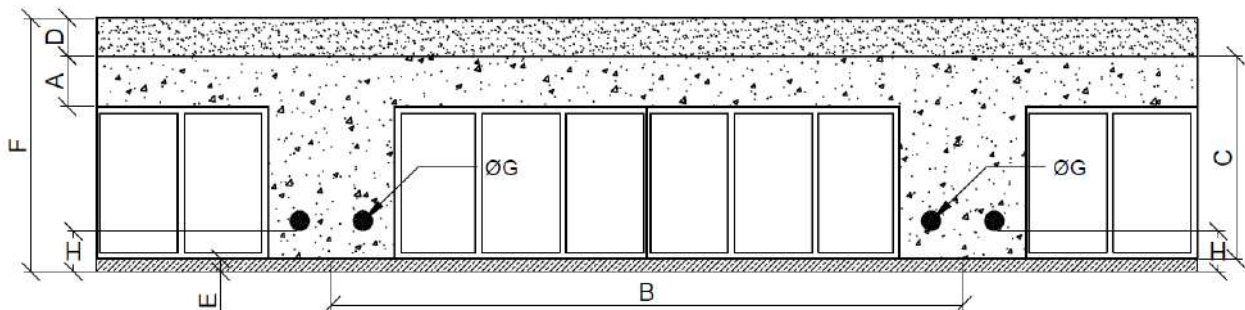


Figure 4. Key components of hollow clay pot floors

A = slab depth; B = span between centre of downstand beams; C = total depth (slab + rib); D = depth of topping; E = thickness of plaster; F = overall depth of construction; G/H = reinforcement specification (diameter + cover)

Table 2. Historic test data for filler joist floor [15]

Test ref.	A	B	C	D	E	F	G/H	Test duration (min)	Mode of failure
F26	38	387	140	0	13	152	2 x 13 @ 19 cover	166	No failure
F27	38	387	140	0	13	152	2 x 13 @19 cover	203	Collapse
F13	38	381	140	73	13	225	1 x 19 @ 19 cover	134	No failure
F14	38	381	140	73	13	225	1 x 19 @ 19 cover	208	Collapse
F15	38	381	140	73	13	225	1 x 19 @ 19 cover	146	Collapse
F32	38	387	140	0	13	152	2 x 13 @ 13 cover	143	Insulation
F59	38	387	140	0	13	152	2 x 13 @ 13 cover	120	No failure
F66	38	387	140	0	13	152	2 x 13 @ 13 cover	120	No failure
F64	38	394	190	0	13	203	2 x 13 @ 25 cover	240	No failure

5 MATERIAL PROPERTIES

Several studies have examined how temperature affects the thermal properties of old concrete. It was found that the thermal properties of concrete, particularly thermal conductivity and specific heat, are influenced by factors such as aggregate type, moisture content, and mix proportions [21-25]. In normal-weight concrete mixes, thermal conductivity typically decreases with increasing temperature until around 700°C, where it stabilises at approximately 0.80–1.20 W/mK. However, the thermal conductivity of lightweight concrete mixes is generally unaffected by temperature variations. This difference is attributed to the increased porosity and voids in lightweight materials, leading to reduced thermal conductivity. The specific heat of concrete was observed to increase between temperatures of 150–400°C due to moisture evaporation, remaining constant beyond that range. These findings highlight the complex relationship between concrete composition and thermal behaviour at elevated temperatures. Figure 5 shows the relationship between various thermal conductivities of concrete and temperature for different types of old concrete and the current and new (λ_{c2022}) Eurocode formulations.

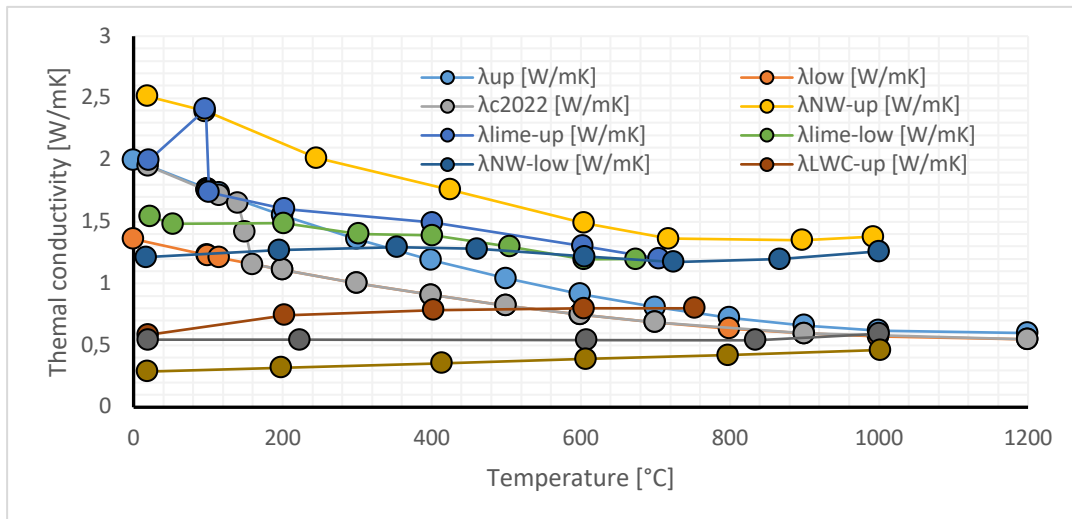


Figure 5. Thermal conductivity for various types of old concrete and the Eurocode formulation

In the early 1800s, cast iron was used as a building material, followed by the introduction of wrought iron. However, after 1850, wrought iron began to be gradually replaced by mild steel, and its usage significantly declined after 1890. Mild steel has many of the properties of wrought iron, with the ultimate tensile and compressive strengths lying roughly between 430-490N/mm² [26]. Based on data presented in the literature, deriving precise values for the mechanical and thermal properties of old concrete and steel at elevated temperatures presents a challenge [27,28]. The yield stress reported in the literature for tension

reinforcement (plain round or deformed) varies between 230N/mm² starting from 1885 to 410N/mm² (square twisted) used in the 1960s [29]. However, a thorough comparison with contemporary design codes found that the thermal and mechanical properties of old steel are in good agreement with the expressions provided in Eurocode 3 [5]. The thermal properties of old concrete are similar to those used for modern concrete, as outlined in Eurocode 2 [4].

6 NUMERICAL VALIDATION

6.1 Filler joist floors

In the validation exercise, the boundary conditions from the test evidence are applied to the numerical model. Figure 6 shows the heat transfer through the filler joist floor section and the time-temperature history of the lower and upper flange and the unexposed face.

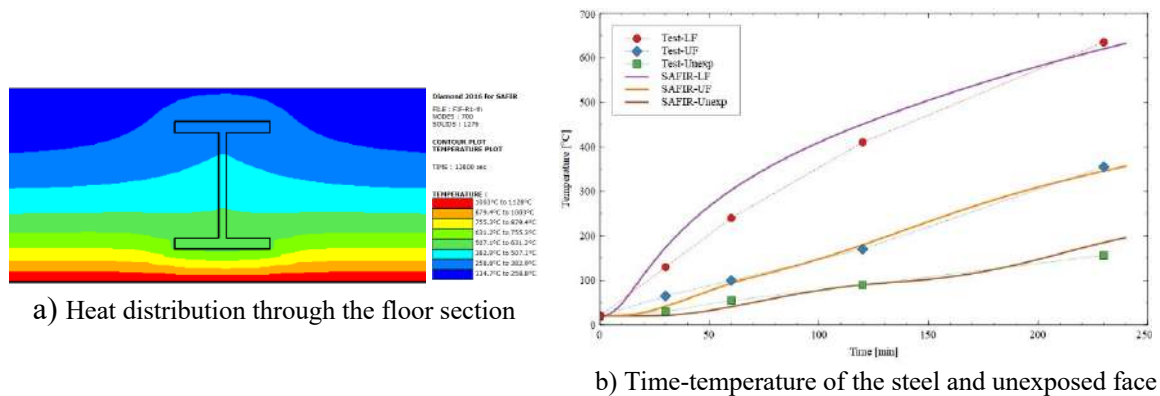


Figure 6. Heat transfer through the section and the time-temperature history through the section

Figure 7 shows a comparison between the measured temperatures during the ten tests with available data (Table 1) and the calculated values. Deviations of $\pm 15\%$ are indicated on the plot. In the early stages of the fire exposure, there is a slight underprediction or overprediction of the temperature distribution. This can be attributed mainly to steam and moisture migration and other phenomena such as crack formation, spalling and fall-off of the plaster layer. In the latter stages of the fire exposure, the temperature predictions of the structural component are within the expected deviation. In this case, the temperature of interest is above 400°C, where strength reduction factors are applicable to the steel member. The overall accuracy of the numerical heat transfer model fits well in the deviation of $\pm 15\%$.

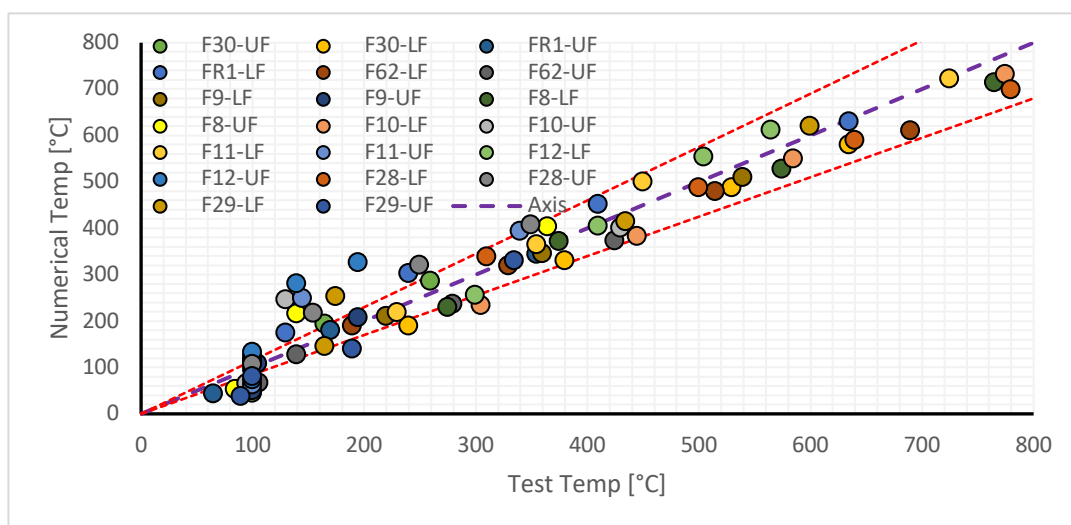
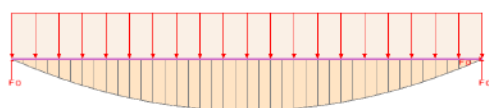


Figure 7. Comparison between calculated and predicted temperatures of the lower and upper flange.

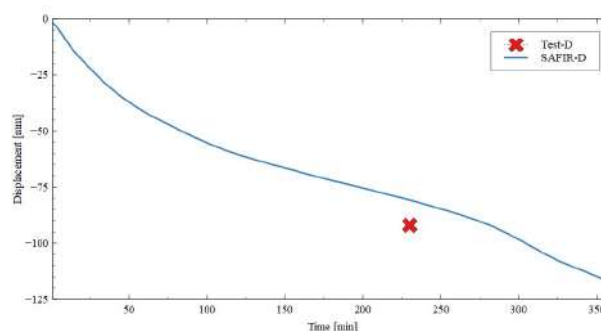
For the structural analysis, the same boundary conditions as those in the standard fire test were applied to the numerical model. The numerical model is simplified to a 2D analysis using beam elements, as shown in Figure 8a. This model assumes a bond between the steel and concrete with a transfer of longitudinal stresses. A summary of the main parameters used in the structural analysis is shown in Table 3 below.

Table 3. Parameters used in the structural analysis for filler joist floors

Test ref.	Density (kg/m ³)	Moisture (%)	Cover (mm)	Conc. Strength (MPa)	Load (kN/m)
F30	2306	5.0	26	26	4.1
FR1	2274	5.2	26	28.8	5.8
F62	2370	7.7	38	28	6.3
F8	2162	4.6	33	22.2	3.5
F9	2242	5.2	33	27.6	3.5
F10	2146	16.1	33	19.3	3.4
F11	1762	10	33	35.3	4.4
F12	1746	8.4	20	24.8	4.4
F28	2259	5.7	26	30.8	1.7
F29	2260	5.9	26	23.8	0.9



a) General view of the 2D model (FR1)



b) Calculated and measured deflection (FR1)

Figure 8. Model geometry following the test boundary conditions and measured and calculated deflection

Figure 8b shows a comparison between the measured deflection at the end of the test and the calculated deflection for case FR1. During the standard fire test, only one deflection measurement is available. The test was stopped at 228 minutes, and no failure mode was recorded. None of the samples tested presented any load-bearing failure (R) during the standard fire exposure. The expected failure mechanism for filler joist floors would be insulation (I) due to the nonlinear heat transfer through the steel section.

Figure 9 shows the duration of fire exposure for the tested samples and the associated failure mechanisms. The numerical analysis was performed for each tested sample and continued for 240 minutes to identify if there was any potential load-bearing failure mechanism for the samples where the test was stopped. In case F62, the test duration was six hours without any loadbearing failure, also captured in the numerical analysis. For the other samples, the numerical analysis is stopped at 240 minutes because there are no requirements in terms of fire resistance above this value.

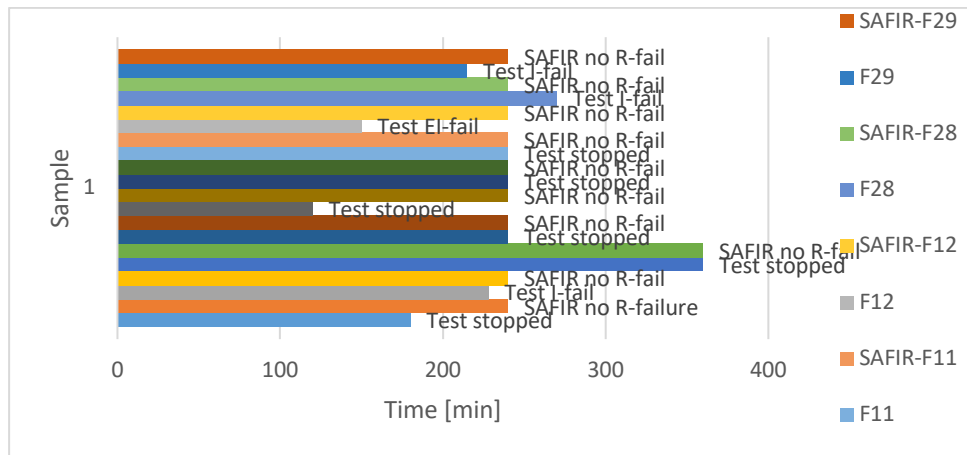
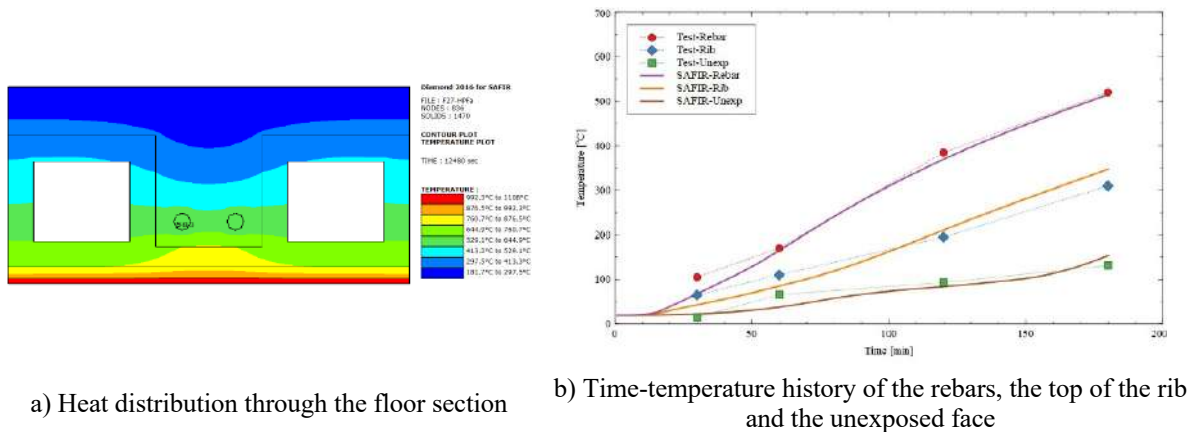


Figure 9. Tested and calculated fire resistance for the filler joist floor samples

6.2 Hollow pot floors

Figure 9 shows the heat transfer through the hollow pot floor section and the measured and calculated time-temperature history of the reinforcement, the upper part of the rib and the unexposed face. A good correlation can be observed between the measured and calculated values.



a) Heat distribution through the floor section

b) Time-temperature history of the rebars, the top of the rib and the unexposed face

Figure 10. Heat transfer through the section and the time-temperature history through the section

Figure 10 shows a comparison between the measured temperature of the main reinforcement during the test and the calculated values for the samples with available data and a deviation of $\pm 15\%$. The overall temperature predictions of the main loadbearing component align with the expected deviation.

For the structural analysis, the same boundary conditions as those in the standard fire test were applied to the numerical model. The numerical model is simplified to a 2D analysis using beam elements, as shown in Figure 11a. A summary of the main parameters used in the structural analysis is shown in Table 4.

Table 4. Parameters used in the structural analysis for hollow pot floors

Test ref.	Density (kg/m ³)	Moisture (%)	Cover (mm)	Conc. Strength (MPa)	Load (kN/m)
F26	2300	5.4	32	42	1.39
F27	2300	5.4	32	41	1.13
F13	2300	5.6	32	30	1.73
F14	2300	5.8	32	25	1.73
F32	2300	5.2	26	53	1.76
F59	2350	5.1	26	44	1.76
F66	2370	4.7	26	45	1.76
F64	2322	5.9	38	30	3.11

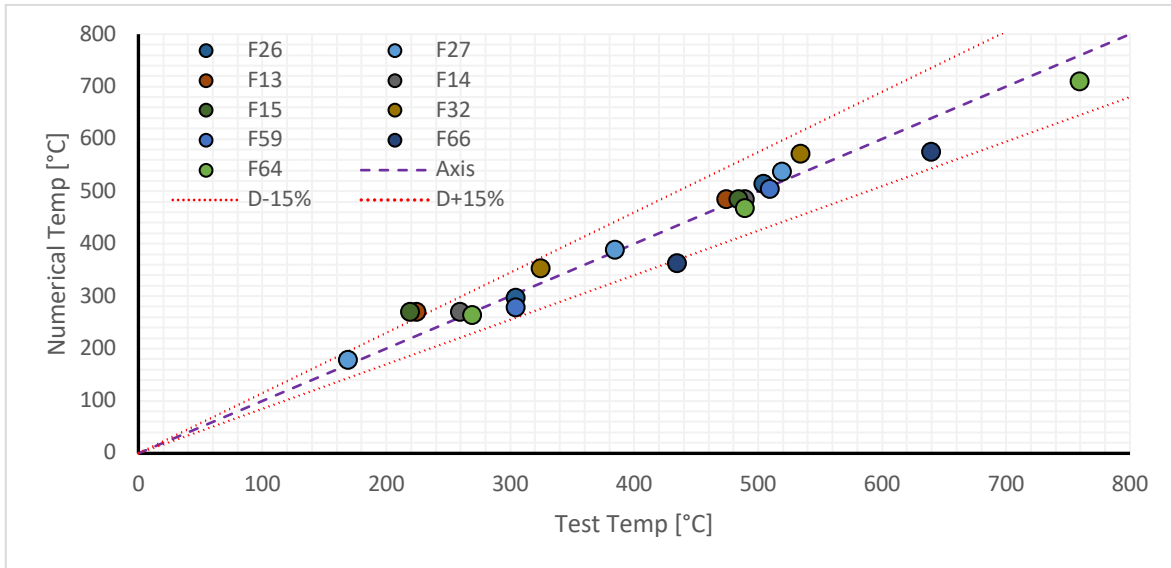
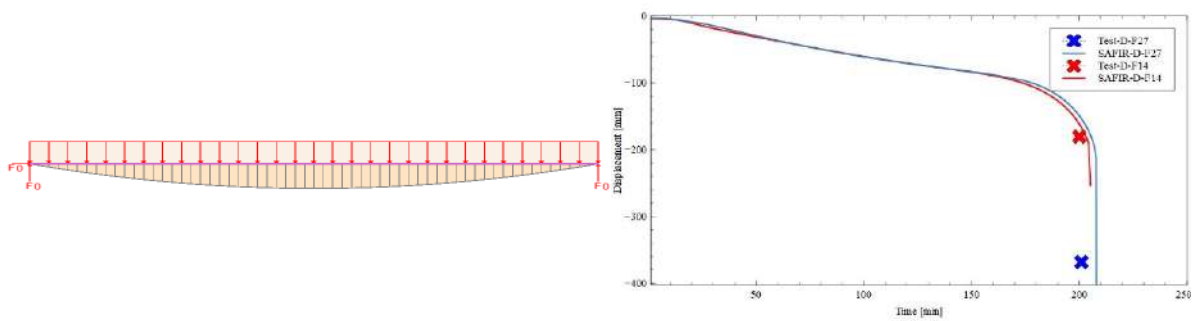


Figure 11. Comparison between calculated and predicted temperatures of the reinforcement layer

Figure 11b shows a comparison between the measured deflection at the end of the tests and the calculated deflection for cases F27 and F14. During the standard fire test, only two deflection measurements were recorded before collapse in the furnace. None of the samples tested presented any load-bearing failure (R) during the standard fire exposure. The expected failure mechanism for filler joist floors would be insulation (I) due to the nonlinear heat transfer through the steel section.



a) General view of the 2D model

b) Calculated and measured deflection (F27, F14)

Figure 12. Model geometry following the test boundary conditions and measured and calculated deflection

Figure 12 shows the duration of fire exposure for the tested hollow pot floor samples and the associated failure mechanisms. The numerical analysis was performed for each tested sample and continued to a load-bearing failure for up to 240 minutes. In most cases, the tests were stopped before any failure mechanism occurred. Two tests had a load-bearing failure after three hours of standard fire exposure. The loadbearing failure in these cases was successfully captured within the numerical model with reasonable accuracy, as shown in Figure 11b.

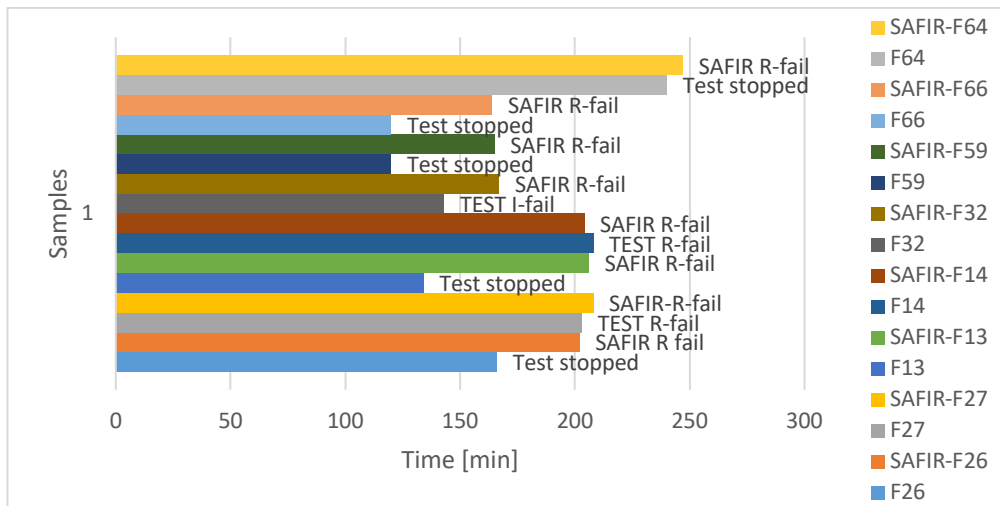


Figure 13. Tested and calculated fire resistance for hollow pot floors

7 DISCUSSIONS AND APPLICABILITY OF THE METHOD

The numerical validation exercise shows the capability of the SAFIR software to capture the thermal distribution through the studied floor systems accurately. The identification of the thermal properties used in the model is essential for its accuracy. The general thermal properties provided by the guidance for concrete, steel, mortar or brick are able to provide accurate results. The analysis found that the lower bound of the concrete thermal properties provides results closer to the measured values from the test.

In some cases, during the early stages of fire exposure, the numerical model overpredicts or underpredicts the temperature distribution. This is because of the complex phenomenon of steam and moisture migration, surface or explosive spalling, crack formation, plaster detachment, etc. These findings align with other studies from the literature [26,27].

The formulation of the concrete thermal properties proposed in the new EN 1992-1-2, which is a combination of the upper and lower bound of the thermal conductivity, is expected to provide more accurate results [30].

The structural analysis of the floor systems was simplified to a 2D model made of beam elements, and the results from the thermal model provided the main input. The loads, material properties and boundary conditions used in the numerical analysis are as close as possible to the samples tested. Where no data was available, assumptions were made based on the literature [27,29]. The stress-strain relationship and associated reduction factors as a function of temperature for the main loadbearing components are based on the formulation from the Eurocodes. The structural analysis performed for the two types of loadbearing floors shows a good correlation between the test data and calculated values.

The expected failure mechanism for the hollow pot floors is the load-bearing capacity (R). There are instances where insulation may be exceeded locally before the loss of capacity, but this is a function of the floor thickness or can be associated with spalling or cracking of the tiles during the fire test.

None of the filler joist floor systems tested presented a load-bearing failure mechanism during the standard fire exposure. Based on the structural analysis, the mechanical behaviour and the floor deflection are captured with a reasonable degree of accuracy.

Insulation failure is the anticipated failure mechanism for the filler joist floors. Loadbearing failure is not a primary failure mechanism because the steel sections encased in concrete have a nonlinear temperature distribution, and the cold side of the section can provide the required level of resistance. The concrete provides insulation and a level of restraint to the steel sections that ensures lateral torsional buckling is not a potential mode of failure of the beams.

Before the analysis, a site investigation must be conducted to identify the nature and extent of any defects. It is also important to determine the condition of the structural elements and if any degradation of materials

has occurred over time. For a more detailed overview of the material properties, destructive testing can be performed on concrete cores and steel coupons (samples).

The construction defects can have a significant impact on the anticipated fire resistance of the floor system. The main visible defects for hollow pot floors are cracked or missing tiles or holes through the tiles where ceilings or installations were present (Figure 13a). Another defect can be the shortfall in cover to the reinforcement or segregation in the concrete. It is recommended that a cover survey is conducted and the concrete in the downstand ribs is inspected by removing tiles in relevant areas. For filler joist floors, the main defects are a shortfall in cover to the bottom flange of the steel joists, poor quality of the infill concrete or corrosion of the steel members exposed (Figure 13b). In many cases, the filler joist floors have been designed to be covered with a plaster layer or protected by a lath and plaster ceiling. The defects should be repaired during the refurbishment process. Depending on the nature and extent of the defects, different solutions can be applied.



a) defects present to the underside of a hollow pot floor system b) defects present to the underside of a filler joist floor system

Figure 14. Examples of defects to the underside of the historic floors considered.

8 CONCLUSIONS

This paper provides a thorough examination of standard fire resistance test data for filler joists and hollow pot floors, which were conducted as part of the Investigation of Building Fires study in the UK during the 1950s. The overarching objective of the paper is to validate the applicability of modern numerical tools such as SAFIR software in evaluating the thermo-mechanical performance of historic forms of construction.

Through the thermo-mechanical analysis and validation exercises, this paper demonstrates the accuracy of advanced numerical techniques in evaluating the fire behaviour of historic forms of construction. Specifically, it aims to validate numerical methods by comparing them against fire resistance test data, focusing on two significant historical floor types: filler joists and hollow pot floors. The analysis presented in the paper shows that the formulation for the material properties (steel, concrete) from the Eurocodes can accurately capture the behaviour in fire of the two floor systems. One limitation is that these numerical methods cannot predict local integrity failure (e.g., cracking or spalling) or the effects of undetected defects. The study presented in the paper highlights the potential of applying advanced numerical techniques to enhance the understanding and evaluation of the fire performance of historical elements of structure. This not only facilitates more accurate assessments of fire resistance but also offers invaluable insights for architects, engineers, and preservationists involved in the conservation and refurbishment of historic buildings.

REFERENCES

1. Franssen, JM., Gernay, T., Modeling structures in fire with SAFIR®: Theoretical background and capabilities, *Journal of Structural Fire Engineering* 8, 300-323 (2017). <https://doi.org/10.1108/JSFE-07-2016-0010>
2. BS EN 13501-2, Fire classification of construction products and building elements, BSI, (2023).
3. Torero, JL., Fire Safety of Historical Buildings: Principles and Methodological Approach, *International Journal of Architectural Heritage* 13, 926-940, (2019). <https://doi.org/10.1080/15583058.2019.1612484>
4. BS EN 1992-1-2, Eurocode 2 Design of concrete structures. General rules. Structural fire design, BSI, (2004).
5. BS EN 1993-1-2, Eurocode 3 Design of steel structures. General rules. Structural fire design, BSI, (2005).

6. DIN EN 1991-1-2/NA, National Annex - National determined parameter – Eurocode 1: Actions on structures – Part 1-2: General actions – Actions on structures exposed to fire, Deutsche Norm, (2010).
7. COSTActionTU0904 Integrated Fire Engineering and Response, Case Studies, Ed. Wald F., Burgess I., Rein G., Kwasniewski L., Vila Real P., Horová K. CTU Publishing Production, Czech Technical University in Prague, (2012). ISBN–9788001050040
8. Ferreira, J., Franssen, JM., Gernay, T., Gamba, A., Validation of SAFIR® through DIN EN 1992-1-2 NA Comparison of the results for the examples presented in Annex CC, University of Liege – ArGenCo – Structural Engineering, (2018).
9. Zaharia, R., Gernay, T., Validation of the advanced calculation model SAFIR through DIN EN 1991-1-2 procedure, International Conference on Advances on Steel Concrete Composite and Hybrid Structures - ASCCS 2012, July 2-4, Singapore, Edited by Liew, JY., and Lee, C.S., ISBN-13: 978-981-07-2615-7, ISBN10: 981-07-2615
10. Ferreira, J.D.R., Gernay, T., Franssen, J.M., Discussion on a systematic approach to validation of software for structures in fire, SiF 2018 The 10th International Conference on Structures in Fire, Fire SERT, Ulster University, Belfast, UK, June 6-8, (2018).
11. Pintea, D., Franssen, J.M., Evaluation of the thermal part of the code SAFIR by comparison with the code TASEF, Proc. 8th Int. Conf. on Steel Structures 2, 636-643, (1997).
12. Miller, J., Conservation compendium. Part 17: Filler-joint floors – development, capacity and typical defects, The Institution of Structural Engineers, (2016).
13. Adams, P., Building Construction, London, UK: Cassells & Co., (1906)
14. Wouters, I., Mollaert, M., Assessing the 19th century 'fire-proof buildings, WIT Transactions on the Built Environment, (2001).
15. National Buildings Studies, Research paper No. 12, Investigations on Building Fires, Part V. Fire tests on structural elements, Her Majesty's Stationary Office, (1953).
16. Fisher, R.W., and Smart, P.M.T., Results of fire-resistance tests on elements of building construction. London, HMSO, Volume 1, (1975).
17. Fisher, R.W., and Smart P.M.T., Results of fire-resistance tests on elements of building construction. London, HMSO, Volume 2, (1977).
18. Lennon, T., Assessing the fire performance of existing reinforced concrete flooring systems, Information paper IP9/12 BRE Press, (2012).
19. BS 8110-2, Structural use of concrete - Part 2: Code of practice for special circumstances, BSI, (1985).
20. BR 128, Guidelines for the construction of fire-resisting structural elements, BRE Press, (1988). Archived
21. Schneider, U., Concrete at high temperatures – a general review. Fire Safety Journal 13, 55–68, (1988).
22. Harmathy, T.Z., Allen, L.W., Thermal properties of selected masonry unit concrete, Am Concr. Inst. Journal 70, 132–42, (1973).
23. Loudon, A.G., The thermal properties of lightweight concrete, Int. Journal of Lightweight Conc. 1, 71–85, (1979).
24. Harmathy, T.Z., Properties of building materials at elevated temperatures, Division of building research, Report no.: 1080, National Research Council of Canada, Ottawa, (1983).
25. Hu, X.F., Lie, T.T., Polomark, G.M., MacLaurin, J.W., Thermal properties of building materials at elevated temperatures, Institute for research in construction, Internal report no.: 643, National Research Council of Canada, Ottawa, (1993).
26. Publication 11/84 Historical structural steelwork handbook, British Constructional Steelwork Association, (1991). ISBN 9780850730159
27. Maraveas, C., Wang, Y.C., Swailes, T., Thermal and mechanical properties of 19th century fire-proof flooring systems at elevated temperatures, Construction and Building Materials 48, 248-264, (2013).doi: 10.1016/j.conbuildmat.2013.06.084
28. Maraveas, C., Wang, Y.C., Swailes, T., Fire resistance of 19th century fire-proof flooring systems: a sensitivity analysis, Construction and Building Materials 55, 69-81, (2014). doi:10.1016/j.conbuildmat.2014.01.022
29. Munter, S., Lume. E., Guide to Historical Reinforcement, CIA Concrete, (2017).
30. Carrascóna. S., Robert, F., Villagrà, C., Some Highlights on the New Version of EN 1992-1-2, (Eurocode 2, Fire part), Hormigón y Acero 74, 223-234, (2023). <https://doi.org/10.33586/hya.2023.3096>

VALIDATION OF NUMERICAL SIMULATIONS FOR HOT-DIP GALVANIZED COMPOSITE BEAMS AND CONNECTION DETAILS WITH EXPERIMENTAL DATA

Maria-Mirabela Firan¹, Justus Frenz², Jie Li³, Annika Kapfhammer⁴, Prof. Jochen Zehfuß⁵,
Prof. Martin Mensinger⁶

ABSTRACT

The results of research on hot-dip galvanized steel [1-3] show that the heating behaviour of steel in the event of a fire is significantly slower than that of uncoated steel profiles. As a result, hot-dip galvanized steel structures, in combination with moderate oversizing, can achieve the required fire resistance class R30 without the need for additional passive fire protection measures. For composite beams, R30 fire resistance can be accomplished with significantly improved material efficiency and economy by using higher strength steels. These effects have been investigated experimentally and are currently being followed up with numerical analysis. The process of model generation and validation with original experimental data in this project is presented.

Keywords: Hot-dip galvanizing; composite beams; high strength steel; connections; numerical modelling

1 INTRODUCTION

The emissivity of steel components treated with hot-dip galvanizing, as per EN ISO 14713-2:2020 [4], differs from the standard emissivity value of $\varepsilon=0.7$ for steel components specified in EN 1993-1-2:2010 [5] and EN 1994-1-2:2010 [6]. Lower emissivities, particularly at component temperatures below 500°C, result in slower heating of the components, allowing for achieving fire resistance rating R30 for compact cross-sections without additional fire protection measures.

During a fire, heat is transferred to steel members through convection and thermal radiation in the form of electromagnetic waves. Initially, convection dominates the heating of steel components, while radiation becomes dominant as the fire progresses. The emissivity of steel becomes significant when heating is primarily due to radiation. A lower emissivity leads to slower component heating. Hot-dip galvanizing can affect emissivity, especially with greater temperature differences between the component surface and furnace temperature, and is particularly beneficial at the onset of a fire and with smaller profile factors.

¹ Doctoral Candidate, Technical University of Munich, TUM School of Engineering and Design, Chair of Metal Structures
e-mail: m.firan@tum.de, ORCID: <https://orcid.org/0000-0002-5879-4515>

² Doctoral Candidate, Technische Universität Braunschweig, Institute of Building Materials, Concrete Construction and Fire Safety (iBMB),
ORCID: <https://orcid.org/0009-0009-2912-7498>
e-mail: j.frenz@ibmb.tu-bs.de

³ Master Student, Technical University of Munich, TUM School of Engineering and Design, Chair of Metal Structures
e-mail: jie.li@tum.de

⁴ M.Sc., Technical University of Munich, TUM School of Engineering and Design, Chair of Metal Structures
e-mail: annika.kapfhammer@gmx.de

⁵ Professor, Technische Universität Braunschweig, Institute of Building Materials, Concrete Construction and Fire Safety (iBMB)
e-mail: j.zehfuss@ibmb.tu-bs.de, ORCID: <https://orcid.org/0009-0004-6547-2479>

⁶ Professor, Technical University of Munich, TUM School of Engineering and Design, Chair of Metal Structures
e-mail: mensinger@tum.de, ORCID: <https://orcid.org/0000-0001-5210-5400>

Hot-dip galvanizing of steel components is conducted in accordance with EN ISO 1461 [7], where steel components are immersed in a liquid zinc bath, leading to the formation of multiple iron-zinc alloy layers due to reciprocal diffusion. EN ISO 14713-2 categorizes galvanizing into four categories based on steel chemical composition: low-silicon area (category A), Sebisty area (category B), Sandelin area (category C), and high-silicon area (category D).

In a research project, small-scale and large-scale fire tests were conducted at the Technical University of Munich to investigate the influence of hot-dip galvanizing on steel component emissivity during fires [8]. Tests compared specimens from categories A to D with different storage conditions after galvanization. Results indicate a more favorable heating behavior of hot-dip galvanized steel components in categories A and B compared to the specified emissivity of $\epsilon=0.70$. Based on the research, a temperature-dependent two-stage emissivity was determined: $\epsilon=0.35$ for component temperatures up to 500°C and $\epsilon=0.7$ for temperatures above 500°C . This temperature-dependent emissivity was incorporated into the revision of EN 1994-1-2.

In [9] large-scale fire tests on composite beams are investigating the impact of hot-dip galvanized steel on fire resistance. The program includes testing large composite beams with various steel sections, each with a reinforced concrete slab. Specific sections, such as halved IPE 500 with optimized lower flanges and hot-dip galvanizing, are tested for R30 fire resistance. Temperature reduction parameters for steel and connections are specified in EN 1994-1-2.

This paper provides an overview of experimental research on the high-temperature behaviour of high-strength steel and fire tests on hot-dip galvanized composite beams and connection details, followed by a description of numerical simulations of the composite beams and connection details.

2 MATERIAL INVESTIGATIONS

2.1 General

In this project, both steady-state and transient tensile tests were carried out at ambient and elevated temperatures. The test specimens were fabricated from the original material of the same steel batch as the full-scale experimental set-up. Water jet cutting was used, as samples were produced from hot-rolled beam flanges for S460M and steel sheets for S690QL. Two sheet thicknesses were considered ($t=20\text{ mm}$ and $t=30\text{ mm}$) for steel grade S690QL. A part of specimen for both S460M and S690QL were hot-dip galvanized after cutting. The tapered test section of the specimen (total length: 1100 mm) had dimensions of $L \times B \times T = 110 \times 15 \times 20\text{ mm}$ and $110 \times 20 \times 30\text{ mm}$ for sample thicknesses of 20 mm and 30 mm respectively. The mounting of the specimen was outside of the furnace (Figure 1).

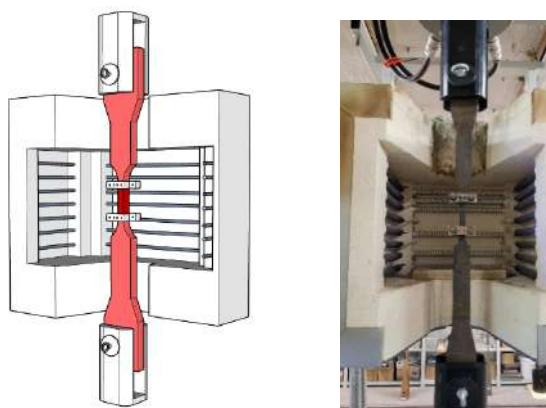


Figure 1. Tensile test setup with electrical furnace and mechanical bearing at TU Braunschweig

From the test data, elastic and plastic limit values, the stress-strain behavior for elevated temperatures and modulus of elasticity were generated and used as input data for the numerical model of the composite beams.

2.2 Steady-state tensile tests

The test regime for the S460M and S690QL included steady-state tests at temperatures of 20, 100, 200, 300, 400, 500, 600 and 700°C. At the start of testing, the specimens were clamped into the testing machine with a minor load of 5 kN, then the furnace heated the test area with a rate of 10 K/min to the target temperature and kept this level for around 30 minutes to allow for uniform spread of temperature throughout the cross-section. After the distribution was achieved, the specimen was loaded by a constant path-controlled speed of 1%/min until failure while maintaining the target temperature. In figure 2, recorded stress-strain relationships at different temperatures are presented for both materials.

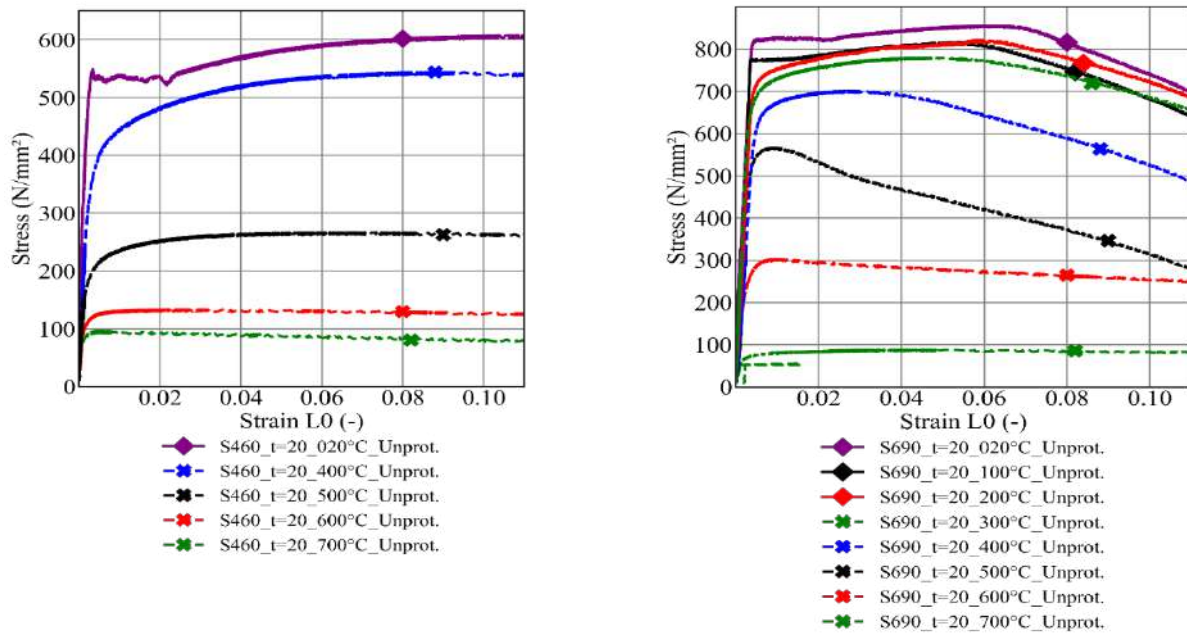


Figure 2. Stress-strain-relationship from steady-state tensile test of S460M (left) and S690QL-t= 20 mm (right)

2.3 Transient tensile tests

For transient tensile tests, investigated load levels included 0%, 20%, 30%, 40%, 50%, 60% and 65% of the yield strength at ambient temperature. The actual corresponding load for each test specimen was calculated from the tensile test at ambient temperature with the same material and the metered test area dimensions from the exact specimen so that imprecisions during cutting may not influence the loading level during the test. In this series, the specimens were loaded to the target load level, which was kept constant throughout the remainder of the test in a force-controlled setting. Then the temperature was progressively increased in the test area at a rate of 10 K/min. Plots of the strain-temperature relationships are presented in figure 3.

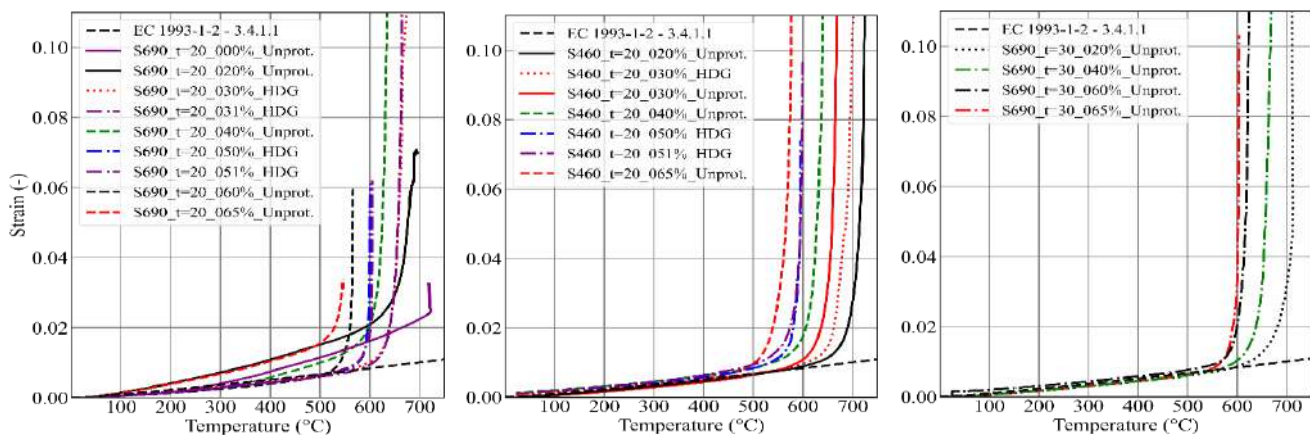


Figure 3. Strain-temperature-relationship from transient tensile test of S460M (left), S690QL-t= 20 mm (middle) and S690QL-t= 30 mm (right)

2.4 Material test data evaluation

From the test data of both the steady-state and transient material tests, elastic and plastic limit values and modulus of elasticity were generated. The derivative reduction factors for yield strength at elevated temperatures are presented in figure 4 at a plastic strain of 0,2% and total strain of 2,0%. As yield strength for elevated temperatures, the stress value at an absolute strain of 2,0% is considered. Data for S460M and S690QL is also in comparison to [10-14]. Further data from the material testing will be published in the final report of the research project (see acknowledgement).

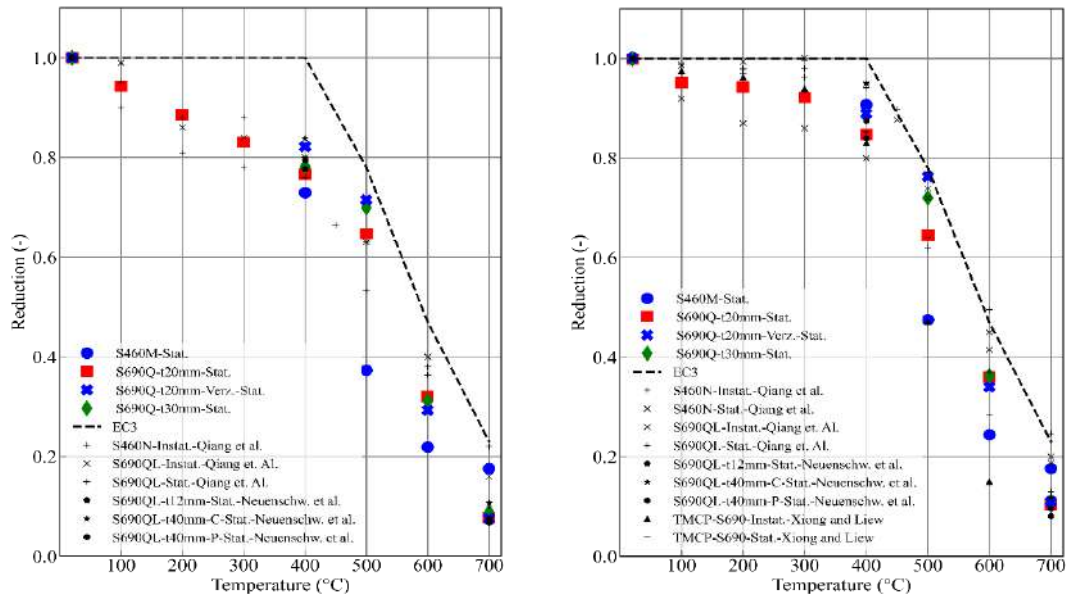


Figure 4. Yield strength reduction at plastic 0,2% strain (left) and total 2,0% strain (right)

All resultant material properties were incorporated into the numerical model to reproduce the full-scale fire testing numerically in this project as the basis to validate the numerical model of the composite beams.

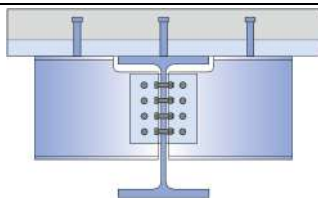
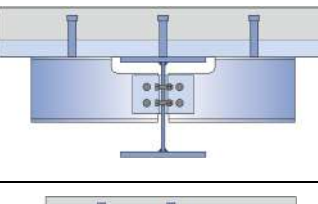
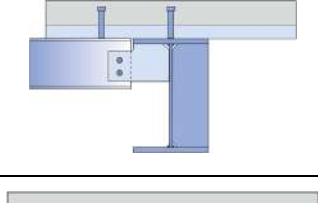
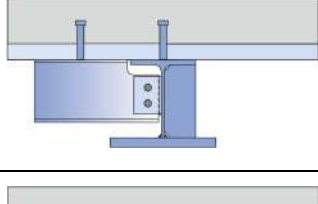
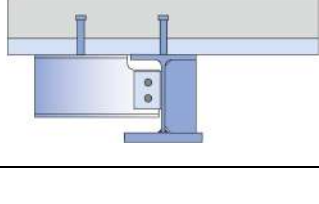
3 FULL-SCALE FIRE TESTS

With the full-scale fire tests a variety of six composite beam configurations with a length of 9.0 m with different steel sections (standard hot-rolled section and optimised welded sections) and a concrete deck width of 1.0 m were investigated. The beams and concrete slab were connected by stud shear connectors (SD 1, $d=22\text{mm}$, $l=125\text{mm}$) welded through the pre-stamped Holorib trapezoidal sheets (HR 51/150, $t = 0.88\text{ mm}$) to the flange of the steel section. The concrete class was C35/45 and the thickness of the concrete slab was 15 cm for the beams 1 to 4 and 20 cm for the beams 5 and 6. Each beam had a secondary beam connected at mid-span (figure 6). For this, different connection types were used. The steel grade was varied between S460M and S690QL for the beams and S355J2 for the secondary beams and connection elements. A summary of the composite beams subjected to the fire tests with the connection details to the secondary beams is given in Table 1.

Table 1. Composite beam configurations and connection details

Beam-no.	Profile main beam	Profile secondary beam	Connection type and no.	Sketch
1	HEB 300 S460M	IPE 200 S355J2	C2-long fin plate $t=10\text{ mm}$	

Table 1. Composite beam configurations and connection details

2	HEB 450 S460M	IPE 330 S355J2	C3-double angles L100x10	
3	Welded section Flange: 16 x 260 Web: 10 x 268 mm S690QL	IPE 200 S355J2	C1-double angles L80x8	
4	Welded section Flange: 20 x 300 Web: 10 x 410 mm S690QL	IPE 200 S355J2	C4-long fin plate t=20 mm	
5	Single Sym. 1/2 IPE500 (S460M) + bottom flange 30 x 340 mm (S690QL)	IPE 200 S355J2	C5-short fin plate t=10 mm	
6	Single Sym. 1/2 IPE500 (S460M) + bottom flange 30 x 250 mm (S690QL)	IPE 200 S355J2	C6-short fin plate t=20 mm	

All steel sections in this project were hot-dip galvanized, however available data from the same test setup in this furnace is available from two other projects where unprotected steel sections (mainly HEB300) of composite beams were investigated [9] and in [15]. This allowed for the comparison of result data for the temperature in the steel section with unprotected beams, presented in [15].

In accordance with EN 1363-1, the tests were conducted in a fire test furnace at TU Braunschweig. The composite beams were loaded vertically from the top using hydraulic presses (total load per beam 240 to 300 kN) and subjected to ISO 834 fire from below in a large test furnace for three-sided fire exposure. A deformation limitation was placed at midspan to prevent total collapse.

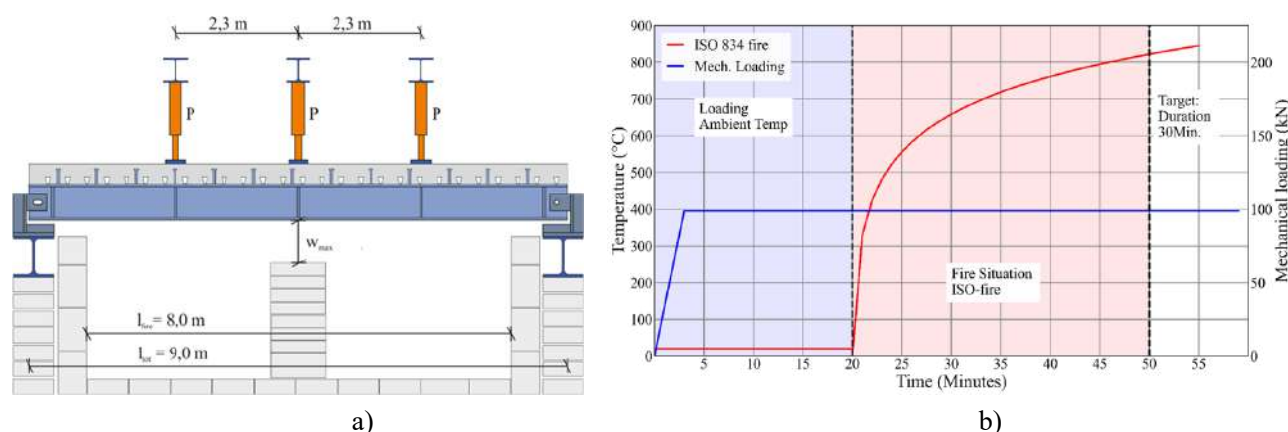


Figure 5. Schematic representation of the test setup (a); test setup (top, left and right) and loading (mechanically and temperature, bottom) (b)

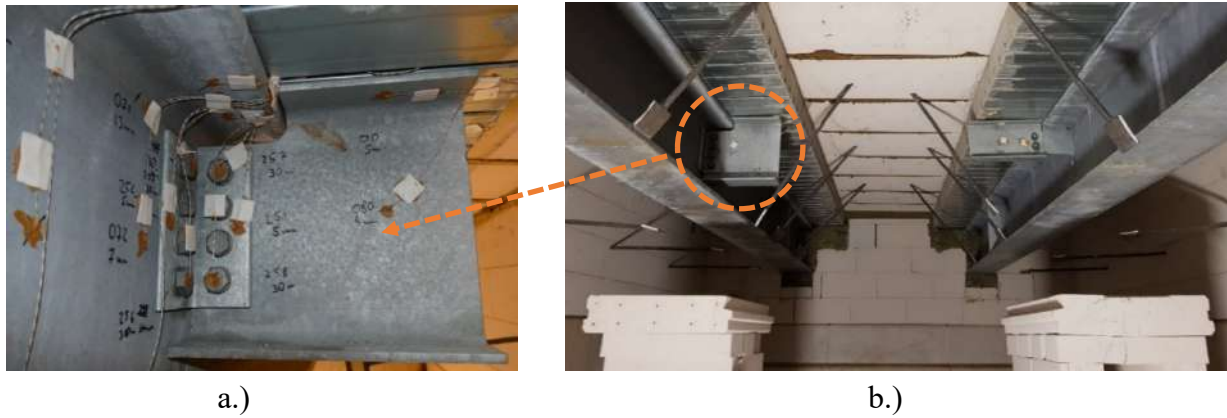


Figure 6. connection detail C3 (a); position of the connection detail (b)

During the fire test, surface plate thermocouples placed uniformly in the furnace directly below the steel sections were used to measure the temperature in the furnace. In this setup, data from loading, temperatures as well as deformation, rotations and slip were recorded. Temperatures were measured throughout the composite beam sections using type K thermocouples. For the hot-dip galvanized beams, thermocouples were placed in small holes (3 mm diameter) at a depth of half the thickness of each section element so that the zinc coating would only be disrupted as little as possible.

To compensate for possible temperature differences due to shading effects, the arrangement of the thermocouples on the steel section was staggered along the length of the beam at six locations and always placed at the top and bottom flange as well as the web. The positions for beam 1 are displayed in figure 7. Throughout the joint detail, an additional number of thermocouples were placed. The positioning of the thermocouples on the secondary beam (also both flanges and web), the fin plate, the web of the main beam and the bolts for the C2 connection detail is shown in figure 7, c.

The loading of the beams with hydraulic presses occurred in a force-controlled regime. Presses were eventually unloaded if structural failure of one beam occurred so that temperature development could be observed further.

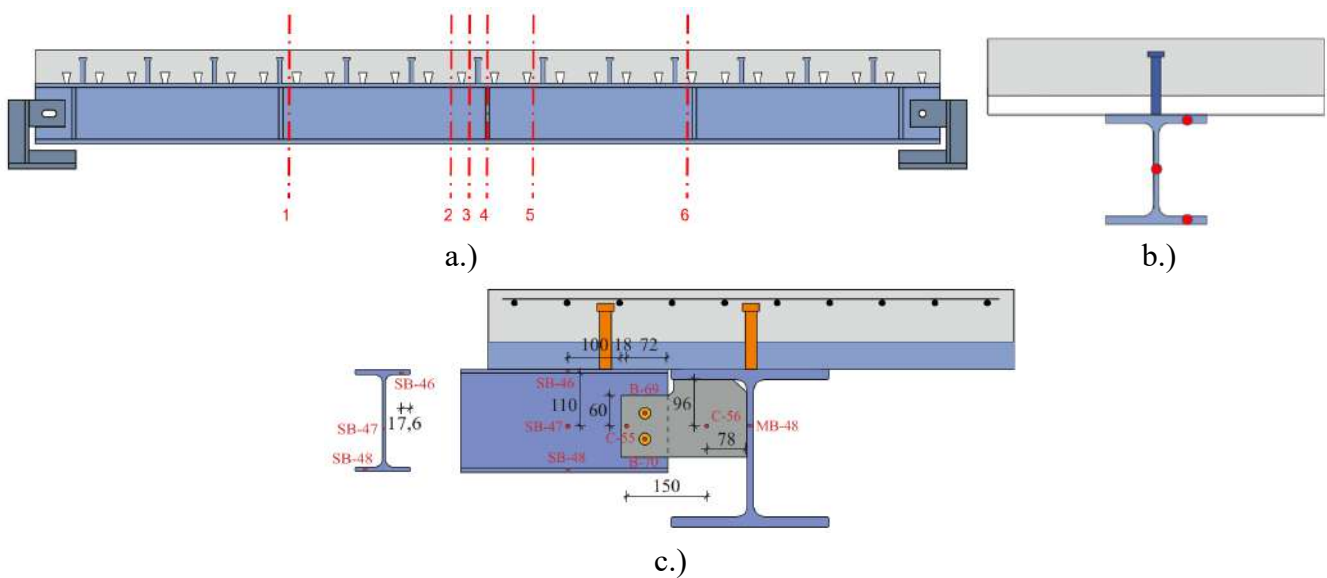
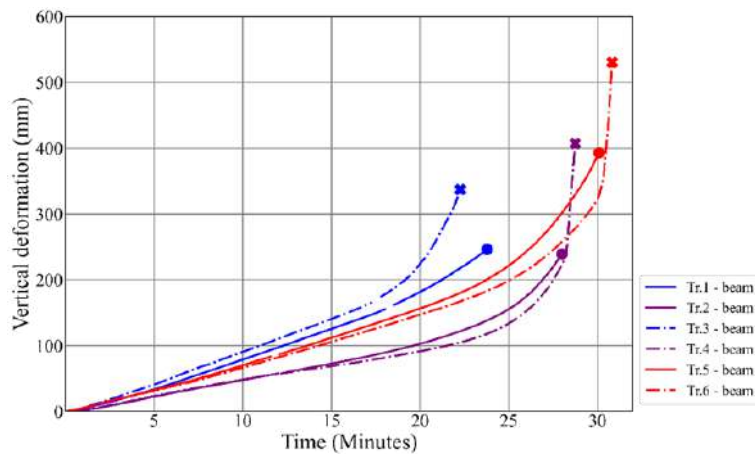


Figure 7. Regions of the temperature measurements (a); thermocouples arrangement on steel beam section (b) and connection detail (c)

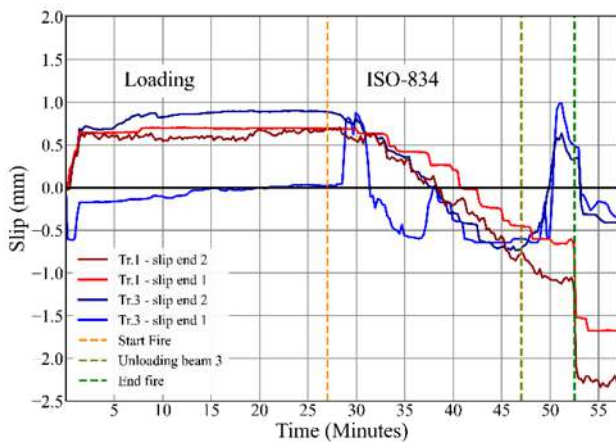
Temperatures were also recorded inside of the concrete slab and at the bottom of the stud shear connections. Before concreting, 18 temperature ladders were placed in the slab, with 6 positioned at midspan and another 6 at each quarter-span points. At every position, 3 ladders were placed in the high rib section of the trapezoidal sheet and 3 ladders in the low rib area. From these 3 ladders, one was positioned in the centreline over the

beam and one in both direction from centreline in a distance of 25 cm. Each ladder consisted of numerous thermocouples (Type K) to record temperatures at increasing depths in the concrete slab. A total of six stud shear connectors were modified with a hole (connector height: 125 mm, hole depth from top: 100 mm) to allow the temperature to be recorded close to the connection point. Vertical deformations of the beam were measured at midspan from an independent transverse beam to the top of the concrete slab of the composite beam. With rising temperatures, the deflection increases almost linearly until, at higher temperature, the rate of sagging increases. In figure 8, vertical deformation data from the experiments is presented.

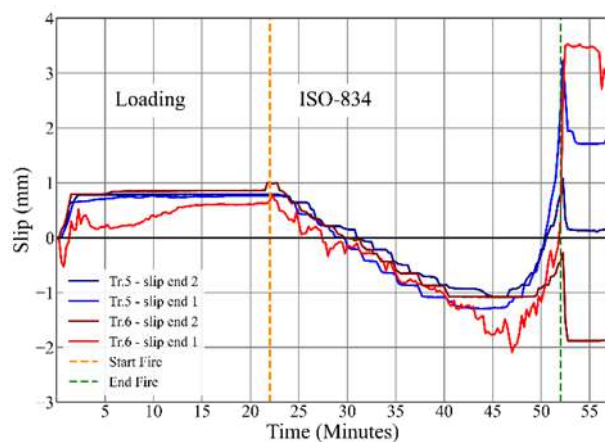
The influence of the hot dip galvanizing is shown by the mean values of the temperature profile development presented in [15]. A good approximation can be obtained by using a simplified method from EN1994-1-2 [8] where steel has an emissivity of 0.35 for steel temperatures below 500°C and 0.7 for steel temperatures over 500°C.



a.)



b.)



c.)

Figure 8. Vertical deformation at mid-span (a), horizontal slip at beam ends of beams 1 & 3 (b) and beams 5 & 6 (c)

The slip of the beams was recorded at each beam end, where the relative movement between concrete slab and steel section was measured during loading, the fire situation and during the cooling phase. Additionally, vertical and horizontal slip between steel section and concrete slab was measured in the midspan of the beams, however the magnitude of this relative movement was minor.

All data generated from the experimental investigations was compared to the numerical results of the simulation to check for an adequate representation of the behaviour by the model.

In figure 9, a comparison of the temperature development for different distances from the axis between all six connection details is shown. The temperature profile plot shows both the longitudinal direction and the transverse direction from the point of connection of the beam.

The discussion about the results may not be presented in this paper but can be found in [16].

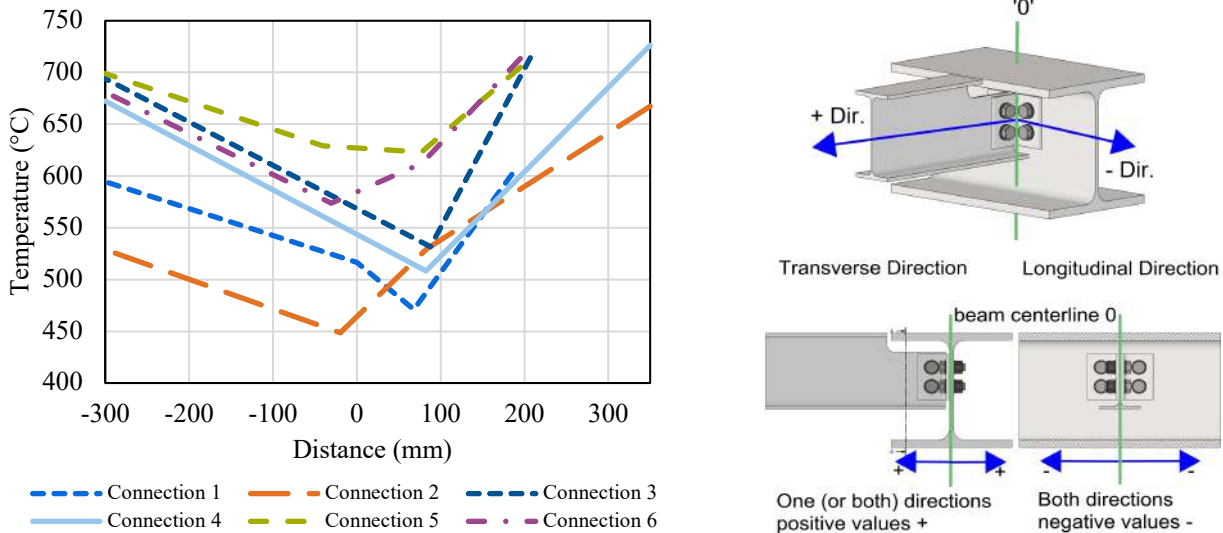


Figure 9. Temperature development for different distances of the connections from the web of the secondary beam to the connection parts and to the web of the main beam (left); trajectory orientation definition in the connection detail (right) [16]

4 NUMERICAL SIMULATIONS

4.1 Simulations of composite beams

The behavior of composite beams under fire exposure is simulated through a thermomechanically coupled analysis with Abaqus [17]. This analysis employs a distributed coupling approach. Initially, the finite element model (FEM) of the composite beam undergoes a heat conduction analysis to determine the temperature development of each element over time (figure 10). Subsequently, the results of this heat conduction analysis are integrated into the mechanical model as a prescribed field and coupled for mechanical analysis (figure 11). The furnace temperature was used to validate the models.

For the thermal simulation, an implicit analysis of heat conduction is conducted with an element size set to 0.03 meters. The thermal model consists of heat conduction elements of type DC3D8 and DC1D2. Mechanical modelling is carried out using implicit static analysis, with 3D stress elements C3D8R and truss elements T3D2 utilized in the FEM.

To minimize computation time, only a quarter model of the composite beam is created, significantly reducing the number of elements. Symmetrical boundary conditions are applied at the center and along the midline of the beam in Abaqus, with only vertical displacements restricted at the beam ends.

The bonding behaviour between the concrete flange and steel profile is mainly considered in tangential and normal directions. Tangential mechanical properties are determined by frictional forces, with a friction coefficient between steel and concrete typically set to 0.15. Additionally, headed studs play a crucial role in force transmission between the concrete flange and steel profile, limiting relative slip and normal separation. Within Abaqus, the bond effect of dowel bolts is simulated using nonlinear spring elements. The nonlinear spring curve, corresponding to the load-slip curve of the dowel bolt, is assumed based on Becker [18] at normal temperature, with a maximum dowel bearing capacity of $P_{Rd,max} = 145$ kN.

Material properties such as the Young's modulus, yield strength, tensile strength, and proportional limit for steel are derived from the tensile fire tests shown above. Similarly, material properties for concrete are determined from accompanying experiments and applied in the simulations. Temperature-dependent material properties such as specific heat capacity and thermal conductivity for the cross-section are used according to EN 1994-1-2. For model validation, visibility factors are determined for considering the burner's location relative to the beam, and emissivity is multiplied when inputting into Abaqus. Emissivity is set according to a two-stage approach with 0.35 up to 500°C and 0.7 from 500°C onwards.

In accordance with the simplified design methods specified in EN 1994-1-2 for the temperature of composite beams under fire conditions, temperature increases are separately calculated for the web and lower flange. The consideration of the two-stage emissivity is achieved by defining two steps in the temperature calculation. In the first step, an emissivity of 0.35 is used up to a component temperature of 500°C, and in the second step, an emissivity of 0.7 is used. The transition point for the emissivity change occurs when the web and the lower flange reach a component temperature of 500°C. To simplify, the average of the two transition points was calculated. The times at which the web and lower flange reach 500°C are taken from experimental data. As the upper flange remains below 500°C, it is only considered in one step.

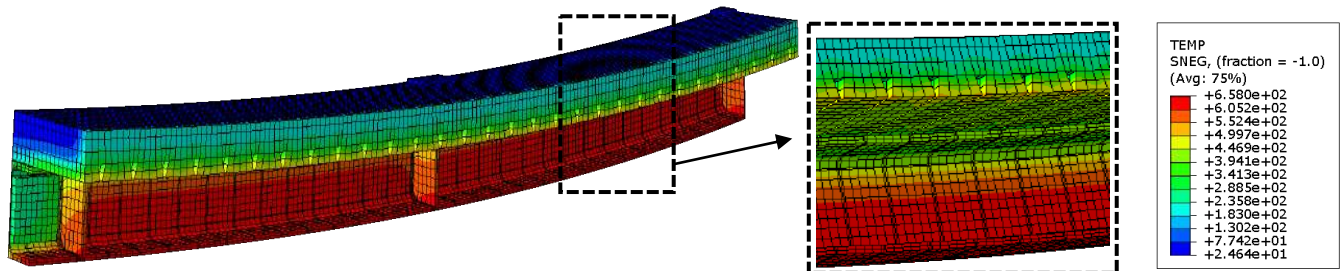


Figure 10: Temperature model beam 1 - temperature development after 30 min fire loading

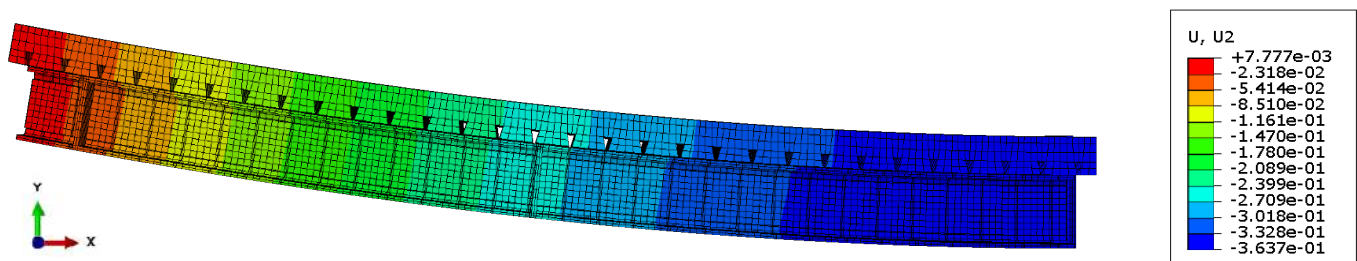


Figure 11. Static model beam 1 - Deformation after 30 minutes of fire test

The experimental fire exposure lasted for 24 minutes, while the simulation assumed a fire exposure duration of 30 minutes. Temperatures obtained from the simulation were compared with the average temperature values measured at external locations of the measurement axis (axis 1 and 6, figure 7) on the upper and lower flanges, as well as on the web (figure 12). The results of the simulations shown in figures 12 and 13 against the experimental data for temperature, vertical deformation and slip show similar results. By validating the models, the two-step approach can be used to account for two-stage emissivity. Further validation models and a parameter study are presented in the final report of the project (see acknowledgement).

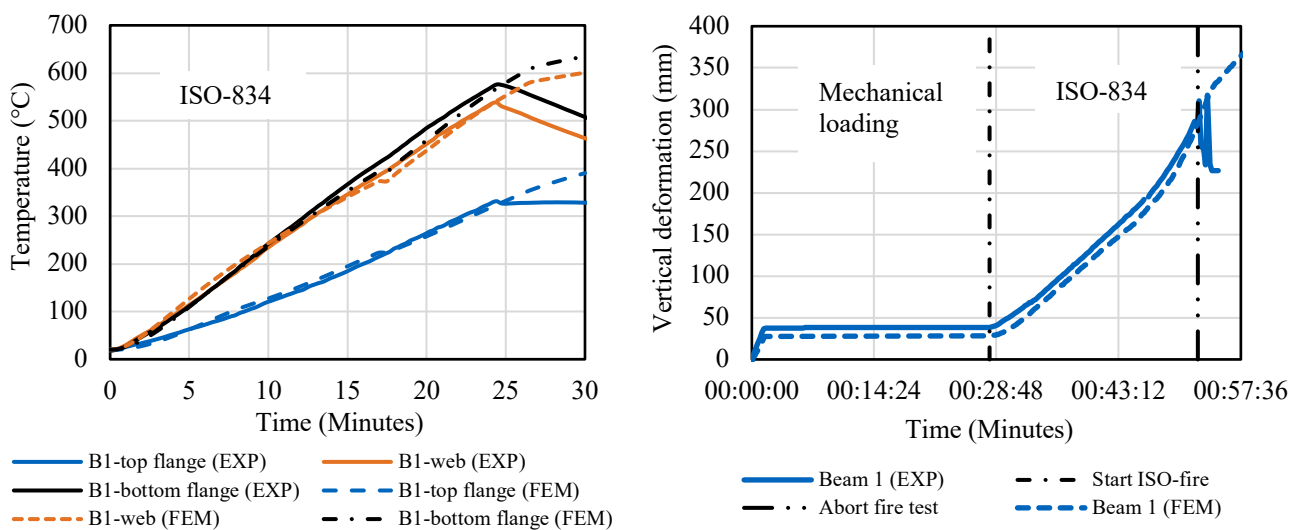


Figure 12. Comparison of the simulation results with the experimental data for Temperature (left) and vertical deformation (right) for beam 1

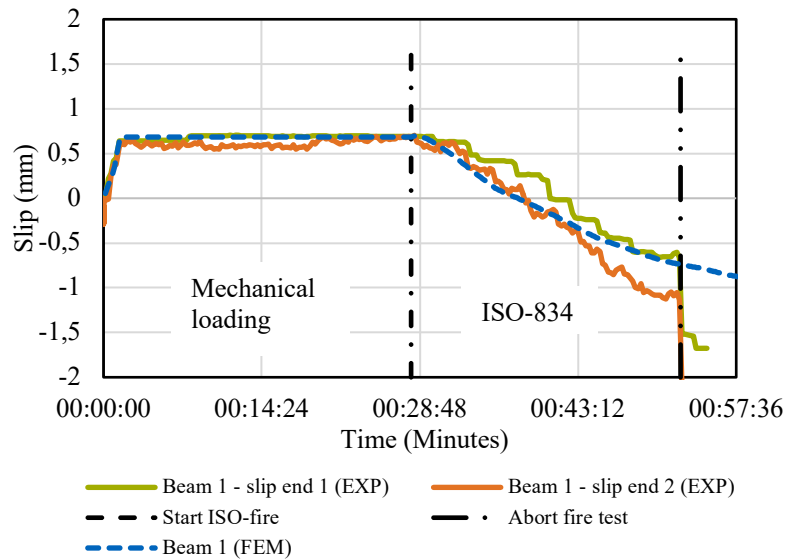


Figure 13. Comparison of the simulation results with the experimental data for slip deformation for beam 1

4.2 Simulations of the connection details on the composite beams

The modeling of the connection details was performed similarly to the modeling of the composite beams. In this case, beam 2 (HEB 450) and connection detail 3 with double angles L 100x10 and two secondary beams were used to validate the model (figure 14).

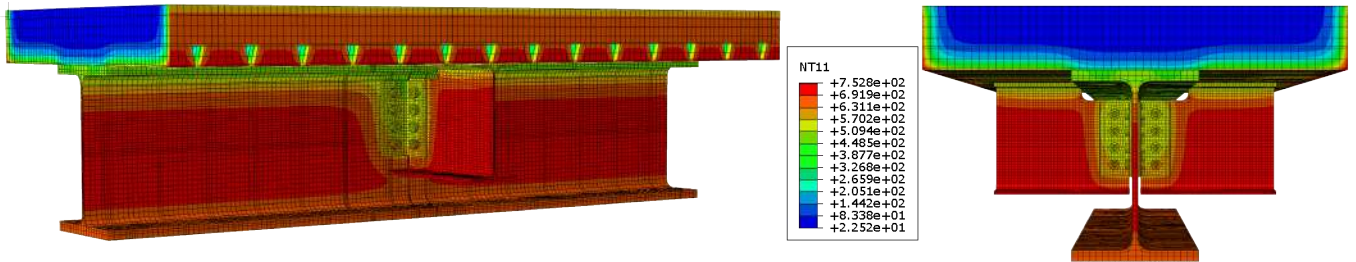


Figure 14. Temperature distribution in the temperature model of connection 3 after 31.2 min (duration of fire test)

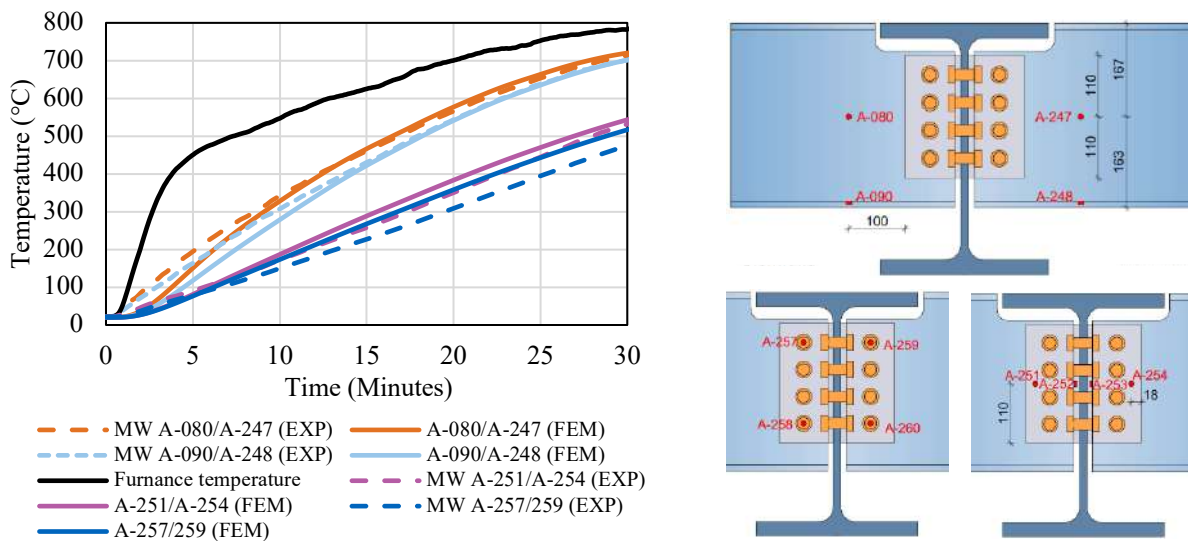


Figure 15. Comparison of the simulation results with the experimental data for Temperature distribution in the secondary beams and connection details

For the connection presented in this paper, a constant emissivity of 0.35 was assumed for the secondary beams, which led to good results compared to the test data (figure 15). Taking into account the visibility factors and shadowing effects caused by the support structure under the main beam and the bottom flanges of the main and secondary beams, the radiation at the angles and bolts was not included in the simulation. Heating only occurs as a result of convection, as the temperature in simulations would otherwise be overestimated. Further influences on the simulations and validation of the connections as well as an extensive parameter study were analysed in [19].

For the parametric study, four connection types were examined: long and short angles, and long and short fin plates. For the long angles, plate thicknesses of 10 mm and 15 mm were investigated. IPE 400 and IPE 600 steel profiles were used for the main beams, and IPE 300 and IPE 400 for the secondary beams. For the short angles, plate thicknesses of 8 mm, 10 mm, and 12 mm were examined. The connections with short and long fin plates were executed with plate thicknesses of 10 mm, 15 mm, and 20 mm. Profiles chosen for the connection configurations with short angles and fin plates were HEA + HEB 300/450/600 for the main beams and IPE + HEA 200/300/400 for the secondary beams. The parametric study was conducted using the ISO 834 fire curve and considering the two-stage emissivity as well as view factors for the case of three-sided fire exposure. Figure 16 shows, for example, the temperature development in connection details with angles and short flag plates for hot-dip galvanized components.

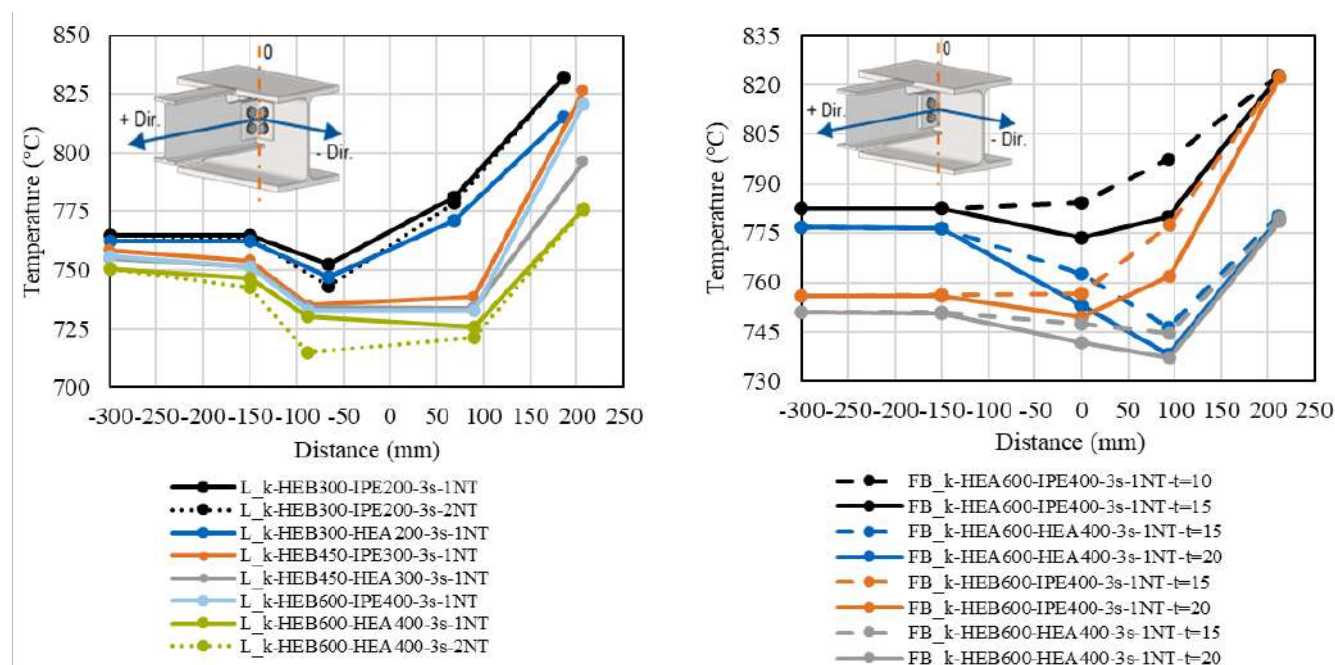


Figure 16. Temperature development after 30 min ISO fire in connection details with short angles (left) and with short fin plates in different thicknesses for a three-sided fire exposure (right); (1NT-one secondary beam; 2NT-two secondary beams)

5 CONCLUSIONS

This research project presents material investigation for high-strength structural steel and full-scale fire tests carried out on simply supported steel-concrete composite beams. The measured temperatures of the galvanized steel profiles show that the approach proposed in [8] is applicable, with a temperature-dependent emissivity that is reduced to $\epsilon_m = 0.35$ up to a component temperature of 500 °C and then increased to $\epsilon_m = 0.7$. A significant proportion of the fire protection measures for R30 requirements can be saved through the positive effect of hot-dip galvanizing and the use of composite construction. The validation of the FE models of the composite beams shows that the effect of hot-dip galvanizing, taking into account the temperature-dependent two-stage emissivity, can be well represented in the simulations. With the parameter study and test data on the hot-dip galvanised connection details, a comparison of the temperature development according to EN 1994-1-2 and with the draft standard will be made and an approach for determining the temperature in the connection details will be proposed.

ACKNOWLEDGMENT

The research project IGF 21536 N from the GAV - Gemeinschaftsausschuss Verzinken e.V., Düsseldorf, FOSTA - e. V., Düsseldorf and DAST Deutscher Ausschuss für Stahlbau e.V., Düsseldorf is supported by the Federal Ministry of Economic Affairs and Climate Action the German Federation of Industrial Research Associations (AiF) as part of the programme for promoting industrial cooperative research (IGF) on the basis of a decision by the German Bundestag. The project is carried out at TU-Munich, TU-Braunschweig and at the RWTH Aachen.

REFERENCES

1. M. Mensinger and C. Gaigl, "Feuerwiderstand verzinkter Stahlkonstruktionen", *Stahlbau* 88, 1, 3–10, 2019.
2. J. Jirku and F. Wald, "Influence of Zinc Coating to a Temperature of Steel Members in Fire", *Journal of Structural Fire Engineering* 6, 2, 141–146, 2015.
3. G. Bihina, B. Zhao, "Hot-dip galvanizing of steel structural members: an alternative to passive fire insulation?", *Proceedings 9. European Conference on Steel and Composite Structures (Eurosteel 2021)*, 1.-3. September 2021, Sheffield, Großbritannien. <https://doi.org/10.1002/cepa.1427>.
4. DIN EN ISO 14713-2 (2020), Zinc coatings - Guidelines and recommendations for the protection against corrosion of iron and steel in structures - Part 2: Hot dip galvanizing; German version.
5. DIN EN 1993-1-2:2010-12, Eurocode 3 (2010) Design of steel structures - Part 1-2: General rules - Structural fire design; German version.
6. DIN EN 1994-1-2:2010-12, Eurocode 4 (2010) Design of composite steel and concrete structures - Part 1-2: General rules - Structural fire design; German version.
7. DIN EN ISO 1461 (2009) Hot dip galvanized coatings on fabricated iron and steel articles - Specifications and test methods (ISO 1461:2009); German version.
8. Martin Mensinger, Christian Gaigl. 2018. Schlussbericht zu IGF-Vorhaben Nr. 18887 N. Feuerwiderstand von feuerverzinkten, tragenden Stahlkonstruktionen im Brandfall.
9. M. Mensinger, S. Pfenning, J. Zehfuß and S. Brunkhorst. 2018. Schlussbericht zu IGF-Vorhaben Nr. 19105 N. Mindestverdübelung von Verbundträgern bei Brand.
10. Neuenschwander, M.; Scandella, C.; Knobloch, M. et al. Modeling elevated-temperature mechanical behavior of high and ultra-high strength steels in structural fire design. In: *Materials and Design* 2017, 2017, 81-102, <https://doi.org/10.1016/j.matdes.2017.09.041>.
11. Qiang, X.; Bijlaard, F.; Kolstein, H. Dependence of mechanical properties of high strength steel S690 on elevated temperatures. In: *Construction and Building Materials* 2012, 2012, 73-79, <https://doi.org/10.1016/j.conbuildmat.2011.12.018>.
12. Qiang, X.; Bijlaard, F.; Kolstein, H. Deterioration of mechanical properties of high strength structural steel S460N under steady state fire condition. In: *Materials and Design* 2012, 2012, 438-442, <https://doi.org/10.1016/j.matdes.2011.11.069>.
13. Qiang, X.; Bijlaard, F.; Kolstein, H. Deterioration of mechanical properties of high strength structural steel S460N under transient state fire condition. In: *Materials and Design* 2012, 2012, 521-527, <https://doi.org/10.1016/j.matdes.2012.04.028>.
14. Xiong, M.-X.; Liew, J.Y.R. Experimental study to differentiate mechanical behaviours of TMCP and QT high strength steel at elevated temperatures. In: *Construction and Building Materials* 2020, 2020, <https://doi.org/10.1016/j.conbuildmat.2020.118105>.
15. Mirabela Firan; Kurt Tutzer; Martin Mensinger; Justus Frenz; Jochen Zehfuß: Temperature development in the cross section of composite beams with galvanized steel compared to uncoated steel. *Proceedings of the 12th International Conference on Structures in Fire, The Hong Kong Polytechnic University 2023*, 180-191. E-ISBN:978-962-367-869-8.
16. Justus Frenz; Jochen Zehfuß; Maria-Mirabela Firan; Martin Mensinger: Temperature increase throughout hot-dip galvanized steel sections and connections of composite beams in the fire situation. *Proceedings of IFireSS 2023 - International Fire Safety Symposium, ALBRASCI, 2023*, 507-516. E-ISBN: 978-65-00-82533-6.
17. Dassault Systèmes (2022) Abaqus 6.14 Documentation [Software].
18. Becker, J. (1997) Beitrag zur Auslegung der Verdübelung von Verbundträgern des Hochbaus unter ruhender und nichtruhender Belastung [Dissertation]. Universität Kaiserslautern.
19. Kapfhammer A. (2024) Numerische Untersuchungen feuerverzinkter Sekundärträgeranschlüsse an feuerverzinkten Verbundträgern (Master's Thesis). Chair of Metal Structures. Technical University of Munich.

VALIDATION OF STRUCTURAL FIRE SIMULATIONS: FROM SMALL-SCALE EXPERIMENTS TO REAL, LARGE-SCALE FIRES

Wulan Shofa Aisyah¹, Augustin Guibaud², Jose Torero³, Alejandra Albuerne⁴

ABSTRACT

Fire is a looming risk in mass timber buildings because structural elements participate in the fire load with consequences for both the fire dynamics and the mechanical stability of the structure. As conducting full-scale experiments is prohibitively costly, modelling tools can be invaluable in understanding the impact of design variations on fire spread and growth in timber construction. To validate the use of numerical tools and highlight their limitations a series of experiments are numerically replicated from the literature. The experiments are chosen to capture fire behaviour across scales, starting with small wood cribs, and then capturing large-scale compartment simulations. Numerical and experimental results are contrasted using the flame spread rate and fields of temperature distribution as criteria of comparison. As a Computational Fluid Dynamics model (CFD) is validated and the sensitivity of the results to the choice of the heat of combustion is established, the model is applied to the real-case scenario of the 2019 fire of Notre Dame, where only indirect observations are available.

Keywords: Structures; Computational Fluid Dynamics; timber.

1 INTRODUCTION

Building fire safety relies on codes and standards developed to achieve life safety in modern constructions. However, these standard approaches can fall short when dealing with unconventional buildings featuring unusual architectural and material characteristics. This is the case in historic buildings, which predate codes and can display an array of geometry and materials that are not common practice in modern construction anymore (for instance high vaulted ceilings, and thatched roofs). In addition, prescriptive codes, which dictate specific requirements, do not fully consider the intrinsic value of structures once life safety is achieved [1,2].

Some traditional construction materials are making a resurgence, driven by environmental and societal concerns. Timber, for instance, is increasingly used due to its potential for sustainable development, reduced energy consumption, and reduced carbon emissions [3]. Still, the use of mass timber in buildings can be particularly problematic as, in addition to bearing the structural load, it also increases the fuel load in case of an accidental fire. As a consequence, there is a need to study the associated fire risk, in a scenario that is not captured by today's standards.

A certain number of experiments have been performed to study timber as a contributing factor in a structural fire. Landmark large-scale experiments include the 'Epernon Fire Test Programme' [4], the RISE

¹ Wulan Shofa Aisyah , University College London
e-mail: wulan.aisyah.22@ucl.ac.uk,

² Augustin Guibaud, University College London
e-mail: a.guibaud@ucl.ac.uk, ORCID: <https://orcid.org/0000-0002-2549-9173>

³ Jose Torero, University College London
e-mail: j.torero@ucl.ac.uk, ORCID: <https://orcid.org/0000-0001-6265-9327>

⁴ Alejandra Albuerne, University College London
e-mail: a.albuerne@ucl.ac.uk, ORCID: <https://orcid.org/0000-0001-6444-9120>

compartment fire [5], and the series of CodeRed experiments [6]. These experiments are crucial to obtaining real data on how the fire and the structure behave, but carrying out experiments is extremely costly. As a result, there is a need to extrapolate the precious data obtained in specific configurations to a wider range of possible layouts representative of the diversity of both the existing building stock and future projects.

This is where the use of computational methods as versatile tools to predict the growth and propagation of a fire inside the building can be particularly useful. The dimensions, use, and intricate details of any timber building can be incorporated into a numerical model to provide architects and engineers with a representation of potential fire events. Traditional numerical tools like zone models are not able to incorporate reactive structural elements [7], prompting a shift to more advanced tools such as Computational Fluid Dynamics (CFD). To this day, a wide range of CFD software has been developed, such as OpenFOAM, Fire Dynamic Simulator (FDS), CFX, PHOENICS, and ANSYS Fluent. By design, these software are flexible enough to address the spectrum of issues at stake in timber construction [8]. Those packages can model complex scenarios but require careful consideration of physical and chemical processes to obtain accurate results.

It is not clear to this day how CFD tools should be adapted to predict large-scale fire scenarios in timber construction. A major challenge is to correctly determine the wide range of parameters defining the properties of the solid phase and of the gas phase to avoid overfitting -and consequently losing the predictive capacity of the model.

In the following, a series of numerical simulations is carried out to reproduce existing results in gradually more complex configurations. First, flame spread over small-scale wood cribs is modelled to define both the chemistry and the meshing required to capture the relevant heat transfer modes. Then, the parameters are used to replicate results from a large compartment fire experiment and underline scaling issues. As the unique charring properties of timber emerge, additional considerations are included to capture the nature of the fully-developed fire. The predictive potential of this method is finally evaluated over a real-case scenario, where the uncertainties associated with the model are compounded with the uncertainties of the measurements.

2 METHODOLOGY

This study relies on the open-source Fire Dynamics Simulator (FDS) model developed by NIST [9], but similar conclusions would be drawn with other CFD software. FDS is selected due to the demonstrated ability to replicate realistic fire scenarios in large environments, such as a subway platform fire [10], fire in a large-elongated compartment [11], and controlled large-scale experiments [12] [13]. Carrying parametric study for different inputs in FDS, the SP Fire 105 study highlights that different parameters being defined in FDS will hugely affect the outcome of the modelling [14]. In spite of these many efforts, the literature still lacks extensive validation studies of numerical tools valid across scales in combustible timber structures.

2.1 Selected experiments

The study starts by reproducing results from lab-scale experiments. To that end, experiments by Delichatsios [14] over wood cribs are studied due to the regularity of the configuration and its ability to accommodate variations in flame spread rates as the fuel dimension and layout change. Delichatsios reports experimental data regarding the burning rate and flame spread rate over 15 wood cribs where the stick length, stick thickness, and the number of layers are varied. Ignited using an acetone pool in the centre of each base, the flame grows vertically and then spreads radially to the sides. The experimental flame spread rates and the numerically obtained flame spread rates are evaluated over four specific configurations of varying sizes, by evaluating the time it takes for the flame to reach the side of the wood cribs. Crib #1, Crib #4, Crib #9, and Crib #13. Crib #1 is explored as the base with a total height of 95.2 mm and Crib #4 comes with different horizontal spacing, both with stick dimensions of 6.35 mm. Crib #9 is the configuration with a dimension in the z direction bigger than the x or y direction, with sticks size of 19.05 mm and a total height of 685.8 mm. Hence, the flow of the hot air rising to the top part of the crib can be observed. In addition to that, Crib #13 is studied due to its thicker stick elements of 31.7 mm. The objective of the wood crib simulations is to validate the use of standard material physical and chemical properties in an early-stage fire situation, using the flame spread rate and the burning rate as the performance criteria.

As longer times are expected in a large-scale fire, other experimental results need to be replicated to evaluate the relevance of the hypotheses of the numerical model. To that end, the CodeRed experiments are analysed [6]. This series of large-scale compartment fires was carried out to understand the flow conditions and temperature distribution in the presence of structural timber elements. The 352 m² compartment replicates a big office space featuring timber columns and a CLT ceiling 3.1 m high, and the fire initially spreads over a large crib ignited at one end, using a set of 12 pools of 0.5 L methanol with the addition of a few fibreboards along 1 meter from the ignition line. For the purpose of this study, the first experiment of the series CodeRed#1 which features glulam columns and CLT panel ceiling as part of the structure, while the main fuel source comes from a large-scale wood crib covering most of the space. This is where the condition of a well-ventilated compartment with CLT being exposed without any encapsulation as well as without any suppression system can be replicated. Temperature measurements are performed using thermocouples located at regular heights across the central axis of the room, to monitor the fire dynamics as well as the thermal exposure of the fuel. The objective of the simulation is to evaluate the sensitivity of the model concerning flame spread mechanisms and temperature distribution within the volume of the compartment.

To gather additional information from real scenarios, the third case study of this analysis is the 2019 Notre Dame fire which destroyed the roof structure of the Parisian cathedral [15]. The roof is made of a complex arrangement of oak trusses, arranged regularly to support a pitched roof made of a layer of oak battens 30 mm thick covered by 3 mm thick lead tiles. As the fire spread through the nave, choir, and transept, oak beams burned through and lost their structural integrity, resulting in the dramatic collapse of the spire approximately 90 minutes after the beginning of the blaze. To simplify the configuration, only the initial phase of fire spread in the choir is investigated. No direct measurements are available to evaluate the progress of the fire, hence indirect measurements relying on the melting of the lead tiles as recorded by external cameras are performed. This indirect measurement at a time when the fire is allowed to burn without any firefighting intervention is of paramount importance and numerical models can provide invaluable insights regarding plausible scenarios within the cathedral roof.

2.2 Numerical model

In the numerical models reproducing the wood crib experiments, the smallest thickness of a stick is 6.35 mm while the biggest is 31.7 mm. The smallest dimension of 6.35 mm is consequently used to develop a regular mesh throughout all four simulations.

This strategy cannot be adopted to reproduce results from the CodeRed compartment fires, as the smaller dimension of 30 mm would result in 43 million cells, computationally prohibitively expensive. Instead, a system of meshes of gradually increased size is introduced, to capture the details of the wood crib while limiting the total number of cells. The model showcases a regular mesh of 30 mm in the lower part of the compartment ($0 \text{ mm} < z < 360 \text{ mm}$), a regular mesh of 60 mm at mid-height ($360 \text{ mm} < z < 720 \text{ mm}$), and a regular mesh of 120 mm at the top part of the compartment ($720 \text{ mm} < z < 3120 \text{ mm}$).

As for the Notre Dame fire, the non-orthogonal nature of the combustible elements limits the benefits of a gradual vertical increase in mesh size. Given the large uncertainties of the model, a 100 mm mesh size is used to capture the reaction within the gas phase as well as the heat transfer in the solid phase of the timber elements. As the thickness of the timber trusses varies from 15 to 30 cm, the regular meshing allows adequate modelling of the structure.

The measurements of the wood crib structure in the Delichatsios small-scale simulation are being replicated in the same way as the experiment as can be seen in Figure 1(a). While in the CodeRed large-scale simulation, the experiments take place in a ventilated compartment 10.27 m wide, 34.27 m long, and 3.1 m high as can be seen in Figure 1(b). The wood cribs are comprised of sticks spaced apart and arranged in layers, with dimensions of 30 mm x 30 mm cross-section timber. The CLT ceiling is constructed from 5 ply with a total of 14 cm thickness. Even though the numerical model in FDS is constructed with the real geometric features in mind, very minor tweaks are made to follow the division of meshes.

From the numerical database developed by the 'Numerical Data' working group of the French CNRS/Ministry of Culture Chantier Scientifique Notre Dame de Paris, timber elements vary in size, and composition, following the work of the original carpenters and the successive restorations. The geometry

of the timber lattice, the lead roof, and the stone masonry ceiling is derived from existing reports and publications [15]. For this specific work, only a part of the choir section is being modelled, which are the second and third frames located at the end of the structure, specifically referred to as Choir Ferme C09 [16] and only for the early phase of the Notre Dame fire. In the simulation, a 9 m x 14 m x 15 m volume is created to accommodate these two main frames with a spacing of 4 m, with several secondary A-frames in between of spacing ranging from 70 cm to 80 cm as can be seen in Figure 1(c). The beam at the base of the frame is 32 cm x 25 cm. The dimensions of the beam appear to be lower for the upper part, ranging from 13 cm x 12 cm to 27 cm x 15 cm.

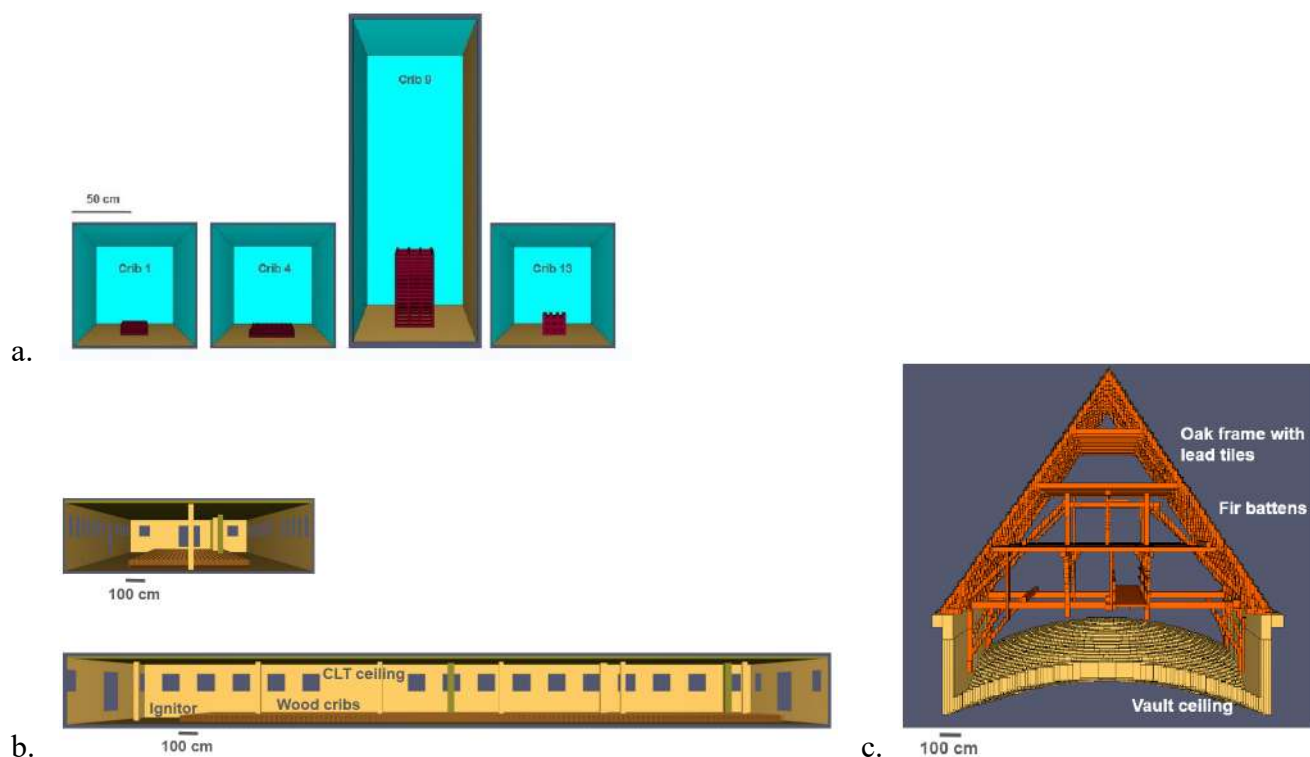
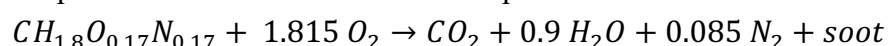


Figure 1. Illustration of the three different numerical configurations studied. a) flame spread over wood cribs, to understand the relevance of literature data; b) fire growth and flame spread in a CodeRed compartment fire, to analyse the influence of structural fuels over a longer period of time; c) fire growth and flame spread in Notre Dame, to evaluate the ability to recover indirect measurements

In the solid phase, heating, conduction, and pyrolysis are considered. The timber pyrolysis model is simple one-step endothermic reaction with a heat of reaction of 430.0 kJ/kg [15]. The charring mechanism is taken into account using the definition of heat of combustion, instead of prescribing the burning rate of the material. This way, a more realistic approach can be obtained as there is a consideration of mass loss rate during the entire reaction.

In the Notre Dame fire, another reaction involved was the melting of the lead tiles covering the roof. Modelling the melting of lead is a critical aspect in replicating the real-life scenario as this will affect the ventilation condition in the roof space. When the lead material melts, it creates openings throughout the roof that allow the fresh air to enter the space and supply more oxygen to the reaction. The parameters being used are the lead melting temperature of 327°C [17] and the heat of fusion of 23.2 kJ/kg [18].

In the gas phase, for Delichatsios small-scale case, since the value of heat of combustion for the wood crib used is absent, the value of 1.5E+4 kJ/kg [19] from the literature is used. However, in the context of the CodeRed large-scale case, it is mentioned that specific cone calorimetric measurement gives the value of around 1.9E+4 kJ/kg, which is replicated in the current simulation. As for Notre Dame's real case scenario, 1.5E+4 kJ/kg is used. All three cases are being set to have the burning of timber with a combustion reaction that assumes an incomplete combustion reaction leads to partial emission of soot and carbon monoxide.



However, as an additional analysis, different values from the literature have been simulated for large-scale CodeRed simulation, from the heat of combustion value of 1.5×10^4 kJ/kg to 1.1×10^4 kJ/kg [19]. The value is varied to get a better understanding of how the heat of combustion affects the burning rate of the material since the flame spread rate will be the focus of the results. This way, the optimum definition of material can be obtained.

In the simulation for the small-scale case, the ignitor being used is an acetone pool which is deactivated after 30 seconds from the total of 60-70 s simulation. In the large-scale case, the simulation is made to replicate this situation by putting an ignitor burner with the power of 115.0 kW/m^2 based on a methanol pool experiment [20]. The ignitor is deactivated after 60 s, which is based on the mass loss rate from the methanol pool calculation. The entire simulation is carried out for 600 s to observe the early mechanism as well as the flashover.

In contrast, the Notre Dame fire is studied based on the assumption that the fire had grown big when it reached the roof. Hence, to model a reasonable incipient fire the model, it was assumed that it started close to the roof where the ignitor is located near the battens. The power is set to 1000 kW/m^2 for 60 s and the total simulation time of 1200 s.

2.3 Outputs

From all the simulations across scales in FDS, small-scale, large-scale, and the Notre Dame real fire, several outputs are obtained with the main focus of the flame spread rate. Flame spread rate is the parameter that can be compared from all different cases. While in addition to that, from CodeRed large-scale simulation, some other outputs such as the temperature field, mixture fraction, and the disappearance of the material give an understanding of how the fire propagates inside the structure.

Unique to the third case: the simulation of the early-stage Notre Dame roof fire, the comparison and the analysis will be slightly different since no direct measurement is available from the real fire. Hence, indirect observations need to be made from various sources. One of the key examples is the disappearance of the material, which in this case is the lead material that can be easily observed from the pictures of the day of the fire with the information gathered about the time stamps. The other important point will be the profile of the fire as well as the profile of the lead disappearance. However, the disappearance of material can give valuable insight into how fast the fire propagates and consumes the materials. At the same time, it also can represent the thermal state of the roof since it shows that the temperature inside the roof is high enough to consume the lead.

At the end, the simulations will be able to depict the mechanism of the fire and provide a better sense of understanding the physics behind the phenomena. Also, the validation across scales can be produced with an emphasis on the benefits and drawbacks of using FDS in different scenarios as well as how to address discrepancies.

3 RESULTS

3.1 Small-scale simulation

Table 1 shows the comparison between the flame spread rate results from the Delichatsios small-scale experiment and the simulation.

Table 1. Flame spread results in mm/s from experiments and simulations over the different wood crib configurations. Experimentally, the flame spread rate of Crib #9 is faster than the other wood cribs, as the heat flux increases with crib height. Numerical results are not able to capture this experimental trend and show a discrepancy up to an order of magnitude regarding Crib #13

Spread rate (mm/s)				
Crib	1	4	9	13
Experiment	1.9	1.3	4.6	2.4
Simulation	4.7	4.6	7.6	2.2

Experimentally, the flame spread rate of Crib #9 is faster than the other wood cribs. It has been mentioned that the lower the number of crib lengths per number of sticks in each layer in the horizontal direction lower the spread rate, as can be seen from the results. For this reason, the flame spread rate in Crib #1 is faster compared to Crib #4. In addition to that, Crib #9 is shown to have the fastest flame spread rate as it has the additional mechanism involving the wood crib: natural convection and radiation.

Numerically, as can be seen from the results of the simulation (based on the flame front detected from the timber ignition temperature of 310°C [21]), the spread rate of the flames is faster in simulation for Crib #1, Crib #4, and Crib #9, but slower for Crib #13, which are still in good agreement with the experiment. The results show that numerical simulations can predict spread rates of the right trend for Crib #1, Crib #4, and Crib #19, with the result from the Crib #13 configuration with much thicker elements showing a very similar spread rate.

In the Crib #13 configuration, the simulation spread rate is notably slower compared to others due to less distance available in the horizontal direction and at the same time also having a thicker dimension that provides more material to the reaction, as illustrated in Table 1. This provides a less exposed area for the material from the radiation of the flames as well as neighbouring elements. Also, as various sizes of ignitor for Crib #13 have been done, it is worth noting that the power of the ignitor affects the reaction. Initially, the ignitor size was too big for the size of the Crib #13 configuration and then refined to match the experiments using different sizes of ignitor for every crib based on their spacing from the experiments.

Crib #1 and Crib #4 show slower results compared to Crib #9 especially because of the configuration of the wood sticks. Having fewer layers in the vertical direction, the flame in Crib #1 and Crib #4 need to consume the wood mostly in the horizontal direction. While in taller configurations, such as in Crib #9, the result of the spread rate is faster as the wood in the top part gets help from the preheating effect from the lower part wood. Hence, in this Crib #9 case, it is easier to reach the ignition point and keep the reaction to be faster, as shown in Table 1.

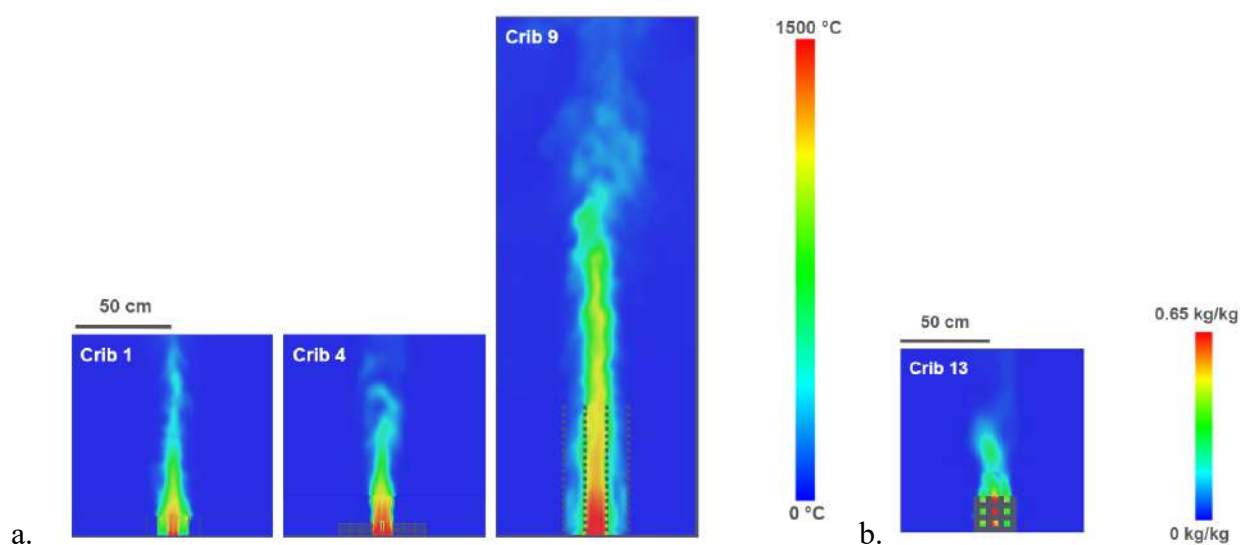


Figure 2 Temperature fields and fuel mass fraction over the wood cribs. a. Comparison of the temperature fields over Crib #1, Crib #4 and Crib #9 simulation, the faster spread rate in Crib #9 is associated to the preheating effect from the lower part of the crib. b. Fuel mass fraction in the Crib #13 simulations: faster spread rate due to less distance travelled in the horizontal direction and more fuel available from thicker sticks

From this series of wood crib small-scale simulations, it can be concluded that FDS gives overall good agreement with the experiment with the flame spread rate as the performance criteria. Different mechanisms such as natural convection and radiation can also be captured in a small-scale environment where the flame rapidly reaches the side of the cribs, which can be considered as early stage development of burning of timber. Several findings are worth considering going forward for the CodeRed large-scale simulation:

- As can be seen from Crib #9 simulation, the preheating effect from both natural convection and radiation takes place which hugely affects the flame spread rate. In the next large-scale CodeRed

simulation, the effect of those mechanisms needs to be captured well by providing adequate meshing, especially in the wood crib area where natural convection and radiation between stick elements greatly affect the results of the flame spread.

- From the Crib #13 simulation, it can be concluded that the size and the power of the ignitor need to be defined carefully so that it will not dominate the reaction. The definition of the ignitor has to be based on the experiment by providing the right power and duration.

3.2 Large-scale simulation

In addition to the flame spread rate, several outputs can be contrasted between the CodeRed large-scale experiment and the simulation, due to various instrumentations available during the experiment. This includes the temperature field as well as the readings of thermocouples throughout different points inside the compartment.

As mentioned before, the first attempt at the first large-scale CodeRed simulation is being made with the value of heat of combustion based on what is specified in the experiment, which is $1.9E+4$ kJ/kg. In this case, the detection of the progression of the fire along CLT in the x direction will then be detected using temperatures. At 11 s, while CLT is being ignited, the specific point of CLT ignition shows $900\text{ }^{\circ}\text{C}$. While in the experiment it was mentioned that the average of the CLT flame spread rate is 0.2 m/s , spreading 30 m in $2\text{ mins } 29\text{ s}$. It was found that in the simulation, CLT reaches the end at 24 seconds, giving the value of a spread rate of 2.35 m/s , much faster than the experiment.

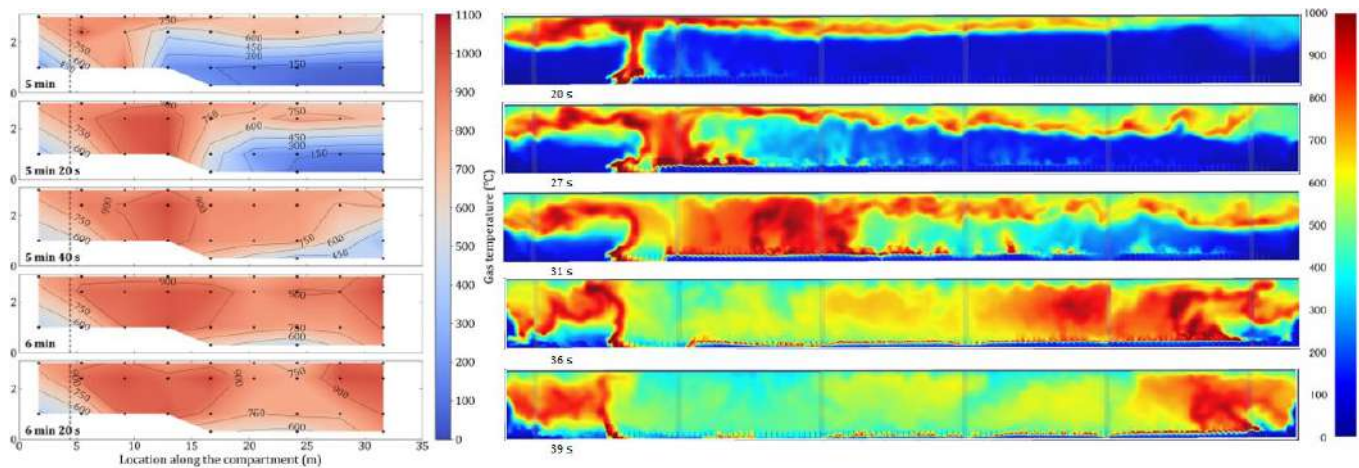


Figure 3. Comparison of temperature field along the central axis from the CodeRed#1 experiment (left) and the associated FDS simulation with the heat of combustion of $1.5E+4$ kJ/kg (right). The experimentally recorded flame spread mechanism is correctly captured in the simulation, as the fire propagates from the ignitor on both the crib and the ceiling, until the ceiling is fully involved, accelerating the flame spread rate over the wood crib. Though the temperature fields display similar patterns, the timeline is significantly different with the numerical temperature fields evolving about 10 times faster

The temperature field can be used to observe the fire dynamics within the compartment. The results shown in Figure 3 are the simulation with $1.9E+4$ kJ/kg. The ignition line is located at the beginning of the compartment, and the flames moving to the end as seen in Figure 2, $t = 20\text{ s}$ in the simulation provides results similar to $t = 5\text{ min}$ in the experiment. Even if in the simulation the flame spread faster than in the experiment, the right mechanism is captured from the ignition to the flashover.

A colder area is observed to the left of the ignition line in both experiments and simulations since there is no available fuel. The openings of two windows and one door to the left create a flow motion carrying hot gas from the fire above that location.

In the experiment, it takes 40 s for the reaction to grow to the point of flashover as can be seen in 5 minutes 40 seconds timestamp. However, in the simulation, this mechanism is reached within 11 seconds as can be seen in 31 seconds timestamp.

Overall, the right sequence of mechanism can be captured well, from the ignition of the CLT to then wood crib, resulting in a sustained combustion that leads to combustion. Around the west part of the model, near

CLT and wood crib ending, there is also the same mechanism between the experiment and material where the hot gases accumulate at the top and escape to the west opening of two windows and one door. Cold air comes from the opening and goes straight to the lowest part near the window.

However, as the first large-scale simulation shows an overestimation of the results, the value of $1.5E+4$ kJ/kg [19] is then used, owing to the fact that this is the value for the heat of combustion of wood. Hence, it is found that in this second attempt of simulation, CLT reaches the end at 40 seconds, giving the value of a spread rate of 0.989 m/s, but still much faster than the experiment.

While still relying on the same study of the heat of combustion of wood, the lowest value of $1.1E+4$ kJ/kg [19] is then explored. However, this third large-scale simulation does not quite capture the mechanism of the experiment, since the low heat of combustion leads to the self-extinction of the wood crib. Then, it seems reasonable to run the simulation with the mid-value of $1.3E+4$ kJ/kg [19]. However, while the flame spread value reasonably fits well with the experiment, which is 0.131 m/s, the temperature field shows far less value compared to the experiment. Hence the conclusion is that a more complex approach needs to be made to define the heat of combustion.

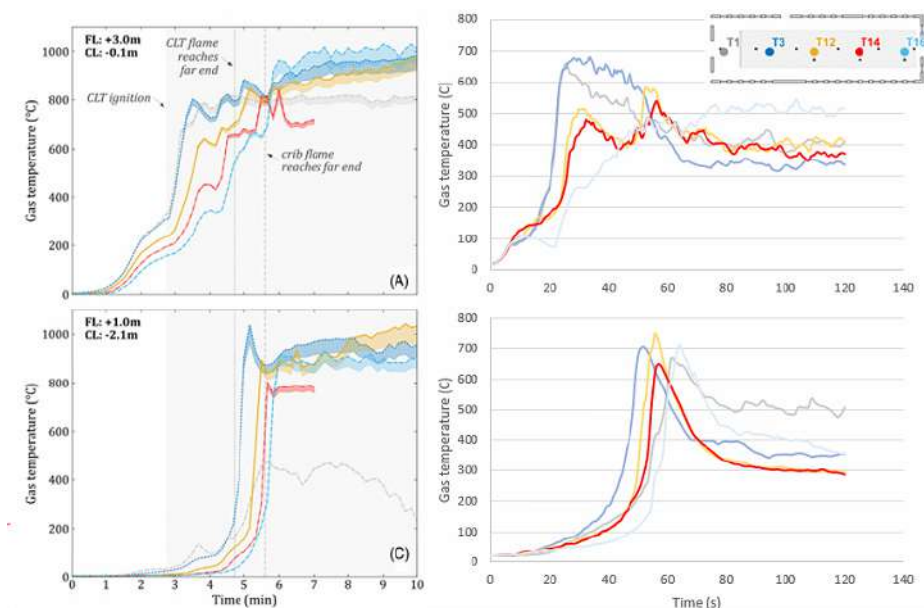


Figure 4. Comparison of temperature along the centreline (1 m and 3 m above the ground) from the experiment (left) and FDS simulation with the heat of combustion of $1.5E+4$ kJ/kg (right). From this result, the much faster rate of the reaction in simulation compared to the experiment is still found. However, there is a difference in the temperature reached, lower in the simulation which shows the peak of 700 °C only

As can be seen from Figure 4, with the heat of combustion of $1.5E+4$ kJ/kg, five different points are measured for their temperature along the main centreline (T1, T3, T12, T14, and T16), at the elevation of 1 m and 3 m from the ground. Overall, the temperature is lower in this simulation compared to the previous one with the heat of combustion of $1.9E+4$ kJ/kg. Also, at 1 m the readings from the simulation, temperature drops quickly after ignition of the CLT, showing that there is a delay in the sequence of ignition, in the experiment the wood crib fire along the floor spread not long after CLT spread, but not the case in the simulation.

In conclusion, from these large-scale simulations, it can be concluded that the material parameters will highly affect the spread of the fire. In addition to the fact that in large-scale cases, more complex mechanisms are present, including the slowing down combustion of the wood material due to longer time as well as the effect of the radiation from the structural timber. Hence, it is always important to capture the right configurations as well as the material to achieve a reasonable result in the modelling. Several findings are worth considering going forward for Notre Dame's real fire simulation:

- In the early development of the fire, the ignitor blows off enough power to ignite the wood cribs as well as later CLT at the top of the ceiling. The fire then propagates horizontally at the CLT part and reaches the end of the compartment faster than the fire within wood cribs. This observation from the simulation agrees well with the experiment. Once the temperature is hot enough, as represented by the temperature field, resulting from the flame as well as the radiation from the ceiling, the flashover mechanism takes place. This confirms that the simulation is able to progress in the same way as the experiment. Also worth noting, is that the reaction is sustained well within the wood crib so that it does not lead to a self-extinguished fire where the heat of combustion is sufficient. Apart from that, the profile of the fire in the simulation shows good replication from the experiment, including the flow of the air entrainment. This mechanism proves the need to consider the boundary condition such as the opening to allow the effect of the airflow into the model. The radiation definition is also key to understanding the temperature throughout the space.
- The most important finding is the definition of the timber material which affects the gas phase as well as the solid phase. Since the heat of combustion is the main parameter that drives the burning rate of the material. Once, the timber pyrolyse, it will generate the fuel which governs the combustion reaction. It is worth noting that, the use of the heat of combustion of $1.9E+4$ kJ/kg CodeRed large-scale simulation still gives much faster flame spread rate results compared to the experiment, while the value under $1.5E+4$ kJ/kg shows lower temperature fields. However, the value of $1.1E+4$ kJ/kg is not sufficient to capture the right mechanism. This will be discussed further in the conclusion section.

3.3 Notre Dame roof simulation

Since the focus of this Notre Dame roof fire study is to replicate the early stage of the fire, the cause or how the fire was initiated is outside the scope of this work. The fire started to reach the choir part with the C04 code [16] at 19 h 13' 20" and continued to burn the nearest frame growing sideways into the direction of the end of the choir. The disappearance of lead showed that in the next few minutes, regions of high temperature grew horizontally, trapped under the roof. Until the timestamp of 19 h 19' 01" the fire started to grow more to burn the fuel in the bottom part of the roof and reach halfway of the height of the roof in 19 h 24' 13". In the horizontal direction, the disappearance of lead had reached between frames C06 and C07. By calculating the timestamp, the fire needed around 653 seconds to consume that amount of fuel, as can be seen from Figure 5.

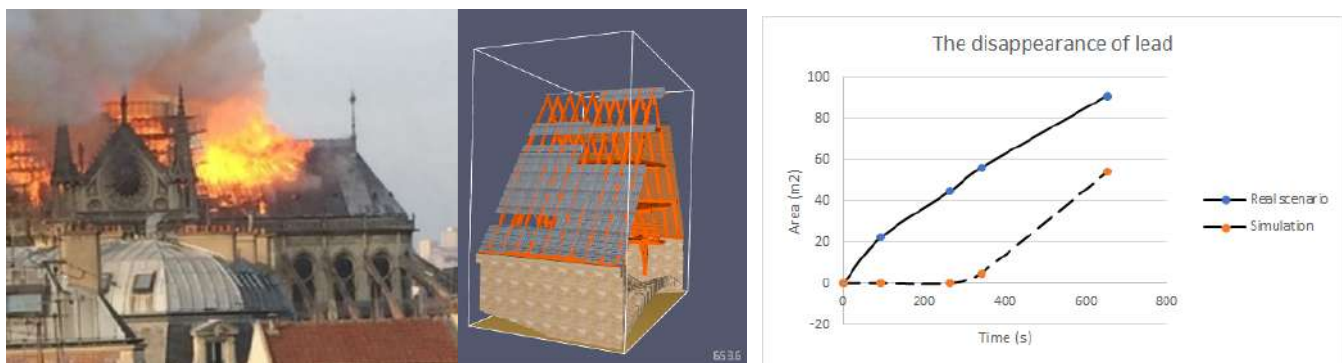


Figure 5. Fire spread in the roof of the Cathedral of Notre Dame in Paris in 2019. The data from the Chantiers Scientifique CNRS/Ministere de la Culture are used to build a numerical model of the structure pre-fire. No direct measurements are available to support numerical simulations, so an indirect evaluation of the gradual melting of the lead tiles is performed. (Credits: François Baudequin)

Firstly, from the mass loss perspective, at $t = 653$ s, the real fire scenario had consumed the lead material for 91-meter squares, while in the simulation 54-meter squares of lead had gone to the fire, with the same thickness. However, the simulation result from $t = 800$ s shows that the flames kept burning and potentially burned more lead if more fuel were available in the horizontal direction. This shows that the prediction of the amount of fuels being burned can potentially be better if the boundaries of the model get bigger. As for

the current model, this value is in the same order of magnitude. It is also worth noting that in the timestamp, the fire was already big hence the amount of lead disappearance was already bigger in the beginning compared to the simulation which started only from the ignitor.

Secondly, another way to assess the fire model is by contrasting the profile of the disappearance of the lead from a real event to the results from the model. The model shows the profile of the lead roof as the fire propagates in the choir.

However, the most important point of this preliminary simulation is the gradient shown in Figure 5. Even though at the early stage, both results from the real scenario and simulation do not seem to start at the same time, they show a good agreement in terms of the rate at which the material disappears. Hence, it can be concluded that the profiles from the simulation can correctly capture the mechanism of the growth of the fire from the real-life scenario.

4 DISCUSSIONS

4.1 Validation study

In terms of the mechanism captured both in the experiment and in the simulation, it can be concluded that FDS is able to model simple small-scale fire experiments where the condition is well controlled. However, there is a critical need to understand a much more complicated mechanism when it deals with a much larger scale where the pyrolysis, as well as the combustion process, are much more complicated due to the nature of the bigger environment, even if it is a well-controlled one. More definitions need to be addressed, such as the heat of combustion, when building the model while trying to replicate every detail of the experiment. In addition to that, an understanding of the underlying phenomena is essential to decide where to improve the model. This can even be more challenging when dealing with fire from a real-life scenario where a much more complex environment is present. In general, the mechanism of both large-scale CodeRed experiment and Notre Dame real fire can be captured well, where the fire grows and consumes the material then the combustion reaction is sustained, that the fire propagates inside the space and leads to flashover, including the profile of the fire where the opening also affects the flow.

However, in terms of the spread rate of the fire between different scenarios can still be improved. The result of the flame spread rate in Delichatsios small-scale simulation gives an overall good agreement, while the flame spread rate in CodeRed large-scale simulation still yields much higher results compared to the experiment. As for Notre Dame, the rate which is represented by the disappearance of the material gives a fairly good agreement but still can be improved in terms of the analysis that can include more duration of the flame so that a more solid comparison can be made. The discrepancies to be expected from these large scales are addressed more in the next section and will be room for improvement for future works.

4.2 Discrepancies to be expected and further study

From the entire simulation across scales, it can be concluded that various parameters in the modelling stage can have a major effect on the results. To compare the Delichatsios small-scale simulation and CodeRed large-scale simulation, while all models captured the right mechanism, the results of the flame spread rate in the CodeRed large-scale simulation show some disparities with the experiment.

The wood crib, as a small-scale case, can be considered as capturing only the burning mechanism in wood material in its early stage of combustion. Hence in CodeRed compartment fire simulation, since the experiments have a much larger scale as well as a longer duration of burning, a more refined approach is needed in defining the heat of combustion.

During the combustion process of timber, there are two distinct phases: flaming combustion and glowing combustion. These two stages have different mechanisms which result in different total energy releases in the form of heat. The heat of combustion during the flaming stage is much higher than the glowing stage, and the glowing stage takes place after the flaming is gone. When timber chars, it creates an additional layer that will inhibit more pyrolyzed gases from being generated hence the combustion with the hot gases can no longer be sustained and the reaction enters the glowing phase.

In the Delichatsios small-scale simulation, the results of the flame spread rate give an overall good agreement with the experiment, due to the fact that the reaction only involves a considerably small amount of fuel and the flame reaches the sides of the crib in an instant while it still in the stage of flaming combustion. In the CodeRed large-scale simulation, the result of the flame spread rate shows a much higher rate compared to the actual experiment. This is due to the whole mechanism of combustion that takes place in the large-scale experiment. The fire grows to the other side of the compartment and consumes the material both CLT and wood cribs. Consequently, during this propagation, the material has undergone changes in which some of the material has already charred and goes into the glowing phase. Hence, the lower value of the heat of combustion during this stage needs to be taken into account while defining the reaction and material parameters.

In the current CodeRed large-scale simulation, the value of heat of combustion of $1.9\text{E}+4$ kJ/kg, $1.5\text{E}+4$ kJ/kg, $1.3\text{E}+4$ kJ/kg and $1.1\text{E}+4$ kJ/kg are used. The values of $1.9\text{E}+4$ kJ/kg and $1.5\text{E}+4$ kJ/kg overestimate the flame spread results, due to too many gases being generated during the combustion reaction which is not the case for the actual fire on such a scale, while $1.1\text{E}+4$ kJ/kg is way too underestimated in that way it does not capture the sustained reaction. However, the lower value of $1.3\text{E}+4$ kJ/kg on the other hand, while showing a closer flame spread rate to the experiment, cannot adequately show the correct temperature field. The way to define the heat of combustion by taking into account both flaming and glowing combustion so that the complex mechanism of combustion is captured still needs to be explored.

From the Notre Dame roof fire scenario, it is clear that the mechanism of this event is closely in the same trend as the CodeRed large-scale experiment, especially in terms of its scale. Hence, this dictates the physics inside the roof structure, including the combustion process which includes both flaming and glowing combustion. Consequently, the definition of the reaction and the material needs to be refined further to capture the right measurement.

5 CONCLUSIONS

Numerical models have been developed to replicate experimental data, and model the fire growth in a real scenario, CFD modelling captures the propagation mechanisms of fire inside a small-scale compartment with wood cribs as the main fuel source. A simple definition of the material and the reaction is enough to capture the flame spread mechanism at a short time scale. As the scale is increased, a more refined approach needs to be made to capture fire spread over timber when charring has time to occur and smouldering is reported. The flaming and glowing combustion mechanisms can be combined via modifications of the heat of combustion. Though the model can still be improved, it is able to reproduce indirect observations regarding the thermal degradation of the lead tiles in the fire of Notre Dame. As such, numerical tools extend the results obtained over experimental configurations and provide insights regarding the growth phase and the temperature conditions within the roof space in a real-case scenario.

REFERENCES

- [1] J.L. Torero, Fire safety of historical buildings: principles and methodological approach, *International Journal of Architectural Heritage* 13 (2019) 926–940.
- [2] E. Carattin, V. Brannigan, Controlled evacuation in historical and cultural structures: requirements, limitations and the potential for evacuation models, in *Proceedings of the 5th International Symposium on Human Behavior in Fire 2012*, Interscience Communication Limited, London, England, 2012, pp. 41-52, 2012.
- [3] B. Östman, D. Brandon, H. Frantzich, Fire safety engineering in timber buildings, *Fire Saf J* 91 (2017) 11–20. [https://doi.org/https://doi.org/10.1016/j.firesaf.2017.05.002](https://doi.org/10.1016/j.firesaf.2017.05.002).
- [4] R. McNamee, J. Zehfuss, A.I. Bartlett, M. Heidari, F. Robert, L.A. Bisby, Enclosure fire dynamics with a cross-laminated timber ceiling, *Fire Mater* 45 (2021) 847–857.

- [5] D. Brandon, J. Sjöström, A. Temple, E. Hallberg, F. Kahl, Fire Safe implementation of visible mass timber in tall buildings—compartment fire testing, (2021).
- [6] P. Kotsovinos, E. Rackauskaite, E. Christensen, A. Glew, E. O’Loughlin, H. Mitchell, R. Amin, F. Robert, M. Heidari, D. Barber, Fire dynamics inside a large and open-plan compartment with exposed timber ceiling and columns: CodeRed# 01, *Fire Mater* 47 (2023) 542–568.
- [7] S.T.W. Kuruneru, E. Marechal, M. Deligant, S. Khelladi, F. Ravelet, S.C. Saha, E. Sauret, Y. Gu, A Comparative Study of Mixed Resolved–Unresolved CFD-DEM and Unresolved CFD-DEM Methods for the Solution of Particle-Laden Liquid Flows, *Archives of Computational Methods in Engineering* 26 (2019) 1239–1254. <https://doi.org/10.1007/s11831-018-9282-3>.
- [8] J.I. Rojas-Sola, C. García-Baena, M.J. Hermoso-Orzáez, A REVIEW OF THE COMPUTATIONAL FLUID DYNAMICS SIMULATION SOFTWARE: ADVANTAGES, DISADVANTAGES AND MAIN APPLICATIONS *, *Journal of Magnetohydrodynamics and Plasma Research* 21 (2016) 417–424.
- [9] K. McGrattan, R. McDermott, J. Floyd, S. Hostikka, G. Forney, H. Baum, Computational fluid dynamics modelling of fire, *Int J Comput Fluid Dyn* 26 (2012) 349–361.
- [10] W. Binbin, Comparative Research on FLUENT and FDS’s Numerical Simulation of Smoke Spread in Subway Platform Fire, *Procedia Eng* 26 (2011) 1065–1075. <https://doi.org/10.1016/j.proeng.2011.11.2275>.
- [11] J. Anderson, J. Sjöström, A. Temple, M. Charlier, X. Dai, S. Welch, D. Rush, FDS simulations and modelling efforts of travelling fires in a large elongated compartment, *Fire Mater* 45 (2021) 699–707.
- [12] P. Blake, H. Phylaktou, G. Andrews, Validating FDS against a full-scale fire test, in: *Fire and Evacuation Modeling Technical Conference*, 2018: pp. 1–3.
- [13] N.L. Ryder, J.A. Sutula, C.F. Schemel, A.J. Hamer, V. Van Brunt, Consequence modeling using the fire dynamics simulator, *J Hazard Mater* 115 (2004) 149–154.
- [14] M.A. Delichatsios, Fire growth rates in wood cribs, *Combust Flame* 27 (1976) 267–278. [https://doi.org/https://doi.org/10.1016/0010-2180\(76\)90028-6](https://doi.org/https://doi.org/10.1016/0010-2180(76)90028-6).
- [15] A. Guibaud, J.-C. Mindeguia, A. Albuerne, T. Parent, J. Torero, Notre-Dame de Paris as a validation case to improve fire safety modelling in historic buildings, (2023).
- [16] C. Trentesaux, Le relevé des charpentes médiévales de la cathédrale Notre-Dame de Paris: approches pour une nouvelle lecture, (2016).
- [17] A.D. Kirshenbaum, J.A. Cahill, A.V. Grosse, The density of liquid lead from the melting, *Journal of Inorganic & Nuclear Chemistry* 22 (1961) 33–38. [https://doi.org/10.1016/0022-1902\(61\)80226-1](https://doi.org/10.1016/0022-1902(61)80226-1).
- [18] J.H. Awbery, E. Griffiths, The latent heat of fusion of some metals, *Proceedings of the Physical Society of London* 38 (1925) 378.
- [19] M. Janssens, Rate of heat release of wood products, *Fire Saf J* 17 (1991) 217–238.
- [20] K. Sung, J. Chen, M. Bundy, A. Hamins, The characteristics of a 1 m methanol pool fire, *Fire Saf J* 120 (2021) 103121. <https://doi.org/https://doi.org/10.1016/j.firesaf.2020.103121>.
- [21] X. Dai, A. Gamba, C. Liu, J. Anderson, M. Charlier, D. Rush, S. Welch, An engineering CFD model for fire spread on wood cribs for travelling fires, *Advances in Engineering Software* 173 (2022) 103213. <https://doi.org/https://doi.org/10.1016/j.advengsoft.2022.103213>.

**OTHER TOPICS RELATED TO
STRUCTURES IN FIRE**

CFD-BASED ANALYSIS OF THERMOCOUPLE MEASUREMENTS IN THE FIRE DECAY AND COOLING PHASES IN RELATION TO THE ADIABATIC SURFACE TEMPERATURE

Florian Put¹, Andrea Lucherini², Ruben Van Coile³, Bart Merci⁴

ABSTRACT

The definition of the thermal boundary conditions is usually the first step in a structural fire engineering calculation and is often represented by a single time-temperature curve, which should be referred to as an Adiabatic Surface Temperature. The validation of thermal boundary condition models is commonly performed based on data from large-scale fire experiments, in which thermocouple measurements provide temperature data, with focus on the post-flashover heating and fully-developed phases of a fire. The present study investigates whether thermocouple data obtained during the decay and cooling phases can serve as input for structural fire engineering calculations, and whether they can be used to compare against Adiabatic Surface Temperature models. To this purpose, a series of canonical FDS simulations is performed, representing the thermal boundary conditions that would be encountered in the fire decay and cooling phases, to study the impact of smoke and radiation on thermocouple measurements. The dynamically changing environment in which the thermocouples are situated during the decay and cooling phases (increased radiation due to dilution of the smoke) is shown to be incompatible with fixed values for the convective heat transfer coefficient and the effective emissivity, as used in the framework of the Adiabatic Surface Temperature.

Keywords: Thermocouple Measurements; CFD Simulations; Heat Transfer; Compartment Fires; Fire Safety; Adiabatic Surface Temperature

1 INTRODUCTION

Structural fire engineering (SFE) commonly encompasses a three-step procedure [1]. The initial step involves delineating the fire exposure scenario. Subsequently, thermal and mechanical analyses are conducted to assess the structure's response under a combination of thermal and mechanical loading [1].

The thermal boundary conditions arising from fire exposure can be expressed in various ways. In the most simplified case, they are represented with a single time-temperature curve. More complicated expressions of the thermal boundary conditions include heat fluxes of various natures, zone-models (either 1- or 2-zone models) or results from Computational Fluid Dynamics (CFD) calculations [1]. When a single time-temperature curve is used, the implicit assumption is that the convective and radiative heat transfer can be replaced by a single temperature, usually associated with the gas phase, and the applied time-temperature

¹ MSc, PhD Researcher, Ghent University, Belgium

e-mail: Florian.Put@UGent.be, ORCID: <https://orcid.org/0000-0002-4522-9015>

² PhD, Senior Researcher, Slovenian National Building and Civil Engineering Institute (ZAG), Slovenia

e-mail: Andrea.Lucherini@zag.si, ORCID: <https://orcid.org/0000-0001-8738-1018>

³ PhD, Ghent University, Belgium

e-mail: Ruben.VanCoile@UGent.be, ORCID: <https://orcid.org/0000-0002-9715-6786>

⁴ Prof., Ghent University, Belgium

e-mail: Bart.Merci@UGent.be, ORCID: <https://orcid.org/0000-0002-2600-0098>

curve represents what is commonly known as the *Adiabatic Surface Temperature* (AST) [2]. This concept relies on a single time-temperature curve, employing fixed values for the convective heat transfer coefficient and effective emissivity, to simplify the expression of the thermal boundary conditions [2].

Literature provides several models to define the thermal boundary conditions with a single time-temperature curve, such as the Eurocode Parametric Fire Curve [3], the BFD-curve [4] and one-zone models such as Ozone. The validation of such models was often based on data from large-scale experiments and mainly focused on the heating and fully-developed phases. Traditionally, the fire decay and subsequent cooling phases were not of interest and therefore neglected. Although the AST can be estimated using a plate thermometer (an idealized plate thermometer would measure the real AST [2]), plate thermometer data is scarce in literature as most large-scale fire experiments primarily use thermocouples to provide temperatures. If thermocouple data is to be used to validate models in the fire decay and cooling phase, a crucial step involves a discussion of the experimental data for temperatures as reported during those phases.

A fire generally consists of several phases (i.e., growth, fully-developed, decay and cooling phases), each with specific thermal boundary conditions [5]. Therefore, it can be expected that the temperatures recorded by thermocouples are also affected in different ways during the different stages of a fire [5]. In particular, the fire decay phase is characterised by a decreasing heat release rate (HRR) of the fire, leading to a reduction in the smoke production and an increased intake of cold air, diluting the smoke. Hence, the optical density of smoke decreases significantly as compared to the fully-developed phase [5]. The cooling phase is characterised by the absence of smoke. The smoke is replaced by cold air, continuously flowing into the compartment, once the fire extinguished, and cooling the structural elements inside [5].

This study focuses on the temperatures as measured by thermocouples, especially during the fire decay and cooling phases, and how they relate to the wide-spread concept of *Adiabatic Surface Temperature*. To this end, the theoretical background of the AST is revisited first. Subsequently, the outcomes of a series of canonical Fire Dynamics Simulator (FDS) calculations are leveraged, focusing on the influence of the smoke and radiation on thermocouple measurements, and their relationship to the AST.

2 ADIABATIC SURFACE TEMPERATURE

2.1 Theoretical background

The thermal boundary conditions of a surface exposed to fire can be characterized by the net heat flux to the surface, typically comprising conductive, convective, and radiative components. When addressing heat transfer between a solid surface and a gas, the conductive aspect is often considered negligible in comparison to the convective and radiative terms. Consequently, the net heat flux can be expressed as [2]:

$$\dot{q}_{tot}'' = \varepsilon (\dot{q}_{inc}'' - \sigma \cdot T_s^4) + h (T_g - T_s) \quad (1)$$

where

\dot{q}_{tot}'' is the total (net) heat flux [W/m²],

ε is the effective emissivity [-],

\dot{q}_{inc}'' is the incoming radiative heat flux [W/m²],

σ is Stefan-Boltzmann's constant [W/m²K⁴],

h is the convective heat transfer coefficient [W/m²K],

T_g is the gas temperature [K]

T_s is the surface temperature [K].

Assuming that the incoming radiative heat flux \dot{q}_{inc}'' can be expressed as a function of the radiation temperature, T_r , equation (1) can be rewritten as [2]:

$$\dot{q}_{tot}'' = \varepsilon \cdot \sigma (T_r^4 - T_s^4) + h (T_g - T_s) \quad (2)$$

The radiation temperature, T_r , is the temperature of a black-body emitter that causes the same incident radiative flux on the surface as q''_{inc} . As convection and radiation represent the dominant modes of heat transfer between elements (solids) and the gas phase during a fire, both equation (1) and equation (2) are generally applicable. The total net heat flux formulation of equation (1) and equation (2) has the drawback that it depends on two variables, \dot{q}''_{inc} (equation (1)) or T_r (equation (2)) and T_g . As a workaround, an adiabatic surface can be considered, which by definition does not absorb any heat due to its thermal equilibrium as it is adiabatic and has a negligible mass [2]. Therefore, the net heat flux to such a surface has to be zero (first law of thermodynamics [6]) and steady-state conditions are implicitly assumed. The heat balance of equation (2) can be rewritten as in equation (3), assuming that the effective emissivity, ε_{AST} , and convective heat transfer coefficient, h_{AST} , are known or have been decided upon.

$$\varepsilon_{AST} \cdot \sigma (T_r^4 - T_{AST}^4) + h_{AST} (T_g - T_{AST}) = 0 \quad (3)$$

By combining the heat transfer equations outlined in equation (2) and equation (3), the total heat transfer can be computed as follows [2]:

$$\dot{q}''_{tot} = \varepsilon_{AST} \cdot \sigma (T_{AST}^4 - T_s^4) + h_{AST} (T_{AST} - T_s) \quad (4)$$

The AST, thus, represents a weighted average of T_r and T_g . The weighting factor is contingent on the ratio $h_{AST}/\varepsilon_{AST}$. As the AST employs a single temperature to express the thermal boundary conditions, the concept is highly appealing for utilization as input in structural fire engineering calculations. The same procedure can theoretically be always applied, across the entire post-flashover fire scenario, encompassing the decay and cooling phases. Yet, special attention with respect to the values of the convective heat transfer coefficient and effective emissivity (and radiation in general) is needed, as explained below in section 2.2.

2.2 Comments on the Adiabatic Surface Temperature

Although the AST is a useful concept that simplifies the thermal boundary conditions of structural elements by representing the total heat transfer by a single temperature, it also has drawbacks regarding applicability. It is a purely mathematical concept, based on the idealized concept of an adiabatic surface, which is usually simplified in an ideal ‘plate thermometer’ and the assumptions made do not reflect the conditions during real fire exposure.

The AST is generally based on fixed values for the convective heat transfer coefficient (e.g., 25 W/m²K for standard fire exposure and 35 W/m²K for natural fire exposure according to EN 1991-1-2 [3]) and the effective emissivity of the emitting and receiving surfaces. These values have been determined for the post-flashover fully-developed phase, but do not consider the changes in thermal boundary conditions once the fire advances into subsequent phases such as the fire decay phase and the cooling phase. Indeed, when the HRR of a fire decreases, the compartment flows induced by the fire also decrease. Hence, the convective heat transfer coefficient should decrease. When the fire has completely extinguished, during the cooling phase, the value should reduce even further as the external source for flows completely disappears and compartment elements cool by natural convection. Therefore, it is incorrect to use experimental data from plate thermometers during the fire decay and cooling phases directly in a calculation with a fixed convective heat transfer coefficient. As the AST is a purely mathematical concept, however, the measured plate thermometer temperatures can be recalculated to fit calculations with a fixed convective heat transfer coefficient, provided that the conditions during the fire (and thus also the real convective heat transfer coefficient) are known.

2.3 Implementation in FDS

FDS is a CFD tool developed by NIST, designed specifically to perform fire simulations. It is a large-eddy simulation code, solving a form of the Navier-Stokes equations for low speed flows, and focusses on the modelling of smoke and heat transfer phenomena [7]. It is widely used in fire safety engineering to predict the behaviour of fire when experiments are not feasible or economical, aiding for example fire risk assessment and evacuation plans.

FDS incorporates two distinct devices to record the AST during a simulation, associated with the output quantities ‘*Adiabatic Surface Temperature*’ and ‘*Adiabatic Surface Temperature Gas*’ [7]. The difference between the two output quantities is subtle, yet of high importance as the results between the two formulations are different.

When a device with the output quantity ‘*Adiabatic Surface Temperature*’ is employed, it should be positioned on the interface between a gas and a solid. To estimate the total net heat flux, with regards to convection, FDS calculates the convective heat transfer coefficient based on the velocity of the flow over the surface at the position where the device is located and the respective temperatures of the gas and surface at that point. In addition, with regards to radiation, FDS assumes that the effective emissivity of the solid also applies to the AST calculation [7]. As a result, the convective heat transfer coefficient is not fixed during the simulation. Instead, it varies throughout the simulation. The calculation of the AST is thus based on continuously changing parameters and to apply the AST in calculations, the values of these parameters should be tracked. This method represents what a plate thermometer would measure in a real experiment.

When a device with the output quantity ‘*Adiabatic Surface Temperature Gas*’ is used, the requirement of positioning it at the interface between a gas and a solid cancels. The device can be freely positioned within the gas phase, but a fixed value for the convective heat transfer coefficient and effective emissivity must be provided [7]. Values for the convective heat transfer coefficient and effective emissivity are chosen and kept constant during the entire fire scenario, even though this may not align with the values during a real fire. This approach resembles the way the concept of AST is typically applied in SFE calculations.

3 NUMERICAL SIMULATIONS SET-UP

To investigate the impact of environmental radiation and smoke on thermocouple measurements during a fire in relation to the AST, a basic setup has been developed in Fire Dynamics Simulator (FDS, version 6.8.0) [7]. The setup consists of a 1 m by 1 m by 1 m cubical box, with small holes of 5 cm by 5 cm in the corners of the floor and ceiling to allow for flow into and out of the cube. The walls are modelled as adiabatic surfaces. Temperatures are recorded by a thermocouple tree, which is positioned in the middle of the cube, as indicated in Figure 1. Thermocouples (output quantity ‘THERMOCOUPLE’) have been positioned on the tree with 10 cm intervals, starting at 10 cm from the ceiling and extending to 10 cm from the floor. Additionally, temperature devices (output quantity ‘TEMPERATURE’) have been added at the same locations to record ‘real’ gas temperatures. In the first part of the analysis, also Adiabatic Surface Temperatures were recorded. Two devices with the output quantity ‘*Adiabatic Surface Temperature*’ were positioned in the middle of the floor and ceiling. Similarly, two devices with output quantity ‘*Adiabatic Surface Temperature Gas*’ were positioned directly in front of the floor and ceiling, with fixed convection coefficient of 35 W/m²K (as specified in [3] for natural fire exposure) and a fixed effective emissivity of 0.9. The mesh cell size was 5 cm, which does not allow for detailed modelling of the inflow and outflow of air and smoke into/from the compartment, but that is not essential for the study at hand as the focus is on thermocouple measurements. A sensitivity analysis has been performed to confirm this and is presented in section 4.4.

The analysis consists of three scenarios, of which the details are presented in Table 1, with varying radiation attenuation coefficient and soot mass fraction in the smoke. To this purpose, the cube is filled with a hot smoke, with different levels of smoke optical thickness and temperature. The optical thickness of the smoke is determined by 2 factors, being the soot mass fraction and the mass extinction coefficient, K_m . The soot mass fraction represents the mass of soot per unit mass of smoke and thus governs the smoke density, while the mass extinction coefficient indicates the attenuation of radiation by smoke per unit of smoke density. In other words, multiplication of the smoke density and mass extinction coefficient, K_m , results in the radiation extinction coefficient, K . Given that K , the incident monochromatic intensity, I_0 , and the travel distance of radiation through the smoke, L , are known, the transmitted intensity, I , of monochromatic radiation through smoke is given by equation (5) [8].

$$I = I_0 e^{-KL} \quad (5)$$

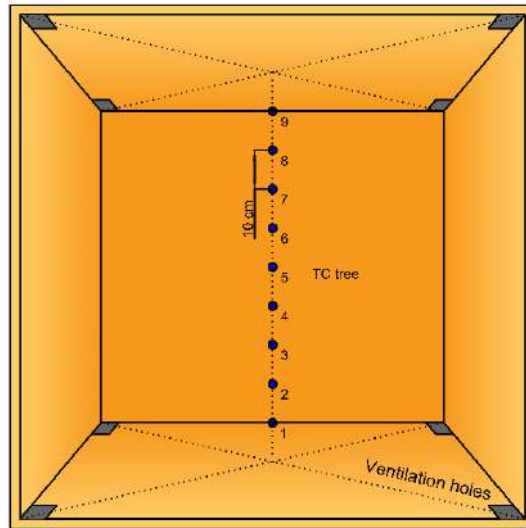


Figure 1. Box geometry used in FDS simulations

Scenarios 1 and 2 represent the onset of the decay phase, immediately after the fully-developed phase, with Scenario 1 having an optically very thick smoke and Scenario 2 having an optically less thick smoke. Scenario 3 represents the onset of the pure cooling phase, immediately after the decay phase has ended. As mentioned before, smoke has left the compartment during this phase, but the linings and structural elements inside are still hot as, due to their thermal inertia, they cool down slower than the compartment gases. Parameters that are not explicitly provided in Table 1 are left according to the FDS default values.

Table 1. Description of decay and cooling phase scenarios

Scenario	T_{ceiling} [°C]	T_{floor} [°C]	T_{smoke} [°C]	Mass Extinction Coefficient, K_m [m ² /kg]	Soot Mass Fraction [-]
1. Onset decay	1000	400	1000	20000	0.1
2. Onset decay	1000	400	750	500	0.005
3. Onset cooling	1000	400	No smoke		

4 RESULTS

4.1 Scenario 1

Scenario 1 marks the transition from a fully-developed phase with an optically very thick smoke to the fire decay phase, which is characterised by a diminishing HRR of the fire. The initial conditions of FDS are such that the thermocouples are initially at ambient temperature (i.e., 20°C), whereas the smoke inside the compartment is initially at elevated temperature (1000°C in this case, as specified in Table 1).

As the smoke is initially hot, buoyancy in the smoke is evident from the onset of the simulation. The hot smoke leaves the compartment immediately after the simulation has started through the holes in the ceiling, while cold air enters the compartment through the holes in the floor. The thermocouples, which are initially cold, increase in temperature immediately after the onset of the simulation as they are surrounded by the hot smoke. Both effects are observed in Figure 2b and Figure 2a respectively, while the large negative values at the onset of the calculation in Figure 2c are caused by the initial conditions in FDS.

The thermocouple measurements at different heights over time are a complex interaction between location (more specifically the distance to radiating surfaces), smoke optical thickness and the corresponding attenuation of radiation, and the smoke temperature. Initially, the smoke has a very high optical thickness (Figure 3a). Radiation from the ceiling and floor cannot affect the thermocouple temperature as radiation is

absorbed by the smoke, which emits radiation based on its own temperature. Once smoke flows out of the box and fresh air enters, the optical thickness in the lower regions is reduced. The onset of this phenomenon can be observed in Figure 3b, while the reduction is more visible in Figure 3c. Thermocouples near the floor exchange heat with both the smoke layer on top and the floor. Radiation from the ceiling is still blocked as the optical thickness of the smoke is still high in the upper regions of the compartment. Given that the smoke clears faster at the bottom, the bottom thermocouples tend to a stabilized temperature faster.

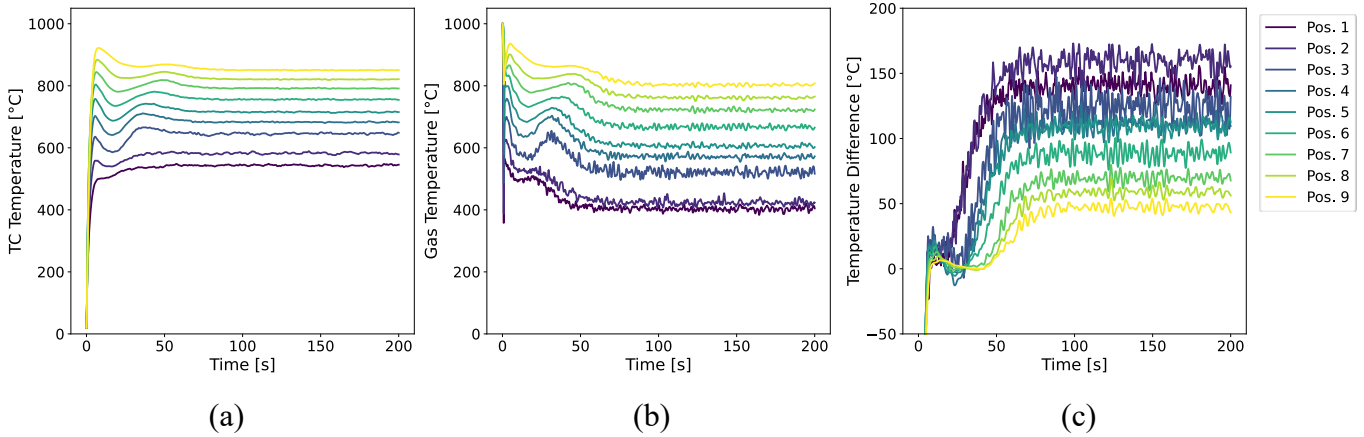


Figure 2. Temperatures measured by (a) thermocouples (TC): T_{TC} and (b) temperature devices (TD): T_g , and (c) the difference $T_{TC} - T_g$ in Scenario 1. Pos. 1 to 9 as specified in Figure 1

Once all the smoke has exited the compartment (see Figure 3d), radiation from the ceiling affects the thermocouple temperatures as air is transparent. The air inside the compartment stratifies due to the presence of the floor and ceiling, which are at different temperatures. There still is a flow inside the compartment as the hot air leaves the compartment due to buoyancy and fresh air enters, but as the optical thickness remains constant (air remains transparent), this flow no longer affects the thermocouple temperatures. At this point, the system has reached steady state, starting from around 90s after the onset of the simulation.

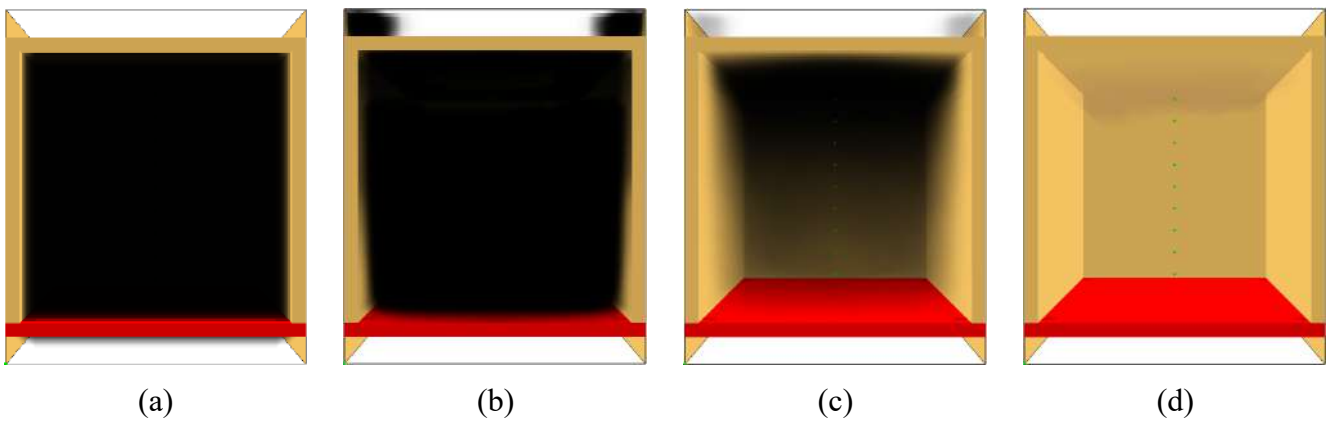


Figure 3. Visualization of smoke density in Scenario 1 at (a) 0s, (b) 20s, (c) 50s, and (d) 90s

Once the smoke has left the compartment and a steady state has been reached, it can be observed that the temperature difference between the thermocouples temperature and the local gas temperature is greater near the floor, even though the view factor from the hottest surface (the ceiling) decreases with distance. Radiative heat transfer depends on both geometry (expressed through the view factor) and the difference in the fourth power in temperatures. Because of the stratification of air within the compartment, the temperature difference between the ceiling and a thermocouple is more pronounced near the floor, leading to increased radiative heat transfer. This phenomenon outweighs the change in view factor caused by

shifting position within the compartment. Consequently, the difference between gas temperature and thermocouple readings increases with distance from the ceiling. Similarly, the AST is higher at the floor than at the ceiling, as depicted in Figure 4. However, positions 1 and 2 show an exception where the temperature difference between thermocouples and gas temperature is larger at position 2 than at position 1 (see Figure 2c). This discrepancy is due to the intake of fresh air, resulting in a relatively small difference in gas temperature between the positions, as evident in Figure 2b. Since the view factor remains constant, the thermocouple at position 2 receives more radiation, leading to a greater temperature disparity.

Under the conditions of Scenario 1, the difference between the output quantities ‘*Adiabatic Surface Temperature*’ and ‘*Adiabatic Surface Temperature Gas*’ is examined. This disparity practically reflects the difference between experimental measurement and use of the AST as parameter in SFE calculations, as discussed in section 2. Figure 4 illustrates how the recorded AST from both outputs diverges over time in relation to the optical thickness of the smoke, represented by the soot density in the air. It is notable that under high soot density, the two AST output quantities almost coincide. However, as the optical thickness of the smoke decreases, disparities emerge between the two formulations. In particular, the ‘*Adiabatic Surface Temperature Gas*’ output exhibits higher values than the ‘*Adiabatic Surface Temperature*’ output near the ceiling, but lower near the floor.

Considering that the emissivity remains constant in both cases (0.9 as specified for the output quantity ‘*Adiabatic Surface Temperature Gas*’, consistent with the default value used in FDS), the observed differences arise from variations in the convective heat transfer. At the ceiling, the overestimation of the convective heat transfer coefficient results in an increase of the AST. Consider the AST to be measured by an infinitesimally small ideal plate thermometer, placed on the ceiling. This device can be conceived as a very thin plate (such that it does not have any heat capacity) of which the backside is perfectly insulated, representing an adiabatic surface. Due to the perfectly insulating layer, the device cannot exchange heat with the surface it is positioned on, but it can exchange heat with the other surfaces in the compartment (only the floor in the considered geometry).

The ideal plate thermometer solely exchanges heat with the floor and not with the ceiling. Hence, it maintains a lower temperature compared to the surrounding gas, which is transparent and does not engage in radiation exchange. Consequently, an overestimated convective heat transfer coefficient results in an increase in adiabatic surface temperature. Conversely, at the floor, an overestimation of the convection coefficient induces a temperature decrease. Here, the ideal plate thermometer solely interacts with the ceiling, and thus maintains a higher temperature relative to the surrounding gas. Consequently, overestimated convection results in cooling of an adiabatic surface and thus also a lower adiabatic surface temperature. Quantitatively, this difference at steady state manifests as approximately 19°C at the ceiling, representing a discrepancy of roughly 2.6%, whereas at the floor, the values are respectively 47°C and 6.0%. As a reference for these values, the temperature increase from ambient (20°C) of the real AST is used (i.e., with varying convective heat transfer coefficient, denoted as AST Ceiling and AST Floor in the legend of Figure 4).

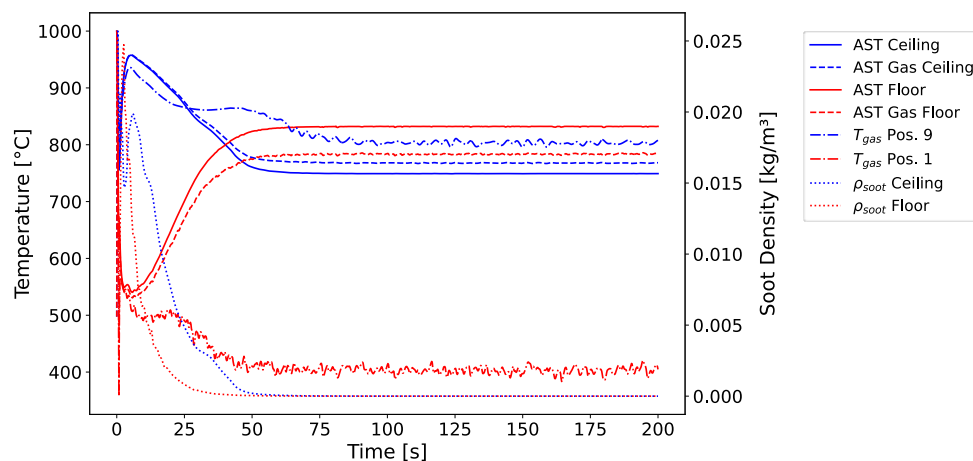


Figure 4. Adiabatic surface temperatures and soot densities in the middle of the ceiling and floor in Scenario 1

4.2 Scenario 2

Similar to Scenario 1, Scenario 2 also depicts the transition from the fully-developed phase to the decay phase. However, the initial optical thickness of the smoke is significantly lower compared to Scenario 1, while the initial smoke temperature is decreased to 750°C (see Figure 5b). The thermocouples are initially at 20°C, as depicted in Figure 5a.

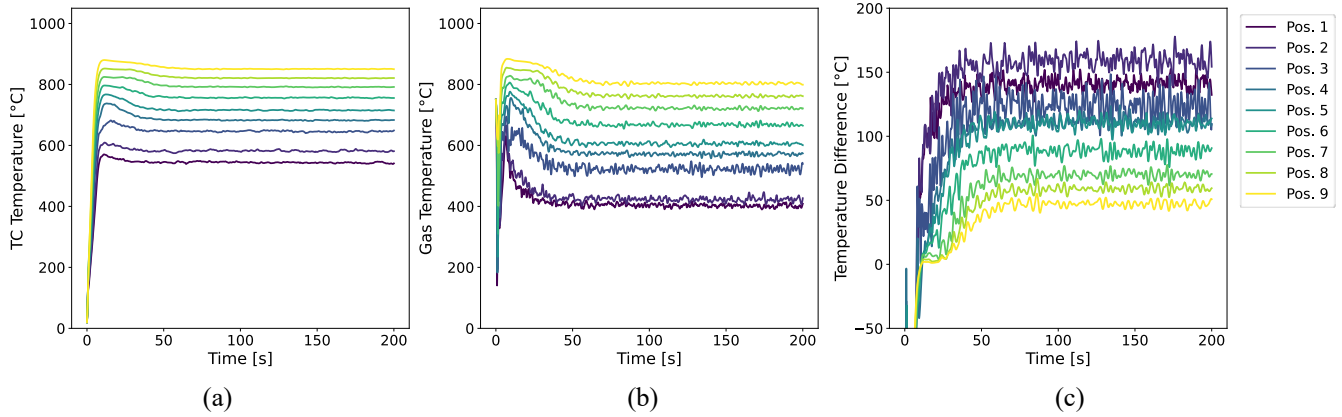


Figure 5. Temperatures measured by (a) thermocouples (TC): T_{TC} and (b) temperature devices (TD): T_g , and (c) the difference $T_{TC} - T_g$ in Scenario 2. Pos. 1 to 9 as specified in Figure 1

At the beginning of the simulation, the same phenomena as in Scenario 1 take place. Due to its elevated temperature, buoyancy in the smoke is evident from the beginning. The smoke leaves the compartment through the holes in the ceiling, while fresh air enters through the holes in the bottom, as can be observed from the transition in Figure 6. Simultaneously, the thermocouples heat up as they are surrounded by hot smoke (see Figure 5a). The overall behaviour is similar to Scenario 1, but steady state is reached more quickly (after approximately 50s compared to 80s in Scenario 1) and the influence of radiation is observed sooner (after about 10s instead of 25s). According to equation (5), a lower extinction coefficient, K , results in a lower attenuation of radiation by smoke. The extinction coefficient, K , is determined by multiplying the mass extinction coefficient, K_m , by the smoke density, which is influenced by the soot mass fraction. As both parameters were initially lower compared to Scenario 1, K was also lower, leading to a head start in the decline in the attenuation of radiation by smoke until it becomes negligible.

Once the smoke has completely left the compartment, both the thermocouple and gas temperatures tend to the same steady-state situation as in Scenario 1. The difference between thermocouple and gas temperatures increases with increasing distance from the ceiling. Similar to Scenario 1, the stratification in the air, induced by the temperature difference between the floor and ceiling, leads to variations in the temperature difference between thermocouples and the radiating surfaces. These variations have a bigger effect than the changes in view factor with position, resulting in a higher difference in temperature between thermocouple and gas as the distance from the ceiling increases.

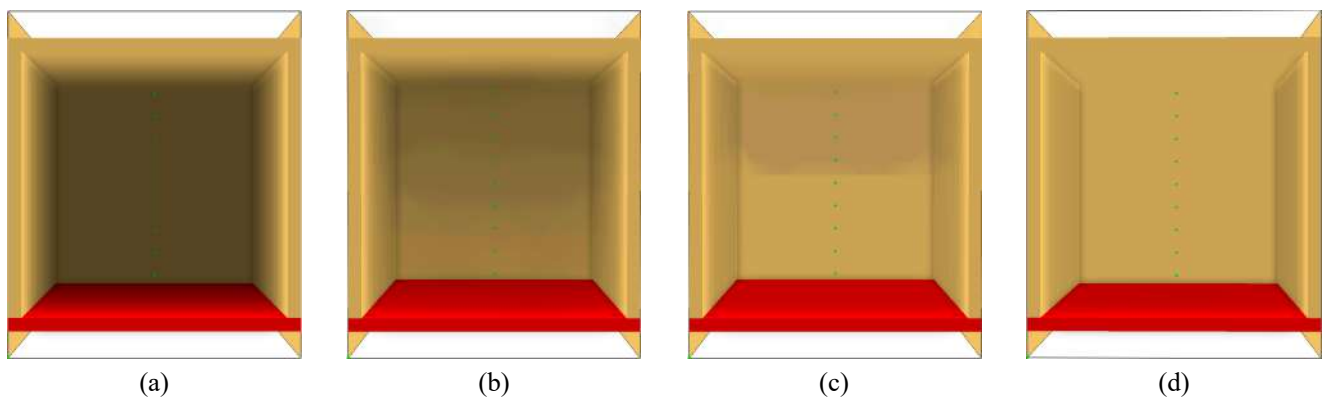


Figure 6. Visualisation of smoke density in Scenario 2 at (a) 0s, (b) 10s, (c) 30s, and (d) 50s

4.3 Scenario 3

Scenario 3 represents a situation in which no smoke is present anymore. Both the thermocouples and gas inside the compartment are initially at 20°C, representing fresh air that cools the linings inside a compartment after a fire. Immediately after the beginning of the simulation, the air inside the compartment stratifies due to the difference in temperature between the ceiling and the floor, as can be seen in Figure 7b. As they are surrounded by air that is increasing in temperature, the thermocouples follow the same trend, as depicted in Figure 7a. The final temperature of the thermocouples at steady state is, however, higher than the local gas temperature due to influence of radiation, which cannot affect transparent air. The resulting steady-state situation is the same as in Scenarios 1 and 2 as the temperatures of the floor and ceiling are the same.

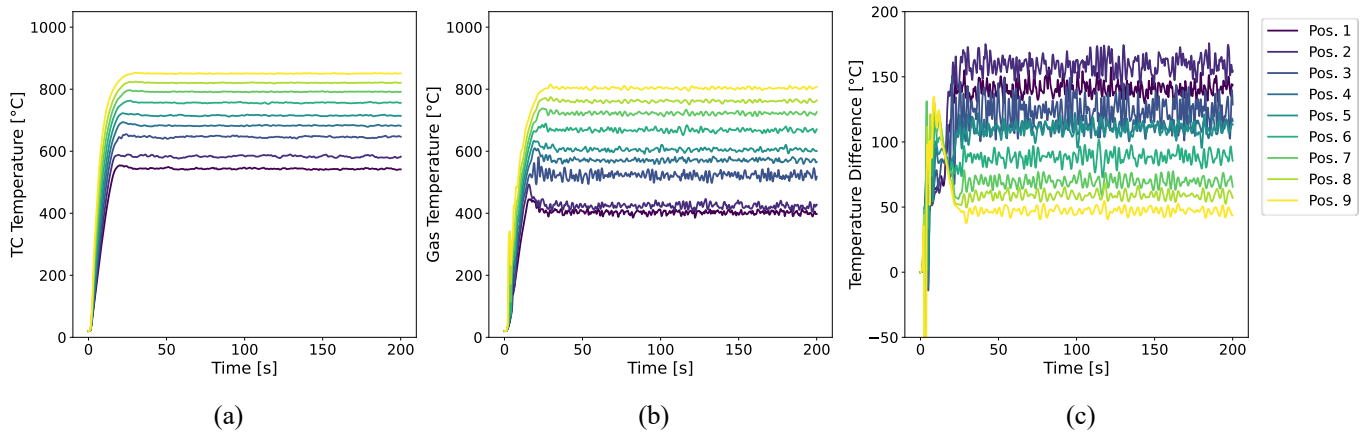


Figure 7. Temperatures measured by (a) thermocouples (TC): T_{TC} and (b) temperature devices (TD): T_g , and (c) the difference $T_{TC} - T_g$ in Scenario 3. Pos. 1 to 9 as specified in Figure 1

4.4 Sensitivity analysis

To ensure that the chosen cell size does not significantly impact the simulation outcomes, a sensitivity analysis is conducted. Specifically, the configuration from Scenario 2 (5 cm cell size) is compared to results from a simulation utilizing a 2.5 cm cell size in Figure 8. This demonstrates that refining the cell size to 2.5 cm does indeed affect the calculated thermocouple temperatures during the dynamic phase of the simulation, but minimal differences are observed in the steady-state values between the the two cell sizes. Moreover, the observed variation is primarily quantitative and is considered overall acceptable: given that the results are utilized for qualitative analysis purposes, the selected mesh cell size is deemed suitable.

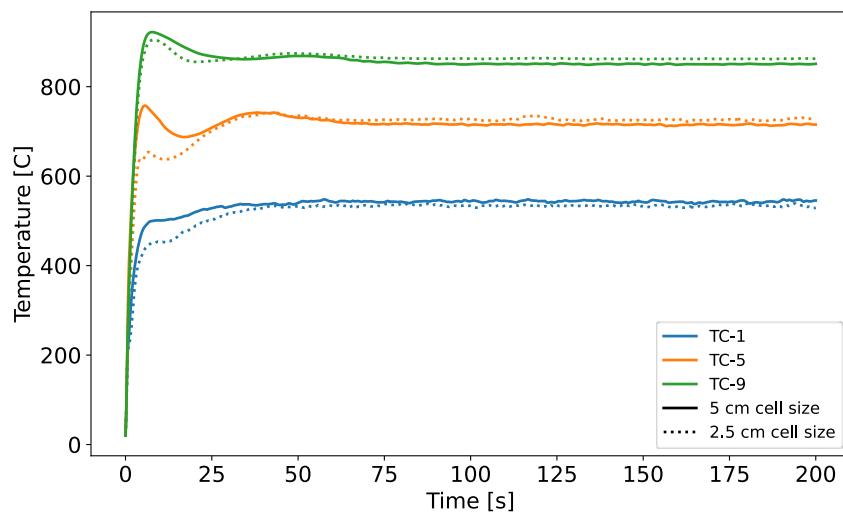


Figure 8. Sensitivity analysis of Scenario 2 employing mesh cell sizes of 5 cm and 2.5 cm

5 DISCUSSION

The three scenarios presented above demonstrated the difficulties inherent to performing and interpreting temperature measurements in large-scale fire experiments. The temperature measured by a thermocouple is heavily affected by the temperature and optical thickness of smoke, the temperature of the linings and the relative position of the thermocouple to radiating surfaces (usually the linings and the smoke layer). Hence, thermocouples can measure significantly different temperatures depending on where they are located inside a compartment, and depending on the stage of the fire, which influences the environmental conditions governing heat transfer.

The changing conditions during the fire decay and cooling phases have important implications on the use of thermocouple data when applied within the framework of the adiabatic surface temperature, which considers fixed values for the convective heat transfer coefficient, h_{AST} , and the effective emissivity, ϵ_{AST} . These values have been determined for the post-flashover heating and fully-developed phases, but not for the decay and cooling phases. During the post-flashover heating and fully-developed phases, the compartment is often assumed to be filled with a hot, optically thick smoke at uniform temperature, preventing radiative heat transfer between temperature measuring devices and the compartment linings. As the optical thickness of the smoke reduces during the decay phase and the smoke is replaced by fresh and transparent air in the cooling phase, the heat transfer equation becomes more complex as the attenuation coefficient of the smoke, the path length of the radiation through the smoke and temperature differences in the smoke need to be considered. Therefore, thermocouple measurements need to be corrected for radiation coming from the compartment linings, considering the optical thickness of the smoke at every point in space and at every instance of time, similar to the method used in [9].

Applying thermocouple data as an AST, with assumed fixed values for the effective emissivity and convective heat transfer coefficient, is inherently incorrect as the net total heat flux in equation (4) will be different when other values for these parameters are used. It was clearly demonstrated in Scenario 1 that significant differences in the AST can be expected when inappropriate values for the convective heat transfer coefficient and effective emissivity are used. This happens mainly during the decay and cooling phases as the suggested values in literature have been derived for the fully-developed phase. This obstacle can be overcome if their values were adjusted to the thermal boundary conditions in the compartment – a task that is far more complex than it appears at first sight. In particular, the value of the convective heat transfer coefficient should be determined based on the velocity of the gas, the temperature of the gas and the temperature of the thermocouple itself. Nevertheless, this information is generally not, or at least insufficiently detailed, available from large-scale fire experiments. A second option would be to predict these values using CFD software such as FDS, although there are also differences between simulations and real experiments.

6 CONCLUSIONS

In this study, it was investigated whether thermocouple measurements can be used directly as input for SFE calculations, using the Adiabatic Surface Temperature to define the thermal boundary conditions, in particular during the fire decay and cooling phases. Firstly, the theoretical background of Adiabatic Surface Temperature was revisited to understand the implicit assumptions of the concept. Secondly, a series of canonical FDS simulations, representing the thermal boundary conditions during the decay and cooling phases, were carried out to investigate the influence of the changing smoke and radiation conditions on the temperatures measured by thermocouples.

The results of the FDS simulations indicated that factors such as smoke temperature, smoke's optical thickness, temperature of the linings and thermocouple position have a significant influence on the readings obtained from thermocouples. When an optically thick smoke is present, thermocouples tend to measure the true smoke/gas temperature. These conditions typically occur during the fully-developed phase of a fire. Given the uniformity of conditions and alignment with the convective heat transfer coefficient and effective emissivity used in calculating the Adiabatic Surface Temperature, during this phase thermocouple measurements can effectively be utilized as inputs for Structural Fire Engineering (SFE) calculations.

The thermal boundary conditions however change significantly when the fire transitions into the decay phase and, subsequently, into the cooling phase. Smoke becomes less optically thick due to dilution with fresh air and a decreasing heat release rate. Radiation from compartment linings and other elements will then affect thermocouple measurements. In addition, the fixed values for the convective heat transfer coefficient and effective emissivity are no longer applicable. Hence, thermocouple measurements for the decay and cooling phases cannot directly be used within the framework of the Adiabatic Surface Temperature.

ACKNOWLEDGMENT

This research has been funded by Research Foundation of Flanders (FWO) within the scope of the research project (Grant number 1137123N) “Characterization of the thermal exposure and material properties of concrete during the fire decay phase for performance-based structural fire engineering”. Dr. Lucherini would also like to gratefully acknowledge the financial support for the FRISSBE project within the European Union’s Horizon 2020 research and innovation program (GA 952395).

REFERENCES

- [1] K. LaMalva and D. Hopkin, Eds., *International Handbook of Structural Fire Engineering*. in The Society of Fire Protection Engineers Series. Cham: Springer International Publishing, 2021. doi: 10.1007/978-3-030-77123-2.
- [2] U. Wickström, *Temperature Calculation in Fire Safety Engineering*. Cham: Springer International Publishing, 2016. doi: 10.1007/978-3-319-30172-3.
- [3] CEN, ‘EN 1991-1-2: Eurocode 1: Actions on structures - Part 1-2: general actions - Actions on structures exposed to fire’. European Committee for Standardization, Brussels, Belgium, 2002.
- [4] C. R. Barnett, ‘BFD curve: a new empirical model for fire compartment temperatures’, *Fire Saf. J.*, vol. 37, no. 5, pp. 437–463, Jul. 2002, doi: 10.1016/S0379-7112(02)00006-1.
- [5] A. Lucherini and J. L. Torero, ‘Defining the fire decay and the cooling phase of post-flashover compartment fires’, *Fire Saf. J.*, vol. 141, p. 103965, Dec. 2023, doi: 10.1016/j.firesaf.2023.103965.
- [6] Y. A. Cengel, ‘Basics of Heat Transfer’, in *Heat Transfer: A Practical Approach*, 2nd ed., New York: McGraw-Hill, 2002, pp. 1–60.
- [7] K. McGrattan, S. Hostikka, J. Floyd, R. McDermott, M. Vanella, and E. Mueller, ‘FDS User’s Guide’, FDS-SMV. Accessed: Nov. 27, 2023. [Online]. Available: <https://pages.nist.gov/fds-smv/manuals.html>
- [8] Y. A. Cengel, ‘Radiation Heat Transfer’, in *Heat Transfer: A Practical Approach*, 2nd ed., New York: McGraw-Hill, 2002, pp. 605–666.
- [9] S. Welch, A. Jowsey, S. Deeny, R. Morgan, and J. L. Torero, ‘BRE large compartment fire tests-Characterising post-flashover fires for model validation’, *Fire Saf. J.*, vol. 42, no. 8, pp. 548–567, Nov. 2007, doi: 10.1016/j.firesaf.2007.04.002.

DELIVERING SUSTAINABLE BUILDINGS: IMPLICATIONS AND CHALLENGES FOR STRUCTURAL FIRE ENGINEERING

Marion Charlier¹, Andrea Lucherini²

ABSTRACT

In the climate emergency context, it is necessary to consider the several existing structural fire engineering (SFE) strategies through the lens of sustainability, i.e. to assess the environmental impact of the current SFE practises to minimize it, based on the project specificities. But it is equally necessary to raise awareness of how sustainability targets may affect the structural performance of a building in the event of a fire. This paper provides observations, analyses and case studies aiming to establish a sound link between the requirements for sustainable structures and the requirements from a structural engineering perspective, focusing on fire safety.

Keywords: Structural fire engineering; sustainable buildings; low carbon materials; case studies

1 INTRODUCTION

Recently, the European Green Deal has set the target of achieving net-zero greenhouse gas emissions by 2050, for which the construction industry will require relevant changes, given its significant impact on global emissions (~40%) [1]. Structural design can no longer be driven only – or even primarily – by criteria such as cost, speed of erection or aesthetics. Instead, sustainability criteria, such as the carbon footprint, recyclability, and optimised use of resources, are increasingly at the core of design decision-making and this new reality is leading to the development and application of novel materials, structural systems, and strategies. In this context, one of the priorities in delivering a sustainable built environment is to reduce its carbon footprint, which can be classified into two parts: the operational carbon (emitted during the operational or in-use phase of a building) and the embodied carbon (associated with the materials and the construction process). As regards to structural engineering, the responsibility is rather linked to the latter. Reducing the embodied carbon of a structure involves several approaches, such as challenging the project brief, opting for efficient structural design which minimize the overall bill of materials, relying on the availability of materials with a lower embodied carbon, and reusing materials. The latter is directly linked to the concept of circularity which fosters keeping materials in circulation through channelling demolition waste into structure inputs. Although some structural elements can be reclaimed after demolition, ensuring an appropriate quantity in a satisfactory (and perhaps optimal) condition requires a specific intervention at the very beginning of the project. This is commonly referred to as “design for disassembly”, where the construction project is envisioned, from the first conceptual engineering steps, to be dismantled in a non-destructive way when reaching its end-of-life [2].

There is an interconnection between many of the innovations for sustainability and fire safety in the built environment. Part of this interconnection is at the fundamental level, as there is often a tension between innovation and safety. Since innovations introduce new systems and technologies for which there is no return of experience, they potentially introduce new unforeseen risks (examples abound where disasters

¹ PhD, Advanced Building Solutions & Sustainability Lead, Steligen Engineering, ArcelorMittal, Luxembourg
e-mail: marion.charlier@arcelormittal.com, ORCID: <https://orcid.org/0000-0001-7690-1946>

² PhD, Senior Researcher, Slovenian National Building and Civil Engineering Institute (ZAG), Slovenia
e-mail: andrea.lucherini@zag.si, ORCID: <https://orcid.org/0000-0001-8738-1018>

have occurred and then led to a “learning from disaster” approach [3]). Even if immediate benefits can be reaped from incorporating a new practice that achieves “better” sustainability without due consideration from safety, these benefits would eventually be nullified by the consequences of a structural failure. Another part is at a technical level: some of the key innovations being introduced have an impact on either the probability of fire events and/or on the structure response when subjected to elevated temperatures, and they therefore need to be carefully studied.

In the next sections, an assessment of the environmental impact of the current SFE practises is proposed and several of the main types of innovations currently emerging to address the climate emergency are discussed in the context of structural fire safety. First, an overview of structural materials with a lower corresponding embodied carbon is provided, discussing the (currently known) implications and challenges of using these materials in fire conditions. A case study of an office building which includes various structural systems is also discussed. Finally, some comments are provided about the challenges that fire safety may introduce when applying circular structural concepts such as design for disassembly and the reuse of elements.

2 WHEN THE OBJECTIVE IS LOW EMBODIED CARBON

2.1 The use of structural materials with a lower embodied carbon

The embodied carbon of a building is associated with the used materials and the construction process: extraction of raw materials, manufacture, transport, erection, and deconstruction of the structural elements and their treatment at the end-of-life [2]. To contribute to the decarbonization effort and to support the reduction of the embodied carbon of the built environment, industries are developing new construction materials with a low corresponding embodied carbon. In other cases, traditional construction materials, such as steel and concrete, have been facing several changes in the manufacturing and production processes in order to reduce their environmental impact.

Bio-based structural materials are inherently low-carbon, and they can contribute to reduce the environmental impact of the built environment. However, as regards to fire safety, bio-based construction materials are typically combustible, and they can impact the fire safety strategy of buildings. For instance, as regards to structural fire engineering (SFE), the combustibility of the load-bearing materials may complicate the structural fire assessment due to the interaction between the fire dynamics and the structural systems [4]. Accordingly, combustible structural materials can constitute an increased level of fuel load (compared to the existing “movable fuel load”), which has to be considered for structural fire calculations to ensure the building stability and integrity during and after a fire. As a consequence, it is fundamental to understand the implications of designing a combustible structure, which would help reduce the environmental impact of a building but may introduce new fire safety hazards and possibly question the resilience, sustainability, and robustness of the building design.

As regards to steel structural elements, low-carbon variants have been developed and achieved through changes of industrial processes, e.g. use of renewable electricity, switch from BF-BOF (Blast Furnace - Basic Oxygen Furnace) to DRI (Direct Reduction Iron) and EAF (Electric Arc Furnace). It is important to highlight that these improvements do not impact the properties of the structural material, which in any case complies with the same product standard (e.g. EN 10025 for hot rolled steel), but they significantly reduce the environmental impact of the manufacturing process [5].

As regards to concrete, many ongoing developments are targeting the improvement of the both the aggregates and the cement. Even though the objective should be to maximize the effort at eliminating waste and therefore maximizing the recycling of the aggregates, the concrete carbon impact challenge mainly is driven by the cement. Indeed, it is responsible for over 60% of its greenhouse gases emissions (and up to 90% depending on the mixture and location) [6]. The current alternatives rely on adapting clinker, which is substituted with GGBS (Ground Granulated Blast furnace Slag) or fly ash. In ambient conditions, the introduction GGBS (replacing a given ratio of cement) affects the early-stage strength and the carbonation [7,8], while the main influence of recycled aggregates applies to the long-term mechanical properties of the concrete. Indeed, it introduces a new weak spot: the interface between old and new mortar around the aggregates which negatively affects the compressive strength [9]. For instance, the effect of the mechanical

properties of concrete containing different volumes of GGBS at elevated temperatures was investigated by Li *et al.* [10]. They found that the relative compressive strength decreased more significantly than ordinary Portland cement concrete, while the modulus of elasticity of concrete was reduced for heating temperatures up to 300°C and the reduction was more obvious for concrete containing higher volumes of GGBS.

2.2 Case study: an office building with different structural systems

Delivering sustainable buildings does not only rely on using low-carbon materials but also on opting for efficient structural design. Playing with the strength of each material, selecting an efficient structural grid, using high-strength materials when relevant can lead to an optimized design and reduction of the global bill of materials. To quantify the embodied carbon of a construction project, a Life-Cycle Assessment (LCA) can be carried out: it is a science-based and standardised [11,12] methodology for quantifying environmental impacts. The LCA procedure is defined by the ISO 14040 standard series and can be applied to support an eco-design, as well as the decision-making process. LCA assesses several environmental impact categories, amongst which the Global Warming Potential (GWP), calculated in carbon dioxide equivalents (CO₂eq.).

In this spirit, de Paula Filho *et al.* [13] presented the comparative results of a “cradle-to-cradle” building LCA of an R+8 (ground-floor and 8 upper levels) office building located in Luxembourg with 50 years of service life (see Figure 1(a)). Three equivalent (i.e. representing the same functional unit) structural systems were designed by independent design office based on the Eurocodes: a prefabricated reinforced concrete variant, a steel-concrete composite variant (Figure 1(b)) and a timber variant (Figure 1(c)). The grid and structural system for each variant was chosen to be representative of the market practice (and of best performance). Amongst several criteria, the GWP were assessed and commented.

When it comes to the structural fire design, the steel-concrete composite and the timber variant imply some strategical choices, which affect the embodied carbon of the whole building. A focus is therefore given below on these two designs to review the possible options and indicate the potential for environmental performance improvement in an SFE context. A low-carbon concrete variant and the corresponding SFE analysis have not yet been developed, as the concrete standard EN 206 (Concrete - Specification, Performance, Production, and Conformity) is currently under revision.



Figure 1. Schematic representation of the (a) R+8 office building, (b) steel-concrete composite variant, (c) timber variant

2.3 Timber structural system: the impact of the total building height

As regards to the timber variant, the structural system is mainly designed using engineering timber products: columns and beams are made of glue laminated timber (GL24h) and floors are in cross laminated timber (layers are made of C24 solid timber). The cores, the two underground floors and the foundations are designed in reinforced concrete. As the building is assumed to be built in Luxembourg, the guidelines from ITM-SST 1503-3 “Prescriptions de prévention incendie – dispositions générales – bâtiments élevés” (i.e. Fire prevention regulations for tall buildings) must be applied. The document differentiates 3 types of tall buildings: Type A (total height above 22 m and lower or equal to 30 m), Type B (total height above 30 m and lower or equal to 60 m), Type C (total height above 60 m and lower or equal to 200 m).

In the brief, the geometric requirements are as given in Table 1 (in the “original” design column): they are based on a 2.7 m free height requirement and the total height of the building exceeds 35 m. Therefore, the building falls into the Type B, which implies that all the structural elements must meet a R120 requirement

(based on ISO-834 standard fire curve). To meet R120, the beams and columns has to have an increased cross-section and the CLT160 slab has to be fire protected with two 12.5 mm layers of type F plasterboards. Some modifications to the brief and to the functional unit of the building itself could make the building become a Type A, implying a R90 fire requirement (and no need of plasterboards to protect the CLT, whose price was evaluated as equivalent to 80% of the cost of an additional floor). Indeed, as shown in Table 1 (in the “suggested” design column), a modification of the free-height from 2.7 m to 2.5 m (which may seem like an acceptable compromise for most end-users) decreases the overall height of the building. This reduction is not sufficient to allow for the total height to remain below 30 m, but with this modification the office building could become Type A if the last level was not built (i.e. if it were to be R+7 instead of R+8), as highlighted in Table 1. Accepting to limit the free height of a typical floor and the total height of the building therefore lead to lower costs and embodied carbon. This threshold of 30 m is specific to the Luxembourgish regulations, but the principle of drawing a line for defining “taller” buildings and enforcing more stringent fire requirements is applied in other countries.

Table 1. Brief requirements and consequences on the total height of the timber building

Brief and geometrical requirements	Original	Suggested	Floor	Original	Suggested
Free height for typical floor [m]	2.7	2.5	R	4.61	4.61
Free height for the ground floor (R) [m]	3.5	3.5	R+1	8.42	8.22
Structural thickness for a typical floor [m]	0.96	0.96	R+2	12.23	11.83
Floor [m]	0.15	0.15	R+3	16.04	15.44
			R+4	19.85	19.05
			R+5	23.66	22.66
			R+6	27.47	26.27
			R+7	31.28	29.88
			R+8	35.09	33.49

As a conclusion, timber structural elements, being made from bio-based material, present several benefits in terms of embodied carbon. But this example showcases that the building height may highly affect these advantages. Indeed, the higher the building, the higher the fire requirements, and the strategy to enhance fire resistance in timber structural elements is to increase their sections and possibly oversize them, as well as at some point to cover them with fire-protective materials, such as plasterboards. For example, the Table 2 provides the increase in cross-section for the glue laminated timber columns (GL24h) of the considered office building to adapt the fire requirements from R90 to R120. Engineers should assess to what extent this increase in dimensions is acceptable or rather jeopardizes the original benefits of designing in timber. For example, Hafner *et al.* [14] mention that cladding timber columns with gypsum plasterboards counteracts these benefits and may cause worse LCA results if compared to reinforced concrete columns.

Table 2. Brief requirements and consequences on the total height of the timber building

Level	Internal columns		External columns	
	R90	R120	R90	R120
R	500x500	500x500	440x440	440x440
R+1	480x480	480x480	400x400	440x440
R+2	440x440	480x480	400x400	420x420
R+3	440x440	440x440	400x400	420x420
R+4	400x400	420x420	360x360	400x400
R+5	360x360	400x400	360x360	400x400
R+6	360x360	400x400	360x360	360x360
R+7	360x360	360x360	360x360	360x360
R+8	280x280	320x320	280x280	320x320

2.4 Steel-concrete composite structural system: three fire assessment strategies

As regards to the steel-concrete composite variant, Figure 2(a) illustrates the foreseen structural system. As the office building is based on a repetition of this structural bay, the latter is considered below for the Life-Cycle-Assessment. It is composed of the following elements:

- Columns: [HE 240 M] (considering the ground floor level);
- Main beams: [Angelina IPE330 / IPEO330] (cellular beams as depicted on Figure 2(b));
- Facade Beams: [IPE400];
- Composite slab with steel deck Cofraplus60;
- Concrete C30/37;
- Overall steel reinforcement (rebars) ratio: 4.77 kg/m².

Three strategies are considered regarding the structural fire assessment: the prescriptive approach (ISO-834 standard fire curve), a first performance-based approach (relying on membrane action [15] with the ISO-834 standard fire curve), and a second performance-based approach (natural fire curve assessment based on the application of zone model OZone [16]). Other scenarios can be considered, but the above-mentioned three scenarios were chosen for this study as they represent the most commonly used practices for office buildings. A Life-Cycle-Assessment is applied for the structural bay represented on Figure 2(a) considering these three different strategies to estimate their respective GWP, and highlight the potential discrepancies or similarities. Two different passive fire protection measures are considered and their influence on the GWP is discussed: plasterboards reinforced with mineral fibers and an intumescent coating in water emulsion consisting of synthetic resin. The purpose of such assessment is not to identify a better design option, but to illustrate the type of analysis which can help assessing the influences of the current SFE practices on the overall embodied carbon, aiming at quantifying and minimizing it. Indeed, it is important to keep in mind that the obtained results are only valid in the considered case study, and under the considered assumptions, which should be adapted case by case based on the considered project specifications.

The three strategies applied for the SFE assessment lead to the following different Bill Of Materials (BOM):

- Prescriptive approach (ISO-834 standard fire curve): passive fire protection for all the steel elements, beams and columns.
- First performance-based approach (membrane action with the ISO-834 standard fire curve): the internal 13 m span beams (i.e. the Angelina IPE 330) are left unprotected, but activating the membrane effect requires extra steel reinforcement in the concrete slab.
- Second performance-based approach (natural fire curve based on zone model): no fire protection required to ensure the stability of the structure under the considered fire scenarios. For this situation, the BOM is therefore similar to the first strategy, except no passive fire protection is accounted for.

When passive fire protection is required, two possibilities have been studied. To evaluate the quantity of plasterboards, the software ABC and A3C were used [17]. The equation 4.27 of EN 1993-1-2 to evaluate the steel temperature development for members insulated by fire protection material is applied and the thickness of plasterboard required for beams and columns to remain below the critical temperature is evaluated (considering commercially available thicknesses of 12.5mm, 15mm, 18mm and 25mm). The protected beams and columns are covered by boards on 3 and 4 sides, respectively. When considering intumescent coatings, a simpler assessment was conducted: the critical temperatures of the elements were not evaluated but the design tables published by Etex Building Performance NV/SA for the product P ROMAPAINTE®-SC4 [18] were used. It provides intumescent coating thicknesses based on the section factor (A_m/V) of the steel profiles, the number of exposed sides and assumed critical temperatures (500°C for a column and 540°C for a beam).

A complete LCA covers all the life stages of a construction: the production of the materials (modules A1–A3), the construction process (modules A4–A5), the end of life (modules C1–C4), and the benefits and loads beyond the system boundary (module D) [10]. Although a complete LCA should be applied when data is available, the illustrative exercise presented below is simplified and focuses on the production stage (A1-A3) only. The life-cycle inventory is composed of Environmental Product Declarations (EPD)

published according to EN 15804. These peer-reviewed and standardized documents provide quantified information on environmental impacts for use in a building LCA. The EPDs considered in this assessment are presented in Table 3 together with their GWP impacts (A1–A3) in terms of their functional unit. The LCA was conducted using the commercial software OneClick LCA.

Table 3. EPD considered for the steel-concrete composite office building and their relative GWP for [A1-A3].

Structural element/component	Data source	Publisher & document number (if available)	Functional Unit (FU)	[A1-3] GWP (kgCO ₂ eq/FU)
Steel sections (“standard”)	OneClick LCA internal data, Structural steel profiles, generic, 20% recycled content, I, H, U, L, and T sections	<u>OneClick LCA</u>	kg	2.51
Steel sections (“low carbon”)	EPD : XCarb® RRP structural steel sections and merchant bars (ArcelorMittal Europe)	<u>IBU</u> EPD-ARC-20210132-CBB2-EN	kg	0.33
Ready-mix concrete C30/37	OneClick LCA internal data	<u>OneClick LCA</u>	m ³	270.88
Steel deck (“standard”)	EPD: Hot-dip galvanized steel coils, Magnelis® (ArcelorMittal Europe)	<u>IBU</u> EPD-ARM-20170140-IBD1-EN	kg	2.57
Steel deck (“low carbon”)	EPD: Hot-dip galvanized steel coils, XCarb® Magnelis® (ArcelorMittal Europe)	<u>EPD International</u> S-P-11914	kg	0.89
Steel rebars (“standard”)	Reinforcing steel (rebar), 7850 kg/m ³ , Krybar® (ArcelorMittal Europe)	<u>IBU</u> EPD-ARM-20210338-CBB1-EN	kg	0.82
Steel rebars (“low carbon”)	EPD: Reinforcing steel bars, XCarb® (ArcelorMittal Europe)	<u>IBU</u> EPD-ARC-20210245-CBA2-EN	kg	0.30
Intumescent coating (fire protection)	intumescent coating, PROMAPAINTE®-SC4 (Promat SpA)	<u>EPD International</u> S-P-08957	kg (wet coating)	2.15
Plasterboard (fire protection) – thickness 12.5mm	Gypsum plasterboard, mineral fibers reinforced, 12.5 mm, GKF (Knauf)	<u>EPD International</u> S-P-01935	m ²	2.54
Plasterboard (fire protection) – thickness 15mm	Gypsum plasterboard, regular, 15 mm, GKB (Knauf)	<u>EPD International</u> S-P-01933	m ²	3.16

A membrane action analysis has been carried out with the pre-design software MACS+ [14] (and with the FEM software SAFIR for the R90 requirement). The beams intersecting columns (i.e. sections IPEO330 and IPE400) are considered as protected while the internal beams (section IPE330) are left unprotected. The following reinforcement meshes allow for different fire requirements with the membrane effect: 257mm²/m (7mm diameter bars, for the longitudinal mesh and for the transversal mesh) for R30, 335mm²/m (8mm diameter bars, for the longitudinal mesh and for the transversal mesh) for R60 and 393mm²/m (10mm diameter bars, for the longitudinal mesh and for the transversal mesh) for R90. To evaluate the total quantity of steel rebars for the considered bay, shown in Figure 2(a), a conservative mesh overlap of 30% is considered. This strategy therefore implies less passive fire protection but an extra quantity of reinforcement.

Several EPDs and products (see Table 3) are considered for the steel as well as for the passive fire protection. The “low carbon” steel products are manufactured via EAF (i.e. recycling route) with renewable electricity, while the “standard” data is either coming from standard products EPDs, either from OneClick LCA generic material data, both representing average materials for the performance criteria defined. Two different products are considered for the passive fire protection: intumescent coating (in water emulsion consisting of synthetic resin especially formulated for fire protection of steel structures) and plasterboards

(made from gypsum: up to 96%, cardboard: up to 2% and additives for less than 2%). Even though the considered plasterboards are commercially available in thicknesses 12.5mm, 15mm, 18mm and 25mm, EPDs are only available for thicknesses 12.5mm and 15mm. Therefore, two layers of 12.5mm boards have been considered in the LCA when the required thicknesses exceed 15mm. The service life of all the elements except the intumescent coating equals the service life of the building (50 years in common building LCA), which means that their impact has to be considered once. For the intumescent coating, the considered EPD mentions a service life of 25 years.

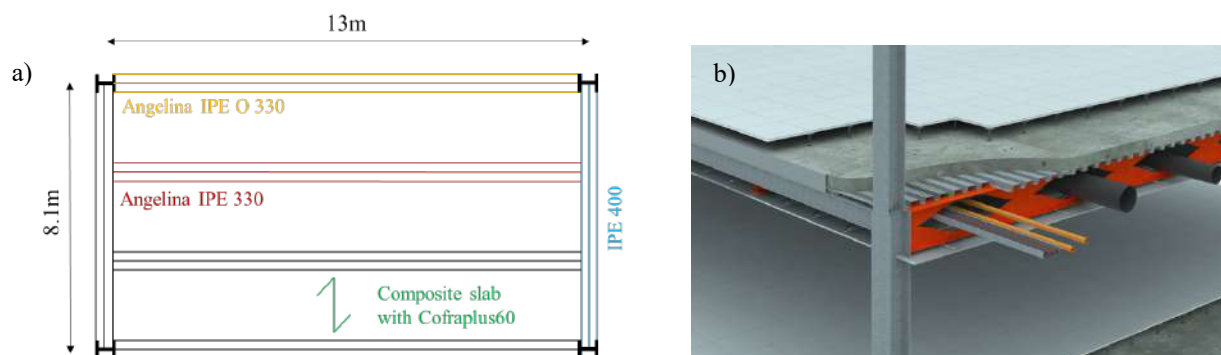


Figure 2. Steel-concrete composite design: (a) Plan view of the structural elements; (b) 3D model

Table 4 provides the results of the LCA analysis for three different fire requirements (R30, R60 and R90, except when applying the natural fire strategy since these requirements do not apply), for the three previously mentioned strategies. The data is structured in sub-tables considering “low carbon” steel products, generic values (“standard”), and the two above-mentioned passive fire protection measures. The “ISO-834 prescriptive” is taken here as the reference strategy; hence, the columns labelled with the symbol Δ in Table 4 provide the relative difference (in embodied carbon) with the two other strategies. The ready-mix concrete is a normal-strength, generic, C30/37 concrete with 10% recycled binders in the cement.

Table 4. Results of the LCA analysis for the steel-concrete composite bay according to different strategies.

“Standard” steel & coating		ISO-834, Prescriptive	ISO-834, Membrane action	Δ	Natural fire	Δ
R30	kgCO ₂ eq	20523	20522	0%	20460	0%
	% rebars	1%	1%		1%	
	% coating	0%	0%		0%	
R60	kgCO ₂ eq	20710	20740	0%	20460	-1%
	% rebars	1%	2%		1%	
	% coating	1%	1%		0%	
R90	kgCO ₂ eq	20920	20950	0%	20460	-2%
	% rebars	1%	2%		1%	
	% coating	2%	2%		0%	

“Low carbon” steel & coating		ISO-834, Prescriptive	ISO-834, Membrane action	Δ	Natural fire	Δ
R30	kgCO ₂ eq	5873	5872	0%	5810	-1%
	% rebars	3%	3%		3%	
	% coating	1%	1%		0%	
R60	kgCO ₂ eq	6060	6050	0%	5810	-4%
	% rebars	2%	4%		3%	
	% coating	4%	3%		0%	
R90	kgCO ₂ eq	6270	6240	0%	5810	-7%
	% rebars	2%	5%		3%	
	% coating	7%	4%		0%	

“Standard” steel & board		ISO-834, Prescriptive	ISO-834, Membrane action	Δ	Natural fire	Δ
R30	kgCO₂eq	20620	20590	0%	20460	-1%
	% rebars	1%	1%		1%	
	% board	1%	1%		0%	
R60	kgCO₂eq	20622	20680	0%	20460	-1%
	% rebars	1%	2%		1%	
	% board	1%	1%		0%	
R90	kgCO₂eq	20750	20810	0%	20460	-1%
	% rebars	1%	2%		1%	
	% board	1%	1%		0%	

“Low carbon” steel & board		ISO-834, Prescriptive	ISO-834, Membrane action	Δ	Natural fire	Δ
R30	kgCO₂eq	5970	5940	-1%	5810	-3%
	% rebars	3%	3%		3%	
	% board	3%	0%		0%	
R60	kgCO₂eq	5972	6000	0%	5810	-3%
	% rebars	3%	4%		3%	
	% board	3%	2%		0%	
R90	kgCO₂eq	6100	6100	0%	5810	-5%
	% rebars	2%	4%		3%	
	% board	5%	3%		0%	

Based on the results presented in Table 4, the following observations can be drawn:

- The performance-based approach based on natural fire demonstrates a lower embodied carbon than for the reference prescriptive strategy, but this effect is almost negligible for “standard” steel products, while benefits become more substantial for “low carbon” steel products. The application of the membrane action globally exhibits similar embodied carbon results than the reference strategy (difference ranging from -1% to 0%).
- For the prescriptive strategy, with the fire requirements becoming more stringent (i.e. increasing from R30 to R90); the discrepancy with the natural fire approach widens for “low carbon” steel. This difference evolution is slightly more pronounced for intumescent coating application compared to the board solution. However, for the lowest considered fire requirement (i.e. R30), the board solution presents a higher difference (i.e. gain) compared to intumescent coating.
- For R30 requirement, the use of boards results in a higher embodied carbon compared to intumescent coating, albeit the variation is extremely minimal because of the low weight of coating required. This is valid both for the reference strategy and for the membrane action strategy. The maximum discrepancy is 2% for the “low carbon” steel products in the reference strategy. Conversely, for R60 and R90 requirements, the board solution demonstrates lower embodied carbon compared to intumescent coating, once more with marginal effect. The maximum discrepancy is 3% for the “low carbon” steel products in the reference strategy (R90).
- The ratio of the GWP impacts from the rebars and the passive fire protection over the total GWP gets higher as the total GWP (of the considered building part) gets lower. In other words, as the GWP of the “standard steel” structure is significantly higher than the GWP of the “low carbon” steel structure, the effect of the additional rebars and/or fire protection becomes negligible.

It is observed that when building with “standard” steel products, the effect of the fire protection becomes negligible in the total environmental footprint of the structure and floor systems. Nevertheless, in a context of industrial decarbonization for construction, systems using “low carbon” materials will become more and more common, and in this case the share of the fire protection will increase. Therefore, deploying efforts on lowering the GWP of fire protection (and/or favour the use of the natural fire safety

concepts) should be pursued. It should be noted that these observations should not blindly be extrapolated to any other situations as they depend on the choice of EPDs (variability in EPDs is particularly notable within the domain of passive fire protection), the structural layout for the membrane (and the number and length of unprotected beams within the structural bay), the loading ratio, etc. This simplified LCA case study is presented to illustrate how such an analysis can help to indicate the potential for environmental performance improvement (i.e., supporting eco-design) in a SFE context.

It is important to realize that the embodied carbon is not the only criterion at stake in a project. For example, two options, A and B, can be considered. If A presents a slightly better (but limited) result in terms of GWP than B but implies a huge cost uplift or increases the fire-related risks, option A should not be considered as the only viable choice. Ideally, engineers should avoid the pitfalls of focusing on a single objective but rather incorporate sustainability and fire implications, through a multi-objective optimisation approach (e.g., Ma *et al.* [19] provide a cost-benefit analysis of fire designs for fire protection costs in composite buildings). Structural fire engineers could be consulted when establishing the conceptual engineering in view of minimizing the embodied carbon of the project without compromising safety or any other constraint related to the design robustness and resilience.

3 WHEN THE OBJECTIVE IS CIRCULARITY

3.1 Design for disassembly

Another strategy to improve the environmental impact of the built environment is through circularity. In the structural engineering context, this approach fosters keeping construction materials in circulation through channelling demolition waste into structure inputs. Even though circularity is linked to what happens at the end-of-life of a building, ensuring an effective reuse of the structural elements when a building is to be deconstructed requires a specific mindset at the very beginning of the project. Indeed, in the “design for disassembly” approach, an early-stage intervention is required because the design of the project itself is directly affected [2]. In this scenario, from the first conceptual engineering steps, the construction project is envisioned to be dismantled in a non-destructive way when reaching its end-of-life. This dismantling allows for, in a subsequent stage, the reuse of the structural elements such as the beams, columns, slab, etc. In view of increasing the reuse of structural elements, a key approach to effectively lower the embodied carbon of buildings and promote a circular economy, designers need to realize that a necessary prior step is to design for disassembly. Indeed, if the building’s structure has not been engineered to be easily dismantled, the adopted deconstruction approach will most likely result in severely damaging the structural elements.

3.2 Reuse of structural elements

Once structural elements are salvaged, they can potentially be reused in a new structure, even further fostering circularity in construction. It has to be noted that this approach strongly depends on the considered materials. For example, Pomponi *et al.* [20] stated that it is potentially best applied to durable materials such as steel and aluminium. Focusing on protected steel sections, when the building is dismantled and the elements are reused in a new application (assuming no fire event took place), boards can be easily removed. Studying whether these boards could be reused as well would be beneficial. However, this involves careful assessment of their condition and ensuring that their performance meets the requirements. When the components are coated, disassembly will pose no challenges. However, if these components are to be reused, the existing protecting layer will likely need removal before applying a fresh coat. Typically, this process can be accomplished through blast cleaning. This step would in any case be necessary to ensure adherence and promote the stickability of the coating even for new steel elements or for unprotected reclaimed steel elements. This was demonstrated in the Mundo Louvain-la-Neuve project, which reused second-hand hot rolled steel sections for its structural frame [2].

Nevertheless, reusing steel sections usually implies an oversizing of the structural elements as the availability of second-hand sections is not as wide as new products offers (it has to be noted that this extra material does not jeopardize the embodied carbon of the structure, as its corresponding GWP is significantly

lower than the one of an equivalent new member). If passive fire protection is required, this overdesign should be considered when quantifying the required protection, as this will possibly lead to a lower utilization ratio, a higher critical steel temperature and therefore lower quantity of fire protection material. Sometimes, it is the building's structure itself (or part of it) which can be reused. This approach implies no (or little) dismantling and is usually associated with refurbishment projects. It can also be sometimes envisaged in case of post-fire situations allowing to re-build parts of the structure, therefore avoiding the unnecessary need to re-fabricate a significant number of structural members. This was the case for the New Zealand International Convention Centre, whose roof was affected by a large fire. The application of a post-fire assessment resulted in the retention of 95% of the roof structure, i.e., approximately 2500 tonnes of steel [21]. Assuming steel produced through the BOF route or through the EAF (i.e. recycling route), this corresponds to a saving of respectively 6250 tons of CO_{2eq} or 1500 tons of CO_{2eq} (embodied carbon).

3.3 Case study: demountable composite beams and adjustable connections

In general, an easy dismantling is usually accessible for non-composite framed structures such as steel or timber frames. Nevertheless, designing overlooking a composite action implies a missed opportunity of playing with the strength of different materials and, therefore, of optimizing the structures. Recently, the European research project REDUCE [22] aimed, as a main objective, at providing practical tools and steel-based technologies to enable the design of steel and concrete composite structures for deconstruction and reuse (a particular focus was given to composite floors, see Figure 3(a)). This project also focused on the development of adjustable and slidable connections, bridging the beam to a wide range of supporting elements of different section dimensions within a planning grid (see Figure 3(b)). A pilot project demonstrating the first practical use of this structural system, “la Petite Maison”, has been designed and built next to the University of Luxembourg in Belval, Luxembourg [23].

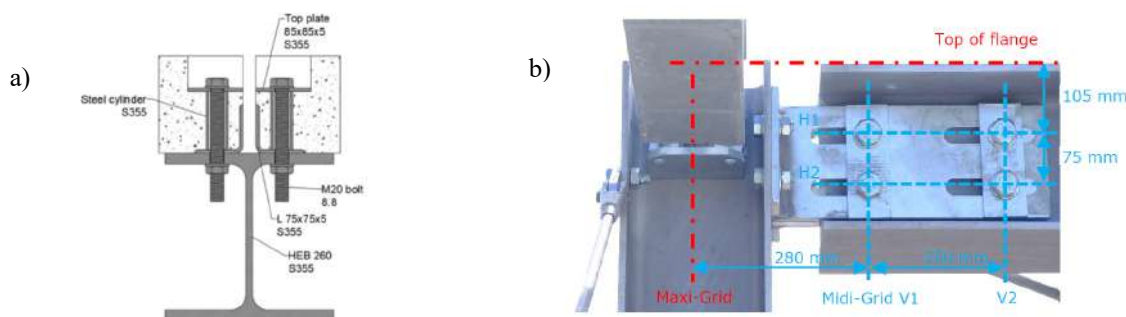


Figure 3. (a) Schematic representation of the demountable shear connectors in steel-concrete composite beams [19]; (b) Photograph of the adjustable connections system in “la Petite Maison” [18]

When it comes to steel concrete composite structures, the behaviour of the structural components under fire are generally well known and described in various standards (e.g. EN 1994-1-2). Nevertheless, further research is needed to assess the behaviour under fire when the members are demountable. Mansilla et al. [24] have conducted an experimental campaign on push-out tests combined with high temperatures, allowing for a characterization of these demountable shear connectors under the combined action of force and elevated temperature (applied by means of heating panels). It was found that the temperature severely impacts the shear resistance of the connectors, and reduction factors were calculated, allowing for a comparison with those proposed for bolts by EN 1993-1-2 Annex D: conservative results were generally obtained. Subsequently, thermo-mechanical numerical model to represent the fire behaviour of steel-concrete composite beams with the above-mentioned demountable shear connectors were developed by [25], to analyse the effectiveness of different fire protection systems. The testing of the whole beam element under elevated temperatures is under preparation by Universitat Politècnica de València.

Another key feature of the REDUCE demountable system involves the adjustable connections utilizing slotted holes and bolts, which are yet to be evaluated in fire scenarios. If required, the type of passive fire protection will have to be carefully selected. Indeed, these connections should remain accessible (since the

aim is to dismantle the structure when reaching its end of life). Most likely, cementitious spray solutions are to be dismissed, leaving boards and intumescent coatings as potential solutions (the use of timber panels could be considered as well, keeping in mind that the latter are combustible and therefore introduce additional complexity/risk compared with insulating boards).

Romero et al. [26] have extended their work on design for disassembly for composite structural systems, considering steel-timber composite beams and flooring systems with the use of LVL (Laminated veneer lumber). Experimental investigations were carried out to assess the system's performance in terms of their load-slip responses, stiffness, and failure mode, and promising results were obtained. These kinds of systems are promising, combining both an efficient structural design, supporting a lower embodied carbon (leveraging on composite action), and a circular approach favouring the reuse of structural components.

4 CONCLUSIONS

Even if sustainability and fire safety objectives may be considered as independent objectives in the short term, they need to be considered jointly to achieve a successful transition towards a sustainable and fire-safe built environment. This paper provides some observations and analyses, aiming to establish links between the requirements for sustainable structures and the requirements from a structural fire engineering perspective. First, an overview of structural materials with a lower corresponding embodied carbon is provided, discussing the implications of using these materials in structures, also including their performance in fire conditions. A case study of an office building is then presented, focusing on a timber and steel-concrete composite structural systems. The implications of design choices on the embodied carbon are discussed, highlighting the influence of the height of the building, materials choice, and the passive fire protection strategy. A focus is finally provided on improving the environmental impact of the built environment through circularity, more specifically by designing demountable composite structural systems and reuse of structural elements, in a structural fire engineering context. This paper is not meant to provide an exhaustive list of all the issues and related solutions arising from the interconnections between fire safety and sustainability, but rather to modestly contribute to highlighting the challenges and existing and currently being developed tools to avoid the pitfalls of focusing on a single objective.

ACKNOWLEDGMENT

Dr Charlier would like to thank José Humberto Matias de Paula, Prof. Christoph Odenbreit, Prof. Thomas Gernay and Prof. Manuel L. Romero for their support. Dr Lucherini would like to acknowledge the financial support for the FRISSBE project within the European Union's Horizon 2020 research and innovation programme (GA 952395).

REFERENCES

1. United Nations. Global Status Report for Buildings and Construction (2021), Available online: <https://globalabc.org/resources/publications/2021-global-status-report-buildings-and-construction>
2. Charlier, M., Vassart, O., A paradigm shift in designing circular steel buildings: Some key principles and pioneering projects. *Steel Construction* 16, No. 4 (2023), <https://doi.org/10.1002/stco.202300033>
3. Bisby, L., Structural fire safety when responding to the climate emergency. *The Structural Engineer*, Volume 99, Issue 2 (2021), <https://doi.org/10.56330/YLVY8201>
4. Nothard, S., Lange, D., Hidalgo, J.P., Gupta, V., McLaggn, M.S., The response of exposed timber in open plan compartment fires and its impact on the fire dynamics, 11th International Conference on Structures in Fire (SiF), Brisbane, Australia: The University of Queensland (2020), <https://doi.org/10.14264/5d97785>
5. Gervasio, H., Simões da Silva, L., D'Antimo, M., The contribution of low carbon steel to the decarbonization of the building sector, Biondini; Frangopol (Eds.) *Life-cycle of structures and infrastructure Systems*. London: CRC Press (2023), DOI: 10.1201/9781003323020-296
6. Miller, S.A., Habert, G., Myers, R. J., Harvey, J.T., Achieving net zero greenhouse gas emissions in the cement industry via value chain mitigation strategies. *One Earth*, Vol. 4 Issue 10 (2021), <https://doi.org/10.1016/j.oneear.2021.09.011>.

7. Witte, A., Garg, N., Quantifying the global warming potential of low carbon concrete mixes: Comparison of existing life cycle analysis tools. *Case Studies in Construction Materials*, Vol. 20 (2024), <https://doi.org/10.1016/j.cscm.2023.e02832>.
8. Proske, T., Hainer, S., Rezvani, M., Graubner, C.-A., Eco-friendly concretes with reduced water and cement contents — Mix design principles and laboratory tests, *Cement and Concrete Research*, Vol. 51 (2013), <https://doi.org/10.1016/j.cemconres.2013.04.011>.
9. Kazmi, S. M. S. , Munir, M. J., Wu, Y. F. ,Recycled aggregate concrete: Mechanical and durability performance. *10 - Recycled aggregate concrete: mechanical and durability performance*. Woodhead Publishing Series in Civil and Structural Engineering, Handbook of Sustainable Concrete and Industrial Waste Management, Woodhead Publishing (2022) <https://doi.org/10.1016/B978-0-12-821730-6.00017-6>.
10. Li, Q., Yuan, G., Xu, Z., Dou, T., Effect of elevated temperature on the mechanical properties of high-volume GGBS concrete. *Magazine of Concrete Research* Volume 66 Issue 24 (2014), <https://doi.org/10.1680/macr.14.00142>
11. ISO 14044 (2006) Environmental management – Life cycle assessment – Requirements and guidelines. International Organization for Standardization. Brussels, Belgium.
12. EN 15978 (2011) Sustainability of construction works – Assessment of environmental performance of buildings – Calculation method. Brussels: CEN.
13. de Paula Filho, J.H.M., D’Antimo, M., Charlier, M., Vassart, O., Life-Cycle Assessment of an Office Building: Influence of the Structural Design on the Embodied Carbon Emissions. *Modelling* (2024), 5, pp. 55–70, <https://doi.org/10.3390/modelling5010004>
14. Hafner, A., Schäfer, S., & Hafner, A., Comparative LCA Study of Different Timber and Mineral Buildings and Calculation Method for Substitution Factors on Building Level. *Journal of Cleaner Production* 167 (2017), pp.630-642. <https://doi.org/10.1016/j.jclepro.2017.08.203>.
15. European Commission, Directorate-General for Research and Innovation, Baniotopoulos, C., Hamerlink, R., Hauke, B. et al., Membrane action in fire design of composite slab with solid and cellular steel beams — valorisation (MACS+) – Final report, Publications Office, 2014, <https://data.europa.eu/doi/10.2777/76136>
16. Cadorin, J.-F., Franssen, J.-M., A tool to design steel elements submitted to compartment fires - OZone V2. Part 1: pre- and post-flashover compartment fire model. *Fire Safety Journal*, Vol. 38(5) (2003)
17. <https://constructalia.arcelormittal.com/en/tools/software>
18. <https://media.promat.com/pi605263/original/-909448742/promapaint-sc4.pdf>
19. Ma, C., Van Coile, R., Gernay, T., Fire protection costs in composite buildings for cost-benefit analysis of fire designs. *Journal of Constructional Steel Research*, Vol. 215 (2024), <https://doi.org/10.1016/j.jcsr.2024.108517>
20. Pomponi, F. et al, Embodied carbon in buildings. Springer International Publishing (2018), <https://doi.org/10.1007/978-3-319-72796-7>
21. Clifton, G. C. et al., Post fire evaluation of the New Zealand International Convention Centre. Proceedings of the 12th International Conference on Structures in Fire (SiF), Hong Kong Polytechnic University (2022), <https://doi.org/10.6084/m9.figshare.22223947.v1>
22. Lawson, M. et al., REDUCE Final Report (Reuse and demountability using steel structures and the circular economy) (2019). European Commission, Research Programme of the RFCS, Grant Agreement 710040.\$
23. Odenbreit, C. et al. A Lego-like steel-framed system for standardization and serial production. *Steel Construction* 16, No. 1 (2023). <https://doi.org/10.1002/stco.202200021>
24. Mansilla, R., Espinós, A., Odenbreit, C., Payá-Zaforteza, I., Romero, M.L., Characterization of the elevated temperature behaviour of demountable shear connectors in steel-concrete composite beams through push-out tests. *Structures*, Volume 59 (2024), <https://doi.org/10.1016/j.istruc.2023.105810>
25. Alberto, V., Espinós, A., Lapuebla-Ferri, A., Romero, M.L., Numerical investigation on different fire protection system for steel-concrete composite beams with demountable shear connectors, 13th International Conference on Structures in Fire (SiF), Coimbra, Portugal (2024)
26. Romero, A., Odenbreit, C., Experimental investigation on novel shear connections for demountable steel-timber composite (STC) beams and flooring systems, *Engineering Structures*, Vol. 304 (2024), <https://doi.org/10.1016/j.engstruct.2024.117620>.

PREDICTION OF STRUCTURAL FAILURES IN A FIRE ACCIDENT FOR FIREFIGHTERS' SAFETY

Aatif Ali Khan¹, Mustesin Ali Khan², Nan Zhuojun³, Asif Usmani⁴

ABSTRACT

Disastrous fire incidents worldwide claim the lives of hundreds of firefighters annually. Several critical events occur in a fire accident which firefighters may encounter during a fire accident. This paper discusses some of the critical events corresponding to structural components that occur in a fire compartment. An artificial intelligence model is developed to predict these critical events for a simple case of a compartment is used. To train the model, the database is generated using CFD fire and FEM simulations. Various compartment parameters, including ventilation size, geometry, fire size, and location, are utilised to create fire scenarios. CFD data in terms of thermal load is used for heat transfer and structural analyses in FEM. The outputs from these analyses are then used to train the AI model to predict critical or precursor events. This methodology serves as a framework for establishing a database for smart firefighting, enabling the forecasting of events before they occur and providing valuable information to firefighters.

Keywords: Firefighter, machine learning, forecasting, structural failure, CFD-FEM

1 INTRODUCTION

The rise of innovative architectural designs, such as those seen in tall buildings and large open spaces, has reshaped the fire threat in the built environment. Conventional design approaches may no longer be suitable given the heightened risk in urban environments. Consequently, firefighters are left facing an unpredictable hazard that they are not trained for, as the London Grenfell Tower fire in 2017 tragically demonstrated[1]. Catastrophic fire incidents continue to occur worldwide, resulting in the loss of hundreds of firefighters annually [2]. The collapse of World Trade Centre Towers 1, 2, and 7 following the terrorist attacks on September 11, 2001, created a precedent for a scenario that had never been seriously considered before, claiming the lives of 343 firefighters. High-rise buildings with thousands of occupants collapsed while emergency services conducted fire control and evacuation operations. No one had any knowledge of the impending collapse of the buildings [3]. The collapse of the Plasco Building in Iran resulted in the tragic loss of 16 firefighters. In the 2016 Hong Kong Ngau Tau Kok mini-storage fire, two firefighters lost their lives. It is unfortunate that engineers often learn more from their mistakes and tragic accidents than their success. For instance, the Great Fire of London in 1666 displaced a significant portion of the city's population. This incident led to setting up an inquiry to strengthen the building regulations to mitigate the risk of such occurrences. Since then, consideration of fire safety has evolved over time. However, due to the large uncertainties with fire and unawareness of real-time information, fire accidents are always life-threatening.

¹ Lecturer, University of Canterbury,
e-mail: aatif.khan@canterbury.ac.nz, ORCID: <https://orcid.org/0000-0001-9181-4795>

² Lecturer, University of Central Lancashire
e-mail: makhan21@uclan.ac.uk, ORCID: <https://orcid.org/0000-0003-2562-9916>

³ Post-doctoral, TU Delft
e-mail: z.nan@tudelft.nl, ORCID: <https://orcid.org/> <https://orcid.org/0000-0001-8189-5448>

⁴ Professor, Hong Kong Polytechnic University
e-mail: asif.usmani@polyu.edu.hk, ORCID: <https://orcid.org/> <https://orcid.org/0000-0003-2454-5737>

The investigation into the 1987 London King's Cross underground station fire highlighted how a flawed understanding of fire growth led to inadequate evacuation procedures. During the explosion in Beirut in 2020, a team of firefighters (9 firefighters and 1 paramedic) responded to a reported fire in a warehouse at the Port of Beirut. Unfortunately, they had no information about the hazard, including the presence of ammonium nitrate and fireworks. This resulted in a catastrophic explosion, claiming the lives of over 200 individuals, including all members of the team. To address these challenges, the development of a practical and feasible smart firefighting system provides an effective solution for fostering a safer built environment. Conventional firefighting methods typically do not incorporate live data to inform intervention strategies due to constraints such as limited information gathering which is generally reliant on human communication, imprecise fire modelling, and slow communication systems. Recently, a *SureFire* system has been proposed for smart firefighting, including cutting-edge technologies such as Artificial Intelligence (AI), Internet-of-Things (IoT), and Digital Twin [4]. This system has demonstrated its capabilities in identifying real-time tunnel fire scenes using sensor data [5], [6] as well as analysing compartment fire scenarios based on video images [7]. Additionally, machine learning techniques have been employed to provide real-time forecasts of fire development in various settings, including tunnels [8], compartments [9], [10], and atriums [11] utilising a high-fidelity fire simulation database.

While responding to a building fire, firefighters may need to enter the building to safely evacuate all occupants. In addition to the exposure to heat and smoke, various critical events related to structural failures or collapses also occur that can jeopardize their safety and impede firefighting efforts. This paper discusses how advanced AI models can predict such critical structural events. By conducting numerous CFD and Finite Element (FE) simulations, a database of fire scenarios and corresponding structural responses within typical compartments is generated to demonstrate the AI tool's prediction capabilities. The framework outlined in this paper enables the creation of a database for machine learning processes and its implementation in smart firefighting methods. A case of a simple fire compartment is presented to illustrate the database generation process and event prediction. This study highlights the feasibility of predicting structural response based on information about compartment geometry, fire size, and temperatures of structural components, which can be integrated into smart firefighting systems.

Table 1. Number of fatalities in the past ten years in the US

Year	2012	2013	2014	2015	2016	2017	2018	2019	2020	2021
Total death	85	109	97	91	92	88	84	62	102*	141*
Death due to Structural Collapse	4	2	1	6	3	0	6	2	4	3

*Data include the firefighters who died due to the exposure during the pandemic (Covid 19) (36 in 2020 and 63 in 2021)

2 FIREFIGHTERS' FATALITIES

During a building fire, firefighters typically bear the responsibility of entering the building. Beyond extinguishing the flames, their primary objective is to locate and rescue any occupants who may be trapped inside, particularly those with physical impairments such as visual impairment, unconsciousness, or other health issues. The spread and dynamics of the fire within the building depend upon numerous factors, including the types and distribution of combustible materials, chemical composition of the fuel, ventilation conditions, and so on. Any change in these variables introduces additional uncertainties in the behaviour, placing firefighters in unprecedented situations.

According to a survey conducted by NFPA, it was found that between 50 to 100 firefighters lose their lives each year in the United States alone (except the year 2001 when 343 firefighters died in the tragedy of the WTC towers in the 9/11 incident). The primary cause of firefighter fatalities during fireground operations in building fires often involves being trapped inside while responding to the fire. Khan et al. [4] outlined the major factors and nature of injuries leading to firefighter deaths, including trauma, asphyxiation, stress,

entrapment, and structural collapse. Given the focus of this paper on structural failures, Table 1 provides a summary of firefighter fatalities resulting from structural collapses in the United States over the past decade.

3 CRITICAL EVENTS

The threat posed by fire spans across various domains, including both structural settings and vehicular contexts, with incidents occurring daily. In terms of building fires or confined structural fires, the initial few minutes following ignition played a critical role in determining the probability of the occurrence of future events. Failure to effectively contain the fire during these early stages—attributable to the failure of detection (whether human or automatic detector) or the malfunctioning of suppression systems such as sprinklers—may fail to prevent the fire growth. A number of incidents may arise due to various reasons, including environmental conditions, structural or non-structural damage or collapse, firefighting interventions, physiological and psychological conditions of firefighters, and so on. A critical event includes any condition, event, or circumstance that influences fire behaviour, poses a threat to the safety of occupants and firefighters, and has the potential to impact on structural and non-structural components of a building. Khan et al. [4] provide a comprehensive list of critical events spanning from the incipient phase of fire to the eventual structural collapse of a building. Nonetheless, due to the uniqueness of each fire incident, this list cannot claim exhaustive completeness. Therefore, it is recommended to continuously revise and update the list based on the experiences encountered by firefighters. This paper focuses on the critical events related to the compartment fire associated with structures.

3.1 Critical event associated with structural components.

Instances of structural component failures, such as beams and columns, are common in fire-related accidents. In severe cases, damaged structural and non-structural elements pose substantial hazards to firefighters, potentially leading to injuries from falling debris and impeding evacuation paths. In fire-damaged structures, firefighters may have only a few moments to recognise an impending structural failure. These collapses often occur suddenly and are challenging to anticipate, presenting considerable uncertainty even to experienced firefighters, thereby making prediction challenging. The forecasting of these critical events holds the potential to enhance urban infrastructure resilience to fire hazards and make smart firefighting practices both reliable and feasible.

In numerous fire incidents, it was observed that structural components such as beams and columns failed. Additionally, support beams or compartment walls may also collapse during fires, potentially obstructing firefighters' access routes. In the worst circumstances, these beams could pose a direct hazard by falling onto firefighters themselves. These localized collapses manifest unpredictably, presenting a significant challenge even to experienced firefighters. Structural components may exhibit precursory signs of impending collapse (precursor events), such as deflection in beams or local buckling of columns, during fire incidents. Identifying these precursor events can help firefighters understand when structural components may fail. Moreover, in certain fire scenarios, the application of water onto the fuel can exacerbate the situation by increasing the dead load on the floor, particularly in the presence of absorbent materials like cotton or foam.

Flames and smoke tend to move towards areas with more oxygen. In many fires, they reach vertical shafts like stairwells or elevator shafts early on, as seen in the 1996 HK Garley Building Fire (due to the stack effect). Apart from making it harder for people to evacuate because of the fire and smoke in the stairwells, the stairs themselves may fail or collapse. This collapse can block the exits, as seen in the Plasco Building fire in 2017 in Iran [12], [13]

One of the most severe structural failures is when floors collapse. When floors are heated for a long time, slabs may collapse, posing a risk to firefighters or occupants inside the building. Instances of floor slab failures are reported in numerous fire incidents [12]. Structures typically suffer damage or collapse during a fully developed fire or when the fire reaches a size where it heats structural components to the point of failure, causing a decrease in their strength. The time to reach this temperature threshold is generally higher than the minimum time required for occupants to safely evacuate (known as Required Safe Egress Time or

RSET). Consequently, only the occupants who are trapped or lose consciousness often remain inside the building during these critical stages of the fire. However, firefighters continue their firefighting efforts during this time. During the local and final collapses of the Plasco building and WTC Towers, numerous firefighters tragically lost their lives as they became trapped inside the building and were crushed beneath the collapsed debris of the structures.

Figure 1 illustrates some of the precursor and critical events linked with the structure failures. Precursor events serve as early warnings indicating the impending onset of critical events. For instance, the buckling of structural components may signal the potential failure of columns, which in turn could result in structural destabilization or total collapse. A comprehensive list of the critical events can be found in the supplementary material. Forecasting such critical and precursor events can aid firefighters in assessing risk in real time. This paper presents a methodology to develop AI models for forecasting such events.

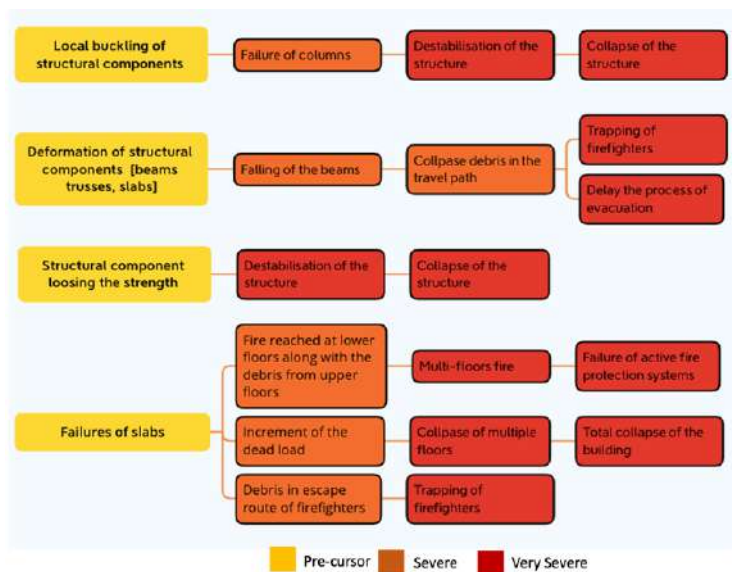


Figure 1. Critical and pre-cursor events corresponding to structural failures

4 SMART FIREFIGHTING

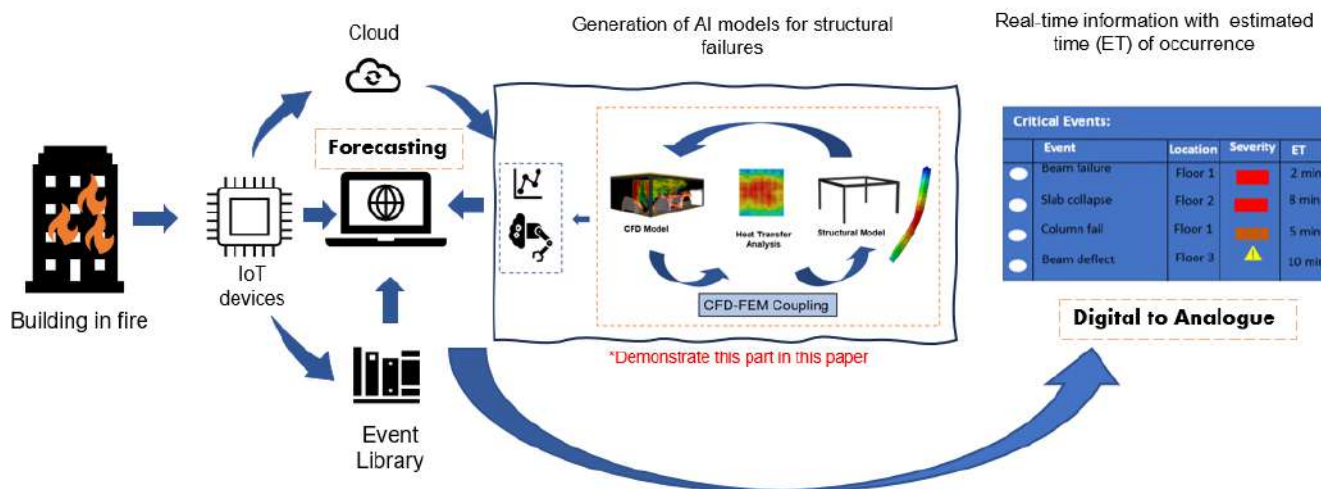


Figure 2. A simple framework for smart firefighting

With the rise of big data and deep learning in the 2010s, there has been a surge in the utilization of AI methodologies, alongside other advanced technologies like remote monitoring, high-resolution sensors, high-speed computation, and data-driven approaches, which have been increasingly applied in fire safety engineering. By using the datasets derived from fire tests and numerical simulations, real-time fire information such as Heat Release Rate (HRR) and the likelihood of flashover can be discerned and forecasted using sensor data. The trained AI model can be embedded with the BIM model to generate the building fire Digital Twin.

Figure 2 illustrates the framework for intelligent firefighting. Within this framework, the event library serves as a repository for storing information in a central system, which also includes AI-trained modules designed to predict events documented in the library. Upon receiving real-time data from IoT devices or sensors—such as temperature, Heat Release Rate, live image feeds, or soot volume—the AI-trained models can forecast critical events, which are then integrated into the software. The data used to train these AI models may include labelled information such as temperature readings, HRR measurements, or images of fire scenes, aimed at predicting future events. When the IoT sensors provide real-time data, the AI-trained model can predict critical events based on the information stored within the event library. The software translates this data into the analogue form, enabling firefighters to access detailed insights about impending events with the estimated time of occurrence, as depicted in Figure 2.

This paper presents the methodology for developing a trained model capable of predicting precursor and critical events. While some researchers have employed prescriptive models for training AI models, these approaches may not accurately present real fires. Thus, it is recommended to utilise Computational Fluid Dynamics (CFD) to generate thermal data for structural analysis. By providing accurate inputs for the CFD model, we can have reasonably accurate thermal data to use for structural analysis. The subsequent section discusses using Computational CFD and Finite Element Method (FEM) to generate a database needed for training AI models.

5 DATABASE GENERATION

As discussed in the previous section, it is required to create a database to train an AI model for the prediction of events. In this study, a large number of compartment fire scenarios are developed using CFD simulations to determine the structural response under these fire scenarios. FDS is used for conducting fire simulations. FDS provides the thermal data that can be transferred to the FEM model for subsequent heat transfer and structural analyses. For carrying out FE simulation, a commercial package, Abaqus, is used in this study. Data transfer from CFD to FEM is not straightforward due to the difference in temporal and spatial resolution in fluid and solid domains. To apply FDS-generated fire scenarios as fire load (gas temperatures, adiabatic surface temperatures [AST] or heat fluxes) to structural models in FE simulations or to enable the CFD-FEM coupling, open-source packages developed by Khan et al. [4] are used, as shown in Figure 3. They presented a methodology applicable to couple FDS with Abaqus and OpenSees.

Before using the CFE-FE tool for this study, validation is conducted using experimental results [14], as shown in Figure 3b. The coupling tool is validated using experimental data from a study by Kamikawa et al. [14], which tested a square hollow section (SHS) column. A CFD model of the experiments was generated, as shown in Figure 3a. Fluid temperatures, expressed in terms of AST were extracted from FDS and converted by using this middleware to an appropriate format to serve as input fields for subsequent heat transfer and thermo-mechanical analysis in Abaqus. For structural analysis, a thermal stress analysis was conducted by importing the temperature history obtained from the heat transfer analysis. Figure 3 presents a comparison of time-vertical deflection behaviour from FE simulation with experiment results. The maximum vertical deflection and failure time derived from the analysis are in close agreement with the experimental values. Further details on the validation study can be found in [15], [16].

5.1 Data repository and AI prediction

To demonstrate the development of AI models for predicting structural failures in smart firefighting applications, a one-story building with a steel beam and composite floors is modelled to generate a database.

A room of 5 by 5m² is representative of an office space within a building, as shown in Figure 4. Various fire scenarios were created to generate the database, as illustrated in Figure 4(b). The parameters include the total heat release rate (HRR), ventilation conditions (size of openings), fire location, and load.

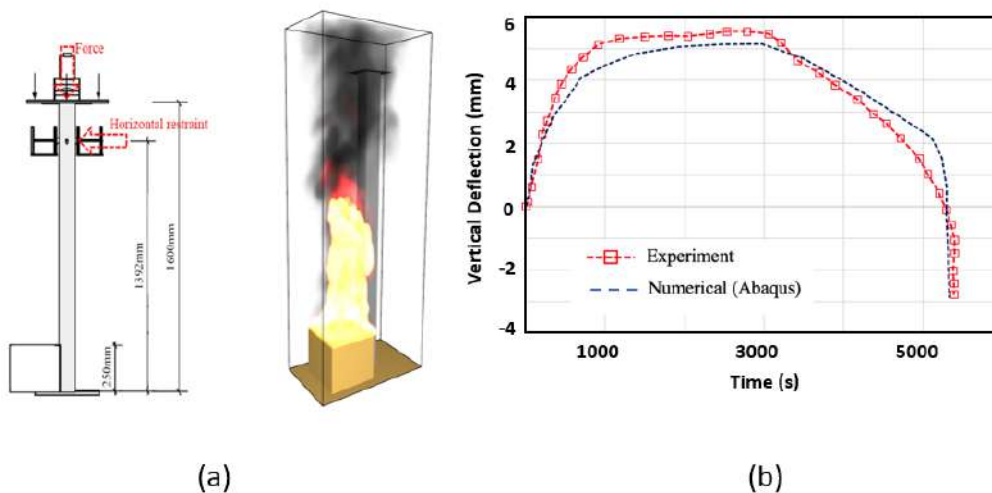


Figure 3. Validation of CFD-FEM with the experiment results

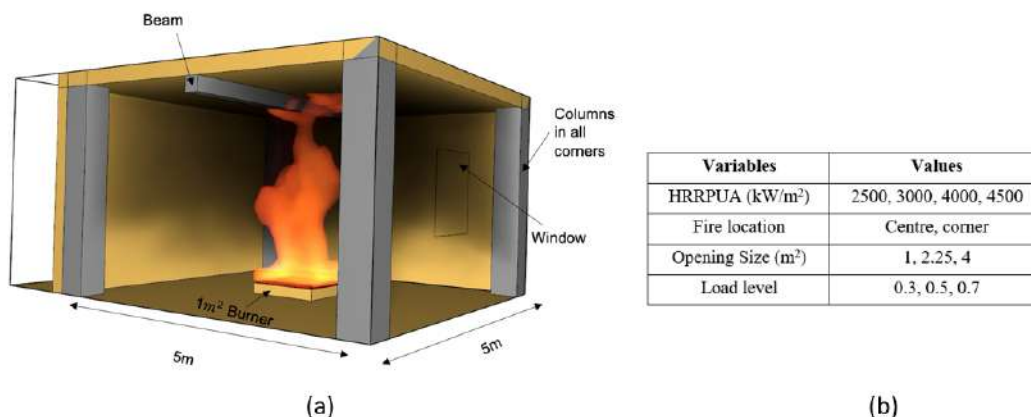


Figure 4. (a) CFD model for fire simulation (b) perimeters used to generate a database for AI model

In the FDS model, HRR is presented as HRRPUA (heat release rate per unit area), so in all cases, a burner of 1m² is used. Heat release rate from 2.5MW to 4.5 MW is used which can be a reasonable representation for an office room containing 2 to 3-seater sofas and chairs. HRR ranging from 2.5MW to 4.5MW is used, which can be a reasonable representation for an office room containing furniture such as sofas and chairs. Similarly, window openings are included to simulate ventilation within the compartment. For this study, the door is assumed to be closed, although future research could explore varying degrees of door opening to further refine the data.

Two fire locations, centre and corner positions, are examined in the study. Regarding structural variables, three load levels are considered, as shown in Figure 4. Subsequent studies could expand the database by incorporating additional parameters such as fire resistive ratings and the thickness of web and flanges.

A total of 72 cases are generated to train the model. While a more extensive dataset is necessary for a robust model, this study serves as a foundational framework for creating an AI model capable of predicting critical events in smart firefighting systems.

The simulations conducted in this study are based on a one-hour fire duration, but future simulations will be extended to align with recommended fire ratings specific to different building (occupancy) types.

5.2 Structure Model

The structural fire response of composite beam exposed to an enclosure fire is studied by developing a FE model based on the experimental configuration described by Wakamatsu et al. [17] as shown in Figure 5. The steel portion of the composite beam, which measured 400 mm in depth and 200 mm in width, had a span of 6 m. The thicknesses of the flange and web were 15 mm and 13 mm, respectively. The 2 m wide and 100 mm thick concrete slab, which was reinforced with nominal reinforcement bars with an 8 mm diameter and spaced 100 mm apart in both directions, was constructed of 35 N/mm² grade concrete. The yield strength of steel girder was 350 N/mm², while the yield strength of steel reinforcement was 450 N/mm².

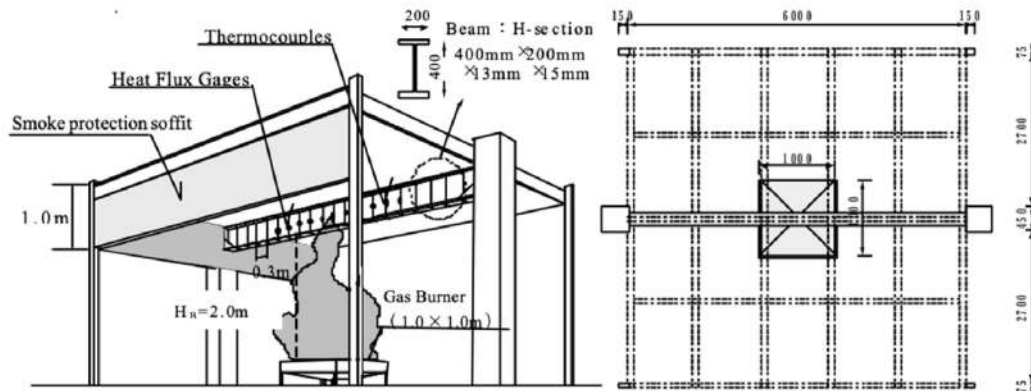


Figure 5. Experimental configuration used by Wakamatsu et al.[17]

In this study, 24 fire scenarios developed by CFD modelling are utilised for performing heat transfer analysis. As mentioned in the previous section, three window sizes, four different HRRPUA and two fire locations are used to develop 24 distinct fire scenarios. The two fire locations used are Centre and Corner of the compartment, and three different HRRPUA as 2500 kW/m², 3000 kW/m², and 4000 kW/m² are utilized. The windows measuring 1 m², 2.25 m², and 4 m² have been chosen to represent various ventilation scenarios.

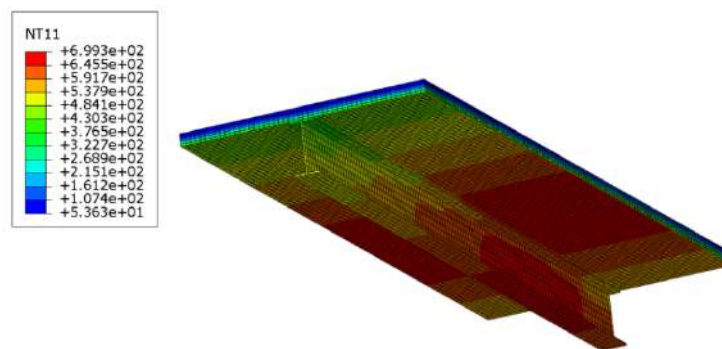


Figure 6. Thermal profile for the case where HRRPUA of 4000 kW/m² and ventilation of 4m²

Temperature output from FDS simulations in the form of adiabatic surface temperature is coupled with the FE heat transfer model using the OpenFIRE framework[18], [19]. This framework allows seamless integration of the FE models with CFD-based fire scenarios, which enables accurate representation non-uniform thermal exposure. Abaqus software is utilised to develop the FE model of the composite beam. Brick elements are used to model the concrete deck and the steel girder. The stringer feature available in Abaqus is used to model the steel reinforcement. The thermal properties of concrete, reinforcing steel and structural steel used are in accordance with Eurocodes [20], [21].

A total of 24 heat transfer analyses are performed corresponding to the fire scenarios developed using FDS simulations. Figure 6 shows the thermal profile for a case with HRRPUA of 4000 kW/m² applied at the centre and a window size of 4m². Three distinct load levels—0.3, 0.5, and 0.7 of the maximum load capacity are incorporated into the thermomechanical FE model. A total of 72 thermomechanical analysis are performed in order to assess the structural response by combining these three load levels with all fire scenarios.

It is observed that higher HRRPUA values (4500 kW/m² and 4000 kW/m²) typically produced larger deflections and higher maximum beam temperatures in comparison to lower HRRPUA values (3000 kW/m² and 2500 kW/m²). This is expected since more severe heating conditions are correlated with higher HRRPUA, which speeds up the deterioration of structural members. Both the fire locations Centre and Corner have an impact on the structural fire response. Fires in the centre of the compartment typically produced larger deflections and higher maximum beam temperatures when compared to fires at the corner. This can be explained by the variations in patterns of thermal exposure as well as the possibility of improved ventilation in the corner locations.

The size of the window controls the ventilation condition inside the compartment and can result in completely different fire scenarios which affects the structural response. Larger window sizes (4 m²) typically resulted in higher maximum beam temperatures and larger deflections in comparison to smaller window sizes (1 m² and 2.25 m²). Greater heat release and burning rate can be intensified by improved ventilation brought on by larger window openings, which can lead to more severe thermal exposure on the structural members. Three load levels 0.3, 0.5, and 0.7 of ultimate load capacity are applied which greatly influenced the structural fire response of composite beam. The maximum vertical displacement increases with an increase in load levels. This is attributed to the fact that initial higher stresses and strains at ambient temperature make the composite beam more prone to deflect in a vertical direction under thermal loading.

In the next section, the ANN model is trained using the data collected from 72 cases. As mentioned in the previous section, HRRPUA, fire location, window size and load level are used as input parameters. Maximum vertical displacement, collapse (if applicable), and maximum beam temperature as output parameters.

6 AI MODEL

AI technologies offer innovative solutions in fire safety engineering. With their unparalleled capabilities in data processing and predictive analytics, Machine Learning (ML) and Deep Learning (DL) show potential for enhancing predictions of structural responses to fire. Notably, pioneering studies have demonstrated the applicability of ML in fire and structural fire engineering [22], [23], [24], [25]. DL models are distinguished not only by their ability to process vast amounts of data but also by their superior performance with smaller datasets. In this paper, we apply a simple Fully Connected Neural Network (FCNN). As depicted in Figure 7, the FCNN model comprises an input layer, three hidden layers with 32 units each, and an output layer. Rectified Linear Units (ReLU) activation functions were incorporated into all hidden layers. The FCNN model, constructed using PyTorch, accepts four input parameters: HRR, fire location, opening size, and load level. It produces three output parameters: time to reach maximum beam deflection (s), max beam deflection at that time (mm), and max beam temperature at that time (°C). The complexity of this problem, underscored by the interactions among fire characteristics, structural features, and critical times, is inherently nonlinear. FCNNs are suited for this work due to their proficiency in modelling complex nonlinear relationships and handling high-dimensional data.

The training, completed after 200 epochs (number of iterations), proved to be sufficient for achieving satisfactory results, while also mitigating the risk of overfitting to the training dataset. The learning rate was set at 0.001 for the training process. A batch size of 16 was chosen to strike an optimal balance between generalization capabilities and the speed of model convergence. Throughout each epoch, the FCNN model was adept at extracting knowledge regarding critical times and structural fire responses from the input parameters. This correlation was encoded within the parameters of each neural unit within the network, with the objective of deploying this acquired knowledge to predict critical structural events to compartment fires. The Adam optimiser was used, along with the Mean Average Error (MAE) loss function, for model training. The generation of the database is discussed in Section 5.1. Data from 72 simulation cases were divided into

training and validation subsets, comprising 80% and 20% of the total data, respectively. The performance of the model on both the training and validation subsets during the training phase is presented in Figure 8.

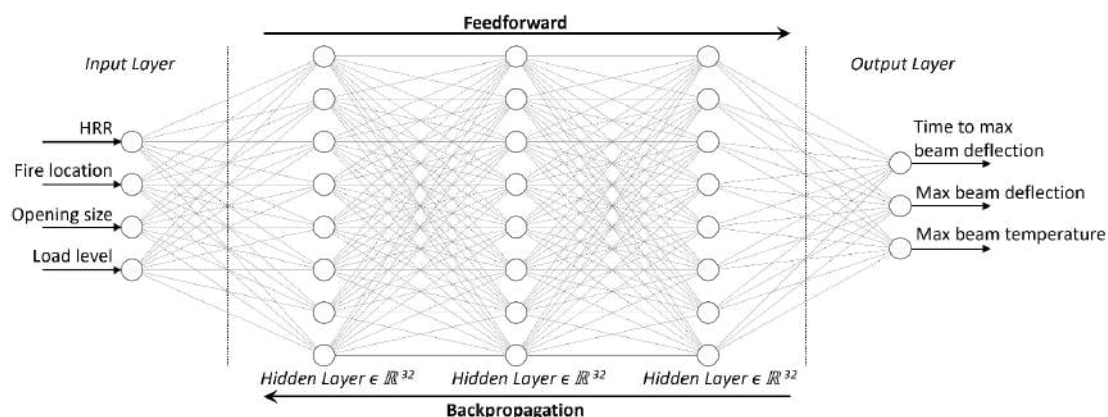


Figure 7. Schematic of the FCNN architecture (R2: Coefficient of Determination)

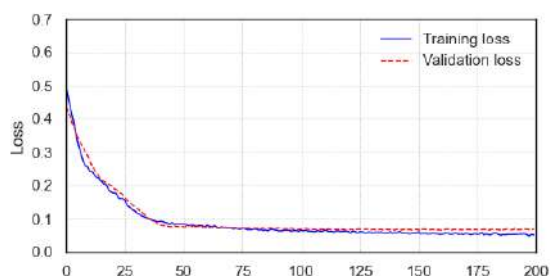


Figure 8. Evaluating the FCNN model performance during training using Mean Average Error (MAE)

The comparisons between AI prediction and simulation results are presented in Figure 9. To facilitate the comparison, an example involving four samples with HRRs of 2500, 3000, 400 and 4500 kW/m², all configured with the fire location of corner, an opening size of 4 m², and a load level of 0.7, was chosen. These examples aim to highlight the predictions of the FCNN model alongside simulation results. Notably, as the HRR increases, there is a corresponding increase in both the max beam deflection and the max beam temperature at the critical time, predictions that the FCNN model accurately made, as shown in Figure 9 (b-c). Nevertheless, the relationship between the HRR and the critical time to reach max beam deflection does not follow a linear pattern. This non-linearity could be attributed to the complex interplay between fire dynamics and structural responses. Under the assumption of constant max beam deflection, an increase in HRR would logically lead to a decrease in the critical time to reach max beam deflection. However, as the HRR rises, the adverse effects on the steel beam intensify, leading to increased max deflection. Thus, the relationship between HRR and the critical time to reach max beam deflection is inherently non-linear. Despite this complexity, the FCNN model adeptly predicted the trend of the changing critical time to reach max deflection with increasing HRR, as shown in Figure 9 (a).

The overall performance of the FCNN model in predicting the critical time to max beam deflection is presented in Figure 10. Figure 10 (a) shows the correlation between simulated and predicted times to reach max beam deflection, with each point representing an individual prediction. The dashed line indicates the ideal prediction, where predicted times perfectly match the actual simulated times. The FCNN model demonstrates good accuracy, showing a relative prediction error of no more than $\pm 30\%$. Furthermore, the mean absolute error is recorded at 194 s, indicating that, on average, the predicted times deviate from the simulated times by approximately 194 s. The distribution of residuals, i.e., the differences between predicted and simulated times, is presented in Figure 10 (b). As evident from Figure 10 (b), the residuals are centred around zero and follow a normal distribution, indicating that the model is well-fitted.

It is important to note that due to the limited size of the dataset, it is challenging to ensure comprehensive coverage of the entire simulated parameter range within the test subset. Specifically, it is difficult to include at least one group of samples that maintains three constant parameters while varying the fourth. Consequently, the test subset was selected randomly from the training and validation subsets. This means that the test scenarios were chosen from an existing database rather than being entirely new or unknown scenarios, which could have contributed to enhanced the performance of the model in predictions. Therefore, it is necessary to expand the database in the future by increasing the number of cases, as well as incorporating additional factors such as compartment sizes, structural layouts, and so on. It is also worth mentioning that the current database does not include cases of structural failure. This might be because the current study focused on demonstrating a case of a typical office room, where fire typically doesn't exceed the values considered in the database. Nevertheless, the present work presents the capability of AI to predict structural fire responses and identify precursor events, thereby informing firefighters of imminent danger. For example, the deflection of the beam is a precursor event of the structural failure. The results clearly illustrate the prediction capabilities of the AI model based on the dataset generated using CFD-FEM models. Our future aim is to predict critical and precursor structural fire events, specifically the failure of key structural elements or progressive fire-induced structural collapses.

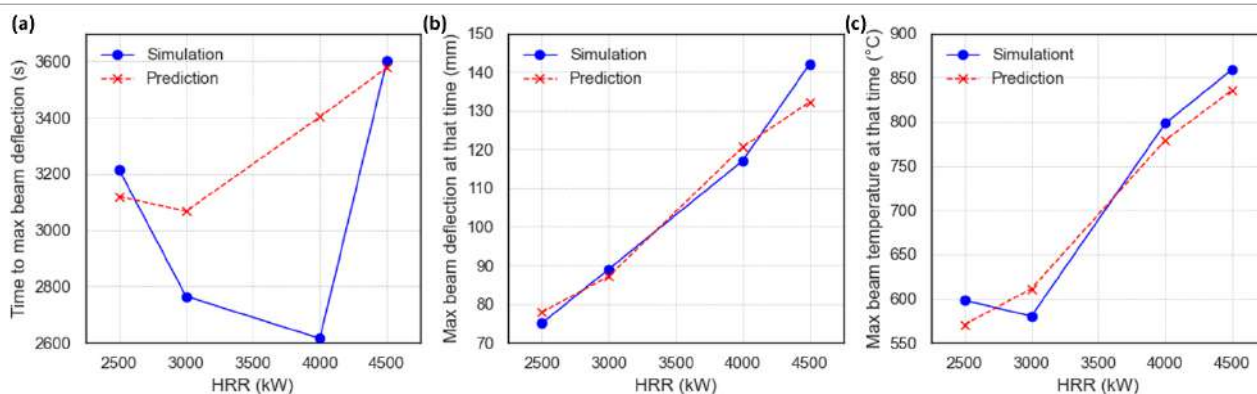


Figure 9. Comparison of the FCNN model predictions and simulations considering the effect of HRR on structural fire responses

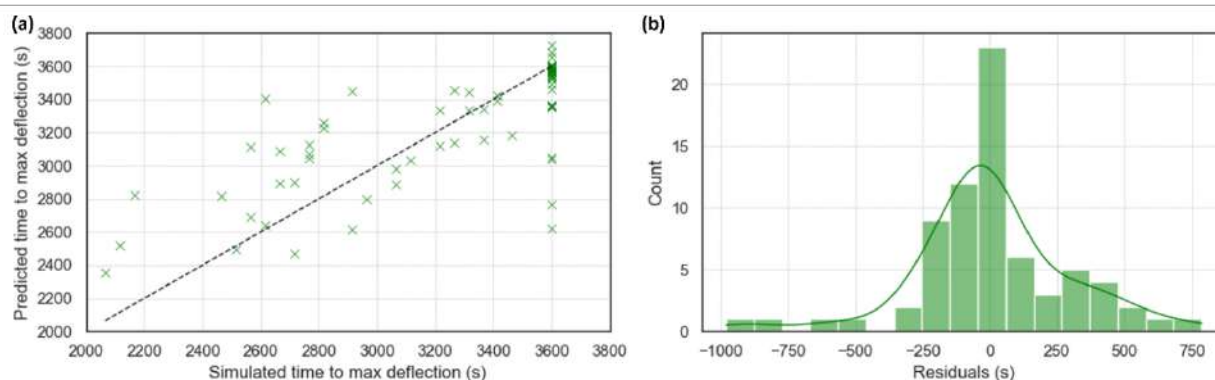


Figure 10. Performance of the FCNN model in predicting the critical time to max beam deflection, (a) comparison of simulated vs. predicted times, and (b) error distribution between simulated and predicted times

7 LIMITATIONS AND FUTURE USE

In addition to the size of the data, the reliability of data is very critical for generating a robust AI model. There are some limitations associated with the current methodology presented in this paper including the uncertainty of fire, inherent limitations of software, unknown variables e.g., the size of the door opened during a fire, and so on. Due to the uncertainty associated with fire, it may not always be feasible to account

for all parameters in CFD simulations. CFD simulations are based on *user inputs*, and if these inputs are not well-understood or relevant factors are not considered, the resulting output will not be reliable. The coupling problem of CFD-FEM presents several limitations due to differences in temporal and spatial discretisation in fluid and solid domains. For instance, in the case of a beam, the size of the CFD mesh may exceed that of the structural component. Typically, only one temperature data point is taken into account for both the web and flanges at a specific location, but they might have different temperatures. However, with careful selection of the inputs and a clear understanding of the required level of accuracy, the current methodology can generate very useful AI models.

In a further study, a generic AI model will be developed by including additional parameters, such as bigger compartment size, fuel load, door opening angle, ceiling height, span lengths of structural components, thickness of fire protection, and so on. Furthermore, this model will be extended to cover broader areas, such as large office floor layouts and warehouses, where fires can be very large and can last for a longer duration. More critical events will be included in future research. This work will be further developed to enable data acquisition from building IoT sensors to predict critical events from the live data and inform firefighters.

8 CONCLUSIONS

In the current paper, a database for a compartment with various fires and structural designs is generated and used to train AI models that can forecast critical events such as deflections, yielding and local or global collapse of structures. It provides a step further in achieving the smart firefighting framework, which can provide information about precursor and critical events before their occurrence and improve operational efficiency and safety of firefighters and help them to assess the risk based on real-time information. This paper uses a case of a typical office compartment to demonstrate the prediction of the precursor and critical events. This framework is applicable regardless of the building's type or size. However, there are limitations associated with the model such as data quality, as software may have inherent constraints, and user input, as users may not fully capture the complexities of real fire scenarios due to the uncertainties associated with fire. In future research, we aim to develop a generic AI model that integrates with building information models and utilises input from IoT sensors to forecast events in real-time and inform firefighters.

REFERENCES

- [1] G. Kernick, "Catastrophe and systemic change: Learning from the Grenfell Tower fire and other disasters.," *Do Sustainability*, 2021.
- [2] U.S. Fire Administration, "Firefighter fatalities in the United States in 2021," 2022.
- [3] A. Usmani, Y. C. Chung, and J. Torero, "How did the WTC towers collapse: a new theory," *Fire Saf J*, vol. 38, no. 6, pp. 501–533, 2003.
- [4] A. A. Khan, M. A. Khan, K. Leung, X. Huang, M. Luo, and A. Usmani, "A review of critical fire event library for buildings and safety framework for smart firefighting," *International Journal of Disaster Risk Reduction*, vol. 83. Elsevier Ltd, Dec. 01, 2022. doi: 10.1016/j.ijdr.2022.103412.
- [5] X. Wu, Y. Park, A. Li, X. Huang, F. Xiao, and A. Usmani, "Smart Detection of Fire Source in Tunnel Based on the Numerical Database and Artificial Intelligence," *Fire Technol*, 2020, doi: 10.1007/s10694-020-00985-z.
- [6] X. Wu, X. Zhang, Y. Jiang, X. Huang, G. G. Q. Huang, and A. Usmani, "An intelligent tunnel firefighting system and small-scale demonstration," *Tunnelling and Underground Space Technology*, vol. 120, no. December 2021, p. 104301, 2022, doi: 10.1016/j.tust.2021.104301.
- [7] Z. Wang, T. Zhang, X. Wu, and X. Huang, "Predicting transient building fire based on external smoke images and deep learning," *Journal of Building Engineering*, vol. 47, no. November 2021, p. 103823, 2022, doi: 10.1016/j.job.2021.103823.
- [8] X. Wu, X. Zhang, X. Huang, F. Xiao, and A. Usmani, "A real-time forecast of tunnel fire based on numerical database and artificial intelligence," *Build Simul*, vol. 15, no. 4, pp. 511–524, 2022, doi: 10.1007/s12273-021-0775-x.

- [9] J. Wang *et al.*, “P-Flash – A machine learning-based model for flashover prediction using recovered temperature data,” *Fire Saf J*, vol. 122, no. April, p. 103341, 2021, doi: 10.1016/j.firesaf.2021.103341.
- [10] T. Zhang, Z. Wang, H. Y. Wong, W. C. Tam, X. Huang, and F. Xiao, “Forecast the compartment fire and flashover based on Deep Learning: A demonstration of reduced-scale experiment,” *Fire Safety Journal (Under Review)*, 2021.
- [11] L. chu Su, X. Wu, X. Zhang, and X. Huang, “Smart performance-based design for building fire safety: Prediction of smoke motion via AI,” *Journal of Building Engineering*, vol. 43, no. March, p. 102529, 2021, doi: 10.1016/j.job.2021.102529.
- [12] A. A. Khan, R. V. V. Domada, X. Huang, M. A. Khan, and A. Usmani, “Modeling the collapse of the Plasco Building. Part I: Reconstruction of fire,” *Build Simul*, vol. 15, no. 4, pp. 583–596, Apr. 2022, doi: 10.1007/s12273-021-0825-4.
- [13] A. A. Khan *et al.*, “Fire modelling framework for investigating tall building fire: A case study of the Plasco Building,” *Case Studies in Thermal Engineering*, vol. 45, May 2023, doi: 10.1016/j.csite.2023.103018.
- [14] D. Kamikawa, Y. Hasemi, K. Yamada, and Nakamura., “Mechanical response of a steel column exposed to a localized fire.,” in *Proc. fourth Int. Work. stuctures fire, Aveiro, Port*, 2006, pp. 225–234.
- [15] A. A. Khan, M. A. Khan, C. Zhang, L. Jiang, and A. Usmani, “OpenFIRE: An Open Computational Framework for Structural Response to Real Fires,” *Fire Technol*, vol. 58, no. 2, pp. 1011–1038, Mar. 2022, doi: 10.1007/s10694-021-01184-0.
- [16] A. A. Khan, M. A. Khan, K. A. Cashell, and A. Usmani, “An open-source software framework for the integrated simulation of structures in fire,” *Fire Saf J*, p. 103896, Aug. 2023, doi: 10.1016/j.firesaf.2023.103896.
- [17] T. Wakamatsu, Y. Hasemi, and A. V Ptchelintsev, “Heating mechanism of building components exposed to a localized fire - FEM thermal and structural analysis of a steel beam under ceiling -,” *Proceedings of the International Conference on Offshore Mechanics and Arctic Engineering - OMAE*, vol. 2, no. m, pp. 51–58, 1997.
- [18] A. A. Khan, M. A. Khan, K. A. Cashell, and A. Usmani, “An open-source software framework for the integrated simulation of structures in fire,” *Fire Saf J*, vol. 140, p. 103896, 2023, doi: <https://doi.org/10.1016/j.firesaf.2023.103896>.
- [19] A. A. Khan, M. A. Khan, C. Zhang, L. Jiang, and A. Usmani, “OpenFIRE: An Open Computational Framework for Structural Response to Real Fires,” *Fire Technol*, vol. 58, no. 2, pp. 1011–1038, 2022, doi: 10.1007/s10694-021-01184-0.
- [20] EUROCODE, *Eurocode 3. Design of steel structures. General rules. Structural fire design*.
- [21] EN 1992-1-2, “Eurocode 2: Design of concrete structures - Part 1-2: General rules - Structural fire design,” *European Committee for Standardization*, 2004, [Online]. Available: [papers2://publication/uuid/1B0960C1-28E7-4B6A-ADFE-19C0455EDFD3](https://www.europecodex.eu/publication/uuid/1B0960C1-28E7-4B6A-ADFE-19C0455EDFD3)
- [22] W. Ji, G. Q. Li, and S. Zhu, “Real-time prediction of key monitoring physical parameters for early warning of fire-induced building collapse,” *Comput Struct*, vol. 272, Nov. 2022, doi: 10.1016/j.compstruc.2022.106875.
- [23] W. Ji, G. Q. Li, and G. B. Lou, “Early-warning methods for fire-induced collapse of single span steel portal frames,” *J Constr Steel Res*, vol. 190, Mar. 2022, doi: 10.1016/j.jcsr.2022.107154.
- [24] Z. Nan, M. A. Orabi, X. Huang, Y. Jiang, and A. Usmani, “Structural-fire responses forecasting via modular AI,” *Fire Saf J*, vol. 140, 2023, doi: 10.1016/j.firesaf.2023.103863.
- [25] A. A. Khan, T. Zhang, X. Huang, and A. Usmani, “Machine learning driven smart fire safety design of false ceiling and emergency response,” *Process Safety and Environmental Protection*, vol. 177, pp. 1294–1306, Sep. 2023, doi: 10.1016/j.psep.2023.07.068.

REVISITING STRUCTURAL FIRE RESISTANCE REQUIREMENTS FOR CARPARKS

Sigurjon Ingolfsson^{1*}, Adam Glew², Julian Mendez³, Eoin O’Loughlin⁴, Alistair Morrison⁵

ABSTRACT

Modern day building codes must respond to the challenges of climate change. Particularly within the last decade, a move towards more sustainable construction and transportation methods has materialised. Some of these innovations present unique fire hazards that need to be considered such that buildings can be designed with appropriate fire safety measures. These measures may be contained within the prescriptive provisions of building codes or be developed by designers to satisfy specific Performance criteria.

This research investigates the key conclusions and limitations of seminal large-scale fire experiments on carparking structures and explores whether the datasets and subsequent guidance arising from those studies are appropriate for contemporary carpark design. Given the changes in cars and carpark design in recent decades, this paper aims to inform how carpark structures should be designed and assessed for fire safety.

Keywords: carparks; fire resistance; modern hazards

1 INTRODUCTION

Since the late 1960s, various research efforts have investigated fires in carparks. This paper revisits their findings and implications, life safety of occupants and firefighters, and property protection. In our research we investigated the key conclusions and limitations of seminal large-scale fire experiments on carparking structures, and explored whether the datasets and guidance arising from those studies are appropriate for contemporary carpark design. Given the changes in cars and carpark design in recent decades, this paper aims to inform how carpark structures should be designed and assessed for fire safety. Other literature, such as the Institution of Structural Engineers’ design guide for carparks [1] as well as public submissions made to the Collaborative Reporting for Safer Structures (CROSS) reporting system in the UK, have questioned the continued validity of these experiments as a basis for design [2], [3].

2 CAR PARK VENTILATION DEFINITIONS

2.1 Open air / Open-deck / closed car parks

Ever since early experimental research on carpark fires, different fire behaviours have been observed in open-air carparks, open-deck carparks, and closed carparks. For the purposes of this paper, car parks are divided into the following categories:

¹ Senior Engineer, Arup, Copenhagen, Denmark
e-mail: sigurjon.ingolfsson@arup.com (*corresponding author)

² Senior Engineer, Arup, Sydney, Australia
e-mail: adam.glew@arup.com, ORCID: <https://orcid.org/0000-0002-3238-6708>

³ Engineer, Arup, Sydney, Australia
e-mail: julian.mendez@arup.com, ORCID: <https://orcid.org/0000-0001-5552-9030>

⁴ Associate, Arup, Dublin, Ireland
e-mail: eoin.oloughlin@arup.com

⁵ Principal, Arup, Sydney, Australia
e-mail: alistair.morrison@arup.com

1. Open-air car park, where the parking spots are not covered by a sheltering construction or a surrounding building. The design of these is not explicitly considered as part of this paper.
2. Open-deck or naturally ventilated car parks, where the parking spots are placed in an enclosure where permanent openings provide a degree of ventilation which provide combustion gases (for day-to-day usability) and smoke with clear passage to the outside.
3. Closed car parks, where parking spots are placed in an enclosure where no or limited permanent openings are provided to the outside.

The primary reason for this distinction (between open-deck and closed car parks) is due to the feasible worst-case fire scenario differing between each type of carpark. In open-deck car parks, the smoke layer is, in theory, cooler than in closed car parks, where there are fewer (note: not always ‘none’) façade openings through which hot gases can escape easily. That will, in turn, result in less radiative feedback from the hot smoke layer to fuel in open-deck car parks, which could lead to slower fire spread than in closed car parks. The distinction between open-deck and closed car parks is in practice made by building codes worldwide. The definition of these terms is therefore crucial. However, what constitutes an ‘open-deck’ carpark varies between countries and is summarised in Table 1 which covers three countries for illustration purposes.

Table 1. Open deck car park definitions

Country	Definition for an ‘open-deck’ car park
Australia	A carpark in which all parts of the parking storeys are cross-ventilated by permanent unobstructed openings in not fewer than 2 opposite or approximately opposite sides, and— <ol style="list-style-type: none"> a. each side that provides ventilation is not less than 1/6 of the area of any other side; and b. the openings are not less than ½ of the wall area of the side concerned.
England	Each storey is naturally ventilated by permanent openings at each car parking level. The aggregate vent area is a minimum of 1/20 of that level’s floor area, at least half of which is provided equally by two opposite walls.
USA (IBC)	For natural ventilation purposes, the exterior side of the structure shall have uniformly distributed openings on two or more sides. The area of such openings in exterior walls on a tier shall be not less than 20 percent of the total perimeter wall area of each tier. The aggregate length of the openings considered to be providing natural ventilation shall be not less than 40 percent of the perimeter of the tier. Interior walls shall be not less than 20 percent open with uniformly distributed openings. Exception: Openings are not required to be distributed over 40 percent of the building perimeter where the required openings are uniformly distributed over two opposing sides of the building.

As illustrated above, comparing three countries results in significant differences. The determination of whether a carpark is open-deck or closed is usually the first step before deriving fire safety design requirements in international codes and standards. As stated at the beginning of this section, experimental research also makes this distinction but the lack of a common definition of these terms makes absolute comparison complex.

3 SEMINAL EXPERIMENTAL RESEARCH ON FIRES IN CARPARKS

3.1 Global research effort before 1985

Since the late 1960s, various research efforts have investigated fires in car parks.

3.1.1 Joint Fire Research Organisation (JFRO), UK

The earliest experimental study on fire behaviour in car parks was completed in the UK at the Joint Fire Research Organisation (JFRO) [4], [5]. Butcher et al. carried out three full-scale burns within a single storey test building, consisting of a steel scaffolding structure and a corrugated iron roof, with a concrete floor slab / ramp. The compartment was approximately 18.5 m × 9 m, with a floor area of approximately 167 m² and a floor-to-ceiling height of approximately 2.25 m. The longer façades had approximately 50% ventilation.

Two of the experiments had the shorter façade completely open, while the third was closed. Each experiment involved nine vehicles in a 3×3 configuration. The steel members were unprotected. The maximum temperature recorded within the steel beams was 275°C , and 360°C within the columns. Butcher et al. reported the wood-equivalent fire load density for a carpark to be 17 kg/m^2 . This research has underpinned the recommendations in [Approved Document] AD B [6], applicable in England and Wales.

3.1.2 Nippon Steel Company, Japan

The Nippon Steel Company of Japan carried out a series of five tests in 1970 with varied ventilation and including an open-deck case [7],[8]. Maximum temperatures in the unprotected steel members did not exceed 245°C [8].

3.1.3 Switzerland

Also in 1970s, five experiments were carried out in an underground carpark building scheduled for demolition in Switzerland [9], [10]. The authors concluded that the main hazard was posed by the dense smoke generated as “the temperatures measured in these tests were not high”. They found that the probability of fire spread was low, and the sprinkler system was effective [8]. The primary research paper is not currently available, so actual temperatures are unknown.

3.1.4 American Iron and Steel Institute (AISI), US

A single open-deck carpark experiment was carried out in the US in 1972 in a previously operational building [11]. Funded by the American Iron and Steel Institute (AISI), Gewain carried out a full-scale experiment in an existing carpark which measured approximately $69 \text{ m} \times 55 \text{ m}$ (i.e., a floor area of $3,800 \text{ m}^2$). The structure was an unprotected steel frame with a concrete deck. However, the experiment involved only three “late-model American automobiles”. The central car, located directly under the exposed steel beam, was ignited. The cars were approx. 600 mm apart. The fire did not spread to either of the adjacent vehicles, and it was concluded that the results of Butcher et al. were confirmed.

3.2 BHP Steel research programme, Australia (1985-1989)

In the 1980s, several developments led to the scrutiny of the earlier experiments: changes in carpark design, increasing car size, growing use of plastics in cars, and an increasing emphasis on light steel carpark structures. The Australian steelmaker BHP conducted a series of experiments between 1985 and 1989, with the aim of addressing doubts about applicability of previous experimental data [12], [13], [14], [15].

3.2.1 Open-deck carparks (1985)

Two experiments were conducted on an open-deck carpark constructed from unprotected steel with a composite (steel and concrete) floor slab (see Figure 1). The aim of the experiments was “to determine whether fire protection of steelwork from fire within the carpark [was] necessary” [42].

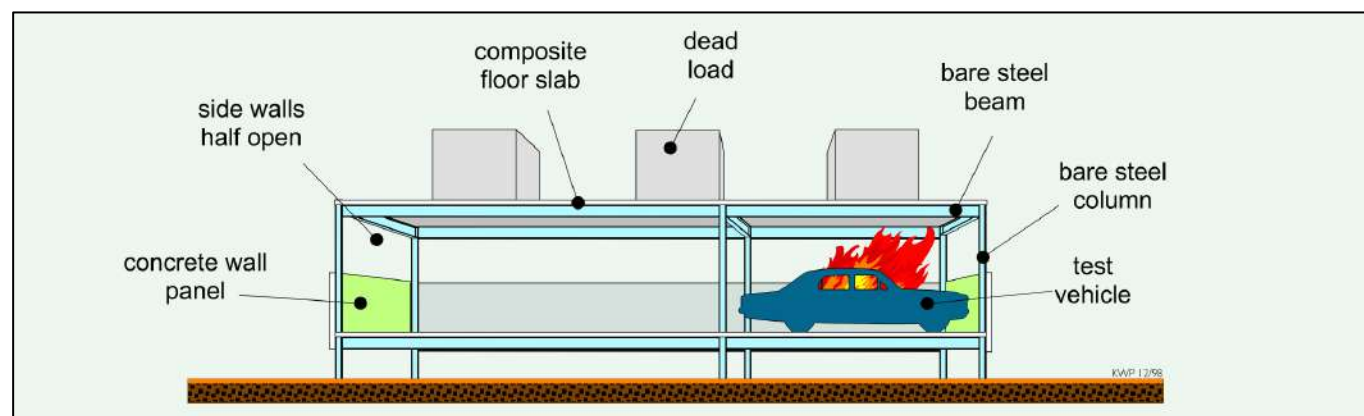


Figure 1. Isometric section drawing showing open-deck carpark experiment arrangement. Reproduced from [49]. © BHP

The structure used thin steel members which aimed to be representative of the smallest members likely to be used in practice, which was not the case in the US tests [41]. The compartment had a floor-to-ceiling height of approximately 2.4 m, and measured approximately 11.4 m × 10.4 m in plan, therefore had a floor area of approximately 120 m². No suppression system was installed. The perimeter walls had 50% ventilation.

Five vehicles were placed within the space; four were parked parallel to each other, with the fifth parked perpendicular (see Figure 2). Fire was started within the test car by igniting rags soaked with petrol placed below the front seat. The front right window was left open to assist with fire development. The front left window of car no 1 (i.e., the window facing the ignited car) was also open to assist fire spread between cars. The cars used in the test were manufactured between 1973 and 1982.

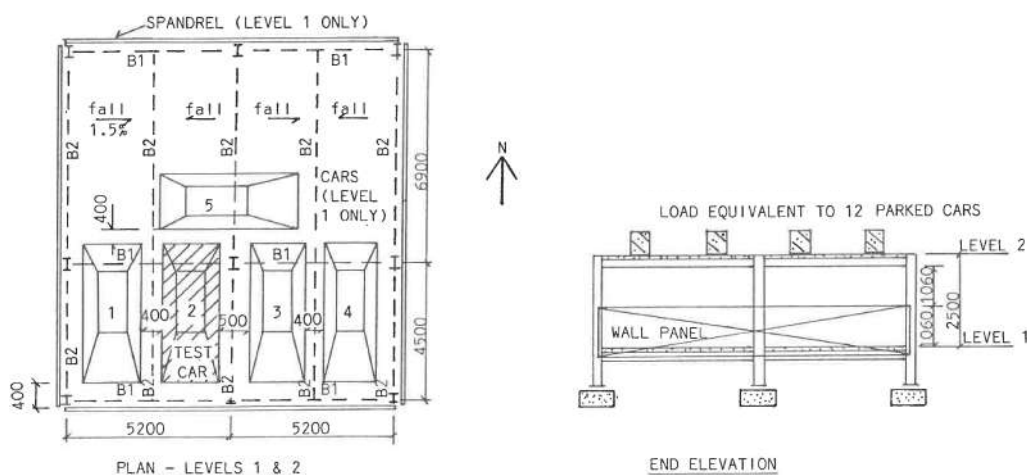


Figure 2. Plan and elevation drawings showing test building. Reproduced from [42]. © BHP

The test car in test one (a Ford Falcon XC Sedan) had a length of 4.9 m, width of 1.9 m and height of 1.4 m. It has a curb weight of 1,475 kg [50]. It is worth noting that this earlier 1979 car didn't have much plastic on its exterior, whereas the 1982 Ford Falcon XD Sedan used in the second test did.

The cars were 400 mm apart, which was described as “closer than normally expected in practice” [42]. Butcher went on to conduct a survey where 300 spacings were measured [51]. The most frequent spacing was found to be 762 mm. A similar survey in the late 1990s studied 18 different carparks in five European countries (Netherlands, Spain, France, Belgium, and Luxembourg), with 1,624 parking distance measurements taken. The data followed a normal distribution, and a mean parking distance of 719 mm was found [38]. Therefore, the cars were relatively tightly packed in the BHP experiments.

Observations

The top flanges of the beams were generally cooler than the web and bottom flange, due to the composite connection to the concrete slab meaning that heat dissipated into the concrete i.e., the slab acted as a heat sink. In test one, the steel reached a peak temperature of 285°C (with a corresponding upper flange temperature of 170°C). In the second test, values of 340°C and 180°C respectively were recorded.

The experiments showed that open-deck carparks can be constructed using unprotected steel without collapsing from a car fire event, under the specific conditions and structural design of these tests.

The results indicated that vehicle-to-vehicle fire spread can vary depending upon wind conditions and the materiality of the vehicle of fire origin, i.e., the quantity and location of plastics around the vehicle exterior and the fuel tank construction.

3.2.2 Closed carparks (1987)

In 1987, BHP adapted and reused the experimental setup to investigate closed carparks [43]. The aim of the experiments was to investigate the effect of a car fire in a closed carpark with either a sprinkler system

installed, a ventilation system installed, or both. The activation of the sprinkler system was automatic in four of the experiments, and manual in the other five experiments. The test setup is shown in Figure 3.

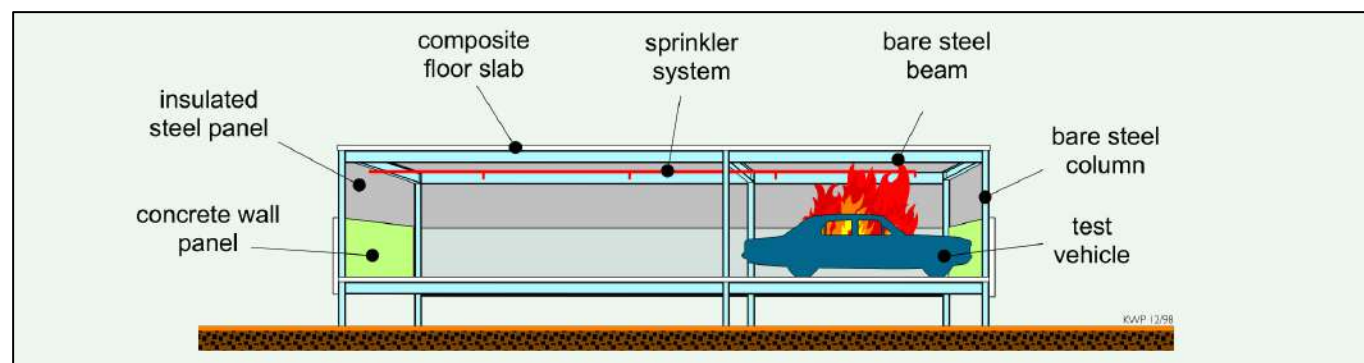


Figure 3. Isometric section showing closed carpark experiment arrangement. Reproduced from [49]. © BHP

The experimental program was created by BHP Research, the Australian Uniform Building Regulations Co-ordinating Council (AUBRCC) and the Australian Institute of Steel Construction (AISC). Interestingly, no dead load was applied to the structure in these experiments, unlike the previous open-deck tests.

The mechanical ventilation system was designed based on what the researchers felt would be acceptable to approval authorities at the time, following AS 1668.2-1980. The design airflow rate of $1 \text{ m}^3/\text{s}$ (which represents approximately 12.7 ac/h, based on a compartment volume of 285 m^3) was based on one in ten cars operating simultaneously.

Due to the prevailing wind conditions during the experiments, the effect of the mechanical ventilation system is reported as being minimal. However, interestingly, two tests (5 and 7) which were the same except 5 had the ventilation system operating and 7 did not, exhibited different results. This is not discussed in the original paper [43]. Test 7 exhibited a “secondary flashover” style temperature-time curve, whereby there is an initial peak, followed by a decay phase (like test 5), but then a period of regrowth and a second, higher peak temperature is observed in test 7. In test 7, the fire eventually burnt out the rear of the car and involved the fuel from the tank.

The tests generally observed that the automatic sprinkler system prevented significant damage to the paint or bodywork of the test car and contained the fire to the test car (i.e., there was no fire spread between vehicles).

A difference was observed between the older cars (with less plastic used in/on their exterior and metal fuel tanks) and the newer cars (with more plastic including the fuel tank). Spread of fire from the test car to other cars only occurred when the newer cars were used.

In the experiments without automatic suppression, burning plastics often dripped to the floor and formed a flaming pool fire.

3.2.3 Summary

BHP carried out 25 experiments in a compartment test building with a floor area of approximately 120 m^2 between 1985-1989. 14 of these experiments used cars as the fuel load. The BHP experiments represent a significant research effort and are still recognised as one of the most comprehensive experimental series on carpark. The National Construction Code (NCC) in Australia was amended following the experiments, and those amendments are still included within the latest revision.

The major influence of these experiments is the concessions subsequently introduced within the NCC which permitted open-deck carpark to be both non-sprinklered and constructed from unprotected steelwork with an exposed surface area to mass per unit length ratio (ESA/M) of $26 \text{ m}^2/\text{tonne}$. This was deemed acceptable by the authors and the code authorities as the steel within this set of experiments (and other prior experiments) remained relatively cool (a peak of 340°C).

3.3 Global research effort post 1990

In 1995, CTICM carried out experiments in France [16]. The Building Research Establishment (BRE) in England in a 2010 report highlighted an elevated risk in split-level car parks with parking spaces located nose-to-nose across a level change [6].

4 LESSONS LEARNT FROM FIRE EXPERIMENTATION

The conclusions from many of these experiments underpin many prescriptive fire codes around the world and are also referenced in performance-based fire engineering design. While reflective of the available knowledge at the time of the studies, these concessions remain within some fire codes today and are cited by some performance-based designs, some 30+ years after the experiments [17].

The experiments reviewed here on both open-deck and closed car parks are still relevant as they represent a significant dataset of large-scale carpark compartment fires. Such experiments are very expensive to undertake (in monetary costs and carbon costs) and should only be completed if absolutely necessary.

The compartments were constructed to represent portions of car parks. The relatively small volumes would mean that heat and smoke could fill the spaces quicker than in a larger building. However, the peak fire size is limited by the size of the building and the number of vehicles within it. In large, open-plan spaces, travelling fires can occur, which may preheat the structure and pose a completely different design fire and subsequent fire exposure than a ‘traditional’ flashover compartment fire. This was highlighted as a possible fire scenario for carpark fires as early as 1999 [38].

Open-deck car parks have received more research attention than closed car parks as it was viewed that they could potentially be built with limited fire resistance and without suppression systems. The BHP experiments on closed car parks and partially open car parks had broadly similar observations. Conditions were “substantially more severe than ... the open-deck tests”. It’s important to note that the BHP experiments concluded that any carpark which does not clearly comply with the requirements set out within the experiments for an open-deck carpark should be treated as a closed carpark.

Peak steel temperatures for the open-deck carpark experiments reviewed are presented in Table 2. Interestingly, the later experiments carried out in France recorded significantly higher temperatures than any of the previous work. This may indicate that more severe fires are to be expected from more modern vehicle fires, involving more plastics. The compartment used by CTICM was much larger than the previous work, so there was greater volume for heat and smoke to dissipate, but further for fresh air to travel before reaching (and cooling) the atmosphere local to the fire.

Table 2: Summary of maximum steel temperatures recorded during open-deck experimental series reviewed

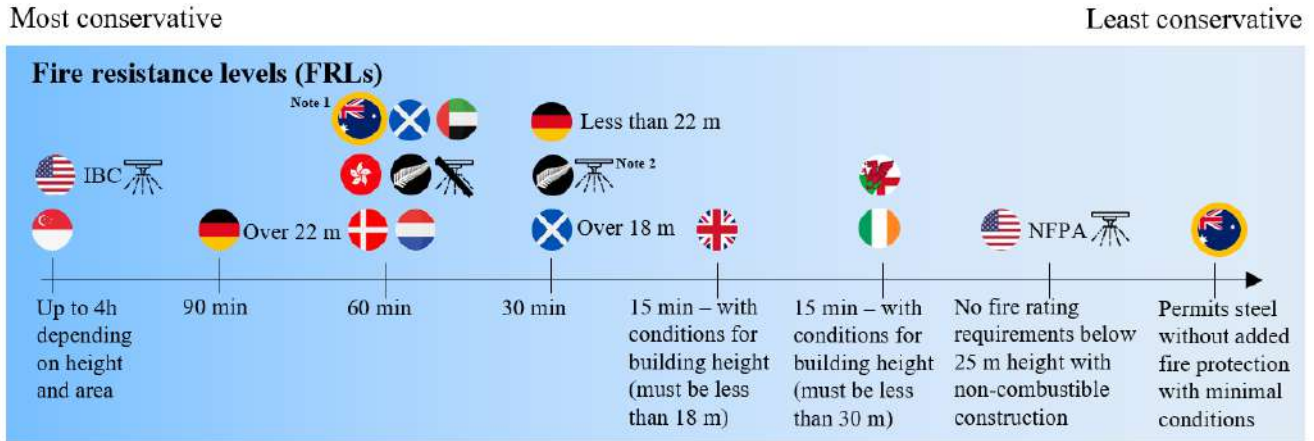
Experiment(s)	Year(s)	Maximum steel temperature recorded (°C)	
		Beam	Column
JFRO, UK [35], [36]	1967	275	360
Nippon Steel, Japan [37]	1970	245	242
AISI, US [41]	1972-1973	226	-
BHP Steel, Australia [42], [43], [44]	1985-1989	340	320
CTICM, France [55]	1995	700	640

5 INTERNATIONAL CODE COMPARISON

Reviewing current fire codes to investigate the impact of the fire test programmes in terms of required fire resistance levels reveals a highly varied approach to prescriptive (noting that many countries permit a performance based approach to design) structural fire resistance requirements for standalone car parks depending on country and whether the carpark is considered to be ‘Open deck’ or ‘Closed’ A high-level

snapshot of the code requirements for standalone carpark is provided in Figure 4 and Figure 5. The requirements vary significantly between countries and regulatory regimes but in general it can be stated that fire resistance requirements for ‘open deck’ carpark are lesser (fire resistance of 0-30 mins permitted) than ‘closed’ carpark (generally requiring a 60-minute fire resistance as a minimum).

5.1 Open-deck carpark

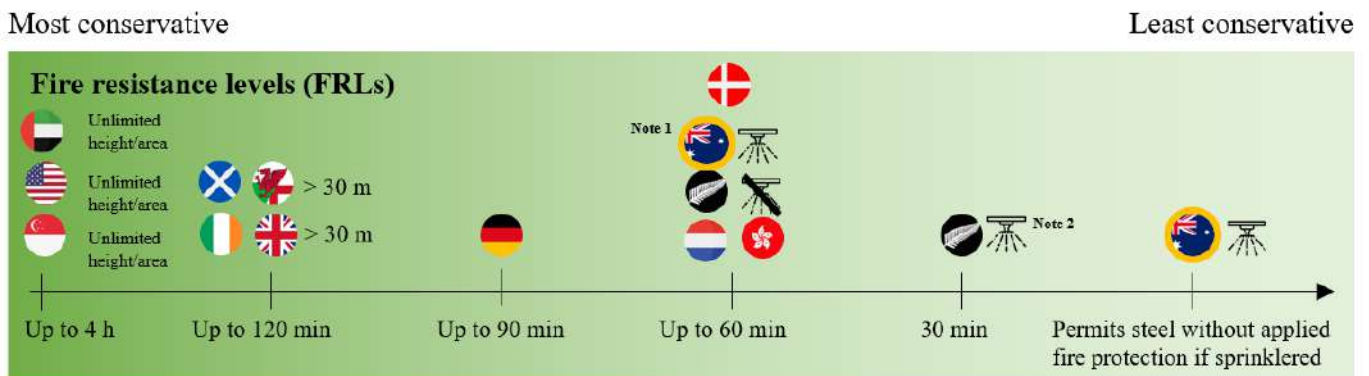


Notes

- 1 – The prescriptive FRL for some elements of Class 7a (carpark) Type A and B buildings is (120)/120/120. However, concessions typically mean (60)/60/60 is a starting point, as discussed within this paper.
- 2 – The sprinkler system can be substituted for cross-ventilation.

Figure 4. Summary of global fire safety prescriptive provisions for open-deck carpark

5.2 Closed carpark



Notes

- 1 – The prescriptive FRL for some elements of Class 7a Type A and B buildings is (120)/120/120. However, concessions typically mean (60)/60/60 is a starting point, as described in Section 2.1.6.
- 2 – The sprinkler system can be substituted for cross ventilation.

Figure 5. Summary of global fire safety prescriptive provisions for closed carpark

6 FIRE HAZARDS IN THE MODERN-DAY CAR PARK

In this review, ‘modern-day’ refers loosely to the 21st century. This period has been chosen because it follows the period within which the seminal experimental research on carpark fires was conducted (between 1967 and 2002). Thus, a clear comparison can be made between the vehicles and carpark of the time (of the experiments), and those of the modern-day.

A recent report by the National Fire Protection Association (NFPA) in the U.S. is widely considered as the most comprehensive document on the topic [54]. It splits modern-day carpark hazards into two categories:

1. Modern vehicles which are larger, heavier and have increased quantities of combustible materials (e.g., fuel, plastics, synthetic materials) when compared to cars manufactured in the 20th century [54], [114], whilst also being parked closer together.
2. Rapid, widespread market growth of alternative fuel vehicles (AFVs).

This paper review follows a similar structure. First, modern internal combustion engine vehicles (ICEVs) are covered, before AFVs are briefly discussed.

6.1 The evolution of the internal combustion engine vehicle (ICEV)

6.1.1 Vehicle size and weight

Modern-day car parks typically optimise spacing of vehicles, and tend to have narrower parking spaces [54]. It is often postulated that modern vehicles are larger and heavier, and that “spaces are smaller”. As part of this paper, the size and weight change between an early model and today’s model of six different vehicles has been assessed (Table 3). To ensure consistent comparisons, the cheapest model of each vehicle was chosen, where an option existed. Three different vehicle types have been covered.

It can be clearly seen that vehicles have gotten larger (in all three dimensions) and heavier. This is evident across all six vehicles analysed, including hatchbacks, SUVs and utility vehicles.

This crude study and observation is generally supported by data recently published by the Australian Government’s Bureau of Infrastructure and Transport Research Economics (BITRE) [128]. Their data shows that sales of SUVs have rapidly (almost exponentially) increased between the end of the 20th century and the beginning of the 21st century, thus taking up a greater portion of the market. A gradual increasing trend in gross vehicle mass (GVM) for total new light vehicles purchased in Australia since the 1980s has also been found, with some fluctuations over time. Their dataset includes cars, SUVs and light commercial vehicles (LCVs).

Table 3. Comparison of size and weight from early models of various vehicles against today’s models

	Size change(H x W x L) [mm]		Weight change[kg]	
	Early model	Today	Early model	Today
Hatchbacks				
Toyota Corolla(1985 to 2023)[116], [117]	1385 x1635 x3970	1460 x1790 x4375	935	1360
VW Golf(1980 to 2023)[118], [119]	1410 x1610 x3815	1456 x1789 x4284	830	1304
SUVs				
Honda CR-V(1997 to 2023)[120], [121]	1675 x1750 x4520	1679 x1855 x4635	1410	1504
Nissan X-Trail(2001 to 2023)[122], [123]	1675 x1765 x4510	1725 x1840 x4680	1395	1540
Utility vehicles (‘utes’)				
Toyota Hilux(1980 to 2023)[124], [125]	1570 x1610 x4305	1750 x1800 x5330	1075	1785
Ford Ranger(2007 to 2023)[126], [127]	1755 x1807 x4841	1886 x1910 x5225	1770	1994

6.1.2 Use of plastics

There has been a steady increase in the use of polymers / plastics in the automotive industry. Cars used to be largely manufactured from metals, but today, plastic is commonly used for wing mirrors, smaller body panels, wheel caps, etc. Boehmer et al. combined two U.S. data sources to plot the amount of plastic in light vehicles over time [54]. Light vehicles are defined as passenger vehicles, excluding trucks. The plot shows a steady increase in plastic weight from around 80 kg per light vehicle in 1980 to 160 kg per light vehicle in 2020. I.e., the amount of plastic in light vehicles appears to have approximately doubled over the past 40 years in the U.S.

Polymers / plastics present a higher fuel load than their metallic alternatives, as they have a higher heat of combustion [130]. It is logical to expect a higher energy release per weight of vehicle, or, in other words, more potential energy in the same volume [131].

6.2 Alternative fuel vehicles (AFVs)

For a few centuries, problems of pollution from ICEVs combined with the climate crisis has led to society seeking AFVs with potential of replacing petrol and diesel vehicles. As AFVs have become more popular, concerns have been raised regarding their unique fire hazards. While some of these concerns are legitimate, others appear to be inflated based on research findings. It is not within the scope of this paper to do a deep dive into this topic. However, the following is noted based on review of contemporary research:

- The current body of evidence does not suggest that the fuel type is the most important factor in determining fire severity.
- Rather the size and mass of the car and its components is more important.
- There are other key conditions which seem to lead to large fire events, namely car parks which are fully occupied, with little spacing between vehicles, and large, deep floorplates and low ceilings.

7 FIRE INCIDENTS

The following table provides a non-exhaustive summary of carpark fire since the turn of the century.

Table 4. Significant recent fire events in car parks. In reverse chronological order

Location	Year	Vehicles involved	Injuries / fatalities	Type	Description
Luton	2023	1300	None	Open	<i>Currently under investigation, led to partial collapse of the structure and a complete demolition of the structure with cars (even unaffected) cars left inside.</i>
Oaklands (Australia) [75]	2023	5	None	Open air	Two vehicles destroyed, another three damaged.
Bankstown (Australia) [76]	2023	6	1 injury (smoke)	Open	Fire controlled by early intervention of fire and rescue services.
Ravensburg (Germany) [73]	2021	4	None	Closed	EV caused the fire. OH2 sprinkler system controlled the fire, before brigade suppressed.
Märsta (Sweden) [77]	2021	200	None	Closed	Roof collapsed, building demolished.
Fremantle (Australia) [78]	2021	4	1 injury (smoke)	Closed	Fire in the underground carpark of a residential block. Did not cause any structural damage.
Geraldton (Australia) [79], [80]	2021	7	None	Open	Caused by an electrical fault. 125,000 AUD damage.
Warsaw (Poland) [81]	2020	22	None	Closed basement	150 residents evacuated. Reoccupation delayed hours by high temps. Considerable spalling.
Epe (Netherlands) [82]	2020	1	None	Closed	EV fire in shopping centre carpark controlled by sprinkler system.
Gaithersburg (MD, USA) [54]	2020	4	None	Open	Significant damage – up to 150,000 USD in losses.
Stavanger (Norway) [61]	2020	200	None	Open	<i>Caused partial collapse of the structure..</i>
Richmond (VA, USA) [54]	2019	3	None	Closed basement	The fire destroyed one vehicle and heavily damaged two others. Heavy smoke spread over several floors of the structure.

Location	Year	Vehicles involved	Injuries / fatalities	Type	Description
Cork (Ireland) [83], [84]	2019	60	None	Open	Fire spread to 60 cars. Prompt evacuation prevented injuries. Part of the structure unsafe and demolished. 30M EUR in damage.
Chicago (IL, USA) [54]	2019	4	None	Open	Fire in a 10-storey carpark.
Houston (TX, USA) [54]	2019	2	None	Open	Smoke spread past nearby high-rise buildings.
Hong Kong [85]	2019	1	None	Closed	Shopping mall carpark EV fire.
Shanghai (China) [54]	2019	3	None	Closed	EV was the ignition vehicle.
Chadstone (Australia) [79], [87]	2018	11	None	Closed	Fire in a shopping centre carpark. Controlled partial evacuation of the shopping centre.
Liverpool (UK) [62], [63], [64], [65], [67]	2017	1400	None	Open	<i>Significant fire causing spalling of the structural system. Damaged structure to the extent that, while it did not collapse, it required demolition post fire.</i>
Jecheon (South Korea) [88]	2017	Unknown	29 deaths, 36 injuries	Closed	Fire began above the carpark. Slab failed, and cars below became involved. Fire then spread through eight storeys above (fitness complex).
Markenhoven (Netherlands) [91]	2013	5	None	Open	Suppression system and the fire service controlled and extinguished fire.
Appelaar (Netherlands) [91]	2010	26	None	Closed	Structural damage led to repairs that took four months.
Stansted (UK) [92]	2010	24	None	Open air	High winds caused the flames to spread rapidly.
Bristol (UK) [68], [69]	2006	22	1 fatality	Open basement	Fire in a lower ground floor carpark which spread to the care home above.
Gretzenbach (Switzerland) [71], [72]	2004	100	7 fatalities, 3 injuries	Closed basement	Parts of the concrete ceiling fell down and buried 10 firefighters during the extinguishing work.
Schiphol (Netherlands) [93]	2002	90	None	Open	Caused by arson. Cars were only 40 cm apart. Some beams collapsed. 5M EUR damage.

7.1 Observations

Upon review of carpark fire events since the turn of the century, it's clear that large-scale fires involving multiple vehicles can and do occur.

The trends in carpark fire events seem to indicate that the distance between vehicles, and the number of vehicles with the carpark, are key factors. A number of fires in carparks involving multiple vehicles have occurred at airports (e.g., Stavanger, Edinburgh, Stansted, Schiphol and, recently, Sydney [94]), where cars are kept for significant periods of time in large carparks, with small distances between vehicles.

As may be expected; suppression (or lack of) influences the fire development. This was found in the BHP research, and further supported by the examples in Ravensburg (Germany), Epe (Netherlands) and Markenhoven (Netherlands) where the sprinkler systems controlled the fire. Timely brigade intervention has also been noted as important. For example, in Bankstown (Australia), early intervention of fire and rescue services was noted as controlling the fire, whereas in Stavanger (Norway), access for fire trucks to the carpark was restricted and the brigade struggled to locate the hydrants, which, in combination with the lack of a sprinkler system, were found as key reasons for the catastrophic fire spread.

Stavanger (Norway) also showed that wind conditions, coupled with the area of openings within the façade (and the positioning of those openings), can lead to much greater fire spread than observed in the smaller-scale experimental research.

The Kings Dock fire in Liverpool (UK) showed that the time until the fire is detected and the alarm is raised is also important, as well as the provision of compartment floors and adequacy of fire-stopping in line with compartmentation.

The experimental research and the case studies commonly made observations that the material used for the vehicle's fuel tank (i.e., whether it is a non-combustible metal, or combustible plastic) is an important factor. Similarly, the amount of combustible material within the vehicle of fire origin and adjacent vehicles will contribute to the likelihood of vehicle-to-vehicle fire spread.

The carpark fire events summarised in this section also demonstrate a fundamental difference in terms of the geometry of actual carpark buildings (including the storey area, depth of the floorplate, and the floor-to-ceiling height) when compared to the previous research upon which codes and standards have been based. Carparks can be very large buildings, with storey areas which are multiple thousand square metres, greatly exceeding the largest experimental research project (CTICM) of around 500 m².

8 CONCLUSIONS

Modern day building codes must respond to the challenges of climate change. Particularly within the last decade, a move towards more sustainable construction and transportation methods has materialised. Some of these innovations present unique fire hazards that need to be considered such that buildings can be designed with appropriate fire safety measures. These measures may be contained within the prescriptive provisions of building codes, or be developed by designers to satisfy specific Performance criteria.

Fire safety measures included within buildings must, amongst other objectives:

- Be appropriate for the risk they mitigate.
- Provide benefit and not be unnecessarily onerous.
- Balance sustainability and fire safety drivers.
- Respond to the drive towards more urbanisation & more multi-level carparks.

The principal findings of this paper are:

- Modern vehicles are larger, heavier, use more plastics and therefore have increased quantities of combustible materials when compared to cars manufactured earlier in the 20th century.
- The experimental research upon which contemporary building codes are still founded, utilised vehicles which were common at the time. Those vehicles are no longer representative of modern vehicles.
- The commonly cited assumption in fire safety literature from the 20th century is that fire spread between cars is a rare event. This is no longer appropriate for the modern car.
- Recently, a number of large-scale fires have occurred in carparking structures around the world. Some have involved multiple hundred or even over a thousand vehicles and led to large economic losses, many occurring at airports where cars are kept for significant periods of time in large carparks with narrow spacings.
- The life safety impacts of carpark fires are currently relatively very small. The case for improvement of fire safety standards is largely driven by increased protection against low probability, high consequence events or for the improvement of fire-fighter ability to fight fire rather than a systematic improvement of occupant life safety. However, as technology evolves and the uptake of technology increases, there is a need to monitor the statistics periodically and keep this under review.

ACKNOWLEDGMENTS

The authors would like to acknowledge the Australian Building Codes Board (ABCB). Arup were appointed by the ABCB in mid-2023 to conduct a literature review on carpark fire safety requirements and

modern vehicle hazards. That work is now complete. This SiF paper would not have been possible without that prior work. It is noted that the presentation of this work does not imply any endorsement of findings or conclusions by the ABCB.

REFERENCES

- [1] M Pundsack et al., Car park design - The Institution of Structural Engineers. The Institution of Structural Engineers, 2023. Accessed: Apr. 08, 2024. [Online]. Available: <https://www.istructe.org/resources/guidance/car-park-design/>
- [2] CROSS-UK, 'Fire in multi-storey car parks', Cross Safety Report, Feb. 2018. Accessed: Apr. 08, 2024. [Online]. Available: <https://www.cross-safety.org/uk/safety-information/cross-safety-alert/fire-multi-storey-car-parks>
- [3] CROSS-UK, 'Fire protection to car park steel frame', Cross Safety Report 1007, Aug. 2022. Accessed: Apr. 08, 2024. [Online]. Available: <https://www.cross-safety.org/uk/safety-information/cross-safety-report/fire-protection-car-park-steel-frame-1007>
- [4] Butcher, E. G., Langdon Thomas, G. J., and Bedford, G. K., 'FRN 678: Fire and the motor car - Results of tests on the propagation of fire in parked cars', 1967.
- [5] Butcher, E. G., Langdon Thomas, G. J., and Bedford, G. K., 'FRN 10: Fire and car-park buildings', 1968.
- [6] BRE, 'BD2552 Fire spread in car parks', 2010.
- [7] Nippon Steel, 'Fire Test with Steel Framed Parking Building', 1970.
- [8] J. Schleich, L. Cajot, and M. Pierre, 'Development of design rules for steel structures subjected to natural fires in closed car parks', European Commission, Directorate-General for Research and Innovation, 1999. [Online]. Available: <https://op.europa.eu/en/publication-detail/-/publication/31860caf-bc55-46b2-8322-2eea65479fad>
- [9] Report on Fire Tests in the Steinenschanze Car Park, Basle, Switzerland. The Department, 1969.
- [10] H. Burgh Schweizerische Feuerwehr, H., 'Fire tests with cars parked in an enclosed car-park building', vol. Zeitung No. 1211970, 1970.
- [11] Gewain, R, 'Fire experience and fire tests in automobile parking structures', 1973.
- [12] I. Bennetts, D. Proe, and R. Lewins, 'Open-deck car park fire tests', BHP Melbourne Research Laboratory, 1985.
- [13] I. Bennetts, V. Dowling, and BHP Research Laboratory, 'Fire and unprotected steel in closed car parks', BHP Steel International, Melbourne, 1987.
- [14] I. Bennetts, I. Thomas, D. Proe, and R. Lewins, 'Fire Safety in Car parks', Structural Steel Development Group, Melbourne, MRL/PS69/89/006, 1989.
- [15] 'Fire in Mixed Occupancy Buildings', 1989.
- [16] D. Joyeux, J. Kruppa, L. Cajot, J. Schleich, P. V. D. Leur, and L. Twilt, 'Demonstration of real fire tests in car parks and high buildings', Europace, 2002, Accessed: Aug. 22, 2023. [Online]. Available: <https://www.semanticscholar.org/paper/Demonstration-of-real-fire-tests-in-car-parks-and-Joyeux-Kruppa/d443b8439694eadfbf8ca9e2ab2361c56a48d032>
- [17] K. Storesund, C. Sesseng, R. F. Mikalsen, O. Holmvaag, and A. Steen-Hansen, 'Evaluation of fire in Stavanger airport car park 7 January 2020', RISE Fire Research, RISE-report 2020:91, Sep. 2020. doi: 10.13140/RG.2.2.24520.14080.
- [18] H. Boehmer, M. Klassen, and S. Olenick, 'Modern vehicle hazards in parking structures and vehicle carriers', NFPA Fire Protection Research Foundation, FPRF-2020-07, Jul. 2020.
- [19] S. Olenick, M. Klassen, and zH Boehmer, 'Changing hazards of modern vehicles in parking structures', presented at the NFPA 125th Anniversary Conference Series, 2021.

SIMULATIONS AND TESTS OF STEEL PLATES PROTECTED BY INTUMESCENT PAINT EXPOSED TO FIRE

Véronique Saulnier¹, Salah Eddine Ouldboukhite², Sébastien Durif³, Abdelhamid Bouchair⁴

ABSTRACT

Intumescent paint is a protective coating used to protect structures against fire. Under the effect of heat, the paint formed an insulation foam and delays steel heating. The aim of this paper is to present tests carry on rectangular plates in an oil burner furnace.

The experimental results are compared to the numerical simulation of paint development during fire exposure.

A finite element modelling with moving mesh done with Comsol MULTIPHYSICS® enable to simulate temperatures rise of steel and to know the behaviour of steel under different heating conditions.

Keywords: Intumescent paint; fire; steel structures, finite element modelling

1 INTRODUCTION

Steel structures are notorious for their vulnerability to high fire-like temperature rises. This is because the mechanical properties of steel degrade at high temperatures. It is estimated that at 400°C the yield strength of steel is 60% of its initial value.

The fire resistance of steel beams is ensured either by a beam of enough size which is calculated so that the critical temperature of the steel is not reached for a specified time, or by an insulating material. The materials generally used are flocking products or sand-lime plates.

Katarzyna Mróz's bibliographic review article [1] presents the different passive fire protections of metal structures.

When it comes to a visible structure with esthetic aspects, it is possible to use intumescent paint [2]. This product has the particularity of forming an insulating meringue under the effect of heat. The foam has the effect of delaying the steel heating. The product is presented as a paint and is used as such, but with a slightly thicker layer. The thickness of the film can range from 100 µm to 1.5 mm [3].

The chemical phenomenon of paint development is perfectly known and mastered [4]. Under the effect of heat, a chemical reaction occurs with the formation of gas bubbles that rise to the surface and cause the formation of a foamy layer. This meringue can reach a thickness of 50 times the initial thickness of paint.

After a review of current knowledge on intumescent paint and experimental conditions, this paper will report on the tests on intumescent paints carried out in a standard fire furnace.

¹ Professeur agrégée et docteur ingénierie des matériaux, Institut Pascal,
e-mail: veronique.saulnier@uca.fr, ORCID: <https://orcid.org/0000-0002-3491-886X>

² Maître de conférence HDR University of Clermont-Ferrand, Institut Pascal
e-mail: salah_eddine.oudboukhite@uca.fr, ORCID: <https://orcid.org/0000-0002-9300-6545>

³ Maître de conférence University of Clermont-Ferrand, Institut Pascal
e-mail: sebastien.durif@uca.fr, ORCID: <https://orcid.org/0000-0002-1202-4179>

⁴ Professeur University of Clermont-Ferrand, Institut Pascal
e-mail: abdelhamid.bouchair@uca.fr, ORCID: <https://orcid.org/0000-0003-2179-421X>

Then the simulations carried out with Comsol MULTIPHYSICS® on the protection of steel by intumescent paint will be presented.

2 THERMAL PROPERTIES OF MATERIALS AND HEAT EQUATIONS

2.1 Intumescent properties

For the test it necessary to knows the conductivity and the specific heat of the intumescent paint. These values come from different studies. Generally thermal conductivity is around 0,3 W/(m.K) for de paint and estimated between 0,01 to 0.05 W/(m.K) for the foam. For the specific heat, the paint before reaction is around 1800 J/(kg.K) and about 1200 J/(kg.K) for the foam. In a first approach the specific heat is taken to be equal at 1000 J/(kg.K) like any insulation. The density is 1300 kg/m³. The density of the foam is estimated to be 50 kg/m³ according Gillet [5].

2.2 Steel properties

The steels used in construction are non-alloy steels of type S, usually S235 or S355 [6]. The properties of the steel used are those given by the Eurocodes [7]. The density of the steel is taken to be equal to 7850 kg/m³. The thermal conductivity of steel evolves according to equation 1 between 0 and 800°C then it remains constant at 27.3 W/(m.K).

$$\lambda a = 54 - 0.033 T a \quad (1)$$

where

λa is the thermal conductivity of steel,

$T a$ is the temperature of steel.

Specific heat varies little overall with temperature and the value of 600 J/kg can be used. But in fact simulations will be done with more precise values given by Eurocodes. The equations take into account the transition from ferrite-pearlitic to austenitic structure around 735°C. In practice, the specific heat curve peaks at 5000 kJ/(kg.K) at 735°C.

2.3 Heat equations

The main physical phenomenon using for the simulations is the heat propagation according to equation 2

$$\rho_{(T)} C_{p(T)} \frac{\partial T(t,x,y,z)}{\partial t} = \text{div}(\lambda_{(T,x,y,z)} \overrightarrow{\text{grad}}(T)) + s(t, T) \quad (2)$$

where

λ is the thermal conductivity,

T is the temperature of steel,

ρ is the density,

C_p is the specific heat,

s is the internal heat source

For steel heating the equation of temperature (Equation 3) rise of steel given by the Eurocode makes it possible to obtain theoretical results close to the experimental results.

$$\Delta T = \frac{q}{\rho_{(T)} \cdot C_{p(T)}} \cdot \frac{S}{V} \Delta t \quad (3)$$

where

q is the specific heat flow,

T is the temperature of steel,

ρ is the density,

C_p is the specific heat,

S/V is the massiveness coefficient,
 t is the time

3 TESTS ON THE INTUMESCENT PAINT

There are many laboratories that have studied the fire protection phenomena of intumescent paints [8]. It is possible to refer to the article by Lucherini and Maluk who make a review on intumescent protections of steel structures [9]

There are mainly two types of tests: with a cone calorimeter (Figure 1) [10] and with a blowtorch like in the articles written by Yew[11] or by Belado [12]. Furthermore, the protection of steel structures against fire is tested in standard fire furnaces [13].

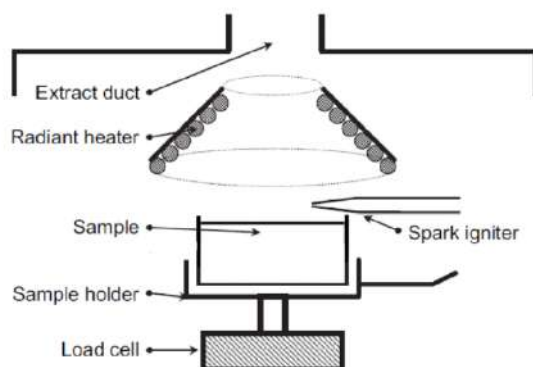


Figure 1. Cone Calorimeter set up [14]

For blowtorch tests, the paint is burned and expands much less than the cone tests [15]. But in both cases (radiant cone heater or blowtorch), the paint has a burnt appearance. On the other hand, when tested in a standard fire oven, the foam has a rather white appearance (Figure 2).

Tests with radiant cone calorimeter are generally done on small square plates 100 millimeters per 100 millimeters

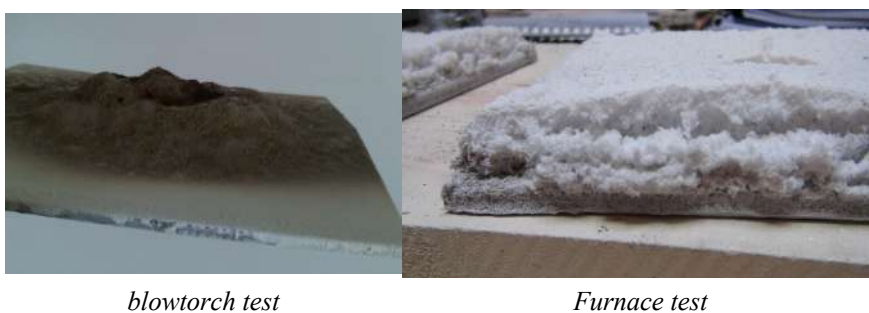


Figure 2. Paint aspect after fire exposition

Samples placed in a furnace under a standard fire with combustion are totally exposed to heat. The conditions are more akin to a fire. Among other things, the oxygen in the environment is primarily consumed by combustion. And unlike the other types of tests (cone calorimeter and blowtorch), the paint is not burned but rather kept in a warm atmosphere.

However, tests under standard fire in a furnace are more complex to perform and some parameters are more difficult to determine.

To perform standard fire tests, an oven must be available in which the samples are placed. All equipment, plates and measurements are exposed to high temperatures. In these conditions, it is difficult to measure some parameters such as the height of the meringue or the mass of the sample during the test.

4 EXPERIMENTAL PART

4.1 Furnace

The furnace used for the tests is a small furnace with a steel shell insulated on the inside with heat-resistant mineral wool (Figure 3). The temperature rises by two oil burners. This device makes it possible to carry out tests under standard fire.



Figure 3. Four d'essai

4.2 Temperature measurement

The temperature measurement in the furnace is carried out by means of several thermoplates. The temperatures of each plate are recorded via K-type thermocouples welded in pairs to the middle of the plate.

4.3 Samples

The tests are carried out on rectangular plates with the dimension 450x100x3 mm³. For each test, there is always an unpainted plate. The samples are with rectangular shape to avoid the edge effects of small square plates. The plates are prepared with an average paint thickness between 0.35 mm and 0.39 mm. The plates are arranged in the furnace above the burners. For the first test One of the specimens is in contact with a support on one face and the second is exposed on all painted faces. A third, unpainted plate is placed on the support. (Figure 4)

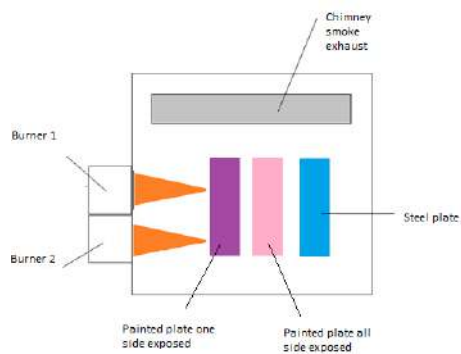


Figure 4. Arrangement of the plates in the furnace for the first test

For the second test, plates are disposed vertically like on the Figure 5.



Figure 5. Arrangement of the plates in the furnace for the first test

The plates are subjected to fire for one hour maximum. At the end of the test, the paint developed into a foam of about 15 millimeters in both cases. (Figure 6)



Figure 6. Plates at the end of the two tests

5 TEST RESULTS AND SIMULATIONS

5.1 First simulations and comparison with results test

Based on initial tests carried out on small 100 mm square plates with a thickness of 8 mm, a preliminary finite element numerical model was developed using Comsol MULTIPHYSICS® during the thesis work [16]. This work made it possible to test and calibrate the model for a plate painted in contact with the support on one side. This model was then applied to the rectangular plate placed on the test stand presented earlier. This simulation is carried out under experimental fire conditions with a radiation limit condition but without convection. Various tests on the models have shown that the convection is zero for these tests. Despite endothermic and exothermic reactions during meringue development, internal sources are neglected. The paint layer is simulated on the side exposed to fire only and not on the edges (Figure 7). The expansion of the foam is simulated by the displacement of the mesh. The speed of movement of the mesh is $2e-5$ m/s for all models and for a temperature interval between 177°C and 567°C . For the contact of the plate with the support, the Eurocode proposes to replace it with a convection coefficient of $4 \text{ W}/(\text{m}^2\cdot\text{K})$. This flat-rate solution was not suitable for test samples. Instead, the plate was simulated with its support. These parameters make it possible to simulate the evolution of the foam thickness and to estimate the final thickness. (Figure 8). The same parameters applied to both tests show agreement between the experimental results and the simulated steel plate temperatures as shown in Figure 9 for the rectangular plate.

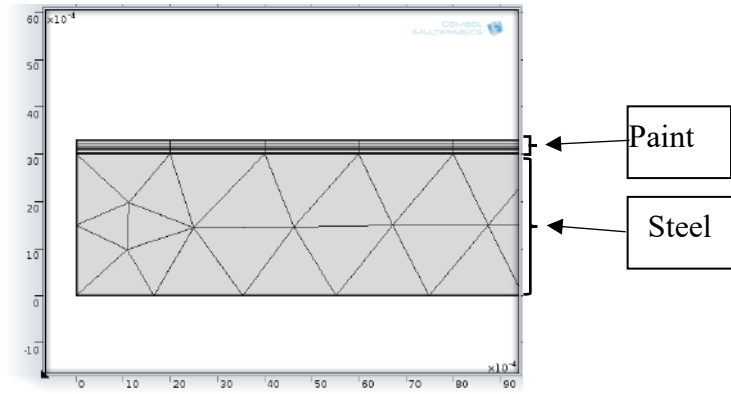


Figure 7. Mesh for steel and paint

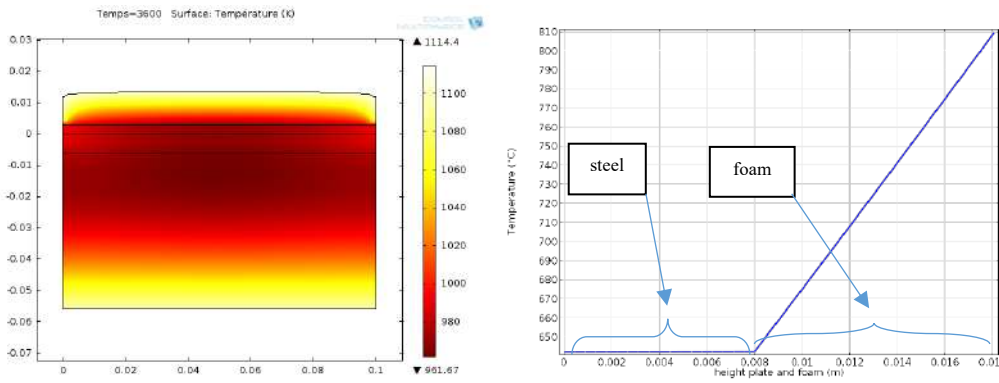


Figure 8. Grow up of foam at the end of the test

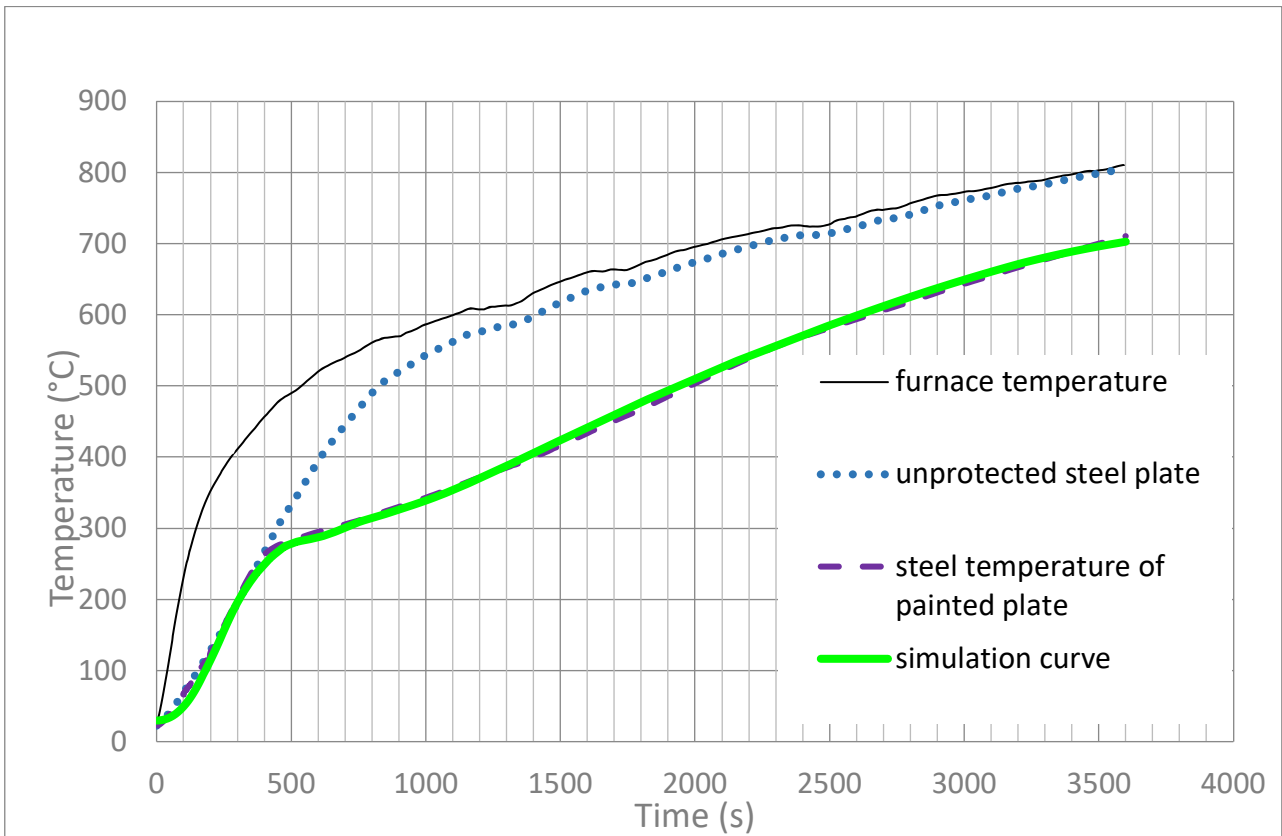


Figure 9. Curve of temperature on steel plate surface comparing the measured and simulated values (steel rectangular plate thickness = 3 mm, intumescent paint thickness = 0.39 mm)

5.2 Simulations for all plate's sides exposed

In this part, the parameters of the previous simulations are repeated, but the paint layer is simulated over the entire section of the plate (Figure 10). Speed of foam is the same. The first simulation with unchanged parameters gives a curve different of the test results. (Figure 11). The steel temperature curve for the simulation does not show an inflection like the experimental curve and the predicted temperature is 100 °C higher than the test temperature. All the thermal characteristics of the paint were then reviewed and set according to the temperature. In particular, the specific heat has a peak value between 227 and 400 °C to simulate the phase change during the development of the foam. New values are in the Table 1. The heating curve of the steel in the simulation is much closer to the experimental curve (Figure 12).

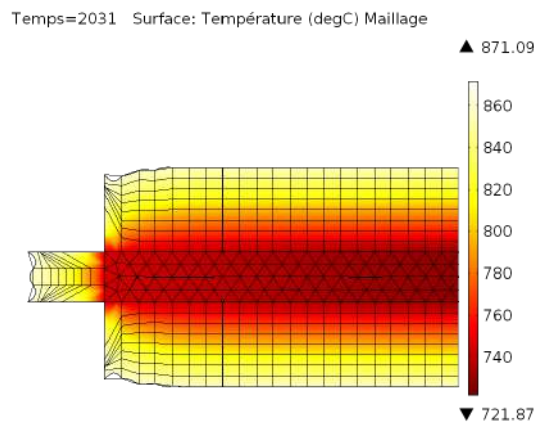


Figure 10. Overview of Foam Development Simulation with Mesh

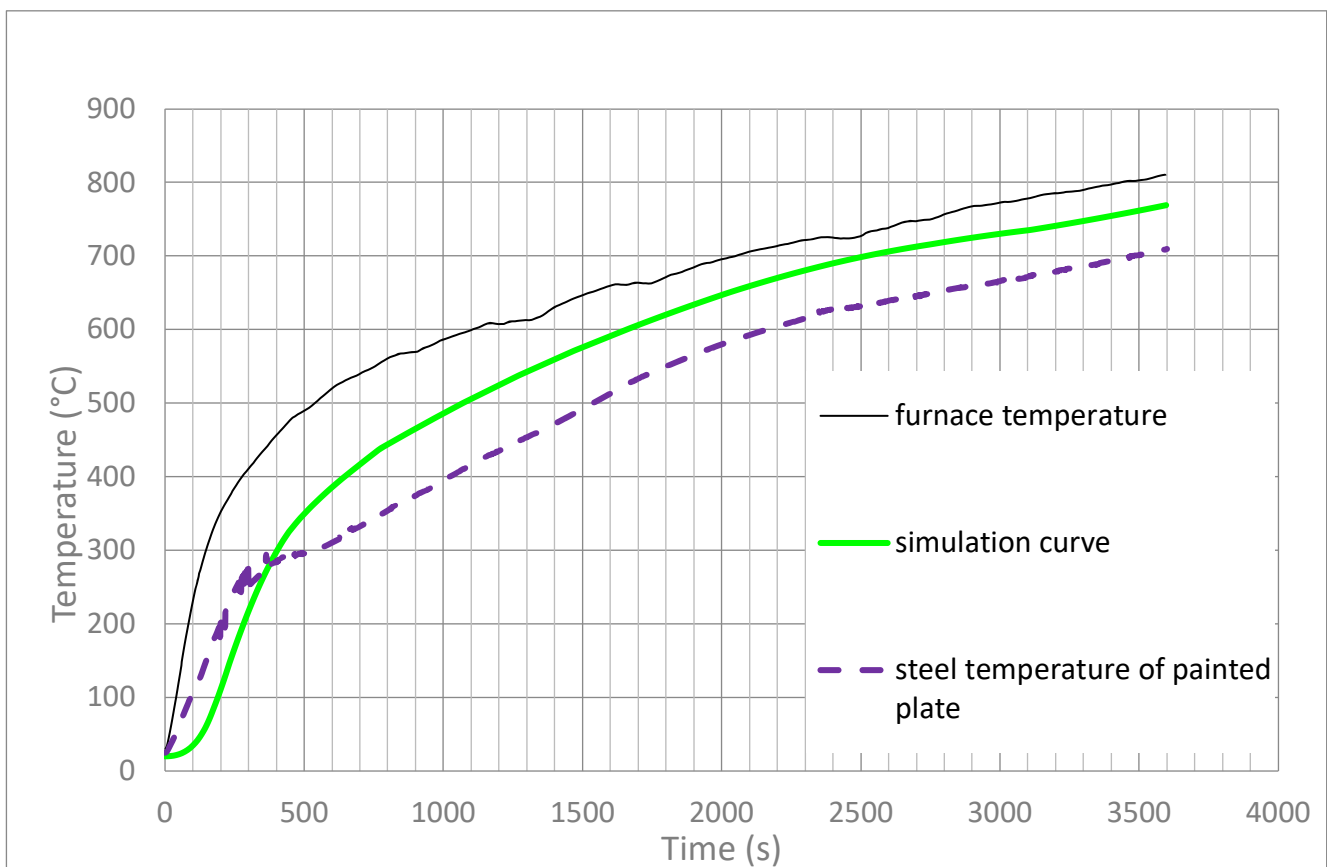


Figure 11. Curve of temperature on steel plate surface comparing the measured and simulated values (steel rectangular plate thickness = 3 mm, intumescent paint thickness = 0.360 mm)

Table 1. Thermal Parameter Values

Parameter of paint	Dee 0 à 100 °C	De 100 à 227 °C	De 227 à 300°C	De 300 à 400°C	Au dela de 400°C
Specific heat Cp en W/(kg.K)	1800	1800	13000	13000	1300
Thermal conductivity en W/(m.K)	0.3	0.08	0.08	0.03	0.03
Density en kg/m ³	1300	50	50	50	50

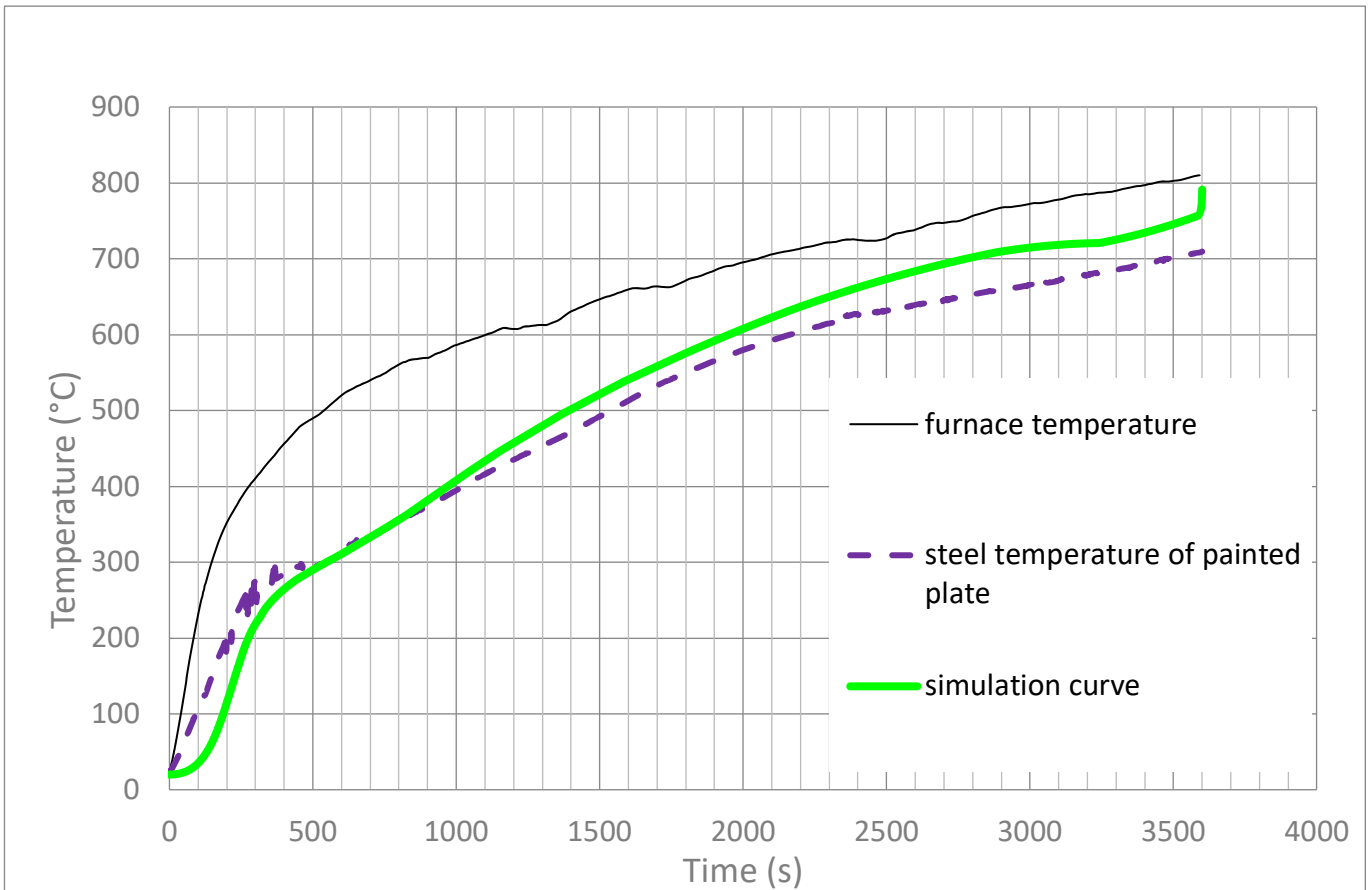


Figure 12. Curve of temperature on steel plate surface comparing the measured and simulated values with adjusting setting (steel rectangular plate thickness = 3 mm, intumescent paint thickness = 0.360 mm)

The test carried out on the vertically arranged plates was carried out under a standard fire for 25 minutes. The test was then stopped because the temperature curve of the steel was above the furnace temperature. The simulation is repeated for this test and compared to the experimental values. This time, the simulation curve is lower than the experimental curve. (Figure 13). The plate disposed vertically heats up more. There are several possible explanations. In the first place, it may be necessary to add the phenomenon of convection for this test. But the simulation curve with convection has lower values than the experimental curve after 15 minutes of testing (Figure 13). On the other hand, there are irregularities in the development of the foam. There is a flow of foam on the lower part of the plate and cracks on the paint in the upper part (Figure 14). It is conceivable that gravity plays a role in the uniformity of foam development.

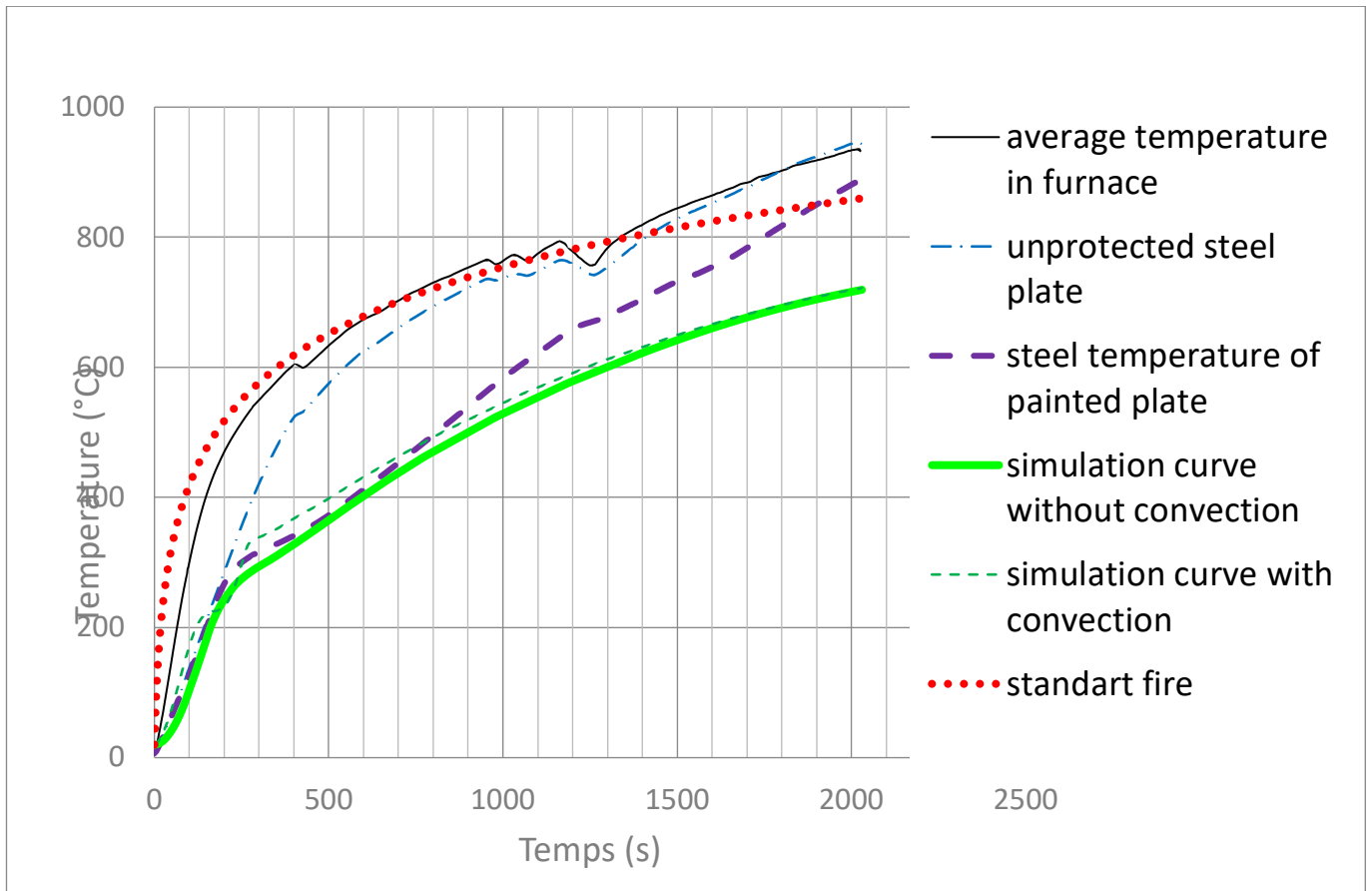


Figure 13. Curve of temperature on steel vertically plate comparing the measured and simulated values with adjusting thermal values (steel rectangular plate thickness = 3 mm, intumescent paint thickness = 0.316 mm)



Figure 14. Foam drips and cracks

6 CONCLUSIONS

The simulations carried out based on the experimental tests allow a better understanding of the experimental results. They made it possible to calibrate some non-measurable parameters.

Each model brings new challenges and challenges the previous model. The numerical simulation for the painted plate exposed on one side does not work for the painted plate exposed on all sides. This study made it possible to refine the previous model and to correct some choices. All thermal characteristics of the paint are dependant of temperature in the new model. In this way, the simulation is independent of the experimental curves. This was not the case before. This new model made it possible to adjust the values of

thermal conductivity and heat by mass. Changes in the conductivity value had no impact on the temperature curves. On the other hand, the increase in the value of the specific heat of the foam made it possible to bring the values of the simulation closer to the experimental values. However, the simulation shows a lack of protection of the paint on the vertical plate. It looks like there's a downward flow of paint. It would be necessary to be able to add a fluidic simulation to determine if the paint drips at the solid-liquid transition and impacts the foam development.

REFERENCES

1. Mróz, K., Hager, I., et Korniejenko, K., Material solutions for passive fire protection of buildings and structures and their performances testing, *Procedia Engineering*, pp. vol. 151, p. 284-291, (2016). <https://doi.org/10.1016/j.proeng.2016.07.388>.
2. Wang, L., Wang, W.Y.C., Li, G., Zhang, Q., An experimental study of the effects of topcoat on aging and fire protection properties of intumescent coatings for steel elements, *Fire Safety Journal*, Volume 111, (2020), 102931, ISSN 0379-7112, <https://doi.org/10.1016/j.firesaf.2019.102931>
3. PROMAT, Protection au feu PROMATECT®-L500 - Poutres et poteaux en acier - R 180, (2022). [En ligne]. Available: <https://www.promat.com/fr-fr/construction/produits-et-systemes/systemes/structures/structures-en-acier/protection-au-feu-promatect-l500-poutres-et-poteaux-en-acier-r-180>.
4. Lucherini, A., Hidalgo, J. P., Torero, J., and Maluk, C., Influence of heating conditions and initial thickness on the effectiveness of thin intumescent coatings, *Fire Safety Journal*, p. p. 103078, (2020). <https://doi.org/10.1016/j.firesaf.2020.103078>
5. Gillet, M., Analyse de systèmes intumescents sous haut flux : modélisation et identification paramétrique, (2009).
6. MURRY, G., *Aciers De Construction Métallique*. Ed. Techniques Ingénieur, (2003). <https://doi.org/10.51257/a-v4-c2501>
7. EN1993-1-2, Eurocode 3: Design of Steel Structures. General rules—Structural fire design. Brussels: European Committee for Standardization. DD ENV, 1-2., (2005).
8. Staggs, J. E. J., Thermal conductivity estimates of intumescent chars by direct numerical simulation, *Fire Safety Journal*, pp. vol. 45, no 4, p. 228-237, (2010). <https://doi.org/10.1016/j.firesaf.2010.03.004>
9. Lucherini, A., Maluk, C., Intumescent coatings used for the fire-safe design of steel structures: A review, *Journal of Constructional Steel Research*, pp. vol. 162, p. 105712, (2019). <https://doi.org/10.1016/j.jcsr.2019.105712>
10. ISO 5660-1 Reaction-to-fire tests - Heat release, smoke production and mass loss rate - Part 1: heat release rate (cone calorimeter method) and smoke production rate (dynamic measurement), ICS : 13.220.50, P 92-190-1, Mai 2015.
11. Yew, M. C., Sulong, N. R., Fire-resistive performance of intumescent flame-retardant coatings for steel.,» *Materials & Design*, , pp. vol. 34, p. 719-724., (2012). <https://doi.org/10.1016/j.matdes.2011.05.032>
12. Beraldo, C. H. M., Da S. Silveira M.R., Baldissera A. F., Ferreira, C. A., A new benzoxazine-based intumescent coating for passive protection against fire. *Progress in Organic Coatings*, pp. vol. 137, p. 105321, (2019). <https://doi.org/10.1016/j.porgcoat.2019.105321>
13. Bailey, C., Indicative fire tests to investigate the behaviour of cellular beams protected with intumescent coatings, *Fire Safety Journal*, pp. vol. 39, no 8, p. 689-709, (2004). <https://doi.org/10.1016/j.firesaf.2004.06.007>
14. Hellebuyck, D.H.L., Functional performance criteria for comparison of less flammable transformer oils with respect to fire and explosion risk, (2013).
15. Yasir, M., Ahmad, F., Megat-Yusoff, P. S., Ullah, S., Jimenez, M., Quantifying the effects of basalt fibers on thermal degradation and fire performance of epoxy-based intumescent coating for fire protection of steel substrate, *Progress in Organic Coatings*, pp. vol. 132, p. 148-158, (2019). <https://doi.org/10.1016/j.porgcoat.2019.03.019>
16. Saulnier, V., Evaluation des performances humo-physiques des protections au feu de structures métalliques et leurs influences sur la résistance mécanique, Montluçon, (2022). <https://theses.fr/2022UCFAC043>

STEEL STRUCTURES IN FIRE

CHARPY IMPACT TEST IN THE POST-FIRE VERIFICATION OF STRUCTURAL STEEL SUSCEPTIBILITY TO BRITTLE FRACTURE

Mariusz Maslak¹, Michal Pazdanowski², Marek Stankiewicz³, Paulina Zajdel⁴

ABSTRACT

Based on the research conducted by the Authors, it has been shown, that instrumented Charpy impact test may constitute an effective and objective tool to verify the specified a priori susceptibility to brittle fracture of steel subjected to a fire episode following any development scenario. Evaluation of this type seems to be the key when a decision has to be made whether the affected material should be kept in extended service after a fire, in particular in bearing elements transferring the loads applied to them. Experimentally determined post-fire impact strength proved to be significantly dependent on the particulars of fire action, and especially on the duration of a fire and the maximum level of temperature reached, the time spent at such temperature level as well as the cooling mode applied in practice. It is conditioned by the internal structure of the material, selected intentionally based on its potential application. The conclusions presented in this paper are based on the interpretation of the F - s curve, where F [kN] represents the force fracturing tested sample while s [mm] is the displacement measured at the force application point and is confronted with the independently determined value of the Lateral Expansion parameter (LE [mm]).

Keywords: Structural steel; post-fire properties; breaking energy; impact strength; brittle cracking.

1 INTRODUCTION

It is a common knowledge, that the properties of structural steel grades specified a posteriori, on cooled material previously affected by a more or less prolonged fire action following certain development scenario, may significantly depart from analogous properties identified for the same material in the as delivered state, i.e. prior to the initiation of fire. Knowledge of the permanent changes induced in given steel grade by the action of fire temperature followed by more or less rapid cooling seems to be the key for drawing reliable conclusions regarding its suitability for extended post-fire service, in particular in bearing elements, which have to be capable of safely bearing the loads applied to them. In the Authors' opinion, in this context identification of post-fire resistance to brittle fracture is of key importance. Detection of susceptibility to brittle fracture in given structural element denotes substantial risk of destruction, initiated rapidly without any prior signs of impending failure. Such a statement, in engineering practice should exclude given steel grade from continued service after fire and enforce replacement by a new component, made of steel not subjected to prior fire exposure.

¹ Prof. Dr Hab. Eng., Cracow University of Technology, Cracow, Poland,
e-mail: mmaslak@pk.edu.pl, ORCID: <https://orcid.org/0000-0003-3592-429X>

² Dr Eng., Cracow University of Technology, Cracow, Poland,
e-mail: michal.pazdanowski@pk.edu.pl, ORCID: <https://orcid.org/0000-0003-1344-1342>

³ M. Eng., Cracow University of Technology, Cracow, Poland,
e-mail: marek.stankiewicz@pk.edu.pl, ORCID: <https://orcid.org/0000-0002-6405-7175>

⁴ Dr Eng., Cracow University of Technology, Cracow, Poland,
e-mail: paulina.zajdel@pk.edu.pl, ORCID: <https://orcid.org/0000-0002-1940-0106>

The risk indicated above so far is little noticed and discussions regarding its importance are scarce in the professional literature. Typical tests of the post-fire steel characteristics are usually concentrated on its mechanical properties affecting strength exhibited post fire. Permanent changes in the yield limit and ultimate strength exhibited by the cooled material are of particular interest here. The Authors of this paper suggest to include the verification of post-fire reduction in ductility exhibited by the tested steel, and understood as susceptibility to unrestricted growth of brittle fractures under load, into the classical set of tests which are advised for execution during expert appraisals of this kind. We recommend the application of classic Charpy impact strength test for this purpose. However, in our opinion, the effectiveness of this test is conditioned by the availability of proper instrumentation capable of automatic registering and processing the results. It is not so important how the fire temperature itself does affect the ductility determined during the test [1-2], but whether and if so how this change is sustained after cooling of the material [3-5].

2 FORCE – DISPLACEMENT OF FORCE APPLICATION POINT RELATIONSHIP AS A BASIS FOR CONCLUSIONS

Impact strength tests conducted by the Authors and described in detail in papers [6-8] had been conducted using instrumented Charpy hammer JB-W450E-L, with 450 J of potential energy (Fig. 1), conforming to the European [9-10] and US standards [11-12]. This hammer is equipped with a converter to record the force applied to the sample, while the corresponding displacement of force application point is recorded by an encoder. Signals generated by both transducers have been gathered and processed by a data logger with high sampling frequency and subsequently analyzed by specialized software designed for this purpose. The result of each test has been presented on an automatically generated graph, depicting the applied force, energy and displacement as functions of time or, alternatively force and energy as functions of displacement. The locations of characteristic limit points have been automatically indicated on these graphs by the software as well.

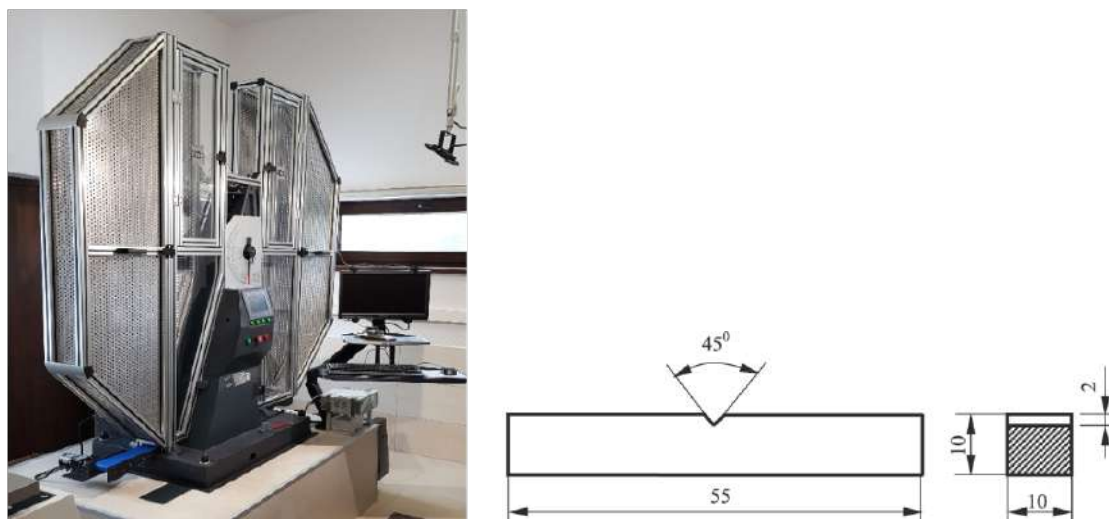


Figure 1. Instrumented Charpy impact strength test. The JB-W450E-L hammer at left, typical sample of normalized shape and dimensions, with V-type notch, at right

Detailed conclusions regarding post-fire resistance of the material to brittle fracture have been drawn based on the shape of experimentally obtained $F-s$ curve, depicting the relationship between the force F [kN], applied to the tested sample and the displacement s [mm] of the force application point (Fig. 2). The F_{gy} force presented on such graph is usually associated with the initiation of plastic process in the developing impact fracture, while the force F_m constituting the global maximum of the analyzed curve determines, together with accompanying displacement, the end of the stable fracture initiation phase. At the displacement increasing further the previously initiated fracture grows in a stable mode, so that its

propagation occurs accompanied by plastic deformation. Initiation of the unstable fracture growth phase occurs at the displacement corresponding to the force F_{iu} . This phase is terminated when the displacement corresponding to the force F_a is achieved. At this moment the self-restriction of the fracture, so far growing in an unstable manner, begins and as a consequence the sample enters the phase of finishing plastic fracture. Particular phases of the sample fracture are accompanied by the components of the fracturing energy $W=KV$ [J], usually juxtaposed on a circular graph (Fig. 2).

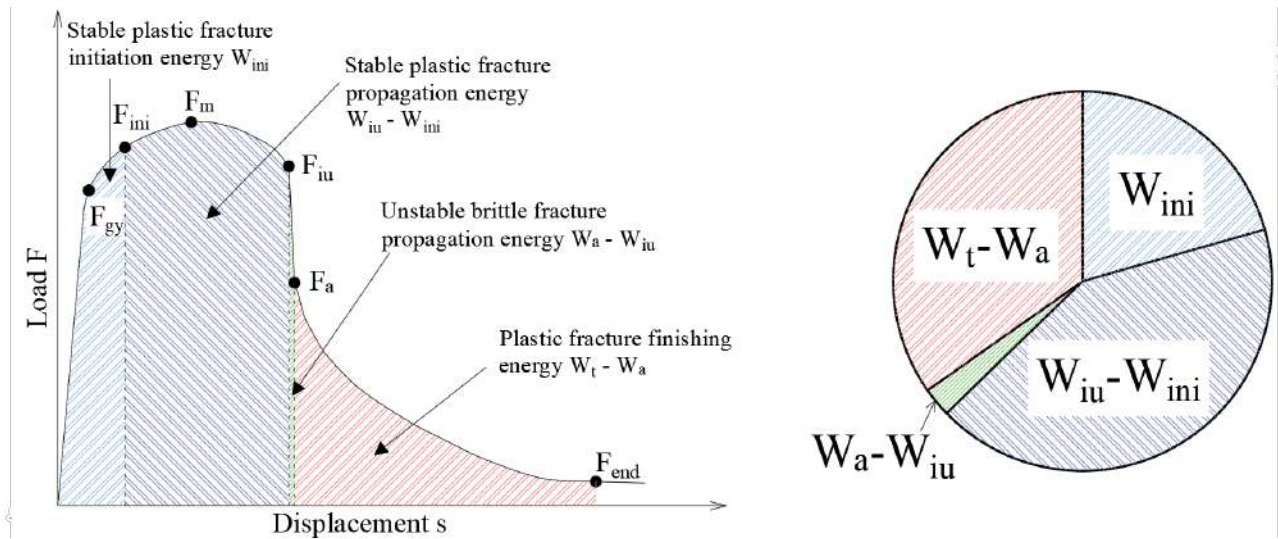


Figure 2. Sample fracturing phases identified on the $F-s$ curve, and fracture energy components determined based on that curve and presented as a pie chart

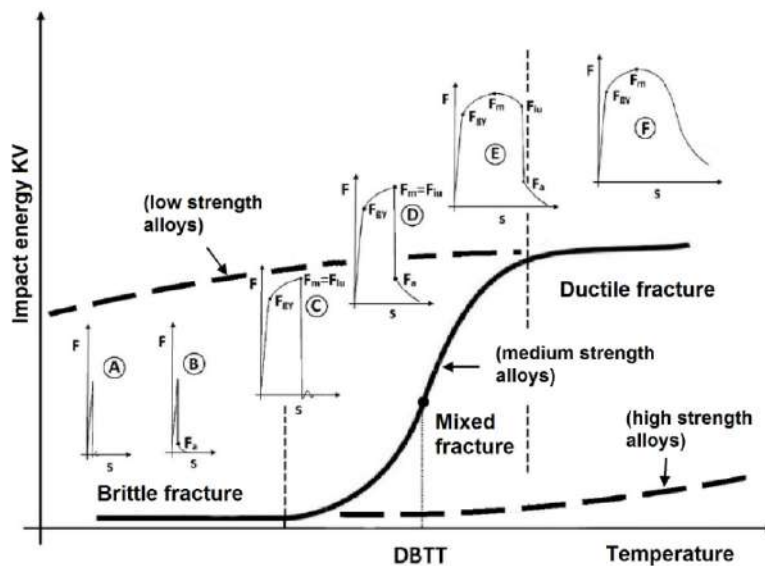


Figure 3. Code shapes of the $F-s$ curves and their distribution on the $KV-T$ graph

Following the code [10], the shape of the resultant $F-s$ curve may be used to draw conclusions by comparison against the templates presented there and denoted with letters A , B , C , D , E and F (Fig. 3). The extreme template type denoted as A , is associated with completely unstable, i.e. brittle fracture growth during the whole process. The other extreme template in this set, located on the opposite side of the spectrum, is denoted by the letter F . The fracturing process conforming to this template does not exhibit unstable growth in any phase. All the fracture growth phases are stable, and this in turn means, that self-arrest of fracture growth is fully effective and efficient. The larger the area under the empirical $F-s$ curve,

however determined only for the displacement higher than the one related to the limit force F_a , the higher the capacity of the material to effectively restrict the unstable growth of previously initiated fracture. This in turn results in relatively larger area of the ductile fracture finishing zone observed on the fractured surface. The templates discussed above have been assigned to corresponding locations on the curve depicting the relationship between the sample fracturing energy (KV [J]) and testing temperature (T [°C]). The conclusions drawn on brittleness of steel samples are related here to the limit fracturing energy $KV_{min}=27$ J, correlated with the ductile-to-brittle transition temperature ($DBTT$). The steel grades, for which at a given temperature the fracturing energy lower than the KV_{min} has been obtained, (i.e. those conforming to the templates A , B , C and D) usually exhibit dominantly brittle character of the fracture. This means, that such steel grades are incapable of self-arresting the developing brittle fractures, and therefore are not recommended for application in the construction industry. The steels exhibiting this capacity (i.e. those conforming to the templates E and F) are characterized by the $F-s$ curves located to the right of the threshold $DBTT$ temperature.

3 LATERAL EXPANSION AS A PARAMETER VERIFYING THE RESULTS OF IMPACT STRENGTH TESTS

During our research the conclusions drawn based on the shape of the $F-s$ curves obtained experimentally during impact strength tests have been confronted against the independently measured magnitude of the so called Lateral Expansion LE [mm]. This parameter was measured each time, directly after the sample had been fractured. The idea of this measurement is illustrated in Fig. 4. As depicted, the higher value of this parameter is accompanied by the higher ratio of plastic fracture observed during the test [13]. Observation of the fracture area, conducted after fracture and identified for each sample, following various testing scenarios allows for identification of particular phases occurring during each test. This allows for verification of the conclusions drawn earlier. Detailed description of this analysis has been presented by the Authors in [7], and due to the limited volume of this paper is not included here. For the same reason the relation of the impact strength tests obtained here to the metallographic analyses discussed in [8] has not been included here as well.

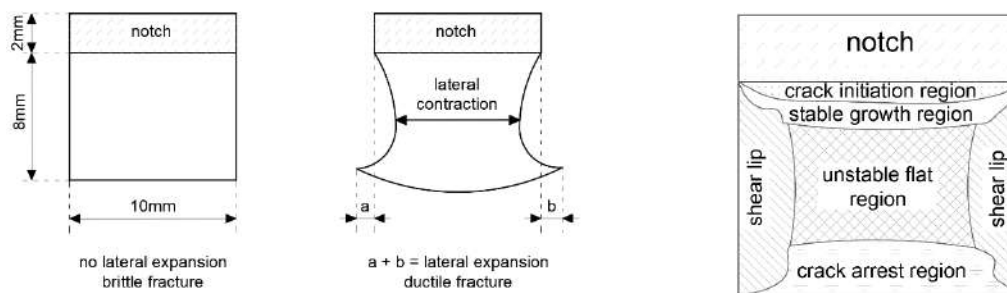


Figure 4. Idea of the Lateral Expansion measurement (LE [mm]) on the impact fracture surface and its interpretation as a measure of plastic fracture component during the impact strength test at left. Stable and unstable fracture growth zones identified on the fracture surface at right

4 IMPACT STRENGTH SAMPLE PREPARATION AND MARKING FOR DIFFERENT TESTING SCENARIOS

As the research presented in this paper was oriented on verification of post-fire susceptibility of tested steel grades to brittle fracture, the samples considered have been subjected to initial heat treatment of prescribed course, simulating a fire action, and after that cooled to the room temperature. The heat treatment has been conducted following the conventional scenario of „steady-state heating regime”, where the sample heated to prescribed temperature is kept at this temperature for a specified amount of time.

Two alternative fire development scenarios have been considered, i.e. a “short” fire with one hour long heating time and a “long” fire with heating time extended to ten hours (Fig. 5). Under both scenarios the

samples have been heated at the beginning with a speed of 100°C/min, until they have reached the prescribed temperature level. The heating temperature levels have been selected intentionally. In the first group of tests the samples had been heated at 600°C, while in the second group this had been increased to 800°C. These levels of temperature are related to the allotropic transition temperature typical for “mild” carbon steels, i.e. transition of the δ ferrite into γ austenite occurring in the $\delta \rightarrow \gamma$ direction with increasing temperature and in the $\gamma \rightarrow \delta$ direction with decreasing temperature. The reference to these steel grades has been enforced by the need to compare the results obtained during our tests on samples made of several steel grades (including those not belonging to the “mild” steels group). Our intent here was to select two temperature levels of which one was too low, while the other one was sufficiently high to initiate and execute with sufficient intensity permanent changes in the microstructure remaining in the material after cooling.

After predetermined heating time hot samples have been effectively cooled. Two alternative cooling modes have been applied, that is slow cooling of the samples left inside cooling muffle furnace – intended to simulate the slow self-extinguishing of a fire, and rapid cooling in water mist – corresponding to typical firefighting action conducted by fire brigade.

The impact strength tests conducted on samples cooled after simulated fire exposure have been performed independently at two different temperature levels, i.e. +20°C – for the first series of tests, and –20°C – for the second series of tests. First of those temperature levels was to simulate the service conditions in summer time, while the second one was to simulate winter service time in the Authors’ intent.

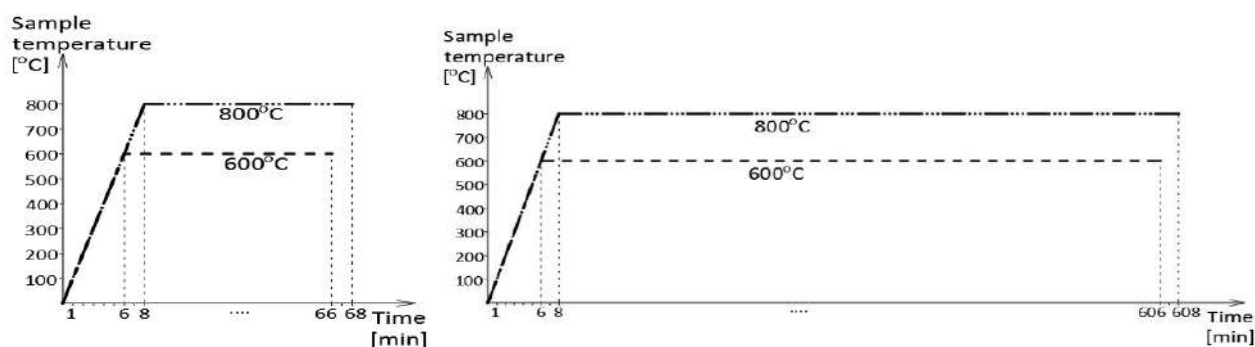


Figure 5. Initial fire exposure simulation scenarios followed during the experiments: “short” fire - at left, “long” fire – at right

Each computational case was tested independently on six impact strength samples to enable proper statistical processing of data obtained during the experiment. The reference samples tested for comparative purposes were made of the material in the as delivered state, that is unaffected by the preliminary heat treatment simulating a fire action.

Samples made of several, intentionally selected, steel grades have been subjected to the tests. These steel grades varied in specifics of their microstructure and chemical composition matched to the intended application. The following steel grades have been subjected to the detailed testing of post-fire impact strength:

- *S355J2+N* steel – as a material representative for conventional structural steels, characterized by a two phase ferritic–pearlitic structure. This steel grade welds well, has increased manganese content, with streaks of pearlite. In the commercial nomenclature it is denoted by the symbol (Werkstoffnummer) 1.0577. Properties of this steel grade are listed in the code [14].
- *X6CrNiTi18-10* steel – as a material representative for stainless acid resistant steels exhibiting single phase austenitic structure. This is a high alloy, chromium–nickel steel with low ferrite content and carbon stabilized by the addition of titanium. It exhibits good corrosion resistance in the natural environment, provided that the chlorine, salt, nitric acid and organic acids content is low. It is particularly used when resistance to intercrystalline corrosion after welding is required. This steel grade represents a group of special steels recommended for application at the temperature up to 600°C (due to the risk of deleterious sigma phase precipitation at the 650-850°C temperature range). In the

commercial nomenclature it is denoted by the symbol (Werkstoffnummer) 1.4541. Properties of this steel grade are listed in the code [15].

- *X2CrNiMoN22-5-3* steel – as a material typical for stainless steels exhibiting two phase austenitic – pearlitic structure of the standard duplex type (SDSS). This is a high alloy chromium–nickel–molybdenum steel grade. It exhibits good resistance to surface and pitting corrosion. This steel grade represents a group of duplex steels recommended for application below 300°C (due to the occurrence of deleterious 475°C brittleness phenomenon). In the commercial nomenclature it is denoted by the symbol (Werkstoffnummer) 1.4462. Properties of this steel grade are listed in the code [15].
- *X2CrMnNiN21-5-1* steel – as a material representative of low alloy stainless steels exhibiting two phase austenitic–ferritic structure of the lean duplex type (LDSS). Steel grades of this type, when compared against traditional standard duplex steel grades, exhibit decreased content of chromium, molybdenum and nitrogen. Their chemical composition is balanced as to obtain good resistance to localized and homogenous corrosion. Microstructure of duplex type contributes to high resistance to fracture, in particular when the stress, intercrystalline and crevice corrosion is advanced. In the as delivered state it is distinguished by high fatigue strength. Due to the risk of brittle fracture it should be applied below 250°C. In the commercial nomenclature it is denoted by the symbol LDX 2101 (Werkstoffnummer 1.4162). Properties of this steel grade are listed in the code [15].

The results obtained have been archived using a four character code to distinguish particular testing scenarios. Interpretation of subsequent characters in the code is described in the Table 1. The cases denoted with single digit only (i.e. 1, 2, 3 and 4) refer to the so called reference cases, obtained during the tests conducted on samples in the as delivered state (that is made of the material not subjected to simulated fire action prior to the impact strength tests).

Table 1. Description mode of samples subjected to impact strength tests

First character of the code – steel grade	Second character of the code – heating temperature	Third character of the code – cooling mode	Fourth character of the code – heating time
1 – <i>S355J2+N</i>	6 – 600°C 8 – 800°C	F – slow cooling in muffle furnace W – rapid cooling in water mist	X – „short” fire Y – „long” fire
2 – <i>X6CrNiTi18-10</i>			
3 – <i>X2CrNiMoN22-5-3</i>			
4 – <i>X2CrMnNiN21-5-1</i>			

Thus 72 qualitatively different testing cases have been considered. For each of the tested steel grades and each of the two testing temperature values (+20°C and –20°C, respectively) eight independent test cases referring to steel cooled after application of simulated fire episode have been taken into account (two heating temperature levels multiplied by two different cooling scenarios multiplied by two different heating periods) and one so called reference case associated with samples made of steel in the as delivered state. Each test has been statistically analyzed on six independent samples in order to obtain sufficiently reliable final estimates of the results. Finally 432 independent impact strength tests have been conducted during this research.

5 PRESENTATION OF SELECTED RESULTS

5.1 *S355J2+N* steel

- Referring to the tests conducted at +20°C and “short” fire simulation (Fig. 6):
 - post-fire impact strength was significantly decreased when compared against the impact strength of reference sample (denoted as 1), regardless of heating temperature and cooling mode,
 - reduction in the post-fire impact strength was more pronounced, when the sample was rapidly cooled in water mist,

- a relatively small reduction in post-fire impact strength observed in the 800°C/1h scenario at slow cooling (the 18FX case), may be attributed to the fact, that after the austenitic transformation occurred under fire conditions, at inverse transformation of austenite into pearlite enforced by material cooling, fragmentation of crystalline matrix grains occurred in the pearlite zones, and this in turn increased impact strength of the material.

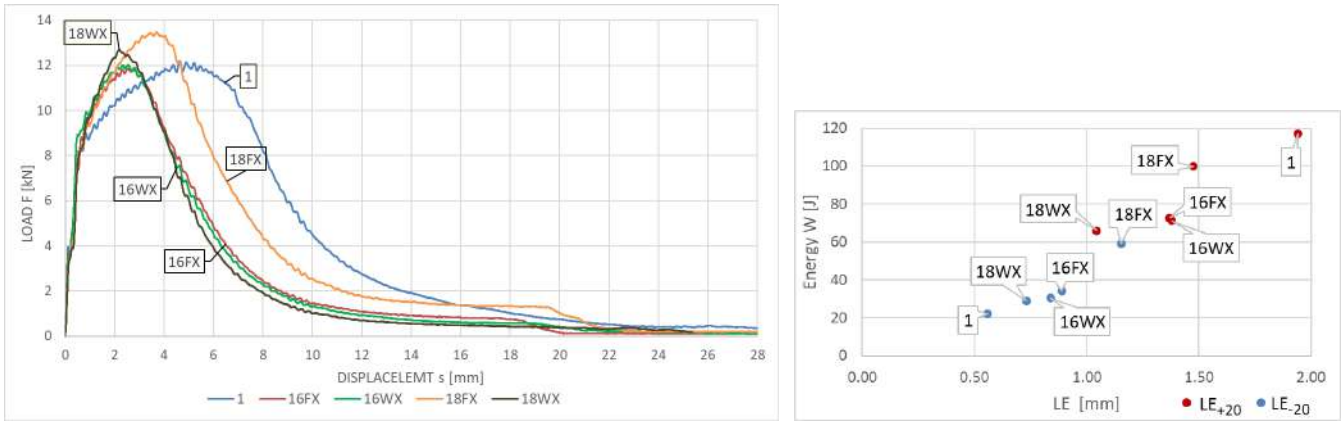


Figure 6. At left: $F-s$ curves obtained during post-fire impact strength tests on samples made of $S355J2+N$ steel following different testing scenarios. “Short” fire simulation. Testing temperature $+20^{\circ}\text{C}$. At right: $LE-W$ relationships determined on the same samples and analogous testing scenarios conducted at $+20^{\circ}\text{C}$ (red dots) and -20°C (blue dots), respectively

- o Referring to the tests conducted at -20°C and “short” fire simulation (Fig. 6, graph at right, blue dots):
 - fire episodes preceding tests conducted on cooled samples, in each testing scenario followed increased post-fire impact strength when compared against impact strength exhibited by reference sample (denoted as 1),
 - improvement in impact strength was more pronounced in the case of slowly cooled specimens.

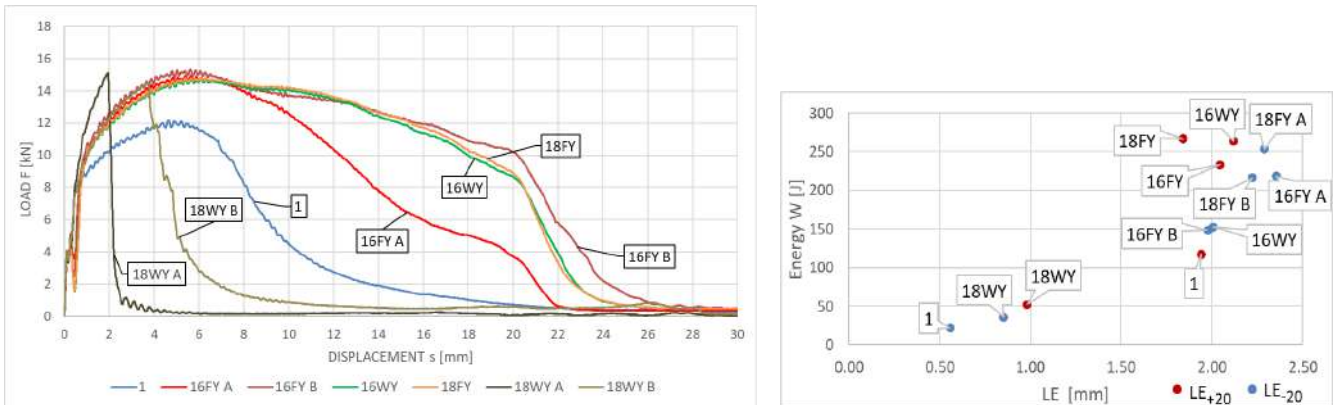


Figure 7. At left: $F-s$ curves obtained during post-fire impact strength tests on samples made of $S355J2+N$ steel following different testing scenarios. “Long” fire simulation. Testing temperature $+20^{\circ}\text{C}$. At right: $LE-W$ relationships determined on the same samples and analogous testing scenarios conducted at $+20^{\circ}\text{C}$ (red dots) and -20°C (blue dots), respectively

- o Referring to the tests conducted at $+20^{\circ}\text{C}$ and “long” fire simulation (Fig. 7):
 - in several testing scenarios alternative responses of the material have been observed, denoted with an additional letter A or B appended at the end of the code,
 - in general post-fire impact strength was higher than the impact strength exhibited by reference sample (denoted as 1), this may be attributed to the fact that sufficiently long heating time allowed sample time for favorable structural changes to occur in the material,
 - at rapid cooling of the sample from 800°C , that is after the austenitic phase change occurred in the material, a significant reduction in impact strength has been observed accompanied by change in the template of $F-s$ curve – this has to be associated with increased risk of brittle fracture occurring in such steel when remaining in service post fire.

- Referring to the tests conducted at -20°C and “long” fire simulation (Fig. 7, graph at right, blue dots):
 - change in testing temperature at sufficiently long fire episode, in spite of significant differences observed on reference samples (denoted as 1), seems not to affect the post-fire impact strength to a significant degree.

5.2 X6CrNiTi18-10 steel

- Referring to the tests conducted at $+20^{\circ}\text{C}$ and “short” fire simulation (Fig. 8):
 - change in the post-fire impact strength exhibited with respect to the reference sample (denoted as 2) was relatively small, regardless of the testing scenario followed,
 - regardless of the cooling mode applied to the hot sample, cooling from 600°C resulted in slightly improved post-fire impact strength,
 - however, when the sample was cooled from 800°C , post-fire impact strength decreased when compared against the reference sample (denoted as 2),
 - these differences may be attributed to the fact, that the activation of diffusion processes in steels exhibiting austenitic structure is easier at higher temperature.

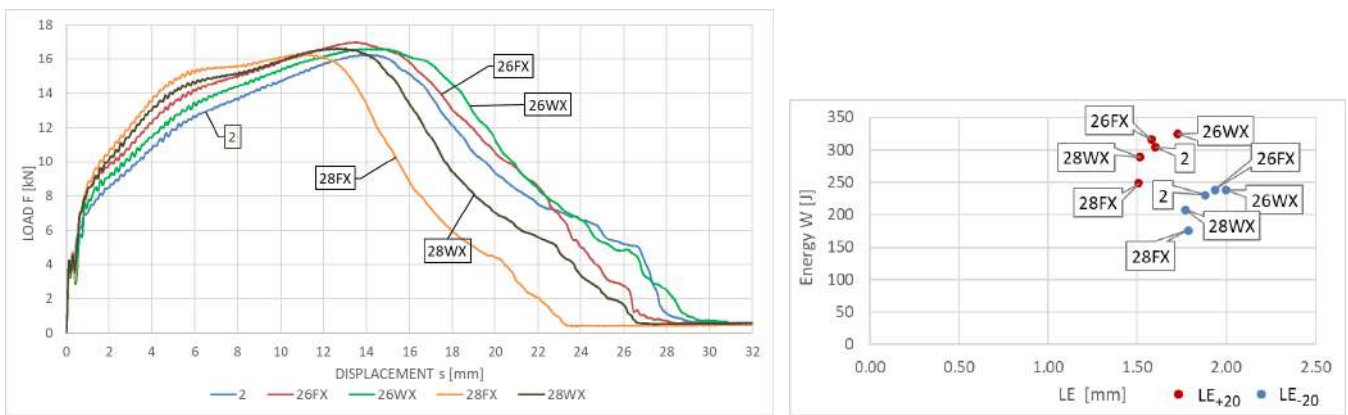


Figure 8. At left: F - s curves obtained during post fire impact strength tests on samples made of $X6CrNiTi18-10$ steel following different testing scenarios. “Short” fire simulation. Testing temperature $+20^{\circ}\text{C}$. At right: LE - W relationships determined on the same samples and analogous testing scenarios conducted at $+20^{\circ}\text{C}$ (red dots) and -20°C (blue dots), respectively

- Referring to the tests conducted at -20°C and “short” fire simulation (Fig. 8, graph at right, blue dots):
 - post-fire impact strength exhibited under these testing conditions was slightly lower than the one determined earlier at $+20^{\circ}\text{C}$,
 - the higher heating temperature resulted in slightly higher reduction of impact strength.

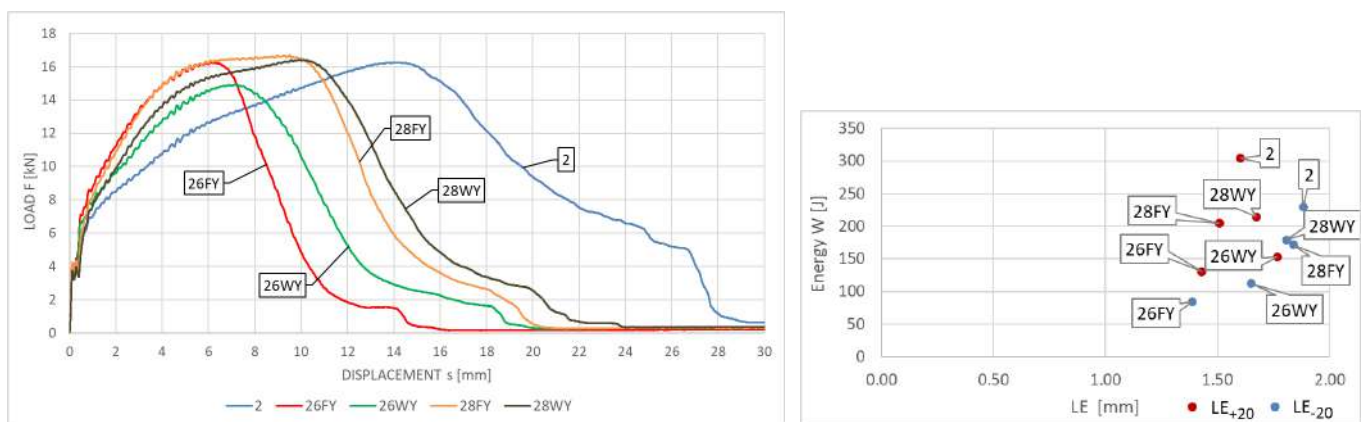


Figure 9. At left: F - s curves obtained during post-fire impact strength tests on samples made of $X6CrNiTi18-10$ steel following different testing scenarios. “Long” fire simulation. Testing temperature $+20^{\circ}\text{C}$. At right: LE - W relationships determined on the same samples and analogous testing scenarios conducted at $+20^{\circ}\text{C}$ (red dots) and -20°C (blue dots), respectively

- Referring to the tests conducted at +20°C and “long” fire simulation (Fig. 9):
 - at sufficiently long simulated fire episode impact strength observed post fire was significantly lower than the one exhibited by the reference sample (denoted as 2),
 - this reduction proved to be visibly smaller when the hot sample was cooled from 800°C, regardless of the cooling mode applied,
 - this is behaviour qualitatively opposite to the one observed on samples subjected to “short” fire,
 - this may be attributed to the fact that at 800°C the solution dynamics of secondary precipitates deleterious to the post-fire impact strength exceeded the formation dynamics of new precipitates; at sufficiently long heating time this dominated the picture.
- Referring to the tests conducted at –20°C and “long” fire simulation (Fig. 9, graph at right, blue dots):
 - impact strength of this steel observed post fire at –20°C was usually slightly lower than the one determined following analogous testing scenarios but conducted at +20°C,
 - the higher heating temperature resulted in slightly lower reduction of impact strength observed.

5.3 X2CrNiMoN22-5-3 steel

- Referring to the tests conducted at +20°C and “short” fire simulation (Fig. 10):
 - a clear plateau observed in certain cases at the finishing stage of fracture (a result of incomplete fracture occurring immediately after hammer hit forcing delayed completion of the fracture when the deformed sample is pushed through the supports of the machine) is a characteristic element in this group of tests,
 - in almost every test case simulated fire episodes preceding impact strength testing resulted in significantly decreased post-fire impact strength observed,
 - the case identified as 36WX proved to be the notable exception, as there material weakening was not observed,
 - this may be explained by the fact, that the heating temperature of 600°C proved to be insufficient to initiate the formation of secondary precipitates in the sample,
 - in addition rapid cooling of the sample in water mist substantially shortened the sample transition time through the 475°C brittleness zone correlated with precipitation of deleterious phases,
 - heating at 800°C/1h scenario resulted in significantly more pronounced reduction in impact strength observed post fire; this reduction was greater when the sample was cooled slowly when compared to the reduction associated with rapid cooling in water mist.

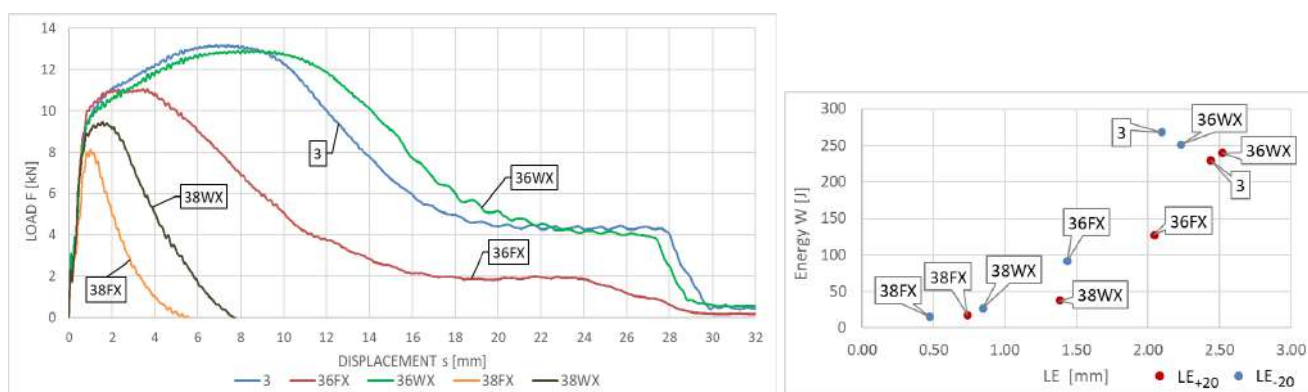


Figure 10. At left: F - s curves obtained during post-fire impact strength tests on samples made of X2CrNiMoN22-5-3 steel following different testing scenarios. “Short” fire simulation. Testing temperature +20°C. At right: LE - W relationships determined on the same samples and analogous testing scenarios conducted at +20°C (red dots) and –20°C (blue dots), respectively

- Referring to the tests conducted at –20°C and “short” fire simulation (Fig. 10, graph at right, blue dots):
 - post-fire impact strength determined for this steel grade at –20°C was for particular testing scenarios very close to the corresponding impact strength determined for the same material at +20°C,
 - the impact strength determined on reference samples tested at –20°C (denoted as 3), proved to be higher than the corresponding impact strength determined at +20°C.

- Referring to the tests conducted at +20°C and “long” fire simulation (Fig. 11):
 - extended sample heating time in both scenarios (600°C/10h as well as 800°C/10h) resulted in further reduction in impact strength,
 - this reduction was more pronounced when material cooled slowly,
 - the cases identified as 38FY and 38WY proved to be the worst, as full scale 800°C brittleness phenomenon was observed here, this was equivalent to complete loss of impact strength.

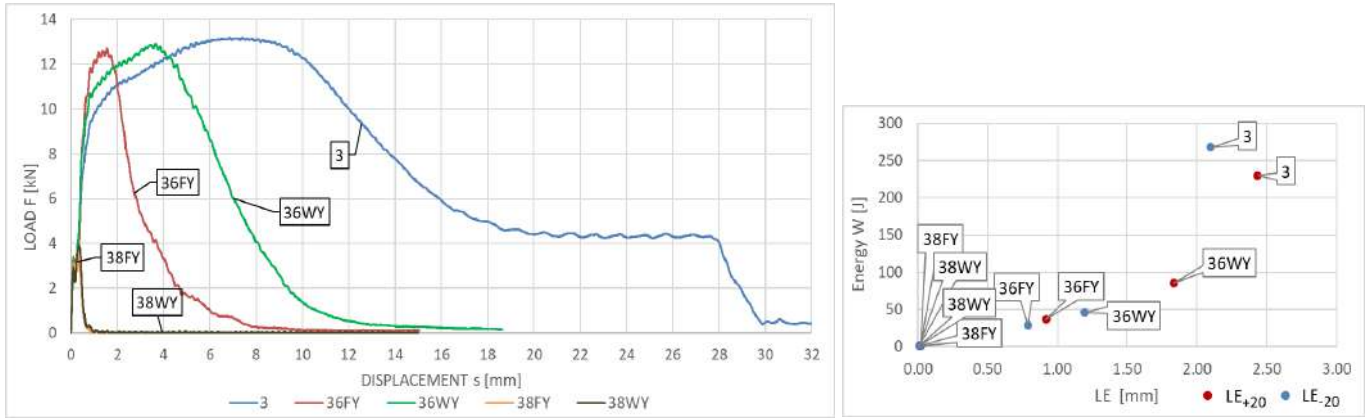


Figure 11. At left: F - s curves obtained during post-fire impact strength tests on samples made of $X2CrNiMoN22-5-3$ steel following different testing scenarios. “Long” fire simulation. Testing temperature +20°C. At right: LE - W relationships determined on the same samples and analogous testing scenarios conducted at +20°C (red dots) and -20°C (blue dots), respectively

- Referring to the tests conducted at -20°C and “long” fire simulation (Fig. 11, graph at right, blue dots):
 - experimentally determined post-fire impact strength proved to be relatively immune to the change in impact strength testing temperature from +20°C to -20°C in all testing scenarios considered.

5.4 $X2CrMnNi21-5-1$ steel

- Referring to the tests conducted at +20°C and “short” fire simulation (Fig. 12):
 - the plateau described above has not been observed in this case, this means that the samples made of this steel grade were effectively fractured directly under hammer impact,
 - the simulated fire episodes applied to the samples significantly negatively affected the impact strength determined after cooling,
 - this reduction was more pronounced for the samples cooled slowly, this may be attributed to the long transition time through the 475°C brittle zone as well as the 800°C brittle zone,
 - the change in the heating scenario from 600°C/1h to 800°C/1h did not result in significant differences observed in the post-fire reduction of impact strength.

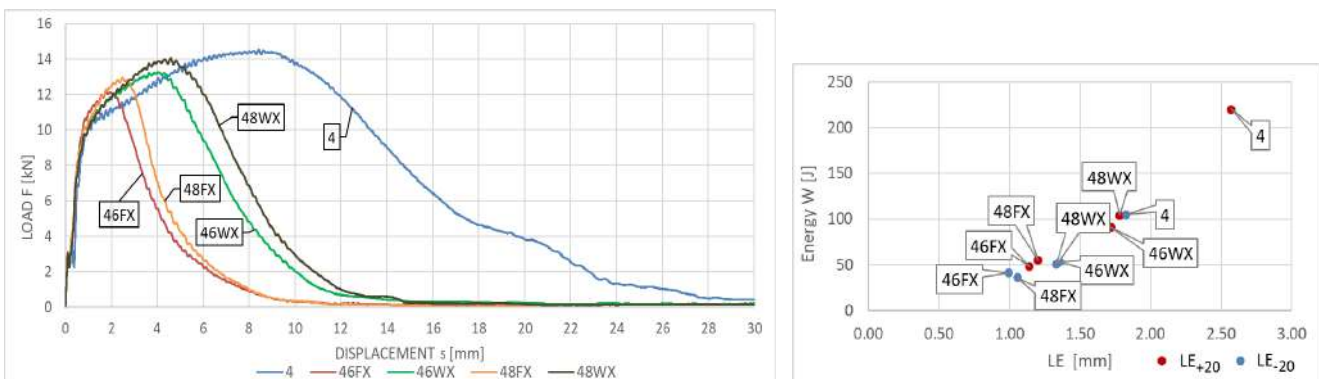


Figure 12. At left: F - s curves obtained during post-fire impact strength tests on samples made of $X2CrMnNi21-5-1$ steel following different testing scenarios. “Short” fire simulation. Testing temperature +20°C. At right: LE - W relationships determined on the same samples and analogous testing scenarios conducted at +20°C (red dots) and -20°C (blue dots), respectively

- Referring to the tests conducted at -20°C and “short” fire simulation (Fig. 12, graph at right, blue dots):
 - the tests conducted at -20°C resulted in the post-fire impact strength exhibited at a slightly lower level; however, this decrease was not as pronounced as in the case of reference samples (denoted as 4).
- Referring to the tests conducted at $+20^{\circ}\text{C}$ and “long” fire simulation (Fig. 13):
 - when the tested sample was heated at $600^{\circ}\text{C}/10\text{h}$, i.e. at the temperature which should be associated with the 475°C brittleness phenomenon, the beneficial influence of rapid cooling in water mist was in principle completely negated (the 46WY case), as a consequence the measured impact strength was close to the one determined earlier in the case of slow cooling inside furnace (the 46FY case),
 - the sample heating temperature of 800°C is not associated with the 475°C brittleness phenomenon, and thus the beneficial influence of rapid cooling in water mist was very pronounced (the 48WY case when compared against the 48FY case).

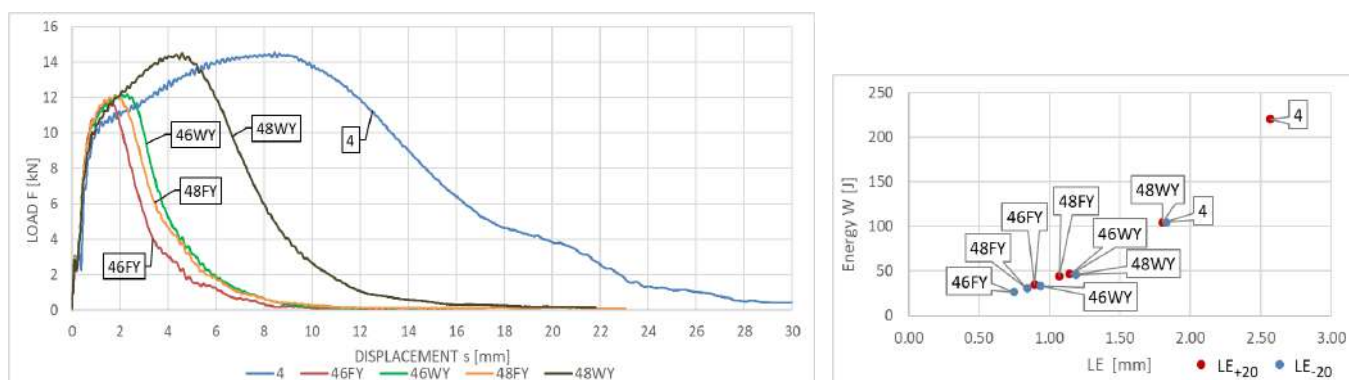


Figure 13. At left: F - s curves obtained during post-fire impact strength tests on samples made of $X2CrMnNiN21-5-1$ steel following different testing scenarios. “Long” fire simulation. Testing temperature $+20^{\circ}\text{C}$. At right: LE - W relationships determined on the same samples and analogous testing scenarios conducted at $+20^{\circ}\text{C}$ (red dots) and -20°C (blue dots), respectively

- Referring to the tests conducted at -20°C and “long” fire simulation (Fig. 13, graph at right, blue dots):
 - the tests conducted at -20°C resulted in slightly lower post-fire impact strength when compared against the results of tests conducted at $+20^{\circ}\text{C}$ (similarly to the “short” fire, the difference observed on samples subjected to the “long” fire scenario was not as pronounced as the one observed on reference samples (denoted as 4)).

6 CONCLUSIONS

In this paper we tried to demonstrate the usefulness of F - s curves obtained experimentally, on samples made of steel, which has survived a fire incident, in instrumented Charpy impact tests in predicting the forecast brittleness in the context of its suitability for prolonged service after fire. In such approach the shape of the F - s curve is correlated with unstable growth and weakly inhibited coalescence of microcracks appearing in the sample, and thus informs the examiner on the risk of brittle failure, that is failure appearing suddenly and not preceded by the signs of imminent danger. Should the thus determined fracturing energy of tested material, constituting the measure of its post-fire impact strength, prove to be close to zero, the material would have to be replaced as the failure risk of keeping it in prolonged service would become unacceptably high.

The samples tested in our experiments yielded F - s curves of varied nature. In general, though not in each case, their shape indicated predominantly plastic fracturing mode. Nevertheless, in each of testing scenarios followed, a very significant change in the impact strength observed post fire, regardless of the simulated fire duration, has been observed when compared against the impact strength exhibited by the material in the as delivered state. The degree of change was affected by not only the temperature and heating time but also by the manner the material was cooled after heating.

A very strong correlation between the results obtained and the microstructure specific for each steel grade has been shown during experiments. Post-fire properties of the samples proved to be a result of permanent structural changes induced in the tested material by a simulated fire episode affecting it. Usually the longer fire exposure allowed for more pronounced disclosure of these influences, in general not observed on samples subjected to the “short” fire scenario. The precipitates of various types decreasing impact strength of tested steel seem to be of particular importance here.

REFERENCES

1. Kharchenko V.V., Kondryakov E.A., Zhamaka V.N., Babutskii A.A., Babutskii A.I., The effect of temperature and loading rate on the crack initiation and propagation energy in carbon steel Charpy specimens, *Strength of Materials*, 38, 5, 535–541, (2006), <https://doi.org/10.1007/S11223-006-0073-Y>.
2. Mirmomeni M., Heidarpour A., Xiao-Ling Zhao, Hutchinson C.R., Packer J.A., Chengqing Wu, Fracture behaviour and microstructural evolution of structural mild steel under the multi-hazard loading of high-strain-rate load followed by elevated temperature, *Construction and Building Material*, 122, 760–771, (2016), <http://dx.doi.org/10.1016/j.conbuildmat.2016.06.122>.
3. Yazhi Zhu, Shiping Huang, Sajid H.U., Micro-mechanisms and modelling of ductile fracture initiation in structural steel after exposure to elevated temperatures. *Metals*, 11, 767, (2021), <https://doi.org/10.3390/met11050767>.
4. Kai Ye, Ozaki F., Impact fracture energy of steel welded connections in fire and post-fire, *Journal of Constructional Steel Research*, 170, 106120, (2020), <https://doi.org/10.1016/j.jcsr.2020.106120>.
5. Kai Ye, Ozaki F., Knobloch M., Impact fracture energies of cold-formed steel square hollow section in and after fire, *Journal of Constructional Steel Research*, 183, 106740, (2021), <https://doi.org/10.1016/j.jcsr.2021.106740>.
6. Maslak M., Pazdanowski M., Stankiewicz M., Zajdel P., Post-fire susceptibility to brittle fracture of selected steel grades used in construction industry – assessment based on the instrumented impact test, *Materials*, 14, 3922, (2021), <https://doi.org/10.3390/ma14143922>.
7. Maslak M., Pazdanowski M., Stankiewicz M., Wassilkowska A., Zajdel P., Zielina M., Impact fracture surfaces as the indicators of structural steel post-fire susceptibility to brittle cracking, *Materials*, 16, 3281, (2023), <https://doi.org/10.3390/ma16083281>.
8. Pancikiewicz K., Maslak M., Pazdanowski M., Stankiewicz M., Zajdel P., Changes in the microstructure of selected structural alloy steel grades identified after their simulated exposure to fire temperature, *Case Studies in Construction Materials*, 18, e01923, (2023), <https://doi.org/10.1016/j.cscm.2023.e01923>.
9. EN-ISO 148-1, Metallic materials – Charpy pendulum impact test, Part 1: Test method, 2006.
10. EN-ISO 14556, Metallic materials – Charpy V-notch pendulum impact test, Instrumented test method, 2015.
11. ASTM E 2298-18, Standard test method for instrumented impact testing of metallic materials, 2018, <https://doi.org/10.1520/E2298-18>.
12. ASTM E 23-92, Standard test methods for notched bar impact testing of metallic materials, 2016. <https://doi.org/10.1520/E0023-18>.
13. Sreenivasan R. Charpy energy – lateral expansion relations for a wide range of steels, *International Journal of Pressure Vessels and Piping*, 83, 498–504, (2006), <https://doi.org/10.1016/j.ijpvp.2006.03.002>.
14. EN 10025-2, Hot rolled products of structural steels, Part 2: Technical delivery conditions for non-alloy structural steels.
15. EN 10088-1, Stainless steels, Part 1: List of stainless steels.

DEEP LEARNING-DRIVEN REAL-TIME PREDICTION OF FIRE-INDUCED COLLAPSE OF STEEL PORTAL FRAMES

Wei Ji¹, Guo-Qiang Li², Shaojun Zhu³, Yong Du⁴, Liu Zhi⁵, Zongjun Xia⁶, Zhifei Chen⁷

ABSTRACT

This paper presents an innovative method for real-time prediction of fire-induced collapse time of steel portal frames, a structural type commonly used yet prone to collapse, to help firefighters. The thermal deep learning (DL) model, trained offline through simulated data acquired from classical fire parametrical models and field simulation, learns the correlation between fire states and gas temperatures. The trained model can implicitly identify fire uncertainties and forecast gas temperature developments through measured gas temperatures and frame dimensions. The structural DL model, trained with data from thermal-structural coupled analysis, learns the mapping relationship between gas temperatures and joint displacements. The trained model can implicitly identify structural uncertainties and predict displacement developments through measured structural responses and both measured and predicted gas temperatures. For a real fire test, the thermal DL model makes temperature predictions with an accuracy exceeding 94.8%, while the structural DL model makes displacement predictions with a determination coefficient exceeding 0.78. The collapse time of the test frame was successfully predicted based on predicted displacements with a prediction error of less than 90 seconds. The proposed method offers firefighters clear insights into the collapse risk of the burning frame, thereby enhancing smart firefighting strategies.

Keywords: smart firefighting, deep learning, gas temperature prediction, frame displacement prediction, parameter identification

1 INTRODUCTION

Building fires results in significant economic and social losses, with firefighters playing a crucial role in mitigating these losses and rescuing occupants. Statistics indicate that the unexpected collapse of burning buildings is a major hazard for firefighters [1], as it is tough to accurately and reliably predict the collapse risk in real time. This is especially the case for large-span building structures such as steel portal frames,

¹ Dr, Tongji University

e-mail: weiji@tongji.edu.cn, ORCID: <https://orcid.org/0000-0001-7423-6612>,

² Professor, Tongji University

e-mail: gqli@tongji.edu.cn,

³ Dr, Tongji University

e-mail: zhushaojun@tongji.edu.cn,

⁴ Dr, Tongji University

e-mail: yongdu_mail@tongji.edu.cn,

⁵ Dr, Tongji University

e-mail: zliu@tongji.edu.cn,

⁶ Mr, China Railway 15th Bureau Group Co., Ltd

e-mail: 1120205123@tju.edu.cn,

⁷ Dr, China Railway 15th Bureau Group Co., Ltd

e-mail: 1913494667@qq.com

due to their low structural redundancy and severe degradation of the material properties of steel at elevated temperatures [2].

Traditionally, firefighters estimate the collapse risk of the burning building through empirical observations on key parameters, such as fire duration time or deformation of key components. These parameters have close relationships with the collapse state, while the relationships are complex and highly affected by the fire and structural states of the burning building. Therefore, a more scientific and accurate method is needed to help firefighters predict fire-induced building collapse in real time, thus reducing fire-related losses and improving firefighting efficiency. With the boom of artificial intelligence (AI) and the Internet of Things (IoT), smart firefighting has been a hot topic for researchers [3, 4]. Based on AI, much research has been conducted on the identification of fire parameters [5, 6] and the prediction of temperature developments [7, 8]. However, most of these findings focus on compartment fires, which are confined to small, enclosed spaces within a building.

In addition, the displacement of key joints is the most direct way to judge the collapse risk, as the collapse of the building is determined by unacceptable deformations [9, 10]. However, current research focuses more on calculating the current displacements based on measured data, rather than predicting the displacement development [11–13]. Moreover, most research calculates displacements based on the structural model in fire safety design, yet real burning buildings present many uncertainties such as load levels and material properties of steel, which usually differ from the design values [14, 15]. These uncertainties significantly affect the collapse behaviour of the burning building structure, and they are challenging to assess on site, thus complicating the prediction of fire-induced displacement.

This paper presents a real-time prediction method for the fire-induced collapse of steel portal frames. The framework employs two deep learning (DL) models, i.e., the thermal DL model and the structural DL model, to cope with the uncertainties of the burning frame and further predict the displacement developments through on-site measured fire and structural responses. The thermal DL model learns the correlation between fire states and gas temperatures and makes temperature predictions based on reliability theory. The structural DL model learns the mapping relationship between gas temperatures and joint displacements and makes displacement predictions after identifying structural uncertainties. These two DL models are validated using a real fire collapse test of a steel portal frame. The successful prediction of displacement progression and the estimation of the remaining collapse time prove their potential in real fire rescue operations.

2 DL FRAMEWORK

2.1 Problem description

Traditional fire safety design evaluates the fire resistance of the designed building based on known structures under standard fires, while a real burning building contains uncertain fire and structural states. The fire state, including fire locations and fire intensity, affects the gas temperature inside the burning building, while the structural state, including load levels and material properties, influences the collapse behaviour under fire. Meanwhile, on-site measured data regarding thermal and structural responses will contain information about the fire and structural state.

Moreover, the fire inside the burning building causes the gas temperatures to increase, which will further heat the steel components, thus leading to thermal expansion and other structural responses. These processes can be simulated using fire dynamic analysis, heat transfer analysis, and thermo-mechanical coupling analysis within computational fluid dynamics (CFD) and finite element (FE) models, which establish the mathematical relationships between fire state, gas temperatures, steel temperatures, and structural responses.

Therefore, the fire-induced collapse of the burning frame can be predicted by analyzing displacements at key joints induced by thermal action. The real fire state and structural state of the burning frame can be identified using data from on-site measurements of fire and structural responses. Then the development of gas temperatures is predicted based on identified fire states, while displacement development is predicted

based on identified structural states and predicted gas temperatures. To achieve this goal, this paper adopts two models, namely the thermal model to deal with implicit fire state identification and gas temperature prediction, and the structural model to deal with implicit structural state identification and key displacement prediction. Deep learning techniques are adopted in the models, as they can give real-time prediction results once properly trained, thus fulfilling the urgent needs of fire rescue operations.

2.2 DL model architecture

The long short-term memory (LSTM) layers [14] coupled with fully-connected (FC) layers were adopted to form the DL models. A sliding window is used to segment the input time-series data, with a time length Δt . Figure 1 shows the architecture of the thermal DL model which identifies fire states and predicts gas temperature developments through measured gas temperatures and geometry dimensions of the burning frame. Figure 2 shows the architecture of the structural DL model, which identifies structural states and predicts displacement developments through measured data and predicted gas temperatures.

In Figure 1 & Figure 2, n_{th} represents the number of gas temperatures, n_{md} is the number of key displacements, n_g is the number of known geometry parameters, n_f is the number of identified fire parameters, n_τ is the number of confidence levels, and these parameters are pre-defined for a specific structure. Parameter n_b refers to the batch size utilized for each training iteration, n_h refers to the size of the hidden state of each layer, and these parameters are set as hyperparameters that require tuning based on the training performance. t represents the time length of the training sample and is typically considered a fixed value in model training. In practical applications, however, t denotes the duration of the fire, which increases as ongoing measurements are taken.

At the fire-induced building collapse forecasting scene, the thermal DL model and structural DL model are combined, as depicted in Figure 3, to enhance prediction capabilities. To achieve extended time-duration prediction, the predicted gas temperatures not only serve as inputs of the structural DL model, but also iteratively feed back into the thermal DL model, thus allowing for continuous updating and refinement of the predictions.

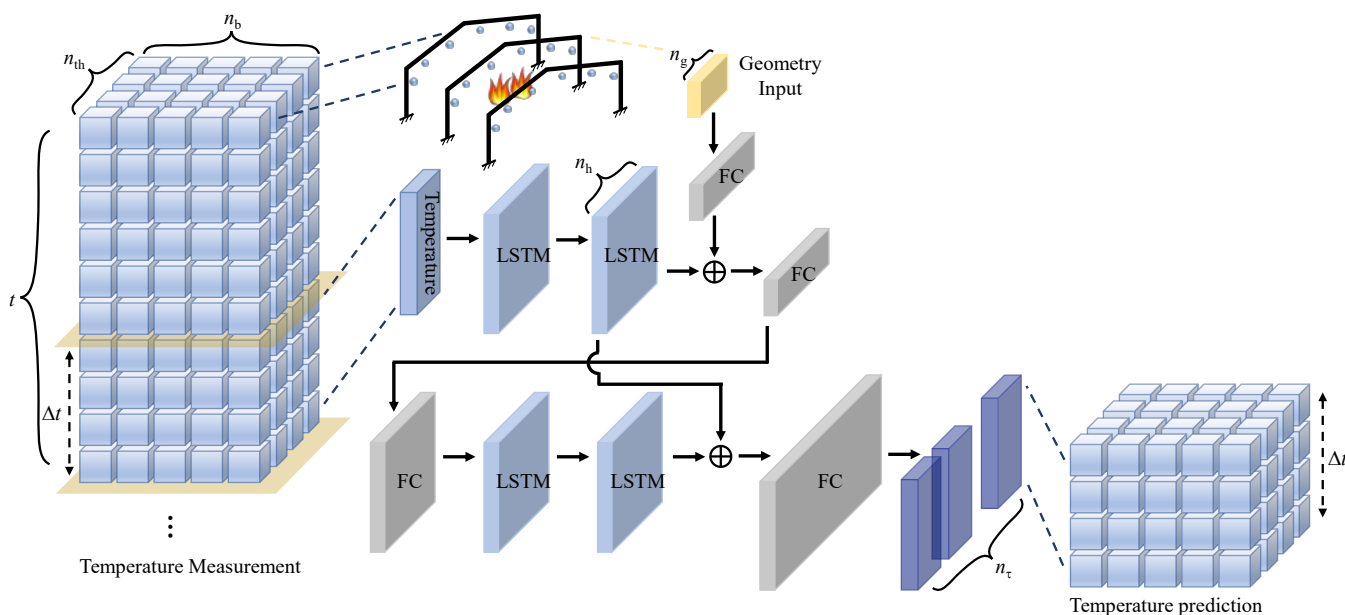


Figure 1. Architecture of thermal DL model

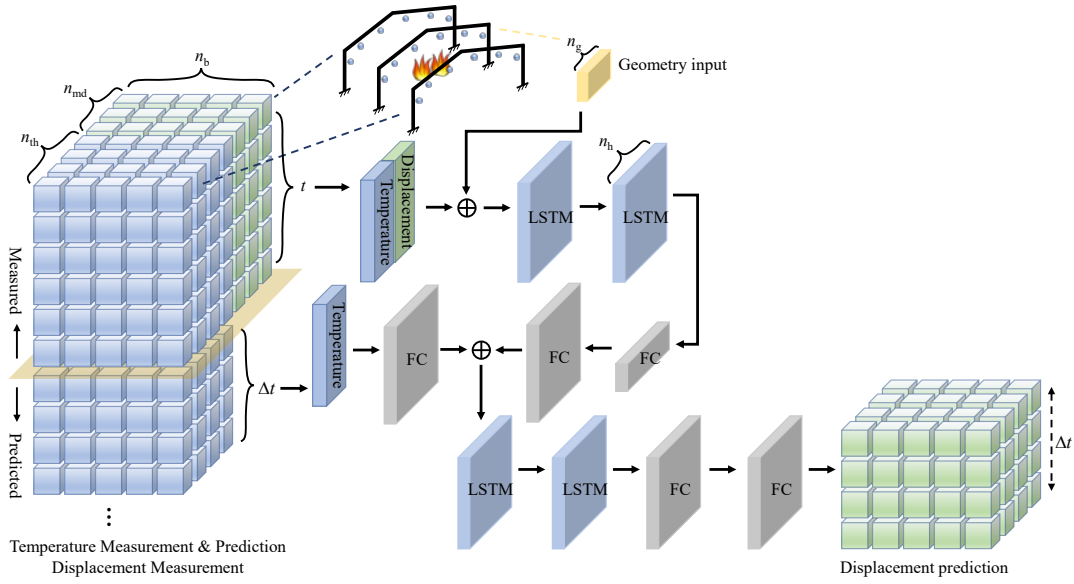


Figure 2. Architecture of structural DL model

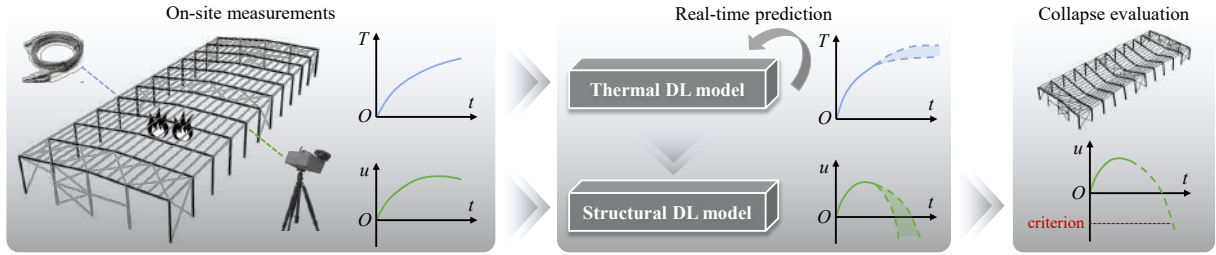


Figure 3. Architecture of structural DL model

2.3 Loss function

The randomness of fire development, which arises from the high nonlinearity of the fire combustion process and the uncertainties of its surroundings, will make the fire state change continuously with time. In the thermal deep learning model, the prediction of gas temperatures is based on the currently identified state of the fire. However, these predictions also encompass uncertainties due to the indeterminacy of future fire states. Therefore, the gas temperature development was predicted based on reliability theory, and quantile loss (QL) functions were chosen to make predictions under a specific confidence level:

$$L_1^\tau = \begin{cases} \frac{1}{\Delta t \cdot n_{th}} \sum_{t=t_0}^{t_0+\Delta t} \sum_{i=1}^{n_{th}} \left[\tau \cdot (T_i^{(t)} - \hat{T}_i^{(t)}) \right] & y_i^{(t)} \geq \hat{y}_i^{(t)} \\ \frac{1}{\Delta t \cdot n_{th}} \sum_{t=t_0}^{t_0+\Delta t} \sum_{i=1}^{n_{th}} \left[(\tau - 1) \cdot (T_i^{(t)} - \hat{T}_i^{(t)}) \right] & y_i^{(t)} < \hat{y}_i^{(t)} \end{cases} \quad (1)$$

where $T_i^{(t)}$ and $\hat{T}_i^{(t)}$ denote the actual and predicted i th temperature at the t th time step, respectively. $\tau \in (0,1)$ is the confidence level, in which case $\tau = 80\%$ means the actual value has an 80% probability of being less than the predicted value. When multiple confidence levels are set in the ML model, an average QL loss can be calculated as

$$L_1 = \frac{1}{n_\tau} \sum_{\tau} L_1^\tau \quad (2)$$

in which n_τ is the number of confidence levels.

For the structural DL model, the loss function L_2 relates to the displacements and velocities to improve the prediction accuracy of large deformations when the frame is about to collapse:

$$L_2 = \frac{1}{\Delta t \cdot n_{\text{md}}} \sum_{t=t_0}^{t_0+\Delta t} \sum_{j=1}^{n_{\text{md}}} \left| \left(u_j^{(t)} - \hat{u}_j^{(t)} \right) \left(v_j^{(t)} - \hat{v}_j^{(t)} \right) \right| \quad (3)$$

where $y_i^{(t)}$ and $\hat{y}_i^{(t)}$ denote the actual and predicted i th displacement at the t th time step, respectively. After calculating the training loss at each training epoch, the network parameters of the DL models are updated using the Adam optimization algorithm [17].

3 NUMERICAL EXAMPLE

3.1 Dataset preparation

The proposed method was illustrated through numerical examples of building fires occurring in single-span steel portal frames, as shown in Fig. 4. To ensure the method's adaptability to the frames, the geometry, structural, and fire parameters of the burning frame were treated as random variables with uniform distributions, as shown in Table 1.

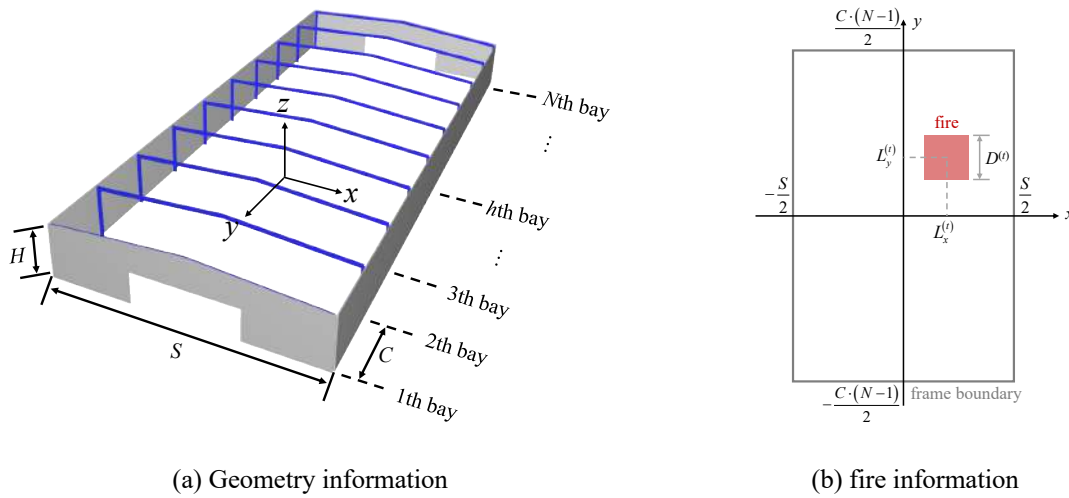


Figure 4. Layout of a typical steel portal frame

Table 1. Parameters of the burning frame

	Random variables	Potential values
Geometry parameters	Span (S)	{12, 15, 18, 21, 24, 27, 30, 33, 36} m
	Eaves height (H)	{6, 7, 8, 9, 10, 11, 12} m
	Column spacing (C)	{6, 7.5, 9} m
	Number of bays (N)	{7, 8, 9, 10, 11}
Fire parameters	Initial fire location ($L_{x,0}$)	$[-0.75, 0.75] \cdot S / 2$
	Initial fire location ($L_{y,0}$)	$[2-N, -2+N] \cdot C / 2$
	fire moving velocity (v_c)	$\pm [0.01, 0.1]^2 \text{ m}\cdot\text{s}^{-1}$
	fire moving direction (I_c)	{0, -1, +1}
	fire start moving time ($t_{c,s}$)	[0, 1800] s
	fire moving duration ($t_{c,m}$)	[0, 1800] s
	heat release rate per area (Q^0)	[200, 1000] kW/m ²
	fire initial side length (D^0)	[0, 2] m
	fire expand velocity (v_d)	$[1, 10]^2 \times 0.002 \text{ m}\cdot\text{s}^{-1}$
	fire moving duration (t_d)	[1200, 3600] s

Table 1. Parameters of the burning frame (cont.)

Structural parameters	thickness of fire-resistant coating (d)	[10, 50] mm
	thermal conductivity of coating (λ)	[0.09, 0.12] W/(m·°C)
	sections of steel components	3 types according to design codes
	vertical load level (q)	[0.3, 0.5] q_u
	yield strength of steel (f_y)	[0.9, 1.1] $f_{y,d}$
	ultimate strength of steel (f_u)	[0.9, 1.1] $f_{u,d}$

For the thermal DL model, the training dataset can be generated by classical fire models, such as the McCaffery fire model [17], and fire dynamic analysis in FDS, using the geometry and fire parameters acquired from Table 1. At fire exposure time t , the location of the fire centre can be calculated as:

$$L_c^{(t)} = \begin{cases} L_c^0 & t < t_{c,s} \\ L_c^0 + I_x \cdot v_x \cdot (t - t_{c,s}) & t_{c,s} \leq t \leq t_{c,m} \\ L_c^0 + I_x \cdot v_x \cdot t_{c,m} & t > t_{c,m} \end{cases} \quad (4)$$

where c denotes the x or y direction, the definitions of other variables can be found in Table 1.

The fire surface is represented as a simplified square plane, which has an initial side length D^0 and a constant heat release rate per area Q^0 . At fire exposure time t , the heat release rate of the fire can be calculated as:

$$Q^{(t)} = \begin{cases} Q^0 \cdot (D^0 + v_d \cdot t)^2 & t < t_d \\ Q^0 \cdot (D^0 + v_d \cdot t_d)^2 & t \geq t_d \end{cases} \quad (5)$$

For the structural DL model, the training dataset will be generated by heat transfer analysis and thermo-mechanical coupling analysis performed in ABAQUS, utilizing the geometry and structural parameters from Table 1, as well as the simulated gas temperatures from the dataset for the thermal DL model.

The geometry dimensions of a constructed frame remain unchanged and can be readily available from design documents, thus serving as the inputs for both thermal and structural DL models:

$$\mathbf{g} = \{S, C, H, N\} \quad (6)$$

The gas temperatures and displacements at eaves can be measured in fire through pre-embedded thermocouples and on-site erected microwave radars, as shown in Figure 5. Therefore, the measured data $\mathbf{x}_h^{(t)}$ and $\mathbf{u}_h^{(t)}$ will serve as the inputs for thermal and structural DL models, respectively:

$$\mathbf{x}_h^{(t)} = \{T_{h,1}^{(t)}, T_{h,2}^{(t)}, \dots, T_{h,6}^{(t)}\} \quad (7)$$

$$\mathbf{u}_h^{(t)} = \{u_{h,1}^{(t)}, u_{h,2}^{(t)}\} \quad (8)$$

where $T_{h,i}^{(t)}$ represents the gas temperatures from the $(t - \Delta t + 1)$ th to the t th time step measured by the i th thermocouple ($i = 1, 2, \dots, 6$), $u_{h,j}^{(t)}$ represents the displacements from fire ignition to the t th time step measured by microwave radar ($j = 1, 2$).

The thermal DL model predicts the gas temperature developments based on the input matrix $[\mathbf{g}, \mathbf{x}_h^{(t)}]$:

$$\mathbf{x}_f^{(t)} = \{T_{f,1}^{(t)}, T_{f,2}^{(t)}, \dots, T_{f,6}^{(t)}\} \quad (9)$$

where $T_{f,i}^{(t)}$ represents the predicted time series data from the t th to the $(t + \Delta t)$ th time step of the i th thermocouple ($i = 1, 2, \dots, 6$).

The structural DL model predicts the displacement developments based on the input matrix $[\mathbf{g}, \mathbf{x}_h^{(t)}, \mathbf{u}_h^{(t)}]$:

$$\mathbf{u}_f^{(t)} = \{u_{f,1}^{(t)}, u_{f,2}^{(t)}, \dots, u_{f,5}^{(t)}\} \quad (10)$$

where $u_{f,j}^{(t)}$ represents the predicted displacements from the t th to the $(t + \Delta t)$ th time step ($j = 1, 2, \dots, 5$).

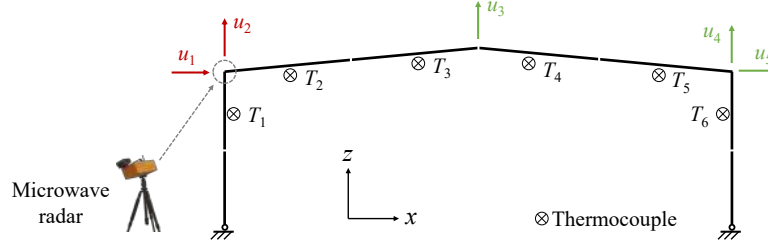


Figure 5. Measurement of gas temperatures and displacements

3.2 Evaluation criteria

At fire exposure time t_0 with a time prediction interval Δt_p , the prediction accuracy of the thermal DL model is evaluated by the relative error between real and predicted gas temperatures $\hat{T}_{f,i}^{(t)}$ under $\tau = 50\%$:

$$AC = 1 - \left| \frac{1}{\Delta t_p \cdot n_{th}} \sum_{t=t_0}^{t_0+\Delta t_p} \sum_{i=1}^{n_{th}} \frac{\hat{T}_{f,i}^{(t)} - T_{f,i}^{(t)}}{T_{f,i}^{(t)}} \right| \times 100\% \quad (11)$$

For the structural DL model, the prediction accuracy can be calculated by the coefficient of determination between the real and predicted displacements $\hat{u}_{f,j}^{(t)}$:

$$R^2 = \frac{1}{n_{md}} \sum_{j=1}^{n_{md}} \left(1 - \frac{\sum_{t=t_0}^{t_0+\Delta t_p} \left(\hat{u}_{f,j}^{(t)} - u_{f,j}^{(t)} \right)^2}{\sum_{t=t_0}^{t_0+\Delta t_p} \left(u_{f,j}^{(t)} - \bar{u}_{f,j} \right)^2} \right) \quad (12)$$

where $\bar{u}_{f,j}$ is the average value of j th displacement. A satisfactory prediction can be concluded when AC and R^2 approach 1.

3.3 Training and evaluation of DL models

Three datasets were generated for model training with a fire duration of 60 min: dataset A with 5000 samples generated by classical fire models, dataset B with 200 samples generated by FDS, and dataset C with 540 samples generated by ABAQUS. These datasets were split into three subsets respectively: the training subset, the validation subset, and the test subset, with ratios of 3: 1: 1. The training and validation subsets will be used for model pre-training to update the network parameters, while the test subset will serve as an entirely unknown dataset for evaluating the pre-trained agent.

The thermal DL model was first trained on dataset A, and the model with the lowest validation error was saved as the best model. Then the best model was transferred for further training using dataset B, where the network parameters of the output layer were updated while other layers were frozen. The window size Δt was set to 5 min. The confidence levels τ were taken as 5%, 50%, 80%, and 90%, respectively. A batch size of 512 was utilized, meaning that in each epoch, 512 samples from the training dataset were randomly selected to update the network parameters. The structural DL model was trained on dataset C with a batch size of 120. All the inputs and outputs of the DL models are scaled in the range of $[-1, 1]$ to enhance the agent's performance.

The model training was performed on a server equipped with an Intel(R) Core(TM) i7-12700k CPU running at 3.60 GHz, accompanied by an NVIDIA GeForce RTX 4090 GPU. Figure 6 shows the training history of the DL models.

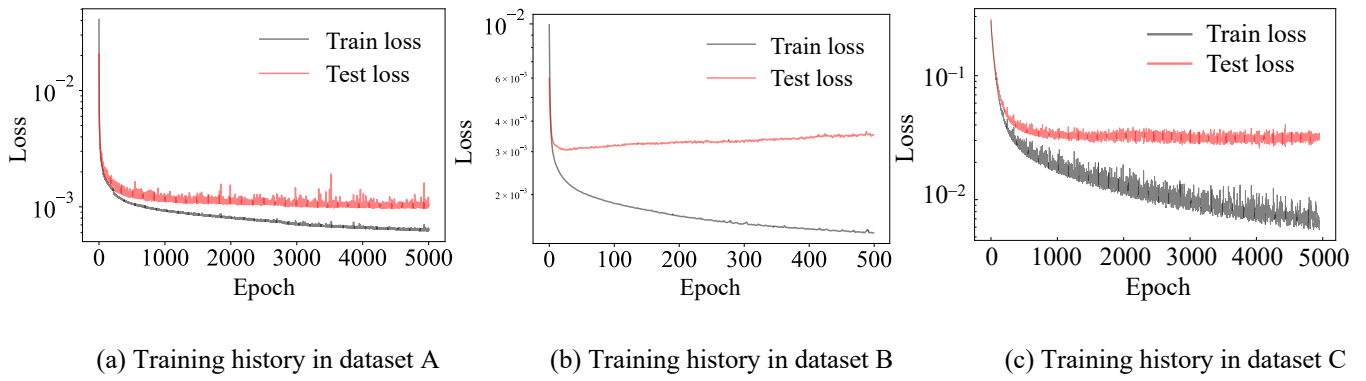


Figure 6. Training history of the DL models

For the thermal DL model, the test subset in dataset B was adopted to evaluate the performance of the trained agent, where an average prediction accuracy exceeding 91% was achieved. Figure 7 shows the temperature prediction results of the trained agent on a typical sample. For the structural DL model, the test subset in dataset C was adopted to evaluate the performances of the trained agent, where an average determination coefficient exceeding 0.8 was achieved. Figure 8 shows the displacement prediction results of the trained agent on a typical sample.

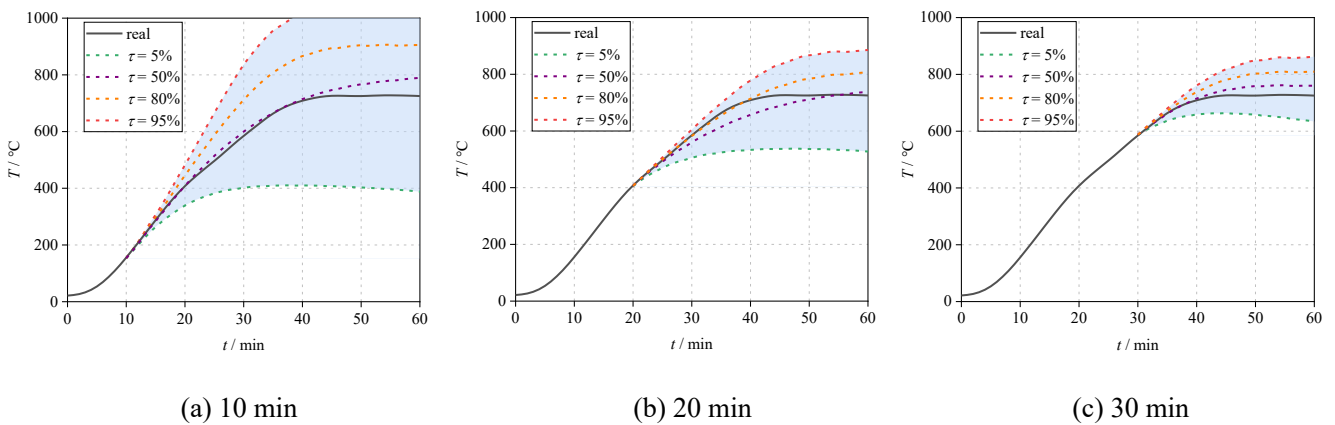


Figure 7. A typical case for temperature prediction of the thermal DL model

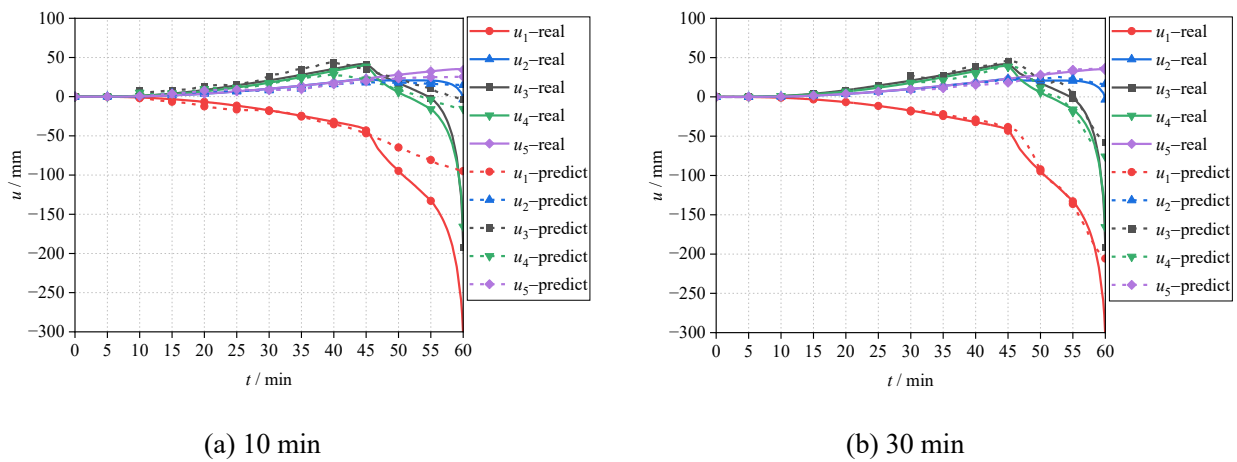


Figure 8. A typical case for displacement prediction of the structural DL model

4 EXPERIMENTAL VALIDATION

4.1 Fire test description

A real fire test was conducted by the authors on a steel portal frame, as shown in Figure 9. The test frame represented three bays from the actual structure, scaled down to 1:4 for simplification, with a span of 7 m, column spacing of 1.5 m, and eaves height of 1.75 m. Heptane was used as the fuel, with two oil trays arranged along the span. The gas temperatures near the heated columns and rafters were measured using thermocouples, as shown in Figure 10(a). The displacements of the apex and eaves were measured using microwave radars, as shown in Figure 10(b). More details of the fire test are available in the literature [18].

The measured data were fed into the trained thermal DL model and structural DL model. Since the test frame had large deformations under a fire exposure time of 5 min, the time scaling technique was adopted to ensure enough input length for the DL models. The smoothed gas temperature-time data and displacement-time data were extended by a ratio of 1:12 before they were fed into the DL models, and then the outputs were scaled in a ratio of 12:1 for comparison.

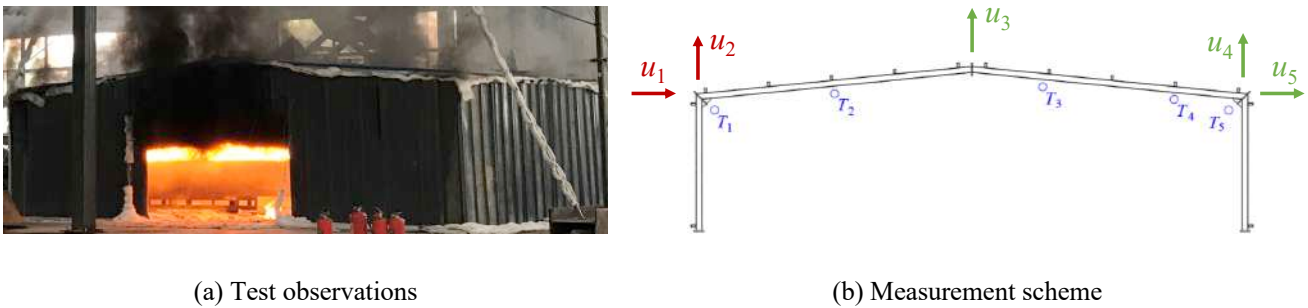


Figure 9. Fire test on a real portal frame

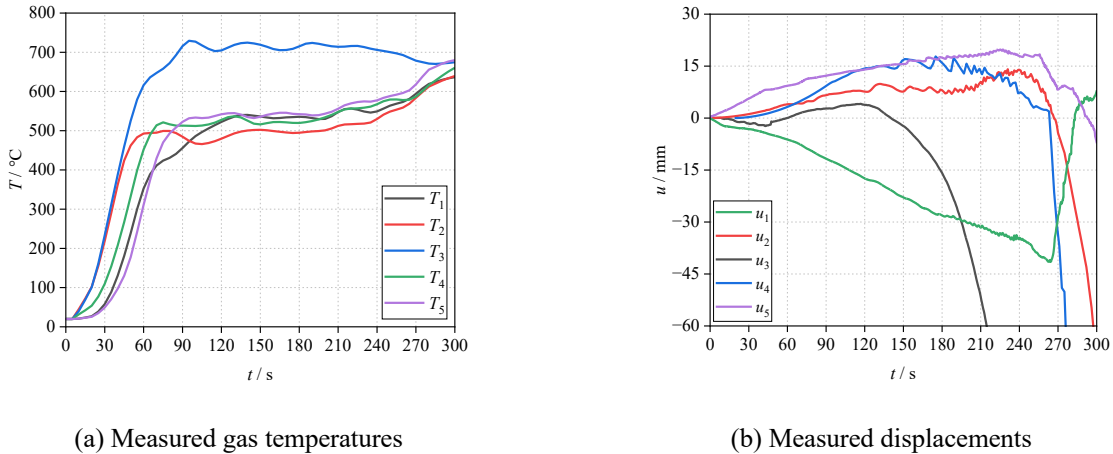


Figure 10. Measured gas temperatures and displacements

4.2 Performance of the thermal DL model

The geometric dimensions were inverse-scaled to match the real frame before being fed into the thermal DL model, and the geometry input was $\mathbf{g} = \{28, 6, 7, 5\}$. The gas temperature input for the test frame was constructed as $\mathbf{y}_0 = \{T_1, T_2, T_3, T_3, T_4, T_5\}$. Figure 11 shows the prediction results of maximum gas temperatures at different fire exposure times, where satisfactory temperature development predictions were achieved. The prediction accuracy is 94.8% and 95.7% at fire exposure times of 1 min and 2.5 min, respectively. The prediction error primarily arises from the size effect and the discrepancy between the thermocouple positions used during the experimental setup and those in the model training.

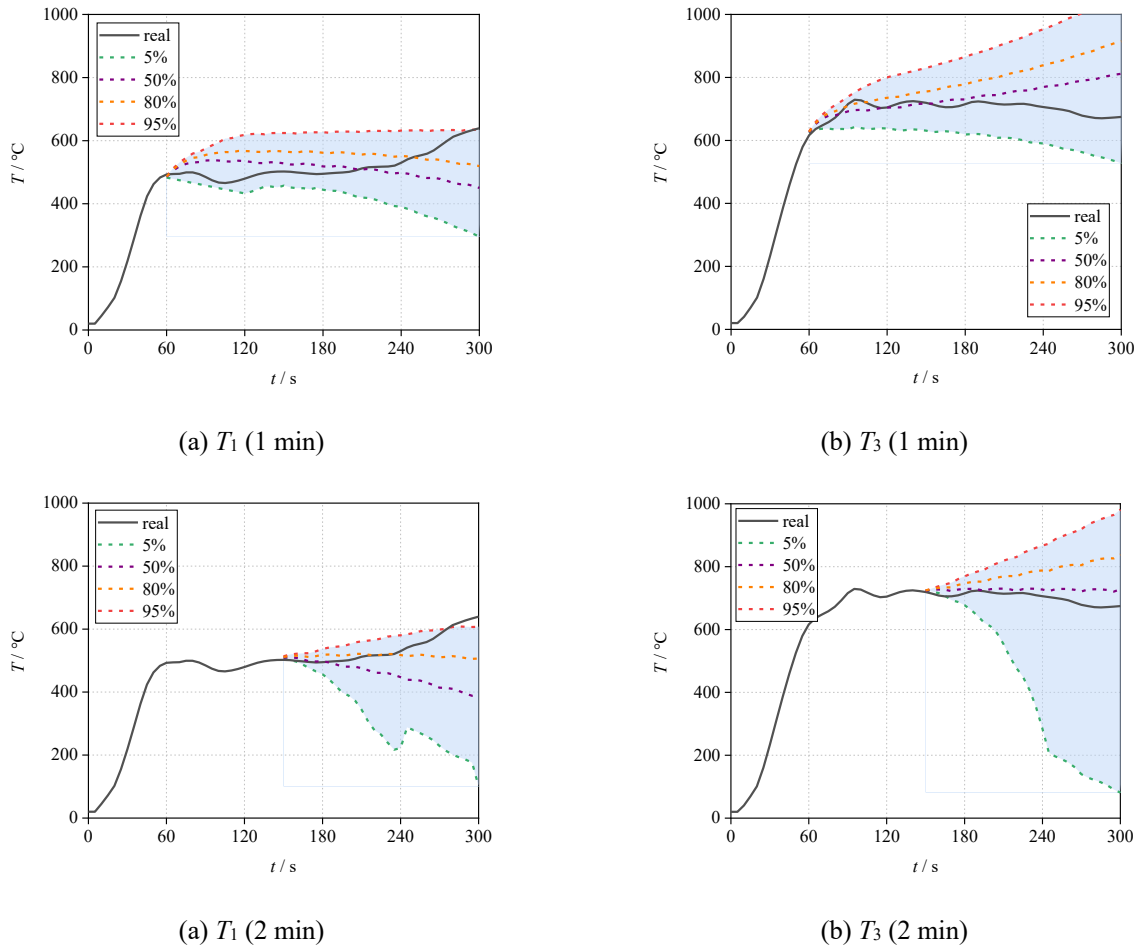


Figure 11. Comparison between predicted and real gas temperatures

4.3 Performance of the structural DL model

The measured gas temperatures and displacements, together with the geometric dimensions, were fed into the structural DL model. Figure 12 shows the predicted displacements at different fire exposure times, where a satisfactory prediction was achieved. The evaluation index R^2 is 0.79 at fire exposure time of 1 min and 0.90 at 2.5 min. The prediction accuracy increases with the fire exposure time, as the abundance of measured responses enhances the identification of the actual structural state over time.

At different fire exposure times, the collapse time of the burning frame can be predicted by the time at which the displacement exceeds the collapse criterion. For this fire test, the allowable deformation was set as 1/20 of the frame's span, and the collapse time of the frame was 310 s. Based on the predicted displacements, the remained collapse time was predicted at fire exposure times of 1 min and 2 min, as shown in Table 2. When the predicted gas temperatures from Figure 11 were used as inputs, the displacements predicted the structural DL model would have the same level of confidence as the temperature predictions, and the predicted remained collapse times are presented in Table 2.

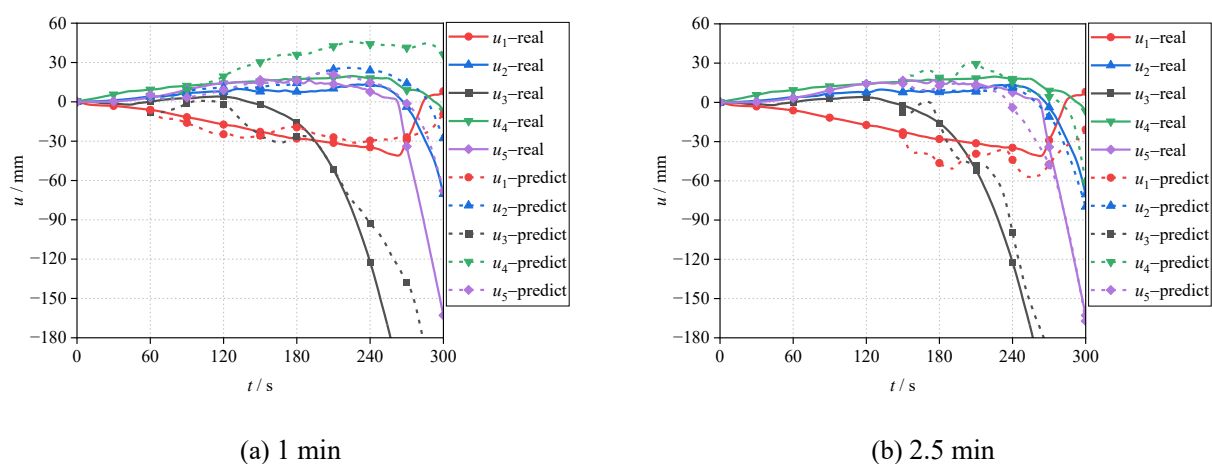


Figure 12. Comparison between predicted and real displacements

Table 2. Collapse prediction results and errors of the test frame

Fire exposure time	Real remained collapse time	Predicted remained collapse time using different temperature inputs		
		Measured temperature	Predicted temperature, $\tau=50\%$	Predicted temperature, $\tau=80\%$
60 s (1 min)	250 s	280 s (+30 s)	340 s (+90 s)	172 s (+78 s)
150 s (2.5 min)	160 s	184 s (+24 s)	148 s (-12 s)	133 s (-27 s)

5 CONCLUSIONS

This paper proposes a real-time prediction method for the fire-induced collapse of steel portal frames. It predicts the gas temperature development and displacement development of the burning frame based on measured thermal and structural responses using pre-trained DL models. The collapse time of the burning frame can be predicted by comparing the predicted displacements with the maximum allowable deformations. The following findings can be concluded:

- (1) The thermal DL model can implicitly identify fire states based on measured gas temperatures and predict the development of these temperatures from the identified fire state. Similarly, the structural DL model can implicitly identify structural states based on measured gas temperatures and displacements, and then predict the displacement development from the identified structural state and the predicted gas temperatures.
- (2) For a real fire test, the trained agent of the thermal DL model can predict temperature developments with an accuracy exceeding 94.8%, while the trained agent of the structural DL model can predict displacement developments with a determination coefficient exceeding 0.79.
- (3) The collapse time of the burning frame can be predicted by comparing the predicted displacements to a predetermined displacement-based collapse criterion. A prediction error of no more than 90 seconds was achieved for predicting the collapse time of the test frame.

REFERENCES

1. Kang, R., Fu G. & Yan J., Analysis of the case of fire fighters casualties in the building collapse. *Procedia Eng* 135, 343-348 (2016). <https://doi.org/10.1016/j.proeng.2016.01.140>.
2. Moss, P., J., Dhakal, R., P., Bong, M., W. & Buchanan, A., H., Design of steel portal frame buildings for fire safety. *J. Constr. Steel Res*, 65(5), 1216–1224 (2009). <https://doi.org/10.1016/j.jcsr.2008.09.003>.
3. Zeng, Y., Li, Y., Du, P. & Huang, X., Smart fire detection analysis in complex building floorplans powered by GAN. *J. Build* 79(15), 107858 (2023). <https://doi.org/10.1016/j.jobe.2023.107858>.

4. Wang, Y., Zheng, R., Hou, L., Li, M. & Li, W., A novel IoT-based framework with prognostics and health management and short term fire risk assessment in smart firefighting system. *J. Build* 78(1), 107624 (2023). <https://doi.org/10.1016/j.jobe.2023.107624>.
5. Huang, P., Chen, M., Chen, K., Zhang, Hao. & Yu, L., A combined real-time intelligent fire detection and forecasting approach through cameras based on computer vision method. *Process Saf Environ* 164, 629–638 (2022). <https://doi.org/10.1016/j.psep.2022.06.037>.
6. Price, M., Marshall, A. & Trouvé, A., A Multi-observable Approach to Address the Ill-Posed Nature of Inverse Fire Modeling Problems. *Fire Technol* 52, 1779–1797 (2016). <https://doi.org/10.1007/s10694-015-0541-7>.
7. Lin, CC., Wang, L. Real-Time Forecasting of Building Fire Growth and Smoke Transport via Ensemble Kalman Filter. *Fire Technol* 53, 1101–1121 (2017). <https://doi.org/10.1007/s10694-016-0619-x>.
8. Mozaffari, M., H., Li, Y. & Ko, Y., Real-time detection and forecast of flashovers by the visual room fire features using deep convolutional neural networks, *J. Build* 64(1), 105674 (2023). <https://doi.org/10.1016/j.jobe.2022.105674>.
9. Li, G., Ji, W., Feng, C., Wang, Y. & Lou G., Experimental and numerical study on collapse modes of single span steel portal frames under fire. *Eng Struct* 245(15), 112968 (2021). <https://doi.org/10.1016/j.engstruct.2021.112968>.
10. Jiang, J., Wang, C., Lou, G. & Li, G., Quantitative evaluation of progressive collapse process of steel portal frames in fire. *J. Constr. Steel Res* 150, 277–287 (2018). <https://doi.org/10.1016/j.jcsr.2018.08.020>.
11. Ji, W., Zhu, S., Li, G. & Chen, B., Synchronous Displacement Acquisition Approach for Early Warning of Fire-induced Collapse of Steel Portal Frames. *Fire Technol* 59, 1613–1645 (2023). <https://doi.org/10.1007/s10694-023-01395-7>.
12. Li, J., Li, G. & Zhu, S., FAST-AlertNet: Early warning fire-induced collapse of large-span steel truss structures. *Eng. Appl. Artif* 126, 106891 (2023). <https://doi.org/10.1016/j.engappai.2023.106891>.
13. Ye, Z., Hsu. S., Real-time prediction of structural fire responses: A finite element-based machine-learning approach. *Automat constr* 136, 104165 (2022). <https://doi.org/10.1016/j.autcon.2022.104165>.
14. Ji, W., Li, G. & Zhu, S., Real-time prediction of key monitoring physical parameters for early warning of fire-induced building collapse. *Comput Struct* 272, 106875 (2022). <https://doi.org/10.1016/j.compstruc.2022.106875>.
15. Ji, W., Li, G. & Lou, G., Early-warning methods for fire-induced collapse of single span steel portal frames. *J. Constr. Steel Res* 190, 107154 (2022). <https://doi.org/10.1016/j.jcsr.2022.107154>.
16. Kingma, D., P., Ba., J., Adam: A method for stochastic optimization. arXiv preprint (2014) <https://doi.org/doi.10.48550/arXiv.1412.6980>.
17. McCaffrey, B., J., Quintiere, J., G. & Harkleroad, M., F., Estimating room temperatures and the likelihood of flashover using fire test data correlations. *Fire Technol* 17, 98–119 (1981). <https://doi.org/10.1007/BF02479583>.
18. Li, G., Ji, W., Feng, C., Wang, Y., Experimental and numerical study on collapse modes of single span steel portal frames under fire. *Eng Struct* 245(15), 112968 (2021). <https://doi.org/10.1016/j.engstruct.2021.112968>.

DSM DESIGN FOR COLD-FORMED STEEL LIPPED CHANNEL BEAMS FAILING IN GLOBAL MODES UNDER FIRE CONDITIONS

Natan Sian das Neves¹, Alexandre Landesmann², Dinar Camotim³

ABSTRACT

Kankanamge and Mahendran [1,2] reported studies on the behaviour of cold-formed steel (CFS) simply supported lipped channel beams (LCB) failing in lateral-torsional (LT) modes at room and elevated temperatures. Their work revealed a clear underestimation of the LCB LT failure moments by the Direct Strength Method (DSM) global design curve (at room temperature) then codified in the Australian/New Zealand and North American specifications. To address this issue, these authors proposed novel DSM strength curves, found to substantially improve the LT failure moment prediction (room and elevated temperatures). This work aims at extending the scope of the previous studies, by analysing a larger LCB set at room and elevated temperatures (up to 800 °C), with (i) various geometries and yield stresses, covering wide LT slenderness ranges, (ii) two end support conditions, differing in the end cross-section warping and wall displacement/rotation restraints (free or fully prevented), and (iii) the Eurocode 3 (Part 1-2) model describing the temperature-dependent CFS material properties. The available results consist of beam LT post-buckling equilibrium paths and failure moments, obtained from ABAQUS shell finite element (SFE) GMNIA with critical-mode (LT) initial geometrical imperfections. The numerical failure moments obtained in this work and in [1,2] are then used to assess the merits of the available DSM global strength curves, a first step towards the final goal of finding an efficient DSM design approach for CFS LCB failing in LT modes at room and elevated temperatures.

Keywords: Cold-formed steel beams; Room and elevated temperatures; Global (lateral-torsional) post-buckling behaviour; Lateral-torsional failure; Shell finite element analysis; Direct Strength Method (DSM) design.

1 INTRODUCTION

CFS structures provide flexible design solutions, due to their fabrication adaptability, structural efficiency and cost-effective production/erection processes – but these advantages come with a trade-off, as CFS members have slender thin-walled open cross-sections, rendering them prone to instability phenomena (local, distortional, global buckling). To address the high buckling susceptibility, design specifications include provisions against the associated failures – e.g., the Direct Strength Method (DSM [3]), adopted by the North American [4] and Australian/New Zealand [5] CFS specifications. In this study, its relevant codified design curve (at room temperature) is the global one, given by

$$M_{nG} = \begin{cases} M_p - (M_p - M_y)[2.70(\lambda_G - 0.23)] & \lambda_G \leq 0.60 \\ \frac{10}{9} M_y \left(1 - \frac{10}{36} \lambda_G^2\right) & 0.60 < \lambda_G < 1.336 \\ M_y \lambda_G^{-2} & \lambda_G \geq 1.336 \end{cases} \quad \text{with} \quad \lambda_G = \sqrt{\frac{M_y}{M_{crG}}} \quad , \quad (1)$$

¹ Ph.D student, Programa de Engenharia Civil, PEC/COPPE/UFRJ, Universidade Federal do Rio de Janeiro, Brasil.
e-mail: natan.neves@coc.ufrj.br, ORCID: <https://orcid.org/0000-0002-4679-0461>

² Full- Professor, Programa de Engenharia Civil, PEC/COPPE/UFRJ, Universidade Federal do Rio de Janeiro, Brasil.
e-mail: alandes@coc.ufrj.br, ORCID: <https://orcid.org/0000-0002-3974-5953>

³ Full-Professor (retired), CERIS, DECivil, Instituto Superior Técnico, Universidade de Lisboa, Portugal
e-mail: dcamotim@civil.ist.utl.pt, ORCID: <https://orcid.org/0000-0002-7994-2687>

where (i) M_{crG} and λ_G are the beam global critical buckling moment and slenderness, and (ii) M_y and M_p are the yield and plastic moments ($M_y = S \cdot \sigma_y$ and $M_p = Z$, where σ_y is the yield stress and S and Z are the cross-section elastic and plastic moduli). This design curve, originally codified about 40 years ago for hot-rolled steel beams [6, 7], comprises three branches, corresponding to low, intermediate and high slenderness. It was almost exclusively based on experimental and numerical studies regarding hot-rolled steel doubly symmetric I-section beams.

The studies on the LT behaviour and design of CFS “non doubly symmetric” beams are scarce (even at room temperature), when compared with those devoted to hot-rolled steel beams, which explains (at least partially) why Eq. (1), developed for hot-rolled steel beams, was adopted by the CFS specifications. At room temperature, it is worth mentioning experimental investigations [8-10], numerical simulations [11-13] and new design proposals against LT failures [14, 15]. At elevated temperature, to the authors’ best knowledge, the only available research work is due to Kankanamge and Mahendran [1, 2]. To assess the merits of Eq. (1) in predicting CFS beam failure moments, these authors [1] studied the behaviour of simply supported LCB under uniform major-axis bending. The beams involved in this numerical study had (i) global (LT) slenderness $0.73 \leq \lambda_G \leq 2.88$, (ii) critical-mode (LT) initial imperfections with $L/1000$ amplitudes (L – beam length) and (iii) “fork-type” end support conditions. After obtaining about 100 LCB numerical LT failure moments, it was found that almost all of them were overestimated by Eq. (1) – the few exceptions were stocky beams, thus extending the findings reported in [10, 13], for plain channel beams.

Kankanamge and Mahendran [1] proposed a novel DSM-based design curve that outperformed Eq. (1) in predicting simply supported LCB LT failure moments. This design curve, similar to the one in the current Australian/New Zealand hot-rolled steel structures code [16], has two branches (instead of 3) and reads (R stands for “reported”)

$$M_{nGR} = \begin{cases} M_y & \lambda_G \leq 0.60 \\ 0.9M_y \left[\sqrt{\lambda_G^4 + 2.05} - \lambda_G^2 \right] & \lambda_G > 0.60 \end{cases} \quad (2)$$

This design curve was shown to predict satisfactorily the available CFS LCB LT failure moments with all slenderness values – the numerical-to-predicted failure moment ratios, with mean and COV of 0.984 and 0.056, respectively, lead to a resistance factor $\phi = 0.892$, marginally below that recommended in [4, 5] for members in bending ($\phi_b = 0.9$). Even if [4, 5] allow accounting for the cross-section inelastic strength reserve, the above authors proposed a M_y plateau for low slenderness ($\lambda_G \leq 0.60$), thus limiting the cross-section resistance to its elastic capacity. It was also said that Eq. (2), with appropriate modifications to account for the temperature influence on the CFS constitutive law, can be used for LCB LT failures at elevated temperatures [2, 17] – this issue is discussed below.

In the context of CFS LCB failing in LT modes at elevated temperatures, Kankanamge and Mahendran [2] extended their previous SFE study [1] to account for elevated temperatures due to fire conditions. They performed an extensive parametric study to gather failure moment data (1060 LCB analysed). The numerical analyses, similar to those carried out in [1] for beams at room temperature, covered beams (i) geometries considered in [1] (ii) at 6 uniform temperatures (200°C to 700°C), and (iii) with three Ramberg-Osgood type experimentally-based CFS material properties at elevated temperatures proposed earlier in [17, 18].

To establish guidelines for the design of LCB failing in LT modes at elevated temperatures, Kankanamge and Mahendran [2] began by using the numerical LT failure moment data gathered to assess the adequacy of Eq. (2) – most performant DSM-based design curve available to handle LCB failures at room temperature (naturally, this design curve was modified to account for the temperature effects) – this approach was explored earlier by other authors [19, 20]. Since it was found in [2] that Eq. (2) yields scattered failure moment predictions in the intermediate slenderness range, they proposed a modification of Eq. (2), termed $M_{nGR,T}$, which reads

$$M_{nGR,T} = \begin{cases} M_{y,T} & \lambda_{G,T} \leq 0.60 \\ 0.9M_{y,T} \left(\frac{k_p}{k_y} \right)^{0.4} \left[\sqrt{\lambda_{G,T}^4 + 2.05 \left(\frac{k_p}{k_y} \right)^{-0.55}} - \lambda_{G,T}^2 \right] & \lambda_{G,T} > 0.60 \end{cases} \quad \text{with } \lambda_{G,T} = \sqrt{\frac{M_{y,T}}{M_{crG,T}}} \quad (3)$$

where (i) $M_{y,T}$ and $M_{crG,T}$ are the beam yield and critical global (lateral-torsional) moments at elevated temperatures, and (ii) k_p and k_y are the proportional limit and yield stress reduction factors reported in [17]. This modification led to failure moment predictions, for elevated temperatures (200-700°C), similar to those yielded by Eq. (2) for LCB

at room temperature: numerical-to-predicted failure moment ratios with mean and COV of 0.983 and 0.068, leading to $\phi=0.886$. This positive assessment prompted recommending Eq. (3) for CFS LCB at elevated temperatures.

Although it was shown in [2, 17] that the above DSM-based LT strength curves (Eqs. (2)-(3)) provide reasonably good failure moment estimates at room and elevated temperatures, it seems fair to argue that their validation procedures had a limited scope, since they involved only (i) one end support condition (“fork-type” supports, with free warping and local displacements/rotations) and (ii) one Ramberg-Osgood type CFS constitutive model at elevated model temperatures [17, 18] and (iii) 12 lipped channel beams with $0.54 \leq \lambda_{G,T} \leq 3.32$. Thus, the aim of this work is extending the scope of the previous study [2], by performing presenting a numerical investigation on the post-buckling behaviour, ultimate strength and DSM design of uniformly bent (about the major-axis) CFS simply supported LCB failing in LT modes at room and elevated temperatures. The beams analysed display (i) two end support conditions (in addition to that considered in [2], simple end supports fully preventing warping and local displacements/rotations – more details in Section 2) and (ii) the temperature-dependent CFS constitutive law based on Part 1-2 of Eurocode 3 (EC3:1-2 [21]) model, adopted in other CFS member numerical simulations (e.g., [20, 22]). Moreover, additional LCB failing in LT modes at room and elevated temperatures (up to 800°C) are analysed, with various geometries and room-temperature yield stresses, chosen to cover an LT slenderness range at least as wide as that in [2] ($0.54 \leq \lambda_{G,T} \leq 3.32$). As done in [2], all the numerical LT failure moments reported in this work (i) concern LCB containing critical-mode (LT) initial imperfections with amplitude $L/1000$ and (ii) are obtained from ABAQUS geometrically non-linear elastic-plastic analyses of beams with initial imperfections (GMNIA), adopting a shell finite element (SFE) model often used by the authors in the past (e.g., [20]).

2 BEAM GEOMETRY SELECTION – BUCKLING BEHAVIOUR

As done in previous studies (e.g., [20]), this work begins by selecting the geometries (cross-section dimensions and lengths) of the single-span CFS LCB to be analysed. Two end support conditions are considered, denoted here SCA and SCB (as in [3]), both simply supported with respect to major and minor-axis bending and having the end cross-section torsional rotations prevented – they differ in the fact that the end cross-section warping and local displacements and rotations are either free (SCA beams – unrestrained end cross-sections) or fully prevented (SCB beams – rigid plates attached to their end cross-sections) – Figs. 1(a)-(b) depict and show the differences between these two support conditions. The selection procedure involves sequences of buckling analyses, carried out in GBTUL [23] (based on Generalised Beam Theory – GBT) or ABAQUS (SFEA) to identify beams buckling and failing in “pure” LT modes – *i.e.*, such that the LT critical buckling moments are well below their local and distortional counterparts. The LCB selection procedure led to the 21 cross-section dimensions (b_w , b_f , b_l and t – see Fig. 1(c)) given in Table 1 – web-to-flange width ratios ranging from 1.5 to 3.75. This table also provides, for each cross-section, (i) the length associated with critical LT buckling (L_G), (ii) the corresponding critical (LT) buckling moment at room temperature (M_{crG}) and (iii) its ratios with respect to the lowest local (M_{crL}) and distortional (M_{crD}) buckling moments – all buckling moments calculated for $E_{20}=210$ GPa (steel Young’s modulus at room temperature) and $\nu=0.3$ (Poisson’s ratio, assumed independent of the temperature). The $M_{crG,T}$ vs. L curves shown

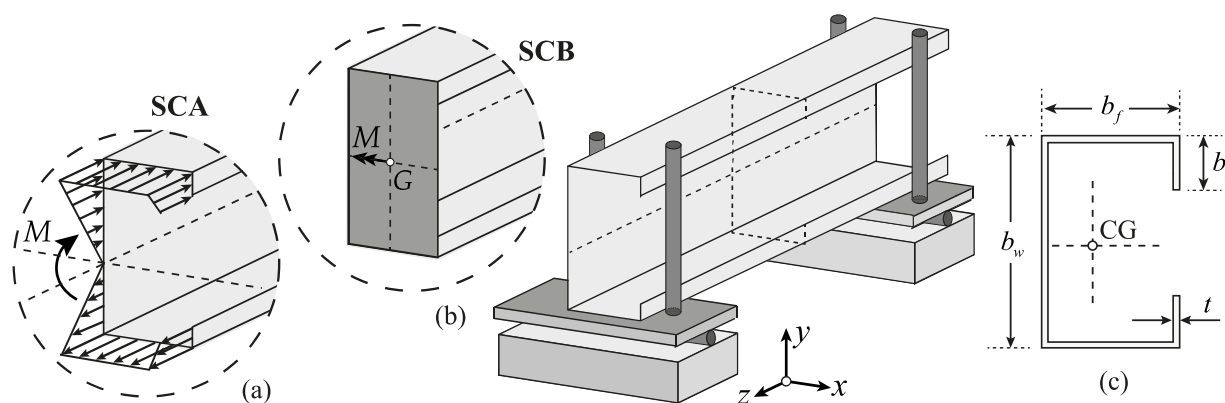


Figure 1. (a) SCA and (b) SCB LCB end support and loading conditions, and (c) LC geometry and dimensions

Table 1. Selected SCA and SCB LC beams failing in “pure” LT modes: geometries (b_w, b_f, b_l, t, L_G – values in mm), critical LT buckling moments (kNcm) and distortional-to-global (R_{GD}) and local-to-global (R_{GL}) critical moment ratios

Beam	SCA								SCB							
	b_w	b_f	b_l	t	L_G	M_{crG}	R_{GD}	R_{GL}	b_w	b_f	b_l	t	L_G	M_{crG}	R_{GD}	R_{GL}
LC1	15.0	10.0	1.20	0.320	500	1075.90	2.1	5.7	12.0	8.0	1.00	0.450	700	874.72	5.1	19.9
LC2	15.0	10.0	1.10	0.325	600	812.60	2.6	7.8	15.0	9.5	1.20	0.350	700	1102.27	2.6	7.9
LC3	15.0	9.0	1.00	0.250	550	507.58	2.4	6.4	16.0	10.0	1.00	0.400	900	992.64	3.5	13.2
LC4	17.0	10.0	1.45	0.360	600	1120.01	3.4	9.2	13.5	8.0	1.00	0.300	700	537.60	3.5	11.1
LC5	17.5	10.0	1.30	0.365	450	1808.17	2.0	6.0	17.5	10.0	1.30	0.405	600	2365.00	2.0	6.5
LC6	18.0	10.0	1.00	0.242	600	632.42	1.8	5.1	12.5	7.0	1.10	0.300	750	349.93	6.2	18.4
LC7	13.0	7.0	1.00	0.300	300	905.40	2.3	7.2	18.0	10.0	1.00	0.400	950	1015.70	3.8	14.7
LC8	16.0	8.0	1.30	0.370	350	1613.09	2.7	8.4	14.0	7.5	1.00	0.450	500	1472.30	3.8	15.2
LC9	19.0	9.0	1.20	0.265	450	1027.20	1.9	5.0	10.0	5.0	1.10	0.300	400	402.43	5.5	18.1
LC10	22.0	10.0	1.66	0.250	500	1296.09	1.8	3.5	20.0	9.0	1.00	0.350	900	832.02	4.2	14.0
LC11	18.5	8.0	1.00	0.360	400	1344.50	2.9	10.3	19.0	8.0	1.10	0.350	850	685.79	5.9	17.7
LC12	25.0	10.0	1.00	0.310	600	1226.85	2.3	7.4	20.0	8.0	1.00	0.450	700	1367.80	5.4	18.9
LC13	10.0	6.0	1.20	0.195	550	119.20	7.2	13.8	10.0	6.0	1.20	0.195	750	117.98	7.4	14.2
LC14	8.0	4.0	1.50	0.190	350	98.85	11.6	19.4	8.0	4.0	1.50	0.190	450	108.73	11.0	17.9
LC15	15.0	10.0	1.00	0.400	700	887.35	3.6	13.3	15.0	10.0	1.00	0.400	950	860.94	3.8	14.0
LC16	10.0	4.0	1.50	0.155	500	50.77	18.2	24.7	10.0	4.0	1.50	0.155	800	38.88	25.9	30.1
LC17	12.0	4.5	1.50	0.155	660	47.60	19.9	26.4	12.0	4.5	1.50	0.155	900	46.76	22.5	24.9
LC18	15.0	4.0	1.50	0.195	750	56.13	33.8	40.3	15.0	4.0	1.50	0.195	850	69.46	27.8	32.0
LC19	9.0	3.0	1.40	0.150	550	24.02	34.7	47.7	9.0	3.0	1.40	0.150	950	15.86	59.1	69.2
LC20	10.0	3.5	1.50	0.190	700	37.54	39.0	62.3	10.0	3.5	1.50	0.190	600	64.37	25.8	34.4
LC21	11.5	4.0	1.50	0.190	650	54.42	28.5	42.6	11.5	4.0	1.50	0.190	750	64.93	26.4	33.6

in Figs. 2(a)-(b) provide the variation of the critical buckling moment at temperature with the length L (logarithmic scale) and temperature T , for SCA and SCB beams with the LC4 cross-section (note that the vertical scales are different in Figs. 2(a) and 2(b)) – (i) four temperatures are considered (20/100°C, 400°C, 600°C and 800°C), and (ii) the EC3:1-2 [21] constitutive model, presented in Section 3, is adopted. Also shown are the critical (LT) buckling modes of the SCA beam with $L_G=600$ cm and SCB beam with $L_G=700$ cm.

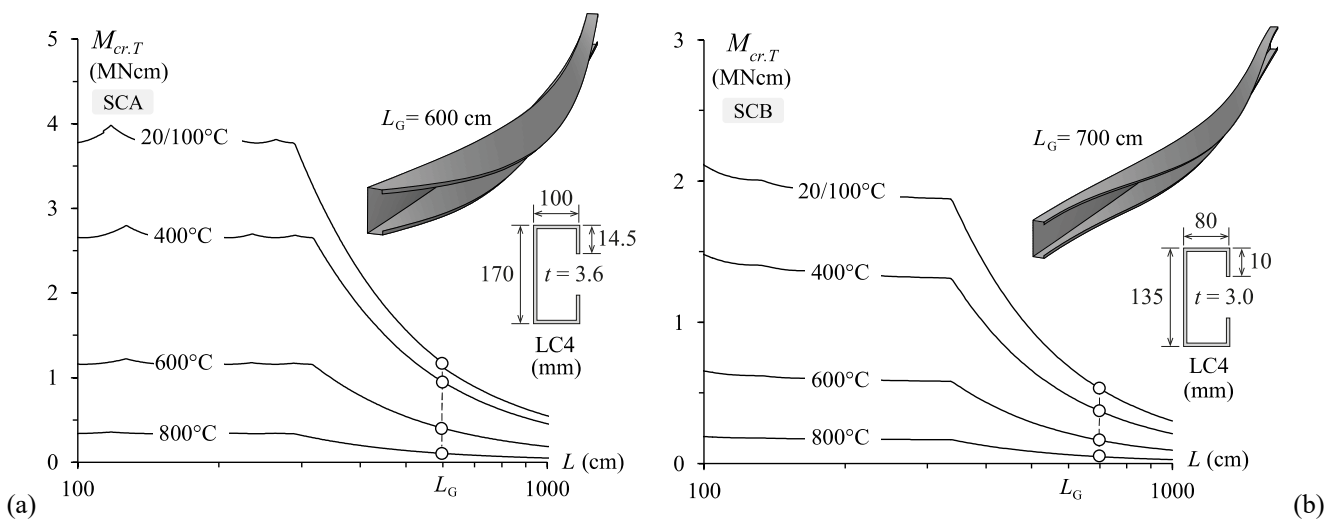


Figure 2. Variation of $M_{cr,T}$ with L and $T=20/100, 400, 600$ and 800 °C for (a) SCA and (b) SCB LC4 beams, adopting the EC3:1.2 [21] CFS constitutive model

3 NUMERICAL MODEL

The beam post-buckling equilibrium paths and failure moments were determined through ABAQUS [24] SFE GMNIA, using validated models employed by the authors in the past (*e.g.*, [20]). The beams were discretised into fine S4 element (ABAQUS nomenclature – 4-node general-purpose SFE with six degrees of freedom per node and full integration) meshes. The analyses (i) were performed by means of an incremental-iterative technique, combining Newton-Raphson’s method with arc-length control, and (ii) simulate the response of beams under constant uniform temperature distributions and then acted by an increasing uniform major-axis bending moment up to failure – steady-state structural analyses providing failure moments.

The simply supported beams analysed have two end support conditions, SCA and SCB (see Figs. 1(a)-(b)) – the latter are modelled by attaching rigid plates to their end cross-sections. The uniform bending moment is applied by means of either (i) concentrated force sets acting on both end cross-section nodes (SCA beams) or (ii) concentrated moments acting on the rigid end-plates (SCB beams). All the beams analysed contain critical-mode (LT) initial imperfections with $L/1000$ amplitudes and involving counter clockwise torsional rotations – the most detrimental, as they lead to lower post-buckling strengths (*e.g.*, [1, 2]). The beam critical buckling modes are yielded by preliminary ABAQUS buckling analyses, performed with the SFE mesh used to carry out the GMNIA. The ABAQUS multi-linear stress-strain curve is adopted to model the steel material behaviour. The CFS constitutive law at elevated temperature adopted is based on the EC3:1-2 [21] model, previously used in the numerical simulations reported in [22, 33].

In order to validate the ABAQUS SFE model used, a fraction of the numerical simulations reported in [2] are replicated. Table 2 gives the data of the LCB considered, namely their cross-section dimensions, length and yield stress means ($b_w \times b_f \times b_l \times t \times L \times \sigma_{y20}$ – mm and MPa): LCB.1 ($90 \times 45 \times 15 \times 1.55 \times 4000 \times 294$), LCB.2 ($125 \times 50 \times 15 \times 1.95 \times 5000 \times 271$), LCB.3 ($115 \times 40 \times 15 \times 1.9 \times 3500 \times 515$) and LCB.4 ($80 \times 40 \times 15 \times 1.9 \times 4000 \times 515$). Table 2 shows that the absolute values of the percentage differences between the beam failure loads reported in [2] ($M_{u.TKM}$) and obtained in this work ($M_{u.TTW}$), for beams at various temperatures, never exceed 2.22% and have a mean equal to 0.78%. In view of this good correlation, the SFE element model employed in this work may be deemed satisfactorily validated.

Table 2. Validation study: comparison between the numerical failure moments reported in [2] and obtained in this work (kNm)

T (°C)	LCB.1			LCB.2			LCB.3			LCB.4		
	$M_{u.TKM}$	$M_{u.TTW}$	D%	$M_{u.TKM}$	$M_{u.TTW}$	D%	$M_{u.TKM}$	$M_{u.TTW}$	D%	$M_{u.TKM}$	$M_{u.TTW}$	D (%)
20	0.634	0.628	0.95%	0.925	0.924	0.11%	1.067	1.073	-0.56%	0.698	0.696	0.29%
200	0.539	0.535	0.74%	0.785	0.785	0.00%	0.907	0.912	-0.55%	0.591	0.586	0.85%
300	0.452	0.45	0.44%	0.661	0.658	0.45%	0.763	0.768	-0.66%	0.5	0.498	0.40%
400	0.367	0.36	1.91%	0.534	0.534	0.00%	0.617	0.622	-0.81%	0.403	0.404	-0.25%
500	0.283	0.279	1.41%	0.41	0.41	0.00%	0.472	0.476	-0.85%	0.308	0.31	-0.65%
600	0.195	0.197	-1.03%	0.286	0.287	-0.35%	0.319	0.324	-1.57%	0.213	0.215	-0.94%
700	0.11	0.111	-0.91%	0.16	0.162	-1.25%	0.18	0.184	-2.22%	0.12	0.122	-1.67%

4 LATERAL-TORSIONAL RESPONSE UNDER ROOM AND ELEVATED TEMPERATURES

4.1 Elastic-Plastic Post-Buckling Behaviour

This section addresses the influence of elevated temperatures on the elastic-plastic LT post-buckling behaviour and failure moment of selected CFS LCB. Figs. 3(a₁)-(a₂) show equilibrium paths M/M_{crG} vs. $|w|/t$, (t is the wall thickness and $|w|$ the beam maximum horizontal displacement absolute value – mid-span compressed flange-web corner) of beams with $\lambda_G=1.5$ at temperatures $T=20/100-200-300-400-500-600-700-800^\circ\text{C}$. The white circles stand for the failure moments $M_{u,T}$ and the room temperature elastic curves are also shown, for comparison purposes. As for Figs. 3(b₁)-(b₂), they show the failure modes deformed and von Mises stress contours at collapse ($M=M_{u,T}$) of the beams at temperatures $T=20/100-300-600-800^\circ\text{C}$. The observation of these figures prompts the following remarks:

- (i) As expected, a temperature increase causes the beam normalised strength and failure moment to drop, regardless of the end support conditions considered (SCA or SCB). This drop is more pronounced between 500 and 600°C.

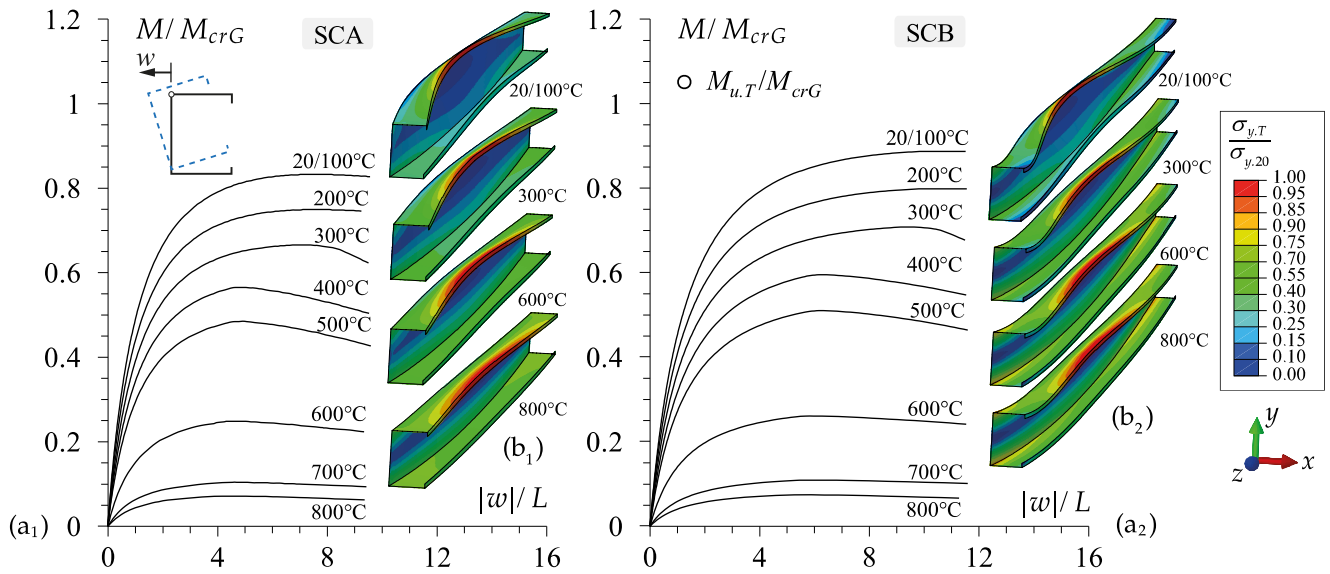


Figure 3. (a) LT post-buckling equilibrium paths M/M_{crG} vs. $|w|/L$ and (b) deformed configurations and von Mises stress contours, at collapse, of the (1) SCA and (2) SCB LC5 beams with $\lambda_G=1.5$ and under temperatures $T=20/100-300-600-800^\circ\text{C}$

(ii) Figs. 3(b₁)-(b₂) confirm that failure modes combine minor-axis bending with counter clockwise torsional rotations – no cross-section distortion is observed. Note that these failure modes and von Mises stress contours are virtually identical for all the beams, regardless of the temperature and end support conditions. The beams collapse after full yielding of the compressed web-flange corners and lip free edge at mid-span, leading to a “LT plastic hinge” – similar observations were reported in [1,2].

4.2 Failure Moment Data

The parametric study carried out involved 4032 beams, all possible combinations of (i) the 21 geometries given in Table 1, (ii) SCA and SCB support conditions, (iii) 8 temperatures ($T=20/100-200-300-400-500-600-700-800^\circ\text{C}$) and (iv) 12 room-temperature yield stresses, covering wide LT slenderness values from 0.125 to 3.6. Fig. 4 shows plots $M_{u,T}/M_{y,T}$ vs. $\lambda_{G,T}$ for the various temperatures considered, each (i) concerning SCA and SCB beams, and

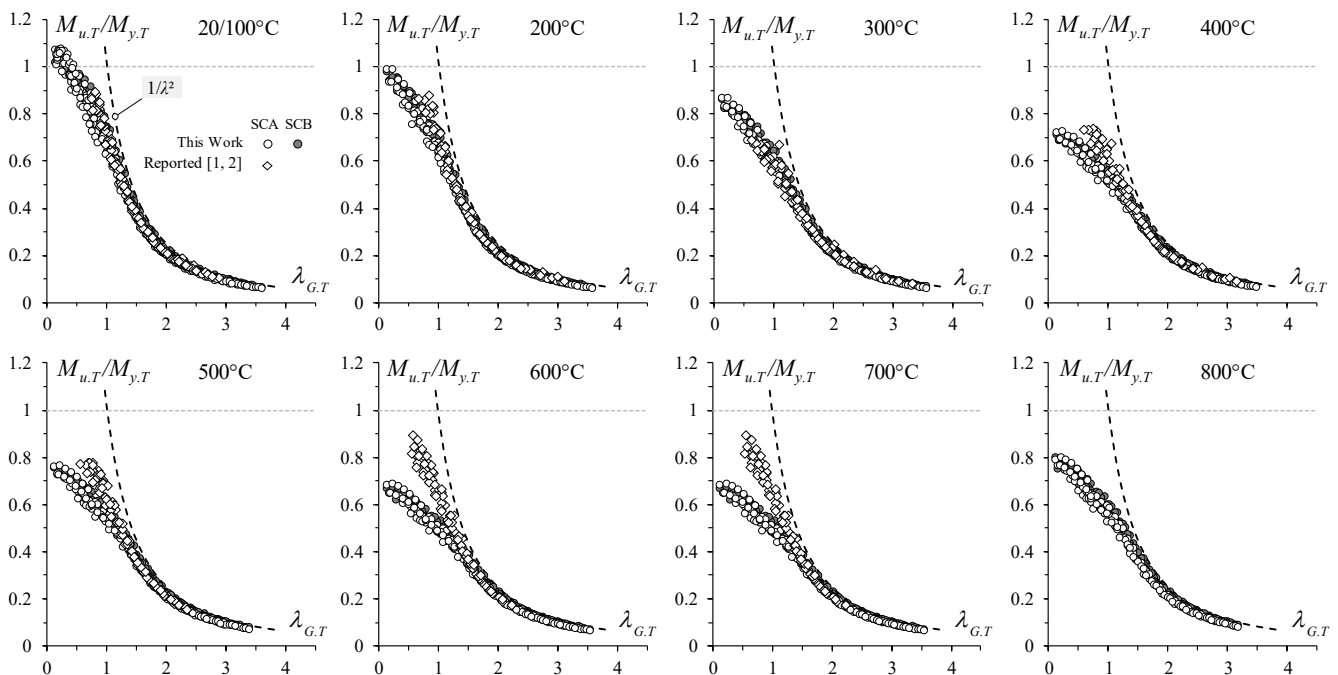


Figure 4. $M_{u,T}/M_{y,T}$ vs. $\lambda_{G,T}$ values concerning all the SCA and SCB LC beams under room and elevated temperatures analysed in this work and in [1,2], and elastic buckling curves

(ii) including, for comparison purposes, the elastic buckling curves $\lambda_{G,T}^{-2} - M_{u,T}$, $M_{y,T}$ and $\lambda_{G,T}=(M_{y,T}/M_{cr,G,T})^{0.5}$ are the beam LT failure moments, yield moments and slenderness values, respectively. Beside the failure moments obtained, Fig. 4 also includes 112 and 494 LT failure moments reported in [1] (room temperature) and [2] (elevated temperatures). The joint observation of these plots leads to the following comments:

- (i) Regarding the beams analysed in this work and for all temperatures, the $M_{u,T}/M_{y,T}$ vs. $\lambda_{G,T}$ values of the SCA and SCB beams are well aligned along “Winter-type” curves, even if some “vertical dispersion” occurs across the whole slenderness range. The numerical values reported in [1,2] (white diamonds), only for SCA beams at temperatures up to 700°C, also align along “Winter-type” curves and “mingle” well with those obtained in this work. But they are a bit higher and exhibit more “vertical dispersion”, particularly stocky beams with $T \geq 400^\circ\text{C}$. Recall also that these numerical results ultimate were obtained with experimentally-based Ramberg-Osgood material models [18,25], differing considerably from the EC3:1-2 [21] model adopted in this work.
- (ii) It is worth noting that, regardless of temperature, the elastic buckling curve lies always above the SCA and SCB beam $M_{u,T}/M_{y,T}$ values, which implies a minute post-critical strength. All the $M_{u,T}/M_{y,T}$ values of beams with low-to-moderate slenderness ($\lambda_{G,T} \leq 1.5$) at elevated temperatures ($T > 100^\circ\text{C}$) are below those concerning the same beams at room/moderate temperature ($T \leq 100^\circ\text{C}$) – the differences tend to increase with the temperature and the elastic buckling curves provide a useful reference to quantify these differences. This feature is not perceptible in the beams with moderate and high slenderness ($\lambda_{G,T} > 1.5$).
- (iii) Concerning the stocky beams at $T > 100^\circ\text{C}$, note that the drop due to the temperature increase does not follow the “logical” temperature sequence, *i.e.*, the decrease with the temperature is not monotonic. Indeed, the reduction is ordered in the sequence $T=20/100-200-300-800-400-700-500-600^\circ\text{C}$ (“out of sequence” values underlined). This unexpected finding, with no obvious mechanical explanation based on the EC3:1-2 [21] CFS constitutive model temperature-dependence, must be investigated (including the possible influence of the ratio k_y/k_E).
- (iv) The above results are promising with respect to the possibility of developing an efficient (safe and reliable) DSM-based design approach to estimate the LT failure moments of CFS simply supported (SCA and SCB) lipped channel beams at elevated temperatures. The DSM design of these beams is addressed next.

5 DSM DESIGN AT ELEVATED TEMPERATURES

The DSM-based prediction of the LT failure moments gathered in Section 4.2, concerning CFS SCA and SCB LCB at elevated temperatures, is addressed in this section. The first step consists of assessing the merits of the available DSM design curve proposed in [2] ($M_{nGR,T}$ —see Eq. (3)), which includes the temperature effects associated with the material model, via the LT buckling ($M_{cr,G,T}$) and yield ($M_{y,T}$) moments (naturally, λ_G also varies with $T - \lambda_{G,T}$). Fig. 5, concerning the failure moments of the LCB analysed in this work and in [2], shows the $M_{u,T}/M_{nGR,T}$ vs. $\lambda_{G,T}$ plots, enabling a quick qualitative assessment of the failure moment prediction quality provided by this DSM-based strength curve. The $M_{u,T}/M_{nGR,T}$ statistical indicators (averages, standard deviations and maximum/minimum values), given

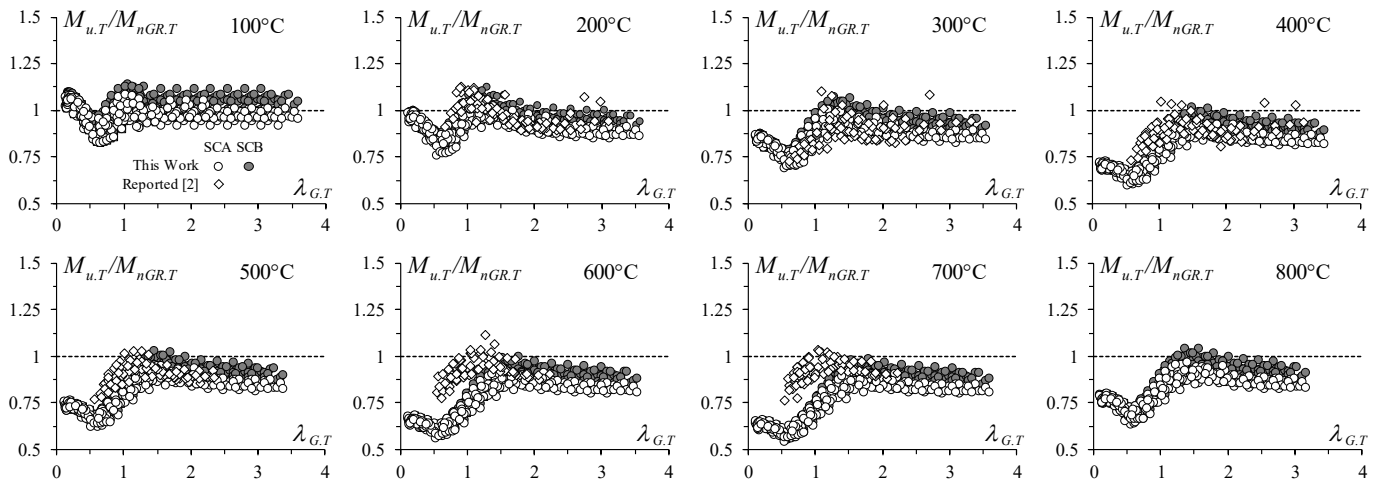


Figure 5. $M_{u,T}/M_{nGR,T}$ vs. $\lambda_{G,T}$ plots concerning the LCB analysed in this work and in [2] at room elevated temperatures

Table 3. $M_{u,T}/M_{nGR,T}$ statistical indicators concerning the CFS LCB analysed in this work and in [2] at elevated temperatures

$M_{u,T}$ $M_{nGR,T}$		$T(^{\circ}C)$	200			300			400			500			600			700			800			
			$\lambda_{G,T}$	≤ 1.5	> 1.5	Any	≤ 1.5	> 1.5	Any	≤ 1.5	> 1.5	Any	≤ 1.5	> 1.5	Any	≤ 1.5	> 1.5	Any	≤ 1.5	> 1.5	Any			
SCA	Reported [2]	<i>n</i>	37	46	83	40	42	82	44	39	83	49	31	80	62	19	81	61	24	85	-	-	-	
		<i>Avr</i>	1.03	0.94	0.98	0.87	0.90	0.88	0.90	0.89	0.89	0.92	0.90	0.91	0.93	0.92	0.93	0.92	0.92	0.92	0.92	-	-	-
		<i>SD</i>	0.05	0.04	0.16	0.09	0.06	0.18	0.07	0.05	0.15	0.06	0.02	0.22	0.07	0.03	0.06	0.06	0.02	0.05	-	-	-	
		<i>Max</i>	1.13	1.09	1.13	1.10	1.08	1.10	1.05	1.04	1.05	1.03	0.95	1.03	1.11	0.99	1.11	1.04	0.98	1.04	-	-	-	
		<i>Min</i>	0.92	0.89	0.89	0.73	0.82	0.73	0.73	0.81	0.73	0.77	0.86	0.77	0.77	0.88	0.77	0.76	0.88	0.76	-	-	-	
		<i>Uns</i>	3	35	38	32	36	68	35	36	71	34	30	64	40	17	57	40	20	60	-	-	-	
	This Work	<i>n</i>	143	109	252	143	109	252	147	105	252	147	105	252	143	109	252	143	109	252	156	96	252	
		<i>Avr</i>	0.92	0.90	0.91	0.83	0.89	0.86	0.73	0.86	0.78	0.75	0.87	0.80	0.69	0.85	0.76	0.67	0.84	0.75	0.78	0.88	0.82	
		<i>SD</i>	0.07	0.03	0.06	0.08	0.03	0.07	0.09	0.03	0.09	0.08	0.03	0.09	0.09	0.03	0.11	0.09	0.03	0.11	0.08	0.03	0.08	
		<i>Max</i>	1.06	1.00	1.06	1.00	0.96	1.00	0.93	0.94	0.94	0.95	0.95	0.95	0.91	0.92	0.92	0.90	0.91	0.91	0.97	0.95	0.97	
		<i>Min</i>	0.76	0.85	0.76	0.69	0.83	0.69	0.60	0.81	0.60	0.62	0.82	0.62	0.56	0.80	0.56	0.54	0.80	0.54	0.64	0.83	0.64	
		<i>Uns</i>	88	99	187	129	105	234	147	105	252	147	104	251	143	109	252	143	109	252	153	96	249	
	All Beams	<i>n</i>	180	155	335	183	151	334	191	144	335	196	136	332	205	128	333	204	133	337	156	96	252	
		<i>Avr</i>	0.94	0.92	0.93	0.84	0.89	0.86	0.77	0.87	0.81	0.79	0.88	0.83	0.76	0.86	0.80	0.75	0.86	0.79	0.78	0.88	0.82	
		<i>SD</i>	0.08	0.04	0.10	0.08	0.04	0.11	0.11	0.04	0.12	0.11	0.03	0.14	0.14	0.04	0.12	0.14	0.04	0.13	0.08	0.03	0.08	
		<i>Max</i>	1.13	1.09	1.13	1.10	1.08	1.10	1.05	1.04	1.05	1.03	0.95	1.03	1.11	0.99	1.11	1.04	0.98	1.04	0.97	0.95	0.97	
		<i>Min</i>	0.76	0.85	0.76	0.69	0.82	0.69	0.60	0.81	0.60	0.62	0.82	0.62	0.56	0.80	0.56	0.54	0.80	0.54	0.64	0.83	0.64	
		<i>Uns</i>	91	134	225	161	141	302	182	141	323	181	134	315	183	126	309	183	129	312	153	96	249	
SCB	This Work	<i>n</i>	143	109	252	143	109	252	147	105	252	147	105	252	143	109	252	143	109	252	156	96	252	
		<i>Avr</i>	0.95	0.96	0.95	0.86	0.94	0.90	0.74	0.92	0.82	0.77	0.93	0.83	0.70	0.91	0.79	0.68	0.90	0.78	0.80	0.94	0.85	
		<i>SD</i>	0.08	0.04	0.06	0.09	0.03	0.08	0.10	0.03	0.12	0.09	0.03	0.11	0.10	0.03	0.13	0.10	0.03	0.13	0.09	0.03	0.10	
		<i>Max</i>	1.13	1.09	1.13	1.07	1.07	1.07	1.02	1.01	1.02	1.03	1.02	1.03	0.95	1.00	1.00	0.94	0.99	0.99	1.04	1.04	1.04	
		<i>Min</i>	0.79	0.89	0.79	0.71	0.87	0.71	0.62	0.85	0.62	0.65	0.86	0.65	0.58	0.84	0.58	0.56	0.84	0.56	0.67	0.87	0.67	
		<i>Uns</i>	69	45	114	118	66	184	142	88	230	140	82	222	141	98	239	143	102	245	140	67	207	
SCA + SCB	All Beams	<i>n</i>	323	264	587	326	260	586	338	249	587	343	241	584	348	237	585	347	242	589	312	192	504	
		<i>Avr</i>	0.95	0.93	0.94	0.85	0.91	0.88	0.76	0.89	0.81	0.78	0.90	0.83	0.74	0.88	0.80	0.72	0.88	0.78	0.79	0.91	0.83	
		<i>SD</i>	0.08	0.04	0.07	0.08	0.05	0.09	0.10	0.04	0.11	0.10	0.04	0.12	0.13	0.04	0.12	0.13	0.04	0.13	0.09	0.04	0.09	
		<i>Max</i>	0.76	0.85	0.76	0.69	0.82	0.69	0.60	0.81	0.60	0.62	0.82	0.62	0.56	0.80	0.56	0.54	0.80	0.54	0.64	0.83	0.64	
		<i>Min</i>	1.13	1.09	1.13	1.10	1.08	1.10	1.05	1.04	1.05	1.03	1.02	1.03	1.11	1.00	1.11	1.04	0.99	1.04	1.04	1.04	1.04	
		<i>Uns</i>	160	179	339	279	207	486	324	229	553	321	216	537	324	224	548	326	231	557	293	163	456	

in Table 3 for the SCA and SCB beams – the failure moment estimates such that $M_{u,T}/M_{nGR,T} < 0.95$ are deemed “clearly unsafe” and denoted “*Uns*”. The observation of the results presented in these figures and tables prompts the following remarks:

- For the beams at $T=100^{\circ}C$ (still “room temperature” for the CFS constitutive model based on EC3.1-2), whose results are not given in Table 3, Fig. 5 shows that Eq. (3) overestimates a large number of SCA LCB failure moments (particularly in the low slenderness range) and also several stocky SCB LCB failure moments.
- Concerning the beams at $T=200^{\circ}C$, most failure moments are visibly overestimated by the $M_{nGR,T}$ DSM design curve along the whole slenderness range – the $M_{u,T}/M_{nGR,T}$ statistical indicators are (ii₁) 0.91-0.06-1.06-0.76 (SCA) and 0.95-0.06-1.13-0.79 (SCB) for the beams analysed in this work, and (ii₂) 0.98-0.16-1.13-0.89, for the (SCA) beams analysed in [2]. However, the overestimation amounts differ for the various beam sets considered – the $M_{u,T}/M_{nGR,T}$ values of the SCA beams analysed in this work are slightly lower than the remaining ones (compare the white circles with the grey circles and white diamonds in Fig. 5).
- Concerning the failure moment estimates for beams at more elevated temperatures ($T > 200^{\circ}C$), it can be generally said that they are virtually all of them are unsafe – the amount of overestimation increases with T and reaches 46% (SCA beams at for $T=700^{\circ}C$). The $M_{u,T}/M_{nGR,T}$ statistical indicators in Table 3 show that the number of “clearly unsafe” failure moment predictions varies from (iii₁) 74% ($T=200^{\circ}C$) to 100% ($T \geq 400^{\circ}C$) for the SCA beams analysed in this work, (iii₂) 45% ($T=200^{\circ}C$) to 91% ($T \geq 400^{\circ}C$) for the SCB beams, and (iii₃) 46% ($T=200^{\circ}C$) to 86% ($T=400^{\circ}C$) for the SCA beams analysed in [2].
- The failure moment prediction quality is not visibly affected by the CFS constitutive model – indeed, the failure moment estimates reported in [2] “mingle” well with those obtained in this work. However, the failure moment predictions of the beams analysed in this work with $\lambda_{G,T} \leq 1.5$ and at $T=600^{\circ}C$ or $T=700^{\circ}C$ are visibly below

those with $\lambda_{G,T} > 1.5$, in contrast with what happens with the beams analysed in [2]. This is probably due to the distinct CFS constitutive models used – in [2], different constitutive models were considered for the G250, G450 and G550 steel grades. The $M_{u,T}/M_{nGR,T}$ statistical indicators concerning the beams analysed in [2] vary from 0.88 (300°C) to 0.93 (600°C), 0.18 (300°C) to 0.06 (600°C), 1.10 (300°C) to 1.11 (600°C) and 0.73 (300°C) to 0.77 (600°C) – see Table 3.

- (v) In view of the above findings, it is clear that the $M_{nGR,T}$ DSM design curve is unable to predict adequately the LT failure moments of LCB at room and elevated temperatures – a large number of failure moment predictions are quite unsafe. To improve the failure moment prediction quality, it is necessary to search for a new DSM-based strength curve. Naturally, the first step of this task consists of improving this quality for the beams at room temperature (note that, in the context of the CFS constitutive law is based on the EC3:1-2 model, this means $T=20/100^\circ\text{C}$).

5.1 Novel DSM-Based Design Curve at Room Temperature

In order to improve the failure moment prediction quality provided by the M_{nGR} values for the failure moments of the SCA and SCB LCB at room temperature considered in this work, namely by reducing the number and amounts of failure moment underestimations (mostly for the beams with $\lambda_G \leq 1.5$ – see Fig. 5, concerning beams at 100°C), a new DSM-based design curve is needed – at this stage, it should be noted that the M_{nGR} values are calculated with Eq. (3), by making $k_p=k_y=1.0$, and not with Eq. (2). For simplicity and uniformity purposes, it was decided to search for a strength curve in the format of the DSM column design curve against global failures [4], which would make it possible to have a common format for CFS columns and beams. This search was successful and, following “trial-and-error” curve fitting procedures involving the LT failure moments obtained in this work and in [1], a novel DSM-based design curve (M_{nLT}) is proposed – it reads

$$M_{nLT} = \begin{cases} M_p (0.643 \cdot a)^{\lambda_G^{1.5}} & \lambda_G \leq 1.5 \\ M_y \left(\frac{b}{\lambda_G^2} \right) & \lambda_G > 1.5 \end{cases} \quad \text{with} \quad \lambda_G = \sqrt{\frac{M_y}{M_{crG}}} \quad , \quad (4)$$

where, (i) $a=(bS/Z)^{0.544}$ is a coefficient calculated to ensure continuity of the design curves (recall that S and Z are the cross-section elastic and plastic moduli, respectively) and (ii) b is a parameter dependent on the beam end support conditions – $b=0.790$, for SCA beams, and $b=0.853$, for SCB beams. Figs. 6(a)-(b) show plots M_u/M_{nGR} vs. λ_G and M_u/M_{nLT} vs. λ_G for the SCA and SCB LCB analysed in this work and in [1] enabling a quantitative assessment of the failure moment prediction improvement achieved. It is observed that the M_u/M_{nGR} vs. λ_G and M_u/M_{nLT} vs. λ_G “clouds” differ substantially for $\lambda_G \leq 1.5$: while the former exhibits a fair amount of failure moment overestimations, the latter displays only a few of them. Indeed, the number of “Uns” failure moment estimates is reduced from 85 to 14 (*i.e.*, from 25% to 4% of the total number of beams considered) – naturally, on the downside, the failure moment underestimations increase (the maximum one moves from 14% to 29%). Concerning the SCA beam failure moments reported in [1], they are slightly underestimated by the novel DSM design curve – the M_u/M_{nGR} and M_u/M_{nLT} statistical indicators are 0.99-0.06-1.12-0.91 and 1.11-0.07-1.29-0.99, respectively (a detailed account can be found in [26]).

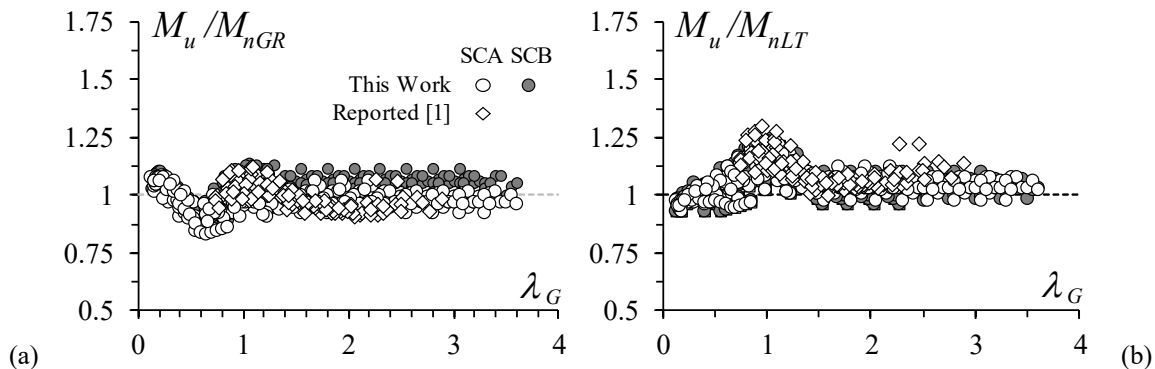


Figure 6. (a) M_u/M_{nGR} vs. λ_G and (b) M_u/M_{nLT} vs. λ_G plots concerning the LCB analysed in this work and reported in [1] at room temperatures

5.2 Novel DSM-Based Design Curve at Elevated Temperatures

This section briefly addresses the work currently under way to look for a DSM-based design approach to predict the failure moments of CFS simply supported SCA and SCB LCB at elevated temperatures [26]. Naturally, the first step consisted of assessing the merits of the M_{nLT} strength curve (see Eq. (4)), appropriately modified to include the temperature effects associated with the EC3:1-2 material model. This strength curve, termed $M_{nLT,T}$, differs from Eq. (4) in the fact that M_p , M_y and M_G are replaced with $M_{p,T}$, $M_{y,T}$ and $M_{G,T}$, respectively (a and b do not depend on the temperature) – it is given by the expressions

$$M_{nLT,T} = \begin{cases} M_{p,T} (0.643 \cdot a)^{\lambda_{G,T}^{1.5}} & \lambda_{G,T} \leq 1.5 \\ M_{y,T} \left(\frac{b}{\lambda_{G,T}^2} \right) & \lambda_{G,T} > 1.5 \end{cases} \quad \text{with} \quad \lambda_{G,T} = \sqrt{\frac{M_{y,T}}{M_{crG,T}}} \quad (5)$$

Fig. 7 shows plots $M_{u,T}/M_{nLT,T}$ vs. $\lambda_{G,T}$ concerning the LCB analysed in this work and in [2], at temperatures ranging from $T=200^\circ\text{C}$ to $T=800^\circ\text{C}$, making it possible to assess the merits of the above DSM-based strength curve – further details about these results can be found in [26]. The observation of these plots prompts the following remarks:

- (i) For LCB having moderate and high slenderness ($\lambda_{G,T} > 1.5$), the $M_{nLT,T}$ values provide reasonably accurate and mostly failure moment estimates, regardless of the temperature. Moreover, in this slenderness range, the failure moment prediction quality is practically not affected by the temperature-dependent CFS constitutive law – indeed, the $M_{u,T}/M_{nLT,T}$ values of the LCB analysed in [2] “mingle” quite well with those obtained in this work.
- (ii) Conversely, for LCB with low and moderate slenderness ($\lambda_{G,T} \leq 1.5$), the $M_{nLT,T}$ values clearly overestimate the failure moments obtained in this work – generally speaking, the amount of overestimation grows with the (elevated) temperature. On the other hand, the failure moments reported in [2] are visibly better estimated, most probably because of the distinct CFS constitutive models adopted – this means that, as it would be logical to expect, the influence of the temperature-dependent CFS constitutive law is felt only in LCB with $\lambda_{G,T} \leq 1.5$. In order to quantify the above assertions, it is worth mentioning that, for LCB with $\lambda_{G,T} \leq 1.5$, the number of “clearly unsafe” failure moment predictions varies (ii₁) from 37% ($T=200^\circ\text{C}$) to over 75% ($T \geq 400^\circ\text{C}$), for the SCA obtained in this work, (ii₂) from 39% ($T=200^\circ\text{C}$) to over 85% ($T \geq 400^\circ\text{C}$), for the SCB beams, and (ii₃) from 0% ($T=200^\circ\text{C}$) to 23% ($T=400^\circ\text{C}$), for the SCA reported in [2].
- (iii) Although the failure moment prediction quality provided by the $M_{nLT,T}$ values is adequate for LCB with $\lambda_{G,T} > 1.5$, this is clearly not the case for LCB with $\lambda_{G,T} \leq 1.5$. Therefore, it is necessary to find a novel DSM-based strength curve that can adequately handle the LCB failure moments at elevated temperatures in the low and moderate slenderness ranges, while retaining the failure moment prediction quality provided by the $M_{nLT,T}$ values for LCB with $\lambda_{G,T} > 1.5$ – the authors are currently investigating this issue and the fruits bore by this research effort will be reported in the relatively near future [26].

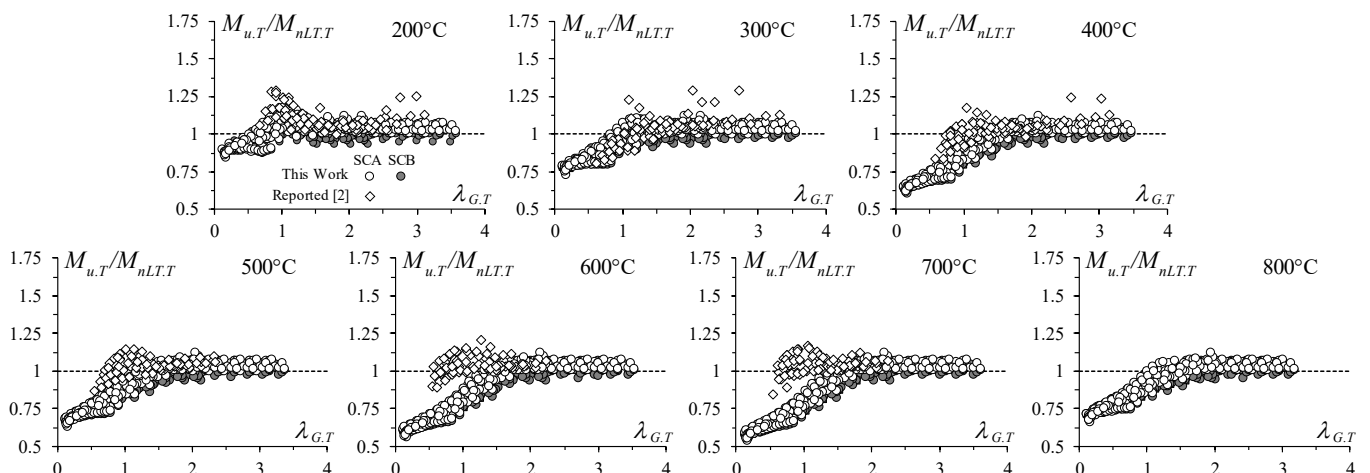


Figure 7. $M_{u,T}/M_{nLT,T}$ vs. $\lambda_{G,T}$ plots concerning the LCB analysed in this work and in [2] at elevated temperatures

6 CONCLUDING REMARKS

This paper reported the most recent results of an investigation, initiated by Kankanamge and Mahendran [1,2] a few years ago, on the post-buckling behaviour, failure moment and DSM design of cold-formed steel single-span simply supported lipped channel beams buckling in LT modes at room and elevated temperatures (typically caused by fire conditions). After addressing the beam geometry selection and the influence of the temperature on the beam LT post-buckling behaviour, numerical failure moment data were obtained for 4032 beams, concerning (i) 21 geometries (cross-section dimensions and lengths), (ii) 2 end support conditions (SCA and SCB – free or fully prevented end cross-section warping and local displacement/rotations), (iii) 8 room-temperature yield stresses, covering wide LT slenderness ranges ($0.125 \leq \lambda_{G,T} \leq 3.6$), and (iv) 8 uniform temperatures ($T=20/100-200-300-400-500-600-700-800^\circ\text{C}$) – the CFS constitutive law based on the EC3:1-2 model was used. The numerical LT failure moments obtained in this work, together with those reported in [1,2], were then used to assess the merits of the DSM design curve proposed in [2] ($M_{nGR,T}$). It was found that this strength curve is not capable of handling adequately CFS (SCA and SCB) LCB failing in LT modes at elevated temperatures, which means that it is necessary to find a more performant alternative to improve this strength curve. Since no satisfactory DSM-based design curve is also available for LCB failing in LT modes at room temperature, it was decided to begin with the LCB at room temperature – once this task is completed, the predictions of the LCB failure moments at elevated temperatures will be addressed.

It was possible to propose a novel DSM-based design curve (M_{nLT}), in the format of a recently developed DSM-based column design curve against global failures [4], that adequately predicts the LT failure moments, at room temperature, of all the SCA and SCB LCB analysed in this work and in [1] (see [26] for further details). However, it was also shown that the above design curve, appropriately modified to account for the temperature effects (replacement of M_p , M_y and M_G with $M_{p,T}$, $M_{y,T}$ and $M_{G,T}$), is not able to predict adequately the LT failure moments, at elevated temperatures, of LCB in the low to moderate slenderness range ($\lambda_{G,T} \leq 1.5$) – the failure moment prediction quality is only adequate for LCB with $\lambda_{G,T} > 1.5$. Therefore, a novel DSM-based strength curve is required for LCB with low and moderate slenderness – an investigation on this issue is currently under way and its findings will be reported fairly soon [26].

Finally, it is worth mentioning that the results presented in this work concern an ongoing investigation whose final goal is to achieve an efficient and general DSM-based design approach for arbitrary CFS beams buckling and failing in LT modes at room and elevated temperatures, namely those caused by fire conditions.

ACKNOWLEDGEMENTS

The first two authors gratefully acknowledge the financial support of the Brazilian institutions (i) CAPES (Coordenação de Aperfeiçoamento de Pessoal de Nível Superior) – Finance Code 001 (both authors), (ii) CNPq (Conselho Nacional de Desenvolvimento Científico e Tecnológico) – 141021/2020-9 (1st author) and 313197/2020-2 (2nd author) and (iii) FAPERJ (Fundação Carlos Chagas Filho de Amparo à Pesquisa do Estado do Rio de Janeiro) –E-26/200.959/2021 (2nd author). The third author gratefully acknowledges the financial support of FCT (Fundação para a Ciência e a Tecnologia – Portugal) – project UIDB/04625/2020 (funding the research unit CERIS).

REFERENCES

1. Kankanamge, ND, Mahendran, M. Behaviour and design of cold-formed steel beams subject to lateral-torsional buckling, *Thin-Walled Structures*, **51**, 25-38 (2012).
2. Kankanamge, ND, Mahendran, M. Behaviour and design of cold-formed steel beams subject to lateral-torsional buckling at elevated temperatures, *Thin-Walled Structures*, **61**, 213-228 (2012).
3. Camotim, D, Martins, AD, Dinis, PB. Towards the next generation design of cold-formed steel structures: the Direct Strength Method (DSM), *Recent Trends in Cold-Formed Steel Construction* (2nd edition), C. Yu (ed.), Woodhead Publishing (Series in Civil and Structural Engineering), Elsevier, Cambridge (MA – USA) and Kidlington (UK), 101-173 (2023).

4. AISI (American Iron and Steel Institute). North American Specification (NAS) for the Design of Cold-Formed Steel Structural Members (2016 edition reaffirmed in 2020 with Supplement 3), AISI-S100-16 w/S3-22, Washington DC. 2022.
5. AS/NZS (Standards of Australia and Standards of New Zealand). Cold-Formed Steel Structures, AS/NZS 4600:2018 (3rd ed.), Sydney-Wellington. 2018.
6. AISC (American Institute of Steel Construction). Load and Resistance Factor Design Specification for Structural Steel Buildings, AISC 328:1986, Chicago IL. 1986.
7. Galambos, TV. Inelastic Buckling of Beams. *Journal of the Structural Division (ASCE)*, **89**(ST5), 217-244 (1963).
8. Put, BM, Pi, YL, Trahair, NS. Lateral Buckling Tests on Cold-Formed Channel Beams. Research Report No. R767, Centre for Advanced Structural Engineering, Department of Civil Engineering, University of Sydney, Australia. 1998.
9. Ellifritt, DS, Sputo, T, Haynes, J. Flexural capacity of discretely braced C's and Z's, Proceedings of Eleventh International Specialty Conference on Cold-Formed Steel Structures, University of Missouri-Rolla,, October. 1992.
10. Ungermann, D, Brune, B. Experimental investigations on plain channels in coupled instabilities, *Steel Construction*, **5**(2), 87-92 (2012).
11. Pi, YL, Put, BM, Trahair, NS.. Lateral buckling strengths of cold-formed channel section beams. *Journal of Structural Engineering (ASCE)*, **124**(10), 1182-1191 (1998).
12. Chu, XT, Kettle, R, Li, LY. Lateral torsional buckling analysis of partial-laterally restrained thin-walled channel-section beams. *Journal of Constructional Steel Research*, **60**(8), 1159-1175 (2004).
13. Ungermann, D, Brune, B. Numerical and analytical investigations on plain channels in coupled instabilities, *Steel Construction*, **5**(4), 205-211 (2012).
14. Lindner, J, Aschinger, R. Load-carrying capacity of cold-formed beams subjected to overall lateral-torsional buckling and local plate buckling. *Journal of Constructional Steel Research*, **31**(2-3), 267-287 (1994).
15. Snijder, H, Hoenderkamp, J, Bakker, M, Steenbergen, H, Louw, C. Design rules for lateral torsional buckling of channel sections subject to web loading. *Stahlbau*, **77**(4), 247-256 (2008).
16. AS/NZS (Standards of Australia and Standards of New Zealand). Steel Structures, AS 4100:2020 (3rd ed.), Sydney-Wellington. 2020.
17. Kankanamge ND. Structural Behaviour and Design of Cold-formed Steel Beams at Elevated Temperatures, PhD thesis, School of Urban Developments, Queensland University of Technology (QUT), Brisbane, Australia, 2010.
18. Kankanamge ND, Mahendran M. Mechanical properties of cold-formed steels at elevated temperatures, *Thin-Walled Structures*, **41**(1), 26-44 (2010).
19. Bandula Heva Y, Mahendran M. Flexural-torsional buckling tests of cold-formed steel compression members at elevated temperatures, *Steel and Composite Structures*, **14**(3), 205-227 (2012).
20. Neves NS, Landesmann A, Camotim D. CFS lipped channel beams buckling in distortional modes at elevated temperatures: behaviour, failure and DSM design, *Thin-Walled Structures*, **196**(March), paper 111366 (2024).
21. CEN (Comité Européen de Normalisation). Eurocode 3: Design of Steel Structures – Part 1.2: General Rules – Structural Fire Design, EN 1993-1-2, Brussels, 2005.
22. Arrais F, Lopes N, Real PV. Fire design of slender cold-formed lipped channel and sigma section members with uniform temperature under compression, *Fire Safety Journal*, **122**(June), paper 103340 (2021).
23. Bebiano, R, Camotim, D, Gonçalves, R. GBTUL 2.0 – a second-generation code for the GBT-based buckling and vibration analysis of thin-walled members, *Thin-Walled Structures*, **124**(March), 235-257 (2018).
24. Simulia Inc.. ABAQUS Standard (version 6.14-1), 2014.
25. Ranawaka T, Mahendran M. Experimental study of the mechanical properties of light gauge cold-formed steels at elevated temperatures, *Fire Safety Journal*, **147**(2), 219-229 (2009).
26. Neves NS, Landesmann A, Camotim D. Lateral-torsional failure and DSM design of CFS lipped channel beams at room and elevated temperatures (in preparation).

EXPERIMENTAL AND NUMERICAL INVESTIGATION ON COLLAPSE MODES AND MECHANISMS OF PLANAR STEEL TRIANGLE TRUSSES EXPOSED TO FIRE

Jinyu Li¹, Guo-Qiang Li², Shaojun Zhu³, Wei Ji⁴, Yao Wang⁵, Honghui Qi⁶, Xiuzhi Zheng⁷, Kun Ding⁸

ABSTRACT

Steel truss structures are widely used in industrial and public buildings, while they may collapse easily in fire due to significant loss in strength of steel at elevated temperatures. Planar steel triangle trusses, often used as the roofs of industrial buildings, have a greater risk of collapse due to low structural redundancy. A real fire test on an existing triangle truss building was conducted to investigate the collapse modes and mechanisms of planar steel triangle trusses in fire. The collapse mode and corresponding collapse mechanisms are analyzed and numerically simulated. Then, a systematic numerical simulation for planar steel triangle trusses is conducted, and four collapse modes are summarized. The findings of this study can help improve the fire resistance of the planar steel trusses and lay a great foundation for further developing the approaches for early warning of the collapse of planar steel triangle trusses exposed to fire.

Keywords: Collapse modes; Fire-induced collapse test; Planar steel trusses

1 INTRODUCTION

Steel trusses are widely used in large-span buildings since the advantages of lightweight, high strength, and a high level of industrialization. Because of the degradation of the strength and stiffness of the steel at high temperatures, steel structures are more likely to be damaged or even collapse under fire. In particular, planar steel truss roof structures, including the triangle trusses, have less structural redundancy. This way, planar steel truss roof structures are more prone to collapse under fire conditions, and the consequences of their fire-induced collapse can be more severe compared with other types of steel structures. Therefore, it is imperative to explore the collapse modes and mechanisms of planar steel trusses and develop early-warning methods for fire-induced collapse in fire. Li *et al.* [1–3] investigated the collapsed modes of the steel portal

¹ Ph.D. Candidate, College of Civil Engineering, Tongji University
e-mail: lijinyu98@tongji.edu.cn

² Professor, College of Civil Engineering, Tongji University
e-mail: gqli@tongji.edu.cn

³ Assistant Professor, College of Civil Engineering, Tongji University
e-mail: zhushaojun@tongji.edu.cn

⁴ Ph.D., College of Civil Engineering, Tongji University
e-mail: weiji@tongji.edu.cn

⁵ Ph.D. Candidate, College of Civil Engineering, Tongji University
e-mail: wangyao2019@tongji.edu.cn

⁶ Ph.D. Candidate, College of Civil Engineering, Tongji University
e-mail: hhqi@tongji.edu.cn

⁷ Ph.D., College of Civil Engineering, Tongji University
e-mail: xiuzhi@tongji.edu.cn

⁸ Mr., Shanghai Industrial Investment North Bund New Landmark Construction and Development Co., Ltd.
e-mail: 31999733@qq.com

frames and planar steel trapezoid trusses in fire and found the number of potential collapse modes is limited. Sun *et al.* [4] explored the collapse mechanisms of steel frames due to column failure under fire conditions and summarized different collapse modes. Jiang *et al.* [5] investigated the fire-induced collapse mechanisms of large-span steel trusses based on a full-scale fire test. Woźniczka [6], Ho *et al.* [7], and Lu *et al.* [8] conducted fire safety assessments of steel trusses from a performance-based fire design perspective. They found that the non-uniform temperature distribution can significantly influence the responses of trusses in fire. Janardhan *et al.* [9] analyzed the behavior of a long truss beam exposed to highly non-uniform temperature fields. Results showed that the truss exhibited various responses, such as thermal bowing, lateral oscillations, efficient load redistribution, local deformations, and global failure. A real fire test on an existing truss building was conducted to investigate the collapse modes and mechanisms of the planar steel triangle truss in fire. Basic information on the test building, procedure, phenomenon, and collapse mode are introduced. The collapse mode is analyzed through numerical simulation with the general FEM software package ABAQUS. Then, a systematic numerical analysis is conducted on the planar steel triangle trusses. The findings of this study can help improve the fire resistance of the planar steel trusses and lay a great foundation for further developing the approaches for early warning of the collapse of planar steel triangle trusses exposed to fire.

2 FIRE TEST

2.1 Basic information

The test building was an actual planar triangle truss plant. The span of the truss was 11.6 m. Since the plant was established in China in the late 1950s, the compressive members of the truss were constructed with reinforced concrete to save steel. The single-angle steel was adopted for tensile members. Figure 1 shows the three-dimensional axonometric view of the test building and the site conditions. The detailed dimensions of the building and the triangle truss can be found in the open-access dataset [10].

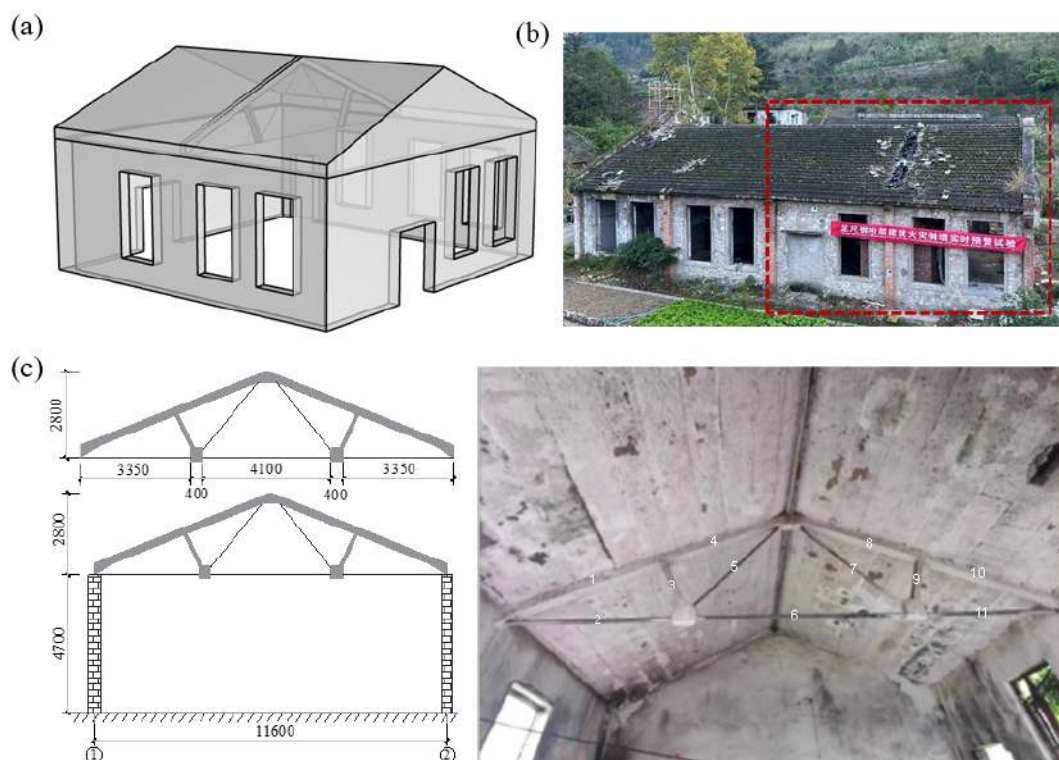


Figure 1. The basic information of the test building. (a) Three-dimensional axonometric view. (b) On-site situation. (c) Detailed information on the triangle truss (unit: mm)

2.2 Test scheme

The loads of the test building include two parts: the dead loads, which include the gravity of the roof panels and the tiles, and the live loads. The dead load per unit area born by the triangle truss was 1.5 kN/m^2 by calculation. To save test time and simulate the live loads experienced by an actual building during the fire, uniform line loads were placed along the truss span subjected to fire, as shown in Figure 2. These loads comprised 100 cast iron weights weighing 25 kg, collectively translating into an approximate uniform line load of 3.5 kN/m .

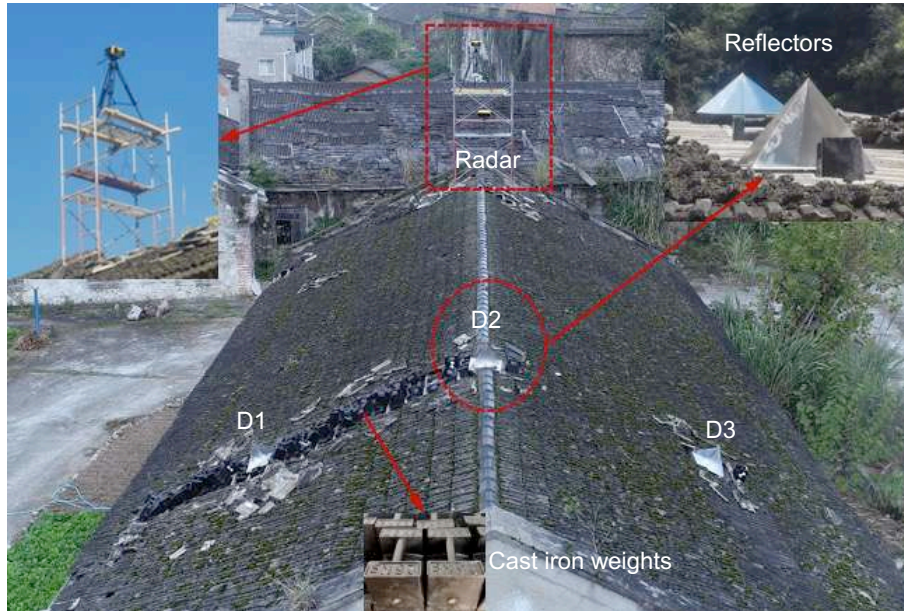


Figure 2. Distribution of the live loads

Since the height of the test building was over 7 m, a platform was constructed for stacking fuels so that the truss could collapse easily and avoid using too many wood strips. The platform was 2.7 m in height, 8 m in length, and 3 m in width. Cedarwood strips, arranged in three stacks, were used as fuel in the fire scenario. Each stack measured 1.55 m in length, 1.55 m in width, and 1.4 m in height. The dimensions of each strip were $0.05 \text{ m} \times 0.05 \text{ m} \times 1.55 \text{ m}$. Each layer contained 16 strips, and there were 28 layers in a stack, with a 0.05 m gap between each strip. There were 1,344 strips occupying a volume of 5.21 m^3 . The moisture content of the firewood was about 13%. The peak value of the heat release rate (HRR) in the fire test per stack was expected to be about 4.8 MW, according to the equation in the literature [11]. The placement of these stacks on the platform is depicted in Figure 3.

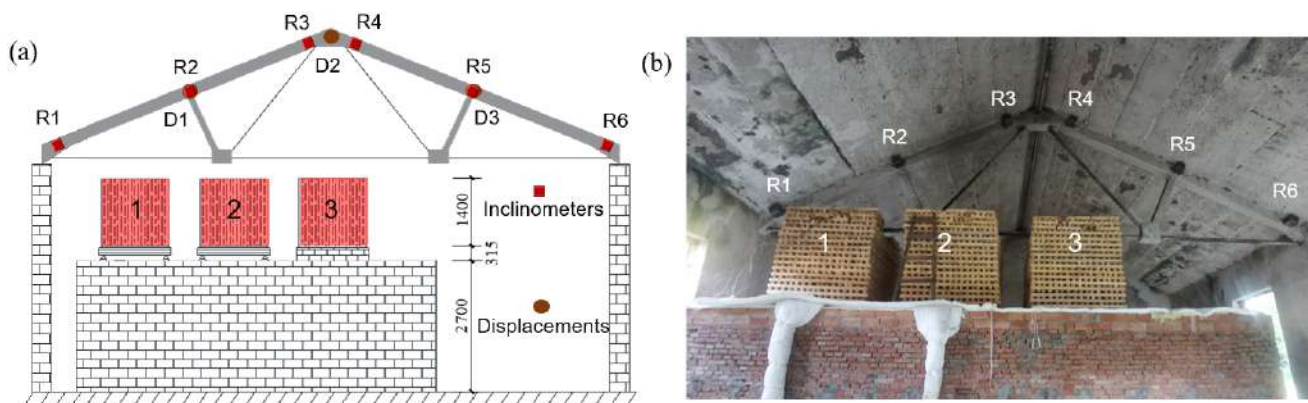


Figure 3 The placement of the stacks. (a) Elevation (unit: mm). (b) On-site photo

2.3 Measuring points and equipment

The K-type thermocouples with a diameter of 3 mm, which can work properly at temperatures under 1200°C , were used to measure the temperature of the truss members and gas. Rotations at the critical

positions of the top chord were measured by the developed inclinometers with high fire resistance, which can be seen in Figure 3. Non-contact measurement technology microwave radar was utilized, as traditional contact measurement technologies can hardly be applied at fire rescue scenes. As shown in Figure 2, aluminum alloy reflectors were positioned at the corresponding position to enhance the reflective intensity at the measured points.

2.4 Test results and collapse mode

The fire test was conducted on 1 November 2023. The detailed test process is given in Table 1 and Figs. 4 and 5. The measured data, including rotations, displacements, and temperatures, can be downloaded in the open-access dataset [10].



Figure 4 The test process of the fire test (Southwest perspective). (a) 2554 s. (b) 3145 s. (c) 3596 s (d) 4253 s

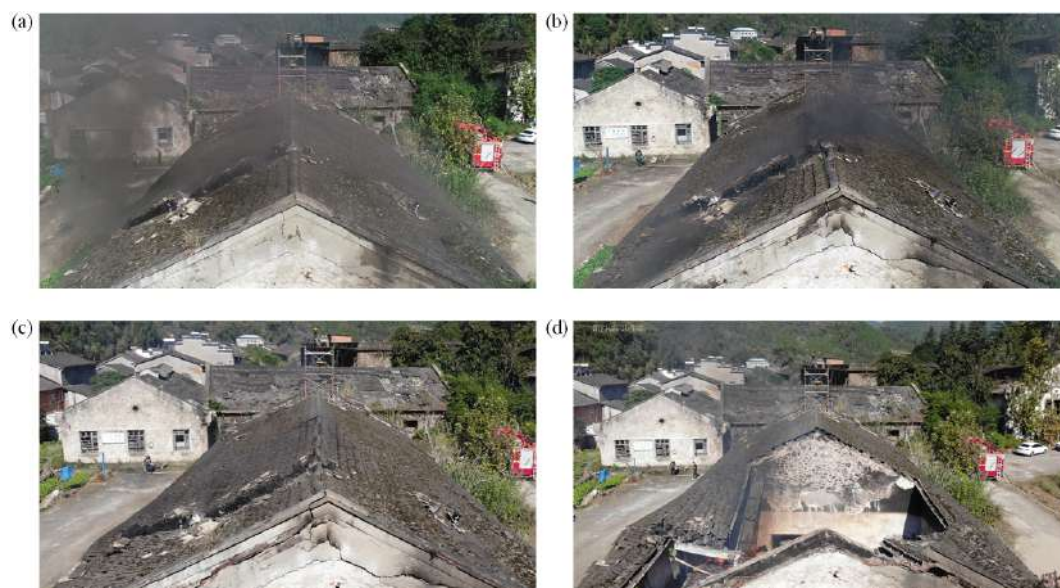


Figure 5 The test process of the fire test (Bird's eye perspective). (a) 1163 s. (b) 3145 s. (c) 4172 s. (d) 4253 s

Table 1. The detailed process of the test

Time	Relative time (s)	Test phenomena
10:09:16	0	The wood crib was ignited, and much dense smoke emerged.
10:28:39	1163	The smoke went from dense to light.
11:01:41	3145	Wood stack 3 collapsed.
11:18:10	4134	The truss exhibited significant deformation.
11:20:09	4253	The truss and the roof panels collapsed totally.

Figure 6 shows the state of the truss after the test. It can be seen that the top chord (member 4), which was directly above the fire source, underwent a bending failure. The concrete in the corresponding position had been dislodged, and the reinforcement bars were visibly bent. The steel members 5 and 6 showed significant buckling damage since the thermal expansion. According to measured data and the collapse mode, we can conclude that the collapse process of the truss is as follows:

- 1) The temperatures of steel members increased quickly after the fire was ignited. However, the thermal expansion of the steel member was constrained by other members and the boundary conditions, resulting in member buckling.
- 2) The top chord had shifted from being primarily under compression to being primarily under bending since the bottom chord buckled and lost its normal functions.
- 3) The support conditions of the trusses could not withstand the vast internal forces of expansion, and there were cracks in the truss support, resulting in apparent horizontal displacement.
- 4) The truss collapsed due to its inability to withstand external loads, resulting from a reduction in strength and stiffness as the temperatures of the truss members increased further.



Figure 6. Collapse mode of the truss

3 NUMERICAL SIMULATION

3.1 Test truss

The numerical model of the test truss was constructed using the general software package ABAQUS. The model is shown in Figure 7. The material properties of the steel truss member at ambient temperature were taken from the tensile test results. The yield strength was 426 MPa, and the ultimate strength was 553 Mpa. The stress-strain model of steel and concrete at high temperatures was determined according to Eurocode 3 [12] and 2 [13], respectively. The compressive strength of concrete at ambient temperature was 24.2 MPa,

tested by the rebound hammer and carbonization depth measuring instruments. The steel bars were embedded in the concrete members. There are three steps in the finite element (FE) analysis:

- 1) Conduct the heat transfer analysis of the concrete truss members based on the measured temperature of the surface of the concrete. The DC3D8 and DC1D2 elements were used for the concrete solids and steel bars.
- 2) Apply the loads to the top chords of the truss and get the static analysis result. The loads were all converted to the line loads applied to the top chords.
- 3) Keep the loads constant, and import the temperature distribution of the concrete members and the steel members. Then, the thermal-structural coupled analysis could be conducted. The C3D8R elements were used for the concrete solid, and the steel members and bars were simulated by the B31 and T3D2 elements, respectively.

Two boundary conditions were considered, i.e., both ends of the truss were fixed; one end was fixed, and another was slid. Here, we should note that the horizontal stiffness of the boundary should be a variant related to the column's lateral stiffness at elevated temperatures, which is hard to determine accurately in fire. Therefore, the actual boundary condition should be between the abovementioned two boundary conditions. Figure 7 shows the collapse process of the truss under different boundary conditions. It is apparent that when both ends are fixed, the bottom chord will buckle as the temperature rises. Then, the truss will form an "arc" effect until the top chords cannot resist the loads and exhibit a bending failure. Under this circumstance, the truss will not have any lateral deformation but better fire resistance. However, if one end of the boundary is slid, the truss can have apparent horizontal displacement, and the fire resistance ability is relatively lower. As the temperature rises, the truss can release internal force by lateral displacement without observing any buckling, and the vertical displacement also increases gradually. Finally, the truss collapses due to the bending failure of the top chord. Figure 8 compares the stress of the top chord at ambient temperatures and before the collapse. Before heating, the top chord mainly resists compression. However, as the temperature rises, the top chord is transferred to a member subjected primarily to bending moments. There is a clear distinction between tensile and compressive stresses in the cross-section of the top chord before the collapse, which can further illustrate that the truss collapsed because of the bending failure of the top chord in both cases.

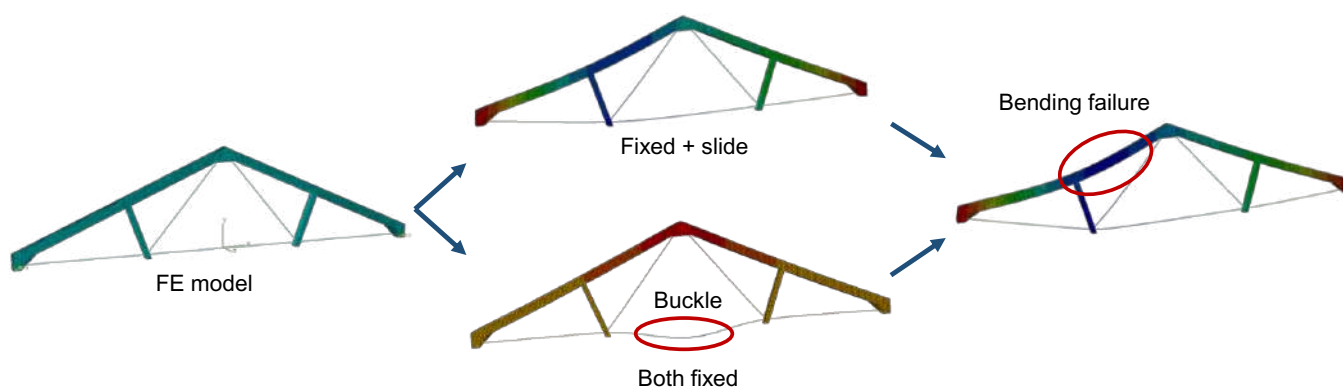


Figure 7. Collapse process obtained by numerical simulation

3.2 Steel triangle truss

The steel triangle truss, whose top chords are also made of steel, is widely used in modern plants. Systematic numerical analysis was conducted to investigate the collapse modes and mechanisms. The basic model of the triangle truss is shown in Figure 9. The B31 element is used to simulate the behavior of the truss members. The detailed configuration of the truss was determined according to the atlas [14]. Different parameters are considered in the numerical analysis.

3.2.1 Numerical simulation scheme

1) Load ratio

To investigate the effect of load ratios on the structural collapse mode, four load ratio conditions, such as 0.3, 0.4, 0.5, and 0.6, are set. The different load ratios are achieved by adjusting the nodal loads converted by the uniform load.

2) Fire scenarios

Five fire locations in the spanwise direction and two fire spreading conditions in the column spacing direction are considered, making ten fire conditions as shown in Table 2. The different fire locations and fire spreading conditions are shown in Figure 10, where S1 indicates that only the middle truss is exposed to fire, S2 indicates that all three trusses are exposed to fire, and it is assumed that the side truss is 3/4 of the temperature of the corresponding location of the middle truss; P1~P5 indicate that the fire source is located at the support directly under the middle truss, 1/4 of the span, the center of the span, 3/4 of the span, and at the other end of the span, respectively. The non-uniform temperature field is calculated using the equation in the literature [15].

3) Boundary conditions

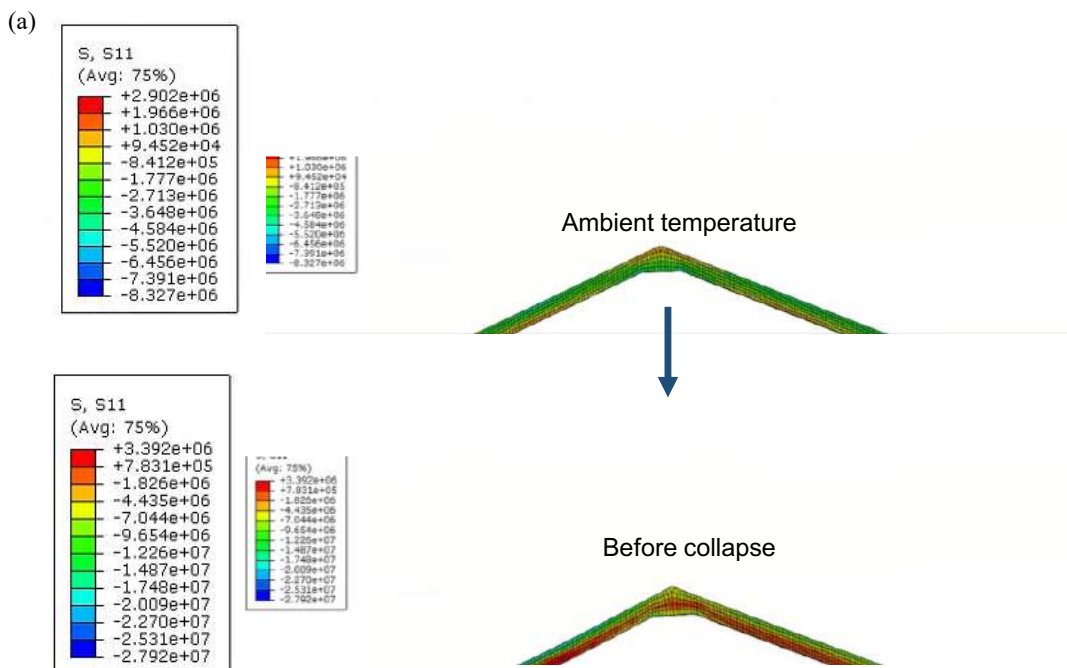
The analysis considers two constraint cases: one with a fixed hinge support at both ends (strong constraint) and the other with a fixed hinge support at one end and a sliding hinge support at the other end (weak constraint).

4) Truss span and spacing

Typical spans of 12 m, 15 m, and 18 m with typical column spacing of 6 m and 7.5 m are selected, and the corresponding forms and sections for trusses with different spans and column spacing are chosen according to the standard atlas 06SG517-1 [14].

5) Fire protections

Five fire protection conditions are considered in the analysis: 2 h, 1.5 h, 1 h, 0.5 h, and no fire protection. For steel members with fire protection, the temperature of the rod is linearly increased from 20°C to the critical temperature according to different fire resistance times [16], and the temperature increase of steel members without fire protection is calculated according to GB 51249-2017 [17].



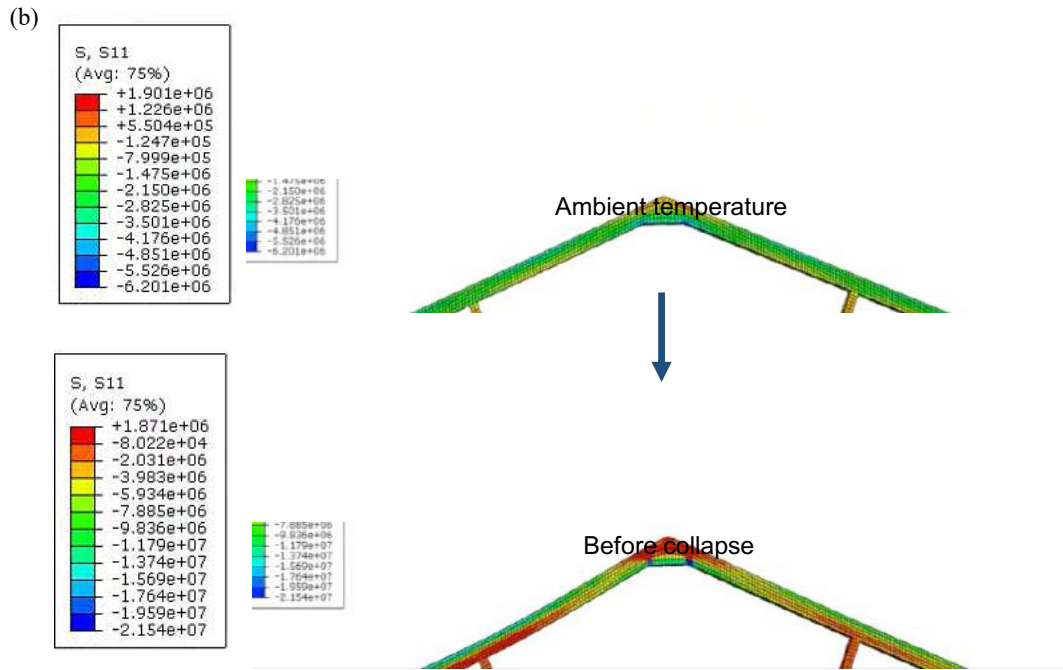


Figure 8. Stress distribution of the concrete members. (a) Fixed + slide. (b) Both fixed

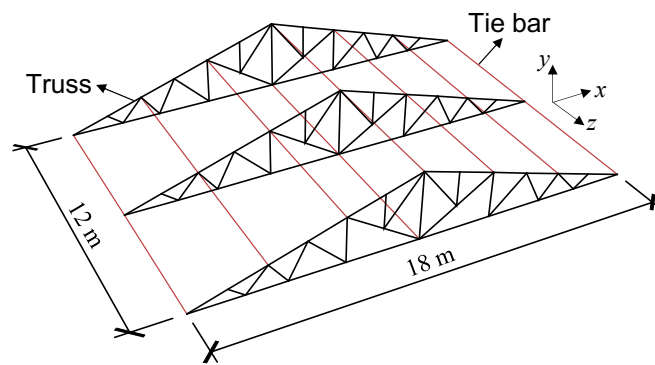


Figure 9. The basic model of the triangle truss

Table 2. Fire scenarios

Fire scenarios	Fire spreading	Fire location
F1	S1	P1
F2	S1	P2
F3	S1	P3
F4	S1	P4
F5	S1	P5
F6	S2	P1
F7	S2	P2
F8	S2	P3
F9	S2	P4
F10	S2	P5

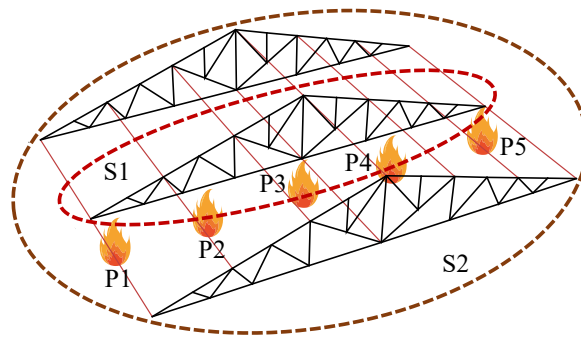


Figure 10. Fire locations and spreads

3.2.2 Collapse modes and mechanisms

Based on the systematic analysis, four collapse modes of planar steel triangle truss can be summarized, including rotation pin collapse mode (SA1), slide surface collapse mode (SA2), post-buckling rotation pin collapse mode (SB1), and post-buckling slide surface collapse mode (SB2). The fire locations and boundary conditions can significantly affect the collapse modes, while other parameters have few effects. This law is identical to the planar steel trapezoid trusses [2]. Figure 11 shows the collapse modes of the planar steel triangle truss.

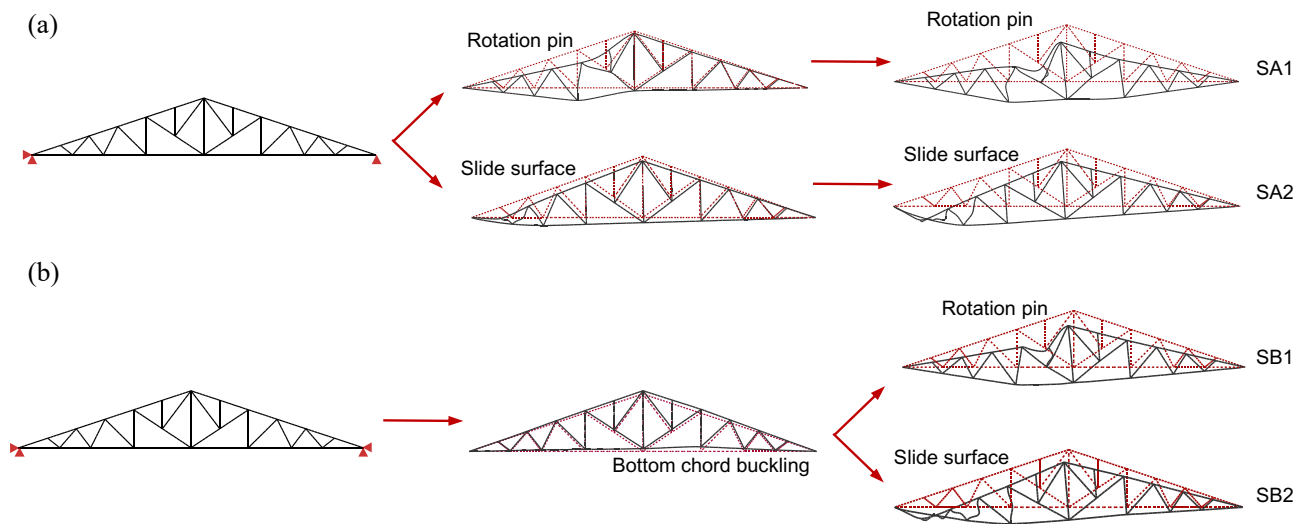


Figure 11. Collapse modes of planar steel triangle trusses

When the supports are weakly constrained, and the fire condition is far from the supports, such as under conditions F2 ~F4 or F7 ~ F9, the temperature of the internal members of the truss is higher. The top chord or web member fails first, leading to the formation of a rotational pin at the lower chord node of the corresponding bay, forming a mechanism. Under fire, this exhibits a rotation pin collapse mode SA1. When the fire condition is close to the supports, such as under conditions F1, F5~ F6, or F10, the temperature at the truss supports is higher, causing the top chord connected to the supports to buckle and fail first. The load cannot be effectively transferred to the supports, forming a slide surface at the corresponding bay, and the remaining members will slide towards the failed side, eventually resulting in a slide surface collapse mode SA2. When the supports are strongly constrained, the bottom chord of the truss is restrained by the supports and cannot deform freely. As the temperature rises, axial compression occurs and leads to buckling; since the lower chord has post-buckling bearing capacity, the truss does not immediately collapse after the lower chord buckles but continues to bear load until the top chord or web member fails, forming a mechanism, and then develops into a post-buckling rotation pin collapse mode SB1 or a post-buckling slide

surface collapse mode SB2. In contrast to test trusses with reinforced concrete top chords, the top chord of a planar steel triangle truss predominantly exhibits buckling failure, as it cannot withstand moments.

4 CONCLUSIONS

Experimental and numerical investigations are conducted on the planar triangle trusses. The collapse modes and mechanisms of the test truss and steel triangle trusses are analyzed and revealed. The findings can be summarized as follows:

- 1) In the case of the test truss with reinforced concrete top chords, the collapse sequence initiates with the buckling of steel tension members and culminates in the bending failure of the top chords.
- 2) Planar steel triangle trusses, comprised entirely of steel components, predominantly exhibit buckling in both chords and braces when collapse, with no observable instances of bending failure.
- 3) Four distinct collapse modes are identified for the planar steel triangle trusses. The specific fire scenarios and boundary conditions are crucial in influencing these collapse modes and their underlying mechanisms. The collapse modes are essential for further developing the approaches for early warning of the collapse of planar steel triangle trusses in fire.

ACKNOWLEDGMENT

The work presented in this paper was supported by Mr. Yongfeng Nie from the Hubei Fire Rescue Brigade and Mr. Qi Luo from the Yichang Fire Rescue Detachment. The authors gratefully acknowledge the financial support provided by the National Key Research and Development Program of China under grant No. 2022YFC3801900 and the Shanghai Pujiang Program under grant No. 22PJ1414000.

REFERENCES

1. Li, G. Q., Ji, W., Feng, C. Y., Wang, Y., & Lou, G. B. Experimental and numerical study on collapse modes of single span steel portal frames under fire. *Eng. Struct.* 245, 112968 (2021). <https://doi.org/10.1016/j.engstruct.2021.112968>.
2. Li, G. Q., Li, J., & Zhu, S. An approach for early-warning collapse of planar steel trapezoid trusses exposed to fire. *Fire Saf. J.* 137, 103778 (2023). <https://doi.org/10.1016/j.firesaf.2023.103778>.
3. Ji, W., Zhu, S., Li, G. Q., Lou, G., & Jiang, S. Approach for early-warning collapse of double-span steel portal frames induced by fire. *Fire Saf. J.* 131, 103628 (2022). <https://doi.org/10.1016/j.firesaf.2022.103628>.
4. Sun, R., Huang, Z., & Burgess, I. W. Progressive collapse analysis of steel structures under fire conditions. *Eng. Struct.* 34, 400-413 (2012). <https://doi.org/10.1016/j.engstruct.2011.10.009>.
5. Jiang, S., Zhu, S., Guo, X., & Li, Z. Full-scale fire tests on steel roof truss structures. *J. Constr. Steel Res.* 169, 106025 (2020). <https://doi.org/10.1016/j.jcsr.2020.106025>.
6. Woźniczka, P. Performance-based analysis of older-type large-space hall in fire. *Arch. Civ. Eng.* 65(1), 17-29 (2019). <https://doi.org/10.2478/ace-2019-0002>.
7. Ho, H. C., Chung, K. F., & Wong, Y. Structural fire engineering study on unprotected long span steel trusses. *Proc. Eng.* 14, 1132-1139 (2011). <https://doi.org/10.1016/j.proeng.2011.07.142>.
8. Lu, L., Yuan, G., Huang, Z., Shu, Q., & Li, Q. Performance-based analysis of large steel truss roof structure in fire. *Fire Saf. J.* 93, 21-38 (2017). <https://doi.org/10.1016/j.firesaf.2017.08.002>.
9. Janardhan, R. K., Shakil, S., Lu, W., Hostikka, S., & Puttonen, J. Coupled CFD-FE analysis of a long-span truss beam exposed to spreading fires. *Eng. Struct.* 259, 114150 (2022). <https://doi.org/10.1016/j.engstruct.2022.114150>.
10. Li, J., Zhu S., Li G.Q., Zhang C., Chen B., Chen N., Yang X., Shan J., Qi H., Ji W., & Wang Y. "Dataset of a Fire-induced collapse test on an existing building with a truss roof by Tongji University", in *Fire-induced collapse test on an existing building with a truss roof by Tongji University*. DesignSafe-CI (2024). <https://doi.org/10.17603/ds2-9bg2-xd96 v3>.

11. Huang, X. L., Xie, Y. Y., Rong, J. Z., & Yang, X. H. Experimental study of heat release rate of wood crib. *Fire Sci. Technol.* 33(05), 484-486 (2014) (in Chinese).
12. Franssen, J. M., & Real, P. V. *EC3: Design of steel structures; Part 1-2: Structural fire design.* John Wiley & Sons (2016).
13. British Standards Institution. *Eurocode 2: Design of concrete structures: Part 1-1: General rules and rules for buildings.* British Standards Institution (2004)..
14. National building standard design atlas: 06SG517-1 light roof triangle steel roof truss (circular steel tube、square steel tube). Beijing: China Planning Press, 2006 (in Chinese).
15. Du, Y., & Li, G. Q. A new temperature–time curve for fire-resistance analysis of structures. *Fire Saf. J.* 54, 113-120 (2012). <https://doi.org/10.1016/j.firesaf.2012.07.004>.
16. Jiang, J., Wang, C., Lou, G., & Li, G. Q. Quantitative evaluation of progressive collapse process of steel portal frames in fire. *J. Constr. Steel Res.* 150, 277-287 (2018). <https://doi.org/10.1016/j.jcsr.2018.08.020>.
17. Code for fire safety of steel structures in buildings: GB 51249-2017. Beijing: China Planning Press, 2018 (in Chinese).

EXPERIMENTAL AND NUMERICAL RESPONSE OF STEEL TRUSSES EXPOSED TO A LOCALIZED FIRE

Kathryn Chin¹, Chloe Jeanneret², Panagiotis Kotsovinos³, John Gales⁴

ABSTRACT

This research focuses on the determination of the stability of a stadium roof structure when a fire occurs to permit timely egress of the occupants. To achieve this objective, a series of experiments were conducted on isolated steel truss systems. The first included testing two small-scale truss systems over a localized, methanol pool fire, designed to mimic potential stadium fire events. Thermocouples were placed at six locations to gather time-temperature data for model validation. An additional thermocouple tree test was used to collect the environment temperatures of a representative methanol pool fire, which was used as model incident heat inputs. The models were simplified to a two-dimensional heat transfer problem, with LS-DYNA being used as the solver. Two modelling attempts were made with varying boundary conditions to determine best modelling techniques. Key findings were that the model overestimates horizontal heat transfer but underestimates vertical heat transfer. The article concludes with a future research framework. Future work should conduct inverse modelling to determine if improper use of heat transfer coefficients is the source of the inaccuracy in modelling heat transfer. In addition, a structural model should be created, which will use the heat transfer model results and produce thermal strains. With a two-part model, other fires and scaled tests can be validated to produce a model which can then be used in fire design and analysis.

Keywords: Steel trusses; localized fire; finite element modelling; stadia

1 INTRODUCTION AND MOTIVATION

The structural fire protection of stadia roof design varies internationally. In Australia, that building code illustrates that stadium roofs do not require fire-resistance, given that the materials used are non-combustible [1]. If the materials are combustible, common practice is to assess the material's performance against various risk factors. In the UK, guidance is through Approved Document B, which provides fire resistance standards for loadbearing components. Roof systems are exempt from this requirement should roof collapse does not lead to structural collapse [2]. Other stadia design guidelines such as the "Green Guide" note that should the roof contain ancillary equipment, a risk assessment should be completed to determine if fire protection is necessary [3]. However, it is important to recognize that the roof is generally part of the stability system for horizontal loads. In addition, these roof systems can support other fire rated construction or critical life safety systems (for example a smoke control or PAVA system). Therefore, the roof's fire scenarios need to be captured in the general design.

¹ Graduate student, York University
e-mail: kchin01@yorku.ca, ORCID: <https://orcid.org/0000-0002-5903-741X>

² PhD Candidate, York University
e-mail: chloej96@yorku.ca, ORCID: <https://orcid.org/0009-0008-0848-8393>

³ Assistant Professor, University of Patras,
e-mail: p.kotsovinos@gmail.com, ORCID: <https://orcid.org/0000-0003-2234-0420>

⁴ Associate Professor, York University
e-mail: jgales@yorku.ca, ORCID: <https://orcid.org/0000-0001-8025-3902>

However, from the review of international guidelines for stadium roof design, the code can be nonspecific. This creates misunderstanding on how to achieve proper fire design and the intention of the code that requires the provision of that fire design. There is a required competency of the practitioner to understand these requirements and research into the relation of human behaviour and structural stability.

In traditional fire safety engineering research – structural stability and evacuation in a fire event are not usually considered in a joint manner and treated in isolated expertise ‘silos’. There are few that couple both disciplines in research despite their relations. This is likely rationalized as structural stability in fire research is considered relevant once a fire has reached its post-flashover stage while evacuation is normally considered relevant in relation to pre-flashover fires. However, there is credence to jointly consider the two disciplines particularly in relation to documented case studies of fires in stadiums and the existing code provision requirements.

While classical case studies such as Bradford [4] certainly demonstrate the dangers of combustible roofing in stadia and the need to better understand well-ventilated fires in these spaces, the authors focus on steel structures for the purpose of this paper but highlight the extension of this study area beyond steel.

A recent illustrative fire demonstrating a gap in knowledge between human behaviour and structural response in a localised fire event can be considered. In this fire, which occurred at a Toronto (Canada) stadium in 2022, an overhead speaker experienced a localized electrical fire during a professional sports game. The fire was adjacent to a large structural steel truss supporting system. This system is typical in stadium and arena design. Spectators were evacuated using a phased approach, starting with those closest to the fire (15 minutes after realization of fire) with extension to a full evacuation (50 minutes after realization of the fire) at the suspension of the sporting event. Tickets were refunded and financial losses were estimated to be more than \$1.5 million CAD. There were no reported or documented issues with the process of evacuation. Once started, it was observed orderly and completed in a timely fashion. However, this fire illustrates two facts 1) that a localized fire is a credible stadium fire scenario exposing structural members to significant heat, and 2) that the timing of egress initiation was of significant time after inception (realization) of the fire. Point two pertains to the first; if a structural system cannot be maintained for the duration of the egress event there is a credible life safety hazard. The two are understudied but not independent. This study is themed on the determination of the stability of an unprotected stadium roof structure when a fire occurs to permit timely egress. To achieve this objective, a series of experimental tests were conducted on isolated steel truss systems with subsequent modelling technologies explored.

2 BACKGROUND LITERATURE

There is limited research pertaining to the importance of engineered structural fire design for roof components and how to implement a safe and optimised structural fire protection design for the roof structure. Studies were reviewed to understand the focus of current literature regarding steel truss roof structures and fire design. First, studies that provided design methodology for fire protection of stadium roof structures were reviewed. Following that, the review was opened to studies regarding fires and steel truss roofing systems of stadia or other large structures.

According to Block and Butterworth [5], most countries’ fire design is determined by prescriptive design such as Approved Document B. However, stadium structures provide unique challenges because the prescriptive design provisions are often inapplicable. The study notes this knowledge gap and provides a risk-based approach for designing stadia structural elements, investigating various scenarios and parameters based on their frequency, probability, and consequence. The result is a fire protection regime of specific structural elements. This study highlights the lack of guidance for stadium roof design. It also provides a method to aid in the design of these structures.

Similarly, Lu et al. [6] discusses the inappropriateness of using traditional prescriptive designs for large structures’ roof design from a fire perspective. They note that regularly, design would require the use of the ISO834 standard fire curve, which is unsuitable. A case study regarding an exhibition centre in China that had a truss roof structure was conducted. Various fire scenarios were modelled generating recommendations for general design of large steel truss roof systems. Overall conclusions were that

structures of an exhibition centre scale provide unique challenges in design because the fire behaviours are complex, particularly the cooling phase.

Few experimental studies have been conducted on steel roof truss structures. However, Jiang et al. [7] completed non-destructive localized fire tests and destructive wood crib fuel tests on a full-scale truss roof system. The non-destructive tests showed no damage that would impact structural integrity, while the destructive tests noted failure modes. The objective was to understand how the trusses behaved both from a thermal and structural perspective. This data was then used in two follow-up studies [8-9]. The two follow-up studies focused on developing two methods to provide early-warning for when a steel truss structure would fail. While these studies were not design for stadia, they were intended for high occupancy buildings. Several studies were found to have conducted post-fire evaluations of steel truss roofing systems of large structures. For example, a post-fire evaluation of a convention centre in New Zealand was conducted by Clifton et al. [10]. The structure was made of steel and concrete and was subject to a fire that burned for over ten days. The study contains key steps required to determine the structural integrity of the building, and then the steps taken to determine how to rehabilitate the structure while maintaining safety. The fire was much larger than what is considered herein, and no focus was placed on egress, since it was a post-fire evaluation focused on structural analysis. However, it provides insight on how to assess a high occupancy building post-fire and how to determine a rehabilitation plan. Muñoz Blanc et al. [11] also created a framework to evaluate the structural integrity of steel structures after a fire. Their methodology was tested using a case study of a stadium fire in Andorra, which had a truss roof structure. The methodology was broken into three milestones: data collection, numerical simulations, and material testing. Data regarding the stadium, its structure and the fire were collected. This information was inputted into a series of simulations including fire simulations, a thermal heat transfer analysis, and a structural analysis model. The structural analysis, the final simulation, along with material testing produced the residual strength of the steel members.

Overall, the reviewed literature shows a plethora of case studies applying various design methods, experiments, and post-fire evaluations. A combination of both localized fire and large-scale fires were considered in various studies. However, it is clear from the reviewed literature that stadium roof studies cannot be designed using a prescriptive method because the guidelines and codes were not intended for that purpose. Instead, a performance-based design must be used. Some studies reviewed provide guidance or methods to do performance-based design, however, they are few. Therefore, the objective of this research is to generate modelling technology and techniques that can predict truss deformation behaviour during and after a fire event. The overarching vision to provide additional tools that can be used to assist in fire designs of stadium roofs and assist analysis that can determine the stability of a stadium structure when a fire occurs to permit timely egress. To achieve this objective, two open web steel joist (OWSJ) sections of similar chemical composition make-up to those typically seen in North America stadia and arenas were tested over a localized fire. An additional thermocouple tree experiment was conducted of the localized fire. As a preliminary stage of research, the first experiments were replicated in a heat transfer analysis LS-DYNA model and the experimental data collected was used for model validation. The second experiment was used as input data for the model. Analysis of the comparison between the experimental and modelling results was conducted to determine best practices when using models for design.

3 EXPERIMENT

3.1 Methodology

In this research, the experiments consisted of two types of scenarios. The first tested two unloaded OWSJ sections using a 30-minute methanol pool fire. The sections are commonly used in Canadian structures only they are of a smaller scale. Often, these types of OWSJ sections will have a yield strength of 350 MPa. Figure 1 shows the dimensions and experimental setup. The trusses were composed of four, 38 x 38 x 4.8 mm, angled members, and a series of cylindrical diagonal members with a diameter of 20 mm. The trusses were 2200 mm and 2100 mm long, however, only the 1350 mm portion of the trusses (see Figure 1) was considered in the experiment and subsequent model. The trusses were placed on concrete masonry units

and secured using both concrete and clay masonry units to prevent torsional effects. The bottom of the truss was 200 mm above the fuel pan.

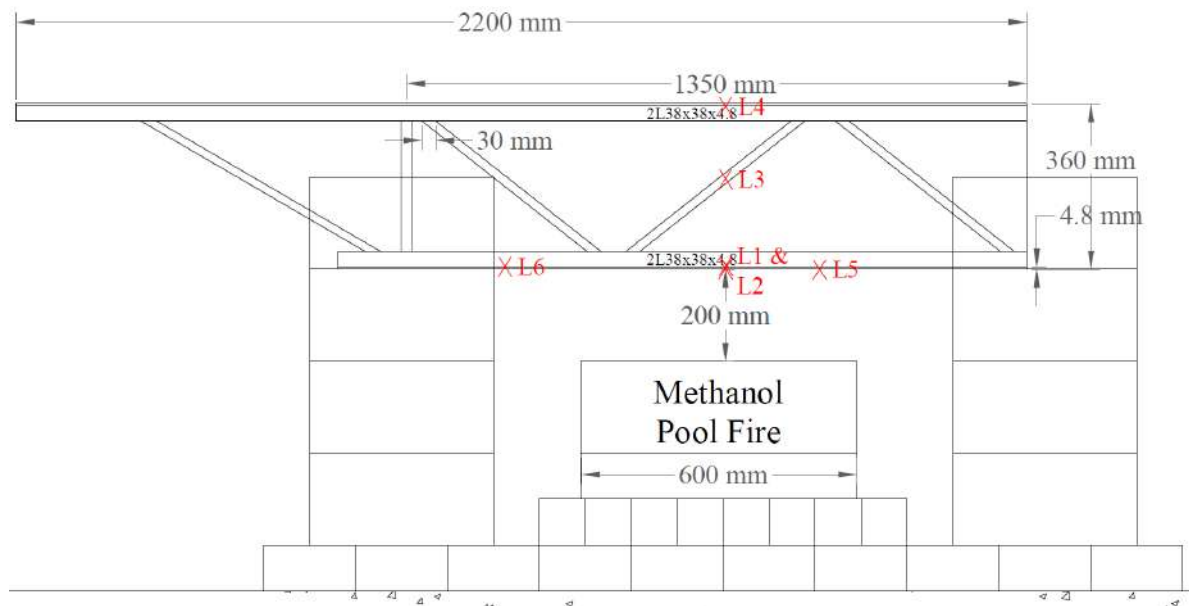


Figure 1. Truss dimensions and experimental setup

A methanol pool fire was chosen because it represents a localized fire scenario, as was seen in the case study. In addition, methanol pool fires have been shown to produce consistent results, meaning that the experiment is repeatable.

K-type thermocouples were used to collect time-temperature data during the test. The instrumentation continued recording during the cooling period, stopping once the steel temperature was below 100°C. While 16 thermocouples were used, eight thermocouples at five locations were chosen to be discussed in the study herein (see Figure 1). Further information on all the thermocouple data and locations can be found in Reference [12]. The first four locations are on the same vertical line, going through the centre of the middle diagonal member. L1 and L2 are located on the top and bottom of the bottom chord. The third and fourth thermocouple locations were chosen to show vertical heat transfer through the truss system, and the remaining thermocouples were chosen to show horizontal heat transfer. All thermocouples were covered with fibre wool, an insulating material, and secured with aluminium tape and nickel-chromium wire.

In addition to setting up thermocouples, a high-resolution camera and narrow spectrum illumination technology [13] were used to collect photos of the truss every five seconds (following Gatien et al. [14]). Narrow spectrum illumination allows for clear images, without visual impairment from the flames (see a side-by-side comparison in Figure 2). The images, along with a speckled pattern painted onto the truss, are used for Digital Image Correlation which can be translated into strain values. The strain values will be used to validate a coupled heat transfer and structural model in the future.

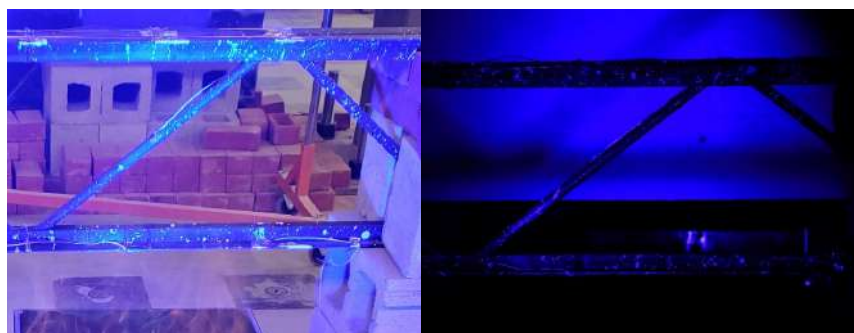


Figure 2. Truss exposed to localized fire without narrow spectrum illumination technology (left) and with narrow spectrum illumination technology (right)

The second test conducted was a methanol pool fire using a thermocouple tree. The setup of the fuel pan was the same as seen in Figure 1, but instead of the specimen, thermocouples were placed at the centre of the fuel pan at heights in increments of 100 mm. They collected time-temperature data during a one-hour burn.

3.2 Results

Results from the first set of experiments can be seen in Figure 3 below. The average from both experiments of all the thermocouples per location were plotted. The locations contained between one to four datasets. L6 had only one dataset because a thermocouple at L4 was moved to L6 during the second test.

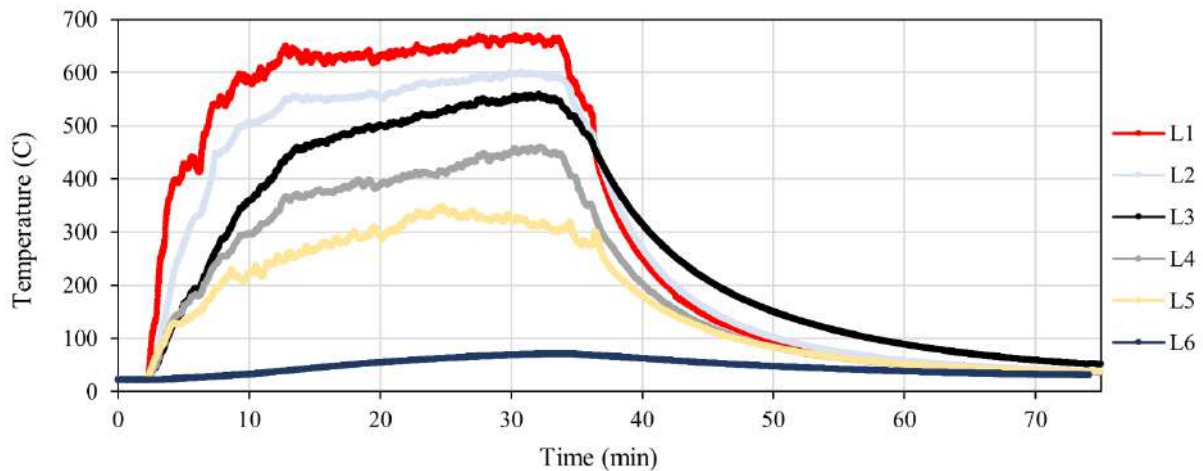


Figure 3. Time-temperature data collected from the truss system experiments

The highest temperatures were found in L1, which was expected, since this was the location nearest to the heat source. When comparing L1 through L4, the temperatures decreased moving away from the fuel source. For horizontal heat transfer, the exposed location L5 experienced higher temperatures than the protected location L6. Note that L5 and L6 were not equidistant to the centre of the fuel source. L5 was closer to the heat source than L6, and, unlike L6, there was no vertical heat transfer prior to reaching L5, resulting in higher temperatures.

Figure 4 shows the data from the second experiment at heights 200 mm to 600 mm from the fuel pan. These values were chosen because they are relevant based on the height of the truss. The closest thermocouple to the heat source (200 mm) experienced the highest temperatures, with the temperatures decreasing moving away from the fuel pan.

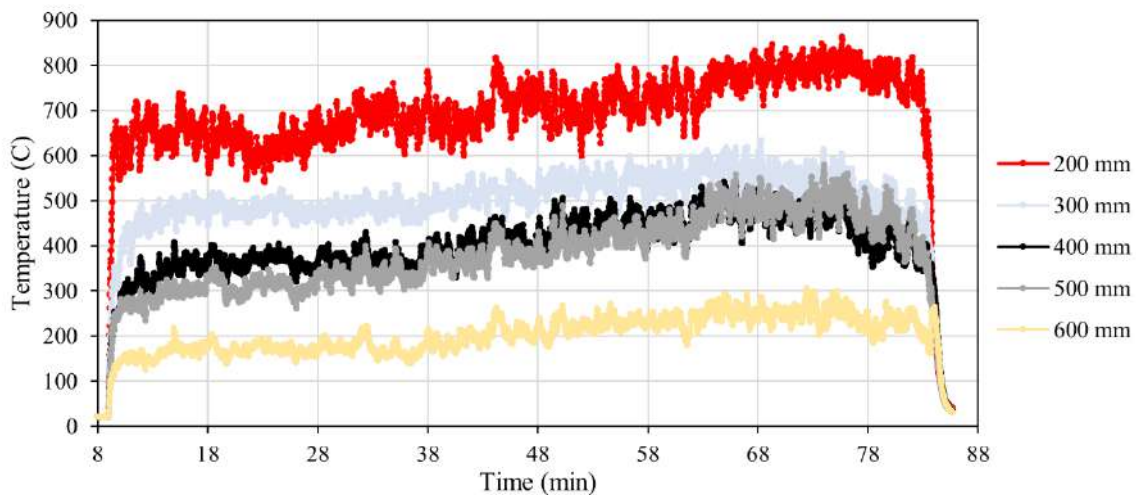


Figure 4. Time-temperature data collected from the thermocouple tree experiment

4 MODEL

4.1 Methodology

Following the experiments, a heat transfer model was developed in LS-DYNA to determine the capability of the software and heat transfer assumptions to compute the expected temperatures and heat transfer as a first stage of research. LS-DYNA was chosen as the solver because of its common use in academia and industry. It has been used in a variety of applications including modelling steel in fire in a structural analysis and heat transfer analysis [15]. Primer was chosen as the pre-processor, and D3Plot and TH/IS as the post-processors. The model represents a simplified two-dimensional heat transfer problem. To do so, the top and bottom chords of the truss were drawn as rectangles representing one leg of one of the L-shape members. The diagonal members were drawn as parallelograms with a width equivalent to the truss specimen's diameter (see Figure 1 for dimensions). A mesh of 1 mm and solid elements were chosen for the preliminary model following Temple et al. [16] and Watson et al. [17].

Material properties were inputted; the density, 7941.176 kg/m^3 , was determined using the Canadian Handbook of Steel Construction [17]. The specific heat capacity and thermal conductivity curves are from Eurocode 3 [19]. The initial temperature of all nodes was set to ambient temperature (20°C).

An explicit, non-linear solution was chosen following Temple et al. [16] and Watson et al. [17]. The models ran for 4750 seconds using an initial one second timestep, with the ability to increase or decrease as the simulation continues. Future work will include both a mesh and time-sensitivity analysis, however, these inputs were considered acceptable for this preliminary stage of the analysis.

For both modelling attempts, the pool fire was represented in the model by using radiative and convective boundary conditions. The surface emissivity, taken from Eurocode 3 was 0.7 [19], and the heat transfer coefficient ($9 \text{ W/m}^2\text{K}$) was taken from Eurocode 1 [20]. Both types of boundary conditions required an environment temperature, which was inputted as a time-temperature curve. This data was taken and modified from the second experiment (see Figure 5). Because the second experiment was a one-hour test, the data from the first half an hour in Figure 4 was used. To facilitate cooling in the simulation, the data moving back to ambient temperature was also used to form a new curve. For the remaining time in the simulation, the temperature was set to 20°C .

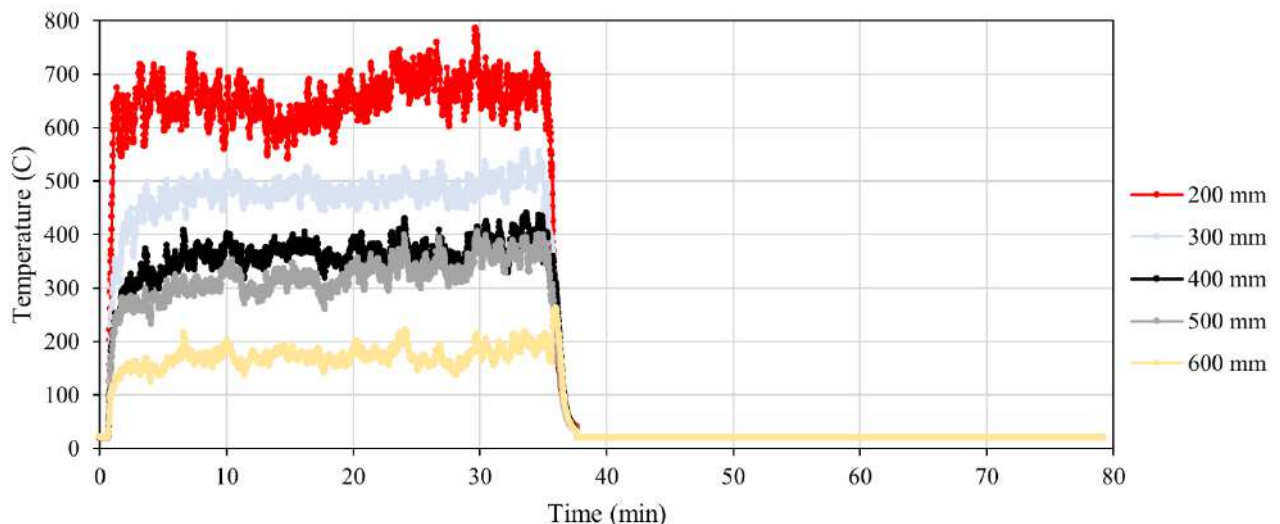


Figure 5. Modified environment time-temperature curve for model input

In the first attempt at modelling, boundary conditions were applied as a line along the bottom chord, the width of the fuel pan (bottom of the black section in Figure 6). Both radiation and convection were applied using the modified data collected at 200 mm for the environment temperature input (see Figure 5). In the second attempt, radiative and convective boundary conditions were applied to every node within the pan width following Watson et al. [17]. The truss was divided into sections using tributary areas, where a different environment time-temperature curve was inputted, depending on the section location (see Figure 6).

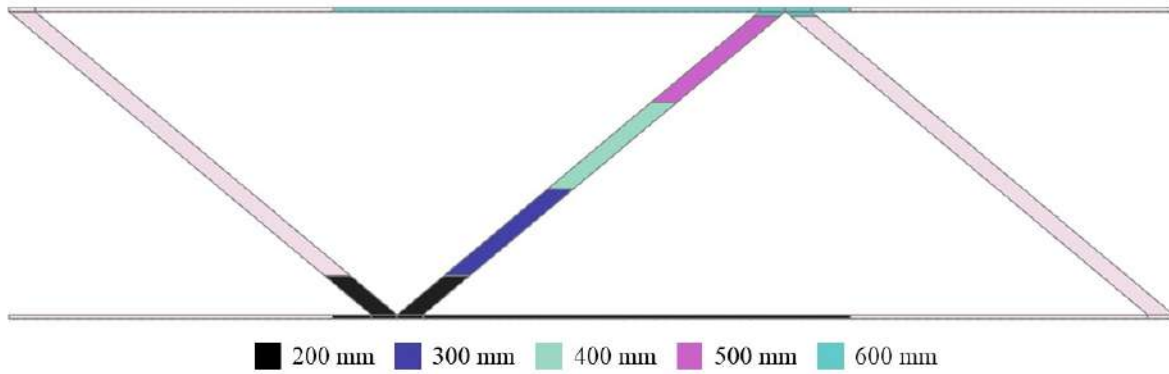


Figure 6. Second model boundary conditions (location and input time-temperature curve)

4.2 Results

Figures 7 and 8 show the comparison of the first model and experimental results. Note that the experimental data was shifted forward by 90 seconds to allow for a proper comparison. When comparing the model to the experiment for L1 and L2, the model has little difference between L1 and L2, whereas the experiment has a difference of approximately 100°C for much of the heating period. The model L1 and L2, reach a similar maximum temperature to the bottom chord location L1 (680°C versus 670°C). The model results for L3 and L4 show little increase in temperature, meaning the model underestimates the heat transfer in the vertical direction. In contrast, the L5 and L6 results show that the model overestimates the heat transfer in the horizontal direction. Both model results for L5 and L6 are significantly higher than the experimental results.

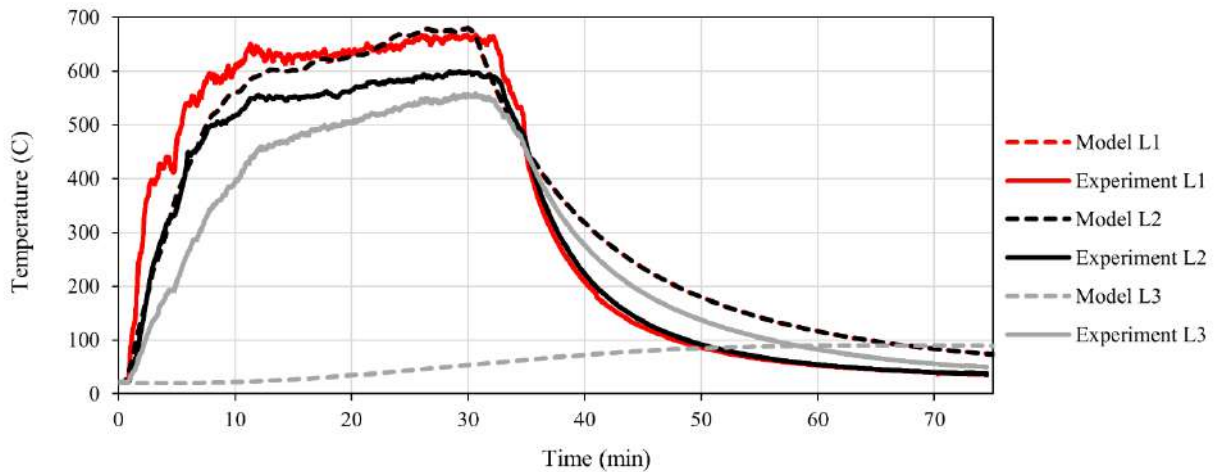


Figure 7. Comparison of the first model and experimental results for Locations 1 to 3

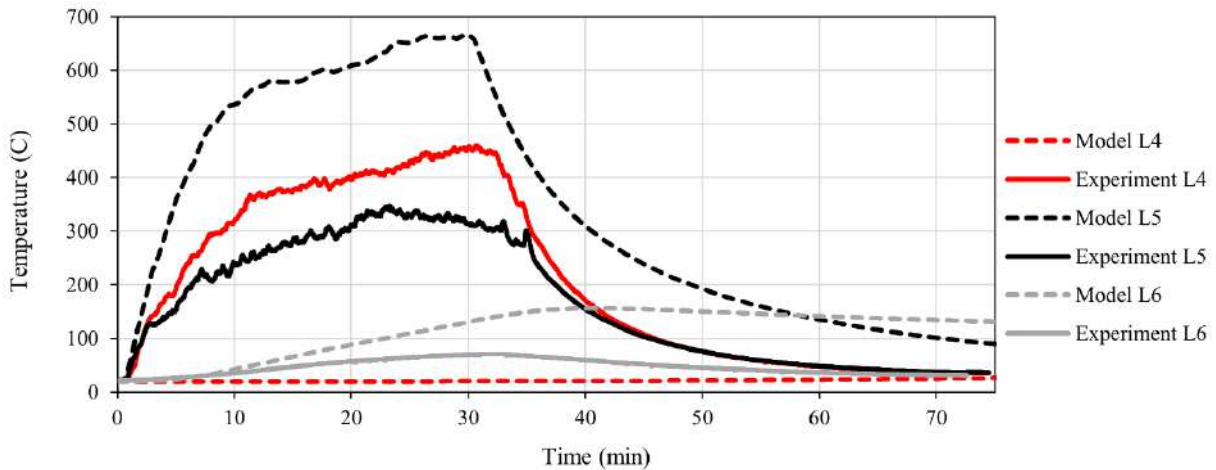


Figure 8. Comparison of the first model and experimental results for Locations 4 to 6

As a response to the results from the first model that illustrated inaccuracies in the assumed model, an additional modelling attempt was made. Improved boundary conditions were applied account for the environment temperatures experienced at various heights. Results from this study can be seen in Figures 9 and 10. Like the first model, there is little difference between the exposed and protected locations along the bottom chord (L1 and L2). However, the model L1 and L2 and the experiment L1, continued reach similar temperatures (693°C versus 670 °C). The vertical heat transfer is more accurate, as shown in the comparison of the data from L3 and L4. However, the model still under predicts the vertical heat transfer. In the same trend as the first model, the second model overestimates the horizontal heat transfer, but to a higher degree, which can be seen in the L5 and L6 data. General trends of this model show that the second model has a faster heating and cooling rate compared to the experiment, which is the opposite of the first model.

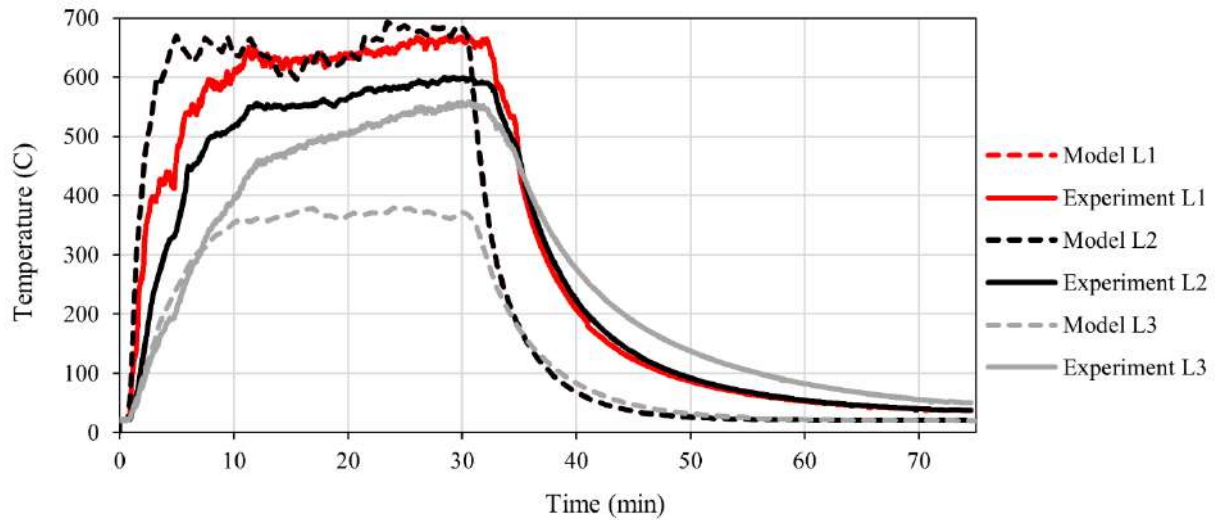


Figure 9. Comparison of the second model and experimental results for Locations 1 to 3

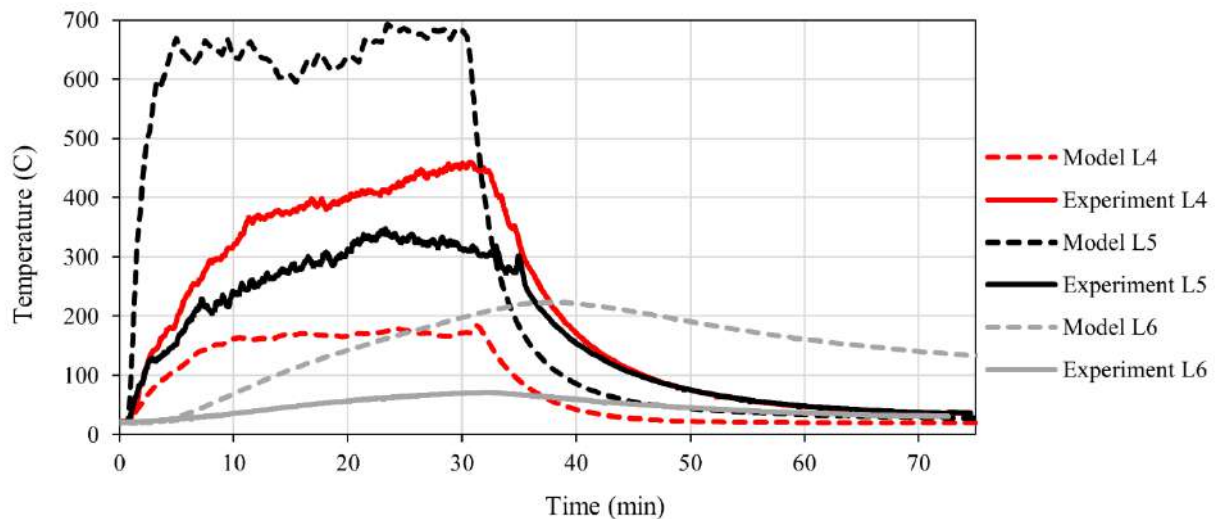


Figure 10. Comparison of the second model and experimental results for Locations 4 to 6

5 DISCUSSION

The completion of both models provides insight into best practices and future work regarding heat transfer models. From the first modelling methodology results, it is evident that applying boundary conditions at a single location cannot accurately represent a localized fire. Localised fires results in increased gas temperatures well beyond their immediate location. In attempt to address this, a second modelling method was completed in which additional boundary conditions were inputted. Convective and radiative boundary conditions were applied to all nodes exposed to the fire. This represented environment temperatures above

the flame, better encapsulating the temperatures experienced by the truss. As a best practice, designers and researchers should be aware of the importance of appropriate boundary conditions to ensure that they do not underestimate the expected temperature values in heat transfer analyses.

Another trend seen in the model results were the different rates of heating and cooling. For the first model, overall, the heating and cooling occurred slower in the model than the experiment. The opposite was seen in the second model. A possible reason why the heating and cooling rates are incorrect could be due to the coefficients used. While the coefficients were taken from various Eurocodes, it is possible that they are not completely representative of the specimen in the study herein. This is because these coefficients were developed for fully developed fires in compartments rather than localised pool fires in large spaces. An inverse modelling approach can be done in the future to verify the actual heat transfer coefficients. Additional experiments studying heat transfer coefficients in similar conditions using appropriate instrumentation would be needed.

In addition, the model overestimates horizontal heat transfer, but underestimates the vertical heat transfer. When simplifying the model, the horizontal chords comprised of two angle members each were simplified to a single rectangle. This rectangle was representative of one leg of one angle. Therefore, while the model results from L1, L2, L5 and L6 are technically correct, the heat transfer through the diagonal chords is only half of what it would be in the experiment. This might explain why the vertical heat transfer is inaccurate. This does not however, explain the overestimation of heat transfer in the horizontal direction.

The study herein contains a heat transfer model of an unloaded steel truss experiment exposed to a localized fire. Future work will include using the time-temperature results from the model as an input for a structural analysis model. The structural model will produce strain values of the truss members which can be validated using DIC results. From there, the scale of steel truss members and effects of longer fire duration will be assessed.

With a two-part model that can produce strain from environment temperatures, the structural integrity of the structure can be assessed. This will provide information for when or if an evacuation is necessary. Preventing unnecessary evacuations will bring financial benefit. From a design perspective, the model can be used to simulate various fire scenarios to understand how the steel will behave. This can also be used as a post-fire tool to determine if repair or demolition and rebuild is required. Preventing unnecessary demolition and rebuilding will also have financial and environmental benefits.

6 CONCLUSIONS

The residual strength of steel structures post-fire can be uncertain. As seen with the case study event, ceiling fires are a credible fire scenario to consider with relevancy to all stages of fire. The uncertainty experienced during the case study showed that financial losses can occur if an unnecessary evacuation occurs, or adequate protection is not provided. Therefore, it is important to provide guidance for stadium roof design, especially since prescriptive-based design is not possible. Additionally, it is important to understand how to analyse the structural stability of a commonly used system such as a truss during and after a fire event to ensure safety. This study explored the prospect of using modelling technology to determine structural stability through a preliminary heat transfer model. The model was compared to a series of experiments which replicated aspects of the case study fire event.

Preliminary results showed that the model overestimated heat transfer in the horizontal direction, but underestimated results in the vertical direction. The study outlined future work required to generate a higher certainty heat transfer model. Once the heat transfer model can accurately predict steel temperatures, the data can be inputted into a structural analysis model which can indicate the structural integrity of the system. Such numerical model, once further validated, can be used by designers, as well as provide guidance to those analysing truss systems during or after a fire.

ACKNOWLEDGMENT

Authors acknowledge the York University Graduate Fellowship award, NSERC Canada through its Discovery and Scholarship Program. ARUP UK is thanked for their technical discussions. Benson Steel is thanked for providing specimens for testing. Sara Guevara Arce is thanked for assisting in experimentation.

REFERENCES

1. Australian Building Codes Board: National Construction Code - Volume One: Building Code of Australia; 2022.
2. HM Government: The Building Regulations 2010 - Fire Safety - Approved Document B; 2010. [Online]. Available: www.gov.uk/guidance/building-regulations-
3. Sports Ground Safety Authority: Guide to Safety at Sports Grounds, 6th ed. London; 2018.
4. Young, T., Gales, J., Kinsey, M., and Wong, W. (2021) Variability in Stadia Evacuation under Normal, High-Motivation, and Emergency Egress. *Journal of Building Engineering* (Elsevier). 40. <https://doi.org/10.1016/j.jobe.2021.102361>
5. Block, F.M., Butterworth, N.A., The Definition of Fire Resistance Requirements for Stadium and Arena Developments Based on Risk. *Int J Steel Struct*, 9, 39–46 (2009). <https://doi.org/10.1007/BF03249478>
6. Lu, L., Yuan, G., Huang, Z., Shu, Q., Li, Q., Performance-based analysis of large steel truss roof structure in fire. *Fire Saf J*, 93, 21-38 (2017). <https://doi.org/10.1016/j.firesaf.2017.08.002>
7. Jiang, S., Zhu, S., Guo, X., Li, Z., Full-scale fire tests on steel roof truss structures. *J Constr Steel Res*, 169 (2020). <https://doi.org/10.1016/j.jcsr.2020.106025>
8. Li, G.Q., Li, J., Zhu, S., An approach for early-warning collapse of planar steel trapezoid trusses exposed to fire. *Fire Saf J*, 137 (2023). <https://doi.org/10.1016/j.firesaf.2023.103778>
9. Jiang, S., Zhu, S., Guo, X., Chen, C., Li, Z., Safety monitoring system of steel truss structures in fire. *J Constr Steel Res*, 172 (2020). <https://doi.org/10.1016/j.jcsr.2020.106216>
10. Clifton, G.C., Hogan, L., Stephens, M.T. et al., Post-Fire Evaluation of the New Zealand International Convention Centre. *Fire Technol* (2023). <https://doi.org/10.1007/s10694-023-01516-2>
11. Muñoz Blanc, C., Obiol Sánchez, A., Fortea Navarro, I., Evaluation of steel structures integrity in a post-fire condition: Case study of the Serradells sports centre in Andorra. *Fire Saf J*, 133 (2022). <https://doi.org/10.1016/j.firesaf.2022.103668>
12. Jeanneret, C., Chin, K., Kotsovinos, P., Gales, J., Chord Shielding Effect in Steel Trusses when Exposed to a Localized Fire. *CSCE Annual Conference, Moncton*; 2023.
13. Smith, CM., & Hoehler, MS. Imaging Through Fire Using Narrow-Spectrum Illumination. *Fire Technol* 54(6), 1705–1723 (2018). doi: 10.1007/s10694-018-0756-5.
14. Gatien, S., Young, T., Hoehler, M.S., Gales, J., Application of narrow-spectrum illumination and image processing to measure surface char formation in lateral ignition and flame spread tests. *Fire Mater*, 43, 4, 358-364 (2019). <https://doi.org/10.1002/fam.2706>
15. Rackauskaite, E., Flint, G., Maani, A., Temple, A., Kotsovinos, P., Use of LS-DYNA for Structural Fire Engineering. *12th European LS-DYNA Conference, Koblenz*; 2019.
16. Temple, A., Walker, G., Flint, GL., Panev, Y., Kotsovinos, P., Verification of 2D heat transfer models developed in LS-DYNA for structural fire engineering applications. *Applications of Fire Engineering*, CRC Press, 361-366 (2017).
17. Watson, S., Nicoletta, B., Kotsovinos, P., Al Hamd, R., Gales, J., Modelling Thermal Performance of Unloaded Spiral Strand and Locked Coil Cables Subject to Pool Fires. *Structural Engineering International* (2022). <https://doi.org/10.1080/10168664.2022.2101969>
18. Canadian Institute of Steel Construction, Handbook of Steel Construction 12th Edition. Toronto; 2021.
19. European Committee for Standardization, EN 1993-1-1: Eurocode 3: Design of steel structures - Part 1-1: General rules and rules for buildings (2005).
20. European Committee for Standardization, EN 1991-1-2: Eurocode 1: Actions on structures - Part 1-2: General actions - Actions on structures exposed to fire (2002).

FAILURE ANALYSIS OF AN ALUMINIUM WAREHOUSE COLUMNS DUE TO TIME-DEPENDENT STRAIN

Marko Goreta¹, Neno Torić², Ivica Boko³

ABSTRACT

This paper presents the parametric analysis of the influence of creep strain induced by transient heating on the column's load-bearing capacity of a typical aluminium warehouse. Due to favourable aluminium properties in terms of lightweight, corrosion resistance and maintained strength ratio compared to structural steel, simple aluminium warehouses are suitable and widely used as temporary structures. However, aluminium's low fire resistance limits its use and application mainly because of strict fire safety regulations and insufficiently researched behaviour of aluminium at high temperatures, especially in transient conditions which are more suited to simulate real structural behaviour under fire exposure. Based on the Eurocode, for fire lasting more than 30 minutes and for the developed temperatures above 170°C the influence of transient induced creep requires explicit consideration. The complexity of the creep phenomenon makes it difficult to determine the creep law valid for all heating conditions which is the main reason the current standards do not cover the influence of creep in transient conditions with sufficient accuracy. The lack of reliable experimental and numerical data supports this fact which is the main reason for a deeper dive on this topic. Observed columns in this study are the outer and the inner columns exposed to transient heating with low heating rates of up to 5°C/min.

Keywords: Creep, fire, aluminium, transient heating, columns

1 INTRODUCTION

1.1 General

Modern demands in civil engineering often require quick and reliable solutions in terms of stable structures prone to reusing, long-lasting and less time-consuming for construction [1]. Aluminium alloys proved themselves to be suited for all the above due to their favourable properties in terms of low density, durability, resistance, load-bearing capacity, and recycling possibility. In comparison to structural steel, the advantage of aluminium with its alloying elements is undeniable. The relative yield strength of the aluminium alloys typically used in civil engineering is around 260 MPa which corresponds to the yield strength of a commonly used structural steel S275 but with nearly three times the weight difference in favour of aluminium. Aluminium is often referred to as "green metal" since it is fully recyclable, so the manufacturing process has a significant reduction in the required energy for production which decreases global pollution and makes it more environmentally acceptable than some other commonly used materials. Aluminium alloys mostly used in civil engineering are from the 5xxx or 6xxx series with Magnesium as an alloying element which ensures corrosion resistance essential for durability. Due to the aforementioned properties, aluminium is recognized as the most suitable material for simple temporary warehouses. However, aluminium's application is currently limited because of its low fire resistance which represents

¹ Senior assistant, PhD, University of Split, Faculty of Civil Engineering, Architecture and Geodesy,
e-mail: marko.goreta@gradst.hr, ORCID: <https://orcid.org/0000-0001-7645-1623>

² Associate Professor, University of Split, Faculty of Civil Engineering, Architecture and Geodesy
e-mail: nenno.toric@gradst.hr, ORCID: <https://orcid.org/0000-0002-7530-7619>

³ Full Professor, University of Split, Faculty of Civil Engineering, Architecture and Geodesy
e-mail: ivica.boko@gradst.hr, ORCID: <https://orcid.org/0000-0003-2282-8362>

its major flaw. In flared-up fires, the aluminium structure often collapses quickly due to its severe fire vulnerability since its load-bearing capacity starts to decrease at temperatures above 100°C, and its melting point is at around 660°C. Due to current strict laws worldwide for modern structures to fulfil sufficient fire safety standards, it is mandatory to use some form of insulated material for fire protection. This paper aims to present the influence of slow-rising temperature on the development of creep strain and the load-bearing capacity of aluminium columns exposed to high temperature. Low heating rates presented in this study simulate fire exposure on insulated aluminium columns exposed to localized fire sources.

1.2 Creep strain

According to Anderberg [2] the total temperature strain is the sum of thermal strain $\varepsilon_{th}(T)$, the strain caused by the external load $\varepsilon_{\sigma}(\sigma, T)$ and the creep strain $\varepsilon_{cr}(\sigma, T, t)$ shown by the following equation (1):

$$\varepsilon_{tot} = \varepsilon_{th}(T) + \varepsilon_{\sigma}(\sigma, T) + \varepsilon_{cr}(\sigma, T, t) \quad (1)$$

Creep is a phenomenon which occurs if the exposed temperature exceeds approximately one third of the metal's melting temperature with the possibility to develop plastic strain even if the effective stress is below the proof strength. Generally, creep strain in metals is dependent on temperature (T), time of exposure (t) and the applied load (σ) as shown in the previous equation. However, the creep process is much more comprehensive since it is also dependent on the crystal structure of the material which depends on the production process and its behaviour is unique for every material. Different thermal and mechanical treatments for each specific aluminium alloy commonly suited and used in civil engineering (series 5xxx and 6xxx) can vary its proof strength from 140 MPa to 350 MPa which is directly related to the creep development.

To adequately represent the influence of the creep strain on the load-bearing capacity of aluminium columns, it is essential to execute the experimental and numerical analyses which can be achieved through the transient or stationary test methodology. The difference in the stress-strain curves attained from the standard transient and stationary coupon tests is presented in Figure 1.

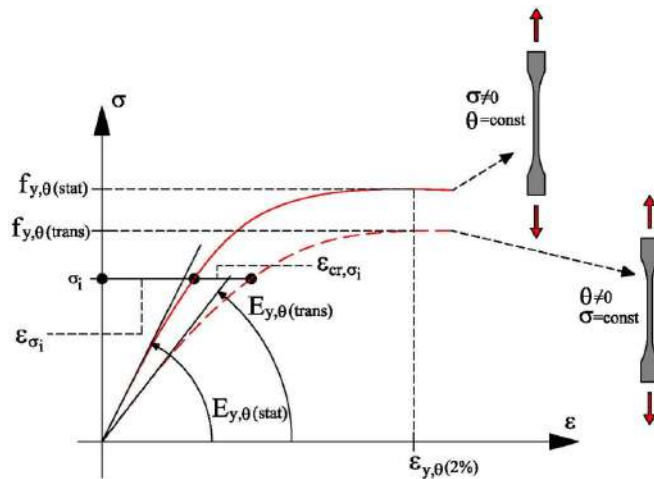


Figure 1. The difference between the transient and stationary tests [3]

The transient tests, which are more suited but less common because of their difficult implementation, can simulate scenario which occurs due to real fire exposure where the temperature increases on the permanently loaded structural element. The stationary tests are carried out for the constant temperature and rising load, and they are mainly used to determine the overall capacity and material properties at a certain temperature.

The deficiency of valid experiments on aluminium alloys and the lack of reliable data emphasize creep as one of the scarcely investigated topics in the scientific community. The current Eurocode for the design of aluminium columns exposed to fire [4] takes creep into account with the 1.2 coefficient which reduces overall column buckling resistance without taking into account the time of exposure, applied load and the heating rate. However, the Eurocode also emphasizes the fact that for the accurate mechanical response of the aluminium column exposed to fire, the transient thermal creep requires explicit consideration for the

temperature above 170°C and the duration of exposure above 30 minutes. It is impossible to fulfil this condition without a detailed experimental and numerical analysis.

2 PREVIOUS RESEARCH

For the past few decades, aluminium has become a material of interest in the scientific community due to its potential for a more frequent implementation in everyday structures. Even with the increased interest and the obvious lack of valid data, it still is a scarcely studied topic.

The first notable studies on the behaviour on the fire exposed aluminium columns and the development of the creep strain were carried out by Nina Kristin Langhelle et al. [5-10]. Circular and rectangular hollow sections of aluminium alloy EN AW 6082 T6 of different tempers (T4 and T6) were tested and numerically validated at ambient and elevated temperatures. They studied the influence of constant heating rate (transient tests) and the constant temperature (stationary tests) for different axial loads. Transient tests were conducted for the heating rates of 12°C/min which showed negligible influence of creep due to the aluminium's low fire resistance. The overall conclusion from their studies was that for the aluminium alloys, the creep is present in the stationary tests for temperatures above 200°C and for the transient tests and heating rates of 12°C/min the influence of creep can be neglected.

The most comprehensive research on aluminium columns exposed to transient heating has been conducted by Maljaars et al. [11-14]. Aluminium alloys from the 5xxx and 6xxx series were tested on more than 100 hollow specimens for various stress levels and heating rates ranging from 1.9°C/min to 11°C/min. Based on their test results, they pointed out that the 1.2 factor proposed by the Eurocode, which should cover the influence of creep on the buckling capacity of the aluminium columns, is a conservative approach for the higher heating rates, and insufficiently accurate for the lower heating rates.

In the absence of valid data for the aluminium I-sections exposed to fire, Torić et al. [15-17] went through the targeted research to test the influence of creep on the EN AW 6082 T6 alloy. Based on the coupon tests they developed an analytical creep model based on the Norton-Bailey law which can predict all creep phases. Afterwards, a total of 17 aluminium columns were tested in the stationary heating conditions for different stress levels and temperatures up to 260°C with a conclusion that significant creep starts to develop at temperatures above 150°C for the specified aluminium alloy [18].

Following this study, Goreta et al. [19-20] calibrated the existing creep model and applied it in the experimental and numerical analysis on the aluminium columns exposed to transient heating. Based on the necessity to use some form of fire protection in everyday structures, the tested heating rate was up to 5°C/min. The creep numerical model matched the results from the experiments with sufficient accuracy and validated the fact that the development of creep strain accelerates the failure of axially loaded columns. Based on the results from this study, numerical simulations on a two-storey aluminium frame structure were carried out with the same creep model [21-22]. A numerical study presented the failure time difference of the most loaded column of the structures between the creep and the creep-free model of up to 28% for the presented low heating rate regime. Due to the low melting temperature of the aluminium and previous research by Maljaars and Langhelle, higher heating rates are insignificant for the load-bearing capacity of the columns. Since simple aluminium warehouses are starting to be used more frequently, there's a need for the preliminary analysis presented in this paper to study the influence of creep on their columns as well.

In a more recent study, Wang et al. [23] pointed out the columns as the critical and the most important structural component since their failure often leads to a collapse of the whole structure. Because of the more frequent use of aluminium alloys in structural engineering, the inability to sufficiently determine the decrease of the load-bearing capacity due to creep acts as a certain barrier to their wider use in everyday structures.

3 NUMERICAL ANALYSIS

3.1 Geometry of the observed structure

The warehouse geometry presented in this parametric analysis was an aluminium frame structure with a total span of twelve meters made of aluminium EN AW 6082 T6 alloy and five meters between the frames which

results in the total length of the structure of twenty meters. The chosen cross-section for the columns was the I section (220 - height; 170 - width; 14 - flange thickness; 8 - web thickness) used to suit the previous research and the obtained creep coefficients for the designed model. The beams (300;170;15;10) and purlins (100;80;8;6) were modelled also with the I section based on the design criterion for the local actions (wind and snow) according to the Eurocode [24-25]. The total height of the structure was five meters.

3.2 Numerical settings and material properties

ANSYS 16.2 [26] was used for numerical modelling of the presented frame structure where the connections were designed as rigid to induce the column failure. High-order SOLID 187 finite elements were used with the capability to display creep, plasticity, large strains, and deflections. The used mesh size was 5 mm with a total of more than 300,000 finite elements. A maximum number of substeps was 100 per iteration for the nonlinear numerical analysis which was carried out to determine the structural behaviour while taking into account the effect of creep and large deflections.

A calibrated Modified Time Hardening (MTH) creep model was used to model creep behaviour which is presented with the following equation (2):

$$\varepsilon_{cr} = C_1 \sigma^{C_2} t^{C_3+1} e^{-C_4/T} / (C_3 + 1) \quad (2)$$

Coefficients C1, C2, C3 and C4 are presented in previous study for temperatures of 150°C, 200°C, 250°C and 300°C [20].

The used material model for simulations was Multilinear Isotropic Hardening which considers creep strain and graphically shows the failure of the column when the plastic strain ratio at a specified temperature is exceeded based on the applied load. The reduction of proof strength, ultimate strength, elastic and shear modulus for used aluminium alloy caused by the rise of temperature is obtained from the previous study [16].

3.3 Applied loads for fire analysis

For the accidental design scenario based on the Eurocode [24], the combination of actions is expressed with the following equation (3):

$$\sum_{j \geq i} G_{k,j} + P + A_d + (\psi_{1,1} \text{ or } \psi_{2,1}) Q_{k,1} + \sum_{i > 1} \psi_{2,i} Q_{k,i} \quad (3)$$

According to the presented equation, the permanent load of 120 kg/m² was combined with the accidental (thermal) load and applied on two differently loaded columns on the structure with a maximum temperature of 350°C caused by the varying heating rate from 1°C/min to 5°C/min presented on Figure 2.

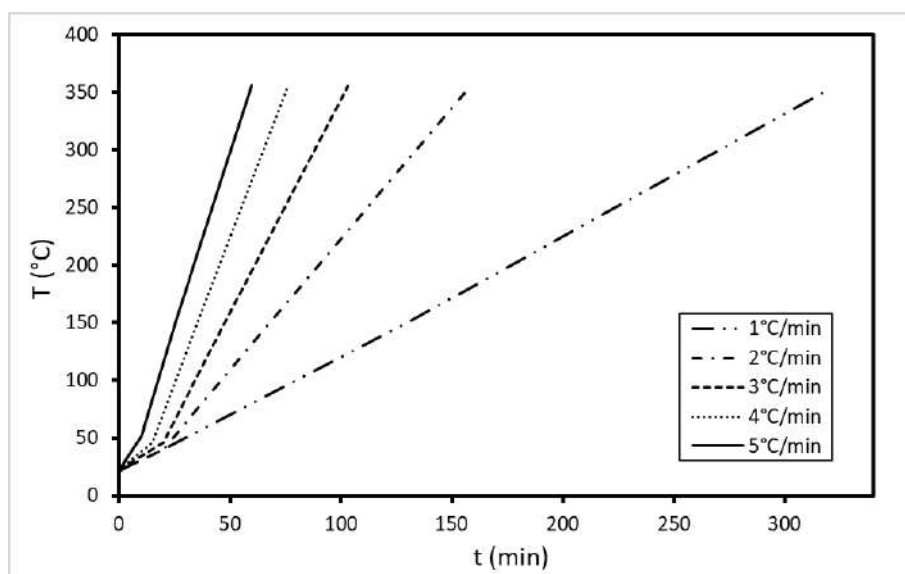
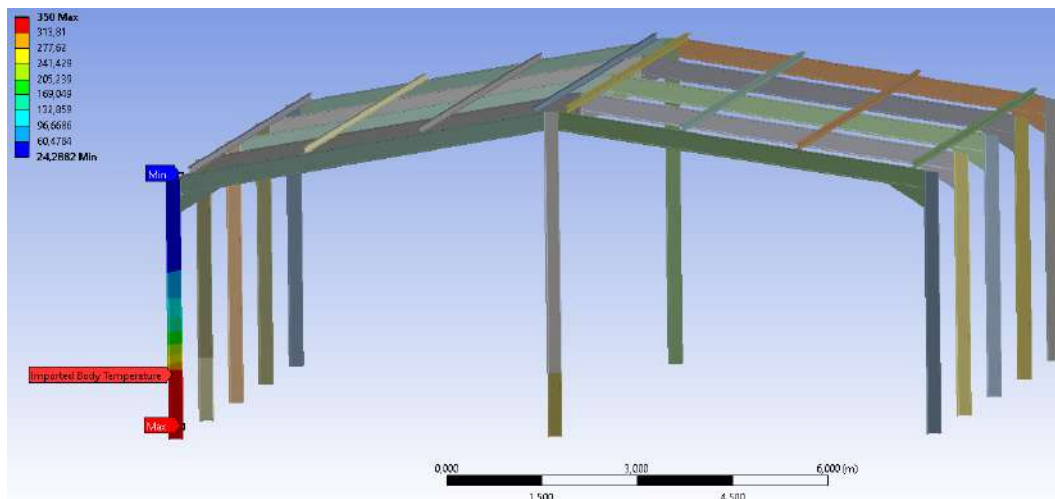
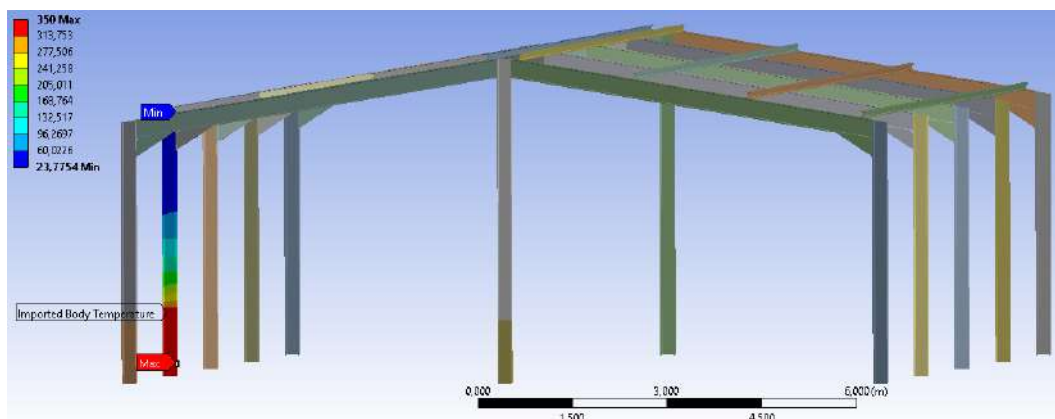


Figure 2. Applied temperatures based on the heating rate

Since the goal is to simulate the scenario which might occur on the existing structure, the applied temperature would suit a localized heating source at the height of approximately one meter above the ground (as a simulation of a point fire load). The observed columns (inner and outer column) were chosen to suit different distributed loads in structure and they are shown in Figure 3.



a) Outer column



b) Inner column

Figure 3. Applied temperatures on the critical columns

The flared-up fires could not isolate one specific column and that fire scenario would probably lead to collapse without the need to consider the creep strain on aluminium columns since their invoked heating rate in that case would exceed $20^{\circ}\text{C}/\text{min}$. Aluminium thermal conductivity determines the developed temperature on the rest of the column (above the heating zone), and it was taken into account in numerical simulations.

3.4 Results

Robust and time-consuming creep calculations on the warehouse structure were carried out with the use of the MTH creep model and compared with the creep-free model. Developed creep strain ϵ_{cr} caused by the applied load and the heating rates from $1^{\circ}\text{C}/\text{min}$ to $5^{\circ}\text{C}/\text{min}$ are presented in Figure 4 for the observed inner (I) and outer (O) columns.

Figure 5. presents developed vertical displacements (u_{vert}) caused by the thermal expansion and ultimately represents failure caused by the influence of creep. The influence of the thermal expansion on the cross-section section level was neglected.

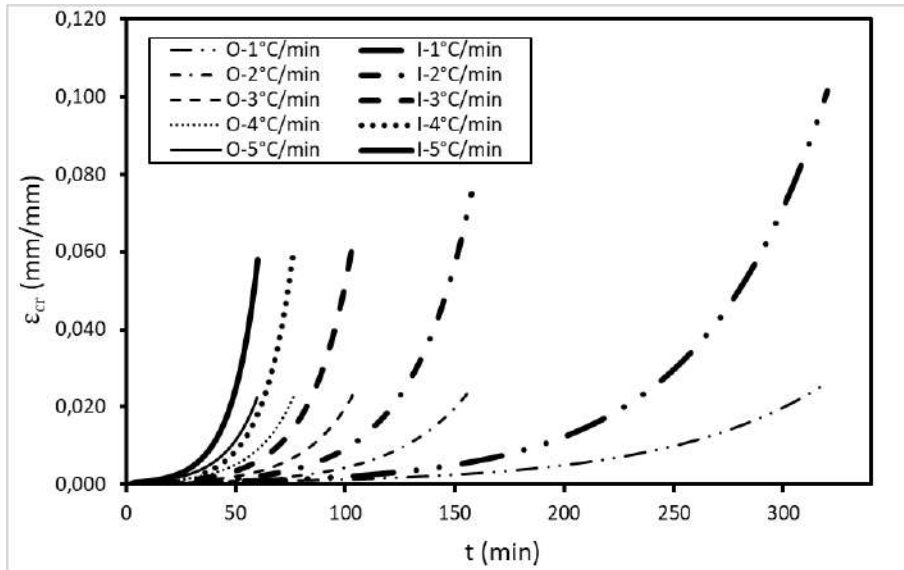
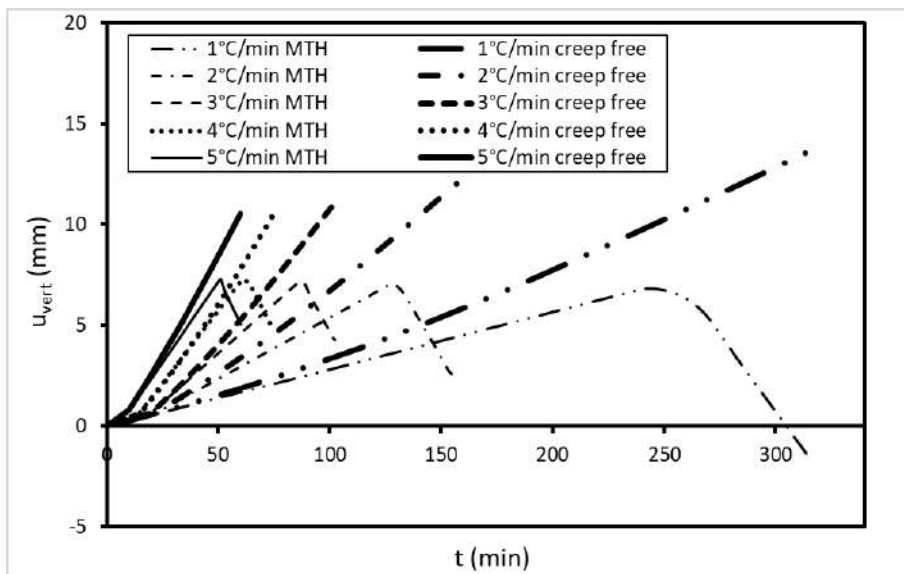
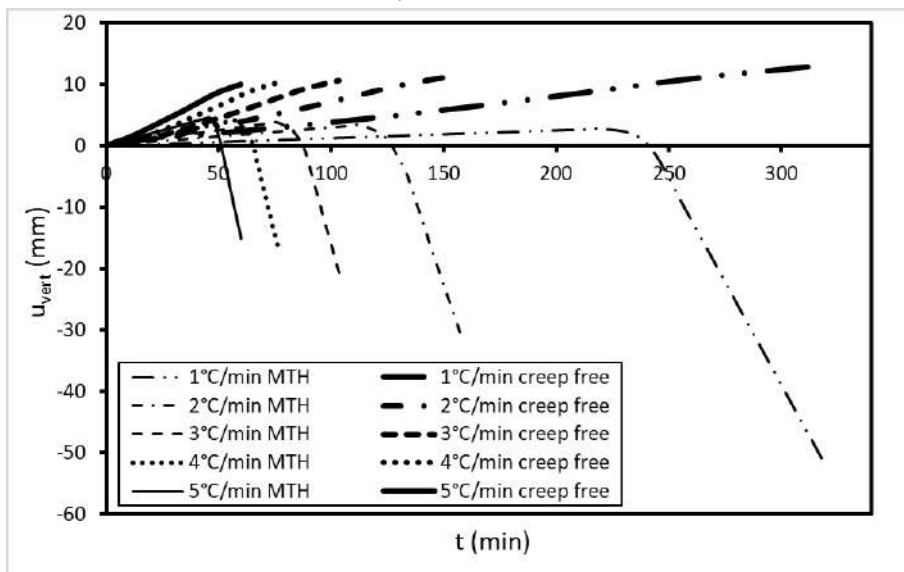


Figure 4. Developed creep strains on the critical columns



a) Outer column



b) Inner column

Figure 5. Developed vertical deflection on the critical columns

4 DISCUSSION OF THE RESULTS

Figure 4. presents the difference between developed creep strains between the outer and inner columns of the simple aluminium warehouse structure. It is visible that the failure methodology is similar for both columns, but the developed creep strain varies from nearly three to five times difference depending on the heating rate. Even the same column endures a significantly higher difference in the developed creep strain when comparing a lower heating rate of 1°C/min with a heating rate of 5°C/min.

From the presented results it is visible that even at the temperature of 350°C, the creep-free model does not cause the failure of the column for presented loads and geometry. On the other hand, the MTH creep model shows the critical point when the column's capacity starts to drop off due to temperature and accumulated creep strain which manifests in the vertical deflections presented in Figure 5. Up to the failure point, the column can sustain strain caused by the thermal expansion due to the sufficient stress reserve in the column. Rigid connections on the structure and sufficient load-bearing capacity of the unheated purlins take over part of the load after the column's failure, which is why the numerical simulations do not cover the complete collapse of the presented structure.

Table 1. presents the difference between the critical temperature and the failure time of the observed columns. The difference between the critical temperature upon failure depends on the heating rates for the applied external load. Based on the results of the presented numerical simulations, the outer column for the same load setup suffers a 30°C difference in the critical temperature upon failure between the heating rate of 1°C/min and 5°C/min while the inner column endures the difference of 23°C. This can be attributed to the previous premise of creep being strictly related to the time of exposure and the stress level caused by the load.

Table 1. Critical temperature and the failure time of the MTH creep model

		Heating rate (°C/min)				
		1	2	3	4	5
Critical temperature (°C)	Outer	270	282	291	296	300
	Inner	248	258	265	269	271
Failure time (min)	Outer	242	127	87	61	51
	Inner	232	112	76	58	47

Column does not fail by the creep-free model while the MTH model causes significant lateral deflection. The difference between the lateral deflections (Δu_{lat}) of the creep-free and the MTH model are presented in Figure 6. The bold line presents the difference of the inner column which fails partially by buckling and the lowering of the column's load-bearing capacity. The outer columns failed around the weaker axis, and the inner column failed along the stronger axis due to the load (un)symmetry.

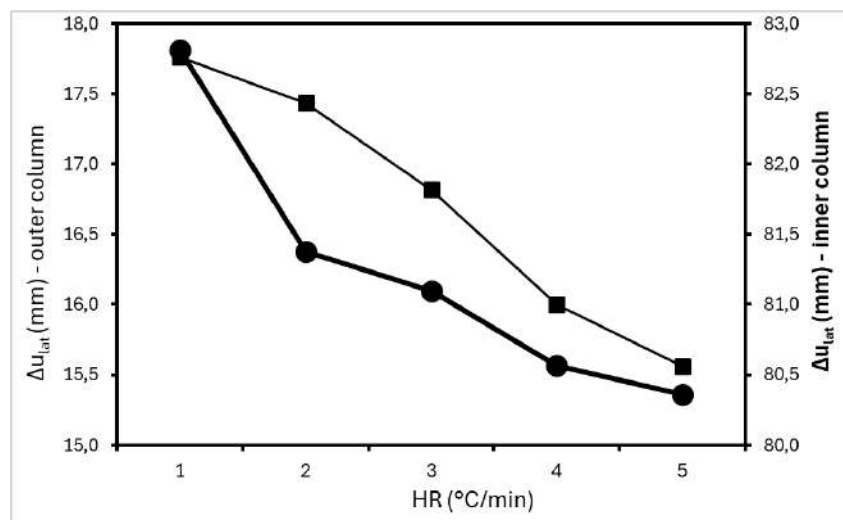


Figure 6. Difference between the lateral deflection of creep and the creep free model

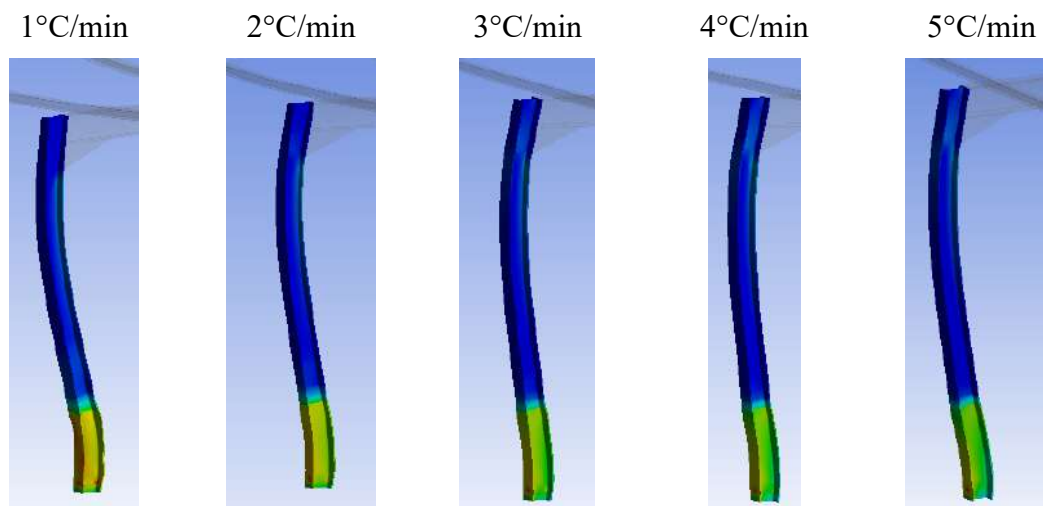


Figure 7. Creep strain in the inner column based on the heating rate

The failure of the inner column and the developed creep strain in the heated zone of the column for every applied heating rate is presented in Figure 7. The failure mechanics for each heating rate is the same but with a visible difference in the developed creep strain as presented in Figure 4. The heated zone of the column withstands local failure followed by the buckling of the column caused by the significant reduction of the mechanical properties and the accumulated creep strain.

5 CONCLUSIONS AND FUTURE WORK

The presented study confirms the importance of the creep strain on the failure time of the aluminium columns exposed to transient heating with a low heating rate regime. The creep accelerates the failure of the column, and it significantly depends on the load and time of exposure.

The main guidelines for future work will be in an experimental manner on coupons and columns with corresponding numerical modelling and include the following:

- To capture the development of the creep strain on aluminium columns with more accuracy, it is necessary to carry out a detailed experimental study on coupons for a narrower temperature span followed by the appropriate load regimes,
- Other aluminium alloys from the 5xxx and 6xxx series which represent mostly used alloys in civil engineering will be tested and compared with the presented EN AW 6082 T6 alloy,
- Since the development of the creep strain varies based on the cross-section type, it would be desirable to carry out a parametric analysis of different hollow-section columns compared with the I-section columns from this and previous studies for the same stress level and temperature regime with the use of the same creep model,
- Obtained results from the planned experimental studies will compare the influence of the MTH creep model with another appropriate creep model to propose the update for future Eurocode 9 which lacks research and data on this topic.

ACKNOWLEDGMENT

This work is partially supported through project KK.01.1.1.02.0027, a project co-financed by the Croatian Government and the European Union through the European Regional Development Fund - the Competitiveness and Cohesion Operational Programme.

This work has been partially supported by Croatian Science Foundation under the project Influence of creep strain on the load capacity of steel and aluminium columns exposed to fire (UIP-2014-09-5711). Any opinions, findings, and conclusions or recommendations expressed in this material are those of the authors and do not necessarily reflect the views of Croatian Science Foundation.

REFERENCES

- [1] X. You *et al.*, “A review of research on aluminum alloy materials in structural engineering,” *Developments in the Built Environment*, vol. 17. Elsevier Ltd, Mar. 01, 2024. doi: 10.1016/j.dibe.2023.100319.
- [2] Y. Anderberg, “Modelling steel behaviour,” *Fire Saf J*, vol. 13, no. 1, pp. 17–26, 1988, doi: 10.1016/0379-7112(88)90029-X.
- [3] N. Torić, A. Harapin, and I. Boko, “Experimental verification of a newly developed implicit creep model for steel structures exposed to fire,” *Eng Struct*, vol. 57, pp. 116–124, Dec. 2013, doi: 10.1016/j.engstruct.2013.09.024.
- [4] European committee for standardization, “EN 1999-1-2: Eurocode 9: Design of aluminium structures - Part 1-2: Structural fire design,” 2007.
- [5] N. K. Langhelle and N. teknisk-naturvitenskapelige universitet, *Experimental Validation and Calibration of Nonlinear Finite Element Models for Use in Design of Aluminium Structures Exposed to Fire*. in Doktor ingeniøravhandling. Department of Marine Structures, Faculty of Marine Technology, Norwegian University of Science and Technology, 1999. [Online]. Available: <https://books.google.hr/books?id=RZR2AAAACAAJ>
- [6] J. Amdahl, E. Eberg, and N. K. Langhelle, “Experimental and theoretical investigation of aluminium tubes in bending at elevated temperatures,” Trondheim, 1993.
- [7] J. Amdahl, E. Eberg, and N. K. Langhelle, “Experimental and theoretical investigation of aluminium tubes subjected to temperature loads,” Trondheim, 1993.
- [8] E. Eberg, N. K. Langhelle, and J. Amdahl, “Experimental investigation of creep buckling behaviour of aluminium tubes subjected to temperature loads,” Trondheim, 1995.
- [9] N. K. Langhelle, J. Amdahl, E. Eberg, and S. Lundberg, “Buckling tests of aluminium columns at elevated temperatures,” in *No. CONF-9606279- American Society of Mechanical Engineers*, New York, US, 1996.
- [10] N. K. Langhelle, E. Eberg, and J. Amdahl, “Comparative study between numerical models and buckling tests of aluminium columns at elevated temperatures,” *Proceedings of the International Conference on Offshore Mechanics and Arctic Engineering - OMAE*. 1998.
- [11] J. Maljaars, F. Soetens, and H. H. Snijder, “Local buckling of aluminium structures exposed to fire. Part 1: Tests,” *Thin-Walled Structures*, vol. 47, no. 11, pp. 1404–1417, 2009, doi: 10.1016/j.tws.2009.02.008.
- [12] J. Maljaars, F. Soetens, and H. H. Snijder, “Local buckling of aluminium structures exposed to fire. Part 2: Finite element models,” *Thin-Walled Structures*, vol. 47, no. 11, pp. 1418–1428, 2009, doi: 10.1016/j.tws.2008.06.003.
- [13] J. Maljaars and F. Soetens, “Structural and Thermal Behaviour of Aluminium Exposed to Fire,” 2006, doi: 10.2749/222137806796184725.
- [14] J. Maljaars, F. Soetens, and L. Twilt, “Heating of aluminium members exposed to natural fire conditions,” in *Sif’06 proceedings of the 4th international workshop structures in fire*, Portugal, 2006, pp. 75–88.
- [15] N. Torić, I. Boko, I. W. Burgess, and M. Goreta, “Experimental analysis of the influence of creep on fire-exposed steel and aluminium columns,” in *The 10th International Conference on Structures in Fire*, Belfast, UK, 2018, p. 6.
- [16] N. Torić, J. Brnić, I. Boko, M. Brčić, I. W. Burgess, and I. Uzelac, “Experimental analysis of the behaviour of aluminium alloy EN 6082AW T6 at high temperature,” *Metals (Basel)*, vol. 7, no. 4, 2017, doi: 10.3390/met7040126.
- [17] N. Torić *et al.*, “High-temperature properties of aluminum alloy EN6082AW T6,” in *The International Conference of Applications of Structural Fire Engineering (ASFE)*, Manchester, UK, 2017, p. 5.

- [18] N. Torić, I. Boko, I. W. Burgess, and V. Divić, “The effect of high-temperature creep on buckling behaviour of aluminium grade EN6082AW T6 columns,” *Fire Saf J*, vol. 112, no. December 2019, 2020, doi: 10.1016/j.firesaf.2020.102971.
- [19] M. Goreta, N. Torić, and I. Boko, “Calibration of an Existing Creep Model for Analysis of Aluminium Members Exposed to Constant Temperature,” *International Journal for Engineering Modelling*, vol. 34, no. 2, pp. 1–15, 2021, doi: 10.31534/engmod.2021.2.ri.01m.
- [20] M. Goreta, N. Torić, I. Boko, and V. Divić, “Behaviour of Aluminium EN AW 6082 T6 Columns Exposed to Transient Heating—Experimental and Numerical Analysis,” *Metals (Basel)*, vol. 12, no. 8, p. 1326, 2022, doi: 10.3390/met12081326.
- [21] M. Goreta, N. Torić, I. Boko, and J. Lovrić Vranković, “The Effect of Creep on Time-Dependent Response of Aluminium Frame Structures,” *Fire Technol*, 2023, doi: 10.1007/s10694-023-01491-8.
- [22] M. Goreta, N. Torić, and I. Boko, “The effect of high-temperature creep on EN6082 T6 aluminium columns exposed to transient heating,” in *Proceedings of the 12th International Conference on Structures in Fire*, Hong Kong, 2022, pp. 491–501.
- [23] Z. Wang *et al.*, “Structural fire behaviour of aluminium alloy structures: Review and outlook,” *Engineering Structures*, vol. 268. Elsevier Ltd, Oct. 01, 2022. doi: 10.1016/j.engstruct.2022.114746.
- [24] European committee for standardization, “EN 1990: Eurocode - Basis of structural design,” 2002.
- [25] European committee for standardization, “EN 1999-1-1: Eurocode 9: Design of aluminium structures - Part 1-1: General structural rules,” 2009.
- [26] A. D. Canonsburg, “ANSYS, PA 15317, Release 16.2.” 2015.

FAILURE ANALYSIS ON THE GLOBAL BEHAVIOUR OF CARBON AND STAINLESS STEEL FRAME STRUCTURES UNDER FIRE CONDITIONS

Nuno Lopes¹, João Cabral², Paulo Vila Real³

ABSTRACT

Stainless steel has superior mechanical properties at high temperatures compared to conventional carbon steel. This can lead to structures with no need of fire protection requirements, making it more competitive for wider range of structural applications. The stainless steel exhibits extensive hardening and ductility at elevated temperatures, characterized by an always non-linear stress-strain relationship. A two-phase Ramberg-Osgood formulation has recently been proposed for modelling that constitutive law in stainless steel structures under fire in the second generation of Eurocode 3 (EC3), which is under preparation. Aiming to increase the knowledge on the fire design of plane frame structures, this work applies advanced calculation methods, through the application of the finite element method (FEM) with the program SAFIR, to analyse and discuss their structural failure through different criteria. Moreover, the obtained resistances of different stainless steel frame structures, subjected to different fire scenarios, are compared with similar cases in carbon steel, to study the influence of the materials different strength and stiffness retentions at high temperatures on their global behaviour. EC3 simplified calculation methods are also considered in the study, including the recently proposed design approaches for inclusion in the second generation of EC3.

Keywords: Stainless steel; Frame structures; Global behaviour; Fire scenarios; Failure criteria analysis

1 INTRODUCTION

The use of stainless steel for structural purposes has been limited to projects with high architectural value, where the innovative character of the adopted solutions is a valorisation factor for the structure. The high initial cost of stainless steel, coupled with lack of knowledge of the additional benefits of its use as a structural material, are some of the reasons that influence designers to avoid the use of the stainless steel in structures [1-4]. However, a more accurate analysis can result on a good performance of stainless steel as a structural material when compared with the conventional carbon steel.

The biggest advantage of stainless steel is its higher corrosion resistance. However, its aesthetic appearance, easy maintenance, high durability and reduced life cycle costs (where it can be considered a longer service life duration, and higher residual value and easier profiles reusability at the end of the structure life) are also important aspects. It is known that stainless steel has a better behaviour at elevated temperatures when compared with carbon steel. However, there is still a need to enhance the understanding of how this advantageous characteristic influences the behaviour of structures during fire situations and avoids the need for their fire protection. The possibility of eliminating the fire protection with the application of stainless steel in structures will result in smaller construction costs and periods, more efficient use of interior spaces,

¹ Prof., RISCO, Civil engineering Department, University of Aveiro,
e-mail: nuno.lopes@ua.pt

² Eng., RISCO, Civil engineering Department, University of Aveiro,
e-mail: joacabral5@ua.pt

³ Professor, RISCO, Civil engineering Department, University of Aveiro,
e-mail: pvreal@ua.pt

healthier work environment, a better aesthetic appearance of the building and elimination of the life cycle costs due to the protection material.

Unlike carbon steel, stainless steel has, at normal temperature and elevated temperatures, an always non-linear mechanical behaviour, even for small stresses values, not exhibiting a clearly defined yield strength. A conventional elasticity limit at 0.2% strain is usually adopted. Table 1 compares mechanical properties of the stainless steels 1.4301 (also known as 304) and 1.4401 (also known as 316), most common grades in practice and used in this paper, with the carbon steel S235, at normal temperature [5-7]. The carbon steel S235 was chosen due to its value of the yield strength, similar to the nominal stresses (0.2% proof stresses) of the stainless steel grades 1.4301 and 1.4401.

Table 1. Steel mechanical properties at normal temperature

Mechanical properties	Carbon steel S235	Stainless steel 1.4301	Stainless steel 1.4401
Yield strength [MPa]	235	210	220
Ultimate strength [MPa]	360	520	520
Ultimate strain	15%	45%	45%
Young modulus [GPa]	210	200	200

Hardening is typically not considered on carbon steel at elevated temperatures, being recently proposed for incorporation in the second generation of Part 1-2 of EC3 (part dedicated to fire design of steel structures) [8] a two-phase Ramberg-Osgood formulation for modelling stainless steel constitutive law at elevated temperatures [9], which considers its extensive hardening and ductility. Moreover the stainless steel strength and stiffness retentions at elevated temperatures are higher than the ones of carbon steel [8]. Figure 1 plots the S235, 1.4301 and 1.4401 stress-strain relationships, proposed in EC3, at 600 °C, where it can be observed significantly better behaviour of the stainless steel grades.

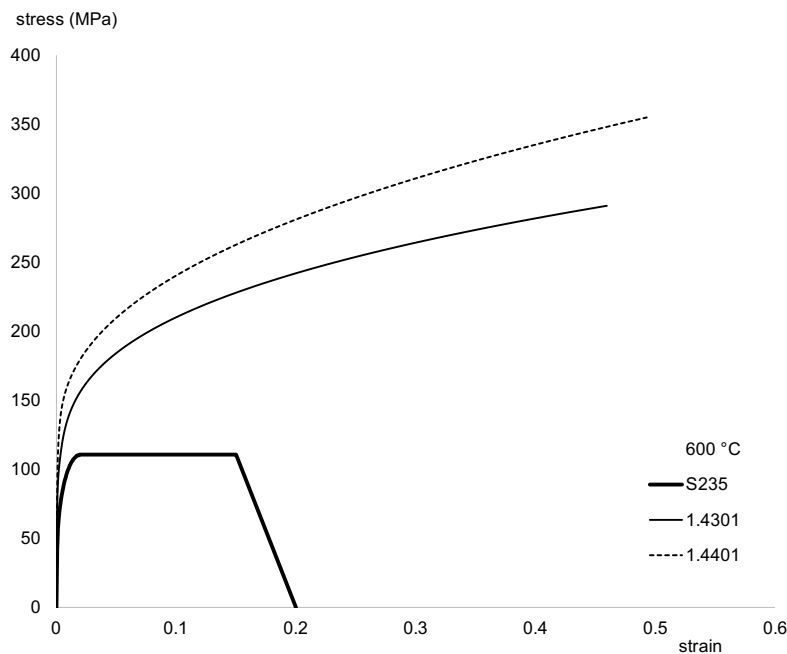


Figure 1. Stress-strain relationships of carbon steel S 235 and stainless steel 1.4301 and 1.4401 at 600 °C [8]

Regarding the materials thermal properties, Figure 2 illustrates the differences between the thermal conductivity and the specific heat of carbon steel and stainless steel [8]. Although the stainless steel has a thermal conductivity lower than the carbon steel, which would make one suppose slower heating speed in stainless steel, the specific heat of the carbon steel is higher, therefore there is a small difference between

the temperature evolutions of both materials, as it can be observed in Figure 4. Finally, the stainless steel thermal expansion is only slightly different from carbon steel (depicted in Figure 2c).

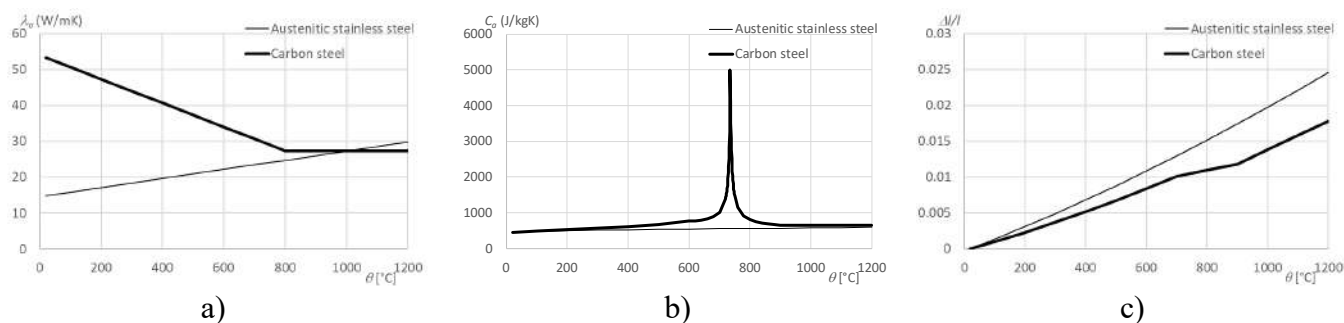


Figure 2. Carbon steel and stainless steel: a) thermal conductivity; b) specific heat; thermal expansion [8]

The fire part of EC3 foresees the application of both simplified and advanced calculation methods for the determination of the fire resistance of steel structures [10].

The simplified rules consist of a set of analytical formulation for the design of members (such as column, beams and beam-columns), considering the materials strength and stiffness reductions at elevated temperatures on their mechanical behaviour and susceptibility to instabilities phenomena, but based on corresponding internal efforts, obtained under accidental limit situation, at normal temperature. The under development second generation of EC3 will include new approaches for the fire design of stainless steel members.

The advanced calculation methods refer to the application of numerical modelling, which can be applied to obtain the fire behaviour of parts or complete structures. The failure criterion of the structure is typically defined as the instant when the stiffness matrix becomes not positive definite, thus becoming impossible to establish the equilibrium of the structure. However, deformations limits may be important to establish safe collapses criteria on the application of these numerical analyses. For example EN1363-1 [11] prescribes the use of limits for the deformation and rate of deformation on experimental fire tests to structural elements (that are consider on the present research work).

Research on the structural behaviour of stainless steel structures under fire has been focused on members, being studies on the global structural behaviour of complete structures still scarce. Attention has started to be given to this subject [12,13], however, more investigations are important to better understand the failure of those steel frame structures under fire conditions.

Aiming to enhance understanding on the behaviour of plane frame structures under fire, this study employs advanced calculation methods, utilizing the finite element method (FEM) with the SAFIR program [14], to analyse and discuss structural failure using different criteria. Furthermore, the study compares the resistance of different stainless steel frame structures, exposed to different fire scenarios, with similar cases in carbon steel. This comparative analysis aims to investigate the influence of their different strength and stiffness retention in materials at elevated temperatures on their overall behaviour. Finally, EC3 simplified calculation methods are also taken into account in this research, with the objective of analysing the approximations provided by those rules to the frame structures numerically obtained ultimate capacities.

2 EVALUATION OF THE FIRE RESISTANCE OF CARBON AND STAINLESS STEEL STRUCTURES

As previously referred, recently, new stainless steel fire design rules have been proposed for inclusion in the second generation of Part 1-2 of EC3 (FprEN1993-1-2:2023) [8], which include a new stress-strain relationship law for numerical modelling and new members fire design approaches, different from the ones in the current version of EN 1993-1-2:2005 [15].

2.1 Eurocode 3 simplified calculation methods

EC3 provides analytical formulations for the fire design of steel axially compressed columns, beams and beam-columns (members under compression plus bending), considering the relevant instabilities phenomena. With these formulations it is possible to obtain the members critical temperatures imposed by the accidental actions combinations, which will be applied to determine the collapse time predictions, from the steel temperature-time evolutions [10].

In EN 1993-1-2:2005, the fire resistance of stainless steel members is calculated using the same procedure as for carbon steel, by changing only the mechanical properties of the material for consideration of the uniform elevated temperatures in the cross-section.

However, FprEN 1993-1-2:2023 [8] proposes new fire design approaches for stainless steel, which include a new methodology of classification into slender and non-slender cross-sections [16], unlike the four classes defined for carbon steel at elevated temperatures [8] and for normal temperature design of both carbon steel and stainless steel members [5,6]. New formulas for verification of stainless steel members were developed based on studies of I-section members [17,18] keeping the main formulation proposed by EC3 but considering the 2% total strain as yield strength, independent of the cross-section classification, and modifying some of the expressions related to buckling reduction factors (such as in columns) and interaction factors (in beam-columns) determinations. The stainless steels yield strength reduction factors at elevated temperatures in FprEN 1993-1-2:2023 are different from those proposed in its current version EN 1993-1-2:2005.

Regarding carbon steel, FprEN 1993-1-2:2023 introduces new design proposals only for members with class 4 sections. The current study considers only class 1 and class 2 sections.

In this work, only some example cases are analysed with these simplified rules, as their accuracy and safety verification should be made in isolated members. The procedure does not take into account thermal expansion on frame structure analysis. In addition, it is expected that frame members buckling lengths vary with the surrounding structure stiffness variation due to fire. In the tested cases, which correspond to non-sway frame structures, the buckling length l_{fi} of a continuous column was taken as $l_{fi} = 0.5L$ in intermediate storeys and as $l_{fi} = 0.7L$ in top storeys, where L is the system length in the relevant storey [8].

2.2 Advanced calculation methods

EC3 also foresees the application of advanced calculation methods for the fire safety verification of steel structures. Geometrically and materially non-linear analysis (GMNIA) considering imperfections can be performed applying finite element method software.

The program SAFIR [14] developed at the University of Liege was used in this work. This program has two distinct calculation modules, one for the thermal analysis of structure and the other for the mechanical behaviour analysis. Consequently, the non-uniform temperature evolution is calculated for each existing section type in the structure, and in a subsequent phase the mechanical module of the program reads these temperatures and determines the thermo-mechanical behaviour of the structure in an incremental static analysis.

In this study beam finite elements were used, being the respective cross-section thermal analysis performed with two-dimensional plane elements. The cross-section of the elements is simulated using a fibre model finite element, the temperature, the stress, the strain and the other material properties being considered constant in each fibre. The thermal conductivity and specific heat presented in Figure 2 are considered in the thermal analyses. The emissivity related to the steel surface should be equal to 0.7 for carbon steel and equal to 0.4.

The mechanical analysis considers the variation of the materials constitutive models with the previously determined elevated temperatures. The new stainless steel material constitutive law at elevated temperatures proposed in FprEN 1993-1-2:2023 was introduced in SAFIR [19]. This beam finite element does not take into account local buckling. The finite beam element presents 3 nodes, with a central node that considers the non-linear axial displacement [12]. The end nodes have three degrees of freedom (two translations and one rotation) and the third node of the beam element one degree of freedom (the axial displacement), in a total of 7 degrees of freedom.

The program step by step analyses (in function of time) stops at the instant when the stiffness matrix becomes not positive definite, thus becoming impossible to establish the equilibrium of the structure. This

has been typically considered the instant of collapse. On these failure analyses, deformation is only indirectly considered by the materials ultimate strains.

Following this, the application of the performance criteria for fire resistance experimental tests to the loadbearing capacity of members (prescribed in EN1363-1[11]), on the numerical analyses of the frame structures, is here also investigated. Support of the test load is determined by both the amount and the rate of deflection calculated.

The following definitions (limiting deflection and limiting rate deflection) are used for flexural loaded elements (in this work, beams):

$$D_{limit} = \frac{L^2}{400d} [\text{mm}] \quad (1)$$

$$\left(\frac{dD}{dt}\right)_{limit} = \frac{L^2}{9000d} [\text{mm}/\text{min}] \quad (2)$$

Being defined for loadbearing vertical elements (in this work, columns) the limiting vertical contraction (negative elongation) and limiting rate of vertical contraction as:

$$C_{limit} = \frac{h}{100} [\text{mm}] \quad (3)$$

$$\left(\frac{dC}{dt}\right)_{limit} = \frac{3h}{1000} [\text{mm}/\text{min}] \quad (4)$$

Based on this, the applied failure criteria were [11]:

- for flexural loaded elements: i) measured deflection $\geq 1.5 \times D_{limit}$ or ii) both D_{limit} and $\left(\frac{dD}{dt}\right)_{limit}$ are exceeded;
- for loadbearing vertical elements: i) measured vertical contraction $\geq C_{limit}$ or ii) $\left(\frac{dC}{dt}\right)_{limit}$ is exceeded.

3 CASE STUDY

A parametric study is presented where plane frame structures, with different geometries (varying the numbers of stories and spans) and dimensions, were analysed, considering different fire scenarios with the standard ISO 834 fire curve [20]. The chosen frame structures are presented in Figure 3. In order to account for the effects of the assembly imperfections, possible eccentricities and geometrical imperfections, an initial sway imperfection has been introduced, according to Part 1-1 of EC3 [5], that corresponds to a rotation angle of 0.0033 rad. No residual stresses were considered in the profiles.

The structures were designed to support actions corresponded to offices buildings, being analysed with unprotected stocky I cross-sections in carbon steel grade S235, and in stainless steel grades 1.4301 and 1.4401 (which have similar yield strength and young modulus at normal temperature).

The chosen cross-sections resulted from numerical analyses at normal temperature aiming at having non-sway structures – critical instability load factor ≥ 10 [5] (applying the software SAP2000 [21] for the respective frames instability analyses) and at providing safe bearing capacities with the numerical model developed in SAFIR for ultimate limit state actions combinations given by EN1990 [22] - equation (5). Self-weight, imposed loads, wind and snow actions were considered according to EC1 [23-25]. Considering buildings with 5 m spacing between frame structures, the most unfavourable loads combinations for ultimate and accidental limit state are presented in Table 2. On the accidental limit state combinations (needed for the fire design) equation (6) is determined according to NP EN 1990 [26], where $\Psi_{1,1}$ is used to consider the possibility of wind loading as main variable action.

$$\sum_{j \geq 1} \gamma_{G,j} G_{k,j} + \gamma_{Q,1} Q_{k,1} + \sum_{i \geq 1} \gamma_{Q,i} \Psi_{0,i} Q_{k,i} \quad (5)$$

$$\sum_{j \geq 1} G_{k,j} + (\Psi_{1,1} \text{ or } \Psi_{2,1}) Q_{k,1} + \sum_{i \geq 1} \Psi_{2,i} Q_{k,i} + A_d \quad (6)$$

Table 2. Chosen cross-sections for each frame structure [kN/m]

Limit state	Vertical uniform loading in the roof beams (q1)	Vertical uniform loading in remaining beams (q2)	Horizontal uniform loading in left exterior columns (q3)
Ultimate	51.5	65.0	4.9
Accidental	36.5	41.0	0.7

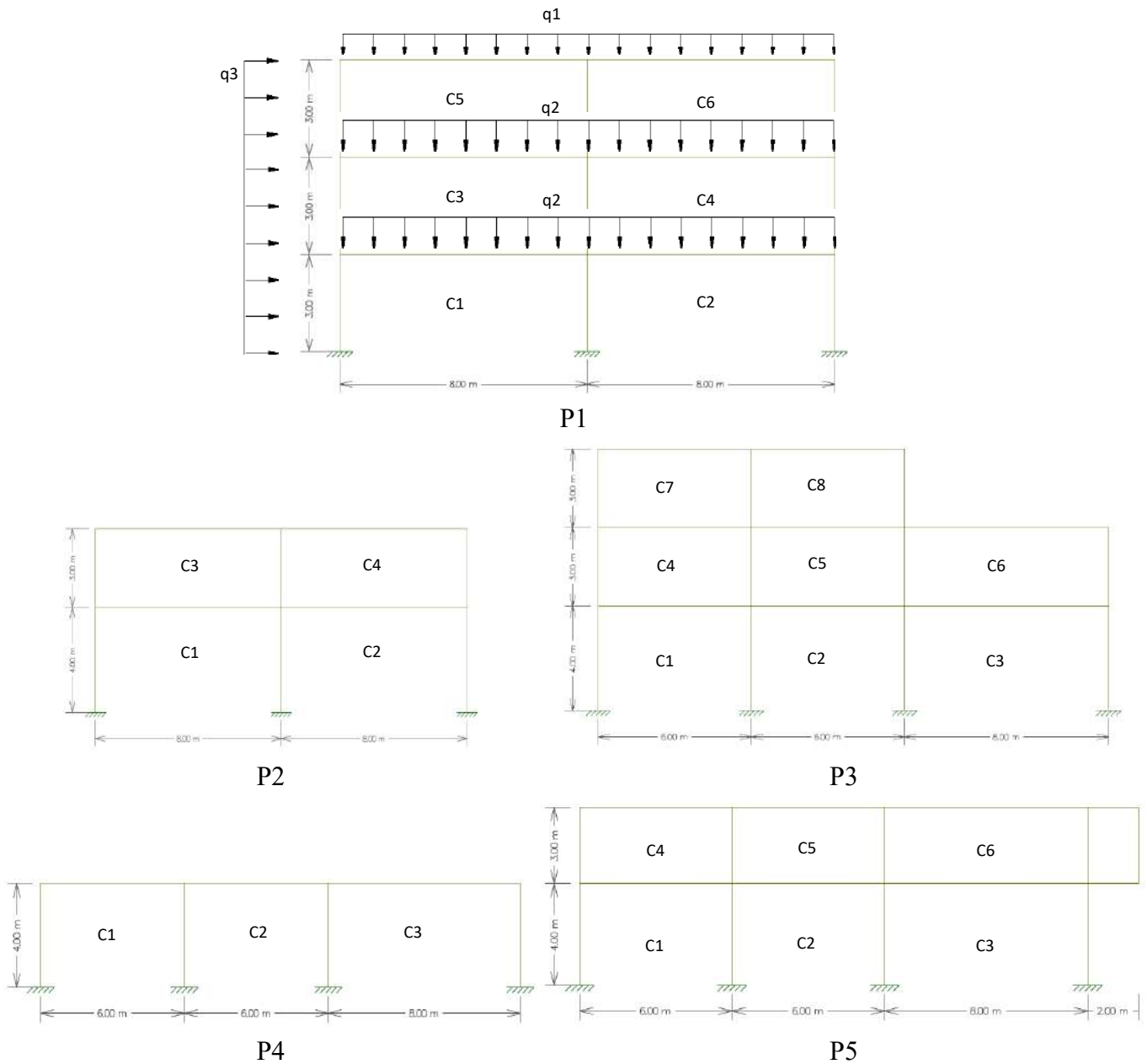


Figure 3. Frame structures analysed

For each frame structure the same I cross-sections (presented in Table 3) were adopted for the different materials S235, 1.4301 and 1.4401.

Table 3. Chosen cross-sections for each frame structure

	P1	P2	P3	P4	P5
Columns	HE260A	HE220A	HE260A	HE220A	HE220A
Beams	IPE500	IPE450	IPE450	IPE400	IPE360

Different fire scenarios were considered for the five frame structures, as shown in Table 4.

Table 4. Considered fire scenarios for each frame structure

Frame structure	P1	P2	P3	P4	P5
Scenario 1	Fire in all compartments	Fire in all compartments	Fire in all compartments	Fire in all compartments	Fire in all compartments
Scenario 2	Fire in compartment C1	Fire in compartment C4	Fire in compartment C5	Fire in compartment C2	Fire in compartment C6
Scenario 3	Fire in compartment C4	Fire in all compartments of the ground floor	Fire in all compartments of the ground floor	-	Fire in all compartments of the ground floor
Scenario 4	Fire in all compartments of the ground floor	Fire in all compartments of the 1 st floor	Fire in all compartments of the 1 st floor	-	Fire in all compartments of the 1 st floor
Scenario 5	Fire in all compartments of the 1 st floor	-	Fire in all compartments of the 2 nd floor	-	-
Scenario 6	Fire in all compartments of the 2 nd floor	-	-	-	-

The I cross-sections of beams located in compartments under fire were considered to be heated under 3 sides, simulating the influence of a concrete slab on its upper flange. The columns that are located between two compartments under fire were heated on their sections 4 sides and the columns that have a compartment under fire only in one side were considered to be heated in 3 sides. The temperature field obtained in the cross-section of the profiles is non uniform. Simplified methods prescribed in Eurocode 3 assume that the temperature field is uniform in the cross section of the profiles, due to the elevated steel thermal conductivity. As it can be easily understood, elevated thermal gradients may be expected in the analysed sections, which can origin significant changes in the thermo-mechanical behaviour.

Figure 4 represents the temperature evolution at a specific point of a beam cross section. It can be verified that the heating curve of the stainless steel is very similar to the heating curve of carbon steel with the exception in the range between 600 °C and 900 °C. The time delay represented for carbon steel is due to the metallurgic phase transformation and accounted by the peak in the specific heat property value of carbon steel, which that does not exists in the stainless steel, as was shown in Figure 2.

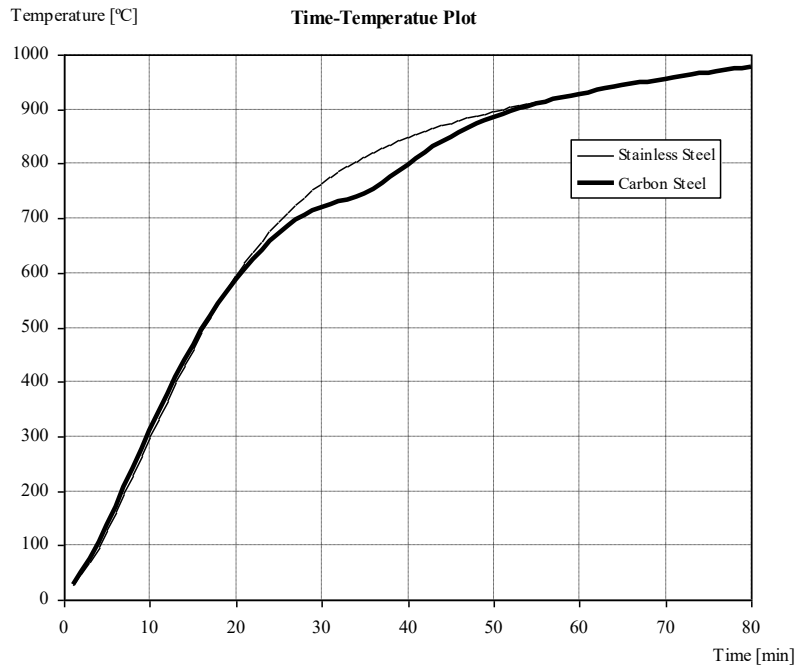
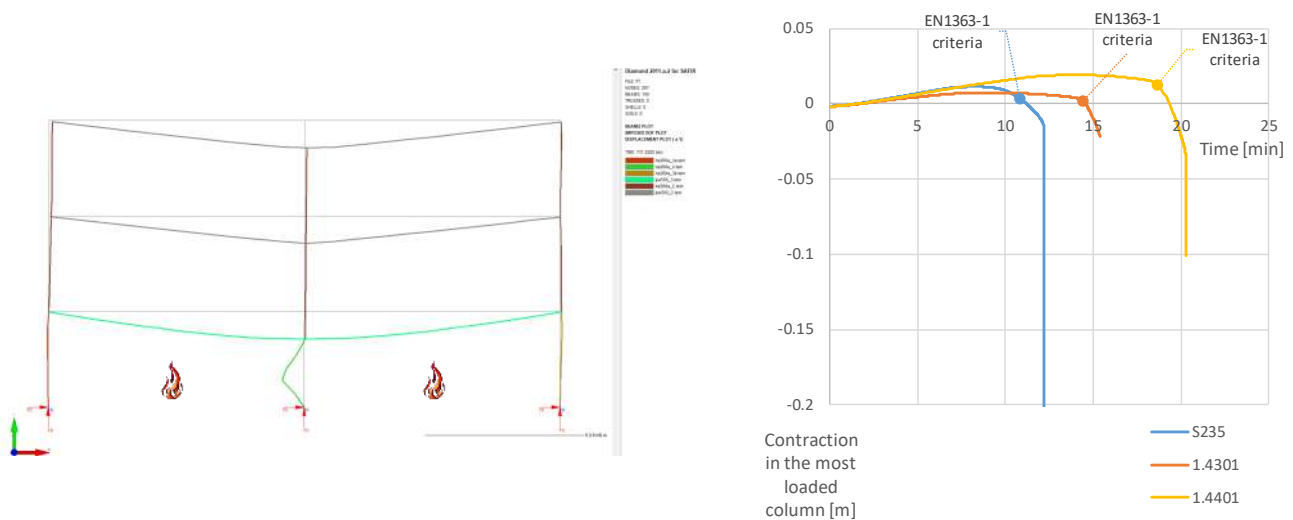


Figure 4. Temperature evolution in a cross section

4 DISCUSSION OF RESULTS

Figure 5 depicts the displacements prior the collapse of two of the tested frame structures (P1 with scenario 4 where collapse occurred in a column and P5 with scenario 2 where collapse occurred in a beam) and corresponded graphs of maximum vertical displacements evolution with time, showing the attainment of the failure criteria in EN1363-1 for fire resistance tests of members (deformation and rate of deformation limits) and the last equilibrium calculation obtained with SAFIR (corresponded to the last plotted instant).



a)

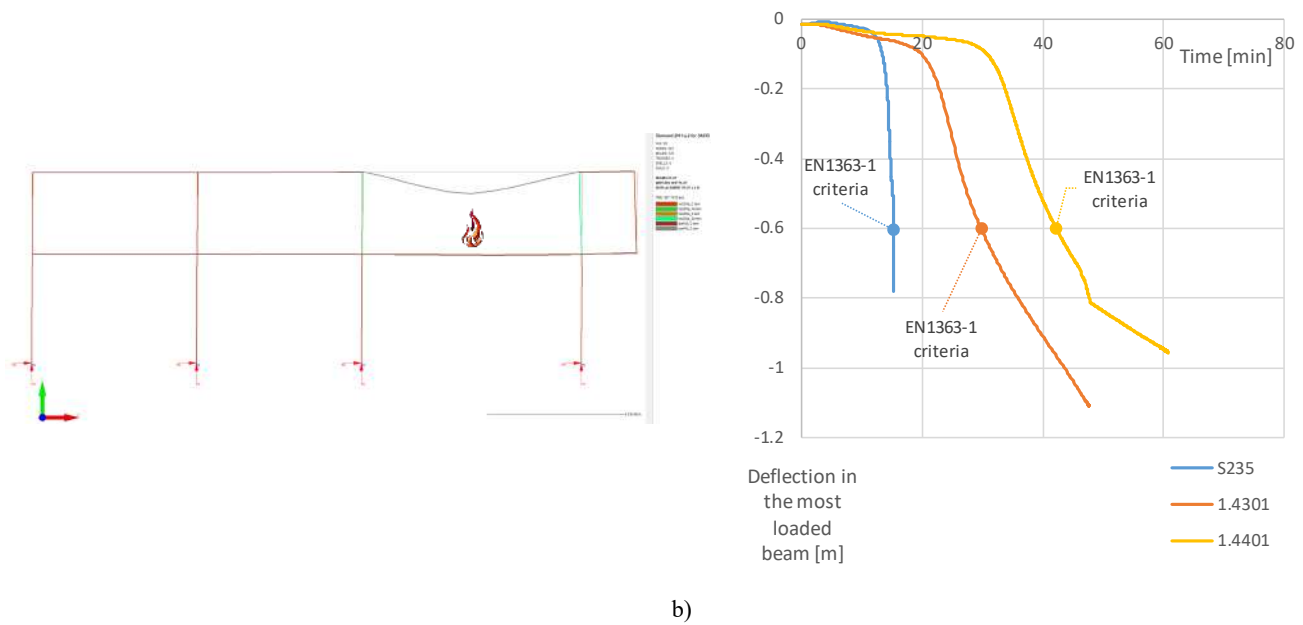


Figure 5. Examples of analysis, deformed shape prior the collapse (x1) and maximum vertical displacements in function of time: a) P1 with scenario 4; b) P5 with scenario 2

Table 5 details the respective results, considering also the design predictions of the current version of EC3 (EN1993-1-2:2005) and its second generation (FprEN 1993-1-2:2023). The proposed method for the second generation of EC3 provides lower fire resistance times for stainless steel, improving EC3 predictions for the case of column design in P1 with scenario 4, but providing too conservative results for P5 with scenario 2, where the failure occurs in the beam.

Table 5. Obtained fire resistance times for the two examples in figure 5 [min]

		Simplified calculation methods		Advanced calculation methods	
		EN1993-1-2:2005	FprEN1993-1-2:2023	EN1363-1 criteria	Loss of equilibrium
P1 with scenario 4	S235	14.6		10.8	12.2
	1.4301	20.3	13.5	14.4	15.4
	1.4401	27.0	19.5	18.7	20.3
P5 with scenario 2	S235	13.8		14.7	15.1
	1.4301	16.6	10.9	25.9	47.6
	1.4401	23.3	17.5	37.3	60.8

Table 5 presents all the complete set of obtained failure times considering the instant that it was not possible to establish the equilibrium of each tested structure with the different fire scenarios. The time corresponded to the attainment of EN1363-1 criteria in each tested case is depicted in Table 7. Below each presented times it is signalled whether the failure was due to the vertical contraction or rate of vertical contraction limits for the columns “C” or due to the deflection and rate of deflection limits for the beams “B”. Figure 6 plots a comparison between all the numerically obtained results considering the two tested different failure criteria.

Table 6. Failure times obtained in SAFIR considering loss of equilibrium [min]

Frame structure	P1			P2			P3			P4			P5		
	S235	1.4301	1.4401	S235	1.4301	1.4401	S235	1.4301	1.4401	S235	1.4301	1.4401	S235	1.4301	1.4401
Scenario 1	11.7	14.6	19.6	10.6	10.9	16.3	13.4	18.4	26.9	11.1	17.4	23.0	10.9	10.1	16.0
Scenario 2	15.2	24.0	29.6	15.0	30.2	42.2	21.9	44.5	52.6	16.4	52.2	76.8	15.1	47.6	60.8
Scenario 3	19.2	28.1	39.5	10.5	10.1	15.4	13.1	17.9	26.0	-	-	-	10.7	9.4	14.0
Scenario 4	12.2	15.4	20.3	15.0	28.7	41.6	15.4	26.9	36.0	-	-	-	14.7	28.3	40.9
Scenario 5	14.2	20.3	27.1	-	-	-	22.0	51.6	69.9	-	-	-	-	-	-
Scenario 6	17.7	39.7	47.8	-	-	-	-	-	-	-	-	-	-	-	-

Table 7. Failure times obtained in SAFIR considering EN1363-1 criteria [min]

Frame structure	P1			P2			P3			P4			P5		
	S235	1.4301	1.4401	S235	1.4301	1.4401	S235	1.4301	1.4401	S235	1.4301	1.4401	S235	1.4301	1.4401
Scenario 1	10.5 C	14.5 C	19.5 C	10.4 C	10.8 C	16.3 C	12.9 C	18.4 C	26.9 C	11.0 B	14.5 B	19.6 B	10.8 C	10.1 C	16.0 C
Scenario 2	14.9 C	16.1 C	23.3 C	14.9 B	25.9 B	37.5 B	21.4 B	41.9 C	51.9 C	16.3 B	37.6 B	47.5 B	14.7 B	25.9 B	37.3 B
Scenario 3	19.0 C	25.6 C	38.3 C	10.2 C	10.1 C	15.4 C	12.7 C	17.9 C	25.4 C	-	-	-	14.3 C	9.4 C	13.9 C
Scenario 4	10.1 C	14.4 C	18.7 C	14.7 B	25.6 B	37.3 B	15.3 C	25.1 C	34.7 C	-	-	-	14.3 C	24.5 B	35.8 B
Scenario 5	12.7 C	19.7 C	27.0 C	-	-	-	21.9 B	47.0 B	69.9 B	-	-	-	-	-	-
Scenario 6	17.6 B	34.7 B	47.4 B	-	-	-	-	-	-	-	-	-	-	-	-

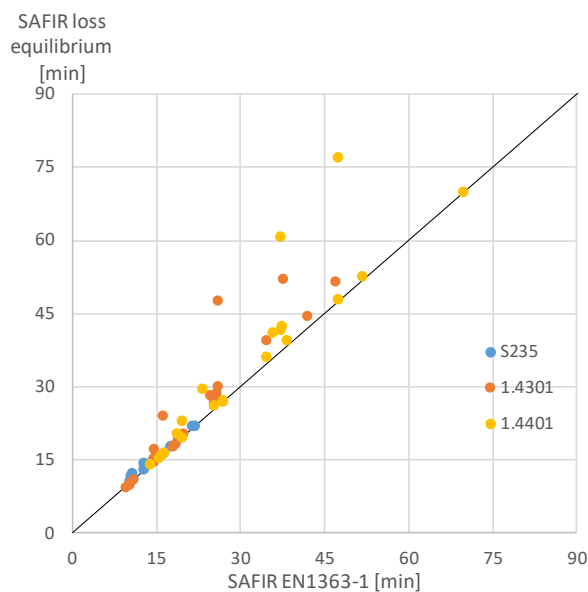


Figure 6. comparison between the numerically obtained results considering the different failure criteria

The failure criteria adopted with the FEM analyses can have a significant influence on the results obtained for stainless steel frame structures, mainly for the fire scenarios where the failure occurs in beams. On those cases, the criteria corresponded to the loss of equilibrium provides significantly higher fire resistance times than EN1363-1 criteria, which can be justified by stainless steel hardening.

Frame structures with scenarios corresponded to fire in only one compartment present typically higher differences between the two tested failure criteria. The lower stiffness reduction on the fire compartment surrounding structure can enable better efforts distribution even when large deformations occur and reduced instabilities susceptibility.

As expected, and although having similar yield strengths and young modulus at normal temperature, the stainless steel structures provide significantly higher fire resistances when compared to the carbon steel structures.

5 CONCLUSIONS

Numerical analyses of the global behaviour of unprotected carbon steel and stainless steel plane frame structures under fire situations were presented.

The main objectives of this research work were to provide a discussion on the failure criteria to be applied on the determination of the fire resistances of frame structures obtained through FEM numerical analyses and to present a wide comparison between carbon steel and stainless steel frame structures ultimate bearing capacities under fire, showing the influence of the stainless steel better mechanical properties at elevated temperatures. It could be concluded that:

- i) Unlike for carbon steel frame structures, the collapse criteria prescribed for experimental fire resistance tests in EN1363-1 of structural members provided significant lower fire resistance times when compared to considering the loss of equilibrium of stainless frame structures. On those cases it is possible to take advantage of stainless steel extensive hardening at elevated temperatures. Nevertheless, it should be noted that the application of a deformation criteria on the analysis of steel frame structures can be important to have safer design choices when needed, as for instance in evacuation routes;
- ii) The studied frame structures in stainless steel 1.4401 provided relatively higher fire resistance times than the same structures in stainless steel 1.4301, which in turn also had significantly higher fire resistance than the same structures in carbon steel S235. These higher resistances may allow for the utilization of stainless steel structures without fire protection, which increases the economic advantage of the stainless steel as a structural material, in the initial cost, maintenance needs and steel residual value (e.g. no need for painting removal after the structure end life).

Finally, comparisons were also made with EC3 simplified calculation methods estimations. These analytical evaluations of the fire resistance of frame structures do not consider steel members thermal expansion and the buckling length factors are constant values that do not reproduce the frames stiffness variation with the temperature precisely.

The results of the practical cases presented in this paper should be seen as preliminary study. There is a wide number of different parameter possible variations (such as frame structures geometries and dimensions, fire scenarios and loading) that should be further considered to validate the general observations presented from this study, considering also 3D structural analyses.

REFERENCES

1. Baddoo, N., "Stainless steel in construction: A review of research, applications, challenges and opportunities", *Journal of Constructional Steel Research*, 64(11), 1199-1206, 2008.
2. Gardner, L., *Stability and design of stainless steel structures – Review and outlook, Thin-Walled Structures*, Elsevier, 141, pp. 208-216, 2019.

3. Steel Construction Institute (SCI), “Design Manual for Structural Stainless Steel”, SCI publication P413 (4th edition), 2017.
4. Mirambell, E., Real, E., “On the calculation of deflections in structural stainless steel beams: an experimental and numerical investigation”, *Journal of Constructional Steel Research*, 54(1), 109-133, 2000.
5. European Committee for Standardisation (CEN), FprEN 1993-1-1, Eurocode 3, Design of Steel Structures – Part 1-1. General rules and rules for buildings. Brussels, Belgium, 2022.
6. CEN, prEN1993-1-4, Eurocode 3, Design of Steel Structures – Part 1-4. General rules – Supplementary Rules for Stainless Steels, Brussels, Belgium, 2023.
7. CEN, EN10088-4, Stainless steels. Part 4: Technical delivery conditions for sheet/plate and strip of corrosion resisting steels for construction purposes, Brussels, Belgium, 2009.
8. CEN, FprEN1993-1-2, Eurocode 3, Design of Steel Structures – Part 1-2. General rules – Structural fire design, Brussels, Belgium, 2023.
9. Liang, Y., Manninen, T., Zhao, O., Walport, F., Gardner, L. Elevated temperature material properties of a new high-chromium austenitic stainless steel, *J. of Constructional Steel Research*, 152, 2019, pp. 261–273.
10. Franssen, J.-M., Vila Real, P., *Fire Design of Steel Structures*, ECCS; Ernst & Sohn, a Wiley Company, 2nd Ed., 2015.
11. CEN, EN1363-1, Fire resistance tests - Part 1: General requirements, Brussels, Belgium, 2020.
12. Segura, G., Arrayago, I., Mirambell, E. Plastic redistribution capacity of stainless steel frames in fire. *Journal of Constructional Steel Research*, Volume 208, 108019, 2023.
13. Segura, G., Pournaghshband, A., Afshan, S., Mirambell, E. Numerical simulation and analysis of stainless steel frames at high temperature. *Engineering Structures*, 227, 111446, 2021.
14. Franssen, J.-M. and Gernay, T. Modeling structures in fire with SAFIR: theoretical background and capabilities *Journal of Structural Fire Engineering*, 8(3), 300–323, 2017.
15. CEN, EN1993-1-2, Eurocode 3, Design of Steel Structures – Part 1-2. General rules – Structural fire design, Brussels, Belgium, 2005.
16. Xing, Z., Kucukler, M. and Gardner, L., Local buckling of stainless steel I-sections in fire: finite element modelling and design. *Thin-Walled Structures*, 161:107486, 2021.
17. Kucukler, M., Xing, Z., Gardner, L., Behaviour and design of stainless steel I-section columns in fire, *Journal of Constructional Steel Research*, Vol. 165, 105890, 2020.
18. Kucukler, M., Xing, Z., Gardner, L., Stability of stainless steel I-section beam–columns at elevated temperatures. *International Journal of Structural Stability and Dynamics*, Vol. 21, No. 3, 2150037, 2021.
19. Pinho-da-Cruz, J., Lopes, N., Vila Real, P., Couto, C. Numerical modelling and benchmark study of fire resistance of stainless steel structural elements. *Journal Fire Technology*, Springer, 2022
20. CEN, NP EN1991-1-2, Eurocódigo 1: Acções em estruturas - Parte 1-2: Acções gerais - Acções em estruturas expostas ao fogo, IPQ, Caparica, Portugal 2010.
21. Computers and Structures, Inc. SAP2000. Version 25, Computers and Structures, Inc., 2024.
22. CEN, EN1990, Eurocode – Basis of structural design, Brussels, Belgium, 2002.
23. CEN, EN1991-1-1, Eurocode 1: Actions on structures - Part 1-1: General actions - Densities, self-weight, imposed loads for buildings, Brussels, Belgium, 2002.
24. CEN, EN1991-1-4, Eurocode 1: Actions on structures - Part 1-4: General actions – Wind actions, Brussels, Belgium, 2005.
25. CEN, EN1991-1-3, Eurocode 1: Actions on structures - Part 1-3: General actions – Snow loads, Brussels, Belgium, 2003.

FIRE DYNAMICS AND STRUCTURAL RESPONSE OF SPRINKLERED WAREHOUSE WITH STEEL TRUSSES USING COMPUTATIONAL MODELLING

Dilip Neupane¹, Zhongcheng Ma²

ABSTRACT

This paper presents the fire dynamics and structural response of a sprinklered warehouse with steel trusses using computer modelling techniques. Different fire scenarios were simulated using the Fire Dynamics Simulator (FDS), both with and without sprinkler systems, considering different fire start locations, the activation temperature, and the flow rate of the sprinkler head. Structural response analyses were conducted using Abaqus to assess the impact of these fire scenarios on the building's stability and integrity. Simulations reveal that the warehouse fires can be effectively controlled by the sprinkler system even if the defects of reduced flow rate exist. Different discharge densities (greater than 50%) will be capable of controlling the fire in the warehouse even if fuels keep burning inside the storage racks. Moreover, the number and location of activated sprinkler heads vary depending on factors such as the fire's ignition surface area and sprinkler head activation temperature. However, the conventional sprinklers, activated by the gas temperature value, have the drawback of excessive activations in other locations than the fire source. The excessive water damage may be induced due to the quick hot smoke accumulation in the sides and corners of fire compartment. The sprinkler system significantly lowered the temperatures in load-bearing structural members and prevent catastrophic structural failure.

Keywords: Steel trusses; warehouse fire; fire dynamics; sprinklers; structural response; FDS; Abaqus

1 INTRODUCTION

The warehouses in Nordic countries are typically constructed from steel frames with tubular trusses and are utilized for storing goods through a rack system. Many of the stored goods consist of materials such as plastic, wood, paper, and other highly combustible materials that are prone to rapid spreading in the event of a fire. Thus, sprinklers were used to control and extinguish a fire, reducing damage to the building, improving the safety of the occupants, and preventing environmental pollution. The sprinkler system in a one-storey building is designed to activate automatically when heat or smoke is detected. In this study, different fire scenarios in a warehouse were simulated using the Fire Dynamics Simulator (FDS), including the fire evolutions with and without sprinkler systems. The effects of the fire start locations, the activation temperature and the flow rate of the sprinkler heads were investigated. Structural response analyses were conducted using Abaqus to assess the impact of these fire scenarios on the building's stability and integrity. The study highlights the critical role of sprinkler systems in the fire safety of steel-framed warehouses and discusses their capacity to control fires with possible defects in the sprinkler system.

¹ Research Engineer, Häme University of Applied Science, Finland
e-mail: dilip.neupane@hamk.fi

² Principle Research Scientist, Häme University of Applied Science, Finland
e-mail: zhongcheng.ma@hamk.fi

2 DESCRIPTION OF A SPRINKLERED WAREHOUSE

The steel-framed one-storey warehouses are usually designed with the tubular trusses or portal frames and have sprinkler systems installed to provide fire protection. A one-storey warehouse in Nordic usually consists of steel frames and the exterior walls using sandwich panels. The warehouse floor is typically constructed from concrete and goods are stored through a rack system. The sprinkler system can be configured for ceiling-only protection or utilized with an in-rack option for enhanced fire safety. The dimensions of the warehouse building in this study are 41m x 35m x 10m. The fire load distribution represents a rack storage typically used in the warehouse. The wooden pallet stacks of 1.22 x 1.22 m x 1.22 m are stored in the rack system. It is assumed that each wooden pallet stack presents the furniture goods in the warehouse. A total of 324 wooden pallet stacks were arranged in the compartment with a spacing of 1.8m between each of the racks. Each rack contains three wooden pallet stacks with a spacing of 280mm along the vertical direction. The average fire load density was 1462 MJ/m². This corresponds to a fire load density greater than 1200 MJ/m², according to the Finnish building code [1]. The warehouse is made of tubular truss frame solution, with the frame spacing of 6m and a wall column height of 9.3m. The pitched roof has a height of 10.2m in the ridge. The sprinkler system considered in this study is a ceiling-only protection configuration, and the sprinklers are located below the bottom chord of the truss frame. The overview of the warehouse is shown in Figure 1(a). Firstly, a fire dynamics model was constructed using FDS to estimate and validate the design parameters of the sprinkler system. Secondly, a FDS model of the entire compartment was developed, and various fire scenarios were planned and simulated. Thirdly, the thermal analysis and structural response analysis were performed. Abaqus, a commercial FEM software, was used to perform 2D heat transfer analysis on selected structural members of the warehouse and to perform 3D structural analyses. The validated thermal and structural analysis methods employed in this study are based on [2] and [3].

3 FIRE DYNAMICS MODELLING

Modelling the one-storey warehouse building with a sprinkler system in Fire Dynamics Simulator (FDS) involves the digital representation of the building and its components and the sprinkler system. The purpose of this modelling is to simulate the behaviour of fire and smoke in the building and evaluate the sprinkler system's performance in controlling the fire. The following steps can be followed:

- Define the building geometry and layout, including the location and arrangement of walls, windows, doors, and other features.
- Assign properties to building materials, such as the thermal conductivity, specific heat capacity, and ignition temperature of the combustible in the warehouse.
- Specify the location, type, and characteristics of the sprinkler system, including the number and distribution of sprinkler heads, flow rate, and water supply pressure.
- Define the initial fire conditions, including the location and size of the fire source and the fuel load in the compartment.
- Run the simulation and analyze the results, including the spreading and growth of the fire, the activation and performance of the sprinkler system, and the smoke and heat distribution in the building.

This process can be repeated with different design scenarios or fire conditions to evaluate the performance of the sprinkler system and make design improvements as needed.

3.1 Computational models of sprinklered warehouse in FDS

Figure 1(b) shows the overview of the warehouse modelled in FDS. The compartment consists of a simplified truss frame structure, walls and ceiling, wall opening, and the wooden pallets stored on the floor and the racks. The wall, ceiling, and truss frame are modelled as non-combustible solid obstructions. The only combustible fuel in the compartment is the wooden pallet stacks. Three wall openings were in the long wall of the warehouse. There are two openings on the front side of the long wall and one opening on the back side of the long wall. The locations of the wall openings in the warehouse are illustrated in Figure

1(b). Boundary walls, ceiling, floor, and truss frame were created as obstructions, and their corresponding surface properties were assigned, and associated material properties of each surface were defined. The computational domain was set to 41m x 35m x 10m, which includes the size of the structure and 2m extended computational domain offset on two sides of the warehouse. The offset allows us to model the gas and heat exchanges with the surrounding environment. The simulations were run using grid resolutions of 20 cm, and the total number of grid cells was 1793750. The computational domain was divided into 32 meshes with an equal number of grid sizes to optimize the computational time. The simulations were performed using Intel(R) Xeon(R) Silver 4210 CPU @ 2.20GHz. The FDS simulation for all fire scenarios was run up to 4500 seconds. The ignition of fire start varies in each fire scenario. Three ignition locations were assumed for the commencements of fires, including centre location 1 with a larger ignition area (1.84 m x 1.84 m), centre location 2 with a smaller ignition area (1m x 1m), and corner location 3 with a larger surface area (1.84m x 1.84m) respectively. The ignition of fire starts with a peak heat release rate per unit area (HRRPUA) of 500 kW/m². The ignition source was modelled by defining a ramp-up time up to 600s. Two different ignition locations (centre and corner) and two ignition surface areas, as shown in Figure 1(b), were studied to compare the effectiveness of the sprinkler system in controlling the fire spread. The fire load distribution represented a rack storage typically used in the warehouse. The heat release rate generated by the burning of a typical wood pallet stack is shown in Figure 1(c). This curve is based on an experimental study presented in [4]. This curve was used to define peak HRR and a ramp-up time for multiple points to model the growth, spreading and extinction of fires. The HRRPUA was derived by dividing the total HRR measured from the test by the external surface area of the wood crib. The fuel surfaces in each wooden pallet were modelled with peak HRRPUA of 493 kW/m² and ignition temperature at 270°C. Figure 1(c) shows the heat release rate of a typical wood pallet used for defining the HRRPUA in this study. For modelling the combustion of fuels, the default simple chemistry reaction model in FDS was used. For the reaction model, a wood fuel species described by chemical formula C_{3.4}H_{6.2}O_{2.5}N, a 1.5% shoot yield, and a heat of combustion of 16 MJ/kg were assumed. Sprinklers were modelled as explained in section 3.2, and a total of 108 sprinklers were designed in the compartment. The sprinklers were placed below 60mm from the truss bottom chord and above the wooden pallets. The spacing between each sprinkler was 3m. The simplified truss element is used in the FDS model.

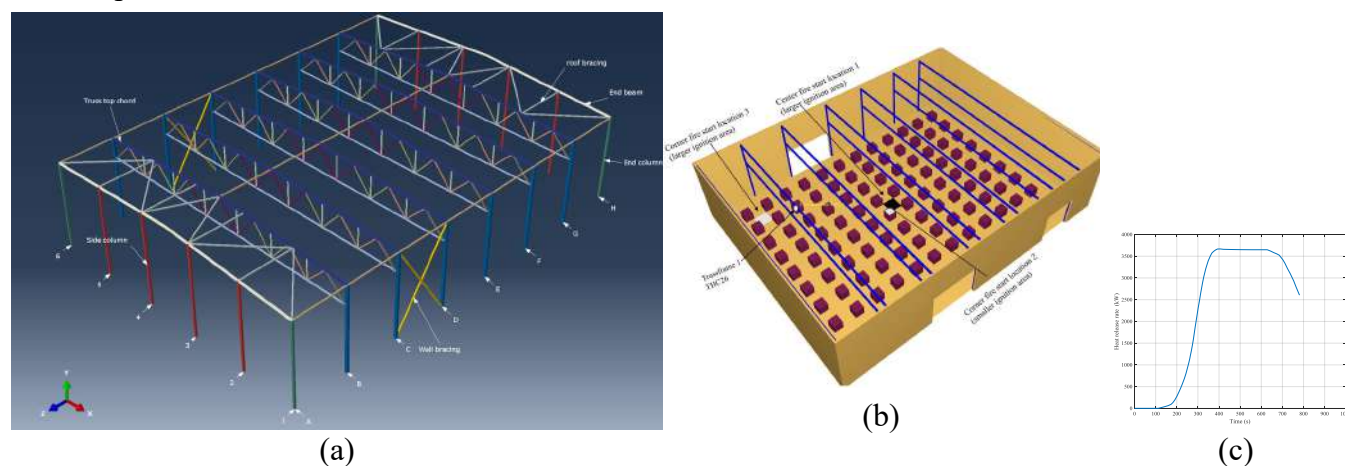


Figure 1. (a) Overview of the warehouse building as a tubular truss frame solution, (b) the ignition locations for different fire scenarios, and (c)HRR of typical wood pallets [4]

3.2 Estimation of sprinklered model parameter for FDS input

TYCO Model ESFR-25 (TY9226) storage pendent sprinkler with a high K-factor of K360 has been selected for this study. This sprinkler is a specialized fire protection system used in high-piled storage facilities, such as warehouses and distribution centres. This sprinkler's key features and characteristics are fast response and early suppression, high K-factor and large orifice size [5]. The information about the orifice diameter is not available in the manufacture catalogue. However, based on the sprinkler CAD (Revit) file from the manufacturer's website [6] the orifice diameter is approximately 23 mm. The maximum and

minimum coverage area of this sprinkler are 9.3 m² and 5.8 m². The maximum working pressure of an ESFR-25 sprinkler [7] is 12.1 bar, and the minimum working pressure for such sprinklers can vary based on several factors, such as the specific design of the sprinkler system, the manufacturer's recommendation, and local fire codes and regulations. Based on the technical data provided by manufacturing, the sprinkler can operate at a minimum pressure of 0.5 bar. In this study, the operating pressure of each sprinkler is assumed to be 1 bar with a flow of 366.4 litres per minute (LPM). The spray profile pattern for the selected sprinkler is shown in Table 1. Modelling a sprinkler spray in FDS required the sprinklers-related numerical parameters such as initial velocity, RTI (response time index), spray cone shapes, volume median diameter (VMD), droplet size distribution, placement of droplets, K-factor, and more. However, due to a lack of detailed information from the manufacturer, these parameters were estimated based on various studies reported in the literature and manufacturer information. Table 1 summarizes the input parameters utilized in FDS. Additionally, an FDS model featuring a sprinkler positioned at the centre within a computational domain of 6m x 6m x 2.6m was created, using the aforementioned parameters for comparing sprinkler spray profile patterns. It was found that approximately 50% of the total discharged mass is concentrated in the centre area. Consequently, the angle specified in the spray table is able to closely approximate the spray profile pattern.

Table 1. Summary of input parameters used in FDS to model sprinklers and validation of sprinkler's parameters

Input parameters		Description
Activation	Activation Temperature (68°C/100°C)	From manufacture document
	Response Time Index (RTI) = 50 (m/s) ^{1/2}	Fast response from [8]
Spray model	Operating pressure (1.0 bar), K-factor (362.9 L/min.atm ^{1/2})	From manufacture document
	Flow rate = 366.4 L/min	Calculated using equation $K\sqrt{p}$
	Initial velocity 14.69 m/s	
	Offset (0.1m), stream type (Spray Table)	
Water particles	Median diameter (1520 µm)	Calculated
	Distribution (Rosin-Rammler Lognormal), Minimum diameter (20µm), Gamma D (2.4)	Default
<p>Spray profile pattern for selected sprinkler Model ESFR-25 [6]</p>		<p>Accumulated mass per unit area collected kg/m²</p>

3.3 Fire scenarios

Several fire scenarios are simulated to evaluate the behaviour of fires and to test the effectiveness of sprinkler system, including uncontrolled fires, fires with limited fire suppression, and fires with different ignition areas at different locations of the compartment. For example, an uncontrolled fire scenario simulates a fire that is not quickly detected and suppressed, while a scenario with limited fire suppression simulates a situation where the water supply or fire suppression system is not functioning correctly. Fire scenarios with varying ignition surface areas are designed to replicate two specific situations: one where

fire ignition initiates within a 1.84 x 1.84 m² area (representing a larger fire source, initially igniting four wooden pallets simultaneously, leading to a higher initial heat release rate), and another where ignition occurs within a 1 m² area (smaller fire, initially igniting only the top surface of a single wooden pallet). Table 2 summarises simulated fire scenarios in FDS.

Table 2. Fire scenarios simulated in FDS

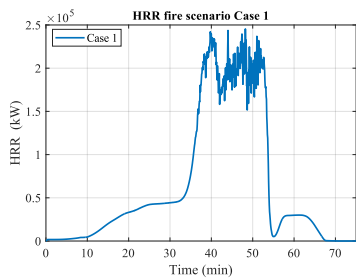
Fire scenario	Fire scenario descriptions
Case 1	Simulation of the warehouse in which no sprinkler system is installed within the compartment, and the fire is uncontrolled and has the potential to result in a catastrophic outcome. The fire initiates at the centre of the compartment with a larger ignition surface area, and the fire travels.
Case 2	Simulation of the warehouse in which sprinklers are present. The fire is controlled, and all the sprinklers are functioning effectively. The flow rate from the sprinkler head is 100%. The activation temperature of the sprinkler is 74°C or 100°C. The fire initiates at the centre of the compartment with a larger ignition surface area.
Case 3	Simulation of the warehouse in which sprinklers are present. The fire is controlled, and all the sprinklers are functioning effectively. The flow rate from the sprinkler head is 50%. The activation temperature of the sprinkler is 74°C or 100°C. The fire initiates at the centre of the compartment with a larger ignition surface area.
Case 4	Simulation of the warehouse in which sprinklers are present. The fire is controlled, and all the sprinklers are functioning effectively. The flow rate from the sprinkler head is 100% or 50%. The activation temperature of the sprinkler is 74°C or 100°C. The fire initiates at the centre of the compartment on the top surface of a wooden pallet, with a smaller ignition surface area.
Case 5	Simulation of the warehouse in which no sprinkler system is installed within the compartment, and the fire is uncontrolled and has the potential to result in a catastrophic outcome. The fire initiates at the corner of the compartment with a larger ignition surface area, and the fire is travelling.
Case 6	Simulation of the warehouse in which sprinklers are present. The fire is controlled, and all the sprinklers are functioning effectively. The flow rate from the sprinkler head is 100% or 50%. The activation temperature of the sprinkler is 74°C. The fire initiates at the corner of the compartment with a larger ignition surface area.

3.4 Results

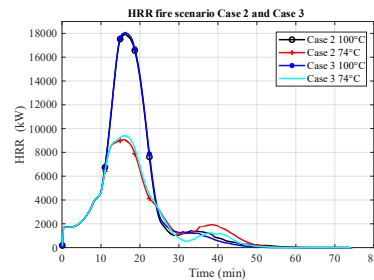
This section discusses the results of the FDS simulations for different fire scenarios. The results of the total heat release rate, temperatures from thermocouples, and sprinkler activation time and sequence. Figure 2 shows the fire heat release rate inside the compartment from fire scenario cases 1-6. Figures 2(a) and 2(d) show the fire heat release rate inside the compartment of fire scenarios Case 1 and Case 5. It can be observed that, in the beginning, the fire heat release rate is about 1692 kW until 2 minutes. This corresponds to the fire ignition definition of 500 kW/m² (HRRPUA) associated with a larger ignition area. In Case 1, after two minutes, the fire starts to propagate through four adjacent wooden pallet fuels located in the central rows of racks and continues to spread to adjacent wooden pallets. With the heating of about 10 minutes, the fire starts to spread quickly, and in about 35 minutes, the fire reaches a flashover and is fully developed. The burning stage of fuel is about 45 minutes. As the fire progresses, it experiences a reduction in intensity due to the presence of smoke and diminished oxygen levels as well. The decay period begins after 52 minutes. Additionally, a backward travel phase is also observed in about 55 minutes. Since this is the case without a sprinkler, it can be observed that the fire is uncontrolled, with higher HRR and higher temperature in the compartment. Similarly, in Case 5, after two minutes, the fire starts to propagate through four adjacent wooden pallet fuels located in the first row of racks (in the corner) and continues to spread radially to adjacent wooden pallets. It can be observed that with the heating of about 15 minutes, the fire reaches a local flashover. The burning stage of fuel continues until the simulation run time. After 20 minutes of burning, the decay period begins. A quasi-steady spreading and decaying process was observed. However, it is noticed that the fire spreads in two directions, and the fire travels, resulting in fluctuations in the heat release rate. Therefore, when considering the varying locations of fire sources, the maximum heat release rate in the compartment for fire scenario Case 1 is approximately ten times that of Case 5. This clearly demonstrates that the location of fire sources significantly impacts fire growth, smoke spread, smoke height,

and temperature development within the compartment. The location notably affects the maximum heat release rate, patterns of fire growth, and fire spread, as well as the smoke's thickness and height.

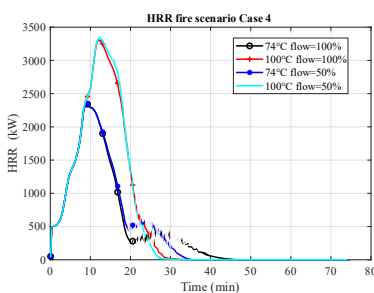
Figure 2(b) depicts the fire heat release rate within the fire compartment of the Fire Scenario Case 2 and Case 3, considering two different sprinkler activation temperatures. It can be observed that, in the beginning, the fire heat release rates for both cases (2 and 3) are similar compared to Case 1. After 2-3 min, the fire propagates through four adjacent wooden pallet fuels in the first row of racks and continues spreading to adjacent wooden pallets. As the fire progresses, the sprinkler system activates and prevents the fire from spreading to adjacent racks and fuels. However, it is observed that there is a significant variation in the maximum heat release rates when the sprinkler system activates at different temperatures.



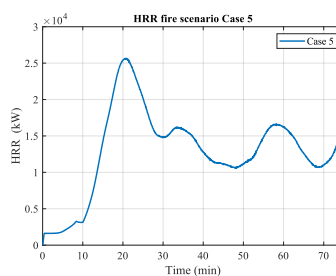
(a) Case 1



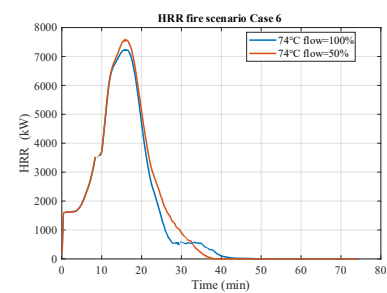
(b) Cases 2 and 3



(c) Case 4



(d) Case 5



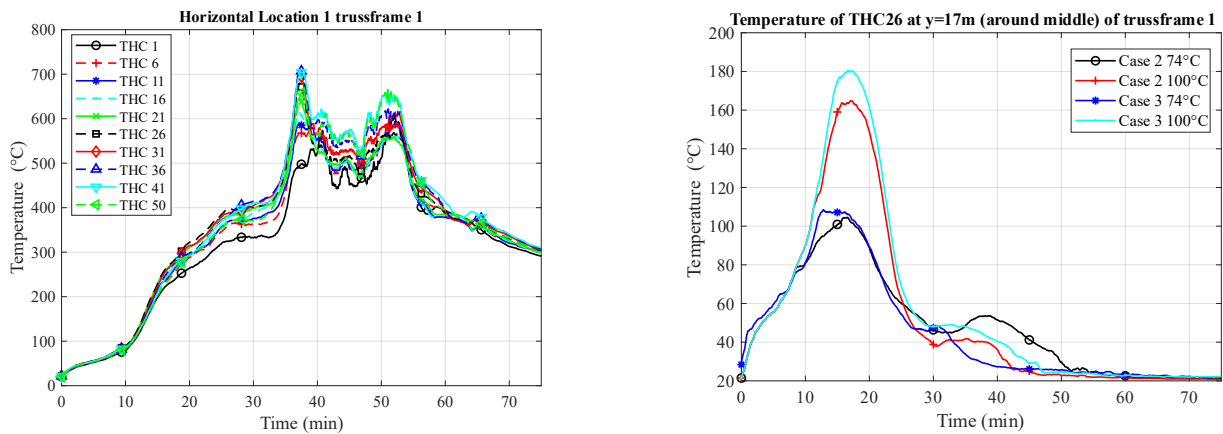
(e) Case 6

Figure 2. Heat release rate in the simulation (Fire scenario cases 1- 6)

When the sprinkler system is set to activate at 74°C, we observe a maximum heat release rate of approximately 9000 kW during the fire event. Similarly, when the sprinkler system is configured to activate at a higher temperature of 100°C, the maximum heat release rate doubles, reaching around 18000 kW. Thus, this will similarly impact the temperature development inside the compartment.

Figure 2(c) shows the fire heat release rate inside the compartment of fire scenario Case 4, considering two different sprinkler activation temperatures and two different flow rates from the sprinkler's head. It can be observed that, in the beginning, the fire heat release rate is about 500 kW until 2 min. This corresponds to the fire ignition definition of 500 kW/m² (HRRPUA) associated with a smaller ignition area (1 x 1 m²). After two minutes, the fire starts propagating through the top surface of the first shelf and the bottom surface of the second shelf in one rack. As the fire progresses, the sprinkler system activates and prevents the fire from spreading to additional racks and fuels. However, it is observed that there is a significant variation in the maximum heat release rates when the sprinkler system activates at different temperatures, similar to Case 2 and Case 3. When the sprinkler system is set to activate at 74°C, we observe a maximum heat release rate of approximately 2241 kW during the fire event. Similarly, when the sprinkler system is configured to activate at a higher temperature of 100°C, the maximum heat release rate reaches around 3344 kW. When considering different flow rates from the sprinkler head, no significant variation in the maximum heat release rate is observed. The maximum heat release rate for Case 4 is similar when the sprinkler activates at different flow rates, with only a slight variation. Based on this observation, we can conclude that the fire was successfully controlled in Case 4 despite different sprinkler activation temperatures and flow rates from the sprinkler's head.

Figure 2(e) shows the fire heat release rate inside the compartment of fire scenario Case 6, considering two different flow rates from the sprinkler's head. After two minutes, the fire starts to propagate through four adjacent wooden pallet fuels located in the first row of racks (in the corner) and continues to spread to adjacent wooden pallets. As the fire progresses, the sprinkler system activates and prevents the fire from spreading to additional racks and fuels. Similar heat release rate curves were obtained when considering different flow rates from the sprinkler's head. It can be observed that with the heating of about 10 minutes, the fire develops quickly and locally and reaches the peak HRRs at 16 minutes. The maximum heat release rate was approximately 7238 kW for a 100% flow rate and 7586 kW for a 50% flow rate, respectively.



(a) The temperatures of the thermocouples near the truss top chord (near the ceiling) of truss frame 1 (Fire scenario Case 1) (b) Comparison of temperature of THC26 located at top chord near truss frame 1 location from fire scenario Case 2 and Case 3, considering two different sprinkler activation temperatures

Figure 3. Comparison of temperature histories of THC26 with and without sprinkler's system (Fire scenario Case 1 and Case 2)

Figure 3 depicts the example of the temperature histories comparison of thermocouple THC26, positioned on the top chord near truss frame one, for two different fire scenarios: Case 1 and Case 2. The THC26 is positioned 17.23m away from the front side of the long wall and 9.09m above the compartment floor, as shown in Figure 1(b). Similarly, thermocouples (THC1, THC6, THC11, THC16, THC21, THC26, THC31, THC36, THC41, and THC50) in Figure 3(a) are situated at distances of (0.73m, 5.23m, 8.23m, 11.23m, 14.23m, 17.23m, 20.23m, 23.23m, 26.23m, and 30m) respectively away from the front side of the long wall, all positioned at a height of 9.09 meters above the compartment floor.

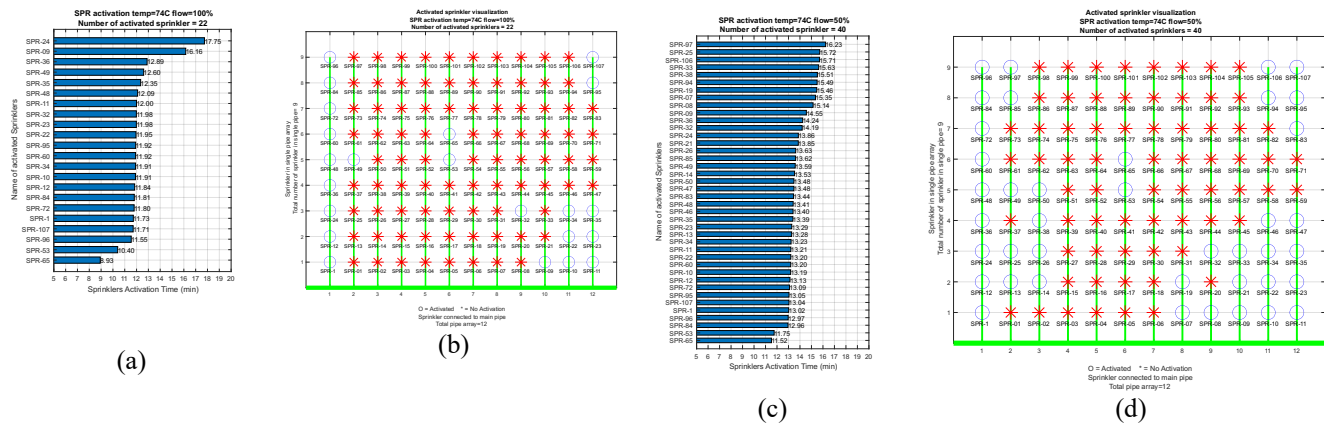


Figure 4. Sprinkler Activation and Visualization for Case 2. Activation Temperatures: 74°C (a and b), and 100°C (c and d). 'O' represents activated sprinklers

In the context of sprinkler activation in Figures 4, it was observed that 22 sprinkler heads were activated in Case 2 and 53 sprinklers activated in Case 3 when the sprinkler activation temperature was set at 74°C. Likewise, when the sprinkler activation temperature was increased to 100°C, a higher number of sprinkler heads activated: 40 in Case 2 and 82 in Case 3. The first sprinkler activation occurred at a similar time and the same activation temperature. Figure 4 displays the names and numbers of activated sprinklers, visualizations of activated sprinklers, their locations, action sequences, and activation times for each activated sprinkler in both Case 2 and Case 3. In both fire scenarios, it is evident that sprinkler activation temperature and the flow rate from the sprinkler heads played a significant role in determining the number of activated sprinklers. Only two sprinkler heads were activated directly above the fire start location. Most sprinklers were activated in the corner of the compartment, likely due to the higher temperature prevailing in that area. This elevated temperature was primarily caused by the accumulation of a thick layer of smoke in the corner.

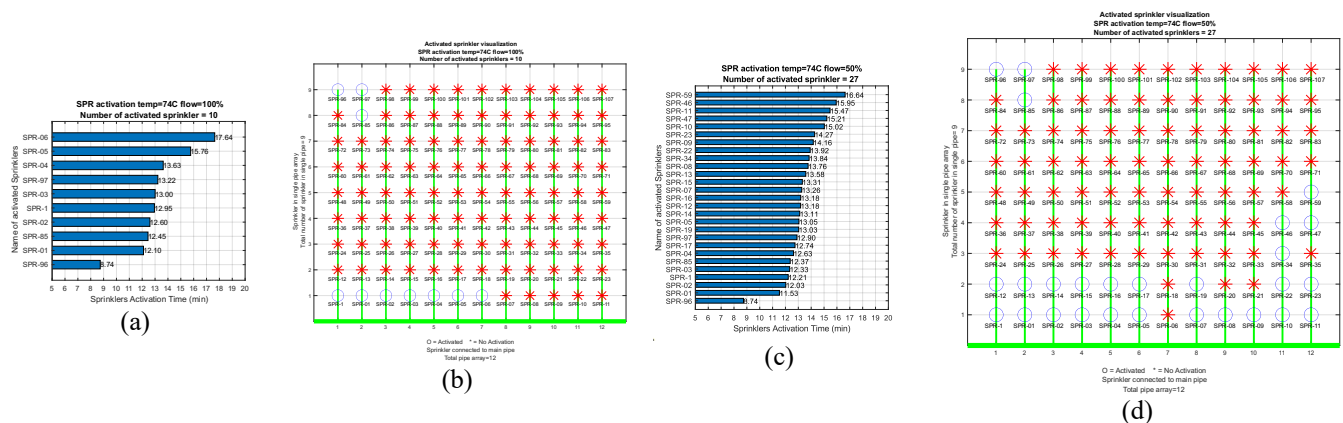


Figure 5. Sprinkler Activation and Visualization for Case 6. (a) and (b) for flow rate of 100%; (c) and (d) for flow rate of 50%. ‘O’ represents the activated sprinklers

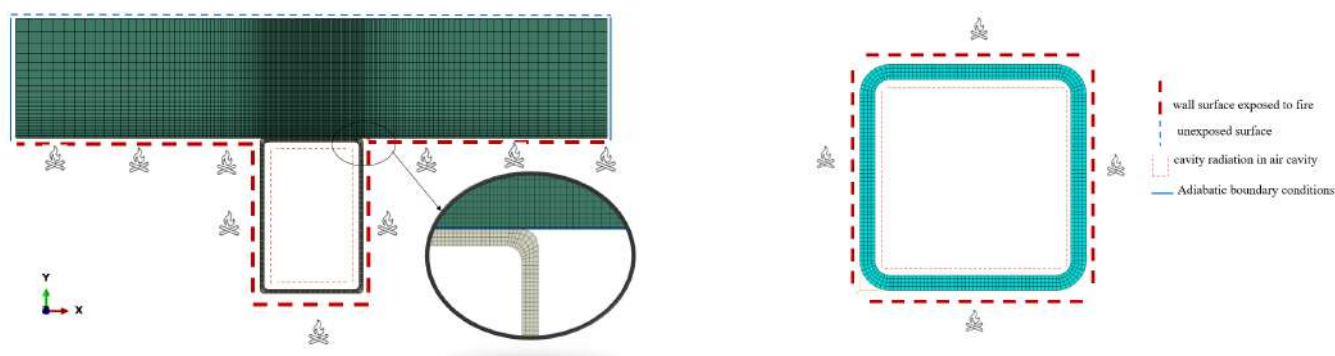
Furthermore, it was observed that only one sprinkler head was activated for Case 4 when the sprinkler activation temperature was set at 74°C or 100°C regardless of two different flow rates from the sprinkler’s head. In Case 6, it was observed that ten sprinkler heads were activated when the design flow rate from the sprinkler head was 100%. Similarly, when the flow rate from the sprinkler head was 50%, it was observed that 27 sprinkler heads were activated. It is evident that the flow rate from the sprinkler heads played a significant role in determining the number of activated sprinklers. Only three sprinkler heads were activated directly above the fire start location. Most sprinklers were activated in the opposite corner of the fire start location, likely due to the higher smoke temperature prevailing in that area. Figure 5 displays the names and numbers of activated sprinklers, visualizations of activated sprinklers, their locations, action sequences, and activation times for each activated sprinkler in Case 6.

4 STRUCTURAL RESPONSE MODELLING

4.1 2D-temperature analysis of structural members of the warehouse

This analysis aims to determine the temperature distribution and the nodal temperature in the cross-section of the wall column, truss top chord, truss bottom chord, and other relevant structural members. This study explicitly conducts thermal analysis for structure members experiencing higher temperatures in two fire scenarios: one without sprinklers and another with a sprinkler system installed. As shown in Figure 6, the wall and end columns were exposed to the hot gases on one side by convection and radiation heat. In the case of structural members within the truss frame, all of them were subjected to fire on all surfaces except the top chord. The red dashed line represents the surface exposed to fire, and the blue dashed line represents the unexposed surface. The elevated temperatures were obtained from the FDS simulation. The density,

temperature-dependent thermal conductivity, and specific heat of steel material are defined according to EN 1994-1-2. Similarly, the temperature-dependent thermal material properties for mineral wool insulation were taken from [9]. DC2D4, a 4-node linear heat transfer quadrilateral element, was used to model the cross-section of the structural member of the warehouse. For all thermal models, the convection coefficient for wall temperature on the exposed side is taken as $25 \text{ W/m}^2\text{K}$ and as $9 \text{ W/m}^2\text{K}$ on the unexposed side, according to EN 1991-1-2 (2005). The emissivity coefficient factor is taken as 0.8 for radiation, according to EN 1993-1-2 (2005) [10]. Cavity radiation was defined in the air cavity (inside the hollow section of the RHS profile) region with a surface emissivity of 0.4. No definition was made for two sides of the wall section (blue solid line). This implies adiabatic boundary conditions, that is, no heat flux through the boundary. An initial temperature of 20°C was defined using a predefined temperature field for all thermal models of RHS profiles and walls. A transient heat transfer analysis was performed for the 2D cross-section of structural members using the Abaqus/Standard heat transfer procedure with an automatic time step for a period of 4500 seconds. Multiple thermal analyses were performed on various structural members with and without sprinkler systems.



(a) Example of a 2D model for a wall column with mineral wool insulation (RHS300x200x8+MW)

(b) Example of a 2D model for bottom truss chord exposed to fire on all sides (RHS120x120x8 profile)

Figure 6. Example of thermal analysis model of a structural member in the warehouse

Figure 7(a) illustrates the temperature contour of the wall column at 9.09m above the floor with sprinklers (Case 2) and without sprinklers (Case 1) at different stages of fire exposure. At approximately 9 minutes of the heating period, in both fire scenarios, the temperature reaches around $62\text{--}63^\circ\text{C}$. In Case 1, as the fire progresses, the temperature begins to rise in the member section, reaching 746°C at the 53-minute. Conversely, in the presence of a sprinkler system, the temperature only reaches around 44°C at 53 minutes. A significant portion of the mineral wool insulation remains at a temperature of 20°C . The presence of the mineral wool insulation causes the temperature at the upper flange to be lower in comparison to the web and lower flange of the RHS profile in the wall column. The temperature histories of wall columns with and without sprinkler systems at 9.09m from the floor are presented in Figure 7(b-c). The temperature histories of the middle of the web, upper flange, and lower flange are compared. As mentioned earlier, the temperature histories of the web and lower flange exhibit similarities, while the temperature history of the upper flange is consistently lower than that of the web and lower flange. Near the ceiling area, temperatures in the web and flanges reach $700\text{--}800^\circ\text{C}$, gradually decreasing along with height until near the floor, where temperatures reach around 300°C . However, in the presence of the sprinkler system, temperatures near the ceiling in the web and lower flange only reach $65\text{--}70^\circ\text{C}$, with a gradual decrease in temperature along the height, eventually reaching around $20\text{--}22^\circ\text{C}$ near the floor.

An example of a temperature contour plot and the temperature histories plot for a truss bottom chord are illustrated in Figure 8. In this scenario, the RHS structural member is exposed to fire from all sides, and there is cavity radiation within the hollow section of the member. Thus, the web, upper flange, and lower flanges experience similar temperature distribution and similar temperature history plots. In Figure 8(b), for Case 1 without a sprinkler system, the peak temperature of the truss bottom chord reaches approximately $600\text{--}700^\circ\text{C}$. Near the ceiling area, temperatures in the web and flanges reach $700\text{--}800^\circ\text{C}$, gradually

decreasing along with height until near the floor, where temperatures reach around 300 °C. However, in the presence of the sprinkler system, temperatures near the ceiling in the web and lower flange only reach 65-70 °C, with a gradual decrease in temperature along the height, eventually reaching around 20-22 °C near the floor. Similar temperature distributions and temperature history plots were obtained for other structural members, although they are not included in this paper. The only difference is the maximum temperature due to variations in the geometry of the structural member cross-section and its location within the truss, ranging from the bottom chord to the top chord.

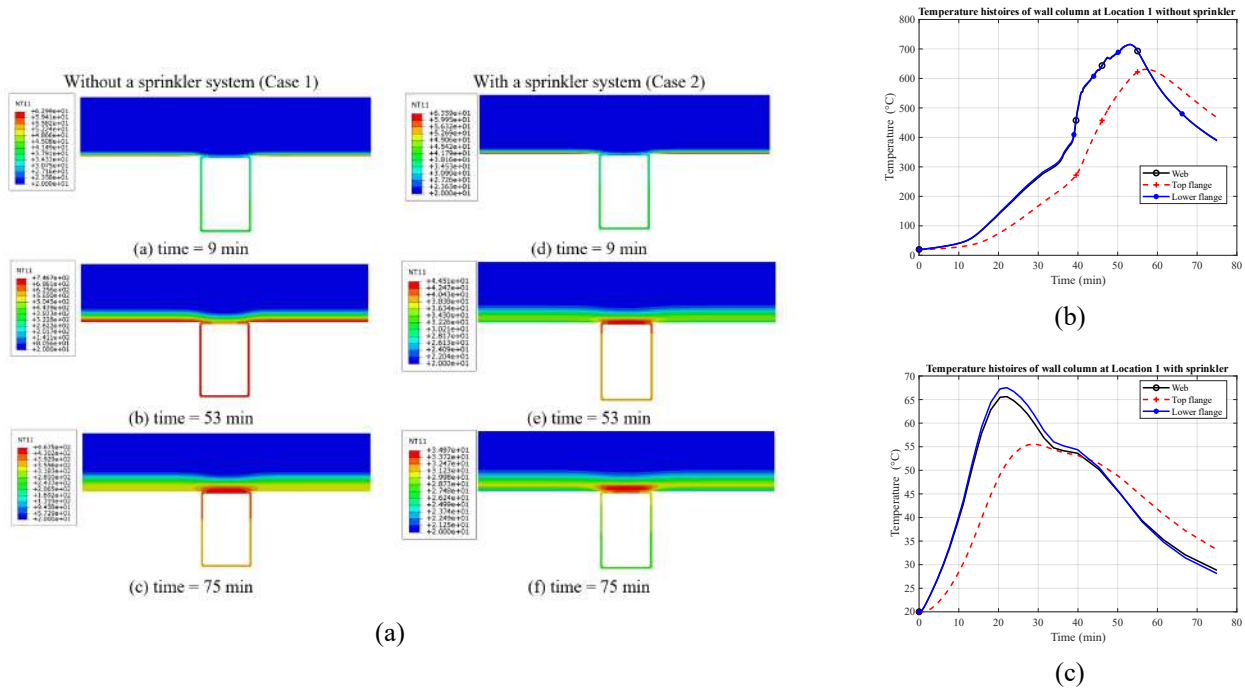


Figure 7. (a) Temperature contour of wall column with and without sprinklers at different stages of fire exposure, (b) and (c) temperature histories of wall column (RHS300x200x8+MW insulation) with and without sprinkler system at 9.09m from the floor

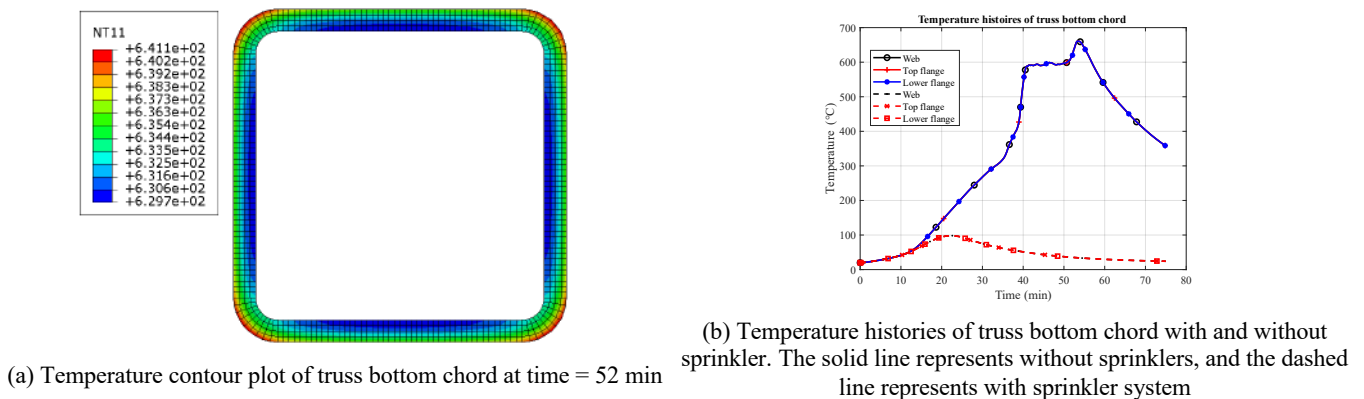


Figure 8. Example of temperature contour plot (Case 1) and temperature history plot for the truss bottom chord

Based on the observed results from the thermal analysis of structural members, the temperatures in load-bearing structural members are higher in the fire scenario without a sprinkler system, leading to great risk of structural failures. Conversely, the temperatures are lower in the fire scenario with sprinkler systems, enabling the structural members to withstand mechanical loads until the sprinkler systems extinguish the fire.

4.2 Structural analysis of warehouse with tubular truss frame solution

The purpose of the structural response model is to investigate the load-carrying capacity of the tubular frame solution of the warehouse. The overall design of the frame is depicted in Figure 1(a). All structural members are S355 steel, and the member profile of the truss frame is made of cold-form rectangular hollow sections. FDS

simulations were performed in different fire scenarios considering the cases with and without sprinkler systems installed in the building. The building is fully engulfed in the fire, and the structural steel members are exposed directly to fire without any fire protection measures. Two-dimensional thermal analyses were performed and are discussed in section 4.1. The fire scenarios (Case 1 and Case 2) were considered in the structural response model. The summary of the geometric data and loads are illustrated in Table 3. Structural analysis of the entire building was only performed using beam elements, and the structure was modelled as a frame structure. The geometry of the warehouse was modelled as a single part, where the entire structure was modelled with line geometry. Mechanical material properties, including temperature-dependent isotropic elasticity, temperature-dependent coefficient of thermal expansion, and temperature-dependent plasticity, are defined according to EN1993-1-2. The tubular frame structure was modelled using the B31 (a 2-node linear beam in a space) beam element. Fixed boundary conditions were defined for the column base. The snow load and permanent load were applied at the nodes of the roof for load case 1 and at the nodes of the roof and wall column for wind loads. The mechanical loading was applied linearly, increasing from zero to maximum in the mechanical loading step and kept constant throughout the fire heating step. Initial temperature and temperature histories due to fire were applied as predefined fields in beam cross-section temperature points. For mechanical loading steps, the uniform temperature of 20°C was defined, whereas, for temperature loading due to fire, the results from the 2D thermal analysis were defined. The structural analysis is performed using the Abaqus/Explicit dynamics procedure. The total simulation time was scaled by a factor of 100. So, the total simulation periods were defined as 45 seconds. The explicit solution was performed using two steps. In the first step, for about 2 seconds, the mechanical load was applied, and in the second step, for about 43 seconds, the heating due to fire was applied.

Table 3. Warehouse geometry as tubular truss frame and loading data

Geometric data and loading information	
Profiles and Material	Wall column: RHS 300 x 200 x 8; End column: RHS 200 x 200 x 6 Truss top chord: RHS 150 x 150 x 8; Truss bottom chord: RHS 120 x 120 x 8; Truss diagonal 1: RHS 120 x 120 x 8; Truss diagonal 2: RHS 100 x 100 x 5; Truss diagonal 3: RHS 80 x 80 x 4; Truss diagonal 4: RHS 70 x 50 x 4; Truss vertical: RHS 70 x 50 x 4 End beam: HEA180; Wall brace: RHS 140 x 140 x 10; Roof brace: RHS 120 x 120x 4; Steel grade: S355
Geometry	Truss frame spacing: 6m, height of the wall column: 9.3m, height of pitched roof: 10.2 m.
Loads	Self-weight of roof: 0.5 kN/m ² ; Self-weight of wall panels: 0.3 kN/m ² ; ground snow load 2.5 kN/m ² , shape coefficient 0.8, wind peak velocity pressure: 0.65 kN/m ²

Figure 9 shows the deformation contour plot shape of the warehouse for the case 1 fire scenario without a sprinkler system. The vertical displacement of frame F (noted in Figure 1a) at the apex is illustrated in 9(b) for a snow load case. In the case of a warehouse building without a sprinkler, the reference building can resist the fire for about 43 minutes before the collapse of the structure without any fire protection on steel structural members. In the presence of a sprinkler system, as in Case 2, no structural collapse of the building was observed. The contribution of the roof system to the fire resistance of truss frames was neglected in the simulation.

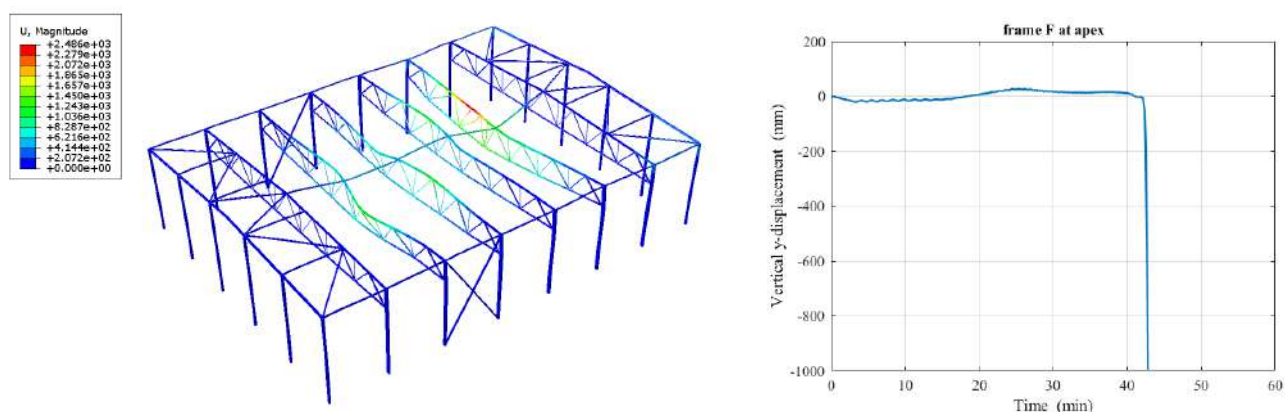


Figure 9. (a) Deformation contour plot of warehouse exposed to natural fire (without sprinkler system), and (b) vertical displacement of frame F at apex with fixed boundary condition for snow loads case

5 CONCLUSIONS

This paper presents the CFD simulation results from different fire scenarios, including the total heat release rate, the gas temperatures, and the sprinkler actions, such as activation times, locations, and sequence. The study shows that the validation of the sprinkler's parameters for modelling accurately the sprinkler spray in FDS is crucial. Simulations reveal that the warehouse fires can be effectively controlled by the sprinkler system even the defects of reduced flow rate in the sprinkler system exists. Different discharge densities (greater than 50%) will be capable of controlling the fire in the warehouse even if fuels keep burning inside the storage racks. Moreover, the number and location of activated sprinkler heads varied depending on factors such as the fire's ignition surface area, sprinkler head activation temperature, and flow rate. However, the conventional sprinklers, activated by the gas temperature value, have the drawback of excessive activations in other locations than fire source. The excessive water damage may be induced due to the smoke accumulation in the sides and corners of the fire compartment. The thermal and structural analyses also show that no additional structural fire protection is needed for single-storey warehouse buildings if sprinkler operations are reliable. The sprinkler system significantly lowered the temperatures in load-bearing structural members, and prevent catastrophic structural failure. The study highlights the critical role of sprinkler systems in the fire safety of steel-framed warehouses and discusses their capacity to control fires initiated from different ignition locations and sizes.

ACKNOWLEDGMENT

The authors would like to acknowledge PSR (Finnish Fire Protection Fund) for providing funding for this study.

REFERENCES

1. E1 the National Building Code of Finland Fire Safety, Ministry of Environment, Finland. Available at: <https://www.edilex.fi/data/rakentamismaaraykset/e1e.pdf> (Accessed: 08 April 2024).
2. D. Neupane (2020). Structural analysis technique of simple steel structures exposed in fire using Abaqus. Master's thesis. LUT University. <http://urn.fi/URN:NBN:fi-fe202102164978>
3. Z. Ma, J. Havula, and M. Heinisuo (2019). Structural fire analysis of simple steel structures by using LS-DYNA. *Rakenteiden Mekaniikka (Journal of Structural Mechanics)*, Vol. 52, No 1, 2019, pp. 1–22.
4. Hurley, M. (2016) *SFPE Handbook of Fire Protection Engineering*. New York: Springer.
5. Tyco (2023) Model ESFR-25 25.2 K-factor pendent sprinkler early ... - johnson controls. Available at: <https://docs.johnsoncontrols.com/tycofire/api/khub/documents/W0rDpx2MV629DYcsCuRHKQ/content> (Accessed: 08 October 2023).
6. Tyco-fire.com (2023a) SPRINKLER SPRAY PATTERNS Refer to the General Description section before applying the spray pattern data. Available at: <https://docs.johnsoncontrols.com/tycofire/api/khub/documents/MbMoAJm4beEEsSDSyfV87g/content> (Accessed: 08 October 2023).
7. Tyco-fire.com (2023b) Tyco-fire.com. Available at: https://www.tyco-fire.com/products-and-solutions/sprinklers-nozzles-and-accessories/storage/esfr-25_fis/model-esfr-25-sprinkler#resources (Accessed: 08 October 2023).
8. Martorano, S. (2006) Automatic Sprinkler Thermal Sensitivity: Clarifying the Terms Fast Response and Quick Response. Available at: <https://www.vikinggroupinc.com/sites/default/files/documents/Automatic%20Sprinkler%20Thermal%20Sensitivity.pdf> (Accessed: 08 October 2023).
9. Z. Ma, J. Havula, F. Wald, K. Cabova (2020). Temperature analysis of steel structures protected by intumescent paint with steel claddings in fire. *Fire and Materials*, 44(7): 897-908. Doi: 10.1002/fam.2890
10. EN1993-1-2 (2005). Eurocode 3: Design of steel structures. Part 1-2: General rules. Structural fire design. European Committee for Standardization (CEN).

FIRE RESISTANCE OF PARTIALLY ENCLOSED STRUCTURAL CARBON STEEL HOLLOW COLUMNS

Luís Laím¹, Aldina Santiago², Helder D. Craveiro³

ABSTRACT

Current building codes often lack the necessary guidance to address fire hazards in performance-based fire design of structures. The existing enclosure fire models employed in fire safety engineering (as indicated by current building codes and regulations) receive only cursory attention and lack thorough evaluation. Additionally, guidance for the fire resistance prediction of structural members with non-linear temperature distribution along and across the structural elements is also not well addressed in the structural codes as it is for uniform conditions. Understanding the impact of real thermal conditions, i.e., the thermal action of physical fires and the real thermal boundary conditions of the structural members is then vital for an adequate evaluation of their fire robustness. The size and location of openings and the arrangement of the structural members related to the secondary construction elements play an important role in the fire resistance of structural members that should be also taken into consideration in fire design, especially of steel structures. Therefore, this research work studied the fire resistance of SHS steel columns embedded on partition walls (with no fire resistance requirements) under simulated fires similar to those in enclosures with opening factors of approximately $0.05 \text{ m}^{1/2}$ (ventilation-limited compartment fires), based on experimental data available by the National Institute of Standards and Technology and on previous research performed by the authors.

Keywords: Computational fluid dynamics; Finite element analysis; SHS; Structural Columns; Walls effect; Performance-based design.

1 INTRODUCTION

Generally steel columns experience non-uniform heating during fires due to their contact with surrounding construction elements, such as walls. This non-uniform heating leads to thermal gradients within the column's cross-section and consequently to varied thermal strains. When one side of a steel column is exposed to heat, it expands more than the cooler side, leading to a curvature or bowing effect towards the heat source. This bending or bowing can cause the column to deviate from its original straight shape. This thermal bowing can then induce additional bending moments and stresses in structural columns, affecting their load-bearing capacity and overall stability during a fire. Under certain conditions (end restraints), the columns after bending towards the heat source, it straightens (coming back to their original location) and eventually failure by bowing in the reverse direction (failing towards the cooler side). Some studies shed light on how factors such as pinned or fixed ends, as well as varying temperature distributions along the length of the column, impact its buckling resistance. Findings indicated that columns with maximum

¹ Professor, University of Coimbra, ISISE, ARISE, Department of Civil Engineering, Coimbra, Portugal
e-mail: luislaim@uc.pt, ORCID: <https://orcid.org/0000-0002-8342-3695>

² Professor, University of Coimbra, ISISE, ARISE, Department of Civil Engineering, Coimbra, Portugal
e-mail: aldina@dec.uc.pt, ORCID: <https://orcid.org/0000-0003-3646-4926>

³ PhD Researcher, University of Coimbra, ISISE, ARISE, Department of Civil Engineering, Coimbra, Portugal
e-mail: heldercraveiro.eng@uc.pt, ORCID: <https://orcid.org/0000-0001-8590-5885>

temperatures at mid-height or near the strongest boundary exhibited the largest reductions in buckling resistance [1-3].

In spite of the fact that the thermal bowing may be generally considered a detrimental effect on the structural resistance of columns under fire conditions, as it can induce larger deformations and stresses in structural elements, these thermal gradients have in the most of the cases a beneficial effect on the fire resistance of structural columns compared to uniform temperature conditions. Advanced numerical simulations and experimental studies have been conducted to better understand the thermal bowing behaviour of steel columns under fire conditions and to develop design guidelines [2-4]. However, structural design guidelines usually rely on simplified assumptions and/or empirical relationships (traditional design approach), which can lead to conservative designs or overlook complex structural behaviours. Conservative assumptions in design guidelines may result in over-designed structures, leading to unnecessary material usage and increased costs, which is a detrimental point for steel structures. Traditional design guidelines may not facilitate optimization of steel structural designs to meet specific performance criteria or cost constraints. Design guidelines for advanced performance-based design should increase and evolve over time to reflect the latest advancements in knowledge, technology, and practices [5-6].

Advanced computational methods, such as the finite element method (FEM) and the computational fluid dynamics (CFD) method with finite volume approach, offer high accuracy in predicting structural behaviour, by accounting for complex geometries, nonlinear behaviour, dynamic loading, and material degradation. Such computational methods enable optimization of structural designs to achieve desired performance criteria, such as minimizing steel weight, maximizing structural resistance, or reducing fire protection cost. They can provide detailed insights into the fire structural behaviour, allowing engineers to identify critical failure modes, assess safety margins, and refine design parameters [7-8]. On the other hand, these computational methods usually require a deep understanding of the numerical methods, the modelling techniques, and structural mechanics. Incorrect modelling assumptions or input parameters in computational analyses can lead to erroneous predictions.

Therefore, this research study brings new insights in advanced performance-based fire design of steel columns, taking into account the contribution of secondary construction elements (internal or external walls) in the fire safety engineering, which allows an efficient and optimized application of fire protection materials in the structural elements and still ensuring their sustainable consumption.

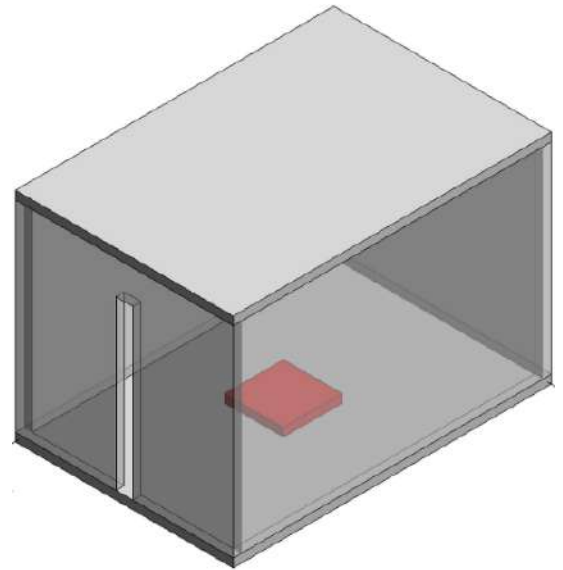
2 FIRE COMPARTMENTS

2.1 Compartment fire tests

Understanding the fire performance of different materials and systems under realistic fire scenarios (non-uniform conditions), it allows the optimization of materials, the improvement of energy efficiency, and it enhances the lifecycle sustainability. It facilitates decision-making concerning material selection, system assemblies, and fire protection measures, fostering the development of more sustainable and resilient built environments. To drive into these goals and predict realistic fire actions in enclosures, computational fluid dynamics (CFD) models were first developed by using the Fire Dynamics Simulator (FDS [9]) where turbulence was treated by means of Large Eddy Simulation (LES), and then results were compared with experimental data available by the National Institute of Standards and Technology (NIST) [10]. A small compartment fire test has been selected (fig. 1) due to the high demands on computational performance and capacity for such analyses. The compartment internal dimensions follow the ISO 9705 standard [11], i.e., its width, length and height were respectively 2.4 m, 3.6 m and 2.4 m. Only one opening was considered, specifically a 2 m by 0.2 m door in order to get the lowest opening factor ($0.0123 \text{ m}^{1/2}$) among the tests described by Lock et al. [10]. All internal surfaces were covered by 5 cm ceramic fiber blankets. A 0.5 m^2 heptane pool fire type scenario was adopted for the CFD model calibration in such a way that the fire load was well defined. In a real compartment fire, fuel sources are physically distributed throughout the compartment, but only one location was adopted in this study, assuming it was always located in the centre of the floor.



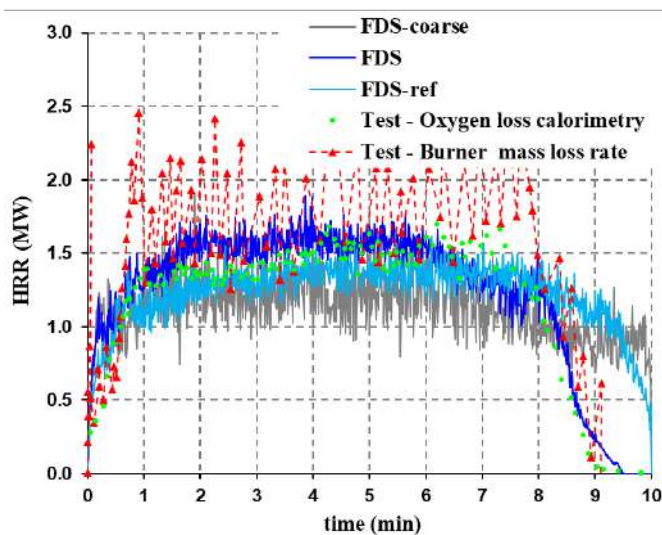
a)



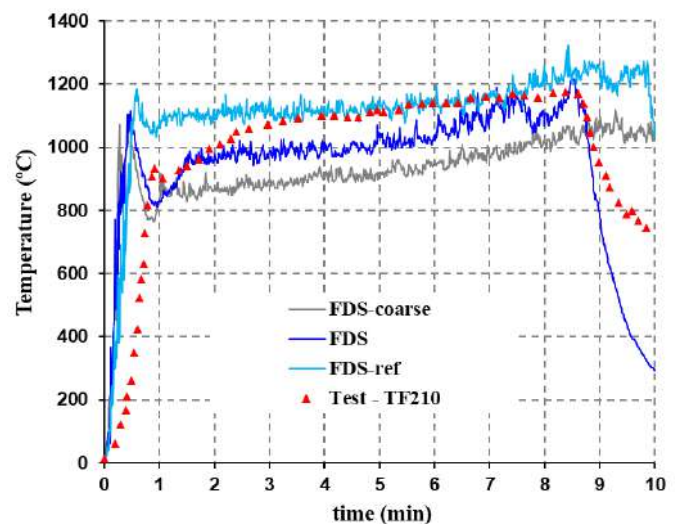
b)

Figure 1. General (a) [10] and schematic (b) view of an ISO 9705 enclosure [11]

Figure 2a shows different heat release rate (HRR) results for the fire scenario described above, including the ideal HRR (measured by the mass loss rate), the measured by oxygen loss calorimetry (given in [10]) and numerical ones, which were estimated by using FDS for different volume mesh sizes: i) 0.025 m (FDS-ref in the fig.), ii) 0.05 m (FDS in the fig.) and iii) 0.10m (FDS-coarse in the fig.). Note that the HRR values fluctuated due to the dynamic and highly turbulent nature of the fire. As suggested by McGrattan et al. [9], a mesh sensitive analysis was performed by gradually refining the mesh until to get appreciable differences between the experimental and numerical results. From the HRR and temperature results (fig. 2), it can be observed that an uniform mesh size with 0.05 m was ideal for numerical simulations in similar compartments with identical heat release rates. The temperature shown in the Figures 2 and 3 were recorded at the position of 0.70 m away from the middle of the opening and 2.10 m from the floor.



a)



b)

Figure 2. Heat release rate (a) and temperature (b) as a function of time in a ISO 9705 enclosure [11] (Test – adapted from [10])

Another crucial parameter to take into account in enclosure fires is the fraction of the fire’s heat release rate released in the form of thermal radiation, commonly referred to as the radiative fraction [9]. This fraction can change over time in a compartment fire due to various factors such as changes in fuel

availability, ventilation conditions, temperature gradients, and combustion efficiency. For example, increased ventilation might lead to more complete combustion and a higher radiative fraction, while decreased ventilation might result in incomplete combustion and a lower radiative fraction, as it is the case of ventilation-limited compartment fires, as this one. While consumed oxygen itself does not directly determine the radiative fraction, its influence on combustion efficiency, flame characteristics, and soot formation indirectly affects the proportion of heat released as thermal radiation. Figure 3b, for example, indicates that similar temperature predictions to the experimental ones were only possible to obtain for low values of radiative fraction of the fuel combustion (about 0.2 or less over time). The initial peak observed in the temperature at the beginning of the simulations resulted from the fact that the radiative fraction was assumed too high at that stage. Initially, during the ignition phase, the radiative fraction should be relatively low as the fire starts and the combustion process is not yet fully developed. Note that in these simulations the maximum radiative fraction was assumed at their beginning (when ventilation conditions were met), instead of starting from zero to take into account the actual initial reaction speed in the simulated fuel combustion. It is still interesting to observe that the hydrocarbon curve [12] predicts reasonably well the maximum temperature in the compartment (which is in according to the selected fuel for this study).

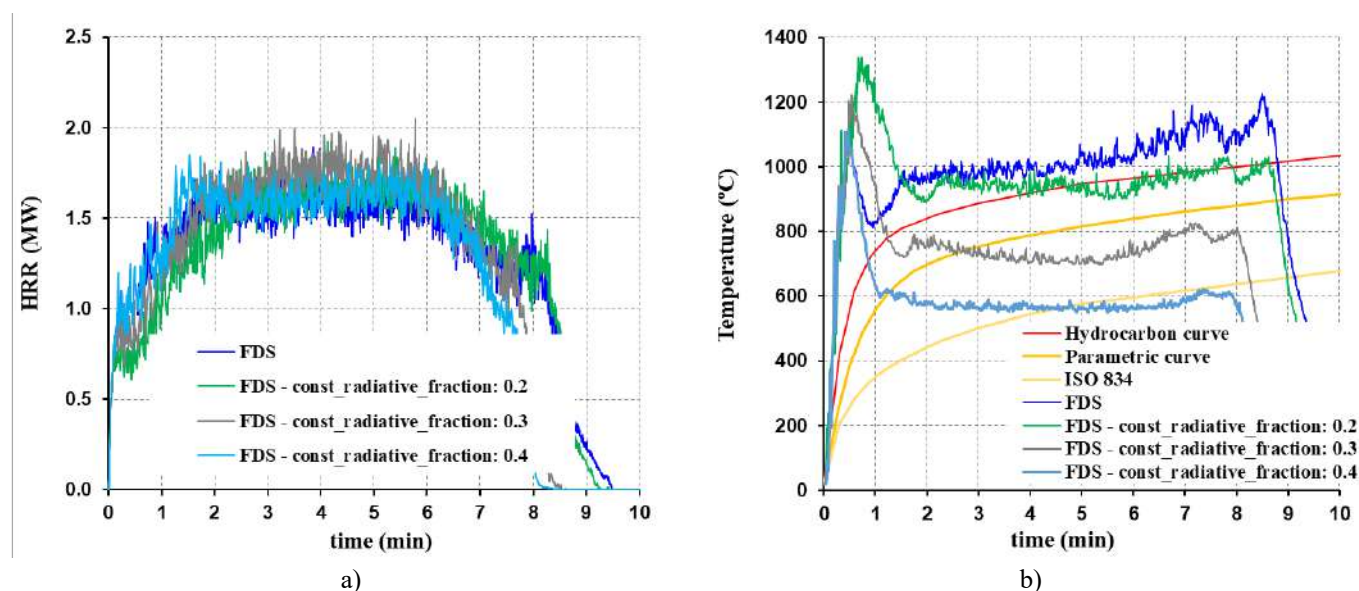


Figure 3. Heat release rates (a) and temperatures (b) for different radiative fractions of the fuel combustion

2.2 Computational fluid dynamics-based fire simulations

After calibrating the CFD-based fire model, two new simulations (CFD-S1 and CFD-S2) were performed with different fire load densities related to the floor area: i) 780 MJ/m² (similar to the average characteristic one defined for dwelling buildings) and ii) 550 MJ/m² (similar to the 85% fractile characteristic one defined for office buildings) [12], respectively for CFD-S1 and CFD-S2. Different floor compartment areas were selected (2.4mx3.6m for the CFD-S1 and 2.4mx5.1m for the CFD-S2) to get similar opening factors, equal to 0.05 m^{1/2}, and similar steady heat release rates to the one obtained in the calibrated model (to use the same mesh resolution). Such opening factor was obtaining for both simulations considering two additional openings on the longest walls of the compartment and located on the top of the wall with 0.40m height and the same length as the wall. The fire location related to the front door was kept. The gas temperatures next to the rear wall and at its centre were them evaluating to predict the gradient temperature along the height of the respective fire compartments (figs. 4 and 5). These fire scenarios are yet far away from the real ones in dwelling and office buildings, but it is a first step to approach to the real conditions. Fire temperatures can be more severe than the standard ones, but they can also be shorter, or the opposite. There are for sure high uncertainties what it comes to fire scenarios, but as the technology continues to evolve and mature, it

is expected to see greater adoption and innovation in the years to come. Digital twins and related technologies can for example be valuable in addressing fire scenarios, since they are becoming an integral part of modern technology ecosystems, offering valuable insights, optimization capabilities, and decision support across a wide range of industries and applications. Fire safety engineering should also make part of that evolution, and research should follow such trends. New guidelines to favour this approach should then be presented. This study, with these cases, clearly shows the benefits to predict the fire action by integrating computational fluid dynamics analysis instead of adopting uniform standard fire conditions. Thermal gradients of 200°C were observed along the compartment height, even for under ventilated conditions (figs. 4 and 5).

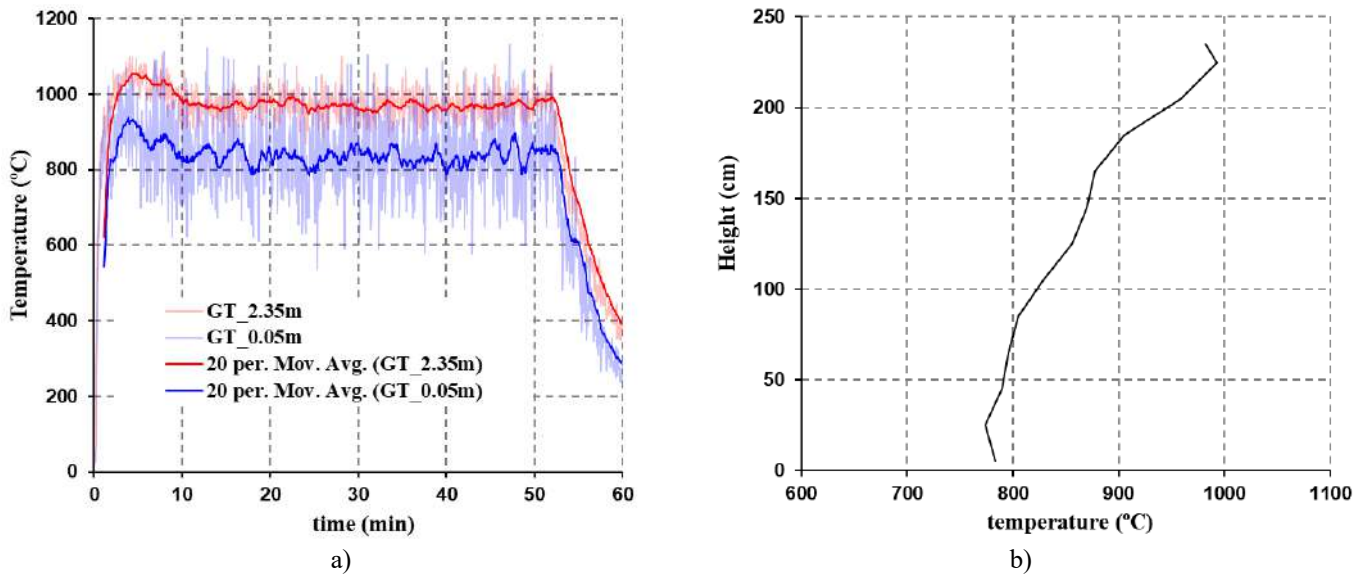


Figure 4. Gas temperature throughout the fire period (a) and along the compartment height next to the rear wall at 50 minutes (b) for the case CFD-S1

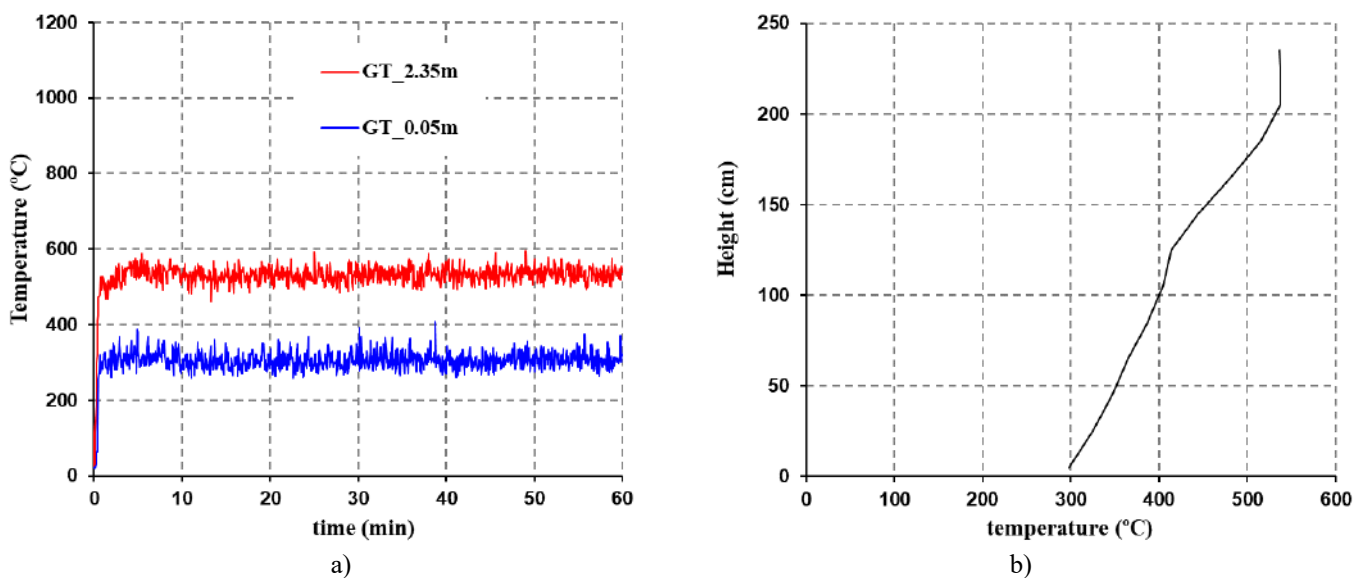


Figure 5. Gas temperature throughout the fire period: (a) and along the compartment height next to the rear wall at 50 minutes, (b) for the case CFD-S2

3 FIRE RESISTANCE OF STEEL COLUMNS

3.1 Fire resistance of isolated steel columns

Finite element analyses (FEA) were then carried out to solve the thermo-mechanical response of isolated and partially enclosed structural carbon steel hollow columns under different simulated fire conditions. Three-dimensional finite element models (FEM) of SHS steel columns under uniform and non-uniform high temperatures were first developed by using the advanced finite element program Abaqus [13]. Secondly, experimental and numerical results of short SHS steel columns under uniform fire conditions were compared, as shown in Figure 6. Such numerical analyses were conducted in three sequential steps: linear buckling analysis, heat transfer analysis and dynamic implicit quasi-static analysis with material and geometric nonlinearity. The thermal analysis allowed to obtain the temperature distribution in the steel columns when subjected to high temperature fields, whereas the linear buckling analysis allowed to achieve an equivalent initial imperfect configuration of the columns by combining their buckling modes, including flexural and local buckling modes. The maximum magnitudes of $L/1000$ and $b/200$ were implemented in the FEM for global and local imperfections, respectively (when considered). Heat transfer from the hot air to the column was modelled using two types of surfaces available in the Abaqus library [13], including “film condition” for heat transfer by convection and “radiation to ambient” for heat transfer by radiation to reproduce the net heat flux on the fire exposed surfaces. On the fire exposed side, a coefficient of heat transfer by convection equal to $25 \text{ W}/(\text{m}^2\text{K})$ and a resultant emissivity to 0.7 were used in the simulations according to EN 1991-1-2 [12] and EN 1993-1-2 [14]. Furthermore, on the fire unexposed side, a coefficient of heat transfer by convection equal to $4 \text{ W}/(\text{m}^2\text{K})$ and an emissivity to 0.8 were adopted. The same emissivity was still implemented in the thermal numerical analysis for the cavity radiation. Conservatively heat losses through both ends of the columns and the walls were neglected. Thermal and mechanical properties at elevated temperatures as established in EN 1993-1-2 [14] for steel were also assumed, with Young's modulus and steel yield strength equal to 210 GPa and 355 MPa (S355), respectively, at ambient temperature [15].

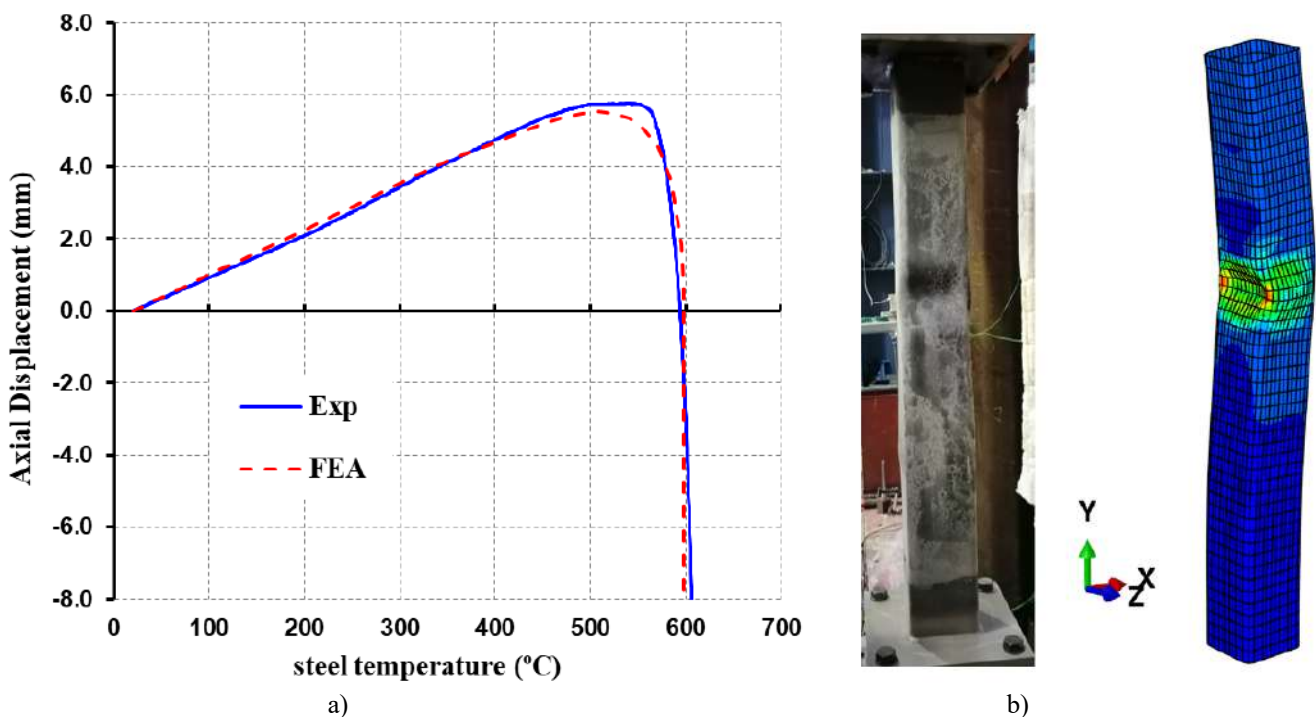


Figure 6. Comparison between experimental [15] and finite element numerical results: axial displacement (a) and failure modes (b)

The dynamic implicit quasi-static analyses with material and geometric nonlinearity and the steel temperatures estimated from the heat transfer analysis were then undertaken. Note that a serviceability load was first applied on the columns. This load level was a percentage (30 or 50%) of the design value of the load-bearing capacity of the columns at ambient temperature, calculated in accordance with the methods proposed in [14]. Finally, the good agreement of FEA results with the experimental ones (fig. 6) may ensure strong confidence of the developed FEM for parametric studies reasonably outside the bounds of the experimental tests.

3.2 Numerical fire resistance of steel columns embedded on walls

Based both on the previous developed finite element models and on the CFD-based fire simulations, a preliminary parametric study outside the bounds of the experimental tests was conducted on 2.4m tall columns with fix-ended boundary support conditions and under axial compression with 50% load level to find out the effect of different parameters on the fire resistance of steel columns under simulated fire conditions, including the presence of walls on opposite sides of the SHS 150x150x8 steel column (fig. 7), global imperfection direction, axial restraint (AR - 40 and 125 kN/mm), wall thickness (75 and 100 mm), wall position (middle or aligned to the exposed surface of the column), serviceability load level (30% and 50% of the design load-bearing capacity of the columns at ambient temperature) and non-uniform fire temperature distribution along the compartment height. For this last scenario a linear thermal gradient of the fire action between the top and the bottom of the column was considered (similar to the fire actions predicted by CFD-S1 and CFD-S2), where the fire action at the top of the column corresponded to the temperatures defined by the ISO 834 fire curve [12] and at the bottom of the column corresponded to 75% of those temperatures.

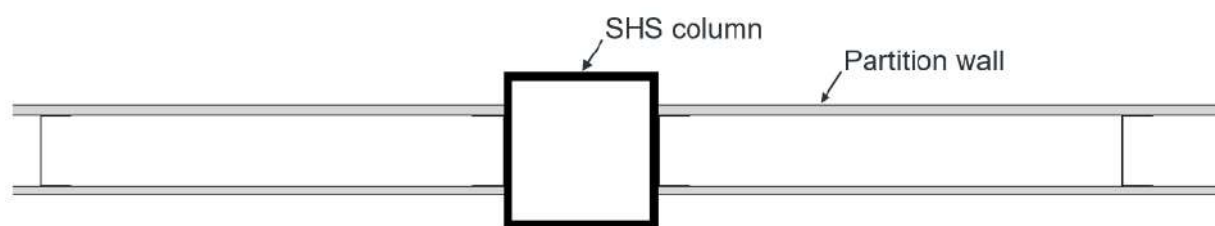


Figure 7. SHS columns embedded on walls

Figure 8 depicts the temperature distribution across the cross-section of the SHS steel column under standard ISO 834 fire curve [12], as an isolated column (fig. 8a), embedded on a 100mm thick wall aligned with both middle axis (fig. 8b) and embedded on a 100mm thick wall aligned with both fire exposed surfaces – façade situation, for example (fig. 8c). In terms of thermal response it is clear the beneficial effect of the presence of a wall. After one hour of fire exposure, whereas the mean temperature of the steel section was 940°C (fig. 8a), the temperature gradient from the exposed surface to the unexposed surface of the section was 265°C (from 565°C to 830°C) for the case where the middle axis of the column was aligned with the middle axis of the wall (fig. 8b) and 285°C (from 530°C to 815°C) for the case where the exposed surface of the column was aligned with the exposed surface of the wall (fig. 8c). In spite of the fact that these gradients were close to each other, note that the extension of cooler region was higher for the case where the exposed surface of the column was aligned with the exposed surface of the wall than for the case where the middle axis of the column was aligned with the middle axis of the wall. Complementary, Figure 9 illustrates the temperature distribution along the column height for the different case studies, i.e., when the column is isolated (no wall - fig. 9a) and when it is embedded on a wall under uniform (fig. 9b), SA, and non-uniform (fig. 9c), non-UF, fire conditions.

On the other hand, Figures 10, 11, 12 and 13 depict the axial displacements of the columns for the different scenarios as a function of time (figs. 10, 11 and 13) and temperature (figs. 12). First of all, the reverse direction of the thermal bowing was only observed when no global imperfection was considered (fig. 10). When the column had its global imperfection configuration ($L/1000$) towards the exposed or the unexposed surface, its fire resistance was lower. A global imperfection of $L/1000$ towards the unexposed surface (worst

case) reduced 7% the fire resistance of the column (fig. 10). Note that the column with restrained thermal elongation is assumed to have failed when the axial compression force in the column returned back to its initial applied load, i.e., when the axial displacement of the column returns to zero.

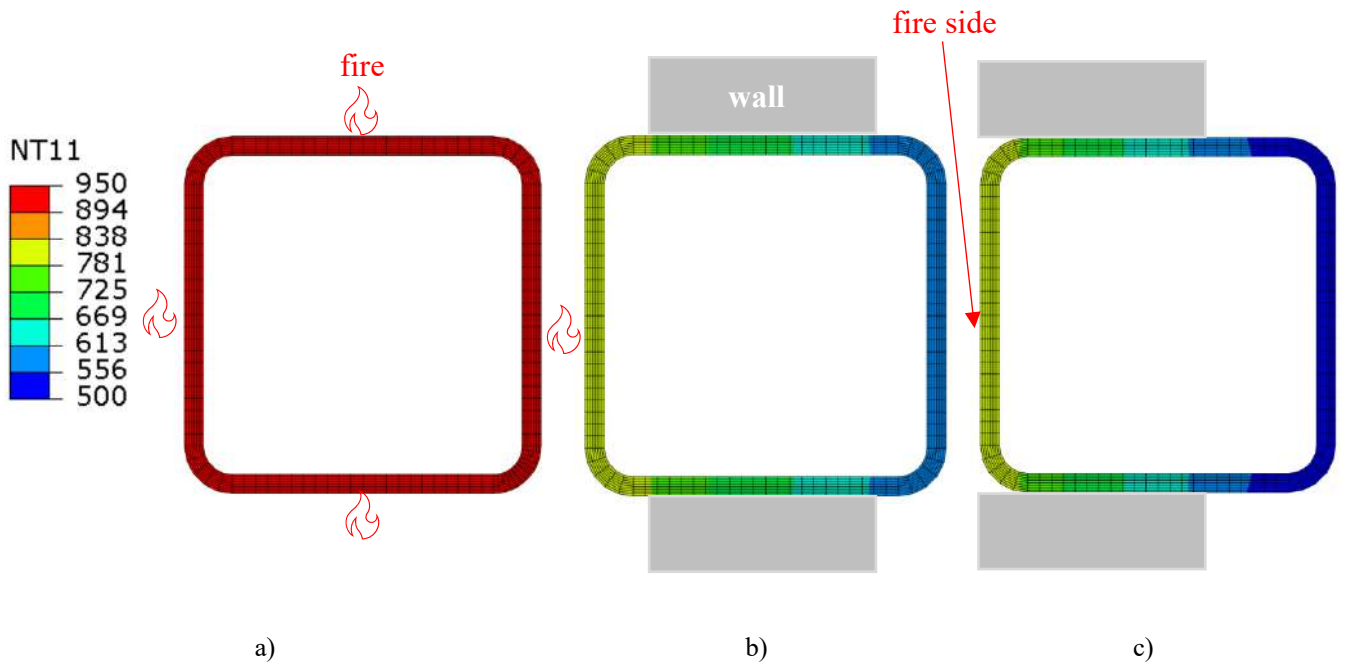


Figure 8. Temperature distribution across the cross-section of SHS steel columns after 60 minutes of fire exposure: a) no wall; b) wall in the middle; c) wall aligned with one side of the column

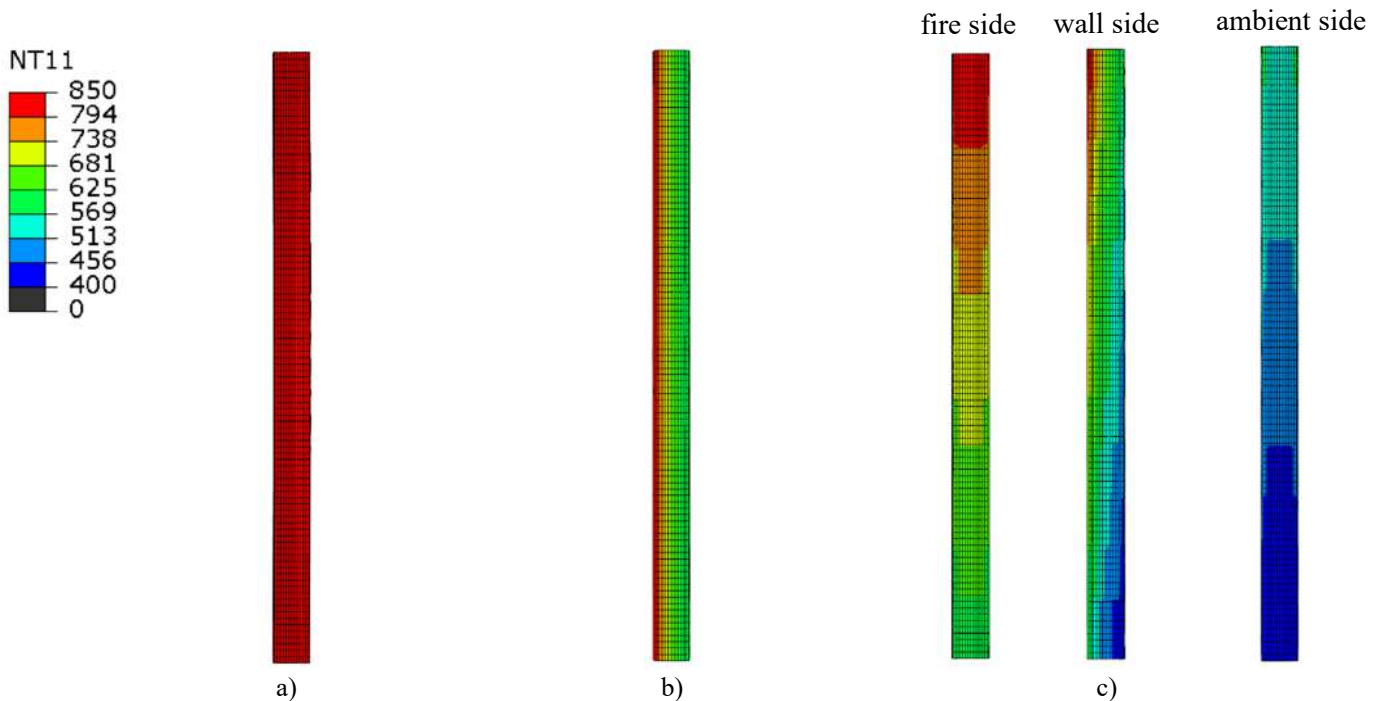


Figure 9. Temperature distribution along the SHS steel columns after collapse: a) fire uniform around the column; b) fire uniform but only one side exposure; c) fire non-uniform and only one side exposure

It can be seen that non-protected isolated steel columns had very low fire resistance (12.8 min), comparing to the ones embedded on walls (fire resistances higher than 30 min - fig. 11). The wall thickness and the

non-uniform fire conditions along the compartment height had a significant impact on the fire resistance of such columns, increasing their fire resistance by 12% (from 29.8 min to 33.5min) when the wall thickness increased from 75mm to 100mm, and by 28% (from 33.5 min to 42.8min) when the temperature distribution along the compartment height shifts from uniform to non-uniform conditions (fig. 11). Regarding the steel temperatures in the column, it was observed that its maximum allowable steel plate temperature increased substantially when embedded on walls under uniform fire conditions (from 565°C to 706°C) and under non-uniform conditions (from 565°C to 751°C), as shown in Figure 12. On the other hand, the axial restraint had no influence on the fire resistance of the columns (either when isolated or when embedded on walls), as expected [16]. While the columns embedded on walls under uniform fire conditions failed by local and global buckling the columns under non-uniform fire conditions failed only by local buckling (fig. 13).

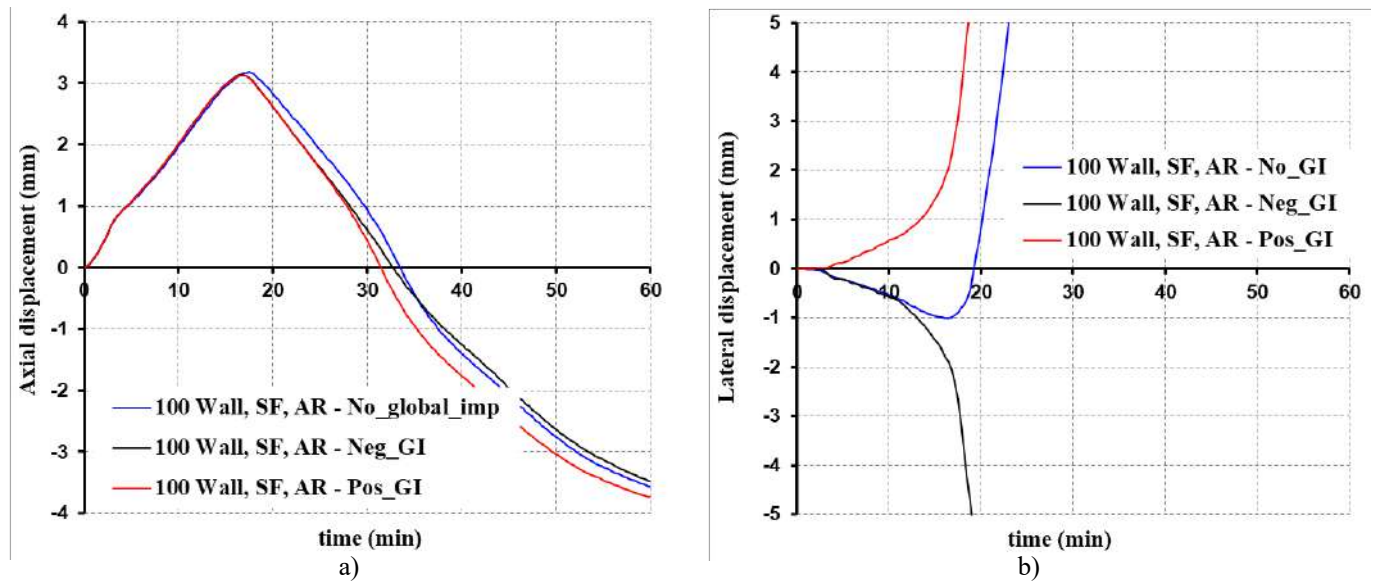


Figure 10. Effect of global imperfections on the axial (a) and lateral (b) displacements of SHS steel columns embedded on partition walls

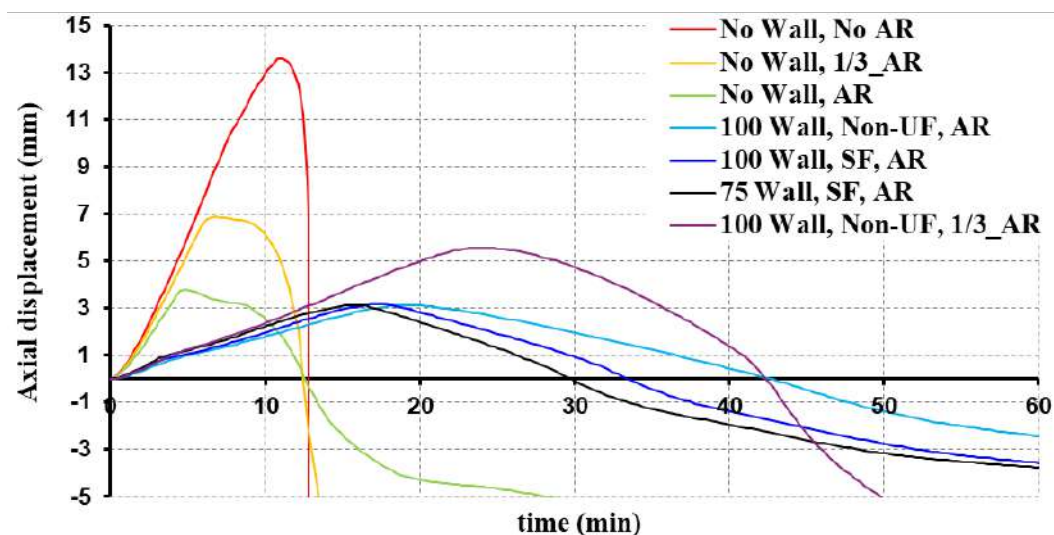


Figure 11. Effect of wall thickness, axial restraint and fire conditions on the structural response of SHS steel columns as a function of time

Last but not least, the fire resistance of such columns may be still withstand the serviceability load without fire protection for longer periods of time when the exposed surface of the column is aligned with the exposed surface of the wall (columns on building façades, for example), instead of their middle axes, or for low load levels (LL) applied on the columns in case of fire, reaching more than one hour of fire resistance (fig. 14).

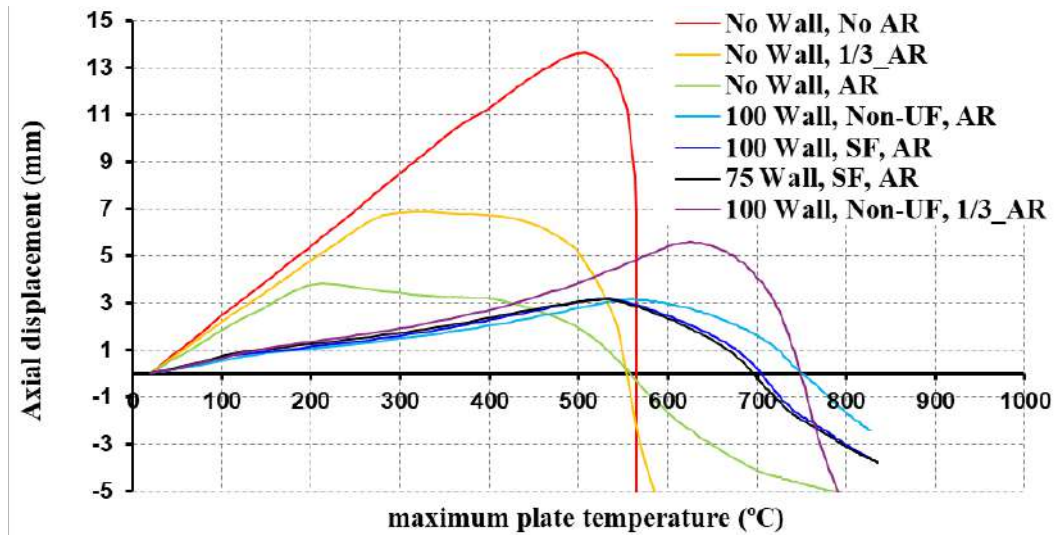


Figure 12. Effect of wall thickness, axial restraint and fire conditions on the structural response of SHS steel columns as a function of their maximum steel plate temperature

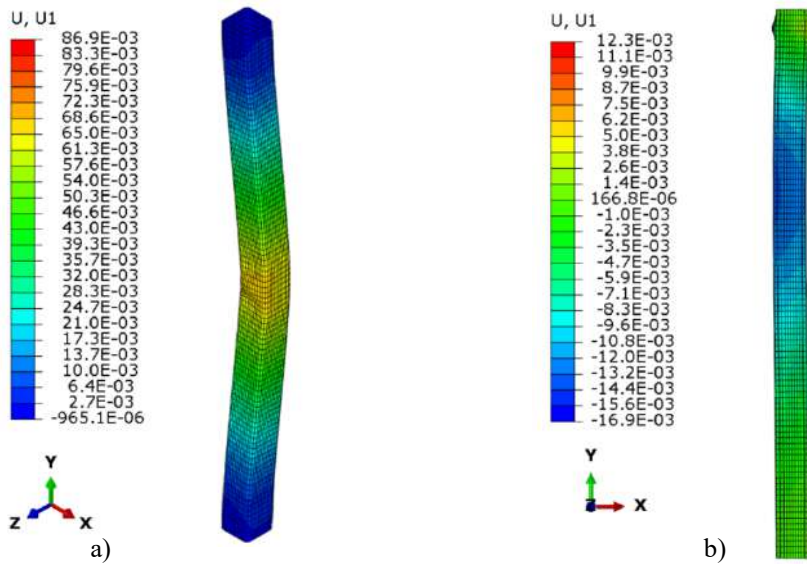


Figure 13. Failure modes of SHS steel columns under uniform (a) and non-uniform (b) temperature conditions.

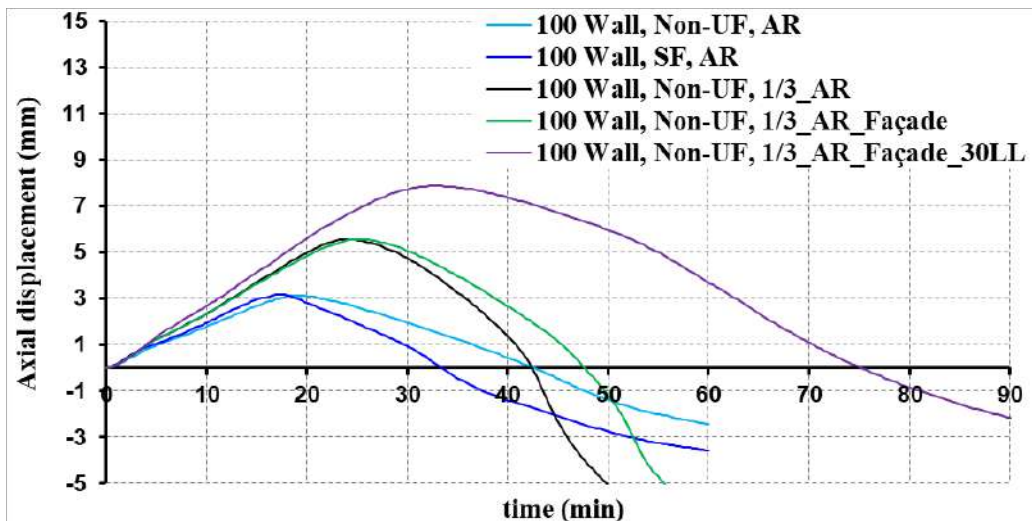


Figure 14. Effect of wall arrangement and load level on the structural response of SHS steel columns as a function of time.

4 CONCLUSIONS

This research work investigated the fire resistance of structural carbon steel hollow columns embedded on walls under simulated fire conditions. Considering the contribution of secondary construction elements by understanding the fire structural response of steel columns embedded on walls is essential for designing resilient and fire-resistant structures that can withstand the challenges posed by fire incidents. It was observed that temperatures from physical fires under certain conditions may be highly severe, but when columns are embedded on walls their fire performance can be significantly increased due to the beneficial thermal gradient effect on the fire resistance of such columns. It was clear that computational fire dynamics and finite element analysis play a crucial role in modern fire engineering not only by enabling the design of fire-resistant structures but also by ensuring optimal performance and safety. Codes and regulations should consider further insights and recommendations based on these findings, ensuring that buildings are designed, constructed, and maintained to the highest standards of fire safety, ultimately protecting lives, property, and the environment from the devastating effects of fire.

ACKNOWLEDGMENT

The authors acknowledge the Foundation for Science and Technology (FCT) for its funding for the research project PTDC/ECI-EGC/31850/2017 (NANOFIRE). This work was also partly financed by FCT / MCTES through national funds (PIDDAC) under the R&D Unit Institute for Sustainability and Innovation in Structural Engineering (ISISE), under reference UIDB / 04029/2020 (doi.org/10.54499/UIDB/04029/2020), and under the Associate Laboratory Advanced Production and Intelligent Systems ARISE under reference LA/P/0112/2020.

REFERENCES

1. Correia, AJP, Rodrigues JPC, Real PV, Thermal bowing on steel columns embedded on walls under fire conditions, *Fire Safety Journal*, 67 (2014), 53-69: <https://doi.org/10.1016/j.firesaf.2014.05.001>.
2. Rocha FM, Rodrigues JPC, Neto JM, Fire behavior of steel and partially encased composite columns embedded on walls, *Journal of Constructional Steel Research*, 149 (2018), 105-118: <https://doi.org/10.1016/j.jcsr.2018.07.014>.
3. Yuan W-b, Ge I P-j, Shen Y-t, Cheng S-s, Yu N-t, Buckling Analysis of Steel H Column with Thermal Gradient Along the Flanges, *International Journal of Steel Structures* (2020) 20(2):677-691: <https://doi.org/10.1007/s13296-020-00314-8>.
4. Charlier, M, Glorieux, A, Vassart, O, Dai, X, Welch, S, Anderson, J & Nadjai, A 2021, 'Travelling fire experiments in steel-framed structure: numerical investigations with CFD and FEM', *Journal of Structural Fire Engineering*: <https://doi.org/10.1108/JSFE-11-2020-0034>.
5. Woo, D.; Seo, J.K. Numerical Validation of the Two-Way Fluid-Structure Interaction Method for Non-Linear Structural Analysis under Fire Conditions. *J. Mar. Sci. Eng.* 2021, 9, 400. <https://doi.org/10.3390/jmse9040400>.
6. Janardhan RK, Shakil S, Lu W, Hostikka S, Puttonen J. Coupled CFD-FE analysis of a long-span truss beam exposed to spreading fires. *Engineering Structures* 259 (2022) 114150. <https://doi.org/10.1016/j.autcon.2022.104574>.
7. Ye Z, Hsu S-C, Predicting real-time deformation of structure in fire using machine learning with CFD and FEM. *Automation in Construction* 143 (2022) 104574. <https://doi.org/10.1016/j.autcon.2022.104574>.
8. Zhou J, Zhou X, Cong B, Wang W, Comparison of different CFD-FEM coupling methods in advanced structural fire analysis. *International Journal of Thermal Sciences* 193 (2023) 108465. <https://doi.org/10.1016/j.ijthermalsci.2023.108465>.
9. McGrattan K, Hostikka S, Floyd J, McDermott R, Vanella M, Fire Dynamics Simulator User's Guide, NIST Special Publication 1019 (Sixth Edition), National Institute of Standards and Technology and VTT Technical Research Centre of Finland, 2022, 402p. <http://dx.doi.org/10.6028/NIST.SP.1019>.
10. A. Lock, M. Bundy, E.L. Johnsson, A. Hamins, G.H. Ko, C. Hwang, P. Fuss, R. Harris (2008), NIST Technical Note 1603: Experimental Study of the Effects of Fuel Type, Fuel Distribution, and Vent Size on

Full-Scale Underventilated Compartment Fires in an ISO 9705 Room. National Institute of Standards and Technology, 113p.

11. ISO9705, Fire Tests - Full-Scale Room Test for Surface Products First Edition. 1993, International Organization for Standardization: Geneva, Switzerland.
12. EN 1991-1-2 (2002), Actions on Structures, Part 1–2, General Actions – Actions on Structures Exposed to Fire, European Committee for Standardisation, Brussels, Belgium.
13. Abaqus/CAE, “Standard user’s manual,” version 2021. USA: Dassault systèm, Simulia Corp.; 2021.
14. EN 1993-1-2; Design of Steel Structures. Part 1–2: General Rules – Structural Fire Design, CEN, Brussels, 2005.
15. Laím L, Santiago A, Caetano H, Craveiro HD, Shahbazian A (2022), Numerical analysis and structural fire design of protected SHS steel columns with thermally enhanced gypsum-based mortars, *Journal of Building Engineering*, Vol. 54, 104629. <https://doi.org/10.1016/j.job.2022.104629>.
16. Laím L, Craveiro HD, Simões R, Escudeiro A, Mota A (2020). Experimental analysis of cold-formed steel columns with intermediate and edge stiffeners in fire. *Thin-Walled Structures* Volume 146, January 2020, 106481. <https://doi.org/10.1016/j.tws.2019.106481>.

FIRE RESISTANCE TESTING OF STEEL TENSION MEMBERS WITH HOLLOW SECTION PROTECTED BY INTUMESCENT COATING

Dustin Häbler¹, Andreas Becker², Richard Fürst³, Sascha Hothan⁴

ABSTRACT

Steel tension members with hollow sections are used in applications such as trusses. To ensure the fire resistance, the steel must be prevented from heating up too quickly. A suitable solution is the application of intumescent coatings. However, the approval-based scope of application of these products generally does not include steel tension members with hollow section. This is mainly due to the lack of a corresponding European test and assessment standard. To investigate the characteristics to be considered when testing these structural members and assessing the contribution of the intumescent coating to the fire resistance, several mechanically loaded fire tests were carried out using a special tension test furnace. The fire tests have shown that intumescent coatings can provide a significant improvement in the fire resistance of steel tension members with hollow section. However, this specific application generally places particularly high demands on the performance of the intumescent coating. This is partly due to the four-sided fire exposure and the mainly filigree cross sections, which both result in high section factors. In addition, there is an increased crack formation due to the tensile load. As a result, the thermal protection of the tested intumescent coating on the tension members decreased compared to columns with the same section factor and fire exposure. Consequently, the presence of a mechanical load in the fire test as well as the type of loading affect the thermal protective performance of the intumescent coating and shall be considered.

Keywords: Fire resistance; fire test; intumescent coating; steel; tension member

1 INTRODUCTION

Steel trusses are a common and suitable type of construction for achieving large spans. The truss components are welded or bolted together and are mainly subjected to axial loads, i.e. compression or tension. In general, both I-sections and hollow sections are used for the truss members. As with all types of steel constructions, appropriate measures shall be taken to ensure fire protection.

Intumescent coatings are commonly used in civil engineering to improve the fire resistance of steel constructions. Due to their profile-following application and the required low coating thickness, these products are particularly suitable for meeting both fire protection and architectural requirements. Under fire exposure, the intumescent coating reacts and forms a thermal protective char around the steel member. Thus, the heating of the steel member is delayed and a higher fire resistance can be achieved.

¹ Dr.-Ing., Bundesanstalt für Materialforschung und -prüfung (BAM), 7.3 Fire Engineering, Unter den Eichen 87, 12205 Berlin, Germany
e-mail: dustin.haessler@bam.de, ORCID: <https://orcid.org/0000-0002-3705-7356>

² Dipl.-Ing.(FH), Bundesanstalt für Materialforschung und -prüfung (BAM), 7.3 Fire Engineering, Unter den Eichen 87, 12205 Berlin, Germany
e-mail: andreas.becker@bam.de

³ PhD, Bundesanstalt für Materialforschung und -prüfung (BAM), 7.3 Fire Engineering, Unter den Eichen 87, 12205 Berlin, Germany
e-mail: richard.fuerst@bam.de, ORCID: <https://orcid.org/0000-0002-4372-5322>

⁴ Dr.-Ing., Bundesanstalt für Materialforschung und -prüfung (BAM), 7.3 Fire Engineering, Unter den Eichen 87, 12205 Berlin, Germany
e-mail: sascha.hothan@bam.de, ORCID: <https://orcid.org/0000-0003-3735-8973>

To determine the contribution of intumescent coatings to the fire resistance in general fire tests are carried out on mechanically loaded and unloaded specimens. However, current normative regulations do not sufficiently address the test and assessment procedure of intumescent coatings applied to steel tension members. Consequently, steel tension members are excluded from the scope of application of these products. More than 10 years ago BAM started the research about this topic and developed appropriate test and assessment recommendations. Fire tests on steel tension bars with solid section protected by intumescent coating were previously presented at *Structures in Fire Conferences* [1, 2]. Following up on this research, the proposed conference paper will focus on real-scale fire testing of steel tension members with hollow section protected by intumescent coating. The paper will describe the test setup and execution as well as discuss the obtained results. Finally, a recommendation regarding the test and assessment procedure will be given.

2 NORMATIVE AND TECHNICAL BACKGROUND

At the European level, normative regulations for fire testing of steel tension bars with solid section have been developed during the last years or are still under preparation. EN 13381-10 [3], which was published in August 2020, describes fire tests of unloaded steel tension members with solid section. As a fundamental requirement for applying this standard, successful testing and assessment according to EN 13381-8 [4] for steel beams and columns with open section (I-, H-, U-, T, L-profiles) or hollow section (rectangular, square or circular profile) is mandatory. Alternatively, the draft standard prEN 13381-11 [5], focuses on fire testing of mechanically loaded steel tension bars with solid section protected by intumescent coating. This document will be a stand-alone standard that does not require additional fire testing according to EN 13381-8.

Regarding steel tension members with open or hollow section, normative regulations to determine the contribution of intumescent coatings to the fire resistance are still missing. As these structural members are typically used in truss constructions, the absence of regulation creates extensive difficulties. To overcome this shortcoming, in Germany the approval-based scope of application for intumescent coatings can be extended to these structural members based on two possibilities: fire resistance test of a mechanically loaded beam or tension member. The beam approach has various limitations, e.g. beam and tension member require the same section type and for the application in practice the tension member's load utilisation factor in case of fire is limited to $\mu_{fi} \leq 0.5$. Because fire tests with mechanically loaded beams are mainly carried out with I- or H-profiles, this approach is primarily used for steel tension members with open section. As an alternative approach fire tests of mechanically loaded steel tension members can be carried out to directly determine the contribution of intumescent coatings to the fire resistance. Due to the lack of a normative test and assessment regulations, it is likely to adopt the procedure developed in draft standard prEN 13381-11. However, the tension member approach has hardly been used so far in Germany for open or hollow sections. The experimental investigations described in this paper provide a valuable insight into this topic and provide important testing experience.

3 EXPERIMENTAL INVESTIGATIONS

3.1 Test programme and specimens

According to the previously described tension member approach an epoxy-based intumescent coating [6, 7] was applied to various rectangular and square hollow sections and afterwards fire tested at BAM. The fire resistance was investigated by mechanically loaded specimens. Additionally, the influence of the member orientations was analysed by unloaded specimens. All specimens were first sand blasted. Afterwards thermocouples were attached. Thereafter, a primer and subsequently the intumescent coating was applied. A top coat was omitted. All specimens are made of hot rolled steel, steel grade S355 and intend

to achieve a fire resistance time of 30 minutes. The fire tests were carried out at the tension test furnace at BAM in real scale using the ISO standard fire curve. The test programme is given in Table 1.

In total, eight mechanically loaded specimens with different cross-sections, section factors (A_m/V), dry film thickness (DFT), and load utilisation factor in case of fire (μ_{fi}) were analysed. The specimens have a total length of 2.05 m, a fire-exposed length of about 1.65 m, and were tested in horizontal orientation. A steel plate was welded at the ends of each hollow section. This allowed the specimen to be attached to the load frame of the tension test furnace by a bolted connection. To measure the steel temperature during the fire test ceramic fibre insulated flexible thermocouples of type K with a fire resistance up to 1200 °C were attached to the specimens prior the application of the intumescent coating. Three measuring stations (MS) with measuring points on all four sides of the cross-section were arranged along the specimen, see Figure 1a. The DFT of the intumescent coating was measured adjacent to the steel temperature measuring points and between the measuring stations at all four sides of the cross-section. Based on these measurements, the actual mean value of the DFT of each specimen was calculated.

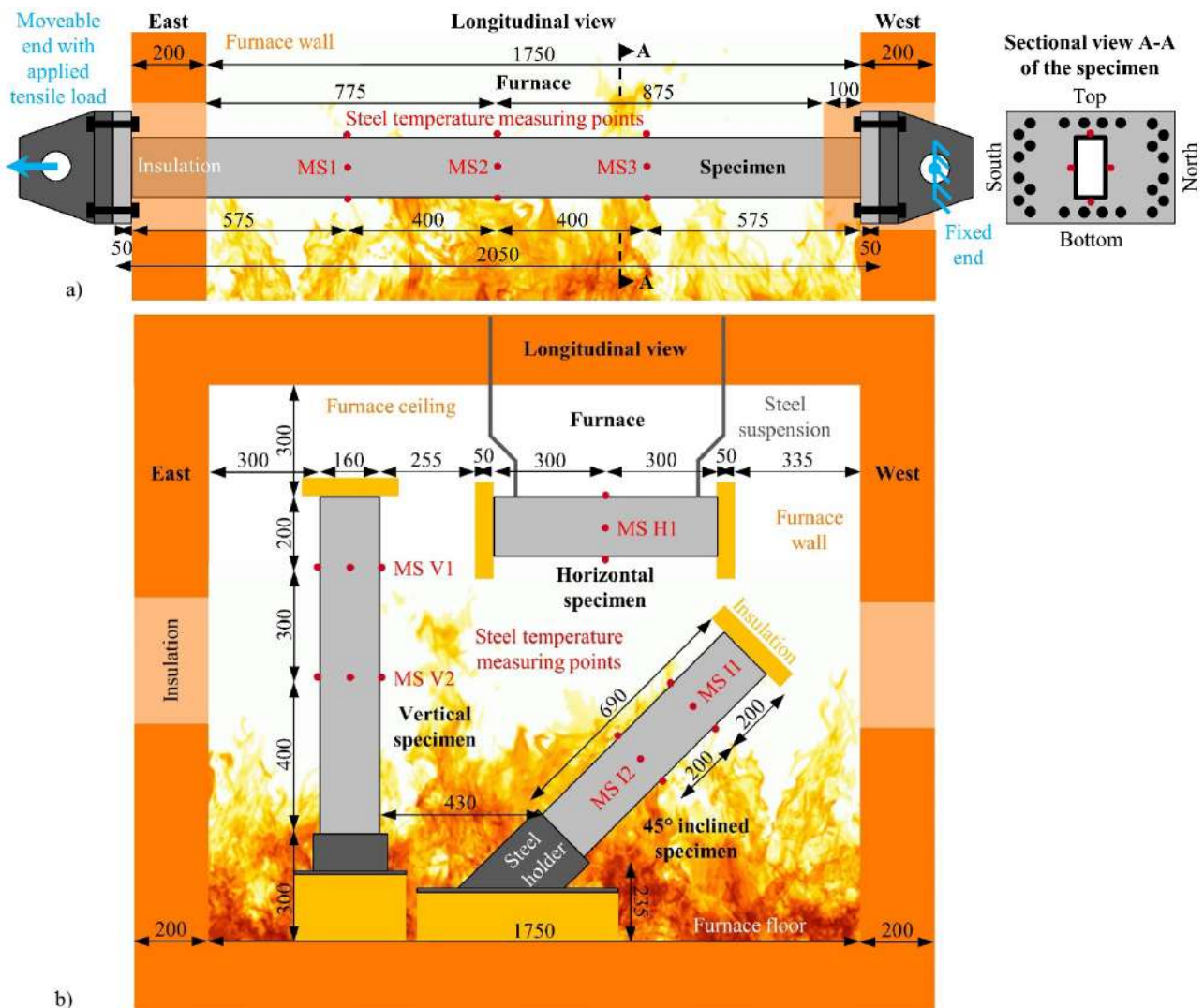


Figure 1. a) Drawing of the mechanically loaded tension member (160x80x6.3 mm³) installed in the tension test furnace; b) Drawing of the unloaded specimens (160x80x6.3 mm³) installed in the tension test furnace; dimensions in mm

In addition, the influence of the member orientation was investigated based on two fire tests with three unloaded specimens arranged in horizontal, 45° inclined and vertical position, see Figure 1b. Due to their

position in the furnace the specimens have a total length of 0.6 m (horizontal), 0.8 m (45° inclined), and 1.0 m (vertical). Just as the mechanically loaded specimens, flexible thermocouples for steel temperature measurement were attached to the unloaded specimens. The measuring stations and measuring points are shown in Figure 1b. The DFT was determined in the same way as for the mechanically loaded specimens.

Table 1. Information about the test programme

Specimen name	Section [mm]	Section factor [m ⁻¹]	Actual mean DFT [mm]	Load utilisation factor in case of fire [-]	Actual steel strength [N/mm ²]		Applied tensile load [kN]
					f _{yield,20°C}	f _{ultimate,20°C}	
1	120x120x5	209	3.15	0.35	461	579	367
2	60x60x4	268	3.85	0.65	425	563	243
3A	220x220x10	105	1.15	0.29	424	560	1020
3B			1.35	0.35			1231
3C			1.90	0.35			1231
4A	160x80x6.3	168	1.55	0.18	499	599	254
4B			2.45	0.35			493
4C			3.00	0.65			915
4AH	160x80x6.3	168	1.60	unloaded			
4AI			1.70				
4AV			1.60				
4CH	160x80x6.3	168	3.30	unloaded			
4CI			3.30				
4CV			3.30				

3.2 Test setup

The fire tests were conducted in the tension test furnace, see Figure 2. This test device consists of a furnace (inner dimension of W=1.8 m; L=1.75 m; H=1.5 m) with two oil burners and an external load frame with two hydraulic actuators (2×750 kN). The mechanically loaded tension members were attached by a bolted connection to the load frame using special attachment devices. The applied tensile load is given in Table 1 and was calculated by multiplying the actual yield strength of the steel at ambient temperature (f_{yield,20°C}) by the cross-sectional area of the hollow section (A_{section}) and the load utilisation factor in case of fire (μ_{fi}). In the fire test with unloaded specimens, the horizontal member was suspended from the furnace ceiling. The 45° inclined and vertical specimens were placed on the furnace floor using special steel holders. The auxiliary construction was protected against fire exposure by high temperature fibre insulation. In addition, the ends of the unloaded specimens were insulated by high temperature fibre insulation and vermiculite boards. Both, mechanically loaded and unloaded specimens were positioned in the centre of the furnace in an east-west direction, see Figure 2. Thus, the specimens are arranged between the burner axes allowing a uniform fire exposure according to ISO standard fire curve. The furnace temperature was measured and

controlled by plate thermocouples (PTC) positioned at a distance of 100 mm (\pm 50 mm) to the surface of each specimen.

In the mechanically loaded fire tests, the specimens were first subjected to the tensile load. Thereafter, the fire test was started by turning on the two oil burners. The mechanical tensile load was kept constant over the entire fire test until the mechanically loaded specimen ruptured. During the fire test photo and video recordings were made. Furthermore, the furnace and steel temperature as well as the applied tensile load and longitudinal deformation of the mechanically loaded specimen were measured and recorded.

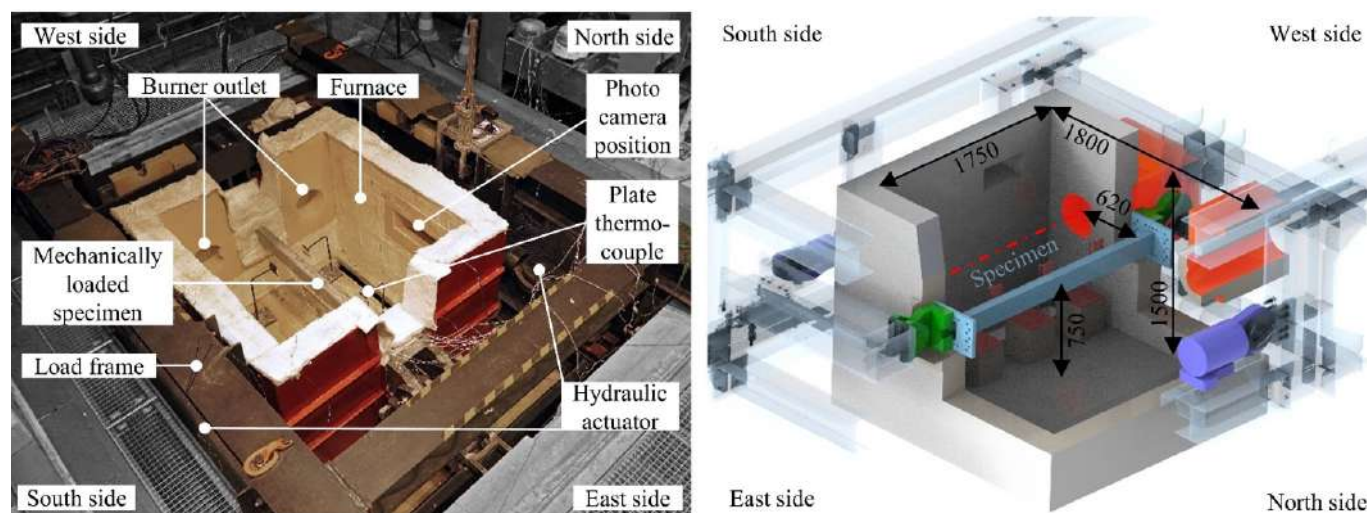


Figure 2. Tension test furnace with installed mechanically loaded specimen 160x80x6.3 mm³ (left); 3D model of the tension test furnace (right), dimensions in mm; furnace ceiling is removed in both pictures

4 RESULTS AND DISCUSSION

The following conclusions apply mainly to the tested intumescent coating [6, 7]. Due to the variety of product types, i.e. water-based, solvent-based and epoxy-based, and the individual product formulations of intumescent coatings, it is difficult to generalise the findings and statements obtained. Nevertheless, the general behaviour shown in the fire tests and the trends derived provide a good insight into how intumescent coatings contribute to the fire resistance of steel tension members with hollow section. To demonstrate the thermal protective performance of a specific product, fire tests are mandatory.

4.1 Char morphology

In all fire tests, the intumescent coating formed a thermal protective char around the steel tension member. The char formation process is characterised by blackening, the creation of small bubbles on the surface as well as a significant volume expansion, see Figure 3a) and 3b). As a result of the expansion cracks occurred. Longitudinal cracks in the char of the intumescent coating were often formed at the sides or at the bottom of the specimen, see Figure 3b) and 3c). Most of the cracks are only superficial and are closed by further foaming. However, the cracks foster a non-uniform char formation across the cross-section of the specimen. The char thickness at the top of the specimen was usually smaller compared to the other sides, see Figure 3d). In longitudinal direction, the specimen showed in general a uniform char thickness, see Figure 4. Therefore, the fire-exposed length is sufficient. The char formation and the related strong expansion ends with the incineration of the intumescent coating, which can be easily recognised by the white colour. During the char forming process and the subsequent incineration, small parts of the char may fall off the specimen. However, unprotected areas have not been observed at the specimens. As some of the char also fell off the specimen due to the impact at rupture, it was only possible to determine the char thickness after the fire test at selected positions.

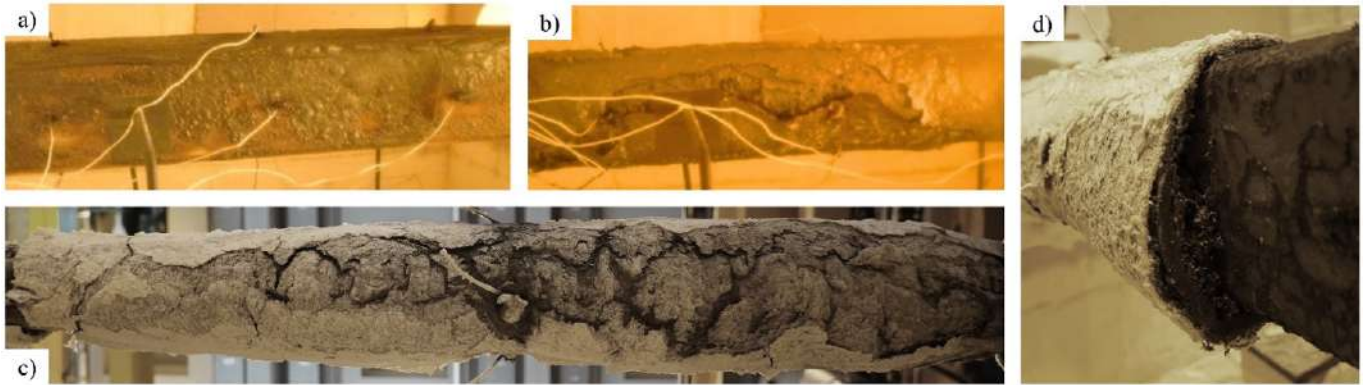


Figure 3. Char formation at mechanically loaded specimens: a) start of the char formation at specimen 3C after the 6th minute of fire exposure; b) longitudinal crack at the north side of specimen 4C after the 8th minute of fire exposure; c) longitudinal crack at the bottom side of specimen 2 after the fire test; d) sectional view of the char at specimen 4C after the fire test



Figure 4. Mechanically loaded specimen before, during and after the fire test; specimen 3C - 220x220x10 mm³ (left); specimen 4C - 160x80x6.3 mm³ (right)

4.2 Steel temperatures

At each measurement station (MS) the steel temperatures were averaged. Incorrect thermocouples were not considered. The assessment is based on the MS with the maximum steel temperature/time curve, which is generally directly or nearest to the location of rupture. The qualitative steel temperature/time curve in the fire tests is similar for all specimens and typical for steel members protected by intumescent coating. Starting from a rapid rise at the beginning of the fire test, the heating rate of the steel slows down due to the reaction of the intumescent coating and the char expansion. Due to the incineration of the intumescent coating, the heating rate increases again, and the steel temperature/time curve becomes almost linear until rupture of the specimen. The quantitative steel temperature/time curve is influenced by several factors, i.e. profile geometry or section factor, DFT and the char morphology. Since the fire tests were conducted with a well reproducible furnace temperature/time curve, see Figure 5, the effects of temperature variations are marginal. The deviations of the furnace temperature, which was measured during the fire test with several plate thermocouples, were in general much smaller than the limits given in EN 1363-1 [8].

Similarly to beams and columns, the thermal protective performance of the intumescent coating applied to tension members generally improves with increasing DFT, see steel temperature/time curves in

Figure 5. As a result of the lower steel temperatures, the time to reach the load-bearing capacity or rupture of the specimen also increases with a higher DFT. At low DFTs, the thermal protective performance of the intumescent coating is due to the reduced ability of a further foaming much more negatively and directly affected by cracks or small parts of the char falling off. An increase in the DFT can be a solution to this problem, but the result may be that the thermal protection of the intumescent coating is not fully utilised.

In general, due to the complex char formation, it is difficult to predict the thermal protective performance of intumescent coatings. For example, this can be shown based on the results of the specimens 3A, 3B and 3C, see Figure 5 (left). The three specimens are geometrically identical and have almost the same load utilisation factor in case of fire. Therefore, at the time of rupture, the steel temperature is about 700 °C. However, the increase in the DFT from 1.15 mm (3A) to 1.35 mm (3B) and to 1.90 mm (3C) has a disproportionate effect on the time when rupture occurs, i.e. 50 min (3A), 58 min (3B) and 67 min (3C). The reasons for this behaviour have been explained in the previous paragraph.

Based on the example of specimen 4A, 4B and 4C, the influence of the load utilisation factor in the case of fire can be assessed. The three specimens are geometrically identical but differ in the applied DFT and level of load utilisation. The load utilisation factor in case of fire increases from 0.18 (4A) to 0.35 (4B) and finally to 0.65 (4C), which represents the maximum load utilisation in case of fire. As a result, the steel temperature at the time of rupture decreases, see Table 2. On the other hand, the DFT applied to the specimens was increased from 1.55 mm (4A) to 2.45 mm (4B) and to 3.00 mm (4C). This resulted in a slower heating of the steel. The results in Figure 5 (right) show that doubling the load utilisation factor in case of fire does not require a doubling of the DFT to achieve a similar time to reach load-bearing capacity.

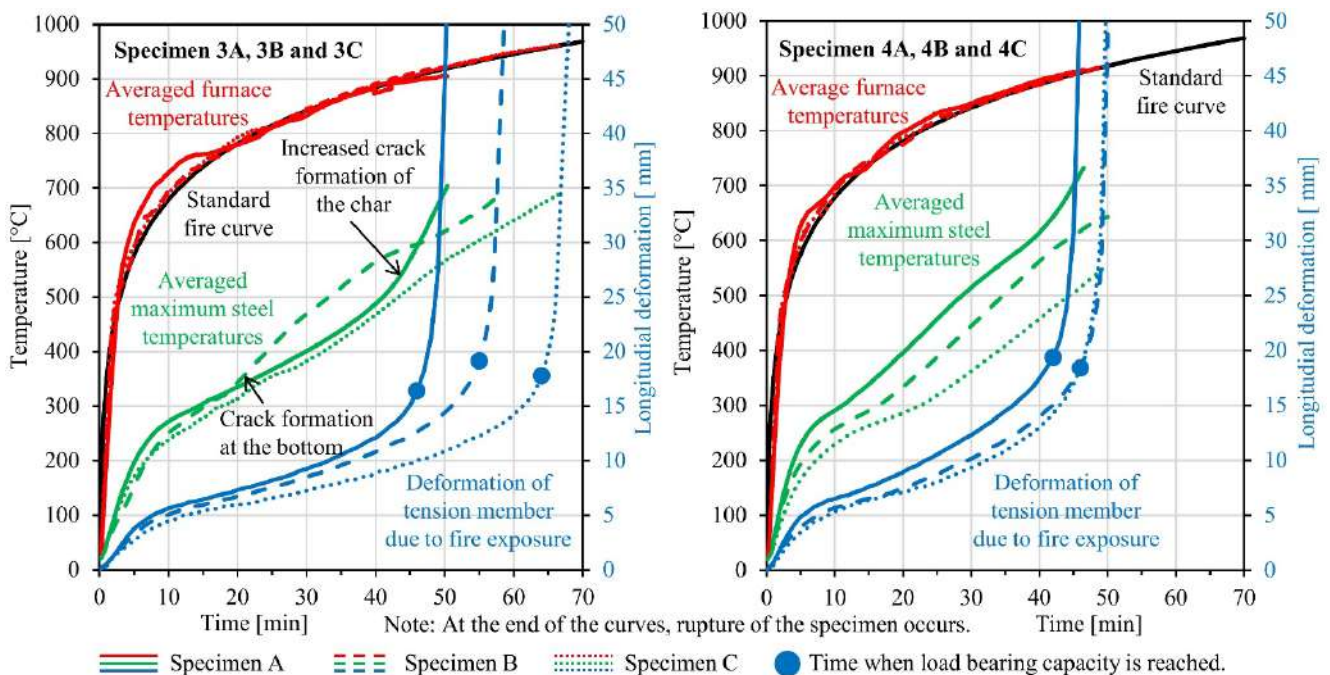


Figure 5. Measured temperature and deformations: specimen 3A to 3C (Left); specimen 4A to 4C (right)

The effect of the section factor can be assessed by comparing specimen 3A, 4B and 2. The specimens have approximately the same load utilisation factor in case of fire, but different cross-sectional dimensions and corresponding section factors. The section factor increases from 105 m⁻¹ (3A) to 168 m⁻¹ (4B) and to 209 m⁻¹ (2). Because steel members with a higher section factor heat up faster compared to those with a low section factor, the DFT applied to the specimens was increased from 1.15 mm (3A) to 2.45 mm (4B) and to 3.15 mm (2). According to Table 2, doubling the section factor requires tripling the DFT to achieve

the same rupture time or respectively time to reach the load-bearing capacity. Slender profiles with a high section factor, such as those often used for steel tension members, are therefore a particular challenge for intumescent coatings. This becomes particularly obvious in case of specimen 1, which has a very high section factor and the maximum load utilisation factor in case of fire. Although this specimen has a very high DFT of 3.85mm, it failed before reaching 30 minutes, see Table 2.

4.3 Deformation behaviour and fire resistance

The fire tests also showed good qualitative agreement regarding the deformation behaviour of the mechanically loaded tension members. In the beginning of the fire tests the longitudinal deformation increases almost linear and is mainly due to the thermal expansion of the steel. At steel temperatures of more than 500 °C, the exact value depends on the load utilisation factor in case of fire, the deformations increase significantly due to mechanical, plastic strains. The rapid increase of the longitudinal deformation and the formation of cracks in the char indicate the rupture of the specimen, see Figure 5. However, it is not the time of rupture that is the decisive factor in the assessment of fire resistance, but the time when the load-bearing capacity is exceeded. To determine this time, the draft standard prEN 13381-11 [5] proposes a rate of deformation criteria, see equation (1). The time to reach the load-bearing capacity is given in Table 2. By reducing the section factor or the load utilisation factor in the case of fire, the time to reach the load-bearing capacity can be extended. The same also applies regarding an increase of the DFT. However, there is no linear relationship between the time and these three parameters. To achieve a certain fire resistance, it may be necessary to adjust several parameters at the same time.

$$\Delta dU/dt_{\text{limit}} = \dot{\epsilon} \cdot L_F \quad [\text{mm} \cdot \text{min}^{-1}] \quad (1)$$

where

$\dot{\epsilon}$ is the strain rate of 0.001 min⁻¹,

L_F is the fire-exposed length in mm of the specimen.

Table 2. Summarised results of the fire tested mechanically loaded steel tension members

Specimen name	Section [mm]	Section factor [m ⁻¹]	Actual mean DFT [mm]	Load utilisation factor in case of fire [-]	Initial deformation due to load application [mm]	Time [min] to reach ...		Steel temperature [°C] at ...	
						Load-bearing capacity	Rupture	Load-bearing capacity	Rupture
3A	220x220x10	105	1.15	0.29	12.7	46	50	595	705
3B			1.35	0.35	15.1	55	58	660	690
3C			1.90	0.35	14.1	64	67	670	695
4A	160x80x6.3	168	1.55	0.18	3.5	42	46	645	735
4B			2.45	0.35	6.5	46	50	620	650
4C			3.00	0.65	12.0	46	50	575	585
2	120x120x5	209	3.15	0.35	5.3	46	49	640	675
1	60x60x4	268	3.85	0.65	5.1	23	25	485	520

Note:

The time to reach load-bearing capacity was determined based on the rate of deformation criteria proposed in the draft standard prEN 13381-11 [5].

4.4 Comparison of steel tension members and columns

Table 3. Comparison of the steel temperatures of tension members and columns with a four-sided fire exposure

Specimen name	Section [mm]	Section factor [m ⁻¹]	Actual mean DFT [mm]	Load utilisation factor in case of fire [-]	Steel temperature in [°C] after ...			
					30 minutes		45 minutes	
					Column ¹	Tension member ²	Column ¹	Tension member ²
3A	220x220x10	105	1.15	0.29	≤ 400	420/400	≤ 550	525/570
3B			1.35	0.35	≤ 375	410/465	≤ 520	525/590
3C			1.90	0.35	<< 350	390/380	≤ 450	490/515
4AV	160x80x6.3	168	1.60	unloaded	≤ 430	500/590	≤ 610 ≤ 550*	n. a. 610*/700*
4AI			1.70		≤ 420	485/480	≤ 600 ≤ 540*	n. a. 585*/570*
4AH			1.60		≤ 430	480	≤ 610 ≤ 550*	n. a. 580*
4A	160x80x6.3	168	1.55	0.18	≤ 435	490/515	≤ 615 ≤ 555*	630/700 585*/615*
4B			2.45	0.35	≤ 365	445/470	≤ 555	610/610
4C			3.00	0.65	<< 350	360/395	≤ 385	505/580
4CH	160x80x6.3	168	3.30	unloaded	<< 350	370	≤ 355	510
4CI			3.30			395/365		515/490
4CV			3.30			415/395		550/525
2	120x120x5	209	3.15	0.35	≤ 350	465/470	≤ 540	690/635
1	60x60x4	268	3.85	0.65	≤ 350	445 [#] /520 [#]	≤ 550	n. a.

Note:

¹ Information regarding the steel temperature is taken from the ETA [6], where unloaded and loaded columns with rectangular hollow section and applied intumescent coating were fire tested according to EN 13381-8 [4]; fire exposure on all sides of the specimens.

² Information is based on fire tests at BAM for unloaded and loaded steel tension members with rectangular hollow section and applied intumescent coating; fire exposure on all sides of the specimens; steel temperature corresponds to measurement station MS1/MS2.

* Steel temperature at a time of 40 minutes.

[#] Steel temperature at a time of 25 minutes.

n. a. – no available data because the fire test has already been terminated.

As already mentioned in Chapter 3.1 the epoxy-based intumescent coating used in the fire tests with steel tension members has an ETA [6] allowing its application to steel columns with rectangular and square hollow section. The data given in this ETA has been determined based on EN 13381-8 [4] at unloaded, 1 m long specimens tested in vertical orientation and exposed at all four sides to the standard uniform fire curve. The temperature data include a stickability correction, which is derived from a comparison of a mechanically loaded column and an unloaded, 1 m long column section with the same geometry and DFT. Table 3 summaries the maximum steel temperature after 30 minutes and 45 minutes fire exposure for tension members and columns. The temperature values for the columns have been taken from the

ETA based on the section factors and the DFT used in the fire tests with steel tension member. Regarding the steel tension member, usually two steel temperatures are given in Table 3. The first value refers to measurement station 1 (MS1) of the mechanically loaded specimens, where the char is in general intact and without cracks. The second value refers to measurement station 2 (MS2), which is often close to the point of rupture. In terms of the analysed fire durations, the comparison shows that in almost all cases the steel temperatures of the tension members are significantly higher compared to the columns. This statement also applies for the tested unloaded specimens, which are regardless of the member orientation about 50 K and more above the steel temperature of columns. The differences may partially result from the test conditions according to EN 13381-8 [4], e.g. different furnaces of the test laboratories. Furthermore, the values given in the ETA [6] are interpolated based on the section factor, i.e. the tested columns differ from those tested under tension. In addition to these points, the significantly higher steel temperatures of in some cases more than 100 K obtained on mechanically loaded tension members are also due to the different type of loading, i.e. tension instead of compression. Consequently, the presence of a mechanical load during the fire test as well as the type of loading affect the thermal protective performance of the intumescent coating and shall be considered. For the same reason, EN 13381-8 [4] distinguishes between beams and columns, not only because of the different fire-exposed areas, but also due to the different type of loading. As a result, separate sets of DFT tables for an intumescent coating are given in an ETA.

Based on the comparison carried out, the test data and resultant set of DFT tables determined for columns is unsafe, and therefore not recommended to be used for tension members. Only the test data obtained on mechanically loaded steel tension members is reliable and appropriate for the intended application of the intumescent coating to these structural members.

5 CONCLUSIONS

The conducted fire tests have shown that the developed test setup is appropriate to assess the fire resistance of steel tension members with hollow section protected by intumescent coatings. Both, a very good reproducibility of the failure mechanisms and a representative char formation of the intumescent coating were achieved. Therefore, specimens with a fire-exposed length of about 1.6 m seem to be sufficient. The test and assessment procedure described in the draft standard prEN 13381-11 [5], which aims at steel tension members with solid section protected by intumescent coating, is generally applicable to hollow sections in tension.

The test results showed that intumescent coatings can provide a significant improvement in the fire resistance of steel tension members with hollow section. Based on the configurations specified in the test programme, the tested tension members with the applied intumescent coating were able to achieve a fire resistance of 30 minutes in almost all cases. A fire resistance of 60 minutes could be obtained in only one case, i.e. a specimen with a low section factor, high DFT and medium load utilisation. In general, the specific application to steel tension members placed particularly high demands on the performance of the intumescent coating. This is partly due to the four-sided fire exposure and the mainly filigree cross sections, which both result in high section factors. In addition, there is an increased crack formation due to the tensile load. As a result, the thermal protection of the tested intumescent coating on the tension members decreased compared to columns with the same section factor and fire exposure. Consequently, the presence of a mechanical load in the fire test, as well as the type of loading affect the thermal protective performance of the intumescent coating and shall be considered. Therefore, only the test data obtained on mechanically loaded steel tension members is reliable and appropriate for the intended application of the intumescent coating to these structural members.

ACKNOWLEDGMENT

The authors would like to thank the colleagues in Division 7.3 who carried out the fire tests and all other external persons involved in the research.

REFERENCES

1. Häßler, D., Hothan, S., Fire tests of reactive fire protections systems applied to steel tension members with solid circular section. 9th International Conference on Structures in Fire, pp.1099-1106 (2016). ISBN: 978-1-60595-320-5.
2. Häßler, M., Häßler, D., Hothan, S., Krüger, S., Performance of intumescent fire protection coatings on steel tension rod systems. 10th International Conference on Structures in, pp. 649-654, (2018). ISBN: 978-1-85923-274-3.
3. EN 13381-10: Test methods for determining the contribution to the fire resistance of structural members - Part 10: Applied protection to solid steel bars in tension (2020).
4. EN 13381-8: Test methods for determining the contribution to the fire resistance of structural members – Part 8: Applied reactive protection to steel members (2013).
5. prEN 13381-11: Test methods for determining the contribution to the fire resistance of structural members - Part 11: Applied protection to solid steel bars in tension based on mechanically loaded fire tests. draft version 12 (2023).
6. ETA-20/1260: European Technical Assessment for the reactive fire protection system “HENSOTHERM® 910 KS”. Element Materials Technology, Rotterdam B.V., Amsterdam (2021).
7. Z-19.51-2273: Reaktive Brandschutzbeschichtung “HENSOTHERM® 910 KS” nach ETA-16/0834 zur Anwendung auf Stahlbauteilen. General construction technique permit (aBG), Deutsches Institut für Bautechnik, Berlin (2018).
8. EN 1363-1: Fire resistance tests - Part 1: General requirements (2020).

FIRE-INDUCED COLLAPSE EARLY-WARNING METHOD FOR PLANAR MULTI-STORY STEEL FRAME STRUCTURES

Yao Wang¹, Guo-Qiang Li², Shaojun Zhu³, Xiuzhi Zheng⁴

ABSTRACT

This paper proposes the overall framework of the fire-induced collapse early-warning method for planar multi-story steel frame structures, involving exploring the potential collapse modes, revealing the evolution laws of key monitoring physical parameters during the whole collapse process, recognition of collapse mode, and the graded early-warning algorithms. At actual fire rescue scenes, combining real-time measured on-site data, the proposed early-warning method can be applied to identify structural collapse mode, evaluate structural collapse state, and early warn the remaining time to collapse, thereby assisting firefighters in making scientific decisions on rescue operations to reduce casualties as much as possible. Moreover, the feasibility and accuracy of the proposed framework are verified by the real fire-induced collapse test of a planar steel frame by comparing the predicted and measured remaining time to collapse.

Keywords: early-warning method; overall framework; multi-story steel frame; remaining time to collapse

1 INTRODUCTION

Multi-story steel frame structures are commonly utilized in large commercial buildings, like supermarkets, commercial complexes, and furniture centres. In large commercial buildings characterized by dense fire loads, fires can quickly escalate, and the intricate internal layout increases the likelihood of individuals being trapped in the fire. For general compartment fires, the air temperature will exceed 600 °C after 10 minutes. At this time, the steel will lose most of its strength, which will greatly increase the fire-induced collapse risk of steel frame structures, and pose a serious threat to the lives of firefighters and trapped people. Therefore, if real-time early-warning information with remaining time to collapse can be provided, it will greatly reduce casualties and property losses, serving as significant demand in the field of structural fire safety and smart firefighting.

Existing studies mainly focus on the collapse behaviours and progressive collapse resistance of steel frames under fire. Research on the collapse mechanism of the large-span floor system under localized fire was conducted by Usmani *et al.* [1–3], in which two progressive collapse modes were summarized, namely the weak floor and strong floor failure modes. Sun *et al.* [4] carried out a series of case studies to further understand the structural collapse mechanism under various fire scenarios. The results showed that different load ratios and beam sections would generate different collapse mechanisms for the un-braced frames. Moreover, the bracing system and higher lateral stiffness were helpful to prevent the frame from progressive collapse. Li *et al.* [5] systematically analyzed collapse modes and mechanisms of planar steel-framed

¹ Ph.D. Candidate, College of Civil Engineering, Tongji University, Shanghai, China
e-mail: wangyao2019@tongji.edu.cn

² Professor, College of Civil Engineering, Tongji University, Shanghai, China; State Key Laboratory of Disaster Reduction in Civil Engineering, Tongji University, Shanghai, China
e-mail: gqli@tongji.edu.cn

³ Assistant Professor, College of Civil Engineering, Tongji University, Shanghai, China
e-mail: zhushaojun@tongji.edu.cn

⁴ Postdoctor, College of Civil Engineering, Tongji University, Shanghai, China
e-mail: xiuzhi@tongji.edu.cn

structures under one-column fire scenarios. Three progressive collapse mechanisms were found, namely the cantilever beam mechanism, pull-in force-induced mechanism, and high load ratio member failure mechanism. Jiang *et al.* [6] found the fire protection of steel members had a significant influence on the resistance of structures against fire-induced collapse. Additionally, they also investigated how the arrangement schemes of vertical and horizontal braces on the resistance of fire-induced collapse [7].

In contrast, there is relatively little research on early warning of fire-induced building collapse, especially for multi-story steel frame structures. Essentially, the fire-induced collapse early warning is an uncertain problem, considering the key parameters such as the loading state, structural material property, fire location, and fire intensity of a real building are generally unknown and hard to determine, which will greatly affect the fire-induced collapse of the building. Lv *et al.* [8] used sensors to measure structural vibration signals under fire. The results showed that the decrease in structural stiffness with the temperature rising would result in a fluctuating decrease in vibration frequency, providing a possible way for collapse early warning. Ye *et al.* [9] and Jiang *et al.* [10] established their early-warning methods based on the component critical temperatures for steel frame and truss structures. However, the structural critical temperatures are relevant to the structural material properties and loading states, which are hard to determine. Recently, combining reliability theory, Li *et al.* [11–13] proposed graded early-warning methods based on displacements and velocities for some relatively simple structural forms, such as steel portal frames and planar steel trapezoid trusses.

In this study, an overall early-warning framework of the fire-induced collapse for planar multi-story steel frame structures is proposed with recognizing the structural collapse mode, evaluating the structural collapse state, and predicting the structural remaining time to collapse. Then, the application process of the early-warning method at actual fire scenes is also discussed. Finally, the feasibility and accuracy of the proposed early-warning framework are proved by comparing the predicted and measured remaining time to collapse of a planar steel frame structure in the fire-induced collapse test.

2 OVERALL FRAMEWORK OF THE FIRE-INDUCED COLLAPSE EARLY WARNING

The fire-induced collapse early-warning method of planar multi-story steel frame structures proposed in this study mainly comprises four key theoretical sections: exploring potential structural collapse modes, selections and evolution laws of key monitoring physical parameters (KMPPs), recognition of collapse mode, and graded early-warning algorithms.

2.1 Potential structural collapse modes

A detailed parametric analysis was conducted to explore all possible fire-induced collapse modes of planar multi-story steel frame structures under various yet reasonable building fire scenarios. Typical topological forms of the moment-resisting steel frames (all beam-column connections are rigid) are selected, involving the regular-span frame as well as large-span frames with different locations or forms of the large-span area, as shown in Figure 1. Moreover, other structural or fire parameters were also considered, including various fire scenarios (one or multiple-column fires, one or multiple-compartment fires, *etc.*), temperature-time curves (standard fire or natural fires), fire protection levels, load cases, component sizes, section temperature gradients, wind loads, *etc.*

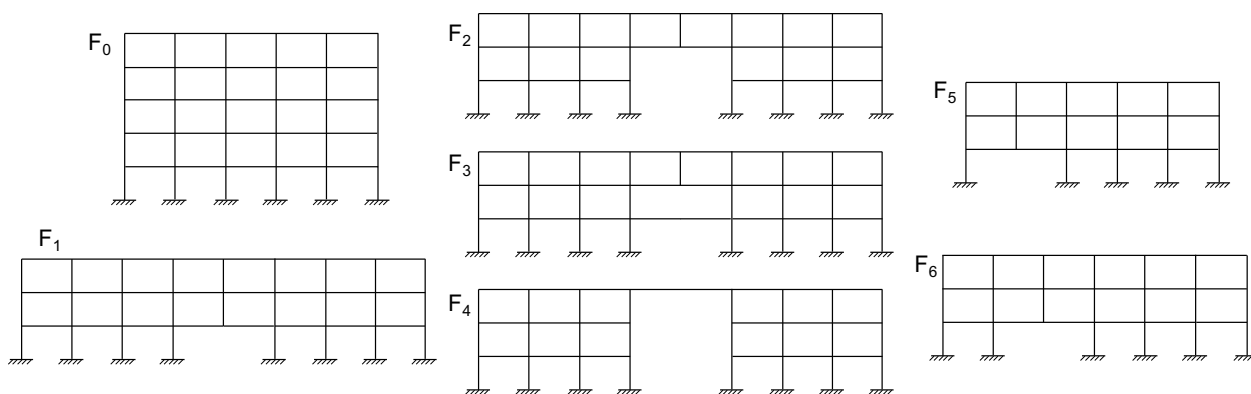


Figure 1. Selected typical topological forms of multi-story steel frames

The coupled thermo-mechanical analysis was carried out with the finite element model in ABAQUS/Explicit to simulate the structural fire-induced collapse process. The stress-strain model of steel at high temperatures was based on EC3 [14] and the dynamic increase factor [15–17] was also considered. Beams and columns were modelled using the B31 element. The sensitivity analysis was conducted on the time scale ratio of analysis steps and element mesh sizes to save computational costs while retaining acceptable accuracy. Three real fire-induced collapse tests of planar steel frames conducted by Jiang *et al.* [18] were used to verify the correctness of the finite element modelling method and the selection of model parameters.

The systematic parametric analysis results indicate that the number of potential fire-induced collapse modes under any reasonable structural parameters and fire scenarios is limited, and the actual frame collapse under fire will ultimately only yield one specific mode, which serves as an important theoretical basis for the early-warning method proposed in this study. Combining the structural collapse mechanisms, a total of eight different collapse modes were found, such as the general inward collapse, partial lateral collapse, heated large-span beam-induced inward collapse, and unheated large-span beam-induced inward collapse, as depicted in Figure 2. Additionally, there are four other collapse modes, namely the rebalancing collapse, restraint failure-induced collapse, overall downward collapse, and overall lateral collapse.

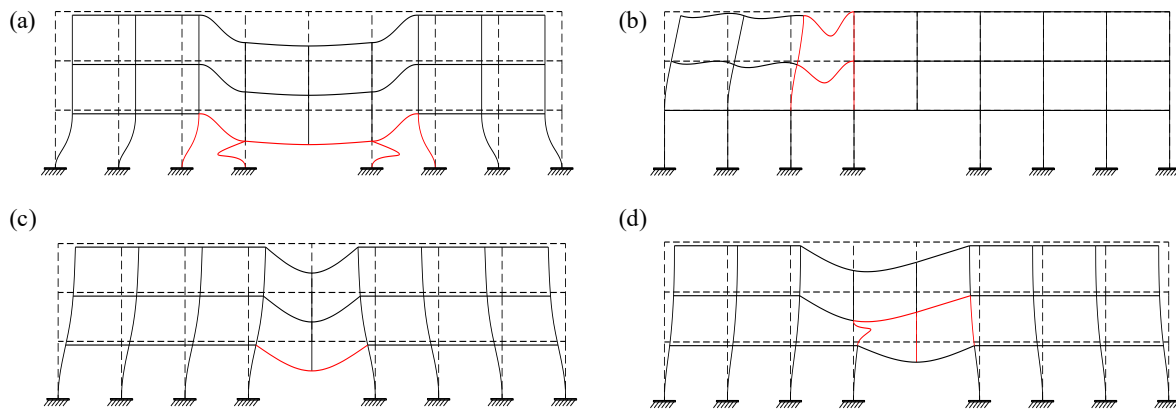


Figure 2. Part of structural collapse modes (a) General inward collapse (b) Partial lateral collapse (c) Heated large-span beam-induced inward collapse (d) Unheated large-span beam-induced inward collapse

2.2 Selection and evolution laws of KMPPs

To break through the bottleneck of building collapse early warning caused by uncertainties in loading action, structural material properties, fire intensities and distribution, the vertical displacements and velocities at the top of columns on the top floor, as well as the horizontal displacements and velocities at the top of edge columns as demonstrated in Figure 3, are selected as KMPPs for steel frame structures to reflect the impact of the actual fire case and uncertain structural state parameters on the structural fire behaviour up to collapse.

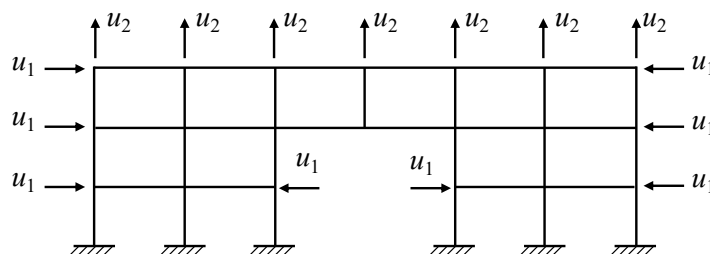


Figure 3. Selections of KMPPs

Further analysis reveals that under one specific collapse mode, the KMPPs will demonstrate unique evolution laws, which is another crucial theoretical foundation for the proposed fire-induced early-warning method. Taking the general inward collapse and partial lateral collapse as examples, for the former, it can

be observed from Figure 4 that only after the vertical displacement at the top of the heated column ($6u_2$ in this case) developed downward to a certain extent, the heated floor would generate significant inward horizontal displacement ($1u_{1-L}$ and $1u_{1-R}$), which indicated that the inward horizontal displacement of the heated floor was caused by the failure of the heated column due to the material degradation at high temperatures. Additionally, the downward development of the vertical velocity at the top of the heated column ($6v_2$) was also obviously earlier and faster than the inward development of the horizontal velocity on the heated floor ($1v_{1-L}$). However, for the latter, the main reason for structural collapse was due to the rapid development of the mid-span deformation of the heated beam driving a significant inward horizontal displacement at the top of the heated column. Therefore, reflected in the evolution laws of KMPPs, the inward horizontal displacement of the heated floor ($2u_{1-L}$), compared to the downward vertical displacement at the top of the heated column ($5u_2$), exhibited a larger absolute value and developed faster as depicted in Figure 5. Moreover, a significant drop in the vertical displacement at the top of the heated column can also be observed as a unique feature of this collapse mode.

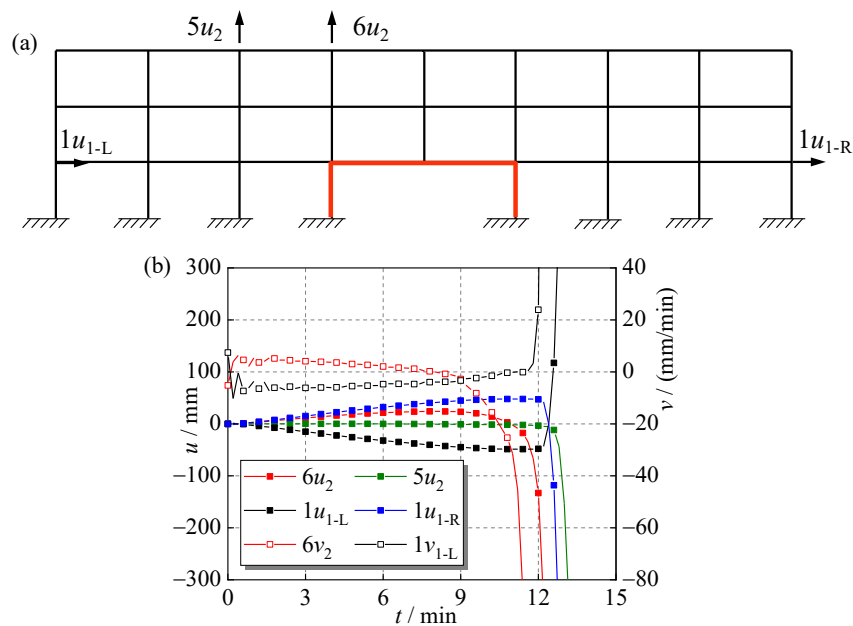


Figure 4. A typical fire case of the general inward collapse (a) Fire area (b) Displacement and velocity-time curves

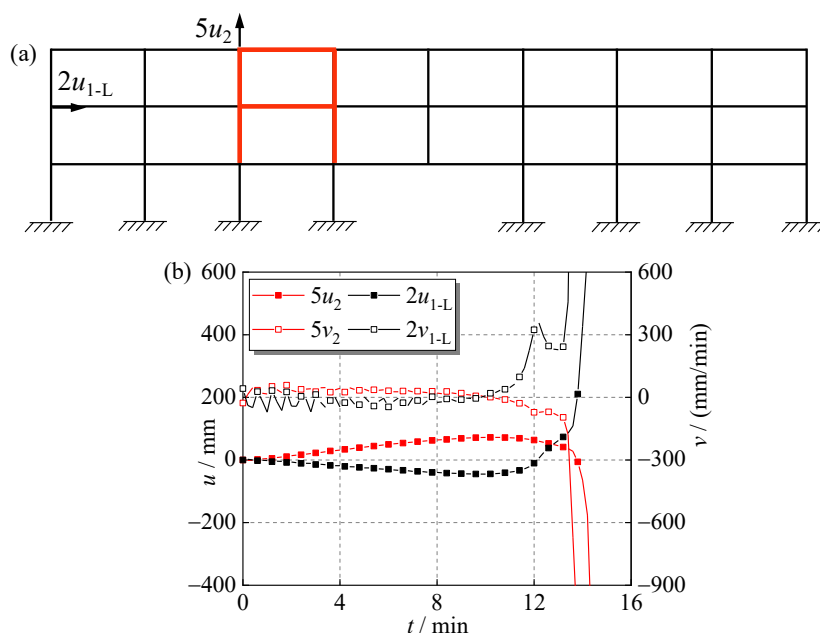


Figure 5. A typical fire case of the partial lateral collapse. (a) Fire area. (b) Displacement and velocity-time curves

2.3 Graded early-warning algorithms

Characteristic points with significant numerical and physical meanings (such as some extreme points or threshold points) on the evolution law curves will be selected as early-warning points. According to the order in which early-warning points appear, three early-warning levels can be established to evaluate the current collapse state of the structure under fire, in which a higher early-warning level indicates the structure is closer to collapse. Using general inward collapse and local lateral collapse as illustrations, the relevant definitions for early-warning points and levels are presented in Table 1, Table 2, Figure 6, and Figure 7, in which $u_{2,i}$ denote the vertical displacement of the i th key joint, which shows significant values among all vertical joint displacements corresponding to heated columns. Similarly, $u_{1,j}$ denotes the horizontal displacement of the j th key joint, which presents significant values among all horizontal joint displacements corresponding to the heated floors involved in the fire. $v_{2,i}$ and $v_{1,j}$ are the velocity curves of $u_{2,i}$ and $u_{1,j}$, respectively.

Table 1. Definitions of early-warning points and levels for the general inward collapse

Early-warning level	Judgment criterion	Early-warning points
1st level	Occurrence of point A	A : $u_{2,p}$ reaches its peak upwards
		B : $u_{2,p}$ returns to 0
		C : $ v_{2,i} $ exceeds 5 times $v_{2,i,OP}$
		D : $ v_{2,i} $ exceeds 10 times $v_{2,i,OP}$
2nd level	Occurrence of point B or C	E : $v_{1,j}$ exceeds 10 times $ v_{1,j,OQ} $
		O : $t = 0$
3rd level	Occurrence of point D or E	P_i : $u_{2,i}$ reaches its peak upwards
		Q_j : $u_{1,j}$ reaches its peak outwards

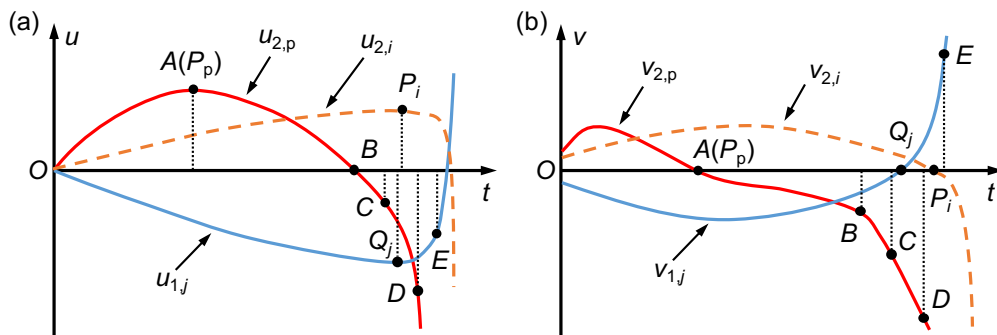


Figure 6. Graph illustration for the early-warning points of the general inward collapse

Table 2. Definition of three early-warning levels for the local lateral collapse

Early-warning level	Judgment criterion	Early-warning points
1st level	Occurrence of any point among points A , B , and C	A : $u_{2,p}$ reaches its peak upwards
		B : $v_{1,j}$ exceeds 5 times $ v_{1,j,OQ} $
		C : $u_{1,j}$ returns to 0
2nd level	Occurrence of any two points among points A , B , and C	D : $ v_{2,i} $ exceeds 10 times $v_{2,i,OP}$
		E : $v_{1,j}$ exceeds 10 times $ v_{1,j,OQ} $
		O : $t = 0$
		P_i : $u_{2,i}$ reaches its peak upwards
3rd level	Occurrence of point D or E	Q_j : $u_{1,j}$ reaches its peak outwards

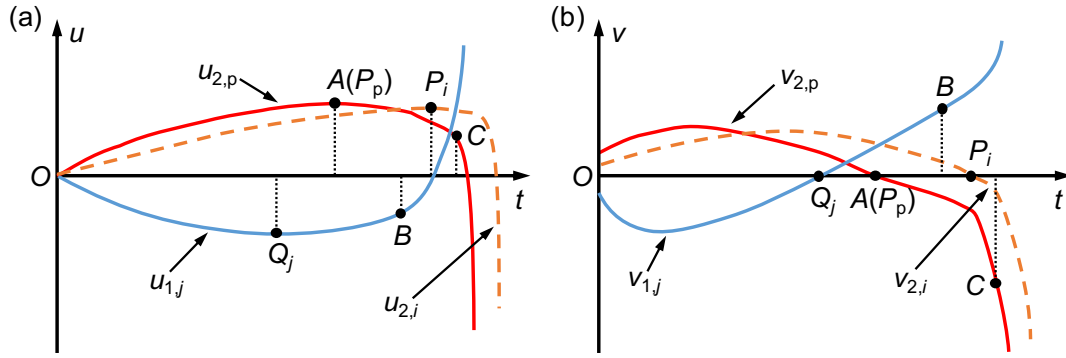


Figure 7. Graph illustration for the early-warning points of the local lateral collapse

In addition to the real-time assessment of the structural collapse state according to different early-warning levels as introduced above, it is more important to predict the remaining time to building collapse. To eliminate the impact of the absolute collapse duration (differing under various structural and fire parameters) on the early-warning results and make the proposed early-warning methods more widely applicable, the dimensionless remaining time ratio at the γ th early-warning level $\tau^{(\gamma)}$ [11,12] is defined as the ratio of the remaining time to collapse $t_{\text{collapse}}^{(\gamma)}$ to the occurrence time of the γ th early-warning level t_γ :

$$\tau^{(\gamma)} = \frac{t_{\text{collapse}}^{(\gamma)}}{t_\gamma} \quad (1)$$

where $\gamma = 1, 2, 3$ represents the early-warning level. The graph explanation for t_γ and $t_{\text{collapse}}^{(\gamma)}$ is shown in Figure 8.

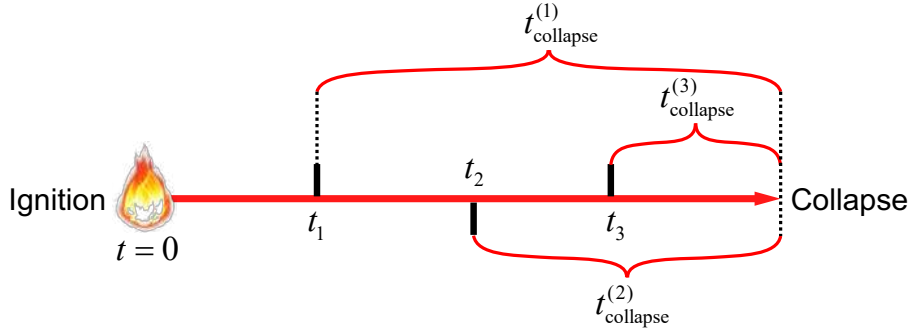


Figure 8. Explanations for t_γ and $t_{\text{collapse}}^{(\gamma)}$

Actually, the remaining time ratio varies under different structural parameters and fire scenarios. $\tau^{(\gamma)}$ represents a general graded early-warning index with reliability significance based on the reliability theory obtained from statistical analysis under various parameters [11,12]. Using $\tau^{(\gamma)}$ and the occurrence time of the γ th early-warning level t_γ , the remaining time to collapse $t_{\text{collapse}}^{(\gamma)}$ can be calculated. In this way, the predicted remaining time to collapse should be more accurate and reliable compared to existing experience-based methods.

2.4 Recognition of collapse mode

However, the above algorithms can be applied in real-life fire only after the actual structural collapse mode is determined. Differences in the evolution laws of KMPPs between various collapse modes, as introduced in Section 2.2, can exactly be utilized to recognize the fire-induced collapse mode. The mode recognition algorithm between the general inward collapse and local lateral collapse is presented as follows:

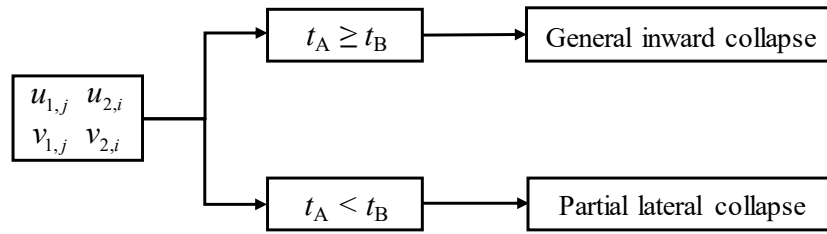


Figure 9. Mode recognition algorithm for the general inward collapse and local lateral collapse

where t_A is the time when $v_{1,j}$ (inwards) exceeds 5 times $|v_{1,j,0Q}|$ firstly, and t_B is the time when $|v_{2,i}|$ exceeds 5 times $v_{2,i,OP}$ firstly. The meanings of other symbols can be found in Figure 7 and Figure 8.

3 PRACTICAL APPLICATION PROCESS OF THE EARLY-WARNING METHOD

As demonstrated in Figure 10, when the proposed early-warning method is applied in a real fire, the required KMPPs-time data will be measured on site and transferred to the early-warning platform in real time first. After accepting relevant data, the embedded mode recognition algorithm in the platform will identify the actual collapse mode based on the evolution laws of KMPPs for different collapse modes. Then, the specific graded early-warning algorithm aimed in the recognized mode will issue three-level early-warning signals in sequence, and predict the corresponding remaining collapse time at each level. Subsequently, this crucial early-warning information will be sent to firefighters at the fire scene to make more accurate, scientific, and efficient rescue decisions to reduce casualties as much as possible.

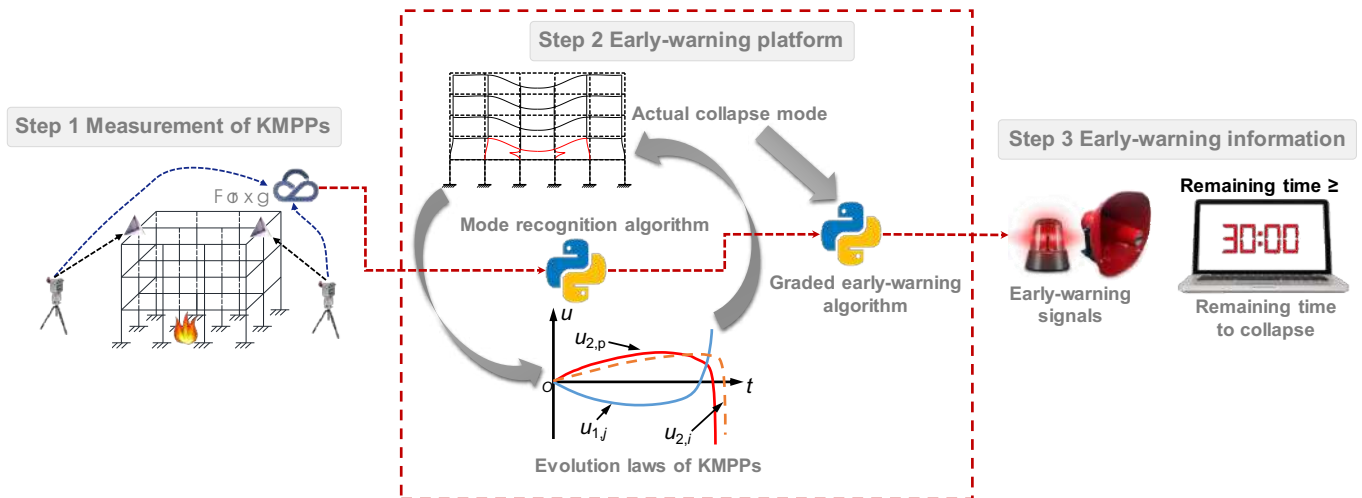


Figure 10. Practical early-warning process

4 TEST VERIFICATION

The real fire-induced collapse test of a planar steel frame structure [18] is used to verify the effectiveness of the proposed early-warning framework for predicting the remaining time to collapse. The two-story, four-span planar steel frame with one column heated is presented in Figure 11. Seamless rectangular steel pipe sections are used for the columns and beams. The section of all steel columns is $50 \times 30 \times 3$ (mm), and the section of all steel beams is $60 \times 40 \times 3.5$ (mm). The loads are applied to the frame in the form of mass blocks, and there are three mass blocks on each span. More detailed information on the test can refer to the original paper.

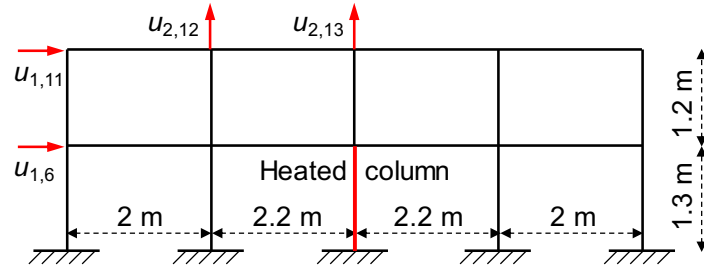


Figure 11. Fire-induced collapse test of a planar steel frame [18]

According to the KMPP-time curves shown in Figure 12 and the mode recognition algorithm depicted in Figure 9, the general inward collapse mode can be identified for this case. Then, based on the early-warning algorithms specifically established for this mode, the predicted results for the remaining time to collapse at each early-warning level with 80% reliability significance can be obtained as tabulated in Table 3. It can be seen that the predicted remaining time to collapse matches well with the measured values for all three early-warning levels, and the predicted value in the final third early-warning level is slightly less than the measured value, which indicates a relatively safe prediction result. These results prove the feasibility and accuracy of the proposed early-warning method to a certain extent.

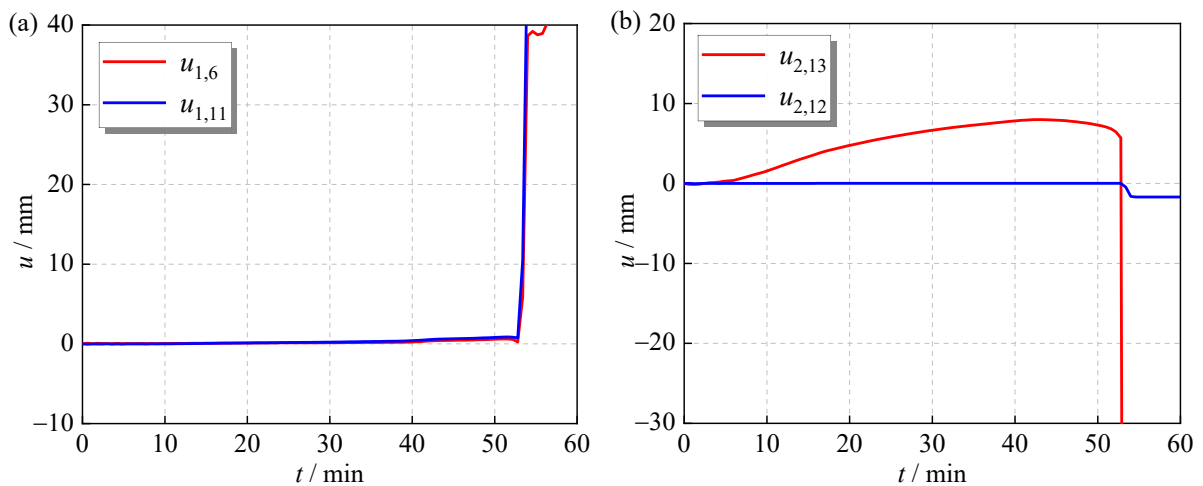


Figure 12. Key displacement-time curves of the test frame

Table 3. Comparisons between measured and predicted remaining time to collapse

Remaining time	1st level	2nd level	3rd level
Measured	910 s	370 s	334 s
Predicted	1044 s	359 s	231 s

5 CONCLUSIONS

The following conclusions can be summarized as follows through this study:

- 1) An overall early-warning framework of fire-induced collapse for planar multi-story steel frame structures based on collapse modes as well as collapse mechanisms, selections and evolution laws of KMPPs, and graded early-warning algorithms, is proposed to identify the structural collapse mode, evaluate the structural collapse state, and early warn the structural remaining time to collapse.
- 2) The practical early-warning process is presented through the real fire test of a planar steel frame, proving the feasibility and accuracy of the proposed early-warning framework with the accurate recognition of the structural collapse mode and a relatively safe predicted value of the remaining time to collapse with 80% reliability significance compared to the measured value at the final third early-warning level.
- 3) In the future, more real fire tests will be supplemented to improve the accuracy and verify the feasibility of the proposed fire-induced collapse early-warning framework. At the same time, the extension of the existing early-warning framework based on the planar frame structures to actual three-dimensional frame structures will be further explored.

ACKNOWLEDGMENT

The authors gratefully acknowledge the financial support provided by the Shanghai Pujiang Program under grant No. 22PJ1414000.

REFERENCES

1. Usmani, A.S., Chung, Y.C., Torero, J.L., How did the WTC towers collapse: a new theory. *Fire Saf. J.* 38(6), 501–533 (2003). [https://doi.org/10.1016/S0379-7112\(03\)00069-9](https://doi.org/10.1016/S0379-7112(03)00069-9).
2. Usmani, A.S., Stability of the World Trade Center Twin Towers structural frame in multiple floor fires. *J. Eng. Mech.* 131(6), 654–657 (2005). [https://doi.org/10.1061/\(ASCE\)0733-9399\(2005\)131:6\(654\)](https://doi.org/10.1061/(ASCE)0733-9399(2005)131:6(654)).
3. Lange, D., Röben, C., Usmani, A.S., Tall building collapse mechanisms initiated by fire: Mechanisms and design methodology. *Eng. Struct.* 36, 90–103 (2012). <https://doi.org/10.1016/j.engstruct.2011.10.003>.
4. Sun, R.R., Huang, Z.H., Burgess, I., Progressive collapse analysis of steel structures under fire conditions. *Eng. Struct.* 34, 400–413 (2012). <https://doi.org/10.1016/j.engstruct.2011.10.009>.
5. Jiang, B., Li, G.Q., Usmani, A.S., Progressive collapse mechanisms investigation of planar steel moment frames under localized fire. *J. Constr. Steel Res.* 115, 160–168 (2015). <https://doi.org/10.1016/j.jcsr.2015.08.015>.
6. Jiang, J., Li, G.Q., Disproportionate collapse of 3D steel-framed structures exposed to various compartment fires. *J. Constr. Steel Res.* 138, 594–607 (2017). <https://doi.org/10.1016/j.jcsr.2017.08.007>.
7. Jiang, J., Li, G.Q., Usmani, A.S., Effect of bracing systems on fire-induced progressive collapse of steel structures using OpenSees. *Fire Technol* 51, 1249–1273 (2015). <https://doi.org/10.1007/s10694-014-0451-0>.
8. Lv, J.L., Dong, Y.L., Sun, J.D., Effect of fire on self-excited vibration characteristic of composite beams of the overall structure. *Appl. Mech. Mater.* 105, 760–764 (2012). <https://doi.org/10.4028/www.scientific.net/AMM.105-107.760>.
9. Ye, Z., Hsu, S.C., Wei, H.H., Real-time prediction of structural fire responses: A finite element-based machine-learning approach. *Autom. Constr.* 136, 104165 (2022). <https://doi.org/10.1016/j.autcon.2022.104165>.
10. Jiang S., Zhu, S., Guo, X., Chen, C., Li, Z., Safety monitoring system of steel truss structures in fire. *J. Constr. Steel Res.* 172, 106216 (2020). <https://doi.org/10.1016/j.jcsr.2020.106216>.
11. Ji, W., Li, G.Q., Lou, G.B., Early-warning methods for fire-induced collapse of single span steel portal frames. *J. Constr. Steel Res* 190, 107154 (2022). <https://doi.org/10.1016/j.jcsr.2022.107154>.
12. Ji, W., Zhu, S., Li, G.Q., Lou, G.B., Jiang. S., Approach for early-warning collapse of double-span steel portal frames induced by fire. *Fire Saf. J.* 131, 103628 (2022). <https://doi.org/10.1016/j.firesaf.2022.103628>.

13. Li, G.Q., Li, J., Zhu, S., An approach for early-warning collapse of planar steel trapezoid trusses exposed to fire. *Fire Saf. J.* 137, 103778 (2023). <https://doi.org/10.1016/j.firesaf.2023.103778>.
14. European Committee for Standardization. EN 1993-1-2: Design of steel structures, Part 1-2: general rules - structural fire design. Brussels: European Committee for Standardization, 2005.
15. Malvar, L.J., Review of static and dynamic properties of steel reinforcing bars. *Mater. J.* 95(5), 609–616 (1998). <https://doi.org/10.14359/403>.
16. Johnson, G.R., Cook, W.H., A constitutive model and data for metals subjected to large strains, high strain rates and high temperatures. *Eng. Fract. Mech.* 21, 541–548 (1983).
17. Cowper, G.R., Symonds, P.S., Strain-hardening and strain-rate effects in the impact loading of cantilever beams. *Small Bus. Econ.* (1957).
18. Jiang, B., Li, G.Q., Li, L., Izzuddin, B.A., Test studies on progressive collapse resistance of steel moment frames under localized furnace loading. *J. Struct. Eng.* 144(2) 04017190. (2018) [https://doi.org/10.1061/\(ASCE\)ST.1943-541X.0001947](https://doi.org/10.1061/(ASCE)ST.1943-541X.0001947).

GUIDANCE FOR INCORPORATING HIGH-TEMPERATURE CREEP IN FIRE-INDUCED PROGRESSIVE COLLAPSE OF STEEL-FRAMED BUILDINGS

Svetha Venkatachari¹, Venkatesh Kodur²

ABSTRACT

High-temperature creep poses a significant risk to the stability of steel structures, particularly when steel temperatures surpass 400°C. It is crucial to adequately address this phenomenon in fire resistance analyses. This paper offers various design approaches to accommodate high-temperature creep in the analysis of steel-framed structures. The first approach, termed the 'creep-not-critical' scenario, suggests disregarding temperature-induced creep strain in structural members experiencing low-stress levels and sectional temperatures. In the 'creep-implicit' scenario, where temperature-induced creep strain is moderate, it can be implicitly integrated into the analysis. For situations where creep is substantial, such as high-stress levels and sectional temperatures, explicit incorporation of creep into the fire resistance analysis is imperative ('creep-explicit' scenario). The feasibility of these approaches in addressing creep in fire resistance analyses is demonstrated through three case studies involving steel-framed structures at various complexity levels.

Keywords: Fire resistance; high-temperature creep; steel structures; progressive collapse; design recommendations

1 INTRODUCTION

The surge in urban population in major cities globally, coupled with limited available space, has led to a growing trend of embracing high-rise buildings as a practical solution. Steel framing is widely adopted in these high-rise structures owing to the enhanced strength, stiffness, and ductility properties of steel. However, steel-framed buildings are more vulnerable in the event of a fire disaster, as steel structures can experience high levels of temperature-induced instability at section, member, or global levels, and under severe fires, this can lead to the progressive collapse of the structure. While significant advances have been made in modelling techniques over the past few decades to evaluate progressive collapse in high-rise buildings under extreme loading events such as blasts, impact, and earthquakes, progressive collapse is not specifically evaluated under fire hazards in most scenarios. This is mainly due to the limited guidance in the current codes and standards, as well as in the literature, for tracing the fire-induced progressive collapse in steel-framed structures.

Progressive collapse under fire conditions depends on several factors including the severity of fire exposure, the extent of burning, steel material properties at elevated temperatures, connection configurations, framing type, and load level [1–3]. Moreover, steel members experience significant creep deformations at elevated temperatures, and thus, high-temperature creep can be more critical to the stability of a fire-exposed steel structure leading to a progressive collapse in severe cases [4]. Several numerical studies have been carried out in the past to determine the fire resistance of steel-framed structures. In many of these studies, high-temperature creep effects in steel are either neglected or considered implicitly through stress-strain relations,

¹ Assistant Professor, Department of Civil Engineering, Indian Institute of Technology Delhi
e-mail: svethav@civil.iitd.ac.in, ORCID: <https://orcid.org/0000-0001-6385-5813>

² University Distinguished Professor, Department of Civil and Environmental Engineering, Michigan State University
e-mail: kodur@egr.msu.edu, ORCID: <https://orcid.org/0000-0003-2058-2725>

such as the Eurocode 3 (EC3) [5] relations. However, such an implicit treatment of transient creep does not capture the full extent of creep deformations that develop under severe fire exposure scenarios [6–8].

Very few studies have considered the high-temperature creep strain explicitly in the analysis. Kodur and Dwaikat [6] evaluated the effect of high-temperature creep on the fire response of restrained beams by explicitly accounting for the high-temperature creep strain using the ANSYS finite element software. This study showed that the load level, heating rate, fire scenario, and fire-induced axial restraint significantly affect the extent of creep deformations that develop at elevated temperatures. Li and Zhang [9] studied the high-temperature creep effects in axially restrained steel columns by using the ANSYS creep model developed by Kodur and Dwaikat [6] to include the creep strains explicitly. The study showed that neglecting creep effects can lead to unrealistic critical buckling temperatures in steel columns subjected to varying levels of axial restraint and heating rates.

Morovat et al. [7] carried out experimental and numerical investigations on steel columns subjected to varying stress and temperature levels. The study indicated that transient creep has a significant influence on the strength (capacity) of steel columns and that the critical buckling load depends not only on the slenderness and temperature level but also on the duration of the applied load. Results showed that the AISC [10] and EC3 [5] predictions underestimate the buckling strength of columns when compared to the test values, especially at steel temperatures above 600°C. Hantouche et al. [11] developed a numerical model in ABAQUS incorporating the creep effects explicitly to study the behavior of a shear tab connection assembly under steady-state and transient heating conditions. The results showed that transient heating scenarios with a slower heating rate and longer cooling durations can lead to high creep deformations.

Recently, Venkatachari and Kodur [4] developed an advanced finite element-based approach in ABAQUS to explicitly account for the high-temperature creep effects in the fire-induced progressive collapse analysis of steel-framed structures. The high-temperature creep strains are accounted for using the Power Law Creep model in ABAQUS. Results from the study indicated that high-temperature creep effects influence the onset of instabilities (and collapse) in a steel-framed structure under severe fire exposure and high-loading (stress) scenarios. The analysis approach presented above yields realistic fire resistance predictions for steel structures; however, such an analysis is highly complex especially when the effects of high-temperature creep are to be considered explicitly at a system level for tracing fire-induced collapse. Thus, the question is in determining when high-temperature creep effects are to be considered in the fire resistance analysis. Depending on the extent of high-temperature creep in a given fire, loading, and restraint scenario, design recommendations are provided in this paper for the treatment of creep in member and system-level analysis.

2 APPROACH FOR INCORPORATING HIGH-TEMPERATURE CREEP IN FIRE-INDUCED PROGRESSIVE COLLAPSE ANALYSIS

2.1 General

A generic approach for accounting for high-temperature creep in the fire resistance analysis of steel-framed structures, and specifically to trace the progressive collapse under fire conditions, is outlined in this section. Accounting for creep through implicit and explicit approaches is discussed in detail.

2.2 Numerical model

For undertaking advanced analysis for tracing the onset of fire-induced instabilities leading to the progressive collapse of a steel-framed building, the use of finite element-based programs such as ABAQUS, ANSYS, etc. is required. The fire-induced progressive collapse analysis involves a three-step procedure. The first step involves determining fire scenarios to be considered for the progressive collapse analysis. At present, in the fire resistance calculations, the fire temperatures are traced using standard or parametric temperature-time relations specified in ASTM E119 [12], ASTM 1529 [13], ISO 834 [14], and Eurocode 1 [15]. Alternatively, for a more realistic evaluation of fire scenarios based on the building characteristics, fuel loads, functions in a building, available fire protection systems, etc., recommendations provided in the SFPE Handbook [16] can be utilized to obtain design fire scenarios for buildings.

In the second step, thermal analysis of the fire-exposed steel members is to be carried out to obtain the cross-sectional temperatures in each member as a function of fire exposure time. The cross-section of the fire-exposed steel member and the associated insulation is discretized using 4-noded quadrilateral elements with temperature as the degree of freedom at each node. The heat transfer from the fire source to the boundary of the structural member is simulated using convection and radiation-type boundary conditions and the heat transfer within the member occurs through conduction. The temperature variation with fire exposure time is obtained at specific nodes in the member cross-section, which subsequently is integrated during the structural analysis for the beam elements. Temperature-dependent thermal property relations specified in EC3 [5] are given as input to the thermal model. Insulation properties are assumed as per [17]. The final (third) step involves the structural analysis of the steel-framed structure at ambient and elevated temperature conditions. In this step, the framing members in the building are discretized using 2-noded beam elements, having six degrees of freedom at each node, i.e., three translations and three rotations. The connections between different members and support conditions in the building are modelled through specified joint constraints and boundary conditions. Partition walls are not considered in the structural model. Two loading sequences are used in the structural analysis. First, the gravity loads, which are obtained as $1.2 \text{ DL} + 0.5 \text{ LL}$ (where DL and LL represent the dead load and live load respectively), and notional lateral loads, evaluated as 0.2% of gravity loading on that floor, are applied gradually to the steel framed building. Second, sectional temperatures obtained as output from the thermal analysis are applied to the fire-exposed members as predefined temperature fields. Temperature-dependent mechanical property relations for steel, as specified in EC3, are given as input to the structural model.

When assigning the stress-strain data for steel in the structural analysis, it is to be specified whether high-temperature creep is accounted for implicitly or explicitly. Further details of the creep model are given in the subsequent section. The progression of instability in the steel-framed structure is to be traced continuously throughout the fire exposure (including the cooling phase) by carrying out a nonlinear quasi-static analysis. The response parameters, including stresses and displacements, are to be traced at various points in the structure including all the fire-exposed members, compartments adjoining the fire compartments, at different floor levels, etc. to trace the progression of instabilities in the building. At each time step, these values are used to check for failure at the member or system level based on the limiting strength and displacement-based failure criteria. A flowchart showing various steps in the analysis regime for evaluating the fire-induced progressive collapse in a steel-framed building is presented in Figure 1.

Further details of the numerical model and validation of this approach against experimental data are given in [4].

2.3 Incorporation of high-temperature creep in the advanced analysis

High-temperature creep in steel can be accounted for in the numerical analysis through one of the two following options. The first option is to account for transient creep effects implicitly wherein only the temperature-induced transient creep strains built into the stress-strain relations of steel (such as the EC3 [5] relations) are automatically incorporated into the analysis. The EC3 [5] stress-strain relations were derived based on transient tests under slow heating rates [18]. In these relations, part of the transient creep strain is included in the resulting temperature-dependent stress-strain curves by underestimating the stress causing the plastic strain in the steel specimen [18]. However, this implicit creep strain includes only primary creep and part of the secondary creep that develops in the early stages of fire exposure. Much of the creep strain that develops beyond steel temperatures of 400°C under prolonged fire exposure, which tends to be governed by secondary and tertiary creep effects, is not accounted for in the EC3 [5] stress-strain relations [6,7]. Moreover, creep strains vary significantly with time, and stress and temperature also vary with time, i.e., duration of fire exposure [6]. Since no explicit calculation of creep strain for a given duration (both absolute time and rates), stress, and temperature level is involved, the implicit creep model (as in the case of EC3 stress-strain relations) does not account for much of the temperature-induced creep strain, particularly close to the failure of a member when stress and temperature levels are high [4]. It should be noted that accounting for secondary and tertiary creep strains is critical for tracing the onset of global instability and thus the progressive collapse of structures.

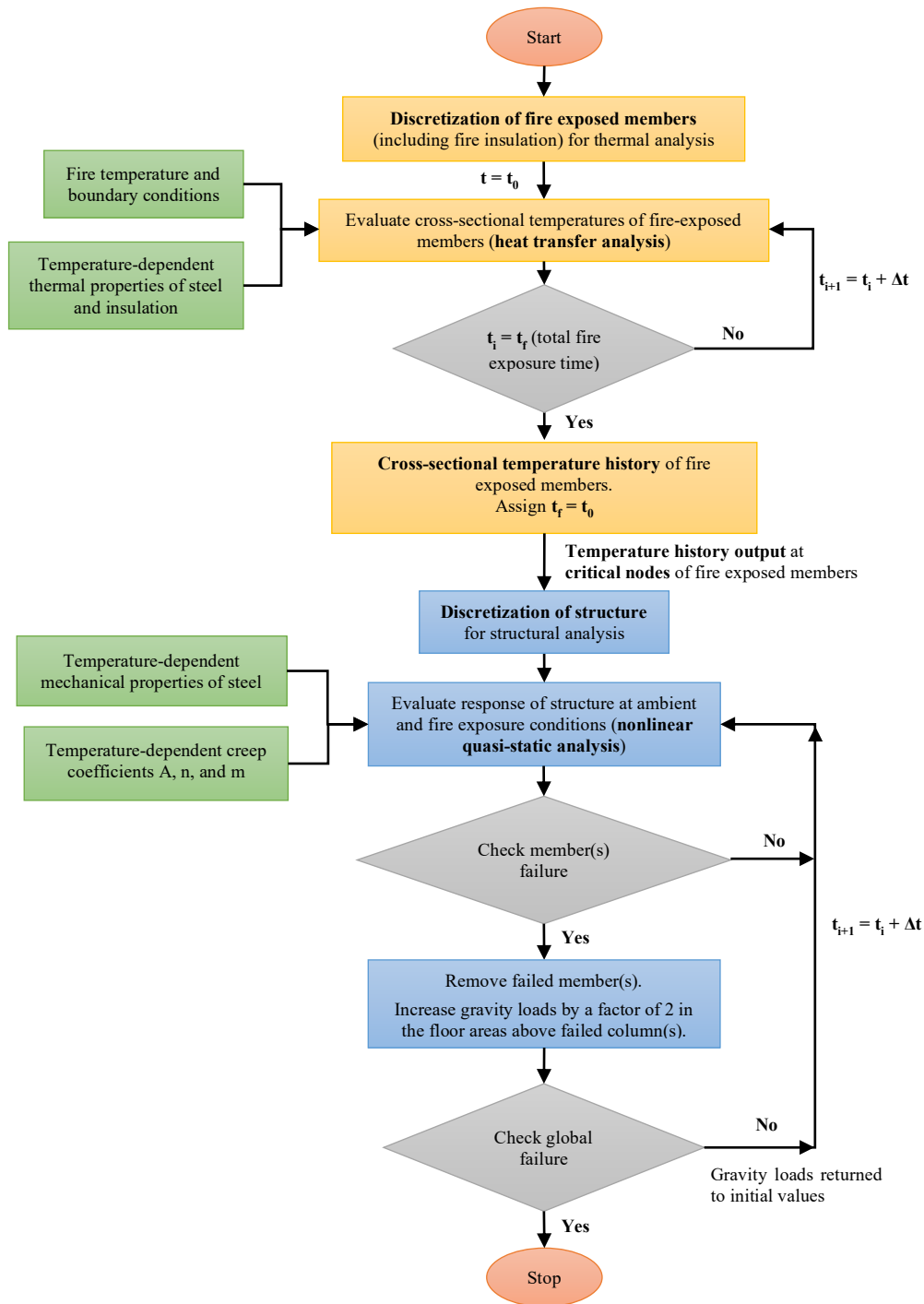


Figure 1. Flowchart illustrating the steps in the fire-induced progressive collapse analysis using the nonlinear quasi-static analysis approach

The second option to account for high-temperature creep effects involves an explicit definition of the full extent of transient creep strain that develops at elevated temperatures through a separate creep model. The built-in creep power law in ABAQUS is used to evaluate the transient creep strain at each time increment for specified stress and temperature levels in this paper. However, other approaches, including the use of a user-defined sub-routine for specifying the creep relations at elevated temperatures can also be adopted. At each time step, the total strain in steel at any given stress and temperature levels is calculated as a linear summation of mechanical, thermal, and creep strain in ABAQUS, as shown in equation (1). The mechanical strain (which includes the elastic and plastic strains) and thermal strain are computed using the constitutive

relations and the expansion coefficient respectively at various temperatures, whereas the transient creep strain is evaluated using the specified creep relations for a given stress and temperature level.

$$\Delta\bar{\epsilon} = \Delta\bar{\epsilon}^{el} + \Delta\bar{\epsilon}^{pl} + \Delta\bar{\epsilon}^{th} + \Delta\bar{\epsilon}^{cr} \quad (1)$$

in which $\Delta\bar{\epsilon}$ is the total strain increment and $\Delta\bar{\epsilon}^{el}$, $\Delta\bar{\epsilon}^{pl}$, $\Delta\bar{\epsilon}^{th}$, and $\Delta\bar{\epsilon}^{cr}$ are the strain components, namely, elastic, plastic, thermal, and creep strain increments respectively.

3 GUIDANCE FOR THE TREATMENT OF CREEP IN FIRE RESISTANCE ANALYSIS

The above-discussed analysis approach is effective in capturing the high-temperature creep effects in the fire-induced progressive collapse of steel-framed buildings, particularly when the creep strains are explicitly included in the analysis. However, such an approach is complex and may not be practical to be applied to every scenario. Hence, recommendations are presented in this section under three scenarios, namely, scenarios where creep effects are minimal and need not be considered, scenarios where implicit treatment of creep through temperature-dependent stress-strain relations is sufficient, and scenarios where explicit consideration of high-temperature creep is required.

3.1 Scenarios where high-temperature creep effects are not critical

Under many practical fire exposure scenarios in a steel-framed building, high-temperature creep effects are minimal and might not govern the onset of instability in a steel member or the building. The fire resistance evaluation of steel structures in current codes and standards is based on simplified approaches that do not give any consideration to transient creep strain in steel. The scenarios where creep effects need not be accounted for in the fire resistance analysis of steel structures are given below:

- When the failure of a steel member is likely to be governed by a force-controlled (strength) limit state rather than deformation-controlled actions (e.g., stub columns), neglecting the transient creep effects does not affect the evaluation of the degraded (reduced) capacity and thus, the fire resistance of the member.
- When the sectional temperatures in a steel member do not exceed 400°C under service stress levels (< 50%), the transient creep strains that develop in the steel member are very minimal and hence can be neglected for the evaluation of fire resistance. E.g., protected steel members exposed to low to moderate design fire scenarios (with peak fire temperatures lower than 800°C and lasting only for 1 to 2 h of duration). Examples of this type of fire scenario are office buildings, apartment buildings, low-rise buildings, etc.

3.2 Scenarios where implicit creep is sufficient

Under certain cases of fire exposure, accounting for transient creep effects implicitly in the fire resistance analysis is sufficient to capture the onset of instability at member and system levels. These scenarios are summarized as follows:

- In unprotected steel members, the steel temperature increases rapidly and the time to failure is low (around 20 to 30 minutes for typical steel columns). Under such short duration and rapid heating rates, the temperature-induced creep deformations tend to be low even under moderate to severe fire exposure scenarios, and hence an implicit consideration of high-temperature creep is sufficient.
- When the average sectional temperature in a protected steel member does not exceed creep critical temperature under service stress levels (< 50%), implicit consideration of creep is sufficient. For a given stress level, the creep critical temperature is defined as the temperature that corresponds to the onset of tertiary creep in steel. Examples of this case are composite floor systems, where the steel beam is connected to a concrete slab. In this case, the sectional temperatures in the beam (near the top flange) tend to be low due to the heat sink effect from concrete.
- In steel columns with slenderness lower than 50 and subjected to low-stress levels (< 40%), the transient creep strain that develops at elevated temperatures is low even under scenarios of moderate to severe fire exposure, and thus implicit creep is sufficient.

- In steel framed buildings, the damage is expected to be minimal when the burning is within one or two compartments on a floor (for instance, less than 20% of the floor area is subjected to fire in a ten-story building). In such cases, the creep deformations are not likely to be critical for the onset of progressive collapse and can be considered implicitly in the FE analysis.

3.3 Scenarios where high-temperature creep is to be considered explicitly

Based on the parametric studies carried out on steel framed structures (refer to [4]), the transient creep effects were found to be significant under conditions of severe fire exposure (with peak fire temperatures reaching beyond 1000°C and lasting for more than 2 h), high loading (stress) scenarios (of 50% and above), and large extents of burning (for example, burning in multiple compartments or floors). In such scenarios, creep deformations are critical to the onset of fire-induced collapse in steel-framed buildings and thus, need to be explicitly incorporated into the fire resistance analysis.

In Figure 2, the average sectional temperatures in a protected W14x53 column (fire rating of 2 h) are plotted under two standard fire scenarios, namely ASTM E119 [12] and ASTM E1529 [13] hydrocarbon, and one design fire exposure scenario, DF-90, with a burning duration of 90 min. Since steel develops only marginal creep strains below 400°C, temperatures below this value are to be considered creep-safe temperatures. When the sectional temperatures rise above 400°C, the creep strain rate increases rapidly and moderate to large creep deformations can occur in the steel column depending on the applied load level. Also, it is evident from Figure 2 that fires with different severity require different times to reach such high temperatures and thus induce creep strains at a rapid pace.

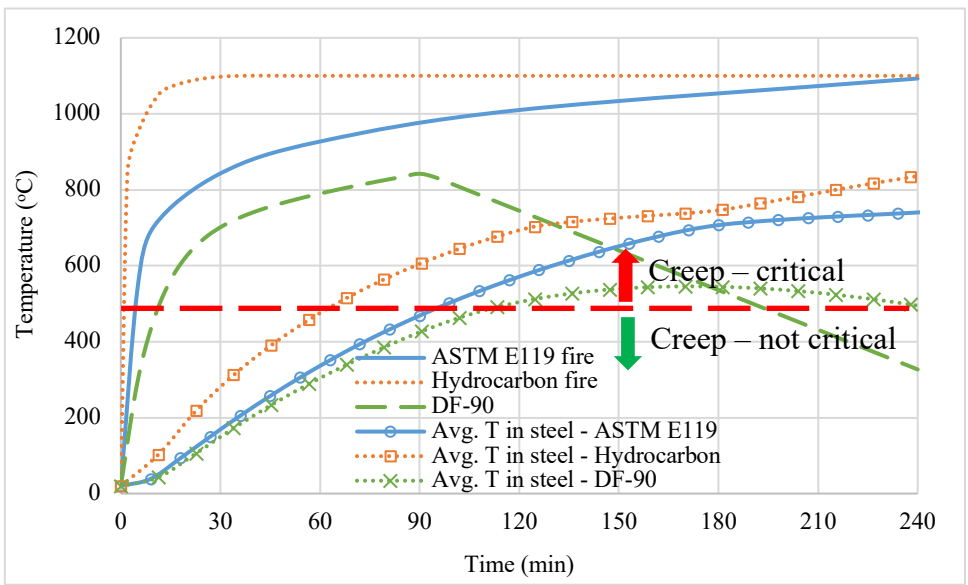


Figure 2. Average sectional temperatures in a steel column (W14x53) under different fire exposure scenarios

In general, the time at which high-temperature creep effects become dominant can be determined based on the time taken for the average temperatures in the steel section to reach the *creep critical temperature*. These *creep critical temperatures* are presented in Table 1 for A992 (Grade 50) steel at different stress levels. These temperatures are evaluated based on the creep test data reported by Morovat et al. [19] for A992 steel at elevated temperatures. For each stress level, the temperature corresponding to the onset of tertiary creep is taken as the *creep critical temperature*. This method of utilizing the *creep critical temperature* to evaluate the extent of creep effects can also be extended to other fire-exposed steel members such as braces and axially restrained beams, which can experience a high level of compression loading. If the average temperatures in these steel members reach the critical temperature as specified in Table 1 for a given stress level, then the creep deformations are more likely to dominate the fire response and need to be considered explicitly through advanced analysis approaches.

Table 1. Creep critical temperatures for A992 steel at different stress levels

Stress level %	Critical Temperatures (°C)
20	640
30	585
40	550
50	525
60	500
70	450
80	400

At a structural level, creep deformations can be critical for predicting the onset of progressive collapse in a steel framed building depending on the severity of fire exposure, burning location, and extent of fire spread. To identify the level of influence that high-temperature creep has on the onset of instability at a structural level, the extent of creep is again classified under three categories: ‘minor’, ‘moderate’, and ‘severe’ based on the severity of fire exposure and extent of burning in a single floor (as shown in Table 2) and in multiple floors with at least 2 compartments (10% floor area) burning in one floor (as shown in Table 3). These recommendations are based on the results of analyses carried out on a braced framed building comprising ten stories and five bays in which the steel members were provided with a 2 h fire rating (based on office occupancy).

Table 2. Extent of creep in steel framed buildings based on fire severity and extent of burning on a single floor

Extent of burning on a single floor	Fire severity		
	Low severity ($T_{\text{peak}} < 800^{\circ}\text{C}$ & duration < 1 h)	Moderate severity ($800^{\circ}\text{C} < T_{\text{peak}} < 1000^{\circ}\text{C}$ & duration of 1-2 h)	High severity ($T_{\text{peak}} > 1000^{\circ}\text{C}$ & duration > 2 h)
< 20%	Minor	Minor	Moderate
20 – 40%	Minor	Moderate	Severe
> 40%	Moderate	Severe	Severe

Table 3. Extent of creep in steel framed buildings based on fire severity and extent of burning on multiple floors

Extent of burning on multiple floors	Fire severity		
	Low severity ($T_{\text{peak}} < 800^{\circ}\text{C}$ & duration < 1 h)	Moderate severity ($800^{\circ}\text{C} < T_{\text{peak}} < 1000^{\circ}\text{C}$ & duration of 1-2 h)	High severity ($T_{\text{peak}} > 1000^{\circ}\text{C}$ & duration > 2 h)
2 floors or less	Minor	Minor	Moderate
3 to 4 floors	Minor	Moderate	Severe
5 floors or more	Moderate	Severe	Severe

It is evident from Table 2 and Table 3 that as the extent of fire spread increases either within a single story or to multiple floors, the severity of creep increases even for low to moderate fire severity. These results are obtained for a ten-story steel framed building with steel members having a 2 h fire rating. For other typical steel framed buildings of similar size and fire resistance rating, the fire severity and extent of burning can be utilized to determine the influence of creep deformations towards the onset of fire-induced collapse.

A summary of the above discussion is presented below.

- When the average sectional temperature in a protected steel column exceeds the *creep critical temperature* as specified in Table 1 for A992 steel at different stress levels, transient creep strain highly influences the onset of instability in the column and hence, the predicted fire resistance.
- For columns with high slenderness (> 50) and/or subjected to high load (stress) levels of 40% or higher, creep effects can be critical.
- When columns are subjected to non-uniform fire exposure (2- or 3-sides), high-temperature creep effects on the onset of instability in the column can be significant.
- Creep effects can be significant when a steel framed building is exposed to severe to very intense fire exposure (peak temperatures exceeding 1000°C and burning for more than 2 h) in 20% of the floor area or more.
- When the extent of fire spread in a single floor of a steel-framed building exceeds 20% of the floor area, large creep deformations are likely to occur, and explicit consideration of creep is required.
- Creep effects can be critical when the fire spreads to more than two stories in a steel-framed building with at least 10% of the floor area subjected to burning on each floor.

The above-discussed recommendations for the treatment of creep in the fire resistance analysis of steel structures are summarized in Table 4 under three categories: ‘*creep-not critical*’, ‘*creep-implicit*’, and ‘*creep-explicit*’.

Table 4. Treatment of high-temperature creep in fire resistance analysis of steel structures

Creep-not critical	Creep-implicit	Creep-explicit
<ol style="list-style-type: none"> 1. When failure of a steel member is evaluated based on strength limit state consideration. 2. When the sectional temperatures in a steel member do not exceed 400°C under service stress levels ($< 50\%$). 3. When fire scenarios are low to moderate ($T < 800^\circ\text{C}$ and duration < 1 h). 	<ol style="list-style-type: none"> 1. In unprotected steel members. 2. When the average sectional temperatures in a protected steel member do not exceed the <i>creep critical temperature</i> under service stress levels ($< 50\%$). 3. For columns with slenderness lower than 50 and lightly loaded (stress level $< 40\%$). 4. For steel framed buildings exposed to moderate fire exposure with burning in one or two compartments ($< 20\%$ of the floor area). 	<ol style="list-style-type: none"> 1. When the sectional temperatures exceed 400°C for stress levels above 60%. 2. When the average sectional temperature in a steel column exceeds the creep critical temperature as specified in Table 1. 3. For columns with high slenderness (> 50), heavily loaded ($> 40\%$), and/or non-uniform fire exposure. 4. When the severity of fire exposure in a steel framed building exceeds the value corresponding to the ‘severe’ creep level as specified in Table 2 and Table 3.

4 CASE STUDIES

To illustrate the applicability of the proposed design alternatives, three case studies are presented in this section. In these cases, the above-discussed recommendations are utilized to determine the level of high-temperature creep required. The model parameters, discretization, and detailed discussion of results for the studies outlined in this section are presented in [4] and are excluded from here for brevity.

4.1 Case 1

In the first case study, a W14x53 steel column that is pinned at both ends and subjected to an axial load of 40% is considered. The column has a fire-resistance rating of 2 hours and is exposed to ASTM E119 [12] fire from one side only. This scenario is representative of an interior column in a steel-framed building that is present in the boundary of the fire-exposed compartments. Thus, the column may only be exposed to fire from one side. Based on the thermal analysis, the average temperature in the column cross-section is likely to remain below 400°C, which is below the creep critical temperature of 550°C for a stress level of 40%.

Therefore, the column in this case will develop negligible high-temperature creep strains, and this case falls under the category of 'creep-not critical' as per the design recommendations proposed in this paper.

The column was analysed using the numerical approach outlined in this paper according to implicit and explicit creep implementation. Figure 3 shows the axial deformation of the column with fire exposure time for the two scenarios. The deformations obtained using the two strategies show a similar trend with very little difference between them. The column continues to expand for most of the fire exposure duration and does not reach a stage where the creep deformations are evident. Hence, the high-temperature creep effects do not influence the response of this column and can be neglected. In this scenario, the fire resistance of the column can also be determined by any of the prescriptive or simplified approaches specified in current codes and standards (e.g., ASCE).

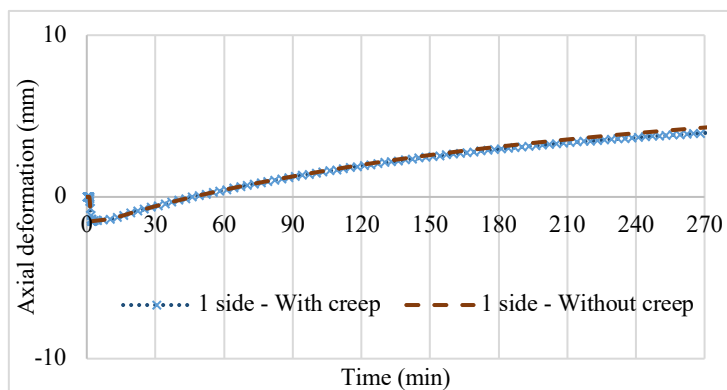


Figure 3. Axial deformation response of the column considered in Case 1

4.2 Case 2

In the second scenario, a ten-story steel-framed building, as shown in Figure 4, that is exposed to a moderate fire scenario, DF-90, is considered. The details of the building can be found in [20]. Fire is contained within the compartments in bays 3-4-5 on Floor 2, which is typical of a high-rise office building fire. The fire is expected to last for a short duration, and the peak temperatures are slightly above 800°C. Based on the thermal analysis, the peak temperatures attained in the cross-section of the steel members are below 550°C, which means that minimal creep deformations are expected to occur during the growth phase of the fire exposure. This scenario falls under the 'creep-implicit' category based on the proposed recommendations.

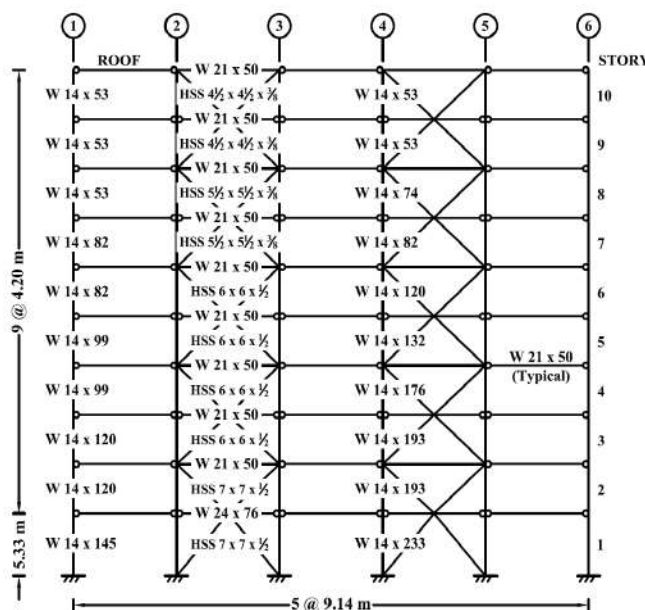


Figure 4. Details of a ten-story steel-framed building considered in the case study

The proposed numerical approach, considering both implicit and explicit creep, is used to analyse the building. The lateral displacement history at the top story level is presented in Figure 5. There are minor differences in the deformation response for the creep-implicit and creep-explicit cases. Since the cross-sectional temperatures in the steel members do not exceed 550°C, no failure is observed at the member level, which means that no global collapse occurs under this fire scenario. Therefore, the implicit treatment of creep strains was found to be sufficient to capture the response of the frame in this case of moderate fire exposure.

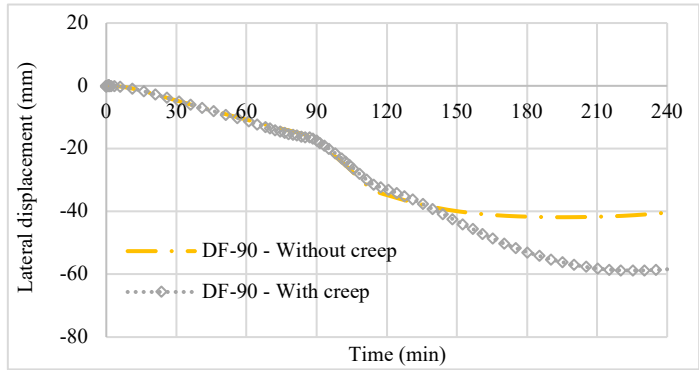


Figure 5. Lateral displacement at the top left corner of the frame for the DF-90 fire scenario considered in Case 2.

4.3 Case 3

For the final illustration, the ten-story braced-framed building shown in the previous case (refer to Figure 4) is considered. In this scenario, the fire is assumed to occur in compartments in bays 3-4-5 on floors 2, 3, and 4. The fire temperatures are assumed to follow the ASTM E119 [12] fire exposure. This situation represents a severe fire scenario in a high-rise building where the fire has spread to multiple stories. In such cases, the active fire protection systems may not be effective, and the response time for firefighting may be high, leading to severe fire exposures of high intensity and duration, and spread to several compartments. Due to these factors, the temperature and stress levels expected in the fire-exposed members are high, and hence, this case falls under the ‘creep-explicit’ category outlined in the design recommendations.

The lateral deformation response evaluated at the top story level for the creep-implicit and creep-explicit cases are compared and plotted in Figure 6. At the beginning of the fire exposure, the lateral deformation response for both cases is similar. However, as the fire exposure time increases, the differences become significant. When burning occurs in more than one story, multiple steel members fail simultaneously, resulting in a rapid increase in the lateral drift of the structure. When creep deformations are explicitly incorporated into the analysis, a greater number of structural members fail at quicker times, significantly increasing the stress levels, and altering the load path. The global failure time predicted by the model “without creep” is 196 minutes, which is much higher than that obtained using the model with creep, i.e. 157 min.

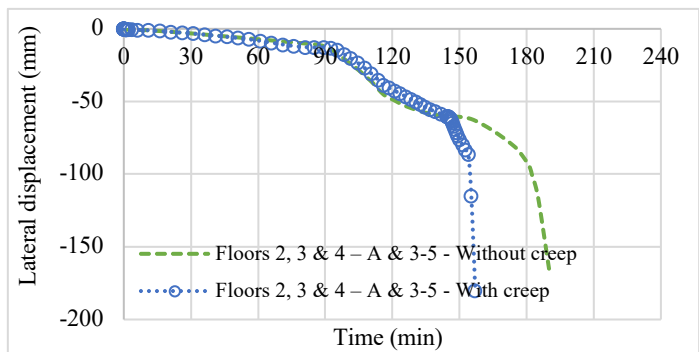


Figure 6. Lateral displacement at the top left corner of the frame for the multi-story fire scenario considered in Case 3.

5 LIMITATIONS

- The recommendations provided for the treatment of high-temperature creep at a system level are based on the studies carried out on a ten-story braced framed building. Additional studies are needed to determine the effect of creep on other types of framing systems such as moment frames, steel-framed buildings with a rigid core, etc. Further, buildings may have different floor layouts, compartment sizes, floor levels, etc. as compared to the buildings considered in this paper. Hence, the recommendations provided based on the extent of burning, fire location, etc. are only approximate and cannot be generalized to all buildings.
- The proposed approach for the explicit treatment of high-temperature creep in the fire-induced progressive collapse analysis can be applied to 2D steel frames only. This is mainly due to the numerous numerical instabilities that can occur while carrying out the analysis using the nonlinear quasi-static regime, as well as high computational effort. Further research is needed to implement the effects of transient creep in 3D building models that include floor slabs and transverse framing with good computational efficiency.

6 CONCLUSIONS

This paper proposes design recommendations to address the limitations related to the treatment of transient creep effects in the fire resistance analysis of steel-framed structures.

- Depending on the extent of transient creep strain that is likely to develop in a fire-exposed steel structure, three alternative scenarios are proposed for incorporating creep in fire resistance analysis (and fire-induced progressive collapse analysis). These scenarios are 'creep - not critical', 'creep - implicit', and 'creep - explicit'.
- The 'creep – not critical' design solution is recommended for scenarios of low to moderate fire exposure and low-intensity loading. In this case, neglecting high-temperature creep does not influence the fire resistance of the steel-framed structure.
- The 'creep - implicit' design solution is for scenarios where high-temperature creep strain has a moderate effect on the fire response of steel members. In this case, accounting for temperature-induced creep strain implicitly through stress-strain relations in the fire resistance analysis is sufficient.
- The 'creep - explicit' design alternative is for the case of fire-exposed steel-framed structures where the temperature-induced creep strain is significant. This can be accounted for by explicitly incorporating creep through advanced analysis.
- Recommendations are given for the explicit consideration of high-temperature creep effects based on creep critical temperature, defined as the temperature above which the tertiary creep strain occurs in steel for a particular stress level.
- The paper also provides three case studies to illustrate the applicability of the proposed guidelines for the treatment of high-temperature creep strains. In these studies, the design alternative selected based on the level of transient creep strain expected in the fire-exposed member accurately predicts failure times (fire resistance).

REFERENCES

1. A. Agarwal, A.H. Varma, Fire induced progressive collapse of steel building structures: The role of interior gravity columns, *Engineering Structures* 58 (2014) 129–140.
<https://doi.org/10.1016/j.engstruct.2013.09.020>.
2. T.T.H. Nguyen, *Composite Framed Buildings under Fire-Induced Progressive Collapse: Computational Analysis and Design Recommendations*, University of Michigan, 2017.
3. S. Venkatachari, V.K.R. Kodur, System level response of braced frame structures under fire exposure scenarios, *Journal of Constructional Steel Research* 170 (2020) 106073.
<https://doi.org/10.1016/j.jcsr.2020.106073>.
4. S. Venkatachari, V. Kodur, Effect of transient creep on fire induced instability in steel framed structures, *Journal of Constructional Steel Research* 181 (2021) 106618.

5. EN 1993-1-2, Eurocode 3-Design of Steel Structures, Part 1-2: General Rules for Structural Fire Design, CEN (European Standards Committee), Brussels, Belgium, 2005.
6. V.K.R. Kodur, M.M.S. Dwaikat, Effect of high temperature creep on the fire response of restrained steel beams, *Mater Struct* 43 (2010) 1327–1341. <https://doi.org/10.1617/s11527-010-9583-y>.
7. M.A. Morovat, M.D. Engelhardt, T.A. Helwig, E.M. Taleff, High-Temperature Creep Buckling Phenomenon of Steel Columns Subjected to Fire, *Journal of Structural Fire Engineering* 5 (2014) 189–202. <https://doi.org/10.1260/2040-2317.5.3.189>.
8. V.K. Kodur, E.M. Aziz, Effect of temperature on creep in ASTM A572 high-strength low-alloy steels, *Materials and Structures* 48 (2015) 1669–1677. <https://doi.org/10.1617/s11527-014-0262-2>.
9. G.-Q. Li, C. Zhang, Creep effect on buckling of axially restrained steel columns in real fires, *Journal of Constructional Steel Research* 71 (2012) 182–188. <https://doi.org/10.1016/j.jcsr.2011.09.006>.
10. AISC (American Institute of Steel Construction), Specifications for structural steel buildings, ANSI/AISC 360-16, Chicago, IL, USA, 2016.
11. E.G. Hantouche, K.K. Al Khatib, M.A. Morovat, Modeling creep of steel under transient temperature conditions of fire, *Fire Safety Journal* 100 (2018) 67–75. <https://doi.org/10.1016/j.firesaf.2018.07.006>.
12. ASTM E119-19, Standard methods of fire test of building construction and materials, ASTM (American Society for Testing and Materials), West Conshohocken, PA, USA, 2019.
13. ASTM (American Society for Testing and Materials), Standard Test Methods for Determining Effects of Large Hydrocarbon Pool Fires on Structural Members and Assemblies, ASTM E1529-14a, West Conshohocken, PA, USA, 2014.
14. ISO (International Organization for Standardization), Fire resistance tests-elements of building construction, ISO-834, Geneva, Switzerland, 1999.
15. EN 1991-1-2, Eurocode 1: Actions on structures - Part 1-2: General actions - Actions on structures exposed to fire, CEN (European Standards Committee), Brussels, Belgium, 2002.
16. Morgan J Hurley, D.T. Gottuk, J.R. Hall Jr, K. Harada, E.D. Kuligowski, M. Puchovsky, J.M. Watts Jr, C.J. Wieczorek, eds., *SFPE Handbook of Fire Protection Engineering*, 5th ed., Springer, New York, NY, USA, 2015.
17. Isolatek International, CAFCO 300 HS ISOLATEK Type 300 HS, (2020). <https://www.isolatek.com/construction/commercial-products/commercial-density/cafco-300-hs-isolatek-type-300-hs/> (accessed September 10, 2020).
18. Y. Anderberg, Modelling steel behaviour, *Fire Safety Journal* 13 (1988) 17–26. [https://doi.org/10.1016/0379-7112\(88\)90029-X](https://doi.org/10.1016/0379-7112(88)90029-X).
19. M.A. Morovat, J.W. Lee, M.D. Engelhardt, E.M. Taleff, T.A. Helwig, V.A. Segrest, Creep properties of ASTM A992 steel at elevated temperatures, in: *Trans Tech Publ*, 2012: pp. 786–792.
20. X. Liang, Q. Shen, S.K. Ghosh, *Assessing Ability of Seismic Structural Systems to Withstand Progressive Collapse*, S.K. Ghosh Associates, Inc., Palatine, IL, USA, 2006.

HEATED STEEL BEARING ELEMENTS CONTINUING THROUGH FIRE COMPARTMENT BOUNDARIES

Anita Ogrin¹, Friderik Knez², Urška Blumauer³

ABSTRACT

In the first part of the paper, experimental research on unprotected steel columns, which continue through the fire compartment boundary, simulated by the top of the furnace, is presented. Temperatures of parts of the columns outside of the furnace are measured and compared for several test configurations. In each of the three tests, three columns are tested. Two of them are positioned below non-heated steel cantilever beams. During the test, the columns thermally expand and come in contact with these cantilever beams. The third column does not have any obstacle above itself and is a control element. The three tests differ in initial distance between the top of the columns and cantilever beams. Influence of a non-heated obstacle on the temperatures of heated elements on the unexposed side of fire compartment boundaries is observed. In the second part of the paper, numerical model of the described experiments is presented. A comparison of numerical and experimental results shows qualitative agreement.

Keywords: Thermo-mechanical contact; fire compartment; insulation ability; protruding bearing elements

1 INTRODUCTION

Standard EN 13501-2 in general describes three elements of fire resistance of structural elements, such as columns, beams and walls: retention of loadbearing capacity (R), retention of integrity (E) and insulation capability (I). Normally, columns and beams are characterized with the retention of loadbearing capacity (R). The standard also prescribes, that a fire compartment boundary has sufficient insulation ability if average temperature rise, compared to initial temperature just before the test commences, on the surface of its unexposed side during standard fire exposure does not exceed 140 K and if temperature rise at any point on the surface of its cool side does not exceed 180 K [1]. This requirement applies to structural construction products, building elements and systems. Columns, integrated in planar structures with fire separating function (as part of fire separating wall) must ensure sufficient thermal insulation in horizontal direction. Similarly, beams, integrated in planar elements with fire separating function (as part of fire separating floors) must ensure sufficient thermal insulation in vertical direction. [1].

In steel frame loadbearing structures, beams continue through vertical boundaries of fire compartment and columns continue through horizontal boundaries of fire compartment. Their fire resistance for each fire compartment is checked, and also, if necessary, they are thermally protected to retain sufficient loadbearing capacity in fire. If needed, fire stopping seals are installed, where fire compartment boundary is penetrated. If a loadbearing element has low utilization factor, i.e., the applied load is low, compared to maximum loadbearing capacity of an element, requirements for load bearing capacity for one fire compartment can

¹ Asst. Prof., University of Ljubljana, Faculty of Civil and Geodetic Engineering,
e-mail: anita.ogrin@fgg.uni-lj.si

² Senior Researcher, Slovenian National Building and Civil Engineering Institute
e-mail: friderik.knez@zag.si

³ PhD, Researcher, Slovenian National Building and Civil Engineering Institute
e-mail: urska.blumauer@zag.si

be satisfied even though the temperature in the element during fire might reach 600 °C and more [2]. Protrusion of a heated beam or column into adjacent, non-heated fire compartment creates a thermal bridge, because of relatively high thermal conductivity of steel. To author's knowledge, such situation is not covered in [1], nor has it been addressed in scientific papers.

During recent experimental research of thermo-mechanical contact of spatial beams, we had an opportunity to measure temperatures in unprotected steel columns, protruding through the top of the furnace (fire compartment boundary). Results have shown that the temperature of the protruding element on the unexposed side of the fire compartment boundary can be notably different, depending on whether there is another, non-heated steel element placed in close proximity to the protruding one on the unexposed side.

The temperature field in the steel column, which is protruding through the fire compartment boundary, has been calculated, using numerical methods and modelling tool for planar thermal analysis of solids, Heatko [3]. Two cases have been analysed; one with a cantilever beam in close proximity of unexposed end of the column and the other without the cantilever beam. Test setup, temperature measurements, numerical model, its results and comparison with experimental results are presented hereinafter.

2 TEST SETUP

The experimental research, presented herein, has been performed at the Fire laboratory of the Slovenian National Building and Civil Engineering Institute. The research included three tests, numbered consecutively ($x = 1,2,3$). In each of the three tests, three S355 steel columns with HEA 140 cross-sections have been positioned inside the furnace, with their tops protruding through the roof of the furnace. Total length of each column was 4.48 m, of which 4.18 m was inside the furnace, the thickness of the roof of the furnace was 0.20 m and 0.10 m of the column has been visible outside of the furnace, as can also be seen in Figure 1. The columns were fixed only at the bottom.

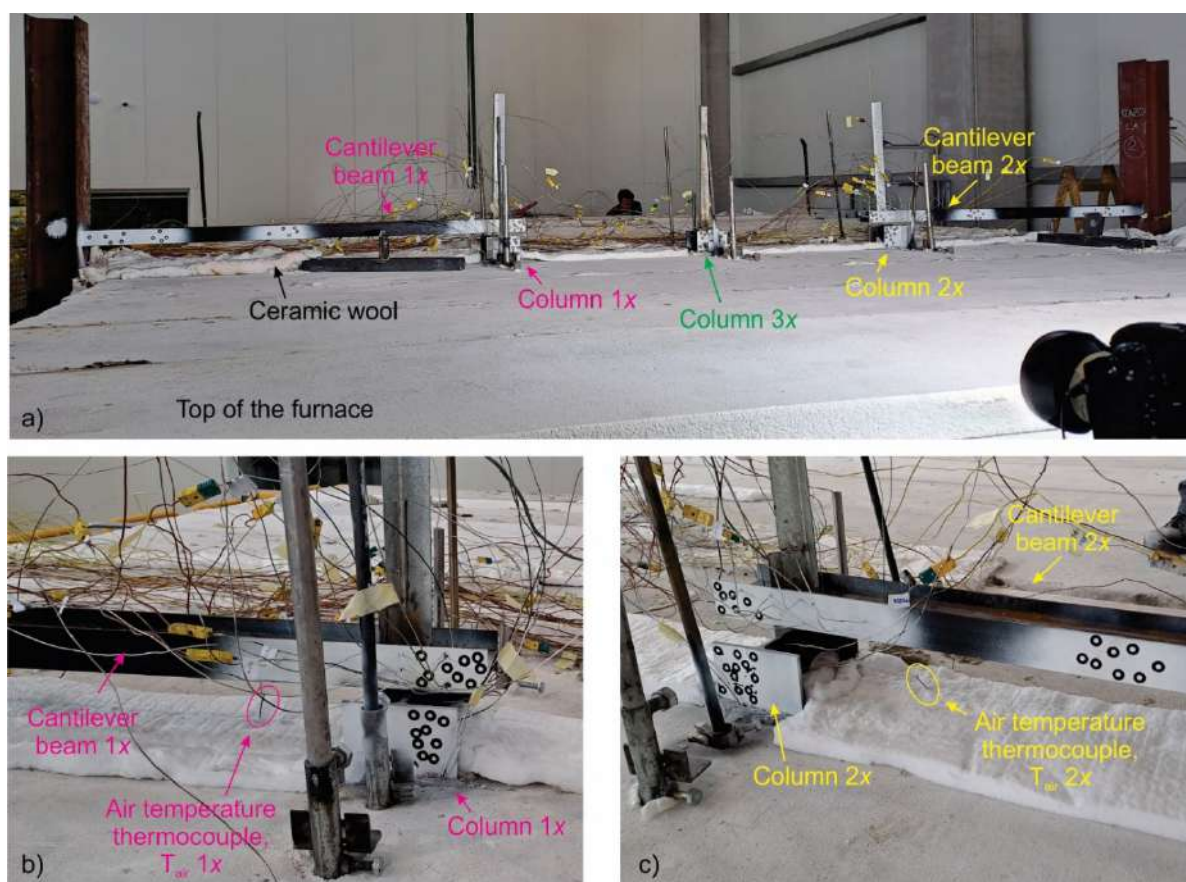


Figure 1. a) Test setup, $x = 3$, b) position of a thermocouple for measuring air temperature under cantilever beam 1 in test 2, $x = 2$, c) position of a thermocouple for measuring air temperature under cantilever beam 2 in test 2, $x = 2$

The top of the left column, named Column 1x, where x denotes the consecutive number of the test, was positioned exactly below the free end of steel cantilever beam, with overturned IPE 100 cross-section (see Figures 1b and 2). It is deemed that the end of the Cantilever beam 1x is fully shadowed by the top of the Column 1x. The initial distance between the top of the column and lowest edge of the cantilever beam, d_{in} , was different in each test and is given in Table 1. During tests, Column 1x thermally expanded and contact with Cantilever beam 1x was created at two small contact areas, causing bending deformations of the Cantilever beam 1x.

Similarly, the top of the right column, named Column 2x, was positioned below the free end of steel cantilever beam, with overturned IPE 100 cross-section. However, the end of the Cantilever beam 2x is only partially, approximately 75% shadowed by the top of the Column 2x (see Figures 1c and 2). The initial distances between the top of the column and lowest edge of the cantilever beam are given in Table 1. During tests, Column 2x thermally expanded and came in contact with Cantilever beam 2x at one small contact area, causing bending and torsional deformations of the Cantilever beam 2x.

The column in the middle, named Column 3x, has been a control element, without any obstacle above its top.

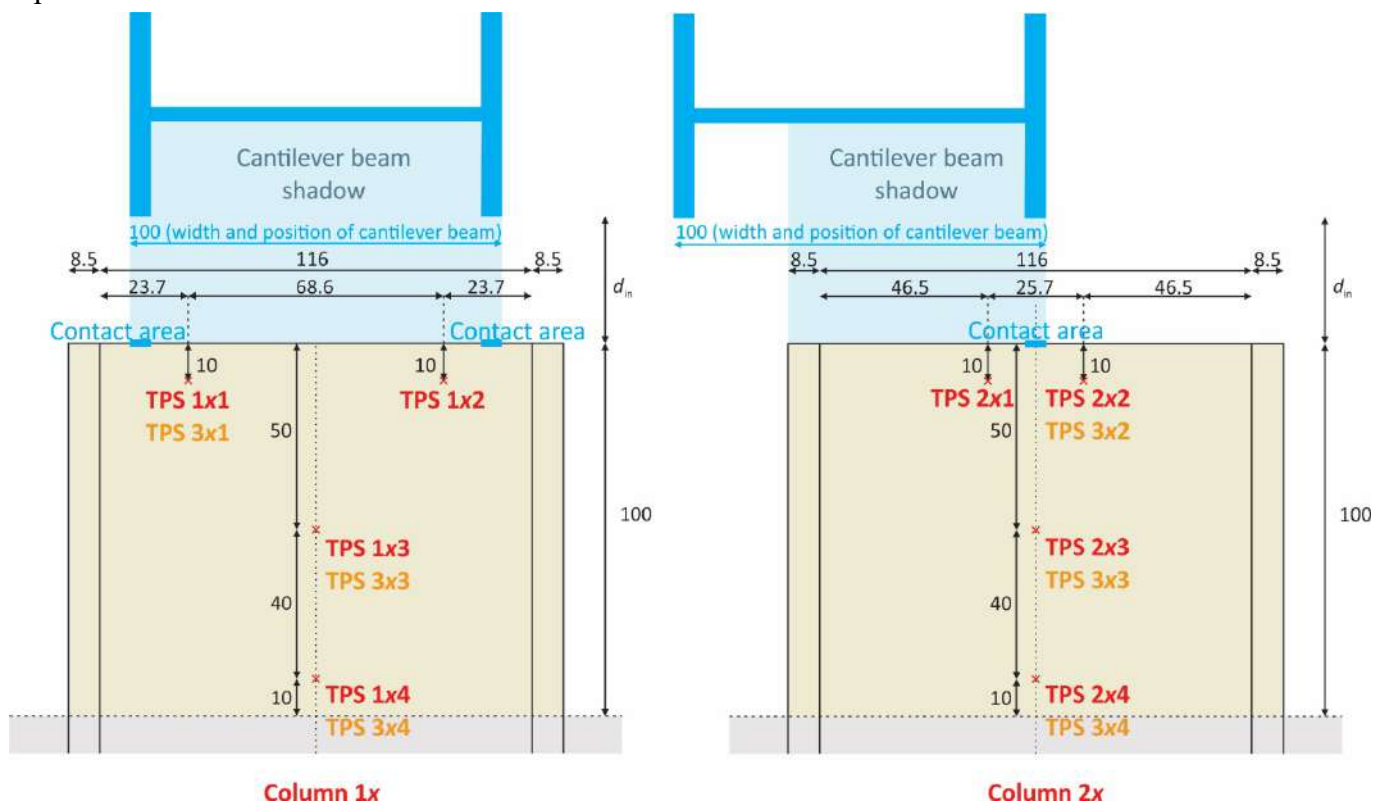


Figure 2. Position of thermocouples on columns 1x and 2x outside the furnace (in red), together with coinciding positions of thermocouples on column 3 (in orange); $x = 1, 2, 3$

Table 1. Differences in the setup of the three tests

Test (x)	$d_{in,1}$ [mm]	$d_{in,2}$ [mm]	Contact at t [min]	Names of columns and cantilever beams		
				Fully-shadowed (left)	Partially-shadowed (right)	Control (middle)
1	4	4	18	11	21	31
2	15	16	70	12	22	32
3	32	29	105	13	23	33

The roof of the furnace, which can be considered as the boundary of the fire compartment, is made of lightweight concrete slabs. Joints between plates and the holes around the column penetration have been filled with ceramic wool.

During the tests, temperatures and displacements of steel elements have been measured. Each column had 7 thermocouples installed: 3 inside the furnace and 4 at the top outside the furnace. Their position is shown in Figure 2. Cantilever beam 1x has been equipped with 24 thermocouples and Cantilever beam 2x with 15. Thermocouples have been tightly attached to steel elements with punching process, approximately 3 mm deep. Temperature inside the furnace has been measured and controlled with 18 plate thermometers. Temperature of air outside the furnace has been measured with one thermocouple beneath each of the cantilever beams, very close to the protruding columns, as shown in Figures 1b and 1c.

The tests have primarily been designed for experimental investigation of thermo-mechanical contact of spatial beam elements. Among other aspects of test setup, this influenced the selected fire curve, which has not been standard fire curve, but rather a slow linear increase of temperatures from 20 °C to 600 °C in the first two hours and constant temperatures in the third hour of the test. Nevertheless, the observed results show interesting insight into temperatures of bearing elements, continuing through fire compartment boundaries.

3 TEST RESULTS

3.1 Results of test 1

The average temperatures of all three columns in test 1 ($x = 1$), measured inside the furnace, are virtually the same for the first 90 min of the test, and there are only small differences not exceeding 25 K between them during the rest of the test (see Figure 3). The steel temperatures inside the furnace are practically uniform and they are very similar to the temperatures of air inside the furnace, because the columns are not thermally insulated.

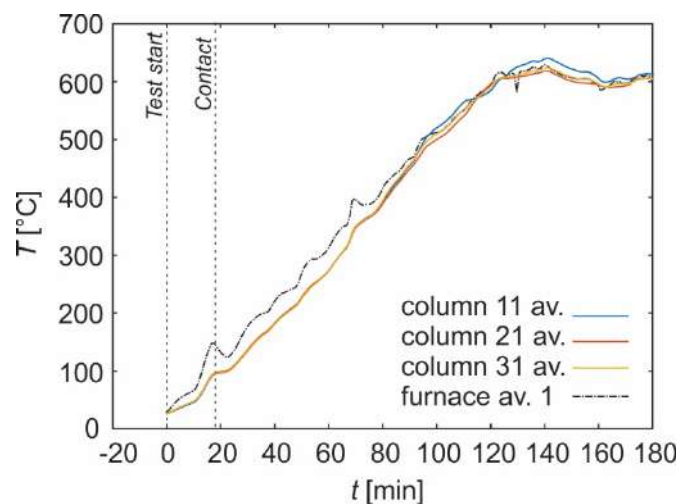


Figure 3. Average temperatures of columns inside the furnace during test 1, together with average temperature of air inside the furnace

Figure 4 shows relevant temperatures measured outside of the furnace during test 1. Thermocouples TPS 111 and TPS 311, which are at identical positions at the top of the columns 11 and 31, respectively, show notably higher temperatures in the column 11. The latter is in contact with Cantilever beam 11 almost entire duration of the test. TPS 112 unfortunately failed. Temperatures, measured at identical positions in columns 21 and 31 (TPS 212 and TPS 312) are not that different, although at the end of the test, temperatures in Column 31 still remain a little lower than those in partially shadowed Column 21. Temperatures of air, measured below both cantilever beams are relatively high and unstable in the second half of the test 1, which implies boosts of hotter air through the joints between slabs of the furnace top. Consequently, the

stripes of ceramic wool, which can be seen in Figure 1 below the cantilever beams, were additionally installed before subsequent tests.

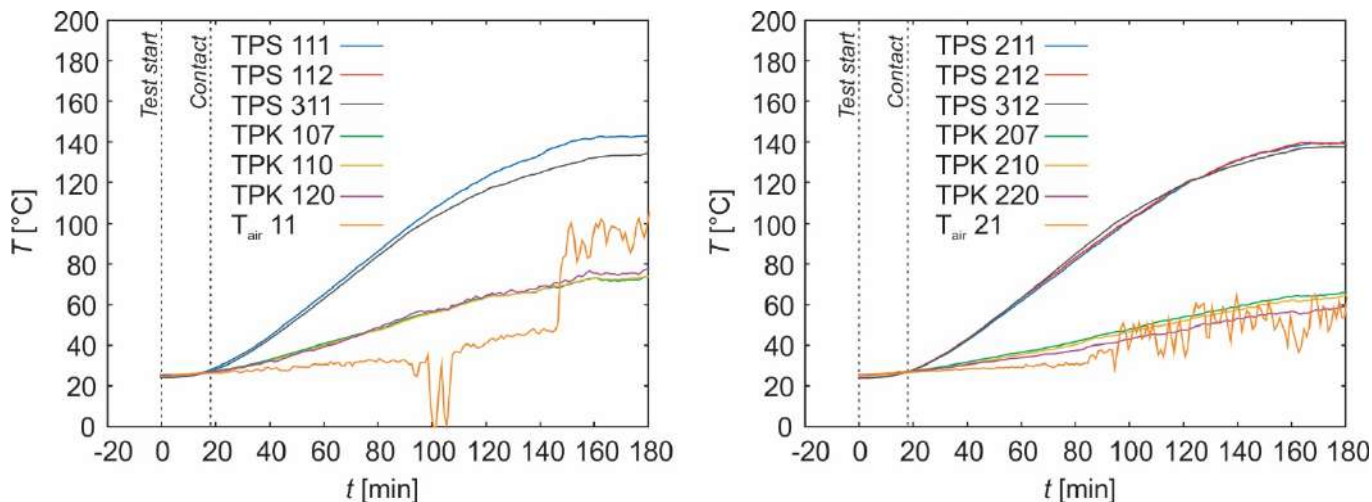


Figure 4. Temperatures in test 1 outside the furnace for columns 11 and 31 (left) and for columns 21 and 31 (right), together with temperatures of air near top of the columns

Temperatures of cantilever beams, measured approximately 1 cm left and right of the contact areas (TPK 107, TPK 110 and TPK 120 for Cantilever beam 11 and TPK 207, TPK 210 and TPK 220 for Cantilever beam 21) are informatively shown in Figure 4.

3.2 Results of test 2

Average temperatures of all three columns inside the furnace during test 2 ($x = 2$) are similar, with exception of temperatures in Column 22 in the second half of the test, which are higher than the temperatures in the other two columns for approximately 30 °C. After the temperature of air inside the furnace reached 600 °C and the “plateau” has begun, the furnace has been shut down for two short time intervals. This can be seen in Figure 5 as two sudden drops of all measured temperatures at 120 and 175 min. Those drops of temperatures, however, seemingly do not affect the temperatures of tops of the columns outside the furnace.

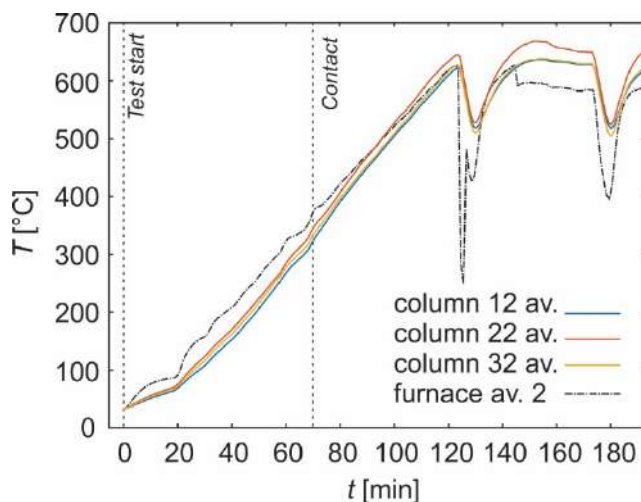


Figure 5. Average temperatures of columns inside the furnace during test 2, together with average temperature of air inside the furnace

Relevant temperatures, measured outside of the furnace during test 2, are shown in Figure 6. The additionally added strips of ceramic wool at the top of the furnace greatly reduced boosts of hot air through fissures in the furnace roof. Again, the temperature in Column 32 remains lower than temperatures in

columns 12 and 22, measured at identical positions. Furthermore, the differences between temperatures of fully shadowed Column 12 and Column 32 are larger than differences between temperatures of partially shadowed Column 22 and Column 32. The differences increase towards the end of the test. Note, that such differences occur in spite of average temperatures of columns 12 and 32 inside the furnace being almost equal and are thus consequence of geometry and not variations in test conditions.

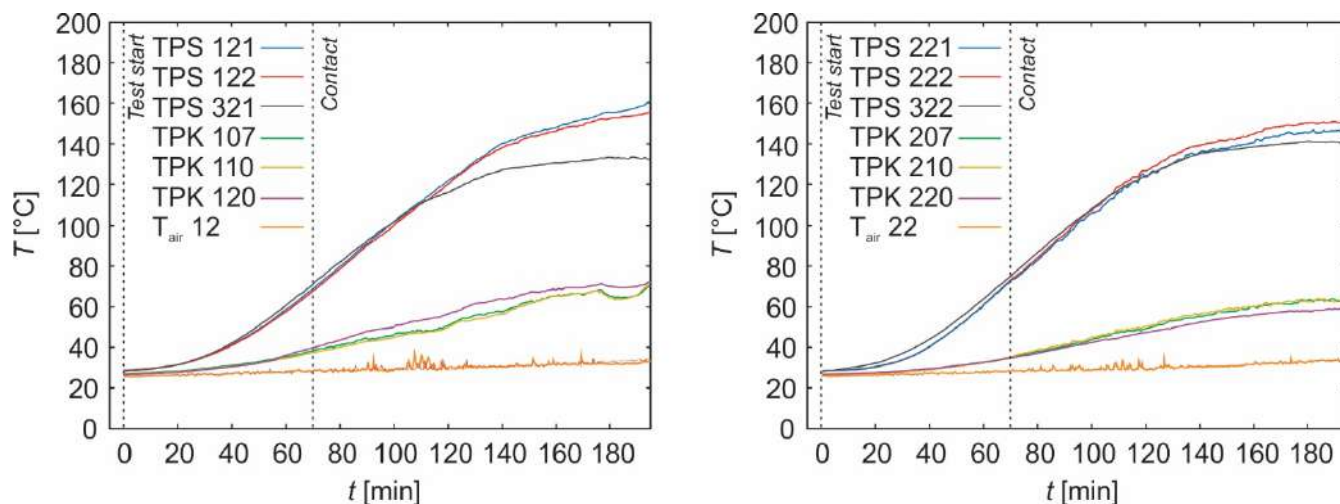


Figure 6. Temperatures in test 2 outside the furnace for columns 12 and 32 (left) and for columns 22 and 32 (right), together with temperatures of air near top of the columns

Temperatures, measured in cantilever beams, start increasing almost immediately after the beginning of the test, more than 50 minutes before the contact occurs. On the other hand, temperatures of air beneath cantilever beams remain almost the same throughout the whole test. This strongly suggests that radiative heat flux between the heated top of the column and non-heated cantilever beam cannot be neglected, despite small area of the top of the column. Another conclusion is, that the air between the top of the column and lower side of the cantilever beam, possibly somewhat heated also by the convective heat flux from the column, stays there in so-called “air-box”. The heat flux from this volume of air to the surrounding air is, assuming from low temperatures of air shown in Figure 6, negligible. This assumption has also been backed by the measurements of air velocity around the column tops during the test, which has been below the detection threshold of the measuring device (0.1 m/s).

3.3 Results of test 3

During test 3 ($x = 3$), the average temperatures of the columns inside the furnace matched very well, and they have been virtually the same for the first 2 hours of the test (see Figure 7).

In Figure 8, relevant temperatures measured outside of the furnace during test 3 are presented. Temperature of air, measured below the cantilevers near the top of the columns remain below 40 °C most of the time, which proves good thermal insulation of furnace roof, although the temperatures are not as stable as in test 2. Nevertheless, outside the furnace the temperatures of Column 13 (TPS 131 and 132) and Column 23 (TPS 231 and 232) increase importantly faster than temperatures of Column 33 at identical measurement positions (TPS 331 and 332). The differences are, once more, present from the beginning of the test and larger for the fully-shadowed Column 13 in comparison with partially-shadowed Column 23. Temperatures at the end of cantilever beam 1 (TPK 107, 110 and 120) and cantilever beam 2 (TPK 207, 210 and 220) again increase above the temperature of air long before the contact, which confirms observations from test 2.

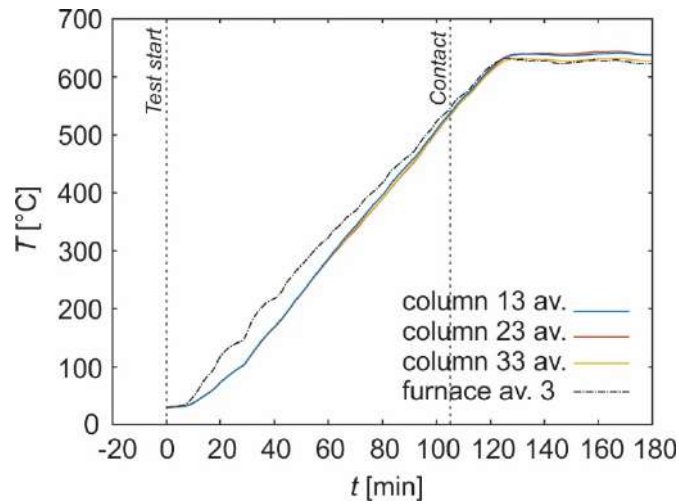


Figure 7. Average temperatures of columns inside the furnace during test 3, together with average temperature of air inside the furnace

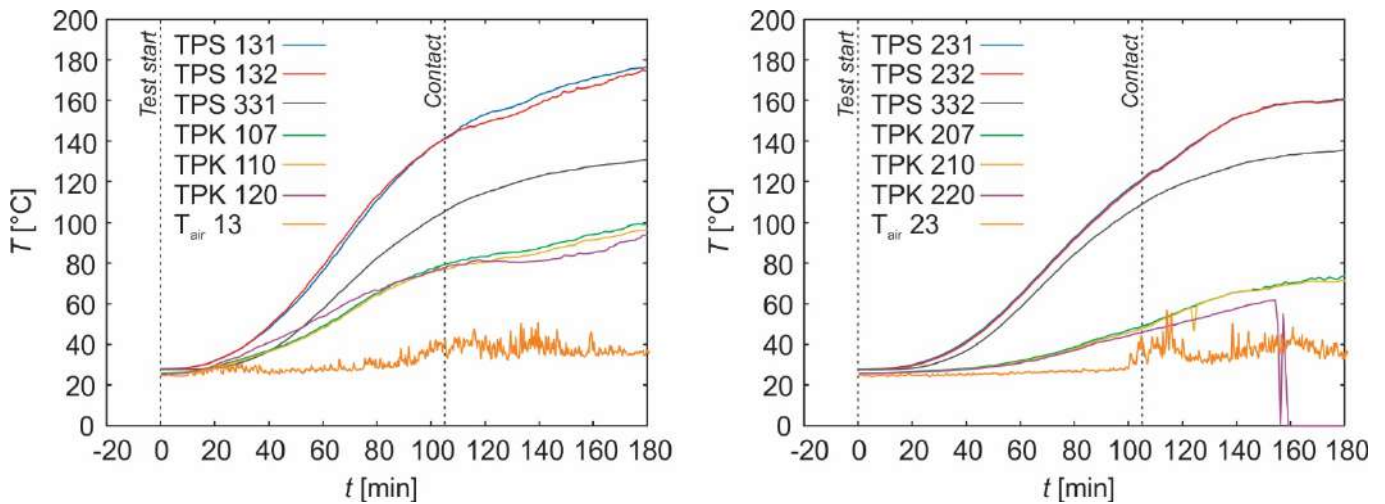


Figure 8. Temperatures in test 3 outside the furnace for columns 13 and 33 (left) and for columns 23 and 33 (right), together with temperatures of air near top of the columns

4 NUMERICAL MODEL

A simple numerical model of thermal interaction between heated column and non-heated cantilever beam has been created in Heatko software. Heatko is a research-oriented software for planar thermal analysis of solids, developed at UL FGG [3], which uses standard 4-node iso-parametric finite elements and implicit one-step time integration method. There have been several modifications of the software, each specifically tailored for modelling different phenomena such as coupled moisture-heat transfer [4], intumescence [5], charring [6] or heat transfer over hollow cross-sections [7]. The later has been taken as the basis in this research. The aim of these numerical analyses has been to qualitatively determine, whether a non-heated element in proximity of the heated one could cause higher temperatures in the heated element. The properties of elements in numerical model reflect the characteristics of elements, used in the experiments, with some simplifications.

The column has been modelled as a rectangle with dimensions $L_c=4.5$ m and $b_c=0.14$ m. Similarly, the cantilever beam has been rectangular with $L_b=1.6$ m and $b_b=0.06$ m. Size of each finite element has been 0.02×0.02 m² (see Figure 9). In order to account for the three-dimensionality of the structural elements, analysed in this planar numerical model, a coefficient k_{3D} was introduced and used to factorize the equations of a heat flux through boundaries. k_{3D} can be described as a ratio between a section factor of planar elements in numerical model and a section factor of 3D elements in experiment. Its purpose was to ensure proper amount of heat flux through the boundaries.

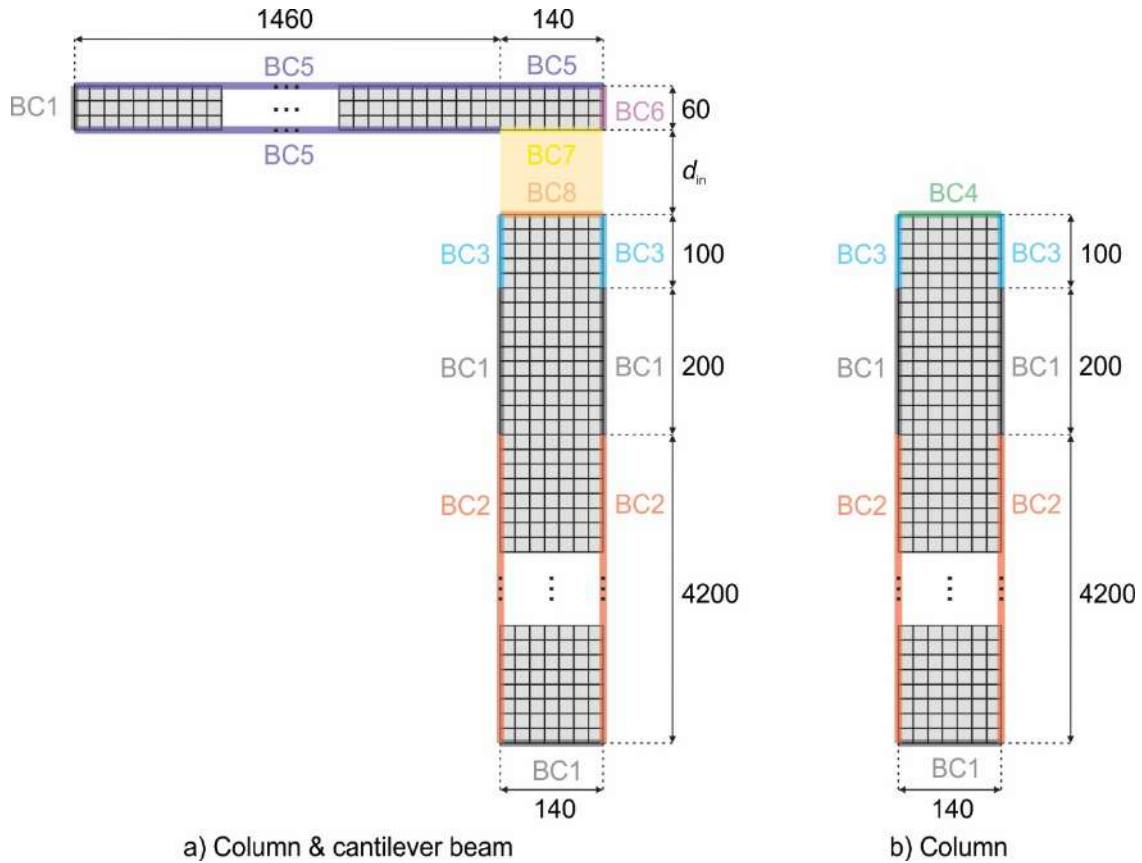


Figure 9. Dimensions [mm] and boundary conditions assumed in numerical models for thermal analyses of a) a column with cantilever beam and b) a column without cantilever beam

Along the length of the elements, k_{3D} was calculated as

$$k_{3D} = \left(\frac{A_m}{V} \right)_i \frac{b_i}{2}, \quad i = b \text{ (beam, IPE 100), c (column, HEA 140),} \quad (1)$$

and at the free ends of the elements, k_{3D} was calculated as

$$k_{3D} = \frac{V_i}{b_i}, \quad i = b \text{ (beam, IPE 100), c (column, HEA 140).} \quad (2)$$

A_m/V is the section factor of unprotected steel members, with A_m being surface area and V being a volume of a member per unit length according to [8]. Despite the definitions in standard, it is easier (and still correct) to perceive A_m as the perimeter of a 2D cross-section and V as the area of this cross-section. Values of k_{3D} are given in Table 2.

Two cases have been considered. First, a single column (i.e., without cantilever beam) has been analysed. The assigned thermal conductivity, specific heat and emissivity of steel, ε_m , were in accordance with EN 1993-1-2 [8]. At the boundaries inside the furnace, the coefficient of heat transfer by convection, α_c , was 35 W/m²K (which is the value for natural fire models according to [9]). At first, the coefficient of heat transfer by convection has been taken 9 W/m²K for unexposed surfaces (outside of the furnace), also according to [9]. However, while calculated temperatures of steel columns inside the furnace reflected the experimental measurements, they were too high at the top of the columns in numerical model. To obtain calculated temperatures in the part of the column outside of the furnace similar to the temperatures in the experiment, at the boundaries outside of the furnace the coefficient of heat transfer by convection, α_c , has been increased to 18 W/m²K. The same α_c has also been applied in the following calculations at all boundaries outside of the furnace, i.e., in case of a column within proximity of a cantilever beam.

Temperature of air at the exposed boundaries raised linearly from 20 °C to 600 °C in the first two hours, and then it remained constant for another hour. Temperature of air at the boundaries outside of the furnace was 20 °C throughout the analysis.

Prescribed boundary conditions are given in Table 2 and their position is visually presented in Figure 9. Note, that boundary conditions BC4 and BC8, both applied at the free end of the column (but in different cases), have identical α_c , ε_m and k_{3D} . The same is true for boundary conditions BC5 and BC7, both applied along the length of the cantilever beam. The only difference is that, in case of a column in proximity of a cantilever beam, boundary conditions BC7 and BC8 “interact” with each other, because those boundaries exchange heat with the same volume of air (later-on referred to as air-box).

Heat flux due to convection and radiation is present on the “column – air-box” and “cantilever beam – air-box” boundaries in accordance with specified boundary conditions. Adiabatic boundary conditions are assumed on the lateral sides of the air-box. Temperature of air inside the air-box is assumed to be uniform and changes linearly within a time step. Consequently, movement of air and related heat flux due to convection inside the air-box are neglected. The shape of the air-box is assumed to be prismatic with volume V_{ab} determined as

$$V_{ab} = \frac{V_c + A_{sh}}{2} d_{in}. \quad (3)$$

Here, A_{sh} denotes rectangular area with sides l_{sh} and cantilever beam height, h_b , and d_{in} denotes initial distance between the column and the cantilever beam. In the presented example, d_{in} was assumed to be 3 cm and inherent V_{ab} was 252 cm³. The temperatures at the top of the column (2 cm below top and 1 cm to the left of the column’s vertical bisector) are presented in Figure 10.

Table 2. Boundary conditions in numerical model

	Description	α_c [W/m ² K]	ε_m	k_{3D}	Interaction
BC1	Adiabatic boundary conditions, at supports and along the depth of the furnace boundary (assumption of perfectly sealed penetration)	/	/	/	/
BC2	Boundary conditions inside the furnace, along the length of the column	35	0.7	18	/
BC3	Boundary conditions outside the furnace, along the length of the column	18	0.7	18	/
BC4	Boundary conditions outside the furnace, at the top of the column, without vicinity of cantilever beam	18	0.7	2	/
BC5	Boundary conditions outside the furnace, along the length of the cantilever beam (with exception of the part above the column)	18	0.7	12	/
BC6	Boundary conditions outside the furnace, at the free end of the cantilever beam	18	0.7	2	/
BC7	Boundary conditions outside the furnace, at the lower side of the cantilever beam, which is above the column	18	0.7	12	With BC8
BC8	Boundary conditions outside the furnace, at the top of the column, which is beneath the cantilever beam	18	0.7	2	With BC7

As can be seen in Figure 10, numerical results qualitatively reflect experimental results. Both numerically determined and experimentally measured temperatures at the top of the column are higher in case with cantilever present in its proximity. Furthermore, both approaches show increase of the temperature differences with time between the cases with and without cantilever beam.

On the other hand, values of numerically determined and experimentally measured temperatures at the top of the column are somewhat different. Some of the differences can be attributed to assumptions and simplifications of the numerical model. It is worth remembering, that just slightly different initial configurations of experiments also led to notably different temperatures at the top of the column.

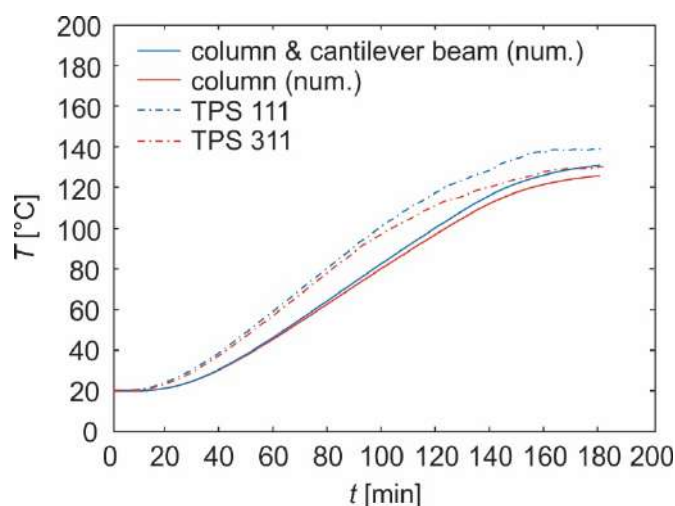


Figure 10. Temperatures at the top of the column with and without cantilever beam; comparison of numerical and experimental results

5 CONCLUSIONS

Higher temperatures, measured in columns with an obstacle (cantilever beam) in its proximity, could suggest that insulation ability of fire compartment boundary is, in certain cases, lower than expected. Test results strongly suggest the dependence of temperature differences on the distance between the column top and an obstacle, as well as on the size of the shadow between interacting boundaries. However, the measured temperature differences cannot be compared to maximum allowed temperature increase by EN 13501-2 [1], because of non-standard heating regime.

ACKNOWLEDGMENT

The research was funded by Slovenian Research Agency (grant number Z2-3203). The financial support is gratefully acknowledged.

REFERENCES

1. EN 13501-2: 2023: Fire classification of construction products and building elements - Part 2: Classification using data from fire resistance and/or smoke control tests, excluding ventilation services. CEN, May 2023.
2. Huang, ZF, Tan, KH, Ting, SK, Heating rate and boundary restraint effects on fire resistance of steel columns with creep. *Engineering Structures* 28(6), 805-817 (2006). <https://doi.org/10.1016/j.engstruct.2005.10.009>.
3. Hozjan, T, Software Heatko: 2-D analysis of heat transfer through solid materials. Ljubljana, University of Ljubljana, Faculty of Civil and Geodetic Engineering, 2009.
4. Pečenko, R., Svensson, S., and Hozjan, Modelling heat and moisture transfer in timber exposed to fire. *Int. J. Heat Mass Tran.* 87, 598–605 (2015).
5. Ogrin, A., Saje, M., Hozjan, T., On a planar thermal analysis of intumescent coatings. *Fire and materials* 42 (2), 145-155 (2018). <https://doi.org/10.1002/fam.2466>.
6. Pečenko, R., Hozjan, T., A novel approach to determine charring of wood in natural fire implemented in a coupled heat-mass-pyrolysis model. *Holzforschung*, Vol. 75 (2), 148-158 (2021). <https://doi.org/10.1515/hf-2020-0081>.
7. Ogrin, A., Dynamical analysis of three-dimensional steel frames in fire. Doctoral dissertation, Ljubljana, University of Ljubljana, Faculty of Civil and Geodetic Engineering, 2017 (in Slovene).
8. EN 1993-1-2: 2005: Eurocode 3: Design of steel structures – Part 1-2: General rules – Structural fire design. CEN 2005.
9. EN 1991-1-2: 2002: Eurocode 1: Actions on structures - Part 1-2: General actions - Actions on structures exposed to fire. CEN 2002.

IN SITU TEST PROCEDURE TO DETERMINE THE FIRE RESISTANCE OF EXISTING STEEL STRUCTURES WITH AGED INTUMESCENT COATING

Richard Fürst¹, Dustin Häßler², Ludwig Stelzner³, Sascha Hothan⁴

ABSTRACT

Intumescent coatings are commonly used in civil engineering to increase the fire resistance of steel structures. In case of a fire, the intumescent coating reacts and forms a thermally protective char around the steel member. Thus, the heating of the steel is significantly delayed, and as a result, a higher fire resistance can be achieved. Throughout the working life, intumescent coatings are aged by climatic factors. To predict durability for several years, the behaviour of the intumescent coatings is extrapolated based on accelerated artificial ageing. The established German and European assessment procedures to test and predict durability assume a working life of at least 10 years. For an extended period, additional evidence is required; yet the procedure and specifications to justify this are not described. Available in situ methods to assess the thermal performance of intumescent coatings are currently limited in their information content. Therefore, BAM is conducting a research project to develop a minimally invasive in situ test procedure to determine the fire resistance of existing steel structures with applied intumescent coating. The paper will describe the test setup, the developed prototype furnace, and the results of the performed test programme with uncoated and coated steel specimens. Based on this, recommendations for the test procedure are given.

Keywords: In situ testing; fire resistance; intumescent coating; steel; thermal protection; durability

1 INTRODUCTION

Intumescent coatings are used to improve the fire resistance of steel structures. The application of these coatings makes it also possible to fulfil architectural design requirements, while the low coating thickness results in marginal additional loads for the structure. Generally, the scope of application and the durability of intumescent coatings are described in European Technical Assessment (ETA) documents or national documents, e.g., in Germany by National Technical Approvals (abZ) or General Construction Technique Permits (aBG). Intumescent coatings usually consist of a primer, an intumescent layer and a top coat. When exposed to elevated temperatures in case of fire, the intumescent coating applied to the steel member expands to multiple times the initial thickness to form a thermally protective char. This char considerably reduces the heating of the underlying steel member and thus delays the deterioration of the mechanical steel properties caused by high temperatures. Hence, the fire resistance of the steel member is improved.

It is an essential requirement for intumescent coatings to ensure the durability of the fire safety throughout the entire working life. The potential ageing of intumescent coatings and a related reduction of the thermal

¹ Ph.D., Bundesanstalt für Materialforschung und -prüfung (BAM), 7.3 – Fire Engineering, Unter den Eichen 87, 12205 Berlin, Germany
e-mail: richard.fuerst@bam.de, ORCID: <https://orcid.org/0000-0002-4372-5322>

² Dr.-Ing., Bundesanstalt für Materialforschung und -prüfung (BAM), 7.3 – Fire Engineering, Unter den Eichen 87, 12205 Berlin, Germany
e-mail: dustin.haessler@bam.de, ORCID: <https://orcid.org/0000-0002-3705-7356>

³ Dr.-Ing., Bundesanstalt für Materialforschung und -prüfung (BAM), 7.3 – Fire Engineering, Unter den Eichen 87, 12205 Berlin, Germany
e-mail: ludwig.stelzner@bam.de, ORCID: <https://orcid.org/0009-0007-3955-7841>

⁴ Dr.-Ing., Bundesanstalt für Materialforschung und -prüfung (BAM), 7.3 – Fire Engineering, Unter den Eichen 87, 12205 Berlin, Germany
e-mail: sascha.hothan@bam.de, ORCID: <https://orcid.org/0000-0003-3735-8973>

protective performance is caused by certain climatic factors, e.g., temperature, humidity, rain, freezing, thawing, acid polluted environment and/or ultra-violet radiation in varying degrees of intensity. The established German [1] and European [2] procedures to assess the durability assume a working life of at least 10 years. Short-term weathering tests, which simulate artificial accelerated ageing, are usually used to predict the durability. For a period of more than 10 years, additional evidence is required [2]; yet the procedure and the specifications to justify this are not described in detail.

In civil engineering practice, there is an increasing demand to verify the fire resistance of existing steel structures with applied intumescent coatings. This might be necessary in several cases, e.g., the working life of 10 years is achieved, the visual appearance of the intumescent coating changed or the label of the product applied is missing. However, there is a lack of suitable test and assessment methods to verify the thermal protective performance of intumescent coatings on site, i.e., in situ. Visual inspection, flame test, adhesive tensile test or chemical analysis can provide only limited information. Consequently, the fire resistance of existing steel members with applied intumescent cannot be determined with these indicative methods. Currently, a reliable determination of the fire resistance is only possible by fire testing in laboratory. This destructive approach requires the extraction of a coated steel member from the existing structure. Hence, the procedure is rarely used.

The ongoing research project "INSIST" [3] at BAM aims to develop a suitable and reliable in situ test procedure to assess the actual thermal protective performance of intumescent coatings and the corresponding actual fire resistance of the related steel member, see Figure 10. A summary of the developed test device and a discussion of the results obtained so far are given in the following chapters.

1.1 Objectives and methods

The developed in situ test procedure aims to determine the actual thermal protection of the intumescent coating directly at the existing structure using a minimally invasive approach. Based on this information the actual fire resistance of the existing coated steel structure can be assessed. The tested steel member will remain in place and undamaged, as well as without a negative effect on its load-bearing capacity during in situ testing by limiting the steel temperature to not exceed 400 °C. The intumescent coating can be locally replaced after the test. The proposed in situ test procedure should be applicable to typical cross-sections and dimensions of steel members, run with standard media and power supply, as well as give reliable and reproducible results. Moreover, the test device requires a compact design to enable a mobile application on site and a high thermal output to activate the intumescent coating similar to a fire exposure. Consequently, various technical aspects need to be addressed to develop an appropriate prototype furnace. The investigation in the research project were divided into four main parts. In this paper, the first and second parts are presented and discussed.

1. **Development of the prototype furnace.** Designing and assembling of the furnace as well as calibration of the heating regime and general test procedure.
2. **Verification and calibration of the test procedure.** The steel temperature of coated and uncoated steel plates and the morphology of the char of coated steel plates tested by the prototype furnace are compared with those results obtained by DIN 4102-8 furnace [5]. Moreover, the effects of the steel plate thickness, dry film thickness (DFT), and heat conduction are assessed.
3. **Testing I-sections with the prototype furnace at.** Coated and uncoated IPE and HEB steel profiles are analysed. In addition, a methodical assessment approach will be developed to extrapolate the steel temperature progression above 400 °C.
4. **Numerical simulation.** The numerical analysis is used to calculate the temperature field of the steel member and to determine the effective thermal conductivity of the intumescent coating. The numerical simulation accompanies the experimental tests carried out with the prototype and intended to enable the verification of the actual fire resistance.

1.2 Development of the prototype furnace

The following requirements and test conditions were defined for the development of the prototype furnace:

- heating regime and thermal output of the prototype furnace must be equivalent to a fire exposure according to the standard temperature/time curve given in EN 1363-1 [4],
 - compact design of the prototype furnace to enable a mobile application on site as well as a broad application to typical cross-sections and dimensions of steel profiles, in particular I-sections,
 - testing of coated steel members with an intended fire resistance of at least 30 minutes,
 - one-sided fire exposure to specimens with a flat test surface, i.e., the coated web of an I-sections,
 - running the prototype with standard media, i.e. three-phase electric power supply and compressed air.
- Depending on these requirements, a prototype furnace with electric heating elements was developed. Figure 1 shows the four main components of the test setup, i.e. prototype furnace, temperature measurement device, temperature controller and laptop for data acquisition.

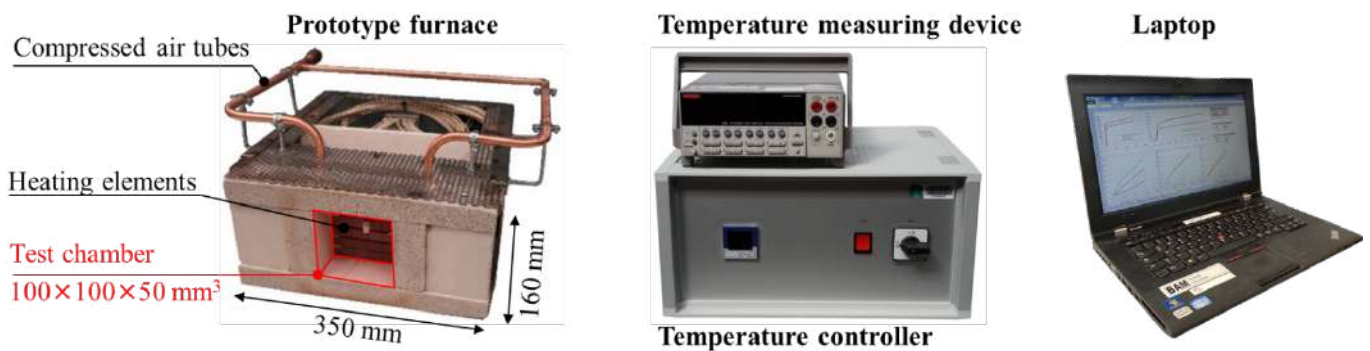


Figure 1. Components of the prototype furnace and geometry

The prototype furnace consists of a thermally insulated test chamber of $100 \times 100 \times 50 \text{ mm}^3$. The device is made of insulation boards, perforated stainless steel sheets and compressed copper tubes. The prototype furnace is mounted on a support construction allowing to adjust the position regarding the tested specimens. The specimen surface is heated primarily by radiant energy, which is emitted by 12 silica-nitride heating elements. A compressed air-cooling system was installed to prevent high temperatures at the electrical connections of the heating elements. The heating elements have a heating rate of approximately 22.5 K/s and can operate up to a maximum temperature of $1000 \text{ }^\circ\text{C}$. They are arranged opposite to the specimen with a surface-to-surface distance of 55 mm . This test setup enables both a high thermal input to the tested area of the specimen to activate the intumescent coating similar to a fire exposure and to obtain a uniform char formation. Specimens can be directly heated up from one side at a local area of $100 \times 100 \text{ mm}^2$. The size of the test area appears to be sufficient, as other approaches of small-scale fire tests [6-10] provided also good results for steel plates with applied intumescent coating.

In contrast to fire tests with oil or gas burners, where the thermal exposure is based on the furnace gas temperature measured by plate thermocouples, the prototype furnace uses the temperature of the electric heating elements. For this purpose, two heating elements are equipped with a sheath thermocouple (TC).

Based on this information the heating regime of all heating elements can be controlled precisely and programmed by the temperature controller. A series of calibration tests have been carried out to ensure that the heating elements of the prototype furnace create a thermal exposure similar to the standard temperature/time curve used in conventional fire testing, see Chapter 1.3. Due to the compact design of the prototype furnace, i.e., dimension of $350 \times 170 \times 350 \text{ mm}^3$ (width \times height \times depth), a broad range of steel profiles can be tested, in particular I-sections. Generally, application limitations are due to the required height of the prototype furnace and a maximum allowed char thickness of about 50 mm , as the heating elements shall not have contact to the char.

1.3 Test programme

The paper presents two series of tests carried out with steel plates of 5 mm and 10 mm thickness. In **test series 1** uncoated steel plates and in **test series 2** steel plates with applied intumescent coating were

tested, see Figure 2. The individual questions to be answered in each task of a test series are summarised in Table 1. Both test series were conducted in the DIN 4102-8 furnace [5] and in the newly developed prototype furnace. To ensure a high reproducibility of results, three specimens were tested for each test setup. **Test series 1** aims to determine an appropriate heating regime for the prototype furnace. For this purpose, the heating regime was iteratively modified, until the steel temperature/time curve of the specimens tested by the prototype furnace was according to those obtained in fire tests in the DIN 4102-8 furnace with standard temperature/time fire exposure [2]. Moreover, also the effects of varying steel plate thicknesses and heat transfer within the specimen, resulting from the limitation of the directly heated area of the specimens, were also analysed. In **test series 2**, steel plates with a commercial water-based intumescent coating [11], applied with a DFT of about 0.5 mm, were tested. The DFT was selected on the basis of an intended R30 fire resistance and the test restriction of the maximum char thickness to less than 50 mm.

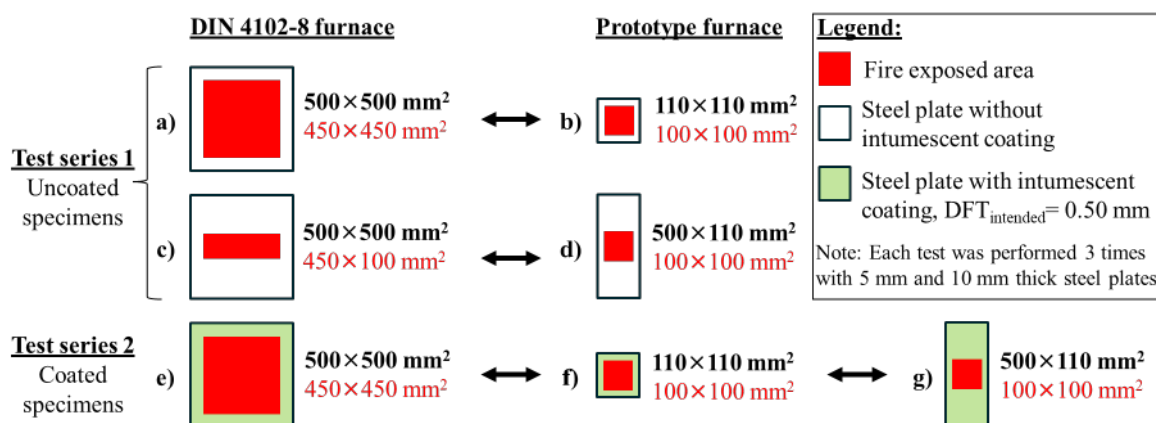


Figure 2. Individual test parts scheme of the test programme

Table 1. Aim of the comparison between individual test series and tasks

	Task	Aim of the comparison
Test series 1	a) and b)	Determination of an appropriate heating regime for the prototype furnace based on uncoated steel plates.
	a) / c) and b) / d)	Identification and comparison of the heat transfer effect at uncoated steel plates.
Test series 2	e) and f)	Verification of the determined heating regime of the prototype furnace at steel plates with applied intumescent coating. Comparison of the morphology of the char obtained after the fire test.
	f) and g)	Investigation of the heat transfer effect at coated steel plates.

1.4 Specimens preparation

All specimens are made of hot rolled steel of grade S235J2 +C. To enable the steel temperature measurement during the fire test, flexible thermocouples (TC) were attached by spot welding on the reverse, unexposed side of the coated and uncoated steel plates. The position of the TC is shown in Figure 3. Regarding the coated specimens, at first the front side of each steel plate was sandblasted. Afterwards the primer and finally the intumescent layer was applied. A topcoat was omitted. The curing time was at least five weeks according to the product technical sheet [9]. After the conditioning phase the DFT of the intumescent coating was determined by an ultrasonic measuring device. Measurement points were taken at the fire exposed area of the specimens to calculate an average actual DFT. The measured DFT values as well as the individual steel plates geometry are given in Table 2.

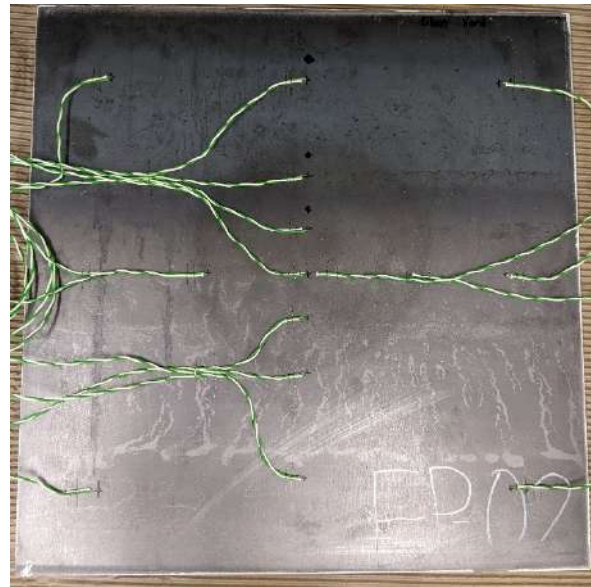
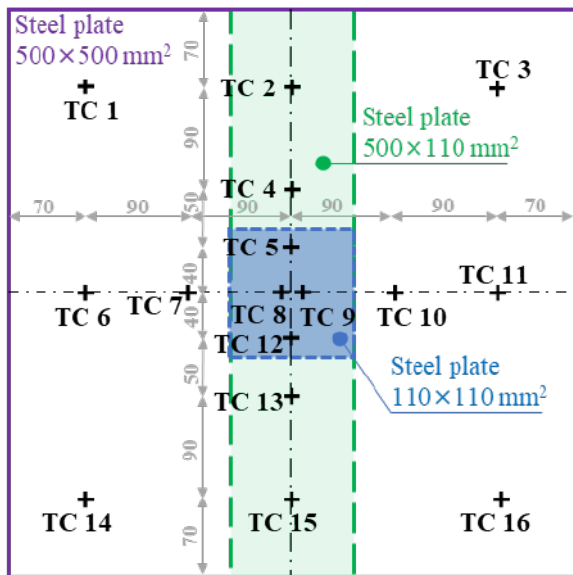


Figure 3. Position of the thermocouples: (left) position of thermocouples for each specimen geometry; (right) example of the thermocouple attachment at the reverse, unexposed side of the steel plate 500×500 mm²; note: dimension in mm

1.5 Test setup and execution

Fire tests carried out at the DIN 4102-8 furnace

In the DIN 4102-8 furnace tests, specimens with a steel plate thickness of 5 mm and 10 mm and a dimension of 500×500 mm² were tested simultaneously. The specimens were installed parallel to the oil burner axis, which has a maximum power of 290 kW. The fire exposed area is given in Figure 2. The non-exposed areas of the specimen were protected by high temperature mineral fibre insulation material and a vermiculite board to avoid heat transfer to the environment. The fire exposure corresponds to the standard temperature/time curve [2]. To control the furnace temperature, two plate thermocouples (PTC) were positioned centrally in front of the specimens at a distance of 100-150 mm to the fire exposed surface. The duration of the fire tests was 30 minutes or until a steel temperature of at least 500 °C was reached. To ensure a uniform emissivity of the steel plate surface, each specimen was subjected to a preliminary fire test to achieve a oxidised surface.

Fire tests carried out at the prototype furnace

In the prototype furnace tests, specimens with a steel plate thickness of 5 mm and 10 mm and a dimension of 110×110 mm² or 500×110 mm² were tested one by one. The fire exposed area is given in Figure 2. Regarding the specimens 110×110 mm² the unexposed circumferential edge at the front is approximately 5 % of the edge length, and therefore has the same ratio as the specimens 500×500 mm² tested in the DIN 4102-8 furnace. At the prototype furnace the specimens were clamped directly in front of the test chamber. To achieve almost adiabatic test conditions, the unexposed areas at the front and reverse side of the specimen were protected by high temperature mineral fibre insulation material. The 5 mm thick layer of high temperature insulation also compensates any unevenness in order to ensure a tight fit between the specimen and the prototype furnace. Moreover, at the reverse side of the specimen also a vermiculite board was added. Similar to the tests performed in the DIN 4102-8 furnace, the duration of the fire tests with the prototype furnace was at least 30 minutes or until a steel temperature of at least 500 °C was reached. Moreover, also for each specimen a preliminary fire test was conducted to achieve a oxidised surface.

After the tests were carried out at the DIN 4102-8 furnace and the prototype furnace the char thickness of all coated specimens was measured by a thin wire. The measuring points were chosen at similar positions as for the DFT measurement. The measured values are given in Table 2.

2 RESULTS AND DISCUSSION

2.1 Uncoated specimens of test series 1

Determination of an appropriate heating regime for the prototype furnace – task a) and b)

Based on the tests carried out in task a) with the DIN 4102-8 furnace and in task b) an appropriate heating regime for the prototype furnace was determined by an iterative process, to obtain almost identical steel temperatures. As in both cases the fire exposure is almost throughout the specimen, the heat transition effect can be neglected. Figure 4 left shows the steel temperature curves averaged from three tests of 5 and 10 mm thick steel plates tested at the DIN 4102-8 furnace and the prototype furnace using the optimised heating regime. For both furnaces, the steel temperature corresponds to the surface centre on the unexposed, reverse side of the specimen, see TC 8 and TC 9 in Figure 2. For both steel plate thicknesses tested, the steel temperature differences between the two furnaces are marginal, i.e. between 5 to 15 K. Therefore, the thermal exposure generated with the specified heating regime for the prototype furnace is equivalent to a standard temperature/time fire exposure. As a result, this heating regime is used in all the following fire tests with the prototype furnace.

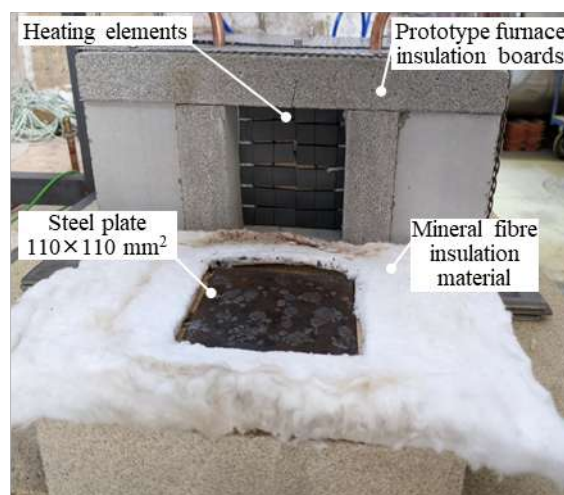
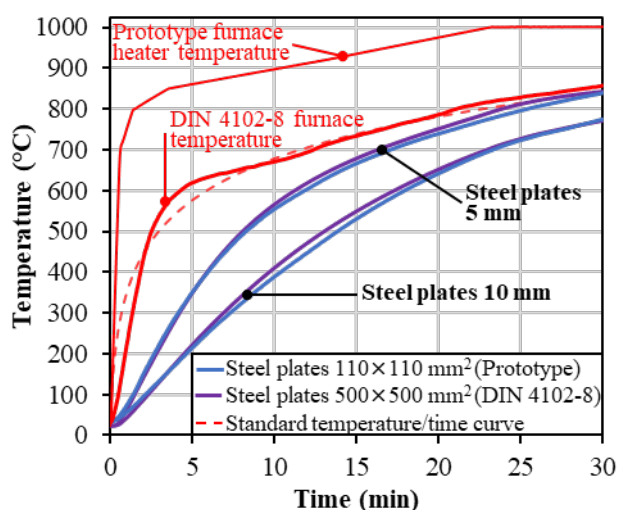


Figure 4. (left) averaged steel temperature from prototype and DIN 4102-8 furnace; (right) steel plate after prototype fire test

Identification of the heat transition effect – task c) to task d)

To analyse the effect of the heat transition within a specimen, 5 and 10 mm thick steel plates were fire tested in task c) at the DIN 4102-8 furnace and in task d) at the prototype furnace. To allow for a heat transition, in the fire tests carried out at the DIN 4102-8 furnace the fire exposed area was reduced from $450 \times 450 \text{ mm}^2$ in task a) to $450 \times 100 \text{ mm}^2$ in task c). In contrast to this, at the prototype furnace the fire exposed area remains unchanged, but instead the dimension of the steel plates was increased from $110 \times 110 \text{ mm}^2$ in task b) to $500 \times 110 \text{ mm}^2$ in task d). Figure 5 compares the steel temperatures measured at the surface centre on the unexposed, reverse side of the specimens. As expected, for both steel plate thicknesses, a significantly slower heating was observed for the specimen with heat transition.

In Figure 6 the steel temperatures of specimens with heat transition tested with the prototype furnace and the DIN 4102-8 furnace are compared. Because in task c) vermiculite boards were installed in front of the specimen to reduce the fire exposed area, the obtained steel temperatures are additionally reduced by shadow effects. The influence of the shadow effect was determined in a separate fire test, where steel plates without heat transition were analysed under same test conditions as in task c). The steel temperature difference between these specimens and the steel plates tested in task a) was used to identify the shadow effect. Based on this, the steel temperatures determined in task c) at the DIN 4102-8 furnace were corrected. The steel temperatures of the specimens with heat transition tested in the prototype furnace and the DIN 4102-8 furnace shown in Figure 6 are almost the same in the first minutes of the fire test, i.e. until 5 minutes

for the 5 mm thick steel plates and until 10 minutes for the 10 mm thick steel plates. Thereafter, the temperature differences increase. After about 25 minutes, the steel temperatures start to converge again. Regarding specimens with heat transition, the specified heating regime of the prototype furnace results partially in higher steel temperatures compared to the testing with the DIN 4102-8 furnace, which is with regards to the determination of the fire resistance of the coated member on the safe side.

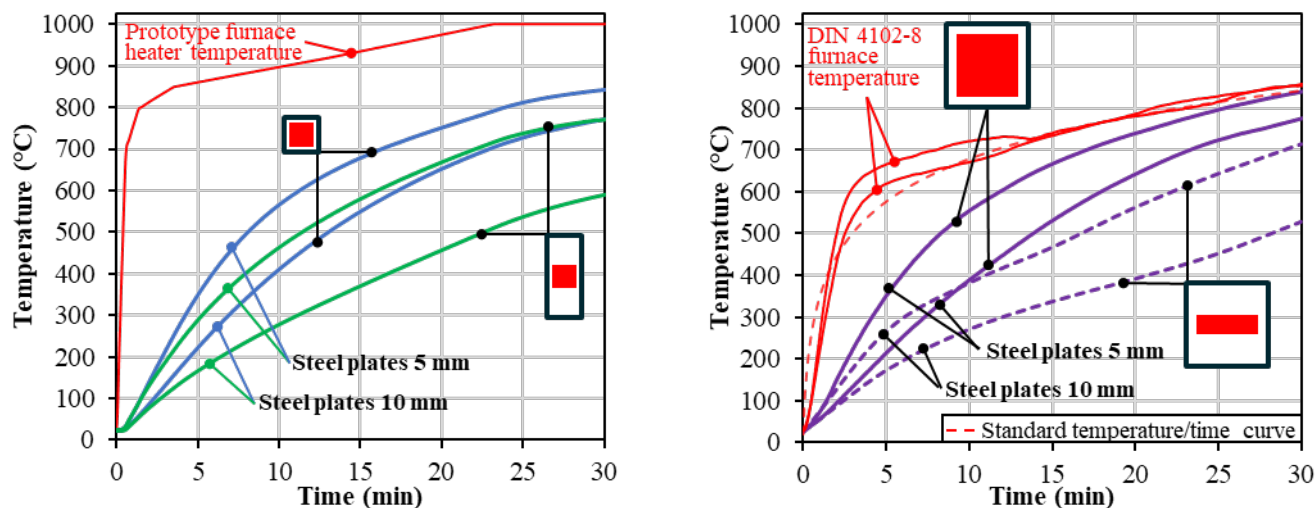
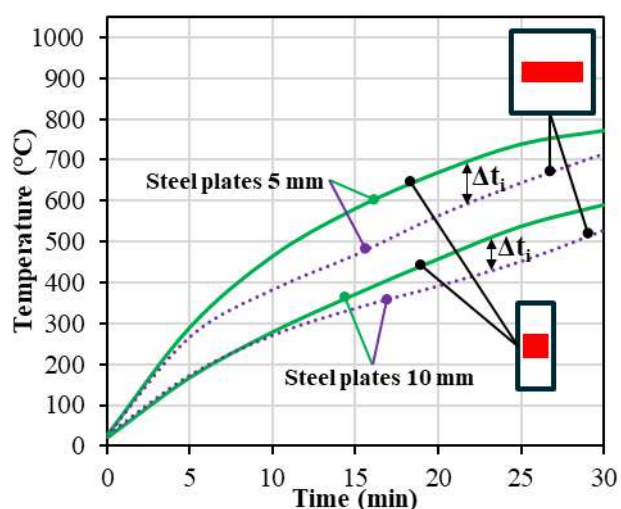


Figure 5. Comparison of the steel temperatures of specimens without and with heat transition: (left) results obtained in prototype furnace; (right) results obtained in DIN 4102-8 furnace



Time of the fire test [min]	Temperature difference Δt_i [K] (Prototype furnace minus DIN 4102-8 furnace)	
	5 mm steel plate	10 mm steel plate
5	23	-6
10	82	7
15	114	33
20	107	65
25	96	85
30	58	62

Figure 6. Comparison of the steel temperatures of specimens with heat transition determined in the prototype furnace and in DIN 4102-8 furnace (after shadow effect adjustment): (left) results shown in a diagram; (right) tabulated results

2.2 Coated specimens of test series 2

The aim was to test whether also for coated specimens the prototype furnace is able to obtain the same steel temperatures and char morphology according to fire tests in the DIN 4102-8 furnace. The tests were conducted in the same manner as in test series 1. The test programme is shown in Figure 2 and Table 1.

Steel temperatures

To set up a reliable basis to compare the test results, it is necessary to take into account the actual DFT of the specimens, see Table 2. For this purpose, the time to reach a certain steel temperature was adjusted according to Equation 1 based on the method given in EN 13381-8, Annex D [12]. The measured steel temperature data was adjusted for all specimens according to the intended DFT of 0.5 mm.

$$t_{adj,i} = t_i \cdot \frac{DFT_{ref}}{DFT_{actual,i}} \quad (1)$$

where

DFT_{ref} is DFT reference value, the intended DFT of 0.5 mm was used,

$DFT_{actual,i}$ is actual DFT of the specimen to be adjusted,

t_i is time to reach a certain temperature of the specimen to be adjusted,

$t_{adj,i}$ is corrected time value of specimen to be adjusted.

Figure 7 (left) shows the measured steel temperatures of coated steel plates tested in task e) and f). As in both cases the fire exposure is almost throughout the entire specimen, the heat transition effect can be neglected. The results of the coated specimens with a steel plates thickness of 10 mm tested in the DIN 4102-8 furnace and the prototype furnace show a good agreement, i.e. the maximum temperature deviation is 22 K. In contrast to this, at the coated specimens with a steel plates thickness of 5 mm the steel temperature obtained after 10 minutes is significantly higher at the prototype furnace compared to those measured in the DIN 4102-8 furnace. This is due to the char formation of the intumescent coating and extensive char expansion at steel temperatures of about 300 °C. Consequently, the distance between the heating elements and the fire exposed surface of the specimen is reduced. Therefore, the energy input into the specimen tested in the prototype furnace increases and results in higher steel temperatures. This happens also at the specimens with a steel plate thickness of 10 mm. However, due to their slower heating the distance effect occurs later and is less significant because of the lower average and maximum char thickness, see Table 2.

In Figure 7 (right) the steel temperatures obtained at coated specimens with heat transition are presented, i.e. results of tasks f) and g) tested at the prototype furnace. Due to the heat transition the coated specimens (500×110 mm²) heat up significantly slower compared to those specimens without this effect (110×110 mm²). Regardless of the steel plate thickness, the temperature difference between the two specimen size is more severe at the coated specimens compared to the uncoated specimens, see comparison of Figure 5 (left) and Figure 7 (right). This is caused by the distance effect described above. Due to the faster heating of the specimens without heat transfer, there is premature char formation and start of the distance effect, which results in an even faster heating of the steel.

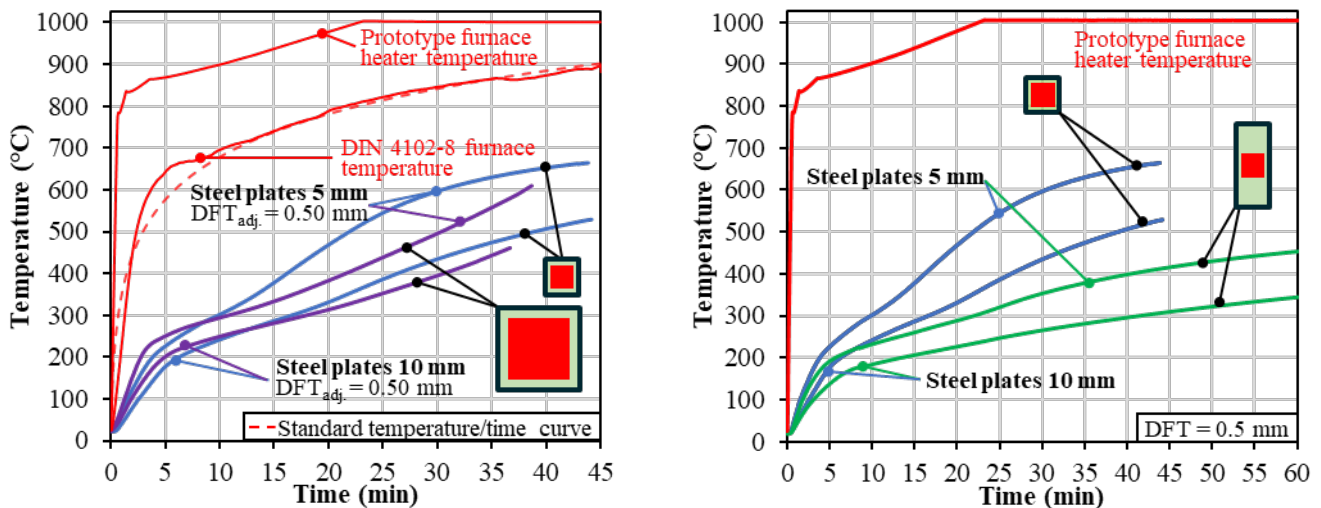


Figure 7. Steel temperatures of coated specimens: (left) results without heat transition effect obtained in the prototype furnace and in the DIN 4102-8 furnace; (right) Comparison of results with and without heat transition obtained in the prototype furnace

Char morphology

The measured char thicknesses after the fire tests are given in Table 2. In general, each specimen shows major differences between the minimum, average and maximum char thickness values, which is mainly

due to big bubbles at the surface, see Figure 8. At the specimens with a steel plate thickness of 5 mm the char thickness was slightly lower when tested in the prototype furnace compared to the DIN 4102-8 furnace. This difference increased at the specimens with a steel plate thickness of 10 mm. In both cases, the greater char thickness obtained at the specimens tested in the DIN 4102-8 furnace can be explained by the higher actual values of the applied DFT. The fact that the prototype furnace is heated primarily by radiation, whereas the DIN 4102-8 furnace is heated by radiation and conduction, may also be a factor.

Even the heating of the steel at specimens with and without heat transition is significantly different when tested in the prototype furnace, the char thickness is similar. This is probably because the char foaming process was completed in both cases. However, the difference in char thickness due to a steel plate thickness of 5 and 10 mm is small for the specimens with heat transfer tested in task g), see Table 2 and Figure 9.

Table 2. Measurements of the actual DFT and the char thickness

Specimen name (Length×Width×Thickness-specimen number)	Task	DFT _{actual} [mm]	Char thickness [mm]				
			Average	Maximum	Minimum		
Tested in DIN 4102-8 furnace							
500×500×5-01	e)	0.55	Char thickness was not measured for this specimen				
500×500×5-02		0.58	13.5	12.9	17.0	16.3	10.0
500×500×5-03		0.59	12.4		15.5		10.0
500×500×10-01		0.61	Char thickness was not measured for this specimen				
500×500×10-02		0.56	14.2	14.8	18.0	19.0	11.0
500×500×10-03		0.67	15.3		20.0		14.0
Tested in prototype furnace							
110×110×5-01	f)	0.51	10.3		22.0		9.0
110×110×5-02		0.53	10.3	11.6	19.0	22.0	9.0
110×110×5-03		0.51	14.1		25.0		12.0
110×110×10-01		0.52	9.9		12.6		6.5
110×110×10-02		0.50	11.4	10.0	14.0	12.5	8.5
110×110×10-03		0.50	8.7		11.0		7.0
500×110×5-01	g)	0.46	9.7		20.0		8.5
500×110×5-02		0.51	10.0	9.4	23.0	20.0	9.5
500×110×5-03		0.50	8.6		17.0		7.0
500×110×10-01		0.51	8.8		19.0		7.0
500×110×10-02		0.50	10.0	9.7	17.0	18.7	8.0
500×110×10-03		0.49	10.3		20.0		9.0

To analyse the morphology more in detail, the char was cut after the fire test. Examples of the sectional views are presented in Figure 8 and Figure 9. Both DIN 4102-8 furnace and prototype furnace specimens have small and large pores in the char. All specimens tested in the prototype furnace showed after the fire tests a white coloured ash throughout the entire char thickness, which means that the intumescent coating has completed its reaction. At the specimens tested in the DIN 4102-8 furnace the char near the steel plate surface is grey or black. Thus, the char formation has not been finished yet. The reason for this might be the slightly higher DFT applied to these specimens and the higher char thicknesses achieved.

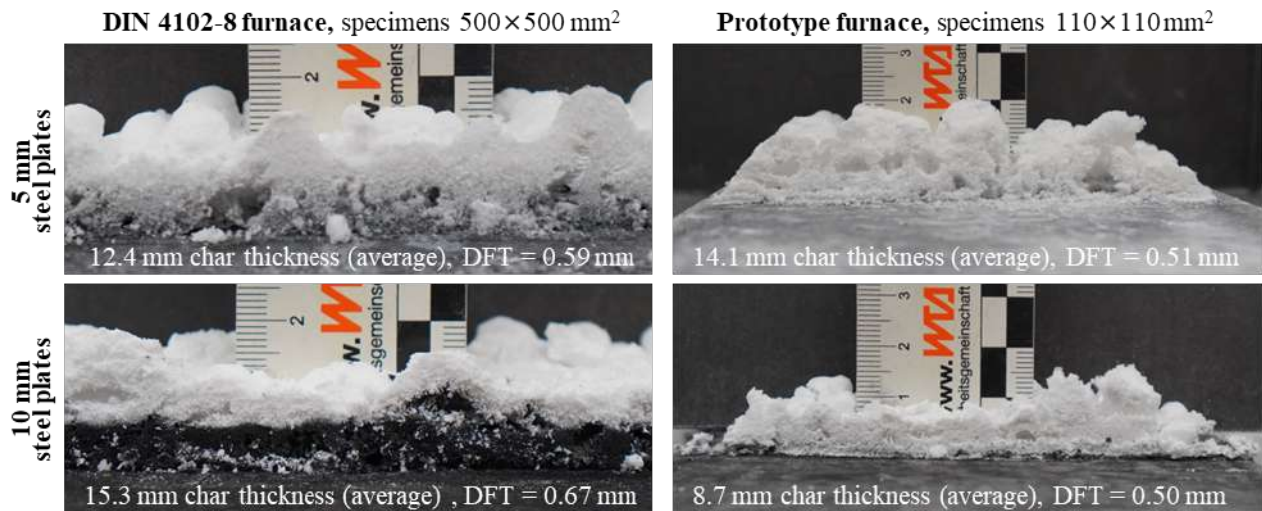


Figure 8. Sectional view of the char after the fire tests: (left) specimen from task e); (right) specimen from task f)

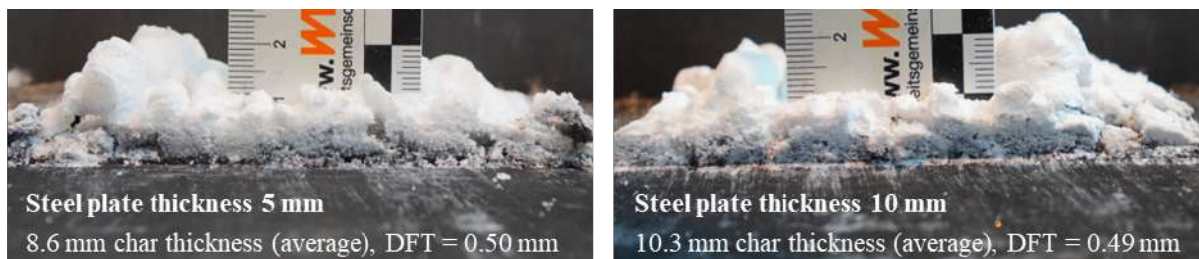


Figure 9. Sectional view of the char of after the fire tests of specimens from task g)

In addition to the fire exposed area of the specimens with heat transition tested in task g), the intumescent coating of adjacent unexposed areas was also visually analysed. The areas beneath the 40 mm wide insulation board of the prototype furnace showed a blackening and thus a minor reaction of the coating. There was no change in the other surrounding areas of the specimen.

In summary, the prototype furnace has demonstrated that the intumescent coating can produce a uniform and representative char, which match to coated specimens fire tested in the DIN 4102-8 furnace.

3 OUTLOOK

Based on the fire tests conducted with the prototype furnace, several possible improvements were identified. For example, a real-time measurement of the actual char thickness during the fire test by a laser distance sensor. This additional information can be used to optimise the heating regime and to consider the change in the distance between the heating elements and the surface of the char. As a result, a better agreement with the DIN 4102-8 furnace test results of coated specimens could be achieved, see Chapter 2.2. In addition, numerical simulations will be carried out to support assessment procedure and enable parametric studies. Moreover, the position of the air tubes for cooling the heating elements shall be modified to allow the prototype furnace to be installed to other specimen geometries, such as I-sections. Similar to the test programme already conducted at steel plates, it is planned to analyse coated IPE 220 and HEB 260 profiles. In this context, also different DFT will be tested. This application case represents the situation on a real structure and aims to demonstrate the applicability of the in situ test procedure, see Figure 10. Different application scenarios regarding the developed test method to assess the fire resistance of existing steel structure with intumescent coating are possible. There may be several reasons that require a re-assessment of the fire resistance of existing steel structures, e.g., the intumescent coating has exceeded its predicted service life, or the performance must be checked for any other reason. Different scenarios are briefly described subsequently:

- **Scenario 1: Direct comparison**

The intumescent coating is known and still available on the market. Thus, it is possible to manufacture a replicate of the existing steel member with the identical section and DFT. Hence a direct comparison of the results derived at the existing structure (aged product) and the replicate (unaged) can be performed to quantify the influence of the ageing.

- **Scenario 2: Direct comparison with reduced DFT**

The circumstances are the same as described in scenario 1 but the measured DFT on the existing structure is less than the value required acc. to the ETA of the product to achieve the prescribed fire resistance. Therefore, the replicate will be manufactured with the reduced DFT. In a first step, analogue to scenario 1, it is quantified if the product on the existing structure suffered a reduction of performance by ageing. If this is the case, please see scenario 3. Otherwise in a second step the fire resistance of the structure can be determined for the actual, i.e. reduced DFT by testing an additional manufactured specimen with the same DFT and geometry. This additional fire resistance test can be replaced by methods of computational fire design procedure acc. to Eurocodes, see scenario 3.

- **Scenario 3: Combination of in situ assessment and FEM simulation**

Information of the intumescent coating is missing or the product is unavailable for any reason. In this case, the temperature data obtained from the in situ tests on the existing structure is used to determine the actual thermal insulation performance of the intumescent coating. Based on the obtained steel temperatures, the effective thermal conductivity of the aged char is calculated by numerical analysis. Then the structures fire resistance is assessed, considering the actual thermal insulation characteristics of the intumescent coating. The fire resistance is determined according to EN 1993-1-2 [13].

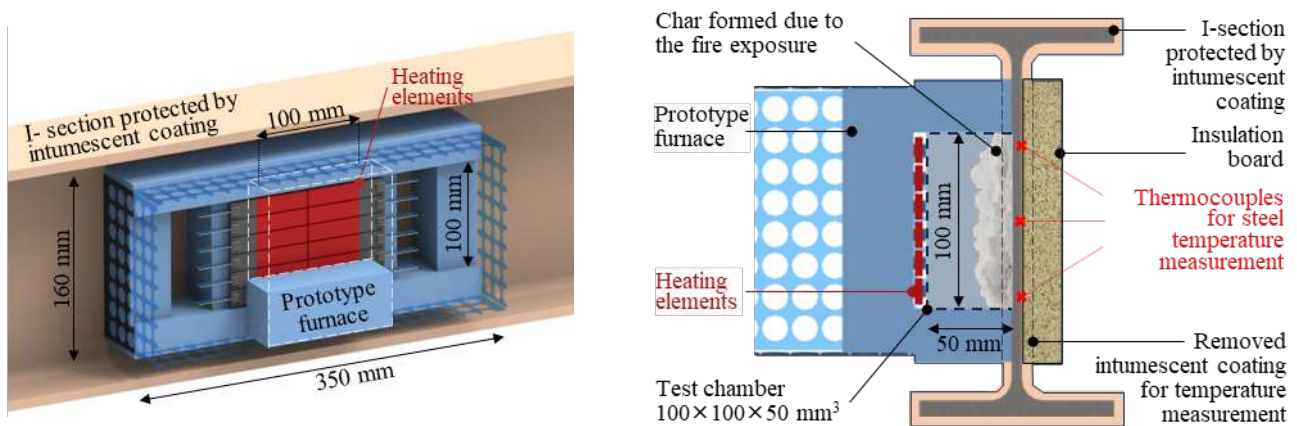


Figure 10. Schema of the in situ test method: position of the prototype furnace at I-section protected by intumescent coating (left); cross section of the test setup (right)

4 CONCLUSIONS

The paper presents the development of an in situ test procedure to assess the actual fire resistance of existing steel structures with applied intumescent coating. For this purpose, a special prototype furnace with an electric heating system was designed. Within the test programme uncoated and coated steel plates were fire tested in the DIN 4102-8 furnace using the standard temperature/time curve. Based on these tests, the prototype furnace was calibrated in order to achieve similar results. In the following the main findings are summarised:

- The prototype furnace is able to generate an equivalent fire exposure as a fire test in DIN 4102-8 furnace using the standard temperature/time curve.
- Regarding the steel temperature, at uncoated steel plates with a thickness of 5 and 10 mm a good agreement between the prototype furnace and the DIN 4102-8 furnace was obtained. In contrast to the

DIN 4102-8 furnace, the prototype furnace heats up the specimen solely by radiation and thus shadow effects can be avoided. Therefore, the specimens with heat transition tested in the prototype furnace have been exposed to higher temperatures and have heated up more quickly. However, this more demanding test condition is conservative and with regards to the determination of the fire resistance of the coated structure on the safe side.

- Based on the specimens with an applied intumescent coating of DFT = 0.5 mm the prototype furnace achieved similar results compared to fire tests in DIN 4102-8 furnace. Due to the char expansion and the resulting reduced distance to the heating elements, specimens heat up faster when tested in the prototype furnace compared to the DIN 4102-8 furnace. To take this effect into account, the char thickness will be measured during the fire test to enable the heating regime to be adjusted. In addition to the steel temperature, the prototype furnace is also able to achieve a uniform and representative char formation, which match to coated specimens fire tested in the DIN 4102-8 furnace.

ACKNOWLEDGMENT

The research is financed by the Deutsches Institut für Bautechnik (DIBt). The authors would like to thank the colleagues of Division 7.3, who supported to prepare and carry out the fire tests.

REFERENCES

1. Deutsches Institut für Bautechnik (DIBt): Zulassungsgrundsätze für reaktive Brandschutz-systeme auf Stahlbauteilen. DIBt Mitteilungen, issue 4, Berlin, Ernst & Sohn, 1998.
2. EAD 350402-00-1106: Fire protective products – Reactive coatings for fire protection of steel elements. European Organization for Technical Approvals, Brussel, 2017
3. BAM: Development of a method for the in-situ assessment of the fire resistance of existing steel structures with intumescent coating (INSIST). project number: P 52-5-4.209-2069/21, Financed by DIBt, Berlin, ongoing project 2021 to 2025.
4. EN 1363-1: Fire resistance tests - Part 1: General requirements, 2020.
5. DIN 4102-8: Fire behaviour of building materials and components - Part 8: Small scale test furnace, 2003.
6. Weisheim, W. Intumescent Coating on Steel Structures Exposed to Natural Fires. Dissertation, Leibniz Universität Hannover (2022). <https://doi.org/10.15488/11732>.
7. Mund, M., Einfluss extensiver Bewitterung auf reaktive Brandschutzsysteme im Stahlbau. Dissertation, Leibniz Universität Hannover (2023). <https://doi.org/10.15488/13557>
8. Mund, M., Häßler, D., Schaumann, P., Hothan, S., Schartel, B., Experimentelle Untersuchungen zur Dauerhaftigkeit von reaktiven Brandschutzsystemen. Stahlbau 92, 93-102, (2023). <https://doi.org/10.1002/stab.202200063>
9. Morys, M., Illerhaus, B., Sturm, H., Schartel, B., Revealing the inner secrets of intumescence: Advanced standard time temperature oven (STT Mufu+)– μ -computed tomography approach. Fire & Materials 41, 927-939 (2017). <https://doi.org/10.1002/fam.2426>
10. Morys, M., Häßler, D., Krüger, S., Schartel, B., Hothan, S., Beyond the standard time-temperature curve: Assessment of intumescent coatings under standard and deviant temperature curves. Fire Safety Journal 112, (2020). <https://doi.org/10.1016/j.firesaf.2020.102951>
11. ETA-20/1228: European Technical Assessment for the reactive fire protection system “HENSOTHERM® 421 KS”. Element Materials Technology, Rotterdam B.V., Amsterdam (2021).
12. EN 13381-8: Test methods for determining the contribution to the fire resistance of structural members – Part 8: Applied reactive protection to steel members (2013).
13. EN 1993-1-2: Eurocode 3: Design of steel structures - Part 1-2: General rules - Structural fire design (2005)

LATERAL-TORSIONAL BUCKLING OF STEEL BEAMS SUPPORTING CROSS-LAMINATED TIMBER SLABS IN FIRE

Aatish Jeebodh¹, Buick Davison², Martyn S. McLaggan³, Ian Burgess⁴, Danny Hopkin⁵, Shan-Shan Huang⁶

ABSTRACT

In recent years, steel-timber hybrid structures with cross-laminated timber slabs and a structural steel frame have become a novel form of sustainable construction in the built environment. This type of hybridization has its benefits as well as challenges, particularly in terms of its structural fire performance. One of the major concerns in fire is the potential lateral-torsional buckling behaviour of the steel beams connected to cross-laminated timber slabs with self-tapping screw fixings which goes beyond the scope of current design guidance. As such, this study explores the use of non-linear finite element analysis to capture the thermo-mechanical response of a 9 m unprotected secondary steel beam with self-tapping screws at 250 mm spacing. The numerical model has been validated using existing test results on heated steel beams. A parametric study is presented to compare the structural behaviour under different degrees of elastic lateral restraint of the screws and axial restraint of the end connections under both uniform and non-uniform heating. In the presence of varying levels of axial restraint, which represents a realistic condition in fire, the beam initially behaves similarly to a corresponding fully laterally restrained beam until the first screw fails and subsequently runaway deflection starts, leading to instability by lateral-torsional buckling. Hence, it is not realistic to assume full lateral restraint condition in the fire design even with an axial restraint of 5% of the initial beam axial stiffness under uniform heating.

Keywords: Steel-timber hybrid structures; fire; lateral-torsional buckling; elastic lateral restraints; end axial restraints

1 INTRODUCTION

Steel-timber hybrid structures are a relatively novel form of construction that combines cross-laminated timber (CLT) slabs with steel beams and columns. In such systems, the CLT floors are typically supported by means of steel beams in downstand or slimfloor arrangements. In a downstand arrangement, the CLT slab is supported and connected to the top flange of the beam. To reduce structural height and intrusion of beams into the floor below, CLT slabs may be supported by the bottom flange of wide flange or shallow sections in a slimfloor arrangement. These types of hybrid construction offer several key environmental and fabrication benefits, but there is a lack of knowledge and understanding regarding their behaviour in

¹ PhD Candidate, University of Sheffield

e-mail: ajeebodh1@sheffield.ac.uk

² Professor of Structural Engineering, University of Sheffield

e-mail: j.davison@sheffield.ac.uk

³ Lecturer in Low Carbon Design, University of Sheffield

e-mail: m.s.mclaggan@sheffield.ac.uk

⁴ Emeritus Professor of Structural Engineering, University of Sheffield

e-mail: ian.burgess@sheffield.ac.uk

⁵ Director, OFR Consultants

e-mail: danny.hopkin@ofrconsultants.com

⁶ Senior Lecturer in Structural Engineering, University of Sheffield

e-mail: s.huang@sheffield.ac.uk

fire, such as: (i) the susceptibility of the steel beams to lateral-torsional buckling in fire, (ii) the degree of composite action between the steel beam and CLT slab at elevated temperatures, and (iii) the potential for fire-induced delamination of CLT due to degradation of the adhesive bond strength with temperature. This paper focuses on the lateral-torsional buckling behaviour of steel-timber hybrid structures in fire and is intended to provide new insights on the thermo-mechanical response of unprotected bare steel beams fixed to CLT slabs with self-tapping screws via finite element modelling. It should be noted that at this point of the study the timber slab is not explicitly modelled but the connection between the steel beam and the timber slab is accounted for through the lateral stiffness provided by the screws. Also in current practice, designers conservatively ignore any potential contribution of CLT panels to composite action and assume the steel beams to resist the full applied loading [1].

In modern steel-timber hybrid construction, CLT panels are fixed to steel beams using partially threaded or fully threaded self-tapping screws at regular spacing not exceeding 600 mm [2]. The screws provide a certain degree of lateral restraint to the lateral-torsional buckling of the steel beam. Merryday et al. [3] conducted a four-point bending test on a simply supported steel-CLT composite beam and reported that lateral-torsional buckling is not a concern at ambient temperature, even with a narrow CLT slab width. However, this assumption may not be valid in fire situations as the lateral stiffness of the screws decreases with increasing temperature due to heating and material degradation of the screw and the surrounding CLT interface. From a design perspective, it is necessary to verify if the screws provide sufficient lateral restraint to prevent beam lateral-torsional buckling in fire and to justify whether the beams should be designed as fully restrained, partially restrained, or unrestrained.

2 FINITE ELEMENT MODELLING

The structural fire performance of steel-timber hybrid structures is mainly influenced by the connection typology, form of shear connection, type of adhesive, and fire safety strategy adopted. As such, a better comprehension of the thermo-mechanical behaviour via experimental and/or numerical studies is essential to develop structural fire engineering approaches, with the aim of determining the best practices to design and construct robust steel-timber hybrid structures for fire conditions. In this study, numerical investigations are presented to assess the influence of elastic restraints representing the screws connecting the top flange of steel beams and the CLT slab on the lateral-torsional buckling behaviour of the beam in fire. In this section, the development of finite element models which are able to replicate the lateral-torsional buckling and restrained behaviour of heated steel beams are validated against experimental results from literature.

2.1 Development of Numerical Models

The numerical models were developed using the finite element analysis software *Abaqus*. The S4R shell element was adopted for meshing in the numerical simulations. The high temperature material properties of carbon steel in terms of non-linear engineering stress-strain relationship and thermal expansion given in Eurocode 3 [4] were adopted. The beam-end boundary conditions shown in Figure 1 were used to mimic fork support conditions (Type 1) and axially/rotationally restrained conditions (Type 2). In Type 1, rigid body constraints connect all nodes of the web to the reference point, whilst the flanges have independent boundary conditions. In Type 2, all nodes of the cross-section are constrained to the reference point. Restraints were simulated using connector elements, which can define a connection between a node and a rigid body.

The high-temperature mechanical analysis was divided into two steps: an ambient-temperature loading step in which the load and a geometric imperfection were applied, followed by a heating step in which steel temperatures increased according to a predefined temperature profile while maintaining the load. The imperfection was included by scaling an eigenmode of a linear buckling analysis on a perfectly straight beam. The static general solver including geometric non-linearity of *Abaqus* was used in both steps. To ensure convergence during the thermal loading step, automatic stabilisation using dissipated energy fraction/damping factor and adaptive stabilisation were utilised to stabilise the unstable quasi-static problem, i.e. lateral-torsional buckling. Adaptive stabilisation was activated to control the ratio of viscous damping energy to the internal energy ($ALLSD/ALLIE \leq 5\%$) and to avoid inaccurate results.

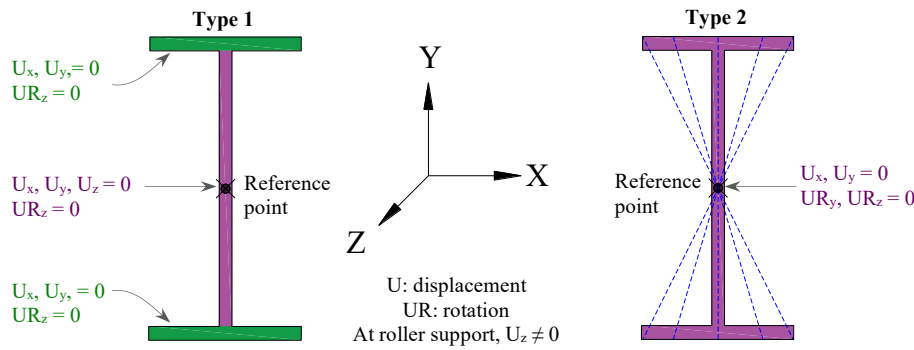


Figure 1: Boundary conditions Type 1 and 2

2.2 Validation of Numerical Models

The validation of the numerical model is performed by comparing the predictions with two sets of experimental data. In the first set, experiments carried out by Mesquita et al. [5] are used for comparison, whereby laterally unrestrained simply supported beams with fork support conditions and uniform temperature distribution were loaded and then heated at a constant rate of 800°C/h until failure by lateral-torsional buckling. The span of the IPE 100 beams varied from 1.5 m to 4.5 m and three tests were carried out for each beam length. Figure 2a compares the numerical results obtained in this study using Type 1 boundary conditions and a half-sine wave geometric imperfection with the experimental data for the beam of 3.5 m span, as well as the predictions made by Kucukler [6]. Based on the test measurements, an imperfection with a maximum amplitude of span/4000 was adopted. It can be observed that the numerical results are in good agreement with the measured path of the midspan deflection; the differences are imperceptible until 621°C. This indicates that the simulation strategy adopted is able to mimic the lateral-torsional buckling response of steel beams in fire.

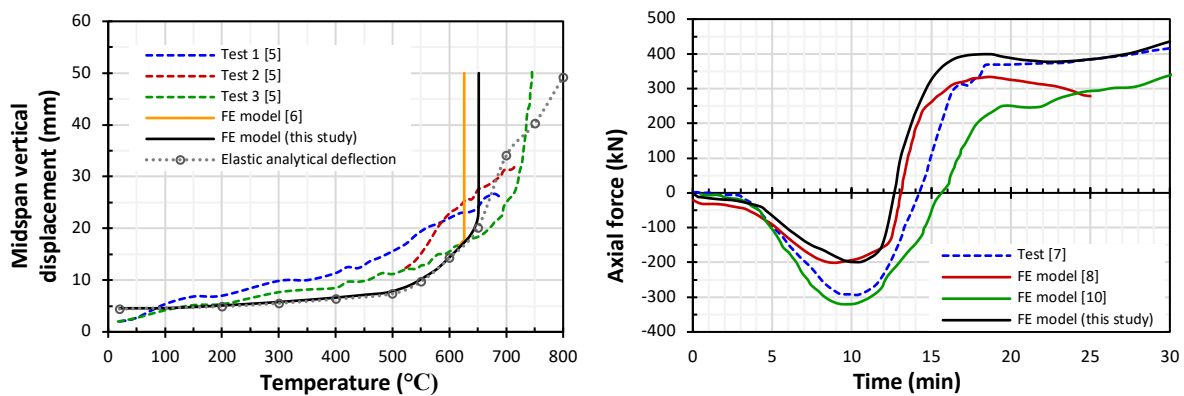


Figure 2: Comparison of (a) midspan vertical displacement with temperature from experiments by Mesquita et al. [5], (b) axial force with temperature from experiments by Li and Guo [7]

In the second set, experiments carried out by Li and Guo [7] are used to model fully laterally restrained beams with non-uniform temperature distribution that display catenary action at large deflections. The span of the H250×250×8×12 beam was 4.5 m. The beam was loaded with two point loads of 130 kN each. The axial and end-rotational stiffness of the beam were 39.5 kN/mm and 1.09×10^8 Nm/rad, respectively [8, 9]. Figure 2b shows the numerical results obtained in this study using Type 2 boundary conditions, including the predictions made by Zhang et al. [8] and Dwaikat and Kodur [10], as well as the experimental data. It can be inferred that the simulation strategy adopted is able to mimic the catenary action of steel beams in fire using both axial and rotational restraints. The discrepancies between the test results and current predictions are mainly due to the simplified boundary conditions assumed in modelling the supports.

3 PARAMETRIC STUDY

The validated numerical models were used to investigate the influence of some key parameters on the thermo-mechanical response of unprotected bare steel beams in steel-timber hybrid structures. As explained earlier in Section 1, the CLT slab is not incorporated in the numerical models but this modelling assumption will still help build up a preliminary understanding of the structural response of steel beams with screw fixations in fire. The parameters considered are the degree of elastic lateral restraint of the screws and the axial restraint of the end connections under both uniform and non-uniform heating.

A hot-rolled steel beam of section UB 457×152×74, grade S355 and 9m span was chosen for the investigation. The 9 m span, giving a span-to-depth ratio of 19.5, was selected to reflect a central secondary beam in a typical steel framing scheme with 9 m × 9 m column grids for a conventional commercial office floor. In terms of applied loading, the dead load is assumed to be 3.0 kN/m² (including self-weight of slab, finishes, and services) and the live load is taken as 5.0 kN/m². Hence, the top flange of the beam is assumed to be loaded with a line load of 24.75 kN/m at the fire limit state from a tributary width of 4.5 m of the slab, giving a load ratio of 0.44 if the beam is assumed to be fully laterally restrained at ambient temperature.

Merryday et al. [1] conducted several monotonic push-out tests using three different brands of self-tapping screws at ambient temperature. The load-slip results from the tests were used to determine the serviceability modulus K_{ser} in accordance with BS EN 26891 [11] equations. It is found that K_{ser} varies approximately between 1500 N/mm and 3500 N/mm per 12 mm nominal diameter screw. Experimental investigations to quantify the longitudinal shear capacity of the steel-timber connections with self-tapping screws in fire are lacking. Therefore, in this parametric study, the high-temperature linear lateral stiffness K_{fi} representing the stiffness of the self-tapping screws in fire is taken as 20% of K_u , which is two-thirds of K_{ser} , for all temperatures, as recommended by BS EN 1995-1-2 [12]. It is assumed that the screws: (i) fail in a brittle manner with a shear deformation capacity of 15mm, and (ii) are staggered at equal spacing of 250 mm on the top flange of the beam. BS EN 26891 [11] recommends that push-out tests may be stopped when the ultimate load is reached, or when the slip is 15 mm, whichever occurs first. Hence, an ultimate slip of 15 mm was adopted for the parametric study and also due to the fact that two of the three brands of screws tested in [1] experienced slippage of at least 15 mm at ambient temperature. However, this may not be valid at higher temperatures and needs to be verified experimentally. To reduce the complexity of the model, the lateral springs were applied at the centre-point of the top flange. The parametric study was performed using the range of linear lateral stiffness K_{fi} as summarised in Table 1. The range of axial restraint adopted is explained later in Section 3.4. The lateral and axial restraints were simulated using connector elements with same technique adopted in Section 2.

Table 1: Range of lateral stiffness for parametric study

K_{ser} (N/mm)	K_u (N/mm)	K_{fi} (N/mm)
75	50	10
188	125	25
375	250	50
750	500	100
1500	1000	200
2500	1667	333
3500	2333	467
Infinity	Infinity	Infinity

The temperature profiles, as shown in Figure 3, were based on the numerical simulations carried by Godoy Dellepiani et al. [13] on steel beams supporting CLT floors on their top flanges subject to a more severe fire exposure than the standard fire curve. It was found that the temperature rose distinctly for different parts of the steel section within the first ten minutes until the temperatures of the web and bottom flange converged. Therefore, for the uniform heating profile, the whole section is assumed to be conservatively at the temperature of the web. In the non-uniform heating profile, the web and bottom flange are assumed to have the same temperature while the top flange is cooler due to the shielding effect of the timber slab. In a

real building fire with a decay phase, the actual heating rates will be different, but the adopted temperature regimes will help to obtain a preliminary understanding of the structural response leading to failure, although to a different timescale.

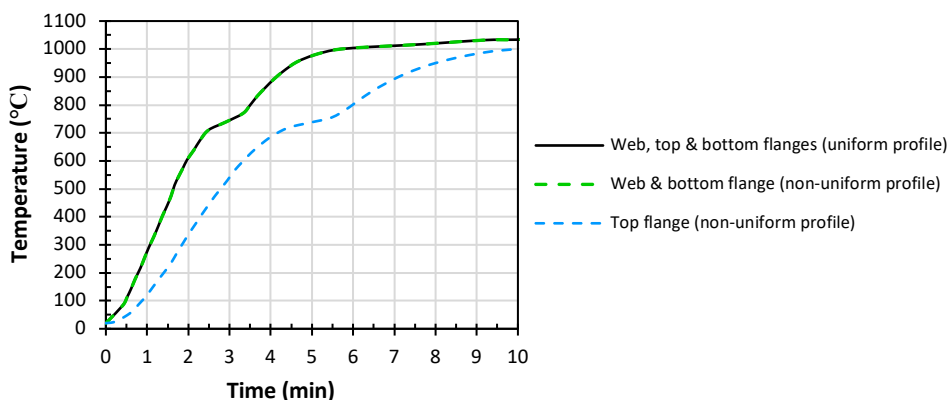


Figure 3: Temperature profiles adopted in the parametric study based on Godoy Dellepiani et al. [13]

3.1 Mesh Sensitivity Analysis

A mesh sensitivity analysis was performed to determine the optimal mesh size to be used for the parametric study. A finer mesh typically results in a more accurate solution but the simulation becomes more computationally expensive. Initially, mesh sizes ranging from 40 mm to 5 mm in *Abaqus* [14] were used to verify the critical linear-elastic buckling moments for different eigenmodes given by *LTBeamN* [15] for the steel beam with elastic lateral restraints of 200 N/mm at 250 mm spacing. The results obtained are shown in Table 2. The results from *Abaqus* are slightly lower than those given by *LTBeamN* as in *Abaqus*, the steel beam was not explicitly modelled to include the fillet radius in order to reduce the complexity of the model. Nevertheless, a mesh size of 20 mm gives an error less than 1.5% for the first eigenmode.

Table 2: Comparison of critical buckling moment in *Abaqus* and *LTbeamN*

Eigenmode	Critical buckling moment (kNm)								
	LTBeamN	Abaqus with different mesh sizes (mm)							
		40	35	30	25	20	15	10	5
1	1035	999	999	1015	1014	1020	1022	1024	1026
2	1116	1081	1081	1094	1093	1098	1099	1101	1102
3	1822	1682	1680	1703	1701	1707	1708	1711	1711

Subsequently, mesh sizes ranging from 40 mm to 10 mm were selected for a further mesh sensitivity analysis for the non-linear high-temperature mechanical analysis. In this phase of the mesh sensitivity analysis, the 5 mm mesh was omitted as it proved to be too computationally expensive with 268,200 elements. The steel beam was loaded with a line load of 24.75 kN/m and subjected to a uniform increase in temperature. The geometric imperfection was initially considered using the half-sine wave of an unrestrained beam. A constant elastic lateral stiffness of 200 N/mm without a fracture limit was adopted to avoid convergence issues. The failure temperature is defined as the temperature at which the vertical deflection reaches span/20 irrespective of the magnitude of the lateral deflection. Table 3 and Figure 4 present the results of this analysis and the error magnitude relative to the smallest mesh size adopted. It indicates that the error is relatively small in all cases. It was, therefore, decided to use a mesh size of 20 mm for the parametric study, which offers both numerical accuracy and computational efficiency.

Table 3: Failure temperature and error magnitude for different mesh sizes

Mesh size (mm)	40	35	30	25	20	15	10
Number of elements	4,180	5,376	7,938	10,800	17,252	30,100	69,300
Failure temperature (°C)	603.41	602.90	603.16	602.59	596.01	596.98	596.62
Error magnitude (%)	1.14	1.05	1.10	1.00	0.10	0.06	0

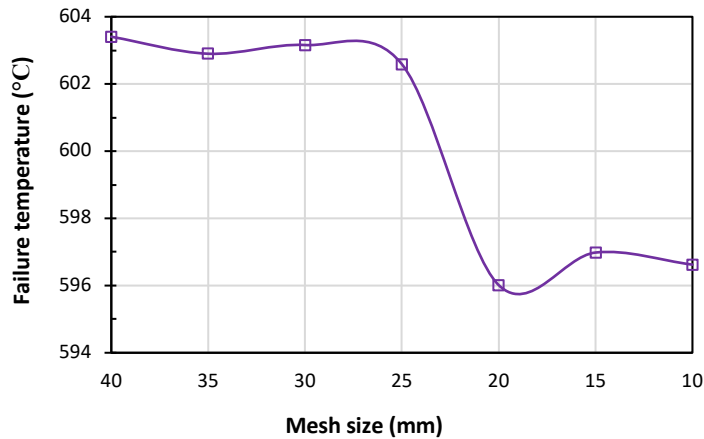


Figure 4: Failure temperature for different mesh sizes

3.2 Imperfection Sensitivity Analysis

Material and geometric imperfections can influence the stability of structural members. Residual stresses, which are generated from the manufacturing process, have been neglected in this investigation as this form of material imperfection decreases with higher temperature levels in a fire. In addition, Vila Real et al. [16] and Kucukler [6] have demonstrated that the buckling resistance of beams is less sensitive to residual stresses with increasing temperature and residual stresses have also been omitted in other high temperature numerical simulations including restrained conditions [17-19].

Geometric imperfection, due to manufacturing, transportation or handling processes, were incorporated in the analysis by performing a prior linear buckling analysis and scaling the buckling eigenmode as necessary. A lateral geometric imperfection based on the first lateral-torsional buckling mode of the beam was considered with a maximum amplitude of 1/1000 of the beam length. This value was adopted based on previous numerical studies [5, 6, 17-20]. It was found that the failure temperature was sensitive to the type of imperfection applied, thus a sensitivity analysis was performed to seek the suitable imperfection type. Similarly, Couto and Vila Real [20] also demonstrated that the shape of the imperfection affects the lateral-torsional buckling resistance of a steel beam. The following imperfections were considered:

- **Imperfection 1:** first eigenmode of a laterally unrestrained beam (half-sine wave);
- **Imperfection 2:** first eigenmode of a partially laterally restrained beam based on K_{fi} .

Table 4 illustrate the effect of imperfection type on the failure temperature of beams for a practical range of K_{ser} of 1500 N/mm to 3500 N/mm and therefore, K_{fi} of 200 N/mm to 467 N/mm. It is typical to assume full lateral restraint at the ambient-temperature due to the high lateral stiffness values of K_{ser} and test observations [3]. However, small lateral movements might occur in the simulations which could affect the shape and magnitude of the imperfection. Hence, the use of the full lateral restraint at the ambient-temperature loading step was also considered. Imperfection 2 was eventually selected for the parametric study, given that it results in the lowest failure temperatures.

Table 4: Effect of imperfection type on predicted failure temperature (i.e. vertical deflection span/20)

K_{ser} (N/mm)	K_{fi} (N/mm)	Failure temperature (°C)		
		Imperfection 1	Imperfection 2	
1500	200	615	594	
2500	333	622	604	
3500	467	642	605	

3.3 Influence of elastic lateral restraints on axially unrestrained steel beams

Secondary steel beams are commonly designed as simply supported members at ambient temperature. This section explores the influence of elastic lateral restraint on the lateral-torsional buckling behaviour of simply supported beams in fire. Figure 5 compares the midspan vertical deflections of the chosen beam for various levels of lateral stiffness K_{fi} of the screws subject to both the uniform and non-uniform temperature profiles described earlier. Type 1 boundary conditions as described in Section 2.1 is adopted and the beam is axially unrestrained and free to expand during heating. The deflection-temperature results are compared to the fully laterally restrained case, as well as to the hand calculated elastic deflection of the beam under uniform heating. In some cases, the analysis stopped prematurely due to convergence issues.

All cases of partial lateral restraint experience runaway deflections. For both the uniform and non-uniform heating cases, the low lateral restraint (10 N/mm) leads to a much lower runaway deflection temperature than all the other cases. All the other partial lateral restraint levels (equal to or above 25 N/mm) result in similar runaway deflection temperatures to those of the fully laterally restrained cases. It should be noted that the practical range of high-temperature K_{fi} is between 200 N/mm and 467 N/mm based on Eurocode 5 [12]. This means that most cases will be similar to a fully lateral restrained case based on the assumptions made in this section. For all the uniformly heated cases, the runaway deflection is caused by lateral-torsional buckling. With the non-uniform temperature distribution, the cooler compression flange provides enhanced structural performance in fire; lateral-torsional buckling occurs after the midspan vertical deflection exceeds span/20 for K_{fi} above 25 N/mm. The effect of thermal bowing can also be observed due to the uneven temperature distribution. However, this simply supported behaviour does not represent real thermo-mechanical response under fire conditions due to the presence of axial restraint offered by adjoining structure.

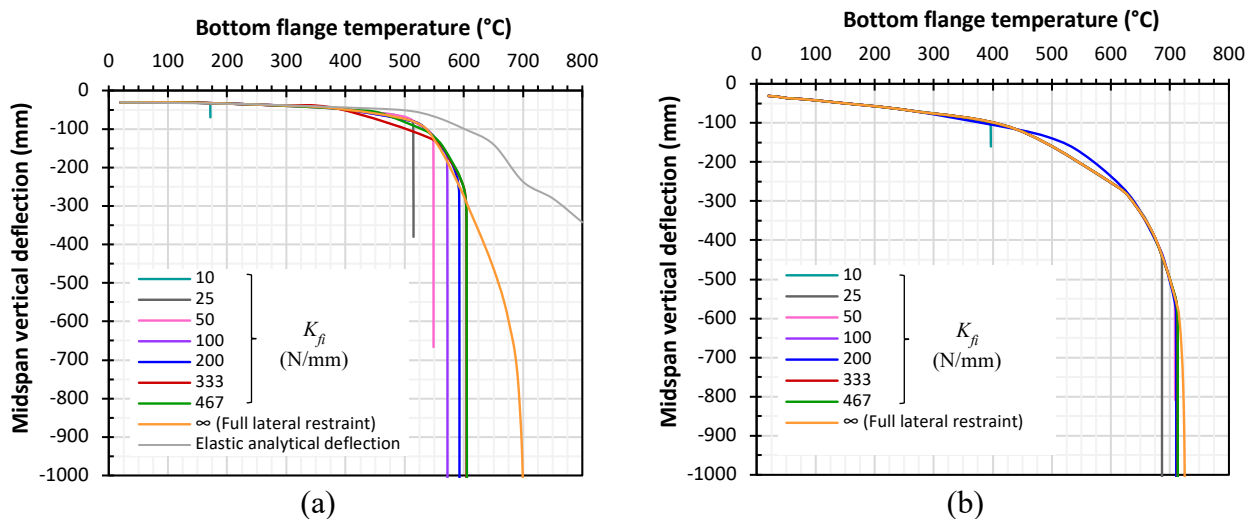


Figure 5: Vertical deflection-temperature relationships with varying lateral stiffness K_{fi} for (a) uniform temperature profile and (b) non-uniform temperature profile

3.4 Influence of elastic lateral restraints on axially restrained steel beams

In real structures, it is well-established that the surrounding support conditions generally restrict the thermal expansion and induce axial compression force followed by tensile force in a fully laterally restrained steel beam exposed to fire [18]. These axial forces in the member provide additional mechanism to resist the external loading at high temperature as material degradation occurs and bending resistance decreases.

In this section, the influence of varying degrees of axial restraint provided by the end connections under both uniform and non-uniform heating is investigated for K_{fi} values of 200 N/mm and 50 N/mm. Seven levels of axial restraint are considered, namely: $0.05K_a$, $0.15K_a$, $0.30K_a$, $0.50K_a$, $1.00K_a$, and ∞ , where K_a is the axial stiffness of the beam at ambient temperature and is 221 kN/mm. The axial restraints are assumed to be linear and unaffected by temperature. Figure 6 and Figure 7 respectively illustrate the evolutions over

heating of the midspan vertical deflection of the bottom flange and the midspan lateral deflection of the top flange with various axial restraints and temperature distributions. The vertical deflection-temperature relationships are also compared to a fully laterally restrained beam ($K_{fi} = \infty$) for the corresponding axial restraints. The full thermo-mechanical response could not be captured in some cases due to non-convergence issues encountered in the numerical analysis.

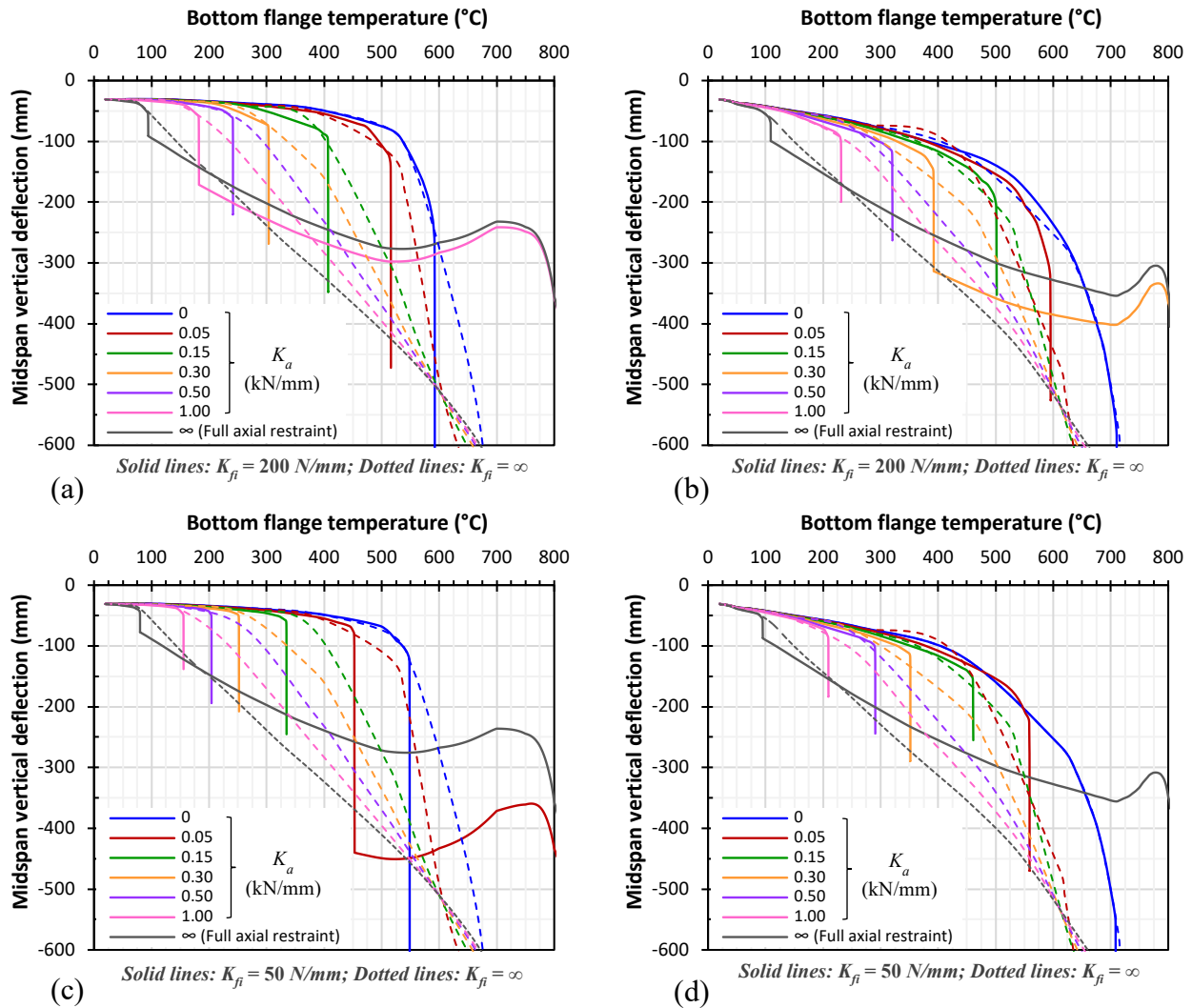


Figure 6: Vertical deflection-temperature relationships for (a) uniform temperature profile with $K_{fi} = 200$ N/mm and infinity, (b) non-uniform temperature profile with $K_{fi} = 200$ N/mm and infinity, (c) uniform temperature profile with $K_{fi} = 50$ N/mm and infinity, (d) non-uniform temperature profile with $K_{fi} = 50$ N/mm and infinity

In general, it can be observed that in the presence of axial restraints, a partially laterally restrained beam initially follows a similar gradient to the fully laterally restrained beam but subsequently undergoes the classical runaway deflection due to lateral-torsional buckling. This is clearly visible in Figure 7 where there is a sudden increase in lateral deflection in the midspan region. A turning point is then reached when the rate of runaway deflection is attenuated due to the development of tensile force in the member, where it starts to behave as a cable.

Figure 8 illustrates the axial forces induced by the different degrees of axial restraint and temperature distributions. The results are also compared to a fully laterally restrained beam ($K_{fi} = \infty$) for the corresponding axial restraints. It can be observed that the curves follow similar gradients to the fully laterally restrained beam until a maximum compression force is attained. In general, the thermo-mechanical response of partially laterally restrained beams with end axial restraints can be described as follows:

- Initially, the beam follows the behaviour of a fully laterally restrained beam until a maximum compressive force is reached when the first screw fails in shear in the midspan region.
- Once the first screw fails, the remaining screws start to fail in succession and the beam undergoes runaway deflection whereby there is a rapid increase in both vertical and lateral deflections along with a very sharp transition from compressive to tensile force in the member.
- The catenary stage is then reached and the tensile force generated provides the mechanism to slow down the rate of runaway midspan deflection. The tensile force remains at a fairly constant magnitude up to a maximum until failure occurs when the tensile capacity of the beam is exceeded.

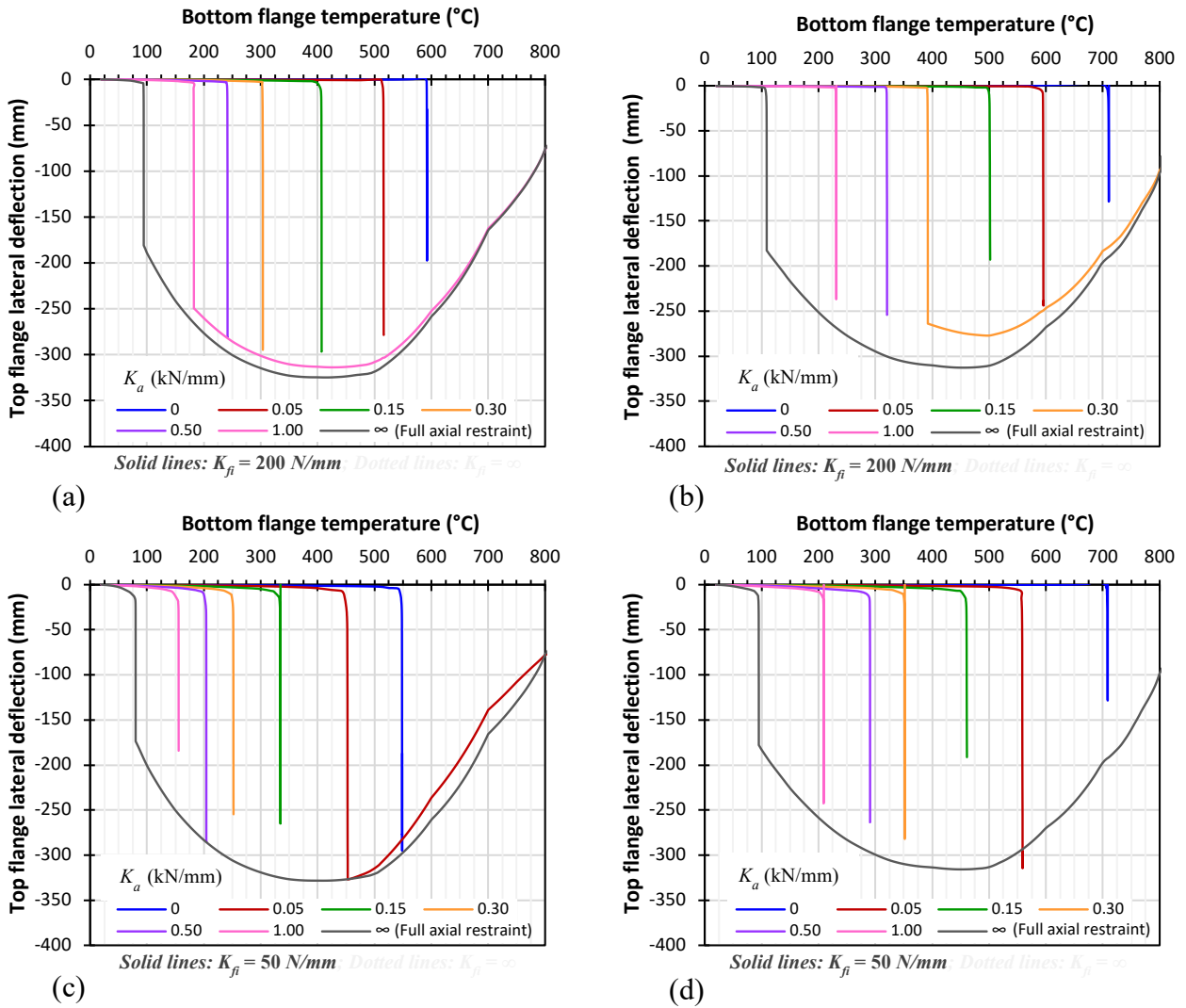


Figure 7: Lateral deflection-temperature relationships for (a) uniform temperature profile with $K_{fi} = 200$ N/mm, (b) non-uniform temperature profile with $K_{fi} = 200$ N/mm, (c) uniform temperature profile with $K_{fi} = 50$ N/mm, (d) non-uniform temperature profile with $K_{fi} = 50$ N/mm

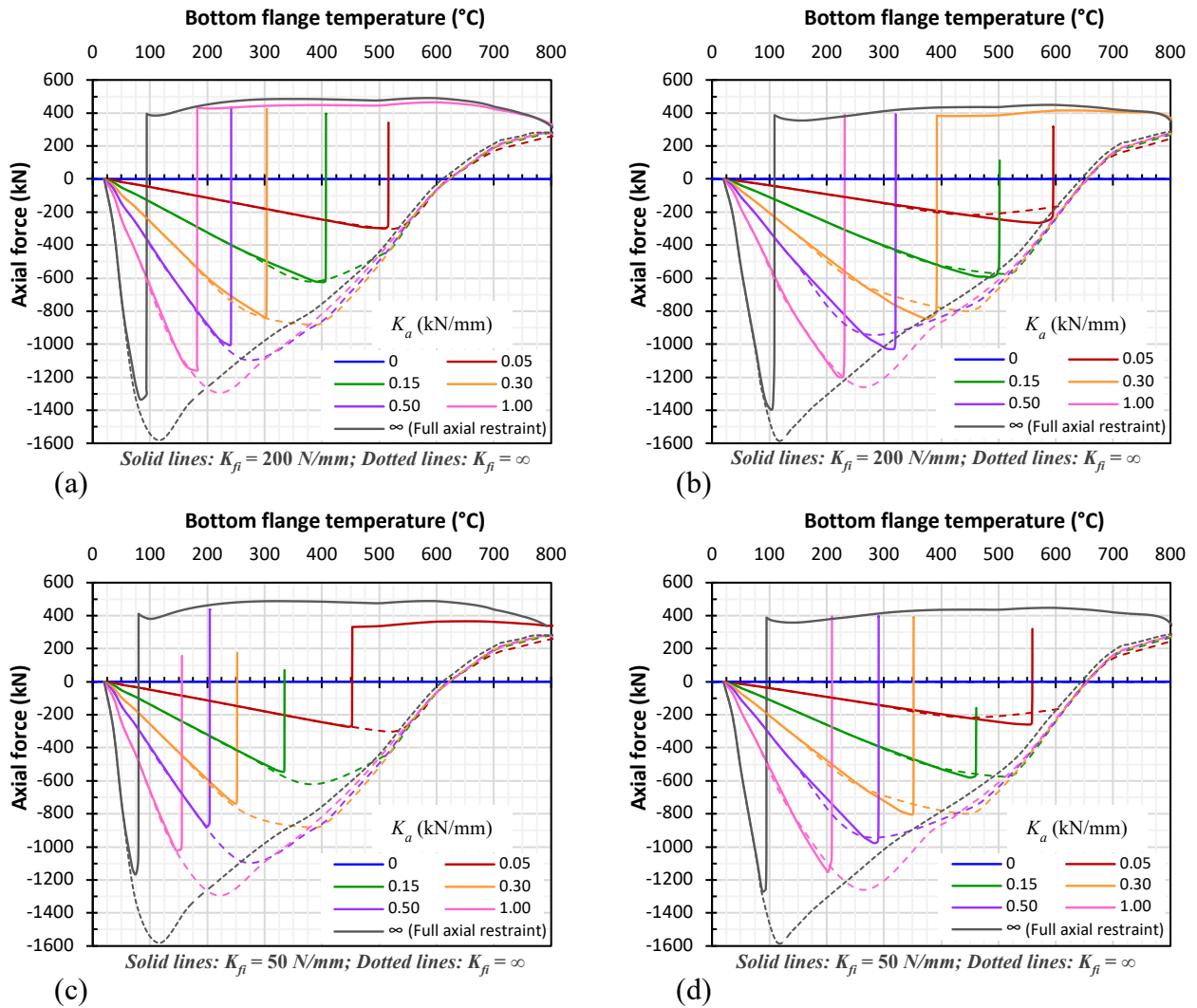


Figure 8: Axial force-temperature relationships for (a) uniform temperature profile with $K_{fi} = 200$ N/mm and infinity, (b) non-uniform temperature profile with $K_{fi} = 200$ N/mm and infinity, (c) uniform temperature profile with $K_{fi} = 50$ N/mm and infinity, (d) non-uniform temperature profile with $K_{fi} = 50$ N/mm and infinity

3.5 Failure Temperature

According to building codes, construction elements must provide one or more of the performance criteria during a specified fire exposure, namely: (a) load resistance or stability, (b) thermal insulation, and (c) integrity. Allied to this, steel-timber hybrid structures must sustain mechanical loads without exceeding large deflections and disproportionate collapse, limit the temperature rise on the unexposed side of the CLT slab and prevent the passage of flames and hot gases through cracks or gaps in the timber floor structure. The CLT slabs must demonstrate compliance with (a), (b) and (c) whereas the steel beams are only required to satisfy the load bearing capacity criterion. For this study, the failure temperature of the steel beam is therefore taken as either of the following, whichever is exceeded first:

- a vertical deflection of span/20 in accordance with BS 476-20 [21]; or
- the temperature at which runaway deflection starts leading to large lateral displacements.

Figure 9 illustrates the deformation of the beam with K_{fi} values of infinity and 200 N/mm for the uniform temperature profile and an axial restraint of $0.05K_a$. It can be observed that the partially laterally restrained beam has failed by lateral-torsional buckling in comparison to the fully laterally restrained beam. Table 5 summarises the failure temperatures of beams with various axial restraints and various lateral restraints under uniform and non-uniform heating. As the axial restraint increases, the failure temperature decreases due to increase in axial compression caused by restrained thermal expansion. As the lateral restraint decreases, the failure temperature decreases, indicating that it is unsafe to assume fully laterally restrained

conditions in fire. However, it must be noted that this study is based on assumed screw characteristic (simplified according to Eurocode 5) that needs to be updated with high temperature push-out tests to capture more realistic response of the beam, which will be further exacerbated with higher load ratios.

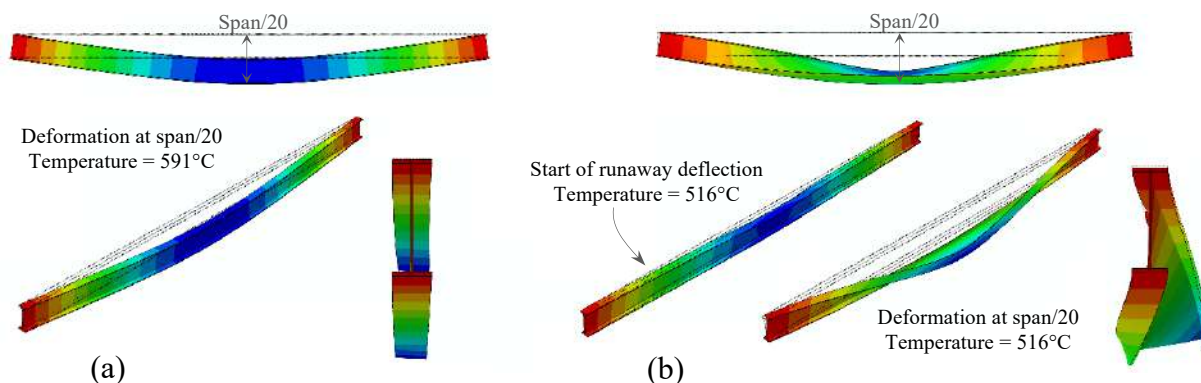


Figure 9: Deformation of beam for uniform profile and axial restraint of $0.05K_a$: (a) $K_{fi} = \infty$, (b) $K_{fi} = 200$ N/mm

Table 5: Assumed bottom flange failure temperature at span/20 or runaway deflection

Axial restraint, K_a (N/mm)	Bottom flange failure temperature (°C)					
	Uniform profile with K_{fi} (N/mm)			Non-uniform profile with K_{fi} (N/mm)		
	∞ [1]	200	50	∞ [1]	200	50
0	647	592	548	689	689 [1]	689 [1]
0.05	591	516	452	602	595	558
0.15	573	406	334	588	501	460
0.30	562	303	251	575	392	351
0.50	556	241	204	567	320	290
1.00	548	182	155	559	231	209
∞	542	94	80	546	109	95

Note 1: Failure temperature taken as vertical deflection at midspan = span/20

4 CONCLUSIONS

This paper investigates the influence of elastic lateral restraints on the lateral-torsional buckling behaviour of secondary steel beams in steel-timber hybrid structures at high temperature, considering the effects of the brittle fracture of the screws and the beam end axial restraints. Based on the results of this investigation, the following conclusions can be drawn:

- In the simply supported condition (no axial restraint), the uniformly heated beam experiences runaway deflection due to lateral-torsional buckling. The structural behaviour is ameliorated under non-uniform heating and lateral-torsional buckling mostly occurs after the vertical deflection exceeds span/20. For both the uniform and non-uniform heating cases, all the partially laterally restrained beams experience similar runaway deflection temperatures to those of the fully laterally restrained cases, except for the lowest lateral restraint (10 N/mm) case.
- A partially laterally restrained beam with axial restraints initially behaves similarly to a corresponding fully laterally restrained beam until failure of the first screw occurs in the midspan region. The beam subsequently undergoes runaway deflection due to lateral-torsional buckling until there is an abrupt transition from compression to tension. The development of the catenary action attenuates the runaway deflection until failure occurs when the tensile capacity of the beam is reached.
- It is not realistic to assume the beams in steel-timber hybrid structures as fully laterally restrained in fire. The screws play a crucial factor in the fire safety of steel-timber hybrid structures and further testing is required to characterise their behaviour.

ACKNOWLEDGMENT

This work was supported by the UK Engineering and Physical Sciences Research Council [grant number EP/T517835/1] in collaboration with OFR Consultants.

REFERENCES

- [1] H. C. Merryday, K. Sener, and D. Roueche, "Pushout Tests on Steel-Timber Connections Using Self-Tapping Screws," *Structures Congress 2023*, pp. 312-327, 2023, doi: <https://doi.org/10.1061/9780784484777.028>.
- [2] D. Barber *et al.*, "Design Guide 37: Hybrid Steel Frames with Wood Floors," American Institute of Steel Construction, USA, 2022.
- [3] H. Merryday, M. Potuzak, D. Roueche, and K. Sener, "Experimental and Numerical Investigations on the Usage of CLT Panels to Form Timber-Steel Composite Floor Systems," in *World Conference on Timber Engineering (WCTE 2023)*, Oslo, Norway, 2023, pp. 3373-3381, doi: <https://doi.org/10.52202/069179-0439>.
- [4] BS EN 1993-1-2, *Eurocode 3: Design of steel structures - Part 1-2: General rules - Structural fire design*. British Standards Institution, 2005.
- [5] L. M. R. Mesquita, P. A. G. Piloto, M. A. P. Vaz, and P. M. M. Vila Real, "Experimental and numerical research on the critical temperature of laterally unrestrained steel I beams," *Journal of Constructional Steel Research*, vol. 61, no. 10, pp. 1435-1446, 2005/10/01/ 2005, doi: <https://doi.org/10.1016/j.jcsr.2005.04.003>.
- [6] M. Kucukler, "Lateral instability of steel beams in fire: Behaviour, numerical modelling and design," *Journal of Constructional Steel Research*, vol. 170, p. 106095, 2020/07/01/ 2020, doi: <https://doi.org/10.1016/j.jcsr.2020.106095>.
- [7] G.-Q. Li and S.-X. Guo, "Experiment on restrained steel beams subjected to heating and cooling," *Journal of Constructional Steel Research*, vol. 64, no. 3, pp. 268-274, 2008/03/01/ 2008, doi: <https://doi.org/10.1016/j.jcsr.2007.07.007>.
- [8] C. Zhang, G.-Q. Li, and A. Usmani, "Simulating the behavior of restrained steel beams to flame impingement from localized-fires," *Journal of Constructional Steel Research*, vol. 83, pp. 156-165, 2013/04/01/ 2013, doi: <https://doi.org/10.1016/j.jcsr.2013.02.001>.
- [9] X. T. Nguyen and J. S. Park, "Design equations for buckling strength of steel I-beam under non-uniform heating condition," *Fire Safety Journal*, vol. 127, p. 103464, 2022/01/01/ 2022, doi: <https://doi.org/10.1016/j.firesaf.2021.103464>.
- [10] M. Dwaikat and V. Kodur, "Engineering Approach for Predicting Fire Response of Restrained Steel Beams," *Journal of Engineering Mechanics*, vol. 137, pp. 447-461., 07/01 2011, doi: [https://doi.org/10.1061/\(ASCE\)EM.1943-7889.0000244](https://doi.org/10.1061/(ASCE)EM.1943-7889.0000244).
- [11] BS EN 26891, *Timber structures. Joints made with mechanical fasteners. General principles for the determination of strength and deformation characteristics*. British Standards Institution, 1991.
- [12] BS EN 1995-1-2, *Eurocode 5: Design of Timber Structures - Part 1-2: General - Structural Fire Design*. British Standards Institution, 2004.
- [13] M. Godoy Dellepiani, G. Roa Munoz, S. J. Yanez, C. F. Guzmán, E. I. Saavedra Flores, and J. C. Pina, "Numerical study of the thermo-mechanical behavior of steel-timber structures exposed to fire," *Journal of Building Engineering*, vol. 65, p. 105758, 2023/04/15/ 2023, doi: <https://doi.org/10.1016/j.jobe.2022.105758>.
- [14] Abaqus, "Abaqus/CAE User's Guide," Dassault Systèmes, 2021.
- [15] CTICM, "Logiciel LTBeamN – Déversement élastique de poutres fléchies comprimées," 2023. [Online]. Available: <https://www.cticm.com/logiciel/ltbeamn/>.
- [16] P. M. M. Vila Real, R. Cazeli, L. Simões da Silva, A. Santiago, and P. Piloto, "The effect of residual stresses in the lateral-torsional buckling of steel I-beams at elevated temperature," *Journal of Constructional Steel Research*, vol. 60, no. 3, pp. 783-793, 2004/03/01/ 2004, doi: [https://doi.org/10.1016/S0143-974X\(03\)00143-3](https://doi.org/10.1016/S0143-974X(03)00143-3).
- [17] Y. Z. Yin and Y. C. Wang, "Numerical simulations of the effects of non-uniform temperature distributions on lateral torsional buckling resistance of steel I-beams," *Journal of Constructional Steel Research*, vol. 59, no. 8, pp. 1009-1033, 2003/08/01/ 2003, doi: [https://doi.org/10.1016/S0143-974X\(03\)00003-8](https://doi.org/10.1016/S0143-974X(03)00003-8).
- [18] Y. Z. Yin and Y. C. Wang, "A numerical study of large deflection behaviour of restrained steel beams at elevated temperatures," *Journal of Constructional Steel Research*, vol. 60, no. 7, pp. 1029-1047, 2004/07/01/ 2004, doi: <https://doi.org/10.1016/j.jcsr.2003.09.005>.
- [19] A. Santiago, L. S. da Silva, P. V. Real, and M. Veljkovic, "Numerical study of a steel sub-frame in fire," *Computers & Structures*, vol. 86, no. 15, pp. 1619-1632, 2008/08/01/ 2008, doi: <https://doi.org/10.1016/j.compstruc.2008.01.006>.
- [20] C. Couto and P. Vila Real, "Numerical investigation on the influence of imperfections in the lateral-torsional buckling of beams with slender I-shaped welded sections," *Thin-Walled Structures*, vol. 145, p. 106429, 2019/12/01/ 2019, doi: <https://doi.org/10.1016/j.tws.2019.106429>.
- [21] BS 476-20, *Fire tests on building materials and structures - Part 20: Method for determination of the fire resistance of elements of construction (general principles)*. British Standards Institution, 1987.

MODELLING THERMAL CREEP OF ULTRA-HIGH-STRENGTH STEELS UNDER STEADY STATE TEMPERATURE CONDITIONS

Sara Uszball¹, Faranak Faghihi², Markus Knobloch³

ABSTRACT

The material behaviour of structural steels at elevated temperatures is strongly influenced by thermal creep which is defined as time-, temperature- and stress-dependent inelastic strain. In advanced fire engineering and design of steel structures, the explicit consideration and precise modelling of thermal creep is of great importance, as creep strains besides other temperature- and rate-dependent thermal-induced phenomena significantly contribute to the deformations of steel structures on cross-sectional, member and structural levels. However, there is still a lack of knowledge on the elevated-temperature creep of high- and ultra-high-strength steels which are increasingly used in sophisticated engineering structures with fire safety requirements like high-rise buildings. This paper presents a comprehensive study on the thermal creep behaviour of ultra-high-strength steels of grades S960QL and S960M. The results of elevated-temperature creep tests at temperatures relevant in terms of material technology and structural fire design are presented. Based on the experimental results, a consistent analytical creep model is developed to determine the creep strains of ultra-high-strength steels using the theoretical creep formulation according to Fields & Fields as a basis and adapting material parameters for the specified materials. The proposed model is implemented further in numerical simulations with the aim of future applications in advanced case studies.

Keywords: Thermal Creep; Ultra-high-strength Steels; Mechanical Material Model; Numerical Implementation

1 INTRODUCTION

The material behaviour of structural steels at ambient temperature is mostly time-independent. However, at elevated temperatures, the material behaviour is strongly influenced by temperature-, time- and rate-dependent phenomena such as thermal creep. In the case of fire, creep strains contribute significantly to the deformations of steel structures and may have implications on the structural performance by buckling or bending of structural members [1, 2]. Therefore, explicit consideration and precise modelling of thermal creep is an essential part of advanced structural fire design methods.

High-strength steels are increasingly used in sophisticated engineering structures with fire safety requirements, e.g. high-rise buildings, due to their favourable characteristics in terms of their strengths-to-weight-ratio and the associated opportunities for material savings and resource-efficient constructions, e.g. as a result of smaller cross-sectional dimensions for structural components. For these steels, however, there is still a lack of knowledge on the elevated-temperature creep behaviour. Thermal creep is defined as time-, temperature- and stress-dependent inelastic strains. Generally, creep tests in which the deformations of a

¹ M.Sc., Ruhr-Universität Bochum,
e-mail: sara.uszball@rub.de, ORCID: <https://orcid.org/0000-0002-6615-5131>

² Dr., Ruhr-Universität Bochum
e-mail: faranak.faghihi@rub.de, ORCID: <https://orcid.org/0000-0001-8061-8430>

³ Prof. Dr., Ruhr-Universität Bochum
e-mail: markus.knobloch@rub.de, ORCID: <https://orcid.org/0000-0002-1289-0691>

specimen are measured under constant mechanical tensile stress and temperature, are used to experimentally determine the creep strains of a material.

Thermal creep has been ongoing research during the last years; several studies have investigated different constitutive creep laws and developed various analytical creep models [3-8]. In state-of-the-art studies, many researchers have so far investigated thermal creep behaviour in different stages and its impact on the design and analysis of steel structures based on their own experimental test data or experimental results of other performed creep tests [2, 9-14]. Meanwhile, only a few studies have addressed the thermal creep behaviour of high- or ultra-high-strength steels [2, 11-14]. In addition, the proposed creep models mainly include stress- and temperature-dependent creep parameters in the exponent coefficients of mathematical creep formulations, which is a limitation for further applications in developing fire and transient elevating temperature conditions.

This paper presents a comprehensive study on the thermal creep behaviour of ultra-high-strength steels of grades S960QL and S960M. The results of comprehensive elevated-temperature creep tests are presented and the creep strains of the quenched and tempered steel are compared to the thermomechanically rolled material. Subsequently, a consistent analytical creep model is developed to determine the creep strains of ultra-high-strength steels at elevated temperatures up to 900°C. The model is based on the theoretical creep formulation according to Fields & Fields [8] and individual material parameters depending on temperature and stress are provided for the adaption of the model to the investigated ultra-high-strength steels. The developed model is further implemented in numerical simulations and the functionality of the numerical model under steady-state temperature and stress conditions is validated against analytically determined strain-time curves and experimental results of creep tests. The study, therefore, provides the scientific basis for explicitly considering thermal creep in advanced numerical simulations. Hence, numerical simulations with the simplified model of this paper provide the basis for future applications in various advanced case studies considering the influence of elevated-temperature creep on the structural performance of steel components.

2 ELEVATED TEMPERATURE CREEP TESTS

2.1 Test Program

Elevated-temperature-creep tests directly provide strain-time curves for a defined temperature and a certain stress level of the specimens. In the present study, the test temperatures of the creep tests (under steady-state temperature conditions) were chosen as $T = 400^{\circ}\text{C}$, 550°C , 700°C and 900°C and the target stress levels were $\sigma = (0.5, 0.8 \text{ or } 0.97) \cdot f_{y,0}$, whereby $f_{y,0}$ is the actual yield strength at the respective test temperature, which was previously determined with elevated-temperature tests under steady-state temperature conditions [15]. In total, 24 creep tests were performed. The test program is summarised in Table 1.

Table 1. Test program of elevated-temperature creep tests

Steel	Temperature T [°C]	$f_{y,0}$ [MPa]	Stress level σ
S960QL	400	903.6	0.5· $f_{y,0}$ 0.8· $f_{y,0}$ 0.97· $f_{y,0}$
	550	692.1	
	700	162.9	
	900	43.4	
S960M	400	854.1	
	550	651.4	
	700	210.4	
	900	49.6	

For the tests, small-scale specimens were manufactured from plate material of ultra-high-strength steels of grades S960QL and S960M. The specimens had a dog-bone-shape with a constant thickness of $t=6$ mm, which is in line with the requirements of the test setup that is shown in Figure 1(a) and, additionally, corresponds to previous studies on the temperature-dependent constitutive behaviour of high- and ultra-high-strength steels [15, 16]. The geometry of the specimens is presented in Figure 1(b).

Test Procedure

Figure 1(a) presents the test setup of the creep tests, which consists of an electromechanical universal testing machine with a maximum load capacity of 250 kN and an electric furnace with three vertically arranged independently controllable heating zones with a maximum temperature of 1200°C per zone. For the creep tests a specimen is heated until it reaches the previously specified target temperature of $T= 400, 550, 700$ or 900°C . The heating is controlled by three mantle thermocouples (type N, $d_1= 1.5$ mm), which are placed on the specimen surface. With three additional mantle thermocouples (type N, $d_2= 3.0$ mm), the air temperature inside the furnace is measured. After a soaking time of 30 min, which ensures the uniform heating of the specimen, a mechanical tensile load is applied in a force-controlled manner corresponding to a target stress level of $\sigma= (0.5, 0.8 \text{ or } 0.97) \cdot f_{y,0}$. The temperature and stress level are kept constant for the duration of the test and the elongation of the specimen is measured using a high-temperature resistant extensometer. The test ends after a duration of 7 h or with the rupture of the specimen if this occurs earlier. The test procedure is shown schematically in Figure 1(c).

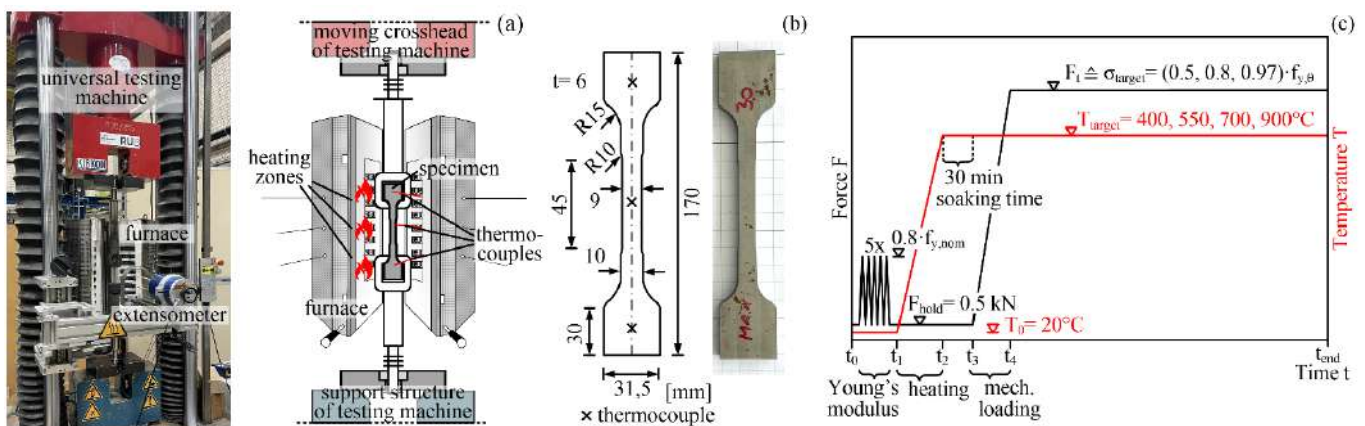


Figure 1. (a) Test setup, (b) geometry of the test specimens and (c) schematic representation of the test procedure

2.2 Test Results

Strain-time curves are obtained directly from creep tests at elevated temperatures for a predefined temperature and a certain stress level of the specimen. After deducting the initial strain resulting from the application of the mechanical load, the temperature- and time-dependent creep strains are obtained.

The creep behaviour of structural steel can usually be divided into three phases: (I) the primary, (II) the secondary and (III) the tertiary creep phases. Figure 2 shows schematically the three characteristic stages of the strain-time curves. In the primary creep stage, the plastic deformations and thus also the creep strains initially increase rapidly. In the further progress of this first phase, the creep rate decreases. The secondary creep phase is characterised by a slower, almost constant creep rate. This stage usually lasts the longest in creep tests. In the tertiary phase, the creep rate and, accordingly, also the creep strains increase rapidly as a result of material damage due to the large plastic deformations. The third creep phase finally ends with the fracture of the specimen.

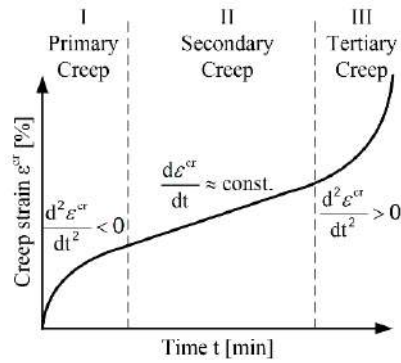


Figure 2. Schematic illustration of characteristic creep strains of structural steel

Figure 3 shows the experimentally determined creep strains of the material S960QL, represented by the black lines, and material S960M, shown in grey, from creep tests at (a) 400°C, (b) 550°C, (c) 700°C and (d) 900°C. It presents the creep strains in a time range from 0 to 400 min after applying the mechanical load for all test temperatures. Each graph contains results from tests at the three predefined stress levels, shown with different line types. Solid lines correspond to stress levels of $0.5 \cdot f_{y,0}$, dashed lines to stress levels of $0.8 \cdot f_{y,0}$ and stress levels of $0.97 \cdot f_{y,0}$ are represented by dotted lines.

Significant creep strains concerning construction practice occur for both ultra-high-strength steels from the test temperature of 550°C (Figure 3(b)) and above and in particular at the stress level above $0.5 \cdot f_{y,0}$. At the lower temperature of 400°C in Figure 3(a) only at the very high stress level of $0.97 \cdot f_{y,0}$ creep strains are measured in the tests. At lower stress levels almost zero creep strains occur.

In addition, in the creep strain-time curves from tests at the temperature of 400°C (Figure 3(a)), the primary and secondary creep phases can be determined for S960QL as well as for S960M. At higher test temperatures, the primary creep phase becomes very short for all investigated temperature-stress combinations and the decrease in creep rate is significantly lower, resulting in higher creep rates in the secondary creep phase for both ultra-high-strength steels. The tertiary creep phase was not reached in the tests at 400°C, but in tests at higher temperatures, this stage could be obtained. In some cases, in particular, at high stress levels and test temperatures, this phase began after very short test durations, so specimen failure occurred after far less than one hour. This underscores the relevance of the adequate consideration of elevated-temperature creep in the assessment of the fire resistance of steel structures with appropriate material models.

The absolute values of the measured creep strains for the two investigated steels differ significantly from each other. The highest creep strains occur for the material S960M in each case; the creep strains for S960QL are generally lower. The thermomechanically rolled steel S960M also shows a higher susceptibility to brittle failure after a short test duration, while the quenched and tempered steel S960QL deforms more slowly under constant loads and temperatures. For steel S960QL, specimen failure can be obtained during the tests only in very few cases, while grade S960M specimens fail after short test durations at high temperatures of 700°C and 900°C (Figure 3(c), (d)) and at high stress levels of $0.8 \cdot f_{y,0}$ or $0.97 \cdot f_{y,0}$.

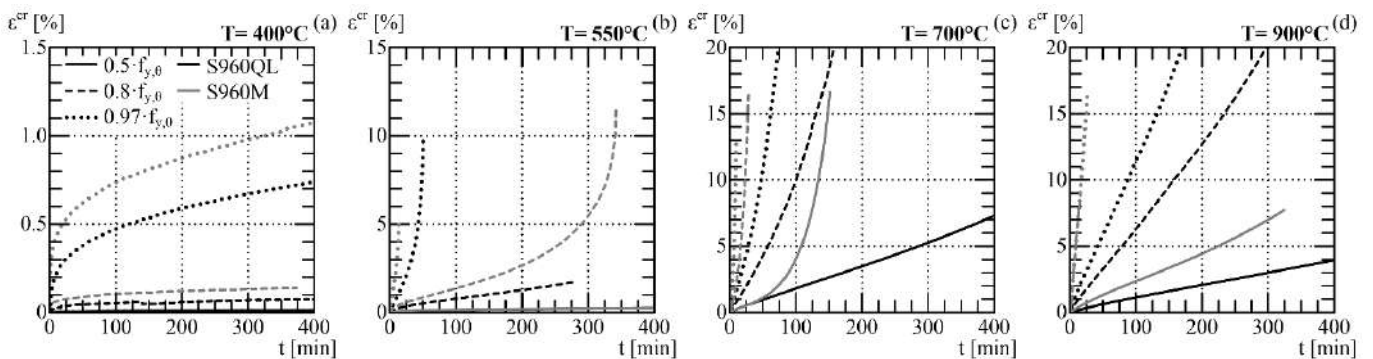


Figure 3. Experimentally determined creep strains of materials S960QL and S960M at (a) 400°C, (b) 550°C, (c) 700°C and (d) 900°C

Figure 4 and Figure 5 show photographs of the specimens from creep tests of steels S960QL (Figure 4) and S960M (Figure 5). For both materials, the specimens at a temperature of 550°C are discoloured and have a visible layer of tinder with spallings on the surface at the temperature of 900°C. In the case of the steel S960M, specimen failure occurs in creep tests at temperatures of 550°C and above. The fracture characteristics at the very high temperature of 900°C are typical for brittle failure with a fracture that is approximately perpendicular to the specimen surface and has a rough texture. In the case of the steel S960QL, only at a temperature of 900°C specimen failure occurs during the tests. The fracture of the specimen at a temperature of 900°C and a stress level of $0.97 \cdot f_y$ in Figure 4(d) is not observed during the test, but occurs during the cooling in the furnace as a result of the constraining stresses caused by the cooling process. The material S960QL deforms more ductile with distinct lengthening in the measuring area. Also, the fracture characteristics at 700°C are typical for ductile failure with a significant necking resulting in a strongly reduced cross-section.



Figure 4. Specimens from creep tests of steel S960QL at a temperature of (a) 400°C, (b) 550°C, (c) 700°C and (d) 900°C

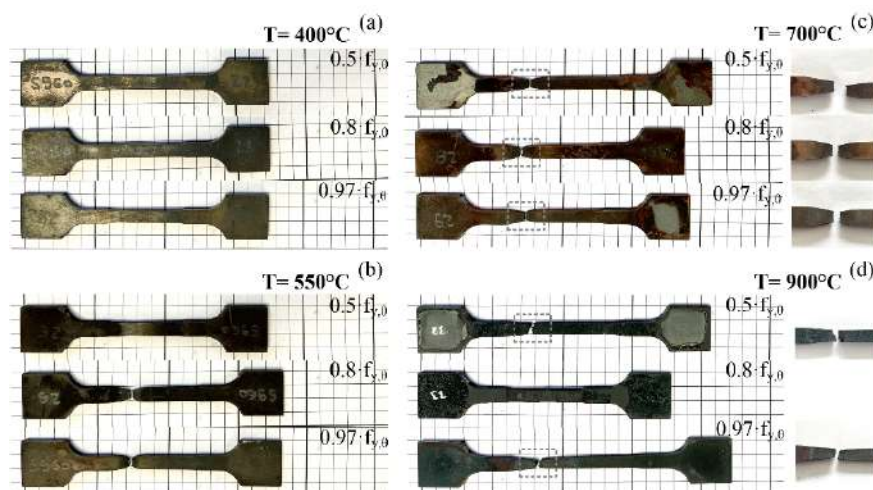


Figure 5. Specimens from creep tests of steel S960M at a temperature of (a) 400°C, (b) 550°C, (c) 700°C and (d) 900°C

3 MODELLING THERMAL CREEP

3.1 Development of an Analytical Creep Model

In this section, a creep model is developed, which captures the effect of thermal-induced creep with the purpose of further application in the fire performance analysis of steel structures. The developed creep model aims to explicitly consider thermal creep effects in different stress and temperature ranges. The model is based on the theoretical and mathematical formulation of Fields and Fields [8] with redefined parameter values fitting the temperature and stress ranges for examined steel grades S960QL and S960M:

$$\varepsilon_{cr} = a \cdot t^b \cdot \sigma^c \quad (1)$$

The creep formulation is based on experimental data from creep tests at elevated temperatures for the abovementioned ultra-high-strength steels and covers primary and secondary creep stages. The tertiary creep stage, which occurred in some of the elevated-temperature creep tests, is not covered by the mathematical formulation of the creep model of Fields and Fields according to eq. (1) and therefore also not included in the developed analytical model in this paper. However, the developed creep model covers the strain ranges relevant to engineering practice in the first two creep phases; so, the third phase of measured creep strains is not essential to be adopted in this application-oriented model. The creep model in this paper considers a unified format for both steel grades but with differences in the parameters of the model.

In the present study, the creep formulation is determined as a unified mathematical format for both investigated ultra-high-strength steels S960QL and S960M using the model according to eq. (1) with the same stress- and temperature-independent creep parameters b_i and c_i in the equations of the exponent parameters b and c for both steel grades. Further, the same equation format considering temperature-independent parameters a_i is used for both steel grades for the determination of parameter a . The determined creep parameters are based on ε_{cr} in [%], t in [min], σ in [MPa] and θ in [°C]. In the developed creep model, the parameters b and c of eq. (1) can be calculated with the following eq. (2) and (3):

$$b = b_0 + b_1 \cdot \theta + b_2 \cdot \theta^2 \quad (2)$$

with values:

$$b_0 = -1.76$$

$$b_1 = 7.09 \cdot 10^{-3}$$

$$b_2 = -4.5 \cdot 10^{-6}$$

$$c = c_0 + c_1 \cdot \theta \quad (3)$$

with values:

$$c_0 = 2.43 \cdot 10^{-1}$$

$$c_1 = 3.92 \cdot 10^{-4}$$

A polynomial formulation and a linear equation are used for the calculation of the parameters b (eq. (2)) and c (eq. (3)), respectively. Thereby, the creep parameters b_i in eq. (2) and c_i in eq. (3) are temperature-independent constant values and fit for the broad range of temperature from $T=400 - 900^\circ\text{C}$, which corresponds to the temperature range of the creep tests of the present study. Further, the parameters b and c are stress-independent.

For the calculation of the parameter a , also a linear formulation as expressed by eq. (4) with respect to the temperature θ as the input variable is determined. The creep parameters a_0 and a_1 in eq. (4) are also temperature-independent constant values. However, the parameter a varies for stress ranges smaller and bigger than $\sigma = 0.8 \cdot f_{y,\theta}$. The parameter a can be calculated as follows:

$$a = a_0 + a_1 \cdot \theta \quad (4)$$

In eq. (4), the parameters a_0 and a_1 are discretely dependent on the ratio of stress to the temperature-dependent yield strength $k_\sigma = \sigma / f_{y,\theta}$ and vary for S960QL and S960M.

For Steel S960QL the aforementioned parameters have the following equations:

$$k_\sigma \leq 0.8: a_0 = -5.73 \cdot 10^{-3} \cdot k_\sigma + 1.18 \cdot 10^{-3} \quad (5)$$

$$k_\sigma > 0.8: a_0 = 1.52 \cdot 10^{-2} \cdot k_\sigma - 1.56 \cdot 10^{-2}$$

$$a_1 = 2.55 \cdot 10^{-5} \cdot k_\sigma - 7.89 \cdot 10^{-6} \quad (6)$$

For steel S960M they follow these relations:

$$k_\sigma \leq 0.8: a_0 = -0.10766 \cdot k_\sigma + 0.051128 \quad (7)$$

$$k_\sigma \geq 0.8: a_0 = 0.024705 \cdot k_\sigma - 0.054746$$

$$k_{\sigma} \leq 0.8: a_1 = 2.766 \cdot 10^{-4} \cdot k_{\sigma} - 13.13 \cdot 10^{-5}$$

$$k_{\sigma} \geq 0.8: a_1 = 58.82 \cdot 10^{-6} \cdot k_{\sigma} + 4.29 \cdot 10^{-5}$$
(8)

3.2 Validation of the Analytical Creep Model with Test Data

The resulting creep strains according to the developed model with eqs. (1)-(8) are compared to the results of the creep tests. Figure 6 compares the analytically determined creep strains (red lines) to creep strain-time curves from tests (black lines) of steel S960QL for the test temperature of (a) 440°C, (b) 550°C, (c) 700°C and (d) 900°C. Figure 7 shows this for material S960M, respectively. The graphs present the strain range of up to 2 % of creep strains, which is especially relevant in structural fire engineering. In Figure 6 and Figure 7 also the creep strains determined from numerical simulations, which are further described in section 4 are presented by the green lines.

The comparison illustrates that the measured creep strains from tests are mainly close to analytically determined creep strains or in some cases almost congruent. The first and second creep phases can therefore be approximated with sufficient accuracy for both investigated materials S960QL and S960M and the temperature- and stress-dependency of creep strains of the ultra-high-strength steels are well captured by the selected approach.

In the case of the temperature 550°C, analytical results have some large deviations from the experimental data for both steel grades S960QL and S960M. However, these are conservative and the model is therefore assessed as fundamentally suitable. As a matter of consistency, no additional adjustment to the model is made. Having temperature- and/or stress-independent constant parameter values in the developed creep model counts as an advantage in comparison to other creep formulations in literature [12-14] which predict thermal creep behaviour in time with dependency on steel grade, temperature and stress range, creep phase and exposure time to elevated temperatures, etc. In addition, the consistent formulation of the model with same material parameters b and c and similar equation format of parameter a provides a high level of expedience.

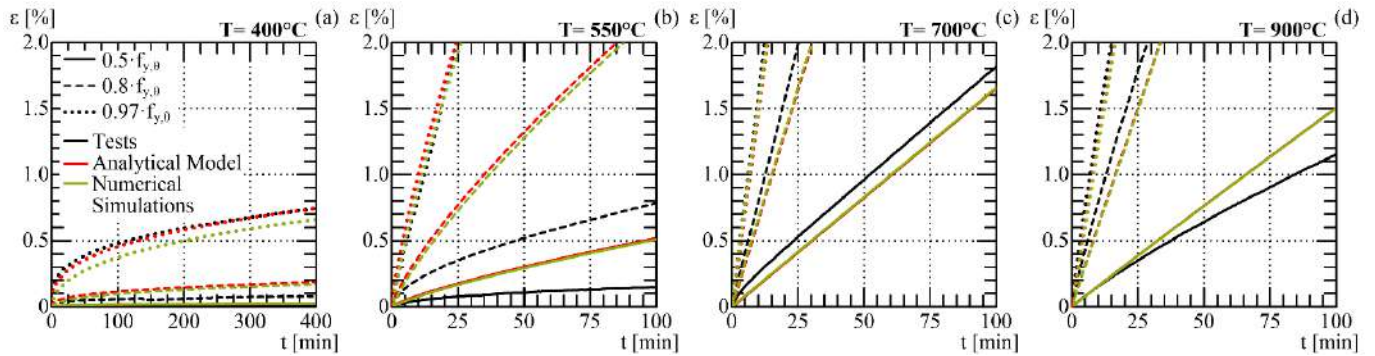


Figure 6. Comparison of creep strains according to the developed creep model with the test data from creep tests on steel S960QL at temperatures (a) 400°C, (b) 550°C, (c) 700°C and (d) 900°C

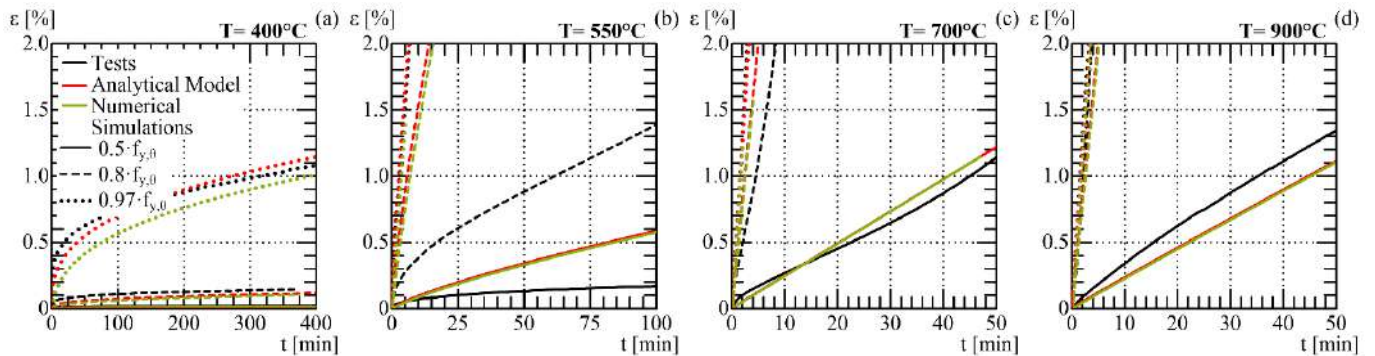


Figure 7. Comparison of creep strains according to the developed creep model with the test data from creep tests on steel S960M at temperatures (a) 400°C, (b) 550°C, (c) 700°C and (d) 900°C

The deviations between analytically determined creep strains and the measured creep strains from tests were statistically analysed. Figure 8 shows the direct comparison of creep strains from tests (a) on steel S960QL and (c) on steel S960M to analytically determined creep strains according to the proposed model. Further, the frequencies of the relative deviations of the creep strains from tests and model proposals $(\epsilon_{cr,Test} - \epsilon_{cr,Model}) / \epsilon_{cr,Test}$ normalised by the total number of measurement points considered n_{tot} are presented in Figure 8(b) for steel S960QL and in (d) for steel S960M. The graphs in Figure 8 consider the strain range up to 2 % creep strains. Table 2 contains the statistical parameters mean value \bar{x} , standard deviation s and variation coefficient COV of the statistical evaluation of relative deviations between test results and creep model presented in Figure 8. The model proposal for S960QL and S960M approximates the creep strains of the investigated ultra-high-strength steels predominantly conservatively. In particular, in the case of the lower temperatures of 400°C as well as at very high temperatures of 700°C and 900°C, the measured strains are accurately determined. The mean values are in general low in those cases with also comparatively small values of the standard variations. In the case of a temperature of 550°C, the deviations between test data and model values are partially large for both materials. However, as these are in the highly conservative range, the proposed models are considered suitable for describing the creep strains of the investigated ultra-high-strength steels. In addition, based on the evaluation, it is justifiable that a future extension of the model to other steel grades is also soundly feasible by slight modifications of the parameter values, which represents a major improvement for explicit creep studies in fire engineering and a safe and reliable prediction of the material and structural behaviour of steel structures in the case of fire.

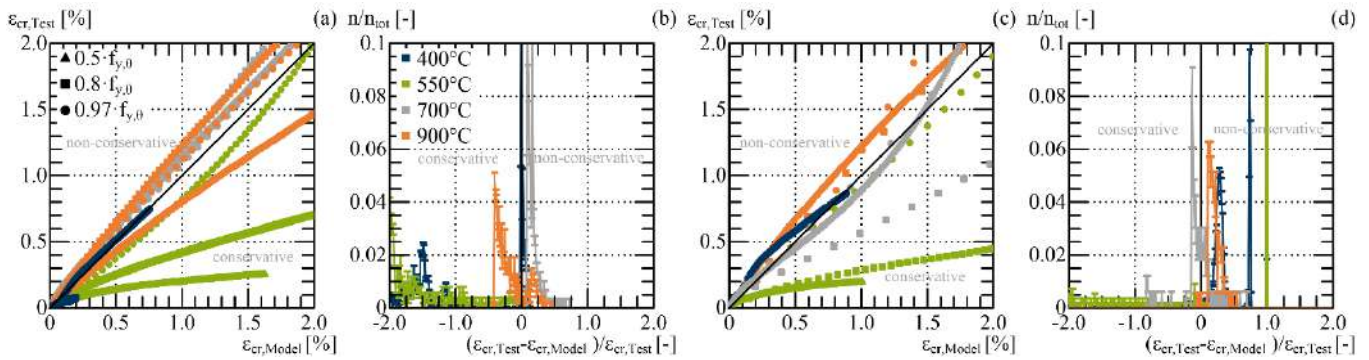


Figure 8. (a) Comparison of creep strains from tests on steel S960QL to analytically determined creep strains, (b) frequency of relative deviations between test data and the creep model for steel S960QL, (c) comparison of creep strains from tests on steel S960M to analytically determined creep strains and (d) frequency of relative deviations between test data and the creep model for steel S960M

Table 2. Statistical parameters of the relative deviations between test results and analytical creep model $(\epsilon_{cr,Test} - \epsilon_{cr,Model}) / \epsilon_{cr,Test}$

	θ	400°C	550°C	700°C	900°C
S960QL	\bar{x}	-1.231	-2.743	0.177	-0.18
	s	1.118	1.343	0.109	0.21
	COV	-0.909	-0.49	0.616	-1.167
	n_{tot}	2216	503	294	469
S960M	\bar{x}	0.349	-1.875	-0.071	0.209
	s	0.293	1.41	0.256	0.091
	COV	0.84	-0.752	-3.624	0.434
	n_{tot}	42154	558	165	175

4 NUMERICAL IMPLEMENTATION OF THERMAL CREEP

4.1 Implementation of the Model in ABAQUS

The overall objective of the study is the reliable assessment of the influence of creep strains on the deformation of steel structures in case of fire and their implications on the structural level by buckling or bending of structural members. Therefore, explicit consideration of thermal creep in advanced numerical simulations is needed. Thus, the ascertained creep model of the present study is implemented in numerical simulations with the FE-software ABAQUS.

The default formulation of a creep model in ABAQUS can be either based on a time-hardening or strain-hardening formulation [3, 4]. The time-hardening is based on the assumption of a uniform stress state in the component over time. In this case, the creep strain rate is described as a function of the time t and the stress σ and is integrated over time to obtain the creep strain. In the strain-hardening approach, on the other hand, the stress in the component changes over time and the creep strain rate is described as a function of the creep strain ϵ_{cr} and the stress σ and is also integrated over time to determine the creep strain. Since the creep model of the present study is determined from creep test results in constant temperatures and stress conditions, which represent an almost steady stress and temperature state, a time-hardening equation can be applied. Time-hardening formulation in the FE-software ABAQUS is stated as the following equation:

$$\dot{\epsilon}_{cr} = A \cdot t^m \cdot \sigma^n \quad (9)$$

For the numerical simulations in ABAQUS, the derivative of eq. (1), eq. (10), can be reformulated according to a time-hardening formulation to eq. (9) which contains temperature-dependent parameters A , m and n based on initially determined constants of the proposed creep model.

With

$$\dot{\epsilon}_{cr} = a \cdot b \cdot t^{b-1} \cdot \sigma^c \quad (10)$$

the parameters for the time-hardening formulation according to the developed model can be calculated as follows:

$$A = a \cdot b = (a_0 + a_1 \cdot \theta) \cdot (b_0 + b_1 \cdot \theta + b_2 \cdot \theta^2) \quad (11)$$

$$m = b - 1 = (b_0 + b_1 \cdot \theta + b_2 \cdot \theta^2) - 1 \quad (12)$$

$$n = c = (c_0 + c_1 \cdot \theta) \quad (13)$$

The values of creep parameters of the time-hardening formulation in different constant elevated temperatures and stresses are derived according to eqs. 11)-(13) considering the model approach with eqs. (2)-(8) and implemented as ABAQUS input values for the definition of the material behaviour in terms of thermal creep of the finite-element model.

For the validation of the functionality of the numerical algorithm with the implemented creep model, a simple finite element model is created in ABAQUS. Modelling in ABAQUS is done with a model as a two-node linear-displacement truss element (labelled in ABAQUS library as T2D2) with a uniform tensile load in cross-section. The dimensions of the numerical model are adopted according to the dimensions of the measuring position of the extensometer with $L \times b \times t = 45 \times 9 \times 6$ mm in the middle of the test specimen shown in Figure 1b. The simulations are performed as quasi-static analysis. The applied forces in the simulations correspond to the creep tests as tensile loads equal to the target stress levels of $\sigma = (0.5, 0.8 \text{ or } 0.97) \cdot f_{y,\theta}$ and the time integration scheme of the simulations is done for a step time in accordance with real-time of the creep tests of the present study. As a result of the numerical simulations creep strain-time curves were obtained which are presented in Figure 6 for steel S960QL and in Figure 7 for S960M.

4.2 Validation of the Numerical Model

As validation of the implementation of the developed creep model into numerical simulations with ABAQUS, the creep strains obtained from numerical simulations are compared to the results of creep tests.

Figure 6 and Figure 7 present the numerical simulation results for which the creep model was used in comparison to analytical and experimental results of creep tests to check whether they comply with each other. For both steel grades, at the moderate temperature of 400°C and in the highest stress range of $0.97 \cdot f_{y,0}$, the numerical simulation results and analytically determined results differ slightly. An explanation for this is the computational solution procedure in the time-hardening approach which is an explicit integration scheme. Nevertheless, in all other cases, the numerical simulation results fit exactly to analytical results of the developed creep equation. In addition, the graphs in Figure 6 and Figure 7 show that despite inevitable error-prone testing, the results of numerical simulations fit appropriately the creep test results with a very sound accuracy. The exceptions are the results at the temperature 550°C (Figure 6(b), Figure 7(b)) which is clarified in section 3.2. That proves the suitability of the creep model to be further applied in the study of thermal creep effects in transient fire conditions as well as structural fire performance analyses.

5 SUMMARY AND CONCLUSIONS

This paper provides the results of a comprehensive study on the thermal creep behaviour of ultra-high-strength steels. The resulting creep strain-time curves from creep tests on ultra-high-strength steels of grades S960QL and S960M are presented and the elevated temperature creep behaviour of quenched and tempered steel is compared to thermomechanically rolled steel. An analytical creep model with a consistent application-oriented formulation of stress- and temperature-dependent material parameters for the investigated ultra-high-strength steels is developed based on experimental results from creep tests. The model proposal is used for numerical simulations under steady-state temperature and stress conditions.

The following findings can be drawn from the comprehensive experimental, analytical and numerical investigations of the study:

At moderately elevated temperatures up to 400°C and also low stress levels, the material behaviour of initially quenched and tempered or thermomechanically rolled ultra-high-strength steels is not influenced by elevated temperature creep to a relevant extent in terms of construction practice as almost zero creep strains occur in those cases.

However, creep tests on ultra-high-strength steels reveal that the adequate consideration of elevated temperature creep is needed in assessing the structural performance of steel structures in the case of fire, as significant creep strains occur at test temperatures of 550°C and above, and in particular at stress levels above $0.5 \cdot f_{y,0}$.

The model proposal based on the mathematical approach of a power law with consistent formulations of material parameters for S960QL and S960M approximates the temperature- and stress-dependency of the creep strains of the investigated ultra-high-strength steels predominantly conservatively. The uniform equation format using temperature- and stress-independent constant parameters to appropriately determine the creep strains of the ultra-high-strength steels represents a major improvement for explicit creep studies in fire engineering. A slight modification of the parameter values can be expected to contribute to a further extension of the application range to additional steel grades.

The validation of the implementation of the proposed creep model into numerical simulations with explicit consideration of creep under steady state temperature and stress conditions against analytical and experimental results provides the basis for future advanced modelling applications in structural fire engineering considering the influence of creep strains on the structural analysis in transient fire conditions as well as the study of the structural behaviour of steel structures in fire.

ACKNOWLEDGEMENT

The research presented in this work is based on the research project IGF 21497 N/ P1502 "Ultra-high strength structural steels in fire – Material behaviour for simplified and advanced calculation models (HighssFire)" from the Research Association for Steel Application (FOSTA), Düsseldorf, which is supported by the Federal Ministry of Economic Affairs and Climate Action through the German Federation of Industrial Research

Associations (AiF) as part of the programme for promoting industrial cooperative research (IGF) based on a decision by the German Bundestag. The project was carried out at Ruhr-Universität Bochum.

REFERENCES

1. V. Kodur, M. Dwaikat: Effect of high temperature creep on the fire response of restrained steel beams, *Material and Structures* 43, pp. 1327-1341 (2010).
2. F Faghihi, M Numanović, M Knobloch: The effect of thermal creep on the fire resistance of steel columns, *Fire Safety Journal*, 2023.
3. Norton, F.H.: *The Creep of Steel at High Temperatures*, McGraw-Hill Inc., New York, 1929.
4. Bailey, R.W.: Creep of steel under simple and compound stress, *Engineering* 121 (1930).
5. Dorn, J.E.: Some fundamental experiments on high temperature creep, *Journal of the Mechanics and Physics of Solids* 8, 85–116 (1954).
6. Harmathy, T.Z.: A comprehensive creep model, *Transactions, A.S.M.E. Journal of Basic Eng.* 89, 496–502, 1967.
7. Williams-Leir, G.: Creep of structural steel in fire: analytical expressions, *Fire and Materials* 7 (2), 1983.
8. Fields, B.A., Fields, R.J.: *Elevated Temperature Deformation of Structural Steel*, National Institute of Standards and Technology, NIST; 1989.
9. Cowan, M., Khandelwal, K.: Modeling of high temperature creep in ASTM A992 structural steels, *Engineering Structures* 80, 426–434 (2014).
10. Fujimoto, M., Furumura, F., Ave, T.: Primary creep of structural steel (SM 50A) at high temperatures, *Journal of Structural Engineering* 306, 148–154 (1981).
11. Fujimoto, M., Furumura, F., Ave, T.: Primary creep of structural steel (SM 58Q) at higher temperatures, *Journal of Structural and Construction Engineering* 319, 147–153 (1982).
12. Li, G.Q., Wang, X.X., Zhang, C., Cai, W.Y.: Creep behaviour and model of high-strength steels over 500 MPa at elevated temperatures, *Journal of Constructional Steel Research* 168 (2020).
13. Lee, J.: *Elevated-Temperature Properties of Steel for Structural-Fire Analysis*, Doctoral thesis, University of Texas; 2012.
14. Wang, W., Yan, S., Liu, J.: Studies on temperature induced creep in high strength Q460, *Materials and Structures* 50 (2017).
15. Uszball, S.; Knobloch, M.: Werkstoffeigenschaften höchstfesten Baustahls S960QL im Brandfall. *Stahlbau*, 92(3) (2023).
16. Uszball, S., Knobloch, M.: Tensile Tests for Material Characterisation of High- and Ultra-High-Strength Steels S690QL and S960QL under Natural Fire Conditions, *Fire Technology*, 2024.

NUMERICAL AND EXPERIMENTAL STUDY ON CRITICAL TEMPERATURE OF AXIALLY LOADED STEEL MEMBERS UNDER FIRE CONDITIONS

Hao Tang¹, Shouchao Jiang², Tingna Zhang³

ABSTRACT

For spatial steel structures in fire, axially loaded members typically buckle due to thermal stress resulting from the thermal expansion restrained by the adjacent members. Existing studies have shown that such members will continue to function after buckling occurs, which means post-buckling behaviour should be considered to define the failure moment. However, quantifying the restraint effect under fire to calculate the critical temperature of axially loaded members is challenging, and there is limited experimental research on this subject. In this paper, an experimental investigation on the performance of six planar steel trusses subjected to localized fire exposure is carried out. An initial analysis of the test data has been implemented and the results, including failure mode, temperature curves, overall deformation curves, and mid-span lateral displacement curves are presented in this paper. Additionally, a simplified method for evaluating the critical temperature of axially loaded members in realistic structures is proposed through finite element analysis. Comparison results indicate that this method is adequate and practical in fire-resistance design.

Keywords: Spatial steel structure; Axially loaded member; Post-buckling; Critical temperature; Thermo-mechanical behaviour

1 INTRODUCTION

Spatial steel structures, such as grid and shell structures, have axially loaded members as their main load-bearing components. Under fire condition, these members are likely to buckle prematurely due to thermal stress, leading to a loss of load-bearing capacity and potentially causing localized or even progressive collapse of the entire structure. The Cardington fire tests [1] have demonstrated that the performance of a separate member under fire is very different from that in an actual structure. Due to the member dimensions, boundary conditions and fire scenarios, as well as other influencing parameters, the fire resistance of steel members in actual multi-story buildings is significantly higher than that of individual members in standard fire tests. The specification requirements for the fire-resistance design of steel structures have shifted from standard tests of individual members to the study of member performance in actual structures currently [2]. Nevertheless, numerical simulation on the behaviour of an entire structure for fire design is time consuming and complicated, and ignoring the failure process, such as the effect of a single member failure on the entire structure, may not be rational, particularly for structures with high redundancy. Therefore, the member-based fire-resistance design method is still necessary, and the key issue is to accurately simulate the real

¹ Mr., College of Civil Engineering, Tongji University, Shanghai, China,
e-mail: 2310046@tongji.edu.cn

² A/Prof, College of Civil Engineering, Tongji University, Shanghai, China,
State Key Laboratory of Disaster Reduction in Civil Engineering, Tongji University, Shanghai, China
e-mail: scjiang@tongji.edu.cn

³ Ms., College of Civil Engineering, Tongji University, Shanghai, China,
e-mail: zhangtn2015@163.com

boundary conditions of the members, so that the computed thermo-mechanical behaviour and failure criteria closely match the real status.

Many scholars have reached a consensus that axially loaded members under fire do not lose their load-bearing capacity completely due to buckling and defined the failure moment as the instant when the restraining force reaches its initial value again [3-6]. Neves et al. [3-4] studied the influence of thermal elongation restraint on the fire resistance of steel columns through the ZWAN program and experiments. The results showed that the restriction of thermal elongation had non-negligible effect on the critical temperature. Thus, the simplification in Eurocodes [7-8], which assumes the action combination at room temperature during fire, may lead to overestimation of the fire resistance of compressed columns in certain cases. Through numerical simulations of the arc length method, Franssen [5] demonstrated that when the axial constraint stiffness ratio exceeded a certain value (2%), increasing it further had almost no effect on the critical temperature. Therefore, the author inferred that it was feasible to calculate the critical temperature based on a totally axial constraint assumption. Wang [6] divided the process of axially loaded steel members under fire condition into three phases: pre-buckling, buckling and post-buckling. A simplified theoretical method was proposed, which required incremental calculation. Wang et al. [9] proposed a simplified design method to calculate the buckling and critical temperatures of restrained columns under axial load or combined axial load and bending moment in fire. However, the effect of rotational constraint was not taken into account among the above studies.

Wang [10] analysed the fire resistance of framed structures using substructures and suggested that when calculating the load carrying capacity of framed columns under fire, adopting built-in support conditions may provide results that were close to realistic situation. This suggestion is also made in Eurocode3 [8] for an intermediate storey column analysis. Then through parametric analysis, Wang [11] demonstrated that the role of axial and rotational constraints didn't need to be clearly represented, when considering the continuity of the structure. This is because their effects on the critical temperature would offset each other. Therefore, the critical temperature can be calculated in accordance with the initial axial force and the unconstrained condition. It is important to note that in this situation, thermal stress is completely disregarded. Valente et al. [12] conducted a numerical simulation to analyse the impact of axial constraint stiffness, rotational constraint stiffness, slenderness ratio, and eccentricity on the critical temperature. The results showed that the critical temperature of the member increased with higher rotational constraint stiffness, but the effect decreased with increasing rotational stiffness. Wang [13] carried out fire tests on no-sway steel columns, and the results showed that by using buckling length ratio of 0.7 and neglecting the initial bending moment, a good fit to the specification results was achieved. However, the axial force and bending moment were ideally constant in the test. Rakshith [14] proposed a linear rotational stiffness method, where the rotational constraint stiffness was linearly reduced to 0 at about 377°C from ambient temperature level, and numerical simulation was conducted to investigate its effect on the stability performance of 720 members under fire. The results demonstrated that the buckling temperature of the members could be lower than 100°C, but they could continue to carry loads. The critical temperature was more significantly influenced by the rotational constraint than by the aspect ratio and axial constraint. The Eurocode3 [8] idealized the effect of rotational restraint as fixed end (the buckling length factor is taken as 0.5) for mid-floor columns. However, this assumption is only valid for members with enough actual restraints [12,14,15]. Gomes et al. [15] proposed alternative formulas to determine the buckling length at elevated temperature, which were an improvement from those presented in [8]. Comparison results showed that the proposed linear solution fitted well with the analytical results. Jiang et al. [16] investigated the effect of rotational constraint on the dynamic performance of columns under fire, and proposed a quantitative index for determining whether the columns exhibit dynamic or quasi-static behaviour under fire. The parametric study revealed that the effect of rotational constraint was equivalent to fixed constraint at both ends when the rotational constraint exceeded a certain value. By comparing the buckling and critical temperature calculated from static and explicit dynamic analysis, Jiang et al. [17] demonstrated that the dynamic effect on restrained columns can be ignored. Ren et al. [18] investigated the buckling and post-buckling behaviour of non-uniform cross-section columns at high temperature in inhomogeneous fire and

proposed a nonlinear governing equation for the whole process of fire. Nevertheless, the application of this method in fire-resistance design is overly complex.

To summarize, it is well recognised that the post-buckling performance of axially loaded members should be considered in fire-resistance design, and the main influential parameters involve slenderness ratio, load ratio, axial restraint and rotational restraint stiffness ratio [19]. The key issue in fire design is to quantify the constraint effect as the other two parameters can be calculated directly. However, only a limited number of fire tests have been conducted to provide necessary information to validate the numerical models. Current studies are usually implemented on isolated members with exact boundaries (one end with beam-column connection at most). This discrepancy with the actual situation may lead to a significant deviation in the critical temperature determined method. Furthermore, little attention has been paid to the members in spatial steel structures, which are subjected to stronger constraint stiffness ratio due to their small section area and high redundancy.

In this paper, numerical and experimental study on critical temperature of axially compressed members in planar steel truss is carried out. Six steel planar trusses were designed to investigate the fire resistance of steel structures with mainly axially loaded members under localized elevated temperature. The obtained results include the temperature distribution of the truss, and the development of structural deformation with temperature. Then, a simplified method for determining the critical temperature of axially loaded members is proposed based on the finite element model and component-based design methodology. The feasibility of this method is verified by comparing it with test results and current mainstream standards.

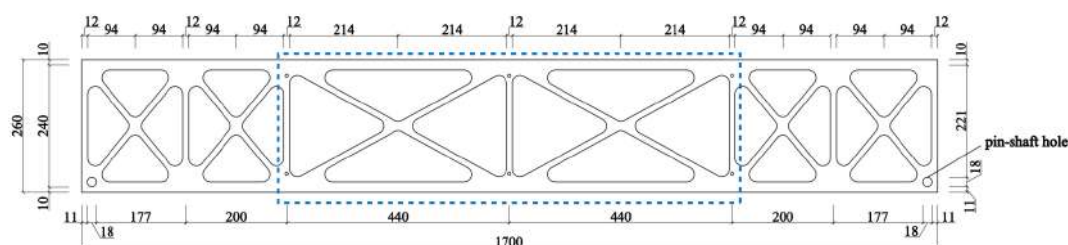
2 EXPERIMENT PREPARATION

2.1 Specimens and test set up

The thermo-mechanical performance of six steel planar trusses subjected to localized elevated temperature was investigated in this experiment. Figure 1 illustrates the specimens and their basic planar dimensions. Each truss had a length of 1.7m and a height of 0.26m. They were fabricated from Q235B steel plates and divided into two groups: group (a) with a thickness of 6mm and group (b) with a thickness of 12mm. All truss members featured a rectangular cross-section, with the height being the larger dimension. The dimensions of both groups were identical except for the thickness. This approach ensured that the lateral slenderness of each member was directly proportional to its thickness, resulting in out-of-plane deflection orientation within the truss plane. This orientation facilitated easier monitoring during the experiment.



(a) Specimens



(b) Basic dimensions

Figure 1. Planar steel trusses

Figure 2 presents a 3D view of the test loading device arrangement employed in the study. Vertical load and temperature effects were applied using a hydraulic jack and an electric furnace, respectively. The trusses were positioned parallel to the side wall of the electric furnace which is depicted by blue dotted

lines in Figure 1, subjected to direct heating. To ensure precise control of the fire-exposure area, fire-proof boards were used to protect the remaining members within the furnace. The trusses were connected to the prefabricated supports through the pin-shaft hole illustrated in Figure 1, and these supports were placed on sturdy piers. To protect the hydraulic jack from high temperatures during testing, a loading short column was incorporated. Moreover, four angle steel components were installed outside the electric furnace, with the upper end firmly connected to the reaction frame and the lower limb tip attached to the vertical plane of the truss. This arrangement effectively prevents out-of-plane overall instability of the truss while maintaining its vertical load carrying capacity.

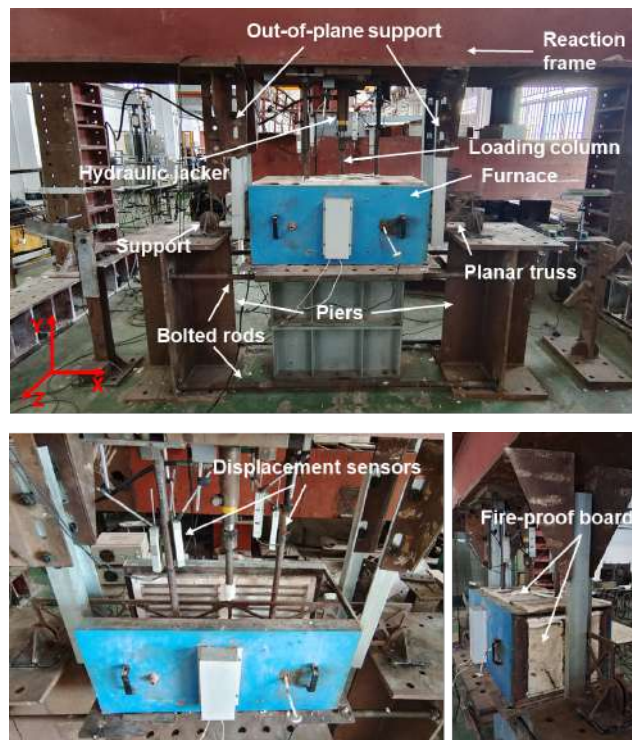


Figure 2. 3D view on test site

2.2 Gauging points and test procedure

Three parameters were mainly measured in this experiment, including temperature, in-plane overall displacement of the truss, and out-of-plane deflection of main members. The location of the measurement points is shown in Figure 3. Temperature was collected by six K-type thermocouples, three for furnace air temperature and the other three for the truss. Displacement was measured using displacement sensors, which were arranged outside the furnace. The directions of the displacements were stipulated by the coordinate axis, which was consistent with that in Figure 2.

In this study, the transient-state condition test was performed (heating the trusses under constant vertical load). The whole experiment was divided into six tests, and test conditions are listed in Table 1. Two connection types between the supports and piers were adopted to form different level of constraint. In the two specimens of group(a), supports were clamped with the piers, which didn't completely restrain the in-plane translation, while the third truss of group(a) adopted three-sides welding method to provide reliable in-plane restraint (shown in Figure 4). The two piers were connected by four steel bolted bars for other four specimens, because the piers were found slightly moved. In three tests of group(b), only the load ratio was different. The load ratio referred to the ratio between the applied load and the design bearing capacity under ambient temperature of the truss, which was based on the Chinese standard GB50017 [20].

The vertical concentrated load was applied to the design value and held for 2 minutes, then the electric furnace was activated. As the duration of a real fire tended to be a quasi-static process [21], the linear heating method of 2h to 900°C was adopted in this experiment. Specifically, test b-3 was set for 3h to 900°C to avoid unforeseen circumstances. When the hydraulic jack could not maintain the initially applied load due to the rate of truss deflection, the furnace would be turned off and the test was terminated.

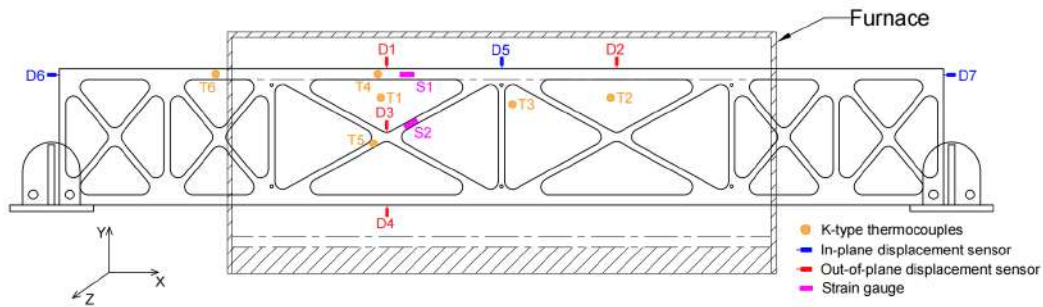


Figure 3. Arrangement of test points

Table 1 Test conditions

Test No.	Load ratio	Concentrated load (kN)	Piers	Support and pier connection type
a-1	0.60	1.68	separate	clamped
a-2	0.60	1.68	connected	clamped
a-3	0.60	1.68	connected	welded
b-1	0.60	11.91	connected	welded
b-2	0.70	13.55	connected	welded
b-3	0.50	9.92	connected	welded



(a) Clamping connection

(b) Three-sides welding

Figure 4. Connection between supports and piers

3 EXPERIMENT RESULTS

3.1 Failure Mode

The six trusses after tests are shown in Figure 5(a-f), and all of them deformed significantly. From Figure 5(a)-(e), it can be seen that in these tests, the structural deformation mainly concentrated on the upper chord and diagonal web members in the mid-span heating area. This suggested that the ultimate failure mode of the truss under this loading condition was initiated by the out-of-plane buckling and loss of load-bearing capacity of the compressed members. The deformation direction appeared in different cases, which was mainly related to the initial defects of the trusses. In test b-3 (Figure 5(f)), the out-of-plane instability occurred in the mid-span vertical web, and this was caused by the insufficient lateral support provided by the loading short columns at elevated temperature.

3.2 Temperature Distribution

Figure 6 shows the measured temperature distribution of the experiment. During the test, air temperature inside the furnace (points T1, T2 and T3) was uniform. The temperature in the centre of the furnace, recorded at T3, was chosen as the representative value of furnace air temperature. At the early stage of

heating, the member temperature slightly lagged behind the furnace air temperature, and the temperature of upper chord was slightly higher than that of diagonal web member. However, when the temperature reached close to 500°C, the discrepancy was negligible. Therefore, the temperature distribution of members in the fire attack area was basically uniform throughout the whole heating stage. The temperature increase of the truss members outside the furnace is primarily due to heat conduction, which will be obtained through heat transfer analysis.

3.3 Displacements

The evolution of the mid-span vertical displacement varied with the member temperature was shown in Figure 7. After static loading, the truss experienced a small vertical displacement downward. The whole fire heating process can be divided into three phases: (1) Arcing stage: as the temperature increased, under the effect of thermal expansion of steel, vertical arching occurred. Gradually, the truss arching reached its peak; (2) Restoring stage: as the temperature increased further, the trend of mid-span vertical deformation changed to downward again and the displacement returned to the value at the beginning of stage(1) within about 100°C; (3) Collapse stage: the vertical displacement increased rapidly. Finally, it was difficult to maintain the vertical load, indicating that the truss lost its bearing capacity and collapsed. Figure 8 shows the mid-span horizontal deformation of members against temperature. It was clearly seen that the out-of-plane deformation of the members in the heating zone of the truss occurred almost simultaneously in each group of tests and it was very close to the time at which the initial vertical position of the truss was restored in Figure 7. This phenomenon indicated that, in the process of heating, with the increase of thermal stress and the reduction of steel material properties, buckling occurred in one of the members in the heated zone. Then the redistribution of the internal force occurred rapidly, causing destabilization of the connected members due to the sharp increase in the axial force, i.e., progressive damage occurred. Subsequently, the out-of-plane horizontal deformation of the members in the heated zone developed further, leading to a continuous decrease in the bearing capacity of the truss and ultimately resulting in collapse damage.

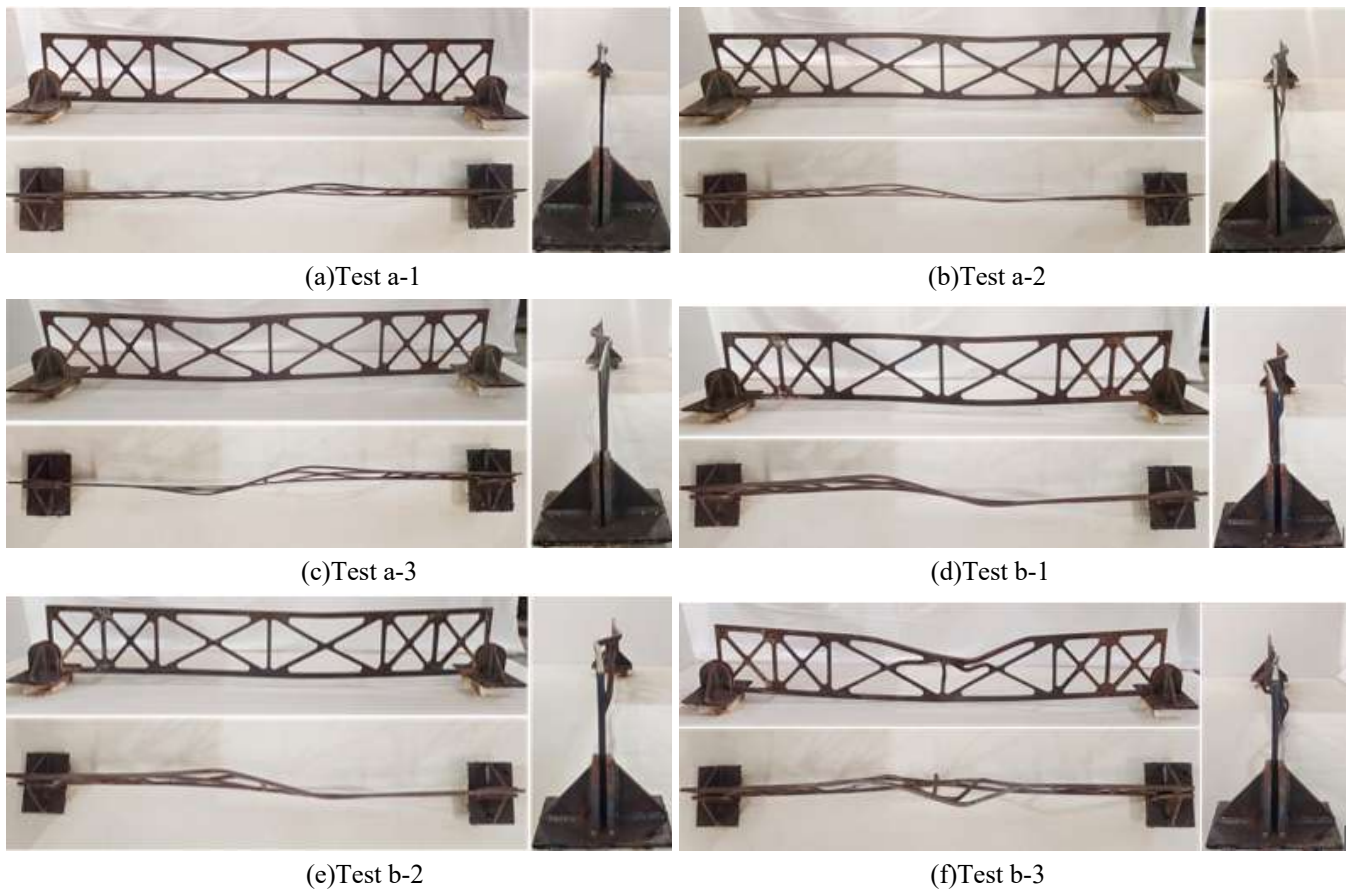


Figure 5. Deformation of trusses after test

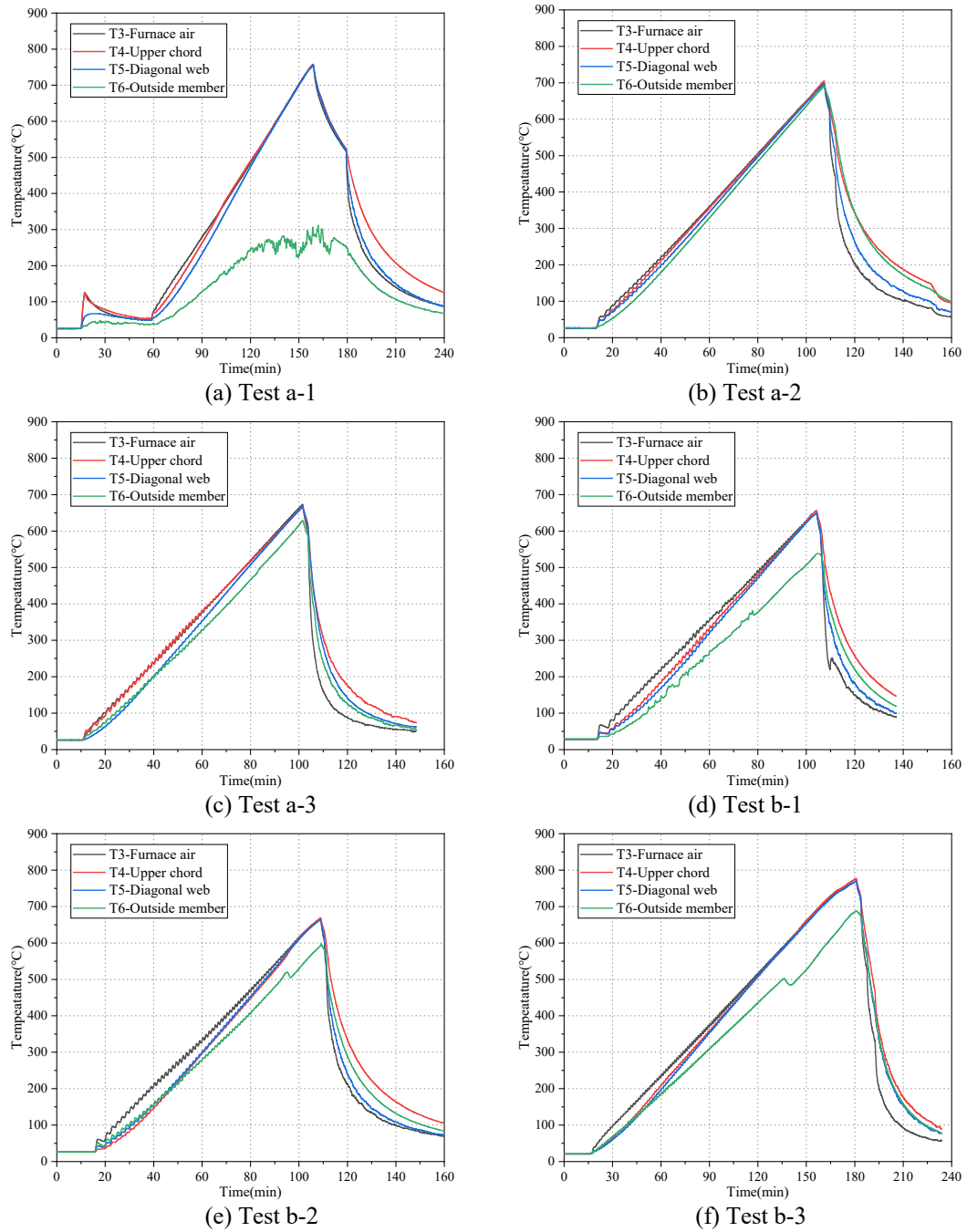


Figure 6. Temperature distribution

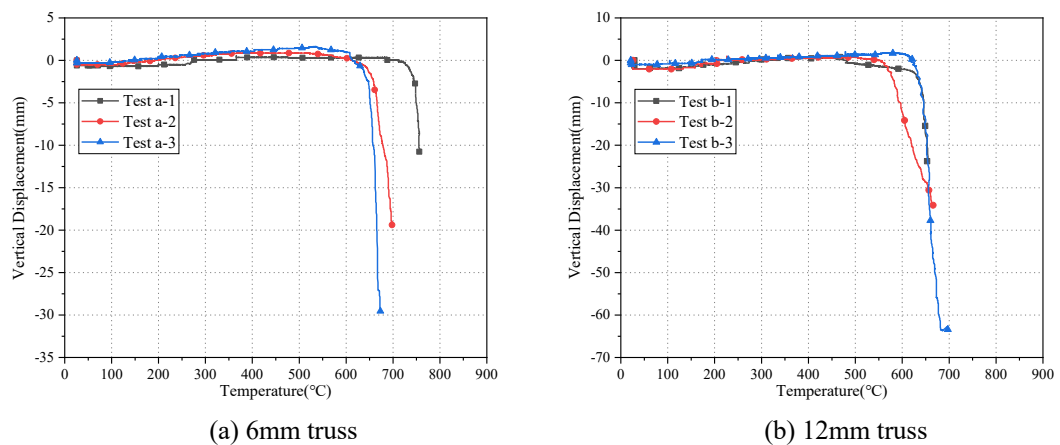


Figure 7. Furnace Temperature-Vertical Displacement in the Mid-Span of Truss

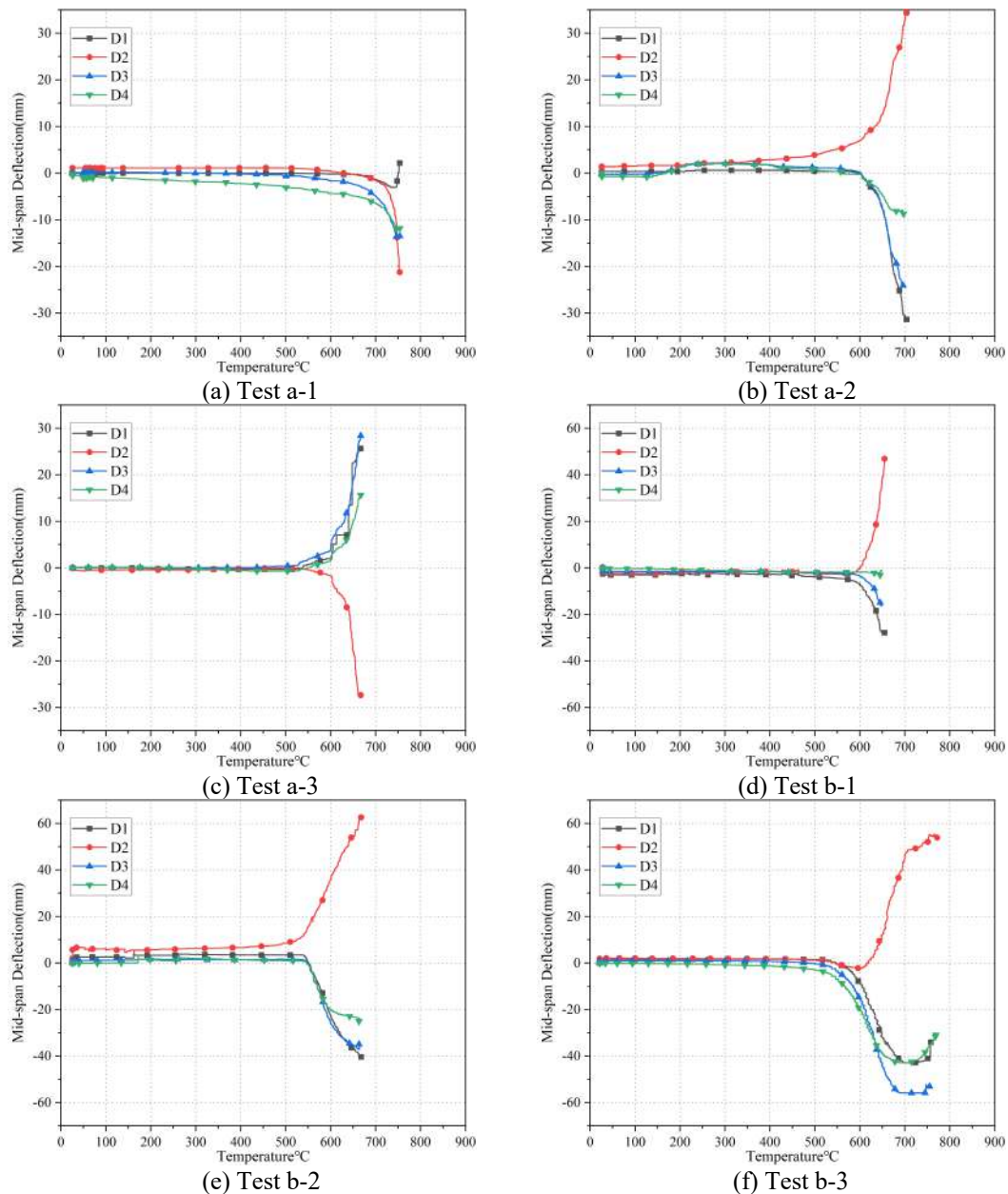
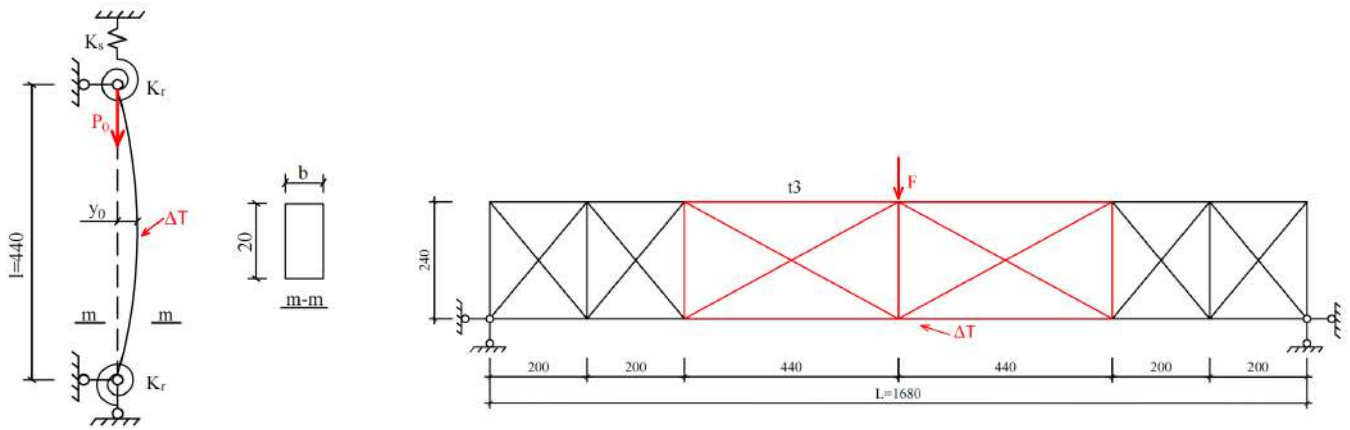


Figure 8. Mid-span Deflection - Member temperature

4 NUMERICAL STUDY

4.1 Numerical model

This section discusses how to consider the axial and rotational constraints when evaluating the critical temperature of axially stressed members in spatial steel structures. The basic strategy is to select a member from the steel truss, impose appropriate boundary conditions and obtain the critical temperature through numerical simulation. Two numerical models with element type B31 and a mesh size of 22mm are established in ABAQUS, illustrated in Figure 9. The upper chord t3 is selected as the object of the study based on the failure mode in fire test. Model A represents the simulated condition of an individual member with idealized constraints, where K_s and K_r represent the axial and rotational constraint by surrounding members, respectively. Model B represents the intact truss model in the experiment and the temperature distribution during the test were imposed by the heat transfer results. In both models, the member initial imperfection is applied and the geometrical imperfection y_0 is idealized as a half-sine wave with a peak amplitude of $l/1000$, where l is the length of the member. In addition, the global initial imperfection is taken as the lowest-order linear buckling mode of the structure in Model B with a magnitude of $L/300$ [20]. L is the span of the truss. The steel material properties in GB51249 [22] and obtained from tensile tests are used in Model A and Model B respectively.

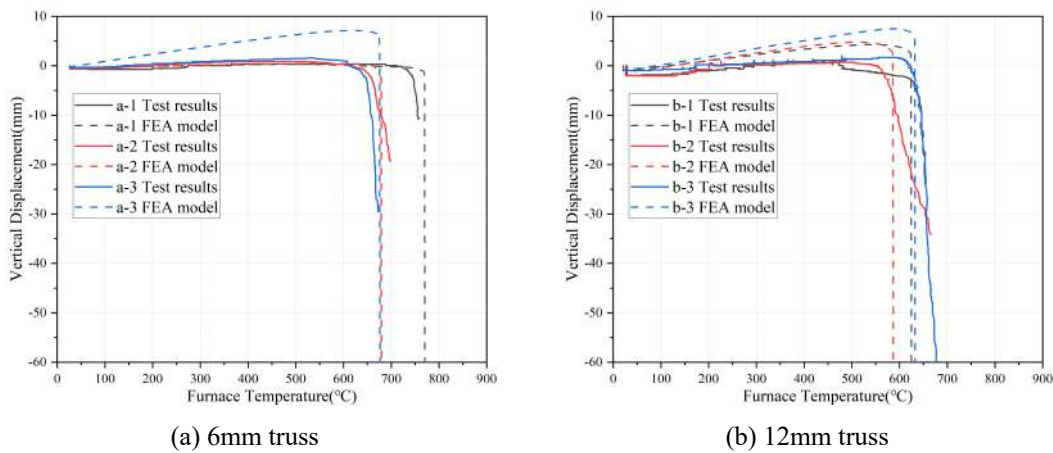


(a) Model A: separate member with idealized constraints (b) Model B: intact truss

Figure 9. Numerical models (dimensions in mm)

4.2 Validation of Model B

To validate the accuracy of the numerical Model B, the vertical displacement-temperature curves of the mid-span of the truss are compared in Figure 10. It can be seen that the displacement-temperature curve obtained by the numerical simulation is in good agreement with the experiment results. Therefore, the FE model established in this paper is reliable. It should be noticed that the arching amplitude are different in the tests with welding connection, but the absolute errors are no more than 6mm.



(a) 6mm truss

(b) 12mm truss

Figure 10. Numerical model validation

4.3 Effect of axial constrain

The axial restraint is mainly idealized by linear springs in existing studies. Its effect can be divided into two contrary aspects. During the pre-buckling phase, the axial compression load increases due to the constraint effect on thermal expansion, which is detrimental. After buckling occurs, the mid-span deflection will not suddenly increase as the contraction trend is inhibited by the idealized constraint, which is beneficial in turn. It is important to note that axially loaded members typically suffer from combined axial load and bending moment because of inevitable initial imperfection. Therefore, the restrained members tend to buckle when the cross-section at mid-height reaches its plastic resistance [9]. If the post-buckling phase is assumed stable in the heating process, then the axial load N_T and mid-span deflection y_T at temperature T satisfy the Equation (1):

$$\frac{N_T}{A} + \frac{N_T y_T}{\mu_T W_x} = f_{yT} \quad (1)$$

where A is the area of the cross section; W_x is the elastic modulus of the cross-section; μ_T is the plastic factor of the section at $T^\circ\text{C}$; f_{yT} is the yield strength of the steel at $T^\circ\text{C}$.

In the linear elastic phase, based on small deflection theory, the mid-span deflection y_T can be calculated by the following equation (2):

$$y_T = y_0 / (1 - N_T / N_{E,T}) \quad (2)$$

where $N_{E,T}$ is the Euler critical load under temperature T °C.

Therefore, although at critical instant the axial load is in the same level compared with the initial ambient temperature situation in current definition, the duration of thermal stress can't be ignored because y_T increases continually, which will lead to premature buckling and failure. The equations above demonstrate that the ignorance of the axial restraint in [8] and [10] may overestimate the fire-resistance capacity.

Figure 11(a) shows the axial load and temperature curves calculated by Model A of the upper chord t3 in test b-1 (of which slenderness is 127 and load ratio is 0.68) with axial constraint stiffness ratio β_s . The axial constraint stiffness ratio β_s is defined in equation (3):

$$\beta_s = K_s / K_{c1} \quad (3)$$

where K_s and K_{c1} represent the axial stiffness of the restraint and member. It is evident that the buckling and critical temperature both decrease with the increasing β_s , but this trend diminishes gradually as the β_s approaches infinity. This finding is consistent with previous research [3,5,6]. Furthermore, the stiffness ratio gradually increases as the material properties of the fired member decay. Therefore, it is reasonable to assume full axial restraint when calculating the critical temperature of axially constrained members.

4.4 Effect of rotational constraint

The effect of rotational constraint is usually equated to the buckling length factor. Similar to axial restraint, there is considerable rotational constraint stiffness of the adjacent members when certain member approaches failure temperature [10]. This implies that the rotational constraint stiffness ratio β_r also tends to be boundless eventually. In Model B, two types of rotational constraint are applied to member t3, including fully released and original condition. Figure 11(b) shows the axial force versus temperature curves. It can be seen that the buckling and critical temperature are significantly higher when rotational restraints exist. Eurocode3 [8] adopts the buckling length factor to consider rotational restraint, with 0.5 for an intermediate storey column and 0.7 for top storey. Calculations in [15] show that the buckling length factor of the intermediate columns gradually converges to 0.5 for different beam-to-column stiffness ratios, regardless whether the upper beams of the fire-exposed columns are heated or not. According to existing studies, for axially loaded members in spatial steel structures, it's rational to simulate the rotational constraint of the adjacent members by fully restrained at both ends.

4.5 Proposed simplified method and validation

Through the above discussion, fix-fix end in Model A is finally adopted for determining the critical temperature of axial loaded members in spatial steel structures, i.e., both axial and rotational are fully restrained. To verify this method, the critical temperature of t3 is calculated by four methods in each test condition, and compared with the experimental results T_{cr} . The methods used include:

1. T_{cr1} : The temperature obtained using the table in GB51249 [22], where thermal stress isn't considered;
2. T_{cr2} : The critical temperature calculated by simplified equation in EC3[8].
3. T_{cr3} : The temperature at which the axial force of t3 decreases to the initial force in Model B;
4. T_{cr4} : The temperature at which the stability capacity of t3 equals to the internal force at elevated temperature in Model B;
5. T_{cr5} : The temperature at which the mid-span vertical displacement returns to initial value in Model B;
6. T_{cr6} : The temperature at which the internal force returns to initial value in Model A with both ends fixed;

If we assume that the stiffness of adjacent members is constant during the fire, the fire-exposed member end returns to its initial position and the restoration of the axial force to its initial value are essentially equivalent. Therefore, based on the definition of the critical temperature, the test result T_{cr} is obtained when the vertical displacement of the truss returned to the value under ambient temperature and load.

Figure 12 shows the comparison results of the critical temperature of member t3 calculated by different methods. The critical temperature T_{cr3} and T_{cr5} obtained from the validated numerical model B are almost

identical, and have a similar trend with the test results T_{cr} . It is shown that the critical temperature definition fits well with the test results. Therefore, the post-buckling behaviour should be considered in fire-resistance design. The difference less than 100°C is mainly because the arcing amplitude in the numerical model is larger than that in the test. For fire-resistance design method, T_{cr6} obtained from the simplified method proposed in this paper is in good agreement with the result from GB51249(T_{cr1}) and EC3(T_{cr2}), and it can give more conservative results when the slenderness of the member is in the range of practical engineering. Therefore, this approach is effective in practice.

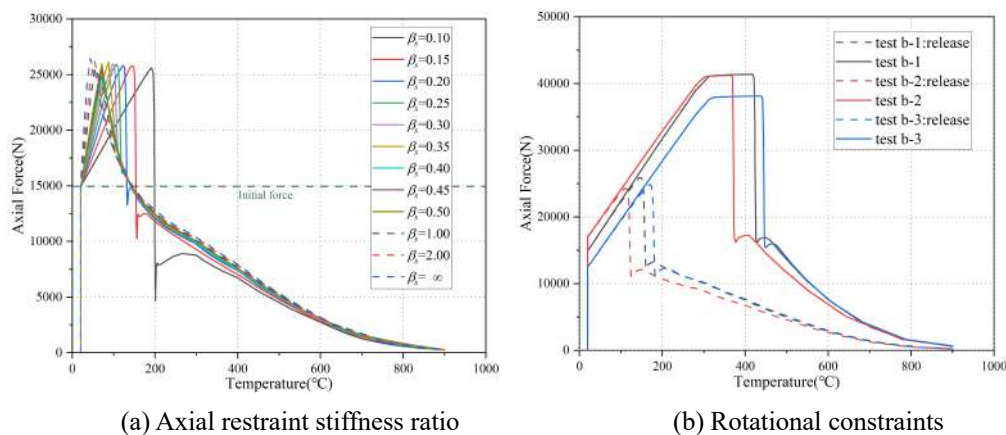


Figure 11. Axial force-temperature curves under different constraints

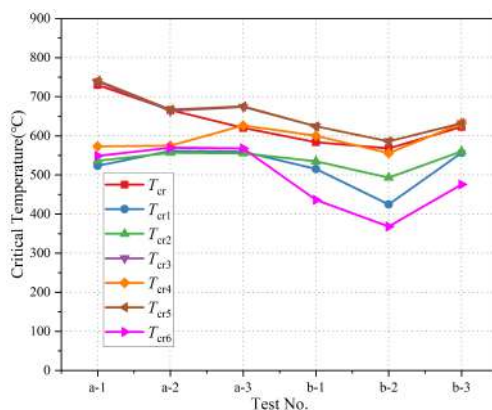


Figure 12. Comparison results of the critical temperature

5 CONCLUSIONS

This paper presents the results of an experimental investigation on the thermo-mechanical behaviour of six planar steel trusses under localized elevated temperature. The numerical models of the specimens are validated by experimental results. A simplified numerical model is proposed to calculate the critical temperature of axially loaded members with restraints at its ends. The findings can be summarized as follows:

1. During the test, the temperature is uniform in the furnace. And the collapse process of the planar steel truss subjected to fire can be divided into three stages, including arcing stage, restoring stage and collapse stage;
2. The specimens behave differently in different boundary and load conditions. The effect of constraint stiffness, load ratio and slenderness can be inferred based on the experiment observations, but should be illustrated clearly by numerical parametric studies in the future;
3. For axially loaded members in fire, the axial and rotational constraint from adjacent members have significant effect on the buckling and critical temperature. Thus, both of them should be taken into account to analyse the thermo-mechanical behaviour;
4. In the proposed simplified method, fix-fix end is imposed on an isolated axially loaded member to calculate critical temperature. The feasibility of the proposed method in predicting critical temperature of steel truss members is verified by experimental results.

REFERENCES

1. BR Kirby. British Steel Technical European Fire Test Program-Design, Construction and Results[A]. 2nd Cardington Conference on Fire, Static and Dynamic Tests of Building Structures[C], 1996.
2. YC Wang. An analysis of the global structural behaviour of the Cardington steel-framed building during the two BRE fire tests[J]. *Engineering Structures*, 2000, Vol.22: 401-412.
3. I.Cabrita Neves. The Critical Temperature of Steel Columns with Restrained Thermal Elongation[J]. *Fire Safety Journal*, 1995, Vol.24(3): 211-227.
4. Rodrigues J, Neves C I, Valente J. Experimental research on the critical temperature of compressed steel elements with restrained thermal elongation[J]. *Fire Safety Journal*, 2000, 35(2):77-98.
5. Jean-Marc Franssen. Failure temperature of a system comprising a restrained column submitted to fire[J]. *Fire Safety Journal*,2000, Vol.34(2): 191-207.
6. Wang YC. Postbuckling Behaviour of Axially Restrained and Axially Loaded Steel Columns under Fire Conditions [J]. *Journal of Structural Engineering*, 2004, 130 (3): 371-380.
7. DC.BS EN 1991-1-2. Eurocode 1. Actions on structures. Part 1-2. General actions. Actions on structures exposed to fire[S].
8. DSF/PREN 1993-1-2. Eurocode 3: Design of steel structures – Part 1-2: General rules – Structural fire design[S].
9. Wang PJ, Li GQ, Wang YC. Behaviour and design of restrained steel column in fire, Part 3: Practical design method[J]. *Journal of Constructional Steel Research*, 2010, Vol.66(11): 1422-1430.
10. YC Wang, T. Lennon, D.B. Moore. The Behaviour of Steel Frames Subject to Fire[J]. *Journal of Constructional Steel Research*, 1995, Vol.35(3): 291-322.
11. Wang YC. Effects of structural continuity on fire resistant design of steel columns in non-sway multi-storey frames[J]. *Fire Safety Journal*, 1997, Vol.28(2): 101-116.
12. Joaquim C. Valente and I.Cabrita Neves. Fire resistance of steel columns with elastically restrained axial elongation and bending[J]. *Journal of Constructional Steel Research*, 1999, Vol.52(3): 319-331.
13. Wang YC, Davies JM. Fire tests of non-sway loaded and rotationally restrained steel column assemblies[J]. *Journal of Constructional Steel Research*, 2003, Vol.59(3): 359-383.
14. Rakshith B.D., Suneel Kumar M.. Behaviour of steel columns with realistic boundary restraints under standard fire[J]. *Structures*, 2020, Vol.28: 626-637.
15. Gomes Fernando C.T., Providência e Costa, Paulo M., Rodrigues João Paulo C., Neves Ildefonso C.. Buckling length of a steel column for fire design[J]. *Engineering Structures*, 2007, Vol.29(10): 2497-2502.
16. Jiang Binhui; Yin Zhongyuan; Zhang Jingzhou; Fan Chuangang; Li Yaozhuang. Effect of rotational restraint conditions on performance of steel columns in fire[J]. *Engineering Structures*, 2021, Vol.238: 112237.
17. Binhui Jiang; Zhengrong Chen; Zhongyuan Yin; Lei Xiao. Buckling and critical temperatures of restrained H-section steel columns in fire considering dynamic effect[J]. *Fire Safety Journal*, 2023, Vol.141: 104006.
18. Ren Yongan; Huo Ruili; Zhou Ding. Buckling and post-buckling analysis of restrained non-uniform columns in fire[J]. *Engineering Structures*, 2022, Vol.272: 1-13.
19. Liu Meijing; Fan Shenggang; Ding Runmin; Chen Guoqiang; Du Erfeng; Wang Kun. Experimental investigation on the fire resistance of restrained stainless steel H-section columns[J]. *Journal of Constructional Steel Research*, 2019, Vol.163: 105770.
20. GB50017-2017, Code for Design of Steel Structures, China Plan Press, Beijing, China, 2017 (in Chinese).
21. Jiang Jian; Li, Guoqiang. Progressive Collapse of Steel High-Rise Buildings Exposed to Fire: Current State of Research[J]. *International Journal of High-Rise Buildings*, 2018, Vol.7(4): 375-387.
22. GB51249-2017, Code for Fire Safety of Steel Structures in Buildings, China Plan Press, Beijing, China, 2017 (in Chinese).

OPENSEES SIMULATION OF THE PLASCO TOWER COLLAPSE USING AN INTEGRATED SIMULATION APPROACH

Ramakanth Domada¹, Aatif Ali Khan², Anwar Orabi³, Asif Usmani⁴

ABSTRACT

The Plasco Tower, a 16-story building constructed in 1962, had been the tallest building in Iran until its collapse in Iran in 2017. This iconic high-rise building known for being the largest garment distribution and production centre in Tehran collapsed due to a fire accident. The fire started on the 10th floor and travelled both vertically and horizontally within the building. The aim of this research work is two-fold i.e., firstly to develop plausible theories explaining the collapse mechanism of the partial collapse of the Northwest corner of the Plasco Tower, a key event during the fire and secondly to demonstrate the open-source integrated approach used for the investigation, which has been developed by Structural Fire Engineering Group at PolyU, Hong Kong. The integrated approach implemented in this work will demonstrate the capabilities of FDS and OpenSEES in performing a complete sequential analysis of fire, heat transfer and thermo-mechanical analysis at a desirable level of fire load resolution.

Keywords: Plasco tower, thermo-mechanical analysis, heat transfer, FDS, OpenSEES, Structural fire engineering

1 INTRODUCTION

Investigation into how buildings collapse under fire is of great importance to engineers in the age where the use of steel is increasing every year. Across the world, both public and private sector organisation are inclined towards constructing tall buildings to maximise the utility of land and other resources. Increase in height of buildings demands designers to consider accidental loadings like earthquake, wind and so on, accordingly, modern design standards provide comprehensive guidance in accounting for such loads. By comparison, the design standards do not provide the same level of comprehensive guidance for the design of tall buildings to resist fire [1].

Structural fire resistance design focuses mainly on the behaviour of materials at high temperatures but generally ignores global structural response that could potentially result in local or global collapse. Previous attempts to understand the vulnerability of structural systems in fire were made by Usmani et al., [2], [3] while studying the collapse of WTC Towers 1 and 2. A clear failure mechanism responsible for global failure of tall buildings was identified. This study aims to model the response of the Plasco building in fire and identify potential failure mechanisms.

¹ PhD student, Building Environment and Energy Engineering
e-mail: ramakanth.domada@connect.polyu.hk, ORCID: <https://orcid.org/0000-0001-9523-4472>

² Lecturer, Civil and Natural Resources Engineering, University of Canterbury
e-mail: aatif.khan@canterbury.ac.nz, ORCID: <https://orcid.org/0000-0001-9181-4795>

³ Lecturer, Faculty of Engineering, Architecture and Information Technology, University of Queensland
e-mail: a.orabi@uq.edu.au, ORCID: <https://orcid.org/0000-0001-5083-3623>

⁴ Professor, Building Environment and Energy Engineering
e-mail: asif.usmani@polyu.edu.hk, ORCID: <https://orcid.org/0000-0003-2454-5737>

2 PLASCO TOWER

2.1 Description of the tower

The Plasco building, from structural engineering point of view, consists of two structures the larger one is a 17-storey main tower and the smaller one is a 5-storey building. The 17-storey building was 30m × 30m in plan and nearly 60m tall with 6m below the ground and the rest 54m above the ground level. It was the taller building that collapsed under fire while the 5-storey building survived with some damage. Plasco building consisted of 48 columns in total with four large columns in the core and the remaining along the periphery. Weaker columns were placed along the periphery to resist lateral loads such as wind and earthquake loads. Whereas thick columns were placed in the centre to safely transfer the gravity loads to the foundation. The corner columns and two perimeter columns at the centre of each face were double in size of the other thinner 34 perimeter columns. Due to the lack of structural drawings and other information during the fire incident, many field inspections were conducted by researchers and engineers to establish the details of all structural members [4]. All the structural members were welded built-up sections, meaning that they were made by welding multiple steel profiles such as channel and angle profiles. The flooring system comprised of a concrete slab with a thickness of 120 mm, which was supported by a series of ceiling trusses in both perpendicular directions forming a dense steel grillage structure.

2.2 State of the tower

The 16-storey building at the time of the collapse was stored with huge quantities of garments and gained a reputation as the largest garment distribution and production centre. The nature of building usage changed from a normal commercial building in the 1970s to an unsafe state as it was in 2017. The building housed shopping areas and restaurants on the ground floor and workshops and garment storage spaces for clothing materials on the upper floors.

Therefore, the primary fuel was the fabric material on the fire floors. The use of the Plasco Building was changed from regular business activities to storage and manufacturing facility, especially on the upper floors (where the fire broke out and spread). The change in occupancy resulted in a much higher fire load than the intended [5]. Behnam [4] argued that at the time of the fire, the fire load was almost four times higher than the designed fire load of the building.

2.3 OpenSees modelling

GiD interface (developed by V Papanikolaou at Aristotle University of Thessaloniki, Greece) [6] which has pre- and post-processing capabilities, was used to build the model and generate *tcl* script for the OpenSees analysis. As the fire affected the top six floors of the tower, only eight floors are modelled for this study. For modelling the truss/beam elements *dispBeamColumnThermal* and for the shells *ShellNLDKGQThermal* element classes of ‘OpenSees for fire’ were used [7], [8]. The connection between the slab and steel truss system was modelled by rigidly connecting the nodes on the beam and shell elements. The meshing size for all elements ranges from 0.3 to 0.5m. Steel was modelled using *Steel01Thermal* material class which uses temperature-dependent properties according to EN 1993-1-2 [9] carbon steel at elevated temperatures whereas concrete was modelled using Concrete Damage Plasticity material model. The fully meshed model consisted of 0.15 million elements of both shells and beams combined. The analysis consumed 30 Gigabytes of RAM while 4.02GHz Intel Xenon CPU worked at 15% utilization.

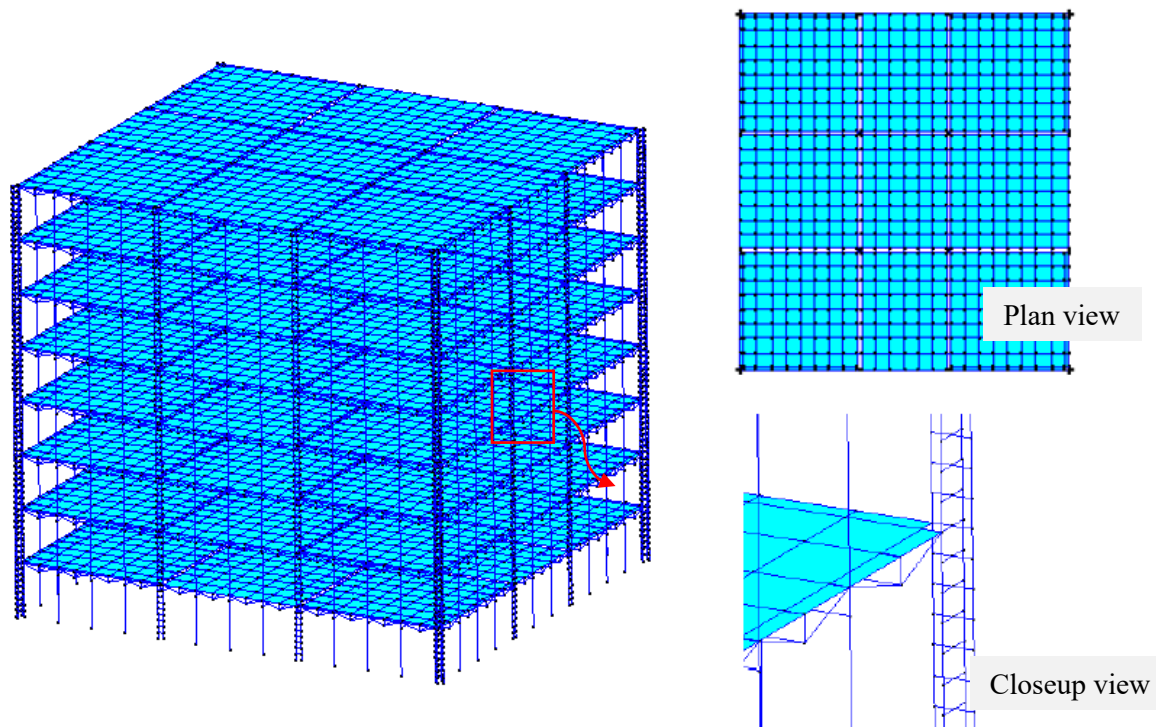


Figure 1. GiD+OpenSees Visualisation of Plasco tower

3 FIRE ACCIDENT TIMELINE

Khan et al. [10] carried out comprehensive fire investigation of Plasco tower fire incident using all sources of information like videos, photos, reports, testimonies of fire fighters and survivors.

For establishing a timeline for critical events, the data in the form of photos and video screengrabs from all the four – East, West, North and South elevations was collected. Evidence of fire signatures like - smoke and fire were used to decide whether fire had travelled past a particular floor, face, or zone or not. The collected data was organized to establish a coherent timeline of fire spread, see Figure 2. The CFD models were calibrated to ensure realistic temperatures and HRR while agreeing with the established timeline of vertical and horizontal fire spread.

The entire 219 minutes of time span of fire incident was divided into 8 events, as (Figure 2), each marking a key aspect related to the fire or the structural damage occurred. The timeline starts with Event 1 which marks the time of fire initiation and ends with Event 10 which indicates the total collapse of the tower. Event 1 to Event 7 indicate various stages of fire spread and firefighting efforts whereas Event 8, 9 and 10 highlight different levels of structural damage. The focus of current study is to simulate the structural response against the fire occurred from Event 1 to Event 8 where the first partial collapse of the NW corner of the tower took place.

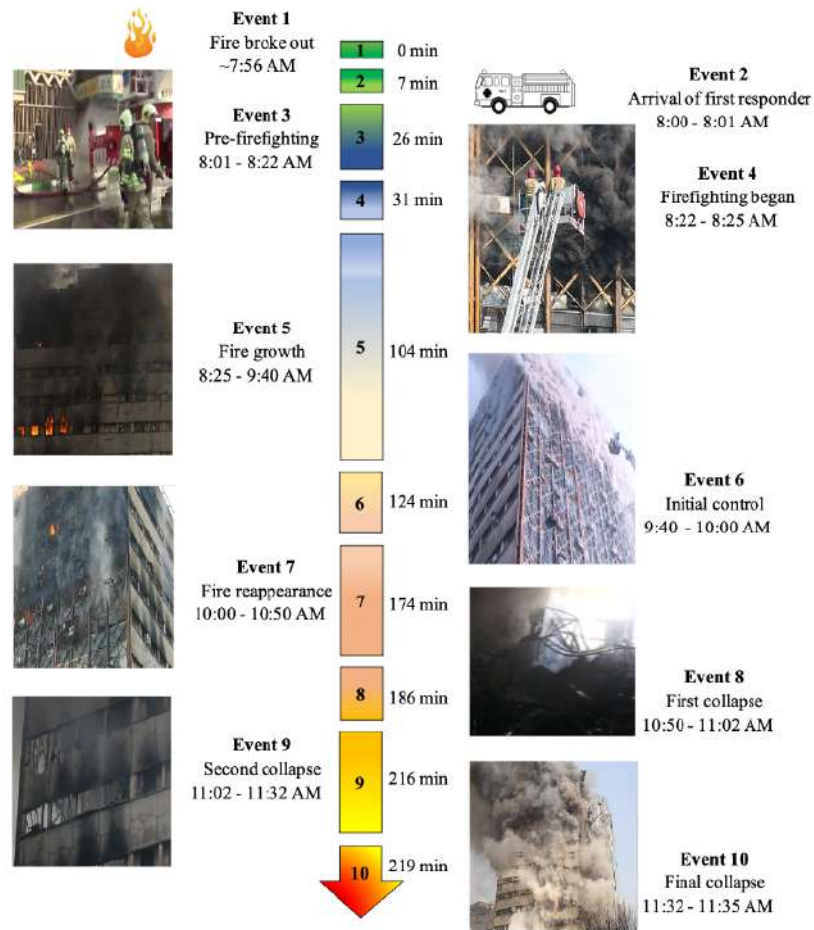


Figure 2. Timeline of the Plasco tower fire accident [8]

4 SOFTWARE INTEGRATION

This study uses an integrated platform for building OpenSees models without needing manual creation of *tcl* scripts. This integrated platform combines functionalities of multiple software to carry out thermo-mechanical analysis of tall buildings [11], [12], [13].

The workflow begins with creation of a BIM model using line and node objects for creating basic geometry of a structure. The BIM model serves as starting point for the subsequent creation of both CFD and finite element models, see Figure 3. The geometry i.e., line and node objects are imported into GiD+OpenSees interface and PyroSim for further model building in respective software. As both software shares same input it is easier to minimize conflicts that arise due to mismatching of inner and outer dimensions, location of columns and orientation of the structure etc. Once both FE and CFD models are created, thermocouple devices are first generated in GiD interface and their data is shared with the CFD model, then gas temperature histories recorded by the thermocouple devices in the CFD model are sent back to the FE model. The GiD+OpenSees interface then invokes heat transfer module of OpenSees and carries out heat transfer analysis on every section assigned with a thermocouple device. The output from this step is then input as thermal load for the final step i.e., thermo-mechanical analysis in OpenSees.

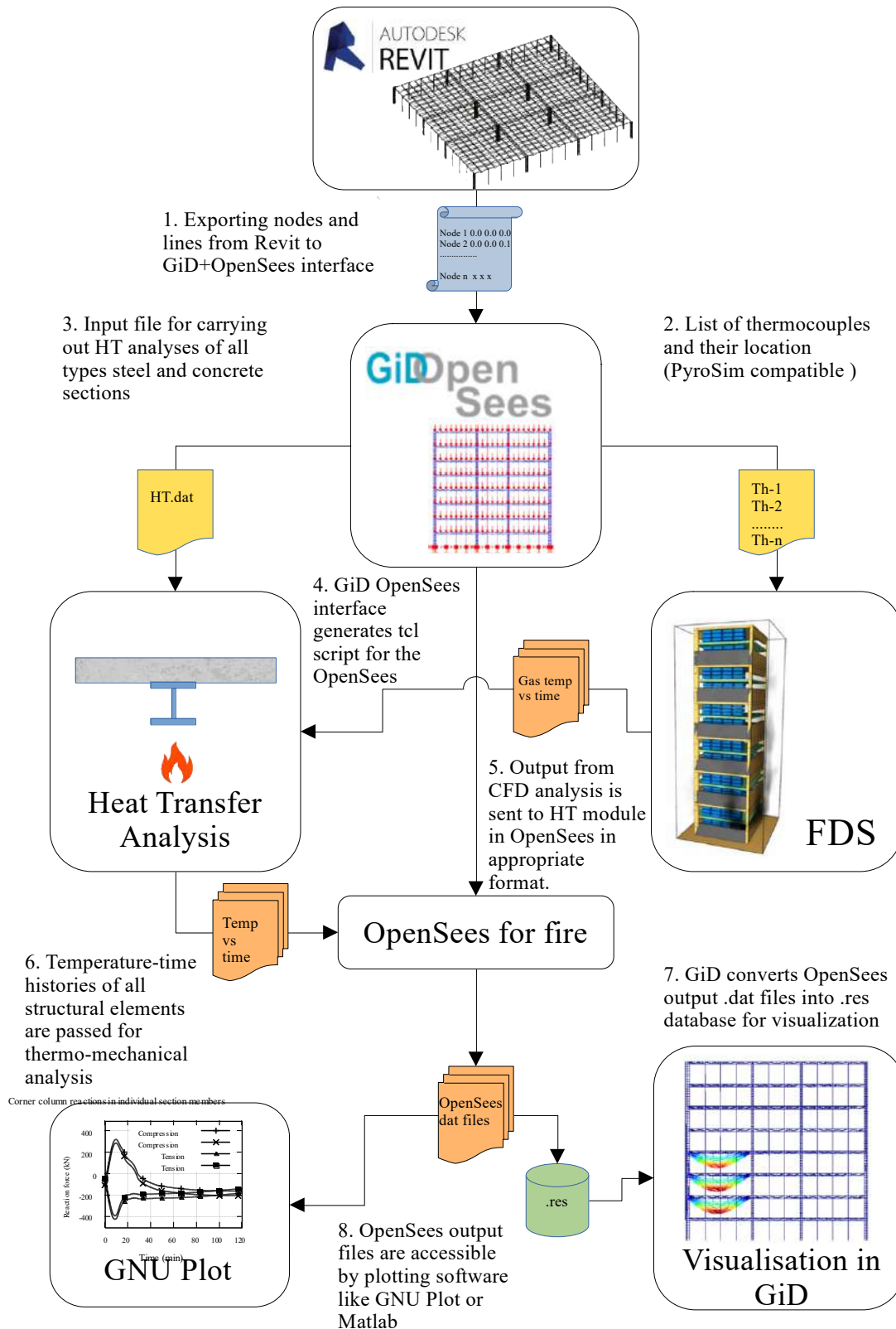


Figure 3. Workflow in the integrated simulation approach

5 MODELLING THE FIRE (EVENT 1 - EVENT 8)

Khan *et al.*, [10], [14], [15] conducted studies on how vertical and horizontal fire spread occurred in the Plasco building. The fire which started in the NW corner travelled in both vertical and horizontal directions. The vertical fire had stayed in the NW corner until the partial collapse of the floors occurred.

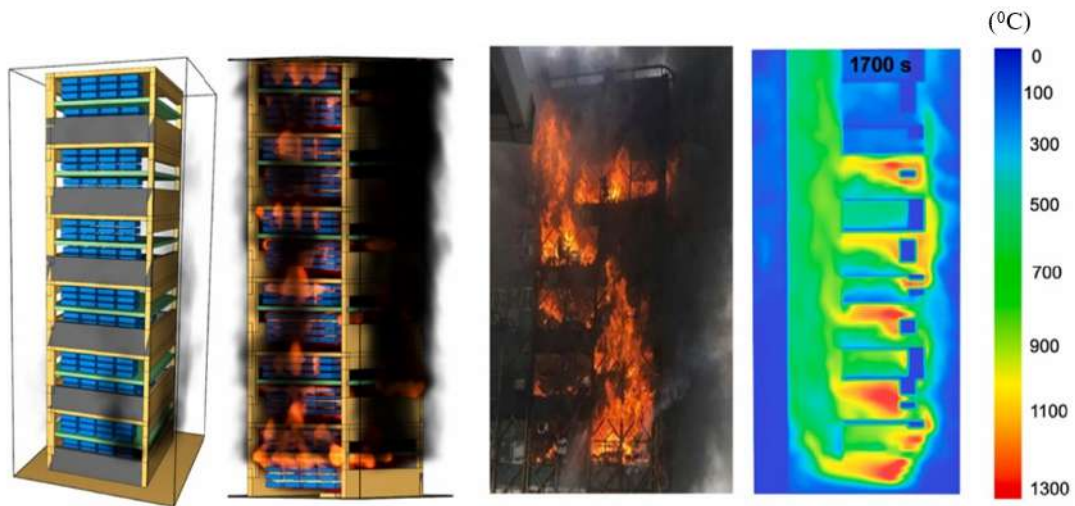


Figure 4. CFD simulation of vertical fire spread and the visual evidence [15].

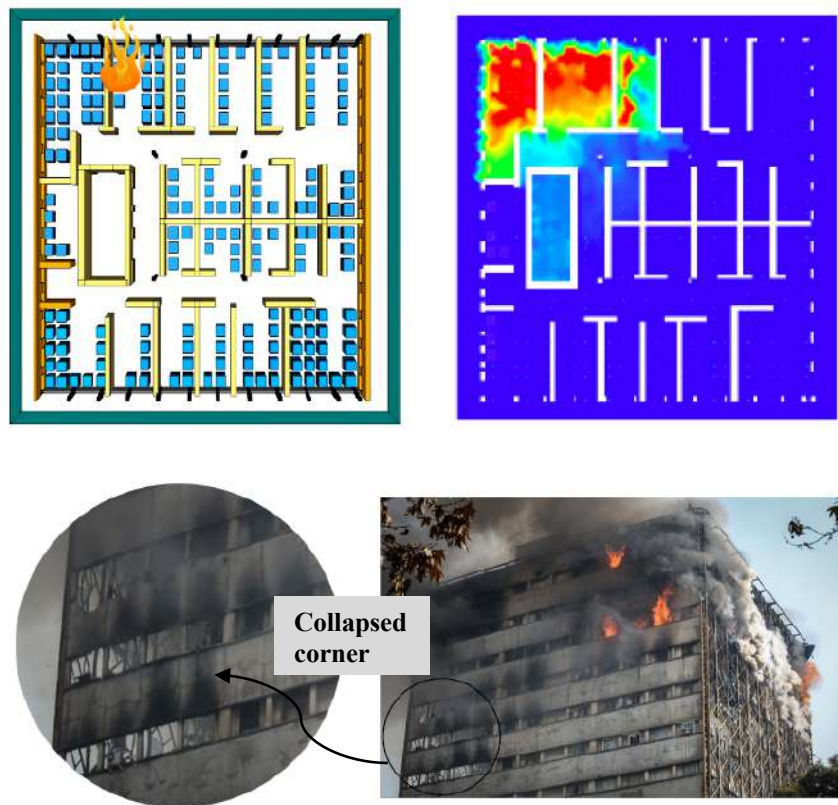


Figure 5. CFD model simulation showing the horizontal fire spread [15]

To carry out this study FDS, a CFD (computational fluid dynamics) based fire simulation tool, was chosen. The fire load characteristics were appropriately chosen to represent tightly stacked fabrics in the storage and ceiling spaces of the building. As the primary combustible material in the Plasco Building were textile material, therefore nylon was considered as fuel for the simulation model and its properties were taken from the SFPE handbook [16]. Other important parameters like ventilation openings, and false ceilings were also considered and modelled; the details of model calibration can be found in the PhD thesis of Khan, A.A. [14]. The authors calibrated the CFD model based on the visual evidence, and witnesses and firefighters' testimonies.

As the fire in the Plasco tower spread both vertically and horizontally, two CFD models were created to simulate both the vertical and horizontal fire spread. For vertical fire spread, the north-western corner of the Plasco Building from the 10th to 15th floors was simulated (Figure 4). The CFD model was calibrated to match the available evidence of the fire. The simulated vertical fire spread closely matched with the available visual evidence, as shown in Figure 5. This vertical fire spread as confirmed by witness testimonies, occurred in the early stages of fire i.e., during the first two hours of the fire incident. The reason for the rapid-fire spread can be ascertained by the easy availability of fuel, ventilation, and sufficient quantity of air. The vertical spread fire modelling provided the time of fire reaching the upper floors. The FDS simulation (Figure 4), shows that the fire reached upper floors within 30 min since the ignition, similar to what was observed during the fire accident. In later stages, the fire was observed spreading horizontally from a similar location (the north-western corner of the building), as shown in Figure 5, agreeing with the visual evidence and testimonies. The vertical fire simulation provides two important pieces of information, i.e., (1) the fire reached the upper floors during the early stages of the fire even before any firefighting operation began, and (2) the fire initiation location was similar at each floor. Therefore, only few floors are needed to calibrate the model and obtain realistic thermal data for all floors. It saves computational cost significantly.

In large open floor plan spaces, fire tends to travel across the floor plates with localized burning, this process is often termed as the traveling fire. In such spaces, fire spreads quickly till all the fuel is consumed. When there are partitions i.e., in a compartment, fire spread is usually slower. In the case of Plasco Tower, the floor was partitioned due to the presence of multiple business units, but the presence of a continuous false ceiling provided faster fire travel. To simulate the horizontal spread, an FDS model is generated to represent the spread of the fire on each floor. The fires on the 10th, 11th and 14th floors were primarily located in the north-western area of the building. Therefore, in FDS, the fire calibrated based on the 10th floor is used to represent the fires on both the 11th and 14th floors. Similarly, the observed flames on the 12th and 13th floors were similar, except for the more intense fire on the 13th floor's south-western side. Thus, only the 13th floor is used to represent the fire. Since the fire on the 15th floor was notably intense compared to other floors, a separate simulation is necessary. However, in this paper, where fire simulation is conducted until Event 8 (the first collapse), the thermal data from the 12th floor simulation is utilized for structural analysis. It is worth noting that although similar fires are simulated across multiple floors, different fire initiation timings are applied by introducing time delays for each floor. Table 1 presents the time delays for the fire to reach upper floors, derived from vertical fire spread modelling. These timings are incorporated into the fire simulation output. For instance, for the 11th floor fire, which utilizes thermal data from the 10th floor fire simulation, the initial fire time is set at 360 seconds (Table 1) to account for vertical fire spread in the structural model.

Table 1. Time delays to be used for applying thermal load on each floor

Floor	10 th floor	11 th floor	12 th floor	13 th floor	14 th floor	15 th floor
Time delay (sec)	0	360	620	900	1100	1300

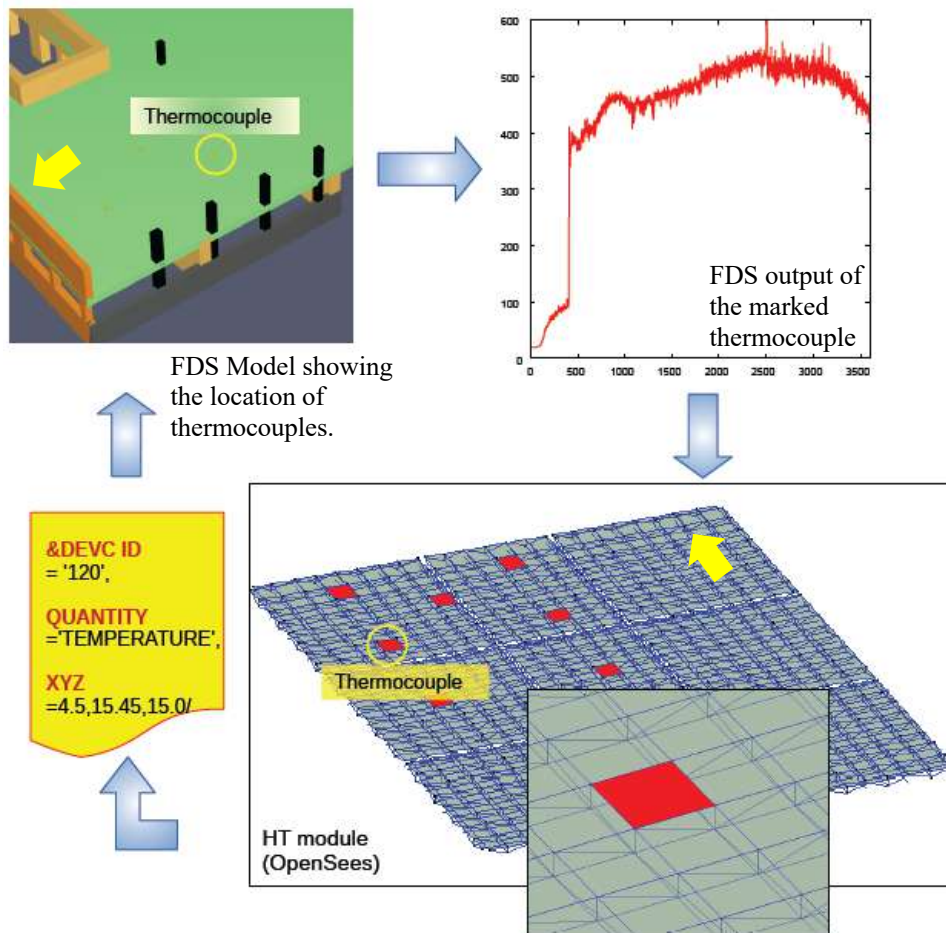


Figure 6. Thermocouple data exchange between the FDS and HT module of OpenSees

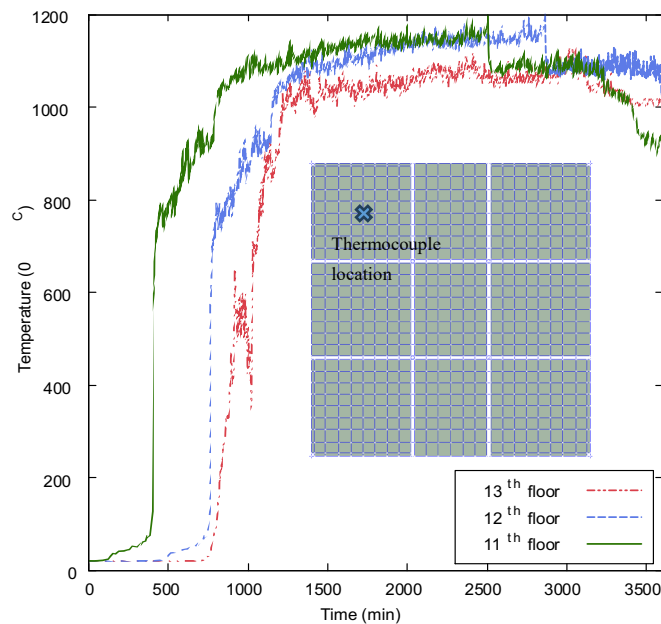


Figure 7. Comparison of temperature vs time data of thermocouples on 11th, 12th and 13th floors

In this study a lower thermocouple resolution was used to study the structural response with an intention to recalibrate the fuel load and gas temperature under the situation where structural response is deviated significantly from the available visual evidence. It is important to highlight that in the context of heat

transfer and structural analyses, the fire on the 10th floor is effectively heating the 11th floor. Consequently, for heat transfer and structural analyses purposes, when referring to the 11th floor, we are essentially considering the fire of 10th floor, and so forth. In the Figure 6, an example for the data communication between HT module of OpenSees and FDS for a particular thermocouple is shown. It can be seen from the FDS output of the marked thermocouple on 12th floor (temperature vs time data) that the temperature was below 100 °C initially and after 500 seconds, the temperature rises to 400 °C indicating the arrival of fire in that area. The initiation and arrival of fire at different locations can be verified by comparing the temperature vs time data from thermocouples those locations. The thermocouple data at NW corner area of three different floors is shown in the Figure 7.

6 BUILDING RESPONSE TO FIRE

The thermomechanical response predicted the failure of nearly 67% percentage of the NW floor area on the 11th and 12th floors of the building, see Figure 8. The deformations observed in the region on both 11th and 12th floors of the structure are more than 600mm. Deformations of 205mm and 110mm are noticed on the West and interior regions of the 11th floor respectively. It is because the fire which started on the 10th floor NW corner moved westwards and was quickly suppressed due to easy reachability (externally) for firefighting. The North face of the tower was not easily reachable hence the region saw quick fire growth and spread.

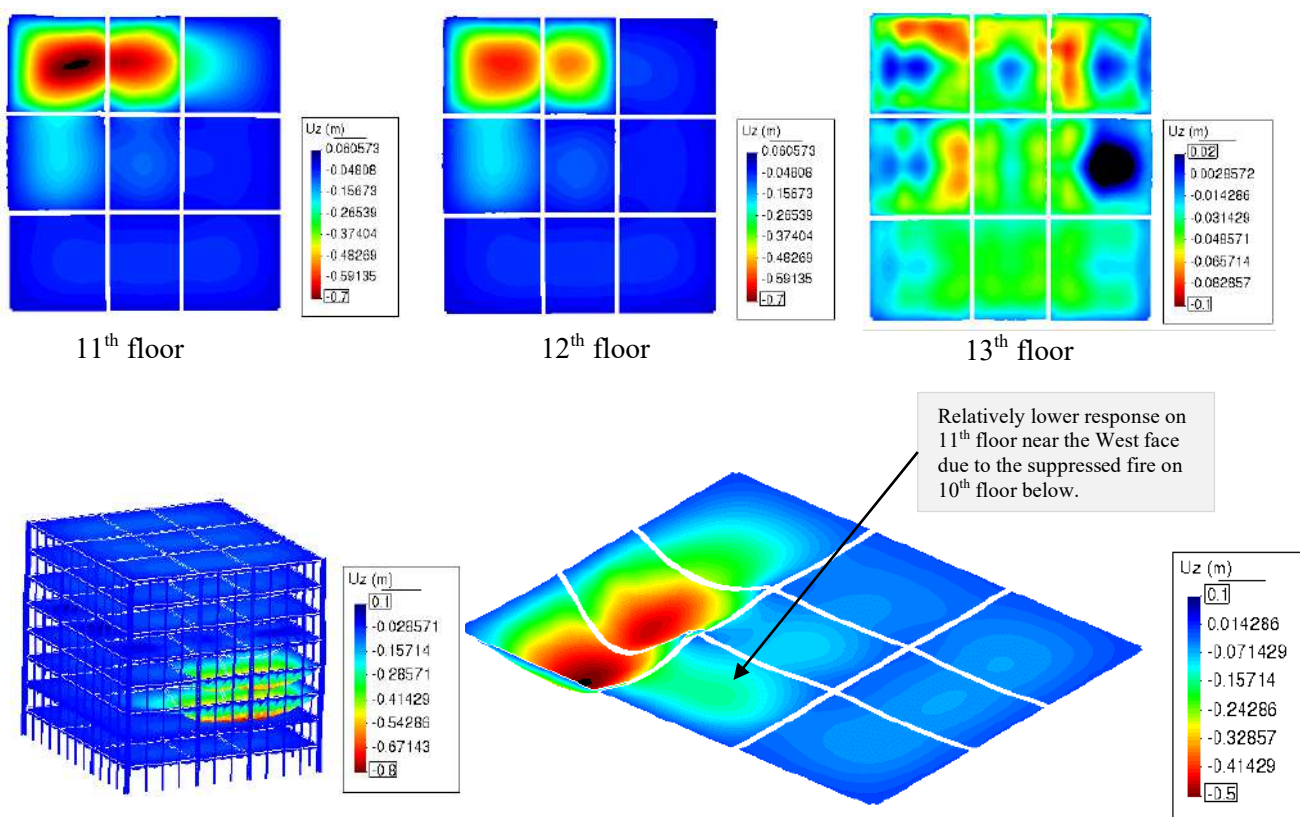


Figure 8. Deformation contour maps of 11th, 12th and 13th floors

The failure of 11th floor marks the Event 8 as shown in the established fire timeline used for this study. Event 9 and Event 10 take place after the failure of damaged 11th floor (Event 8) and both these events involve significant damage on the 13th floor. In this exercise the deformation contours showed only the arrival and fire spread on the 13th floor but did not show deformations of comparable scale. Therefore, an investigation is carried into the FDS and HT analyses done on the 13th floor. It was realized that there is a need to recalibrate the temperature input on 13th floor by managing the cooling part of the temperature vs

time data of thermocouples. Since this study focuses on the first collapse (till Event 8), where reduction in temperatures due to cooling was not an issue as fire in this zone re-emerged even after initial suppression and persisted till the first collapse.

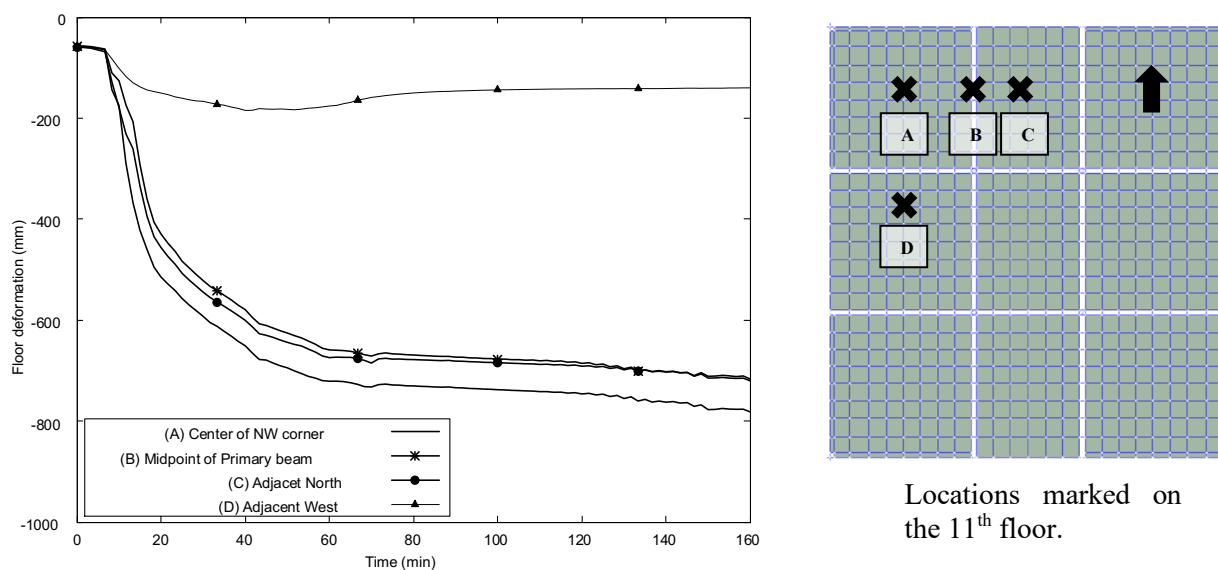


Figure 9. Plot showing deformations at different locations on 11th floor

The deformations on the 11th floor at different locations, see Figure 9, shows the failure of NW corner and adjacent area on the North side. The adjacent side on the West shows relatively lower deformations (200mm). The thermomechanical response indicating the failure of 2/3rd of the North side of the 11th floor agrees well with the visual evidence thus proving the accuracy of the fire modelling. The fire load on 13th floor and remaining floors (14-16) should be calibrated, before analysing Event 9 and Event 10.

7 FUTURE WORK

In the current paper, only a limited number of thermocouples are positioned at various locations to monitor thermal gradients on each floor. However, the research will use more detailed data from CFD, increasing the resolution of thermocouples on all floors to capture the structural response more accurately. Fire will be calibrated for upper floors (13th floors and above) to simulate the structural response of Event 9 and Event 10. Using the data from all fire simulations, the progressive collapse of the building will be simulated with respect to the traveling fire phenomenon.

8 CONCLUSIONS

It is important to understand the how a structure responds during a fire accident. This paper presents a methodology to carry out the structural analysis for a fire accident using the thermal data from FDS fire simulations. The output from FDS is used to perform heat transfer and thermomechanical analyses. The integration between FDS, the HT module, and the thermomechanical analysis module of OpenSees is demonstrated. Multiple floor fires involving the 11th, 12th, and 13th floors of the Plasco tower are simulated using the thermal data acquired from FDS. This study used a low-resolution thermocouple distribution, and the model accurately predicts the response of the 11th floor to fire, i.e., the arrival of the Event 8 numerically. Vertical and horizontal fire spread is presented using FDS where vertical fire spread provides arrival time of the fire on upper floor, which eventually introduces the delay in the timescale of thermal mechanical response. Thermal data is transferred from the FDS to OpenSees to conduct heat transfer and structural analyses. The simulations shows that the West side of the 11th floor did not see run away failure like the North side, therefore the fire modelling and thermal load application was reasonable.

In future studies, higher resolution thermal data will be utilized for each floor, and additional events such as the second collapse and progressive collapse will be analysed using the methodology outlined in this paper.

REFERENCES

- [1] A. A. Khan, A. Usmani, and J. L. Torero, "Evolution of fire models for estimating structural fire-resistance," *Fire Safety Journal*, vol. 124. Elsevier Ltd, Sep. 01, 2021. doi: 10.1016/j.firesaf.2021.103367.
- [2] A. S. Usmani, Y. C. Chung, and J. L. Torero, "HOW DID THE WTC TOWERS COLLAPSE: A NEW THEORY."
- [3] A. S. Usmani, J. M. Rotter, S. Lamont, A. M. Sanad, and M. Gillie, "Fundamental principles of structural behaviour under thermal effects," *Fire Saf J*, vol. 36, no. 8, pp. 721–744, Nov. 2001, doi: 10.1016/S0379-7112(01)00037-6.
- [4] B. Behnam, "Fire Structural Response of the Plasco Building: A Preliminary Investigation Report," *International Journal of Civil Engineering*, vol. 17, no. 5, pp. 563–580, 2019, doi: 10.1007/s40999-018-0332-x.
- [5] NFPA, *Fire Protection Handbook*, 21st Edition. NFPA, 2023.
- [6] T. K. Kaounis, "GiD+ opensees interface: a major extension to nonlinear finite element analysis." 2017.
- [7] A. Orabi, A. Khan, and AS. Usmani, "An Overview of Opensees for Fire," in *OpenSEES Days Eurasia, The Hong Kong Polytechnic University*, Hong Kong, 2019.
- [8] L. Jiang, M. A. Orabi, J. Jiang, and A. Usmani, "Modelling concrete slabs subjected to fires using nonlinear layered shell elements and concrete damage-plasticity material," *Eng Struct*, vol. 234, p. 111977, May 2021, doi: 10.1016/J.ENGSTRUCT.2021.111977.
- [9] Eurocode 3, "Design of Steel Structures," Part 1-2: General Rules, Structural Fire Design, , 2006.
- [10] A. A. Khan *et al.*, "Fire modelling framework for investigating tall building fire: A case study of the Plasco Building," *Case Studies in Thermal Engineering*, vol. 45, May 2023, doi: 10.1016/j.csite.2023.103018.
- [11] M. A. Orabi, A. A. Khan, L. Jiang, T. Yarlagadda, J. Torero, and A. Usmani, "Integrated nonlinear structural simulation of composite buildings in fire," *Eng Struct*, vol. 252, Feb. 2022, doi: 10.1016/j.engstruct.2021.113593.
- [12] A. A. Khan, M. A. Khan, C. Zhang, L. Jiang, and A. Usmani, "OpenFIRE: An Open Computational Framework for Structural Response to Real Fires," *Fire Technol*, vol. 58, no. 2, pp. 1011–1038, Mar. 2022, doi: 10.1007/s10694-021-01184-0.
- [13] A. A. Khan, M. A. Khan, K. A. Cashell, and A. Usmani, "An open-source software framework for the integrated simulation of structures in fire," *Fire Saf J*, p. 103896, Aug. 2023, doi: 10.1016/j.firesaf.2023.103896.
- [14] A. A. Khan, "Reconstruction of tall buildings fires for thermal response analysis," The Hong Kong Polytechnic University, Hong Kong, 2021.
- [15] A. A. Khan, R. V. V. Domada, X. Huang, M. A. Khan, and A. Usmani, "Modeling the collapse of the Plasco Building. Part I: Reconstruction of fire," *Build Simul*, vol. 15, no. 4, pp. 583–596, Apr. 2022, doi: 10.1007/s12273-021-0825-4.
- [16] SFPE, *SFPE Handbook of Fire Protection Engineering*, 5th Edition. 2016.

PROGRESSIVE COLLAPSE OF STEEL FRAMES SUBJECTED TO PARAMETRIC FIRE CURVES

Luca Possidente¹, Boban Cvetanoski², Nicola Tondini³, Fabio Freddi⁴

ABSTRACT

Extreme events such as terrorist attacks, vehicle impacts, and fires cause local damage to the buildings, which may spread from element to element, inducing progressive collapse. Steel structures are characterised by a high risk of progressive collapse owing to their high vulnerability (*e.g.*, low structural redundancy, joint behaviour), high hazard, and exposure (*e.g.*, they are often employed for large industrial or strategic buildings occupied by a large number of people). Therefore, steel structures should be carefully designed to mitigate the risk of progressive collapse. Despite being a rare event, fire may lead to the progressive collapse of the structure, and this paper investigates the progressive collapse of a seismically designed 9-storey steel moment-resisting frame subjected to different parametric fire scenarios and various loading levels. The response of critical components was validated against experimental data and standard prescriptions to accurately simulate both beam-type (*i.e.*, ductile plastic hinges and catenary action) and column-type (*i.e.*, non-ductile buckling) mechanisms. Various parametric fires and scenarios affecting ground-storey columns were considered. It is shown that the fire affecting one column may induce buckling of the adjacent ones (*i.e.*, column-type mechanism). This is in contrast with the typical considerations on progressive collapse at ambient temperature, which assume beam-type mechanisms. The mechanisms of collapse are described in detail and the influence of the fire parameters and the loading levels are outlined.

Keywords: Progressive collapse; Parametric fires; Steel structures; Risk mitigation

1 INTRODUCTION

Extreme events may cause local damage to building structures, which may spread from element to element, leading to the collapse of the entire structure or a large part of it [1], *i.e.*, progressive collapse. Among these extreme events, short-duration events, like blasts and impacts, cause sudden damage to the structure involving dynamic actions that may severely stress the structure. Conversely, long-duration events, such as fires, damage the structure with slow-developing actions, which can typically be investigated with static analyses. A general simplified threat-independent approach for short-duration events involves static analyses in which the damaged elements are removed and factors to account for the dynamic effects, *i.e.*, Dynamic Increase Factors (DIF), are applied to the gravity loads. However, recent studies have shown that such an approach is not appropriate for fire-induced progressive collapse (long-duration events) [2] and that the structural response needs to be carefully investigated, explicitly simulating the effects of fire. Indeed, the degradation of the mechanical properties with temperature and thermal expansion cannot be accurately accounted for with a notational element removal scenario. Moreover, fire might be critical as progressive collapse may be caused by mechanisms significantly different from those in other situations.

¹ PhD, Post-doctoral Fellow, Department of Civil, Environmental and Geomatic Engineering, University College London, UK
e-mail: l.possidente@ucl.ac.uk, ORCID: <https://orcid.org/0000-0002-4179-1860>

² MSc, MSc Student, Department of Civil, Environmental and Mechanical Engineering, University of Trento, Italy

³ PhD, Associate Professor, Department of Civil, Environmental and Mechanical Engineering, University of Trento, Italy
e-mail: nicola.tondini@unitn.it, ORCID: <https://orcid.org/0000-0003-2602-6121>

⁴ PhD, Associate Professor, Department of Civil, Environmental and Geomatic Engineering, University College London, UK
e-mail: f.freddi@ucl.ac.uk, ORCID: <https://orcid.org/0000-0003-2048-1166>

For instance, columns may lose their lateral restraints due to fire-induced floor collapse, as presumably occurred in the World Trade Center [3], or experience additional tension forces in the cooling phase [2,4]. Steel structures have a higher risk of progressive collapse compared to other building types. Indeed, being risk defined as the convolution of vulnerability, hazard, and exposure, the three components of risk are highly present in steel frames. The vulnerability of steel structures is high as they are usually designed with a low level of redundancy, with sections optimised for specific design actions. The joints may not be able to withstand the additional tie forces. The hazard and the exposure are high as steel structures are often employed for large strategic or industrial buildings occupied by a large number of people or devoted to the provision of fundamental services. In this context, investigating fire-induced progressive collapse is very relevant for steel structures, and extensive studies are necessary to effectively design resilient buildings and propose actions to mitigate the progressive collapse risk.

This paper addresses the problem of fire-induced progressive collapse of steel moment-resisting frame (MRF) by performing an extensive parametric study. A 9-storey steel MRF is considered for case study purposes. Different scenarios involving several parametric fires affecting ground-storey columns were investigated. The intensity of the gravity loads was varied to explore the response of the structure under different loading levels. The case study structure was modelled in OpenSees [5,6], with particular attention to components significantly affecting the response under fire and large inelastic deformations. The response of beams and columns was validated against experimental data and European design standards [7,8] to accurately simulate beam-type and column-type collapse mechanisms. Global and local imperfections were included as well to capture the potential loss of stability of the structure. The governing collapsing mechanisms are described in detail for representative scenarios. In contrast with the typically considered beam-type ductile mechanisms in progressive collapse analyses of steel frames, the investigated structures show a progressive collapse initiated by the buckling of the columns adjacent to the heated one (*i.e.*, column-type mechanism). It is also demonstrated that the seismic design confers to the investigated frame a sufficient capacity to resist progressive collapse when the fire combination is considered, while by increasing the loads by 10% or 20%, progressive collapse occurs depending on the fire scenario. The present study provides significant insights toward the understanding and knowledge of fire-induced progressive collapse of steel MRF. In particular, the influence of each single fire parameter and the loading level are assessed.

2 NUMERICAL STUDY

2.1 Case Study Structure

Figure 1 shows the 9-storey seismically designed MRF considered for case study purposes. This MRF was already examined in previous research focusing on progressive collapse [9,10], and detailed information can be found in Gerasimidis *et al.* [11]. The structure is characterised by an inter-storey height of 3 m and a total height of 27 m. The plane frames consist of 4 bays with 5 m spans, with the steel sections oriented along the major axis. The bay span in the transversal direction was considered equal to 7 m. Beam-column joints were designed as rigid, full-strength welded joints. Steel S235 was used for the steel components (*i.e.*, yield strength $f_y = 235$ MPa, Young's modulus $E = 210000$ MPa, and Poisson ratio $\nu = 0.3$). Table 1 summarises the steel cross-sections for columns and beams. The seismic design was performed according to the Eurocode recommendations [7,12,13] for a building located in Greece with a horizontal peak ground acceleration equal to 0.16g. The structure was considered unprotected against fire, which generally would not be true for a multi-storey building. However, this aspect does not alter the results, given that steel structures can be assessed in the temperature domain. The focus is not on the time of collapse but on identifying the mechanisms leading to progressive collapse. Thus, the time indicated in the figures must not be considered a measure of assessing the vulnerability of the case study.

Table 1. MRF design. (Adapted from Gerasimidis *et al.* [11])

Storey	1	2	3	4	5	6	7	8	9
Columns	HE500B			HE280B			HE220B		
Beams	IPE550	IPE500		IPE450			IPE400		IPE360

A Dead Load (DL) equal to 5.0 kN/m² was applied on all floors, consisting of 3.0 kN/m² for the self-weight of the concrete slab and 2.0 kN/m² to account for the non-structural permanent components. The additional DL for the self-weight of beams and columns was applied directly to these elements. The building was assumed to be an office; hence, a Live Load (LL) of 2.00 kN/m² was applied on all floors. The only exception is the roof, which considered a Snow Load (SL) equal to 0.69 kN/m² based on Eurocode guidelines [12] for the Greek climate region in Zone III, 200 m of altitude and standard conditions. The analyses were performed considering the fire load combination defined according to the EN1990 [14] reported in Eq. 1 as follows.

$$q_d = 1.0DL + 0.3LL + 0.0SL \quad (1)$$

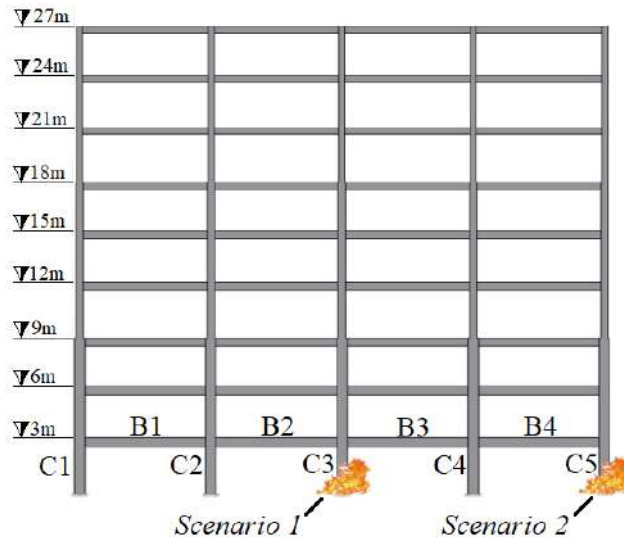


Figure 1. Case study steel moment-resisting frame (MRF) and fire scenarios

2.2 Fire scenarios and parametric analysis

Two scenarios were considered to investigate the effects of fire on the progressive collapse resistance of the frame. Columns are typically identified as the elements that are more critical to structural stability and whose failure maximises the progressive collapse risk. Hence, fire was assumed to affect the central ground-storey column in Scenario 1 and a perimetral ground-storey column in Scenario 2. Figure 1 shows the frame and the fire-affected columns for the two scenarios.

For each scenario, a parametric analysis was performed to identify the parameters governing the progressive collapse of the MRF. Several parametric fires were defined according to EN 1991-1-2 [15], considering an opening factor of 0.044 m^{1/2} for Scenario 1 and 0.051 m^{1/2} for Scenario 2. Ventilation-controlled parametric fires were defined by varying the thermal inertia b and the fire load density $q_{f,d}$ within the range $b = 900$ -1500 J/m² s^{1/2} K and $q_{f,d} = 500$ -1000 MJ/m². Figure 2a and Figure 2b show the influence of these parameters on the gas temperatures for Scenario 1.

Finally, the variability of the loads was considered in the parametric analysis. Different loading levels, due to possible alternative load configurations were adopted, varying the value of the load factor λ . The load factor λ was defined as follows:

$$\lambda = \frac{\sum_{i=1}^n R_i}{Q_{tg}} \quad (2)$$

where $\sum_{i=1}^n R_i$ is the sum of the n vertical base reaction forces of the frame, and Q_{tg} is the load target the structure is supposed to bear according to the load combination in Eq. 1. The load factor λ was varied from 1.0 to 1.3. Table 2 summarises the parameters varied in the numerical simulation.

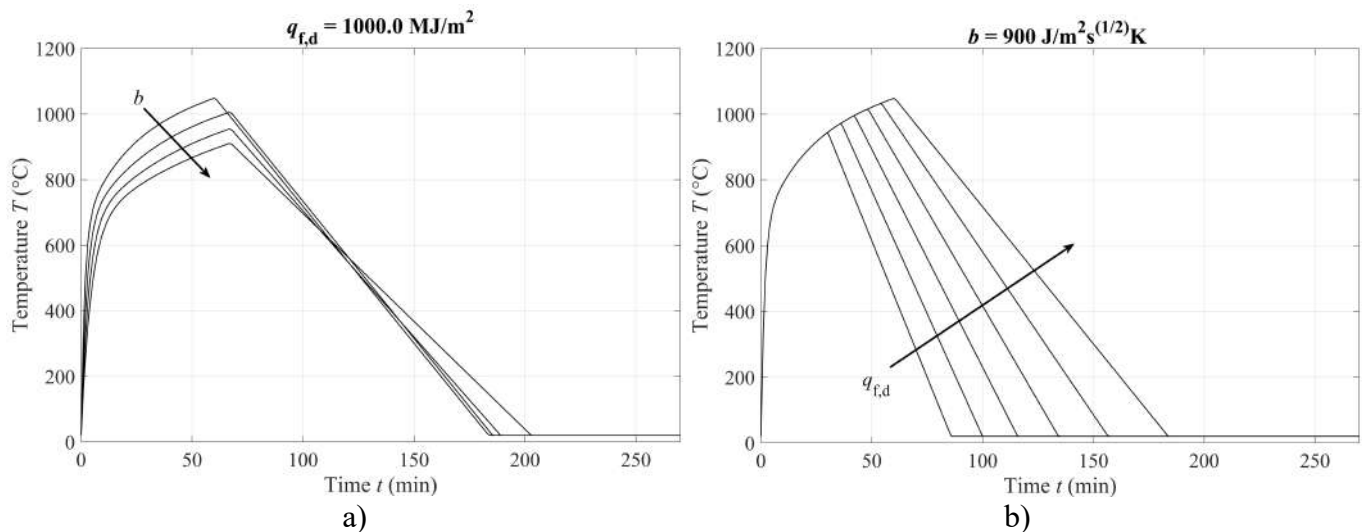


Figure 2. Parametric fire curves for Scenario 1: a) Influence of b ; b) Influence of $q_{f,d}$

Table 2. Configurations varied in numerical simulation

Fire scenarios	Fire curves	Load factors
1) Fire on the central ground-storey column 2) Fire on a perimetral ground-storey column	$b = 900 - 1500 \text{ J/m}^2 \text{ s}^{1/2} \text{ K}$ $q_{f,d} = 500 - 1000 \text{ MJ/m}^2$	$\lambda = 1.0 - 1.3$

2.3 Numerical model

3D numerical models of the plane MRF were developed in OpenSees [5] and OpenSees for fire [6]. The ground-storey columns were fixed in the x -direction and hinged in the y -direction. Lateral restraints were introduced on the beam-column joints of each floor to prevent a global out-of-plane loss of stability and account for the lateral stiffness of the transversal beams and the slab. Similarly, it was assumed that the slab provides effective restraints for lateral-torsional buckling of the columns. Conversely, the possible positive contribution of the slab to the progressive collapse resistance was conservatively neglected. The possible loss of stability of the structure and the buckling of columns were considered based on the EN1993-1-1 [7] recommendations. A global equivalent imperfection in terms of initial column rotation Φ was applied to the structure, and both in-plane and out-of-plane local imperfections with a local magnitude e_o were considered. Masses were concentrated on the floor and at half the columns' length.

A distributed plasticity approach was considered for columns. The elastic shear stiffness of the columns was included using the 'Section Aggregator' command. A lumped plasticity approach was used for beams, concentrating plastic hinges at the beams' ends. Plastic hinges were modelled with the 'Parallel Plastic Hinge' (PPH) approach proposed by Lee *et al.* [16]. This approach considers flexural and axial behaviour via two springs. It is, therefore, particularly suited for progressive collapse scenarios, in which both flexural and catenary actions contribute to the resisting mechanism. Beam-column joints were modelled through two independent flexural springs connected to two orthogonal rigid links, whose extension is representative of the height of the column and beam steel sections. The flexural springs were employed to define a 'Scissor Model' [17] to simulate the deformability of the column web panel and flanges. The main parameters of this model were determined according to Charney and Downs [18].

OpenSees for fire was extensively validated against experimental results and was shown to be able to correctly capture the behaviour of heated columns [6]. Conversely, the response of beams and columns at ambient temperature was validated and calibrated against experimental results. A brief description of the validation is provided here, while detailed information can be found in Possidente *et al.* [10]. Figure 3a shows the validation of the PPH model against the experimental results provided by Dinu *et al.* [19]. In such tests, a beam-column connection was investigated by testing a steel subassembly subjected to a column

removal scenario. Figure 3a shows a good agreement in the evolution of the axial force with the vertical displacement δ , measured at the actuator simulating the column removal. A conservative behaviour is observed for the flexural response, which is consistent with the plastic bending moment capacity M_{pl} of beams. A similar model was implemented in the FE model of the entire structure and calibrated based on the dimensions of the connections. Figure 3b shows the validation of the numerical model for column buckling. The capability of the model to simulate buckling is essential for progressive collapse scenarios and was carefully checked in the present study. For this purpose, GMNIA (Geometrically and materially nonlinear analysis with imperfections included) analyses were performed to reproduce the buckling resistance provided in EN1993-1-1 [7] of compressed members $N_{y,b,Rd}$. Indeed, various research studies [20,21] showed that a good match between numerical results and buckling curves could be achieved for the strong axis buckling by introducing the imperfection $e_{o,\eta} = k\alpha(\bar{\lambda}-0.2)$, indicated also in the EN1993-1-1 [8]. In such an equation, $k=W_{el}/A$ is the kernel radius, defined as the ratio between the elastic section modulus W_{el} for the strong axis and the area A of the section, while α and $\bar{\lambda}$ are the imperfection factor and the non-dimensional slenderness according to EN1993-1-1 [7], respectively. Analyses were performed by varying the length of simply supported columns made of HE400B section with steel S235 (*i.e.*, same as the ground-storey columns of the case study structure). Lateral restraints were introduced to avoid buckling on the weak axis, and each column was modelled with 6 fibre elements. Figure 3b shows that the numerical results are in good agreement with the buckling curve. Hence, the model was deemed sufficiently accurate to reproduce the effect of buckling, and the same discretisation was employed in the FE model of the entire structure.

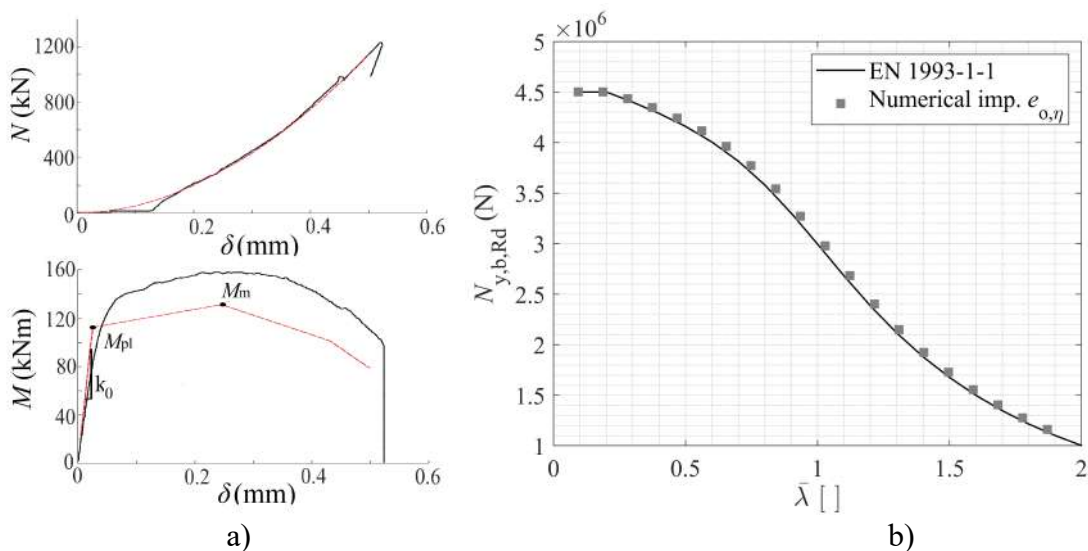


Figure 3. Model validation. a) Experimental validation for the PPH; b) Numerical validation for the columns

2.4 Analysis procedure

The analyses were performed with OpenSees and involved both thermal and mechanical analyses. First, thermal analyses were performed to determine the temperature inside the steel sections [6]. Analyses were carried out for the columns heated in the two scenarios, considering all the different fire curves. The same temperature distribution was assumed along the column height.

The mechanical analyses were performed in two steps: 1) the gravity loads according to the selected load factor λ were applied to the MRF. As in this stage, the structure remained essentially in the elastic range, the results of the analyses are not shown in detail in the following section; 2) the temperature evolution obtained from the thermal analyses was applied to the heated columns, and the structural response of the MRF was investigated. Dynamic analyses were carried out to capture the final collapsing phase and understand the collapse mechanism. Fire analyses were performed considering both scenarios.

3 RESULTS

For brevity, the results are shown in detail only for a few representative cases of Scenario 1. Figure 4 shows the relevant results for a load factor $\lambda=1.1$ and the parametric curve defined with $b=1500 \text{ J/m}^2 \text{ s}^{1/2} \text{ K}$, and $q_{f,d}=500 \text{ MJ/m}^2$. The axial force in the ground-storey columns and the average steel temperature $T_{s,avg}$ in the heated column are shown in Figure 4a. The axial force in the heated column (*i.e.*, column C3) increases owing to the restrained thermal expansions until it reaches the buckling capacity at about 250°C . After that, the capacity is reduced due to the degradation of the mechanical properties caused by the further temperature increase, and the column is unloaded. The axial force reduction continues in the cooling phase, where tension forces appear due to thermal contraction. Throughout the analysis, the loads previously carried by the heated column are redistributed to the adjacent columns C2 and C4, while a very small portion of the loads is redistributed to the perimeter columns C1 and C5. The columns C2 and C4 experience buckling in the cooling phase when the average steel temperatures $T_{s,avg}$ are lower than 250°C and the axial force reaches the buckling resistance $N_{b,Rd,MN}$, calculated incorporating the effects of the bending moments according to EN1993-1-1 [7]. Nevertheless, the MRF does not collapse as the catenary mechanism activates, and the slight load increase induced by restrained thermal contraction is effectively redistributed to the perimeter columns. Figure 4b shows that the beams are not critical as the bending moments in the beams above the heated column (*i.e.*, beams B2 and B3) remain below the maximum bending moment M_m defined in the PPH model.

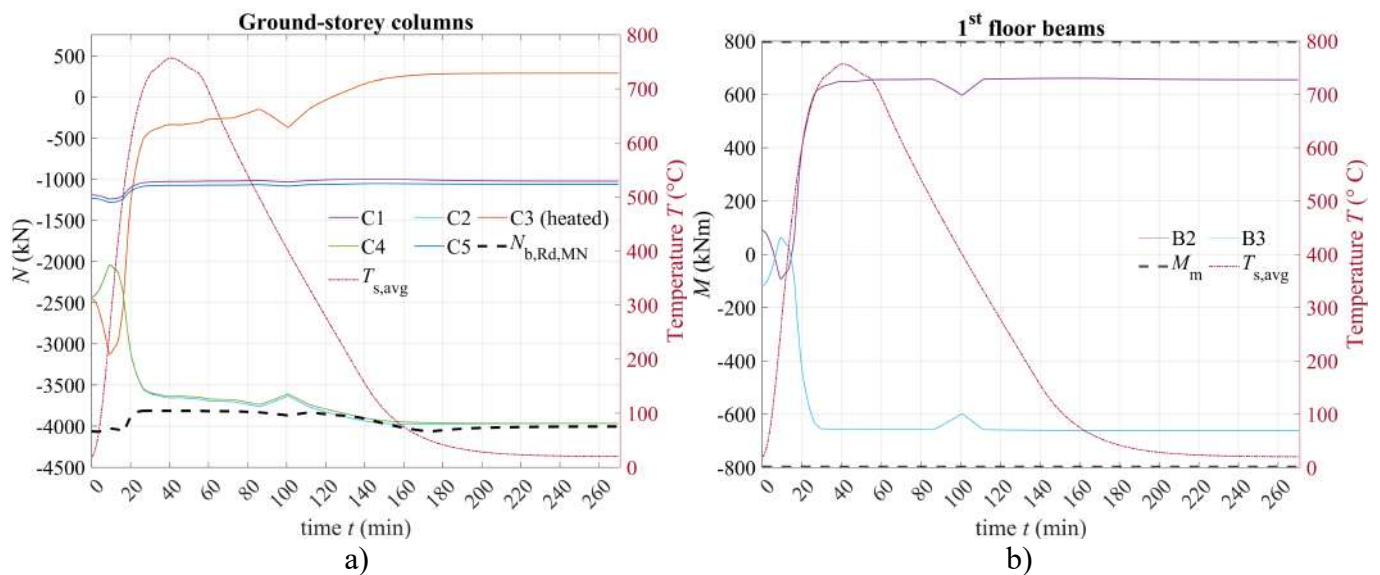


Figure 4. Scenario 1, $b=1500 \text{ J/m}^2 \text{ s}^{1/2} \text{ K}$, $q_{f,d}=500 \text{ MJ/m}^2$, $\lambda=1.1$: a) Axial forces in the ground-storey columns; b) Bending moment in the beams above the heated column

Similarly, Figure 5 shows the axial force in the ground-storey columns and the bending moment in the beams B2 and B3 in the case of $\lambda=1.3$. It can be observed that the increase in the load factor causes the collapse of the structure. Figure 5a shows that the axial force in the heated column is reached at about 210°C and that the load redistribution triggers column buckling in the adjacent columns at about 630°C . In this case, the out-of-plane runaway deflections caused by buckling of columns C2 and C4 cannot be effectively prevented, causing the collapse of the MRF in the heating phase. As shown in Figure 5b, the beams are not critical as the bending moment in the beams B2 and B3 is well below the maximum moment M_m . Hence, the buckling of columns C2 and C4 initiates the progressive collapse of the frame.

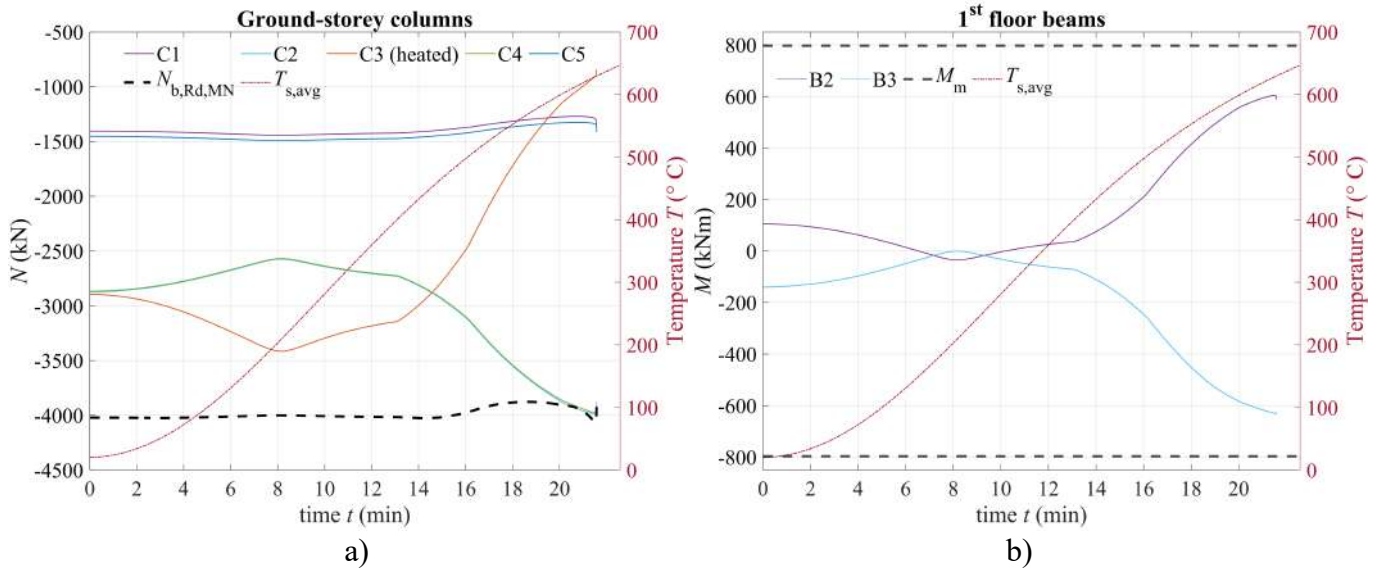


Figure 5. Scenario 1, $b=1500 \text{ J/m}^2 \text{ s}^{1/2} \text{ K}$, $q_{f,d}=500 \text{ MJ/m}^2$, $\lambda=1.3$: a) Axial forces in the ground-storey columns; b) Bending moment in the beams above the heated column

Figure 6a and b compare the axial forces in beams B1 and B2 to track the development of catenary actions for all load factors considered in the parametric study. The measured tension forces are very small and well below the axial capacity of the beams. For $\lambda < 1.3$, the beam's tension forces effectively redistribute the gravity loads during the entire fire exposure, even when buckling occurs in the C2 column for $\lambda = 1.1$ and $\lambda = 1.2$. Conversely, for $\lambda = 1.3$, the load redistribution mechanism stops being effective at about 630°C , as the higher loads induce a more rapid increase in the tension force. In this situation, a further temperature increase in column C3 induces a deformed configuration that, combined with the gravity loads, causes the loss of stability of the MRF.

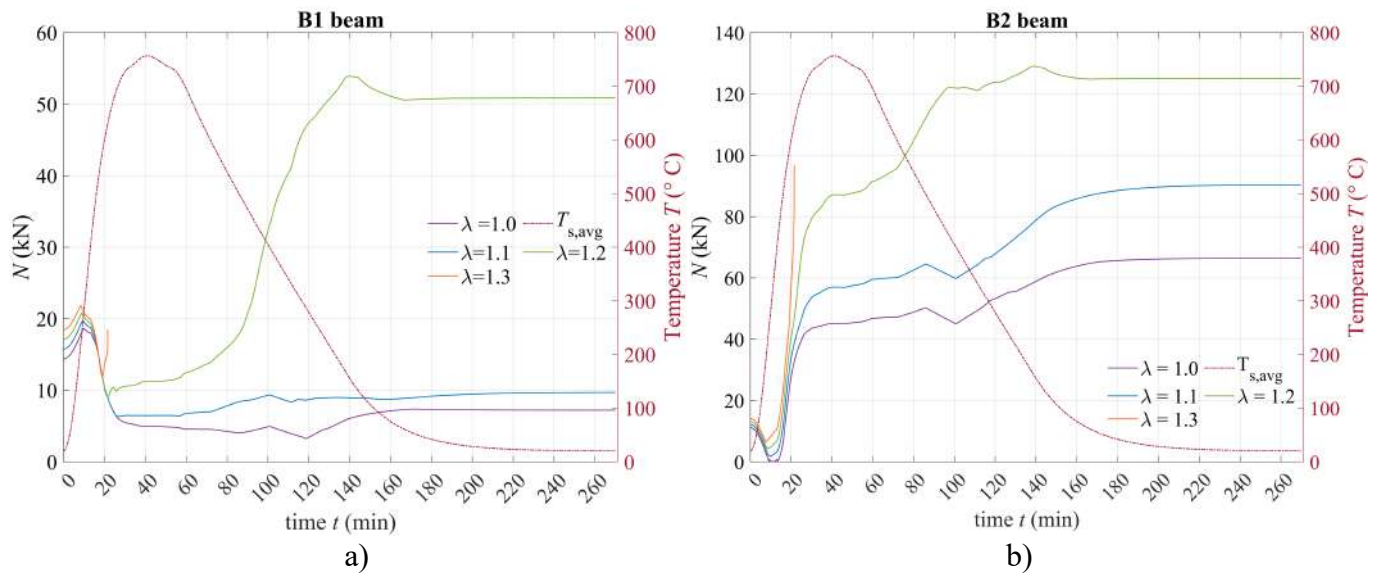


Figure 6. Scenario 1, $b=1500 \text{ J/m}^2 \text{ s}^{1/2} \text{ K}$, $q_{f,d}=500 \text{ MJ/m}^2$: a) Axial forces in the B1 column; b) Axial forces in the B2 beam

Figure 7 shows the results of the parametric analysis in terms of time of collapse, *i.e.*, the time of fire exposure before the collapse. As aforementioned, considerations in the domain of the temperature were provided as the time of collapse would differ from the one provided if a more typical situation for high building with protected steel elements were to be considered. Nevertheless, it seems relevant to assess the influence of the different parameters on the time of collapse. Trends of the collapse-retarding effect of the parameters remain valid in the case of protected steel elements. Hence, despite the structure will be

protected, Figure 7 gives insight on the influence of b and $q_{f,d}$. The time of collapse was defined as the time at which no converged solution could be found in the numerical analyses due to a loss of stability of the structure.

Figure 7a shows that for Scenario 1, the collapse is observed only for $\lambda > 1.1$. In particular, $\lambda = 1.2$ entails collapse times spanning from 22 to 38 minutes, while for $\lambda = 1.3$ collapse occurs between 14 to 22 minutes. All collapses were observed in the heating phase, as when buckling occurred in the columns adjacent to the heated one during the cooling phase, it was always possible to redistribute loads to the perimetral columns. Hence, the fire load $q_{f,d}$ shows no impact on the time of collapse. Indeed, for heating curves with the same value of thermal inertia b , collapse is triggered in the heating phase by exceeding a critical average steel temperature value $T_{s,avg}$, and therefore, the only possible effect of reducing $q_{f,d}$ is to avoid collapse by preventing from reaching such critical temperature in the steel section (see Figure 2b). This is the case when $q_{f,d}$ is reduced from 600 to 500 for $b = 1500 \text{ J/m}^2 \text{ s}^{1/2} \text{ K}$ and $\lambda = 1.2$. Figure 7b shows that Scenario 2, which involves the heating of column C1, is more severe and collapse occurs already for a load factor $\lambda = 1.1$. Similar considerations as the ones for Scenario 1 apply in this situation. The collapse times span from 21 to 37 minutes for $\lambda = 1.3$, 15 to 23 minutes for $\lambda = 1.2$ and 13 to 20 minutes for $\lambda = 1.1$.

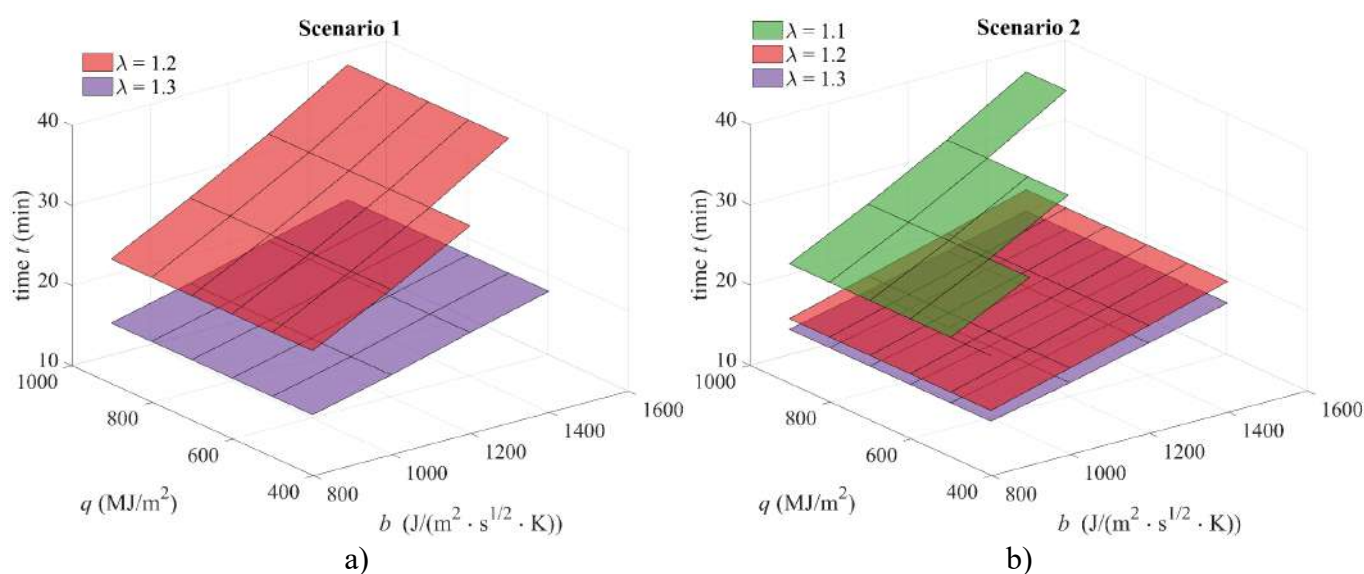


Figure 7. Time of collapse: a) Scenario 1; b) Scenario 2

In general, it can be concluded that for the loads considered in this study, the fire combination is not sufficient to induce the collapse of the structure, as no collapse was observed for $\lambda = 1.0$. Hence, the seismic design of the structure seems adequate to provide sufficient capacity to the structure also in fire situation. Nevertheless, the DL and the LL on the structure may change owing, for instance, to the use of the structures for different purposes or the reorganisation of internal non-structural components. In this case, a careful check of the design is required as the fire combination may become critical for progressive collapse. Finally, it is noteworthy that preliminary analyses performed with the alternate path method (APM) showed that for a progressive collapse load combination according to the recommendations provided in the UFC [22], the MRF is not able to withstand the removal of the central or perimetral column, owing to the dynamic effects induced by the sudden removal of the column [23].

4 CONCLUSIONS

This paper presents and discusses the results of a parametric study on the fire-induced progressive collapse of steel structures. Non-linear thermomechanical analyses were performed to investigate the progressive collapse in a 9-storey Moment Resisting Frame (MRF) considering various fire scenarios and parametric fire curves affecting the ground-storey columns. To better capture the progressive collapse response of the MRF, and accurately simulate both beam-type (ductile plastic hinges and catenary action) and column-type

(non-ductile buckling) mechanisms, beam and columns were validated against experimental data and design standards. The study shows that the structure is sufficiently robust to withstand the fire scenarios when the fire combination is considered. However, by increasing the gravity loads by up to 30%, *i.e.*, employing load factors λ up to 1.3, progressive collapse occurs depending on the scenario and the fire curve. In particular, progressive collapse may be triggered with a loading level $\lambda \geq 1.2$ when the central column is heated and $\lambda = 1.1$ when the perimetral column is heated. As collapse occurred in the heating phase, less severe parametric curves, *i.e.*, with higher b or lower $q_{f,d}$, may hinder from attaining the critical steel temperature $T_{s,avg}$ causing collapse, *e.g.*, for $\lambda = 1.1$ in Scenario 1 and $\lambda = 1.2$ in Scenario 2. The thermal inertia b , may also have the effect of postponing the time of the collapse. In contrast with the typical consideration based on the ductile behaviour of beams, the progressive collapse was always triggered by the buckling of the columns adjacent to the heated column. It is noteworthy that the attainment of the buckling capacity in such columns did not always induce the collapse of the structure. Indeed, especially when buckling occurs during the cooling phase of the fire curves, the MRF shows sufficient capacity to further redistribute the loads from the columns adjacent to the heated one to the other elements. This situation is rare in the case of higher load factors, in which the higher loads prevent effectively redistributing the force previously carried by the buckled columns through catenary action in the beams. In future applications, different steel structures and scenarios will be investigated, to generalise results. Among the others, MRFs more sensitive to the beam mechanism will be analysed. These analyses aim to further investigate the redistribution capacity of the frames, particularly in the case of multiple buckled columns, and explore the potential for progressive collapse during the cooling phase.

ACKNOWLEDGEMENT

The first author was supported by the UK Research and Innovation Institution (UKRI) in the framework of the project RESTORE “Retrofit strategies for Existing Structures against progressive collapse” (grant EP/X032469/1). Any opinions, findings, and conclusions or recommendations expressed in this paper are those of the authors and do not necessarily reflect the views of UKRI.

Nicola Tondini gratefully acknowledges the support received from the Italian Ministry of Education, University and Research (MIUR) in the frame of the ‘Departments of Excellence’ (grant L 232/2016).

REFERENCES

1. SEI/ASCE 7-16. (2016). Minimum Design Loads for Buildings and Other Structures. ASCE, Reston, VA, USA.
2. Gernay, T., Gamba, A. Progressive collapse triggered by fire induced column loss: Detrimental effect of thermal forces. *Eng Struct* 172: 483–496 (2018).
3. Usmani, A.S., Chung, Y.C., Torero, J.L. How did the WTC towers collapse: a new theory. *Fire Safety J* 38: 501–533 (2003).
4. Sun, R., Huang, Z., Burgess, I.W. The collapse behaviour of braced steel frames exposed to fire. *J Constr Steel Res* 72: 130–142 (2012).
5. Mazzoni, S., McKenna, F., Scott, M.H., Fenves, G.L. Open System for Earthquake Engineering Simulation User Command-Language Manual, OpenSees Version 2.0, University of California, Berkeley, CA, (2009).
6. Jiang, J., Jiang, L., Kotsovinos, P., Zhang, J., Usmani, A., McKenna, F., and Li, G.-Q. OpenSees software architecture for the analysis of structures in fire, *Journal of Computing in Civil Engineering*, 29(1) (2015).
7. CEN (European Committee for Standardization), Eurocode 3: Design of steel structures – Part 1–1: General rules and rules for building. EN 1993–1–1. Brussels, Belgium, 2005.
8. CEN (European Committee for Standardization), Eurocode 3: Design of steel structures – Part 1–1: General rules and rules for buildings. ENV 1993–1–1. Brussels, Belgium, 2004.
9. Freddi, F., Ciman, L., Tondini, N. Retrofit of existing steel structures against progressive collapse through roof-truss. *Journal of Constructional Steel Research*; 188: 107037 (2022).
10. Possidente, L., Freddi, F., Tondini, N. Dynamic increase factors for progressive collapse analysis of steel structures considering column buckling. *Engineering Failure Analysis*, 160, 108209 (2024).

11. Gerasimidis, S., Bisbos, C., Baniotopoulos, C. Vertical geometric irregularity assessment of steel frames on robustness and disproportionate collapse, *J. Constr. Steel Res.*, 74: 76–89 (2012).
12. CEN (European Committee for Standardization), Eurocode 1: Actions on structures – Part 1–1: General actions - densities, self-weight, imposed loads for buildings. EN 1991–1–1. Brussels, Belgium, 2002.
13. CEN (European Committee for Standardization), Eurocode 8: Design of Structures for Earthquake Resistance. Part 1: General Rules, Seismic Action and Rules for Buildings. EN 1998–1. Brussels, Belgium, 2005.
14. CEN (European Committee for Standardization), Eurocode: Design of steel structures – Part 1–1: General rules and rules for building Basis of structural design. EN 1990. Brussels, Belgium, 2005.
15. CEN (European Committee for Standardization), Eurocode 3: Design of steel structures – Part 1-2: General rules - Structural fire design. EN 1993–1–2. Brussels, Belgium, 2005.
16. Lee, C.-H., Kim, S., Lee, K. Parallel axial-flexural hinge model for non linear dynamic progressive collapse analysis of welded steel moment frames, *J. Struct. Eng.* 136(2): 165–173 (2009).
17. Castro, J.M., Elghazouli, A.Y., Izzuddin, B.A., Modelling of the panel zone in steel and composite moment frames, *Engineering Structures.* 27: 129–144 (2005).
18. Charney, F.A., Downs, W.M., Modeling procedures for panel zone deformations in moment resisting frames, in: *Proc. Conference on Connections in Steel Structures V: Innovative Steel Connections*, Amsterdam, the Netherlands, 2004.
19. Dinu, F., Marginean, I., Dubina, D., Petran, I. Experimental testing and numerical analysis of 3D steel frame system under column loss. *Engineering Structures*, 113: 59–70 (2016).
20. Jönsson, J., Stan, T.-C. European column buckling curves and finite element modelling including high strength steels, *J. Constr. Steel Res.* 128: 136–151(2017).
21. Possidente, L., Tondini, N., Battini, J.-M.. Torsional and flexural-torsional buckling of compressed steel members in fire. *J. Constr. Steel Res.* 171 (2020)
22. DOD (United States Department of Defense), Unified Facilities Criteria (UFC) – Design of Structures to Resist Progressive Collapse. 4–023-0314. July 2009 – Change 3, 1 November 2016, Arlington, Virginia.
23. Possidente, L., Freddi, F., Tondini, N. Numerical investigation of retrofit measures to mitigate progressive collapse in steel structures. SECED 2023 Conference, 14-15 September 2023, Cambridge, UK.

RESISTANCE MODELS FOR THIN-WALLED STEEL BEAMS UNDER NON-UNIFORM TEMPERATURE USING MACHINE LEARNING

Carlos Couto¹, Qi Tong², Thomas Gernay³

ABSTRACT

The resistance of thin-walled steel beams in fire is governed by a complex interaction between the buckling of the plates and the lateral-torsional buckling (LTB) of the member, combined with the temperature-induced reduction of steel properties. Besides, in many applications, steel beams are subjected to non-uniform thermal exposure which creates temperature gradients in the section. There is a lack of analytical design methods to capture the effects of temperature gradients on the structural response, which leads to overly conservative assumptions thwarting optimization efforts. Meanwhile, data-based Machine Learning (ML) methods have been widely recognized for their ability to learn from complex dataset and generate predictive models. This paper describes the development of four different ML models for thin-walled steel beams subjected to thermal gradients. A parametric heat transfer analysis is first conducted to characterize the thermal gradients that develop under three-sided fire exposure. Nonlinear finite element simulations with shells are then used to generate the resistance dataset. The ML models, trained using physically defined features, show significant improvement in predictive capacity over the Eurocode methods. The ML-based models can be used to improve existing design methods for non-uniform temperature distributions.

Keywords: Machine learning; Thin-walled beams; Fire; Temperature gradient; Shell finite elements

1 INTRODUCTION

This paper investigates opportunities from application of ML methods to the problem of thin-walled steel beams in fire subjected to non-uniform temperature gradients. Recently, ML models have been successfully developed for thin-walled members [1–3], but the effect of thermal-gradients has not been yet accounted for. While the development of ML models requires sophisticated modelling and large datasets, which may not be always available, once a ML model is developed its application to practical design situations within the limits of its validity is straightforward.

Existing analytical methods have undeniable advantages, such as confidence from accrued experience and link to physical key parameters, which allow calibration for target reliability and interpretability (“white-box”) for generic applicability. Yet analytical methods have failed so far to solve some complex issues in fire, including those arising from the effects of temperature gradient. In particular, there are few studies devoted to investigation of the effect of non-uniform temperature gradients in beams [4–7]. In addition, the inclusion of novel developments into design standards is a lengthy process, for example the present version of Eurocode 3 Part 1-2 was issued in 2005 [8]. For these reasons, innovations are held back as there is no

¹ Assistant Researcher, RISCO, Civil Engineering Department, University of Aveiro, Portugal
e-mail: ccouto@ua.pt, ORCID: <https://orcid.org/0000-0003-0865-2225>

² Department of Civil and Systems Engineering, Johns Hopkins University, Baltimore, USA
e-mail: qtong5@jhu.edu

³ Assistant Professor, Department of Civil and Systems Engineering, Johns Hopkins University, Baltimore, USA
e-mail: tgernay@jhu.edu, ORCID: <https://orcid.org/0000-0002-3511-9226>

legal basis for practitioners to apply recent methods with a negative impact on the industry. This motivates exploration of ML methods.

The approach in this study starts by deriving a comprehensive dataset where the samples were obtained from parametric analysis using nonlinear Finite Element (FE) with shell elements and capture the different structural failure modes (local buckling and LTB). The FE model includes non-uniform temperature distributions resulting from thermal gradients, based on an assessment of the temperature distributions in the flanges and webs occurring from three-side thermal exposure of protected beams. Then, ML-based models are derived for predicting the capacity of these thin-walled steel members at elevated temperature. The ML models include artificial neural networks (ANN), support vector regression (SVR), random forests (RF) and polynomial regression (PR). An overview of the existing analytical design rules in the Eurocode 3 Part 1-2 [8], and improved proposals [9], for predicting the capacity of these members at elevated temperature is provided with discussion of the input parameters (or features). Given that these analytical methods are based on a uniform temperature distribution in the section, the effect of different assumptions regarding their applicability to non-uniform temperature distributions is also discussed.

2 CURRENT ANALYTICAL MODELS FOR THIN-WALLED BEAMS IN FIRE

2.1 Effective cross-section

For beams with thin-walled sections, the evaluation of load carry capacity at elevated temperature must consider the effect of local buckling. Part 1.5 of Eurocode 3 provides expressions of reduction factors for plate buckling resistance under compression, based on the concept of effective width method accounting for geometric imperfection and residual stresses [10]. Couto et al. [11] proposed an updated formula to account for the local buckling of slender steel members (Class 3 and Class 4) at elevated temperature and replaced the use of design yield strength corresponding to the 0.2% proof strength with the yield strength at 2% total strain for Class 4.

The effective width of plates at elevated temperature can be calculated as:

$$b_{eff} = \rho_{\theta} \times b \quad (1)$$

The new expression [11] for a plate reduction factor of internal compression elements (e.g., web) is:

$$\rho_{\theta} = \frac{(\bar{\lambda}_p + \alpha_{\theta})^{\beta_{\theta} - 0.055(3+\psi)}}{(\bar{\lambda}_p + \alpha_{\theta})^{2\beta_{\theta}}} \leq 1.0 \quad (2)$$

For outstand compression elements (e.g., flanges) it is:

$$\rho_{\theta} = \frac{(\bar{\lambda}_p + \alpha_{\theta})^{\beta_{\theta} - 0.188}}{(\bar{\lambda}_p + \alpha_{\theta})^{2\beta_{\theta}}} \leq 1.0 \quad (3)$$

$\bar{\lambda}_p$ is the non-dimensional slenderness of a plate given by:

$$\bar{\lambda}_p = \frac{b/t}{28.4\epsilon\sqrt{k_{\sigma}}} \quad (4)$$

where k_{σ} is the buckling coefficient of plates, b and t are the width and thickness of the plates, ψ is the stress ratio between two ends. Coefficients α_{θ} and β_{θ} are given in Table 2 in the reference [11] for internal compression elements and outstand compression elements. ϵ is calculated as:

$$\epsilon = \sqrt{\frac{235}{f_y}} \sqrt{\frac{E}{210000}} \text{ in which } f_y \text{ and } E \text{ in Mpa} \quad (5)$$

According to the current Eurocode 3 Part 1-2 [8], the effective section is calculated for $\alpha_{\theta} = 0$ and $\beta_{\theta} = 1$.

2.2 Lateral-torsional buckling

Once the effective width of the plates is calculated and the effective properties of the section determined, the load-carrying capacity of the beam is evaluated by making allowance for lateral-torsional buckling using equation (6) according to Part 1-2 of Eurocode 3 [8].

$$M_{b,fi,t,Rd} = \chi_{LT,fi} \cdot M_{fi,Rd} / \gamma_{M,fi} = \chi_{LT,fi} \cdot W_{eff} \cdot k_{\theta} \cdot f_y / \gamma_{M,fi} \quad (6)$$

where W_{eff} is the effective section modulus calculated using the effective width of the plates, k_{θ} is the reduction factor for the yield strength at elevated temperatures, f_y is the yield strength, $\gamma_{M,fi}$ is the safety factor taken as 1.0. According to the present version of the Eurocode 3 Part 1-2, for Class 4 sections, k_{θ} is taken as the reduction factor for the 0.2% proof strength of steel at elevated temperatures ($k_{p,0.2,\theta}$).

The lateral-torsional buckling reduction factor for flexural buckling $\chi_{LT,fi}$ is calculated as:

$$\chi_{LT,fi} = \frac{1}{\phi_{LT,\theta} + \sqrt{\phi_{LT,\theta}^2 - \bar{\lambda}_{LT,\theta}^2}} \quad \text{and} \quad \chi_{LT,fi} \leq 1.0 \quad (7)$$

$\bar{\lambda}_{LT,\theta}$ is the non-dimensional slenderness at elevated temperature and $\phi_{LT,\theta}$ is calculated as:

$$\phi_{LT,\theta} = 0.5[1 + \alpha_{LT}\bar{\lambda}_{LT,\theta} + \bar{\lambda}_{LT,\theta}^2] \quad (8)$$

and α_{LT} is the imperfection factor calculated as $\alpha_{LT} = 0.65\varepsilon = 0.65\sqrt{235/f_y}$. The non-dimensional slenderness at elevated temperature $\bar{\lambda}_{\theta}$ is calculated as:

$$\bar{\lambda}_{LT,\theta} = \sqrt{\frac{W_{eff} \cdot k_{\theta} \cdot \frac{f_y}{\gamma_{M,fi}}}{k_{E,\theta} M_{cr,20}}} \quad (9)$$

where $k_{E,\theta}$ is the reduction factor for Young's modulus at elevated temperatures, and $M_{cr,20}$ is the elastic critical capacity at ambient temperature which is based on the full section.

2.3 New generation of Eurocode 3 Part 1-2

In the new generation of Eurocode 3 Part 1-2 (EN 1993-1-2 New Generation) [9], the overall capacity of laterally unrestrained beams with slender cross-sections is calculated following the same procedure presented in the previous section, except that the reduction factor $\chi_{LT,fi}$ calculated using equation (7) is determined by replacing $\phi_{LT,\theta}$ in equation (8) with the $\phi_{LT,\theta,NG}$ calculated according to equation (11),

$$\phi_{LT,\theta,NG} = 0.5[1 + \alpha_{LT,NG}(\bar{\lambda}_{LT,\theta} - 0.2) + \bar{\lambda}_{LT,\theta}^2] \quad (10)$$

where the values of the imperfection factor $\alpha_{LT,NG}$ depend on the limits of the Effective Section Factor (ESF), defining three different LTB design curves named L1, L2 and L3. The ESF is the ratio between the effective modulus ($W_{eff,y}$) and the elastic modulus ($W_{el,y}$) of the cross-section and captures the role of the local buckling on the lateral-torsional buckling resistance of the beams at elevated temperature [12]. The $\alpha_{LT,NG}$ is 1.25ε , 1.0ε and 0.75ε , according to the limits, $\frac{W_{eff,y}}{W_{el,y}} > 0.9$, $0.8 < \frac{W_{eff,y}}{W_{el,y}} \leq 0.9$ and $\frac{W_{eff,y}}{W_{el,y}} \leq 0.8$, respectively, defining the curves L1, L2 and L3.

The model discussed here does not incorporate the effect of non-uniform temperatures. The Eurocode 3 Part 1-2 specifies that (clause 4.2.3.4(3)) conservatively, the temperature θ in Eq. (6) can be assumed to be equal to the maximum temperature. Further discussion on this aspect is provided in Section 6.

3 ANALYSIS OF NON-UNIFORM TEMPERATURE DISTRIBUTION IN THE SECTIONS

In many applications, steel beams will be subjected to non-uniform thermal exposure resulting in temperature gradients in the section. Here, heat transfer analyses with the finite element method (FEM) is used to analyze the temperature distribution in steel cross-sections heated by the ISO 834 fire on three sides.

The fourth side of the steel profile is either in contact with a concrete slab, or with air at ambient temperature. The parametric thermal analyses are conducted in SAFIR [13] considering a range of section dimensions, insulation thickness, and the presence of the slab. The insulation is a sprayed material with a conductivity of 0.4 W/mK, specific heat of 900 J/kgK, specific mass of 40 kg/m³, water content of 1 kg/m³, and emissivity of 0.8. Figure 1 shows the temperature distribution in two steel profiles protected with 12.7 mm of insulation after 30 minutes of exposure to the ISO 834 fire. The analyses determine the temperature evolution in each node of the section, which is then averaged into one (transient) temperature for each plate of the cross-section. The non-uniform temperature distribution is then defined through 2 parameters: (i) the temperature of the lower flange exposed to the fire, $\theta_{fl,hot}$, and (ii) the temperature of the unexposed upper flange, $\theta_{fl,cold}$. The temperature of the web, θ_{web} , is also examined and is related to the flange temperatures. The study aims at evaluating the difference in the average temperatures between the flanges, $\theta_{fl,hot} - \theta_{fl,cold}$.

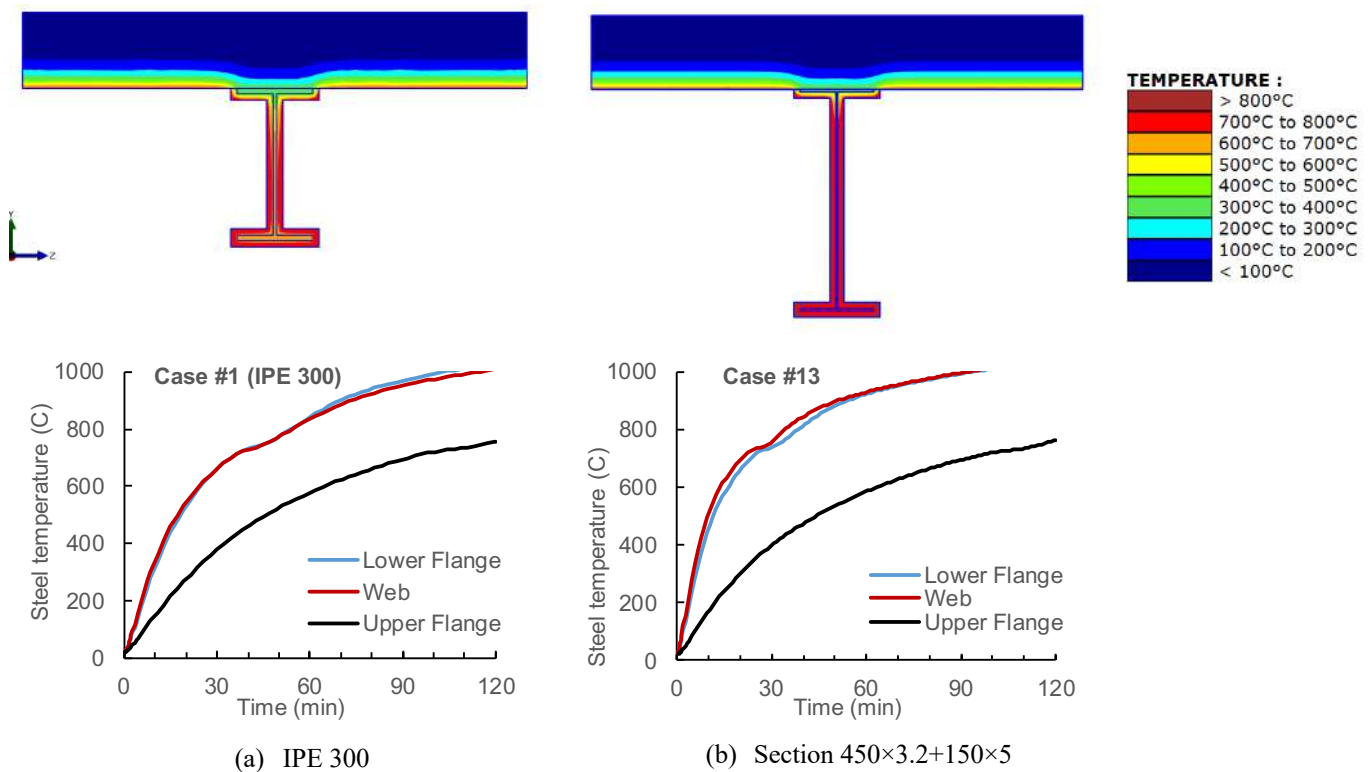


Figure 1. Temperature distribution in protected steel beams subjected to ISO 834 fire exposure on three sides

A sample of results are plotted in Figure 2. This plot shows, for fourteen cases, the average temperature in each of the plate after 30 min and 60 min of exposure, respectively. Cases 7 to 12 do not have a slab. It is found that the temperature of the web (θ_{web}) is consistently very close to the temperature of the lower flange ($\theta_{fl,hot}$). The θ_{web} will thus be assumed as the same as $\theta_{fl,hot}$. The difference between the flange temperatures increases when a concrete slab is present. The difference is also larger for the thin-walled section than for compact hot-rolled sections. A reasonable estimate of the temperature gradient between the flanges is found as $\theta_{fl,hot} - \theta_{fl,cold} = 150\text{ }^{\circ}\text{C}$ for profiles without slab and $\theta_{fl,hot} - \theta_{fl,cold} = 250\text{ }^{\circ}\text{C}$ for profiles with a concrete slab. Based on these analyses, four temperature distribution cases will be considered for constructing the numerical database for elevated temperature resistance of the steel beams, namely $(\theta_{fl,hot}; \theta_{fl,cold})$ equal to (650 °C; 500 °C), (650 °C; 400 °C), (550 °C; 400 °C), (550 °C; 300 °C).

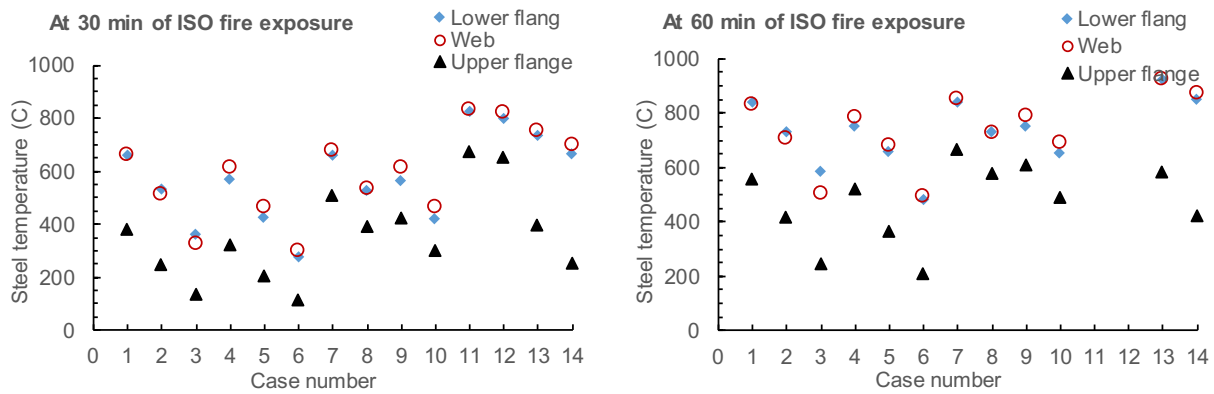


Figure 2. Calculated temperature distributions at different times of ISO fire exposure

4 NUMERICAL MODEL AND DATASET

4.1 Finite element model

Numerical modelling was used to analyse beams made of I-shaped slender cross-sections subjected to major-axis bending at elevated temperatures. The numerical models were built using shell elements in the nonlinear finite element software SAFIR [13]. Beams with different plate slenderness, lengths and non-uniform thermal gradients were modelled. A sensitivity analysis on the mesh size was conducted to have a sufficiently refined mesh while preserving an appropriate computational cost.

The constitutive model included in the simulations followed the non-linear stress-strain relationship and reduction factors defined in Eurocode 3 Part 1-2 [8]. Steels with grades S235 and S355, corresponding to yield strength of 235 and 355 MPa at ambient temperature were used in the numerical models. Young's modulus of elasticity at ambient temperature was taken as 210 GPa and Poisson's ratio as 0.30.

Both geometric imperfections (global and local) and material imperfections, in the form of residual stresses, were included in the models. For global imperfection, the amplitude followed the design recommendation, i.e. $L/1000$, where L is the length of the member. For local imperfection, the amplitude was calculated as 80% of the geometric fabrication tolerances [14]. The global imperfection and local imperfection were combined following the recommendation of Annex C in Part 1-5 of Eurocode 3 [10]. In accordance with the recommendations of this Annex, the full amplitude was considered for the leading imperfection while that of the accompanying imperfections was reduced to 70%. The shape of these imperfections was obtained from a linear buckling analysis (LBA), using Ansys [15], following the same modelling assumptions as described here. For the residual stresses, the pattern for welded beams [14] was included in the models.

Fork-supports were used at both ends of the structural member to prevent the displacements in y-direction and z-direction. To prevent rigid body movement, the displacements in x-direction were constrained at mid-span. The loading was applied by nodal forces to produce end-moments at both ends. Additionally, a layer of thicker elements was included at the extremities to ensure correct load distribution (see Figure 3) as done in [16].

The ultimate load-bearing capacity of the beams was calculated with SAFIR considering steady-state conditions i.e., by first uniformly increasing the temperature in the section up to the target value and then progressively loading the members until failure was reached.

An example of the collapse shape of a slender beam with $450 \times 3.2 + 150 \times 5$ and the corresponding boundary conditions are provided in Figure 3. More details about the numerical model can be found in [14,16].

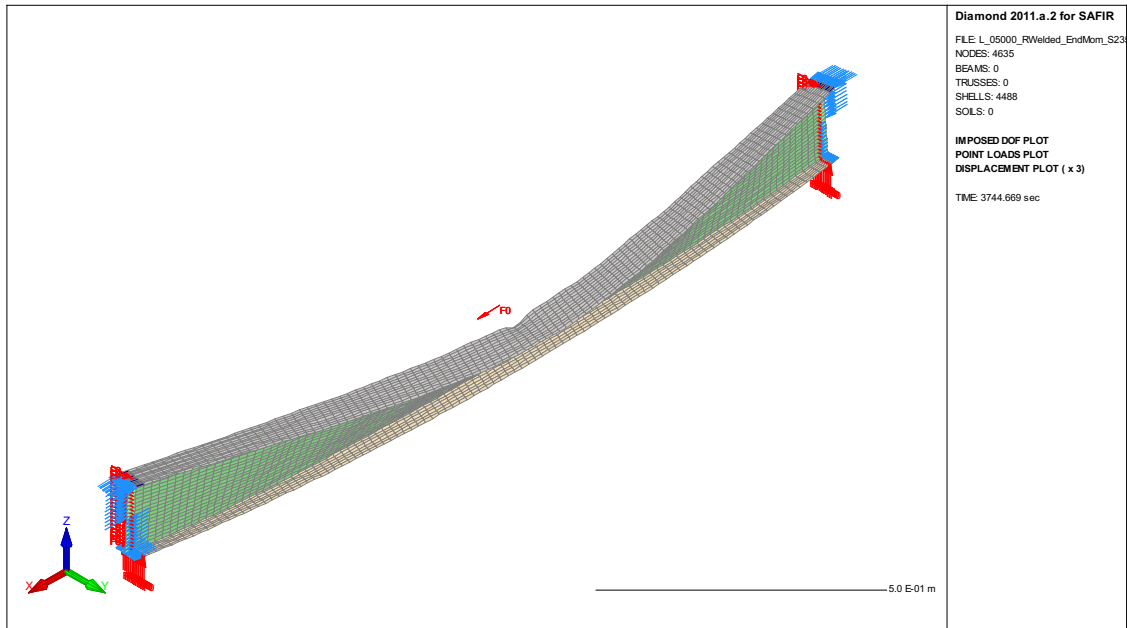


Figure 3. Collapse shape of beam 450×3.2+150×5 (S235) with L=5.0 m, $\theta_{fl,cold} = 300^\circ\text{C}$ and $\theta_{fl,hot} = 550^\circ\text{C}$

4.2 Dataset

A dataset was defined where the data points were calculated using the numerical model described in the previous section. FE simulations were run to failure. The dataset includes 6348 FE simulations.

The selection of features was carried out using a procedure that combined prior knowledge about the parameters potentially influencing the mechanical response (mechanistic-informed) and a quantitative trial-and-error approach to find the most suitable combination of features. The process of feature selection dealt with both inclusion and exclusion of parameters and their combination, and the best model was selected as the one with fewest parameters for a given accuracy. The ranges of values for the input parameters are listed in Table 1, defining 8 features for the ML models.

Table 1. Input parameters/features of dataset used for the ML models training

Notation	Feature	Input values	Min.	Max.
	x_1	h_w/t_w	75	200
	x_2	b/t_f	9	37.5
	x_3	h_w/b	1	6.67
	x_4	t_w/t_f	0.08	1.6
	x_5	f_y/E	(235/E)	(355/E)
	x_6	$\theta_{fl,cold}$	300°C	500°C
	x_7	$\theta_{fl,hot}$	550°C	650°C
	x_8	$(M_{pl,20}/M_{cr,20})^{0.5}$	0.16	8.25

In this table, the h_w/t_w and b/t_f are the adimensional web and flange dimensions, f_y/E is the adimensional yield strength for beams. $M_{pl,20}$ is the section plastic capacity, $M_{cr,20}$ is the elastic critical load at ambient temperature. The range of feature values considered in the dataset was chosen to cover a common range of design parameters for slender section steel beams in building structures.

The output was defined as $y = M_{ult,fi}/M_{pl,20}$ with $M_{ult,fi}$ being the ultimate capacity of a beam. The frequency distribution for each feature is plotted in Figure 4.

The 6348 samples were randomly divided on a proportion of 9:1 to create the training and testing subsets, thus 5713 cases were considered for training and 635 cases for testing.

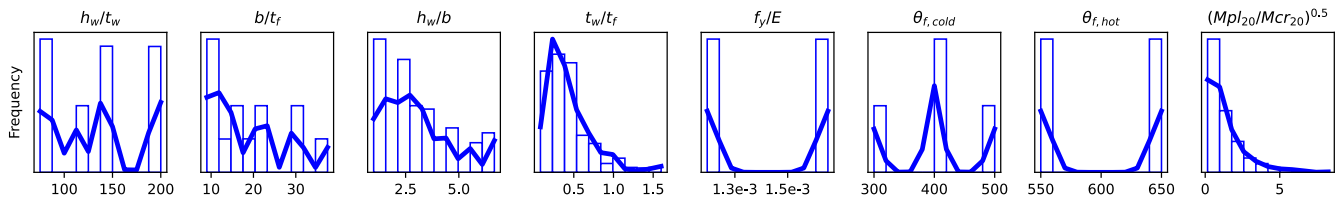


Figure 4. Frequency distribution for the different features

5 MACHINE LEARNING MODELS

Four different machine learning models were considered in this study, namely Artificial neural networks (ANN), Support vector regression (SVR), Random forests (RF) and Polynomial regression (PR). These models were chosen based on previous experience in their application to regression problems of thin-walled sections in fire [1–3].

The ANN models were implemented using the *pyrenn* [17], which relies on the mean squared error as the loss function and the Levenberg-Marquardt as the optimization algorithm. Among the different architectures, with one or two hidden layers, that were tested, the best performing one was the $8 \times 64 \times 4 \times 1$ corresponding to two hidden layers with 64 and 4 neurons.

To train and develop the SVR and RF models, *scikit-learn* library [18] was used. A grid search technique was applied to tune the hyperparameters. Table 2 and Table 3 highlight the hyperparameters that were considered for SVR and RF, respectively, marking with (*) the best ones.

Table 2. Table of hyperparameters used in the SVR [18] (* indicates the best).

kernel	degree	gamma	C	epsilon
Rbf*	1*, 3,	scale, auto	1,	0.1, 0.05
	5, 10,	0.049*, 0.1, 0.0049	10*,	0.01, 0.005*
	100, 1000	0.001, 0.00049	100,	0.0001
			1000	

Table 3. Table of hyperparameters used in the random forests [18] (* indicates the best).

n_estimators	max_depth	min_samples_split	max_features	max_leaf_nodes
10,20,	10, 50,	2 *, 8,	auto*	none*
50, 100,	100*, 500,	16, 24,	log2	10
250, 500,	1000	32, 64	sqrt	100
1000*				500

Finally, the same library was also used to train and develop the PR model. In this case, since models with higher degrees may closely fit most of the data in the training dataset, but possibly at the cost of over-fitting resulting in a larger error on the testing dataset, ridge regression was applied to fit the polynomial feature matrix. We found that a degree 5 polynomial is capable of predicting the resistance of beams within the range of features provided in Table 1 of the numerical dataset.

6 RESULTS AND DISCUSSION

In this section the performance of both analytical and machine learning models is evaluated using different metrics, namely the coefficient of determination R^2 , the mean absolute error (MAE) and the mean squared error (MSE). The R^2 measures how well the observations are replicated by a model and a R^2 close to 1 is preferred. The mean absolute error (MAE) quantifies the average magnitude of errors between predicted and actual values, providing a measure of the model's accuracy. On the other hand, the mean squared error (MSE) calculates the average squared differences between predicted and actual values, emphasizing larger errors due to squaring. It is particularly sensitive to outliers and deviations from the predicted values. While

both MAE and MSE provide insights into the model's performance, they offer different perspectives on the accuracy and precision of the predictions, and a lower value is preferred. For the sake of this comparison, the actual and predicted values are considered in terms of the ultimate capacity of the beam $M_{ult,fi}$. Predictions from the shell FE models are considered as ground truth; validation is available in Refs [19,20]. Figure 5 plots the graphical representation of the accuracy obtained with the ML models, for both the training and testing sets. Values of R^2 are given in the figure. The MAE and MSE are given in Table 4.

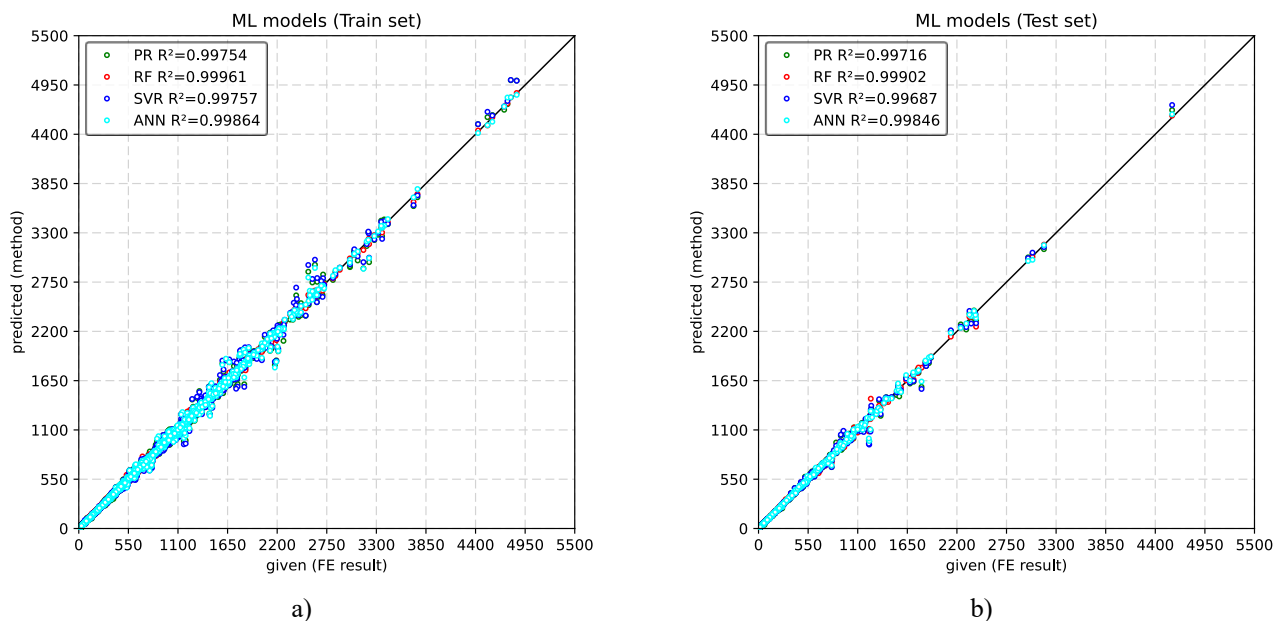


Figure 5. Graphical representation of the accuracy obtained with the machine learning models for the a) training and b) testing sets (see Table 4 for MAE and MSE). Values are for ultimate capacity in kN.m

Table 4. Results of different evaluation metrics for the training and testing sets of ML models

Model	Set	R^2 [-]	MAE [kN·m]	MSE [(kN·m) ²]
ANN	Train	0.99864	5.63021	18.16122
	Test	0.99846	7.05563	20.25923
SVR	Train	0.99757	8.80275	24.24885
	Test	0.99687	11.29989	28.89603
RF	Train	0.99961	4.30033	9.72442
	Test	0.99902	6.03555	16.18913
PR	Train	0.99754	10.19526	24.39320
	Test	0.99716	12.21141	27.52662

The results show that all the models have good accuracy and are able to predict the capacity of the thin-walled beams under thermal gradients. The best-performing models are the ANN with R^2 of 0.99864 and 0.99846 for training and testing sets, respectively, and RF with R^2 of 0.99961 and 0.99902. In terms of MAE and MSE these are also the models with lowest values. However, it is noticeable that in the ANN the MAE and MSE are more consistent between training and testing sets, with an increase of $7.05563/5.63021 \approx 1.25$ and 1.11, while the RF holds 1.40 and 1.66, for MAE and MSE, respectively. A further inspection based on the domain knowledge was carried out using a representation in terms of buckling curves, by plotting the capacity $M_{ult,fi}$ as a function of a slenderness parameter $(M_{pl,20}/M_{cr,20})^{0.5}$. The latter was considered as a feature of the dataset. Note that because of thermal gradients it is simpler to represent the slenderness parameter at normal temperature. Figure 6 plots the results for beams with two different sections.

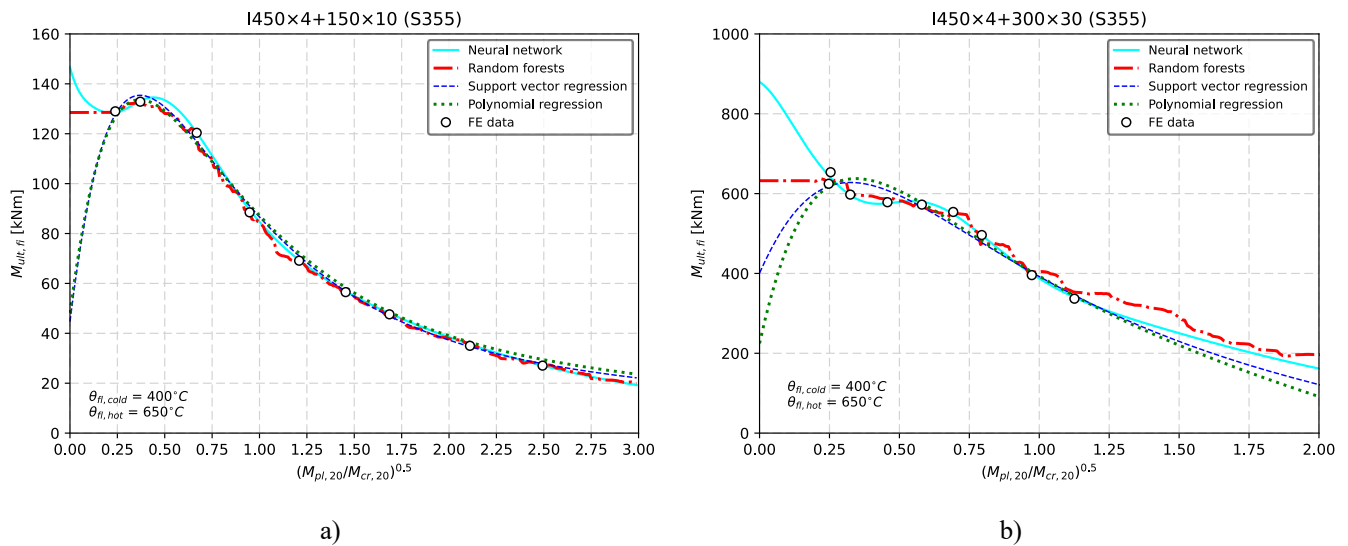


Figure 6. Buckling curve representation of the prediction models based on machine learning models for beams with a) $I450\times4+150\times10$ and b) $I450\times4+300\times30$ sections

The RF despite being the model with better results in terms of metrics denotes problems when the buckling curve representation is considered. Indeed, we see that the RF model exhibits some jumps/odd behaviour (e.g. at slenderness of 1.0) which is not physically meaningful. In particular, for the $I450\times4+300\times30$ beam (Figure 6 b)) we observe that for longer spans the model is diverging. This observation is likely linked with the increase in MAE and MSE that was observed in the results provided in Table 4. On the other hand, the ANN for smaller slenderness values is also overpredicting the beam capacity. The reason for this is related to missing values in the dataset for slenderness below 0.16 (see feature x_8 in Table 1), which can be addressed by increasing the dataset to cover smaller ranges of slenderness. Notwithstanding, the ANN are deemed adequate to be used within the feature range provided in Table 1.

For the analytical models described in section 2, different assumptions were considered in order to compare the results with those obtained numerically and predicted by the machine learning models. Because these analytical models assume a uniform temperature across the section and member length, two extreme cases were considered with a constant temperature equal to the hot flange ($\theta_{fl,hot}$) and cold flange ($\theta_{fl,cold}$). Figure 7 plots the accuracy obtained for these results (for MAE and MSE metrics, see Table 5).

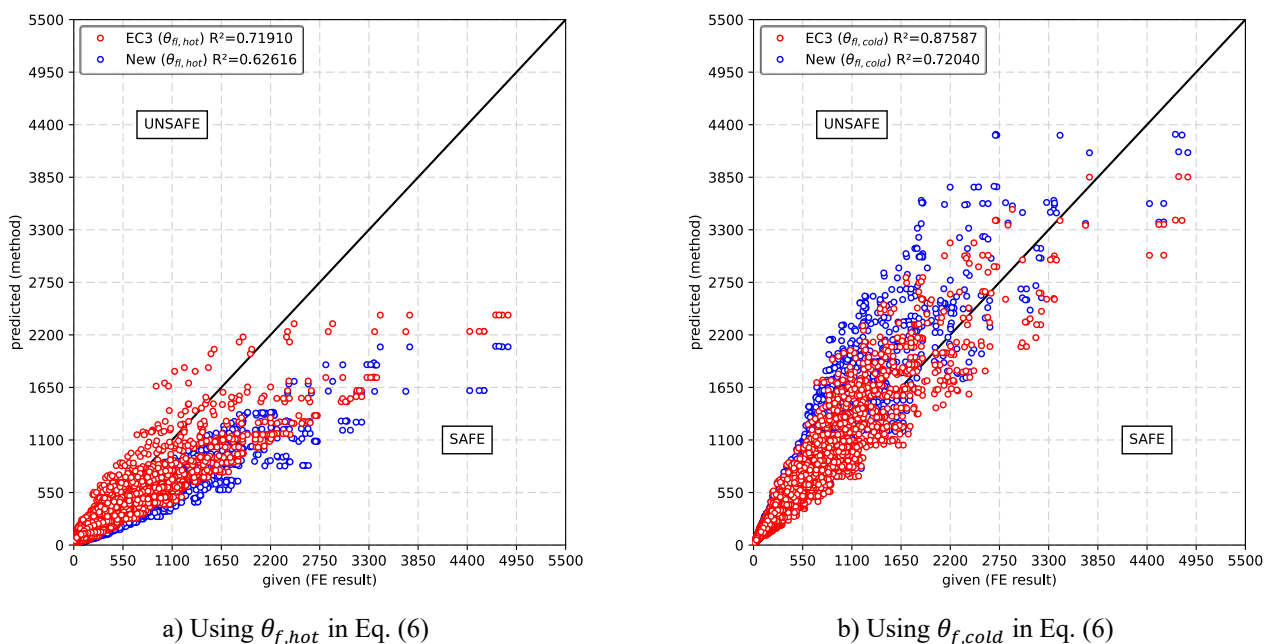


Figure 7. Accuracy obtained with the analytical methods assuming uniform temperature distribution based on either flange

As expected, both models (EC3 and New generation) fail to adequately predict the beam capacity. The New generation model, with the safe assumption of considering the highest temperature $\theta_{fl,hot}$ everywhere in the section, results in a safe-sided approach but too uneconomical with a R^2 of 0.63.

To test if the lateral-torsional buckling analytical models can predict the beam capacity under thermal gradients, a third assumption was considered where $M_{fi,Rd}$ and $M_{cr,fi}$ are numerically determined from the FE analysis. In this latter approach, it is not possible to assess the limits of ESF to choose the correct buckling curve (L1, L2 or L3) thus the least severe one (L3) was considered for the sake of this comparison. Figure 8 plots the results obtained and Table 5 give the metrics for all the model and assumptions regarding the consideration of the analytical models.

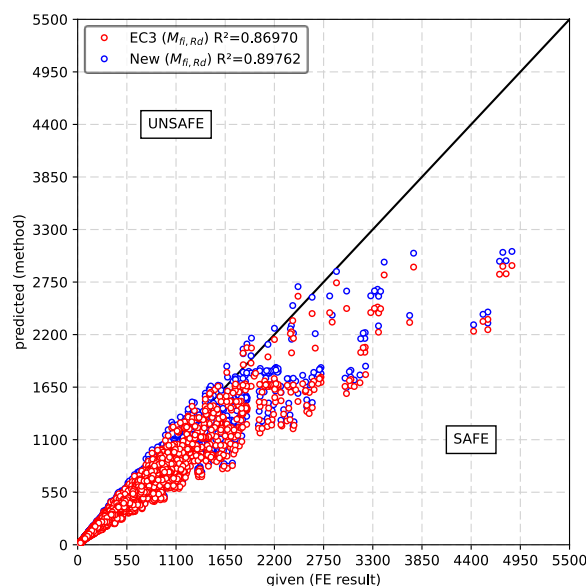


Figure 8. Accuracy obtained with the analytical methods with section resistance and elastic critical moment obtained numerically (note: New generation with curve L3)

Table 5. Results of the accuracy of analytical methods with different assumptions

Model	Assumption	R^2 [-]	MAE [kN·m]	MSE [(kN·m) ²]
EN1993-1-2	Uniform temperature equal to $\theta_{fl,cold}$	0.87587	99.92005	174.26332
	Uniform temperature equal to $\theta_{fl,hot}$	0.71910	144.11253	262.14421
	$M_{fi,Rd}$ and $M_{cr,fi}$ from FEA (numeric)	0.86970	77.24774	178.54238
New generation	Uniform temperature equal to $\theta_{fl,cold}$	0.72040	145.37009	261.54127
	Uniform temperature equal to $\theta_{fl,hot}$	0.62616	174.10493	302.42116
	$M_{fi,Rd}$ and $M_{cr,fi}$ from FEA (numeric) & L3	0.89762	63.01273	158.26233

The results show that accuracy increases, with R^2 of 0.89762 and 0.86970 obtained for the New generation and EN 1993-1-2 models. This suggests that analytical approaches aiming to increase the accuracy of the section capacity prediction, as well as the elastic critical moment, when thermal gradients are present can be used with the analytical models for the lateral-torsional buckling resistance. In addition, for a more economical model, it might be necessary to further calibrate the lateral-torsional buckling model. For the sake of comparison, Figure 9 plots the results of the analytical models for the different assumptions considered in the form of buckling curves.

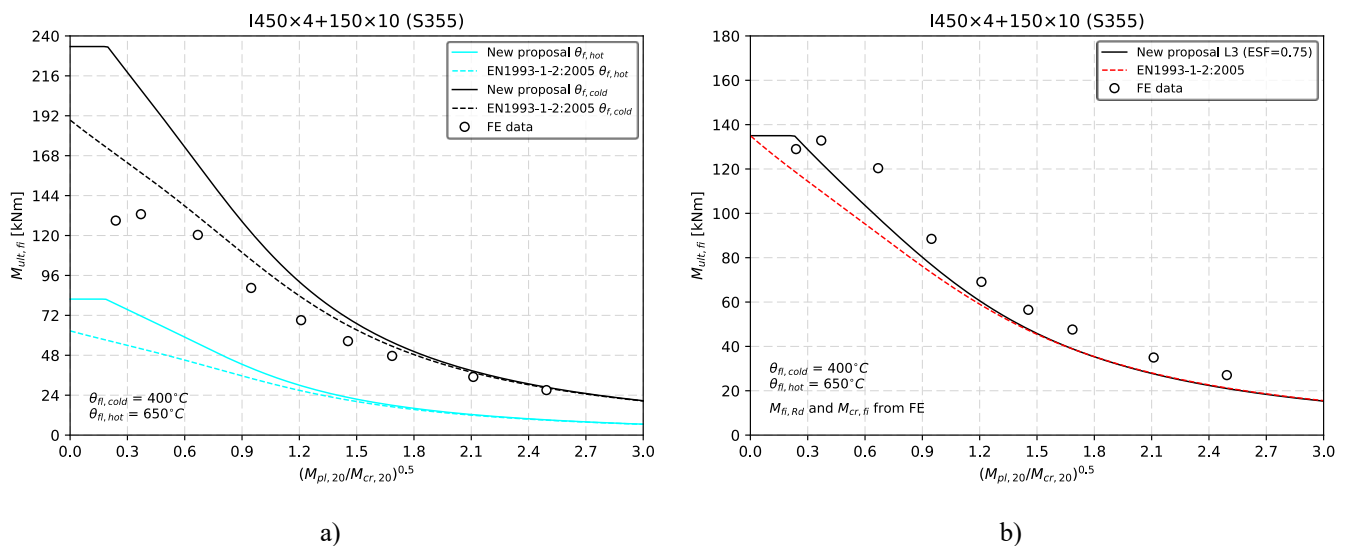


Figure 9. Buckling curve representation of the analytical models based on a) uniform temperature of either $\theta_{fi,hot}$ or $\theta_{fi,cold}$ and b) section resistance and elastic critical moment obtained numerically

7 CONCLUSIONS

As predicting the ultimate strength of laterally unrestrained slender steel beams subjected to fire on three sides remains an elusive problem, we have adopted here Machine Learning (ML) models to investigate the ability to capture the key features and predict the behaviour influenced by local buckling, lateral torsional buckling, and thermal gradients. The key findings are summarized hereafter.

A numerical thermal analysis performed to investigate the thermal gradients that develop in beams heated on three sides found that, when no slab is present, the gradient between the flanges typically ranges between 150 °C and 250°C. The temperature of the web is similar to that in the exposed flange. These results were obtained on a range of protected steel profiles under ISO 834 fire. When a slab is present, lateral-torsional buckling may be prevented but the thermal gradients may reach values higher than 250°C in very slender profiles, which warrants further studies for such conditions.

For the mechanical resistance, a numerical study based on validated nonlinear shell FEM was conducted to build a dataset of 6348 data points for beams with a range of cross-sections, member length, temperatures, and yield strength. The dataset was used to train and test ML models to predict the elevated temperature capacity of the beams. Four ML models were applied to the beam, namely based on artificial neural network (ANN), support vector regression (SVR), random forests (RF) and polynomial regression (PR).

The ML models can fit the results of the shell FE models more closely than the state-of-the-art analytical methods to be included in the next generation of the Eurocodes. The ML models can predict the resistance at elevated temperature, for both the training and testing dataset, with a R^2 greater than 0.990 for all the models. Further inspection based on domain knowledge and buckling curve representation shows, however, that these models might overpredict the capacity for slenderness ranges outside the training range. These observations also demonstrate that domain knowledge is fundamental to investigate the accuracy of ML models in addition to the usual metrics that are used.

For the analytical models, different assumptions were considered to enable the comparison with the FE results and ML model's prediction. However, these models were not found capable of delivering accurate and economical methodologies despite different simplifying assumptions. One possibility is to develop improved section capacity prediction models when thermal gradients are present, but it might be necessary still to adjust the lateral-torsional buckling models to deliver more economic methodologies.

This work shows that ML models can accurately predict the resistance of beams under non-uniform heating while also being computationally efficient. In future works, beams with higher thermal gradients and with restrained lateral-torsional buckling will be investigated to study cases where a slab is present, as well as beams under different loading conditions.

ACKNOWLEDGMENT

Carlos Couto acknowledges the funding from FCT – Fundação para a Ciência e a Tecnologia, I.P., under the Scientific Employment Stimulus – Institutional Call – CEECINST/00026/2018, and Rede Nacional de Computação Avançada, within the scope of the exploratory research project 2022.15930.CPCA.A1.

Under a license agreement between Gesval S.A. and the Johns Hopkins University, Dr. Gernay and the University are entitled to royalty distributions related to the technology SAFIR described in the study discussed in this publication. This arrangement has been reviewed and approved by the Johns Hopkins University in accordance with its conflict of interest policies.

REFERENCES

1. Couto, C, Tong, Q, Gernay, T: Predicting the capacity of thin-walled beams at elevated temperature with machine learning. *Fire Saf J* (2022). doi:10.1016/j.firesaf.2022.103596.
2. Couto, C, Tong, Q, Gernay, T: Comparing analytical and machine-learning-based design methods for slender section steel members in fire. 12th Int. Conf. Struct. Fire, Hong Kong (2022)
3. Tong, Q, Couto, C, Gernay, T: Applying Machine Learning to Evaluate the Performance of Thin-Walled Steel Members in Fire, 363–84 (2024). doi:10.1007/978-3-031-48161-1_15.
4. Wong, MB: Adaptation factor for moment capacity calculation of steel beams subject to temperature gradient. *J Constr Steel Res* 63:1009–15 (2007). doi:10.1016/j.jcsr.2006.10.004.
5. Li, G, Wang, P, Shouchao, J: Non-linear finite element analysis of axially restrained steel beams at elevated temperatures in a fire. *J Constr Steel Res* 63:1175–83 (2007). doi:10.1016/j.jcsr.2006.11.009.
6. Pi, Y-L, Bradford, MA: Thermoelastic lateral-torsional buckling of fixed slender beams under linear temperature gradient. *Int J Mech Sci* 50:1183–93 (2008). doi:10.1016/j.ijmecsci.2008.04.004.
7. Ragheb, WF: Local buckling capacity of steel I-section beams subjected to uniform or linear temperature gradient. *Thin-Walled Struct* 119:304–14 (2017). doi:10.1016/j.tws.2017.06.017.
8. CEN: EN 1993-1-2, Eurocode 3: Design of steel structures - Part 1-2: General rules - Structural fire design (2005).
9. CEN: FprEN 1993-1-2, Eurocode 3: Design of steel structures - Part 1-2: General rules - Structural fire design (2023).
10. CEN: EN 1993-1-5, Eurocode 3 - Design of steel structures - Part 1-5: Plated structural elements (2006).
11. Couto, C, Vila Real, P, Lopes, N, Zhao, B: Resistance of steel cross-sections with local buckling at elevated temperatures. *J Constr Steel Res* 109:101–14 (2015). doi:10.1016/j.jcsr.2015.03.005.
12. Couto, C, Vila Real, P, Lopes, N, Zhao, B: Numerical investigation of the lateral–torsional buckling of beams with slender cross sections for the case of fire. *Eng Struct* 106 (2016). doi:10.1016/j.engstruct.2015.10.045.
13. Franssen, J-M, Gernay, T: Modeling structures in fire with SAFIR®: theoretical background and capabilities. *J Struct Fire Eng* 8:300–23 (2017). doi:10.1108/JSFE-07-2016-0010.
14. Couto, C, Vila Real, P: The influence of imperfections in the critical temperature of I-section steel members. *J Constr Steel Res* 179 (2021). doi:10.1016/j.jcsr.2021.106540.
15. ANSYS®. Academic Research Mechanical, Release 18.2 2018.
16. Couto, C, Vila Real, P, Lopes, N, Zhao, B: Numerical investigation of the lateral torsional buckling of beams with slender cross-sections for the case of fire. *Eng Struct* 106:410–21 (2016).
17. Atabay, D: pyrenn: A recurrent neural network toolbox for Python and Matlab. Inst Energy Econ Appl Technol Tech Univ München, Http://Pyrenn Readthedocs Io/En/Latest (2024).
18. Pedregosa, F, Varoquaux, G, Gramfort, A, Michel, V, Thirion, B, Grisel, O, et al: Scikit-learn: Machine learning in Python. *J Mach Learn Res* 12:2825–30 (2011).
19. Prachař, M, Lopes, N, Couto, C, Jandera, M, Vila Real, P, Wald, F: Lateral torsional buckling of Class 4 Steel Plate Girders Under Fire Conditions: Experimental and Numerical Comparison. In: Wald F., Burgess I., Kwasniewski L., Horová K. CE, editor. Benchmark Stud. - Exp. Valid. Numer. Model. fire Eng., CTU Publishing House, Czech Technical University in Prague 21–33 (2011).
20. FIDESC4: Fire Design of Steel Members with Welded or Hot-Rolled Class 4 Cross-Section, RFCS-CT-2011-00030, (2014).

STRUCTURAL BEHAVIOUR OF AUTOMATED RACK SUPPORTED WAREHOUSES IN FIRE SITUATION

Margherita Autiero¹, Donatella de Silva², Naveed Alam³, Emidio Nigro⁴

ABSTRACT

This work deals with the fire modelling and structural thermo-mechanical assessment of Automated Rack Supported Warehouses (ARSWs), which are a particular type of steel racks that combines the structural efficiency of steel constructions with automated machines for handling stored products. The study is composed of two phases: the first one regards the investigation of the fire modelling which can be used in a multi-depth ARSW structure, by adopting localized fire models, zone models, and Computational Fluid Dynamics models. A fire model that allows vertical and horizontal propagation, starting from a localized fire, evaluated and validated against experimental results available in the literature, is proposed. Also, a criterion to evaluate the vertical and horizontal propagation times is provided. The second part of the work focuses on the study of the structural collapse mechanism and on the methodologies of analysis that the designer should adopt to properly interpret it. Several thermo-mechanical analyses were carried out by using all the results of the proposed fire model and compared with different fire models available in the literature. To correctly analyse the progressive mechanism of collapse, an iterative procedure is proposed by using several subsequent implicit analyses carried out with SAFIR software and comparing this one with an automatic procedure performed through the software ABAQUS CAE, which allows the implementation of implicit/explicit analyses.

Keywords: Automated Rack Supported Warehouses; cold-formed steel members; numerical simulations.

1 INTRODUCTION

The warehouses are typical buildings where many goods can be stored after their production and before their distribution to the consumers. The demand for storage space is growing, due to increasing production and increasing consumption levels, therefore highly optimized and reliable warehouses are needed. Automated Rack Supported Warehouses (ARSWs) are used in industrial facilities to optimize storage spaces; these structures combine the structural efficiency of steel construction with automated machines for handling stored products.

A fundamental difference exists between traditional Steel Racks (SRs) ARSWs. SRs are designed to carry on the structural self-weight and the weight of the stored goods. ARSW are self-bearing rack structures committed to support, besides self-weight and weight of products, also environmental loads (i.e., wind, snow, and seismic action) and all the other non-structural elements such as clads, equipment, etc. A typical structure during its construction is shown in the following Figure 1a. The traditional structural steel racking

¹M.Eng, PhD candidate Department of Structures for Engineering and Architecture, University of Naples Federico II (Italy),
e-mail: margherita.autiero2@unina.it,

² PhD, Assistant Professor Department of Structures for Engineering and Architecture, University of Naples Federico II (Italy),
e-mail: donatella.desilva@unina.it,

³ PhD, Assistant Professor FireSERT, Built Environment Research Institute, School of the Built Environment, Ulster University, (United Kingdom),
e-mail: n.alam@ulster.ac.uk,

⁴ PhD, Full Professor Department of Structures for Engineering and Architecture, University of Naples Federico II (Italy),
e-mail: eminigro@unina.it.

system is characterized by two principal directions and by a regular sequence of frames composed of several shoulders, made of two uprights (the vertical members), connected in the DA direction by pallet beams devoted to bringing the goods and in the CA direction by horizontal beams and by a bracing system to provide lateral stability of the structure in this direction. In the CA direction, all the frames are connected by an upper truss (see Figure1a).

In the ARSW the handling of the pallets can be done by using two systems, AS/RS, and shuttle systems. In the case of AS/RS, a stacker crane moves on a rail back and forth along the DA direction. The shuttle system is composed of two parts: a shuttle carrier and a shuttle, the shuttle carrier moves back and forth on the aisle along the DA direction, and when it has reached the unit load, the shuttle starts moving on rail beams underneath pallets to reach these ones. Three building types of ARSW can be defined depending on the pallet disposal: single-depth, double-depth, and multi-depth. In the single-depth configuration, there is one unit load line per frame; in the double-depth configuration, there are two unit load lines per frame. In this work, the focus is given to Automated Multi-Depth Shuttle Warehouses (AMSWs), as a specific ARSW type (see Figure1b). AMSWs are compact systems providing large surface occupation and maximum storage density, where the handling of unit loads is realized by a system of shuttles that move goods along rails in the warehouse DA and CA directions.

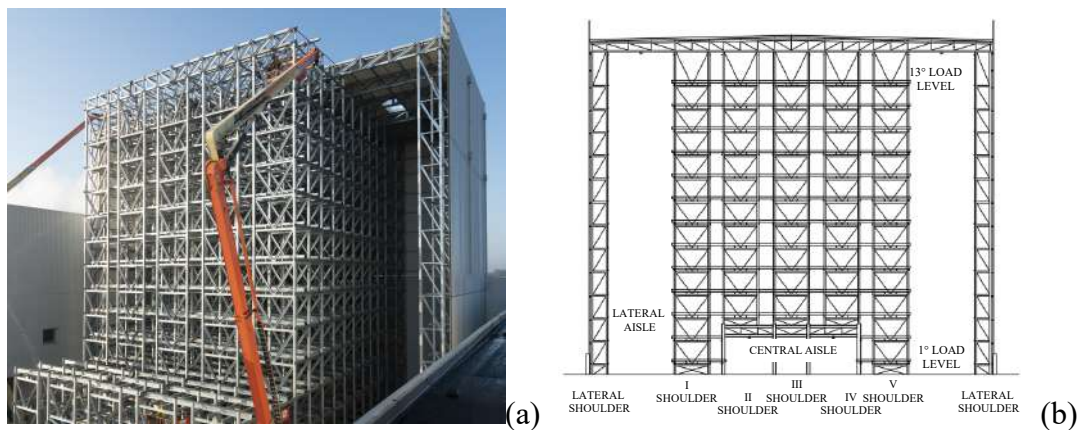


Figure 1. (a) an ARSW during its construction. (b) cross-aisle direction (Source: ROSSS s.p.a.)

To design ARSW, the reference regulations are EN1993-1-1 [1] and EN1993-1-3 [2] for steel structures and EN1998-1-1 [3] for seismic action. Moreover, the designers usually refer also to specialist regulations such as EN15512 [4] which provides principles for the structural design of pallet racking systems, and EN16681 [5] which indicates principles for the seismic design of pallet racking systems. of pallet racking systems, and EN16681 which indicates principles for the seismic design of pallet racking systems. The Italian Building Code “Norme Tecniche per le Costruzioni” NTC2018 [7] must be considered. Hence, while well-established principles and rules supported by experimental evidence and theoretical research are available and presented in Bernuzzi et al. (2015) [6] for the usual SR, for the ARSWs, which are systems larger, taller, and more complex than usual SR, manufacturers and designers have questioned the suitability of the available regulations for ARSWs, for years. Recently, in Italy new guidelines providing a framework in terms of procedures, for the design, improvement, and adaptation of industrial metal racks in the earthquake zone are available [8]. The guidelines identify the references and regulatory limits for the design of new racks and provide the first elements for assessing the seismic vulnerability of existing racks. ARSWs are characterized, on one hand, by a peculiar structural configuration, that strongly influences global behaviour and, on the other hand, by unique non-standard structural components and connections. Indeed, these structures mainly consist of thin-walled sections obtained by cold-forming thin metal sheets that, on one hand, optimize the structural performance by reducing the steel weight, the costs, and the assembly time. On the other hand, these types of sections are usually classified as class 4 cross-section, according to EN1993-1-1 [1], so they have much lower strength and stiffness than hot-rolled steel members, these members can fail by a variety of buckling modes including global, local, and distortional buckling and their interactions. For this reason, usually, racks are made with channel sections and stiffened with additional

folds (called “lip”) to reduce local and distortional buckling phenomena caused by the small thickness of the sections (typically from 1.5 mm to 3.0 mm). However, an ARSW can be characterized even by hollow square sections depending on the dimensions and the requested load. In the last decades, the global structural behaviour of traditional racks has been investigated focusing especially on a seismic point of view. Caprili et al. (2018) [9] investigated the efficiency of Eurocodes’ design and analysis rules for ARSW, in terms of feasibility, structural performance and costs demonstrating how the capacity design requirements for ARSW are challenging to satisfy especially in terms of the maximum difference of the over-strength factor between load levels, requested in the case of X-braces steel-structures. These problems have led designers to consider ARSW as “non-dissipative” structures. Only in recent years capacity design approaches specifically made for ARSWs were proposed (Natali et al. (2022)) [10], defining rules and hierarchies that consider the characteristics of these structural systems. At ambient temperatures, EN1993-1-5 [11] gives two methods to consider the effects of local buckling in the design, i.e., the “effective width method” and the “reduced stress method”, while the distortional buckling strength is considered by using a reduced thickness in the edge stiffener and/or deformed part of the compression flange. The behaviour of thin-walled steel members in centric and eccentric compression and particularly of cold formed steel members (CFS) have been widely investigated by many researchers through experimental tests. Test on fixed-ended cold-formed steel rack-section columns were carried out to investigate the local–distortional interaction (Dinis et al. (2014)) [12]. Methods to evaluate the buckling behaviour of cold-formed sections (CFS) are still an actual topic. The latest trend is to move from simplified design models to design procedures based on “whole section” analysis, avoiding the use of the effective width method (Schafer. 2000) [13]. This paper provides an assessment of a self-supporting automated multi-depth warehouse under fire conditions. The first part focused on establishing the fire modelling necessary for assessing the mechanical response and analysing the collapse mechanism in the second part of the study.

2 DESIGN OF ARSWS IN FIRE CONDITIONS

In the contest of the new Italian fire regulation [14], the fire resistance is defined as a passive fire protection measure to guarantee load bearing and compartmentation capabilities to the structures according to performance levels, selected by the designer to achieve the defined fire safety objectives. Five performance levels (PL) depending on the importance of the building, are defined, the PLI could be required for ARSWs, indeed, among the criteria required to fall into the PL I, there is the request that the building is not involved in activities concerning the presence of people, except for the occasional and short-term activity of highly trained workers. The latter is generally the condition of every ARSW. Different design solutions can be chosen to comply with the PL, based on prescriptive or performance-based approaches, PA and PBA respectively. The analytical evaluation the bearing capacity, in case of fire, can be divided into six phases, from the i) definition of fire scenarios; ii) evaluation of fire action; iii) evaluation of the thermal response (thermal analysis); iv) evaluation of the mechanical action (load combinations), v) evaluation of the mechanical response (type of structural analysis and mechanical analysis); vi) verification of fire resistance, that is the level of safety expressed by the structure. These steps are the same for both PA and PBA approaches, with some simplification for the prescriptive one; the main difference between the prescriptive and the performance-based approaches is that the first one requires nominal fire curves. On the other hand, the PBA considers the complexity of structures using specific natural fire curves, which can be generally obtained by through simplified or advanced models. In ARSWs structures to consider the PBA, is essential because they generally require a minimum fire resistance performance for structural elements that lead to the use of traditional passive fire protection systems, which in the case of these metal profiles are difficult to apply, because of their high section factors (A_m/V). Under fire conditions, the thin thickness of the CFS profiles, combined with the high thermal conductivity of the steel, induces a fast increase in the steel temperature with a significant loss in material stiffness and strength. At present, fire design methods for CFS members are not as investigated as for hot-rolled ones. At elevated temperatures, to account for local buckling the actual EC3 part 1-2 [15] suggests for Class 4 cross-sections a default critical temperature of 350 °C is considered, if no fire design is conducted, which means that even for a requirement of R15, passive fire protection should normally be used for current profiles. Alternatively, the informative Annex

E of the EC3 part 1-2 [15] suggests (i) using an effective cross-section (A_{eff}) calculated with the effective width method, according to EC3 part 1-5 [11], by considering the steel properties at ambient temperature, which means that the effective properties of a steel plate should be kept unchanged as the one as at ambient temperature, (ii) taking the 0.2% proof strength ($f_{0.2p,\theta}$) for the design yield strength of steel instead of the stress at 2% total strain (f_y), as normally used in the fire design of other cross-sectional classes. This means that the design buckling resistance of a compressed member with a non-uniform temperature distribution for the actual Eurocode can be evaluated as follow:

$$N_{b,fi,t,Rd} = \chi_{fi} \sum_i A_{eff} k_{0.2p,\theta} \frac{f_y}{\gamma_{M,fi}} \quad (1)$$

Where, χ_{fi} the reduction factor for flexural buckling in the fire design situation provided in EC3 part 1-2; A_{eff} effective cross-sectional area; $\gamma_{M,fi}$ is the partial safety factor for the relevant material property, for the fire situation, taken as equal to 1; $k_{0.2p,\theta}$ is the reduction factors for the 0.2% proof strength at elevated temperatures.

Couto et al. (2014) [16] proposed new expressions to determine the effective width of steel sections at high temperatures. This design curve has been calibrated as close as possible to the existing design curve by introducing the factors α_θ and β_θ on the expressions of EC3 part 1-5, hence the influence of the imperfections is taken into account as in the original formulas developed by Winter (1947) [17] and additionally the non-linear steel constitutive law at elevated temperatures is also accounted for, furthermore by using the factor ε_θ steel grade is also taken into account in this new proposal. Moreover, by using these expressions, the strength at a total strain of 2% ($f_{y,\theta}$) can be used to calculate the resulting effective cross-sectional resistance, instead of using the 0.2% proof strength ($f_{0.2p,\theta}$).

The new expressions are temperature-dependent leading to a variation in the effective cross-section properties under fire situations. For this reason, a simplified proposal, not temperature dependent, was investigated by the authors [18], based on the assumption that the influence of the temperature on the range of the critical temperatures usually expected for steel members (from 350 °C to 750 °C) are negligible leading to a simpler yet accurate design. These expressions are proposed for the new drafts of the next generation of structural Eurocodes. This means that the design buckling resistance of a compressed member for the new Eurocode can be evaluated as follow:

$$N_{b,fi,t,Rd} = \chi_{fi} \sum_i A_{eff} k_{y,\theta} \frac{f_y}{\gamma_{M,fi}} \quad (2)$$

Where in this case the effective cross-sectional area determined according to the new equations explained before. Moving in the context of a PBA, the absence of external consequences due to structural collapse must be demonstrated, which means that the designer must prove analytically that the collapse mechanism is inward, and implosive. Many authors pointed out how the study of the mechanism of collapse is related to the fire model adopted and the types of methodologies of analysis that the designer must adopt to properly interpret it. Zaharia and Franssen (2002) [19] studied the case of a two-dimensional ARSW built in Belgium, affirming that a natural fire scenario might be more realistic, but under this fire curve, the progressive collapse of the structure cannot be avoided, in fact, the local collapse of rack uprights, causes the global collapse. Mei et al. (2023) [20] provides a robustness evaluation and highlights some possible aspects to be considered in the structural design to avoid a progressive collapse in the event of a fire.

3 FIRE MODELLING OF ARSW STRUCTURE

As analysed by Mei et al. (2023) [20] fire scenarios for ARSW will consider primarily the chance of an electrical malfunction that causes the burning of the stacker crane, at the lower building level; this choice is made because rack uprights are more stressed at the lower level. Since they are large and high structures a fully developed fire seems unrealistic and for this reason the fire model that better fits in this case could be the localized fire model, therefore, ARSW single or double depth the fire scenario at the base within the aisles for stacker cranes can be modelled by considering the localized fire (LOCAFI model [21]). On the other hand, in the case of multi-depth ARSW because of their configuration and the presence of the shuttle systems, the fire could start like a localized fire also within the load levels and could develop into a traveling fire both in

horizontal and vertical directions. Fire design methods for vertically traveling fires are not as developed as for horizontal ones, indeed, in the last decade, vertically traveling fires have been analyzed like multi-floor fires in high-rise buildings Usmani et al. (2009) [22], which represents a different condition than the ARSWs. For these reasons, to study the fire behaviour of the ARSW, it was necessary to obtain a fire model that allowed the vertical and horizontal propagation of localized fires to be considered, for this purpose some experimental results were looked for in the scientific literature. The work used as principal references for validating the fire model was carried out by Lönnemark and Ingason (2005) [23], which performed several scale fire tests, to investigate the fire spread from an initial fire in rack storage to adjacent racks without any suppression system. These tests were simulated by using the software CFAST (Jones et al. 2006 [24]) which is a two-zone fire model that predicts the thermal environment caused by a fire within a compartmented structure, and that allows the modelling of different compartments that can communicate to each other. The results of test series 1 (cone calorimeter tests of the cardboard boxes) allowed obtaining the Heat Release Rate (HRR) curves of a single cardboard box, and starting from these input curves, it was possible to model test series 2 (fire spread tests with one small rack) and validate the CFAST model for a single rack. In this way, it was possible to simulate test series 5, which consists of the study of the vertical and horizontal fire propagation in a group of 4 racks, modelling the propagation of a localized fire, indeed this test was the only one that provided the vertical and horizontal propagation times between levels of the racks. This propagation was considered in the CFAST model by assigning time delays to the HRR curves, starting from the HRR curve of a single level. Thanks to the simulation of these experimental tests, it was possible to find that: vertical time propagation is equal to the time for the flame to reach the upper level of the racks, calculated by using the flame lengths L_f proposed in EC1 part 1-2, moreover since the main assumption of the zone model is that the temperature is uniform in each compartment, to obtain different temperature distributions within the structure it was necessary to divide the whole geometry of the fire model into different cells as the load level of structure, i.e., where the combustion material (UDC) is present. Therefore, the final model of the ARSW was created in CFAST, as shown in Figure 2a, where a first large compartment that represents all structure volume was modelled. Within this one, one transversal cross section was modelled, by modelling the 5 racks shoulder and 1 steel compartment representing the bottom steel frame. For the central three shoulders, the first six load levels which were directly affected by the presence of a fire, were modelled as a single compartment/cell but communicated among them thanks to horizontal openings (ceiling/floor vent). The result was a model with seven compartments for each shoulder: six single compartments related to the first six levels where, with several delays, the fire develops and the seventh compartment grouping the remaining load levels where no fire was defined. The lateral shoulders were not modelled as a compartment because they were considered cold. Figure 2b shows the temperature distributions recorded by the CFAST thermocouples placed at the first seven levels near the horizontal elements i.e., the hot zone. By analysing temperature results, it is possible to appreciate, how the time delay imposed for the HRR curves was found also in the natural fire curves. All the curves reach a maximum temperature equal to about 1120 °C.

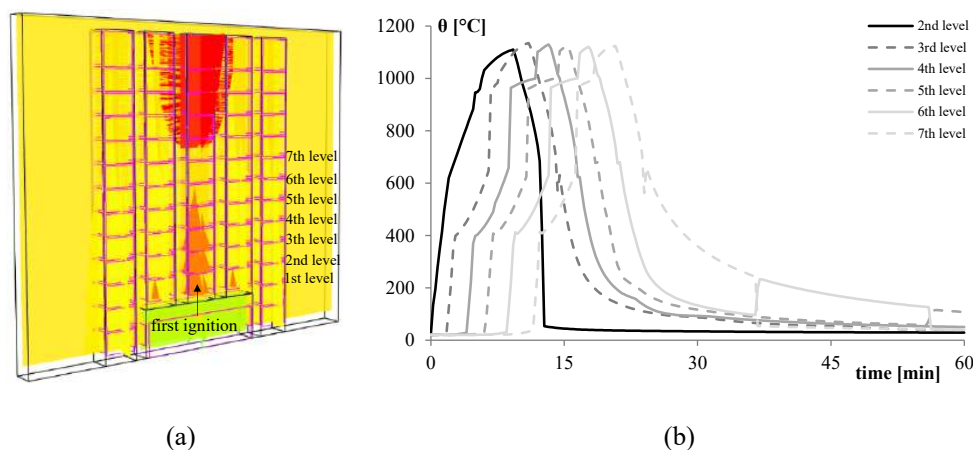


Figure 2. (a) CFAST model (b) temperature distributions recorded by the thermocouples placed at the first 7 levels near the horizontal elements

4 THERMO-MECHANICAL MODELLING

4.1 Finite element model by using SAFIR software.

A typological frame, in the CA direction, of the ARSW structure shown previously, was modelled in SAFIR software by using *beam* elements. The structure was analyzed in 3D space by blocking out-of-plane displacements thanks to restraints. At the structural base, fixed restraints were considered while the braces, horizontal beams of the shoulders, and diagonal and vertical elements of the truss were modelled as pinned beams (see Figure 3a). The exceptional load combination was considered, and dynamic analyses were carried out by considering the nonlinear geometry and material nonlinearity, and for a more correct modelling of Class 4 steel elements through beam elements, a modified constitutive law was considered to consider in beam-based numerical models, local instabilities that can occur in thin sections (Franssen et al. 2014) [25].

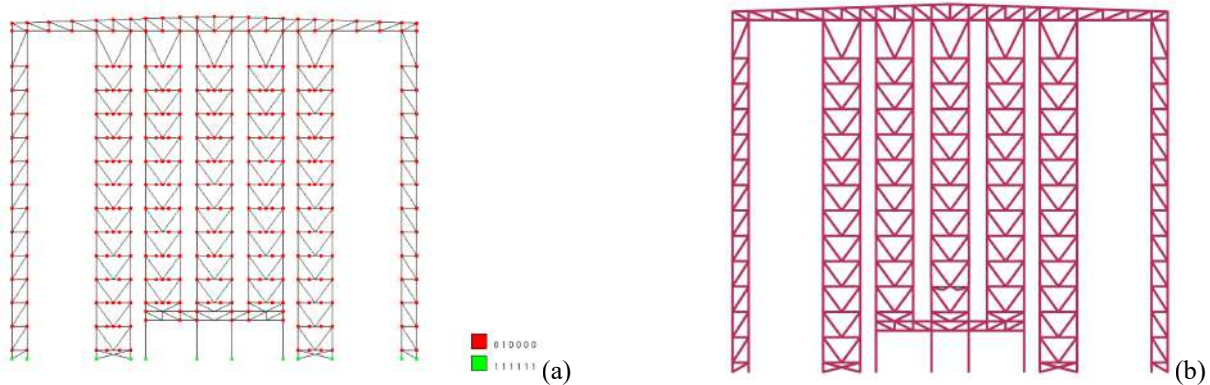


Figure 3. (a) The cross-aisle view of the FE model in the GID environment; (b) deformed shape at 5.8 minutes in the Diamond environment

Since the literature assesses that the most indicated simplified fire model for a member outside the fire area is the localized model [21], the thermo-mechanical analysis was carried out by considering different fire models for different structural elements. For all the uprights the LOCAFI model was used while for all the other structural elements, the results of the proposed multi zone model were used. The following Figure. 3b shows the deformed shapes of the structure at 336 seconds (i.e., 5.6 minutes), which is the last step of the structural analysis provided by SAFIR. At this time the critical element could be the transversal beam of the central shoulder at the 2nd load level, which is a coupled C150x50x15mm and 2mm thickness, which shows a buckling shape. Figure. 4a shows the temperature distribution within the cross-section, obtained from the thermal analysis, where it is possible to appreciate a little temperature difference among the web, the flanges, and the lips. Figure. 4c shows the temperature distribution along the first level of the upright, obtained with LOCAFI, in comparison, with the one obtained from the thermal analysis carried out with the CFAST natural fire curve. By analyzing the results, it is possible to see that LOCAFI provides different temperatures along the vertical development of the column, unlike by using the zone model where it is possible to obtain only one uniform temperature, on the other hand, it is possible to see that CFAST could be seen as a mean value of the LOCAFI one. To investigate the achievement of the capacity of the beam, the compression resistance axial force at different exposure times was calculated with both capacity methods (the actual EC3 part 1-5 and the new EC3). For this reason, the first step was the evaluation of the effective cross-sectional area, Table1 shows the comparison between the area for the coupled C150x50x15mm and 2mm thickness and the effective cross-area calculated with the effective width method, according to both capacity methods.

Table 1. Effective cross-sectional area for the coupled C section 150x50x15x2mm according to the two capacity methods

A	A _{eff, actual EC3}	A _{eff, new EC3}	reduction	reduction
[mm ²]	[mm ²]	[mm ²]		
1080	842	562	48%	22%

Once the A_{eff} is known it was possible to evaluate the design buckling resistance at different exposure times by using the Eq1 and Eq2. The results are shown in the following Figure.4c in comparison with the axial force provided by SAFIR, where a positive axial load indicates compression in the beam element. This comparison confirms that the critical element is the selected transversal beam, the thermal action has induced an increment of the initial compression load which corresponds to an expansion of the beam, after 3 minutes the load starts to decrease, and the beam starts to deflect inward, at this point the section has reached a temperature equal to 400°C more or less and so the steel resistance starts to decrease. The load decreases until 5.6 minutes with an inward deflection for a tension load, with a little catenary effect, for the beam. Moreover, it is possible to see that the two capacity methods provide different results within the first 2 minutes, with lower values obtained with the new EC expressions, while after this time the results are very similar to each other.

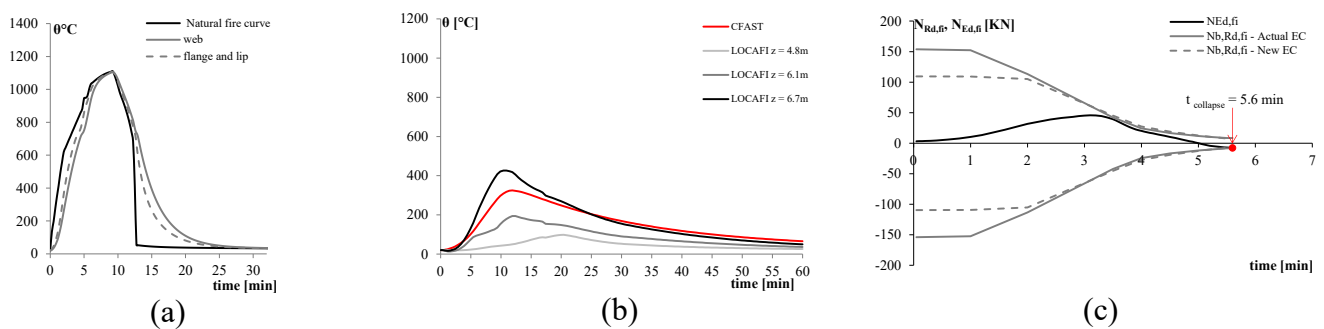


Figure 4. (a) temperature distribution within cross section of the beam over time (b) Temperature distributions along the 1st level of the upright, comparison between LOCAFI model and CFAST one (c) comparison between stress and resistance

The thermo-mechanical analysis has shown that the collapse time for this type of structure is of the order of a few minutes, and to study the collapse it is essential not only to carry out advanced analyses but also to refine them as much as possible, for example to investigate the achievement of the capacity of the beam in terms of compression resistance axial force, the non-uniform temperature distribution had to be considered, combined with the assessment of the effective width to consider the local instability, and the assessment of χ coefficient to consider the global instability in compression. Moreover, the analysis stopped at the achievement of the capacity of the most stressed elements. For this reason, it was not possible to analyse the global collapse and the correct collapse time. This is due to the type of analysis that SAFIR allows to implement, which is dynamic analysis, but it is an implicit analysis, which stops when convergence problems are reached. All these aspects lead to affirm that to correctly estimate the collapse times and the shape of the global mechanism, it could be necessary to go beyond the time provided by SAFIR, manually eliminating the elements that gradually fail. Starting from the analysis carried out with the zone model, since it was demonstrated that the element that led the analysis to stop was the horizontal beams of the 2nd level, another structural model was built by removing this element and applying the internal forces as times changes, that the previous thermos-mechanical analysis had provided. The following Figureures show the results of this analysis without the beam of the 2nd load level. In particular, Figure.5a show the comparison among the axial force provided by SAFIR in the beam element and the buckling resistances calculated with both capacity methods. The first thing that it is possible to appreciate is the fact that the last step of the analysis increased from 5.8 to 7.8 minutes, in this way, the beam of the 3rd level has continued its heating corresponding to an increase of the horizontal displacements, and the axial load in compression, until 7 minutes when the load starts to decrease, and the beam starts to deflect inward, at this point the section has reached a temperature equal to 600°C more or less and so the steel has lost about half of its strength. The load decreases until 7.8 minutes with an inward deflection for a tension load, with a little catenary effect for the beam. By assessing that the global behaviour of the structure without one element is not changed, the load and the displacements are the same in shape and entities until the last step of the previous analysis. For these reasons, another structural model was built by removing both the 2nd and 3rd horizontal beams of the central shoulder and applying the internal forces as times change, that the previous thermos-mechanical analysis had provided. This procedure was continued until

to reach a structural model without the beam at the 2nd, 3rd, and 4th load levels and the truss' diagonal. The following Figure 5 shows the results of this analysis without these elements, in particular Figure. 5b shows the deformed shapes of the structure at last step 742.5 seconds (i.e., 12.4 minutes). From the deformed shape it is possible to see that at that time the critical element was the transversal beam of the central shoulder at the 5th load level, which is a coupled C section 150x50x15mm and 2mm thick-ness, which shows a buckling shape. Figure.4c shows the comparison between the axial force provided by SAFIR in the beam element and the buckling resistances calculated with both capacity methods. The first thing that it is possible to appreciate is the fact that the last step of the structural analysis provided by SAFIR time increased from 10.2 to 12.4 minutes, moreover the comparison confirms the critical element is the selected transversal beam of the 5th level, which has continued its heating corresponding to an increase of the horizontal displacements, and the axial load in compression, until 9 minutes when the load starts to decrease. The beam starts to deflect inward, at this point the section has reached a temperature equal to 600°C and so the steel has lost about half of its strength. The load decreases until 12.4 minutes with an inward deflection for a tension load, with a little catenary effect for the beam. Currently, it is possible to also see that the uprights belonging to the central shoulder without the horizontal beams that have collapsed, show a global buckling.

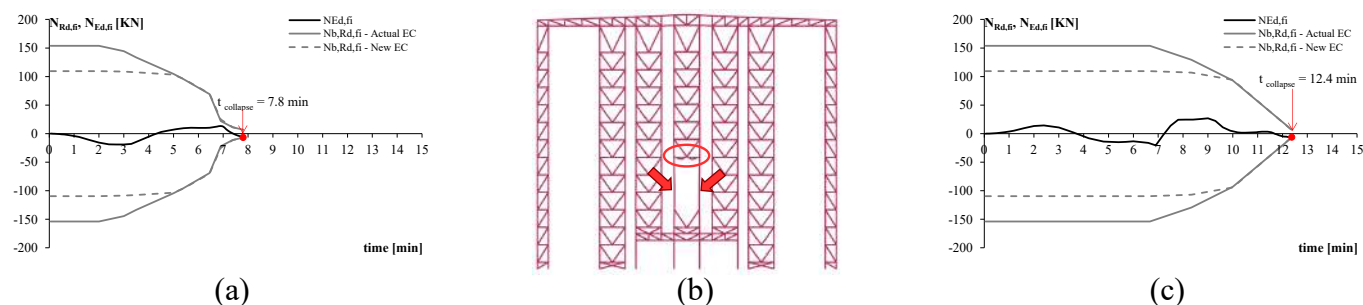


Figure 5. (a) comparison between stress and resistance (b); deformed shape at 12.4 minutes in the Diamond environment of the structure without the beam at the 2nd, 3rd, and 4th load levels and the truss' diagonal; (c) comparison between stress and resistance

Finally, the shown proposed procedure has confirmed that to correctly estimate the collapse times and the shape of the global mechanism, it is necessary to go beyond the last step of the structural analysis provided by an implicit analysis, by manually eliminating the elements that collapse. Indeed, since SAFIR implements only implicit analysis, this type of analysis stops when convergence problems are reached that usually correspond to the collapse of the most stressed structural elements.

4.2 Finite element model by using ABAQUS CAE software

As shown before, assessing the collapse of steel structures due to fire requires an analysis capable of processing numerical singularities, such as buckling of elements, plastic hinges, and large displacements. The explicit algorithm can be a helpful tool for solving these problems. As deeply shown in Mei et al [20] a fire input can be more than 60 minutes long, so an entirely explicit analysis can be computationally expensive and time-consuming. Classical strategies such as time or mass scale can be tricky to solve this problem because they can introduce unrealistic inertial effects in large models during collapse, for this reason the authors proposed a nonlinear procedure based on 3-step process: static, dynamic implicit, dynamic explicit. In the first phase, non-structural loads (such as load unit loads) are applied to the structure using a static procedure; when the fire begins to heat frames, the analysis switches to dynamic implicit. Then, the last phase is the explicit analysis, where frames undergo large displacements and deformations until the complete collapse. Moreover, since racks have a peculiar load distribution, with point masses representing pallet loads placed at the beam-to-upright intersection, the dynamic procedure permits better capturing the dynamic effects due to concentrated masses in the collapse phase.

Abaqus/Standard uses the Hilber-Hughes-Taylor time integration. The stiffness matrix is computed and inverted, and the non-linear system of equations is solved in each time increment iteratively using Newton's

method. The method is unconditionally stable, which is advantageous compared to conditionally stable explicit methods. It is also faster for typical structural analysis but computationally less efficient due to the inversion process for the stiffness matrix. On the contrary, Abaqus/Explicit uses a central-difference integration rule. As it is conditionally stable because the time step should withstand the Courant Condition of Equation (21), it is a computationally more efficient process as the integration method requires the inversion of the mass matrix only.

The 2D finite element model has been built in ABAQUS using B21 beam elements (see Figure 6).

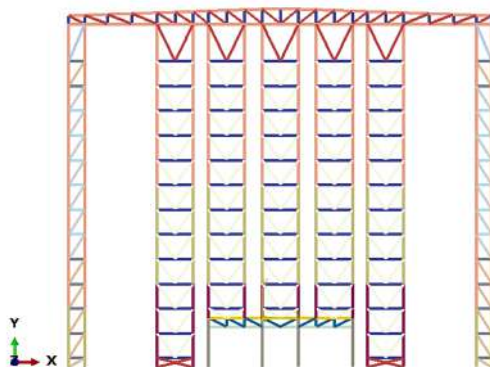


Figure 6. The cross-aisle view of the FE model in the ABAQUS CAE environment

To replicate the conditions of pinned beams for braces, truss diagonals, it is impossible to use a “truss” T21 in the model since it cannot consider the buckling eventuality of the element. For this reason, an assembled connector was used, made by a Join and a Rotation connector. The Join connector constraints displacements in the two directions, X and Y, and does not activate rotational DoF, while the Rotation connector makes the rotation in the XY plane available. Uprights were considered pinned in the cross-aisle direction and fixed in the down-aisle direction. The analyses were carried out considering nonlinear geometry and material nonlinearity. The EC3 part 1-2 formulation was adopted for the latter and a linear interpolation was adopted between two temperature values given by the Eurocode. The nonlinear procedure before was considered to run the analyses. In the same way of SAFIR method, the unit load loads were applied as concentrated forces at the four intersections between uprights and beams. The analysis was carried out by considering the results of the zone model proposed and shown before it is worth understanding that the thermal analysis was not carried out by using ABAQUS, but the results of the thermal analyses provided by SAFIR were used, in this way for each element a uniform temperature was applied as predefined fields. Moreover, in order to compare the implicit analysis with the SAFIR results, no ABAQUS General contact was activated.

The deformation sequence is reported in the following Figure 7. Referring to this figure, the collapse sequence for some of the significant time steps is as follows: 324 seconds, about 3.9 minutes: end of the implicit part. From the deformed shape, it is possible to see that at that time the critical element was the horizontal beam of the central shoulder at the 2nd load level, which showed a collapse shape. At that time the temperature of that beam was at about 690°C, while the temperatures in the other elements were still increasing. 402.2 seconds, about 6.7 minutes, thanks to the explicit part of the analysis it is possible to see that, as with the previous horizontal beam, now the beam of the 3rd level collapsed in the same way as the previous one and at the same temperature at about 689 (the yellow one). Since the beam of 2nd level has collapsed, it is not present in the structure anymore. 988.3 seconds, about 16.5 minutes, also the horizontal beam of the 7th level collapsed; it is possible to see that the uprights of the central shoulder, without the horizontal beams that collapsed, showed a global buckling. 1096.9 seconds, about 18.3 minutes end of the analysis.

From the previous considerations, it is possible to affirm that the results obtained with this implicit/explicit procedure are in line with the SAFIR ones. The sequence of the progressive collapse (the elements that collapse and their times) is the same as obtained with SAFIR, i.e., an iterative procedure only based on subsequent implicit analyses: however, in this case the procedure is automatic while with SAFIR it was necessary for every step to remove manually the critical element by replacing it with their reactions.

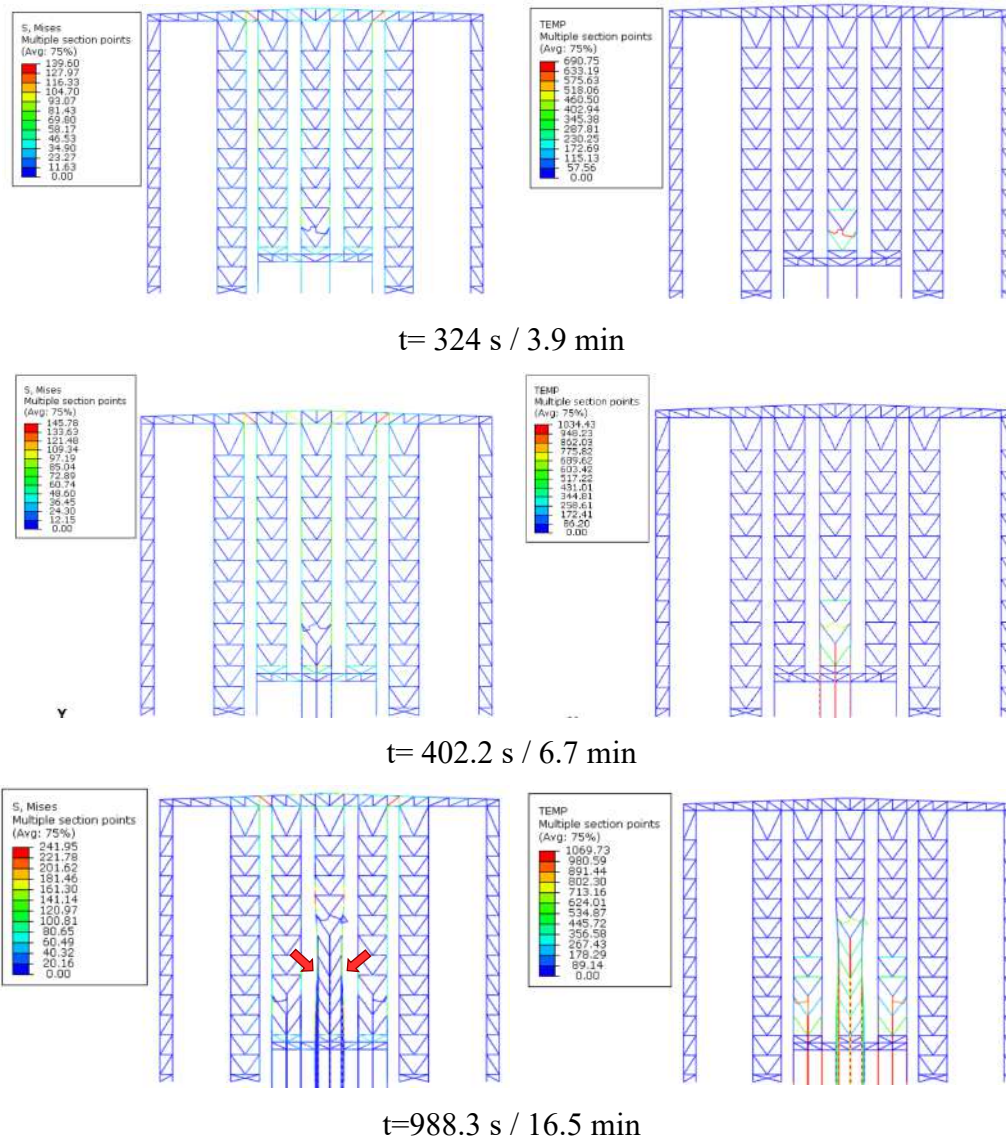


Figure 7. Deformation sequence. Left: Von-Mises stresses; Right: Temperatures

In the following Figure 8 some comparisons are shown, to validate the previous considerations and the model reliability.

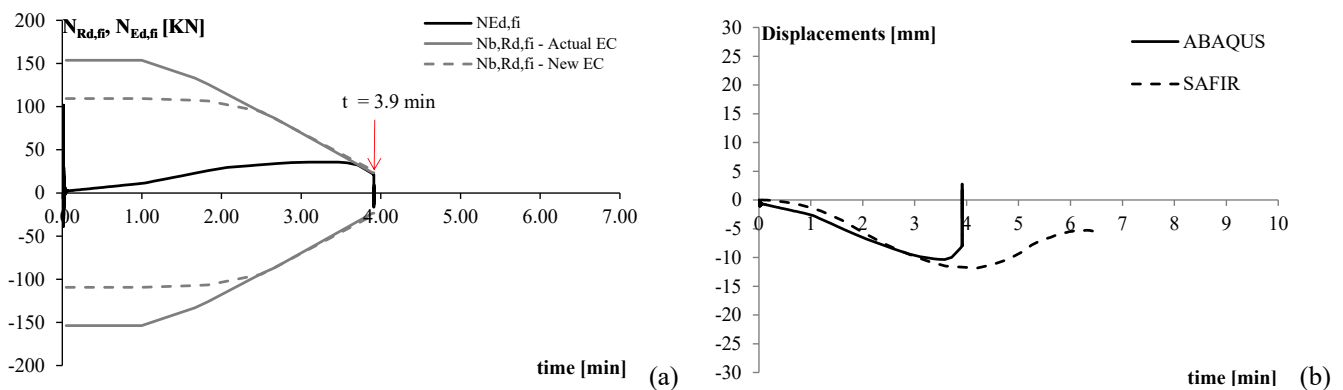


Figure 8. (a) Comparison between stress and resistance at the last step of the implicit part. (b) Benchmark between ABAQUS and SAFIR displacements at the end of beam of the 2nd load level

The Figure 8a shows the comparison between the axial force provided by ABAQUS as a result of the implicit analysis, with the buckling resistance calculated with both capacity methods for the beam belonging to the 2nd level of the central shoulder. This comparison confirms that, in the examined case-study, the critical element is the selected transversal beam. The thermal action leads to an increment of the initial compression load due to the thermal expansion of the beam: after 3 minutes the axial load starts to decrease, and the beam starts to deflect inward; at this point the section has reached a temperature equal to 400°C more or less and so the steel resistance starts to decrease. The axial load decreases until it reaches the collapse at 3.9 minutes with an inward deflection. The implicit part of the analysis conducted in ABAQUS gives results in line with the SAFIR ones one showed in Figure 5b, but in ABAQUS the collapse is anticipated by a few minutes, confirming that SAFIR, despite stopping at the collapse of the first most stressed elements, considers a redistribution of the internal stresses. This aspect is shown and confirmed also in terms of comparison between the displacement at the end of the beam, shown in Figure 8b. The two displacements are similar in the first phase; in the second phase the ABAQUS one increase quickly with a beam collapse at 3.9 minutes, while the SAFIR's one still increasing with a collapse at 5.8 minutes. Finally, the two deformed shapes obtained with ABAQUS (Figure 7), and Safir (Figure 5b) are in a good agreement to each other, confirming that to analyse the collapse of these structure by using an implicit analysis removing the collapsed elements, is necessary to go beyond the time provided by the first implicit analysis.

5 CONCLUSIONS

This work presents the study of a typological ARSW, from the definition of the fire modelling to the study of collapse mechanism. A fire model that allows vertical and horizontal propagation, starting from a localized fire, evaluated and validated against experimental results available in the literature, is briefly shown.

Several thermo-mechanical analyses were performed by using the SAFIR software, which allows modeling Class 4 steel elements like beam elements but considering the local instabilities that can occur in these slender sections. These analyses were carried out by considering different fire models for different structural elements (LOCAFI and zone models' results). The results showed that collapse time for this type of structure is within a few minutes: for the thermo-mechanical analysis it is essential to carry out advanced analyses refining them as much as possible, taking into account, for example, the field of non-uniform temperature distribution and all the instability phenomena. Moreover, the analyses stopped at the collapse of the most stressed elements, and for this reason, it was not possible to analyze the real global collapse and the correct collapse time. This is due to the type of analyses that SAFIR allows to implement, which are dynamic implicit analyses that stop when convergence problems are reached. Since ARSWs are characterized by elements with a reduced deformed capacity (class 4 sections), that does not allow the development of a full plastic stress distribution in the section and leads to an incomplete plastic redistribution along the members in the structure. Therefore, to correctly estimate the fire collapse times and the shape of the global mechanism, to go beyond the time of collapse provided by an implicit analysis by SAFIR, it is necessary manually eliminating the elements that collapse. The reliability of this iterative procedure, based on subsequent implicit analyses, has been examined and validated by modelling the same structure with a second structural software, ABAQUS CAE, that allows the implementation of both implicit and explicit analyses. The implicit part of the analysis conducted in ABAQUS gave results in line with the SAFIR ones, but in ABAQUS the collapse was anticipated by a few minutes, because SAFIR better considers the redistribution of the internal stresses until the collapse of the first most stressed elements. Finally, the explicit analysis conducted by ABAQUS allowed to follow a progressive collapse and a global collapse mechanism, like those obtained by means of the iterative subsequent procedure implemented with SAFIR: in that case, however, the procedure is automatic and does not require removing manually the collapsed elements by users.

REFERENCES

1. EN 1993-1-1. 2004. Eurocode 3: Design of steel structures - Part 1-1: General rules and rules for buildings.
2. EN 1993-1-3. 2005. Eurocode 3, Design of Steel Structures - Part 1-3: supplementary rules for cold formed thin gauge members and sheeting.

3. EN 1998-1-1. 2004. Eurocode 8: Design of Structures for earthquake resistance - Part 1: General rules, seismic actions and rules for buildings.
4. CEN European Committee for Standardization. 2009. EN 15512 Steel static storage systems—Adjustable pallet racking systems—Principles for structural design.
5. CEN European Committee for Standardization. 2016. EN 16681 Steel static storage systems—Adjustable pallet racking systems—Principles for seismic design.
6. Bernuzzi C, Draskovic N, Simoncelli M. 2015. European and United States approaches for steel storage pallet rack design. Part 2: practical applications. *Thin-walled Structures* vol. 97, pp.321–341.
7. C. S. LL. PP. 2018. Aggiornamento delle Norme Tecniche per le Costruzioni - D.M. 17 /01/2018”, (in Italian).
8. C. S. LL. PP. 2023. Linee guida per la progettazione, esecuzione, verifica e messa in sicurezza delle scaffalature metalliche, (in Italian).
9. S. Caprili, F. Morelli, W. Salvatore, and A. Natali. 2018. Design and Analysis of Automated Rack Supported Warehouses, *Open Civil Engineering Journal*, vol. 12, no. 1, pp. 150-166.
10. A. Natali, F. Morelli, and W. Salvatore. 2022. On the Seismic Design and Behaviour of Automated Rack Supported Warehouses”, *Bulletin of Earthquake Engineering* 20, pp. 1247–1295.
11. EN 1993-1-5. 2006. Eurocode 3: Design of steel structures - Part 1-5: General rules - Plated structural elements.
12. P.B.Dinis, B.Young, D.Camotim. 2014. Local–distortional interaction in cold-formed steel rack-section columns, *Thin-Walled Structures*, vol. 81, pp. 185–194.
13. B. W. Schafer. 2000. Distortional Buckling of Cold-Formed Steel Columns, *The American Iron and Steel Institute*, final report.
14. D.M. 3 agosto 2015 Approvazione di norme tecniche di prevenzione incendi, ai sensi dell’articolo 15 del decreto legislativo 8 marzo 2006, n. 139, GU n. 192 del 20/8/2015 – S.O. n. 51 (in Italian).
15. EN 1992-1-2, “Eurocode 2: Design of concrete structures - Part 1-2: General rules - Structural fire design” 2004.
16. C. Couto, P.V. Real, N. Lopes, B. Zhao. 2014. Effective width method to account for the local buckling of steel thin plates at elevated temperatures, *Thin-Walled Structures*, vol. 84, pp. 134–149.
17. G. Winter. 1947. Strength of thin steel compression flanges, *Transactions of the American Society of Civil Engineers*, vol. 112.
18. C. Couto, P.V. Real, N. Lopes, B. Zhao. 2015. Resistance of steel cross-sections with local buckling at elevated temperatures, *Journal of Constructional Steel Research*, vol. 109, pp. 101–114.
19. R. Zaharia and J.-M. Franssen, 2002. Fire design study of a high-rise steel storage building, in *International Colloquium on Stability and Ductility of Steel Structures*, pp. 745-752.
20. A. Mei, M. Orlando, L. Salvatori, K, Thiele. 2023, Fire-Induced Collapse of Automated Rack-Supported Warehouses. *ce/papers*, 6: 2167-2172.
21. O. Vassart, F. Hanus, M. Brasseur, R. Obiala, J.-M. Franssen, A. Scifo, B. Zhao, C. Thauvoye, A. Nadjai, and H Sanghoon. 2016. Temperature assessment of a vertical steel member subjected to localised fire, acronym LOCAFI, Report RFSR-CT-2012-00023, European Commission.
22. A. Usmani, C. Roben, A. Al-Remal, A. 2009. A Very Simple Method for Assessing Tall Building Safety in Major Fires. *International Journal of Steel Structures*, vol. 9(1), pp. 1-15.
23. A. Lönnermark, H. Ingason, 2003. Fire Spread in Large Industrial Premises and Warehouses, in *BRANDFORSK project 630-021*.
24. W. W. Jones, G. Forney, R. D. Peacock, and P.A. Reneke. 2003. A Technical Reference for CFAST: An Engineering Tool for Estimating Fire and Smoke Transport”, *Technical Note*, (NIST TN), National Institute of Standards and Technology, Gaithersburg, MD, May 2.
25. Franssen J.M., Cowez B, Gernay T., 2014. Effective stress method to be used in beam finite elements to take local instabilities into account, *Fire safety science-proceedings of the eleventh international symposium* pp. 544-557.

TIMBER STRUCTURES IN FIRE

AN EMPIRICAL MODEL OF FALLOUT OF CHAR LAYER OF GLUE LAMINATED TIMBER WALLS HEATED BY ISO 834 STANDARD FIRE FOR VARIOUS DURATION

Shoma Makino¹, Anyang Sun², Kazunori Harada³, Daisaku Nii⁴

ABSTRACT

It is widely known that heavy timber construction element is fire resistant. As the heating continues, char layer is formed on the heated surface. The char layer acts as an insulator to protect the core of the element. As the heating duration is longer, the surface char layer gets thicker, and more insulation is expected. However, if the char layer gets too thick, surface char block may fallout due to its self-weight. If fallout occurs, fresh surface is exposed to fire and burns intensely. Thus, the stability of char layer is important to obtain fire resistance. Even though fallout of char is often observed, the behaviour is poorly understood, especially the behaviour of fallout during cooling phase. In this study, 100 mm or 150 mm thick glue laminated timber walls were heated in accordance with ISO 834 standard fire for various durations, i.e., 30, 45, 60, 90 and 120 minutes, and cooled down for 0, 60 and 180 minutes. After extinction, the remaining surface geometry was measured by laser displacement meter. The width, interval and depth of the crack and fallout spots of char layer were identified as functions of heating and cooling durations. An empirical relationship was developed to predict the fraction of fallout as a function of char layer thickness.

Keywords: char layer; char fallout; ISO 834 fire; glue laminated timber; empirical model

1 INTRODUCTION

To construct large scale buildings, structural elements must be fire resistant. In case of timber construction, large-sectioned element is used to obtain necessary fire resistance. It is widely known that heavy timber construction element is fire resistant [1]. As the heating continues, char layer is formed on the heated surface. The char layer acts as an insulator to protect the core of the element. As the heating duration is longer, the surface char layer gets thicker, and more insulation is expected. However, if the char layer gets too thick, surface char block may fallout due to its self-weight. If fallout occurs, fresh surface is exposed to fire and burns intensely. Thus, the stability of char layer is important to obtain fire resistance. Even though fallout of char is often observed, the behaviour is poorly understood, especially the behaviour of fallout during cooling phase. To account for crack formation and fallout of char layer, EuroCode [2] applies an apparent thermal conductivity. The thermal conductivity of wood char is increased at above 500 °C in order to account for loss of integrity of char layers implicitly. To account for the effect of heat penetration through crack, Parker developed an one-dimensional heat conduction model of heat transfer in wood material

¹ M. Eng, Oayashi Corporation (Formerly, graduate student of Kyoto University),
e-mail: ue-makino@archi.kyoto-u.ac.jp

² Dr. Eng., Assistant Prof., Dept. of Architecture & Architectural Eng., Kyoto University
e-mail: sun@archi.kyoto-u.ac.jp, ORCID: <https://orcid.org/0000-0003-0456-8835>

³ Dr. Eng., Prof., Dept. of Architecture & Architectural Eng., Kyoto University
e-mail: harada@archi.kyoto-u.ac.jp, ORCID: <https://orcid.org/0000-0001-8270-1692>

⁴ Dr. Eng, Associate Prof., Dept. of Architecture & Architectural Eng., Kyoto University
e-mail: nii@archi.kyoto-u.ac.jp, ORCID: <https://orcid.org/0000-0002-5821-7494>

considering the shrinkage of char, formation of crack and subsequent heat transfer through the crack [3]. The model was applied mostly to initial stage of burning. Thus, no consideration was made on the effect of fallout of char layer. For two dimensional problems, Harada developed a finite element model of heat conduction considering the effect of heat penetration through crack [4]. For detailed analysis of charring, heat and mass transfer is considered [5][6]. However, fallout of char was not considered explicitly. Many analytical models do not explicitly consider the fallout of char because of the lack of reliable models. Boe et al. developed a model of recession of combustible insulation materials for I-joist [7], but the scope is focussed on specific range, but not applicable to broad range.

In this study, to develop a model of char fallout, 100 mm or 150 mm thick glue laminated timber walls were heated in accordance with ISO 834 standard fire for various durations, i.e., 30, 45, 60, 90 and 120 minutes, and cooled down for 0, 60 and 180 minutes. After extinction, the remaining surface geometry was measured by laser displacement meter. The width, interval and depth of the crack and fallout spots of char layer were identified as functions of heating and cooling durations. An empirical relationship was developed to predict the fraction of fallout as a function of char layer thickness.

2 EXPERIMENTAL METHOD

2.1 Objective

The objective of the experiments is to examine the degree of cracking of surface char layer and the degree of fallout of char layers. Wall specimens were heated by fire resistance furnace and cooled down. Then the surface geometry of char layer, including crack and fallout spots, were measured [8,9]. The results were summarized and correlated with char layer thickness.

2.2 Experimental setup and procedure

The experiments were conducted using wall specimens made of glue laminated larch. Fourteen tests were conducted in total by varying the heating and cooling durations. The thickness was 100mm for 30- and 45-minutes of heating, 150mm for 60, 75, 90 and 120-minutes of heating. The specimens were heated by a box furnace as shown in Figure 1.

After cooled down and remaining glowing combustion was extinguished, the geometry of surface char layer was measured. As shown in Figure 2, the specimen was put horizontally, and the remaining thickness was measured by scanning laser displacement meter from top to bottom of the wall.

Finally, the specimens were cut at the centre to measure the burnt-out, charred and coloured depths. The depths were measured by tape with eye observation.



Figure 1. View of the ISO 834 standard fire test using a small box furnace

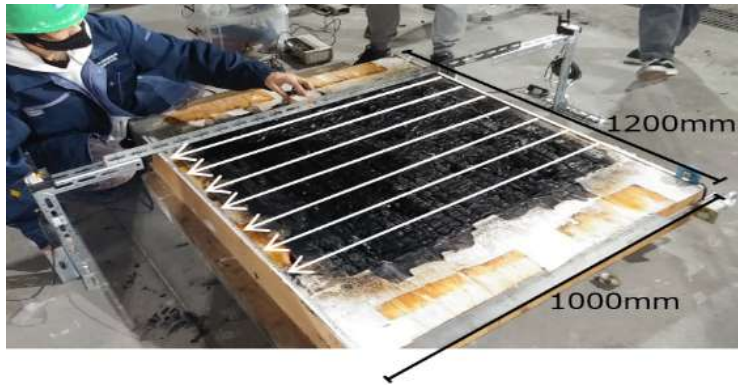


Figure 2. View of the measurement of surface geometry

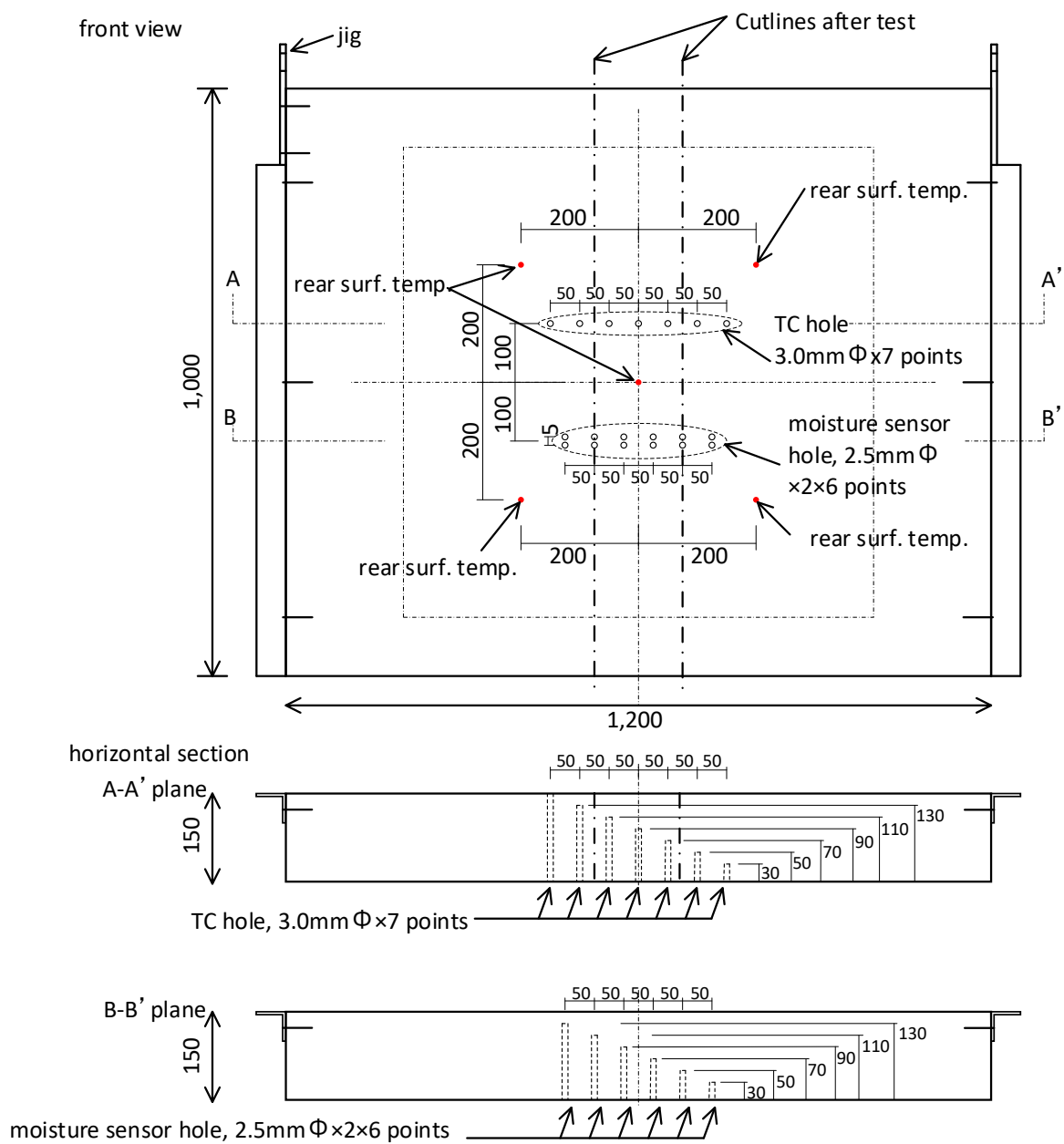


Figure 3. schematics of specimen (150mm thick)

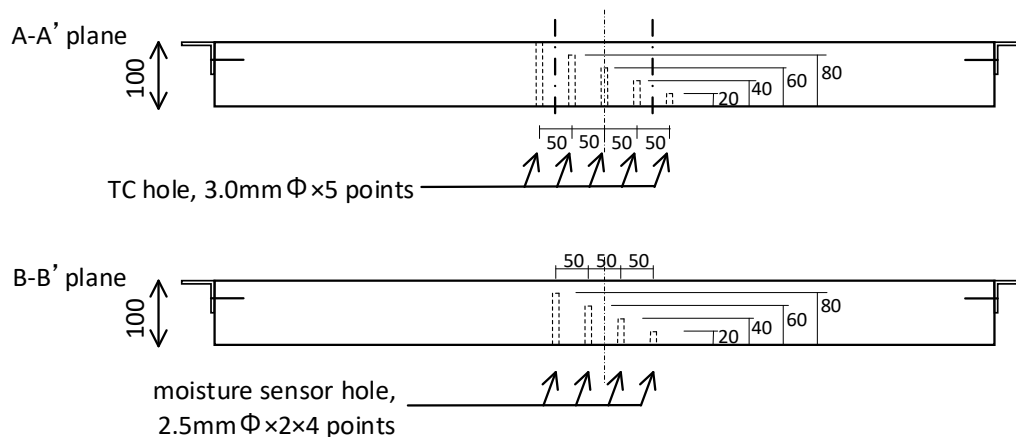


Figure 4. schematics of specimen (150mm thick)

2.3 Specimen

The specimens were 100mm or 150mm thick glue laminated walls made of larch. The schematics of specimens are shown in Figures 3 and 4. Specimen size was 1,200 x 1,000. The central part, 800 x 800 mm, was exposed to furnace and heated in accordance with ISO 834 standard fire.

Specimen temperatures and moisture contents were measured at every 20mm interval from the exposed surface. Temperatures were measured by sheathed type K thermocouples. Water content was measured by using a hand-made moisture sensor based on electric resistance measurements [10].

2.4 Experimental conditions

The experiments were carried out for 14 times, changing the heating and cooling durations. Heating duration was selected between 30 and 120 minutes. Cooling duration was selected among 0, 60 and 180 minutes. To investigate the crack and fallout during heating, the experiments with 0 min. of cooling were analysed. To investigate the effect of cooling, the data for 60 min. and 180 min. of cooling were compared with those with 0 min. of cooling.

Due to the convenience of preparation, five 100mm thick specimens and nine 150mm thick specimens were prepared. The density and initial moisture contents were slightly different unfortunately.

Table 1. Experimental conditions

symbols	thickness [mm]	oven-dry density [kg/m ³]	water cont. [%-wt.]	heating duration [min.]	cooling duration [min.]
30+0	100	461	13.1	30	0
30+180			12.9	30	180
45+0			13.3	45	0
45+180			13.8	45	180
60+60			12.5	60	60
60+0			14.4	60	0
60+180			13.5	60	180
75+0			12.8	75	0
75+180	150	520	11.7	75	180
90+0			11.8	90	0
90+60			12.7	90	60
90+180			13.4	90	180
120+0			12.5	120	0
120+180			10.4	120	180

3 EXPERIMENTAL RESULTS

3.1 An example of experiment, 120min of heating with 180min of cooling

As an example, the results for 120+180 (120 min. of heating with 180 min. of cooling) is presented in Figures 5, 6 and 7. As shown in Figure 5, the specimen temperature increased to 120 minutes. The surface temperature is close to furnace temperature especially after 30 minutes. As the measuring position was apart from the exposed surface, the temperature rise was smaller and slower. At 60mm and beyond, the maximum temperature appeared after 120 minutes, when the furnace heating was already stopped.

Figure 6 shows the change of water content with time. The water content is increased during the period when the temperature is around or slightly above 100°C.

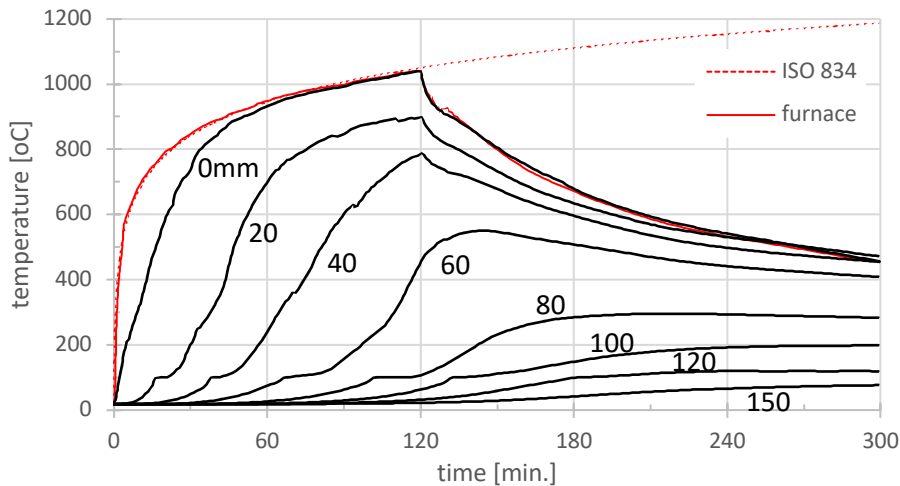


Figure 5. Measured temperatures at 120 min. of heating with 180 min. of cooling

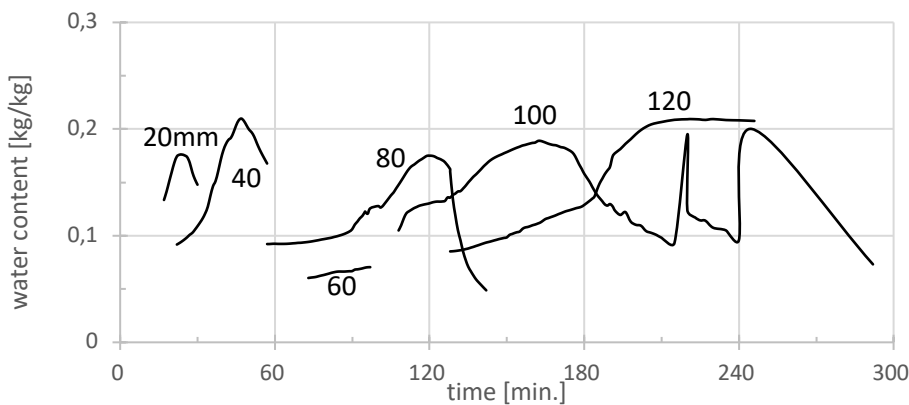


Figure 6. Measured moisture content at 120 min. of heating with 180 min. of cooling

After the heating and cooling, the surface geometry of specimen was measured by the method shown in Figure 2. The result is shown in Figure 7. The left figure corresponds with the geometry of char surface along the measured line shown in the right figure. As shown, approximately 30mm from original surface was burnt out. Along the char surface, many narrow and deep cracks can be identified. At the same time, large portion of char is missing as indicated by circles in the figure. These are the result of fallout.

3.2 Geometries of char layer surface

The measured geometries of char layer surface are shown in Figure 8 and 9. Same with the left side of Figure 7, the diagram was created by the method shown in Figure 2. Figure 8 shows the data for the experiments without cooling phase. Figure 9 corresponds with the experiments with 180minutes of cooling phase. The total thickness was 100mm for 30 and 45 minutes of heating, 150m for longer heating period.

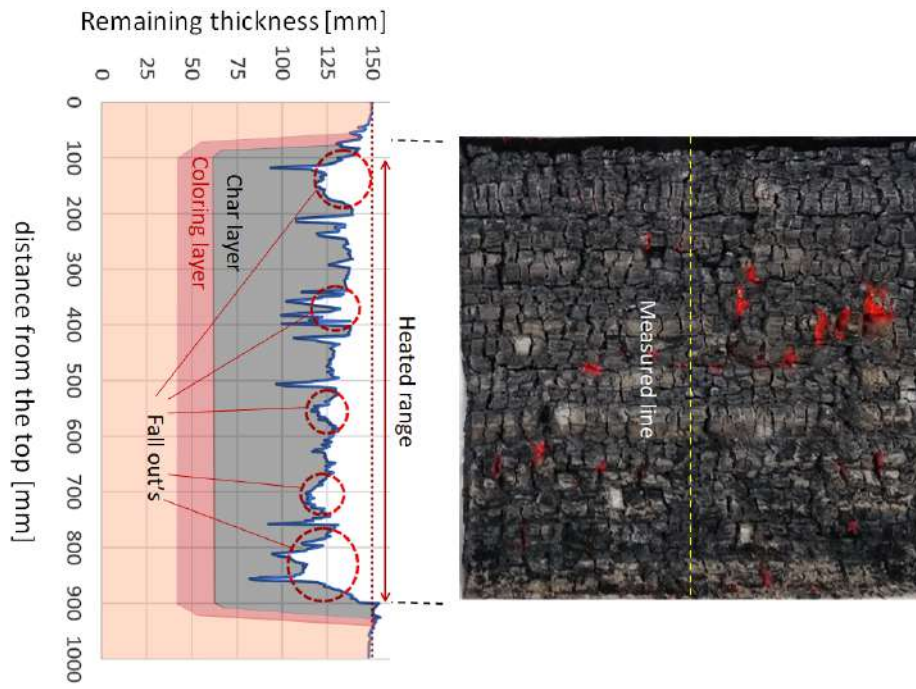


Figure 7. Measured surface crack pattern after 120 min. of heating and 180 min. of cooling

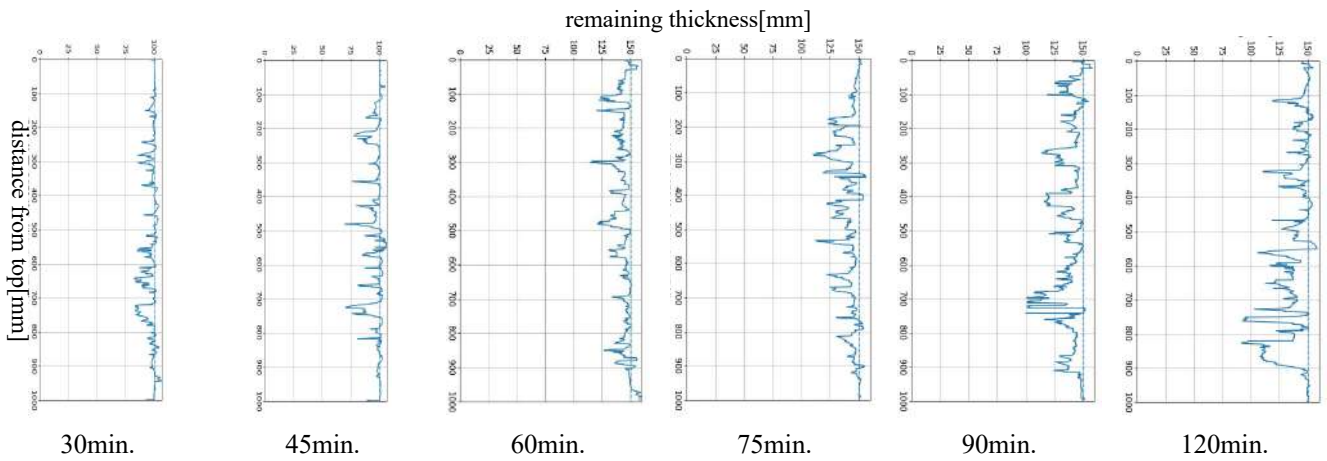


Figure 8. Measured geometries of char layer surface after various heating duration without cooling

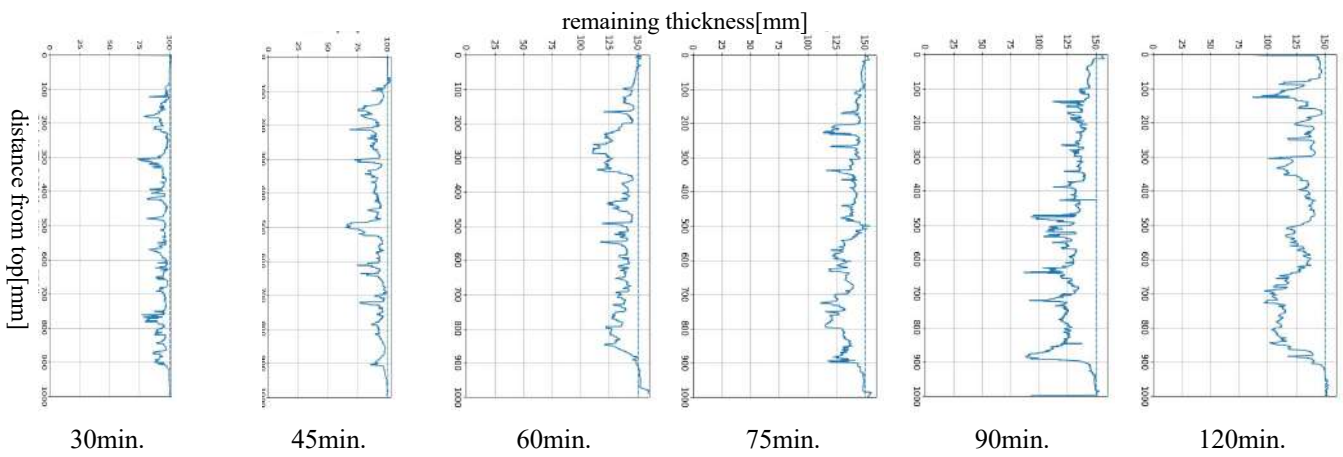


Figure 9. Measured surface crack pattern at various heating duration with 180 min. of cooling

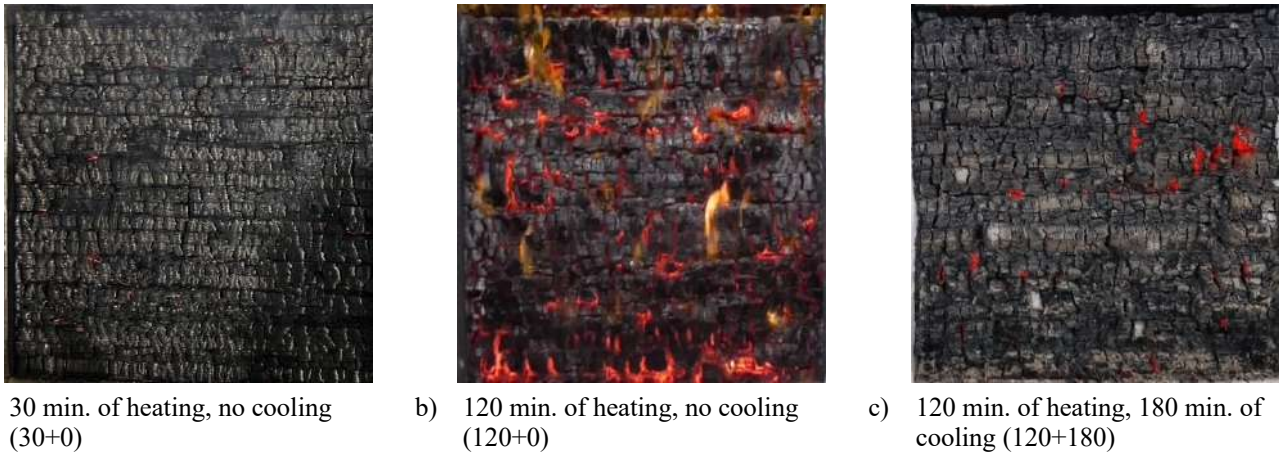


Figure 10. Condition of exposed surface after tests

In case of the experiments without cooling phase, Figure 8, the crack and fallout are increased as the heating duration is longer. After 30 minutes of heating, the surface was slightly cracked, and the fallout was not significant. As the heating duration was over 45 minutes, crack formation was obvious. As the heating duration was over 60 minutes, fallout was obvious.

The overall tendency is similar in case of 180 minutes cooling after heating as shown in Figure 9. However, the degree of fallout was increased compared with those for heating without cooling phase shown in Figure 8. In cases of fire duration more than or equal to 60 minutes, fallout was significant. Especially in case of 120 minutes heating, large portion of char layer has fallen out in the bottom region. The photographs of exposed surface after tests are picked up in Figure 10 for cases of 30+0, 120+0 and 120+180. In case of a) 30+0, the surface char layer remains unaffected. Several fallout spots are seen but limited. In case of b) 120+0, the fallout spots are extended to overall region. In case of c) 120+180, large portion of surface char layer had severely fallen out especially at the lower part of the specimen.

4 DISCUSSION OF RESULTS

4.1 Cracks

Among the geometry of char surface, crack pattern was analysed. The results are shown in Figures 11 to 13. As shown in Figures 11 and Figure 12, crack width and depth increases with heating duration. The cooling period increases the width of crack slightly. At 120 minutes of heating, the increase seems to be saturated, and width and depth are almost the same as those at 90 minutes of heating. As a result, the shape of crack is unchanged. As shown in Figure 13, the depth/width ratio (= depth of crack / width of crack) does not significantly depend on heating duration. At the same time, the interval of cracks is almost constant. In summary, it can be said that the surface crack is initiated at a uniform interval, and the width and depth are increased at the same position as the heating period is increased.

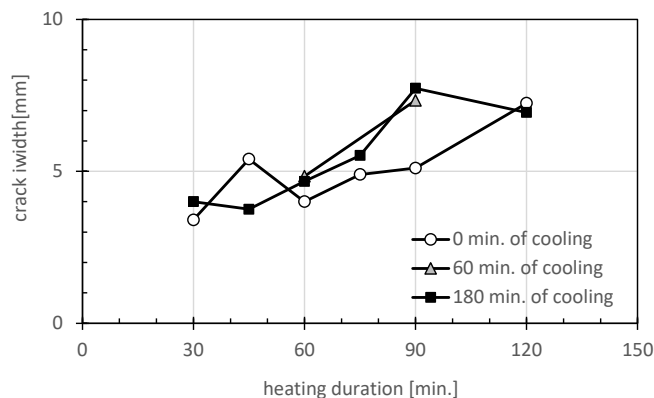


Figure 11. crack width as functions of heating duration

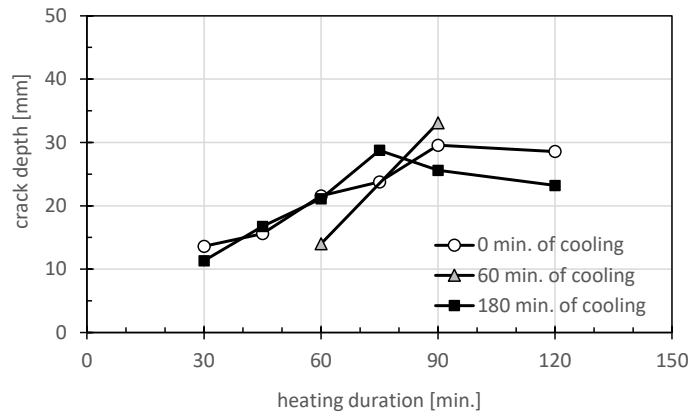


Figure 12. crack depth as functions of heating duration

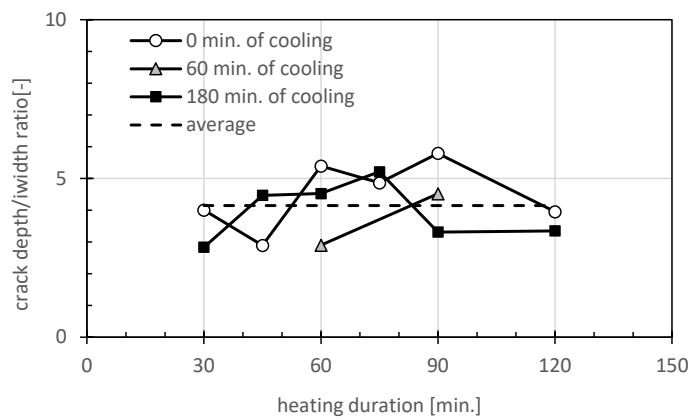


Figure 13. crack depth/width ratio as functions of heating duration

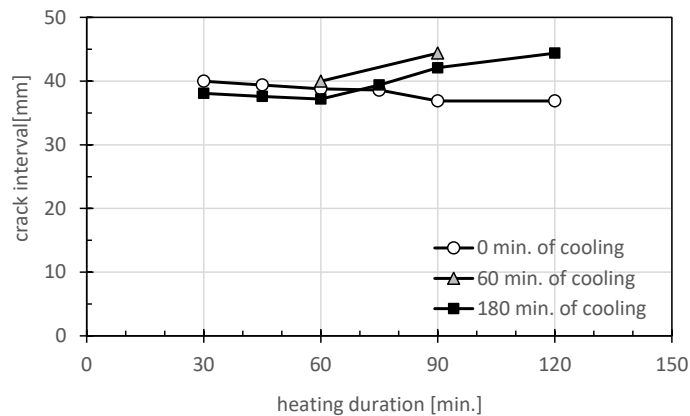


Figure 14. crack interval as functions of heating duration

4.2 Fallout spots

Apart from cracks, fallout patterns were also analysed. The results are shown in Figures 15 to 18.

As shown in Figures 15, the fallout width is increased with heating duration. The effect of cooling is also clear. Comparing the data for 0 min. of cooling and 180 min. of cooling, the fallout width is clearly larger in case of 180 min. cooling. The depth of fallout is shown in Figure 16. The depth increased slightly up to 60 minutes of heating. Thereafter, the depth seems to be unchanged. As shown in Figure 17, fallout fraction (=area of fallout / total area) was increased with heating duration. The number of fallout spots is almost unchanged with heating duration as shown as in Figure 18.

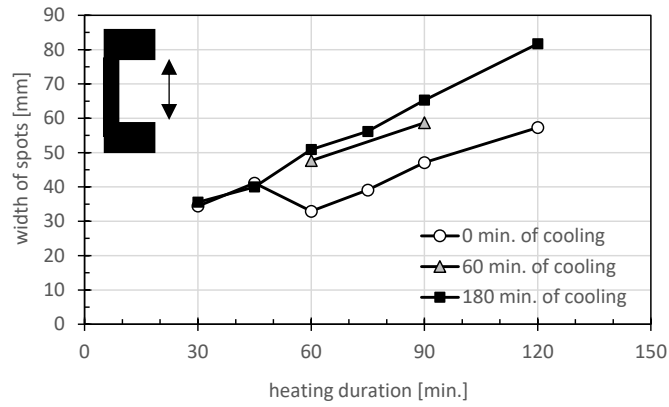


Figure 15. width of fallout spots as functions of heating duration

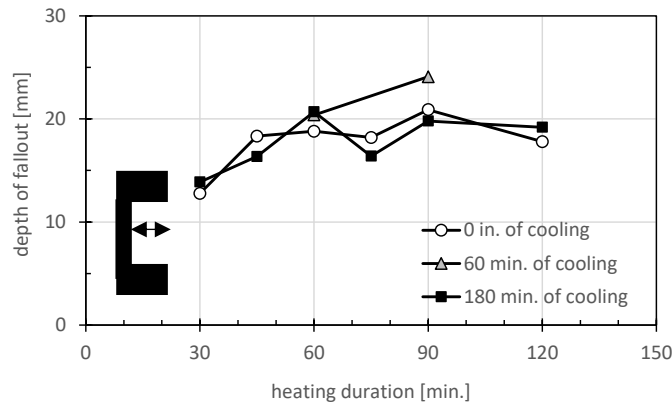


Figure 16. depth of fallout spots as functions of heating duration

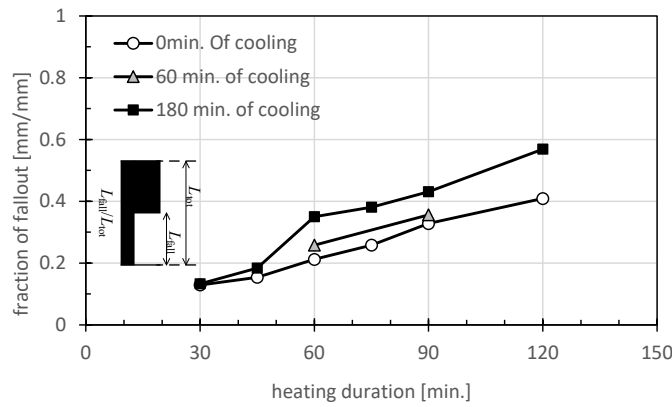


Figure 17. fraction of fallout area as functions of heating duration

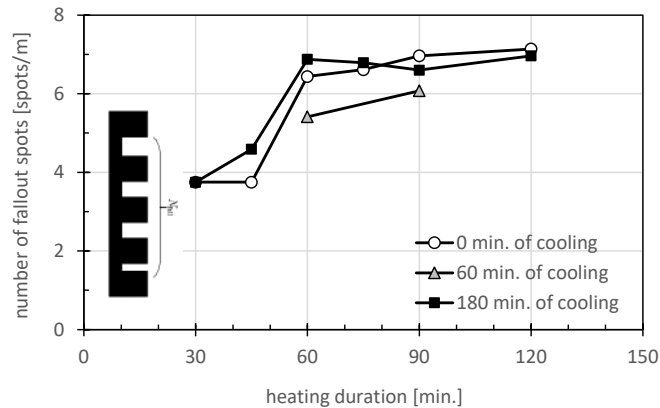


Figure 18. number of fallout spots as functions of heating duration

In summary, it can be said that the number of fallout spots are increased slightly up to 60 minutes of heating duration, but the number does not change afterward, but the width of each fallout spot is increased. As a result, the fraction of fallout is increased with heating duration.

4.3 Burnt-out/ charred/coloured/ depths

To measure the burnt-out depth, charred depth and coloured depth, the specimen was cut at the centre and the depths were measured by tape with eye observation. An example is shown in Figure 19. Results of all the specimens are shown in Figure 20. As expected, the depths are increased monotonically with heating duration. The burnt depth was 12mm for 120min heating of heating duration without cooling. The effect of cooling is obvious. The burnt depth was increased about double by 180 minutes of cooling. It means that burning continues during cooling phase, regardless of flaming combustion or glowing combustion. The effect is not negligible.

As the charred depth, the charred depth is roughly proportional to heating duration. In case of 120min of heating, charred depth was 73mm for no cooling, 82mm for 180 minutes of cooling. The effect of cooling period is not negligible also for charring depth.



Figure 19 An example of cut section of specimen after test (120+180)

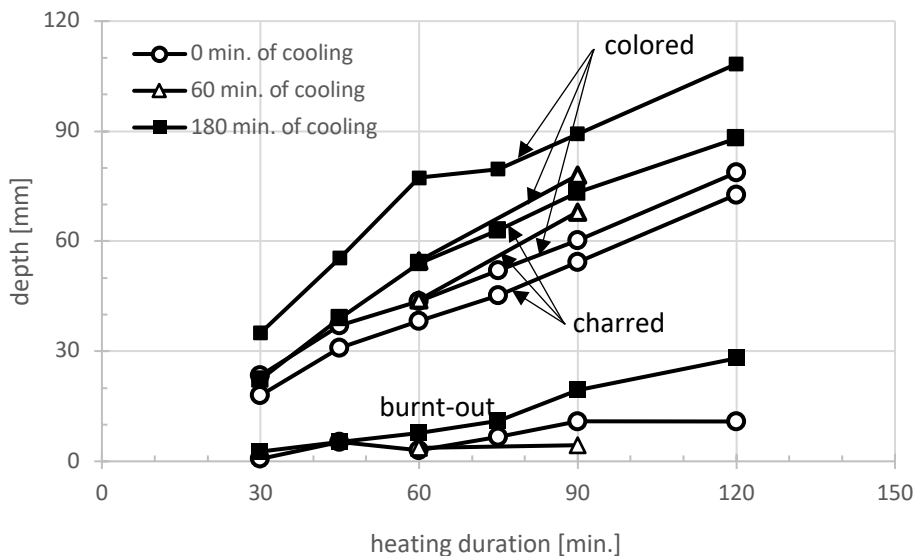


Figure 20 Burnt-out/ charred/coloured/ depths as functions of heating duration

4.4 Correlation of fallout properties with char layer thickness

It is convenient for analytical models to use an empirical relationship describing the char fallout characteristics. It is expected that part of char layer tends to fallout as the total char layer thickness is increased. To derive the relationship, fallout depth and fallout fractions were correlated with char layer

thickness (= charred depth – burnt-out depth) as shown in Figure 21. As expected, the fallout depth is increased linearly with char layer thickness. The dependence of cooling is minor on this correlation.

$$d_{fallout} = 0.114d_{char} + 13.1 \tag{1}$$

where

$d_{fallout}$ is the depth of fallout spot [mm],

d_{char} is the char layer thickness (= charred depth – burnt-out depth) [mm].

Similarly, the fallout fraction is correlated with char layer thickness as shown in Figure 22. Linear correlation was obtained against char layer thickness.

$$f_{fallout} = 0.00685d_{char} \tag{2}$$

where

$f_{fallout}$ is the fraction of fallout area [-].

Referring the figure 22, equation (2) is applicable in the range of $15\text{mm} < d_{char} < 65\text{mm}$. Even though, enough data is not available, it is guessed that the fraction of fallout will be drastically increased for char layer thickness greater than 65mm as shown by dashed line in Figure 22.

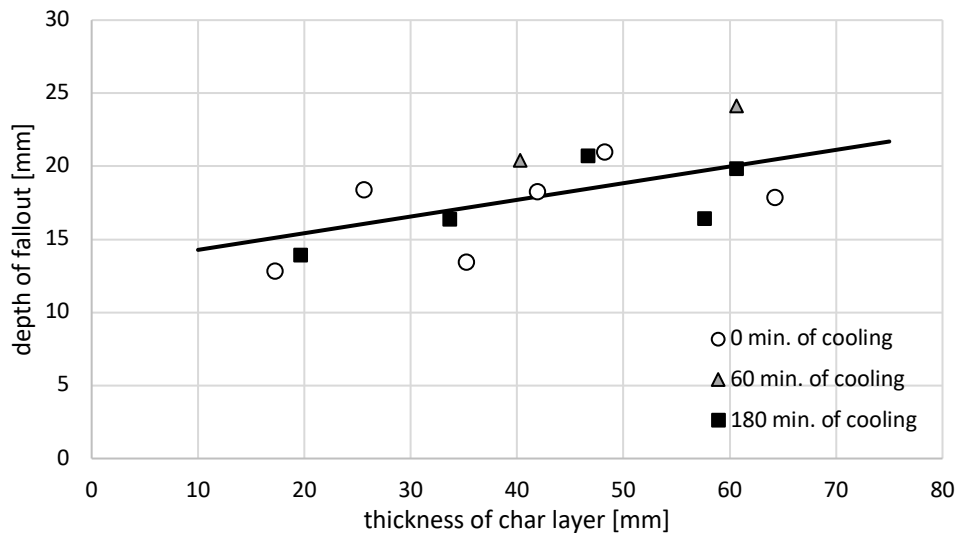


Figure 21 correlation of fallout depth with char layer thickness

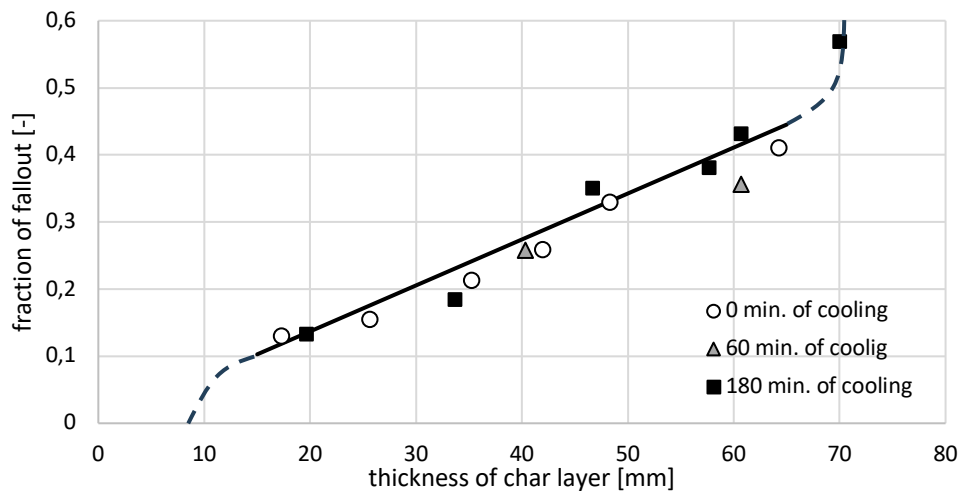


Figure 22 correlation of fallout fraction with char layer thickness

5 CONCLUSIONS

Fire resistance tests of glue laminated timber walls of larch were carried out varying heating and cooling durations. The degrees of crack and fallout of char layer were measured by laser displacement meter. As the heating time is increased, fallout fraction and width were increased. The number of fallout spots did not change drastically, but the depth of fallout spot was slightly increased with time. Fallout of char layer is significant during heating period, but fallout continues during cooling period as well. By summarizing the data, empirical formulae for depth and fallout fraction were developed.

ACKNOWLEDGMENT

This work was supported by JSPS (Japan Society for the Promotion of Science) KAKENHI Grant Number 21H01490. The experiments were carried out at General Building Research Corporation of Japan. Technical support by the corresponding staff is greatly appreciated.

REFERENCES

1. Brandon, D., Hopkin, D., Emberley, R., Wade, C., Timber Structures, International Handbook of Structural Fire Engineering, Chapter 8, Society of Fire Protection Engineering, Springer, 2021
2. EN 1995-1-2:2004, Eurocode 5 – Design of timber structures, Part 1-2: General; - Structural fire design, 2004
3. Parker, W. J.: Prediction of the Heat Release Rate from Basic Measurements, Heat Release in Fires, pp. 333-355, Elsevier Applied Science, 1992
4. Harada, K., A calculation method of temperature profile of a timber structural element during whole process of fire, International Workshop on Advances in Fire Engineering 2018, 6-7 December 2018, Huaqiao University
5. Pečenko, R., Hozjan, T., Huč, S., Modelling charring of timber exposed to natural fire, Journal of Wood Science, 69:19, 2023, <https://doi.org/10.1186/s10086-023-02091-4>
6. Sun, A., Harada, K., Nii, D., Numerical model for simulating heat and mass transfer process of wood under fire heating, summaries of technical papers, Annual meeting of Architectural Institute of Japan (AIJ), fire safety, pp. 309-301, 2023 (in Japanese)
7. Bøe, A., Mager, K., Friquin, K., Just A., Experimental Study of the Charring of I-Joists and Recession of Combustible Insulation in Light Timber Frame Assemblies with Comparison to Eurocode 5, Fire Technology, 59, 3283–3325, 2023
8. Harada, K., Sun, A., Makino, S., Nii, D., Experiments on burning and dropping of char layer of timber walls heated by ISO 834 and cooled down, part 1-3, Annual meeting of Japan Association for Fire Science and Engineering, pp. 129-134, 2023 (in Japanese)
9. *ibid.*, part 4-6, to be published in May, 2024 (in Japanese)
10. Sun, A., Harada, K., Nii, D. Experimental Research on Moisture Transfer, Burning and Charring Behavior of Glue Laminated Larch Under Fire Heating Using Cone Calorimeter. Fire Technology (2024). <https://doi-org.kyoto-u.idm.oclc.org/10.1007/s10694-024-01545-5>

APPLICATION OF THE EUROPEAN CHARRING MODEL TO CROSS LAMINATED TIMBER IN PARAMETRIC FIRE

Alanen Mika¹, Malaska Mikko², Pajunen Sami³

ABSTRACT

The Eurocode sets out a method for determining the charring rate and depth of solid wood in parametric fire exposure [1]. Cross laminated timber (CLT) is an engineered wood product made of lumber boards glued together in perpendicular layers. Many manufactures use polyurethane-based adhesives (PUR), making it possible for the adhesive to lose its stickability during the fire, leading to fall-off and delamination of the charring layers. After the protecting char layer falls off, the charring rate increases. The current Eurocode approach to determining the design charring depth does not consider char fall-off, and it can only be applied to solid wood and engineered wood where bond line integrity is maintained. The new generation of Eurocode EN 1995-1-2 will include this, but only for CLT members exposed to the standard ISO834 fire [2, 3]. The development of a new method for parametric fire exposure requires experimental research and results. This article presents the implementation and results of eight fire tests to determine the charring of CLT structures exposed to parametric fire. The study also examines how the test results differ from those of the current Eurocode model and evaluates how the Eurocode model should be developed so that it would also work for CLT structures when the bond line integrity is not maintained.

Keywords: Cross laminated timber; CLT; charring; parametric fire; European charring model

1 INTRODUCTION

In many countries, compliance with essential technical fire safety requirements can be demonstrated by using either prescriptive requirements or design fire scenarios. Prescriptive requirements generally provide load-bearing and integrity requirements based on building height and size, the material of load bearing structures, building use, and occupation. For example, in Finland, prescriptive requirements for a wooden multi-storey apartment building, less than 28 meters in height, stipulate that the load-bearing capacity must sustain 60 minutes of standard fire (R60). Additionally, most internal surfaces need to be covered with a class K₂30 protective surface made from A2-class products. Buildings in Finland can also be designed based on the performance-based design approach. When this approach is applied, the load-bearing structures must be able to withstand the entire design fire, including the cooling phase [4]. When using the effective cross-section method for the structural fire design of load-bearing timber structures, information on the charring performance and charring depth is required.

The parametric fire model represents a compartment fire scenario, including the post-flashover and cooling phases. Standard EN 1991-1-2 [5, Annex A] gives formulae to calculate parametric fire scenario, which

¹ Doctoral researcher, M.Sc, Metal and Lightweight Structures, Tampere University, Korkeakoulunkatu 5, 33720 Tampere, Finland
e-mail: mika.alanen@tuni.fi, ORCID: <https://orcid.org/0000-0001-7215-4138>

² Prof. D.Sc, Metal and Lightweight Structures, Tampere University, Korkeakoulunkatu 5, 33720 Tampere, Finland
e-mail: mikko.malaska@tuni.fi, ORCID: <https://orcid.org/0000-0002-8215-9765>

³ Prof. D.Sc, Metal and Lightweight Structures, Tampere University, Korkeakoulunkatu 5, 33720 Tampere, Finland
e-mail: sami.pajunen@tuni.fi, ORCID: <https://orcid.org/0000-0003-2498-8749>

has been the most popular parametric approximation since its release [6]. Recently, this scenario has been compared to measurements from compartment fire tests [7,8]. The obtained results indicate that the calculated temperatures during the heating phase of parametric fire scenario [5] can differ from compartment fire temperatures by up to 200 °C, and also that the linear descending cooling phase is too fast [7]. Zehfuss and Hosser [9] presented an alternative fire curve (iBMB) that has since been added into the German National Annex of EN 1992-1-2 [8]. McNamee et al. [7] and Rackauskaite et al. [8] compared the compartment fire test results also against iBMB, and it gave reasonable predictions for temperatures when the CLT in the compartment was considered in the fire load. Still, this method overpredicted the fully developed phase in ventilation controlled fires and thus, further research was recommended.

Solid timber charring in standard fire can be considered constant [1,10]. Many wood properties affect this nominal charring rate value, like species, density, and moisture content. Charring rate also depends on compartment fire dynamics. Parametric fire curves demonstrate these conditions and include a cooling phase where charring rate decreases until it stops. In EN 1995-1-2 [1] parametric scenario, charring rate for solid timber depends on time factor (Γ) and begins to decrease linearly at a time depending on the fire load and opening factor. Unintuitively, this charring rate decrease begins before then maximum temperature is reached.

CLT-panels behaviour in fire differs from solid wood when the bond line integrity of face bonds is not maintained during the fire exposure. If the char layer falls off, the charring rate in the following layer increases, until a new char layer is formed. This needs to be taken account similar way as the falling of fire protection [11]. The European Charring Model (ECM) takes into account the char fall-off in standard fire by increasing charring rate when char depth reaches bond line [2]. In the ECM, after the following lamella is charred 25 mm, returns the charring rate to nominal value, due to the new protective char layer is formed. Falling off layers can also affect compartments fire dynamics. In the medium scale tests by Gorska [12] this falling off layers prevented auto-extinction. When one wall was unprotected in these tests and the first layer fell-off before the burnout of movable fire load, and even 17% unprotected wood was enough to maintain the fire. In order for self-extinguishing to be possible in CLT structures where the bond line integrity is not maintained, the area of visible and unprotected wood surfaces must be limited.

This paper presents the experimental study conducted to gather information on the temperature development and charring of CLT panel structures exposed to standard and parametric fire conditions. The study focused on initially unprotected CLT products, which do not maintain bond line integrity of face bonds in fire. The test series included four different fire scenarios and two panels composed of lamella layers of varying thicknesses. The experimental results have been utilised to investigate how the charring of structures exposed to standard fire and parametric fires differs. It was also studied whether it would be possible to determine the charring depth for the parametric fire by applying a method similar to the one outlined in EN 1995-1-2 [1] for solid timber, and by using the phased charring rates of ECM instead of the notional charring rate of solid wood.

2 EXPERIMENTAL FIRE TESTS

The charring of CLT panel products was studied by exposing the panels to different fire curves including the standard temperature-time curve of EN 1991-1-2 [5], parametric temperature-time curves according to Annex A of EN 1991-1-2 [5], and iBMB parametric curves from Zehfuss and Hosser [9]. In the calculation of the temperature-time curves, the mean thermal absorptivity (b) of the fire compartment was set to $606 \text{ J/m}^2\text{s}^{0.5}\text{K}$. Fire load and number of openings were varied in different scenarios to adjust the temperature and duration of fire.

The panels were fabricated as 10 m x 3.2 m CLT elements, from which the test specimens were then cut. The size of a specimen was 500 mm x 1600 mm (width x length). All specimens consisted of five lamella layers, and the outer lamella layers were parallel to the longer dimension of the test specimen. The width of a lamella was 115 mm. Panel surfaces were finished, and sanding had reduced the thickness of the outer lamellas by 1 mm. Measured gaps between the lamellae on the exposed face were less than 1 mm wide. The first layer of lamella to be exposed to fire was sawn across at a distance of 50 mm from the furnace

wall to allow the lamellae to fall-off freely. The saw cuts were filled with ceramic fibre paper. In total, eight specimens were tested in a horizontal position. The CLT panel configurations, temperature-time curves, and variables related to parametric fires are presented in Table 1.

Table 1. Geometrical details of the test specimens and main parameters of the temperature-time curves

Ref.	Lamella thicknesses [mm]	Fire curve	Time factor Γ [-]	Time of fire growth to 1 MW [s]	Opening factor O [$m^{1/2}$]	Maximum rate of heat release (vent. contr.) [MW]	Fire load density related to	
							Floor area $q_{f,d}$ [MJ/m^2]	Total surface area $q_{t,d}$ [MJ/m^2]
EN-20	20-20-20-20-20	EN 1363-1	-		-		-	-
P3-20	20-20-20-20-20	EN 1991-1-2	3		0.036		550	101
P7-20	20-20-20-20-20	EN 1991-1-2	7		0.055		550	101
i-20	20-20-20-20-20	iBMB		300	0.055	3.9	786	
EN-40	40-20-40-20-40	EN 1363-1	-		-		-	-
P2-40	40-20-40-20-40	EN 1991-1-2	2		0.03		550	101
P7-40	40-20-40-20-40	EN 1991-1-2	7		0.055		950	174
i-40	40-20-40-20-40	iBMB		300	0.055	3.9	786	

The panels were made of spruce (*Picea abies*) with a strength class of C24. The dry density of the panels was 420 kg/m^3 . The panels were glued with one-component polyurethane (PUR) adhesive. The adhesive was applied to the faces of the lamellae in their main bond line and without edge bonding. The moisture content of the specimens on the day of testing was 8.7–10.7 dry weight-%.

2.1 Test set-up

A test specimen was installed across the 1200 mm wide opening of the furnace chamber, which had internal dimensions of 3000 mm x 3000 mm x 1200 mm (height x width x depth). The long vertical side faces of the specimens were protected with mineral wool and timber board to limit the heat flow between the specimen and the surrounding furnace roof construction and the excessive charring near specimen corners, as shown in Figure 1. The tests were conducted in accordance with EN 1363-1 [13]. The brick walls of the furnace were covered with a 25 mm thick layer of ceramic insulation to allow better control of the furnace temperature during the heating and cooling phases. The standard fire tests were terminated, and the burners were shut off when temperature measurements at the second bond line exceeded $300 \text{ }^\circ\text{C}$. A crane located above the furnace chamber was used to lift the panels into a pool of water. Parametric fire tests were continued until the temperatures inside the specimens had stabilised.

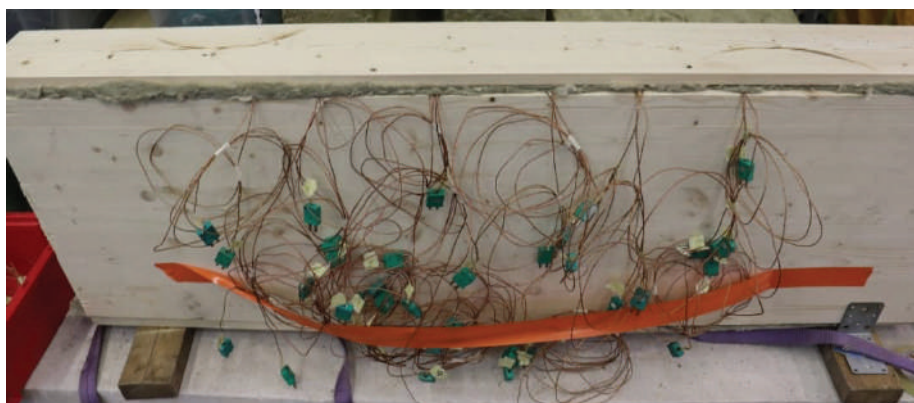


Figure 1. Overview of a test specimen showing the thermocouple wires drill-installed from the side face of the specimen and fire protection to limit heat flow and excessive charring near specimen corners.

During the tests, furnace temperature, specimen temperatures, oxygen content within the furnace, and the pressure differences between the furnace and test hall were monitored. The pressure difference was set to 20 Pa at the level 100 mm below the exposed face of the specimen. The oxygen concentration 300 mm below the furnace roof was measured using a Dräger EM200-E multi gas detector. The char fall-off of the lamellae layers was observed visually with a video camera.

2.2 Application of thermocouples

All thermocouple wires were placed parallel to the isotherms (horizontally), and they were installed in holes drilled into the side faces of the specimens. Holes were created using a pillar drill and a 4 mm diameter drill bit. Fibreglass-wrapped thermocouple wire (K-24-2-305) was then inserted into a hole using a 3 mm diameter wooden stick to ensure good contact between the thermocouple and the wood. The end of the stick was cut diagonally and the welded junction of the thermocouple was mounted on the bevelled surface, so that the thermocouple was wedged tightly against the CLT structure when the stick was pushed against the bottom of the hole, refer to the detail in Figure 2. In the first lamella layer, the drilling depth was 75 mm, while in all other layers, it was 100 mm. Schematic views of the test furnace, a specimen and the positioning of thermocouples are presented in Figure 2. The vertical spacing of the thermocouples was around 5 mm, and the consecutive thermocouples formed a measurement station. Two or three measurement stations were used in a specimen. During the preparation of the test series, the effect of drill diameter on installation accuracy was studied. Because the mounting accuracy of the thin drill bits was found to be too low due to their bending, a 4 mm diameter bit and a 100 mm drilling depth were chosen. The installation accuracy was checked after tests by cutting the specimens and measuring the hole locations visible in uncharred wood sections.

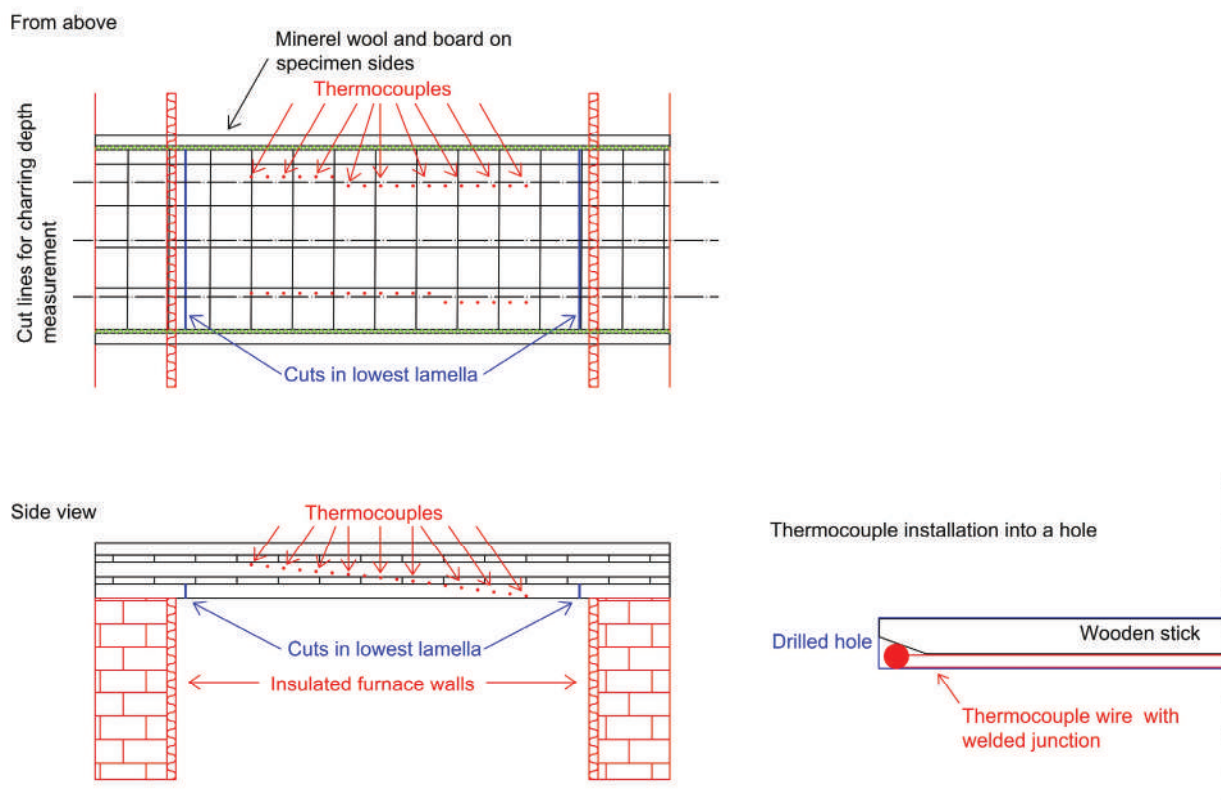


Figure 2. Schematic views of the test furnace, a specimen and positioning of thermocouples: (a) plan and (b) vertical side views of the specimen, and (c) a thermocouple installation into a hole.

2.3 Test results

Figure 3 shows the temperature-time curves used in the tests and the measured average furnace temperatures during the tests. In all tests, the temperatures followed reasonably well the calculated temperature-time curves. The cooling phase is more challenging to control because then the temperature has to be controlled by the using the burners and by opening the furnace roof elements. Although the furnace walls were lined with ceramic wool insulation, it was difficult to get the temperatures to fall below 400°C as quickly as the calculated curves would have required. A similar situation is also possible in real fires. Depending on the thermal characteristics and thermal inertia of the compartment enclosure and ventilation, the temperature of the fire compartment may remain higher than the calculated curve suggests.

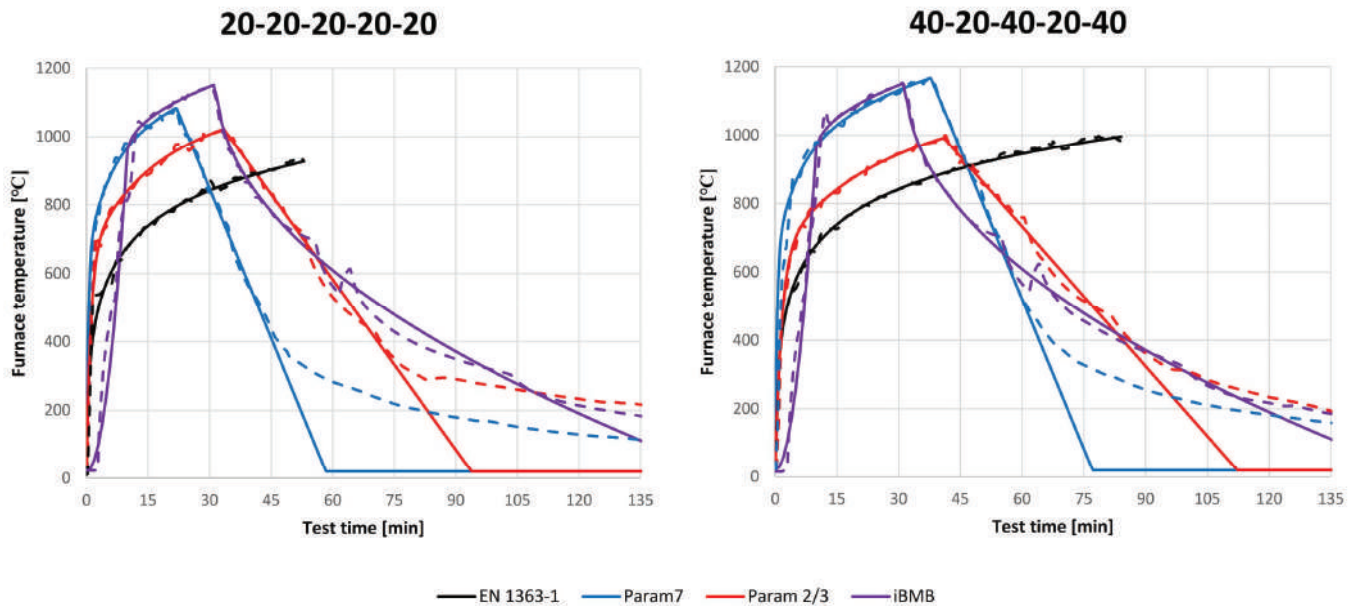


Figure 3. Solid lines present the target heating curves and dashed the measured average furnace temperatures.

The oxygen concentrations measured in the tests are presented in Figure 4. At the beginning of the standard fire tests, the oxygen concentration dropped quickly to around 8%. Within an hour, the concentration steadily decreases to about 6%. With faster heating curves, oxygen concentration inside the furnace decreased as the time factor increased. According to earlier experience, in standard fire curve tests using a furnace chamber without insulation on the walls, the oxygen concentration drops to around 6% at the beginning of test and continues to decrease during test. Adding insulation to the furnace walls probably reduced the required gas feed into the furnace, resulting in higher oxygen levels. Drops in oxygen concentrations are connected to char fall-off times. During the cooling phase, turning off some burners increased oxygen concentration in the furnace. A similar increase is noticed in compartment fire tests after the fuel load is burned and the temperature decreases [14,15]. In iBMB test, the oxygen content dropped to zero and the CO concentration exceeded the sensor's capacity, causing the sensor to stop measurement. The measurement was started several times again. At 30 minutes before the temperature begins to decrease, CO still exceeded sensor capacity. After the first burners were turned off, the measurement could be started again. For P2-40, the oxygen measurement isn't available before 17 minutes.

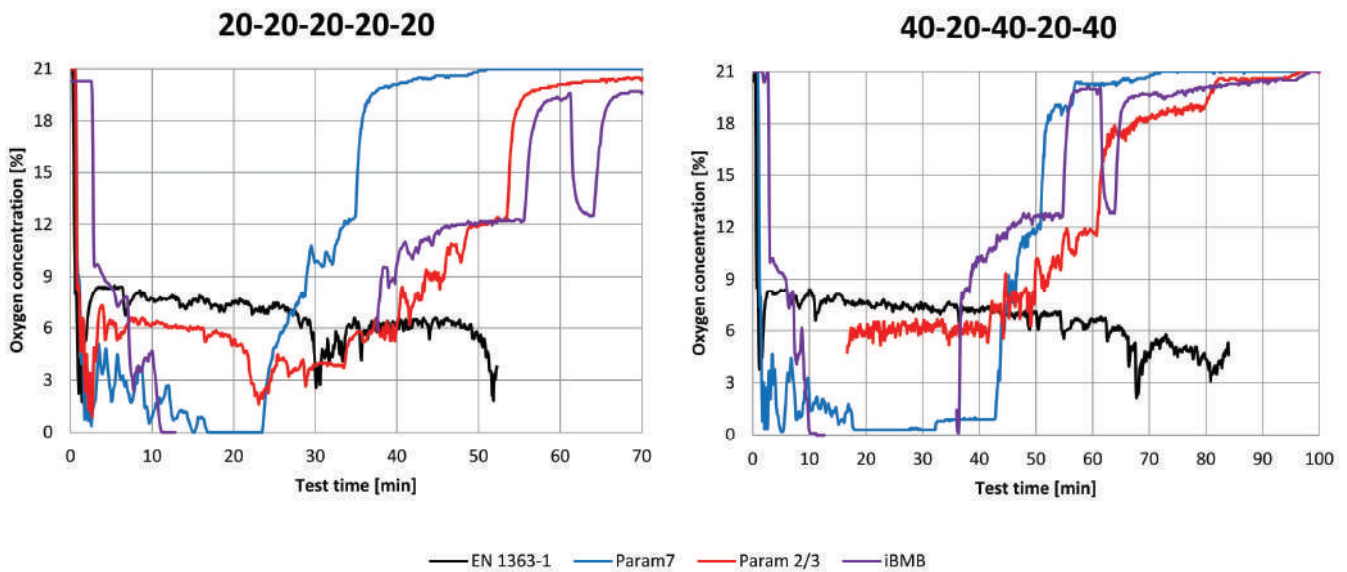


Figure 4. Oxygen concentration in furnace with different heating curves.

The char depths and charring rates were determined indirectly from the temperatures measured inside the specimens during the test. Char depth is assumed to correspond with a 300 °C temperature [1] and the charring rate is considered constant between measurement points. Measurement points are not in a single line orthogonal to the exposed surface. Sometimes temperature in deeper measurement point reached 300 °C before previous points. This could be due to uneven charring in the specimen, falling of a lamella or crooked drilling. In these cases, charring is considered to reach the deeper point and the previous point is disregarded.

The char depth development is presented in Figure 5. The greyed area represents the first layer fall-off close to measurements points. With 20 mm lamellas, both sides fall-off occurred almost the simultaneously. However, with 40 mm lamellas, different sides have differences in fall-off times. In the P7-40 test, the camera was damaged during the test, and lamella fall-off times weren't recorded. In the i-40 test, the first layer fall-off wasn't noticed over measurement points. Recorded layer fall-off times align well with the times when charring reaches the bond line. In some cases, layer fall-off occurs before charring reaches the bond line, and the temperature at an adjacent measurement point reaches 300 °C within a short interval. In the i-20 test, charring exceeded the last measurement depth. For other specimens, charring stopped between measurement depths.

The char depths at the end of the test were studied visually and measured with a calliper. The panels were cut into four parts using three cut lines presented in Figure 2. These cut lines were parallel to the span. The residual cross-section was measured at 17 points, 50 mm apart, on each cut line. The minimum, maximum, and mean values of the measured char depths are reported in Figure 5.

When the burners were turned off and oxygen content in the furnace increased, in the i-40 and P2-40 tests, specimen flaming and glowing continued locally. After the test, this was also clearly visible in the measured char depths. The char depth at the flaming locations was higher. The fall-off lamellae wasn't connected to this flaming. At the end of the test, after the temperature should have decreased below 400 °C, the furnace temperature remained higher than the chosen design curves. Based on temperature measurement, charring had stopped before furnace temperature deviated from the design curves. Therefore, the difference in furnace temperature didn't affect temperature based charring depth. The higher temperature at the end of the test could have caused greater charring depth in the measured cross-sections.

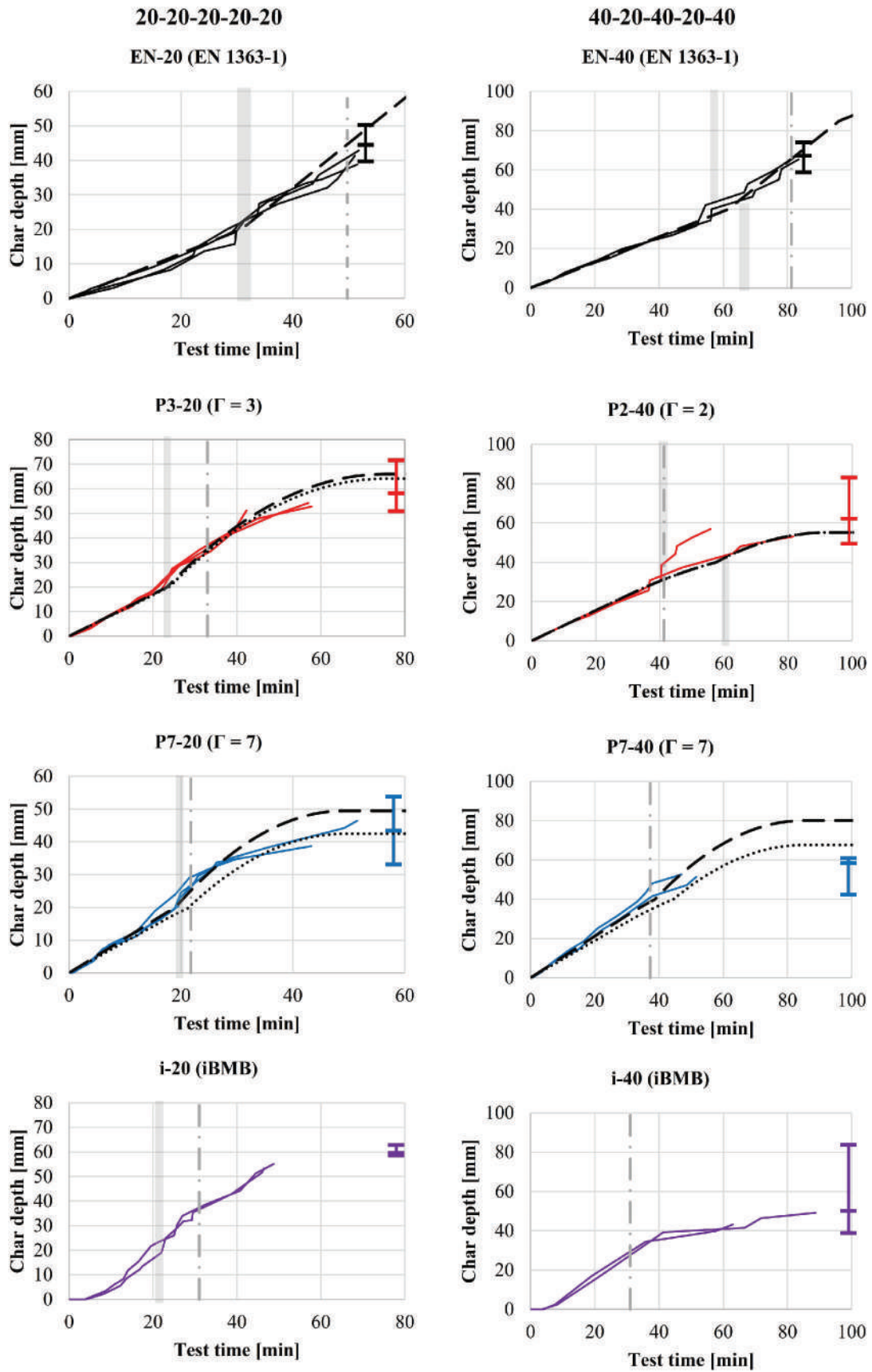


Figure 5. Temperature based charring depth are presented as solid lines. Dotted line is ECM based charring rate combined with current Eurocode parametric charring. Dashed line is ECM combined with proposed charring rate [16,17]. Time of furnace temperature decrease is marked at dash-dot line. Vertical lines with horizontal marks present measured mean char depth and range.

The thermocouples hole locations in the remaining cross-section were measured from the cut line and the specimen's edge. Total 67 uncharred holes were measured, and the standard deviation between edge and measurement depth was 0.93 mm. After the test, some char was found to be attached to thermocouple wires, but based on measured remaining cross-section in the middle of the specimen and the location close to thermocouples, there was no significant difference in char depths.

3 COMPARISON OF EXPERIMENTAL RESULTS WITH DESIGN MODELS

The experimental results were compared to charring depths and rates determined using the charring models of EN 1995-1-2 [1] and modified model by Brandon et al. [16] presented in design guide [17]. The model of EN 1995-1-2 [1] can be used to determine the charring depth and charring rate of initially unprotected solid timber members exposed to parametric temperature-time curves given in Annex A of EN 1991-1-2 [5]. In this research, the model was applied to determine the charring characteristics of the first lamella layers. According to EN 1995-1-2 [1], the charring rate during the heating phase of the parametric fire curve can be calculated from Equation 1. This equation has been proposed to be changed to Equation 2 format in the next Eurocode update [16,17]. Table 2 shows the charring rates calculated by the parameters in Table 1 and determined from the experimental test results.

$$\beta_{par_EC2004} = 1,5 \beta_n \frac{0,2\sqrt{\Gamma}-0,04}{0,16\sqrt{\Gamma}+0,08} \quad (1)$$

$$\beta_{par_Br} = \beta_n \Gamma^{0,25} \quad (2)$$

where

Γ is the time factor function,

β_n is the nominal charring rate.

Since the Eurocode methods do not consider the char fall-off, the charring rates calculated with them apply only to the first lamella layers of the panels. The experimental results for the first layer are calculated by dividing the time from ignition of the furnace to the time when the temperature on the first bond line exceeds 300 °C. In the EN-20, EN-40 and P2-40 tests, temperature rises quickly at two consecutive measurement depth close to the bond line. In these tests, charring is calculated using time and depth from a measurement point closer to the exposed surface. For the EN-20 and P2-40 tests, this quick charring can be connected to layer fall-off. In the EN-40 test, the fall-off occurred later, but it has been assumed that the layer has partly detached and caused a temperature increase in the bond line. The charring rate for the second layer is calculated up to the last measurement point where charring has reached before the furnace temperature begins to decrease. The second layer charring rate at stations where fall-off occurred before the char depth has reached the bond line is calculated using the start time and depth where the first layer calculation ended.

Table 2. Calculated and experimentally determined charring rates for first and second lamella layers [mm/min]

Specimen ref.	EN 1995-1-2 [1]	Modified Brandon et al. [16, 17]	Station 1		Station 2		Station 3	
			1 st layer	2 nd layer	1 st layer	2 nd layer	1 st layer	2 nd layer
EN-20	0.65	0.65	0.65	0.84	0.53*	1.03	0.66	1.06
P3-20	0.84	0.86	0.92	1.54	0.94	1.23	0.85	1.56
P7-20	0.95	1.06	1.04	-	1.03	-	1.23	1.66
EN-40	0.65	0.65	0.61*	1.25	0.61*	1.13		
P2-40	0.77	0.77	0.77*	-	0.83	-		
P7-40	0.95	1.06	1.10	-	1.17	-		

*First layer charring rate is determined up to the depth where there is a clear increase in rate, prior to char front reaching the bond line. The following layer rate calculation begins from the same depth.

Oxygen concentration was higher in performed tests when the time factor was smaller. Higher oxygen concentration can affect char contraction, thereby increase the charring rate. The limit of significant glowing combustion is between 10% - 15% [18]. Although, other studies have reported differing charring rates between 4% and 8-10% oxygen concentrations [19]. Neither of the used calculation methods consider the effect of oxygen concentration.

In Figure 5, the calculated charring rates are presented using the current method [1] and the proposed calculation method [16,17] as dotted line and dashed line, respectively. For smaller heating factors, charring rates are close to each other, but with higher time factor values, the new proposed method gives faster charring rates and follows test results more accurately, as can be seen in Table 2.

In the ECM, the charring rate is doubled when the bond line is reached and returns to nominal after 25 mm protective char layer is formed. In Figure 5, charring rates seem to increase when charring exceeds lamella interface. Charring rates in the second layer until the furnace begins cooling are presented in Table 2. A factor of 2 seems conservative compared to the results. It is only exceeded in the EN-40 test, where high charring rate includes first layer detachment before charring has reached the bond line. Locations where charring has exceeded the bond line by a few millimetres are left out because possible thermocouple installation error could have a significant effect on these results.

The ECM can predict charring depth in standard fire. When the ECM is combined with parametric charring rate, the result has some similarities with test data, but the final charring depth cannot be accurately predicted. Test with higher time factors give a smaller final charring depth than the calculation. The charring rate seems to decrease faster than formulas predict. Data were analysed, and the furnace temperature where charring stopped varied greatly, from 240 °C to 720 °C. The measurement point installation interval wasn't dense enough to determine this more accurately. Additionally, the remaining char layer will affect this temperature. Even with small specimens, burning and charring continued locally during the cooling phase. Normally, structures have corners or other installation that can increase the risk of local burning.

According to Eurocode charring begins to decrease when most of the fire load is burned at a time t_0 and stops at time $3 \times t_0$. The reason why charring would decrease before the temperature decreases isn't clear. This reduced charring rate is not visible in test results, as expected. If the formula assumes that the heat release rate decreases when fuel load is low, and this decrease is assumed to affect the temperature, it hasn't been added to the fire curve temperature formula. In the furnace, the temperature is controlled with burners, and low fire load doesn't decrease the heat release rate or temperature, and therefore it doesn't influence the charring rate.

For the iBMB heating curve, there is no determined charring rates to use in this analysis. The temperature in the iBMB curve increases slowly at the beginning, and there's some delay before charring begins. This slowly beginning is difficult to carry out in a furnace. The cooling phase in iBMB is slower, and the furnace seemed to follow this curve quite well, until differences between the calculated curve and furnace occurred around 200 °C.

Timber structures cannot be designed solely based on charring depth, but the weakened layer also need to be taken into account. After charring has stopped, temperatures deeper within the panel continue to increase. This paper hasn't analysed how temperature fields below 300 °C progress during the cooling phase.

CONCLUSIONS

Eight fire tests were conducted to investigate the temperature development and charring of CLT panel structures exposed to standard and parametric fire conditions. The study focused on initially unprotected CLT products, which do not maintain bond line integrity of face bonds in fire. Based on the findings of this study:

- The sequenced charring phases of the ECM in standard fire conditions align well with the experimental results of this study. This is clearly demonstrated in the results of the specimens EN-20 and EN-40 in Figure 5.
- The equations of EN 1995-1-2 [1] (Equation 1) and the one proposed by Brandon et al. [16,17] (Equation 2) can be used to calculate the charring rates of solid timber exposed to parametric fire conditions. These formulae can also be applied to determine the charring characteristics of the first lamella layer in CLT. The method by Brandon et al. yields more accurate results than the current Eurocode formula provided in EN 1995-1-2 [1].
- In a CLT structure exposed to parametric fire conditions, the charring rate of a lamella layer behind the bond line increases, as in standard fire conditions (refer to the experimentally determined charring rates for the first and second layers in Table 2).
- When the phased ECM and the parametric charring rate equations of Brandon et al. are combined, the calculated charring depths in most cases yield higher charring depth values than measured in the tests. In the test results, the charring rates tend to decrease faster than expected by the equation, see Figure 5.
- Thermocouple installation into holes drilled on the side face of the specimen introduces measurement depth uncertainty. The standard deviation for the installation depth using a pillar drill was 0.93 mm, considering 100 mm long holes and 4 mm diameter drill bit.

REFERENCES

1. EN 1995-1-2:2004 + AC:2009, Eurocode 5. Design of Timber Structures. Part 1-2: General. Structural Fire Design. CEN European Committee for Standardization, Brussels (2004)
2. Just, A., Abu, A., Barber, D., Dagenais, C., Klippel, M. and Milner, M. "Load-bearing Timber Structures," In Fire Safe Use of Wood in Buildings. Global Design Guide, A. Buchanan and B. Östman, Eds. Boca Raton: CRC Press, pp. 227-276. (2022). <https://dx.doi.org/10.1201/9781003190318-7>.
3. ISO 834-1. Fire Resistance Tests – Elements of Building Construction. International Organization for Standardization. Geneva. Switzerland. (1999).
4. Ministry of the Environment, 848/2017 Ympäristöministeriö asetus rakennusten paloturvallisuudesta. Helsinki, Finland. (2017).
5. EN 1991-1-2:2002 + AC:2013, Eurocode 1: Actions on Structures. Part 1-2 : General Actions. Actions on Structures Exposed to Fire. CEN European Committee for Standardization, Brussels. (2002).
6. Lucherini, A., Coile, R.V. & Merci, B., Background and Limitations of the Eurocode Parametric Fire Curves, Including the Fire Decay Phase. Applications of Structural Fire Engineering, 10-11 June 2021, Ljubljana, Slovenia. (2021).
7. McNamee, R, Zehfuss, J, Bartlett, AI, Heidari, M, Robert, F & Bisby, LA. Enclosure Fire Dynamics with a Cross-laminated Timber Ceiling. Fire and Materials. 45, 847–857 (2021). <https://doi.org/10.1002/fam.2904>.
8. Rackauskaite, E., Kotsovinos, P. & Barber, D., Letter to the Editor: Design Fires for Open-Plan Buildings with Exposed Mass-Timber Ceiling. Fire Technol 57, 487–495. (2021). <https://doi.org/10.1007/s10694-020-01047-0>.

9. Zehfuss, J. & Hosser, D., A Parametric Natural Fire Model for the Structural Fire Design of Multi-storey Buildings. *Fire Safety Journal* 42, 115–126 (2007). <https://doi.org/10.1016/j.firesaf.2006.08.004>
10. Frangi, A. & Fontana, M., Charring Rates and Temperature Profiles of Wood Sections. *Fire Mater* 27, 91–102 (2003). <https://doi.org/10.1002/fam.819>.
11. Frangi, A., Fontana, M., Knobloch, M. & Bochicchio, G., Fire Behaviour of Cross-laminated Solid Timber Panels. *Fire Safety Science*. 9, 1279–1290. (2008) <https://doi.org/10.3801/IAFSS.FSS.9-1279>.
12. Gorska, C., Fire Dynamics in Multi-scale Timber Compartments (PhD Thesis). The University of Queensland. (2020). <https://doi.org/10.14264/uql.2020.795>.
13. EN 1363-1, Fire Resistance Tests – Part 1: General Requirements. CEN European Committee for Standardization, Brussels. (2020).
14. Su, J., Lafrance, P.-S., Hoehler, M. & Bundy, M., Fire Safety Challenges of Tall Wood Buildings – Phase 2: Task 2&3 – Cross Laminated Timber Compartment Fire Tests. National Research Council of Canada. FPRF-2018-01-REV. (2018).
15. Épernon Fire Tests Programme. Synthesis report. Report no EFTP-2020/01. (2020). www.epernon-fire-tests.eu.
16. Brandon, D., Just, A., Lange, D. & Tiso, M., Parametric fire design – zero-strength layers and charring rates. Presented at the INTER International Network on Timber Engineering Research Proceedings. August 2017, Kyoto, Japan. ISSN 2199-9740. (2017).
17. Wade, C., Dagenais, C., Klippel, M., Mikkola, E. & Wertner, N., “Fire Dynamics” In *Fire Safe Use of Wood in Buildings. Global Design Guide*, A. Buchanan and B. Östman, Eds. Boca Raton: CRC Press, pp. 63-115. (2022). <https://dx.doi.org/10.1201/9781003190318-3>.
18. Schmid, J., Santomaso, A., Brandon, D., Wickström, U. & Frangi, A., Timber under real fire conditions – the influence of oxygen content and gas velocity on the charring behavior. *Journal of Structural Fire Engineering* 9, 222–236. (2018). <https://doi.org/10.1108/JSFE-01-2017-0013>.
19. Babrauskas, V., Charring rate of wood as a tool for fire investigations. *Fire Safety Journal* 40, 528–554. (2005). <https://doi.org/10.1016/j.firesaf.2005.05.006>.

BURNING BEHAVIOUR OF A TIMBER CEILING: A BENCH-SCALE INVESTIGATION

Joshua Madden¹, Mabelle Kriel², Felix Wiesner³, Wenxuan Wu⁴, Ryan Hilditch⁵, Adam Ervine⁶,
David Lange⁷

ABSTRACT

Recent large-scale open-plan testing has highlighted the rapid change in fire dynamics within the compartment following the ignition of an exposed timber ceiling. There is no standard approach, nor is there any significant research that has been undertaken to understand what impact inverting an exposed surface to a ceiling orientation has on the time to ignition and charring rates. Utilising the Fire Propagation Apparatus (FPA), a novel methodology is implemented to research these phenomena at bench-scale for an inverted orientation. When comparing the piloted ignition study for a normal orientation to that of an inverted (i.e. ceiling) orientation, inverting the sample is found to have a noticeable impact on the time to ignition of the Cross-Laminated Timber (CLT) specimens, with no clear impact on the critical heat flux of ignition, nor on the charring rates. The findings have implications for a building's fire safety strategy that must be considered.

Keywords: Ignition; Charring Rates; CLT; Ceiling

1 INTRODUCTION AND MOTIVATION

The fire dynamics inside a compartment constructed using mass timber will be significantly different compared with those observed in a non-combustible structure compartment because the additional fuel load from the timber structure alters the fire dynamics [1, 2]. The consequences of this have the potential to overcome the buildings' fire safety strategy whereby the hazards such as increased fuel loads will likely impact the burnout duration, increase the potential for internal and external fire spread, ultimately increasing thermal exposure to the structure and affecting its ability to maintain structural stability [3, 4]. The requirement for the structure to maintain structural adequacy post-burnout is fundamental to most fire safety strategies [5, 6] and as such, this must be understood to design these buildings to ensure that relevant performance requirements are met.

¹PhD Student, The University of Queensland, Brisbane, Australia
e-mail: joshua.madden@uq.net.au, ORCID: <https://orcid.org/0009-0001-2150-4553>

²Mabelle Kriel, The University of Queensland, Brisbane, Australia
e-mail: m.kriel@uq.net.au

³Assistant Professor, The University of British Columbia, Vancouver, Canada
e-mail: felix.wiesner@ubc.ca, ORCID: <https://orcid.org/0000-0002-0231-4244>

⁴PhD Candidate, The University of Queensland, Brisbane, Australia
e-mail: wenxuan.wu@uq.net.au, ORCID: <https://orcid.org/0000-0002-5692-6051>

⁵Director of Fire Safety (Australia), Hydrock Pty Ltd.
e-mail: ryanhilditch@hydrock.com.

⁶Director, Bloom Fire Consulting
e-mail: adam.ervine@bloomfireconsulting.com.

⁷Associate Professor, The University of Queensland, Brisbane, Australia
e-mail: d.lange@uq.edu.au, ORCID: <https://orcid.org/0000-0002-4551-1045>

Mitchell et. al. [7] in their review paper of experimental mass timber compartment tests identified a wide range of charring rates of between 0.4-3.5 mm/minute, including reported rates of 2.25 mm/min for a ceiling. Butler [8] in the 1970's investigated the charring rates on slabs of wood in an oxygenated environment exposed to an incident black-body radiant heat flux of 200 kW/m² (i.e. representing a typical compartment temperature of the order of ~1100°C). Charring rates in the order of 4.4 mm/minute were calculated from this work, showcasing a significant disparity to those observed under exposure to a standard fire in fire resistance tests.

The decay and cooling impacts of fire on a timber structure should also be accounted for as part of the design due to the delay in the propagation of the thermal wave resulting in a further decrease in load-bearing capacity even after the fire associated with both the moveable fuel load and structure has burnt out [9, 10]. This has been shown experimentally for timber columns subjected to standard fire exposure by Gernay [11]. It was found by Gernay that the duration of heating that a timber column could be subjected to without failing was significantly less than that derived from standard fire-exposure when post-fire cooling was considered due to delayed heating and loss in mechanical properties at low temperatures.

The necessity to holistically design engineered timber structures for fire taking into account all stages of the fire from ignition to burnout, through to post-cooling could not be clearer, as highlighted by many authors [2, 12-16]. Wiesner et al. [17] concluded further that the compartment fire dynamics and the coupled thermal and structural response must be considered as part of a holistic design, and that the existing conventional fire resistance framework "*hinders the application of structural fire safety engineering as part of a holistic fire safety design approach*".

At a range of scales, numerous authors [18-23] have observed that following the ignition of a combustible ceiling, a rapid change in the compartment fire dynamics has occurred often resulting in a rapid transition to flashover. This has the potential to impact all stages of the fire safety strategy, whereby if this occurred during the evacuation, tenable conditions within the compartment would be compromised. Subsequently, this also has a significant impact on the structural design of the building. If the structure is exposed to more onerous conditions than designed for (i.e. standard fire exposure) then this could impact upon both fire brigade intervention and also the structural stability under the increased burning rates. As such, understanding the ignition and burning behaviour of a combustible surface such as Cross Laminated Timber (CLT) in an inverted orientation is important for the performance-based design of mass timber buildings.

An abundance of research surrounding the ignition of wood has been undertaken at a range of scales, with both with horizontal and vertical orientations as described by Babrauskas [24] in their review of the ignition of wood. It appears that the only investigation into the ignition of timber in a ceiling orientation was done by Shields et. al. [25], who found that times to ignition were 2-3 times greater for piloted ignition, and 5-13 times greater for non-piloted ignition when compared to a horizontal surface.

Nothard et. al. [19] undertook a mid-scale study to investigate the fire dynamics in an open-plan compartment. In this study which compared a non-combustible ceiling to that of a combustible ceiling, and evaluated the impact of down stands, the residence time (i.e. the time that fuel vapours will remain in the reaction zone) was hypothesised to impact the time to ignition. In the absence of ceiling obstructions, high momentum-driven flows due to the ceiling jet from the movable fuel load reduced the residence time, delaying the time for a combustible mixture to be formed and the subsequent ignition of the ceiling to occur. In this instance, there was a delay of several minutes between the heat flux to the ceiling from the fire involving the movable fuel exceeding the critical heat flux for piloted ignition of timber, and the time at which ignition of the ceiling occurred. A similar phenomenon was observed by Bøe et. al. [22] who observed delayed sustained ignition of the ceiling.

Given the significant role of ceiling ignition on the fire dynamics inside an engineered timber compartment, this scarcity of research on the understanding of how the orientation impacts the ignition and burning behaviour of a timber ceiling has led us to develop a bench-scale methodology to test and investigate the ignition and burning behaviour of a timber surface at an inverted surface (i.e. ceiling orientation).

2 METHODOLOGY

2.1 Background Theory

Flaming combustion of a fuel is complex, however can be simplified into a discussion around two processes: pyrolysis and oxidation [26]. Pyrolysis is a process that occurs to organic materials such as timber. When heated, timber will chemically decompose, releasing flammable volatiles and leaving a solid carbon-rich porous material referred to as char [27]. Factors such as the fuel, heating rate and intensity, all impact this highly complex and irreversible process [28].

Oxidation can occur in the gas or solid phase. Oxidation of pyrolysis gases generally results in flaming combustion (whereas oxidation in the solid phase will generally result in smouldering combustion - as this is not the primary focus, of this study, smouldering combustion will not be explored further and reference to ignition will be in the context of flaming combustion) [26].

With respect to flaming combustion, to ignite a solid such as timber, when heated, a sufficient concentration of pyrolysates must be released and mixed with a sufficient concentration of an oxidizer, typically air, to create a flammable fuel/oxidiser mixture. There is a strong positive correlation between temperature and production rates of pyrolysis gases [28]. This mixture must also be at a sufficient temperature to enable auto-ignition, or piloted ignition, and must be supplied at a sufficient rate to enable sustained flaming combustion to occur as a result of feedback of heat from the combustion process to further contribute to the decomposition and volatilisation of the solid [29].

The charred timber insulates the virgin timber behind the char front and as such, higher temperatures are required at the surface to enable a sufficient flow of volatiles to support sustained flaming combustion [27]. Fernandez-Pello [30] is understood by the authors of this paper to be one of the first to describe the concept of ‘ignition delay time’, which is the summation of the pyrolysis time and gas induction time. This was improved [31] and is given in equation (1):

$$t_{ig} = t_p + t_m + t_i \quad (1)$$

where

t_{ig} is the time to reach ignition or ignition delay time (s),

t_p is the to reach pyrolysis (s),

t_m is the being the time to create a flammable mixture (s),

t_i is the time to reach a sustained ignition (s).

Refer to Quintiere [32] for a detailed description of ignition delay time.

The SFPE handbook [28] further details general ignition theory beyond that detailed above, such that when the induction time, t_i , and the mixing time, t_m , are small, ignition is considered to occur when pyrolysis occurs and these are discounted. Long et al. [31] details that a change in the convective flow, such as inverting the surface, the mixing time, t_m , must be considered. When a strong pilot is provided such as a spark or pre-mixed gas flame commonly used apparatuses to test ignition [33], in conjunction with ambient oxygen concentrations, the induction time, t_i , can be considered to be negligible [31], This ‘ignition delay time’ from equation (1) can now be simplified and given in equation (2):

$$t_{ig} = t_p + t_m \quad (2)$$

Piloted ignition is a simplification made to study the ignition phenomena as it simplifies both the gas phase and the external environment, as opposed to auto-ignition [28]. Testing by way of piloted ignition enables the assumption to be made that the pyrolysis time, t_p , (i.e. time for a solid to reach pyrolysis temperature) can be equated to t_{ig} the time to pyrolysis/ignition is obtained from equation (3) [32]:

$$t_p \approx t_{ig} = \frac{\pi}{4} k \rho c \frac{(T_{ig} - T_0)^2}{\dot{Q}_R''^2} \quad (3)$$

Where

- t_p is the time to reach pyrolysis (s),
 t_{ig} is the time to reach ignition or ignition delay time (s),
 k is the thermal conductivity (kW/m K),
 ρ is the density (kg/m³),
 c is the specific heat (J/kg K),
 T_{ig} is the ignition temperature (K)
 T_0 is the ambient temperature (K),
 \dot{Q}_R'' is the incident radiative heat flux (kW/m²).

Equation (3) is a simplification of the phenomena described above, and the approximation is consistent with the assumption that the induction and the mixing time are negligible. However numerous factors may impact the concentration of a sufficient mixture of volatiles, such as the orientation and other changes to the boundary conditions. The location of the surface undergoing pyrolysis also has a significant impact. Close to the surface, the fuel/oxidiser ratio will be above the upper flammability limit, and at a certain distance from the surface, will be below the lower flammability limit. This highlights the criticality of pilot location when testing such a phenomenon.

It is therefore postulated that a change in orientation of a combustible surface such as at a ceiling orientation, is likely to have a considerable impact on the time to create a flammable mixture, t_m . Subsequently, a novel method for measuring the ignition and burning behaviour of an inverted surface has been undertaken to investigate the phenomena governing the ignition of an inverted surface.

2.2 Experimental Setup

This study explores the burning behaviour, nominally the ignition and charring rates, of CLT at an inverted surface (i.e. the exposed surface facing downwards), compared to that of a normal surface (i.e. horizontally with the exposed surface facing up).

The Fire Propagation Apparatus (FPA) was chosen to undertake bench scale testing as modifications can be made to invert the sample enabling a quantitative comparative analysis on the impact of orientation on the ignition delay time.

Shorter wavelengths (i.e. <2 μm) are emitted from the lamps of the FPA compared to those seen in actual fires [33], and less radiation is absorbed by the wood under tungsten lamp radiation compared to that from the cone calorimeter or from flaming radiation lamps being reflected [34, 35]. This is a limitation of the chosen apparatus. However, the absorptivity of charred wood is higher than virgin wood [36, 37], such that this will likely only impact the initial heating of the wood, and not the post-ignition burning behaviour.

No modifications are made to the FPA for the normal orientation, as indicatively shown in *Figure 1a*. It is noted that the air distribution chamber and quartz tube were not used for this testing as the tests were at ambient oxygen concentrations. Furthermore, the quartz tubes were not used due to potential increases in the error margin due to its ability to filter wavelengths above 2 μm [35].

For the inverted orientation, testing was conducted nearly identically to that of the normal orientation. The tungsten lamps were reorientated such that a uniform heat flux distribution at the exposed inverted surface (further detailed in Section 2.2.5) was achieved. A new sample holder was manufactured to enable the sample to be inverted and heat flux mapping to be undertaken at this exposed surface level. The sample holder was supported by a steel channel section and threaded rods, connected to the supports of the FPA, as shown in *Figure 1b*. The use of load cells (S-Type Low Capacity – AWSL– 2kg) enabled mass-loss to be recorded over the duration of the testing period. Both the steel channel and threaded rods were insulated to minimise thermal impacts on the holder.

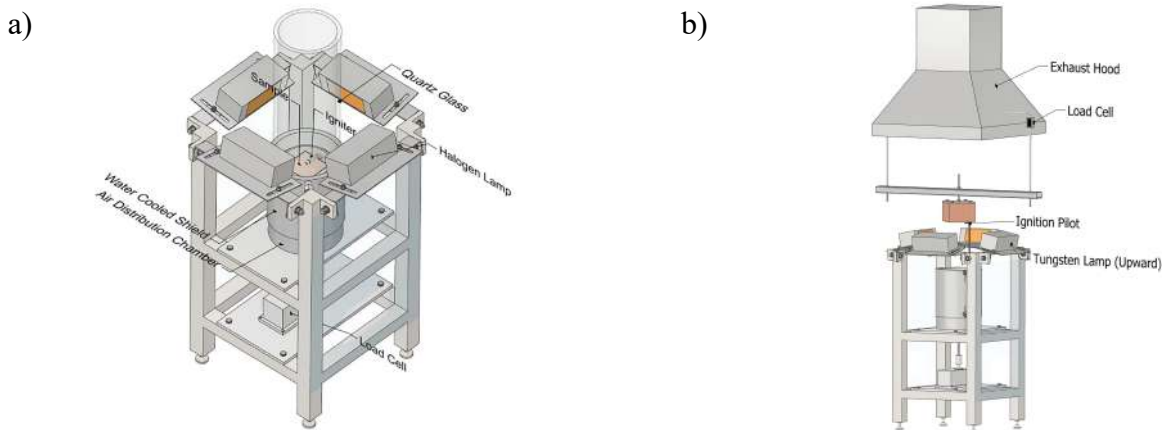


Figure 1. The Fire Propagation Apparatus (FPA)– a) Normal Orientation - The combustion chamber component of the FPA b) Modified Inverted Orientation –The combustion chamber component of the FPA and new sample holder

2.2.1 Sample Preparation

Three-ply commercially available CLT with a depth of 125 mm (45/35/45 mm) was chosen for this comparative experimental investigation. These samples were cut such that the exposed surface was 100 mm x 100 mm, with the depth remaining as 125 mm.

Prior to testing the CLT, which was all taken from the same slab to reduce the likelihood of material variability, samples were stored in a non-airconditioned naturally ventilated space for several months.

To enable charring rates to be calculated based on the 300°C isotherm [38, 39], stainless steel probe mineral insulated 1.5 mm diameter Type K thermocouples with a sheath of 150 mm were inserted into the sample. Based on the work by Pope et al. [40] to minimise thermal disturbance errors, 2 mm diameter holes were drilled by a CNC router parallel to the heated surface (parallel to the thermal wave) at distances of 3, 6, 10, 15, 12, 30, 42.5, 62.5, 77.5, and 102.5 mm from the heated surface, to a depth of 50 mm. The locations were chosen such that all thermocouples were located within the middle third of the sample, with at least 10 mm separation as also recommended by Pope et al. [40], with thermocouples primarily concentrated around the heated surface where temperature gradients are high during the initial stages of ignition and burning.

During the testing period, the moisture content of samples was tested twice weekly by the oven-drying method whereby the samples were placed in an oven set to $103 \pm 2^\circ\text{C}$. The geometry and mass of the samples were recorded prior to the test, with the mass weighed until there was no change. It was calculated that these specific samples had a moisture content of 10.81% (standard deviation 0.39%), with a density of 457 kg/m^3 (standard deviation of 22.65 kg/m^3). Samples with any visible defects within the first lamella of the CLT such as knots, cracks, splits, finger joints or edge joints were discounted from ignition testing to minimise variability between samples and keep conditions consistent between orientations.

Prior to testing, samples were wrapped with a 4 mm thick layer of Ceramic Paper ($\text{SiO}_2\text{Al}_2\text{O}_3$) and a reflective aluminium tape to minimise heating of the lateral surfaces [41]. In tests where thermocouples were inserted into samples, this was done after wrapping of the ceramic paper to minimise the likelihood of a cavity between the sample and the ceramic paper promoting pyrolysis and flaming ignition along the lateral face.

2.2.2 Testing Conditions

As the primary aim of this study was to analyse the ignition and charring rates of CLT samples at a normal and inverted orientation, the samples were exposed to a constant uniform heat flux for the duration of the test, to analyse the burning behaviour for the entire test duration or to observe if flaming self-extinction

occurred due to the increase in char layer thickness. Surface heat flux deviation conformed to the tolerances within ASTM E2058-13a [42].

A test duration of 2,700 seconds (~45 minutes) was calculated to be sufficient for sample testing such that the semi-infinite solid assumption for the sample could be retained [27].

A minimum of three repeatability tests were undertaken for each incident heat flux at both sample orientations. Samples were subjected to heat fluxes of 20, 30, 40, 50 and 60 kW/m² in both orientations, with the critical heat flux of ignition for each orientation obtained by bracketing heat fluxes in the vicinity of this value.

2.2.3 Procedures

The procedures detailed within ASTM E2058-13a [42] were generally followed for this experimental campaign. As per the requirements of this standard, for the normal orientation, a pilot flame was placed 10 mm above the exposed surface and 10 mm from the perimeter of the sample. For the inverted surface, the same occurred except the flame was located 10 mm below the exposed surface face. The flow of the pre-mixed ethylene/air fuel/oxidiser mixture was modified to achieve a 10 mm flame length such that pre-heating the sample via flame was minimised. The location of the pilot relative to the surface is very likely to have an impact on the ignition of an inverted surface, however, this was not investigated as part of this study.

Prior to testing, the halogen lamps were required to heat up for a period of two minutes for the voltage to stabilise. For the normal orientation, the water-cooled jacket (refer *Figure 1a*) protected the sample from being exposed to this incident heat flux for the period whilst heating up, whilst for the inverted surface, this could not be used so a 13 mm thick plasterboard covered in the aluminium tape was manually positioned between the lamps and the sample and removed at inception of the test.

Once the voltage had stabilised, the water-cooled jacket or the ad-hoc board were removed, exposing the sample to the set incident heat flux. The time to ignition is then recorded for the specimen once sustained flaming across most of the surface occurs for a period of four seconds. As per ASTM E2058-13a [42], if ignition did not occur within 900 seconds (i.e. 15 minutes) following initial exposure to the incident heat flux, the test was stopped.

At least three of the tests conducted to determine the time to ignition for each orientation contained in-depth thermocouples (located as defined in *Section 2.2.1*) to record the in-depth temperatures from the commencement of each test.

3 RESULTS

3.1 Ignition

Tests were carried out as per the conditions described in *Section 2.2.2* to determine the piloted ignition time for the CLT specimens. Three tests were conducted at each of 18 and 19 kW/m² to determine the critical heat flux for ignition for periods below 900 seconds. Results for these tests are presented in *Figure 2*, with the average time to ignition for each incident heat flux at each orientation provided within *Table 1*.

Table 1. Average Time to Piloted Ignition for Each Incident Heat Flux at a Normal and Ceiling Orientation (s)

Orientation	Incident Heat Flux (kW/m ²)				
	20	30	40	50	60
Normal	498 s	152 s	77 s	42 s	30 s
Ceiling	616 s	232 s	112 s	73 s	40 s
Average Time Difference	118 s	80 s	35 s	31 s	10 s
Percentage Difference (%)	~24	~53	~45	~73	~33

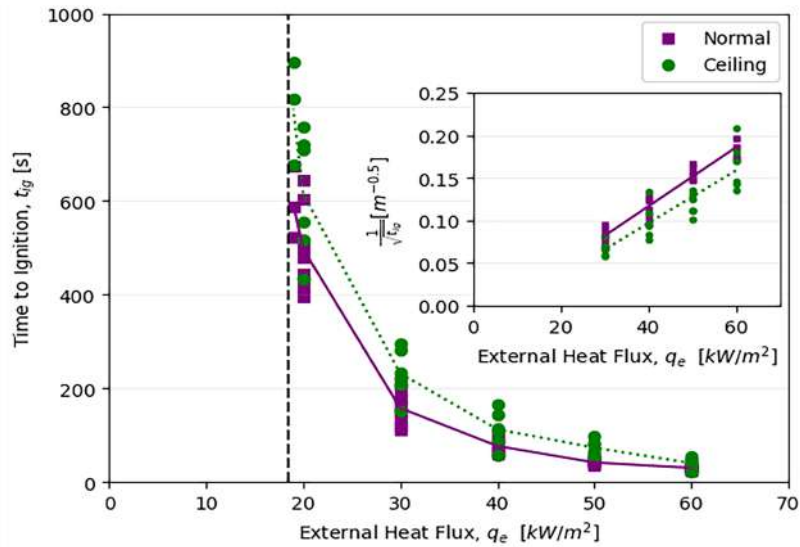
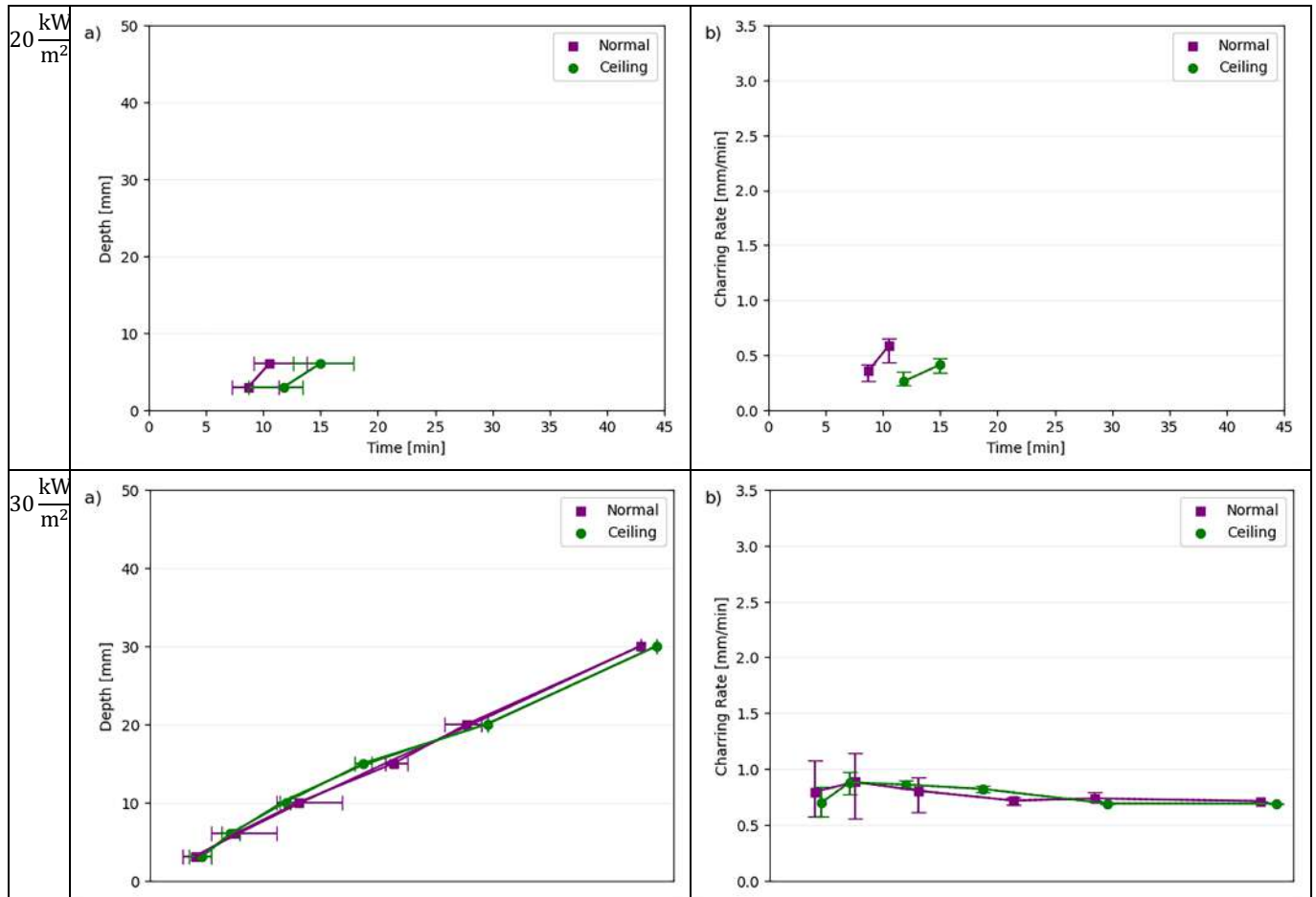


Figure 2. Time to piloted ignition for different incident heat fluxes on cross-laminated timber tested in the FPA in horizontal upwards (normal) or downwards orientation (ceiling). Note that for the inset figure, where ignition times are greater than 5 minutes (i.e. at or below 20 kW/m² for this data), these have been removed as non-linearities are found at low heat-fluxes with long ignition times [27]

3.2 Charring Rates

In-depth temperatures measured for the samples can be used to evaluate char front and subsequently charring rates based on the 300°C isotherm [38, 39]. These results are presented in *Figure 3* for heat fluxes of 20, 30, 40, 50 and 60 kW/m², respectively. Error bars on these plots represent a lower and upper bound of the recorded times to reach the 300°C isotherm at the varying depths, and a lower and upper bound of the calculated specimen charring rates.



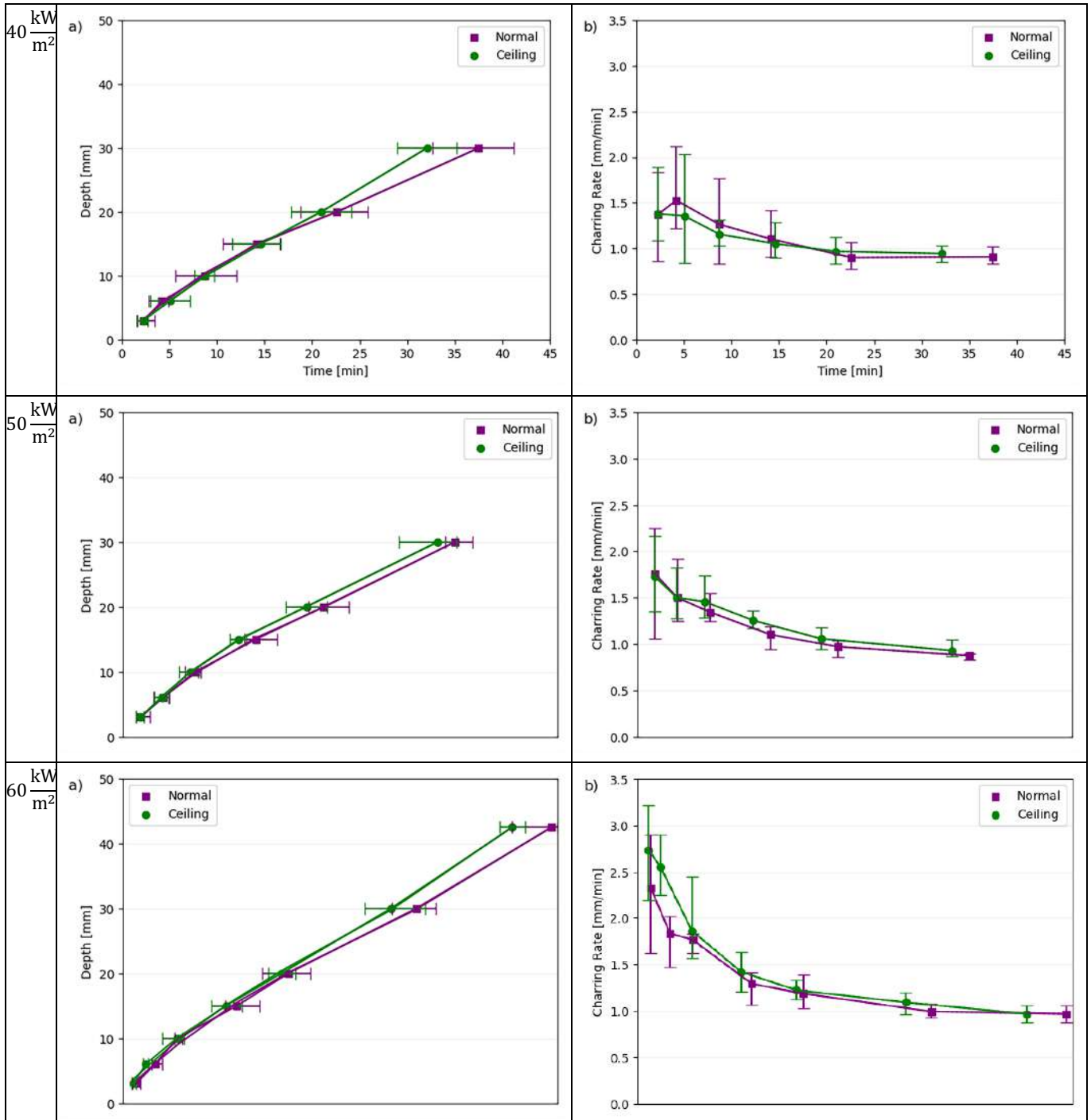


Figure 3. At Varying Heat Fluxes - a) Average Times to Reach 300°C Isotherm at Thermocouple Depths b) Average Charring Rates

4 DISCUSSION

4.1 Ignition

4.1.1 Critical Heat Flux of Ignition

Results illustrated in *Figure 2* show that both the normal and inverted heat fluxes had a critical heat flux of ignition of 18.5 kW/m². As a linear correlation between the density of wood and time to ignition as found by Wiesner et. al. [43], times to ignition of timber samples would be reasonably expected to be similar if tested in the same environment and with a similar density. The results for the normal orientation correlate well with data presented by Bartlett [44] for times to ignition below 900 seconds. This comparison is

reasonable as both studies used the FPA to determine the time to ignition, and despite different species, the densities of the samples are markedly similar (457 kg/m^3 in this study, and 447 kg/m^3 from Bartlett [44])

However, caution should be taken to this as this was calculated with a sample size of only three per heat flux (i.e. 18 or 19 kW/m^2), per orientation, with a maximum permitted time of 900 seconds. Further, it can be seen within *Figure 2* that as this apparent critical value is approached, there is a significant difference between the times to ignition of the inverted samples to that of the normal samples.

Samples of Sitka spruce (with a density similar to radiata pine used in this study) were measured by Shields et. al [25] in the normal orientation and showed a similar critical heat flux of ignition at 20 kW/m^2 . However, for the inverted orientation, in the study by Shields et. al [25], no samples were tested below 50 kW/m^2 due to significant variance in times to ignition at heat fluxes below this, hence no determination can be made on the basis of that work as to the impact of orientation on the critical heat flux of ignition.

Further work could be undertaken to calculate this critical heat flux for times greater than 900 seconds to determine the applicability of this finding.

4.1.2 Time to Ignition at Heat Fluxes Above the Critical Heat Flux for Ignition

For all incident heat fluxes investigated as part of this study, the time to ignition of a sample in an inverted orientation was generally greater than that of a normal sample, as shown in *Figure 2*.

On average, this increase in the time to ignition from the normal sample to the inverted sample ranged from a minimum 24% at an incident heat flux of 20 kW/m^2 to 73% at 50 kW/m^2 . However, the greatest percentage difference between ignition times is generally observed at lower heat fluxes. As shown in Table 1, no obvious correlation exists between the delay associated with inverting the sample and the incident heat flux.

For Sitka spruce, Shields et. al [25] found that the time to ignition was 2-3 times greater for heat fluxes above 50 kW/m^2 when orientated in an inverted orientation, as opposed to a normal orientation. Results from this study follow the same trend whereby there is an increase in the time to ignition when invertedly orientated, however, results from this study were not as marked. It is difficult to ascertain exactly how many repetitions were performed by Shields et. al [25], making a comparison to this work difficult.

The inset figure in *Figure 2* shows $1/\sqrt{t_{ig}}$ plotted as a function of the external heat flux. The gradient of this linearised data represents the effective thermal inertia as described in ignition theory [28]. The lines are approximately parallel to one other confirming that this effective thermal inertia is the same for both orientations. The vertical separation between these trendlines is attributed to the additional impacts of the mixing time, as described in equation (2) confirming that the change in orientation had an impact on the time to ignition due to the increased mixing time required to enable sustained flaming combustion.

The change in orientation is postulated to change the boundary layer thickness as well as the mixing times leading to increased times to ignition of the CLT. In a normal orientation, at the boundary layer, the pyrolysates and the oxidiser are diffused through natural turbulent convection [32]. When this occurs, at their interface, the pyrolysate/air mixture rises due to buoyancy forces entraining towards the centre of the plume. When there is a change to an inverted orientation, this boundary layer becomes thinner resulting in a steeper gradient of pyrolysates in the vicinity of the surface and an interface that is not so strongly impacted by buoyancy forces, which thus requires more mixing time before a sufficient fuel/oxidiser mixture can be achieved for sustained flaming combustion. This phenomenon was observed and reported by Zhou and Fernandez-Pello [45] when analysing flame spread across a PMMA ceiling.

4.1.3 Charring Rates

The progression of the char front and subsequent charring rates based on the 300°C isotherm [38, 39] results presented in *Figure 3* generally showed good agreement for charring rates at both a normal and inverted surface. For low heat fluxes such as 20 kW/m^2 , it appears that the average time to reach the 300°C isotherm was quicker for the normal sample. A consequence of this is the resulting charring rates whereby steeper

and faster charring rates reached on average in the order of 0.6mm/minute. The 300°C isotherm did not reach the thermocouple located 10 mm from the exposed surface, as a result of flaming self-extinction from the char insulating the virgin timber. This slight difference at 20 kW/m² can be attributed to the long times to ignition, resulting from greater heat losses from the exposed surface due to the impedance of the heat transfer when the heated surface in a colder environment faces downwards [46]

For higher heat fluxes between 30 to 60 kW/m², both the in-depth temperature profile and the charring rates for the normal and inverted surface follow the same trend, albeit noting that at 60kW/m² the 300°C isotherm for the inverted surface appears to on average be reached in a shorter period than that of the normal with consequently slighting higher charring rates recorded at a comparatively shorter period of time.

The average peak charring rates for 60 kW/m² were recorded to be 2.7 mm/minute during the initial stages of the fire, before reaching a steady state of approximately 1.0mm/minute after 30 minutes of exposure.

The above data has been generated based on a sample size of three to four per heat flux, per orientation making it difficult to conclude that orientation appears to have little impact on the charring rates. Further investigation into the peak heat release rates, total energy released, and mass loss rates may provide a greater insight into the burning behaviour of an inverted surface.

4.2 Implications for the Structural Design of Timber Buildings for Fire

Concerning ignition, and in the context of an open-plan timber building with an exposed ceiling, pyrolysates are trapped by the ceiling, and not permitted to naturally ventilate as in this experiment. In the event of a moveable fuel load fire, however, 58momentum-driven flows reduce the residence time of the volatile thus delaying ignition still further [19]. As such, the ignition delay time in an actual compartment fire with a combustible ceiling could be expected to be even greater than observed in this study which may help to further explain the delayed ignition observed in literature [19, 22].

Testing was conducted in an oxygenated environment with generally ambient conditions (i.e. 21%). It has been summarised [7] that across a number of engineered compartment fire tests with an exposed ceiling, that charring rates within the ceiling were generally less than that observed at a wall which was attributed to the reduction in oxygen concentration. However, heat fluxes in an actual compartment may be greater than those tested to, with peak heat fluxes in some compartment tests reaching 270 kW/m² [23].

An important note to make was that no char or lamella fall off was observed, despite using a glue that has been reported to experience issues at elevated temperatures, as the thermocouples did not allow for such an event to occur. In an actual compartment, there is potential for char fall off or lamella fall off which would expose virgin timber, complicating the observed behaviour.

5 CONCLUSION

The need to undertake a performance-based design for timber in fire has been highlighted by many authors [2, 12-16], which has been reinforced even further with recent testing at various scales highlighting a rapid transition to flashover within a mass timber compartment following the ignition of the exposed timber ceiling [18-23].

An abundance of research surrounding the ignition of wood has been undertaken at a range of scales, under both horizontal and vertical orientations as described by Babrauskas [24] in their review of the ignition of wood. Surprisingly, limited research has been undertaken investigating the ignition of an inverted surface (i.e. ceiling orientation), with Shields [25] appearing to be the only researcher to investigate the ignition of timber in this orientation, with times to ignition between 2-3 times greater for piloted ignition, when compared to a horizontal surface.

In this study, the FPA was modified to enable the study to determine what impact inverting the orientation of a CLT specimen has on the time to ignition and subsequent charring rates.

This comparative study demonstrates that by inverting the specimen, there is a significant increase in the mixing time of the fuel and oxidiser required to result in the piloted ignition of the specimen. This change

in mixing time is postulated to be due to the change in the boundary layer, which becomes thinner when inverted resulting in a steeper gradient of pyrolysate requiring more mixing to result in piloted ignition.

It was found that there is no significant impact of orientation on the critical heat flux of ignition nor on the charring rates of the CLT at a range of incident heat fluxes. However, caution should be applied to this conclusion due to the small sample sizes for these studies.

In the context of an actual building, momentum-driven flows associated with a moveable fuel load fire may further reduce the residence time of the pyrolysates than observed in this study without any forced convective flows, therefore a greater delay in the ignition of a ceiling may occur. Further research, including greater sample size, is required to validate the findings of this study.

ACKNOWLEDGMENT

This research was conducted by the *Australian Research Council Research Hub to Advance Timber for Australia's Future Built Environment* (project number IH220100016) funded by the Australian Government. We also acknowledge Sergio Zarate and Stewart Matthews for their support.

REFERENCES

1. Hadden, R.M., et al., *Effects of exposed cross laminated timber on compartment fire dynamics*. Fire Safety Journal, 2017. **91**: p. 480-489.
2. Schmidt, L., et al. *Explicit Fire Safety for Modern Mass Timber Structures - From Theory to Practice*. in *World Conference on Timber Engineering (WCTE 2023)*. 2023. Oslo, Norway: WCTE 2023.
3. Östman, B., D. Brandon, and H. Frantzich, *Fire safety engineering in timber buildings*. Fire Safety Journal, 2017. **91**: p. 11-20.
4. Pettersson, C., *Fire Safety in Timber Buildings-A review of existing knowledge*. 2020: Brandforsk.
5. Emberley, R., et al., *Critical heat flux and mass loss rate for extinction of flaming combustion of timber*. Fire Safety Journal, 2017. **91**: p. 252-258.
6. Gernay, T., *Response to "Commentary on DHP concept"*. Fire and Materials. **n/a**(n/a).
7. Mitchell, H., et al., *Review of fire experiments in mass timber compartments: Current understanding, limitations, and research gaps*. Fire and Materials, 2023. **47**(4): p. 415-432.
8. Butler, C., *Notes on charring rates in wood*. Fire Research Notes, 1971. **896**.
9. Lucherini, A., et al., *Thermal characterisation of the cooling phase of post-flashover compartment fires*. International Journal of Thermal Sciences, 2024. **199**: p. 108933.
10. Wiesner, F., et al., *Structural fire engineering considerations for cross-laminated timber walls*. Construction and Building Materials, 2022. **323**: p. 126605.
11. Gernay, T. and J.-M. Franssen, *A performance indicator for structures under natural fire*. Engineering Structures, 2015. **100**: p. 94-103.
12. Bartlett, A.I., et al. *Needs For Total Fire Engineering of Mass Timber Buildings*. in *2016 World Conference on Timber Engineering (WCTE 2016)*. 2016. Vienna.
13. Law, A. and R. Hadden, *We need to talk about timber: fire safety design in tall buildings*. The Structural Engineer, 2020. **98**(3): p. 6.
14. Brandon, D., et al., *Timber Structures*, in *International Handbook of Structural Fire Engineering*, K. LaMalva and D. Hopkin, Editors. 2021, Springer International Publishing: Cham. p. 235-322.
15. McNamee, M. and B.J. Meacham, *Conceptual Basis for a Sustainable and Fire Resilient Built Environment*. Fire Technology, 2023.
16. Xu, H., et al., *Large-scale compartment fires to develop a self-extinction design framework for mass timber—Part I: Literature review and methodology*. Fire safety journal, 2022. **128**: p. 103523.
17. Wiesner, F., et al., *Structural capacity in fire of laminated timber elements in compartments with exposed timber surfaces*. Engineering Structures, 2019. **179**: p. 284-295.
18. Emberley, R., et al., *Description of small and large-scale cross laminated timber fire tests*. Fire Safety Journal, 2017. **91**: p. 327-335.
19. Nothard, S., et al., *Factors influencing the fire dynamics in open-plan compartments with an exposed timber ceiling*. Fire Safety Journal, 2022. **129**: p. 103564.
20. Hidalgo, J.P., et al., *The Malveira fire test: Full-scale demonstration of fire modes in open-plan compartments*. Fire Safety Journal, 2019. **108**: p. 102827.

21. Hopkin, D., et al., *Large-Scale Enclosure Fire Experiments Adopting CLT Slabs with Different Types of Polyurethane Adhesives: Genesis and Preliminary Findings*. Fire, 2022. **5**(2): p. 39.
22. Bøe, A.S., et al., *Fire spread in a large compartment with exposed cross-laminated timber and open ventilation conditions: #FRIC-01 – Exposed ceiling*. Fire safety journal, 2023. **140**: p. 103869.
23. Kotsovinos, P., et al., *Fire dynamics inside a large and open-plan compartment with exposed timber ceiling and columns: CodeRed #01*. Fire and Materials, 2023. **47**(4): p. 542-568.
24. Babrauskas, V., *Ignition of Wood: A Review of the State of the Art*. Journal of Fire Protection Engineering, 2002. **12**(3): p. 163-189.
25. Shields, T.J., G.W. Silcock, and J.J. Murray, *The effects of geometry and ignition mode on ignition times obtained using a cone calorimeter and ISO ignitability apparatus*. Fire and Materials, 1993. **17**(1): p. 25-32.
26. Rein, G., *SFPE Handbook of Fire Protection Engineering*. 2016, Springer New York: New York, NY. p. 581-603.
27. Drysdale, D., *Ignition: The Initiation of Flaming Combustion*, in *An Introduction to Fire Dynamics*. 2011. p. 225-275.
28. Torero, J., *SFPE Handbook of Fire Protection Engineering*. 2016, Springer New York: New York, NY. p. 633-661.
29. Babrauskas, V., *Ignition handbook : principles and applications to fire safety engineering, fire investigation, risk management and forensic science*, ed. E. Society of Fire Protection. 2003, Issaquah, WA : Bethesda, Md.: Fire Science Publishers Society of Fire Protection Engineers.
30. Fernandez-Pello, A.C., *Combustion Fundamentals of Fire: The Solid Phase*, in *Chapter*, G. Cox, Editor. 1995, Academic Press Limited: London. p. 31-100.
31. Long Jr, R.T., et al. *Scale and Transport Considerations on Piloted Ignition of PMMA*. in *Fire Safety Science*. 2000.
32. Quintiere, J.G., *Fundamentals of Fire Phenomena*. 2006.
33. Janssens, M., *Calorimetry*, in *SFPE Handbook of Fire Protection Engineering*, M.J. Hurley, et al., Editors. 2016, Springer New York: New York, NY. p. 905-951.
34. Wesson, H.R., J.R. Welker, and C.M. Sliepcevich, *The piloted ignition of wood by thermal radiation*. Combustion and Flame, 1971. **16**(3): p. 303-310.
35. Girods, P., et al., *Comparison of Pyrolysis Behavior Results between the Cone Calorimeter and the Fire Propagation Apparatus Heat Sources*. 2011. **10**.
36. Kashiwagi, T., T.J. Ohlemiller, and K. Werner, *Effects of external radiant flux and ambient oxygen concentration on nonflaming gasification rates and evolved products of white pine*. Combustion and Flame, 1987. **69**(3): p. 331-345.
37. Janssens, M., *Piloted ignition of wood: A review*. Fire and Materials, 1991. **15**(4): p. 151-167.
38. White, R.H., *Analytical Methods for Determining Fire Resistance of Timber Members*, in *SFPE Handbook of Fire Protection Engineering*, M.J. Hurley, et al., Editors. 2016, Springer New York: New York, NY. p. 1979-2011.
39. Bartlett, A.I., R.M. Hadden, and L.A. Bisby, *A Review of Factors Affecting the Burning Behaviour of Wood for Application to Tall Timber Construction*. Fire technology, 2019. **55**(1): p. 1-49.
40. Pope, I., J.P. Hidalgo, and J.L. Torero, *A correction method for thermal disturbances induced by thermocouples in a low-conductivity charring material*. Fire Safety Journal, 2021. **120**: p. 103077.
41. Cuevas, J., et al., *Complexities of the Thermal Boundary Conditions when Testing Timber using the Fire Propagation Apparatus*. 2019.
42. Materials, A.S.f.T.a., *ASTM E2058 - 13a*, in *Standard Test Methods for Measurement of Material Flammability Using a Fire Propagation Apparatus (FPA)*. 2013, ASTM International: West Conshohocken, PA.
43. Wiesner, F., et al., *Bushfire performance of native Australian wood species*. Fire Safety Journal, 2023. **140**: p. 103884.
44. Bartlett, A.I., *Auto-extinction of engineered timber*. 2018, The University of Edinburgh.
45. Zhou, L. and A.C. Fernandez-Pello, *Turbulent, concurrent, ceiling flame spread: The effect of buoyancy*. Combustion and Flame, 1993. **92**(1): p. 45-59.
46. Cengel, Y. and A.J. Ghajar, *Heat and Mass Transfer: Fundamentals and Applications*. 6 ed. 2019, NY: McGraw-Hill US Higher Ed USE.

DETERMINATION OF CHAR LAYER DENSITY PROFILE DURING STRUCTURAL TIMBER FIRE EXPERIMENTS

Fernando Pérez Pérez¹, Joachim Schmid², Andrea Frangi³

ABSTRACT

This paper evaluates several non-destructive experimental methods for determining the char thickness and density profile in structural timber samples exposed to standard ISO 834 fire curve experiments. Microwave echo scanning, ultrasonic echo pulse, X-ray computed tomography and resistance drilling were evaluated. Their results were compared against photogrammetry results. Preliminary tests on partially charred cold timber samples showed that X-ray computed tomography can accurately predict the char density profile and that the resistance drilling technique can determine the char layer thickness. For the first time, the results of char layer thickness evolution during a 105 minutes ISO 834 fire curve experiment on a structural timber element are presented.

Keywords: Fire experiment; Char layer; Structural timber; Resistance drilling; Computed tomography

1 INTRODUCTION

An increase in the use of timber as structural material is being promoted to compensate for the high greenhouse gas emissions of traditional construction methods [1] and help the construction industry move towards the UN Sustainable Development Goal 11 [2]. One of the differences between timber and other traditional construction materials is that timber is combustible. Therefore, although unlikely, a severe fire event is a key design scenario to be considered when designing timber structures.

Performance based design methods are frequently needed to satisfy the structural fire design [3]. These methods require the designer to consider the contribution of the structural timber as a fuel during the duration of the fire [4 - 7]. The correct definition of the action and resistance sides of the model is key to achieving an efficient design while maintaining an equivalent level of safety to other construction methods.

For example, a proposed new Eurocode advanced model includes in the action side the contribution of all timber section above the 300 °C isotherm [8]. This may be a conservative approach as the char attached to solid timber elements is not necessarily fully combusted immediately after is formed. It has been shown that adding the contribution of the char layer to a structural fire model increases its accuracy [5].

It is important to determine the properties of the char layer experimentally to validate models that include its contribution. In particular, the evolution of the char layer density during a fire experiment would inform its combustion rate. However, the literature on this subject is very limited. Most authors focus on other parameters such as charring depth, which they refer to as char depth [9, 10]. This paper evaluates several state-of-the-art methods and tests them for their ability to determine the char density profile during a fire experiment.

¹ Mr., Institute of Structural Engineering, ETH Zurich, 8093 Zurich, Switzerland
e-mail: fernando.perez@ibk.baug.ethz.ch, ORCID: <https://orcid.org/0000-0002-4035-5004>

² Dr., Institute of Structural Engineering, ETH Zurich, 8093 Zurich, Switzerland
e-mail: schmid@ibk.baug.ethz.ch, ORCID: <https://orcid.org/0000-0002-4460-8638>

³ Prof. Dr., Institute of Structural Engineering, ETH Zurich, 8093 Zurich, Switzerland
e-mail: frangi@ibk.baug.ethz.ch, ORCID: <https://orcid.org/0000-0002-2735-1260>

Figure 1 highlights the current standardised names for a charred timber section and includes the new term ‘total residual depth’ to define the thickness equal to the residual depth plus the char layer thickness.

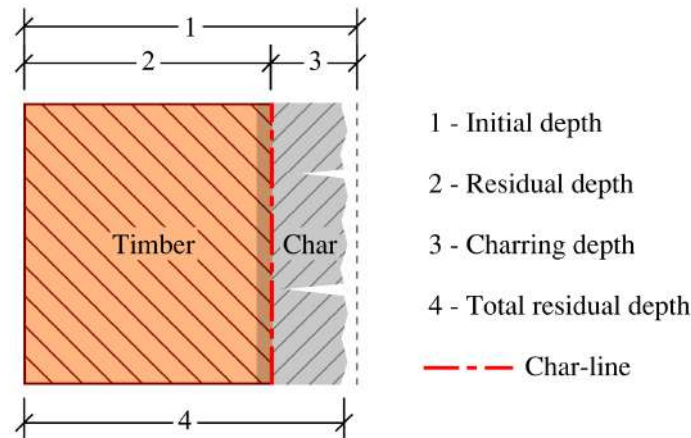


Figure 1. Depth definitions for a timber member exposed to fire on one side

2 MATERIALS AND METHODS

Table 1 shows the different non-destructive testing methods selected in a desktop study to determine the char density profile from the unexposed side of the timber sample. They were then evaluated on charred timber samples in three experimental phases described in this section. All methods were tested in a preliminary phase. Those that produced results were selected and validated on cold charred structural timber samples using the photogrammetry method. Finally, the selected suitable method was tested in a standard fire test on a cross laminated timber wall element.

Table 1. Test methods evaluated

	Destructive	Non-destructive
Deferred	Photogrammetry	X-ray computed tomography
In-situ		Resistance drilling Microwave Ultrasonic X-ray

2.1 Preliminary phase

The methods selected in the desktop study to estimate the char density profile were: (A) resistance drilling, (B) microwave pulse echo scanning, (C) ultrasonic pulse echo scanning and (D) X-ray scanning. The results of each method were compared with the photogrammetry result.

Photogrammetry uses photographs of a specimen from different perspectives, which are reconstructed into a geometric mesh of points using a software package [11]. In this study, Autodesk Recap was used, post-processed with a MATLAB script to extract the relevant points of the mesh and compute their statistical representation. The method can be applied before and after manual removal of the char layer from the specimen with a steel wire brush to obtain the total residual depth and residual depth, respectively. The average char density $\rho_{c,m}$ can be calculated from equation (1) using the mass of the sample with and without char.

$$\rho_{c,m} = \frac{m_c - m_r}{(h_{t,res} - h_{res}) * A_s} \quad (1)$$

where

m_c is the mass of the timber sample with char

m_r is the mass of the timber sample without char

$h_{t,res}$ is the average total residual depth

h_{res} is the average residual depth

A_s is the area of the timber sample

Resistance drilling consists of measuring the resistance to the advance of a thin drill bit rotating and advancing at a constant high speed through the section of timber. The tip of the drill bit is 3 mm wide and its flexible shaft of approximately 1.5 mm diameter is available in lengths between 200 and 1000 mm. The tool records the amplitude of the resistance to drilling along the length of the drill. The resistance reading has been correlated to the density of the material [12]. Although each test leaves a hole in the sample, the volume of material removed from the section can be considered negligible. For example, holes at 100mm centres would represent a section loss of 0.07%.

There are currently two main suppliers, IML and Rinntech. Figure 2 shows the drills used: IML-RESI PowerDrill 400 (RD-I) with 33.33 m/s feed speed and 2500 rpm drilling speed and the Rinntech RESISTOGRAPH® Series 3 (RD-R) with slower speeds manufactured from 1999 to 2005. The older RD-R model was used as it was expected to be more sensitive in the lower density ranges, being able to measure amplitudes related to densities in the range 50 to 900 kg/m³. The reading is combined into one value every 0.01 mm. The RD-I reading is split into resistance to drilling and resistance to feed (advance) every 0.1 mm. The RD-I was initially tested on a 400 x 300 x 120 mm charred glulam sample.

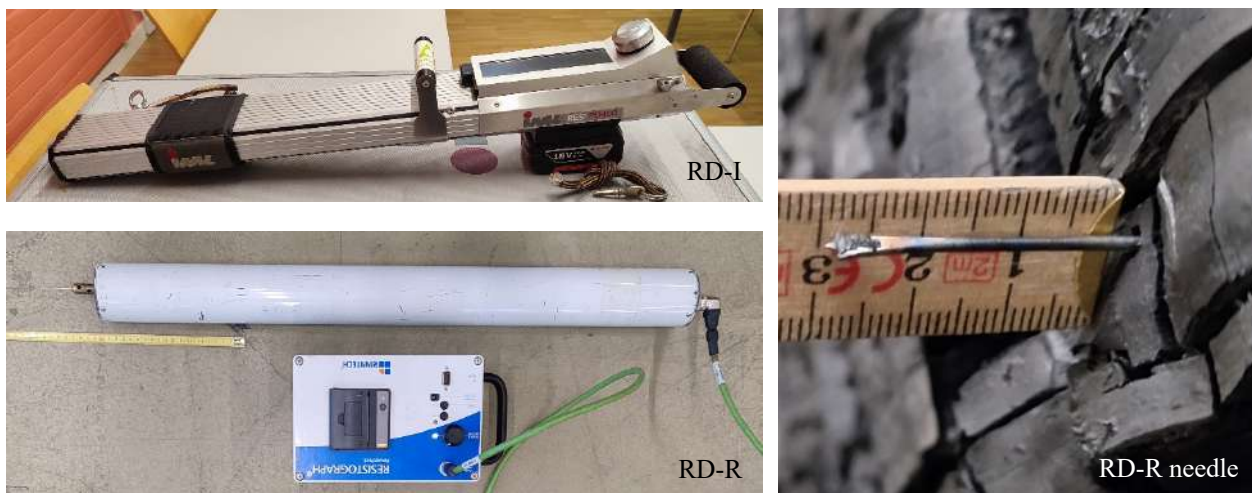


Figure 2. RD-I and RD-R drills and RD-R needle through charred CLT

The most commonly used microwave scanning techniques are based on the transmission of an electromagnetic wave between a transmitter and a receiver on either side of the sample, sending a pulse and measuring the attenuation and delay in reception based on the interaction with the sample [13]. The pulses sent through the sample are more energetic, have a shorter wavelength and can provide higher resolution than radar scans. Microwave scans used to image wood samples operate in the range of 1-25 GHz [14].

In microwave pulse echo scanning (MPE), the same antenna transmits the pulse and receives the reflection produced when the dielectric conductivity of the material in the sample changes [15]. Tests were carried out along 4 different locations on the same sample used for the RD-I tests with an antenna with a bandwidth of 10 GHz and a peak width of 12 mm at SUPSI-ISEA, as shown in Figure 3 a).

Ultrasonic sensors measure the time taken for the sound pulse to travel between the emitter and the receiver. Sound is a mechanical vibration that propagates through timber at different speeds depending on density and stiffness [16]. There are two main methods of measurement. The direct method involves placing the emitter and receiver on opposite sides of the specimen and measuring the time taken for the longitudinal sound wave to pass through. It has previously been used to detect delamination in glulam beams [17]. In ultrasonic pulse echo (UPE), the emitter and receiver are on the same side of the specimen and the shear wave reflection peaks when it encounters a sudden change in material properties [18]. Two different UPE handheld sensors - ACS M2502 in Figure 3 b) and Proceq PD8050 - were used to estimate the thickness of the char layer on the same charred glulam sample described above.

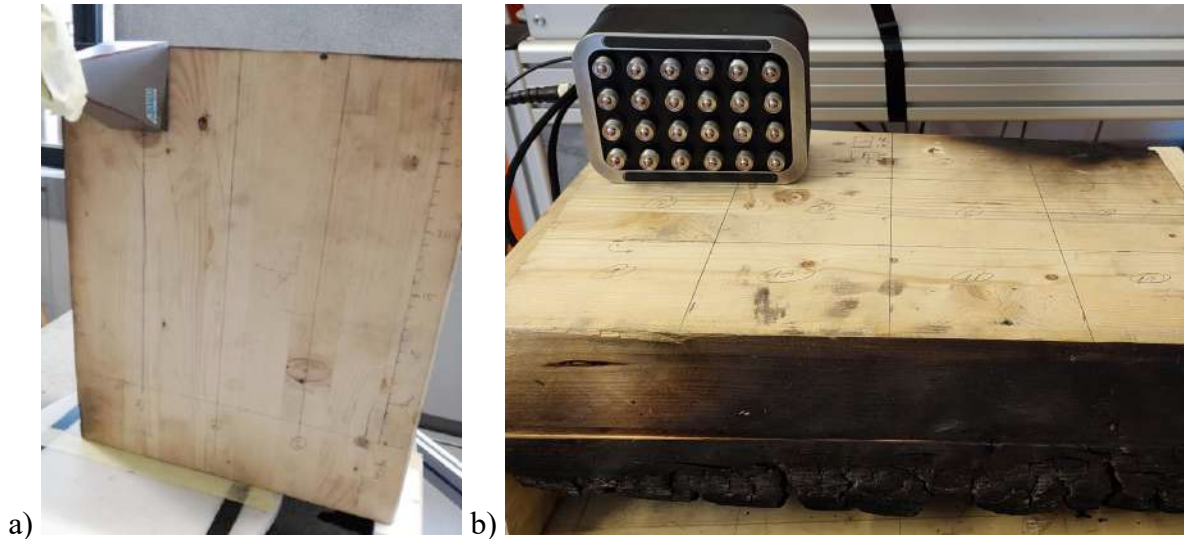


Figure 3. a) SUPSI-ISEA MPE and b) UPE ACS M2502

X-ray radiation is the process of exposing a sample to an electromagnetic wave in the range of 3×10^{16} Hz to 3×10^{19} Hz. This technique is often used in non-destructive testing as a transmission technique, where the sample is located between the X-ray beam (emitter) and the detector (receiver). The emitter radiates the sample. Some of the energy of the wave is attenuated by the material. The detector then records the attenuated radiation. The total attenuation is the difference between the wave in the vacuum and the wave through the material. For thick materials, the attenuation through the material is the sum of the attenuation through each of the differential sections in the direction of the wave.

X-ray computed tomography (XCT) scans are multiple individual X-ray scans of a thick sample. The computer then analyses the response received and digitally reconstructs the sample by calculating the attenuation of each voxel within it. XCT scans are typically used in the literature to validate the results of other test methods [13], [17].

Lindgren showed that X-ray attenuation coefficients are correlated with timber density [19]. Boigné calibrated wood and char densities with attenuation coefficients and used the same linear regression for both materials from XCT attenuation results [20]. In this paper, the densities of the timber and char layers for each voxel were calculated from their XCT grey values using equation (2) based on the linear regression from the water and air XCT mean results described in Figure 4.

$$\rho_i = 0.018461 \times G_i - 134.67 \quad (2)$$

where

ρ_i is the mean density of voxel i

G_i is the grey value of voxel i

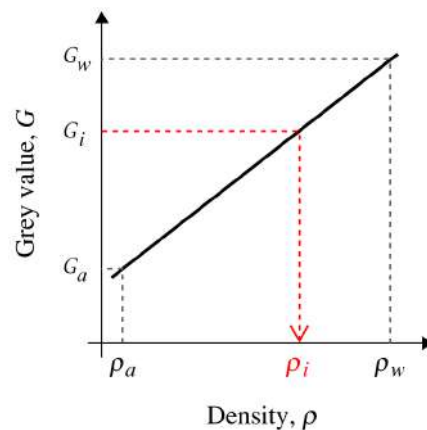


Figure 4. Determination of density from XCT grey value for voxel i based on known values for water (w) and air (a)

In the preliminary phase, a small cylindrical sample of 40 mm diameter by 60 mm height, cut from cross laminated timber (CLT) made with *Picea abies* boards, was partially charred and then tested on 2 different XCT scanners at the ETHZ. One was a Scanco μ CT 45 scanner with an irradiation energy of 45 kV and the other was a GE Phoenix v|tome|x s scanner with an irradiation energy of 60 kV.

2.2 Experiments on partially charred timber after a fire experiment

A 2 m x 1.5 m x 160 mm thick 5-layer (40/20/40/20/40) CLT panel made with *Picea abies* and polyurethane (PUR) adhesive type I according to EN 15425 was exposed horizontally as a slab to the ISO 834 fire curve for 45 minutes. The specimen was then removed from the furnace and cooled with water spray. It was then cut into 300 x 300 mm samples.

Both the RD-I and RD-R drills were used on one of these samples at 10 randomly selected locations based on the Latin Hypercube Sampling (LHS) method. Each instrument drilled 5 locations. The sample was then scanned with a larger XCT than that used in the preliminary series. Finally, the photogrammetric method was applied to the sample before and after removal of the char layer.

The XCT used was a floor-mounted uDetect scanner with a 300 kV Finetech X-ray microfocus tube, collimator, rotary table and a PerkinElmer XRD 1611 CP3 digital flat-panel detector. The scan irradiance was 240 kV and 400 μ A with a cone beam angle of 40 degrees. The distance from the centre of the object to the source focal point was 849.96 mm and from the source focal point to the detector was 1407.57 mm. The detector had 4096 x 4096 pixels with a pixel size of 100 μ m. The scan parameters were 1000 ms exposure time per frame with 4050 projections and 2 frames averaged for each projection. The reconstruction software used was Rx Solutions X-Act to generate 3841 horizontal slices with a voxel size of 60.39 μ m.

2.3 Experiments on partially charred timber during a fire experiment

A CLT panel with the same characteristics as the one described in section 2.2 was used as a vertical wall in the same furnace during a 105 minutes fire test according to the standard ISO 834 fire curve. During the test, an RD-R tool was used to drill into the specimen 48 times, an average of once every 2 minutes, to estimate the evolution of the total residual depth. At the end of the test, the total residual depth of the sample is determined using the RD-R and the photogrammetry method.

3 RESULTS AND DISCUSSION

The microwave echo and ultrasonic pulse echo scanning techniques did not identify the thickness or density profile of the char layer. Both lack sufficient resolution to clearly distinguish between the char layer and air. The test results for the partially charred samples are not shown and are not discussed further in this paper. This paper focuses on the results of the RD-I, RD-R and XCT in determining the thickness and density profile of the char layer.

3.1 Char layer thickness

Figure 5 shows the RD-R results on the charred timber sample after the fire test where 0 mm represents the unexposed timber side. The resistance readings were scaled so that the average in the air zone after the char layer is equal to 100. Figure 5 a) shows the 7 readings taken through solid char, denoting three different amplitudes for the timber, char and air zones.

After drilling through the wood and char, when the needle is in the air, there is a residual reading. The empirical 95th percentile of this residual reading in this zone between 160 and 170mm is calculated for each drill individually. The total residual thickness is then taken where the 95th percentile of the air value meets the last significant drop in the resistance reading. Figure 5 b) shows the derivation of the total residual depth on one of the drills.

30% of the drills in the cold specimen tested with both DR-I and RD-R went directly from the timber to the air through cracks in the char layer. The same percentage was achieved in the additional specimen tested 10 times with the RD-R only. Thus, the success rate for drilling through solid char was typically 70%.

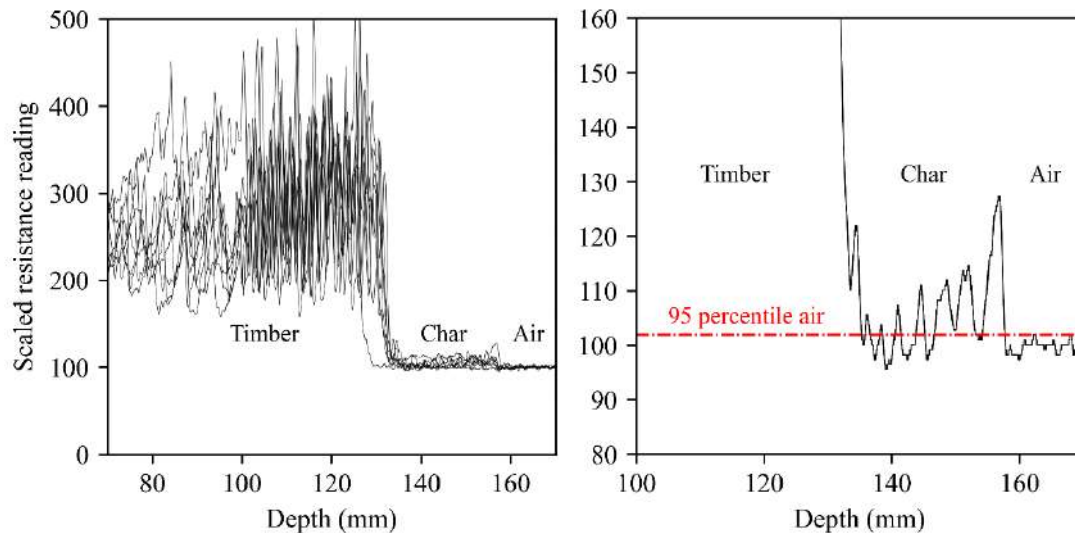


Figure 5. RD results of a) 7 readings overlapped and b) individual reading zoomed in the char layer

The XCT scan of the charred sample tested with the RD-I and RD-D produced a 3D array of approximately 3800 x 3800 x 3800 voxels. Each voxel had a grey value representing the attenuation of the X-ray through its volume. Figure 6 shows in the background of the graph a grey map of a 2D XCT slice in which one of the RD-R drill holes was made. A 3 mm square region of interest (ROI) orthogonal to the 2D slice was selected close to the drilling zone. The average of the values on the square ROI at each voxel in depth was calculated and plotted as a dashed line. The RD-R result was then plotted as a solid line with a running average of 10 measurements (0.1 mm).

The RD-R reading shows good correlation with the XCT ROI results, highlighting the density peaks of the latewood rings and the change in amplitude patterns of the different boards. Both show a clear drop in magnitude at the end of the char layer. This result demonstrates for the first time the suitability of the RD technique for measuring total residual depth.

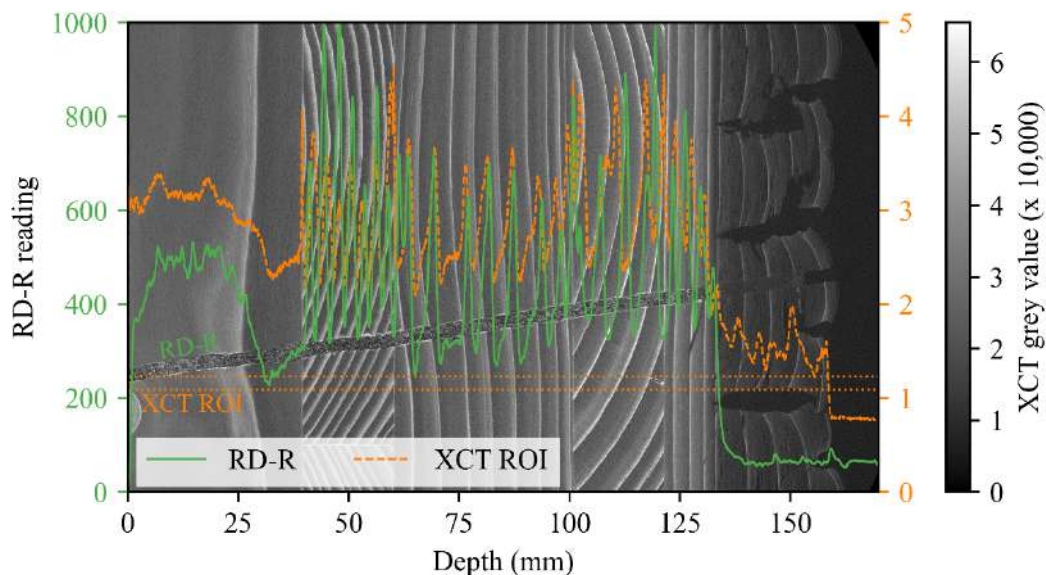


Figure 6. XCT slice in grey scale map in the background with ROI reading in dashed line and RD-R reading in solid line

The RD is perpendicular to the specimen before each drill is started. However, as shown in Figure 6, in practice there is a small deviation from the orthogonal line. The angle of deviation from each drill with the RD-I was 4.30 (+3.22, -2.90)°. This indicates that the RD gave 0.547 (+0.841, -0.500) mm longer results on this specimen.

Table 2 summarises the results of the 4 methods without any correction factor. RD-I and RD-D results were calculated using the 95 percentile method. XCT results were obtained from 1 cm square ROIs at 10 random LHS locations. The total residual depth was taken as the depth where the average grey value fell below the 95 percentile air values. The photogrammetry results are presented with the empirical 90% confidence limits as a reference.

Table 2. Total residual depth (mm)

	RD-I	RD-R	XCT	Photogrammetry
Mean	165.2	157.9	160.6	159.25 (+5.20, -5.84)
Standard deviation	2.2	2.8	4.7	3.64

Both XCT and RD-R results are in best agreement with the photogrammetry results. Their mean value is within less than one standard deviation of the reference value. The RD-I results are further away from the reference value. Their mean value is not within one standard deviation of the reference value, even when the maximum correction from the insertion angle described is applied.

Based on these results, the RD-R was used to determine the char thickness evolution during an ISO 834 fire curve test on a CLT wall with a PUR adhesive. Figure 7 a) shows the results of the 44 drills done during the 105 minutes of fire test and the average of 3 results at minute 105, after the sample was cooled down with water. The residual depth is plotted for all drills together with the theoretical one dimensional charring rate of 0.65 mm/min for a solid softwood member [21].

Total residual depth was calculated using the 95 percentile air method for the 36 drills that had a clear horizontal trend in their readings through the air layer. The char depth was then calculated and the lowest 30% of values were excluded to account for the hit and miss rate through char gaps experienced in the cold tests. The final values, based on the average of 3 post-test readings, are plotted with blank markers at minute 105.

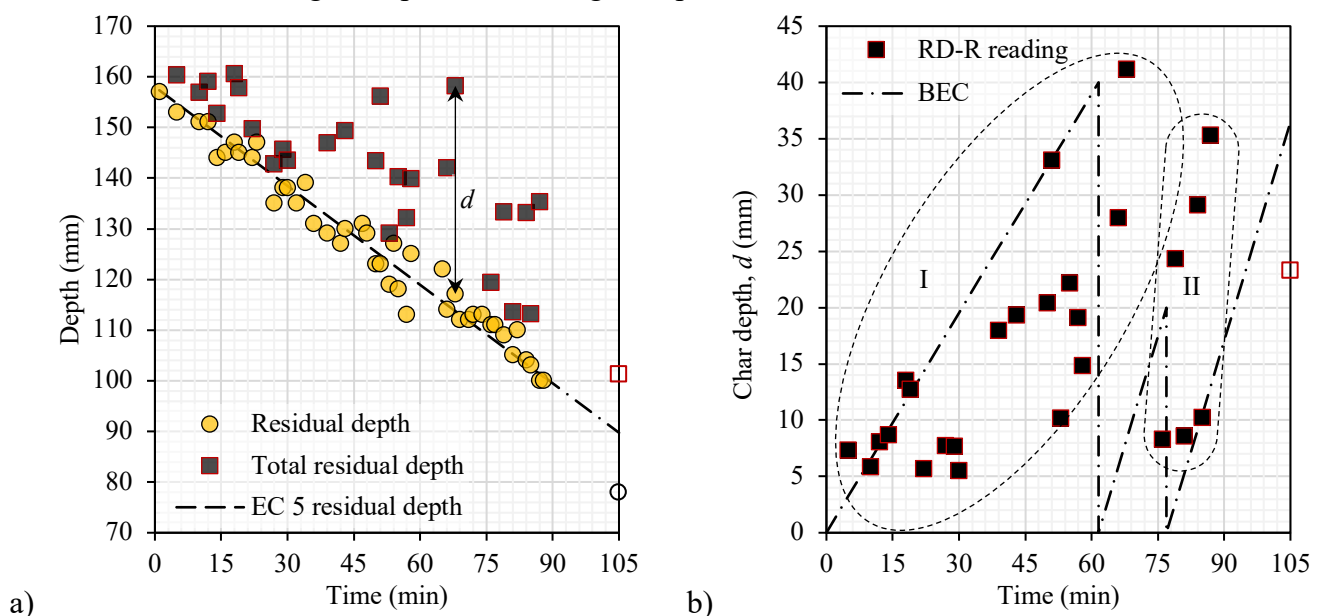


Figure 7. RD-R a) total residual depth and residual depth readings and b) char layer thickness during an ISO 834 fire test

The longest period without a clear reading of the total residual depth occurs between minutes 68 and 76. This gap coincides with the period when the residual depth is consistently below 120 mm, where the first glue line is located. The adhesive used on this CLT panel is not certified to pass the GLIF test. It is deduced that this lack of results coincides with the fall of the first lamella. When the panel was removed, there was a significant pile of smouldering char at the bottom of the furnace by the CLT panel. Furthermore, the

residual depth of 78 mm at minute 105 is based on the average of 4 drills and confirms the faster charring rate of this CLT panel compared to the Eurocode rate for solid timber.

Figure 7 b) shows the char depth results d from the RD-R readings during the fire test and the calculated char thickness based on Eurocode 5, Annex B (referenced as BEC model). The increased charring rate of 1.35 mm/min was used after the residual depth reached the bond lines. At this point it was assumed that the full depth of carbon would fall off uniformly. The end of the residual depth is the char layer exposed to 1200 °C in accordance with Appendix B [21] which is not reached during the 105 minutes test. The average remaining char depth from 3 RD-R readings after the fire test is plotted with a blank marker at the last minute.

The char depth results in Figure 7 b) show a steady increase in the first period (I), generally below the calculated char depth value. Then the zone between 68 and 76 minutes mentioned earlier coincides with the thinner 20 mm lamella, which theoretically experiences 2 fall off events within 15 minutes. After this period, zone II denotes an area with two groups of low and high char depths during the period of increasing char rate of the central 40 mm lamella. These scattered zone II results could be due to partial fall off where there were some areas of thicker char that did not fully fall off.

3.2 Char layer density profile

RD does not have sufficient resolution to detect the char density profile. Figure 8 shows that the distributions of the RD-R char and air readings overlap more than those of the XCT. Therefore, the XCT results on the charred sample after the fire tests were used to evaluate the char density profile.

The density profile was calculated based on the average readings within 1 cm² regions through the sample at 10 random locations selected by the LHS method. The profiles at all locations were then shifted to set the 0 mm char depth at the empirical 5 percentile value from the readings on the whole timber specimen. Figure 9 shows the density ratio between the mean char density at all random locations and the mean density of the wood. The maximum and minimum char density ratios for the 10 sites are also plotted. The char layer densities were scaled down to account for the 9% moisture content of the char sample at the time of scanning, which was determined by drying 4 char samples of approximately 40 x 40 x 20 mm in an inert atmosphere furnace at 150 °C for 6 hours.

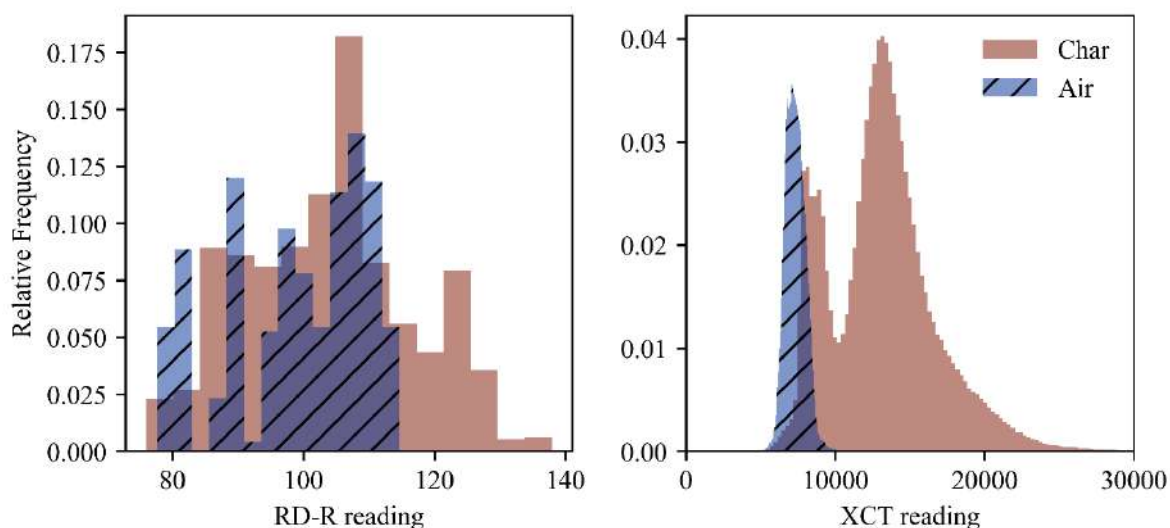


Figure 8. Histogram from char and air readings on a cold charred sample for RD-R and XCT

Figure 9 also shows a calculated char density profile (BEC) based on the temperature dependent timber properties of Annex B of Eurocode 5 [21]. The temperature distribution within a timber sample of 405 kg/m³ density was calculated in Abaqus using a unidirectional transient heat transfer model with a surface temperature boundary condition equal to the ISO 834 time temperature curve. The profile temperature at 45 minutes was then correlated with the Eurocode density ratio at each mm in depth.

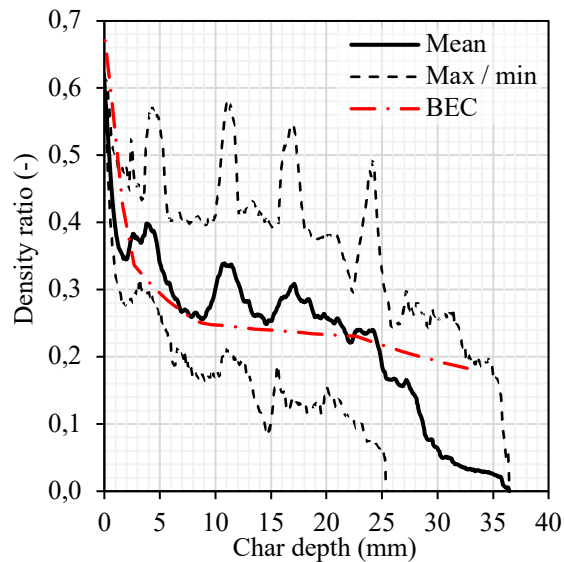


Figure 9. Density ratio of XCT char layer results compared to a SAFIR model based on EN 1995-1-2 parameters

The average char density ratio from the photogrammetry results was 0.245. The average ratio for the BEC model was 0.267 and for the XCT was 0.274. The results from the BEC model and the XCT are similar and both approximately 10% above the photogrammetry results. It is unclear where the brush cleaning method would stop removing char. When the BEC and XCT results of the char layer are taken from the 350 °C isotherm instead of the 300 °C isotherm, the average densities drop to values similar to the photogrammetry results.

Comparing the BEC and XCT results, the density ratio for the first 25 mm is higher for the XCT and then drops sharply below the BEC values for the last 10 mm. This could be improved by implementing char combustion parameters in the BEC models and increasing the initial density ratio.

4 CONCLUSIONS

Different methods for determining the char thickness and density profile during and after a fire experiment have been presented. It is concluded that:

1. XCT is the only non-destructive method tested that can determine the density profile of the char layer. The application of this method is currently limited to the period after the fire experiment.
2. The RD technique can determine the char thickness during and after the fire experiment.
3. Further experiments should be carried out with the RD technique to validate its accuracy and increase its precision. It is recommended that these experiments are carried out with solid timber panels lying horizontally and drilling vertically from the unexposed face of the timber panel.

ACKNOWLEDGMENT

The authors acknowledge all those people, companies and institutes that helped carrying out some of the testing related to this project. In particular: Martin Viertel at ETHZ, Frank Rinn at Rinntech-Metriwerk GmbH; Robert Zboray, Kiarash Tajbakhsh and Roman Furrer at Empa, Samuel Poretti and Tommaso Pagani at ISEA-SUPSI, Matthias Brunner AG, and Proceq. This work is done in the framework of a PhD funded by the SNF grant 200020_207498.

REFERENCES

- [1] Core Writing Team, Hoesung Lee, and José Romero, 'Climate Change 2023: Synthesis Report. Contribution of Working Groups I, II and III to the Sixth Assessment Report of the Intergovernmental Panel on Climate Change', Panmao Zhai, Geneva, 2023. doi: 10.59327/IPCC/AR6-9789291691647.

- [2] Independent Group of Scientists appointed by the Secretary-General, ‘Global Sustainable Development Report 2023: Times of crisis, times of change: Science for accelerating transformations to sustainable development’, New York, 2023.
- [3] STA special interest group, ‘Structural timber buildings fire safety in use guidance - Volume 6 - Mass timber structures - Building Regulation compliance B3(1)’, Alloa, May 2023. [Online]. Available: www.structuraltimber.co.uk
- [4] C. Wade, ‘A theoretical model of fully developed fire in mass timber enclosures’, Doctor of Philosophy, University of Canterbury, Christchurch, 2019. doi: 10.13140/RG.2.2.15162.13764.
- [5] J. Schmid and A. Frangi, ‘Structural timber in compartment fires – the timber charring and heat storage model’, *Open Engineering*, vol. 11, no. 1, pp. 435–452, Jan. 2021, doi: 10.1515/eng-2021-0043.
- [6] D. Brandon, A. Temple, and J. Sjöström, ‘Predictive method for fires in CLT and glulam structures - A priori modelling versus real scale compartment fire tests & an improved method’, Borås, 2021.
- [7] L. Girompaire and C. Dagenais, ‘Fire Dynamics of Mass Timber Compartments with Exposed Surfaces: Development of an Analytical Model’, *Fire Technol*, 2024, doi: 10.1007/s10694-023-01528-y.
- [8] CEN Enquiry, ‘EN 1995-1-2 (Eurocode 5): Design of timber structures — Part 1-2: Structural fire design’, 2023.
- [9] P. Kotsovinos et al., ‘Fire dynamics inside a large and open-plan compartment with exposed timber ceiling and columns: CodeRed #01’, *Fire Mater*, vol. 47, no. 4, pp. 542–568, Jun. 2023, doi: 10.1002/fam.3049.
- [10] A. S. Bøe, K. L. Friquin, D. Brandon, A. Steen-Hansen, and I. S. Ertesvåg, ‘Fire spread in a large compartment with exposed cross-laminated timber and open ventilation conditions: #FRIC-01 – Exposed ceiling’, *Fire Saf J*, vol. 140, p. 103869, Oct. 2023, doi: 10.1016/J.FIRESAF.2023.103869.
- [11] J. Schmid et al., ‘Charring of timber-determination of the residual virgin cross section and charring rates’, Red Hook, NY, 2021, pp. 1081–1089. Accessed: Apr. 09, 2024. [Online]. Available: https://www.researchgate.net/publication/348389904_CHARRING_OF_TIMBER_-_DETERMINATION_OF_THE_RESIDUAL_VIRGIN_CROSS_SECTION_AND_CHARRING_RATES
- [12] F. Rinn, F. H. Schweingruber, and E. Schar, ‘Comparative Evaluation of Resistograph and X-Ray - Density Charts for different wood species’, *Holzforschung*, vol. 50, no. 4, pp. 303–311, 1996.
- [13] L. Hansson, N. Lundgren, A. L. Antti, and O. Hagman, ‘Microwave penetration in wood using imaging sensor’, *Measurement (Lond)*, vol. 38, no. 1, pp. 15–20, Jul. 2005, doi: 10.1016/j.measurement.2005.03.007.
- [14] M. Pastorino et al., ‘A microwave tomographic system for wood characterization in the forest products industry’, *Wood Mater Sci Eng*, vol. 10, no. 1, pp. 75–85, Jan. 2015, doi: 10.1080/17480272.2014.898696.
- [15] J. E. Mast, H. Lee, and J. P. Murtha, ‘Application of microwave pulse-echo radar imaging to the nondestructive evaluation of buildings’, *Int J Imaging Syst Technol*, vol. 4, no. 3, pp. 164–169, 1992, doi: 10.1002/ima.1850040304.
- [16] P. Niemz, A. Teischinger, and D. Sandberg, Eds., *Springer handbook of wood science and technology*. Springer Nature Switzerland AG, 2023. doi: 10.1007/978-3-030-81315-4.
- [17] J. Neuenschwander, S. J. Sanabria, P. Schuetz, R. Widmann, and M. Vogel, ‘Delamination detection in a 90-year-old glulam block with scanning dry point-contact ultrasound’, *Holzforschung*, vol. 67, no. 8, pp. 949–957, Dec. 2013, doi: 10.1515/hf-2012-0202.
- [18] A. Hasenstab, M. Krause, and B. Hillemeier, ‘Defect localisation in wood with low frequency Ultrasonic Echo Technique’, p. 466, May 2005.
- [19] O. Lindgren, ‘Medical CT-scanners for non-destructive wood density and moisture content measurements’, Doctoral Dissertation, Luleå University, Skellefteå, 1992.
- [20] E. Boigné, N. R. Bennett, A. Wang, K. Mohri, and M. Ihme, ‘Simultaneous in-situ measurements of gas temperature and pyrolysis of biomass smoldering via X-ray computed tomography’, in *Proceedings of the Combustion Institute*, Elsevier Ltd, 2021, pp. 3899–3907. doi: 10.1016/j.proci.2020.06.070.
- [21] CEN, ‘EN 1995-1-2 (Eurocode 5) (2010): Design of timber structures, Part 1-2: General – Structural fire design’, BSI, Brussels, 2010.

EMBEDMENT STRENGTH OF DOWELLED CONNECTIONS OF GLULAM TIMBER AT HIGH TEMPERATURES

Shunsuke Saito¹, Takayuki Kikuchi², Yukito Nakayama³, Marina Totsuka⁴, Takeo Hirashima⁵

ABSTRACT

Dowelled connections are commonly employed in mass timber constructions. In fire-exposed dowelled connections, its resistance is determined by the embedment strength of the timber, not the yield strength of the dowels, as the dowels transfer heat and elevate the temperature of the adjacent timber. Therefore, it is essential to comprehend the embedment strength of the timber at high temperatures. This study investigated heating methods using dowels as a heat source and carried out the load-increasing tests under steady-state conditions at constant temperature (steady-state test, ST test) and temperature-increasing tests under constant stress (transient-state test, TR test). This study proposes a reduction factor for embedment strength based on the results of the TR test, indicating that the strength decreases to 50% at 100 °C and 0% at 300 °C, both parallel and perpendicular to the grain. The results of the ST test showed that specimens compressed parallel to the grain exhibited brittle behaviour from ambient temperature to 150 °C and ductile behaviour from 200 °C to 300 °C. Specimens perpendicular to the grain exhibited ductile behaviour from ambient temperature to 300°C. Finite element analysis indicated that stresses were concentrated in the embedment area, and the influence of temperature distribution was minimal for the specimen compressed parallel to the grain. Meanwhile, stresses spread in the width direction, and the influence of the temperature distribution was significant for the specimen compressed perpendicular to the grain.

Keywords: Dowelled connections; embedment strength; high temperature; glulam timber; anisotropy

1 INTRODUCTION

In recent years, the demand for medium- and large-scale timber constructions has increased for environmental reasons. Dowelled connections represent a common method employed in mass timber construction. Their load-carrying capacity has been evaluated using Johansen's yield equation, which is a prevalent approach in European and American contexts [1, 2]. Similarly, in Japan, the load-carrying capacity of dowelled connections is evaluated using Johansen's yield theory, considering factors such as the length, diameter, and strength of the dowel, as well as the embedment strength of the timber [3].

¹ Graduate Student, Graduate School of Science and Engineering, Chiba University, Japan
e-mail: 23wm3118@student.gs.chiba-u.jp

² Technical Staff, Faculty of Engineering, Chiba University, Japan
e-mail: kikuchi.takayuki@chiba-u.jp, ORCID: <https://orcid.org/0000-0001-9972-6386>

³ Graduate Student, Graduate School of Science and Engineering, Chiba University, Japan
e-mail: yukiton@chiba-u.jp, ORCID: <https://orcid.org/0000-0002-3814-4902>

⁴ Assistant Prof., Graduate School of Engineering, Chiba University, Dr.Agr., Japan
e-mail: mtotsuka@chiba-u.jp, ORCID: <https://orcid.org/0000-0001-8548-4996>

⁵ Prof., Graduate School of Engineering, Chiba University, Dr.Eng., Japan
e-mail: hirashima@faculty.chiba-u.jp, ORCID: <https://orcid.org/0000-0003-1462-5370>

In the case of a fire in timber construction, dowelled connections play a crucial role in transferring heat, consequently elevating the temperature of adjacent timber components. The strength of the dowels exhibits minimal alterations at temperatures up to 300 °C [4]. In contrast, the strength of timber experiences a notable decline with increasing temperature, with its strength halved at 100 °C [5]. If the dowelled connection is subjected to fire heating, its resistance is not determined by the yield strength of the dowel, but by the embedment strength of the timber. Therefore, it is essential to understand the reduction factor of embedment strength of the timber at high temperatures.

Several tests have been conducted on the embedment strength of timber at high temperatures [6 – 8]. Moraes et al. [6] conducted experiments on dowelled connections in European red pine (*Pinus sylvestris*) and obtained data on embedment strength parallel and perpendicular to the grain at temperatures ranging from 20 °C to 240 °C. They indicated that the embedment strength was 70% of the ambient temperature at 80 °C, followed by strength recovery due to drying, reaching 85% at 140 °C and decreasing to 40-50% at 240 °C. Moss et al. [7] conducted experiments on bolted connections of LVL, and the experimental results showed the reduction factor of the embedment strength at temperatures from 20 °C to 300 °C. They pointed out that the embedment strength decreased to about 61% at 110 °C, 72% at 200 °C, and 22% at 270 °C. Kawarabayashi et al. [8] conducted experiments on dowelled connections in Japanese cedar (*Cryptomeria japonica*) and Japanese larch (*Larix leptolepis*) and obtained data on the embedment strength and embedment stiffness parallel and perpendicular to the grain at temperatures from 20 °C to 150 °C. The embedment strength parallel to the grain decreased by 37-44% up to 100 °C. The embedment strength perpendicular to the grain decreased by 60-65% up to 100 °C. However, there are no defined methods for high-temperature tests.

In some cases, the heating and loading were carried out in a furnace; in others, the test specimens were heated in an oven before being taken out and loaded. However, there were several problems with these methods. When load was applied in the furnace, it was difficult to measure the displacement. When test specimen heated in an oven was taken out and loaded, the temperature decreases before the embedment strength at high temperatures was obtained.

In this study, a heating method using the dowels as a heat source was investigated to replicate the situation at the dowelled connections during a fire, where the dowels transfer heat and increase the temperature of the adjacent timber. This heating method allowed two types of compression tests to be conducted. One was a load-increasing test under steady state at constant high temperature (steady-state test, ST test), as performed in the previous tests. The other was a temperature-increasing test under continuous load (transient-state test, TR test), which is more similar to a fire situation.

This study aims to investigate the embedment strength at high temperatures of glulam timber subjected to heating from a dowel and to consider the reduction factor of the embedment strength.

2 EMBEDMENT TESTS

2.1 Test conditions

The test conditions are shown in Table 1. For the ST test, the load was applied from the time the target temperature was reached until failure to obtain the load-displacement relationships at a constant temperature (see Figure 1(a)). The temperature of timber subjected to embedment was used as the reference temperature for starting the test, and one specimen was tested every 25 to 50 °C from ambient temperature up to 300 °C. For the TR test, to reproduce conditions more similar to a fire, a certain load is applied in advance, and heating is continued until the load can no longer be maintained to obtain the displacement-temperature relationships (see Figure 1(b)). The main parameter of the TR tests was the load ratios. The load ratio was the ratio to the yield load obtained in the ambient temperature test. The load direction was parallel and perpendicular to the grain in both tests, as bending moments and shear forces act in the direction parallel to the grain and perpendicular to the grain, respectively, at the beam end of the column-beam connection. In addition, temperature measurement tests were carried out without loading before the embedment tests at high temperatures were carried out.

Table 1. Test conditions

Steady-state tests (ST tests)									
Load direction	Constant Temperature [°C]								
	AT	50	75	100	125	150	200	250	300
Parallel to the grain	5	1	1	1	2	1	1	1	1
Perpendicular to the grain	5	1	1	1	1	1	1	1	1
Transient-state tests (TR tests)									
Load direction	Constant load ratios [-]								
	1/3	1/2	2/3	5/6					
Parallel to the grain	1	1	1	1					
Perpendicular to the grain	1	1	1	1					

note : The numbers in the table are the number of specimens.

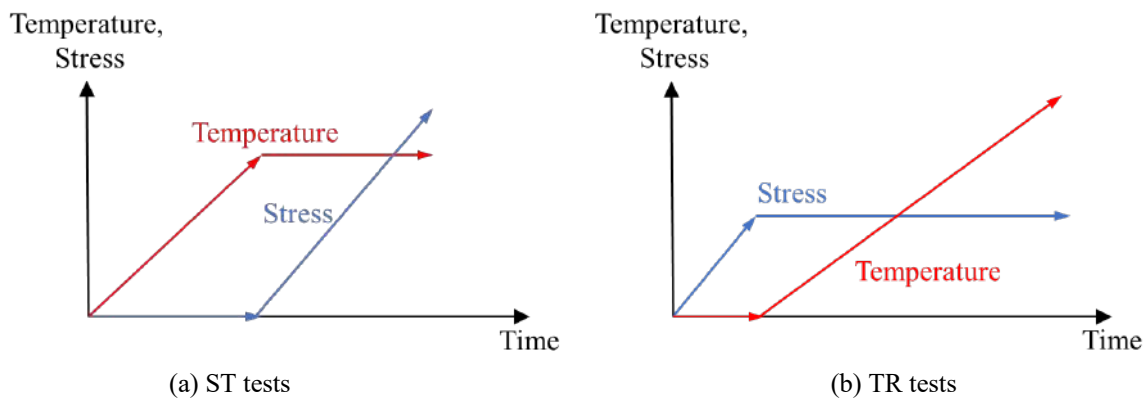


Figure 1. Test outline of ST and TR tests

2.2 Test specimens

The specimens were made of Japanese larch (*Larix kaempferi*) with a reference strength of 20.3 MPa. The material properties of the glulam are shown in Table 2. The density was 0.46-0.51 g/cm³, and the water content was 9.0-10.4%.

The specimens were prepared as dowelled connections, as shown in Figure 2. Due to its closer resemblance to actual fire conditions at the connections, a full-hole test was adopted in this study. Regarding the difference between the full-hole and half-hole tests, Ottenhaus et al. [9] mentioned that the stress distribution in the full-hole tensile tests was not uniform and was similar to the stress state of actual timber connections.

The specimens compressed parallel to the grain have three layers of 25 mm thick lamina (Figure 3(a)), and the specimens perpendicular to the grain have five layers of 30 mm thick lamina (Figure 3(b)). The dowels have a diameter of 16 mm and a length of 90 mm. When the specimens were compressed, they were secured at eight points with metal fittings to prevent rotation at the connections and splitting at the edges of the dowels.

Table 2. Material properties of the test specimen

Load direction	Number of specimens	Density (g/cm ³)	Water content (%)	Compressive strength (N/mm ²)	Young's Modulus (N/mm ²)
Parallel to the grain	3	0.49	9.3	28.3	8596
Perpendicular to the grain	6	0.47	10.3	3.0	485

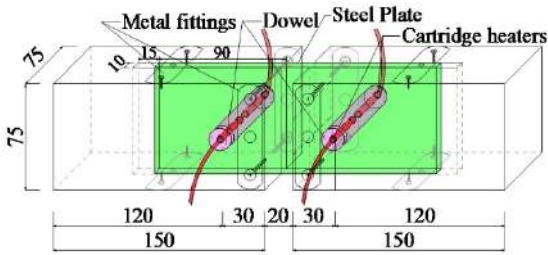
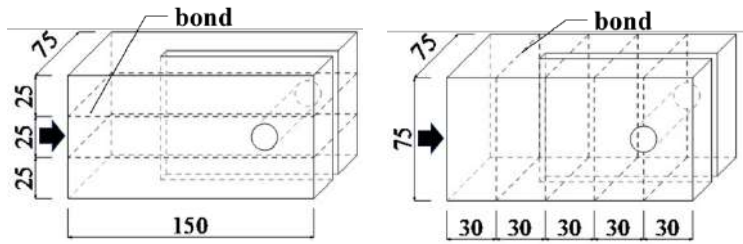


Figure 2. Test specimen



(a) Parallel to the grain (b) Perpendicular to the grain
Figure 3. Load direction

2.3 Heating and compression methods

The test setup is shown in Figure 4. A compression machine was used to apply the force. A load cell was installed at the bottom of the specimen to measure the load. A compressometer with two displacement transducers was used to measure the relative displacement of 150 mm, and the average of the two displacement transducers was used as the displacement. In the ST test, the load was applied at a 0.9 mm/min speed. In the TR test, the load was maintained, and a constant load was within ± 2.5 kN.

Cartridge heaters were used to heat the specimen in order to reproduce a fire situation where the dowel transfers heat. A $\phi 5.0 \times 40$ mm hole was drilled at both ends of the inserted $\phi 16 \times 90$ mm dowel (Figure 5 (a)), and a $\phi 4.0 \times 40$ mm cartridge heater (Figure 5 (b)) was inserted into the hole from both ends. The dowels shown in Figure 5 (a) were not drilled in the contact area (10 mm) with the steel plate, and the deformation of the contact area was suppressed. A $\phi 1.0 \times 50$ mm sheathed thermocouple was inserted into the approximately 1 mm gap created when the cartridge heater was inserted into the dowel to measure and control the temperature.

The temperature measurement points of the specimen for temperature measurement are shown in Figure 6. A glass-coated type k thermocouple was used to measure the temperature of the specimen. The temperature distribution inside the specimen was checked by measuring the temperature at the intersection of the steel plate and the dowel (steel plate temperature: 1, 2), the temperature of the timber section receiving the embedment (embedment temperature: 3 – 6) and the temperature of the timber section around the dowel (timber temperature: 8 – 14). Timber temperatures were measured at 9.4 mm and 18.8 mm from the surface of the specimen at points 10, 20, 30 and 50 mm away from the outer diameter of the dowel. Four points were measured on the specimens in the ST and TR tests at No. 1, 2, 5 and 6 in Figure 6, and the temperatures at No. 5 and 6 were used as reference temperatures in the experiments. The measurement position of the embedment temperature was located on the opposite side of the loading direction to avoid the influence of the load.

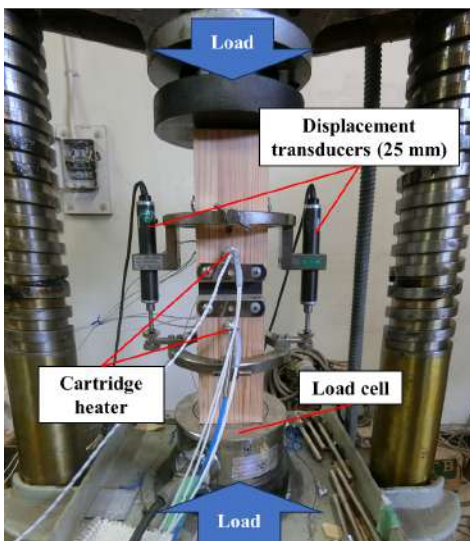
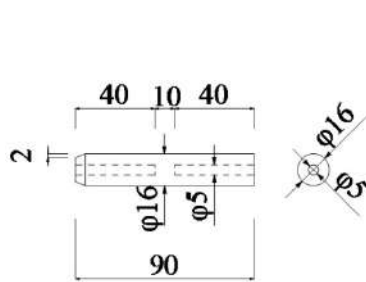


Figure 4. Test setup



(a) Dowel with hole



(b) Cartridge heater

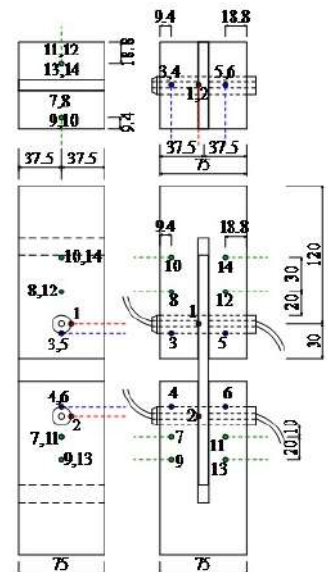


Figure 6. Temperature measurement points

Heating was carried out by increasing the cartridge heater by 2 °C per minute to compare the ST and TR tests and for ease of temperature control.

3 TEMPERATURE MEASUREMENT RESULTS

The temperature measurement results of the non-loaded specimen are shown in Figure 7, corresponding to the measurement points shown in Figure 6. The temperature could be controlled at almost 2 °C per minute constantly.

The embedment temperature reached 260 °C for 140 min (1.64 °C/min) in the specimen compressed parallel to the grain and 145 min (1.59 °C/min) in the specimens compressed perpendicular to the grain. The embedment temperature-time relationships were almost the same for the specimens compressed parallel and perpendicular to the grain.

However, the temperature-time relationships were different for the specimens compressed parallel and perpendicular to the grain far from the dowels. The temperatures of the timber located 10mm away from the dowel reached 81-83 °C in 60 minutes in the specimen compressed parallel to the grain and that reached 51-64 °C in 60 minutes in the specimen compressed perpendicular. The timber temperatures of the specimen compressed parallel to the grain tended to increase more quickly than those of the specimen compressed perpendicular to the grain. This is due to the anisotropy of thermal conductivity, as the thermal conductivity parallel to the grain is considered to be about twice that perpendicular to the grain [10].

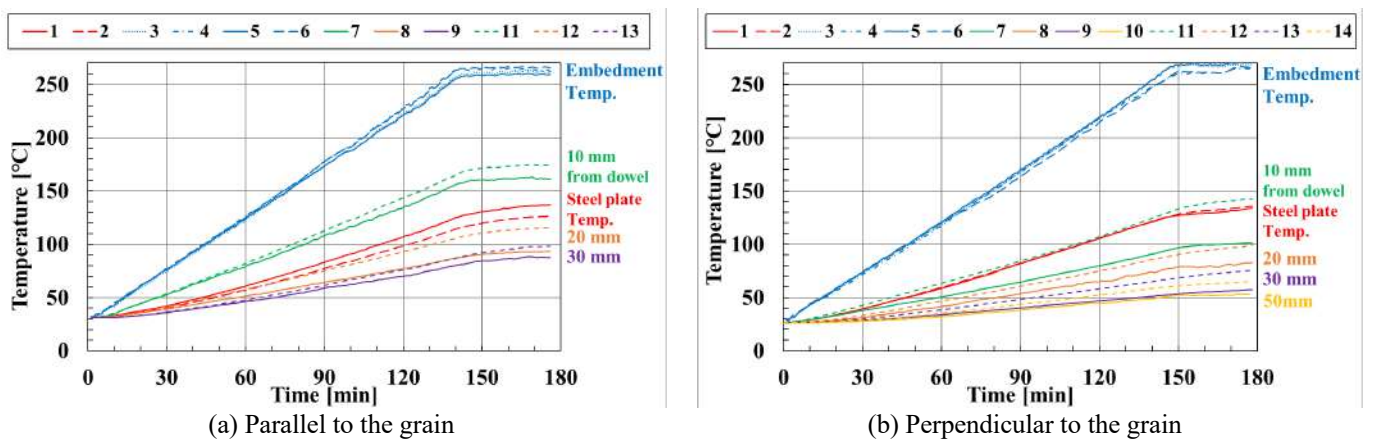


Figure 7. Results of temperature measurement of non-loaded specimens

The embedment temperature results of the ST test are shown in Figure 8. The temperatures could be controlled at almost 2 °C per minute constantly. After reaching the target temperature, the load was started and a gap was created between the timber and dowel. The embedment temperature decreased because the thermocouple at the embedment temperature separated from the dowel. Since the timber at the embedment section is in contact with the dowel, it is likely that the temperature is maintained at the beginning of loading. Therefore, in the discussion, the temperature at the beginning of loading was used as the temperature at embedment strength.

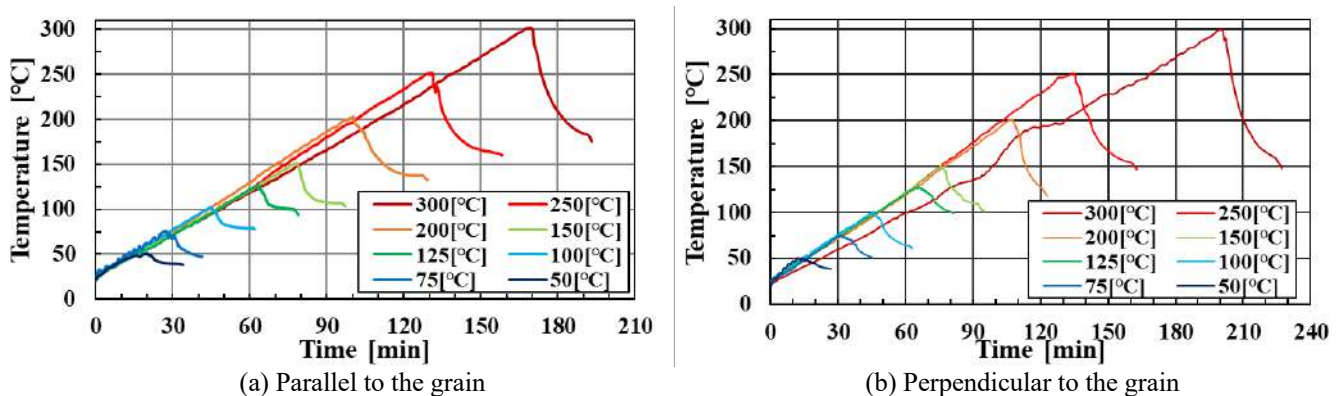


Figure 8. Results of embedment temperature from ST tests

The embedment temperature results of the TR test are shown in Figure 9. The temperatures was controlled at almost 2 °C per minute constantly. At the point where the rate of temperature increase changed, it is likely that the timber yielded, creating a gap between the dowel and the wood. It is possible that the temperature corresponding to the failure time could be evaluated lower than the actual embedment temperature if the temperature in Figure 9 is used to evaluate the temperature. Therefore, in the discussion, the temperature of the non-loaded specimen in Figure 7 is used as the embedment temperature at the failure time of the TR test.

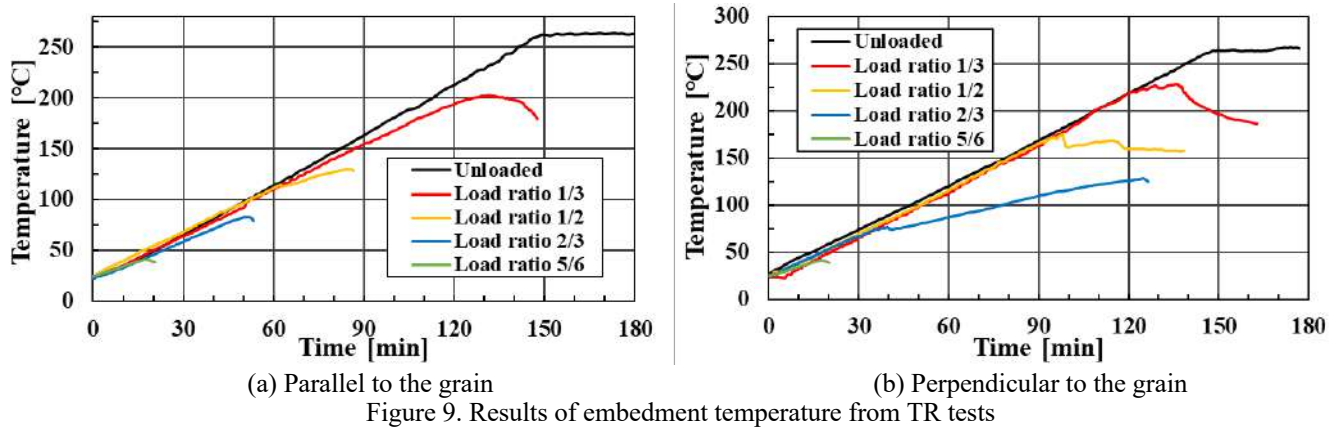


Figure 9. Results of embedment temperature from TR tests

4 EMBEDMENT TEST RESULTS

4.1 Load–displacement relationships in ST tests

The load-displacement relationships in the ST tests are shown in Figure 10. For both specimens compressed parallel and perpendicular to the grain, the stiffness and maximum strength were almost the same from 100 °C to 200 °C. However, the stiffness and maximum strength decreased after reaching temperatures above 200 °C. As shown in Figure 10(a), the specimens compressed parallel to the grain exhibited brittle behavior because of cracking after yielding from ambient temperature to 150 °C. However, they transitioned to ductile behavior from 200°C to 300°C. As shown in Figure 10(b), the specimens compressed perpendicular to the grain consistently exhibited ductile behaviour, with the load increasing steadily from ambient temperature to 300 °C. In addition, the dowels did not yield and deform in the specimens compressed parallel and perpendicular to the grain.

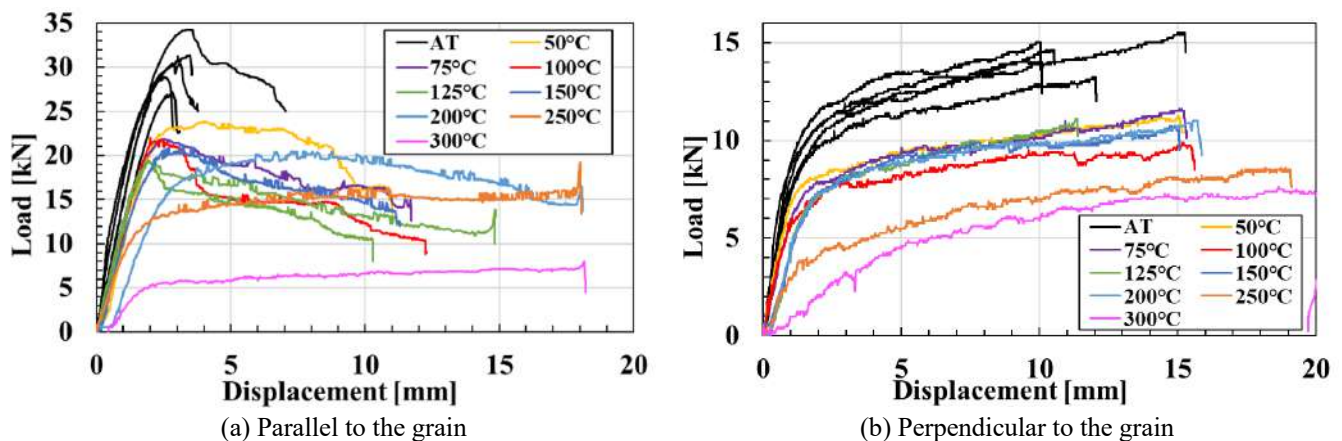


Figure 10. Load–displacement relationships

Embedment strength in the ST tests was calculated using the following equation.

$$\sigma_{y,em} = \frac{P_y}{d \cdot l_{em}} \quad (1)$$

where,

$\sigma_{y,em}$ is the embedment strength,

P_y is the yield load,

d is the diameter of the dowel,

l_{em} is the length of the dowel and timber embedment.

As shown in Figure 11, the yield load was calculated using the 5%-offset method [11]. The initial slope was determined by a straight line passing through two points representing 10% and 40% of the maximum load. The yield point was defined as an intersection point between a parallel shifted line of the initial slope and the load-displacement curve, where the load at this point is called the yield load, and the displacement is called the yield displacement. Considering that the specimen had two dowels, the amount of parallel displacement was 10% of the dowel diameter (1.6 mm). In addition, embedment stiffness defined the initial slope.

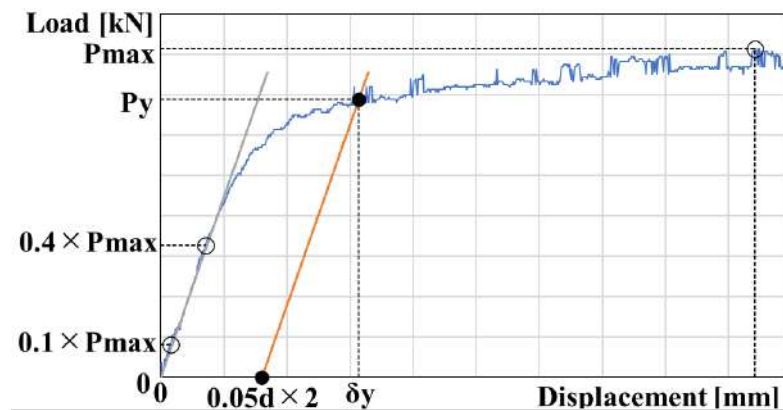


Figure 11. Determination of yield point (Example: Parallel, 250 °C)

Results of the embedment strength at ambient temperature are shown in Table 3. The mean value of embedment strength at ambient temperature was 27.2 N/mm² for specimens compressed parallel to the grain and 10.8 N/mm² for specimens compressed perpendicular to the grain.

Table 3. Embedment strength results at ambient temperature

Load direction	Embedment strength [N/mm ²]					Average [N/mm ²]	Standard deviation [N/mm ²]
	1	2	3	4	5		
Parallel to the grain	27.6	29.7	21.4	25.4	32.1	27.2	3.67
Perpendicular to the grain	11.5	10.0	10.7	10.8	11.1	10.8	0.50

4.2 Displacement–embedment temperature relationships in TR tests

The displacement-embedment temperature relationships in the TR test are shown in Figure 12. The temperatures at end of loading of the specimens compressed parallel to the grain were 45 °C for a load ratio of 5/6, 105 °C for a load ratio of 2/3, 165 °C for a load ratio of 1/2, and 260 °C for a load ratio of 1/3 (Figure 12(a)). The displacement increased due to cracking in the load ratios of 5/6, 2/3, and 1/2. The specimens with lower load ratios failed at higher temperatures compressed parallel to the grain. The temperatures at end of loading of the specimens compressed perpendicular to the grain were 230 °C for a load ratio of 5/6, 225 °C for a load ratio of 2/3, 243 °C for a load ratio of 1/2, and 265 °C for a load ratio of 1/3 (Figure 12(b)). The specimens compressed perpendicular to the grain maintained their load up to temperatures exceeding 200 °C across all load ratios. In addition, regardless of the load direction, there was a tendency for displacement to increase rapidly above 200 °C.

The black dot in Figure 12 is the yield displacements obtained at each temperature in the ST test. The broken line in Figure 12 is a line connecting the mean values of the yield displacements. The yield temperature was determined by the temperature at the intersection point of the broken line and the displacement-embedment temperature curve in Figure 12.

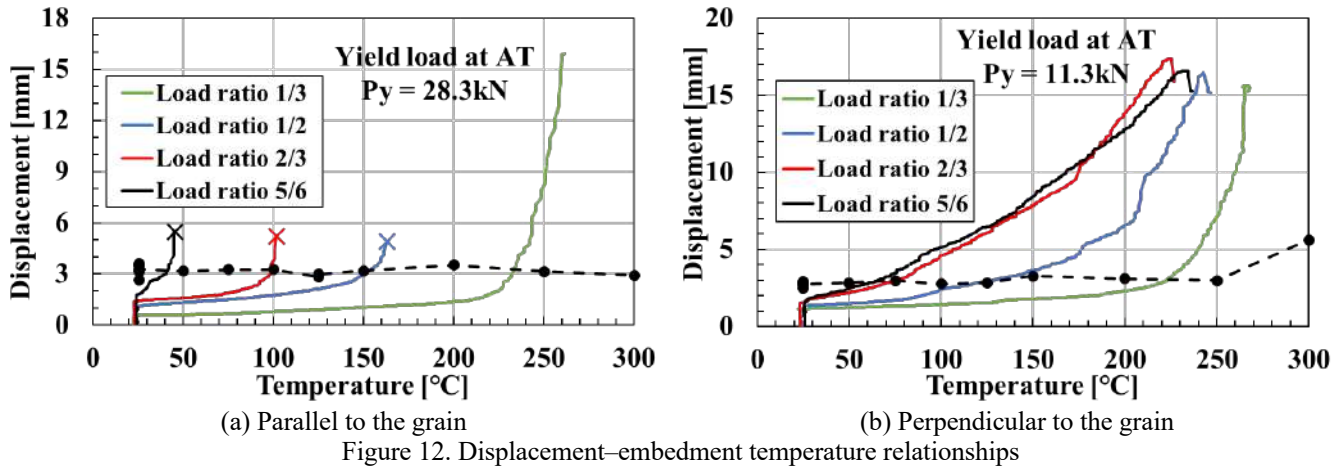


Figure 12. Displacement–embedment temperature relationships

5 REDUCTION FACTOR

5.1 Embedment strength

The reduction factors of embedment strength are shown in Figure 13. From the ST tests (Figure 13(a)), the embedment strength of the specimens compressed parallel to the grain decreased to about 60% of the ambient temperature strength at 125 °C, then slightly recovered with drying at 150 °C, and then decreased to about 50% strength at 250 °C and about 20% strength at 300 °C. The embedment strength of specimens compressed parallel to the grain from TR tests decreased to 67% of ambient temperature strength at 100 °C, with no strength recovery, and decreased to 50% at about 150 °C and 33% at about 230 °C. The reduction factors of embedment strength obtained from the ST and TR tests were similar up to 100 °C, while after 100 °C, the embedment strength of the TR test tended to be smaller than that of the ST test. Although Moss et al. [7] and this study's heating methods differed, the embedment strength reduction factor was roughly the same. Moreover, the reduction factor of the embedment strength in this study tended to be larger than that in Kawarabayashi et al. [8]. This study suggests the reduction factor of embedment strength parallel to the grain, where the strength decreases to 50% at 100 °C and 0% at 300 °C. After 100 °C, the reduction factor of embedment strength is based on the results of TR tests because it is close to the situation during a fire.

As shown in Figure 13(b), the embedment strength of specimens compressed perpendicular to the grain from ST test decreased to about 73% of the ambient temperature strength by 50 °C, with no significant decrease in strength between 50 and 200 °C. The strength decreased significantly to about 40% at 250 °C, with no further decrease in strength between 250 and 300 °C. The embedment strength of specimens perpendicular to the grain from TR tests decreased to 67-83% of ambient temperature strength by about 75 °C, with no stagnation of strength, and further decreased to 50% at about 130 °C and 33% at about 220 °C. The reduction factors of embedment strength obtained from the ST and TR tests showed a similar trend for specimens compressed parallel to the grain, with similar embedment strength up to 100 °C, while

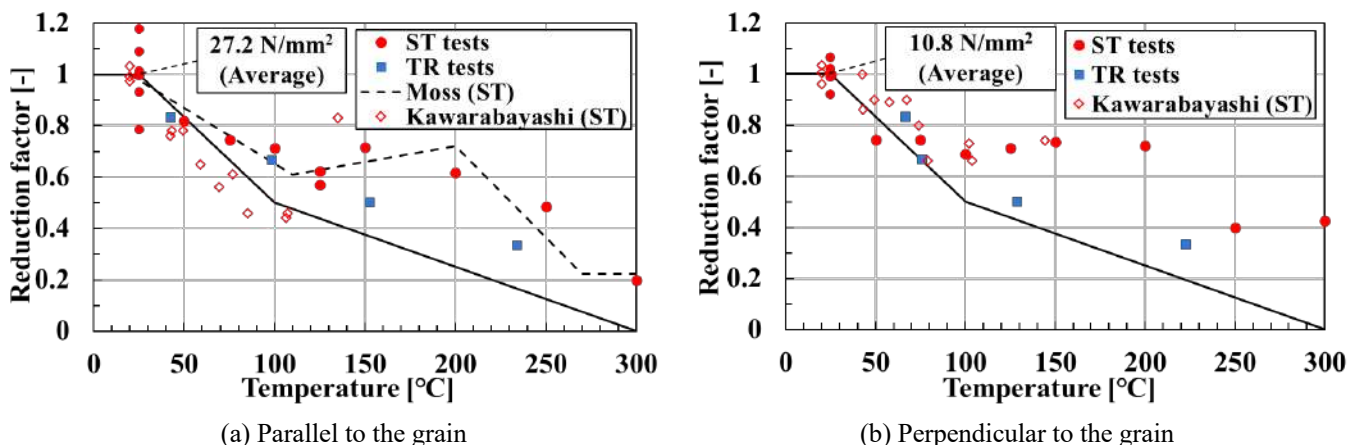


Figure 13. Reduction factor of the embedment strength

after 100 °C, the embedment strength of the TR test tended to be smaller than that of the ST test. The difference in the reduction factor of embedment strength between the ST and TR tests after 100 °C was probably due to transient creep, which increases with temperature. The reduction factor of embedment strength in this study and Kawarabayashi et al. [8] was roughly the same in the specimens compressed perpendicular to the grain. This study suggests the reduction factor of embedment strength perpendicular to the grain, where the strength decreases to 50% at 100 °C and 0% at 300 °C.

5.2 Embedment stiffness

Results of the embedment stiffness at ambient temperature are shown in Table 4. The mean value of the embedment stiffness at ambient temperature was 34.5 N/mm³ for specimens compressed parallel to the grain and 19.0 N/mm³ for specimens compressed perpendicular to the grain. Embedment stiffness of specimens compressed parallel to the grain showed variability.

Table 4. Embedment stiffness results at ambient temperature

Load direction	Embedment stiffness [N/mm ³]					Average [N/mm ³]	Standard deviation [N/mm ³]
	1	2	3	4	5		
Parallel to the grain	53.3	38.5	22.9	26.2	31.6	34.5	10.77
Perpendicular to the grain	19.2	15.5	16.1	24.1	20.1	19.0	3.10

The reduction factors of the embedment stiffness are shown in Figure 14. As shown in Figure 14(a), the embedment stiffness of specimens compressed parallel to the grain decreased to about 70% of the ambient temperature stiffness by 75 °C, and then stiffness did not decrease from 75 °C to 150 °C. The stiffness decreased to about 50% at 200-250 °C, and the stiffness decreased to about 25% at 300 °C. Similar to the embedment strength, the reduction factor of this study in the embedment stiffness tended to be larger than that of Kawarabayashi et al. [8].

As shown in Figure 14(b), the embedment stiffness of the specimens perpendicular to the grain decreased to about 70% of the ambient temperature by 50 °C, with no significant decrease in stiffness between 50 and 200 °C. The stiffness decreased to 33% at 250 °C and 12% at 300 °C. Similar to the embedment strength, the reduction factor of the embedment stiffness in this study and in Kawarabayashi et al. [8] was generally the same. In addition, the reduction factors of the embedment stiffness parallel and perpendicular to the grain were similar.

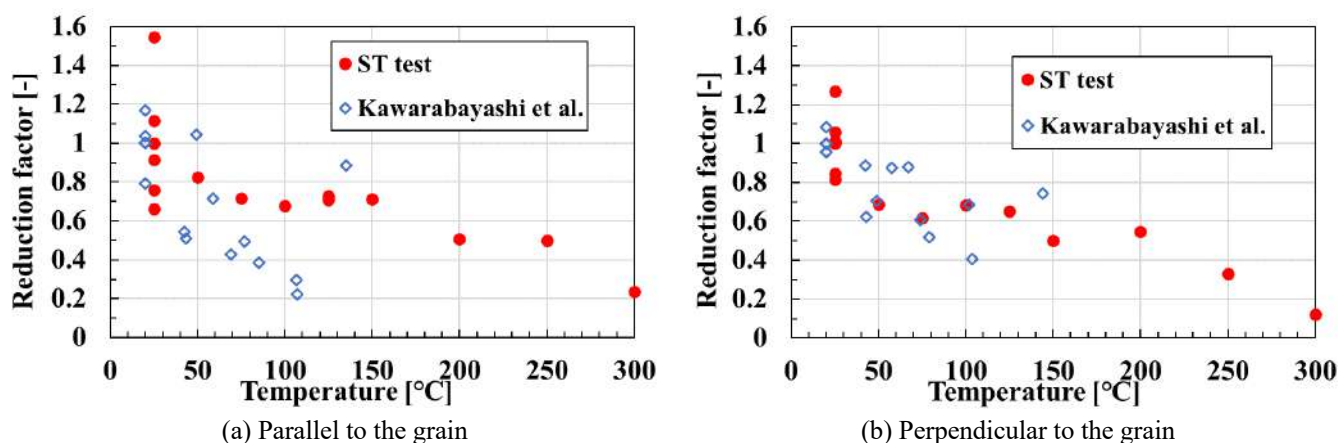


Figure 14. Reduction factor of the embedment stiffness

6 INFLUENCE OF TEMPERATURE DISTRIBUTION AROUND THE DOWEL

6.1 Finite element model

A finite element analysis was carried out for TR test to understand the effect of temperature distribution around the dowel. The analysis was performed using the non-linear FE analysis software Marc [12]. The

analysis model is shown in Figure 15. Because the specimen was symmetrical, it was modelled as one-half of the specimen. The analysis models were based on the Damage Zone model (Parallel to the grain) and the Split model (Perpendicular to the grain) presented by Kawai et al. [13]. The Damage Zone model has a low stiffness area of about 3 mm in length from the embedment area (see Figure 16). The Distribution model provided the temperatures for each measurement point, as shown in Figure 16 (one for each of the four temperature zones). The Homogeneous model provided the embedment temperature throughout the model.

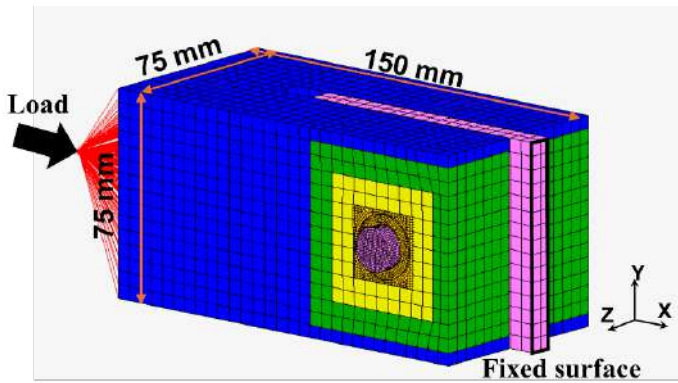


Figure 15. Analysis model

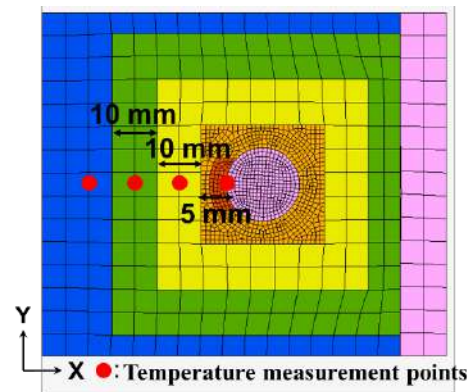


Figure 16. Models around the dowel

Material properties of the timber at ambient temperature are shown in Table 5. Young's modulus, Poisson's ratios, and yield stress were obtained from the compression test. Young's modulus and Poisson's ratio have a constitutive equation relationship, and the shear modulus was obtained from a constitutive equation [14]. Hill's yield equation was used for the yield. Material properties of timber at high temperatures were determined using the reduction factor on modulus of elasticity and the reduction factor for compressive strength, as given in Eurocode 5 [5]. Young's modulus of steel was set at 205 kN/mm² and Poisson's ratio at 0.3.

Table 5. Material properties of the timber

Young's modulus (N/mm ²)			Poisson's ratios (-)			Shear modulus (N/mm ²)			Yield stress (N/mm ²)		
E_L	E_R	E_T	ν_{LR}	ν_{RT}	ν_{TL}	G_{LR}	G_{RT}	G_{TL}	$\sigma_{y,L}$	$\sigma_{y,R}$	$\sigma_{y,T}$
8596	485	320	0.56	0.86	0.028	433	114	293	28.3	3.0	2.7

6.2 Analysis results and discussion

The results of the FE analysis are shown in Figure 17. As shown in Figure 17 (a), the displacement corresponded to the experimental values up to about 50 °C using the Damage Zone model for specimens compressed parallel to the grain. The failure temperature was also roughly the same between the analysis and the experimental values at 100 °C. In addition, there was no difference in the increase in displacement between the Homogeneous and Distribution models.

As shown in Figure 17(b), the displacement curves of analysis values for the Distribution model and the experimental values were roughly the same for the specimen perpendicular to the grain. Differences in displacement increase were observed between the Homogeneous and Distribution models, with the latter retaining load up to higher temperatures more than the former. The influence of temperature distribution around the dowel was not significantly observed parallel to the grain but was evident perpendicular to the grain.

Stress distributions are shown in Figure 18. Stress concentration was observed in the embedment area for the specimen compressed parallel to the grain (Figure 18 (a)). In contrast, stresses were spread across the width of the specimen for the specimen compressed perpendicular to the grain (Figure 18 (b)). Therefore,

the reason for the influence of temperature distribution in the specimen compressed perpendicular to the grain was that the timber at a low temperature away from the dowel resisted the axial forces.

The specimens after the test are shown in Figure 19. Similar to the stress distribution obtained from the FE analysis, the deformation was concentrated in the embedment area for the specimen compressed parallel to the grain, whereas the deformation was spread to the specimen compressed perpendicular to the grain.

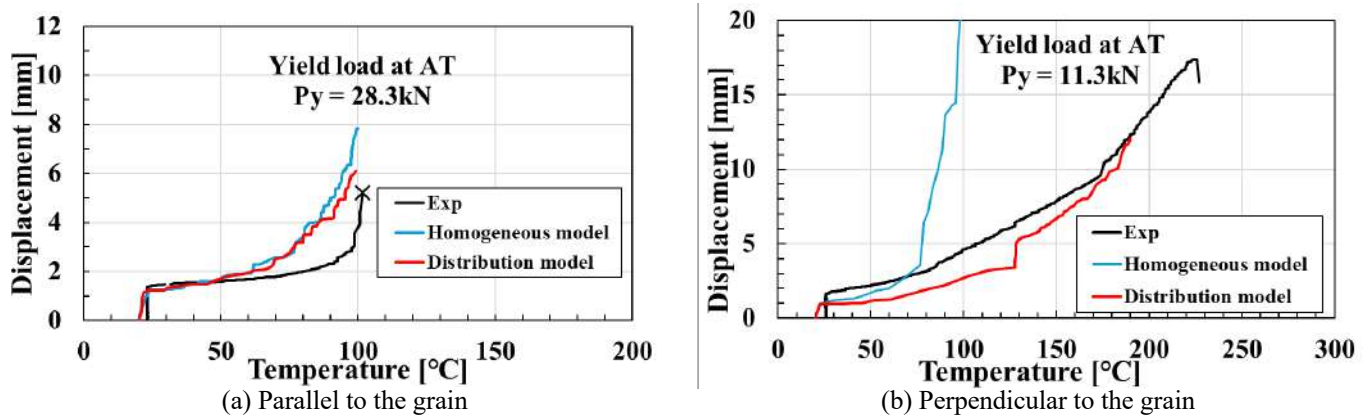


Figure 17. Displacement-embedment temperature relationships (load ratio 2/3)

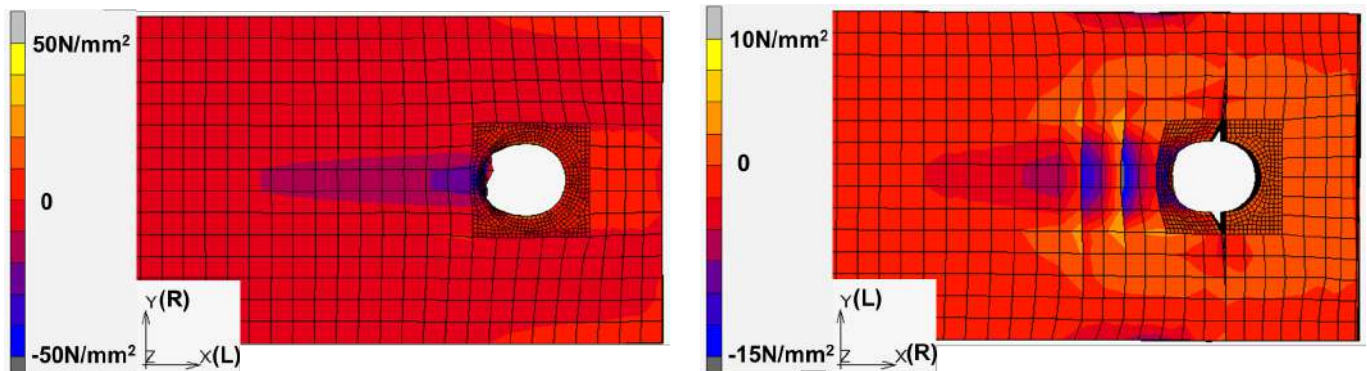


Figure 18. Stress distribution (Temperature distribution model, At maximum displacement)



Figure 19. Specimen after the test (TR tests, load ratio 2/3)

7 CONCLUSION

This study tested glulam timber subjected to heating from dowels to obtain the embedment strength at high temperatures. The findings are summarized as follows:

- 1) The reduction factor of the embedment strength, obtained from the steady-state tests, exhibited a slight decrease in strength between 100 °C and 200 °C for specimens compressed parallel and perpendicular to the grain. In contrast, the reduction factor obtained from the transient-state tests continued to decrease

after 100 °C. This was probably due to the effect of transient creep, which tended to increase with temperature. Based on the transient-state test results, the reduction factor of the embedment strength was proposed which decreased to 50% at 100 °C and 0% at 300 °C.

- 2) The specimens compressed parallel to the grain exhibited brittle behaviour because of cracking after yielding from ambient temperature to 150 °C. However, they transitioned to ductile behaviour from 200°C to 300°C. The specimens compressed perpendicular to the grain consistently exhibited ductile behaviour, with the load increasing steadily from ambient temperature to 300 °C.
- 3) The specimen compressed parallel to the grain with a higher load ratio failed at around 100 °C. Conversely, compressed perpendicular to the grain, specimens maintained their load at all load ratios up to temperatures exceeding 200 °C. In the results of the FE analysis, for specimens compressed parallel to the grain, stresses were concentrated in the embedment area, with minimal impact from the temperature distribution. In contrast, for specimens compressed perpendicular to the grain, stresses were distributed across the width and resisted in the timber away from the dowel, where the temperature was lower.

ACKNOWLEDGEMENT

This study was supported by the JSPS KAKENHI (grant numbers JP22H04232 and JP22H01636). The analysis was carried out using computer resources offered under the category of General Projects by the Research Institute for Information Technology, Kyushu University.

REFERENCES

1. Johansen, K.W., Theory of Timber Connections, Int. Assoc. Bridge and Struct. Eng., Vol. 9, pp. 249–262, 1949.
2. EN1995-1-1 : Eurocode 5 : Design of Timber Structures – Part 1-1 : General – Common Rules and Rules for Buildings, 2004
3. Architectural Institute of Japan, Standard for Structural Design of Timber Structures, 2006 (in Japanese).
4. EN1993-1-1 : Eurocode 3 : Design of Steel Structures – Part 1-2 : General Rules – Structural Fire Design, 2005.
5. EN1995-1-2 : Eurocode 5 : Design of Timber Structures – Part 1-2 : General – Structural Fire Design, 2004
6. Moraes, P.D., Rogaume, Y., Bocquet, J.F. and Triboulot, P., Influence of Temperature on the Embedding Strength, Holz als Roh – und Werkstoff, Vol. 63, pp. 297–302, 2005.
7. Moss, P., Buchanan, A., Fragiacomio, M. and Austruy, C., Experimental Testing and Analytical Prediction of the Behavior of Timber Bolted Connections Subjected to Fire, Fire Technology, Vol. 46, pp. 129–148, 2010.
8. Kawarabayasi, F., Kikuchi, T., Totsuka, M. and Hirashima, T., Embedding Behaviors of a Dowelled Connection in Structural Glulam Timber at High Temperature, J. Stust. Constr. Eng., Architectural Institute of Japan, Vol. 87, No. 795, 2022, pp.498–509 (in Japanese).
9. Ottenhaus, L.M., Li, Z. and Crews, K., Half Hole and Full Hole Dowel Embedment Strength: A review of International Developments and Recommendations for Australian Softwoods, Construction and Building Materials, 344 (2022) 128130.
10. Maku, T., Studies on the Heat Conduction in Wood, Wood Research, No. 13, pp. 1–80, 1954
11. Sawata, K. and Yasumura, M., Determination of Embedding Strength of Wood for Dowel-Type Fasteners, Journal of Wood Science, 48 (2002) 138–146.
12. MSC Software Corporation, MSC.MARC User’s Manual. Vol. A : Theory and User Information, Stockholm, Sweden, 2017
13. Kawai, Y., Totsuka, M. and Hirashima, T., Elastoplastic Analysis of Timber Connections with Dowel-Type Fasteners at Ambient and High Temperatures, Forests, 14, 373, 2023
14. Norman, E.D., Mechanical Behavior of Materials : Engineering Methods for Deformation, Fracture, and Fatigue, Pearson Prentice Hall, 2007

EXPERIMENTAL FIRE STUDIES COMPARING THE CHARRING BEHAVIOUR OF TIMBER PROTECTED WITH THIN INTUMESCENT COATINGS AND FIRE RATED PLASTERBOARD

Stavros Spyridakis¹, Felix Wiesner², Anwar Orabi³, Cristian Maluk⁴

ABSTRACT

The experimental fire studies presented herein investigate the influence in the charring behaviour of mass timber structures with thin intumescent coatings and fire rated plasterboard layers as a means of passive fire protection. CLT samples tested within the scope of this research are characterised as: (a) bare timber, (b) timber coated with one of two types of thin intumescent coatings and (c) timber encapsulated with either one, or two, layers of fire rated plasterboard. For the coated timber, a thin film of 2.45 ± 0.15 mm for Coating A and 2.25 ± 0.15 mm for Coating B was applied, while for the encapsulated samples the thickness of each plasterboard layer was 13 mm. A total of 45 CLT samples were tested using the H-TRIS method for a duration of 60 min at three incident radiant heat fluxes of 25, 50, and 75 kW/m². The outcomes demonstrated that intumescent coatings did not prevent timber from charring (assumed when timber reaches 300 °C) for the specified heat exposure. However, they delayed considerably the overall heat transferred into the timber, with their protective efficacy being inversely proportional to the heat flux intensity. For the encapsulated samples, it was deduced that once the plasterboard layer dehydrated and timber began to char, the resulting char depth increment is steep, leading to even higher charring rates than the coated samples. Lastly, for timber samples with two plasterboard layers charring was only observed at 75 kW/m², while samples with Coatings A, B, or one plasterboard layer experienced charring at all three heating conditions.

Keywords: Mass timber; thin intumescent coating; fire rated plasterboard; timber charring; H-TRIS.

1 INTRODUCTION

The influence exposed (unprotected) timber may have in the response of a building during and after a fire, remains a key challenge to mass timber construction. In the event of a fire, exposed mass timber elements, such as slabs, walls, columns, or beams, could experience flaming combustion; this is probably the most direct impact. However, the nature of this impact is complex and plays an important role in every phase of a fire. During the growth phase, flaming combustion of timber may result in a faster fire growth, while in the fully developed phase, the flaming of exposed timber may result in a more intense fire [1]. Lastly, during the decay phase, the burning of the mass timber structure may lead to a sustained fire and longer burnout duration, therefore releasing heat beyond the burnout of furniture and other moveable fuel load. The above pose a challenge to several aspects which are at the core of a fire safety strategy for a building. For instance, they may lead to the spread of the fire beyond the floor of fire origin, as well as compromising

¹ PhD Candidate, School of Civil Engineering, The University of Queensland, Australia
e-mail: s.spyridakis@uq.edu.au, ORCID: <https://orcid.org/0000-0003-1978-0556>

² Assistant Professor, Faculty of Forestry – Department of Wood Science, The University of British Columbia, Canada
e-mail: felix.wiesner@ubc.ca, ORCID: <https://orcid.org/0000-0002-0231-4244>

³ Lecturer, School of Civil Engineering, The University of Queensland, Australia
e-mail: a.orabi@uq.edu.au, ORCID: <https://orcid.org/0000-0001-5083-3623>

⁴ Technical Director, Semper, UK
e-mail: c.maluk@sempergrp.com, ORCID: <https://orcid.org/0000-0002-1662-6943>

the stability of the load bearing structure during and after the fire. In modern mass timber construction, the predominant fire safety engineering solution used to mitigate the above challenges is the partial or complete encapsulation of timber using fire rated plasterboards. The main purpose of mass timber encapsulation is to prevent the ignition of timber, thus eliminating its contribution to the spread and severity of the fire. Subsequently encapsulation delays the initiation of charring – a phenomenon conventionally assumed to occur when timber reaches a temperature of 300 °C [2], with the charred portion of the structural element assumed to have negligible mechanical properties.

Thin intumescent coatings, widely employed in the steel construction industry as a substitute to traditional passive fire protection such as fire rated plasterboards, could be used as an alternative means of fire protection to address the challenges associated with timber burning [3]. When exposed to heat, intumescent coatings can intumesce up to 50 times their original thickness. These coatings are typically applied as a thin film with a thickness of up to 3 mm, referred to as Dry Film Thickness (DFT) [4]. Intumescent coatings offer several key advantages over other passive fire protection methods. Perhaps the most notable of these advantages is the enhanced aesthetics and application flexibility – onsite or offsite [5, 6]. However, before applying thin intumescent coatings as a fire protection solution for mass timber, it is imperative to acquire a fundamental understanding of the underlying principles governing their efficacy for mass timber in fire, thus instilling the same level of confidence placed in more traditional passive fire protection solutions.

2 RESEARCH METHODOLOGY

This experimental fire study investigates how thin intumescent coatings and encapsulation with fire rated plasterboard layers, influences the charring of mass timber substrates. Specifically, it considers the timber-coating and timber-plasterboard responses at varied heating conditions, benchmarking them against bare timber. The fire tests involved Cross Laminated Timber (CLT) samples, characterised as: (a) bare timber, (b) timber coated with one of two types of thin intumescent coatings and (c) timber encapsulated with either one, or two, fire rated plasterboard layers. Both intumescent coating types had an opaque finish, with Coating A (solvent-based) being a commercial flagship for passive fire protection of steel structures, while Coating B (water-based) formulation was developed for use on timber. For the encapsulated samples, commercially available fire rated plasterboards with a thickness of 13 mm were used.

Empirical correlations were also developed comparing the influence of the coating DFT and plasterboard thickness to the (i) onset of charring delay and (ii) charring rate reduction for the protected timber, while accounting for the effects associated with the variation of the heating condition. A similar investigation was briefly undertaken by Hartl et al. [7], however, those tests focused on the onset of charring only (i.e., terminated when the protected timber reached 300 °C or after one hour of testing) and were limited to one intumescent product. The experimental study herein expands upon these findings through systematic testing and analysis, providing increased confidence to assess the charring behaviour of timber, quantitatively and qualitatively, focusing on coated and encapsulated timber samples.

2.1 Testing apparatus and instrumentation

Bench-scale fire experiments were conducted with a Heat-Transfer Rate Inducing System (H-TRIS) [8], consisting of four radiant panels with total dimensions of 300×400 mm². This enabled imposition of incident radiant heat fluxes in the range of 5 to 100 kW/m². Key components of the apparatus are shown in Figure 1 below. The H-TRIS was mechanically controlled, therefore allowing for the position of the radiant panels to be corrected during testing of the coated samples by capturing the swelling effect, to ensure that the target incident radiant heat flux on the surface of the sample remains constant. The swelling behaviour of the coatings was recorded by a high-resolution camera and captured in a monitor during each test, allowing the live correction of heat flux, thus improving the consistency of results between repeat tests. Similarly, the in-depth temperatures of all timber samples were measured using thermocouples, placed along the sample's depth. In addition, a spark igniter was mounted on the sample holder to pilot the ignition, effectively establishing a lower bound ignition criterion replicating likely ignition conditions in real fires.

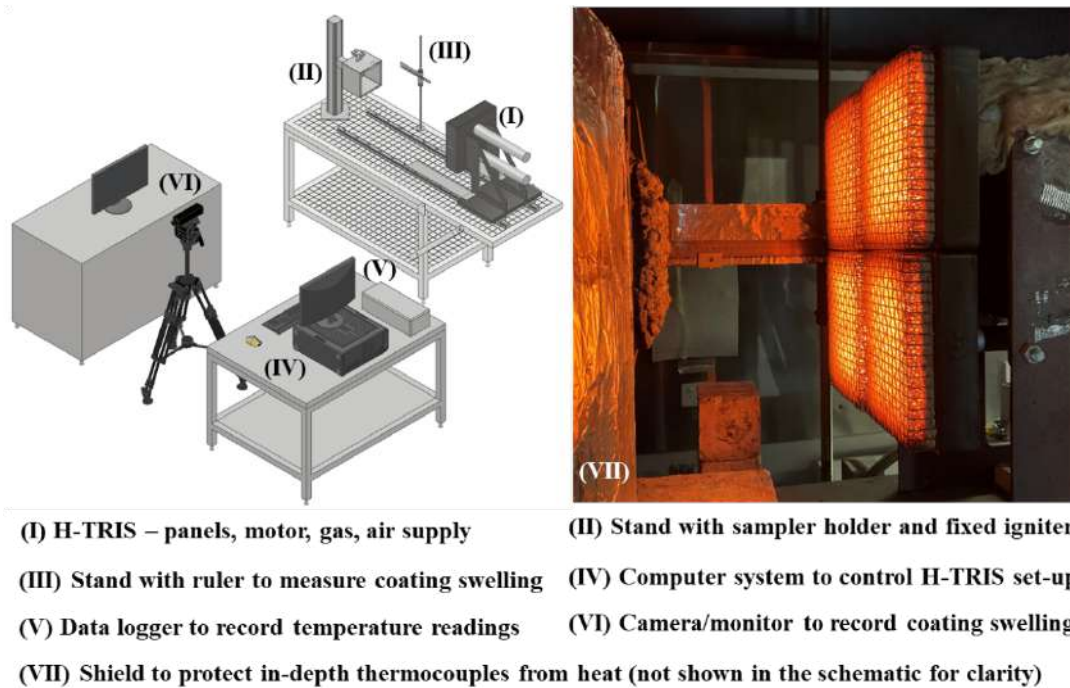


Figure 1. (Left) Technical drawing showing the H-TRIS experimental setup with key peripheral instrumentation; (Right) Close-up view of H-TRIS during testing of an intumescent-coated timber sample

2.2 Testing procedure and sample preparation

Fire experiments were conducted at three different, constant, incident radiant heat fluxes of (A) 25 kW/m², (B) 50 kW/m², (C) 75 kW/m². This range of heat fluxes allowed assessing the fire behaviour of the samples from; (A) – fire exposure conditions above those for bare timber piloted ignition (13-14 kW/m²) [9] to conditions approximating auto-ignition of cellulosic materials (≥ 20 kW/m²) [10]; and (B) – above bare timber self-extinction for the charring effect to continue (> 45 kW/m²) [11]. Lastly, (C) – the 75 kW/m² heat flux condition was selected to further examine the sustained fire performance of the intumescent coatings and fire rated plasterboards during significantly elevated temperatures.

Each fire test was carried out for 60 min, to collect sufficient data considering the available apparatus and size of the samples. The test duration, or the test results, are not equivalent to standard fire testing or the ISO standard fire curve. The fixed heat fluxes were selected to illuminate fundamentals rather than direct fire safety approvals – i.e., to highlight the dependency of the charring behaviour in timber (protected or bare) to the severity of the heat flux condition that it is exposed to. Additionally, this allows for a direct comparison for different types of samples and heating conditions, which is not necessarily possible in a standard fire test, considering in a standard fire test the imposed heat flux varies depending on the material being tested, as does the fuel load needed to maintain the ISO standard fire curve.

For bare timber, the igniter was switched-off once sustained flaming was established at the exposed surface of the sample – characterised as continuous flaming for at least 30 sec; this is longer than required in a standard reaction-to-fire test [12]. For the coated timber samples, the pilot was switched-off after the first 5 min of the test to assess the response of the coating during the swelling stage. To ensure a consistent testing approach with the encapsulated timber sample tests, the pilot was also kept on for the first 5.

Square timber samples with length 200 mm were prepared from 110 mm deep CLT panels of Australian radiata pine (*pinus radiata*). Each CLT sample comprises three lamellas with 32.5 mm, 45 mm, and 32.5 mm thickness. For the coated samples, the intumescent product was applied on the surface of the samples by a registered professional using an airless spray gun. For the encapsulated samples, plasterboard layers of 200×200 mm² were affixed onto the timber surface using screws. A total of 45 samples were tested as part of this experimental fire study, with nine samples per surface type (i.e., bare, coated, and encapsulated timber), resulting in three tests per heat flux condition. Figure 2 shows typical samples prior to being tested, with their sides wrapped using ceramic wool and aluminium foil tape. This minimised any transversal heat exchange from the sample holder, thus creating one-dimensional heat transfer conditions.

Each sample was drilled from its side using a CNC machine for accuracy, creating 100 mm deep holes with a diameter of 2 mm. This enabled the insertion of 1.5 mm Type K thermocouples with an error margin of ± 2.2 °C [13], with their tip at the centre of the sample's surface. This position, in-depth from the centre of the exposed surface, corresponded to the maximum incident radiant heat flux. This was verified through the calibration process of the apparatus. The thermocouples were staggered along the central axis from the side of the sample to minimise thermal disturbances from each other (Figure 2 e)). Their insertion perpendicular to the main heat flux direction and thus parallel to the isotherms further reduced thermal disturbances that would arise from the difference in conductivity between TCs and timber [14, 15]. For the coated and bare timber samples, the thermocouples were inserted at varying depths from the exposed surface to the back of the sample at: 3, 5, 10, 20, 33, 50, 78, and 110 mm. As shown in Figure 2 e), for encapsulated timber samples an additional thermocouple was placed between the timber front surface and the underside of the plasterboard layer, at 0 mm. Similarly, for the samples with two layers of plasterboard a thermocouple was also inserted between the two boards.

The DFT for each coating was measured with an electronic gauge with a probe for timber substrates. The mean DFT values, along with the max. and min. intervals, are reported in Table 1 below. The target DFT for Coating A was selected based on the max. DFT allowed for Coating B as per manufacturer's guidelines. Additionally, the moisture content for the 45 samples (i.e., a total of five campaigns, each including nine samples per surface type) was tracked weekly by using sacrificial timber samples, as each testing campaign was completed on a weekly basis. The sacrificial samples were stored at ambient temperature conditions in the same laboratory environment as the tested samples, and following the oven dry method [16].

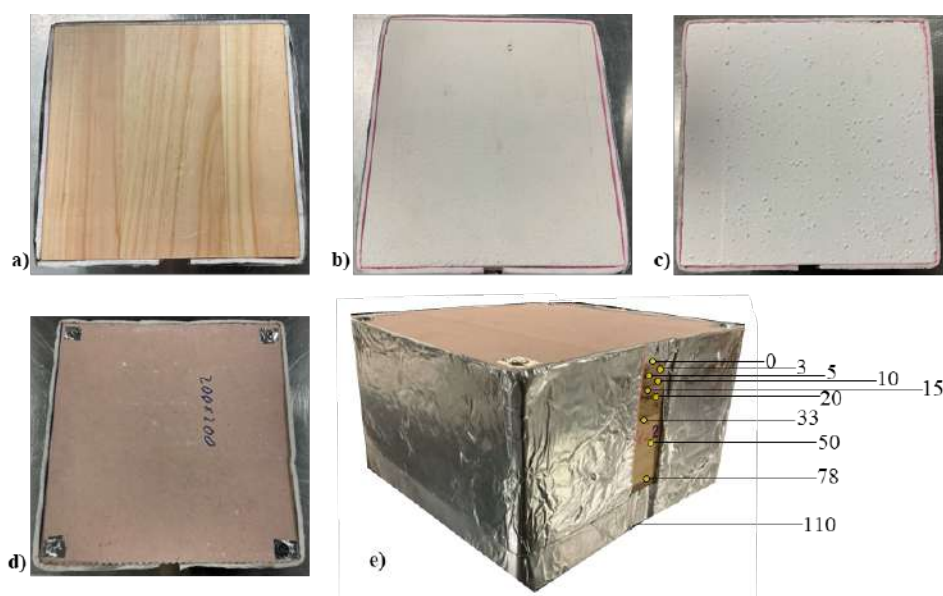


Figure 2. Typical samples used for testing for a) Bare timber, b) Coating A, c) Coating B, d) Plasterboard and (d) ISO view of a wrapped timber sample with the thermocouple locations shown in millimetres, with one layer of plasterboard affixed on top

Table 1. Moisture content of tested samples and thickness of intumescent coating and plasterboard layer

Surface type	Timber moisture content [%] (by mass)	Fire protection thickness [mm] (at ambient conditions)
Bare Timber	9.1	N/A
Intumescent Coating A	9.5	2.45 ± 0.15
Intumescent Coating B	9.3	2.25 ± 0.15
Plasterboard – One Layer	11.1	13
Plasterboard – Two Layers	10.1	26

3 EXPERIMENTAL RESULTS

The char of timber (bare, coated, and encapsulated) was measured during post-processing of the in-depth temperature readings of the tested samples. This was done by tracking the 300 °C isotherm of the timber samples using a smoothing spline fit [17, 18], assuming the char front aligns with the 300 °C in-depth temperature evolution. The mean char depth for the tested samples at 25 kW/m², 50 kW/m² and 75 kW/m² is presented in Figure 3, Figure 4, Figure 5, respectively. This is based on three repetitions per sample type for each heating condition, with the max. and min. char depth values also shown in a shaded format. There is a clear distinction in the char depth increment plots between bare timber and coated or encapsulated timber. Protected timber experienced not only a reduced char depth by the end of the tests (60 min) but also a significant delay in the onset of charring. The latter is associated with pyrolysis initiation of the timber and thus the reduction of its mechanical properties, which was taken as the time that the first in-depth thermocouple, i.e. at 3 mm from the timber’s front surface, reached 300 °C.

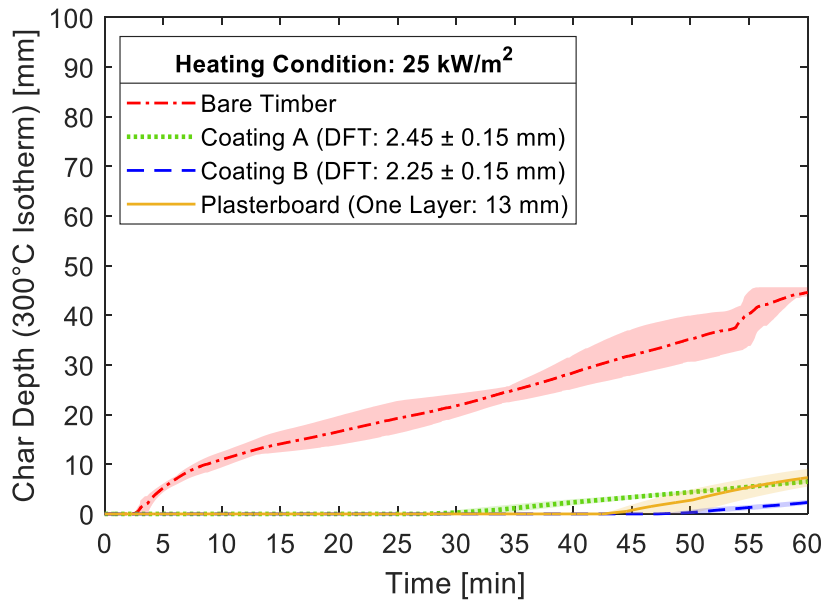


Figure 3. Mean char depth with max. and min. intervals highlighted for tested samples at 25 kW/m²

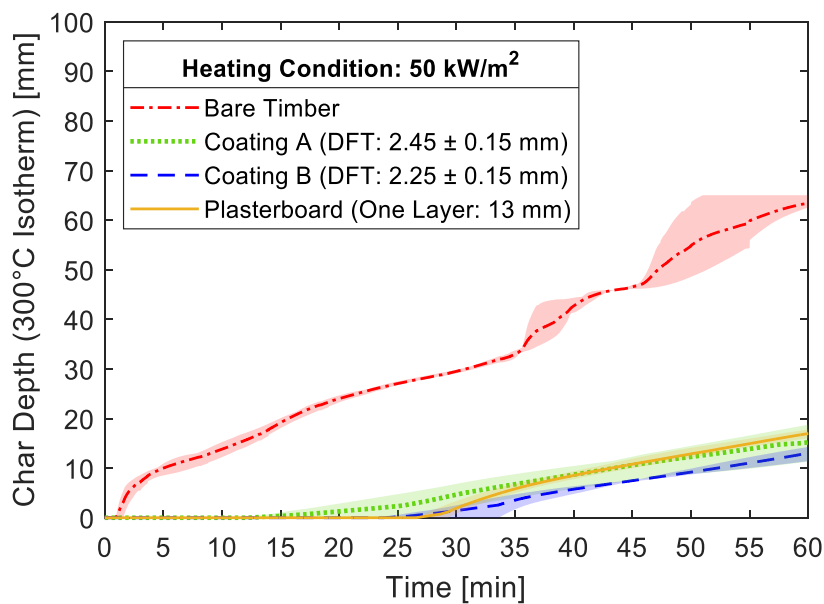


Figure 4. Mean char depth with max. and min. intervals highlighted for tested samples at 50 kW/m²

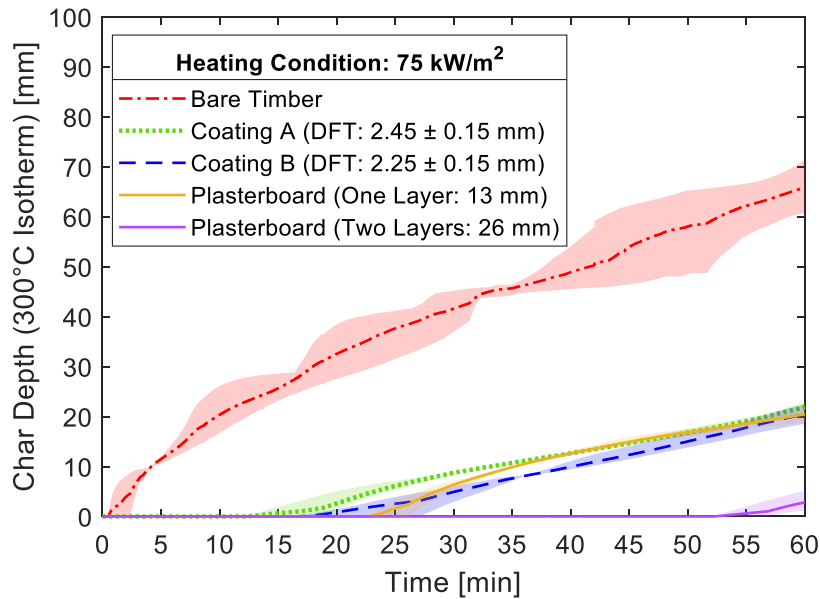


Figure 5. Mean char depth with max. and min. intervals highlighted for tested samples at 75 kW/m²

3.1 Onset of timber charring

The mean measured values for the onset of timber charring are presented in Table 2 below. For samples with two layers of plasterboard, charring during the specified test time for these timber samples was only observed at 75 kW/m², hence why no char depth data are shown for those in Figure 3 and Figure 4. Further, Coating B was the second most effective thermal buffer (compared to two layers of plasterboard) at 25 kW/m² to delay the initiation of timber charring. At 50 kW/m², Coating B and one layer of plasterboard samples had a similar insulating effect, followed by Coating A.

However, for the most onerous heating scenario (75 kW/m²), the one layer of plasterboard samples began to char at a later stage of the test compared to coated samples. Although small variations were observed in the onset of charring data between repeat tests of the same type of samples under the same heating condition, they had practically no impact on the final char depth (at 60 min) for coated and encapsulated timber samples. Conversely, variances in the data between repeat tests were more pronounced for bare timber samples due to significant and continuous flaming and char fall-off from the early stages of the test.

Table 2. Mean onset of timber charring for bare, coated, and encapsulated timber samples at three different heat fluxes

Surface type	Measured onset of timber charring [min] (time-to-300 °C at 3 mm from the front surface)		
	25 kW/m ²	50 kW/m ²	75 kW/m ²
Bare Timber	3.0	1.4	1.3
Intumescent Coating A	30.5	17.8	16.1
Intumescent Coating B	49.4	27.7	20.7
Plasterboard – One Layer	45.8	28.2	24.3
Plasterboard – Two Layers	-	-	52.2

It is also worth noting that once a plasterboard layer dehydrated it lost quite rapidly its insulating properties. This can be observed from the char depth plots of the one layer of plasterboard data, where once charring is initiated the resulting char depth increment becomes quite steep compared to the coated timber samples.

For instance, it took approx. 45 min for timber samples with one layer of plasterboard to start to char at 25 kW/m²; for Coating A samples this time was approx. 30 min, however, the mean char depth at the end of the test (60 min) for Coating A was very similar to the one layer of plasterboard samples – 6.5 mm for Coating A and 7.3 mm for one layer of plasterboard. Further, plasterboard fixings leading to premature delamination of the individual layers was not considered as part of this comparative assessment.

3.2 Rate of timber charring

Based on the char depth data, the charring rate of timber was calculated as the first derivative of the 300 °C isotherm, from the onset of charring to the end of the experiment (60 min) for each individual test. Although the charring rate naturally varies during a test as it can be seen from the slope of the char depth data plots (Figure 3 to Figure 5), the charring rate for each individual test was derived based on the best-fit line of the char depth slope allowing the comparison between the different types of samples. The mean charring rate values for the tested timber samples (bare, coated, and encapsulated timber) are presented in Table 3, including the max. and min. intervals, derived from three sample repeats per heat flux. The calculated charring rates and their variation per heat flux condition for all timber samples are shown in Figure 6 below.

Table 3. Mean charring rate values with max. and min. bounds for tested timber samples at three different heat fluxes

Surface type	Measured charring rate of timber [mm/min] (slope of 300 °C isotherm along the solid's depth)		
	25 kW/m ²	50 kW/m ²	75 kW/m ²
Bare Timber	0.72 ± 0.09	0.98 ± 0.12	1.00 ± 0.11
Coating A	0.23 ± 0.02	0.37 ± 0.03	0.49 ± 0.04
Coating B	0.21 ± 0.01	0.33 ± 0.03	0.46 ± 0.04
Plasterboard – 1L	0.49 ± 0.02	0.51 ± 0.01	0.52 ± 0.01
Plasterboard – 2L	-	-	0.36 ± 0.01

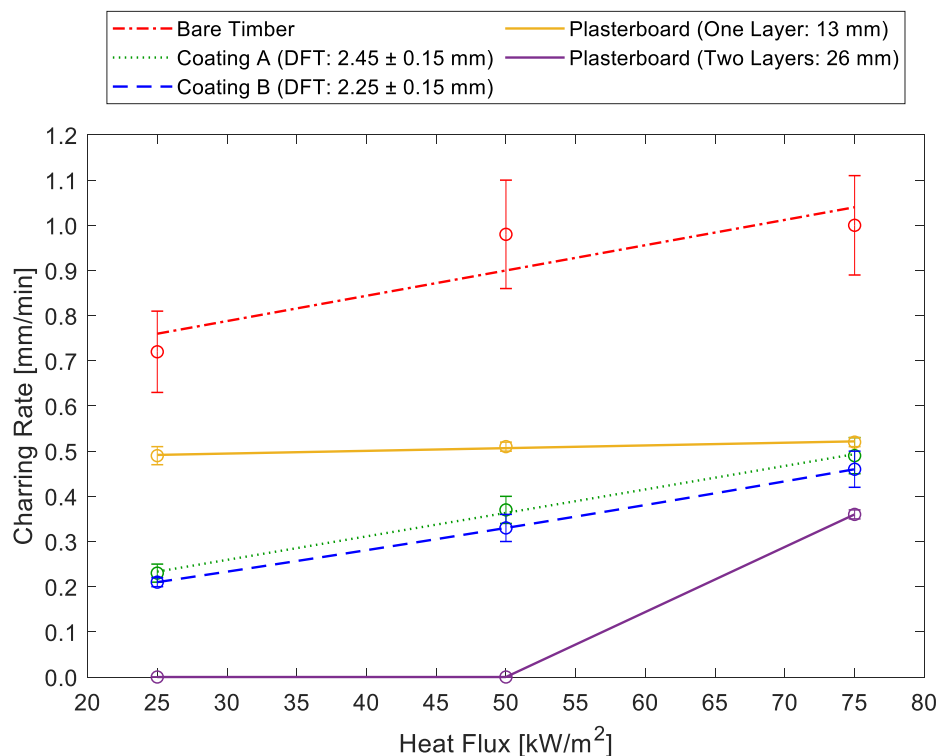


Figure 6. Heat flux versus mean charring rate (slope of 300 °C isotherm) with max. and min. error bars for tested samples

For the 60 min test duration, no charring was observed at 25 kW/m² and 50 kW/m² for timber encapsulated with two layers of plasterboard, while at 75 kW/m² the charring rate was significantly reduced compared to bare timber. Although the charring rates were also reduced for the coated timber samples when compared to bare timber, the effectiveness of the coating was found proportional to the severity of the heating condition. Conversely, timber samples with one layer of plasterboard had an increased mean charring rate compared to coated timber samples (Coating A and B) across all three heating conditions; this difference was less pronounced as the heating severity increases to 75 kW/m² due to the heightened dependency of the coating protective efficacy to the heat flux intensity.

It is evident from the Table 3 data and plots presented in Figure 6 that, in comparison to bare timber samples, coated timber samples experienced a reduction in charring rate of approx. 70 % at 25 kW/m² and 60 % at 50 kW/m² and just over 50 % at 75 kW/m². For the encapsulated timber samples, one layer of plasterboard provided approx. 30 % reduction in the charring rate of the timber at 25 kW/m² and just under 50 % at 50 kW/m² and 75 kW/m², respectively. Charring was neither observed nor measured for timber samples tested at 25 kW/m² and 50 kW/m² with two layers of plasterboard, with a marked reduction in charring rate of at least 60 % at 75 kW/m².

3.3 Visual test observations

As shown in Figure 7 below, bare timber samples at 75 kW/m² ignited very early into the test (within the first 15 sec), experienced flaming and charring, with charred sections falling-off at later test stages. In contrast, flaming in the coated timber was only observed towards later stages of the test. This occurred mainly on the perimeter of the samples, which is likely due to thermal degradation and subsequent shrinkage of the coating and timber underneath, therefore exposing the bare timber sides of the sample to direct radiant heat. Similarly, flaming was witnessed for tests with one layer of plasterboard along the edges of the sample. This is believed to have resulted from dehydration and shrinkage of the plasterboard layer and timber underneath. However, samples with two layers of plasterboard only experienced charring near the front surface of the timber sample, with no flaming occurring for the 60 min duration of the fire tests.

The fire behaviour of the plasterboard layers associated with dehydration in a fire event was also noted in a previous experimental study conducted by Hasburgh et al. [19] on CLT panels exposed to a standard fire curve using different encapsulation methods. It was shown that CLT samples protected with plasterboard resulted in increased charring rates once the timber started to char compared to bare timber samples, even though the onset of charring for the plasterboard samples was significantly reduced in comparison to bare timber. The application of intumescent coatings was also studied, however, their findings are not comparable to this study, as the intumescent products used are the cementitious type, applied at much higher thicknesses than the thin film coating types in this study.

The fire behaviour of all the tested samples, bare, coated, and encapsulated timber, is further highlighted in Figure 8, which provides temperature evolution plots along the depth of the samples at discrete times during testing for each heat flux condition. A considerable delay in the in-depth temperature rise was observed for the coated and encapsulated timber samples when compared to bare timber. The latter exhibited significant variance in the thermocouple profiles due to extensive flaming at the exposed surface of the sample early on during the test, and char fall-off in later stages, thus exposing thermocouples to the gas phase. This gas phase data from the exposed thermocouples falls outside the scope of this work and was truncated from the figures, to focus on the timber solid phase.

Flaming in the perimeter of the coated and encapsulated timber samples was also observed at later stages of the tests at 75 kW/m², resulting from significant thermal degradation and shrinkage of the coating or plasterboard edges, hence exposing the virgin timber to direct radiant heat. However, side flaming for the coated and encapsulated samples had a negligible effect on the temperature readings (taken at the centre of the sample) compared to the fully involved surface for the bare timber samples. Flaming on the sides of the samples is considered mostly an artifact of the test setup – e.g., the lip of the metal holder around the edges of the samples acting as a heat sink by absorbing and transferring heat locally at a faster rate than the directly exposed surface of the coating or plasterboard.

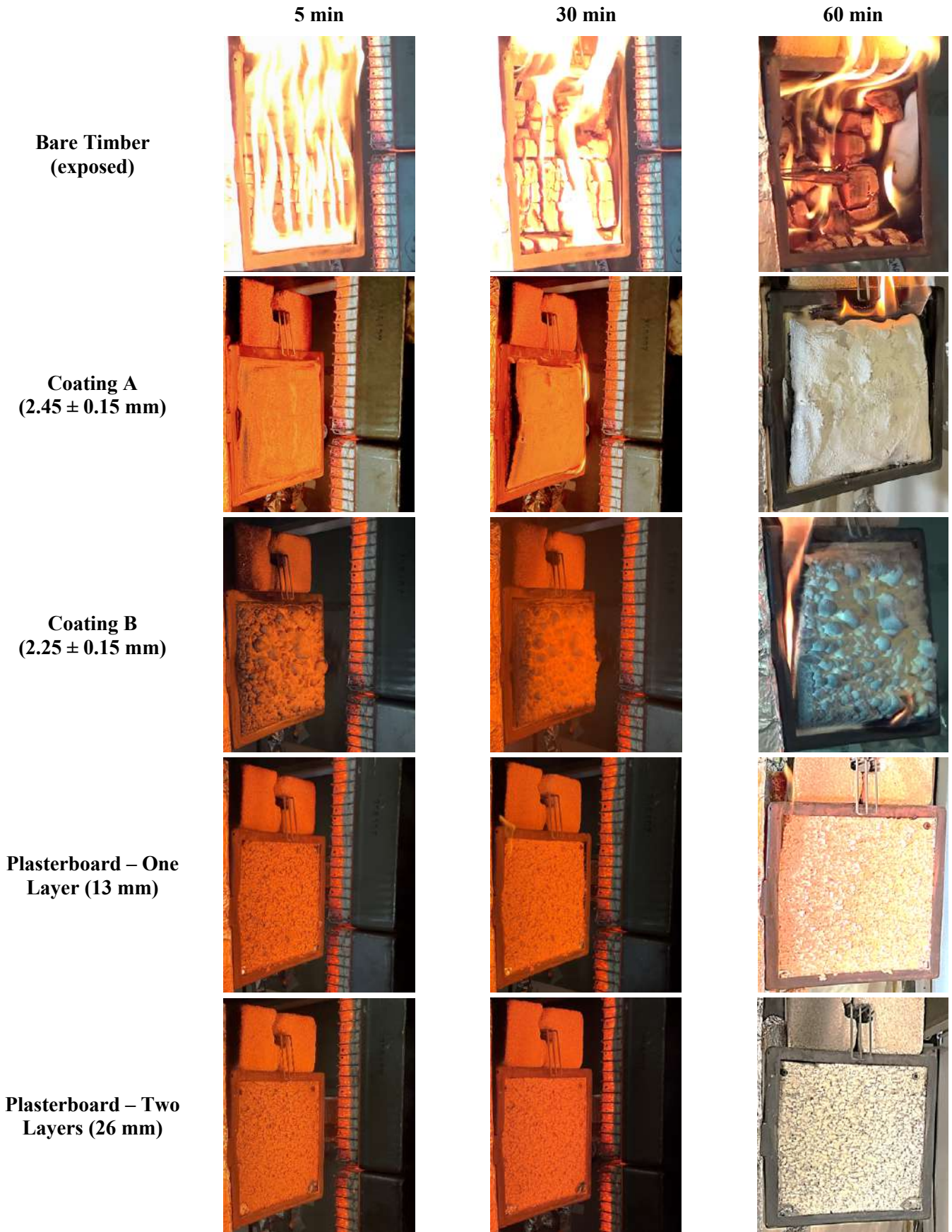


Figure 7. Typical sample photos taken at three different time intervals during fire testing at 75kW/m^2

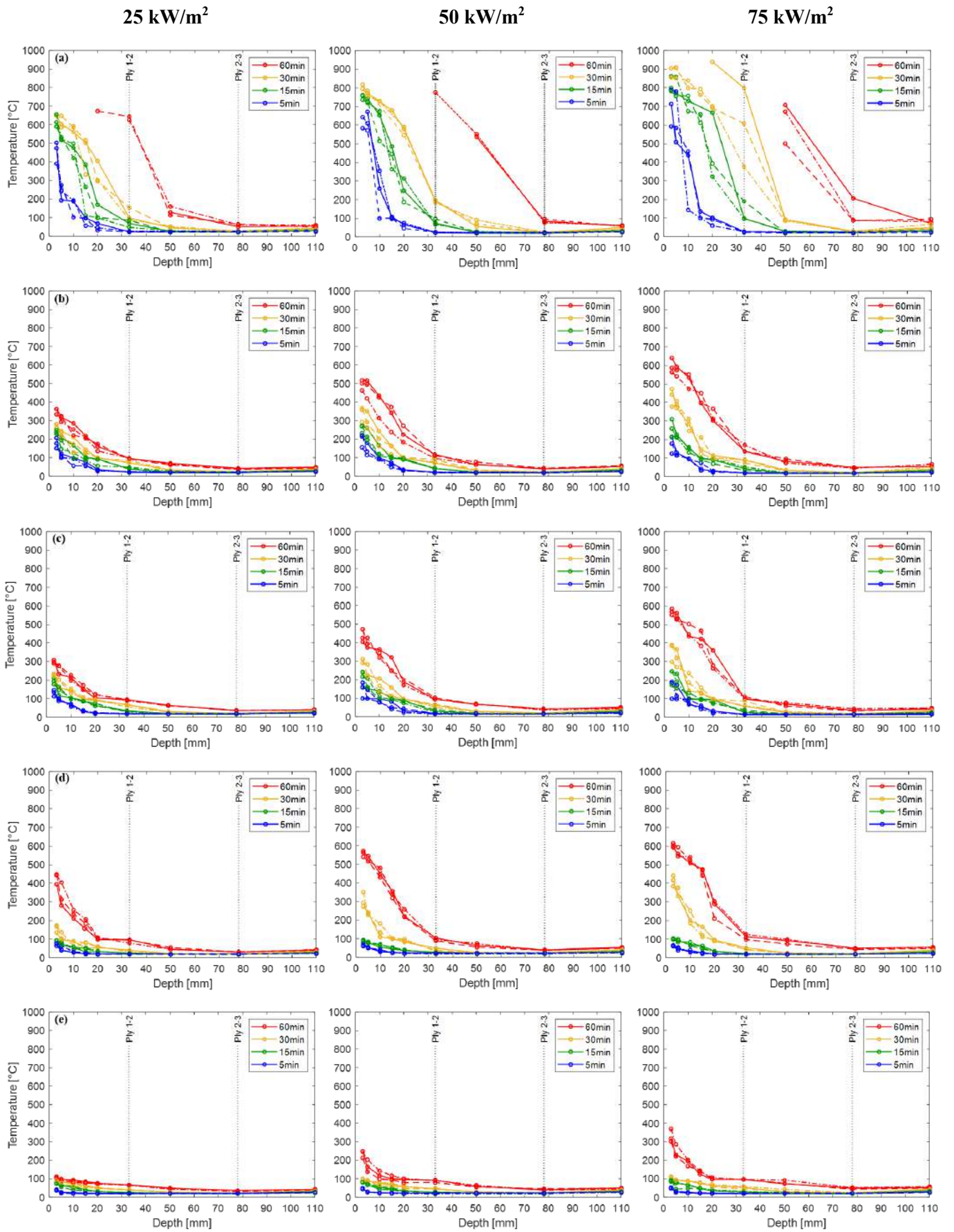


Figure 8. Temperature evolution graphs along the depth of the timber samples at discrete time intervals during fire testing for: (a) Bare timber; (b) Coating A; (c) Coating B, (d) Plasterboard – One layer; (e) Plasterboard – Two layers. Note: Dash and dash-dot lines represent repeat tests; Ply 1-2, ply 2-3 refer to lamella intersection of the CLT samples

4 CONCLUSIONS

The main experimental findings of this study relating to the charring behaviour of timber protected with thin intumescent coatings and fire rated plasterboard, exposed to three different heating conditions, are:

- As expected, it was demonstrated that both the application of thin intumescent coatings and fire rated plasterboard can effectively (1) delay the onset and (2) reduce the rate of charring in mass timber.
- The application of thin intumescent coatings did not prevent the onset of timber charring for the duration of the heat exposure (60 min), irrespective of the applied heat flux. However, the overall heat transferred into the timber as a function of the heat flux severity was slowed down considerably. Meaning, the ability of the coating to act as thermal buffer to delay the onset of charring or reduce the charring rate of the protected timber is inversely proportional to the intensity of the heating condition.
- Contrary, the use of fire rated plasterboard prevented (two-layer application, at 25, 50 kW/m²) or significantly delayed (one-layer application) the onset of timber charring up to the point in the fire test where the plasterboard layer dehydrated. Once this occurred and timber started to char, the resulting char depth increment was quite steep compared to the coated timber samples, leading to even higher charring rates than the coated samples.
- Bare timber samples underwent significant thermal degradation and began to char in the very early stages of the fire tests, i.e., between 1.3-3.0 min depending on the heat flux condition. For timber samples with two layers of plasterboard, charring was only observed for the most onerous heating condition (75 kW/m²), while samples protected with Coatings A, B, or one layer of plasterboard experienced charring at all three heating conditions.
- Coating B was the second most effective thermal buffer (compared to two layer of plasterboard samples) in delaying the onset of charring at 25 kW/m², while at 50 kW/m² Coating B and one layer of plasterboard provided a similar insulating effect, followed by Coating A. However, at 75 kW/m² timber samples with one layer of plasterboard began to char at a later stage of the test, as opposed to coated samples due to the heightened dependency of the coating protective efficacy to the heat flux intensity.
- The reduction in the charring rate for coated timber samples was similar between Coating A and B, with Coating B providing a slightly better insulating effect than Coating A, even though the mean applied DFT for Coating B was approx. 0.20 mm less than Coating A. Generally, when compared to bare timber, coated timber samples experienced a reduction in the charring rate of approx. 70 % at 25 kW/m², at least 60 % at 50 kW/m² and just over 50 % at 75 kW/m².
- For timber samples protected with plasterboard, one layer of plasterboard provided approx. 30 % reduction at 25 kW/m² and just under 50 % at 50 kW/m² and 75 kW/m², respectively. Charring was neither observed nor measured for timber samples tested at 25 kW/m² and 50 kW/m² with two layers of plasterboard, with a marked reduction in charring rate of at least 60 % at 75 kW/m².

ACKNOWLEDGMENT

The authors would like to acknowledge and thank XLam Australia for the donation of testing material and wish to extend their gratitude to Wenxuan Wu and Julian Mendez for the insightful discussions regarding data processing and graphical presentation of empirical data. The authors are also grateful to the Australian Research Council Research Hub to Transform Future Tall Timber Buildings (IH150100030) and the Fire Safety Engineering Group, especially Assoc. Prof. David Lange in the School of Civil Engineering at the University of Queensland, as without their valuable financial support this work wouldn't have been realised.

REFERENCES

1. R. M. Hadden *et al.*, "Effects of exposed cross laminated timber on compartment fire dynamics," *Fire Safety Journal*, vol. 91, pp. 480-489, 2017.
2. M. Violette, "Memoire sur les Charbons de Bois," *Ann. Chim. Phys*, vol. 32, p. 304, 1853.
3. A. Lucherini, Q. S. Razzaque, and C. Maluk, "Exploring the fire behaviour of thin intumescent coatings used on timber," *Fire Safety Journal*, vol. 109, p. 102887, 2019.
4. T. Mariappan, "Recent developments of intumescent fire protection coatings for structural steel: A review," *Journal of fire sciences*, vol. 34, no. 2, pp. 120-163, 2016.
5. R. G. Puri and A. Khanna, "Intumescent coatings: A review on recent progress," *Journal of Coatings Technology and Research*, vol. 14, no. 1, pp. 1-20, 2017.
6. A. Lucherini and C. Maluk, "Intumescent coatings used for the fire-safe design of steel structures: A review," *Journal of Constructional Steel Research*, vol. 162, p. 105712, 2019.
7. A. Hartl, Q. S. Razzaque, A. Lucherini, and C. Maluk, "Comparative study on the fire behaviour of fire-rated gypsum plasterboards vs. thin intumescent coatings used in mass timber structures," 2020.
8. C. Maluk, L. Bisby, M. Krajcovic, and J. L. Torero, "A heat-transfer rate inducing system (H-TRIS) test method," *Fire Safety Journal*, vol. 105, pp. 307-319, 2019.
9. D. Drysdale, *An introduction to fire dynamics*. John Wiley & sons, 2011.
10. R. D. Peacock, P. A. Reneke, R. W. Bukowski, and V. Babrauskas, "Defining flashover for fire hazard calculations," *Fire Safety Journal*, vol. 32, no. 4, pp. 331-345, 1999.
11. R. Emberley *et al.*, "Description of small and large-scale cross laminated timber fire tests," *Fire Safety Journal*, vol. 91, pp. 327-335, 2017.
12. I. O. f. Standardization, "ISO 5660-1: 2015 Reaction-to-Fire Tests—Heat Release, Smoke Production and Mass Loss Rate—Part 1: Heat Release Rate (Cone Calorimeter Method) and Smoke Production Rate (Dynamic Measurement)," ed: International Organization for Standardization Geneva, Switzerland, 2015.
13. S. ASTM, "E230/E230M: Standard Specification and Temperature-Electromotive Force (EMF) Tables for Standardized Thermocouples," 2017: ASTM.
14. J. V. Beck, "Thermocouple temperature disturbances in low conductivity materials," 1962.
15. I. Pope, J. P. Hidalgo, R. M. Hadden, and J. L. Torero, "A simplified correction method for thermocouple disturbance errors in solids," *International Journal of Thermal Sciences*, vol. 172, p. 107324, 2022.
16. R. Boone and E. Wengert, "Guide for using the oven-dry method for determining the moisture content of wood," *Forestry Facts*, vol. 89, no. 6, pp. 1-4, 1998.
17. MATLAB, *version 9.5.0944444 (R2018b)*. Natick, Massachusetts: The MathWorks Inc., 2018.
18. F. Wiesner, R. Hadden, and L. Bisby, "Influence of Adhesive on Decay Phase Temperature Profiles in CLT in Fire," in *Proceedings of the 12th Asia-Oceania Symposium on Fire Science and Technology (AOSFST 2021). Presented at the 12th Asia-Oceania Symposium on Fire Science and Technology (AOSFST 2021), The University of Queensland, Online. <https://doi.org/10.14264/a023d21>*, 2021.
19. L. Hasburgh, K. Bourne, C. Dagenais, L. Ranger, and A. Roy-Poirier, "Fire performance of mass-timber encapsulation methods and the effect of encapsulation on char rate of cross-laminated timber," in *World Conference on Timber Engineering*, 2016, p. 10.

FIRE DEVELOPMENT IN LARGE COMPARTMENTS WITH MIXED-TIMBER-SECTION CEILING

Cheng Chen¹, Tianwei Chu², Guillermo Rein³, Asif Usmani⁴, Liming Jiang^{5,*}

ABSTRACT

Timber as a structural material has attracted increasing interest in modern building designs as it could potentially replace traditional construction materials for its excellent load-bearing capacity, aesthetic appearance, and carbon-negative feature. The major barrier of using timber is its combustibility and the risk of fast fire spread. Even in large open-plan compartments expecting slow travelling fire behaviour, the full-scale fire tests have shown that the compartment with a timber ceiling is engulfed in flames within five minutes after the ignition of the timber ceiling. This is due to the burning of pyrolysis gases emitted from the heated timber ceiling, leading to rapid flame spread along the ceiling and then in the floor fuel bed. In order to mitigate this rapid flame spread mechanism, this paper proposes and investigates a mixed ceiling section design comprising timber and insulation strips. Full-scale CFD fire models have established with reference to the original Malveira fire test, which were then extended for accommodating different ceiling configurations including full-timber ceiling and mixed sections of different widths. The simulation results demonstrate the effectiveness of the mixed ceiling strategy in delaying rapid flame spread. The mixed ceiling in large open compartments can even achieve localized burning, when the floor fuel bed is discontinuous. These research findings could facilitate the fire-safe use of mass timber in floor slabs.

Keywords: Timber ceiling; fire dynamics; fire simulation; timber burning; fire safety design

1 INTRODUCTION

Timber is widely preferred in the construction owing to its inherent natural affinity. Its aesthetic appeal and renewable properties make it a potential substitute for traditional construction materials. Moreover, engineered timber products such as cross-laminated timber (CLT) and glued laminated Timber (Glulam) exhibit stable and superior structural performance along with low-carbon prefabrication capabilities. Based on the advantages, timber materials have been used as structural components such as beams, columns, and floor slabs. In modern architectural design, driven by principles of low-carbon and architectural aesthetics, the integration of exposed timber elements with buildings has become the preferred choice. However, this poses challenges in terms of fire safety requirements for structural timber components.

¹ PhD student, The Hong Kong Polytechnic University
e-mail: cheng363.chen@connect.polyu.hk, ORCID: <https://orcid.org/0000-0003-4347-0718>

² PhD student, The Hong Kong Polytechnic University
e-mail: tianwei.chu@connect.polyu.hk, ORCID: <https://orcid.org/0000-0003-3286-6856>

³ Professor, Imperial College London
e-mail: g.rein@imperial.ac.uk, ORCID: <https://orcid.org/0000-0001-7207-2685>

⁴ Professor, The Hong Kong Polytechnic University
e-mail: asif.usmani@polyu.edu.hk, ORCID: <https://orcid.org/0000-0003-2454-5737>

⁵ Assistant Professor, The Hong Kong Polytechnic University
e-mail: liming.jiang@polyu.edu.hk, ORCID: <https://orcid.org/0000-0001-8112-2330>

The current fire safety design of timber components is usually based on Eurocode 5 [1], which estimates heat transfer or charring depth under standard fire exposure conditions. To investigate the behavior of timber structural components under realistic fire scenarios in compartments, appropriate models need to be established for numerical simulations at different stages. Considering the impact of timber combustion on the internal heat transfer of the components, Chen et al. [2] developed a layered heat transfer model applicable to timber material based on the open-source platform OpenSees [3] to predict the thermal response of timber sections exposed to realistic fires, based on the thermal response of timber sections exposed to a series of fixed as well as varying heat fluxes. Additionally, based on the implementation of heat transfer simulations of timber sections under non-standard fire conditions, Chen et al. [4] established thermal-mechanical analysis models for various timber structural components, such as timber slabs with one-side fire exposure or timber beam with three-side fire exposure, using beam elements or shell elements in the OpenSees for fire platform [5]. They also made preliminary attempts to combine the CFD simulations to model the fire impact in compartments and the thermal-mechanical analysis based on OpenSees for fire platform to do modelling work for timber-concrete composite slabs. Additionally, the natural combustibility of timber materials causes exposed timber components additional sources of fuel in compartment fires, thereby influencing the dynamics of such fires. Consequently, various research institutions have conducted a series of compartment fire experiments at different scales to evaluate the impact of exposed timber elements with varying compositions on compartment fire dynamics. Pope et al. [6] recently conducted a series of experiments within a timber compartment measuring 3.15 m × 3.15 m × 2.70 m, featuring a door with dimensions of 0.85 m in width and 2.10 m in height. The primary objective of these experiments was to evaluate the contribution of exposed timber walls during the fully developed fire. However, with the popularity of large open-plan compartments in modern architectural design, the limitations inherent in defining compartment sizes of the traditional compartment fire designs have constrained the applicability of fire dynamics research findings to large open-plan compartments. Hence, it is necessary to undertake investigations into the fire dynamics of modern compartments to gradually understand and establish the reference code for the fire design of such compartments. To capture the natural behavior of fires within large open compartments, Rackaukaite et al. [7] executed the x-ONE fire experiment within a 380 m² open compartment. Notably, the observed fire dynamics exhibited notable distinctions from those observed in traditional small-scale compartments and from the conventional assumptions for structural design. These distinctions included an accelerated rate of flame propagation and combustion. However, regarding this fire dynamics, the localized fire models employed in the latest traveling fire methods are based on localized fire experiments with unconfined ceiling boundaries, which do not account for the smoke effects generated by the fire. Aatif et al. [8] conducted CFD simulations of localized fire experiments to assess the thermal impact on structural components and extended the simulation models and analysis methods to localized fires in large compartments. Additionally, Nan et al. [9] developed a generic structural model in OpenSees for fire [citation] to examine the thermal impact on structural components under various traveling fire scenarios with different traveling parameters, fire travelling directions, and beam sizes. . Additionally, given that fuel is typically non-uniformly distributed in building environments, Nan et al. [10] investigated the impact of non-uniform fuel distribution on the development of fully ventilated compartment fires. The results indicated that assuming a uniform distribution of fuel load may underestimate the fire hazard, and they recommended considering scenarios with non-uniform fuel load distribution in performance-based fire safety design. Furthermore, the observation of "traveling fire" behavior in large compartment fire tests [11] with initial window openings, characterized by slow fire development, is advantageous for fire safety design. Therefore, Chu et al. [12] proposed a strategy of active opening strategy for modern large compartments commonly equipped with glass panels to regain ventilation conditions, which can effectively mitigate compartment fire development. Subsequently, considering the impact of window glass on large open compartment fires in realistic modern building, Chu et al. [13] proposed a 'standard control' model to simulate the interaction between glazing failure and fire behaviour in CFD fire models. Furthermore, in alignment with the concept to reduce carbon emissions, the presence of timber elements within a structure could potentially increase fire intensity. Although current regulations aim to maintain residual load-bearing capacity by facilitating the formation of a char layer through partial timber consumption [1], the CodeRed #01 fire tests, conducted by Kotsovinos et al. [14] within a large open compartment featuring fully exposed CLT ceilings, demonstrated that a fire could rapidly penetrate the CLT ceiling and spread to

the opposite end of the compartment in mere 3 minutes, subsequently engulfing a compartment measuring 34 m in length and 10 m in width. The rapid development of the fire is attributed to the release of pyrolysis gases from the timber ceiling and the ignition under the impingement of the localised fire. Subsequently ignited areas sustainably preheat adjacent unignited regions, leading to rapid flame spread across the ceiling. Ultimately, the fully burning timber ceiling interacts with the floor fuel load through radiation, thus leading the catastrophic fires within large compartments characterized by extensive floor areas and sufficient ventilation provided by surrounding windows.

In view of the fire development mechanisms and fire simulation results of large open compartments with timber ceilings, this paper aims to explore a conceptual novel design to mitigate such fast fire spread using mixed surface with timber and insulation strips. In addition, different full-scale fire simulation models have been developed and conducted, including compartments with concrete ceilings, timber-insulation mixed ceilings and full-timber ceilings, respectively. Furthermore, the effect of different designs of strips widths has been explored as the preliminary attempt to help the development of fire-safe timber slabs for large open plan compartments.

2 FIRE DEVELOPMENT IN LARGE OPEN-PLAN COMPARTMENT

Regarding the fire safety of buildings with large open-plan compartments, it is essential to understand the fire dynamics during the fire development. Due to its possible localised burning feature induced by sufficient ventilation, modelling fire development behaviour in large compartment pose unique. It would be further complexed if the compartments involve the use of combustible materials as structural elements, such as timber ceilings. The initial localised fire at floor would cause the emission and ignition of pyrolysis gases while heating the ceiling slab. The localised fire is then significantly intensified and causes the fast heating of floor fuel bed, which will routinely lead to a “chained reaction” of burning in a large open plan compartment from floor fuel to ceiling timber members.

2.1 Travelling fire behaviour in compartment with non-combustible ceiling

In contrast to the relatively uniform temperature distribution characteristic of fully-developed small compartment fires, the behaviour of fires in large open-plan compartments with sufficient ventilation and only floor fuel is remarkably different. These fires often exhibit non-uniform burning patterns and would not experience global flashovers. Instead, a travelling fire may occur in such compartments, while the fire impact can be characterized as a near field representing intense burning and a far field representing the heating of a smoke layer. The burning front within the intense burning region usually moves along the floor plan, accompanied by a receding burnt-out front. This phenomenon, commonly referred to as a "travelling fire," has been introduced in the literatures [15, 16]. Experimentally, a travelling fire has been observed in the Malveira fire test [11], which was conducted in a large open compartment of a size of 21 m × 4.7 m × 2.85 m. The slow move of the intense burning region as shown in Figure 1 lasted for nearly four hours. This pattern of development contrasts with the traditional design fire models assuming uniform distribution of fire impact that are suitable for describing small compartment fires. An interesting phenomenon in Malveira fire test [11] is the point that the moving localised fire ignited the ceiling cork layer, which immediately caused zonal intense burning as shown in Figure 1.



Figure 1. Travelling fire exhibited in Malveira fire tests with non-combustible ceiling [11]

2.2 Fast fire development in compartment with combustible timber ceiling

As mentioned previously, timber slabs have been increasingly used in modern structures and have caused new challenges on fire spread and fire-safe designs. Usually, timber is used as the lower section of timber-concrete composite slabs since the lower section of timber can provide excellent tensile resistance and serve as formwork for the casting of upper concrete section. The current fire safety design of timber sections mostly adopts the reduced cross-section method considering charring as given in Eurocode 5 [4]. This methodology accepts the loss of a portion of the timber section thickness to form a char layer of a lower thermal conductivity and to maintain the effective residual section of timber during a fire, thereby preserving an adequate load-bearing capacity. When calculating the load resistance of such slabs, the thickness of the growing char layer should be excluded as it is nearly of no strength. Other than the structural fire resistance, another alarming phenomenon has been observed in recent full-scale fire tests in the large compartment with timber ceilings. The fire spread was found very rapid after the ignition of floor wood crib, which result in a massive fire engulfing the whole large compartment. For instance, in CodeRed#01 experiment [14] conducted in 2021, the fire developing to the whole 352 m² compartment in 5 minutes as shown in Figure 2.

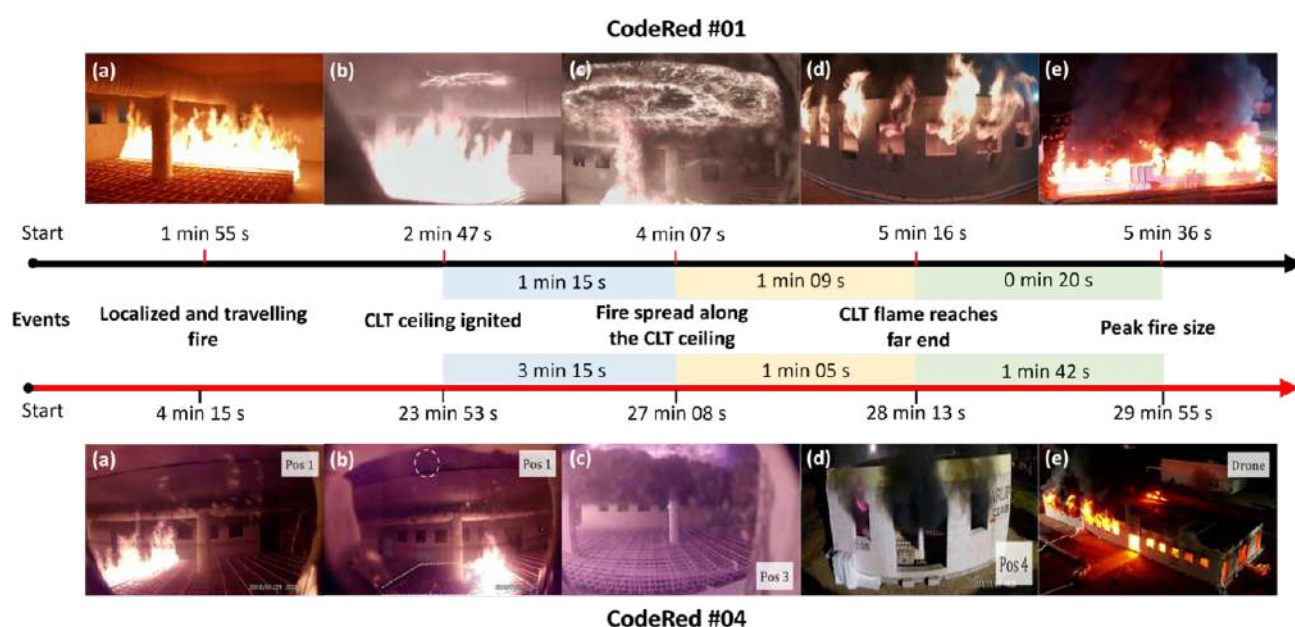


Figure 2. Faster fire development in large and open-plan compartment with timber ceiling components: CodeRed#01 fire experiment [14] and CodeRed#04 fire experiment [17]

Observing the photo evidence given in the reference paper [14], the combustion of ceiling timber due to the ignition of pyrolysis gas occurred around 2 min 47 s after the start of the test, which was followed by the flame spread over the surface lasting for about 2 min 24 s. Subsequently, the interaction between the burning ceiling components and the floor fuel load in this compartment led to the formation of a massive fire with an additional 20 s. If comparing this fire test to the Malveira fire test [11] in a large open-plan compartment of a similar size but with non-combustible ceiling, the timber ceiling has caused significantly faster fire spread with a much severer fire threat.

In addition to CodeRed #01 fire experiment [14] with full CLT ceiling, the compartment was configured to a ceiling of 50% of CLT and 50% of fire protection in CodeRed #04 fire experiment [17] to observe the fire spread on a partially protected timber ceiling. In the test, the central area occupying 50% of ceiling area was protected. However, only the ignition was slightly delayed due to the encapsulation of the ceiling above the ignited wood crib, whereas the fire flames propagated rapidly throughout the compartment similar to CodeRed#01 fire experiment [14]. According to the reference paper, the duration of the fire, peak temperatures, and heat fluxes were similar to those observed in the CodeRed#01 experiment [14]. Therefore, using the whole block of fire protection seems incapable to mitigate the fast fire spread induced by ceiling timber burning.

2.3 Mechanism of the fast fire development in large compartment with timber ceiling

Based on the above brief discussion on the compartment fire dynamics under different ceiling configurations, it may be possible to describe such fast fire spread using a ‘chained reaction’ concept. As illustrated in Figure 3, when compartments are equipped with continuous timber ceilings and exposed to localized fires at the beginning of fire, the timber ceiling begins to partially pyrolyze and release combustible gases as the fire impinges the ceiling. Simultaneously, the high-temperature smoke generated by localized fire gradually accumulates at the surface of the ceiling, preheating the entire timber ceiling. When the localized flames ignite the top of the timber ceiling, it is accompanied by a larger area of ceiling flames compared to the compartment fire with non-combustible ceiling. This along with the preheating by high-temperature smoke layer leads to propagation of flames along the ceiling from the area above the localised fire to the adjacent areas. This larger fire at the ceiling would inevitably cause higher radiation to the floor fuel bed and then the spread of flames of the original localised fire to adjacent wood crib blocks. This growth routinely induces heating and ignition of ceiling timber, and a massive fire could be formed within a very short period due to such ‘‘chained reaction’’ fire spread mechanism. Hence, mitigating such fast fire spread should aim for cutting off the ‘‘chained reaction’’. In the following sections, a conceptual design using mixed strips of timber and fire protection is introduced for this purpose.

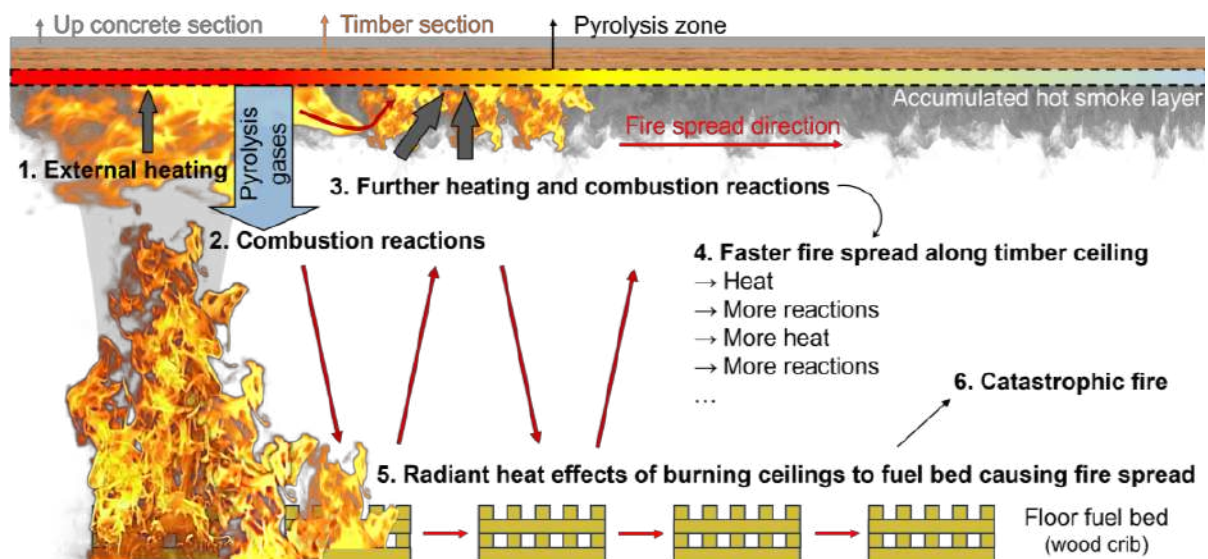


Figure 3. Schematic illustration of the mechanism of ‘‘chain reaction’’ for the faster development of compartment fires with the full-timber ceiling

3 NUMERICAL SIMULATION FOR LARGE OPEN-PLAN COMPARTMENT

3.1 Description of CFD fire models

The simulation of large compartment fires to explore the mixed-strip design is carried out using FDS version 6.8.0. The compartment from the Malveira Fire Test [11] is chosen as the prototype, whose layout is illustrated in Figure 4. This compartment is 21.1 m long, 4.7 m wide with an effective height of 2.6 m and it is constructed as a concrete frame structure with masonry block infill. These enclosing walls is set to have a thickness of 0.3 m in the CFD fire models, with its density 1375 kg/m³, specific heat 0.753 kJ/kg·K, and thermal conductivity 0.42 W/m²·K. In this fire test, a fuel bed of pine crib of 16.8 m in length and 2.4 m in width is deployed as the fuel load within the compartment. It was constructed from wood sticks of 1.2 m in length, with a cross-section of 0.05 m by 0.05 m, stacked in three layers. The spacing between sticks on the top layer was 0.15 m, while the spacing for the other two layers was 0.05 m. The global density of fuel bed was reported as 510 kg/m³ with a moisture content of 19 ± 6 %. The fuel load density was therefore estimated to around 420 MJ/m², which conforms with the recommended fuel loads in modern offices in EN 1991-1-2 [18].

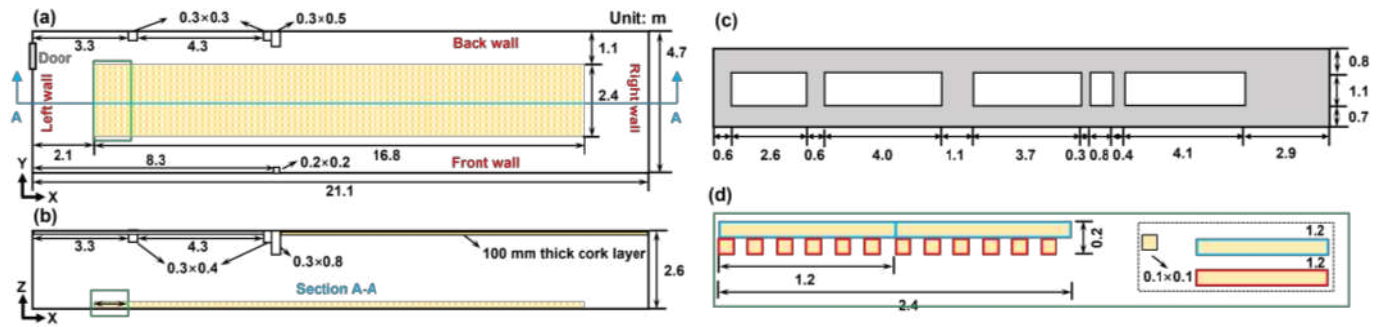


Figure 4. Diagram of the CFD model for Malveira fire test: (a) Top view; (b) Section A-A; (c) Front view; (d) Detailed dimensions of sub-cribs

Table 1. Thermal and chemical parameters used in the pyrolysis model

Properties	Unit	Dry wood	Char	Moisture
Density ρ	kg/m ³	510	135	1000
Specific heat c_p	kJ/kg · K	20°C – 0.85 800°C – 2.73	1.08	4.18
Thermal conductivity λ	W/m · K	20°C – 0.07 800°C – 0.37	0.13	0.1
Emissivity e	–	0.95	1.0	–
Pre-exponential factor A_a	s ⁻¹	2.01×10^3	–	6.16×10^{16}
Activation energy E_a	kJ/mol	8.97×10^4	–	1.36×10^5
Order of reaction n	–	1.69	–	3.31
Heat of reaction ΔH_r	kJ/kg	250	–	2500

In CFD modelling, the burning process of wood sticks with a cross-section of 0.05 m by 0.05 m requires considerable computational costs due to the needs of finer mesh resolution. To tackle this challenge, the equivalent wood crib method proposed by Janardhan and Hostikka [19] and its subsequent expansion by Chu et al . [12] are utilized to effectively reduce the computational cost while ensuring the validity of the outcomes. Specifically, the fuel bed in the simulations is simplified to two layers of sticks, where the cross-section of each stick is appropriately modified to 0.1 m by 0.1 m, and the spacing between sticks is set to 0.1 m. Additionally, the input parameters AREA_MULTIPLIER (AM) and BULK_DENSITY (BD) are employed to correct for the reduced exposed area caused by adjustments of the geometry of wood sticks and ensure the designed fuel load density, respectively. The combustion modelling of wood sticks is addressed through a single-step pyrolysis model that encompasses two parallel reactions: the pyrolysis of dry wood producing fuel vapor and char, and the evaporation of moisture content producing water vapor. This is implemented in the CFD fire model by designating the fuel surface as a dry wood layer and a moisture layer according to the moisture content. The relevant thermal and chemical parameters listed in Table 1. Similarly, the combustion reactions of timber ceilings mentioned later are also achieved in this manner. The energy required to ignite the fuel bed is provided by a linear burner of 0.48 m² on the floor. The heat release rate per unit area of this burner is set to linearly increase to 4200 kW/m² over 30 s, then maintained at a constant value of 4200 kW/m² for 180 s, and finally, it linearly decreases to 0 at 420 s.

3.2 Validation of the CFD fire model

In this subsection, numerical simulation analyses were conducted for the CFD model established based on the experimental parameters of the Malveira test, serving as the base model of fire dynamics analyses. Two key variable representing the fire development [20], the mass loss rate of fuel and the overall compartment heat release rate, were utilized for assessing the appropriateness of the simulation model.

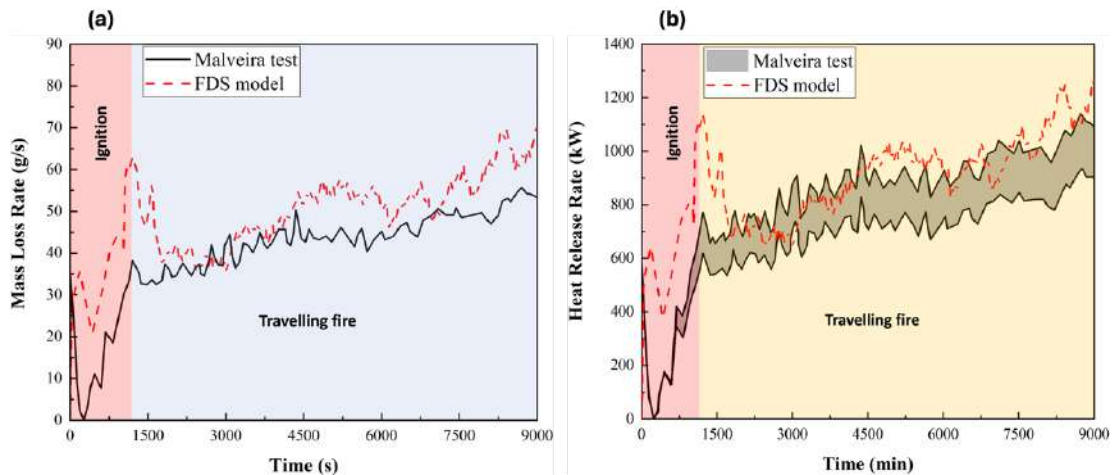


Figure 5. Validation of the FDS model against Malveira fire test [11]: (a) Evolution of the mass loss rate of reaction fuel; (b) Evolution of compartment heat release rates and the error bars correspond to the minimum and maximum HRR using 12.8 and 20.4 MJ/kg as the heat of combustion for timber material

As depicted in Figure 5, the simulation results indicate that the established model effectively reproduces the fire development within the compartment during the initial 9000 s following ignition. It is noteworthy that the discrepancy observed during the first 1200 s is due to the unavailability of information regarding the initial ignition power of the wood cribs from the experimental reports. Subsequently, the overall mass loss rate (MLR) and heat release rate (HRR) of the fuel load closely approximate the measured values from the tests. Furthermore, according to relevant experimental reports, although the fire subsequently propagated to the latter half of the compartment and ignited the cork ceiling, this portion of the ceiling was not included in the subsequent calculations of mass loss rate. Therefore, the comparison of simulation results in this subsection is limited to the initial 9000 s, during which the cork ceiling decoration in the latter half of the compartment did not participate in the stage of compartment fire development.

3.3 Adoption of timber-insulation mixed ceiling design in validated CFD fire model

While observing the fire dynamics in large compartments with full timber ceiling, the rapid spread of fire flames was initiated by a localized fire at floor but significantly intensified by the pyrolysis gas emitted from the fire-heated timber ceiling. To mitigate such rapid fire spread in such compartments, as illustrated in Figure 6, this paper proposes a conceptual design of timber ceilings composed of mixed surfaces of timber strips and insulation strips. This design is to counter the spread mechanism by reducing the heating area of timber ceiling exposed to a localised fire, decreasing the preheating of adjacent timber strips as a gap (insulation strip) is introduced between timber strips. Consequently, the flame spread underneath the ceiling is mitigated, which simultaneously reduces the heating towards floor fuel. Therefore, the “chained reaction” of fire spread could be delayed and mitigated.

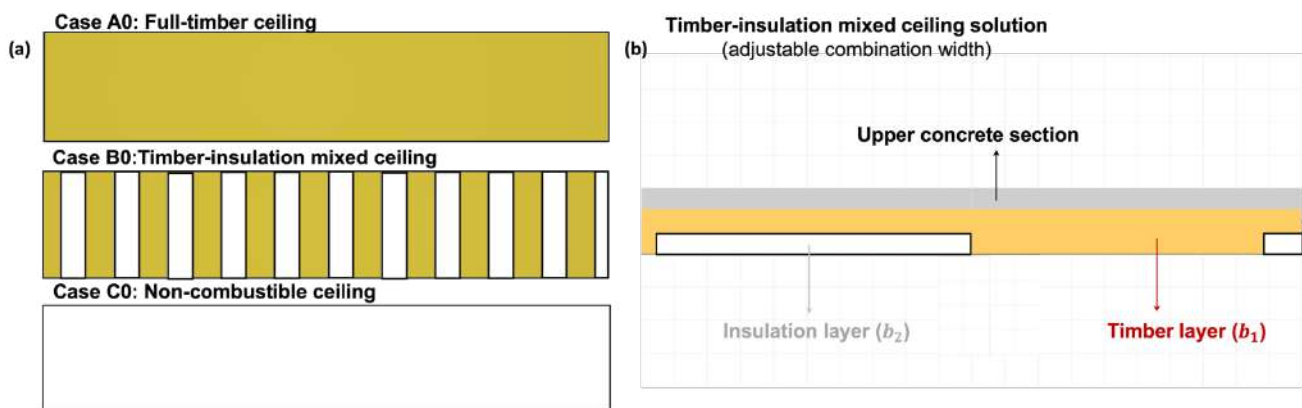


Figure 6. The conceptual design of timber-insulation mixed ceiling for fire mitigation in large open compartments: (a) Floor system with different arrangements; (b) Vertical mixed ceiling section

In this conceptual design, the widths of timber strip (b_1) and insulation strip (b_2) as illustrated in Figure 6(b) could be altered, which shall produce different fire mitigation effects. To examine the effectiveness of the proposed mixed-strip ceiling, the following section will investigate the fire development dynamics in large open compartments with different ceiling configurations using CFD simulation, including full-timber ceilings (Case A0), timber-insulation mixed ceilings (Case B0), and non-combustible ceilings (Case C0) under the continuous fuel load as mentioned in section 3.1. It should be noted experimental validation has been conducted by the authors, but the results were not included in this paper due to length limit.

4 EFFECTS OF MIXED-STRIP TIMBER CEILING TO LARGE COMPARTMENT FIRE

Based on the aforementioned CFD fire model, this section conducted further investigation and comparative analysis of the fire dynamics in the large compartments featuring three distinct ceiling configurations. While keeping all other model parameters identical, the widths of the timber strips (b_1) and insulation strips (b_2) are set as 0.4 m, 0.8 m, and 1.6 m. Particularly the mixed-strip model of Case B0 shown in Figure 6 is of 0.8 m widths for timber strips and insulation strips.

4.1 Fire behaviour in large open compartment with different ceiling configurations

The numerical simulation for each case is carried out separately on a workstation, and the simulation results exhibiting different fire behaviour in the given large compartments are shown in Figure 7. In Case A0 with full-timber ceiling, rapid spread of flames was observed at the floor and underneath the ceiling to the other end of the compartment within 600 s. Subsequently, from 600 to 1600 s, the fire swept the whole compartment due to the “chained reaction” between the burning of ceiling timber and ground fuel. In contrast, in compartments with timber-insulation mixed-strip ceiling (Case B0), the fire spread was much slower. At 600 s, flames remained localised on the initially ignited wood cribs, and the localized burning pattern is similar to Case C0 (compartment with non-combustible ceiling) as observed from 0 to 1600 s. In Figure 7, the time steps of 600 s and 1800 s are deliberately chosen to compare the timeline of compartment fire development under the different ceiling configurations. It is clearly shown that the mixed-strip timber ceiling of 0.8 m width could mitigate the fire development for at least 1600s and prevent the full development of fire as found in Case A0.



Figure 7. Fire development of the compartments with different ceiling arrangements under continuous fuel load

Based on the fire dynamics within the compartment under three different ceiling configurations, the associated compartment fire development mechanisms were further explored by the compartment fire dynamic output variables. As shown in Figure 8(a), in the case of a mixed ceiling compartment, the virtual heat flux gauges were set up in the CFD models on the surface of the adjacent wood cribs ($x = 3.7$ m) to the ignited wood crib and on the surface of the adjacent timber strip ($x = 4.4$ m) above the ignited wood crib. As shown in Figure 8(b), the comparison of the compartment heat release rate variations for the three ceiling configurations is presented, which reveals that the rapid development of the heat release rate was delayed by nearly 17 minutes in the compartment with the mixed ceiling compared to the compartment

with the full-timber ceiling. As shown in Figure 8(c) and (d), comparative analyses of surface radiative heat flux monitored by heat flux gauges at different locations indicate that the mixed ceiling effectively reduces the incident heat flux on adjacent wood cribs and surrounding adjacent timber strip surfaces. Therefore, the pyrolysis process of timber strips is much less than that in Case A0, and then significantly preventing the fire spread over the wood crib bed.

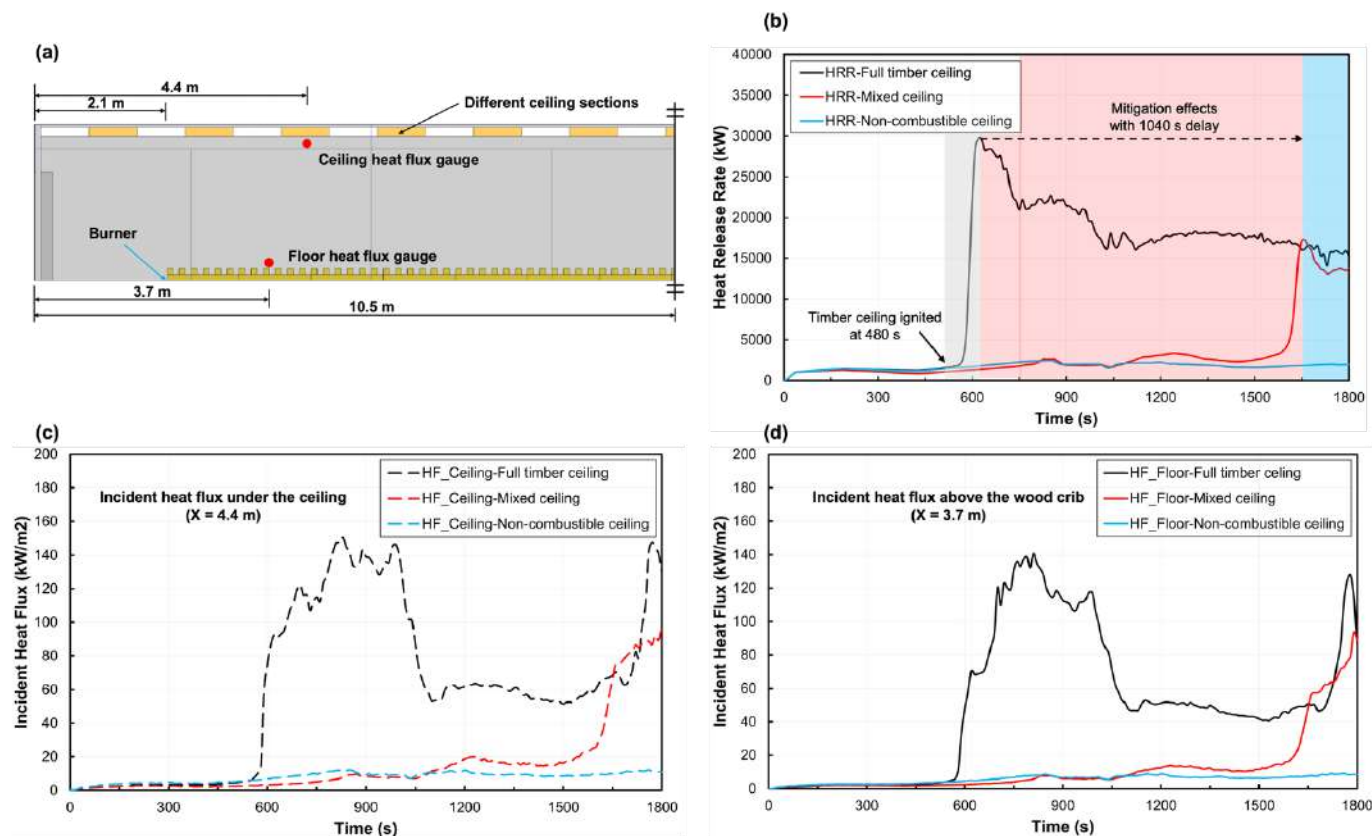


Figure 8. Diagrams: (a) Compartment half-section and heat flux gauge settings; (b) Development of the heat release rate for compartment with different ceiling configurations; (c)(d) Incident heat flux evolution at different monitoring locations

4.2 Implementation of mixed-strip ceiling in large open compartments with discrete fuel load

In addition to the continuous fuel bed in large open plan compartments, the effect of discontinuous fuel bed is studied. In real building compartments, fuel load may be located in a discrete pattern. As demonstrated by recent fire experiments on discontinuous fuel loads conducted by Nan et al. [10], it was found that altering the gaps between wood cribs under the same fuel load conditions can effectively change or even prevent the spread of fire. Therefore, for large open-plan compartments with different ceiling configurations, while maintaining the same fuel load density, the floor wood crib was discretely distributed as a number of blocks. The corresponding analysis of compartment fire dynamics have been conducted, including full-timber ceilings (Case A1), timber-insulation mixed ceilings (Case B1), and non-combustible ceilings (Case C1) under the discontinuous fuel load. Due to the discrete fuel bed, it is expected to observe better mitigation effect of the mixed-strip timber ceiling. More discussion to address discontinuous and non-uniform fuel load distribution will be presented in a journal paper later.

As depicted in Figure 9(a), particular attention may be directed to the initial development of localized fire upon impinging the ceiling within different compartments. It can be observed that at 550 s, an array of localized fire over the wood crib blocks was formed. Subsequently, in Case A1 (compartment with full-timber ceiling), the timber ceiling was ignited at 680 s, and flames were observed spreading along the ceiling to the other end of the compartment at 850 s. The side view of fire development is illustrated in Figure 9(b). From 850 s to 1800 s, the fire entered full development stage. In contrast, the progression of compartment fire in Case B1 employing timber-insulation mixed ceiling is significantly slower, which

exhibits localised burning similar to the compartment equipped with non-combustible ceiling. Specifically, through the use of a mixed surface, the flaming area underneath the ceiling is much smaller than that in Case A1 at 800 s, which quickly turns to a fully-sweeping fire at 850s as shown in Figure 9.

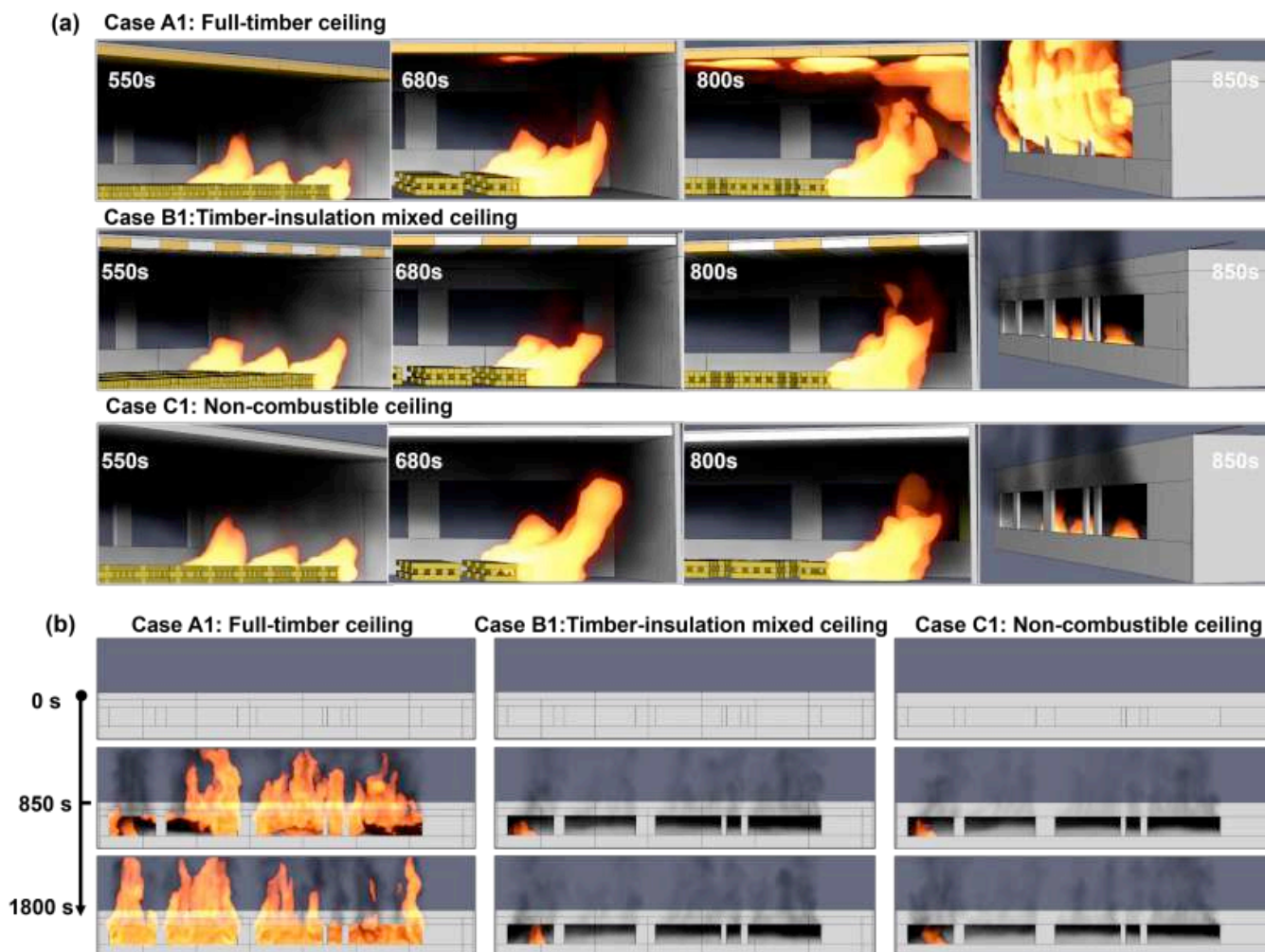


Figure 9. Images captured from the simulated cases: (a) The initial development of the localized fire impinging on the ceiling; (b) Timeline of the numerical simulation cases of large compartment fire development with different ceiling configurations under discontinuous fuel load

4.3 Effects of strip combination width on large open compartment fire dynamics

As described in Section 3.3, the proposed mixed ceiling strategy, with adjustable widths of relevant strips, greatly enhances the flexibility of this design. As depicted in Figure 10(a), while maintaining the ratio of timber strips to insulation strips at around 1:1, this section analyses the impact of three different combinations of strip widths (0.4 m, 0.8 m, and 1.6 m) on the compartment fire dynamics.

From the comparison of compartment heat release rates in Figure 10(b), it can be observed that all three combinations of strip widths mentioned above have mitigated the rapid development of compartment fires compared to Case A1 with full timber ceiling. Among them, the 0.4-meter strip combination (Case B2) and the 1.6-meter strip combination (Case B3) exhibit similar mitigation effects, both effectively delaying the rapid compartment fire by approximately 6 minutes. From the simulation results, it is found a low peak of HRR appeared at 850 s, which was followed by slight decrease of HRR. It is noticed that the 0.8-meter strip in Case B1 successfully limited the rapid spread and development of compartment fires within 1800 s, exhibiting localized burning similar to compartment with non-combustible ceilings (Case C1). Conversely, the other two cases using 0.4m strips (B2) and 1.6m strips (B3) could only delay the rapid fire development by 1200s, which were followed by rapid increases of HRR.

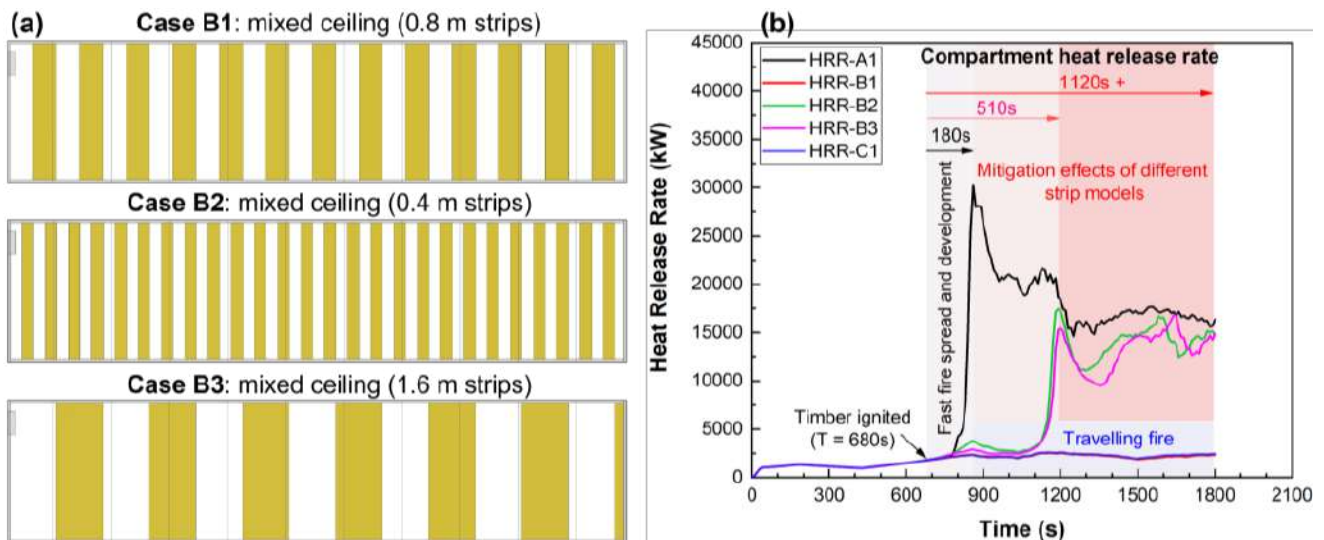


Figure 10. Compartment fire dynamic simulation results under discontinuous fuel load distribution: (a) Mixed ceiling layout with three strip combinations; (b) Compartment heat release rate evolution

5 CONCLUSIONS

The paper presents the numerical exploration on fire dynamics development in large open-plan compartments using the novel timber-insulation mixed-strip ceilings, which are aimed at mitigating the rapid spread of fires in large compartments with timber ceilings. Based on the CFD simulation models extended from the base model validated by Malveira test, the fire dynamics in large open-plan compartments with different ceiling configurations were simulated and compared, including compartments with a full-timber ceiling, timber-insulation mixed ceiling, and non-combustible ceiling. By analysing the results of simulation results, the beneficial effects of the mixed-strip ceiling design in mitigating fire propagation were validated. The preliminary findings of this study are outlined as follows:

1. Comparing to the fire development in the large compartment with a full-timber ceiling, the mixed-strip ceiling strategy enabled a notable delay of fast fire spread for almost 17 mins in a compartment with a fuel load density of 420 MJ/m^2 .
2. For the large compartment with the mixed-strip timber ceiling and discrete fuel load, successful mitigation of rapid-fire spread can be achieved within 1800 s, exhibiting a slow propagation of localized fire similar to the compartments utilizing non-combustible ceilings.
3. The investigation of compartment fire development under different combination modes based on the flexibility of strip combinations in the timber-insulation mixed ceiling strategy highlights the necessity of exploring rational strip designs.
4. Limitations of the current study should be clarified, which includes the detailed designs of timber-concrete composite slabs and the effects of compartment configurations. Nevertheless, this conceptual design may provide an opportunity of designing fire-safe timber slab solutions for future buildings.

REFERENCES

1. CEN., BS EN 1995-1-2:2004: Eurocode 5. Design of timber structures. General. Structural fire design. 2004.
2. Cheng, C., et al., "Modelling Heat Transfer of Timber Sections Subjected to Non-standard Fire Actions," Fire Technology. (Pending to submission). 2024.
3. McKenna, F., Fenves, G., & Filippou, F OpenSees. 2010, University of California, Berkeley: nd.
4. Chen, C., et al., "OpenSees development for modelling timber structural members subjected to realistic fire impact," Fire and Materials. 47(4): p. 461-478. 2022.

5. Jiang, L. and A. Usmani, "Towards scenario fires – modelling structural response to fire using an integrated computational tool," *Advances in Structural Engineering*. 21(13): p. 2056-2067. 2018.
6. Pope, I., et al., "Fully-developed compartment fire dynamics in large-scale mass timber compartments," *Fire Safety Journal*. 141. 2023.
7. Rackauskaite, E., et al., "Fire Experiment Inside a Very Large and Open-Plan Compartment: x-ONE," *Fire Technology*. 58(2): p. 905-939. 2021.
8. Khan, A.A., et al., "Model characterisation of localised burning impact from localised fire tests to travelling fire scenarios," *Journal of Building Engineering*. 54. 2022.
9. Nan, Z., et al., "Application of travelling behaviour models for thermal responses in large compartment fires," *Fire Safety Journal*. 134. 2022.
10. Nan, Z., et al., "Fire spread and burning dynamics of non-uniform wood crib for evolved design fire scenarios," *Fire Safety Journal*. 140. 2023.
11. Hidalgo, J.P., et al., "The Malveira fire test: Full-scale demonstration of fire modes in open-plan compartments," *Fire Safety Journal*. 108. 2019.
12. Chu, T., L. Jiang, and A. Usmani, "Introducing an active opening strategy to mitigate large open-plan compartment fire development," *Fire Safety Journal*. 141. 2023.
13. Chu, T., et al., "Integrating glass breakage models into CFD simulation to investigate realistic compartment fire behaviour," *Journal of Building Engineering*. 82. 2024.
14. Kotsovinos, P., et al., "Fire dynamics inside a large and open-plan compartment with exposed timber ceiling and columns: CodeRed #01," *Fire and Materials*. 47(4): p. 542-568. 2022.
15. Stern-Gottfried, J. and G. Rein, "Travelling fires for structural design-Part II: Design methodology," *Fire Safety Journal*. 54: p. 96-112. 2012.
16. Stern-Gottfried, J. and G. Rein, "Travelling fires for structural design-Part I: Literature review," *Fire Safety Journal*. 54: p. 74-85. 2012.
17. Kotsovinos, P., et al., "Impact of partial encapsulation on the fire dynamics of an open-plan compartment with exposed timber ceiling and columns: CodeRed #04," *Fire and Materials*. 47(4): p. 597-626. 2023.
18. CEN., BS EN 1991-1-2: 2002 Eurocode 1: Actions on structures- Part 1-2: General actions -Actions on structures exposed to fire. 2002.
19. Janardhan, R.K. and S. Hostikka, "When is the fire spreading and when it travels? – Numerical simulations of compartments with wood crib fire loads," *Fire Safety Journal*. 126. 2021.
20. Dai, X., et al., "An engineering CFD model for fire spread on wood cribs for travelling fires," *Advances in Engineering Software*. 173. 2022.

INFLUENCE OF ADHESIVE TYPE ON HEAT INDUCED DELAMINATION IN TENSION LOADED SHEAR LAP CROSS LAMINATED TIMBER SAMPLES EXPOSED TO RADIANT HEAT FLUX

Čolić A.¹, Wiesner F.², Spearpoint M.³, Hopkin D.⁴, Bisby L.⁵

ABSTRACT

Heat induced delamination (HID) is a phenomenon in engineered wood products which may result in the detachment of the bonded timber lamellae before charring propagates to the bond line interphase. This study aims to correlate the thermal degradation of two 1-c-polyurethane adhesives at the microscale to the thermo-hydro-mechanical behaviour of tension shear lap cross laminated timber at an intermediate scale. The performance criteria studied are the failure mode, time to failure, and bond line temperature at failure. The variables considered are the adhesive type (standard adhesive (Loctite HB S) and an adhesive with an improved performance fire (Loctite HB X), initial moisture content, and severity of thermal exposure. Results indicate that both adhesive types exhibited HID, with temperatures at failure being influenced by heat flux severity and initial moisture content variations. The study also correlates the responses with microscale analyses using differential scanning calorimetry (DSC) and dynamic thermo-mechanical analysis (DTMA).

Keywords: Structures; finite element modelling; compartment fires; fire tests

1 INTRODUCTION

1.1 Problem statement

Maintaining composite action between the bonded layers of engineered wood products (EWP) is a critical structural performance criterion in both ambient and fire conditions. Failure in EWP can be categorised into either timber or bond line failures. The terminology ‘bond line’ herein includes the adhesive phase and the timber-adhesive interphase (i.e. the timber fibres in proximity of the bond line which are penetrated by the adhesive).

Failure within the timber, away from the bond line, is a cohesion failure, whilst failure within the bond line can be either adhesion (timber-adhesive interphase) failure, or cohesion (adhesive bulk) failure. Adhesive bulk failure results in a smooth surface within the adhesive zone, whilst the interphase failure exhibits a rough surface with areas of exposed timber fibres. Cohesion failure in the timber is a common failure mode at ambient temperature for EWPs, provided that appropriate adhesives are used. However, the stiffness and strength of both polymer adhesives and timber reduce under elevated moisture and temperature conditions,

¹ PhD student, The University of Edinburgh, School of Engineering, Edinburgh, Scotland
e-mail: A.Colic@sms.ed.ac.uk, ORCID: <https://orcid.org/0000-0002-9341-2623>

² Assistant Professor, The University of British Columbia, Vancouver, Canada
e-mail: felix.wiesner@ubc.ca, ORCID: <https://orcid.org/0000-0002-0231-4244>

³ Director, OFR consultants, UK
e-mail: danny.hopkin@ofrconsultants.com, ORCID: <https://orcid.org/0000-0002-3632-4870>

⁴ Research Leader, OFR consultants, UK
e-mail: michael.spearpoint@ofrconsultants.com, ORCID: <https://orcid.org/0000-0002-2559-3581>

⁵ Professor, The University of Edinburgh, School of Engineering, Edinburgh, Scotland
e-mail: Luke.Bisby@ed.ac.uk, ORCID: <https://orcid.org/0000-0001-8293-4322>

potentially impacting the failure modes; failure typically shifts towards adhesive cohesion or interphase adhesion failure, whilst the wood failure percentage decreases [1–3].

Under ambient temperature conditions, delamination is detachment at the bond line, typically due to environmental changes, i.e. cyclic exposure to dry and wet conditions, that cause a loss of composite action. In elevated temperature or fire conditions, heat induced delamination (HID) may occur due to a combination of hydro-thermo-mechanical stresses. The bond line is exposed to a moving moisture front emanating from the heated surface, thermal degradation due to thermal penetration, and mechanical normal and/or shear stresses which may increase due to thermal expansion or dehydration shrinkage. Such loss of composite action can occur before a visual failure [4], or as a visual failure where the bonded lamellae pieces detach *before* the char front has propagated to the bond line. Detached lamella fragments consist of both virgin and charred timber [3] and therefore HID differs from only char fall off [5]. The occurrence of HID not only causes the remaining timber cross section to be exposed to more severe fire conditions, but causes a more progressive loss of effective cross section and loss of structural capacity.

1.2 Research methods related to the adhesive performance

Experimental research methods used to study(1-c-polyurethane) bond line performance in fire conditions are presented in Table 1; differing in (i) the applied load value and load type, (ii) load application transience, (iii) heating application method, and (iv) the thermal profile induced. Small scale testing typically involves bench-scale experiments, intermediate testing often assesses a single structural element using radiant panel or furnace tests, while large scale testing generally encompasses compartment-scale sizes.

Table 1. Experimental methods used to assess the (1-c-polyurethane) adhesive performance in fire conditions

	Bond line Structural load	Appl. sequence	Load transience	Thermal profile	Heat source	Performance criteria	Ref
Small	Shear lap/ Finger joint Tension	H->L	Ramp	Uniform	Oven	Strength reduction, wood failure percentage	[2,6–12]
	EWP block compression	H+L	Constant	Transient		Strength, strain	[1,3]
				Uniform		Strain rate (creep)	[10,13]
	EWP Beam Bending	H->C->L	Constant	Transient		Failure time, Deformation, BLT ¹	[10,14–16]
				Constant -> Transient		Residual strength	[17]
EWP block	H	N/A	Transient	Flame test	Delamination length	[18]	
Intermediate	EWP Slab No load	H	N/A	Transient	Furnace	Charring rate, MLR ² , BLT	[19,20]
	EWP block /wall No load				Cone calorim. Radiant panel	Thermal penetration	[3,21]
	EWP block/wall Compression	H+L	Constant	Transient	Furnace	Charring rate, deflection, thermal penetration	[22–24]
	EWP Beam / Slab Bending						
EWP Beam Bending	H->C->L	Ramp	Constant-> Transient	Pool fire	Residual strength	[1]	
Large	EWP Beam / Slab Bending	H	N/A	Transient	Natural gas, wood cribs, furniture	Thermal penetration, Visual observation, BLT	[25–27]
	EWP wall Compression	H+L	Constant				[28–31]

¹ BLT: bond line temperature | ² MLR: mass loss rate

H->L: heated then loaded | H+L: heated and loaded simultaneously | H->C->L: heated, cooled and then loaded | H:heated

Performance criteria used to assess adhesives through small-scale studies are typically ultimate stress and/or strain rate increase when tested at a specific uniform bond line temperature, wood failure percentage, and/or delamination length in the flame test. Figure 1 summarises small scale studies of 1-c-polyurethane adhesive included in Table 1 with transient loading and constant elevated temperature. When the authors [12] publish only the curve fit with no independent data points, the data is included in the plot as such. Despite the similar heating (oven) and applied displacement rates (1–2 mm/min), the data are scattered, with no discernible pattern between different test series, likely due to changes in the adhesive composition and sample manufacturing. However, the shear capacity drops below 20 % for temperatures above 200 °C for all studies (20 % considered as a reasonable ambient temperature upper service load utilisation level).

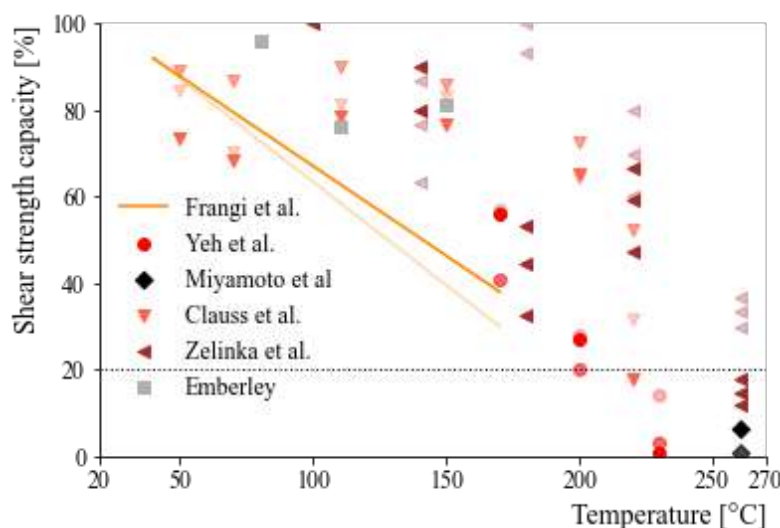


Figure 1. Shear strength reduction in shear lap experiments under uniform [2,6,10–12] and transient temperature profiles [3], Marker transparency varies for the 1-c-polyurethane adhesives used in the study (i.e. 0%: 1-c-PUR1, 20%: 1-c-PUR2, etc.)

The literature from intermediate and large-scale testing depicted in Table 1 discussed time of failure, deflection, and corresponding bond line temperature. However, there is some uncertainty in determining elevated temperature adhesive performance using large scale experiments as HID may occur at positions with no temperature measurements or where adhesive stresses are low. The reported bond line temperatures at HID failure for intermediate and large-scale experiments reported in the literature are shown in Figure 2. These varied depending on the load and heating conditions. Additionally, the initial moisture content in the timber in most of the studies was 9–15 % by mass, and the 1-c-polyurethane adhesives used for the analysis presented varied in their chemical composition, both of which will influence the results. The results fall within a range from 100–350 °C and 20–160 min. The mean failure temperature and the mean failure time are presented as grey lines, with their respective standard deviations shown as shaded regions (5-70 min, 86-231 °C). The temperatures above 250 °C were reported mostly from standardised furnace testing.

Neither failure time nor temperature could not be correlated to the load application, but this could also be due to the large scatter in the load applied. In the legend in Figure 2, the load is presented as the calculated utilised bending/compression/shear capacity based on the load specified in the study. Calculations were run with CLTdesigner software [32] according to the effective-cross section method. The study specified load was used in calculation as a live load in non-factored load combination (1.0*dead load + 1.0*live load) to define the bending and shear stresses within the cross-laminated (CLT) beams. The calculated capacity is only an approximation, based on the authors interpretation of the load applied. When the ultimate capacity of a tested sample was cited concurrently with the applied load, the two were simply divided. This unifying approach to load highlighted a large range of possible utilisations for the results in Figure 2 (3–30 % for shear capacity (SC), 30–69 % for tension capacity (TC), 10–23 % for bending capacity (BC).

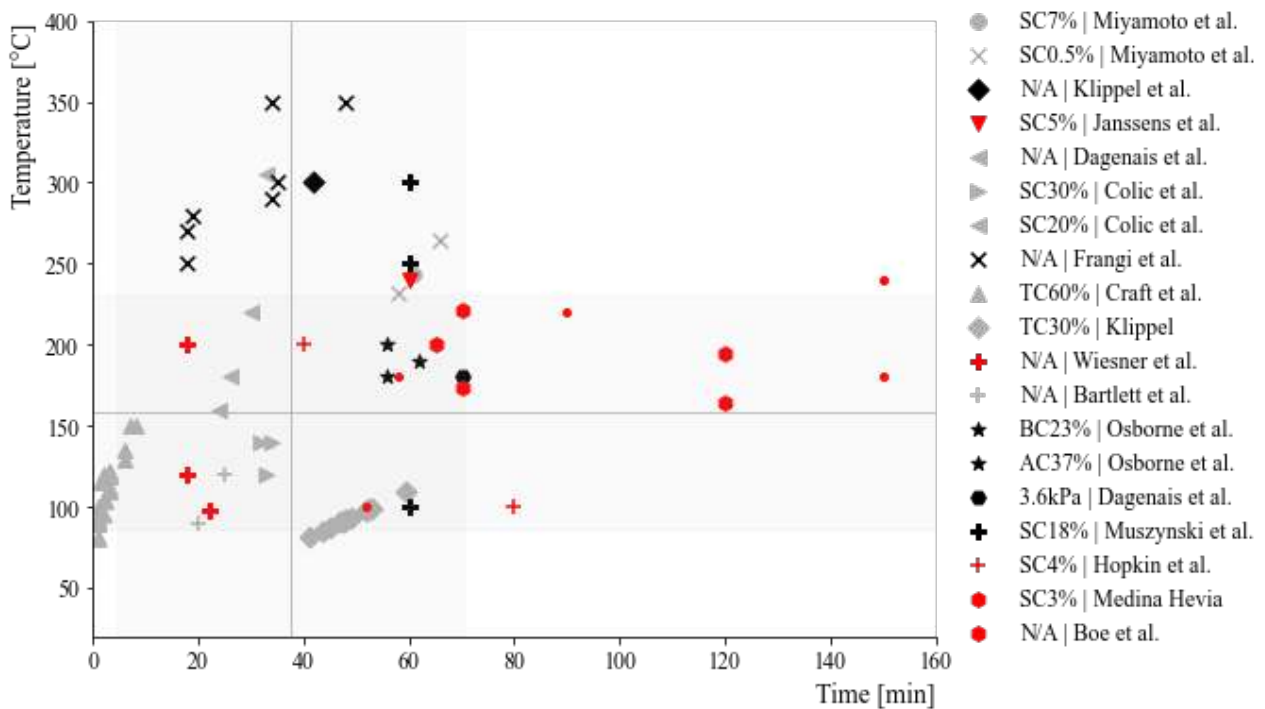


Figure 2. Heat induced delamination time and corresponding bond line temperature based on the small (grey,[5,10,13,15,18,21]), intermediate (black, [19,20,22–24]) and large scale studies (red, [25–31]) performed under transient heating conditions without (n/a) and with the application load (%)

Adhesive choice

Due to variations in chemical compositions across 1-component polyurethane adhesives, this current study focuses on the performance of two adhesives commonly used to produce cross-laminated timber (CLT) products; standard adhesive (HB S), and adhesive with improved performance at elevated temperature and in fire (HB X).

In a small-scale study by Zhang et al. [7] block samples with HB x bonded embedded steel plates were heated to an elevated temperature and the plates were pulled out to estimate bond line shear strength. The samples retained 40% of their shear strength after linearly decreasing during a temperature increase from 20 °C to 80 °C, the test limit of 100 °C meant that the outcomes do not capture more severe fire conditions. Small scale experiments by Hopkin et al. [33] suggested that use of HB X may reduce effective charring rates and improve adhesion in CLT at elevated temperature.

In a furnace testing method proposed by Klippel et al. [19], CLT panels with 25 mm and 35 mm lamellae thickness glued with HB X experienced ‘no significant’ and ‘no’ char fall off and HID respectively with 1.17 and 1.07 times higher mass loss rate (MLR) than solid timber panel. Lamellae (25 mm) bonded with HB S did exhibit char fall off and HID, with 1.73 times higher MLR, and were not tested with thicker lamellae. The authors suggested that the HB X system underperformed with smaller thicknesses due to the macroscopic shrinkage effects leading to thin char pieces bending. However, the samples in that study [19] were unloaded.

In a large scale loaded compartment study by Hopkin et al. [30], 40 mm lamella was used and char fall off was observed for both HB S and HB X, however HID was only observed for HB S. Severe HID of 20 mm lamellae with HB S was confirmed in an unloaded compartment fire experiment by Wiesner et al. [27].

Given the relative novelty of HB X, more data are needed to confirm the ability of HB X to mitigate HID.

The diverse adhesive formulations and testing load selections notably impact adhesive performance, leading to substantial variation across assessments. However, none of the globally applied methods address the loss of composite action or the influences of structural load, moisture content fluctuation, and heating conditions on failure mode, time, stresses, and temperatures at failure.

2 OBJECTIVES

The main objectives of this work are to (i) assess the temperature distribution near the bond line at the time of failure (i.e. adhesive cohesion or timber-adhesive adhesion failure near the bond line), (ii) shed light on the position of the in-depth moisture front at the time of aforementioned failure., and (iii) compare the performance of HB S and HB X under consistent and controlled heating and loading conditions. HB S is widely used in the CLT manufacturing industry has been shown to be susceptible to heat induced delamination [25–31]. HB X, was developed to deliver improved performance at elevated temperatures and in fire. Thus far this performance assessment has mainly focused on char fall off or changes in fire dynamics rather than HID.

The parameters varied in this study are the (i) adhesive type (HB S or HB X), (ii) initial moisture content of the timber, and (iii) imposed external heat flux intensity. Mechanical loading was conservatively maintained as constant and at a relatively high bond line utilisation.

3 METHODOLOGY

3.1 Materials

Shear lap samples were cut from cross laminated timber slabs with three lamellae as shown in Figure 3. The samples were $130 \times 130 \times 400 \text{ mm}^3$ with three plies $42.5/35/42.5 \text{ mm}$. Two notches (each 20 mm wide) were cut from the front and from the back to isolate the bond line between the first and second lamellae. The upper notch protruded only to the front (exposed) lamella (42.5 mm) while the lower notch was cut from the back (unexposed side), protruding two lamellae deep (77.5 mm). The notches were filled with mineral wool insulation. The sample was wrapped in aluminium foil apart from the $120 \times 130 \text{ mm}$ area which was exposed to radiant heating as shown in Figure 3). Three $\text{Ø}12$ holes were pre-drilled at the top and bottom of the sample to clamp it to a tension rig using M10 bolts, as shown in Figure 4.

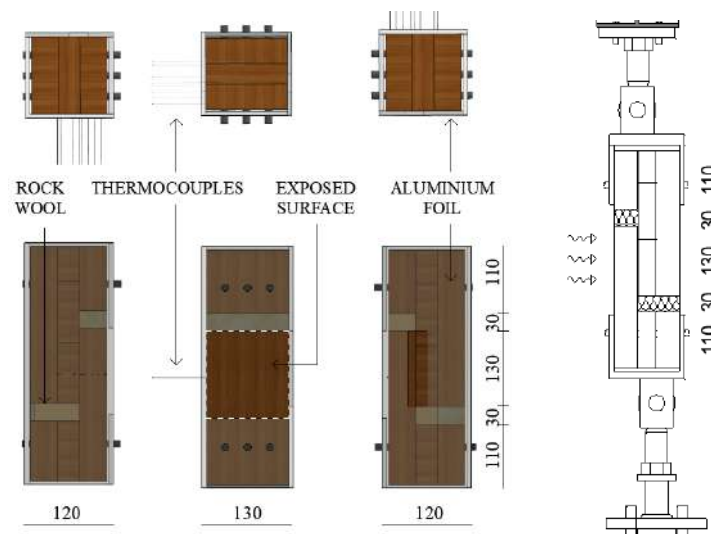


Figure 3. Sample dimensions (mm) (left side view, front view (heated surface), right side view) the rig fitting (right)

The experimental matrix was defined by the adhesive used, external heat flux severity, and initial moisture condition, as presented in Table 2. The CLT panels from which the samples were cut were manufactured by the same supplier but using HB S or HB X. All samples were manufactured using Radiata Pine.

Table 2. Experimental matrix

	Ambient	25 kW/m ²	50 kW/m ²
MC 9%	HB S (2) HB X (2)	HB S (4) HB X (3)	HB S (5) HB X (5)
MC 14%	HB S (2) HB X (2)	HB S (5)	HB S (5) HB X (3)

Samples were conditioned at 21 °C and one of two relative humidity (RH) conditions, namely 65 % and 80 %, so as to achieve two different initial moisture contents of 9 and 14 %, respectively. Control samples were tested at ambient temperature conditions and also under two different external heat fluxes (25 and 50 kW/m²). The number of experimental repeats is presented in brackets in Table 2.

3.2 Equipment and measurements

The experimental setup is shown in Figure 4. A reaction frame was fitted with an actuator at the bottom which was connected to a hydraulic power pack to impose a sustained tension load. The sample clamps were positioned asymmetrically, aiming to minimise normal stresses on the bond line and induce mainly shear stresses; the bottom clamp was aligned with the first (front) bond line and the upper clamp with the second (rear) bond line, as per Figure 4.

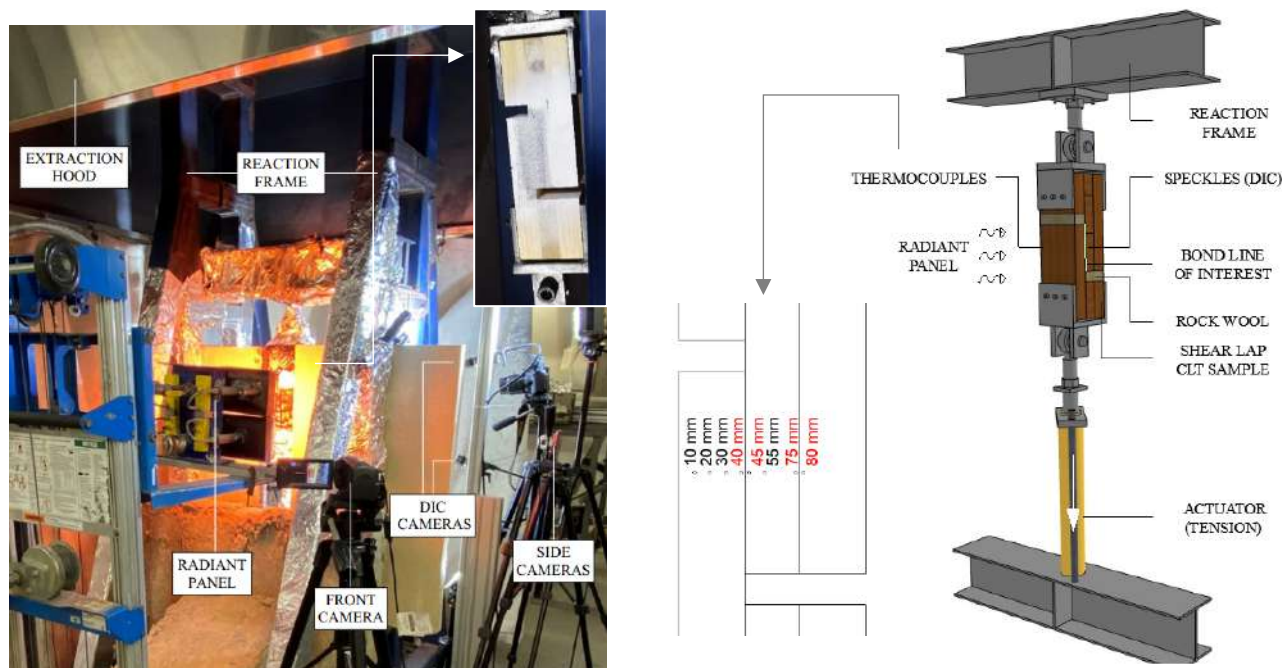


Figure 4. Experimental setup (left), scheme (centre), installed sample tested in ambient conditions (right)

Samples were first tested under ambient temperature conditions in tension, at a loading rate of 1 kN/min, to determine their ultimate strength. For the experiments at elevated temperatures, samples were exposed to a constant incident heat flux whilst under a sustained load of 20 % of their ambient temperature ultimate capacity. This is considered an onerous test condition with a severe shear stress effect and minimised normal stresses in the bond line, so as to pinpoint differences in response amongst the varied parameters. It is considered unlikely that such severe shear stresses would be present in a typical CLT building under service loads.

A front video camera and a side camera were used to capture the behaviour, the failure mode, and the time of failure. The samples were also painted with a speckle pattern with the aim of tracking strains and displacement using Digital Image Correlation; however, these data are not included here. Thermocouples were installed with wires running parallel to the in-depth isotherms to measure bond line temperatures. Thermocouples were placed at a side-depth of 75 mm, at 10, 20, 30, 40, 45, 55, 75 and 80 mm from the exposed face, as shown in Figure 4.

4 RESULTS

4.1 Failure mode

Two failure modes were observed; HID and ‘mixed mode’ (Figure 5). The former manifests as a relatively smooth surface with visible uncharred sections of the detached lamella. Mixed mode appears as a more

localised and uneven failure combined from HID and wood failure. Other observed failure modes are marked as N/A modes initiated outside the bond line region and assigned to the inherent variability of methodological errors (i.e. equipment malfunction, poor installation of the sample), etc.

A distribution of failure modes depending on the group tested is shown in Figure 5. HID occurred for 60 % of all 30 samples (11 HB X, 19 HB S) tested in fire conditions, 6 for HB X and 12 for HB S samples. The rest of the samples experienced either a mixed mode (30 %) or an N/A failure mode (10 %).



Figure 5. Failure modes (left) and their distribution with the subsets depending on the applied heat flux and moisture content (right)

Mixed mode failures were prevalent for HB S samples tested at lower heat fluxes, and at lower moisture contents, and for HB X samples tested at higher moisture contents and higher heat fluxes. The occurrence of HID increased with increased heat flux and moisture contents for HB S. The variability in failure modes reflects the inherent variability of the timber samples. Both the wood failure and HID results can be used to discuss adhesive performance as a function of moisture content and heat flux, whilst the N/A results are disregarded in assessing the results.

4.2 Failure time

Figure 6 shows failure times together with bars showing maximum and minimum values for each sample set. The correlation between adhesive type and failure time can be deduced depending on the increase in heat flux (Figure 6, left) and moisture content (Figure 6, right).

In all cases an increase in heat flux led to shorter failure times, due to the faster char front movement and temperature increase in the bond line region. The failure time decrease was most pronounced for samples with lower moisture content (9 %). At lower heat fluxes, more HB X 9 % samples experienced HID compared with the HB S 9 % samples, also with an overall earlier mean failure time (52 minutes versus 61 minutes).

At higher heat flux this trend was reversed (30 minutes and 35 minutes for HB S 9 % and HB X 9 %, respectively). The change in the mean failure time with heat flux was less pronounced for samples conditioned at 14% (HB S 14 % failed after 48 minutes at 25 kW/m², and at 38 minutes at 50 kW/m²).

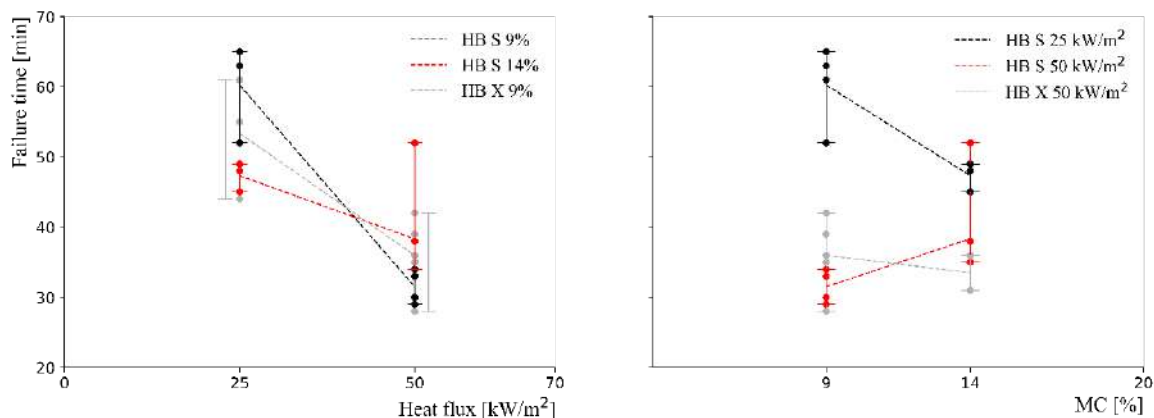


Figure 6. Failure time for HB S and HB X groups depending on the applied heat flux (left) and moisture content (right)

It is considered that two competing mechanisms are relevant when assessing the potential role of moisture in EWP. It is expected that the higher moisture contents would slow thermal penetration due to the latent heat of evaporation of water. However, the heat flux dependent moisture front position, and its interaction with the adhesive, could contribute to premature failures.

The two adhesives showed opposing trends with an increase in moisture content, as per Figure 6 (right). The moisture content dependent failure time for the two adhesives is compared for the higher heat flux only because 14 % HB X samples were not tested at the lower heat flux. Whilst HB S showed earlier mean failure times at the lower MC (32 minutes versus 37 minutes), this was reversed at the higher MC (39 versus 34 minutes). At the higher heat fluxes, an increase in MC had a positive influence on HB S (i.e. failure time was delayed from 32 to 38 minutes) and a negative influence on HB X (failure time decreased from 36 to 32 minutes). However, testing HB S at lower heat fluxes resulted in a negative correlation, showing the heat flux dependence. The scatter in failure time was not correlated to the change in heat flux and moisture content. However, in all cases, a higher scatter was noted for HB X.

To conclude, general trends in failure time were affected by both change in moisture content and heat flux, albeit more by the latter. The variables were shown to be interdependent. Whilst increases in heat flux led to substantially faster failure times, a positive correlation between the increase in MC and failure time was both adhesive and heat flux dependent, and hence this needs to be investigated for more conditions with a larger number of samples to draw definitive conclusions.

4.3 Bond line interphase temperatures

Figure 7 shows the failure temperatures recorded 2.5 mm in advance of the bond line (i.e. 40 mm depth) and 2.5 mm behind the bond line (i.e. 45 mm depth) for all samples that experienced either delamination or mixed failure mode. Each set of markers corresponds to one trial i.e. each pair of the equivalent shape with the same colour but different transparency are the temperatures in the same sample at 40 and 45 mm (black and grey for HB X and red and pink for HB S). Two complementary microscale methods, dynamic thermo-mechanical analysis (DTMA) and differential scanning calorimetry (DSC), were used to identify possible temperature ranges over which both timber and adhesive materials experience transitions and thermal degradation. Moisture evaporation was found to occur from 50–120 °C, glass transition in the temperature range 160–180 °C for HB S and 180–210 °C for HB X (based on the tan delta increase in DTMA and DSC), softening of HB S adhesive from 220–260 °C (based on DSC), and Radiata Pine pyrolysis from 230–300 °C (based on DSC).

In the DSC results, for the specified range, HB S showed an endothermic increase (a dip) related to the mass loss rate plateau in the thermogravimetric analysis in both nitrogen and air, suggesting that the HB S adhesive softens before it undergoes pyrolysis. HB X experienced no such dip before the onset of pyrolysis.

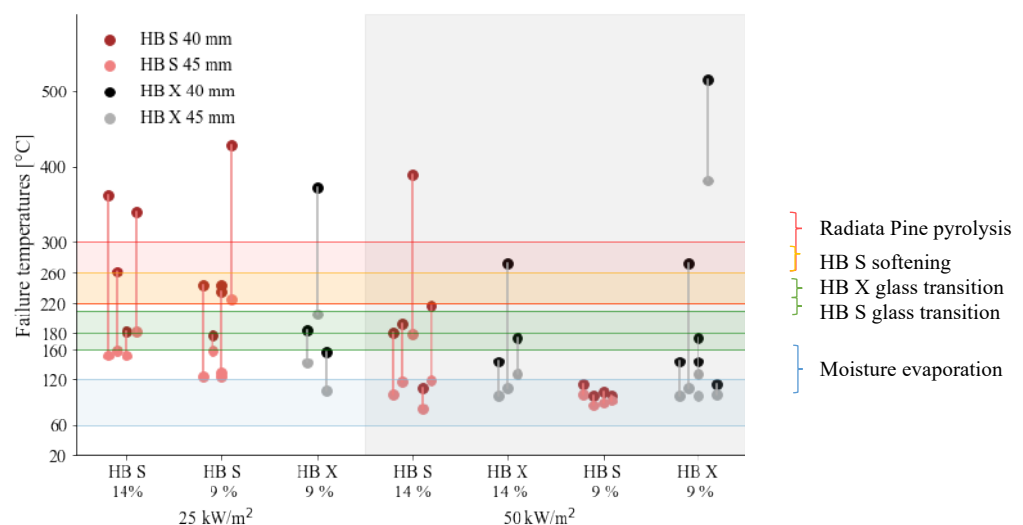


Figure 7. Temperature rang +/- 2. 5mm around the bond line at the time of failure with the adhesive and timber transition and thermal degradation temperatures according to DSC and DTMA analysis

From the temperatures at the time of failure, considerable variation between the samples was observed. Whilst some (6 of 26) temperatures at 40 mm fall within or beyond the timber pyrolysis region, their corresponding temperatures at 45 mm and the temperatures of all other tested samples fall below 260 °C. The high bond line temperatures in HB X conditioned at 9 % (400–500 °C), presented in Figure 8, are considered to be outliers. It is possible that a crack occurred at or close to the thermocouple location which resulted in it being exposed to higher temperatures. Also, it must be remembered that temperatures were monitored only at one discrete location over the bond surface, and considerable variability in temperatures is considered likely given the inherent variability and cracking behaviour of charring timber.

For all samples exposed to higher heat fluxes, failure occurred once the moisture front had passed the bond line and the temperatures measured at the thermocouple behind the bond line (i.e. 45 mm depth) correspond to moisture evaporation. This is confirmed by considering bond line temperature development in time, shown in Figure 8, where for the case of the higher heat fluxes it is evident that the failure occurred when the moisture evaporation plateau had passed the bond line.

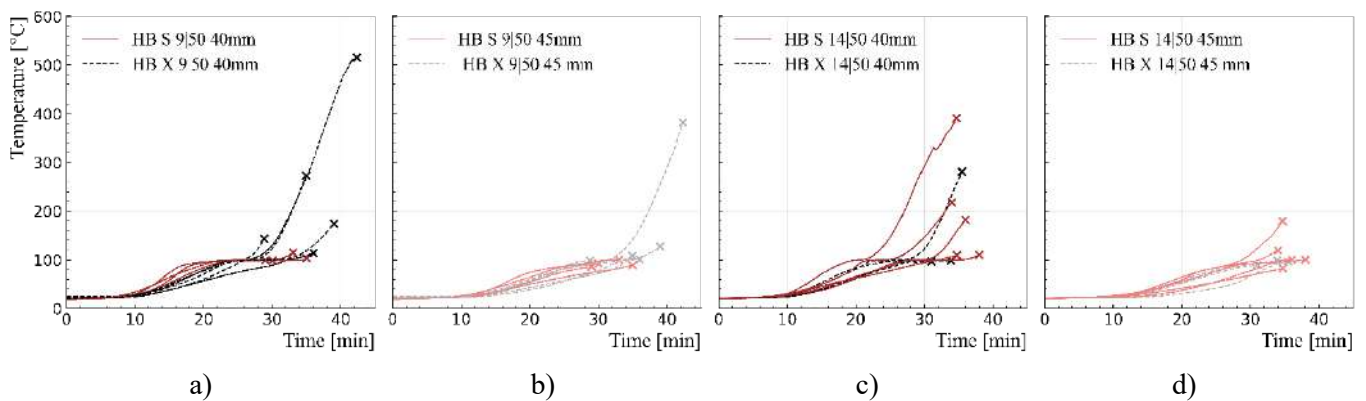


Figure 8. Temperature-time curves (a,c) ahead of the bond line at 40 mm and (b,d) behind the bond line at 45 mm for samples tested at 50 kW/m² and conditioned at (a,b) 9% and (c,d) 14%

For the same heat flux both adhesives exhibited similar bond line temperatures at failure. In Figure 8 one would expect the same failure time for HB S and HB X. However, since failure times for HB X were longer, this may indicate different influence of moisture for HB X than for HB S. However, at higher heat fluxes the moisture plateau was longer for HB S than for HB X, whilst it was similar at lower heat fluxes.

Temperatures ahead of the bond line varied for both adhesive groups, but more scatter was evident due to increases in initial moisture content (100–400 °C, Figure 8) and the lower heat flux (160–450 °C,

Figure 9). The lower heat flux exposures also led to higher failure temperatures recorded after the bond line (100–200 °C), approaching the adhesive glass transition temperatures, as indicated in

Figure 9. This suggests that there a single bond line temperature criterion cannot be used in design; rather it may depend on the heating history of the sample.

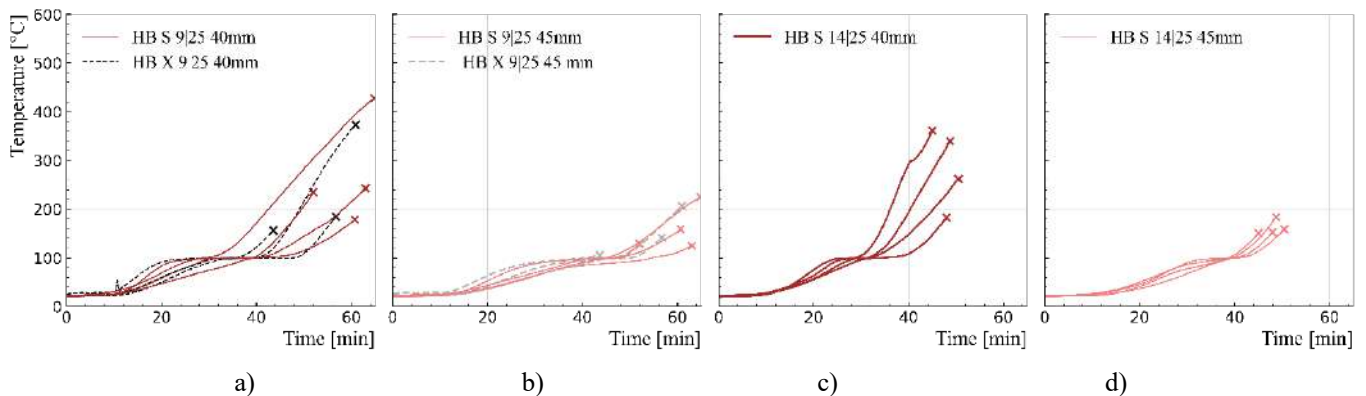


Figure 9. Temperature-time curves (a,c) ahead of the bond line at 40 mm and (b,d) behind the bond line at 45 mm for samples tested at 25 kW/m² and conditioned at (a,b) 9% and (c,d) 14%

Finally, the influence of the heat flux severity and moisture content on the failure temperatures (calculated as a mean from the temperatures at 40 mm and 45 mm) is shown in Figure 10. Bond line temperatures were reduced with an increase in heat flux, and increased with an increase of initial moisture content.

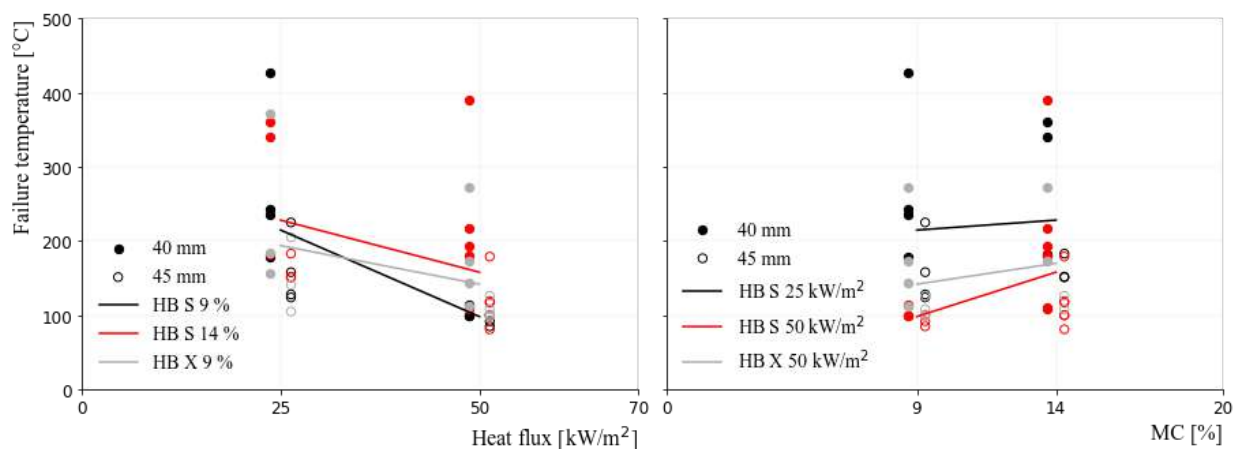


Figure 10. Linear fit for the averaged temperatures before (40 mm depth) and after (45 mm depth) the first bond line at the time of failure, depending on the heat flux (left) and moisture content (right)

Better performance of HB S 9 % with slightly higher failure temperatures than HB X 9 % at 25 kW/m² cannot be rationalised at this point and it might be from the inherent variability in the data results, perhaps compounded by the presence of an outlier at 400 °C. At 50 kW/m² HB X failed at higher temperatures than HB S 9% but not HB S 14 %. Temperatures trends show that HB S 9% was significantly affected by heat flux change (average 117 °C reduction in failure temperature), followed by HB S 14 % and HB X 9 % (average 70 °C and 52 °C reductions in failure temperature, respectively). Additionally, a positive correlation between the average bond line temperatures and MC increase was most pronounced for the HB S 50 kW/m² (average 60 °C higher failure temperature with MC increase), followed by HB X 50 kW/m² (28 °C higher failure temperature), and HB S 25 kW/m² (13 °C higher failure temperature).

The hypothesis posits that higher heat flux accelerates the moisture front, leading to lower failure temperatures, particularly for HB S. This implies heightened degradation of HB S adhesive under the influence of intensified moisture fronts induced by temperature and pressure gradients, but the reason behind HB X's superior performance under these conditions remains unknown to the author. Additionally, if more moisture is expected to cause higher degradation of HB S adhesive, one would expect lower failure temperatures for the HB S 14 %. The considerable specific heat of the water could lead to the longer section cooling, potentially delaying the failure, consequently resulting in elevated temperatures at the bond line. However, it is notable in Figure 6 that the HB S 14% adhesive exhibited earlier failure. Thus, the rationale underlying the rise in average bond line temperature with moisture content remains elusive. Further experimentation with a larger sample size is warranted to validate the observed trends depicted in Figure 10 (right).

When compared, the results do not suggest a consistently and significantly better behaviour of HB X against HB S (i.e. longer failure times or higher failure temperatures). Overall, the data suggests that the failure temperatures for the HB S adhesive are more dependent on both the change in heat flux and moisture conditions, whereas the HB X adhesive temperatures are more heat flux dependent.

5 CONCLUSIONS

This study has studied the dependence of heat-induced delamination on various factors, including adhesive type, heating conditions, loading parameters, and the initial moisture content of engineered wood products (EWP). Despite intentionally imposing severe bond line shear stresses in the experiments so as to create a credible worst-case mechanical loading scenario, the observed temperatures at which bond line failures occurred remained highly scattered and within a wide range from 80 to 230 °C; this accords with temperatures quoted within the available literature (Figure 2) for mass timber elements tested under transient heating conditions.

Heat induced delamination occurred for both of the 1-c-polyurethane adhesives used in this study, with HB S performing better at lower heat fluxes, and HB X at higher heat fluxes, in terms of longer failure times and higher bond line temperatures at failure. Under the given test conditions there is no clear advantage in the performance of HB X over HB S.

The performance of 1-c-PUR adhesives could not be captured with a single testing condition or summarised into a single critical temperature as a bond line temperature performance criterion for all scenarios. However, temperatures behind the bond line appeared to provide less variability in the data across all scenarios. At higher heat fluxes, adhesive failure was attributed to moisture front movement, occurring within the moisture evaporation range (80–120 °C). Conversely, at lower heat fluxes, the moisture front traversed through the adhesives, allowing time for glass transition, thereby shifting failure to higher temperatures (160–180 °C for HB S and 180–210 °C for HB X).

Both HB X and HB S show similar trends; failure temperature decreased with heat flux and increased with moisture content. However, the variation in the performance with the increased moisture content are unclear and more samples need to be tested to confirm the trends.

ACKNOWLEDGMENT

The authors would like to acknowledge the contribution of COST Holistic Design of Tall Timber buildings (HELEN) Action CA20139, who awarded the main author with a grant for a Short Term Scientific Mission to perform part of the experimental campaign at the University of Queensland, where she collaborated with Jeronimo Carrascal, Dr Felix Wiesner and Dr David Lange. Microscale studies were done in collaboration with Henkel AG & Co. KGaA, and the authors would like to thank Gordian Stapf and Dr Sebastien Josset for their support. We would like to gratefully acknowledge UQ PhD students Sergio Zarate, Thomas Bravo, and Wenxuan Wu as well as the skilled technicians at UQ including Chris Russ, Van Thuan Nguyen, Shane Walker, Jason Van Der Gevel, Stewart Matthews, Frazer Reid, and John Stafford.

REFERENCES

- [1] H. Quiquero, B. Chorlton, J. Gales, “Performance of adhesives in Glulam after short term fire exposure” . In: *Int. J. High-Rise Build.* 7 (2018) , pp.299–311. <https://doi.org/10.21022/IJHRB.2018.7.4.299>.
- [2] S.L. Zelinka, K. Sullivan, S. Pei, N. Ottum, N.J. Bechle, D.R. Rammer, L.E. Hasburgh, “Small scale tests on the performance of adhesives used in cross laminated timber at elevated temperatures” . In: *Int. J. Adhes. Adhes.* 95 (2019). <https://doi.org/10.1016/j.ijadhadh.2019.102436>.
- [3] R. Emberley, *Fundamentals for the fire design of cross laminated timber buildings*, The University of Queensland, 2017. <https://doi.org/10.14264/uql.2017.163>.
- [4] R. Emberley, A. Nicolaidis, D. Fernando, J.L. Torero, “Changing failure modes of Cross-Laminated Timber” . In: *9th Int. Conf. Struct. Fire.* (2016) , pp.643–649.
- [5] A. Čolić, F. Wiesner, L. Bisby, J.P. Hidalgo, Delamination and char fall-off in fire exposed cross-laminated timber loaded in shear, in: *Proc. 12th Asia-Oceania Symp. Fire Sci. Technol. (AOSFST 2021)*, The University of Queensland, Brisbane, Australia, 2021. <https://doi.org/10.14264/a067f63>.
- [6] B. Yeh, R. Brooks, “Evaluation of adhesive performance at elevated temperatures for engineered wood products” . In: *9th World Conf. Timber Eng. 2006, WCTE 2006.* 2 (2006) , pp.1068–1076.
- [7] R. Zhang, H. Dai, G.D. Smith, “Investigation of the high temperature performance of a polyurethane adhesive used for structural wood composites” . In: *Int. J. Adhes. Adhes.* 116 (2022) , pp.102882. <https://doi.org/10.1016/j.ijadhadh.2021.102882>.
- [8] R. Balkova, J. Vanerek, M. Smak, R. Drochytka, “Time-temperature resistance of transverse stressed lap joints of glued spruce and thermal analysis of adhesives” . In: *Int. J. Adhes. Adhes.* 104 (2021) , pp.102760. <https://doi.org/10.1016/j.ijadhadh.2020.102760>.
- [9] M. Klippel, A. Frangi, M. Fontana, “Influence of the adhesive on the load carrying capacity of glue laminated timber members in fire” . In: *Fire Saf. Sci.* (2011). <https://doi.org/10.3801/IAFSS.FSS.10-1219>.
- [10] B. Miyamoto, N.J. Bechle, D.R. Rammer, S.L. Zelinka, “A small-scale test to examine heat delamination in cross laminated timber” . In: *Forests.* 12 (2021) , pp.1–11. <https://doi.org/10.3390/f12020232>.

- [11] S. Clauß, M. Joscak, P. Niemz, “Thermal stability of glued wood joints measured by shear tests” . In: *Eur. J. Wood Wood Prod.* 69 (2011) , pp.101–111. <https://doi.org/10.1007/s00107-010-0411-4>.
- [12] A. Frangi, M. Fontana, A. Mischler, “Shear behaviour of bond lines in glued laminated timber beams at high temperatures” . In: *Wood Sci. Technol.* 38 (2004) , pp.119–126. <https://doi.org/10.1007/s00226-004-0223-y>.
- [13] S.T. Craft, R. Desjardins, L.R. Richardson, “Development of small-scale evaluation methods for wood adhesives at elevated temperatures” . In: *10th World Conf. Timber Eng. 2008.* 2 (2008) , pp.583–590.
- [14] D.R. Rammer, S.L. Zelinka, L.E. Hasburgh, S.T. Craft, “Ability of finger-jointed lumber to maintain load at elevated temperatures” . In: *Wood Fiber Sci.* 50 (2018) , pp.44–54. <https://doi.org/10.22382/wfs-2018-005>.
- [15] M. Klippel, Fire safety of bonded structural timber elements, ETH, 2014. <https://doi.org/10.3929/ethz-a-010782581>.
- [16] A. Čolić, F. Wiesner, L. Bisby, J.P. Hidalgo, Delamination and char fall-off in fire exposed cross-laminated timber loaded in shear, in: 12th Asia–Oceania Symp. Fire Sci. Technol., 2021: pp. 7–9.
- [17] B. Källander, P. Lind, Strength properties of wood adhesives after exposure to fire, Borås 2001, 2001.
- [18] C. Dagenais, L. Ranger, Revisiting heat delamination characteristics of adhesives in cross-laminated timber, in: WCTE 2018 - World Conf. Timber Eng., 2018.
- [19] M. Klippel, J. Schmid, R. Fahrni, A. Frangi, “Assessing the adhesive performance in CLT exposed to fire” . In: *WCTE 2018 - World Conf. Timber Eng.* (2018).
- [20] A. Frangi, M. Fontana, E. Hugi, R. Jübstl, “Experimental analysis of cross-laminated timber panels in fire” . In: *Fire Saf. J.* 44 (2009) , pp.1078–1087. <https://doi.org/10.1016/j.firesaf.2009.07.007>.
- [21] A. Bartlett, K. Gajewski, R. Hadden, N. Butterworth, L. Bisby, “Fire-Induced Delamination of Cross-Laminated Timber Fire-Induced Delamination of Cross-Laminated Timber” (2015). <https://www.researchgate.net/publication/308653056%0AFire-Induced>.
- [22] L. Osborne, C. Dagenais, N. Benichou, Preliminary CLT Fire Resistance Testing Report by, 2012.
- [23] C. Dagenais, L. Ranger, N. Benichou, J. Su, “Fire performance of cross-laminated timber with adhesives conforming to 2018 edition of ANSI/APA PRG-320” (2019).
- [24] L. Muszynski, R. Gupta, N. Osborn, B. Pickett, “Fire resistance of unprotected cross-laminated timber floor assemblies produced in the USA” 107 (2019) , pp.126–136. <https://doi.org/10.1016/j.firesaf.2018.12.008>.
- [25] F. Wiesner, L.A. Bisby, A.I. Bartlett, J.P. Hidalgo, S. Santamaria, S. Deeny, R.M. Hadden, “Structural capacity in fire of laminated timber elements in compartments with exposed timber surfaces” . In: *Eng. Struct.* 179 (2019) , pp.284–295. <https://doi.org/10.1016/j.engstruct.2018.10.084>.
- [26] A. Sæter, K. Leikanger, D. Brandon, A. Steen-hansen, I.S. Ertesvåg, “Fire spread in a large compartment with exposed cross-laminated timber and open ventilation conditions : # FRIC-02 - Exposed wall and ceiling” 141 (2023). <https://doi.org/10.1016/j.firesaf.2023.103986>.
- [27] A. Sæter, K. Leikanger, D. Brandon, A. Steen-hansen, I.S. Ertesvåg, “Fire spread in a large compartment with exposed cross-laminated timber and open ventilation conditions : # FRIC-01 – Exposed ceiling” 140 (2023). <https://doi.org/10.1016/j.firesaf.2023.103869>.
- [28] M. Janssens, Development of a fire performance assessment methodology for qualifying cross-laminated timber adhesives, San Antonio, Texas, USA, 2107.
- [29] J. Su, M. Hoehler, M. Bundy, “Fire Safety Challenges of Tall Wood Buildings -Phase 2: Task 2&3 - Cross Laminated Timber Compartment Fire Tests” (2018).
- [30] D. Hopkin, M. Spearpoint, I. Fu, H. Krenn, T. Sleik, D. Hopkin, W. Wojciech, “Large-Scale Enclosure Fire Experiments Adopting CLT Slabs with Different Types of Polyurethane Adhesives : Genesis and Preliminary Findings” (2022).
- [31] A. Medina Hevia, Fire resistance of partially protected CLT rooms, Carleton University, Ottawa, 2014.
- [32] A. Thiel, G. Schickhofer, “CLTdesigner - A software tool for designing cross laminated timber elements: 1D-plate-design” . In: *11th World Conf. Timber Eng. 2010, WCTE 2010.* 2 (2010) , pp.1742–1747.
- [33] D. Hopkin, C. Gorska, M. Spearpoint, I. Fu, H. Krenn, T. Sleik, G. Stapf, Experimental characterisation of the fire behaviour of CLT ceiling elements from different leading suppliers, in: Appl. Struct. Fire Eng., Ljubljana, Slovenia, 2021.
- [34] F. Wiesner, M. Klippel, C. Dagenais, A. Dunn, B. Östman, M.L. Janssens, K. Kagiya, Requirements for engineered wood products and their influence on the structural fire performance, in: WCTE 2018 - World Conf. Timber Eng., 2018.
- [35] PRG 320-2019: Standard for Performance-Rated Cross-Laminated Timber, United States, n.d.

INFLUENCE OF SURFACE SLOT SHAPE ON THE TEMPERATURE RISE AND BURNING BEHAVIOR OF WOOD UNDER INTENSE HEATING

Anyang Sun¹, Kazunori Harada², Daisaku Nii³

ABSTRACT

Cone calorimeter tests were conducted to investigate the effect of surface crack on temperature rise and burning behavior of wood. Laminated larch wood specimen with 99*99mm size in heating surface and 50mm in depth were used. Pre-processed slot on the surface were used to simulate surface crack, and 4 types of specimens with difference slot sizes (no slot, 5*25 mm, 5*40mm, 10*40mm) were created. Two types of experiments with different heating intensity, the heating experiments and the burning experiments, were conducted. In the heating experiments, specimens were heated by 6kW/m² intensity for 30 minutes, then 12kW/m² for 30 minutes. In the burning experiments, specimens were heated by 50kW/m² intensity for 20 minutes. The existence of slot had made the internal temperature rise further when subjected to the same intensity of heating. The greater the heating intensity, the more obvious this tendency is. The maximum value of heat release rate were not affected by slot, while heat release rates during the steady combustion stage were 20~25% higher in case of specimens with a slot than specimens without slot. The charred depth and colored depth of the specimens with slots also increased by about 20 to 25% compared to the specimens without a slot.

Keywords: Timber; Radiative heat transfer; Surface slot; Cone calorimeter; Char layer; Heat release rate

1 INTRODUCTION

Wood is an environmentally friendly and sustainable material, and it is widely used in constructions and building engineering in many countries. However, wood is flammable. When wood was exposed to high temperature, pyrolysis of wood continues to occur, turns virgin wood into char, combustible pyrolysis gas, and other products like tar[1]. Heat generated by the combustion of flammable reaction products will become the heat source of further pyrolysis, allowing the reaction to continue and finally result in the failure of timber elements. Therefore, it is greatly significant to study the fire safety of timber elements used in building and constructions.

Char layer will be formed on the surface of wood due to pyrolysis after heated intensely. It is widely believed that these formed char layer has the effect of preventing the internal temperature of virgin wood from increasing further, and delays the charring of wood[2], since the thermal conductivity of char is lower than unreacted wood. The thermal conductivity of wood is about 0.08~0.15W/m·K[3] at room temperature, while the thermal conductivity of char is lower than this, say about 0.04W/m·K reported by Wijayanti[4], about 0.09/m·K reported by Gupta[5]. However, the protective effect of the char layer on virgin wood will

¹ Assistant Professor, Department of Architecture and Architectural Engineering, Graduate School of Engineering, Kyoto University
e-mail: sun@archi.kyoto-u.ac.jp, ORCID: <https://orcid.org/0000-0003-0456-8835>

² Professor, Department of Architecture and Architectural Engineering, Graduate School of Engineering, Kyoto University
e-mail: harada@archi.kyoto-u.ac.jp, ORCID: <https://orcid.org/0000-0001-8270-1692>

³ Associate Professor, Department of Architecture and Architectural Engineering, Graduate School of Engineering, Kyoto University
e-mail: nii@archi.kyoto-u.ac.jp, ORCID: <https://orcid.org/0000-0002-5821-7494>

change over time. When the specimen was heated, shrinkage in size will occur as pyrolysis proceeds[6][7]. As a result, cracks will be formulated on the charred layer near heated surface. Heat flux from external heat source can flow directly through these cracks, which causes the internal temperature of the wood element to rise further and accelerates the charring rate [8]. Due to the mentioned phenomenon, it is necessary to investigate the effect of surface crack on internal temperature and burning behavior of timber element under high temperature heating.

Much research about surface crack on timber specimen exposed to intense heating were reported. Konig *et al.*[9] proposed a set of effective thermal conductivity expressing the strengthening effect of crack on heat transfer. Proposed values were calibrated based on experimental data on temperature measured in standard fire tests. Zhang *et al.*[10] conducted heating experiments on small timber specimens, and found that the transition from smoldering combustion to flaming combustion occur at about 830°C under external airflow. They believed that the occurrence of this phenomena is caused by the interaction between cracks undergoing smoldering and airflow in the external environment. Watanabe and Chatani[11] conducted fire resistance test on laminated larch and cedar wall specimens with pre-processed slot, to investigate the effect of slot opening size on temperature rise. They found that for slots with 30mm depth, when the slot width is greater than 3mm, the maximum temperature at 30mm location rose sharply. There are also some research focuses on the formation process of surface crack. Lee *et al.* [12] proposed a mathematical model using critical stress criterion and energy conservation theory, to predict the number of surface cracks. Shen *et al.* [13] conducted heating experiments on softwood and hardwood specimens to measure the depth and pattern of cracks under radiant exposure with different durations. Empirical formulas on crack depth related to heating intensity and heating time were proposed.

However, there are still some problems should be investigated on the effects of crack on fire resistance of timber specimen under intense heating. Research on the influence of crack on burning behavior (heat release rate, etc.), charring behavior, and temperature increase is not sufficient. These data are very important while developing and calibrating numerical models of wood combustion considering surface cracks.

In this paper, cone calorimeter tests on laminated larch wood specimens were conducted to investigate the effect of crack on burning behavior and temperature rise. Since it is hard to control the size, shape and number of cracks generated according to pyrolysis and shrinkage, and the temperature near the location where the crack exists is very difficult to measure because the carbonized layer is thin and fragile, pre-processed slot on the surface of specimen were used to simulate cracks in this experiment. Temperature, heat release rate and burnt-out/charred/colored depths were measured to investigate the effect of pre-processed slot on burning behavior. The outcome and results of this research is important in structural fire engineering and can be useful in the cases such as developing and validating numerical models to simulate timber wall or connections under fire heating considering surface cracks.

2 MATERIALS AND METHODS

2.1 Experimental outline

The experiments were conducted using a Cone Calorimeter[14]. The photograph of ongoing experiment is shown in Figure 1. Specimen was exposed to radiant heating from top. Two types of experiments with different heating intensity were conducted, and they were named as heating experiment and burning experiment. In the heating experiment, specimens were heated at 6kW/m² intensity for 30 minutes, then 12kW/m² for 30 minutes. Time to switch the heating intensity is approximately 2.5 minutes. In the burning experiment, specimens were heated under 50kW/m² intensity for 20 minutes. Heating experiments were conducted once for each condition. For burning experiment, two duplicate runs were conducted on each condition.

During the experiment, heat release rate from the burning specimen, temperature inside the specimen, temperature inside slot and the heated surface temperature of specimen were measured.

Before conducting the heating experiment, a piece of aluminium foil was placed on the specimen to prevent radiant heat from penetrating through the gap of the baffle, to prevent the rise of specimen's temperature before the start of experiment.

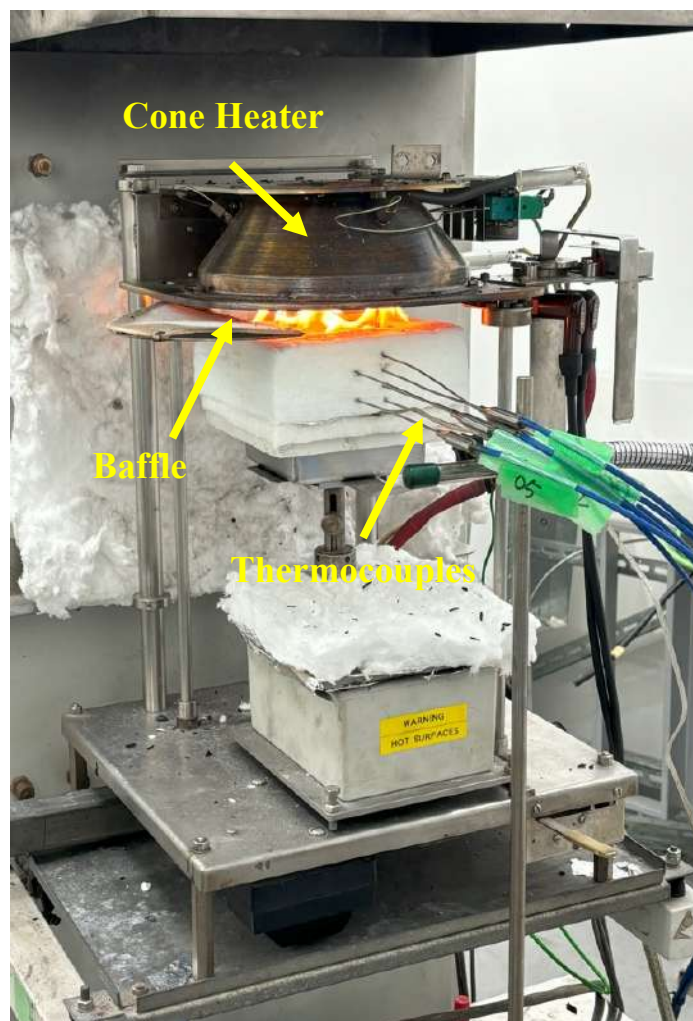


Figure 1. Photograph of the ongoing experiment

2.2 Specimens

The size of specimen used in this experiment is the standard size of cone calorimeter experiment, with a heating surface of 99 x 99 mm. Thickness of specimen is 50mm. Specimen was made of laminated larch wood, and the laminar thickness is about 25mm. Four types of specimens were used in this experiment, with different shapes of slots created in the centre of the heating surface. Summary of the dimension of slots are shown in Table 1. The four types of specimens were named as specimen P (plain), NS (narrow and shallow), ND (narrow and deep), and WD (wide and deep), according to the size of the slot.

Table 1. Summary of different types of specimens

Specimen type no.	Slot length[mm]	Slot width [mm]	Slot depth [mm]
P (Plain, No slot)	0	0	0
NS (Narrow and shallow slot)	50	5	25
ND (Narrow and deep slot)	50	5	40
WD (Wide and deep slot)	50	10	40

The images of specimens are shown in Figure 2. Radiant heat was applied from top of the specimen. The direction of radiant heat flow is represented by the red arrows.

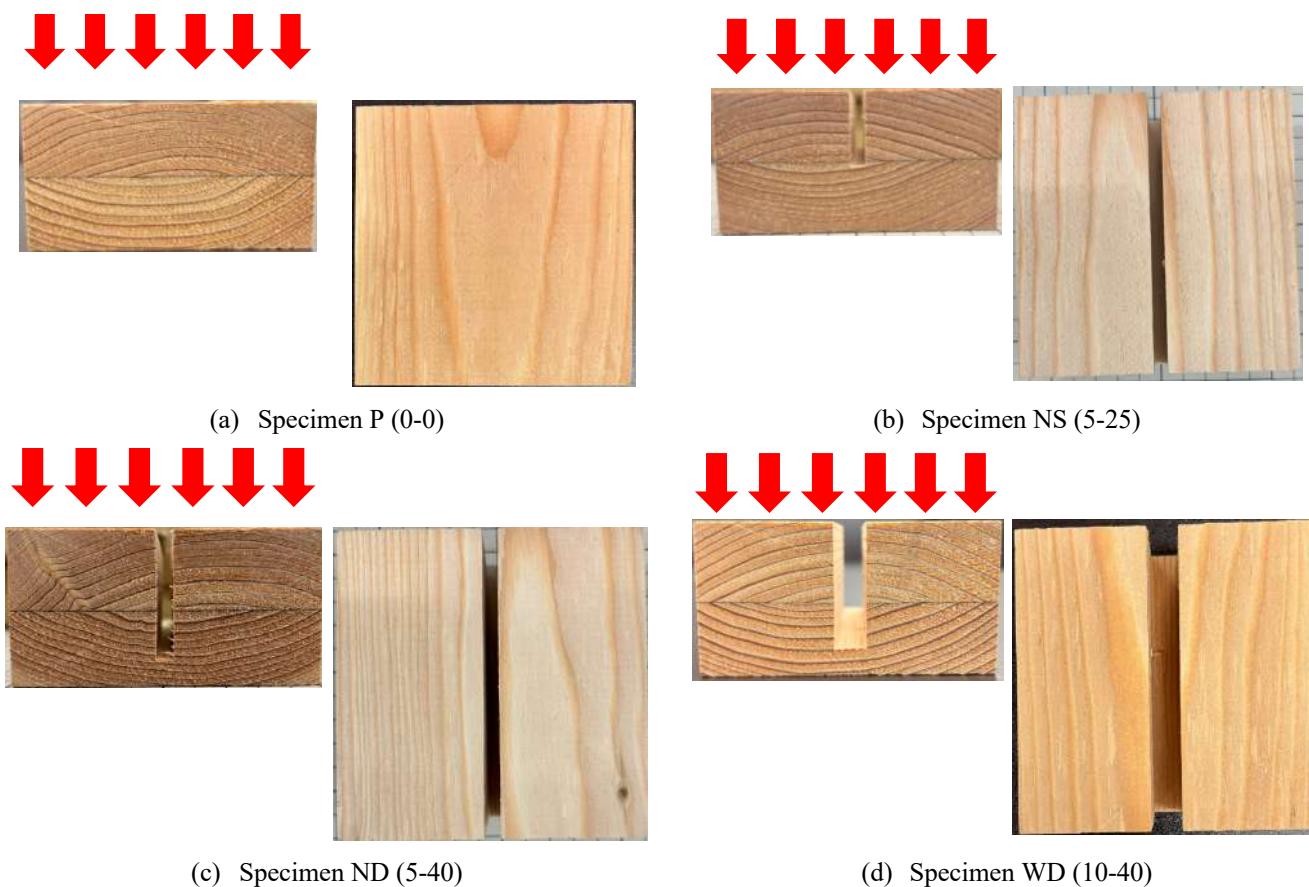


Figure 2. Image of specimens

Side surfaces of specimens were sealed by aluminium foil tape, to reduce heat exchange and combustion from side surface. Specimen was placed in a holder made by ceramic fibre, as shown in Figure 1. Thermocouples were set inside the specimen through the ceramic fibre and fixed on a supporting stand. Specimens were cured in a room with steady temperature (23°C) and humidity (50%) before the experiment. Initial moisture content and mass of specimen were measured before heating. Initial moisture content was measured by high frequency moisture meter. The result was 10.0 ± 0.6 wt.% (average \pm standard derivation). Air-dry density of specimens was $428.1 \pm 4.9 \text{ kg/m}^3$, and the oven dry density estimated by initial moisture content and air-dry density was $389.3 \pm 3.4 \text{ kg/m}^3$.

As mentioned in section 2.1, two types of experiments, the heating experiment and burning experiment, were conducted for each type of specimens. Experiments were named as the following format, slot width-slot depth-runs. For example, 5-40-1 represent the first experiment using specimen ND (slot width 5mm, slot depth 40mm). For experimental runs, the first run represents the heating experiment, while the second run and the third run represent the burning experiment. Summary of experimental conditions is shown in table 2.

Table 2. Summary of experimental conditions

Experiment type	Specimen P (0-0)	Specimen NS (5-25)	Specimen ND (5-40)	Specimen WD (10-40)
Heating Experiment	0-0-1	5-25-1	5-40-1	10-40-1
Burning Experiment	0-0-2	5-25-2	5-40-2	10-40-2
	0-0-3	5-25-3	5-40-3	10-40-3

2.3 Measurement methods

Heat release rate was measured by cone calorimeter equipment during the experiment base on oxygen consumption method.

Temperature of specimen was measured by K-type thermocouples. Interval of thermocouples is 10mm, and the measurement was conducted at 10, 20, 30, 40, 50mm from the heating surface. For specimens with slots, air temperature of the slot was also measured at the middle height and at the bottom. Surface temperature was measured by infrared camera. Summary of the locations of thermocouples are shown in Table 3. Depth of hole for placing thermocouples varies with the type of measurement location. For thermocouples measuring temperature inside the slot, the depth was 50mm, and for thermocouples measuring temperature inside the specimen, the depth was 40mm. A schematic of specimen and measuring points is shown in Figure 3.

Table 3. Summary of locations of thermocouples (unit: mm from heating surface)

Temperature measurement type	Specimen P (0-0)	Specimen NS (5-25)	Specimen ND (5-40)	Specimen WD (10-40)
Inside specimen	10, 20, 30, 40, 50	10, 20, 30, 40, 50	10, 20, 30, 40, 50	10, 20, 30, 40, 50
Inside the slot	N/A	12, 24	20, 38	20, 38

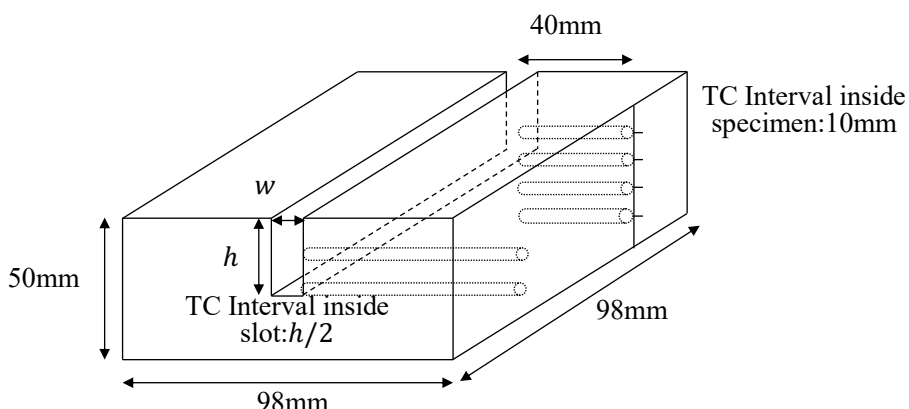


Figure 3. A schematic of specimen and measuring points

After the experiment, specimens were cut perpendicular to the direction of slot. Burnt-out depth, charred depth and coloured depth were measured from the cut section.

3 EXPERIMENTAL RESULTS

3.1 Temperature in heating experiments

Temperature measured in the heating experiments are shown in Figure 4. The temperature at 0mm was the result measured by IR camera, while other results were measured by thermocouples. Solid lines represent the temperature inside specimen, while dashed lines represent temperature inside the slot.

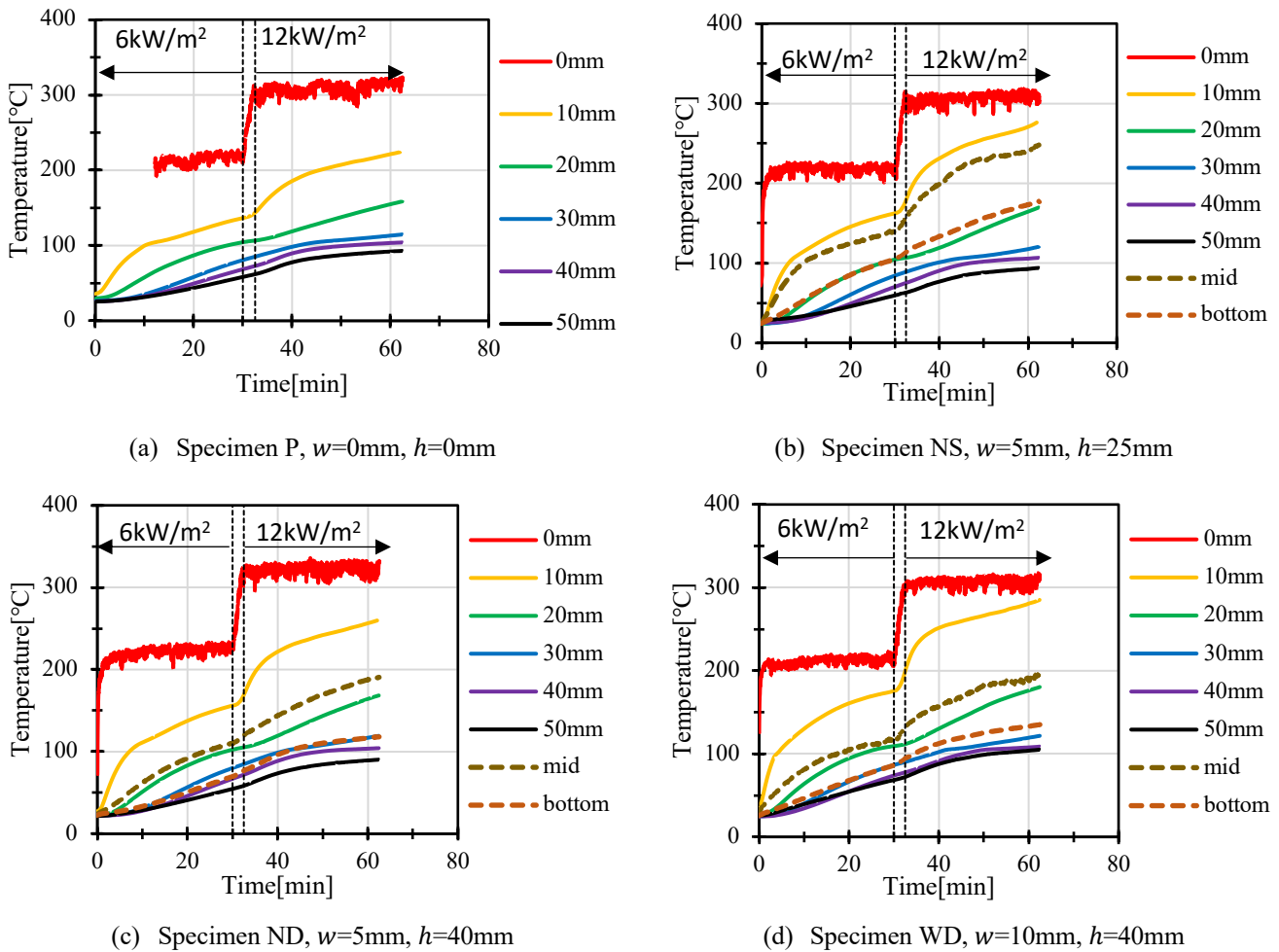


Figure 4. Temperature measured in heating experiment

It can be observed that the size of slot inside specimen did not influence the surface temperature. Surface temperature of specimen heated by 6kW/m^2 intensity is about $200\sim 220^\circ\text{C}$. The value is about $300\sim 320^\circ\text{C}$ for intensity of 12kW/m^2 . This is because the surface of the specimen is in direct contact with the outside air. The surface temperature is related only to the heating intensity since the ambient temperature remains basically unchanged.

It is obvious from Figure 4(a) and Figure 4(b) that internal temperature increased due to the existence of slot on the specimen. At the end of 6kW/m^2 heating period (30min), the temperature at 10mm location in specimen P is 136°C , while the temperature at 10mm location in specimen NS is about 162°C . Temperature difference increased further after heating intensity increased to 12kW/m^2 . Temperature at 10mm location at the end of experiment is 225°C for specimen type P and 278°C for specimen type NS.

Similar tendency is also observed on temperature at 20mm. For intensity of 6kW/m^2 , temperatures in specimen P and specimen NS are almost the same. For intensity of 12kW/m^2 , temperatures are 159°C for specimen P and 170°C for specimen NS. Noticeable difference were not observed at 30~50mm locations.

From experimental results mentioned above, it can be concluded that the effect of slot on the temperature rise inside the specimen is only limited to the locations near heating surface. As the intensity of heating increases, the depth of the affected area also increased. Greater heating intensity is therefore required to show significant temperature differences.

By comparing temperatures between Figure 4(b) and Figure 4(c), it can be concluded that increasing the depth of the slot has basically no effect on the temperature at locations farther from the heating surface, since temperature at 30~50mm locations are basically the same. For results in Figure 4(c) and Figure 4(d), it is shown that temperatures in specimen type WD shown in Figure 4(d) is higher than temperature in

specimen type ND in general. This shows that when the depth of the slot is constant, the smaller the width-depth ratio, the more obvious the effect of the slot on heating.

3.2 Temperatures in burning experiments

Temperatures measured in burning experiments are shown in Figure 5. Solid lines and dotted lines represent the temperature inside the specimen measured in the first and second runs of the burning experiment, while dashed lines and dash-dotted line represent the temperature inside the slot measured in the first and second runs measured in burning experiment.

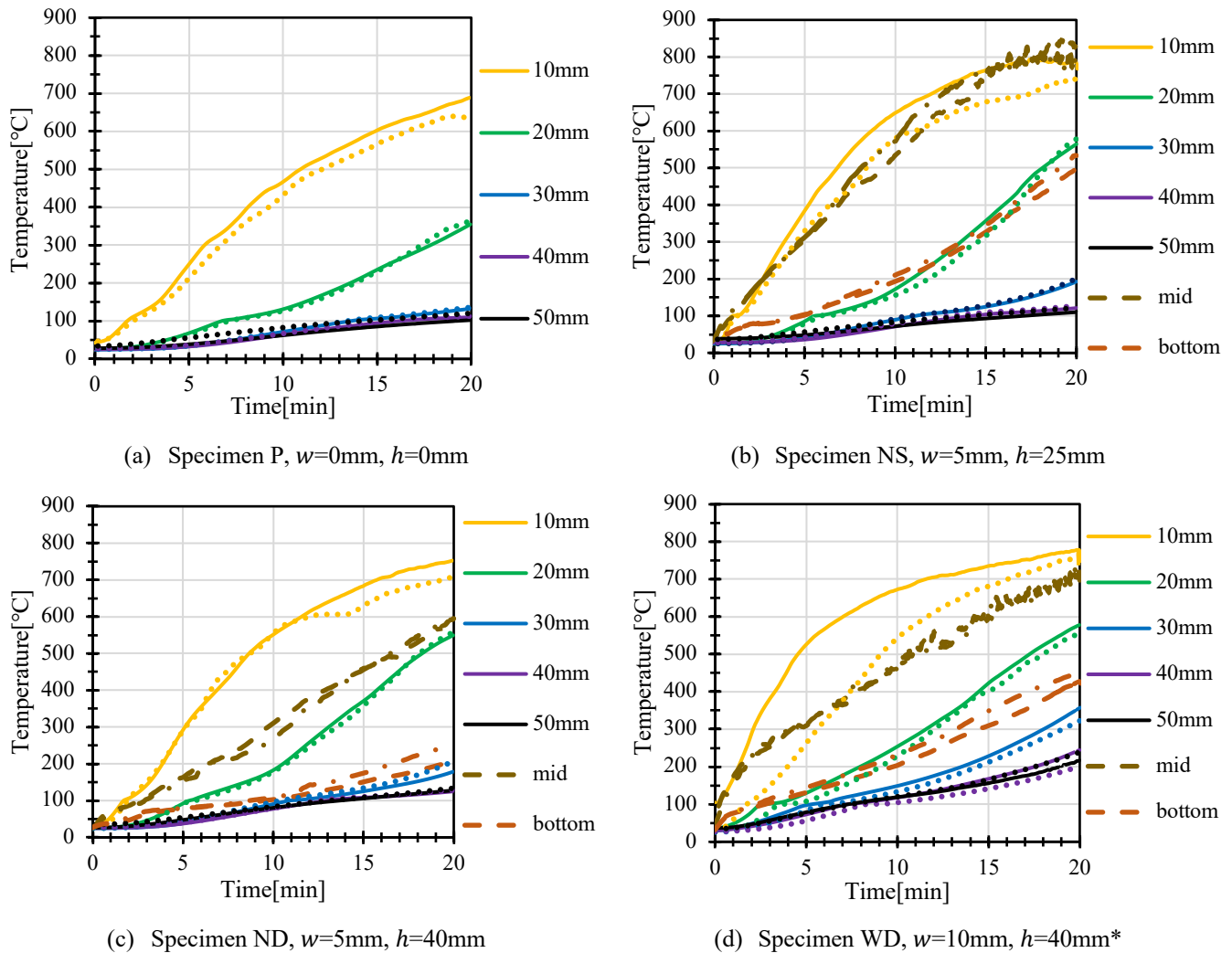


Figure 5. Temperature measured in burning experiment

*Aluminium foil was not successfully set in experiment 10-40-2, so the temperature at 10mm in the early stage is very high.

Comparison between specimen P and specimen NS shows that when the heating intensity is very high, the effect of the surface slot on the internal temperature rise of the specimen is obvious. Temperature difference between the two groups of experiments under different conditions began to appear after 3 minutes after the experiment started. The temperature difference gradually increased after that. At the end of the heating experiment (20min), temperature at 10mm in specimen NS (5 x 25 slot) is about 100°C higher than specimen P (no slot). For 20mm location, temperature difference is about 200°C.

Comparison between specimen NS and specimen ND shows that when the opening of the slot is narrow, the effect of slot on temperature rise is almost the same regardless of the depth of slots. As shown in Figure 5 (b) and (c), although the slot in specimen type C is 15 mm deeper than specimen type B, the temperature history in specimen type B and type C follows almost the same pattern.

Comparison between specimen type ND and specimen type WD shows that increasing the opening size of slot increased the effect on internal temperature of specimen. The temperature difference is more obvious at the 20~50mm positions, compared to 10mm position. This is because the 10mm position is relatively close to the heating surface. Even for small opening slots with a small deep-width ratio, external heat radiation can enter relatively easily.

From figure 5(c) and figure 5(d), for the same distance from the surface, the temperature inside the slot is higher than the temperature inside the specimen. The temperature difference is about 100°C for specimen ND at 20mm and about 200°C for specimen WD at 200°C. The temperature changes inside the slot are also drastic. The temperature in the middle of the slot is about 300 to 400 degrees higher than the temperature at the bottom of the slot. This shows that when simulating the temperature rise of the specimen caused by the slot, temperature gradient inside the slot should be considered rather than assuming that the temperature inside the slot is uniform.

By summarizing the results in Figure 4(a)~(d) and Figure 5(a)~(d), it can be said that the existence of slot will cause the internal temperature of the specimen to rise faster. The degree of influence varies with heating intensity and the size of slot opening. However, the effects mentioned above are limited to the locations close to the heating surface.

3.3 Heat release rate

Heat release rates (HRR) measured in burning experiments are shown in Figure 6.

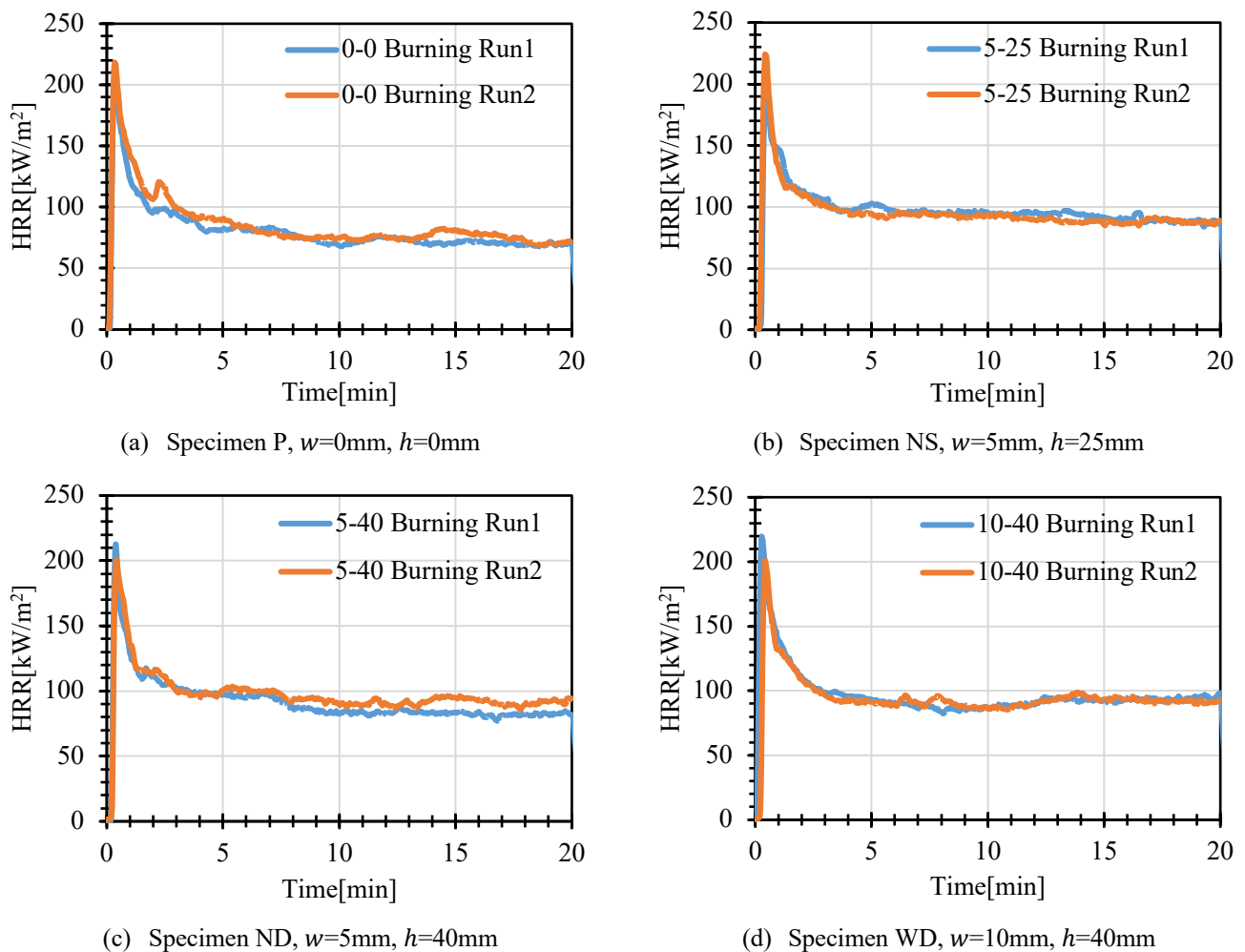


Figure 6. Heat release rate measured in burning experiments

The heat release rate of 4 types of specimens shows similar trends. HRR rapidly increased right after ignition and reached to its peak at about 200kW/m² within 1 minutes, then decreased gradually. After 5~10minutes, the HRR values are almost stable. For specimens with slot (specimen NS, ND, WD), the steady HRR values are higher than specimen without slot (specimen P). This is because specimens with slots can be heated through slot directly by radiation, leading to more intense combustion.

The average HRR during the steady combustion period in each experiment were summarized in Table 4. At here, the steady combustion period was defined as 10~20minutes after the start of heating. The HRR's of specimens with slot are about 20~25% higher than that of specimen without a slot.

Table 4. Average HRR during the steady combustion period (unit: kW/m²)

	Specimen P $w=0\text{mm}, h=0\text{mm}$	Specimen NS $w=5\text{mm}, h=25\text{mm}$	Specimen ND $w=5\text{mm}, h=40\text{mm}$	Specimen WD $w=10\text{mm}, h=40\text{mm}$
Run 1	71.3 kW/m ²	91.7 kW/m ²	82.7 kW/m ²	92.5 kW/m ²
Run 2	75.4 kW/m ²	88.9 kW/m ²	91.4 kW/m ²	91.9 kW/m ²

3.4 Burnt, charred and coloured behaviour

Specimens were cut vertically after the experiment. Figure 7 shows the scanned section images of cut specimen.

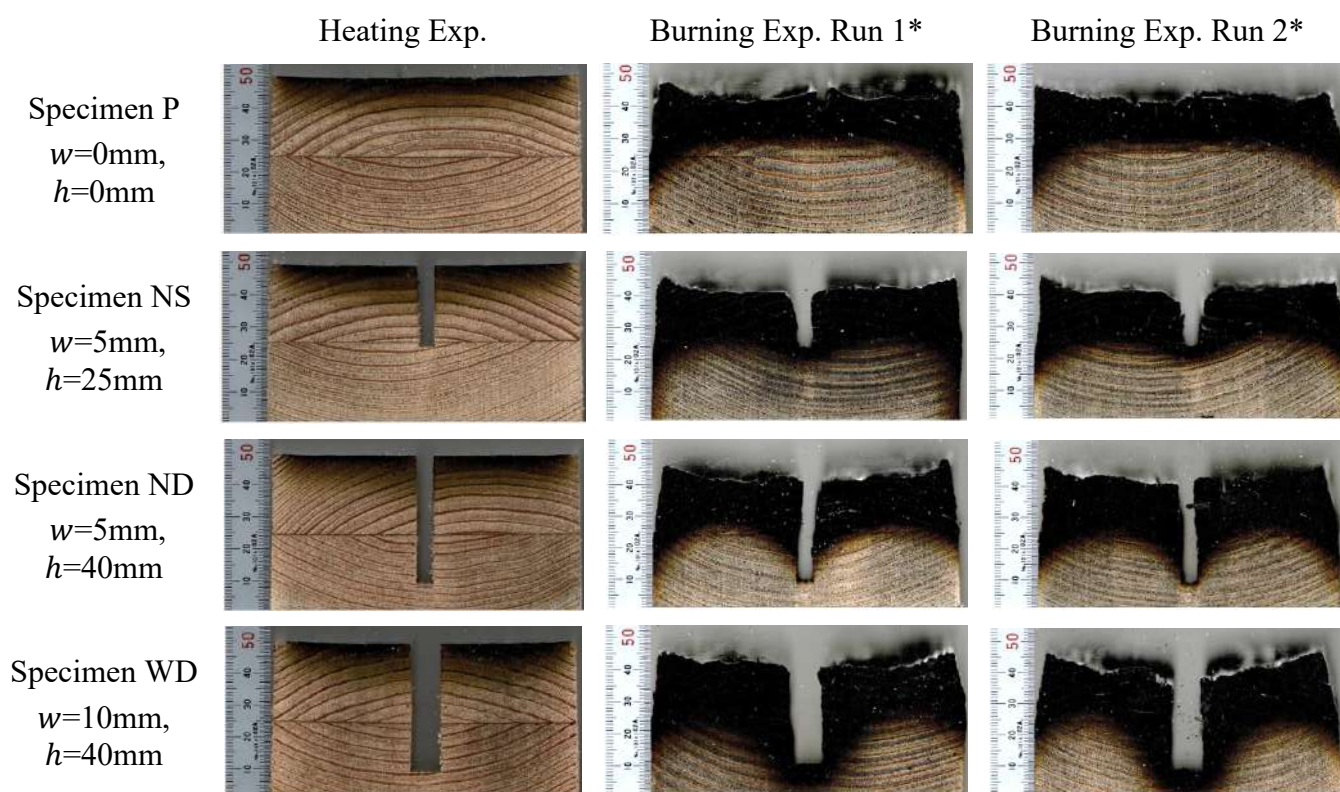


Figure 7. Charring behaviour of heated specimens

*Since thick charring layer exists on the surface of specimens used in the burning experiment, the originally scanned picture cannot be seen clearly. Therefore, the contrast of images for specimens in burning experiment were adjusted in the same way

Charring and colouring states of specimens after heating experiments are relatively similar. Since the heating intensity is relatively low and maximum value of specimen surface temperature is only slightly higher than the pyrolysis temperature, charred layer exists only at about 3~5mm on the surface layer of the specimen. Obvious burnt out was not observed. Coloured depth is about 12~15mm, while the specimen

WD with slot size of 10mm x 40mm has the deepest coloured depth. For charring and colouring situation of specimens after burning specimens, charred depth and coloured depth of specimens with slot is much greater than that of specimen without slot.

Burnt out depth, brittle charred depth, charred depth and coloured depth of specimens after heating and burning experiment were summarized in Table 5 and Table 6, respectively. These depths were calculated based on equation (1).

$$L = 50 - l \quad (1)$$

Where L is burnt out/brittle charred/charred/coloured depth[mm] and l is the distance from burnt out/brittle charred/charred/coloured front to the bottom surface of the specimen. Burnt out front were defined as the top position of specimen. Brittle charred front was defined as the location of the charred layer which can be carved by nail. Charred front was defined as the position where specimen looked charred. Colored depth was defined as the location where specimen colored. Location of burnt-out front, charred front and colored front was determined visually. Two measurements were conducted while measuring the location of burnt out/brittle charred/charred/coloured front. For specimen with slots, the shapes of fronts are curved. The highest point of the curve was used to determine the front location.

Table 5. Burnt out, charred and coloured depth of specimens after heating experiment

	Specimen P $w=0\text{mm}, h=0\text{mm}$	Specimen NS $w=5\text{mm}, h=25\text{mm}$	Specimen ND $w=5\text{mm}, h=40\text{mm}$	Specimen WD $w=10\text{mm}, h=40\text{mm}$
Burnt out depth[mm]	0.5	0.5	0.5	0.5
Brittle charred depth[mm]	1.0	1.5	1.0	2.3
Charred depth[mm]	2.0	2.0	1.8	3.0
Coloured depth[mm]	9.3	9.0	10.0	9.8

Table 6. Burnt out, charred and coloured depth of specimens after burning experiment

	Specimen P $w=0\text{mm}, h=0\text{mm}$	Specimen NS $w=5\text{mm}, h=25\text{mm}$	Specimen ND $w=5\text{mm}, h=40\text{mm}$	Specimen WD $w=10\text{mm}, h=40\text{mm}$
Burnt out depth[mm]	7.6	8.1	9.3	9.0
Brittle charred depth[mm]	17.9	20.1	20.1	22.4
Charred depth[mm]	19.6	22.0	22.9	24.5
Coloured depth[mm]	25.0	27.6	27.3	30.3

From the data in Table 5, it can be observed that the existence of slot can be almost neglected during the heating experiment with low heating intensity. Burnt out depth, brittle charred depth, charred depth, and colored depth in four types of specimens is almost the same. This is because the temperature of the specimen is low during low-intensity heating, and only the part very close to the surface reached to the pyrolysis temperature. Therefore, even if the internal temperature of the specimen increased slightly due to the existence of the slot, the impact of this change on the charring and coloring condition is negligible.

According to Table 6, it can be concluded that the existence of slot can increase the amount of burnt out, charring and coloring of specimen. Comparing specimens NS and ND, it can be concluded that when a slot already exists on the specimen surface, charring and coloring condition will not be affected while increasing

the slot depth. This phenomenon is basically consistent with the phenomenon observed in section 3.2 that increasing the depth of slot has weak influence on temperature changes at locations far from the surface.

Comparing specimens ND and WD, it can be concluded that increasing the width of slot do not have any effect on the burnt-out front, which is very close to the heating surface. However, it will progress the charred front and colored front. This is because radiant heat can reach the bottom of slot easier for specimen with wide slot opening, which leads to the increase on temperature and progress of charring or coloring front.

To summarize, the existence of slot on the specimen will increase the progression speed of charred front and colored front. Charred and colored depth will be increased by increasing width of slot opening.

4 SUMMARY

4.1 Conclusions

In this paper, cone calorimeter tests were conducted on glue laminated larch specimens to investigate the effect on burning behaviour of surface cracks. Pre-processed slot was used to simulate surface crack. Four types of specimens with different surface slot patterns (no slot, 5 x 25mm slot, 5 x 40mm slot, 10 x 40mm slot) were used. Two types of experiments were conducted, including the heating experiment and the burning experiment. In the heating experiment, specimen was heated at 6kW/m² intensity for 30 minutes and 12 kW/m² intensity for 30 minutes. In the burning experiment, specimen was heated by 50kW/m² intensity for 20 minutes. Temperature inside the specimen and slot were measured by K-type sheathed thermocouples. Heat release rate from the surface were measured by oxygen consumption method using cone calorimeter equipment. Burnt-out depth, charred depth and coloured depth of specimens were measured by cutting the specimen after the experiments.

Temperature inside the specimen were affected by the existence of slot. The effect of slot on temperature increased as the heating intensity increased. For temperature at 10mm location, the temperature difference between specimen with slot and without slot is about 25°C at 6kW/m² heating and about 100°C at 50kW/m² heating. As the distance from the surface is increased, the effect of the slot on the temperature gradually decreased. In the burning experiment, at the same depth from the surface, the temperature inside the slot is about 50 to 100 °C higher than the temperature inside the specimen. This value increases as the opening width of the slot increases, which is because the change of configuration factor of opening seen from bottom of slot. After the heating was stopped in burning experiment, temperature difference of about 300 °C between the middle of slot and bottom of slot were observed.

The heat release rate (HRR) in four types of specimens changed in similar ways in the burning experiments. Maximum value of heat release rate, about 200kW/m², reached soon after ignition. HRR become steady after 5~10 minutes. Average heat release rate in steady stage on specimen without slot was about 70~75W/m², while the HRR on specimen with slot was about 90kW/m². About 20~25% increase on HRR were observed due to the existence of surface slot. The effect of shape of the slot on HRR in the stable combustion stage was negligible.

There is no significant difference in the burnt-out, charring and coloring behavior of the specimens used in the heating experiment regardless the size of slot, since the surface temperature exceeds pyrolysis temperature only slightly. For specimens in burning experiment, burnt-out depth, charred depth and colored depth in specimen with slot was approximately 20~25% higher than specimens without slot.

4.2 Future works

The effect of surface slot on temperature rise and burning behaviour were analysed in this work qualitatively in this research. Further research should be conducted on analyzing these effect quantitatively, to make the research results more useful and available to actual situations. In addition, it is also necessary to develop a wood combustion model that considers the impact of surface crack on mass and heat transfer.

ACKNOWLEDGMENT

This work was supported by JSPS Grant-in-Aid for JSPS Fellows, Number JP 22KJ1844. Experiments were conducted at General Building Research Corporation of Japan, supported by Mr. Masato Komiya and Ms. Takako Oue. The authors appreciate all the supports received.

REFERENCES

- [1] T. Fateh, T. Rogaume, J. Luche, F. Richard, and F. Jabouille, “Characterization of the thermal decomposition of two kinds of plywood with a cone calorimeter - FTIR apparatus,” *J. Anal. Appl. Pyrolysis*, vol. 107, pp. 87–100, 2014, doi: 10.1016/j.jaap.2014.02.008.
- [2] T. Harada, “A Study on the Combustibility and the Fire Resistance of Wood,” *Bull. For. For. Prod. Resource Institute*, vol. 378, pp. 1–85, 2000.
- [3] T. Ouchi, “Mokuzaino kouonjino netsudendouritsu (Thermal conductivity of wood at high temperatures, in Japanese),” *Archit. Inst. Japan, Res. reports*, pp. 785–786, 1987.
- [4] W. Wijayanti, “The physical properties (enthalpy and thermal conductivity) of mahogany wood induced by pyrolysis temperature process,” *Appl. Mech. Mater.*, vol. 664, pp. 215–220, 2014, doi: 10.4028/www.scientific.net/AMM.664.215.
- [5] M. Gupta, J. Yang, and C. Roy, “Specific heat and thermal conductivity of softwood bark and softwood char particles,” *Fuel*, vol. 82, no. 8, pp. 919–927, 2003, doi: 10.1016/S0016-2361(02)00398-8.
- [6] K. O. Davidsson and J. B. C. Pettersson, “Birch wood particle shrinkage during rapid pyrolysis,” *Fuel*, vol. 81, no. 3, pp. 263–270, 2002, doi: 10.1016/S0016-2361(01)00169-7.
- [7] A. Sun, K. Harada, D. Nii, E. Kuroda, and Y. Chatani, “Karamatsu to Sugi no Teionkanetsu niyoru Shushukuryou Sokutei (Measurement of Shrinkage of Larch and Japanese Cedar During Constant Temperature Heating, in Japanese),” *Archit. Inst. Japan, Kinki Branch, Res. reports*, 2021.
- [8] K. Li, Y. Zou, S. Bourbigot, J. Ji, and X. Chen, “Pressure effects on morphology of isotropic char layer, shrinkage, cracking and reduced heat transfer of wooden material,” *Proc. Combust. Inst.*, vol. 38, no. 3, pp. 5063–5071, 2021, doi: 10.1016/j.proci.2020.07.072.
- [9] J. König and L. Walleij, “One-dimensional charring of timber exposed to standard and parametric fires in initially unprotected and postprotection situations,” 1999.
- [10] Z. Zhang, P. Ding, S. Wang, and X. Huang, “Smouldering-to-flaming transition on wood induced by glowing char cracks and cross wind,” *Fuel*, vol. 352, no. April, p. 129091, 2023, doi: 10.1016/j.fuel.2023.129091.
- [11] S. Watanabe and Y. Chatani, “Measurement of Internal Temperature of Grooved Laminated Wood Exposed to Fire,” *Summ. Tech. Pap. Annu. Meet. Fire Safety, Archit. Inst. Japan*, pp. 139–140, 2022.
- [12] K. Li, M. Mousavi, and S. Hostikka, “Char cracking of medium density fibreboard due to thermal shock effect induced pyrolysis shrinkage,” *Fire Saf. J.*, vol. 91, no. April, pp. 165–173, 2017, doi: 10.1016/j.firesaf.2017.04.027.
- [13] D. K. Shen, S. Gu, K. H. Luo, and A. V. Bridgwater, “Analysis of Wood Structural Changes under Thermal Radiation,” *Energy and Fuels*, vol. 23, no. 2, pp. 1081–1088, 2009, doi: 10.1021/ef800873k.
- [14] International Standard Organization, “ISO5660-1 Reaction-to-fire tests — Heat release, smoke production and mass loss rate,” vol. 2015, 2015.

NUMERICAL INVESTIGATIONS ON FIRE PERFORMANCE OF TIMBER FRAMES WITH DOWEL-TYPE CONNECTIONS

Yukito Nakayama¹, Marina Totsuka², Takeo Hirashima³

ABSTRACT

For moment-resisting dowel-type timber connections, it has been shown by recent experimental evidence that their ductile semi-rigid behaviour can be maintained even in fire. However, there is currently a lack of both experimental and numerical investigations into the influence of semi-rigidity on the overall structural fire behaviour of timber structures. The present paper first provides a series of fire tests on large-scale timber frames with semi-rigid dowel-type connections as well as simply supported timber beams under ambient, heating, and cooling conditions. Then, a new numerical model for fire response analysis of timber structures assuming the semi-rigid behaviour is developed and used to obtain the time evolution of bending moment distribution and stress distribution within the specimens. Based on the test and numerical results, the failure time of the semi-rigid specimen was 70 min longer than that of the pinned specimen when cooled after heating and 11 min when exposed to continuous heating. It was shown that guaranteeing ductility of connections by appropriate dowel spacings and timber plugs can significantly extend the failure time of the connected beam, particularly during the cooling phase, as the prior formation of a plastic hinge delays the brittle bending failure of the beam.

Keywords: Timber frames; dowel-type connections; numerical modelling; fire tests

1 INTRODUCTION

The advancement in timber building design over recent decades has been considerable, evolving from conventional timber-framed houses to mid- and high-rise mass timber construction with the advent of high-quality engineered wood products. In mass timber construction, the most common type of connections is dowel-type connections owing to their ease of installation, aesthetic appearance, and high strength. However, a design challenge with dowel-type connections is their semi-rigid moment–rotation response, which falls between that of pinned and rigid connections [1, 2]; furthermore, recent experimental evidence, particularly in [3–5], indicates that they maintain the semi-rigidity even in fire. Thus, comprehensive understanding of the semi-rigid behaviour of dowel-type connections in fire as well as accurate modelling of the structural fire behaviour of timber structures are key.

Based on the fire test results on dowel-type connections under shear and bending forces [6, 7], their behaviour is significantly dependent on multiple factors such as dowel length and position and clearance between the beam and column, as heat flux from the clearance and the steel dowels with high heat conductivity is sensitive to connection configurations. In efforts to reduce the heat flux, several experimental studies were performed using glued-in timber plugs for fire protection [8]. The study conducted by Okunroumu [5] showed that dowel-type moment-resisting connections, fire-protected by 30-mm-long timber plugs and reinforced with self-tapping screws, withstood 60 min of the Canadian

¹ Ph.D. Candidate, Graduate School of Science and Engineering, Chiba University, Japan,
e-mail: yukiton@chiba-u.jp, ORCID: <https://orcid.org/0000-0002-3814-4902>

² Assistant Professor, Graduate School of Engineering, Chiba University, Japan,
e-mail: mtotsuka@chiba-u.jp, ORCID: <https://orcid.org/0000-0001-8548-4996>

³ Professor, Graduate School of Engineering, Chiba University, Japan,
e-mail: hirashima@faculty.chiba-u.jp, ORCID: <https://orcid.org/0000-0003-1462-5370>

standard fire with their rotation angles exceeding 0.1 rad, even though the applied load was higher than the design load as suggested by Eurocode 5. This result implies the effectiveness of timber plugs in ensuring adequate ductility to guarantee stress redistribution. In addition, the phase of fire can also have a major impact on the way the connections respond. As presented by Kinjo [9], the mechanical behaviour of timber differs in the cooling phase from that in the heating phase as timber continues to combust after a fire is extinguished, using itself as fuel. These available experimental investigations, however, have focused on dowel-type connections in isolation during the heating phase. For the numerical modelling of semi-rigid connections, two common approaches exist for adopting semi-rigidity into a fire response analysis. The first technique is to introduce the three-dimensional finite element method (3D FEM) to consider varying connection configurations and the distinct thermal and mechanical properties of timber and steel. Notably, to date, the application of 3D FEM has been limited to thermo-mechanical analysis of connections in isolation [3, 4, 6], due to its time- and memory-consuming nature. The second approach, known as the “component-based model”, has been generally adopted for steel structures [10, 11], which mechanically model connections as an assembly of non-linear springs that exhibit load-displacement response of the joineries. Although this method is unquestionably simpler than the 3D FEM, its application to timber structures is unprecedented. Thus, the effect of semi-rigidity on structural fire performance is neglected in many cases, and the influence of the semi-rigidity of these connections on the overall structural fire behaviour of timber frames both during and cooling phase is unexplored.

Therefore, the present study first provides a series of tests on large-scale timber frames with semi-rigid dowel-type connections as well as simply supported timber beams under ambient, heating, and cooling conditions. Then, a simple yet accurate numerical methodology for fire response analysis of timber frames assuming the semi-rigid behaviour of dowel-type connections is developed by combining the component-based model for non-linear moment-rotation response of dowel-type connections developed by the authors [12] and the fire response analysis program applying beam-column elements, FIRES-RC, developed by UC Berkley [13]. Finally, the proposed method is used to obtain the time evolution of bending moment distribution and stress distribution within the specimens, aiming to investigate the influence of the semi-rigidity on fire performance of timber frames.

2 FIRE TESTS ON TIMBER FRAMES WITH DOWEL-TYPE CONNECTIONS

2.1 Test specimens

Figure 1 shows the two types of specimens used in the test: simply supported timber beams (pinned specimen) and timber frames with dowel-type connections (semi-rigid specimen). Both specimens shared the same supporting span of 6000 mm and loading span of 1200 mm and beam cross-sections, differing only in the beam end restraint conditions, either pinned or semi-rigid, to evaluate the extension of the fire resistance time by the semi-rigidity. Both glulam beams and columns were prepared from Japanese larch (*Larix kaempferi*) with an average density of 0.543 g/cm³ and a stress grade of 30 N/mm². The cross-sectional dimension of the glulam beam and column was 210 mm (width) × 420 mm (depth) and 300 mm (width) × 300 mm (depth), respectively. Figure 2 shows the dimensions of the connection utilized in the test. A T-stub steel plate manufactured with 9-mm-thick plate was fastened to the column using six 20-mm-diameter bolts. At both beam ends, a slotted cut was prepared with a 10.5-mm width to accommodate the 9-mm-thick web of the T-stub steel plate. The depth of the slotted cuts was 370 mm from the beam’s top surface to employ 50-mm-deep timber layers that insulated the steel plate bottoms. The web of the T-stub steel plate was sandwiched between two timber side members and fastened together with four 16-mm-diameter dowels. The circular holes for the dowels were drilled using a 17-mm drill for the steel plate and a 16-mm drill for the beam. The spacings of the dowels, such as end distance, edge distance, and spacing between dowels, were designed to meet the requirements of the Japanese design standard [14]. The length of the dowels was 130 mm, which was 80 mm less than the width of the beam, to accommodate 40-mm-long glued-in timber plugs used as fire protection for the dowel heads. The clearance between the column and beam end was less than 2 mm to minimize heat flux from the clearance to the beam end.

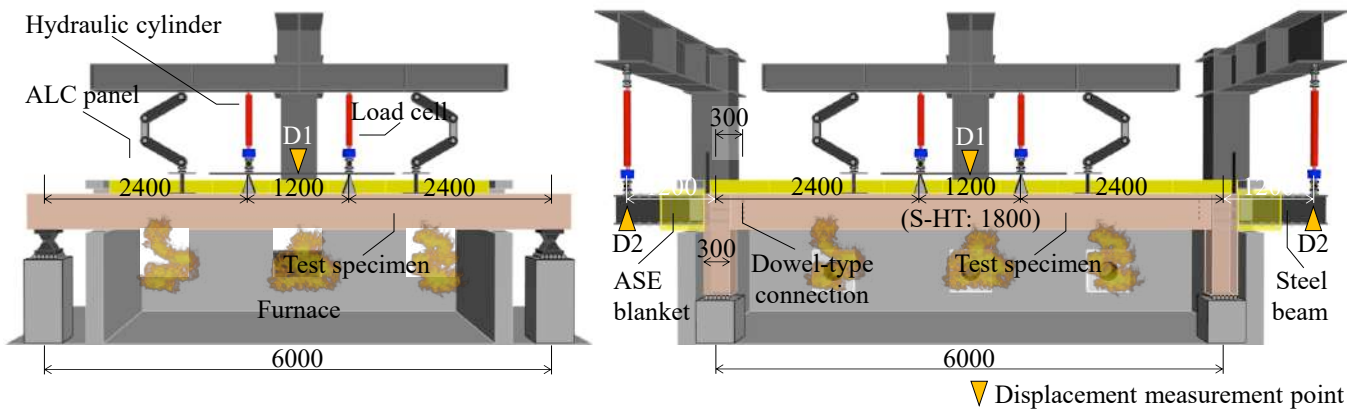


Figure 1. Test specimen (dimensions in mm)

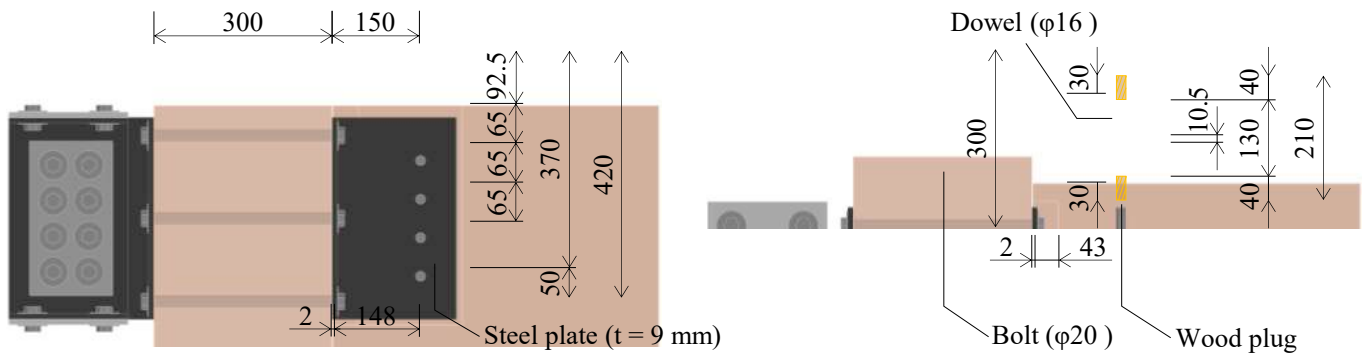


Figure 2. Connection configuration (dimensions in mm)

2.2 Test-setup and procedure

Table 1 lists the test conditions. To obtain the load-carrying capacity of the specimens, load-carrying tests under ambient temperature were conducted on both pinned and semi-rigid specimens (P-AT, S-AT). In addition, fire tests in which pinned and semi-rigid specimens were heated for 60 min and then cooled in a furnace until failure (P-60, S-60) and in which a semi-rigid specimen was heated until failure were conducted (S-HT). For the set-up of the semi-rigid specimens, steel beams were attached to the opposite side of the six bolts that connected the T-stub steel plate to the column. Temperatures within the cross-section of the beam's midspan and the left-side connections were measured by type-K thermocouples inserted to the measurement points (see Figure 3). Draw-wire displacement transducers installed outside the furnace were used to measure the vertical deflections of the measurement points illustrated in Figure 1. To apply vertical load on the beams and the free ends of the cantilevered steel beams, hydraulic cylinders were mounted above the furnace to a robust steel loading frame. The distance between the applied load was 1200 mm in P-AT, S-AT, P-60, and S-60, and 1800 mm in S-HT. During the tests on the semi-rigid specimen, the deflection of the D2 points was monitored and maintained at 0 to ensure that the dowel-type connections exhibited semi-rigidity throughout the tests, with the use of the hydraulic cylinders connected to manually controlled hydraulic pumps. In the tests P-60 and S-60, two specimens were preloaded to 70 % of the design load for the 60-min fire-resistant timber structures in accordance with the Japanese standard [14] (16.7 kN). The heating was commenced after the pre-loading and terminated in 60 min, followed by the cooling phase. The applied load ratio of 70 % was determined with the aim of allowing the specimens to fail during the cooling phase rather than during the heating phase, referring to the previous load-carrying fire tests on simply supported glulam beams made of Japanese larch [9]. On the other hand, in the test S-60, the specimen was preloaded to 100 % of the design load (28.5 kN). In these three fire tests, the loads applied on the beam were monitored and maintained constant, and the failure criterion was assumed to occur when the loads decreased to 95% of the preload. Further, 100-mm-thick ALC panels were mounted on the specimens to replicate the existence of a slab on the beam, exposing all sides except the top one to elevated temperatures that followed the ISO standard fire time–temperature curve. Slits with an interval of 750 mm were prepared in the ALC panels to prevent them from bearing the bending moment. The results

obtained through the five tests were previously reported by the authors. Refer to [15] for detailed test results and discussions.

Table 1. Test conditions and results

Test	Specimen		Heating condition	Loading condition	Loading span	Maximum load / failure time
	Type	Connection				
P-AT	Pinned	Pinned connection	Ambient temperature	Until failure	1200 mm	70.9 kN
S-AT	Semi-rigid	Dowel-type connection	Ambient temperature	Until failure	1200 mm	91.0 kN
P-60	Pinned	Pinned connection	60 min + cooling	16.7 kN	1200 mm	60 + 114 min
S-60	Semi-rigid	Dowel-type connection	60 min + cooling	16.7 kN	1200 mm	60 + over 180 min
S-HT	Semi-rigid	Dowel-type connection	Until failure	28.5 kN	1800 mm	92 min

3 HEAT TRANSFER ANALYSIS

The three-dimensional heat transfer analysis was previously conducted by the authors [16] to obtain the temperature distribution within the connections and the beam's midspan for the specimens. This section mainly focuses on validating the temperature results obtained through the heat transfer analysis, as the present paper aims to mechanically model the fire behaviour of timber frames with dowel-type connections. Refer to [16] for a detailed description of the heat transfer model. Figure 3 compares the time-temperature curves obtained by the heat transfer analysis and the thermocouples. Both numerical and experimental results in tests S-60 and S-HT exhibited a similar trend of increased temperatures with time; however, differences between the numerical and measured temperatures in test P-60 were observed particularly at TC1, 5, and 6, as the test results showed relatively lower temperatures compared to those in test S-60.

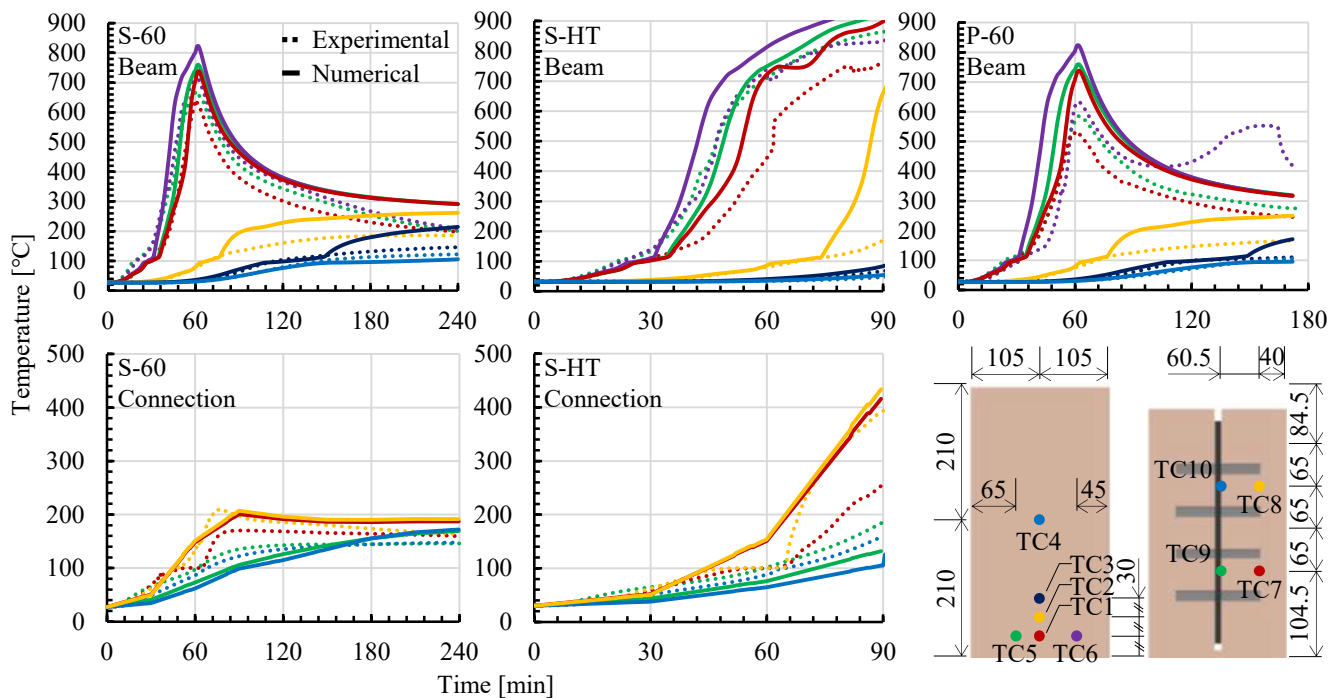


Figure 3. Numerical and experimental temperatures

4 MECHANICAL MODELLING

4.1 Model of specimens

The mechanical model for the structural fire behaviour of timber frames outlined in this section is based on the fire response analysis program developed by UC Berkley [13]. In addition to the use of original beam-column elements, the proposed method employs component-based connection elements, enabling the consideration of semi-rigid beam-end restraint conditions while using the direct stiffness method. Figure 4

illustrates the mechanical model for the specimens. In a two-dimensional plane, the specimens' members are divided into finite-length beam-column elements with three degrees of freedom, which are further subdivided into fibres as illustrated in Figure 4. On the contrary and based on the component method, the dowel-type connections connect the adjacent beam-column elements as an assembly of zero-length non-linear springs experiencing axial, shear, and bending forces (connection element). This connection model is based on the numerical model for the non-linear $M - \theta$ relationships of dowel-type connections developed by the authors [12], which was expanded to include the springs that resist axial force, shear force, and contact force between the column and the beam end.

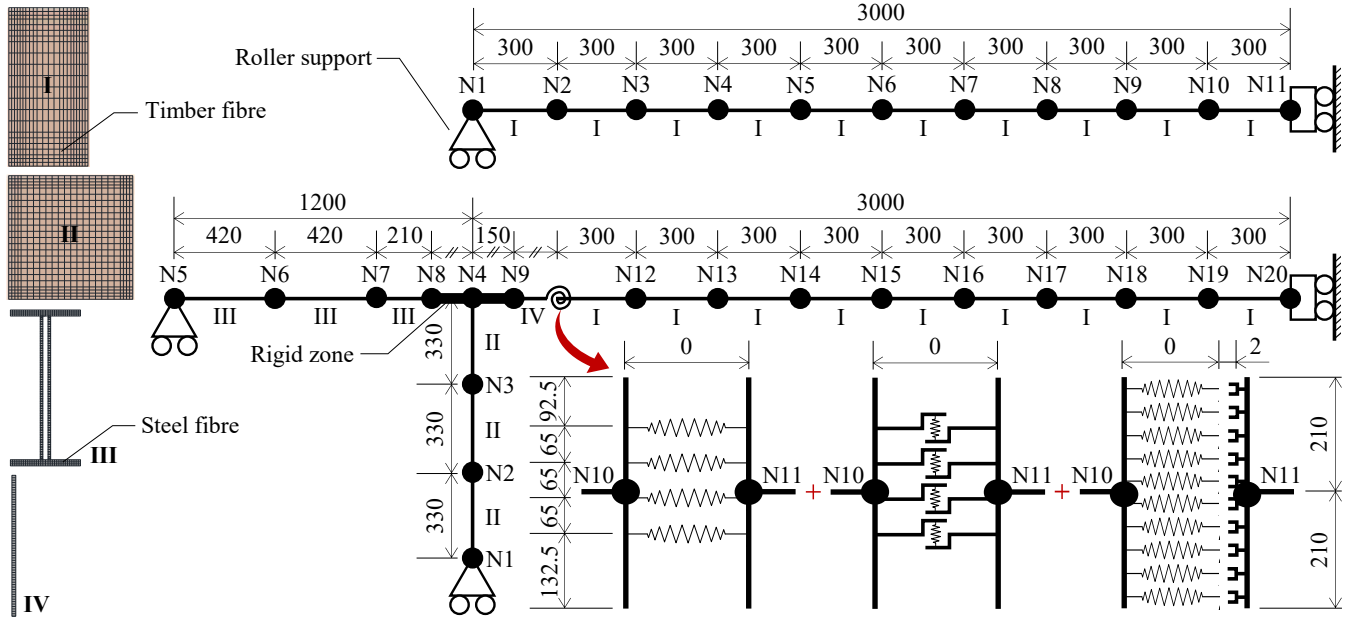


Figure 4. Mechanical model of the specimens

4.2 General approach

Figure 5 illustrates the flow chart for the calculation procedure. The nodal deformation vector U_i is the unknown function to be determined in a time-incremental procedure. Within a given time step i , the time-dependent deformed shape of timber structures with respect to the nodal force vector R_i can be expressed as Equation (1) using the current temperature distribution T_i and the current structural stiffness matrix K_i .

$$\Delta R_i = K_i(U_i, T_i) \cdot \Delta U_i \quad (1)$$

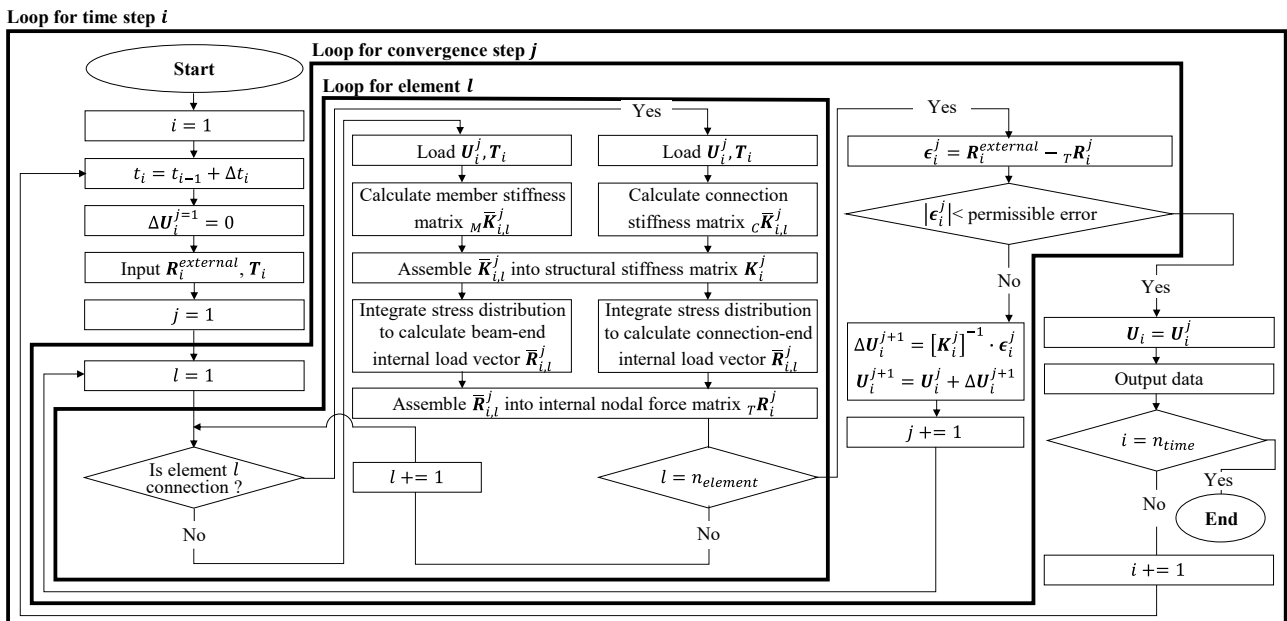


Figure 5. Flow chart for the calculation procedure

The solution of Equation (1) requires an iterative procedure within a given time step i , as the structural stiffness matrix is dependent on the deformed shape and current temperature distribution. The accuracy of the estimated deformed shape \mathbf{U}_i^j in a convergence step j can be checked through the calculation of the out-balance forces $\boldsymbol{\epsilon}_i^j$, which is defined as the error between the external nodal force vector $\mathbf{R}_i^{external}$ and the internal nodal force vector ${}^T\mathbf{R}_i^j$. Convergence can be determined with the out-balance force compared to a permissible error level. The current structural stiffness matrix \mathbf{K}_i is obtained by first calculating each element's stiffness matrix based on its current deformation, and then by assembling the element stiffness matrices using the direct stiffness matrix.

4.3 Beam-column elements

The derivation of the element stiffness matrix for beam-column elements ${}_M\bar{\mathbf{K}}$ assumes that they have fully restrained beam-end conditions [13]. Due to the dependence of ${}_M\bar{\mathbf{K}}$ on the deformed shape and temperature distribution, the effective cross-sectional properties such as axial and bending stiffness are calculated by adding the current effective modulus of fibres, which exhibit the stress-strain relationship developed by Richard [17] as shown in Figure 6. The available material test data [18] was used to determine the reduction factors for elastic modulus and strength of timber fibres, as those specified in Eurocode 5 [19] may be overly conservative, especially in the case of compressive strength [20].

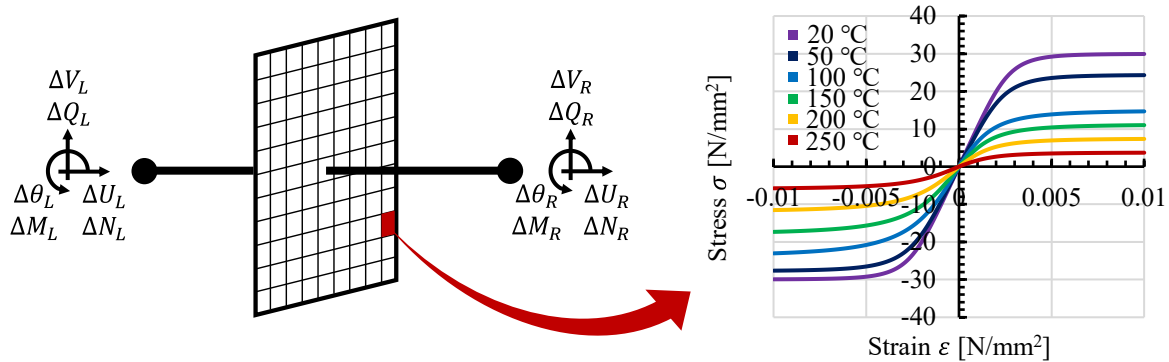


Figure 6. Stress-strain relationship of fibre

4.4 Component-based connection elements

In the proposed method, the load-slip relationship of dowels is represented as non-linear springs (slip springs), as shown in Figure 7. In addition, the axial and bending forces generated by the contact between the beam end and column are modelled as non-linear springs that resist only compressive force (contact springs). Equation (2) shows the element stiffness matrix of connection elements ${}_c\bar{\mathbf{K}}$.

$$\begin{bmatrix} \Delta N_L \\ \Delta Q_L \\ \Delta M_L \\ \Delta N_R \\ \Delta Q_R \\ \Delta M_R \end{bmatrix} = \begin{bmatrix} K_{11} & 0 & K_{13} & -K_{11} & 0 & -K_{13} \\ & K_{22} & 0 & 0 & -K_{22} & 0 \\ & & K_{33} & -K_{31} & 0 & -K_{33} \\ & & & K_{11} & 0 & K_{13} \\ \text{Sym.} & & & & K_{22} & 0 \\ & & & & & K_{33} \end{bmatrix} \begin{bmatrix} \Delta U_L \\ \Delta V_L \\ \Delta \theta_L \\ \Delta U_R \\ \Delta V_R \\ \Delta \theta_R \end{bmatrix} \quad (2)$$

$$K_{11} = \sum_{k=1}^{n_s} sK_{//,i,k}^j + \sum_{k=1}^{n_c} cK_{i,k}^j \quad (3)$$

$$K_{22} = \sum_{k=1}^{n_s} sK_{\perp,i,k}^j \quad (4)$$

$$K_{13} = K_{31} = \sum_{k=1}^{n_s} sK_{//,i,k}^j (y_k - e_i^j) + \sum_{k=1}^{n_c} cK_{i,k}^j (y_k - e_i^j) \quad (5)$$

$$K_{33} = \sum_{k=1}^{n_s} sK_{//,i,k}^j (y_k - e_i^j)^2 + \sum_{k=1}^{n_c} cK_{i,k}^j (y_k - e_i^j)^2 \quad (6)$$

$$e_i^j = \left(\sum_{k=1}^{n_s} {}_sK_{//,i,k}^j \cdot y_i + \sum_{k=1}^{n_c} {}_cK_{i,k}^j \cdot y_i \right) / K_{11} \quad (7)$$

Where ${}_sK_{//}$, ${}_sK_{\perp}$: stiffness of slip springs parallel and perpendicular to grain
 ${}_cK$: stiffness of contact springs
 k : spring number
 n_s, n_c : total number of slip springs and contact springs
 y : coordinate of spring around centroid axis
 e : coordinate of neutral axis around centroid axis
 $N_{L,R}, Q_{L,R}, M_{L,R}$: element end axial, shear, and bending forces
 $U_{L,R}, V_{L,R}, \theta_{L,R}$: element end horizontal, vertical, and rotational displacements

The stiffness of slip springs is defined as the slip modulus of the non-linear load-slip relationship, which is determined based on the calculation procedure developed by the authors [12] using finite-element model consisting of a series of elastoplastic beam elements on elastoplastic foundation (see Figure 7). Using Foschi's approach [21], the stress–displacement relationship of the elastoplastic foundation parallel to the grain ${}_s\sigma_{//}(u, T)$ was assumed to take the exponential form of Equation (8). On the other hand, timber typically exhibits plastic stiffness when subjected to embedding force in the grain orthogonal direction [22]. Therefore, the stress-displacement relationship of elastoplastic foundation resisting shear force ${}_s\sigma_{\perp}(u, T)$ includes an influence of secondary embedding stiffness k_u as expressed in Equation (9).

$${}_s\sigma_{//}(u, T) = \begin{cases} k_{\sigma}(T) \cdot \sigma_e \left[1 - \exp\left(\frac{-k_e(T) \cdot k_s \cdot u}{k_{\sigma}(T) \cdot \sigma_e}\right) \right] & (u \geq 0) \\ -k_{\sigma}(T) \cdot \sigma_e \left[1 - \exp\left(\frac{-k_e(T) \cdot k_s \cdot |u|}{k_{\sigma}(T) \cdot \sigma_e}\right) \right] & (u < 0) \end{cases} \quad (8)$$

$${}_s\sigma_{\perp}(u, T) = \begin{cases} (k_{\sigma}(T) \cdot \sigma_e + k_e(T) \cdot k_u \cdot u) \left[1 - \exp\left(\frac{-k_e(T) \cdot k_s \cdot u}{k_{\sigma}(T) \cdot \sigma_e}\right) \right] & (u \geq 0) \\ -(k_{\sigma}(T) \cdot \sigma_e + k_e(T) \cdot k_u \cdot |u|) \left[1 - \exp\left(\frac{-k_e(T) \cdot k_s \cdot |u|}{k_{\sigma}(T) \cdot \sigma_e}\right) \right] & (u < 0) \end{cases} \quad (9)$$

Where k_{σ}, k_e : reduction factor for embedding strength and embedding stiffness
 σ_e : embedding strength
 k_s, k_u : initial embedding stiffness and secondary embedding stiffness
 u : displacement

Multiple non-linear springs distributed on the contact surface in its width and height directions replicate the contact force, such that by determining their stiffness with respect to the temperature distribution, the charring of the contact surface can be considered. The model for the contact behaviour is based on the assumption that the contact surface is fully a rigid foundation compressing elastoplastic foundation with the stress-displacement relationship perpendicular to the grain, owing to higher embedding stiffness and strength parallel to the grain than those perpendicular to the grain (see Figure 7). Due to a fabrication clearance c between the beam end and column, contact force needs to be generated in the case that the connection rotation proceeds to a certain level. Therefore, the stress-displacement relationship of the elastoplastic foundation ${}_c\sigma_{\perp}(u, T)$ takes the form of Equation (10), which produces stress when the displacement exceeds the clearance, such that by differentiating the function, the stiffness of a contact spring can be defined as expressed by Equation (11). The reduction factors for embedding stiffness and strength were determined so that the stress-displacement curves fit into the available test data provided in reference [22].

$${}_c\sigma_{\perp}(u, T) = \begin{cases} 0 & (u \geq -c) \\ -[k_{\sigma}(T) \cdot \sigma_e + k_e(T) \cdot k_u \cdot |u + c|] \left\{ 1 - \exp\left[\frac{-k_e(T) \cdot k_s \cdot |u + c|}{k_{\sigma}(T) \cdot \sigma_e}\right] \right\} & (u < -c) \end{cases} \quad (10)$$

$${}_c K_{i,k}^j = A_k \cdot \frac{\partial {}_c \sigma_{\perp}}{\partial u} \Big|_{u=u_{i,k}^j, T=T_{i,k}} \quad (11)$$

$$u_{i,k}^j = (\theta_{L,i,k}^j - \theta_{R,i,k}^j)(y_k - e_i^j) \quad (12)$$

Where A : contact surface area of contact spring

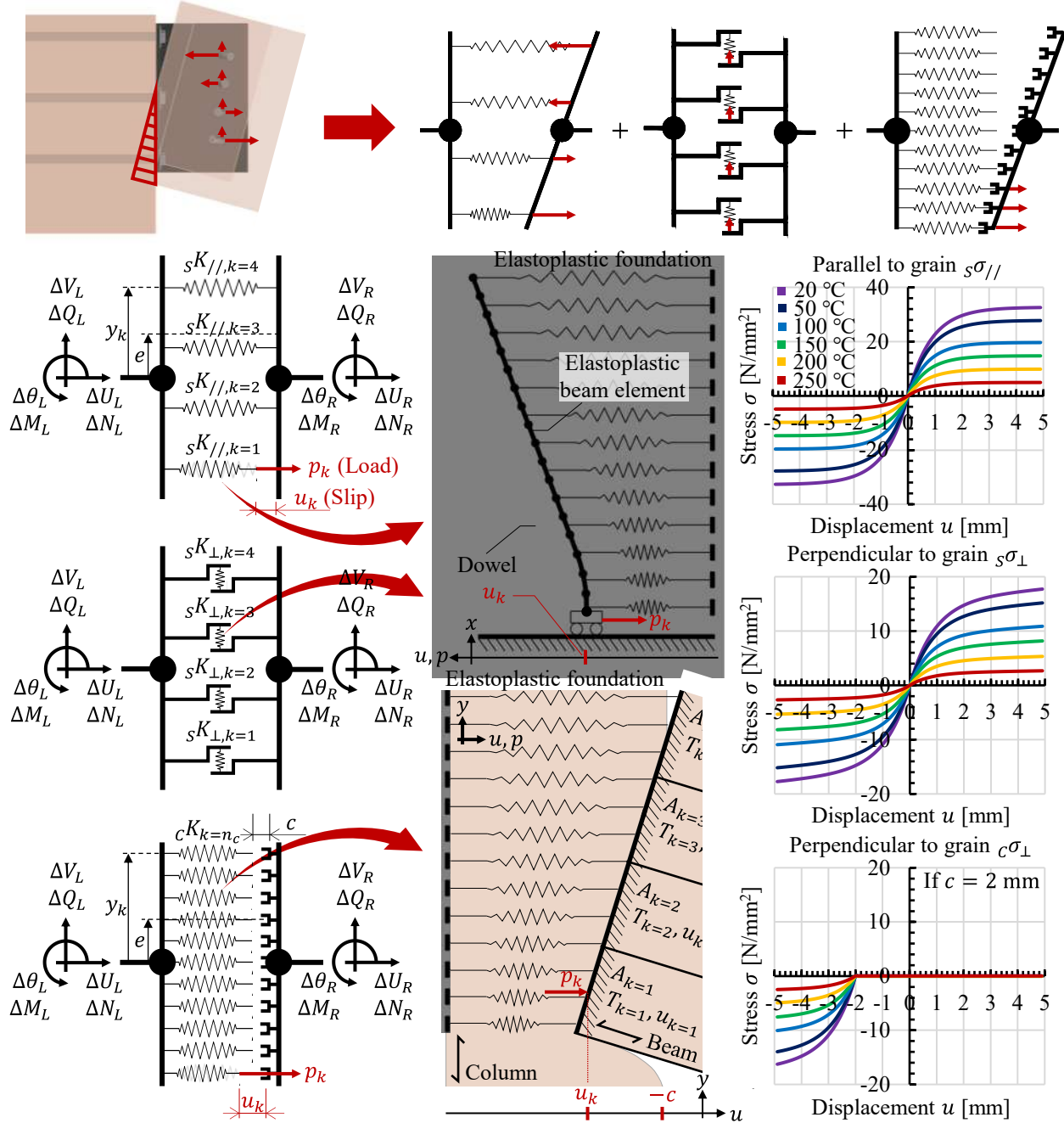


Figure 7. Model of dowel-type connections

5 RESULTS AND DISCUSSION

5.1 Load-displacement relationship

Figure 8 compares the load-deflection curves obtained from the analysis with those obtained with the use of the load cells and the transducer at point D1. The maximum loads in tests P-AT and S-AT were 70.9 kN and 91.0 kN, respectively. Both specimens lost their load-carrying capacity due to the failure of the finger joints located at the bottom of the beam. Therefore, the calculation was stopped when one fibre recorded

the tensile failure strain (0.0028%), which was defined as the quotient of tensile strength and elastic modulus. The proposed model predicted the failure loads within 8% relative error of the test results.

5.2 Time-deflection relationship

The time to failure for the pinned specimen (P-60) was recorded at 174 min; however, no failure of the semi-rigid specimen (S-60) was observed even at 240 min, so the test was continued beyond this point with the applied load gradually increased. As a result, the failure of the semi-rigid specimen was observed at 246 min when the load reached 21.9 kN. The time to failure for the semi-rigid specimen exposed to continuous heating (S-HT) was recorded at 92 min, which was higher than the design fire resistance time specified as 60 min. Based on the post-test observation, the failure of all specimens was due to bending failure in the uniform bending span. On the contrary, due to the use of 40-mm-thick timber plugs as fire protection and the appropriate dowel spacings, the tested connections never experienced any brittle failure such as splitting or shear throughout the tests. Both numerical and test results for the two tests on semi-rigid specimens, S-60 and S-HT, exhibited a similar trend of increased deflection with S-HT having a 9 min error for the failure time (see Figure 8); however, the numerical result for test P-60 underestimated the failure time by approximately 40 min due to the difference between the temperatures obtained from the heat transfer analysis and those recorded by the thermocouples. The time required for completing the calculation was less than 15 min for all cases, and this indicates that employing the component-based connection model significantly reduces the time required for analysis while successfully guaranteeing accuracy.

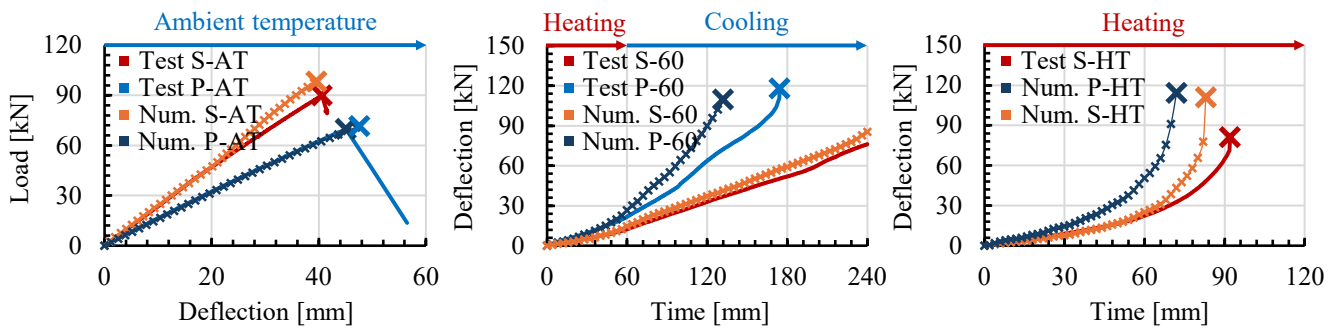


Figure 8. Load-deflection and time-deflection curves

5.3 Moment redistribution

The bending moments at the connection $M_{connection}$ and beam's mid-span M_{beam} (nodes N11 and N20) obtained in the analysis were used to plot the time-moment curves as illustrated in Figure 9. Up to 60 min in both tests S-60 and S-HT, the temperatures at the dowel centres, which have a critical effect on the bending stiffness of the connection, remained below 80°C owing to the wood plugs used as fire protection. However, the temperatures at TC1, 5, and 6 exceeded the charring temperature of 300 °C at 40 min (see Figure 3). In addition, the temperatures at TC2 and TC3, which are both close to the tensile edge of the beam, experienced a rapid increase before 60 min and as a result, the decline in its bending stiffness was faster than that of the connection and led to the continuous moment distribution to the connection.

The gradual decline in the bending moment at the connection observed during the cooling phase is mainly due to the formation of a plastic hinge at the connection. The cross-sectional stress distribution at the beam's mid-span (element in between nodes N19 and N20) and the stress produced by the elastoplastic foundation parallel to the grain under all four dowels are plotted in Figure 10. The dotted line in these figures illustrates the strength level at that time step. The stress on all four dowels almost reached embedding strength after 120 min while the residual cross-section of the beam remained almost linear at 120 min. Owing to the appropriate dowel spacings and the use of the timber plug as fire protection, the connection continuously sustained the bending moment without any brittle failure and reduced the bending moment at the beam's mid-span, which delayed the bending failure of the beam. As a result, the semi-rigid specimen exhibited a failure time that was approximately 70 min longer than that of the pinned specimen and did not fail even after 60 min of heating and 180 min of cooling. Due to the higher load ratio, the stress on the four dowels

in test S-HT reached embedding strength at 60 min while the residual cross-section of the beam remained almost linear, which resulted in the moment redistribution to the beam afterwards. At the failure point of 83 min, a three-hinge failure occurred as the beam reached its bending capacity and resulted in the bending failure of the beam. Therefore, the failure time of the numerical result for the semi-rigid specimen was recorded as 11 min longer than for the pinned specimen. This implies that guaranteeing ductility of connections by means of appropriate dowel spacings and timber plugs can significantly extend the failure time of the connected beam, particularly during the cooling phase, as the prior formation of a plastic hinge delays the brittle bending failure of the beam.

In addition, the failure mode of the dowels in tests S-60 and S-HT was determined only by the embedding failure of the adjacent timber, and not by the plasticization of the dowels. Therefore, the dowel can be assumed to be a rigid body in the ultimate stage of a fire, which can contribute to a significant simplification of the calculation.

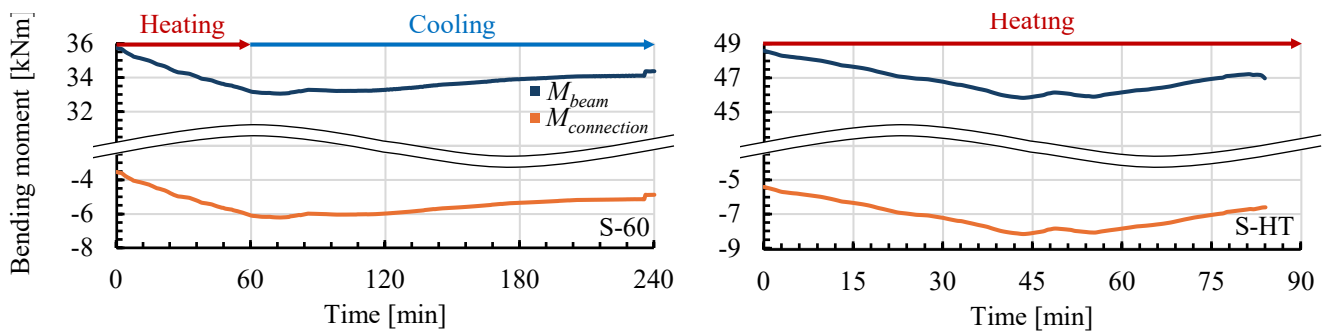


Figure 9. Time-moment curves

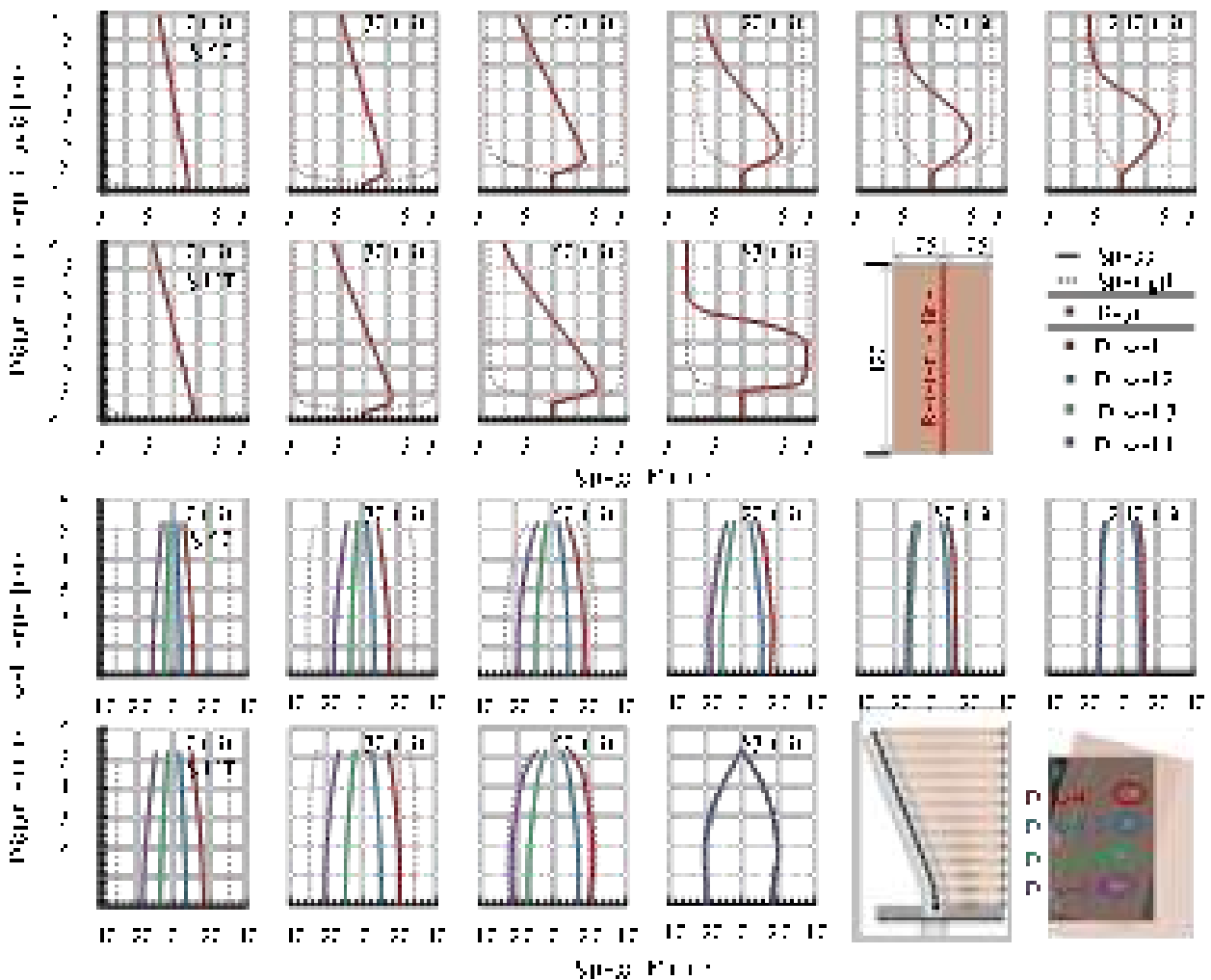


Figure 10. Stress distribution within the beam's mid-span and the connection

5.4 Contact between beam end and column

Figure 11 shows the bending moment burden rate of five resisting mechanisms: the four dowels and the contact between the beam end and column. Most importantly, the burden rate for the contact was zero throughout test S-60, as the charring speed from the beam bottom was faster than the increase in the contact surface area. On the contrary and due to a higher load ratio, an increase in the burden rate for the contact was observed at 40 min in test S-HT and subsequently resulted in the downward transition of the neutral axis position; however, the burden rate immediately decreased to zero at 50 min due to the charring of the beam bottom. This indicates that the contact between the beam end and the column has little influence on the fire performance of timber structures and can be ignored.

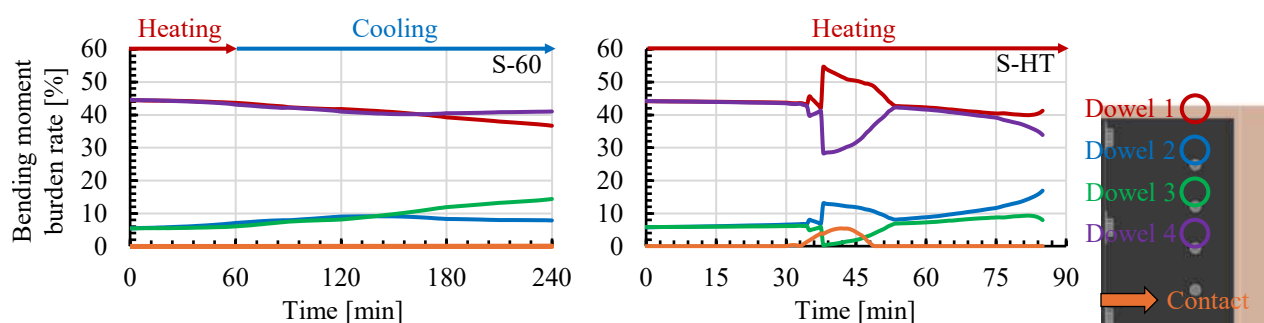


Figure 11. Bending moment burden rate

6 CONCLUSIONS

Fire tests on large-scale timber frames with semi-rigid dowel-type connections as well as simply supported timber beams under heating and cooling conditions were conducted. The time to failure for the pinned specimen heated for 60 min and then cooled in a furnace was recorded at 174 min; however, no failure of the semi-rigid specimen under the same heating condition was observed even at 240 min. The failure time for the semi-rigid specimen exposed to continuous heating was recorded at 92 min. To numerically investigate the influence of the semi-rigidity on the overall structural fire performance, a new numerical model for structural fire behaviour of timber structures assuming the semi-rigid behaviour of dowel-type connection was developed and validated using the test results. The proposed model employs traditional beam-column elements and component-based connection models that consist of non-linear springs to consider semi-rigid restraint conditions while using the direct stiffness method in a time-incremental procedure. Both numerical and test results for the two tests on semi-rigid specimens exhibited quite a similar trend of increased deflection. In addition, the time required for completing the calculation was less than 15 min for all cases, and this indicated the possibility that the proposed model can significantly reduce the time required for analysis compared to the conventional three-dimensional finite element method. The developed model was then used to obtain the time-moment curves and stress distribution within the beam and connection. It was shown that guaranteeing ductility of connections by means of appropriate dowel spacings and timber plugs can significantly extend the failure time of the connected beam, particularly during the cooling phase, as the prior formation of a plastic hinge delays the brittle bending failure of the beam. Further, the contact between the beam end and the column, one of the resistance mechanisms of dowel-type connections, has little influence on the fire performance of timber structures and can be ignored.

REFERENCES

1. Chen, Z., Zhao, J., Zhao, S., Wang, X., Liu, H., Zhang, L. and Xu, Q., Experimental study and theoretical analysis on the rotational performance of large-size bolted joints with slotted-in steel plates, *Construction and Building Materials*, Vol. 341, (2022). <https://doi.org/10.1016/j.conbuildmat.2022.127785>.
2. Liu, Y. and Xiong, H., Lateral performance of a semi-rigid timber frame structure: theoretical analysis and experimental study. *Journal of Wood Science*, Vol. 64, 591–600 (2018). <https://doi.org/10.1007/s10086-018-1727-7>.

3. Dhima, D., Audebert, M. and Bouchaïr, A., Analysis of the Thermo-Mechanical Behaviour of Steel-to-Timber Connections in Bending, *Journal of Structural Fire Engineering*, Vol. 5 No. 2, 97–112 (2014). <https://doi.org/10.1260/2040-2317.5.2.97>.
4. Luo, J., He, M., Li, Z., Gan, Z., Wang, X. and Liang, F., Experimental and numerical investigation into the fire performance of glulam bolted beam-to-column connections under coupled moment and shear force, *Journal of Building Engineering*, Vol. 46, (2022). <https://doi.org/10.1016/j.jobe.2021.103804>.
5. Okunroumu, O., Salem, O.(S). and Hadjisophocleous, G., Fire performance of hybrid mass timber beam-end connections with perpendicular-to-wood grain reinforcement, *Journal of Structural Fire Engineering*, Vol. 13 No. 4, 433–450 (2022). <https://doi.org/10.1108/JSFE-06-2021-0036>.
6. Audebert, M., Dhima, D., Taazount, M. and Bouchaïr, A., Numerical investigations on the thermo-mechanical behavior of steel-to-timber joints exposed to fire, *Engineering Structures*, Vol. 33, Issue 12, 3257–3268 (2011). <https://doi.org/10.1016/j.engstruct.2011.08.021>.
7. Palma, P., Frangi, A., Hugi, E., Cachim, P. and Cruz, H., Fire resistance tests on timber beam-to-column shear connections, *Journal of Structural Fire Engineering*, Vol. 7 No. 1, 41–57 (2016). <https://doi.org/10.1108/JSFE-03-2016-004>.
8. Nagaoka, T., Kobayashi, M., Hanai, A., Naruse, T., Suzuki, J. and Kagiya, K., Development of wood beam joints with 90-minute quasi-fire-resistance (Part 1) Loading heating test, *Summaries of Technical Papers of Annual Meeting, Architectural Institute of Japan*, 235–236, (2020). (in Japanese).
9. Kinjo, H., Horio, T., Hirashima, T., Katakura, Y., Saito, K. and Yusa, S., Deflection behaviour and load bearing capacity of larch glued laminated timber beams exposed to standard fire heating during the cooling phase, *Journal of Structural and Construction Engineering*, Vol. 81, No. 726, 1355–1361 (2016). <https://doi.org/10.3130/aijs.81.1355>. (in Japanese)
10. L Simões da Silva, Aldina Santiago and Paulo Vila Real, A component model for the behaviour of steel joints at elevated temperatures, *Journal of Constructional Steel Research*, Vol. 57, Issue 11, 1169–1195 (2001). [https://doi.org/10.1016/S0143-974X\(01\)00039-6](https://doi.org/10.1016/S0143-974X(01)00039-6).
11. Sarraj, M., The behavior of steel fin plate connections in fire, *Sheffield University, Ph. D. Thesis*.
12. Nakayama, Y., Kikuchi, T., Totsuka, M. and Hirashima, T., Analytical model for non-linear M- θ relationships of dowel-type timber connections exposed to fire, *Fire Technology*, (2024). <https://doi.org/10.1007/s10694-024-01546-4>.
13. Becker J. and Bresler B., A computer program for the fire response of structures - reinforced concrete frames, *Fire Research Group, Report No. UCB FRG 74-3, University of California, Berkeley*, 1974.
14. *Architectural Institute of Japan, Standard for Structural Design of Timber Structures*, 2015. (in Japanese)
15. Nakayama, Y., Kikuchi, T., Yotsumoto, N., Kawarabayashi, F., Totsuka, M. and Hirashima, T., Experimental study on fire performance of glulam timber frames (part 3) influence of rotational resistance of dowel-type connections on fire performance of timber frames, *Journal of Structural and Construction Engineering*, Vol. 89, No. 816, 223–234 (2024). <https://doi.org/10.3130/aijs.89.223>. (in Japanese)
16. Ishida, Y., Hirashima, T. and Totsuka, M., Three-dimensional heat transfer analysis of dowelled type connections for timber structures, *Summaries of Technical Papers of Annual Meeting, Architectural Institute of Japan*, 159–162 (2022). (in Japanese)
17. Richard, R.M. and Abbot, B. J., Versatile elastic-plastic stress-strain formula, *Journal of Engineering Mechanics*, Vol. 10, No. 4, 511–515 (1975). <https://doi.org/10.1061/JMCEA3.0002047>
18. Kikuchi, T. and Hirashima, T., Influence of moisture on compressive behaviour of Japanese cedar and larch structural glulam timbers at elevated temperature, *Journal of Structural and Construction Engineering*, Vol. 86, No. 781, 513–523 (2021). <https://doi.org/10.3130/aijs.86.513>. (in Japanese)
19. EN 1995-1-2, *Eurocode 5: Design of timber structures – Part 1-2: General – Structural fire design*.
20. Garcia-Castillo Ester, Gernay Thomas, and Paya-Zaforteza Ignacio, Probabilistic models for temperature-dependent compressive and tensile strengths of timber, *Journal of Structural Engineering*, Vol. 149 (2022). <https://doi.org/10.1061/JSENDH.STENG-11369>
21. Foschi, R. O., Load-slip characteristics of nails. *Wood Science*, Vol. 7, 69–76 (1974).
22. Saito, S., Kikuchi, T., Nakayama, Y., Totsuka, M. and Hirashima T., Embedment strength of dowelled connections of glulam timber at high temperatures, *Proceedings of the 13th International Conference on Structures in Fire* (2024).

NUMERICAL MODELLING OF THE CHARRING PERFORMANCE OF CROSS-LAMINATED TIMBER EXPOSED TO STANDARD FIRE

Mika Alanen¹, Topi Julin², Mikko Malaska³, Mikko Salminen⁴, Aleksi Ojala⁵

ABSTRACT

The fire resistance assessment for timber and cross laminated timber (CLT) structures is typically based on fire testing or on rational fire resistance calculation methodology, which are based on first principles such as charring rate and effective reduced cross-sections. There are also a great number of applications where advanced finite element methods and numerical simulations can assist in technical assessment exercises and in complementing full scale tests that are resource demanding and expensive. Advanced methods have already been successfully applied to timber and CLT structures [1, 2, 3]. In the case of CLT, the analysis is complicated by the char fall-off and delamination of the charring layers, which decrease the fire protective function provided by the charcoal and increase the charring rate compared to solid wood members. When simulating the temperature distribution of CLT cross-sections and estimating the location of the char front, it is necessary to know at what temperature the adhesive fails and loses its stickability and integrity at the bond lines. Due to the lack of experimental data the char fall-off is often not included in the analysis models. The research presented in this article aims to use experimental fire test results to assess the temperature level where the adhesive fails and to determine how the failure temperature affects the numerical simulation results. A numerical model has been developed to incorporate the effects of heat transfer and char fall-off performance in a CLT panel exposed to standard fire.

Keywords: timber; CLT; adhesive; char fall-off; fire test; finite element modelling

1 INTRODUCTION

Research has been conducted on numerical simulations of CLT structures exposed to the standard fire conditions in accordance with ISO834 [1] and advanced methods have already been successfully applied to CLT structures [2-4]. The thermal properties for wood and the char layer are typically taken from standard EN 1995-1-2 [5]. However, research has shown that applying these features to CLT structures is not a viable solution. Kleinhenz et al. [2] conducted thermal simulations of CLT rib panels using SAFIR software [6]. Their research stated that after removing fallen-off layers in the finite element model, the time-temperature dependence of the thermal properties must be different, since the relationship between

¹ Doctoral researcher, M.Sc, Metal and Lightweight Structures, Tampere University, Korkeakoulunkatu 5, 33720 Tampere, Finland
e-mail: mika.alanen@tuni.fi, ORCID: <https://orcid.org/0000-0001-7215-4138>

² Fire Safety Engineer, Jensen Hughes, Runeberginkatu 5 B, 00100 Helsinki, Finland, Finland
e-mail: topi.julin@jensenhughes.com

³ Prof. D.Sc, Metal and Lightweight Structures, Tampere University, Korkeakoulunkatu 5, 33720 Tampere, Finland
e-mail: mikko.malaska@tuni.fi, ORCID: <https://orcid.org/0000-0002-8215-9765>

⁴ Structural Fire Engineering Lead for Europe, Jensen Hughes, Aleksanterinkatu 32 B, 33210 Tampere, Finland
e-mail: mikko.salminen@jensenhughes.com

⁵ Title Service Line Leader Mass Timber (Europe), Jensen Hughes, Aleksanterinkatu 32 B, 33210 Tampere, Finland
e-mail: aleksi.ojala@jensenhughes.com

time and temperature differs compared to the standard time-temperature of ISO834 [1]. The temperature level where the adhesive was assumed to fail was set to 300 °C. The use of material properties of EN 1995-1-2 [5] together with char layer fall-off leads to too conservative results in the case of CLT. The paper proposed a new set of thermal properties for CLT, where thermal conductivity and specific heat are different than in EN 1995-1-2 [5]. They proposed a new set of thermal properties for CLT exposed to standard fire from one side. The following properties of the current EN 1995-1-2 [5] were changed:

- An endothermic reaction heat during pyrolysis
- The effect of thermal insulation by increasing the char layer

Research by Brandon et al. [4] represents a predictive method focusing on post flashover compartment fire including the decay phase and extinction of flaming combustion. An iterative approach is introduced including a single-zone model which uses an energy equilibrium approach to obtain gas temperatures and surface temperatures of compartment boundaries, and a thermal model calculating the temperature-time history of the timber structural element. However, in this research, no attempt was made to equip the model to account for char fall-off. The observations reported for the detachment of plasterboard fire protection is also well suited for modelling the CLT structure.

This paper focuses on the numerical simulations of the charring behaviour of CLT floor panels under ISO834-standard fire exposure on one side taking into account the char fall-off. The attempt was to investigate how well a one-dimensional numerical thermal analysis model implemented in SAFIR-software simulates the fire performance of CLT structures. Moreover, the objective was also to investigate the differences in the results of the model and tests, and their potential reasons to understand how the model could be improved further.

2 EXPERIMENTAL INVESTIGATIONS

The charring performance of CLT panels exposed to standard fire was investigated using panel products from two different CLT manufacturers, both of which use polyurethane-based adhesives. The panels were made of spruce (*Picea abies*) with a strength class of C24. The panels were glued with one-component polyurethane (PUR) adhesive. The adhesive was applied to the faces of the lamellae in their main bond line and without edge bonding. The geometrical details, dry wood densities and moisture contents of the specimens are reported in Table 1. All the specimens were 1600 mm long.

Table 1. Geometrical details of the test specimens, the methods used for thermocouple installation

Specimen reference	Panel thick. [mm]	Lamella thicknesses [mm]	Panel width [mm]	Thermocouple installation	Dry wood density [kg/m ³]	Moisture content [%]
Test 1a	100	20-20-20-20-20	835	Inlaid	420	9.2
Test 1b	100	20-20-20-20-20	835	Inlaid	426	10.0
Test 2	100	20-20-20-20-20	500	Drilled	408	9.1
Test 3	160	40-20-40-20-40	500	Drilled	430	9.2

2.1 Test set-up

The specimens were tested in a horizontal position and exposed to standard fire conditions in accordance with EN 1363-1 [7]. The internal dimensions of the furnace chamber were 3 m x 3 m x 1.2 m (height x width x depth), and the specimen was installed across the 1.2 m-wide opening of the chamber. The rest of the chamber was covered with aerated concrete slabs. The tests were conducted unloaded. Schematic vertical cross-sections of the test set-up and specimen are shown in Figure 1. In Tests 1a and 1b, the outer lamella layers were perpendicular to the 1.2 m span. In Tests 2 and 3, the outer layers were parallel to the

span, and the first lamella layers were saw-cut near the supporting walls. The cuts were filled with ceramic fiber paper. The specimens were extinguished by immersing them in a pool of water after the termination of the test and the charring depths were determined by measuring the residual panel cross-sections.

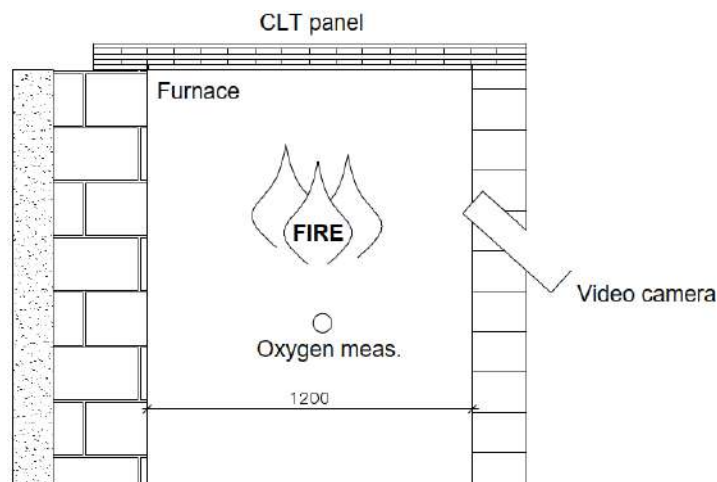


Figure 1. Schematic view of the vertical cross-section through the test furnace and specimen

During the tests, furnace temperature, specimen temperatures, oxygen concentration 300 mm below the furnace ceiling, and the pressure differences between the furnace and test hall were monitored. The char fall-off of the lamellae layers was observed visually with a video camera. Furnace temperature was measured using four plate thermometers located 150 mm below the soffit of the specimen.

2.2 Instrumentation of the specimens

Fibreglass-wrapped Type K24-2-305 thermocouples with a welded junction were used to determine the temperatures inside the specimens. All the thermocouple wires were placed parallel to the isotherms (horizontally). In the specimens of Tests 1a and 1b, inlaid thermocouple wires were installed during the CLT manufacturing process before the lamellae were glued together under hydraulic pressing. The wires were installed in 1.5 mm x 2 mm grooves milled on the lamellae. The gaps around the wires were assumed to be filled with PUR during the gluing process. Five measurement stations having five overlapping thermocouples in each (see Figure 2a) were used in a specimen. For Tests 2 and 3, the thermocouples were installed in 100 mm deep holes drilled in the laboratory. In order to ensure accurate installation, a 4.0 mm diameter drill bit was used. Good contact between the thermocouple and wood was ensured by mounting the thermocouple using a 3.0 mm diameter wooden sticks. Wooden sticks also filled the hole. Side views of the specimens with indicated locations of inlaid and drilled thermocouples are shown in Figure 2b. Also, additional tests were carried out using 1.5 mm thick sheathed type K thermocouples, but the variation in those results was considered too high.

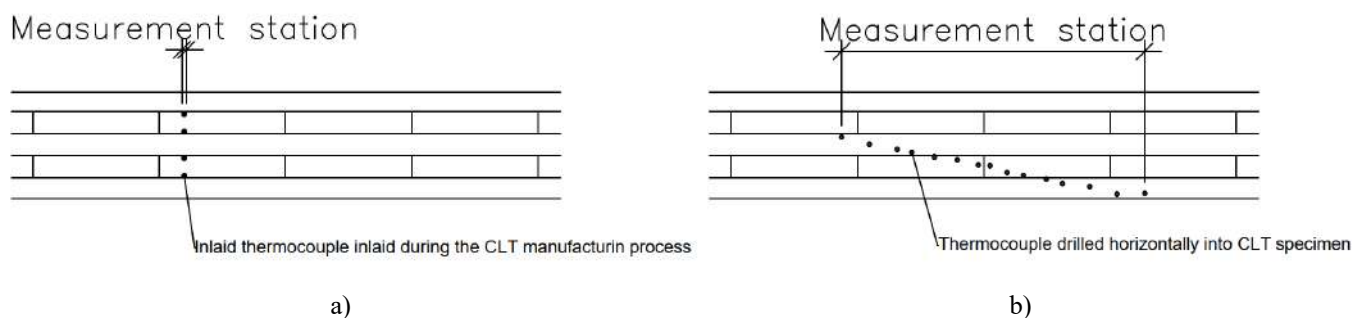


Figure 2. Schematic views of the specimen and positioning of thermocouples a) inlaid thermocouples inside the specimens of Tests 1a and 1b and b) on the side elevation of the specimens of Tests 2 and 3

The char layer formed on the fire-exposed surface acts as an insulating layer, protecting the uncharred wood behind it. The charring rate decreases up to a certain limit as the thickness of the char layer increases. Consequently, the charring rate is not linear [8, 9]. In the specimens of Test 1a and Test 1b, temperatures were measured only at the interfaces between lamellae, and it was considered that a constant rate value within a lamella provide sufficiently accurate results for the comparisons made in this research. In the specimens of Test 2 and Test 3, thermocouples were installed also inside the lamellae and the results provide information on the non-linear charring performance within the lamella layers.

2.3 Test results

Figure 3 shows the average furnace temperatures and oxygen concentration levels monitored during the tests. At the beginning of the tests, the oxygen concentration dropped quickly to around 6–7%. The concentration levels decreased steadily during the tests, reaching around 5-6 % at the end of the tests.

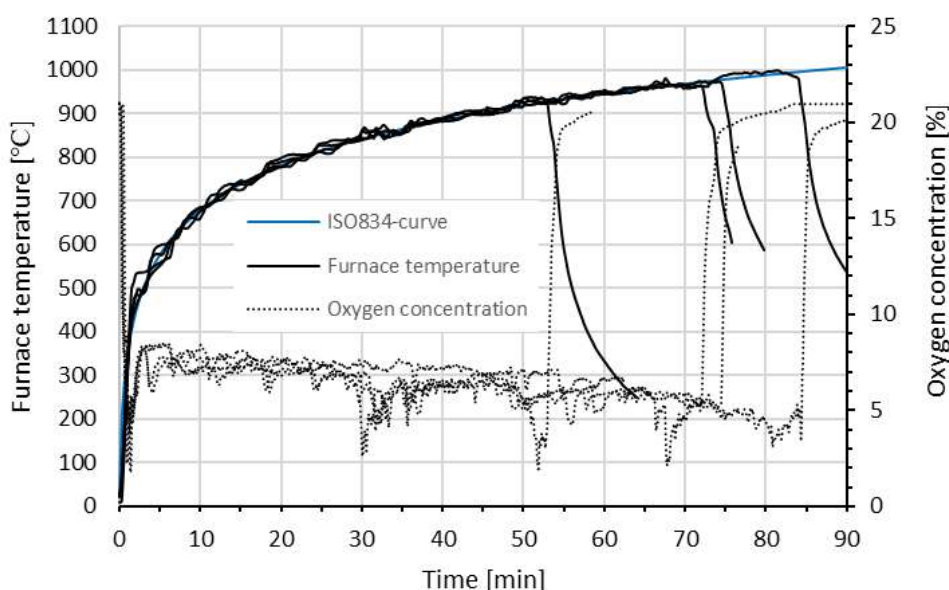


Figure 3. Furnace temperatures and oxygen concentrations measured during the fire tests

Wood temperatures measured over time at different measurement stations and distances from the fire-exposed side are reported in Figure 4. In many temperature curves, a noticeable plateau can be observed at 100–150 °C. At this temperature, free water begins to evaporate, and the moisture slows the temperature rise as the energy supplied is used for evaporation rather than heating [10].

The greyed area in Figure 4 represents the char fall-off of different lamella layers, based on video footage from the furnace. The figure also displays the time ranges when temperatures at various measurement stations within a lamellae interface exceeded 300 °C. According to the visual observations, the char fall-offs occurred either simultaneously or shortly after the 300 °C isotherm surpassed the lamellae interface. Identifying an exact temperature for the bond failure is challenging, but based on these observations, 300 °C was deemed to be a representative temperature. This is also well in line with other studies.

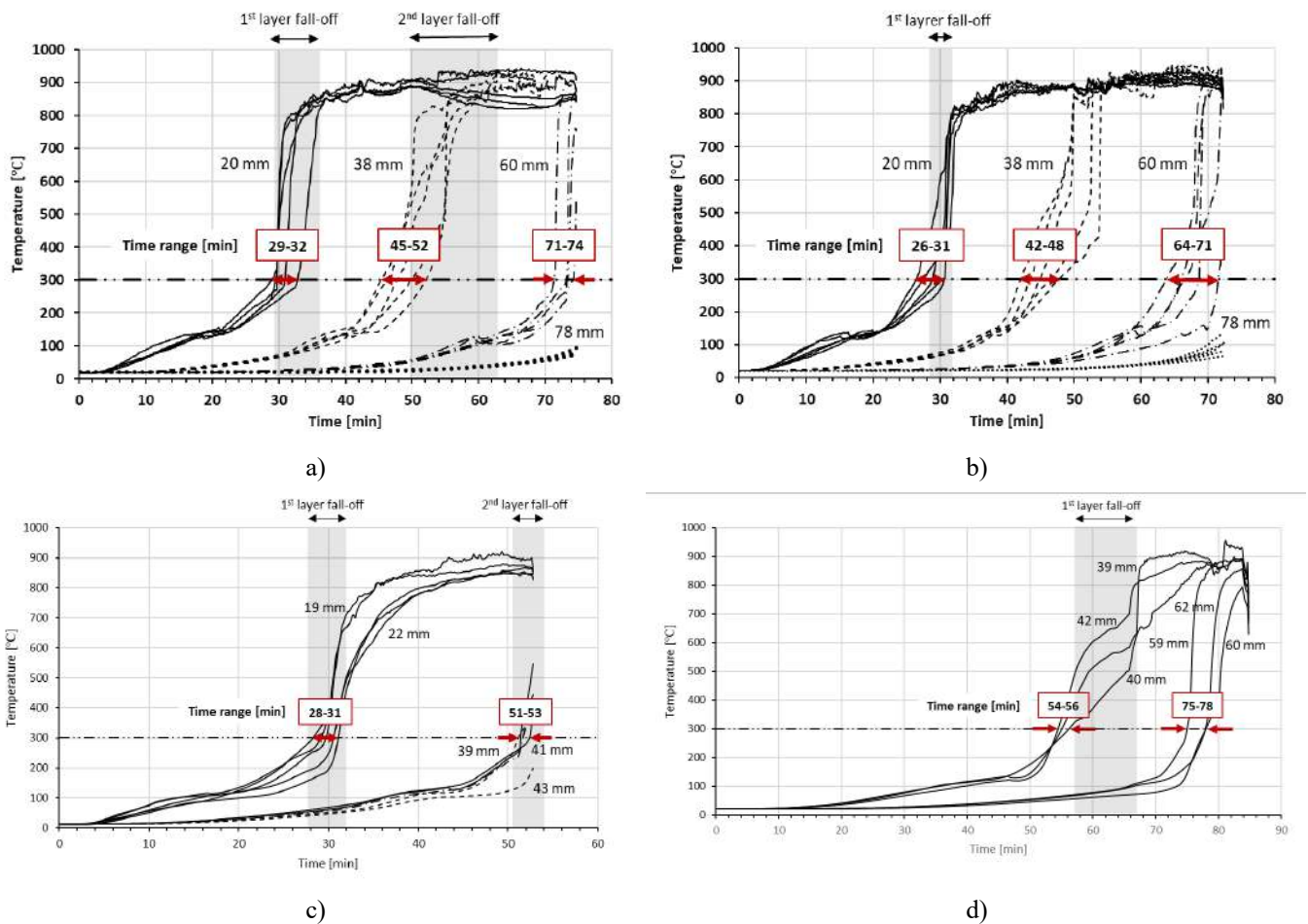
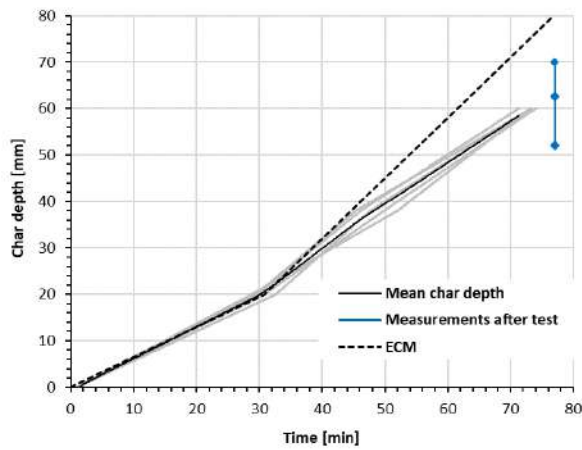
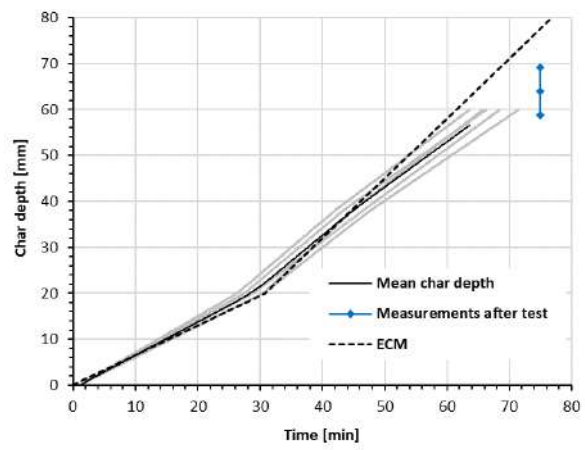


Figure 4. Experimental temperature distributions measured at different thermocouple locations: a) Test 1a; b) Test 1b; c) Test 2; d) Test 3. The numbers next to the line indicate the distance to the fire-exposed surface, and the greyed areas present char fall-off of a specific layer

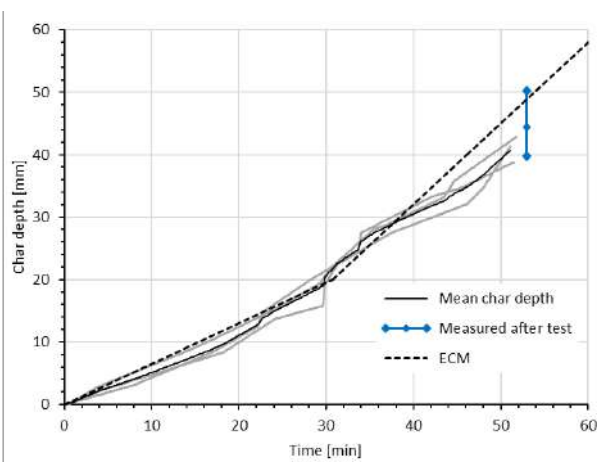
The char depth development in CLT members was estimated based on temperatures measured inside the specimens during the test and on visual observations made after tests. The position of the char line in the test specimen was assumed as the position of the 300 °C isotherm [5]. Figure 5 represents the mean char depth development curves based on experimental temperature distributions of panels. The grey curves represent the char depths based on measurements at different measurement stations. The black curve represents the mean char depth and is based on the measurement station results at specific times. In blue colour are the char depths measured manually after tests: minimum value, mean value and maximum value. The dotted line (ECM) represents the phased char depth according to EN 1995-1-2 [5]. The results of Tests 2 and 3 show clearly that the charring rate increases near the bond lines. In tests 1a and 1b the char depth development is more linear as the temperatures were measured at the bond lines only.



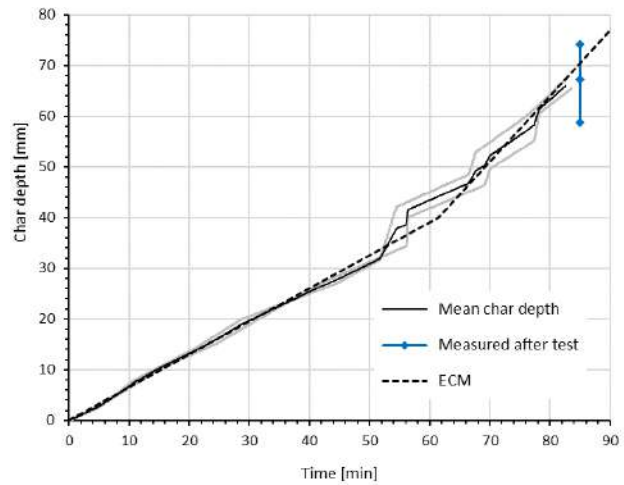
a)



b)



c)



d)

Figure 5. The mean char depth development curves based on experimental temperature distributions of panels and the char depths measured after tests: a) Test 1a; b) Test 1b; c) Test 2; d) Test 3. The grey curves represent the char depths based on measurements at different measurement stations. The black curve represents the mean char depth and is based on the measurement station results at specific times

Based on the European charring model (ECM) the charring of a CLT panel can be represented as a combination of sequenced charring phases [11,12]. When the bond line integrity of face bonds is not maintained, fall-off of the charring layer occurs when the charring depth reaches the bond line leading to an increased charring rate for the following layer. The dashed black lines in Figure 5 represent the charring depths calculated by using ECM and a post-protection factor k_3 of 2. The experimental results are in line with the ECM.

3 NUMERICAL SIMULATIONS

A one-dimensional thermal model is used for predicting the heat transfer in CLT panels exposed to standard fire including the variation of thermal properties of timber material during the heating process and the char fall-off. The analysis is executed using SAFIR-software [6].

3.1 Numerical model

The element size and time step used in the analysis were chosen so that the results do not significantly differ, if smaller elements or time steps were chosen. Temperatures were determined at 1.0 mm centres throughout the panel depth and the time step was limited to a maximum value of 1.0 sec.

Boundary conditions, convection coefficients and the emissivity of timber and the furnace for these analyses were in accordance with EN 1991-1-2 [13] and Annex B of EN 1995-1-2 [5]. One side was exposed to standard fire while the opposite side was at ambient (20 °C) conditions. Surface emissivity of $\epsilon_m = 0.8$ was assumed for wood. On the unexposed side the coefficient of heat transfer was taken as $\alpha_c = 4 \text{ W/m}^2\text{K}$ and on the exposed side, $\alpha_c = 25 \text{ W/m}^2\text{K}$ was applied.

The dry wood density used was $408,5 \text{ kg/m}^3$. The initial moisture content considered in the analyses was 9,1 %. The values given in EN 1995-1-2 are given for a moisture content of 12 % and, therefore, the specific heat capacity values were adjusted accordingly using a method by Brandon et al. [3]. The specific heat values at 100 °C and 120 °C were hence $10,479 \text{ kJ/(kgK)}$ and $10,373 \text{ kJ/(kgK)}$, respectively. The thermal properties used are reported in Table 2.

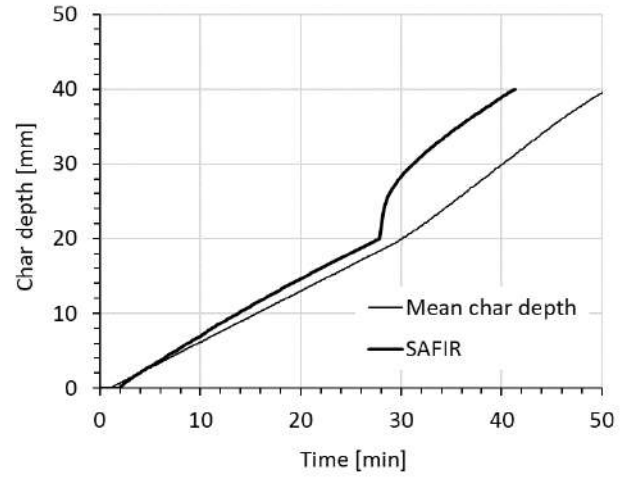
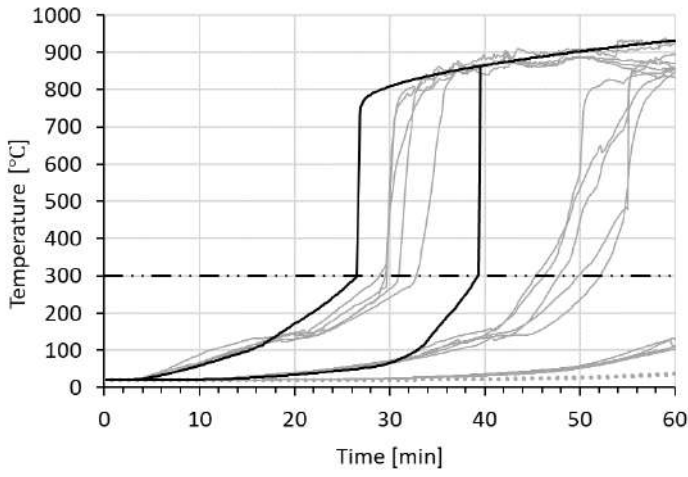
Table 2. Thermal properties used for CLT. ω is the moisture content [3,14]

Temperature [°C]	Thermal conductivity [W/(mK)]	Specific heat capacity [kJ/(kgK)]	Ratio of dry density to dry density at 20 °C [-]
20	0.120	1.53	$1 + \omega$
99	0.133	1.77	$1 + \omega$
99	0.133	$13.60 + (\omega - 12) * 1.076$	$1 + \omega$
120	0.137	$13.50 + (\omega - 12) * 1.076$	1.00
120	0.137	2.12	1.00
200	0.150	2.00	1.00
250	0.120	1.62	0.93
300	0.100	0.71	0.76
350	0.070	0.85	0.46
400	0.080	1.00	0.38
500	0.090	1.20	0.28
600	0.180	1.40	0.26
800	0.350	1.65	0.23
1200	1.500	1.65	0.00

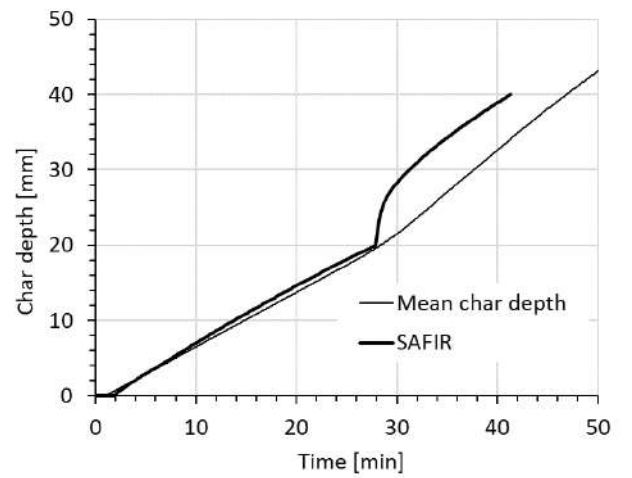
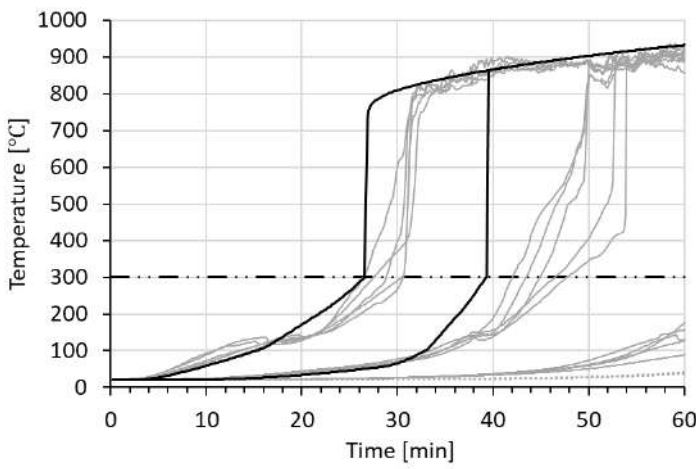
Fall-off of lamella layers is simulated by removing the exposed lamella from the model when temperatures in the bond line reach 300 °C and using sequentially chained models. In the simulations, the exposed layer was removed when the bond line temperature exceeded 300 °C. The effects of the temperature are analysed in more detail in Chapter 4. The model assumes that the ash layer (wood temperatures higher than 300 °C) is not removed by either flow or gravity.

3.2 Results from numerical analysis

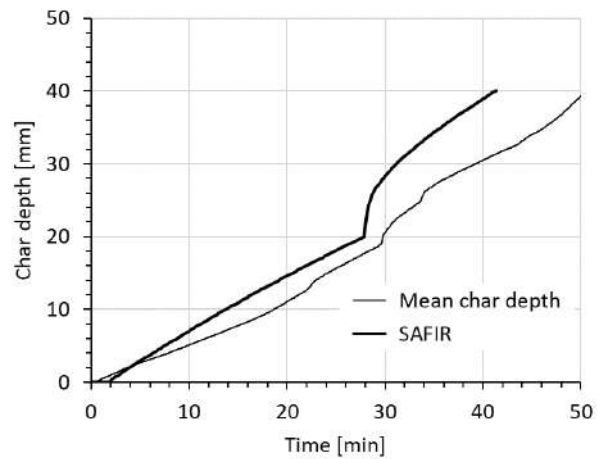
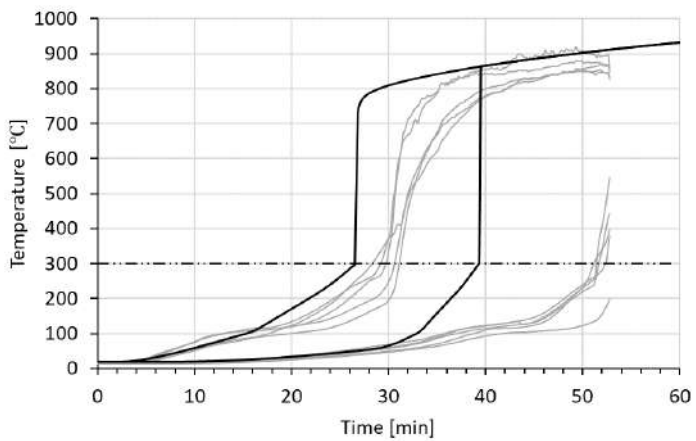
Figures 6 and 7 below depict the results from numerical analysis and compare them to the experimental test results.



a)



b)



c)

Figure 6. Experimentally and numerically determined bond line temperatures and the corresponding char depths of 100 mm thick CLT panels: a) Test 1a, b) Test 1b, c) Test 2

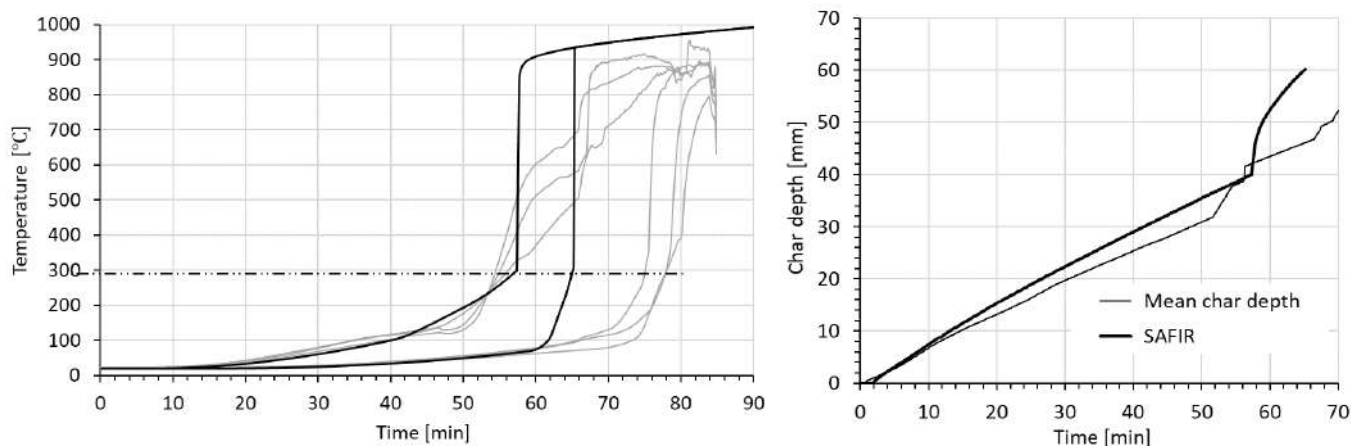


Figure 7. Experimentally and numerically determined bond line temperatures and the corresponding char depths of a 160 mm thick CLT panel: Test 3

4 DISCUSSION

The critical temperature for the fall-off of first lamella was calibrated by comparing experimentally measured data reported in Section 2. These tests include panel products from two different CLT manufacturers. Further research is needed to validate the simulation model against other research, panel products, adhesives, wood densities, moisture contents. In this research, the following observations were made:

- The applied model predicts the fall-off the first lamella layer well.
- The applied model overestimates the charring rate after the fall-off the first lamella layer. Consequently, the fall-off times for the next lamella layers are too conservative.

Numerical analysis can be useful tool to determine the fire resistance of CLT-structures in Structural Fire Engineering (SFE) projects as there are no simple methods to design timber CLT -structures for natural fires and/or to resist the full burnout. Developing a consistent, conservative and accurate procedure for numerical analysis is therefore important.

Comparison between results from tests and numerical analysis suggest that building a consistent and accurate numerical model may be challenging. A potential option to increase the accuracy of the numerical results is to further modify the material properties of timber. It is considered that modifying char layer fall-off temperature might also be an option to match better to the test results. The following approaches are considered potential options in SFE project to design CLT structure for other than standard fire:

1. Use the current EN 1995-1-2 [5] Annex B material properties with the modified values for specific heat to take the moisture content better into account.
2. Develop material properties (thermal conductivity and specific heat) further, as presented in Kleinhenz's paper [2].
3. Modify the char layer fall-off temperature to match better with the test results.
4. Attempt to develop more complicated models of charring.

The options listed above are discussed below.

The first option (using current EN 1995-1-2 [5] Annex B material properties and modified specific heat) seems to give relatively conservative results after the fall-off of first lamella layer.

The second option (developing / using different material properties as presented e.g. in Kleinhenz's paper [2]) might make the results more accurate. It is understood that the material properties of timber presented in EN 1995-1-2 Annex B [5] are so-called "effective" properties. However, modifying the material properties does not necessarily make sense as they should be independent on the product (CLT or solid wood). Moreover, using different material properties for different layers does not seem consistent. In work of Kleinhenz the modification of thermal properties served the purpose of reducing the sharp increase in charring rate after char fall-off. However, the experiments presented in this paper show that the sharp rise in charring rate

sometimes appears in experimentally determined charring rates. This suggests that the reason for the charring rate rise is something related to the mechanism of char fall-off, not pyrolysis reactions.

The motivation for modifying material properties is to include the effect of various physical phenomena not included in the numerical model. The effective properties of EN 1995-1-2 [5] already attempt to take into account, e.g. the radiative heat transfer in the pores of wood char and cracking of the char layer. Additional consideration could be given to the energy needed to heat up water and pyrolysis gases from the pyrolysis temperature to furnace temperature. The energy absorbed by the released gases will increase as the furnace temperature grows, offering a possible explanation for the relatively slower charring rate after delamination observed in experiments.

The third option (modifying the fall-off temperature of the lamella layers) may be worth investigating more. In the fire tests, the fall-off of the lamella layers occurs at different times at different locations. The numerical model naturally considers this as a uniform event which eventually leads to too conservative results. It might make sense to increase the fall-off temperature in the model so that it would correspond to the time when e.g. half of the fall-off has occurred. However, more investigations in this issue are needed.

5 CONCLUSIONS

The results of four fire tests on CLT panels exposed to standard fire conditions were investigated to assess the charring and char fall-off performance of the panels. Also, a numerical model has been developed to incorporate the effects of heat transfer and char fall-off performance. Numerical one-dimensional thermal simulations were conducted using SAFIR software, and the agreement between experiments and numerical analysis predictions were in general very good. The following was concluded from the comparative study between the numerical results and the test results:

- The predicted temperatures were generally underestimated for the fully developed phase of the fire by approximately 100°C. However, the accuracy of the temperature predictions are considered to be reasonable.
- The predicted time at which delamination occurs corresponds well with the experimental results.
- The increase in charring rate due to delamination was overestimated by the model. This is likely due to the assumption that the char fall off is instantaneous. However, similar sharp increase of charring rate is seen in some experiments, suggesting that there is considerable variability in the mechanism of char fall-off.
- The applied model predicts the fall-off the first lamella layer well.
- The applied model overestimates the charring rate after the fall-off of the first lamella layer. Consequently, the fall-off times for the next lamella layers are too conservative.

The numerical model predicts a sharp increase in charring rate after char fall-off that tapers relatively quickly towards the average charring rate. This same increase does not appear in all tests, suggesting that the char fall-off process itself changes between tests.

REFERENCES

1. ISO 834-1, Fire resistance tests – elements of building construction. Geneva. Switzerland. International Organization for Standardization. 1999
2. Kleinhenz, M., Just, A., Frangi, A., Temperature-dependent thermal properties for cross-laminated timber exposed to standard fire, Conference: INTER - International Network on Timber Engineering Research, Meeting 8 (INTER Meeting 2021), August 16-19, 2021
3. Brandon, D., Klippel, M., Frangi, A., Glueline integrity in fire, RISE Report 2021:107, Division Safety and Transport, Fire Research, RISE Research Institutes of Sweden. 2021
4. Brandon, D., Temple, A., Sjöström, J., Predictive method for fires in CLT and glulam structures – A priori modelling versus real scale compartment fire tests & an improved method, RISE Research Institutes of Sweden AB, RISE Report 2021:63. 2021
5. EN 1995-1-2:2004 + AC. Eurocode 5: Design of timber structures – Part 1-2: General – Structural fire design. 2nd ed. Brussels: European Committee for Standardization.

6. Franssen, J.M., Gernay, T., Modeling structures in fire with SAFIR®: Theoretical background and capabilities, *Journal of Structural Fire Engineering*, pp. 300-323, 2017, <https://doi.org/10.1108/JSFE-07-2016-0010>
7. EN 1363-1:2020, Fire resistance tests. Part 1: General requirements, Brussel, European committee for standardization, 47 p., 2020
8. Frangi, A., Fontana, M., Knobloch, M. & Bochicchio, G., Fire behaviour of cross-laminated solid timber panels. In: Karlsson, B. (Ed.) *Fire Safety Science – Proceeding of the ninth international symposium*. Karlsruhe, Germany. 21-26 September 2008. International Association for Fire Safety Science, pp. 1279-1290. 2008. doi: 10.3801/IAFSS.FSS.9-1279
9. Pope, I., Hidalgo, J.P., Hadden, R.M. & Torero, J.L. A simplified correction method for thermocouple disturbance errors in solids. *International Journal of Thermal Sciences*, 172. 2022. doi: 10.1016/j.ijthermalsci.2021.107324
10. Bartlett, A. I., Hadden, R. M. & Bisby, L. A. (2019). A review of factors affecting burning behaviour of wood for application to tall timber construction, *Fire Technology*, 55, pp.1-49. doi: 10.1007/s10694-018-0787-y
11. Klippel, M., Schmid, J. & Frangi, A. Fire Design of CLT. In: Falk, A., Dietsch, P. & Schmid, J. eds. *Proceedings of the joint conference of COST Actions FP1402 & FP1404 “Cross laminated timber – A competitive wood product for visionary and fire safe buildings”*. Stockholm, Sweden. 10-11 March 2016. KTH Royal Institute of Technology. pp. 101 – 122. ISBN 978-91-7729-043-8.
12. Just, A., Abu, A., Barber, D., Dagenais, C., Klippel, M. & Milner, M. (2022). Load-bearing timber structures. In Buchanan, A. & Östman, B. eds. *Fire safe use of wood in buildings. Global design guide*. Boca Raton, Florida, USA: CRC Press, pp. 227-276. doi: 10.1201/9781003190318-7
13. EN 1991-1-2 :2003 Eurocode 1: Actions on structures. Part 1-2: General actions. Actions on structures exposed to fire. European committee for standardization. Brussels
14. Franssen, J.M., Gernay, T., User’s manual for SAFIR 2022, A Computer program for analysis of structures subjected to fire, Part 5: material properties. Liege University, 2022, https://www.uee.uliege.be/cms/c_8478223/en/manual-of-safir-2022-5-material-properties

PARAMETRIC EXPERIMENTAL STUDY ON GLT COLUMNS STABILITY DURING NATURAL FIRE TESTS INCLUDING THE COOLING PHASE

Silvio Renard¹, Thomas Gernay², Fabienne Robert³, Jochen Zehfuß⁴, Robert McNamee⁵, Patrick Bamonte⁶, Jean-Marc Franssen⁷

ABSTRACT

This paper is about the behaviour of glue laminated timber (GLT) columns subjected to physically based fires which include a decay phase. A summary is first given of the results of numerical analyses, of furnace tests made in a controlled environment following the parametric fire model of Eurocode 1 and of a series of seven tests made in a naturally vented compartment with wood cribs used as fire load.

This paper then presents in detail the results of five additional tests performed in the same fire compartment with some variation of the parameters compared to the previously presented series. One test conducted with the same 280 × 280 mm² section as the previous series but with lower compartment temperatures, led to collapse after 45 minutes, not yet in the decay phase. Three tests were made on an increased section of 400 × 400 mm². These three specimens survived for more than 11 hours but collapsed thereafter due to localised zones of increased charring and combustion, essentially at the base of the columns. The final test investigated the effect of fire service intervention. In this test on the 280 × 280 mm² section, the column did not collapse owing to the intervention of fire fighters after 35 minutes of fire.

Keywords: Timber; loaded columns; Glue laminated timber; compartment fires; tests

1 INTRODUCTION

The ability of load-bearing members to withstand fire exposure is typically evaluated through the concept of fire resistance rating (FRR), as outlined in Eurocode 1 in Europe [1]. This grading system involves loading the element and subjecting it to a standardized, continuously increasing, temperature-time curve. It is well understood that the FRR, although it is expressed in minutes, must not be mistaken for the actual survival time of the structure to which the member belongs in a real fire. Notwithstanding all its limitations,

¹ Research Engineer, CERIB Fire Testing Centre, France

e-mail: s.renard@cerib.com, ORCID: <https://orcid.org/0009-0007-7807-042X>

² Assistant Prof., Department of Civil and Systems Engineering, Johns Hopkins University, USA

e-mail: tgernay@jhu.edu, ORCID: <https://orcid.org/0000-0002-3511-9226>

³ Deputy head, CERIB Fire Testing Centre, France

e-mail: f.robert@cerib.com, ORCID: <https://orcid.org/0009-0008-1963-5037>

⁴ Prof., Institute of Building Materials, Concrete Construction and Fire Safety (iBMB), Technische Universität Braunschweig, Germany

e-mail: J.Zehfuss@ibmb.tu-bs.de, ORCID: <https://orcid.org/0009-0004-6547-2479>

⁵ Reserch developer, RISE Research Institutes of Sweden & Adjunct senior lecturer, Lund University

e-mail: robert.mcnamee@ri.se, ORCID: <https://orcid.org/0000-0002-0380-9548>

⁶ Associate Professor, Department of Civil and Environmental Engineering (DICA), Politecnico di Milano, Italy

e-mail, patrick.bamonte@polimi.it, ORCID: <http://orcid.org/0000-0002-4967-1089>

⁷ Prof., Liege University, Belgium

e-mail, jm.franssen@uliege.be, ORCID: <https://orcid.org/0000-0003-2655-5648>

this concept nevertheless forms the base of many fire regulations, probably because of the unwritten but accepted hypotheses that:

- 1) For a given type of member, either be it a steel, a timber, or a reinforced concrete member, increasing its FRR will result in a better performance in a real fire that may occur in the future, no matter what this fire may be.
- 2) Different types of members, either be it a steel, a timber, or a reinforced concrete member, which have the same FRR will have a similar performance in a real fire.

Whereas there is no reason to question the first hypothesis, the second one is already questionable if only the eventuality of collapse during the heating phase of a fire is considered. Real fires which are more severe or less severe than the standardized fire curve may affect different types of members in a different manner. Spalling in concrete, kinetics of the chemical reactions of intumescent products, charring rate in timber [2] may indeed be influenced differently by a variation of the fire temperature history compared to that of the standardized fire curve.

There are other reasons which may indicate that the second hypothesis is particularly questionable if the fire curve involves a descending branch, which is always the case in a real fire, and the structure has survived the heating phase of the fire:

- the fact that some types of members have their temperature decreasing nearly as soon as the fire temperature decreases whereas others experience a temperature increase for a significant time after the peak of the fire curve, at least in the central zones of the section [2, 3],
- the fact that some materials recover their strength or part of it when they cool down whereas others have an irreversible loss of mechanical properties [4],
- the fact that some materials are not severely affected when the temperature in the central zones of the section reach levels around 400°C whereas others may be severely affected or destroyed for much lower temperatures.

Because of these differences, the FRR may not give a good indication of the capability of a member to survive a fire that comprises a decay phase.

Yet, if the structure collapses during the decay phase or, even worse, during the cooling phase when the fire is completely down, this poses a significant hazard for both the occupants who may not have evacuated and for the firefighters and rescue services who may still be on the scene.

The concept referred to as "burnout resistance" addresses the challenge of load-bearing members having to withstand a complete fire event. This concept is the central focus of an international research program which aims to establish a methodology to describe the performance of structural members more accurately, namely throughout the entire duration of a fire. The goal of this research is to provide the necessary tools for designing non-protected timber members that maintain stability during the entire duration of the fire, until the end of the cooling phase.

This paper presents the result of 5 experimental fire tests performed in 2023 on full scale glue laminated timber columns in a compartment constructed at the Fire Testing Centre of CERIB in France where the fire source consisted of wood cribs.

2 PREVIOUS WORKS

2.1 Numerical simulations

To complement the concept of FRR, Gernay proposed an alternative normalised fire curve to characterise the behaviour of structural members subjected to a fire that comprises a heating and a decay phase [5]. This concept called DHP is based on the parametric fire model of Eurocode 1 in which the time factor Γ is taken as 1 (and the heating phase being thus very close to that of the ISO 834 curve). The DHP of a structural member is the duration of the heating phase of the longest parametric fire model that the member can be subjected to without collapse, even after an infinite duration. A parametric fire with a duration of the heating phase shorter or equal to the DHP will be survived by the member; whereas, if

the duration of the heating phase is longer than the DHP, the member will collapse, either in the heating phase, in the decay phase or even in the cooling phase (when the temperature in the compartment is back to ambient).

Gernay performed numerical simulations with the software SAFIR® [6] on timber columns, using thermal and mechanical properties of Eurocode 5 [7] assumed during cooling to be fixed at the value of the maximum temperature. His conclusion was that the DHP of timber columns varies from 20% to 50% of their FRR [3]. In other words, a timber column with a FRR of 60 minutes will not survive a parametric fire if the heating phase is longer than 30 minutes. In some conditions, collapse can occur during the decay or the cooling phase if the heating phase has been slightly longer than only 12 minutes.

2.2 Experimental tests under parametric fire curves

Experimental tests were performed at the Technische Universität Braunschweig on 8 similar 3.72 meters long glued laminated timber columns with a section of $280 \times 280 \text{ mm}^2$ which were supported hinged-hinged (Euler case 2) [8]. The applied load of 322 kN amounts to 15% of the load bearing capacity of 2160 kN measured at ambient temperature on a companion specimen of the same production. The FRR was first determined by two tests as 55 and 58 minutes, slightly shorter than the 60 minutes which were estimated (on the base of declared resistance class) by the simple model of Eurocode 5 with a charring rate of 0.70 mm/min and a zero-strength layer of 14 mm. The other specimens were subjected to the parametric fire of Eurocode 1 with heating phase of various durations. Two columns subjected to a heating phase of 15 minutes followed by a decay phase with a constant rate of -10.4 K/min collapsed after 98 and 153 minutes. Two columns subjected to a heating phase of 10 minutes survived the complete fire duration and the long cooling phase which followed. These results are within the range estimated by the numerical simulations of reference [3].

2.3 Experimental tests under wood crib fires

Tests were performed on similar columns at the Fire Testing Centre of CERIB, in France, in a compartment built for this purpose, with dimensions $L \times l \times H$ of $6.00 \times 4.00 \times 3.10 \text{ m}^3$, various opening factors and various fire loads. The length of the columns was 3.60 m, five of them with the same section as the tests performed in Braunschweig, one with the section increased to $340 \times 340 \text{ mm}^2$, and one with the section increased to $360 \times 360 \text{ mm}^2$. The load was maintained at 322 kN for all tests. The main results of the tests are presented in Table 1 in which T_{\max} refers to the maximum in time of the average temperature in the compartment. More details are given in [9] (the value of 90 minutes given for Test 12 in [9] is a typing error).

Table 1. Main results of the previous tests with wood crib fires [9]

Test	A [mm ²]	T _{max} [°C]	End of heating phase [min.]	Collapse [min.]
9	280 × 280	1 000	30	71
10	280 × 280	1 150	30	47
11	280 × 280	1 200	29	35
12	340 × 340	1 150	28	87
13	360 × 360	1 180	30	>98 ^(*)
14	280 × 280	600 ^(**)	36	66
15	280 × 280	1 250	40	37

^(*)Instability of the loading system, ^(**)1 000°C during the first 7 minutes

Figure 1 presents the evolution of the average temperature (from 9 plate thermometers) in the compartment as a function of time, up to the moment of failure of the column in each test.

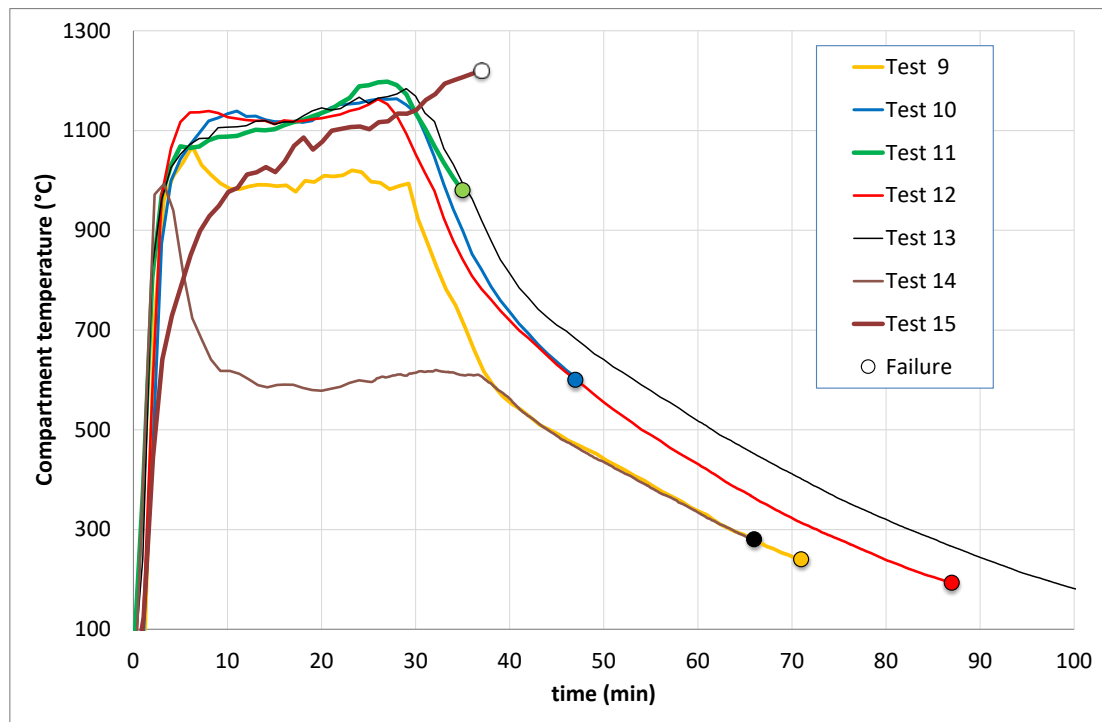


Figure 1. Evolution of the temperature in the compartment for 7 tests in timber columns

These tests confirmed that timber columns can fail during the decay phase of a fire, not only in the controlled environment of a furnace, but also in a naturally vented compartment in which the fire load is made of wood cribs. It has yet to be noted that, except for test 14 performed with a reduced fire load, the temperatures in the compartment in the heating phase were higher than those of the ISO curve. Nevertheless, failure in the decay phase was also observed for this test 14 and for test 12 where the section had been increased by 47%.

3 NEW SERIES OF TESTS

3.1 Modification of the compartment temperature

From the observation that the temperature in the heating phase was higher than the ISO curve in most of the tests described in Section 2.3, a new test (Test 17) was performed on the $280 \times 280 \text{ mm}^2$ section with a modified fire load. Instead of wood cribs made of 10 layers of 5 sticks of $90 \times 90 \times 1\,000 \text{ mm}^3$ spaced by 138 mm, the cribs were now made of 5 layers of 5 sticks of $120 \times 120 \times 1\,000 \text{ mm}^3$ spaced by 100 mm, while the total fire load was maintained at 780 MJ/m^2 and the opening factor at $0,065 \text{ m}^{1/2}$. The total amount of heptane used in the initial phase of the fire was also reduced from 18 liters to 3 liters. In this Test 17, collapse occurred after 45 minutes, whereas the compartment temperature kept on increasing until 915°C , reached after 55 minutes when the decay phase started.

It would be interesting, from a fire dynamics point of view, to examine how the compartment temperature development was influenced by the type and amount of fire load and by the value of the opening factor, and eventually by the wind intensity and direction with respects to the openings. Yet, in this paper, the focus is on the structural behaviour of the timber columns. This is why Figure 2 shows the average compartment fire development for the 6 tests made on similar $280 \times 280 \text{ mm}^2$ columns subjected to the same loading up to the moment of collapse of the specimen.

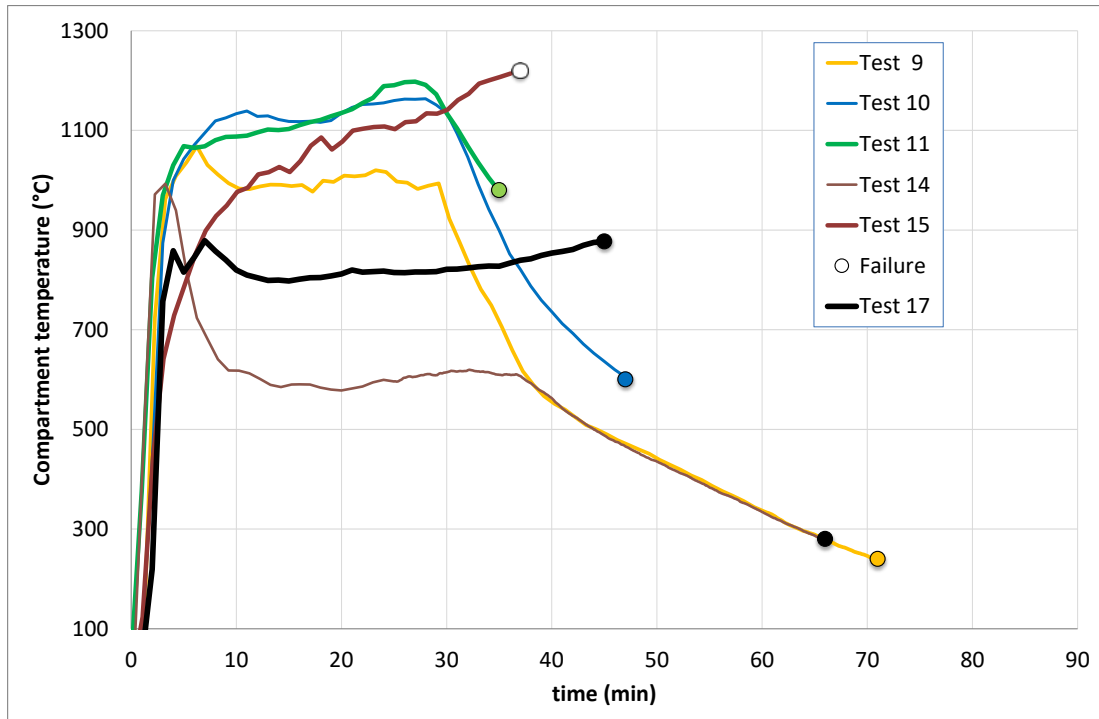


Figure 2. Evolution of the temperature in the compartment for the 6 tests on $280 \times 280 \text{ mm}^2$ sections

These results form a unique set of results on similar specimens subjected to different compartment fire histories and should form a statistically meaningful base for the development of a calculation method for timber columns subjected to physically based fires. This is at least the case if the compartment temperature is the main driving parameter of the temperature development in the section and, hence, of the structural behaviour. The evolution of oxygen concentration has also been measured and is given for this test 17 in Figure 3. The detailed results for all tests are available on the web site “burnout-resistance.eu”.

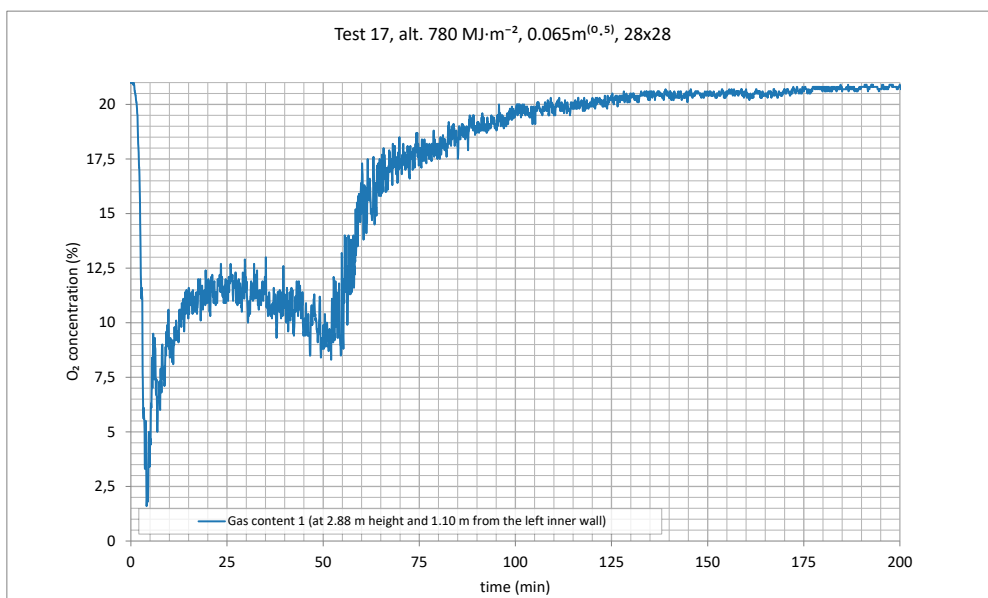


Figure 3. Evolution of the oxygen concentration in the compartment for test 17

3.2 Tests with increased section size

Three tests were then performed with a section increased to $400 \times 400 \text{ mm}^2$, based on numerical modelling predictions made with SAFIR[®] indicating that this size would be sufficient for the column to survive the

fire after the end of the decay and the cooling phase. The cross-sectional area was thus more than doubled compared to the reference section of $280 \times 280 \text{ mm}^2$ while the intensity of the load was kept the same.

Test 18 was performed with the same fire load arrangement and fire load density (780 MJ/m^2) and the same opening factor ($0.065 \text{ m}^{1/2}$) as the reference case of test 10. The compartment temperature reached $1\ 080^\circ\text{C}$ after 12 minutes, then increased to $1\ 200^\circ\text{C}$ after 31 minutes when the decay phase started. The column seemed to be surviving the whole fire duration when collapse occurred suddenly 11 hours and 28 minutes after the beginning of the test, at a time when the compartment temperature was at 34°C .

It has yet to be mentioned that a defect in the construction of the specimen had been detected before the test in the form of a longitudinal gap between two halves of the column as can be seen in Figure 4-a. This gap, which was as much as 35 mm deep in some places was filled with an intumescent product for a length of 69 cm on one side and 197 cm on the other side. This did not save the situation as can be seen by the local glowing visible in Figure 4-b at mid-level of the column, and by the difference in residual sections visible on Figure 4.c when the two halves of the column have been separated after the test. In this Figure, the vertical dark line in the centre of each half is the groove which contained the wires of the thermocouples located inside the section.

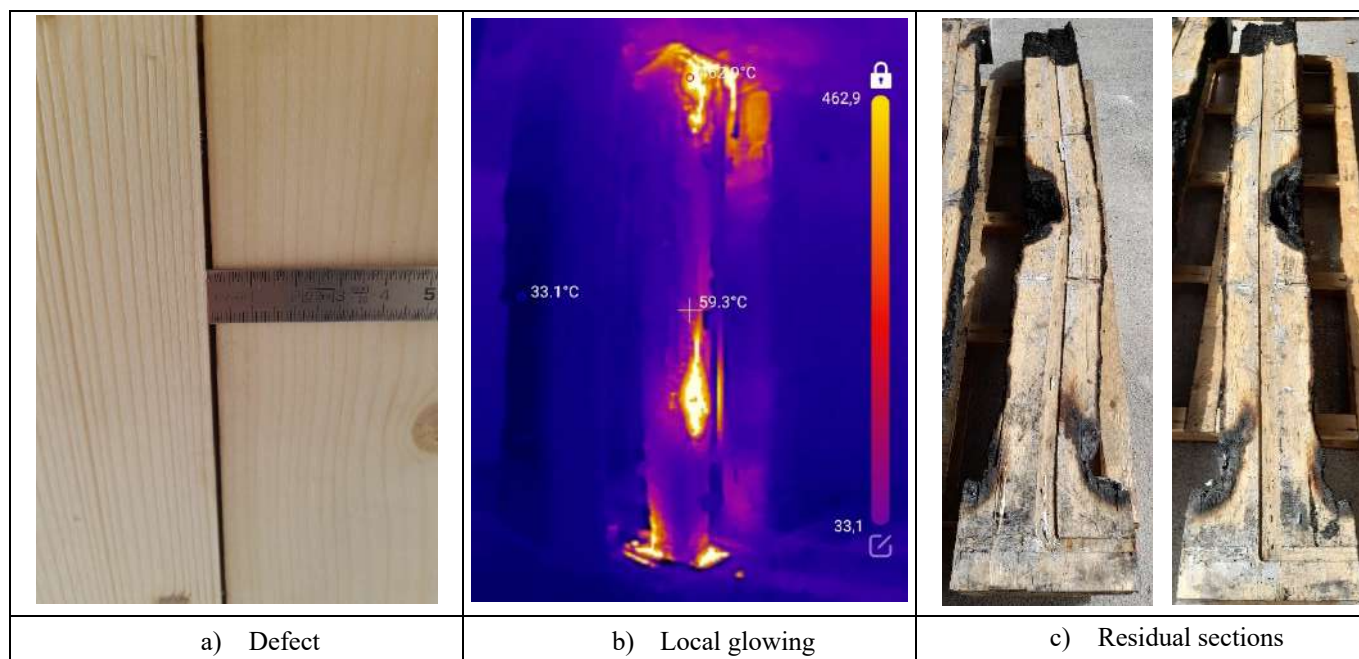


Figure 4. Test 18 specimen before, during and after the fire test

It may be questioned whether any structural member would remain uninspected for more than 11 hours in a real fire event. Still, this test highlighted the detrimental influence that defects in gluing planes of GLT sections can have in case of fire, and the importance to have a deep inspection of the structure as soon as possible after a fire and not to neglect the dramatic consequences that local glowing may have on its stability; a fast extinction seems to be a must.

Test 19 was performed under the same compartment conditions as test 18 and on a $400 \times 400 \text{ mm}^2$ section, but on a specimen that did not contain any thermocouple inside the section. This was to eliminate the possibility to have a defect in the gluing plane of the two halves of the column and to rule out the hypothesis that, even without any visible defect, this gluing plane may be different from the gluing planes that nevertheless exist between all lamellae of the GLT, and would perhaps be a weak point in the specimen. This also eliminated any possible negative influence of the groove and of the thermocouple wires.

The compartment temperature reached $1\ 050^\circ\text{C}$ after 5 minutes, then increased to $1\ 170^\circ\text{C}$ after 27 minutes when the decay phase started. The column seemed to be surviving the whole fire duration when collapse

occurred suddenly 16 hours and 18 minutes after the beginning of the test, at a time when the compartment temperature was at 28°C.

After the test, it was observed that charring and combustion of the section have been much more severe at the foot of the column than in the rest of the column as can be seen in Figure 5 which presents the foot of the column before and after the test. Note that late failure of structural timber members due to continued smouldering have been reported by other authors; [10]: “Scenario 2 collapsed 29 h after the onset of heating; this was attributed to continued smouldering within the slab after the fire had effectively burned out within the compartment ”; [11] “Structural failures due to smouldering were studied, including the formation of holes in the ceiling and encapsulation, and the collapse of a column. ”.

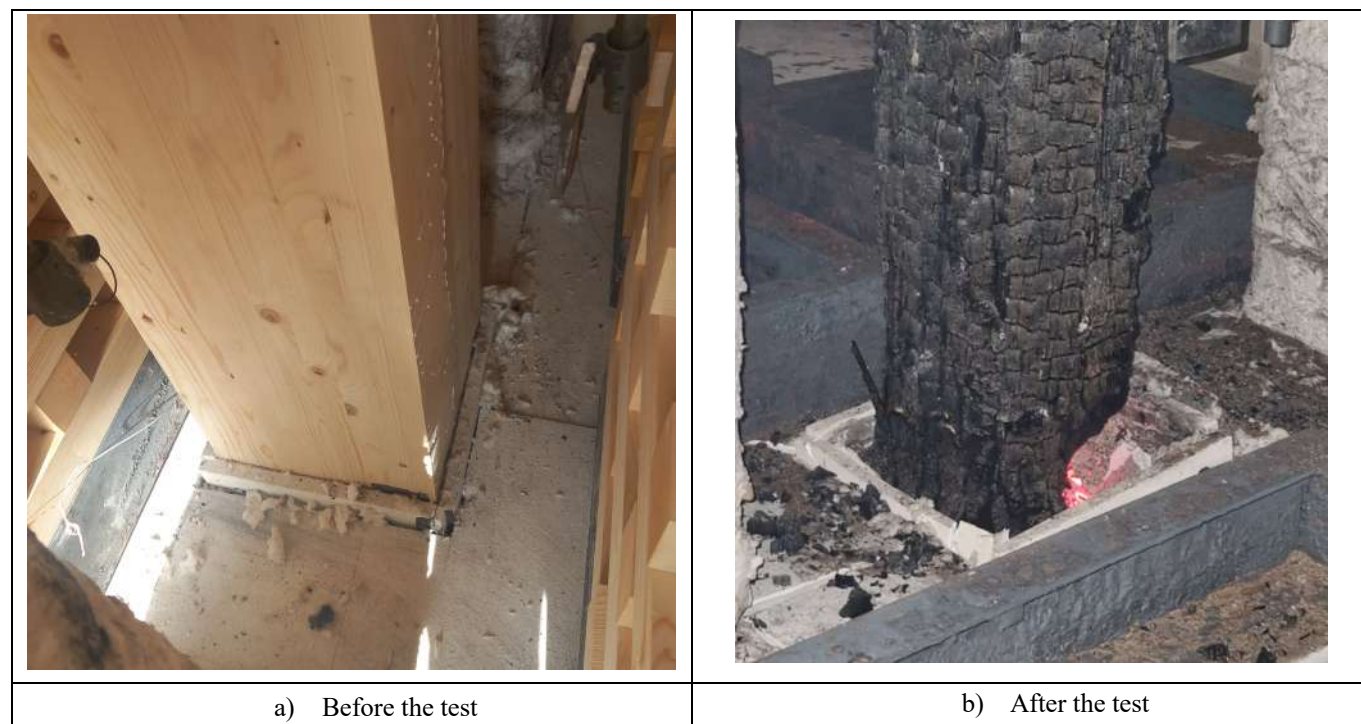


Figure 5. Foot of the column of Test 19

Figure 6 shows the residual section of the column after the test at different heights after the charred layers had been removed. Whereas around 0.08 m² of the initial section of 0.16 m² remained for most of the sections, there remained only 0.035 m² of it at the base of the column.

After this test 19 had shown the detrimental effect of the extensive charring at the base of the column, examination of pictures from test 18 showed that this effect may have been present also in this test, see Figure 4-b, although it was overwhelmed in this case by the more severe influence of the local defect at mid height of the column.

The reason for this extensive charring and combustion at the foot of the columns are not known. Possible leads are:

- Extensive radiation from the ambers of the fire load laying on the floor.
- Radiation from the floor surface (although the same effect should exist from the ceiling, which was not the case).
- Gravity current of fresh air containing oxygen flowing on the floor.

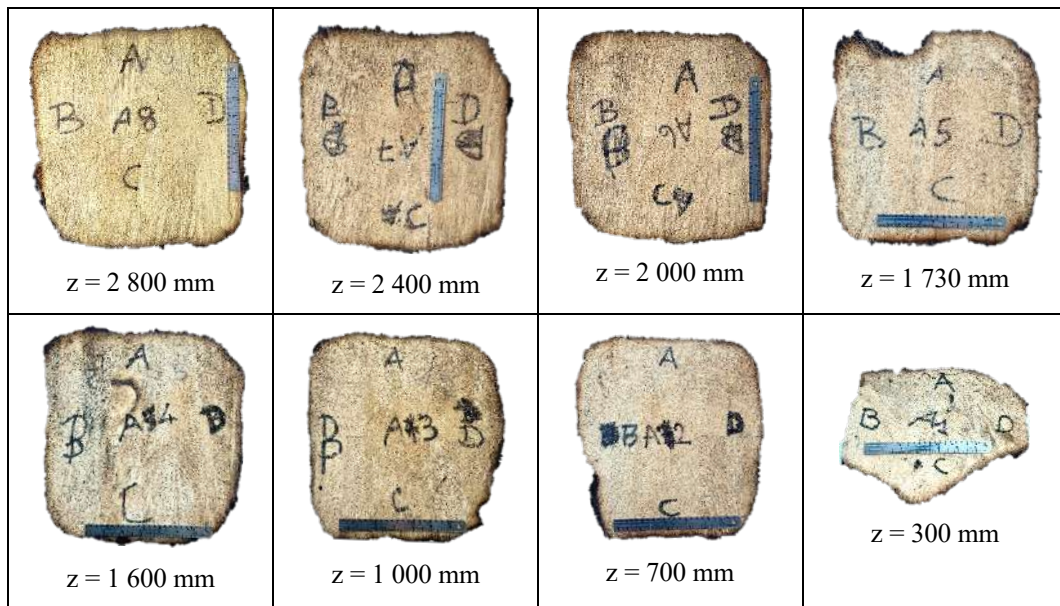


Figure 6. Residual sections of Test 19 at different heights

Test 20 was performed in an attempt to reach survival to the complete burnout. The effect of an increased cross section of $400 \times 400 \text{ mm}^2$ and of reduced compartment temperatures by using thicker sticks of $120 \times 120 \text{ mm}^2$ were combined, while the opening factor of $0.065 \text{ m}^{1/2}$ and fire load of 780 MJ/m^2 were maintained.

The average temperature in the compartment varied between 770°C and 850°C for 59 minutes when, at 780°C , the decay phase started. The column seemed to be surviving the whole fire duration when collapse occurred suddenly 12 hours and 18 minutes after the beginning of the test, at a time when the compartment temperature was at 34°C with, again, a severe reduction of the section at the base of the columns, as can be seen in Figure 7.



Figure 7. Foot of the column of Test 20 after the test

Figure 8 shows as full lines the compartment temperature evolution in the three tests to which the $400 \times 400 \text{ mm}^2$ sections survived for more than 11 hours before collapsing due to local intense charring and combustion.

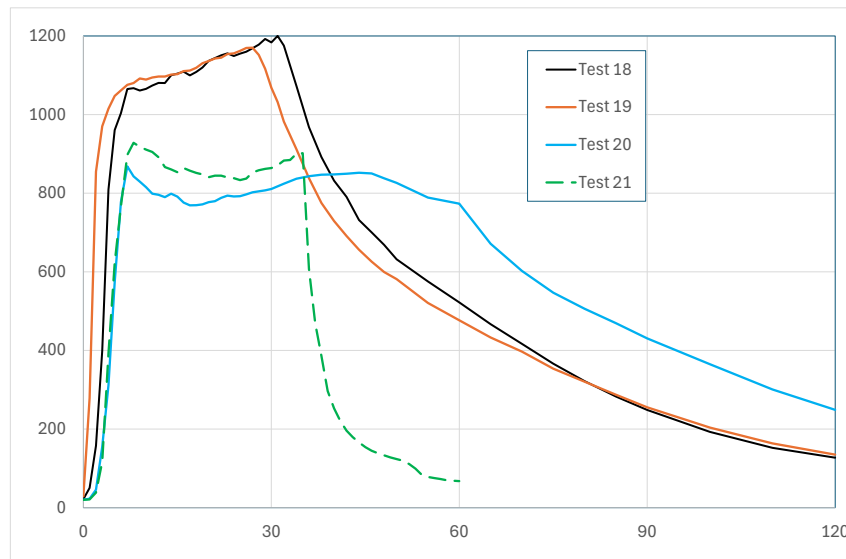


Figure 8. Compartment temperature for tests on $400 \times 400 \text{ mm}^2$ sections (full lines) and for Test 21 (dotted line)

3.3 Fire fighters intervention

Test 21 was performed as a repetition of test 17 in which failure occurred after 45 minutes, but with an intervention of fire fighters planned after 35 minutes. At this time, fire fighters sprayed water in the compartment from the outside with a water hose to extinguish the wood cribs, then sprayed the column and finally entered in the compartment to scratch the charred layers away from the column. The amount of water used in the intervention was 1 m^3 . Figure 8 shows, as a dotted line, the rapid decrease of the compartment temperature that was measured immediately after the beginning of the intervention. The column did not collapse.

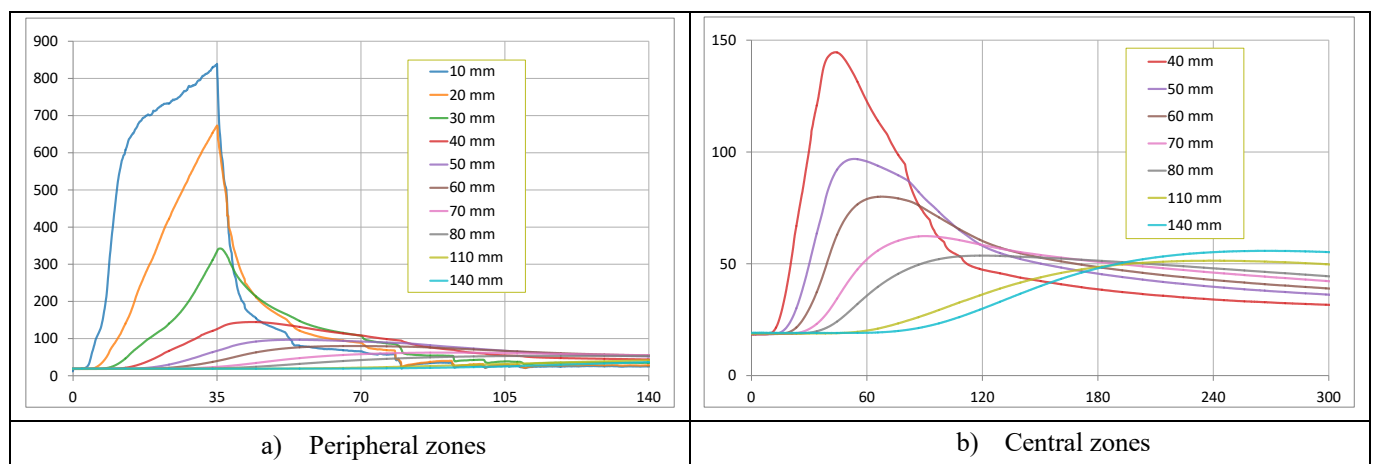


Figure 9. Temperature evolution in the section of tests 21 at different depths

Figure 9 shows the evolution of the temperature inside the section with each curve being the average of 6 measurements, two at three different heights. Figure 9-a shows that the temperatures inside the section at a depth of 10, 20 and even 30 mm from the surface decrease nearly immediately after the intervention. It must be noted that these distances are with respect to the initial geometry of the section and the section may have shrunk and the surface have cracked during the first 35 minutes of the fire. Figure 9-b shows that,

on the contrary, temperatures continued to increase in the central zones of the section, and the time of the maximum value was all the more important that the depth was important. At the centre of the section, at a depth of 140 mm, it took more than 4 hours for the temperature to reach its maximum, notwithstanding the fact that a layer of char estimated (from Figure 9 a) at 30 mm had been removed, taking away with it the thermal energy that it contained, and reducing the distance from the central zones to cold air. Despite this continued heating of the inner part of the section, this test showed that the intervention of the fire fighters was successful in achieving resistance to full burnout of the timber column.

3.4 Summary

The main parameters and results of the new series of tests are summarized in Table 2 whereas Figure 10 gives an overview of all tests made in this research work in a naturally vented compartment.

Table 2. Main results of the new tests with wood crib fires

Test	A [mm ²]	Tmax [°C]	End of heating phase [min.]	Collapse [min.]
17	280×280	915	55	45
18	400×400	1 200	31	686
19	400×400	1 170	27	978
20	400×400	850	45	738
21	280×280	900	35 ^(*)	-

*fire fighter intervention

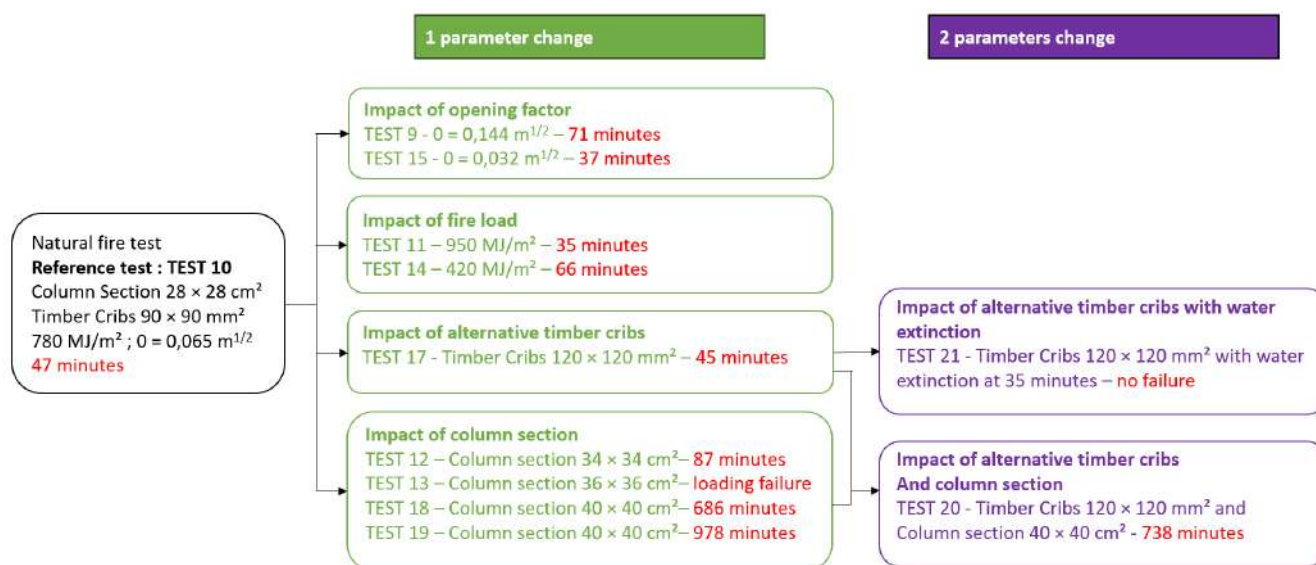


Figure 10. Overview of the tests made in a naturally vented compartment

4 CONCLUSIONS

This paper describes five new experimental tests performed in a naturally vented compartment on full scale glue laminated columns.

Two tests were on specimens of 280 × 280 mm² cross-section. In the first test, the column collapsed after 45 minutes, still in the heating phase of the fire. In the other test, the fire was extinguished after 35 minutes and the column did not collapse.

Increasing the section from $280 \times 280 \text{ mm}^2$ to $400 \times 400 \text{ mm}^2$ allowed the three next specimens to survive for more than 11 hours, well after the decay phase of the fire. Yet, all three specimens collapse at a later stage, slightly after 11, 12 and 16 hours, due to an extensive charring and combustion that developed locally at the base of the columns and, in one test, at mid-level due to a defect in the construction of the specimen. These experimental results form, with those previously reported, a significant and well documented basis for the development of design methods which should ensure that, when required, non-encapsulated timber columns can survive to the complete duration of a real fire or a physically based fire model.

The reasons for the intensive localised charring observed in three tests is still investigated. A point of great interest is whether such phenomena would occur in a real fire in a real building. These results nevertheless indicate that a thorough inspection of the whole structure should be undertaken without any delay after the decay phase of the fire and that any glowing area should be extinguished as soon as possible, which corroborates recent findings from other full-scale experiments.

A rapid extinction of the fire and of the combustible structure is of course beneficial, although the optimum operational procedures still remain to be established if the amount of timber members involved is significant and it may not be possible to dedicate all required attention to all of them immediately as was the case here.

ACKNOWLEDGMENT

The support from the French Federation of insurers FRANCE ASSUREURS is gratefully acknowledged.

REFERENCES

1. Eurocode 1: Actions on structure – Part 1-2: General actions – Actions on structures exposed to fire, CEN Brussels, 2002.
2. Bartlett, A, Hadden, R, Bisby, L & Law, A: Analysis of cross-laminated timber charring rates upon exposure to non-standard heating conditions. *Fire Mater*, 667-681, 2015.
3. Gernay, T: Fire resistance and burnout resistance of timber columns, *Fire Safety Journal*, 122, 2021.
4. Li, YH, Franssen, JM: Test results and model for the residual compressive strength of concrete after a fire. *Journal of Structural Fire Engineering*, 2(1), 29-44, 2011.
5. Gernay, T, Franssen JM: A performance indicator for structures under natural fire, *Engineering Structures*, 100, 94–103, 2015.
6. Franssen, JM, Gernay, T: Modeling structures in fire with SAFIR®: Theoretical background and capabilities. *Journal of Structural Fire Engineering*, 8 (3), 300-323, 2017.
7. Eurocode 5: Design of timber structures Part 1.2: General – Structural Fire Design, CEN, Brussels, 2004.
8. Gernay, T, Zehfuß, J, Brunkhorst, S, Robert, F, Bamonte, P, McNamee, R, Mohaine, S, Franssen, JM: Experimental investigation of structural failure during the cooling phase of a fire: Timber columns, *Fire and Materials*, doi: 10.1002/fam.3110, oct. 2022
9. Robert, F , Franssen, JM, Zehfuß, J ,Brunkhorst, S ,Bamonte, P, Renard, S ,McNamee, R, Gernay, T: Natural fire tests on GLT columns including the cooling down phase, in World Conference on Timber Engineering (WCTE 2023), Oslo, Norway, 2023, p. 1848-1854. doi: 10.52202/069179-0244.
10. Wiesner, F., Bartlett, A., Mohaine, S., Robert, F., McNamee, R., Mindeguia, J. C., & Bisby, L. (2021). Structural capacity of one-way spanning large-scale cross-laminated timber slabs in standard and natural fires. *Fire Technology*, 57(1), 291-311.
11. Mitchell, H., Amin, R., Heidari, M., Kotsovinos, P., & Rein, G. (2023). Structural hazards of smouldering fires in timber buildings. *Fire safety journal*, 140, 103861.

PROBABILISTIC MODELLING OF WOOD CHARRING RATES: A PARAMETRIC STUDY AND NEXT STEPS

Jakub Šejna¹, Dominik Štraus², Kamila Cábová³, František Wald⁴

ABSTRACT

This paper presents a parametric study of the probabilistic modelling of wood charring rate under the various fire scenarios, building on prior research on wood pyrolysis and the development of charred layer. Using room corner test setups, the study assesses different thermal loads on wood columns to determine charring depths. By a probabilistic approach, it analyses the evolution of charred layer on spruce columns, considering thermal load a stochastic methodology derived from earlier studies. The main idea is to verify the PyCiF model on presented data, which aims to accurately predict charred layer without relying on traditional isotherm 300°C. This method accounts for the variability of the properties of wood over time under different thermal conditions. The findings of numerical analyses and the comparison of parametric studies with standard methods offer information for refining probabilistic models of the development of the charred layer in timber columns. In addition, this work prepares the knowledge for subsequent research on different types of fire effects on wood behavior and therefore represents a step forward in the field of fire safety engineering of timber structures.

Keywords: Wood Charring; Probabilistic Modelling; Fire Safety; Room Corner Test; Timber Structures.

1 INTRODUCTION

In recent years, wood has emerged as a preferred construction material due to its sustainability and environmental friendliness. With the increasing application of wood in the construction industry, ensuring adequate fire resistance is paramount. A major challenge lies in determining the depth of charring during fires, as the rate of charring is not constant [1]. A probabilistic approach is considered necessary for more accurate estimations [2], particularly under realistic natural fire conditions [3]. Despite the availability of various calculation methods, simplified or prescriptive models often do not account for the variable nature of fire conditions and the dynamic properties of wood [4]. Enhanced accuracy in calculating charring depths is critical for optimizing the wood structure fire resistance in natural or orientated fires.

This study introduces a parametric investigation into the evolution of the charring layers in wood columns under orientated fire conditions, building on and expanding the research conducted by Šejna [5] on modelling wood pyrolysis in room corner tests (RCT). Full-scale fire experiments using RCT were used to simulate orientated fire scenarios, which are crucial to monitoring the initial response of wood to fire and

¹ Jakub Šejna, Department steel and timber structures, Faculty of Civil Engineering, Czech technical university in Prague, Czech republic, e-mail: jakub.sejna@fsv.cvut.cz, ORCID: <https://orcid.org/0000-0002-9968-2026>

² Dominik Štraus, Department steel and timber structures, Faculty of Civil Engineering, Czech technical university in Prague, Czech republic, e-mail: straudom@student.cvut.cz,

³ Kamila Cábová, Department steel and timber structures, Faculty of Civil Engineering, Czech technical university in Prague, Czech republic, e-mail: firstname.lastname@address, ORCID: <https://orcid.org/0000-xxxx-xxxx-xxxx>

⁴ František Wald, Department steel and timber structures, Faculty of Civil Engineering, Czech technical university in Prague, Czech republic, e-mail: firstname.lastname@address, ORCID: <https://orcid.org/0000-xxxx-xxxx-xxxx>

the development of the charred layer. These experiments offer invaluable insights into the behavior of wood under travelling fire conditions.

Following a previously conducted parametric study that explored the temperature evolution in spruce columns under various thermal stresses and sample locations, this investigation utilizes the findings to further examine the evolution of pyrolysis. Using a probabilistic analysis, this study scrutinizes the development of a charred layer on spruce columns, informed by heat load data derived from prior parametric analyses. Through extensive statistical examination, it evaluates numerous factors affecting charred layer formation and probabilistically assesses the fire safety of timber structures. This approach underscores the significance of probabilistic methodologies in the advancement of wood fire safety.

The paper concludes by detailing the results, focusing on charring rates and the development of char layers through probabilistic methods underpinned by experimental RCT data. The aim of this paper is to elucidate insights from numerical calculations and to outline subsequent steps to advance probabilistic models of charred layer evolution in timber columns. This includes considerations of incident heat flux, wood moisture content, heat and water vapor transport through wood, and even air oxygen levels, thereby setting the stage for future research endeavors.

2 CHARRING RATE

2.1 Advancing from Deterministic to Stochastic Modelling

The need for stochastic models, which account for the randomness of parameters, is evident despite their complexity. Studies by Pečenko et al. [6], [7], [8] have gone into stochastic analyses of wood burning, considering variables such as thermal properties and boundary heat flux coefficients, but relying on simplified models for charred layer determination. Determining the charred layer, the position of the 300 ° C isotherm is often used; However Pečenko and Hozjan [7] highlight its variability depending on the temperature curve. The PyCiF model [9], which combines wood pyrolysis with a "heat-mass" model. Mass conservation equations for bound water and mass conservation equations for bound water vapor more accurately determine the depth of charring without the need to use the 300 ° C isotherm. The model has been successfully validated for both standard and natural fires, providing precise results compared to experimental data.

Hietaniemi [2], on the basis of Mikkola's foundational equations [10], developed an advanced probabilistic approach to calculate the charring rate of wood. This methodology uniquely incorporates varying factors such as heat flux, oxygen concentration, and humidity, employing probability distributions to model these variables. Such an approach allows for the consideration of wood's heterogeneous properties over time and under different temperature conditions. Significantly, Hietaniemi's calculation method extends beyond the limitations of standard fire progressions, making it applicable to a broad range of fire scenarios. This versatility is encapsulated in Equation (1), which is not confined to typical fire models but can adapt to diverse fire dynamics.

$$\beta = f(\chi_{O_2,t}) \frac{C \dot{q}_e^n(t)^p}{[(\rho + \rho_0)(A + B\omega)]} \exp\left(\frac{-t}{\tau}\right) \quad (1)$$

where

β	is charring rate [mm·min ⁻¹],
$f(\chi_{O_2,t})$	is a function that characterises the dependence of the charging rate on oxygen concentration [-],
C	is coefficient for the probabilistic approach in the range of [2] [kW·m ⁻²],
$\dot{q}_e^n(t)$	is heat flux through wood as a function of time [kW·m ⁻²],
p	is calculation parameter,
ρ	is wood density [kg·m ⁻³],
ρ_0	is dry wood density [kg·m ⁻³],
A	is coefficient for the probabilistic approach in the range of [kJ·kg ⁻¹],
B	is coefficient for the probabilistic approach in the range by [2] [kJ·kg ⁻¹],
ω	is wood moisture content [%],

t is time [min],

τ is time constant in the [2] range [min].

The Eurocode EN1995-1-2:2005 thermal property values for wood are criticized for their limits in various fire scenarios, prompting the development of more nuanced models. In particular, the PyCiF model by Peenko and Hozjan [7], [9] marks an advance by integrating a thermal mass with a pyrolysis model, bypassing the need for the 300 °C isotherm criterion to determine char depth.

Furthermore, Wade [11], [12] introduced a detailed model considering additional variables such as oxygen concentration and mass loss during burning, although it requires calibration against natural fire experiments. Kamenická et al. [13] contrasted various calculation methods, including those of Mikkola and Hietaniemi [2], highlighting the accuracy of the latter in early fire phase predictions.

The shift towards stochastic models reflects the growing recognition of their necessity in accurately simulating wood burning under fire conditions, acknowledging the limitations of deterministic approaches and the potential of probabilistic analyses to offer more realistic predictions.

3 PROBABILISTIC MODEL OF CHARRED LAYER DEVELOPMENT FOR VERIFICATION OF THE PEČENKO MODEL

Equation (1) was selected as the basis to compare the results of the previous numerical CFD model [5] with the probabilistic evaluation of the charred layer. CFD models and the effect of pyrolysis are described by Šejna [5]. This solution is justified by the different approach used by [2] in defining the input parameters for the probabilistic approach, which includes a set of coefficients. According to Equation (1), the charring rate shows an initial increase followed by a decrease, a phenomenon attributed to the insulating properties of the charred layer. This relationship and its implications are illustrated in Figure 1. In this investigation, the Python programming language was used for the numerical calculations. For example, it takes approximately 51 mins to perform 100,000 calculations.

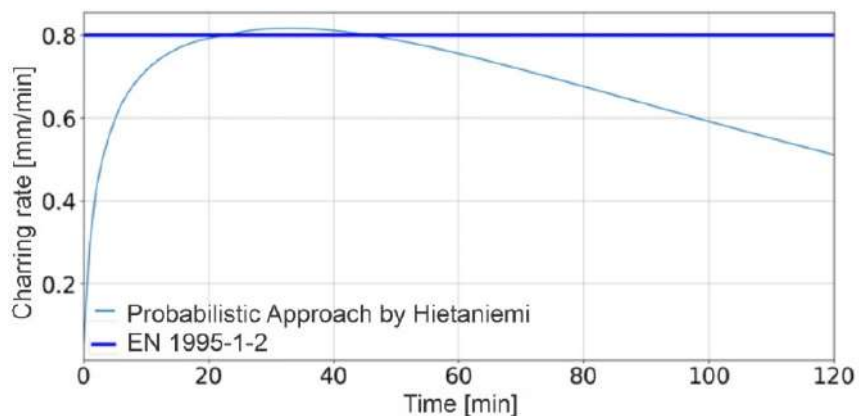


Figure 1 Comparison of the development of the charring rate in the standard approach and the probabilistic approach according to Hietaniemi [2]

Initially, it was necessary to import the necessary equations and determine the basic parameters, including the calculation duration, the structure of the data table and other basic definitions. Subsequently, Equation (1), which represents the formula of the charring rate defined by Hietaniemi [2], was incorporated into the calculation of the development of the charred layer. To ensure the completeness and precision of this equation, all probabilistic values given in [2] were incorporated.

3.1 General calculation

The computational model was developed initially applied to simulate a comprehensive general state that encompasses all potential factors that may arise in a fire scenario. Before the parametric study was conducted, the model was tested using the nominal standard temperature curve. This curve provided a benchmark for

verifying the accuracy of our model setup, as the expected charring rate curve for this specific temperature profile is well established. According to observations and as shown in Figure 1, the charring rate initially escalates rapidly, but then starts to decrease. This decrease is attributed to the insulating properties of the charred layer, which increasingly impedes the fire's ability to penetrate the raw wood.

In Figure 2, the results of 100 such calculations are compared against the standard charring rate defined by EN 1995-1-2 [4], represented by a thick blue dashed line in the figure. This comparison reveals that the charring rate, as defined by Hietaniemi [4], initially increases as the raw wood begins to burn but then slows down because of the formation of a protective charred layer. Of the 100 numerical calculations performed as part of this calculation, the average depth of the charred layer was found to be 110 mm. This depth variance, both below and above normative values, underscores the complexity of accurately predicting the development of the charred layer in fire scenarios.

However, it is important to note that the rate of charring is also affected by the potential development of the charred layer. If parts of this layer fall off, the raw wood underneath will remain exposed and unprotected, which can lead to a renewed increase in the charring rate. The analysis of the charred layer, as shown in Figure 3, is based on the same computational model. This Figure presents that the increase in the depth of the charred layer is more gradual compared to the conventional approach where an initial approximation of the charred layer is usually made. The graph shows that in some cases the values set by the standard norms were not only not met but in other cases exceeded. Out of the 100 runs performed as part of this calculation, the average depth of the charred layer was found to be 110 mm. This depth variance, both below and above the standard values, highlights the complexity of accurately predicting the development of the charred layer in fire scenarios.

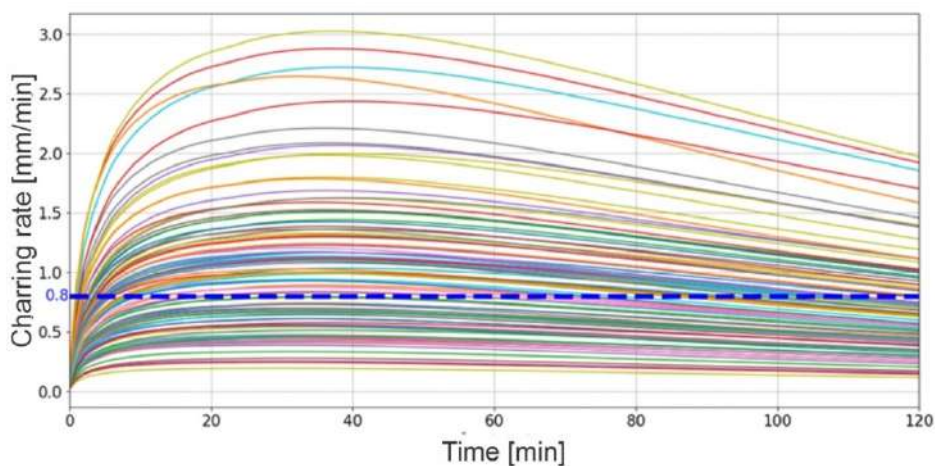


Figure 2 Comparison of the development of the charring rate considering the probabilistic variation of the wood properties [2]

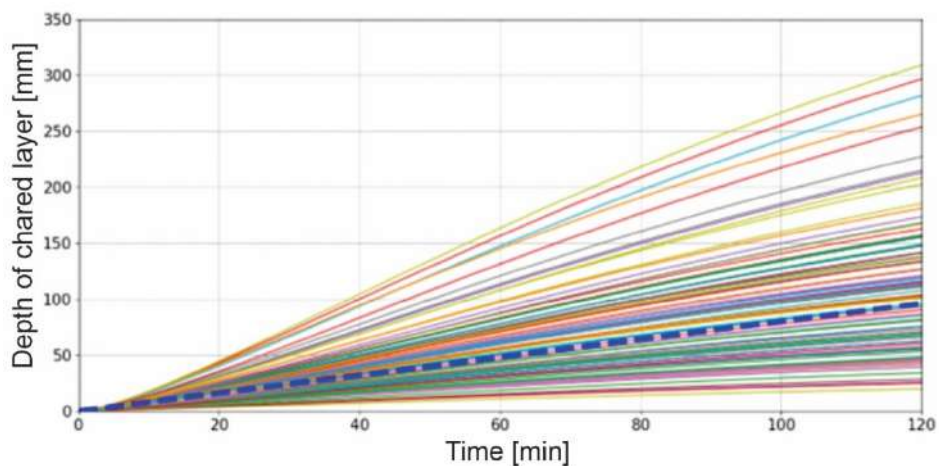


Figure 3 Calculated charred layer for 100 calculations in relation to Figure 2

3.2 Refinement of the General Model

The comparison of the numerical calculations involved comparing the calculated values of the charred layer with the values obtained by experimental measurements. This comparison focused primarily on the final depth of the charred layer, as it provides a key indicator of the applicability and accuracy of the model in different segments of the column. Examination of the numerical model focused primarily on the means and variances within the charred layer.

Temperature profiles observed by thermometer sensors during the experiment were included to refine the calculations. The aim of this crucial step was to align the model with the actual temperature conditions of the fire. However, it should be noted that one of the thermometers stopped working at the 28th minute of the experiment. This factor was considered in the final analysis.

The temperatures for the calculation of the charring rate to adjust the computational model were taken from an experiment in an RCT where 3 spruce columns were placed. The exact positioning of the members of the experiment is shown in Figure 4.

The sand propane burner located in the corner of the furnace served as the heat source. To observe the development of the differential temperature, both experimental setups were repeated. Column 1, which was closer to the burner in each arrangement, received the most heat. The burner power was consistently set at 100 kW for the first 10 minutes, then increased to 300 kW for the next 20 minutes, for a total of 30 minutes of each experiment.

The thermocouples type K were placed to measure a range of temperature values at various depths and heights. Specifically, they were embedded below the wood surface at depths of 5, 15, 25, and 50 mm. For the columns, these measurements were taken at heights of 1000 and 1920 mm.

In addition to measuring the temperature within the timber elements, the gas temperature in the RCT fire tests was meticulously recorded using a thermocouple tree (TC tree) and additional thermocouples placed on the ceiling and above the burner, as mandated by the RCT fire test standard. The TC tree was equipped to measure temperature data at seven different heights within the furnace, ranging from 0.67 to 2.1 m.

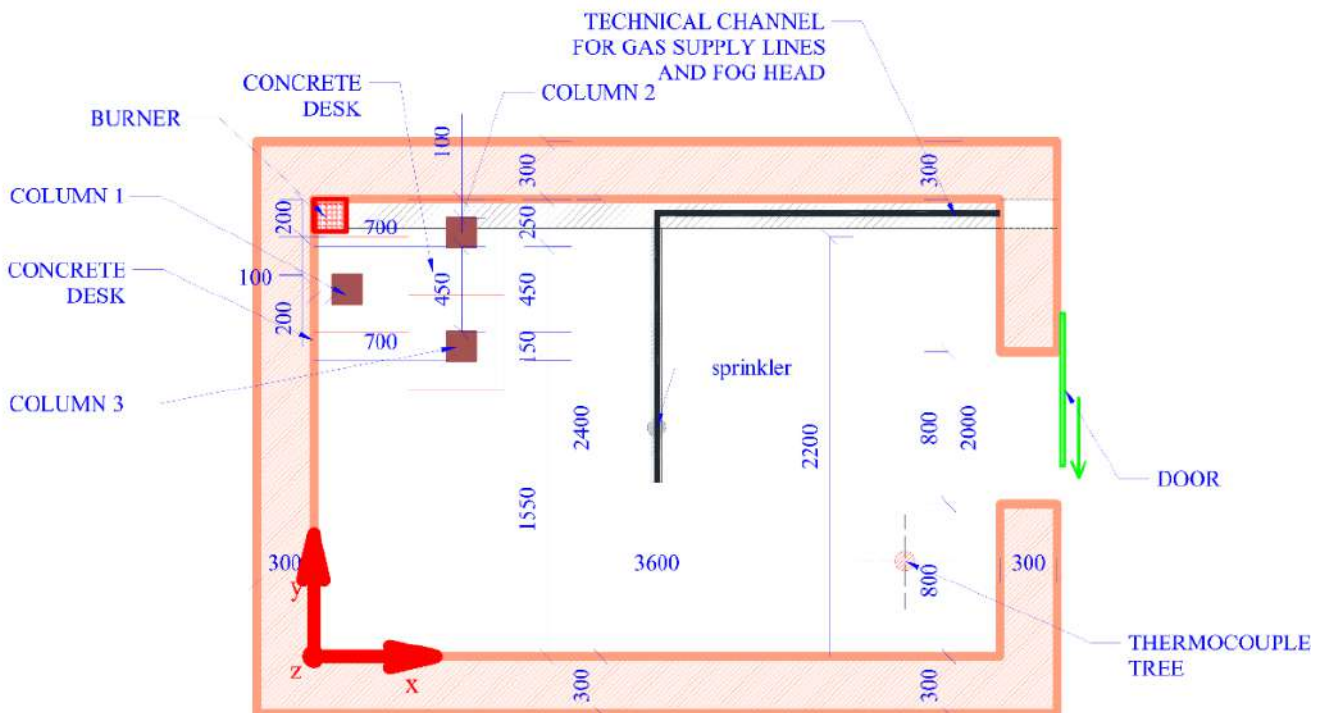


Figure 4 Floor plan of experiment

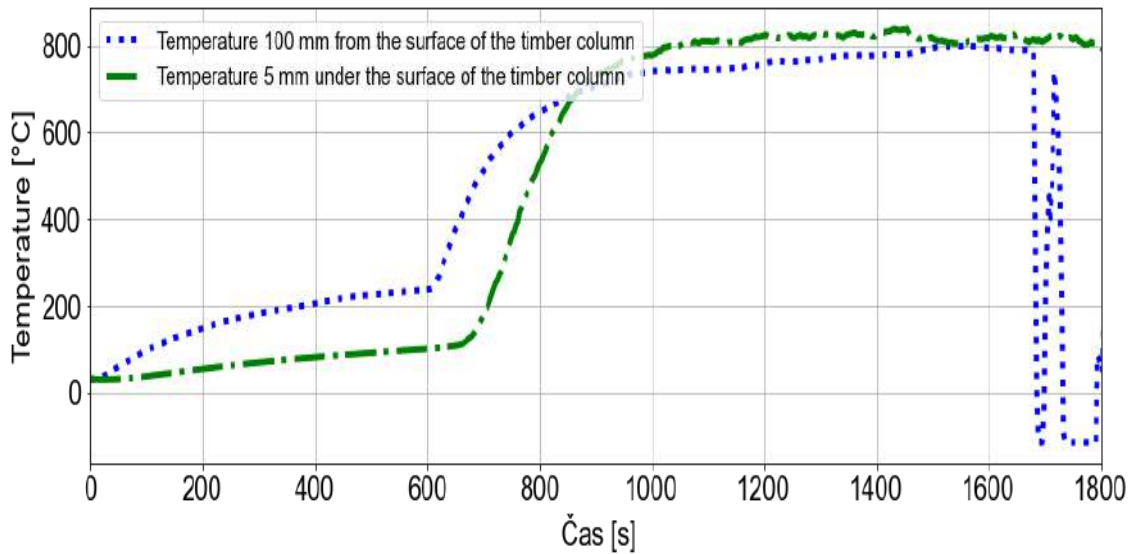


Figure 5 Temperatures measured in the experiment and used for the calculation

Subsequent refinement of the computational model revealed deviations in the charring rate profile and subsequently in the depth of the charred layer compared to the general model. These deviations are attributed to the different temperature behaviour observed during the fire. For example, while the standard temperature curve reached approximately 680 °C during the first 10 minutes, the experimental temperature only increased to approximately 240 °C. Figure 6 shows the charring rate calculated by the numerical model considering the temperature data from the experiment. It should be noted that during the first 10 min the charring rate did not follow the typical charring rate, even at its maximum. The average charring rate in the 10th minute based on 100,000 calculations was 0.15 mm·min⁻¹ with a standard deviation of 0.07 mm·min⁻¹. At the 28th minute, the average value increased significantly to 0.88 mm·min⁻¹ with a standard deviation of 0.52 mm·min⁻¹. Minimal charring depth was observed during the initial phase of the fire. However, in the following phase, which was characterized by an increase in burner power and consequent furnace temperatures, the charring layer developed more rapidly. This relationship is illustrated in Figure 7, which shows the calculated charring depth using a numerical model that includes experimental temperature data.

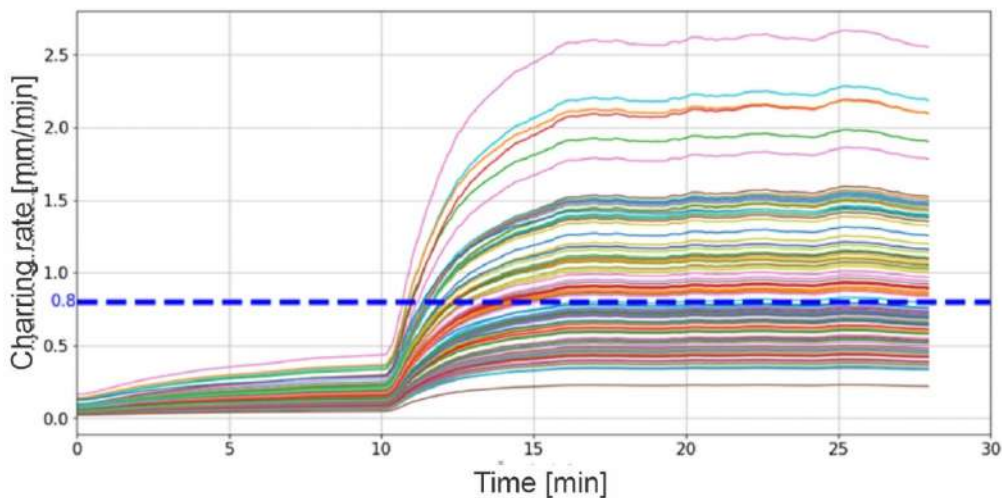


Figure 6 Graph shows 100 calculations of the charred layer according to the procedures defined by [2] for the experimental temperature profile compared to the normal charred layer profile

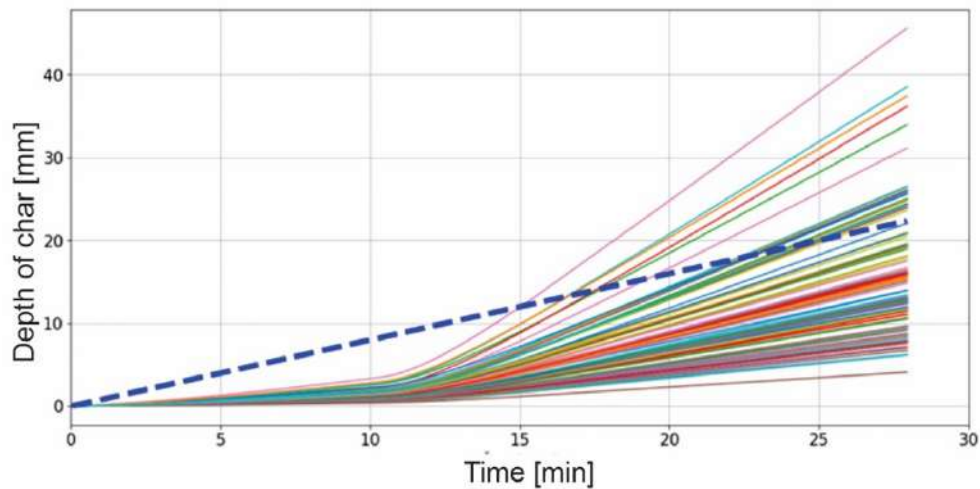


Figure 7 The graph shows 100 calculations of the charred layer according to the procedures defined by [2] for the experimental temperature profile compared to the normal charred layer profile

In this model, the average charring depth at the 10th min, based on 100,000 calculations, was 1.17 mm with a standard deviation of 0.54 mm. By the 28th min, the average depth had increased significantly to 15.76 mm with a standard deviation of 8.93 mm. These results underscore the dynamic nature of the carbon layer evolution in response to fluctuations in furnace temperature.

3.3 Probabilistic model of charred layer development for verification of the PyCiF model

For the parametric study that examined the impact of the fire scenario, different burner powers were used, but the layout of the experiment remained the same as in [5]. The aim was to induce various types of fires that would differ over time. Its intention was to achieve fire scenarios with varying development rates, different lengths of the descending phase, and other characteristics. In all simulations, the same maximum burner power of 300 kW was used, which is the same as in the experiment studied [5]. The same maximum powers ensure some comparability of the results.

The first simulation (Study 1) is the same as the experiment studied [5], that is, for the first 10 minutes the power is 100 kW and for the remaining 20 minutes the power is 300 kW. The second simulation (Study 2) only differs in the duration of the initial phase, where the power is set to 100 kW for 20 minutes and for the remaining 10 minutes the power is 300 kW. These simulations represent fires with only an increasing phase. The third simulation (Study 3) is a model with a power of 300 kW. The fourth and fifth simulations (Study 4 and 5) simulate a fire including its descending phase, where the original power of 300 kW decreases to 0 or 100 kW at different times. The sixth simulation (Study 6) simulates a fire with increasing and decreasing phases.

The temperatures calculated from the CFD models considering the individual burner settings are shown in Figure 8. These are the temperatures directly above the burner, which were supplied to the solved computational model. This is a parametric study that compares the impact of burner power on the depth of charring and, therefore, it was possible to use data from previous research. Figure 8 shows the temperature profiles, which mimic the temperature course calculated according to [5]. These are not the exact values measured during their calculations, but a simplified course defined by a linear progression of temperatures they measured. The temperature profile follows the temperature profile calculated by the FDS programme, where the maximum temperatures at different times are preserved, and these peaks are connected by linear equations. This approach is sufficient for sensitivity analysis as the result should show the effect of burner performance on the final charring depth.

Into the computational model, simplified temperature courses were sequentially entered, for which mean values and standard deviations were then calculated. These values were then used to evaluate the parametric study. The results are presented in Table 1.

Table 1. Final depth of charred layer at 30 min [mm]

Study	Minimum	Maximum	Mean Value
Study 1	9.36	26.68	18.02
Study 2	6.21	16.83	11.52
Study 3	13.32	38.86	26.09
Study 4	4.45	11.51	7.98
Study 5	7.81	21.37	14.59
Study 6	3.72	9.46	6.59

Figure 9 shows a comparison of the mean values for the simulations calculated in this comparative study. The trend of the charring rate is temperature dependent. From the resulting values shown in Fig. 10, the dependence of the burner power and the resulting charring depth is evident. The charring rate curves partly follow the temperature curves for the wooden members. Even if the same maximum power is set everywhere, the course and duration of the maximum power are also very important, as the resulting charring depths vary in all cases. The highest values are achieved in Study 3, where the burner power is always set to 300 kW. Charring depths range from 13.32 to 38.86 mm. Study 2 and 5 are the opposite, and it is clear from the resulting values that it also depends on when the maximum power is applied. In Study 2, the wood was first burnt at a lower power and a charred layer was formed on the wood; therefore, the maximum power did not have the same effect on the wood as in Study 5, where the unburnt wood was affected by the temperatures of the maximum power of the burner.

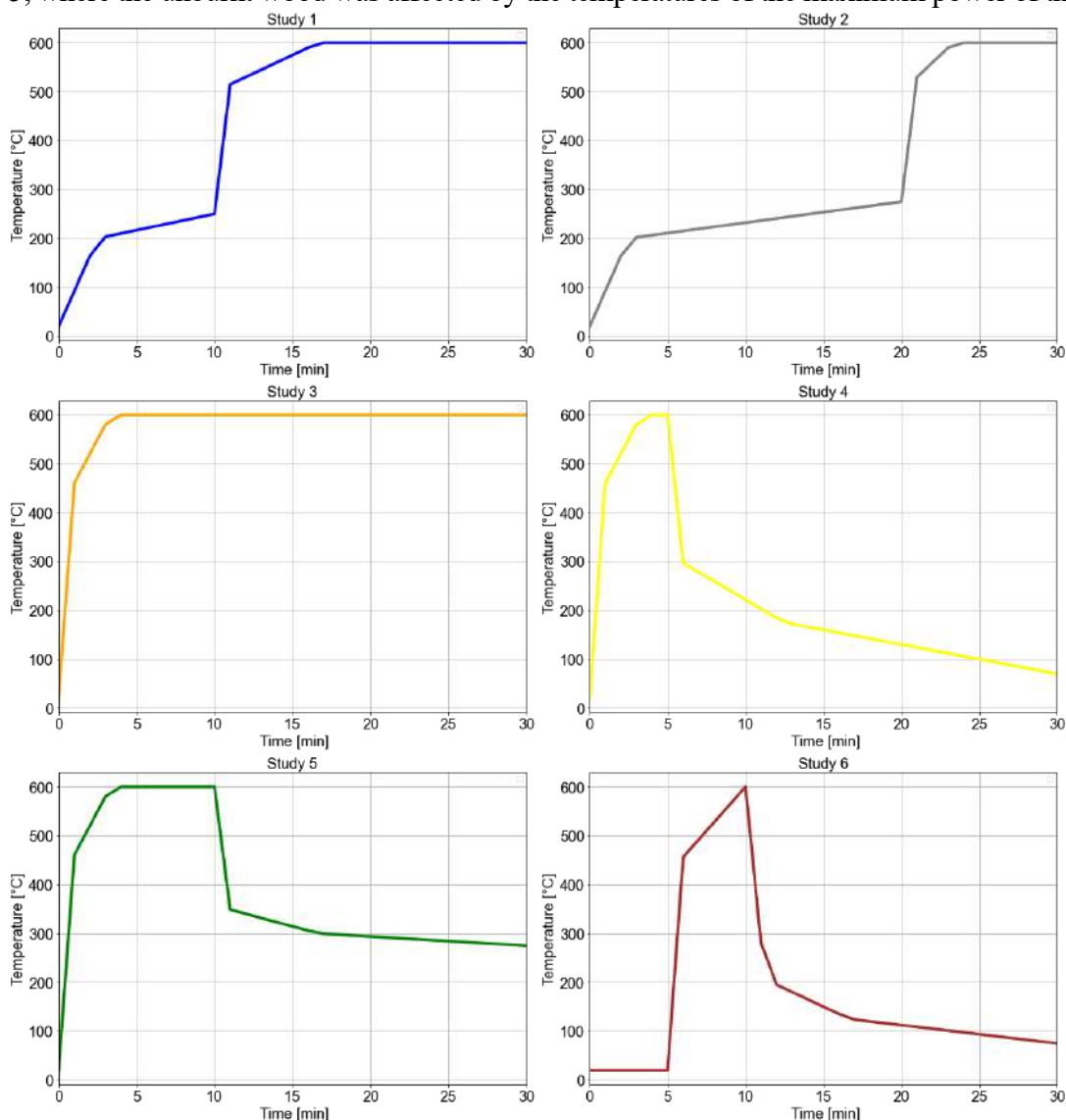


Figure 8 Temperatures chosen for parametric study

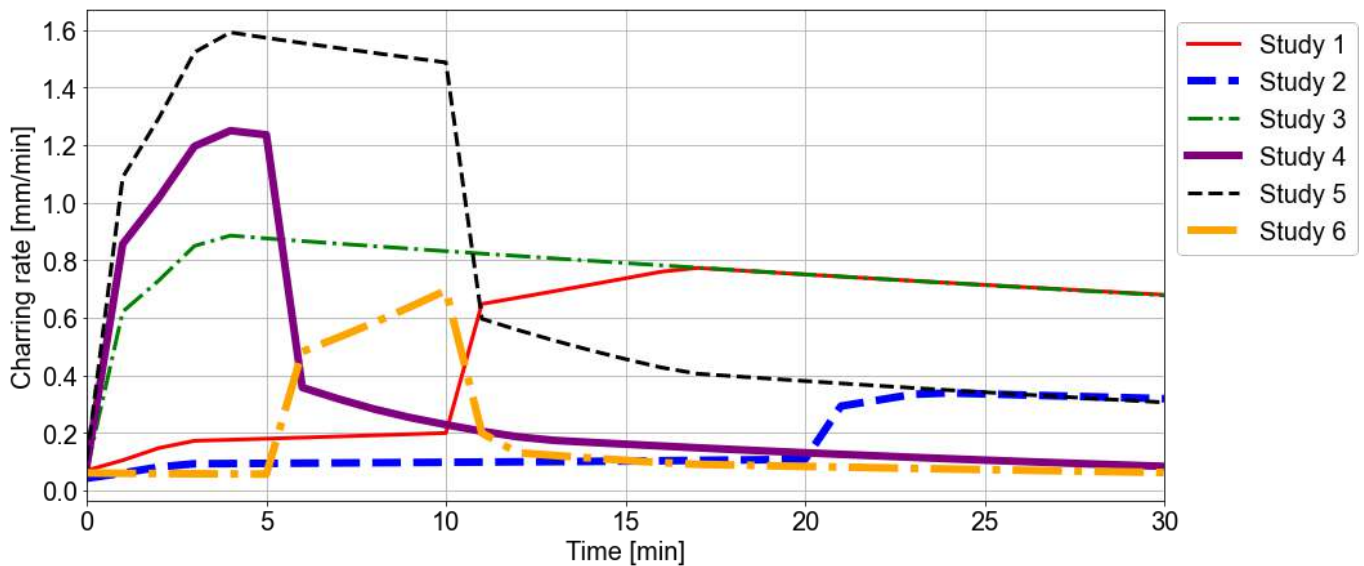


Figure 9 Development of charring rates for individual studies

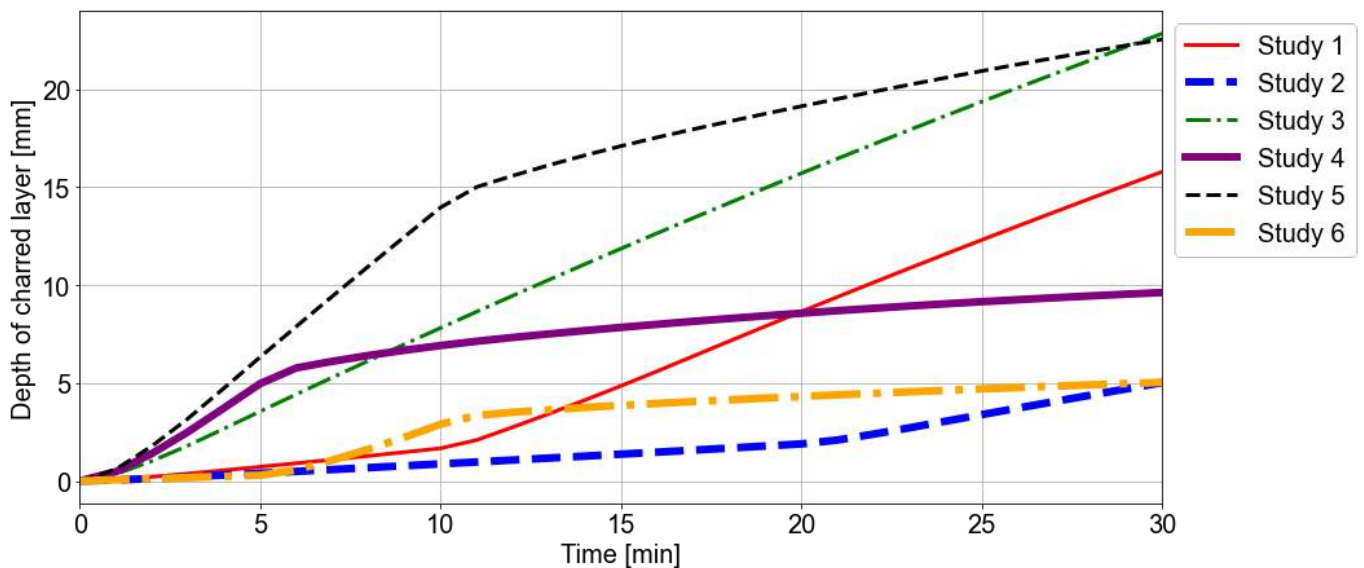


Figure 10 Development of the depth of the charring layer based on the charring rates in Figure 9

4 CONCLUSIONS

Research confirmed the significant effect of fire behavior on burning of wood and noted the influence of various fire parameters. Empirical calculations of charring depth, despite their simplicity, include basic fire characteristics and offer a quick and generally safe method. Advanced methods based on physical principles are essential to accurately model natural fires and understand the temperature distribution in a cross section of wood. Models such as PyCiF, which do not rely on the 300 ° C isotherm criterion, require carefully chosen and calibrated thermal properties of the wood. The exothermic nature of wood combustion and the associated heat generation are key factors in these models.

The study also examines the effect of burner performance on charring rate and emphasizes that even if only one parameter is focused on, other factors such as wood properties, moisture content, and thermal inertia cannot be ignored. These factors have a direct influence on the reaction of the wood and the formation of the charring layer. The parametric study reveals a complex relationship between burner performance, wood temperatures, and other fire parameters.

This study may be valuable for further investigation of a probabilistic approach to determining the charring rates of solid wood members. Subsequent work will focus on comparing the calculated charring rates using different procedures against the developed PyCiF model.

ACKNOWLEDGMENT

This research was funded by Czech Science Foundation, grant GF21-30949K“ Charring of timber under fully developed natural fire – stochastic modeling ”.

REFERENCES

1. Buchanan, A. H., Abu A. K.: Structural design for fire safety. Second edition. Chichester: West Sussex, 2017. ISBN 978-047-0972-892.
2. Hietaniemi, J. A: Probabilistic Approach to Wood Charring Rate. VTT Building and Transport. Julkaisija - Utgivare publisher, 2005, 2005(1), 1-54. ISSN 951-38-6583-5.
3. PEČENKO, R., HOZJAN T.: A novel approach to determine charring of wood in natural fire implemented in a coupled heat-mass-pyrolysis model. *Holzforschung*. 2021, 75(2), 148-158. ISSN 1437-434X. doi:10.1515/hf-2020-0081
4. EN 1995-1-2. Eurocode 5: Design of timber structures - Part 1-2: General - Structural fire design. 2. 2020.
5. Šejna, J., Cábová K., Pečenko R., Hozjan T., Křišťanová M., Wald F.: Validation of a virtual room corner fire test with spruce members and the development of the char layer. In: Proceedings of the 12th International Conference on Structures in Fire. Hong Kong: The Hong Kong Polytechnic University, 2022, s. 1093-1102.
6. Pečenko R., Svensson S., Vensson, Hozjan T.: Modelling heat and moisture transfer in timber exposed to fire. *International Journal of Heat and Mass Transfer*. 2015, 87, 598-605. ISSN 00179310. doi:10.1016/j.ijheatmasstransfer.2015.04.024
7. Pečenko R., Planinc I., Laninc, Svensson S., Vensson, Hozjan T.: Implementing coupled heat and moisture transfer model in the fire analysis of timber beams. *Fire Safety Journal*. 2019, 107, 170-178. ISSN 03797112. doi:10.1016/j.firesaf.2018.11.007
8. Huč S., Pečenko R., Hozjan T.: Predicting the thickness of zero-strength layer in timber beam exposed to parametric fires. *Engineering Structures*. 2021, 229. ISSN 01410296. doi:10.6028/NIST.TN.1842
9. Pečenko, R., Hozjan T., Huč S.: Modelling charring of timber exposed to natural fire. In: *Journal of Wood Science*. 2023, , s. 14. ISSN 1611-4663. doi:10.1186/s10086-023-02091-4
10. Mikkola E.: Charring Of Wood Based Materials. *Fire Safety Science*. 1991, 3, 547-556. ISSN 18174299. doi:10.3801/IAFSS.FSS.3-547
11. Wade C. A.: A theoretical model of fully developed fire in mass timber enclosures. Department of Civil and Natural Resources Engineering, 2019. Doctoral Thesis. University of Canterbury, Christchurch, New Zealand.
12. Wade, C.A., Hopkin D., Spearpoint M., Fleischmann Ch.: Calibration of a coupled post-flashover fire and pyrolysis model for determining char depth in mass timber enclosures. In: Proceedings of the 11th International Conference on Structures in Fire (SiF2020). Brisbane, Australia: The University of Queensland, 2020. ISBN 9781742723433. doi:10.14264/20b5cf6
13. Kamenická Z., Sandanus J., Blesák L., Cábová K., Wald F.: Methods for Determining Charring rate of timber and their mutual comparison. *Wood Research*. 2018.

STUDY ON THE FIRE DESIGN METHOD OF TIMBER MEMBERS TREATED WITH SURFACE PLASTERING APPLICATION

Lingzhu Chen¹, Xi Chen², Qingfeng Xu³, Mingqian Wang⁴, Yubing Leng⁵, Fuwen Zhang⁶

ABSTRACT

Timber members in the Chinese traditional timber buildings are commonly protected with surface plastering treatment. Their fire design methods are not currently available. This paper presents an experimental and theoretical study aimed at evaluating the fire performance of timber beams and columns treated with surface plastering application exposed to three-side and four-side standard fire conditions. Twenty-two fire tests were carried out including ten fire tests on timber beams and twelve fire tests on timber columns. Test parameters include surface treatment type, fire exposure duration and geometry. Timber members protected with surface plastering treatment exhibited different surface charring characteristics with unprotected timber member. The finish paint of the surface plastering application began to peel off after being exposed to fire for 20 minutes, and a white covering appears after being exposed to fire for 40 and 60 minutes. Charring depth was measured for all specimens after tests and charring rate was calculated. Result shows that the surface plastering treatment significantly reduced the charring rate of the timber. A simplified method based on the reduced cross-section method is proposed to determine the charring rate and fire resistance of timber members treated with surface plastering application.

Keywords: Fire design method; surface plastering application; charring rate; timber members

1 INTRODUCTION

There are a large number of traditional timber structures existing in Asia that contain important historical and cultural values, which are also an important carrier for the inheritance of human civilization. As timber is combustible, fire is one of the main disasters faced by traditional timber structures. Famous buildings such as Yuanzhi Temple in China, Chongli Gate in South Korea, Notre Dame Cathedral in Paris, and the National Museum in Brazil have all suffered serious fires, causing a large amount of property loss, which

¹ Professor-level senior engineer, Shanghai Key Laboratory of Engineering Structure Safety, Shanghai Research Institute of Building Sciences Co. Ltd, Shanghai, China.

e-mail: 20040392chen@163.com, ORCID: <https://orcid.org/0009-0009-5588-7829>

² Professor-level senior engineer, Shanghai Key Laboratory of Engineering Structure Safety, Shanghai Research Institute of Building Sciences Co. Ltd, Shanghai, China.

e-mail: chenxi@sribs.com

³ Professor-level senior engineer, Shanghai Key Laboratory of Engineering Structure Safety, Shanghai Research Institute of Building Sciences Co. Ltd, Shanghai, China.

e-mail: xudingfeng73@163.com, ORCID: <https://orcid.org/0000-0002-2679-7498>

⁴ Senior engineer, Shanghai Key Laboratory of Engineering Structure Safety, Shanghai Research Institute of Building Sciences Co. Ltd, Shanghai, China.

e-mail: glulam_wmq@163.com, ORCID: <https://orcid.org/0000-0001-5445-7389>

⁵ Senior engineer, Shanghai Key Laboratory of Engineering Structure Safety, Shanghai Research Institute of Building Sciences Co. Ltd, Shanghai, China.

e-mail: leng_yb@163.com

⁶ Professor-level senior engineer, Shanghai Key Laboratory of Engineering Structure Safety, Shanghai Research Institute of Building Sciences Co. Ltd, Shanghai, China.

e-mail: zhangfuwen@sribs.com

is unrecoverable. Therefore, study on fire resistance performance of traditional timber structures is an important task for the protection of cultural heritage buildings worldwide [1].

The fire performance of modern timber structures has been carefully studied by many researchers through experimental and theoretical analysis. Fire design method based on the reduced cross-section method was commonly accepted for timber structures worldwide [2], such as design codes in Europe, the United States, China and Australia. Charring performance of timber is an important factor for the fire performance of timber members. Therefore, many studies are focused on the charring properties of timber. Cone calorimeter tests and fire tests were commonly employed to investigate the charring properties of timber. Tran et al. [3], White et al. [4, 5], Yang et al. [6], Frangi et al. [7] and Xu et al. [8] studied the charring performance of timber, and test results showed that the charring depth was approximately linearly related to the fire exposure time, and the charring rate tended to be constant with the increase of the fire duration. The charring rate is also related to timber species, density, and moisture content. It was found that the charring rate decreased with the increase of moisture content and density. Tsantaridis et al. [9] found that fire-proof gypsum board can delay the time when timber begins to charring. Nussbaum et al. [10] and Zhang et al. [11] studied the charring performance of timber treated with fire retardant coating, and pointed out that fire retardant coating have a certain improvement on the fire performance of timber. Zhang et al. [12, 13] and White et al. [14] conducted a study on the charring performance of timber members coated with fire retardant coatings on the surface. The results showed that fire retardant coatings can delay the start time of charring, and the charring rate of timber members is significantly reduced after applying fire retardant coatings.

For the fire performance of timber members, Ni et al. [15], Xu et al. [16] and Chen et al. [17] studied the fire resistance performance of timber beams exposed to three-side fire through fire tests, and results showed that the lower corner of the timber beams became curved due to charring from two directions, and the vertical charring rate was slightly higher than the horizontal charring rate. The fire resistance rating of timber beams exposed to three-side fire decreased significantly with the increase of load ratios and increased with the increase of cross-sectional size under the same load ratio. Lange et al. [18] studied the effect of different fire development curves on the fire performance of glulam beams exposed to three-side fire, and pointed out that the fire resistance rating of timber beams was relatively small when exposed to a rapid fire. Li et al. [19], Malhotra et al. [20], Ali et al. [21], and Chen et al. [22] studied the fire resistance rate of timber columns subjected to fire on all four sides. The study showed that the fire resistance rating of timber columns decreased significantly with the increase of load ratios and increased with the increase of cross-sectional size under the same load ratio. Xu et al. [23] conducted a study on the fire resistance rating of timber beams protected with fire retardant coatings when exposed to three-sided fire. The study showed that the fire resistance rating of the timber beams was slightly improved. However, Malhotra et al. [20] pointed out that the effect of surface application of fire retardant coatings or flame retardant treatment on the fire resistance rating of timber columns is not significant. Xu et al. [16] and Li et al. [19] conducted tests on the fire resistance rating of timber beams treated with lime plaster exposed to three-side fire and timber columns exposed to four-side fire. The results showed that lime plaster can greatly improve the fire resistance rating of timber beams and columns.

Despite many fire tests carried out to study the fire performance of modern timber structures, there are few results available in the literature for fire performance of traditional timber structures. Timber members in the Chinese traditional timber buildings are commonly protected with surface plastering treatment, as shown in Figure 1(a). The commonly used craftwork of surface plastering treatment is craftwork of one hemp fibre and five plastering application, as shown in Figure 1(b), which is made of brick ash, blood, lime, white flour, soil seeds, camphor tree, raw oil, light oil, ash oil, oil filling, and fibre. The surface plastering application was supposed to protect the timber members from fire and erosion like fire retardant coating for steel structures. Wang et al. [24] conducted a study on the effect of surface plastering treatment on the fire resistance rating of round timber columns. The study showed that all columns exhibited buckle failure and the fire resistance rating of round timber columns increased with the surface plastering treatment. Chen et al. [25] studied the fire performance of timber beams with surface plastering treatment. Bending failure was observed for all timber beams, and the fire resistance rating of timber beams was also found increased with the surface plastering treatment. The post-fire performance of timber beams and columns were also

studied by Xu et al.[26, 27]. Despite fire tests have been conducted to study the fire performance of timber members with surface plastering treatment, their fire design methods are not currently available, which is crucial for the preventive protection of traditional timber buildings.

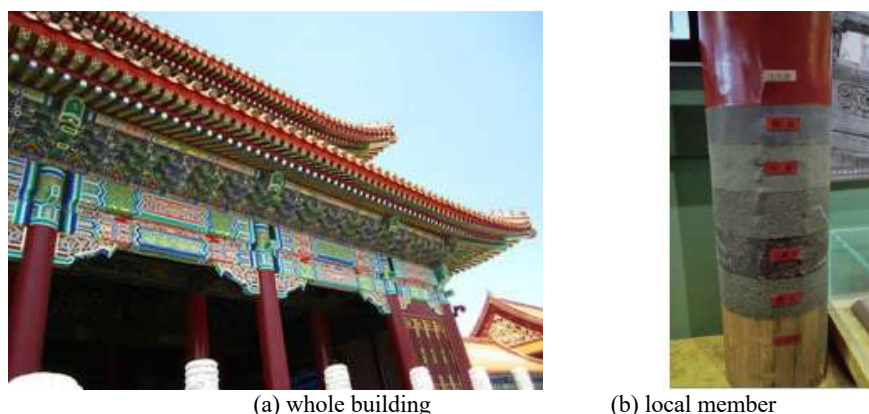


Figure 1. The craftwork of one hemp fibre and five plastering application

In this context, the objective of this paper is to develop a fire design method for timber members treated with surface plastering application based on the analysis of experimental results. The charring performance of timber members with surface plastering treatment was carefully studied with fire tests and a fire design method based on reduced cross-section method was proposed for timber members with surface plastering treatment.

2 EXPERIMENTAL PROGRAMME

2.1 Test specimens

In total, ten timber beams and twelve timber columns were prepared and tested. Parameters including the cross-section dimensions, fire exposure durations, and surface treatment types were considered. Ten timber beams all have an overall length of 2000 mm, and have a cross-section dimensions of 100mm deep×200 mm wide and 200mm deep×400 mm wide, respectively. Twelve timber columns all have an overall length of 600 mm, and have a cross-section dimensions of 200 mm diameter and 350 mm diameter, respectively. These cross-section dimensions are commonly used in traditional timber structures in China, and the length of specimens was taken in consideration of the requirement of loading tests after the fire exposure, which has been introduced in references [26, 27]. The fire exposure durations are 20 mins, 40 mins and 60 mins, respectively. Part of specimens were treated with surface plastering treatment. Table 1 lists the detail information of test specimens.

Table 1. Summary of test specimens

Member type	Specimen No.	Geometry/mm	Surface treatment	fire exposure durations /mins
Timber beams	S100B20	100×200×2000	no	20
	S100B40	100×200×2000	no	40
	S100BII20	100×200×2000	surface plastering application	20
	S100BII40	100×200×2000	surface plastering application	40
	S200B20	200×400×2000	no	20
	S200B40	200×400×2000	no	40
	S200B60	200×400×2000	no	60
	S200BII20	200×400×2000	surface plastering application	20
	S200BII40	200×400×2000	surface plastering application	40
	S200BII60	200×400×2000	surface plastering application	60
Timber columns	S200C20	A200×600	no	20
	S200C40	A200×600	no	40

Table 1. Summary of test specimens

Member type	Specimen No.	Geometry/mm	Surface treatment	fire exposure durations /mins
	S200C60	A200×600	no	60
	S200CII20	A200×600	surface plastering application	20
	S200CII40	A200×600	surface plastering application	40
	S200CII60	A200×600	surface plastering application	60
	S350C20	A350×600	no	20
	S350C40	A350×600	no	40
	S350C60	A350×600	no	60
	S350CII20	A350×600	surface plastering application	20
	S350CII40	A350×600	surface plastering application	40
	S350CII60	A350×600	surface plastering application	60

2.2 Material properties

The wood species of both timber beams and columns is Southern Pine (genus *Pinus*). The measured density and moisture content are 681 kg/m³ and 18.2 %, respectively. The commonly used craftwork of one hemp fibre and five plastering application was employed in the study, which includes one layer of hemp and five layers of ash, with a total thickness about 4 mm.

The craftwork of surface plastering application is divided into six processes: seam catching ash, sweeping ash, using hemp, pressing hemp ash, medium ash, and fine ash, as shown in Figure 2. Five layers of ash are mixed and stirred by a certain mass ratio of raw paint, tile ash, and gypsum powder, and are then evenly applied to the surface of timber members. Table 2 lists the raw material ratio of each layer of ash. Using hemp is to soak the hemp cloth in clean water for two to three minutes, then lay it flat on the top of the sweeping ash, and use a board to press the fluffy hemp to tightly hook the hemp cloth with the sweeping ash.

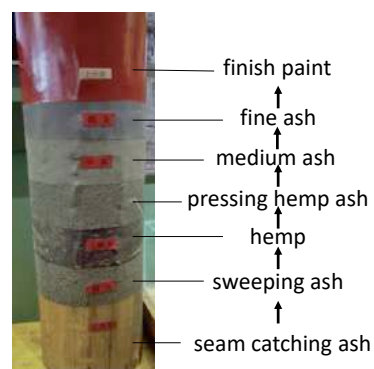


Figure 2. The demonstration of craftwork of one hemp fibre and five plastering application

Table 2. The raw material ratio of each layer of ash

Process name	Mass ratio			
	raw paint	gypsum powder	tile ash	hemp
seam catching ash	1	1	/	/
sweeping ash	1	1	/	/
using hemp	/	/	/	1
pressing hemp ash	1	1	1	/
medium ash	1	1	/	/
fine ash	1	1	/	/

2.3 Test program

Fire tests were conducted in the vertical furnace of Shanghai Key Laboratory of Engineering Structure Safety. All the specimens were placed in the furnace and exposed to an ISO 834 standard fire. The top surface of the beams was protected with mineral wool during the fire exposure to simulate the three-side fire of beams in a real fire, while the timber columns were exposed to fire at four sides. All specimens were heated without load. Following fire exposure for the prescribed time (see in Table 1), the furnace fire was stopped, and specimens were extinguished with water. The residual geometry of the fire-exposed beams and columns was then measured from 50 mm-thick pieces cut from the beams at third points and columns at half point after the charring layer was removed. The difference of the original geometry and the average undamaged geometry was recorded as the charring depth. It is worth to note that, to investigate the influence of the fire on the mechanical performance of timber beams and columns, loading tests were also conducted on these specimens before the measurement of the charring rate. Detail information of the loading test results can be found in references [26] and [27].

3 TEST RESULTS AND DISCUSSION

3.1 Test observation

Figure 3 shows the photos of typical specimens after fire exposure. A charring layer can be observed on the fire-exposed surfaces of all specimens. The charring layer cracked along the longitudinal and transversal directions. A layer of white covering appeared on the surface of the timber members treated with the craftwork of one hemp fibre and five plastering application after exposed to fire. The comparison of charring characteristics among different specimens can be seen in Figure 4, which clearly shows the pyrolysis of the surface plastering application. The finish paint of the surface plastering application began to peel off after being exposed to fire for 20 minutes, and a white covering appears after being exposed to fire for 40 and 60 minutes.



(a) timber beams after 20 mins' fire



(b) timber beams after 40 mins' fire



(c) timber beams after 60 mins' fire



(d) timber columns after 20 mins' fire



(e) timber columns after 40 mins' fire



(f) timber columns after 60 mins' fire

Figure 3. Photos of typical specimens after fire

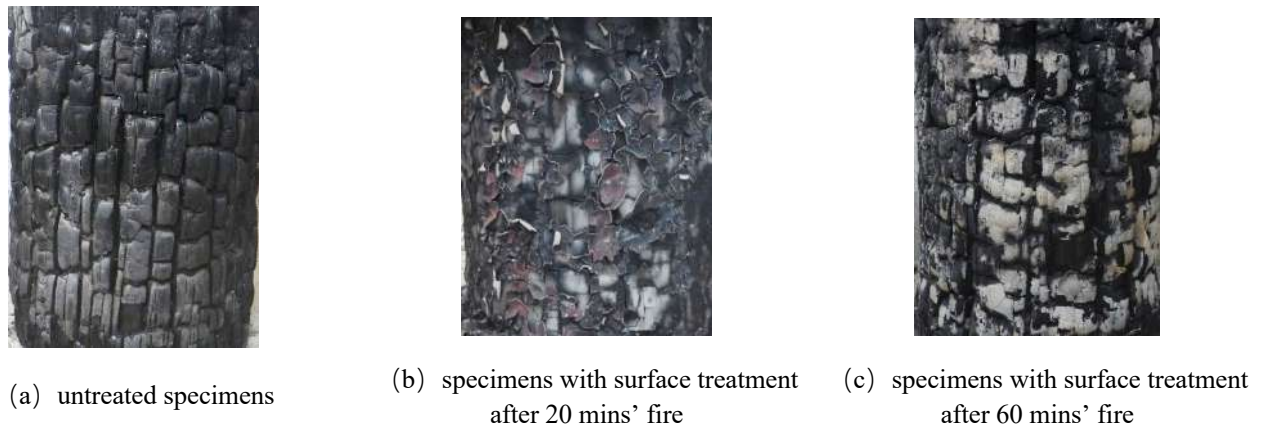


Figure 4. Comparison of charring characteristics among different specimens

3.2 Charring rate

After being exposed to fire, the cross-section of the timber can be divided into three zones: a charring layer, a pyrolysis and elevated temperature affected layer, and a normal zone [4, 5]. The charring layer forms when the temperature reaches about 300 °C, and effectively reduces the burning rate of timber. The temperature of the pyrolysis layer is in the range of 200–300 °C, and the elevated temperature affected layer has the temperature range of 50–200 °C. The mass and strength of the pyrolysis and elevated temperature affected layer is smaller than normal timber not subject to fire or elevated temperature. Finally, for the interior normal zone, the strength of the timber remains unaffected.

To investigate the development of charring depth, the residual geometry of the fire-exposed beams and columns from 50 mm-thick pieces cut from the beams at third points and columns at half point after the charring layer was removed were carefully measured. As shown in Figure 5(a), for both beams with or without surface plaster application, the bottom corners which were subjected to heat transfer from two directions, exhibited greater section loss due to charring leading to a rounding effect. Average values were listed in Table 3 and the rounding effect was not considered in the measurements to unify the measurement. The cracks were caused by the loading process after fire exposure. Timber columns with circular cross-section remain approximately circular after charring. Some specimens show slightly larger charring depth at the location of the defects such as cracks and knots. Average values of diameters from three directions along 120° were listed in Table 3. Knowing the original section geometry, the extent of charring was calculated, as listed in Table 3. The measured charring rate data for timber beams with cross-section of 200mm×400mm was lost. To increase the sample numbers for analysis, the measured charring depth from the study by authors [24, 25] from the fire resistance tests of the timber members were also listed in Table 3.

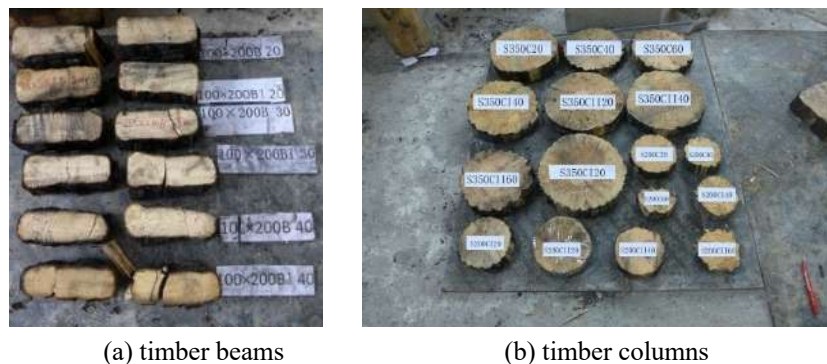


Figure 5. Residual cross-sections of typical specimens

It can be observed from Table 3 that for timber beams, the vertical charring rate is slightly higher than the horizontal charring rate, which is similar to the observations in other studies [15-17]. The average charring rate of timber members without surface treatment and with surface plastering treatment are about

0.76mm/min and 0.54mm/min, respectively. The surface plastering treatment significantly reduced the charring rate of the timber. This may be mostly attributed to the delay of the burning time of the timber due to the protection of the surface plastering application. The average charring rate of the timber members without fire prevention is slightly larger than the suggested nominal charring rate in Chinese code [28] and American code [29], which is 0.63 mm/min, and slightly lower than the suggested nominal charring rate in Eurocode 5 [30], which is 0.8 mm/min.

Table 3. Charring rate of specimens

Member type	Specimen No.	Fire duration/min	Initial geometry/mm		Charred geometry		Charring rate/mm/min	
			b	h	b'	h'	β_b	β_h
Timber beams	S100B20	20	107	204	79.0	187.4	0.70	0.83
	S100B40	40	105	204	47.0	170.0	0.73	0.85
	S100BII20	20	113	208	95.4	195.5	0.44	0.63
	S100BII40	40	112	210	74.4	184.0	0.47	0.65
Timber beams[25]	E100B30	40.0	104	204	57.5	173.5	0.58	0.76
	E100B50	28.0	105	204	68.3	182.0	0.66	0.79
	E100BII30	51.0	112	211	65.3	176.5	0.46	0.68
	E100BII50	38.5	111	211	73.8	184.0	0.48	0.70
	E200B30	82.0	204	404	106.3	348.5	0.60	0.68
	E200B50	56.0	203	405	134.0	368.5	0.62	0.65
	E200BII30	99.5	211	410	127.8	354.5	0.42	0.56
Timber columns	S200C20	20	203		174		0.74	
	S200C40	40	205		146		0.74	
	S200C60	60	204		116		0.73	
	S200CII20	20	208		189		0.48	
	S200CII40	40	208		157		0.64	
	S200CII60	60	208		137		0.59	
	S350C20	20	354		317		0.93	
	S350C40	40	355		292		0.79	
	S350C60	60	357		251		0.89	
	S350CII20	20	358		335		0.59	
	S350CII40	40	359		320		0.49	
	S350CII60	60	353		287		0.55	
Timber columns[24]	E200C30	39.7	201		147		0.69	
	E200C50	8.7	202		186		0.87	
	E200CII30	56.1	203		128		0.67	
	E200CII50	19.9	204		183		0.52	
	E350C30	94.2	352		218		0.71	
	E350C50	62.6	352		244		0.86	
	E350CII30	123.7	354		243		0.45	
	E350CII50	94.8	356		269		0.46	

4 FIRE DESIGN METHOD

4.1 Charring depth

For timber members without surface treatment, the charring depth was commonly calculated with linear or power function model. For example, the linear model was proposed in Eurocode 5 [30], while in Chinese code [28] and American code [29], the charring depth was suggested to be calculated with power function model as shown in equation (1).

$$d = \beta_n t^{0.813} \quad (1)$$

Where

d is the charring depth (mm),

β_n is the nominal charring rate for timber without surface treatment, linear charring rate based on 1-hour exposure (mm/h), and is suggested to be taken as 38 mm/h,

t is the fire exposure time (h).

To in comply with the Chinese standard, equation (2) was proposed to calculate the charring depth of timber members with surface plastering treatment based on equation (1).

$$d_p = \beta_n (t - 0.15)^{0.813} \quad (2)$$

Where,

d_p is the charring depth of timber members with surface plastering treatment (mm),

β_n and t have the same meaning with equation (1).

Comparison between the test results and the prediction from equation (2) was shown in Figure 6. The test results by authors in reference [24] and [25] were also plotted in Figure 6. Good agreement can be observed, showing that equation (2) can be further applied to calculate the fire resistance rating of the timber members treated with surface plastering application.

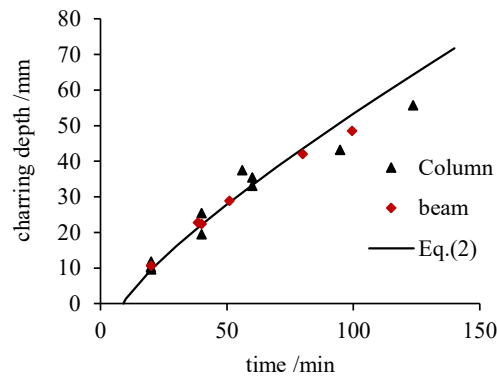


Figure 6. Comparison between the measured and calculated charring depth

4.2 Fire resistance

The fire design method based on reduced cross-section method was applied in the design codes of timber structures in many countries. In Chinese code [28] and American code [29], the effective charring depth was suggested to be calculated with equation (3). And it is specified that section properties shall be calculated using standard equations for area, section modulus, and moment of inertia using the reduced cross-sectional dimensions. The dimensions are reduced by the effective char layer thickness for each surface exposed to fire.

$$d_{ef} = 1.2\beta_n t^{0.813} \quad (3)$$

Where,

d_{ef} is the effective charring depth (mm),

β_n and t have the same meaning with equation (1).

The effective charring depth of timber members with surface plastering treatment is suggested to be calculated with equation (4).

$$d_{ef}^p = 1.2\beta_n(t - 0.15)^{0.813} \quad (4)$$

Where,

d_{ef}^p is the effective charring depth of timber members with surface plastering treatment (mm),

β_n and t have the same meaning with equation (1).

Figure 7 shows the good agreement between the measured and predicted fire resistance rating. The prediction from the Chinese code for timber members without surface treatment was also shown in Figure 7. The error of the prediction was decreased using equation (4).

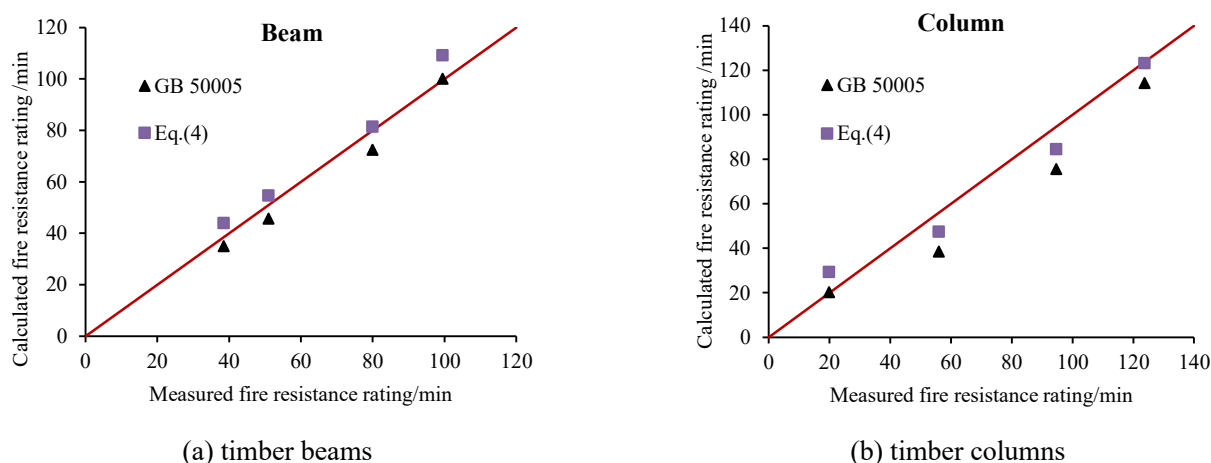


Figure 7. Comparison between the measured and calculated fire resistance rating

5 CONCLUSIONS

This paper has presented the results of an experimental and theoretical study to investigate the fire resistance performance of timber beams and columns treated with surface plastering application. In total, twenty-two fire tests were carried out including ten fire tests on timber beams and twelve fire tests on timber columns exposed to a standard fire. Charring characteristics was carefully analysed and charring depth was measured after the tests. A simplified method based on the reduced cross-section method were developed to calculate the charring rate and fire resistance rating of timber members treated with surface plastering application. The following conclusions are drawn:

- (1) Timber members with surface plastering treatment exhibited different surface charring characteristics with unprotected timber member. The anti-corrosion paint of the surface plastering application began to peel off after being exposed to fire for 20 minutes, and a white covering appears after being exposed to fire for 40 and 60 minutes.
- (2) Greater charring is observed at the bottom corners of timber beams, which were subjected to heat transfer from two directions, leading to rounding of the cross section. Timber columns with circular cross-section remain approximately circular after charring.
- (3) The surface plastering treatment significantly reduced the charring rate of the timber, due to the delay of the burning time of timber. The average charring rate of timber members without surface treatment and with surface plastering treatment are about 0.76mm/min and 0.54mm/min, respectively.
- (4) A simplified method based on the reduced cross-section method is proposed to determine the charring rate and fire resistance of timber members treated with surface plastering application.

ACKNOWLEDGMENT

This work was financially supported by the National Key R&D Program of China (Grant No. 2023YFF0906100) and National Nature Science Foundation of China (No. 52378522).

REFERENCES

1. Xue, Y., Study on Fire Protection Alteration of Timber Historical Buildings. Tianjin: Tianjin University, 2007. (in Chinese)
2. Schmid, J., Klippel, M., Just, A. & Frangi, A., Review and Analysis of Fire Resistance Tests of Timber Members in Bending, Tension and Compression with Respect to the Reduced Cross-Section Method. *Fire Safety J*, 68: 81-99(2014). DOI:10.1016/j.firesaf.2014.05.006.
3. Tran, H. C., White, R. H., Burning Rate of Solid Wood Measured in a Heat Release Rate Calorimeter. *Fire & Materials*, 16: 197-206(1992). DOI:10.1002/fam.810160406.
4. White, R. H., Tran, H. C., Charring Rate of Wood Exposed to a Constant Heat Flux. *Wood Fire Safety: 3rd International Scientific Conference*, 175-183(1996).
5. White, R. H., Nordheim, E. V., Charring Rate of Wood for ASTM E119 Exposure. *Fire Technol*, 5-30(1992).
6. Yang, T. H., Wang, S. Y., Tsai, M. J. & Lin C. Y., The Charring Depth and Charring Rate of Glued Laminated Timber After A Standard Fire Exposure Test. *Building & Environment*, 44(2): 231-236(2009). DOI:10.1016/j.buildenv.2008.02.010.
7. Frangi, A., Fontana, M., Charring Rates and Temperature Profiles of Wood Sections. *Fire & Materials*, 27(2): 91-102(2003). DOI:10.1002/fam.819.
8. Xu, Q., Chen, L., Harries, K. A., Zhang, F., Liu, Q. & Feng J., Combustion and Charring Properties of Five Common Constructional Wood Species from Cone Calorimeter Tests. *Construction and Building Materials*, 96: 416-427(2015). DOI:10.1016/j.conbuildmat.2015.08.062.
9. Tsantaridis, L. D., Ostman, B. L., Charring of Protected Wood Studs. *Fire & Materials*, 22: 55-60(1998). DOI:10.1002/(sici)1099-1018(199803/04)22:2<55::aid-fam635>3.0.co;2-t.
10. Nussbaum, R. M., The Effect of Low Concentration Fire Retardant Impregnations on Wood Charring Rate and Char Yield. *Journal of Fire Sciences*, 6: 290-307(1988). DOI:10.1177/073490418800600405.
11. Zhang, S., Cheng, L., Liu, J., Fire Resistant Performance of Chinese Northeastern Larch. *Structural Engineers*, 29(4): 140-145(2013). DOI:10.15935/j.cnki.jggcs.2013.04.001. (in Chinese)
12. Zhang, J., Xu, Q., Li, W., Li, X., Shang, J., Experimental Study on The Charring Rate and Residual Flexural Capacity of Timber Beams after Exposure to Four-Side Fire. *China Civil Engineering Journal*, 46(2): 24-33(2013). DOI:10.15951/j.tmgcxb.2013.02.008. (in Chinese)
13. Zhang, J., Xu, Q., Shang, J., Experiment on Residual Bearing Capacity of Wood Columns with One-Side or Two-Adjacent-Side Fire Exposure. *Journal of Shenyang University of Technology*, 35(4): 461-468(2013). (in Chinese)
14. White, R. H., Use of Coatings to Improve Fire Resistance of Wood. *Fire Resistive Coatings: The Need for Standards*. ASTM STP 826, 24-39(1983).
15. Ni, Z., Peng, L., Qiu, P., Zhang, H., Experimental study on fire resistance performance of timber assemblies. *China Civil Engineering Journal*, 45(12): 108-113(2012). DOI:10.15951/j.tmgcxb.2012.12.018. (in Chinese)
16. Xu, Q., Zhang, J., Shang, J., Li, X., Li, W., Experimental research on fire endurance of timber beams exposed to three-side fire. *Building Structure*, 42(12): 127-130(2012). DOI:10.19701/j.jzjg.2012.12.029. (in Chinese)
17. Chen, L., Xu, Q., Wang, X., Experimental Study on Fire Endurance of Glulam Beams Exposed to Three-side Fire. *Structural Engineers*, 34(4):109-116(2018). DOI:10.15935/j.cnki.jggcs.2018.04.016. (in Chinese)
18. Lange, D., Bostrom, L., Schmid, J., Albrektsson, J., The Influence of Parametric Fire Scenarios on Structural Timber Performance and Reliability. Sweden: SP Technical Research Institute of Sweden, 2014.
19. Li, X., Li, S., Xu, Q., Xu, Q., Zhang, J., Experimental Research on Fire Endurance of Timber Columns Exposed to Four-Side Fire. *Building Structure*, 40(3): 115-117(2010). DOI:10.19701/j.jzjg.2010.03.031. (in Chinese)
20. Malhotra, H. L., Rogowski, B. F., Fire Resistance of Laminated Timber Columns. *Fire Research Note No.671*, Borehamwood, UK: Fire Research Station, 1967.

21. Ali, F., Kavanagh, S., Fire Resistance of Timber Columns. *Journal of the Institute of Wood Science*, 17(2): 85-93(2005).
22. Chen, L., Xu, Q., Hu, X., Experimental Research on Fire Endurance of Moderately Long Glulam Columns Exposed to Four-Side Fire. *Journal of Building Structures*, 41 (1): 95-103(2020). DOI:10.14006/j.jzjgxb.2018.0518. (in Chinese)
23. Xu, Q., Han, C., Hu, X., Chen, L., Leng, Y., Experimental Research on Fire Endurance of Glulam Beams with Different Fire Retardant Coating Exposed to Three-Side Fire. *Building Structure*, 48(10):73-78+97 (2018). DOI:10.19701/j.jzjg.2018.10.015. (in Chinese)
24. Wang, Z., Xu, Q., Han, C., Chen, L., Hu, X., Experimental Study on Fire Endurance of Round Timber Column with Traditional Craftwork with One Hemp Fiber and Five Plastering Application. *Building Structure*, 47(17): 14-19(2017). DOI:10.19701/j.jzjg.2017.17.003. (in Chinese)
25. Chen, L., Xu, Q., Han, C., Wang, Z., Leng, Y., Chen, X., Experimental Study on Fire Endurance of Timber Beams with Treatment of One Hemp Fiber And Five Plastering Exposed to Three-Side Fire. *Journal of Building Structures*, 42(9): 101-109(2021). DOI:10.14006/j.jzjgxb.2020.0074. (in Chinese)
26. Xu, Q., Han, C., Chen, L., Wang, Z., Leng, Y., Experimental Research on Mechanical Behavior of Round Timber Columns Protected with Traditional Craftwork after Fire. *China Civil Engineering Journal*, 52(7): 90-99(2019). DOI:10.15951/j.tmgcxb.2019.07.009. (in Chinese)
27. Xu, Q., Han, C., Chen, L., Wang, Z., Leng, Y., Experimental Study on Mechanical Behavior of Timber Beams Treated with Traditional Plastering Application after Exposed to Three-Side Fire. *Building Structure*, 51 (9): 92-97+29(2021). DOI:10.19701/j.jzjg.2021.09.015. (in Chinese)
28. 2018 National Design Specification for Wood Construction-ANSI /AWC NDS-2018, American Wood Council, Leesburg, VA, 2018.
29. Standard for Design of Timber Structures GB 50005-2017, China Architecture & Building Press, Beijing, 2017. (in Chinese)
30. Eurocode 5: Design of timber structures–Part 1-2: General–Structural fire design EN 1995-1-2, Brussels: European Committee for Standardization, 2004.

TOWARDS ALTERNATIVE FIRE DESIGN SOLUTIONS FOR WOOD-TO-WOOD CONNECTIONS

Anne Davidson¹, Ethan Phillion², Lilyana Mladenova³, Rwayda Al Hamd⁴, Beth Weckman⁵, John Gales⁶

ABSTRACT

A lack of available reference data exists for modelling wood structures in fire. This is of importance where protection schemes are evaluated as part of an alternative solution process for new and old structures. Herein, a mortise and tenon connector (Eastern Hemlock of heritage value) was subjected to a localised pool fire exposure of approximately thirty minutes. Interior connection temperature was measured. Narrow Spectrum Illumination technologies were utilised to characterize the char layer formation and the generation of embers which may contribute to fire spread. Results indicated that in this experiment the observed char rate was faster than codes prescribe and was non-linear. A dynamic char rate model may be needed for accurate fire performance calculations of wood members. The corner-rounding effect is more severe at interior interfaces suggesting that the heat flux generated from the burning wood could be a large contributor to char rate. Although the mechanical integrity of a traditional all-wood mortise-and-tenon connection appears largely maintained post-fire, current codes may not accurately predict post-fire outcomes.

Keywords: Concrete; corrosion; fire performance; structural performance; Digital Image Correlation – DIC; narrow spectrum (in DIC)

1 INTRODUCTION

Historical timber frame structures exist worldwide and hold intangible value within many of their communities. Unfortunately, one of the greatest risks to these valuable structures is their inherent susceptibility to fire. When they burn, the physical and emotional loss is catastrophic. Such was the case with the Notre Dame Cathedral Fire in 2019. It is obvious that these wooden structural frames must be protected from fire, but it is not obvious as to how to evaluate their performance in fire. To retain the heritage value of the building, the character-defining elements such as mass timber wood members and their often-crafty connections must be preserved and thereby left visually unimpaired and often unprotected [1]. Similar demands in contemporary structures also exist to leave the structure and connections exposed. Many fire codes do not consider traditional all-wood connections sufficiently. This requires the development of alternative solutions.

¹ Graduate Student, Department of Civil Engineering, York University (Canada)
e-mail: annedavidson1203@gmail.com

² PhD. Student, Department of Civil Engineering, York University (Canada)
e-mail: ephillion@yorku.ca, ORCID: <https://orcid.org/0009-0001-7116-6935>

³ PhD. Student, Department of Civil Engineering, Abertay, Scotland
e-mail: lmladenova1900@abertay.ac.uk, ORCID: <https://orcid.org/0009-0006-2399-0539>

⁴ Lecturer, Department of Civil Engineering, Abertay, Scotland
e-mail: r.al-hamd@abertay.ac.uk, ORCID: <https://orcid.org/0000-0002-8702-0279>

⁵ Professor, Department of Mechanical and Mechatronics Engineering
e-mail beth.weckman@uwaterloo.ca, ORCID: <https://orcid.org/0000-0002-1978-8892>

⁶ Associate Professor, Department of Civil Engineering, York University (Canada)
e-mail: jgales@yorku.ca, ORCID: <https://orcid.org/0000-0001-8025-3902>

A common approach in Canada to evaluating the fire resistance of a mass timber member is by considering the reduced cross-section, where the wood beneath the char layer and its original properties are used to calculate the structural resistance. This approach relies heavily on the material's char rate. Charring rates vary for different species, under different conditions, and over time [2]. Currently, codes use all-encompassing linear char rates, which have been taken as the average char rate of wood exposed to a standard fire-resistance test [3]. However, the United States has accepted a non-linear char rate model developed by White and Nordheim [4]. All these tests and models however are based on testing of limited species. To the author's knowledge, data pertaining to the char rate of Eastern Hemlock is lacking, a commonly used wood species in historical timber-frame structures in Canada. The researchers of this paper aim to develop requisite data which may be then used for developing alternative solutions (based upon a future model) for evaluating the fire performance of heritage and mass timber structures so that proper planning of protection or exposure strategies can be achieved. To develop a reliable model which can form the basis for an alternative solution, this research aims to better define the parameters contributing to char formation in heritage wood. While the data will have use for consideration of first-phase models of contemporary timber, the paper here describes the heritage application so as to place the narrative of the studies current use into context.

A full-scale fire test of a salvaged heritage Eastern Hemlock mortise-and-tenon connection was considered to examine the effects of geometry and all-wood construction techniques on char rate (Figure 1). The full-scale burn test was also used to examine the wood's contribution to ember generation; an important but understudied critical contributor to fire spread in old and new structures alike [5]. The authors have previously investigated ember generation using a lateral ignition and flame spread test radiant heater on contemporary glulam and were able to track the creation of flaming embers (see Figure 2 from the study seen in reference [6]).

While the specimens are being analysed for char formation, once fire-exposed, the connector is to be tested mechanically to failure and compared in strength to a non-fire-exposed counterpart. While Canadian focused, results herein will be of international use.

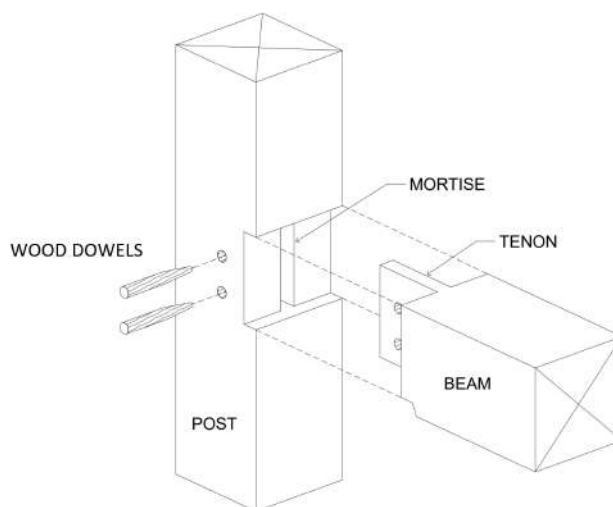


Figure 1. A typical mortise-and-tenon connection



Figure 2. Ember generation of glulam sample tested with a radiant heater (circled) [6]

2 LITERARY BACKGROUND

In a literature review, Garcia-Castillo et al. [7] assessed 125 studies on heritage structures and fire safety ranging from 1985 – 2022. It was found that the studies could be separated into six general categories. The distribution is as follows: 11% on fire safety regulations, 23% fire risk assessment, 23% fire protection and mitigation measures, 12% spread of both fire and smoke and evacuation, 17% thermomechanical behaviour of historic structures or materials, and 14% fire safety engineering design. This demonstrates that there is still a deficiency in understanding how a heritage fire spreads and how the structure performs. For further context, of the 125 studies examined in the literature review, 64 were related to heritage timber. Of those 64 studies, 5 of them investigated the thermal and thermo-mechanical performance. From the literature review, it was deemed that the fire performance of heritage timber is unclear, signifying the need for these studies to take place.

From an overall perspective, many researchers agree that fire safety design of historic timber structures requires a performance-based approach. Some researchers such as Petriniet et al. [8] have done case studies on heritage timber frames using a probabilistic risk performance-based engineering framework commonly found in engineering of other hazards such as earthquakes. In their study, the fire scenarios were analysed for probability of occurrence using a customized methodology conceived by the authors for heritage wood structures, and a fire hazard analysis using an event tree model along with advanced nonlinear thermomechanical finite element models [8]. Another case study by Pau, Duncan, and Fleischmann [9] used another method of performance-based design by adopting the Verification Method C/VM2 (an RSET ASET approach) with a ‘Nearly As is Reasonably Practicable’ for the special consideration of heritage. Both case studies use Performance Based Fire Design (Pbfd) approach with special modifications which account for the heritage aspect of the structure.

To perform Pbfd however, assumptions must be made regarding fire load, heat release rate, and other material properties such as heat capacity and density. These properties however can differ between species, age, and the condition of the wood. Such differences are largely understudied. Some recent research examining the differences on a kinetic, chemical, and physical level include a study by Wanga et al. [10]. The study examined the combustion kinetics and gas product release of ancient pine compared to new pine using TG-FTIR-MS and found that the aged wood had a different carbon composition containing less combustible components than the newer wood [10]. In another study investigating the thermal stability of four kinds of Chinese heritage wood, Huai et al. [11] found that the activation energy of the historical wood species is lower than most fresh wood. In both studies, the wood samples were pulverized into a powder for testing. The studies also emphasize how both age and species result in different outcomes.

In terms of flame spread testing, Chorlton et al. [12] observed that heritage wood outperformed contemporary glulam in a Lateral Ignition and Flame Spread Test (LIFT) with regards to char depth and that the flame stopped spreading sooner on the historic specimens. However, the glulam had a less extensive char front as well as a slower rate of flame spread [12].

The current level of deterioration of contemporary and heritage samples has importance when placing the results in general applicability. Solid wood mass timber elements often display discrete cracking (aka. checking) which occurs when the wood dries, shrinks, and consequently, the fibres tear to relieve the internal stresses. Large solid wood members are often present in heritage structures, and with reduced moisture content over time, presence of checking is more likely. Harun et al. [1] investigated the effects of radial cracks (checking) on the fire performance of heritage timber. In full-scale member tests, it was observed that pre-existing cracks increased in width during a fire and that the crack impacted the development of the pyrolysis and char front [1]. Char depths which occurred away from the crack were 64% less than char depths observed at the crack [1]. The level of deterioration however can extend beyond just radial cracking (checking) or shakes. In heritage timber frame structures other deterioration mechanisms can be present such as moisture damage, rot, biota (damage by insects), and human inflicted defects such as exposed notches and the presence of nails which can conduct heat in the event of fire.

In addition to considering the effects of species, age, and condition, the effects of a structure’s connections must be considered as their performance often dictates the overall building’s performance. Load transfers from members often cause concentrated stresses in the connections which make them more vulnerable to

structural failure. Additionally, it has been observed that damage due to fire is more severe at wood connections [13]. This phenomenon has been observed by conservators who remove the char before proceeding with preservation and repair techniques [13]. This suggests that the incident heat flux coupled with the nature of the connection has a major impact on the char rate of wood.

Most research on the fire performance of connections for mass timber construction focus on steel-to-timber joints for engineered glulam. Zhang et al. [14] developed a numerical model to assess the thermos-mechanical response of all-wood dovetail connections and validate it with full scale tests under ISO 834 [15] fire conditions [15]. The wood used in this experiment though was engineered glulam rather than a solid and/or aged timber. Even research on the mechanical performance of wood-wood connections using wooden dowels, such as the mortise and tenon are lacking [16]. Brandon [16] compared a wood dowel connection to a metallic dowel connection and found that when the connection was cut in half, the wood dowel did not allow for char to propagate into the connection, whereas the wood surrounding the metal dowel experienced charring [16]. Brandon also tested for creep of wood doweled connections for which there is very little research. All the experiments in Brandon's PhD dissertation [16], however, did not include traditional timber samples, and were also glue-laminates.

3 MATERIAL SPECIMEN COLLECTION

In addition to modern counterparts, the York University Fire Research team has had success in procuring aged construction specimens which can have heritage value for fire testing (see [1] and [12] as examples). Essentially, a process considered facadism is undertaken for various heritage structures where the interior of the structure is demolished and exterior of the structure can be preserved. The process is considered controversial in the sense that the interior of the structure still holds heritage value. Recognizing the loss of these structures, these researchers have made concentrated efforts to procure aged construction specimens in the Toronto and surrounding area with the assistance of demolition organisations. In this cooperation, the materials are more carefully removed during the demolition process and preserved as they would have been constructed. To date this has included samples from structures being demolished dating as early as 1830 and as late as 1880 where the samples are now stored at the York University lab. Samples exhibit an aging process (cracking from loads etc) but are significantly limited in number and hence restrictive in test protocol despite these efforts. These samples are in good condition, however; they are largely free of checks and large visible cracking, there are no presence of rot or insects. In addition to assisting in projects of heritage value they have added value as reference points for solid wood studies.

In the context of this paper, there are numerous properties in the surrounding Toronto area which have been slated for demolition, particularly after abandonment. In this case, an early nineteenth century farmstead was identified of interest and with the assistance of local authorities, a selection of construction frames was made available to researchers from this structure (see Figure 3).



Figure 3. Heritage farmstead structure dating to early 1800s (Author's photo)

The dwelling on the property in Figure 3 was considered heritage. Dwellings on the property included a selection of various construction materials beyond early Canadian uses of concrete and masonry examples. The farmstead was primarily constructed using wood. The wood was carefully removed during the demolition of one farmstead structure and brought back to the York University fire lab. The wood was identified using Environment Canada’s “Key for Microscopic Identification of Woods Commonly Used in Canada” and was identified as Eastern Hemlock. Within the members collected, there were two identical formed wood-wood connections. The samples being tested are Eastern Hemlock fully housed mortise and tenon connection (figures 1,4, and 5). This type of connection is technically semi-rigid, but for structural analysis, is standardly considered pinned. The column member with the mortise is a hewn timber, meaning it was shaped and formed using an axe. The beam member with the tenon was rough sawn. This indicated that the column member is likely older than the beam member and repurposed. This agrees with the unused notches in the column member as seen in Figure 3. Due to the hewn characteristic and the vertically aligned 1-1/2” pins (Ontario barns in the early 18th century used dowels or pins that were between 1-1/4” and 2” in diameter), it is likely that this member dates back to the early 1800s, when the dwelling was on site. The sawn beam and metal brace were likely added somewhere in the mid to late 1800’s because though the beam is sawn, the pins, or dowels, are large, and the metal brace seen in Figure 4 was for holding in place a wagon-rack-lifter (which was in storage beside the procured connection).

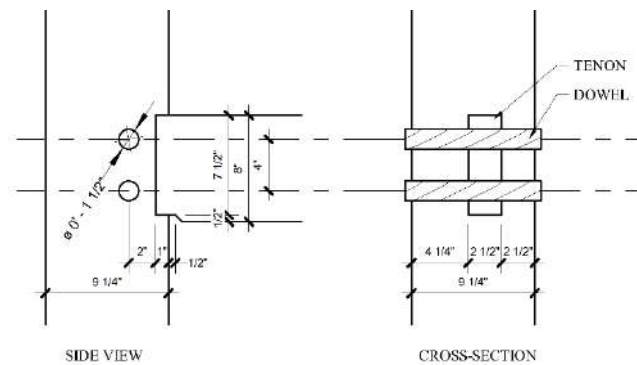


Figure 4. Connector Schematic

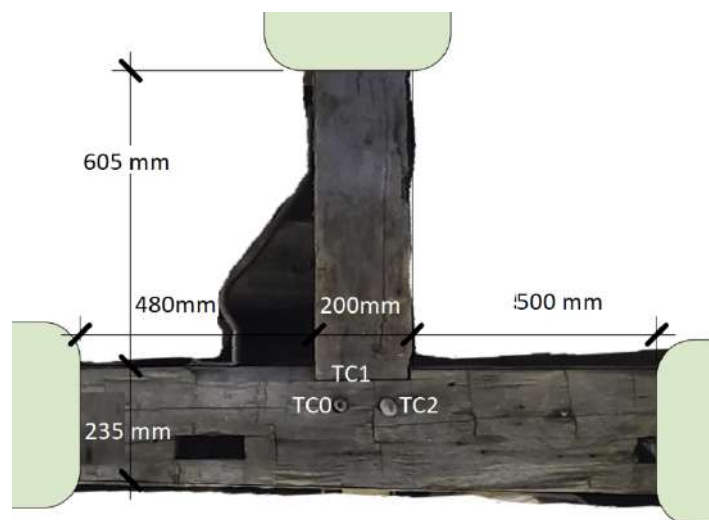


Figure 5. Eastern Hemlock fully housed mortise and tenon connection

4 FIRE TESTING METHODOLOGY

Once procured, all samples were wrapped in plastic tarp. They were then slowly conditioned in a room at 21°C and 12% RH. By calculating the moisture content in-situ samples had a 9.8% MC, while conditioned

in the lab prior to testing they plateaued at 7.5% MC. Before any preparations, the two connectors were completely recorded using photography and hand measurements. The connection for fire testing was prepared where the ends were wrapped in rockwool insulation so that the fire could be isolated to the connection only. Non-destructively, three thermocouples were placed into the fire testing connection: one in each dowel, and one in the centre, between the two members. Each thermocouple was placed approximately 1" into the crevices. However, thermocouple TC2 is placed closer to the surface than TC0 due to the tight fit between the dowel and the dowel hole. Additional thermocouples were not installed as the authors did not wish to disturb the sample and the focus was more on the generation of char and its evaluation post-fire.

A full-scale fire test examined the geometrical contributions to charring behaviour by exposing a beam-to-column mortise-and-tenon connection to an approximate 30-minute methanol pool fire burn. Pool fires were used as they are considered repeatable heat exposures and maintain a degree of sample visibility, and thus safety, for the researcher conducting the experiment. They can be easily quantified and established as an input fire into a requisite finite element analysis. They also allow the specimen to be viewed unobscured.

Although the originally planned test duration was for 30 minutes, there was visual concern of the connection member failing before that time. This prompted an earlier end to the test than was originally planned and disrupted the ability to monitor the structure during the cooling phase of the experiment. The fuel pan was covered (smothering the fire) at 26 minutes 17 seconds. The fire was extinguished from the connection at 28 minutes 22 seconds. The authors intended to test longer, however the stability of the connection in the restraining frame above the fire was of concern, albeit only visually.

Once the thermocouples had achieved 10 minutes of baseline data, 8 L of methanol fuel was added to the fuel pan and ignited. At 28 minutes the fire was put out and the connection was doused with water by gently pouring rather than spraying to avoid damage to the char.

It was found that at 200 mm above the fuel pan, a decently consistent exposure temperature of 700-750°C occurred. Therefore, it is specified that the bottom of the connection be supported by concrete masonry units (CMU) 200 mm above the fuel pan to ensure quick ignition and to simulate exposure to a real fire. The connection was positioned on its side, which would not be the usual case if it were in a real fire scenario. However, in this way, the connection is exposed to a more severe fire scenario and allows for a more stable test set-up. Future tests are underway to confirm the influence of the heated sample above on the rate of burning and determine whether this is negligible in terms of the rate of fuel consumption.

The fire test and instrumentation were set-up in the configuration shown in Figure 6. A high intensity blue light is emitted onto the specimen. Figure 7 illustrates the bottom view of the connector during the fire test. The camera in the centre with direct view of the mortise and tenon had a blue light filter attached to it, generating the images seen in the results section. This allows the light emitted from the flames to be filtered out of the photos. This method is called narrow spectrum illumination. Narrow spectrum illumination technologies [18, 19] were used to examine the charring mechanisms beneath the flames and in an effort, for the first time, to monitor the sample for ember generation and quantification. It is important to remark that obscuration from heat haze and smoke cannot be removed from the image. Temperature measurements were made within the connector itself for the duration of the fire. The connection then had the char removed post-fire to examine the real reduced cross-section of the connection prior to loading. An identical "twin" connection was left un-burned for mechanical performance comparison post-fire with the burned sample. Both the fired and non-fired connector are planned to be tested mechanically to failure to understand the consequences of this type of damage to the connector. Applied load and deformation, such as connection rotation, will be monitored using Digital Image Correlation. The data from both test series would be used to support data requests as it could be used for Finite Element Analysis model validation in future research. The char was carefully removed once the connection was back at York University's lab and photographed. This was done using palm sanders. A grit of 80 was used initially to get the bulk of the char, and then 120 grit was used. For tighter spaces, the char was sanded off by hand rather than using a palm sander. Sanding was discontinued once the wood grain was visible. The result is the reduced cross section after the burn. Sanding inside the mortise and any other voids was avoided.

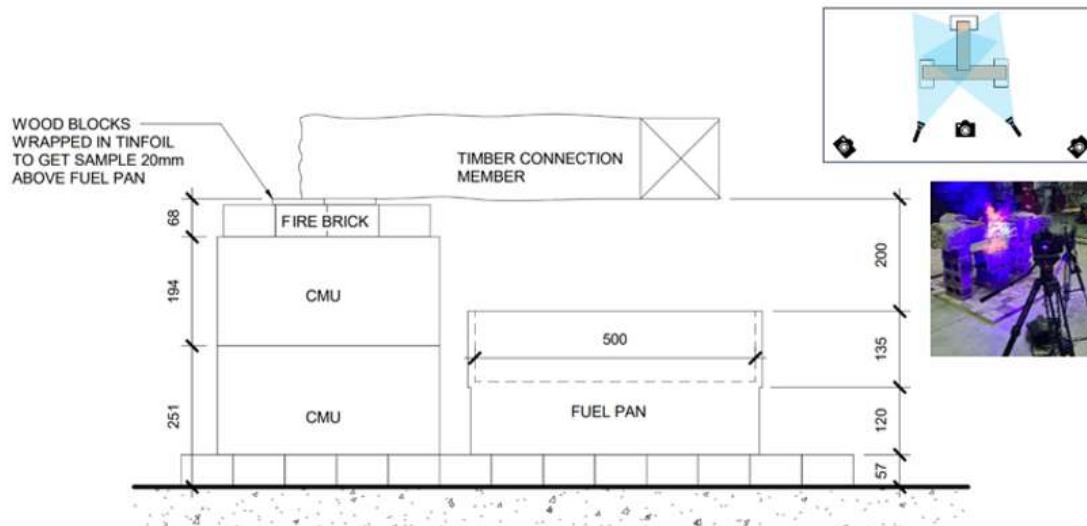


Figure 6. Diagram of Burn set up



Figure 7. Underside of Connector during fire test

5 RESULTS AND DISCUSSION

As the initiation of analysis, Narrow Spectrum illuminated images were overlaid on top of the first reference image. This way image showing charring can be directly compared against the connection's original state. From beginning to end, the positioning of the tenon inside the mortice remains relatively unchanged which suggests that the member is not deflecting. Figure 8 shows an enlarged photo of the connection at the end of the test. The faint red line is the outline of the connection before the burn. An image of the connection after the burn is overlaid on top, showing the extent to which the char has retreated from the original dimensions. On top of the charred connection image is an overlay of the connection after the char was removed. As shown in Figure 8, despite the char remaining close to the original dimensions, once removed, the reduced cross section is apparent. Scaling the photograph above confirmed measurements made on site before and after removing char. The cross-sectional dimension shown reduces from 235 mm to 224 mm, to 184 mm with the char removed. This equates to a charring rate of about 0.85 mm/min on the bottom face and 1.11 mm/min on the top.



Figure 8. Connector with Original and Damaged States Overlaid

Studying the progression of photos describes the charring and decomposition phenomena. At 2 minutes 25 seconds into the test the connection is fully involved in charring. As the wood fibres become dehydrated, they shrink and contract. At 3 minutes 30 seconds, the wood fibres are still intact, in the next photo, at 4 minutes 55 seconds, it can be seen that small fissures have occurred across the grain. As the wood dehydrates more, more stress is created, and the larger the “cracks” or char mounds become. Early on, smouldering is captured in the connection (at ~1 min). Throughout the entire test, it seems as though heat gets captured in the mortise, creating a kind of oven. This observation is supported by continued smouldering in the same location after the connection is no longer burning. This is likely to cause significant damage to the tenon. In under three minutes the exterior of the connection is completely charred. The progression of photos also illustrates the behaviour of embers as the wood burns. Almost instantaneously, embers are seen leaving the surface of the wood (0.67 minutes). Mostly ‘larger’ embers were observed at first. As the connection started burning at a steadier rate, the embers became smaller. Throughout the test, some pieces of char would dislodge, but usually they were heavy enough to fall to the ground rather than be carried away into the air as an ember.

The mortise and tenon are shown in Figure 9B. This did not have the char removed from it, but here it can be seen that the mortise has become larger due to charring within it. The tenon, although still intact, also appears significantly charred. The original dowels in Figure 9B, were cut to be level with the surface for testing. This was the side exposed to fire. During char removal, the mortise, tenon, and dowels were avoided, but once the char was removed surrounding the dowels, the dowels crumbled away with the char, leaving what is shown in Figure 9C-D. In Figure 9D, one can see more easily the extent of damage to the left peg, which had loose char falling out at an additional depth of about 25 mm. What is interesting about these photos is that the old nails in the member are shown protruding now that the char has been removed, whereas before the burn (Figure 9B) the nails were slightly inset. The nails themselves provide a useful way to measure the various char depths across the member. Corner rounding is apparent in the below photos; however, it is more significant at the interior corners where the two members connect (Figures 9C & D). Despite this greater than anticipated corner rounding damage, the connection while handling, remained rigid. It should be noted that current methods to consider corner rounding typically are not this

detailed. Figure 10 illustrates the difference in corner rounding observed in the experiment and how prescriptive standards would predict the corner rounding.



Figure 9. Connector after Char Removal

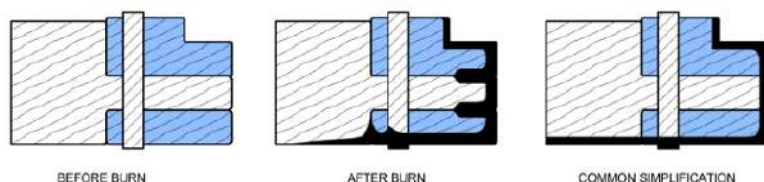


Figure 10. Cross-section of connection showing the charring (black) of the dowel (white) through the mortise (blue) and tenon (white), comparing the charring which occurred during testing to the simplification made in prescriptive standards.

Temperatures recorded using the thermocouples placed within the connection are shown below in Figure 11. The time in minutes on the plot has been adjusted so that the point at which the fuel was ignited is time=0. Interestingly, Figure 11 shows that the thermocouple placed in the crevasse between the two connecting members starts experiencing higher temperatures relatively quickly, then slows to a rate of just over 1°C/min. The thermocouples in the left and right dowels increase at a steadier rate with no initial jump in temperature. This suggests that the interface between the dowels and the members are tight connections while the interface between the two members is not as snug, thereby allowing more heat to infiltrate. The likely reason why the right dowel experiences greater temperatures is because the thermocouple in that dowel was placed at a shallower depth than the one on the left, thereby being closer to the source of heat.

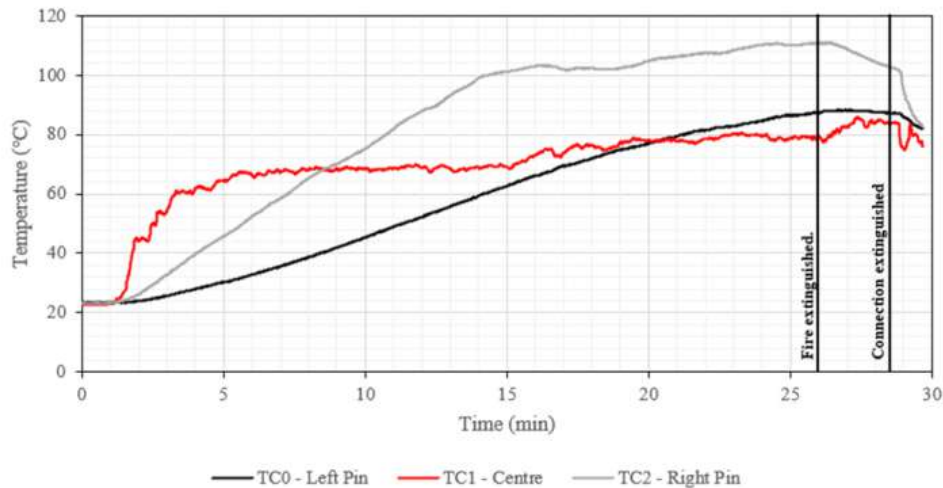


Figure 11. Connector temperature evolution

6 CONCLUSIONS AND FUTURE RESEARCH

While not discussed in the paper, a range of cone sample testing was also performed on Hemlock samples. The data is important as it allows the validation of models at various scales and heat intensities to be examined, particularly considering the few specimens that are available to test. The resulting cone testing and heritage tests also give important reference markers for contemporary counterparts where modelling is also desired. Future work will consider and describe the analysis of these samples in relation to other heritage species and contemporary engineered counterparts. The authors caution that the samples tested herein are of largely good quality, whereas many heritage buildings will have significant damage caused by rot or insects which may influence the applicability of these results. As such, they are considered a good reference point for understanding the deterioration of mass timber in fire with general applicability in goal of developing modelling tools in mind.

The research is still limited as the load testing is required to see the structural effect on the samples. With this data, more robust modelling techniques can be validated. Once the validation is completed it would be possible to use the techniques in order to develop alternative design procedures for real heritage buildings not undergoing plans for demolition but of new use. However, it must be recognized that modelling technologies for timber engineering need significant development and understanding to better determine what parameters most effect their reliability.

The results of the research carried out within this paper indicate that the char rate of heritage Eastern Hemlock is faster than codes prescribe and is non-linear. A dynamic char rate model is needed for accurate fire resistance calculations of wood members. Aged timber material chars at a faster rate than non-aged timber, but more research is required. The corner-rounding effect is more severe at interior interfaces suggesting that the heat flux generated from the burning wood is a significant contributor to char rate (see Figure 9). This phenomenon is not considered in prescriptive codes. Narrow Spectrum Illumination can effectively identify released embers but the use of this technology for this purpose needs to be further developed as it may also have applicability in testing of modern counterparts as observed in other testing.

Although, the mechanical integrity of a traditional all-wood mortise-and-tenon connection is largely maintained post-fire, current codes may not accurately predict post-fire outcomes. From these results, current models for calculating fire performance of traditional timber frame connections may be challenged and a modelling endeavour is needed to generate an alternative solution. The framework for such a model will be presented in future research. There is importance in also assessing these modelling techniques for appropriateness of contemporary counterparts, however such an endeavour will provide a suitable reference approach.

ACKNOWLEDGMENT

Rene Champagne and Parks Canada are thanked for facilitating the procurement of samples in relation to this study. NSERC CGS, Discovery and Alliance funding is acknowledged.

REFERENCES

1. Harun, G., Chorlton, B., Richter, F. & Gales, J. The Effects of Radial Cracks on the Fire Performance of Heritage Timber. *Fire and Materials* 47(3), 1-14 (2022). <https://doi.org/10.1002/fam.3104>.
2. Cavalli, A., Cibecchini, D., Togni, M., & Sousa, HS. A Review of the Mechanical Properties of Aged Wood and Salvaged Timber. *J. Build. Mat.* 114, 681-687 (2016). <https://doi.org/10.1016/j.conbuildmat.2016.04.001>.
3. U.S. Department of Agriculture. *The Encyclopaedia of Wood*, Washington: Skyhorse Publishing, Inc., 2007.
4. White, RH., & Nordheim, EV. Charring Rate of Wood for ASTM E 119 Exposure. *Fire Technol.* 28(1) 5-30 (1992). <https://doi.org/10.1007/BF01858049>.
5. Kodur, V., & Naser, MZ. *Timber Structures*, in *Structural Fire Engineering*, 1st Ed. New York: McGraw Hill, 2020. <https://www.accessengineeringlibrary.com/content/book/9781260128581/chapter/chapter10>.
6. Chorlton, B., and Gales, J. Elative Fire Performance of Heritage and Contemporary Timber. 15th International Conference and Exhibition on Fire Science and Engineering. Royal Holloway College, Windsor, United Kingdom. 2019. 2039-2048.
7. Garcia-Castillo, E., Paya-Zaforteza, I., & Hospitaler, A. Fire in Heritage and Historic Buildings, a Major Challenge for the 21st Century. *Developments in the Built Environment* 13, 100102 (2023). <https://doi.org/10.1016/j.dibe.2022.100102>.
8. Petrini, F., Aguinagalde, A., & Bontempi, F. Structural Fire Risk for Heritage Buildings by the Performance-Based Engineering Format. *International Journal of Architectural Heritage* 17(7), 1171-1194 (2022). <https://doi.org/10.1080/15583058.2021.2022249>.
9. Pau, D., Duncan, C., & Fleischmann, C. Performance-Based Fire Engineering Design of a Heritage Building: McDougall House Case Study. *Safety* 5(45), 2019. <https://doi.org/10.3390/safety5030045>.
10. Wanga, H., Chen, X., Tian, Y., Gao, Y., Fan, C., Liu, Z., & Nong, C. Study on the Thermodynamic Characteristics of Wood Combustion in Historical Buildings. *Journal of Cultural Heritage* 63, 32-41 (2023). <https://doi.org/10.1016/j.culher.2023.07.008>.
11. Huai, C., Xie, J., Liu, F., & Liu, J. Study on the Thermal Stability and Degradation Kinetics of the Historical Wood: Restoration Residues Collected from Chinese Heritage Buildings," *International Journal of Architectural Heritage* 18(1), 164-176 (2024). <https://doi.org/10.1080/15583058.2022.2130839>.
12. Chorlton B., & Gales, J. Fire Performance of Cultural Heritage and Contemporary Timbers. *Engineering Structures* 201, 109739 (2019). <https://doi.org/10.1016/j.engstruct.2019.109739>.
13. Ridout, B. Timber Decay in Buildings: The Conservation Approach to Treatment. *APT Bulletin* 32(1), 58-60 (2001). <https://doi.org/10.2307/1504694>.
14. Zhang, J., Wang, Y., Li, L., & Xu, Q. Thermo-mechanical Behaviour of Dovetail Timber Joints Under Fire Exposure. *Fire Safety Journal* 107, 75-88 (2019). <https://doi.org/10.1016/j.firesaf.2017.11.008>.
15. International Organization for Standardization: ISO 834-11: Fire resistance tests - Elements of building construction - Part 11: Specific requirements for the assessment of fire protection to structural steel elements. 2014.
16. Brandon, D. Fire and structural performance of non-metallic timber connections. PhD Dissertation, University of Bath, 2015.
17. Smith, CM., and Hoehler, MS. Imaging Through Fire Using Narrow-Spectrum Illumination. *Fire Technol* 54(6), 1705–1723 (2018). doi: 10.1007/s10694-018-0756-5.
18. Gatien S., Young, T., Hoehler M., and Gales, J. Application of Narrow-Spectrum Illumination and Image Processing to Measure Surface Char Formation in Lateral Ignition and Flame Spread Tests. *Fire and Materials* (John Wiley). 43(4), 358-365. (2019) <https://doi.org/10.1002/fam.2706>

19 to 21 June, 2024

Department of Civil Engineering

University of Coimbra

Coimbra – Portugal

Organized by



UNIVERSIDADE D
COIMBRA



Institute for Sustainability and
Innovation in Structural Engineering